Challenges in Chemistry for Sustainable Development

PACCON
PURE AND APPLIED CHEMISTRY INTERNATIONAL CONFERENCE 2010

PROCEEDINGS

Pure and Applied Chemistry International Conference 2010

January 21-23, 2010

Ubon Ratchathani University

Ubon Ratchathani

THAILAND

PURE AND APPLIED CHEMISTRY INTERNATIONAL CONFERENCE 2010
PROCEEDINGS

CHALLENGES IN CHEMISTRY FOR SUSTAINABLE DEVELOPMENT

JANUARY 21-23, 2010
UBON RATCHATHANI, THAILAND

ISBN: 978-974-523-230-3

LIST OF CONTENT

Section **Page**

Analytical Chemistry

Preparation of Co/SiO_2 fiber catalysts by electrospinning technique

S. Promduang[1], C. Chaiya[2], C. Samart[3] and P. Reubroycharoen[4,5*]

[1]Petrochemistry and Polymer Science, Faculty of Science, Chulalongkorn University, Bangkok 10330, Thailand
[2]Division of Chemical Engineering, Faculty of Engineering, Rajamangala University of Technology Krungthep, Bangkok 10120
[3]Department of Chemistry, Faculty of Science and Technology, Thammasat University Pathumthani 12121, Thailand
[4]Department of Chemical Technology, Faculty of Science, Chulalongkorn University, Bangkok 10330, Thailand
[5]Center for Petroleum, Petrochemicals and Advanced Materials, Chulalongkorn University, Bangkok 10330, Thailand

[*] E-mail: prasert.r@chula.ac.th

Abstract: Co/SiO_2 fiber catalysts were successfully prepared via electrospinning and impregnating technique. Tetraethyl orthosilicate and $Co(OAc)_2$ were selected as a source of Co/SiO_2 fiber catalysts. Poly (vinyl-pyrolidone) or PVP was used as a binder to control fiber diameter during the electrospinning step. The Co/SiO_2 fiber catalysts were characterized by SEM, XRD, EDS, and TPR. SEM results showed that the average diameter of SiO_2 fibers was in submicron (0.468 μm). The average diameter of fibers depended on the percentage of PVP content. The higher the PVP content, the smaller the average diameter of fiber is obtained.

Introduction

Electrospinning is a process to produce polymer nanofibers with diameter lower than 100 nm and lengths up to kilometres [1]. Electrospinning occurs when the electrical forces at the surface of a polymer solution or melt overcome the surface tension and cause an electrically charged jet to be ejected. When the jet dries or solidifies, an electrically charged fibre remains. This charged fibre can be directed or accelerated by electrical forces and then collected in collector [2] as shown in Scheme 1 [3].

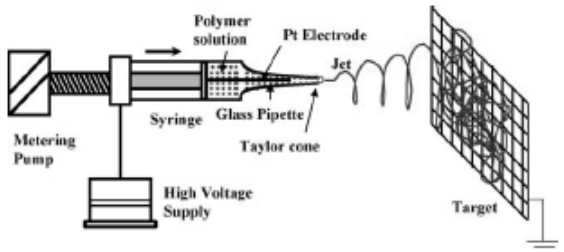

Figure 1: Schematic of the electrospinning apparatus utilized to electrospin polymer solutions.

Fischer–Tropsch synthesis (FTS) is a promising way to convert coal, biomass and natural gas to clean fuels and chemicals via syngas. Cobalt-based catalysts attract most of the current attention for the direct conversion of syngas in FTS because of their high activity, high selectivity for long chain paraffins, and low water gas shift activity. Besides cobalt, some supports such as SiO_2 are indispensable. The chemical and textural properties of the support influence the catalytic activity and product selectivity of Co catalysts, via their modifications on the reducibility and dispersion of cobalt or the formation of well-fined phases. Synthesis of highly dispersed Co catalysts requires strong interaction between the support and the Co precursor, but in turn such strong interactions generally lower the reducibility of such precursors. Different from silica tend to have a strong interaction with cobalt precursor causing highly dispersed Co and limited reducibility [4].

In this work, we have studied the preparation of Co/SiO_2 fiber catalysts by electrospinning technique and impregnation. The effects of various factors such as polymer loading, needle size and Co loading were studied to optimize the fiber diameter and catalytic properties.

Materials and Methods

1. Preparation of Polymer solution

Polymer solution was prepared from poly(vinyl-pyrolidone) (PVP) and ethanol. The ratio of PVP:ethanol was 1:5, 1.5:5, 2:5, 2.5:5, 3:5, 4:5, 5:5, 6:5, and 7:5. PVP and ethanol was pre-mixed at the given ratios under stirring for 10 min.

2. Preparation of silica sol-gel

A silica sol was prepared from tetraethyl orthosilicate (TEOS), ethanol, distillated water and HCl. The molar ratio of TEOS:ethanol:H2O:HCl was 1:2:2:0.01. TEOS and H_2O was mixed, then added conc. HCl following by ethanol. The mixed solution was kept at 55°C for 35 min under stirring. Polymer solution was added to the solution in the final step.

3. Electrospinning condition

The electrospinning condition in this study was the different needle size and various polymer solution. The needle size was 0.6 and 0.4 mm. The polymer solution at different ratio of (PVP):ethanol was 5, 10, 20, 30, 40, 50, 60, and 70wt.%. TCD and voltage was fixed at 15 cm and 15 kV, respectively. The electrospun fibers were collected and calcined at 600°C for 2 h for removed the PVP from the fiber.

4. Impregnation

The Co/SiO_2 catalyst was prepared by impregnation method at different cobalt loading of 5, 10, 15 and 20 wt.%. The prepared fiber were impregnated with the various percent loading of cobalt nitrate solution, then dried at 110°C for 12 h. Finally, the catalyst was calcined at 600°C for 2 h.

5. Catalyst characterizations

The morphology and average diameter of silica fibers were examined by SEM. Temperature programmed reduction (TPR) was used to study reduction behavior and interaction between the active phase and the support.

Results and Discussion

1. Effect of electrospinning conditions

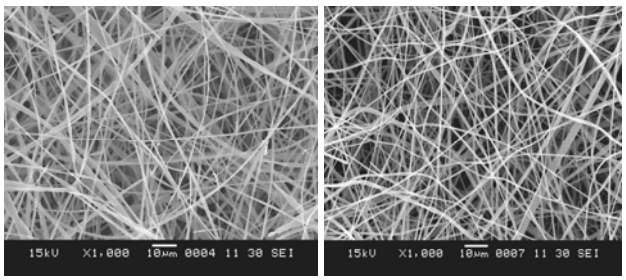

(a) PVP/SiO_2 fibers (b) calcined at 600°C

Figure 2: The SEM photographs of PVP/SiO2 composite fibers (a) and the fibers calcined at 600°C (b)

Figure 2 shows electrospun fibers before and after calcined at 600°C. The diameters of electrospun fiber before calcined at 600°C was 0.8-2.2 μm and the diameters of electrospun fiber after calcined was decreased to range of 0.4-2.1 μm after calcined due to the removal of PVP [5].

Table 1: The average diameter of fibers with various needle size, TCD = 15 cm and applied voltage = 15 kV

PVP:EtOH (wt.%)	Needle size (mm)	
	0.6	0.4
	Average diameter (μm)	
5	2.105	
10	1.867	
15	1.782	
50	1.785	
25	1.612	0.820
30		0.713
40		0.685
50		0.659
60		0.515
70		0.468

Table 1 shows average fiber diameter prepared from different needle size (0.6 and 0.4 mm) at TCD of 15 cm and voltage of 15 kV. The ratio of PVP:ethanol was 25 wt.% comparison between needle size 0.6 mm and 0.4 mm found that the average diameter of fiber prepared from 0.6 mm needle was larger than that prepared from 0.4 mm needle. This can be attributed to the needle size 0.4 mm was appropriate condition to produce the smallest fiber in this experiment. Then using needle size 0.4 mm and vary PVP content. At the same needle, the average fiber diameter was decrease to smaller with increasing the PVP content in the solution. The results implied that the average diameter of fiber could be easily controlled by the PVP content. The smallest fiber diameter was 0.468 μm when using needle size 0.4 mm and 7 g of PVP solution.

2. The TPR behaviors of cobalt/silica fibers and cobalt/silica porous

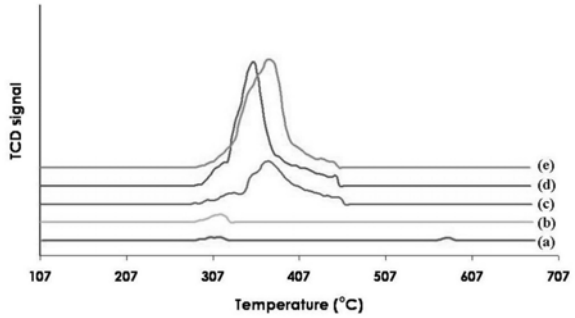

Figure 3: The TPR profile of (a) 10wt.% Co/SiO_2 porous, (b) 5wt.% Co/SiO_2 fiber, (c) 10wt.% Co/SiO_2 fiber, (d) 15wt.% Co/SiO_2 fiber and (e) 20wt.% Co/SiO_2 fiber

The TPR profiles of Co/SiO_2 fiber catalyst with various Co loading (5-20%) compared with the 10wt.% Co/SiO_2 porous catalyst are shown in Scheme 3. The CoO of porous support showed two peaks [6] whereas the fiber catalyst with the same cobalt loading showed one peak of reduction. Comparison between 10wt.%Co/SiO_2 porous catalyst and 10wt.%Co/SiO_2 fiber catalyst found that the temperature of reduction of Co/SiO_2 fiber catalyst is lower than Co/SiO_2 porous catalyst.

Table 2: The H_2 TPR results.

% Metal loading	Degree of Reduction (%)
5 wt.% Co fiber	2.08
10 wt.% Co fiber	29.28
15 wt.% Co fiber	63.68
20 wt.% Co fiber	63.96
10 wt.% Co porous	1.30

Table 2 shows comparison between 10wt.%Co/SiO_2 porous catalyst and 10wt.%Co/SiO_2 fiber catalyst found that the degree of reduction of 10wt.%Co/SiO_2 fiber catalyst is more than 10wt.%Co/SiO_2 porous catalyst. The degree of reduction of 20wt.%Co/SiO_2 fiber catalyst is highest indicating that the fiber catalyst was easily reduced than the porous catalyst.

Conclusions

The Co/SiO_2 fiber catalyst was successivly prepared by electrospinning with impregnation. The diameters of the fibers after calcined were decreased after calcination. The average diameter of fibers depended on the percentage of PVP content. The higher the PVP content, The smaller the average diameter of fiber is obtained. The TPR profile of

cobalt/silica fiber catalysts shifted to the lower temperature compared to that of cobalt/silica porous catalyst indicating that the fiber catalyst was easily reduced than porous catalysts.

References

[1] A. Frenot, I. S. Chronakis, *J. Current Opinion in Colloid and Interface Science*. **8** (2003), pp. 64–75.

[2] H.R. Darrell and C. Iksoo, *J. Nano*, **7** (1996), pp. 216-223.

[3] P. Guptaa, C.Elkinsb, T. E. Longb and G. L. Wilkes, *J. Polymer*, **46** (2005), pp. 4799–4810.

[4] S. Hinchiranan, Y. Zhang; S. Nagamori, T. Vitidsant, N. Tsubaki, *Fuel*, **89** (2008), pp. 455-459.

[5] Ch. Shao, H.-Y.g Kim, J. Gong, B. Ding, D.-R. Lee and S.- J. Park, *J.of Chinese chem. lett*., **4** (2004), pp. 492-494.

[6] S. Sun., N. Tsubaki and K. Fujimoto, *Appl. Catal. A*, **202 (2000)**, pp. 121-131.

Anodic stripping analysis of cadmium (II) and lead (II) ions by bismuth–carbon nanotube modified electrodes

N. Pikroh and P. Vanalabhpatana*

Department of Chemistry, Faculty of Science, Chulalongkorn University
Bangkok 10330, Thailand

*E-mail: parichatr.v@chula.ac.th

Abstract: Synthesized by polyol process, bismuth–carbon nanotube (Bi–CNT) composites have been developed as working electrodes for the determination of cadmium (II) and lead (II) ions at ppb level by means of anodic stripping voltammetry. Physical and electrochemical characterization of Bi–CNT composites were confirmed by X-ray diffraction technique and cyclic voltammetry, respectively. Various factors (*e.g.*, bismuth concentration, deposition time, and deposition potential) influencing the detection of both metals were thoroughly investigated. Furthermore, in comparison with *in situ* bismuth film modified onto CNT electrodes, the Bi–CNT modified electrodes can yield larger stripping signals for cadmium (II) and lead (II) ions. According to these results, we have tried to optimize several experimental parameters to improve the ability of the Bi–CNT modified electrodes towards the determination of the metal ions in real samples.

Introduction

Anodic stripping voltammetry has been applied to the determination of a wide variety of trace metals [1–3]. Mercury electrodes in film and drop forms have been traditionally used for metal detection with high sensitivity and reproducibility [4]. However, due to the extreme toxicity of mercury and its salts employed for the electrode preparation, intensive researches have been attempted to investigate mercury-free electrodes. In 2000, bismuth film electrode was initially proposed as an alternative to the mercury electrodes [5] since its toxicity is negligible. Furthermore, the bismuth film electrode displayed comparable performance to mercury electrodes for the electrochemical analysis. Recently, Hwang *et al*. [6] reported that, owing to high electrical conductivity, high surface area, and good chemical stability of carbon nanotubes (CNTs), the bismuth film modified CNT electrode exhibited superior performance in comparison with the bismuth film electrodes modified on activated carbon, graphite, and glassy carbon electrode (GCE). Since typical bismuth film electrodes require additional step for film preparation by using the solution of bismuth (III) ions, it is sometimes inconvenient to utilize bismuth film electrodes in real sample analysis. Hence, in this work, a new and easy-to-prepare type of bismuth electrode, bismuth–CNT (Bi–CNT) composite modified electrode has been selected for the determination of cadmium (II) and lead (II) ions by means of square wave anodic stripping voltammetry (SWASV). Bi–CNT composites were simply synthesized by polyol process [7], which uses a poly alcohol as a solvent and a reducing agent to produce bismuth particles deposited onto CNTs from the mixture of bismuth (III) ion solution and CNTs.

Methodology

1. Composite Preparation

Bi–CNT composites were prepared via the following procedure. Calculated bismuth (III) nitrate pentahydrate ($Bi(NO_3)_3{\cdot}5H_2O$) was added into ethylene glycol to form a solution, followed by the addition of CNTs. Then, the $BiNO_3$–CNT mixture was sonicated and heated for several hours. When the mixture was cooled down, its pH was adjusted with acidic solution. After that, the mixture was refluxed to settle the Bi–CNT which was subsequently filtered, washed, and dried. Additionally, the prepared Bi–CNT was characterized by X-ray diffraction (XRD) method (Bruker D8 ADVANCE, Germany).

2. Electrode Preparation

GCE modified with Bi–CNT composite or CNTs was used as a working electrode and prepared by the following protocol. Desired amount of Bi–CNT composite or CNTs was sonicated in a solvent to form a slurry. Then, the slurry was placed onto the surface of GCE and the solvent was left to evaporate at room temperature for 10 min.

3. Voltammetric Measurement

Stripping voltammetric measurements were performed without deaerating an analyte solution. At the preconcentration step, Bi–CNT modified electrode was usually held at –1.10 V in a solution of cadmium (II) and lead (II) ions for 120 s. After that, the voltammo-gram in a square wave mode was recorded with an anodic scan from –1.10 to +0.30 V. At the end, the electrode was cleaned at +0.30 V for 30 s. Note that all potentials are quoted with silver/silver chloride reference electrode.

For comparison, the electrochemical performance of *in situ* bismuth film modified CNT electrode was also observed. In a solution containing bismuth (III), cadmium (II), and lead (II) ions, the CNT modified GCE was set at the potential of –1.10 V to allow the formation of bismuth film and its alloys (BiCd and

BiPb). Similar to the Bi–CNT modified electrode, square wave voltammogram was then obtained prior to electrode cleaning.

Results and Discussion

1. XRD Characterization of Bi–CNT Composite

Bi–CNT composite and CNTs were confirmed by XRD investigation as shown in Fig. 1a and 1b, respectively. The diffraction peaks at 2θ = 24.5° correspond to the plane (002) of graphite [8], indicating the presence of CNTs. While the other diffraction peaks in Fig. 1a represent the planes of bismuth. This result exhibited the successful deposition of bismuth onto CNTs.

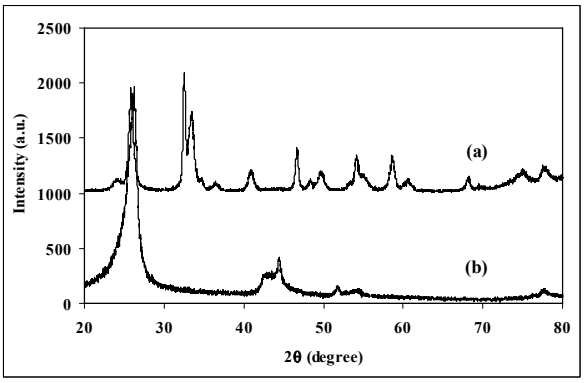

Figure 1 XRD patterns of (a) Bi–CNT composite and (b) CNTs.

2. Electrochemical Characterization of Bi–CNT Modified Electrode

Fig. 2 displays cyclic voltammogram of the GCE modified with Bi–CNT composite scanned in 0.1 M acetate buffer solution (pH 4.5) from +0.80 to –1.20 V and –1.20 to +0.80 V at the scan rate of 100 mVs^{-1}. The cathodic and anodic peaks of bismuth (III)–bismuth (0) redox couple [9] were observed with the peak potentials of –0.89 and –0.08 V, respectively. This result not only confirmed that bismuth was successfully deposited on the surface of CNTs by our selected method, but revealed that the GCE modified with Bi–CNT could be fabricated.

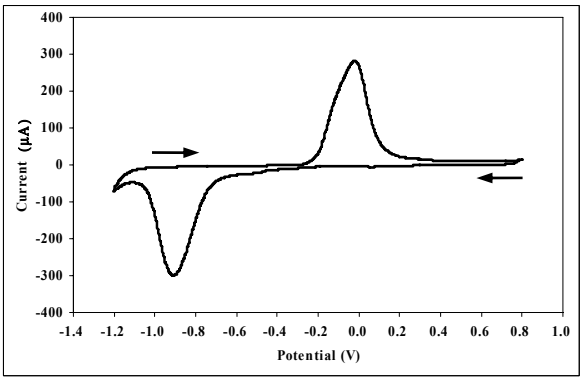

Figure 2 Cyclic voltammogram of 0.1 M acetate buffer solution (pH 4.5) recorded by the Bi–CNT modified GCE at the scan rate of 100 mVs^{-1}.

3. Electrochemical Responses of In Situ Bismuth Film Modified CNT Electrode, CNT Electrode, and GCE towards Cadmium (II) and Lead (II) Ions

To understand the effect of bismuth film towards the determination of cadmium (II) and lead (II) ions by SWASV, the stripping voltammograms for 40 μgL^{-1} of these metal ions recorded with *in situ* bismuth film modified CNT electrode (Fig. 3a), CNT electrode (Fig. 3b), and bare GCE (Fig. 3c) were obtained. For the bismuth film modified electrode, the anodic peaks of cadmium (II), lead (II), and bismuth (III) ions appeared at the potentials of –0.86, –0.65, and –0.22 V, respectively, during the positive scan. On the contrary, only the tiny peak of cadmium (II) ions was observed at the bare CNT electrode and no peaks corresponding to the metal ions were found at GCE, implying that the presence of bismuth film is significant for the stripping analysis of the target metal ions. Our findings about the necessity of bismuth are in agreement with the results in earlier literatures [5,10].

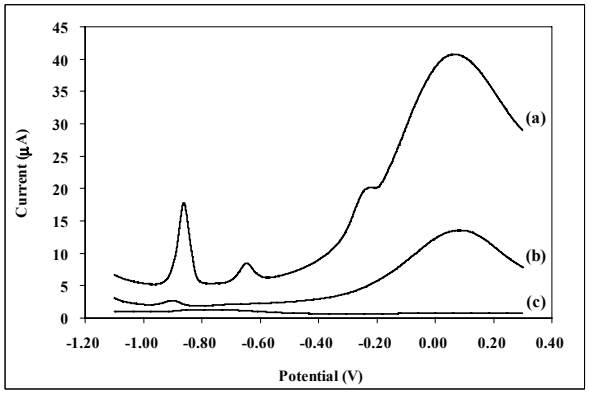

Figure 3 SWASV signals obtained from (a) *in situ* bismuth film modified CNT electrode, (b) CNT electrode, and (c) GCE for 0.1 M acetate buffer solution (pH 4.5) containing 40 μgL^{-1} of cadmium (II) and lead (II) ions with the deposition potential of –1.10 V, the deposition time of 120 s, and the scan rate of 7.5 mVs^{-1}.

4. Optimization of Deposition Conditions for In Situ Bismuth Film Modified CNT Electrode

For stripping voltammetric analysis by *in situ* bismuth film modified CNT electrode, the influence of bismuth (III) ion concentration on the peak currents of cadmium (II) and lead (II) ions are shown in Fig. 4. Bismuth (III) ion concentration was investigated in the range of 250 to 2,000 μgL^{-1} for a solution containing 25 μgL^{-1} of cadmium (II) and lead (II) ions. Similar to previous work [10], the concentration of bismuth (III)

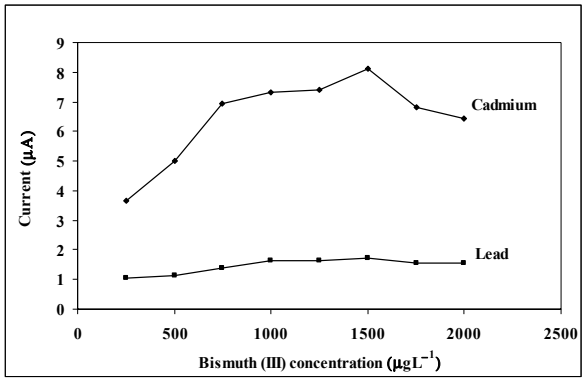

Figure 4 Effect of bismuth (III) ion concentration on the peak currents of 25 μgL^{-1} cadmium (II) and lead (II) ions recorded with *in situ* bismuth film modified CNT electrode in 0.1 M acetate buffer solution (pH 4.5) by SWASV using the deposition potential of –1.10 V, the deposition time of 120 s, and the scan rate of 7.5 mVs^{-1}.

ions controlled the thickness of the bismuth film, but it did not affect the peak positions of both heavy metal ions. A bismuth (III) ion concentration of 1,500 μgL^{-1} was used for subsequent analytical work by the *in situ* bismuth film electrode since this concentration provided the highest peak currents for both heavy metal ions.

To obtain better stripping signals for cadmium (II) and lead (II) ions, the effect of the deposition potential

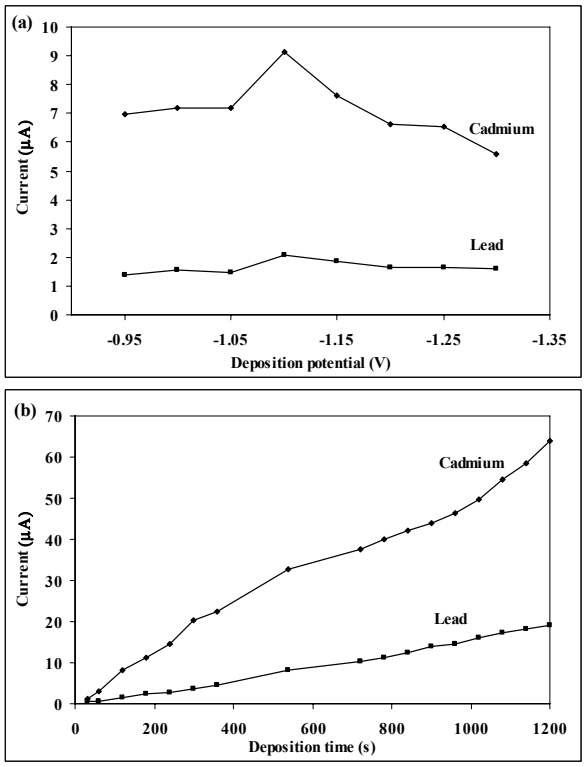

Figure 5 Effects of (a) the deposition potential and (b) the deposition time on the stripping peak currents of cadmium (II) and lead (II) ions recorded with *in situ* bismuth film modified CNT electrode by SWASV.

was probed in the range from –0.95 to –1.30 V and the result is given in Fig. 5a. Since the peak currents of both heavy metal ions had the maximum values when the deposition potential of –1.10 V was used, this deposition potential was then chosen throughout the work.

Furthermore, the deposition time for the stripping analysis of cadmium (II) and lead (II) ions were changed from 30 to 1,200 s and its effect towards the stripping currents are demonstrated in Fig. 5b. The peak currents of both heavy metal ions increased proportionally with the deposition time. Thus, the whole range of 30 to 1,200 s could be effectively used as the deposition time; however, 120-s deposition time was selected in this work to obtain rapid and efficient analysis.

For the purpose of direct comparison, these optimized deposition conditions for *in situ* bismuth film electrode were applied to the Bi–CNT modified GCE in subsequent investigation.

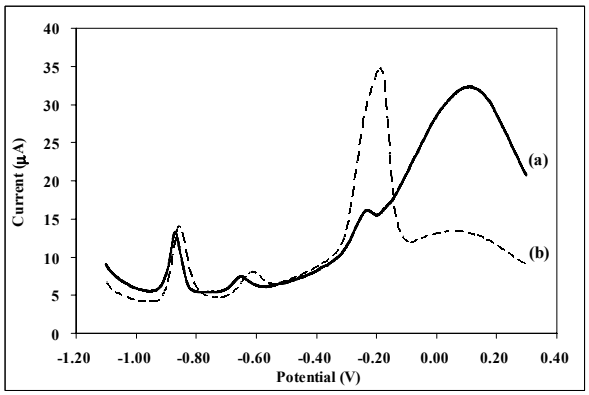

Figure 6 SWASV signals obtained from (a) *in situ* bismuth film modified CNT electrode and (b) Bi–CNT modified GCE for 0.1 M acetate buffer solution (pH 4.5) containing 25 μgL^{-1} of cadmium (II) and lead (II) ions with the deposition potential of –1.10 V, the deposition time of 120 s, and the scan rate of 7.5 mVs^{-1}.

5. Electrochemical Performance Comparison between In Situ Bismuth Film Modified CNT Electrode and Bi–CNT Modified Electrode

Fig. 6 displays typical anodic stripping voltammograms for 25 μgL^{-1} of cadmium (II) and lead (II) ions obtained from (a) *in situ* bismuth film modified CNT electrode and (b) Bi–CNT modified GCE. The peak potentials of cadmium (II) and lead (II) ions were approximately the same at these electrodes. With 120-s deposition at –1.10 V, well-defined and sharp stripping peaks were observed at both electrodes. For cadmium (II) ion, the peak currents of 7.80 μA and 10.19 μA were obtained from *in situ* bismuth film modified CNT electrode and Bi–CNT modified GCE, respectively. For the stripping peak current of lead (II) ion, the bismuth film modified electrode gave 0.37 μA whereas the Bi–CNT modified electrode led to 1.94 μA. Our results have shown that, compared to the *in situ* bismuth film modified CNT electrode, the Bi–

CNT modified GCE yielded slightly larger stripping signals for these heavy metal ions. Therefore, due to simpler preparation and better electrochemical performance, we have tried to optimize various experimental parameters to improve the ability of the Bi-CNT modified GCE towards metal determination.

Conclusions

In this research, the Bi–CNT composites were synthesized by polyol process. XRD and voltammetric results confirmed the deposition of bismuth onto CNTs and the successful fabrication of Bi–CNT modified GCEs. For the determination of cadmium (II) and lead (II) ions at low μgL^{-1} levels using SWASV, the Bi–CNT modified electrodes exhibited more attractive voltammetric response than the *in situ* bismuth film modified CNT electrodes. Currently, we are trying to optimize several experimental parameters to improve the ability of the Bi–CNT modified electrodes towards the determination of the heavy metal ions in real samples.

Acknowledgement

This research has been supported by Asia Research Center (ARC), Chulalongkorn University, Thailand.

References

[1] G. Kefala, A. Economou, and A. Voulgaropoulos, *Analyst* **129** (2004), pp. 1082–1090.
[2] G. J. Lee, H. M. Lee, Y. R. Uhm, M. K. Lee, and C. K. Rhee, *Electrochem. Comm.* **10** (2008), pp. 1920–1923.
[3] K. Tyszczuk, M. Korolczuk, and M. Grabarczyk, *Talanta* **71** (2007), pp. 2098–2101.
[4] T. H. Lu, H. Y. Yang, and I. W. Sun, *Talanta* **49** (1999), pp. 59–68.
[5] J. Wang, J. Lu, S. B. Hocevar, and P. A. M. Fa-rias, *Anal. Chem.* **72** (2000), pp. 3218–3222.
[6] G. H. Hwang, W. K Han, J. S. Park, and S. G. Kang, *Talanta* **76** (2008), pp. 301–308.
[7] Y. Yu, L. Ma, W. Huang, J. Li, P. Wong, and J. C. Yu, *J. Solid State Chem.* **178** (2005), pp. 488–494.
[8] N. Yanna, Y. Jun and J. Mingshan, *Mat. Lett.* **62** (2008), pp. 2092–2095.
[9] A. Economou, *Trends Anal. Chem.* **24** (2005), pp. 334–340.
[10] X. He, Z. Liping, H. Dekun, X. Yuezhong, and J. Litong, *Food Chem.* **109** (2008), pp. 834–839.

Determination of cadmium and lead in human hair samples by cloud point extraction and atomic absorption spectrophotometry

S. Suntithunyaroj[1] and S. Kungwankunakorn[1*]

[1]Department of Chemistry, Faculty of Science, Chiangmai University, Chiangmai, 50200 Thailand

E-mail: ksukjit@hotmail.com

Abstract: A simple and versatile methodology based on cloud point extraction (CPE) was applied as a preconcentration step for determination the amount of cadmium and lead in human hair samples and subsequent analysis by atomic absorption spectrophotometry (AAS). Cadmium and lead were complexed with 1-(2-pyridylazo)-2-naphthol (PAN) to form hydrophobic chelates, using octylphenoxypolyethoxyethanol (Triton X-114) as surfactant and quantitatively extracted into a small volume of the surfactant-rich phase after centrifugation. Then, the mixture was cooled in order to increase the viscosity of surfactant-rich phase. The chemical variables that affect the cloud point extraction, such as Triton X-114 concentration, complexing agent concentration, equilibration temperature and time, pH of the sample solution and the viscosity affecting the detection process were investigated. Under optimized condition, the cloud point is formed at 40°C, only 10 ml of sample solutions was used in the presence of 2×10^{-4} mol l^{-1} PAN and 0.04% v/v Triton X-114 at pH 3. The method permitted the limit of detection of 0.029 and 0.62 μg ml^{-1} cadmium and lead, respectively. The proposed method has been applied to the FAAS determination of cadmium and lead in human hair samples after cloud point extraction.

Introduction

In recent years, human hair has been interested as a clinical sample and attracted the interest of researchers from the forensic science increasingly. Human hair has been used as an evident in suicide and homicide police cases to prove that the cause of death is from poison or not. There are many advantages on the use of human hair as sample in heavy metal analysis, such as most of the toxic elements are accumulated in hair higher than in other human organs, hair is an inert and chemically homogeneous sample, sampling is carried out easily and painlessly. Moreover, the composition of hair does not change measurably and repeated determination can be performed easily over times [1-3].

For the determination of trace elements, preconcentration can provide the amount of analyte to get a higher confidence level. Normally, classical preconcentration technique such as liquid-liquid extraction (LLE), ion-exchange techniques and solid-phase extraction (SPE) consumes large amounts of sample and high purity solvents, also produces large amounts of waste which creates a severe environmental problem. Alternative approach to the sample preconcentration for trace elements is cloud point extraction (CPE). CPE is becoming a practical application in the use of surfactants in analytical chemistry, it reduces the consumption of solvent, disposal costs and extraction time.

The role of CPE is based on the property of most non-ionic surfactants in aqueous solutions to form micelles and to separate into a surfactant-rich phase and an aqueous phase when heated to the temperature known as cloud point temperature. CPE is a green method due to it consumes less amounts of reagents and surfactants are not toxic. This work used flame atomic absorption spectrophotometry (FAAS) for determination the amount of Cd and Pb in human hair samples [4-8].

Materials and Methods

Apparatus and Reagents

Flame atomic absorption spectrophotometer, model Analyst 680 (Shimadzu, Kyoto, Japan) was used for Cd and Pb measurements. Microwave digestion system, model Ethos Sel (Milestone Ethos, Italy) was used for sample decomposition. A non-ionic surfactant Triton X-114 (Fluka, Buches, Switzerland) was used without further purification. A solution of $4x10^{-3}$ mol l^{-1} 1-(2-pyridylazo)-2-naphthol (PAN): $C_{15}H_{11}N_3O$ (Carlo Erba, Italy) was prepared by dissolving appropriate amount of this reagent in absolute ethanol (E. Merck, Darmstadt, Germany). Stock standard solutions of Cd and Pb at concentration of 1000 μg ml^{-1} were obtained from (Fluka, Buches, Switzerland). Working standard solutions were obtained by appropriate dilution of the stock standard solution. All other reagents were of analytical-reagent grade (E. Merck, Darmstadt, Germany) and all solutions were prepared with deionized water. The laboratory glassware was kept in dilute nitric acid at least overnight and subsequently washed with deionized water.

Cloud Point Extraction Procedure

For Cd determination, aliquots of 10.0 ml of the solution containing the analyte 1 μg ml^{-1}, PAN $2x10^{-4}$ mol l^{-1} and Triton X-114 0.04% (v/v) and for Pb determination, aliquots of 10 ml solution containing

the analyte 10 μg ml^{-1}, PAN $2x10^{-4}$ mol l^{-1} and Triton X-114 0.04% (v/v) were subjected to CPE. Then the mixture was adjusted to pH 3 by acetate buffer solution and heated at 40 ºC for 30 min. Separation of the two phases was achieved by centrifuging at 3400 rpm for 10 min. On cooling in an ice–acetone mixture for 10 min, the surfactant-rich phase became viscous and the supernatant aqueous phase was separated by the aid of a syringe. The surfactant-rich phase was treated with 500 μl methanol containing 0.1 mol l^{-1} HNO_3 in order to reduce its viscosity and facilitate sample handling. The final solution was introduced into a flame atomic absorption spectrophotometer.

Preparation of Hair Samples

Human hair samples were cut into 2 cm with a stainless steel scissors. Firstly, human hair samples were washed with acetone. Then, hair samples were washed with deionized water for three times before washed with acetone one more time. The samples were then oven-dried at 110 ºC for 16 hrs.

Hair Samples Decomposition

A 0.50 g of sample was treated with 10.00 ml of concentrated HNO_3 in the microwave-digestion oven (PTFE digestion vessel) under the following conditions: (1) power 250%, time 6 min; (2) power 350%, time 6 min; (3) power 500 %, time 10 min; (4) power 250 %, time 6 min; (5) power 0%, time 2 min. After cooling to room temperature, the solutions were transferred into beakers. To each sample, 0.50 ml of 30% H_2O_2 was added dropwise and heated for some minutes. The solutions obtained were made up to 50.00 ml with deionized water.

Results and Discussion

1 Effect of PAN Concentration

The effect of PAN on analytical signal is shown in Fig. 1. The concentration of PAN was evaluated over the range of $2x10^{-5}$–$1x10^{-3}$ mol l^{-1}. In both cases of cadmium and lead, the absorbance decreased from $2x10^{-5}$ mol l^{-1} to $1x10^{-4}$ mol l^{-1}, later increased up to the maximum at $2x10^{-4}$ mol l^{-1} and then the absorbance decreased after $2x10^{-4}$ mol l^{-1}.

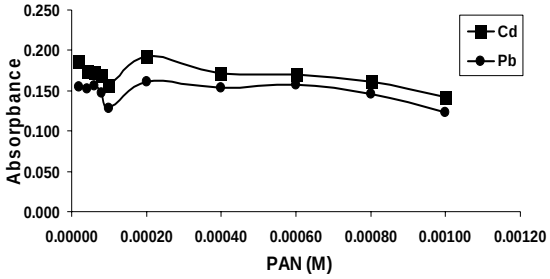

Fig 1. Effect of PAN concentration on the analytical signal of the Cd (1 μg l^{-1}) and Pb (2 μg l^{-1}). Condition: 0.04% (v/v) Triton X-114 and pH 3 at 40 ºC.

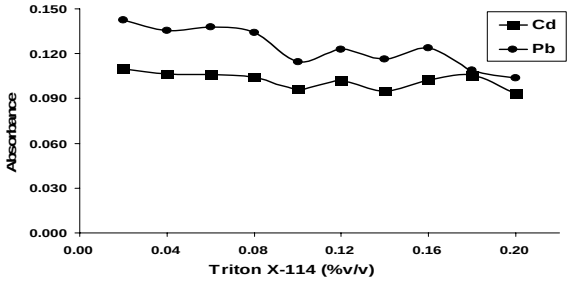

Fig 2. Effect of Triton X-114 concentration on the analytical signal of the Cd (1 μg l^{-1}) and Pb (2 μgl^{-1}). Condition: $2x10^{-4}$ mol l^{-1} PAN and pH 3 at 40 ºC.

Therefore, the concentration of PAN $2x10^{-4}$ mol l^{-1} was chosen as optimum concentration for the determination of both elements.

2 Effect of Triton X-114 Concentration

Fig. 2 shows the effect of Triton X-114 concentration on analytical signal**.** The preconcentration efficiency was evaluated in the range of 0.02-0.20 %(v/v) Triton X-114. The highest absorbance was obtained with 0.02% (v/v) Triton X-114, but at the concentration of Triton X-114 lower than 0.02 %(v/v) the preconcentration efficiency of the complex was not reproducible, due to assemblies that were inadequate to quantitatively entrap the hydrophobic complex. Also, the higher concentration of Triton X-114 can be deteriorated the analytical signal due to the increase of viscosity. Therefore, the concentration of 0.04% (v/v) Triton X-114 was selected for the rest of this work.

3 Effects of Equilibration Temperature and Time

The effect of equilibration temperature and time on the analytical signal was studied in the range of 30–50ºC and 15–60 min, respectively. Since, it is desirable to employ the lowest possible equilibration temperature and the proper equilibration time, a temperature of 40 ºC and an equilibration time of 30 min were chosen for further experiments.

4 Effect of pH

Fig. 3 shows the effect of the pH values on analytical signal.

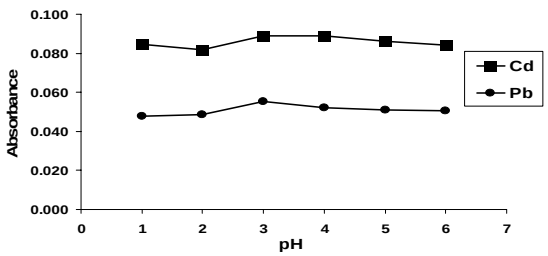

Fig 3. Effect of pH on the analytical signal of the Cd (1 μg l^{-1}) and Pb (2 μg l^{-1}). Condition: $2x10^{-4}$ mol l^{-1} PAN and 0.04% (v/v) Triton X-114 at 40 ºC.

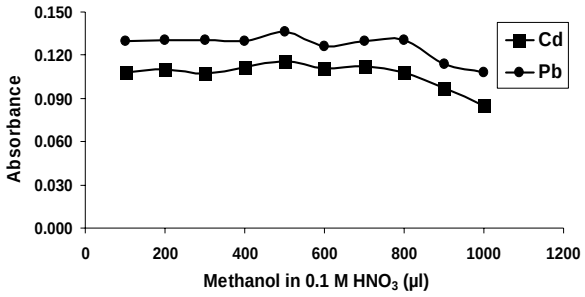

Fig 4. Effect of the viscosity to the analytical signal of the Cd (1 µg l^{-1}) and Pb (2 µg l^{-1}). Condition: $2x10^{-4}$ mol l^{-1} PAN, 0.04% (v/v) Triton X-114 and pH 3 at 40 ºC.

The preconcentration efficiency was evaluated in the range of pH 1-6, because after pH 6 the solutions were precipitated. It can be seen that for pH value in the range of 3-6, the absorbance was almost constant. Therefore, pH 3 was chosen for the rest of this work in order to reduce the interference effects.

5 Effect of Viscosity on Analytical Signal

Since the surfactant-rich phase obtained after CPE is rather viscous, methanol containing 0.1 mol l^{-1} HNO_3 was added to the surfactant-rich phases in order to decrease the viscosity and facilitate the introduction
of the sample into the atomizer of spectrophotometer. Fig. 4 shows the change of absorbance normalized as a function of the volume of methanol containing 0.1 mol $l^{-1}HNO_3$ added into the surfactant-rich phase. The optimum volume of methanol containing 0.1mol l^{-1} HNO_3 was 500 µl with respect to cadmium and lead. For smaller volume of methanol containing 0.1 mol l^{-1} HNO_3, the signals are rather lower because the viscosity remains high. For larger volume of methanol containing 0.1 mol l^{-1} HNO_3, the absorbance was reduced, due to the dilution effects. Therefore, 500 µl of methanol containing 0.1 mol l^{-1} HNO_3 was selected for the rest of this work.

6. Analysis of Human Hair Samples

The determination of Cd and Pb in human hair samples were performed by spiked method. The amounts of Cd (1 µg l^{-1}) or Pb (10 µg l^{-1}) standard solutions were added into human hair samples followed with cloud point extraction procedure and the final solutions were detected by flame atomic absorption spectrophotometer. Good recoveries in the range of 95.04–101.70 and 98.23-106.06% were obtained for Cd and Pb, respectively. The results show that the cloud point methodology can be successfully applied to the determination of Cd and Pb in human hair samples.

Conclusions

In this work, the use of CPE as a preconcentration step for cadmium and lead offers high recoveries of both elements. The methodology also offers several advantages including low cost, simple, sensitive and non-polluting alternative to other separation or preconcentration techniques.

Further, in comparison with solvent extraction methods, it is much safer, since only a small amount of surfactant which has a low toxicity is used. The surfactant-rich phase can be easily introduced into a flame atomic absorption spectrophotometer after treated with methanol containing 0.1 mol l^{-1} HNO_3. The proposed method can be applied to determination of trace cadmium and lead in human hair samples.

Acknowledgements

The authors would like to thank Department of Chemistry, Faculty of Science, Chiang Mai University and Centre for innovation in Chemistry: Postgraduate Education and Research Program in Chemistry (PERCH-CIC) for financial support.

References

[1] J. Kubova, V. Hanakova, J. Medved and V. Stregko, *Anal. Chim. Acta* **337** (1997), pp. 329-334.
[2] J.L. Manzoori and A.B Tabrizi, *Anal. Chim. Acta* **470** (2002), pp. 215-221.
[3] K.S. Rao, T. Balaji, T.P. Rao, Y. Babu and G.R.K. Naidu, *Spectrochim. Acta, Part B.* **57** (2002), pp. 1333–1338.
[4] J.L. Manzoori and A.T Bavili, *Microchem. J.* **72** (2002), pp. 1-7.
[5] J.L. Manzoori and G.N. Karim, *Anal. Sci.* **19** (2003), pp. 579-583.
[6] P.Liang, H. Sang and Z. Sun, *J. Colloid Interface Sci.* **304** (2006), pp. 486–490.
[7] K. Madej, *Trends Anal. Chem.* **28** (2009), pp. 436-446.
[8] L.M. Coelho and M.A.Z. Arruda, *Spectrochim. Acta, Part B* **60** (2005), pp. 743–748.

Separation and purification of fulvic acid from leonardite

K. Sangsorn[1], P. Sooksamiti[2] and O. Arquero[1,*]

[1]Department of Chemistry, Faculty of Science, Chiang Mai University, Chiang Mai, Thailand 50200
[2]Department of Primary Industry and Mine Office Region 3,Chiang Mai, Thailand 50200

E-mail: noi2495@hotmail.com*

Abstract: The isolation and purification of the fulvic acids from soil have been a challenging task for researchers. In this research work, fulvic acids have been extracted from a low rank coal (leonardite) obtained from Mae Moh Lignite Mine in Lampang province, by using alkali extraction with sodium hydroxide solution. Fulvic acid was separated from humic acid by acid solution (0.1 M HCl, 0.1 M HNO_3 or 0.1 M CH_3COOH). The greatest yield of fulvic acid was obtained from 0.1 M HNO_3. Then, the crude fulvic acid was purified by precipitation procedure with $AlCl_3$ at pH 5. The mechanism forming the precipitates includes a complexation reaction of carboxylic groups of the fulvic acids with aluminium ion (ligand exchange reaction). The fulvic acid samples were identified to confirm their compositions by the Fourier-transformed infrared spectroscopy (FT-IR) analysis. The spectral features obtained from FT-IR were similar to those reported for humic substances from the other sources.

Introduction

Leonardite is an oxidized form of lignite coal that originated on the surface of lignite deposits by post-sedimentary oxidation. Humic substance, the biologically refractory degradation components are classified into three groups: humic acid, fulvic acid and humin. Humin has very high molecular weights and is not soluble in water at any pH. Humic acid is soluble in water only under alkaline conditions and has a smaller molecular weight than humin. Fulvic acid has the smallest molecular weight and is soluble in water under all pH conditions [1]. Humic and fulvic acids can be obtained by extraction from leonardite. Humic substances are known to play an important role in plant growth, several environmental, geochemical reactions and ubiquitous in natural environments [2]. Among these, the fulvic acid fraction has the highest solubility in water, and this part of fraction can form soluble complexes with metals and hydrophobic organic chemicals. Fulvic acid is used as carrying agents and complexing media affect the transport and bioavailability of environmental contaminants such as heavy metals, polycyclic aromatic hydrocarbons and other chemicals [3]. Therefore, fulvic acid can be applied to neutralize toxic waste and improve soil work ability. Preparation of the fulvic acids has not been easy because they are soluble in both alkaline and acidic solution [4]. The most extraction was achieved humic plus fulvic acids fraction using liquid-liquid extraction with alkali solution. Then, fulvic acid was separated by acid solution such as HCl [1, 3], H_2SO_4 [6] or HNO_3 [7] for precipitation humic acid and supernatant of fulvic acid fraction. A fulvic acid fraction is obtained in an aqueous solution that usually contaminated with a large amount of salts (crude fulvic acid fraction). Several procedures have been employed to purify fulvic acid such as adsorption on hydrophobic resin [1, 3, 7], precipitation [4, 5], thin-layer chromatography (TLC), reverse phase HPLC and size-exclusion chromatography (SEC) [8]. In the International Humic Substances Society (IHSS) method, hydrophobic fulvic acid is isolated from the crude fulvic acid fraction using an adsorption procedure on a hydrophobic resin such as XAD-8, DAX-8 or other equivalent resins and followed by elution with 0.1 M NaOH. This procedure is effective in removing salts and water from the crude fulvic acid fraction, but it could also remove hydrophilic fulvic acid. Precipitation is another method for fulvic acid separation. This method successfully recovered hydrophilic plus hydrophobic fulvic acids from crude fulvic acid fractions [3]. The mechanism of the high recovery of the precipitation method would be a co-precipitation of the fulvic acid fraction with aluminium hydroxide in weakly acidic to neutral pH conditions [4].

The aim of this work is to separate fulvic acid from leonardite by co-precipitation with aluminium hydroxide and characterize by Fourier transform infrared spectroscopy (FT-IR) [9].

Materials and Methods

Apparatus and Reagents

The leonardite material was obtained from Mae Moh Lignite Mine in Lampang province. All chemicals used (NaOH, HCl, HNO_3 and CH_3COOH) are of analytical reagent grade. The Fourier transform infrared (FT-IR) using KBr pellet (BRUKER tenser 27) was used to characterize the fulvic acid.

Preparation of Leonardite Sample

Leonardite was collected from Mae Moh Coal Mine, Lampang Province, Thailand. The sample was ground, air dried and sieved through 100 mesh by sieving machine.

Extraction of humic and fulvic acids

10 g of leonardite was extracted with 100 mL of 0.2 M NaOH and stirred for 1 min. The pH of the suspension was then adjust and maintained at 13 by

addition of NaOH (20%, w/v), and allowed to stand for 3 h. The mixture was centrifuged at 3500 rpm for 15 min in order to eliminate the precipitation. The supernatant was then acidified with acid solution (HCl, HNO_3 or CH_3COOH) and stirred for 1 min. The pH of the suspension was adjusted to 1 by the addition of acid solutions (20%v/v of either HCl or HNO_3), and it was allowed to stand for over night. Both fulvic acid (supernatant) and humic acid (precipitate) fractions were separated by centrifugation at 3500 rpm for 15 min and rinsed once with distilled water. The supernatant (crude fulvic acid fraction) was filtered through a 0.45-µm pore-sized filter membrane.

Purification of the crude fulvic acid fraction

1. **Precipitation procedure as influenced by equilibrium pH**

The crude fulvic acid fraction solution (pH 1.0, equivalent to an extract from 10 g leonardite) was precipitated with 20 mL of 0.5 M $AlCl_3$ solution at several pH values (pH 4-8) by addition of NaOH solution.

2. **Precipitation procedure as influenced by equilibrium concentration of $AlCl_3$**

The crude fulvic acid fraction solution was precipitated by addition of 20 ml of $AlCl_3$ solution (0.1-0.5 M) at pH 5 condition. The precipitated fraction was rinsed once with distilled water. The humic and fulvic acids were dried at 60 ^oC, and the major functional groups of the solid humic acids were characterized by Fourier Transform Infrared (FT-IR) Spectroscopy.

The FT-IR spectra were recorded in the transmission mode by a FT-IR (BRUKER tenser 27) spectrophotometer using KBr pellet containing 1% of fulvic acid.

Results and Discussion

Results showed that the greatest yield of crude fulvic acids (1.994 g) was obtained when using 0.1 M HNO_3 to precipitate the humic acid, while the lowest yield (1.534 g) was obtained from 0.1 M HCl as shown in Fig. 1. In the precipitation method for separation humic acid from fulvic acid with acetic acid, the pH was adjusted using HCl. Therefore, the yield of crude product including salts from both HCl and acetic acid was higher than when using only HCl. The crude fulvic acids obtained in an aqueous solution that contaminated with a large amount of salts. Therefore, purification with precipitation method is necessary for removing salts and water from the crude fulvic acid fraction.

The precipitation method of fulvic acid with aluminium hydroxide includes pH-adjustment of the fulvic acid solution from slightly acidic to neutral (pH range 4-8). It was found that the fulvic acid could be precipitate in the form of complex from the solutions of HNO_3 or HCl, but no precipitate was obtained from the solution of CH_3COOH. The yields of the precipitated fulvic acid from the crude fulvic acid solution prepared from leonardite were determined as a function of equilibrium pH (Fig. 2).

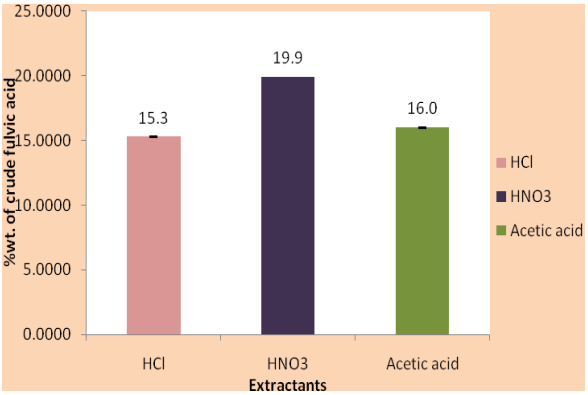

Figure 1 The %wt. of crude fulvic acids extracted from 10 g of leonardite with HCl, HNO_3 and CH_3COOH

The results showed that the yields in the precipitation method at equilibrium pH 5.0 were higher than the others pH. In this study, the effect of concentration of $AlCl_3$ was studied in the range of 0.1-0.5 M. When the concentration of $AlCl_3$ was higher than 0.5 M, the solution became cloudy due to $Al(OH)_3$ formation. Therefore, the precipitant might be more contaminated by $Al(OH)_3$. It was shown that the greatest yield of precipitated fulvic acid was obtained at 0.5 M $AlCl_3$ (Table 1).

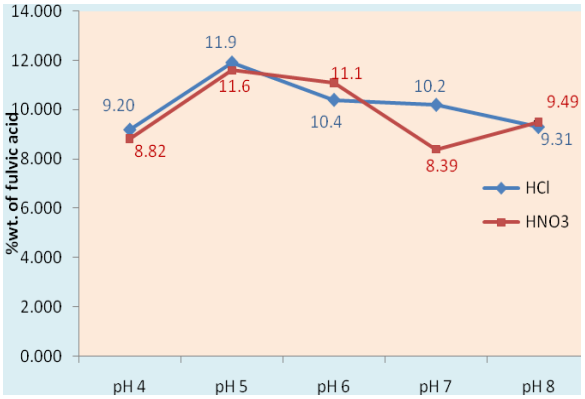

Figure 2 The %wt. of fulvic acids after precipitation with 0.5 M $AlCl_3$ in HCl and HNO_3 at different pH

The mechanism of the precipitation method would be a co-precipitation of carboxylic groups of the fulvic acids with aluminium in weakly acidic to neutral pH conditions. This mechanism is identical to that for the retention of fulvic acids in many soils. These results suggest that the precipitation method is very effective in isolating fulvic acids as solid phase.

Table 1 %wt. of fulvic acid precipitated with $AlCl_3$ solution at pH 5.0

Concentration of $AlCl_3$ (M)	The %wt. of fulvic acid (g)	
	0.1 M HCl	0.1 M HNO_3
0.1	2.82 ± 0.01	2.74 ± 0.01
0.2	4.93 ± 0.02	5.03 ± 0.01
0.3	6.47 ± 0.01	8.37 ± 0.01
0.4	9.75 ± 0.01	9.87 ± 0.01
0.5	13.0 ± 0.01	12.6 ± 0.02

The FT-IR spectrum of extracted fulvic acid is shown in Fig. 3. It was found that the mains of the adsorption broad bands of fulvic acid were around 3,400 cm^{-1}, which corresponds to O-H stretching of hydroxyl groups. Other bands around 1,600 cm^{-1} was attributed to the C=C vibrations of aromatic structures. Band at around 1,200 cm^{-1} was C-O stretching of aliphatic OH. Refer to table 2, it may be confirmed that the FT-IR spectrum obtained is fulvic acid, because each peak corresponds with the functional groups present in fulvic acid. However, the small peaks in FT-IR spectra were disappeared because aluminium ion entrapped carboxylic groups of fulvic acid leading to decrease the stretching in the molecule. The FT-IR evidence suggested that the extracted fulvic acid was relatively rich in carboxylic and phenolic groups.

Table 2 Assignment of FT-IR absorption bands of the fulvic acid

Wave number (cm^{-1})	Peak	Assignment
3400	Broad peak	H-bonds; OH groups
2919	Small peak	C-H asymmetric; C-H stretch of –CH; C=O of COOH
1717	Small peak	C=O of COOH
1606	Broad peak	C=C in aromatic structure; COO^-
1399	Small peak	COO^-
1217	Broad peak	C-O stretch of aliphatic OH

From H. Fu, X. Quan / Chemosphere 63 (2006) 403–410

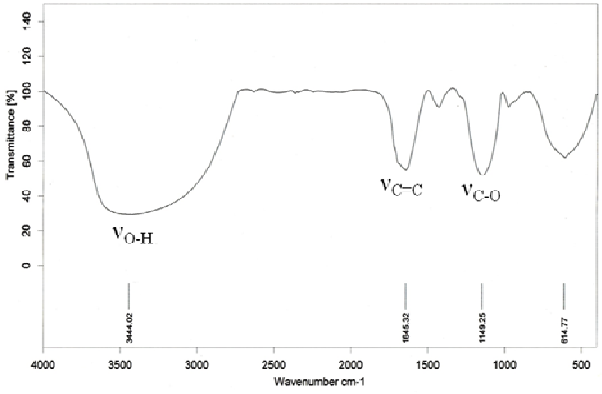

Figure 3 FT-IR spectra of fulvic acid from leonardite.

Conclusions

The highest and lowest yields of the crude fulvic acids were obtained when extracted 10 g of leonardite with 0.1 M HNO_3 and 0.1 M HCl, which yielded 1.994 g and 1.534 g, respectively. To remove salts and water, the fulvic acid was co-precipitated with aluminium hydroxides at pH 5.0. The presence of carboxylic acids and other functional groups such as alcohols and aromatic rings was indicated.

Acknowledgements

The authors wish to thanks Mae Moh Lignite Mine in Lampang province for leonardite, the National Research University, the Center of Excellence for Innovation in Chemistry (PERCH-CIC), Commission on High Education, Ministry of Education, and the Graduate School, Chiang Mai University for financial support.

References

[1] J. Dai, W. Ran, B. Xing, M. Gu and L. Wang, *Geoderma.,* **135** (2006) 284-295.

[2] J.C.A. de Wuilloud, R.G. Wuilloud, B.B.M. Sadi and J.A. Caruuso, *Analyst*., **128** (2003) 453-458.

[3] S. Hiradate, T. Yonezawa and H. Takesako, *Soil Sci. Plant Nutr*., **53** (2007) 413-419.

[4] S. Hiradate, T. Yonezawa and H. Takesako, *Geoderma*., **132** (2006) 196-205.

[5] M. Fukushma, A. Kikuchi, K. Tatsumi and F. Tanaka, *Anal. Sci*., **22** (2006) 229-233.

[6] A. Jouraiphy, S. Amir, P. Winterton, M. El Gharous, J-C. Revel and M. Hafidi, *Bioresour. Technol*., **99** (2008) 1066-1072.

[7] M. Krog and C. Gron, *Sci. Total Environ*., **172** (1995) 159-162.

[8] X. Ma and S. A. Green, *Chemophere*, **72** (2008) 1425-1434.

[9] C. Plaza, N. Senesi, G. Brunetti, D. Mondelli, *Bioresour. Technol*., **98** (2007) 1964-1971.

[10] H. Fu andX. Quan, *Chemosphere,***63** (2006) 403-410.

Aqueous two-phase extraction and spectrophotometric determination of benzoate in fermented rice noodle (Knomjeen)

W. Praditweangkum[1*] S. Mitkosum[1]

[1]Department of Chemistry, Faculty of Science, King Mongkut's Institute of Technology Ladkrabang, Ladkrabang, Bangkok, Thailand

*E-mail: kprwiboo@kmitl.ac.th

Abstract: An aqueous two-phase system (ATPS) of poly(ethylene glycol) (PEG) and ammonium sulphate $(NH_4)_2SO_4$ was employed in a separation and spectrophotometric determination of benzoate in fermented rice noodle (Knomjeen). The phase diagrams of the aqueous two-phase system of PEG-salt-water were determined by turbidometric titration method. It was found that the best volume ratio of 1:1:1 (sample solution : PEG1000 (50% w/v) : $(NH_4)_2SO_4$ (50% w/v)) gave 94.35-103.21% extraction efficiency, and therefore this ratio was selected in the method development. At the optimum condition, 5.0 mL of the slurry sample was mixed thoroughly with 5.0 mL of PEG1000 (50%w/v) and 5.0 mL $(NH_4)_2SO_4$ (50% w/v) in a test tube. Two clear phases and a layer of white precipitate between the phases were formed. The calibration graph of benzoate (as sodium benzoate) was linear in the range of 50 to 1000 mg/L with coefficient of determination (r^2) was 0.9992. The limit of detection and limit of quantitation for sodium benzoate were 39 mg/L and 130 mg/L, respectively. The recoveries of the spiked standards for the analytes were 98.48-104.91% with relative standard deviation of 0.11-2.52%. The results demonstrated the suitability of ATPS method to analyze benzoate in fermented rice noodle. The method is rapid and environmentally friendly.

Introduction

Fermented rice noodle (Knomjeen) was generally consumed in Thailand for favorite food among people of all ages, especially during annual festivals or ceremonies. The fermented rice noodle was susceptible to rapidly deteriorate during storage. In the manufacturing process, preservation from detrimental effect of microorganisms was attempted. Some chemical food preservatives such as benzoic acid, sodium benzoate, sodium metabisulphite and potassium metabisulphite were commonly used for this purpose [1]. Benzoic acid and sodium benzoate have been used to inhibit microbial growth in foods [2]. Benzoic acid was much less soluble in water than sodium benzoate. For the latter reason the sodium benzoate is preferred for used in most foods [3]. The oral administrations of sodium benzoate at rates of 5-10 g for several days had no adverse effect on health, the reason for low toxicity and have an efficient detoxification mechanism for benzoate [2]. The compounds are conjugated with glycine in the liver to form hippuric acid, which is the excreted in the urine [3]. However, most food preservatives may only be used in limited quantities in certain food under the notification of the Ministry of Public Health. The legal allowance of benzoate in pre-cooked noodle is 1000 ppm (as benzoic acid) [4].

The methods of Association of Official Analytical Chemists (AOAC), 1995, procedures 960.38 and 963.19 for determination of benzoic acid in food with extensive extraction procedures, were involved by large amounts of reagents [5]. Some analytical methods have been reported for the determinated benzoic acid and sodium benzoate in food, beverage and other matrices, such as gas chromatography (GC) [6], high performance liquid chromatography (HPLC) [7-9] and spectrophotometric method [10]. Many of these methods have significant disadvantage, requires derivatization technique, use of toxic organic solvent and that consumed long time for extraction and analysis. Aqueous two-phase system (ATPS) as a useful extraction technique is formed by mixing two aqueous solutions of structurally different polymers or by mixing a polymer and salt [11]. More recently, aqueous two-phase systems were applied for purification of biological materials [12-13] and extraction of metal ion from many samples [14-15]. The aim of this study was to develop a simple and used green solvent extraction method based on aqueous two–phase systems for separation and determination of benzoate in fermented rice noodle (Knomjeen).

Materials and Methods

Apparatus: A UV-visible spectrophotometer (Jasco V-630) with 10 mm cells was employed for the absorbance measurement.

Reagent: PEGs (molecular mass 400, 1000 and 4000) were obtained from Fluka, Panreac Sintesis and Asia Pacific Specialty Chemical Limited, respectively. Solid PEGs of various molecular mass were accurately weighed and dissolved separately with deionized water to obtain stock solution of PEG. The stock solution of inorganic salts, $(NH_4)_2SO_4$ and Na_2SO_4 from Rankem, were similarly prepared. The various concentrations of NaOH and HCl solutions (from Calrlo Erba) were prepared. Sodium benzoate (from Fluka) was accurately weighed and dissolved in deionized water to obtain stock solution of 10,000 mg/L. All reagents were of analytical reagent grade.

Preparation of phase diagram: Each portions of 50%(w/w) of PEG stock solution and 30%(w/w) salt

stock solution were accurately weigted into a test tube and mixed thoroughly until turbidity and a two-phase system was formed. This test tube was weighed. Then, deionized water was added dropwise to the test tube to get a clear one-phase system. The final weight was recorded. The weight of added water was determined by subtraction. The compositions of this mixture at the point of phase transition were calculated. These point liens on the binodal curve. Other points were obtained same as this procedure but different weight ratio of PEG stock solution and salt stock solution at the start.

Preparation of aqueous two-phase system: Each 5.0 mL portions of standard solution (sodium benzoate 50-1000 mg/L), 50%(w/v) PEG stock solution and 50%(w/v) $(NH_4)_2SO_4$ stock solution were added to a test tube. The mixture was shaken to mix thoroughly, then let to stand for 10 min and two clear phases were formed. Benzoate was enriched in the PEG top phase and salt was enriched in bottom phase. The absorbance of the upper PEG-rich phase was scanned from 200 to 400 nm. The corrected absorbance, $Abs_{269.5}$-$[(Abs_{265.5}+Abs_{275.5})/2]$, was calculated using baseline technique. The extraction efficiency (%E) (defined by $E=(V_uC_u/m_s)$ where V_u is the volume of the upper phase, C_u is the concentration of benzoate in the upper phase and m_s is the amount of bezoate added)

Preparation of sample: Fermented rice noodle sample was chopped into small pieces. Mixed the sample thoroughly. Accurately weighed 20.0 g of this prepared sample into 100.0 mL graduated cylinder. Added 16.70 mL of 6.0 M NaOH into this cylinder and diluted to 100.0 mL with deionized water. Stirred thoroughly, left to stand for 30 min. Transfer 25.0 mL of the cloudy solution from cylinder into volumetric flask and diluted with deionized water to 50.0 mL. Pipet 5.0 mL of each portions; diluted sample, 50% (w/v) PEG1000 and 50% (w/v) $(NH_4)_2SO_4$ into a test tube and mixed thoroughly. Two clear phases and a layer of white precipitate between the phases were formed. The absobance of upper PEG-rich phase were determined for benzoate using spectrophotometer.

Results and Discussion

Phase diagrams: Generally, the formation of aqueous two-phase system of PEG and a certain inorganic salt can be explained on the competition for hydration between the two components [16]. The addition of an inorganic salt increases the dehydration of the polymer chains, due to the salting-out effect and phase separation. Thus, two immiscible aqueous phases are obtained: an upper one-rich in PEG, having the same role as the organic phase in traditional extraction systems, and a lower one, rich in the inorganic salt. Three types of phase separation salts were selected to make phase diagrams with comparing the molecular mass of PEG as results were shown in Figure 1. The area above the binodal curve was the two-phase area. Below the binodal curve was the homogeneous phase area. The results were illustrated that the abilities of the salts studies for phase separation were in same order of $Na_2SO_4 \approx NaOH > (NH_4)_2SO_4$ for either PEG1000 or PEG4000 used. For the same salts, minimum amount of salt for the phase separation decreased with the increased of PEG molecular mass. The larger the difference in the molecular mass between the two PEG, the more asymmetrical is the binodal curve. For PEG400 with lower molecular mass, the phase diagram cannot be obtained if concentration of salt was lower than 20%(w/w). The precipitate was formed when NaOH was used. This may be the precipitation of PEG in high concentration of NaOH. The relative effectiveness of cations in inducing two phase was: $Na^+ > NH_4^+$ for sulphate salts.

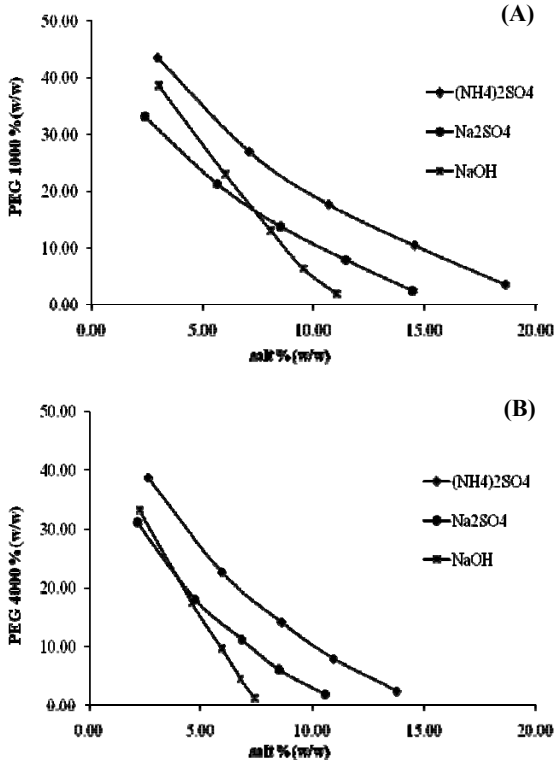

Figure1. Phase diagrams of PEG-salt aqueous two-phase systems: (A) PEG1000/salt, (B) PEG4000/salt.

The concentrations of the phase forming components were selected according to the phase diagram of the system, that the system remains two-phased throughout all experiments. The preparation of aqueous two-phase system can be made more practical by volume measurement than weight measurement. PEG stock solution and salt stock solution should be prepared in high concentration at 50%(w/v). The 50%(w/v) Na_2SO_4 stock solution cannot be prepared because its solubility in water is lower than that of $(NH_4)_2SO_4$. As a result, PEG1000/$(NH_4)_2SO_4$ and PEG4000/$(NH_4)_2SO_4$ aqueous two-phase systems were selected for the following study.

Effect of the PEG molecular mass: The best volume ratio of 1:1:1 (sodium benzoate solution : 50%(w/v) PEG stock solution : 50%(w/v) $(NH_4)_2SO_4$ salt stock solution) was selected to prepare aqueous

two-phase system. The partition of the solute in such an aqueous two-phase system depends both on the characteristics of the formed system (nature and concentration of the inorganic salt, molecular mass and concentration of the polymer) and the hydration properties of the solute (the solute extraction increase with decreasing of the solute hydration) [17]. The effect of polymer molecular mass on extraction efficiency (%E) was examined with the aqueous two-phase conditions of 5.0 mL of benzoate solution (200 and 400 mg/L sodium benzoate), 5.0 mL of 50%(w/v)PEG and 5.0 mL of 50% (w/v)$(NH_4)_2SO_4$. As shown in Figure 2, PEG1000 gave higher extraction efficiency of benzoate than that of PEG4000.

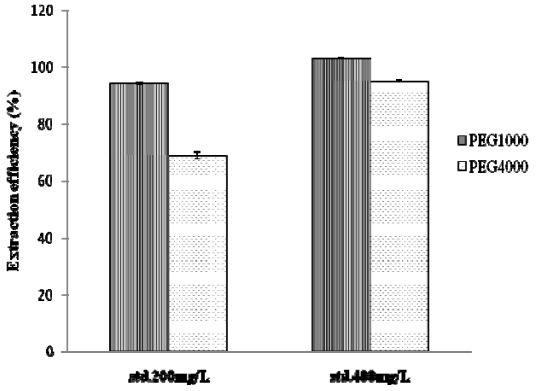

Figure 2. Effect of the PEG molecular mass on extraction efficiency (n=3), extraction conditions: 5.0 mL of sodium benzoate 200 and 400 mg/L, 5.0 mL of 50%(w/v)PEG solution and 50%(w/v)$(NH_4)_2SO_4$ solution.

The effect of polymer molecular mass on extraction efficiency is usually attributed to increasing hydrophobic chains on PEG molecular mass increase. Due to the effect, the general tendency expected would be and increase of extraction efficiency as the PEG molecular mass increase. However, benzoate had hydrophilic head and may be form dimer molecule but no longer hydrocarbon chain. This short hydrophobic chain of benzoate should interact with lower PEG molecular mass (PEG1000) than that of higher PEG molecular mass (PEG4000). Another tendency should be bear in mind that increase of PEG molecular mass will strengthen the viscosity of system and result in bad reproducibility. Therefore, PEG1000 was chosen as the phase separation polymer in following study.

Extraction of benzoate: Benzoate was extracted into the upper phase of an aqueous two-phase system. Absorbance of the upper PEG-rich phase was scanned from 200 to 400 nm. Absorption spectra of benzoate standrad solution was shown in Figure 3(A). The corrected absorbance, $Abs_{269.5}$-[($Abs_{265.5}$+$Abs_{275.5}$)/2], was calculated using baseline technique. The calibration graph was a plot of corrected absorbance vs. benzoate concentration, as shown in Figure 4.

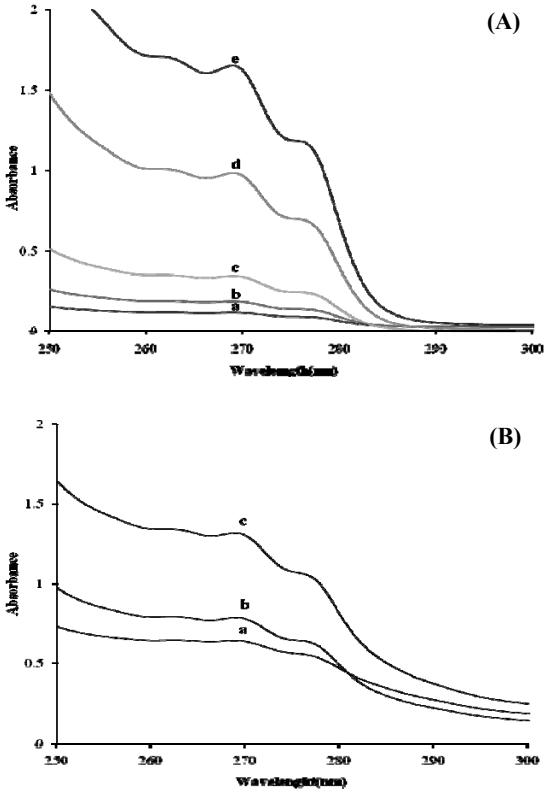

Figure 3. Absorption spectra of extracted benzoate in PEG-rich phase. (A) benzoate standard solution. a: 50, b: 100, c: 200, d: 600 and e: 1000 mg/L.
(B) fermented rice noodle sample. a: sample, b: spiked sample 100mg/L and c: spiked sample 200 mg/L.

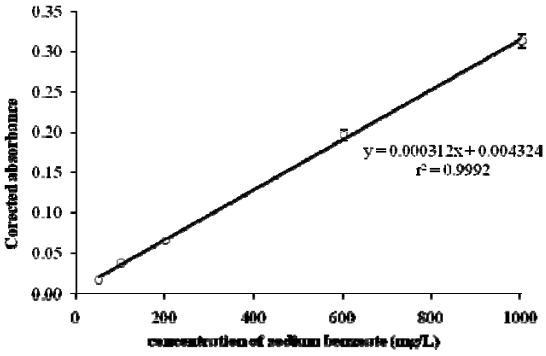

Figure 4. Calibration graph of benzoate.

Dissolving of sample: Chopped sample of fermented rice noodle was soaked in various concentrations of HCl and NaOH solutions in order to test the dissolving of sample. The samples were dissolved to suspendible powder form in 5.0 M and 6.0 M HCl, but cannot dissolve in 1.0 M to 4.0 M HCl. This suspended sample should be filtered before the extraction process was done. The slurry samples can be done in 1.0 M and 2.0 M NaOH, but cannot dissolve in concentration of NaOH higher than 3.0 M. As this result, 1.0 M NaOH was selected to hydrolyze fermented rice noodle sample. The extraction of this slurry sample can be processed without the filtration step.

Method evaluation: For the optimal condition, the calibration graph of sodium benzoate was linear in 50-1000 mg/L concentration range with coefficient of determination (r^2) was 0.9992. The limit of detection and limit of quantitation for sodium benzoate were 39 mg/L and 130 mg/L (concentration that corresponded to $y_{intercept} + 3s_{y/x}$ and $y_{intercept} + 10s_{y/x}$), respectively. The accuracy and precision of the proposed method were determinated. The extraction efficiency of 94.35-103.21% with relative standard deviation of 0.28% (n=3) were obtained. The performance of the method was shown in Table 1. The developed method has satisfactory reproducibility and accuracy for the determination of benzoate in samples in a wide range of concentration.

Table 1. Performance of the method

Parameters	**Value**
Calibration equation	y=0.000312x + 0.004324 (r^2 =0.9992)
Linearity	50-1000 mg/L
LOD	39 mg/L
LOQ	130 mg/L
Extraction efficiency	94.35-103.21%
R.S.D (n=3)	0.28%

Table 2. Results of the analysis of benzoate in fermented rice noodle samples.

sample	**Concentration (mg/L) added**	**found**	**Recovery (%)**	**RSD (%)**
1	0	ND	-	-
	100	98.56	98.56	0.38
	200	201.36	100.68	2.52
	400	393.91	98.48	2.49
2	0	68.79	-	0.42
	100	98.90	98.90	0.21
	200	204.36	102.18	0.11
3	0	130.56	-	2.51
	100	103.85	103.85	1.38
	200	201.37	104.91	2.11

Application of the method: This extraction with aqueous two-phase system could be applied to analysis of benzoate in fermented rice noodle. The results obtained were shown in Figure 3(B) and Table 2. In the optimal condition, 5.0 mL of the turbid sample was added to the optimum aqueous two-phase systems. Two clear phases and a layer of white precipitate between the phases were formed. The upper PEG-rich phase was determined with spectrophotometric method. Figure 3(B) showed the absortion spectra of benzoate. The hydrolyzed flour in cloudy sample solution was coagulated in the white precipitate layer and two phases were clear. Standard benzoate was added to sample, processed under the proposed extraction technique. As shown in Table 2, the recoveries of the spiked standard for the analytes were 98.48-104.91% with relative standard deviation of 0.11-2.52% (n=3). The proposed method could be applied to the quantitative determination of benzoate in fermented rice noodle.

Conclusions

The proposed extraction method based on aqueous two-phase system of PEG1000/$(NH_4)_2SO_4$ following with spectrophotometric measurement was demonstrated to be a the suitability for determination of benzoate in fermented rice noodle. This extraction process can be done in one-step without filtration process, so this method is simple and more rapid than that of traditional liquid-liquid extraction. Due to using of PEG1000 instead of toxic organic solvent and the dominating component in both phases is water, this extraction method is environmentally friendly. The developed method is convenient to be used as routine analysis.

References

[1] S.Suwansri and P.Ratanatriwong , Production of noodle and fermented rice noodle from rice, Faculty of Agriculture, Natural Resources and Environment, Naresuan University, (2006).

[2] A.L. Branen, P.M. Davidson and S. Salminen, Editors, *Food Additives*, Marcel Dekker, New York (1990), pp. 83.

[3] A.L. Branen, P.M. Davidson, S. Salminen and J. H. Thorngate III, Editors, *Food Additives*, Marcel Dekke, New York (2002), pp. 582.

[4] P. Buranapim and V. Areekul, *Effect of benzoate and sorbate on growth of fungi isolated from rice noodle*, 35th Congress on Science and Technology of Thailand, Chonburi, Thailand, 2009, pp. 2.

[5] AOAC International, *Official Methods of Analysis* 16th *Ed*, Vol II, Cunniff, P. (ed), Arlington, VA. (1995).

[6] Z. Pan, L. Wang, W. Mo, C. Wang, W. Hu and J. Zhang, *Anal. Chim Acta*. 545 (2005), pp. 218–223.

[7] Y. A. Onishi, C. Yomota, N. Sugimoto, H. Kubota and K. Tanamoto, *J. Chromatogr. A*. 1040 (2004), pp. 209–214.

[8] S.A.V. Tfouni and M.C.F. Toledo, *Food Control.* 13 (2002), pp. 117–123.

[9] H. M. Pylypiw Jr and M. T. Grether, *J. Chromatogr. A*, 883 (2000), pp. 299 –304.

[10] I. Ahmad and F. H. Vaid, *J. Pharm. Sci*. 22 (2009), pp.18-22.

[11] S. Li, C. He, F. Gao, D. Li, Z. Chen, H. Liu, K. Li and F. Liu, *Talanta* 71 (2007), pp. 784–789.

[12] I.B.R. Ramirez, S. Mebrahtu and B. Jergil., *J. Chromatogr*. *A.* 971 (2002), pp. 117.

[13] I.P. Trindade, M.M. Diogo, D.M.F. Prazeres and J.C. Marcos., *J. Chromatogr.A*. 1082 (2005), pp.176.

[14] Y. Akama and A. Sali., *Talanta*. 57 (2002) , pp 681.

[15] N. Yoshikuni, T. Baba, N. Tsunoda and K. Oguma., *Talanta.* 66 (2005), pp. 40.

[16] H. Cabezas, Jr., *J. Chromatogr. B.* 680 (1996), pp. 3.

[17] R. D. Regers, A. H. Bond, C. B. Bauer, J. Zhang and S. T. Griffin, *J. Chromatogr. B.* 680 (1996), pp. 221.

Optimization of extraction and purification conditions of sericin from silk cocoon

P. Ratanasongtham*, S. Watanesk

Department of Chemistry, Faculty of Science, Chiang Mai University,
239 Huai Kaeo Rd, A. Mueang Chiang Mai, Thailand 50200

* Email: fah_ut@hotmail.com

Abstract: Modification of an extraction method of sericin from Thai silk cocoon (Nang Noi Srisakate) in order to obtain better yield with high purity has been studied. The raw silk cocoons was degummed by boiling at 95 °C for 30 min in a mixture of 0.1 M sodium carbonate (Na_2CO_3), 0.1 M sodium hydrogen carbonate ($NaHCO_3$) then sodium dodecyl sulphate (SDS) solution was added at different concentrations at pH about 10. It was found that the addition of 2 % w/v SDS yielded the highest % degumming ratio which showed the improvement of degumming efficiency. For separation of sericin, the degumming solution was then precipitated with various precipitants such acetic acid and ethanol. The acid precipitation using 5 % v/v acetic acid as a precipitant at pH 4 provided the highest sericin yield. The sericin solution was then dialyzed for 24 hours with distilled water followed by freeze drying to obtain sericin powder. The silk sericin was structurally characterized by Fourier Transform Infrared Spectroscopy (FT-IR)

Introduction

Silk cocoon from silkworm, *Bombyx mori*, is one of the most important materials extensively used in the textile industry. Silk processing from cocoons to the finished clothing consists of a series of steps. Degumming is a key process during which sericin is removed by thermo-chemical treatment of the cocoon [1]. In Thailand, there are many silk-yarn factories and rural industries of silk textile handicrafts that produce huge amounts of silk waste every year. At present, sericin, a major component of silk fiber has been selectively removed during the silk manufacturing process to make silk lustrous and the removed sericin goes as waste. If this sericin protein is recovered and recycled, its value can contribute to significant economic and social benefits [2]. Raw silk fibers, produced by *Bombyx mori* silkworm, consist of major proteins such as fibroin (about 70 %) and sericin (about 30%). Sericin comprises a group of serine rich-proteins produced in the middle silk gland of silk worm. Sericin contains three major and two minor proteins of which the molecular weights range from 20 to 400 kDa [3]. Sericin envelops the fibroin fiber with successive sticky layers that help in the formation of a cocoon. Sericin protein is useful because of its special properties, i.e. anti-oxidative, antibacterial, UV resistant, moisture absorbing and desorbing characters. Thus, because of its properties, sericin can be applied in many fields such as cosmetics, polymer and pharmaceutical products as well as for biomaterials manufacturing [2,4]. Removal of sericin from silk cocoon is accomplished by a process called "degumming" and the degumming solution is precipitated with various precipitants such as alcohol, acid and ammonium sulphate (a protein precipitant) in order to obtain high amount of purified sericin yield. For concentrating sericin, the sericin solution is dialyzed and freeze-dried to convert the extracted sericin from liquid state to powder [5]. There have been numerous reports relating to extraction and purification of sericin from silk cocoon. Gamo [6] extracted sericin from silk cocoon by boiling in water, then divided it into insoluble and soluble fractions. These studies, however, could neither prove the heterogeneity of sericin nor achieve molecular separation, because the report showed that sericin was degraded by boiling water. Yamada, et al. [7] suggested different degumming conditions that could be operated in a medium of various degumming solutions such as hot water, Na_2CO_3, soap solution, urea and enzyme. Degumming condition was carried out with different concentrations of degumming solution, heating temperatures and lengths of heating time. The conditions for degumming silk cocoon were listed i.e. using hot water at 120 °C for 5 min, 0.05 % w/v Na_2CO_3 at 100 °C for 15 min and 8 M urea at 80 °C for 10 min. Soap and enzyme degumming procedures was demonstrated that these treatments caused decomposition of silk fiber and fibroin. The highest amount of weight loss (which corresponded to the amount of removed sericin) can be obtained by treatment with condition of 0.05 % (w/v) Na_2CO_3. Dash et al. [8] isolated sericin from silk cocoon by the method described by Takasua et al. [9] which used Na_2CO_3 solution in degumming procedure, with a slight modification. The finely cut silk cocoons pieces were soaked in degumming solution containing 8M urea, 1% SDS v/v and 2% v/v mercaptoethanol at room temperature. Sericin solution was in supernatant. After that, sericin was precipitated by adding ethanol, then, HCl solution was added to dissolve the precipitate. Nouri and Heidari [9] reported the procedures for extraction of sericin from silk degumming wastewater and its application. They used a mixture of Na_2CO_3 and $NaHCO_3$ as degumming solution and then extracted sericin by using acetic acid for precipitating silk protein. The highest percent efficiency of sericin

extraction was obtained when the pH of solution was 4. For purifying and concentrating sericin, sericin solution was dialyzed and freeze-dried. In this research, two different alkaline solutions were used for removing sericin from silk cocoon including sodium carbonate (Na_2CO_3), and mixture of sodium hydrogen carbonate ($NaHCO_3$) and sodium carbonate (Na_2CO_3). For separation of sericin, various precipitants such as acetic acid and ethanol were trialed by adding into the degumming solution to precipitate the sericin, then dialyzing and freeze-drying. The modification of the conditions of solvent extraction were studied by adding some appropriate surfactants in order to get a better crude extract yield and more purified product.

Materials and Methods

Materials

The yellow cocoons of a polyvoltinerace (called locally as Nangnoi) of Thai silkworms, *Bombyx mori* were obtained from The Queen Sirikit Sericulture Centre, Chiang Mai Province, Thailand.

All other chemicals were reagent-grade products obtained commercially.

Degumming treatment

The raw silk cocoons were cut into pieces and condi-tioned with various alkaline solutions such as Na_2CO_3 and a mixture of Na_2CO_3 and $NaHCO_3$. The sodium dodecyl sulphate (SDS) solution was then added at different concentrations in order to see the synergistic effect of the cleaning agent. Treatment temperature and time was 95°C and 30 minutes, respectively. Degum-ming ratios (%) were calculated by the equation described by Chang et al. [10]

$$\text{Degumming ratio (\%)} = 1 - \frac{W_D}{W_U} \times 100 \quad (1)$$

Where W_D is the mass of degummed cocoon (g) and W_U is the mass of untreated cocoon (g).

Extraction of sericin

The sericin was precipitated from the degumming solution by adding various precipitants such as 5 % v/v acetic acid at different pH (2, 4, 6 and 8) and ethanol at different concentrations (30, 50, 70, 80, 90 % v/v) separately. The degumming solution was centrifuged at 6000 rpm for 10 minutes to remove the colloid. The appropriate precipitant and precipitating condition was investigated.

Purification of sericin solution

The sericin solution was dialyzed in distilled water for 24 hours and then freeze-dried in order to purify and concentrate the sericin. The yellow sericin powder was obtained. The extraction yield (%) of sericin can be calculated according to Eq. (2)

$$Y_{Ext}(\%) = \frac{W_S}{W_C} \times 100 \quad (2)$$

Where Y_{Ext} is the extraction yield (%), W_s is the mass of extracted sericin (g) and W_C is the mass of silk cocoon (g).

Results and Discussion

Degumming ratio

The degumming process was achieved by solvent extraction to obtain sericin. To compare the degum-ming ratios (%) obtaining by using different degum-ming solvents, the results are shown in Table1.

Table1 Degumming ratios (%) of silk cocoons treated with various degumming conditions

Degumming solvent	Degumming ratio (%)
0.1M Na_2CO_3	20.0
0.1M Na_2CO_3 and 0.1M $NaHCO_3$	23.1

It can be observed that higher degumming ratio was obtained when a mixture of sodium carbonate and sodium hydrogen carbonate was used as a degum-ming solvent. The sodium dodecyl sulphate (SDS) solution was then added at different concentrations. SDS is a strong surfactant that is widely used in protein sample preparation. It was considered that the mutual effects of having hydrophobic alkyl chains and the surface charges or electrostatic interaction surrounding SDS chains can enhance the protein recovery. Effect of SDS concentrations on degumming ratio is shown in Figure 1

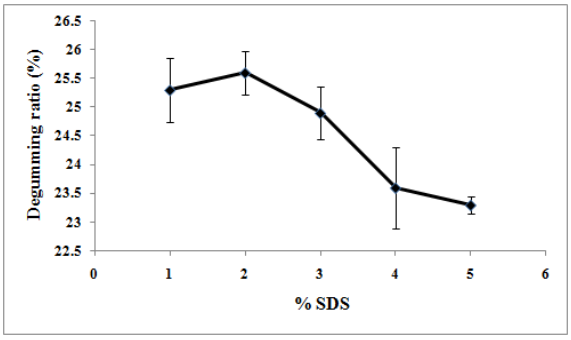

Figure1. Effect of SDS concentration on degumming ratio

It was found that the presence of SDS affected the degumming ratio. The degumming ratio was observed to be highest at the concentration of SDS of 2 % w/v and it decreased with the increase of SDS concentration.

Extraction yield of sericin

Extraction of sericin could be done by acid and alcohol precipitation of the degumming solution. The extraction yields of sericin for acid and alcohol precipitation are shown in Figure 2 and 3.

Extraction of sericin could be done by acidifying the degumming solution. From Figure 2, it is observed that extraction yield of sericin depends on pH of the degumming solution. It increases with the increase of pH, when pH of the solution is up to 4, the extraction yield decreases. Sericin, like other proteins, has an

isoelectric point in which the solubility of sericin is the lowest.

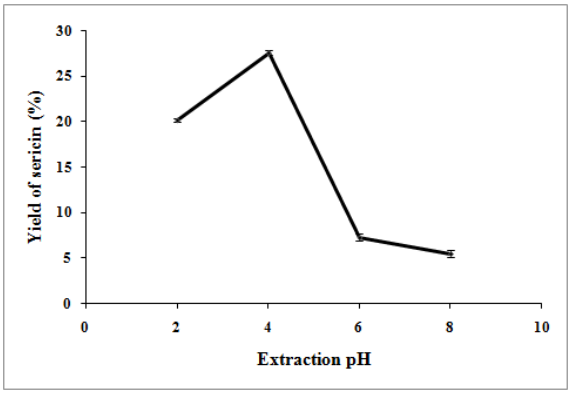

Figure2. Effect of pH on extraction yield of sericin

On the basis of the results, it is clear that pH 4 could be regarded as the isoelectric point of sericin.

Figure 3 denotes that the extraction yield of sericin is increased with the increase of ethanol concentration. Due to the fact that silk sericin is a kind of water-soluble natural protein, it can be maintained in the solution by the interaction of surface hydrophilic groups with water solvent. So, adding ethanol which is less polar than water could reduce the solvent polarity and sericin tends to become less soluble, thus we could separate sericin from silk wastewater by centrifugation.

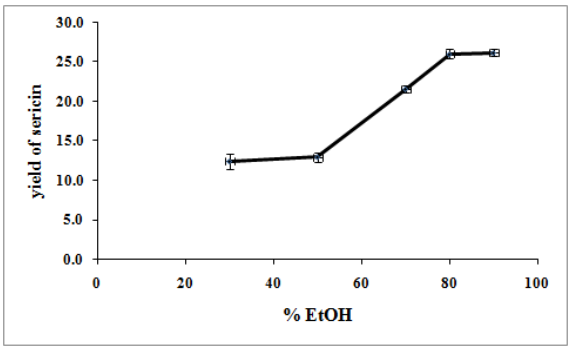

Figure3. Effect of ethanol concentration on extraction yield of sericin

Results of the extraction yield of sericin by acid and alcohol precipitation of the degumming solution showed that sericin yield from acid precipitation (27.4%) was higher than alcohol precipitation (26.2%). However, the amount of sericin has not clearly been reported in term of % yield. The silk sericin was then structurally characterized by Fourier Transform Infrared Spectroscopy (FT-IR). Figure 4 shows the FTIR spectrum of the extracted sericin at pH 4. It is clear that –NH stretching bands occur at 3424 cm^{-1} and 1551 cm^{-1}, -OH stretching band at 3600 cm^{-1}, C=O stretching band at 1655 cm^{-1} and C=O symmetry stretching at 1384 cm^{-1} are the same as being reported previously [9].

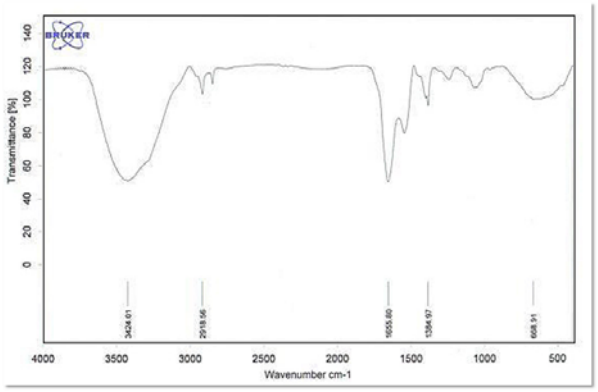

Figure4. IR spectrum of extracted sericin

Conclusions

In this work, we modified an extraction procedure in order to recover sericin from Thai silk cocoon by using a mixture of alkaline solution and acid precipitation method. It was proven to be effective and simple. Addition of an appropriate surfactant concentration can improve the degumming ratio of sericin extraction. The highest degumming ratio was obtained under the condition using a mixture of 0.1 M $NaHCO_3$ and 0.1 M Na_2CO_3 containing 2 %w/v SDS. The acid precipitation using 5 %v/v acetic acid as precipitant at pH 4 provided the highest extraction yield of sericin.

Acknowledgements

The authors would like to thank the Center of Excellence for Innovation in Chemistry (PERCH-CIC) for supporting a scholarship, the Graduate School, Chiang Mai University for partial funding and Department of Chemistry, Faculty of Science, Chiang Mai University for facilities provision.

References

[1] A.S. Bianchi and G.M. Colonna, Melliand Textilberichte 73 (1992), 68–75.
[2] M. Mondal, K. Trivedy and S. Nirmal Kumar, J. Env. Sci., 5 (2007), 63-76.
[3] Y.Takasua, H. Yamada, T. Tamura, H. Sezutsua, K.Mita and K. Tsubouchia, Insect. Biochem. Molec., 37 (2007), 1234–1240.
[4] Y-Q. Zhang, J. Biotech., 20 (2002), 91–100.
[6] T. Gamo, T. Inokuchi and H. Laufer, Sericult. Sci. Jpn., 42 (1973), 17-23.
[7] H. Yamada, H. Nakao, Y. Takasu and T. Tsubouchi, Mater. Sci. Eng., 14 (2001), 41–46.
[8] R. Dash, S. Mukherjee and S.C. Kundu, Int. J. Biol. Macromol., 38 (2006), 255–258.
[9] M. Nouri and P. Heidari, (15 June 2009). The use of natural silk sericin in textile processing, http://research.guilan.ac.ir/research/doc/c1064.pdf
[10]S.K. Chang, J.W. Kim, H.J. Oh, K.H. Lee, Y. H. Park, Int J Biol Macromol., 41 (2007) 346–353.

Determination of volatile substances in polystyrene foam food packaging by NIR spectroscopy

S. Homdumrongvong[1,3*], S. Ekgasit[1], and O. Chailapakul[1,2]

[1] Sensor Research Unit, Department of Chemistry, Faculty of Science, Chulalongkorn University, Bangkok 10330, Thailand
[2] Center of Excellence for Petrochemicals, and Advanced Materials, Chulalongkorn University, Bangkok 10330, Thailand
[3] Bureau of Quality and Safety of Food, Department of Medical Sciences, Ministry of Public Health, Nonthaburi 11000, Thailand

[*] E-mail: sasitornhom@yahoo.com

Abstract: In this study, volatile substances in polystyrene foam were detected and quantified using near-infrared (NIR) diffuse reflectance infrared Fourier transform spectroscopy. Spectra were scanned from 1,000 to 2,500 nm, 30 scans per spectrum at a resolution of 4 cm^{-1}. The gas chromatographic method was assumed to provide the reference value of the analytes for calibration. Partial least squares regression (PLSR) was used to construct calibration models. Spectra were pre-treatments by using multiplicative signal correction (MSC) and second derivative. The correlation coefficient (R), root mean square error of calibration (RMSEC), root mean square error of prediction (RMSEP) and bias was found to be 0.9677, 35.1 mg/kg, 49.7 mg/kg and -4.23 respectively.

Introduction

Styrene is produced mainly by catalytic dehydrogenation of ethylbenzene and is used mainly for production of polystyrene and styrene copolymers [1]. General purpose, polystyrene is widely used in food packaging applications. Examples would include foamed trays for meat, clear trays for candy and cookies, and film for wrapping produce.

In Notification of the Ministry of Public Health No. 295 (B.E.2548(2005))[2] regulated for volatile substances (toluene, ethyl benzene, isopropyl benzene, n- propyl benzene and styrene) in polystyrene packaging is not more than 5,000 mg/kg.

Quantitative analysis of volatile substances was performed by GC [3-5], which it is time-consuming, destructive, using reagents and wastes produced.

Near-infrared (NIR) spectroscopy has been proven to be a powerful analytical tool used in the agricultural, nutritional, petrochemical, textile and pharmaceutical industries [6-14]. It is a fast, accurate, non-destructive technique, without using any chemical reagent and friendly environment. Quantitative NIR measurements are usually based on the correlation between sample composition, as determined by defined reference methods, and the absorption of light at different wavelengths in the near infrared region measured by either reflectance or transmission spectroscopy [15].

The absorption peak of NIR spectra are broad and overlap, making single wavelength calibration impossible due to large hidden information in spectral data. Useful multivariate calibration tools such as partial least-squares (PLS) are available. PLS is an analysis method that relates changes in spectral data [16]. The calibration equation can be applied to unknown samples once the calibration is established by PLS from samples where the analyte is determined by another acceptable method [17]. PLS regression is a multivariate method. It has no restriction in using the number of wavelengths that can be selected for the calibration to make the model suitable to extract the maximum information from the spectra. The information extracted can be condensed in the latent variables or factors which are used in the calibration and prediction steps [18].

In this study, NIR spectroscopy was applied to assess its potential for quantitative determination of volatile substances in polystyrene foam food packaging. Calibration models were developed from GC as a reference method and NIR spectral data a using PLS regression.

Materials and Methods

Sample: A total of 83 polystyrene foam food packaging samples were purchased from the local market in Donmuang City, Bangkok and Muang City, Nonthaburi Province. The samples were divided into two groups. The first group consisted of 51 samples used for developing the calibration model. The second group consisted of 32 samples used for prediction models. The range of reference measurements results of volatile substances in the calibration set almost covers the range in the validation set. Therefore, the distribution of the samples was appropriate in calibration and validation set [19].

Chemical analysis: As a referenced method refer to JETRO [20], volatile substances are measured by gas chromatography (GC17-A gas chromatograph Shimadzu, Japan), with flame ionization (FID). The used column was a VertiBond^{TM} WAX (30m x 0.32mm x 0.5um).

Spectra collection: The NIR spectra were collected in the diffuse reflectance mode using FT-NIR spectrometer (Antaris II Analyzer, Thermo electron Corporation, USA) with an integrating sphere sample module. All of the sample non-destructively analyzed by diffuse reflectance FT-NIR spectroscopy between 1,000 to 2,500 nm. (10,000-4,000 cm^{-1}), 30 scans per spectrum at a resolution of 4 cm^{-1}.

Pre-processing and construction of calibration model: Partial least squares regression (PLSR) was used to construct calibration models. Spectra were pre-

treatments by using multiplicative signal correction (MSC) and second derivative. Calculations were performed with TQ Analyst version 7.2

Results and Discussion

The range of volatile substances in polystyrene foam containers were from 341- 883 mg/kg. In Table 1 showed the characteristic of the sample in calibration set and validation set to develop the calibration equation.

Table 1: characteristic of the sample in calibration and validation set.

Variable	Calibration set	Validation set
Number of sample	51	32
Volatile substances	341-883	386-831
Mean	585	569
Standard deviation	134	115
Unit	mg/kg	mg/kg

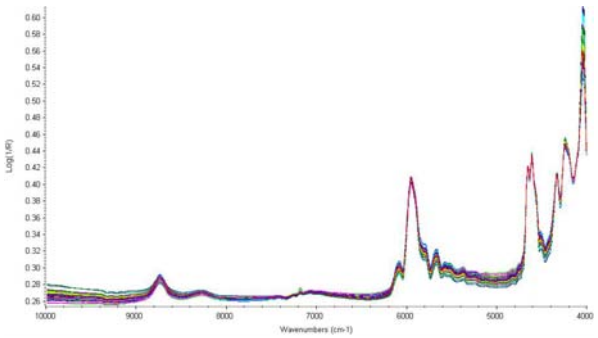

Figure 1, raw spectra

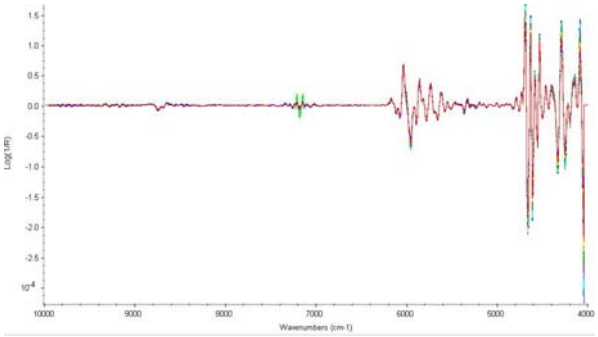

Figure 2, spectra were pre-treatments by using MSC+ second derivative

Figure 1 shows the 83 original spectra collected for the foam packaging samples. Figure 2 shows the spectra were pre-treatments by using multiplicative signal correction (MSC) and second derivative which multiplicative signal correction (MSC), treatments allow someone to analyze samples with different pathlength when it is difficult or impossible to obtain an independent measure of sample pathlength and in the case of diffuse reflectance measurements, they may also be used to compensate for variations in sample thickness that are caused by particle size and scattering [21]. Also, transformation with Savitzky-Golay second derivative was use to remove baseline shift, overlapping peak and resolution broad absorbance band on the reflectance spectra [22].

Table 2: Calibration and Validation Result from PLSR Models for volatile substances

	R	RMSEC	RMSEP	Bias
Volatile substances	0.9677	35.1	49.7	-4.23

Table 2 shows the performance of the NIR calibration model with pre-processing methods. The correlation coefficient (R), root mean square error of calibration (RMSEC), root mean square error of prediction (RMSEP) and bias was found to be 0.9677, 35.1mg/kg, 49.7 mg/kg and -4.23 respectively.

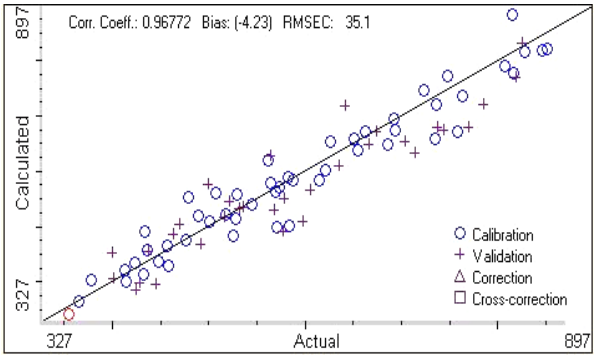

Figure 3, Correlation statistics between the measured values and calculated values of volatile substances in polystyrene foam.

Figure 3 shows the correlation between the values determined by the reference analysis method [GC] and the values predicted by the NIR spectroscopy technique on the whole sample set of polystyrene foam. The cycle points refer to calibration samples, and the plus points refer to validation samples. This method used in this work is less accurate than GC.

Conclusions

The results in this research show the potential of NIR spectroscopy to detect volatile substances in polystyrene with the reference method of gas chromatography. Compared to GC method, the parameters for evaluating models such as accuracy were not very perfect. However, the combination of NIR spectroscopy has been found to be a convenient, versatile method. It has the ability to dramatically reduce consuming time and cost of monitoring without using any chemical reagent although GC has to be preferred due to its sensitivity.

Acknowledgements

The authors would like to thank Department of Chemistry, Faculty of Science, Chulalongkorn University and Bureau of Quality and Safety of Food,

Department of Medical Sciences, Ministry of Public Health.

References

[1] W. Tang, I. Hemm, and G. Eisenbrand, *Toxicol.* **144** (2000), pp. 39-50.

[2] Notification of the Ministry of Public Health No.295 *Qualities or Standards of Plastic Containers.* (B.E.2548 (2005)).

[3] S.L. Vaner and C.V. Breder, *J. Assoc. Off. Anal.* **64** (1981), pp. 1122-1130.

[4] S.L. Vaner, C.V. Breder and T. Fazio, *J. Assoc. Off. Anal.* **66** (1983), pp. 1067-1072.

[5] M.L. Garrigos, M.L. Marin and A. Sanchez, *J.Chromatogr.* **1061** (2004), pp. 211-216.

[6] J. M. Esteban-Diez, C. Gonzalez-saiz and Pizarro, *Anal. Chim. Acta.* **514** (2004), pp. 57-67.

[7] K. Kachrimanis, V. Karamyan. and S. Malamataris, *Int. J. Pharm.* **250** (2003), pp. 13-23.

[8] Y. A. Woo, H. J. Kim, K. R. Ze and H. Chung, *J. Pharmaceut. Biomed. Anal.* **36** (2005), pp. 955-959.

[9] Y. Dou, Y. Sun, Y. Q. Ren, P. Ju and Y. L. Ren, *J. Pharmaceut. Biomed. Anal.* **37** (2005), pp. 543-549.

[10] C. W. Huck, W. Guggenbichler and G. K. Bonn, *J. Pharmaceut. Biomed. Anal.* **538** (2005), pp. 195-203.

[11] R. De Maesschalck and T. V. Kerkhof, *J. Pharmaceut. Biomed. Anal.* **37** (2005), pp. 109-114.

[12] C. J. Clark, V. A. McGlone and R. B. Jordan, *J. Pharmaceut. Biomed. Anal.* **28** (2005), pp. 87-96.

[13] Y. A. Woo, H. J. Kim and H. Chung, *J. Pharmaceut. Biomed. Anal.* **33** (2003), pp. 1049-1057.

[14] V. A. McGlone, R. B. Jordan, R. Seelye and P. J. Martinsen, *Potharvest Biol.* **26** (2002), pp. 191-198.

[15] D. Cozzolino, M. J. Kwiatkowski, M. Parker, W. U. Cynkar, R. G. Dambergs, M. Gishen, M. J. Herderich, *Anal. Chim. Acta*. **513** (2004), pp. 73-80.

[16] C. Coury and A. M. Dillner, *Atmosp. Environ.* **42** (2008), pp. 5923-5932.

[17] L. D. Gautz, P. Kaufusi, M. C. Jackson, H. C. Bittenbender and C. Tang, *J. Agric. Food Chem.* **54** (2006), pp. 6147-6152.

[18] F. J. Rambla, S. Garrigued and M. de la Guardia, *Anal. Chim. Acta.* **344** (1997), pp. 41-53.

[19] Q. Chen, J. Zhao, H. Zhang and X. Wang, *Anal. Chim. Acta.* **572** (2006), pp. 77-84.

[20] Japan External Trade Orgaization. Specifications, Standards and Testing, Methods for Foodstuffs, Implements, Containers and Packaging, Toys, Detergents. Japan. (2006), pp. 94-5, 114.

[21] J. Moros, I. Llorca, M. L. Cervera, A. Pastor, S. Garrigues, and M. de la Guardia, *Anal. Chim. Acta.* **344** (1997), pp. 41-53.

[22] P. William, K. Norris, Near- Infrared Technology in the Agricultural and Food Industries, 2nd ed. America Association of Cereal Chemists,Inc. St. Paul, Minnesota, USA, 2001, pp 296.

Simultaneous determination of carbamate and polar organophosphate in mangosteen using liquid chromatography - tandem mass spectrometry with dispersive –SPE mix sorbent

W. Meecharoen[1], N. Tayaputch[2], and N. Leepipatpiboon[1]*

[1]Chromatography and Separation Research Unit, Department of Chemistry, Faculty of Science, Chulalongkorn University, Bangkok , Thailand.
[2]Central Laboratory (Thailand) Co. Ltd., Bangkok , Thailand.

* E-Mail: natchanun.l@chula.ac.th

Abstract: **A liquid chromatography – tandem mass spectrometry was established for the simultaneous determination of 13 carbamates and 8 polar organophosphate compounds in mangosteen by using acetonitrile as the extractant and primary secondary amine (PSA) and alumina N mix sorbent in ratio 1:1 as dispersive-SPE clean up technique. Method performances for the analysis of carbamate and polar organophosphate pesticides are: limit of detection 0.005 mg/kg, limit of quantification 0.01 mg/kg, recoveries 66-116%, RSD 9-26% for carbamate and recoveries 75-97%, RSD 5-20% for polar organophosphate which is compliance to the benchmark parameters of Directive EC 396/2005.**

Introduction

The organophosphate and carbamate pesticides are widely applied on fruit and vegetable crops to protect pests and preserve quality for post-harvest storage. To ensure food safety for consumers and international trade, the strict regulation on low concentration levels were enforced by importing countries. Therefore, a selection and sensitive methods are required.

The organophosphate residues are routinely analyzed using gas chromatography with flame photometric detector (GC/FPD) method [1-3] while the most widely used method for the analysis of carbamate residues in foods is HPLC with post-column derivatization and fluorescence detector[2] or liquid chromatography–mass spectrometry[4-5]. Each method gives better specific for their groups. A liquid chromatography–tandem mass spectrometry was employed for the simultaneous determination of both groups and it has proven to be a sensitive and selective detector. Multiple reaction monitoring (MRM) with two mass transitions was used for quantification and confirmation of all studied compounds.

Mangosteen is one of major fruits exported from Thailand to foreign markets; especially the European Union (EU). Since September 1, 2008 the European Union has implemented regulation EC 396/2005 which 27 member states are mandated to have one unified limit for any pesticide residues that their MRLs (Maximum residue Limit) were not listed as default MRLs at 0.01 mg/Kg [6]. The pesticide residues in mangosteen including pulp and peels are required to prove that the product is safe in compliance to Good Agricultural practice (GAP). However, the trace analysis of pesticide residues in a whole mangosteen is quite complicated due to its intensive colored and plenty of high molecular weight components such as polyphenols and wax in the peel. Therefore, additional cleanup is demanded for obtaining the reliable analysis result. Currently, QuEChERS (quick, easy, effective, rugged and safe) method has demonstrated to be a very effective sample clean-up procedure for simultaneous analysis of pesticides in a variety of fruit and vegetable matrices [7]. The method is recognized by AOAC for the analysis of grapes, lettuces, and oranges [8] but no representive matrix has been done on mangosteen.

In this study we modified and optimized QuEChERS method for simultaneous determination of 13 carbamate and 8 polar organophosphate residues in mangosteen and determination was carried on by using liquid chromatography-tandem mass spectrometry technique.

Materials and Methods

Sample preparation:

The stems of fresh mangosteen fruits were removed and the whole fruit including pulp and peel were homogenized in a high speed blender for 3-5 min.

Sample Extraction:

The carbamate and polar organophosphate were extracted from 10 g of homogenized mangosteen with 10 mL of acetonitrile in 50 mL centrifuge tube. Anhydrous magnesium sulfate, sodium chloride, and anhydrous sodium acetate (4:1:1) were added into the mixture to remove water, induced polarity range and phase separation. The acetonitrile layer was transferred into another tube for a clean-up with dispersive solid phase extraction using mixed sorbents of 25 mg PSA and 25 mg Alumina-N, shake, centrifuge and take clear aliquot to analyzed by LC-MS/MS.

Standard: Quantitative analysis was performed by using matrix-matched (standards added to blank extracts) calibration standard.

Fortification: In recovery studies, the mixture of all studied pesticide standards in acetonitrile was spiked to each 10 g blank sample at 0.005, 0.01, 0.02, 0.05, 0.10 mg/Kg level. The tubes containing spiked samples were vortexed for 30 sec and left standing for 10 min to allow timing for pesticides interact with matrix.

Determination by LC-MS/MS:

The residue analyses were performed by liquid chromatography-tandem mass spectrometry (LC-MS/MS). The HPLC separation was performed by injecting 10 µL via autosampler on a Luna C-18 (2.0 mm x 150 mm x µm) column (Phenomenex, USA) connected with guard column, maintained at 40 ^{o}C at the flow rate 0.2 ml/min. The mobile phase was composed of (A) 0.01 M ammonium acetate and (B) methanol; set linear gradient from 0 %B to 95 %B in 14 min and held for 6 min. The MS parameters included ion spray voltage of 4000 V, cone gas flow 50-55 L/hr., Desolvation gas flow 600-650 L/hr., Desolvation temp.350^{o}C and the ion source temperature 120 ^{o}C. Estimation of the residues was performed by multiple reaction monitoring (MRM), with two mass transitions for each pesticide; one for quantification and the other for confirmation. The detail of MRM transitions of all analytes were shown in Table 1.

Results and Discussion

The method can analyze 13 carbamate residues and 8 polar organophosphate residues in mangosteen by LC-MS/MS condition. The extraction and clean-up steps were optimized. After the modified sample preparation steps, the clear solution was subjected for liquid chromatography-tandem mass spectrometry (LC-MS/MS) analysis.

Effect of extraction solvent and buffer:

The extraction solvents, type of salts and amounts were evaluated for their extraction efficiency. The comparison between using acetonitrile and 1% acetic acid in acetonitrile as extractant was shown in Figure 1 (A). The different of % recovery when using (a) 4 g of $MgSO_4$+ 1 g of NaCl, (b) 4 g of $MgSO_4$ + 1 g of NaCl + 1 g of trisodium citrate dehydrate + 0.5 g disodium hydrogen citrate sesquihydrate and (c) 4 g of $MgSO_4$ + 1 g of NaCl + 1 g of anhydrous sodium acetate were also shown in Fig 1 (B). The best recovery was obtained when using 100% acetonitrile and added mixture of 4g magnesium sulfate, 1 g sodium chloride and 1g anhydrous sodium acetate in the extraction solution.

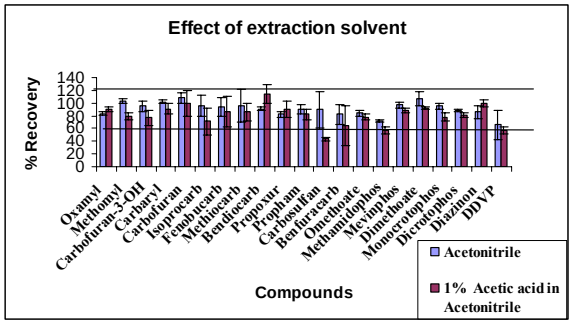

(A)

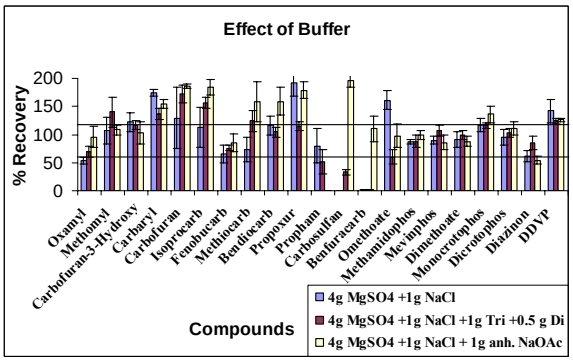

(B)

Figure 1: Effect of extraction solvent and buffer showed in mean recovery data (n=3).

(A) Carbamate and polar organophosphate residues spiked at 0.1 mg/kg extracted with acetonitrile and 1% acetic acid in acetonitrile.

(B) Carbamate and polar organophosphate residues spiked at 0.1 mg/kg extracted with acetonitrile plus added salts.

Effect of sorbent clean-up in dispersive-SPE step:

Polar interferences and large molecules such as fatty acids and wax can be further removed by dispersive-SPE adding sorbent. Five different dispersive-sorbent types of primary secondary amine (PSA), alumina N, florisil, MCX, SAX were tested. PSA, alumina N and florisil worked very well for removing interferences of fatty acids and wax in the matrix, as showed in Figure 2

Table1: The MRM transition and performance of method in recovery data (%mean recovery, n =10) obtained for 21 pesticides in the mangosteen matrix.

Pesticide	The MRM transition					The performance of method									
	Quantitation MRM 1	Confirmation MRM 2	Collision energy1 (V)	Collision energy 2 (V)	R^2	0.01 mg/Kg		0.02 mg/Kg		0.05 mg/Kg		0.10 mg/Kg		LOD (mg/Kg)	LOQ (mg/Kg)
						Mean	%RSD	Mean	%RSD	Mean	%RSD	Mean	%RSD		
Oxamyl	237.01>71.99	237.01>89.94	10	8	0.9609	66	18.39	134	19.94	83	15.84	76	10.58	0.005	0.01
Methomyl	162.98>88.01	162.98>105.96	8	8	0.9773	82	25.52	90	25.48	90	7.71	101	6.32	0.005	0.01
Carbofuran-3-OH	238.05>162.97	238.05>181.03	18	10	0.9921	100	23.79	75	22.15	78	12.99	88	7.12	0.005	0.01
Carbaryl	202.04>117.04	202.04>145.04	20	13	0.9339	88	15.06	98	17.14	86	8.01	94	16.05	0.005	0.01
Carbofuran	222.07>122.99	222.07>164.96	20	12	0.9749	110	11.83	101	19.59	101	7.82	98	7.10	0.005	0.01
Isoprocarb	194.07>95.04	194.07>137.04	13	8	0.9662	111	10.07	108	9.05	75	24.42	87	5.01	0.005	0.01
Fenobucarb	208.12>95.08	208.12>152.07	13	8	0.9711	106	10.13	99	19.50	83	19.79	106	12.46	0.005	0.01
Methiocarb	226.04>121.07	226.04>169.02	18	10	0.9396	111	11.19	95	12.66	78	13.45	89	9.23	0.005	0.01
Bendiocarb	224.08>109.04	224.08>167.01	15	8	0.9911	116	12.16	118	11.55	75	22.98	93	11.00	0.005	0.01
Propoxur	210.09>111.03	210.09>168.02	13	8	0.7594	92	14.09	111	9.40	91	17.18	93	10.28	0.005	0.01
Propham	180.05>120.04	180.05>138.03	15	8	0.9559	79	21.24	113	8.98	79	18.86	88	9.34	0.005	0.01
Carbosulfan	381.16>118.08	381.16>160.13	18	13	0.9918	86	8.54	89	9.58	108	31.06	70	6.50	0.005	0.01
Benfuracarb	411.06>195.01	411.06>252.10	23	15	0.9849	87	13.85	76	19.96	74	15.58	75	10.52	0.005	0.01
Omethoate	214.03>142.97	214.03>182.98	18	12	0.9947	90	19.58	68	5.98	76	14.98	76	8.81	0.005	0.01
Methamidophos	142.03>112.01	142.03>124.97	10	12	0.9887	75	5.98	63	6.23	70	6.03	69	3.54	0.005	0.01
Mevinphos	225.04>126.96	225.04>193.03	15	8	0.9843	84	17.76	75	16.74	102	13.15	78	6.46	0.005	0.01
Dimethoate	229.99>170.98	229.99>198.97	15	8	0.9847	97	15.11	97	19.96	81	15.91	100	10.41	0.005	0.01
Monocrotophos	224.09>127.03	224.09>192.98	15	8	0.9930	84	8.48	80	7.30	89	7.02	81	3.75	0.005	0.01
Dicrotophos	238.03>112.05	238.03>127.01	13	15	0.9963	89	8.73	104	7.55	93	9.02	93	5.13	0.005	0.01
Diazinon	305.06>153.08	305.06>169.06	20	20	0.9773	77	7.96	82	5.87	85	20.67	93	5.97	0.005	0.01
DDVP	221.08>108.96	221.08>127.02	15	15	0.9701	87	14.14	73	13.01	95	8.64	93	7.28	0.005	0.01

Mixture of PSA and alumina-N was proved to be very good for cleaning up by removing the interferents of mangosteen matrix. Ratio of mix sorbent was evaluated the optimum quantity, showed in figure 3. The data indicated that a mixture of PSA & alumina-N and PSA & florisil sorbents were evaluated in term of precision of 10 replicates at 0.01 mg/kg spiked level. PSA and alumina N mix sorbents have higher precision at RSD 5.98-25.52 % for PSA:alumina-N(25:25mg) and RSD 4.74-39.08 % for PSA : florisil (25:25mg) mix sorbents.

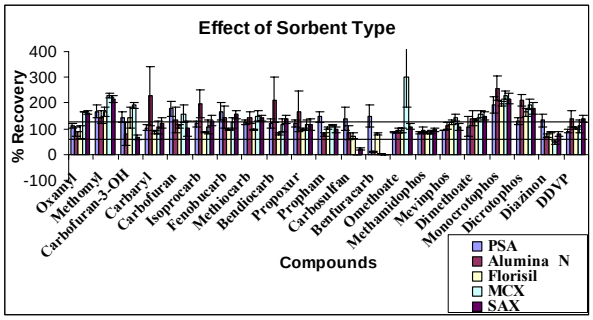

Figure 2: Effect of sorbent type : Mean recovery (n=3), of 21 pesticides spiked at 0.1mg/Kg cleaned up with PSA, alumina N, florisil, MCX, SAX.

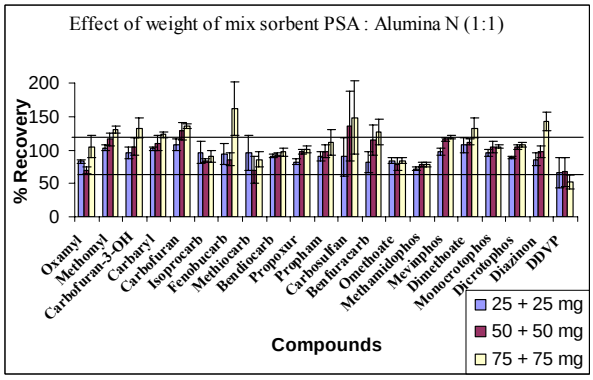

(A)

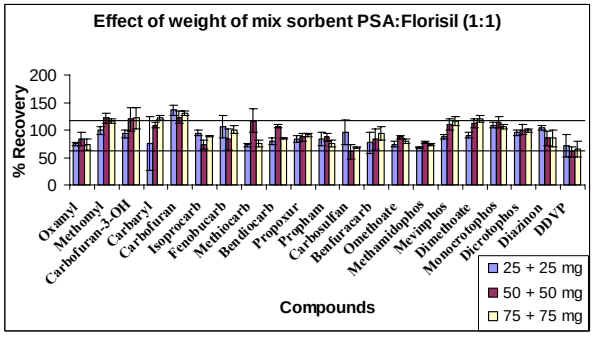

(B)

Figure 3: Extraction efficiency of mixed sorbent and amount employed. Mean recovery (n=3) of 21 pesticides spiked at 0.1 mg/kg cleanup with mixture of PSA:alumina-N (A) and PSA:florisil (B) at 3 levels**.**

The performances of method were studied at concentration range from 5-125 µg/L. The spiked samples were evaluated ten replicates of signal to noise level (3 S/N) was defined as the limit of detection (LOD) at spiked level 0.005 mg/Kg. Ten replicates for accuracy and precision data at spiked level 0.01, 0.02, 0.05 and 0.10 mg/Kg were shown on table 1.

Conclusions

A modified QuEChERS procedure was proved to be satisfactory for the extraction of carbamate and polar organophosphate residues in whole mangosteen. The optimum method employed acetonitrile added with combination of salt and buffering agent to induce liquid phase separation as well as stabilize acid and base labile pesticides. PSA and alumina-N (1:1) were used as dispersive mix sorbent to clean-up the polar interferences and fatty acids in the matrix. The validation data demonstrated good method performance with satisfactory recovery range from 66-116 % and RSD 25.52 % at limited of quantification (LOQ) 0.01 mg/Kg. The limit of detection (LOD) was 0.005 mg/Kg. The method is safe and quick for simultaneous determination of 21 compounds of carbamate and polar organophosphate residues in mangosteen.

Acknowledgments

This research is supported by the Thailand Research Fund, Central Laboratory (Thailand) co, Ltd. and the Center for Petroleum, Petrochemicals, and Advanced Materials at Chulalongkorn University.

References

[1] H. Steinwandter, *Fresenius J. of Anal. Chem.* **322** (1985), pp. 752-754.

[2] M. Luke, J.E. Frobery, H.T. Masumoto, ***J. AOAC Int.*** **58** (1975), pp. 1020-1026.

[3] M. Okihashi, Y. Kitagawa, K. Akutsu, H. Obana, and Y. Tanaka, *J.Pestic.Sci.*. **30** (2005), pp. 368-377.

[4] M. Fernandez, Y. Pico, J. Manes, *J. of Chromatography A.* **871** (2000), pp. 43-56.

[5] L. Min, Y. Hashi, S. Yuanyuan, L. Jinming, *Chin J Anal Chem*. **37** (2006), pp. 941-945.

[6] Regulation(EC) No. 396/2005 of The European Parliament and of The Council on Maximum Residue Levels of Pesticides in or on Food and Feed of Plant and Animal Origin and Amending Council Directive 91/414/EEC, (2005).

[7] M. Anastassiades, S. J. Lehotay, D. Stainbaher, and F. Schenck, *J. AOAC Int.* **86** (2003), pp. 412-431.

[8] *AOAC International,* AOAC Official Method of Analysis, AOAC Official Method **2007.01**, Chapter10 (2007), pp. 17-26.

Phosphate recovery via ion exchange chromatography and chemical precipitation

S. Yodsoongnern* and C. Chotratanadilok

King Mongkut's University of Technology North Bangkok, Department of Industrial Chemistry, Faculty of Applied Science, Bangkok, Thailand 10800

*E-mail: saowapa.yod@dpu.ac.th

Abstract: Phosphate discharged into the water reservoir accelerates eutrophication environment in which excessive growth of organisms such as algae. It decreases the soluble oxygen concentration in water and causes detrimental effects on aquatic life. The treatment of phosphate can be achieved by physical, chemical and biological methods. The aim of this research is to reduce the amount of phosphate from industrial wastewater. This research is divided into two parts: the removal of phosphate by ion exchange chromatography and the recovery of phosphate by chemical precipitation process. To achieve the first part, Dowex marathon MSA resin was used to determine optimal condition for an effective removal of phosphate. It could be easily operated, economical and rapid. For these reasons, the use of resin would be the worth of method for phosphate removal. Synthetic wastewaters were prepared from KH_2PO_4. 25 mL Synthetic wastewaters at 200 mg P L^{-1} were passed through the adsorption column at a flow rate 0.5 mL min^{-1}. It was found that the optimal condition for removing phosphate from the column were 1.0 g resin and 10 mL 0.1 M HNO_3 eluent at the elution rate of 0.5 mL min^{-1}. All solutions were analyzed by molybdenum blue method using UV-vis spectrophotometer at 890 nm for the analysis of phosphate. The efficiency of resin was extremely high. The second part of this research was carried out by adding $CaCl_2$ or $Ca(OH)_2$ to the exhausted desorption solution in order to form calcium phosphate. To determine optimal condition for precipitation reaction, the different values of Ca/P mole ratio and the time of precipitation were examined for the recovery of phosphate process. In order to reduce the use of commercial reagents, the natural wastes such as eggshell and cockleshell were also studied as the sources of calcium ion to form calcium phosphate. The compositions of the structure of the solid precipitate were investigated by infrared spectroscopy technique.

Introduction

Phosphorus is an important element that is widely used in agriculture and industry. It is commonly found in phosphate form. Large quantities of phosphate are used in many industrial applications include detergents, food and drinks, metallurgy, electroplating etc. Discharge of high concentration of phosphate into the lake, water reservoir or river causes eutrophication phenomenon. This directly affects water quality through oxygen depletion and harm to fish including other aquatic life.

The phosphate removal processes have been developed by physical, biological and chemical treatment process. Physical process such as reverse osmosis and electrodialysis has a drawback of high costs [1-3]. Biological process requires highly skilled operation techniques regarding microbial adaptation, and strict anaerobic and aerobic conditions. It is very difficult to operate the process stably in the actual phosphate removal treatment [4-7]. Chemical precipitation is widely used for phosphate removal process using the common precipitants: $Ca(OH)_2$, $Al_2(SO)_4$ and $FeCl_3$ [8-11].

The aim of this research is to reduce the amount of phosphate from industrial wastewater. To achieve this objective, our research was divided into two parts: the phosphate removal by ion exchange chromatography and the phosphate recovery by chemical precipitation process. In order to reduce the use of commercial reagents, some natural wastes such as eggshell and cockleshell were also studied as the sources of calcium ion to form calcium phosphate.

Materials and Methods

Materials

Dowex Marathon MSA resin was purchased from Sigma-Aldrich (20-50 mesh, chloride form). Phosphate solution was prepared from KH_2PO_4 in distilled water. Calcium solutions were prepared from calcium hydroxide and calcium chloride. All chemicals used were analytical grade.

Preparation of synthetic waste water

The stock solution of synthetic waste water (1000 mg L^{-1} of Phosphorus, Chloride and Nitrate were prepared separately by dissolving appropriate quantities of analytical grade potassium dihydrogen phosphate , Sodium chloride and Ammoniumnitrate in deionized water. The stock solutions were further diluted to suitable concentrations.

Analysis

A UV-Vis spectrophotometer (Lambda 2S) was used for the analysis of phosphate in accordance with the standard methods (molybdenum blue method) [12].

The pH was measured by a digital (Cyber Scan pH 510 instruments) pH-meter and adjusted with 1 M NaOH and 1 M HCl. Precipitates produced were identified by using infrared spectroscopy and X-Ray diffraction technique.

Phosphate sorption by Dowex Marathon MSA resin

25 mL of phosphate solutions (200 mg P L^{-1} of KH_2PO_4) were fed at a flow rate of 0.5 mL min^{-1} to a glass column (i.d. 1 cm, length 20 cm) packed with 1 g of Dowex Marathon MSA resin.

Loading capacity of Dowex Marathon MSA resin

Phosphate solution (200 mg P L^{1-}) was fed to a glass column packed with 1 g of Dowex Marathon MSA resin at a flow rate of 0.5 mL min^{-1}. The loading solution was collected every 5 mL for analysis of phosphate with the standard methods by UV-Vis spectrophotometer.

Phosphate desorption and column regeneration

The adsorbed phosphate ion on the glass column was eluted with 10 mL of various eluents (HCl, HNO_3, NaCl and NaOH) with different concentrations (0.01, 0.1, 1, 5 M) at a flow rate of 0.5 mL min^{-1}. To regenerate the resin to the chloride form, 10 mL of NaCl solution at various concentrations (4, 6, 8 and 10 %w/v) were studied after the column was completely washed with the distilled water to be neutral.

Phosphate precipitation

Calcium stock solutions were prepared from $Ca(OH)_2$ and $CaCl_2$ (their concentration was 500 mg Ca L^{-1}) and were added into the phosphate solution (100 mg P L^{-1} of KH_2PO_4). The mixture was maintained under vigorous stirring (at 200 rpm) during 30 min. The precipitate was separated from the turbidity through the cellulose nitrate membrane filter, 0.45 µm. The collected precipitate was dried at room temperature.

Cockleshell and eggshell as a precipitant for calcium phosphate precipitates

Prepared precipitant

Cockleshells were collected from local restaurants located in the city of Bangkok. The shells were washed several times and dried in an oven (Universal oven WB 14, Memmert) at 80ºC for 6 h. 15 g of cockleshell were put in furnace (Furnace 48000, Burnstead Thermolyne) at 900ºC for 8 h. Then, it was milled and sieved to 200 µm.

Eggshells were collected from bakehouses in the city of Bangkok. The shells were washed several times and dried in an oven (Universal oven WB 14, Memmert) at 80ºC for 4 h. After it was milled and sieved to 200 µm, calcium in eggshell was extracted in the form of calcium chloride by hydrochloric acid [13]. 10 g of eggshell were mixed into 150 mL of 4%w/v HCl. The mixture solution was stirred at room temperature every 30 min for 3 h. Then, it was centrifuged (2000 rpm/min) for 10 min. The centrifugate was heated to precipitate the protein at 90ºC for 30 min. The precipitate was separated by further centrifuge. The last centrifugate was evaporated on hot plate at 90ºC until white powder was observed.

Precipitation

0.5 g of natural waste precipitant (prepared from cockleshell or eggshell) was added into the 250 mL of distill water. Then, the solution was mixed with 250 mL of phosphate solution (100 mg P L^{-1} of KH_2PO_4). The mixture was maintained under vigorous stirring (at 200 rpm) during 30 min. The precipitate was separated from the turbidity through the cellulose nitrate membrane filter, 0.45 µm. The collected precipitate was dried at room temperature.

Results and Discussion

Phosphate sorption by Dowex Marathon MSA resin

In the study of effective of resin for ion exchange, Fig. 1 shows concentration of phosphate in column effluent as a function of elution volume. Removal of phosphate by Dowex Marathon MSA resin was 5 mg P (g resin)$^{-1}$ when 200 mg P L^{-1} was used as feeding solution. This concentration was prepared according to the range of phosphorus concentration in waste water from electroplating industry.

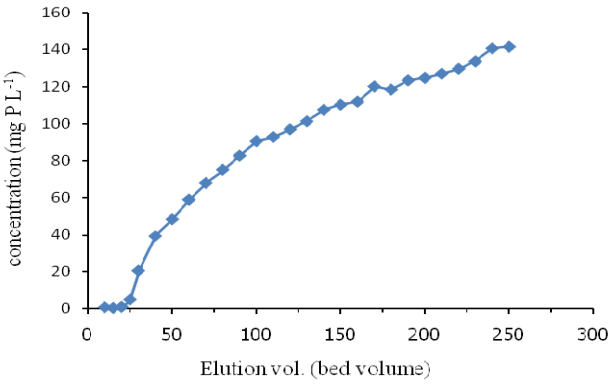

Fig. 1 Phosphate sorption graph using 200 mg P L^{-1}. Flow rate = 0.5 mL min^{-1}, 1 g Dowex Marathon MSA resin.

Desorption of phosphate

According to the effects of eluents on phosphate removal, Fig. 2 shows the various eluents of sorbed phosphate at 500 mg P L^{-1} onto 1 g Dowex Marathon MSA resin.

It was found that the use of 1 M of HCl, HNO_3 and NaOH could be removed the sorbed phosphate higher than 90%. While 1 M NaCl could be removed the sorbed phosphate only 40%. Therefore, the optimal concentration of HCl, HNO_3 and NaOH were carried out for the proper eluents.

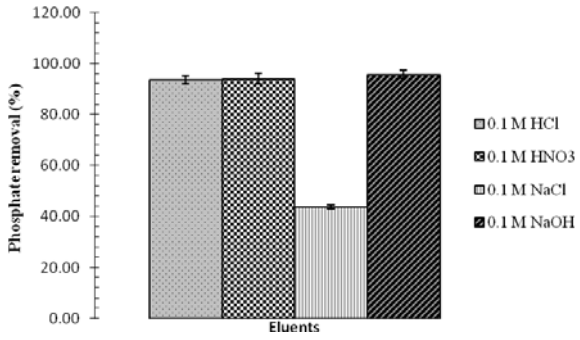

Fig. 2 Elution of sorbed phosphate from 1 g Dowex Marathon MSA resin at various eluents. Flow rate = 0.5 ml/min

Effect of concentration of eluents

The percentage of phosphate removal was higher than 80% when HCl and HNO_3 were used at 0.1, 1 and 5 M. The percentage of phosphate removal was also higher than 80% when NaOH was used at 1 and 5 M. Meanwhile, the use of NaOH at 0.1 M could remove phosphate only 13%. However, All eluents (HCl, HNO_3 and NaOH) could remove phosphate lower than 2% at 0.01 M concentration. The results are shown in Fig. 3. It was found that the effective eluent were 0.1 M HNO_3 and 0.1 M HCl. However, 0.1 M HNO_3 was chosen as an eluent for further studies.

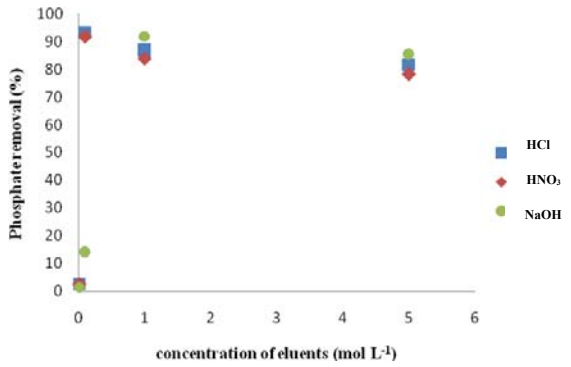

Fig. 3 Elution of sorbed phosphate from 1 g Dowex marathon MSA resin at various eluents (0.01, 0.1, 1 and 5 M). Flow rate=0.5 ml/min.

Regeneration of column

After eluting with 0.1 M HNO_3 and rinsing with distill water, the resin was further rinsed with NaCl in order to convert it back to the chloride form. Resin in the column was regenerated and can be reused.

Fig. 4 shows the concentration of NaCl on the percentage of phosphate removal. 4%w/v NaCl was chosen as the proper regenerant concentration. The regeneration process was studied to obtain the efficiency of the exhausted Dowex Marathon MSA resin. After repeating 30 times, it was found that the efficiency of resin was extremely high. It could be regenerated for 24 times as shown in Fig. 5.

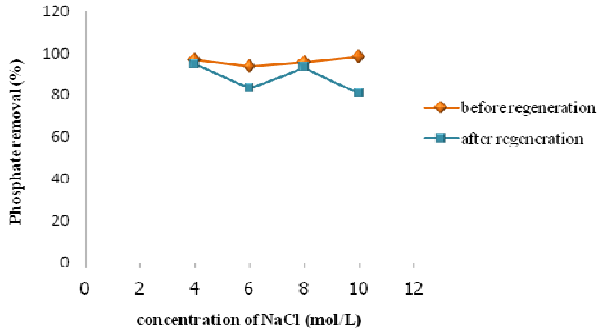

Fig. 4 Effect of concentration of NaCl on phosphate removal percentage

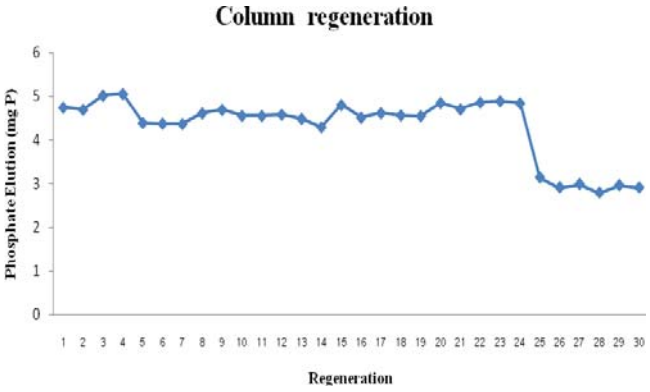

Fig.5 Phosphate removal percentage during regeneration of Dowex Marathon MSA resin

Effect of mole ratio Ca/P

Phosphate removal was investigated by increasing mole ratio as shown in Fig. 6. At the fixed pH 11, phosphate removal increases with increasing Ca/P mole ratio. The percentage of phosphate removal passes from 60% to 99% when Ca/P passes from 1 to 1.5 and 2. However, the Ca/P mole ratio for phosphate removal was chosen at 2 to complete the precipitation reaction.

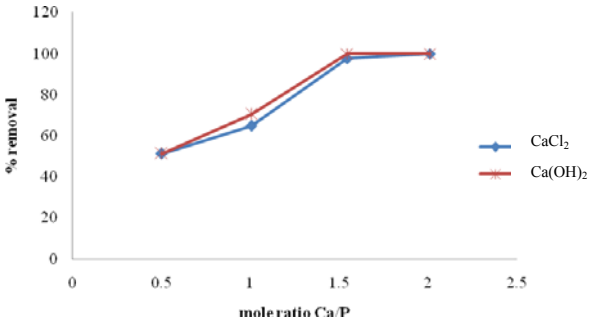

Fig. 6 Effect of phosphate removal with various mole ratio at pH 11

Effect of time of precipitation

The time influence of phosphate removal by $CaCl_2$ and $Ca(OH)_2$ was also observed. The variation of the

time of precipitation is shown in Fig. 7. It shows that the precipitation of phosphate at Ca/P mole ratio=2 cause more effective. The percentage of phosphate removal was not affected by time of precipitation that equal to 99% in every time of precipitation. For the further studies, the time of precipitation was used at 30 min.

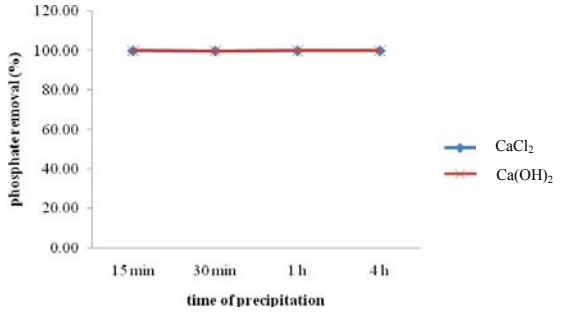

Fig. 7 Effect of phosphate removal with various time of precipitation at pH 11

Cockleshell and eggshell

Cockle shell and eggshell could be used as the calcium source for phosphate precipitation. It can remove phosphate upper to 99%. Fig. 8 shows the IR spectra of the precipitates obtained by precipitation of phosphate ion by calcium from cockleshell and eggshell. The spectrum shows sharp characteristic peaks of PO_4^{3-} at 1036 and 564 cm^{-1} in Fig. 8(a), 1038 and 565 cm^{-1} in Fig. 8(b). Indeed, the spectrum of the precipitates heated at 600 ºC (Fig. 8(c),(d)) shows the characteristic bands of the OH at 3423 (Fig. 8(c)) and 3433 cm^{-1}(Fig. 8(d)). The presence of these bands proves the formation hydroxyapatite.

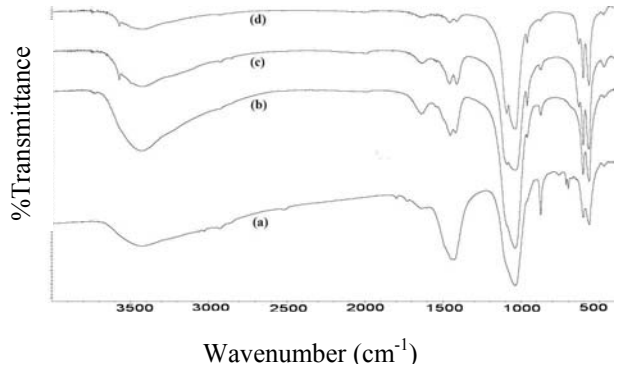

Fig. 8. FT-IR spectra of precipitate obtain by precipitation of phosphate ion by calcium from (a) cockle shell at room temperature (b) eggshell at room temperature (c) eggshell after calcination at 600 ◦C (d) cockle shell after calcination at 600 ◦C

This proposed method has several advantages when compare with the conventional method : for example, easy to operate and maintenance, economical compact and rapid. The price of resin is approximately 20 Baths per 1 g resin. For water treatment cost, it would be about 60 Baths per 300 ml P L^{-1}.

Conclusions

Dowex Marathon MSA resin is highly selective and efficient for phosphate removal from wastewater. This resin is easily regenerated. It can be repeatedly used with little loss of performance. Removal of phosphate is rapid and efficient. For the recovery of phosphate by chemical precipitation process, an optimum value of Ca/P mole ratio for phosphate removal is equal to two while the percentage phosphate removal was not affected by time of precipitation. Cockleshell and eggshell could be as a precipitant for phosphate precipitation that could remove phosphate upper to 99%.

Future work

The characteristic of hydroxyapatite will be confirmed with x-ray diffraction. The effect of other ions which could be adsorbed by Dowex Marathon MSA resin will also be studied. Furthermore, the optimal condition will be used to analyse the waste water from electroplating industry.

Acknowledgement

The authors wish to thank Graduate College King Mongkut's University of Technology North Bangkok for partially financial support. The authors would also like to thank Industrial Chemistry Department and Industrial Physics and Medical Instrumentation Department, Faculty of Applied Science, Kink Mongkut's University of Technology North Bangkok .

References

[1] M. Kumar, M. Badruzzaman, S. Adham, *Wat Res.* 41 (2007), pp. 2211 – 2219.
[2] S. Karaca, A. Gürses, M. Ejder, M. Açıkyıldızb, *J.Colloid Interf. Sci.* 277 (2004), pp. 257–263 .
[3] Sh. Ch. Akyeva, L. K. Berkelieva, and Kh. N. Evzhanov *J. Water Chem and Tech.* 30 (2008), pp. 246–250.
[4] T. Mino, M. C. M. Van Loosdrecht, J. J. Heijnen. *Wat Res.* 32 (1998), pp. 3193-3207.
[5] H. Carlsson, H. Aspegren, N. Lee, A. Hilmer, *Wat Res.* 31 (1997), pp. 1047-1055.
[6] D. Mulkerrinsa, A.D.W. Dobsona, E. Colleran, *Environ Interna*. 30 (2004), pp. 249– 259.
[7] S. Srivastava, A. K. Srivastava, *Proc Biochem*. 41 (2006), pp. 624–630.
[8] R. J. Banu, K. U. Do, I. T, J. *Environ Sci Technol*. 5 (2008), pp. 93-98.
[9] K. Hosni, S.B. Moussa, A. Chachi, M. B. Amor, *Desalination*, 223 (2008), pp. 337-343.
[10] T. Clark, T. Stephenson, P. A. Pearce, *Wat Res*. 31 (1997), pp. 2557-2563.
[11] C. F. Brothersen, N. F. Olson, T. Richardson , *J Dairy Sci*. 65 (1982), pp. 17-23.
[12]http://wwwchem.uwimona.edu.jm/lab_manuals/c10expt 36.html. 2006.
[13] A. Changpuak, W. Garnjanagoonchorn, Production calcium chloride from egg shell, Master's Thesis, Kasetsart University, 1998.

An automatic phosphate analyzer by cross injection analysis

S. Janya[1,2], P. Sastranurak[1,2], T. Mantim[1,2], N. Chauyprasatwattana[3], C. Boonpanaid[1,3], N. Choengchan[1,4], D. Nacapricha[1,2], K. Uraisin[1,2*]

[1]Flow Innovation - Research for Science and Technology Laboratories (FIRST Labs.).
[2]Department of Chemistry and Center for Innovation in Chemistry, Faculty of Science, Mahidol University, Bangkok, Thailand, 10400.
[3]Department of Industrial Chemistry, Faculty of Applied Science, King Mongkut's Institute of Technology North Bangkok, Bangkok, Thailand ,10800
[4]Department of Chemistry, Faculty of Science, King Mongkut's Institute of Technology Ladkrabang, Bangkok, Thailand, 10520

[*] E-mail :sckur@mahodol.ac.th

Abstract: A new flow-based technique, so called "Cross Injection Analysis" or CIA was developed for determination of phosphate in water samples based on the formation of molybdophosphoric acid and subsequent reduction to molybdenum blue with stannous (II) chloride. The blue complex was monitored at 690 nm. The major potential interfering substance for this chemical detection was silicate which could be reduced by controlling pH of solutions and the addition of tartaric acid in order to decompose the molybdosilicic acid. Several physical and chemical parameters affecting to the sensitivity were studied. Under the optimal conditions, the system provided working range of 0.5-5 mgP/L. The tolerance limit of silicate interference was found at 1,200 mgSi/L. The precision of CIA method was satisfactory good with low R.S.D. of 1.13 % (3 mgP/L, n = 10). Quantitative recoveries ranging from 88 to 103% were obtained in water samples.

Introduction

Phosphorus is a necessary element for all life including plant and photoplankton. Phosphorus exists in different form in waters and the dominant species is orthophosphate (PO_4^{3-}) that is the most bioavailable form in aquatic systems [1]. The concentration of phosphate in water is an important quality factor of water. Phosphate is usually not toxic to people or animal unless they are present in very high level. Under natural conditions, concentration of phosphorus compounds in ground water and surface water is generally lower than 0.1 mgP/L [2]. An excessive phosphorus concentrations can lead to acceleration of eutrophication (excessive algal growth), which can be harmful to environment, because it reduces the amount of free oxygen in water. Therefore, the method for analysis of phosphate content in natural and waste water is important for environmental monitoring.

There are a number of different methods for the determination of phosphate comprise of HPLC [3-4], polarographic method [5], voltammetric ion-channel sensor [6], ETAAS [7], ICP-MS [8] and ICP-OES [9]. Spectrophotometric methods are the most widely used for phosphate determination [10-15], often in combination with flow injection analysis (FIA) [16-19]. The high accuracy and precision with low detection limit were obtained from FIA method; however, it has a weak point due to the continuously pumping of solution that consume large amount of reagent and sample. Moreover, FIA technique requires high cost of injection valve to introduce sample into system.

In this work, a cost effective technique so called Cross Injection Analysis (CIA) was presented. The system requires reagent and sample consumption less than FIA while refuse the utilization of injection valve. The CIA was developed for analysis of phosphate in natural waters using the molybdenum blue chemistry using Tin (II) chloride as the reductant. The effect of silicate interference was reduced by the addition of tartaric acid.

Materials and Methods

Reagents and solutions

All chemicals used in this work were analytical reagent grade. Deionized-distilled water was used throughout and was directly obtained from a milli-Q system (Millipore,USA). A 100 mgP/L stock solution was prepared by dissolving 0.4393 g (oven dried for 1 h at 105 °C) of potassium dihydrogen orthophosphate (Merck, Germany) in 1 L of deionized-distilled water. Working standards in the range 0.5 -5 mgP/L were prepared by applicable dilution from the stock solution. The silicate standard were prepared by dilution of stock silicate solution 10,000 mgSi/L (43.4996 g of Na_2SiO_3 (Merck) in 1 L of deionized-distilled water) to the appropriate concentration as required in studies of silicate interference.

Ammonium molybdate 0.03 M was prepared by dissolving 37.08 g ammonium molybdate (Fluka, Switzerland) in 1 L of 1 M sulfuric acid. Stannous (II) chloride 5.6×10^{-3} M was achieved by dissolving 0.3 g tin (II) chloride (BDH, England) and 1 g hydrazinium sulphate (Merck) in 1 L of 0.5 M sulfuric acid. Tartaric acid solution (0.016 M) was prepared by dissolving 2.4 g tartaric acid (Fluka) in 1000 mL deionized-distilled water.

Instrumentation

The CIA platform is a flow-conduit that was made of a small piece of acrylic (1.5 x 4 x 3 cm), as shown in

Fig. 1. It was designed to have a cylindrical main channel for horizontal flow and other four crossing channels were drilled perpendicularly to main channel. Crossing channel was filled with three reagents and a sample or standard by vertical-cross flow, whereas the main channel was filled with carrier using horizontal flow. All channels can be tight connected to pump tube by using screw-nuts (Upchurch, USA).

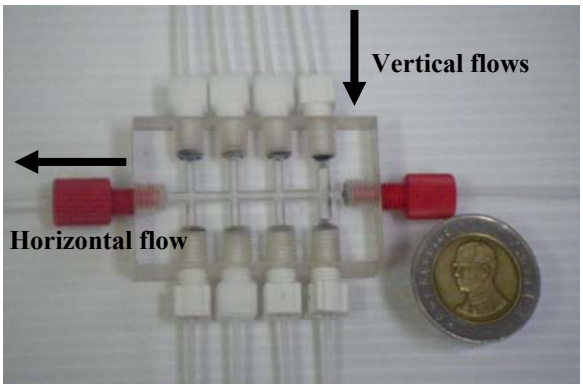

Figure 1. Illustration of the CIA platform showing the actual size of platform compare with ten bath coin.

The cross injection manifold used in this work is shown in Fig. 2. Two peristaltic pumps (Ismatec SA, model ISM843, Switzerland) were used to control the horizontal and vertical flow which was automatically manipulated by laboratory-made micro-controller incorporated with Visual Basic software. All tubing used in manifold for carrier, reagent and sample were 0.95 mm i.d. Tygon tubes (Ismatec).

Procedure

Firstly, two-way valve (modelV-101L, USA) was closed and then turn on two peristaltic pumps for 20 s in order to simultaneously introduce minute zones (µl level) of all reagents and standard into the crossing space of the conduit. After that all pumps was stopped for 20 s to pre-mix reagents and standard. Molybdenum blue complex of phosphate was occurred inside the CIA channel. Finally, two-way valve was opened and pump P2 was turned on to propel the blue complex product into detector which can be monitored at 690 nm using UV-VIS spectrophotometer (Agilent, model 3851, Germany)

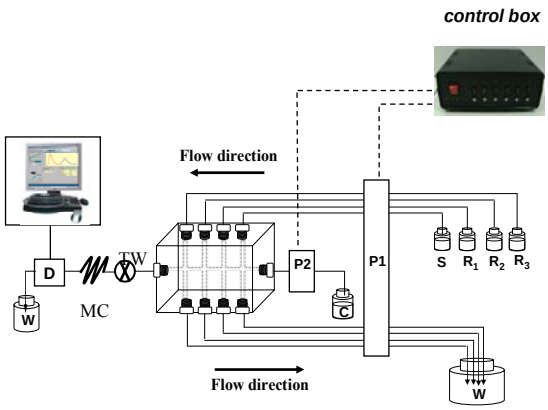

Figure 2. Schematic diagram of CIA manifold for determination of phosphate where S: sample or standard, R_1: $16x10^{-3}$ M tartaric acid, R_2: 0.03 M ammonium molybdate in 1 M sulfuric acid R_3: 5.6 x 10^{-3} M stannous (II) chloride in 0.5 M sulfuric acid, C: water carrier, TW: Two way valve, MC : Mixing coin.

Results and discussion

This method is based on reaction of phosphate with acidic molybdate to form a yellow molybdophosphoric acid which subsequently reduces to molybdenum blue complex by stannous (II) chloride, as following reaction.

$$PO_4^{3-} + 12MoO_4^{2-} + 27H^+ \longrightarrow H_3PO_4(MoO_3)_{12} + 12H_2O$$

$$H_3PO_4(MoO_3)_{12} + Sn^{2+} \longrightarrow \text{Molybdenum blue} + Sn^{4+}$$

This product can be monitored using a visible spectrometer at 690 nm which the absorbance depends on the concentration of phosphate.

Optimization of the CIA manifold

Several physical parameters affect to the sensitivity and analysis time were studies by repetitive injection of standard phosphate in the range of 1-5 mgP/L. The conditions provide the best sensitivity with appropriate analysis time were chosen as optimum condition. The results are summaried in Table 1.

Table 1 Summary of optimum condition for physical parameters in CIA manifold

Parameter	Studied range	Optimum condition
Sample volume (µl)	4.97 - 5.18	5.18
Reagent volume (µl)	4.97	4.97
Flow rate of horizontal channel (ml/min)	1 - 4	3
Flow rate of vertical channel (ml/min)	1	1
The length of mixing coil (cm)	32 - 120	32
Stop time in unit (sec)	10 - 25	20

Several chemical parameters were examined. The effect of concentration of molydate, stannous (II) chloride and sulfuric acid on the sensitivity of phosphate determination were studied by repetitive injection of standard phosphate 3 mgP/L. Results were shown in Fig. 3. The effect of molybdate concentration was examined over the range of 0.005 – 0.03 M. The result in Fig. 3A shows that the signal of standard phosphate increase with an increasing in molybdate concentration. However, increment of blank signal was obtained. Therefore, 0.03 M molybdate was selected as a compromise between sensitivity and blank signal.

Alteration of the sulfuric acid concentration over the range of 0.5 – 3 M affect to sensitivity of phosphate analysis. Higher concentration of sulfuric give lower sensitivity of phosphate analysis (Fig 3B). In this experiment, the concentration of sulfuric acid lower than 1 M was used because it provides high sensitivity.

Stannous (II) chloride acts as a reductant for reducing molybdophosphoric acid to form molybdenum blue complex. The effect of stannous (II) chloride was studied in the range between 2.8 and 16.8 mM. The result in Fig. 3C demonstrates that concentration of this reagent is slightly effect on the signal. However, blank signal was increased with an increment of stannous (II) concentration. Therefore, in this work 5.6 mM stannous (II) chloride was chosen.

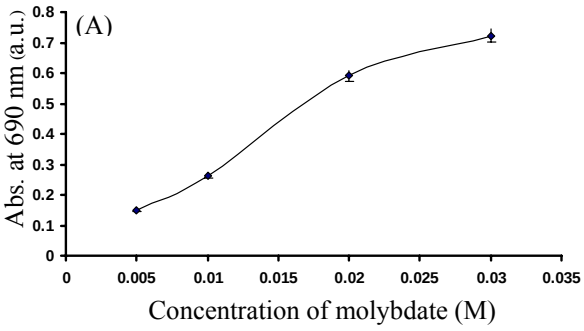

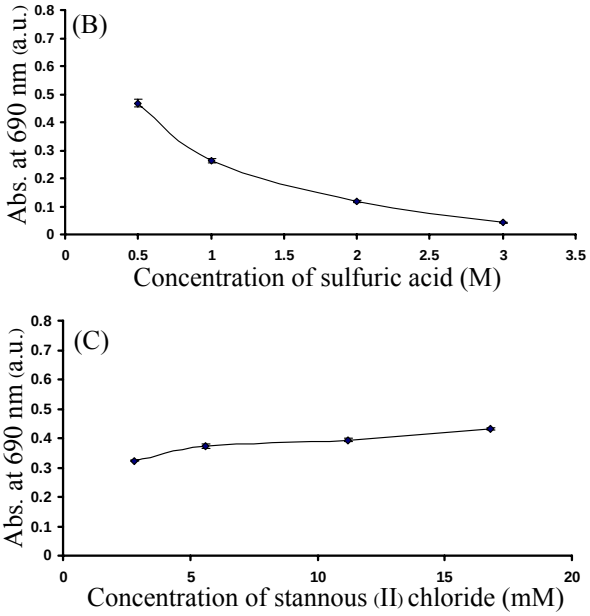

Figure 3. Effect of chemical parameters:(A) molybdate concentrations, (B) sulfuric acid concentrations, and (C) stannous (II) chloride concentrations.

Interference

Silicate is well-known as the major interfere for the analysis of phosphate using molybdenum blue method because silicate form similar blue complex with molybdate. The interference of silicate on phosphate was normally minimized by adding tartaric acid as masking agent. In this work, 0.016 M of tartaric acid was used in reagent line (R_1) for elimination of silicate. In order to determine the tolerance limit of the CIA system for silicate, various concentrations of silicate standard were spiked into a phosphorus solution (2 mgP/L). The tolerance limits for silicate is defined as the change in signal of phosphate at three times of standard deviation (3SD). According to the result in Fig. 4, the tolerance limits for silicate were found at 1,200 mgSi/L. The concentration of silicate that normally found in natural water are ranging from 0-2.8 mgSi/L [20]. These concentrations are much lower than the tolerance limits of the developed CIA. Therefore, silicate does not interfere in determination of phosphate in natural water.

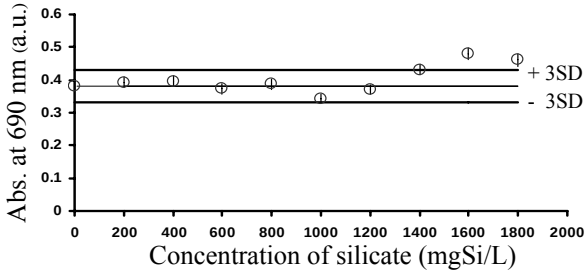

Figure 4. Tolerance limits of CIA system for silicate studied on 2 mgP/L with 0.016 M tartaric acid as masking agent.

Analytical features

A calibration graph was obtained over the concentration range of 0.5 – 5 mgP/L (r^2 = 0.999). A typical CIA signal and calibration are shown in Fig. 5. Reproducibility was good with R.S.D.s of 1.13% for ten replicate injections of 3 mgP/L. The sample throughput was 32 injection / hr.

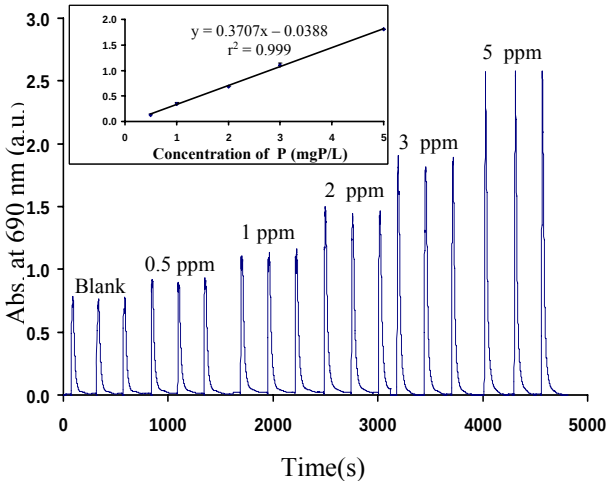

Fig. 5. Typical CIA signal and calibration curve using phosphate standard in the range 0.5 to 5 mg P/L. Error bars ± SD, n =3.

3.2 Application to real sample and recovery

Water samples were collected from the canal around Mahidol University. Samples were filtered through 0.45 µm cellulose nitrate membrane prior analysis. The results shown in Table 2 indicate that the concentration of phosphate found in water sample higher than the limit of problematic excessive algal growth in water (0.1 mgP/L), so these canal is in eutrophication condition. This causes phytoplankton to grow rapidly, resulting in algal bloom. Recovery tests were made with eight water samples by addition of 1 mgP/L. The recoveries were found in the range of 88 – 103.5 %. Therefore, this method is well satisfied which implied that the foreign ions were not interfered with the proposed method.

Table 2 Recovery tests for determination of phosphate

Sample no.	Conc. of P in sample	Added (mgP/L)	Found (mgP/L)	% Recovery
1	0.95 ± 0.01	1.00	2.02 ± 0.03	103.5
2	0.66 ± 0.03	1.00	1.61 ± 0.03	90.77
3	1.12 ± 0.01	1.00	2.05 ± 0.03	88.94
4	0.61 ± 0.02	1.00	1.57 ± 0.04	92.03
5	1.36 ± 0.04	1.00	2.30 ± 0.03	90.58
6	0.99 ± 0.01	1.00	1.98 ± 0.02	95.06
7	1.07 ± 0.02	1.00	1.99 ± 0.01	88.00
8	1.21 ± 0.04	1.00	2.20 ± 0.07	95.51

Conclusions

The developed CIA method for phosphate analysis in water sample is automatic and simple with less consumption of reagents and sample. The system provides high sample throughput of 32 injections / hr. The CIA system can be used as an alternative method for analysis of phosphate in natural water with satisfactory results.

Acknowledgements

The authors would like to acknowledge the financial supports of this project from the Thailand Research Fund, the Center of Excellence for Innovation Chemistry (PERCH-CIC), Commission on Higher Education, Ministry of Education, National Research Council of Thailand and the institute for the Promotion of Teaching Science and Technology: Project for the Promotion of Science and Mathematics Talented Teachers (PSMT) for their financial support.

References

[1] Y.B. Spivakov, A.T. Maryutina, H..Muntau, *Pure.Appl. Chem.* **71** (1999), pp. 2161–2175.
[2] U.S. Environmental Protection Agency, Quality Criteria for water, Office of water (1986), Variously paged.
[3] N. Yoza, K. Ito, Y. Hirai, S. Ohashi, *J. ChromatogrA.* **196** (3), (1980), pp. 471– 480.
[4] D. Jolley, W. Maher, P. Cullen, *Wat.Res.***32** (3), (1998), pp. 711–716.
[5] R. Pardo, E. Barrando, P.B. Sanchez, *Talanta.***30** (1983), pp. 655–658.
[6] H. Aoki, K. Haseawa, Y. Umezawa, *Biosensor Bioelectronics.* **18**, (2003), pp. 261-267.
[7] J. Alvardo and R. Christina, *J.Anal.Atom.Spectrom.* **10**, (1995), pp. 483-486.
[8] Y. Chiao-Hui, J. Shiuh-Jen, *Spectrochimica Acta,Part B* . **59B**(9), (2004), pp. 1389-1394.
[9] Q. Cai and Z. Yang , *Anal.Sci.* **17** (2001), pp. 853–856.
[10]J. Ruzicka,D.G. .Marshall, *Anal.Chim.Acta.* **237**,(1990), pp. 329-343.
[11] S. Motomizu, M. Oshima and A. Hirashima, *Anal .Chim. Acta.* **211**,(1998), pp. 119-127.
[12] L.K. Linge and E.C. Oldham, *Anal.Chim.Acta.* **450**, (2001), pp. 247-252.
[13] A. Munoz and V. Cerda, *Anal .Chim . Acta.* **350**,(1997), pp. 21-29.
[14] D.J. Ingle and R.S. Crouch, *Anal.Chem.* **43**,(1971), pp. 7-10.
[15] M. Korn, M.P. Primo and S.C. Sousa , *J.Microchemical.* **73**,(2002), pp. 273-277.
[16] W. Tiyapongpattana, P. Pongsakul, J. Shiowatana, D. Nachapricha, *Talanta.* **62** (4), (2004), pp. 765–771.
[17] K. Grudpan, P. .Ampon and J. Ruzicka, *Talanta.* **58**, (2002), pp. 1319–1326.
[18] O. Tue-Ngeun, D.I. Mckelvie and K. Grudpan, *Talanta.* **66**, (2005), pp. 453–460.
[19] S. Motomizu, M. Oshima and N. Katsumura, *Anal. Sci.and Tec.* **8**,(1995), pp. 846-848.
[20] Z. J. Zhang, J.C. Fischer, B.P. Ortner, *Talanta.* **49** (2), (1999), pp. 293–304.

Selective determination of acetaldehyde by membrane permeation with spectrophotomertic flow injection

P. Inpota[1,2], A. Kongsakphaisal[2], D. Nacapricha[1,3] and N. Choengchan[1,2]*

[1] Flow Innovation-Research for Science and Technology Laboratories (FIRST Labs),
[2] Department of Chemistry, Faculty of Science, King Mongkut's Institute of Technology Ladkrabang, Bangkok, 10520 Thailand
[3] Department of Chemistry and Center of Excellent for Innovation in Chemistry, Faculty of Science, Mahidol University, Bangkok, 10400 Thailand

*E-mail: nchoengchan@gmail.com

Abstract: This work describes method development for selective determination of acetaldehyde. The method is based on using gas-diffusion flow injection (GD-FI) with spectrophotometric detection. . Detection principle is based on monitoring of a blue-colored product of the reaction between diffused acetaldehyde with nitroprusside and morpholine. By the developed system, linear correlation between absorbance reading at 600 nm and acetaldehyde concentration (0.5 to 5.0 mM) was achieved. Application of the method to determine trace acetaldehyde in Thai alcoholic beverages was investigated for the sake of food safety. Results are compared with the results obtained from gas chromatographic (GC) method. They were successfully validated. The method also provided high precision (RSD = 3.7 % for 1 mM and 2.9 % for 5 mM), high accuracy (Recovery = 92-101 %) and high throughput (40 samples/ h). By means of GD, samples were determined selectively and directly without any pretreatment or dilution.

Introduction

Acetaldehyde is toxic and is carcinogenic substance which can raise cancer risk for human, according to the International Agency for the Research on Cancer (IARC) [1]. Trace acetaldehyde can be contaminated in foods and beverages. For alcoholic drinks, acetaldehyde can be produced by further oxidation of ethanol by yeast during fermentation. Level of acetaldehyde in beverage should be legally under regulation. In Thailand, its quantity has to be lower than 160 ppm (approximately 4 mM) [2]. Therefore, measurement of acetaldehyde in beverage is necessary in term of quality control and food safety.

There are a great number of analytical methods for quantitative analysis of acetaldehyde. Electrochemical techniques with different detection patterns, such as conductometry, potentiometry and cyclic voltammetry, have been reported [3-5]. Colorimetry has also been presented for determination of acetaldehyde in variety of sample matrices [6-11]. Advantages of the colorimetric methods are their simplicity. However, the absorbance measurement is strongly perturbed by sample color and its matrix. Sample pretreatment step such as distillation before detection was essentially included for selectivity improvement [6, 7].

The other analytical methods for specific analysis of acetaldehyde are separation techniques. Some researchers proposed gas chromatography (GC) for separation of acetaldehyde from sample containing high acetic acid concentration [12]. Whilst another presented the GC with headspace as a method for direct analysis of acetaldehyde in food packaging [13]. Liquid chromatography with electrochemical detection for monitoring of acetaldehyde derivative was also reported [14]. Although the mentioned methods were selective, they consumed long analysis time which is not appropriate for routine work. Flow injection (FI) technique [15] then becomes more attractive due to its rapidity and automation. Usually for selective determination of acetaldehyde by the spectrophotometric-FI, the immobilized enzyme reactor was incorporated into the system [16-18]. Not only high selectivity but also high sampling frequency were achieved [16, 17]. Nevertheless, the cited enzyme-based FI method required dilution of beverage samples (>100 times) in order to eliminate interferences from sample color and matrices. This could lead to high risk of contamination and error.

In this work, a non enzymatic FI method for spectrophotometric determination of acetaldehyde is presented. Selective analysis can be accomplished by using gas-diffuion (GD) unit, fitted with gas permeable membrane. Diffused acetaldehyde was scrubbed into the acceptor stream of nitroprusside and morpholine. A blue-colored product was developed and was subsequently monitored at 600 nm. Application to alcoholic beverages and validation of the proposed method were also investigated.

Materials and Methods

Standards and reagents

All chemicals used were of analytical-reagent (AR) grade. Deionized-distilled water was used throughout.

Acetaldehyde standard (1 M) was prepared from 99.5 % (v/v) acetaldehyde (Riedel-de Haën, Germany) and was standardized according to iodometry.

Calibrators were prepared by appropriate dilution of stock standard with water.

Acceptor stream (AS in Figure 1) was freshly prepared by mixing 2.5 % (w/v) of sodium nitroprusside (AnalaR, Australia) and 5 % (v/v) of morpholine (Fluka, Germany).

The GD-FI manifold

The manifold of the GD-FI system is depicted in Figure 1. The system was established with Teflon™ tubing (0.5 mm i.d.). A peristaltic pump (P1) (Ismatec, Switzerland) was employed for delivering the streams of carrier (CS) and acceptor (AS). An AS-90 auto-sampling with another peristaltic pump (P2) (Perkin-Elmer, USA) was used for automatically loading standard or sample solutions into an injection loop of 300 µl. A flat type GD unit (Methrohm, Switzerland), fitted with a circular PTFE membrane (47 mm diameter, pore size = 0.45 µm; Sartoriuos, Germany), was used. Detection was carried out by a 630-UV-Vis. Spectrophotometer (Jasco, US).

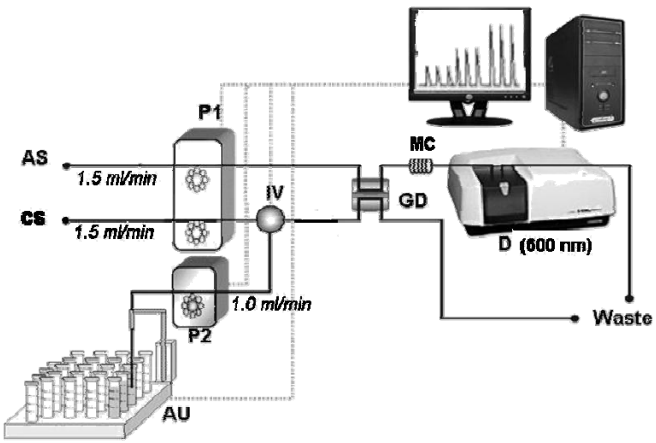

Figure 1. Manifold of the GD-FI system for determination of acetaldehyde. AU: Auto-sampler unit, P1, P2: Peristaltic Pump, IV: Injection Valve, MC: Mixing Coil, D: Detector, GD: Gas-diffusion unit with PTFE membrane, CS: Water and AS: Nitroprusside (2.5 % w/v) + Morpholine (5 % v/v).

Results and discussion

Absorption spectrum of detection reaction

The reaction between acetaldehyde with nitroprusside and morpholine was firstly proposed by F. Feigl [19] for qualitative analysis of acetaldehyde.

In this work, absorption spectra of the blue-colored product was monitored. Results are illustrated in Figure 2. Maximum absorption wavelength (λ_{max}) appears at 600 nm. This wavelength was therefore selected for all next investigation.

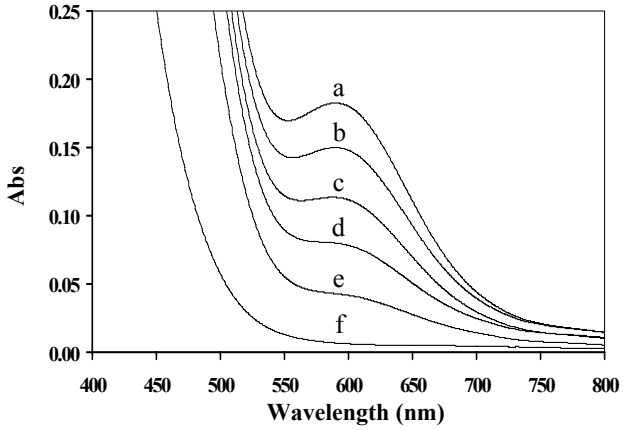

Figure 2. Spectra of standard acetaldehyde (a to e). a: 5, b: 4, c: 3, d: 2 and e: 1 mM. Spectrum of 0.6 % w/v nitroprusside, mixed with 1.2 % v/v morpholine (f).

Optimization of the GD-FI system

All chemical and physical parameters affecting sensitivity of the method were investigated by uni-variable approach. Each effect was discussed in subsections below. Summary of the studied ranges and the optimal values are shown in Table 1.

Effect of acceptor concentration

Effect of concentration of the acceptor stream is shown in Figure 3 and 4. Results in Figure 3 demonstrate that increasing in nitroprusside concentration results in improvement of sensitivity. Similar to the effect of morpholine (Figure 4), the sensitivity is increased with concentration of morpholine (upto 5 % v/v). At grater concentration (10 % v/v), the solution became more viscous. This leads to significant dropping in sensitivity. In addition, higher concentration of morpholine brought about strong alkaline solution. This can also affect the method sensitivity *(See effect of pH of the acceptor stream)*. Concentration of 2.5 % (w/v) nitroprusside and of 5 % (v/v) morpholine is considerably appropriate since they gave adequate sensitivity.

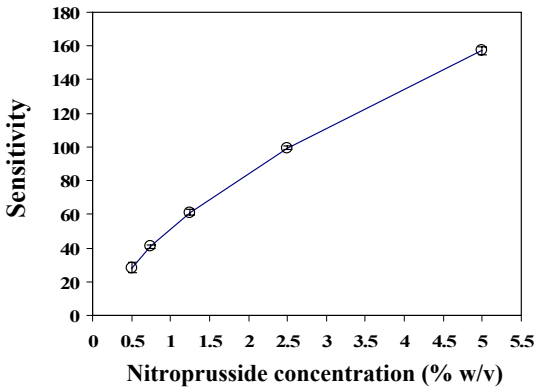

Figure 3. Effect of nitroprusside concentration.

Effect of sample volume

As expected, when sample size was increased from 100 to 500 µl, sensitivity was also increased. An

aliquot of 300 µl was selected as compromising between sensitivity and consumption of sample.

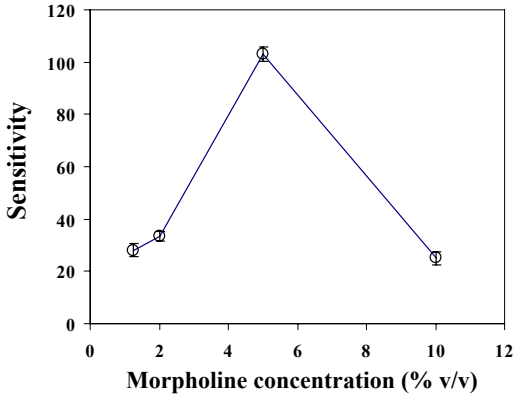

Figure 4. Effect of morpholine concentration.

Effect of donor and acceptor flow rate

The flow rate of donor and acceptor streams were examined simultaneously for the sake of simplicity. Sensitivity was noticeably declined when flow rate of the donor and acceptor stream were increased from 0.5 to 2.0 ml/min since residence time was decreased. The flow rate of 1.5 ml/min was selected with regards to sensitivity and sample throughput.

Effect of mixing coil length

When the length of mixing coil was prolonged from 50 to 300 cm, sensitivity was also enhanced. This was because of increasing in reaction time. However, at longer length (400 cm), sensitivity was slightly diminished due to dispersion. By taking into account for sensitivity and sampling frequency, a 300-cm mixing coil was chosen as suitable length.

Table 1: Studied and selected parameters of the GD-FI for determination of acetaldehyde.

Parameters	Studied range	Selected value
Chemical parameters		
Concentration of nitroprusside/ % w/v	0.5-5.0	2.5
Concentration of morpholine/ % v/v	1.25-10	5
Physical parameters		
Sample volume/ µl	100-500	300
Donor and acceptor flow rate/ ml/min	0.5-2.0	1.5
Mixing coil length/ cm	50-400	300

Effect of pH of the acceptor stream

M. Khanmohammadi *et. al.* [11] presented that the reaction rate between nitroprusside and morpholine was inhibited by acetaldehyde itself in strong alkaline medium (pH 9.5). While the other researchers [8] reported that hypsochromic shift (blue shift) was occurred when the reaction was taken place in acidic solution. This brought about pink-colored product instead of blue.

In this work, pH of the acceptor solution with various mopholine concentrations was measured. Very high (10 % v/v) or low (2 % v/v) concentration of morpholine resulted in alkaline (pH 10.1) or acidic (pH 3.5) solution, respectively. Low sensitivity was observed when pH was not appropriate. Highest sensitivity was achieved with 5 % (v/v) morpholine. By this concentration, pH of the acceptor solution was 6.9. This can be an evidence for the highest sensitivity obtained when this concentration was exploited.

Analytical performances

Under the optimal condition, in Table 1, linear correlation between absorbance and acetaldehyde concentration (0.5 to 5 mM) was obtained with the following regression equation: Abs_{600nm} = 99.5[acetaldehyde] + 0.0039, r^2=0.999. Example of profiles when standard acetaldehyde was injected are shown in Figure 5.

Relative standard deviation (RSD, n=10) were 3.7 and 2.9 % when 1 and 5 mM were studied, respectively. Limit of detection (LOD, 3S/N) was 0.42 mM. This was below regulation concentration of acetaldehyde in beverages [2]. This can guarantee that the developed method is capable for investigation the contaminated acetaldehyde in this kind of sample.

Accuracy of the method was also investigated in term of analytical recovery. It was found that recovery of seven samples was ranging from 92 to 101 %. This implies that the proposed system was not perturbed by sample matrix. Regarding sampling frequency of the system, throughput of 40 samples/ h was achieved.

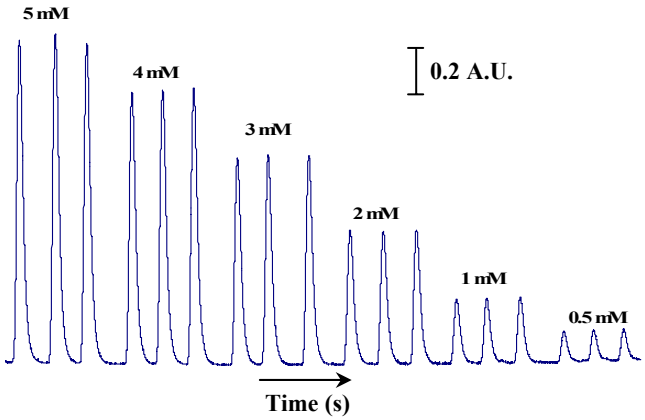

Figure 5. Profiles of standard acetaldehyde.

Interference study

D. J. Clancy *et. al.* [8] revealed that the detection reaction was positively interfered by formaldehyde. In this work, effect of foreign species, namely the other aldehydes, (formaldehyde (0.04 M) and propionaldehyde (0.02 M), were examined.

Results indicated that signal alteration was within ± 3SD of the averaged absorbance of 5 mM acetaldyhyde when high concentration of interferences (value in parenthesis) were studied. These concentration levels are much greater than their naturally found contents in beverages. This suggests that the method was not interfered by the investigated species.

Application to samples and validation

Synthetic (trace acetaldehyde in medium of high ethanol concentration) and real samples (wines and whisky) were determined. Red and fruit wines were made in Thailand, accordingly to *'OTOP'* project. All samples were directly introduced into the GD-FI system without neither sample pretreatment nor any further dilution. The acetaldehyde concentration was validated against the GC method in which its operating condition was described elsewhere [20]. Results are presented in Table 2.

Table 2: Comparison of acetaldehyde concentration in alcoholic drinks, determined by the proposed method and by GC.

Sample	Acetaldehyde concentration*/ mM	
	This method	GC
Synthetic sample 1 (1 mM in 20 % Ethanol)	0.93 ± 0.001	1.09 ± 0.009
Synthetic sample 2 (2 mM in 30 % Ethanol)	2.12 ± 0.006	2.04 ± 0.007
Synthetic sample 3 (3 mM in 40 % Ethanol)	3.07 ± 0.002	3.11 ± 0.001
Red wine	0.68 ± 0.003	0.63 ± 0.001
Lychee wine	1.41 ± 0.001	1.36 ± 0.002
Strawberry wine	1.27 ± 0.003	1.30 ± 0.005
Whisky	1.18 ± 0.005	1.21 ± 0.007

** mean ± SD, n = 3 replicates*

Results in Table 2 are not significant difference by means of statistical paired *t*-test [21] ($t_{critical}$ = 2.45, t_{obs} = 0.37) at degree of 95 % confidence. This specifies that the proposed method gave high accuracy. In addition, the acetaldehyde levels of all real samples are also lower than regulation limit (4 mM).

Conclusions

The FI system was developed for spectrophotometric determination of acetaldehyde in alcoholic beverages. Selective analysis was achieved by using membrane permeation technique instead of enzymatic method. The system allows *'on-line'* separation of acetaldehyde from sample matrices. This can lead to direct analysis of samples without any prior preparation.

The proposed method was successfully validated against GC. It also provided high precision with high sampling frequency. Therefore, the method can be considered as an alternative method for determination of acetaldehyde in routine analysis of beverages.

Acknowledgements

The authors would like to thank financial supports from the Thailand Research Fund (Grant no. MRG 5080264, given to NC) and from Faculty of Science, King Mongkut's Institute of Technology Ladkrabang, Bangkok, Thailand (given to PI and NC). The authors would also like to express their appreciations to FIRST Labs., Mahidol University for contribution.

Dr. Warawut Tiyapongpattana (Thammasart University) and Ms. Thitima Bhusrisom (Mahidol University) are also acknowledged for their suggestion and helps on preliminary experiment on GC.

References

[1] http://www.iarc.fr.
[2] Declaration of Ministry of Industry of Thailand. Issue 118, pp. 21.
[3] I. A. Capuano, *Anal. Chem.* **32** (1960), pp. 1025-1027.
[4] A. Avramescu, T. Noguer, M. Avramescu and J. L. Marty, *Anal. Chim. Acta.* **458** (2002), pp. 203-213.
[5] V. S. Rodgher, L. L. Okumura, A. A. Saczk, N. R. Stradiotto and M. V. B. Zanoni, *J. Anal. Chem.* **61** (2006), pp. 889-895.
[6] M. A. Joslyn and C. L. Comar, *Ind. Eng. Chem.* **10** (1938), pp. 364-366.
[7] M. C. Bowman, M. Beroza and F. Acree Jr., *Anal. Chem.* **33** (1961), pp. 1053-1055.
[8] D. J. Clancy and D. E. Kramm, *Anal. Chem.* **35** (1963), pp. 1987-1988.
[9] G. P. Arsenault and W. Yaphe, *Anal. Chem.* **38** (1966), pp. 503-504.
[10] S. Flamerz and W. A. Bashlr, *Anal. Chem.* **54** (1982), pp. 1734-1735.
[11] M. Khanmohammadi, H. Vahid, N. Moazzen, A. B. Garmarudi and R. Alijanianzadeh, *J. Anal. Chem.* **63** (2008), pp. 1164-1167.
[12] H. J. Rhodes, D. W. Bode and M. I. Blake, *Anal. Chem.* **46** (1974), pp. 1584.
[13] L. Gramiccioni, M. R. Milana, S. Di Marzio and S. Lorusso, *Chromatographia*. **21** (1986), pp. 9-11.
[14] A. A. Saczk, L. L. Okumura, M. F. de Oliveira, M. V. B. Zanoni, and N. R. Stradiotto, *Anal. Sci.* **21** (2005), pp. 441-444.
[15] http://www.flowinjection.com
[16] A. M. Almuaibed and A. Townshend, *Anal. Chim. Acta.* **198** (1987), pp. 37-44.
[17] F. Lazaro, M. D. L. de Castro and M. Valcarcel, *Anal. Chem.* **59** (1987), pp. 1859-1863.
[18] H. Mori, Y. Sekine and Y. Takahashi, *J. Health Sci.* **49** (2003), pp. 55-58.
[19] F. Feigl, *Spot Tests in Organic Analysis,* Elsevier, The Netherlands (1960).
[20] T. Bhusrisom, Selective quantitation of ethanol in beverage using some membraneless vaporization apparatuses, Master's Thesis, Mahidol University, 2009.
[21] J. N. Miller and J. C. Miller, *Statistics and Chemometrics for Analytical Chemistry*, fourth ed., Pearson Education, Essex, 1993.

A HPLC method using UPLC™ column for simultaneous determination of alpha- and beta-arbutin in cosmetics

M. Mala[1,2*] and P. Varanusupakul[2]

[1]Devision of Cosmetic and Hazardous Substances, Department of Medical Sciences, Ministry of Public Health, Muang, Nontaburi, Thailand 11100. E-mail: muntinee.m@dmsc.mail.go.th
[2]Chromatography and Separation Research Unit, Department of Chemistry, Faculty of Science, Chulalongkorn University, Patumwan, Bangkok, Thailand 10330.

*muntinee.m@dmsc.mail.go.th

Abstract: Hydroquinone has prohibited in cosmetic products because of its severe effects on the human skin. Arbutin is among alternative whitening agents available in the market. It is a derivative of hydroquinone that is present in two configurations; i.e., beta- and alpha-arbutin. Beta-arbutin is a natural product whereas alpha-arbutin is a synthetic. Both are skin lightening active but alpha-arbutin offers higher stability and more efficiency, acts faster than beta-arbutin so that it is more expensive. Some manufacturers may take an advantage by misleadingly advertising that their products contain alpha-arbutin to increase their sale prices. For health consumer protection, it is necessary to develop a reliable method to assure that the cosmetic products contain such arbutins as it is claimed. This presentation shows a method for simultaneous determination of alpha- and beta-arbutin by using UPLC™. The method was performed on Waters ACQUITY UPLC® HSS T3 column (1.8 µm particle size, 2.1 x 150 mm) with gradient elution of 0.1% acetic acid and methanol as a mobile phase. The flow rate was 0.3 mL/min. The arbutins were detected and quantified by UV/VIS spectrometry at 283 nm. The analysis time was less than 6 min. The linear working ranges for both arbutins were 2-30 µg/mL (r = 0.9999). The recoveries of spiked synthetic cosmetics in various matrices such as lotion, cream and gel were between 98-102% with %RSD less than 0.6%. Our method offered better resolution, speed and sensitivity than a typical HPLC method.

Introduction

Sunlight is the main cause for appearance of brown-spots on the human skin such as freckle and melasma which are not desirable to some people. The alternative for this disorder can be reduced using the skin-whitening products. In the past, hydroquinone was used for topical application in skin whitening products to decrease freckle and melasma by inhibiting enzyme tyrosinase in melanin production but it has been banned due to its effect to the skin irritation, mild itching, reddening and permanent skin damage if continually used for a long period of time [1]. Arbutin, which is a derivative of hydroquinone, has become an alternative whitening agent. Beta-arbutin (Figure 1) is a natural product that is extracted from bearberry plant [8], it does not cause a skin irritation and other side effects. Although it is inexpensive but not stable in a very acidic condition and may cause color change in a final product if storage for a long time. In the year of 2002, a synthetic alpha-arbutin (Figure 1) has been introduced that offers higher stability and more efficiency than beta-arbutin [9-10]. Its color and odor does not change during storage but it is about 8 times more expensive than beta-arbutin. So, some manufacturers may have been deceptively advertising that their cosmetic products contain alpha-arbutin in order to raise the sale prices. For health consumer protection and product quality control purposes, it is necessary to develop a reliable method for simultaneous determination of beta- and alpha-arbutin. The method will provide confidence for consumers to obtain product containing active ingredient as labeled.

Several methods have been reported for determination of beta-arbutin in whitening cosmetic products [2-5]. Most of them were based on HPLC methodology. None of them has reported for determination of alpha-arbutin yet. Since they are isomers, it would be very difficult to achieve a complete separation using such a conventional HPLC method. This work aims to develop a method for simultaneous determination of beta- and alpha-arbutin by using ultra performance liquid chromatography (UPLC™), which offers much more separation efficiency than the conventional HPLC system [6-7]. The separation performance is based on the use of the smaller size particle column (1.8 µm compared to 3-5 µm of the conventional HPLC column), of which the number theoretical plates (N) are much improved, according to the Van Deemter equation, resulting to high resolution power with fast flow rate. The UPLC™ system comes with the high pressure pump (15,000 psi pressure limit) and uses about 10 times less system volume than the HPLC system allowing much shorter analysis time, less waste and high sample throughput, which are suitable for routine analysis.

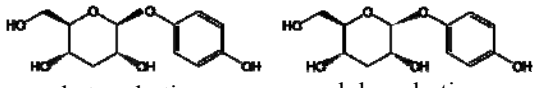

beta-arbutin alpha-arbutin

Figure 1. The chemical structures of beta-and alpha-arbutin.

Materials and Methods

UPLC™ system equipped with a Waters Acquity UPLC™ Binary Solvent Manager, Sample Manager and PDA detector (Waters, USA) were employed and personal computer with an Empower 2 software program was used to process all chromatographic data. An ACQUITY UPLC® HSS T3 (High Strength Silica C 18), 1.8 µm, 2.1 x 150 mm column (Waters, USA) was used for separation of both arbutins. The mobile phase was prepared from HPLC-grade methanol (Fisher Scientific, Canada) and AR-grade acetic acid (Merck, Germany). Beta-arbutin (99.60% purity) was purchased from Bioland (USA). Alpha-arbutin (97.70% purity) was purchased from Pentapharm (Switzerland). Working standard solutions of beta- and alpha-arbutin ranging from 2-30 µg/mL were prepared in 95% of 0.1% acetic acid : 5% methanol for a calibration. Three matrices of skin whitening cosmetic samples (cream, lotion and gel) containing 2% w/w of beta- and alpha-arbutin each were prepared in the laboratory for method validation. The sample was extracted with methanol and the final solution was prepared in 95% of 0.1% acetic acid : 5% methanol. Both standard and sample solutions were filtered through 0.2 µm PVDF syringe filters into a 2 mL vial prior to analysis. The method was validated for system suitability, linearity, precision, accuracy and limit of detection.

Results and Discussion

Since beta- and alpha-arbutin are organic compounds that are very well soluble in water and alcohol, reversed phase separation mechanism with high content aqueous mobile phase was investigated. The ACQUITY UPLC® HSS T3 column, a reversed phase column which is designed for separation of organic compounds that are in a high aqueous environment or a 100% aqueous solution was chosen. A non-linear gradient elution profile was optimized for simultaneous analysis of beta- and alpha-arbutin as summarized in Table 1 and the chromatogram was illustrated in Figure 2.

Table 1. The non-linear gradient elution profile for simultaneous separation of beta- and alpha-arbutin on the ACQUITY UPLC® HSS T3 column.

Time (min)	Flow rate (mL/min)	Mobile phase fraction (%)	
		0.1% HOAc	MeOH
0.0	0.3	93.0	7.0
3.0	0.3	97.0	3.0
3.4	0.3	90.0	10.0
4.2	0.3	93.0	7.0

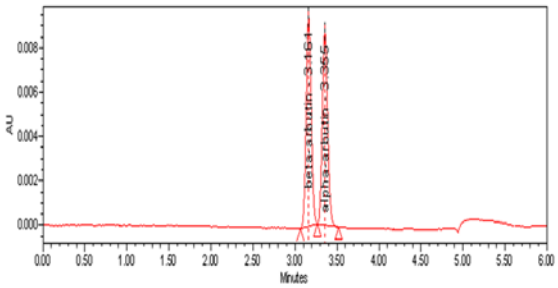

Figure 2. The chromatogram of simultaneous separation beta- and alpha-arbutin by the UPLC™ method.

The system suitability for five replicate injections of beta- and alpha-arbutin mixture standard solution was shown in Table 2. The analysis time for simultaneous determination of beta- and alpha-arbutin was less than 5 min and the resolution (Rs) of more than 1.5 were achieved.

Table 2. The system suitability for simultaneous determination of beta- and alpha-arbutin by the UPLC™ method.

Whitening agent	System suitability			
	RT (min)	Capacity factor (k')	Tailing factor	Resolution (Rs)
Beta-arbutin	3.17	11.66	1.06	-
Alpha-arbutin	3.36	12.44	1.10	1.71

Figure 3 and Figure 4 showed the system linearity of standard beta- and alpha-arbutin. The coefficient of determination (R^2) of 0.9999 was achieved for the concentration range of 2-30 µg/mL. The maximum %RSD of five replicated injections at each concentration level was 1.41 and 1.05 for beta- and alpha-arbutin, respectively. The limit of detection (LOD) was defined as the concentration corresponding to the peak area at y-intercept + 3 x standard deviation of slope. The LOD of this method for both arbutins were 0.005 % w/w.

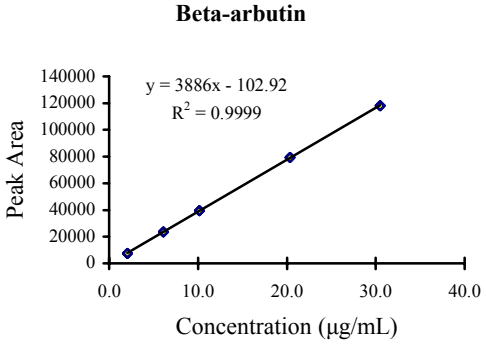

Figure 3. Linear regression of standard beta-arbutin.

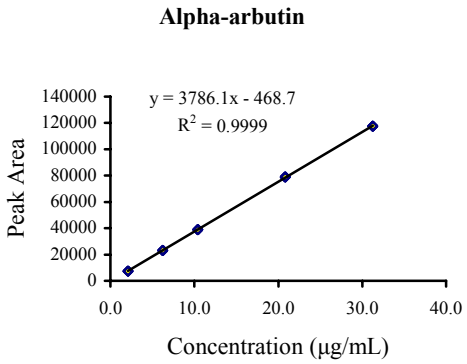

Figure 4. Linear regression of standard alpha-arbutin.

The method linearity, accuracy and precision were determined from spiked cosmetic samples. The linearity was expressed as the correlation coefficient (r). The accuracy, expressed as %recovery, was calculated from $[(S-U) \times 100]/C_{SA}$; S was the concentration of the arbutin in spiked sample (%w/w); U was the concentration of the arbutin in unspiked sample (%w/w); C_{SA} was the concentration of arbutin added, (%w/w). The recoveries of arbutin spiked samples at three level concentrations were in the range of 98-102%. The method reproducibility was determined from duplicate spiked samples. The relative percent difference (%RPD) was less than 0.6%. The method repeatability (intra-day) was determined from five replicated analyses. The relative standard deviation (RSD) was less than 0.5%. The intermediate precision (inter-day) was obtained from five days (n=5) and the relative standard deviation (RSD) was less than 0.6%. Table 3 summarized the method linearity, method accuracy and method precision for each kind of matrix.

Table 3. The method linearity, accuracy and precision of the UPLC™ method for simultaneous determination of beta- and alpha-arbutin.

Parameter	Beta-arbutin			Alpha-arbutin		
	cream	lotion	gel	cream	lotion	gel
Method linearity : Correlation coefficience (r)	0.9995	0.9997	0.9995	0.9993	0.9995	0.9997
%Recovery (3 levels, 5 replicates /level)	98-102	98-101	98-102	98-102	98-101	98-102
Repeatability: %RSD (5 replicates)	0.34	0.50	0.19	0.14	0.10	0.12
Intermediate precision %RSD (5 days)	0.34	0.50	0.49	0.15	0.14	0.29

Conclusions

The HPLC with UPLC™ column for simaltaneous determination of beta- and alpha-arbutin in whitening cosmetics was developed. The method was able to separate arbutin isomers with resolution greater than 1.5 for less than 5 min. The method exhibited very good performance for determination of arbutin isomers in several kinds of matrices that would be beneficial for routine analysis in a product quality control laboratory as well as for health consumer protection purposes.

References

[1] Notification of Ministry of Public Health, (No. 39) B.E. 2538.
[2] M.L. Chang and C.M. Chang, *J. Pharm. Biomed. Anal.***33** (2003), pp. 617-626.
[3] Han, Z.; Zheng, Y.; Chen, Na; Luan, L.; Zhou, C.; Gan, L.; Wu, Y., *J Chromatogr A*, **2008**, 1212, 76-81.
[4] C.H. Lin, H.L. Wu and Y.L. Huang, *J Chromatogr B*, **829** (2005), pp. 149-152.
[5] Y.H. Lin, Y.H. Yang, and S.M. Wu, *J. Pharm. Biomed. Anal.* **44** (2007), pp. 279-282.
[6] E.M. Paliakov, B.S. Crow, M.J. Bishop, D. Norton, J. George and J.A. Bralley, *J Chromatogr B*, **877** (2009), pp. 89-94.
[7] www.en.wikipedia.org
[8] www.pentapharm.com
[9] www.makingcosmetics.com

Remediation of heavy metals in wastewater sludge using EDTA extraction

P. Pawanna[1] and S. Kungwankunakorn[1*]

[1]Department of Chemistry, Faculty of Science, Chaing Mai University, Chaing Mai, 50200 Thailand

*E-mail: ksukjit@hotmail.com

Abstract: The removal of toxic metals in sludge is very important for the resolution of the limited sludge application. Thus, the objective of this research is the study on the possibility of EDTA as extractant for heavy metals from artificially contaminated sludge sample. The sludge sample contains a high level of Cd, Cr, Cu and Pb. The sequential extraction method according to the guidelines of BCR (Community Bureau of Reference) was applied for metal fractionation, as well as the analysis of chemical forms, of interested heavy metals in artificially contaminated sludge sample. The results showed that Cd, Cr, Cu and Pb were distributed in four fractions (exchangeable, reducible, oxidizable and residual) with various concentrations. Investigation of the effect of operating variables on EDTA extraction, including contact time, concentration of EDTA and pH of extractant, was the major focus of this work. The contact time study was performed within 1-48 hours. The rapid desorption of metals occurred within 4-16 hours and then the gradual release occurred in the following hours. The removal efficiency of metals increased progressively with increasing EDTA concentration, when the dose of EDTA was less than the sludge requirement. Only small increases of removal efficiency was observed when the EDTA concentrations were above 0.05 M, 0.15 M, 0.20 M and 0.15 M for Cd, Cr, Cu and Pb, respectively. For most values of contact time study and EDTA concentration study, the percentage of metal removal followed the order Cd > Pb > Cu > Cr. For the study on the pH of extractant, the removal efficiency of target metals decreased with increasing pH in the range of 3-12 (except Cd).

Introduction

The increasing of wastewater sewage sludges due to increase in population density and the number of industry, is considered as a serious problem when sludges are discharged on the environment. Disposal of sludge by incineration and landfill has been performed in many countries for many years. However, incineration is less economical method because it always needs supplementary fuel. Until a few years ago, the recycling of sludge for land application by means of agricultural application is a useful alternative to incineration because there are lots of the valuable nutrients and organic matter, which can improve the physical, chemical and biological properties of soil. Moreover land application is an inexpensive method [1-2]. However, sewage sludge not only consists of valuable components but also pollutants such as heavy metals, which are the major limitation to applications. The retained heavy metals in sewage sludge cause a variety of environmental problem from land application such as soil and groundwater contamination, which become toxic to plants, animals and humans [3]. Currently, there are several techniques for heavy metals removal from sludge, including thermal treatment, chemical extraction, cementation, electroreclamation and bioleaching treatment. Chemical extraction has received extensive attention because it is simple operation, short extraction time and high removal efficiency [4]. The chemical reagents commonly used to extract heavy metals fall generally within the following groups: acids, buffered salts, unbuffered salts and chelating agents [5,6]. Chelating agents have been widely used to remove heavy metals from various solid samples because they can form very stable water soluble complexes with a wide range of cations. Among a lot of chelator, ethylenediamine tetraacetic acid (EDTA) is the most commonly used as reagent. EDTA has been shown to be the most effective agent for heavy metals. Moreover, EDTA is regarded as less toxic and non carcinogen. The extraction efficiency depends on many factors, including sample properties (e.g., sample pH and sample composition), extraction process parameters (e.g., chelant dosage, solution pH and contact time) and contaminant-related parameters (e.g., metal type, metal concentration and chemical form) [7-9].

The objective of this research is the study on the possibility of EDTA as extractant for heavy metals from artificially contaminated sludge sample. The sludge sample contains a high level of Cd, Cr, Cu and Pb. In this experiment, the effect of operating variables including contact time, concentration of EDTA and pH of extractant were investigated.

Materials and Methods

Sludge sample

The artificially contaminated sludge sample was prepared by adding Cd, Cr, Cu and Pb into original sludge, collected from wastewater treatment plant. The solution containing metal nitrate was added to a portion of dried-raw sludge at a ratio of 100 mL/10 g in conical flask. The suspension samples were placed on a mechanical shaker operated at 150 rpm and at room temperature (27-31°C) for 48 h. At the end of 48 h, the suspension was separated solid from solution.

Table 1. Operating conditions required in modified BCR sequential extraction method

Fraction	Extraction agent	Shaking time[a]
F1. Exchangeable	20 mL CH_3COOH (0.11 M)	10 h
F2. Reducible	20 mL NH_2OH-HCl (0.5 M, pH = 1.5)	10 h
F3. Oxidizable	5 mL H_2O_2 (30%) heat to 85 °C for 1 h (twice) and then 20 mL CH_3COONH_4 (1 M, pH = 2)	10 h
F4. Residual	10 ml aqua regia (HCl/HNO_3, 3:1)	Microwave digestion

[a] Shaking was applied at 30 rpm.

The contaminated sludge was washed with double deionize water to remove the entrapped solution in the sludge. Before analysis, the particle size of air-dried sludge was reduced by grinding. Sample was then sieved using a U.S. no. 20 sieve (0.8 mm) for the generic characterization and EDTA extraction and below 63 µm for metal fractionation.

pH and conductivity of sludge were measured by detecting the homogenate of sludge and ddH_2O at the ratio of 1:10 (w/v) using pH meter and conductometer. Organic matter and inorganic matter were estimated by loss on ignition at 450 °C for 3 h in muffle [2]. The total heavy metals content and major element content were determined by X-ray fluorescence spectrometry (XRF).

The BCR sequential extraction procedure modified by Arain et al. [10] was selected to study chemical form of interested heavy metals (Cd, Cr, Cu and Pb) in the artificially contaminated sludge sample into fractions namely exchangeable, reducible, oxidizable and residual. The extraction procedure carried out in this study is presented in Table 1 for approximately, 0.5 g sludge sample. Flame atomic absorption spectrometer (FAAS) was used for quantification of heavy metal levels in different fractions.

Extraction procedure

The extraction tests were conducted using EDTA solution at various contact times, concentrations and solution pH. The extraction solution was prepared from analytical-grade disodium ethylenediaminetetra acetate (Na_2EDTA). The polyethylene flask containing 0.5 g sample and a measured volume of EDTA was placed on a mechanical shaker operated at 150 rpm and at room temperature (25–31 °C) for a given time. The suspensions were separated the solid phase from solution by centrifuged at 4500 rpm for 10 min (twice). The concentrations of heavy metals in the supernatants were determined by AAS.

The contact time study was performed with 0.05 M Na_2EDTA (L/S = 10, pH 7) in 1, 2, 4, 6, 8, 10, 12, 16, 20, 24, 30, 36, 42 and 48 h time periods. Seven different concentrations: 0.01, 0.05, 0.10, 0.15, 0.2, 0.25, 0.30 M of Na_2EDTA (L/S = 10, 16 h) were chosen for the concentration study. In the pH start experiment, the extractions were conducted using 0.15 M Na_2EDTA solution (L/S = 20, 16 h) at different pH values (3-12) adjusted with HCl or NaOH solution. All extraction experiments were performed in triplicates and the results are presented as averages of the triplicate extracts.

Results and Discussion

Sludge characterization

The artificially contaminated sludge sample was weak acidic with a pH of 5.66 ± 0.02 and moderate electrical conductivity (645 ± 18 µS/cm). The results reveal a high organic matter content (60.50 ± 0.11%) and high level of macronutrients such as Ca, K and Mg. Table 2 shows the mean values of total and fraction concentrations of metals in sludge sample. The sum of four fractions of interested heavy metals is similar to the total contents determined by XRF.The recovery in the sequential extraction procedure was calculated as follows:

$$\% \text{ Recovery} = \frac{(\sum \text{Metal in the individual fractions}) \times 100}{\text{Total metal content}}$$

The recoveries of metals were in the range of 76 - 83%. Moreover, the results shown Cd, Cr, Cu and Pb were distributed in four fractions with different concentrations. Figure 1 shows the percentages, in relation to the sum concentration, of each of metal fractions obtained after sequential extraction.

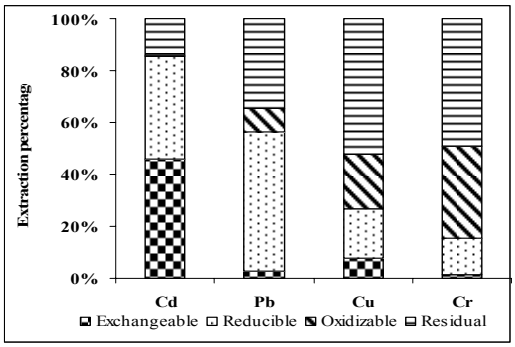

Figure 1. Distribution of fractions for each metal in sludge

Cu and Cr were principally between the two less mobile fractions, oxidizable and residual. The large quantities were extracted from residual fraction, 43% of Cu and 42% of Cr. About 17% of Cu and 30% of Cr were recovered in oxidizable fraction. On the

Table 2. The values of total and fraction concentrations (mg kg^{-1}, dry weight) of metals in sludge sample (mean ± SD, n = 3)

Metals	Cd	Cu	Cr	Pb	Total element content (g/kg)[b]	
Exchangeable	1058.2 ± 67.4	427.9 ± 6.7	51.0 ± 2.5	64.2 ± 3.3	Mg	46.89
Reducible	919.7 ± 60.1	1040.9 ± 70.2	596.3 ± 16.3	1355.9 ± 49.8	Mn	1.65
Oxidizable	9.48 ± 1.3	1145.7 ± 88.9	1477.3 ± 56.5	221.2 ± 29.9	Fe	47.64
Residual	289.6 ± 21.5	2459.3 ± 197.6	1892.3 ± 186.8	722.7 ± 40.6	Zn	8.50
Total metal [b]	2730	6640	4970	2880	Ca	10.05
Recovery (%)	83	76	81	81	Al	59.13

[b] Total element content was determined by XRF method.

contrary, Cd presented the greatest degree of mobility as seen from the high percentage of metal extracted in the exchangeable (39%) and reducible (34%) fraction. For Pb, the quantities in easily mobile fraction were similarly to two less mobile fractions.

Exchangeable metals are the most available for plant uptake and leading to possible contamination of groundewater and soil because they associated with weakly bond and can be dissolved in water and acid. Also reducible metals, they are unstable under reducing conditions and can transfer to available from for plant. Finally, metals in oxizable and redual fractions are not expected to be released under normal condition [6].

Effect of operating variables

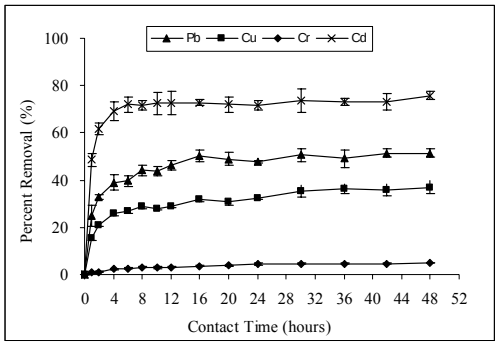

Figure 2. Removal efficiency of different contact times (0.05 M Na_2EDTA, liquid/solid = 10, pH 7)

Desorption of metals from solid particle is a kinetic equilibrium process, thus contract time plays a very important role in metal removal from sludge. The contact time study was performed at 0.05 M Na_2EDTA within 1-48 hours for four types of metals: Cd, Cu, Cr and Pb. Rapid desorption occurred in first time period and then the gradual release occurred in the following hours. As shown in Figure 2, the release of heavy metals was rapid such that reached an equilibrium within 4-16 h. The extraction efficiencies obtained at 16 h were 31.7% of Cu, 3.6% of Cr, 72.7% of Cd and 50.2% of Pb. With more contract time, the removal approached a plateau after 4–16 h and remained almost constant. A further increase of the contact time had little effect on the total removal. Therefore, an extraction time of 16 h was chosen for the remainder of this study.

EDTA is combined with metal ions in 1:1 molar ratio complexes. However, this ratio should not calculate from the concentration of EDTA and the concentration of target metals. Because EDTA is a non specific chelating agent thus the other cations in the sludge such as Fe, Mg and Zn, that originally present in the sludge, may complete with target metals for combination with EDTA [9,11]. Therefore, the molar concentration of EDTA must higher than the concentration of all metals presented in the sample. In our experiment, the effect of EDTA concentration on extraction of four metals was investigated and the results are shown in Figure 3. The removal efficiency increased progressively with increasing concentration of EDTA, when the dose of EDTA was less than the sludge requirement. The little effect of EDTA concentration on the removal efficiency was observed when the EDTA dose was above the sludge requirement. The removals of Cd and Cu were constant level at around 66% and 36% when the concentrations were above 0.05 M and 0.20 M, respectively. For Cr and Pb, the removal increased slightly when the concentration was above 0.15 M (from 14.4% to 20.4% and 51.9% to 54.3% for Cr and Pb, respectively).

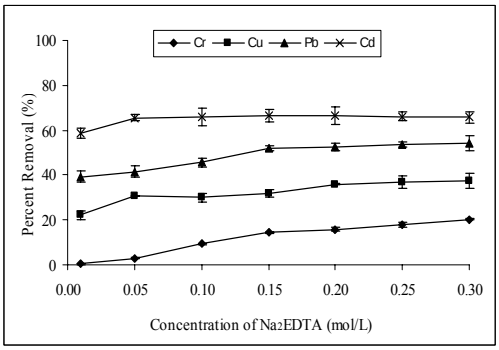

Figure 3. Removal efficiency of different concentrations of Na_2EDTA (liquid/solid = 10, pH 7, 16 h)

The pH of extractive solution is important operating variables to estimate the efficiency of metal removal. Because it can affect the retention of metals in solid by adsorption and influence the capability of chelating agent to extract the heavy metal from solid sample through different mechanisms, including the conditional

stability constants of metal–EDTA complexes (aqueous metal species concentration), the solubility of chelating agents, ion exchange phenomena and trace metal sorption/desorption [7,9]. In general, a lower pH of extractive solution gives higher metal removal efficiency because of protons (H^+) can promote the dissolution of metal- hydrous oxide in sludge. On the contrary, as the solution pH becomes more alkaline, the ability of EDTA to enhance the solubility of metal (especially metal-oxide) decreases because hydrolysis is favoured more than complexation by EDTA [7,9,12]. Thus, above mentioned can explain why removal efficiency in the low solution pH is higher than removal efficiency in high solution pH.

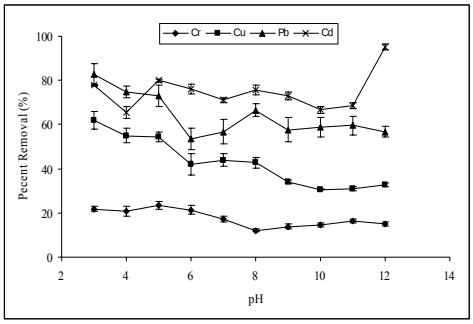

Figure 4. Influence of pH on extraction of metals using 0.15 M Na_2EDTA (liquid/solid = 20, 16 h)

In this research, the effect of solution pH on extraction of heavy metals was investigated. The extraction experiments were performed at different pH values in the range of 3-12 and the results are reported in Figure 4. The removal efficiency of almost metals decreased with increasing pH in the range of 3-12, especially Cu. High removal efficiency of Cu, Cr and Pb were obtain in pH range 3-5 (about 24% Cr, 62% Cu and 82% Pb). The highest removal efficiency of Cd was obtained at pH 12 (about 95%). This is probably due to the solubility of Cd in high pH solution by negative charge ($Cd(OH)_3^-$ and $Cd(OH)_4^{2-}$) [12], while other metal-hydroxides were precipitated in high pH solution.

Conclusion

In this work, the effect of operating variables including contact time, concentration of EDTA and pH of extractant were investigated. The artificially contaminated sludge was prepared to use as sample. The results from BCR sequential extraction method showed that Cd, Cr, Cu and Pb were distributed in four fractions with various concentrations. The contact time study was performed within 1-48 hours for four types of metals, Cd, Cu, Cr and Pb**.** The rapid desorption of metals occurred within 4-16 hours and then the removal efficiency slightly increased. The removal efficiency increased progressively with increasing concentration of EDTA, when the dose of EDTA was less than the sludge requirement. Only small increase was observed when the dose was higher than the sludge requirement. The removal efficiency of Cu, Cr and Pb decreased with increasing pH in the range of 3-12. High removal efficiency was obtained in pH range 3-5. For Cd, the highest efficiency was obtained at pH 12. The percentage of metal removal followed the order Cd > Pb > Cu > Cr respectively, that similarly to the order of two easily mobile fractions. From our study, EDTA was used as an extraction reagent for heavy metal removal from sludge containing high level of Cd, Cu, Cr and Pb.

References

[1] A. Fuentes, M. Llorens, J. Saez, A. Soler, M.I. Aguilar, J.F. Ortuno and V.F. Meseguer, *Chemosphere*, **54** (2004), pp. 1039-1047.

[2] P.F. Wang, S.H. Zhang, C. Wang, J. Hou, P.C. Guo and Z. Lin, *Afr. J. Biotechnol.*, **7** (2008), pp. 1329-1334.

[3] J. Peng, Y. Song, P. Yuan, X. Cui and G. Qiu, *J. Hazard. Matet.,* **161** (2009), pp. 633–640.

[4] J. Deng, X. Feng and X. Qiu**,** *Chemical Engineering J.* **152** (2009), pp. 177–182**.**

[5] G. Rauret, *Talanta*, **46** (1998), pp. 449-455.

[6] J.R. Dean*, Methods of Environmental Trace Analysis*, John Wiley & Sons, USA (2003), pp. 76-88.

[7] A. Polettini, R. Pomi and E. Rolle, *Chemosphere*, **66** (2007), pp. 866–877.

[8] B. Sun, F.J. Zhao, E. Lombi and S.P. McGrath, *Environ. Pollut*., **113** (2001), pp. 111-120.

[9] Z. Zou, R. Qiu, W. Zhang, H. Dong, Z. Zhao, T. Zhang, X. Wei and X. Cai, *Environ. Pollut*., **157** (2009), pp. 229-236.

[10] M.B. Arain, T.G. Kazi, M.K. Jamali, H.I. Afridi, N. Jalbani, R.A. Sarfraz, J.A. Baig, G.A. Kandhro and M.A. Memon, *J. Hazard. Matet.,* **160** (2008), pp. 235–239.

[11] D.A. Skoog, D.M. West, F.J. Holler and S.R. Crouch, *Fundamental of Analytical Chemistry*, 8Ed, Brooks Cole, USA (2004), pp. 458-461.

[12] L.D. Palma and P. Ferrantelli, *J. Hazard. Matet.,* **B122** (2005),pp.85–90.

Oxidative and antimicrobial properties of bamboo vinegar extracts

P. Wannaprapha, M. Sriuttha, S. Chanthai, C. Ruangviriyachai*

Department of Chemistry, Faculty of Science, Khon Kaen University, Muang, Khon Kaen, 40002, Thailand

*E-mail: chal_ru@kku.ac.th

Abstract: The oxidative and antimicrobial properties of commercial bamboo vinegar from the Kiengmool Wood Energy Society in Ubonratchathani (Thailand) was studied. For sample preparation, the vinegar was loaded into a Strata-X solid phase extraction sorbent and eluted with various organic solvents including hexane (F1), dichloromethane (F2), iso-butanol (F3), ethyl acetate (F4) and methanol (F5). After removal solvent from each fraction using a rotary evaporator, the residues were dissolved in methanol and then evaluated their properties. The Ferric-ion-based total antioxidant capacity method of 1,10-phenanthroline (Phen) was used for determination of antioxidant capacities of each extracts in bamboo vinegar. The relative order of antioxidant capacities for these fractions was F4 > F5 > F2 > F3 > F1 respectively. Moreover, the antimicrobial activities of extracted bamboo vinegar against the growth of some food poisoning bacteria including *Xanthomonas axonopodis, Xanthomonas campestris* and *Xanthomonas malvacearum* were tested by disc diffusion method. It was found that the extracts from bamboo vinegar showed good activity against *Xanthomonas axonopodis*, *Xanthomona campestris* and *Xanthomonas malvacearum.* The results of this study indicated that the extracted bamboo vinegar would be applied in food and agricultural fields. In addition, this can support and increase the value-added OTOP products.

Introduction

There is an increasing interest in the role of free radical-mediated damage in the etiology of human diseases. Free radicals formed during oxidation process occurring in various products and biological systems are known to be responsible for oxidative deterioration, health damage and accelerated aging [1-2]. Consequently, phenolic compounds, which are secondary metabolites in plant material are known to be responsible for antioxidant effect. Recent epidemiological studies have strongly suggested that consumption of certain plant materials may reduce the risk of chronic diseases related to oxidative stress on account of their antioxidant activity and promote general health benefits [3-4].

Antioxidants are compounds that can delay or inhibit the oxidation of lipids or other molecules by inhibiting the initiation or propagation of oxidizing chain reactions [5-6]. The antioxidant activity of phenolic compounds is mainly due to their redox properties, which can play an important role in adsorbing and neutralizing free radicals, quenching singlet and triplet oxygen, or decomposing peroxides. In addition, antioxidant protection in biological systems has been a growing topic in biomedical sciences [7]. The number of research articles containing the word antioxidant in their titles has increased by more than 340% in the past 10–12 years [8]. This partially is due to the increase in data supporting oxidative damage as a contributing factor in diseases like cancer and cardiac disorders as well as in the process of aging [9-10]. In general, there are two basic categories of antioxidants, natural and synthetic. Interest has increased considerably in finding naturally occurring antioxidants for use in foods or medicinal materials to replace synthetic antioxidants, which are being restricted due to their carcinogenicity [11].

Many natural additive, preservatives have been widely used in food such as spices, herb and essential plant oils. Some preservatives act as antimicrobial agents, some acts as antioxidants and some can perform both functions [12]. Wood vinegar or pyroligneous acid is the name of the crude condensate produced from the distillation of smoke generated in the process of making charcoal. Pyroligneous acid was first developed in Japan when scientists and researchers discovered that wood vinegar from some trees has powerful detoxifying abilities [13]. In Thailand, wood vinegar has been used for ages as sterilizing agents, deodorizers, fertilizers, antimicrobial and growth promoting agents. In addition, the production and consumption of wood vinegar have been increasing recently. To the best of our knowledge, however, little information is available about the antioxidant properties of commercial bamboo vinegar. This has led researcher and food processors to look for natural food additive with a broad spectrum of antioxidant properties including antimicrobial activity [14].

The aim of the present study was to evaluate the total phenolics content, antioxidant capacity and antimicrobial activity of commercial bamboo vinegar. The antioxidant activity was determined using by Folin Ciocalteau assay and Phenanthroline method. The antimicrobial activity was examined using disc diffusion method

Materials and Methods

Chemicals: Gallic acid was obtained from Sigma (Sigma-Aldrich, USA). Ferric chloride ($FeCl_3.6H_2O$), Ferrous sulfate ($FeSO_4.7H_2O$) and Folin Ciocalteu's reagent were purchased from Carlo Erba, Italy. Sodium carbonate (Na_2CO_3) was obtained from BDH, England. Methanol was AR grade, Lab Scan, Thailand. 1,10-phenanthroline (99%) was obtained from Fluka, Switzerland. All another chemicals and

reagents used were analytical grade and the water used was deionized.

Materials and sample preparation

Materials: The clear reddish brown color of commercial bamboo vinegar was purchased from the Kiengmool Wood Energy Society in Ubonratchathani, Thailand.

Sample preparation of bamboo vinegar extracts: A sample of bamboo vinegar was filtered through Whatman No. 1 filter paper. The 5 mL of obtained filtrate was loaded into a Strata-X solid phase extraction sorbent (200 mg) and then eluted with 60 mL (20 mL x 3) of various organic solvents including hexane (F1), dichloromethane (F2), iso-butanol (F3), ethyl acetate (F4) and methanol (F5). Organic solvents from each fraction were removed by using a Buchi Model R-114 rotary evaporator at 40 ^{o}C. The residues were dissolved in methanol and then evaluated their properties.

Determination of total phenolic contents

The total phenolic contents in the sample were estimated by a colorimetric assay based on the procedure described by Ademiluyi and Oboh [15] with a modified technique. Gallic acid was used as standard [16]. Briefly, 0.2 mL of the standard or extracted sample solution was added to a 5 ml volumetric flask, then filled with 1 mL of 10 % Folin–Ciocalteu's reagent. After that, 0.8 mL of 7 % Na_2CO_3 solution was added, and the deionized water was adjusted to final volume of 5 ml. The mixture was stored in the dark at room temperature for 30 minutes. The absorbance was measured at 765 nm using a Jenway Model 6400 Spectrophotometer (England). Total phenol contents were examined in triplicate, and expressed as mg of gallic acid equivalents per g of sample extracts.

Antioxidant capacity determination

Phenanthroline method: The Ferric-ion-based total antioxidant capacity method of 1,10-phenanthroline (Phen) was used for determination of antioxidant capacities of each extracts in bamboo vinegar. The antioxidant capacities were determined by coloration of a methanolic solution of 1,10-phenanthroline (Phen) proposed by Szydlowska-Czerniak *et al.* [17] with little modification. Briefly, 0.5 mL of extracted solutions of bamboo vinegar sample, 1 mL of 0.2% $FeCl_3$ solution in methanol and 0.5 mL of 0.5% 1,10-phenanthroline solution in methanol were placed into a 5 mL volumetric flask and made up to volume with methanol. The obtained solution was mixed and left at room temperature in a dark. After 20 min, the absorbance of an orange-red solution was measured at 510 nm against a reagent blank (1 mL of $FeCl_3$ (0.2%) and 0.5 mL of Phen (0.5%) made up to 5 mL with methanol). Calibration curves were prepared using working solutions of $FeSO_4.7H_2O$ between 25 –150 ppm for Phen method.

1,10 phenantroline method (Phen) was used to determination of antioxidant capacities of bamboo vinegar extracts. The chemical reaction of the Phen method should be presented by following equation :

$$\text{Fe(III)–L} + \text{antioxidant} \rightarrow \text{Fe(II)–L} + \text{oxidized antioxidant}$$

where L is the ferrous-selective chromogenic ligand (1,10-phenanthroline).

Antimicrobial activity

Microbial strains: Some food poisoning bacteria including *Xanthomonas axonopodis, Xanthomonas campestris* and *Xanthomonas malvacearum* were obtained from the collection of the Department of Microbiology, Faculty of Science, Khon Kaen University, Khon Kaen, Thailand.

Antimicrobial screening: Antibacterial activity of sample extracts were tested by the paper disc diffusion method according to the slightly modified by Ćavar, *et al.* [18]. The bamboo vinegar extract from each solvent fraction in the concentration of 2000 ppm was individually tested against the growth of some food poisoning bacteria including *Xanthomonas axonopodis, Xanthomonas campestris* and *Xanthomonas malvacearum* by using methanol as the contlol. Briefly, a suspension of the test microorganisms were spread over the surface of Mueller Hinton agar (MHA) in Petri dishes with a diameter of 9 cm. Filter paper disks (6 mm diameter) were placed on the surface of the MHA, then loaded each sample (15 µl) using auto-micropipette. Test plates were incubated at ambient temperature for 24 h. The diameters of the inhibition zones were measured in millimeters. The developing inhibition zones were compared with the control disc.

Results and Discussion

Determination of total phenolic contents

Various types of organic solvents were used to extract phenolic compounds from bamboo vinegar (Figure 1). The highest phenolic levels were observed in ethyl acetate fraction (F4), due to a behavior explained by specific introductions between ethyl acetate and solute phase. The results were expressed as milligram of gallic acid equivalents (mg GAE) per gram of sample extract. The total phenols content in F1 to F5 were 323.18, 519.80, 445.55, 587.83 and 538.69 mg GAE/g sample extract, respectively. The total phenolic of each fraction exhibited the descending order of F4 > F5 > F2 > F3 > F1. To extract phenolic compounds from vegetable oils, black currant leaves and wood vinegar of *Rhizophora apiculata*, the most efficient solvents are methanol and dichloromethane [17, 13, 19]. The results suggest that

the bamboo vinegar is a rich source of polyphenolic compounds.

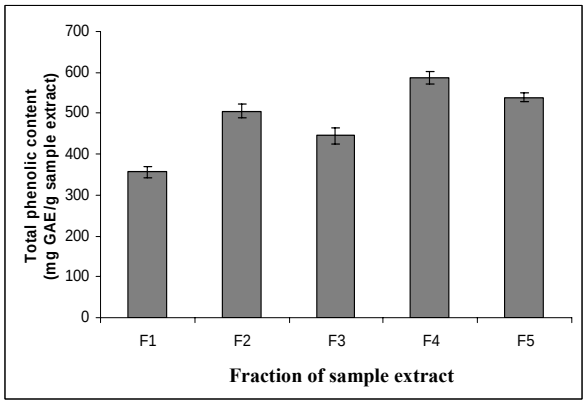

Figure 1. Comparison of total phenolic contents of extracted bamboo vinegar; hexane extract (F1), dichloromethane extract (F2), iso-butanol extract (F3), ethyl acetate extract (F4) and methanol extract (F5).

Antioxidant capacity

The obtained results were listed in Figure 2. The ability of F1, F2, F3, F4 and F5 to reduce Fe^{3+} to Fe^{2+} were 841.23, 1114.91, 923.68, 1279.83, 1251.75 mg Fe/g sample extract, respectively. The antioxidant capacity of bamboo vinegar extracts by five solvents decrease in the following order: F4 > F5 > F2 > F3 > F1. Ethyl acetate was the highest efficient solvent for extraction of antioxidants from bamboo vinegar. These results suggest that the antioxidant activity in bamboo vinegar was due to the presence of phenolic components. The same relationship was also observed between phenolic contents and antioxidant activity in sample extracts [20-22].

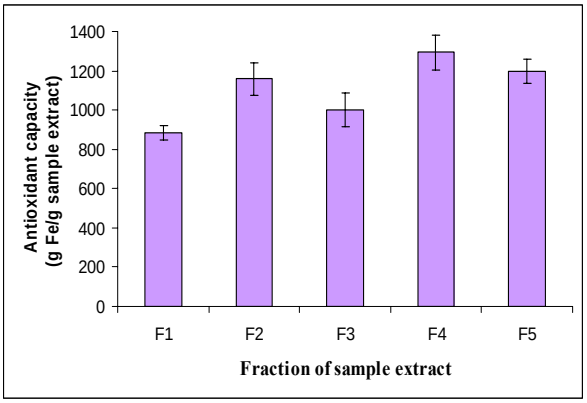

Figure 2. Comparison of antioxidant capacity of extracted bamboo vinegar; hexane extract (F1), dichloromethane extract (F2), iso-butanol extract (F3), ethyl acetate extract (F4) and methanol extract (F5).

Antimicrobial activity

The antimicrobial activities of extracted bamboo vinegar against the growth of some food poisoning bacteria including *Xanthomonas axonopodis, Xanthomonas campestris* and *Xanthomonas malvacearum* were tested by disc diffusion method. The inhibition zones were shown in the Table 1. The extracted fraction of ethyl acetate (F4) had greater potential as an antimicrobial agent against all these strains of food poisoning bacteria. However, the extracted fraction of dichloromethane (F2) can not inhibit the growth all of these strains, it may be due to the chemical components that role play to antimicrobial property no dissolve well in dichloromethane. The result indicated that the ethyl acetate extracted was good fraction for antioxidant and antimicrobial properties. Several researches suggest that the antimicrobial activity of wood vinegar is attributed to the presence of compound like phenols, carbonyl, and organic acid [23-25].

Table 1: Antimicrobial activity of bamboo vinegar extracts.

Bacteria	Diameter of inhibition zones in mm[a]				
	F1	F2	F3	F4	F5
Xanthomonas axonopodis	- [b]	-	8.2 ± 1.0	10.3 ± 0.6	8.7 ± 0.3
Xanthomonas campestris	10.1 ± 2.4	-	9.4 ± 1.3	11.5 ± 1.1	20.2 ± 1.6
Xanthomonas malvacearu	-	-	9.7 ± 1.2	13.2± 0.9	-

The tests were done in duplicate. [a] Each value is expressed as mean ± SD ,[b] (-) no inhibition zone

Conclusions

The antioxidative and antimicrobial properties of the bamboo vinegar extracts were evaluated. The extract fraction from ethyl acetate (F4) evidently showed the highest total phenolic contents and antioxidant capacity when compared to different organic solvents. The F4 extract was also a potent antioxidant since it has high phenolic content. In addition, the extracted bamboo vinegar exhibited good activity against the growth of some food poisoning bacteria including *Xanthomonas axonopodis, Xanthomonas campestris* and *Xanthomonas malvacearum*. The present study provides additional data to support using bamboo vinegar as natural antimicrobial and antioxidant agents in smoke curing of food including ham, sausages and fish. Moreover, this work showed that bamboo vinegar was possible

used to be sources of natural antioxidant for pharmaceutical and food applications.

Acknowledgements

We also thank to Khon Kaen University, Faculty of Science, Department of Chemistry and Nong Khai Campus. Financial support from the Centre for Innovation in Chemistry (PERCH-CIC), Commission on Higher Education, Ministry of Education and Project for the Promotion of Science and Mathematics Talented Teachers (PMST) are gratefully acknowledged.

References

[1] Z. Zhang, L. Liao, J. Moore, T. Wu and Z. Wang, *Food Chem.* **113** (2009), pp. 160-165.
[2] O. I. Aruoma, *J. Am. Oil Chem. Soc*. **75** (1998), pp. 199–212.
[3] M. Kosar, B. Bozan, F. Temelli and K. H. C. Baser, *Food Chem*. **103** (2007), pp. 952-959.
[4] B. Halliwell, *Nutr. Rev.* 55 (1997), 544-552.
[5] W. Zheng and S. Y. Wang, *J. Agric. Food Chem.* **49** (2001), pp. 5165-5170.
[6] Y. S. Velioglu, G. Mazza, L. Gao and B. D. Oomah, *J. Agric. Food Chem.* **46** (1998), pp. 4113-4117.
[7] S. M. Phipps, M. H. M. Sharaf and V. Butterweck, *Pharmacopeial Forum.* **33** (2007), pp. 810-814.
[8] R. L. Prior and G. Gao, *J. AOAC Int*. **83** (2000), pp. 950-955.
[9] M. Valko, C. J. Rhodes, J. Moncol, M. Izakovic and M. Mazur, *Chem. Biol. Interact*. **160** (2006), pp. 1–40.
[10] C. Ceconi, A. Boraso, A. Cargnoni and R. Ferrari, *Arch. Biochem. Biophys.* **420** (2003), pp. 217-221.
[11] N. Ito, S. Fukushima, A. Hasegawa, M. Shibata and T. Ogiso, *J. Natl. Cancer Inst*. **70** (1983), pp. 343-347.
[12] E. I. Korotkova, O. A. Avramchik, T. M. Angelov and Y. A. Karbainov, *Electrochim. Acta*. **51** (2005), pp. 324-332.
[13] A.Y. Loo, K. Jain and I. Darah, *Food Chem.* **104** (2007), pp. 300–307.
[14] R. A. Holley and D. Patel, *Food Microbiol*. **22** (2005), pp. 273-292
[15] A. O. Ademiluyi and G. Oboh, *Afr. J. Biotechnol.* **7** (2008), pp. 3138-3142.
[16] O. K. Chun and D. O. Kim, *Food Res. Int.* **37** (2004), pp. 337-342.
[17] A. Szydłowska-Czerniak**,** C. Dianoczki, K. Recseg, G. Karlovits, E. Szłyk, *Talanta*. **76** (2008), pp. 899-905.
[18] S. Ćavar, M. Maksimovic´, M. E. Šolic´, A. Jerkovic´-Mujkic´ and R. Bešta, *Food chem.* **111** (2008), pp. 648-653.
[19] J. Tabart, C. Kevers, A. Sipel, J. Pincemail, J. O. Defraigne and J. Dommes, *Food Chem*. **105** (2007), pp. 128-1275.
[20] A. C. Akinmoladun, E. O. Ibukun, E. Afor, B. L. Akinrinlola, T. R. Onibon, A. O. Akinboboye, E. M. Obuotor and E. O. Farombi, *Afr. J. Biotechnol.* **6** (2007), pp. 1197-1201.
[21] X. Gao, M. Ohlander, N. Jeppsson, L. Bjork and V. Trajkovski, *Food Chem.* **48** (2000), pp. 1485–1490.
[22] P. D. Duh, Y. Y. Tu and G. C. Yen, *Lebnesm. Wiss. Techno*. **32** (1999), pp. 269-277.
[23] E. Sunen, C. Aristimuno and B. Fernandez-Galian, *Food Res. Int.* **36** (2003), pp. 111–116.
[24] N. G. Faith, A. E. Yousef and J. B. Luchansky, *J. Food Safety.* **12** (1992), pp. 303-304.
[25] M. Vitt, B. H. Himelbloom and C. A. Crapo, *J. Food Safety*. **2** (2001), pp. 111-125.

Improvement of a process for the purification of glycerine residue from transesterification of *Jatropha curcas* oil

S. Supakarn, W. Tongpoothorn, S. Chanthai and C. Ruangviriyachai*

Department of Chemistry, Faculty of Science, Khon Kaen University, Khon Kaen 40002, Thailand.

*E-mail: chal_ru@kku.ac.th

Abstract: Glycerine residue derived from biodiesel production possesses very low value because of its contaminants. Therefore, further purification of glycerine residue is necessary. The aim of this research is to investigate the improved method for purification glycerine in order to reduce steps and lost glycerine in conventional method. Glycerine residue was obtained from transesterification of *Jatropha curcas* seed oil by using NaOH as a catalyst. The purification process was carried out by both conventional and improved method. The purity was expressed as percentage of glycerol content. The determination of glycerine compositions was performed by the International Organization for Standardization Method and present in the term of glycerol content, ash content, moisture content and matter organic non-glycerol (MONG). The improved method, based on cation exchange chromatography, was carried out by batch experiment with optimized conditions as follow: 1:3(w/w) of ratio of exchanger to glycerol, 3 hours of contact time and 150 rpm of agitation rate, respectively. The analyses showed that the average composition of the purified glycerol obtained from conventional method was: 70.35% glycerol, 12.92 % ash, 10.76% water and 5.97% MONG. By improved method, the purified glycerol comprised 74.25% glycerol, 10.95% ash, 9.69% water and 5.11% MONG.

Introduction

The commonly used method for produce biodiesel from *Jatropha curcas* oil is the transesterification. The results of this reaction are methyl or ethyl esters and glycerine as a by-product. The glycerine residue was obtained approximately 45 % wt of this oil. However, glycerine residue derived from biodiesel production possesses very low value because of the impurities including water, monoglycerides, diglycerides, salt, soap, catalyst residues and some residues of esters. Further purification of the glycerine residue depended on the economy of production scale and the availability of a glycerine purification facility. [1-2]. Previous studied have been reported that the glycerol purification based on many steps of physical and chemical treatment followed by distillation [3]. Nevertheless, the primary disadvantage of these processes is capital and energy intensive. In addition, purification of glycerol by this method makes many steps. From this point of view, therefore, the main objective of this work was to improve a process for purify glycerol obtained from transesterification of *Jatropha curcas* oil to reduce time and lost of glycerol during purification step.

Materials and Methods

Glycerine residue was obtained from transesterification of *Jatropha curcas* oil. All the reagents (hexane and sulfuric acid, 95-97%) and chemicals (sodium hydroxide and sodium periodate) used were analytical grade. Amberlite IR-120 (hydrogen form), strongly acidic cation exchange resin, was used in this study.

The purified glycerol was characterized by it contents of glycerol, ash, MONG and water. Moreover, density, pH and FT-IR spectrum of purified glycerine were also determined. The analyses were carried out in duplicate by the International Organization for Standardization Methods as below:

(a) Glycerol content: UV-Vis Spectrophotometer-Colorimetric method.
(b) Ash content: Standard method ISO 2098-1972.
(c) MONG: Standard method ISO 2464-1973.
(d) Water content: Standard method ISO 2098-1972.
(e) pH. A solution of 20.0 g purified glycerol in 100.0 ml distilled water was measured with a pH meter (Thermo Orion, model 420 APLUS, USA).
(f) Infrared spectroscopic analysis: FT-IR Spectrophotometer, Spectrum one, Perkin Elmer, Germany with KBr pellet.

Purification of glycerine residue by conventional method

The conventional purification [4] of glycerine residue was carried out by acidified, using 6% sulfuric acid to split the soap and neutralize the residual NaOH. The charred substances obtained were filtered off. The sample was then decanted to recover the crude fatty acids, and the aqueous glycerine solution was neutralized using 50% sodium hydroxide. Subsequently, it was evaporated to concentrate the glycerine solution. The salt crystallization was removed by decantation. To purify and concentrate the solution in the next procedure, it was extracted and filtered to remove the residual salt. Finally, the solution was evaporated to obtain the purified glycerine. The conventional method for purification of glycerine residue was shown in Scheme 1.

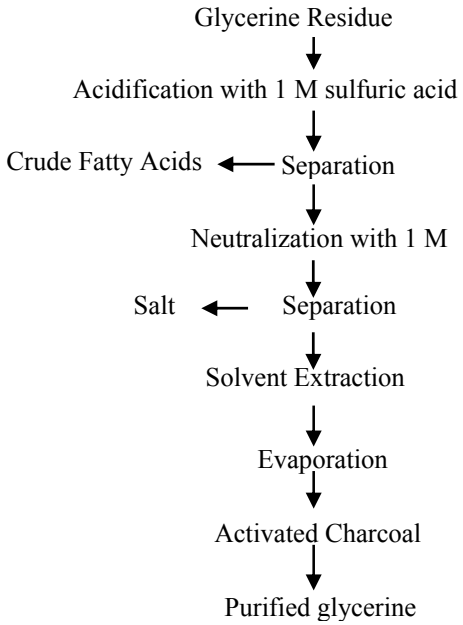

Scheme 1. Schematic diagram of conventional method for purification of glycerine residue.

Purification of glycerine residue by improved method

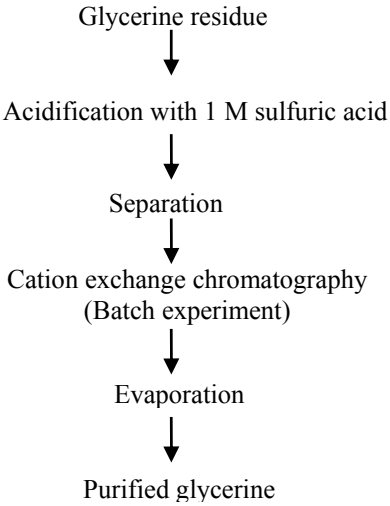

Scheme 2. Diagram of improved method for purification of glycerine residue.

Improved method was performed by following steps: acidification by adding 1 M sulfuric acid to split the soap and neutralize the residual NaOH. Subsequently, the glycerine solution was mixed with cation exchanger. By this method, the optimization condition was investigated. The varying parameters were ratio of cation exchanger to glycerine residue (1:1, 1:2, 1:3 and 1:4 w/w), contact time (3, 6, 12 and 24 hours) and agitation rate (50, 150 and 250 rpm). The eluates obtained from batch experiment were then evaporated to remove methanol. The final products were also called purified glycerine.

Results and Discussion

Chemical compositions of glycerine standard and glycerine residue are present in Table 1. It was found that the purity of glycerine residue obtained from transesterification of *Jatropha curcas* oil (50.05%) was relative low when compared with glycerine standard (99.50%).

Table 1. Chemical compositions of glycerine standard and glycerine residue

Sample	Glycerol (%)	Ash (%)	Water (%)	MONG (%)	Density (g/cm^3)	pH
Glycerine standard	99.50	0.001	0.44	0.025	1.25	6.86
Glycerine residue	50.05	23.71	9.98	16.26	0.81	10.11

Chemical compositions of purified glycerine from conventional method are shown in Table 2. The analyses showed that the average compositions of the purified glycerine obtained were: 70.35% glycerol, 12.92% ash, 10.76% water and 5.97% MONG. It was observed that the glycerol content of purified glycerine was increased. However, water content was slightly increased. It probably due to glycerol is hygroscopic, thus it absorbs moisture from its surrounding. On the other hand, ash content and MONG were decreased when compared with glycerine residue. Because salts, such as NaCl and Na_2SO_4, mainly constituted the ash, were removed by acidification and neutralization steps in conventional method. In addition, glycerine residue contained some organic matter including soap and methyl esters which removed by acidification step.

Table 2. Chemical compositions of purified glycerine obtained from conventional method

Samples	Glycerine (%)	Ash (%)	Water (%)	MONG%	Density (g/cm^3)	pH
1	70.01	12.89	10.56	6.54	1.37	6.92
2	70.75	12.92	10.84	5.49	1.02	6.21
3	70.29	12.95	10.89	5.87	1.27	6.60
Average	70.35	12.92	10.76	5.97	1.22	6.57

The results of optimization conditions for improved method are demonstrated in Figure 1, Figure 2 and Figure 3.

It was indicated that the optimized conditions for batch experiment were 1:3(w/w) of ratio of cation exchanger to glycerol, 3 hours of contact time and 150 rpm of agitation rate, respectively. The purified glycerol from optimized conditions of improved method comprised 74.25% glycerol, 10.95% ash, 9.69% water and 5.11% MONG as summarized in Table 3.

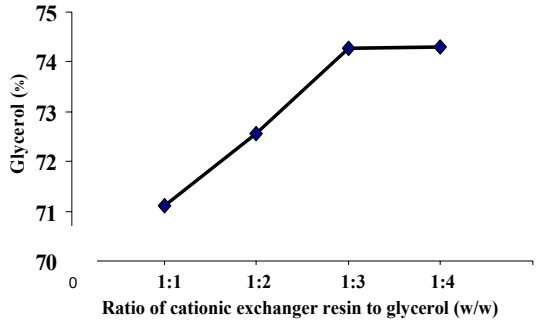

Figure 1. Effect of the ratio of cationic exchanger resin to glycerol on percentage of glycerol content

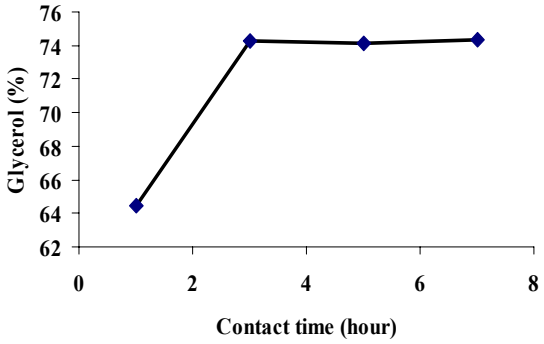

Figure 2. Effect of contact time on percentage of glycerol content

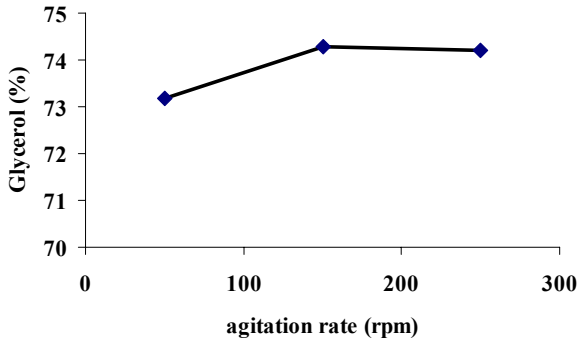

Figure 3. Effect of agitation rate on percentage of glycerol content

Table 3. Chemical compositions of purified glycerine obtained from optimized conditions for improved method

Samples	Glycerine (%)	Ash (%)	Water (%)	MONG (%)	Density (g/cm^3)	pH
1	74.35	10.85	9.85	5.05	1.19	6.97
2	74.13	10.83	9.62	5.18	1.26	6.71
3	74.27	11.17	9.59	5.10	1.24	6.85
Average	74.25	10.95	9.69	5.11	1.23	6.84

The results from Table 3 suggested that the improved method had effectively removed the impurities in glycerine residue. Because cation exchanger can be exchange positive charge ions from ionization of salts and other impurity, constituted the ash. Therefore, ash content was decreased resulting in the higher purity of glycerine was obtained by improved method. Moreover, MONG, which comprised mainly partial glycerides, free fatty acid, oxidation products and the polymerized compounds of glycerine, was reduced. Because some MONG was removed by acidification step as shown in scheme 2. Although, percentage of glycerol content of purified glycerol obtained from improved and conventional method was not significant. However, by conventional method, it was take too much time about 16 h for overall steps. On the other hand, it can be reduced steps, which implied the reduction of glycerol lost, by improved method.

FT-IR spectra of standard glycerine and purified glycerine obtained from conventional and improved method are shown in Figure 4. The presence of OH group in all samples was evidenced by fundamental mode of O-H stretching at 3400 cm^{-1}. It was found that C-H stretching at 2880 and 2940 cm^{-1}. The presence of some impurities was shown by the absorption peak at 1648 cm^{-1} (C=O group). The glycerol moiety of the standard glycerine is evidenced by the absorption peak at 1400 to 1460 cm^{-1}, assigned to overlapping of the C-H in-planed and O-H bending in the glycerol molecule. Furthermore, C-O stretching from 1040 to 1120 cm^{-1} and O-H bending at 920 cm^{-1} were observed in FT-IR spectra of standard glycerine [5-8]. FT-IR spectra of purified glycerine obtained from both conventional and improved method also showed almost similar absorption patterns but with a broader absorption band at 3387 cm^{-1}. This was probably due to the hydroxyl groups from water.

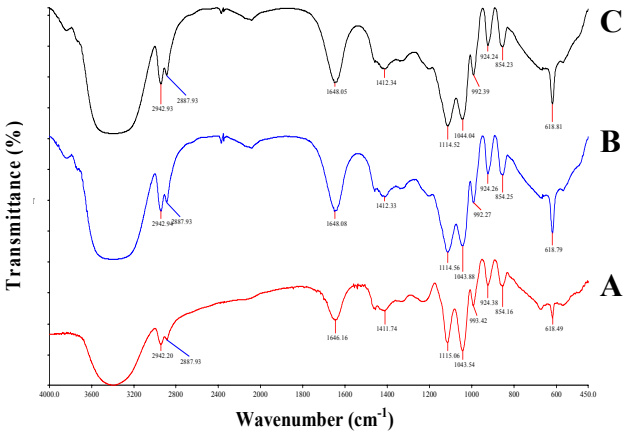

Figure 4. FT-IR spectra of standard glycerine (A), purified glycerine obtained from conventional (B) and improved method (C).

Conclusions

In this study improved method, based on ion exchange chromatography, was carried out by batch experiment with optimized conditions as follow: 1:3 of cationic exchanger resin to glycerol ratio, 3 h of contact time and 150 rpm of agitation rate, respectively. The analyses showed that the average composition of the purified glycerol obtained from improved method were 74.25% glycerol 10.95% ash, 9.69% water and 5.11% MONG. The purified glycerine from this method had higher glycerol content (74.25% vs. 50.05%) than glycerine residue. Moreover, FT-IR spectrum of the purified glycerine from this method also show almost similar absorption patterns with FT-IR spectra of standard glycerine. It was suggested that this method had effective removed the impurities. Although, percentage of glycerol content of purified glycerol obtained from improved and conventional method was not significant. However, by improved method, it can be reduced steps, which implied the reduction of glycerol lost.

Acknowledgements

The financial support from the Center of Excellence for Innovation in Chemistry: Postgraduate Education and Research Program in Chemistry (PERCH-CIC) are gratefully acknowledged.

References

[1] R. Brockmann, L. Jeromin, W, Johaannisbauer, H. Meyer, O. Michel and J. Plachenka. (1987). *Patent No.* **4.** pp. 655, 879.
[2] H. B. Hass and J. A. Patterson. *Ind. Eng. Chem. Res.* **33** (1941), pp. 615–616.
[3] J.E. Aiken. (2006). *Patent No.* **7**, pp. 126, 032.
[4] T.L. Ooi, K.C. Yong, K. Dzulkefly, W.M.Z. Wan yunus and A.M. Hazimah. *J. Oil Palm Res.* **13** (2001), pp.16-22.
[5] K.C. Yong, T.L. Ooi, K. Dzulkefly, W.M.Z. Wan yunus and A.M. Hazimah. *J. Oil Palm Res.* **13** (2001), pp 39-44.
[6] A.M. Hazimah, T.L. Ooi and A. Salmiah. *J. Oil Palm Res.* **15** (2003), pp 1-5.
[7] T.L. Oil, K.C. Yong, A.H. Hazimah, K. Dzulkefly and W.M.Z. Wan Yunus. *J. Oleo Sci.* **53** (2004), pp 29-33.
[8] K.C. Yong, T.L. Ooi, K. Dzulkefly, W.M.Z. Wan yunus and A.M. Hazimah. *J. Oil Palm Res.* **13** (2001), pp. 1-6.

The problematic of structural characterization of benzo(a)pyrene monoclonal antibody by FT-ICR-MS

P. Songsermsakul[1]* D. Knopp[2] B.Kanawati[3]

[1]Faculty of Pharmaceutical Sciences, Khon Kaen University, Khon Kaen, 40002 Thailand
[2]Chair for Analytical Chemistry, Institute of Hydrochemistry ,
Technische Universität München, Marchioninistr. 17, D-81377 Munich, Germany
[3]Institute of Ecological Chemistry, Helmholtz Center Munich,
German Research Center for Environmental Health,
Ingolstädter Landstr.1, D-85758 Neuherberg, Germany

* E-Mail: spiyad@kku.ac.th

Abstract: Contamination of benzo(a)pyrene, a pollutant and carcinogen, in food and water causes health problems. Besides chromatographic method such as GC and HPLC, bioanalysis by application of monoclonal antibody in ELISA is an alternative approach for benzo(a)pyrene detection. Structural characterization of monoclonal antibody can be performed by mass spectrometry. However this study shows the problematic of benzo(a)pyrene monoclonal antibody characterization by Fourier-transform ion cyclotron resonance mass spectrometry (FT-ICR-MS). Benzo(a)pyrene monoclonal antibody solution (100 ppm in water) was injected directly into the electrospray ionization source. The highest mass detected was approximately 40 kDa (m/z 710.1, 58+ charges). The mass measurement of benzo(a)pyrene monoclonal antibody by MALDI-TOF/TOF showed molecular weight around 148 kDa. Therefore the ion found in FT-ICR-MS did not correspond to the intact antibody. Digestion by papain was performed to minimize the size of molecule. Papain cleaves antibodies at the heavy chain hinge region into three fragments, one Fc and two identical antigen-binding fragments (Fab). After papain digestion, Fab was separated from the other fragments by immobilized protein A. The Fab solution in water was injected directly into the ionization source. The spectrum showed only peaks of 1+ charge ion. A matrix effect existed and affected the ionization of the intended protein fragments in the ESI. In conclusion an intact monoclonal antibody is a large molecule (approximately 150 kDa). Mass limit might be the problem of FT-ICR-MS. The next approach for this study should focus on an important part of the antibody molecule for example paratope peptide and Fab fragment. Extensive sample preparation is still needed even using the highly sophisticated instrument like FT-ICR-MS for structural characterization.

Introduction

Benzo(a)pyrene is a pollutant and carcinogen. Contamination of benzo(a)pyrene in food and water can cause health problems. Due to the carcinogenic nature of benzo(a)pyrene, monitoring of this substance in water and susceptible foods should be carried out regularly. The sensitive and reliable analytical method has to be developed to determine benzo(a)pyrene in low level. Besides chromatographic method like GC and HPLC, bioanalysis by application of monoclonal antibody in ELISA is an alternative approach.

Even though benzo(a)pyrene is a small molecule (molecular weight = 252.3), its conjugate with protein can stimulate immune response [1]. Matschulat et al. has described the production of benzo(a)pyrene monoclonal antibody and its application on ELISA [1].

Monoclonal antibodies have been used in both medical and analytical purposes. Structural characterization of monoclonal antibody can be carried out by mass spectrometry (MS) such as FT-ICR-MS and orbitrap [2]. Structural characterization of the molecule needs fragmentation. When fragmentation occurs in solution by using enzyme digestion, the mass spectrometer is used to analyze each fragment. The molecule is constructed based on information obtained from these fragments: this approach is an up-type method. On the other hand, when the fragmentation occurs in the gas phase inside the instrument, the mass spectrometer is used to analyze the entire molecule directly, and this approach is a down-type method.

Zhang et al. [2] summarized the different MS-based techniques for structural characterization of monoclonal antibodies as shown in Figure 1.

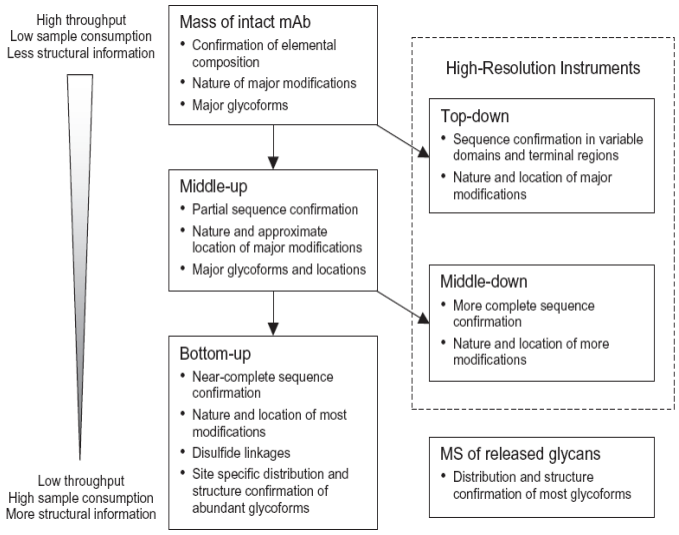

Figure 1. A summary of different MS-based techniques for structural characterization of monoclonal antibodies [1].

At first the present study had aimed to perform top-down analysis of benzo(a)pyrene monoclonal antibody. However the problems occurred. Therefore the problematic of structural characterization of benzo(a)pyrene monoclonal antibodies by FT-ICR-MS will be shown and discussed.

Materials and Methods

FT-ICR-MS (Bruker Daltonics, Bremen, Germany) with 12 T magnet (Magnex, UK) was used in this study. Electrospray ionization source (ESI) (Apollo II, Bruker Daltonics, Bremen, Germany) was used in the positive ionization mode to ionize the analyte. The instrument was calibrated by Arginine before use. Benzo(a)pyrene monoclonal antibody was produced as described by Matschulat et al. [1]. 500 µL of 100 ppm Benzo(a)pyrene monoclonal antibody in water was prepared. 20 µL of 2% formic acid was added afterward to help generate the ion. The solution was desalted by centrifugation and injected directly to the ionization source by using a microliter pump at flow rate of 2 µL/min.

Since the top-down analysis of the intact molecule could not be performed. Digestion by papain was the next approach to reduce the size of the antibody. Immobilized papain (Pierce, Rockford, USA) was equilibrated with digestion buffer (20 mM sodium phosphate, 10 mM EDTA and 20 mM cysteine pH 7.0, freshly prepared). Benzo(a)pyrene monoclonal antibody was mixed with the activated papain and incubated overnight. The digest was separated from the immobilized enzyme by centrifugation and washed by 10 mM Tris.HCl pH 7.5. The Fab fragments were separated from undigested antibody and Fc fragments by using Protein A recombinant immobilized on 6% fast-flow beaded agarose (Sigma-Aldrich, Taufkirchen, Germany). The Fab fragments were collected as the flow-through. The sample was concentrated and desalted with 10 kDa membrane vivaspin® 500 spin column (Sartorius, Stockport, UK). 20 µL of 2% formic acid was added into Fab solution in water and injected directly to the ionization source.

Results and Discussion

Analysis of benzo(a)pyrene monoclonal antibody

The benzo(a)pyrene monoclonal antibody solution was injected directly to the ionization source. The highest mass detected was m/z 710.1 (58+ charges) as can be seen in Figure 2.

The highest mass obtained was approximately 41185.8 Da (710.1x58) or 40 kDa. The mass measurment of benzo(a)pyrene monoclonal antibody by MALDI-TOF/TOF showed molecular weight of 148 kDa approximately (148252, 148302 spectra not shown). Therefore the ion found in FT-ICR-MS does not correspond to the intact antibody. This means that no intact antibody molecular ion could be isolated. This phenomenon could be due to salt, impurities and stability of the sample. The 40 kDa ion could be a small fragment or degradation product of the intact antibody. Moreover, mass limit can be the problem of FT-ICR-MS as describe by Bogdanov [3]. The high mass molecule analysis has been achieved for chondroitinase I, a 997 amino acid protein with a molecular weight of 112,508 Da [3]. As a stronger magnetic fields (e.g., 12 T) was used in this study, analysis of 150 kDa was supposed to be possible. However, the result shows that an intact molecular ion of antibody could not be isolated.

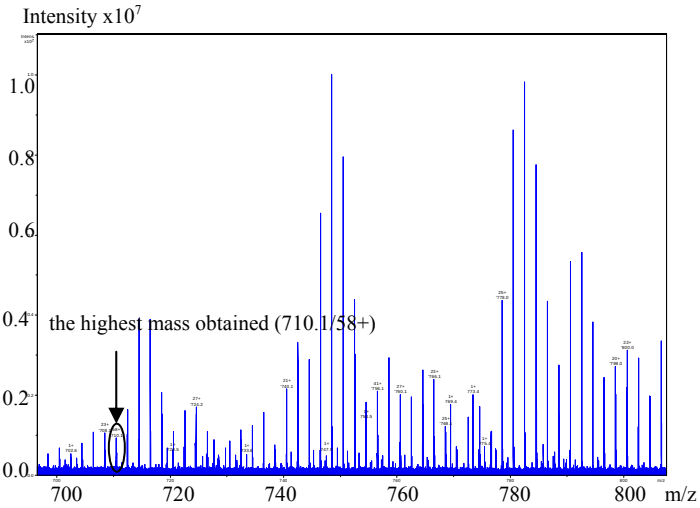

Figure 2. Benzo(a)pyrene monoclonal antibody spectrum with 250 scans

Analysis of Fab fragment

Fab, the antigen binding fragment, is useful in analysis of antigen-antibody interaction. As the top-down analysis of the intact molecule could not be performed, Fab, a smaller protein fragment, was the next target in this study. Fab fragments can be produced from monoclonal antibody by enzymatic digestion with papain or pepsin [4]. Papain is a thiol protease that cleaves IgG antibodies at the heavy chain hinge region into three fragments, one Fc and two identical Fab fragments as shown in Figure 3. The size of Fab and Fc are similar, approximately 50 kDa [4].

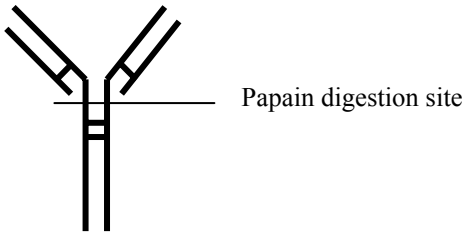

Figure 3. The digestion site of papain on antibody

After enzymatic digestion and purification, the Fab solution in water was injected directly to the ionization source. The spectrum of Fab analysis can be seen in figure 4. The spectrum shows only peaks of 1+ charge molecular ion. There was no 50 kDa molecular ion isolated. There were many small molecules inside the sample. A matrix effect existed which affected the

ionization of the intended protein fragments in the electrospray source. The Fab fragments (50 kDa) should be purified and isolated from all small molecules by the use of special chromatographic columns for proteins. Zhao et al. suggested that further purification after protein A column should be performed [4]. Since direct injection of the sample into the ionization source without any separation step was carried out in this study, the purification of the sample was a critical point. Moreover the low amount of substrate at the digestion step could lead to the uncompleted digestion or low concentration of Fab fragments. The concentration might be lower than detection limit of the instrument. Digestion with papain needs high amount of substrate. When production of monoclonal antibody is complicated and expensive, sufficient substrate cannot be provided.

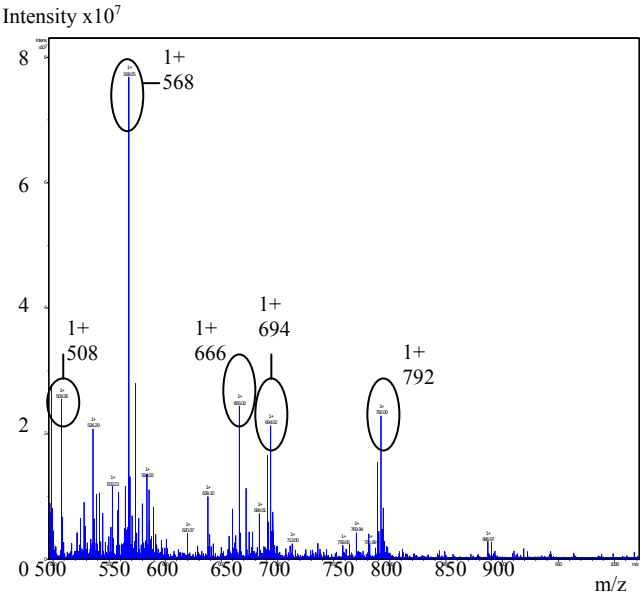

Figure 4. Fab fragment spectrum with 250 scans

Zhao et al. [4] proposed 2 ways of Fab production and purification as can be seen in figure 5. Immobilized protein A is not the end process of the purification. Further chromatographic step is needed. The alternative process of Fab generation is transient expression in mammalian cells which needs recombinant DNA technologies. Although high resolution instrument like FT-ICR-MS was used in this study, extensive sample preparation is still needed. The results in figure 4 showed only peaks of small molecules. This means immobilized protein A and the spin column cannot purify the sample. Sample preparation is still an analytical bottleneck in some aspects.

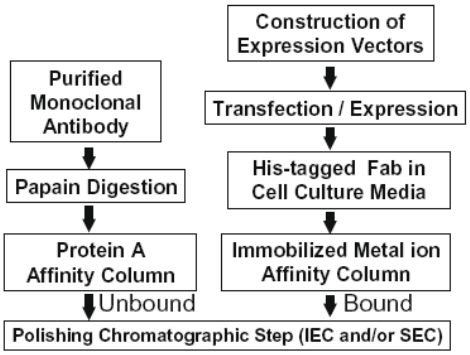

Figure 5. Overview of two routes for Fab production and purification [4].

Conclusions

Top down analysis of benzo(a)pyrene monoclonal antibody cannot be performed with FT-ICR-MS in this study. The causes could be due to mass limit of FT-ICR-MS and the sample preparation process. FT-ICR-MS was successfully used for elucidation of antibody paratope (the antigen binding site) structure [5]. However the extensively sample preparation was performed such as preparation of antigen column. Moreover MALDI was used to aid in the process and the software for protein database search has to be installed.

Top down analysis of an intact monoclonal antibody has been accomplished by using hybrid linear quadrupole ion trap-orbitrap (LTQ orbitrap) [6]. Nano-ESI infusion, step elution and RP HPLC were tested as sample delivery methods. Variable regions of monoclonal antibodies were analyzed by LTQ-Orbitrap [7]. However the exclusively sample preparation was needed by using HPLC size exclusion column.

In conclusion mass spectrometry has been a powerful tool for structural characterization of proteins including antibodies. However an appropriate sample preparation should be considered. An intact monoclonal antibody is a large molecule (approximately 150 kDa). The signal intensities both in FT-ICR-MS and Orbitrap will be lower with a bigger molecule analysis. The next approach in this study should focus on an important part of the antibody molecule such as paratope peptide and Fab fragment. The identification of paratope sequences from intact antiboies would also imply the binding of benzo(a)pyrene on the antibody as well. Fab fragment can be generated as described above however further clean-up after immobilized protein A should be performed.

Acknowledgements

P. Songsermsakul gratefully thanks Deutscher Akademischer Austauschdienst (*DAAD*) for awarding a fellowship. The authors would like to thank *Dr. Philippe Schmitt-Kopplin for his comments and suggestions on this study.*

References

[1] D. Matschulat, A. Deng, R. Niessner and D. Knopp, *The Analyst.* 130 (2005), pp. 1078–1086.
[2] Z. Zhang, H. Pan, and X. Chen, *Mass Spectrom. Rev.* 28 (2009), pp. 147–176.
[3] B. Bogdanov and R.D. Smith, *Mass Spectrom. Rev.* 24 (2005), pp. 168–200.
[4] Y. Zhao, L. Gutshall, H. Jiang, A. Baker, E. Beil, G. Obmolova, J. Carton, S. Taudte and B. Amegadzie, *Protein Expression Purif.* 67 (2009), pp. 182-189.
[5] R. Stefanescu, R.E. Iacob, E.N. Damoc, A. Marquardt, E. Amstalden, M. Manea, I. Perdivara, M. Maftei, G. Paraschiv and M. Przybylski, *Eur. J. Mass Spectrom.* 13 (2007), pp. 67-75.
[6] P.V. Bondarenko, T.P. Second, V. Zabrouskov, A.A. Makarov and Z.Zhang, *J. M. Soc. Mass Spectrom.* 20 (2009), pp. 1415-1424.
[7] Z. Zhang and B. Shah, *Anal. Chem.* 79 (2007), pp. 5723–5729.

Spectrofluorometric study for the determination of salicylic acid via complexation with As(III)

P. Ketkaew*, M. Singwattana[1] and T. Taopalee[1]

[1]Department of Chemistry, Faculty of Science, King Mongkut's University of Technology Thonburi, Bangkok, 10140, Thailand

*E-mail: nitaya.ket@kmutt.ac.th

Abstract: Salicylic acid (SA) was analyzed by spectrofluorometric method via complexation with As(III). The experimental factors for the complexation step including the amount of As(III) and sodium dodecyl sulfate(SDS), reaction time and the optimum conditions for salicylic acid extraction were studied. It was found that the appropriate excitation wavelength (λ_{ex}) at 293 nm and the emission wavelength (λ_{em}) at 404 nm were the same for both SA and SA-As (III) complex but the fluorescence intensity of the complex was much higher than that of the SA . The solution for optimum complexation involved 1.00 cm^3 of 1.0 x 10^{-4} M As (III) solution and 5.00 cm^3 of SA (2000.0 ppm) without adding SDS, and the reaction time was 15 minutes. The SA-As(III) complex was then extracted one time with 10.00 mL of 1% acetic acid in chloroform. Quantitative study parameters were as follows: linearity was obtained in the concentration range of 0.025- 13.00 ppm (SA-As(III) complex) with R^2 of 0.9991, the limit of quantitation was 25 ppb. The average percentage recovery and % RSD (n = 6) were 99 % and 1.05 % respectively. This method was applied to determine SA in fermented green cabbages. In addition, the comparison between the SA-As(III) complex and direct SA spectrofluorometric measurements were also studied, and the quantitative results from both methods were insignificant differences.

Introduction

Salicylic acid [$C_6H_4(OH)COOH$] is a beta hydroxy acid (BHA), that occurs as white or colorless crystals and widely used in medicine and cosmetics.The medicinal properties of salicylic acid and its derivatives are pain and fever relief. Like other BHA, salicylic acid (SA) is a key ingredient in many skin care-products for the treatment of acne, calluses, corns, keratosis pilaris and warts. Also, it is used in several shampoos for anti-dandruff purposes. Additionally, salicylic acid has ability to inhibit the growth of bacteria and fungi, and it was used as a food preservative. In Thailand, it is prohibited to use in all kind of foods since 1993. However, this acid is still used as antimicrobial in foods, especially in fermented fruits and vegetables products from many small factories. The harmfulness results from the intake of salicylic acid more than 170 mg/ kg of body weight and the acute toxicity occurs if there is salicylic acid in blood more than 25-35 mg/100 mL. Various analytical methods have been used to determine salicylic acid and its derivatives including HPLC-CL[1], electro-chemical oxidation [2], flow injection analysis –AAS [3], and spectrofluorimetric – PLS [4], [5].

This work aims to determine SA in fermented vegetables using spectrofluorometric measurement of SA-As(III) by studying the optimum conditions for complexation, sample extractions and comparing the quantitative results with the direct spectrofluoro-metric measurement of SA.

Materials and Methods

Reagents and solutions: All reagents were of analytical reagent grade. Stock standard solution of 2000.00 ppm was prepared by dissolving 0.2000 g of SA in 100.00 mL of solvent (1% v/v acetic acid in chloroform), and then appropriate diluted to a required concentration. Solutions of $1.0x10^{-4}$M As_2O_3 and $1.0x10^{-3}$ M SDS were prepared in 1% NaOH and deionized water respectively. Solutions of 2% w/v benzoic acid, citric acid and ascorbic acid were separately prepared for interferent effect studies.

Instrument: Fluorescence measurements were carried out on Hitachi F-500 Fluorescence spectro-photometer equipped with xenon lamp and using 1 cm quartz cell to obtain the fluorescence intensities of solutions.

Working solution: Five milliliters of SA standard solution, 1.00 mL of $1.0x10^{-4}$ M As(III), and 1.00 mL of $1.0x10^{-3}$ M SDS were mixed in 10 mL volumetric flask and stood for 10 min. The solution was then made up to 10.00 mL with deionized water and mixed well. After phase separation was completed, the aqueous phase was measured the fluorescence intensity against the reagent blank (solution with no SA) to determine the optimum excitation and emission wavelengths.

Optimum condition studies: Factors affecting the complexation between SA and As(III): volume of $1.0x10^{-4}$ M As(III), volume of $1.0x10^{-3}$ M SDS, and complexation time (5-20 min) were varied in order to determine the optimum condition.

Extraction: Thirty milliliters of 0.05 ppm SA standard solution was extracted one time with 1% acetic acid in chloroform (5,10,15, 20 mL) for 15 min. Pipet 5.00 mL of organic layer to prepare the working solution using the parameters obtained at optimum condition. The experiments were repeated by varying the extraction time (5, 10, 15, 20 min).

Sample preparation: Twenty five grams of ground fermented green cabbage was extracted with 30.00 mL

of 1% acetic acid in chloroform, and 30.00 mL of the fermented solution sample was extracted according to the extraction procedure at optimum condition. The extracted SA was then spectrofluorometric analysis via SA-As(III) complex.

For direct SA measurement, 10.00 mL of the extracted solution obtained from sample preparation step was evaporated to remove chloroform, then redissolved the extracted SA with methanol and made up the volume to 10.00 mLwith deionized water.

Results and Discussion

1. Fluorescence excitation and emission spectra

Fluorescence excitation and emission spectra of both SA-As(III) complex and SA were similar in shape and maximum wavelength for excitation and emission . It was found that the excitation spectrum of SA-As(III) complex depended on the concentration of SA and was resolved into two peaks while the emission spectra showed only one peak with maximum wavelength at 404 nm as shown in Table 1. The interferent effects of benzoic acid, citric acid and ascorbic acid on complexation were insignificant when using optimum excitation wavelength at 293 nm and emission wavelength at 404 nm (fluorescence intensities of the interferent acid-complexes were 0.94,0.00 and 0.00 respectively).

.

Table 1 Excitation and emission wavelengths at different concentrations of SA-As (III)

SA-As(III) concentration (ppm)	Excitation wavelength (nm)	Emission wavelength (nm)
20.00	293*	404*
50.00	287	404
500.00	265/ 323	402
1000.00	259/ 330	402
As(III)- citric acid	282	312 /326
complex**	293*	404*
As(III)-benzoic acid	290	320
complex**	293*	404*

* optimum wavelengths used in this study
** concentration was 2000.0 ppm

2. Optimum conditions for complexation

The fluorescence intensity of SA-As(III) complex at optimum wavelengths was about four times higher than that of the SA. The experimental results in Figure 1-3, showed that the solution for optimum complexation involved 1.00 mL of 1.0 x 10^{-4} M As (III) solution in 5.00 mL of SA (2000.0 ppm) without adding SDS, and the reaction time was 15 minutes.

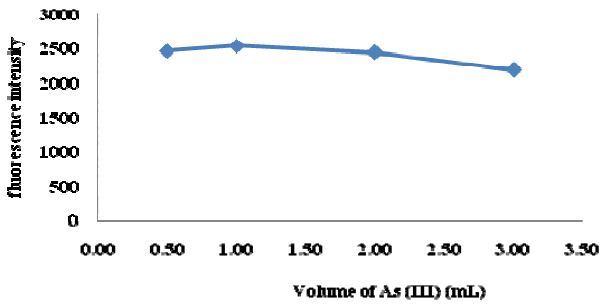

Figure 1. Effect of As(III) concentration on fluorescence intensity of SA- As(III) complex .

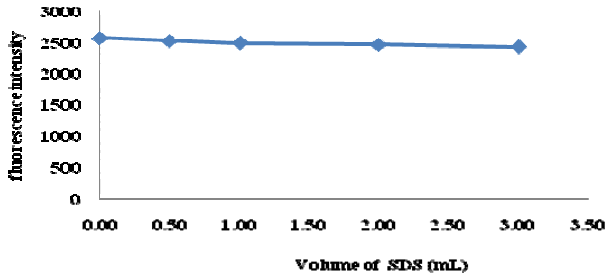

Figure 2. Effect of SDS concentration on fluorescence intensity of SA- As(III) complex .

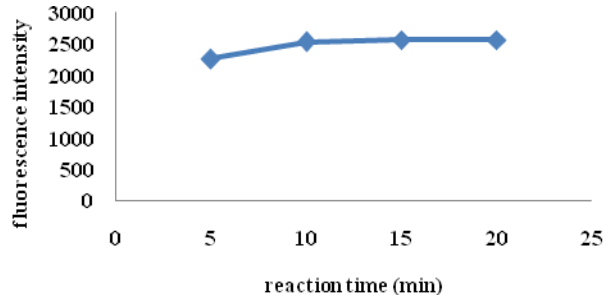

Figure 3. Effect of reaction time on fluorescence intensity of SA- As(III) complex

3. Extraction conditions

The extraction condition of using 10.0 mL of 1 % acetic acid in chloroform to extract SA from 30.00 mL of known aqueous solution one time for 15 min gave the highest percentage recovery of SA, (Figure 4-5).

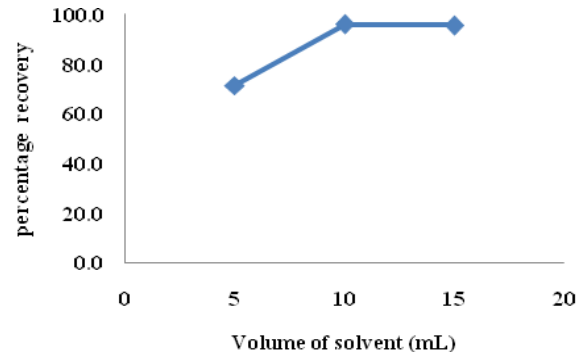

Figure 4. Effect of solvent volume on the extraction of SA from aqueous solution.

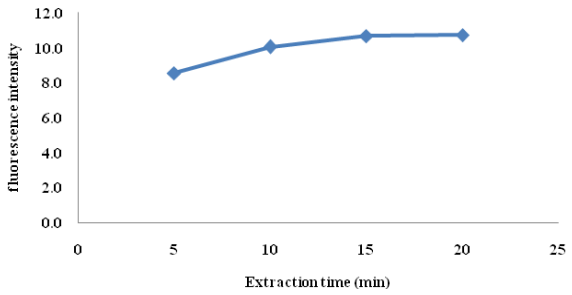

Figure 5. Effect of extraction time on the extraction of SA from aqueous solution

4. Direct SA measurement

Though the SA gave fluorescence spectra under the optimum wavelengths but its fluorescence intensity was much lower than that obtained when adding As(III) into SA solution. This resulted in the higher limit of quatitation (LOQ) in comparison to the SA-As(III) complex.

5. Analytical parameters

Calibration curves of both SA and SA-As(III) were carried out under the same optimum wavelength i.e. λ_{ex} = 293 nm, λ_{em}= 404 nm, and optimum conditions for complexation. Linear calibration curves were obtained for both SA and SA-As(III) with different in concentration range as shown in Fig. 6. Percentage recoveries were obtained by adding standard SA concentration to the samples of known analysis quantities. The relative standard deviation (%RSD) calculated from six repeated measurements of 2.1 mg/L and 10.5 mg/L of SA were 1.45% and 0.65 % respectively. The limit of quantitation (LOQ) for The direct SA measurement was about ten times higher than that from SA-As(III) complex but the linear concentration range was longer. The analytical parameters of calibration curves were summarized in Table 2.

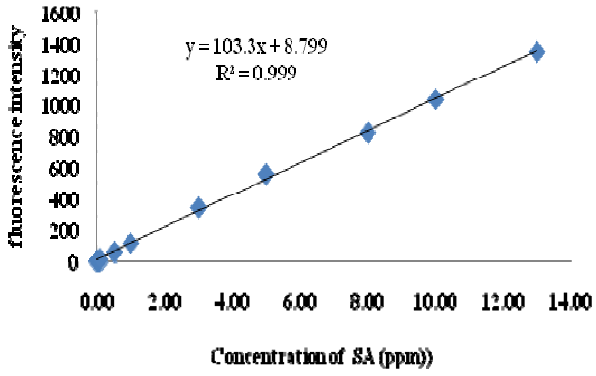

Figure 6. Calibration curve of salicylic acid in form of SA-As (III) complex (0.025-13.00 ppm)

Table 2. Analytical parameters of calibration curves

Parameters	SA-As(III) complex	SA
Calibration curve		
Linear range (ppm)	0.025 – 13.00	0.25-20.00
R^2	0.999	0.9985
Equation	y = 103.3x + 8.799	y = 24.7x + 3.333
LOQ (ppm)	0.025	0.25
LOD (ppm)	0.025	0.25
% RSD	0.65 – 1.45	1.32 – 2.30
% Recovery	98.58 – 101.64	97.83 – 98.83

6. Analysis of salicylic acid in samples

Fermented green cabbages and solution samples were from different open markets. The samples were extracted and analyzed by the studied method at optimum conditions via SA-As(III) complex and direct measurement of SA. The quantitative results from both spectrofluorimetric measurements were in good agreement. The concentration ranges of SA found in fermented green cabbages samples and fermented solution samples were 2.4-12.6 mg/kg and 0.3-2.1 mg/L respectively.

Conclusions

This study provides the use of simple spectro-fluorometric method and instrument to determine salicylic acid with the addition of As(III) to enhance the fluorescence intensity which gains the sensitivity of the measurement. The LOQ and LOD from this study were equal 0.025 ppm and the quantitative results are accurate and reliable which results from high percentage recoveries and low % RSD. However, some of disadvantages are time consuming in the complexation step (~30 min, including complexation time of 15 min) and wastes from the use of arsenic and chloroform.

References

[1] H. Cui, J. Zhou, F. Xu, C. Ze Lai and G.H.Wan, Anal. Chim. Acta., **511**(2004), pp.273
[2] A.A.J. Torriero, J.M. Luco,L. Sereno and J. Raba, Talata, **62**(2004), pp. 247
[3] G.A. Rivas and J.M. Calatayud, Talanta, **42**(1995), pp. 1285

[4] N.R. Martos, A.M. Diaz, A. Navalon, I. De Orbe Paya and L.F. Capitan Vallvey, *J. Pharm. Biomed. Anal.*, **23** (2000), pp. 837-844.
[5] M.M. Karim, H.S. Lee, Y.S. Kim, and H.S. Bae, *Anal.Chim. Acta.*, **576(**2006), pp. 136-139.

Tandem FFD-GrSPLITT system for separation of silica gel particles

N. Paothong[1], T. Nasingha[1], W. Veerasai[1] and N. Tantidanai[1,2*]

[1] Department of Chemistry, and Center of Excellence for Innovation Chemistry, Faculty of Science, Mahidol University, Bangkok, Thailand 10400
[2] Mahidol University, Kanchanaburi campus, 199 Saiyok, Kanchanaburi, Thailand 71150

[*] E-Mail: scntt@mahidol.ac.th

Abstract: Tandem Full-Feed Depletion Gravitational Split flow thin cell (Tandem FFD-GrSPLITT) fractionation, a newly developed system for rapid separation of particles in different properties such as size, mass, shape and density by series combination of the two or more GrSPLITT channels proposed by Nasingha et al [1]. Particle suspension can be separated to obtain three different size fractions by setting two different cutoff diameters of the two GrSPLITT channels within one step. The separation is based on settling velocities and laminar flow velocities on each particle within the channels. In this work, the Tandem FFD-GrSPLITT system was tested for its efficiency with silica gel which is a spherical sample in size range 1-20 micrometers. Six cutoff-diameters were varied at 5, 7, 10, 13, 15 and 17 micrometers. Seven fractions: (1) <5 μm, (2) 5-7 μm, (3) 7-10 μm, (4) 10-13 μm, (5) 13-15 μm, (6) 15-17 μm, and (7) >17 μm can be collected. All fractions and the original suspension were quantitatively imaged and sized for plotting their particle size distributions (PSDs). All PSDs were presented and compared. Their theoretical and experimental mid-diameters presented that all experimental mid-diameters greater than their theoretical mid-diameters in range 0.0-0.5 micrometers. It may cause of the deflection during the microscope imaging and sizing of the silica particles.

Introduction

Gravitational Split-flow thin cell (GrSPLITT) fractionation is a rapid and continuous fractionation separation method. This method can be operated in two different modes consisted of (1) transport mode (TS) and (2) full-feed depletion mode (FFD) [2-5]. The FFD mode is an advanced mode that no effect of dilution during the separation.

The separation process of the Tandem FFD-GrSPLITT fractionation is similar to the FFD-GrSPLITT mode. It depended on two gradient velocities at each particle, which is different of size, mass, shape and density. First the gradient flow velocities in x-axis and the second is the gradient of Earth's gravities. The partway of each particle depended on its result between the two perpendicular velocities vectors in each time as shown in Figure 1.

The Tandem FFD-GrSPLITT system can be set up a series of cutoff diameters (d_c), which is depended on the number of the GrSPLITT channels.

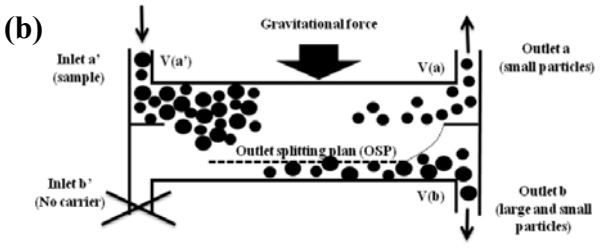

Figure 1. Schematic side view of the GrSPLITT channel operated in; (a) transport (TS) mode and (b) full feed depletion (FFD) mode.

The simple diagram for two GrSPLITT channels of the Tandem FFD-GrSPLITT system was presented in Figure 2.

The Tandem FFD-GrSPLITT (two channels) system was marked that it is more advantage over the previous system, FFD-GrSPLITT system (one channel). They can be set the different two cutoff-diameters. The separation was occurred continuously during the suspension sample flow through the GrSPLITT channels. Consequently, in the first cycle, three different size fractions were obtained as shown in Figure 2. The concept and application of the Tandem FFD-GrSPLITT system with marl particle (irregular shape) was compared and reported by Nasingha et al in 2009 [1].

In this work, the Tandem FFD-GrSPLITT system was applied with the silica gel particles which are a spherical particle sample. Six cutoff diameters were operated with in three cycle steps. Seven fractions were also obtained and their PSDs were plotted and calculated for the experimental mid-diameters. To prove the effect of shape and density on the theoretical mid-diameters, the experimental mid-diameters would be compared and discussed with the theoretical mid-diameters.

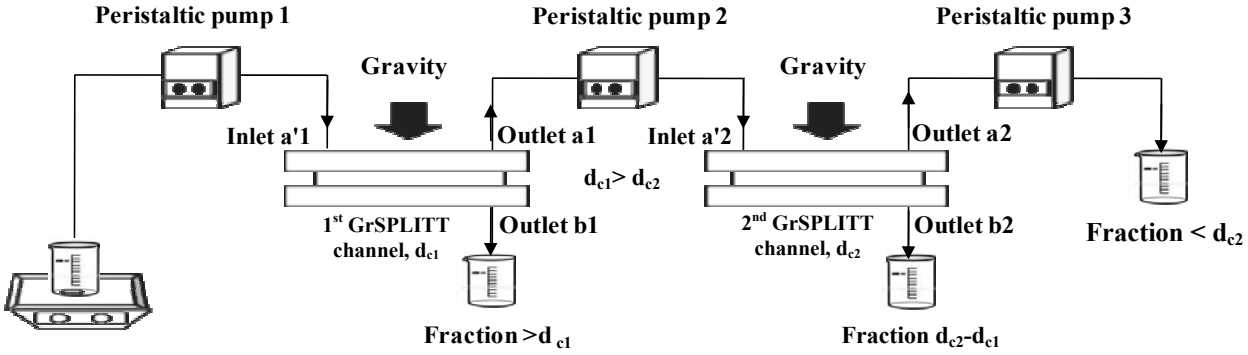

Figure 2. The diagram of Tandem FFD-GrSPLITT system for two GrSPLITT channels, which is set up of two cutoff-diameters (d_{c1} and d_{c2}, where $d_{c1} > d_{c2}$) using three peristaltic pumps. Three different fractions can be obtained: (1) fraction > d_{c1}, (2) fraction d_{c2}-d_{c1}, (3) fraction < d_{c2}. The suspension sample is stirred on the magnetic stirrer during the separation.

The SPLITT cell apparatus

The components of the GrSPLITT cell were showed in Figure 3. The cell consists of the two plastic spacer planes sandwich to a stainless-steel splitter plane. They are kept tight between the two acrylic plates.

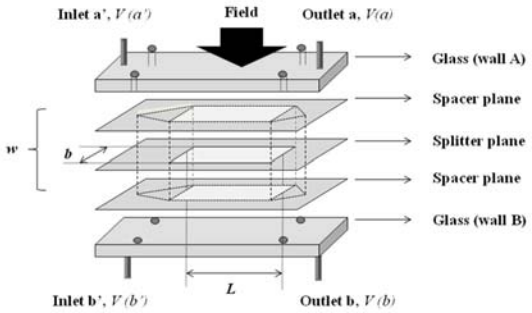

Figure 3. The SPLITT cell apparatus, the cell dimensions are the length: L = 10 cm, the width of the stainless steel splitter: b = 1.5 cm and the channel thickness: w = 0.076 cm (combined thickness of two spacers plane and a stainless-steel splitter plane).

The Tandem FFD-GrSPITT fractionation using to this work were a homemade and the commercial SPLITT channel that is a Model SF1000 Salt Lake city, USA. Three peristaltic pumps were used to control the inlet and outlet flow rate, consist of two MasterFlex, L/S Model 7523-25 and a Gilson Minipuls, Middleton, WI.

Materials and Methods

Preparation of silica suspension

A commercial silica particle was suspended in degassed and distilled water at 0.2% w/v. Then the particle larger than 20 micrometers in the suspension was removed to prevent the channel clogging during the separation using gravitational settling method (GrSettling) based on Stoke's law as presented in Equation 1.

was collected and waited for the Tandem FFD-GrSPLITT fractionation.

$$d_c = \sqrt{\frac{18\eta x}{g\Delta\rho t}} \qquad \text{..... (1)}$$

Where d_c is the cutoff diameter, η is the fluid viscosity (kg.m^{-1}.s^{-1}), x is depth from liquid surface to removal position (cm), t is settling time (min), g is the gravitational acceleration (cm.s^{-2}), and $\Delta\rho$ is the difference in densities of the particle and the fluid (g.cm^{-3}).

Methods of Tandem FFD-GrSPLITT fractionation

Six cutoff diameters at d_c = 5, 7, 10, 13, 15, and 17 micrometers were set into three cycle steps as showed in Figure 4. Seven different size fractions were obtained for PSDs analysis. The PSDs data were used to calculate the experimental mid-diameters. The experimental mid-diameters were compared with the theoretical mid-diameters. The assumption is that the more closely the two source of the mid-diameters, the more ideally the separation theory and the experiment using the spherical shape and the unity of density of silica particle. The cutoff diameters were controlled by the ratio between inlet and outlet flow rates in each channel based on Equation 2, proposed by J.C. Giddings [6], as presented below:

$$d_c = \sqrt{\frac{18\eta(v_{a'} - v_b)}{bLg\Delta\rho}} \qquad \text{..... (2)}$$

Where d_c is the cutoff diameter (μm), η is viscosity of medium (kg.m^{-1}.s^{-1}), b is the breadth of channel (cm), L is the distance between splitting planes (cm), g is the gravitational acceleration (cm.s^{-2}), $\Delta\rho$ is the difference in densities of the particle and medium (g.cm^{-3}) and v_a', v_b are the flow rates of the upper inlet and the lower outlet (ml.min^{-1}) respectively.

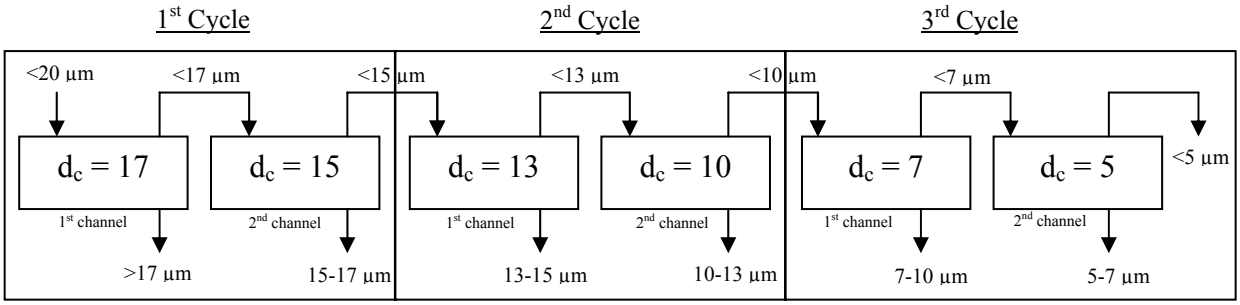

Figure 4. Experimental designs for setting six cutoff diameters with in three cycle steps using the Tandem FFD-GrSPLITT system (two GrSPLITT channels) at d_c= 5, 7, 10, 13, 15, and 17 µm. Seven fractions were obtained: (1) <5 µm, (2) 5-7 µm, (3) 7-10 µm, (4) 10-13 µm, (5) 13-15 µm, (6) 15-17 µm, and (7) >17 µm.

Optical Microscopes with Image Analysis

Trinocular microscope power 1000 (OLYMPUS U-CMAD3 and OLYMPUS cx-31 & Moticam 2000, Japan) and image analysis with Motic Images Plus 2.0 ML program. All fractions were imaged and sized by using Trinocular microscope with Motic Images Plus 2.0 ML program.

Results and Discussion

The seven silica fractions: (1) <5 µm, (2) 5-7 µm, (3) 7-10 µm, (4) 10-13 µm, (5) 13-15 µm, (6) 15-17 µm, and (7) >17 µm were imaged 30 photomicrographs per each fraction to gain data for plotting their PSDs. The example of all photomicrographs in each fraction and the silica suspension smaller than 20 micrometer were presented in Figure 5. The PSD curves were plotted between calculated volume based on spherical shape and mid-diameter, as showed in Figure 6. Which the mid-diameter and volume of particle in the mid-range diameter (*di*) can be calculated follow Equation 3 and 4 respectively.

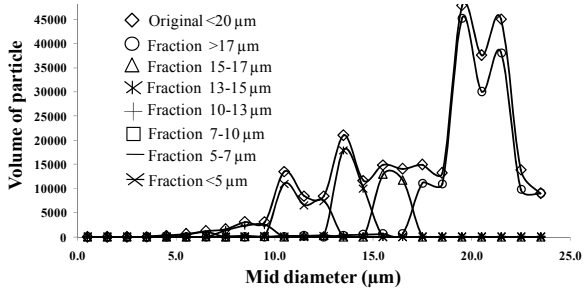

Figure 6. Particle size distribution curves of seven silica fractions separated using two GrSPLITT channel of Tandem FFD-GrSPLITT fractionation at six cutoff-diameters 5, 7, 10, 13, 15 and 17 µm with in three cycle steps.

$$\text{Mid-range diameter } (di) = \frac{\text{Min diameter} + \text{Max diameter}}{2} \quad \text{.....(3)}$$

$$V_{di} = \frac{N_{di} \times \pi di^3}{6} \quad \text{.....(4)}$$

where min and max diameter is minimum and maximum diameter respectively.
where V_{di} and N_{di} are the volume and number of particle in the *di* median diameter, respectively.

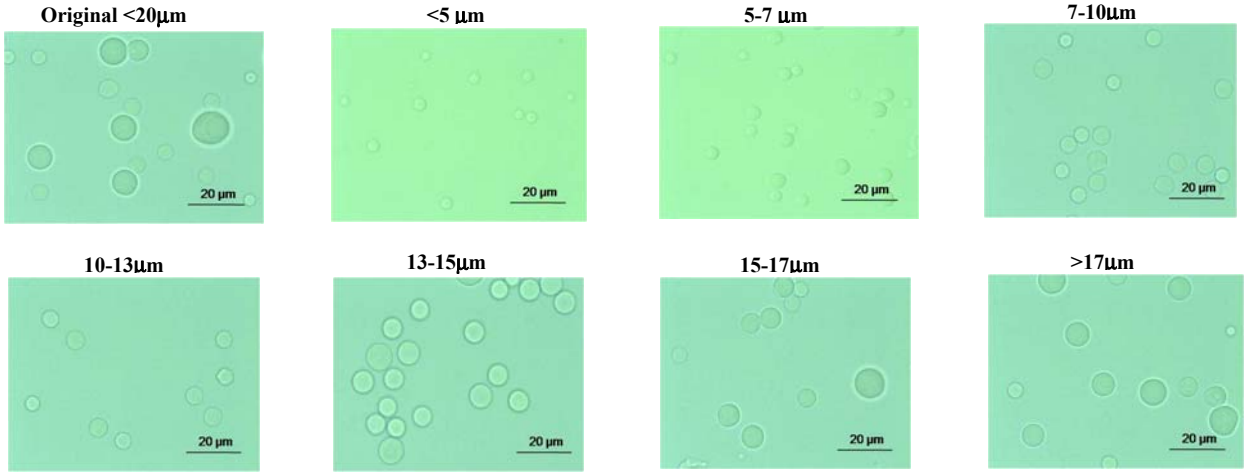

Figure 5. An example of all photomicrographs of original silica gel (<20 µm) and seven fractions: (1) <5 µm, (2) 5-7 µm, (3) 7-10 µm, (4) 10-13 µm, (5) 13-15 µm, (6) 15-17 µm, and (7) >17 µm, respectively. All fractions separated by using Tandem FFD-GrSPLITT fractionation at setting cutoff diameters (d_c) 17, 15, 13, 10, 7, and 5µm.

The *di* is the mid-range diameter of particle *di* that calculated form Equation 3. For example, diameter range 0.1-1.0 µm, *di* is 0.5.

The comparison of theoretical and experimental mid-diameters was presented in Table 1. The results of the experimental mid-diameters where different to the theoretical mid-diameters. The experimental mid-diameters were significantly upper than the theoretical mid-diameters in 0.0-0.5 micrometers.

Table 1: Comparison of theoretical and experimental mid-diameters based on particle volume of silica particles, **n = 3**.

Expected Fractions [a] (µm)	Theoretical mid-diameter [b] (µm)	Experimental mid-diameter [c] (µm)	Different mid- diameter [d] (µm)
17-24	20.5	20.5	0.0
15-17	16.0	16.5	0.5
13-15	14.5	14.5	0.5
10-13	11.5	11.5	0.0
7-10	8.5	9.0	0.5
5-7	6.0	6.5	0.5
1-5	3.0	3.5	0.5

[a] Fraction from figure 4.

[b] $[(\text{Minimum } d_{Th} - \text{Maximum } d_{Th})/2]$ of the expected fraction

[c] $[(\text{Minimum } d_{Exp} - \text{Maximum } d_{Exp})/2]$ of the experimental fraction

[d] Different mid-diameter = $d_{Exp} - d_{Th}$

Conclusion

Even if, the experimental mid-diameters were greater than the expected mid-diameters in range 0.0-0.5 micrometers for all fractions, the Tandem FFD-GrSPLITT fractionation presented that it can be used to separate the silica particles relatively to the theory by J.C. Giddings. This may cause the reflection of imaging and sizing method using microscope.

Acknowledgements

The authors thank to the Thailand Research Fund (TRF), Young Scientist Research Fund from faculty of Science Mahidol University and Center of Excellence for Innovation in Chemistry (PERCH-CIC).

References

[1] T. Nasingha, W. Veerasai, N. Tantidanai, *Pure and Applied Chemistry International Conference* (2009), pp. 66-69.

[2] G. Blo, C. Contado, F. Fagioli and F. Dondi, *J. Anal. Chem.* **125** (2000), pp. 1335-1339.

[3] N, Tantidanai, W. Veerasai, R. Beckett, *J. Sep. Sci. Techno.* **41** (2006), pp. 3003-3025.

[4] A. Momi, J. R. Lead, *J. Environ. Sci. Technol*. **41** (2006), pp 6738-6743.

[5] C. Contado, F. Dondi, R. Beckett, J. C. Giddings, *J. Anal. Chim. Acta.* **345** (1997), pp. 99-110.

[6] C. Contado, F. Riello G. Blo, and F. Dondi, *J. Anal. Chem.* **845** (1999), pp. 303-316.

Classification of thai honey origins by their mineral contents

S. Junklun[2], J. Lewatchararongjarorn[1], P. *Ritthiruangdej*[1] and N. Tantidanai[1,2]*

[1] Mahidol University, Kanchanaburi campus, Lumsum Kanchanaburi, 71150, Thailand.
[2] Department of Chemistry and Center of Excellence for Innovation Chemistry, Faculty of Science, Mahidol University, Bangkok, 10400, Thailand.

*E-mail: scntt@mahidol.ac.th

Abstract: Honey is a sweet product generated food made by some insects using nectar from flowers and nectar of plants, as well as from honeydew. Honey composition depends on great extent on the nectar sources. Contents of minerals affect physical and chemical properties of honey such as color, smell, precipitation, dissolution, taste, quality. Contents of Ca, K, Mg, Na, and Zn have been reported that they are indicating parameters for classifying the origin of honeys. Therefore, the mineral contents are very significant to the quality and the application of honey. Little information is available, about the mineral contents in Thai honey which is gained from various botanic and sources. To understand and add more value information to the Thai honey, the characterization of mineral contents in Thai honey should be studied to originate the source of the honey and to relate the mineral characterization with the qualities and applications of the honey. In this work, different types of honey in Thailand were characterized on the basis of their mineral contents for classification of honey origins. Five different botanics of Thai honeys: longan (LG), lychee (LC), multiflower (MF), sunflower (SF) and wild flower (WF) were determined for Ca, K, Mg, Na, and Zn contents using flame atomic absorption spectrometer (FAAS). The relationship between the mineral concentrations and the known botanic origins of all honey (95 samples) were plotted and discussed about on their patterns characteristics of the mineral contents

Introduction

Honey, a natural sweet product elaborated by honeybees, contains mostly simple sugars or monosaccharide, of which fructose and glucose are the major components 65% of and 18% of water content, approximately. Proteins, flavonoids, flavor and aroma, phenolic compounds, free amino acids, organics acids, and vitamins comprise minor components of honeys. The quantity and variety of minerals in honeys is depended on sources of nutrients such as types and environmental locations of plant. Thereby, the excess or deficiency of certain chemicals in the soil or water will have repercussions in the chemical compositions of the plants and then in the nectar.

Mineral content can be highly indicative of the geographical origin of honey and can be used as environmental indicators. Honeybees may continuously be exposed to present contaminants in the area surrounding the apiary for the duration of their foraging activity.

Many publications reported that the mineral contents such as Ca, Cu, K, Mg, Na and Zn were very important indicators to relate with the honey properties [5, 6, and 7].

Thai honeys have been one of the most export products in Thailand because the varieties and characteristic of Thai botanic is unique. However, little information of Thai honey is known. To valuate the Thai honey, the understanding of sources and mineral composition of honey should be done.

In this work, The mineral contents of Ca, K, Mg, Na and Zn were determined for 95 honey samples and repeated for three times(n=3). Then the metal patterns in each type of honey were discussed using the simple relationship between the mineral concentrations and the known botanic origins. Including, the differences of standard deviation in each type of honey, which is a simple grouping stand, were used to classify botanic origins.

Materials and Methods

Apparatus: Elemental analysis was carried out on GBC model 932 plus atomic absorption spectrometer with the oxidant-fuel ratio (Air: Acetylene) of 5:1.

Reagents and solutions: All the applied chemicals were of analytical grade or better quality. The 65% HNO_3 and 30% H_2O_2 (Merck, Darmstadt, Germany) were of AR grade. The solutions were diluted with de-ionized water

Sample preparation procedures: Five different botanic origins of Thai honey were determined their mineral contents of Ca, K, Mg, Na and Zn. The honey sources were presented in table 1. The samples were stored in polypropylene bottles at room temperature sheltered from light until analysis. The honey samples were weighed for 0.5018 g. The honey samples were digested with 1 ml of H_2O_2 and 0.5 ml of HNO_3 in ultrasonic bath for 10 min to assure the homogenization of the solutions. Then, each sample solution was adjusted the final volume to 50.0 mL by deionized water.

Table 1: Sources and types of botanic honeys

Type of honey	samples	Band/company
Lychee (LC)	LC1-2	Ambrosia
	LC3-13	Supa honey farm
Longan (LG)	LG1-2	Bualuang
	LG3-4	Thailanna
	LG5-7	Ambrosia
	LG8-10	Tappakdee
	LG11-12	Supa honey farm
	LG13-28	Chiang Mai
	LG29-30	Watit farm
Sunflower (SF)	SF1-3,23-27	Ambrosia
	SF4-9	Tappakdee
	SF10-22	Lungsa-at
	SF28	Kidnakoon
	SF29	Nook Chainat
	SF30	Supa honry farm
Wildflower (WF)	WF1-3,15-17	Ambrosia
	WF4-5,7-8,18	Bualuang
	WF6	Supa honey farm
	WF9-12	Chiang Mai
	WF13-14	Watit farm

Calibration and analytical efficiency: Calibration curves of Ca, K, Mg, Na, and Zn were determined and plotted. Then, their slope and correlation coefficient were presented in Table 2.

Table 2: The slope and correlation coefficient of five minerals(Ca, K, Mg, Na, and Zn) obtained by their calibration curves

Parameter	Ca	K	Mg	Na	Zn
Working rang(ng m $L^{-1)}$	0.5-4.0	0.5-4.0	0.1-0.4	0.3-1.0	0.01-0.07
Slope (A ml ng^{-1})	0.053	0.293	0.417	0.316	0.413
Correlation coefficient	0.996	0.999	0.989	0.986	0.998

*** A=** Absorbance Units

Results and Discussion

All honey samples were determined of their mineral concentrations. The data were plotted to relate between their mineral concentration and types of the botanic origins as shown in Table 3.

The stardard deviation (SD) were calculated by n=3 for each honey sample and were used as a simple rule for grouping the mineral contents in each botanic of all honey sample.

Table 3: The relationship between average concentrations (ng mL^{-1}) of Ca, K, Mg, Na, and Zn and different type of botanic ; Lychee(LC), Longan(LG), Multiflower(MF), Sunflower(SF), and Wild flower(WF).

Types of honeys	Average concentration of Minerals (mg kg^{-1}) ± SD	
	Ca	
	Group 1	Group 2
LC	367±11 (13)[b]	-
LG	80±27 (30)[b]	-
MF	86±5 (4)[b]	-
SF	103±29 (30)[b]	-
WF	146±18 (12)[b]	75±12 (6)[b]
Types of honeys	**Average concentration of Minerals (mg kg^{-1}) ± SD**	
	K	
	Group 1	**Group 2**
LC	244±140 (13)[b]	-
LG	499±80 (30)[b]	-
MF	540±91 (4)[b]	-
SF	402±169 (24)[b]	758±66 (6)[b]
WF	812±294 (18)[b]	-
Types of honeys	**Average concentration of Minerals (mg kg^{-1}) ± SD**	
	Mg	
	Group 1	**Group 2**
LC	12±3 (13)[b]	-
LG	19±6 (30)[b]	-
MF	23±3 (4)[b]	-
SF	19±5 (24)[b]	32±4 (6)[b]
WF	14±3 (16)[b]	39±1 (2)[b]
Types of honeys	**Average concentration of Minerals (mg kg^{-1}) ± SD**	
	Na	
	Group 1	**Group 2**
LC	48±1 (4)[b]	19±1 (9)[b]
LG	23±5 (30)[b]	-
MF	45±6 (4)[b]	-
SF	41±19 (30)[b]	-
WF	46±19 (18)[b]	-
Types of honeys	**Average concentration of Minerals (mg kg^{-1}) ± SD**	
	Zn	
	Group 1	**Group 2**
LC	1.55±0.43 (13)[b]	-
LG	3.95±0.27 (8)[b]	2.81±0.94 (22)[b]
MF	1.49±0.30 (4)[b]	-
SF	1.27±0.47 (30)[b]	-
WF	1.38±0.43 (18)[b]	-

average concentration $=(Conc._1+Conc._2+\ldots+Conc._n)/N$

[b] number of sample in the group

From the table 3, the concentrations of Ca and K presented strongly dependent on the honey botanical origins. While as the concentrations of showed the strongly highest (3.9±0.3 ng ml^{-1}) in Longan(LG)

honey which was compared to the others(in range of 1.3-1.6±0.5 ng mL^{-1}).For the concentrations of Mg, these showed the several groups with in each type of botanic honey. Therefore, the other parameters such as source of companies, colour of the honey should be considered. While as, the Na concentrations showed insignificantly different for each botanic honey. Except for Sunflower SF28 from (Kidnakoon) and Wild flower WF7 from (Bualuang), WF9-12 from (Chiang Mai) presented the strongly higher than the others. It may cause of the different sources of the honey samples. The different sources of honey samples may obtain the honey from different time of honey gather, storage method, location of the botanic etc.

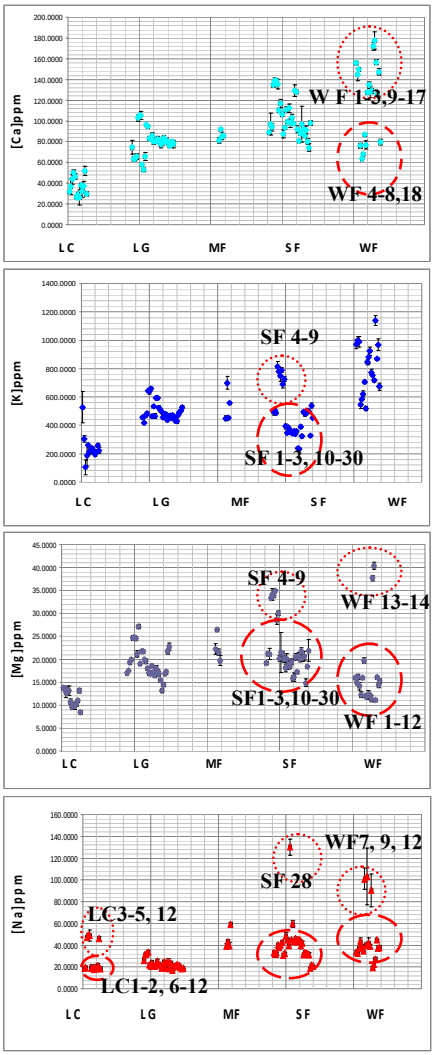

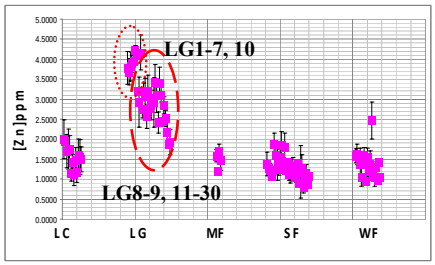

Group 1 Group 2

Figure 1: Relationship between five different types of Thai honey: (1) Lychee (LC), (2) Langan(LG), (3) Multiflower(MF), (4)Sunflower (SF)and (5)Wild flower(WF).

The relationship between the mineral concentrations and the known botanic origins (five botanics) of all honeys were plotted and discussed on their characteristics of the mineral contents to be able to classify types of Thai honey as shown in Figure 1.To able classified type of Thai Honey.

Conclusions

In this work, a challenge to establish a classification of some Thai honeys from different botanical and geographical origin was made using the different concentrations of five minerals (Ca, K, Mg, Na, and Zn) pattern recognition techniques. The origins of Thai honey can be simply classified by their mineral contents. The different concentrations of minerals in the same type of botanic origins may cause of several parameters such as (1) different areas for growth plant, (2) different storage method and different location of botanics. It refered that these parameter may affect the honey's quality and color.

References

[1] O.M.; Hernandes, J.M.G.; Fraga. *J. Food Chem.* **93**, (2005),pp. 449-458.

[2] M.J.; Latorre, R.; Pena. *J. Food Chem.* **66**, (1999), pp. 263-268.

[3] R. Fernandez-Torres. *Talanta* . **65**, (2005), pp. 686-691

[4] Rodriguez-Otero, J. L., Pasrio, P., Simal, J. and Cepeda, A.: 'Mineral content of the honeys produced in Galicia (north–west Spain)' *Food Chem.* **49**, (1994), pp. 169–171.

[5] Poiana et al., 1996 A. Poiana, S. Fudo, E. Manzini, S. Postarino and B. Mincione, Ricerche sui mieli commercializatti in Italia: la componente minerale, *Ind Alim* **35** (1996), pp. 522–530.

[6] Feller-Demalsy et al., 1989 M.J. Feller-Demalsy, B. Vincent and F. Beaulieu, Teneur en mineraux et origine geographique des miels du Canada, *Apidologie* **20** (1989), pp. 77–91.

[7] Terrab, A., Pontes, A., Heredia, F.J., Díez, M.J. A preliminary palynological characterization of Spanish thyme honeys. *Botanical Journal of the Linnean Society* **146** (3) (2004),pp. 323-330.

A copolymer of aniline and *m*-ferrocenylaniline: electrochemical copolymerization, electric properties and electrocatalysis

W. Sriraksa and S. Chairam*

Department of Chemistry, Faculty of Science, Ubon Ratchathani University, Warinchamrap, Ubon Ratchathani, Thailand 34190

*E-Mail: chairam019@yahoo.com

Abstract: A poly(aniline-*co*-*m*-ferrocenylaniline) was successfully synthesized by electrochemical polymerization of 0.1 M aniline and 0.005 M *m*-ferrocenylaniline on glassy carbon electrode using the scan potential range between −0.3 and 0.9 V (vs. Ag/AgCl) in an aqueous 0.5 M H_2SO_4 solution containing 30% (v/v) acetonitrile. When studying the cyclic voltammetric behavior in a 0.1 M H_2SO_4 solution, the electric property of the as-prepared poly(aniline-*co*-*m*-ferrocenylaniline) was better than that of the parent polyaniline. The cyclic voltammograms of the copolymer in an aqueous 0.5 M Na_2SO_4 solution with various pH values from 3 to 8 were performed at the same potential range of the synthetic process. The results indicated that the copolymer still hold an electrochemical property in acid, neutral and even alkaline media, although the electrochemical property slightly decreased with increasing of the pH values. A poly(aniline-*co*-*m*-ferrocenylaniline) coated glassy carbon electrode also exhibited an electrocatalytic response to the electrochemical oxidation of ascorbic acid in citrate buffer solution of pH 5. The results showed that the anodic peak potential of ascorbic acid shifted from 0.6 V at bare glassy carbon electrode to 0.2 V at poly(aniline-*co*-*m*-ferrocenylaniline) coated glassy carbon electrode with a greatly enhanced current response.

Introduction

Conducting polymers have attracted much scientific and technological interest in recent years. Among various conducting polymers, polyaniline (PANi) is one of the most promising conducting polymers due to its high conductivity, good redox reversibility, swift color change with applied potential and good stability in aqueous solutions and air. These properties also provide favorable conditions for its potential applications in rechargeable batteries [1], electrocatalysis [2], electrochromic devices [3,4], corrosion prevention [5], conversion of light to electricity [6], and super capacitor [7]. Unfortunately, PANi has low conductivity and redox activity at pH > 5, limiting its applications to other fields, such as biochemical industries, chemical sensors, biosensors, and contaminated water treatment. As known, the pH dependence of the conductivity and redox activity of PANi is a very important factor for considering its practical applications. The copolymerization of aniline (ANi) and other monomers offers a possibility to prepare a new polyaniline type of copolymer that not only retains the good properties of polyaniline itself, but also possesses new properties. The general procedures in the chain-growth copolymerization of ANi and its derivatives have been carried out using chemical and electrochemical methods. It is noted that the electrochemical method can quickly diagnose the electrochemical properties of the polymer during the polymerization process and conveniently provides the optimal copolymerization conditions. Therefore, this method is especially suitable for initial studies of new systems. Ferrocene (Fc) and its derivatives are attracting keen interest in the area of electroanalysis for their unique redox behavior. Because Fc is one of the most popular electrochemical active species and the redox reaction of Fc/Fc+ is completely reversible, many researchers have used it for the modification of many electrodes to determine the analytes [8,9].

An ascorbic acid (AA) is of vital importance in processes of oxidation and reduction in human organism, participating of several metabolic reactions [10-13]. Moreover, it is present in many biological systems and multivitamin preparations, which are commonly used to supplement inadequate dietary intake. Nevertheless, it is widely used in foods as an antioxidant with subsequent extension of the storage time of the products [14]. Thus, the determination of ascorbic acid content is particularly important in the pharmaceutical and food industry.

In this work, the electrochemical method was used to synthesize the copolymerization of aniline and *m*-ferrocenylaniline. The electrochemical activity of as-synthesized copolymer was studied at different values of pH, and a poly(aniline-*co*-*m*-ferrocenylaniline) coated glassy carbon electrode was then used to carry out the electrocatalytic oxidation of ascorbic acid.

Materials and Methods

Chemicals and Solutions: The aniline (ANi) was distilled twice and stored at 4 °C in dark when not in used. Deionized (DI) water (R ≥18.2 MΩ-cm) purified with a Nanopore ultrapure water system was used to prepare solutions. The *m*-ferrocenylaniline (*m*-FcANi) was synthesized according to the literature [15]. Ethanol (EtOH), acetonitrile (ACN), sulfuric acid solutions (H_2SO_4), ascrobic acid (AA) and sodium sulphate (Na_2SO_4) were purchased from Sigma-Aldrich. Other reagents were of analytical grade and used as received without purification. All the electrochemical experiments were carried out at room temperature (25 °C).

Apparatus: All the electrochemical experiments were carried out using an AUTOLAB PGSTAT 12

with a conventional three-electrode cell, consisting of either glassy carbon electrode (GCE, Φ 3.0 mm) or the PANi-*m*-FcANi film coated GCE (PANi-*m*-FcANi/GCE) as a working electrode, a platinum (Pt) wire as an auxiliary electrode, and a Ag/AgCl (sat. 3 M KCl) electrode as a reference electrode.

Preparation of Polymer-Modified Electrode: GCE was polished carefully with alumina powder (1.0 µm, 0.5 µm and 0.03 µm, respectively) on a soft polishing cloth. After sonicating in absolute EtOH and water, respectively for 10 min, the GCE was cleaned by potentially cycling between −1.0 and 1.0 V at scan rate of 50 mVs^{-1} in 0.1 M H_2SO_4, until a stable cyclic voltammogram was obtained. The electrochemical copolymerization was performed by cyclic scanning for 10 cycles within the potential range of −0.3 to 0.9 V at 50 mVs^{-1} in an aqueous 0.5 M H_2SO_4 solution, containing 30% (v/v) ACN, 0.1 M ANi and 0.005 M *m*-FcANi. After rinsing of the electrode with EtOH and water, PANi-*m*-FcANi/GCE was obtained for further studies.

Results and Discussion

Electrochemical polymerization of PANi and PANi-m-FcANi

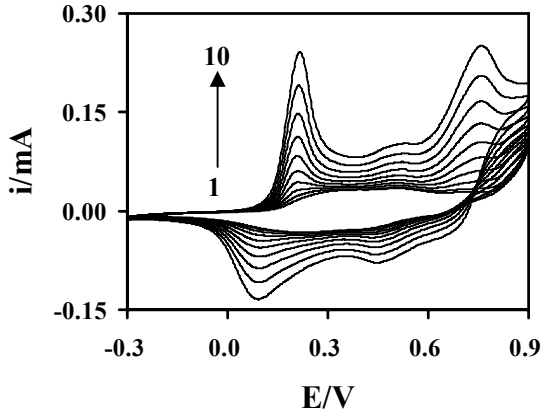

Figure 1. The film growth of 0.1 M ANi at GCE in aqueous 0.5 M H_2SO_4 solution containing 30% (v/v) ACN at scan rate of 50 mVs^{-1}

Figure 1 shows the cyclic voltammograms of the electropolymerization of 0.1 M Ani on GCE in 0.5 M sulfuric acid containing 30% (v/v) acetonitrile in the potential range from −0.3 to 0.9 V at 50 mVs^{-1}. The two sets of anodic-cathodic peaks located at 0.21/0.09 V and 0.73/0.67 V correspond to redox process of leucoemeraldine/emeraldine salt and emeraldine salt/pernigraniline transformations, respectively. The third pair of peaks in the middle is attributed to the defects in the linear structure of the polymer [16]. The current of these peaks increases with the number of scaning cycles, indicating the formation of the polymer. After the electropolymerization a dark green film of PANi was observed on GCE and used as the working electrode for further studies.

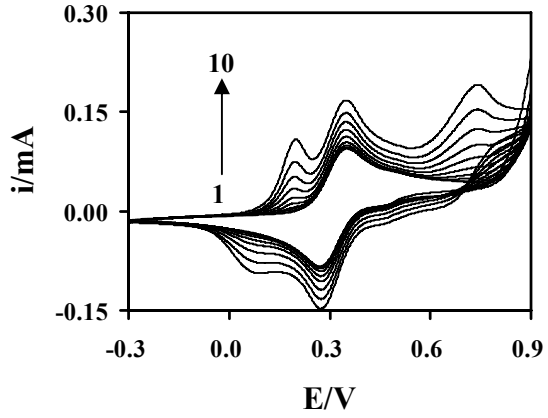

Figure 2. The film growth of 0.1 M ANi and 0.005 M *m*-FcANi at GCE in aqueous 0.5 M H_2SO_4 solution containing 30% (v/v) ACN at scan rate of 50 mVs^{-1}

Figure 2 shows the cyclic voltammograms for the electrochemical copolymerization of 0.1 M Ani and 0.005 M *m*-FcANi in 0.5 M H_2SO_4, containing 30% (v/v) ACN in the same conditions for synthesis of PANi. At the begining of cycling, there were one anodic and one cathodic peaks on the first circle. The first anodic peak at 0.35 V and cathodic peak at 0.27 corresponds to the oxidation and reduction of Fc/Fc+ in the *m*-FcANi molecule. When increasing in the number of scaning cycles, the two more sets of redox peaks located around 0.21/0.09 V and 0.73/0.67 V were observed on the cyclic voltammograms, indicating the film growth of the copolymer PANi-*m*-FcANi.

Cyclic voltammograms of PANi– m-FcANi

Figure 3 shows the cyclic voltammograms of the PANi (curve 1) and PANi-*m*-FcANi (curve 2) in 0.1 M H_2SO_4 at 50 mVs^{-1}, respectively. As can be seen, the cyclic voltammogram of PANi-*m*-FcANi is very similar in shape to that PANi parent. This results indicated that the electrochemical property of PANi-*m*-FcANi is very analogues to PANi in the acid solution [16,17]. However, based on the areas of curve 1 and 2, the PANi-*m*-FcANi has a good electrochemical characteristic more than PANi. The main difference of curve 1 from curve 2 is that a sharp cathodic peak at 0.07 and 0.62 V, respectively. The copolymer bearing ferrocene as the more easily oxidized substituent group was observed to be sensitive to pH changes. Therefore, the presence of Fc species on curve 2 is a main cause for increasing in the electrochemical property of the coplymer compared with curve 1.

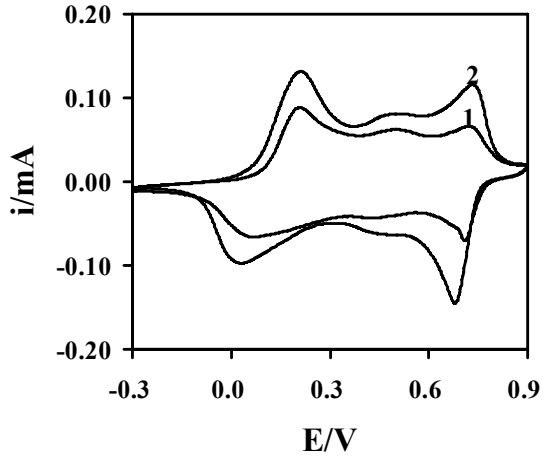

Figure 3. The cyclic voltammograms of (1) PANi/GCE and (2) PANi-*m*-FcANi/GCE in 0.1 M H_2SO_4 solution at scan rate 50 mVs^{-1}

Redox electroactivity of PANi- m-FcANi

In order to investigate the application of the copolymer PANi-*m*-FcANi, the electrochemical activity was verified at the different pH values. Figure 4 shows the cyclic voltammograms of the copolymer PANi-*m*-FcANi in a 0.5 M Na_2SO_4 solution with different pH values. The broad anode peak and the broad cathode peak were observed on curve 1-6. It can be described that the redox peaks shift towards more positive-negative potentials with increasing the pH values. This reveals that the redox process of the copolymer PANi-*m*-FcANi was related to the proton concentration in the solution [18]. In addition, the anodic and cathodic peak currents slightly decrease with increasing the pH values from 3.0 to 8.0. This reversible redox process must be accompanied by a proton exchange between the copolymer and the solution, which plays an important role in adjusting the pH value in the vicinity of the copolymer-coated electrode. The catalytic activity of polyaniline are limited by pH, and polyaniline has a little redox electroactivity at pH >3. Considering the sensitivity, the pH 5.0 citrate buffer (CB) solution as the supporting solution was selected for further investigation, because the copolymer still hold a good redox electroactivity.

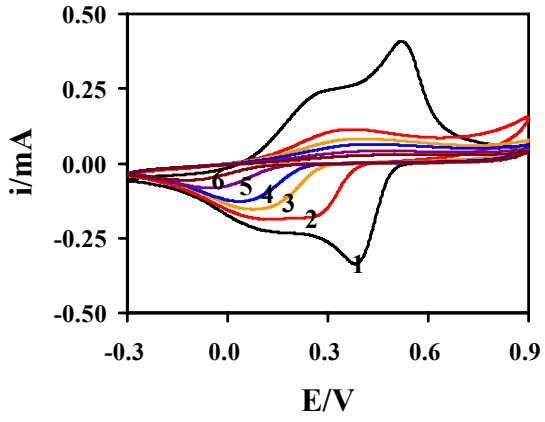

Figure 4. The cyclic voltammograms of the PANi-*m*-FcANi in 0.5 M Na_2SO_4 solution with different pH values: (1) pH 3.0, (2) pH 4.0, (3) pH 5.0, (4) pH 6.0, (5) pH 7.0, and (6) pH 8.0 at scan rate 50 mVs^{-1}

Electrocatalytic oxidation of ascorbic acid

Figure 5 shows the cyclic voltammograms on either bare GCE or PANi-*m*-FcANi modified GCE with different concentration of AA in 0.1 M CB (pH 5.0). As can be seen, Figure 5b showed that the oxidation peak of AA was very broad occured at 0.6 V on bare GCE. In contrast, the dramatically increased oxidation current and the negatively shifted anodic potential indicated the strong electrocatalytic function of the PANi-*m*-FcANi modified GCE for the electrocatalytic oxidation of AA when compared with bare GCE. The AA was oxidized at the low potential, which is an advantage of PANi-*m*-FcANi modified GCE for solving the interference problem, such as hydrogen peroxide or dopamin. Thus, PANi-*m*-FcANi modified GCE can be used for the determination of AA in the further investigation.

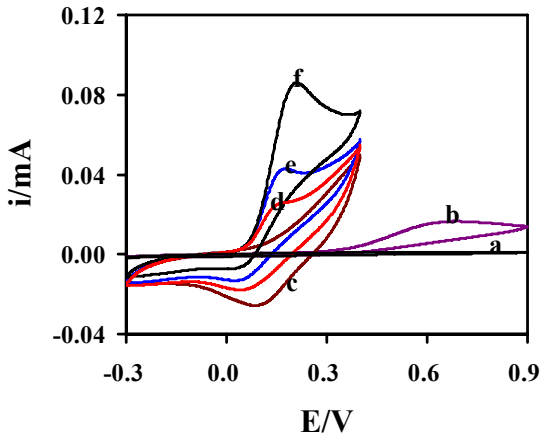

Figure 5. The cyclic voltammograms on bare GCE with different concentrations of AA: (a) 0 mM and (b) 2 mM in 0.1 M CB (pH 5.0), respectively at scan rate 50 mVs^{-1}. CVs on the PANi-*m*-FcANi modified GCE with different concentrations of AA: (c) 0 mM, (d) 2 mM, (e) 4 mM, and (f) 8 mM in 0.1 M CB (pH 5.0).

Conclusions

A copolymer PANi-*m*-FcANi was successfully synthesized by electrochemical polymerization of 0.1 M Ani and 0.005 M *m*-FcANi on GCE using the scan potential range between −0.3 and 0.9 V (vs. Ag/AgCl) in an aqueous 0.5 M H_2SO_4 solution containing 30% (v/v) ACN. The electric property of the as-prepared PANi-*m*-FcANi was better than that of the parent PANi. Moreover, the copolymer still hold an electrochemical property in acid, neutral and even alkaline media, although the electrochemical property slightly decreased with increasing of the pH values. A PANi-*m*-FcANi coated glassy carbon electrode also exhibited an electrocatalytic response to the electrochemical oxidation of AA in CB solution (pH 5.0). The anodic peak potential of AA shifted from 0.6

V on bare GCE to 0.2 V on the PANi-*m*-FcANi/GCE with a greatly enhanced current response.

Acknowledgements

The authors wish to acknowledge the financial support of this paper from the promotion project for teacher production in science and mathematics, Center of Excellence for Innovation in Chemistry (PERCH-CIC) and Faculty of Science, Ubon Ratchathani University.

References

[1] K. Ghanbari, M.F. Mousavi, M. Shamsipur and H. Karami, *J. Power Sources* **170** (2007), pp. 513–519.
[2] K. L. Nagashree and M. F. Ahmed, *Synth. Met.* **158** (2008), pp. 610–616.
[3] C.H.Yang, T. L. Wang and Y.-T. Shieh, *Electrochem. Commun.* **11** (2009), pp. 335–338.
[4] H. Li, K. Xie, Y. Pan, M. Yao and C. Xin, *Synth. Met.* **159** (2009), pp. 1386–1388.
[5] E. Hur, G. Bereket and Y. Sahin, *Prog. Org. Coat.* **57** (2006), pp. 149–158.
[6] Q. Li, J. Wu, Q. Tang, Z. Lan, P. Li, J. Lin and L. Fan, *Electrochem. Commun.* **10** (2008), pp. 1299–1302.
[7] C. A. Amarnath, J. H. Chang, D. Kim, R. S. Mane, S.H. Han and D. Sohn, *Mater. Chem. and Phys.* **113** (2009), pp. 14–17.
[8] J. Qiu, H. Peng and R. Liang, *Electrochem. Commun.* **9** (2007), pp. 2734–2738.
[9] S. Wang and D. Du, *Sens. and Actuators B* **97** (2004), pp. 373–378.
[10] P. Zhang and S. T. Omaye, *Toxicol. in Vitro* **15** (2001), pp. 13–24.
[11] J. Frank, A. Flaccus, C. Schwarz, C. Lambert and H. K. Biesalski, *Free Radic. Biol. Med*. **40** (2006), pp. 827–836.
[12] Y. M. Ha, M. K. Park, H. J. Kim, H. G. Seo, J. H. Lee and K. C. Chang, *Cancer Lett.* **277** (2009), pp. 48–54.
[13] M. Garland and W. W. Fawzi, *Nutr. Res*. **19** (1999), pp. 1259–1276.
[14] L. A. Pacheco-palencia, P. Hawken and S. T. Talcott, *Food Res. Int.* **40** (2007), pp. 620–628.
[15] L. Chaicharoenwimolkul, A. Munmai, S. Chairam, U. Tewasekson, S. Sapudom, Y. Lakliang and E. Somsook, *Tetrahedral Lett.* **49** (2008), pp. 7299–7302.
[16] L. Zhang and J. Lian, *J. Electroanal. Chem*. **611** (2007), pp. 51–59.
[17] S. Mua, Y. Zhang and J. Zhai, *Electrochim. Acta* **54** (2009), pp. 3923–3929.
[18] J. Zhang, D. Shan and S. Mu, *Polymer* **48** (2007), pp. 1269–1275.

Screen-printed electrode modified with nano-ZnO dispersed in polyaniline nanowires for hydrogen peroxide biosensor

S. Chaiyasith[1]* W. Phoohinkong[1]

[1] Department of Chemistry, Faculty of Science, King Mongkut's Institute of Technology Ladkrabang, Ladkrabang, Bangkok, Thailand 10520

*E-mail: kcsuwan@kmitl.ac.th

Abstract: The development of hydrogen peroxide biosensor using screen-printed carbon electrode (SPCE), nano-ZnO and polyanaline. The SPCE ware modified by using the composite of nano ZnO-polyaniline (PANI) and nano-ZnO dispersed on polyaniline nanowires (PANI-NWs). The surface morphology of electrode was characterized by field-emission scanning by scanning electron microscopy (FE-SEM) and electrochemical impedance spectroscopy (EIS). The performances of the resulting hydrogen peroxide sensor were studied by using cyclic voltammetric and amperometric measurements. The results of EIS and CV showed that the modified hydrogen peroxide biosensors using dispersed nano-ZnO in PANI-NWs were more high sensitivity and easy preparation then the ZnO-PANI composite modified electrode. The detection limit of nano-ZnO dispersed in PANI-NWs biosensor was found to be 160 µM based on signal-to-noise ratio of 3. Linear responses over the concentration range between $2x10^{-4}$ to $9x10^{-3}$ M of H_2O_2 were observed. This biosensor can be used as portable device and showed advantage in many applications such as in chemical, biological, and environmental analysis etc. since its required small sample size and easily to operate.

Introduction

The determination of hydrogen peroxide is widly applies in chemical, biological, environmental analysis [1] food industries pharmaceutical [2], clinical and particulary in health care by determining hydrogen peroxide in human blood plasma, serum [3] and in freshly voided human urine etc [4-5].

Horseradish peroxidase (HRP), which can catalyze the oxidation of a variety of substrates by hydrogen peroxide or related compounds, is one of the most commonly used metalloenzymes for the construction of electrochemical biosensors [6]. It is the most studied enzyme among plant peroxidases due to its wide application in different biotechnological processes, especially for analytical purposes. In previous work demonstrated that direct electronic contact between a number of electrode materials and HRP is possible creating the basis for the development of HRP-modified electrodes for detection of hydrogen peroxides [7].

Zinc oxide (ZnO) is a versatile semiconductor material, which has attracted attentions for its wide range of applications, such as solar cells, as well as luminescent, electrical and acoustic devices [8-10]. Zinc oxide nanoparticle has been found to be an interesting for immobilization of desired biomolecules because of the wide bandgap semiconductor with good biological compatibility, low cost and easy availability etc. Zinc oxide nano particles (ZnO NPs) could also be served as the matrix for immobilization of biomolecules. Li et al. [11] have reported the immobilization of tyrosinase on ZnO nanoparticles and found that the adsorption can be facilitated by the electrostatic interactions. Xiaoli et al. [12] reported the nano ZnO microperoxidase (MP) on the surface of the pyrolytic graphite electrode for hydrogen peroxide biosensor. The immobilizing HRP in ZnO has been achieved in nano sized flower-like ZnO as matrix for hydrogen peroxide biosensor [13], flowerlike ZnO-gold nanoparticle-Nafion nanocomposite for hydrogen peroxide biosensor [14] and electrodiposition of ZnO nanoflowers onto carbon nanotubes film electrode [16,17].

Polyaniline (PANI) is an important electric conducting material and has been extensively studied. Because of its unique properties, low-cost, ease in synthesis, high stability and interesting electrochemical property. Generally, the preparation of nanostructured PANI involves polymerization of aniline-monomer in acidic solutions, accomplished either by chemical template-based synthesis or via electrochemical deposition routes. The Pickering emulsion polymerization of aniline can be achieved in the nano ZnO/polyaniline composite [18]. The direct-growth polyaniline nanowires via electrochemical deposition method have been achieved by preparing on a stainless steel [19-21], titanium electrode [21], and carbon cloth electrode [22]. Ying-Ying et al. [22] have been reported the electropolymerization for direct-growth of polyaniline nanowires on carbon cloth (CC) for enzyme-immobilization and found that PANI-NWs can proved the defect-free interface with the support CC, significantly improve the electron-transfer efficiency and large specific surface area of PANI-NWs improved the efficient immobilization of enzyme. In this work, HRP was firstly immobilized on ZnO-PANI composite and PANI nanowire-ZnO nanoparticles on SPCE for detection of hydrogenperoxide. ZnO-PANI composite synthesized via chemical oxidation of aniline and PANI nanowires synthesized by electrochemical deposition on SPCE.

Moreover, the large specific surface area of PANI-NWs can provide the efficient immobilization of HRP and facilitate a highly sensitive glucose-sensor

Materials and Methods

Chemicals： ZnO NPs were purchased from Zonof Company. HRP type VI was purchased from Sigma Chemical Co. Aniline from E. Merck was distilled under vacuum, obtaining a colourless liquid.

Other chemicals were purchased in analytical grade and used without further purification. All solutions were prepared with double distilled water, which was purified with a Milli-Q purification system (Branstead, USA) to a specific resistivity of >18 MΩ cm.

Preparation of ZnO-PANI composite: Composite of polyaniline/ZnO were prepared via chemical oxidation of aniline in aqueous solution of 0.5 M phosphoric acid. 2% of ZnO nanoparticles were dispersion in 0.5 M H_3PO_4 solution and stirred for 30 min. Then add 1 ml of aniline and stirred for 30 min. The 2.49 g of $(NH_4)_2S_2O_8$ (APS) in 20 ml of 0.5 M H_3PO_4 was slowly added dropwise to the suspension mixture with a constant stirring. The polymerization was allowed to proceed for 12 h at room temperature and washing the suspension eith deionized water and ethanol and dried at 60°C for 24 h.

Preparation of PANI nanowires: The electrochemical deposition was performed using auto-lab PGSTAT 20 instrument connected to a SPE. Deposition of PANI-NWs onto surface of SPCE was performed by electrochemical oxidation of aniline (0.2 M) in HCl (0.5 M), The deposition of polyaniline was carried out at the constant potential of 0.75 V for 20 minutes. Finally, the electrode was washed in distilled water and dried in oven at 40 °C for a day.

Preparation of H_2O_2 biosensor: HRP were prepared in 0.1 M of phosphate buffer solution at pH 6.7. Two types of biosensors were used in this work.

A. Nafion/HRP/nano ZnO-PANI composite/SPCE

10 µL of 2% nano ZnO-PANI composite in 0.1 M of phosphate buffer solution pH 6.7 and 10 µL of the enzyme solution was added into 20 µL of 2% nafion in ethanol solution. The mixture was mixed throughly for 30 min. Then 2 µL of the resulting solution was pipetted onto the surface of a SPCE and dried 12 h at 4 °C.

B. Nafion/HRP/nano ZnO/PANI-NWs/SPCE

ZnO nano powders were dispersed in 0.1 M of phosphate buffer solution pH 6.7 , Then the mixture was sonicated for 30 min after stirring for 1 h. 10 µL of 2% of nano ZnO dispersed in phosphate buffer solution (above mixture), 10 µL of the enzyme solution and 20 µL of 2% Nafion solution were mixed together for 30 min. Then 2 µL of mixture solution was pipetted onto the surface of polyaniline nanowires SPCE and dried 12 h at 4 °C.

Characterizations: Microstructure and morphology were investigated using field-emission scanning electron microscopy (FESEM, JEOL-6700), and electrochemical measurements were performed using a potentiostat (Autolab/PGSTAT20).

Results and Discussion

Characteristics of PANI-ZnO composite and PANI-NWs on surface of SPCE: SEM image (Figure.1) exhibit the large-area, three-dimension network of polyaniline nanowires on the surface of SPCE, the average dimeter from the SEM images is estimated to be 130-150 nm.

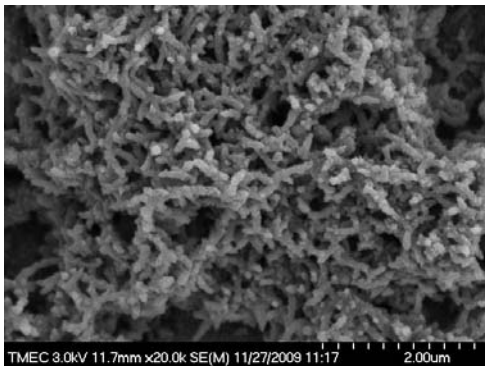

Figure.1 SEM image ot PANI-NWs on surface of SPCE.

It indicated that electrochemical process is effective in the deposition of polyaniline nanowires uniformly cover over a large area and highly homogenize and easily prepares compairing to the Pickering emulsion polymerization process for SPCE H_2O_2 biosensor. The size of nano ZnO-PANI composite paticles in method A is estimated to be 10 – 200 µm (not show the picture). The blocking electron transfer of nano ZnO modified electrodes is analysis by the AC impedance mesurements. Figure.2 shows the electrochemical impedance spectra of the bare electrode and the different modified electrodes. These results were fit to the equivalent circuit shown in the figure.2.

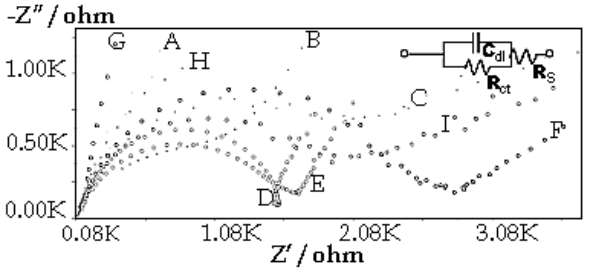

Figure.2 Impedance spectra of (A) Nafion/HRP/nano ZnO-PANI composite/SPCE (B) Nafion/HRP/nano ZnO/PANI-NWs/SPCE (C) Nafion/nano ZnO-PANI composite/SPCE (D) PANI-NWs/SPCE (E) Nafion/nano ZnO/PANI-NWs/SPCE (F) bare SPCE (G) HRP/SPCE (H) Nafion/HRP/nano ZnO/SPCE (I) Nafion/HRP/SPCE in a drop (50 µL) of phosphate buffer solution (0.1 M, pH 6.7) containing $[Fe(CN)_6]^{3-/4-}$(30mM).

The results show that impedance spectra are distinct different in patterns with different modified

surface of screen-printed electrodes. The Nyquist diameter of each electrode suggests that substance is coated or immobilized on the surface of SPCE. The nano-ZnO/PANI-NWs/SPCE has lower impedance than nano-ZnO/SPCE. Indicated that the PANI-NWs improve electron transfer of nano-ZnO.

Cyclic voltammetric (CV) response investigating for redox reaction of potassium ferricyanide $K_3[Fe(CN)_6]$ of difference electrodes is shown in figure.3. The results show that PANI-NWs improve the current peak of nano-ZnO.

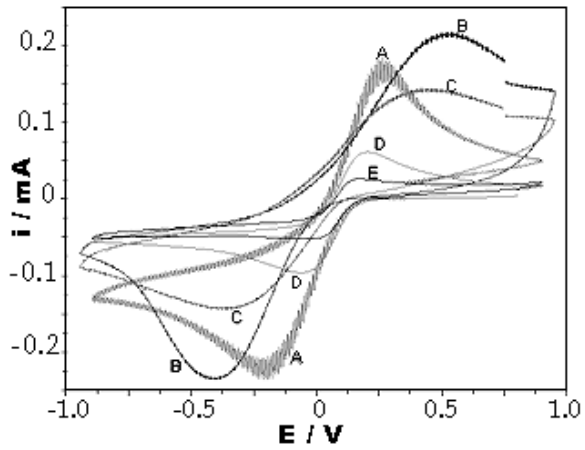

Figure.3 CVs of different electrodes in 50 µL of 30 mM $K_3[Fe(CN)_6]$ in 0.1 M KCl at 0.5 Vs^{-1} : (A) bare SPCE (B) PANI-NWs/SPCE (C) Nafion/nano ZnO/PANI-NWs/SPCE (D) Nafion/nano ZnO-PANI composite/SPCE (E) Nafion/HRP/nano-ZnO/SPCE.

Electrochemical sensing of hydrogen peroxide:
The Nafion/HRP/nano ZnO/PANI-NWs/SPCE (method B) was very low impedance and higher current peak than Nafion/HRP/nano ZnO-PANI composite/SPCE (method A), which also resulted in the inherent thickness of ZnO-PANI composite particles was inhibit electron transfer [23]. Considering these factors, the biosensor used in the hydrogen peroxide determination was prepared by method B.

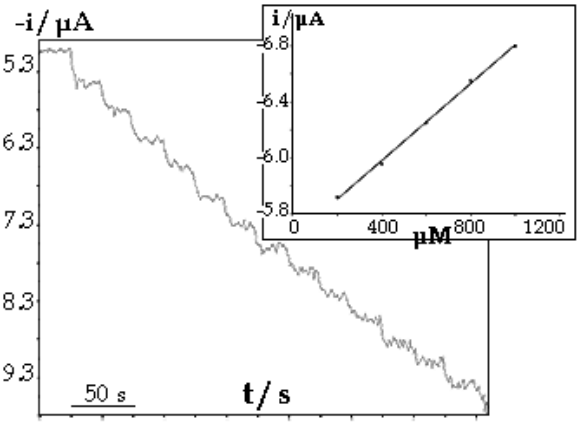

Figure.4 The amperometric i-t current of Nafion/HRP/nano-ZnO/PANI-NWs/SPCE for detect H_2O_2 at concentration between 100 µM to 9 mM the working potential of -500 mV. Figure.4 (inset) shows the H_2O_2 response of Nafion/HRP/nano-ZnO/PANI-NWs/SPCE biosensor.

The amperometry i-t of Nafion/HRP/nano-ZnO/PANI-NWs/SPCE for detect the reduction reaction at surface of electrode. As the other electroactive species normally are present at lower potential. The linear range is 100 µM to 9 mmol/L of H_2O_2 with correlation of 0.9946 (n=18). The detection limits 30 µM with the signal-to-noise ratio of three.

Conclusions

Electropolymerization for direct- growth of PANI-NWs on surface of SPCE has been successfully developed, can improve surface area and electronic property of SPCE due to enhanced facilitate of electron transfer from convention drop-coating PANI onto screen-printed electrodes method. The large specific surface area of PANI-NWs also provides the efficient immobilization of HRP. Then nano-ZnO dispersed on phosphate buffer solution, HRP and Nafion was droped on PANI-NWs to prepare a nano-ZnO/PANI-NWs/SPCE. This modified SPCE biosensor can improve the efficiency of SPCE for direct electron transfer of hydrogen peroxide produces enhanced sensitivity, wide linear range and lower detection limit. In addition, we are using the cheap nano-ZnO to prepare peroxide biosensors.

References

[1] R. M. Peña, S. García, C. Herrero and L. Tomás, *Atmospheric Environment*. **35**(2001), pp. 209-219.
[2] L. Campanella, R. Roversi, M. P. Sammartino and M. Tomassetti, *J. Pharm. Biomed. Anal*. **18**(1998), pp.105-116.
[3] W. Qin, Z. Zhang, B. Lia and S. Liua, *Anal. Chim. Acta*. **372**(1998), pp. 357-363.
[4] D. Banerjee, J. Jacob, G. Kunjamma, U.K. Madhusoodanana and S. Ghosh, *Anal. Chim. Acta*. **350**(2004), pp 233-236.
[5] B.Halliwell, M. V. Clementb and Lee H. Long, *FEBS Lett*. **486**(2000), pp. 10-13.
[6] Y. Liu, J. Qian, X. Fu, H.Liu, J. Deng and T. Yu, *Enzyme Microb. Technol*. **21**(1997), pp. 154-159.
[7] Y. J. Teng, S. H. Zuo and M. B. Lan, *Biosens. Bioelectron*. **24**(2009), pp. 1353-1357.
[8] J.J. Chena, F. Zenga, D.M. Lia, J.B. Niub and F. Pan, *Thin Solid Films*. **485**(2005), pp. 257-261.
[9] A. Arora, A. Aroraa, V.K. Dwivedia, P. J. Georgeb, K. Sreenivasc and V. Gupta, *Sens. Actuator A*. **141**(2008), pp.256-261.
[10] Y. Yoshino, T. Makino, Y. Katayam and T. Hata, *Vacuum*. **59**(2000), pp. 538-545.
[11] Y-F. Li, Z.-M. Liu, Y.-L. Liu, Y.-H. Yang, G.-L. Shena and R.-Q. Yu, *Anal. Biochem*. **349**(2006), pp. 33-40.
[12] X. Zhu, I. Yuri, X. Gan, I. Suzuki and G. Li, *Biosens. Bioelectron*. **22**(2007), p. 1600-1640.

[13] Y.-L. Liu, Y.-H. Yang, H.-F. Yang, Z.-M. Liu, G.-L. Shen and R.Q. Yu, *Inorg. Biochem.* **99**(2005), pp. 2046-2053.
[14] C. Xiang, Y. Zou, L.-X. Sun and F. Xu, *Sens. Actuator B.* **136**(2009), pp. 158-162.
[15] T. Tangkuaram, C. Ponchio, T. Kangkasomboon, P. Katikawong and W. Veerasai, *Biosens. Bioelectron.* **22**(2007), pp. 2071-2078.
[16] H. P. Bai, X. X. Lu, G. M. Yang and Y. H. Yang, *Chin. Chem. Lett.* **19**(2008), pp. 314-318.
[17] X. Ren, C. H. Jiang, D. D. Li and L. He, *Mater. Lett.* **52**(2008), pp. 3114-3116.
[18] J. Jeng, T.-Y. Chen, C.-F. Lee, N.-Y. Liang and W.-Y. Chiu, *Polymer*. **49**(2008), pp. 3265-3271.
[19] V. Gupta, N. Miura, *Electrochem. Commum*. **7**(2005), pp. 995-999.
[20] Y. Guo and Y. Zhou, *Eur. Polym. J*. **43**(2007), pp. 2292-2297.
[21] H. Zhoo, J. Wen, X. Ning, C. Fu, J. Chen and Y. Kuang, *Synth. Met*. **157**(2007), pp. 98-103.
[22] Y.-Y. Hong, Y.-K. Hsu, A. Ganguly, C.-C. Chen, L.-C. Chen and K.-H. Chen, *Electrochem. Commun.* **11**(2009), pp. 850-853.
[23] M. Aoife, W. Frank, N. Orawan, E. M. Simon, J. K. Anthony, G. W. Gordon, and R. S. Malcolm, *Electrochem. Commun*. **7**(2005), pp. 317-322.

Optimization for determination of esters in biodiesel oil by spectrophotometric method

M. Kitiphatmontree[1*], K. Yindeechat[1], W. Youlamyai[1] , A. Retvereeyasakul[1]

[1] Department of Chemistry, Faculty of Science and Technology, Rajamangala University of Technology Thanyaburi (RMUTT) Pathumthani, Thailand 12110

[*] E-mail: mkitiphatmontree@hotmail.com

Abstract: The simple spectrophotometric method for the determination of esters has been developed. The procedure is based on the quantitative determination of ferric hydroxamate generated from the reaction of esters, hydroxylamine hydrochloride in basic solution at 120 °C, and ferric chloride. The formed complex was monitored through absorbance at 517 nm. The parameters affecting the absorbance value were explored for optimum analytical performance. The optimum conditions were 1.50 cm^3 of 0.5M hydroxylamine hydrochloride, 0.40 cm^3 of 6M sodium hydroxide, 1.00 cm^3 of 3M hydrochloric acid and 0.50 cm^3 of 5 % ferric chloride. The method exhibits linear response upto 7.50%wt. and a detection limit of 0.23%wt. The linear range and working range were used at the same range 1.25 to 7.50%wt. The proposed method can be applied to biodiese(B100) for the measuring the esters quantity in the percentage unit of biodiesel oil.

Introduction

Biodiesel is a renewable fuels, alternative diesel oil produced from vegetable oils, animal fats and recycled cooking oil, that is reacted with alcohol in the presence of a catalyst. Biodiesel can consist of up to 100 different fatty acid methyl esters depending on the sources of oil used during production. Addition, this non-alkyl esters of long chain fatty acid and may be used alone or blended with petroleum based diesel oil. Gas Chromatography (GC) is commonly adopted to quantitative pure biodiesel(B100) according to the following standard methods. This GC analysis provides verification that the esters content in biodiesel(B100) is great than 96.5 %w/w [1]. The calculation of the percentage of esters is achieved with calibration that this method is suitable for esters which contain total esters in biodiesel.

The hydroxamic acid test is generally identification of ester function group of ester compounds. The esters react with hydroxylamine hydrochloride in the presence of sodium hydroxide under boiling solution to form the sodium salt of the corresponding hydroxamic acid. On acidification and addition of ferric chloride the magenta-coloured iron (III) complex of the hydroxamic acid is formed [2,3,4]. The preparation of ferric(III) hydroxamate are as represented by the reaction below:

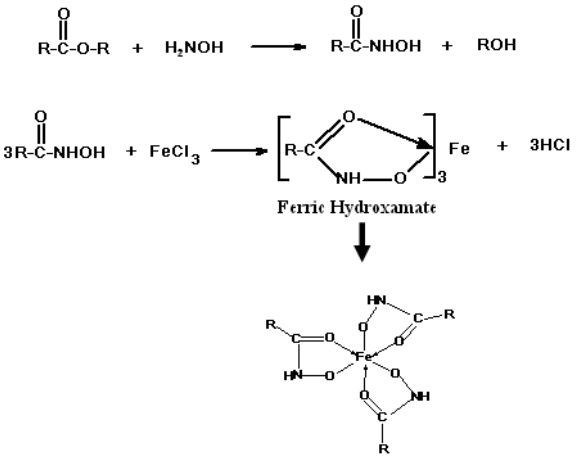

Where R = Alkyl of long chain fatty acid

This method can be determined triglyceride quantity of a partitioning study of olive oil in microemulsion-based gels[5]. This project is then focus determine the esters quantity from ester function group of fatty acid methyl esters (FAME) in biodiesel and biodiesel blends. Notice of the reaction above, the hydroxamic acid was reacted to pass ester bond that methyl or ethyl was not brought to form hydroxamic acid. This work was studied probability of determination the esters quantity in biodiesel by spectrophotometric method. This simple method may be further developed it to detect total esters in biodiesel oil or biodiesel blends (B5 or B20).

Materials and Methods

Ethyl carprylate was represented standard ester for optimization and purchased from Aldrich. Absolute ethanol was used the solvent and purchased from Scharlau. Sodium hydroxide and hydrochloric acid were purchased from BDH. Ferric chloride and hydroxylamine hydrochloride were obtained Fluka and UNILAB Company respectively. All other reagents were of Analytical reagent grade. Except, ethanol 95% for dilution was of commercial grade. It was purified by single distillation. Water was doubly distilled. Standard biodiesel(B100) was obtained from one company. The purity of fatty acid methyl ester in biodiesel(B100) was examined by GC. Acceptable values were assigned to be 98.74% which is the standard range for biodiesel(B100).

The absorbance was measured on Shimadsu UV-visible spectrophotometer series UV1601. While, the solution was mixed by Voltex mixer series Vortex Genie 2 and boiled from heater of Heidolph.

In this method, ethyl carprylate was used to optimize condition throughout preliminary studies. The standard material for calibration curve was created from biodiesel(B100).

The preparation of $Fe(C_8H_{16}O_2)_3$ complex from the aliquot was made as follows: Dissolved a portion of 10 µl aliquot sample (Ethyl carprylate) in a test tube containing 1 cm^3 of absolute ethanol. Accurately added 1.00 cm^3 of 0.5M hydroxylamine hydrochloride in 95% ethanol and 0.40 cm^3 of 6M sodium hydroxide solution. Heated the mixture to boil for 1 minute, and slowly cooled down to room temperature. The mixture was then acidified by slightly adding 1 cm^3 of absolute ethanol and 1 cm^3 of 3M hydrochloric acid solution, prior to an addition of 0.50 cm^3 of 5% ferric chloride solution. After well shaking, $Fe(C_8H_{16}O_2)_3$ complex was formed. The complex solution was made up to 25 ml with 95% ethanol and measured the absorption spectra[5].

Preliminary studies for optimize condition were aimed to study the effect of amount of reagent which produced maximum absorbance. Dissolved a portion of 50 µl aliquot sample (Ethyl carprylate) in a test tube containing 1 cm^3 of absolute ethanol. The main reagents were varied as follows: The amount of 0.5M hydroxylamine hydrochloride was varied from 0.50, 1.00, 1.50 and 2.00 cm^3. The 6M NaOH was varied from 0.10, 0.20, 0.30, 0.40, and 0.50 cm^3. 3M hydrochloric acid was varied from 0.50, 1.00, 1.50, 2.00, 2.50, 3.00, 3.50, 4.00, and 4.50 cm^3. And the 5% ferric chloride was varied from 0.10, 0.20, 0.30, 0.40, 0.50, 0.60, 0.70, 0.80, 0.90, and 1.00 cm^3. The complex solution was made up to 25 ml with 95% ethanol and measured the absorption spectra. The suitable volume of each reagent was chosen to use follow the data which produce maximum absorbance. A blank was treated in the same way as the sample. They concentration the reform can be measured spectrophotometrically by investigating the absorbance at its maximum wavelength, 517 nm.

After optimization, the standard calibration curve was prepared based on quantities of biodiese(Bl100) as follows: The stock of standard biodiesel was diluted from 1.25 g biodiesel(B100) in 100 cm^3 absolute ethanol. After that, calibration graphs for the biodiesel were obtained over the range 50-300 mg/25cm^3 of sample from stock of standard.

The detection limit for the analytical procedure was measured from a suitable blank value. It was obtained from calculation of reagent blank signal.

Results and Discussion

The ethyl caprylate was determined by using the hydroxamic acid method in which the concentration of complex solution formed from a mixture of ethyl caprylate and hydroxylamine hydrochloride/ferric chloride, $Fe(C_8H_{16}O_2)_3$ complex, is measured.

The figure 1 shows the absorption spectra of complex solution. The complex possessed a maximum absorption in visible region at 517 nm.

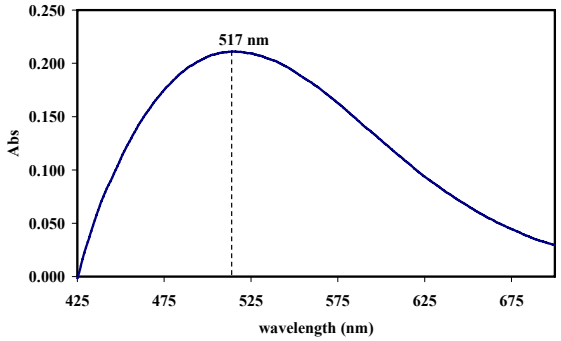

Figure 1. the absorption spectra of ferric (III) hydroxamate as $Fe(C_8H_{16}O_2)_3$ complex solution from ethyl caprylate.

When variation component, was measured the following results were obtained:

1. The effect of variation hydroxylamine hydrochloride volume. There is an optimum 0.5M hydroxylamine hydrochloride content of about 1.50 cm^3 that produce maximum absorbance; increasing the hydroxylamine hydrochloride beyond this is not benefited, that is shown in figure 2.

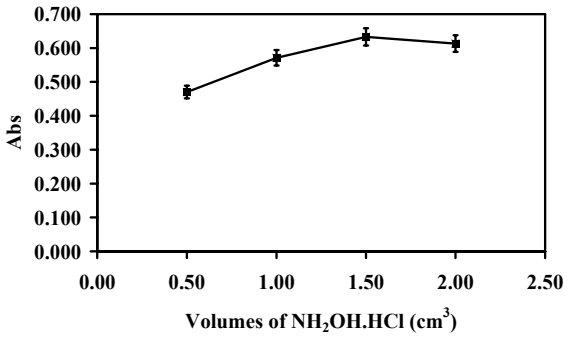

Figure 2. Effect of 0.5M hydroxylamine hydrochloride content on the absorbance at its maximum wavelength , A_{517}.

At the optimum volume, the hydroxylamine hydrochloride was reformed under basic to the hydroxamate that it is involved in the coordination to ferric(III) ion complex suitably.

2. The effect of variation sodium hydroxide solution volume. When volume of 6M NaOH is further increased up to a value 0.50 cm^3 a decrease in the absorbance is observed. This result shows a suitable pH of solution which is solubility of complex. Normally, each of complex compounds was reacted under the special pH range.

That is shown in figure 3. There is an optimum 6M sodium hydroxide solution content of about 0.40 cm^3 that produce maximum absorbance; increasing or decreasing the sodium hydroxide beyond this is not benefited.

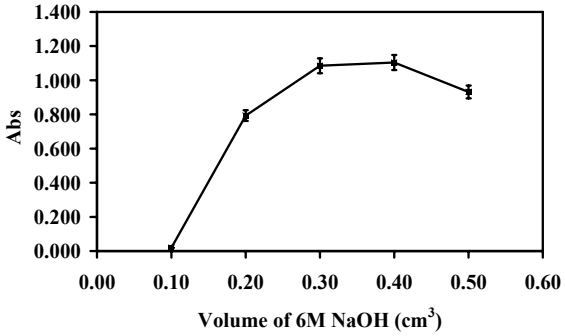

Figure 3. Effect of 6M sodium hydroxide solution content on the absorbance at its maximum wavelength , A_{517}.

3. The effect of variation hydrochloric acid solution volume. There is an optimum 3M hydrochloric acid solution content of about 1.00 cm^3 that produce maximum absorbance; increasing the hydrochloric acid beyond this is not benefited, that is shown in figure 4.

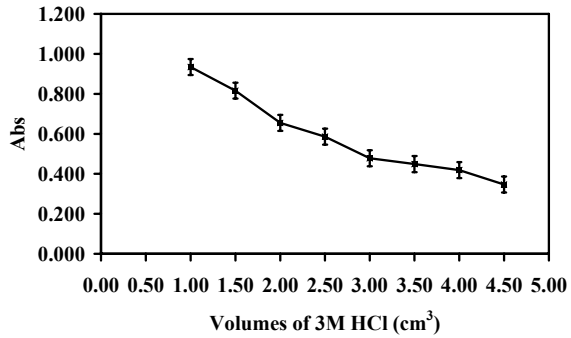

Figure 4. Effect of 3M hydrochloric acid solution content on the absorbance at its maximum wavelength , A_{517}.

When volume of 3M HCl is further increased up to a value 4.50 cm^3 a decrease in the absorbance is observed. This result shows a suitable pH of solution which is formed complex.

4. The effect of variation ferric chloride solution volume. There is an optimum 5%w/v ferric chloride solution content of about 0.50 cm^3 that produce maximum absorbance. It was found that increasing the 5%w/v ferric chloride solution beyond this is almost independent of the maximum absorbance, that is shown in figure 5.

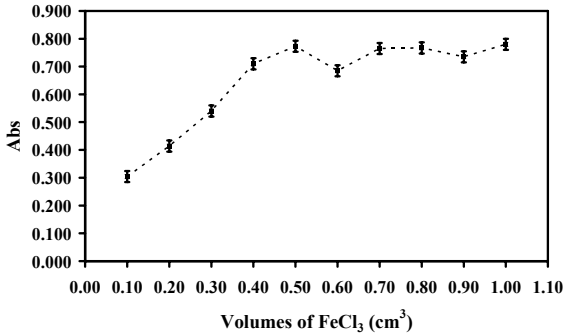

Figure 5. Effect of 5%w/v ferric chloride solution content on the absorbance at its maximum wavelength, A_{517}.

The figure 6 is a plot of pH in the solution against variation of volumes $FeCl_3$. It shows an increase in the initial pH when the amount of $FeCl_3$ is increased, which shows the completely complex formed and the increasing amount of ferric chloride beyond this is decrease pH. On account of, the remainder of ferric (III) ion can be not reacted to the $Fe(C_8H_{16}O_2)_3$ complex. To cause the hydrolysis of ferric(III) ion is increase acidic in solution. It was explained following equation (1) that shown pKa ≈ 2.2 [6]. The pH was obtained decrease when increased ferric (III) ion.

$$Fe^{3+} + H_2O \rightleftharpoons Fe(OH)^{2+} + H^+ \quad \text{.....(1)}$$

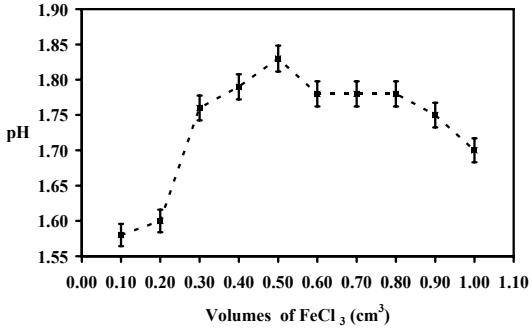

Figure 6. Effect of variation 5% ferric chloride solution content on pH influence.

The optimization condition can be summarized as shown in table 1.

Table 1. Variables ranges studied and optimum values for reaction of $Fe(C_8H_{16}O_2)_3$ complex.

Variables	Range studied	Value chosen
0.5M hydroxylamine hydrochloride	0.50 – 2.00 cm^3	1.50 cm^3
6M sodium hydroxide	0.10-0.50 cm^3	0.40 cm^3
3M hydrochloric acid	1.00 – 4.50 cm^3	1.00 cm^3
5% ferric chloride	0.10 – 1.00 cm^3	0.50 cm^3

To determine the total esters in the biodiesel standard on complex formed is shown in figure 7. This is the ability of the method to give a response which is proportional to the concentration of biodiesel.

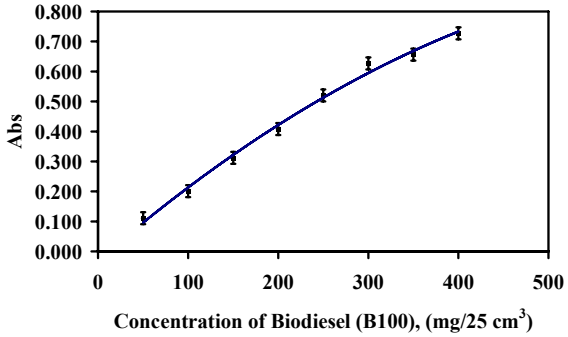

Figure 7. Effect of Biodiesel(B100) concentration on linear range.

A spectrophotometric method was used to measure the concentration of esters in biodiesel. The spectrophotometer response is shown to be linear from 50 to 400 mg/25cm^3 of sample (1.25 to 10.00%wt). Therefore, the method has a working range from 50 to 300 mg/25cm^3 of sample (1.25 to 7.50%wt) biodiesel(B100) concentration as shown in figure 8.

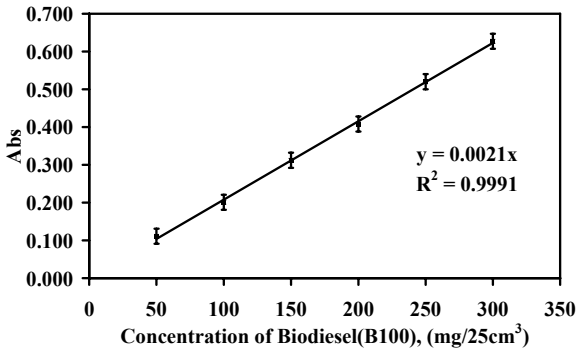

Figure 8. Calibration curve for absorbance versus biodiesel(B100).

The calibration, measurement and calculation of results were as described under figure 8. The esters content were obtained by reference to the calibration curve. The results are calculated from the calibration curve and converted in the percentage unit of biodiesel.

The limit of detection, was derived from the smallest measure of blank, LOD = 0.23%wt, that can be detected with reasonable certainty for a given analytical procedure. It was calculated from 3SD of reagent blank signal.

Conclusions

This work presents the optimal condition for reaction between ester and reagents to $Fe(C_8H_{16}O_2)_3$ complex. They was prepared as follows then method. The biodiesel(B100) have component of esters function group in material that can be measured esters quantity from this spectrophotometric method under the optimal condition. A calibration curve is drawn using the stock biodiesel(B100) solution in the range 50 to 300 mg/25cm^3 of sample. The results can be calculated concentration of sample from calibration curve in mg/25cm^3 of sample unit and to convert percentage unit. In addition, this method can easily be prepared to determine total esters quantity in biodiesel oil but the problem about matrix effect have studied. However, this project will study the method validation further experiments.

References

[1] EN 14214: 2003 Automotive fuels-Fatty Acid Methyl Esters(FAME) for diesel engins.

[2] A.O. Aliyu, J.N. Nwabueze., *J. Physi. Sci.* **3(1)**, (2008), pp. 018–021.

[3] Brian S. Furniss, Antony J. Hannaford and Peter W.G. Smith, *Vogel's Textbook of Practical Organic Chemistry*, Fifth edition, ELBS, (1989).

[4] http://www.chem.uwimona.edu.jm/lab-manual. January 2003.

[5] M. Kitiphatmontree,The Kinetic Study of Lipase Catalysed Hydrolysis of Olive Oil in Microemulsion-Based Gels, Master's Thesis, Ramkhamhaeng University, **1997**.

[6] K.B. Agashe, J.R. Regalbuto., *J. Colloid and Interface science.* 185,(1997), pp.174-189.

Flow injection chemiluminescence for the determination of cephalexin, cefaclor and cefadroxil using acidic potassium permanganate and formaldehyde system

C. Thongpoon[1]*, B. Liawruangrath[2] and T. Machan[3]

[1] Program of Chemistry, Faculty of Science and Technology, Pibulsongkram Rajabhat University, Phitsanulok, Thailand 65000
[2] Department of Pharmaceutical Sciences, Faculty of Pharmacy, Chiang Mai University, Chiang Mai, Thailand 10900
[3] Program of Applied Chemistry, School of Science, Mae Fah Luang University, Chiang Rai, Thailand 57100

* E-mail: g4370029@yahoo.com,

Abstract: Flow injection chemiluminescence (FICL) system was designed, fabricated and investigated for the determination of three cephalosporin antibiotics (cephalexin, cefaclor and cefadroxil). The method was based on the chemiluminescence (CL) emitting reaction between each cephalosporin and potassium permanganate ($KMnO_4$) in an acid medium, which was greatly enhanced by formaldehyde. The optimum conditions for CL reaction were studied in detail using flow injection (FI) system. Under the optimum conditions, calibration graphs over the ranges of 0.1-8.0 μg ml^{-1} for cephalexin and cefaclor, and 0.1-10.0 μg ml^{-1} for cefadroxil were obtained. The limits of detection (3σ) for cephalexin and cefaclor were 0.05 μg ml^{-1}, and for cefadroxil was 0.02 μg ml^{-1}. The relative standard deviation (R.S.D.) were less than 2% (n=11) with the percentage recovery of 99.4 ± 1.7%, 99.0 ± 1.5% and 99.2 ± 1.4% for cephalexin, cefaclor and cefadroxil, respectively. The method was successfully applied to the determination of cephalexin, cefaclor and cefadroxil in pharmaceutical formulations with no evidence of interference from common excipients. The results compared favourably with those obtained by the official methods, and were in agreement with the declared compounds. The method can be used for quality control assay of the studied cephalosporins.

Introduction

Cephalexin, cefaclor and cefadroxil are some of the first-generation cephalosporin antibiotics characterized by a broad antibacterial spectrum and a resistance to beta-lactamase-producing organisms in addition to its antimicrobial activity [1]. The structures of them are illustrated in Figure 1.

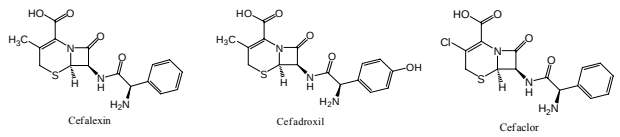

Figure 1 Chemical structures of the investigated drugs

Many methods have been reported for the determination of cephalosporins, such as HPLC [2-4], CE [5], spectrophotometry [6-8], spectrofluorometry [9,10], and polarlography [11].

Chemiluminescence (CL) is the emission of radiation, usually in the visible or near-infrared region, as a result of chemical reaction. One of the reaction products is formed in an electronic excited state, and emits the radiation on falling to the ground state. CL is becoming a powerful analytical tool with widespred application in various fields owing to its high sensitivity, wide dynamic range and simple instrumentation [12-15]. The advantages of flow injection analysis (FIA) has been one of the reasons for the increasing number of applications of CL. The use of FICL as a simple means for pharmaceuticals detection and has been applied to many drugs, such as morphine [16], buprenorphine hydrochloride [17], loprazolam [18], tetracycline [19] and amoxicillin [20]. Since then, a few of such reactions have been reported mainly in cephalosporin analysis [21-24].

The present paper described a simple FICL method for the determination of cephalexin, cefaclor, and cefadroxil. The method was based upon the enhancing effects of these antibiotics on the CL reaction of formaldehyde with potassium permanganate in acid condition which shows lower detections limits and wider calibration ranges. The method was applied to the determination of cephalexin, cefaclor, and cefadroxil in pharmaceutical preparations with satisfactory results.

Materials and Methods

Instruments : The FICL manifold was designed and fabricated as shown in Figure. 2. The reaction reagents were pumped to the three-line manifold by a peristaltic pump (Gilson, Miniplus 2) at a total flow rate of 6.0 ml min^{-1} through poly(tetrafluoroethylene) (PTFE) flow tubes (Tygon, 0.8-mm i.d. resistant to acid). The water carrier stream, and the reagent streams (4.0 M formaldehyde solution in H_2SO_4 and $KMnO_4$ oxidant) both at flow rate of 2.0 ml min^{-1}. A 100 μl sample or standard of cephalosporin was injected into water carrier stream. Acidic 0.50 mM $KMnO_4$ was used as the oxidant and 5%v/v formaldehyde solution in 4.0 M H_2SO_4 as enhancing reagent.

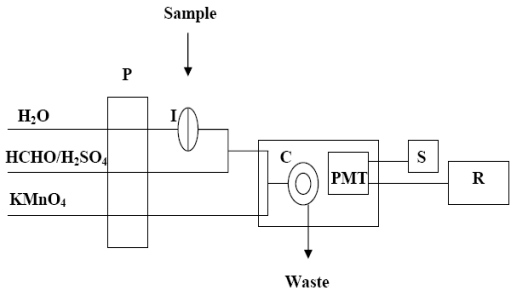

Figure 2 FICL manifold designed for determination of cephalexin, cefaclor, and cefadroxil. (P) peristaltic pump; (I) injection valve; (C) flat spiral-coiled glass tube flow cell; (PMT) photomultiplier tube; (S) photomultiplier source power supply; (R) chart recorder.

A home-made detector was used which comprised three components: a T-piece where reagent and carrier streams come together, a flat spiral flow cell and a photomultiplier tube (PMT) was operated at 0.55 kV, provided by a stable high voltage power supply; detector components were placed inside a closed black box to avoid light input. A chart recorder recorded the signal and the peak height was measured for quantification.

Reagents: All of solutions and chemicals were prepared from analytical reagent grade materials using distilled, deionised water. Cephalexin, cefaclor and cefadroxil standards were purchased from Sigma, Poole, Dorsest, UK.

A stock standard solution containing 1000 μg ml^{-1} of each cephalosporins were prepared by dissolving 100 mg of each drug in 100 ml of water.

Potassium permanganate ($KMnO_4$) and sulfuric acid (H_2SO_4) were obtained from Fisher Chemicals (Loughborough,UK). The stock standard solution of $KMnO_4$ was prepared daily and protected from light using amber glass bottles.

A solution of 5%v/v formaldehyde was prepared by dissolving formaldehyde (Fisher Scientific Chemicals, UK) in 4.0 M H_2SO_4.

Pharmaceutical products containing the investigated drugs were purchased from commercial sources in Phitsanulok and Chiang Mai Province, Thailand.

Optimization studies: The optimization of experimental conditions was carried out by means of a univariate method, using cefadroxil as a model molecule. The optimized FICL system for the determination of cefadroxil is represented in Figure 2, which is consisting of three channels FI manifold. The optimized conditions consisted of the water carrier stream, 4.0 M H_2SO_4 as the oxidant stream and a third stream of 5%v/v formaldehyde dissolved in 4.0 M H_2SO_4 to provide an acidic medium and act as an enhancer. The total flow rate of the carrier, the oxidant and the acidic streams were 6.0 ml min^{-1}. A 100 μl of cefadroxil standard or sample solutions were injected into the water carrier stream. The CL emission intensity from the reaction of cefadroxil with 0.50 mM $KMnO_4$ in sulfuric acid medium, enhanced by formaldehyde was monitored. The CL signals were outputted to a recorder. The typical calibration graphs were obtained by plotting CL intensity (mV) against cefadroxil concentration.

Results and Discussion

Effect of different acid concentrations:

It was observed that the CL signal of $KMnO_4$-formaldehyde system was stronger in acid solution than in neutral or basic solution. Four different acids (i.e. HCl, HNO_3, H_3PO_4, and H_2SO_4) of different concentrations, as the mediums for $KMnO_4$, over the range of 0.05-7.0 M were studied. The results showed maximum CL intensity was obtained with 4.0 M H_2SO_4. The effect of H_2SO_4 is shown in Figure 3.

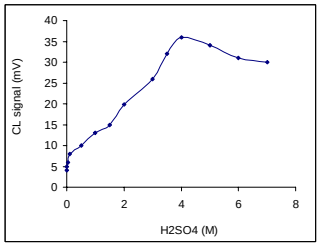

Figure 3 Effect of H_2SO_4 of concentrations on CL intensity. Conditions: cefadroxil 50.0 μg ml^{-1}, formaldehyde 2%v/v in 0.10 mM $KMnO_4$.

Effect of $KMnO_4$ concentration:

The effects of $KMnO_4$ concentration on the CL reaction of cefadroxil have been studied over the range of 0.05-2.0 mM. The CL intensity continued to increase with increasing $KMnO_4$ concentration up to 0.50 mM. The experimental results showed that 0.50 mM $KMnO_4$ could give rise to the larger CL response and lower background signal. Larger concentration of $KMnO_4$ could lower the CL intensity. Thus, 0.50 mM $KMnO_4$ was used in this work.

Effect of formaldehyde concentration:

The influence of formaldehyde concentration was studied over the range 0.1-12% v/v; by dissolving formaldehyde in H_2SO_4 solution. Standard solution of cefadroxil (50.0 μg ml^{-1}) with a volume of 100 μl was injected into the FICL manifold (Figure 2).

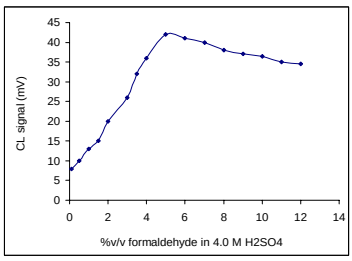

Figure 4 Effect of formaldehyde concentrations on CL intensity. Conditions: cefadroxil 50.0 μg ml^{-1}, 0.10 mM $KMnO_4$.

It was shown that peak heights increased with increasing formaldehyde concentration over the range 0.1-5% v/v, above which the CL signal decreased

gradually, as shown in Figure 4. Therefore, 5% v/v of formaldehyde in 4.0 M H_2SO_4 was applied for subsequent studies.

Effect of flow rate:

The flow rate in each channel is an important parameter influencing on the CL signal of cefadroxil, because the time taken to transfer the excited product into the flow cell is critical for maximum collection of the emitted light. Too low or too high flow rates result in a decrease or even absence of CL signal. At a low flow rate, the residence time for each sample was long and the dispersion was large leading to the reduction of peak height. On the other hand, a high flow rate resulted in a shorter time required for each sample passing through the FI system, a poor precision of the peak height and a large volume of reagent consumption were obtained. In this work, total flow rates between 1.5 and 9.0 ml min^{-1} (with 0.5–3.0 ml min^{-1} /channel) were studied. The optimum total flow rate chosen was 6.0 ml min^{-1} (2.0 ml min^{-1} for each channel)and this was used throughout the experiments. Increasing the flow rate above 6.0 ml min^{-1} does not significantly enhance the peak intensity, which will increase the pressure in the tubing and the consumption of the reagents.

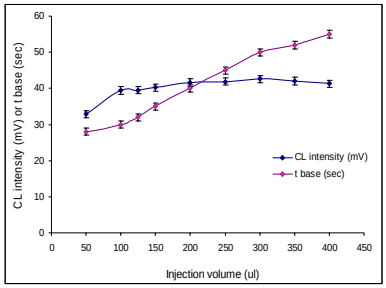

Figure 5 Effect of sample injection volume

Effect of injection volume:

The effect of injection volume was investigated by changing the sample loop over the range 50-400 µl and was found to have an important effect on the signal. The CL signal increased with increasing injection volume and reached the maximum signal at 100 µl. With further increases in sample volume up to 400µl, the CL intensity increases very slightly (Figure 5), and is then decreased whereas the t_{base} or peak width continues to increase rather rapidly and significantly with each increase in sample volume. This is because larger volumes of sample in the carrier stream mix with the reagents over a longer period of time causing alterations of the CL emission profile

So, the selected sample loop in this FICL system was 100 µl because it gave high sensitivity with reasonable sample throughput (120 h^{-1}) and the consumption of standard or sample solutions injected.

Effect of the photomultiplier tube (PMT) voltage:

The effect of the PMT voltage was investigated ranging from 0.4 to 0.7 kV (maximum recommended by the manufacture). Ten injections of water, 0.10 and 0.20 µg ml^{-1} cefadroxil standard solution were performed. There was an exponential relation between the CL intensity and the PMT voltage, both noise and analytical signal increased as the PMT voltage increases; the signal-to-noise ratio reached a maximum value at 0.55 kV and above 0.55 kV the background noise increased considerably. Thus, 0.55 kV was selected as the optimum value to give a high signal with acceptable noise. The influence of PMT voltage on the cefadroxil CL signal was illustrated in Figure 6.

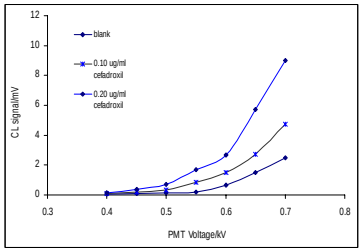

Figure 6 Effects of PMT voltage on the cefadroxil CL signal at concentration of 0.10 and 0.20 µg ml^{-1}.

Interferences Study:

In order to assess the selectivity of the proposed method, the effect of some common inorganic ions and organic compounds was studied by preparing solutions containing 5 µg ml^{-1} of cefadroxil. It was considered not to interfere if a foreign material caused a relative error of less than ± 5% during the determination of 5 µg ml^{-1} cefadroxil. The results showed that no interference had been found when including up to a 1000-fold Na^+, K^+, Mg^{2+}, Ba^{2+}, Ca^{2+}, SO_4^{2-},NO_3^-,PO_4^{3-} ,glucose, lactose, sucrose, citric acid, saccharin, sorbitol, and starch.

Summary of Optimized Experimental Conditions:

The ranges over which the variables involved in the proposed FICL system studied and their optimum conditions are listed in Table 1.

Table 1 The optimized of the FICL conditions for the determination of cephalexin, cefaclor and cefadroxil

Variables	Studied range	Optimum conditions
$KMnO_4$ concentration (mM)	0.05 - 2.0	0.5
H_2SO_4 concentration (M)	0.05 - 7.0	4.0
Formaldehyde concentration (%v/v)	0.1 - 12	5
Injection volume (µl)	50 - 400	100
Total flow rate (ml min^{-1})	1.5 - 9.0	6.0
PMT voltage (kV)	0.40 - 0.70	0.55

Analytical Applications:

The proposed FICL method was successfully applied to the determination of cephalexin, cefaclor and cefadroxil in commercial pharmaceutical formulations. The results are presented in Table 2.

It was found that the results obtained were in agreement with thosed obtained by the phamacopoeia method, which is based on HPLC [25].

Table 2 Results for the determination of cephalosporins in samples by the proposed and official methods (n=5)

Preparation	FICL method (% content)	Official method (% content)
Cephalexin capsules 1	101.4 ± 2.2	101.1 ± 2.0
Cephalexin capsules 2	98.4 ± 2.1	100.4 ± 1.9
Cephalexin powder 3	99.5 ± 1.9	100.2 ± 1.6
Cefaclor capsules 1	102.2 ± 1.8	99.8 ± 2.0
Cefaclor capsules 2	101.2 ± 1.8	103.2 ± 1.9
Cefadroxil capsules 1	102.5 ± 2.0	100.2 ± 1.8

Analytical characteristics for cephalosporins analysis:

Under the optimum conditions, calibration graphs over the ranges of 0.1-8.0 μg ml^{-1} for cephalexin and cefaclor, and 0.1-10.0 μg ml^{-1} for cefadroxil were obtained. The limits of detection (3σ) for cephalexin and cefaclor were 0.05 μg ml^{-1}, and for cefadroxil was 0.02 μg ml^{-1}. The relative standard deviation (RSD) for replicate injections (n=11) of 4.0 μg ml^{-1} of the investigated drugs were found to be 1.23 %, 1.20% and 1.07% for cephalexin, cefaclor and cefadroxil, respectively. This is indicating that the method was very reproducible. The accuracy of the proposed method was verified by 5 replicate injections of 100 μl of commercial drug sample solutions at concentrations of 2.0 μg ml^{-1}. Commercial formulations were spiked with known amounts of the drug in the concentration ranges 0.1-3.0 μg ml^{-1}. The percentage recovery of 99.4□1.7%, 99.0□1.5% and 99.2□1.4% for cephalexin, cefaclor and cefadroxil, respectively, were obtained.

Possible reaction mechanism:

It has previously been suggested [26] that $KMnO_4$ could react with some reductants in the presence of formaldehyde to produce $^1O_2{}^1O_2(^1\Delta_g{}^1\Delta_g)$, a dimeric oxygen molecule in the singlet state, which emits light as it relaxes to $^3O_2(^3\Sigma_g)$, a triplet state oxygen. During the transformation, it could produce CL and the formaldehyde could accelerate oxidation reaction rate [27]. Thus, it is possible that the singlet excited molecular oxygen species is an emitter in the present system, formed by the transfer of energy from oxidized cephalosporins to dissolved oxygen. Based on the above discussion, a possible mechanism for this process is:

1. $MnO_4^- + H^+ + CH_2O$ + cephalosporins → $H_2O + Mn^{2+}$ + oxidized cephalosporins intermediate
2. $^3O_2(^3\Sigma_g)$ + oxidized cephalosporins intermediate → $^1O_2(^1\Delta_g)$ + oxidized cephalosporins product
3. $2\ ^1O_2(^1\Delta_g) \rightarrow {}^1O_2{}^1O_2(^1\Delta_g{}^1\Delta_g)$
4. $^1O_2{}^1O_2(^1\Delta_g{}^1\Delta_g) \rightarrow 2\ ^3O_2(^3\Sigma_g) + h\nu$

Conclusions

Based on the chemiluminescence reaction of the studied cephalosporins with $KMnO_4$ in sulfuric acid, sensitized by formaldehyde, a novel flow injection CL methods was developed for the determination of cephalexin, cefaclor and cefadroxil. The proposed method was simple, rapid and sensitive, and was successfully applied to quantitative analysis of these cephalosporins in pharmaceutical preparations and compared with pharmacopoeia method.

Acknowledgements

The authors gratefully acknowledge to Prof. A. Townshend and Dr. R.A.Wheatley (Chemistry Department, University of Hull, UK) for allowing this work to be carried out in laboratories. The authors are thankful to the Chemistry and Applied Chemistry Research Unit, Faculty of Science and Technology and the Institute of Research and Development, Pibulsongkram Rajabhat University (PSRU) for providing facilities and also supporting partial finance for presenting this work .

References

[1] D. Bassetti, Chemioterpici, Antiffettivi e Loro Impiego Razionale, fourth ed., Lomardo, Rome, Italy, 1986.
[2] V.F. Samanidou, E.A. Hapeshi, I.N. Papadoyannis, *J.Chromatogr. B.* **788** (2003), pp. 147.
[3] L.K. Sorensen, L.K. Snor, *J.Chromatogr. A.* **882** (2000), pp. 145.
[4] M. Kai, H. Kinoshita, M. Morizono, *Talanta.* **60** (2003), pp. 325.
[5] Y. Mrestani, R.H.H, Neubert, *J. Pharm. Biomed. Anal.* **24** (2001), pp. 637.
[6] C.S.P. Sastry, K.R. Rao and D.S. Prasad, Mikrochim. Acta **126** (1997), pp. 167.
[7] S.M. El-Ashry, F. Belal, M.M. El-Kerdawy and D.R. El Wasseef, *Mikrochim. Acta.***135** (2000), pp.191.
[8] H. Salem and G.A. Saleh, *J. Pharm. Biomed. Anal*. **28** (2002), pp.1205.
[9] M. Hefnawy, Y. El-Shabrawy and F. Belal, *J. Pharm. Biomed. Anal.* **21** (1999), pp.703.
[10] X.W. He, B. Tang, H.X. Shen, *Chem. J. Chin. Univ.* **16** (1995), pp. 26.
[11] A. Ivaska and F. Nordstrom, *Anal. Chim. Acta.* **146** (1983), pp. 87.
[12] W.R. Seitz, C.R.C. Crit, *Rev. Anal. Chem.* **13** (1981), pp. 1.
[13] A. Townshend, *Analyst.* **115** (1990), pp.495.
[14] M.L. Grayeski, *Anal. Chem.* **59** (1987), pp.1243A.
[15] K. Robards, P. Worsfold, *Anal.Chim.Acta.* **266** (1992), pp. 147.
[16] R.W. Abbott, A. Townshend, R. Gill, *Analyst.* **111** (1968), pp.634.
[17] A.A. Alwarthan, A. Townshend, *Anal.Chim.Acta.* **185** (1986), pp. 329.
[18] A.R.J. Andrews, A. Townshend, *Anal.Chim.Acta.* **227** (1989), pp. 65.
[19] A. Townshend, W. Ruengsitagoon, C. Thongpoon, S.

Liawruangrath, *Anal.Chim.Acta.* **541** (2005), pp. 105.
[20] C. Wei, Y. Jing-He, S. Chang-Xia, C. Yan-Jing, G. Qing-Fei, *Luminescence.* **20** (2005), pp.20.
[21] C.Thongpoon, B. Liawruangrath, S. Liawruangrath, R.A. Wheatley, A. Townshend. *Anal.Chim.Acta*. **553** (2005), pp. 123.
[22] C.Thongpoon, B. Liawruangrath, S. Liawruangrath, R.A. Wheatley, A. Townshend.*J. Pharm. Biomed. Anal.* **42** (2006), pp. 277.
[23] Y. Sun, Y. Tang, H. Yao, X. Zheng. *Talanta.* **64** (2004), pp. 156.
[24] F.A. Aly, N.A. Alarfaffj, A.A. Alwarthan. *Talanta.* **47** (1998), pp. 471.
[25] The British Pharmacopoeia, HMSO, London, 1998, Volume 1.
[26] N.T. Deftereos, A.C. Calokerinos, C.E. Efstathiou, *Analyst*, **118** (1993), pp. 627.
[27] D. Slawinska and J. Slawinski, *Anal. Chem*, **47** (1975) , pp.210.

Effect of ethanal percentage in gasohol fuel vapour evaluated by electronic nose technique

T. Rutirawut*, R. Jaisutti, T. Kerdcharoen and T. Osotchan

Center of Nanoscience and Nanotechnology, Department of Physics, Faculty of Science,
Mahidol University, Ratchathewi, Bangkok, Thailand

* Corresponding Author tamdefault@gmail.com

Abstract: An amount of ethanol content in gasohol fuel leading to the different characteristics of odor can be detected by various gas detectors in electronic nose technique. In this research, the vapour of gasohol fuels with systematically varied ethanol amounts was measured and analysed by using a home-built electronic nose system with four different gas sensors. The respond signals from each sensor have different characteristic for each odor. The vapour with varied percentage of ethanol including 0%, 10%, 20%, 30%, 40%, 50%, 60%, 70%, 80%, 90% and 100% were used as a database for principle component analysis (PCA) and the pattern from PCA at the percentage between 0% to 30% and 70% to 100% can be separated clearly. This is sufficient to determine the ethanol in commercial gasohol fuels in class E10 and E20 while the commercial diesel response located in well separated position in PCA pattern. The data for all contents of ethanol located along the straight line of PC2 = 0.56 PC1 +0.37. The PCA pattern can be applied to identify the key feature response used in extracting the percentage of ethanol by using coordinate transformation. It can be demonstrated that the decay characteristics of two proper sensors can provide the major feature while the maximum response value of these two sensors contributed much less than those from decay values with the about 7% of relative components on the identified axis.

Introduction

The gasohol, gasoline-ethanol mixture, is one of nowadays alternative fuels. It can be mixed with ethanol in various ratios for use in different gasoline engine while the conventional ratio measurements [1,2] still depend on complicated chemical reactions and expensive instrument. The different ethanol contents have result in properties of vapour. Therefore, it would be a great advantage if we had access to relatively cheap, uncomplicated, and non-waste substance devices determining the ratio of gasohol.

The "electronic nose" technology [3] has potential to meet these previous requirements. The electronic nose consists of a matrix of metal oxide semiconductor gas sensors and having partial selectivity coupled with an appropriate data analysis system. This enables the characterization of complex gas mixtures by recognition of sensor response patterns. Potential applications of these instruments are related to food and beverage, cigarette, car, pharmaceutical, and paper industry, biotechnology, medicine, wastewater treatment plants, monitoring of indoor air and odour pollution from pig and chicken slurry and sewage treatment works.

This work evaluated the effect of ethanol content in gasohol fuel with analysis of characteristic of response signal. The principal component analysis (PCA) method is consequently applied to classify patterns of response signal because this method is acceptable one of all classification method.

Materials and Methods

The sensory cell of home-built electronic nose system consists of four commercially gas sensors manufactured from Figaro, i.e. sensor TGS2620 (sensor for alcohol and organic solvent vapors), TGS2600 (sensor for general air contaminants), TGS822 (sensor for organic solvent vapors) and AF63 (sensor for ethanol). They were used to measure and classify 16 types of fuel including gasoline (GSH E00), gasohol E10 (GSH E10), E20, E30, E40, E50, E60, E70, E80, E90, pure ethanol (GSH E100), commercial gasoline octane 91(C91 E00), commercial gasohol E10 octane 91(C91 E10), commercial gasohol E10 octane 95(C95 E10), diesel (DSL) and diesel B5 (DSL B5).

In the measurement, 0.2 ml of gasohol odors was introduced in a flask and maintained at room temperature. The pumped air was used to convey the odor to the sensor which is controlled its flow rate by mass flow controller. The output voltage across load resistor connected in series with gas sensor resistor was monitored, acquired and stored in a computer for further analysis.

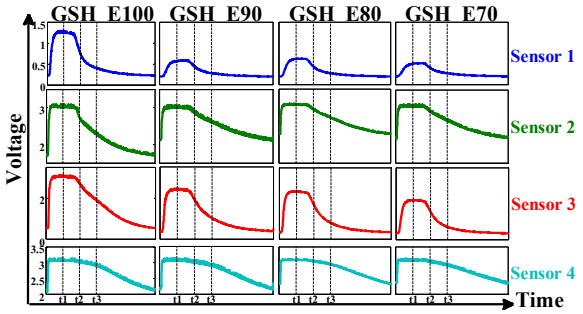

Figure 1. Dynamic response of four types of sensors during exposed to pure ethanol, gasohol E90, E80, and E70 and the represent parameters were extracted from response signal at time of 2, 4 and 6 minute for further PCA analysis.

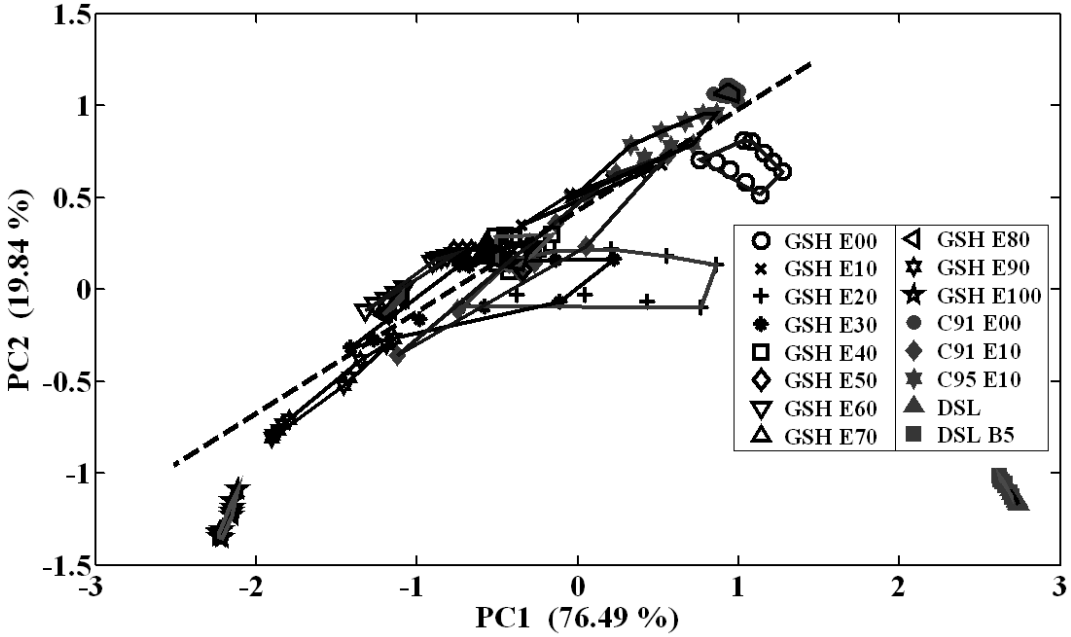

Figure 2. Classification pattern of various ratios of gasohol fuel and commercial fuels

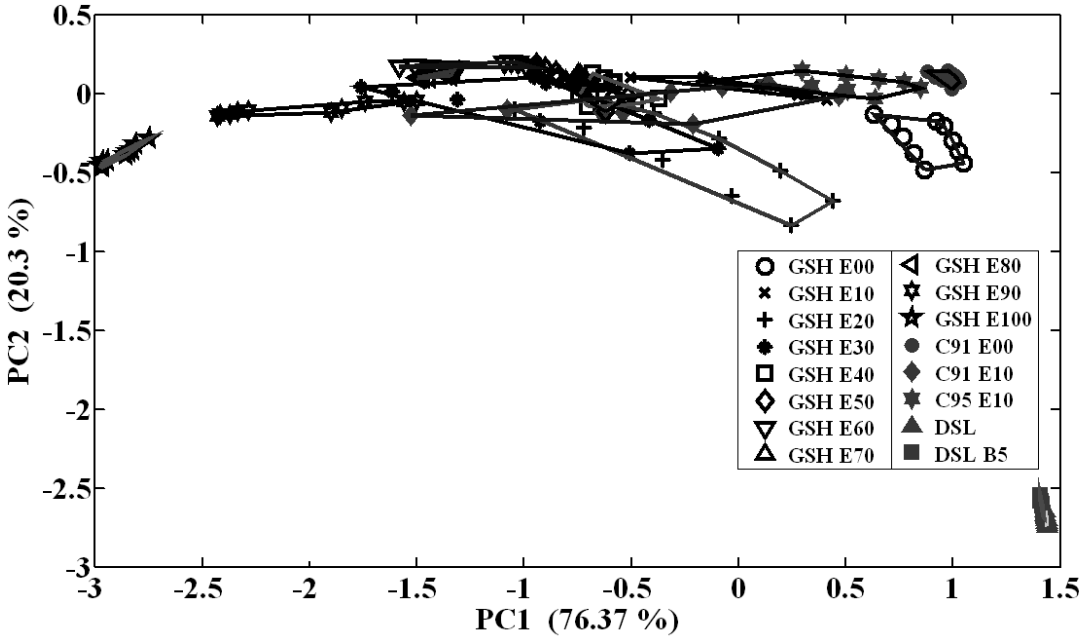

Figure 3. Coordinate transform of classification pattern of various ratios of gasohol fuel and commercial fuels

In order to study sensor response pattern under difference types of odor sample, a single period of each measurement (2784 points) is collected from the sensor response. Then, few data points were used to represent the response by selecting the average response at time of 2, 4 and 6 min as illustrated in Figure 1. These selecting data were used as the input of PCA [4] calculation for classifying the type of sample.

Results and Discussion

The shapes of measured respond curves depend on the type of odors and sensors as shown in Fig. 1. Each sensor has different maximum response and recovering period with the same odor. The sensor4 has faster responding to gasohol odor than those in sensor2, sensor3 and senso1, respectively. However, their recovery periods indicated the inverse characteristics. The sensor1 has the fastest recovering rate while the

sensor4 shows very slow recovering characteristics. For different percentage of ethanol in gasohol fuel, there are two main types of responding characteristic. The sensor1 and sensor3 show decreasing in maximum response voltage when percentage of ethanol was decreased, while their recovery responses show approximately the same values. The sensor2 and sensor4 has approximately the same value in maximum response voltage but their recovering periods are different. The decreasing percentage of ethanol mixed in gasohol fuel leads to decrease a recovery rate of sensor.

The sensor responses are analyzed by selecting three response voltages at the time of 2, 4 and 6 min. The selected coefficients can be used to derive the feature for classifying the type of odors and it can be concluded that this can be extracted from the whole curve both in steady state and decay information.

The data from several repeated measurement were used as the input of PCA training calculation. The PCA pattern of 10 types of gasohol (the mixtures with varied the ratio of the ethanol) and 5 types commercial fuels were calculated and demonstrated in Figure 2. In this analysis graph, the distinct marker represents each type of fuel which tends to group together and indicated by the loop line in the graph. The marker arrangements of gasohol including mixtures and commercial products are looked like a straight line. By using the linear fit, this line can be described by equation of PC2 = 0.56 PC1 + 0.37 and represented in the graph by dash line.

Most groups of marker are arranged along this line by ratio ordering especially for the gasohol with very high and very low percentage of ethanol. Gasohol types with very high percentage ethanol (i.e. GSH E70 to E100) are aligned on dash line with lower PC1 value than that of low percentage ethanol. Commercial gasoline and gasohol are located at near position of this mixture with the same percentage of ethanol. Furthermore, both commercial diesels are located in far separated position from all type of gasohol.

Figure 3 shows the coordinated transformation of the result in Figure 2. This transformation can be used to calculate the percentage of ethanol from unknown gasohol fuel. The result also shows that diesel fuel is clearly separated from gasohol. However it can not distinguish the percentage of ethanol in middle range of the gasohol fuel.

The coefficient from the first two PCs of four sensors plotted with sensor type was shown in Figure 4. The result shows that most of significant feature of calculation come from selecting data at time2 both in PC1 and PC2. The extracted feature from the recovery time usually provides more informative than those in the maximum value.

Conclusions

The vapour of gasohol fuels with systematically varied ethanol amounts was measured and analyzed by using the electronic nose system and PCA. The result from PCA indicate that gasohol with percentage of ethanol between 0% to 30% and 70% to 100% can be clearly separated.

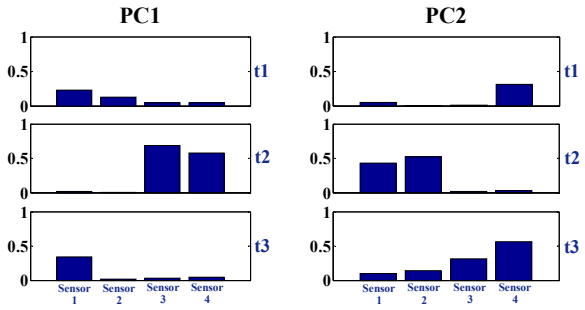

Figure 4. Coefficient components of PCA pattern of various ratios gasohol fuel

This separation is sufficient to determine the ethanol in commercial gasohol fuels in class E10 and E20. The PCA pattern can be applied to identify the key feature response used in extracting the percentage of ethanol by using coordinate transformation. It can be demonstrated that the decay characteristics of two proper sensors can provide the major feature while the maximum response value of these two sensors contributed much less than those from decay values with the about 7% of relative components on the identified axis.

Acknowledgment

One of authors would like to acknowledge the Development and Promotion of Science and Technology Talents Project (DPST) for scholarship. This research was partially supported by National Nanotechnology Center.

References

[1] T.R.L.C. Paixão, J.L. Cardoso and M. Bertotti, *Fuel* **86** (2007), pp.1185-1191.

[2] T. Sobański, A. Szczurek, K. Nitsch, B.W. Licznerski and W. Radwan, *Sens. Actuators* B **116** (2006), pp.207-212

[3] J.W. Gardner and P. N. Bartlett, *Electronic Noses: Principles and Applications*, Oxford University Press, Oxford, 1999.

[4] S.T.R. Ozaki, N.K.L.Wiziack, L.G. Paterno and F.J. Fonseca, *Classification of fuels using multilayer perceptron neural networks*, Olfaction and Electronic Nose 13th Inter. Symp. Proc., 2009.

Determination of selenium in seafood by cyclic instrumental neutron activation analysis and flame atomic absorption spectroscopy

S. Pumsawai[1,2], A. Busamongkol[1]
N. Ruangket[2], P. Sangpattaranet[2] and C. Boonpanaid[2*]

[1]Thailand Institute of Nuclear Technology, Research and Development Division, Bangkok, Thailand.
[2]King Mongkut's University of Technology North Bangkok, Department of Industrial Chemistry, Faculty of Applied Science, Bangkok, Thailand.

*E-mail:cbn@kmutnb.ac.th, Tel:085-931-1719

Abstract: Determination of selenium by neutron activation in the system of Cyclic Instrumental Neutron Activation Analysis(CINAA) measurement and Flame Atomic Absorption Spectroscopy(FAAS) technique were interested. The optimum conditions of CINAA such as irradiation time, decay time, counting time, cooling time between consecutive cycles and number of cycles were investigated. Analytical features of this method were evaluated by analyzing the certified reference materials: SRM 1566b (Oyster Tissue, NIST). This work also developed sensitivity for absorbance measurement in FAAS technique by addition of some transition metals to promote the stability of selenium in flame. The analytical results for determination of selenium in seafood samples by both techniques were not significantly different in the range of 1.24-3.27 mg.kg^{-1} dry weight. Detection limit investigated by CINAA and FAAS was 0.65 and 0.83 mg.kg^{-1} respectively. It was found out that the former method needs no sample preparation and it has low detection limit, with high accuracy and short analysis time.

Introduction

Selenium (Se) is an essential mineral for all mammalian species. Selenium is incorporated into proteins to make selenoproteins, which are important antioxidant enzymes. These antioxidant properties can prevent cellular damage from free radicals that may contribute to the development of chronic diseases such as cancer and heart disease [1]. As selenium is one of the important nutrients, the Recommended Dietary Allowance (RAD) of 55 μg/day for adult females and 70 μg/day for males has been established in the United States [2]. In Canada, the Recommended Nutrient Intake (RNI) level is 50 μg/day for adults [3]. Although selenium is one of the recommended daily diets, we need it in only small amounts. If we take it to excess, there may be some terrible side effects. The United States Environmental Protection Agency (USEPA) has found that selenium potentially causes some health effects, such as hair and fingernail changes, damage to the peripheral nervous system, fatigue and irritability, when people are exposed to it at levels above the MCL for relatively short periods of time. For a lifetime exposure at levels above the MCL, selenium also has the potential to cause some effects which are, for example, hair and fingernail loss, damage to kidney and liver tissue, and problems with the nervous and circulatory systems. Therefore, it is necessary to determine selenium in food in order to make sure that the level of selenium does not exceed the recommended daily intake of selenium.

Neutron activation analysis (NAA) has been reported for the determination of selenium in food as well as other biological samples. Cyclic Instrument Neutron Activation Analysis (CINAA) is a NAA method of activation analysis for elemental analysis in which a sample is irradiated, decayed, counted, then irradiated again, and this process is repeated for a number of cycles. The spectrum from each counting is being summed to give a final total spectrum. By this process, the counts of a short-lived nuclide of interest are considerably increased and the analytical sensitivity of elements is significantly improved. The CINAA by irradiation with thermal, epithermal, and fast neutrons produced from a nuclear reactor, accelerator, or isotopic neutron flux are most often used for this purpose. At least 20 elements which produce short-lived nuclides (half-life less than 100s) by thermal neutron bombardment, and also more than 10 elements which produce nuclides with half-lives of 100-600s can be determined by thermal and epithermal neutron cyclic activation analysis [4]. Nevertheless, the neutron bombardment instrument is not available in a simple laboratory. Furthermore, several analytical reports for the determination of selenium are spectrophotometric techniques[5,6]. One of the most respective methods is atomic absorption spectrometry or atomic emission including vapour generation system. However, the settle of hydride vapour generation equipment is expensive. Flame atomic absorption spectrometry (FAAS) is a widely accepted technique for determination of trace metals but it is seldom employed in determination of selenium because of limiting of sensitivity. Recently, the ordinary flame with the new high-resolution continuum source was an effective method of determination of sulfur [7,8]. Therefore, this work is interested in applying this instrument to selenium detection.

The aim of the present work was to develop optimum conditions of FAAS and CINAA for the determination of Se in seafood samples. The method in this paper has been shown to be a valid method by analyzing certified reference materials namely: NIST 1566b (Oyster Tissue) by CINAA and FAAS techniques.

Materials and Equipments

The TRR-1/MI Research Reactor at the Thailand Institute of Nuclear Technology, Bangkok, Thailand (TINT) was used for samples and standard irradiations. For short-lived nuclides, a pneumatic system was utilized to transfer the sample into the reactor core at a thermal neutron flux of 1×10^{13} $n.cm^{-2}.s^{-1}$. The associated facility for activity measurements is a gamma-ray data acquisition system by ORTEC. It consists of a high-purity germanium (HpGe) detector with a relative efficiency of 30%. The resolution of the detector is 1.85 keV at 1332.5 keV of ^{60}Co. The multi-channel analyzer (MCA) used was DSPEC PLUS program, a digital gamma ray spectrometer. The Analytic Jena atomic absorption spectrometer, model ContrAA 300, flame atomic absorption system has been struggled to get better sensitivity in Se detection.

Working standard solutions for analysis were prepared by diluting with 0.1%v/v HNO_3 to the appropriate amount from 1000 mgSe/L standard solution. The SRMs 1566b, standard reference materials of oyster tissue from National Institute of Standard and Technology were used for evaluation of detection limit, precision and accuracy in both techniques.

Results and Discussion

CINAA conditions studies

SRMs and seafood samples were placed in clean polyethylene vials and heat-sealed before measured. The samples were irradiated using a pneumatic transport system at the TRR1/M1. After the irradiation, the gamma energy at 161.9 keV of Se-77m with the half-life of 17s is measured throughout the experiment. The optimum conditions for short-lived nuclides are summarized in Table 1.

Table 1 optimum condition for the analysis of Se by CINAA

Irradiation Times (s)	Decay times (s)	Count times (s)	Delay time (s)	Cycle
8	30	30	112	6

The LOD was calculated by using Gilmore and Hemingway's equation (1). From the equation, LOD was determined by using standard peak and background from sample spectrum. In this study, selenium peak and background value were obtained of the SRM spectrum using optimum conditions obtained earlier. Figure 1 demonstrated the standard peak area for LOD calculation.

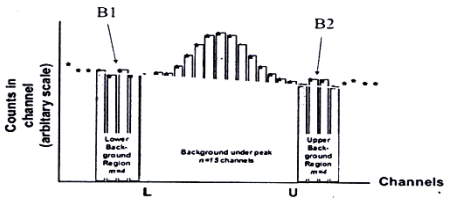

Figure 1 Standard peak area for LOD calculation

$$LOD = 2.71 + 3.29\sqrt{B\left(1 + \frac{n}{2m}\right)} \quad (1)$$

$$\text{Where; } B = (B1+B2)\frac{n}{2m} \quad (2)$$

B1 = summation of count in the channels beyond the lower channel for m channels
B2 = summation of count in the channels beyond the upper channel for m channels
n = number of channels within the peak region
m = number of channels within the background region

LOD values evaluated according to Gilmore and Hemingway [7] in this study was 0.65 mgSe/L.

Treatment of samples

Weighed seafood samples of 0.500 – 1.000 g are treated with 10 mL of a 9:1 of concentrated HNO_3–H_2SO_4 mixture in the microwave oven with the following programs: 5 min at 250 W, 10 min at 450 W and finally 12 min at 650 W. The same procedure was adopted for mineralizing the protein fraction by addition of 8 mL concentrated HNO_3 and digestion until grease dissolved. After the suitable volume reduction, 2 mol/L HCl was added and digested with the following instrumental programs: 3 min at 250 W, 3 min at 450 W, 3 min at 650 W. The analyzed samples were adjusted to the suitable volume with 0.1 mol/L HNO_3.

FAAS conditions studies

The AAS instrument used in this study did not include any hydride generation equipment therefore Se free atom in solution was detected directly in flame at wavelength 196.0267 nm. It is claimed that Se can be detected by FAAS at this wavelength. However, it is questionable whether the resolution of CCD detector of this instrument is that high. The best possible signal achieved from flow ratio of acetylene and air at 60 mL per hour, nebulizer uptake rate at 8 mL per minute concerning in reading time along with replication times at 4 second and 3 times respectively. The stabilizing actions of different modifiers such as Mg^{2+}, Sr^{2+}, Cu^{2+}, Co^{2+}, Ni^{2+}, Sn^{4+} and Ti^{4+} were compared in terms of Se in seafood samples. The performance of each chemical was established by considering maximum absorbance, precision and interrupted signals. It is expected that an addition of a modifier will further stabilize Se to higher pyrolysis temperature. Besides, amount of chemical modifiers were also varied. The results showed that the signal was increased by 39% when the concentration ratio of Ni^{2+} is four times more than the concentration of Se. Therefore Ni^{2+} was chosen as the modifier for the whole experiments.

A Calibration graph for Se was prepared under the optimized conditions from above. The linearity range of the curve was 0.50 – 6.0 mgSe/L. Typical regression line was Abs = 0.012 [Se] + 0.001 (r^2 = 0.998). The limit of detection of this system was 0.83 mgSe/L which is calculated as the triple of standard deviation of the blank measurement (n=6) per slope of the calibration graph.

FAAS interferences studies

The effect of interfering species on the absorbance signal of Se was tested. Different amounts of common cations were added to the tested solution containing two main components of Se mass concentration of 25 mgSe/L and Ni^{2+} mass concentration of 100 mgNi/L as modifier. The tolerance limits were accepted for the maximum error in the range of 95-105% recovery. The results from these studies are collected in Table 2. The tolerance limits of Na^+, K^+ and Ca^{2+} presented as matrix in real sample was 10 times whereas Cu^{2+}, Mg^{2+} and Mn^{2+} were seriously effective with twice times concentration ratio. Nevertheless, these phenomena could not be described clearly in pyrolysis state including Ni^{2+} as a modifier.

Table 2 Tolerance limits of interfering species for the determination of Se (n=3)

Ion	Maximum concentration (mg/L)	%Recovery
Na^+	250	105.72±3.64
K^+	250	105.36±3.44
Ca^{2+}	250	108.36±4.43
Zn^{2+}	125	91.12±1.07
Fe^{2+}	100	95.80±7.90
Cu^{2+}	50	98.32±3.73
Mg^{2+}	50	114.78±4.60
Mn^{2+}	25	93.20±3.28

Analysis of seafood samples

The applicability of the developed methods were evaluated by analyzing 10 seafood items. The experimental results are included in Table 3. The results obtained from FAAS were fewer than CINAA in all cases however T-test (level of significant, α=0.01 and 99%) confirmation showed no significant difference.

Table 3 Determination of selenium in various seafood samples with CINAA and FAAS methods. (n=3)

Sample	Selenium found (mg Se/ Kg sample)		t
	CINAA	FAAS	
Shrimp 1	1.596±0.261	1.309±0.242	2.550
Shrimp 2	1.877±0.283	1.583±0.244	2.488
Dried salted prawn	1.507±0.258	1.269±0.193	2.236
Oyster	1.744±0.276	1.438±0.241	2.279
Crabmeat	1.236±0.229	1.012±0.198	2.340
Dried fish	1.951±0.287	1.743±0.271	1.666
Squid	2.754±0.423	2.482±0.396	0.810
Mackerel	3.272±0.452	3.106±0.433	0.839
Shellfish	1.765±0.279	1.594±0.253	1.436
Blood Cockle	2.245±0.387	2.037±0.295	1.352

Conclusions

The present study reports a way to improve analytical performance in view of limit of detection and linearity range in Se determination. The new CINAA method helps to save time however it is an extraordinary instrument and specialists are in need of it. Whereas FAAS is an available routine instrument, it is insensitive to Se analysis. Therefore, it is interesting to investigate whether Ni as a modifier could increase interested signals. In addition, the results showed adequate sensitivity that could analyze Se in seafood samples. Both methods are feasible provided that some detailed research precedes the application.

References

[1] SB. Goldhaber, *Regulatot Toxicology and Pharmacology*, **38** (2003), pp. 232-242.

[2] National Research Council, *Recommended Dietary Allowance,*10th ed. National Academy Press, Washington. (1989), pp. 230-234.

[3] Health and Welfer Canada, *Nutrition Recommendations,* Canadian Government Publishing Center, Ottawa, (1990), pp. 165-167.

[4] H. Xiaolin, *Cyclic Activation Analysis*, Encyclopedia of Analytical Chemistry., 2002, pp. 1247-12459.

[5] K. Suvardhan, K. Suresh Kumar, D. Rekha, K. Kiran, B. Jaya Raj, G.K. murthy Naidu and P. Chiranjeevi, *Food Chemistry*. **103** (2007), pp. 1044-1048.

[6] B. Walz, *Anal. Bioanal. Chem*. **381** (2005), pp. 69-71.

[7] H. Becker-Ross, S. Florek, U. Heitmann, M.D. Huang, M. Okruss and B. Radziuk, *Spectochimica Acta Part B*. **61** (2006) pp. 1015-1030.

[8] H.D. Revanasiddappa and T.N. Kiran Kumar, *Anal Bioanal. Chem*. **374**(2002), pp.1121-1124.

[9] G. Gilmore and D. J. Hemingway, *Practical Gamma-Ray Spectrometry*. John Wile

Biological / Biophysical Chemistry and Chemical Biology

A kinetic approach to evaluate the effects of 3, 3′-diaminobenzidine on N mineralization in soils

B. Jalili[1], F. Nourbakhsh[1*] and M. Ghiasi[2]

[1]Department of Soil Sciences, College of Agriculture, Isfahan University of Technology, Isfahan, 84156-83111, Iran
[2] Department of Chemistry, Isfahan University of Technology, Isfahan, 84156-83111, Iran

*Email: farshid@cc.iut.ac.ir

Abstract: It has been demonstrated that, azo dyes the xenobiotics widely use in industries can pose threats to public health. 3, 3' – diaminobenzidine (DAB), as a benzidine analogue, is generated from reduction of azo dyes by intestinal or environmental microorganisms. The compound was applied at doses of 0 and 100 mg DAB kg^{-1} to two soils (Juzdan and Shervedan) and the effects were evaluated on N mineralization kinetics. Kinetic behavior of N mineralization in either the control or the DAB-treated soils consistently followed first-order models. In the early 7-10 days of the incubation period, net N mineralization was adversely influenced by DAB. Following the short period, DAB was started to degrade as the accumulation of inorganic N was greater in DAB-treated soils than those of control soils. Potentially mineralizable N in Juzdan and Shervedan soils were 1.1 and 1.4 times greater than those of controls, respectively. Similarly, initial potential rates of N mineralizations in the DAB-treated soils were 1.3 and 1.1 times greater than those of controls, respectively. About 95 and 82 % of the initial DAB-N has been mineralized to inorganic N after 60 days of aerobic incubation. Overall, DAB can be a potential toxic xenobiotic for soil N mineralization shortly after application and that the rate of its inhibition or stimulation is time-dependent.

Introduction

Soil is a complex microhabitat regulating plant productivity and the maintenance of biogeochemical cycles by the activity of microorganisms able to degrade organic including xenobiotics [1]. It has been comprehensively shown that azo dyes can pose threats to public health [2]. Azo dyes are synthetic organic colorants used for research purposes and in the textile, hair dying, paper making and food industries [3]. One of the analogues of benzidine is 3,3'- Diaminobenzidine (DAB). DAB is an aromatic compound with a molecular weight of 214.27 that shows an important potential toxicity and carcinogenic properties. This substance, as other benzidine analogues, is generated from the reduction of azo dyes by intestinal or environmental microorganisms [4,5].

Considerable amounts of information currently exist about the effects of DAB on animal cells and human health [4,6]. The toxicity of azo dyes for microbial populations and the processes of biotransformation and mineralization of organic compounds in aquatic environments is well documented [5], but far less is known about the effects of this substance on soil biological activities [7]. The negative effects of DAB on the growth and nitrogenase activity of Azotobacter vinelandii and Azotobacter chroococcum strains are previously reported [8,9]. Lower nitrogenase activity, ATP content and growth of Azotobacter and lower number of nitrifying and denitrifying bacteria [7] were also reported when exposed to 5-50 mg DAB kg^{-1} [9]. In contrast, soil dehydrogenase, phosphatase and arylsulfatase activities were responded positively to DAB [7].

There is a lack of information about the effects of DAB on N availability in soil. Since DAB is an N containing compound, it can be hypothesized that DAB provides soil microbiota with a source of N that is presumably mineralizable to inorganic N. For this purpose, a kinetic approach is required to investigate the fate of DAB-N in soil. Therefore, the objective of this study was to investigate the effects of DAB on the kinetic parameters of N mineralization in soils.

Material and methods

Two samples (0-15 cm) were collected from soils developed in the arid climate of Central Iran. The Juzdan soil was taken from an agricultural field (31° 30′ N, 51° 55′E) under irrigated alfalfa cultivation. The Shervedan soil was taken from Isfahan University of Technology Research Station in Shervedan (32° 30′ N, 51° 36′E). This soil was under irrigated conventional corn (Zea mays L) monoculture. Both soils are calcareous and belong to the arid regions of Central Iran with 120 mm mean annual precipitation. The general properties of the soils are summarized in Table 1.

Table 1. General properties of the soils studied

Soil	Texture	pH	SOC g/kg)	EC_e ds/m	SP g/kg	CCE g/kg
Juzdan	SCL	7.5	17.7	5.1	43.8	46.5
Shervedan	C	8.0	17.4	1.8	57.7	37.0

SCL: sandy clay loam; C: clay; SOC: soil organic carbon; EC_e: electrical conductivity
SP**:** saturation percentage; CCE: Ca-carbonate equivalent.

Triplicates of 100 g of sieved soil were placed in sterile glass vials. DAB was dissolved in acetone and the stock solution was added to the dishes, in order to reach concentration of 100 mg DAB kg^{-1} of dry weight

soil. After thorough mixing, the treated soils were incubated at 25°C and 50% water holding capacity (WHC) under aerobic conditions for 60 days. Controls without DAB received the same amounts of distilled water and acetone. During the 60 days of incubation, inorganic N was monitored by destructive sampling on 12 occasions at 0, 1, 2, 4, 7, 10, 15, 20, 25, 30, 40 and 60 days after incubation. Inorganic N was extracted with 2 M KCl and measured by steam distillation procedure [10].

A first order kinetics equation was used to calculate the potentially mineralizable N (N_0) and N mineralization rate constant (k):

$$N_m = N_0 (1\text{-}e^{-kt})$$

Where N_m is the N mineralized at any specific time (t), and k is the first-order rate constant. The initial potential rate of N mineralization was calculated as $N_0 \times k$ [11].

Results and discussion

The amounts of N mineralized in Juzdan soil are shown for the DAB-treated and the control soils (Fig 1). During the early 7 days of incubation no significant difference was observed between the two treatments however, the amounts of inorganic N released in the control soil was insignificantly greater than the DAB-treated soil. Similar trend was also observed for Shervedan soil, so that N mineralized in the DAB-treated and the control soils during the first 10 days of incubation was not significantly different although, the amounts of inorganic N released was slightly greater in the control soil (Fig 2). This implies that DAB has not been contributed to N mineralization process during the first 7 (in Juzdan soil) and 10 (in Shervedan soil) days of incubation. Moreover, the rate of N mineralized during the period was slightly greater in the control soil compared to the soils treated with 100 mg DAB kg^{-1} (Figs 1 and 2) which, indicate that DAB can slightly inhibit N mineralization during the early period. Since N mineralization process is

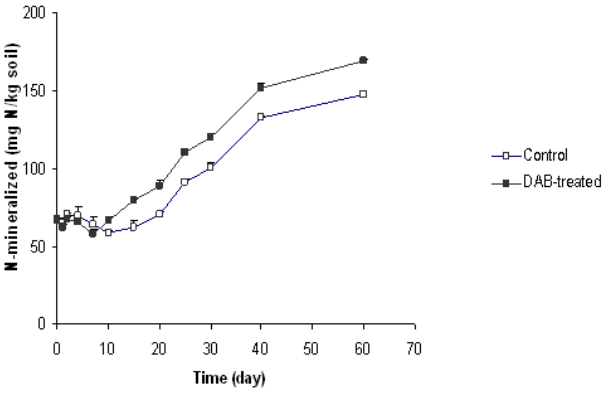

Figure 1. Inorganic nitrogen mineralized in Juzdan soil during the incubation time.

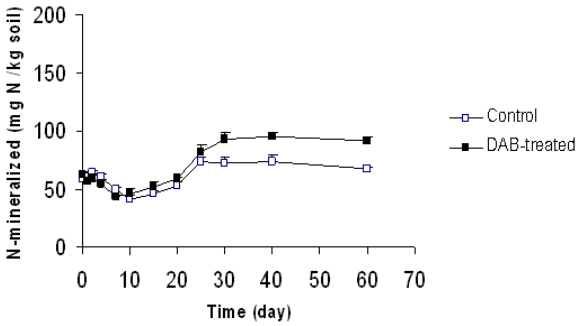

Figure 2. Inorganic nitrogen mineralized in Shervedan soil during the incubation time.

basically a microbilally-mediated process [12], it can be hypothesized that N mineralizing populations of soil are adversely affected.

Following the early period (7-10 days), DAB application resulted in increasing the amounts of N mineralized in both soils (Figs. 1 and 2). The difference between DAB-treated and control soils remained significant during the rest of incubation period in both soils (Fig 1 and 2). It has been shown that the DAB has enhanced the growth of viable soil bacteria and that for all tested doses (0- 50 mg kg^{-1}), heterotrophic counts were significantly higher compared with control after 14 days of treatments [7]. The promoting effects of benzidine and benzidine analogues on the growth and biological activity of Azotobacter have also been reported indicating that these microorganisms can tolerate high concentrations of benzidine [9]. These results are in agreement with our findings and indicate that DAB can stimulate the activity of soil microorganisms which participate in N mineralization processes. The positive effects of DAB on soil dahydrogenase are also reported [7]. Soil dehydrogenase activity and soil microbial biomass are associated [13] therefore, it can be concluded that DAB has enhanced soil microbial biomass. To our knowledge, the effect of DAB on the soil enzymes contributing to N mineralization (i.e. amidohydrolases) has not been investigated.

The effects of xenobiotic compounds on soil biological properties are time dependent [7, 14]. Viera et al. (2007) showed that as time elapsed, the negative effects of sulfentrazone herbicides on soil microbial biomass C decreased [15]. We observed that the pattern of DAB effects on N mineralization varied with time (Figs 1 and 2). While the cumulative concentration of inorganic N mineralized were statistically similar for control and DAB-treated soil during early 7-10 days, DAB-treated soil supported greater amounts of inorganic N after the early period (Figs 1 and 2) . This finding is consistent with that of Pozo et al. (2003) which showed that the maximum difference of bacterial population between control and DAB-treated soil occurred after 14 days of incubation [7]. Apparently, a time lag is required for soil microbiota to start degradation of DAB and consequently to release its N as inorganic N. The mechanism underlying the lag time is not well understood and warrant further researches.

All results of N mineralization from DAB treated soils conformed well to the exponential model $N_m = N_0 (1-e^{-kt})$ described earlier. The first-order kinetic model has been widely used in literature to describe the C [16, 17] and N mineralization kinetics [18, 19].

The values of potentially mineralizable N (N_0) and initial potential rates of N mineralization (kN_0) are shown in Table 2. The N_0 values in DAB treated soils were consistently greater than those of control in both soils. In the Juzdan and Shervedan soils, the average values of N_0 for DAB-treated soils were 1.1 and 1.4 times greater than those of controls, respectively. Similar trend was observed for kN_0. In the Juzdan and Shervedan soils, the average values of kN_0 for DAB-treated soils were 1.3 and 1.1 times greater than those of controls, respectively.

Table 2. Potentially mineralizable N (N_0) and initial potential rates (KN_0) of DAB-treated and control soils

Soil	DAB (mg kg^{-1} soil)	N_0	kN_0
Juzdan	0	175.9 (1.60)	5.3 (0.05)
	100	192.5 (2.20)	7.1 (1.05)
Shervedan	0	74.4 (1.70)	5.7 (0.31)
	100	102.1(1.74)	6.1 (0.11)

In the current study the values of N_0 has been calculated according to a 60 day aerobic incubation. These results imply that during the incubation period, DAB has gradually been used as a source of N by the soil microbial population. The effects of management practices on N mineralization in soil have been extensively investigated [19, 20]. The greater rate of N mineralization in organic amendment-treated soils has been attributed to the higher availability of organic N [21].

Therefore, the greater levels of aerobic N mineralization indices (N_0 and kN_0) in the DAB-treated soils can be attributed to the higher input of N which has entered into the soils as DAB-N. The DAB-induced inorganic N (ΔNi) was calculated as:

$$\Delta Ni\ (mg\ kg^{-1}) = Ni_{(DAB)} - Ni_{(C)}$$

Where, $Ni_{(DAB)}$ and $Ni_{(C)}$ are the inorganic N in the DAB treated and control soils, respectively. Dividing ΔNi by the total N that was initially added to the soils as DAB-N would provide the percentage of DAB-N that is mineralized to inorganic N during the incubation period. It was observed that 95 and 82 % of the initial DAB-N has been mineralized to inorganic N after 60 days of aerobic incubation (data not shown). Most of DAB-N has obviously been converted to inorganic N however; the fate of the rest of DAB molecule (C skeleton) in soil is still obscure.

Overall, our results clearly declare that in a short period of time (early 7-10 d of the incubation) DAB has a potential inhibitory effect on N mineralization but following gradual degradation of DAB in soil, most of DAB-N would be released as inorganic N. The results have supported our hypothesis suggesting that DAB can be used as N containing substrate by native soil microbiota. Our results have been obtained from two calcareous soils which predominantly exist in arid and semi-arid areas. To have a better understanding form the dynamic of DAB in soil, a study can be performed in acidic and/or tropical soils. Moreover, recognition of the transient organic molecules that are generated in DAB contaminated soils is of great importance for further studies.

References

[1] P. Nannipieri, J. Ascher, M. T. Ceccherini, L. Landi, G. Pietramellara and G. Renella, Eur. J. Soil Sci. 54 (2003), PP. 655-670.

[2] A. Pielesz, I. Baranowska, A. Rybak and A. Wochowicz, Ecotox. Environ. Safe. 53 (2002), PP. 42-47.

[3] U. Meyer, FEMS Symp. 12 (1981), PP. 371-385.

[4] K. T. Chung, S. E. Stevens and C. E. Cerniglia, Crit. Rev.Microbiol. 18 (1992), PP. 175–190.

[5] K. T. Chung and S. E. Stevens, Environ. Toxicol. Chem. 12 (1993), PP. 2121-2132.

[6] G. Choudhary, Chemosphere. 32 (1996), PP. 267-291.

[7] C. Pozo, M. V. Martinez- Toledo, B. Rodelas and J. Gonzalez- Lopez, Appl. Soil. Ecol. 23 (2003), PP. 119-126.

[8] K. T. Chung, S. C. Chen, T. Y. Wong and C. Wei, Environ. Toxicol. Chem. 17 (1998), PP. 271-275.

[9] C. Pozo, M. V. Martinez-Toledo, V. Salmeron, B. Rodelas and J. Gonzalez- Lopez, Appl. Soil. Ecol. 14 (2000), PP. 183-190.

[10] D. R. Keeney and D. W. Nelson, In: A. L. page, R. H. Miller, D. R. Keeney (Eds.), Methods of soil analysis. Part 2. American Society of Agronomy. Madison, WI. USA. 1982, PP. 643-698.

[11] J. Z. Burket and R. P. Dick, Biol. Fertil. Soils. 27 (1998), PP. 430-438.

[12] R. L. Tate, Soil Microbiology. John Wley & Sins. New York, USA (2000).

[13] R. P. Dick, D. P. Breakwell and R. F. Turco In: J. B. Doran and A. J. Jones (Eds.), Methods for Assessing Soil Quality. Soil Science Society of America, Madison, WI, USA, 1996, PP. 410-475.

[14] X. H. Yoa, H. Min, Z. H. Lu and H. P. Yuan, Soil Biol. 42 (2006), PP. 120-126.

[15] R. F. Viera, M. S. Silvia and P. D. Silveira, Plant Soil. 300 (2007), PP. 95-103.

[16] H. A. Ajwa and M. A Tabatabai, Biol. Fert. 18 (1994), PP. 175-182.

[17] C. E. Martinez and M. A. Tabatabai, Environ. Qual. 26 (1997), PP. 625-632.

[18] M. El-Gharous, R. L. Westerman and P. N. Soltanpour, Soil Sci. Soc. Am. J. 54 (1990), 438-443.

[19] F. Nourbakhsh and A. Alinejadian, J. Plant Nutr. Soil Sci. 172 (2009), PP. 127-133.

[20] S. P. Deng and M. A. Tabatabai, Biol. Fertil. Soils. 31 (2000), PP. 211-218.

[21] M. Zaman, M. Matsushima, S. X. Chang, K. Inubish, L. Nguyen, S. Gotao, F. Kaneko and T. Yoneyama, Biol. Fertil. Soils. 40 (2004), PP. 101-109.

Salmonella typhi detection using dot blot assay based on gold nanoparticles

P. Preechakasedkit[1], W. Siangproh[2], W. Chaicumpa[3], P. Tongtawe[4] and O. Chailapakul[5,6]*

[1] Program in Biotechnology, Faculty of Science,Chulalongkorn University Bangkok 10330, Thailand.
[2] Department of Chemistry, Faculty of Science, Srinakharinwirot University, Sukhumvit 23, Wattana, Bangkok 10110, Thailand.
[3] Department of Parasitology, Faculty of Medicine, Siriraj Hospital, Mahidol University, Bangkok 10700, Thailand.
[4] Faculty of Allied Health Sciences, Thammasat University, Pathumthani 12120, Thailand.
[5] Department of Chemistry, Faculty of Science, Chulalongkorn University, Patumwan, Bangkok 10330, Thailand.
[6] Center of Petroleum, Petrochemicals, and Advanced Materials, Chulalongkorn University, Bangkok 10330, Thailand.

*E-mail: corawon@chula.ac.th

Abstract: An analytical system of dot blot assay based on gold nanoparticles was developed for Salmonella typhi (S. typhi) detection. Polyclonal rabbit antibodies to S. typhi O901 labeled with gold nanoparticles were used to visualize the results. Conjugations of polyclonal antibodies with gold nanoparticles were characterized by UV-vis spectroscopy and transmission electron microscopy (TEM). The dot blot assay was constructed by immobilizing S. typhi in dot onto nitrocellulose membrane. After blocking with blocking solution (3% BSA), gold nanoparticles-labeled polyclonal antibodies bound to S. typhi to form red-wine dots. The results obtained could be visually assessed by naked eye. Therefore, this method is low-cost, rapid and simple for S. typhi detection.

Introduction

Typhoid fever is an infectious disease caused by a bacterium called Salmonella typhi, a major cause of morbidity and mortality worldwide, with an estimated 21 million new infections and 0.2 million deaths each year [1, 2]. Early, it was estimated to be 16 million with over 600,000 deaths [3]. This clearly shows in morbidity with a decrease in mortality. The possibility of having laboratory tests done rapidly and results available immediately is essential for potentially life-threatening disease, which requires prompt medical intervention. Currently, general methods for analysis are polymerase chain reaction [4], pulsed-field gel electrophoresis [5], amperometric immunosensors [6] and enzyme-linked immunosorbent assay [7]. The above methods are effective but simple and rapid method is required. Dot blot assay is alternative methods with simple, rapid and low-cost analysis. Dot blot assay is biochemical that performed on nitrocellulose membrane test using the reaction of an antibody or antibodies to its antigen. For positive results, the colored dot appears on nitrocellulose membrane which can be visually assessed by naked eye. The advantage of this method is rapid, simple and low-cost. For dot blot assay, the labels are used to visualize the results such as alkaline phosphatase (ALP) [8], horseradish peroxidase (HRP) [9], gold nanoparticles [10] and others. The use of enzyme labels (ALP, HRP) as a label requires an additional step for the detection itself using an unstable substrate. Thus, gold nanoparticle is chosen as a label for dot blot assay.

Gold nanoparticles have been used in different immunoassay techniques over the past several years, because of their easily controllable size distribution, long-term stability, and friendly biocompatibility with antibodies, antigen, proteins, DNA, and RNA [11]. Gold particles of any accurately defined size can be manufactured reproducibly under the appropriate manufacturing conditions. Different sizes may be used for different applications. Gold is essentially inert and forms almost perfectly spherical particles when properly manufactured. Proteins bind to the surfaces of these gold particles with enormous strength when correctly coupled, thus providing a high degree of long-term stability.

In this works, dot blot assay based on gold nanoparticles was developed to S. typhi detection with rapid simple and low-cost. The details of the optimization and performance of our methods are presented in the following sections.

Materials and Methods

2.1 Reagents

Polyclonal rabbit antibodies for polysaccharides of S. typhi O901 were obtained from Siriraj Hospital. Hydrogen tetrachloroaurate (III) and albumin bovine serum (BSA) were obtained from the Sigma Chemical Co. (St. Louis, MO). Sodium chloride, potassium chloride, potassium dihydrogen phosphate, disodium hydrogen phosphate, sodium bicarbonate, sodium citrate were obtained from Merck (Germany).

The incubation and washing buffer consisted of 137 mM sodium chloride, 2.7 mM KCl, 2 mM KH_2PO_4, 10 mM Na_2HPO_4 (pH 7.4). All of the solutions were prepared using Milli-Q 18MΩ water (Millipore purification system).

2.2 Preparation and characterization of gold nanoparticles

The gold nanoparticles were prepared according to the method reported in ref. [12]. First, 1 mL of 1% (w/v) hydrogen tetrachloroaurate (III) ($HAuCl_4$) solution was mixed with 100 mL of ultrapure water and boiled under stirring. Then 2.5 mL of 1% (w/v) sodium citrate was added into solution under continuous heating and stirring for 15 min until the

color of solution changed to red-wine. The gold nanoparticles solution was left to cool at room temperature under stirring and was later stored in dark bottles at 4 ^{o}C. The solution of gold nanoparticles was characterized by UV–vis spectrophotometer and transmission electron microscopy (TEM).

2.3 Preparation and optimization of antibody-gold nanoparticles conjugate

The amount of polyclonal rabbit antibody for polysaccharides of S. typhi O901 was optimized from 0 to 1 mg/mL. An appropriate volume of stock solution was added to 2 mL of gold nanoparticles solution and the solution was incubated under stirring at room temperature for 1 h. Then 100 µL of 3% (w/v) BSA (pH 7.4) was added to minimize nonspecific reaction and incubation under stirring at room temperature for 1 h. The antibody-gold nanoparticles conjugate was centrifuged at 15,000 rpm for 10 min, and the soft sediment was washed and suspended in 3% BSA (pH 7.4). The antibody-gold nanoparticles conjugate was stored at 4 ^{o}C. The solution of conjugate was characterized by UV–vis spectroscopy. The absorbance of 520 nm at different concentrations of antibody (0-1 mg/mL) was recorded and plotted to determine the optimal of antibody concentration.

After obtaining optimal concentration of antibody, the antibody-gold nanoparticles conjugate was prepared as above-mentioned method.

2.4 Dot blot assay

The dot blot diagram was shown in Figure 1. First, 1 µL of S. typhi in serial two-fold dilutions was dotted on nitrocellulose membrane (Whatman, UK) for 30 min and air-dried. The strips were blocked with 3% BSA (pH 7.4), incubated on a rocking platform at room temperature for 1 h, and washed with washing buffer. To visualize the results, strips were placed in antibody-gold nanoparticles conjugate for 20 min at room temperature. The reaction was stopped by washing nitrocellulose membrane with ultrapure water and then air dried. The results of the assay could be visually assessed by naked eyes.

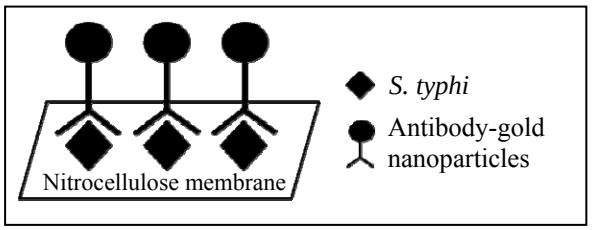

Figure 1. Schematic of dot blot assay for S. typhi detection

Results and Discussion

3.1 Preparation and characterization of gold nanoparticles

The gold nanoparticles were produced by chemical condensation using reduction of hydrogen tetrachloroaurate (III) ($HAuCl_4$). The sodium citrate was used to reduce hydrogen tetracloroaurate (III) to neutral gold atoms. The gold precipitated in the form of gold nanoparticles and the colored of solution changed from yellow to red-wine. To characterize the gold nanoparticles, UV-vis spectra of hydrogen tetrachloroaurate (III) and gold nanoparticles were recorded (Figure 2). The maximum absorbance of the gold nanoparticles occurred at the wavelength of 520 nm, which similar to other reports [12, 13]. From TEM photographs, the average particles size of gold nanoparticles was 15 nm (Figure 3).

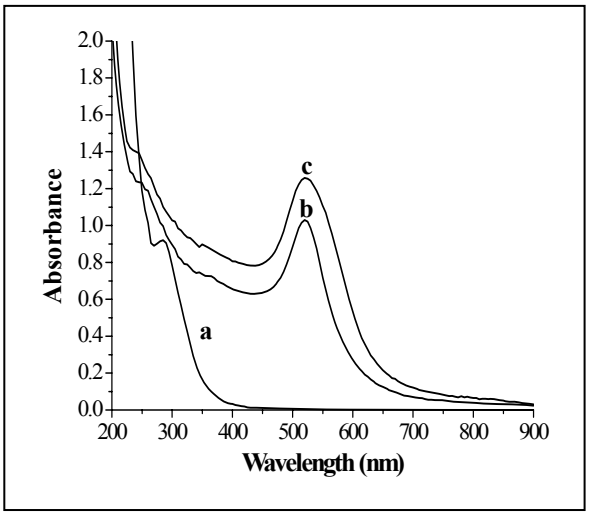

Figure 2. UV-vis spectra of the $HAuCl_4$ (a), gold nanoparticles (b) and the antibody-gold nanoparticles conjugate (c)

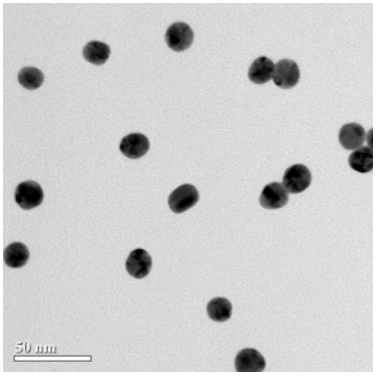

Figure 3. TEM photographs of gold nanoparticles sizes

3.2 Preparation and optimization of antibody-gold nanoparticles conjugate

For the preparation of antibody-gold nanoparticles conjugate, it was found that the antibody could bind with gold nanoparticles. The UV-vis spectra of antibody-gold nanoparticles gave the maximum absorbance at the wavelength of 520 nm (Figure 2). There were no significant changes in the absorption spectrum between antibody-gold nanoparticles and gold nanoparticles, this could be explained that gold still presented nanosized after binding.

Light absorption of conjugate at different antibody concentrations from 0 to 1 mg/mL was shown in Figure 4. The absorbance increased from 0 mg/mL to 0.5 mg/mL of antibody and the the absorbance decreased. The maximum absorbance of antibody-gold nanoparticles conjugate occurred at the antibody concentration of 0.5 mg/mL. Therefore, the optimal concentration of antibody to stabilized gold nanoparticles was 0.5 mg/mL.

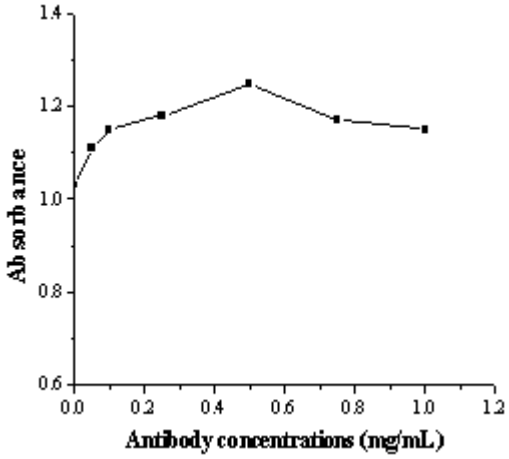

Figure 4. Light adsorption of conjugate at different antibody concentrations (0 to1 mg/mL)

3.3 Dot blot assay

The dot blot assay for S. typhi detection was shown in figure 5. The antigen-antibody interaction was detected using antibody-gold nanoparticles conjugate. For positive results, the red-wine dot appeared on nitrocellulose strip. From Figure 5, the weak red-wine dot was visualized until 0.14 mg/mL of S. typhi. Thus, the limit of detection (LOD) of S. typhi detection by dot blot assay was 0.14 mg/mL which could be visually assessed by naked eye.

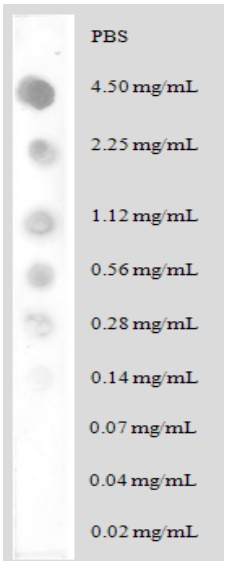

Figure 5. Dot blot assay of S. typhi detection at the concentration of 0 (PBS) to 4.5 mg/mL

Conclusions

In this works, we have described a successfully method for S. typhi detection by dot blot assay based on gold nanoparticles conjugate. Optimal condition for the preparation of antibody-gold nanoparticles conjugate was 0.5 mg/mL for the antibody concentration. The particle size of gold nanoparticles was 15 nm. The limit of detection of S. typhi was 0.14 mg/mL. The dot blot assay based on gold nanoparticles was simple, rapid and low-cost to S. typhi detection. This method proposes some advantages over the dot blot using enzyme labeled [8] for S. typhi detection. These include rapidity and simplicity. Thus, this method is effective for rapid, simple and low-cost diagnosis.

Acknowledgement

This work was financially supported by the Thailand Research Fund through Basic Research Grant, TRF-Master Research Grant (MRG-WII525S010), the 90th Anniversary of Chulalongkorn University Fund (Ratchadaphiseksomphot Endowment **Fund**) and CU. Graduate School Thesis Grant.

References

[1] A. Fraser, M. Paul, E. Goldberg, C.J. Acosta and L. Leibovici, Vaccine **25** (2007), pp. 7848-7857.
[2] T.H. Abdoel, R. Pastoor, H.L. Smits and M. Hatta, **Trans. R. Soc**. Trop. Med. Hyg. **101** (2007), pp. 1032-1038.
[3] T. Pang, M.M. Levine, B. Lvanoff, J. Wain and B.B. Finlay, Trends Microbiol. **6** (1988), pp. 131-133.
[4] A. Kumar, V. Arora, A. Bashamboo and S. Ali, **Infect**. Genet. Evol. **2** (2002), pp. 107-110.
[5] K. Thong, Y. Cheong and T. Pang, Int. J. Infect. Dis. **1** (1996), pp. 95-97.
[6] V. Kameswara, G. Rai, G. Agarwal and S. Suresh, Anal. Chim. Acta, **531** (2003), pp. 173-177.
[7] T. Quiroga, M. Goycoolea, R. Tagel, F. Gonzalez, L. Rodriguez and L. Villarroel, Diagn. Microbiol. **15** (1992), pp. 651-656.
[8] W. Chaicumpa, W. Ngren-ngarmlert, T. Kalambaheti, Y. Ruangkunaporn, M. Chongsa-nguan, P. Tapchaisri, V. Desakorn, and O. Suthienkul, Asian Pacific J. Allergy Immunol. **13** (1995), pp. 159-166.
[9] E. Cesar, B.J. Nadala and P. C. Loh, J. Virol. Methods **84** (2000), pp. 175-179.
[10] I.A. Lyubavina, A.A. Zinchenko, I. S. Salomatina, A.V. Zherdev and B.B. Dzantiev, Russ. J. Bioorg. Chem. **30** (2004), pp. 178-183.
[11] S. Hou, H. Chen, H. Cheng and C. Huanf, Anal. Chem. **79** (2007), pp. 980-985.
[12] W. Dungchai,W. Siangproh, W. Chaicumpa, P. Tongtawe and O. Chailapakul, Talanta **77** (2008), pp. 727-732.
[13] S. Xiulan, Z. Xiaolian, T. Jian, J. Zhou and F. Chu, Int. J. Food Microbiol. **99** (2005), pp. 185-194.

[15] H.D. Rode, D. Eisel, I. Frost, Apoptosis, Cell Death and Cell Proliferation Manual, **3rd** ed., Roche Applied Science (2004)
[16] S. Julia, Cytotoxic test of protein fraction of Erythrina fusca Luor (Cangkring) leaf toward HeLa cell, Skripsi, Fakultas Farmasi Universitas Gadjah Mada, Yogyakarta (2001)
[17] http://www.biotech.ist.unigue2003
[18] M. Arcinas, C.A. Heckman, J.W. Mehew, and L.M. Boxer, Cancer Res., 61, (2001), pp. 5202-5206.

Differential responses of flavonoids to abiotic stress in rice seedling cultivars

S. Chutipaijit[1*], S. Cha-um[2] and K. Sompornpailin[3,4]

[1]Department of Chemistry, Faculty of Science, Srinakharinwirot University, Sukumvit 23 Road, Wattana, Bangkok 10110, Thailand
[2]National Center for Genetic Engineering and Biotechnology, National Science and Technology Development Agency, 113 Thailand Science Park, Klong Luang, Pathumthani, 12120, Thailand
[3]Department of Applied Biology, Faculty of Science, King Mongkut's Institute of Technology Ladkrabang, Bangkok, 10520, Thailand
[4]College of KMITL Nanotechnology, King Mongkut's Institute of Technology Ladkrabang, Bangkok, 10520, Thailand

[*] Corresponding Author; E-mail: sutee@swu.ac.th

Abstract: Drought, a type of abiotic stress, affects rice growth and productivity among Asian countries. Responses of flavonoid accumulations to drought stress were comparatively studied in four cultivars of rice (Oryza sativa L.) differing in sensitivity, two of them (KK and BSR) are tolerant to drought and the others (D and TD49) are sensitive to drought. The seedlings of four rice cultivars were cultured into photoautotrophic system for 4 days in NB containing 100 mM mannitol solution as drought stress treatment. Under drought condition, the growth reduction presented in shoot and root length and the elevated levels of lipid peroxidation in KK and BSR are lower than those in D and TD49. Contents of flavonoid (flavanone, flavones, flavonols and anthocyanins) were measured during the stress treatments. Flavanone was decreased at 4 days after stress treatments in all rice cultivars. Flavones and flavonols were greatly enhanced at 4 days after drought stress treatment in the two drought-tolerant cultivars but they were reduced in two drought-sensitive cultivars in the same condition. Contents of anthocyanins were greatly increased in the drought-tolerant cultivars while slightly increased in drought-sensitive cultivars after drought stress. The results indicated that tolerance to drought in rice cultivars is well associated with the enhanced capacity of flavones and flavonols under drought condition.

Introduction

World population is increasing at a rapid rate whereas food productivity is decreasing due to the effect of abiotic stresses. Therefore, it is important to elucidate the abiotic tolerance mechanisms of plant species in order to improve their agronomic performances and to obtain more resistant cultivars. Drought is among the major abiotic stresses, which adversely affect plants growth and productivity; hence it is important to develop and study stress tolerant crops, including rice. Drought stress in fact is the principal cause of crop failure world wide, dipping average yields for most major crops by more than 50% [1]. Drought stress can cause the promotion of reactive oxygen species (ROS) in plant, including superoxide, singlet oxygen, hydroxyl, and hydrogen peroxide, which can be detrimental to proteins, lipids, carbohydrates, and nucleic acids [2]. Plants have evolved both enzymatic and non-enzymatic defense systems for scavenging and detoxifying ROS. Flavonoids are one of the importance non-enzymatic antioxidants in plant stress.

Flavonoids are a family of diphenylpropanes found ubiquitously in plant as well as in food products and beverages derived from plants such as olive oil, tea, and red wine. Physiological of flavonoids are generally thought to be due to their antioxidant and free radical scavenging properties [3]. Maintaining a high level of antioxidative activities may contribute to drought tolerance by increasing the capacity better protection mechanisms against oxidative damage [4]. However, changes in activities of these antioxidant compounds under drought stress depend on plant species, cultivars and stress intensity and duration [5].

Therefore, the objective of this study was investigate the change of plant growth (shoot and root length) and the accumulation of MDA and flavonoid patterns in tolerant- and sensitive-seedlings of rice cultivars under drought stress.

Materials and Methods

Plant materials and stress condition

Seeds from four cultivars of rice [Oryza sativa L. cv. Klumkhonkaen (KK) and Black sticky rice (BSR)-drought tolerant cultivars; Dang (D) and TD49-drought sensitive cultivars] were obtained from the Pathumthani and Sakolnakorn Rice Research Center (Rice Research Institute, Department of Agriculture, Ministry of Agriculture and Coorperative, Thailand). Seeds were sterilized with 70% ethanol, 5% Clorox® (5.25% sodium hypochlorite, The Clorox Co., USA) for 40 min, 30% Clorox® for 30 min and washed extensively with distilled water. Surface-sterilized seeds were germinated on NB medium [6] containing 3% (w/v) sucrose and 0.8% (w/v) agar and were grown at 25±5 °C, 85-90% relative humidity and 60±5 $\mu molm^{-2}s^{-1}$ photosynthetic photon flux (PPF) with 16 hd^{-1} photoperiod. Seven-day-old rice seedlings were transferred to NB-liquid medium under photoautotrophic system (CO_2 as a carbon source) using vermiculite as a supporter. The number of air-exchanges of photoautotrophic system was adjusted to 2.32 h^{-1} by punching a hole on plastic cap (Ø 1 cm) and covering the hole with a microporus filter (0.20 μm) of pore size. After 7 days of growth under photoautotrophic system, the mannitol concentration of the medium was adjusted to 0 or 100 mM mannitol. After 4 days culture, rice seedlings were harvested and frozen in liquid nitrogen and stored at -80°C prior to analysis.

Growth determination

Shoot length and root length of seedlings were measured for analyze growth characteristics.

Lipid peroxidation

The levels of lipid peroxidation in rice seedling sample were determined in terms of malondialdehyde (MDA) content according to the method of Hodges et al. [7].

Flavonoid levels

Flavonoid contents were determined according to Harborne [8]. Rice seedlings were ground in liquid nitrogen and extracted with 1% (w/v) HCl in methanol for 2 h at room temperature and subsequently added 1 mL chloroform. The supernatant was collected and assayed by UV-visible spectrophotometer at wavelength 300 nm for flavanone, 350 nm for flavones, 378 nm for flavonols and 525 nm for anthocyanin.

Statistical analysis

The experiment was designed as Completely Randomized Design (CRD) with five replicates (n=5). The mean values were compared by t-test and analyzed by SPSS software (SPSS for Windows version 15, SPSS Inc., Chicago, USA).

Results and Discussion

Drought is an important abiotic factor that could influence the growth and physiological traits of plants [9, 10]. The results showed the shoot length of tolerant cultivars (KK and BSR) and sensitive cultivars (D and TD49) dropped to 4.41-7.06% and 12.68-13.25%, whereas the root lenght of those cultivars dropped to 4.84-8.16 and 12.68-15.07%, respectively under drought stress when compared to the controls (Figure 1).

Lipid peroxidation level in the seedlings of the rice cultivars, measured as the content of MDA. The MDA content was increased 19.04-41.41% and 66.82-71.27% in stressed-tolerant and stressed-sensitive cultivars, respectively when compared to the controls (Figure 2). Drought stress induced the reduction of plant growth and elevation of lipid peroxidation which observed from shoot length, root length and MDA content. The results indicated KK and BSR (drought-tolerant cultivars) could endure to cellular membrane damages due to the growth reduction and MDA accumulations were less than D and TD49 (drought-sensitive cultivars). Higher MDA accumulation in various sensitive cultivars under abiotic stress conditions has been reported earlier [11-13]. Drought stress, due to its osmotic and oxidative effects in agricultural habitats can induce a wide variation of plant responses ranging from growth inhibition and accumulation of MDA content. The increase of lipid peroxidation correlated to accumulation of MDA content, indicating that the membrane injury caused by drought stress is resulted from the oxidative damage [14]. It was similarly observed in many investigations that have demonstrated that the cellular injury to plants by abiotic stresses is oxidative damage [15, 16].

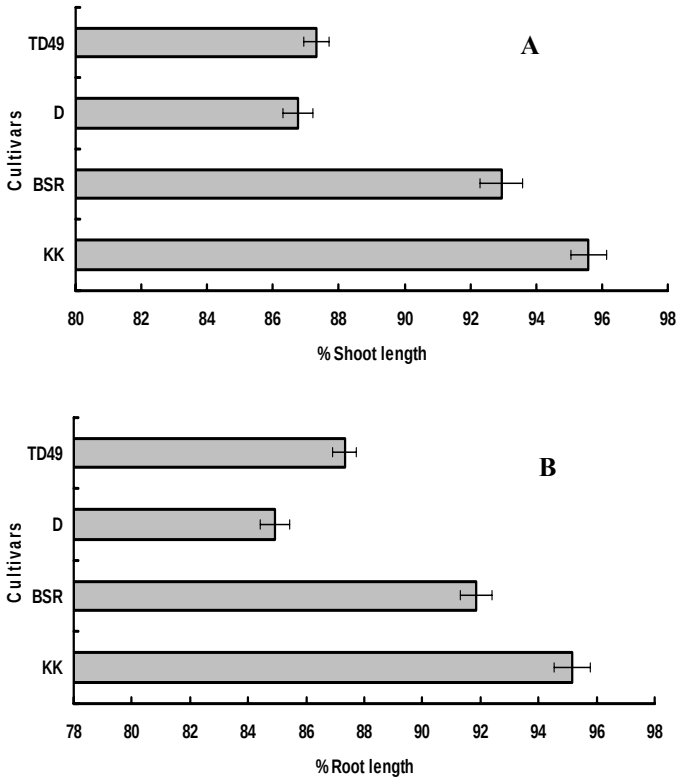

Figure 1. Effects of 4 days drought stress on the percentage of shoot length (A) and root length (B) in the stressed-seedlings of rice cultivars when compared to unstressed treatment set as 100%. Vertical bars show ± S.E.

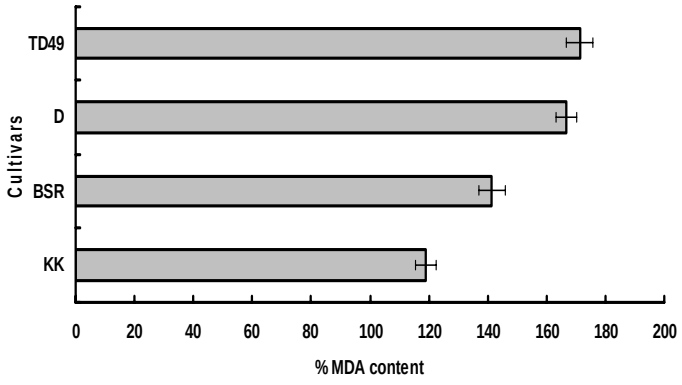

Figure 2. Effects of 4 days drought stress on the percentage of malondialdehyde (MDA) content in the stressed-seedlings of rice cultivars when compared to unstressed treatment set as 100%. Vertical bars show ± S.E.

To be able to endure oxidative or ROS damage under stress conditions, plants possess antioxidants such as ascorbic acid, glutathione, α-tocopherol, carotenoid, flavanoids and antioxidant enzymes [17]. Under drought stress, the results presented the decrease of flavanone content (3.05-13.78%) in all stressed-seedling cultivars (Figure 3A). This compound was decreased in the stressed-tolerant cultivars (11.54-13.78%) more than in the stressed-sensitive cultivars (3.05-3.28%). The enhanced production of flavones (6.81-15.53%) and

flavonols (12.40-15.23%) was only observed in stressed-tolerant cultivars whereas these compounds were decreased 8.89-9.35% and 6.12-7.13% in stressed-sensitive cultivars, respectively (Figure 3B and C). Increases of anthocyanin contents up to 19.16-23.91% and 3.84-7.84% were found in the stressed-tolerant and stressed-sensitive cultivars, respectively when compared to the control (Figure 3D). When subjected to environmental stress, plants also form some protective mechanisms by increasing antioxidant contents. The ability to alter flavonoid production under abiotic stress condition could help plants to protect themselves from harmful effects. Thus, changes of flavonoid metabolites in plant tissue protect the stressed-seedlings from serve as a ROS scavenger [18, 19]. It could function as a free radical scavenger to prevent cell membrane, organelle damage and protein denaturation [20]. In our study, supply significantly increased flavone, flavonol and anthocyanin contents (Figure 3B, C and D), which may provide an ecological adaptation for drought stressed-seedlings.

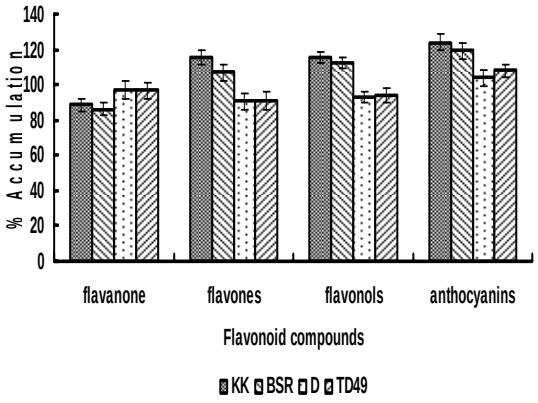

Figure 3. Effects of 4 days drought stress on the percentage accumulation of flavanone, flavones, flavonols and anthocyanins in the stressed-seedlings of rice cultivars when compared to unstressed treatment set as 100%. Vertical bars show ± S.E.

Conclusions

Drought stress increased certain ROS productions which induced lipid peroxidation in rice seedlings. These affected plant growth observed by the reduction of shoot and root length in stressed-seedlings compared to unstressed-seedlings. The increased or decreased accumulations of flavonoid compounds were generally observed under drought stress. The flavanone content was decreased in all stressed-seedlings cultivars. Drought stress enhanced the level of flavones and flavonols in drought-tolerant cultivars, while drought-sensitive cultivars were decreased. All stressed-seedlings cultivars was induced the increase of anthocyanin levels. The differential responses of stress tolerance level suggested dissimilar flavonoid metabolisms in rice seedlings exposed to drought conditions, especially flavone and flavonol compounds.

References

[1] E.A. Bray, J. Bailey-Serres, E. Weretilnyk, in: W. Gruissem, B. Buchannan, R. Jones (Eds.), Biochemistry and Molecular Biology of Plants, American Society of Plant Biologists, Rockville, MD, 2000, pp. 158-1249.
[2] N. Smirnoff, New Phytol. 125 (1993), pp. 27-58.
[3] K. Ishige, D. Schubert and Y. Sagara, Free Rad. Biol. Med. 30 (2001), pp. 433-446.
[4] P. Sharma and R.S. Dubey, Plant Growth Regul. 46 (2005), pp. 209-221.
[5] M. DaCosta, and B. Huang, J. Am. Soc. Hortic. Sci. 132 (2007), pp. 319-326.
[6] L. Li, R. Qu, A. De Kochko, C. Frauquet and R.N. Beachy, Plant Cell Rep. 12 (1993), pp. 250-255.
[7] D.M. Hodges, J.M. DeLong, C.F. Forney and R.K. Prange, Planta 207 (1999), pp. 604-611.
[8] J.B. Harborne, Phytochemical methods: a guide to modern techniques of plant analysis, Chapman & Hall, London, UK (1998).
[9] J. Ren, W.R. Dai, Z.Y. Xuan, Y.A. Yao, K. Helena and C.Y. Li, Forest Ecol. Manage. 239 (2007), pp. 112-119.
[10] D. Bartels and R. Sunkar, Crit. Rev. Plant Sci. 4 (2005), pp.23-58.
[11] J.A. Hernandez, A. Jimenez, P. Mullineaux, and F. Sevilla, Plant Cell Environ. 23 (2001), pp. 853-862.
[12] Q.S. Wu, Y.N. Zou and R.X. Xia, Eur. J. Soil Biol. 42 (2006), pp. 166-172.
[13] I. Turkan, M. Bor, F. Ozademir, and H. Koca, Plant Sci. 168 (2005), pp. 223-231.
[14] M. Jain, G. Mathur, S. Koul, and N.B. Sarin, Plant Cell Rep. 20 (2001), pp. 463-468.
[15] M. Huang, and Z. Guo, Biol. Plant. 49 (2005), pp. 81-84.
[16] O.T. Del Longo, C.A. Gonzalez, G.M. Pastori, and V.S. Trippi, Plant Cell Physiol. 34 (1993), pp. 1023-1028.
[17] M.M. Chaves, J.P. Maroco, and J.S. Pereira, Funct. Plant Biol. 30 (2003), pp. 239-264.
[18] D.G. Cooper, Phytochem. 56 (2001), pp. 229-236.
[19] M.L. Dionisio-Sese and S. Tobita, Plant Sci. 135 (1998), pp. 1-9.
[20] V. Alexieva, I. Sergiev, S. Mapellis and E. Karanov, Plant Cell Environ. 24 (2001), pp. 1337-1344.

Identification of monacolins in red yeast rice from thai glutinous rice fermentated with monascus purpureus CMU001.

S. Taweekasemsombut[1, 3] G. Chairote [2, 3] *

[1] Department of Biotechnology, Faculty of Graduate School, Chiang Mai University, Chiang Mai, Thailand
[2]Department of Chemistry, Faculty of Science, Chiang Mai University, Chiang Mai, Thailand
[3] Center for Innovation in Chemistry faculty of Science, Chiang Mai University, Thailand

* E-mail: griangsa@science.cmu.ac.th

Abstract: Monacolins were known as the cholesterol-lowering compounds, which are produced by Monascus spp. in red yeast rice products. In this study, red yeast rice was prepared from Thai glutinous rice (Oryza sativa.) cv. Sanpatong 1. It was fermented with Monascus purpureus CMU 001 using the solid-state fermentation method. The analysis for the presence of monacolins from red yeast rice extract was performed by HPLC. The presence of several monacolins were confirmed with reference compounds in previous studied and by LC-MS. The chromatogram and mass spectrum show the presence of monacolin K, monacolin K acid form, monacolin X, monacolin X acid form, dehydro-monacolin K, monacolin L, dihydromonacolin L and monacolin M. A dominant compound with the molecular weight of 353 was also detected but could not be identified. This compound will be separated and identified in the future study.

Introduction

Red yeast rice or red mold rice also known as Ang-kak has been used as a traditional food and medicine in China and East Asian countries (such as Japan, Taiwan, Thailand, Indonesia and Philippines) for thousand years [1]. It was produced by solid-state fermentation of rice substrates fermented with Monascus sp. [2-3]. This microorganism was screened firstly from red yeast rice by van Tieghem (1884) [4]. Red yeast rice has been used as a dietary supplement and medicine. Which has pharmaceutical effect to promote blood circulation, reduce blood cholesterol level, improve digestion and has antibacterial activity [2, 4, 6]. Many secondary metabolites such as monacolins, γ-aminobutyric acid (GABA), natural pigments, glucosamine, lecithin, flavonoids, and dimerumic acid are produced in red yeast rice. There are several useful compounds, which have medical activities as above mentioned. However, mycotoxin citrinin which is an unuseful compound was found [2-3, 7].

Monacolins which are interesting secondary metabolites are produced by species of the genus Monascus in the form of polyketides. Monacolins were discovered firstly as a HMG-CoA reductase inhibitor in form of monacolin K and it was purified from the metabolites of M. ruber and Aspergillus terreus by Endo [8-9]. This compound has a significant function on reducing cholesterol level in blood. The biosynthesis of monacolin K (mevinolin or lovastatin: $C_{24}H_{36}O_5$) proceeds in Monascus sp. via the derivatives monacolin L, monacolin J and monacolin X. Therefore, Komagata et al. [12] found that the production of M. ruber M 4681 monacolin L is the precursor of monacolin J, and the enzyme monooxygenase involved in the conversion of monacolin L to monacolin J in hydroxylation reaction. Subsequently, Nakamura et al. [14] found that 4,5-dihidromonacolin L converted to 3α-hydroxy-3,5-dihydromonacolin L by hydroxylation reaction and 3α-hydroxy-3,5-dihydromonacolin L can be converted spontaneously to monacolin L under acidic condition. Later, Kimura et al. [13] discovered that the formation of monacolin K was derived from esterification of monacolin J with α-methylbutyryl-CoA. Another possibility mechanism was that monacolin J was the first esterified with α-methylbutyryl-CoA, followed by reduction, dehydration, and reduction of the side chain ester moiety. However, Monascus sp. producing monacolin K are less than the other pigment producers. Monacolin K is produced as a mixture of a lactone and a free hydroxyl acid. Numerous monacolins were used to inhibit cholesterol biosynthesis. The reversible competitive inhibition of the microsomal 3-hydroxy-3-methyl-glutaryl coenzyme A reductase (HMG-CoA reductase) results in the reduction of HMG-CoA to mevalonic acid (mevalonyl-CoA or mevalonate) and formation of cholesterol as well as other compounds such as ubiquinones. This enzyme is the rate-determining enzyme of the cholesterol biosynthesis pathway. Therefore, monacolins have been known as a blood-reducing cholesterol substance for controling blood cholesterol level. Among the monacolins, monacolin K is the most efficacious compound to decrease cholesterol in the plasma when compared with other monacolins [2-3, 6-7].

In previous studied, Chairote et al. [2] prepared red yeast rice from several type of Thai glutinous rice (Oryza sativa L.) cv. Korkor 6 (RD6), Kam (Kam), and Sanpatong1 (SPT1) and compared with red yeast rice which was prepared from non-glutinous rice and commercial Chinese red yeast rice. They found that red yeast rice from Thai glutinous rice had more intense monacolins peaks than non-glutinous rice and commercial Chinese red yeast rice but their chromatographic profiles were similar. The results from chromatograms showed the presence of several monacolins (monacolin K acid form, compactin, monacolin M acid form, monacolin K, monacolin M, and dehydromonacolin K) and an unidentified main compound with the molecular weight of 358. The

highest amount of monacolin K were 33.79 mg/g, produced from Oryza sativa L. cv. Korkor 6 (RD6).

In this study, aim to produce monacolins by solid-state fermentation of Thai glutinous rice with M. purpureus CMU001. The monacolins crude extract will be separated by silica gel column chromatography and analyzed by liquid chromatography and mass spectrometry (LC-MS).

Materials and Methods

Materials

Thai glutinous rice, O. sativa L. cv. Sanpatong 1 (SPT1) were purchased from a local market to be used in fermentation of red yeast rice.

Monacolin K (mevinolin) was purchased from Sigma-Aldrich, Germany.

Isolated Monascus purpureus strain CMU001 on PDA slant was obtained from the Department of Biology, Faculty of Science, Chiang Mai University.

Fermentation of red yeast rice

The grain of polished glutinous rice cultivar were soaked in distilled water for 8 hour and then water was removed. The soaked rice grain was separately steamed in a cooking pot for 20 min. After that, streamed glutinous rice 50 g was put in a 250 ml Erlenmeyer flask and sterilized in autoclave at 15 psi and 121 °C for 20 min. After sterilization the sterile of glutinous rice was cooled. One week old precultured of M. purpureus CMU001 spores were inoculated in to the stream rice. The inoculate rice were incubated at 30 °C for 3 weeks. The fermented of glutinous rice product was dried in an oven at 70 °C to obtain dry red yeast rice. Dry red yeast rice was ground to a powder by blender for extraction of monacolins.

Sample preparation

An extraction of sample was performed by using 1 g of red yeast rice powder. It was mixed with 20 ml of 75% ethanol and put into a centrifugal tube, then use a vortex mixture. The solution was sonicated in an ultrasonic bath for 60 min. The suspension was centrifuged at 3000 rpm for 10 min at 4 °C. The supernatant was collected, the extraction was repeated three times and all of the extracted were mixed together. Finally, the extract was filtrated with 0.2 µm nylon membrane into a vial for monacolins analysis.

For column chromatography, the extracts were evaporated under vacuum rotary evaporator. The concentrated crude extract was separated further by chromatography using silica gel column, eluting with a stepwise solvent gradient of hexane to hexane/dichloromethane (90:10), dichloromethane/ethylacetate (90:10), ethylacetate/methanol (90:10) and methanol. Several separated fraction of eluted solution from silica gel column were collected and filtered with 0.2 µm nylon membrane into a vial for monacolins analysis.

Analysis of monacolins by HPLC and LC-MS

The presence of monacolins in the samples were determined by HPLC (Agilent HP 1100) with Inertsil ODS-3 column (5 µm 4.6x150 mm 6BI85146) and photodiode array detector. The chromatography was performed using of acetonitrile as a solvent A and 0.1% trifluoroacetic acid (TFA) as a solvent B. Linear gradient elution (0.5 ml/min) from 35% to 75% A in 30 min and keeping at 75% A from 30 to 40 min was applied with total analysis time of 50 min. The chromatogram was detected at 237 nm with sample injection volume of 10 µl.

The samples containing monacolins were analyzed by LC-MS (HP 1100 Binary/G1946A). The mass spectrometer with an electrospray ionization (API-EI) source was operated in the positive ion mode. The eluents, injection volume and flow rate were the same as for HPLC analysis.

Results and Discussion

Identification of monacolins in red yeast rice

The results from obtained extracted samples at 237 nm show several monacolins in HPLC chromatograms shown in Figure 1. Mass spectrometry was used to confirm the presence of monacolins based on the molecular weight of monacolins. In this study, we found 8 kinds of monacolins. The results identified by LC-MS are shown in Table 1. A peak of interesting compound (number 8) with the molecular weight of 353 could not be identified.

Table 1: Monacolins were identified from red yeast rice extract.

Peak No.	Compound	MW
1	Dihydromonacolin L[10]	306
2	Monacolin X acid form[10]	436
3	unidentified	-
4	Monacolin X[10]	418
5	Monacolin K acid form[10]	422
6	Monacolin L[11]	304
7	Monacolin K[8]	404
8	unidentified	353
9	Monacolin M[5]	406
10	Dehydromonacolin K[4]	386
11	unidentified	-
12	unidentified	-
13	unidentified	-

In previous studied, Li et al. [5] reported 12 kinds of monacolins in red yeast rice. These include monacolin K, monacolin J, monacolin L, monacolin M, monacolin X, monacolin X acid form, monacolin K acid form, monacolin J acid form, monacolin L acid form, monacolin M acid form, dehydromonacolin K, dihydromonacolin L and compactin.

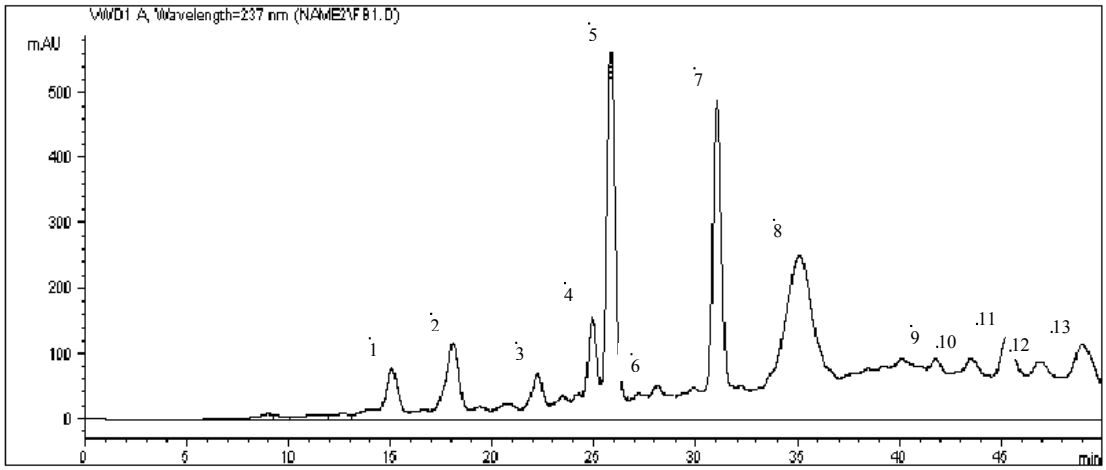

Figure 1. Chromatogram of monacolins in red yeast rice sample extracted.

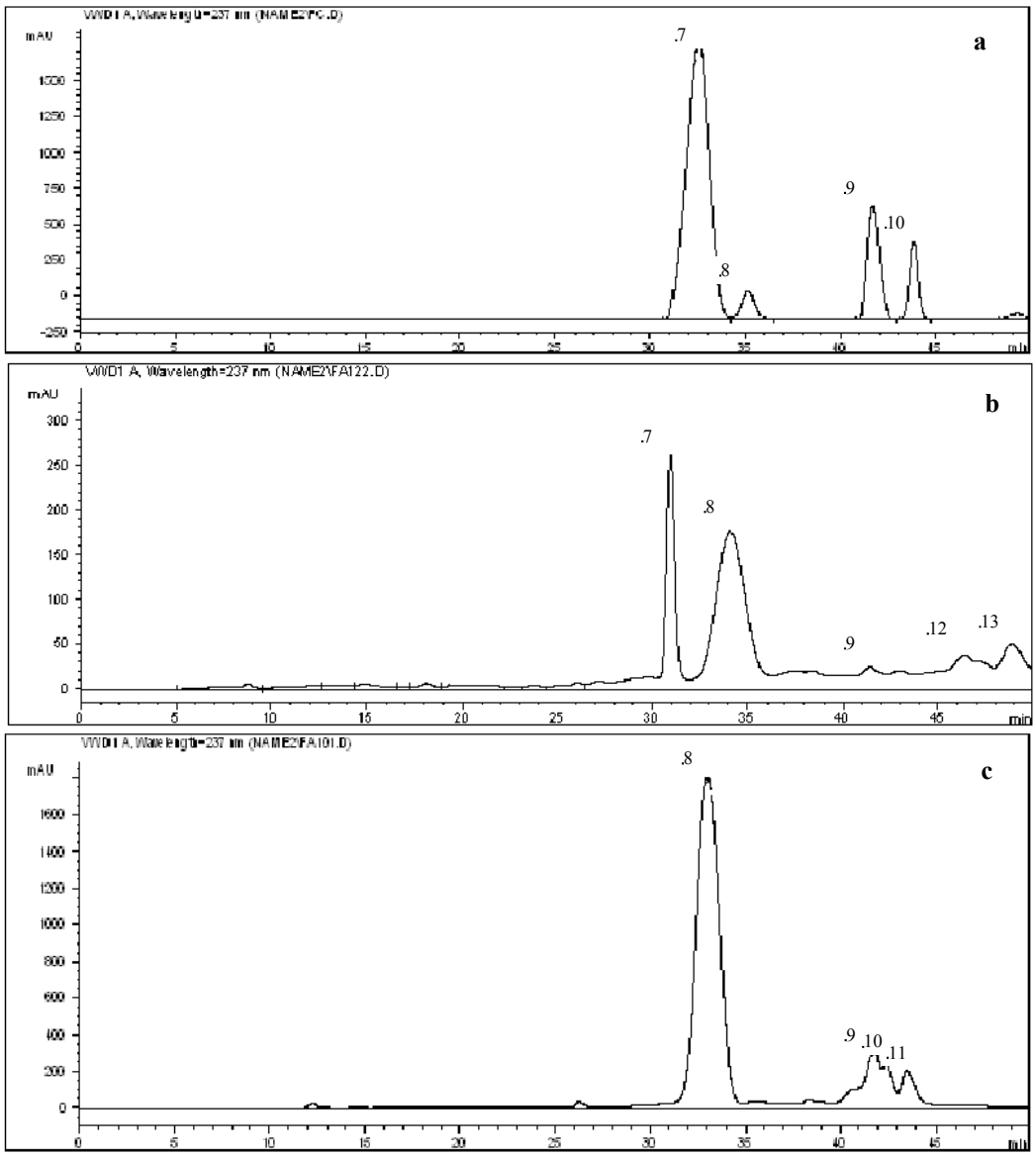

Figure 2. Chromatogram of monacolins were separated by silica gel column chromatography**.** (a) number 7 (monacolin K), number 8 (unidentified compound), number 9 (monacolin M**),** number 10 (dehydromonacolin K), (b) number 7 (monacolin K), number 8 (unidentified compound), number 9 (monacolin M), (c) number 8 (unidentified compound), number 9 (monacolin M).

In order to have better results, red yeast rice extract was separated by silica gel column chromatography. The chromatogram of separated fraction are shown in Figure 2. The condition of eluting should be developed in future study in order to purify this compound more effectively.

Conclusions

Several monacolins identified from red yeast rice production from Thai glutinous rice are monacolin K, monacolin K acid form, monacolin X, monacolin X acid form, dehydro-monacolin K, monacolin L, dihydromonacolin L and monacolin M. Another interesting compound with the molecular weight of 353 is obtained. This compound will be separated and identified in the future study.

Acknowledgements

The authors are grateful to the Faculty of Graduated School, Chiang Mai University and Center of Excellence for Innovation in Chemistry (PERCH-CIC) for financial supports.

References

[1] Y.-C. Su, J.-J. Wang, T.-T. Lin and T.-M. Pan, J. Ind. Microbiol. Biotechnol. **30** (2003), pp. 41-46.
[2] E. Chairote, G. Chairote, H. Niamsup and S. Lamyong, World J. Microbiol. Biotechnol. **24** (2008), pp. 3039-3047.
[3] P. Pattanagul, R. Pinthong, A. Phianmongkhol and S. Tharatha, Int. J. Food Microbiol. **126** (2008), pp. 20–23.
[4] J. Ma, Y. Li, Q. Ye, J. Li, Y. Hua, D. Ju, D. Zhang, R. Cooper and M. Chang, J. Agric. Food Chem. **48** (2000), pp. 5220–5225.
[5] Y.-G. Li, F. Zhang, Z.-T. Wang and Z.-B. Hu, J. Pharm. Biomed. Anal. **35** (2004), pp. 1101-1112.
[6] Y.-G. Li, H. Liu and Z.T. Wang, J. Pharm. Biomed. Anal. **39** (2005), pp. 82–90.
[7] J.-J. Wang, C.-L. Lee and T.-M. Pan, J. Ind. Microbiol. Biotechnol. **30** (2003), pp. 669–676.
[8] A. Endo, J. Antibiot. **32** (1979), pp. 852-854.
[9] A. Endo, J. Antibiot. **33** (1980), pp. 334–336.
[10] A. Endo, K. Hasumi, T. Nakamura, M. Kunishima and M. Masuda, J. Antibiot. **38** (1985), 38: 321-327.
[11] A. Endo, K. Hasumi and S. Negishi, J. Antibiot. **38** (1985), pp. 420-422.
[12] D. Komagata, H. Shimada, S. Murakawa and A. Endo, J. Antibiot. **42** (1989), pp. 407-412.
[13] K. Kimura, D. Komagata, S. Murakawa and A. Endo, J. Antibiot. **43** (1990), pp. 1621-1622.
[14] T. Nakamura, D. Komagata, S. Murakawa, K. Saki and A. Endo, J. Antibiot. **43** (1990), pp. 1597-1600.

Synthesis of avidin-fingerroot peroxidase conjugate for lectin detecting method

J. Ketvaraporn[1, 3], P. Sangthong[2], M. Pattarawarapan[2, 3] and L. Shank[2, 3]*

[1] Department of Biotechnology, Faculty of Graduate School, Chiang Mai University, Chiang Mai, Thailand 50200
[2] Department of Chemistry, Faculty of Science, Chiang Mai University, Chiang Mai, Thailand 50200
[3] Center for Innovation in Chemistry faculty of Science, Chiang Mai University, Chiang Mai, Thailand 50200

* E-mail: lalida_shank@yahoo.com

Abstract: Fingerroot, Boesenbergia Rotunda (L.) Mansf. , is a new found source of peroxidase. Fingerroot peroxidase (FRP) purified by affinity chromatography was conjugated with avidin and used in the biotin-avidin system for detection of galactose binding lectin. The avidin-FRP conjugate was prepared by a chemical reaction employing periodate. The activity of avidin-FRP conjugate was compared with the conjugate prepared from commercial horseradish peroxidase, HRP, using the same reaction conditions. The detection of galactose binding lectin was carried out by coating lectin from jackfruit, Artocarpus heterophyllus, on microwell plates, followed by addition of biotin-galactose conjugate and avidin-peroxidase conjugate. The final step of the detection was completed by addition of 2,2'-Azino-bis(3-ethylbenzothiazoline-6-sulfonic acid (ABTS), a peroxidase substrate. The affinity purified fingerroot peroxidase was successfully conjugated with avidin and subsequently used in the lectin detecting method as reported in this study.

Introduction

Peroxidase is widely used as labeling enzyme due to its ability to oxidize various chromogenic substrates in the presence of hydrogen peroxide. Peroxidase can be conjugated with antibody specific to the molecule of interest. [1] In addition, peroxidase labeled avidin and streptavidin are commonly used in the avidin (streptavidin)-biotin interaction system [2]. Biotinylated sugar molecules were used in the screening of lectin-sugar binding activity. Wetprasit et al. (1997) determined sugar specificity of jackfruit lectin, Jacalin, by using a simple biotinylated sugar-lectin binding assay and streptavidin-HRP reporting system [3]. Wang et al. (2009) screened lectin from papaya (Carica papaya) seeds, longan (Euphoria longana) seeds and sorghum (Sorghum bicolor) by a sugar-polymer-biotin based enzyme-linked adsorbent assay. Commercial streptavidin-labeled HRP was also used as a detecting agent [4].

Recently the interest in application of peroxidases from alternative sources has increased. Berlina et al. (2007) employed peroxidase from soybean, Glycine max, conjugated with streptavidin for biotinylated antibody binding to report the presence of sulfamethoxipyridazine in milk [5]. Correspondingly, this proposed study aims to apply peroxidase from fingerroot, Boesenbergia rotunda (L.) Mansf., in lectin detection system. Avidin-HRP conjugate, avidin-FRP conjugate and biotinylated galactose were systhesized for detection of galactose binding lectin using jackfruit lectin as a test model. The development of protocols and comparative results between traditional HPR and alternative FRP conjugates are hereby discussed.

Avidin and strptavidin are both biotin binding tetrameric proteins. Avidin is a glycoprotein found in egg whites, while streptavidin, a non-glycoprotein, is isolated from Streptomyces avidinii. Avidin or streptavidin is labeled with a detectable molecule, e.g., peroxidase catalyzing a color reaction, fluorescent or radioactive probes. Biotin presents another binding partner (such as antibody, nucleotide, and sugar) that specifically links to the target molecule in the samples offering the labeling system. The avidin (streptavidin)-biotin complex assists the detection of the targeted analytes both to locate and to quantify upon the introduction of substrate or other means of visualization [6]. Lectins are carbohydrate binding glycoproteins. Lectin can bind to glycosyl groups on the cell membrane of the lining in the digestive tract resulting in damage of the membrane. Lectins from different sources have unique carbohydrate group binding properties. Hence, the screening of lectins in potential food sources is a preventive necessity [7].

Materials and Methods

Materials Bovine serum albumin (BSA) and o-dianisidine were purchased from Fluka. Horseradish peroxidase (HRP), avidin, biotin hydrazide, galactose, jackfruit lectin (JFL), sodium borohydride, and 2,2'-azino-bis(3-ethylbenzthiazoline-6-sulphonic acid) were purchased from Sigma. All other chemicals used were analytical grade and obtained from local suppliers.

Purification of fingerroot peroxidase (FRP) Roots of fingerroot were cut into small pieces and blend with 0.01 M phosphate buffer, pH 6.0. The crude extract was centrifuged at 6000 x g for 20 min to remove insoluble debris. Ammonium sulfate was added to the supernatant up to 20% saturation. After centrifugation at 6000 x g for 20 min, the supernatant was removed. Additional ammonium sulfate was introduced to the supernatant to achieve a solution with 40% salt saturation. The protein precipitate was collected by centrifugation at 6000 x g for 20 min and resuspended in 0.01 phosphate buffer, pH 6.0. The fingerroot extract was dialyzed with the same buffer. The dialyzate was loaded onto the Con A-sepharose

4B column (1.4x18 cm). The eluent buffer was a gradient of 0.0-0.5 mM D-(+)-mannose in 0.01 M phosphate buffer, pH 6.0 containing 0.5 mM each of $MgCl_2$, $MnCl_2$ and $CaCl_2$. Protein content was determined by the method of Bradford [8]. Peroxidase activity was determined according to the procedure modified from that of González using o-dianisidine (ε_{460} 11.3 $mM^{-1} \cdot cm^{-1}$) as substrate [9]. Peroxidase activity unit (U) was calculated using the following formula according to that used for calculation of HRP conjugates by EY laboratories. [10].

$$U = \frac{(OD460/min) \times ml \text{ of reaction mixture}}{11.3}$$

Preparation of avidin-peroxidase conjugates Sodium periodate was added to 1 ml of HRP solution (1 mg/ml) to a final concentration of 8 mM. The periodate oxidation was left in the dark for 20 min at room temperature. The oxidized peroxidase was purified by sephadex G-25 to remove the excess oxidant. The eluent buffer was 0.01 M sodium phosphate, 0.15 M NaCl, pH 7.2. The collected fractions (0.5 ml) were monitored for heme protein at 404 nm using known concentrations (mg/ml) of HRP as a standard curve. The oxidized peroxidase was dialyzed with 0.2 M sodium carbonate, pH 9.6, overnight at 4ºC. The concentration of the obtained peroxidase solution was calculated to determine the amount of peroxidase present. The amount of avidin in 0.2 M sodium carbonate buffer, pH 9.6 was prepared to be one quarter of the amount of HRP used. The avidin solution was added to the peroxidase solution and incubated at room temperature for 2 hr with constant stirring. Freshly prepared 5.0 M sodium borohydride was added at 30 µl per milliliter of reacting protein solution and the reaction was left for 30 min at room temperature to form Shiff base interactions. The unreacted aldehyde sites were blocked by adding 50 µl of 1.0 M ethanolamine, pH 9.6, per milliliter of protein conjugate solution. Lastly, the solution was dialyzed with 0.01 M sodium phosphate, 0.15 M NaCl, pH 7.2 and stored at 4ºC. FRP solution obtained from affinity chromatography was quantified according to the heme method described above and undergone the same conjugation procedure as HRP.

Preparation of biotin-galactose conjugates A solution of 50 mM galactose in 10 mM phosphate buffer saline (PBS), pH 7.4 was added to the fresh periodate solution to a final concentration of 10 mM. The reaction was left for 30 min at 4ºC in the dark with constant stirring. Periodate oxidation was terminated by addition of sodium sulfite to a final concentration of 20 mM and left to react for 5 min at room temperature. A solution of Biotin hydrazide in dimethylsulfoxide was mixed with the oxidized galactose solution to a final concentration of 15 mM. The mixture solution was constantly stirred for 2 hr at room temperature. The mixture solution was purified by gel filtration with Sephadex G-50 column (1x50 cm) and eluted with 10 mM PBS, pH 7.4. The collected fractions were screened for biotinylated galactose and galactose by phenol-sulfuric acid assay according to the procedure of Dubois [11].

Electrophoresis Native-PAGE was performed using 7.5% polyacrylamide slab gels at constant Voltage of 40 Volts. Guaiacol was used for peroxidase activity detection.

Sugar-lectin binding assay 150 µl of lectin solution at 0.1, 1.0 and 10.0 µg/ml (in 50 mM sodium carbonate buffer, pH 9.6, containing 0.02% sodium azide) was placed into the wells of microtiter plates and incubated at 4ºC overnight. The plate was washed three times with 10 mM PBS, pH 7.4 containing 0.05% Tween 20 to remove the unbound lectin. Then the wells were coated with 250 µl of 3% periodate treated BSA in 10 mM PBS, pH 7.4 and incubated at 4ºC overnight. The plate was then washed three times and the wells were supplemented with 150 µl of 0.32 mM biotin-galctose conjugate in 10 mM PBS, pH 7.4, containing 1 mM $MgCl_2$, 1 mM $MnCl_2$, 1 mM $CaCl_2$. Microplates were incubated at room temperature overnight. After removal the unbound conjugates, the wells were supplemented with 150 µl of the conjugate avidin-peroxidase solution in 50 mM Tris-HCl buffer, 0.15 M NaCl, pH 7.4. The plates were incubated at room temperature for 2 hr and then washed three times. The wells were supplemented with 150 µl of the substrate containing ABTS (0.8 mg/ml) and hydrogen peroxide (0.032%) in 50 mM citrate buffer, pH 4.2, and incubated for 1 hr at room temperature to determine the optical density values at 415 nm.

Results and Discussion

FRP was partially purified by affinity chromatography via Con A-sepharose 4B column. The chromatographic profile was shown in figure 1. Fraction no. 21 and 22 were pooled together. The specific activity of FRP in the solution was determined to be 12.0 U per mg protein.

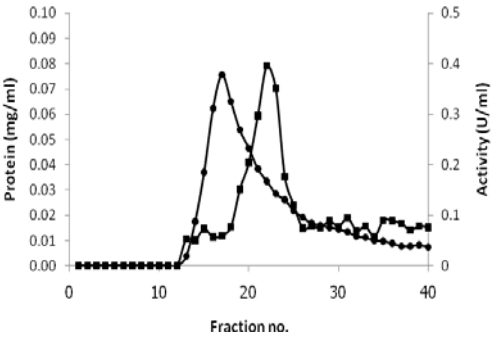

Figure 1 Chromotographic profile of FRP from Con A-Sepharose 4B affinity chromatography (solid circle represents protein (mg/ml) and solid square represents activity (U/ml).

In the next step, avidin-HRP conjugate and avidin-FRP conjugate were synthesized via the process of periodate oxidation and reductive amination. Conjugation employing 0.7 mg of HRP according to the heme group quantification method resulted in the avidin-HRP conjugate with activity of 190.3 U per microliter of solution (using o-dianisidine as

substrate), FRP solution with 17.3 mg of heme protein resulted in FRP-avidin conjugate with the activity of 0.27 U per microliter of solution. This may be the result of the much higher purity of commercial HRP compared to the affinity purified FRP which may contain other heme proteins. It is also known that HRP has much higher catalytic efficiency than peroxidases from other sources. This is also possible as HRP could be more stable and can withstand the conjugation reaction condition better than FRP. However, the application of FRP and FRP conjugates remained to be explored. Native-PAGE was used to observe peroxidase activity and patterns of the enzyme from both sources before and after the reaction as shown in figure 2. The orange bands indicate the formation of tetraguaiacol which is a product of the catalytic reaction by peroxidase on the oxidation of guaiacol. This in turn locates protein bands with peroxidase activity. Lane 1 in figure 2 contained commercial horseradish peroxidase as positive control which gave an intense orange band and another slight orange band closer to the stacking gel. This result agrees with a report by Dunford (1999) that two neutral isoenzymes (mixture of B and C) are usually present in commercial peroxidase [12]. Lane 2 contained avidin-HRP conjugate which appeared as several orange bands suggesting that molecular weights of HRP have increased as the conjugation with avidin occurred and more than one form of the conjugates existed. However, some forms may also be the result of alternation of pI after reaction. Lane 3 contained BSA as a negative control which did not produce tetragiacol, but could be visualized when the same gel is stained by Coomassie Brilliant Blue, a protein dye. Lane 4 contained the avidin-FRP conjugate appearing as a wide orange band close to the stacking gel. When this result is compared to that from lane 5 which contained affinity purified peroxidase (two orange bands), it is likely that the shift in the pattern is resulted from molecular weight addition due to the conjugation rather than a simple PI alteration alone. This also suggests that affinity purified FRP from the 20-40% saturation of ammonium sulfate precipitation is likely to contain two major isoenzymes.

Next, biotin-galactose conjugate was synthesized and purified by gel filtration chromatography. The fractions were examined for the presence of biotin-galactose conjugate by a phenol-sulphuric acid assay. One major peak and one minor peak were obtained (data not shown). The major peak which came out first was collected. The binding of biotinylated galactose to HRP-avidin conjugate or FRP-avidin conjugate and also to JFL were confirmed by the sugar-lectin binding assay.

To compare the activity between the horseradish peroxidase conjugates and the fingerroot peroxidase conjugate, a standard jackfruit lectin, was selected as a test model to verify the biotinylated galactose binding ability.

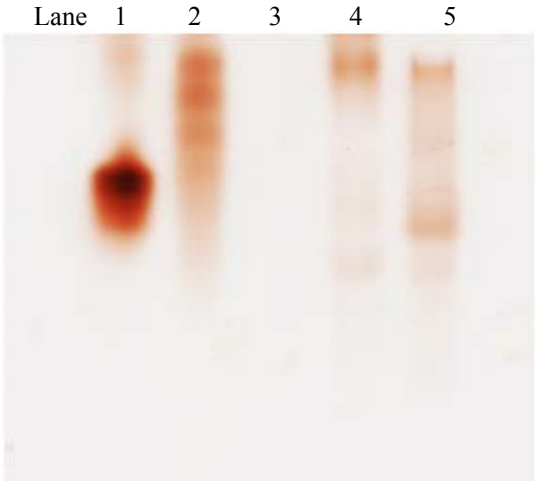

Figure 2 Native-PAGE of avidin-HRP conjugates and avidin-FRP conjugates, lane 1: HRP (0.25 µg), lane 2: avidin-HRP conjugates (0.43 µg), lane 3: BSA, a negative control (1.25 µg), lane 4: avidin-FRP conjugates (10.50 µg) and lane 5: FRP (41.66 µg)

JFL was coated on the plates and detected by addition of biotin-galactose conjugate, avidin-peroxidase conjugate and followed by addition of ABTS, a substrate of peroxidase, to generate the color. The result is shown in the figure 4.

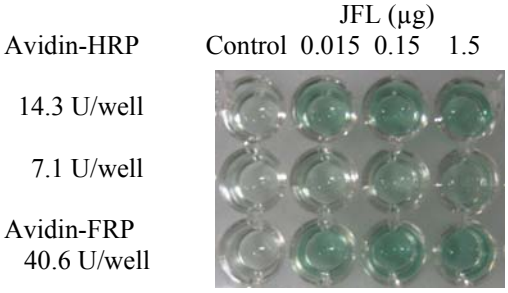

Figure 3 Comparison of sensitivity between avidin-HRP and avidin-FRP in lectin detecting method.

Peroxidase activity unit per microliter of avidin-HRP and avidin-FRP conjugates previously calculated was used for the preparation of sugar-lectin binding assay. Figure 3 is a representative picture of the assay performed in microtiter plate among the triplicate experiment. Control samples in figure 3 contained all other substances except JFL which did not produce the oxidation of ABTS substrate due to the absence of avidin-peroxidase. At 7.1 U per well avidin-HRP conjugate gave detectable color change, but the difference among different amounts of lectin tested were only detectable by spectrophotometer. Once 14.3 U per well of such conjugate was used, it was more visible as the green color of the product became more intense as the amount of JKL was increased. The binding of biotinylate-galctose on JKL on the plate and the binding of avidin-HRP conjugate to the

biotinylated galactose were verified here. Avidin-FRP conjugate at 40.6 U per well produced color change at the similar levels as those obtained from 14.3 U per well of avidin-HRP conjugate. This suggests that although avidin-HRP conjugate synthesized from commercial HRP has higher activity, Fingeroot peroxidase can be used to prepare avidin-FRP conjugate that can be used in the sugar-lectin binding assay as well as other applications requiring peroxidase conjugates.

Conclusions

Lectin detecting method was prepared to report the presence of lectin, a sugar binding protein, by using biotinylated sugar-lectin and avidin-peroxidase system. Avidin-FRP conjugate was successfully synthesized and used in biotinylated galactose-avidin system for detection of the galactose binding activity of Jacalin, the jackfruit lectin. Fingerroot which is local to Thailand can be used as a source of peroxidase and FRP-avidin conjugate can be used in lectin screening and in many other biotin-avidin systems as biotin can be linked to various types of molecules.

Acknowledgements

The authors are grateful to the Thailand Research Fund (TRF), the Faculty of Graduate School, Chiang Mai University and Center of Excellence for Innovation in Chemistry (PERCH-CIC) for financial supports.

References

[1] S.S. Deshpande, Enzyme immunoassays, From concept to product development, Chapman & Hall, New York, USA, 1996, pp. 164-189.
[2] E. P. Diamandis and T. K. Christopoulos, Clin. Chem. **37** (1991), pp. 625-636.
[3] N. Wetprasit and M. Chulavatnatol, Biochem. Mol. Biol. Int. **42** (1997), pp. 399-408.
[4] T.-H. Wang, M.-H. Lee and N.-W. Su, Food Chem. **113** (2009), pp. 1218-1225.
[5] A. N. Berlina, A. V. Zherdev, B. B. Dzantiev and I. Y. Sakharov, Applied Biochem. Microbial. **43** (2007), pp. 550-555.
[6] G. T. Hermanson, Bioconjugate Techniques, Academic Press, San Diego, USA (1996).
[7] I. M. Vasconcelos, J. Tadeu and A. Olivrira, Toxicon. **44** (2004), pp. 385-403.
[8] M. M. Bradford, Anal. Biochem. **72** (1967), pp. 248-254.
[9] E. M. González, B. Ancos and M. P. Cano, J. Agric. Food Chem. **48** (2000), pp. 5459-5464.
[10] EY laboratory data sheet catalog no. H-2402-1, EY laboratories, INC. San Mateo, CA, USA.
[11] M. Dubois, K. Gill, J. Hamilton, P. Roberts and F. Smith, Anal. Chem. **28** (1965), pp. 350-356.
[12] H. B. Dunford, Heme peroxidase, John Wiley & Sons, New York, USA, 1999, pp. 92-95.

Acetylcholinesterase inhibitors and antioxidant activity in some thai plants

P. Chada[1,3] and N. Rakariyatham[2,3]*

[1]Department of Biotechnology, Faculty of Graduate School, Chiang Mai University, Chiang Mai, Thailand 50200
[2]Department of Chemistry, Faculty of Science, Chiang Mai University, Chiang Mai, Thailand 50200
[3]Center for Innovation in Chemistry faculty of Science, Chiang Mai University, Thailand 50200

* Corresponding Author E-mail Address: nuansri1@yahoo.com

Abstract: Oxidative modifications are associated with subtle inflammatory processes in the brain in Alzheimer's disease and acetylcholinesterase inhibitor (AChEI) is currently still the best available pharmacotherapy for Alzheimer patients. This study aims to evaluate the antioxidant and the acetylcholinesterase inhibitory activity of some Thai herb extracts. Different Thai herbs, grown for traditional food in Thailand, were extracted by using ethanol, methanol and boiling water. The antioxidant and acetylcholinesterase inhibitory activity of Thai herb extracts were measured by the DPPH test and Ellman's method. The results showed that methanol extracts of Chionantus parkinsonii **(Hutch) Bennet & Raizada possessed the highest free radical-scavenging activity with 95% inhibition whereas the highest activity of acetylcholinesterase was found in the water extract of Zanthozylum Limonella Alston with 59% inhibition.**

Introduction

Alzheimer's disease (AD) occurs regularly in elderly people because of the malfunctioning of different biochemical pathways [1]. It is a progressive disease that causes memory loss, behavioral changes, disorientation, depression and death. There are several causes of this disease. The causes and progression of Alzheimer's disease are not well understood; one is cholinergic hypothesis [2]. Adsersen et al.(2006) indicate that the disease is associated with plaques and tangles in the brain[3].

The enzyme acethylcholinesterase (AChE) is concerned with the nervous systems and this enzyme rapidly hydrolyzes the active neurotransmitter acetylcholine into inactive compounds choline and acetic acid [4]. The principal role of AChE to terminate of nerve impulse transmissions at the cholinergic synapses by rapid hydrolysis of acetylcholine [5].

Moreover another possible cause of AD is oxidative stress which causes damage to cell function with aging and is involved in a number of age-related disorders. In AD, there are increasing of oxidative brain lipids, carbohydrates, proteins, and DNA [6]. Amyloid beta (Aβ) is a major source of oxidative free radicals and/or toxic agents in AD and Smith et al.(2000) suggested that both Aβ and neurofibrillary tangles (NFT) may be cellular compensations for the increase in oxidative stress and to serve antioxidative functions[7].

To date, only a few inhibitors of AChE, such as tracine, donepezil and rivastigmine, are used in medicine for the treatment of AD symptoms by counteracting the ACh level in the brain[8]-[9]. There may be adverse effects including gastrointestinal disturbances and problems associated with bioavailability. There are many plants which contain natural antioxidants that respond to the endogenous production of free radicals and other species [10]. The aims of this study are to emphasize evaluation of antioxidant and acetylcholinesterase inhibitory activity of some Thai herb extracts.

Materials and Methods

Preparation of the extracts

Fifteen dry plant materials (Momordica charantia Linn, Phyllanthus acidus skeels, Bauhinia purpurea Linn, Cassia siamea Britt, Morinda citrifolia Linn, Zanthozylum Limonella Alston, Piper nigrum Linn, Capsicum anuum Linn var annuum, Capsicum annuum Linn var. acuminatum Fingerh, Capsicum Frutescens Linn, **Chionanthus parkinsonii** (Hutch) Bennet & Raizada, Solanum aculeatissimum Jacq, Solanum melongena Linn, Solanum torvum Swatz and Zingiber officinale Roscoe) were dried by sunlight and then ground in to powder. The obtained powder was pre-extracted with n-hexane. After that each sample was mercerated with ethanol, methanol and boiled-water. The extracts were filtered through Whatman paper. Water extracts were lyophilized. Ethanol and methanol extracts were evaporated to dryness. After being dissolved in solvent, the extracts were screened for acetylcholinesterase (AChE) inhibitory activity and antioxidant activity by the DPPH test.

Acetylcholinesterase activity

The enzyme activity was measured using an adaptation of the method described in Ingkaninan et al. (2003). To 325 µl of Tris–HCl buffer (pH 8), 100 µl of sample solutions and 25 µl of an enzyme solution containing 0.28 U/ml were incubated for 15 min. Subsequently, 75 µl of a solution of acetylthiocholine iodide (AChI) 0.023 mg/ml and 475 µl of 3 mM 5,5'-dithiobis-(2-nitrobenzoic acid) (DTNB) were added and the final mixture was incubated for another 30 min at room temperature. Absorbance of the mixture was measured at 405 nm. Inhibition in %, was calculated as:

$$I\ (\%) = 100 - [(A_{sample}/A_{control}) \times 100]$$

Antioxidant activity

The free radical scavenging was measured using DPPH assay. To 5 ml of a methanol solution of 2, 2'-diphenylpicrylhydrazyl (DPPH) 0.002% in methanol, 50 µl of extract solutions were added and the mixture was incubated at room temperature for 30 min. The absorbance was measured at 517 nm. The inhibition percentage of free radical DPPH (I %) was calculated as:

$$I\ (\%) = 100 - (A_{sample}/A_{control}) \times 100$$

Results and Discussion

Acetylcholinesterase activity

Fifteen plant species were selected for investigation and a total of 45 extracts were tested for AChE inhibitory activity. The results obtained with 1 mg/ml of all plant extracts are shown in Table 1.

The inhibitory activity of extract samples was divided into 3 groups: low (< 25%), moderate (25-50%) and high (> 50%). Thirteen samples of boiled-water extracts exhibited inhibitory activity. Z. Limonella Alston and C. Frutescens Linn exhibited high inhibitory activity.

Eleven of the methanolic extracts exhibited inhibitory activity. S. melongena Linn exhibited high inhibitory activity while M. charantia Linn, Z. Limonella Alston, C. anuum Linn var annuum, C. annuum Linn var. acuminatum Fingerh, C. Frutescens Linn, S. aculeatissimum Jacq and S. torvum Swatz exhibited moderate inhibitory activity.

However, six samples of ethanolic extracts exhibited low inhibitory activity. Other ethanol extracts were not detected.

The results showed that the boiled-water extract of Z. Limonella Alston exhibited the higest acetylcholinesterase inhibitory activity. The AChE inhibitory activity of Z. Limonella Alston have never been reported before. This activity has been found in Feroniella lucida and Citrus paradise [11] and Ruta graveolens [3].

Antioxidant activity

The extracts (1 mg/ml) were submitted to be evaluated for antioxidant activity using DPPH assay and the results are shown in Table 2. All samples, except the boiled-water extract of P. nigrum Linn, possessed various level of antioxidant activity. The DPPH scavenging property of boiled-water extract was 1.59 to 89.94% and Z. Limonella Alston showed the highest. The potential activity was found in the methanolic extracts of 4 samples, Z. Limonella Alston, **C. parkinsonii** (Hutch) Bennet & Raizada, S. aculeatissimum Jacq and S. torvum Swatz which exhibited antioxidant activity greater than 90%. High antioxidant activity was also found in the ethanolic extracts of S. aculeatissimum Jacq (77.32%) and S. torvum Swatz (73.96). However, the methanolic extract of **C. parkinsonii** (Hutch) Bennet & Raizada showed the greatest activity (95.37%). The plant in the genus **Chionanthus** was reported to contain secoiridoids possessing antioxidant properties[12].

Conclusions

This study reported the screening of AChE inhibitory and antioxidant activity in edible Thai plants. Among the fifteen analyzed plants, several showed acetylcholinesterase inhibitory activity and antioxidant activity. The methanolic extracts of **C. parkinsonii** (Hutch) Bennet & Raizada possessed the highest antioxidant activity while the boiled-water extract of Z. Limonella Alston exhibited highest AChE inhibitory activity, as well as high antioxidant activity. Plants showing simultaneous AChE inhibitory activity and also antioxidant activity could be considered to be foods, having some potential function besides their traditional value, which makes them a possible medicinal soure in preventing AD.

Acknowledgements

This research was supported by the Graduate School, the Department of Chemistry, Faculty of Science, Chiang Mai University and also thanks PERCH-CIC, the Department of Chemistry, Faculty of Science, Chiang Mai University, Thailand.

References

[1] A. Ferreira, C. Proenca, M.L.M. Serralheiro and M.E.M. Araujo, J. Ethnopharmacol. **108** (2006),pp. 31-37.
[2] H.Q. Lin, M.T. Ho, L.S. Lau, K.K. Wong, P.C. Shaw and D.C.C. Wan, Chemico-Biological Interaction. **175** (2008), pp.352-354.
[3] A. Adsersen, L. Gudiksenand and A. K, Jager, J. Ethnopharmacol, **104** (2006), pp. 418-422.
[4] C.F.D. Jong, R.J.E. Derks, B. Bruyneel, W. Niessen, and H. Irth, J. Chromatogr A, **1112** (2006), pp. 303-310.
[5] P.K. Mukherjee, V. Kumar, M. Mal and P.J. Houghton, **14** (2007), pp. 289-300.
[6] W.R. Markesbery, Archneurol, **56** (1999), pp. 1449-1452.
[7] M.A. Smith, C.A. Rottkamp, A. Nunomura, A.K. Raina, and G. Perry, Biochemica Biophysica Acta, **1502** (2000), pp. 139-144.
[8] S. Lopez, J. Bastida, F. Viladomat, and C. Codina, Life Sci, **71** (2002), pp. 2521-2529.
[9] H. Wang, G. Zhou, X. Gao, Y. Wang, and W. Yao, Food chem, **105** (2007), pp. 24-27.
[10] A.T. Mata, C. Proenca, A.R. Ferreira, M.L.M. Serralheiro, J.M.F. Nogueira and M.E.M. Araujo, Food Chem, **103** (2007), pp. 778-786.
[11] K. Ingkaninan, P. Temkitthawon, K. Chuenchom, T. Yuyaem and W. Thongnoi, J. Ethnopharmacol, **89** (2003), pp.261-264.
[12] I. Gülçin, R. Elias, A. Gepdiremen and L. Boyer, Eur. Food Res. and Technol., **223** (2006), pp. 759-767.

Table 1: Effect on AChE activity, % of inhibition, of ethanolic , methanolic and boiled-water extracts (1 mg/mL)

Family	Plants	Part used	%Inhibition of acetylcholinesterase		
			(boiled-water extracts)	(ethanolic extracts)	(methanolic extracts)
Cucurbitaceae	Momordica charantia Linn	Fruit	34.02	-	37.35
Euphorbiaceae	Phyllanthus acidus skeels	Fruit	-	1.82	6.26
Leguminosae	Bauhinia purpurea Linn	Leaf	7.66	-	-
	Cassia siamea Britt	Leaf	18.14	-	-
Rubiaceae	Morinda citrifolia Linn	Leaf	2.93	-	-
Rutaceae	Zanthozylum Limonella Alston	Fruit	59.43	17.84	48.84
Piperaceae	Piper nigrum Linn	Seed	18.60	-	-
Solanaceae	Capsicum anuum Linn var annuum	Fruit	46.59	-	49.63
	Capsicum annuum Linn var. acuminatum Fingerh		2.28	4.50	27.27
	Capsicum Frutescens Linn	Fruit	56.40	-	35.46
	Chionanthus parkinsonii (Hutch) Bennet & Raizada	Fruit	7.49	3.40	17.45
	Solanum aculeatissimum Jacq	Fruit	39.39	15.02	42.16
	Solanum melongena Linn	Fruit	35.35	5.86	50.94
	Solanum torvum Swatz	Fruit	23.22	-	42.70
Zingiberaceae	Zingiber officinale Roscoe	Rhizome	-	-	9.86

Table 2: Antioxidant activity (%) of ethanolic, methanolic and boiled-water extracts (1 mg/mL)

Family	Plants	Part used	% Inhibition of free radical DPPH		
			(boiled-water extracts)	(ethanolic extracts)	(methanolic extracts)
Cucurbitaceae	Momordica charantia Linn	Fruit	4.62	4.79	3.46
Euphorbiaceae	Phyllanthus acidus skeels	Fruit	28.62	16.74	33.49
Leguminosae	Bauhinia purpurea Linn	Leaf	9.87	3.29	10.84
	Cassia siamea Britt	Leaf	12.13	3.11	6.49
Rubiaceae	Morinda citrifolia Linn	Leaf	3.47	3.47	4.15
Rutaceae	Zanthozylum Limonella Alston	Fruit	89.94	57.25	90.14
Piperaceae	Piper nigrum Linn	Seed	-	17.31	23.77
Solanaceae	Capsicum anuum Linn var annuum	Fruit	27.46	36.92	72.18
	Capsicum annuum Linn var. acuminatum Fingerh	Fruit	55.08	48.16	79.96
	Capsicum Frutescens Linn	Fruit	23.93	16.81	27.37
	Chionanthus parkinsonii (Hutch) Bennet & Raizada	Fruit	15.24	67.56	95.37
	Solanum aculeatissimum Jacq.	Fruit	26.30	77.32	93.08
	Solanum melongena Linn	Fruit	29.15	49.36	82.85
	Solanum torvum Swatz	Fruit	22.98	73.96	92.27
Zingiberaceae	Zingiber officinale Roscoe	Rhizome	1.59	18.39	66.00

Anti cancer activity of ampelopsin H from stem bark of hopea odorata

N. Aznam* , S. Atun, and R. Arianingrum

Department of Chemistry Education, Faculty of Mathematic and Natural Science, Yogyakarta State University, Karangmalang, Yogyakarta 55281, Indonesia

*E-mail: nurfina_uny@yahoo.com

Abstract: Ampelopsin H was isolated from the stem bark of Hopea odorata, Dipterocarpaceae family. The structure of this compound was elucidated by NMR spectroscopy, including 1D and 2 D NMR. The invitro cytotoxicity of ampelopsin H against human cancer cell lines indicated that this compound had cytotoxic effect against HeLa, Raji, and Myeloma cell with the IC_{50} values of 129.718; 91.075; and 165.959□g/ml respectively and had no cytotoxic effect against Vero human cell (IC50 305.652□g/ml). The antiproliferative mechanism toward these human cancer cell lines showed that ampelopsin H influenced on cell cycle progression by defered doubling time cell. Also, this compound was able to induce apoptosis by influenced the expression of p53.

Introduction

Dipterocarpaceae is a large family found in Indonesia. There is about sixteen genera and six hundred species [1] and nine genera of which found in Indonesia extending from Aceh to Papua with the greatest population in Kalimantan. Hopea is one of genera largely found in Indonesia, at least about one hundred species [2,3].

Based on many research, it had been reported that terpenoid, phenylpropanoid, flavanoid, benzofuran derivative, fenolic acid, and oligostilbenoid were compounds commonly found in some species of Dipterocarpaceae. Some of oligostilbenoid exhibited the interesting biological activity, such as resveratrol. It is the first compound found and isolated in 1977 as phytoalexin, antimicrobial product from the leaves of Vitis vinifera plant as reaction against infection or another physiologic stimulus [4]. The other research also indicated that resveratrol had chemo preventive activity against cancer cells [5]. Many other biological activity of oligostilbenoid had been reported, such as ε-viniferin and copaliferol A exhibiting antimicrobial activity against some micro-organism [6]. Some of these oligostilbenoid also showed cytotoxic activity against certainly strain, for example (-)-ampelopsin A and hopeaphenol had cytotoxic activity against KB epidermoid carcinoma cell [7-10], while malibatol A and malibatol B had cytotoxic activity against CEM SS cell in antiviral test.

We have been isolated a number of oligostilbenoid from steam bark of Hopea odorata [12]. The elucidation structure by NMR spectroscopy, including ID and 2D NMR showed that these compounds were Balanocarpol (**1**), Ampelopsin H (**2**), Hopeafenol (**3**), and Hemlesyanol C (**4**) (Figure 1). This paper reports the cytotoxic activity, anti proliferative effect, and how the anti proliferative mechanism of Ampelopsin H that have been isolated from steam bark of H.odorata against HeLa S3, and Raji, human cancer cell lines, and Vero.

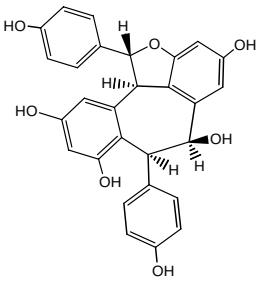

Balanocarpol (**1**)

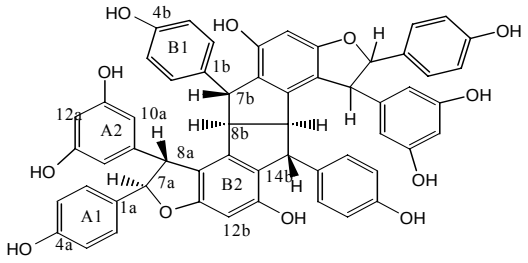

Ampelopsin H (2)

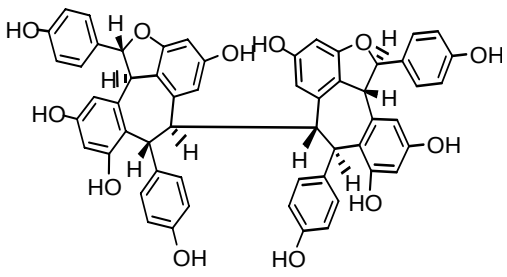

Hopeafenol (3)

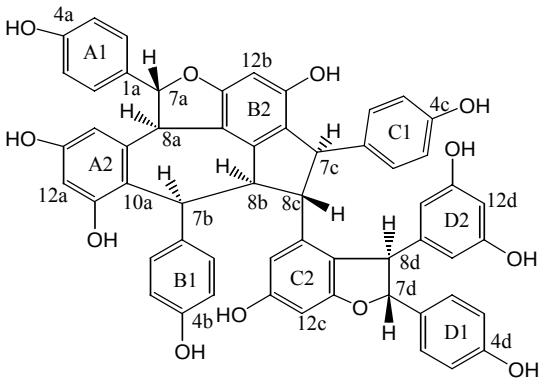

Hemlesyanol (4)

Figure 1. Compounds have been isolated from H. odorata : Balanocarpol (**1**), Ampelopsin H (**2**), Hopeafenol (**3**), and Hemlesyanol (**4**)

Materials and Methods

Materials : Ampelopsin H has been isolated from stem bark of H. odorata (from garden of attempt of Dramaga and Jasinga, Bogor at June 2007.

In-vitro cytotoxicity test : The in-vitro cytotoxicity test was investigated using 96 wells plate with cell density $2x10^4$ cells per ml for HeLa S3 and Raji human cancer cell lines, and $1x10^4$ cells per ml for vero cell. Into each well was added with 100 µl cells in culture medium (87.5% RPMI 10,4 g/L; 2% penstrep; and 10% FBS) and was then incubated in CO_2 incubator for 12-24 hours at 37^0C. Each sample was dissolved in culture medium containing 0.05% DMSO, and 100 µl of each sample in the different concentrations was added into each well in triplicate and was then incubated in CO_2 incubator for 12-24 hours at 37^oC. MTT solution (10 µl per 100 µl medium) was added to all wells of an assay, and plates were incubated for 4 hours at 37^oC in CO_2 incubator. As much as 100µl formazon (10% SDS and 0, 01 N chloride acid) was added into each well and mixed on a shaker for 5 minutes. The wells were incubated in the dark room for 12-24 hours at room temperature. The absorbance was measured using multiwell scanning spectrophotometers (ELISA reader) at wavelength 595 nm. The absorbance is directly proportional to the number of living cells. So the dead cell could be calculated to determine LC_{50}.

Doubling time test: The cell was fasted (distarvation) for 24 hours in culture medium containing 0.5% FBS. Then they were grown in multiple dishes containing compound in low concentration ($\leq LC_{50}$). The sampling was done at 24, 48 and 72 hours. The living cell in each well was measured using multi well scanning spectrophotometers (ELISA reader) at wavelength 595 nm. The absorbance is directly proportional to the number of living cells. The curve between the number of living cell and incubation time indicated how the anti proliferative effect. The difference of doubling time was measured from the slope of log the number of cell versus incubation time curve.

Determination of Apoptosis: The determination of induction apoptosis was investigated by DNA cellular coloration using ethidium bromide/acrydine orange and observed on fluorescence microscope**.** The living cell give bright green colour and the apoptosis cell give orange colour. Futhermore the expression of p53 was determination by immunohistochemical analysis [15].

Results and Discussion

The cytotoxic activity of the Ampelopsin H against HeLa S3, Raji, and Vero cell measured as LC_{50} were provided in Table 1.

Table 1: LC_{50} of Ampelopsin H against HeLa S3, Raji, Myeloma, and Vero cell

Cell Lines	**LC_{50} (□g/mL)**	**Note**
HeLa S3	129.71	Active
Raji	34.69	Very Active
Myeloma	165.95	Less Active
Vero	305.65	Less Active

HeLa-S3, a continuous cell line that living as adherent cell, is a cell derivate of ephythell cell of human cervix cancer [16]. While Raji cell is a lymphoblast cell found by R.J.V Pulvertaft (1963) from Burkitt's lymphoma at the left of upper jaw of negro boy oldest 11 years [17].

Table 1 showed that the highest cytotoxic activity of Ampelopsin H is on Raji cell.

Based on doubling time test showed that Ampelopsin H reduce the growing of HeLa S3 (Figure 2), Raji (Figure 3), and Myeloma (Figure 4) cell compared with non treatment cell (control). It also showed that the slope curve of log number of cell versus incubation time with Ampelopsin H treatment smaller than control. It proved that Ampelopsin H caused a doubling time deferment. The doubling time value of HeLa S3, Raji, and Myeloma cell with Ampelopsin H treatment have been provided in Table 2. It mean that Ampelopsin H inhibit proliferate cell through cell cycle progression as well as transduction signal.

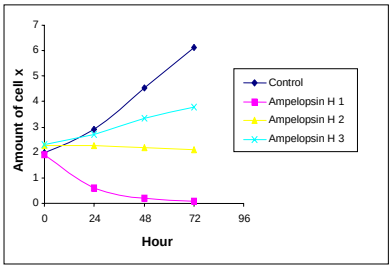

Figure 2. The growing profile of Hela S3 cell without treatment (control), and with Ampelopsin H (concentration 135, 67.5, and 33.75 µg/mL).

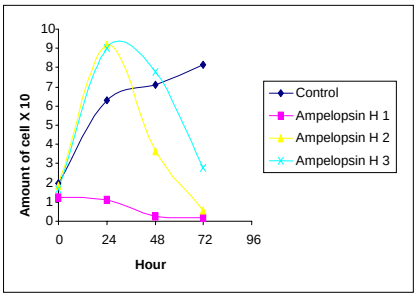

Figure 3. The growing profile of Raji cell without treatment (control), and with Ampelopsin H (concentration 90, 45, and 22.5 µg/mL).

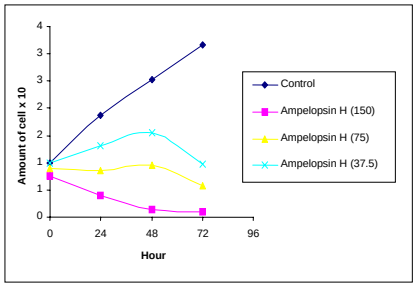

Figure 4. The growing profile of Myeloma cell without treatment (control), and with Ampelopsin H (concentration 150, 75, and 37.5 µg/mL).

Table 2: The equation curve of log number of cell vs time and the value of doubling time of HeLa S3, Raji, and Myeloma cell

Ampl (□g/mL)	Equation curve of log number of cell vs time	**Slope**	**Doubling time (hour)**
A. HeLa			
0	y = 0.0069x + 4.3048	0.0069	43.087
67.5	y=-0.0004x + 4.3571	-0.0004	-
135	y= -0.0186x+ 4.2381	-0.0186	-
33.75	y= 0.0027x + 4.3680	0.0027	110.852
B. Raji			
0	y = 0.0078x + 4.4337	0.0078	21.577
90	y =-0.0127x + 4.1532	-0.0127	-
45	y = -0.0084x+ 4.6828	-0.0084	-
22.5	y = 0.0026x + 4.5345	0.0026	-
C. Myeloma			
0	y = 0.0068x + 4.4098	0.0068	36.946
150	y =-0.0132x + 3.8796	-0,0132	-
75	y = -0.008x + 3.9407	-0.0023	-
37.5	y = 0.0029x + 4.0146	0.0029	768.087

The ethidium bromide/acrydine orange coloration indicated that Ampelopsin H also inhibits cell through apoptosis mechanism in HeLa S3 (Figure 5), Raji (Figure 6), and Myeloma cell (Figure 7).

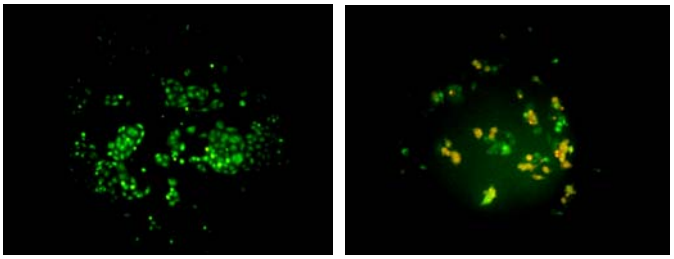

Figure 5. The acridine orange coloration of : (A) HeLa S3 cell without Ampelopsin H, and (B) HeLa S3 cell with 135 µg/mL Ampelopsin S3.

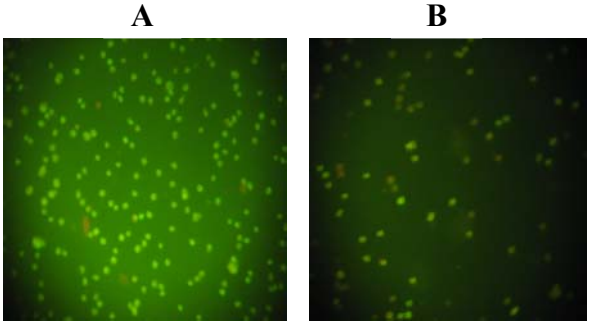

Figure 6. The acridine orange coloration of : (A) Raji cell without Ampelopsin H, and (B) Raji cell with 34.69 µg/mL Ampelopsin H.

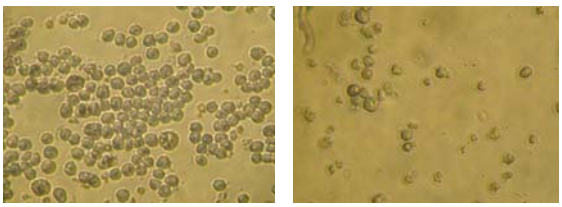

Figure 7. The acridine orange coloration of : (A) Myeloma cell without Ampelopsin H, and (B) Myeloma cell 100 µg/mL Ampelopsin H.

The effect of Ampelopsin toward the DNA change of Raji cells were indicated in Figure 6b. The living cell with intact nucleus gives the bright green color, while the apoptosis cell gives orange color. The Figure show that Ampelopsin H treatment cause cell become apoptosis therefore give orange color, and also indicate the morphology of apoptosis characteristic as cell become small, membrane bleeding, and nucleus fragmentation.

As we know that HeLa S3 cell is immortal cell because there is E6 protein that degrades p53, and E7 that degrades pRb. Therefore cell lost the growing cell protein. Until now there is no information about Ampelopsin H activity can repress E6 and E7 expression. Based on some anticancer compound like curcumin, it is possible that the antiproliferative activity of Ampelopsin H is initiated by bounding between this compound and protein. Therefore it cause the protein was recognize by proteosome that it degrade this protein. Furthermore, the expression of p53 was analyzed by immunohistochemical. It show that HeLa cell without treatment has a blue colour . It's mean that there are no expression of p53. The other way, HeLa S3 cell by adding Ampelopsin H show a brown colour, that it's mean that there was expression of p53.

Conclusions

In this paper we conclusion that Ampelopsin H isolated from the steam bark of H. odorata have cytotoxic effect against HeLa S3, Raji, Myeloma cell lines, and relatively no toxic effect to Vero cell . This compound gives the highest cytotoxic effect against Raji cell. It also have antiproliferative effect by induced apoptosis toward HeLa S3, Raji and Myeloma cell. This compound was able to induce apoptosis by influence the expression of p53 in HeLa cell.

References

[1] A. Cronquist , An Integrated System of Classification of Flowering Plants (1981), Columbia In Press, New York, pp. 316 – 318

[2] K. Heyne, Tumbuhan berguna Indonesia (1987). Badan Litbang Kehutanan, Jakarta, jilid III, pp. 1390 – 1443

[3] I. Soerianegara, R.H.M.J. Lemmens, Plant resources of South East Asia, 5 (1), timber trees : major commercial timbers (1994), Prosea, Bogor, Indonesia, pp. 166- 193

[4] P.Langcake and R.J. Pryce, Phytochemistry, **16 (**1977), pp. 1193 –1196

[5] M. Jang, G.O. Lining Cai, K.V. Udeani, C. F . Slowing, C.W.W. Thomas, H.S. Beecher, N.R. Fong, A. D. Farnsworth, R.G. Kinghorn, R.C Mehta, J.M. Moon, Pezzuto. Science. **275 (**1997), pp. 218- 220

[6] S. Sotheeswaran, and V Pasuphaty, Phytochemistry, **32** (1993), (**5**), pp.1083-1092

[7] T. Tanaka, K. Ito, M. Nakaya, Y.Iinuma, H. Takashi, N. Naganawa, M. Matsuura, Ubukata. Vatikanol D, a novel resveratrol hexamer isolated from Vatica rassak, Tetrahedron Letters, **41** (2000), pp.7929 – 7932

[8] T. Ito, K. Tanaka, M. Nakaya, Y. Iinuma, H. Takahashi, M. Naganawa, Y. Ohyama, K.F. Nakanishi, Bastow, Kuo-Hsing Lee, Tetrahedron Letters, **42** (2001), pp.5909-5912

[9] T. Ito, Y. Tanaka, K. Ido; M. Nakaya, Y. Iinuma, H. Takashi, M. Naganawa, Y. Ohyama, K.F. Nakanishi, K.H. Bastow, Lee, Tetrahedron, **57** (2001), pp. 7309-7314

[10] E.K. Seo, H.L Chai , V.R. Constant, R. Santisuk, W.W. Vichai, N.R. Christopher , G.A. Farnsworth , J.M. Cordell, A.D. Pezzuto, Kinghron, J. Org. Chem. , **64** (1999), pp.6976-6983

[11] S. Atun**,** N. Aznam, R. Arianingrum, JPMS, **X**, (2005), No. 2.

[12] S. Atun**,** N. Aznam, R. Arianingrum, M. Niwa, Indo. J. Chem, **5** (2005) (3), pp. 211-214

[13] S. Atun**,** N. Aznam, R. Arianingrum, M. Niwa, Indo. J. Chem, **6** (2006) (1), pp. 75-78

[14] S. Atun**,** A.A. Sjamsul, N. Aznam, R. Arianingrum, M. Niwa, Biochem. System. And Ecol, **34** (2006), pp. 642-644

[15] H.D. Rode, D. Eisel, I. Frost, Apoptosis, Cell Death and Cell Proliferation Manual, **3rd** ed., Roche Applied Science (2004)

[16] S. Julia, Uji Sitotoksisitas Fraksi Protein Daun Erythrina fusca Luor (Cangkring) Pada Sel HeLa, Skripsi, Fakultas Farmasi Universitas Gadjah Mada, Yogyakarta (2001)

[17]http://www.biotech.ist.unigue200

Production of geranylgeraniol by metabolically engineering escherichia coli

A. Klamrak[1], P. Promdonkoy[2], S. Tanapongpipat[2], N. Nualkaew[1*], N. Guennewich[4], W. De-Eknamkul[3] and T.M Kutchan[4, 5]

[1]Faculty of Pharmaceutical Sciences, Khon -Kaen University, Khon –Kaen, Thailand
[2]Microbial Cell Factory Laboratory, Bioresource Technology Unit, National Center of Genetic Engineering and Biotechnology, 113 Thailand Science Park, Pathumthani, Thailand
[3]Faculty of Pharmaceutical Sciences, Chulalongkorn University, Bangkok, Thailand
[4]Leibniz Institute of Plant Biochemistry, Halle/Saale D-06120, Germany
[5]Donald Danforth Plant Science Center, St. Louis, MO 63132, USA

*nnatsa@kku.ac.th

Abstract: Geranylgeraniol (GGOH) is a potent apoptotic inducer in various cancer cells lines such as human lung adenocarcinoma cell, colon cancer cell, etc[1]. It is also only one intermediate of the biosynthetic pathway of plaunotol, an anti ulcer drug from Croton stellatopilosus[2]. However low yield and mixture of terpenoids were obtained from recombinant E. coli harboring PDPase alone and chemical synthesized of this compound. To overcome these problems we have used pathway engineering approach for reconstruction of GGOH biosynthetic pathway in E.coli BL21 (DE3) RIPL to increase its GGOH accumulation. Therefore, the recombinant plasmid pETDuet-1 harboring both genes encoding two enzymes involved in GGOH biosynthetic pathway was constructed. The first gene is geranylgeranyl diphosphate synthase (GGPPS) which is responsible for rate determining step **of GGPP biosynthesis in E. coli[3]. The last gene is prenyl diphosphate phosphatase (PDPase) that catalyzes** de-phosphorylation **of GGPP yielding GGOH. Here we described the construction of a vector for the co-expression of 2 genes (GGPPS and PDPase), and the detection of GGOH as its phenotype of co-expression and single gene expression in E. coli BL21 (DE3) RIPL by using HPLC. The results showed clearly that GGOH was accumulated in E. coli cells of both clone harboring co-expression vector and single gene GGPPS, but not PDPase alone. The higher amount of GGOH from the co-expression strain revealed that it could enhance GGOH production by the increase level of GGPP through functional expression of GGPPS. It is possible that pool of GGPP serve as a critical point for GGOH production in E. coli.**

Introduction

GGOH is an acyclic diterpene alcohol. It possesses potent anticancer activity in various cancer cell lines such as human leukemia 60 (HL60), human lung adenocarcinoma A549 cell, human leukemia U937 cell and colon cancer cell [1]. GGOH is also used as the starting material in the production of vitamin E. In addition, it is the only one intermediate in biosynthetic pathway of plaunotol, an anti ulcer drug from Croton stellatopilosus Ohba (Plau-noi). Feeding experiment of stable isotope indicated that GGOH was derived from deoxyxylulose-5-phosphate pathway [2]. Although GGOH can be preceded by means of chemical synthesis, racemic mixtures of other terpenoids and low yield of GGOH have been obtained.

Heterologous expression of genes involved in the secondary metabolite production by using microorganisms received much attention in the last few decades. Especially, E.coli and S. cerevisiae have been widely used as cell factories for production of various compounds such as taxadiene, artemisinin and carotenoids, through metabolic engineering technique. Expression of genes in E. coli has shown many advantages such as high level proteins production, easily grown in media consisting of inexpensive carbon sources, and capable manipulated by molecular biology tools [3]. For these reasons, E. coli is suitable for metabolic engineering works.

The biosynthetic pathway of GGOH is included 2 genes, geranylgeranyl diphosphate synthase (GGPPS), and prenyl diphosphate phosphatase (PDPase) that catalyzes **de-phosphorylation** of GGPP yielding GGOH. GGPPS is probably be a critical point of isoprenoid production, therefore the heterologous expression of this gene may increase GGPP, which serve as substrate of GGOH.[4-6] Coexpression of more than one gene together with gene related to the rate limiting step of biosynthetic pathway can be used to increase secondary metabolite production, such as coexpression of isopentenyl pyrophosphate isomerase (IPP isomerase) couple with mutant form of farnesyl diphosphate synthase (IspAm) in E. coli JM101 [7]; and the overexpression of HMG CoA reductase along with IPP isomerase, GGPP synthase, and diacylglycerol diphosphate phosphatase in Saccharomyces cerevisiae [8].

From our previous experiment, the expression of phosphatase gene alone could not enhance GGOH accumulation in E. coli. Therefore, in this study we conducted coexpression of 2 genes involved in GGOH biosynthesis pathway, (GGPPS and PDPase) in E. coli BL21 (DE3) RIPL. The phenotype of the engineered E. coli carrying 2 genes and single gene were also investigated by GGOH detection.

Materials and Methods

Construction of recombinant plasmid pETDuet/GGPPS/PDPase: Construction of recombinant plasmid pETDuet harboring GGPPS and PDPase was accorded to Tolia and Tor [9] with slightly

modification. The process can be divided in two steps, Firstly, a PDPase from pET101TOPO/PDPase, was doubly digested with NdeI and EcoRV, and cloned into pETDuet-1 coexpression vector (Novagen) at the corresponded sites in MCSII. Then, the plasmid pETDuet/PDPase was transformed into E. coli DH5α. The insert was verified by digestion and automated sequencing (Macrogen, Korea). Secondly, the truncated gene of GGPPS was amplified from plasmid pTZ57R/GGPPS, after that, it was treated with BamHI and SalI, and subcloned into pETDuet/PDPase which had been treated with the same enzymes. The plasmid pETDuet/GGPPS/PDPase which contained 2 genes was obtained. The in frame fusion was confirmed by automated sequencing using pairs of primer (pETUpstream primer and DuetDownI primer) according to manufactured recommend. The plasmid constructions used in this study are summarized in Table 1.

Table1: Plasmid constructions used in this study.

Plasmid construction	Gene	Description
pETDuet/*GGPPS/PDPase*	Geranylgeranyl diphosphate synthase and Prenyl diphosphate phosphatase	Coexpression
pETDuet/*GGPPS*	Geranylgeranyl diphosphate synthase	Single gene expression
pETDuet/*PDPase*	Prenyl diphosphate phosphatase	Single gene expression
pETDuet-1 (empty vector)	None	Negative control

Heterologous gene expression: The plasmid constructions from Table 1 were expressed separately in E. coli BL21 (DE3) RIPL cells (Novagen). They were cultivated in LB medium containing 50 μg/ml carbenicillin and 34 μg/ml of chloramphenicol, at 200 rpm, 37 ^{O}C until OD_{600} reached 0.6-0.8. The expression was induced by using 1 mM IPTG, and then continued culturing at 16 ^{O}C for 18 hrs. After that, the cultures were harvested by centrifugation at 8,000 rpm for 30 min, 4 ^{O}C and stored at -20 ^{O}C until used.

Determination of intracellular GGOH by HPLC**:** The intracellular GGOH level in E. coli was measured by HPLC method according to Huang et al, 1993 with slightly modification [10]. Pellets were resuspended in 10 mL lysis buffer (50 mM Tris-HCl, 0.2% Triton X-100, and pH 7.5), and sonicated 30 sec pulse 1 min in 3 cycles. Then, the cells lysate were centrifuged at 10,000 g for 30 min, 4 ^{O}C to remove cell debris. The supernatant was applied onto the MCI GEL CHP20P column (Mitsubishi) and eluted with linear gradient of 0, 10, 30, 50, 80, and 100% (V/V) MeOH, respectively. The fraction of 100% MeOH was collected, concentrated under gently stream N_2 gas, and adjusted to final volume 500 μL with absolute EtOH. GGOH was determined by HPLC using RP-18 column (4.0 mm x 250 mm, 5 μm: Phenomenex, Germany) at 25^{O}C using linear gradient of 0-100% acetonitrile (flow rate 1ml/min), for 40 min with UV detection at 214 nm.

Result and Discussion

As shown in Figure 1, plasmid for coexpression of GGPPS and PDPase was constructed. The GGPPS was inserted in the proper reading frame of MCS1 which contain an N-terminal His Tag, meanwhile, the PDPase was inserted in the proper position of MCSII which contain S Tag at C-terminal. The partial purification of GGOH from cell lysate of E. coli was performed and determined for GGOH accumulation. GGOH production could be detected only from clones carrying GGPPS, (pETDuet/GGPPS/PDPase and pETDuet/GGPPS), whereas clones harboring pETDuet/PDPase and pETDuet empty vector shown no production of GGOH. It could be explained that, expression of GGPPS and PDPase were fluxed from endogenous FPP toward GGOH. On the other hand, the expression of GGPPS alone could be produced GGOH via catalytic activity of endogenous phosphatase. No GGOH production from the clones harboring PDPase alone might due to the insufficient pool of endogenous GGPP. Interestingly, farnesol (FOH) appeared in all constructs including clone harboring pETDuet empty vector. It is possible that, temporary accumulation of endogenous FOH serve as conventional control mechanism for regulation the level of FPP. When cells need to up regulate for the higher terpenoids level, FOH can be converted back to FPP by FPP kinase [11, 12].

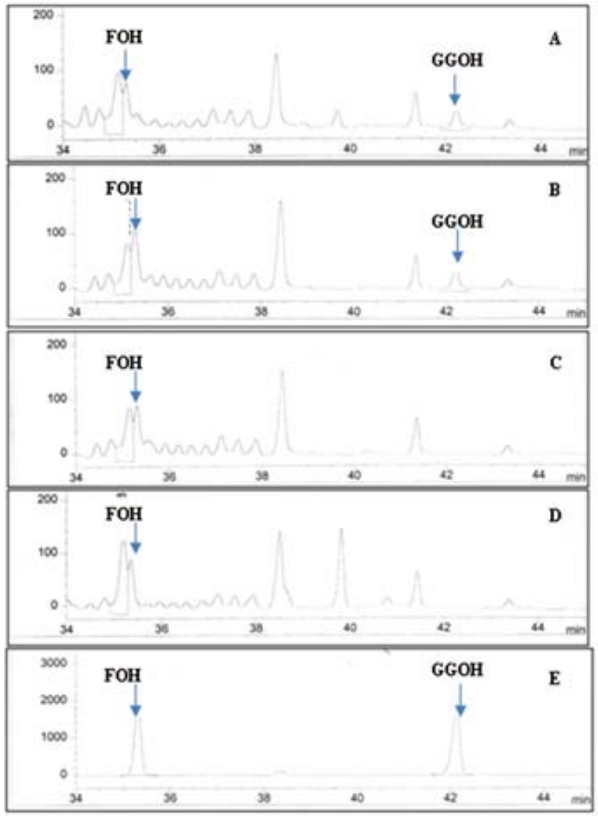

Figure 2. HPLC analysis of GGOH from the engineered E. coli BL21 (DE3) RIPL. **A**, E. coli [pETDuet/GGPPS/PDPase]; **B**, E. coli [pETDuet/GGPPS]; **C**, E.coli [pETDuet/PDPase]; **D**, E.coli carrying pETDuet-1empty vector, as a negative control; and **E**, authentic FOH (Sigma) and GGOH (Sigma).

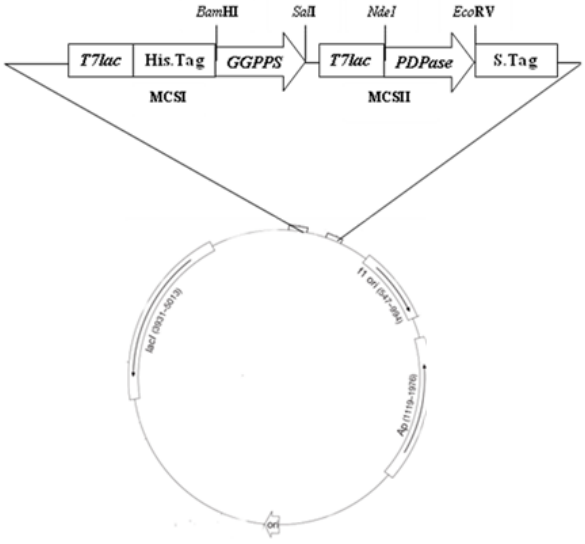

Figure 1. Map of recombinant plasmid pETDuet/GGPPS/PDPase. The GGPPS gene was inserted at BamHI and SalI in multiple cloning sites 1 (MCSI) and the PDPase gene was introduced at NdeI and EcoRV in multiple cloning sites 2 (MCSII). Heterologous genes were expressed under control of T7 promote and lac repressor protein.

Conclusion

The coexpression plasmid containing 2 genes responsible for the GGOH biosynthetic pathway was successfully constructed, and expressed in E. coli BL21 (DE3) RIPL. The GGOH investigation by HPLC analysis showed the presence of GGOH in E. coli harboring plasmid pETDuet/GGPPS/PDPase and pETDuet/GGPPS, whereas the clone carrying pETDuet/PDPase shows no accumulation of GGOH. The results indicated that, introducing of heterologous GGPPS leads to the increasing of GGPP level, which serve as available pool for GGOH production in E. coli.

Acknowledgments

The authors would like to thank Dr. Somsak Nualkaew (Faculty of Pharmaceutical Sciences, Mahasarakham University) for his support HPLC column and this work was supported by TRF-Master research fund (Grant No. MRG-WII505S037).

References

[1] H. Ohizumi, Y. Masuda, S. Nakajo, I. Sakai, S. Ohsawa ans K. Nakara, J. Biochem. **117** (1995), pp. 11-13.
[2] J. Wungsintaweekul and W. De-Eknamkul, Tetrahedron Lett**. 46** (2005), pp. 2125-2128.
[3] P.K. Ajikumar, K. Tyo, S. Carlsen, O. Mucha, T.H. Phon and G. Stephannopoulos, J. Mol. Pharm. **5** (2008), pp. 167-190.
[4] A. Ruther, N. Misawa, P. Boger and G. Sandmann, J. Appl Microbiol Biotechnol. **48** (1997), pp. 162-167.
[5] C.W. Wang, M.K. Oh and J.C. Liao, J. Biotechnol and Bioeng. **62** (1999), pp. 235-241.
[6] T. Vallon, S. Ghanegaonkar, O. Vielhauer, A. Miller, C. Albermann, G. Sprenger, M. Reuss and K. Lemuth, J. Appl Microbiol Biotechnol. **81** (2008), pp. 175-182.
[7] C. Ohto, M. Muramatsu, S. Obata, E. Sakuradani and S. Shimizu, J. Biosci. Biotechnol. Biochem. **73** (2009), pp. 186-188.
[8] K. Tokuhiro, M. Muramatsu, C. Ohta, T. Kawaguchi, S. Obata, N. Muramoto, M. Hirai, H. Takahashi, A. Kondo, E. Sakuradani and S. Shimizu, J. Appl. Environ. Microbiol. **75** (2009), pp. 5536-5543.
[9] N.H. Tolia and L.J Tor, J. Nat Methods.**3** (2006), pp. 55-64.
[10] D. Zhang and C.D. Poulter, J. Anal. Biochem. **213** (1993), pp. 356-361.
[11] S. Ohnuma, M. Watanabe and T. Nishino, J. Biochem. **119** (1996), pp. 541-547.
[12] H. Fuji, T. Koyama and K. Okura, J. Biochim Biophys Acta. **712** (1982), pp. 716-718.

Tyrosinase inhibitory and antioxidant activities of wastewater from paper mulberry pulps production

M. Kanlayavattanakul* and N. Lourith

School of Cosmetic Science, Mae Fah Luang University, Chiang Rai 57100, Thailand

* E-mail: mayuree@mfu.ac.th

Abstract: Wastewater from production of paper mulberry (Broussonetia papyrifera) was subjected to study. The biologically active principles were isolated by liquid-liquid extraction and the crude EtOAc extract posed the strongest antioxidant (IC_{50} = 0.4408 mg ml^{-1}) and tyrosinase inhibitory (IC_{50} = 1.634 mg ml^{-1}) activities with the highest ferulic acid content (4.450 ± 0.0077 ppm). It was further chromatographic fractioned, the bioassay-guided was done on all of the obtained 5 fractions at 1 mg ml^{-1}. The fraction eluted with EtOAc:n-Hexane (70:30, v v^{-1}) was found strongest inhibited free radical (92.33%). This fraction was further evaluated on its IC_{50} against free radical and tyrosinase which were 0.075 and 0.042 mg ml^{-1}, respectively. In addition, ferulic acid was found only in this fraction (45.310 ± 0.115 ppm). The biological activities of the were found increased and confirmed ferulic acid as a marker. This wastewater treatment successfully isolated biologically active compounds which appropriated for skin lightening and anti-wrinkles product developments and overwhelmed the drainage pollution from pulps manufacturing.

Introduction

Paper mulberry or Broussonetia papyrifera L. Vent. is widely distributed in East and Southeast Asia [1] including Thailand. Traditional processing of coarse-textured parchment from the paper mulberry's inner bark has been extensively conducted for supply into the handcraft industry. Therefore, large volume of the drainage wastewater is a serious environmental problem [2] as a strong base (NaOH) which was used to digest the fiber. The basic hydrolyzed lignins and p-hydroxycinnamic acid derivatives [3] which are biologically active compounds in wastewater were subjected to study in an attempt to search for a possible and environmental friendly treatment with additional benefit. Antioxidant and tyrosinase inhibitory effects and the total flavonoids and phenolics contents were evaluated to correlate the biological activities with the principle active compounds and characterization of phenolics and flavonoids in the wastewater extracts as well.

Materials and Methods

Wastewater extract preparations: All of the solvents used were reagent grade unless otherwise stated. Wastewater (pH 14) from the digestion process was collected from a local paper processing plant (Siam Northern Paper Co., Ltd., Chiang Rai, Thailand) and filtered to separate the fibers. The filtrate was lyophilized to produce a pale brownish powder which was then dissolved in MeOH (1:8 w v^{-1}, pH 8.20) which was equally divided into two parts. The first part was evaporated to dryness under vacuo yielded crude MeOH (not partition). The other part was partitioned with n-Hexane (1:3 v v^{-1}, ×3), the organic layers were combined and neutralized by washing with saturated brine. The neutralized organic layer was then concentrated to dryness and labeled as the n-Hexane extract. The aqueous phase was partitioned with EtOAc (1:3 v v^{-1}, ×3), washed and concentrated to obtain the EtOAc extract. The residue was concentrated to facilitate MeOH (partition) extract. The EtOAc was further applied onto column chromatography eluted with a gradient mobile phase (EtOAc:n-Hexane; 50:50 and 70:30 v v^{-1}, EtOAc, MeOH:EtOAc; 1:99, 5:95, 15:75, 30:70 and 50;50, MeOH)

Free radical scavenging activity assay: The antioxidant activities were measured using the free radical, 1, 1-Diphenyl-2-picrylhydrazyl (DPPH) [4]. DPPH was prepared in absolute EtOH at a concentration of 6×10^{-5} M. EtOAc extracts concentrated 0.25 to 4.0 mg ml^{-1}, MeOH (partition) and MeOH (not partition) extracts concentrated 0.5 to 6.0 mg ml^{-1} were tested. Ascorbic acid (vitamin C), concentrated 1.0 to 8.0 µg ml^{-1}, was used to prepare a standard curve (Figure 1). Briefly, a portion of the sample solution was mixed with equal volume of 6×10^{-5} M DPPH in absolute EtOH and was kept in the dark at room temperature for 30 min. The absorbance was then measured at 517 nm with a microplate reader (ASYS/UVM340, UK). Free radical scavenging activity was measured using the following equation:

% of free radical scavenging activity = $[(A_{control} - A_{sample})]/A_{control}$

where A is the absorbance

The IC_{50} values were calculated by linear regression of plots where the x-axis represented the concentrations of the extracts and the y-axis represented the percentage of free radical scavenging activities.

Tyrosinase inhibitory activity (enzyme-inhibitor pre-incubation method) assay: The tyrosinase inhibitory activity of the extracts was determined by the spectrophotometric method, as described by Chan et al. (2008) [5], using a modified dopachrome method with L-Dopa as the substrate [6]. All samples were first dissolved in absolute EtOH to concentrations of 10 to 15 mg ml^{-1}. Sample (40 µl) was added into 20 mM phosphate buffer (pH 6.8, 80 µl) and mushroom tyrosinase (240 unit ml^{-1}, 40 µl) in one well of a 96-

well plate. The solution in each well was mixed and pre-incubated at 25 ^{o}C for 10 min; 40 µl of 0.85 mM L-DOPA was then added followed by a continued incubation at 25 ^{o}C for 20 min. There was a corresponding blank for each sample, and this blank contained all components except for the mushroom tyrosinase. The absorbance was measured at 490 nm, using kojic acid as a positive control as shown in Figure 2. Each assay was performed in triplicate and the inhibition of tyrosinase activity was calculated using the following equation:

$$\% \text{ inhibition} = (A - B)]/A \times 100$$

where A is the absorbance at 490 nm without test sample, and B is the absorbance at 490 nm with test sample.

Total phenolics content determination: The total phenolic content of three wastewater extracts were measured as previously described [7]. The Folin-Ciocalteu reagent and gallic acid were used as standards. The standard curve was generated by using of gallic acid (0.125 to 1.00 mg ml^{-1}). The total phenolics content was measured in the samples (37.5 mg ml^{-1}). Each sample (0.1 ml) was added to 3.9 ml of distilled water and 1 ml of the Folin-Ciocalteu reagent, and the resultant solution was mixed by shaking. Two h prior to the absorbance measurement, 2% Na_2CO_3 (0.5 ml) was added. The absorbance was then measured at 760 nm. Each assay was performed in triplicate and all measurements were reported as gallic acid equivalents per 100 g of extract.

Total flavonoids content determination: The total flavonoids content was measured based on a published protocol [8] with certain modifications described herein. The standard curve was generated by using of quercetin (0.1 to 5.0 mg ml^{-1}). The total flavonoids content was measured in each extract (1.0 mg ml^{-1}) by mixing of sample (20 µl) with distilled water (80 µl) and 15% $NaNO_2$ (6 µl), respectively. After 6 min of incubation with shaking, 6 µl of 10% $AlCl_3$ was added. Shaking and incubation was continued for another 6 min followed by the addition of 80 µl of 4% NaOH to the mixture. Water (8 µl) was added to adjust the final volume to 200 µl. Thereafter, the mixture was thoroughly mixed with shaking for 15 min before measurement of the absorbance at 510 nm. Each assay was performed in triplicate and all measurements were reported as quercetin equivalent per 100 g crude extract.

Analysis of p-hydroxycinnamic acid derivatives: Characterization of the phenolics and flavonoids was done be means of HPLC on a Waters 2695 equipped with a Waters 2996 photodiode array detector using a reversed phase column (Alltech, Prevail C_{18} 5 µm, 250 × 4.6 mm, stainless steel with Alltech, Prevail all-guard cartridge C_{18} 5 µm, 7.5 × 4.6 mm) controlled through Waters Empower II software. All solvents were HPLC grade. The compounds were successively separated by a mobile phase which was a mixture of AcCN and 3% aq. AcOH (1:1 v v^{-1}) and flowed at 1 ml min^{-1}. Ferulic and caffeic acids and quercetin (Aldrich, USA) were used as standards. Calibration curves were obtained from the standards concentrated 1-500 ppm in AcCN ($R^2 > 0.999$). Analytes concentrated 10,000 ppm were prepared in AcCN. All of the measurement was done in triplicate.

Results and Discussion

The extractive yield was found highest in the crude MeOH extract followed by the MeOH (partition), EtOAc and n-Hexane extracts in descending order (Table 1). The total phenolics and flavonoids contents were not evaluated in the n-Hexane extract since most of the biologically active compounds possessed moderate to high polarity. The MeOH (partition) extract had a higher phenolic content than both the EtOAc and MeOH (not partition) extracts. However, the flavonoids content was found highest in the EtOAc extract followed by the MeOH extracts. In addition, the EtOAc extract showed the highest inhibition against the free radical scavenging and tyrosinase activities (Figure 1 and 3; Table 1).

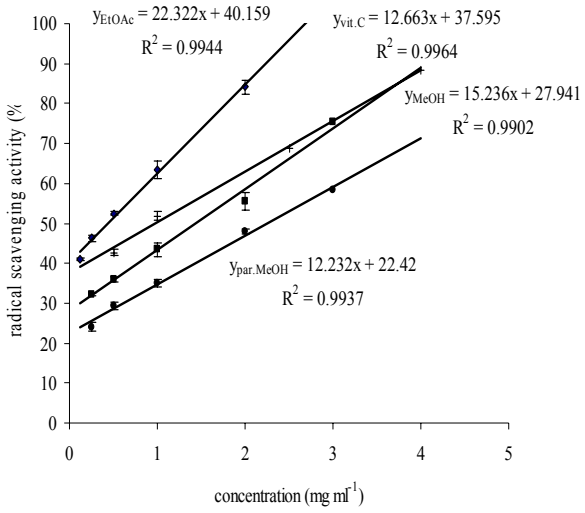

Figure 1. DPPH scavenging activity of samples; [EtOAc extract (♦), MeOH (not partition) extract (■), MeOH (partition) extract (●), Vitamin C (+)]

Table 1: Extractive yield, biological activities, total phenolics, flavonoids and ferulic acid contents of wastewater extracts

Extract	Yield (%, w w^{-1})	Radical scavenging activity (IC_{50}, mg ml^{-1})	Tyrosinase inhibitory activity (IC_{50}, mg ml^{-1})	Total phenolics (mg GAE 100g $extract^{-1}$)	Total flavonoids (mg QE 100g $extract^{-1}$)	Ferulic acid (ppm)
n-Hexane	0.53	-	-	-	-	-
EtOAc	0.58	0.441	1.634	1,306.667 ± 0.0007	9,819.523 ± 0.0021	4.450 ± 0.0770
MeOH (partition)	4.07	2.254	2.843	1,413.33 ± 0.0150	2,310.383 ± 0.0001	0.237 ± 0.0250
MeOH (not partition)	5.17	0.840	1.845	906.667 ± 0.0041	2,317.251 ± 0.0013	0.641 ± 0.0350
Vitamin C	-	0.001	-	-	-	-
Kojic acid	-	-	0.024	-	-	-

Characterization of phenolics and flavonoid was further carried out. Caffeic and ferulic acid were used as reference compounds as they are cell wall bound substances [9,10] and quercetin was chosen as it was extracted from paper mulberry in high amount over other flavonoids [11]. However, only ferulic acid was found in the extracts (Table 1) whereas caffeic acid and quercetin were undetectable under this condition. The EtOAc extract which was the best radical scavenger and tyrosinase inhibitor contained the highest ferulic acid content followed by the MeOH (not partition) and MeOH (partition), respectively.

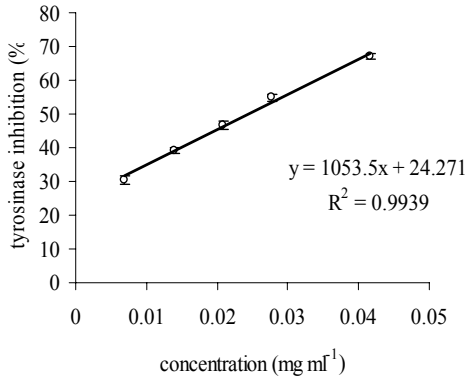

Figure 2. Tyrosinase inhibitory effect of standard (Kojic acid)

Antioxidant activity was correlated with flavonoids (R^2 = 0.450) and particularly ferulic acid (R^2 = 0.536) content similar to tyrosinase inhibitory effect (flavonoids; R^2 = 0.404, ferulic acid; R^2 = 0.489). Interestingly, ferulic acid content was closely related with total flavonoids (R^2 = 0.993) rather than the phenolics contents (R^2 = 0.055). Others have observed differences in the antioxidant activity of plant extracts and have attributed these differences to the different qualitative and quantitative compositions of the phenolic constituents [12]. Phenolic compounds, through the formation of intermolecular hydrogen bonds, inhibit tyrosinase by sterically hindering the enzyme's binding to receptor. Phenolic compounds can also induce a conformational change in tyrosinase resulting in the enzyme's deactivation [13].

Table 2: Radical scavenging and tyrosinase inhibitory activities and ferulic acid content of fractions from EtOAc extract

Fraction	Radical scavenging activity		Tyrosinase inhibitory activity	Ferulic acid content
	% at 1 mg ml^{-1}	IC_{50} (mg ml^{-1})	IC_{50} (mg ml^{-1})	(ppm)
1	71.97	-	-	ND
2	92.33	0.075	0.042	45.310 ± 0.0115
3	87.96	-	-	ND
4	58.05	-	-	ND
5	42.30	-	-	ND

ND; Not Determined

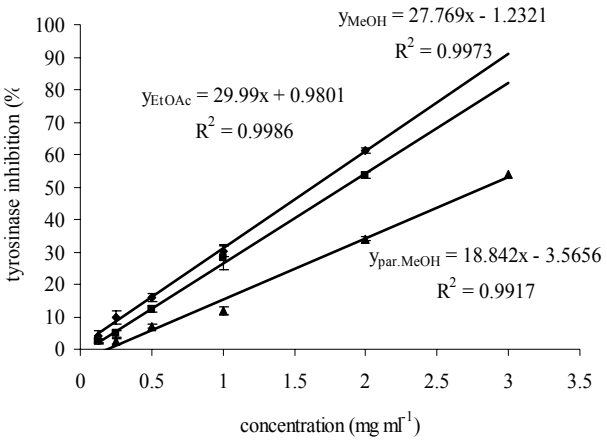

Figure 3. Tyrosinase inhibitory effect of samples; EtOAc extract (♦), MeOH (not partition) extract (■), MeOH (partition) extract (▲)

In an attempt to archive the biological activity and purity of the wastewater extract. The most potent biologically active extract (EtOAc) was further purified by means of column chromatography and monitored by using of TLC. Five fractions were obtained and further tested on antioxidant activity. The bioassay-guided was performed on each fraction at the concentration of 1 mg ml^{-1}. The strongest antioxidant was found in fraction no. 2 (3.78 % yield) which was eluated by EtOAc:n-Hexane (70:30) (Table 2) This fraction was further evaluated on its IC_{50} and tyrosinase inhibitory effect. However, although all

fractions were quantified on the ferulic acid content. It was found only in fraction no. 2. In addition, biological activities and ferulic acid content were enhanced following chromatographically fractioned particularly the tyrosinase inhibitory activity (38.90 folds).

Conclusions

This wastewater treatment addresses potentially solution of a serious environmental problem in pulps production. Biologically active principles were extracted and ferulic acid was characterized as a reference compound which is promising for pharmaceutics and cosmetics developments [14] particularly anti-wrinkles and skin lightening products. Furthermore, irritation test should be performed to ensure safety of the standardized wastewater extract.

Acknowledgements

The authors would like to thank Siam Northern Paper Co., Ltd., Chiang Rai, for wastewater from paper mulberry pulps production. Mrs. Sinthorn Chomboon, Nisara Sumeaing, Panisa Kongoum and Warattaya Kassakul are acknowledged on their assistances in research works.

References

[1] K. Saito, B. Linquist, B. Keobualapha, T. Shiraiwa and T. Horie, Agroforest. Syst. (2009) DOI 10.1007/s10457-009-9206-1.
[2] A.U. Buranov and G. Mazza, Ind. Crops Prod. **28** (2008), pp. 237-259.
[3] R.C. Sun, X.F. Sun, S.Q. Wang, W. Zhu and X.Y. Wang, Ind. Crops Prod. **15** (2002), pp. 179-188.
[4] S. Milardović, D. Ivekovic, and B.S. Grabarić, Bioelectrochem. **68** (2006), pp. 175-180.
[5] E.C.W. Chan, Y.Y. Lim, L.F. Wong, F.S. Lianto, S.K. Wong, K.K. Lim, C.E. Joe and T.Y.Lim, Food Chem. **109** (2008), pp. 477-483.
[6] T.Y. Lim, Y.Y. Lim and C.M. Yule, Food Chem. **144** (2009), pp. 594-599.
[7] B. Tepe and A. Sokmen, Biores. Technol. **98** (2007), pp. 3076-3079.
[8] A. Ardestani and R.Yazdanparast, Food Chem. **104** (2007), pp. 21-29.
[9] E. Adler, Wood Sci. Tech. **11** (1977), pp. 169-218.
[10] K. Krygier, F. Sosulski and L. Hogge, J. Agric. Food Chem. **30** (1982), pp. 330-334.
[11] Z.P. Zheng, K.W. Cheng, J. Chao, J. Wu and M. Wang, Food Chem. **106** (2008), pp. 529-535.
[12] F. Conforti, S. Sosa, M. Marrelli, F. Menichini, G.A. Statti, D. Uzunov, A. Tubaro and F. Menichini, Food Chem. **112** (2009), pp. 587-594.
[13] I. Kubo, Q.X. Chen and K. Nihei, Food Chem. **81** (2003), pp. 241-247.
[14] P.A. Kroon and G. Williamson, J. Sci. Food Agric. **79** (1999), pp. 355-361.

Antibacterial activity of ellagitannins isolated from nephelium lappaceum peel

N. Thitilertdecha[1] N. Rakariyatham[2]*

[1] Division of Biotechnology, Graduate School, Chiang Mai University, Chiang Mai, 50200, Thailand
[2] Department of Chemistry, Faculty of Science, Chiang Mai University, Chiang Mai, 50200, Thailand

* E-Mail Address: nuansri1@yahoo.com

Abstract: Infectious diseases are the major problem to world population and antimicrobial drugs may have an adverse effect on human health. Recently, there is an increased interest in finding antibacterial substances from plant materials. The present research aims to purify the phenolic constituents from methanolic extract of Nephelium lappaceum peels and to determine their antibacterial activity. Ellagic acid, corilagin and geraniin were successfully isolated from the methanolic extract of Nephelium lappaceum using Sephadex LH-20 column chromatography. The antibacterial activity was assessed by disc diffusion and microdilution assays. These purified compounds possessed antibacterial activities against five pathogenic bacteria, Salmonella typhi, Vibrio cholerae, Enterococcus faecalis, Staphylococcus aureus and Staphylococcus epidermidis. Staphylococcus epidermidis was the most sensitive strain inhibited by corilagin and geraniin (MIC 250 µg/mL). This study suggests that Nephelium lappaceum peels could be an alternative source of antibacterial phenolics.

Introduction

Microbial infections cause significant health problems throughout the world. In recent years, there has been an increasing concern regarding microbial resistance toward antiobiotics. Antiobiotics which are widely used to remedy microbial infections are sometimes associated with adverse effects to human health [1]. These have highlighted the necessity to develop new antimicrobial agents from natural sources, especially plants.

Phenolic compounds are the main secondary metabolites naturally occurring in plants [2] ranging from simple compounds to high polymerized molecules, such as tannins. Ellagitannins are hydrolysable tannins, which are widely distributed in plants. They were reported to exhibit many biological functions, as well as cytotoxic, xanthine oxidase inhibition, antiviral, antioxidant and antimicrobial activities [3-7]. The agricultural residues, such as grape seeds and peels and/or pomegranate peels [8-11] have also been evaluated as rich sources of natural phenolic compounds. The separation of phenolic compounds can be performed by Sephadex LH-20 which is extensively used [12-13].

Nephelium lappaceum L (rambutan), belonging to Sapindaceae, is a tropical fruit widely distributed in South-East Asia. Its consumption results in the production of vast amounts of waste from seeds and peels of the rambutan fruit. The peels account for 53% of the ripe fruit weight. Recently, its peel has been evaluated as a potent natural source of phenolics [14-16] which could contribute to solving waste disposal problems and simultaneously evaluate this fruit for its greater value.

The aim of this study was to report the separation of phenolic constituents from methanolic extract of N. lappaceum peel by Sephadex LH-20 column chromatography. The antibacterial activity based on disc diffusion and microdilution methods of these major components were also determined.

Materials and Methods

1. General

HPLC was performed in an HP1100 series liquid chromatography system. Fractions were analyzed on a C_{18} Vertisep column (5 µm, 4.6 × 150 mm). Sephadex LH-20 from Amersham Biosciences (Uppsala, Sweden) was used as the adsorbent for column chromatography. 2-(4-iodophenyl)-3-(4-nitrophenyl)-5-phenyltetrazoliumchloride (INT) were purchased from Sigma-Aldrich (Steinheim, Germany). Other chemicals were purchased from commercial sources and were of analytical purity.

2. Extraction and purification of phenolic compounds from N. lappaceum peel

Extraction procedures were performed according to the method previously described by Thitilertdecha et al. (2008) [15]. The lyophilized peel powder of N. lappaceum L. (120 g) was extracted with ethyl ether (three times). The residue was then extracted with methanol (three times). After the filtering of methanol extract, methanol was evaporated to absolute dryness and this portion was separated using Sephadex LH-20 column chromatography (4 × 55 cm) eluted with methanol. Methanolic fractions (10 mL each) were collected and read at 280 nm to afford eight fractions designated as F1-F8. These fractions were further analyzed for purity by reverse-phase HPLC, eluted with gradient elution using water (solvent A) and 80% acetonitrile (solvent B) [0-50 min, 0-44% B; 50-55 min, 44-100% B, flow rate 1.0 mL/min] [17].

3. Bacterial culture

The microorganisms used in this study consisted of eight strains of pathogenic bacteria, viz. Escherichia coli, Klebsiella pneumoniae, Pseudomonas aeruginosa,

Salmonella typhi, Vibrio cholerae, Enterococcus faecalis, Staphylococcus aureus and Staphylococcus epidermidis. All bacterial strains were obtained from the Department of Clinical Microbiology, Faculty of Associated Medical Sciences, Chiang Mai University. The bacteria were grown and maintained on nutrient agar slants. The inoculated agar slants were incubated at 37 °C.

4. Antibacterial assays

The antibacterial activity was based on the disc diffusion method [18] using a bacterial cell suspension whose concentration was equilibrated to a 0.5 McFarland standard. 100 µL of each bacterial suspension was spread on a Mueller-Hinton agar plate. Sterile paper discs (6 mm diameter) were impregnated with 20 µL of each sample dissolved in methanol at 125 mg/mL. The discs were allowed to dry and then placed on the inoculated agar. Discs with methanol were used as negative control and 10 µg streptomycin discs were used as positive controls. The plates were incubated at 37 °C for 24 h. After incubation, the zone of inhibition was measured.

Minimum inhibition concentrations **(**MICs**)** of the samples were evaluated for the bacterial strains which were determined as being sensitive to the samples in the disc diffusion assay. A broth microdilution method was used [19] with some modification. Stock solutions of the samples and streptomycin were prepared from 1,000 µg/mL to 1.95 µg/mL. Aliquots (100 µL) of each dilution were transferred into 96-well plates and an equal volume of double strength Nutrient Broth was then added. These were inoculated with 5 µL of bacterial inocula incubated at 37 °C for 24 h. Visible growth was first detected and then afterward by the addition of 20 µL of an alcoholic solution (1 mg/mL) of INT. The plates were incubated at 36 °C for 3 h, INT changed from yellow to purple where bacterial growth occurred. The MIC was determined as the lowest concentration (µg/mL) of the samples that inhibited the bacterial growth.

Result

In this study, separation on Sephadex LH-20 column chromatography of major phenolic compounds in methanolic extract of Nephelium lappaceum peel was reported. The separations of phenolic compounds were performed using Sephadex LH-20 column chromatography. The elution profile of the methanolic extract on Sephadex LH-20 column is illustrated in Figure 1 exhibiting eight maxima (recorded at 280, 330 and 365 nm) designated as F1-F8. A mixture of phenolic components was found in fractions F2-F5, specifics of which are unknown. Three main fractions (F6-F8) containing phenolic compounds illustrated a single peak and were ellagitannins, ellagic acid, corilagin and geraniin (Figure 2), respectively.

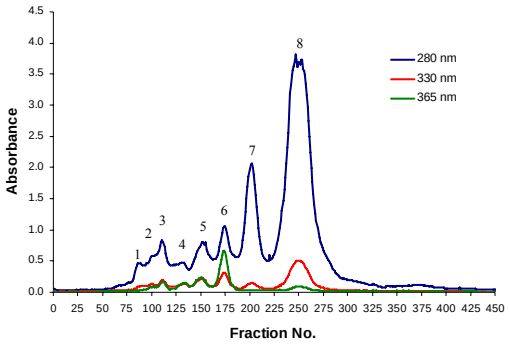

Figure 1. Elution profile of Sephadex LH-20 chromatography of the methanolic extract of Nephelium lappaceum L. peel eluted with methanol; flow rate 1 mL/min (fraction volume: 10 ml).

The antibacterial activities were determined based on disc diffusion assay. The antibacterial activities of the isolated phenolic compounds were effective against bacterial strains which were determined based on disc diffusion assays (Table 1). V. cholerae, S. epidermidis were sensitive to ellagic acid and corilagin while S. typhi and S. aureus were less sensitive. Geraniin not only exhibited activity against these four strains but also E. faecalis.

Table 1: Antibacterial activity of the isolated phenolic compounds from N. lappaceum L. was determined based on disc diffusion method (Inhibition zone in diameter, mm)

Compounds	**Microorganism**				
	S. t.	V. c.	E. f.	S. a.	S. e.
Ellagic acid	6.7 ± 0.2	10.6 ± 0.1	-	7.1 ± 0.1	14.2 ± 0.1
Corilagin	7.4 ± 0.7	12.4 ± 0.3	-	7.0 ± 0.4	28.0 ± 2.9
Geraniin	7.3 ± 0.6	11.1 ± 0.5	7.9 ± 0.8	12.8 ± 0.5	24.3 ± 2.1
Streptomycin	17.3 ± 0.9	16.9 ± 0.6	7.2 ± 0.5	18.0 ± 0.8	11.8 ± 0.9

S.t.: S. typhi, V.c.: V. cholerae, E.f.: E. faecalis, S.a.: S. aureus, S.e.: S. epidermidis.
Values are means ± S.D. (mm).

In comparing the sensitivity of the bacterial strains to the tested compounds, the phenolics that inhibited the growth of bacterial strains in disc diffusion assay were submitted to the minimum inhibition concentrations (MICs) test based on a microdilution assay. The MIC values of the phenolic components and the antibiotic drug, streptomycin, are illustrated in Table 2. S. epidermidis was still the most sensitive to the tested compounds (ellagic acid; 500 µg/mL, corilagin and geraniin; 250 µg/mL) and V. cholerae was also inhibited by corilagin at low concentration level (250 µg/mL). In the case of ellagic acid, the activity was observed but with slightly less efficiency than corilagin and geraniin.

Table 2: The minimum inhibition concentration (MIC) values[a] of the isolated compounds from N. lappaceum L. peels

Compounds	Microorganism				
	S. t.	V. c.	E. f.	S. a.	S. e.
Ellagic acid	> 1,000	1,000	ND	1,000	500
Corilagin	1,000	250	ND	500	250
Geraniin	> 1,000	500	250	500	250
Streptomycin	125	31.2	31.2	15.6	7.8

S.t.: S. typhi, V.c.: V. cholerae, E.f.: E. faecalis, S.a.: S. aureus, S.e.: S. epidermidis.
ND; not determined.
[a] Expressed in μg/mL of isolated compounds and streptomycin.

Discussion

The antibacterial substances from natural sources, such as plants, are still important due to the fact that synthetic antibiotic drugs can be associated with adverse effects to human health [1]. Phenolic compounds are secondary metabolites which are distributed in substantial quantity to all parts of the plant [2]. Previous research has revealed that the agricultural waste and/or residue contain potent sources of natural phenolics which possess antibacterial property [8-10]. Rambutan peels have also been evaluated as an excellent phenolic source exhibiting antioxidant, antibacterial and cytotoxic activities [14,16]. The methanolic extract of Nephelium lappaceum peel was reported to exhibit the most antibacterial properties due to its high phenolic constituent content [15].

For the separation of phenolics from plants, sephadex LH-20 column chromatography is used due to efficiency of separation [12,13]. Phenolic constituents of methanolic extract from N. lappaceum peel was successfully separated on Sephadex LH-20 column in one step separation to obtain three individual compounds, ellagic acid, corilagin and geraniin. These isolated compounds were reported to exhibit a broad spectrum of biological activity, as well as cytotoxic, antiviral and antioxidant properties [5,7,20].

These results indicated that these three constituents are responsible for the antibacterial property in the methanolic extract of N. lappaceum peels. Corilagin and geraniin are already well known to inhibit the growth of bacteria [4,6]. Tannins and their hydrolyzed products have been revealed to delay the growth of microorganisms by sequestering metal ions critical for their growth and metabolism [21]. Hydrolysable tannins are thought to exert their antibacterial property by disruption of the plasma membrane of the bacterial cell [22]. These results revealed that corilagin did not exhibit strong antibacterial activity compared to streptomycin, however, Shimizu et al. (2001) [23] reported that corilagin possessed the synergistic reduction of the MICs for oxacillin against methicillin-resistance Staphylococcus aureus not only having a bacteriostatic effect but also acted as a bactericidal.

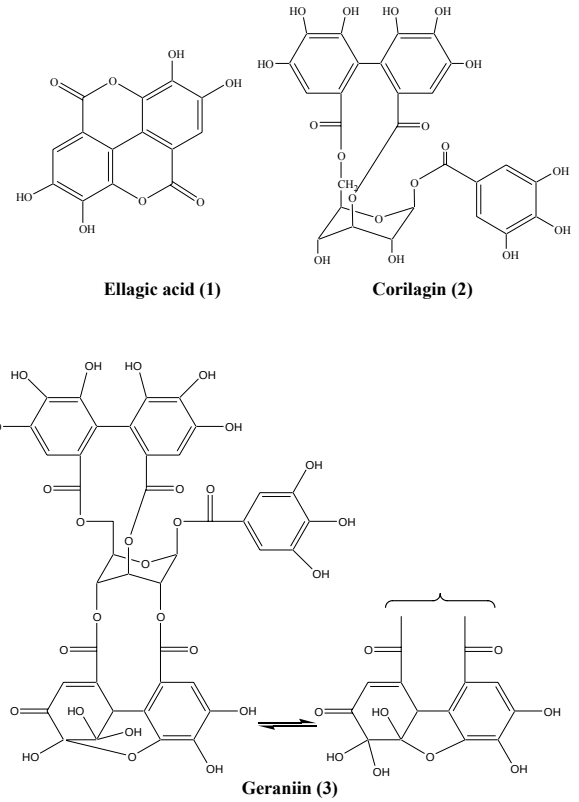

Figure 2. The structures of ellagic acid (**1**), corilagin (**2**), and geraniin (**3**).

Conclusions

This study demonstrated chromatographic separation of phenolic components from N. lappaceum L. peels and their antibacterial properties. All individual ellagitannins exhibited antibacterial activities. Therefore, N. lappaceum peel could be considered as an alternative source of antibacterial substances derived from plants as well as being applied as a food preservative or as a medicinal application.

Acknowledgements

This research was financially supported by the Thailand Research Fund (TRF) through the Royal Golden Jubilee Ph. D. Program, and from the Graduate School and the Department of Chemistry, Faculty of Science, Chiang Mai University, Thailand. The authors thanks Mr. James F. Maxwell, Department of Biology, Faculty of Science, Chiang Mai University, for the plant identification and PERCH-CIC, Department of Chemistry, Faculty of Science, Chiang Mai University and School of Chemistry, Faculty of Engineering, Science and Mathematics, University of Southampton for HR-MS and NMR service.

References

[1] M. Georgieva, R. Pancheva and V. Tzaneva, Pediatriya. **49** (2009), pp. 32-35.

[2] D.E. Pratt, in: I.M.T. Huang, C.T. Ho, C.Y. Lee, (Eds.), Phenolic compounds in food and their effects on health, American Chemical Society, New York, 1992, pp. 54-72.
[3] Y. Kashiwada, J. Nat. Prod. **55** (1992), pp. 1033-1043.
[4] A.A. Gohar, M.F. Lahloub and M. Niwa, Verlag Z. Naturforsch. **58** (2003), pp. 670-674.
[5] F. Notka, G. Meier and R. Wagner, Antiviral Res. **66** (2004), pp. 241-247.
[6] B. Fogliani, P. Raharivelomanana, J.-P. Bianchini, S. Bouraïma-Madjèbi and E. Hnawia, Phytochem. **66** (2005), pp. 241-247.
[7] M.K. Reddy, S.K. Gupta, M.R. Jacob, S.I. Khan and D. Ferreira, Planta Med. **73** (2007), pp. 461-467.
[8] R.P. Singh, K.N.C. Murthy and G.K. Jayaprakasha, J. Agric. Food Chem. **50** (2002), pp. 81-86.
[9] C. Negro, L. Tommasi and A. Miceli, Bioresource Technol. **87** (2003), pp. 41-44.
[10] G.K. Jayaprakasha, T. Selvi and K.K. Sakariah, Food Res. Int. **36** (2003), pp. 117-122.
[11] A. Ghosh, B.K. Das, A. Roy, B. Mandal and G. Chandra, J. Nat. Med. **62** (2008), pp. 259-262.
[12] U. Wanasundara, R. Amarowicz and F. Shahidi, J. Agric. Food Chem. **42** (1994), pp. 1285-1290.
[13] Y.Y. Soong and P.J. Barlow, J. Chromatogr. A. **1085** (2005), pp. 270-277.
[14] U. Palanisamy, H.M. Cheng, T. Masilamani, T. Subramaniam, L.T. Ling and A.K. Radhakrishnan, Food Chem. **109** (2008), pp. 54-63.
[15] N. Thitilertdecha, A. Teerawutgulrag and N. Rakariyatham, LWT-Food Sci. Technol. **41** (2008), pp. 2029-2035.
[16] S. Okonogi, C. Duangrat, S. Anuchpreeda, S. Tachakittirungrod and S. Chowwanapoonpohn, Food Chem. **103** (2007), pp. 839-846.
[17] R.R. Montealegre, R.R. Peces, J.L.C. Vozmediano, J.M. Gascueňa and E.G. Romero, J. Food Compos. Anal. **19** (2006), pp. 687-693.
[18] A.W. Bauer, W.M.M. Kirby, J.C. Sherris and M. Truck, Am. J. Clin. Pathol. **45** (1966), pp. 493-496.
[19] C.S.G. Kitzberger, A. Smânia Jr., R.C. Pedrosa and S.R.S. Ferreira, J. Food Eng. **80** (2007), pp. 631-638.
[20] C.-M. Yang, H.-Y. Cheng, T.-C. Lin, L.-C. Chiang and C.-C. Lin, J. Ethnopharmacol. **110** (2007), pp. 555-558.
[21] M. McDonald, I. Mila and A. Scalbert, J. Agric. Food Chem. **44** (1996), pp. 599-606.
[22] K. Funatogawa, S. Hayashi, H. Shimomura, T. Yoshida, T. Hatano, H. Ito and Y. Hirai, Microbiol. Immunol. **48** (2004), pp. 251-261.
[23] M. Shimizu, S. Shiota, T. Mizushima, H. Ito, T. Hatano, T. Yoshida and T. Tsuchiya, Antimicrob. Agents Chemother. **45** (2001), pp. 3198-3201.

Production of volatile compounds in fermented mungbean protein by starter culture of Bacillus spp.

S. Wittanalai[1], P. Kitsawatpaiboon[2] and N. Rakariyatham [2]*

[1] Division of Biotechnology, Graduate School, Chiang Mai University, Chiang Mai, 50200, Thailand
[2]Department of Chemistry, Faculty of Science, Chiang Mai University, Chiang Mai, 50200, Thailand

* Corresponding Author: nuansri1@yahoo.com

Abstract: This study contributes to the selection of starter cultures for the production of vegetarian condiments with improved quality, especially in terms of odor. Bacillus spp. (IS4 and IS10) isolated from Thai shrimp paste were used as starter culture to ferment mungbean protein from the vermicelli plant. Volatile compounds in unfermented (UFM) and fermented mungbean protein and commercial fermented soybean were extracted by using solid-phase microextraction (SPME) and analyzed by gas chromatography and mass spectrometry (GC-MS). A total of 52 volatile compounds were found and classified into 9 groups (aldehyde, alcohol, ester, acid, N-containing compound, aromatic compound, furan, miscellaneous compound and hydrocarbon). The major compound group found in fermented mungbean by Bacillus spp. IS4 (FMIS4) was hydrocarbon while fermented mungbean by Bacillus spp. IS10 (FMIS10) and commercial fermented soybean (CFS) produced acid as the main constituent. Comparing the fermented products, the fermented mungbean by IS10 produced more volatile compounds than that produced by IS4. It indicates that Bacillus spp. IS10 are considered as suitable starter cultures for vegetable condiments under the controlled conditions.

Introduction

Thailand produces various kinds of food condiments which are important ingredients in many traditional Thai dishes. Most Thai condiments are used as flavoring agents, and are produced from seafood products such as nam pla (fish sauce) and kapi (fermented shrimp paste). Nowadays, there has been an increase in the numbers of people who identify themselves as vegetarians. Vegetarian diets consist of plant foods, such as grains, legumes, fruits, vegetables and nuts. Light sauce or salt fermented soybean products based on seafood products are often used as food condiments to substitute for the majority of condiments.

Several Bacillus species have been found to be associated with fermented soybean products such as thua nao (Thailand), kinema (India) and soy-daddawa (Nigeria) [1, 2, 3]. However, no studies have reported the fermentation of mungbean protein by Bacillus spp. This work focuses on the use of mungbean protein as a substrate for producing new types of food condiments by selected starter cultures to develop a more satisfying food condiment for vegetarian diets. The aim of this work was to identify the volatile compounds in fermented mungbean protein when produced by different starter cultures and compared with the commercial fermented soybean.

Materials and Methods

The starter cultures used in this study were isolated from traditional shrimp paste and both isolates were indicated as Bacillus spp. by biochemical assays. Inoculum preparations by each strain (Bacillus spp. IS4 and Bacillus spp. IS10) were precultured in nutrient broth medium for 16 h. at 37°C and cells were suspended in 0.85 % NaCl solution at the density of 10^8 cells/ml.

Mungbean protein, obtained from a vermicelli plant in Lampang Province, was centrifuged at 1500 rpm for 15 min. Thirty grams of mungbean protein precipitate were added to Erlenmeyer flasks, stopped with cotton wool and aluminium foil and sterilized at 121 °C for 20 min. After sterilization, 3 ml of inoculum was added and incubated for 12 days at 37°C.

Volatile compounds were identified in unfermented mungbean protein (UFM), fermented mungbean protein by Bacillus spp. IS4 (FMIS4), fermented mungbean protein by Bacillus spp. IS10 (FMIS10) and commercial fermented soybean (CFS) by solid-phase microextraction (SPME) followed by gas chromatography and mass spectrometry (GC-MS).

Results and Discussions

The volatile compounds detected in UFM, FMIS4, FMIS10 and CFS are listed in table 1 and the relative amounts of the volatile groups are shown in figure 1. A total of 52 volatile compounds were found and classified into 9 groups including aldehyde, alcohol, ester, acid, N-containing compound, aromatic compound, furan, miscellaneous compound and hydrocarbon. The dominant volatile compound in UFM was alcohol. While the dominant volatile compound in fermented FMIS4 and IFIS10 was hydrocarbon and acid, respectively. The common compounds produced by both strains were benzaldehyde, acetic acid, butanoic acid, pentanoic acid, 2,4-bis(1,1-dimethyl)phenol, 2-pentylfuran, chloroform, tridecan, 1-tetradecane and pentadecane. Moreover, FMIS4 released a higher amount of hydrocarbon compounds than FMIS10 which might be responsible for differences in the overall flavor of the fermented products.

The CFS produced the different profile of volatile compounds from FMIS4 and FMIS10. The dominant

volatile compound in CFS was acid. However, aldehyde, alcohol, ester, acid and N-containing compound in CFS were also found in higher amounts than in FMIS4 and FMIS10. Similar fermented soybean products like natto and thua-nao have been previously studied [4] and the major volatile compounds identified in these products was ketone, acids and pyrazines. Azokpota et al. reported that ketones and aldehydes are generally formed via Maillard reactions and it is possible that carbohydrates of the substrates have been degraded to saccharides and then contributed to the formation of aldehyde, ketone and alcohol in condiments from Benin [5]. Pyrazines were reported to be formed by Maillard reactions though Strecker degradations from various nitrogen sources such as amino acids [4].

Conclusions

The present study examined the fermentation of mungbean protein by different starter cultures with a view to determine the volatile compound production in fermented products. The result showed that Bacillus spp. IS4 and IS10 have different abilities to ferment mungbean protein, leading to the difference in profile of the volatile compounds. This study provides information on the properties of Bacillus spp. strains for selection potential starter culture for food condiment fermentation.

Acknowledgements

The authors are grateful for the financial support by the Thailand Research Fund (TRF) through the Royal Golden Jubilee Scholarship Program, Thailand. The authors also gratefully acknowledge the Graduate School, the Department of Chemistry, Faculty of Science, PERCH-CIC, Department of Chemistry, Faculty of Science, Chiang Mai University, Thailand

References

[1] P. Chantawannakul, A. Oncharoen, K. Klanbut, E. Chukeatirote and S. Lumyoung, ScienceAsia. 28(2002); pp. 241-245.
[2] J.P. Tamang and S. Nikkuni, World J. Microbiol. Biotechnol. 12(1996): pp. 629-635.
[3] B.O. Omafuvbe, S.H. Abiose and O.O. Shohukan, Food Microbiol .19 (2002): pp. 561-566 .
[4] J.D. Owens, N. Allagheny, G. Kipping and J.M. Ames, J. Sci. Food Agric. 74(1997): pp.132-140.
[5] P. Azokpota, J.D. Hounhouigan, N.T. Annan, M.C. nago and M. Jakobsen, World J. Microbiol. Biotechnol. 24(2008): pp. 879-885.

Table 1: Volatile compounds of unfermented mungbean protein (UFM), fermented mungbean protein by Bacillus spp. IS4 (FMIS4), fermented mungbean protein by Bacillus spp. IS10 (FMIS10) and commercial fermented soybean (CFS)

		Relative amounts compound (%)[a]			
RT	**Compound**	**UFM**	**FMIS4**	**FMIS10**	**CFS**
	Aldehyde				
2.05	3-methyl butanal	-	-	-	1.91
2.10	2-methyl butanal	-	-	-	1.65
5.65	benzaldehyde	-	2.82	4.67	0.95
16.13	5-methyl-2-phenyl-2-hexenal	-	-	-	0.89
	Alcohol				
1.58	ethanol	2.17	-	-	19.73
2.22	dimethyl silanediol	16.29	-	7.76	-
2.57	3-methyl 1-butanol	-	-	-	6.25
4.23	1-hexanol	8.84	-	-	-
6.30	1-octen-3-ol	-	-	-	0.91
8.82	phenylethyl alcohol	-	-	-	1.20
	Ester				
1.90	ethyl acetate	-	-	-	5.33
	Acid				
1.81	acetic acid	12.1	3.37	5.54	4.41
2.81	2-methyl-,ethyl propanoic aicd	-	-	-	1.63
3.03	butanoic acid	5.96	3.40	4.61	
3.92	3-methyl butanoic acid	-			9.85
3.96	2-methyl-ethyl butanoic acid	-			1.74
3.99	3-methyl-ethyl butanoic acid	-			2.83
4.07	2-methyl butanoic acid	-			3.07
4.48	pentanoic acid	7.99	5.94	7.82	-
5.72	4-methyl-pentanoic acid	-	-	-	1.58
5.98	ethyl ester hexanoic aid	-	-	-	1.93
6.66	ethyl ester octanoic acid	-	-	-	1.50
10.08	ethyl ester benzoic acid	-	-	-	5.76
13.56	ethyl ester benzenepropanoic acid	-	-	-	7.25
17.19	isobutyl tridecyl carbonic acid	-	1.59	-	-
17.66	1,2-benzenedicarboxylic acid	-	-	15.30	-
24.16	ethyl ester hexadecanoic acid	-	-	-	0.89
	N-Containing compounds				
2.21	propyl hydrazine	-	5.01	-	-
4.86	2,5-dimethyl pyrazine	-	-	-	1.70
6.60	trimethyl pyrazine	-	-	-	4.34
8.25	2-ethyl-3,5-dimethyl pyrazine	-	-	-	1.10
8.38	2,3,5,6 tetramethyl pyrazine	-	-	-	5.22
9.97	2,3,5-trimethyl-6-ethylpyrazine	-	-	-	1.01
	Aromatic compounds				
2.93	toluene	-	-	2.06	-
16.68	2,4-bis(1,1-dimethyl) phenol	2.44	2.33	4.04	-
	Furan				
6.62	2-pentylfuran	3.92	6.20	3.62	--
	Miscellaneous				
1.91	chloroform	16.36	11.96	18.21	

- not detected

[a] % concentration of volatile compounds relative to the total concentration of volatile compounds identified

Table 1: Volatile compounds of unfermented mungbean protein (UFM), fermented mungbean protein by Bacillus spp. IS4 (FMIS4), fermented mungbean protein by Bacillus spp. IS10 (FMIS10) and commercial fermented soybean (CFS) (continue)

RT	Compound	Relative amounts compound (%)[a]			
		UFM	FMIS4	FMIS10	CFS
	Hydrocarbons				
11.23	dodecane	-	1.73	-	-
12.73	3,6-dimethyl octane	-	1.27	-	-
13.21	tridecane	2.73	9.70	5.08	1.38
14.19	6-methyl-tridecane	-	1.90	-	-
14.33	tetradecane	-	2.11	-	-
14.43	8-methyl-heptadecane	-	2.96	-	-
14.55	dodecane	-	3.16	-	-
14.70	tridecane	-	3.79	-	-
14.89	1-tetradecane	-	4.52	7.50	-
14.89	2-tetradecene	13.46	18.47	-	-
15.09	tetradecane	4.10	-	7.93	2.01
16.24	2,3,7-trimethyl-decane	-	2.99	-	-
16.84	E,E-alpha-farnesene	3.65	-	-	-
16.86	pentadecane	-	4.79	2.34	-
17.18	1-undecene	-	-	3.53	-

- not detected

[a] % concentration of volatile compounds relative to the total concentration of volatile compounds identified

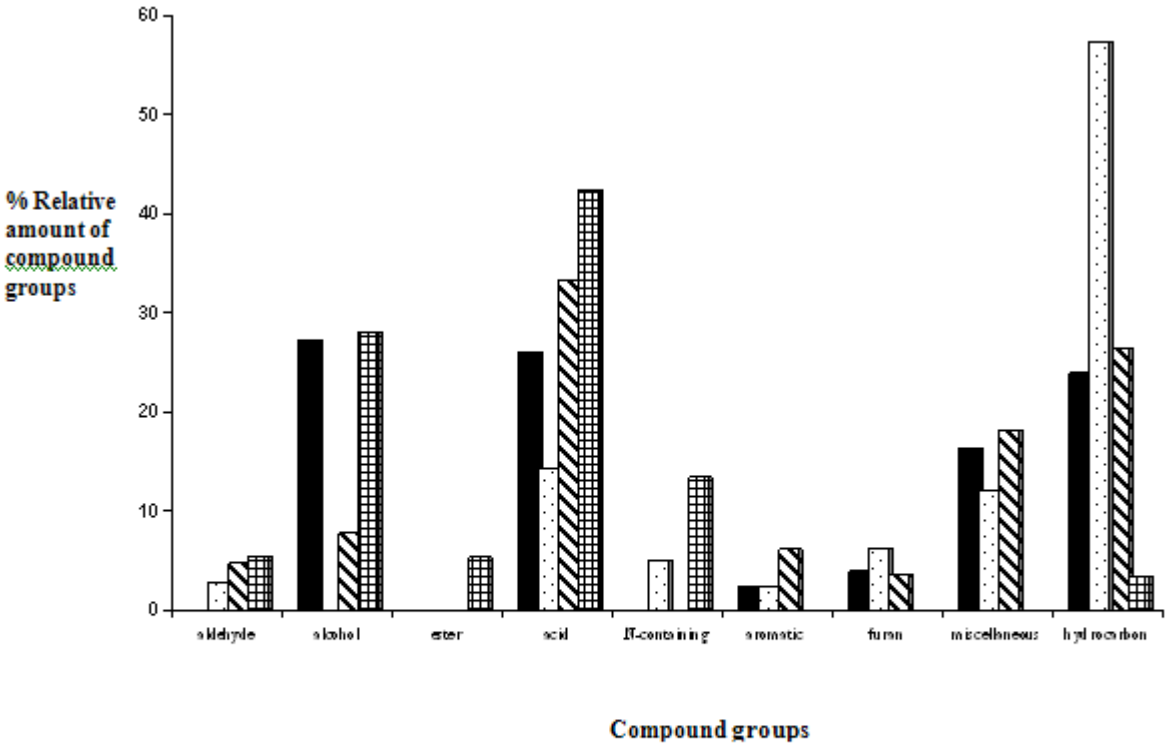

Figure 1. Relative amounts of volatile compound groups of unfermented mungbean protein (UFM: ■), fermented mungbean protein by *Bacillus* spp. IS4 (FMIS4; ⁘), fermented mungbean protein by *Bacillus* spp. IS10 (FMIS10; ▨) and commercial fermented soybean (CFS; ▦).

In-silico designed neuraminidase inhibitors based on derivatives of oseltamivir

N. Pattarapongdilok[1,2], Y. Sritana-anant[1], and P. Sompornpisut[2*]

[1]Organic Synthesis Research Unit, Department of Chemistry, Faculty of Science, Chulalongkorn University, Bangkok, Thailand
[2]Computational Chemistry Unit Cell, Department of Chemistry, Faculty of Science, Chulalongkorn University, Bangkok, Thailand

E-mail: sporntheᵃhotmail.com

Abstract: (D/L)-Gabaculine and 31 oseltamivir analogs were designed based on a synthesis of gabaculine-based intermediates towards oseltamivir. These analogs were designed by stereochemical and functional variations of substituents, where R^1 is OH, NH_2, NH_3^+ or NHAc, and R^2 is NH_2 or NH_3^+. By taking stereochemistry into consideration, 34 structures of the analogs were subsequently constructed using Hartree-Fock geometric optimization with 6-31G* basis set. To predict binding interactions between neuraminidase (NA) and the built analogs, the crystallographic structure of N1-oseltamivir complex (2HU4) obtained from the protein data bank was used as a drug target model. Molecular dockings of N1-oseltamivir (a control) and its in-silico designed analogs have been performed using a polar hydrogen force field with united and non-united atomic charge models of N1. The results showed that the lowest binding free energy (ΔG) of each docked complex using united atomic charge model was better than that of the complex obtained from non-united atomic model. In terms of ΔG, four analogs were found to be slightly better than oseltamivir. The best binding energy tended to associated with the oseltamivir analogs that adopt R-configuration at C_5 and NH_2 or NH_3^+ substituted at the position of R^1.

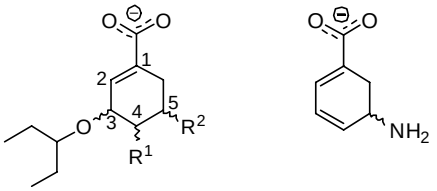

Figure 1. The core structures of oseltamivir analogs and gabaculines

Introduction

Neuraminidase (NA) is one of the two surface glycoproteins of influenza virus which plays an essential role in the release of progeny virus from infected cell [1]. NA is thus an ideal drug target for the prevention of influenza infection. Oseltamivir is the important anti-influenza drug which inhibits the catalytic activity of NA enzyme that cleavages the sialic acid residues from glycoproteins and liberates the budding virion from the infected cell [2]. It is one of a few agents effective against most viral flu subtypes and is highly recommended for stockpiling in preparedness for pandemics. Due to its significance but limited production for global demand, alternative routes besides the current total synthesis of oseltamivir have become an intensive research subject.

Among many synthetic strategies, gabaculine derivatives are one of the most interested intermediates reported in many recent total synthesis of oseltamivir (Figure 2). Corey's synthesis is the first route through a gabaculine derivative [3]. The key advantage of the method is the use of alternative starting materials to the increasingly limited supply of (-)-shikimic acid used in conventional synthesis. In addition, modifications to other derivatives could be carried out at the positions 3 and 4 of the gabaculine derivative with potential binding groups to NA. More accesses to gabaculine derivatives have also appeared in recent reports [4-5].

For the present study, a number of oseltamivir-like structures was designed and modeled based on the potential to obtain these compounds from gabaculine through the related synthetic pathways. Molecular docking technique was used to predict interaction energy and binding of the designed compounds to the protein target. The results could help guiding the laboratory synthesis of potentially improved NA inhibiters.

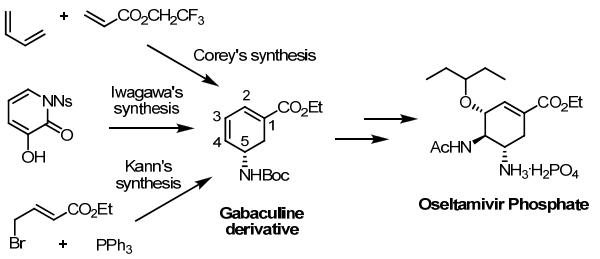

Figure 2. Oseltamivir synthesis through a derivative of gabaculine intermediate

Methods

Molecular docking: The AutoDock4.0 [6] was chosen to dock the oseltamivir analogs and D/L-gabaculine into the active site of neuraminidase. AutoDock tools (ADT) were used to set up input docking parameters for the ligands (created with HyperChem Program and optimized with Gaussian program (6-31G*)) and the protein. The NA model was the x-ray structure (PDB code: 2HU4) [7], to which polar hydrogens were added. Two types of atomic charges, united and non-united (Kollman united atoms charges) atomic models, were used to test the docking parameters. A grid box with the dimensions 90 x 90 x

90 points was constructed around the binding site, based on the location of the oseltamivir-NA complex from the x-ray structure. All bond rotations and torsions for the ligand were automatically set in the ADT. The Lamarckian genetic algorithm (LGA) procedure was employed and the docking runs were set to 500. The rest of the parameters were taken as default.

Table 1: Substituents and their configurations on oseltamivir analogs

Com-pound	Config. of C_2	R^1	Config. of C_4	R^2	Config. of C_5
1	R	$NH(CO)CH_3$	R	NH_3^+	S
4			S		S
5			S		R
6			R		R
7	S		S		S
8			S		R
9			R		S
10			R		R
11	R	NH_2	S	NH_3^+	S
12			S		R
13			R		S
14			R		R
15	S		S		S
16			S		R
17			R		S
18			R		R
19	R	NH_3^+	S	NH_2	S
20			S		R
21			R		S
22			R		R
23	S		S		S
24			S		R
25			R		S
26			R		R
27	R	OH	S	NH_3^+	S
28			S		R
29			R		S
30			R		R
31	S		S		S
32			S		R
33			R		S
34			R		R

Analysis of the results: A scoring function was introduced to help the analysis. The probability score is computed in a form of an exponential function comparable to the Boltzmann, introduced previously by Sotrifer et al [8] to evaluate the results of docking simulations. On the basis of the interaction energy of NA-oseltamivir complex, PSE function is introduced as shown in Eq(1). PSE is based on energy comparison between the NA-compound and the NA-oseltamvir complexes. By analogy, the position of oseltamivir in the NA active site was taken into consideration to compute the probability score, PSR, on the basis of distance between the center of mass of oseltamivir and compound in the bound state as shown in Eq(2). PSE and PSR were plotted by selecting the docking output of the first rank and the highest frequency.

$$PSE = \frac{H}{N}\exp(-\Delta E / wRT) \quad \ldots\ldots\ldots\ldots\ldots\ldots (1)$$

$$PSR = \frac{H}{N}\exp(-R_{CMS} / wRT) \quad \ldots\ldots\ldots\ldots\ldots\ldots (2)$$

Where PSE is the energy-based probability score, PSR is the distance-based probability score, ΔE is the difference in docked energy between ligand-NA and the reference oseltamivir-NA complexes ($\Delta E = E_{lig} - E_{ref.}$, $E_{ref.}$ is the docked energy of the reference oseltamivir-NA complexes, E_{lig} is the docked energy of the oseltamivir analogs and D/L-gabaculine), H is the number of docked conformations in the cluster, N is the total number of the runs (N = 500), R is the gas constant (1.9858775 cal K^{-1} mol^{-1}), T is 310 K, and R_{CMS} is the distance between the center of mass of the ligand and that of oseltamivir in the selected docked conformations, w is weighting factor.

Results and discussion

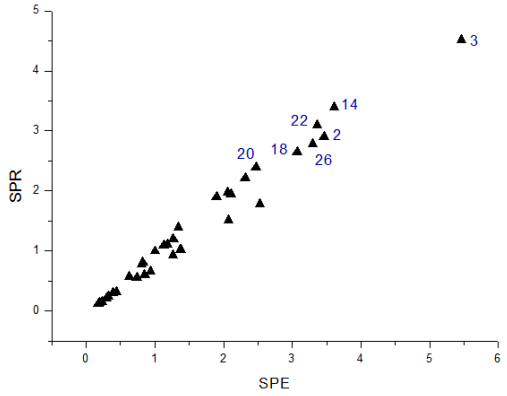

Figure 3. PSE and PSR of the first rank of non-united atomic model's results

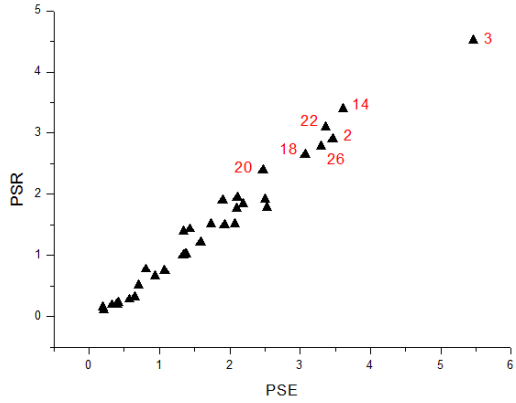

Figure 4. PSE and PSR of the highest frequency of non-united atomic models' results

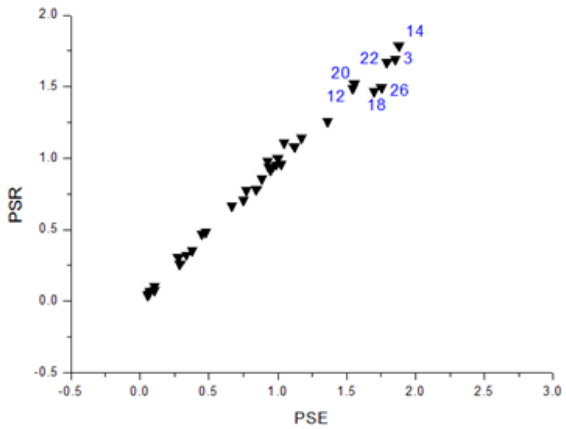

Figure 5. PSE and PSR of the first rank of united polar atomic models' results

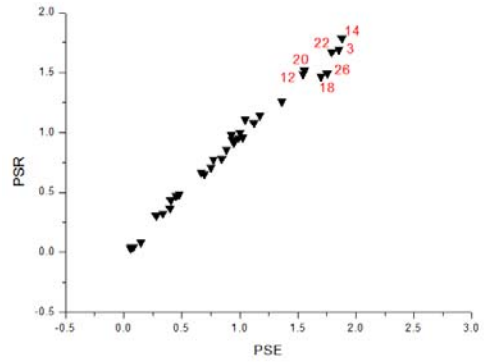

Figure 6. PSE and PSR of the first rank of united atomic models' results

Table 2: Results of the first rank cluster of top eleven compounds using non-united atomic models' results

Compound	Lowest binding energy (kcal/mol)	Mean binding energy (kcal/mol)	Frequency (500 run)
26	-7.98	-6.87	258
18	-7.64	-6.68	245
14	-7.36	-6.81	293
22	-7.35	-6.77	273
3	-7.22	-7.19	447
25	-7.08	-6.57	174
2	-6.85	-6.67	290
21	-6.73	-6.18	53
12	-6.66	-6.11	196
20	-6.46	-5.91	212
1	-7.98	-6.87	86

Table 3: Results of the first rank cluster of top eight compounds using united atomic models' results

Compound	Lowest binding energy (kcal/mol)	Mean binding energy (kcal/mol)	Frequency (500 run)
26	-9.86	-8.83	411
18	-9.63	-8.85	404
14	-9.16	-8.64	460
22	-9.16	-8.54	439
25	-8.91	-8.5	255
12	-8.56	-7.93	392
21	-8.56	-7.86	96
1	-8.44	-7.91	256

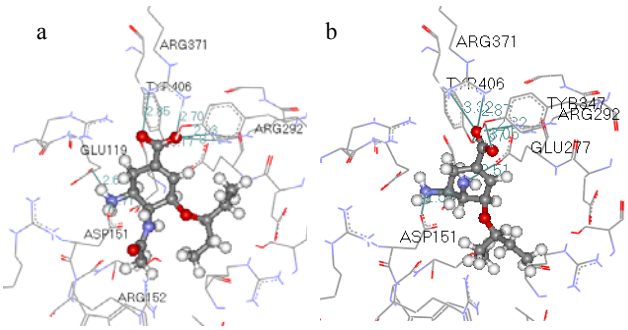

Figure 7. Binding of compound **1** (a) and **14** (b) to NA

Table 4 : The presence of H-bonds from the binding of oseltamivir **1**, compounds **3** and **14** to NA

Amino acid residue	Non-united atomic model		United atomic model	
	1	**3**	**1**	**14**
ARG118		/		
GLU119	/		/	
ASP151	/		/	/
ARG152	/		/	
GLU277		/		/
ARG292	/	/	/	/
TYR347				/
ARG371	/	/	/	/
TYR406	/	/	/	/

From the results, docking with united atomic model gave difference in the binding energy and the number of runs with the same cluster (frequency) as compared to that with non-united atomic model (Table 2 and 3). For docking with non-united charge set, compounds **2**, **3**, **14**, **18**, **20**, **22** and **26** exhibited the highest PSE and PSR whereas compounds **3**, **12**, **14**, **18**, **20**, **22** and **26** gave the best PSE and PSR for docking with united atomic model. It should be noted that these compounds shared some common features. These included the R-configuration at C_5 of oseltamivir core structure and the preference of amino or ammonium group at R^1. The presence of amino or ammonium group made the analogs bound to NA better than amide and hydroxyl group substituted at C_4 of oseltamivir analog (Table 4).

It appeared that docking results obtained from united atomic model gave a lower binding energy and greater frequency as compared to those obtained from non-united atomic model. An experimental inhibition constant (K_i) of oseltamivir-NA was reported to be 0.32 nM which corresponded to ΔG = 12.93 kcal/mole at 298K [9]. This suggested that docking with united atomic model gave closer results to the experimental value.

In addition, **14** became the compound of most interest. It formed hydrogen bonding with up to 4 amino acid residues of NA: ASP151, ARG292, ARG371, TYR406 similar to those in oseltamivir **1**-NA complex (Figure 7 and Table 4), although compound **1** (oseltamivir) and **14** were different in their docked conformations. Compound **14** also exhibited the stronger binding energy than compound **1** and appeared to be an attractive target towards further development. The laboratory synthesis and bioactivity tests of some of these oseltamivir analogs are under investigation.

Conclusions

The predictions of binding of H5N1 neuraminidase enzyme oseltamivir-based analogs have been performed by molecular docking method. The lowest binding free energy (ΔG) of each docked complex using united atomic model was mostly lower than that of the same complex using non-united atomic model and was closer to the experimental K_i value. The effective analogs were chosen based on the probability score which a comparison of oseltamivir docking

results was taken into consideration. It appears that the selected analogs contain either amino or ammonium group at the C_5 and C_4 positions of the core structure of oseltamivir. The substitution at C_5 with R-configuration is likely to have a better binding to NA. In addition, compound **14** was found to have the highest affinity to NA.

References

[1] V. Farina and J. D. Brown, Angew. Chem. Int. Ed. **45** (2006), pp. 7330-7334.

[2] G. T. Wang, Expert Opin. Ther. Patents **12** (2002), pp. 845.

[3] Y. Y. Yeung, S. Hong and E. J. Corey, J. Am. Chem. Soc. **128** (2006), pp. 6310-6311.

[4] T. N. Kipassa, H. Okamura, K. Kina, T. Hamada and T. Iwagawa, Org. Lett. **10** (2008), pp. 815-816.

[5] K. M. Bromfield, H. Gradén, D. P. Hagberg, T. Olsson and N. Kann, Chem. Commun. **30** (2007), pp. 3183-3185.

[6] G. M. Morris, D. S. Goodsell, R. S. Halliday, R. Huey, W. E. Hart, R. K. Belew and A. J. Olson, J. Comput. Chem. **19** (1998), pp. 1639–1662.

[7] R. J. Russell, L. F. Haire, D. J. Stevens, P. J. Collins, Y. P. Lin, G. M. Blackburn, A. J. Hay, S. J. Gamblin and J. J. Skehel, Nature **443** (2006), pp. 45-49.

[8] C. A. Sotriffer, R. H. Winger, K. R. Liedl, B. M. Rode and J. M. Varga, J. Comput.-Aided Mol. Design **10** (1996), pp. 305.

[9] Y. Ha, D. J. Stevens, J. J. Skehel and D. C. Wiley, Proc. Natl. Acad. Sci. USA (2001) **98**, pp. 11181–11186.

Efficacy of plant extracts in controlling of cruciferous insect pests

N. Prathummintr[1]* K. Issakul[1] W. Laosripaiboon[2]

[1*]Department of Science, Faculty of Liberal Arts and Science, Kasetsart University, Kamphaeng Saen Campus, Nakhon pathom, 73140, Thailand.
[2]Department of Chemistry, Faculty of Liberal Arts and Science, Kasetsart University, Kamphaeng Saen Campus, Nakhon pathom, 73140, Thailand.

*E-mail: nattanicha31@hotmail.com

Abstract: The objectives of this research were to investigate the efficacy kinds of Thai plants extracts on growth inhibition and controlling cruciferous insect pests. Each part of Thai plants (1 kg) was extracted with hexane, dichloromethane and methanol, respectively at room temperature for 48 h. Also the biological activity of the Spodoptera exigua (Hübner) and Plutella xylostella (L) which are the important of cruciferous insect pests to screening of the test samples were carried out at higher dosages (50,000 ppm). Bioassay procedure by using leaf dipping method was employed for oral toxicity and topical application for contact toxicity studied, and were tested the second and third instar larvae were used in our experiments. The results showed that the efficacy most of the Thai plants were active was extracted with dichloromethane have effect mortality to the Spodoptera exigua and Plutella xylostella tested at the 48 h contact time; for example seed of Durio zllbethinus Murr., leaf of Ruellia tuberosa **(Linn.), shoot of Rottboellia cochinchinensis (Lour.) and stem of Calotropis gigantean (Linn.). The results of the present study would be useful when find Thai plants extracts have potential for controlling cruciferous insect pests and development Thai plants extracts to insecticidal products.**

Introduction

Biopesticides are an important group of naturally occurring, often slow-acting crop protectants that are usually safer to humans and the environment than conventional pesticides, and with minimal residual effects. Biopesticides can be biochemical or microbial. Biochemical pesticides may include plant-derived pesticides (botanicals) that can interfere with the growth, feeding, or reproduction of pests or insect pheromones applied for mating disruption, monitoring or attract-and-kill strategies. [1]

Botanical or plants extracts, and varietal resistance can reduce beet armyworm populations and larval damage to crop plants, but conventional pesticides and insect growth regulators have been the mainstays of crop protection against beet armyworms at the commercial scale.[2,3,4]

The diamondback moth, Plutella xylostella (L.), is a serious pest of crucifer cropsis and wellknown destructive insect pest of brassicaceous crops worldwide. It globally requires over US$ 1.0 billion in estimated annual management costs [5,6]

The beet army worm, Spodoptera exigua (Hübner), is a widespread and very polyphagous lepidopteran pest causing severe economic damage in both dicotyledon (chrysanthemum, sugarbeet, alfalfa, cotton) and monocotyledon crops (rice) [7]

The common cutworm, Spodoptera litura (Fabricius), is a polyphagous insect pest that is widely distributed in the subtropical and temperate regions of Asia and Oceania. This insect occurs as a serious pest throughout Japan, except in Hokkaido and the northern areas of Honshu, causing substantial loss of forage crops, vegetables, and ornamental plants [8]. Chemical control of S. litura is difficult because it has developed resistance to many chemical insecticides [9,10,11]

In the present paper we investigate the efficacy bioactivities of some Thai plant extracts on growth inhibition and controlling cruciferous insect pests against two important agricultural pests, The beet army worm, Spodoptera exigua, the common cutworm, Spodoptera litura and the diamondbackmoth, Plutella xylostella.

Material and methods

Plant materials: The plant in this study were grown in Thailand. Thai plants were dried in oven at 45 ºC for 48 h, ground to a powder. Each part of plant (1 kg) was extracted with hexane, dichloromethane and methanol, respectively at room temperature for 48 h by using ultrasound apparatus. Before using, extracts were evaporated to dryness to give crude extract.

Insects: Larvae of three species of insects S. exigua S. litura and P. xylostella were taken form laboratory cultures maintained on artificial diet or Chinese cabbages in the laboratory. All experiments, larvae and adults were grown on laboratory cultures at 25 ± 1, 65% relative humidity and 14:10 light/dark cycle by using. Generally second and third instar larvae were used in our experiments

Bioassay procedure:

A leaf dipping method and Topical application bioassay was used to evaluate the toxicity of the 8 Thai plants extracts to larvae of S. exigua S. litura and P. xylostella. In preliminary experiments to screening at higher dosages (5%) and diluted with acetone to make up to 10, 7, 5, 3 and 1 % of Thai plants extracts against larvae cruciferous insect pests. Controls were treated with aqueous solution and positive controls were treated with cypermethrin.

Leaf dipping method**:** we punched 1.0 cm^2 discs from Chinese cabbages leaves and leaf dipped of aqueous allelochemical solution emulsified with Tween-80 (0.1%) to each side. The leaf discs were dried at room temperature. The testing was carried out three replicates each of 10 insects for each concentration leave at room temperature for 48 h. Mortality was recorded at 24 h and 48 h. [12]

Topical application: Aliquots of 0.5 µL of the dilutions were topically applied onto the thorax of third instar larvae were used in our experiments. The solvent was allowed to evaporate and the treated insects were transferred to box artificial diet or Chinese cabbages. Mortality was recorded every 24 h until end-point mortality when the number of dead insects no longer increased with time. [13,14]

Statistical analysis: Data from all bioassays were determined the mortality by using Abbott's formula. [15] The percentage mortality and lethal concentration (LC_{50}) were calculated by using Probit analysis program [16]

Phytochemical screening: The screening method was according to Professor Farnsworth's method. [17] The alkaloids, flavonoids, saponins, tannins, phenolic compound, carotenoids and anthracene were examined.

Results and discussion

The efficacy of 8 Thai plants extracts against larvae of S. exigua S. litura and P. xylostella. Bioassay procedure by using leaf dipping method was employed for oral toxicity and topical application for contact toxicity. The plants extracts such as seed of Areca catechu, stem, leaf, flower of Calotropis gigantean, seed of Durio zllbethinus, fruit of Diospyros mollis, bark of Garcinia mangstana, leaf of Pluchea indica, shoot of Rottboellia cochinchinensis and leaf of Ruellia tuberose. (Table 1)

Leaf dipping method

The results of the leaf dipping method screening at 5% bioassay was used to evaluate the toxicity of the 8 Thai plants extracts to larvae of S. exigua S. litura and P. xylostella in Table 1. The results showed that the 4 Thai plants was extracted with dichloromethane have the most efficacy to the larval mortality to the S. exigua S. litura and P. xylostella tested at the 48 h contact time. The toxic effect seed of Durio zllbethinus extracted with dichloromethane most of mortality to the S. exigua (83.3%) P. xylostella (83.3%) and S. litura (73.3 %), respectively. The toxic effect leaf of **Ruellia tuberosa**, extracted with dichloromethane most of mortality to the P. xylostella (70.0%) S. litura (70.0%), and S. exigua (63.3%), respectively. The toxic effect shoot of Rottboellia cochinchinensis extracted with dichloromethane most of mortality to the P. xylostella (66.6%) S. exigua (60.0%) and S. litura (60.0%), respectively. The toxic effect stem of Calotropis gigantean extracted with dichloromethane most of mortality to the P. xylostella (73.3%) S. litura (70.0%) and S. exigua (66.6%), respectively. (Table 1)

Topical application

Topical application screening at 5% bioassay was used to evaluate the toxicity of the 8 Thai plants extracts to larvae of S. exigua S. litura and P. xylostella. The results showed that have the most efficacy of the 8 Thai plants were active was extracted with hexane dichloromethane and methanol have effect 100% to the larval mortality to S. exigua S. litura and P. xylostella. tested at the 24 h contact time. (Not show results)

Oral toxicity (leaf dipping method)

The results of the leaf dipping method in Table 1. The 4 Thai plants was extracted with dichloromethane have the most efficacy make up to 10, 7, 5, 3 and 1 %, mortality was recorded at 24 h and 48 h and calculated lethal concentration (LC_{50}).

Oral LC_{50} values for the 4 Thai plants extracts tested at the 24 h and 48 h contact time are shown in Table 2. For P. xylostella larvae were tested at 48 h Calotropis gigantean was the most toxic plants extracts (LC_{50} = 7,900 ppm), followed by Durio zllbethinus (LC_{50} = 9,200 ppm), **Ruellia tuberose** (LC_{50} = 9,500 ppm) and Rottboellia cochinchinensis (LC_{50} = 13,000 ppm). S. exigua larvae were tested at 48 h Calotropis gigantean was the most toxic plants extracts (LC_{50} = 17,000 ppm), followed by **Ruellia tuberose** (LC_{50} = 18,000 ppm), Durio zllbethinus (LC_{50} = 21,000 ppm) and Rottboellia cochinchinensis (LC_{50} = 35,000 ppm). S. litura larvae were tested at 48 h Durio zllbethinus was the most toxic plants extracts (LC_{50} = 13,000 ppm), followed by Rottboellia cochinchinensis (LC_{50} = 17,000 ppm), **Ruellia tuberose** (LC_{50} = 21,000 ppm) and Calotropis gigantean (LC_{50} = 24,000 ppm).

Most of the botanical or plants extracts tested proved to be strong growth inhibitors, acutely toxic and active feeding deterrents against both lepidopteran species. [14] However, plants extracts form Durio zllbethinus, leaf of **Ruellia tuberose**, shoot of Rottboellia cochinchinensis, and stem of Calotropis gigantean was extracted with dichloromethane have have effect highter mortality to the S. exigua S. litura and P. xylostella tested at the 48 h contact time.

Phytochemical screening

The phytochemical screening from the 8 Thai plants contained the alkaloids, phenolic compound flavonoids, saponins, tannins, anthracene, and carotenoids

Alkaloids were found in seed of Durio zllbethinus, leaf of **Ruellia tuberose**, stem of Calotropis gigantean and shoot of Rottboellia cochinchinensis, and other sample plant that the contained different constituents as shown in that Table 3.

Table 1: Efficacy of Thai plants extracts in leaf dipping method screening at 5% against Spodoptera exigua, Spodoptera litura and Plutella xylostella

Plant species	Sample	Solutions	Mortality (mean ±SE, %)					
			S. litura		S. exigua		P. xylostella	
			24 h	48 h	24 h	48 h	24 h	48 h
control			0.0±0.0	0.0±0.0	0.0±0.0	0.0±0.0	0.0±0.0	0.0±0.0
cypermethrin			53.3±3.3	63.3±3.3*	66.6±3.3	83.3±3.3*	36.6±3.3	50.0±0.0*
Areca catechu	seed	a	23.3±3.3	36.6±3.3	20.0±0.0	36.6±3.3	13.3±3.3	26.6±3.3
		b	26.6±3.3	43.3±3.3	20.0±0.0	40.0±0.0	23.3±3.3	30.0±5.7
		c	23.3±3.3	40.0±0.0	20.0±0.0	33.3±3.3	26.6±3.3	36.6±3.3
Calotropis gigantean	stem	a	33.3±3.3	43.3±3.3	20.0±0.0	43.3±3.3	20.0±5.7	63.3±3.3
		b	53.3±3.3	70.0±0.0*	26.6±3.3	66.6±3.3*	33.3±3.3	73.3±3.3*
		c	30.0±0.0	46.6±3.3	20.0±0.0	43.3±3.3	33.3±3.3	60.0±0.0
	leaf	a	26.6±3.3	36.6±3.3	20.0±0.0	33.3±3.3	20.0±0.0	43.3±3.3
		b	30.0±0.0	46.6±3.3	23.3±3.3	43.3±3.3	20.0±0.0	46.6±3.3
		c	23.3±3.3	40.0±0.0	20.0±0.0	33.3±3.3	23.3±3.3	43.3±3.3
	flower	a	26.6±3.3	40.0±0.0	20.0±0.0	33.3±3.3	20.0±0.0	50.0±0.0
		b	26.6±3.3	43.3±3.3	23.3±3.3	43.3±3.3	23.3±3.3	60.0±0.0
		c	23.3±3.3	36.6±3.3	20.0±0.0	33.3±3.3	23.3±3.3	56.6±3.3
Durio zllbethinus	seed	a	46.6±3.3	53.3±3.3	20.0±0.0	46.6±3.3	36.6±3.3	80.0±0.0
		b	53.3±3.3	73.3±3.3*	33.3±3.3	83.3±3.3*	30.0±5.7	83.3±3.3*
		c	26.6±3.3	56.6±3.3	26.6±3.3	50.0±5.7	20.0±0.0	60.0±0.0
Diospyros mollis	fruit	a	20.0±0.0	36.6±3.3	20.0±0.0	36.6±3.3	13.3±3.3	30.0±0.0
		b	26.6±3.3	43.3±3.3	20.0±0.0	43.3±3.3	20.0±0.0	53.3±3.3
		c	26.6±3.3	40.0±0.0	20.0±0.0	40.0±0.0	13.3±3.3	33.3±3.3
Garcinia mangstana	bark	a	33.3±3.3	53.3±3.3	20.0±0.0	33.3±3.3	13.3±3.3	26.6±3.3
		b	46.6±3.3	56.6±3.3	20.0±0.0	40.0±0.0	23.3±3.3	30.0±5.7
		c	23.3±3.3	40.0±5.7	20.0±0.0	30.0±0.0	26.6±3.3	36.6±3.3
Pluchea indica	leaf	a	23.3±3.3	40.0±0.0	20.0±0.0	30.0±5.7	20.0±0.0	46.6±3.3
		b	30.0±0.0	43.3±3.3	20.0±5.7	36.6±3.3	26.6±3.3	60.0±0.0
		c	26.6±3.3	40.0±0.0	23.3±3.3	33.3±3.3	30.0±0.0	43.3±3.3
Rottboellia cochinchinensis	shoot	a	23.3±3.3	40.0±0.0	20.0±0.0	46.6±3.3	13.3±3.3	56.6±3.3
		b	36.6±3.3	60.0±0.0*	20.0±0.0	60.0±0.0*	23.3±3.3	66.6±3.3*
		c	23.3±3.3	43.3±3.3	20.0±0.0	53.3±3.3	13.3±3.3	50.0±0.0
Ruellia tuberosa	leaf	a	23.3±3.3	50.0±5.7	26.6±3.3	50.0±5.7	23.3±3.3	66.6±3.3
		b	53.3±3.3	70.0±0.0*	20.0±0.0	63.3±3.3*	30.0±5.7	70.0±0.0*
		c	33.3±3.3	46.6±3.3	20.0±0.0	50.0±0.0	23.3±3.3	53.3±3.3

* Means hight mortality was extracted with dichloromethane in recorded at 48 h.

a: Means was extracted with hexane, b: Means was extracted with dichloromethane, c: Means was extracted with methanol

Table 2: Lethal dose concentration (LC_{50}) were tested leaf dipping method against Spodoptera exigua, Spodoptera litura and Plutella xylostella

Plant species	LC_{50} (ppm)[a]					
	S. exigua		S. litura		P. xylostella	
	24 h	48 h	24 h	48 h	24 h	48 h
Acetone	0.0	0.0	0.0	0.0	0.0	0.0
cypermethrin	$3.0*10^4$	$1.6*10^4$	$2.1*10^4$	$1.6*10^4$	$5.7*10^4$	$3.8*10^4$
Calotropis gigantean	$5.0*10^4$	$2.4*10^4$	$4.1*10^4$	$1.7*10^4$	$3.6*10^4$	$7.9*10^3$
Durio zllbethinus	$5.2*10^4$	$1.3*10^4$	$4.2*10^4$	$2.1*10^4$	$2.3*10^4$	$9.2*10^3$
Rottboellia cochinchinensis	$6.6*10^4$	$1.7*10^4$	$5.9*10^4$	$3.5*10^4$	$5.6*10^4$	$1.3*10^4$
Ruellia tuberosa	$7.6*10^4$	$2.1*10^4$	$4.8*10^4$	$1.8*10^4$	$4.9*10^4$	$9.5*10^3$

[a] Means Lethal dose concentration (LC_{50}) by using Probit analysis program [16]

Table 3 Phytochemical screening of dried 8 Thai plants

Plant species	Sample	Compounds[a]						
		Car.	Phe.	Alk.	Fla.	Sap.	Tan.	Anth.
A. catechu	seed	-	+	+	+	+	+	-
C. gigantean	stem	+	-	+	-	-	-	+
	leaf	+	-	-	-	+	+	+
	flower	+	+	+	+	-	+	+
D. zllbethinus	seed	-	-	+	-	+	-	-
D. mollis	fruit	-	+	+	+	+	+	-
G. mangstana	bark	-	+	+	+	+	+	+
P. indica	leaf	+	+	+	-	+	+	+
R. cochinchinensis	shoot	+	+	+	+	+	+	+
R. tuberosa	leaf	+	+	+	-	+	+	+

[a] Car.: carotenoids, Phe.: phenolic compound, Ark.: alkaloids, Fla.: flavonoids, Sap.: saponins, Tan.: tannins, Anth.: anthracene

Conclusions

The efficacy of the 8 Thai plants extracted were tested with S. exigua S. litura and P. xylostella by using leaf dipping method. The results showed that the 4 Thai plants which were extracted with dichloromethane have the most efficacy to the larval mortality; for example, stem of Calotropis gigantean, seed of Durio zllbethinus, shoot of Rottboellia cochinchinensis, and leaf of Ruellia tuberose.

Oral LC_{50} values for the stem of C. gigantean recorded at 48 h shows the most efficacy for P. xylostella (LC_{50} = 7940 ppm).

Thai plants extracts have potential for controlling cruciferous insect pests and can be developed Thai plants extracts to insecticidal products.

Acknowledgements

This experiment was financially supported by Department of Science, Faculty of Liberal Arts and Science and Department of Chemistry Kasetsart University, Kamphaeng Saen Campus, Nakhon pathom, Thailand.

References

[1] L.G. Copping and J.J. Menn, Biopesticides: a review of their action applications and efficacy. Pest Manag Sci. **56** (2000), pp. 651–676.

[2] M. Berdegué, K.K. White and J.T. Trumble, Environ. Entomol. **26** (1997), pp. 912–919.

[3] W.L. Yee and N.C. Toscano, J. Econ. Entomol. **91** (1998), pp. 56–63.

[4] G.T. Bottger and R. Patana, J. Econ. Entomol. **59** (1966), pp. 1166–1168.

[5] E.Q. Javier, Foreword In: N.S. Talekar, (Eds.), Diamondback Moth and Other Crucifer Pests. Proceedings of the Second International Workshop, 10–14 December 1990. Asian Vegetable Research and Development Center, Tainan, Taiwan, (1992), pp. 11.

[6] N.S. Talekar and A.M. Shelton, Biology, ecology and management of the diamondback moth. Annual Review of Entomology. **38** (1993), pp. 275-301.

[7] D. S. Hill, Agricultural Insect Pests of Temperate Regions and their Control. Cambridge University Press, Cambridge (1987).

[8] A. Mochida and T. Okada, A bibliography of Spodoptera spp. (Lep.: Noc.). Misc. Bull. Kyushu Natl. Agric. Exp. Stn. (in Japanese). **49**, (1974), pp. 1–110.

[9] T. Hirose, Jpn. J. Appl. Entomol. Zool. (in Japanese with an English abstract). **39**, (1995), pp. 165–167

[10] T. Kasai and K. Ozaki, On the resistance of Prodenia litura Fabricius to several insecticides. Bull. Kagawa Agric. Exp. Stn. (in Japanese). **26**, (1975), pp. 25–28.

[11] M. Takai, Insecticide susceptibility of Spodoptera litura in Kochi Prefecture. Proc. Assoc. Pl. Protec. Shikoku (in Japanese).**26**, (1991), pp. 67–76

[12] K. D. Tewary, A. Bhardwaj and A. Shanker, Pesticidal activities in five medicinal plants collected from mid hills of western Himalayas**.** Industrial Crops and Products. **22** (2005), pp. 241-247.

[13] Y. Huang, and S.H. Ho, J. Stored Prod. Res. **34** (1999), pp. 11-17.

[14] L.A. Hummelbrunner and M.B. Isman, J. Agric. Food Chem. **49** (2001), pp. 715-720.

[15] W.S. Abbot, J. Econ. Ent. **18** (1925), pp. 265–267.

[16] D.J. Finney, Probit Analysis, third ed. Cambridge University Press, London, UK, (1971), pp. 38.

[17] NR. Farnsworth, J Pharm Sci. **55:3** (1966), pp. 225-269.

Biofunctionalization of acrylic acid-modified colored nanoparticles: method comparison and their agglutination reaction

R. Thiramanas[1], P. Piyakulawat[1], U. Asawapirom[1], K. Jangpatarapongsa[2] and D. Polpanich[1]*

[1]National Nanotechnology Center, National Science and Technology Development Agency, Thailand Science Park, Pathumthani, Thailand 12120
[2]Department of Clinical Microbiology, Faculty of Medical Technology, Mahidol University, Bangkok, Thailand 10700

* Corresponding Author E-Mail Address: duangporn@nanotec.or.th

Abstract: Here, blue colored carboxylated polystyrene (PS) nanoparticles were synthesized by miniemulsion polymerization and the carboxyl group originated from the added acrylic acid monomer was used for biomolecule immobilization. The obtained deep blue acrylic acid-modified PS nanoparticles were well characterized in terms of particle size, zeta potential and morphology. Afterwards, the nanoparticles were biofunctionalized with human polyclonal anti-malaria IgG antibody specific to Plasmodium falciparum malaria parasite by three different methods including physical adsorption, covalent coupling and affinity binding. To prepare the stable biofunctionalized latex, optimization of the factors affecting the antibody adsorbed amount such as pH medium and the antibody concentration in each immobilization procedure was performed. In physical adsorption, the adsorption buffer at pH 8.0 was the optimum pH medium. For covalent coupling and affinity binding methods, the particle stability was greatly depended on the amount of antibody presented on the particle's surface, i.e., the stability of the latex was dramatically decreased when the amount of antibody loaded more than 10 µg to 1 mg bead. However, the amount of antibody can reach 150 µg to 1 mg bead when using the physical adsorption. Then, the stable biofunctionalized latexes were applied for the agglutination reaction tested with the malaria patient plasma and normal plasma as negative control. Efficiency for parasite detection in terms of sensitivity and specificity will be investigated.

Introduction

Functionalized nanoparticles (NPs) have been widely used in the biomedical applications. In diagnostic field, to find causing of illness as fast as possible, various rapid diagnostic tests (RDTs) have been researched and developed for easy-to-use at field work, less time interpretation and low instrument utilizing. Polymer based NPs were extensively used as suitable solid support especially in latex agglutination test (LAT) [1-3]. The LAT is performed by reacting antigen (Ag) or antibody (Ab) immobilized onto the NP surface with specific Ab or Ag in the specimen to form network structure resulting in the particle clumping which can be observed via naked eyes [4]. To develop the diagnostic kit, the immobilization of biological recognition molecules is critical to maintain their binding site for reacting with specific molecule and preserve the biofunctionalities. Moreover, the appropriate immobilization method does not preserve only colloidal stability but also promote dispersability of the NP. Available methods for protein immobilization onto the polymeric surface have been intensively studied [2]. In this work, we focused on three methods. The first method was physical adsorption onto the latex surface In which, the orientation of the adsorbed biomolecules is uncontrollable due to their random and non-specific immobilization, however, this method exhibits good performance in biosensor [5,6]. The second one was strong affinity binding via streptavidin (SA)-biotin system (affinity constant ca. 10^{15}/M) [7]. The last method was covalent coupling via EDC/NHS which was compatible with the carboxylated particle surface. Here, the blue colored carboxylated polystyrene (PS) NPs were synthesized by miniemulsion polymerization and the carboxyl group for biomolecule immobilization was originated from the added acrylic acid (AA) monomer. Besides the AA provides the carboxylic groups on the latex surface, it functions as a steric stabilizer of the latex [8]. To compare the biomolecule immobilization methods, the well-characterized AA-modified PS NPs were biofunctionalized with human polyclonal anti-malaria IgG antibody specific to Plasmodium falciparum by three different methods as mentioned above and applied in the LAT.

Materials and Methods

Chemical Reagents: Styrene (St) (Fluka, Purum) was purified by passing through the alumina columns and then stored at 4°C until use. All other chemicals were used without further purification: AA (Aldrich), potassium persulfate (KPS) (Fluka, Puriss), hexadecane (HD) (Fluka, Purum), sodium dodecyl sulfate (SDS) (Merck), 1-ethyl-3-[3-dimethyl aminopropyl]carbodiimide hydrochloride (EDC) (Sigma-Aldrich), N-hydroxysulfosuccinimide (Sulfo-NHS), 2-(N-morpholino)ethanesulfonic acid (MES) (Fluka), biotin (Sigma-Aldrich) and SA from S. avidinii (Invitrogen). Deionized water was used throughout the work.

Synthesis and Characterization of Colored Nanoparticles: The colored NPs were prepared by miniemulsion polymerization based on the copolymerization of St, AA and 2,3,6,7-tetra(2,2'-bithiophene)-1,4,5,8-naphthalenetetracarboxylic-N,N'-di(2-methylallyl)bisimide (ALN8T), a blue dye monomer. Briefly, a mixture of St (6.0 g), ALN8T (0.025 g), AA (0.18 g) and HD (0.250 g) was added

into the deionized water (24.0 g) containing SDS (0.072 g). After 1 h of emulsification, the mixture was sonicated in an ice bath for 180 s at 90% amplitude (Sonics). The reaction was started by adding of an aqueous solution of KPS (0.100 g) at 80°C. After 5 h the deep blue PS/AA-ALN8T latex was obtained. Morphology of the colored NP was investigated by scanning electron microscope (SEM) (Hitachi, S-3400N). Hydrodynamic diameter (D_h) and zeta potential (ζ) of the PS/AA-ALN8T NPs diluted in NaCl (1 mM) were determined by using Zetasizer (Malvern Instruments, Nano ZS) at 25˚C.

Immobilization of Anti-malaria IgG Antibody onto the Colored Nanoparticles: Acutely P. falciparum infected plasma were collected from patients at Malaria Clinic, Mae Sod, Tak province, Thailand. Then, the protein was precipitated with saturated ammonium sulfate and the IgG was purified by Protein G column (Nunc, USA). For Ab immobilization by physical adsorption, the latex (2% (w/v), 5 µl) was mixed with the purified malaria IgG (20 to 100 µg/ml) in adsorption buffer (0.01 M Tris-Cl pH 8.0) to make the total volume of 500 µl. The mixture was incubated at 25°C for 2 h with shaking. For Ab immobilization by SA-biotin bridge, the latex (0.5 mg) was coated with SA (50 µg/ml) in the presence of EDC (2 mM) and sulfo-NHS (5 mM) in MES (25 mM, pH 6.0) at 25°C for 3 h. After blocking with 50 mM glycine and washing with PBS, the washed latex was bioconjugated with biotinylated anti-malaria IgG while shaking at 25°C for 3 h. For covalent coupling via EDC/NHS, the latex (0.5 mg) was activated with EDC (2 mM) and sulfo-NHS (5 mM) in MES (25 mM, pH 6.0) containing the purified Ab at 25°C for 3 h. The blocking and washing steps were performed as described in SA-biotin bridge. Amount of adsorbed antibody (Γ_{ads}) in each immobilization methods was optimized. Zeta potential of the prepared Ab-latex conjugate was measured to determine the particle stability.

Latex Agglutination Test: The Ab-latex conjugate (1% (w/v), 5 µl) was dropped onto a glass slide and the malaria plasma (0.5 µl) was subsequently added. The slide was swirled and the mixture was mixed thoroughly for 2 min, and then the agglutinates were investigated under an inverted OM (IX71, Olympus). The PBS was used as negative control. The results were classified as 3+, 2+ and 1+ if agglutination was occurred within 30 s, 1 and 2 min, respectively. The sensitivity and specificity were calculated as followed in equation (1) and (2).

$$\%\ sensitivity = \frac{True\ positive}{True\ positive + False\ negative} \times 100 \qquad (1)$$

$$\%\ specificity = \frac{True\ negative}{True\ negative + False\ positive} \times 100 \qquad (2)$$

Results and Discussion

Characteristics of PS/AA-ALN8T Latex: The prepared deep blue colored NP having D_h and polydispersity index (PDI) of 99.7 ± 0.4 nm and 0.018 ± 0.015, respectively. From SEM micrograph in Fig. 1, the spherical shape and size uniformity of the NPs were demonstrated. The zeta potential (ζ) value of the obtained NP was -44.8 ± 2.5 mV indicated that the good colloidal stability of the NPs was obtained.

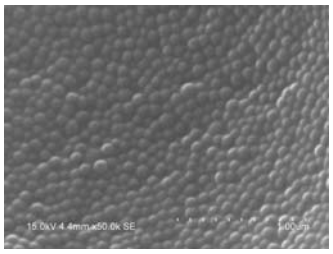

Figure 1. SEM micrograph of PS/AA-ALN8T NPs.

Characteristics of Antibody-Latex Conjugate: The different ratios of Ab to the bead for Ab immobilization by physical adsorption, SA-biotin linkage and covalent coupling were prepared and measured the zeta potential values at various pHs to determine the latex stability as shown in Figs. 2, 3 and 4. It can be observed that there was no significant different in zeta potential values at various ratios of Ab:bead for SA-biotin immobilization method, while the high amounts of adsorbed Ab seemed to decrease the latex stability in the case of physical adsorption and covalent coupling. So, the initial Ab concentration applied in immobilization step was chosen at maximum concentration that exhibited agglutination and gave the high latex stability as followed: 100, 20 and 15 µg Ab:1 mg bead for physical adsorption, SA-biotin linkage and covalent coupling.

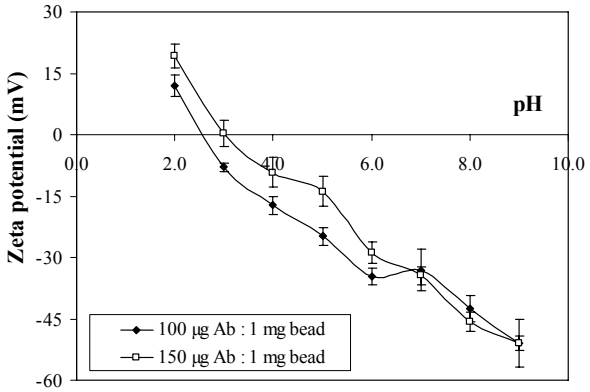

Figure 2. Zeta potential values of Ab-latex conjugate prepared by physical adsorption at various pHs.

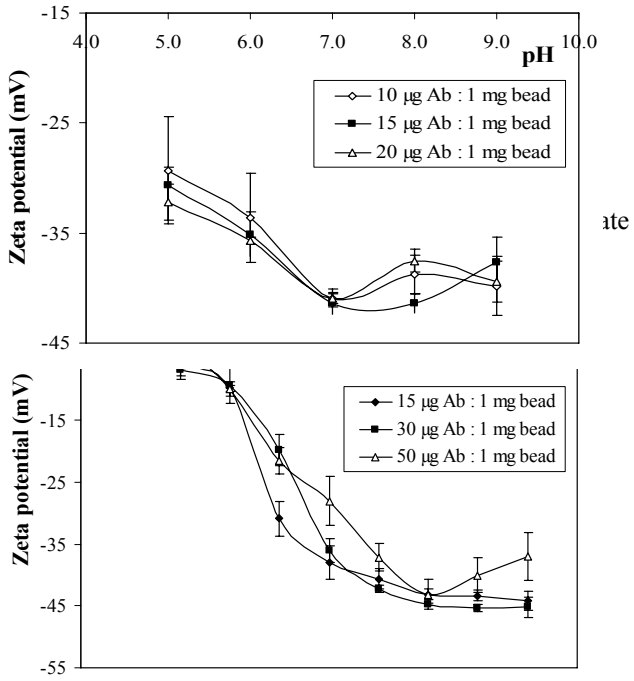

Figure 4. Zeta potential values of Ab-latex conjugate prepared by covalent coupling at various pHs.

Latex Agglutination Test: The agglutination results are summarized in Table 1. The results obtained by testing three biofunctionalized latex with 19 cases of the P. falciparum patient plasma showed 100% sensitivity. The agglutinate can clearly be seen via naked eyes within 2 min and the average agglutinates' size determined by OM was about 30 µm as shown in Fig. 5 (1c, 2c and 3c).

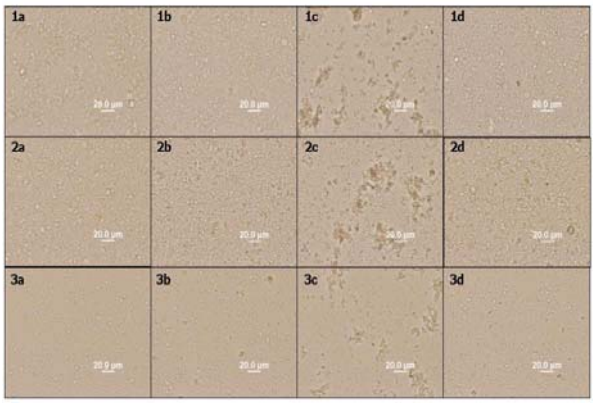

Figure 5. OM images of the immunoagglutination reaction of the Ab-latex conjugate prepared by physical adsorption (row 1), SA-biotin (row 2) and covalent coupling methods (row 3) (5.0 µl) in the presence of PBS (a), normal plasma (b), P. falciparum infected plasma (c) and P. vivax infected plasma (d) (0.5 µl).

However, the slow agglutination compared with P. falciparum infected plasma against P. vivax infected plasma and some cases of the normal plasma can also be observed in all Ab-latex conjugates. Due to cross-reaction of Ab on the particle surface and the Ag presenting in the P. vivax infected plasma, the percentage of specificity were rather low as 18.6, 23.3 and 14.0 for physical adsorption, SA-biotin and covalent bead, respectively. This might be resulted from the low specificity of polyclonal anti-malaria IgG purified from acutely P. falciparum infected plasma. However, from the degree of agglutination results, the SA-biotin bead exhibited false positive results with the lowest degree of agglutination compared to the rest two methods when tested with P. vivax infected plasma and normal control. It might be because the orientation of the adsorbed Ab by SA-biotin interaction was in such a way that the Ab binding site was facing to aqueous media which facilitated the antigen recognition [7]. From these results, this was suggested that the SA-biotin bead showed a good possibility to increase the specificity of the LAT compared to the other beads.

Table 1. The summary of agglutination results

Sample	Agglutination results	Methods to prepare Ab-latex conjugate		
		Adsorption	SA-biotin	Covalent
P. falciparum infected plasma	3+	7	7	6
	2+	10	8	11
	1+	2	4	2
	Negative	0	0	0
P. vivax infected plasma	3+	8	6	3
	2+	4	3	8
	1+	10	13	10
	Negative	1	1	2
Normal plasma	3+	6	0	1
	2+	4	3	0
	1+	3	8	15
	Negative	7	6	4
% Sensitivity		100	100	100
% Specificity		18.6	23.3	14.0

Conclusions

The biofunctionalized blue colored NPs immobilized with IgG antibody by three different methods including physical adsorption, covalent coupling via EDC/NHS and affinity binding via streptavidin-biotin system were prepared. There was no significant different in zeta potential values at various ratios of Ab:bead in SA-biotin conjugated latex, whereas, the stability of the biofunctionalized beads prepared from physical adsorption and covalent coupling was decreased when increasing the Ab adsorbed amount. The prepared Ab-latex conjugates showed 100% sensitivity with 19 cases of P. falciparum infected plasma, although, the low specificity due to cross-reaction between Ab on the particles' surface and the Ag in the P. vivax infected plasma was observed. For further study, the specificity of the assay might be improved by using specific monoclonal anti-malaria Ab.

Acknowledgements

This research work was supported by National Nanotechnology Center (NANOTEC), NSTDA, Thailand.

References

[1] J.M. Goddard and J.H. Hotchkiss, Prog. Polym. Sci. **32** (2007), pp. 698-725.

[2] O. Lazcka, F.J.D. Campo and F.X. Munoz, Biosens. Bioelectron. **22** (2007), pp. 1205-1217.

[3] J.E. Smith, L. Wang and W. Tan, Trends Anal. Chem. **25** (2006), pp. 848-855.

[4] L.B. Bangs, Pure Appl. Chem. **68** (1996), pp. 1873-1879.

[5] A.A. Karyakin, G.V. Presnova, M.Y. Rubtsova and A.M. Egorov, Anal. Chem. **72** (2000), pp. 3805–3811.

[6] S. Tombelli and M. Mascini, Anal. Lett. **33** (2000), pp. 2129–2151.

[7] TechNote 101. ProActive Microspheres. Bang Laboratories, Inc. (2008).

[8] C. Pichot, Curr. Opin. Colloid Interface Sci. **9** (2004), pp. 213–221.

Fungal fermentation to enhance the prebiotic protential of rice

P. Saman* and S. Artjariyasripong

Bioscience Department, Thailand Institute of Scientific and Technological Research
35 M3 Technopolis, Khlong 5, Khlong Luang, Pathum Thani. 12120, Thailand

* Corresponding Author E-Mail:premsuda@tistr.or.th

Abstract: The production of prebiotic oligosaccharides by fungal fermentation using two Thai rice varieties, waxy rice RD6 and non-waxy rice KDM **105, as substrates were investigated. Solid-state fermentation with Aspergillus oryzae TISTR 3108 was used as a source of enzymes for rice starch hydrolysis instead of direct amylolytic enzyme application. The effects of the main parameters such as incubation time, temperature, pH, fungal spore inoculum size and moisture content were also studied individually to maximise the prebiotic-oligosaccharides yield. The optimal conditions of amylolytic activities during fermentation were found at moisture content of 70% with pH 6 and incubated at 30°C for 4 days. The fermentation of waxy rice RD6 produced higher levels of maltose, glucose and isomalto-oligosaccharides than the fermentation of non-waxy rice KDM 105, while both their amylolytic activities were similar. The fermented waxy rice was selected and used further in mashing for the production of rice syrup. The rice syrup with high concentrations of isomaltose, panose and isomaltotriose was obtained at the end of the process.**

Introduction

Solid-state fermentation (SSF) is gaining interest in recent years due to potential advantages in manufacturing products such as enzymes in high yield, at high concentrations and with high specificity. Various fungi have been used in order to produce amylolytic enzymes for starch degradation. Possessing a high amylolytic enzyme activity, Aspergillus oryzae has been determined to be a suitable culture for food and beverages products. Furthermore, A. oryzae has been recommended as one of the potential probiotics in poultry [1, 2].

This study was designed to investigate the potential use of rice to produce prebiotic oligosaccharides using the process of fungal fermentation. The effects of the main parameters such as rice variety, incubation time, temperature, pH, fungal spore inoculum size and moisture content were studied individually to maximise the isomalto-oligosaccharides yield.

Materials and Methods

Substrate preparation

Two cultivars of Thai rice (Oryza sativa L.), RD6 and KDM 105, were used in the experiment. The 300 g (on a dry basis) of waxy rice RD6 and non-waxy rice KDM 105 was weighed separately into a 2-l Erlenmeyer flasks and distilled water was added and adjusted to 70% moisture level. The contents of the flasks were mixed thoroughly and autoclaved at 121°C for 15 minutes.

Solid-state fermentation

The sterilised solid substrate was inoculated with one ml of the prepared inoculum. The contents were mixed thoroughly and incubated at 30°C. Samples of triplicate flasks were withdrawn after desired incubation.

Effect of incubation time

SSF was carried out using rice RD6 and KDM 105 to optimise the time-course of incubation. Initial moisture content of the substrate was 70%. The sterilised solid substrate was inoculated with one ml of the prepared inoculum having 10^8 spores/ml and maintained at 30°C. Samples were withdrawn at regular intervals up to 7 days after inoculation.

Effect of initial pH

The effect of initial pH of SSF on amylolytic enzyme production was studied by adjusting the initial pH from 3.5 to 7. The cultures were incubated at 30°C and collected after 4 days.

Effect of incubation temperature

SSF was carried out at different incubation temperatures ranging from 20 to 50°C. The cultures were maintained under optimal conditions and extracted after 4 days.

Effect of inoculum size

A master spore suspension was made from a PDA slant and varying levels of inoculum size was achieved by the method of serial dilution. SSF was carried out with samples that were inoculated with one ml of these spore suspensions that had varying levels of viable spores (10^5-10^8 spores/g). All cultures were incubated under optimal conditions and extracted after 4 days.

Effect of moisture content

The influence of initial moisture of the substrate was studied by carrying out SSF at varying levels of moisture (50 to 80%). The cultures were incubated under optimal conditions and extracted after 4 days.

Mashing

The fermented mass was mixed into water to form the slurry of 30% w/v. One litre of the slurry was added with 0.03 g of $CaCl_2$ and adjusted to pH 6 by using 0.1 M lactic acid. Mashing was carried out by following the method of Okafor and Iwouno [3].

Measure of total reducing sugar (TRS) and free amino nitrogen (FAN)

The samples of fermented rice were diluted with distilled water and analysed for TRS and FAN following the methods of Miller [4] and Lie [5] respectively.

Enzyme activity

Crude enzyme from the fermented mass was extracted and measured for amylolytic using the Terashima method [6].The α-amylase activity was measured following the increase of reducing sugars with time [7].The α-glucosidase activity was determined using a modified method of McCue and Shetty [8].

Determination of sugars by high performance liquid chromatography (HPLC)

The samples of sugars and oligosaccharides were diluted and analyzed by HPLC using an Inertsil NH2 column (5 µm, 250×4.6 mm, Shimadzu, Japan) maintained at 40°C. The injection volume was 20 µl, and the flow rate 1.2 ml/min. The elution of sugars was carried out with 75% acetronitrile with detection with an ELSD (ELSD 800, Alltech, USA)

Results and Discussion

SSF using RD6 and KDM 105 as raw materials was demonstrated to optimise the time-course of incubation. Initial moisture content of each substrate was 70%. Both SSF were inoculated with one ml of the prepared inoculum having 10^8spores/ml and maintained at 30°C. Results in Figure 1 show that the highest concentration of TRS was obtained from SSF of RD6 at day 4 while the highest concentration of FAN was obtained from SSF of KDM105. The initial pH decreased from 5.6 to 4.5 in SSF of KDM105 and from 5.6 to 4.2 in SSF of RD6. The highest activities of amylolytic enzyme, α-amylase and α-glucosidase were observed in SSF of RD6.

From these results, it might be concluded that waxy rice RD6 has a higher potential to be used as the substrate of SSF. Besides, the 4-day period was the optimum incubation time for SSF. The next experiment was designed to investigate the other optimal conditions of SSF to obtain the maximal yields of enzyme activities.

Effect of pH

After selecting waxy rice as the substrate, the optimal initial pH of SSF was investigated for the best yield of enzyme activities. Eight different SSF with pH ranging from 3.5 to 7 were carried out at 30°C. The initial moisture content was adjusted to 70% and the samples were extracted after 4 days. The amylolytic activity maximised at pH 6.

Effect of incubation temperature

SSF was carried out at different incubation temperatures ranging from 20 to 50°C. The fungus showed its best performance for enzyme production in the mesophilic range at 30°C.

Effect of inoculum size

Four different inoculum sizes ranging from 10^5 to 10^8spores/g were carried out at 30°C. Less difference was observed in the level of enzyme activities between the inoculum sizes of 10^7 and 10^8spores/g. Therefore, the 10^7 spores/g was applied in further studies.

Effect of moisture content

The effect of initial moisture of the substrate was observed by carrying out SSF at varying levels of moisture. The fungus showed its best performance with the highest enzyme activities at initial moisture content of 70%.

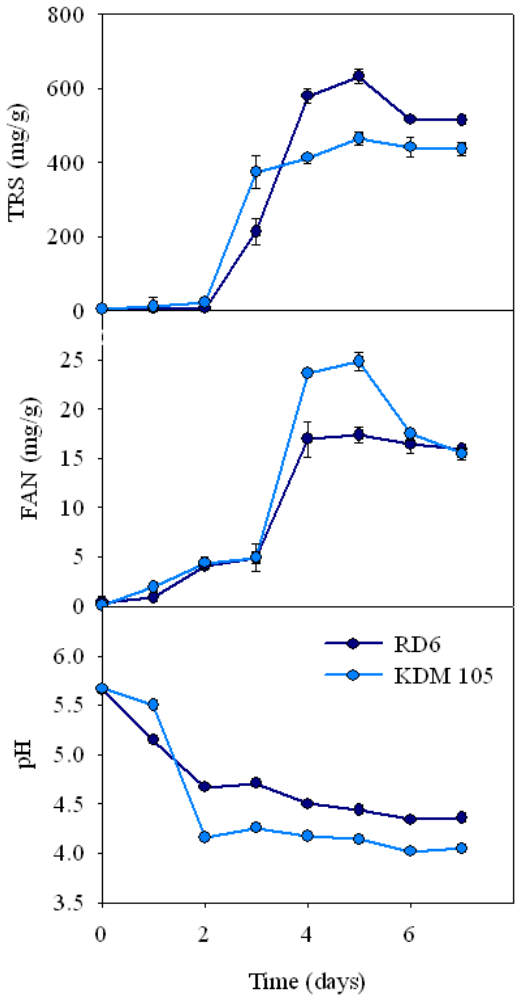

Figure 1. Evolution of TRS, FAN and pH in RD6 and KDM105 during fermentation at 30°C.

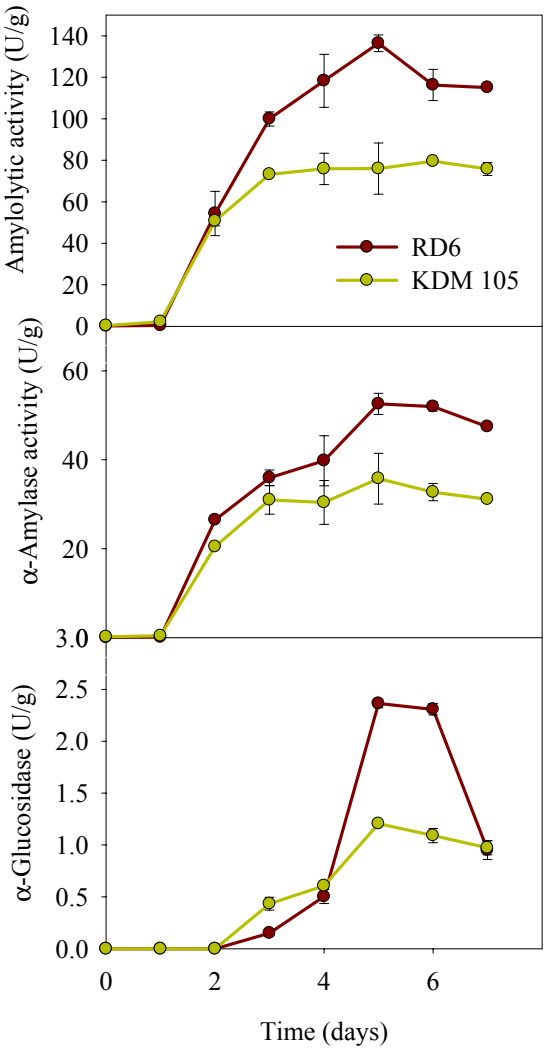

Figure 2. Evolution of amylolytic activity, α-amylase and α-glucosidase in RD6 and KDM 105 during germination at 30°C.

Production of the rice syrup

Different parameters were comparatively investigated to reveal the optimal conditions for the production of rice syrup. Results show the best yield of fermentable sugars and enzyme activities when SSF was performed at 70% moisture content with the inoculum size of 10^7 spores/g and at pH 6. The incubation condition was maintained at 30°C for 4 days.

In order to digest the remaining starch in the fermented rice slurry, mashing was conducted latterly to the process. The resultant rice syrup contained large amounts of fermentable sugars, especially glucose and maltose. The high levels of isomalto-oligosaccharides (isomaltose, panose and isomaltotriose) were also observed after mashing.

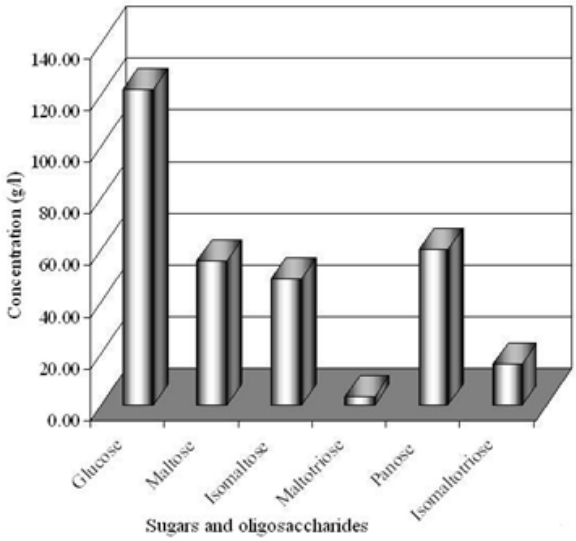

Figure 3. Concentrations of glucose, maltose, isomaltose, maltotriose, panose, isomaltotriose and maltotetraose in the rice syrup

Conclusions

It can be concluded that rice, in particular waxy rice RD6 is a suitable substrate for SSF with fungi for the production of amylolytic enzymes. The fermented material with a high enzymatic activity could be directly mashed for the production of prebiotic isomalto-oligosaccharides. The syrup obtained after mashing contained a high concentration of isomalto-oligosaccharides and higher amounts of glucose and maltose

References

[1] K. W. Lee, S. K. Lee, and B. D. Lee, Journal of Poultry Science **5** (2006), pp.1-3.
[2] S. W. Han, K. W. Lee , B. D. Lee and C. G. Sung, Asian Aust. J.Anim. Sci. **12** (1999), pp.417-421.
[3] N. Okafor and J. Iwouno, World Journal of Microbiology and Biotechnology. **6**(1990), pp.187-194.
[4] G. L. Miller, Analytical Chemistry. **31**(1959), pp.426-428.

[5] S. Lie, J Inst Brew. **79** (1973), pp.37-41.
[6] M. Terashima, A. Kubo and M. Suzawa, Eur. J. Biochem. **226**(1994). pp.249-254.
[7] Z. Sun and C.A. Henson, Arch Biochem Biophys.**1284**(1991), pp. 298-305.
[8] P. McCue and K. Shetty, Food Biotechnology. **17** (2003), pp.27-37.

Characterization of ammonium sulfate precipitant peroxidase from ivy gourd

S. Kongwithtaya[1*], G. Chairote[1] and S. Laloknam[2,3]

[1] Department of Chemistry, Faculty of Science, Chiang Mai University, Chiang Mai, Thailand
[2] Department of General Science, Faculty of Science, Srinakharinwirot University, Bangkok, Thailand
[3] Research Unit on Science Technology and Environment for Learning, Faculty of Science, Srinakharinwirot University, Bangkok, Thailand

[*]Email: sombat_k2@hotmail.com

Abstract: This study aimed to investigate the screening of peroxidase activity from 10 kinds of vegetables, Shallot (Allium accalonicum Linn.), Bitter gourd (Momordica charantia Linn.), Chinese cabbage (Brassica pekinensis Linn.), Lettuce (Lactuca sativa Linn.), Cabbage (Brassica oleracea Linn.), Mustard (Brassica chinensis Linn.), Chinese Kale (Brassica alboglabra Linn.), Coriander (Foeniculum vulgare Mill.) and Ivy gourd (Coccinia grandis Voigt) and to compare with Horseradish root (Armoracia lapathifolia Linn.). All samples were extracted by phosphate buffer, pH 7.0 and crude extracts were measured for peroxidase activity using a reaction mixture consisting of 4-aminoantipyrine, phenol and hydrogen peroxide. The condition for reaction of phenol was at 30°C, 10 minutes. Ivy gourd showed highest peroxidase activity, 349.95 units/mg protein. The Ivy gourd crude extract was fractioned by ammonium sulfate precipitation at percentage saturation ranged of 0 – 20, 20 – 40, 40 – 60, 60 – 80, and 80 – 100, respectively. Ammonium sulfate fractionation ranged of 60 – 80% saturation was the highest peroxidase activity, 1522.25 units/mg protein. Percentage of ammonium sulfate fractionation at 20 – 80% saturation was selected to precipitate of peroxidase from Ivy gourd crude extract. Yield and Purity of ammonium sulfate precipitant peroxidase were 60% and 4.08 folds, respectively. Ammonium sulfate precipitant peroxidase has an optimum pH and temperature, were 6 and 45°C, respectively. Kinetic studies of this enzyme for phenol showed that phenol has shown K_m and V_{max} were 140 μM and 21,000 nmol/min.mg protein. Peroxidase activity was enhanced by Cu^{2+} and strongly inhibited by Cr^{3+} and Hg^{2+}, respectively. Ivy gourd had stability in the presence of urea and sodium dodecyl sulfate.

Keywords: Peroxidase, Characterization, Ivy gourd, Ammonium sulfate precipitation

Introduction

Peroxidases (E.C. 1.11.1.7) are enzyme to catalyse substrates using oxido-reduction reaction with hydrogen peroxide. They are widely used in several fields such as treatment of waste water containing phenolic compounds, synthesis of aromatic chemicals, removal of peroxide from materials and part of the defence system against stress conditions such as infections [1, 2]. The sources of peroxidases are found in various sources microorganisms, animals, and plants [3 – 9]. Recently, Horseradish root tubers and carrot hairy root cell are a source of peroxidase, especially; horseradish root tubers are commonly used as a commercial source for peroxidase production [5, 6, 10]. However other plant species may has peroxidase enzymes exhibiting similar or better properties, and can provide and produce in local country because an application for biosensor to detect and determine phenolic compounds in expected sources [11 – 12].

Coccinia grandis Linn is a member of the family Cucurbitaceae, commonly called Pak Tum Lunk in Thai and Ivy gourd in English. Ivy gourd is a vegetable found commonly in India and Thailand as well as in tropical areas such as Hawaii. It is a medicinal plant to show antidiabetic activity and treatment of diabetes mellitus, bronchitis, skin diseases, tongue-sores and ear ache [13 – 14]. A phytochemical determination indicated the presence of proteins, fibers, flavonoids, fatty acids, and a moderate source of calcium as well as rich in β-carotene [15 – 17].

The preliminaries work to screen of plants (vegetables) have peroxidase activity and therefore is selected the vegetable showed highest peroxidase activity to produce of the enzyme. Leaves of 10 kinds of vegetables, Shallot (Allium accalonicum Linn.), Bitter gourd (Momordica charantia Linn.), Chinese cabbage (Brassica pekinensis Linn.), Lettuce (Lactuca sativa Linn.), Cabbage (Brassica oleracea Linn.), Mustard (Brassica chinensis Linn.), Chinese Kale (Brassica alboglabra Linn.), Coriander (Foeniculum vulgare Mill.) and Ivy gourd (Coccinia grandis Voigt) were used as a source of peroxidase production, which has not been attempted before. These could be an alternative commercial source of high activity peroxidase. Ivy gourd is the vegetable which representing highest peroxidase activity.

However, extraction of enzyme is a limitation to enzyme production because reduce enzyme activity and yield. Conventional initial purification steps, ammonium sulfate precipitation was selected for this research to reduce process time, low energy consumption and biocompatible environment to the biomolecule due to the presence of large amounts of water in the extraction systems. Therefore, in the present study, we have investigated the property of ammonium sulfate precipitant peroxidase from ivy gourd to use enzyme source for phenolic compound biosensor.

Materials and Methods

Materials: Vegetables; Shallot (Allium accalonicum Linn.), Bitter gourd (Momordica charantia Linn.),

Chinese cabbage (Brassica pekinensis Linn.), Lettuce (Lactuca sativa Linn.), Cabbage (Brassica oleracea Linn.), Mustard (Brassica chinensis Linn.), Chinese Kale (Brassica alboglabra Linn.), Coriander (Foeniculum vulgare Mill.), Ivy gourd (Coccinia grandis Voigt) and Horseradish root (Armoracia lapathifolia Linn.) were purchased from department store or local markets. Ammonium sulfate, sodium chloride and Sephadex G-25 were from Pharmacia Fine Chemicals (Piscataway, NJ, USA) and Comassie brilliant blue G-250, 4-aminoantipyrine (4-AAP) and hydrogen peroxide (H_2O_2) were from Fluka Chemie AG (Buchs, Switzerland). All other chemicals used were of analytical grade.

Vegetable crude extract samples: The crude extract was prepared in the following manner. The fresh leaves were washed thoroughly with distilled water at room temperature. One hundred grams of the fresh leaves were cut into small pieces and homogenized with 10 ml of 50 mM phosphate buffer, pH 7.0 for 5–10 min at room temperature. The extract was filtered using a cheese cloth (arranged in four folds or layers) to remove suspended fibrous solid particles. The clear filtrate was used as crude extract for further experiment. Crude extract was also stored at 4°C until used.

Peroxidase assay and protein concentration determination:
The enzyme activity was determined by a colrimetric method following modified in [18]. A reaction mixture containing 50 mM phosphate buffer (pH 7.0), 2 mM 4-AAP, 2 mM phenol, 4 mM hydrogen peroxide and 1.0 g/l Triton X-100 in a total volume of 5.0 ml was incubated at room temperature (30^{o}C) for 10 min. The reaction was then started by adding 0.1 ml of diluted enzyme solution, and the initial increase in absorbance was monitored at 500 nm using UV/VIS-spectrophotometer Model Jenway 6405 (Jenway, UK). One unit of peroxidase activity was defined as the amount of the enzyme consuming 1 μmol of hydrogen peroxide per minute under the assay conditions. Protein was determined by Comassie brilliant blue G-250 method, using bovine serum albumin as standard [19].

Ammonium sulfate precipitation: The partial purification procedure began by a filtration of ivy gourd crude extract after leaves were homogenized. A specific peroxidase activity of 349.95 U/mg protein was measured. The filtered crude extract was centrifuged at 3,000 rpm/min for 10 min at 4^{o}C and then ammonium sulphate was added to precipitate ranged of 0 – 20, 20 – 40, 40 – 60, 60 – 80, and 80 – 100 %saturation. After centrifugation, the pellet was dissolved in 50 mM acetate buffer (pH 4.5) and desalted by chromatography on Sephadex G25. The active fractions, i.e. those showing a peroxidase activity, were pooled, concentrated and stored at 4°C until used.

Optimum pH, Optimum temperature and Enzyme kinetic: The ivy gourd ammonium precipitant peroxidase was determined for optimum pH at pH range of 4 – 9 and optimum temperature at range of 4 – 100^{o}C, respectively. Kinetics was studied with ammonium sulfate precipitant peroxidase using phenolic acid as substrate. The inset is the Lineweaver–Burk plot for K_m and V_{max} estimation.

Effect of urea, Sodium dodecyl sulfate and Cations: Ivy gourd (0.5 U/mL) was incubated with increasing concentration of urea (0.0 – 2.0 M) for 1 h in 50 mM phosphate buffer, pH 6.0 at 45^{o}C. Peroxidase activity was determined after each incubation period. The activity of the untreated enzyme was considered as control (100%) for calculating percent activity. Ivy gourd (0.5 U/mL) was incubated with increasing concentration of SDS (0.0 – 10.0 mM) for 1 h in 50 mM phosphate buffer, pH 6.0 at 45^{o}C. Peroxidase activity was determined after each incubation period. The activity of the untreated enzyme was considered as control (100%) for calculating percent activity. Also the effects of cations was examined using different cations, Zn^{2+}, Cu^{2+}, Cd^{2+}, Ni^{2+}, Cr^{3+}, Fe^{2+}, Fe^{3+}, Mg^{2+}, Hg^{2+}, Ca^{2+}, K^{+}, Na^{+} and Mn^{2+}, respectively. Ivy gourd (0.5 U/mL) was incubated with increasing concentration of various cations for 1 h in 50 mM phosphate buffer, pH 6.0 at 45^{o}C. Peroxidase activity was determined after each incubation period. The activity of the untreated enzyme was considered as control (100%) for calculating percent activity.

Results and Discussion

Screening of peroxidase in various: In this study, ten kinds of vegetables; Shallot (Allium accalonicum Linn.), Bitter gourd (Momordica charantia Linn.), Chinese cabbage (Brassica pekinensis Linn.), Lettuce (Lactuca sativa Linn.), Cabbage (Brassica oleracea Linn.), Mustard (Brassica chinensis Linn.), Chinese Kale (Brassica alboglabra Linn.), Coriander (Foeniculum vulgare Mill.), Ivy gourd (Coccinia grandis Voigt) were selected for peroxidase activity assay.

The crude samples were then characterized for peroxidase activity. The peroxidase activity was determined follow materials and methods. All samples showed peroxidase activity (data not shown); the highest peroxidase activity crude extracts were ivy gourd, 349.95 units/mg protein. For horseradish, peroxidase activity was 425.23 units/mg protein.

Partial purification by ammonium sulfate precipitation: The filtered crude extract was added by ammonium sulfate to precipitate ranged of 0 – 20, 20 – 40, 40 – 60, 60 – 80, and 80 – 100 %saturation. The result showed that Ammonium sulfate fractionation ranged of 60 – 80% saturation was the highest peroxidase activity, 1522.25 units/mg protein and ammonium sulfate precipitation ranged of 20 – 80%

saturation was selected for partial purification of Ivy gourd peroxidase data as shown in Table 1.

Table 1: Purification table of Ivy gourd peroxidase

Step	Enzyme Yield (%)	Specific activity (units/mg protein)	Purity (fold)
Crude	100	349.95	1.00
0 – 20 % $(NH_4)_2SO_4$	6.24	157.48	0.45
20 – 40 % $(NH_4)_2SO_4$	29.21	1253.37	1.53
40 – 60 % $(NH_4)_2SO_4$	32.21	871.37	2.49
60 – 80 % $(NH_4)_2SO_4$	28.64	1522.25	4.34
80 – 100 % $(NH_4)_2SO_4$	5.70	118.98	0.34
20 – 80 % $(NH_4)_2SO_4$	60.00	1427.80	4.08

Optimum pH: Ammonium sulfate precipitant peroxidase from ivy gourd showed a pH optimum of 6.0 and stability at wide pH ranged of 5.5 – 8.5 data as shown in Figure 1. Stability at wide range of 5.5 – 8.5 suggests that the enzyme can function in an acidic and basidic environment, such as peroxidase in rice, tomato, soybean, coconut and strawberry [20 – 24].

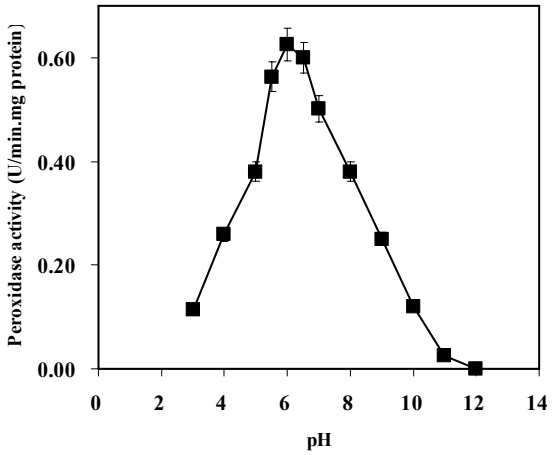

Figure 1. Effects of pH on Ivy gourd peroxidase activity

Effect of Themperature: Ivy gourd leaf peroxidase exhibited temperature optimal at 45°C and can express peroxidase at low temperature (10°C) and high temperature (70°C) by remaining peroxidase activity about 20% data as shown in Figure 2. Also, effect of temperature had been reported in oil palm leaf, cotton [25], strawberry [23] and coconut [24]. It was also suggested that the higher temperature to denature enzyme protein and groups of peroxidase active site [26].

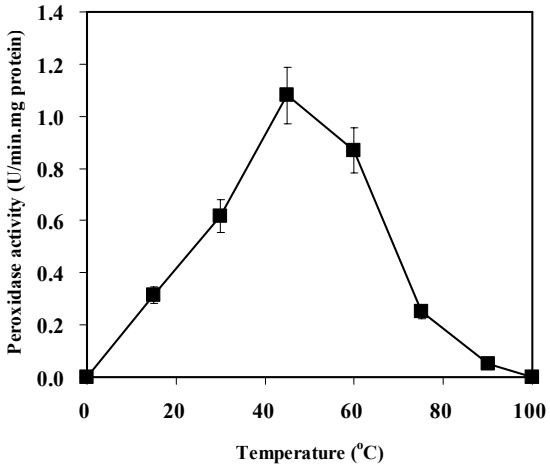

Figure 2. Effects of temperature on Ivy gourd peroxidase activity

Kinetic of Ivy gourd peroxidase: The apparent kinetic parameters for ammonium sulfate precipitant peroxidase are shown in Figure 3. The plot shown is for phenol. The K_m and V_{max}values for ivy gourd peroxidase were 140 µM and 21,000 nmol/min.mg protein, respectively. Other reported for K_m values of peroxidase from pear and Araucaria seeds showed lower substrate specificity than Ivy gourd [27 – 28].

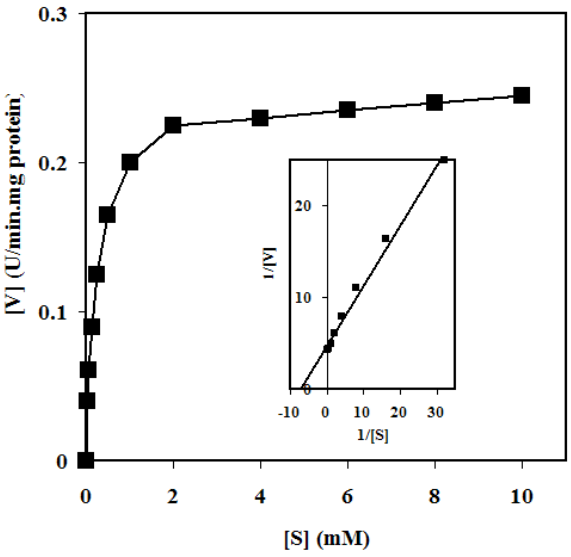

Figure 3. Kinetic of Ivy gourd peroxidase activity

Effect of urea, Sodium dodecyl sulfate and Cations:
Effect of urea, SDS and cations: Urea, SDS and some cations was examined for peroxidase activity. There was no change in activity of peroxidase when increasing concentration of urea (data not shown). SDS, an anionic detergent on the activity of peroxidase indicated that enzyme can remain activity at SDS range of 0 – 1 mM. At 3 mM SDS had peroxidase activity as a half of untreated condition (data not shown). Monocation, Na^+ and K^+ had no effected to peroxidase activity. Peroxidase activity was enhanced under

condition contained Cu^{2+} and Fe^{2+} because of some heavy metal acts as cofactor for enzyme reaction. Also, enzyme activity was strongly inhibited by Hg^{2+} and Cr^{3+} (data not shown) because of heavy metals precipitated the protein and denatured enzyme protein).

Conclusions

In this work, Ivy gourd showed the highest peroxidase activity from various sources in this research. The ivy gourd crude peroxidase was partial purification using ammonium sulfate precipitation and some enzyme property was determined. Peroxidase indicated stability against the denaturizing induced by heat, pH, urea and SDS. The activity of was enhanced by Fe^{2+} and Cu^{2+} and strongly inhibited Hg^{2+} and Cr^{3+}. Future work, Ivy gourd peroxidase was purified and compared to Horseradish peroxidase which can be easily substituted to replace of Horseradish peroxidase in biochemical, environmental and biotechnological applications.

Acknowledgements

We gratefully acknowledge PERCH-CIC for the financial assistance in research and presentation at PACCON 2010, Ubolrachathani, Thailand.

References

[1] E. Agostini, M.J. Medina, R. Silvia, M.D. Forchetti, and H. Tigier, Properties of anionic peroxiase isoenzymes from turnip (Brassica napus L.) roots. J. Agric. Food Chem. **45** (1997), pp. 596 – 598.

[2] R. Hammerschmidt, E.M. Nuckles, and J. Kuc, 1982. Association of enhanced peroxidase activity with induced systemic resistance of cucumber to Colletotrichum lagenarium. Physiol. Plant Pathol. **20** (1982), pp. 73 – 82.

[3] Y.H. Kim, and J.J. Yoo, Peroxidase production from carrot hairy root cell culture. Enzyme Microb. Technol. **18** (1996), pp. 531 – 535.

[4] Y. Yamada, S. Kobayashi, K.Q. Watanabe, and U. Hayashi, Production of horse radish peroxidase by plant cell culture. J Chem. Tech. Biotechnol. **38** (1987), pp. 31 – 39.

[5] K.G. Welinder, Superfamily of plant, fungal and bacterial peroxidases, Curr. Opin. Struct. Biol. **2** (1992), pp. 388 – 393.

[6] H.B. Dunford, Heme peroxidase nomenclature, Plant Peroxidase Newsl. **13** (1999), pp. 65 – 71.

[7] M. Zamocky, Phylogenetic relationships in class I of the superfamily of bacterial, fungal, and plant peroxidases, Eur. J. Biochem. **271** (2004), pp. 3297 – 3309.

[8] M. Habetha, and T.C. Bosch, Symbiotic Hydra express a plant-like peroxidase gene during oogenesis, J. Exp. Biol. **208** (Pt 11) (2005), pp. 2157 – 2165.

[9] T. Cavalier-Smith, Only six kingdoms of life, Proc. Biol. Sci. **271** (2004), pp. 1251 – 1262.

[10] T. Saitou, H. Kamada, and H. Harada, Isoperoxidase in hairy roots and regenerated plants of horse radish (Armoracia lapathifolia). Plant Sci. **75** (1991), pp. 195 – 201.

[11] I.S. Alpeeva, M. Niculescu-Nister, J.C. Leon, E. Csoregi, and I.Y. Sakharov, Palm tree peroxidase-based biosensor with unique characteristics for hydrogen peroxide monitoring. Biosens. Bioelect. **21** (2005), pp. 742 – 748.

[12] S. Gaspar, I.C. Popescu, I.G. Gazaryan, G., Bautista, G. Ardila, I.Y. Sakharov, B. Mattiasson, and E. Csoregi, Biosensor based on novel plant peroxidases: a comparative study. Electrochem. Acta **46** (2000), pp. 255 – 264.

[13] H.D. Brahmachari, and K.T. Augusti, Orally effective hypoglycemic principles from Coccinia indica. J. Pharm. Pharmacol. **15** (1963), pp. 411 – 412.

[14] G.V. Satyavati, M.K. Raina, and M. Sharma, Medicinal Plants of India, vol. 1. Indian Council of Medical Research, New Delhi, 198pp (1987).

[15] I.A. Siddiqui, S.M. Osman, M.R. Subbaram, and K.T. Achaya, Fatty acid components of seed fats from four plant families. J. Oil Technol. Assoc. India **5** (1973), pp. 8 – 9.

[16] A.B. Brua, and B.C. Goswami, Carotenoides of Cephalandra indica (Coccinia indica). Curr. Sci. **48** (1979), pp. 630 – 632.

[17] M.M. Vaishnav, and K.R. Gupta, Ombuin 3-O-arabinofuranoside from Coccinia indica. Fitoterapia **67** (1996), pp. 80.

[18] H. Wright, J.A. Nicell, Characterization of soybean peroxidase for the treatment of aqueous phenol. Biores. Technol. **70** (1999), pp. 69 – 79.

[19] M. Bradford, A rapid method for the quantification of microgram quantities of proteins utilizing the principle of protein-dye binding. Anal. Biochem. **72** (1976), pp. 248 – 254.

[20] D.J. Sessa, and R.L. Anderson, Soybean Peroxidase: purification and some properties. J. Agric. Food Chem. **29** (1981), pp. 960 – 965.

[21] H. Ito, N. Hiraoka, A. Ohbayashi, and Y. Ohashi, Purification and chracterization of rice peroxidases. Agric. Biological. Chem. 55 (1991), pp. 2445 – 2454.

[22] J.J. Jen, A. Seo, and W.H. Flurkey, Tomato peroxidase: purification via hydrophobic chromatography. J. Food Science **45** (1980), pp. 60 – 63.

[23] P.M. Civello, G.A. Martinez, A.R. Chaves, and M.C. Anon, Peroxidase from strawberry fruit (Fragaria ananassa Duch): partial purification and determination of some properties. J. Agric. Food Chem. **43** (1995), pp. 2596 – 2601.

[24] C.V. Mujer, E.M.T. Mendoza, and D.A. Ramirez, Coconut peroxidase isoenzymes: isolation, partial purification and physio chemical properties. Phytochem. **22** (1983), pp. 1335 – 1340.

[25] B. Triplett, and J.E. Mellon, Purification and characterization of anionic peroxidases from cotton (Gossypium hirsutum L.). Plant Science **81** (1992), pp. 147 – 154.

[26] L. Vamos-Vigyazo, Polyphenol oxidase and peroxidase in fruits and vegetables. Critical Reviews in Food Science and Nutrition 15 (1981), pp. 49 – 127.

[27] F.C. Richard-Forget, and F.A. Gauillard, Oxidation of chlorogenic acid, catechins and 4-methylcatechol in model solutions by combinations of pear (Pyrus communis Cv Williams) polyphenol oxidase and peroxidase: A possible involvement of peroxidase in enzymatic browning. J. Agric. Food Chem. **45** (1997), pp. 2472 – 2476.

[28] A. Riquelme, and L. Cardemil, Peroxidases in the cell-walls of seeds and seedlings of Araucaria araugana. Phytochem. **31** (1993), pp 15 – 20.

Efficiency of indigenous plant extracts in northeastern of Thailand for inhibiting the growth of the pathogen Colletotrichum sp.

S. Taveepanich[1]*, P. Suwanakood[2], U. Polngam[2] and P. Lootianan[1]

[1]Department of Chemistry, Faculty of Science, Ubon Ratchathani University, Warinchamrap, UbonRatchathani, Thailand
[2]Department of Biological science, Faculty of Science, Ubon Ratchathani University, Warinchamrap, UbonRatchathani, Thailand

*E-mail: somjintana@yahoo.com

Abstract: Colletotrichum sp. was isolated and identified as causal agent of anthracnose in chilli, tomato and banana from 3 plantations in UbonRatchathani province. The results showed that twenty isolates of Colletotrichum sp. were collected. Crude extracts of 37 dry indigenous plants were extracted with hexane, ethylacetate and 95 % methanol, respectively and tested for the efficiency on growth inhibition of Colletotrichum sp. by paper disc diffusion method on double layer Potato Dextrose Agar (PDA). The results indicated that ethylacetate and 95% methanol extracts showed greater activity on Colletotrichum sp. It was found that methanolic extracts from seven species of indigenous plant extracts namely Limnophila aromatica Merr., Centella asiatica Urban., Azadirachta indica Juss., Crateva adansonii Roxb., Ficus benjamina Linn., Memecylon edule Linn. **and Leucaena leucocephala de Wit. at 100,000 ppm could inhibit the growth of Colletotrichum sp. and showed typically inhibition zone. However, only Limnophila aromatica Merr. was excellent efficiency to inhibit every isolates of collected Colletotrichum sp. Thus, this material might be possible as new sources of controlling the growth of plant pathogenic fungi in the future.**

Introduction

Colletotrichum is one of the most important plant pathogens worldwide causing the economically important disease anthracnose in diverse tropical vegetable crops, which causes low yield and poor quality of the crops [1].

Owing to technology evolution, chemical substance is a necessary part in agricultural production processes, because they are used to inhibit plant pathogens which are important enemies of agricultural products. However, chemical substances not only afford damage to environment, but they provide direct effect to human as well. Hence, mitigation of chemical substances using is the best path to solve these problems. The medicinal plant extracts is one of the interesting ways to substitute chemical substances for inhibition of plant pathogens which does not render wicked problems to environment and living being in the world [2]. Although plant based pesticides are cheep, locally available, non-toxic and easily biodegradable limited efforts have been made to screen plants that are suspected to possess antimicrobial properties for effect against Colletotrichum. sp. Higher plants may contain secondary compounds that could effectively control plant diseases, but which are yet to be exploited and used as pesticides [3].

Although there is a growing interest in the use of medicinal plants to control plant diseases, only about 2,400 plant species among more than 250,000 higher plants have been screened for phytoactivity [4-6]. This research is to extract crudes from 37 indigenous plants for inhibiting the growth of the pathogen Colletotrichum sp. Not only can this research diminish pollutant from chemical substances, but it establishes more benefits from local resources as well.

Materials and Methods

Plant materials: Thirty seven kinds of indigenous plants (Limnocharis flava Linn. Buch., Mangifera indica Linn., Nymphoides parvifolia, Markhamia stipulata Seem., Anacardium occidentale, Momordica charantia Linn., Cratoxylum formosm, Centella asiaica Urban., Morinda citrfolia Linn., Phyllanthus acidus Linn. Skeels., Aganosma marginata (Roxb.) G. Don., Trichosanthes anguina Linn., Sauropus androgynus Linn. Mert., Cassia siamea Britt., Morinda citrifolia Linn., Paper samentosum Roxb., Azadirachta indica Juss.Var. siamensis Valeton., Limnophila aromatica Merr., Syzygium gratum Wight S.N.Mitra ar.gratum., Crateva adansonii DC. subsp. trifoliata (Roxb.) Jacobs., Diplazium esculentum., Aganonerion polymorphum Pierre ex Spire., Ficus benjamina Linn., Amaranthrs Spinosus Linn., Sesbania grandiflora (L.) Pers., Lasia spinosa Thw., Neptunia oleracea Lour., Symplocos cochinchinensis Lour., Symplocos sp.Moore., Polygonum odoratum Lour., Careya sphaerica Roxb., Barringtonia acutangla (Linn.) Gaertn., Leucaena leucoce-phala Lamk. de Wit., Passiflora foetida Linn, Tiliacora triandra Diels., Cissampelos pareira L. var hirsute, Cassia alata Linn., Cleome gynandra Linn., previously recorded with antimicrobial effects were selected for this experiment. Plants were purchased from various local markets in Northeastern of Thailand in June to October 2008.

Plant Extract Preparation: The selected parts of different indigenous plants were air-dried, then dried in an oven at 50 ^{o}C and, after that, finely powdered. Each plant (100 g) was extracted with hexane (500 mL) in a glassed bottle for 3 days. The hexane solution was filtered and then the marc was extracted with the fresh hexane (500 mL) in the previous glassed bottle for 3 days. The whole hexane solution was concentrated to dryness under reduced pressure at 30 ^{o}C using rotary evaporator. Then it was air-dried at room temperature to afford the crude hexane product as dark brown gum. In the same way, the marc was continuously extracted with ethylacetate

to provide crude ethylacetate product as dark green gum and further extracted with 95 % methanol to render the crude methanol product as dark brown gum.

Pathogen isolation: Chilli, tomato and banana with anthracnose lesions were collected from 3 plantations in UbonRatchathani province in June 2008 and isolated Colletotrichum sp. by tissue transplanting method. These crops were washed with tap water, and small portions (0.5 cm^2) of contaminated epidermis were cut off and then sterilized with a 10% solution of sodium hypochlorite (trade name Cloralex) for 3-4 min. After sterilization, tissue portions were washed thoroughly three times with sterile distilled water (SDW). The sterile pieces were blotted dry using sterile filter papers and placed on Potato Dextrose Agar (PDA) in 9cm Petri dishes. The dishes were incubated at ambient conditions of light and room temperature for 3 days until fungal growth was observed. Fungus structures (conidia and mycelia) were observed with a scanning electron microscope (SEM), and identification was according to a published description [7]. When used as proof that the fungi causing the disease by Koch's postulation [8]. These fungi were grown on PDA plate at 28 ^oC and maintained with periodic sub-culturing at 4 ^oC.

Antifungal Assay: The plant extracts were tested for the efficiency on growth inhibition of Colletotrichum sp. by paper disc diffusion method on double layer Potato Dextrose Agar (PDA) [9]. Double layer PDA was prepared by pouring 4 ml of liquefied into a sterile Petridish and allowed the agar to set as the basal layer. The top layer was prepared by mixing 1 ml of Colletotrichum sp suspension with 9 ml of liquefied PDA. These preparations should be used for efficacy test immediately. Plant extracts (1 g) were dissolved individually in ethylacetate (9 mL)and an aliquot (10 µL) was dropped on a 0.6 cm diameter sterile paper disc by micropipette to obtain a final concentration of 1 g/mL and placed the disc on the surface of double layer by using ethylacetate as control. Incubation period of 48 hours at room temperature was maintained for observation of antifungal activity of plant extracts. The antifungal activity was evaluated by measuring zones of inhibition of fungal growth surrounding the plant extracts. Each assay was replicated three times and results expressed as the mean of three replicates.

Results and Discussion

Chilli, tomato and banana with anthracnose lesions were collected from 3 plantations in UbonRatchathani province in June 2008 and isolated Colletotrichum sp. by tissue transplanting method. The results of pathogen isolation showed that twenty isolates of Colletotrichum sp. were isolated from chilli 15 isolates (C1-C15), tomato 3 isolates (TM1-TM3), and banana 2 isolates (BA1-BA2). The example isolated colony of Collectotrichum sp. with a scanning electron microscope (SEM) are shown in Figure 1.

Antifungal activity of thirty seven plant extracts was assayed by paper disc agar diffusion method, it was observed that ethylacetate and 95% methanol extracts showed greater activity on Colletotrichum sp. It was observed that extracts showed significant differences in their efficacy to inhibit the growth of Colletotrichum sp. All the extracts tested gave significant inhibition of mycelial growth of Colletotrichum sp. over control. It was found that methanolic extracts from seven species of indigenous plant extracts namely Centella asiatica Urban., Azadirachta indica Juss., Limnophila aromatica Merr., Crateva adansonii DC. subsp. trifoliata (Roxb.) Jacobs., Ficus benjamina Linn., Symplocos sp. Moore. and Leucaena leucocephala de Wit. at 100,000 ppm could inhibit the growth of Colletotrichum sp. and showed typically inhibition zone in Table 1 and Figure 2.

Table 1 Efficacy of seven indigenous plant crude extracts on growth inhibition of Colletotrichum sp.

No	Indigenous plants	Family	Inhibitory zone		
			Chilli CA7	**Tomato** TM2	**Banana** BA1
1.	Centella asiatica Urban	Umbelliferae	-	-	+
2.	Azadirachta indica Juss.	Meliaceae	+	-	-
3.	Limnophila aro matica Merr.	Scrophulariaceae	+	+	+
4.	Crateva adansonii DC. subsp. trifoliata (Roxb.) Jacobs	Capparicadeae	-	-	+
5.	Ficus benjamina Linn.	Moraceae	-	+	+
6.	Symplocos sp. Moore.	Symplocaceae	-	+	+
7.	Leucaena leucocephala Lamk. de Wit	Leguminosae-mimosoideae	+	+	+

Table 1 showed that three methanolic extracts namely Azadirachta indica Juss., Limnophila aromatica Merr. and Leucaena leucocephala de Wit. could inhibit the growth of Colletotrichum sp. isolated from chilli CA7 and four methanolic extracts namely Limnophila aromatica Merr., Ficus benjamina Linn., Symplocos sp. Moore. and Leucaena leucocephala de Wit. could inhibit the growth of Colletotrichum sp. isolated from tomato TM2. While inhibition the growth of Colletotrichum sp. isolated from banana BA1 was six methanolic extracts of Centella asiatica Urban., Limnophila aromatica Merr., Crateva adansonii DC. subsp. trifoliata (Roxb.) Jacobs., Ficus benjamina Linn., Symplocos sp. Moore. and Leucaena leucocephala de Wit. However, only Limnophila aromatica Merr. was excellent efficiency to inhibit every isolates of collected Colletotrichum sp.

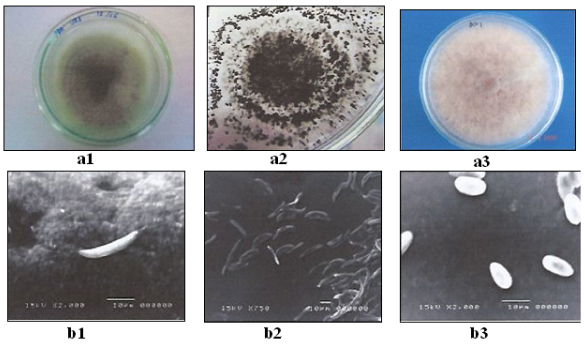

Figure 1 a. Colonies of CA7 isolate (a1), TM2 isolate (a2), BA1 isolate (a3). b. Conidia of Collectotrichum sp. were isolated from CA7 (b1), TM2 (b2), BA1(b3)

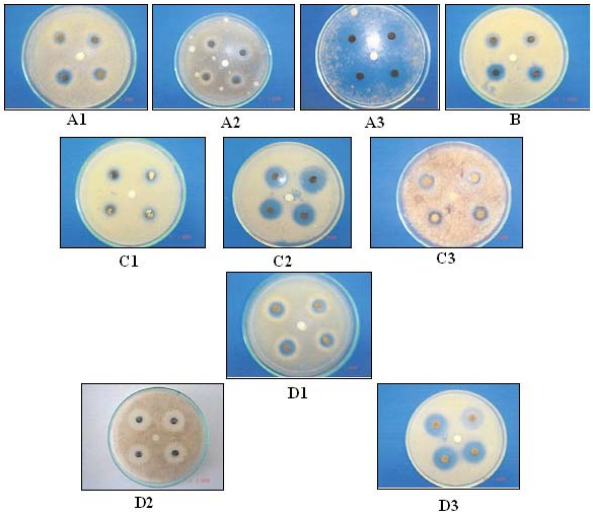

Figure2 Inhibition zone from various plants on growth of Collectotrichum sp. were isolated from CA7, TM2 and BA1.
A) Azadirachta indica Juss. Var. siamensis Valeton.(A1), Ficus benjamina Linn.(A2), leucocephala Lamk. de Wit.(A3), on growth of Collectotrichum sp. from CA7 isolate.
B) Symplocos Moore. (B) on growth of Collectotrichum sp. from TM2 isolate.
C) Centella asiatica Urban.(C1), Crateva adansonii DC. subsp. trifoliata (Roxb.) Jacobs. (C2), Symplocos Moore.(C3), on growth of Collectotrichum sp. from BA1 isolate.
D) Limnophila aromatica Merr. on growth of Collectotrichum sp. of CA7 isolate, TM2 isolate, BA1 isolate.

Conclusions

From thirty seven kinds of indigenous plant extracts tested seven alcoholic extracts could inhibit the growth of Colletotrichum sp. by paper disc agar diffusion method. Limnophila aromatica Merr. was excellent efficiency to inhibit every isolates of collected Colletotrichum sp. Thus, this material might be possible as new sources of controlling the growth of plant pathogenic fungi in the future.

Acknowledgements

We would like to express our sincere thanks to Faculty of Science, Ubonratchathanee University and National Research Council of Thailand for financial support.

References

[1] J. A. Bailey, M. J. Jeger, Colletotrichum: Biology, Pathology and Control. Commonwealth Mycological Institute, Wallingford, (1992), pp.388.
[2] R. P. Leite, S. K. Jr and Mohan, Crop Protection, **9** (1) (1990), pp. 3-7.
[3] V. Kurucheve, E. J. Gerard, J. Jayaraj, Indian Phytopythology, **50** (2) (1997), pp. 235-241.
[4] S. A. Oluwalana, M. F. Adekunle, Journal of Tropical Forest Resources, **14** (1) (1998), pp. 120-136.
[5] S. A. Oluwalana, N. A. Adetoro, M. F. Adekunle, S. Momoh, Bioprospector, **1**(2) (1999), pp. 1-10.
[6] I. K. Khafagi and A. Dewedar, Journal of Ethnopharmacology, **71** (2000), pp. 365-376.
[7] H. L. Barnett, B. B. Hunter, Illustrated Genera of Imperfect Fungi, 4th ed.; MacMillan Publishing: New York, (1986), p. 218.
[8] G. N. Agrios, Plant pathology, Academic press. New York, (1997), pp. 635.
[9] T.C. Hui, Y. H. Cheng, C. L. Wu, S. T. Chang, T. T. Chang, Y. C. Su, Bioresource Technology, **99** (2008), pp. 6266-6270.

Production of 1,3-propanediol from a biological fermentation of glycerol by Clostridium butyricum DSM 5431 in an anaerobic moving-bed bioreactor

J. Wuttisarnsukit [1] and K. Nootong[1,*]

[1]Department of Chemical Engineering, Faculty of Engineering Chulalongkorn University, Bangkok 10330, Thailand

* E -mail: kasidit.n@chula.ac.th

Abstract: Clostridium butyricum DSM 5431 immobilized on BCN-009 were used for a continuous glycerol fermentation to produce 1,3-propanediol (1,3-PDO) in an anaerobic moving-bed bioreactor. Effects of varying dilution rates (i.e., 0.3 to 0.6 hr^{-1}) and fixed inlet glycerol concentration at 40 g/L were investigated. The result indicated that the optimal condition measured in term of 1,3-PDO concentrations was observed when the dilution rate maintained at 0.4 hr^{-1}. The corresponding 1,3-PDO concentration, productivity, and product yield were determined at 23.31±1.21 g/L, 9.32±0.48 g/L/hr, and 0.71, respectively. The ability of moving-bed bioreactor to enhance external mass transfer resulted in a better pH control in bulk liquid in comparison to using fixed-bed column bioreactor.

Introduction

Biodiesel is becoming favorable due to variation of petroleum prices and environmental concerns about global warming. During biodiesel production, the tranesterification of plant oils or animal fats generates glycerol. As the demand for biodiesel increases, a large number of biodiesel plants are now being built and operated actively, thereby resulting in an excessive supply of glycerol in the market that subsequently reduces glycerol price rapidly. One of promising options for glycerol utilization is a synthesis of 1,3-propanediol (1,3-PDO), a higher valued chemical, which can be used as a onomer of many biodegradable polymers and in many industrial applications. Production of 1,3-PDO is possible from either chemical or biological processes. Chemical process derives 1,3-PDO from ethylene and propylene under high temperature and pressure, whereas in biological process, it was produced from biological fermentation of glycerol by various microbial strain namely Citro-bacter fruendii, Klebsiella pneumoniae, and Clostridium butyricum [1,2,3]. Among these strains, Clostridium butyricum is able to produce the highest yield of 1,3-PDO. Currently, the bio-logical fermentation of glycerol to produce 1,3-PDO is often performed in suspension over immobilization despite the latter can offer several advantages namely the higher cell concentrations, the elimination of washout at high dilution rates, the protection against shear damage, and the possibility of cell reuse and ease of separation [4]. However, the majority of research on microbial immobilization to produce 1,3-PDO was based on either an encapsulation of bacteria in gel-matrix or an adsorption onto the surface of polymeric supporting materials such as polyurethane, polystyrene, and loofa sponges [3,5,6,7,8]. It should point out that only several of previous works have employed any immobilizing techniques on C. butyricum. In addition, this bacterial strain does not require a special safety precaution unlike K. pneumoniae and C. freundii, which are opportunistic patho-gens [9]. In the previous work by [7], fixed-bed bioreactors integrating loofa sponges were employed to immobilize C. butyricum DSM 5431 to convert glycerol to 1,3-PDO. The maximum 1,3-PDO concentration and productivity were determined at 29.08 g/L and 6.23 g/L/hr, respectively. Setback associated with this study was the ineffectiveness in main-taining proper pH between 6.5 and 8 especially in the middle and upper sections of fixed-bed column, thereby resulting in microbial growth inhibition. In response to a challenge stated earlier, a moving-bed bioreactor was chosen to carry out the fermentation of glycerol by C. butyricum DSM 5431 to produce 1,3-PDO. This bioreactor scheme should be advantageous from immobilization and able to control the pH of bulk liquid effectively.

Materials and Methods

Materials

Microorganisms and Inoculation

A bacterial strain Clostridium butyricum DSM 5431, obtained from the American Type Culture Collection (ATCC) BAA-557^{TM}, was used in this study. The stocked culture of C. butyricum DSM5431 was stored at -20 °C in a reinforced clostridial medium (RCM). The RCM was mixed with 10% glycerol in a ratio of 1:1 by volume, sterilized in an autoclave for 15 minutes at 121°C, then gassed with nitrogen for 6 minutes at 0.1 vvm. The RCM medium containing 10% by volume of C. butyricum DSM 5431 was transferred into a preculture medium constituting of glycerol 20 g/L; K_2HPO_4 1 g/L; KH_2PO_4 0.5 g/L; $(NH_4)_2SO_4$ 2 g/L; $MgSO_4 \cdot 7H_2O$ 0.2 g/L; $CaCl_2 \cdot 2H_2O$ 15 mg/L; $FeSO_4 \cdot 7H_2O$ 5 mg/L; $CaCO_3$ 2 g/L; and yeast extract 1 g/L. Preculture was incubated at 33 °C for 18 hours under anaerobic condition without an agitation. After 18 hrs, the inoculation of C. butyricum DSM 5431 was to continue for another 12 hours in a 1 L glass fermentor, which was fed with 630

mL of 20 g/L of pure glycerol and 70 ml of preculture medium described previously. Anaerobic condition in a fermentor was achieved by constantly purging nitrogen gas at a rate of 0.1 vvm. The agitation speed and temperature were maintained at 100 rpm and 33 °C, respectively. The pH was adjusted to 7.0 by an automated controlled addition of 2 M NaOH.

Moving-Bed Bioreactor

Moving-bed bioreactor (inner diameter: 19 cm; height 25.1 cm) used in this study was made from transparent acrylic to achieve an effective volume of 4 L. Four baffles were also constructed on side wall to enhanced mixing. The top of bioreactor was tightly seal to prevent air penetration and also used to accommodate glycerol feed line, nitrogen gas line, and NaOH line. Bioreactor was sterilized with steam for 20 minutes before packing with the cell supporting materials. In this study, commercial packing plastic called BCN-009 (HDPE; 834 m^2/m^3) was used to immobilize C. butyricum DSM 5431. Prepared BCN-009 was washed in boiling water for 15 minutes, washed in 95% ethanol then sterilized by steam for 15 minutes.

Bioreactor Startup and Continuous Operation

Approximately 0.8 L of active preculture of C. butyricum DSM 5431 and 3.2 L of fresh glycerol at 40 g/L were fed into moving bed bioreactor to attain a working volume of 4.0 L. Bioreactor was operated in batch mode for 48 hrs before it was drained and refilled with the same amount of preculture and fresh glycerol. The same procedure was repeated until biofilm formation was clearly visible. After a complete draining of liquid in bioreactor, the system was ready to be operated under a continuous feeding of 40 g/L glycerol at the dilution rate of 0.3 hr^{-1}. Dilution rates chosen at 0.3, 0.4, 0.5, and 0.6 hr^{-1} and the initial glycerol concentration at 40 g/L were main experimental variables, which were manipulated to examine the performance of moving bed bioreactor. At a given dilution rate, bioreactor was operated until it reached steady state as indicated by relatively constant concentrations of 1,3-PDO and glycerol. Mixing in bioreactor was accomplished by using magnetic stirrer operated 100 rpm and baffles located on the side wall. The temperature was kept at 33 ºC and pH was maintained at 7.0 by an automated addition of 2.0 M NaOH.

Analytical Methods

Concentrations of 1,3-PDO and glycerol were quantified HPLC at the Scientific and Technological Research Equipment Center of Chulalongkorn University. Samples were injected at the volume of 50 µL into a column (Lichrocart C18) with the length of 250 mm and outer diameters of 4 mm. Operating conditions were as followed: 20 mM H_3PO_4 as a mobile phase, flow rate 1.2 ml/min, column temperature at 25 ^oC. Immobilization and microorganism morphology on BCN-009 was confirmed and examined by a scanning electron microscope (SEM)

.

Results and Discussion

Bioreactor Startup

Immobilization of C. butyricum DSM 5431 was initiated by feeding 40 g/L of fresh glycerol and preculture into anaerobic moving bed bioreactors with BCN-009 as media. This particular cell supporting material had been successfully used to immobilized C. butyricum DSM 5431 to produce 1,3-PDO [7] as well as in the applications of biological nitrogen removal from wastewater. After three batch repetitions (i.e., 144 hrs), murky white-colored biofilm started to develop on the surface of media and slight odors of butyric acid and gas bubbles were also detectable. Scanning electron micrograph (SEM) revealed a successful immo-bilization of C. butyricum DSM 5431 that appeared to form dense colonies, which were widely distributed over media surface (Figure 1). Morphologies of attached cells were mixed between rod shape and long filament. It was also necessary to point out that bacterial attachment was denser on an inner surface of BCN-009 compared to the outer surface, which was directly exposed to liquid circulation. By the end of startup period, relatively constant 1,3-PDO and glycerol concentrations in the effluent were reported at 18.27 ± 0.505 g/L and 8.42 ± 2.140 g/L, respectively. Suspended biomass in the effluent was insignificant measured at 0.25 g/L.

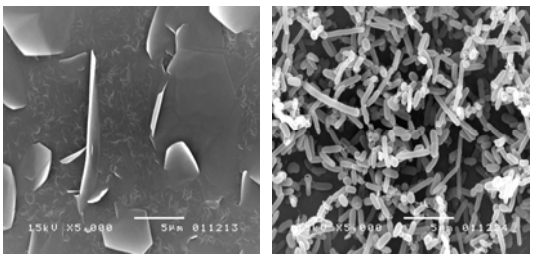

Figure 1. Immobilization of C. butyricum DSM 5431; (left) non-acclimated BCN-009 (right) immobilized C. butyricum DSM 5431 on BCN-009 during the system startup.

Steady State Continuous Operation

The steady state continuous operation of moving-bed bioreactor integrating BCN-009 as cell supporting materials was conducted after startup period. During the 1,3-PDO synthesis, organic acids were produced naturally as by-products and were able to reduce the pH of bulk liquid into acidic domain if production systems lacked pH controlling devices. It was reported that 1,3-PDO synthesis by C. butyricum DSM 5431 exhibited an inhibitory effect when pH of liquid decreased below 6.5 [2]. In this study, there was no pH gradient existed in bioreactor and the pH can be

effectively maintained at 7.05 ± 0.66 throughout the study. The use of magnetic bar and baffles in moving-bed bioreactor clearly improved the external mass transfer in bulk liquid, thereby enhancing neutral-lization between hydrogen ions produced and buffer. The ability to maintain proper pH in moving-bed bioreactor was clearly an improvement from a previous experiment [7] that employed fixed- bed column and experienced failure in pH controls despite the system equipped with automated pH control. Range of dilution rates (i.e., 0.3, 0.4, 0.5, 0.6 hr^{-1}) and initial glycerol inlet at 40 g/L were tested and the result was demonstrated in Table 1. The maximum 1,3-PDO concentration was measured at 23.31 ± 1.21 g/L after the bioreactor was maintained at the dilution rate of 0.4 hr^{-1}. The corresponding product yield and remaining glycerol concentration, and 1,3-PDO productivity were determined at 0.71, 7.37 ± 0.66 g/L, and 9.32 ± 0.48 g/L/hr, respectively. At high dilution rate, it was likely that immobilized bacteria were unable to acquire glycerol quick enough in comparison to the rate of liquid withdrawal from bioreactor. From past studies that employed different cell immobilizing techniques to produce 1,3-PDO. Clearly, the performance of this bioreactor system, measuring in terms of 1,3-PDO productivity and concentration, was slightly better than the previous experiments [7,6,3,8]. Part of the explanation may be related to maintaining inlet glycerol concentration below inhibitory threshold reported at 80 g/L [2,6] and the ability to provide suitable condition (i.e., pH and temperature) for bacteria.

Table 1. Continuous operation of anaerobic moving-bed bioreactor with BCN-009 as carriers to immobilize C. butyricum DSM 5431 to produce 1,3-PDO

Parameters	**Dilution Rate (hr^{-1})**			
	0.3	**0.4**	**0.5**	**0.6**
Feed Glycerol Concentration (g/L)	40	40	40	40
Effluent Glycerol Concentration (g/L)	8.63± 0.61	7.37± 0.66	9.1± 0.47	10.72± 0.37
1,3-PDO Concentration (g/L)	20.33± 1.31	23.31± 1.21	19.6± 0.72	17.62± 0.77
Productivity (g/L/hr)	6.1± 0.39	9.32± 0.48	9.65± 0.36	10.57± 0.46
Yield	0.65	0.71	0.62	0.6

Conclusions

Production of 1,3-PDO based on immobilization of C. butyricum DSM 5431 on BCN-009 in anaerobic moving-bed bioreactor was possible. Variation of dilution rates affected the performance of moving-bed bioreactor. The ability of moving-bed bioreactor to effectively control pH within optimal growth condition was also essential to microbial synthesis of 1,3-PDO. Based on the data obtained, the maximum 1,3-PDO concentration and productivity were determined at 23.31±1.21 g/L and 9.32±0.48 g/L/hr, respectively, the values that were slightly better than past experiments

References

[1] Chen, X., Xiu, Z., Wang, J., Zhang, D., Xu, P. (2003). Stoichiometric analysis and experimental investi-gation of glycerol bioconversion to 1,3-propanediol by Klebsiella pneu-moniae under micro aerobic conditions. Enzyme and Microbial Technology, 33, 386-394.

[2] Gunzel, B., Yonsel, S., Deckwer, W.-D. (1991). Fermentative production of 1,3-propanediol from glycerol by Clostridium butyricum up to a scale of 2 m^3. Appl. Microbiol Biotechnol, 36(3), 289-294.

[3] Pflugmacher, U. Gottschalk, G. (1994). Development of an immo-bilized cell reactor for the production of 1,3-propanediol by Citrobacter freundii. Appl. Microbiol Biotechnol, 41, 313-316.

[4] Shuler, M.L, Kargi, F. (1992). Biopro-cess Engineering Basic Con-cepts. Prentice-Hall, Eaglewood Cliffs, New Jersey.

[5] Griffiths. M.S., Bosley J.A. (1993). Assessment of macroporous poly-styrene-based polymers for the immo-bilization of Citrobacter freundii. Enzyme Microb Technol, 5, 109-113.

[6] Pullsirisombat, J. (2007). γ-Alumina doped alginate gel for cell immo-bilization in fermentation processes. Master's degree thesis of Chemical Engineering. Chulalongkorn Univer-sity, 1-97.

[7] Suratago, T. (2009). Immobilization of Clostridium butyricum DSM 5431 on loofa sponges in fixed bed bioreactors for the production of 1,3-propanediol. Master's degree thesis of Chemical Engineering. Chulalongkorn University, 1-51.

[8] Zhao, Y.-N., Chen, G., Yao S.J. (2006). Microbial production of 1,3-propanediol from glycerol by encapsulated K. pneummoniae. Bio-chem. Eng. J, 32, 93-99.

[9] Deckwer, W.D. (1995). Microbial conversion of glycerol to 1,3-propanediol. FEMS. Microbiology Reviews, 16, 143-149.

Optimal nutrient requirement of Entomoneis sp. cultivated under batch and fed-batch

K. Nootong [1*], T. Viriyayingsiri [1], and S. Powtongsook [2,3]

[1] Chulalongkorn University, Department of Chemical Engineering, Faculty of Engineering, Phrayathai Road, Prathumwan District, Bangkok, 10330, Thailand
[2] Chulalongkorn University, Center of Excellence for Marine Biotechnology, Department of Marine Science, Faculty of Science, , Phrayathai Road, Prathumwan District, Bangkok, 10330, Thailand
[3]National Center for Genetic Engineering and Biotechnology, Nation Science and Technology Development Agency, Pathum Thani, 12120, Thailand

[*] Corresponding: address: kasidit.n@chula.ac.th

Abstract: Entomoneis sp. is a shell-covered diatom that our research team was successfully isolated from many aquaculture systems in Thailand. Early assessment of this diatom demonstrated its potential for mass cultivation, which is depending on many parameters such as temperature, light intensity, salinity and especially quantity of nutrition given to the diatom. Since the outer shell of typical diatom usually has silica as its component, thus the amount of nutrition in culture medium is very crucial for its growth. This study, therefore, aims to investigate the nutrient requirement aspect of Entomoneis sp. and to obtain other useful information that need to be considered during mass production. Preliminary result revealed that the specific growth rate and maximum cell density of Entomonies sp. subjected to batch cultivation in modified F/2 medium were at 1.61 day^{-1} and 2.24 × 10^5 cell/ml, respectively. Modification of silica supplement to fed-batch mode improved the specific growth rate and maximum cell density of this diatom to 1.76 day^{-1} 2.98×10^5 cell/ml, respectively. Analysis of macronutrients (nitrate, phosphate, and silicate) suggested that modified F/2 medium should be adjusted with reduction of nitrate, and increasing phosphate and silicate contents.

Introduction

The idea of using microalgae as a source of biofuel is now being taken seriously because of the uncertainty in petroleum price [1]. Entomoneis sp. is a shell-covered diatom that has been successfully isolated from many aquaculture systems in Thailand. Preliminary assessment of this diatom indicates its potential for mass cultivation for biofuel production purpose. The shell-covers of this diatom consists of mainly silica and many organic contents including lipids, which constitutes as high as 47 % of total diatom dried weight [2]. This diatom also yields oil contents approximately 6 to 12 times higher than other energy crops, and has relatively large cell size and weight, thereby making it to be separated from water by means of gravitational sedimentation. Therefore, it is the objective of this article to describe the following preliminary information including: (1) growth data of Entomoneis sp. (2) optimization of Si requirement and the method of supplying it to Entomoneis cultures.

Materials and Methods

Microalgae and culture conditions

Entomoneis sp., isolated from commercial shrimp aquaculture pond in (Thailand), was used in this study. Diatom was inoculated in 250 ml flasks with the modified F/2 Guillard's medium [3] which composed of $NaNO_3$ (75 g/L), $NaH_2PO_4 \cdot H_2O$ (5 g/L), $Na_2SiO_3 \cdot 9H_2O$ (30 g/L), trace metal solution and vitamin solution. Initial cell concentration was measured at 1-2× 10^4 cell/ml after 10 day incubation. These incubated cells are transferred to 1.0 Duran glass bottle filled with artificial seawater (30 PSU) to increase cell number. Conditions inside Duran bottles were kept as followed: illumination at 5,000 lux by two fluorescent lamps; and carbon dioxide from air flow through microfilters (0.2 mm) at 115 L/hr.

Batch Culture of Entomoneis sp.

Batch culture of Entomoneis sp. was conducted to obtain growth information including specific growth and cell number. The experiment was performed in batch mode in 1.0 L Duran bottles (0.95 working volume), which were inoculated with modified F/2 medium and 10% (v/v) of diatom described in section 2.1. Light and airflow were maintained at 5,000 lux and 115 L/hr, respectively. Daily water sample from Duran bottles were obtained and immediately determined for cell number and concentration of macronutrient (i.e., nitrate, phosphate, and silicate) according to Strickland and Parson (1972) [4] and Greenberg et al., (1992) [5].

Fed-batch Culture of Entomoneis sp.

Preliminary study in fed-batch culture of Entomoneis sp. was carried out to assess the method of supplying silicate to diatom. The experiment was performed in 1.0 L Duran bottles (0.95 working volume), which were inoculated with modified F/2 medium without silicate content and 10% (v/v) of diatom described in section 2.1. Silicate solution (0.497 mg Si/L) at approximately 1.0 ml was added into Duran bottles on a daily basis to ensure that the

same amount of silicate was supplied as in batch operation. Illumination and airflow were maintained at 5,000 lux and 115 L/hr, respectively. Daily water sample from Duran bottles were obtained and immediately determined for cell number and concentration of macronutrient (i.e., nitrate, phosphate, and silicate) according to Strickland and Parson (1972) and Greenberg et al., (1992).

Determination of macronutrients

For analyze of nitrate, using screening method [3], by measure the absorption at the wavelengths 220 and 275 nm. For measurement of phosphate and silicate using method of Strickland and Parson (1972) by measure the absorption at the wavelengths 885 and 810 nm, respectively.

Results and Discussion

Batch cultivation

The specific growth rate of Entomoneis sp., determined during the exponential growth phase (i.e., day 1 and 2), was found at 1.61 day^{-1} and the maximum cell density was determined at 2.24×10^5 cell/ml were shown in Figure 1.

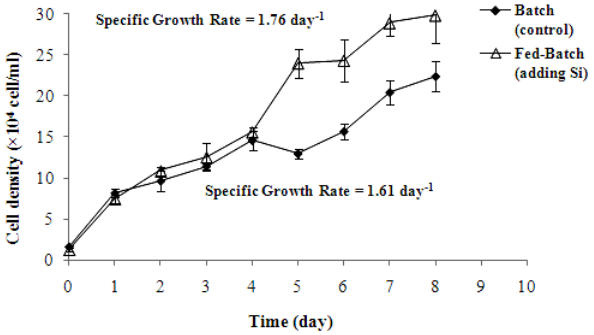

Fig 1. Growth of Entomoneis sp. comparing batch and fed-batch cultivation

Analysis of macronutrients as shown in Figure 2 indicated the decreasing trend of nitrate, phosphate and silicate until the stationary phase was reached after day 6. The remaining nitrate concentration was still available in significant quantity measured at approximately 4.0 mg/L. Remaining phosphate and silicate concentrations, in contrary, were almost exhausted. Clearly, the initial amount of nitrate in modified F/2 medium was sufficient for growth for this particular diatom and possibly could be reduced, whereas the initial phosphate and silicate contents were limiting even on the first day of experiment. The reason for nutrient limitation, particularly silicate, could be linked to silicate sedimentation at the bottom of glass bottles.

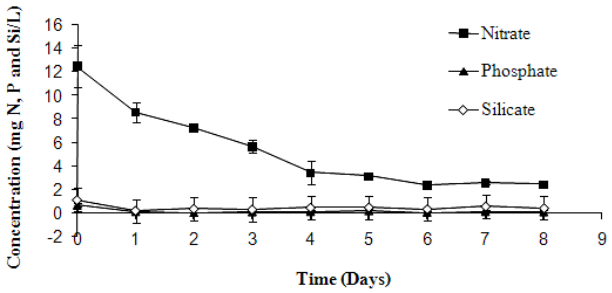

Fig 2. Macronutrients analysis during batch cultivation of Entomoneis sp.

Fed-batch cultivation

It was important to emphasize that silicate solution was supplied into culture vessels on a daily basis, hence the name fed-batch. By performing this modification, lesser amount of silicate was lost via sedimentation and diatom should be able to utilize the nutrient more effectively. Entomonies sp. was able to grow better in fed-batch environment compared to batch culture, demonstrating the specific growth rate and cell density at 1.76 day^{-1} and 2.98×10^5 cell/ml, respectively. Figure 3 depicts the result of macronutrient analysis during fed-batch cultivation. The general pattern of concentration profiles was similar to that of batch culture. Nitrate was still in excess compared to silicate and phosphate, which became limiting since the first day of the experiment. The similarity of macronutrient profiles obtained from both batch and fed-batch operations implied that the current formula of modified F/2 medium was unsuitable for optimal growth of Entomoneis sp. An initial amount of nitrate in the medium can be reduced to lower the cost of cultivation, whereas silicate and phosphate contents should be increased to meet the demand of diatom.

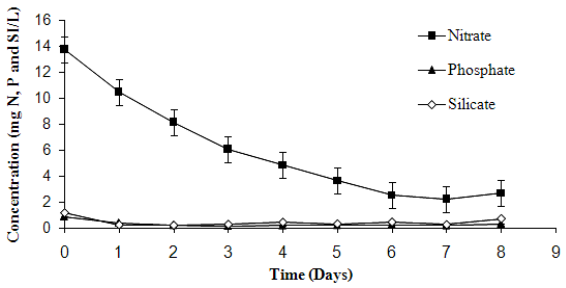

Fig 3. Macronutrients analysis during fed-batch cultivation of Entomoneis sp.

Conclusion

Entomoneis. sp. cultivation with modified F/2 medium could be improved by mode. The result of this study indicated changing nutrient addition into fed-batch that fed-batch addition of silicate was able to increase the specific growth rate of this diatom to 1.76

day^{-1}. In addition, macronutrient analysis suggested a further study to optimize the compositions of media

Acknowledgements

All the equipments and facilities in this research were provided by the Center of Excellence for Marine Biotechnology, Department of Marine Science, Faculty of Science, Chulalongkorn University.

References

[1] Y. Chisti, Biotechnology Advances, **25** (2007), pp 294–306.
[2] H.C. Hong, A. Mazumder, M.H. Wong and Y. Liang, Water Research. **42** (2008), pp 4941 – 4948.
[3] R.R.L. Guillard, Culture of Marine Invertebrate Animals. Plenum Press, New York, 1975.
[4] J.D. Strickland and T.R. Parson (2nd edition), A Practical Handbook of Water Analysis. Fishery Research Board of Canada, Otawa, 1972.
[5] A.E. Greenberg, L.S. Clesceri and A.D. Eaton, Standard Method for the Examination of Water and Wastewater. Victor Graphic, Maryland, 1992.

Development of closed recirculating system integrating nitrifying and denitrifying biofilters for rearing tilapia larviculture

T. Suwannarat[1], K. Nootong[1]* and S. Powtongsook[2,3]

[1]Department of Chemical Engineering, Faculty of Engineering, Chulalongkorn University, Phrayathai Road, Prathumwan District, Bangkok 10330, Thailand.
[2]Center of Excellence for Marine Biotechnology, Department of Marine Science, Chulalongkorn University, Bangkok 10330, Thailand
[3]National Center for Genetic Engineering and Biotechnology, National Science and Technology Development Agency, Pathumthani 12120, Thailand

*E-mail: kasidit.n@chula.ac.th

Abstract: This study focused on the development of nitrification system as part of a complete water recirculating scheme based on nitrification and denitrification for the tilapia larviculture. Nitrifying system was intended to integrated biofilters directly into cultured tank as means to lowering aeration and pumping cost and reduce areal requirement for construction. Preliminary result indicated that the current design of nitrifying system was unsuitable for long term operation due to the accumulations of suspended solids (i.e., fishmeal) on the floor and biofilter surface, subsequently creating toxic hydrogen sulfide. Determining the frequency of biofilter cleaning and/or appropriate cleaning method or redesigning the system by separating biofilters from cultured tank would be likely choices for future development.
Keywords: Nitrification, Aquaculture, Nitrogen, Tilapia.

1.Introduction

Thailand, nursery of tilapia larva is commonly performed using cage culture or in large outdoor ponds. Problems such as fish disease and stress from uncontrolled environment are generally found. Closed-system cultivation is advantageous due to the ability to attain extremely high productivities, the reduction of disease infection, and the lowering environmental impacts associated with wastewater discharges. An intrinsic problem of closed-aquaculture systems is a rapid accumulation of toxic inorganic nitrogen species (i.e., ammonia and nitrite). This cannot be avoided since aquatic stocks assimilate only 20 to 30% of feed proteins while the rest is excreted as urea, which subsequently undergoes a biological degradation into ammonia [5, 7, 13]. In most recirculating systems, ammonia removal is usually accomplished via nitrification, which is an aerobic biological process that converts toxic ammonia into far less toxic nitrate. Cultivation of commercial aquatic species in water with high nitrate concentration for a long period is not recommend since nitrate can retard their growth. Apart of toxicity on aquatic animals, nitrate discharge can create environmental problems. This article, therefore, focuses on the development of nitrifying system as part of a complete water recirculating system based on nitrification and denitrification. Spe-cifically, the paper describes: (1) the inorganic nitrogen concentrations in the nitrifying unit of prototype system, and (2) the operational difficulties encountered during the system evaluation and the possible scenarios for future improvement.

2.Materials and Methods

2.1 Biofilter Acclimation.

Fibrous Biocord^{TM} biofilters (i.e., polypropylene; specific surface area: 2.8 m^2/m or 82.35 m^2/kg-biofilter) used in the study by [8] were employed as nitrifying biofilters in this study. To ensure a complete nitrification, Biocord^{TM} bio-filters were re-acclimated according to the procedure slightly modified from [8]. A periodic addition of shrimp diets (30% proteins) was performed for once every two days as means to provide ammonium at 2.0 mg N/L while NH_4Cl at equivalent ammonium concentration was used as a substitute on day 7, 20, 37, and 50. Four diffusive stone aerators were used to provide the dissolved oxygen at least 4.0 mg/L. Alkalinity and pH were maintained from 100 to 150 mg/L $CaCO_3$ and from 7 to 8.2 by a periodic supplement of $NaHCO_3$. Daily grasp samples of water in acclimating tank were immediately ana-lyzed for NH_4-N, NO_2-N, and NO_3-N concentrations according to [2].

2.2 Experimental Setup.

Plastic ponds (HDPE; 2,000 L working) were used to conduct the closed-water tilapia larviculture. At the center of plastic pond, a rectangular nylon cage (width: length: depth 0.8 m × 0.8 m × 0.5 m) were installed and completely submerged below water surface. Acclimated Bio-cord^{TM} biofilters (60 pieces, 50 cm per pieces) were evenly distributed outside the nylon cage by connecting to a metal frame lying on the floor. Water salinity was adjusted to 3 psu while alkalinity and pH ranges were maintained from 100 to 150 mg/L $CaCO_3$ and from 7 to 8.2 by periodic addition of $NaHCO_3$. Eight dif-fusive stone aerators were used to keep DO greater than 4.0 mg/L. Water samples from plastic ponds were obtain on a daily basis and

immediately analyzed for NH_4-N, NO_2-N, and NO_3-N concentrations according to [2].

2.3 Zero-Water Exchanged Tilapia Larviculture.

Zero-water exchanged tilapia larviculture was conducted for 24 days in the controls (i.e., only ponds and nylon cage) and recirculating systems described in section 2.2. For both systems, tilapia at average initial weight of 0.01 g/tilapia was released into a nylon cage to obtain a stocking density of 4,000 tilapia/m^3. Fishmeal at 50% proteins was used as tilapia diet. Feeding was performed at 5 to 6 times per day, maintaining daily ration at 15% of total fish weight. Water salinity was adjusted to 3 psu while alkalinity and pH were maintained in the ranges from 100 to 150 mg/L $CaCO_3$ and from 7 to 8.2 by periodic addition of $NaHCO_3$. The DO concentration is also kept at greater than 4.0 mg/L for the entire experiment. Water samples from the controls and experimental treatments obtain were obtained at least 3 time per week and immediately analyzed for NH_4-N, NO_2-N, and NO_3-N concentrations according to [2].

3.Results and Discussion

3.1 Biofilter Acclimation.

Figure 1 illustrates inorganic nitrogen profiles of water in acclimating tank. Clearly, addition of shrimp diets and NH_4Cl resulted in an increase of ammonium concentrations in water. Relatively small accumulation of nitrite during the startup (i.e., day 2 and 3) was also noticeable. Nitrate formation proceeded immediately after initializing the biofilter acclimation. Complete nitrification established after day 20 as can be confirmed by negligible ammonium and nitrite (i.e., NH_4-N < 0.2 and NO_2-N < 0.2 mg N/L) and continued nitrate production. At the end of acclimation, an independent batch test revealed that acclimated Biocord^{TM} biofilters exhibited ammonium degra-dation rate at 36.6 mg N/m^2/day.

3.2 Zero-Water Exchanged Tilapia Larviculture.

The general water parameters of both the controls and treatments were within the optimal range (i.e., temperature = 26.8 ± 1.51 °C; pH = 7.84 ± 0.52; alkalinity = 120 ± 28 mg/L $CaCO_3$; DO > 4 mg/L) for tilapia [3]. Water in the controls, which featured zero biofiltration, was not transparent but appeared brownish with suspended solids from fishmeal floating. Figure 2 displays the result of water analysis from the controls and treatments. In the controls, ammonium and nitrite remained below an acceptable level of 1.0 mg N/L for 12 days. Excessive accumulation of ammonium and nitrite as high as 4.8 and 7.2 mg N/L was observable by the end of experiment, respectively. Buildup of ammonium was the consequence of ammonification of unconsumed feeds and animal excretion while the proliferation of ammonia oxidizing bacteria was likely responsible for the accumulation of nitrite. In contrary to ammonium and nitrite, nitrate did not demonstrate an obvious trend and its concentration only increased from 3.5 to 7.2 mg N/L during the period of 24 days. It was quite interesting to point out that as high as 90% of tilapia survival rate was observed in the controls despite excessive ammonium and nitrite concentration (i.e., NH_4-N > 1.0 mg/L and NO_2-N > 1.0 mg/L) lingered in the systems for more than a week since day 16. This result was somewhat unexpected since it was generally known that excessive ammonium and nitrite levels can retard growth and cause death in tilapia [8]. The average daily growth for tilapia fingers was determined at 0.01 g/day.

Nitrification also exerted a crucial role on inorganic nitrogen control in the treatments since it was able to maintain negligible levels of ammonium and nitrite below 1.0 mg N/L for 19 days while nitrate gradually increased from 15 to 20 mg N/L. However, ammonium started to exhibit an increasing trend after day 20 and the final concentration was determined at 2.5 mg N/L. Similar trend was noticeable for nitrite but its concentration still remained below 1.0 mg N/L. Significant numbers of tilapia was observed to stop eating and surfacing on day 18, leading to substantial death several days later. The mortality rate for the treatment was calculated at 85%. High death rate was the believed to be the result of hydrogen sulfide production. The ability of Biocord^{TM} biofilters to effectively retain small fishmeal particles on their surface and the accumulation of fishmeal below the nylon cage may contribute to the occurrence of anaerobic pockets and the production of hydrogen sulfide. The average daily growth for tilapia fingers in the treatments varied from 0.095 to 0.099 g/day, which is indifferent to that from the controls.

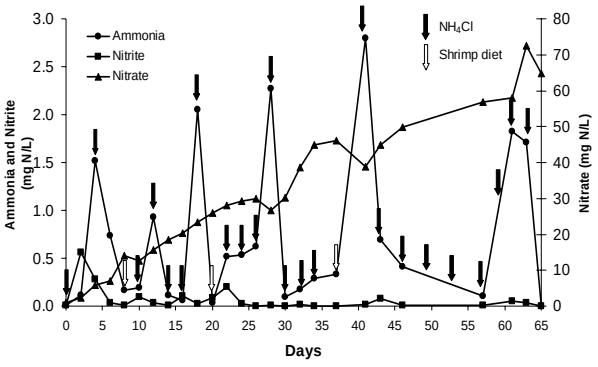

Figure 1 Inorganic nitrogen profiles during reacclimation of Biocord^{TM} biofilters

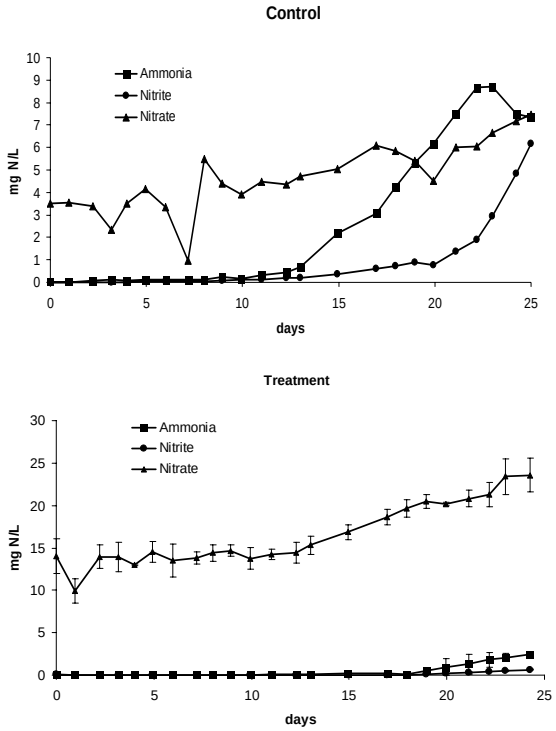

Figure 2. the results of the water analysis from each tilapia cultivating pond showing the concentration profiles of inorganic nitrogenous compounds. The results from treatment (integrated with acclimated biofilters), control has no biofilter.

Conclusions

1. Shrimp diets were possible substrate for establishing nitrification. Accli-mated biofilters are required to re-activate their nitrifying activity after prolonged idle.
2. The current design of nitrifying system with Biocord^{TM} biofilters di-rectly integrated into cultured tank was not appropriate for tilapia larviculture since the accumulation of fishmeal in the system can generate hydrogen sulfide As a result, de-termining the frequency of biofilter cleaning or appropriate cleaning method or redesigning the system by separating biofilters from cultured tank would be likely choices for future development.

References

[1] Alexssandro G. Becker, Bibiana S. Moraes, Charlene C. Menezes, Vania L. Loro, Danilo R. Santos, Jose M. Reichert, Berrnardo Bald isserotto, Ecotoxicology and Environmental Safety 72 (2009): 1734-1739.

[2] AWWA-APHA-WPCE, Standard Method for the Ex-amination of water and Wastewater, 20th ed. Washing-ton, DC (1998).

[3] A. F. M. Sayed, Abdel-fattah, M. El-Sayed, Tilapia Culture, United States: C A B lntl. (2006).

[4] Catherine Lyssenko, Fred Wheaton, Aquaculture Engineering 35 (2006): 26-37.

[5] M.E. Azim, D.C. Little, Aquaculture 283.(2008): 29-35.

[6] P.De Schryver, R. Crab, T. Defoirdt, N. Boon, W. Verstraete., Aquaculture 277 (2008): 125-137.

[7] Roselien Crab, Yoram Avnimelech, Tom Defoirdt, PeterBossier, Willy Verstraete., Aquaculture 270 (2007): 1-14.

[8] Thanathon Sesuk, Sorawit Pow-tongsook, Kasidit Nootong, Bioresource Technology 100 (2009): 2088-2094.

[9] Yoram Avnimelech, Aquaculture Engineering 34 (2006):172-178.

Molecular docking of HSV-1 for identification of sulfolipid (SQDG) targeted protein

P. Kaewmanee[1], S. Hannongbua[5,6], P. Saparpakorn[5,6], K. Porkaew[1,3], V. Chumchua[7], N. Chirasuwan[4], M. Ruengjitchatchawalya[1,2]*

[1] Bioinformatics and Systems Biology program; [2] School of Bioresources and Technology;
[3] School of Information Technology; [4] Pilot Plant Development and Training Institute,
King Mongkut's University of Technology Thonburi (KMUTT), Bangkok 10140, Thailand
[5] Department of Chemistry, Faculty of Science;
[6] Center of Nanotechnology, Kasetsart University, Bangkok 10900, Thailand
[7] National Institute for Child and Family Development,
Mahidol University, Nakhon Pathom 73170, Thailand.

*E-mail: marasri.rue@kmutt.ac.th

Abstract: The binding of non-ionic (L1) and ionic (L2) forms of sulfo-quinovosyl-diacyl-glycerol (SQDG) structure, in three target protein structures of Herpes Simplex Virus Type 1 (HSV-1), i.e. HSV-1 DNA polymerase (HSV-1 DNAPol); Glycoprotein D (gD); and Thymidine kinase (TK),were investigated using GOLD program. Results showed that both L1 and L2 posed the high fitness score with HSV-1 DNAPol chain B (46.49 and 44.49, respectively) and the binding site 2 of gD (48.44 and 41.53, respectively). Amino acid containing positively charged sidechain, i.e. arginine (Arg), was found to be important in the binding to hydrophilic region of sulfonyl group, while amino acid containing hydrophobic sidechain revealed the interaction to hydrophobic region, fatty acid chains, of the sulfolipid.

Introduction

Herpes simplex virus 1 and 2 (HSV-1 and HSV-2) are ubiquitous and contagious, via direct contact with a lesion or body fluid of an infected individual. Infection may cause only a single outbreak of sores, but in many cases the person will have more outbreaks. There are approximately 45-98% of the world population who live under the HSV infection [1]. Though the disease cannot be cured and no approved vaccines are available, the HSV infection are also more increasing, including in Thailand. Thus, management and developing of drug(s) become important in treating of the viral infection. Presently, structures of many proteins such as DNA polymerase (DNAPol), thymidine kinase (TK) and glycoproteins (gD) of the HSV are available. The viral DNAPol and TK were found as only the preferred targets of all HSV treatment and the drug development. Generally, drugs that are used for the treatment of this disease are acyclovir and pencyclovir which are the most widely used [2,3]. However, a serious problem of the use of acyclovir is drug resistance and toxic side effects. Hence, continuous search for new compounds as more effective antiviral agents is important [3]. Sulfolipid compound, known as sulfo-quinovosyl-diacyl-glycerol (SQDG), was discovered in 1959 [4]. It is a sulfonic analog of monosaccharide as glucose bound to glycerol bearing fatty acids, found abundantly in thylakoid membrane of photosynthetic organisms [4]. This compound is of interest in drug discovery because of its high biological activities, including antiviral against such as HSV-1 and 2, HIV-RT, anti-tumor [5].

Spirulina platensis, a cyanobacterium, is known as a rich source of nutritional value and bioactive compound, such as sulfolipid (SQDG), γ-linolenic acid (GLA), sulfated polysaccharides and c-phycocyanin [6]. Chirasuwan et al. (2009), reported that the SQDG showed anti-HSV-1 activity in vivo, potently inhibited with an IC_{50} value of 6.8 μg/ml and very low toxicity [5]. However, the inhibition mechanism of the SQDG are unclear. Furthermore, target protein of HSV-1 for SQDG has not been revealed yet. We thus aim to find the candidate target protein of HSV-1 and investigate interaction between the ligand and target protein by docking model.

Materials and Methods

Ligand preparation

The structure of ligands, non-ionic (L1) and ionic (L2) forms of SDQG, were prepared and optimized using AM1 method in Hyperchem. Each ligand was optimized with the higher level of calculation by Hartree-Fock method (HF) using the 6−31G basis set from Gaussian03 program.

Protein preparation

The x-ray structures of target proteins of HSV were obtained from Protein Data Bank (PDB codes 2GV9; HSV-1 DNA polymerase; 2C3A; Glycoprotein D; and 2KI5; Thymidine kinase). All possible binding sites of the proteins were collected/listed and used for docking. Protein structures were prepared by adding hydrogen and/or removing ligand and water on the structures using DSVisualizer program.

Protein-ligand docking

Docking was performed with Genetic Optimization for Ligand Docking, GOLD version 4.0, using genetic

algorithm (GA). Each ligand–protein was docked 15 independent GA runs, and other parameters using default of the program. The docking scheme was performed as shown in Figure 1. The highest fitness score of GOLD indicated good convergence was the best docked conformations.

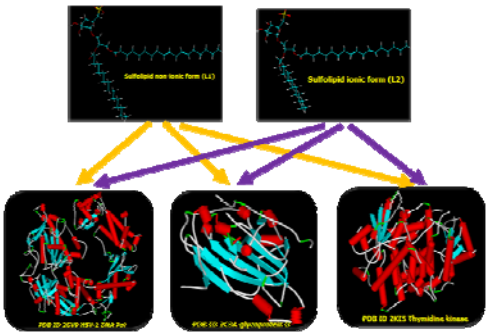

Figure 1 Docking experiment designed in this study.

Results and Discussion

Determination of SQDG binding site in target proteins of HSV-1

To search the target protein for SQDG, the SQDG L1 and L2 were docked into three target proteins of HSV-1, i.e. HSV-1 DNAPol (pdb code 2GV9), gD (pdb code 2C3A) and TK (pdb code 2KI5). Both SQDG forms docked with different binding site of each protein are summarized (Table 1). Docking results of HSV-1 DNAPol chain B with SQDG L1 and L2 showed a similar fitness scores, 46.49 and 44.49, respectively. Concurrently, the docking between binding site 2 (BDS2) of gD with SQDG L1 and L2 showed fitness scores of 48.44 and 41.53, respectively. Whereas, docking result of the other protein, TK, with different binding site(s) no binding occurred.

Interaction of SQDG-protein complex

To study the interaction of SQDG- protein complex, SQDG showing the high fitness score in the complexes with HSV-1 DNAPol chain B and gD at BDS2, as shown in Table 1, were collected and analyzed. Binding position of HSV-1 DNAPol chain B complex with SQDG L1 (Figure 2A) indicating the binding site of this docking model interacted was Arg469 with hydrophilic region of sulfonyl group, while the fatty acids appeared to bind to Ile504, Ser 507, Tyr526. The interaction between SQDG L1 and gD at BSD2 was shown in Figure 2B. Amino acid as Arg36 was found to interact with oxygen of sulfonyl group, while hydrophobic region as fatty acid chains were interacted with Pro31, Pro32, Pro78.

Table 1 The fitness score of ligands and different binding site of proteins.

Molecule forms	PDB/ID Protein names	Binding site	Fitness score
Sulfolipid non-ionic form (L1)	2GV9/ HSV-1 DNA Pol	Chain A	NB
	2GV9/ HSV-1 DNA Pol	Chain B	46.49
	2C3A/ Glycoprotein D	BDS1	NB
	2C3A/ Glycoprotein D	BDS2	48.44
	2KI5 Thymidine kinase	BDS1	NB
	2KI5 Thymidine kinase	BDS2	NB
Sulfolipid ionic form (L2)	2GV9 HSV-1 DNA Pol	Chain A	NB
	2GV9 HSV-1 DNA Pol	Chain B	44.49
	2C3A Glycoprotein D	BDS1	NB
	2C3A Glycoprotein D	BDS2	41.53
	2KI5 Thymidine kinase	BDS1	NB
	2KI5 Thymidine kinase	BDS2	NB

Note: BDS = Binding site, NB = No binding

For complex of proteins and SQDG L2, the docking result showed that the complex of HSV-1 DNAPol chain B and ligand L2 (Figure 2C). The hydrophilic region as sulfonyl group interacted with Arg620. Interaction with fatty acid chains in this docking model were Ile468, Ile504. Finally, the gD with binding site 2 and SQDG L2 complex (Figure 2D) formed hydrogen bonds in hydrophobic region with residue Pro31, Gly33, Pro78.

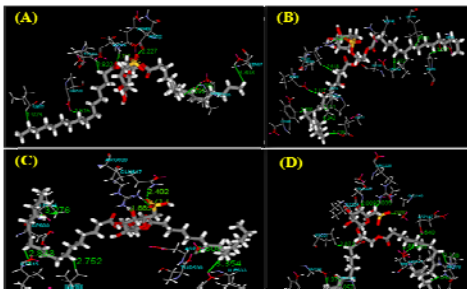

Figure 2 Interaction of SQDG-protein complex, (A) between SQDG L1 and HSV-1 DNAPol chain B; (B) between SQDG L1 and gD with BDS2; (C) between SQDG L2 and HSV-1 DNAPol chain B; (D) between SQDG L2 and gD at BDS2.

Conclusion

Both of HSV-1 DNA polymerase (HSV-1 DNA Pol) and glycoprotein D (gD) were predicted to act as target proteins for SQDG, both non-ionic (L1) and ionic (L2) forms, dued to their high fitness scores of individual docking. Sufonyl group of both forms of the sulfolipid was predicted to interact with amino acid containing positively charged sidechain which located on hydrophilic region, whereas fatty acid chain most interacted to amino acid containing hydrophobic sidechain.

Acknowledgements

We thank Bioinformatics and Systems Biology program, KMUTT and BIOTEC, NSTDA for facilities and scholarship support. S.H. and P.S. are grateful to the Thailand Research Fund (RTA5080005, and MRG5080267). Center of Nanotechnology at Kasetsart University, Laboratory for Computational and Applied Chemistry (LCAC), and National Center of Excellence for Petroleum, Petrochemicals, and Advanced Materials (NCE-PPAM) are also gratefully acknowledged for research facilities and computing resources.

References

[1] M. Fatahzadeh and R.A. Schwartz, J. Am. Acad. Dermatol. **57** (2007), pp. 737- 763.
[2] D.M. Coen and P.A. Schaffer, Nat. Rev. Drug Discovery **2** (2003), pp. 278-288.
[3] F. Morfin and D. Thouvenot, J. Clin. Virol. **26** (2003), pp. 29-37.
[4] A.A. Benson, H. Daniel and R. Wiser, Proc. Natl. Acad. Sci. **45** (1959), pp. 1582-1587.
[5] N. Chirasuwan, R. Chaiklahan, P. Kittakoop, W. Chanasattru, M. Ruengjitchatchawalya, M. Tanticharoen and B. Bunnag, Science Asia **35** (2009), pp. 137-141.
[6] M.F. Ramadan, M.S. Asker and Z.K. Ibrahim, Czech J. Food. Sci. **26** (2008), pp. 211-222.

Structural optimization of Ca-spirulan target on glycoprotein-D of HSV-1

C. Sonthirod[1], P. Saparpakorn[5,6], N. Waraporn[1,4], R. Palangsuntikul[2], S. Hannongbua[5,6] and M. Ruengjitchatchawalya [1,3*]

[1]Bioinformatics and Systems Biology program; [2]Biological Engineering program;
[3]School of Bioresources and Technology; [4]School of Information Technology,
King Mongkut's University of Technology Thonburi (KMUTT), Bangkok 10140, Thailand
[5]Department of Chemistry, Faculty of Science; [6]Center of Nanotechnology, Kasetsart University, Bangkok 10900, Thailand

[*]E-mail: marasri.rue@kmutt.ac.th

Abstract: To optimize structure of Ca-spirulan (Ca-SP), a sulfate polysaccharide isolated from Spirulina platensis, as an anti-herpes simplex viruses type 1 (HSV-1) focusing to its envelope glycoprotein-D (gD), their structures were prepared by Hyperchem and Discovery Studio Visualizer porgram. Docking by Autodock program to identify binding site, we found that Ca-SP bound with a group of basic amino acid by hydrogen bonding in gD, espectially arginine (Arg) and lysine (Lys). The result showed with -8.85 kcal/mol of binding free energy in Arg130. Sequentially, structural optimization by Genetic Algorithm (GA) revealed that the modified structure of Ca-SP showed a stronger binding affinity than that of its natural structure, suggesting the inhibition of HSV-1 infection requires a specific sulfation pattern.

Introduction

Nowadays, herpes simplex virus (HSV) infection is common worldwide. Type 1 (HSV-1) infection is common pandemic, with 45% to 98% of the world population and 40% to 63% of the people in the United States reportedly seropositive [8]. In Thailand, numbers of HSV-1 infected patients were increasing every year. Hence, this problem is considered to be one of a critical health issue in our country. It was recently reported that using acyclovir, a DNA base analog, for long-term, resistant virus strains have emerged [6]. Therefore, searching of novel anti-HSV-1 agent is important.

Ca-SP, a sulfate polysaccharide chelating calcium ion extracted from Spirulina platensis, can act as an inhibitor of herpes simplex virus-1 (HSV-1) [3]. Previous studies reported an importance of sulfate content involving in antiviral potency [5]. Infection process of HSV into host cells is a complex process initiated by the specific interaction between host-cell-surface receptors and viral envelope glycoproteins, such as glycoprotein-C (gC), glycoprotein-B (gB), and glycoprotein-D (gD). The infection of HSV seems to be mediated through function of gC/gB. Before virus entry requires the activity of the gD, which can interact with entry mediator(s)/ receptor(s) and with specific sites in heparan sulfate (HS) [2]. Although, several

sulfated polysaccharides have been shown to inhibit the replication of various enveloped viruses, including not only HSV, human cytomegalovirus, and HIV [5]. Ca^{2+} might be a specific metal cation which can form a potent antiviral molecule, according to the antiviral activity and cytotoxicity [4]. In this study, to develop a new generation of anti-HSV-1 agent from sulfate polysaccharide targeting on gD with anti-HSV activity improvement, structure optimization of Ca-SP using genetic algorithm (GA) is reported.

Materials and Methods

Methodology in this work can be divided into two main parts. The first was docking between Ca-SP and gD of HSV-1 to identify binding site. The second was optimizing sulfate pattern on structure of Ca-SP using GA.

Ca-SP and gD structures preparation: Ca-SP polysaccharide consists of 1,3-linked rhamnosyl, 1,2-linked 3-O-methyl-rhamnosyl, 1,4- and 1,3,4-linked hexuronosyl residues and sulfate groups substituted at C-2 of 1,3-linked rhamnosyl and at C-4 of 1,2-linked 3-O-methyl-rhamnosyl residues (Fig 1). In this study, 3D-structure of the Ca-SP was prepared by using Hyperchem program, whereas the gD, pdb code 2C3A, was downloaded from Protein Data Bank (PDB). The structure Ca-SP was optimized by Gaussian 03 program using semi-empirical AM1 method.

Identification of binding site of Ca-SP:gD: Autodock 4.2 program was used for docking Ca-SP into gD of HSV-1. To view the identified binding site and the interaction, Discovery Studio (DS) visualizer program was used.

Optimization of Ca-SP structure: Genetic Algorithm (GA) was used to find new sulfate pattern of Ca-SP. We used JGAP, a genetic algorithm and programming package provided as a Java framework, to implement the GA. SMILES string was applied to represent structure of Ca-SP, before converted to 3D-structure using Openbabel program. Autodock Vina program [7] was used to dock and evaluate binding energy of Ca-SP new generations. The algorithm was terminated till 20 repeats/generations.

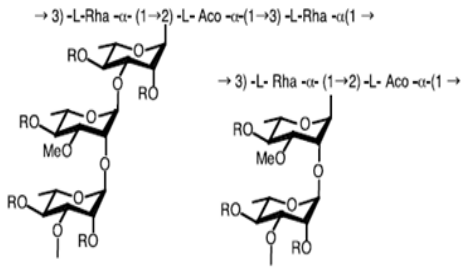

Figure 1. Ca-SP structure [5]

Results and Discussion

Identification the binding site of Ca-SP : gD: Using Autodock 4.2 program, 100 structures of Ca-SP were generated (Fig 2), Ca-SP model 41 showed a minimal binding energy of -8.85 kcal/mol. Table 1 shows about amino acids in the gD that can interact with Ca-SP model 41 with distance between them. We found that most amino acids that interact with gD were basic amino acid, such as Lys 122 and Arg 130. Final intermolecular energy demonstrated that the model 41 possese the lowest binding energy (data not shown). In addition, the Ca-SP model 41 showed the strongest interaction with Arg 130 binding site on gD. The result corresponds to a binding site reported in previous report [3] that of two binding site on gD for the modified heparan sulfate gD receptor were Arg 130 and Lys 190, suggesting that Arg 130 may be binding site on gD of HSV-1 of Ca-SP.

Table 1: Interaction between amino acid of the gD with Ca-SP model 41

Amino acid	Distance (Å)
Lys122	1.919, 2.422, 2.312
Arg130	2.105, 2.189
Asn148	2.391
Leu28	3.332

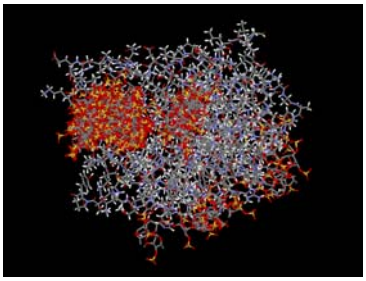

Figure 2. Ca-SP 100 structures bound to gD of HSV-1

Structure optimization of Ca-SP using GA: SMILES string representing Ca-SP (Fig.3) was tested by an online tool, "Online SMILES Translator and Structure File Generator". Result of genes on chromosome using GA contained SMILES strings of random sulfate group (F1~F5, in Fig 3). Therefore, there are 5 genes (sulfate groups) on each chromosome (Ca-SP) structure. New populations (100 chromosomes/ generation) generated by selection and crossing over by GA (20 generations) were converted to 3D-structure and then evaluated their fitness by Autodock Vina. Table 2 shows some good affinity of Ca-SP with sulfate patterns. After structural optimization, stronger binding affinity of new sulfate pattern Ca-SP bound to gD of HSV-1 were obtained (Table 3). The best binding energy was -7.4 kcal/mol, according to mode 1 in Table 3, compared to -6.6 kcal/mol (mode 1 in Table 2).

COC1C(O(**F1**))C(C)OC(OC2C(O(**F2**))C(C)OC(O)C2O(**F3**))C1OC3OC(C)C(O(**F4**))C(O)C3O(**F5**)

Figure 3. SMILES string representing Ca-SP structure

Table 2: List of binding energy (affinity) of generated sulfate pattern Ca-SP bound to gD, before structural optimization.

mode	affinity (kcal/mol)	dist from best mode rmsd l.b.	rmsd u.b.
1	-6.6	0.000	0.000
2	-6.2	21.181	24.811
3	-6.2	2.234	4.561
4	-6.0	22.347	25.523
5	-6.0	21.284	25.336
6	-5.8	1.881	5.402
7	-5.8	20.885	24.743
8	-5.8	26.889	29.934
9	-5.7	13.682	16.621

Table 3: List of binding energy (affinity) of new generated sulfate pattern Ca-SP bound to gD, after structural optimization.

mode	affinity (kcal/mol)	dist from best mode rmsd l.b.	rmsd u.b.
1	-7.4	0.000	0.000
2	-7.3	1.820	2.560
3	-7.3	2.061	2.621
4	-7.2	2.362	7.510
5	-7.0	21.597	26.364
6	-6.9	22.165	26.427
7	-6.8	2.100	7.305
8	-6.6	23.110	28.108
9	-6.6	24.073	28.860

Conclusions

New generation of Ca-SP using Autodock 4.2, model 41 showed binding site on gD located in basic amino acid, specifically Arg 130. Structural optimization using GA and Autodock Vina, new sulfate pattern of Ca-SP

were generated having a stronger binding affinity to gD of HSV-1 than non-optimized Ca-SP. The result suggested a possibility of HSV-1 inhibition by blocking the viral entry by sulfate polysaccharides of which a specific sulfate pattern.

Acknowledgements

We thank Bioinformatics and Systems Biology program, KMUTT and BIOTEC, NSTDA for facilities and scholarship support. S.H. and P.S. are grateful to the Thailand Research Fund (RTA5080005, and MRG5080267). Center of Nanotechnology at Kasetsart University, Laboratory for Computational and Applied Chemistry (LCAC), and National Center of Excellence for Petroleum, Petrochemicals, and Advanced Materials (NCE-PPAM) are also gratefully acknowledged for research facilities and computing resources.

References

[1] A. Carfi, S.H. Willis, J.C. Whitbeck, C. Krummenacher, G.H. Cohen, R.J. Eisenberg, and D.C. Wiley, Mol. Cell, **8** (2001), pp. 169-179.
[2] T. Ghosh, K. Chattopadhyay, M. Marschall, P. Karmakar, P. Mandal and B. Ray, Glycobiology**, 19** (2009), pp. 2–15.
[3] K. Hayashi, T. Hayashi, and N. Morita, Phytotherapy. Res., **7** (1993), pp. 76-80.
[4] J.B. Lee, T. Hayashi, K. Hayashi, and U. Sankawa, J. Nat. Prod., **63** (2000), pp. 136–138.
[5] J.B. Lee, X. Hou, K. Hayashi, and T. Hayashi, Carbohydr. Polym, **69** (2007), pp. 651–658.
[6] M.J. Levin and J.J. Leary, Clin. Infect. Dis., **39** (2004), pp. 248-257.
[7] O. Trott., Glycobiology, **19** (2009), pp. 2-15.
[8] Y. Xiang and Y. Pei, Virol. Sin., **23** (2008), pp. 305-314.

Investigation of the His120Asn mutant of the oxygenase component of *p*-hydroxyphenylacetate hydroxylase

C. Tongsook[1*], K.Thotsaporn[1], N. Ruangchan[1], J. Sucharitakul[2], and P. Chaiyen[1]

[1] Department of Biochemistry and Center of Excellence in Protein Structure and Function, Faculty of Science, Mahidol University, Rama VI Rd, Ratchathevi , Bangkok 10400, Thailand
[2] Department of Biochemistry, Faculty of Dentistry, Chulalongkorn University, Henri-Dunant Rd, Patumwan, Bangkok, 10300,

[*] E-mail: sc_chanakan@yahoo.com

Abstract: *p*-hydroxyphenylacetate hydroxylase from *Acinetobacter baumannii* is a flavoprotein monooxygenase that catalyzes hydroxylation of *p*-hydroxyphenylacetate (HPA) to form 3,4-dihydroxyphenylacetate (DHPA). This enzyme is a two-protein enzyme system containing a smaller reductase component (C_1) and a larger oxygenase component (C_2). Based on crystal structures of the oxygenase component (C_2), His120 was speculated to be a residue that may be important for binding of the substrate, HPA, since His120 can interact with the hydroxyl group of HPA via H-bonding. The interaction of His-120 and HPA may facilitate the binding of HPA in the deprotonated form. In this study, His120 was mutated into Asn (H120N) in order to investigate the functional role of this residue. Results indicated that formation of a C(4a)-hydroperoxy flavin intermediate occurred with a rate constant of 6.2×10^5 M^{-1} s^{-1} in the absence of HPA and 6.7×10^5 M^{-1} s^{-1} in the presence of HPA. Both rate constants are about half of the value of C_2 wild-type enzyme in the absence of HPA (1.1×10^6 M^{-1} s^{-1}). These results also indicated that the rate constant of the C(4a)-hydroperoxy flavin formation of the mutant was unaffected by the presence of HPA, implying that HPA may not bind to H120N mutant. Results from this study indicate that His120 is important for the HPA binding, possibly via a H-bond interaction.

Introduction

Flavoprotein monooxygenases contain a non-covalently bound flavin as a cofactor, mainly in the form of flavin adenine dinucleotide (FAD) or flavin mononucleotide (FMN). They catalyze a wide variety of reactions including regio-selective hydroxylations, biodegradation of aromatic compounds, and antibiotic systheses [1]. Two types of flavoprotein monooxygenases were identified: single-component and two-component flavoprotein monooxygenases. The single-component flavoprotein monooxygenases have been well studied for 40 years; in the past decade, many two-component monooxygenases have been identified and shown to be involved in a wide variety of biological reactions [2, 3]. The two-component monooxygenase enzymes require two protein components for their function, a reductase and a oxygenase component, where the reductase provides reduced flavin for the monooxygenase component to be used in hydroxylation of a substrate. Examples of two-component flavoprotein monooxygenases include *p*-hydroxyphenylacetate hydroxylase (HPAH) [4-9], phenol hydroxylase [10], chlorophenol-4-monooxygenase [11], EDTA oxygenase [12], alkane sulfonate monooxygenase [13], nitrilotriacetate monooxygenase [14], and oxygenases involved in biosynthesis of actinorhodin [15], pristinamycin IIA [16], valinomycin [17] , and rebeccamycin [18].

Our study here focuses on the enzyme *p*-hydroxyphenylacetate hydroxylase (HPAH) from *Acinetobacter baumannii* [4, 19] comprising of a small reductase component (C_1) and a larger oxygenase component (C_2). C_1 is a flavoenzyme having FMN bound tightly (K_d ~ 0.006 μM). HPA, a substrate of C_2 component, acts as an effector on C_1 by binding to it and stimulate reduction of FMN by NADH to generate reduced FMN ($FMNH^-$) [20]. The $FMNH^-$ in C_1 is transferred to C_2 via free diffusion with the release of reduced FMN as the rate-limiting step [21]. C_2, a monooxygenase of *p*-hydroxyphenylacetate hydroxylase, catalyzes hydroxylation of HPA by allowing the bound $FMNH^-$ to react with molecular oxygen to form C4a-hydroperoxy-FMN that hydroxylates HPA to form 3,4-dihydroxyphenylacetate (DHPA) and H_2O [22].

Previous investigation on the reaction of C_2 has determined rate constants for each step of catalysis [22]. Reaction of the C_2:$FMNH^-$ complex with oxygen forms C(4a)-hydroperoxy-FMN with a bimolecular rate constant of 1.1×10^6 $M^{-1}s^{-1}$. However, in the presence of HPA, the rate constant for formation of the C(4a)-hydroperoxy-FMN was decreased to 4.8×10^4 $M^{-1}s^{-1}$. This result can be explained by the structural data showing that binding of HPA may obstruct a pathway for oxygen diffusion into the active site [23, 24]. Kinetic mechanism of C_2 is a preferential random-order type, where HPA or oxygen can initially bind to the C_2:$FMNH^-$ complex but the preferential pathway is oxygen reacting with C_2:$FMNH^-$ to form C(4a)-hydroperoxy-FMN prior to the binding of HPA [Scheme 1]. Hydroxylation of HPA to form DHPA occurs with a rate constant ~ 17-22 s^{-1}, transferring a hydroxyl group from the C(4a)-hydroperoxy intermediate to form DHPA and C(4a)-hydroxy. The last step of the reaction of C_2 is elimination of water from C(4a)-hydroxy-FMN to yield oxidized FMN that dissociates after completion of the catalytic cycle as in scheme 1. Crystal structures of C_2 in apo form and in complex with $FMNH^-$ and $FMNH^-$ plus HPA have been reported [23]. Molecular

dynamics simulations have shown that oxygen diffuses from the enzyme

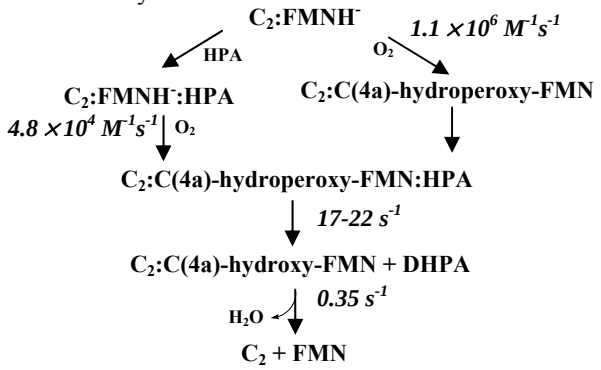

Scheme 1. Kinetic mechanism of the oxygenase component (C_2) of HPAH from *A. baumanii [22]*

surface to the active site by multiple diffusion pathways [24]. HPA enters to the active site via the site of Phe266. This residue is also important for substrate binding; it rotates to create the pocket for the HPA binding [23].

In this study, the role of His120 speculated to be important for binding of HPA was investigated by site-directed mutagenesis into Asn, H120N. His120 may help in binding with HPA through H-bonding which in turn facilitates the electrophilic aromatic substitution reaction of HPA and C(4a)-hydroperoxy-FMN.

Materials and Methods

Reagents: NADH, glucose, glucose oxidase were from Sigma-Aldrich. FMN was prepared by conversion of FAD to FMN with snake venom from *Crotalus adamanteus* [20, 25]. Concentrations of the following compounds were determined using the known absorption coefficients at pH 7.0: $\varepsilon_{340} = 6.22 \times 10^3$ $M^{-1}cm^{-1}$ for NADH; $\varepsilon_{446} = 1.22 \times 10^4$ $M^{-1}cm^{-1}$ for FMN; $\varepsilon_{277} = 1.5 \times 10^3$ $M^{-1}cm^{-1}$ for HPA [4], and $\varepsilon_{458} = 1.28 \times 10^4$ $M^{-1}cm^{-1}$ for C_1 enzyme [20]. The concentration of H120N was estimated from the absorption coefficient (based on amino acid sequence) of $\varepsilon_{280} = 5.67 \times 10^4$ $M^{-1}cm^{-1}$.

Site-Directed Mutagenesis: The plasmid pET-H120N was constructed by Mr. Kittisak Thotsaporn. Site-directed mutagenesis at position His120 was performed by using QuickChange® II Site-Directed Mutagenesis Kit. The mutagenic forward primers 5'-GGGCATTTAGTCTTCTTTGTACTGTGAGCCATCA AATTGCG-3' and the mutagenic reverse primer 5'-CGCAATTTGATGGCTCACAGTACAAAGAAGACT AAATGCCC-3' were from Sigma-Prolico (Singapore). The plasmid pET-11a was used as a template for mutagenic PCR (GeneAmp PCR system, Applied Biosystem, model 2004 or MyCycler™, Thermal Cycler, Biorad). The plasmid was analyzed DNA sequencing by using T7 forward and reverse primers performed by MACROGEN (Korea).

Expression and Purification of H120N: The plasmid pET-11a containing H120N gene was transformed into *E.coli* BL21(DE3). *E.coli* cells were cultured in Luria-Bertani broth medium containing 50 μg/mL of ampicillin and induced by addition of 1 mM IPTG at the culture with OD_{600}~1.0 at 25 °C. Cells were harvested when the OD_{600} reached ~4.0. Purification process for the recombinant H120N was according to the methods previously described for the wild-type enzyme [4] with slight modification, using Sephacryl S-200 gel filtration chromatography instead of G-150 gel permeation chromatography.

Enzyme Activity: H120N mutant activity during the purification process was monitored using the protocol described in [4] by coupling with the reaction of 3,4-dihydroxyphenylacetate oxygenase (DHPAO). DHPAO catalyzes conversion of the product, DHPA, to form 5-carboxymethyl-2-hydroxymuconate semialdehyde (CHS) which is a yellow compound with ε_{max} at 380 nm ($\varepsilon_{380} = 3.8 \times 10^4$ $M^{-1}cm^{-1}$ at pH 8.0).

Rapid-Reaction Experiments: Reactions of H120N with or without HPA were investigated at pH 7.0, 4 °C. Rapid kinetics measurements were performed with a Hi-Tech Scientific Model SF-61DX2 stopped-flow spectrophotometer in single mixing-mode with 1 cm path-length. The stopped-flow apparatus was made anaerobic by flushing the flow system with an anaerobic buffer and incubating overnight with a solution containing 400 μM of glucose, 1mg/mL of glucose oxidase (15.5 unit/mL), and 4.8 μg/mL of catalase in 50 mM sodium phosphate pH 7.0. This solution was made anaerobic by equilibrating in an oxygen-free nitrogen glovebox (Belle Technology). Before the experiments were carried out, the flow unit was rinsed with anaerobic buffer bubbled with oxygen-free nitrogen that had been passed through an Oxyclear oxygen removal column (Labclear). This method has been used routinely in our laboratory and shown to efficiently maintain good anaerobic condition. In the reaction of H120N at pH 7.0, solutions of enzyme or enzyme substrate complex with oxidized FMN in 50 mM sodium phosphate buffer, pH 7.0 were made anaerobic before reduction by equilibrating them in the anaerobic glovebox. The anaerobic solution was stoichiometrically reduced with a solution of dithionite (~5 mg/ 1mL in 100 mM potassium phosphate pH 7.0). A diode array spectrophotometer in the glove box was used to monitor the reduction of FMN. Then, the reduced enzyme solution was transferred into anaerobic glass tonometer. Solutions of various concentrations of oxygen were prepared by equilibrating buffers with air and certified oxygen in nitrogen gas mixtures. The stopped-flow reactions were monitored absorbance changes at the wavelengths 390 and 446 nm to detect kinetics of formation and decay of intermediates and the final species (oxidized FMN). Analysis of kinetic data were conducted by fitting the data to exponential equations to calculate apparent rate constants (k_{obs}) using Marquardt

algorithm in Program A, developed by Rong Chang, Jung-yen Chiu, Joel Dinverno, and D.P. Ballou at the University of Michigan (Ann Arbor, MI). Determination of rate constants were obtained from plots of k_{obs} versus substrate concentrations using Marquardt-Levenberg non-linear fitting algorithms that are included in the KaleidaGraph software (Synergy Software).

Results and Discussion

Site-directed mutagenesis: The recombinant plasmid pET-11a containing H120N gene was constructed by site-directed mutagenesis as described in Materials and Methods. The correct mutation at the position 120 were confirmed by DNA sequence analysis (Macrogen). The PCR products and the plasmid containing the H120 mutant gene was run on 0.8% agarose gel and the result showed DNA of ~ 6.97 kb compared to the DNA molecular size markers (Figure 1).

Expression and purification of the recombinant H120N: The purification procedure used was quite effective and efficient since it yielded the purified H120N of 377 mg per 4 L of cell culture. Purified H120N mutant showed a single band on SDS-PAGE analysis and had the same subunit molecular mass as the wild-type enzyme, 47 kDa. Results of the purification were summerized in Table 1

Reaction of H120N:FMNH$^-$ complex with oxygen: Kinetics of the reaction of H120N:FMNH$^-$ with oxygen was investigated in a similar fashion as the reaction of the C_2 (WT) [23]. H120N exhibited biphasic kinetics (Figure 2) as in the wild-type reaction. The first phase was formation of C(4a)- hydroperoxy as shown by an increase of absorbance at 390 nm. Observed rate constants of this phase were oxygen-dependent and consistent with a bi-molecular rate constant of 6.2×10^5 $M^{-1}s^{-1}$ (k_1, Inset in Figure 2).

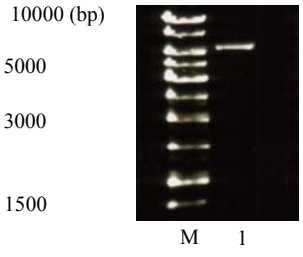

Figure 1. Agarose gel electrophoresis of PCR products. Lane M: 1 kb DNA ladders, Lane 1: PCR product of the plasmid harboring the gene of H120N

Table 1 Purification table of H120N

Purification step	Total protein (mg)	Yield (%)
Crude extract	1931	100
20-40% $(NH_4)_2SO_4$ precipitation	1193	62
DEAE-Sepharose	678	35
Sephacryl S-200	377	20

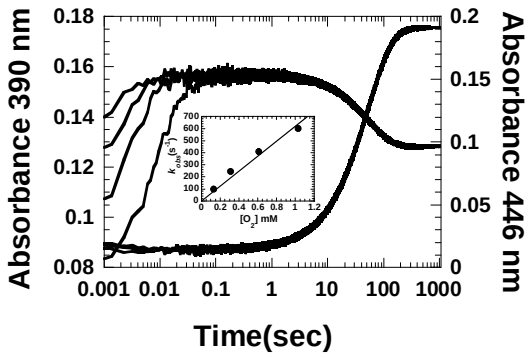

Figure 2. Kinetics of the reaction of H120N:FMNH$^-$ complex with oxygen. A solution of H120N (40 μM) plus FMNH$^-$ (16 μM) in 50 mM sodium phosphate buffer, pH 7.0 was mixed with the same buffer containing various concentrations of oxygen: 0.13 mM, 0.31 mM, 0.61 mM, and 1.03 mM (from the lower to the upper traces at 390 nm). The inset shows a plot of k_{obs} of C(4a)-hydroperoxy-FMN formation versus oxygen concentrations. The second-order rate constant was derived from the slope of the plot to be 6.2×10^5 $M^{-1}s^{-1}$.

The value is half of that of the WT. A small decrease of absorbance at 390 nm and a large increase of absorbance at 446 nm during the second phase indicated that the C(4a)-hydroperoxy-FMN decays to form FMN_{ox} and generate H_2O_2 at a rate constant of 0.019 s^{-1}(k_2). These results can be summarized as in Scheme 2.

Reaction of the H120N:FMNH$^-$:HPA complex with oxygen: Reaction of the H120N:FMNH$^-$:HPA complex with oxygen at pH 7.0, 4°C was investigated by mixing a solution of 40 μM H120N, 16 μM FMNH$^-$ and 2 mM HPA in 50 mM sodium phosphate buffer pH 7.0 with the same buffer containing various concentrations of oxygen (0.13 mM, 0.31 mM, 0.61 mM, and 1.03mM) and 2 mM HPA. Kinetic traces in Figure 3 at the wavelengths 390 and 446 nm showed only two phases. The first phase was an increase of

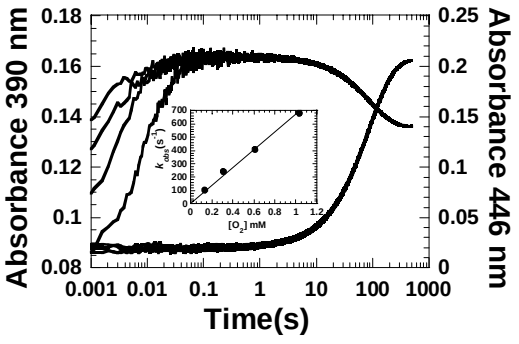

Figure 3. Kinetics of the reaction of H120N:FMNH$^-$:HPA complex with oxygen. H120N (40 μM):FMNH$^-$ (16 μM):HPA (2 mM) was mixed with buffers containing 2 mM HPA and various concentrations of oxygen: 0.13 mM, 0.31 mM, 0.61 mM and 1.03 mM (From the lower to the upper traces). The inset shows a plot of k_{obs} of C(4a)-hydroperoxy-FMN

formation against oxygen concentrations. The rate constant was calculated from a slope of the plot to be 6.7×10^5 $M^{-1}s^{-1}$.

Table 2. Summary of rate constants of the reactions of H120N and WT

Samples	Rate of C(4a)-hydroperoxy-FMN formation (k_1) ($M^{-1}s^{-1}$)	Rate of flavin re-oxidation (k_2) (s^{-1})
C_2-WT (no HPA)	1.1×10^6 $M^{-1}s^{-1*}$	0.003*
C_2-WT (+ HPA)	4.8×10^4 $M^{-1}s^{-1*}$	0.35*
H120N (no HPA)	6.2×10^5 $M^{-1}s^{-1}$	0.019
H120N (+HPA)	6.7×10^5 $M^{-1}s^{-1}$	0.012

* Data from [22] and Nantidaporn Ruangchan's data, 2008

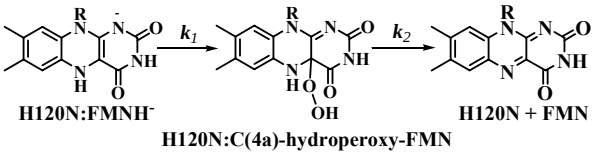

Scheme 2. Kinetic mechanism of H120N mutant

absorbance at 390 nm. This phase, represented the reaction of H120N:$FMNH^-$ with oxygen to form a C(4a)-hydroperoxy-FMN intermediate. k_{obs} of formation of C(4a)-hydroperoxy-FMN was linearly dependent on oxygen concentration. A bimolecular rate constant of the plot is 6.7×10^5 $M^{-1}s^{-1}$ (k_1) as shown in inset in Figure 3. These value is similar as that of the reduced H120N reacting with oxygen in absence of HPA, indicating that HPA included may not bind to the enzyme. The second phase was a decrease of absorbance at 390 nm and a large increase of absorbance at 446 nm. This phase represented the decay of C(4a)-hydroperoxy-FMN to yield oxidized FMN and H_2O_2 at a rate constant of 0.012 s^{-1} (k_2). These results can be summarized as in Scheme 2. Rate constants of the second phase was also similar to those of the reactions without HPA, again supporting that HPA might not bind to H120N. Therefore, mutation of H120N possibly disrupts the binding of HPA in C_2.

Results of the WT are described below for comparison In WT, the the reaction of C_2:$FMNH^-$:HPA with oxygen at pH 7.0 resulted in 4 phases. The first phase is a small fraction of the enzyme witout HPA bound reacting with oxygen to form C(4a)-hydroperoxy-FMN with a rate constant of 1.1×10^6 $M^{-1}s^{-1}$. The second phase is formation of C(4a)-hydroperoxy-FMN:HPA with a rate constant of 4.8×10^4 $M^{-1}s^{-1}$. Therefore, with HPA pre-bound, the reaction of C_2 with oxygen was significatly slower than in absence of HPA. Hydroxylation of HPA occurs in the third step and the fourth phase is dehydration of C(4a)-hydroxy-FMN with a rate constant of 0.35 s^{-1}. Rate constants of the reactions of H120N and WT were summarized in Table 2.

Conclusion

Investigation of the reaction of reduced H120N with oxygen with and without HPA using stopped-flow spectrophotometry shows that HPA may not bind to H120N mutant since the same rate constants for formation and decay of C(4a)-hydroperoxy-FMN intermediate were obtained in absence and presence of HPA (Table 2). In H120N, H-bonding interaction with HPA may be disrupted. These results suggest that H120 is important for the substrate binding.

References

[1] W.J.H. van Berkel, N.M. Kamerbeek and M.W. Fraaije, *J. Biotechnol*. **124** (2006), pp. 670-689

[2] B.A. Palfey and V. Massey, Flavin-dependent enzyme, in *Comprehensive Biological Catalysis* (Michael, S., Ed.). **Vol.3** (1998), pp. 83-153, Academic Press, San Diego, CA

[3] D.P. Ballou, B. Entsch and L.J. Cole, *Biochem. Biophys. Res. Commun.* **338** (2005), pp. 590-598

[4] P. Chaiyen, C. Suadee and P. Wilairat, *Eur. J. Biochem.* **268** (2001), pp. 5550-5561

[5] B. Galan, E. Diaz, M.A. Prieto and J.L. Garcia, *J. Bacteriol.* **182** (2000), pp. 627-636

[6] U. Arunachalam, V. Massey and C.S. Vaidyanathan, *J. Biol. Chem.* **267** (1992), pp. 25848-25855

[7] J.F. Hawumba, V.S. Brozel and J. Theron, *Curr. Microbiol.* **55** (2007), pp. 480-484

[8] A Gibello, M. Suárez, J.L. Allende and M. Martin, *Arch. Microbiol.***167** (1997), 160-166

[9] S. Chakraborty, M.Ortiz-Maldonado, B. Entsch and D.P. Ballou, *Biochemistry.* **49** (2010), 372-385

[10] U. Kirchner, A.H. Muller and W.J.H. van Berkel, *J Biol. Chem.* **278** (2003), pp. 47545-47553

[11] M.R. Gisi and L. Xun, *J. Bacteriol*.**185** (2003), pp. 2786-2792

[12] Y. Xu, M.W. Mortimer, T.S. Fisher, M.L. Kahn, F.J. Brockman and L. Xun, *J. Bacteriol.* **179** (1997), pp.1112-1116

[13] E. Eichhorn, J.R. van der Ploeg and T. Leisinger, *J. Biol. Chem.* **274** (1999), pp. 26639-26646

[14] T. Uetz, R. Schneider, M. Snozzi and T. Egli, *J. Bacteriol.* **174** (1992), pp. 1179-1188

[15] J. Valton, L. Filisetti, M. Fontecave, V. Nivière, *J. Biol. Chem.* **279** (2004), pp. 44362-44369

[16] D. Thibaut, N. Rater, D. Bisch, D. Faucher, L. Debussche and F. Blanche, *J Bacteriol.* **177** (1995), pp. 5199-5205

[17] R.J. Parry and W. Li, *J. Biol. Chem.* **272** (1997), pp. 23303-23311

[18] E. Yeh, L.J. Cole, E.W. Barr, J.M. Bollinger, D.P. Ballou and C.T. Walsh, *Biochemistry*. **45** (2006), pp. 7904-7912

[19] K. Thotsaporn, J. Sucharitakul, J. Wongratana, C. Suadee and P. Chaiyen, *Biochim. Biophys. Acta.* **1680** (2005), pp. 60-66

[20] J. Sucharitakul, P. Chaiyen, B. Entsch and D.P. Ballou, *Biochemistry.* **44** (2005), pp.10434-10442

[21] J. Sucharitakul, T.Phongsak, B. Entsch, J. Svasti, P. Chaiyen and D.P. Ballou, *Biochemistry.* **46** (2007), pp.8611-8623

[22] J. Sucharitakul, P. Chaiyen, B. Entsch and D.P. Ballou,*J. Biol. Chem.* **281** (2006), pp. 17044-17053

[23] A. Alfieri, F. Fersini, N. Ruangchan, M. Prongjit, P. Chaiyen, A. Mattevi, *Proc. Natl Acad Sci USA.* **104** (2007), pp. 1177-1182

[24] R. Baron, C. Riley, P. Chenprakhon, K. Thotsaporn, R.T. Winter, A. Alfieri, F. Forneris, W.J.H. van Berkel, P. Chaiyen, M.W. Fraaije, A. Mattevi, *Proc. Natl. Acad. Sci. USA.* **106** (2009), pp. 10603-10608

[25] D.S. Duch and M.Sr. Laskowski, *Anal. Biochem*. **44** (1971), pp. 42-48

Chemical Education

Synthesis of silver nanoparticles/carbon composite by a simple carbonization using a Bunsen burner

S. Chairam[1*] and E. Somsook[2]

[1] Department of Chemistry and Center for Innovation in Chemistry, Faculty of Science, Ubon Ratchathani University, Warinchamrap, Ubon Ratchathani, Thailand 34190
[2] NANOCAST Laboratory, Department of Chemistry and Center of excellent for Innovation in Chemistry, Faculty of Science, Mahidol University, Rama VI Rd. Rachathewi, Bangkok, Thailand 10400

[*] Corresponding Author E-Mail Address: chairam019@yahoo.com

Abstract: Starch vermicelli was used to incorporate the metal salts inside the helical structure of starch by using the microwave heating method. In this procedure, the experiment did not require any external reducing agent during the synthesis processes, because starch provided the active functionalized sites for reducing Ag(I) ions to Ag(0) species. The resulting product was characterized by using UV-Vis spectrophotometer, scanning electron microscope (SEM) attached with energy-dispersive X-ray spectroscopy (EDS) and X-ray powder diffractometer (XRD). After microwave heating, the resulting starch vermicelli obviously changed from colourless to yellow, indicating the formation of starch vermicelli capping AgNPs. The strong absorption peak of the colloidal solution monitored by using UV-Vis spectrophotometer was observed with λmax at 421 nm. The SEM micrograph showed that AgNPs were stabilized by starch vermicelli. Then, the synthesis of the nano-Ag/C composite was successfully prepared by a simple carbonization of the starch vermicelli-stabilized AgNPs using a commercial Bunsen burner. For further analysis, the SEM micrograph showed clearly that AgNPs were stabilized by carbon black confirmed by EDS spectrum. The XRD diffractogram of the carbonized sample showed clearly the presence of AgNPs. Because of a green approach, the method was convenient and suitable for an experiment in teaching nanotechnology laboratory in the school and undergraduate levels.

Introduction

The nanoscale-sized materials have been attracting considerable interests due to their properties such as size and shape. Nanostructures, such as nanorods, nanowires and nanoparticles, have also been synthesized using different physical and chemical methods by scientific interest including education [1]. Among various noble metal nanoparticles, silver nanoparticles (AgNPs) have been much of considerable interest because of their properties and potential applications. In the field of chemical education, many nanotechnology experiments for teaching in the laboratory have also been published [2-5]. The synthesis of AgNPs can be achieved at the school and undergraduate levels. There have been various methods for the synthesis of AgNPs. In general, most of methods for fabricating AgNPs require the reducing agent for the reduction of Ag(I) to Ag(0) species. However, these experiments spent a large amount of toxic reagents that may cause problems to humans and the environment during sythetic processes.

An increasing number of researchers and colleagues are concerning and developing the green nanotechnology experiments in teaching the chemistry laboratory for young students. [6-8]. From metal ions to metal nanoparticles, it is essential to have a biomacromolecule that itself can provide active sites without using an external reducing agent, and also stabilize nanoparticles. Though it is cheap and widely used, less attention has been paid to the construction of nanoarchitectures in the structure of starch [9].

The synthetic strategies for producing metal/carbon composite have been a hot topic due to its potential importance to science and technology such as electrodes, electronic devices, sensors, fuel cells, etc. However, most of the currently available methods for the synthesis of carbon materials require the use of sophisticated electronic instruments. In addition, these may not be suitable for carrying the experiments by young students in the school and undergraduate levels in a three-hour laboratory period. As known, the Bunsen burner is a common laboratory instrument used for heating, sterilization, and carbonization. In this work, the synthesis of AgNPs/C composite was selected to demonstrate to students by a simple carbonization of the starch vermicelli-stabilized AgNPs within using a commercial Bunsen burner.

Materials and Methods

Instrument and Starting Materials: A Sumsung household microwave oven (model M181GN, output power 100/850 W, and operating frequency 2,450 MHz) was used. The experimental setup for a simple carbonization is composed of a commercial Bunsen burner, clamp and stand, and alumina crucible. Silver nitrate ($AgNO_3$, ≥99%) was purchased from Sigma-Aldrich, and used without further purification. Starch vermicelli (100% mung bean; Kaset Brand) was purchased form a local supermarket in Thailand. The de-ionized (DI) water (R ≥18.2 MΩ-cm) was purified with a Nanopore ultrapure water system.

Synthesis of Starch Vermicelli-Stabilized AgNPs: In a typical procedure, a 0.1 g of starch vermicelli was added into a 50-mL Erlenmeyer Pyrex flask containing 30 mL of DI water. The reaction flask was placed in microwave oven, and also soaked by using a

microwave power of 100 W for a minute [9]. Starch vermicelli was observed as transparent, and no color change of starch vermicelli was observed during this procedure. Then, a 3 mL of 0.01 M $AgNO_3$ solution was added to start the reaction. After the microwave heating at a higher power setting for few minutes, the colour of starch vermicelli was observed to change obviously from the colourless to yellow, indicating the formation of the starch vermicelli capping AgNPs.

Synthesis of Silver Nanoparticles/Carbon Composite: The starch vermicelli-stabilized AgNPs was placed in alumina crucible and then carbonized using a commercial Bunsen burner in air. Finally, the black precipitate powder was collected for further characterization.

General Characterization: The visible spectrum of the colloidal silver solution was recorded on UV-Vis scanning spectrophotometer (HP-8453 Hewlett-Packard). The SEM micrographs were recorded using a scanning electron microscope (JEOL JSM-5910, 15 kV). The XRD diffractogram was recorded on a X-ray powder diffractometer (D8 Advance Bruker, 40 kV, 40 mA) with CuKα wavelength as the source.

Results and Discussion

Microwave oven is a noninvasive and clean processing tool that has been widely used to activate or accelerate chemical reaction. Microwave heating is a means of rapidly introducing energy into a chemical system in a manner different from the traditionally thermal heating [9,10]. Because of the selective heating of microwave, it was possible to perform reactions quickly for the synthesis of nanoparticles, and to reduce the time constraint of three-hour laboratory session.

There were several advantages to use of transparent starch vermicelli, including a clear, cheap and natural material. The AgNPs were successfully prepared using starch vermicelli which played the significant role as a stabilizing and reducing agent. While Ag(I) ions were stabilized by hydroxylated functional groups, the aldehyde terminal of starch was used to reduce Ag(I) ions to AgNPs. After microwave heating, the resulting starch vermicelli was observed in yellow color due to the formation of nano-silver(0) species as shown in Figure 1. The starch temple-assisted synthesis of AgNPs was described in our recent report [9].

The absorption spectrum of the clear yellow colloidal solution of silver nanoparticles was monitored using UV-Vis spectrophotometer due to a surface plasmon absorbance. The spectrum of the clear yellow colloidal solution of silver nanoparticles is shown in Figure 2. The strong absorption peak was observed with λ_{max} at 421 nm which is similar to the literature [9].

Figure 1. Vial containing starch vermicelli-stabilized AgNPs

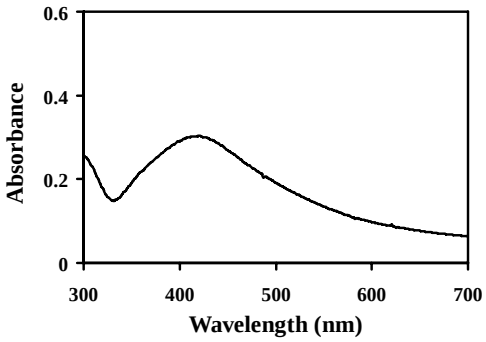

Figure 2. UV-Vis absorption spectrum of the clear colloidal solution of AgNPs

In order to investigate the surface of starch vermicelli, the resulting material was characterized by the SEM observation. The SEM micrograph of a region of AgNPs stabilized by starch vermicelli was shown in Figure 3a. The starch vermicelli-stabilized AgNPs was carbonized using a commercial Bunsen burner, leading to the formation of AgNPs/C composite as shown in Figure 3b, which was confirmed by EDS spectrum. It could be described that the organic structure of starch vermicelli was carbonized in air into carbon black, which could form the AgNPs/carbon composite. The results obtained here were found to be similar to our recent report in the literature [11].

The black precipitate powder was ground and then characterized by the powder XRD diffractometer. As shown in Figure 4, three diffraction peaks were observed with the 2θ of 38.4, 44.5, and 64.7, which can be indexed to (111), (200), and (220) planes of face-centered cubic silver (JCPDS file no.04-0783). These positions of the diffraction peaks for silver nanoparticles/carbon composite showed a match with the reported results in the literature [9].

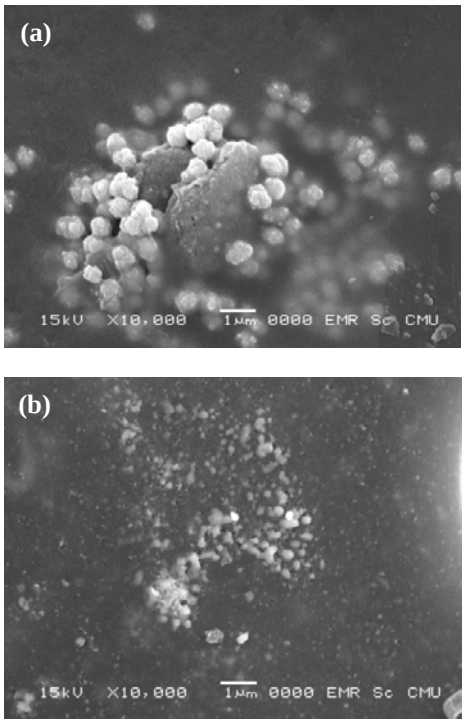

Figure 3. SEM micrographs of (a) before (b) after carbonization of starch vermicelli-stabilized AgNPs.

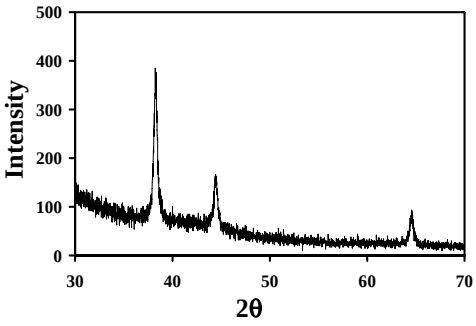

Figure 4. The XRD diffractogram of AgNPs after carbonization

Hazards: $AgNO_3$ is corrosive causing burn in contact with the skin and eyes. Special care should be taken with heavy metal solutions used in this experiment. In a typical synthesis of metal nanoparticles, safety goggles and gloves are always worn for all times when working chemistry experiment.

Conclusions

In summary, after microwave heating the colour of starch vermicelli was observed to change obviously from the colourless to yellow. The yellow colloidal solution of silver exhibited the UV-Vis spectrum with a peak at 421 nm. The SEM micrograph showed that AgNPs were stabilized by starch vermicelli. After carbonization, the SEM micrograph indicated that AgNPs was supported on carbon black. Also, the XRD diffractogram of carbonized sample showed the presence of AgNPs. The synthesis of silver nanoparticles/carbon composite can be prepared by a simple carbonization of starch vermicelli-stabilized AgNPs in which starch vermicelli was used as a carbon source confirmed by EDS spectrum. So, it was convenient and suitable for an experiment in teaching nanotechnology laboratory in the school and undergraduate levels, this experiment provided a green approach, and reduced the synthesis time for synthesizing AgNPs/C composite.

Acknowledgements

This research was mainly supported from Ubon Ratchathani University through the division of research promotion Ubon Ratchathani University, and partially supported by the Center for Innovation in Chemistry: Postgraduate Education and Research Program in Chemistry (PERCH-CIC).

References

[1] A.G. King, *J. Chem. Educ.* **82** (2005), pp. 666-669.
[2] A.D. McFarland, C.L. Haynes, C.A. Mirkin, R.P. Van Duyne and H.A. Gowin, *J. Chem. Educ.* **81** (2004), 544A.
[3] C.D. Keating, M.D. Musick, M.H. Keefe and M.J. Natan, *J. Chem. Educ.* **76** (1999), pp. 949-955.
[4] K.E. Dungey, D.P. Muller and T. Gunter, *J. Chem. Educ.* **82** (2005), pp. 769-770.
[5] S.D. Solomon, M. Bahadory, A.V. Jeyarajasingam, S.A. Rutkowsky and C. Boritz, *J. Chem. Educ.* **84** (2007), pp. 322-325.
[6] D.L. Hjeresen, D.L. Schutt and J.M. Boese, *J. Chem. Educ.* **77** (2000), pp. 1543-1547.
[7] A. Richardson, A. Janiec, B.C. Chan and R.D. Crouch, *Chem. Educator* **11** (2006), 331-333.
[8] P. Anastas, F. Wood-Black, T. Masciangioli, E. McGowan and L. Ruth, *Exploring opportunities in green chemistry and engineering education*, National Academies Press, Washington, DC, USA (2007).
[9] S. Chairam, C. Poolperm and E. Somsook, *Carbohydr. Polym.* **75** (2009), pp. 694-704.
[10] Z. Dong, D. Richardson, C. Pelham, and M.R. Islam, *Chem. Educator* **13** (2008), pp. 240-243.
[11] S. Chairam and E. Somsook, *J. Magn. Magn. Mater.* **320** (2008), pp. 2039-2043.

Inquiry-based experiments to enhance student conceptual understanding of organic acid-base extraction and purification

S. Supasorn*

Department of Chemistry Faculty of Science, Ubon Ratchathani University, Ubon Ratchathani, Thailand

*saksri.supaorn@gmail.com

Abstract: The inclusion of inquiry-based learning approach in the chemistry laboratory has been highly advocated in the last three decades to improve students' chemistry conceptual content knowledge and also process of learning. As a result, two 3-hour inquiry-based experiments concerning acid-base extraction and recrystallization were implemented as a part of the *organic chemistry Laboratory I* course at Ubon Ratchathani University. 64 chemistry students enrolled in the course were engaged in the situation in which they were asked to separate the mixture of benzoic acid, *p*-nitroaniline and naphthalene by acid-base extraction and to purify the extracted compounds by recystallization in an appropriate condition. The concept of basic organic extraction was provided through the interactive caffeine extraction simulated experiment or ICESE. The data collected in this study consisted of conceptual understanding and experiment diagram as well as mental models of acid-base extraction. The paired-sample T-test analysis showed that the students obtained post-experiment score for each of the conceptual test, the experiment diagram, and the mental models of acid-based extraction process statistically higher than the pre-experiment score at $p<0.001$. Although most students had planed their experiments carefully, many students revealed alternative conceptions through their pre-mental models and pre-diagram of acid-based extraction. However, most of them corrected their alternative conception after performing the inquiry-based experiment.

Introduction

Traditional cookbook experiments are often effective in developing student's observational skills and illustrating a key connection between theory and practice in chemistry. However, cookbook experiments are not effective in developing the scientific process called science inquiry or scientific investigation [1]. On the other hand, inquiry-based experiments emphasize the explicit use of the whole process of science inquiry. In this approach, students have to define the problem to be investigated, generate hypotheses, devise a plan and conduct the investigation, and making explanations from experimental evidence [2]. Therefore, inquiry-based experiments provide an opportunity to not only imitate the experiment, but also to practice how scientists really do science, and to deeply understand key concepts in chemistry [1].

Inquiry-based laboratory, or inquiry in terms of *skills* and *abilities* by National Science Education Standards, refers to laboratory that provide students with opportunity for asking scientifically oriented questions, forming hypotheses, designing and conducting scientific investigations, making scientific explanations from experimental evidence, and communicating and defending scientific arguments [3]. This student-centered laboratory is central to science and can promote students' meaningful learning, conceptual understanding, inquiry skills, and understanding the nature of science when properly developed and implemented [4].

The inquiry-based experiments have been proven to be effective approach in learning chemistry laboratory and highly advocated in the last 2-3 decades [5]. The inquiry-based experiments have advantages over traditional experiments since students are challenged to practice using learning resources and working in group to enhance their analytical and critical thinking skills. In addition, they have an opportunity to practice chemistry research and to do science [6].

Many institutions in Thailand including Ubon Ratchathani University have highly advocated implementing inquiry-based experiments in chemistry laboratory. Lab manual and instructor in this learning approach are no longer the main source of knowledge but are the facilitator to motivate and challenge their students to be able to complete the experiment through science inquiry process which is important and essential for doing their further science research [7,8].

It is advisable that implementation of inquiry-based laboratory with inexperience students should begin with familiar techniques such as liquid-liquid extraction, but make it more complicated and challenging [9]. In this study, liquid-liquid extraction was considered because it is a common and relevant technique for chemistry students and they already performed the basic extraction of a single compound from a given solution. In a new task, students were asked to separate a mixture of acid, basic and neutral organic compound from a given solution. This is intellectual challenge since there is no procedure and equipment list given, while they have to integrate what they have learned with information from literature search of how to separate each compound from the mixture. This learning process can support students' development of both understanding and inquiry process skills.

Research Methodology

Goals and Objectives: The main goal of this study was to develop and implement inquiry-based separation and purification experiment to promote students' scientific process skills. This study was intended not to compare the inquiry-based laboratory over the traditional one, but to investigate how the inquiry laboratory works with students who had limited experience with inquiry approach laboratories. More specifically, the objective of this study was to investigate student conceptual understanding and mental models (presentations of the mind constructed by incorporating relevant conceptual understanding into existing knowledge to explain how a specific process functions or works [11, 12]) of separation and purification of a mixture of acid, base and neutral organic compounds before and after experiencing with the inquiry-based separation and purification experiments.

Settings and Participants: The participants were 64 second-year chemistry students enrolled in *Organic Chemistry Laboratory II* during 2/2008 semester at a Ubon Ratchathani University. They all have learned and performed basic extraction in *Organic Chemistry Laboratory I* during the 1/2008 semester.

Implementation: This study was a pre-experimental design; therefore, all participants were treated similarly. The inquiry-based acid-base extraction and purification experiment were implemented as 2 lab periods (6 hours). They were asked to participate in the following process:

1) A week prior to the laboratory, the participants were noticed that no lab direction is given for the next 2 experiments. The task is to individually design their own experiments to separate and purify a mixture of benzoic acid, *p*-nitroaniline, and naphthalene. They have to hand in their lab planner three days prior to the lab hour for suggestion from lab instructors. The basic organic extraction concepts and experiments are available through the Interactive Caffeine Extraction Simulated Experiment, *ICESE* [10].

2) Before conducting the experiment, they spent 15 minutes to complete a set of pretest including conceptual test and diagram of experiment process. Example of higher-order cognitive skill questions is illustrated in Figure 1. They were asked to draw their understanding (called mental models) of organic acid-base separation (modified from [11]) as shown below.

> *"Please draw series of pictures to represent your understanding about what happens in a submicroscopic level when you are extracting a mixture of benzoic acid (△), p-nitroaniline (□), and naphthalene (○) dissolved in dichloromethane by HCl followed by NaOH solutions. Changing in molecules can be indicated by color or solid icon. "*

They then took about 150 minutes to separate the mixture of the three compounds regarding their designed experiment. Crude crystals of the three compounds should be obtained in this step.

3) Students took 150 minutes to purify their crude crystals by recrystallization in the appropriate solvent. Then determine the melting point of the fine crystal of the 3 compounds compared to the crude crystals.

4) During the last 30 minutes of the three-hour lab period, they completed the set of post-test (same difficulty and parallel to a set of pretest). They were encouraged to review and correct their mental models.

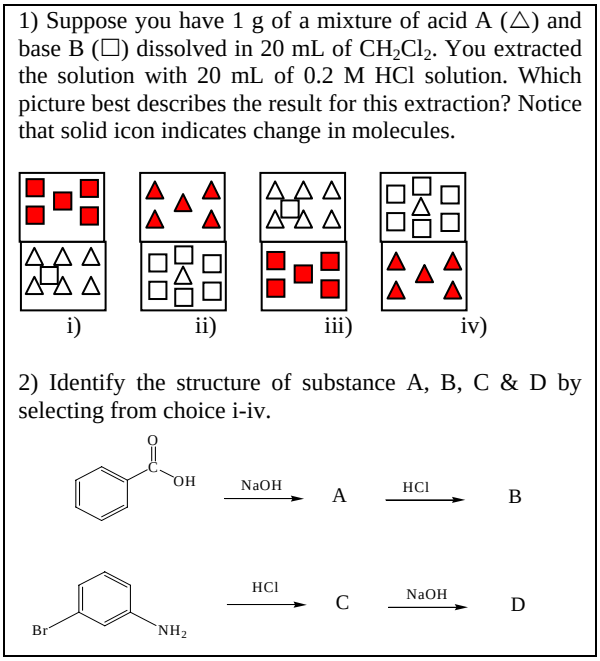

Figure 1. Example of HOCS questions in the conceptual test of experiment

Data Analysis: The collected data during this study including pre- and posttest test scores, pre- and post-experiment diagram, and pre- and post-mental models (coding and then scoring) of organic acid-based separation and purification were analyzed. Since this study was a pre-experimental design (one group pretest-posttest), paired-sample *T*-test analysis was performed to identify mean differences between pre- and post- scores.

Results and Discussion

The study results showed that the averaged post-conceptual test scores ($\bar{X}$ =6.47, *SD*=1.47) of separation and purification of the mixture of acid, base and neutral organic compounds was statistically higher than each of the averaged pre- conceptual test score ($\bar{X}$ =5.03, *SD*=1.65) at *p*-value <0.001 (see Table 1). The post- experimental diagram score ($\bar{X}$ =4.29, *SD*=1.60) was statistically higher than each of the averaged pre- experimental diagram score ($\bar{X}$ =2.59, *SD*=1.61) at *p*-value <0.001.

Table 1. Pre- and post-scores on conceptual test (CT), experimental diagram (ED), and submicroscopic mental models (MM)

Test	Pretest		Posttest		T-Test	
	$\bar{X}$	*SD*	$\bar{X}$	*SD*	*T*	*p*
CT	5.03	1.65	6.47	1.47	5.21	< 0.001
ED	2.59	1.61	4.29	1.60	5.99	< 0.001
MM	4.86	1.50	6.80	1.62	7.03	< 0.001

Maximum score for each of CT, ED & MM was 10, 6 & 10 respectively (n=64).

There were a few questions that students often answered them wrong. One of them was to calculate a partition coefficient of a given extraction system. This may be due to the fact that the partition coefficient was not covered in a lecture part. The other question was to select the appropriate solvent for the extraction when provided solubility of a substance in each solvent and miscibility of a solvent in a mixture solution being extracted. This may occur because they just selected the 2nd solvent from solubility property and omitted the miscibility of the 2nd solvent in the 1st solvent (if the two solvents are miscible, the extraction system will not separate into two layers).

Since the guided inquiry experiments engaged and challenged students in all steps of the experimental process (searching literature, planning and conducting their own experiment, and analyzing and discussing experimental data), their conceptual understanding and mental models of the experiment concepts were enhanced [1].

In the same fashion, the averaged post- mental models score ($\bar{X}$ =6.80, *SD*=1.62) was also significantly higher than the pre- mental models score ($\bar{X}$ =4.86, *SD*=1.50) at *p*-value <0.001. Many students showed the most likely correct conceptual understanding in their pre-model. This may be due to the fact that they have interacted with the *ICESE* which was carefully designed based on a constructivist learning environemnts to support student development of conceptual understanding and mental models [11]. However, some students expressed some alternative conceptions at submicroscopic level. Major alternative conceptions are shown below;

- *p*-nitroaniline and/or benzoic acid molecules were transferred to the aqueous layer without any change in molecule (Figure 2a),
- *p*-nitroaniline still left in the organic layer after extracted with HCl solution (Figure 2b),
- naphthalene molecule were changed and left in the organic layer (Figure 2c),
- *p*-nitroaniline and benzoic acid were mixed in the aqueous layer after extracted with HCl and NaOH solutions, and
- about 70% of students showed that 100% of molecules were transferred to the other layer (acceptable conception, Figure 2d), while 30% realized that not 100% of molecules were transferred (corrected conception, Figure 2e).

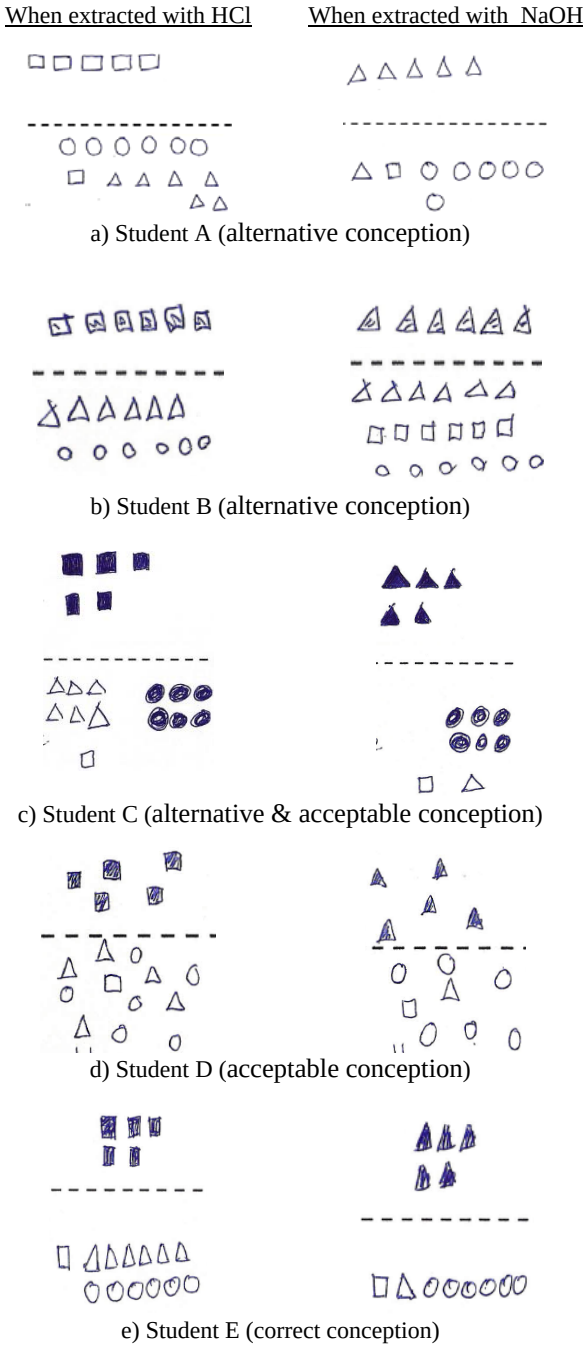

a) Student A (alternative conception)

b) Student B (alternative conception)

c) Student C (alternative & acceptable conception)

d) Student D (acceptable conception)

e) Student E (correct conception)

Figure 2. Examples of experiment mental models of the separation of a mixture of benzoic acid (△), *p*-nitroaniline (□) and naphthalene (○)

After performing the hands-on experiment, most of them corrected their alternative conception and obtained the more correct mental models [11]. Many students realized that there should be a few molecules left in the old layer after extraction, not 100% transferred (Figure 2e). Most of them recognized that *p*-nitroaniline and benzoic acid transferred from organic layer to aqueous layer because they were changed from organic acid and base compounds (soluble in organic solvent) into salts (soluble in water). They also noted that no change in naphthalene molecule after extracted with HCl and NaOH

solutions, so they were still dissolved in the organic layer. However, some of them tended to accommodate their alternative conceptions. In this case, lab instructor had to discuss further to help them obtain the acceptable conceptions.

The instructor observation during lab period accompanied with analyzing lab plan and report implied that science inquiry, scientific investigation and thinking of the students were continually improved. Moreover, they were confident of planning and conducting the experiment as they were less rely on the lab manual during performing the experiment. Although the students obtained the scores on the conceptual test and mental models of organic acid-base separation and purification, they planned and conducted the experiment sucessfully with few facilitating from the lab instructor. The two major problems encountered in the experiment were;

- they sometimes confused which layer will be re-extracted because they were familiar with extracting substance from aqueous to organic layer, and
- they evaporated solvent from naphthalene solution by heating it on a hot plate so some naphthalene were sublimated.

Conclusions

The results of this study verified that inquiry-based learning approach is in chemistry laboratory. This laboratory style can effectively improve student conceptual understanding as well as science inquiry skills including designing and conducting scientific investigations, making scientific explanations from experimental evidence, and communicating and answering corresponding scientific questions [3]. This supported that lab manual and instructor are no longer the main source of knowledge about experiments [7,8]. Moreover, student mental models of what is happening at a submicroscopic level during each step of the experiment can be enhanced. This can help students to really understand key concepts in chemistry especially at a submicroscopic world [12].

This study may have implication to chemistry lab instructors to consider implementing inquiry-based experiments in their chemistry laboratory. It will be a great help to enhance student scientific investigation skills if they have a chance to practice 2-3 inquiry experiments per a semester.

In the future, effects of inquiry-based experiments on student progression of science inquiry and other scientific process skills will be studied throughout the organic chemistry I and II courses.

Acknowledgement

This study was funded by the seed grant for new faculty member, Ubon Ratchathani University. Special thank to the Innovative Learning Development (ILD) Network at Ubon Ratchathani University for the relevant suggestion and comment on the study.

References

[1] W.J. Green, C. Elliott, and R.H. Cummins, *J. Chem Educ*. **2004**, 81, pp. 239-241.
[2] B. Hand, and C. Keys, *Sci. Teach*. **1999**, 66, pp. 27-29.
[3] National Research Council. *Inquiry and the National Science Education Standards: A Guide for Teaching and Learning*, National Academy Press, Washington DC (2000).
[4] M. Kipnis, and A. Hofstein, *Int. J. Sci. Math. Educ*. **2007**, 6, pp. 601-627.
[5] M. Sanger, *J. Chem. Educ.* **2008**, 85, pp. 297-302.
[6] S.L. Black, *J. Chem. Educ.* **1996**, 73, pp. 776-778.
[7] K.M. Deters, *J. Chem. Educ.* **2005,** 82, pp. 1178-1180.
[8] A. Hampp, *J. Chem. Educ.* **2008**, 73, pp. 1172.
[9] I. Montes, C. Lai, and D. Sanabria, *J. Chem. Educ.* **2003**, 80, pp. 447-449.
[10] http://www.chem.sci.ubu.ac.th/e-learning/extraction_en/
[11] S. Supasorn, P.J. Suits, L.L. Jones and S. Vibuljan, *Chem. Educ. Res. Pract.*, **2008**, 9, pp. 169-181.
[12] G.M. Bodner In: G.M. Bodner & M. Orgill, Editors, *Theoretical Frameworks for Research in Chemistry/Science Education*, Prentice-Hall, Upper Saddle River, pp. 1

The element rhythm

S. Phonchaiya

The Institution for the Promotion of Teaching Science and Technology/ Primary Science Department, Bangkok, Thailand

E-Mail Address: sopho@ipst.ac.th

Abstract: An activity called the element-rhythm game was developed to help secondary school students recognize the element symbols as well as their metallic properties. Initially, the rhythm notes such as Ta, Titi and Hus were introduced, and then students created the pattern consisting of four beats in one measure. Later, students generated the pattern using the chemical elements instead of musical rhythm notes. The simple musical instruments were also designed to make the learning more enjoyable. After this activity, students were able to recognize the element symbols along with their metallic properties. They could also create their own rhythm using other chemistry concepts. Moreover, students enjoyed this learning pedagogy.

Note: Here is an example of a pattern that one measure has four beats.

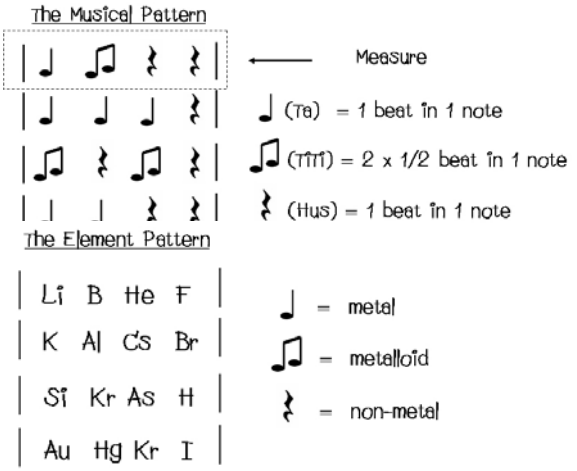

Introduction

Secondary school students may feel intimidated when they are introduced to the element symbols. They are also frustrated when they have to memorize those symbols along with the metallic properties. This may cause students to lack motivation and fear coming back to class. To make students more interested in learning about the element symbols and their metallic properties, an activity called the element-rhythm game was developed. This activity incorporates music, which is an important feature of today's world [1], into the chemistry classroom. Students are also provided opportunities to work collaboratively and create their own patterns [2] from this activity.

Science and music have been described in opposite ways for over a century: Science mostly involves logical thought rather than feelings. In contrast, music is often regarded as driven by intuition and passion rather than by reason. Indeed, this view of music and science as opposite one another is not always true. Good science always involves creativity, intuition and inspiration. Scientists may sometimes work via their hearts rather than their heads [3].

Currently, there are some reports concerning the incorporation of music into science classroom [1, 3-4]. Teachers may create songs addressing science concepts in lyrics, and students are encouraged to learn science through songs. This approach has already been tested and found to be successful in helping students learn or memorize some science concepts. Students also enjoy this learning method [1-4].

This report describes an alternative pedagogy of the incorporation of music into science (chemistry) classroom. Besides learning the element symbols, periodic table and metallic properties, students are introduced to some musical terms. These terms include beat, tempo, measure and rhythm [2]. An example of rhythm notes are shown in Table 1.

Table 1: The "Ta" rhythm language

Quarter note	♩	Ta	1 beat in 1 note
Silent quarter note	𝄽	Hus	1 silent beat in 1 note
Two eights note	♫	Titi	2 half beats in 1 note
Half note	𝅗𝅥	Taa	2 beats in 1 note
Dotted half Note	𝅗𝅥.	Taaa	3 beats in 1 note
Whole note	𝅝	Taaaa	4 beats in 1 note

With the rhythm notes, beat and measure, a pattern can be created. A pattern is a set of measures that usually consist of four or eight beats. Figure 1 illustrates an example of a pattern that one measure has four beats (also four rhythm notes in this case).

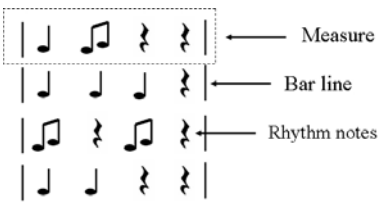

Figure 1. An example of a pattern

Materials and Methods

This activity was implemented to 74 secondary school students (M.1) from Samsen Wittayalai School. The activity was divided into three parts:

First: students learned the element symbols, periodic table, and metallic properties from worksheets and exercises.

Second: students were introduced to the musical terms which were pattern, measure, beat and rhythm. In this activity, only the three rhythm notes: Ta, Titi, and Hus were emphasized. Initially, a teacher acted as a conductor and students clapped their hands according to the notes in the pattern. Later, the simple musical instruments were created: The Maracas were created by putting pebbles into drinking-water bottles. The wooden Castanet was made from chopsticks and Drum was simply created by hitting a bottle of water with a chopstick. Students had to decide when to use these instruments. An example of a pattern with the musical instruments is shown in Figure 2.

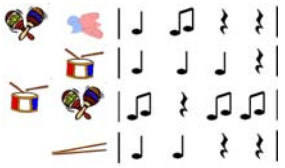

Figure 2. An example of a pattern with musical instruments

Third: Students created the pattern using the chemical elements instead of musical rhythm notes. In this case, metal, metalloid and non-metal were used as Ta, Titi and Hus, respectively. A pattern in Figure 2 might be re-written as that in Figure 3. After a pattern was created, each group performed the music in front of the class.

Figure 3. An example of an element pattern

Each student's recognition of element symbols as well as their metallic properties was assessed by his/her musical performance. The student's satisfaction about this learning activity was assessed by a questionnaire using the Likert scale where 5, 4, 3, 2 and 1 are strongly agree, agree, neutral, disagree and strongly disagree, respectively.

Results and Discussion

1. The student's recognition of element symbols as well as their metallic properties

Two examples of student rhythm patterns are shown in Figure 4. Most students were likely to create the pattern as in Figure 4a. However, one group of students made a unique pattern as the words were also created in their pattern (Figure 4b).

a)

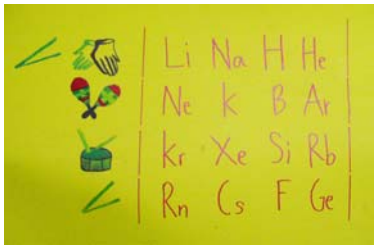

b)

Figure 4. Examples of student rhythm patterns

By observation, students performed the music well with their element pattern. In addition, when they were asked to perform the music by using another group's pattern, they still played well. This could imply that the element symbols and their metallic properties were well recognized by students through this learning activity.

4.2 The student's satisfaction regarding the activity.

The results from the questionnaire are shown in Table 2. By analyzing the questionnaire, the mean range is 3.57 – 4.14. This refers to an agreement of students for all items (3.51 – 4.50 is classified as an agreement). This could imply that this activity is fun, improves students' thinking ability, encourages students to design pieces of work and makes them work collaboratively. The majority of students (63%) would also recommend their teachers implement such learning activity into their classrooms.

Table 2. Mean and standard deviation (SD) of a questionnaire (N = 74)

Description	Mean ± SD
1. This activity helped me improve my thinking skill.	3.97 ± 0.72
2. I had opportunities to design my own experiment or work piece by myself.	4.07 ± 0.81
3. I worked collaboratively.	4.14 ± 0.81
4. A teacher encouraged me to ask questions.	3.58 ± 0.89
5. I can link what I have learned to my everyday life.	3.57 ± 0.95
6. I can link what I have learned to other subjects.	3.63 ± 0.91
7. I have learned chemistry contents.	3.91 ± 0.79

8. The activity was fun.	3.83 ± 0.92
9. This activity improves my attitude toward chemistry.	3.79 ± 0.82
10. I like such learning approach.	3.83 ± 0.95

Conclusions

To help secondary school students (M.1) recognize the element symbols as well as their metallic properties, an activity called the element rhythm game was developed. This activity incorporated music into the chemistry classroom. Students initially learned the element symbols, periodic table and metallic properties from their worksheets. Then students were introduced to the musical terms. To perform the music, a teacher acted as a conductor and students clapped their hands according to the notes in the pattern. The simple musical instruments were also designed to make the learning more enjoyable. Lastly, students generated the pattern using the chemical elements instead of musical rhythm notes. They also had to figure out when each instrument would be used. When a pattern was created, students were asked to perform the music in front of the class. They had to play the music using their own pattern and the patterns from other groups. Based on performance, it could be implied that students could recognize the element symbols and the metallic properties well. By analyzing questionnaire, students enjoyed such learning activity and would recommend it to their teachers for use in their classrooms.

Acknowledgements

The author wishes to thank the Institute for the Promotion of Teaching Science and Technology (IPST) for financial support.

References

[1] C. Molyneux, *Science in School.* **5** (2007), pp. 32-35.
[2] E. Serbro, *Documents from the workshop (Learning mathermatics through music in early chilhood).* 12-16 October, IPST, Bangkok..
[3] http://www.clta.uci.edu/documents/article2.pdf
[4] M. Kumbar, *J.Chem.Educ*. **84**(2007), pp 1933-1936.

Experimental kit: soft drink's secret

K. Nugultham[1], A. Siripinyanond [2], and J. Shiowatana[2*]

[1]Institute for Innovative Learning, Mahidol University, 999 Phuttamonthon 4 Road
Nakhon Pathom, 73170, Thailand
[2]Department of Chemistry and Center of Excellence for Innovation in Chemistry, Faculty of Science
Mahidol University, Rama VI Rd., Bangkok, 10400, Thailand

*E-mail: scysw@mahidol.ac.th

Abstract: This presentation aims to develop a low-cost experiment kit for secondary school teaching. The major part involves developing testing kits and using instructions to help students use the kits effectively. The kits are based on colorimetric and turbidimetric analyses. The experimental kit was designed to support students exploring issues associated with soft drink and consists of instructional manuals, lesson plans, assessment items and testing kits (pH, phosphate and CO2). Inquiry-based learning has been promoted in the experimental kit and encouraged students to collect their own data and explored their results in practical work. By self experiment, students will learn by themselves that their favorite soft drinks contain only sugar and food additives some of which may not be beneficial to their health. In addition, students will learn about the concept of solution, gas and their properties. It is expected that the developed experimental kit could also help raise awareness of health problem from overconsumption of carbonated drink.

Introduction

According to The Thai Health Promotion Foundation and other health organizations all over the world, the common health problems of school student include obesity and nutritional deficiencies typically suffered by heavy soda drinkers. From the survey of the frequency of carbonated beverage consumption, it showed that Thai students under 18 years age group in 14 provinces consumed in average 50 liters per year per person of carbonated drink[1]. Consequently, obesity, reducing in bone mass, and decayed tooth can occur leading to poor health[2]. Experimental kit, named ChemKits, hands-on practical chemistry, microlabs and test kit, have been successfully introduced at secondary school and university level to facilitate student learning[3]. It can be appropritately designed and managed to fit in science contents. The advantages of experimental kit are to make science and chemistry real and interesting, to make concepts more understandable, to learn science process, and to practice scientific skills. Moreover, science is an important subject that student can explore knowledge through practical work and relate science toward other subjects for example health science, and environmental science.

This project proposed on experimental kit to investigate components of soft drink. The results of measurement are used for learning some basic concepts in chemistry and raising awareness of the fact that popular drinks among chlidren school contain many additives with no nutritional value but can be harmful to health. It outlined the development and evaluation of experimental kit. The initial target of the experimental kit was secondary schools students. The designing of an experimental kit was aimed to support teachers' teaching and students' learning and exploring towards achievement of learning of solution and acid-base concepts by introducing inquiry into learning process. The experimental kit consists of instructional manuals for both teachers and students, activities, lesson plans, assessment items as well as low cost test kits in one package. The knowledge in the content of beverages can lead to awareness of effect of additives on health.

Materials and Methods

A widely used principle for developing chemical kit is colorimetry in which a specific color reaction for an element or substances is used for color generation and color comparison for quantitative evaluation[4].Three test kits for phosphate, CO_2 and pH, were developed as investigating tool in exprimental kit to find out chemical composition in soft drinks. For phosphate test kit, molybdenum blue reaction was used to detect amount of phosphate in a range of 0-5 ppm within 2 min. Carbon dioxide test kit was developed using turbidimetric method which can detect carbon dioxide in a range of 0-8 mg CO_2 within 1 min. pH test kit was developed using extract of butterfly pea's petal in water prepared in an appropriate concentration to distinguish pH in the range of 1-7. Other materials included low-cost supplies that were available locally such as reagent and reaction bottles, plastic syringes and droppers. The use of reagents and samples was realized in small scale to reduce cost and waste generation.

Figure 1. The experimental kit package

The experimental kit, "soft drink's secret", has been developed to help students connect science to their surrounding. Students used the kit to measure pH, phosphate and CO_2 concentrations in the drink and were expected to learn about pH scale in relation to acid concentration, and discussion on the relationship between pH, phosphate, CO_2 and the properties of solution and chemical equilibria can be encouraged. The learning process was designed to translate "Inquiry" into "Activity"[5]. Additional activity to engage students included, observation of Coke fountain demonstration experiment, preclass questions such as "What's in Coke?"and role play as journalist to consider research columns and news on soft drinks consumption problems then they discussed about properties of solution and were encouraged to ask scientific questions. After they investigated the amount of CO_2, pH and phosphate, the questions can be answered by the result of the testing to evidence in responding to questions by using test kits. Finally they calculated the pH of solution from concentration of acids in the drinks. They compared the calculated pH with the measured values of pH as shown in Table 1. The measured pH of Mirinda, Sprite and Fanta differed from calculated pH because the only carbonic and phosphoric acids were considered on this calculation. In reality, citric acid and benzoic acid are added as fruit flavour and preservative, respectively, which could not be ignored in the calculation provided that correct pH values are expected. In addition, students communicated their results and discussed about the effect of phosphate content leading to health problems. For assessment, pre-test and post test , data worksheet and questionnaire were designed.

Table 1: Results of composition of soft drink (N=3)

Soft drink	CO_2 (mg)/10 mL ±SD	Phosphate (ppm P) ±SD	pH ±SD
Coke	7 ± 0	186 ± 11	2.7 ± 0.5
Pepsi	6.7 ± 0.3	193 ± 11	2.7 ± 0.5
Mirinda (orange)	6.8 ± 0.3	0 ± 0	3 ± 0
Sprite	6.8 ± 0.3	0 ± 0	4 ± 0
Capico soda	2.7 ± 0.6	40 ± 34	4 ± 0
Fanta (orange)	6.5 ± 0	0 ± 0	3 ± 0

Results and Discussion

The experimental kit was tried out in a classroom, grade 8 with 111 students (26 % male and 74% female). When the learning process was over, students had to complete the post test and questionnaires. It appeared that the most favorite subjects of students were science (42.9%) and music (32.1%). 12.0 % of students never attended science group, science club or science project.Yet, they can learn and perform experiment with no problem. 80% of the students had no exprerience to use test kit in the classroom. They enjoyed using the kit and the activity.

For the awareness of health, students learn about adverse effect of soft drinks and on the correlation between soft drink consumption and the increased risk of bone fractures, obesity, nutritional deficiencies, and tooth decay through information sheets and hands-on experience in the determination of the amount of phosphate, CO_2, and pH. Investigation on behavior change as affected by this activity showed that student average consumption of carboneted drink before this activity was 2 cans/week. After the class, student's consumption of soft drinks reduced to 1 can/week.

Conclusions

The experimental kits were considered to be useful in inquiry learning in classroom. Although lesson plan and activities were previously designed completely in this project, teachers can modify them to fit their students and classroom environment. The most effectiveness of this experimental kit was that students were able to investigate, discuss and relate the data through their scientific knowledge. Moreover the experiment kit could be useful as a tool to promote health drinking habit in school children.

References

[1] http://www.songkhlahealth.org/paper/288
[2] L. Marr, *J. Nutr. Educ. Behave*. **36**(2004), pp. 258-265.
[3] J.D. Bradley,*Pure. Appl. Chem.* **71**(1999), pp. 817-823.
[4] D.F. Boltz. *Colorimetric Determination of Nonmetals*. Interscience publishers, USA, 1958.
[5] R.A. Huber and C.J. Moore, *School Science and Mathematics*, **101**(2001), pp. 32-41.

Solving absorption peaks overlap with excel

S. Wongnawa [1]* , R. Waranyoupalin[1], K. Chaithanadul[1], P. Chooto[1], M. Wongnawa[2]

[1] Department of Chemistry and Center for Innovation in Chemistry, [2] Department of Pharmacology, Faculty of Science, Prince of Songkla University, Hat Yai, Songkhla, Thailand 90112

[*] Corresponding E-mail: sumpun.w@psu.ac.th

Abstract: In studying chemical reactions using spectrophotometric technique, quite often may encounter absorption peaks from more than one components overlapping with each other. Overlap may be partial or complete overlap. If overlap cannot be solved, further studies beyond this stage are not possible or one must turn to other methods instead. To overcome the overlap obstacle usually rely on softwares that are commercially available. In this work, the utilization of MS Excel – the software that comes bundled with MS Windows – will be described based on the data of metal-curcumin complexes. In the system of metal-curcumin complex, the absorption peak of the remained curcumin overlaps with that of the complex newly formed in the system. By this method, one compiles data of curcumin absorption at various concentrations in the Excel format and uses them to simulate the absorption peak of curcumin at any desired concentration. The simulated peak then is used to subtract from the original overlapped profile to obtain the absorption of another species, presumably the new complex. From here, other studies beyond this point become possible, e.g. reading of peak positions and intensities, finding the composition of the complex by the Job's method, calculating the complex formation constant, etc.

Introduction

UV-Vis spectroscopy is one of the oldest methods in molecular spectroscopy. The method owes its importance not least to its varied applications in chemistry, physics, and biochemistry. It can be applied to analytical problems, to the investigation of chemical equilibria and to the kinetics of chemical reactions, including photokinetics [1]. In chemistry, UV-Vis spectroscopy can be considered as one of the most basic techniques one usually encounters in his/her early years. It is quite certain that almost all of the undergraduate students will have done some kind of experiment utilizing this technique before their graduations. The use of this technique is not difficult to comprehend for students. It is rather straightforward and accurate as long as the absorption peaks are clearly discernible and far apart. However, if the peaks are very close together and overlapping takes place this can be a nightmare for analysts. The overlap prevents accurate reading of absorbances of the target peaks, hence, further manipulation of data based on absorbances will be difficult and less accurate. The problem of overlapping peaks and how to resolve them mathematically has been discussed by Abdollahi and Nazari [2]. In many cases, to avoid confronting with this problem, researchers turned to other methods that do not depend on reading absorbances such as voltammetry [3]. There are many softwares available commercially in the market to help solve this problem (see an example in Ref [4]). Those softwares are rather expensive though. Nowadays PCs have become an integrated part of every laboratories and one software, the Excel, is usually preinstalled in them. Our research group, hence, came up with a method to maximize the use of this widely available software with the problem of peak overlapping instead of having to rely on the commercial specialized softwares for the purpose.

Materials and Methods

Chemicals

All the chemicals were of AR grade: curcumin ($C_{21}H_{20}O_6$), Code no. C-1386 (Sigma, USA), copper chloride dihydrate ($CuCl_2 \cdot 2H_2O$), Code no. 2802 (APS Finechem, Australia), mercuric chloride ($HgCl_2$), Code no. 461005 (Carlo Erba, Italy), methanol (CH_3OH), Code no. 1.06009.2500 (Merck, Germany).

Stock solution of curcumin (2.0×10^{-4} M) in 50% MeOH (methanol: deionized water) was freshly prepared before measurement. Since the solubility of curcumin is low in water, curcumin powder was first dissolved in absolute methanol then the deionized water was added to make a final solution be 50% MeOH. In order to minimize the effects of light on these solutions, all the experiments were carried out in the dark.

Stock solution of metal ion (2.0×10^{-4} M) was also prepared in 50% MeOH.

Construction of data base to simulate the absorption spectra of unreacted curcumin

From the stock solution of curcumin several lower concentrations were prepared (from 4.0×10^{-5} to 4.0×10^{-6} M). Absorption spectra of these solution were obtained using SPECORD S100 spectrophotometer (Analytik Jena GmbH, Germany) equipped with a thermoelectrically temperature-controlled cell holder (Themostat, Lauda® A100, Germany). The data were output in the Excel format (example shown in Table 1). The data were obtained in triplicate and averaged before being used in the next stage.

Table 1 Output of spectral data

Wavelength (nm)	*Absorbance of curcumin at various concentrations (M)*				
	Conc. 1	Conc. 2	Conc. 3	…	…
Wavelength 1	Abs. 11	Abs. 21	Abs. 31	…	…
Wavelength 2	Abs. 12	Abs. 22	Abs. 32	…	…
Wavelength 3	Abs. 13	Abs 23	Abs. 33	…	…
…	…	…	…	…	…
…	…	…	…	…	…

The correlation between absorbance and concentration of curcumin at each wavelength was obtained by graphical method using absorbance as y-axis and concentration as x-axis. The Excel built-in function was used : Format → trendline → Options → choose "Set intercept = 0"; and choose "Display equation on chart". The usual linear equation is in the form: y = (slope.x) + intercept, which can be translated to our case as :

Absorbance = (slope.concentration) + 0 (1)

This process must be carried out for every wavelength to obtain the slope at each wavelength. The slope values are the important parameter from this stage after which they will be used to calculate the absorbance and simulate the absorption spectrum of unreacted curcumin at any desired concentrations.

Subtraction and simulation of new peak

Absorbances at all wavelengths of the unreacted curcumin can be obtained by inserting the slope values obtained in the preceeding paragraph into eq. (1) with initial "guess" value of concentration. The process requires reiteration until the "best" value of absorbances were obtained. (The "best" value was judged by inspecting one particular point in the original spectrum with the lowest absorbance which after the subtraction remained unchanged.) These absorbances then were used to subtract from the absorbances of the original overlapped spectrum. The resulting new absorbance values are those of the new unknown complex just formed in the solution. These new absorbances if plotted against wavelengths will give a profile of new spectrum exhibited by the new unknown complex.

Results and Discussion

A system of curcumin and Hg(II) ion will be a good example to show the application of this method. Curcumin in methanolic-aqueous solution shows a broad characteristic UV-Vis absorption around 300-500 nm with maximum absorption band at wavelength 430 nm and shoulders near 360 and 460 nm, and a weak absorption band at 260-280 nm. (Figure 1, line 1), while Hg(II) has no absorption. When solutions of Hg(II) and curcumin were mixed (2.5×10^{-5} M of each) in an attempt to study the complex formation, the spectrum of the mixture was obtained (Figure 1, line 2) . By using the method described here, an absorption peak of unreacted curcumin in the system can be simulated (practically, the same as line 1, in Figure 1). Subtraction of absorbance at each wavelength of simulated line 1 from its corresponding wavelength of line 2 yielded a new set of absorbance which when plotted against the wavelengths gave spectrum as shown in Figure 1, line 3. This, presumably, is the absorption peak of the new complex that formed in the system.

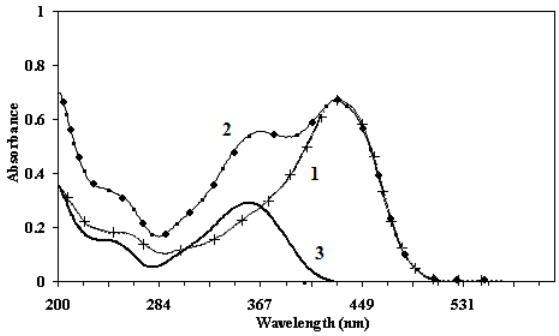

Figure 1 Absorption spectra of : (1) initial curcumin (or simulated curcumin), (2) curcumin + Hg(II) mixture, and (3) new complex

As an example, if we started with equimolar of curcumin and Hg(II) solutions, 2.5×10^{-5} M. After calculation as outlined above, the concentration of unreacted curcumin remaining in the system was arrived (after some reiteration) at 1.37×10^{-5} M and the plotted spectrum of the new complex, line 3 in Figure 1, has the maximum absorption at wavelength 359 nm.

Up to this point, one can obtain a clear spectrum of the new species (line 3 in Figure 1) which otherwise could not have been obtained due to overlapping with the unreacted curcumin. One can go further as to obtain the composition of the complex, the concentration of the new species and other species involved that exist together in this solution at equilibrium, and to calculate the equilibrium constant [5]. Examples of these results have been reported elsewhere [6].

Conclusions

The overlap of peaks from two components in the solution can be resolved by using of the MS Excel software combined with the spectrophotometer capability to export the data in the Excel format. The system of curcumin-Hg(II) is illustrated in this work where the original spectrum of the mixture is suffered badly from the overlap of the peaks of new complex formed and that of the unreacted curcumin. With this method the latter can be simulated and subtracted from the original spectrum to yield the desired spectrum of the new complex.

Acknowledgements

Financial supports from the Center for Innovation in Chemistry : Postgraduate Education and Research Program in Chemistry (PERCH-CIC), Commission on Higher Education, Ministry of Education, the Graduate School and the Research Foundation of Prince of Songkla University are gratefully acknowledged.

References

[1] H.-H. Perkampus, "UV-VIS Spectrscopy and its applications", translated by Grinter, H. C.; Threlfall, T.L., Springer-Verlag, Berlin, Germany (1992).
[2] H. Abdollahi and F. Nazari, *Anal. Chim. Acta.* **2003**, 486, pp. 109-123
[3] K. Ogura, Y. Fukusima and I. Aomizu, *J. Electroanal. Chem*. **1980**, 107, pp. 271-279.
[4] B. Tang, L. Ma, H.-Y. Wang and G.-Y. Zhang, J. Agric. Food. Chem. **2002**, 50, pp. 1355-1361
[5] M.A. Rauf, Z. Akhter and S. Kanwal, Dyes and Pigm. 67 (2005), pp. 77-79
[6] R. Waranyoupalin, S. Wongnawa, M. Wongnawa, C. Pakawatchai, P. Panichayupakaranant and P. Sherdshoopongse, *Cent. Eur. J. Chem.* **2009**, 7, pp. 388-394.


PACCON
Pure and Applied Chemistry International Conference 2010

Cosmetics

Antioxidant activity of phycocyanin from *Spirulina platensis*

W. Khamrat[1*], P. Leelapornpisid[1] and D. Santiarworn[1]

[1]Faculty of Pharmacy, Chiangmai University, Chiangmai , Thailand 50200

*E-mail: w_wara09@hotmail.com

Abstract: This study aimed to purify and determine antioxidant activities of different fractions obtained during the purification process of phycocyanin from *Spirulina platensis*. The dried powder of *Spirulina platensis*, after ground with sands, was extracted with 50 mM sodium phosphate buffer pH 6.8 before centrifuged to precipitate unwanted proteins. Then the supernatant was separated by celit column to obtained phycocyanin. The purity of phycocyanin was monitored by measuring the absorbance, spectrum from 200 to 700 nm. Its purity ratio A_{620}/A_{280} were determined. The antioxidant activities of the obtained phycocyanin were determined by 2,2'-azino-bis(3-ethylbenzthiazoline-6-sulphonic acid) ABTS assay and lipid peroxidation (linoleic acid) assay. The purity ratio of phycocyanin in the *Spirulina* crude extract was 0.36 and increased to 2.68 after purification. The fraction with highest purity ratio of phycocyanin demonstrated hightest antioxidant activities. For ABTS assay, it presented the VCEAC value of 0.0405 ± 0.0002 mg of ascorbic acid/mg of sample and the TEAC value of 0.0485 ± 0.0002 mg of trolox/mg of sample respectively. The result from lipid peroxidation assay exhibited IC_{50} value of 5.9336 ± 0.2565 mg/ml. The purification of *Spirulina platensis* crude extract obtained from this study increased the purity ratio of phycocyanin and its antioxidant activities. This will be further investigated for the development into anti-aging cosmetic products.

Introduction

Spirulina platensis, is a multifilamentous prokaryotic cyanobacterium and can be easily monocultured and harvested. Phycocyanin is the major phycobiliprotein in *Spirulina platensis*. Phycocyanin is water soluble, blue color and used as fluorescent markers in biomedical research [1], nutrient ingredients and natural dry for food and cosmetics[2]. and antioxidant activity. Although several methods have been developed for the purification and antioxidantion activity of phycocyanin from *Spirulina platensis* [3-7].

The present work has been carried out the purification and antioxidant activity of phycocyanin from *Spirulina platensis*. The purity was monitored at each stage of purification by absorption spectroscopy. Antioxidant activity of each stage was determined by ABTS radical cation decolourization assay and inhibition of peroxidation of linoleic acid. Thus, this work is expect phycocyanin could befurther investigated for the development into anti-aging cosmetic products.

Materials and Methods

Preparation of crude extract of phycocyanin

A 1 g sample of *Spirulina platensis* dried powder was add to 5 ml of 0.5 mM phosphate buffer pH 6.8. The mixture was ground with 5 g of sand by ball mill for 30 min. The mixture was then centrifuged at 10,000 rpm at 4 ◦C for 20 min to separate the phycocyanin from the cell debris. The blue supernatant was collected stored at 4 ◦C for further use.

Purification of phycocyanin

The crude extract of phycocyanin was separated by celit column to obtained phycocyanin. Then precipitation with powderd ammonium sulfate to obtain 60% saturation with continuous stirring for 1 h. The resulting solution was kept overnight and centrifuged at 10,000 rpm at 4 ◦C for 20 min. The pellet was resuspended in 10 ml of 0.5 mM phosphate buffer pH 6.8, in order to have sample celit column. Dialyzed sample overnight againt water, and freeze-dried for storage in darkness at 4 °C.

For ease of operation we labled crude extract, celite column elute, 60% ammonium sulfate precipitates and celite column elute sample as stages I, II and III sample, respectily.

Spectroscopic measurements

Absorbance spectra of phycocyanin was measured using UV-visible Spectrophotometer.The ratio of A_{620}/A_{280} give the purity of phycocyanin and while A_{620}/A_{280} give that of phycocyanin wherin A_{620} is the maximum absorbance of phycocyanin and A_{280} is the maximum absorbance of total proteins.

Determination of antioxidant activity $ABTS^{\bullet+}$ Assay

The total antioxidant activity of each stag was measure by ABTS radical cation decolourization assay $ABTS^{\bullet+}$ use in the assay was generated from ABTS salt, in which 2.45 mM potassium persulfate ($K_2S_2O_8$) was reaced with 7 mM ABTS salt in DI water for 16 h at room temperature in the dark[8]. The resultant $ABTS^{\bullet+}$ radical cation was dilute with water, to give an absorbance of 0.700 ± 0.002 at 734 nm. The standard and sample were dilute 100× with $ABTS^{\bullet+}$ solution to total volume of 1 ml and allowed to react for 1 h. Control (without a standard or sample) was use blank. Trolox and ascorbic acid (vitamin C), served as a standard, and results of

assay were expressed as trolox equivalent antioxidant capacity (TEAC)and vitamin C equivalent antioxidant capacity (VCEAC).

Lipid peroxidation (linoleic acid) assay

The antioxidant activity of the extracts from *Spirulina platensis* was assayed by a linoleic acid system [9]. One millilitre of five milligrams sample, 4 ml of 0.05 M sodium phosphate buffer (pH 7.0),One millilitre of anhydrous ethanol and 2 ml distilled water were mixed with 2 ml of 2.5% (v/v) linoleic acid in ethanol.The preoxidation was initiated by the addition of 0.4 ml of 0.1 M AAPH and carried out at 37 °C in the dark.The degree of oxidation was measured by reading the absorbance at 500 nm after colouring with $FeCl_2$ and ammonium thiocyanate[10]. Trolox in deionized water were used as references.The control was absolute ethanol.The percentage of lipid peroxidation of each sample was expressed as IC_{50}.

Results and Discussion

At each stage of purification show in Table 1.The crude extract (stage I) was obtained by centrifugation at 10,000 × g at 4 °C for 20 min. The supernatant obtained showed its highest absorption pick at 620 nm indicating. At this stage the A_{620}/A_{280} ratio was 0.36 (stage I). Celite column, size exclusion column was dialyze protein. The blue colour phycocyanin started eluting untill colourless, indicating an absence of phycocyanin. At this stage the A_{620}/A_{280} ratio was 1.15(stage II). The 60% ammonium sulfate precipitates phycocyanin overnight at 4 °C, centrifuged at 10,000 × g at 4 °C for 20 min. Sample was to have celit column, dialyzed sample overnight, changes of water to enchance dialysis process. Pure water phycocyanin was collected separately (stage III).The A_{620}/A_{280} ratio was 2.68.

Table 1. The purity of phycocyanin in various stages

Purification stage	Purity ratio A_{620}/A_{280}
stages I	0.36
stages II	1.15
stages III	2.68

Success of purification was also revaled by UV-vis overlay show in Fig.1. A sharp increase in a single peak at 620 nm suggested absorbance maxima phycocyanin while the decrease in absorbance at 280 nm suggested the removal of proteins other than phycocyanin.

The antioxidant activity of each stage was assayed by $ABTS^{\bullet+}$ method, it expressed as trolox equivalent antioxidant capacity (TEAC) and vitamin C equivalent antioxidant capacity (VCEAC), and results are show in Table 2. The results of $ABTS^{\bullet+}$ method the antioxidant activity increased in each stage for final stage (III) show that VCEAC value of 0.0405 ± 0.0002 mg of ascorbic acid / mg of sample

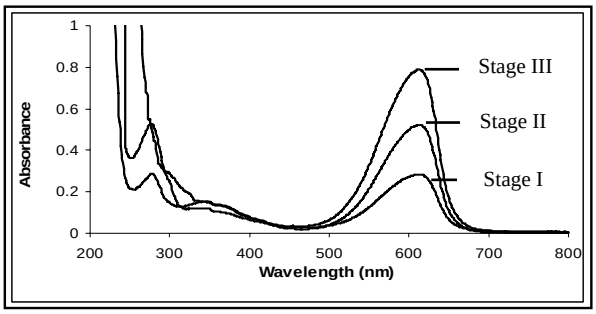

Figure 1. UV-vis absorption overlay spectra of phycocyanin from *Spirulina platensis* at each stage of purification. Stages: I crude extract; II, celit column; III, 60% ammonium sulfate precipitate and separated by celit column. The singer peak at 620 nm suggested the absorbance maxima of purified phycocyanin.

and the TEAC value of 0.0485 ± 0.0002 mg of trolox / mg of sample respectively.

The antioxidant activity of each stage was assayed by inhibiting peroxidation of linoleic acid method. As expected, with the increase of the phycocyanin, the antioxidant activity increased in each stage results are show in Table 2. The values of IC_{50} were8.8745 ± 0.2685, 7.5609 ± 0.2646 and 5.9336 ± 0.2565 mg/ml for stage I, stage II and stage III respectively.

Conclusion

Using the purification protocol presented here, we were obtain pure phycocyanin from *Spirulina platensis*. Also increase in the amount of phyccyanin is related to the increase in the antioxidant activity in each stage. This will be further investigated for the development into anti-aging cosmetic products.

Acknowledgements

The authors gratefully thank the Thailand Research Fund (TRFMAG) for financial support.

Table 2. The antioxidant activity by ABTS method and Lipid peroxidation of phycocyanin in various stages

Purification stage	ABTS		IC_{50} (mg/ml) of lipid peroxidation
	TEAC	VEACE	
stages I	0.0202 ± 0.0004	0.0172 ± 0.0003	8.8745 ± 0.2685
stages II	0.0278 ± 0.0002	0.0235 ± 0.0002	7.5609 ± 0.2646
stages III	0.0485 ± 0.0002	0.0405 ± 0.0002	5.9336 ± 0.2565

References

[1] A.N. Glazer, *Appl. Phyco.* 6 (1994), 105-112.
[2] A.Yoshida, Y. Takagaki, & T. Nishimune. 60 (1996), 57- 60.
[3] P. Ganapathi, S. Chethana, A.S. Sridevi & K.S.M.S. *Chromatography*. 1127 (2006),76 – 81.
[4] R. Manian, N. Anusuya. P. Siddhuraju & S. Manian. *J. Food Chemistry*. 107 (2008), 1000 – 1007.
[5] P. Estrada, B. Bescos, & V. Del. *J. IL Farnaco*. 56 (2001), 497-500.
[6] P.Anamika, M. Sandhya, P. Richa & P.K. Ghosh. *Protein Expresstion and Purification*. 40 (2005), 248-255.
[7] R. Re, N. Pellegrini, A. Proteggente, A. Pannala, M. Yang & C. Rice Evanc. *Free radical Biology and Medicine*. 26 (1999), 1231-1237.
[8] R. Huang, E. Mendis and S. Kim. *J.Biological Macromolecules*. 36 (2005), 120-127.
[9] L. Wang, B. Pan, J. Sheng, J. Xu & Q. Hu *J.Food Chemistry*. 105 (1993), 36-41.
[10] H. Kikuzaki & N. Nakatami.*Food Science*. 58 (1993), 1407-1410.

Emotional and psychophysiological effects of thai fragrances in aromatherapy/cosmetic products

T. Hongratanaworakit

Department of Pharmaceutical Chemistry, Faculty of Pharmacy, Srinakharinwirot University, Ongkharak, Nakhonnayok, Thailand

Corresponding Author E-Mail Address: tapanee@swu.ac.th

Abstract: This study was designed to assess the impact of Thai fragrances in aromatherapy/cosmetic products on emotion and psychophysiology in healthy volunteers. Ylang ylang oil (*Cananga odorata*), jasmine oil (*Jasminum sambac*), and rose oil (*Rosa damascena*) were used as Thai fragrances in aromatherapy massage oil. Human psychophysiological parameters, i.e. blood pressure, pulse rate, blood oxygen saturation, breathing rate, and skin temperature, were recorded as indicators of the arousal level of the autonomic nervous system. Emotional responses, i.e. relaxation, vigor, calmness, attentiveness, mood, and alertness, were assessed by visual analogue scales. Eighty healthy participants took part in the experiments. Subjects were tested in individual sessions and randomly assigned to one of four independent groups, i.e. control group, ylang ylang oil group, jasmine oil group, rose oil group, according to random numbers. In the experimental group, 1 mL of a 20% (w/w) solution of fragrance in sweet almond oil was applied to the skin of the lower abdomen of each subject and the subjects self-massaged the fragrance into the skin. In the control group, 1 mL of the placebo oil, pure sweet almond oil, was used. Compared to placebo, ylang ylang oil caused significant a decrease of blood pressure and an increase of skin temperature which indicated a decrease of autonomic arousal. At the emotional level, subjects in the ylang ylang oil group rated themselves as more calm and more relaxed than subjects in the control group. Compared to placebo, rose oil caused significant decreases of breathing rate, blood oxygen saturation, systolic blood pressure, and an increase of skin temperature which indicated a decrease of autonomic arousal. At the emotional level, subjects in the rose oil group rated themselves as more calm, more relaxed and less alert than subjects in the control group. Compared to placebo, jasmine oil caused significant increases of breathing rate, blood oxygen saturation, and blood pressure, which indicated an increase of autonomic arousal. At the emotional level, subjects in the jasmine oil group rated themselves as more alert, more vigorous and less relaxed than subjects in the control group. These findings suggest the relaxing/sedating effect of the ylang ylang oil and rose oil as well as the stimulating/activating effect of the jasmine oil. In conclusion, our results provide evidence for Thai fragrances use in aromatherapy/cosmetic products for the relief of depression and stress as well as uplifting mood in humans.

Introduction

Presently, Thai essential oils, i.e. ylang ylang oil (*Cananga odorata*, Annonaceae), jasmine oil (*Jasminum sambac* L., Oleaceae), and rose oil (*Rosa damascene* Mill, Rosaceae) are widely used as a fragrance in perfumery and cosmetic industries. In medicine the interest in the usage of these fragrances as therapeutically active agent has grown considerably. Especially in aromatherapy, ylang ylang oil has been used as an antidepressant in cases of depression and nervousness as well as used for reducing the blood pressure in the case of hypertension [1, 2]. Jasmine oil is used in aromatherapy as a holistic treatment for apathy, fear, hysteria, depression, balancing, uplifting mood and inspiring confidence [1, 2]. Rose oil reported helps to improve memory and brings a feeling of well-being. In addition, rose oil is also used for insomnia, headache, migraine, nervous tension and stress-related emotion [1, 2].

Thai fragrances in aromatherapy/cosmetic products are increasingly being used for the improvement of the quality of life, as well as for the relief various symptoms in patients, but scientific evaluation of the effects of those products in healthy volunteers is rather scarce. Up to now, no experiments on the effects of ylang ylang oil, jasmine oil, and rose oil in massage oil on human psychophysioloigcal parameters and on emotional responses after transdermal administration have been carried out. Therefore, the main objective of the present study was designed to assess the impact of of Thai fragrances in aromatherapy/cosmetic products on emotion and psychophysiology in healthy volunteers.

Materials and Methods

Subjects and essential oils: Eighty healthy volunteers took part in the experiments. Subjects were tested in individual sessions and randomly assigned to one of four independent groups, i.e. control group, ylang ylang oil group, jasmine oil group, rose oil group according to random numbers. Each group consisted of 20 subjects. Ylang ylang oil (fraction II) was obtained by steam distillation of the dry, fresh picked flowers of *C. odorata (DC.) Hook. f. et Thoms.* Jasmine oil was obtained by enfleurage of fresh petals of *J. sambac.* Rose oil was obtained by steam distillation of fresh petals of *R. damascene.* These oils were analyzed by GC/FID and GC/MS.

Essential oil administration: In the experimental group, 1 mL of a 20% (w/w) solution of each Thai fragrance in sweet almond oil was applied to the skin

of the lower abdomen of each subject and the subjects self-massaged the oil into the skin for 5 min. Afterwards, the massage area was covered with a plastic film in order to prevent evaporation of the oil. In the control group, 1 mL of the placebo oil, pure sweet almond oil, was used.

Experimental procedure: The experimental procedure has been previously used by our group [3-8]. One session consisted of two trials of 20 min each. At the beginning and at the end of each trial, emotional responses were assessed by visual analogue scales (VAS). Psychophysiological parameters, i.e., breathing rate (BR), blood oxygen saturation (BOS), pulse rate (PR), skin temperature (ST), systolic and diastolic blood pressure (SBP, DBP), were recorded continuously during each trial. In the first trial, which served as a control for influences of the experimental setup, the placebo substance was administered to all subjects. In the second trial the placebo was again administered to the control group, whereas in the experimental group the appropriate fragrance was administered.

Acquisition of psychophysiological parameters: Psychophysiological parameters were measured using MP100WSW hardware (Biopac Systems, Inc., Santa Barbara, California, USA). Details of the recording system and procedure have been described elsewhere [3-8]. VAS, i.e., relaxation, vigor, calmness, attentiveness, mood and alertness, were used to assess psychological responses. Each subject was asked to mark his or her feeling for each item between the two possible extremes.

Statistical Analysis: SPSS was used for data analysis. Taking into account the great inter-individual variability and the rather small sample size, only non-parametric test (i.e. Mann-Whitney-U-Test) was used in this study. The effects of fragrances on psychophysiological and emotional parameters were determined by comparing the difference scores between the control group and the experimental group.

Results and Discussion

In the present study Thai fragrances in aromatherapy massage oils were administered transdermally to healthy subjects. Psychophysiological parameters, i.e. systolic blood pressure (SBP), diastolic blood pressure (DBP), pulse rate (PR), blood oxygen saturation (BOS), breathing rate (BR), and skin temperature (ST), were recorded as indicators of the arousal level of the autonomic nervous system. In addition, subjects had to rate their mental and emotional condition in terms of relaxation, vigor, calmness, attentiveness, mood, and alertness in order to assess subjective behavioral arousal.

Ylang ylang oil: The mean difference scores and SEM of psychophysiological parameters between the second and first trials for the control group and the ylang ylang oil group are presented in Figure 1. Comparison of these difference scores revealed significantly larger decreases of SBP and DBP in the ylang ylang oil group than in the control group (p<0.05). In addition, comparison of these difference scores revealed a significantly larger increase of ST in the ylang ylang oil group than in the control group (p<0.05). The mean difference scores and SEM of emotional parameters between the second and first trials for the control group and the ylang ylang oil group are presented in Figure 2. Comparison of these difference scores revealed significant increases of subjective calmness and relaxation in the ylang ylang oil group as compared to the control group (p<0.05).

Rose oil: The mean difference scores and SEM of psychophysiological parameters between the second and first trials for the control group and the rose oil group are presented in Figure 1. Comparison of these difference scores revealed significantly larger decreases of SBP, BR, BOS in the rose oil group than in the control group (p<0.05). In addition, comparison of these difference scores revealed a significantly larger increase of ST in the rose oil group than in the control group (p<0.05). The mean difference scores and SEM of emotional parameters between the second and first trials for the control group and the rose oil group are presented in Figure 2. Comparison of these difference scores revealed significant increases of subjective calmness and relaxation in the rose oil group as compared to the control group (p<0.05). In contrast, comparison of these difference scores revealed a significant decrease of subjective alertness in the rose oil group as compared to the control group (p<0.05).

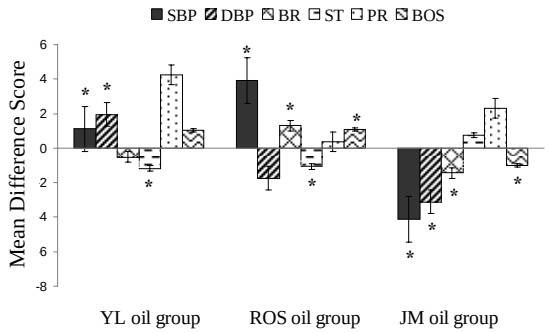

Figure 1: The mean difference scores and SEM of psychophysiological parameters for the ylang ylang oil (YL), rose oil (ROS), and jasmine oil (JM). * on the top of the bars indicates significant differences (p<0.05)

Both the ylang ylang oil and the rose oil showed a significant decrease of blood pressure. Since blood pressure is determined by the activity of the sympathetic branch of the autonomic nervous system (ANS), a decrease in blood pressure shows a decrease in sympathetic tone, i.e., a decrease of autonomic arousal [9-10]. Moreover, both fragrances showed a

significant increase of skin temperature. Skin temperature is controlled indirectly by the sympathetic division of the ANS via the contraction or relaxation of the smooth muscles which surround the blood vessels and regulate blood supply to distinct skin areas. When these muscles are contracted skin temperature is lower because less blood reaches there. On the other hand, when these muscles are relaxed, skin temperature is higher because more blood is supplied there. Therefore, the increase of skin temperature in both fragrances indicates a decrease of ANS arousal [9-10]. Subjects in the ylang ylang oil and the rose oil rated themselves more relaxed and more calm than subjects in the control group. This finding points towards a decrease of arousal in terms of self-evaluation [9-10].

Transdermal absorption of ylang ylang oil and rose oil reduced the level of arousal of the ANS, i.e. decreases of SBP, DBP, BR, BOS, and an increase in ST. Moreover, massage of ylang ylang oil and rose oil led to deactivation at the behavioral level, i.e. subjects feel more calm, more relaxed and less alert than before the administration of the oil. This finding points towards a decrease of arousal in terms of self-evaluation. Thus, the effects of ylang ylang oil and rose oil by means of percutaneous administration may be characterized by the concept of relaxation, which has also been described for sandalwood [4, 6].

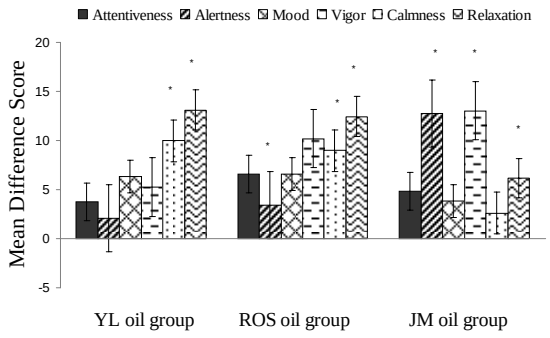

Figure 2: The mean difference scores and SEM of emotional parameters for the ylang ylang oil (YL), rose oil (ROS), and jasmine oil (JM). * on the top of the bars indicates significant differences (p<0.05)

Jasmine oil: The mean difference scores and SEM of psychophysiological parameters between the second and first trials for the control group and the jasmine oil group are presented in Figure 1. Comparison of these difference scores revealed significantly larger increases of SBP, DBP, BR, and BOS in the jasmine oil group than in the control group (p<0.05). The mean difference scores and SEM of emotional parameters between the second and first trials for the control group and the jasmine oil group are presented in Figure 2. Comparison of these difference scores revealed significant increases of subjective alertness and vigor in the rose oil group as compared to the control group (p<0.05). In contrast, comparison of these difference scores revealed a significant decrease of subjective relaxation in the jasmine oil group as compared to the control group (p<0.05).

The jasmine oil group showed significant increases of blood pressure. Since blood pressure is determined by the activity of the sympathetic branch of the ANS, an increase in blood pressure shows an increase in sympathetic tone, i.e., an increase of autonomic arousal [9-10]. In addition, transdermal absorption of jasmine oil led to significant increases of BR and BOS. In general, the cardiovascular system has a relationship with the respiratory system. Muscle sympathetic nerve activity is associated with respiratory function, namely, an increase in respiratory rate leads to an increase of muscle sympathetic activity [11]. Furthermore, an increase in breathing rate may cause a decrease of baroreceptor sensitivity and an increase of blood oxygen saturation [12]. Subjects in the jasmine oil group rated themselves more vigorous, more alert and less relaxed than subjects in the control group. This finding points towards an increase of arousal in terms of self-evaluation [9-10].

Transdermal absorption of jasmine oil increased the level of arousal of the ANS, i.e. increases of SBP, DBP, BR, and BOS. Moreover, massage of jasmine oil led to activation at the behavioral level, i.e. subjects feel more vigorous, more alert and less relaxed than before the administration of the oil. This finding points towards an increase of arousal in terms of self-evaluation. Thus, the effects of jasmine oil by massage may be characterized by the concept of stimulating/activating effects, which has also been described for kaffir lime oil [7], rosemary oil [8], and sweet orange oil [5].

Conclusions

These findings suggest the relaxing/sedating effect of the ylang ylang oil and rose oil as well as the stimulating/activating effect of the jasmine oil. Our results provide evidence for Thai fragrances use in aromatherapy/cosmetic products for the relief of depression and stress as well as uplifting mood in humans.

References

[1] M. Lis-Balchin, *Aromatherapy science: a guide for healthcare professionals*, Pharmaceutical Press, London, UK (2006).
[2] Y.L.Albert and F. Steven, *Encyclopedia of common natural ingredients 2nd ed.* John Wiley & Sons, Inc., New York, USA (1996).
[3] E. Heuberger, T. Hongratanaworakit, C. Boehm, R. Weber, G. Buchbauer, *Chem. Senses* **26** (2000), pp. 281-292
[4] T. Hongratanaworakit, E. Heuberger, G. Buchbauer, *Planta. Med.* **70** (2004), pp. 3-7.
[5] T. Hongratanaworakit and G. Buchbauer, *Acta. Hort.* ***679*** (2005), pp. 75-81.

[6] E. Heuberger, T. Hongratanaworakit, G. Buchbauer, *Planta. Med.* **72** (2006), pp. 792-800.
[7] T. Hongratanaworakit and G. Buchbauer, *Flavour Fragr. J.* **22** (2007), pp. 443-449.
[8] T. Hongratanaworakit, *Sci. Pharm.* **77** (2009), pp. 375-387.
[9] J.L. Andreassi, *Psychophysiology: human behavior & physiological response*, Lawrence Erlbaum Associated, London, UK (2000).
[10] K. Hugdahl, *Psychophysiology: the mind-body perspective.* University Press, England (1995).
[11] Y. Goso, H. Asanoi, H. Ishise, T. Kameyama, T. Hirai, T. Nozawa, *Circulation* **104** (2001), pp. 418-423
[12] L. Bernadi, C. Porta, L. Spicuzza, J. Bellwon, G. Spadacini, A.W. Frey, *Circulation*, **105** (2002), pp. 143-145.

Influence of vesicle sizes on in vitro release and skin permeation of dual flavonoids-loaded niosomes

B. Yingngam[1], N. Supaka[2], W. Rungseevijitprapa[1*]

[1] Department of Pharmaceutical Chemistry and Technology, Faculty of Pharmaceutical Sciences, Ubonratchathani University, Ubonratchathani, Thailand
[2] National Nanotechnology Center (NANOTEC), National Science and Technology Development Agency (NSTDA), Thailand Science Park, Pathumthani, Thailand

[*] Corresponding Author: wandeeim@yahoo.com

Abstract: The purposes of this research were to investigate *in vitro* release and skin permeation of niosomes with varying vesicle sizes. Quercetin-3-rhamnoglucoside and quercetin were chosen as glucoside and aglycone model and were co-loaded into niosomes using film hydration method following vesicle size reduction by high pressure homogenization. The influence of vesicle size on the release rate of flavonoids was studied *in vitro* with dialysis tubes. *In vitro* percutaneous absorption experiments were performed on new born porcine abdominal skin with Franz diffusion cells. The influence of vesicle sizes on flavonoids permeation into skin layers was investigated and the flavonoid contents were analyzed using high performance liquid chromatography. Four niosome sizes were grouped as follows: 100±3, 206±5, 505±57 and 828±23 nm. It was shown that the rate of flavonoid release was strongly dependent on the vesicle size and hydrophilicity of the encapsulated active. The dual flavonoid-loaded in smaller vesicle sizes exhibited faster release rate in comparison to the niosomes with larger size and hydrophobic aglycone was released faster than hydrophilic glucoside. The permeation of flavonoids-loaded larger vesicular sizes than 500 nm was limited to superficial layer of the skin. The highest potential skin permeation was observed in vesicles having sizes of 100 ± 3 nm. However, absorption of niosome vesicles to systemic should be carefully concerned. Niosomes with vesicles size of 206±5 nm optimized transportation of the flavonoids through the stratum corneum into deeper skin layer while no absorption to systemic circulation was observed. Thus, niosomes with vesicles in the size range of 100-200 nm were most appropriate candidates as percuteneous cosmetic carriers for flavonoid delivery.

Introduction

Among several bioactive compounds, flavonoids are the second mostly used plant metabolites for many anti-aging skin products [1, 2, 3]. In nature, flavonoid glucosides are the abundant form found in flavonoid extract than aglycones. Their high water solubility and large molecular weight are the major drawback for skin absorption. On the contrary, flavonoid aglycones are higher lipid soluble substances that readily penetrate through stratum corneum. However, their aqueous insolubility limits skin absorption [4]. The combination of both glucosides and aglycones has been commonly used in anti-aging-skin products to enhance synergistic of action.

In order to improve bioavailability of those flavonoids, these substances should be able to penetrate into the deeper skin layer of epidermis but should not absorb to systemic circulation. Several studies reported that niosomes can promote the penetration of bioactive compound into the deeper skin due to their ability to decrease the skin barrier by either disrupting or fluidizing the lipid lamellar of the stratum corneum. Moreover, the vesicles increase the solubility of the bioactive compounds in the stratum corneum. However, there are no data available for selecting optimum size ranges of niosomes for the delivery of both flavonoid glucosides and aglycones into the target sites with minimize systemic circulation effect.

The objective of this study was to investigate the *in vitro* release and skin permeation of flavonoid glucoside and its aglycone co-loaded niosomes with varying vesicle sizes. The obtained data will be useful for selecting the optimal sizes to be used in cosmetic application. Quercetin-3-rhamno glucoside (QR) and quercetin (Q) were chosen as glycoside and aglycone model, respectively, due to their widely existence in most plant flavonoids (Figure 1).

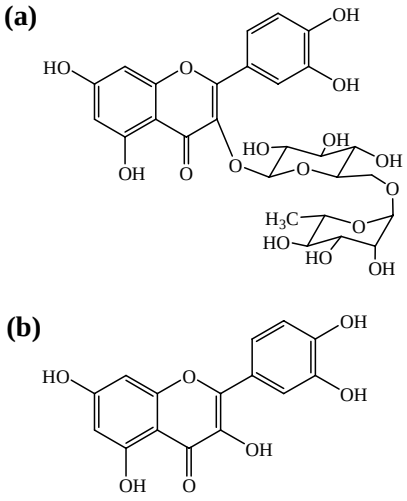

Figure 1. Chemical structure of (a) QR and (b) Q

Materials and Methods

Materials: The following chemicals were used in this study: Tween 61, QR and Q (Sigma-Aldrich, Inc., St. Louis, MO, USA), cholesterol (Carlo Erba Reagenti SpA, Italy). All other chemicals were of analytical or higher grade.

Niosome preparation: Niosomes containing QR and Q (QR/Q-niosomes) with different vesicle sizes were prepared using film hydration method, following vesicle size reduction by high pressure homogenization. Briefly, Tween 61, cholesterol and flavonoids were co-dissolved in the mixture of ethanol and chloroform. The dried film was formed under reduce pressure and kept overnight under vacuum, subsequently hydrated with an ultrapure water. The obtained dispersions were passed through high pressure homogenizer (APV 1000, Invesys APV Products, Denmark) with varying homogenization times to prepare different sizes of nisomes.

In vitro release study: Release profiles of QR/Q-niosomes were analyzed using dialysis tubing technique in a mixture of ethanol and phosphate buffer saline (PBS) pH 7.4 (1:1, v/v) at 37 °C. At the predominant time, sample was withdrawn periodically and the flavonoid content was analyzed by high performance liquid chromatography (HPLC).

In vitro skin permeation study: Skin permeation of loaded flavonoids from niosomes was determined using Franz diffusion cells in a mixture of PEG 400 and PBS (1:1, v/v) at 37°C. Prior to study, the integrity of the full thickness porcine abdominal skin was checked by measuring total epidermal water loss using Tewameter (Courage & Khazaka, Germany). After incubation, the flavonoid content in skin and receptor medium was analyzed by HPLC.

Results and Discussion

The influences of vesicle sizes and flavonoid forms on the *in vitro* release of QR and its aglycone co-loaded niosomes were investigated and the results are shown in Figure 2a and b. The release rate of flavonoids was apparently biphasic pattern with rapid flavonoid release, followed by a slower release phase. The faster release from niosomes was observed for Q than that of its glucoside. This pattern could be explained by hydrophilic-lipophilic property of those flavonoids and their path of diffusion. Q is a lipophilic compound, thus having more affinity to deposit between the alkyl chains of the Tween 61 in the bilayer formed niosomal vesicles. On the contrary, QR is a polar molecule and was mainly trapped in the polar head region inside the vesicles. Q with the shorter path of diffusion led to rapid ionization and release. The longer path diffusion of the trapped glucoside in the core structure of niosomes allowed the release of glucoside longer than that of its aglycone which deposited between the lipophilic bilayer membranes.

It was obvious that increasing vesicle size of niosomes from 100±3 nm to 828±23 nm markedly reduced the release rate of QR ($p < 0.05$) (Figure 2a). This could be ranked in the following order: 828±23 nm < 505±57 nm < 205±5 < 100±3. Similarly to the release pattern of Q (Figure 2b), the release rate of that aglycone loaded into the niosomes with smaller size was significantly different from the larger one ($p < 0.05$). This phenomenon could be explained by the diffusion path within the vesicle and layer of the vesicles. Based on the hydrodynamic diameter described above, the diffusion path of vesicles containing both QR and its aglycone in the smaller vesicles was shorter than the larger sizes. In addition, the lamellar number of the niosomes having sizes of 505±57 nm and 828±23 nm contained several concentric spheres of lipid bilayers rather than the oligolamellar or large unilamellar vesicles of the niosomes having sizes of 205±5 and 100±3 nm, led to the lower diffusion of the loaded flavonoids than the smaller vesicular sizes.

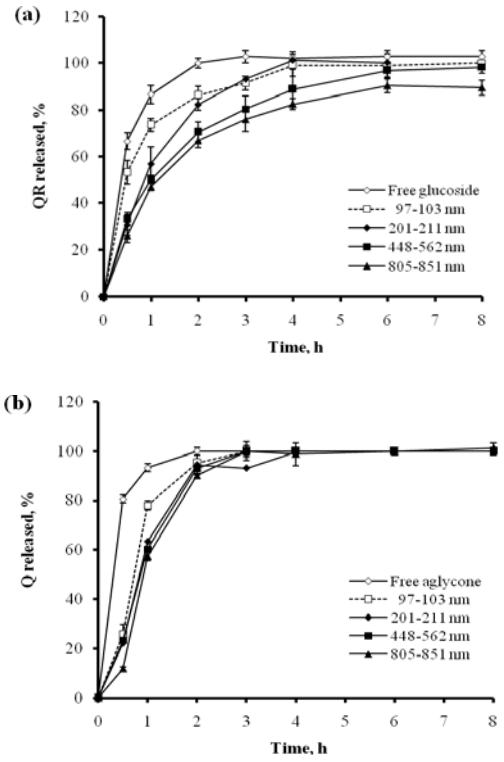

Figure 2. Effect of vesicle sizes of niosomes on the *in vitro* release of dual flavonoids against the mixture solution of PBS (pH 7.4) and ethanol (1:1, v/v): (a) QR and (b) Q. Data are expressed as % dose dialyzed ± S.D., n =3.

Figure 3a and b show effect of vesicle sizes of niosomes on the permeation of QR and Q into the stratum corneum. The absorption of flavonoid-loaded niosomes with smaller sizes into the stratum corneum exhibited higher amount than that of the larger sizes. The niosome formulations having sizes of 100±3 nm and 206±5 nm, could penetrated through the stratum corneum into the viable epidermis and the dermis. However, the flavonoids loaded into niosomes with

sizes of 100±3 nm were found in receptor medium after 2 h of incubation period while the release from other vesicle sizes was not observed. This study suggested that absorption of flavonoids in niosomes having sizes of 100±3 nm to systemic circulation should be carefully concerned. The permeation of flavonoid co-loaded niosomes with larger vesicular sizes than 500 nm was limited to superficial layer of the skin.

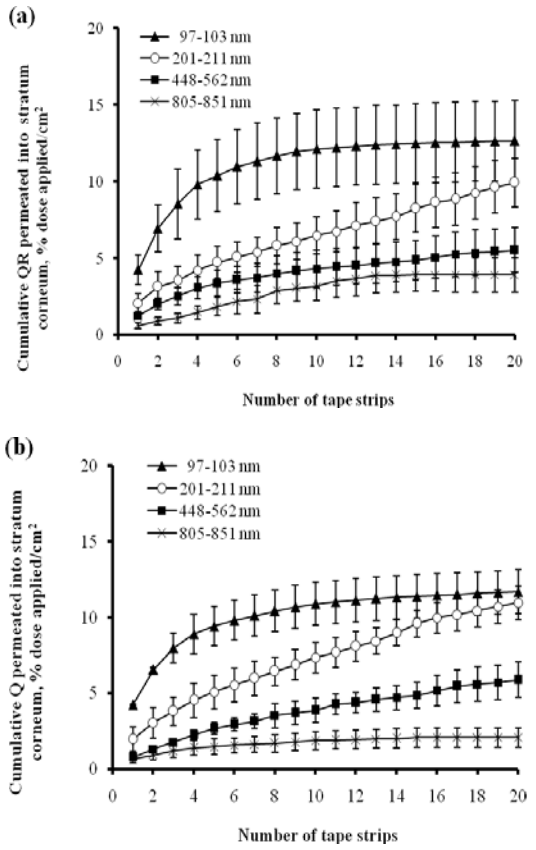

Figure 3. Stratum corenum strip profiles of niosomes having different vesicle sizes on the penetration of QR (a) and Q (b) after 8 h formulation application. Data are expressed as cumulative % dose applied/cm^2 ± S.D., n =3.

Conclusions

It can be concluded that flavonoid glucoside mainly deposited in the polar core region while its aglycone intercalated into the lipophilic area in the bilayer structures. The niosomes prepared with smaller sizes exhibited burst release effect of loaded flavonoids higher than that of the larger one. This result suggested that niosomes with the sizes of 100-200 nm gave high skin penetration of loaded flavonoids and were the most appropriate candidates as cosmetic carriers for flavonoids delivery.

Acknowledgments

This study was partially financial supported by the National Science and Technology Development Agency (NSTDA) through the Thai Graduate Institute of Science and Technology (TGIST) (Grant No. TG-55-24-49-070D) and Ubonratchathani University.

References

[1] R. Casagrade, S.R. Georgetti, W.A. Verri, Jr, D.J. Dorta, A.C. dos Santos and M.J.V. Fonseca, *J. Photochem. Photobiol. B: Biol*. **84** (2006), pp. 21-27.

[2] T. Gebre-Mariam, K. Asres, M. Getie, A. Endale, R. Neubert and P.C. Schmidt, *Eur. J. Pharm. Biopharm.* **60** (2005), pp. 31-38.

[3] J.P.E. Spencer, M.M.A.E. Mohsen and C. Rice-Evans, *Arch. Biochem, Biophys*. **423** (2004), pp. 148-161.

[4] F.T. Vicentini, T.R. Simi, J.O. Del Ciampo, N.O. Wolga, D.L. Pitol, M.M. Iyomasa, M.V. Bentley and M.J. Fonseca, *Eur. J. Pharm. Biopham*. **69(3)** (2008), pp. 948-957.


PACCON
Pure and Applied Chemistry International Conference 2010
Environmental Chemistry

Treatment of textile industrial wastewater from water jet loom machine

K. Charoenlarp*

Rajamangala University of Technology Krungthep /Textile Chemistry Department, Asso Prof.,Bangkok,Thailand.

* khanittha.C@rmutk.ac.th

Abstract: The objective of this research was to investigate the optimum condition for treatment of textile industrial wastewater from water jet loom machine by chemical coagulation and electrocoagulation methods. The variables of chemical coagulation method were type and amount of chemicals, pH and stirring rate. For electrocoagulation method, the variables were electrode materials, electric potential and contact time. It was found that the optimum condition of chemical coagulation method was 10% w/w of aqueous solution of aluminum sulphate 80 mL and 0.1% w/w of aqueous solution of coagulant aids, cationic polymer 32 mL per 4 L of wastewater at pH 8. The mixture solution was rapidly stirred with 120 rpm for 1 min and then slowly stirred with 20 rpm for 20 min. The removal efficiency of turbidity, COD and oil content were 88.88%, 85.20% and 77.72%, respectively. For electrocoagulation method, the optimum condition was using aluminum electrode with 35 volts and 150 min of contact time. The removal efficiency of turbidity, COD and oil content were 98.86%, 91.63% and 89.84%, respectively. It can be concluded from this study that the textile industrial wastewater treatment from water jet loom machine with electrocoagulation method is more efficient than that with chemical coagulation method.

Introduction

Recently it is obvious that economic and industrial situation have appeared with high competition including production, marketing and product design. Trade regulations especially environmental management reduction of pollution has been the main factor which takes a major role in industrial sector. Meanwhile textiles industry has been considered as a cause of water pollution. Weaving with water jet loom machine has caused high quantity of wastewater which has been contaminated with oil from machine and sizing agent. This sizing agent contains polyvinyl alcohol, acrylic, lubricant substances which are stable organic. It is hard to be biodegraded. The oily wastewater from factory processing is discharged into water resource and is able to be separated and floated on the water surface. The oily wastes discharged into the environment typically has deleterious effects. The oily wastes discharged may have objectionable odors and cause undesirable appearance. Bioassay data indicate that oil is toxic to fish. In greater quantities, it limits oxygen transfer and hindering biological activity.

The appropriate treatment of wastewater is necessary in order to reduce the impact of its discharge. Several methods have been used for the treatment of these wastes, such as coagulation [1], dissolved air floatation [2], and membrane processes [3,4]. A review literature indicated a certain number of studies which showed the success of the oil separation from oily rejections by using electrocoagulation [5,6,7]

The present work was aimed at investigating the efficiency of the method for treatment of wastewater from water jet loom machine by comparison between chemical coagulation and electrocoagulation.

Coagulation is one of the most commonly used method. In coagulation operations, a chemical substance is added into an organic colloidal suspension to cause its destabilization by reduction of forces that keep them apart. It involves the reduction of surface charges responsible for particle repulsions. This reduction in charge causes flocculation. Particles with larger size are then settled and clarified effluent is obtained. However, this technology usually needs additional chemicals which produce a huge volume of sludge [8,9]. Water treatments based on the electrocoagulation method have been recently proved to circumvent most of these problems, while also economically attractive[10].

Electrocoagulation (EC) is an electrochemical method of treating polluted effluent whereby sacrificial anodes (aluminum or iron electrodes) corrode to release active coagulant precursors into solution. These molecules produce insoluble metallic hydroxide flocs which can remove pollutants by surface complexation or electrostatic attraction [11]. The use of electrocoagulation for the treatment of wastewater has been reported by various authors. It is indicated that electrocoagulation is an efficient process for different waste, e.g. soluble oils, liquid from the food, textile industries and effluents from the paper industry [12,13,14]. The most common used materials for electrocoagulation are aluminum or iron. However, aluminum was found to be a more appropriate electrode material according to the iron electrode performance [15].The electrocoagulation reactions with aluminum as anode may be summarized as follows:

At the anode:

$$M(s) \longrightarrow M^{3+}(aq) + 3e^- \quad (1)$$

At the cathode:

$$3H_2O + 3e^- \longrightarrow 3/2H_2 + 3OH^- \quad (2)$$

In the solution:

$$M^{3+}(aq) + 3H_2O \longrightarrow M(OH)_3(s) + 3H^+(aq) \quad (3)$$

$M^{3+}(aq)$ and OH^- ions generated by the electrode reactions (1) and (2) respectively, to form various monomeric species, depending on pH range, which finally transform into $M(OH)_3$ according to complex precipitation kinetics. Freshly formed amorphous $M(OH)_3$ with large surface areas are beneficial for a rapid adsorption of soluble organic compounds and trapping of colloid particle [16]. The aggregates formed can be removed by decantation or floatation.

This study focuses on the improvement in wastewater treatment for the wastewater generated by a water jet weaving plant located in Chonburee Province, Thailand. The woven fabric produced plant generates 154 m^3/day of wastewater. In order to determine the optimum operating condition, the chemical coagulation method was examined under various variables as: type and amount of coagulant, type and amount of coagulant aids, pH and stirring rate. For comparison, the electrocoagulation method was used. The variables to examine was electrode materials, electric potential and contact time. Obtained experiment data was compared between each treatment method.

Materials and Methods

Analysis of wastewater from jet loom machine

The weaving wastewater from jet loom machine in Chonburee Province, Thailand was used in this study. The properties of wastewater to be analyzed were turbidity, suspended solid (SS), total solid (TS), oil content and chemical oxygen demand (COD). The properties of SS, TS, oil content and COD were carried out to the Standard Methods for Examination of Water and Wastewater [17]. JENWAY naphelometer and CYBERSCAN 2500 pH meter used to measure turbidity (NTU) and pH value, respectively.

Chemical coagulation experiment

Chemical coagulation was evaluated using the standard jar testing technique, with 10% w/w of aqueous solutions of $Al_2(SO_4)_3.18H_2O$, Fe_2SO_4 and $FeCl_3$ as the chemical coagulant and 0.1% w/w of aqueous solution of cationic and anionic polymer as the chemical coagulant aids. The amount of coagulant, coagulant aids, pH of solution and stirring rate were given in Table 1.

Electrocoagulation experiment

A laboratory-scale batch rectangular acrylic with 13cm x 25cm x 16cm was used. Two types of electrode (Fe or Al) were used as both anode and cathode materials. The distance between electrodes was 3 cm and dimension of the electrode was 3cm x 12.5cm x 0.6cm. They were connected to a direct current power supply with variable ranges of 0-6 A for current and 0-35 V for voltage. Electrocoagulation experiments were run as follows; electrode type, electrical potential and contact time as shown in Table 1. After each experiment, the electrocoagulation reactor and electrodes were carefully rinsed twice with 20% nitric acid and finally with distillation water.

Table 1: Experiment Condition

Method	Condition	Value
Chemical coagulation	Amount of 10% aqueous of coagulant (mL)	1.0, 2.0, 3.0, 4.0, 5.0 and 6.0
	Amount of 0.1 % aqueous of coagulant aids (mL)	1.0,2.0 and 3.0
	pH	4.0, 5.0, 6.0, 7.0, 8.0 and 9.0
	Rapid stirring rate (rpm)	100, 120 and 150
	Slow stirring rate (rpm)	20, 30 and 40
Electro coagulation	Electrode materials	Al, Fe
	Electrical potential (V)	20, 25, 30 and 35
	Contact time (min)	30, 60, 90, 120, 150 and 180

Results and Discussion

Properties of wastewater from water jet loom machine

The advantages of water jet loom machine are decreasing of noise and damaged yarn. However the disadvantages are high amount of wastewater with high turbidity, COD, SS, TS, and oil content. The wastewater from water jet loom machine was analyzed and the results were shown in Table 2.

Table 2: Properties of Wastewater From Water Jet Loom Machine

Parameter	Value				STD value
	min	max	X	SD	
pH (25°C)	7.30	7.7	7.5	0.2	5.5-9
Turbidity (NTU)	184.5	194.3	188.7	4.1	-
COD (mg/l)	1218.6	1866.7	1601.1	317.5	120.00
SS (mg/l)	140.0	172.5	157.0	12.0	<50.0
TS(mg/l)	2885.0	3127.5	2969.0	98.6	<3,000.0
oil content (mg/l)	512.0	660.0	571.8	64.8	5.00

As shown in Table 2, the properties of the wastewater were over the limit of standard regulation. Therefore, it need to have treatment before discharge. Then chemical treatment should be considered as an appropriate method.

Influence factors for chemical coagulation method

To explore the influence factors of the chemical coagulation condition, the mean turbidity of treated water by various factor were used with F-test at 0.05 level of significance and were presented in Table 3. The result shown that, type and amount of coagulant, type of coagulant aids, pH, and stirring rate were affected significantly with the efficiency of turbidity removal. The order of the coagulant ability was $Al_2(SO_4)_3$ > $FeCl_3$ > Fe_2SO_4. Turbidity removal efficiency increased with increasing the amount of $Al_2(SO_4)_3$ up to 5 mL, increasing the pH up to 8.0 and then decreased. In addition, it could be observed that, the $Al_2(SO_4)_3$ with cationic polymer were more

efficient than the $Al_2(SO_4)_3$ with anionic polymer. This behavior can be explained that, the oil drops have negative electrical charges, the cationic polymer induce flocculations by means of the neutralization of the particle surface charges.

Table3: The Mean Turbidity of Treated Water by Various Chemical Coagulation Factors.

Factors		N	X	SD	P-value
Coagulants type	$Al_2(SO_4)_3$	10	27.50	0.38	<0.001
	Fe_2SO_4	10	58.38	0.45	
	$FeCl_3$	10	28.44	0.70	
10% $Al_2(SO_4)_3$ (mL)	1.00	10	59.28	0.24	<0.001
	2.00	10	50.24	0.53	
	3.00	10	50.38	0.54	
	4.00	10	32.58	0.58	
	5.00	10	22.60	0.61	
	6.00	10	27.50	0.38	
pH	4.0	10	71.62	0.28	<0.001
	5.0	10	67.12	0.49	
	6.0	10	51.06	0.36	
	7.0	10	47.76	0.42	
	8.0	10	21.14	0.55	
	9.0	10	23.16	0.52	
Coagulant aids	Anionic polymer	10	47.28	0.59	<0.001
	Cationic polymer	10	20.58	0.38	
Rapid stirring rate (rpm)	100	10	24.40	0.57	<0.001
	120	10	20.98	0.69	
	150	10	21.90	1.32	
Slow stirring rate (rpm)	20	10	20.98	0.69	<0.001
	30	10	21.92	0.34	
	40	10	24.77	0.83	

Influence factors of the electrocoagulation method

To explore the influence factors of the electrocoagulation condition, the mean turbidity of treated water by various factor were used with F-test at 0.05 level of significance and were presented in Table 4.

Table 4:The Mean Turbidity of Treated Water by Various Electrocoagulation Factors.

Factors		N	X	SD	P-value
Electrode materials	Fe	10	20.84	0.90	<0.001
	Al	10	15.66	0.45	
Electric potential	20.00	10	15.66	0.42	<0.001
	25.00	10	12.98	0.61	
	30.00	10	6.33	0.32	
	35.00	10	2.15	0.21	
Contact time	30	10	16.20	0.38	<0.001
	60	10	9.70	0.45	
	90	10	4.62	0.43	
	120	10	3.11	0.28	
	150	10	2.15	0.15	
	180	10	2.01	0.09	

As shown in Table 4, Electrode materials, electric potential and the contact time were affected significantly with the efficiency of turbidity. The result found that the optimum electrode material was aluminum. Aluminum electrode dissolves at the anode and hydrogen gas is released at the cathode. The coagulation agent combines with pollutants to form large size flocs. As the bubbles rise to the top, they adhere to particle suspended in the water and float them to the surface. Turbidity removal efficiency increased with increasing the contact time and applied electric potential. This is ascribed to the fact that a high electric potential will generate significant amount of oxidized aluminum, resulting in a greater amount of precipitate for removal of colloids particles. The increase in turbidity removal efficiency slow down after 150 min contact time.

Conclusions

This study has shown the possibility to use electrocoagulation method to treatment the wastewater from water jet loom machine compare to chemical coagulation. The following conclusion could be drawn from the experiment study;

The type and dosing of coagulant, coagulants aids, initial pH and stirring rate have a significant influence on the treatment efficiency of chemical coagulation. The optimum condition of chemical coagulation method was 10% w/w of aqueous solution of aluminum sulphate 80 mL and 0.1% w/w of aqueous solution of coagulant aids, cationic polymer 32 mL per 4 L of wastewater. The mixture solution was rapidly stirred with 120 rpm for 1 min and then slowly stirred with 20 rpm for 20 min. The removal efficiency of turbidity, COD and oil were 88.88%, 85.20% and 77.72%, respectively.

The electrode materials, electric potential and the contact time have a significant influence on the treatment efficiency of electrocoagulation. The optimum condition was using aluminum electrode with 35 volts and 150 min of contact time. The removal efficiency of turbidity, COD and oil content were 98.86%, 91.63% and 89.88%, respectively.

The textile industrial wastewater treatment from water jet loom machine with electrocoagulation method is more efficient than that with chemical coagulation method.

For further study, studying life time of electrode, space between electrode, and comparison of the effectiveness and the cost of water treatment by coagulation with chemicals and with electrical current.

Acknowledgement

The author would like to thank Rajamangala university of Technology Krungthep for the financial support and also grateful to Assis.Prof. Dr. Waraporn Tanakulrangsarn for her valuable comments and suggestions.

References

[1] A. Pinotti, A. Bevilacqua and Zaritzky, *Waste manage*. **21** (2001), pp. 535-542.

[2] A.A. Al Shamrani, A. James and H. Xiao, *Colloids Surf.* **A 209** (2002), pp. 15-26.

[3] K. Scott, R.J. Jachuck and D. Hall, *Sep. Purif. Technol.* **22** (2001), pp. 431-441.

[4] N. Moulai-Mostefa, A. Brou, L. Ding and M.Y. Joffrin, *Mecanique&Industries*. **6** (2005), pp. 203-210.

[5] S.E. Burns, S. Yiacoumi and C. Tsouris, *Sep. Purif. Technol.* **16** (1999), pp. 193-203.

[6] X. Chen, G. Chen and P.L. Yue, *Environ. Sci. Technol.* **36** (2002), pp. 778-783.

[7] M. Tir and N. Moulai-Mostefa, *J. Hazard. Matter*. **158** (2008), pp. 107-115.

[8] T.H. Kim, C. Park and E.B. Shin, *Desalination.* **150** (2002), pp. 165-175.

[9] M. Bayramoglu, M. Eyvaz and M. Kobya, *J Chem.Eng*. **128** (2007), pp. 155-161.

[10] A.H. Esssdki, M. Bennajah, B. Gourich and H. Delmas, *J Chem.Eng*. **47** (2008), pp. 1211-1223.

[11] P.K. Holt, G.W. Barton and C.A. Mitchell, *Chemosphere.* **59** (2005), pp. 355-367.

[12] L.S. Calvo, J.P. Leclerc, G Tnguy,M.C. Cames, G. Paternotte, G. Valentin, A. Rostan and F. Lapicque, *Environmental Progress.* **22** (2003), pp.57-65.

[13] M. Carmona, M. Khemis, J.P. Leclerc and F. A. Lapicque, *Chemical Engineering Science.* **61** (2006), pp. 1237-1246.

[14] P. Canizares, C. Martinez, C. Saez and M. Rodrigo, *Journal of Hazardous Materials*. **151** (2008), pp.44-51.

[15] M. Kobya, H. Hiz, E. Senturk and E. Demirbas, *Desalination*. **190** (2006), pp. 201-211.

[16] M. Yousuf, A. Mollah, R. Schennach, J.R. Parga and D.L. Cocke, *J.Hazard.Matter.* **84** (2001), pp. 29-41.

[17] APHA (American Public Health Association). Standard Methods for the Examination of Water and Wastewater. 20th ed. Washing, DC (1998)

Cadmium, lead, and manganese in PM10 in the air environment of Phitsanulok trade areas

N. Meechaiyo and P. Thongsanit*

Department of Civil Engineering, Faculty of Engineering, Naresuan University, Muang, Phitsanulok, Thailand 65000

*E-mail: Pajareethongsanit@yahoo.com

Abstract: This research is an attempt to study the concentration of Cadmium, Lead, and Manganese in the dust of which sizes are smaller than 10 micron (PM10) within the commercial areas of Nakhon Pitsanulok Municipality. The research aims to study the concentration of hazardous heavy metals such as Cadmium, Lead, and Manganese in PM10. Samples were collected from two locations. The first location is Boromtrilokkanat road of which the traffic rate is 5,000 vehicles within 12 hours (7.00 a.m.-7.00 p.m.). The second location is Ekatossarot road where there were 6,500 vehicles within 12 hours (7.00 a.m.-7.00 p.m.). PM10 samples were collected by using the High Volume Air Sampler for 24 hours. In the hot season and rainy season, samples were collected every 12 days. The dust concentration was analyzed by the gravimetric method while the quantity of heavy metals such as Cadmium, Lead, and Manganese were examined using the Flame Atomic Absorption Spectroscopy instrument. It was found that in hot season the average concentration of PM10 were 62 and 68 microgram per cubic meter in the sampling locations on Boromtrilokkanat and Ekatossarot road respectively. The PM10 concentration did not exceed the standard value of 120 microgram per cubic meter. The average concentration PM10 in the rainy season was found to be lower than that of the hot season. The concentration of heavy metals such as Cadmium, Lead, and Manganese were examined. The Lead's concentration was found to be in a range of 0.048-0.070 and 0.049-0.076 microgram per cubic meter in the two sampling locations on Boromtrilokkanat and Ekatossarot road respectively. These values do not exceed the standard value set by the Pollution Control Department (PCD) at 1.5 microgram per cubic meter. Meanwhile, the intensity of Cadmium and Manganese were found to be very low.

Introduction

At present, the traffic in Nakhon Pitsanulok Municipality is quite dense. There are private cars, buses, and motorcycles. Therefore, it increases environmental impacts and, importantly, causes the problem of the particulate matter that is smaller than 10 micron (PM10). This problem affects the respiratory system and human health. Moreover, this small particle dust can be an important accumulated source of heavy metals in the environment. Some heavy metals have adverse effects whereas other heavy metals are essential to human health but can be toxic if taken in excess quantity. As a guideline for the study of environment in the habitation and a guideline for the risk assessment of people's health in the area of Nakhon Pitsanulok Municipality, this research emphasized on the study of the quantity of toxic heavy metals which were cadmium, lead and manganese in PM10 and the study of the quantity of PM10 in trade area of Nakhon Pitsanulok Municipality.

Materials and Methods

2.1 Studied locations: collected the samples on the roadsides from 2 locations, e.g., Boromtrilokkanat road at the opposite side of Nanchao Hotel and Ekatossarot road at the BanKhak intersection which were in Nakhon Pitsanulok Municipality. PM10 dust samples were collected by the high volume air sampler in every 12 days and, in each round, the PM10 dust samples were collected 24 hours, continuously.

2.2 Research Period the research period was divided into 2 phases as follow;

(1) In dry season from the middle of February until the middle of May 2009

(2) In rainy season from the middle of May until September 2009

2.3 Sampling: collected the dust sample of which sizes are smaller than 10 micron by the glass fiber filter, collected the samples using the high volume air sampler, install the dust samplers at the studied locations as specified above.

2.4 Studies parameters and sample analysis

(1) The concentration of the dust of which sizes are smaller than 10 micron in 24 hours was analyzed by weight measurement (Gravimetric Method).

(2) The composite elements, i.e., cadmium (Cd), lead (Pb), and manganese (Mn) were analyzed by Flame Atomic Absorption Spectrophotoscopy (FAAS).

Results and Discussion

3.1 Concentration of PM10 in the air environment

The statistical summary of the daily PM10 data from two sites in Phitsanulok across the period January 2009 to September 2009 is show that the data minimum value of 24.53 microgram per cubic meter, recorded on 15 July 2009 at Boromtrilokkanat road site, to a maximum value of 90.80 microgram per cubic meter, recorded on 6 March 2009 at Ekatossarot road site. The daily PM10 concentrations were not exceeded the standard value at 120 microgram per cubic meter.

The measurement results of the average concentration of the dust of which sizes are smaller than 10 micron (PM10) in the studied location:

Boromtrilokkanat road in both seasons showed that, in dry season, the concentration of the dust of which sizes are smaller than 10 micron ranged from 38.75-87.27 microgram per cubic meter. The average concentration was 61.83±17.70 microgram per cubic meter. In rainy season, the concentration of the dust of which sizes are smaller than 10 micron ranged from 24.53-44.33 microgram per cubic meter. The average concentration was 33.26±7.33 microgram per cubic meter.

The measurement results of the average concentration of the dust of which sizes are smaller than 10 micron in the studied location: Ekatossarot road in both seasons showed that, in dry season, the concentration of the dust of which sizes are smaller than 10 micron ranged from 52.12-90.80 microgram per cubic meter. The average concentration was 67.81±13.17 microgram per cubic meter. In rainy season, the concentration of the dust of which sizes are smaller than 10 micron ranged from 25.98-53.32 microgram per cubic meter. The average concentration was 39.21±7.91 microgram per cubic meter.

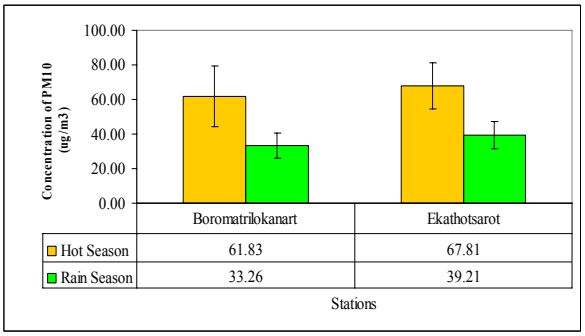

Figure1. Concentration of PM10 in the air environment

3.2 Concentration of Cadmium, Lead, and Manganese in PM10

The measurement results of the average concentration of metals: Cd, Pb, and Mn in the dust of which sizes are smaller than 10 micron in the studied location: Boromtrilokkanat road in both seasons showed that, in dry season, the average concentrations of Cd, Pb, and Mn in PM10 were 0.0042±0.0011, 0.0595±0.0073 and 0.0064±0.0012 microgram per cubic meter, respectively. In rainy season, the average concentrations of Cd, Pb, and Mn in PM10 were 0.0027±0.0012, 0.0499±0.0041 and 0.0045±0.0009 microgram per cubic meter, respectively.

The measurement results of the average concentration of metals: Cd, Pb, and Mn in PM10 in the studied location: Ekatossarot road in both seasons showed that, in dry season, the average concentrations of Cd, Pb, and Mn in PM10 were 0.0046±0.0013, 0.0605±0.0107 and 0.0070±0.0016 microgram per cubic meter, respectively. In rainy season, the average concentrations of Cd, Pb, and Mn in PM10 were 0.0023±0.0013, 0.0516±0.0041 and 0.0060±0.0015 microgram per cubic meter, respectively.

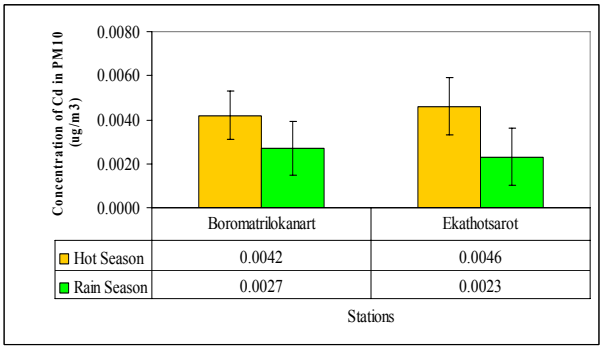

Figure2. Concentration of Cadmium in PM10 in the air environment

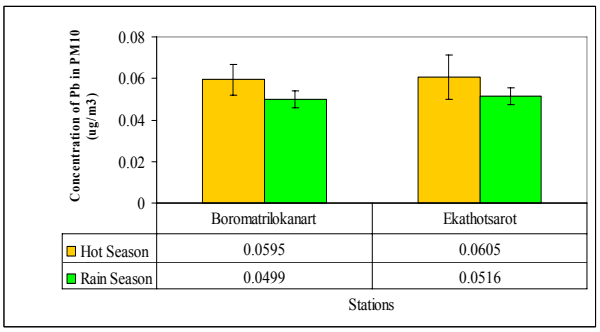

Figure3. Concentration of Lead in PM10 in the air environment

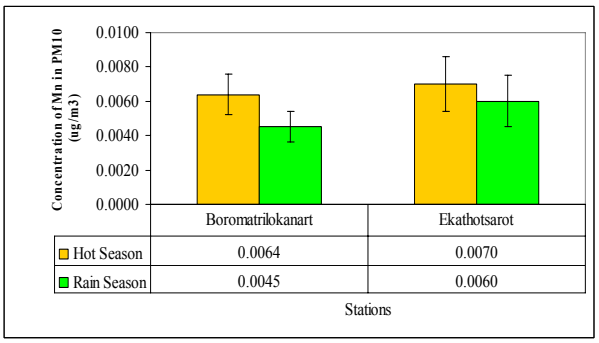

Figure4. Concentration of Manganese in PM10 in the air environment

Conclusions

From the measurement of the average concentration of the dust of which sizes are smaller than 10 micron from 2 studied locations which were Boromtrilokkanat and Ekatossarot road in both dry and rainy season, it was found that the average values were not exceed the quality standard in the air environment. It could be seen that the average concentration of the PM10 in each studied locations decreased in rainy season due to the rain erosion process which increased the precipitation of the accumulated dust and could reduce the concentration of the dust concentration in the air environment. There were cadmium (Cd), lead (Pb) and manganese (Mn) in every studied location. When comparing the average concentrations of these 3 heavy

metals in the PM10, lead (Pb) was found in the highest quantity and cadmium (Cd) was found in the lowest quantity. In rainy season, it was found that the average concentrations of these three heavy metals decreased because of the rain erosion process as well. This showed the same trend as the quantity of PM10.

Acknowledgement

This study was funded by the Faculty of Engineering, Naresuan University. The authors wish to thank all of staffs of the department of civil engineering for their support and providing research equipments. We thank Academic office in the faculty of engineering, Naresuan University, for their facilities support

References

[1] U. Chotpong, The study of particulate matter levels impact on respiratory system. *Research Report of Environmental Research Institute*. Chulalongkorn University, Bangkok. (1998).

[2] S. Melaku, V. Morris, D. Raghavan and C. Hosten, *Env. Pol*. **155** (2008), pp. 88-98.

[3] M. Thakur, M. Kantideb, S. Imai, Y. Suzuki, K. Ueki and A. Hasegawa, *Env. Mon. and Assess.***95** (2004), pp. 257-268.

[4] C. Y. Kuo, J. Y. Wang, S. H. Chang and M.C. Chen, *Atm. Env***.xxx** (2009), pp. 1-7.

[5] C. S. L. Lee, X. D. Li, G. Zhang, J. Li, A. J. Ding and T. Wang, *Atm. Env*. **41** (2007), pp. 432-447.

Purification of biodiesel using natural diatomite and diatomite doped with MnO_2

N. Saengprachum[1], S. Pengprecha[2*]

[1]National Center of Excellence for Environmental and Hazardous Waste Management, Chulalongkorn University, Bangkok, Thailand

[2] Department of Chemistry,Faculty of Science, Chulalongkorn University, Bangkok, Thailand

[*]E-mail: somchai.pe@chula.ac.th

Abstract: Biodiesel is an alternative fuel derived from vegetable oils or animal fats by using transesterification/ esterification reaction. In order to meet the high purity requirements laid down on the standard for biodiesel fuel, a purification process is needed. The common process to purify biodiesel is water washing. However, the water-washing process has several disadvantages such as yields loss in effluent; high soap levels that cause emulsification, and wastewater that cause environmental problem. To solve these problems, this research studies the adsorption of contaminants in crude biodiesel by using natural diatomite adsorbent (D). The sorption capacity of natural diatomite was further improved by doping diatomite with manganese oxide. The MnO_2-doped diatomite (DDM) was done by impregnating the diatomite surface with manganese oxide. The high performance exhibited by modified diatomite was attributed to increased surface area and higher negative surface charge. The surface area of diatomite and MnO_2-doped diatomite calculated using B.E.T method were 66 and 137 m^2g^{-1}, respectively. Moreover, MnO_2-doped diatomite adsorbent has advantage of reusable adsorbent. The optimal adsorption process was obtained by varying the ratio of adsorbent to biodiesel, contact time and temperature. Maximum sorption was achieved at 50°C with 4 % (w/w) of adsorbent and contact time of 20 min, which gave treated biodiesel that meet the major specification of biodiesel standards.

Introduction

Previously, the price of petroleum and the environmental concerns about air pollution coming from the car and industrial releasing continue to increase. Alternative fuel is the most possible way to solve these problems. Biodiesel, which defined as a fuel consist of mono-alkyl esters of long chain fatty acids derived from vegetable oils or animal fats by using transesterification/ esterification reaction, is one of the possible ways for this propose.

The conventional purification of biodiesel is water-washing. However, the water-washing process has several disadvantages; for example, yields loss in effluent, high soap levels that cause emulsification and high cost of treatment. In addition, water-washing process normally uses large amount of water which will generate wastewater that cause environmental problem.

To solve these problems, the research to date has tended to focus on using various adsorbents such as CaO, MgO, Mg_2CO_3, magnesium silicate, activated charcoal and bentonite to purify biodiesel instead of water-washing process. In this study, natural diatomite, alternative low cost sorbent available in Thailand, will be used. Furthermore, the effect of surface modification of diatomite by treating the diatomite with manganese chloride and sodium hydroxide on removal of glyceride will be studied.

Materials and Methods

The adsorbent: Natural diatomite was obtained from Amphur Mae Tha, Lampang province, Thailand. The Diatomite was washed with distilled water to remove fine particles and other impurities, dried at 100^0C, desiccated and stored in tightly capped glass bottle for future use. The chemical composition of diatomite was given in Table 1.

Surface modification: 15 g of natural diatomite was immersed in sufficient 6M sodium hydroxide at 80°C for 2 h. The diatomite was then placed in 100 mL of 1.5M manganese chloride (pH adjusted to 1–2 with hydrochloric acid) at room temperature for 10 h. The supernatant of this mixture was then discarded and the manganese-soaked diatomite was immersed in 6M sodium hydroxide at room temperature for 10 h. The supernatant was decanted and the diatomite was left to contact with air for 48 h. The sample was then washed, dried at 100°C, desiccated and stored in tightly capped glass bottle. This modified diatomite will be referred to MnO_2 doped diatomite [2]. The amount of Mn(IV) oxides doped on the diatomite was determined by dissolving the MnO_2 doped diatomite in 4 M hydrochloric acid at 40°C in a hot water bath. Manganese ions were determined by Inductively Coupled Plasma Atomic Emission Spectrometry (ICP) technique. The effect of chemical modification on diatomite was characterized using x ray diffraction (XRD) technique [4]. The surface area for the MnO_2 doped diatomite was estimated by B.E.T. method.

Synthesis of biodiesel from palm oil via base-catalyzed process: 400 g of palm oil was added into a 1000 mL round bottom flask equipped with condenser. After the oil was heated to 65°C, the solution of sodium hydroxide (4.0g) in methanol (115.85 mL) was slowly added into the reaction and then the mixture was heated to 65°C for 1 h. The reaction mixture was transferred to a separatory funnel, and allowed glycerin to separate. The excess methanol in crude biodiesel was removed by rotary evaporator, and then the crude biodiesel was brought to purification process.

Selection of adsorbents: Three types of adsorbents, natural diatomite, MnO_2 doped diatomite and activated charcoal, were studied. The size of all adsorbents was separated by passing through a screen (100 meshes).

Adsorbent treatment: In an effort to adsorb glycerin, five concentrations of each adsorbent: 1, 2, 3, 4 and 5 %wt were used. In a 150 mL flask, 100 g of crude biodiesel was treated with each adsorbents at 50 ^oC, with stirring at 150 rpm and contact time at 10, 20, and 30 minutes in water bath. Then the adsorbent was removed by filtration. Sorption capacities of all adsorbents were compared with traditional adsorbent (activated charcoal) and control (without adsorbent).

Analytical methods: (A two-step) Titration method is used to determine the amount of glycerin and unreacted catalyst. In Step 1, 3 g of crude biodiesel was dissolved in 100 mL of isopropyl alcohol with 2 mL of 1% phenolphthalein as an indicator. The mixture was titrated with 0.01N hydrochloric acid until the color of the solution changed from red to colorless. Then in Step 2, 1 mL of 0.04%bromophenol blue was added into the mixture. The solution was further titrated with 0.01N hydrochloric acid until the color of the solution changed from blue to yellow. This amount of 0.01N hydrochloric acid solution is referred as "B" [5]. The mount of unreacted NaOH can be calculated by using equation 1:

$$\text{g of NaOH / g of crude biodiesel} = \frac{A \times 0.01 \times 40.0}{W \times 1000} \quad (1)$$

where:
A = volume of hydrochloric acid used in step 1.
W = weight of crude biodiesel used (g).

And the amount of glycerin in the biodiesel can be calculated by using equation 2:

$$\text{g of glycerin /g of crude biodiesel} = \frac{B \times 0.01 \times 304.4}{W \times 1000} \quad (2)$$

where:
B = volume of hydrochloric acid used in step 2.
W = weight of crude biodiesel used (g).

Results and Discussion

Characterisation of natural diatomite: The chemical composition of natural diatomite determined by x-ray florescence (XRF) technique was shown in Table1. The main constituent of diatomite samples is SiO_2 (72.5 %). The surface area of natural diatomite calculated by B.E.T. method was estimated to be approximately 66 m^2/g.

Characterisation of modified diatomite: The amount of manganese oxides loaded on the surface of diatomite was 0.38 g/g diatomite assuming a birnessite type oxides ($Na_4Mn_{14}O_{27}\cdot 9H_2O$) formed on the surface [4]. This loading value was calculated from desorbing of Mn^{2+} ion from the MnO_2 doped diatomite surface. The surface area of modified diatomite calculated by B.E.T. method was estimated to be approximately 138 m^2/g.

Effect of contact time: The effect of contact time on sorption of glycerin was studied. By using 2%wt. of adsorbent, 30 g of treated biodiesel, and agitating at 150 rpm for 10-30 min. at 50^oC, the concentration of glycerin decrease from 0.005 to 0.0027, 0.0026, and 0.0023 g glycerin/g crude biodiesel with natural diatomite, activated charcoal, and MnO_2 doped diatomite respectively. The results were shown in Figure 1. The optimum contact time was found to be 20 min.

Effect of sorbent dosage: Figure 2 showed the glycerin content vs. various % adsorbent in the purification of biodiesel at 50^oC. By treating crude biodiesel with 1-5%wt. of adsorbents, the content of glycerin decreased from 0.005 to 0.0020, 0.0025, and 0.0011 g glycerin/g crude biodiesel with 4% of natural diatomite, activated charcoal, and MnO_2 doped diatomite, respectively.

Effect of methanol: In Table 2, the results showed that sorption without methanol could remove glycerin better than sorption with the presence of methanol. For MnO_2 doped diatomite, the glycerin content could be removed 12 times better than the presence of methanol and 25 times better for natural diatomite.

All treatments with natural diatomite and modified diatomite resulted in glycerin level to be below the value of the specification of biodiesel standard (0.0025g/g).

Table 1: Chemical composition of natural diatomite.

Oxide	Composition (%)
SiO_2	72.5
Al_2O_3	11.42
Fe_2O_3	5.81
MgO	0.25
CaO	1.48
Na_2O	7.21
K_2O	0.69

Table 2: Effect of methanol on adsorption process.

Adsorbent	Glycerin content (g glycerin/ g crude biodiesel)	
	With methanol	Without methanol
MnO_2 doped diatomite	1.8×10^{-4}	0.15×10^{-4}
Natural diatomite	5.36×10^{-4}	0.21×10^{-4}

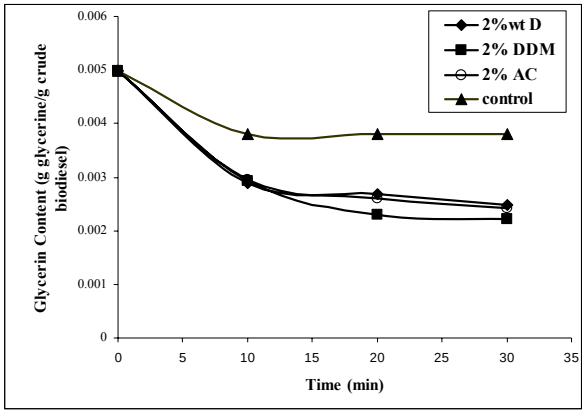

Figure 1. Glycerin content vs. time with various adsorbents at 50°C and stirring at 150 rpm.

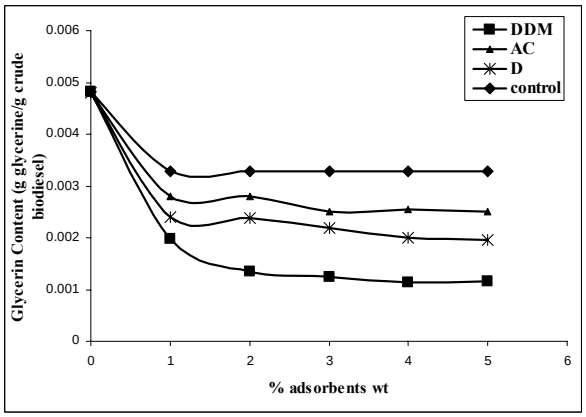

Figure 2. Glycerin content vs. various % adsorbent at 50°C and stirring at 150 rpm.

Conclusions

Low cost natural diatomite could be used as adsorbent for purifying biodiesel as it has capacity to adsorb contaminants in biodiesel as well as activated charcoal. Sorption capacity of diatomite is considerably improved after modification. By using 4 %wt. of adsorbent at 50°C with contact time of 20 min., the level of glycerin is lower than of the specification of biodiesel standard (0.0025g/g).

References

[1] M. Berriosa, R.L. Skeltonb, *Chem. Eng.J.***144** (2008), pp. 459–465.
[2] M.A.M. Khraisheh, Y. Al-degs., Wendy and A.M. Mcminn.*Chem. Eng. J.* **99** (2004), pp. 177–184.
[3] M. Maskan and H. Bagci, *Eur Food Res Technol*. **217** (2003), pp. 215– 218.
[4] Y. Al Degs, M. A. M. Khraisheh and M. F. Tutunji, *Water Res*. **35**, (2001), pp. 3724-3728.
[5] J. Van Gerpen, B. Shanks, R. Pruszko, D. Clements and G. Knothe, Biodiesel Analytical Methods, *National Renewable Energy Laboratory*, (2004), NREL/SR-510-36240.
[6] M. A. Al-Ghouti , Y. S. Al-Degs , M. A.M. Khraisheh, M. N. Ahmad and S. J. Allen, *Journal of Envi Manage*. **90** (2009), pp. 3520-3527.
[7] Y.S. Al-Degs and M.F. Tutunju, *Sep. Sci. And Tecchnol*. **35**(14), (2000) pp. 2299-2310.
[8] M. Al-Ghouti , M.A.M. Khraisheh , M.N.M. Ahmad and S. Allen , *Journal of Coll. and Inter. Sci.* **287** (2005), pp. 6–13.
[9] P. Moslehi and P. Nahid, *IJE Transactions B*. **20**, (2007), pp. 141-146.
[10] J.M. Marchetti, V.U. Miguel and A.F. Errazu, *Renew Sust Energy Rev* **11** (2007), pp 1300-1311.
[11] S. Nassreddine, A. Karout, M. Lorraine Christ and A.C. Pierre, *Apply. Catal. A* **344** (2008), pp. 70-77.
[12] A.L. Ahmad, S. Bhatia, N. Ibrahim and S. Sumathi, *Brazil. Journal of Chem. Eng.* **22** (2005), pp 371-379.
[13] A.P. de A. Vieira, M.A.P. da Silva and M.A.P. Langone, *Latin American Apply. Res.* **36** (2006), pp. 283-288.
[14] O.S. Amuda and A.O. Ibrahim, *African jounal. of Biotech*. **5** (2006), pp. 1483-148

Life cycle assessment study for two different phenol production processes

W.Ponkham[1]*, P. Kittisupakorn [1]

[1]Life Cycle Engineering Laboratory , Department of Chemical Engineering, Faculty of Engineering, Chulalongkorn University, Phayathai, Bangkok, Thailand 10330

*E-mail: Wilaiwan.P@Student.chula.ac.th

Abstract: In this research studies on phenol production processes by using two different phenol production processes which are cumene oxidation (Hock process)[1] and toluene oxidation (Dow process)[2]. In order to study in environmental impacts, Life Cycle Assessment (LCA) is applied to evaluate environmental impacts of phenol production processes. Environmental impacts are evaluated according to cradle-to-gate approach by using SimaPro 7.1 software for Life Cycle Assessment . Approach by IMPACT 2002+ . The result shows that cumene process is more environmentally favorable than toluene process. Environment impacts are Non-renewable energy, Global warming, Respiratory inorganics and Carcinogens respectively.

Keywords: Phenol, Cumene,Toluene,Hock process,Dow process

Introduction

Life cycle assessment (LCA) methodology is used to evaluate the impact of processes or products on the environment. The inclusion of every stage of the process or product's life cycle is fundamental to this analysis. In the case of products, every stage from the production of the raw materials to the end of their useful lives and their use and maintenance should be included. Thus, all significant environment impacts in their life cycle (cradle to grave) analysis is impossible and the analysis must terminate at an intermediate stage (gate to gate). [3]

Phenol, hydroxybenzene, carbolic acid, C_6H_5OH, discovered in 1834 by F.Runge, is the parent substance of a homologous series of compounds with the hydroxyl group bonded directly to the aromatic ring. Phenol occurs as a free component or as an addition product in natural products and organisms. For example, it is a component of lignin, from which it can be liberated by hydrolysis. As a metabolic product it is normally excreted in quantities of up to 40 mg/L in human urine. Higher quantities are formed in coking or low-temperature carbonization of wood, brown coal, or hard coal and in oil cracking. Initially phenol was extracted exclusively from hard coal tar, and only after consumption had risen significantly was it also produced synthetically. The earlier methods of synthesis have been replaced by modern processes, mainly by the Hock process starting from cumene. Phenol has achieve considerable importance as the starting material for numerous intermediates and finished products. [4]

Small quantities of phenol (cresylic acids) are isolate from tars and coking plant water produced in the coking of hard coal and the low temperature carbonization of brown coal as well as from the wastewater from cracking plants. By far the largest proportion in obtained by oxidation of benzene or toluene. Although direct oxidation of benzene is in principle possible, the phenol formed in immediately oxidized further. Therefore, alternative routes must be chosen, e.g. via halogen compounds which are subsequently hydrolyzed or via cumene hydroperoxide which in then cleaved catalytically. The following processes were developed as industrial syntheses for the production of phenol:

1 Cumene oxidation (Hock process).

2 Toluene oxidation (Dow process).

Physical Properties

Phenol has a melting point of 40.9°C,crystallizes in colorless prisms and has a characteristic, slightly pungent odor. In the molten state it is a clear, colorless, mobile liquid. In the temperature range up to 68.4 °C its miscibility with water is limited, above this temperature it is completely miscible. The melting and solidification points of phenol are lowered quite considerably by water. A mixture of phenol and ca 10 wt% water is called phenolum liquefactum, because it is liquid at room temperature. Phenol is readily soluble in most organic solvents (aromatic hydrocarbons, alcohols, ketones, ethers, acids, halogenated hydrocarbons, etc.). Other physical data of phenol follow:

Table 1: physical data of phnol

M_r g/mol	94.11
B_p (101.3kPa)	181.75 °C
Mp	40.9°C
Relative density g/cm^3	
0°C	1.092
20°C	1.071
50°C	1.050
Vapour density air =1	3.24

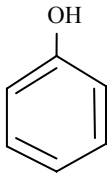

Figure 1. The chemical structure of Phenol

Materials and Methods

1. Cumene oxidation (Hock process)

The cumene – phenol process is based on the discovery of cumene hydroperoxide and its cleavage to phenol and acetone published in the 1944 by H.HOCK and S.LANG. This reaction was developed into an industrial process shortly after World War II by the Distillers Co. in the United Kingdom and the Hercules Power Co. in the United States. Cumene is produced commercially through the alkylation of benzene with propylene over an acid catalyst. Over the years, many different catalysts have been proposed for this alkylation reaction, including, and phosphoric acid. Cumene processes were originally developed between 1939 and 1945 to meet the demand for high octane aviation gasoline during World war II. In 1989, about 95% of cumene demand was used as an intermediate for the production of phenol and acetone. A small percentage is used for the production of α-methylstyrene. The demand for cumene has risen at an average rate of 2-4% per year from 1970 to 2003. This trend is expected to continue though at least 2010.[5]

Two reaction steps from the basis of the production of the phenol from cumene:

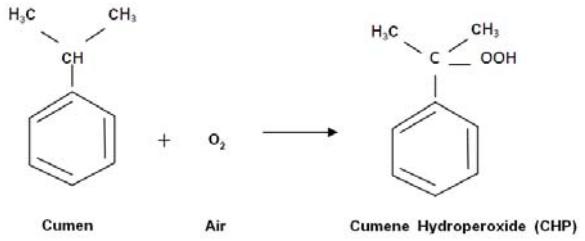

Figure 2. Oxidation of cumene to Cumene Hydroperoxide (CHP)

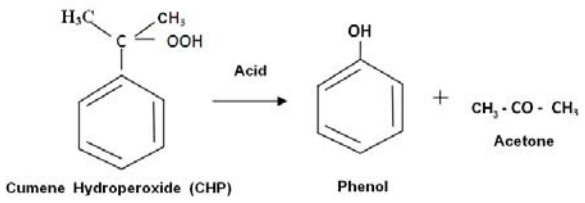

Figure 5. Reaction for phenol and acetone production

Table 2: Data in the SimaPro 7.1 software which the phenol product 1 kg. (Hock process)

		Name	Amount	Unit
Input	Cumene		1.340	kg
	Oxygen		0.358	kg
Output	Emission to air	Carbon dioxide	0.191	kg
		Cumene	0.002	kg
		Heat (waste)	1.200	MJ
	Emission to water	Water (waste)	10.000	mg
		Cumene	0.006	kg

2. Toluene oxidation (Dow process).

The Dow phenol Process utilizes toluene as feedstock. In two separate steps, toluene is first oxidized to benzoic acid; thereafter benzoic acid is converted to phenol, using copper benzoate as the principal catalyst. In the first stage toluene is oxidized with atmospheric oxygen in the presence of a catalyst to benzoic acid in the liquid phase. In the second stage the benzoic acid isolated is decarboxylated catalytically in the presence of atmospheric oxygen to produce phenol.

The oxidation occurs in the liquid phase at 150°C and 0.5 Mpa the toluene is converted into benzoic acid. The selectivity is 90%. The oxidation decarboxylation of benzoic acid proceeds via Cu benzoate, which reacts further to give benzoylsalicylic acid. The latter then either hydrolyzes to salicylic acid and benzoic acid or decarboxylates to phenyl benzoate.

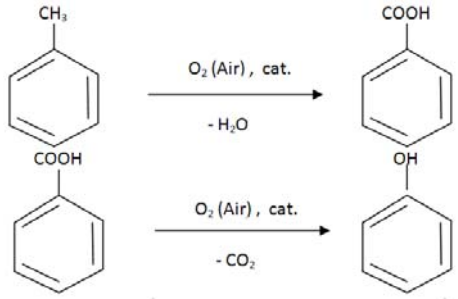

Figure 3. Reaction for phenol from toluene oxidation.

The oxidizing decarboxylation of benzoic acid proceeds via Cu (II) benzoate, which reacts further to give benzoylsalicylic acid. The latter then either hydrolyzes to salicylic acid and benzoic acid or decarboxylates to phenol benzoate. Phenyl benzene hydrolyzes in the presence of water to phenol and benzoid acid, Cu (II) is reduced to Cu (I) which is present as Cu (I) benzoate. Copper (I) is reoxidized to Cu (II) with atmospheric oxygen at a very high reaction rate. The reaction proceeds at 250°C under normal pressure or a small excess pressure (up to 0.25 MPa). The selectivity is ca. 90%.

Table 3: Data in the SimaPro 7.1 software which the phenol product 1 kg. (Dow process)

Data		*Name*	*Amount*	*Unit*
Input	*Toluene*		*1.440*	*kg*
	Oxygen		*0.476*	*kg*
Output	*Emission to air*	*Carbon dioxide*	*10.300*	*mg*
		Carbon monoxide	*31.000*	*mg*
		Nitrogen dioxide	*1.900*	*g*
		Phenol	*22.000*	*mg*
		Toluene	*23.000*	*mg*
		Heat (waste)	*0.800*	*MJ*
	Emission to water	*Water (waste)*	*20.000*	*mg*
	Emission to soil	*Copper*	*322.000*	*mg*

Results and Discussion

Evaluated the environmental impacts by SimaPro software. Life cycle assessment for Phenol production process from cumene or Hock process which use indicator IMPACT 2002+ .

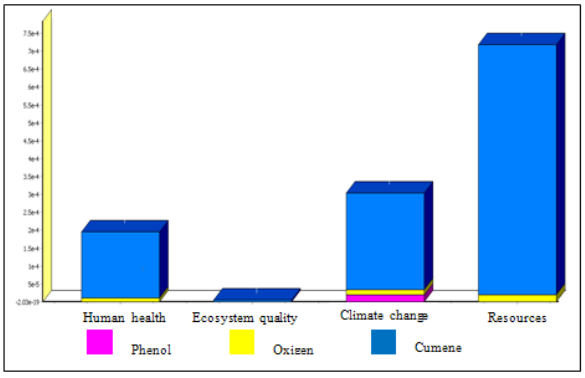

Figure 4. Life cycle assessment for phenol production process from cumene (Human health , Ecosystem, Climate change and Resources)

Table 4: Data in the SimaPro 7.1 software for Impact category of hock process

Impact category	Total	Phenol	Oxygen	Cumene
Carcinogens	4.95E-05	0.00E+00	1.69E-07	4.94E-05
Non-carcinogens	1.02E-05	5.93E-08	2.85E-07	9.87E-06
Respiratory inorganics	1.33E-04	0.00E+00	9.73E-06	1.23E-04
Ionizing radiation	9.84E-07	0.00E+00	3.57E-07	6.27E-07
Ozone layer depletion	7.37E-09	0.00E+00	1.04E-09	6.33E-09
Respiratory organics	1.47E-06	4.19E-07	3.91E-09	1.05E-06
Aquatic ecotoxicity	1.18E-07	0.00E+00	1.54E-08	1.03E-07
Terrestrial ecotoxicity	3.50E-06	0.00E+00	2.97E-07	3.20E-06
Terrestrial acid/nutri	2.42E-06	0.00E+00	1.33E-07	2.28E-06
Land occupation	2.42E-08	0.00E+00	7.62E-09	1.66E-08
Global warming	3.03E-04	1.93E-05	1.41E-05	2.69E-04
Non-renewable energy	7.18E-04	0.00E+00	1.93E-05	6.98E-04
Mineral extraction	1.92E-09	0.00E+00	1.53E-10	1.77E-09

Figure 4. show that phenol production process environmental impacts everyway as human health , Ecosystem quality, Climate change and Resources etc. Cumene more than phenol and oxygen in all way.

Main impacts in table 4 are cumenae impacts to Non-renewable energy, Global warming, Respiratory inorganics and Carcinogens respectively. Oxygen in process impacts to Global warming, Non-renewable energy and Respiratory inorganics respectively. Phenol impacts to Global warming .

Evaluated the environmental impacts by SimaPro software. Life cycle assessment for Phenol production process from toluene or Hock process which use indicator IMPACT 2002+ method.

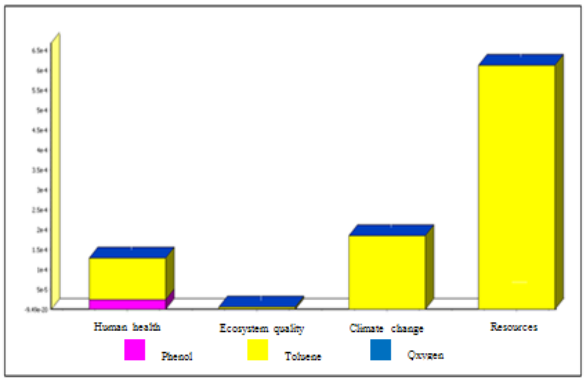

Figure 5. Life cycle assessment for phenol production process from toluene (Human health , Ecosystem, Climate change and Resources)

Table 5: Data in the SimaPro 7.1 software for Impact category of dow process

Impact category	Total	Phenol	Toluene	Oxygen
Carcinogens	2.63E-05	1.85E-13	2.63E-05	2.25E-13
Non-carcinogens	1.25E-06	2.15E-09	1.25E-06	3.79E-13
Respiratory inorganics	1.00 E-04	2.39E-05	7.66E-05	1.29E-11
Ionizing radiation	5.91E-10	0.00E+00	5.91E-10	4.74E-13
Ozone layer depletion	9.91E-12	0.00E+00	9.91E-12	1.39E-15
Respiratory organics	5.00E-07	4.41E-09	4.96E-07	5.20E-15
Aquatic ecotoxicity	7.43E-08	2.41E-08	5.02E-08	2.04E-14
Terrestrial ecotoxicity	2.95E-06	1.29E-06	1.66E-06	3.95E-13
Terrestrial acid/nutri	2.28E-06	7.92E-07	1.49E-06	1.77E-13
Land occupation	2.46E-09	0.00E+00	2.46E-09	1.01E-14
Global warming	1.85 E-04	1.05E-09	1.85 E-04	1.87E-11
Non-renewable energy	6.11 E-04	0.00E+00	6.11 E-04	2.56E-11
Mineral extraction	5.50E-10	0.00E+00	5.50E-10	2.04E-16

Figure 5 main impact to environment as human health , Ecosystem quality, Climate change and Resources etc. Toluene impact to everyway more than phenol and oxygen.

Table 5 show that toluene impacts to Non-renewable energy, Global warming, Respiratory inorganics and Carcinogens respectively.
Oxygen in process impacts to Non-renewable energy, Global warming, Respiratory inorganics and Carcinogens respectively. And phenol impacts to Respiratory inorganics .

Conclusions

Environmental impacts are evaluated according to cradle-to-gate approach by using SimaPro 7.1 software for Life Cycle Assessment . Approach by IMPACT 2002+ . The result shows that cumene process is more environmentally favorable than toluene process which main impacts are Non-renewable energy, Global warming, Respiratory inorganics and Carcinogens etc show that in figure 4 and figure 5.

So phenol production process will be better off toluene process or dow process but in Thailand has cumene process which impacts to environment very much so be using Life Cycle Assessment for decreasing environment impacts.

References

[1] Robert J.; Schmidt. Industrial catalytic process phenol production. *Applied Catalysis*. 2005, 280, 89-103.

[2] W.Buijs. The mechanism of phenol formation in the Dow phenol Process. *Industrial Chemistry*. 1999, 146, 237-246. [3]

[3] Alejandro Josa , A. A., Arnaldo Cardim ,Ewan Byars "Comparative analys is of the life cycle impact assessment of available cement inventories in the EU." 2007: 781-788.

[4] "Encyclopedia of industrial chemistry volumn 25." 589-602.

[5] Schmidt, R. "Industrial catalytic processes phenol production." 19 October (2005): 89–1.

Cutting oil removal by continuous froth flotation under low interfacial tension conditions: effects of packing media

A. Bunturngpratoomrat[1*], S.Nitivattananon[1,3] and S.Chavadej[2,3]

[1]Department of Chemical Technology Faculty of Science Chulalongkorn University, , Phaya Thai, Bangkok, Thailand 10330
[2]The Petroleum and Petrochemical College, Chulalongkorn University, , Phaya Thai, Bangkok, Thailand 10330
[3]Center for Petroleum, Petrochemicals and Advanced Materials, Chulalongkorn University, , Phaya Thai, Bangkok, Thailand 10330

*E-mail: apitch_pe4r@hotmail.com

Abstract: Froth flotation is an effective process for oil removal from wastewater especially at low oil concentrations. The aim of this research was to apply a packing media in a froth flotation column for oily wastewater treatment and to investigate the relationship between interfacial tension (IFT), foam characteristics and the efficiency of cutting oil removal from water in a continuous froth flotation operation. The effects of operational parameters including height of packing media, salinity, air flow rate, and hydraulic retention time (HRT) on the cutting oil removal were investigated in a continuous froth flotation column. In this research, a sodium dodecyl sulfate (SDS) concentration of 0.1 % by weight which provided the highest cutting oil removal was used as the base operation condition. The froth flotation column without packing media gave oil removal of 88.1 % and the oil removal increased to 98.10 % and then declined to 90.60 % with 50% and 100% packing media, respectively. The optimal operational condition was found at 50% packing media, 6 % by weight NaCl, 500 ppm oil content, 200 ml/min air flow rate, and 60 minutes HRT. The presence of packing media in the froth flotation column simply retained the air bubbles in the column, leading to a higher mass transfer rate. However, if it was too high fraction of packing media, it might reduce the effective liquid holding volume in the column, resulting in the reduction of oil removal efficiency.

Introduction

In general there are three steps in wastewater treatment system. The first step is the preliminary treatment in order to screen out disposable garbage using bar screens or grit chambers. The primary treatment is the second step in wastewater treatment for the separation of suspended solids and greases to be treated as sludge. The last step is the secondary treatment or biological treatment process to remove dissolved organic matter from wastewater.

Cutting oil is a complex combination of hydrocarbons produced by the distillation of crude oil. It consists of hydrocarbons having carbon number predominantly in the range of C_{15}-C_{24} and having a boiling point higher than 316ºC. The cutting oils are normally used in during the mechanical operations of cutting and shaping metals. A cutting fluid usually contains a mineral oil, a surfactant mixture, and various additives. These cutting fluids lose their effectiveness because of their thermal degradation and the presence of the suspended matters. Hence, it is necessary to carry out their replacement periodically and to get rid of the worn effluents, therefore resulting in producing oily wastewater.

There are several technologies for oily wastewater treatment such as centrifuge, rotary drum vacuum filter, biological treatment and froth flotation processes. This research focused on the froth flotation process, which is primary treatment process, due to simple method, high efficiency and low operating cost. The air is introduced at the bottom of a froth flotation column. Emulsified oils can co-adsorb at the air-water interface and be carried over the top of the column. Surfactants play an important role in the froth flotation by inducing foam formation, reducing the coalescence rate of bubbles within the liquid phase, and increasing the retention time of bubbles in the column. Besides the surfactant, there are additional factors effects on separation efficiency of the froth flotation process such as salinity, oil-to-water ratio, foam height, air flow rate, and hydraulic retention time, (HRT). These factors have previously studied in several works. The packing material often used in industries to provide intimate contact between two phases in separation processes. Therefore, this research will focus on the packing media volume in the froth flotation column. The objective of this research is to investigate the effects of packing media volume on cutting oil removal by continuous froth flotation system and find the optimal operational condition.

Materials and Methods

Materials: Sodium dodecylsulfate (SDS) used in this work is an anionic surfactant with a negatively charged sulfate head group and an alkyl chain length of twelve carbon units, which was obtained from Carlo Erba Reagenti with purity in the range of 94–98%. All experiment was carried at the constant concentration of SDS at 0.1% by weight. Analytical grade sodium chloride (NaCl) was used as an electrolyte and obtained from Labscan Asia Co., Ltd. with a purity of 99%. All chemicals were used as received without further purification. Deionized water was used to prepare all aqueous solutions.

Interfacial tension measurement: the interfacial tension (IFT) between the surfactant solution and the oil phase which were in equilibrium at different

conditions was measured using a spinning drop tensiometer (SITE 04, Kruss) in order to localize precisely the microemulsion phase boundary at very low surfactant concentrations.

Froth flotation system: Figure 1 shows a schematic of the continuous froth flotation apparatus used in this study. The apparatus consisted of a glass cylindrical column with 5 cm inside diameter and 120 cm height, and it was operated in continuous mode. Compressed air was first filtered to remove all particles, water, and oil before entering the flotation column. The flow rate of the filtered air was regulated by a mass flow controller (GFC171S, Aalborg). The filtered air was introduced into the bottom of the column through a sinter glass disk with pore diameters of about 16–40 mm. A well-mixed solution was fed continuously at a desired flow rate into the froth flotation column by using a peristaltic pump (Easy-load II, Masterflex). The level of the solution in the column was adjusted by a three-way flexible outlet tube in order to vary the foam height. The air bubbles ascended through the solution generated foam. The foam overflown from the column was collected 10 minute intervals, and then the collapsed froth was analyzed for cutting oil and surfactant concentrations in the froth. The effluent samples were collected for analysis of cutting oil and surfactant concentrations by using the methylene chloride extraction method and the titration with methylene blue chloride method (ASTM D1681-92), respectively. Percentage of cutting oil removal was calculated using equation (1);

$$\% \text{ Oil removal} = \frac{([\text{oil}]\text{in} \times \text{feed flow rate}) - ([\text{oil}]\text{out} \times \text{treated water flow rate})}{([\text{oil}]\text{in} \times \text{feed flow rate})} \times 100 \quad (1)$$

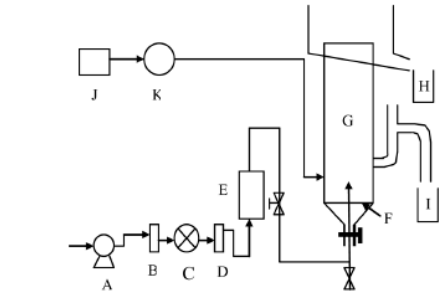

A :Compressor
B :Water filter
C :Air regulator
D :Oil filter
E :Mass flow controller
F :Sintered glass disc
G :Flotation column
H :Foam receiver
I :Effluent receiver
J :Feed tank
K :Peristatic pump

Figure 1. Schematic of the continuous mode froth flotation apparatus [5].

Results and discussion

Effect of Salinity: The effect of NaCl concentration on IFT is shown in Figure 2. The concentrations of NaCl was varied from 3 to 8 wt.% The IFT was dramatically decreased as the salt concentration increased in the range of 3-6 wt.%. This is because the repulsive force between anionic head group of surfactant decrease leading to an increase in aggregation number as well as increasing solubilization of oil into inner core of micelles. It was found that at 6 wt.% the IFT value was lowest and was selected to study for the performance of froth flotation.

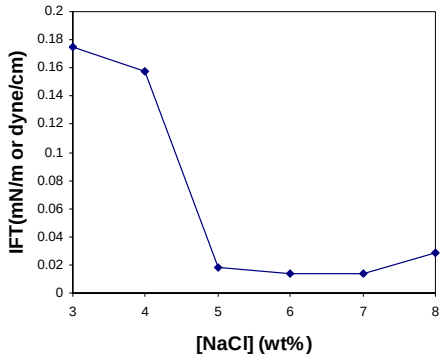

Figure 2. Effect of NaCl concentration on the interfacial tension.

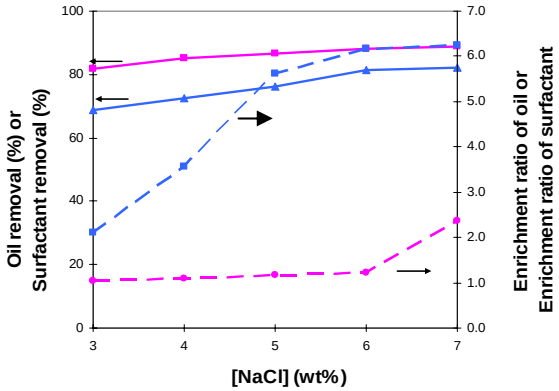

Figure 3. Effect of NaCl concentration on process parameters for continuous froth flotation.

Figure 3 shows effect of NaCl concentration on oil and surfactant removal in the left y-axis and on enrichment ratio of oil and surfactant in the right y-axis. For non packing media experiment, it was found that the increasing of NaCl concentration leads to higher oil and surfactant removal due to the lower repulsive force between anionic head group of surfactant. The highest oil removal is 88% at 6 wt.% NaCl. This phenomenon could explain as following. The surfactant molecules adsorb into air bubble more easily leading to a higher amount of oil to be carried over into the collapsed froth. As a result, the enrichment ratio of oil and surfactant increases with increasing NaCl concentration.

Effect of air flow rate: The effect of air flow rate and percent oil removal at various packing media volumes using 6 wt.% NaCl and 60 minutes HRT is shown in Figure 4. In without packing media system, the highest oil removal was 88.1% at 150 ml/min air flow rate. It was observed that at a lower range air flow

rates (150-250 ml/min.), the percentages of oil removal was higher as air flow rate increased. However, the oil removal efficiency was found to decrease as the air flow rates increased in the range of 250-300 ml/min. The best condition was found at 200 ml/min air flow rate and 50% of packing volume where the oil removal efficiency was as high as 98.10%. It can be explained that the packing media hold the air bubbles in the column therefore the oil droplets agglomerated better with the bubbles. However, at 75% and 100% packing volume and 250 ml/min air flow rate, the oil removal decreased to 91.90% and 90.60%, respectively. This might be because the time spent in the column of the bubbles was too long leading to higher change of bubbles breaking before reaching the top of the column. For this reason the oil droplets failed down to the solution once again resulting lower efficiency at high packing volumes.

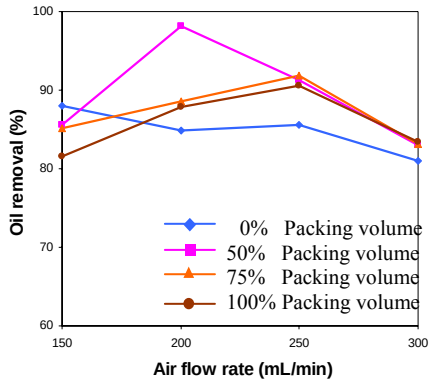

Figure 4. Effect of air flow rate on cutting oil removal

Figure 5 shows effect of air flow rate on enrichment ratio of cutting oil at various packing media volumes using 6 wt.% NaCl and 60 minutes HRT. As the air flow rate increased, the tendency of the enrichment ratio of cutting oil is decreased due to the short drainage time of water from the foam phase. The highest enrichment ratio was found at 75% packing volume.

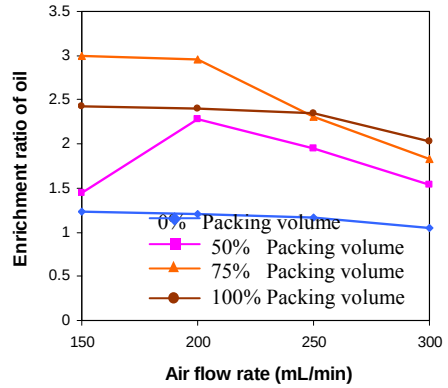

Figure 5. Effect of air flow rate on enrichment ratio of cutting oil

Figure 6 shows that foam production rate increased with increasing in air flow rate. The foam production rate was highest in the system without packing media. In contrast the lowest foam production rate was found in a system of 100% packing volume at the same air flow rate. An increasing of packing media volume leads to a higher change of bubble breaking and system turbulent. As can be seen in Figure 5, the column with packing media gave higher enrichment ratio of oil. At low foam production rate, the froth zone has longer time for water drainage. As a result, the concentration of oil in this zone was higher. In Figure 5, the enrichment ratio of oil in the system with 100% packing volume was lower than that of the system with 75% packing volume at air flow rate less than 250 ml/min. In such system (low air flow rate and high packing volume), the air bubbles remained excessively in the column and are easily to break up before float up. Consequently, an amount of oil in the top of the colun

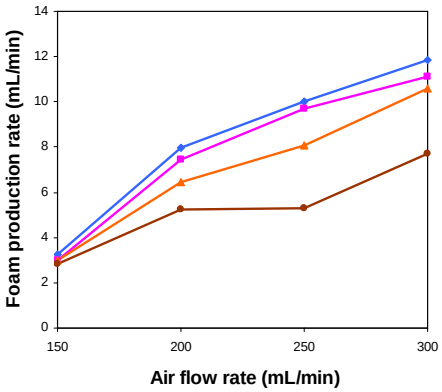

Figure 6. Effect of air flow rate on foam production rate

Effect of HRT: Figure 7 illustrates the effect of HRT on oil removal at various packing volume using 6 wt.% NaCl and 200 ml/min air flow rate. The oil removal tended to increase with increasing HRT since the cutting oil has longer residence time in the column resulting in higher coalescing between air bubbles and oil in the solution. The highest oil removal efficiency was found at 60 minutes HRT in the system containing 50% packing volume. For 75% and 100% packing volume systems, the oil removal efficiency reduced because of less liquid holding volume in the column. However, at 80 minutes HRT oil removal was found to decrease for all packing systems. The explanation of this action will be in the next section.

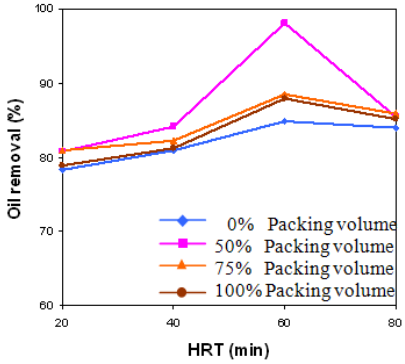

Figure 7. Effect of HRT on cutting oil removal

Figure 8 shows the effect of HRT on enrichment ratio of oil. At 0% packing volume, the increased of HRT caused only a slight increased in enrichment ratio of oil. At 50% packing volume, the enrichment ratio tended to increase with increasing HRT from 20 to 60 minutes. At high HRT (lower feed flow rate), the oil has longer residence time in the columns leading to more contact with the air bubbles. However, enrichment ratio of oil decreased after 60 minutes HRT. It is from the fact that the surfactant concentration is too low to remove oil from the solution into the froth zone. Figure 8 also shows that at 75% and 100% packing volume, the enrichment ratio of oil gradually decreased as HRT increased. The volume of packing media reduced the solution volume and surfactant concentration. For this reason the enrichment ratio was found to decrease in these two packing systems.

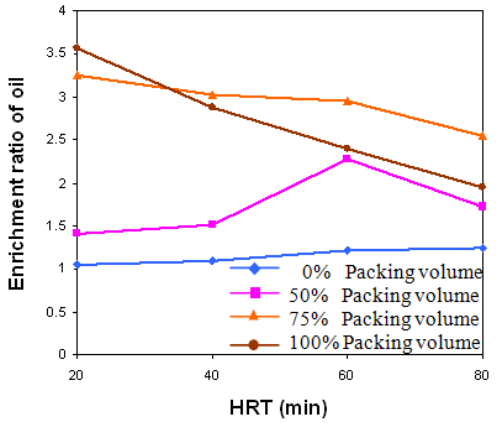

Figure 8. Effect of HRT on enrichment ratio of cutting oil.

Figure 9 shows the effect of HRT on foam production rate. The foam production rate decreased in all systems as HRT increased. This behavior was due to the effect of lower feed flow rate when HRT increased. It should be pointed out that the foam production rate in the systems without packing volume was higher than those of systems with packing media.

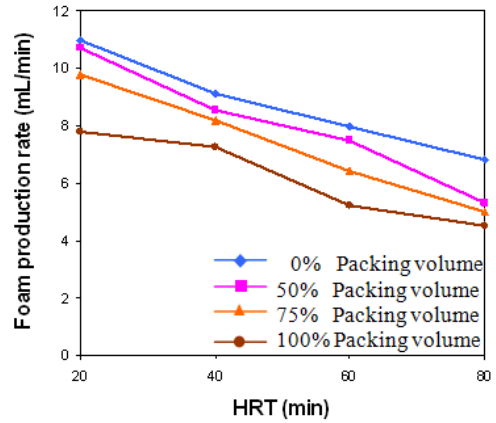

Figure 9. Effect of HRT on foam production rate

Conclusion

A continuous froth flotation column with packing media was successfully performed for oily wastewater treatment. Without packing media, the highest oil removal was 88.1% at 0.1wt.% SDS, 6 wt.% NaCl, 500 ppm oil content, 150 ml/min air flow rate, and 60 minutes HRT. The highest oil removal increased to 98.10% in the system with 50% volume of packing media at 0.1 wt.% SDS, 6 wt.% NaCl, 500 ppm oil content, 200 ml/min air flow rate, and 60 minutes HRT. The packing media leads to a high mass transfer rate between oil and bubbles. In conclusion, the froth flotation performance was improved by using packing media in a continuous system.

Acknowledgement

This work was fully supported by Department of Chemical Technology Faculty of Science Chulalongkorn University and the Petroleum and Petrochemical College, Chulalongkorn University.

References

[1] Rosen, M.J., Wiley J., Surfactants and Interfacial Phenomena, 2nd Ed., New York (1989), pp. 276–303.

[2]Chavadej, S., Ratanarojanatam, P., Wisakha Phoochinda,W., Ummarawadee Yanatatsaneejit, U., and Scamehorn, J.F., *Clean-up of Oily Wastewater by Froth Flotation: Effect of Microemulsion Formation II: Use of Anionic/Nonionic Surfactant Mixtures* Separation and technology 39 (2004), pp. 3079–3096

[3] Yanatatsaneejit, U., Witthayapanyanon, A., Rangsunvigit, P., Acosta, E.J., Sabatini, D.A., Scamehorn, J.F., and Chavadej, S., *Ethylbenzene removal by Froth Flotation under conditions of middle-phase microemulsion formation I: Interfacial tension, foamability, and foam stability*, Separation Science and Technology 40 (2005), pp. 1553-1537

[4] *Yanatatsaneejit, U., Chavadej, S. and Scamehorn, J.F.*, Diesel Oil Removal by Froth Flotation Under Low Interfacial Tension ConditionsI: Foam Characteristics, and Equilibration Time, *Separation Science and Technology 43 (2008), pp.1520–1534*

[5] Watcharasing, S., Chavadej, S. and Scamehorn, J.F., *Diesel Oil Removal by Froth Flotation Under Low Interfacial Tension Conditions II: Continuous Mode of Operation*, Separation Science and Technology, 43 (2008), pp. 2048–2071

pH response to NaCl toxicity in anaerobic digestion

N. Hudayah[1], B.Suraraksa [2*], P. Kullavanijaya [1] and P. Chaiprasert [3]

[1] Pilot Plant Development and Training Institute (PDTI),
King Mongkut's University of Technology Thonburi, Bangkuntien, Bangkok 10150, Thailand
[2] Excellent Center of Waste Utilization and Management (EcoWaste),
National Center for Genetic Engineering and Biotechnology (BIOTEC),
Thakham, Bangkhuntien, Bangkok 10150, Thailand
[3] Division of Biotechnology, School of Bioresources and Technology,
King Mongkut's University of Technology Thonburi, Bangkhuntien, Bangkok 10150, Thailand

[*] E-mail : benjaphon@biotec.or.th

Abstract: Saline wastewater is one of the high strength wastewaters which is difficult to be treated because of its high organic matter and salt content. Although anaerobic digestion (AD) is well known as the most appropriate method for treating high organic matter, high salt concentration in that wastewater can inhibit the activity of microorganism. pH factor was commonly used to indicate the performance of AD. Determining the effect of pH on salt toxicity, pH was controlled at pH 6.5, 7.0 and 7.5 with synthetic wastewater containing 0, 5 and 10 g/l of NaCl. The results of each pH showed that an increase of NaCl concentration negatively affected on starch degradation, methane production, COD degradation and methane yield. At high NaCl concentration, volatile fatty acids (VFA) tend to be accumulated resulting to the increase of total volatile acid (TVA) to alkalinity ratio. Determining the effect of pH on salt toxicity, it mostly related to the optimum pH for each microbial group. At NaCl concentration of 10 g/l, the activity of hydrolytic and acidogenic bacteria at pH 6.5 was inhibited (9% and 12% inhibition, respectively) lower than that at pH 7.0 and 7.5. Whereas the activity of acetoclastic methanogens at NaCl concentration of 10 g/l was the lowest inhibition (30% inhibition) at pH 7.0. According to those activity tests, it can also be concluded that acetoclastic methanogens was the most sensitive microorganism to NaCl toxicity than hydrolytic and acidogenic bacteria. At each concentration of NaCl, pH 7.0 tend to provide a good condition to prevail over NaCl toxicity which were indicated by high production of methane yield and low inhibition on the activity of acetoclastic methanogens.

Introduction

Saline wastewater is a type of strength wastewater which is difficult to be treated due to its organic matter and salt content. Commonly, industries such as agro-food, petroleum, starch modified, and leather industries generate that kind of wastewaters [1]. Anaerobic digestion (AD) is one of more promising and sustainable development technologies among other treatments such as physio-chemical and aerobic biological treatment for its several advantages such as save energy consumption, save nutrient addition, less sludge production and biogas production.

However, high salt content in saline wastewater can inhibit AD treatment [2,3,4,5,6]. High NaCl concentration negatively affect on the activity of microbial groups in anaerobic digestion. The activity of acetoclastic methanogens was the most sensitive microorganism to NaCl toxicity than the activity of hydrolytic and acidogenic bacteria [7]. The increase of salt concentration caused the microorganism deterioration by the difference of osmotic pressure and the damage of bacteria cell membrane [8,9].

Several factors such as pH, alkalinity, temperature, and toxic substances, affect on the performances of AD. Impropriety of those factors will influence on pH inside of AD reactor. Thus, pH is an important factor affecting bacterial growth and its activity in anaerobic digestion. The change in the dominant volatile fatty acids production in AD was affected by various pH treatments [10]. There was a few works which studies the effect of pH in AD treating saline wastewater. In this research, pH was maintained at various conditions in order to know its effect on salt toxicity. The study of NaCl toxicity was preferred to be conducted at batch operation mode than continuous mode because batch operation mode offered abruptness of the exposure to NaCl and optimum contact between biomass with toxic substance. The performances of AD such as starch degradation, methane production rate, VFAs profile, and COD degradation rate were analyzed to evaluate the salt toxicity.

Materials and Methods

Microorganism: Seed sludge was obtained from open treatment pond at tapioca starch factory in Chonburi Province, Thailand.

Synthetic saline wastewater composition: The wastewater used was based on Smolders et al. [11] (as shown in Table 1). Alkalinity was initially adjusted at concentration of 2.5 g/l as $CaCO_3$ by $NaHCO_3$ addition.

Reactor: The reactor was BIOSTAT $^{(R)}$ B Plus type reactor with height 285 mm, width 230 mm, and depth 270 mm. Reactor's working volume was 2.5 l. Reactor was equipped with pH, temperature, and agitation controller.

Experimental condition: The experiments were conducted in anaerobic batch reactor. Seed sludge of 5 g VSS/l was inoculated into synthetic wastewater in

various NaCl concentrations (0, 5, and 10 g/l). The synthetic saline wastewater and seed sludge were fed at the beginning of AD (batch digestion type). The reactor was equipped with gas and sludge sampling ports to take the sample in a certain time for determining starch concentration, COD concentration, methane production, and VFA concentration. The pH was set at pH 6.5, 7.0, and 7.5 by addition of HCl 1 N and NaOH 1 N. The temperature was maintained at 37 ^{o}C during anaerobic digestion. AD was operated for 4 days (96 hours). Microbial activities, i.e. hydrolytic bacteria, acidogenic bacteria, and acetoclastic methanogens, were also analyzed at the initial and the end of AD [12]. The activities of microorganism inside anaerobic reactor were analyzed based on Soto et al., [12] by using specific substrate such as starch (hydrolytic bacteria), glucose (acidogenic bacteria), and acetic acid (acetoclastic methanogens).

Table 1 Synthetic wastewater composition [11]

Composition (mg/l)		Nutrient solution (g/l)	
$(NH_4)_2SO4$	132	$CoCl_2.H_2O$	0.15
$NaH_2PO_4.H_2O$	75.5	KI	0.18
Soluble starch	2000	$CuSO_4.5H_2O$	0.03
$CaCl_2.H_2O$	50	$MnCl_2.4H_2O$	0.12
$MgSO_4.7H_2O$	90	$ZnSO_4.7H_2O$	0.12
Yeast extract	10	$FeCl_3.H_2O$	1.50
Nutrient solution	0.3	H_3BO_3	0.15
(ml/l)		EDTA	10.0
pH 7.2		$Na_2MoO_4.2H_2O$	0.06

Analytical methods: Several parameters such as starch degradation rate, methane production rate, COD degradation rate, VFAs concentration, methane yield, microbial activity, and microbial population were analyzed in order to know the effect of pH on salt toxicity in anaerobic digestion. Acid hydrolysis was used to analyze starch concentration in wastewater [13]. Glucose concentration resulted from starch hydrolysis was analyzed by using YSI 2300 Lactate-glucose analyzer. Total volatile acid (TVA) and alkalinity were analyzed based on standard method [14]. Composition of volatile fatty acids (VFAs) was analyzed by GC 14B chromatography (flame ionization detector). Gas composition including methane and carbon dioxide was analyzed by GC 9A chromatography (thermal conductivity detector). Gas production was analyzed by water replacement method.

Results and discussions

Starch degradation rate: Starch degradation represents the ability of hydrolytic microorganism for utilizing starch as their carbon source. Therefore, the starch degradation was determined in this research to understand the hydrolysis at various pH and NaCl concentration. The results were found that an increase of NaCl concentration negatively affected on starch degradation rate (first 36 hours) in all pH condition (Table 2). The highest inhibition of starch degradation was found at NaCl concentration of 10 g/l which were in range 33.5-50.5%. According to the inhibition of starch degradation rate, pH 7.0 tend to provide good condition for starch degradation which was showed by low inhibition at high NaCl concentration of 10 g/l.

Table 2 Starch degradation rate at various pH and NaCl concentration

NaCl	Starch degradation rate (g starch/l.d)			Inhibition (%)		
(g/l)	pH 6.50	pH 7.00	pH 7.50	pH 6.50	pH 7.00	pH 7.50
0	1.15	1.10	1.05	-	-	-
5	0.90	1.00	0.95	18.5	9.5	8.5
10	0.65	0.70	0.50	44.5	33.5	50.5

Profile of Volatile fatty acids (VFAs): Determining VFAs profile and their concentration can be useful as an indicator for the imbalance of AD system. Accumulation of VFAs indicates that at least one microbial group is inhibited.

The results were found that the most VFAs produced in AD by microorganism are acetic acid, propionic acid, and butyric acid. Moreover, an increase of NaCl concentration at each pH caused VFAs accumulation except that at pH 7.5, which showed a decrease of VFAs accumulation at NaCl concentration of 10 g/l. (Table 3). This result was due to that the starch degradation was highly inhibited at this condition (as shown in Table 2). As such the VFAs production at pH 7.5 was the lowest.

Table 3 VFAs accumulation at 96 hours under various pH and NaCl concentration

pH	NaCl (g/l)	HAc (mg/l)	HPr (mg/l)	HBu (mg/l)
6.5	0	0	30	275
	5	190	65	250
	10	330	80	325
7.0	0	250	80	115
	5	135	160	125
	10	410	180	150
7.5	0	130	145	0
	5	405	190	0
	10	85	100	100

Remark: HAc = Acetic acid; HPr = Propionic acid; HBu = Butyric acid

In addition pH mostly affected the profile of VFAs produced in AD. At pH 6.5, butyric acid seemed to be dominant in every NaCl condition. At pH 7, the dominant VFAs were acetic acid and butyric acid. At pH 7.5, acetic acid and propionic acid were dominant VFA. These results can be explained by the research of Horiuchi et al. [10], which had investigated the effect of pH shifts on acidogenesis phase in anaerobic digestion. The results showed that the main products were changed from butyric acid to acetic acid and

propionic acids, depending on the culture pH from 5.0 to 8.0. The possibility of the change in the dominant microbial population in AD occurred because the optimum pH was different for the bacterial groups producing each organic acid. Some kind of propionic acid had an optimum pH of 7-8 for cell growth, while pH 6 was optimum for many other bacteria in the reactor.

COD degradation: COD concentration in anaerobic digestion involved the concentration of starch and VFAs in the system. Therefore, COD degradation at the end of AD can represent the substrate (organic matter) degradation to be biogas. From the results, the highest COD degradation rate at every NaCl concentration was found in pH 7.0. This result also related to starch degradation in which the highest of starch degradation rate was also found in pH 7.0. At the highest NaCl concentration (10 g/l), the COD degradation rate was the highest at pH 7.5. This result was related with the accumulation of VFAs inside reactor which at pH 7.5, the accumulation of VFAs was lower than that of at pH 6.5 and pH 7.0 with the same NaCl concentration of 10 g/l.

Table 4 COD degradation rate at various pH and NaCl concentration

NaCl (g/l)	COD degradation rate (g COD/l.d)		
	pH 6.5	pH 7.0	pH 7.5
0	0.82	0.93	0.67
5	0.49	0.64	0.55
10	0.18	0.25	0.32

Methane production: Since methane is produced by methanogens, determining methane production can represent the methanogenic activity in anaerobic treatment. The increase of NaCl concentration obviously decreased methane production. At treatment without NaCl, the methane production was 155, 485, and 245 ml at pH 6.5, 7.0, and 7.5, respectively. While at NaCl concentration of 10 g/l, the methane production dramatically decreased to 45, 95, and 35 ml at pH 6.5, 7.0, and 7.5 ml, respectively. Lee et al. [15] stated that sodium concentration ranging from 2 to 10 g/l inhibited the methanogenic activity moderately and a concentration above 10 g/l strongly inhibited the methanogenic activity.

The indication of lag phase of methane production was achieved at NaCl concentration of 5 and 10 g/l at all pH conditions (graphs not shown). Lag phase was defined as the time required by bacteria to acclimate to their new high stress environment which in batch experiment, daily gas production was recorded, and the lag period was the phase prior to exponential gas production [16,17]. Consequently, methanogens needed to adapt on the saline environment before they produced methane which were showed after 24 hours.

Various pH values slightly influenced methane production under saline condition. The apparent differences of methane production under various pH were shown at the treatment without NaCl concentration. At pH 7.0, methane production was higher than that of at pH 6.5 and pH 7.5 which were 485, 155, and 245 ml, respectively. Similar observations had been investigated by Chen et al. [2007] whose study showed that most methanogenic microorganism functions in a pH range of 6.6-7.6 with an optimum near pH 7.0. When the pH decreased from 6.6 or increase from 7.6, the methane production therefore was decreased.

Methane yield: Methane yield represents the amount of methane produced for a quantity of organic matter removed. Methane yield is the result of the activity of the anaerobic consortium of microorganism.

Table 5 Methane yield at various pH and NaCl concentration

NaCl (g/l)	Methane yield (m^3CH_4 /kg $COD_{removed}$)		
	pH 6.5	pH 7.0	pH 7.5
0	0.04	0.23	0.15
5	0.04	0.11	0.04
10	0.02	0.08	0.02

The treatment at pH 7.0 without NaCl addition showed the methane yield about 0.23 m^3CH_4/kg $COD_{removed}$, while at pH 6.5 and 7.5 were 0.04 and 0.15 m^3CH_4/kg $COD_{removed}$. Methane yield at pH 6.5 was the lowest compared with methane yield at pH 7.0 and pH 7.5 at NaCl concentration of 0 g/l. Ratio of CH_4:CO_2 (30:70) at pH 6.5 was also lower than that of at pH 7.0 (65:35) and pH 7.5 (80:20). This result indicated that there was a disturbance of anaerobic digestion to produce methane which was showed by high CO_2 production. The slight different of methane yield were also shown at NaCl concentration of 5 and 10 g/l in different pH. This result indicated that anaerobic digestion was proper to be performed at pH 7.0. Lee et al. [15] stated that the reduction in methane yield at high sodium concentration could be attributed to the high sodium gradient between internal and external cellular environments then it could eliminate the water and other essential nutrients from within the cells, thereby diminishing the growth and activity of the microorganism significantly. The difference of organic matter degradation also caused the different value of methane yield. Vyrides and Stuckey [19] found the extracelluler polysaccharide (EPS) increased as response of the biomass to counteract the high sodium toxicity (osmotic stress). Cell consumed a significant amount of energy to adapt to the high osmotic environment the produced less methane.

Microbial activity: Different substrates were used for analyzing pH effect on microbial activity including hydrolytic bacteria, acidogenic bacteria, and acetoclastic methanogens. The microbial activities were considered at the fastest phase of substrate degradation. To represent the effect of pH and NaCl

concentration, the difference of microbial activities at the initial and the end of experiment were investigated. The increase of NaCl concentration decreased the activity of microorganism inside anaerobic digester including hydrolytic bacteria, acidogenic bacteria, and acetoclastic methanogens. The results showed that the most sensitive microorganism to NaCl toxicity was acetoclastic methanogens. At NaCl concentration of 10 g/l, the inhhibition of microbial activities in all conditions were 8.85-27.05%, 11.55-13.65%, and 30.10-42.0% for hydrolytic bacteria, acidogenic bacteria, and acetoclastic methanogens, respectively. Fusuwankaya [7] also reported similar results which showed that acetoclastic methanogens was the most sensitive to NaCl toxicity than hydrolytic and acidogenic bacteria.

pH significantly affected on the activity of hydrolytic bacteria which the increase of pH enhanced NaCl inhibition on the activity of hydrolytic bacteria. At NaCl concentration of 10 g/l, the highest of NaCl inhibition on the activity of hydrolytic bacteria was found at pH 7.5 with 42.0% inhibition, whereas various pH did not significantly affect on NaCl toxicity in the activity of acidogenic bacteria and acetoclastic methanogen. This result was indicated by insignificant different of NaCl inhibition on the activity of acidogenic bacteria and acetoclastic methanogens at the same NaCl concentration and different pH condition. Lefebvre et al. [1] also stated that increasing NaCl concentration had a huge impact on the biodegradation rate of microorganism but not on the composition of biomass.

Conclusion

The increase of NaCl concentration negatively affect on the performance of anaerobic digestion including starch degradation rate, methane production, COD degradation rate, methane yield and the activity of microorganism in all pH conditions. The optimum pH for starch degradation rate and methane production was pH 7.0 which showed the lowest inhibition than that of others. The effect of pH seemed to more influence on the dominant VFAs production. At pH 6.5, butyric acid was dominant whereas at pH 7.0 and pH 7.5, acetic acid and propionic acid were dominant, respectively.

pH more affected on the activity of hydrolytic bacteria than that of acidogenic bacteria and acetoclastic methanogens. The activity of hydrolytic bacteria showed to decline along with the increase of pH while the other microorganism, i.e., acidogenic bacteria and acetoclastic methanogens showed insignificant inhibition of their activities caused by high NaCl concentration at various pH.

References

[1] O. Lefebvre and R. Molleta, *Water Res.* **40** (2006). pp. 3671-3682

[2] I.J. Kugelman, I.J and P.L. McCarty, *J. WPCF*. **37(1)** (1965), pp. 97-115

[3] Z. Mudryk, and W. Donderski, *Estuaries*, **14(4)**(1991), pp. 495-498

[4] F. Kargi and A.R. Dincer, *Enzyme and Microb. Tech*, **19** (1996). Pp 529-537

[5] G. Feijoo, M. Soto, R. Mendez,, and J.M Lema, *Enzyme and Microb. Tech*.**17** (1995), pp.180-188

[6] O. Levebvre, N. Vasudevan, M. Torrijos, K. Thanasekaran, and R. Moleta, *Water Res*, **39(8)** (2005), pp. 1471-1480

[7] K. Fusuwankaya, *Master Thesis, School of Bio-resources and Technology* (2006) King Mongkut's University of Technology Thonburi

[8] L.A. De Baere, M. Devocht, and P. Van Asche, *Water Res*, **18(5)** (1984), pp. 543-548

[9] M.H. Gerardi, *The microbiology of anaerobic digestion*, John Willey and Sons, Inc. New Jersey, 2003, pp. 81-115

[10] J.I. Horiuchi, T. Shimizu, K. Tada, T. Kanno, and M. Kobayashi, *Biores. Tech*, **82** (2002), pp. 209-213

[11] G.J.F. Smolder, J.V.D Meiji, M.C.M.V. Loosdrecht, and J.J. Hejinen, *Biotech. and Bioeng.*, **43**, (1994), pp.461-470

[12] M. Soto, R. Mendez, and J.M. Lema, *Water Res.*, **27(8)**, (1993) pp. 1361-1376.

[13] AOAC, *Official methods for analysis of AOAC international, 13th ed*, Association of Official Analytical Communities. Washington, DC, (1990). USA

[14] APHA, *Standard method for the examination of water and wastewater. 20th*, APHA/AWWA/WEF. (1996), Washington

[15] D.H. Lee, S.K. Behera, J.W. Kim, and H.S. Park, *Waste Manage*, 29(2) (2009), pp. 876-882

[16] E. Metcalf, *Wastewater engineering treatment and reuse. fourth edition*, McGraw Hill, Inc, (2003), New York

[17] R. Riffat, and K. Krongthamchat, *Environ. Sci. Tech*, **2(4)** (2006), pp. 291-299

[18] Y. Chen, S. Jiang, H. Yuan,Q. Zhou, and G. Gu, *Water Res.* **41**, (2007), pp. 683-689

[19] I. Vyrides, and D.C Stuckey, *Enzyme and Microb. Tech.* **44**, (2009), pp. 46-51

Isotherm and kinetics study of nonylphenol polyethoxylate and nonylphenol adsorption onto *Rastrelliger neglectus*

N. Thongkon[1*], V. Sutthithum[1] and S. Premsri[1]

[1]Department of Chemistry, Faculty of Science, King Mongkut's University of Technology Thonburi, Bangmod,Thungkru, Bangkok, Thailand 10140

* E-mail: nisakorn8@yahoo.com

Abstract: Adsorption of nonylphenol polyethoxylate (NPnEO; n = 9) and nonylphenol (NP) onto an alternative biomaterial, the fish scales from *Rastrelliger neglectus*, has been investigated. To determine the importance that the two main fractions (the organic and the inorganic fraction) of their materials play in this adsorptive capacity, the original thermally pretreated fish scales were subjected to a warm 30% w/v KOH and a warm 20% v/v HCl solution treatment to modify the organic/inorganic matter ratios present. Batch sorption experiments showed that the adsorptive capacity of NP9EO and NP depended on inorganic fraction of fish scales and the initial concentration of NP9EO (1.0 - 7.0 mg L^{-1}) and NP (0.3 – 3.0 mg L^{-1}). Inorganic-rich materials produced via a basic treatment had a higher adsorptive capacity than organic-rich materials. The equilibrium sorption isotherms have been analyzed by Langmuir and Freundlich models. The experimental data were correlated reasonably well by the Langmuir isotherms for nonylphenol and by the Freundlich model-for nonylphenol polyethoxylate with R^2 values ranging from 0.9703 to 0.9912. The adsorption kinetics of NP and NP9EO on KOH treated fish scales can be depicted with the pseudo-second-order kinetic model. In this work, the concentration of NP and NP9EO was measured by HPLC with C_{18} reversed-phase column and equipped with fluorescence detector.

Introduction

Nonylphenol polyethoxylates (NPnEO) are very common water pollutants because of their widely present in the effluents such as those generated from industrial uses, detergents, cosmetics, shampoos, and surfactants [1,2]. NPnEO are transformed in the environment by microorganism to form nonylphenol and short-chain nonylphenol polyethoxylates [3]. Some researchers indicate that these biodegradation compounds persist in rivers, sediment, groundwater and finally accumulates in aquatic organisms [4,5]. The toxic effect of these compounds is associated to their ability to mimic natural estrogens and disrupt the endocrine systems of living organisms [6]. They may hinder reproduction, growing and survival of certain animals such as salmon and oysters [7]. NP and NPnEO have been banned in the European Union as a hazard to human and environmental safety but they are still widely used in Thailand and other Asian countries.

Variety techniques for removing the small quantities of NP and NPnEO in various samples have been investigated [8,9]. Adsorption, as one of these techniques, provides a simple and universal approach to effectively removing these compounds from aquatic solution. Many researchers have studied the use of adsorption techniques, especially those using activated carbon [10], mesoporous materials and suspended particulate matters (SPM) [11]. However, cost-effectiveness is the main limitation for widely application.

In the present work, an alternative biomaterial from fish scales of short-mackerel (*Rastrelliger neglectus*) was tested. This fish species are commercially exploited and consumed with/without removing scales by the population of Thailand. Experiments have been carried out to estimate the isotherm and kinetics of NP9EO and NP from solutions using the thermally pretreated fish scales with different organic/inorganic fraction of fish scales.

Materials and Methods

Adsorbent biomaterials

The raw fish scales of short-mackerel were collected from the waste of fish cleaning that is originated in Thai markets. The material was first washed and thermally treated in deionized water at a temperature ranging of 80-90 ^{o}C for 1 h. The thermally pretreated fish scales were dried in an oven at 80^{o}C for 3 h and then refrigerated at 4 ^{o}C. In this research, the thermally pretreated scales were divided into 3 parts. The first part was control scales without any treatment. The second and the third part were treated with 20% v/v HCl and 30% w/v KOH, respectively at 60^{o}C for 240 min in order to obtain scales with different organic and inorganic fraction [12]. KOH treated scales and HCl treated scales were washed with deionized water to reach pH 6-7 and dried in an oven at 90 ^{o}C for 5 h. All scales were kept in desiccators.

Adsorbates

Nonylphenol (NP, analytical grade) and Nonylphenol polyethoxylate (NPnEO; n=9, analytical grade) were products of Fluka, Thailand). All Organic solvents were supplied by Fisher, Thailand).

Instruments

Varian Model PROSTAR 230 liquid chromatograph system coupled with a fluorescence detector (F2500 Hitachi) was utilized for chemical analysis in this study. A Zorbax SB-C_{18} column (25 cm x 0.46 cm I.D. 5 μm packing, Zorbax, Thailand) was used for separation of NP and NP9EO.

Gravimetric calcinations method

Each adsorbent material was calcined at 700 ^{o}C for 15 min. The organic fraction was the volatile fraction while the inorganic fraction was the remaining residue.

Biosorption study

Sorption isotherms of NP and NP9EO on the thermally pretreated fish scales were investigated using batch experiments. Each experiment was conducted in triplicate. Initial concentrations were of 0.30/1.0, 0.50/2.0, 0.70/3.0, 1.0/5.0, 2.0/6.0 and 3.0/7.0 mg L^{-1} for the mixture of NP/NP9EO. The thermally pretreated fish scales (0.10 g) were added to 10 mL of the mixture of NP/NP9EO in 50 mL flasks. The flasks were placed on a shaker (300 rpm, room temperature) for 540 min. Upon equilibrium, the NP and NP9EO uptake was calculated by using:

$$q_e = \frac{(C_o - C_e)}{m} \times V \quad \text{.....(1)}$$

where C_o and C_e are the initial and equilibrium concentrations of NP or NP9EO solution, q_e is the amount of adsorption at equilibrium (mg g^{-1})

Batch kinetic experiment

Kinetic experiments were performed in continuously stirred flasks containing 10 mL NP/NP9EO solution at the concentration of 0.70/ 3.0 mg L^{-1} and 0.10 g of the thermally pretreated fish scales. The solutions were stirred for 30, 90, 150, 240, 360, 540 and 720 min. The uptake of the NP/NP9EO on the thermally pretreated fish scales at time t, q_t was calculated according to the following equation:

$$q_t = \frac{(C_o - C_t)}{m} \times V \quad \text{.....(2)}$$

Determination of NP and NP9EO in solution

After adsorption, the thermally pretreated fish scales were separated by filtering through a membrane filter (Whatman No.4) and the concentration of NP and NP9EO in solution was analyzed using a HPLC system coupled with a fluorescence detector by monitoring the peak area. Calibration curves were plotted between peak area and concentration of NP or NP9EO.

Results and Discussion

Organic/inorganic fraction in the thermally pretreated fish scales

From a gravimetric calcination method, the ratios of inorganic and organic fractions in control scales, KOH treated scales and HCl treated scales are shown in Table 1. Calcination method of thermally pretreated scales showed that the content of inorganic matter was about 81.3% higher in scales after being treated with KOH solution for up to 240 min than in control scales without a basic treatment. HCl treated scales had a higher organic fraction (74.5%) than control scales without an acidic treatment.

Table 1 Inorganic/ Organic fraction ratios in the thermally pretreated fish scales

Control scales	KOH treated scales (Inorganic-rich)	HCl treated scales (Organic-rich)
Inorganic / Organic	**Inorganic/ Organic**	**Inorganic/ Organic**
0.509 / 0.491	0.923 / 0.077	0.143 / 0.857

HPLC analysis

Figure 1 displays C_{18} reversed-phase LC chromatogram obtained by analyzing the mixture of NP and NP9EO. The mixture was eluted and baseline separated as two major peaks. Quick elution and efficient separation of NP from NP9EO at room temperature was achieved by using the methanol: acetonitrile: deionized water (80:2:18) mobile phase at a flow rate of 1.3 mL min^{-1}. The fluorescence detection was achieved at the excitation and emission wavelength of 227 nm and 300 nm, respectively. The described analytical method was used to determine the remaining concentration of NP and NP9EO in solution after adsorption on the thermally pretreated fish scales.

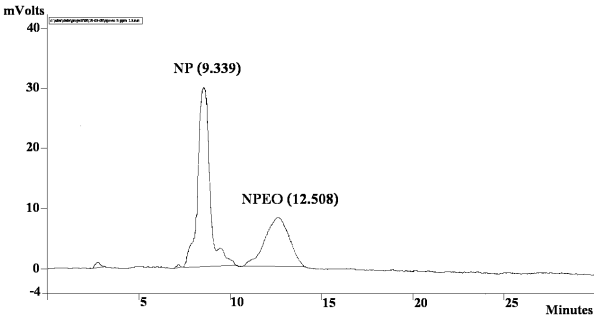

Figure 1. HPLC Chromatogram of NP and NP9EO standards

Effect of contact time

Figure 2 shows the contact time on the biosorption of NP and NP9EO onto control scales, KOH treated scales and HCl treated scales.

Batch sorption experiments showed that the adsorptive capacity of NP and NP9EO depended on inorganic fraction of fish scales. From the graph, it is clear that the maximum adsorptive capacity of NP/ NP9EO concentration 0.70/3.0 mg L^{-1} was achieved for KOH treated scales, which have the highest inorganic content. The inorganic fraction, mainly composed of hydroxyapatite [HAP; $Ca_{10}(PO_4)_6(OH)_2$]- is more responsible on the adsorption of NP and NP9EO than organic fraction. NP is more lipophilic and less amphiphilic than NP9EO, giving less sorption capacity than NP9EO. NP9EO has both hydrophilic and hydrophobic functional groups; therefore, hydrogen bonding, hydrophobic, hydrophilic and Van der Walls interactions could play an important role for the NP9EO adsorption.

KOH treated scales were used as an adsorbent for adsorption and kinetic isotherm studies due to the highest sorption capacity of both NP and NP9EO.

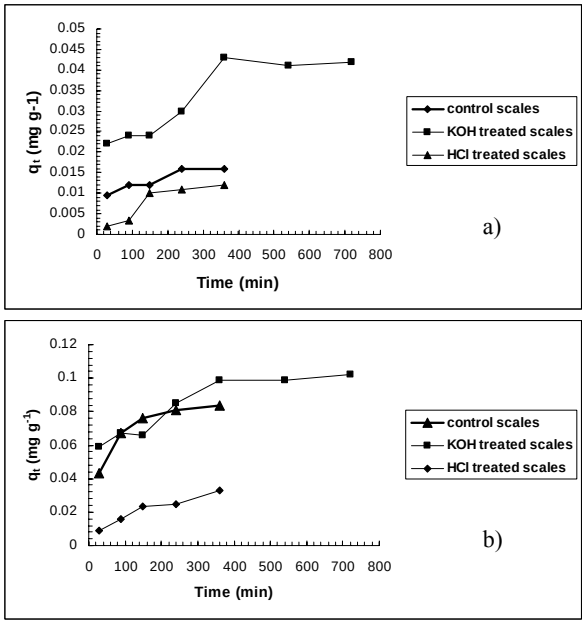

Figure 2. Effect of contact time on the biosorption of a) NP and b) NP9EO onto all types of fish scales

Effect of initial NP and NP9EO concentration (C_o)

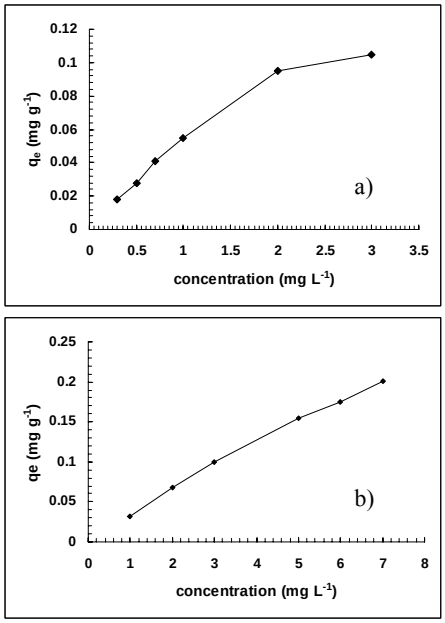

Figure 3. Effect of initial concentration of NP and NP9EO on the biosorption of KOH treated scales; contact time 540 min

From Figure 3, it was observed that the values of q_e increased with increasing C_o. This indicates that an increase in C_o enhanced the sorption capacity and the interaction between NP/NP9EO and KOH treated scales. The C_o provided the driving force to overcome the resistance to the mass transfer of these compounds between the solution and KOH treated scales.

Adsorption isotherm

To gain a better understanding of the biosorption process of NP and NP9EO, two isotherm equations have been establish the most appropriate correlation for the equilibrium data. The Langmuir isotherm model, which assumes monolayer sorption onto a surface and is given by

$$\frac{C_e}{q_e} = \frac{C_e}{q_m} + \frac{1}{K_L q_m} \quad \text{.....(3)}$$

where q_m (mg g^{-1}) is a constant related to sorption capacity; and K_L (L mg^{-1}) is a constant related to the affinity of the binding sites and energy of adsorption.

The Freundlich equation is an empirical describing the adsorption onto a heterogeneous surface. It is expressed as:

$$\log q_e = \log K_f + \frac{1}{n} \log C_e \quad \text{.....(4)}$$

where K_f and n are the Freundlich constants related to the adsorption capacity and the adsorption intensity of the adsorbent, respectively.

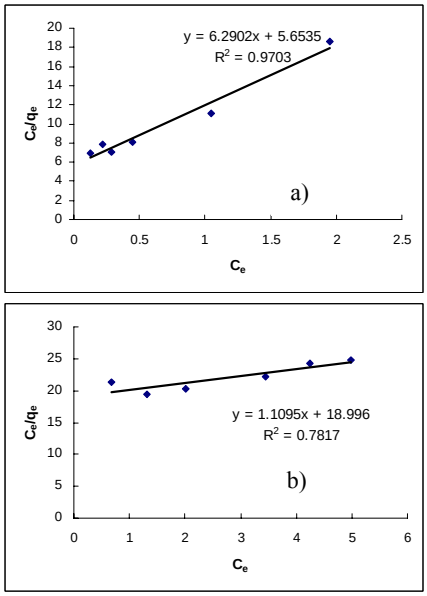

Figure 4. Langmuir isotherm plots for the biosorption of a) NP and b) NP9EO onto KOH treated scales

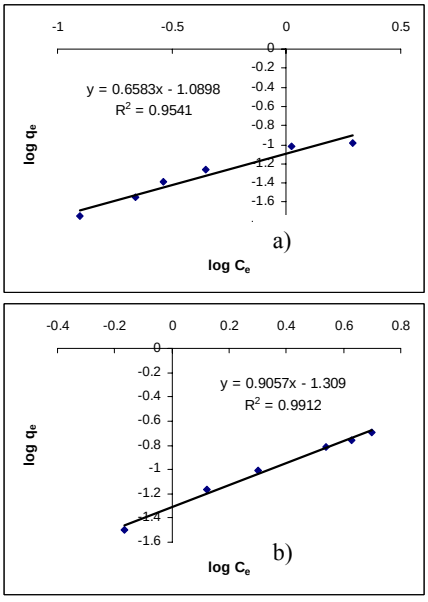

Figure 5. Freundlich isotherm plots for the biosorption of a) NP and b) NP9EO onto KOH treated scales

Figure 4 indicates the linear relationship between the amount of NP and NP9EO adsorbed per unit mass of KOH treated scales against the concentration of NP and NP9EO remaining in solution. Figure 5 shows the Freundlich isotherms obtained for the biosorption of NP and NP9EO onto KOH treated scales.

Table 2 Parameters of adsorption isotherms of NP and NP9EO on KOH treated scales

	Langmuir model			Freundlich model		
	q_m	K_L	R^2	K_f	1/n	R^2
NP	0.159	1.112	0.9703	0.081	0.658	0.9541
NP9EO	0.901	0.058	0.7817	0.049	0.906	0.9912

The higher coefficients of determinations (R^2) for Langmuir isotherm predicted the monolayer coverage of NP on KOH treated scales. This model suggests sorption on a surface without interaction between NP. On the other hand, the higher R^2 for Freundlich isotherm predicted a monolayer sorption with a heterogeneous energetic distribution of active sites, accompanied by interactions between NP9EO. Therefore, KOH treated scales had better adsorbing capacity (q_m) for NP9EO than NP. Moreover, the lowest value of K_L indicating that NP9EO had a high binding affinity for KOH treated scales. The 1/n values were between 0 and 1 indicating that biosorption of NP and NP9EO onto KOH treated scales was favorable at studied conditions.

Biosorption kinetics

A study of adsorption kinetics provides information about the mechanism of adsorption, which is important for the efficiency of the process. In order to clarify the biosorption kinetics of NP and NP9EO onto KOH treated scales, two kinetic models, the pseuso-first-order Largergren equation and the pseudo-second-order kinetics equation given below as (5) and (6), respectively.

$$\log (q_e - q_t) = \log q_e - \frac{K_1}{2.303} t \qquad \text{.....(5)}$$

$$\frac{t}{q_t} = \frac{1}{K_2 q_e^2} + \frac{t}{q_e} \qquad \text{.....(6)}$$

where K_1 and K_2 are the rate constants for the pseudo-first-order (min^{-1}) and for the pseudo-second-order (g mg^{-1} min^{-1}), respectively

Table 3 Kinetic parameters obtained from the pseudo first-order and the pseudo second-order for the NP and NP9EO biosorption

	pseudo first-order			pseudo second-order		
	K_1	q_e	R^2	K_2	q_e	R^2
NP	2.76×10^{-3}	0.020	0.8721	0.257	0.043	0.8584
NP9EO	4.84×10^{-3}	0.047	0.8192	0.185	0.098	0.9546

In general, the pseudo-first-order kinetics is usually used to describe the initial stage of the adsorption process. The pseudo-second-order model is more likely to predict kinetic behavior of biosorption with chemical sorption being the rate controlling step. Since the value of R^2 nearer to one indicates that the respective equation better fits the experimental data. The pseudo-first-order model was concluded to be preferred model for the kinetic process of NP. The adsorption kinetic for NP9EO was well explained by the pseudo-second-order kinetics. From Table 3, the calculated rate constants for both NP and NP9EO biosorption were closer to unity for the pseudo-second-order kinetic model than the pseudo-first-order kinetic model. Moreover, the calculated values of q_e obtained from the pseudo-second-order agreed more perfectly the value of $q_{e(exp)}$, 0.041 and 0.099 mg g^{-1} for NP and NP9EO, respectively. Therefore, the sorption reaction of NP could be approximated more favourably by the pseudo-second-order kinetic model when the values of R^2 were slightly different between the pseudo first and the pseudo second order equation.

Conclusions

This study focused on the biosorption of NP and NP9EO onto the thermally pretreated fish scales. The operating parameter, contact time and initial concentration, were effective on the biosorption capacity of NP and NP9EO. The obtained results shows that inorganic fraction in the thermally pretreated fish scales was responsible on the adsorption properties. Adsorption isotherms of NP and NP9EO were explained by Langmuir and Freundlich models, respectively. Kinetic behavior of NP and NP9EO biosorption was more likely to predict with chemical sorption of these compounds onto KOH fish scales.

Acknowledgement

The work described in this article was supported by department of chemistry, faculty of science, King Monkut's University of Technology, Thonburi, Thailand.

References

[1] M. Ahel, J. McEvoy and W. Giger, *Environ. Pollut*. **79** (1993), pp. 243-248.

[2] M.J. Scott and M.N. Jones, *Biophys. Acta.* **1508**, (2000), pp. 235-251.

[3] M. Ahel, W. Giger and M. Koch, *Water Res*. **28** (1994), pp. 1131-1142.

[4] R.M. Mann and M.R. Boddy, *Chemosphere.* **41**, (2000), pp. 1361-1369.

[5] G.G. Ying, B. Williams and R. Kookanan, *Environ. Int*. **28**, (2002), pp. 215-226.

[6] A. Kollmann, A. Brault, I. Touton, J. Dubroca, V. Chaplain and C. Mougin, *J. Environ. Qual.* **32** (2003) pp. 1269-1276.

[7] P.L. Keen, D.A. Higgs, K.J. Hall and M. Ikonomou, *Sci. Total. Environ.* **349** (2005), pp. 81-94.

[8] M. Franskaa, R. Franskib, A. Szymanskia and Z. Lukaszewskia, *Water Res.* **37**, (2003), pp. 1005-1014.

[9] M. Allali-Hassani, O. Dusart and M. Mazet, *Water Res.* **24**, (1990), pp. 699-708.

[10] D.M. Nevskaia and A. Guerrero-Ruiz, *J. Colloid Interf. Sci.* **234**, (2001), pp. 316-321.

[11] H. Shao-gang, S. Hong-wen and G. Yuan, *Chemosphere.* **63**, (2006), pp. 31-38.

[12] J.F. Villanueva-Espinosa, M. Hernandez-Esparza and F.A. Ruiz-Trevino, *Ind. Eng. Chem. Res.* **40**, (2001), 3563-3569.

Removal of heavy metal ions in water using aminated polystyrene

W. Mingvanish[1*] W. Pattanaworrasate[1] B. Sangchakr[1] N. Thongkon[1]

[1] Department of Chemistry, Faculty of Science, King Mongkut's University of Technology Thonburi, 126 Pracha-utis Rd., Thung-kru, Bangkok, Thailand 10140

[*] E-mail: withawat.min@kmutt.ac.th

Abstract: The potential of aminated polystyrene (APS) as an adsorbent for heavy metal ion adsorption has been investigated by batch experiments. APS was synthesized from polystyrene via a sequence of nitration and reduction with $SnCl_2$/HCl. The chemical structure of APS was characterized by FTIR. The effects of various experimental parameters on adsorption studies, i.e. initial pH, metal ion concentration, and contact time, were examined. At initial concentration of metal ion 50 mg L^{-1} and pH 4.0, the removal efficiencies of Ni(II), Cu(II), and Zn(II) ions were 33.4%, 43.9%, and 46.5%, respectively. The adsorption isotherms of Ni(II), Cu(II), and Zn(II) ions onto APS could be described by both the Langmuir and Freundlich models.

Introduction

Heavy metals discharged from industries into the aqueous ecosystem may be the cause of serious environmental and public health problems due to their toxicity. This is because heavy metal ions are non-biodegradable and have a tendency to accumulate in living tissues, causing various diseases and disorders as absorbed into the body. The important sources of heavy metal ions in industrial wastewaters include metal plating, mining activities, smelting, paint manufacture, and petroleum refining industries, etc. [1-2]. Therefore, they must be removed before discharge. Various methods for removing either or both dissolved and suspended heavy metal ions from industrial waters and wastewaters include reduction, precipitation, ion exchange, filtration, electrochemical treatment, membrane technology and evaporation removal, all of which may be either ineffective or cost unacceptable [3-5]. Among all the treatment processes mentioned, adsorption is one of the physico-chemical treatment processes found to be high efficient for the removal of the toxic metals present in low concentrations in aqueous solutions [6].

Activated carbons are widely used as an adsorbent due to their porous structure and surface functional groups. However, polymeric adsorbents are thought as the alternative for activated carbons. Various polymeric adsorbents have been used to remove metal ions and organic compounds from aqueous solutions [7-10]. To develop more polymeric adsorbents, our present work attempts to synthesize aminated polystyrene, APS, for adsorbing Ni(II), Cu(II), and Zn(II) metal ions in aqueous solutions.

Materials and Methods

Materials

Polystyrene (PS) with the average molecular weight of about 110,000 g mol^{-1}, a starting material for preparing aminated polystyrene (APS), was donated by Siam Polystyrene Co., Ltd., and was used without any further purification. Standard stock solutions of copper(II) chloride, nickel(II) chloride and zinc(II) chloride (1000 mg L^{-1}) were purchased from Carlo Erba Co. Other chemicals used in this study were of analytical grade purity and were purchased either from Asia Pacific Specialty Chemicals Ltd. or from E. Merck Co. Deionized water was used throughout experiments.

Synthesis of aminated polystyrene (APS) adsorbent

Aminated polystyrene (APS) was prepared by the nitration reaction of polystyrene (PS), and followed by the reduction reaction of the resulting nitrated polystyrene (NPS) with $SnCl_2$/conc. HCl.

A solution of PS (60 g) in dichloromethane (800 mL) was added drop by drop into a three-necked round bottom flask containing a mixture of conc. HNO_3 (65 mL) and conc. H_2SO_4 (70 mL) at 0^oC with stirring. The reaction mixture was refluxed for 3 h. under N_2 atmosphere. The resulting mixture was first extracted with sat. $NaHCO_3$ solution and then washed with deionized water until pH of the aqueous layer was neutral. The organic layer was evaporated by the rotary evaporator. NPS was dried in vacuum at 75^0C at 40 kPa until the weight of NPS remained constant. In order to prepare APS, the obtained NPS (40 g) was redissolved in THF (500 mL) and was placed into a three-necked round bottom flask. A solution of $SnCl_2$ (153 g) in conc. HCl (135 mL), which was diluted with THF (300 mL), was added. Then, the reaction mixture was refluxed with stirring for 1 h under N_2 atmosphere. After that, the product was first extracted with 2M NaOH and then washed with deionized water until pH of the aqueous layer was neutral. The organic layer was evaporated by the rotary evaporator. APS was then dried in vacuum at 75^0C at 40 kPa to a constant weight. After that, the dried APS was grounded and sieved to obtain APS with the paticle size of 100-200 mesh. The sieved APS was kept in a dessicator until used.

Structural characterization

FT-IR spectroscopy was used to characterize the chemical structure of the polymers. FT-IR spectra of the polymers were recorded from 4000-400 cm^{-1} with Bio-Rad FTS 175 Fourier Transform Infrared spectrophotometer (Hewlett Packard) using potassium bromide disks.

Adsorption Procedure

Heavy metal ion adsorption from the single metal aqueous solutions was studied using batch adsorption experiments. The effects of the contact time, initial pH of the solution and initial metal ion concentration on the adsorption capacity of the adsorbent were also investigated. In each adsorption experiment, 0.1000 g of APS was mixed with a 50 mL of aqueous metal ion solution of known concentration and pH in a 250 mL erlenmeyer flask. The solution pH was adjusted with 6 M HCl or 6 M NaOH to a desired value. The solution was shaken at 250 rpm on the shaker bath, which was controlled at room temperature (30°C). After shaking for a predetermined time interval, the metal ion solution was separated from the adsorbent by filtration. The remaining concentration of metal ions in a solution was determined by using AAanalyst 300 flame atomic absorption spectrophotometer. The adsorption capacity of APS was calculated and presented in term of percentage of metal ion removal (% Removal), which represents as the ratio between the amount of metal ions adsorbed by APS and the starting amount of metal ions. Each experiment was made in triplicate.

Results and Discussion

Characterization of polystyrene derivatives

The preparation of aminated polystyrene or aminopolystyrene (APS) contained two main steps:

1. the addition of nitro groups ($-NO_2$) into PS to yield nitrated polystyrene or nitropolystyrene (NPS) and

2. the conversion of nitro groups ($-NO_2$) into amine groups ($-NH_2$) with $SnCl_2$/conc. HCl.

The incorporation of nitro and amine groups into the polystyrene derivatives was analyzed with FT-IR spectrophotometer. The FT-IR spectra of NPS and APS are shown in Figure 1.

Figure 1a is the FT-IR spectrum of NPS. The characteristic IR peaks observed at 1348 and 1521 cm^{-1} are due to the N-O stretching, that can be attributed to the existence of nitro groups on benzene ring of NPS [11]. For the FT-IR spectrum of APS (Figure 1b), two new peaks observed at around 3300-3400 cm^{-1} and at 1620 cm^{-1} correspond to the N-H stretching and N-H bending vibrations of the amine groups on APS, respectively [11]. In addition, the N-O stretching peak intensities of nitro groups at 1348 and 1521 cm^{-1} decreased as compared with those of NPS. Theses results indicated the presence of the amine groups on APS.

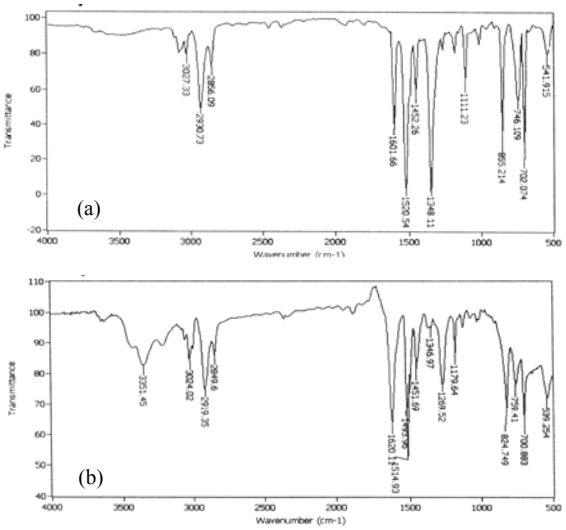

Figure 1. FT-IR spectrum of (a) NPS and (b) APS

Effect of contact time

The effect of contact time on the adsorption of Ni(II), Cu(II) and Zn(II) ions by APS is shown in Figure 2. As seen from Figure 2, a tendency of the adsorption of Ni(II), Cu(II) and Zn(II) ions by APS was similar. The percent removal of Ni(II), Cu(II) and Zn(II) ions by APS increased with contact time and reached equilibrium at 6 h. However, for any further experiments, the contact time taken for studying the adsorption of metal ions by APS was 24 h.

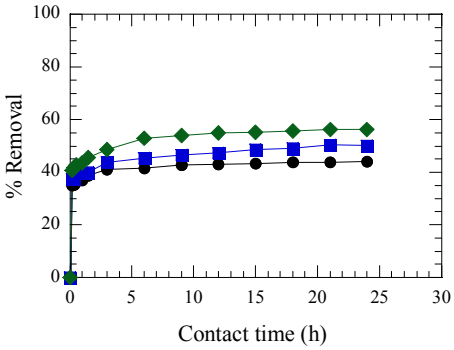

Figure 2. Effect of contact time on (●) Ni(II), (■) Cu(II) and (♦) Zn(II) ion adsorption by APS (initial metal ion concentration: 50 mg L^{-1}; adsorbent dosage: 2 g L^{-1}; initial pH: 6.5 for Ni(II) and Zn(II) ions and 5 for Cu(II) ion)

Effect of initial pH

The solution pH has remarkably influenced on adsorption process, particularly on the adsorption capacity of an adsorbent. The variation of the adsorption of metal ions was studied in the range of pH 2.5-7.5 for Ni(II) and Zn(II) ions, 2.5-5.5 for Cu(II) ion, and the results are shown in Figure 3. As seen from Figure 3, the influence of the pH of the metal ion solution on the removal capacity of Ni(II), Cu(II) and Zn(II) ions by APS found to be the same. An increase in initial pH of the system increased the metal-ion removal capacities of APS. Beyond pH 3.5, the metal ion adsorption was almost constant. As pH of the system decreased, the amine groups ($-NH_2$) could be

protonated as a form of $-NH_3^+$. Consequently, the number of amine groups acting as adsorbent sites decreased and the number of positively charged adsorbent sites in the form of $-NH_3^+$ increased, which did not favor the adsorption of positively charged metal ions due to electrostatic repulsion forces. For any further experiments, the solution pH values suitable for the adsorption of metal ions by APS were 6.5 for Ni(II) and Zn(II) ions, and 5.0 for Cu(II) ion.

Comparison of the removal efficiencies of Ni(II), Cu(II) and Zn(II) ions by APS was done at the initial solution concentration of 50 mg L^{-1} and at pH 4. It was found that the removal efficiencies of Ni(II), Cu(II), and Zn(II) ions were 33.4%, 43.9%, and 46.5%, respectively. The total capacity of APS towards investigated metal ions increased in order Ni(II) < Cu(II) ≈ Zn(II). However, there was little observable difference in the percentage of metal ion removal by APS; this may imply the adsorption mechanism of each metal ion by APS was similar.

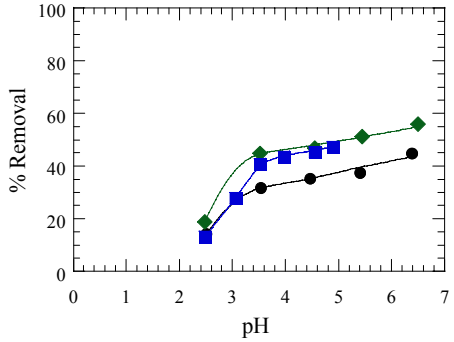

Figure 3. Effect of pH on (●) Ni(II), (■) Cu(II) and (♦) Zn(II) ion adsorption by APS (initial metal ion concentration: 50 mg L^{-1}; adsorbent dosage: 2 g L^{-1}; contact time: 24 h)

Effect of metal ion concentration

The effect of metal ion concentration on the adsorption capacity of APS was also examined. Figure 4 showed that the percentage of metal ion removal by APS decreased with increasing the metal ion concentration. This is because as metal ion concentration increases, the adsorption process of metal ion onto the surface of APS may become limited due to the unavailability of the free active adsorption sites on the surface [12].

Adsorption isotherm

The comparison of the adsorption capacities of Ni(II), Cu(II) and Zn(II) ions by APS was be carried out according to the Langmuir [13] and Freunlich [14] isotherm models.

The Langmuir equation can be written as follows:

$$\frac{C_e}{q_e} = \frac{1}{bQ^0} + \frac{C_e}{Q^0}$$

where C_e is the equilibrium concentration of metal ion solution (mg L^{-1}), q_e is the amount of metal ions adsorbed on APS, Q^0 is the maximum amount of metal ions adsorbed on APS per unit weight of APS (mg g^{-1}) and b is the Langmuir constant (L mg^{-1}). Q^0 and b are related to the maximum adsorption capacity and energy of absorption, and can be determined from the slope and intercept of the linear plot of C_e/q_e against C_e, respectively (see Figure 5).

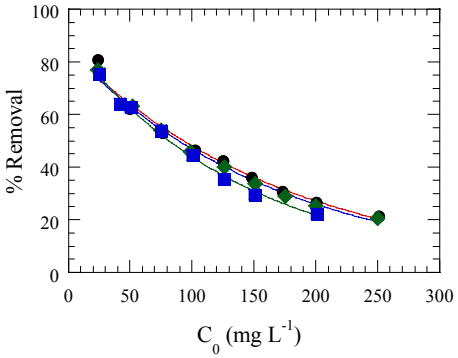

Figure 4. Effect of metal ion concentration on (●) Ni(II), (■) Cu(II) and (♦) Zn(II) ion adsorption by APS (adsorbent dosage: 2 g L^{-1}; contact time: 24 h; initial pH: 6.5 for Ni(II) and Zn(II) ions and 5 for Cu(II) ion)

The linear form of the Freundlich isotherm equation is shown below:

$$\log q_e = \log K_F + \frac{1}{n}\log C_e$$

where K_F is the Freundlich constant (mg g^{-1}) and 1/n is an empirical constant. K_F and n are related to the adsorption capacity and intensity and can be obtained form the intercept and the slope of the linear plot of log q_e against log C_e, respectively (see Figure 6).

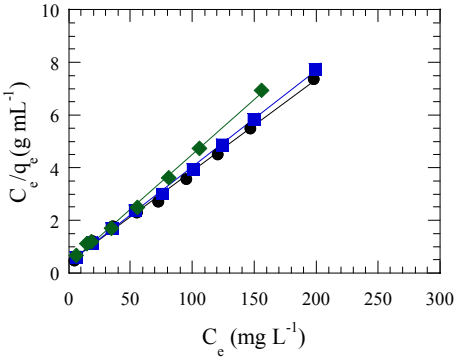

Figure 5. The Langmuir adsorption isotherms of the (●) Ni(II), (■) Cu(II) and (♦) Zn(II) ion adsorptions on APS

Table 1 gives the coefficients for the linearized forms of the isotherm models for adsorption of each metal ions on APS. The results in Table 1 pointed out that the adsorption isotherms of metal ions fitted with both the Langmuir and Freundlich models ($R^2 > 0.95$). In addition, the present study showed that the maximum adsorption capacities Q^0 *and* K_F estimated from both of the adsorption isotherm models for each metal ion were similar. The Q^0 values for the adsorption of Ni(II), Cu(II) and Zn(II) ions were 28.78, 27.35 and 24.03 mg g^{-1}, respectively, and the K_F values for the adsorption of Q^0 values for Ni(II), Cu(II) and Zn(II) ions were 5.63, 5.37 and 5.24 mg g^{-1}, respectively.

Table 1. Linearised isotherm parameters for the Langmuir and Freundlich fits at 30°C

Metal ion	Langmuir adsorption isotherm			Freundlich adsorption isotherm		
	Q^0 (mg g^{-1})	b (L mg^{-1})	R^2	K_F (mg g^{-1})	n	R^2
Ni(II)	28.78	0.09	0.9984	5.63	2.8	0.9961
Cu(II)	27.35	0.09	0.9994	5.37	2.8	0.9854
Zn(II)	24.03	0.12	0.9986	5.24	2.8	0.9748

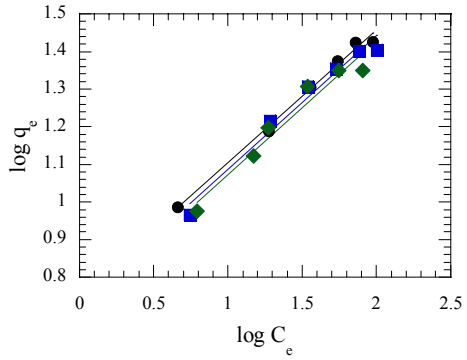

Figure 6. The Freundlich adsorption isotherms of the (●) Ni(II), (■) Cu(II) and (♦) Zn(II) ion adsorptions on APS

Conclusions

The present study showed that APS was a moderately effective adsorbent for removing Ni(II), Cu(II) and Zn(II) ions from aqueous solutions. Furthermore, the results indicated that the removal capacities of heavy metal ions by APS have been considerably affected by initial metal ion concentration, pH, and contact time. At initial concentration of metal ion 50 mg L^{-1} and pH 4.0, the removal efficiencies of Ni(II), Cu(II), and Zn(II) ions by APS were 33.4%, 43.9%, and 46.5%, respectively, at 30°C. The isothermal data fitted well with both Langmuir and Freundlich adsorption models**.**

Acknowledgments

The authors were grateful to the financial support by the Master degree program in Industrial chemistry in the Department of Chemistry, Faculty of Science, KMUTT, Thailand.

References

[1] C.J. Williams, D. Aderhold and G.J. Edyvean, *Water Res.* **32** (1998), pp. 216-224.
[2] K. Kadirvelu, K. Thamaraiselvi and C. Namasivayam, *Bioresour. Technol.* **76** (2001), pp. 63-65.
[3] A. Özcan, A.S. Özcan, S. Tunali, T. Akar and I. Kiran, *J. Hazard. Mater. B* **124** (2005), pp. 200-208.
[4] D.W. O' Connell, C. Birkinshaw and T.F. O' Dwyer, *Bioresour. Technol.* **99** (2008), pp. 6709-6724.
[5] W.S. Wan Ngah and M.A.K.M. Hanafiah, *Bioresour. Technol.* **99** (2008), pp. 3935-3948.
[6] Y.F. Jia, K.M. Thomas, *Langmuir* **16** (2000), pp. 1114-1122.
[7] T. Shiraishi, M. Tamada, K. Saito and T. Sugo, *Radiat. Phys. and Chem.* **66** (2003), pp. 43-47.
[8] P.K. Roy, A.S. Rawat and P.K. Rai, *Talanta* **59** (2003), pp. 239-246.
[9] H.A. Abd El-Rehim, E.A. Hegazy, and A. El-Hag Ali, *React.Funct. Polym.* **43** (2000), pp. 105-116.
[10] B. Pan, B. Pan, W. Zhang, L. Lv, Q. Zhang and S. Zheng, *Chem. Eng. J.* **151** (2009), pp. 19-29.
[11] V.L. Covolan, L.H.I. Mei and C.L. Rossi, *Polym. Adv. Technol.* **8** (1996), pp. 44-50.
[12] D. Özer, G. Ducsum and A. Özer, *J. Hazard. Mater.* **144** (2007), pp. 171-179.
[13] I. Langmuir, *J. Am. Chem. Soc.* **38** (1916), pp. 2221-2295.
[14] J.M. Smith, *Chemical Engineering Kinetics*, 3rd ed., McGraw-Hill, Singapore (1981).

Purification of biodiesel using rice husk ash

V. Kaewpaluek [1], S. Pengprecha [2*]

[1] Inter-department of Environmental Science, Graduate School, Chulalongkorn University, Bangkok, Thailand 10330
[2] Department of Chemistry, Faculty of Science, Chulalongkorn University, Bangkok, Thailand 10330

[*]E-mail: somchai.pe@chula.ac.th

Abstract: Biodiesel is an alternative fuel that is produced from vegetable oils or animal fats. Transesterification of oil with methanol using alkali catalysis is a common process used to produce biodiesel. To purify biodiesel, it was subjected to wash with water for several times, this can cause environmental problem. To avoid this problem, this research aim to remove glycerin in biodiesel synthesized from palm oil via a base-catalyzed process by using rice husk ash as adsorbent including white rice husk ash, black rice husk ash, black rice husk ash activated by sodium hydroxide and black rice husk ash activated by zinc chloride. The optimal adsorption process was obtained by varying ratio of adsorbent to biodiesel, contact time and temperature. The result showed that all rice husk ash can remove glycerin efficiently by using temperature at 50°C, contact time for 10 minutes and with amount of 4% adsorbents. In comparison of all adsorbents, white rice husk ash give the most efficiency for removing of glycerin in biodiesel.

Introduction

The consumption of diesel fuel in Thailand is being rather continuously increased. Nowadays the prices of petroleum and natural gas dramatically increase and vacillate regarding the resource reduction. Thus, the alternative sources of energy are vital importance.

Biodiesel is an alternative fuel that is produced from vegetable oils or animal fats. Transesterification of oil with methanol using alkali catalysis is a common process used to produce biodiesel. To purify biodiesel, it was subjected to wash with water for several times, this can cause environmental problem. To avoid this problem, absorbents such as magnesium silicate, activated charcoal used to wash biodiesel replace water.

The objective of this research is to compare efficiency for adsorption of glycerin in biodiesel by using rice husk ash as absorbent including white rice husk ash(WRHA), black rice husk ash(BRHA), black rice husk ash activated by sodium hydroxide(BRHA-NaOH) and black rice husk ash activated by zinc chloride(BRHA-$ZnCl_2$).

Materials and Methods

Synthesis of biodiesel from palm oil via base-catalyzed process: 300 g of palm oil was added into 1000 ml of round bottom flask equipped with condenser. After the oil was heated to 65 °C, the solution of sodium hydroxide (3.0 g) in methanol (86.89 ml) was slowly added into the reaction and then the mixture was heated to 65°C for 1 h. The reaction mixture was transfered to a separatory funnel, and allowed glycerin to separate. The methyl ester layer was brought to purification process.

Preparation of adsorbents: Rice husk was washed with distilled water to remove fine particles and other impurities and dried at 110°C for 24 hours. Then it was subjected to heat at 700°C for 1 hour in opened system to produce white rice husk ash. Black rice husk ash was obtained by a method analogous to white rice husk ash, but heating rice husk at 350°C for 1 hour in closed system.

NaOH-activated black rice husk ash was prepared by soaking black rice husk ash in saturated sodium hydroxide solution using 1:2 weight ratio of black rice husk ash to sodium hydroxide for 12 hours. After this period, the mixture was heated at 700ºC for 1 hour, successively washed with hot water until the pH of wash water is around 6.5-7.5, dried at 110ºC. $ZnCl_2$-activated black rice husk ash was obtained by a method analogous to NaOH-activated black rice husk ash, but using $ZnCl_2$ instead of NaOH.

All of adsorbents were desicated and stored in tightly capped glass bottle for futher use.

Selection of adsorbents: Five types of adsorbents, WRHA, BRHA, BRHA-NaOH, BRHA-$ZnCl_2$ and activated charcoal, were studies. The size of all adsorbents was 100 μm.

Adsorbent treatment: In an effort to adsorb glycerin, 2, 4, 6 and 8%wt of each adsorbents were used. In 150 ml of flask, 100 g of untreated biodiesel was treated with each of adsorbents at 50°C, with stirring rate at 150 rpm and contact time at 5, 10, and 20 minutes in water bath. Then the adsorbent was removed by filtration.

Analytical methods: Titration method is used to determine the amount of glycerin and unreacted catalyst. Step 1, 3 g of untreated biodiesel was dissolved in 100 ml of isopropyl alcohol with 2 ml of 1% phenolphthalein as an indicator. The mixture was titrated with 0.01N hydrochloric acid until the color of the solution changed from red to clear color. Step 2, Then 1 ml of 0.04%bromophenol blue was added into the mixture solution and titrated with 0.01N hydrochloric acid until the color of the solution changed from blue to yellow. This amount of 0.01N hydrochloric acid solution is referred as "B". The amount of unreacted catalyst can be calculated by using the equation 1:

g of NaOH / g of untreated biodiesel= $\frac{Ax\ 0.1\ x\ 40.0}{W\ x\ 1000}$ (1)

where:
A = volume of hydrochloric acid used in step 1 (mL)
W = weight of untreated biodiesel used (g)

And the amount of glycerin in the biodiesel can be calculated by using the equation 2:

g of glycerin /g of untreated biodiesel=$\frac{B\ x\ 0.1\ x304.4}{W\ x\ 1000}$ (2)

where:
B = volume of hydrochloric acid used in step 2 (mL)
W = weight of untreated biodiesel used (g)

Results and Discussion

Effect of contact time: The effect of contact time on sorption of glycerin was studied. As shown in Figure 1, by using 2%wt. of adsorbents, WRHA, BRHA, BRHA-NaOH, BRHA-$ZnCl_2$ and activated charcoal, 30 g of untreated biodiesel, and agitating at 150 rpm for 10-30 min. at 50 ^oC, the glycerin content was decreased from 0.0045 to 0.0024, 0.0026, 0.0029, 0.0023 and 0.0032 g glycerin/g untreated biodiesel, respectively. The optimum contact time was found to be 10 min.

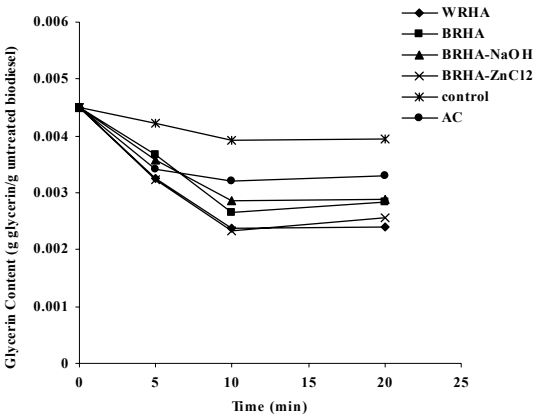

Figure 1. glycerin content vs. time with 2%wt of various adsorbents at 50 ^oC

Effect of sorbent dosage: In Figure 2 showed the glycerin content vs. various % adsorbent. By treating untreated biodiesel with 2, 4, 6 and 8%wt of adsorbents, WRHA, BRHA, BRHA-NaOH, BRHA-$ZnCl_2$ and activated charcoal, the glycerin content was decreased from 0.0049 to 0.0018, 0.0022, 0.0023, 0.0019 and 0.0025 g glycerin/g untreated biodiesel, respectively. The results showed that 4%wt of adsorbents gave the most efficiency in each cases.

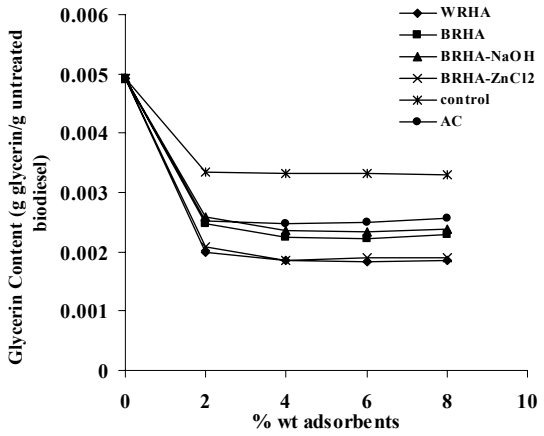

Figure 2. glycerin content vs. various % adsorbent at 50^oC for 10 min.

Conclusions

Rice husk ash can be used as an adsorbent for purifying biodiesel as it has capacity to adsorb contaminants in biodiesel. White rice husk ash and black rice husk ash activated by zinc chloride are the most efficient adsorbents for removing glycerin. By using 4%wt of adsorbents at 50^oC with contact time of 10 min., the level of glycerin is lower than of the specification of biodiesel standard.

References

[1] B.Bertram, C.Abrams and B.S.Cooke, *U.S.Patent Aplication No20050081436*. (2005).
[2] T.Bryan, *Biodiesel magazine*. (2005), pp. 40-43.
[3] J.Charoensinvorakul, *Petrochemistry and Polymer Science.* Chulalongkorn University. (2006).
[4] J.M.Marchetti, V.U.Miguel and A.F.Errazu, *Renew Sust Energy Rev* **11** (2007), pp. 1300-1311.
[5] J.Van Gerpen, B.Shanks, R.Pruszko, D.Clements and G.Knothe, *National Renewable Energy Laboratory*, (2004), NREL/SR-510-36240.
[6] Selkirk and W.Robert, *U.S. Patent No.20070175088*, (1997).
[7] N.Wang and M.J.D.Low, *Materials Chemistry and Physics,* **26** (1990), pp. 117-130.
[8] Y.Guo, J.Qi, S.Yang, K.Yu, Z.Wang, and H.Xu, *Materials Chemistry and physics,* **78** (2002), pp.132-137.
[9] N.Yalcin, and V.Sevinc, *Carbon*. **38**(2000), pp. 1943-1945.

A new surface ionic-imprinted biosorbent for selective adsorption of Cd(II) metal ions

A. Shofiyani[1,3*], Narsito[1], S.J. Santosa[1], S. Noegrohati[2], T.A. Zaharah[3], E. Sayekti[3]

[1] Department of Chemistry, University of Gadjah Mada, Yogyakarta, Indonesia
[2] Faculty of Pharmacy, University of Gadjah Mada, Yogyakarta, Indonesia
[3] Department of Chemistry, University of Tanjungpura, Pontianak, Indonesia

[*]E-mail : anisof@yahoo.com

Abstract: A new Surface-Ionic Imprinted Biosorbent (SIIB), which can considerably enhance the adsorption selectivity and capacity of Cd(II) ions is presented in this paper. The biosorbent was prepared by coating Cd(II)-imprinted chitosan hydrogel onto *Chlorella* sp biomass surface followed by crosslinking procedure. Then, the imprinted ions were desorbed using EDTA solution to provide a specific template for Cd(II) binding sites. Batch adsorption was conducted to study the characteristics adsorption of Cd(II) onto SIIB and surface non-imprinted biosorbent (SNIIB) as comparison. By Langmuir isotherm analysis, chemisorption considered as predominant mechanism for the Cd(II) adsorption onto SIIB as well as SNIIB. Competitive adsorption of multi-ions studies displayed that SIIB had superior selectivity for Cd(II). It showed metal ion affinity in the competitive conditions of Cd(II)>Cu(II)>Cr(III).

Introduction

Cadmium is heavy metal with great potential hazard in water environmental. Toxicity and un-biodegradability are the two properties of this metal, which need its recovery from solution. Many techniques have been employed for recover this metal, including chemical precipitation, ion-exchange, filtration, electrochemical treatment, membrane technologies and adsorption [1]. At present years, many kinds of biosorbent was developed due to their biodegradability, biocompatibility and chelating ability to adsorb heavy metals.

Chitosan, poly (N-acetyl-D-glucosamine), is deacetylated product of chitin, the second most abundant polysaccharides in nature. Due to its large content of $-NH_2$ and –OH groups that can chelate with many heavy metal ions such as Cd(II), Pb(II), Cd(II), Zn(II), and Ni(II), chitosan had been widely applied for remove heavy metal ions in wastewater. The disadvantage of using chitosan for industrial wastewater treatment is that it dissolves in dilute acids. This can be avoided by crosslink chitosan with many kinds of bi/poly-functional agent chitosan e.g. glutaraldehyde [2], epichlorohydrin [3]3], and ethylene glycol diglycidyl ether [4]4]. Crosslinking procedure can improve the stability of chitosan in acid media but the capacity significantly decrease because most of $-NH_2$ active sites consumed by crosslinking agent.

Using the molecular imprinting methods introduced by Ekberg and Mosbach, Tan *et al*. [5]5] prepared imprinted chitosan resin to adsorb Ni(II) ions. Molecular imprinting is an inexpensive technique for preparing adsorbent which have a specific space for molecular recognition, so the adsorption selectivity of desired molecule is enhanced. For metal ions, molecular imprinting can be interpreted as ionic imprinting exactly i.e. preparing such template for metal ions recognition. By this methods, active sites of chitosan was firstly shielded with metal ions before crosslinked so the stability of this resin increased without losing of its adsorption capacity. Su *et al*., [6,8,9] improved this technique to synthesis of surface molecular imprinted chitosan adsorbent by using biomass of *Penicillium chrysogenum* as core materials. Surface molecular imprinting is one of the important types of molecular imprinting. Surface molecular imprinted adsorbent (SMIA) not only posseses high selectivity but also avoids problem with mass transfers [7].

Inspired by Su *et al*., we developed a Surface-Ionic Imprinted Biosorbent (SIIB) by coating imprinted-chitosan on *Chlorella* sp biomass surface. This microalgae was chosen as support material for imprinted-chitosan due to its abundant and compatibility with chemical structure of chitosan.

The SIIB prepared in this paper was used for selective adsorption of Cd(II) ion. The capacity of SIIB was compared with non-imprinted one (SNIIB) to evaluate the effect of imprinting method toward ability of biosorbent. The selectivity coefficient of biosorbent in the multi mixture ions also calculated to study the applicative prospect of SIIB.

Materials and Methods

Materials

Chitosan (from crab shells 90% DD) was purchased from Sigma-Aldrich. $CdCl2.H_2O$, EDTA and all other chemicals were of analytical grade. Biomass of Chlorella sp collected from Lampung Bay, Bandar Lampung, Indonesia, washed thoroughly with water and deionized water to neutral pH, dried till constant weight then sized by 80-mesh sieve for further use.

Preparation of Surface-Ionic Imprinted Biosorbent

SIIB was prepared according to the reported procedure [6,8] and our improved work. Firstly, 0.5 g chitosan (dry weight) was dissolved in 10 mL dilute acetic acid solution of 2,5% (v/v). Then a 5000 mg/L of 10 mL $CdCl_2$ was added into the chitosan solution and stirred for 6 h to get an equilibrium adsorption of Cd(II) ions. 1.0 g (dry weight) biomass of *Chlorella* then added into the above solution and stirred for 30 minutes. The mixture dropped into 0,2 M NaOH solutions, stirred for about 1h, filtered and washed three times using distilled water.

The beads then poured into epichlorohydrin for crosslinking procedure, stirred and allowed to react for 6 hours at room temperature. After 6h reaction, beads were filtered, washed thoroughly with distilled water and then crushed. Cd(II) ions on the chitosan surface was desorbed by treating with 0.2M EDTA solution for 5 hours in a rotational shaker at room temperature. Regeneration was carried out by dipping the biosorbent into 0.1M NaOH solution for 1 hour. Subsequently, the suspensions filtered using vacuum filtration and then washed several times with deionized water until the washings were neutral, then crushed, and dried in a oven at 60^0C. The dry biosorbent was sized by an 80-mesh sieved and stored at a sealed bottle for further use.

Adsorption experiments

Batch adsorption studies were conducted by mixing 0.05 g (dry weight) adsorbent with 10 mL metal solution at pH 5.5-5.7 in a 100 mL erlenmeyer flasks, shaking at 120 rpm for 3 hour using a rotational shaker at room temperature. The relation between varying Cd(II) initial concentration (0-1000 mg/L) and its adsorption equilibrium data for Cd(II)-SIIB and SNIIB was studied.

Selectivity of biosorbents was investigated by doing competitive adsorption on multi mixture of Cd(II)/Cd(II)/Cr(III) solutions with each initial concentration of 100 mg/L in a batch system.

Results and Discussion

Adsorption Studies

The adsorption of Cd(II) on SIIB, SNIIB and IIB (Ionic Imprinted Biosorbent but without surface) was carried out with 0.05 g biosorbents. Figure 1 shows the experimental equilibrium isotherm for adsorption of Cd(II) on SIIB, SNIIB and IIB, respectively.

The isotherm on all type of biosorbents were similar in shape. It can be seen that adsorption has a rapid increase in first concentration because it still much opened active sites so Cd(II) ions reached the sites effectively. Adsorption reached the relatively constant state after concentration of 500 mg/L for SIIB and IIB and 750 mg/L for SNIIB, indicating the equilibrium of adsorption and desorption process.

The adsorption behavior of the Cd(II) ion can be described by the Langmuir adsorption equation, as follow :

$$\frac{C_e}{Q_e} = \frac{C_e}{Q_{\max}} + \frac{1}{b\,Q_{\max}} \qquad (1)$$

Where C_e is the equilibrium or final concentration of Cd(II) (mg/L), Q_e is the adsorption capacity of Cd(II) adsorbed per unit weight of adsorbent (mg/g), Q_{max} is the theoretical maximum adsorption capacity (mg/g) and b is the Langmuir adsorption equilibrium constant (L/mg).

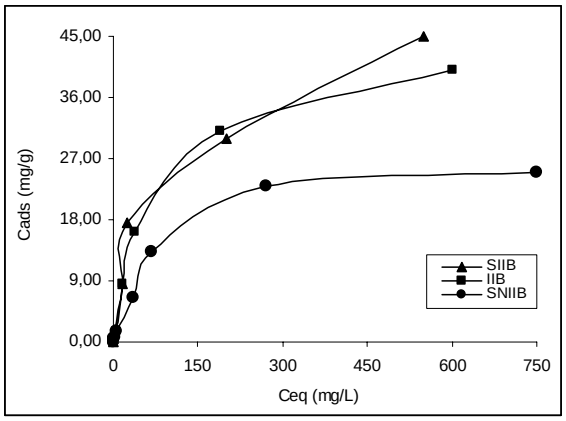

Fig. 1: Equilibrium isotherm adsorption of Cd(II) on SIIB, SNIIB and IIB

A linearized plot of C_e/Q_e versus C_e gives Q_{max} and b. The calculated results showed in Table 1.

Table 1. Langmuir constant for Cd(II) adsorption

Adsorbent	Q_{max} (mg/g)	b (L/mg)	R^2
SIIB	47.3933	0.0232	0.9704
SNIIB	27.3973	0.0916	0.9673
IIB	44.4444	0.0355	0.9507

From the table, it can be seen that Langmuir equation fits well for Cd(II) adsorption on the SIIB, SNIIB and also IIB (R^2>0.95) under the concentration range studied. The adsorption capacity of the SIIB developed in the presence study are about 15 percent higher than that of SMIA developed by Su *et al*. [6]. Su and co-workers synthesized the SMIA (Surface Molecular Imprinted Adsorbent) based on chitosan and biomass of *Penicllium chrysogenum* with Ni(II) as metal ions template. It had been found that adsorption capacity of Ni(II) to SMIA prepared is only 84% compared to chitosan imprinted resin, while this research found that the capacity of SIIB 6.2% higher instead of that IIB (chitosan imprinted resin). It is considered that the higher adsorption capacity of SIIB toward IIB is attributed to the role of biomass. The presence of biomass as surface support for chitosan enable to expose more active sites of polymer that allows the enhancement adsorption ability of biosorbent. Another reason is that the functional groups of algae biomass may also took parts in the Cd(II) adsorption.

It also seen that adsorption capacity of SIIB is almost twice higher than SNIIB. This fact confirmed that imprinting process successfully create such kind of template for Cd(II) ions. By controlling the ratio of chitosan:concentration of Cd(II) solution and chitosan:crosslinking agent, most of active sites were chelated by metal ion imprinted (on the formation of biosorbents template) and only a few of it was used for crosslinking reaction. So the adsorption capacity still high without losing its stability in acid media.

Selectivity Studies

In order to prove the selectivity of biosorbent, competitive adsorption of Cd(II)/Cu(II) and Cd(II)/Cr(III) from the multi mixture solution was investigated in a batch system. The constants such as adsorption capacity (Q), distribution ratio (*D*) and selectivity constant (α) were determined and calculated using the following equation :

$$Q = \frac{(C_0 - C_e)V}{W} \qquad (2)$$

Where Q is the adsorption capacity (mg/g), C_0 and C_e are initial and equilibrium concentration of metal ions (mg/L), V is the volume of solution (L) and W is the mass of biosorbent (g).

The distribution ratio (D) was determined using Q of each metal ion.

$$D = \frac{Q}{C_e} \qquad (3)$$

While the selectivity coefficient (α) was calculated according to :

$$\alpha_{Cd/X} = \frac{D_{Cd}}{D_X} \quad [X = Cu(II), Cr(III)] \qquad (4)$$

α represents the adsorption selectivity of Cd(II) ions in the presents of another competitor ions in solution. The larger α value indicates a stronger selectivity of Cd(II) than another ions.

The capacities of SIIB and SNIIB for each ion of Cd(II), Cu(II) and Cr(III) under competitive adsorption are summarized in Table 2.

Table 2. Adsorption capacity, distribution ratio and selectivity coeeficient of Surface-Ionic Imprinted Biosorbent

Ion	Q	*D*	α
Cd(II)	40.0	4.00	-
Cu(II)	19.9	1.99	2.01
Cr(III)	3.8	0.38	10.59

From the table, it was clear that the adsorption capacity SIIB for Cd(II) was higher than that of other ions. When the mixture ions exists in the same solution, a competition will happened for the same active sites of biosorbent. It can be seen that the Cd(II)-SIIB had superior affinity for Cd(II) ion by selectivity order of Cd(II)>Cu(II)>Cr(III) under the same competitive condition.

From this data, it is proven that surface imprinted biosorbent can provide the specific template for Cd(II) ion spesies target. It may happened as a result of rearrangement of ligand (active sites of biosorbent) during the preparation of SIIB.

Conclusions

The surface ionic imprinted biosorbent based on chitosan and biomass of microalgae *Chlorella sp* can be prepared by simple and rapid methods. The adsorption capacity of Cd(II) ions onto SIIB was much higher than that on SNIIB, considered as formation of specific template for metal ion during imprinting process. Competitive adsorption of multi-ions studies showed that Cd(II)-SIIB had superior selectivity for Cd(II) by affinity order of Cd(II)>Cu(II)>Cr(III). This founding data offers good practical prospects of SIIB in the wastewater treatment.

References

[1] J. Wang and C. Chen, "Biosorbents for Heavy Metals removal and Their Future", *Biotech. Adv*., **27** (2009), pp. 195-226.

[2] T.Y. Hsien and G.L. Rorrer, "Heterogenous Cross-Linking of Chitosan Gel Beads: Kinetics, Modeling, and Influence on Cadmium Ion Adsorption Capacity," *Ind. Eng. Chem. Re.,* **36** (1997), pp.3631-3638.

[3] Y. Baba, Y. Kawano, and H. Hirakawa, "Highly Selective Adsorption Resin: Preparation of Chitosan Derivatives Containing 2-Pyridiyl-methyl, 2-Thienylmethyl, and 3-(methylthio) propil Groups and Their Selective Adsorption of Precious Metals, *Bull. Chem. Soc. Japan*, **69** (1996), 1955-1960.

[4] W.S.W. Ngah, A.B. Ghani, and S. Kamari, "Adsorption Behavior of Fe(II) and Fe(III) Ions in Aqueous Solutions on Chitosan and Cross-Linked Chitosan Beads, *Bioresour. Technol,* **96**, pp. 443-450.

[5] T. Tan, X. He, and W. Du, "Adsorption Behaviour of Metal Ions on Imprinted Chitosan resin," *J.Chem.Technol. Biotechnol*., **76** (2001) pp 191-195.

[6] H.J. Su, Z. Wang, and T.W. Tan, "Adsorption of Ni^{2+} on The Surface of Molecularly Imprinted Adsorbent from *Penicillium Chysogenum* Mycellium, *Biotechnol. Lett*, **25**, (2003), pp. 949-953, 2003.

[7] X. Chang, *et al*., Solid-Phase Extraction of iron(III) with an Ion-Imprinted Functionalized Silica Gel Sorbent Prepared by a Surface Imprinting Technique, *Talanta*, **71** (2007), pp. 38-43.

[8] H.J. Su, Z.X. Wang, and T.W. Tan, Preparation of Surface Molecular Imprinted Adsorbent for Ni Based on *Penicillium chysogenum*, *J. Chem. technol. Biotechnol*, **4** (2005), pp. 439-444.

[9] H.J. Su, Y. Li, and T.W. Tan, "Biosorption of Ni^{2+} by the Surface Molecular Imprinting Adsorbent, *Process. Biochem*, **41** (2006), pp. **1422-1426**.

Evaluation of the possibility in applying jatropha curcas seedcake as fertilizer in chinese kale

V. Punsuvon[1*], R. Nokkaew[2] and I. Sooksathan[3]

[1] Department of Chemistry, Faculty of Science, Kasetsart University, Jatuchak, Bangkok, Thailand 10900
[2] Center of Excellence-Oil Palm, Kasetsart University, Bangkok, Thailand 10900
[3]KU-Biodiesel, Kasetsart University, Bangkok, Thailand 10900

E-mail: fscivit@ku.ac.th

Abstract: The possibility in applying Jatropha curcas seedcake as fertilizer for growing Chinese kale was studied in term of total yield, plant growth, plant analysis in elemental contents, soil analysis, and phorbol esters which co-carcinogen compound. In this experiment, eleven treatments of the difference amount of seedcake mix with chemical fertilizer, farm manure, and one control were studied compared with applying chemical fertilizer, farm manure, and seedcake alone. The quantitative analysis of phorbol esters was analyzed the residue concentration in chinese kale and in soil after harvesting by HPLC-UV and confirmation by LC-MS/MS with multiple reaction monitoring (MRM) mode. This mode used the ionization of parent ion with mass 711 to daughter ion with mass 311 and 293 respectively. The result of experiment showed that the application of high rate Jatropha seedcake mix with chemical fertilizer in half rate of recommendation gave the highest yield comparable to the application of full rate of chemical fertilizer. In addition, no phorbol esters residued in both Chinese kale and soil after harvesting.

Introduction

Jatropha curcas seedcake contained high content of nitrogen element that could be used as organic fertilizer for growing different vegetables. This seedcake not only contained nitrogen but also contained toxic phorbol esters compound which act as cocarcinogen, so to make sure the safety application of seedcake as fertilizer for grower and consumer, it was necessary to determine the concentration of phorbol esters residue in vegetable that growing with this seedcake and in soil after harvesting..

From literature review, Wink et al (2000) identified phorbol esters in Jatropha curcas oil by using ESI-MS/MS. The spectrum of phorbol esters showed the parent ion had 711 of molecular mass and daughter ion at 693, 383, 311, 293 of molecular mass respectively. Punsuvon et al (2008) analyzed the concentration of phorbol esters by using HPLC-UV with TPA as external standard and confirmed phorbol esters compound by using LC-MS/MS with multiple reaction monitoring mode from ionization of parent ion with mass 711 to daughter ion with mass 331 and 293 respectively. In addition the amount of seedcake as fertilizer is necessary to know for the highest yield of vegetable product too.

The objective of this research is to determine the residue of phorbol esters toxic compound of Jatropha curcas seedcake which used as organic fertilizer, in Chinese kale and in soil after harvesting. The investigation of total yield, plant growth, plant and soil analysis is also analysis.

Materials and Methods

Jatropha curcas seedcake used in this experiment had phorbol esters content equal 0.3281 mg/g. The experiments was conducted during May to September 2008 at Ayutthaya province, Thailand. In each experiment unit, twenty four days seedings were transplanted to 5 x 1.5 m pot size for 6 rows with row by plant spacing of 25 x 20 cm. Harvest area was 4 m^2 of middle 4 rows. The experimental design was randomize completed block with 3. replications of 12 treatments. Thus, the whole trial consisted of 36 experimental units. Twelve treatments were shown as table 1

Table 1: Treatments of twelve experiments

Treatments	Conditions
1	Control (No seedcake)
2	Chemical fertilizer (95 recommendation) Basal of 15-15-15 rate 312.50 Kg/ha at land preparation. Top dress of 46-0-0 rate 156.25 Kg/ha at 25 days after transplanted
3	Farm manure as basal rate 9.4 t/ha
4	Jatropha seedcake (low rate) 2.5 t/ha
5	Jatropha seedcake (medium rate) 5.0 t/ha
6	Jatropha seed cake (high rate) 10 t/ha
7	Chemical fertilizer (as half rate of recommendation) Basal of 15-15-15 rate 156.25 Kg/ha + Jatropha seedcake (low rate) 2.5 t/ha
8	Chemical fertilizer at half rate + Jatropha seedcake (medium) 5.0 t/ha

Treatments	Conditions
9	Chemical fertilizer at half rate + Jatropha seedcake (high rate) 10 t/ha
10	Farm manure at half rate (4.7 t/ha) + Jatropha seedcake (low rate) 2.5 t/ha
11	Farm manure at half rate (4.7 t/ha) + Jatropha seedcake (medium rate) 5.0 t/ha
12	Farm manure at half rate (4.7 t/ha) + Jatropha seedcake (high rate) 10 t/ha

For phorbol esters analysis, 10 g of each dry Chinese kale and soil after harvesting were extracted with 250 ml CH_3OH in soxhlet extractor for 4 hours. After that the extract solvent was further evaporated by vacuum rotaevaporator until 10 ml of solution was obtained. One portion of solution was analyzed concentration of Phorbol esters by HPLC-UV followed Punsuvon et al (2008). Another portion of solution was further evaporated to 1 ml of solution. The solution was confirmed by LC-MS/MS with multiple reaction monitoring (MRM) mode. The mode used the ionization of parent ion with molecular mass 711 to daughter ion with molecular mass 311 and 293 respectively.

Results and Discussion

Chinese Kale healthy seeding of 24 days old were transplanted to experimental field plot on June, 14, 2008 and after transplanted for 25 days, the green leafy vegetables were harvested. Plant growth and fresh vegetable yield were recorded and presented in table 2

Table 2: Average growth characters and fresh vegetable yield of Chinese kale as the effect of different treatments.

Treatments	Leaf length (cm)	Leaf width (cm)	Plant height (cm)	Canopy height cm)	Canopy width (cm)	Total yield (t/ha)
1	10.87	8.70	7.39	19.83	13.27	4.12
2	14.83	12.26	15.83	29.27	21.27	9.87
3	11.18	8.58	7.73	20.47	17.00	2.02
4	9.75	7.05	7.26	18.37	13.57	1.77
5	9.63	7.04	7.83	17.60	12.33	4.08
6	11.35	9.63	9.06	2.91	14.42	3.77
7	12.10	10.03	10.13	20.90	14.23	7.07
8	9.76	8.00	8.30	19.07	12.60	4.55
9	14.23	12.40	10.57	27.87	19.67	9.08
10	10.43	7.63	8.05	20.77	15.40	2.60
11	12.07	8.26	9.60	23.27	15.23	4.12
12	11.50	9.16	8.85	23.30	15.20	3.99

From table 2, plant growth was presented as leaf length, leaf width, plant height, canopy height and canopy width. The responses of all 5 characters to treatments showed the same trend. The best performance mostly obtained from treatments by chemical fertilizer (treatment 2), chemical fertilizer at half rate + jatropha seedcake (high rate) 10 t/ha (treatment 9) followed by chemical fertilizer at (half rate) + jatropha seedcake (low rate) 2.5 t/ha (treatment 7), farm manure at half rate 4.7 t/ha + jatropha seedcake (medium rate) 5.0 t/ha and (low rate) 2.5 t/ha (treatment 11, 10) and jatropha seedcake at high rate 10 t/ha (treatment 6) respectively. The other treatments including control (treatment 1) showed low performance of growth.

For total yield, the highest total yield (9.87 t/ha and 9.08 t/ha) were obtained from the treatment of chemical fertilizer (treatment 2) and chemical fertilizer half rate + jatropha seedcake (high rate) 10 t/ha (treatment 9). These results showed high potential of high rate application of jatropha seedcake to reduce the cost of vegetable production especially for replacement of the high price of chemical fertilizer. The chemical fertilizer at half rate + jatropha seedcake (low rate) (treatment 7) showed medium yield (7.07 t/ha). The rest treatments including control gave lower yield.

For plant analysis, the result presented in table 3 Chinese kale analyzed for total percentage of N, P and K as the effects of different treatment.

Table 3: Plant analysis of Chinese kale for total percentage N, P and K as affected by different treatments

Treatments	N^1(%)	P^2(%)	K^3(%)
1	2.30	0.56	3.06
2	2.14	0.61	2.64
3	2.27	0.63	2.62
4	1.92	0.54	2.97
5	2.27	0.59	3.51
6	2.34	0.58	2.81
7	1.92	0.64	3.12
8	1.78	0.51	2.39
9	2.24	0.68	4.18
10	2.32	0.58	2.36
11	2.81	0.80	3.47
12	3.19	0.70	4.12

Note; method analysis:
[1] Total N: Semi microkjeldehl method
[2]Total P: Vanado molybdophosphoric acid yellow method
[3]Total K: Atomic absorption spectro photometer

To consider vegetable quality, nutritional value of total N, P and K should be more or less in the balance level. The result showed high level of N, P and K were obtained from the application of farm manure + Jatropha seedcake (high rate) 10 t/ha (treatment 12) followed by those of farm manure + Jatropha seedcake

(medium rate) 5 t/ha (treatment 11) and chemical fertilizer + Jatropha seedcake (high rate) (treatment 9) respectively. Treatments of Jatropha seedcake (low rate) and chemical fertilizer + Jatropha seedcake (medium rate) (treatment 4 and treatment 7) gave the lowest performance.

For soil analysis, the result presented in table 4. Soil sample from preplanning and after Chinese kale harvesting (post) were analyzed to compare the effects of different treatments. The result of soil analysis was shown in table 4.

Table 4: Soil analysis for pH, organic matter, available P and K of preplanning and postharvest

Treatments	pH[1]	OM[2](%)	P[3](mg/kg)	K[3](%)
Preplanting Postharvest	7.0	2.61	49.04	271.69
1	7.4	2.47	70	580
2	7.4	2.33	73	470
3	7.6	2.67	75	480
4	7.5	2.33	120	360
5	7.4	2.63	87	570
6	7.3	2.33	79	450
7	7.3	2.30	70	570
8	7.4	2.33	68	500
9	7.2	2.53	77	530
10	7.5	2.67	80	560
11	7.5	2.70	79	440
12	7.4	2.80	85	580

Note; method analysis:
[1] Total N: Semi microkjeldehl method
[2]Total P: Vanado molybdophosphoric acid yellow method
[3]Total K: Atomic absorption spectro photometer

The result of pH value showed slightly increased in all treatments. Organic matter percentage showed slightly increased in treatments with farm manure applicaton (both farm manure alone and farm manure + Jatropha seedcake). For available N, P and K, all treatments showed higher concentration over the soil sample from preplanting soil. However, there were not much different concentration of N, P and K as affected by different treatments.

The result of phorbol esters analysis. Phorbol esters peak in seedcake that used in this experiment presented at the retention time between 8-12 minutes as showed in figure 1.

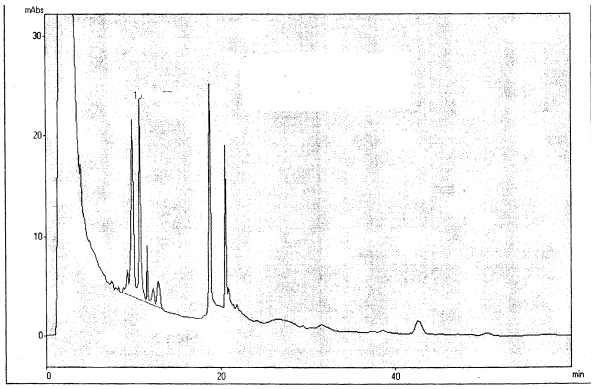

Figure 1. Chromatogram of phorbol esters in seedcake

The concentration of phorbol esters which calculate by using TPA (Phorbol-12-myristate-13-acetate) as external standard was 0.3246 mg/g and the oil content of seed cake was 0.74%. The result of confirmation by LC-MS/MS with MRM mode of phorbol esters in seedcake presented two peak at the time 2.49 and 2.48 minutes of chromatogram as showed in figure 2

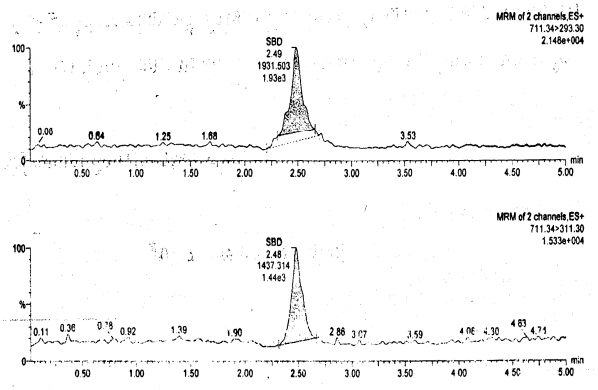

Figure 2. Chromatogram of phorbol esters from LC-MS/MS

The first peak showed phorbol esters as molecular mass 711 ionized to molecular mass 293 and the second peak showed molecular mass 711 ionized to molecular mass 311. The result from analyzed Chinese kale and soil after harvesting at the best treatment (Chemical fertilizer at half rate + Jatropha seedcake (high rate) 10 t/ha by HPLC-UV showed the chromatogram in figure 3 and figure 4 and the concentration of phorbol esters content around 0.063 mg/g, and 0.0086 mg/g in Chinese kale and soil respectively. But after confirmation the peak by LC-MS/MS, they had not occurred two peaks of ionization at the retention time 2.49 and 2.48 minutes. So, it mean no phorbol esters residued in Chinese kale and soil sample.

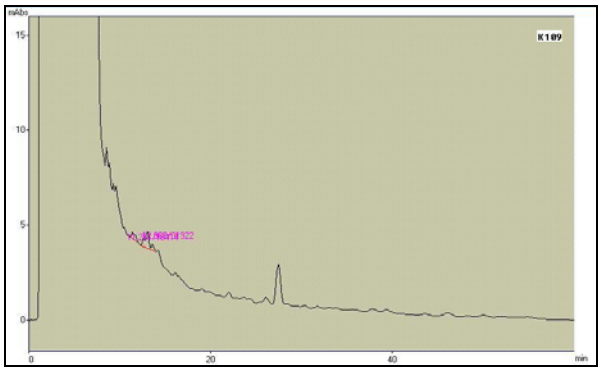

Figure 3. Chromatogram of Chinese kale extract

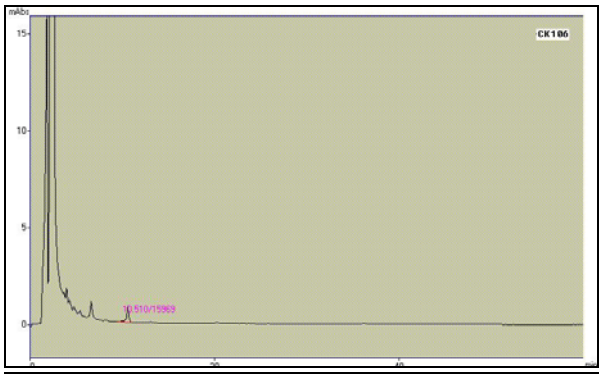

Figure 4. Chromatogram of Soil extract

Conclusions

The best treatment in applying Jatropha curcas seedcake as fertilizer in Chinese kale was applying chemical fertilizer at half rate (Basal 15-15-15 rate 156.25 Kg/ha and top dress of urea 78.125 Kg/ha) + Jatropha seedcake (high rate) 10 t/ha. This treatment gave total yield at 9.08 t/ha and no phorbol esters residued in both Chinese kale and soil after harvesting. The summary result showed that Jatropha seedcade can be applied as fertilizer with safety for growing Chinese kale.

References

[1] R. Nokkaew, V. Punsuvon and P. Vaithanomsat, *Proceeding in Pure and Applied Chemistry International Conference* (2008), pp. 202-207.
[2] M. Wink, C. Grimn, C. Koschmieder, F. Sporer and O. Bergeot, *Chemoecology* (2000), pp. 179-187

Acknowledgement
This research is supported by D1 Oil Company.

Life cycle assessment study for environmental impacts assessment of chitosan production processes

S. Kaewseelam[1*] and P. Kittisupakorn[1]

[1] Life Cycle Engineering Laboratory , Department of Chemical Engineering, Faculty of Engineering, Chulalongkorn University, Phyathai, Bangkok, Thailand 10330

[*] E-mail: manornae@hotmail.com

Abstract: Chitosan, a copolymer of D-glucosamine and N-acetyl-D-glucosamine with β-(164) linkage is obtained by alkaline or enzymatic deacetylation of chitin and an abundant polymeric product in nature. Chitosan is an important raw material and product of industry (pharmacology, agriculture, waste water treatment etc.). In this research, the chemical method has been studied in order to provide the environmental impact and three chitosan production processes studied are based on different raw materials: shrimp shells, crab shells and squid pens. Life Cycle Assessment (LCA) has been applied to evaluate environmental impacts of processes. SimaPro software consisting of 19 categories such as resources, global warming, ozone depletion etc. waste has been used to quantify the environmental impacts. The results have shown that the environmental impacts for the process using crab shells as raw material is lowest environmental impacts.

Introduction

Chitin is derived from the Greek word chiton, which means a coat of nail. It is the major component of the exoskeleton of invertebrates, crustaceans, insects, and the cell wall of fungi and yeast in which chitin acts as a supportive and protective component. Chitin, poly-(164)-N-acetyl-D-glucosamine, is a cellulose-like biopolymer found in a wide range of products in nature.

Chitosan is found in different morphological forms such as a primary, unorganized structure, crystalline and semicrystalline forms. For different reasons, especially problems of environmental toxicity, these two biopolymers are considered interesting substances for producing polymers. Because of their unique structures, they possess high biological and mechanical properties as they are biorenewable, biodegradable, and biofunctional. Two methods, namely chemical and enzymatic, are known for preparation of chitin, chitosan and their oligomers, with different degrees of deacetylation, polymerization, and molecular weight (MW). The molecular weight of natural chitin is normally higher than 1,000,000 Da and that of commercially available chitosan is around 100,000–1,200,000 Da. Numerous forces during commercial production may influence the MW of chitosan. Factors such as high temperature (>280 0C thermal degradation of chitosan occurs and the polymer chains quickly break down), dissolved oxygen concentration, and shear stress may cause these changes to occur.

Life cycle assessment (LCA) is a method for assessing various aspects associated with development of a product and its potential impact throughout a product's life from raw material acquirement, processing, manufacturing, use and finally its disposal. LCA studies should systematically and sufficiently address the environmental aspects of products/systems. The depth of the details and time frame of and LCA study may vary to a large extent, depending on the definition of goal and scope. The scope, assumptions, description of data quality, methodologies and output of LCA studies should be transparent. LCA methodology should be agreeable to inclusion of new scientific findings and improvement in the state-of-the-art of the technology. The result are also related for the use of a product, which allows comparison between alternatives.

Life cycle assessment is a systematic approach used to manage the potential environmental impacts of product and service systems. It is applied methodologically to build a quantitative inventory of environmental burdens or releases, evaluate their potential impacts, and consider alternatives to interpret the results or improve environmental performance. LCA can be used to identify critical life cycle stages or burdens for which additional environmental assessment tools (such as risk assessment) may be applied to fully understand the potential impacts and risks.

In any application, LCA considers the potential environmental impacts along the continuum of a product's life (i.e., cradle to grave or cradle to cradle), from raw materials acquisition to production, use, and disposal or recovery. The potential environmental impacts to consider include resource depletion, human health, and ecological health.

LCA consists of four iterative phases:

1. Goal and Scope Definition: Defining the aims, product system, and reach of the study.
2. Life cycle Inventory Analysis: In which extractions and emissions related to the product system are quantified and related to the product function.
3. Life cycle Impact Assessment: In which the outcome of the inventory is analyzed with respect to their environmental relevance and is aggregated within a smaller number of relevant environmental issues.
4. Interpretation: In which the results are compared with the goal of the study.

Life cycle assessment use result from the assessment goes to adjust the procedure produces for

the procedure produces and the products that are good quality and friendly with environment. Furthermore, use comparison of each products that the product suit to usable and have an affect to the environment least. Besides, choice expansion in the procedure produces which decrease the effect to the environment and bring about to using resource efficiently.

Thailand has a lot of seafood consume and export which these are factor increase regarding from shrimp shells, crab shell etc. In present, these waste sell to the animal food industry. The cost of selling wastes are 3-4 baht/kg. But if produced chitosan, it will increase value are 200-2500 baht/kg depend on quality of chitosan.Chitosan has many application for industry such as medical, food, agriculture etc. In this research, Life cycle assessment (LCA) has been applied to evaluate environmental impacts of chitosan production processes. Based on different raw materials: shrimp shells, crab shells and squid pens

Methodology

Chitosan production processes based on different raw materials: shrimp shells (case I), crab shells (case II) and squid pen (caseIII) are studied. In this research, the information regarding the process has been gathered based on previous related researches carried out in laboratory. Mass balances of each process are derived and simulation has been carried out to obtain relevant data used in the SimaPro software. SimaPro software is applied to evaluate the environmental impacts of all processes.

Show flow diagram of research methodology in figure 1.

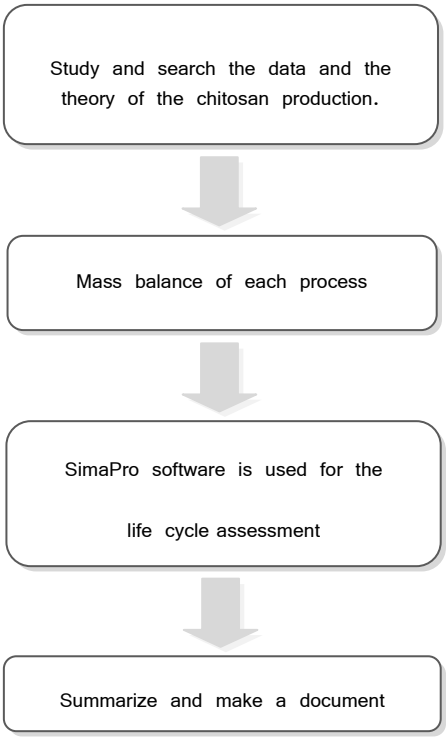

Figure 1. Flow diagram of research methodology

Results and Discussion

The chitosan production processes using shrimp shells (case I), crab shells (case II) and squid pens (case III) as raw material (1 kg. each) are studied. The input and output of the processes are shown in table 1.

Table 1 The input and output of the chitosan production processes

Amount (kg)	Case I	Case II	Case III
Product			
Chitosan	0.27	0.32	0.10
Input			
Sodium hydroxide	36.60	46.86	0.55
Hydrochloric acid	11.80	11.80	0.35
Ethanol	6.31	3.95	0
water	0.13	0.08	0.16
Calcium carbonate	0.32	0.29	0.36
Output			
Sodium hydroxide	22.46	22.98	0.43
Hydrochloric acid	11.57	11.59	0.09
Ethanol	6.31	3.95	0
Water	0.23	0.16	0.24
Calcium chloride	0.35	0.32	0.40
Carbondioxide	0.14	0.13	0.16

The amount of output water and chemicals from each unit are recovered and recycled for the next process.

We evaluated the environmental impacts by SimaPro software. The proportions of chemical reagent, product and environmental impacts for case I, case II and case III are shown in Fig.2, Fig.3 and Fig.4, respectively.

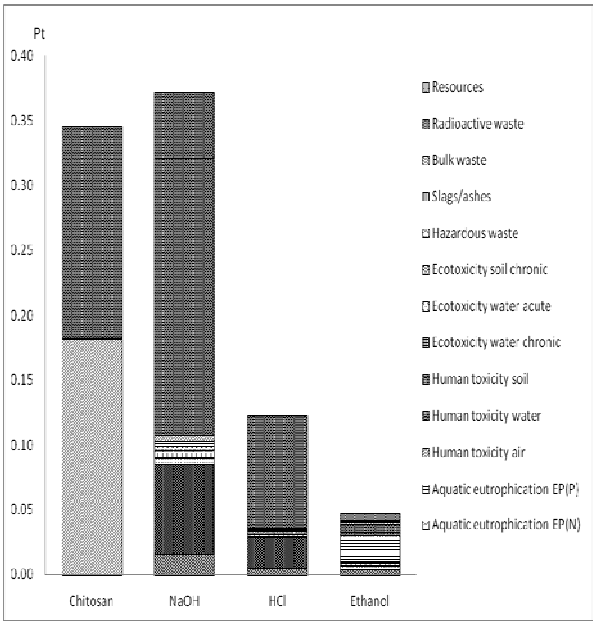

Fig. 2 Environmental impacts of the chitosan production process of case I

Form Fig.2, main impacts of chitosan are human toxicity air and human toxicity soil. Main impacts of NaOH are global warming, ozone depletion, human toxicity water and human toxicity soil. Main impacts of HCl are ozone depletion, human toxicity water and human toxicity soil. Main impacts of ethanol are aquatic eutrophication EP (P). Total impacts of case I is 0.89 Pt.

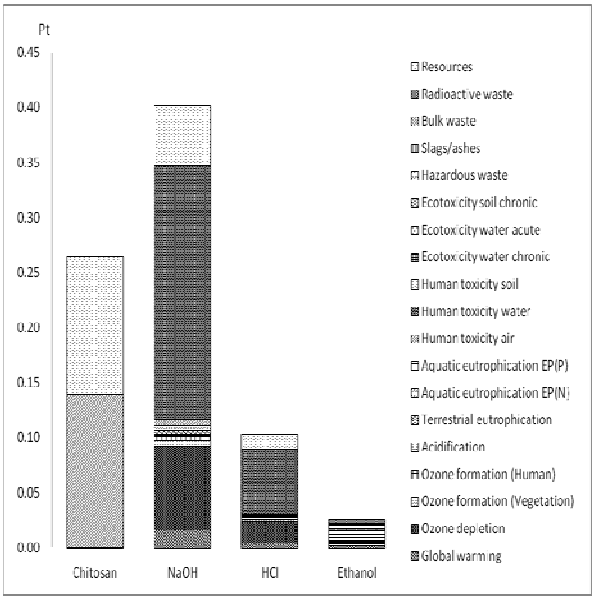

Fig. 3 Environmental impacts of the chitosan production processes of case II

Form Fig.3, main impacts of chitosan are human toxicity air and human toxicity soil. Main impacts of NaOH are global warming, ozone depletion, human toxicity water and human toxicity soil. Main impacts of HCl are ozone depletion, human toxicity water and human toxicity soil. Main impacts of ethanol are aquatic eutrophication EP (P). Total impacts of case II is 0.79 Pt.

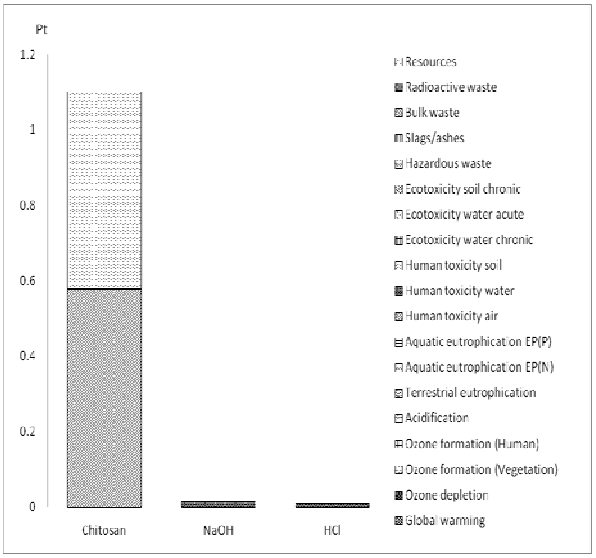

Fig. 4 Environmental impacts of the chitosan production processes of case III

Form Fig.4, main impacts of chitosan are human toxicity air and human toxicity soil. Main impacts of NaOH and HCl are human toxicity water. Total impacts of case III is 1.13 Pt. (Case III didn't use ethanol because it produced white chitin.)

Conclusions

The environmental impact of chitosan production processes are studied. It was found that the environmental impact of the production process using crab shells as raw material is lowest environmental impacts; the main impacts are global warming, ozone depletion, aquatic eutrophication EP (P), human toxicity air, human toxicity water and human toxicity soil.

Although this chitosan production based on a chemical mechanism method needs large amount of chemical reagents which affect the environment but in comparison to the enzymatic method, the chemical method has been used in the real industry because it takes easier to control. Therefore, in this research, the chemical method has been studied in order to provide the environmental impact information for further consideration in developing the process.

In this research, benefits of the life cycle assessment are strategy for improving the chitosan production process as well as decreasing the environmental impacts corresponding to the production.

References

[1] Yaowapa Waiprip, Chitin and Chitosan production from shrimp shells, Department of food technology, Faculty of science, Chulalongkorn university. 1991. ISBN 974-578-609-8X.

[2] Ming Tsung Yen, Joan Hwa Yang and Jeng Leun Mau., Physicochemical Characterization of chitin and chitosan from crab shells. *Carbohydrate Polymers* **75** (2009), pp. 15-21.

[3] R. Shepherd, S. Reader and A. Falshaw. *Chitosan functional properties*. **14** (1997), pp. 535-542.

[4] Majeti N. V. Ravi Kumar, A review of chitin and chitosan applications, *Reactive & Functional Polymers* **46** (2000), pp. 1–27.

[5] Entsar S. Abdou, Khaled S. A. Nagy and Maher Z. Elsabee. Extraction and characterization of chitin and chitosan from local sources. *Bioresource Technology* **99** (2008), pp. 1359-1367.

[6] A. Tolaimate, J. Desbrie`res, M. Rhazi, A. Alagui, M. Vincendon and P. Vottero., On the influence of deacetylation process on the physicochemical characteristics of chitosan from squid chitin., *Polymer* **41** (2000), pp. 2463-2469.

[7] Pawadee Methacanon, Malinee Prasitsilp, Thanawit Pothsree and Junya Pattaraarchachai., Heterogeneous N-deacetylation of squid chitin in alkaline solution, *Carbohydrate Polymers* **52** (2003), pp. 119–123.

[8] M. Susana Cortizo, Carla F. Berghoff and Jose Luis Alessandrini., Characterization of chitin from Illex argentinus squid pen, *Carbohydrate Polymer* **74** (2008), pp. 10-15.

[9] Ruth Hagen Rodde, Aslak Einbu and Kjell M. Va rum., A seasonal study of the chemical composition and chitin quality of shrimp shells obtained from northern shrimp (Pandalus borealis), *Carbohydrate Polymers* **71** (2008), pp. 388–393.

[10] N. Acosta, C. Jimenezt, V. Boraut and A. Heras., Extraction and Characterization of Chitin from Crustaceans. *Biomass and Bioenergy* **Vol.5, No.2** (1993), pp. 145-153

Development of low cost solid sorbent using agriculture wastes for CO_2 sequestration: a study on the effect of mixing amines and glycerol

T. Jarunchart, P. Mangosol, M. Krikrabkreaw, M. Kittiyawat and P. Toochinda *

Sirindhorn International Institute of Technology/School of Bio-Chemical Engineering and Technology, Thammasat University, P.O. Box 22, Pathumthani, Thailand 12121

* E-mail: pisanu@siit.tu.ac.th

Abstract: The development of low cost amine-enriched solid sorbent from agriculture wastes was studied for CO_2 sequestration in automobiles and small industry. The agriculture wastes have the high potential as supports for CO_2 capture solid sorbents due to the high availability, low cost, light weight, and ability to be shaped into various forms. The agriculture wastes used as support in this study were bagasse and activated carbon derived from bagasse. Different types of amines could be used to provide the different benefits and effects for CO_2 capture for the solid support. The adsorption rate of CO_2 over sorbent can be boosted by using primary and secondary amines over tertiary amine. On the other hands, the tertiary amine could provide higher CO_2 capture capacity per site over primary and secondary amines. This study focuses on the effect of different types of amines and the mixing ratio in order to enhance the performance of CO_2 capture over amine-enriched solid sorbent. The amines used in this study are primary amine (monoethanolamine; MEA), secondary amine (diethanolamine; DEA), and tertiary amine (2-amino-2-methyl-1-propanol; AMP). The study of the glycerol promotion was also investigated in order to improve the performance of mixed amine-enriched solid sorbent. The agriculture waste supports were treated with 1.0 M NaOH and mixed with 20 weight percent of amines. The combinations of different amines were used to study the performance of CO_2 capture of sorbents as follows; the MEA/AMP, DEA/AMP, MEA/AMP/glycerol, and DEA/AMP/glycerol. The performances of CO_2 capture of solid sorbents were conducted in tubular reactor at pressure of 1 atm at the adsorption temperature range between 298K and 323K. The CO_2 capture capacities of the solid sorbents were determined by Gas Chromatography (GC) at desorption temperature range between 373K and 423K. The results show that the mixed amine of the DEA/AMP could capture CO_2 more than MEA/AMP. The optimum composition of mixed amines (MEA, DEA and AMP) and glycerol for the active CO_2 capture solid sorbent was investigated. The roles of different amine types and glycerol shall be discussed.

Introduction

Global warming is now considered as one of the top priorities within the world society. Challenges in decreasing the atmospheric CO_2 turns to be an urgent research interest. The effective methods that could be used to capture and sequestrate atmospheric CO_2 from the combustion have been an attractive and challenging topic during up until the present.

One of the CO_2 reduction methods is the adsorption of CO_2 over solid sorbent. The combination of mixed amines in liquid absorption of CO_2 also provides the high potential in CO_2 sequestration process. The principle of this study is to adopt these two ideas together by using the mixed amine treated on agricultural waste support to develop the mixed anime enriched solid sorbent. The combination of different amines in proper contents could utilize the benefits of individual. Primary amine (monoethanolamine) and secondary amine (diethanolamine) could provide the high CO_2 adsorption rate while tertiary amine (N-methyldiethanolamine or 2-amino-2-methyl-1-propanol provide the high capacity of CO_2 capture.
S. Bandyopadhyay et.al. reported that AMP has the same high CO_2 capture capacity per site compared to MDEA, but has a higher rate constant for reaction with CO_2 [1-5].

Another way in order to improve the efficiency of CO_2 capture sorbents is adding the hydroxyl group. Ming Bo Yue et.al. reported that hydroxyl groups can promote the formation of the intermediate between CO_2 and the amine and also promote the capture of CO_2 of mesoporous silica SBA-15 (SP) with mixed amine (TEPA and DEA). This work also used glycerol to mix with tetraethylene pentamine (TEPA) to study the promotion of hydroxyl group from glycerol on the CO_2 adsorption of this synthesized SBA-15 [6].

So the objectives of this work are focused on the effect of different types of amines and the proper mixed ratio of amines in order to study the performance of CO_2 capture over amine-enriched solid sorbent. The sorbents were developed by depositing primary amine (monoethanolamine; MEA), secondary amine (diethanolamine; DEA), and tertiary amine (2-amino-2-methyl-1-propanol; AMP) on the supports of bagasse and activated carbon derived from bagasse. The study of the glycerol promotion was also investigated in order to improve the performance of mixed amine-enriched solid sorbent. The CO_2 capture of solid sorbent by using combinations of MEA, DEA, and AMP with glycerol could provide the attractive choice for atmospheric CO_2 reduction.

Experimental Section

1.1.1 Support Material Preparation:

The agriculture wastes used as support in this study were bagasse and activated carbon derived from bagasse. The supports were treated with 1 M of NaOH (Aldrich) at 298 K for 12 h for cleaning purpose. The supports were dried in the oven at 333 K for 12 h.

Sorbents Preparation:

The mixed amine-enriched solid sorbents were prepared by the incipient wetness impregnation of the mixtures of MEA/AMP, DEA/AMP, MEA/AMP/glycerol, and DEA/AMP/glycerol. They were solubilized in methanol solution. In this work, mixed amines were dissolved in methanol at the ratio of mixed amines/methanol of 1/3. Both supports were treated with mixed amines at a fixed ratio of 20% with varying the ratio of glycerol.

CO_2 Capture Capacity:

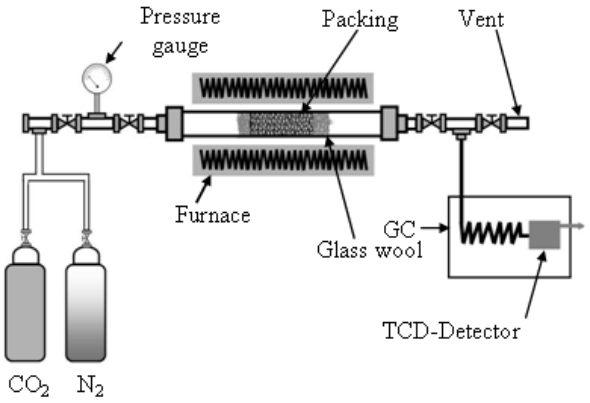

Figure 1: Schematic of experimental setup for the study of CO_2 capture capacity

Figure 1 illustrates the schematic of the experimental set up for CO_2 capture capacity. The experiments over various solid sorbents were conducted in a fixed-bed reactor. Two grams of sorbent were packed with glass wool in the tubular reactor. The CO_2 capture was performed by keeping the sorbents in CO_2 atmosphere and kept in batch mode at 298 K and 1 atm for 1, 3 and 5 hours. The solid sorbent were flushed with 30 ml/min N_2 flow for 1 h to get rid of the CO_2 physisorptions. Sorbents were heated at 393 K by furnace (model TF150) with PID controller under atmospheric pressure for 45 min. to desorb all CO_2 chemisorptions from the sorbent. The gas samples were collected and quantified the amounts of CO_2 chemisorptions from the sorbent which are the CO_2 capture capacities by gas chromatography (GC), Perkin Elmer-Autosystem XL, coupled with Porapak Q column (Supelco) and thermal conductivity detector (TCD).

Results and Discussions

Table 1: The study of the effect of various amine types, glycerol promotion and adsorption time (pure amine and pure amine with glycerol)

Amine Composition	Adsorption time (h)	CO_2 Capture Capacity (µmol/ g. Sorbent)
MEA	1	583
	3	610
	5	609
DEA	1	1167
	3	1186
	5	1189
AMP	1	285
	3	886
	5	883
MEA: Gly. = 4:1	1	899
	3	903
	5	908
DEA: Gly. = 4:1	1	1533
	3	1537
	5	1541
AMP: Gly. = 4:1	1	612
	3	992
	5	990
MEA + AMP (1:1)	1	788
	3	956
	5	961
MEA + AMP (1:1) : Gly. = 4:1	1	903
	3	1097
	5	1094
DEA + AMP (1:1)	1	804
	3	981
	5	976
DEA + AMP (1:1) : Gly. = 4:1	1	947
	3	1224
	5	1229
MEA + AMP (1:2)	1	523
	3	909
MEA + AMP (1:2): Gly. = 4:1	1	627
	3	1020
MEA + AMP (2:1)	1	863
	3	1057
MEA + AMP (2:1) : Gly. = 4:1	1	1079
	3	1261
DEA + AMP (1:2)	1	732
	3	1130
DEA + AMP (1:2) : Gly. = 4:1	1	869
	3	1262
DEA + AMP (2:1)	1	891
	3	1083
DEA + AMP (2:1) : Gly. = 4:1	1	1233
	3	1419

Table 1 shows that 20 wt% DEA-enriched solid sorbent at the adsorption time at 1 h can exhibit the highest performances of CO_2 capture among other amines (MEA, DEA and AMP = 583, 1134 and 285 µmol/g. sorbent, respectively). This study also shows that when increasing adsorption time from the sequence of 1 h, 3 h and 5 h, MEA and DEA has a

similar trend in CO_2 capture capacity (MEA adsorption time at 1 h = 583 μmol/g.sorbent and 3 h = 610 μmol/g.sorbent and DEA at 1 h = 1167 μmol/g.sorbent and 3 h = 1186 μmol/g.sorbent), though the CO_2 capture capacity of AMP has a different pattern which increased dramatically at the adsorption time of 1 h to 3 h and maintains the amount at 5 h. (AMP at 1 h, 3 h and 5 h of adsorption time = 285, 886 and 883 μmol/g. sorbent, respectively) This clearly confirms that the primary and secondary amines provides a high reaction rate and tertiary amine provides a high CO_2 capture capacity but low reaction rate [1, 2, 4]. AMP structure has the high branches, which is sterically hindered amine, can provide steric effect influence to the stability of the carbamates formed by the amine with CO_2 [1]. The CO_2 loading in AMP comes near a value of 1.0 mol of CO_2 per mole of amine [2].

Processes that include glycerol can enhance CO_2 capture capacity of these sorbents. In table 1, it is obvious that the result that includes glycerol outputs a higher CO_2 capture capacity than the original amine composition. This can be explained that glycerol provides hydroxyl groups, which can boost CO_2 capture capacity as mentioned in the previous work [6]. The formation reaction of carbamate type zwitterions may be promoted in terms of adding hydroxyl group; [6]

$$CO_2 + R\text{-}OH + R_2\text{-}NH = R\text{-}OH^+ + 2R_2\text{-}NCOO^-$$

,where R-OH = *glycerol and* R_2-NH = *amines*

Table 1 also illustrates other types of amine composition by mixed amines along with glycerol promotion. The results of this study have the same trend comparing to the previous result. Process shows that MEA/AMP over bagasse at adsorption time of 1 h, 3 h and 5 h are 788, 956 and 961 μmol/g.sorbent; the 903, 1097 and 908 μmol/g. sorbent of MEA/AMP/Gly. over bagasse; the 804, 981 and 976 μmol/g. sorbent of DEA/AMP and the 947, 1224 and 1229 μmol/g. sorbent of DEA/AMP/Gly. over bagasse, respectively.

The optimum ratio of the mixture of MEA/AMP, MEA/AMP/Gly., DEA/AMP and DEA/AMP/Gly. has a ratios of 2:1 (CO_2 capture capacity of MEA/AMP, MEA/AMP/Gly., DEA/AMP and DEA/AMP/Gly. at the adsorption time of 3 h = 1057, 1261, 1083 and 1419 μmol/g.sorbent, respectively. This implies that at the beginning of the adsorption time, primary and secondary amines can affect CO_2 capture capacity more than tertiary amine, but when the adsorption time increases at a certain rate, tertiary amine provides a higher CO_2 capture capacity more than primary and secondary amines.

Table 2: The study of adsorption profiles of amine-enriched solid sorbents using different supports**:**

Amine Composition	**CO_2 Capture Capacity (μmol/g.Sorbent) Adsorption Time = 3 h**
DEA + AMP (4:1)	1256
DEA + AMP (4:1): Gly.. = 4:1	1342
DEA + AMP (4:1)	1284
DEA + AMP (4:1): Gly.. = 4:1	1403

Note: *Fixed weight of mixed amines at 20 wt% per g.support + 5 wt% glycerol per g.support*

Table 2 illustrates the effect of mixed amines of DEA/AMP and DEA/AMP/Gly. at the ratio of 4:1 to CO_2 capture capacity on bagasse (BG) and activated carbon derived from bagasse (AC, BET surface area = 900 m^2/g). Results show that at the same ratio of mixed amines and mixed amines with glycerol, the AC support provides a higher CO_2 capture capacity than BG support. This could be explained by a high surface area of the support.

Table 3: The study of the optimum ratio of glycerol **:**

Support	**The Ratio of the DEA + AMP (4 : 1) : Glycerol**	**CO_2 Capture Capacity (μmol/g. Sorbent) Adsorption Time = 3h**
BG	4 : 1	1342
	4 : 2	971
	4 : 3	914
	4 : 4	700
AC	4 : 1	1403
	4 : 2	798
	4 : 3	787
	4 : 4	709

Note: *Fixed weight of amines at 20 wt% per g. support + 5 wt% glycerol per g.support*

Table 3 illustrates in finding the optimum ratio of glycerol. The results of this study show that at the ratio of the DEA + AMP (4:1)/Gly. = 4:1 is the most optimum ratio of glycerol. Results could be explained that for the support of used BG, increasing the ratio

results in a lower CO_2 capture capacity due to a limited surface area. This can be explained by adding an exceeded amount of loading in both mixed amines and glycerol which blocks the pore of the support, along decreasing the CO_2 capture capacity [7-8]. The results of CO_2 capture capacity of the DEA+AMP (4:1) with glycerol at various ratios of mixed amines and glycerol of 4:1, 4:2, 4:3 and 4:4 over the BG support at the adsorption time of 3 h are 1324, 971, 914 and 700 μmol/g. sorbent, respectively, and the CO_2 capture capacity of 1403, 798, 787 and 709 μmol/g. sorbent, respectively, for the AC support.

Conclusions

In this study, 20 wt% DEA-enriched solid sorbent at the adsorption time at 1 h can exhibit the highest performances of CO_2 capture among other amines. When increased adsorption time from 1 h , 3 h and 5 h, MEA and DEA almost have the same CO_2 capture capacity, but CO_2 capture capacity of AMP is increased at the adsorption time of 3 h and maintain at this level at 5 h. This can clearly confirm that primary and secondary amines have high reaction rate and tertiary amine has the high CO_2 capture capacity but low reaction rate. This study also shows that glycerol can enhance CO_2 capture capacity of these sorbents. It could be explained that glycerol provides hydroxyl groups, which can help to boost CO_2 capture capacity as mentioned in the previous work. The optimum ratio of the mixture of MEA/AMP, MEA/AMP/Gly., DEA/AMP and DEA/AMP/Gly. is 2:1. The AC support can provide the higher CO_2 capture capacity than BG support. In the study of optimum ratio of glycerol, the results of this study show that at the ratio of the DEA + AMP(4:1)/Gly. = 4:1 is the optimum ratio of glycerol. This could be explained from the limited surface area. The high loading of both mixed amines and glycerol could block the pore of support, which lead to the decreasing of CO_2 capture capacity. The results of this study could lead to the development of novel amine-enriched CO_2 capture solid sorbent that is high performance and low cost.

Acknowledgement

Our thanks to Thammasat University Research Fund for the financial support.

References

[1] B.P. Mandala, A.K. Biswasb, S.S. Bandyopadhyay, *Chem.Eng.Sci.* ***58*** (2003) pp. 4137-4144
[2] B.P. Mandala, M. Guhab, A.K. Biswasb, S.S. Bandyopadhyaya, *Chem.Eng.Sci.* ***56*** (2001) pp. 6217- 6224
[3] B.P. Mandal, A.K. Biswas, S.S. Bandyopadhyay, *Separation and Purification Technology* ***35*** (2004) pp. 191-202
[4] B.P. Mandala, S.S. Bandyopadhyay, *Chemical Engineering Science* **60** (2005) pp. 6438-6451
[5] Zhang Pei, Shi Yao, Wei Jianwen, Zhao Wei, Ye Qing, *Journal of Environmental Sciences* ***20*** (2008) pp. 39-44
[6] Ming Bo Yue, Lin Bing Sun, Yi Cao, Zhu Ji Wang, Ying Wang, Qing Yu, Jian Hua Zhu, *Microporous and Mesoporous Materials* ***114*** (2008) pp. 74–81
[7] M. Mercedes Maroto-Valer, Zhe Lu, Yinzhi Zhang , Zhong Tang, *Waste Management*, **28** (2008) 2320– 2328
[8] 342M.G. Plaza, C. Pevida, A. Arenillas, F. Rubiera, J.J. Pis, *Fuel* **86** (2007) 2204–2212

Roles of urea and zirconia in Cu-Zn/Al_2O_3 for methanol-steam reforming

C. Siriruang, P. Vacharapong, S. Ajavakom, T. Sumonsart and P. Toochinda*

Sirindhorn International Institute of Technology/School of Bio-Chemical Engineering and Technology, Thammasat University, P.O. Box 22, Pathumthani, Thailand 12121

* E-mail: pisanu@siit.tu.ac.th

Abstract: The active impregnated catalyst could be an attractive catalyst for the hydrogen production from methanol-steam reforming in term of low use in metal contents and cost of preparation. The activity of impregnated Cu-Zn/Al_2O_3 catalyst could be enhanced by using urea and Zirconia. The addition of urea in the impregnation process could reduce the size of metal clusters and improve the metal dispersion over Al_2O_3 support, which results in a higher hydrogen yield. The high activity of the catalyst could also be enhanced furthermore by the addition of Zirconia into the impregnated Cu-Zn/Al_2O_3. The hydrogen production performances of various Cu-Zn/Al_2O_3 catalysts with different Zirconia compositions were tested in order to study the effect of Zirconia and determine the optimized compositions. The catalytic methanol-steam reforming was conducted in tubular reactor at the temperature range of 453-523 K. The hydrogen effluent gas was analyzed by gas chromatography (GC). The catalysts were characterized by XRD before and after reaction to identify the phases of metal on the catalyst. Metal cluster size and dispersion over the catalysts were identified by SEM-EDS. The results show that Zirconia promoted catalyst with urea could exhibit the hydrogen yield better than the non-promoted catalyst of 29.3% at 453 K and 36.3% at 523 K. XRD and SEM-EDS data show that the Zirconia promoted catalyst with urea exhibit smaller metal cluster and metal crystal as well as better dispersion over non-promoted catalyst. The catalyst from this study could provide an alternative catalyst for hydrogen production from methanol-steam reforming, which is high performance, low cost and easy in preparation. The roles of urea and Zirconia in Cu-Zn/Al_2O_3 for methanol-steam reforming will be discussed.

Introduction

Hydrogen fuel cell is considered as an attractive choice of energy for the future. Hydrogen fuel cell is generates electrical energy from electrochemical reaction of hydrogen with atmospheric oxygen and yield water, which is the environmental benign product. Therefore, one of the most important parts in energy production by the fuel cell is hydrogen resources. The production of hydrogen is very important and the hydrogen could be produced from reforming reaction of hydrocarbons. Methanol is mostly considered as resource of hydrogen production for fuel cell due to their properties, low cost, low boiling point, high energy density, high H/C and easy storage [1-2]. The reaction is shown as;

Methanol Steam Reforming:

$CH_3OH + H_2O \rightarrow 3H_2 + CO_2 \qquad \Delta H_0 = 49.5$ kJ/mol

This reaction is a heterogeneous catalytic reaction with the Cu-Zn based catalyst. Most of the Cu-Zn based catalysts are prepared by co-precipitation method which requires high Cu and Zn contents of 60-90 weight percent in order to serve as the active catalyst for methanol steam reforming [3-4]. The incipient wetness impregnation is one of the simple catalyst preparation methods, which requires low content of active metal relative to other preparation methods. The lower of metal content in catalyst with the competitive performance could lower the cost of catalyst production. The impregnation of Cu and Zn with urea on the support such as alumina could exhibit a high activity of hydrogen production without using a high metal loading on the catalyst. The major drawback of impregnation method is the dispersion of metal loading on the support. In order to solve this problem, urea has been used to allow the formation of precipitates to have better homogeneity of metal cation distribution in the solution [5-6]. In addition, several literatures have been used the other metal as a promoter to increase the performances of the catalyst such as Zr, Ce, Pd, Pt and Cr. Zirconia (ZrO_2) has been used to promote the precipitated Cu-Zn/Al_2O_3 to increase the catalyst activity [7]. Unfortunately, very few works investigate the effect of these promoters in the impregnated catalysts with urea and the roles of the promoters still remain unclear.

The objective of this work is to develop high activity of Cu-Zn/Al_2O_3 by impregnation method in order to provide the lower cost and ease in preparation. Zirconia was used as a promoter for the Cu-Zn/Al_2O_3 with urea. The roles of Zirconia and urea in the impregnation method are investigated. The results of this study could lead to develop the novel impregnated catalysts for hydrogen production from the methanol steam reforming process.

Materials and Methods

Catalyst Preparation: Cu-Zn based catalysts over Al_2O_3 were prepared by incipient wetness impregnation methods. The catalysts were prepared with Zirconia and 2 moles of urea were synthesized by impregnating the aqueous solution of $Cu(NO_3)_2 \cdot 3H_2O$, $Zn(NO_3)_2 \cdot 6H_2O$ and $ZrO(N_2O_6) \cdot xH_2O$) with an addition of urea (99%, Carlo Erba) over Al_2O_3. Table 1 lists the composition of Cu, Zn , Zr and urea used in the catalyst prepapration in this study. The activity of Cu-Zn catalyst using NaOH instead of urea was also tested in order to study the effect of basicity of the

metal salt solution to the activity of the catalyst. The catalyst prepared with NaOH (CZNa) was synthesized by impregnating the aqueous solution of $Cu(NO_3)_2 \cdot 3H_2O$ and $Zn(NO_3)_2 \cdot 6H_2O$ with the addition of NaOH (≥ 98%, Sigma-Aldrich) over Al_2O_3. The pH of metal salt solution was adjusted using NaOH to be equivalent with the pH value of metal salt-urea solution. The impregnated samples were dried in air at 373 K for 12 hrs and then calcined at 573 K for 3 hrs. The commercial catalyst used for comparison was $Cu\text{-}Zn/Al_2O_3$ prepared by precipitation method from Süd-Chemie AG (München, Germany).

Table 1: The composition of Cu-Zn catalyst for methanol-steam reforming

Catalyst	Composition ($Cu/Zn/Al_2O_3$) (%wt)	Urea (mole/mole Cu)	Zirconia (%wt of Cu)
CZ	10/10/80	0	0
4Zr-CZ	10/10/79.6	0	4
CZNa	10/10/80	0	0
CZU	10/10/80	2	0
1Zr-CZU	10/10/79.9	2	1
2Zr-CZU	10/10/79.8	2	2
4Zr-CZU	10/10/79.6	2	4

Methanol-Steam Reforming in Tubular Reactor: The methanol steam reforming reaction for the hydrogen production was studied on the prepared catalysts in a stainless steel tubular reactor which has an inside diameter of 1 cm. Two grams of catalyst were packed between quartz wool in the reactor. The catalyst was reduced with 30 ml/min of 10% H_2: N_2 balanced at 453 K for 1 hr prior to the methanol reforming reaction test. The reactor was flushed with 30 ml/min N_2 flow at 453 K for 30 min to get rid of adsorbed hydrogen from the reduction process. The mixture of methanol and water solution was loaded into a saturator which was heated to 333 K. The compositions of methanol and water in the liquid phase are 0.125:0.875 molar ratios. The composition of solution was calculated by the Aspen Plus simulation program (Aspen Technology Inc., Burlington, Mass., USA) to ensure that the composition of the mixture in the vapor phase is a 1:1 molar ratio at the outlet from the saturator. The vapor of the mixture within the saturator was carried out at 20 ml/min N_2, and sent into the reactor at 453 K and 523 K in a continuous system. Therefore, the time spent in the packed bed reactor in continuous system was about 6 seconds. The product was collected and the production of hydrogen was determined via gas chromatograph (GC).

Analysis sections: A Perkin Elmer (Waltham, Mass., USA) Autosystem XL gas chromatograph (GC) with Porapak Q column (Supleco, Bellefonte, PA, USA) coupled with a thermal conductivity detector (TCD) was used to determine the amount of hydrogen production.

Morphology of the catalysts was inspected by a scanning electron microscope (SEM, JEOL JSM-5410, Jeol Inc., Tokyo, Japan). The elemental composition of the catalyst surface was determined by energy dispersive spectrometry (EDS, Oxford, Oxford Instrument, Oxfordshire, United Kingdom) which the SEM was equipped with.

The catalysts were characterized by the X-ray diffraction technique (XRD, JEOL JDX-3530, Jeol Inc., Tokyo, Japan) using Cu Kα1 radiation, 30° - 41° 2-theta, 0.04° step size, 1 sec step time. JADE software (Jade Software Corporation Ltd., Christchurch, New Zealand) was used to determine the crystallize size of the CuO by using the broadening of peak at 38.8° 2-theta. JADE software was also used to identify phases of the catalysts before and after calcination with the references of X-ray diffractogram database from the International Centre for Diffraction Data (Newtown Square, PA, USA).

Results and Discussion

Activity of the Catalysts for Methanol Reforming:

The activities of catalysts for the hydrogen production from the methanol steam reforming reaction are listed in table 2. Percent H_2 yields were calculated using the following equation derived from stoichiometric coefficients of methanol and hydrogen from the balanced chemical reaction:

$$\%H_2\ yield = \frac{1}{3}\frac{mol\ of\ H_2}{mol\ of\ CH_3OH\ fed} \times 100$$

Table 2 shows that addition of urea in preparation method could increase the performance of catalyst. The catalyst that prepared by using urea (CZU) exhibited higher hydrogen yield than catalyst without urea (CZ). The addition of Zirconia could also increase the activity of catalyst, which is evidenced by the higher activity of Zirconia promoted catalyst (4Zr-CZU) than that of non-Zirconia promoted catalyst (CZ). Unlike the addition of urea, the data shows that there is no improvement in catalyst activity with the addition of NaOH, which is also indicated by the CZU exhibit higher activity than those of CZNa. The data can show that the improvement of catalytic activity of CZU catalysts does not result from the basicity of the metal salt solution in the impregnation process.

Table 2 also shows the increasing of Zirconia promoted with urea in preparation method catalysts (1Zr-CZU, 2Zr-CZU, and 4Zr-CZU) could lead to increasing of hydrogen yield. The 4% of Zirconia over Copper catalyst (4Zr-CZU) could exhibit the highest hydrogen yield (40.2 % H_2 yield) and higher hydrogen yield than the non-promoted (CZU) catalyst of 29.3% at 453 K, 36.3% at 523 K.

Table 2: Hydrogen production from methanol reforming over various catalysts at 453 K and 523 K.

Cu-Zn-Al_2O_3 Catalysts	Temperature (K)	% Hydrogen yield
CZ	453	12.9
4Zr-CZ		14.0
CZNa		13.0
CZU		14.7
1Zr-CZU		16.4
2Zr-CZU		18.1
4Zr-CZU		19.0
CZ	523	22.1
4Zr-CZ		23.9
CZNa		23.0
CZU		29.5
1Zr-CZU		34.6
2Zr-CZU		36.6
4Zr-CZU		40.2

Catalysts Characterization:

Figure 1 shows the SEM-EDS images of the 4Zr-CZU. The image shows that the Cu, Zn and Zr are deposited in the form of small clusters on the Al_2O_3 surface. The EDS profiles indicate clearly that the small clusters are composed of Cu, Zn and Zr located on Al_2O_3.

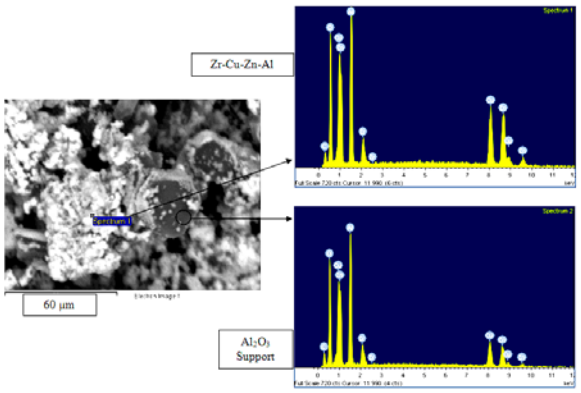

Figure 1. SEM image and EDS profiles of the impregnated Cu-Zn with Zirconia and urea over Al_2O_3 catalyst.

Figure 2 shows the SEM images of catalysts without urea and Zirconia, catalyst with urea and catalyst with urea and Zirconia. The SEM image of CZ (Fig. 2.a) shows the agglomeration of a large Cu-Zn compounds cluster (> 10 µm) over Al_2O_3. The distribution of Cu-Zn compounds clusters is inconsistent throughout the surface of Al_2O_3. The SEM images of CZU (Fig. 2.b) and 4Zr-CZU (Fig. 2.c) show smaller Cu-Zn compounds clusters (≈ 0.2-1 µm) and better dispersion of Cu-Zn compounds clusters over Al_2O_3 than that of CZ. These result exhibited that using urea in catalyst preparation method could provide a better metal dispersion over the support, which is correspond with hydrogen yield.

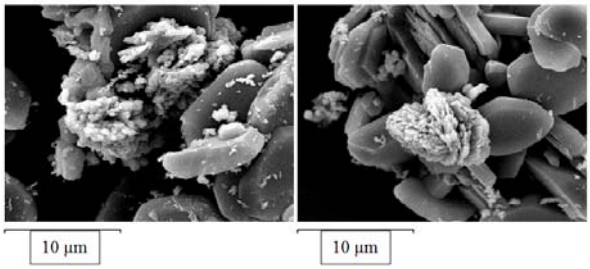

(a) CZ (catalyst without urea and Zirconia)

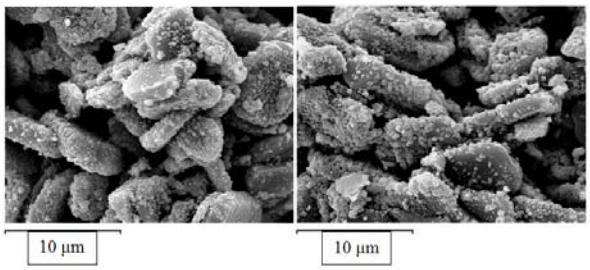

(b) CZU (catalyst with urea)

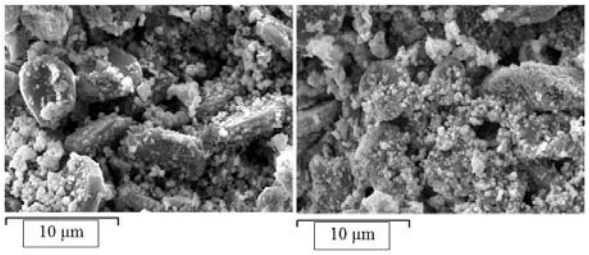

(c) 4Zr-CZU (Catalyst with urea and Zr)

Figure 2. SEM images of the impregnated Cu-Zn base catalyst, (a) CZ (catalyst without urea and Zr), (b) CZU (catalyst with urea), (c) 4Zr-CZU (catalyst with urea and Zirconia).

Role of Urea in Cu-Zn/Al_2O_3:

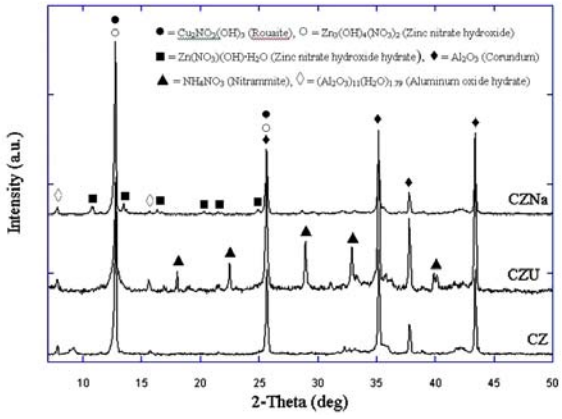

Figure 3. X-ray diffractogram of the impregnated catalysts before calcinations.

Figure 3 shows the X-ray diffractogram of the CZ, CZU and CZNa catalysts. The diffractogram of these catalysts exhibit similar patterns. The major phase of these catalysts was composed of copper and zinc nitrate hydroxide. The diffractogram of CZU exhibits the presence of ammonium nitrate (NH_4NO_3) as a

minor phase, which was not found in CZ and CZNa. The urea that was added into the metal salt solution for impregnation can react with copper nitrate ($Cu(NO_3)_2$) and zinc nitrate ($Zn(NO_3)_2$) as in the following reactions to form NH_4NO_3.

$$CO(NH_2)_2 + H_2O \rightarrow 2NH_4^+ + HCO_3^- + OH^-$$

$$2NH_4^+ + Cu(NO_3)_2 \rightarrow 2NH_4NO_3 + Cu^{2+}$$

From these reactions, the dissociation of urea can further react with metal nitrates to form NH_4NO_3, which is evidenced in the XRD diffractogram of CZU. The XRD pattern of NH_4NO_3 disappeared after calcinations. NH_4NO_3 was reported to aid the synthesis of silver, nickel and ruthenium in the form of nanoparticles from the spray-pyrolysis process. The literature also reports the ability of NH_4NO_3 to undergo explosive decomposition during the calcination process [8-9]. The NH_4NO_3, which is produced in the catalysts with urea, can provide the ability to reduce the size of Cu-Zn compounds clusters and also improve the distribution of Cu-Zn compounds clusters over Al_2O_3 during the calcinations.

Table 3: Estimated crystallize size of CuO

Sample	Estimated crystallize size of CuO* (nm)
CZ	29
CZNa	24
CZU	14
4Zr-CZU	6

*determined by XRD using peak at 2-theta equal to 38.8°

Table 3 shows the estimated crystallize size of CuO on the catalysts. The data shows that the present of urea used in the catalyst impregnation process can yield a smaller crystallize size of CuO. The crystallize size of CuO on the Cu-Zn catalyst using NaOH (CZNa) does not significantly decrease compared to Cu-Zn catalyst without NaOH (CZ). Therefore, the basicity of the metal salt solution from NaOH in the impregnation process does not significantly affect the size of a crystallized CuO. Unlike NaOH, urea can be added into the metal salt solution, not only to reduce the size of Cu-Zn compounds cluster on the catalysts, but also to reduce the crystallize size of CuO.

Role of Zirconia in Cu-Zn/Al_2O_3:

Literatures report the presence of Zirconia in catalyst can lower the reduction temperature and speed up the reduction process. Zirconia could provide the high activity in converting CuO on the surface to be Cu and Cu^+ by redox mechanism in methanol synthesis. Cu and Cu^+ are considered as the active metal sites for methanol steam reforming [7]. The facility of reducibility could be the important factor in determining the activities of the catalysts.

In Table 3, the 4Zr-CZU shows the smallest estimated crystallize size of CuO (6 nm) among all the catalysts in this study. Literature reported that Zirconia promotion can weaken the interaction between CuO/ZnO and Al_2O_3. This effect could provide the ease in dissociation of Cu-Zn metal site on Al_2O_3, which results in a smaller crystalline of CuO. Literature also reported the oxygen ion vacancy in Zirconia (ZrO_2) which could influence in the dispersion of Copper resulting in better dispersion of Cu metal site over the support [10]. The detailed mechanistic study of Zirconia role in impregnated Cu-Zn catalyst will be further investigated.

Conclusions

This study shows that the addition of urea in the impregnation method can improve the activity of Cu-Zn/Al_2O_3 for methanol steam reforming reaction. The SEM-EDS images show that the Cu and Zn are deposited as a cluster over Al_2O_3. Images also show that the use of urea can reduce the size of Cu-Zn compounds clusters and provide better dispersion of Cu-Zn compounds clusters throughout Al_2O_3 surface which results in a higher activity of hydrogen production. This phenomenon can be explained from the presence of NH_4NO_3 produced by the reaction of urea and metal salt solution. NH_4NO_3 can reduce the size of Cu-Zn compounds clusters over Al_2O_3 and also the crystallize size of CuO determined via XRD. The addition of Zirconia could also improve the activity of catalyst. The Zirconia promoted catalyst prepared by impregnation using urea provides the highest hydrogen production and the smallest CuO crystallize size in this study. The results of this study could lead to the development of novel catalysts for hydrogen production from the methanol steam reforming process.

Acknowledgement

Our thanks to Thammasat University Research Fund for the financial support.

References

[1] James R. Lattner and Michael P. Harold, *Applied Catalysis B: Environmenta,l* 56(2005),149–169.
[2] Ayman Karim, Jaime Bravo, David Gorm, Travis Conant and Abhaya Datye, *Catalysis Today* 110 (2005) 86–91.
[3] Patel S, Pant KK, *Chem. Eng Sci* **62** (2007), 5436-5443.
[4] Shishido T, Yamamoto Y, Morioka H, Takehira K, *J Mol Catal A: Chem* **268** (2007), 185-194.
[5] M. Turco, G. Bagnasco, U. Costantino, F. Marmottini, T. Montanari, G. Ramis, G. Busca, 2004. *J Catalysis* **228** (2004), 43–55.
[6] Murcia-Mascaros S, Navarro R M, Gomez-Sainero L, Costantino U, Nocchettiy M, Fierro J L G, *J Catalysis*, **198** (2001), 338-347.
[7] John P. Breen, Julian R.H. Ross, *Catalysis Today*, **51** (1999) 521-533.
[8] Balcerowiak W, Perkowski I, *J Thermal analysis* **32** (1987), 1777-1779.
[9] Morozov I V, Fedorova A A, Knotko A V, Valedinskaja O R, Kemnitz E, *Mendeleev Commun*. **14(4)** (2004)**,** 138-139.
[10] Li Yong-Fenga, Dong Xin-Fab, Lin Wei-Mingb, *International Journal of Hydrogen Energy*, **29** (2004) 1617-1621.

Removal of orthophosphate from aqueous solution using natural zeolite

Y. Karemdabeh[1] and U.Onthong[1]*

[1] Computational Chemistry Research Unit, Department of Chemistry, Faculty of Science, Thaksin University, Pathalung, 93110 Thailand

*E-mail:usa@tsu.ac.th

Abstract: This study was focused on orthophosphate adsorption on natural zeolite was obtained from South of Thailand have been carried out by Vanadomolybdo-phosphoric Acid and using spectrophotometry technique. The phosphate solution were prepared artificially by adding certain quantities of KH_2PO_4 in water at the initial orthophosphate concentration of 5, 10 and 20 mg/L. While the adsorbent quantity was 1 g. of natural zeolite per 50 ml. aqueous solution NaOH 1N and HCl 1N solutions were used as pH regulators. The effect of equilibrium pH, Adsorbent Mass and contact time was studied. Adsorption isotherms for phosphate on natural zeolite were prepared at pH 6-12 in this study. The results showed that natural zeolite adsorption efficiency 99.18%, 99.33% and 99.02% (5, 10 and 20 mg/L), respectively a pH of 12 and a contact time of 30 minutes at 298 K. Efficiency of absorption all will be reduced by pH values lower. Moreover, the isotherm can be used to evaluate the capacity and nature of the interaction between a sorbent and a sorbate. This work considers the Langmuir and Freundlich isotherm. Based on the R^2 of adsorption isotherm studies the adsorption data for phosphate fitted well the Freundlich isotherm for natural zeolite (R^2=0.99), with multi-layer adsorption. The results are in good agreement with recent theoretical data.[1]

Introduction

Phosphate is essential in the growth of weed. It is one of the most important elements and is the main factor responsible for eutrophication may be defined as the enrichment of a water body by plant nutrients.[7] Orthophosphate is one of the important plant nutrients involved in the eutrophication process and phosphate ions are responsible for the algal bloom in receiving water bodies and aesthetic problems in drinking water. From the environmental and economic points of view, management of such a contaminant and valuable resource is very important.[3] Phosphorus usually occurs in wastewater and surface water in the form of organic phosphates (e.g. detergents) and inorganic phosphates (ortho- and poly-phosphates).[4] There are various techniques have been employed for reducing the levels of phosphate in water with chemical precipitation and biological nutrient removal begin the most commonly applied methods. Adsorption is a robust and effective technique used in water and wastewater treatments. The success of an adsorption depends on the choice of an appropriate sorbent treatment and various conditions. The zeolite sorbents were then characterized and their phosphate adsorption behavior was studied under varying experimental conditions such as adsorbent mass, solution pH, coexisting ions, and initial concentration. The results are presented in terms of equilibrium isotherm [5] of natural zeolite as adsorbents to adsorb orthophosphate in prepared wastewater.

Materials and Methods

Materials

Artificial orthophosphate solutions were used throughout the adsorption tests. Initially, a stock solution of 50 mg/L in orthophosphate was prepared by dissolving a certain amount of chemically pure KH_2PO_4 in water. Analytical reagent grade chemicals were used throughout and were purchase Vanadate-molybdate reagent (Sigma-Aldrich, Germany) Sodium hydroxide (Ajax Finechem, Australia) Hydrochloric acid (Baker, Thailand) Potassiumdihydrogenphosphate (Fluka, Switzerland) Natural zeolite (South of Thailand).

Adsorption Procedure

Batch experiments were used for this study. All the adsorption experiments were performed by using 0.5, 1, 2 and 5 g. of adsorbent and 50 ml of phosphate ion solution of known concentration and pH. The initial solution pH was adjusted to the desired value with NaOH 1 N or HCl 1N solution was used to elucidate the adsorption parameters, contact time, adsorbent dosage, initial solution pH and initial concentration of adsorbent. [2] Detector (Shimadzu, UV-1700) Prior to the study of orthophosphate adsorption, natural zeolite A gram of each adsorbent was added into KH_2PO_4 solution at the concentrations 5, 10 and 20 mg/L.[4] The solutions were shaken in a shaking bath at the speed of 160 rpm at room temperature until the adsorption reached equilibrium. Then, adsorbents were separated out from the solutions by the leftover orthophosphate in the solutions was analyzed by one of colorimetric method, called Vanado-molybdophosphoric Acid method. The absorbance of each solution was measured using UV/VIS spectrophotometer at wavelength of 420 nm to determine the orthophosphate concentration.

Results and Discussion

The results of bath experiments adsorptive removal of inorganic phosphate ions from aqueous solutions hasbeen studied. were pH, time and orthophosphate/ adsorbent ratio. The results are cited below.

Effect of Adsorbent Mass

The effect of adsorbent mass was studied by varying the amount of each adsorbent from 0.5 to 5 g. The amount of each zeolite type was added to 50 mL phosphate solution contained in plastic bottles. The bottles were placed in a thermostatic shaker and were agitated at 298 K for 30 min.[5] The results of the residual phosphate concentration against amounts of different natural zeolites are shown in Figure 1. The residual phosphate concentration decreased with an increase in the amount of adsorbent due to an increase in the number of active sites. From an initial concentration of 5 mg/L, the zeolites were able to remove phosphate to concentrations below detectable levels.

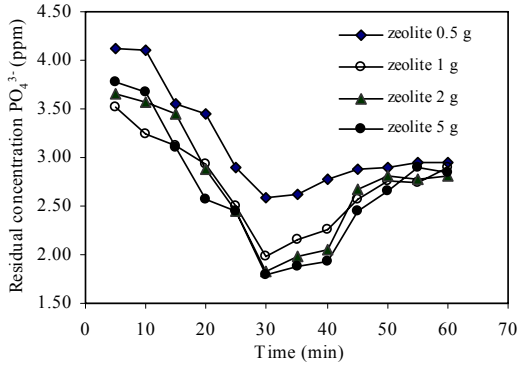

Figure 1. Effect of adsorbent mass on phosphate removal from wastewater at 298 K:initial concentration, 5 mgPO_4^{3-} /L

Effect of contact time

The effect of contact time on natural zeolite adsorption capacities is shown in Figure 2. The natural zeolite adsorption rate was increased with increasing contact time and reached a maximum value at about 30 min.

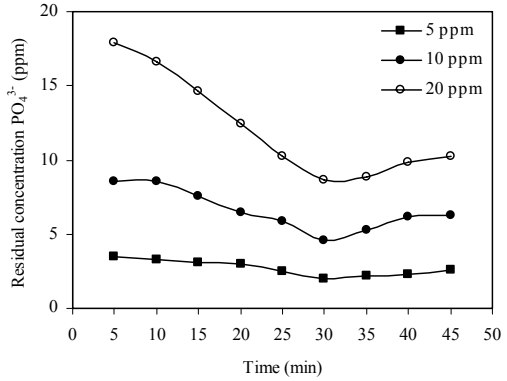

Figure 2. Effect of contact time orthophosphate adsorption onto natural zeolite

Effect of initial solution pH

The effect of pH on the removal of orthophosphate species, through adsorption onto natural zeolite, was examined in the pH region between 6 and 12. The tests were carried out at constant experimental conditions with an initial solution concentration 5, 10 and 20 mg/L in orthophosphate and 1 g of adsorbent. All the tests were carried out at constant retention time, fixed at 30 min. The effect of pH is illustrated in Fig. 3.

The results show that pH is an important factor regarding orthophosphate adsorption onto natural zeolite. The orthophosphates uptake is comparatively lower in the slightly basic pH it increases for higher pH values and becomes complete in the vicinity of pH 12. Correspondingly, the supernatant remaining concentration decreases with pH. Orthophosphates are completely removed from solution in the basic pH region around 12.

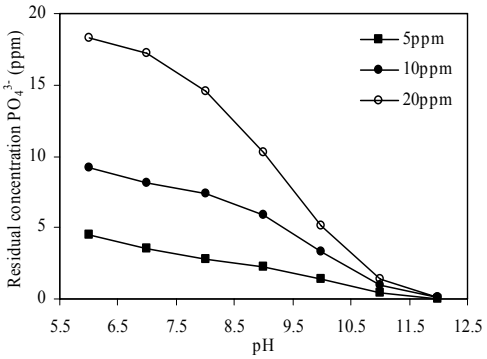

Figure 3. Effect of pH on orthophosphate adsorption onto natural zeolite and supernatant concentration, contact time: 30 min; adsorbent mass 1 g.

Batch tests were carried out with various contaminant /solid ratios at pH 12. In all the cases, the solid mass was maintained constant at 1 g while the initial concentration in orthophosphates was increasing The retention time was 30 min. The results are illustrated in Figure 4.

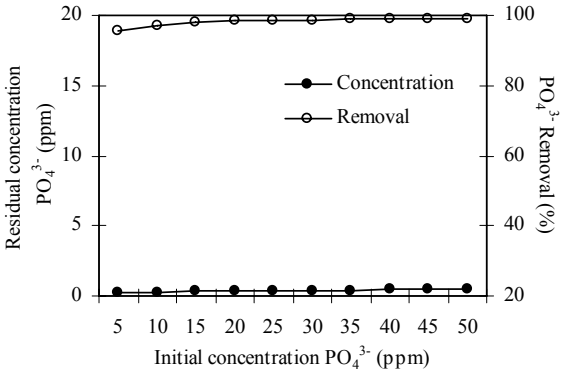

Figure 4. Effect of initial concentration on orthophosphates removal and remaining concentration at pH 12 (adsorbent mass 1 g)

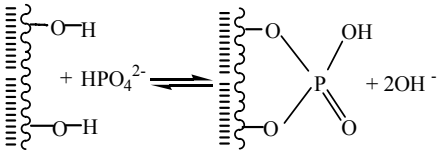

Figure 5. Hypothesis of phosphate removal by natural zeolite adsorbent

Adsorption Isotherm

The adsorption isotherm studies the Langmuir and Freundlich models were used to study the adsorption isotherm orthophosphates on natural zeolite. The Langmuir equation is given as follows:

$$\frac{C_e}{q_e} = \frac{1}{bQ^0} + \frac{C_e}{Q^0}$$

where C_e is the equilibrium concentration of aqueous solution (mgl^{-1}), q_e is the amount of aqueous adsorbed on natural zeolite per unit weight of natural zeolite at equilibrium, Q^0 is the maximum amount of aqueous adsorbed on natural zeolite (mgg^{-1}). b is the Langmuir constant (Lmg^{-1}). Q^0 and b can be determined from the slope and the intercept of linear plot of C_e/q_e against C_e, respectively. [5] The correlation coefficients (R^2), Q^0 and b are tabulated in Table.

The Freundlich equation is given as follows:

$$\log q_e = \log K_F + \frac{1}{n} \log C_e$$

where q_e is the amount of phosphate ion adsorbed onto adsorbent at equilibrium (mgg^{-1}), C_e is the equilibrium concentration of phosphate ion ($mg\ L^{-1}$), K_F is the Freundlich constant (mgg^{-1}) and $1/n$ is an empirical constant. $1/n$ and K_F can be obtained from the slope and the intercept of the linear plot in Figure 6. The correlation coefficients (R^2), K_F and $1/n$ are tabulated in Table. [6]

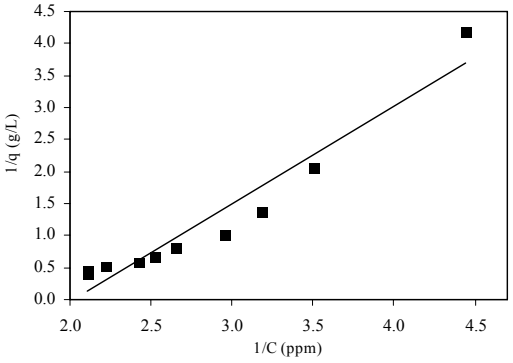

Figure 5. The langmuir adsorption isotherm of orthophosphate onto natural zeolite

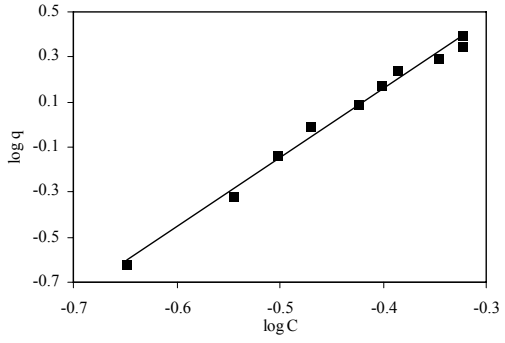

Figure 6. The Freundlich adsorption isotherm of orthophosphate onto natural zeolite

Table : Summary of Equilibrium Isotherm Parameters for Phosphate Uptake

Natural Zeolite Adsorbent					
Langmuir Adsorption Isotherm			Freundlich Adsorption Isotherm		
Q^0 (mgg^{-1})	b (Lmg^{-1})	R^2	K_F (mgg^{-1})	$1/n$	R^2
0.66	0.50	0.93	24.10	3.06	0.99

The correlation coefficient showed that the data were better fitted in the Langmuir isotherm model (R^2=0.93) than the Freundlich isotherm model (R^2=0.99). Even though, the Langmuir and Freundlich constant Q^0 and K_F have different meanings, they led to the same conclusion the experimental data with the sorption model,[5] together with regression coefficients, were extracted and are summarized in Table the Langmuir parameters b and Q^0 are 0.50 Lmg^{-1} and 0.66 mgg^{-1} for natural zeolite and the Freundlich parameters together with regression coefficients are summarized in Table the Freundlich isotherm give the best representation to data points. The value of the constants K_F and $1/n$ are 24.10 mgg^{-1} and 3.06 for natural zeolite, respectively. This shows that a multilayer of phosphate was formed on the surface of natural zeolite.

Conclusions

Adsorption of orthophosphate onto natural zeolite of batch experiments and fixed bed operation showed that adsorptive removal of inorganic phosphate ions from aqueous solution has been studied A natural zeolite with high been internal surface area. Among the parameters studied, pH is proved to be the key variable for orthophosphate uptake and a decrease in sorbent mass. Equilibrium data were well-fitted with Freundlich isotherms.

The results showed that natural adsorption efficiency 99.18%, 99.33% and 99.02% (5, 10 and 20 mg/L), respectively a pH of 12 and a contact time of 30 minutes. at 298 K Efficiency of absorption all will be reduced by pH values lower. Moreover, the isotherm can be used to evaluate the capacity and nature of the interaction between a sorbent and a sorbate. This work considers the Langmuir and Freundlich isotherm. Based on the R^2 of adsorption isotherm studies the adsorption data for phosphate fitted well the Freundlich isotherm for natural zeolite (R^2=0.99), with multilayer adsorption.

Acknowledgment

This work was supported by the Computational Chemistry Research Unit, Department of Chemistry, Faculty of Science, Thaksin University and Graduate School, Thaksin University.

References

[1] Abubakar, SM., Marcus, DM., Lee, JC., et al. *Langmuir*. 2006, **22**(10), pp. 4846-4852.

[2] Chen, J., Kong, H., Wu, D., Hu, Z., Wang, Z., Wang, Y. *J. Colliod Interface Sci*. **300**(2006), pp.491-497.

[3] Ebner, C., Onthong, U., Probst, M. *J. Mol. Liquids*. **118**(2005), pp.15-25.

[4] Karageoriou, K., Paschalis, M., Anastassakis, G. *J. Hazard. Mater*. **139**(2007), pp. 447-452.

[5] Onyango, M.; Kuchar, D.; Kubota, M.; Matsuda, H. *Eng. Chem. Res.* 2007, **46**, pp. 894-90.

[6] Ping, N., Hans, B., Bing, L., Xiwu, L., Yong, Z. *J. Environ Sci.* **20**(2008), pp.670-674.

[7] Ugurlu, A., Salman, B. *Environ Int*. **24**(1998), pp.911-918.

Effect of diatomite heat treatment on glycerin adsorption in biodiesel

P. Wungsila[1*] and S. Pengprecha[2]

[1] Chulalongkorn University, Interdisciplinary program of Environmental Science, Graduate School, Bangkok, Thailand 10330
[2] Chulalongkorn University, Department of Chemistry, Faculty of Science, Bangkok, Thailand 10330

*E-mail:somchai.pe@chula.ac.th

Abstract: The purpose of this research is to improve the adsorption efficiency of diatomite by heat treatment for purifying biodiesel. All heat-treated diatomite were subjected to adsorption of glycerin in biodiesel synthesized from palm oil via a base-catalyzed process. The optimal adsorption was obtained by varying the ratio of adsorbent to biodiesel, contact time and temperature. By using 2% wt of adsorbents at 50°C for 30 minutes, the glycerin in biodiesel could be drastically removed and meet the specification of biodiesel standards. Furthermore, in among of heat-treated diatomites, heat-treated diatomite at 800°C for 6 hours is the most preferable adsorbent.

Introduction

Nowaday, biodiesel has received much attention as the alternative energy particulary in Thailand. Since there is abundant vegetable oil e.g. coconut oil, palm oil ,and sunflower oil, for using in diesel oil substitution in Thailand, development of biodiesel production technology based on the national resources can , therefore, provide many advantages :

a) reduce the diesel utilization in agriculture
b) substitute the imported diesel
c) improve the market prices of the vegetable oil and agricultural products.

In biodiesel production, there is a problem in glycerin separation process. To purify the biodiesel, dry process is applied to remove glycerin biodiesel production. Diatomite is an efficient adsorbent materials composed of silica. Since diatomite has the high porosity and large surface area, it is suitable for filtation application. Moreover, heat treatment of diatomite exhibits the generation of large amount of negative charges resulted in the higher adsorption efficiency in glycerin separation. The aim of this research is to improve the adsorption efficiency of diatomite by heat treatment . Because glycerin has a positive charge if diatomite was heated and negative charge increase. It will make more absorbable.

Materials and Methods

Natural diatomite was obtained from Amphur Mae Tha, Lampang province, Thailand. The Diatomite was washed with distilled water to remove fine particles and other impurities, dried at 100 ^{0}C, desiccated and stored in tightly capped glass bottle for future use. The chemical composition of diatomite was given in Table 1.

Heat-treat(ed) adsorption 1) Natural diatomite was heated at varied temperatures: 200, 400, 600, and 800^{o}C for 6 h.To test in an absorpability of colour with the spectrophotometer before having glycerin absorb.

Synthesis of biodiesel from palm oil via base-catalyzed process: 200 g of palm oil was added into 500 mL of round bottom flask equipped with condenser. After the oil was heated to 65 °C, the solution of sodium hydroxide (2.0 g) in methanol (57.92 mL) was slowly added into the reaction and then the mixture was heated to 65^{o}C for 1 h. The reaction mixture was transferred to a separatory funnel, and allowed glycerin to separate. The methyl ester layer was brought to purification process. By doing nothing with methanol , then take it to adsorp diatomite immediately.

Adsorbent treatment: In order to adsorb glycerin, five concentrations of each adsorbent: 2, 4 6, 8 and 10 %wt By do increase 2% each to obsrerve the tendency of an adsorpbent efficiency. were used. In 250 mL of flask, 50 mL of crude biodiesel was treated with each of adsorbents at 50 ^{o}C, with stirring at 150 rpm and contact time for 10, 20, and 30 minutes in water bath. Then the adsorbent was removed by filtration.

Analytical methods: Titration method is used to determine the amount of glycerin and unreacted catalyst.

Step 1, 1 g of untreated biodiesel was dissolved in 100 mL of isopropyl alcohol with 2 mL of 1% phenolphthalein as an indicator. The mixture was titrated with 0.01N hydrochloric acid until the color of the solution changed from red to colorless

Step 2, Then 1 mL of 0.04%bromophenol blue was added into the mixture the solution was titrated with 0.01N hydrochloric acid until the color of the solution changed from blue to yellow. This amount of 0.01N hydrochloric acid solution is referred as “B”. The mount of base catalyst cannot finish reaction .There is some amount of base remains did not ract to synthesis biodiesel. catalyst can be calculated by using equation 1:

$$\text{g of NaOH / g of untreated biodiesel} = \frac{A \times 0.01 \times 40.0}{W \times 1000} \quad (1)$$

where:
A = volume of hydrochloric acid used in step 1 (mL)
W = weight of untreated biodiesel used (g).

And the amount of glycerin in the biodiesel can be calculated by using equation (2):

$$\text{g of glycerin /g of untreated biodiesel} = \frac{B \times 0.01 \times 304.4}{W \times 1000} \quad (2)$$

where:
B = volume of hydrochloric acid used in step 2 (mL)
W = weight of untreated biodiesel (g).

Results and Discussion

Characterisation of natural diatomite: The chemical composition of natural diatomite determined by x-ray diffraction technique was shown in Table 1. The main constituent of diatomite samples is SiO_2 (72.5 %). The surface area of natural diatomite calculated by B.E.T. method was estimated to be approximately 66 m^2/g.

Effect of contact time: The effect of contact time on sorption of glycerin was studied. In order to the quanlity of diatomite being stable through the experiment to be best time suitable the adsorption. By using 5%wt of adsorbents, 40 g of crude biodiesel, and agitating at 150 rpm for 10-30 min. at 50 °C, the concentration of glycerin decrease from 0.0195 to 0.0005 g glycerin/g crude biodiesel with heat–treated diatomite at 800°C. The results were shown in Table 2. The optimum contact time was found to be 30 min.

Effect of sorbent dosage: Figure 1 shows the glycerin content vs. various % adsorbent in the purification of biodiesel at 50 °C. By treating untreated biodiesel with 2-10%wt. of adsorbents, the content of glycerin decreased from 0.0048 to 0.0011g glycerin/g crude biodiesel. The result showed that large amount of glycerin content could be removed by using 2% wt adsorbents.

Table 1: Chemical composition of natural diatomite

Oxide	Composition (%)
SiO_2	72.5
Al_2O_3	11.42
Fe_2O_3	5.81
MgO	0.25
CaO	1.48
Na_2O	7.21
K_2O	0.69

Table 2: Glycerin content vs. time with 5%wt heat – treated diatomite at 800 °C .begining is 1.9467×10^{-2}

Time (min)	Weight of untreated biodiesel (g)	Titrant HCl (mL)	Glycerin content (g glycerin/ g crude biodiesel)
10	18.21	3.8	5.20×10^{-4}
20	26.29	5.9	5.60×10^{-4}
30	30.02	6.4	5.02×10^{-4}

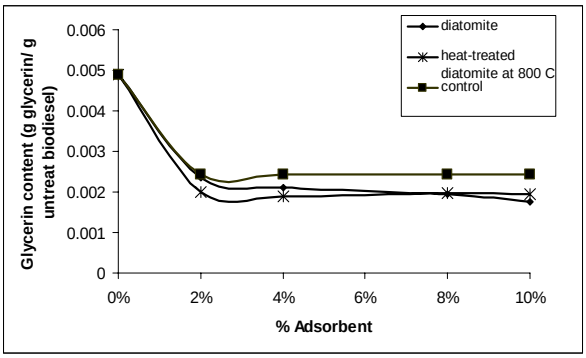

Figure 1. Glycerin content vs. various adsorbents at 50 °C for 30 min.

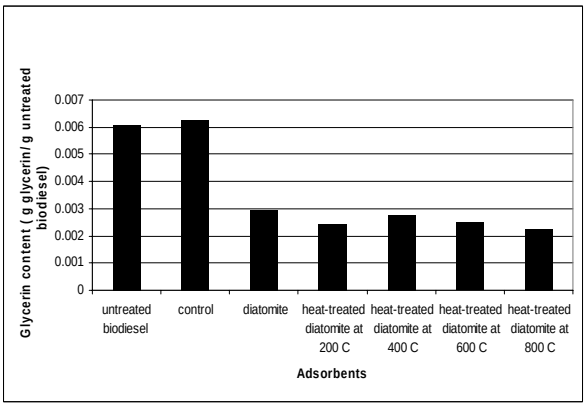

Figure 2. Glycerin content vs. various adsorbents at 50 °C for 30 min.

In Figure 2, the efficiency of various adsorbents were observed. Under the optimal adsorption condition, heat-treated diatomite at 800 °C gave the best result and removed glycerin Standerd of glycerin is 0.25%

Conclusions

In the present study, natural diatomite and heat-treated diatomite at 800 °C could be used as adsorbent to adsorb glycerin. The optimal conditions were 2% wt, contact time 30 min at 50°C.

References

[1] G.Antolin, *Biores. Techno.* **83** (2002), pp. 111-114.
[2] B.Bertram, C.Abrams, B.S. Cooke,*U.S. Patent Application*.**20050081436** (2005).
[3] W.Cao, H.Han, and J. Zhang, 2005. *Fuel*. **84** (2005), pp. 347-351.
[4] A.Dermirbas, *Energy Conversion and Management*. **43** (2002), pp. 2349-2359.
[5] V.J. Gerpen, and K. Menges, *Final report to the Dallas Group of America*. (2004).
[6] M.A. Ghouti, M.A. Khraisheh, , S.J. Allen, and M.N. Ahmad, *Journal of Environmental Management*. **69** (2003), pp. 229-238.
[7] K.J. Hsien, , W.T. Tsai, , Y.M.Chang, and C.C. Lo, *Biores. Techno.* **96** (2005), pp. 657-663.
[8] H. Katsumata , S. Keneco, T. Suzuki , and K.Ohta , *Analytica Chimica acta* .**577** (2006),pp. 214-219.
[9] D. Kusdiana, and S.Saka, *Bioresource Technology* .**91** (2004), pp. 289-295.
[10] J.R.Munson, B.L.Bertram, J.D. Caldwell, *U.S. Patent*. **5597600** (1997).
[11] Selkirk and R. William, *U.S. Patent*. **20070175088** (1997).
[12] W.T. Tsai , C.W. Lai , and K.J.Hsien, *Journal of Colloid and interface Science*. **297**(2006), pp. 749-754.

A study for the effectiveness of chitosan on granulation process and UASB efficiency in wastewater treatment at thermophilic condition

B. Nuntakumjorn[1], W. Ruenglertpanyakul[1], W. Songkasiri[2] and C. Phalakornkule[3]*

[1] Department of Chemical Engineering, Faculty of Engineering, King Mongkut's University of Technology Thonburi, Thungkhru, Bangkok 10140, Thailand
[2] National Center for Genetic Engineering and Biotechnology, Biochemical Engineering and Pilot Plant R&D Unit, Bangkuntien, Bangkok 10150, Thailand
[3] Department of Chemical Engineering, Faculty of Engineering, King Mongkut's University of Technology North Bangkok, Bangsue, Bangkok 10800, Thailand

* Corresponding Author E-Mail Address: cpk@kmutnb.ac.th, cphalak21@yahoo.com

Abstract: Chitosan with degree of deacetylation of 94% and molecular weight of $3.5x10^5$ dalton, yielding high flocculation efficiency (85-100% flocculation) and broad flocculation region (2 to 45 mg/g suspended solids), was selected for enhancing the performance of thermohilic UASB reactor treating wastewater from a palm oil mill processing industry. Twenty four mg of chitosan were applied per liter of bioreactor on the first day of operation and the performance of the UASB was investigated for 123 operating days. In comparison with the UASB without chitosan addition, the UASB had 2-8% higher COD removal, 6-23% lower biomass washout and up to 24% higher biogas production rate. Based on the current prices of chitosan and Bunker C fuel oil, the extra biogas produced could compensate well for the cost of chitosan added to the system.

Introduction

The upflow anaerobic sludge bed (UASB) process enables anaerobic degradation of organic matter in wastewater and subsequent solid-liquid-gas separation to occur in a single reactor [1]. Wastewater is supplied from the bottom of the reactor and the organic matter is digested by the biomass granules as the wastewater moves up to the top. UASB reactor is able to treat wastewater with a high suspended solid content. This type of reactor also provides a high methane production. However, if seed sludge is not granulated, the start-up periods can be long [2]. UASB system has been widely applied for treating a variety of industrial effluents [2].

Chitosan is a modified polysaccharide comprised of copolymers of D-glucosamine and N-acetyl-D-glucosamine. It is mainly produced by alkaline deacetylation of chitin. Chitosan has been found to enhance sludge granulation and shorten the start-up periods of UASB systems [3-5]. El-Mamouni et al. [4] illustrated the use of 25 mg chitosan/g suspended solids to enhance sludge granulation in UASB-like reactors used for treating synthetic wastewater. In their study, a total of 4 injections was carried out during the course of their study which lasted for 5 weeks. It was found that chitosan yielded a granulation rate as high as 56 □m d^{-1}. In Lertsittichai et al. [5], chitosan with specific characteristics was selected for accelerating granulation in a 30-liter UASB treating wastewater from a tropical fruit-processing industry. The chitosan was implemented on the second and on the thirty-seventh operating day during the start-up at a dose rate of 2 mg/g suspended solids. In comparison with a UASB without chitosan addition, the use of chitosan was found to enhance granulation, leading to larger granules, and that a higher density sludge was then retained in the reactor. In addition, the addition of chitosan to the UASB led to a 9-59% lower effluent COD, a 4-10% higher removal efficiency, an approximately 3 liters per day higher biogas production rate, and a 16-68% lower washout of biomass.

The previous studies of chitosan utilization described above were all performed under mesophilic conditions (30-35^{o}C). It has been shown that operating temperature is a major factor that greatly influences digester performances [2, 6-7]. Thermophilic operation of anaerobic reactors has been reported to provide some advantages over mesophilic operation in areas such as higher rates of substrate degradation and biogas production. However, it has also been reported that mesophilic reactors can be preferable because of greater process stability [2, 8-10].

In this paper, results are given of studies on the effectiveness of chitosan as a sludge granulation accelerator under thermophilic UASB operation (57^{o}C). The present work investigated the effects of chitosan addition on the performance of a 5-liter UASB for wastewater treatment of a palm oil mill processing industry. Palm oil mill effluent (POME) has a high biochemical oxygen demand (BOD) and chemical oxygen demand (COD) and contains a wide-range of biopolymers including starches, hemicelluloses to simple sugars, proteins to amino-acids, dissolved oil and fatty acids, glycerin, crude oil solids and short fibers [9]. POME also contains soluble materials that are harmful to an environment. POME was selected for the study because it is usually discharged at temperatures around 80-90^{o}C. The high discharge temperatures mean that both mesophilic and thermophilic treatments are possible [8, 10-12].

In this study, the UASB performances were monitored over a period of 123 operating days for a chitosan dosage of 24 mg chitosan per liter of bioreactor. The performance was measured through analyses of chemical oxygen demand (COD) removal, washout of biomass and biogas production rate and methane content.

Materials and Methods

Sludge suspension: The sludge used as a source of the biological inoculum was an anaerobic sludge obtained from Nong-Khaem Water Quality Control Plant (Bangkok, Thailand). This is a domestic wastewater treatment plant operated under mesophilic conditions. The sludge was screened with a sieve of 500 µm (mesh no. 35) to remove material that would not biodegrade in a UASB. The sludge had a volatile suspended solid (VSS) concentration of approximately 20.6 g VSS l^{-1}.

Chitosan: The chitosan was provided by Taming Enterprises Co., Ltd. (Thailand) and its characteristics are as follows: %DD = 94.2; MW = $3.5x10^5$ dalton; moisture content = 8.0%; ash content = 0.91%; protein content = 2.79%; viscosity = $33.20x10^{-3}$ Pa.s (33.2 cps). Chitosan solution (1% w/v) was prepared by mixing 1 g of chitosan in 100 ml of 1% acetic acid. The solution was mixed at 200 rpm for 24 hr.

Wastewater feed: The POME wastewater was obtained from Suksomboon Palm Oil Co., Ltd. (Chonburi province, Thailand). The raw POME was collected from the wastewater collection tank of the company. The POME was then filtered through two-layer cheesecloth to remove dirt, plant cell debris, fibers and other solids whose size was in the order of millimeters. The POME was then allowed to stand overnight to allow precipitation. The supernatant portion of the POME was then separated. It was then pretreated to remove oil and grease by adding aluminum sulfate to achieve a final concentration of 25 ppm. The suspension was rapidly mixed at 150 rpm for 5 min and then slowly mixed at 30 rpm for 30 min. The wastewater was then allowed to settle for 6 hr and the supernatant was separated and stored in a cold room at 4°C. The characteristics of the POME before and after the pre-treatment are shown in Table 1.

In preparing the substrate for UASB operation, five samples of the pre-treated POME were prepared by diluting with tap water at the POME:water ratios of 1:10, 2:10, 3:10, 4:10 and 5:10. These 5 samples were used for treatments at operating temperatures of 37, 42, 47, 52 and 57°C. $NaHCO_3$ was added to the samples to obtain an alkalinity concentration of 500 mg l^{-1} and 6 N NaOH was added to obtain a pH of 7.

Reactor system: Two identical UASB reactors (Fig. 1), with a working volume of 5.3 L, were a cylindrical shape, 14 cm in diameter and 40 cm in height and had 4 sampling ports located at 4, 14, 24, and 37cm from the bottom, respectively. The chitosan was added to the reactor (R1) and the other reactor (R2) had no chitosan added and served as a control.

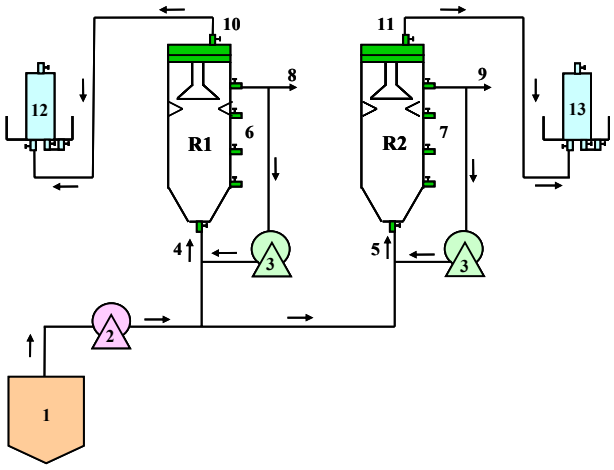

Fig. 1. Schematic diagram of the UASB reactor system with two reactors running in parallel.

1 Influent wastewater tank; 2,3 Peristaltic pump; 4,5 Influents; 6,7 Sampling ports; 8,9 Effluents; 10,11 Biogas out; 12,13 Gasometers

Table 1: Chemically characteristics of POME

Parameter	Raw POME	Settled POME	Chemically-treated POME
pH	4.4 - 4.6	4.4 - 4.6	4.3 – 4.5
Alkalinity (mg $CaCO_3$ l^{-1})	50 - 150	50 - 150	50 - 150
TVFA (mg CH_3COOH l^{-1})	300 – 500	300 - 500	300 - 500
COD $_{(soluble)}$ (mg l^{-1})	55,000 – 60,000	53,000 - 55,000	52,000 - 54,000
COD $_{(total)}$ (mg l^{-1})	80,000 – 95,000	68,000 - 83,000	60,000 - 64,000
TS (mg l^{-1})	58,000 - 62,000	56,500 - 60,000	50,000 – 55,000
SS (mg l^{-1})	50,500 - 53,000	16,000 - 21,000	10,000 - 15,000
Oil and grease (mg l^{-1})	4,600 - 5,100	4,500 - 5,000	1,500 – 2,500

Acclimation, start-up and operation: Sludge with an initial volatile suspended solid (VSS) concentration of 12 kg VSS m^{-3} was inoculated into the reactors. The POME substrate prepared by diluting POME with tap water at a ratio of 1:10 (pretreated POME:tap water) was fed to both R1 and R2 with hydraulic retention time (HRT) of 2.4 days and an upflow velocity of 0.3 m hr^{-1}. The starting temperature was 37°C. After the COD removal of a reactor was greater than 80% for at least 3 times the HRT, the temperature of both reactors was increased by a step of 5°C to 42°C and the organic loading rate (OLR) of both reactors was simultaneously increased by feeding the 2:10 diluted substrate. The process was then repeated for temperatures of 47°C, 52°C and 57°C and feeds of 3:10, 4:10 and 5:10, respectively. The effluent from the reactors was recirculated to the reactors with the ratio of influent:effluent to 1:50 in order to maintain the upflow velocity of 0.3 m hr^{-1}. The temperatures were maintained by circulating hot water through the reactors' jacket.

At the first day of operation, chitosan solution 1% (w/v) was injected to R1 at a dosage of 2 mg chitosan per g VSS. The concentration of the dosage was based on an optimum dosage reported by Kaseamchochuang et al. [13].

Analytical methods: The influent and effluent samples from the UASB reactors were collected every 3 day for analyses of pH, COD, VSS according to the Standard Methods [14]. Gas composition was determined by a gas chromatograph (GC) equipped with a thermal conductivity detector (GC-2014; SHIMADZU, Japan), a stainless steel packed column and a helium carrier gas with a flow rate of 50 ml min^{-1}. The amount of generated biogas was recorded using liquid displacement gas meters and the pH value was measured every day.

Reproducibility: In this study, each measurement was of triplicate performance. The standard errors of the mean were all within 10%. Test of significant difference based on paired t-statistic was performed using Basic Statistics, MINITAB (Minitab Inc., USA): non-significant difference if (Probability; $P>0.05$) and a significant difference if ($P<0.05$).

Results and Discussion

Organic loading rate and reactor stability: Fig. 2 presents the applied OLR during the start-up of the UASB reactors. The OLR ranged between 2.2-9.5 kg COD m^{-3} d^{-1}. The sludge that the reactors were inoculated with was diluted to the same VSS concentration of 20.6 g VSS l^{-1} at the start of the study. Fig. 3 shows the influent and effluent pH of both reactors. The influent pH was adjusted to 7. A pH value near neutral is the optimum for anaerobic digestion and below 6.8 methanogenic activity is inhibited. Acidogenic bacteria, through the production of acids, reduce the pH of the system. The effluent pH was steadily higher than 7, ranging between 7.3-8.0 for both reactors. The steady pH values indicated a good stability of the reactors since pH can be a cause of inhibition if present above certain value can halt the digestion process.

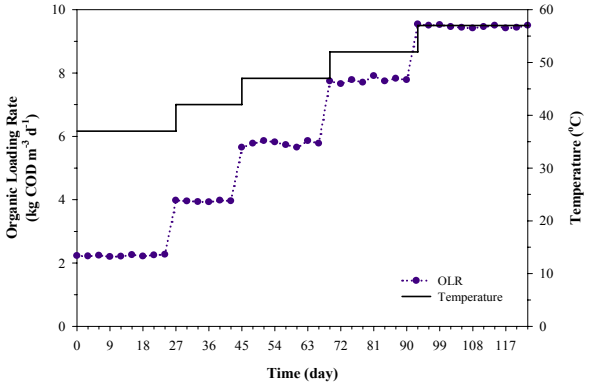

Figure 2. Organic loading rate and temperature against time.

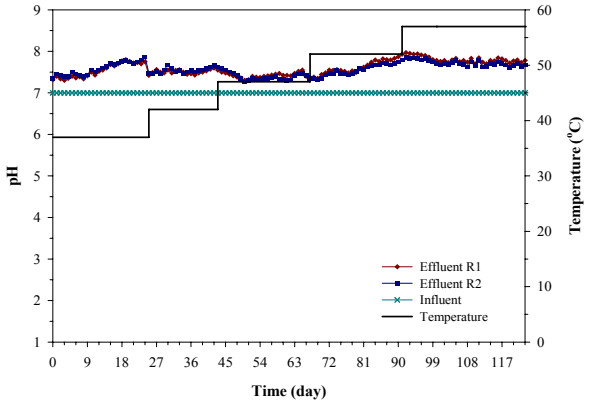

Figure 3. pH influent and effluent against time.

Biogas and methane production: Fig. 4 illustrates that biogas production of R1 continuously increased to 18 liters per day, while that of R2 to 16 liters per day during the period of study. The paired t-test analysis of the biogas production rates yielded ($P<0.05$), indicating that R1 and R2 produced biogas at significantly different rates. Fig. 5 shows the methane content in the biogas. The methane content of both reactors was similar, on an average of 78% and 76% for R1 and R2, respectively.

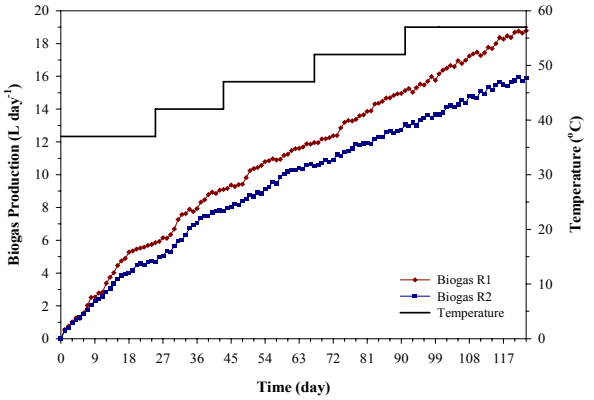

Figure 4. Biogas production against time.

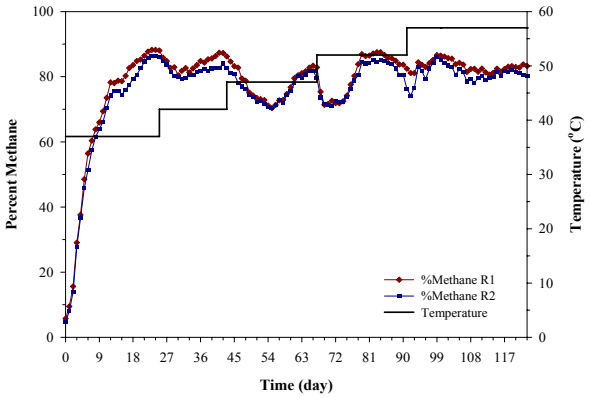

Figure 5. Methane composition against time.

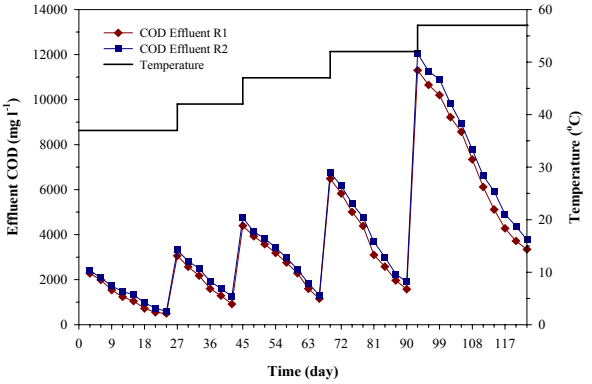

Figure 6. COD effluent against time.

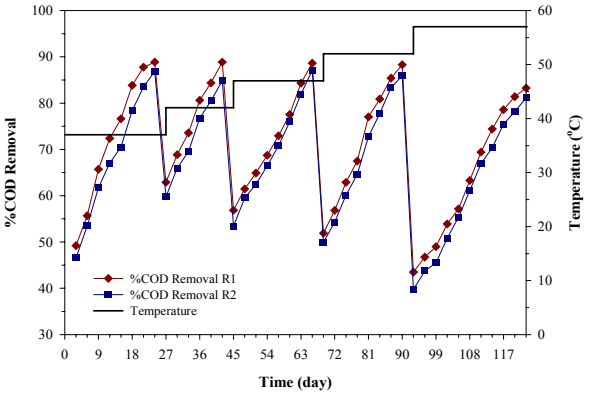

Figure 7. COD removal efficiency against time.

COD effluent and removal efficiency: The COD variation in the reactor influent and effluent and the COD removal efficiency during the 123 operating days are shown in Figs. 6 and 7, respectively. The acclimation period enabled the system to rapidly adjust itself to the wastewater at HRT of 2.4 days. The initial OLR was 2.3 kg COD m^{-3} d^{-1}. Within 24 days after the startup, the COD removals reached 89% and 87% for R1 and R2, respectively. The soluble COD effluent of R1 and R2 were 500 and 590 mg l^{-1}, respectively. The OLR was then increased to 4.0 kg COD m^{-3} d^{-1}. The increase in OLR resulted in a decrease in COD removal efficiency; however, the system adapted to the new condition within 9 and 12 days for R1 and R2, respectively. That is, the COD removal of R1 reached 80% on Day 36, and the COD removal of R2 reached 80% on Day 39. The OLR was then increased to 5.7 kg COD m^{-3} d^{-1} on Day 45. Both R1 and R2 required 18 days for the COD removal to reach higher than 80%. The process was repeated again. The OLR was then increased to 7.8 kg COD m^{-3} d^{-1} on Day 69. R1 required 15 days for the COD removal to reach higher than 80%, while R2 required 18 days. On Day 93, the OLR was then increased to 9.5 kg COD m^{-3} d^{-1} on Day 93. Both R1 and R2 required 27 days for the COD removal to reach higher than 80%. Every increase of OLR resulted in a decrease in COD removal efficiency. However, typically, the systems can adapt to the new condition within 18 days for R1 and R2. However, for the last OLR investigated in this study, both systems needed 27 days. From the first to the last day reported in this study, the COD removal efficiency of R1 was 2-8% higher than that of R2. The paired t-test analysis of the COD effluents and the COD removals yielded ($P<0.05$), indicating that R1 and R2 had significantly different effluent COD values and COD removals.

Biomass washout: Biomass washout represented by effluent VSS is shown in Fig. 8. It should be noted that effluent VSS may not perfectly represent the biomass grown in the reactors since the influent contained certain degrees of VSS. The increase in OLR resulted in an increase of biomass washout. However, both systems can adapt to the new OLR, resulting in a decrease of biomass washout within 18 days. However, the biomass washout kept increased with increasing OLR. In the last OLR investigated in this study, the biomass washout became near 300 mg VSS l^{-1} and higher than 300 mg VSS l^{-1}. The biomass washout of R1 was continuously lower than that of R2 (6-23% lower biomass washout). The paired t-test analysis of the effluent VSS yielded ($P<0.05$), indicating that R1 and R2 had significantly different VSS at the reactor effluents.

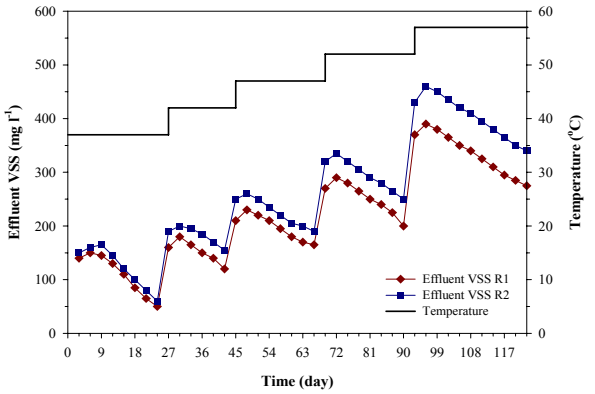

Figure 8. Washout of biomass represented by VSS at the effluent against time.

Conclusions

From our knowledge, this study reports the minimal usage of chitosan to enhance the performances of thermophilic UASB systems all in terms of COD removal, biogas production and biomass washout. Chitosan was presumed to help sludge pellet development, which led to faster sludge formation and higher density sludge retained in the reactor. The higher density sludge was presumed to lead to higher COD removing activities and higher biogas production. Biogas could replace fuel oil in supplying energy in a factory such as a facility boiler.

Based on the current prices of chitosan and Bunker C fuel oil ($20/kg and $0.25/liter, respectively) and the heating values of biogas and Bunker C fuel oil (24 MJ/m^3 and 40 MJ/liter, respectively), Table 2 illustrated that the more biogas produced (3 liters per day) could compensate well for the cost of chitosan added to the system.

Table 2. Estimated heat, quantity and cost of Bunker C fuel oil that can be compensated by exceeded biogas.

Item	Values
Unit price of chitosan	$20/kg
Exceeded biogas produced due to chitosan addition	3 liters/day
Heating value of biogas	24 MJ/m^3
Heat due to exceeded biogas	7.056 MJ
Heating value of Bunker C fuel oil	40 MJ/liter
Cost of Bunker C fuel oil	$0.25/liter

Acknowledgements

The authors are grateful to Thailand Research Fund (TRF-Master Research Grant, Grant No. MRG-OSMEP505E225) for financial support. We would like to thank Nong-Khaem water quality control plant for providing sludge and Suksomboon Palm Oil Co., Ltd. for wastewater samples. Special thanks to Taming Enterprises Co., Ltd. for providing chitosan samples.

References

[1] G. Lettinga, S.W. Hobma, L.W. Hulshoff Pol, W. de Zeeuw, P. de Jong, P. Grin and R. Roersma, *Water Sci. Technol*. **15** (1983), pp. 177-195.
[2] P.E. Poh and M.F. Chong, *Bioresource Technol.* **100** (2009), pp. 1-9.
[3] J. Thaveesri, D. Daffonchio, B. Liessens, P. Vandermeren and W. Verstraete, *Appl. Environ. Microbiol.* **61** (1995), pp. 3681-3686.
[4] R. El-Mamouni, R. Leduc and S.R. Guiot, *Water Sci. Technol*. **38** (1998), pp. 341-347.
[5] S. Lertsittichai, P. Lertsutthiwong and C. Phalakornkule, *Water Environ. Res*. **79** (2007), pp. 801-807.
[6] H.-Q. Yu, H.H.P. Fang and G.-W. Gu, *Process Biochem*. **38** (2002), pp. 447-454.
[7] W. Choorit and P. Wisarnwan, *J. Biotechnol.* **10** (2007), pp. 376-385.
[8] J. Quarmby and C.F. Forster, *Enzyme Microbial Technol.* **17** (1995), pp. 493-498.
[9] E.O. Ugoji, *Renew. Energ.* **10** (1997), pp. 291-294.
[10] S. Mustapha, B. Ashhuby, M. Rashid and I. Azni, *Process Saf. Environ*. **81** (2003), pp. 262-266.
[11] G.D. Najafpour, A.L. Zinatizadeha, R. Mohameda, Isa M. Hasnain and H. Nasrollahzadeh, *Process Biochem*. **41** (2006), pp. 370-379.
[12] Y. Zhang, L. Yan, L. Chi, X. Long, Z. Mei and Z. Zhang, *J. Environ. Sci*. **20** (2008), pp. 658-663.
[13] C. Kaseamchochoung, P. Lertsutthiwong and C. Phalakornkule, *Water Environ. Res.* **78** (2006), pp. 2010-2016.
[14] American Public Health Association, *Standard Methods for the Examination of Water and Wastewater*. Washington, DC: American Public Health Association, (1998).


PACCON
Pure and Applied Chemistry International Conference 2010

Food Safety

Sequential-injection on-line solid-phase extraction coupled with HPLC using boron-doped diamond electrode for the determination of sulfonamides

P. Chantarateepra[1], W. Dungchai[1], O. Chailapakul [1,2,*], W. Siangproh[3] , N. Ngamrojanavanich[1], and S. Motomizu[4]

[1] Department of Chemistry, Faculty of Science, Chulalongkorn University, Patumwan, Bangkok, Thailand
[2] National Center of Excellence for Petroleum, Petrochemicals and Advanced Meterials, Chulalongkorn University, Patumwan, Bangkok, Thailand
[3] Department of Chemistry, Faculty of Science, Srinakharinwirot University, Sukhumvit 23, Wattana, Bangkok, Thailand
[4] Department of Chemistry, Faculty of Science, Okayama University, 3-1-1 Tsushimanaka, Okayama, Japan

*Corresponding authors: corawon@chula.ac.th

Abstract: In this work, sequential-injection on-line solid-phase extraction (SPE) coupled with HPLC for the separation and determination of sulfonamides has been developed. A homemade microcolumn SPE was automated by sequential-injection analysis to perform on-line sample clean-up and extraction. A SIA system consisting of a syringe pump and multi-position valve was constructed. Our method can continuously extract sulfonamides from aqueous samples followed by the separation of sulfonamides using HPLC coupled with boron-doped diamond electrode as electrochemical detection. The conditions for on-line SPE including eluent, flow rate of sample loading and elution, and zone of eluate were investigated. An eluent composition of methanol was selected. The optimal flow rate of sample loading and elution was found to be 10 µL/s and optimal elution time was 20-23 s. Under optimal conditions, a linear relationship between peak height and sulfonamides concentration was obtained in the range of 0.01-8 ppm. Our results demonstrate that our method is simple, rapid and highly sensitive for the automated extraction, separation, and determination of sulfonamides.

Introduction

Sulfonamides are among the most widely used antibacterial agents because of their low cost, low toxicity, and excellent activity against common bacterial diseases [1-2]. They are used for therapy, prophylaxis, and growth promotion in animals. However, long-term use of the sulfonamides shows serious side effects such as emiction and hemopoiesis turbulence [3-7]. Antibacterial druggery in food can cause anaphylaxis in irritability patients and pathogenic organism to produce antibodies [8]. The European Union (EU) has set up the maximum residue levels of 100 ng/g in edible tissues and milk [9]. The conventional methods for the separation and determination of sulfonamides such as gas chromatography (GC), gas chromatography-mass spectrometry (GC/MS), capillary electrophoresis (CE) [10-11], enzyme-linked immunosorbent assay (ELISA) [12], thin-layer chromatography (TLC), high-performance liquid chromatography–mass spectrometry (HPLC/MS), and high-performance liquid chromatography (HPLC) [13-20] have been reported. The common detectors used for the detection of sulfonamides such as ultraviolet (UV) [21-28] and fluorescennce [1,29] which exhibits high sensitivity and selectivity. Even though those methods provide high sensitivity and selectivity, there is a high cost for the equipment and laboratories. Moreover, they still need sample preparation techniques, such as solid phase extraction (SPE) [1,13,15-19,27] and liquid phase extraction (LPE) [25,30] that significantly increase analysis time. Nowadays, HPLC coupled with on-line solid phase extraction (SPE) has been reported [31-36]. On-line SPE is an attractive sample preparation technique because it can reduce sample preparation time and increase sample throughput [29]. Sequential injection analysis (SIA) is a suitable technique for on-line SPE. Moreover, SIA can be coupled with electrochemical detection (EC). Electrochemical detection is not only utilizes low cost instrumentation but it is also fast and highly sensitive [30,37]. Here, our aim is to develop on-line SPE coupled with sequential injection analysis for the separation and determination of seven sulfonamides including sulfaguanidine, sulfadiazine, sulfamethazine, sulfamonomethoxine, sulfamethoxazole, sulfadimethoxine, and sulfaquinoxaline by HPLC using electrochemical detection. We used a silica-based monolithic column for the sulfonamide separation because of its high tolerance for organic solvent, low back-pressure relative to traditional columns.

Experimental

Reagents and standards

All solvents and reagents used were HPLC or analytical grade. Acetonitrile was purchased from Sigma-Aldrich (MO, USA). Ethanol was purchased from Carlo Erba (Val de Reuil, France). Methanol was obtained from Merck (Darmstadt, Germany). Water was purified ($R \geq 18.2$ MΩ cm^{-1}) by a Milli-Q system (Millipore). Potassium dihydrogen orthophosphate (KH_2PO_4) was obtained from BDH (VWR International Ltd., England). Disodium hydrogen phosphate dehydrate (Na_2HPO_4) and citric acid were obtained from Merck (Darmstadt , Germany). Ethylenediaminetetraacetic acid disodium salt dehydrate (Na_2EDTA) was purchased from Sigma–

Aldrich (St. Louis, MO, USA). The extraction solution (Na_2EDTA–McIlvaine buffer, pH 4) was prepared by dissolving 13.52 g of Na_2HPO_4, 13.02 g of citric acid and 3.72 g of Na_2EDTA in 1 liter of Milli-Q water. All solutions and solvents were filtered with 0.45 µm Nylon membranes before use.

Sulfadiazine, sulfadimethoxine, sulfamethazine, sulfamethoxazole, sulfamonomethoxine, and sulfaquinoxaline were purchased from Sigma–Aldrich (MO, USA). Sulfaguanidine was obtained from ICN Biomedicals Inc. (USA). A stock standard solution (100 µg mL^{-1}) of each SAs was prepared by dissolving 3 mg of SA in 30 mL of an acetonitrile:Milli-Q water (50:50; v/v) solution in a volumetric flask and stored at 4 ºC in the dark. The working solutions were prepared by diluting the stock standard solutions with the mobile phase.

Materials and instrumentations

Oasis HLB with particle size of 30 µm was obtained from Water (MA, USA). A homemade microcolumn SPE (40 mm × 1.59 mm i.d.) packed with 47 mg of Oasis HLB was used for the sample clean-up and extraction of SAs in solution. SIA coupled with SPE for automated extraction consisted of 8-port selection valve (Hamillton, Nevada, USA), 6-port switching valve (Rheodyne MXT 715-000, USA), and syringe pump (Hamillton, Nevada, USA). A sample loop between 8-port selection valve in SIA system was constructed 34 µL from PTFE tubing (0.5 mm i.d.).

The HPLC-EC system consisted of an HPLC compact pump model 2250 (Bischoff, Germany) and a thin-layer flow cell (GL Sciences, Inc.). A thin-layer flow cell is used as an amperomertic detector consisted of three electrodes: a BDD working electrode, an Ag/AgCl reference electrode (Bioanalytical system Inc., USA), and a stainless steel tube counter electrode. The chromatographic column was a Chromolith® Performance RP-18e silica-based monolithic column (100 mm × 4.6 mm i.d.) from Merck (Darmstadt, Germany). The HPLC was carried out in the mobile phase, which consisted of a phosphate buffer solution (0.05 M KH_2PO_4, pH 3), acetonitrile, and ethanol in the ratio of 80:15:5 (v/v/v), with an applied potential of 1.2 V versus Ag/AgCl. The flow rate was set at 1.5 mL min^{-1}. The experiment was performed at room temperature (25 °C). The Palm Sens PC vs2.11 (IVIUM technologies, Eindhoven, Netherland) was used for amperometric controlling and signals processing.

On-line SPE-HPLC procedure

A schematic diagram of the on-line SPE-HPLC-EC for the determination of SAs in shrimp is shown in Fig. 1. The on-line SPE-HPLC-EC consists of three parts. Part I is on-line SPE-SIA including a syringe pump (2.5 mL), 8-port selection valve, 6-port switching valve, holding coil (2.5 mL), sample loop (34 µL), and SPE microcolumn. Part II is HPLC system including a HPLC pump and analytical column. Part III is an EC detector consisting of a thin-layer flow cell and a data acquisition system (palm sens PC). The on-line SPE procedure consists of four steps including loading, washing, elution, and reconditioning. In the first step, 1 mL of sulfonamides solution is applied to the SPE microcolumn. In the second step, 1 mL of deionize water is loaded into the column to remove interferences from analytes retained in the SPE microcolumn. In the third step, 0.2 mL of methanol is delivered to column for the elution of sulfonamides from the sorbent, and then eluate was retained in sample loop. Finally, 7.5 mL of methanol and 1 mL of Na_2EDTA–McIlvaine buffer are sequentially passed through the SPE microcolumn to solvate the functional groups of the sorbent and recondition of the SPE microcolumn. During the reconditioning, eluate was transferred to the analytical column using a switching valve. The separation was performed on the analytical column.

Sample preparation

The apparatuses for sample preparation consisted of a vortex mixer (Mixer Uzusio LMS. Co. Ltd., Japan), an ultrasonic bath (ESP chemicals, Inc., MA, USA), and a centrifuge (Cole Parmer, illinois, USA). Shrimp were obtained from a local supermarket. Two grams of a homogeneous shrimp sample was placed in a 15 mL amber glass bottle, and 10 mL of Na_2EDTA–McIlvaine's buffer solution was then added into the bottle. The mixture was well mixed on a vortex mixer for 10 min at high speed. Then, the mixture was placed in an ultrasonic water bath for 10 min following centrifugation at 3500 rpm for 10 min. The collected supernatant was cleaned up and extracted with automated on-line SPE microcolumn. Prior to load supernatant into SPE microcolum, they were filtered through a 0.45 µm Nylon membrane filter.

Results and Discussion

The optimization of SPE conditions

Effect of eluent

We eluted seven sulfonamides from SPE and directly flow to electrochemical detection so the eluent has directly effect on the efficiency of elution, sensitivity of electrochemical signal, and performance of separation. In this work, we used Methanol as eluent. Hence, we first studied the effect of methanol to mobile phase ratio from 50:50 to 100:0 (v/v). The peak height for seven sulfonamides increased with increasing methanol ratio as shown in Figure 1. Moreover, good resolution of seven sulfonamides was obtained at 100% of methanol. Therefore, we selected at 100% of methanol as eluent to compromise between good resolution and high sensitivity.

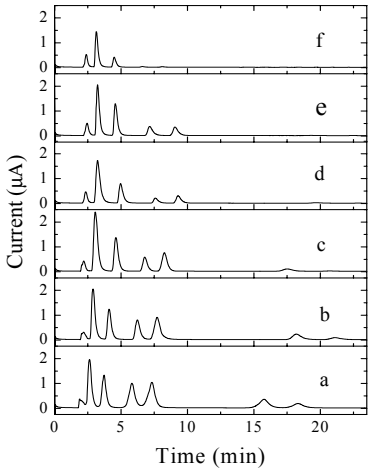

Figure 1 HPLC chromatograms of sulfonamides (10 ppm) at different ratio of methanol and mobile phase. (a) methanol, (b) methanol and mobile phase 90:10, (c) methanol and mobile phase 80:20, (d) methanol and mobile phase 70:30, (e) methanol and mobile phase 60:40, (f) methanol and mobile phase 50:50.

Effect of sample loading and eluting rate

Sample loading and elution was used at the same flow rate in each process. We studied the effect of sample loading and elution rate in the range of 8-11 μL/s. Figure 2 shows that the peak height of the seven sulfonamides increased when sample loading and elution rate increased up to 10 μL/s. Furthermore, the resolution of seven sulfonamides was not affected by changing either flow rate. Therefore, we selected the optimal sample loading and elution rate of 10 μL/s.

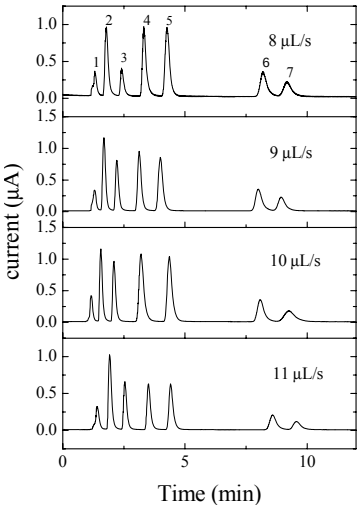

Figure 2 HPLC chromatograms of seven sulfonamides (10 ppm) at different sample loading flow rates and eluting flow rate. (1) sulfaguanidine, (2) sulfadiazine, (3) sulfamethazine, (4) sulfamonomethoxine, (5) sulfamethoxazole, (6) sulfadimethoxine, (7) sulfaquinoxaline.

Effect of eluate zone

After elution of sulfonamides from the SPE column, the eluate was retained in the sample loop and flowed to analytical column using the switching valve. Each elute zone has different concentration of sulfonamides. We collected the concentrated zone of eluate in sample loop (34 μL) and delivered the rest of the eluate zone to analytical column and waste (port 2 of switching valve). The effect of the eluate zone was also studied. The result was shown in Figure 3 where elution zone is represented by elution time. Elution time was calculated from start to stop of the elution step. We found that peak current for the seven sulfonamides decreased with increasing of the elution time. Hence, the optimal condition was selected at 20-24 s for the next experiment.

Analytical performance

Using the optimal conditions, calibration curves were obtained by plotting the peak areas of each compound versus concentrations of each sulfonamide. The studied concentration ranges were 0.05-10 μg mL^{-1}. The calibration curves were found to be linear in the concentration range 0.01-8 μg mL^{-1} for sulfaguanidine, sulfadiazine, sulfamethazine, sulfamonomethoxine, and sulfamethoxazole and 0.1-8 μg mL^{-1} for sulfadimethoxine and sulfaquinoxaline. The correlation coefficients generally exceeded 0.994 for seven sulfonamides as shown in Table 1.

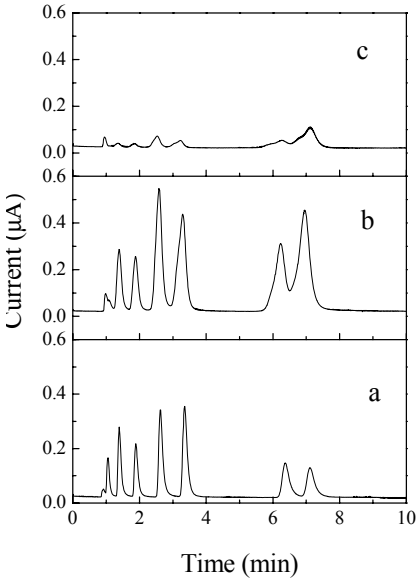

Figure 3 HPLC chromatograms of sulfonamides at different zone of eluate. (a) zone of eluate at time 20-24 s, (b) zone of eluate at time 25-29 s, (c) zone of eluate at time 30-34 s.

Table 1 Linearity, limit of detection and limit of quantitation of the method

Analyte	Linearity (μg/mL)	Slope (peak area units /ppm)	Intercept (μA)	R^2	LOD (ng/mL)	LOQ (ng/mL)
Sulfaguanidine	0.01-8	0.5277	0.1085	0.9943	33.6	11.2
Sulfadiazine	0.01-8	7.6757	0.0403	0.9982	1.2	4.0
Sulfamethazine	0.01-8	6.5834	0.0769	0.999	1.3	4.2
Sulfamonomethoxine	0.01-8	5.2178	0.3764	0.9965	1.5	5.0
Sulfamethoxazole	0.01-8	2.4536	0.0679	0.9994	2.9	9.8
Sulfadimethoxine	0.1-8	2.397	0.2668	0.9957	3.1	10.3
Sulfaquinoxaline	0.1-8	0.8786	0.0419	0.9997	7.4	24.6

Conclusions

In this work, we developed an on-line solid phase extraction (SPE) coupled with sequential injection analysis for the separation and determination of sulfonamides in shrimp samples. The proposed method could reduce sample preparation time and reagent consumption and enable effective preconcentration and clean-up of sample. The sensitivity of seven sulfonamides obtained from this method was higher than the previous publications. The results show that our method is simple, rapid and highly sensitive for the determination of sulfonamides.

Acknowledgements

The authors gratefully acknowledge the support from The 90TH Anniversary of Chulalongkorn University Fund and Innovation for the improvement of food safety and food quality for new world economy project.

References

[1] T.A. Gehring, B. Griffin, R. Williams, C. Geiseker, L.G. Rushing, P.H. Siitonen, J. Chromatogr. B 840 (2006) 132.

[2] G. Fang, J. He, S. Wang, J. Chromatogr. A 1127 (2006) 12.

[3] W.H. Xu, L.M. Lin, X.T. Wang, J. Instrum. Anal. Chin. 5 (2004)

[4] Y. Tang, H. He, J. Instrum. Anal. Chin. 1 (2005) 96.

[5] Y. Qin, M.J. Zhang, H.D. Lin, J. Instrum. Anal. China 4 (2004) 88.

[6] R.F. Yang, Z.G. Shi, Y.Q. Feng, Acta Pharm. Sin. 38 (2003) 129.

[7] K.E. Maudens, W.E. Lambert, J. Chromatogr. A 1047 (2004) 85.

[8] G. Diaz, Anal. Lett. 23 (1990) 607.

[9] Commission of the European Community, The rules governing medical products in the European Community IV, Brussels, 1991.

[10] T. You, X. Yang, E. Wang, Analyst 123 (1998) 2357.

[11] M.S. Fuh, S. Chu, Anal. Chim. Acta 499 (2003) 215.

[12] X. Wang, K. Li, D. Shi, N. Xiong, X. Jin, J. Yi, D. Bi, J. Agric. Food Chem. 55 (2007) 2072.

[13] H. Chang, J. Hu, M. Asami, S. Kunikane, J. Chromatogr. A 1190 (2008) 390.

[14] E.L. McClure, C.S. Wong, J.Chromatogr. A 1169 (2007) 53.

[15] R. Sheridan, B. Policastro, S. Thomas, D. Rice, J. Agric. Food 3509.

[16] U. Koesukwiwat, S. Jayanta, N. Leepipatpiboon, J. Chromatogr. 102.

[17] M.S. Díaz-Cruz, M.Js. García-Galán, D. Barceló, J. Chromatogr. 50.

[18] H. Li, P.J. Kijak, S.B. Turnipseed, W. Cui, J. Chromatogr. B 836

[19] Z. Ye, H.S. Weinberg, M.T. Meyer, Anal. Chem. 79 (2007) 1135.

[20] K. Choi, S. Kim, C. Kim, S. Kim, Chemosphere 66 (2007) 977.

[21] N. Furusawa, Anal. Chim. Acta 481 (2003) 255.

[22] R.H.M.M. Granja, A.M.M. Ni˜ no, F. Rabone, A.G. Salerno, Anal. Chim. Acta 613 (2008) 116.

[23] M. Gratacós-Cubarsí, M. Castellari, A. Valero, J.A. García-Regueiro, Anal. Bioanal. Chem. 385 (2006) 1218.

[24] J. He, S. Wang, G. Fang, H. Zhu, Y. Zhang, J. Agric. Food Chem. 56 (2008) 2919.

[25] J.E. Roybal, A.P. Pfenning, S.B. Turnipseed, S.A. Gonzales, Anal. Chim. Acta 483 (2003) 147.

[26] Y. Wen, M. Zhang, Q. Zhao, Y.Q. Feng, J. Agric. Food Chem. 53 (2005) 8468.

[27] H. Niu, Y. Cai, Y. Shi, F. Wei, J. Liu, S. Mou, G. Jiang, Anal. Chim. Acta 594 (2007) 81.

[28] B. Roudaut, M. Garnier, Food Addit. Contam. Part A 19 (2002) 373.

[29] K.E. Maudens, G. Zhang, W.E. Lambert, J. Chromatogr. A 1047 (2004) 85.

[30] A. Preechaworapun, S. Chuanuwatanakul, Y. Einaga, K. Grudpan, S. Motomizu, O. Chailapakul, Talanta 68 (2006) 1726.

A rapid on-line solid phase extraction coupled with LC-MS method for the determination of sudan I-IV in chilli products

K. Sonamit[1, 2] and O. Chailapakul[2, 3*]

[1] Bureau of Quality and Safety of Food, Department of Medical Sciences, Ministry of Public Health, Muang, Nonthaburi, Thailand
[2] Department of Chemistry, Faculty of Sciences, Chulalongkorn University, Patumwan, Bangkok, Thailand
[3] Center of petroleum, Petrochemicals and Advanced Materials, Chulalongkorn University, Patumwan, Bangkok, Thailand

[*] E-Mail: corawon@chula.ac.th

Abstract: A rapid liquid chromatography-mass spectrometry (LC-MS) using on-line solid phase extraction (SPE) has been developed and validated for the determination of sudan I-IV in food samples. Chilli products were first extracted with acetone and then an on-line SPE system were used for analyte enrichment before determination by LC-MS. Sudan dyes were eluted using a gradient elution program (0.1% formic acid aqueous solution / 0.1% formic acid acetonitrile) followed by electrospray MS analysis. All four sudan dyes were separated in less than 8 min. Linearity was obtained with the coefficient of determination (R^2) greater than 0.9998. Limits of detection (LOD) and quantitation (LOQ) for sudan I, II and IV were 0.03 and 0.05 mg kg^{-1}, respectively, and for sudan III were 0.04 and 0.1 mg kg^{-1}, respectively. The intra- and inter-day recoveries of the four sudan dyes in chilli powder were found to be 90.1-101.6% and 90.2-102.0%, with intra- and inter-day precision (RSD) between 0.01-0.16% and 0.04-0.20%, respectively. Food samples including chilli sauce, roasted chilli paste and dried chilli were spiked at three levels of standard sudan dyes; the recoveries obtained were more than 90%. The present method is rapid, sensitive, and reliable that could be applicable for the determination of sudan dyes in chilli products.

Introduction

Sudan azo-dyes are synthetic colorants, also known as sudan I-IV (Figure 1) that widely used as colouring agents in oils, waxes, petrol, shoes and floor polishes [1]. Sudan dyes are classified by the International Agency for Research on Cancer (IARC) as category 3 carcinogens [2] that have been proved through laboratory experiment to cause cancer to animals and human. Therefore, sudan dyes at any level are considered unsafe for human consumption. Because of these problems, the EU and the US do not permit the use of these colorants as food additives. The EU has set the detection limit at 0.5-1 mg kg^{-1} for sudan dyes [3]. As the illegal use of dyes is the big problem for food industries in world-wide as well as an impact on public health. For this reason, a sensitive, simple, accurate, reliable and rapid analytical method for the determination of sudan dyes in food still is significative for the assurance of consumer health.

Variety analytical methods have been developed for the determination of sudan dyes in food-stuffs. Most of common methods are based on LC combined to UV, DAD, MS, electrochemical and chemiluminescent detection [4-10]. Due to the important problem for

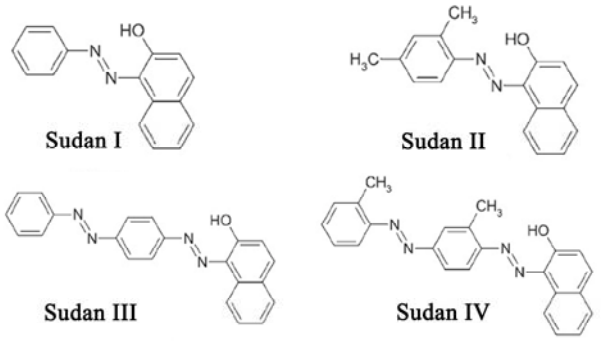

Figure 1 Chemical structures of the four Sudan dyes

the determination of sudan dyes in food is the matrix. Therefore, sample extraction techniques are required before analysis. Thus, sample preparation methods have been included such as GPC [11], DSSBME and HF-LPME [12]. Although these methods have been successfully applied to determine sudan dyes at trace levels, however, they suffer from tedious sample preparation led to the long analysis times. In addition, they used large amounts of organic solvents. Thus, the development of simple, rapid and efficient sample preparation technique for the trace analysis of sudan dyes is truly important.

Solid-phase extraction (SPE) is a method of sample preparation that concentrates and purifies analytes from complex samples [13]. This extraction technique has been developed in the on-line mode with column switching to improve sample throughput. On-line SPE not only offers an exceptional opportunity to reduce the analysis time comparing to manual off-line SPE but also requires minimal reagent and sample consumption. This method allows the samples to be directly injected into a fully automated HPLC system. Because of these reasons, the on-line SPE was applied for analysis sample in many fields such as pharmaceutics [14-16], environments [17-19], biologics [20, 21] and food [22].

The purpose of the present study was to develop a simple, rapid and reliable on-line SPE-LC-MS method for the determination of sudan I-IV in chilli products without additional pre-purification steps. The method provides high recovery and short analysis time when compared to those of existing methods. In final step, the method was applied to analyze sudan dyes in various chilli samples.

Materials and Methods

Materials and reagents: Sudan I, II, III and IV were purchased from Sigma-Aldrich (Steinheim, Germany). The purities of all standards were greater than 90%. Acetonitrile and methanol (HPLC grade) were purchased from Fisher Scientific (Loughborough, UK). Water was purified with a Purelab Ultra system (Elga Labwater). Formic acid, acetone and ethyl acetate (analytical reagent grade) were purchased from Fisher Scientific. (Loughborough, UK). The solvents for HPLC were filtered with a nylon membrane filter (0.2 µm, 47 mm, Vertical) prior to use. The sample was filtered by nylon syringe filter (0.2 µm, 13 mm, Vertical) prior to inject.

Calibration standards: Individual stock standard solution (100 µg mL^{-1}) of sudan I-IV were prepared by dissolving the standard in acetonitrile/water (90/10, v/v), except sudan III and IV were dissolved in a small amount of ethyl acetate and followed by dilution with acetonitrile/water (90/10, v/v). All stock standard solutions were kept at 4ºC in the dark. Freshly working standard mixture solutions were prepared by mixing desired volume of individual stock standard solution and successively diluting to different levels with acetonitrile.

Instrumentation: The instrument set up is shown in Figure 2. The LC-MS system was Agilent 1100 series LC-MSD-Trap-XCT (Agilent Technologies, USA) the configuration used here consisted of a binary pump system with separately operated pump A and B with degasser, an autosampler, and a column thermostat compartment with a 6-port 2-position switching valve and MSD ion trap detector. The analytical column was a reversed phase C_{18} column (Fortis C_{18}, 150 mm x 2.1 mm id., 3 µm), and the column temperature was maintained at 40 ºC throughout the experiments. The SPE cartridge used for an on-line enrichment column (Alltech, USA) was contained with C_{18} sorbent (15-40 µm particle size, Vertical). The mass spectrometer was operated in positive ion mode. The ESI interface conditions for all target analytes were as follow: drying gas temperature 325 ºC, drying gas flow rate 10 L min^{-1} and nebulizer pressure of 45 psi. The MS analysis was divided into four segments each containing one of the analytes and used manual MS^2 mode.

Extraction: The chilli products (1 g) were weighed and extracted with 10 mL acetone; the solution was filtered with 0.2 µm nylon syringe filter before injection to the on-line SPE-LC-MS system. No additional clean up of the sample solution was performed.

On-line SPE-LC-MS procedure: The instrumental configuration used here is displayed in Figure 2. For enrichment, pump A supplied eluent A (MeOH/water, 50/50 v/v) and is required for sample introduction and rinsing step at a flow rate 1.0 mL min^{-1}. 20 µL of sample supernatant was injected onto the enrichment column. When loading was complete, the valve was switched as shown in Figure 2b. Then, pump B begins the solvent composition program at flow rate 0.4 mL min^{-1} to back flush the analytes to the analytical column

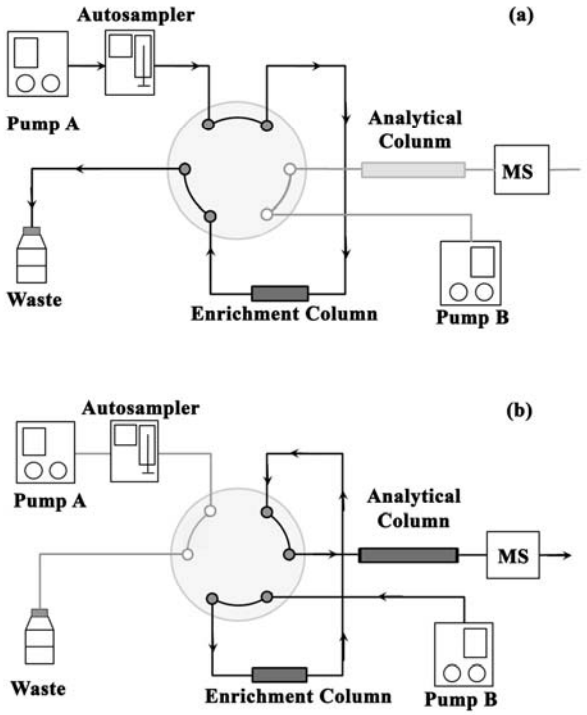

Figure 2. Schematic view of the on-line SPE-LC-MS system (a: sample enrichment and rinsing step, b: analyte elution and transfer to analytical column and analysis by MS)

Table 1: The HPLC gradient program of pump B and switching valve position

Time (min.)	Switching valve position	Pump B	
		%A	%B
0-0.5	1	8	92
0.5-4	2	2	98
4-5	2	0	100
5-7	2	0	100
7-8	2	8	92
8-12	1	8	98

A: 0.1% formic acid in H_2O, B: 0.1% formic acid in Acetonitrile
1: Enrichment column, 2: Analytical column

and mass spectrometer. After the analytes were eluted, the valve was returned to the load position (Figure 2a) and initial solvent was used to condition the re-equilibration for the next sample. The solvent composition program of pump B and the switching valve program are shown in the Table 1.

Results and Discussion

LC-MS for sudan I-IV: Typical on-line SPE-LC chromatogram and mass spectrum of sudan I-IV are presented in Figure 3. The four sudan dyes were separated in less than 8 min. From literature reviews, we found that most publications using LC-MS (/MS) techniques required at least 15 min or more for the separation four of them. These times are not inclusion of

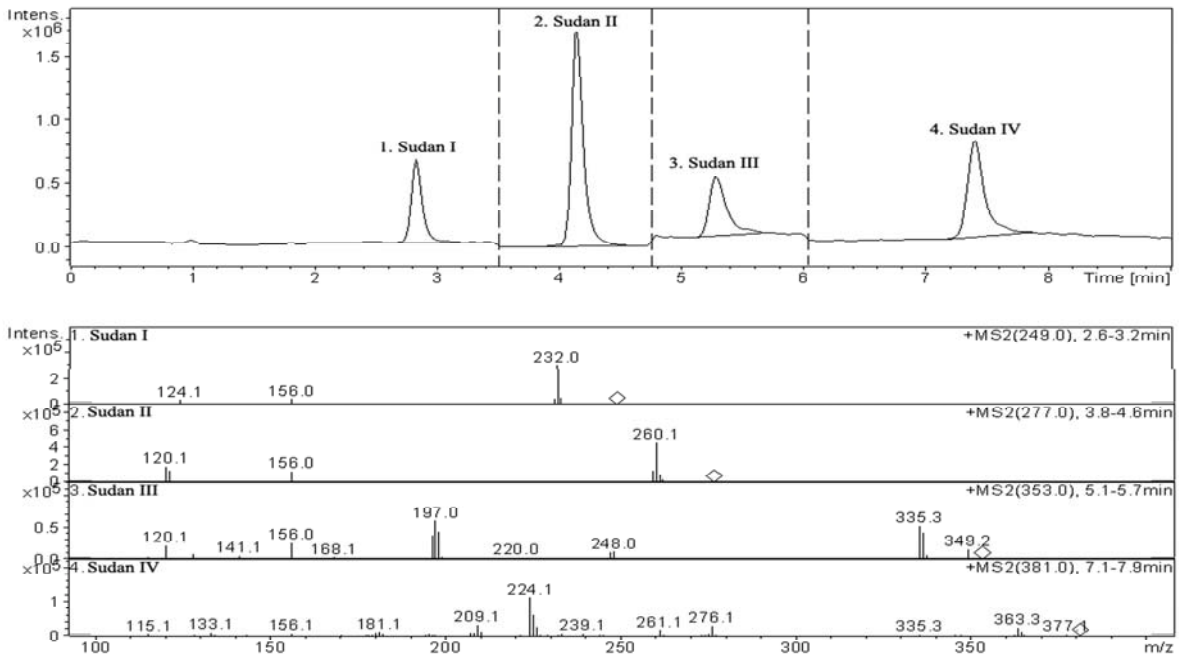

Figure 3. Typical on-line-SPE-LC-MS chromatograms and mass spectrums for blank chili powder spiked with the standard mixture of Sudan I-IV (0.5 mg kg^{-1})

sample preparation steps. Comparison to this developed experiment, the total analysis time is 12 min (include re-equilibration). This indicated that the present method is successfully improved by reducing the total analysis time using the optimized on-line SPE-LC-MS.

The choice of SPE sorbent: Generally, SPE materials significantly affected to the recovery. Therefore, in this work we compared SPE columns packed with C_{18}, silica and HCP-SC using an off-line method. The conditions of the use of SPE were 5 mL of MeOH, followed by 5 mL of water. Next, 1 mL of a 0.5 µg mL^{-1} sudan dyes standard mixture solution, prepared in acetone was loaded and 5 mL of MeOH:water (50:50, v/v) was used to wash the column. Finally the sudan dyes were eluted from the SPE cartridge with 0.1% formic acid in acetonitrile. From the results, it was found that the C_{18} cartridge provided the high recoveries of sudan II, III and IV, but for Sudan I, the C_{18} cartridge provided a lower recovery than the HCP-SC cartridge. This phenomenon can be explained by the polarity difference of sudan I versus the remaining dyes. The silica cartridge has the lowest recoveries because it was suitable for a polar compound and worked extremely well with non polar solvents such as n-hexane or methylene chloride. On the other hand, sudan dyes were non polar compounds and acetone was used as organic solvent so the recoveries obtained from silica cartridge was low (data not shown). However, the C_{18} cartridge was chosen for the suitable on-line SPE material because it provided the high recoveries for three of dyes.

Method validation: The on-line SPE-LC-MS method was validated in accordance with the guidelines for validation method. Typical acceptable criteria for validation of an analytical method such as limit of detection (LOD), limit of quantitation (LOQ), linearity, recovery and precision were determined.

Linearity: Standard calibration curves were generated from standard solutions at different concentrations of sudan dyes (I-IV). For sudan I, II and IV, the linear range was found to be 0.005-1.0 µg mL^{-1} and sudan III was 0.01-4.0 µg mL^{-1}. The coefficients of determination of each equation were greater than 0.9998.

Limit of detection (LOD) and limit of quantitation (LOQ): The LOD was determined by analyzing ten blank chilli powder samples at levels that provide signals at three times above the background noises. In a similar way, the LOQ was identified at signal-to-noise ratios equaled to 10. The LOD for sudan I, II and IV was 0.03 mg kg^{-1} and sudan III was 0.04 mg kg^{-1}. The LOQ for sudan I, II and IV was 0.05 mg kg^{-1} and sudan III was 0.1 mg kg^{-1}. Although the LOD and LOQ values are not lower than that of the methods reported previously, however, they are lower than the EU standard [3]. Therefore, it was sensitive enough to support this evaluation.

Intra-day, inter-day recovery and precision: The intra-day recovery and precision were investigated on spiked samples for five times in 1 day at three different concentrations. The inter-day recovery and precision was performed on different days by analyzing spiked samples at three different concentrations. Using the data of matrix, it indicated that intra-day and inter-day recoveries were found to be in range of 90.1-101.6% and 90.2-102.0%, respectively, with intra-day and inter-day precision (RSD) of 0.01-0.16% and 0.04-0.20%, respectively. The results demonstrated that the method has a good precision and a high recovery.

Table 2: Recoveries for the spiked chili products (n=3)

Compound	Spiked level (mg kg^{-1})	Recovery (%)		
		Chili sauce	Roasted chili paste	Dried chili
Sudan I	0.05	101.2	101.1	100.0
	1	95.6	95.5	95.5
	10	99.3	98.9	100.0
Sudan II	0.05	100.4	100.5	97.0
	1	97.2	94.6	101.4
	10	98.1	91.2	94.2
Sudan III	0.1	100.8	101.5	101.5
	4	99.7	96.8	97.9
	40	98.4	100.6	98.9
Sudan IV	0.05	100.7	101.4	100.2
	1	95.0	98.6	91.0
	10	98.8	97.8	99.6

Real sample analysis: Food samples including chilli sauce, roasted chilli paste and dried chilli from local supermarkets were analyzed by on-line SPE-LC-MS. None of the samples contained the sudan dyes. To demonstrate the method feasibility, the recovery experiments were carried out using spiked samples with the sudan dyes standards at three levels. It was found that recoveries of greater than 90% were obtained for sudan I-IV (Table 2).

Conclusions

An on-line SPE-LC-MS method was successfully developed for simultaneous determination of sudan I-IV in chilli products. This method allowed the possibility for the determination of these dyes within a short analysis time compared to those previous works, with a simple and efficient sample preparation technique. The results obtained from validation showed a satisfactory value of LOD, LOQ, recovery and precision. Moreover, it could be applicable for the determination of sudan dyes in variety of food-stuff sample for the assurance of consumer healthiness.

Acknowledgements

This work was financially supported by the Innovation for the improvement of food safety and food quality for new world economy project, the Ratchadaphisek Somphot Endowment Grant, Chulalongkorn University and the Department of Medical Sciences. The authors also thank the Regional Medical Sciences Center Nakhonratchasima and the Bureau of Quality and Safety of Food for instrument support.

References

[1] http://www.food.gov.uk/safereating/chemsafe/sudani/
[2] International Agency for Research on Cancer. (1975). Monographs on the evaluation of carcinogenic risks to humans and their supplements (Vol.8, pp.225-241). (IARC).
[3] http://www.ift.org/news_bin/news/archiveFrames.php?view=5-2005
[4] E. Ertas, H. Özer, C. Alasalvar, Food Chem. 105 (2007) 756.
[5] V. Cornet, Y. Govaert, G. Moens, J.V. Loco, J.M. Degroodt, J. Agric. Food Chem. 54 (2006) 639.
[6] F. Calbiani, M. Careri, L. Elviri, A. Mangia, L. Pistarà, I. Zagnoni, J. Chromatogr. A 1042 (2004) 123.
[7] F. Calbiani, M. Careri, L. Elviri, A. Mangia, I. Zagnoni, J. Chromatogr. A 1058 (2004) 127.
[8] M. Ma, X.B. Luo, B. Chen, S.P. Su, S.Z. Yao, J. Chromatogr. A 1103 (2006) 170.
[9] O. Chailapakul, W. Wonsawat, W. Siangproh, K. Grudpan, Y. Zhao, Z. Zhu, Food Chem. 109 (2008) 876.
[10] Y.T. Zhang, Z.J. Zhang, Y.H. Sun, J. Chromatogr. A 1129 (2006) 34.
[11] H.W. Sun, F.C. Wang, L.F. Ai, J. Chromatogr. A 1164 (2007) 120.
[12] C. Yu, Q. Liu, L. Lan, B. Hu, J. Chromatogr. A 1188 (2008) 124.
[13] E.M. Thurman, M.S. Mills, Solid-Phase Extraction: Principles and Practice, Wiley, New York, 1998.
[14] A. Schellen, B. Ooms, D. Lagemaat, R. Vreeken, W.D. Dongen, J. Chromatogr. B 788 (2003) 251.
[15] Y.C. Barrett, B. Akinsanya, S.Y. Chang, O. Vesterqvist, J. Chromatogr. B 821 (2005) 159.
[16] A. Castro, M. Fernandez, M. Laloup, N. Samyn, G. Boeck, M. Wood, V. Maes, M. López-Rivadulla, J. Chromtogr. A 1160 (2007) 3.
[17] A. Asperger, J. Efer, T. Koal, W. Engewald, J. Chromatogr. A 960 (2002) 109.
[18] H. Bagheri, A. Mohammadi, A. Salemi, Anal. Chim. Acta 513 (2004) 445.
[19] S. Wang, W. Huang, G. Fang, J. He, Y. Zhang, Anal. Chim. Acta 606 (2008) 194.
[20] T. Koal, M. Deters, B. Casetta, V. Kaever, J. Chromatogr. B 805 (2004) 215.
[21] X. Ye, L.J. Tao, L.L. Needham, A.M. Calafat, Talanta 76 (2008) 865.
[22] A. Bacaloni, C. Cavaliere, A. Faberi, E. Pastorini, R. Samperi, A. Lagana, J. Agric. Food Chem. 53 (2005) 5518.

Study on the occurrence of maillard browning reaction in thai herb medicine

P. Muangthai[1] * and A. Kanthuskampol[2]

[1] Srinakharinwirot University , Department of Chemistry ,Associate Professor , Bangkok , Thailand
[2] Srinakharinwirot University , Department of Chemistry ,Graduate Student,Bangkok,Thailand

* Corresponding Author E-Mail Address:pornpi@swu.ac.th

Abstract: Thai herb medicine is one of the popular drug in Thailand for a long time. Some drugs contain honey as a binder substance. The drugs showed dark brown color after storage.The dark brown color sometime occured from nonenzymatic browning reaction known as Maillard browning reaction. The aim of this work is to detect nonenzymatic browning reaction by analysis the hydroxymethylfurfuraldehyde(HMF) content in Thai herb medicine. HMF was one of toxic substance and was accept to be a good indicator to interpret the quality of honey in Europe. However, fresh new honey should contain HMF content not exceed than 1 ppm. The experiment was divided into 2 parts.The first part , the HMF content in pure honey was analysed by heating honey at various temperature (40 – 100 ^{o} C) and time(20 – 120 minutes) using Highperformance liquid chromatography with diode array detector.In the second part ,the HMF was analysed in some Thai herb medicine samples which were collected from the herb store drug in Bangkok.The results showed that the HMF content in pure honey was 0.45 ± 0.02 ppm. HMF content increased to 4.50 ± 0.03 ppm after the honey was heated at 100 ^{o} C for 120 minutes. HMF content in Thai herb medicine samples were 3.87 – 45 ppm.Those drugs showed a high content of HMF,this presented that the dark brown color of Thai Herb medicine occurred from Maillard browning reaction. Thus, the human should aware about the toxic of some Thai herb medicine.

Introduction

Thai Herb medicines were used for Thai people for a long time. There are many Thai herb medicine from Thai wisdom knowledge and also used as many types such as bolus or spherical shape form, flat plate and liquid solution.[1]. However ,all or some Thai herbal medicine may contained honey in their component especially in bolus form. New fresh honey from Bee showed yellow color and darken brown to almost black color after storage for a long time. Since the occurrence on browning reaction which was known as Maillard reaction[2]. Maillard reaction is an nonenzymatic browning reaction , which occur from the reaction between a carbonyl group of reducing sugar and amino group from amino acid[3]. There are many products from Maillard browning reaction, the one product that used to be an indicator for this reaction is 5-hydroxymethylfurfuraldehyde(HMF). HMF has been detected in a wide variety of heat-processed foods including milk, fruit juices, spirits, honey, etc.[4]. HMF is also used as an indicator of heat treatment and storage time in honey. However,HMF is also formed by fructose degradation in the presence of an acid. Heat increases the speed of this reaction. The increase in speed is exponential with increasing heat with the age and heat treatment on honey[5]. However, HMF should not be detected in new honey but permission content not exceed than 1 ppm[6].There has the regulation to control HMF in honey in could not exceed than 15 ppm in many countries as German, Belgium, Italy, Austria and Spain [7]. There was no report about the HMF content in Thai herb medicine but there was found only the report of HMF in pharmaceutical drug[8].So,the aim of this work is to analyse the HMF content in Thai herb medicine.The HMF in honey and heated honey were also studied.

Materials and Methods

Part 1. Analysis of HMF in Honey.

1.1Preparation of standard HMF calibration curve.

Standard HMF(HPLC grade purchase from Fluka) was prepared for 100 ppm in milli Q water (stock solution) ,then it was prepared as solution series by variation of HMF concentration between 10 -100 ppm. Those standard solution were filtered through 0.45 µm cellulose acetate membrane filter by SPE technique.The standard purified filtrate was injected through RP C_{18} column (Bondeclone 10 µ, 300 x 390 mm.) 100 µl to HPLC Chromatography (HP1100).The eluate was eluted by systems of the water : acetonitrile = 97 : 3 (modified from reference [5])The elution system was isocratic system and control rate of flow at 1 ml/min.The signal was detected by diode array detector at 280 nm. The chromatogram of the standard was recorded for the inspection of the appropriate condition.

1.2. Analysis of HMF content in pure honey.

The honey (Chrtralada Brand) was weighed for 5.000 g and heated on hot plate at 40^{0}C for 30 min.The heated honey was treated by addition 25 ml. of water and 0.5 ml. of carrez I solution.The mixing solution was mixed with 0.5 ml. of carrez II solution and diluted again to 50 ml. solution by milliQ water.[9]. The clearance solution of honey sample was filtered through 0.45 µm cellulose acetate membrane filter and injected to RP C_{18}column.Then the solute was eluated by the system of water : acetonitrile = 97 : 3 (modified from reference [5]) .The chromatogram of

honey was recorded and compared with the standard calibration curve of standard HMF.

1.3 Study the factors that effect on heated honey.

1.3.1 Effect of heating temperature on honey

The honey (Chrtralada Brand) was weighed for 5.000 g and heated on hot plate at 40^{0}C for 30 min.The heated honey was treated by addition 25 ml. of water and 0.5 ml. of carrez I solution.The mixing solution was mixed with 0.5 ml. of carrez II solution and diluted again to 50 ml. solution by milliQ water.[9]. The clearance solution of honey sample was filtered through 0.45 µm cellulose acetate membrane filter and injected to RP C_{18}column.Then the solute was eluated by the system from part 1 and recorded the chromatogram. The heating systems were studied with the new honey as above by heated the honey at 60 ^{o}C , 80^{o}C and 100^{o}C. All systems were trial for 5 replications.

Note: carrez I was the solution of 15 % of $K_4Fe(CN)_6$ carrez II was the solution of 30 % of $Zn(OAc)_2$

1.3.2 Effect of heating time on honey

The honey was weighed for 5.000 g and heated on hot plate at 100^{0}C for 20 ,40, 60,80, 100 and 120 min. and treated as 2.1

Part 2. Analysis of HMF in Thai herb medicine samples.

Thai herbal drugs were purchased from Thai herb store at Tha phra Chan nearby Thammasart University,Bangkok and general drug store that sold Thai herbs. Those drugs were collected about 25 examples as liquid form , bolus and pellet form. The drugs were weighed 5.0000 g and dissolved in 50 ml.of water.The drug solutions were treated with carrez I and carrez II as on experiment part 2.1. The chromatogram of samples were recorded and calculated the content of HMF in drugs. All experiments were carried out in 3 replicates.

Results and Discussion

From part 1, the standard HMF was prepared and injected to RP C $_{18}$ column and the chromatogram of standard HMF was recorded as in figure 1. Tha chromatogram of pure honey presented in figure 2.The standard calibration curve showed in figure 3.

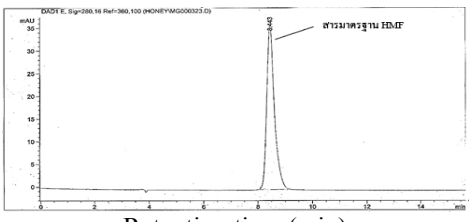

Retention time (min)

Figure 1 Chromatogram of Standard HMF

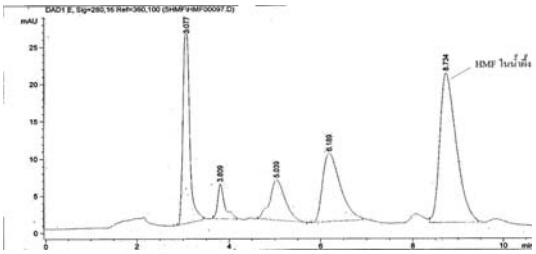

Retention time (min)

Figure 2 Chromatogram of pure honey

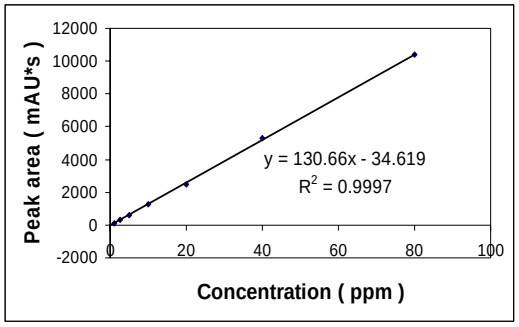

Figure 3 Standard calibration curve of standard HMF

From the regression equation of the standard calibration curve of standard HMF was y = 130.66 x -34.62 , with the R^2 = 0.9997. The areas of HMF peak from part 3.1 and 3.2 were calculated by the above regression to evaluate the HMF contents in heating honey showed in table 3 and 4.

Table 3 The HMF value of heated honey at various temperature

Heating temperature(^{o}C)	HMF content (ppm)	% RSD (n=6)
Room temperature	0.45 ± 0.02	3.90
40	0.47 ± 0.01	4.86
60	0.48 ± 0.01	5.41
80	0.49 ± 0.02	3.11
100	0.93 ± 0.03	2.43

Table 4 The HMF value of heated honey at various time

Heating time (min)	HMF content (ppm)	% RSD (n=6)
20	0.59 ± 0.02	4.50
40	1.06 ± 0.05	6.66
60	1.46 ± 0.07	4.60
80	2.97 ± 0.15	4.88
100	4.20 ± 0.13	3.10

From the table 3, the HMF content still constant from room temperature to the heating at 80^{o}C and increase 2 times at 100 ^{o}C of heating. The relation between the heating temperature and HMF content as showed in figure 4 was the polynomial relation with R^2 = 0.90

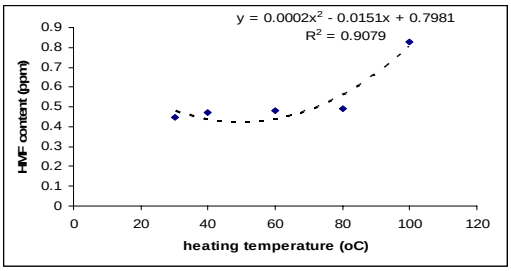

Figure 4 The relation between heating temperature and HMF content in heating honey

This experiment presented HMF in honey will increase as a polynomial form when the honey was heated at high temperature as 100 ^{o} C which had the same trend as referred by [10]. Thus, if the honey was heated at high temperature HMF will increase too much. So the Thai herbal drug which contains honey as its component or binder also contains HMF too.

The relation between heating time and HMF content in heated honey showed in figure 5 was the exponential form.

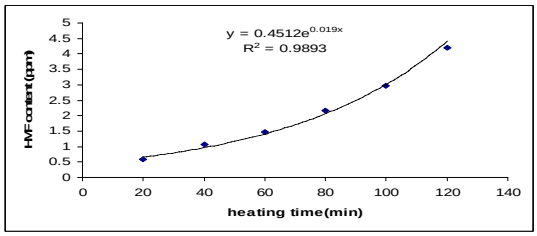

Figure 5 The relation between heating time and HMF content in heating honey

From the relation between heating time and HMF content found in figure 5 also showed the exponential relation as $R^2 = 0.99$. The heating time also effected on the HMF content in heating honey and more effect than heating temperature on honey which support the result from [11,12].

In this part of the experiment revealed that the HMF occurred in honey and after used the heating honey in herbs as their component or binder, there are possibility to detected HMF in high content. After, an application of method in analysis HMF content in honey with the true Thai herbal medicines 30 samples , the chromatogram of Thai herbal medicines were recorded as showed an example in figure 6 and the results showed in table 5.

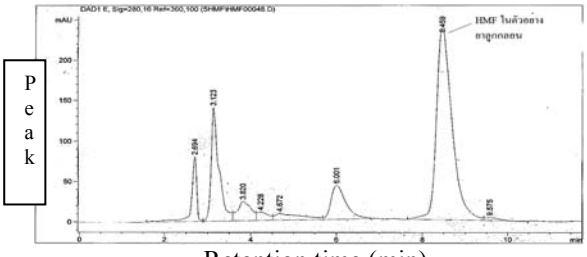

Figure 6 The Chromatogram of HMF in Thai herb drugs.

Table 5 The HMF content in Thai herb drugsamples.

Sample number	Physical state of drugs	HMF content(ppm)
1	Dark brownLiquid	1.51 ± 0.05
2	Dark brownSolid	0.65 ± 0.01
3	Dark brownSemisolid	1.85 ± 0.03
4	Dark brown plate	1.47 ± 0.02
5	brown Semisolid plate	0.87 ± 0.02
6	Brown Semisolid plate	0.71 ± 0.02
7	BrownSemisolid plate	0.67 ± 0.02
8	Brown Semisolid plate	0.24± 0.02
9	Dark brown plate	3.12 ± 0.02
10	Dark brown plate	1.07± 0.02
11	Dark brown tablet	1.52 ± 0.15
12	Dark brown tablet	3.02 ± 0.12
13	Dark brown tablet	4.52 ± 0.23
14	Brown tablet	0.65 ± 0.15
15	Black tablet	20.85 ± 0.03
16	Brown tablet	0.47 ± 0.18
17	Dark brown tablet	5.58 ± 0.05
18	Pale brown tablet	0.05 ± 0.02
19	Brown tablet	0.56 ± 0.04
20	Pale brown tablet	0.05 ± 0.01
21	Dark brown tablet	8.89 ± 0.08
22	Dark brown tablet	6.29 ± 0.14
23	Black tablet	23.28 ± 0.27
24	Dark brownLiquid	1.16 ± 0.11
25	Dark brownLiquid	3.17 ± 0.20
26	Dark brownLiquid	3.24 ± 0.05
27	Black bolus	22.30 ± 0.14
28	Black bolus	44.95 ± 0.50
29	Dark brown bolus	5.08 ± 0.21
30	Dark brownbolus	3.87 ± 0.09

From the value of HMF content in Thai herbal medicines which had pale brown color to black colour and the liquid form to solid form were 0.05 – 44.95 ppm.Those Thai herb medicines contained HMF from the production of the producer, however there was noticed that the black color medicine contained the higher HMF content than the paler color.Since there was no regulation for control the quality of those Thai herbs medicines and the effect from the producer used the heated honey to produce Thai herbal medicines,so the people who eat those drugs should cared about the toxic of HMF content in the drugs.HMF is the one that was claimed to be a carcinogen in animal[11], it may dangerous for health of human.Eventhough , there was no regulation for control the HMF content in nowadays , but in the future the HMF was controlled in honey as the aboard countries[9].

Conclusions

All this research proved that the honey contained some of HMF content. After, the result from the studied an effect of heating time and heating temperature on honey revealed that the HMF depend on both parameters. This showed that whenever the

heated honey was used as a component in Thai herb medicines or as a binder , there had a probability to get the HMF. After the analysis method was applied to the real Thai herbal medicines for 30 samples which had many form such as liquid , bolus and pellet and also 4 shades of color such as pale brown , brown , dark brown and black color, the results showed that those drugs contained the HMF from low level about 0.05 ppm to highest level as 44.95 ppm. The darken in color of drugs contained the higher level of HMF value. However, the HMF content is the one parameter to control the honey quality and there has some report about the toxicity of HMF, so the people who eat drugs which contained honey should be care with HMF value.

Acknowledgement

The authors are grateful to the faculty of Science ,Srinakharinwirot University by financial support for this experiment.

References

[1]S. Putiyanon,*Fundamental Knowledge of Thai wisdom plant* . 3 rd ed. Thahan ban suk Press. Bangkok. (1999)

[2]S.Bogdanov,International Honey Commission. Honey quality and international regulatory standards: review by the International Honey commission. Bee-World, **80:** 2,(1999)pp 61-69.

[3]I.Kubis and I. Ingr. *Czech-Journal-of-Animal-Science.* **43**: 8, (1998)pp 379-383.

[4].Y.Román-Leshkov,N.Juben.Chheda,and A. James Dumesic . *Science* **312** (5782): (2006).pp1933–1937.

[5]A.Aal-ESM,HM.Ziena and MM. Youssef.*Food-Chemistry*; **48** (2)(1986).pp 209-212.

[6] HM.Wen, J.C.Chern, S.Chen,HM. Wen,JC. Chern and SH. Chen . *Journal-of-Food-and-Drug-Analysis.* **3:** 4,(1995).pp. 295-305

[7]Codex Alimentarius.*Standard for Honey*. Ref.Nr.Cl.1993/ 14-SH FAO and WHO.(1993) Rome.

[8]M.A. Espinosa,P.A. Munoz. andF. Salinas, (2005). *Journal of the AOAC International.* **76**(6) (2005). pp1255-1261.

[9].K.Kukurova,G.Karoviova,G.,Greif, G.Kohajdova and J.Lehkozivova.*Chemical Paper*, **60**(3) (2006). pp: 295-305.

[10] N.Singh andP.K. Bathm.*Food Chemistry*.**58**: 1-2 (1997),pp 129-133.

[11] F.L.Coco,C.Valentin, V.Novelli andL. Ceccon. *Journal-of-Chromatography,-A.* **749**: 1-2,(1996) pp 95-102.

[12]. H.Wen.Mei., J.C.Chern,S.H.Chen, H.M.Wen, and J.C.Chern. *Journal-of-Food-and-Drug-Analysis*., **3**: 4, (1995)pp. 295-305.

Effect of sodium metabisulfite and ascorbic acid on browning control of sugar palm seed in syrup and safety level of the products available on the market

P. Suthiluk[1*], T. Theppakorn[1] and A.Chantaraboon[2]

[1]School of Agro-Industry, Mae Fah Luang University, 333 M.1, Thasud, Muang, Chiang Rai 57100, Thailand
[2]Rajamangala University of Technology Lanna, Nan Campus, 59 M.12, Faikaew Sub-district, Phupieng, Nan 55000, Thailand

[*]E-mail: phunsiri.a@mfu.ac.th

Abstract: The effect of sodium metabisulfite ($Na_2S_2O_5$) and ascorbic acid treatment on browning control of sugar palm seed in syrup was investigated to clarify the safety level of using $Na_2S_2O_5$ and the feasibility to substitute ascorbic acid for $Na_2S_2O_5$. Sugar palm seed were treated in $Na_2S_2O_5$ and ascorbic acid solutions at different concentrations (0.05, 0.5, 1.0, 2.0, 4.0% and 0.2, 0.5, 1.0, 2.0, 5.0%, respectively) for 24 hours, followed by preserving. Whiteness and sulfite residue were measured after treatment and preserving. Results showed that higher $Na_2S_2O_5$ concentration provided more whiteness and also high level of sulfite residue. The 0.5% $Na_2S_2O_5$ treatment obtained the whiteness value nearby the sugar palm seed in syrup available on the market with 77 ppm sulfite residue. Sugar palm seed treated with ascorbic acid had whiteness value more than untreated. However, after preserving, the whiteness value of all ascorbic acid treatment were not significantly different *(P<0.05)*. The use of $Na_2S_2O_5$ in appropriate concentration could be considered for commercial application to control browning of sugar palm seed in syrup during storage and distribution. In addition, the whiteness stability after $Na_2S_2O_5$ treatment should be confirmed in further experiment. The sulfite residue in sugar palm seed products available on the market is between 80-672 ppm. Therefore the safety level of these products must be concerned.

Introduction

Sugar palm (*Arenga westerhoutii*, Tao) as shown in Figure 1 is a native wild plant naturally found over a wild area of the Asian tropics, from northeastern India, Thailand, Myanmar, peninsular Malaysia, Cambodia, Laos and adjacent southern China [1]. Sugar palm seed (young endosperms) in syrup also in the form of dried product are consumed throughout Thailand as a dessert or for ice cream topping [2]. After harvest, the seeds are lost their bright white color and turn brown, resulting in the use of chemical agents in the processing step. Nevertheless, the cause of browning in sugar palm seed has not been clarified yet. Sulfites are inorganic salts popular used as anti-browning and preservative in foods. Many compounds produce sulfite, called sulfiting agents including sulfur dioxide, sodium sulfate, sodium and potassium bisulfites and metabisulfits. They have been applied to many foods to prevent both enzymatic and nonenzymatic browning. The intake of sulfur dioxide and related compounds (Acceptable Daily Intake: ADI) approved by WHO is 0-0.7 mg/kg body weight.

Figure 1 Fruit, cross-section and seed of sugar palm

However, some groups of sulfite agent are not allowed for application in food including over limit of using can be dangerous to human health, especially in sulfite-sensitive people or asthmatic patients. The awareness in safety level sugar palm seed products must be concerned. Therefore, alternatives chemical agents of browning control without toxic effects are needed. Several researches focused on the used of non-sulfite anti-browning agents such as L-cysteine, ascorbic acid and its derivatives, sodium erythorbate, EDTA, citric acid. Nevertheless, no reports have been carried out on studying the effect of sodium metabisulfite ($Na_2S_2O_5$) and ascorbic acid on browning control of sugar palm seed in syrup. Moreover, the data about safety of sugar palm seed products has not yet available.

The main purposes of this study were to clarify the safety level of using $Na_2S_2O_5$ and the feasibility to substitute ascorbic acid for $Na_2S_2O_5$ in attempt to find the most safety and effective treatment on browning control of sugar palm seed in syrup and also provide the information of safety level of sugar palm seed products available on the market in term of residual sulfite.

Materials and Methods

Experimental Design: This study was divided into two parts. Part I to determine the sulfite residue in sugar palm seed product available on the market (5 brands is sugar palm seed in syrup and 3 brands is dried preserved sugar palm seed). Part II to study the effect of $Na_2S_2O_5$ and ascorbic acid on browning control of sugar palm seed in syrup.

Collection of Samples: Eight of sugar palm seed products (S1-S8 in Figure 2) were sampled from different markets in the North of Thailand. All samples were stored at room temperature as is usual in the retail shops.

Figure 2 Sugar palm seed products sampling from the local market in the North of Thailand

Determination of Sulfite Residue: Fifty grams of sample was chopped and added to 25 ml of 1N NaOH. The mixture was allowed to stand for 10 min and then added 10 ml of diluted sulphuric acid (H_2SO_4: H_2O = 1 : 3) and starch solution. After that the mixture was titrated with 0.05N iodine. The sulfite residue was expressed in term of total sulphur dioxide calculated from Equation (1):

$$\text{Sulphur dioxide (ppm)} = \frac{\text{Titration} \times 0.0016 \times 10^6}{50} \quad (1)$$

Plant Material and Preparation: Sugar palm seed was supplied from Rattanapanit Den-Chai Ltd., Phrae Province, Thailand and stored at -20°C for further experiment. Samples were thawed and washed in tap water prior to treatment.

Effect of $Na_2S_2O_5$ and Ascorbic Acid on Browning Control: Three hundred grams of sample was treated in 300 ml of $Na_2S_2O_5$ solution at different concentrations (0.05, 0.5, 1.0, 2.0 or 4.0%) or ascorbic acid solution (0.2, 0.5, 1.0, 2.0 or 5.0%) and left overnight. The treated samples were drained and washed in tap water and then blanched for 10 min. After that, 200 g of refined sugar and 150 ml of water were added into each treated samples and left overnight. The mixture (sugar palm seed, refined sugar and water) was then heated with stirring for 10 min. Finally, 0.65 g of citric acid was added to adjust the pH of sugar palm in syrup to smaller than 4.5 [3]. Sample treated in tap water was used as control. The experiment was repeated twice.

Color Measurement: Color of sugar palm seed (L*, a* and b* values) product, after treatment and preserving was obtained from the center of each half sliced using Hunter Lab Color Quest XE. Ten replications were measured for each sample or treatment. Results were expressed as the whiteness calculated from Equation (2):

$$\text{Whiteness} = 100 - [(100-L^*)^2 + a^{*2} + b^{*2}]^{1/2} \quad (2)$$

Statistical Analysis: Results were expressed as the mean value $\pm$ standard deviation *(n=10)*. Data were statistically analyzed using Statistical Package for the Social Sciences (SPSS). Duncan's multiple range test were performed to determine any significant difference among various treatment at the $P<0.05$ level.

Results and Discussion

The color in terms of whiteness and sulfite residue in sugar palm seed products sampling from the retail shop in the North of Thailand are shown in Table1. S-1 to S-5 is sugar palm seed in syrup and S-6 to S-8 is dried preserved sugar palm seed.

Table 1 Color and sulfite residue in sugar palm seed products available on the market

Product	Whiteness	Sulfite Residue (ppm)
S-1	46.32* $\pm$ 3.94	80
S-2	60.98 $\pm$ 1.85	128
S-3	60.32 $\pm$ 4.36	88
S-4	51.75 $\pm$ 5.00	112
S-5	65.62 $\pm$ 4.88	93
S-6	68.76 $\pm$ 2.54	672
S-7	69.05 $\pm$ 2.26	240
S-8	66.50 $\pm$ 3.32	400

*Results are Mean$\pm$SD *(n=10)*

The whiteness value of all products was within 46-69 while sulfite residues ranged from 80 to 672 ppm, the lowest was for sugar palm seed in syrup and dried preserved sugar palm seed had the highest. These data revealed that in the process of dried preserved sugar palm seed product may use high level of sulfite agent. The maximum level of sulfiting agents 1,500 mg/kg is approved by Food and Drug Administration of Thailand to be used in dried or preserved fruits and vegetables. Although sulfite treatment levels in foods vary widely by application, the residue levels should not usually exceed several hundred ppm [4,5]. These results indicated that safety level of sugar palm products must be concerned.

Since sulfite agents have shown the most effective widespread used for control of browning due to both enzymatic and non-enzymatic browning. It also acts as bleaching agent, antioxidants or reducing agents [4, 5]. The results are shown in Table 2. $Na_2S_2O_5$ were found to be effective in retarding browning of sugar palm seed. Various concentration of $Na_2S_2O_5$ provided significantly different *(P<0.05)* in the whiteness of seed sample. The value ranged from 56.42 to 61.64. After preserving, 0.5, 1.0, 2.0 and 4.0% $Na_2S_2O_5$ treated samples had the whiteness value more than after treatment which the range extended from 61.99 to 67.62, respectively. As the pH value of 3.5-5.0 is proper to function of $Na_2S_2O_5$, citric acid added in heating step may not only reduce pH value but also enhance the effectiveness of $Na_2S_2O_5$ on browning control.

Figure 3 shows the amount of sulfite residue in sugar palm seed in syrup. The sulfite residue was found to be higher in sample treated with 4.0% $Na_2S_2O_5$ (468

ppm). Even though high concentration of $Na_2S_2O_5$ provided higher whiteness value, they can also harm human health due to high level of sulfite residue. From these results, 0.5% of $Na_2S_2O_5$ was recommended for browning control of sugar palm seed in syrup.

Table 2 The color of sugar palm seed after treated with different concentration of $Na_2S_2O_5$

% $Na_2S_2O_5$	Whiteness	
	After Treatment	After Preserving
0	48.93^{d}* ± 1.51	47.31^{d} ± 1.07
0.05	56.42^{c} ± 2.25	54.02^{c} ± 1.89
0.5	**58.02^{bc} ± 3.73**	**61.99^{b} ± 2.39**
1.0	59.43^{ab} ± 1.58	64.05^{b} ± 1.42
2.0	60.57^{ab} ± 0.54	67.7^{a} ± 1.32
4.0	61.64^{a} ± 0.80	67.62^{a} ± 1.53

Results are Mean±SD *(n=10)*
*Mean in the same column with different letters are significantly different *(P<0.05)*

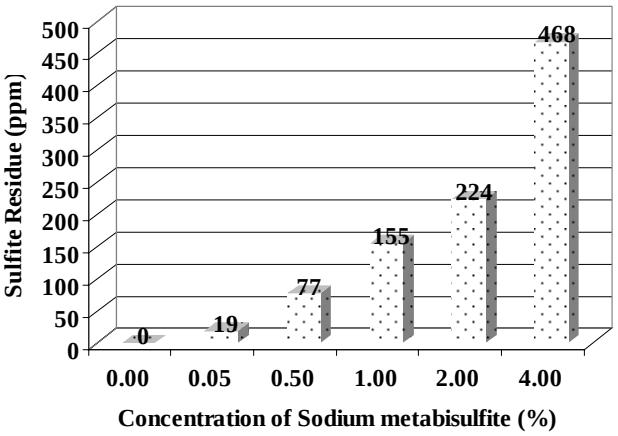

Figure 3 The amount of sulfite residue in sugar palm seed in syrup after treated with different concentration of $Na_2S_2O_5$

However, food safety concern and the current restrictions to the use of sulfite agents in food inspired many researchers to develop the sulfite substitutes. The well known alternative to sulfite agents is ascorbic acid which is highly inhibitor of enzymatic browning due to its ability to reduce quinones, generated by PPO-catalyzed oxidation of polyphenols, back to phenolic compounds before they can undergo further reaction to form pigments [6]. Ascorbic acid has been widely used as an anti-browning agent in fruits and vegetables. Table 3 shows the whiteness of the sample treated in ascorbic acid solution at different concentration (0, 0.2, 0.5, 1.0, 2.0 and 5.0%). After treatment, the whiteness of treated samples was significantly different from the control sample. The value ranged from 62.06 to 68.87. These data revealed that ascorbic acid at 0.5 and 1.0% appeared to effectively control browning. Treatment of 5% ascorbic acid obtained the whiteness value nearby the control. The suitable concentration of ascorbic acid plays alternative roles on browning control nevertheless the used of high concentration probably cause browning in the products. This result was similar with the previous research of fermented bamboo [7].

Table 3 The color of sugar palm seed after treated with different concentration of ascorbic acid

% Ascorbic Acid	Whiteness	
	After Treatment	After Preserving
0	61.87^{c}* ± 1.42	57.87^{a} ± 3.97
0.2	67.06^{ab} ± 2.45	56.48^{a} ± 3.00
0.5	68.87^{a} ± 2.83	58.76^{a} ± 2.58
1.0	68.26^{a} ± 2.14	57.82^{a} ± 4.88
2.0	66.02^{b} ± 3.07	58.36^{a} ± 3.93
5.0	62.06^{c} ± 1.80	57.08^{a} ± 4.41

Results are Mean±SD *(n=10)*
*Mean in the same column with different letters are significantly different *(P<0.05)*

After preserving, there was no significant difference between control and treated samples. Ascorbic acid is not usually as effective as sulfite agents because of the greater stability and better penetration of the latter [6] and also exposure to oxygen, metals, light or heat destroys ascorbic acid. However, soaking sugar palm seed in 0.5-1.0% ascorbic acid solution before preserving can be alternative way to minimize the use of sulfite agents. The combination of ascorbic acid and $Na_2S_2O_5$ on browning control will be studied in the future.

Conclusions

The amount of sulfite residue presented in sugar palm seed products sampling from local market in the North of Thailand indicate that safety level of sugar palm seed products available on the market must be concerned. From this experiment, the use of $Na_2S_2O_5$ clearly defined as the browning control agent in sugar palm seed in syrup with the concentration not exceeds 0.5% w/v. The feasibility of using ascorbic acid to inhibit browning was also demonstrated.

In addition, other sulfite substitute agents such as ascorbic acid derivatives, cysteine, sorbates salts, ethylenediamine tetraacetic acid (EDTA) and citric acid and combination agents should be studied in further experiment in attempt to find out the most effective and safety treatment for control of browning in sugar palm seed products and maintain quality and safety during storage and distribution.

Acknowledgements

The financial support provided by Office of the Higher Education Commission. The authors wish to thank Scientific and Technological Instruments center and School of Agro-Industry, Mae Fah Luang University, Chiang Rai province, Thailand for the research facilities and also thanks to Ms. Jiraporn Raiputta for her support to the present work.

References

[1] L. R. Robert and C. Paul, *An Encyclopedia of Cultivated Palms*, Timber Press, Incorporated. (2003).

[2] R. Pongsattayapipat and A. Barfod, *PALMS*. **49(1)** (2005), pp 5-14.

[3] http://www.tisi.go.th/otop/pdf_file/tcps1219_49.pdf

[4] G. M. Sapers, *Food Technol*. **47(10)** (1993), pp. 75-84.

[5] S. L. Taylor, N.A. Higley, R. K. Bush, *Adv. Food Res.* **30** (1986), pp. 1-76.

[6] http://www.okyanusbilgiambari.com/Bilim/Okyanus-BrowingInFoods.pdf

[7] W. Jirapakkul, *The reduction of sulfiting agents in risk foods*. (2005).

Biosurfactant production by *Pichia anomala* PY1 in batch fermenter

M. Aoenkaew*, S. Chanprateep and J. Thaniyavarn

Chulalongkorn University /Department of Microbiology, Faculty of science, Bangkok, Thailand

* Akitam_ih@hotmail.com

Abstract: The production of a biosurfactant by *Pichia anomala* PY1 was studied. Culture conditions were examined for their effects on biosurfactant production involved variations in carbon and nitrogen sources and different of carbon to nitrogen (C/N) ratios in the shake flask at constant temperature 30 ºC with initial pH of 5.0 for 7 days. To further improve the biosurfactant yield, a batch stirred and aerated tank bioreactor were performed by using optimal medium and operating conditions (30 ºC, pH 5.0) obtained from shake flask experiment. In this study, the effects of oxygen transfer rate and mass transfer efficiency on biosurfactant production were also investigated by employing various combinations of aeration and agitation rate. The highest efficiency was achieved when using glucose and soybean oil as carbon sources, $NaNO_3$ and Yeast extract as nitrogen sources respectively with an optimal C/N ratios (in %wt/wt) of 16/0.7, giving minimum surface tension of 29.17 mN m^{-1} and oil displacement activity of 31.15 cm^2. Batch fermentation was able to produce biosurfactant up to 0.83 g/l by maintain aeration rate at 1.5 vvm and agitation rate at 400 rpm. After 7 days of cultivation the biosurfactant produced minimum surface tension of 29.16 mN m^{-1}, oil displacement activity of 43.37 cm^2 and the critical micelle concentration (CMC) of 162.18 mg/l. Analytical thin layer chromatography of the crude extracted biosurfactant revealed 3 major peaks with Rf of 0.89, 0.76 and 0.69 (F1-F3) respectively.

Introduction

In present, the production volume of surfactants steadily increases, belonging to the most important classes of industrial chemicals with a current total world production of about 10 million ton per year [1]. Surfactants can be used in a broad range of industrial applications, particularly the textile, paper and food processing industries, cosmetics, health care and agriculture, etc. However, the large majority of the currently used surfactants are synthesised by petroleum-based. These compounds are often toxic to the environment and may lead to significant ecological problems [2]. The aim of decreasing the amount of chemically-synthesised surfactant in food, pharmaceutical and household products are considered due to the increase of the environmental awareness [3]. Therefore, another class of surfactant is interested, biosurfactant, produce by microorganisms especially bacteria and yeasts. Most of biosurfactants are complex molecules, comprising different structures including glycolipids, lipopeptides, polysaccharide protein complex, fatty acids and phospholipids [4]. Some advantages of biosurfactant over synthetic ones such as biodegradability, low toxicity, ecological acceptability, ability to be produced from renewable and cheaper substrates [5, 6], specific activity at extreme temperature, pH and sanility [7]. However, biosurfactant have not been yet employed extensively in industry because of their high production costs. The development of improved technologies for reduced the production costs are necessary such as studied an optimal medium composition, methods to produce biosurfactant in high concentration and the production methods in bioreactor.

Pichia anomala PY1 is the newly isolated strain which can produce biosurfactant as indicated by LC-MS spectrum correspond to sophorolipid compound containing fatty acid of $[C22]_{Lactone}$ and $[C22{:}1]_{Lactone}$ [8]. From literature review has been described for yeast cultures with two carbon sources that the production was significantly higher than only one carbon source [9]. This strain is able to produce biosurfactant when grown in a modified medium containing both water-soluble and water-insoluble carbon sources: glucose and soy bean oil, respectively.

This study aims to develop the optimal medium composition leading to the maximal of biosurfactant production by *Pichia anomala* PY1 in shake flask. Furthermore, we investigated the parameters for culture optimization in small scale batch fermenter.

Materials and Methods

Microorganism: The strain used in this study was *Pichia anomala* PY1, isolated from Thai fermented food in central part of Thailand [10]. Yeast strain was maintained on yeast extract/ malt extract (YM) agar slant at 4 ºC and subcultured every month.

Culture medium and fermentation conditions:

Cultures were grown on a modified medium containing **:** KH_2PO_4 0.02%, $MgSO_4{\cdot}7H_2O$ 0.02% , NaNO3 0.35%**,** Yeast extract 0.35%, Glucose 5.33% and Soy bean oil 10.67% **.** The initial pH of the medium was adjusted to 5 and sterilized by autoclaving at 121 ºC for 20 min. The inoculum of *Pichia anomala* PY1 was prepared by transferring two loops of cells grown on YM plate to 250 ml Erlenmeyer flasks containing 50 ml of YM broth at pH 4.5. The seed culture was incubated in a rotary shaker 200 rpm at 30 ºC for 18 h and added to the fermentation medium at an 8% concentration (v/v).

Batch fermentations were performed in a 5-l laboratory scale fermenter (Eyela, model EPC-100) with a working volume of 2.5 l for 168 h. The operation conditions were as follows: initial pH 5;

temperature 30 ºC; agitation rate 400 rpm; aeration rate 1, 1.5 vvm. Samples were withdrawn for analyses the growth of culture and biosurfactant production during the fermentation.

Analytical methods:

*Surface activities.*Culture samples were centrifuged at 8,000 rpm for 20 min for cell removal and the cell-free broth was obtained to measure surface activity. Surface tensions were determined with a Krüss Tensiometer (model K6, Hamburg, Germany) using du Nouy ring method at room temperature. The critical micelle concentration (CMC) was determined by measuring the surface tension of serial dilution of the isolated biosurfactant dissolved in 50 mM Tris-HCl pH 8. The CMC value obtained from the plot between surface tension versus the logarithm of the concentration.

Isolation of biosurfactant. A 200 ml sample of fermentation broth was centrifuged at 4 ºC, 8000 rpm for 20 min to remove the microbial cells. The obtained supernatant was placed into a 500 ml separating funnel, and 2 ml hexane was added to remove fatty acids. The lower phase was extracted with an equal volume of ethyl acetate, two times, for complete recovery of glycolipids. The ethyl acetate was evaporated by roto-evaporator under vacuum at 37 ºC. The residue was washed with methanol and then dried in the centrivaporator to a contant weight.

Thin-Layer Chromatography. Silica gel (Merck) plates, 0.2 mm thick, were used. The following solvent system was used: Chloroform/methanol/water (65: 25:4, by volume). The components were detected by the iodine vapors.

Results and Discussion

Effects of carbon and nitrogen sources on biosurfactant production

From previous study revealed that the glucose and soy bean oil as carbon source, $NaNO_3$ and Yeast extract as nitrogen source were the effective substrates for growth and biosurfactant production by *P. anomala* PY1. This study started with the investigation of carbon to nitrogen (C/N) ratios in the shake flask at constant temperature 30 ºC with initial pH of 5.0 for 7 days. The best results were obtained at the C/N ratios of 16/0.7 (in %wt/wt) was giving minimum surface tension of 29.17 mN m^{-1} (Highest value of Δ surface tension at 28.23 mN m^{-1}) and oil displacement activity of 31.15 cm^2 (Fig1).

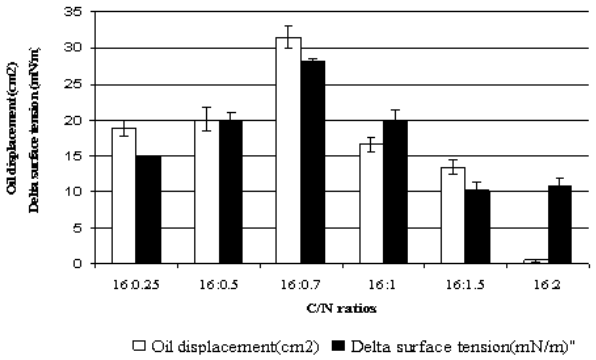

Fig 1. The effect of carbon to nitrogen (C/N) ratios on biosurfactant production with *P. anom*ala PY1.

Table 1 shows the effect of various C/N ratios on the final biomass yields and pH after cultivation for 7 days. Although the C/N ratios of 16/0.7 had reached highest activity in both surface tension reduction and oil displacement test, the biomass yield and pH of C/N 16/0.25-16/1 were slightly different.

Table 1: Effect of C/N ratios on biomass and final pH during biosurfactant production by *P. anomala* PY1

C/N ratios	Biomass(g/l)	pH
16:0.25	20.62 ± 1.22	7.74 ± 0.22
16:0.5	15.45 ± 0.56	7.83 ± 0.21
16:0.7	16.92 ± 0.86	7.56 ± 0.25
16:1	14.49 ± 0.63	7.05 ± 0.37
16:1.5	7.08 ± 0.57	3.71 ± 0.02
16:2	8.29 ± 0.92	3.66 ± 0.05

Biosurfactant production with batch fermentation

Biosurfactant production in batch-mode fermentor was performed using the optimized medium obtained from previous experiment with pH at 5 and 30 ºC during the cultivation time. However, foam formation was not a serious problem because soy bean oil can be used as both carbon source and antifoam agent After the end of cultivation, the batch cultured with the combination of aeration rate of 1.5 vvm and agitation rate 400 rpm produced biosurfactant up to 0.83 g/l, minimum surface tension of the medium was lowered from 50 mN/m to 29.16 mN/m and oil displacement activity of 43.37 cm^2 which higher than that obtained from the combination of aeration rate of 1 vvm and agitation rate 400 rpm. Fig 2. shows the biosurfactant production during the growth and production phase. The biosurfactant was extracellular production which produced from the stationary phase of cell growth and rapidly increased after 132 h and not growth associated.

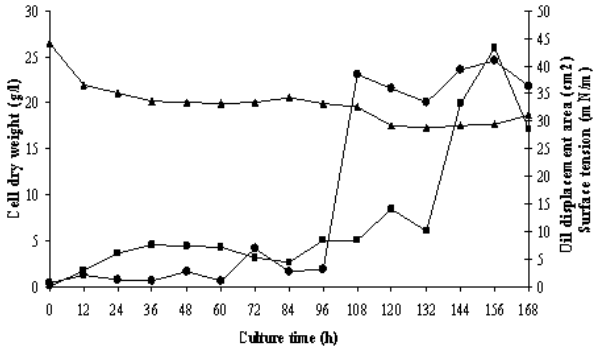

Fig 2. Time course of biosurfactant production by *P. anomala* PY1 in batch culture. Cells were cultured in a 5 l fermentor at aeration rate 1.5 vvm and agitation rate 400 rpm. (●) Cell dry weight (g/l); (■) Oil displacement area (cm^2); (▲) Surface tension (mN/m)

Isolated biosurfactant properties

Crude biosurfactant reduces the superficial air-water tension. This effect is proportional to surfactant dilution until this reaches the Critical micelle concentration (CMC), the value of the concentration that corresponds to the moment at which the biosurfactant molecules begin to form micelles [11]. Surface tensions (ST) versus serial dilutions of the crude biosurfactant dissolved in 50 mM Tris-HCl pH 8 were plotted as shown in Fig 3. The CMC appears as an intercept point in the surface tension and was found to be 162 mg/l and minimum surface tension of biosurfactant at CMC was found to be 27 mN/m and similar values were reported with sophorolipid produced from a corn-oil processing byproduct by *Candida bombicola* 22214, 150 mg/l [12]. The CMC values of isolated biosurfactant was higher than that obtained from the chemical surfactants such as Chemtec 307, Triton X-100 and Sodiumdodecyl sulfate; 2,042, 537, and 2,630 mg/l, respectively [8].

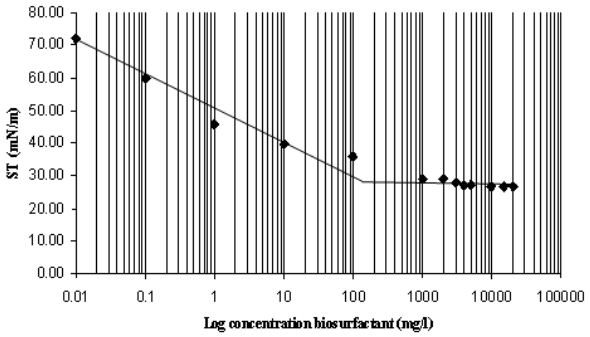

Fig 3. Surface tension versus serial dilutions of the crude biosurfactant produced by *Pichia anomala* PY1.

After 7 day of cultivation, the crude extract of biosurfactant was examined. It was analyzed by thin layer chromatography (TLC) and visualized with iodine vapor showing positive spots at R_f of 0.89, 0.76 and 0.69 (F1-F3), respectively.

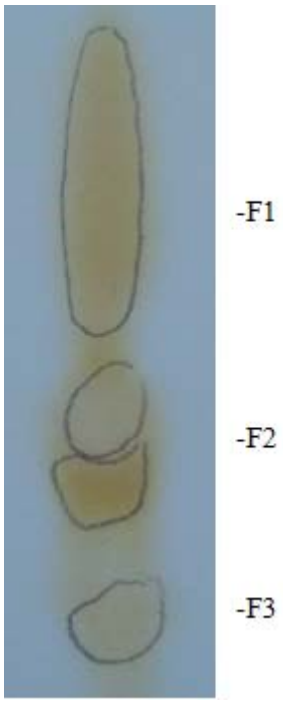

Fig 4. TLC profile of the crude extract biosurfactant from *P. anomala* PY1 when cultivated in modified medium. F1-F3 are positive spots with iodine vapor.

Conclusions

This work demonstrated that the biosurfactant of 0.82 g/l was produced by *P.anomala* PY1 when grown on glucose and soy bean oil as carbon sources at carbon to nitrogen (C/N) ratio of 16/0.7 with the combination of aeration rate of 1.5 vvm and agitation rate 400 rpm in batch fermentation. And these studies revealed the relationship between oxygen conditions and biosurfactant production in lab scale fermentor. The higher aeration rate where a further increase in dissolved oxygen resulted in an increase in product formation.

Acknowledgements

This work was supported by the Integration Project: Innovations for the improvement of Food Safety and Food Quality for New World Economy, The government Researh Budget of Thailand, and Chulalongkorn University.

References

[1] I. N. A. Van Bogaert, K. Saerens, C. De Muynck, D. Develter, W. Soetaert, E. J. Vandamme, *Appl. Microbiol. Biotechnol.* 76 (2007), 23-34.
[2] R. M. Mann, J. R. Bidwell, *Environ. Pollution*. 114 (2001), 195-205.
[3] M. Adamczak, W. Bednarski, *Biotechnol. Lett*. 22 (2000), 313-316.
[4] M. Nitschke, G. M. Pastore, *Bioresour. Technol*. 97 (2006), 336-341.
[5] J. D. Desai, I. M. Banat, *Microbiol. Mol. Biol. Rev*. 61 (1997), 47-64.

[6] R. S. Makkar, S. S. Cameotra, *A review J. Surf. Det.* 2 (1999), 237-241.
[7] M. Abouseoud, R. Maachi, A. Amrane, S. Boudergua, A. Nabi, *Desalination*. 223 (2008), 143-151.
[8] P. Ratchamontree, Effect of sugar supplementation on the production of biosurfactant by *Pichia anomala* PY1 and characterization there of. Master's Thesis, Chulalongkorn University, 2008.
[9] L. A. Sarubbo, C. B. B. Farias, G. M. C. Takaki, *Cur. Microbiol.* 54 (2007), 68-73
[10] J. Thaniyavarn, T. Chianguthai, P. Sangvanish, N. Roongsawang, K. Washio, M. Morikawa and S. Thaniyavarn, *Biosci. Biotechnol. Biochem*. 72 (2008), 2061-2068.
[11] M. Ron, E. Rosenberg, *Environ. Microbiol*. 3 (2001), 229-236.
[12] H. S. Kim, Y. B. Kim, B. S. Lee, E. K. Kim, *J. Microbiol. Biotechnol.* 15 (2005), 55-58.


PACCON
Pure and Applied Chemistry International Conference 2010
Industrial Chemistry and Innovation

Acid impregnation and steam explosion of oil palm frond for ethanol production

R. Nokkaew[2], V. Punsuvon[1,2*], P. Vaithanomsat[3] and T. Khunrong[2]

[1] Department of Chemistry, Faculty of Science, Kasetsart University, Jatuchak, Bangkok, Thailand 10900
[2] Center of Excellence-Oil Palm, Kasetsart University, Bangkok, Thailand 10900
[3]Kasetsart Agricultural and Agro-Industrial Product Improvement Institute, Kasetsart University, Bangkok, Thailand 10900

[*]E-mail: fscivit@ku.ac.th

Abstract: The pre-treatment of oil palm frond for ethanol production was studied using of acid-catalyzed steam explosion technique. Oil palm frond chips which impregnated in 0.14 M H_2SO_4 for one night was steamed at temperatures varying between 180 °C, 191 °C and 203 °C for 2 min., 3 min. and 5 min. The steam fiber was washed with hot water to yield a solution rich in hemicellulose-derived mono and oligosaccharides. The effects of these steam pre-treatment conditions were assessed by measuring monomers (glucose and xylose) and oligomer solubilization. Fibers under every condition were further hydrolysis by commercial enzyme. The results showed that the condition at 191 °C for 2 min. of explosion time gave the highest percentage of enzyme hydrolysis. The fiber obtained from this optimum condition was also further studied ethanol yield by separate hydrolysis and fermentation (SHF).

Introduction

Lignocellulosic material represents renewable resources for production of fuel ethanol from sugar. Among lignocellulosic materials, the use of agricultural residue is of particular interest because it has also the benefit of disposal of problematic solid wastes which usually do not have any economic alternative. The utilization of lignocellulosic materials in a bioconversion process requires a pre-treatment step in order to break down the various physical and chemical barriers that greatly inhibit their susceptibility to bioprocess such as enzymatic hydrolysis and fermentation. Pre-treatment, recognized from an economic point of view as a key step in the bioconversion process, must improve the formation of sugars, avoid the degradation or loss of carbohydrate, avoid the formation of inhibitory products to the subsequent hydrolysis and fermentation processes and, finally, be cost-effective. Among the different existing pre-treatment methods, steam explosion is one of the most commonly used for fractionation of biomass components. In steam explosion pre-treatment biomass is exposed to pressurized steam followed by rapid reduction in pressure. The treatment results in substantial breakdown of the lignocellulosic structure, hydrolysis of the hemicellulosic fraction, depolymerization of the lignin components and defibration. Therefore, the accessibility of the cellulose components to degradation by enzymes is greatly increased. Compared with alternative pre-treatment methods, the advantages of steam explosion include a significantly lower environmental impact, lower capital investment and less hazardous process chemicals (Ruiz, 2008).

The oil palm frond appears as wastes on trimming the oil palm tree. In Thailand, oil palm frond represents a very abundant, inexpensive and renewable source and its utilization has not been intensively studied. The increase of oil palm frond could cause pollution in the future thus the development of technology for value added product such as ethanol production of this biomass is urgently needed to study.

The objective of this work is to evaluate the effect of temperature and exploded time of steam explosion pre-treatment of acid impregnated oil palm frond chip, including the susceptibility of enzymatic hydrolysis of the cellulose residue and the hemicellulosic-sugar recoveries.

Materials and Methods

Raw material

Oil palm fronds were cut into pieces with approximate 25 x 25 x 5 mm. These chips were used to steam explosion pre-treatment.

Steam explosion pre-treatment

Oil palm fronds chips were impregnated in 0.14 M H_2SO_4 for one night. The chips were steam in a steam explosion of Nitto Koatsu Company Japan that it showed in figure 1. An amount of 150 g of soak chips were placed in 2.5 L batch reactor. Saturated steam from the boiler was then allowed to enter the reactor and heat the material to the desired temperature (180, 191and203°C) for 2, 3 and 5 min. and then the reactor was suddenly depressurized. The exploded material was filtered for liquid and solid recovery. The solid fraction was water-washed and used for enzymatic hydrolysis. The water soluble fraction (hydrolysate) was analyzed sugar and sugar-degradation products compositions.

Figure 1. Steam explosion apparatus.

Enzymatic hydrolysis

The washed water-insoluble residue of pre-treated oil palm frond was further enzymetically hydrolysed by a cellulolytic complex (celluclast 1.5 L). Cellulose enzyme loading was 74 FPU/g substrate. Fungal β-glucossidase (Novozyme 188) was used to supplement the β-glucosidase activity with an enzyme loading of 365 international unit (IU)/ml substrate. Enzymatic hydrolysis was performed in 0.05 M sodium citrate buffer (pH 4.8) at 50°C on a shaker at 150 rpm for 72 h and at 2% (w/v) pretreated material concentration. Sample was taken at 72 h for glucose concentration determination.

Analytical methods

Composition of raw material was determined according to standard Tappi method. Glucose and xylose content was determined after a two-steps acid hydrolysis procedure to fractionate the fibber. A first step mixed 72% H_2SO_4 and fibers for 60 min. In a second step, the hydrolysis reaction by autoclaved at 121°C for 1 h which it was diluted to 4% H_2SO_4. Sugars composition analyzed by high performance liquid chromatography (HPLC: shimazu) with RID detector. An AMINEX HPX87P carbohydrate analysis column (Bio-Rad, Hercules, CA) operating at 85°C ,deionized water as a mobile-phase (0.6 ml/min). Furfural and 5-hydroxy methyl furfural (HMF) content were analysed by HPLC with Bio-Rad HPX-87H column, operating at 65°C with 0.005N H_2SO_4 at flow rate of 0.6 ml/min.

Results and Discussion

The oil palm frond consisted of 57.11% glucose and 16.37% lignin. This result indicated that high glucose content in oil palm frond was appropriate for ethanol production.

Acid impregnation and steam explosion pre-treatment

The raw material was impregnated in 0.14 M H_2SO for one night after that it was subjected to steam explosion pre-treatment at 180, 191and 203°C for 2, 3 and 5 min. The result of fiber and hydrolysate obtained after pre-treatment shown in figure 2. Table 1 showed the total gravimetric recovery yield (solid remaining after pre-treatment divided by original oven dried weight) and the composition of glucose and lignin content at the different conditions of pre-treatment.

Figure 2. (a) Oil palm fronds fibers and (b) hydrolysate that they were pre-treatment with steam explosion process.

Table 1: Total gravimetric recovery yield (%) and composition of water-insoluble fiber resulting from steam explosion pre-treatment

Temperature (°C)	Time (min.)	Yield (%)	Glucose (%)	Lignin (%)
180	2	44.35	69.54	29.33
180	3	43.62	60.58	29.23
180	5	40.35	65.13	31.40
191	2	40.09	62.57	31.20
191	3	40.25	63.03	32.67
191	5	35.39	59.15	35.47
203	2	38.91	57.42	30.92
203	3	35.91	58.22	31.10
203	5	31.77	57.92	41.89

The percentage yield ranged between 31 and 44%. As expected, a decrease of yield was detected as the pre-treatment temperature increased. At the same temperature of pre-treatment, the yield was decreased as the pre-treatment time increased too. This was mainly attributed to the decrease of hemicellulose fraction which contented in oil palm frond raw material. For the cellulose as glucose content in solid, it decreased as pre-treatment temperature increased. And at the same temperature of pre-treatment, glucose content was decreased when pre-treatment time increased too. The overall yield of glucose content was in the range 57-69%. The content of lignin of the solid pretreated residue showed increase as the pre-treatment temperature increased. The yield of lignin content was in the range 29-41%

Hydrolysate composition

Sugars (glucose as well as hemicellulose-derived sugars) were recovered mainly in the water-soluble fraction. The amount of monosaccharides was detected as a result of the effect of acid impregnation because acid would increase the hydrolysis reaction of hemicellulose during steam explosion pre-treatment. In addition during steam explosion not only to produce sugars but also the inhibitors for yeast fermentation

such as furfural and hydroxyl methylfurfural (HMF) could produce too. The result of the composition of the hydrolysate was shown in Table 2.

Table 2: Sugars and toxics composition of the hydrolysate from steam explosion conditions (g/100 g raw material).

Condition	Glucose	Xylose	Gatactose	Arabinose	Manose	HMF	Furfural
180°, 2 min	2.46	10.01	1.49	2.74	0.97	0.08	0.38
180°, 3 min	2.40	10.45	1.30	2.42	0.97	0.09	0.60
180°, 5 min	2.98	8.91	1.14	2.29	0.79	0.21	1.31
191°, 2 min	3.19	8.60	1.08	2.10	0.84	0.12	0.75
191°, 3 min	3.48	9.45	1.34	2.48	1.10	0.18	1.20
191°, 5 min	4.40	7.47	1.24	2.07	1.13	0.31	1.60
203°, 2 min	3.54	9.83	1.42	2.43	1.10	0.19	0.73
203°, 3 min	3.56	7.90	1.17	2.25	1.02	0.27	1.38
203°, 5 min	6.05	6.10	0.95	1.67	0.92	0.52	1.81

The results from table 2 showed that sugars contained in hydrolysate were glucose, xylose, galactose, arabinose and manose. Xylose was the main product in hydrolyzed from hemicellulose composition by acid used for impregnation. HMF and furfural were products of hexose and pentose degradation, respectively. Both compounds were presented in trace amounts when compared with the amount of sugars. These compounds were necessary to remove before fermentation because these compounds were act as inhibitors for yeast growth.

Enzymatic hydrolysis of pretreated fiber

The water insoluble pretreated residue was submitted to enzymatic hydrolysis by a cellulose complex (celluclast 1.5L) supplemented with β-glucosidase (Novozyme 188). The concentration of glucose was determined every 4 h during a 72 h-period of enzymatic action. Table 3 shows the enzymatic hydrolysis yields, determined from the glucose concentration in solution divided by glucose concentration in pretreated fiber and multiple with one hundred.

Table 3: Enzymatic hydrolysis of pretreated fiber from steam explosion pre-treatment at different conditions.

Condition	%enzyme hydrolysis at the time (h)					
	4	8	12	24	48	72
Raw material	13.83	17.5	17.98	18.61	18.69	19.74
180°, 2 min	19.32	20.05	23.68	31.85	31.94	34.75
180°, 3 min	14.08	18.24	21.54	26.59	30.79	3.43
180°, 5 min	14.49	17.97	21.00	24.58	28.09	29.21
191°, 2 min	17.45	23.24	29.16	37.32	43.23	48.14
191°, 3 min	20.83	25.12	28.39	33.95	35.18	37.82
191°, 5 min	16.62	21.15	25.00	27.33	30.94	32.71
203°, 2 min	16.60	21.15	24.99	27.33	30.94	32.71
203°, 3 min	17.40	22.60	25.63	31.07	34.49	36.24
203°, 5 min	21.77	24.03	27.64	41.87	46.31	45.81

From table 3, enzymatic hydrolysis was also carried out on raw material not subjected to steam pre-treatment. Hydrolysis yield at 72 h of enzymatic action was 19.74%. But enzymatic hydrolysis yields were improved by steam explosion pre-treatment at any conditions. The maximum hydrolysis yield at 72 h (48.14%) was found in the water in soluble fiber obtained at 191°C, 2 min of pre-treatment condition. In addition the table 3 showed the percentage of enzyme hydrolysis increased with the time of hydrolysis increase too.

Separate hydrolysis and fermentation (SHF)

The glucose solution from enzyme hydrolysis at 191°C, 2 min. of pre-treatment condition was selected to further study on fermentation. The glucose solution was concentrated to 50 g/L and fermented with saccharomyces cerevisiae yeast at 30°C of temperature and pH 5.5. The concentration of ethanol was determined every 12 h during 72 h-period of fermentation time by Gas Chromatography (GC). The result of ethanol yield (%) was shown in table 4.

Table 4: Ethanol yield from separate hydrolysis and fermentation (SHF)

Fermentation time (h)	**Ethanol concentration (g/L)**	**Ethanol yield (%)**
12	6.20	24.32
24	11.70	45.92
36	17.19	67.42
48	19.34	75.86
60	19.36	75.92
72	19.37	75.98

From table 4, the ethanol yield increased sine 0-36 h of fermentation time and after that the ethanol yield began constant from 48-72 h of fermentation time. The highest ethanol yield of fermentation at 72 h was 75.98%.

Conclusions

Acid impregnation followed steam explosion pre-treatment is an interesting option for using oil palm frond in ethanol production scheme. The optimize steam explosion pre-treatment at 191°C, 2 min improves enzymatic hydrolysis yield from 19.74 to 48.14% (unpretreated material to pretreated material) and renders a relatively concentrated glucose broth suitable for fermentation. In the water soluble filtrate, the highest concentration of sugar in monomeric form along with a low presence of inhibitors is found for an acid impregnation and steam explosion pre-treatment. This is the benefic of this technique because the global process economy and the utilization of the feedstock will be improved by considering the monomeric form of sugar (mostly xylose) in the hydrolysate for fermentation to ethanol production.

Acknowledgement

The work was support by Kasetsart Research and Development Institute, Kasetsart University.

References

[1] Ruiz., C. Ca1ra., P.Manzanares.,M. Ballesteros., and E.Castro. Enzymeand Microbial Technology (2008). pp. 160-166.
[2] M. Ballesterus., J.M. Oliva., M.J. Negro., P.Manzanares., and I. Ballesteros. Process Biochemistry (2004). pp. 1843-1848.

Study of azo disperse dyeing on polyester/elastane blend

L. Chuaybamrung[1], P. Suwanruji[1*] and J. Suesat[2]

[1]Department of Chemistry, Faculty of Science, Kasetsart University, Jatuchak, Bangkok, Thailand 10900
[2] Department of Textile Science, Faculty of Agro-Industry, Kasetsart University, Jatuchak, Bangkok, Thailand 10900

[*] E-Mail: fscipjs@ku.ac.th,

Abstract: Selected monoazo disperse dyes, either commercial or synthesized dyes, were used in this study. The commercial dyes were purified by extraction with refluxing monochlorobenzene. The synthesized dyes were characterized by thin layer chromatography (TLC), ^{1}H NMR and elemental analysis. The disperse dyes were applied on polyester and elastane fabrics, having a ratio of 9:1 as a typical polyester/elastane blend, in the same dyebath by high temperature (HT) exhaust dyeing. The dye concentrations of 0.1, 0.5 and 2% on weight of fabric (%owf) and dyeing times of 0, 30, and 60 min were used. The extracted dye concentrations from each dyed fabric were used to evaluate the partition ratios and the migration of the disperse dyes in polyester and elastane fabrics before the reduction clearing process. From partition ratios, the amount of disperse dyes was more on elastane than polyester fiber. Secondary forces formed between disperse dye molecules and fibers caused different substituent groups, such as cyano and nitro on a diazo component of the disperse dyes to give different degrees of dye uptake on each fiber. The amounts of most disperse dyes on polyester increased as the dyeing times increased because the fiber was more accessible. Conversely, the lower glass transition temperature of elastane provided easy access for the dyes at the beginning but then the dyes could also easily migrate out of the fiber as the dyeing time increased. These results will be compared with the outcomes after reduction clearing.

Introduction

Elastane fibers or Spandex are also familiar under their trade name, Lycra. Elastane is a synthetic fiber known for its extraordinary elasticity. The fiber is a segment polymer comprised of at least 85% segmented polyurethane. The structure is built from alternating hard segments, which contain ureylene and urethane groups, and soft segments that are macroglycols, either a polyester (PET) or polyether [1-4]. In the textile industry, PET/elastane blends have gained importance because of their functionality in the areas that require a high degree of elasticity, for example, in tights, sportswear and swimwear [4-6]. Elastane is typically used only in fairly small amounts in blends for added comfort and freedom of movement.

Disperse dyes are used for dyeing PET/elastane blends [7-9]. However, disperse dyes have a very high affinity for elastane fiber and stain them heavily when the blends are dyed. This problem also causes the blends to have poor wet fastness [10-12]. Therefore, azo disperse dyes with different substituents were used in this work for dyeing PET and elastane fabrics in the same dyebath. Then, the distribution and migration of the dyes between both fabrics during the dyeing under high temperature were investigated. The results of the present study will be useful to compare with the results obtained from the fabrics after the reduction clearing process.

Materials and Methods

1. Materials

Elastane fabrics (weft-knitted fabrics, 70 denier) were scoured in a bath containing 1g/l non-ionic surfactant and 1g/l sodium carbonate at 70°C for 15 min. The liquor ratio used was 30:1. The scoured fabric was then rinsed with water and air-dried.

Polyester fabrics (weft-knitted filament fabrics, 70 denier) were scoured at 80°C for 15 min in a bath containing 1g/l non-ionic surfactant and acetic acid with a pH of 5. The liquor ratio was 30:1. The scoured PET fabric was rinsed with water and air-dried.

C.I. Disperse Blue 165 (B1)

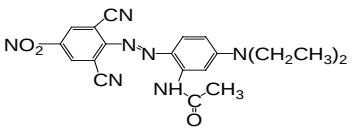

C.I. Disperse Blue 284 (B2)

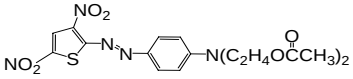

C.I. Disperse Red 82 (R1)

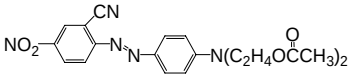

R2

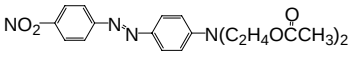

R3

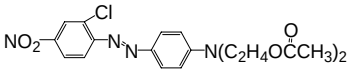

Figure 1. Structures of azo disperse dyes

Five azo disperse dyes were used in this study as shown in Figure 1. Three commercial disperse dyes, B1, B2 and R1, were purified by extraction with refluxing monochlorobenzene. The other two disperse dyes, R2 and R3, were systhesized and characterized by TLC, melting point, ^{1}H NMR and

elemental analysis. The eluent system for TLC was ethyl acetate:tolulene (7:3). Melting points were determined using a FISHER-JOHNS melting point apparatus. ^{1}H NMR spectra were obtained from a VARIAN^{unity} INOVA 400 MHz. Elemental analysis was performed by a CHNS-932 LEGO elemental analyzer.

2. Dye synthesis

The diazo components of R2 and R3 were 4-nitro aniline and 2-chloro-4-nitro aniline, respectively. Each diazo component was dissolved in a mixture of acetic acid and propionic acid (43:7). The diazotisation was performed by the addition of nitrosyl sulfuric acid to the diazo component solution at 0-5°C. N,N-bis-β-acetoxyethyl aniline used as the coupling component for both R2 and R3 was prepared by dissolving it in an acetone/water mixture. Then the prepared diazo component was added dropwise to the coupling component at 0-5°C. The reaction was stirred continuously for 2 h. The dye precipitate was filtered out and dried. After that, the dye was purified by recrystallization in 2-methoxyethanol. Table 1 showed the results from characterization of R2 and R3.

Table 1: Characterization of the synthesis dyes

Dye	R_f	m.p. (°C)	Elemental analysis (%) Cal/Found		
			C	H	N
R2	0.76	140	57.96 59.96	5.35 5.68	13.52 13.42
R3	0.76	123	53.52 55.21	4.72 5.00	12.48 12.31

Dye	^{1}H NMR (in DMSO) δ/ppm
R2	1.99(6H, s, CH_3); 3.77(4H, t, CH_2); 4.23(4H, t,CH_2); 7.07(2H, d, J=9.32, ArCH); 7.87(2H, d, J=9.22, ArCH); 7.96(2H, d, J=9.11, ArCH); 8.38(2H, d, J=9.12, ArCH)
R3	1.99(6H, s, CH_3); 3.78(4H, t, CH_2); 4.24(4H, t,CH_2); 7.01(2H, d, J=9.38, ArCH); 7.77(2H, d, J=8.92, ArCH); 7.86(2H, d, J=9.28, ArCH); 8.25(2H, d, J=8.94, ArCH); 8.44(1H, s, ArCH)

3. Dye application

Two pieces of fabric, 4.5g of pre-scoured PET and 0.5g of pre-scoured elastane, were dyed in the same dyebath at 130°C. The liquor ratio used was 30:1. The disperse dyes were applied on the fabrics at three different depth of shades, 0.1, 0.5 and 2% owf, and different dyeing times, 0, 30 and 60 min. Figure 2 showed the dyeing profile of disperse dyes.

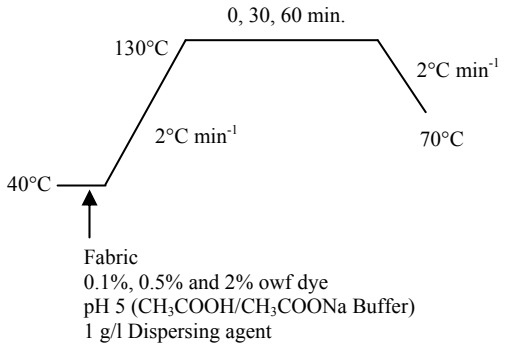

Figure 2. Dyeing profile

4. The amount of disperse dye on fabrics

The dyes were extracted from PET and elastane fabrics separately by refluxing monochlorobenzene until the fabrics became colorless. The amount of dyes was determined by UV-VIS spectrophotometer.

The percentage of dye exhaustion (%) was calculated using equation (1).

$$\%\,E = \frac{D_f}{D_b} \times 100 \qquad (1)$$

Where D_f = the total amount of dye extracted from both PET and elastane fabrics, mg

D_b = the initial amount of dye in the dyebath, mg

Partition ratio (P.R.) was calculated from equation (2).

$$P.R. = \frac{D_P}{(D_E \times 9)} \qquad (2)$$

Where D_P = the amount of dye extracted from PET fabric, mg

D_E = the amount of dye extracted from elastane fabric, mg

Results and Discussion

1. Migration of the disperse dyes

The amount of disperse dyes extracted from dyed PET and elastane fabrics at different dyeing time, 0, 30 and 60 min, was shown in Figure 3. As the dyeing time increased from 0 to 60 min, the amount of most dyes on PET increased whereas those on elastane decreased. The longer the dyeing time, the more accessible the PET fabric was. On the other hand, elastane fabric which had lower glass transition temperature (T_g) than PET provided easy access for the disperse dyes at the initial dyeing time. The T_g of elastane and PET fabrics used in this study are -23°C and 80°C, respectively. As the dyeing time increased, the dye molecules can also easily migrate out of the fiber. The results of 0.1 and 0.5% owf were similar. However, the results from a 2% applied dye concentration on both substrates were anomalous. It is possible that dye is being destroyed (hydrolysed) in

the dyebath. Therefore, this work will focuses on a 0.1 and 0.5% owf dyeing.

Five disperse dyes gave different dye uptakes on PET and elastane fabrics. The order of the dye uptake on PET and elastane were B1>B2>R2>R3>R1 and R2>R3>B2>B1>R1, respectively. The secondary forces, such as dipole-dipole or H-bonding, formed between the dyes and the fabrics depended on the substituted groups on both diazo and coupling components.

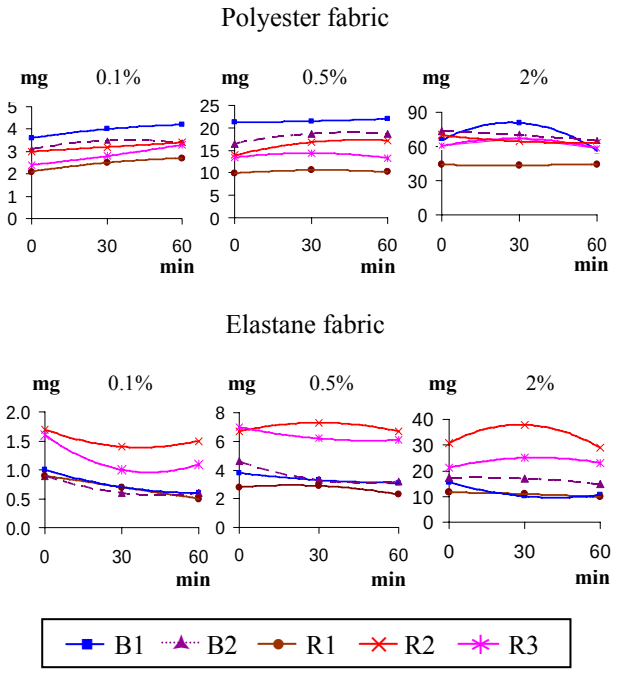

Figure 3. Migration of disperse dyes on PET and elastane fabrics

2. Dye exhaustion

The percentages of dye exhaustion at 0.1 and 0.5% owf were shown in Table 2. The amount of dyes on the fabrics almost reached an equilibrium at 30 min. After dyeing for 60 min, many cases showed that the exhaustion decreased as compared to those at 30 min. As the depth of shade increased five times from 0.1 to 0.5% owf, the exhaustion values of most dyes were slightly higher except R1. The exhaustion of R1 was only 50-60% so that the dye uptake of R1 was lowest on both fabrics as shown in Figure 3.

Table 2: The percentages of exhaustion of the azo disperse dyes

Dye	0.1%			0.5%		
	0 m	30 m	60 m	0 m	30 m	60 m
B1	92.0	94.0	96.0	97.2	98.0	99.6
B2	80.0	82.0	80.0	84.4	88.0	87.6
R1	60.0	62.0	62.0	50.8	54.0	50.0
R2	94.0	92.0	98.0	86.4	96.4	95.6
R3	80.0	76.0	88.0	81.6	82.4	77.6

3. Partition ratio

All partition ratios in Table 3 were less than one which indicated that if the same masses of PET and elastane fabrics were used, the disperse dyes preferred to go into elastane. For instance, 0.1% owf B1 at 0 min had a partition ratio of 0.4 which indicated that the ratio of dye in PET to elastane was 0.4 to 1. In other words, it was 2.5 times the amount of dye in elastane than in PET. By increasing the dyeing time, the partition ratios were also increased. The disperse dyes initially favored the elastane fabric but redistributed after 30 to 60 min to PET. Considering the results of 0.1% owf B1, the partition ratio was only 0.4 at 0 min and then increased to 0.78 at 60 min. The heavier shade also gave a higher partition ratio than the paler shade.

Table 3: Partition ratio of the azo disperse dyes

Dye	0.1%			0.5%		
	0 m	30 m	60 m	0 m	30 m	60 m
B1	0.40	0.63	0.78	0.76	0.80	0.84
B2	0.38	0.65	0.63	0.40	0.63	0.65
R1	0.26	0.38	0.58	0.39	0.41	0.49
R2	0.20	0.25	0.25	0.25	0.26	0.29
R3	0.17	0.31	0.33	0.21	0.26	0.24

Conclusions

Dyeing a 9:1 ratio of polyester and elastane fabrics at 130°C with selected monoazo disperse dyes showed that the partition of dye on elastane portion was higher than on PET portion. At 0.1 and 0.5% owf, the amount of most dyes on PET increased whereas those on elastane decreased when the dyeing time increased. The substituents on both diazo and coupling components effected the attractive forces between the disperse dyes and the fabrics. The results showed that B1 and B2 had good affinity on PET but did have poor affinity on elastane. Consequently, B1 and B2 were the best options for dyeing PET/elastane blends from this part of the study. However, the behavior of the dyes after reduction clearing needs to be studied. For good wet fastness of PET/elastane blends, the disperse dyes should be effectively removed from elastane and also still have good affinity on PET in the reduction clearing process.

Acknowledgment

The authors would like to thank the Thailand Research Fund (MRG 5180086) for financial support of this research. Special thanks is given to Senior Research Scholars (RTA 5080005), and the National Center of Excellence for Petroleum, Petrochemicals, and Advanced Materials (NCE-PPAM).

References

[1] H.F. Qian and X.Y. Song, *Dyes Pigm*. **74** (2007), pp. 672-676.

[2] H.F. Qian and X.Y. Song, *Color Technol*. **125 (**2009**)**, pp. 146-150.

[3] J.I. Kroschwitz, *Polymer: Fibers and Textiles, A Compendium*, A Wiley-Interscience, Canada (1990), pp. 305-311.

[4] M.L. Joseph, *Introductory Textile Science*, 2nd ed., Holt, Rinehaet and Winston, Inc., USA (1966), pp. 170-174.

[5] M. Humphries, *Fabric Reference*, 3rd ed., Pearson Prentice Hall, New Jersey (2004), pp. 69-71.

[6] B.P. Corbman, *Textiles: Fiber to fabric*, 6th ed., McGraw-Hill Book Company, Singapore (1983), pp. 429-430.

[7] J.J. Pizzuto, *Fabric Science*, 7th ed., Fairchild Publications, Inc., New York (1999), p. 77.

[8] A. Ujhelyiová, E. Bolhová, K. Vaľková, A. Marcinčin, *Dyeability of blend polypropylene/polyester fibers with disperse dyes*, *Vlákna a textil* **12** (2) (2005), pp. 48-50.

[9] K. Lacasse and W. Baumann, *Textile Chemicals Environmental Data and Facts*, Springer, Germany (2004), p. 200.

[10] H.F. Qian and X.Y. Song, *Color Technol*. **125 (**2009**)**, pp. 141-145.

[11] J.H. Choi and A.D Towns, *Color Technol*. **117 (**2001**)**, pp. 127-133.

[12] http://www.alaincharles.com/pdf/Articles/Aftex/aftex203.pdf

Platinum recovering from gold industrial wastewater via solvent extraction

N. Chankong*, W. Patthaveekongka

Department of Chemical Engineering, Faculty of Engineering and Industrial Technology, Silpakorn University, Nakhon Pathom, Thailand 73000.

* E-mail: yo_natt@hotmail.com

Abstract: Platinum, a precious metal was found in gold industrial wastewater. The set of experimental was taken to investigate the optimum condition of solvent extraction via large hydrocarbon molecule extractant (D2EHPA, Lix84I, TBP, Aliquat 336) and stripping to recover Pt from wastewater. This work reports the effect of different extractants and conditions consist of concentration of extractant, pH of feed solution, rate of agitation, type and concentration of stripping agent to the recovering of Pt compared to other metals. The wastewater from gold process was extraction by various extractants in kerosene for different conditions. The sample from aqueous phase before and after extraction was taken to measured amount of Pt, Pd, Au, Ag, Fe and Cu by ICP-AES. The recovered platinum was calculated by mass balance and compared to the other metals extraction. The highest extraction percentage of Pt for D2EHPA, Lix84I, TBP and Aliquat 336 were 93, 62, 27 and 90 % respectively. D2EHPA had the highest extraction percentage but poor selectivity adverse from Aliquat 336. For stripping, 0.3 mol/l of nitric acid solution can get maximum recovery of 78% platinum ion from organic phase.

Introduction

Platinum is a member of platinum group metals (PGM) that consist of ruthenium, rhodium, palladium, osmium, iridium, and platinum. They are rare elements and platinum is the most common occurring of about 10^{-6} %, whereas the others have abundances of the order of 10^{-7} % of the earth's crust. PGM are commonly associated with major base metals as well as gold and silver. PGM together with gold and silver form the family of precious metals [1]. In the past few decades, precious metals have found new applications outside the jewellery and decorative industries due to its excellent physical and chemical properties. The most common use of platinum is as catalyst in chemical reactions. The important application of it is in automobiles as a catalytic converter. It is also used in the petroleum cracking process and used as a hydrogenation catalyst. With the physico chemical and electronic properties platinum is used as an alloying agent for various metal products, including fine wires, noncorrosive laboratory containers, medical instruments, airplane engine part, jewelry, dental equipment, electrical contacts, and thermocouples[2][3]. The traditional process to recovery platinum from acidic solution involves series of selective precipitation that have to use a lot of chemicals, time and equipments. Solvent extraction is a technique that has the potential to be used in industrial-scaled. The extractive separation via large hydrocarbon molecule extractants are used to recover precious metals in acidic solution with better selectivity than older process.

In the gold industrial wastewater, platinum was found with number of metals[4]. To recover the valuable Pt, reactive extraction was used in this work and the optimum conditions of separation was studied.

Materials and Methods

Reagents: Waste water of gold process was taken from Precious Classic Co., Ltd. Bangkok, Thailand. Di (2-ethylhexyl) phosphoric acid (D2EHPA, Fluka), Lix84I (Cognis), tributyl phosphate (TBP, Merck) and Aliquat336 (Sigma-Aldrich) as extractants. Kerosene was used as organic diluent for each extractant. All other chemicals used in this work were reagent grade.

Metal Extraction: The metal extraction experiments were carried out in batch experiments at room temperature. Equal volumes, 50 ml, of aqueous and organic solution were mixed with magnetic-stirrer (VELP SCIENTIFICA model AREX) at 700 rpm for 30 minutes. After phase separation in separatory funnel, metal concentrations in the aqueous phase were determined by ICP-OES (VARIAN model VISTA-MPX CCD Simultaneous), amount of metal in organic phase was calculated by mass balance.

Metal Stripping: Metal stripping tests were carried out in batch experiments at room temperature. Firstly, 50 ml of wastewater were contacted with 50 ml of organic solution containing extractant dissolved in kerosene for 30 minutes in order to load the metal on organic phase. Then, immediately after separating both phases, 50 ml of strippant reagent were added to the rich metal organic phase and were agitated vigorously for 30 minutes. The metal concentrations after the extraction and stripping steps in aqueous phase were determined by ICP-OES.

Table 1: Metals in gold industrial wastewater

Metal	App. Conc.(ppm)
Pt	20
Pd	20
Au	5
Ag	1
Fe	2
Cu	300

Results and Discussion

Effect of type and concentration of extractant:

The wastewater in this study has pH about 2 and approximated concentration of metals as show in table 1.

From the experiments of extraction via D2EHPA, Lix84I, TBP and Aliquat336 in various concentrations in kerosene as organic phase. The highest extraction percentage of Pt for D2EHPA, Lix84I, TBP and Aliquat336 were 93, 62, 27 and 83 % respectively as can be seen in Figure 1.

The percentage of extracted metals in experiments on range of extractant concentration for D2EHPA, Lix84I, TBP and Aliquat 336 are shown in Figure 2 to 5.

The extraction of metals increase as increase of concentration of D2EHPA for this range. D2EHPA could nearly complete extract Pt but poor in selectivity as can be seen in Figure 2.

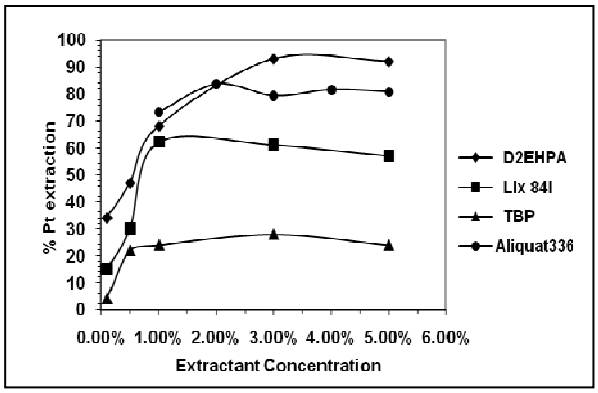

Figure 1. Pt extraction percentage on various concentrations of extractans

Lix 84I had relative high Pt extraction percentage with good selectivity to separate Pt from other metals (Figure 3) with concentration of 1.0 %(v/v) but extraction of Cu in the same condition was extracted up to 15%. Because relative high concentration of Cu in initial wastewater, amount of Cu that was loaded in organic after extraction was too high.

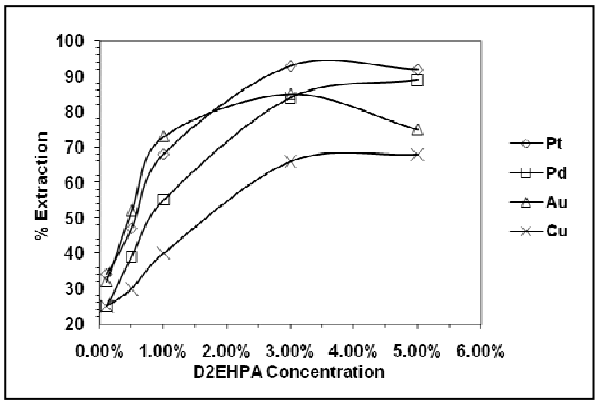

Figure 2. % metal extraction in various conc D2EHPA

The maximum Pt extraction of TBP was the lowest, compared to other extractants in this work, with maximum Pt extraction was only 27% at concentration of 3%(v/v) and had poor selectivity.

Aliquat336 had 83% Pt extraction at 2%(v/v) concentration that quite high and with good separation from Cu. Therefore Aliquate336 was selected for further study in effect of pH.

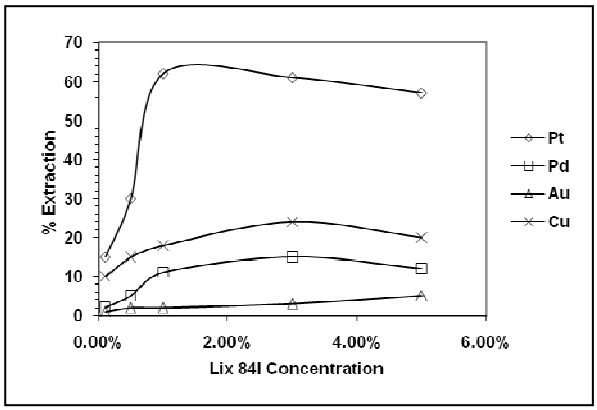

Figure 3. % metal extraction in various conc Lix84I

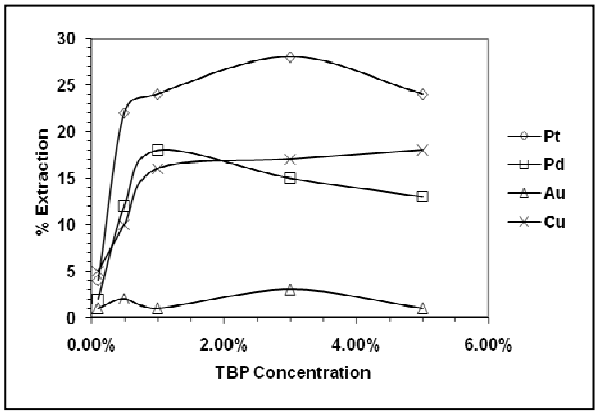

Figure 4. % metal extraction in various conc TBP

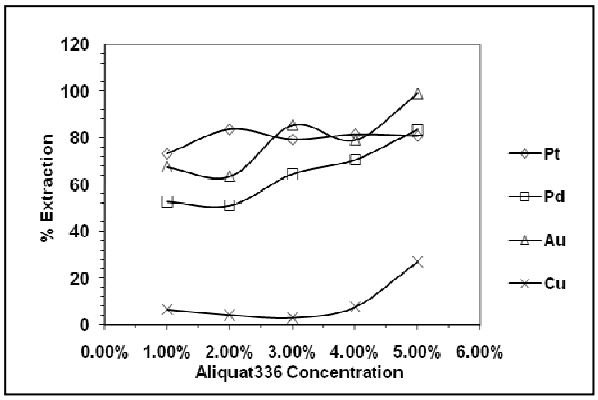

Figure 5. % metal extraction in various conc Aliquat336

Effect of pH to Aliquat336:

Wastewater that was adjusted pH by ammonia and HCl solution was extracted with Aliquat336. We found that low pH favored extraction of Cu. Platinum can be extracted about 80% in pH 1-6 but when adjusted pH above 5, precipitate was observed and solid could interfere the extraction and concentration analysis. Thus pH 4 was the optimum condition to separate Pt from Pd and Cu.

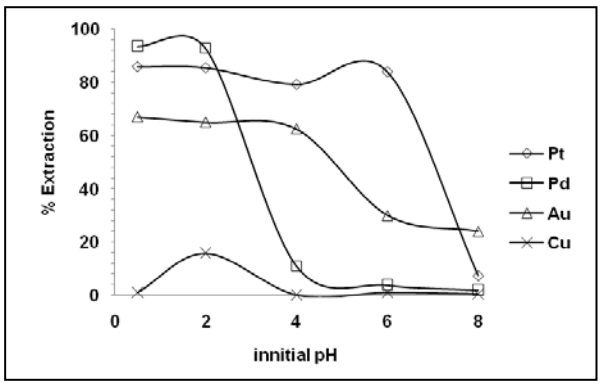

Figure 6. % metal extracted by Aliquat336 in different pH

Stripping:

The loaded organic phase from extraction in pH4 was used in this study. 4M ammonia solution as Stripping agent was used to strip loaded organic phase two time. We found it can recovery Pt from organic phase 69 and 12% in first and second contact respectively. Aqueous solution from second stripping had Pt in metal weight fraction of 0.86.

Conclusions

TBP didn't be selected because the lowest Pt extraction only 27% at the maximum and had poor selectivity.

The highest Pt extraction are 93 % in experiment of 3 %(v/v) D2EHPA but it has poor selectivity and Cu that was the major impurity was extracted in very high amount (65%). For Lix 84I, Cu was extracted up to 17%. Therefore when considered in the same way D2EHPA and Lix 84I were not suitable for separate Pt from Au Pd and Cu.

Aliquat 336 has a good selectivity but for completed Pt separation, the separation during stripping are needed.

For the conditions - feed solution's pH is 4.0, A/O ratio equal to 1:1 by vol. and agitation rate is 700 rpm in Pt extraction from gold industrial wastewater by Aliquat336 can recovery Pt up to 80% . For stripping by two stage of 4 M ammonia solution can recovery 80% of platinum ion from organic phase.

We found that satisfied recovery process could be achieved in lab test. The optimum conditions of extraction and stripping should be applied to use in industrial unit.

Acknowledgement

This work was supported by TRF-MAG project of the Thailand Research Fund. We are grateful to Precious classic Co, Ltd. and Bangchak Petroleum Public Co., Ltd. for kindly donating kerosene.

References

[1] F.A. Cotton, and G. Wilkinson, *Advanced Inorganic Chemistry*, John Wiley & Sons, New York (1980).

[2] R. E Krebs, *Platinum The History and Use of our Earth's Chemical Elements*, Greenwood Press, (1998).

[3] R.V. Parish, *The Metallic Elements,* Longman, London, (1977).

[4] W. Patthaveekongka, N. Vijitchalermpong and U. Pancharoen, *Korean J. Chem. En.* **6** (2003), pp.1092 – 1096.

The optimal conditions of gel electrolyte for valve-regulated lead-acid battery

T.Tantichanakul[1*], N.Tantavichet[1,2]

[1]Department of Chemical Technology, Faculty of Science, Chulalongkorn University, Bangkok, Thailand, 10330
[2]Fuels Research Center, Center of Excellence for Petroleum, Petrochemicals, and Advanced Materials, Chulalongkorn University, Bangkok, Thailand, 10330

*E-mail: T.titipon@hotmail.com

Abstract: Valve regulated lead acid batteries with gel electrolyte (Gel-VRLA Battery) have proven their excellent performance due to no leakage of acid mist, long service life, high reliability under deep-discharge cycles and low corrosion problem. In addition, they are maintenance-free since they do not need to add water during their service life as a result of oxygen-recombination cycle. Optimal conditions for gel electrolyte preparation for VRLA battery have been investigated by mixing fumed silica, sulfuric acid and sodium sulphate using a controlled high-speed mixer. The results show that silica concentration, acid concentration, mixing speed and mixing time affect the gelling time, but sodium sulfate does not. Besides the basis ingredients for gel formation, several additives such as vaniline and poly (methyl methacrylate) have been added and their effect has been studied. The preparing conditions that yield more than 3 hours of gelling time were selected to fill into the 4 Ah VRLA batteries to test the battery performance under 100% Depth of discharge. The results show that although the conventional Liquid-VRLA battery initially has higher discharge capacity than does Gel-VRLA battery, its performance declines gradually with the discharge cycle and eventually has the discharge capacity lower than does the Gel-VRLA battery after about 5 discharge cycles. Without additional additive, the gel electrolyte prepared with 5%w/v fume silica was found to yield the highest performance. An addition of additive was found to affect the gelling process, gel electrolyte properties and battery performance.

Introduction

Compared to the conventional lead-acid batteries, valve-regulated lead-acid (VRLA) battery offers many advantages such as its design to prevent electrolyte loss through evaporation which eliminates the need for addition of water, preventing stratification and providing high power density. One major component in the VRLA battery that influences these benefits is an immobilizing electrolyte. Nowadays, there are two types of the immobilizing electrolytes commercially available:

(i) a starved sulfuric acid solution in absorptive glass-mat (AGM) separator, called AGM battery.
(ii) a gelled electrolyte, which is prepared by mixing of sulfuric acid solution and silicon dioxide (SiO_2) to get the thixotropic structure, called gel VRLA battery.

The gel VRLA battery has many advantages over AGM battery. Such as ability to use in any orientations, no leakage of sulfuric electrolyte, maintenance-free operations, long service life and slower self-discharge [1-5].

Nomally, the fumed silica is used as a gelling agent, where most of its isolated surface silanols link to form weak hydrogen bonds with each other. This gives a three-dimensional network gel structure. The properties of this three-dimensional silica gelled electrolyte significantly affect the processability during battery assembly, capacity and cycle life of gel-VRLA battery [1, 6]. During the gel formation, gelling time is an important parameter that affects the electrolyte processability during battery assembly (filling and formation of electrolyte) [7]. Then, it should be considered as a crucial factor along the performance of the gel-VRLA battery.

The aim of this work is to study the factors influencing the gelling time and the performance of Gel-VRLA battery.

Materials and Methods

Electrolyte preparation: Gel electrolyte (GE) was prepared by mixing fumed silica, sulfuric acid and sodium sulphate using a controlled high-speed mixer. Various ratio of 2-6 % weight by volume (%w/v) fumed silica, 40-70 %w/v sulfuric acid and 1.5 – 15 %w/v sodium sulphate were used in this study. The prepared electrolyte was then agitated at 1500-3000 rpm between 10-25 minutes. After agitation, the mixed suspension was measured the gelling time by measuring the penetration of 3 mm dimeter (0.3 g) lead ball every 30 minutes. The depth of the falling lead ball was monitored and an acceptable gel texture was defined when the penetrated depth was constant.

Battery testing: For performance test of the batteries, small sized VRLA battery modules rated 12 V/4Ah were employed. Gel electrolytes for filling in batteries were preparation by mixing various amounts of fumed silica, sulfuric acid using a controlled high-speed mixer at 2000 rpm for 10 minutes. All prepared gel electrolytes filled in the batteries were included 13.25g/l sodium sulphate to improve the battery rechargeability [7].

Prepared electrolyte was filled in the battery using a vacuum system to improve the gel distribution. A cycling performance tests under 100% depth of

discharge (DOD). Details of the cyclic test alogrithm are presented in Table 1.

Table1: Cyclic test for Liquid-VRLA Battery and Gel-VRLA Battery (12V/4Ah) at 100% DOD at 10-h rate

Step	Test algorithm
1	Charge (0.8A/14.1 V/7 hr)
2	Rest (5 h)
3	Discharge (0.4 A/10.5 V)
4	Charge(0.8A/14.1 V/11 hr)
5	Cycle from step 3 to step 4 for seven times
6	Rest (24 hr)
7	Go to step 3 to step 5

Results and Discussion

Factors affecting gelling time:

Concentration of fumed silica: The results of penetration depth of the lead ball at different times in the electrolyte prepared using difference %si are shown in figure 1. Figure 1 shows that the concentration of fumed silica (as a gelling agent) affects the penetration depth. Where high concentrations of fumed silica lead to shorter penetration depth.

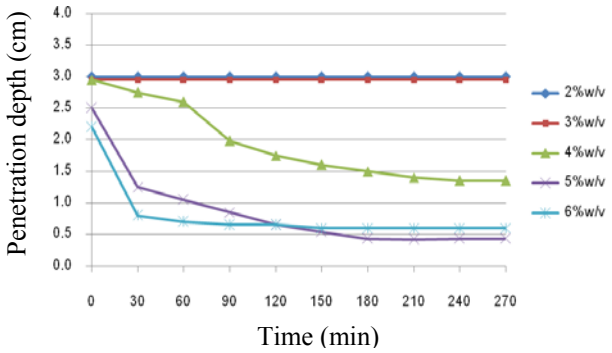

Figure 1. Penetration depth of lead balls in gel electrolytes containing 2 to 6%w/v fumed silica, 65%w/v sulfuric acid at 3000 rpm for 10 minutes

Table 2 shows gelling times of prepared gel electrolyte containing different amounts of fumed silica. As expected, concentration of fumed silica was found to affect the gelling time. The gelling time was shorter for high concentration of fumed silica. For the electrolytes containing 2% and 3% w/v fumed silica, their gelling times were over than 4 hour.

Table 2: Gelling time of gel electrolytes containing 2 to 6%w/v fumed silica, 65%w/v sulfuric acid after stirring at 3000 rpm 10 minutes

Concentration of fumed silica (%w/v)	Gelling time (hr : min)
2	>4
3	>4
4	4
5	3
6	2:30

Concentration of sulfuric acid: The result shows that the concentration of sulfuric acid has influence, but not as significant as the concentration of the fumed silica; on the penetration depth of the lead balls. Figure 2 shows the penetration depth of the lead balls at different times in the 40 to 70%w/v sulfulric acid, 6%w/v fumed silica after stirring at 3000 rpm 10 min.

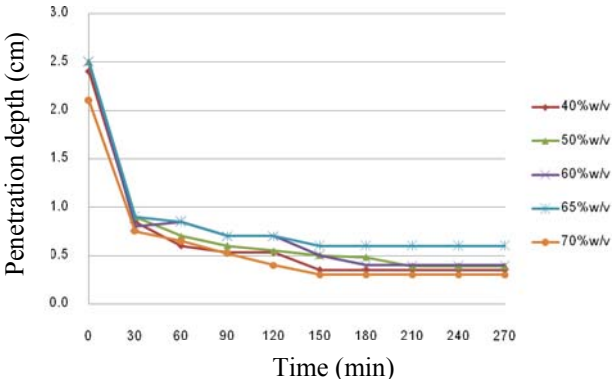

Figure 2. Penetration depth of lead balls in gel electrolytes containing 40 to 70%w/v sulfuric acid, 6%w/v fumed silica after stirring at 3000 rpm for 10 minutes

Table 3 shows gelling times of prepared gel electrolyte containing different amounts of sulfuric acid. The results show that a higher concentration of sulfuric acid reduces the gelling time.

Table 3: Gelling time of gel electrolytes containing 40 to 70%w/v sulfuric acid, 6%w/v fumed silica after stirring at 3000 rpm 10 minutes

Concentration of sulfuric acid(%w/v)	Gelling time (hr:min)
40	3:30
50	3:30
60	3
65	3
70	3

Concentration of sodium sulphate: The adventage to using sodium sulphate as an additive in electrolyte is to improve the battery rechargeability at low state of charge (SOC) [7]. As shown in Figure 3, the concentration of sodium sulphate used in this study

(1.5-15% w/v) does not affect the penetration depth and gelling time.

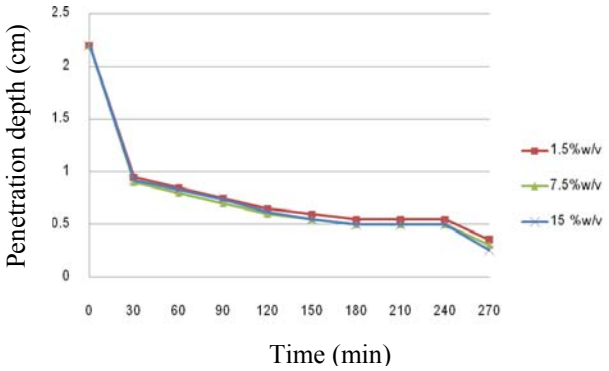

Figure 3. Penetration depth of lead balls in gel electrolytes containing 1.5 to 15%w/v sodium sulphate, 5%w/v fumed silica and 65%w/v sulfuric acid after stirring at 3000 rpm for 10 minutes

Mixing speed: Figure 4 shows relationship between penetration depth and time gel electrolyte containing 5%w/v fumed silica, 65%w/v sulfuric acid at after the prepare electrolytes were stirred at different speeds for 10 minutes. The result shows that an increase in a mixing speed decreases the penetration depth and longer gelling time. For the mixing speed at 1500 rpm, the penetration depth is constant indicating gelling time is longer than 4 hours.

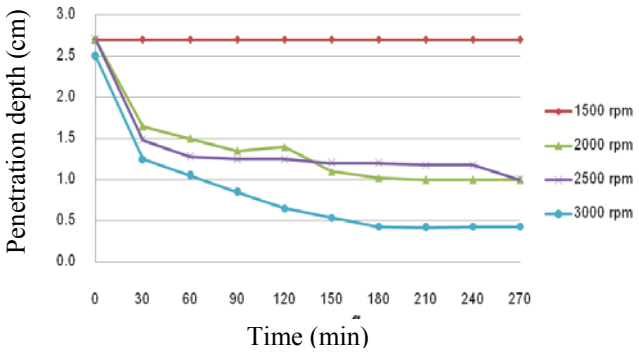

Figure. 4 Penetration depth of lead balls in gel electrolytes containing 5%w/v fumed silica, 65%w/v sulfuric acid after stirring at 1500 to 3000 rpm for 10 minutes

The results shown in table 4 show fumed silica in electrolytes became more homogeneous when a higher mixing speed was used

Table 4: Gelling time of gel electrolytes containing 5%w/v fumed silica, 65%w/v sulfuric acid after stirring at 1500 to 3000 rpm for 10 minutes

Mixing speed (rpm)	Gelling time (hr:min)
1500	>4
2000	3:30
2500	3
3000	3

Mixing time: Figure 5 shows the penetration depth of gel electrolytes containing 5%w/v fumed silica, 65%w/v sulfuric acid at after stirring for 10 to 25 minutes. The results show that an increase in a mixing time decreases a penetration depth after stirring for 20 minutes sine the gelling process improves with in the mixing time.

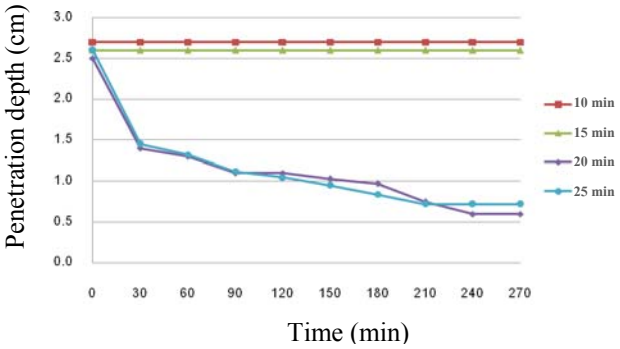

Figure 5. Penetration depth of lead balls in gel electrolytes containing 5%w/v fumed silica, 65%w/v sulfuric acid after stirring at 1500 rpm after stirring for 10 to 25 minutes

Table 5 shows that increase the mixing time shorten the gelling time. The gel electrolytes having the short mixing times (10 and 15 minutes), their gelling times were long than 4 hours.

Table 5: Gelling time of gel electrolytes containing 5%w/v fumed silica, 65%w/v sulfuric acid after stirring at 1500 rpm for 10 to 25 minutes

Mixing time (min)	Gelling time (hr:min)
10	>4
15	>4
20	4
25	3:30

Additives:Two additives were selected to added in the electrolyte in this study. Vanilline was reported to inhibite the hydrogen evolution which can occure during overcharged process, while poly (methyl methacrylate) was reported to increase the ionic conducting of electrolyte [8,9].

.

Table 6: Gelling time of gel electrolytes containing 4%w/v fumed silica, 56.84%w/v sulfuric acid after stirring at 2000 rpm 10 minutes

Concentration of Vaniline(%w/v)	Gelling time (hr:min)
0	>4
0.01	>4
0.03	>4
0.05	2:30
0.1	1

Table 6. shows gelling time at 0.01-0.05%w/v vanilline, 4%w/v fumed silica, 56.84%w/v sulfuric acid after stirring at 2000 rpm 10 minutes. We found that the concentration of vanilline added affected the gelling time. Where we use a high concentrations of vanilline decrease the gelling time. For the electrolyte containing 0.01% and 0.03% w/v vanilline, their gelling time were over than 5 hour. Additive is poly (methyl methacrylate) not effect gelling time

Battery testing: To test the performance of batteries, gel electrolyte with 3-5% w/v fumed silica (0% w/v fumed silica indicates conventional liquid electrolyte) was added to VRLA batteries (12v/4Ah). The batteries were test using a cyclic performance at 10 hours rate discharge 100% DOD (shown in table 1).

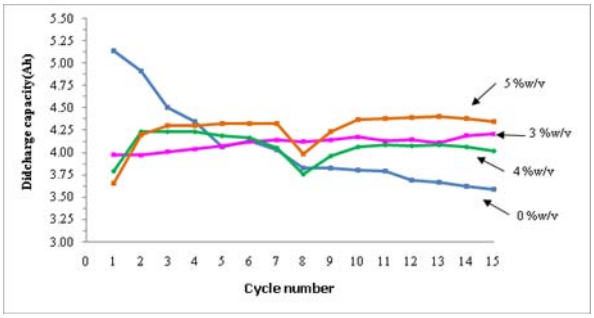

Figure 6. Discharge capacity of VRLA battery (12v/4Ah) for different concentrations of fumed silica gelling agent during 15 testing cycles under 100% DOD at 10-h rate.

A discharge capacity results are shown in figure 6. The results show that although the conventional liquid-VRLA battery initially has higher discharge capacity than do gel-VRLA batteries, its performance declines gradually with the discharge cycle and eventually has the discharge capacity lower than do the gel-VRLA batteries after about 5 discharge cycles. The gel electrolyte prepared with 5%w/v fume silica was found to yield the highest performance.

Table 7: Performance test results of 12V/4Ah batteries having different electrolyte formulations

Electrolyte formulation	**Initial capacity (Ah)**	**Final capacity (Ah)**	**Average efficient (%)**
Liquid-VRLA battery	5.138	3.589	94.09
Gel-VRLA battery			
5%si	3.653	4.348	89.18
4%si	3.797	4.021	92.61
3%si	3.974	4.206	97.08
4%si 0.005%vanilline	3.518	4.016	94.45
5%si 0.5 %PMMA	2.956	3.448	85.92

The results of the initial capacity, the final capacity and the averge efficient after 15 cycles (%dischange/change) are summarize in table 7. The gel electrolytes contained more fumed silica have lower initial capacity and average efficient. Gel-VRLA battery prepared with 3%w/v fumed silica was found to have highest average efficient. Additives added in gel electrolyte is decrease battery capacities but vaniline was found to improve efficient of the gel-VRLA battery slightly.

Conclusions

The silica concentration, acid concentration, mixing speed,mixing time and vanilline additive were found to influence the gelling time, but sodium sulfate was not. The results show that although the conventional liquid-VRLA battery initially has higher discharge capacity than does gel-VRLA battery, its performance declines gradually with the discharge cycle and eventually has the discharge capacity lower than do the gel-VRLA batteries after about 5 discharge cycles. Without additional additive, the gel electrolyte prepared with 5%w/v fume silica was found to yield the highest final carpacity, whereas gel-VRLA battery prepared with 3%w/v fumed silica was found to yield the highest average efficient. Path additives used in this study decreases battery performance but vaniline slightly improve efficient of the gel-VRLA battery.

Acknowledgement

The authors are gratefully acknowledge the funding support from Center of Excellence for Petroleum, Petrochemical and Advanced Materials, Thailand Research Fund and N.V. Battery Ltd., Part.

References

[1] Lambert, D.W.H.; Greenwood, P.H.J.; Reed, M.c., *J.Power Sources* 107 **2002** 173-179
[2] Culpin, B.; Peters, K., J.Power Sources 158 **2006** 1077-1083.
[3] Tang, Z.; Wang, J.; Mao, X.-X.; Shao, H.; Chen, Q.; Xu, Z.; Zhang, J . *J. Power Sources*. **2007**, 168, 49–57.
[4] Tang, Z.; Wang, J.-M.; Mao, X.-X.; Chen, Q.-Q.; Shen. C.; Zhang, J.-Q. *J.Appl. Electrochem*. **2007** , *37*, 1163-1169
[5] Guo, Y.; Hu, J.; Huang, M. J. Power Sources. **2006**, 158, 991–996.
[6] Chen, M.Q.; Chen, H.Y.; Shu, D.; Li, A.J.; Finlow, D.E. *J. Power Sources*. **2008**, 181, 161–171.
[7] Hern´andez, J.C.; Soria, M.L.; Gonz´alez, M.; Garc´ıa-Quismondo, E.; Mu˜noz, A.; Trinidad, F. *J. Power Sources*. **2006**, 161, 851–863.
8] Dietz, H.; Hoogestraat, G.; Laibach, S.; Von Borstel. D.;\ Wiesener, k. *J. Power Sources*. **1995**, 53, 359-365.
[9] Rajiv. K,; Sekhon. S.S. *J Appl Electrochem*. **2009**, 39, 439–445

Build-up characteristics and fastness properties of azo disperse dyes on poly(lactic acid) and poly(ethylene terephthalate) fibers

T. Mungmeechai[1], J. Suesat[2*] and P. Suwanruji[1]

[1]Department of Chemistry, Faculty of Science, Kasetsart University, Jatuchak, Bangkok, Thailand 10900
[2] Department of Textile Science, Faculty of Agro-Industry, Kasetsart University, Jatuchak, Bangkok, Thailand 10900

[*] E-mail: Jantip.s.@ku.ac.th

Abstract: A series of azo disperse dyes was synthesized and their structures were confirmed by thin layer chromatography, melting point, ^{1}H NMR and elemental analysis. The dyes were dyed onto the fabrics derived from PET and PLA fibers. The dyeing properties of the dyes on both fibers were also studied. The dyes exhibited a high degree of exhaustion on the fibers. The higher % exhaustion was observed on PLA fiber. In addition the K/S values of the dyed PLA fiber were higher but λ_{max} was lower than the dyed PET fiber. Build-up properties of the dyes on PLA were different from those on PET. Most of the dyes exhibited lower build-up on PLA. A larger difference of build-up properties among the dyes used on PLA may be due to a relatively lower dye-fiber affinity related to types of substituted groups on the dye molecules as compared with PET. The study on fastness properties of the dyes showed that the dyes PLA had an inferior heat and light fastness to the dyed PET. The lower heat fastness of the dyes on PLA may be explained by a lower affinity of the dyes toward PLA fiber. Also, the higher UV transmittance of PLA impaired the light fastness of the dyes.

Introduction

Poly(ethylene terephthalate) (PET) fiber is the major synthetic fiber used in textile industry. However, its manufacture from petroleum-based resources is not sustainable. For this matter, a natural resource-based polyester, poly(lactic acid) (PLA), has attracted great attention as a more environmentally friendly polyester for textiles. The technical properties of PLA fiber are nearly similar to PET fiber. PET and PLA fibers are disperse dyeable [1-3]. The disperse dyeing conditions of PET and PLA are different. PET is conventionally dyed at 130°C while PLA must be dyed at lower temperature, generally at 110°C for 30 minutes. The visual shade of the disperse dyes obtained on PLA differed from that of PET. Lighter and brighter shade was observed on PLA as compared to PET [1-3].

In this work, the dyeing and fastness properties of the azo disperse dyes having different substituted groups on PET and PLA fabrics were studied. The build-up characteristics of the dyes on the two fabrics were investigated.

Materials and Methods

Materials

2,4-dinitro aniline laboratory grade purchased from ACROS ORGANICS was used as diazo components. The coupling components were N,N-diethyl aniline, N,N-bis-β-acetoxyethyl aniline, N,N-diethyl-m-toluidine, and N,N-bis-β-acetoxyethyl-m-toluidine laboratory grade purchased from ACROS ORGANICS. The 30 Ne. single-jersey knitted fabrics derived from PET and PLA fibers were used.

Synthesis of Azo Disperse Dyes

A series of azo disperse dyes was synthesized using 2,4-dinitro aniline as diazo component. The coupling components were N,N-diethyl aniline, N,N-bis-β-acetoxyethyl aniline, N,N-diethyl-m-toluidine, and N,N-bis-β-acetoxyethyl-m-toluidine. Diazotization was performed by adding nitrosyl sulfuric acid to the solution of the diazo component. The solution was stirred and the temperature was kept in the range of 0-5°C. The solution of the coupling components was prepared separately by dissolving the coupling component in acetone/water mixture. The coupling reaction was performed by slow addition of the diazonium salt to the coupling solution at 0-5°C and stirring about 2 hours. After that, the dye was filtered out and then washed with distilled water. The dyes were purified by recrystallizating in 2-methoxyethanol and the purity of the synthesized dyes was analyzed by TLC**,** melting points were determined using FISHER-JOHNS melting point apparatus. ^{1}H NMR spectra were obtained from a VARIAN^{unity} INOVA 400 MHz, while UV-VIS absorption spectra were measured on a Spectronic G5. Elemental analysis was performed using CHNS-932 LEGO elemental analyzer.

Dyeing of the Synthesized Dyes onto Polyester Fabrics

The dyes were applied onto PET and PLA fabrics at 0.2% owf depth of shade. The 1g/l Sera Sperse (Dystar) was used as a disperseing agent. The pH of the dyebath was adjusted to 5 using acetic acid/ sodium acetate buffer solution. The dyeing was carried out at 110°C and130°C for PLA and PET, respectively. After

that, the dyed fabrics were rinsed with water. The subsequent reduction clearing of the dyed fabrics was performed in a bath containing 2g/l sodium dithionite and 2g/l sodium carbonate at liquor ratio of 10:1. The reduction clearing of dyed PLA and PET fabrics were carried out for 15 minutes at 60 and 70°C, respectively.

Measurement of the Degree of Exhaustion and the Visual Color Yield of the Dye on Polyester Fabric

The visual color yield of the dyed fabrics was assessed in terms of K/S values using a Macbeth Color-Eye 7000 spectrophotometer. The degree of exhaustion of the dyes onto the polyester fabrics was determined by dissolution and dilution the dyebath with acetone. The absorbance of the dye solution was measured using a UV-visible spectrophotometer [1,2]. The exhaustion percentage was calculated using the following equation.

$$\%E = \left(\frac{A_o - A_1}{A_o}\right) \times 100$$

Where % E is the exhaustion percentage, A_o and A_1 is the absorbance of dyes in original dyeing bath and the residual dyeing bath, respectively.

Study of the Build-Up Properties of the Dye on Polyester fabrics

The dyes were applied onto PET and PLA fabrics at 0.5, 1, 2 and 4 % owf depths of shade. The K/S values of the dyed fabrics were measured and the build-up curves of the dyes were created by plotting the graph between K/S values and the depth of shade applied.

Fastness Properties of the Dyed Polyester fabrics

The PET and PLA fabrics were dyed to the same visual color yield (K/S 10). The color fastnesses to light and dry heat of the dyed PET and PLA fabrics were then determined according to ISO 105-B02:1994(E) and ISO 105-P01:2006(E) (150°C), respectively.

Results and Discussion

Synthesis and Characterization

The chemical structures of the synthesized dyes depicts in Table 1. The purity of the synthesized dyes and chemical structure were confirmed using melting point, ^{1}H NMR and elemental analysis. The results are shown in Table 2.

Table 1: Chemical structure of the synthesized dyes

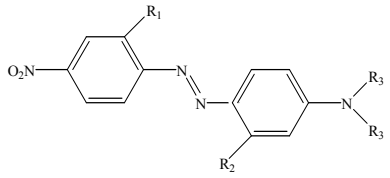

Dye	R_1	R_2	R_3
1	NO_2	H	C_2H_5
2	NO_2	H	$C_2H_4OCOCH_3$
3	NO_2	CH_3	C_2H_5
4	NO_2	CH_3	$C_2H_4OCOCH_3$

Dyeing Properties of the Synthesized Dye on Polyester Fabrics

The results in Table 3 indicated that all of the azo disperse dyes showed good exhaustion level on the two polyester fabrics. At about the same degree of exhaustion, most dyes exhibited higher K/S values on PLA indicating a deeper shade obtained on PLA as compared with PET. Dyes 1. and 3. having stronger electron-donating power on R_3 groups (C_2H_5) showed higher K/S values on both PET and PLA fabrics. The λ_{max} of all dyes on PET were longer (bathochromic shift) than the corresponding PLA. In addition, lighter and brighter shade obtained on PLA. On both fabrics, the dyes having stronger electron-donating power on R_2 and R_3groups (CH_3 and C_2H_5, respectively) exhibited longer λ_{max}.

Table 2: Characterization result of the synthesized dyes

Dye	M.p (°C)	Elemental analysis (%) Cal/Found			^{1}H NMR (in DMSO) δ/ppm
		C	H	N	
1	155-158	55.97 54.21	4.99 4.85	20.40 19.79	1.17(6H, t, CH_3); 3.53(4H, q, CH_2); 6.88(2H, , J=9.44, ArCH); 7.77(1H, d, J=9.34, ArCH); 7.91(2H, d, J=9.01, ArCH); 8.50(2H, d, J=8.99, ArCH); 8.83(1H, s, ArCH)
2	115-118	52.29 51.45	4.61 4.47	15.24 15.34	1.99(6H, s, CH_3); 3.80(4H, t, CH_2);4.24(4H, t, CH_2); 7.04(2H, d, J=9.31, ArCH); 7.80(1H, d, J=9.06, ArCH); 7.92(2H, d, J=8.96, ArCH); 8.54(2H, d, J=8.91, ArCH); 8.88(1H, s, ArCH)
3	139-143	57.14 55.66	5.36 5.13	19.60 19.80	1.17(6H, t, CH_3); 2.07(4H, q, CH_2);2.58(3H, s, $ArCH_3$); 6.74-6.68(2H, m, ArCH); 7.64(1H, d, J=9.30, ArCH); 7.93(1H, d, J=9.01, ArCH); 8.48(2H, d, J=9.00, ArCH); 8.80(1H, s, ArCH)
4	174-176	53.28 53.34	4.90 4.84	14.79 14.79	1.99(6H, s, CH_3); 2.61(3H, s, $ArCH_3$); 3.79(4H, t, CH_2); 4.24(4H, t, CH_2); 6.86(2H, d, J=9.38, ArCH); 7.62(1H, d, J=9.09, ArCH); 7.94(1H, d, J=8.97, ArCH); 8.52(2H, d, J=8.97, ArCH); 8.84(1H, s, ArCH)

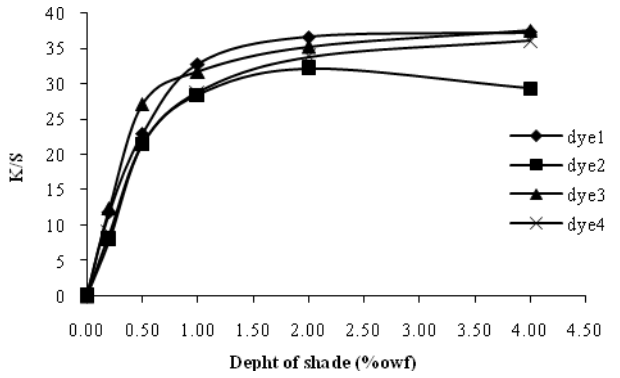

Figure 1. Build-up curve of the dyes on PET fabric

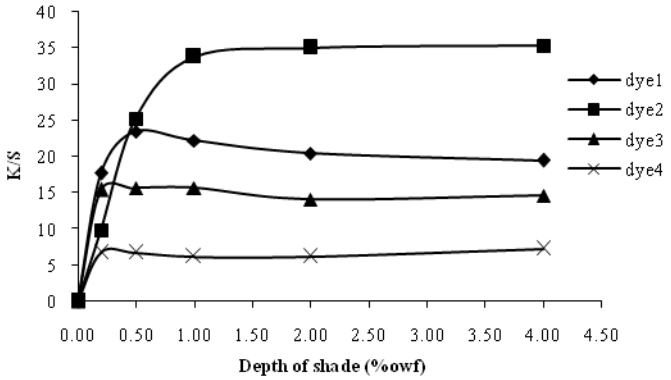

Figure 2. Build-up curve of the dyes on PLA fabric

Figures 1. and 2. showed that build-up properties of the dyes on PLA were different from those on PET. Most of the dyes exhibited lower build-up on PLA. A larger difference of build-up characteristics among the dyes on PLA may be due to a relatively lower dye-fiber affinity relating to types of the substituted groups on the dye molecules as compared with PET.

Fastness Properties of the Dyed Polyester Fabrics

Table 4 indicates the light and heat fastness properties of the dyes on the polyester fabrics. The dyed PLA exhibited slightly lower light fastness properties as compared with the dyed PET. This was presumed to be due to the greater transmittance of PLA in the ultraviolet range compared to PET [1, 2, 4]. The dyes having stronger electron-withdrawing R_3 group ($C_2H_4OCOCH_3$) showed better light fastness on PLA However, all the dyes exhibited the same level of light fastness on PET. Heat fastness of the dyed on PLA tended to be lower than that of the dyed PET. The dyes having R_3 group as $C_2H_4OCOCH_3$ showed better heat fastness on PLA as compared with those dyes having R_3 group as C_2H_5. This might be explained by the presence of stronger electron-donating C_2H_5 group on R_3 of dye 2.

Conclusions

A series of azo disperse dyes was synthesized. Dyeing properties of the synthesized dyes on PET and PLA were different. The dyes exhibited bathochromic shift when being dyed onto PET as compared with PLA. As a result, the shade difference was observed on the dyed PET and PLA fabrics. All of the dyes showed good exhaustion on PLA and PET but higher K/S was obtained on PLA, indicating a deeper shade on the fiber. A larger difference of build-up properties among the dyes used on PLA may be due to a relatively lower dye-fiber affinity related to types of the substituted groups on the dye molecules as compared with PET. The study on fastness properties of the dyes showed that the dyed PLA had an inferior heat and light fastness to the dyed PET. The lower heat fastness of the dyes on PLA may be explained by a lower affinity of the dyes toward PLA fiber. Also, the higher UV transmittance of PLA impaired the light fastness of the dyes as compared to PET.

Acknowledgement

A great thankfulness to The Thailand Research Fund and Office of The Higher Education Commission, for financial support throughout this research. Special thanks is given to Senior Research Scholars (RTA 508005) and The National Center of Excellence for Petroleum, Petrochemicals and Advanced Materials (NCE-PPAM).

References

[1] J.H. Choi, M.H. Kim, J.S. Park, J.M. Jeon, D.O. Kim, A.J. Towns, *J. Fibers and Polymers*. **8** (2007), pp. 37-42.

[2] J.H. Choi, W.Y. Seo, *J. Fibers and Polymers*. **7** (2006), pp. 270-275.

[3] S.M. Burkinshaw, D.S. Jeong, *J. Dyes and Pigments*. **77** (2008),pp. 180-190.

[4] S.D. Kim, E. J. Park, *J. Fibers and Polymers*. **2** (2001),pp. 159-163.

Table 3: Dyeing Properties of The Dyes on PET and PLA fabric at 0.2% owf

Dye	On PET			On PLA		
	%Exhaustion	K/S	λ_{max}(nm)	%Exhaustion	K/S	λ_{max} (nm)
1	96.43	11.94	550	99.30	17.67	530
2	91.55	7.97	520	98.30	9.82	490
3	98.48	12.46	550	99.12	15.41	540
4	98.27	8.93	520	99.10	6.78	510

Table 4: Light and Heat Fastness of Dyed PET and PLA fabric at (K/S 10)

Dye	Light fastness		Heat fastness (150°C)			
	Color change		On PET		On PLA	
	PET	PLA	Staining to nylon	Staining to polyester	Staining to nylon	Staining to polyester
1	4-5	4	4-5	4	3-4	3-4
2	4-5	4-5	4-5	4-5	4-5	4-5
3	4-5	4	4-5	4-5	3-4	3-4
4	4-5	-	4-5	4-5	-	-

Effects of relative humidity on performance of pt/zeolite-chitosan membrane in pem fuel cell

A. Angkatreerat[1,2] and K. Soontarapa[2,3]*

[1]Program of Petrochemistry and Polymer Science, Faculty of Science, Chulalongkorn University, Patumwan, Bangkok, Thailand
[2]Center of Excellence for Petroleum, Petrochemicals, and Advanced Materials, Chulalongkorn University, Patumwan, Bangkok, Thailand
[3]Fuel Research Center, Department of Chemical Technology, Faculty of Science, Chulalongkorn University, Patumwan, Bangkok, Thailand

*E-mail: khantong@sc.chula.ac.th

Abstract: This research studied the effects of relative humidity on performance of Pt/zeolite-chitosan membrane in PEM fuel cell. The studied membranes were uncrosslinked chitosan, uncrosslinked chitosan-zeolite, crosslinked chitosan, crosslinked chitosan-zeolite, doped crosslinked chitosan and doped crosslinked chitosan-zeolite membrane. Zeolite A contents were in the range of 10 – 30% by weight of chitosan. It was found that the ion exchange capacity; %water uptake and proton conductivity was increased with zeolite contents however the tensile strength was decreased. The fully hydrated proton conductivities in planar view at 60°C of 30% zeolite of uncrosslinked, crosslinked, and doped crosslinked chitosan-zeolite membranes were 0.021±0.003, 0.043±0.006, and 0.123±0.024 S/cm, respectively. After Pt plating by electroless technique at 60°C for 90 min, they were increased to 0.130±0.002, 0.160±0.002, and 0.040±0.010 S/cm, respectively. However, those in cross section view of their MEA were 0.006±0.011, 0.011±0.020, and 0.012±0.007 S/cm, respectively. In single cell testing, it was found that the external humidifier could be eliminated. This was the beneficial of its high hydrophilicity. The current density at 0.5 V of 30%doped crosslinked chitosan-zeolite membrane was increased from 6.7±0.004 at fully hydration (RH 100%-100%) to 9.9±0.007 mA/cm^2 for zero hydration (RH 0%-0%) on both sides. In partial hydration, its current density at 0.5 V was in the range of 7.5 – 9.3 mA/cm^2.

Introduction

Operation of PEMFCs at high temperature is considered to be the next generation due to its effective way on improving performance in terms of reaction kinetics, catalyst tolerance, heat rejection, and water management [1-4]. With respect to water management to obtain a practical performance, an external humidification subsystem is required to ensure water retention in the membrane electrode assembly (MEA). Such a humidifier, which requires both space and a heat supply, causes a drop in system efficiency and is thus a burden to the fuel cell system. The operation without external humidification is believed to be an effective way to simplify the system [5-8].

In this study, various chitosan based membranes; i.e., uncrosslinked chitosan, uncrosslinked chitosan-zeolite, crosslinked chitosan, crosslinked chitosan-zeolite, doped crosslinked chitosan and doped crosslinked chitosan-zeolite membrane, were prepared and characterized. Platinum catalyst was loaded on both sides of membranes by electroless plating technique as catalyst layers of membrane electrode assembly (MEA). The effect of relative humidity on fuel cell performance of Pt/zeolite-chitosan membrane was then investigated.

Materials and Methods

1. Materials

Chitosan with a deacetylation degree of 90.0±5.0%, and Zeolite A, having a Si:Al ratio (w/w) of 1.1 were supplied domestically. Sulfuric acid (H_2SO_4), sodium hydroxide (NaOH) and acetic acid (CH_3COOH) were commercial grade. Platinum chloride solution ($PtCl_2$), ammonia solution ($NH_3 \cdot H_2O$), hydrazine (N_2H_4) and disodium ethylene diaminetetraacetate (Na_2EDTA) were AR grade. All materials were used as received.

2. Membrane preparation

A 3% (w/w) chitosan solution was prepared in 3% (v/v) aqueous acetic acid and then poured onto a glass plate and dried completely in an air oven at 40 – 60 °C. The formed membrane was immersed in a 4% (w/w) NaOH solution until equilibrated, and then washed with water and dried. These membranes are referred to as uncrosslinked chitosan membranes. Crosslinked chitosan membranes were made by immersing the uncrosslinked chitosan membranes in a 4% (w/w) H_2SO_4 solution until equilibrated, and then drying. The chitosan-zeolite membranes were prepared by adding the required amount of zeolite to attain a final concentration of 10, 20 or 30% (w/w; relative to the chitosan), to the chitosan solution before casting and drying as detailed above. For doped membranes, the membranes were immersed in a 2% (w/w) H_2SO_4 solution until equilibrated with the excess solution at the membrane surface removed by padding with tissue paper.

3. Characterization of membranes

Ion exchange capacity

Ion exchange capacity was measured by immersing 20 mg of the membrane in a 25 mL solution of 0.005 N NaOH overnight, with continuous stirring. A 10 mL aliquot was back-titrated with 0.005 N HCl to a pH of 7.0. Ion exchange capacity was reported as a milli-equivalent per gram of dry membrane.

% Water uptake

Water uptake was determined from the different weight of the membrane before and after equilibrating in distilled water and removing the excess water at the membrane surfaces by padding with tissue papers.

Proton conductivity

The membrane proton conductivity in planar view was measured by the direct current, four-point-probe method under 100% humidity hydrogen atmosphere at 60°C. The four-point-probe cell consists of two platinum foil outer current-carrying electrodes and two platinum wire inner potential-sensing electrodes. Membrane samples were cut into strips having 1×4 cm and preconditioned in distillated water for 10 min. prior to mounting in the cell. The cell was then placed in a thermo-controlled humidic chamber.

Tensile strength

Tensile strength at break was measured according to ASTM D638 by a universal testing machine (Lloyd, LR 5 K) at a crosshead speed of 50 mm/min.

4. Electroless plating of platinum

The plating solution consisted of $PtCl_2$ 5g/L, Na_2EDTA 40.1 g/L, 28% (w/w) $NH_3{\cdot}H_2O$ 198 mL/L and N_2H_4 6 mL/L. Both sides of membrane were plated at 60°C for 90 min. The plated area was controlled at a gas diffusion layer (GDL) area for example of 2.3×2.3 cm in this work.

5. Membrane electrode assembly (MEA)

The membrane electrode assembly (MEA) was prepared by hot pressing together, the carbon paper/anode, Pt-plated membranes and carbon paper/cathode at 37 – 40°C and 30 kg/cm^2 for 1 min. The MEA was assembled as a single cell with two unipolar plates. The cell resistance on proton transportation was measured and reported as its proton conductivity in cross section view. The cell performances of 60°C were tested at various relative humidity for comparison by feeding 100 sccm. of hydrogen and air each into anode and cathode side, respectively. Polarization data was plotted from stable cell voltage under each current density.

Results and Discussion

1. Ion exchange capacity (IEC)

The IEC of crosslinked chitosan membrane was 3.43±0.05 meq/g. It was increased to 3.71±0.05 meq/g for 30% zeolite-crosslinked chitosan membranes, due to the effect of net negative charge of zeolite.

2. % Water uptake

The capability on water uptake of crosslinked chitosan membrane was 74.7±1.6%. It was increased to 90.7±1.1% for 30% zeolite-crosslinked chitosan membranes. Comparing to only 16.6±0.005% of Nafion117 membrane, the external humidifier might be eliminated by the effect of self humidification of chitosan based PEMFC.

3. Proton conductivity

The fully hydrated proton conductivities in planar view at 60°C of 30% zeolite of uncrosslinked, crosslinked, and doped crosslinked chitosan-zeolite membranes were 0.021±0.003, 0.043±0.006, and 0.123±0.024 S/cm, respectively, as shown in Figure 1. After Pt plating, they were increased to 0.150±0.006, 0.235±0.003, and 0.312±0.008 S/cm, respectively, as shown in Figure 2. That of Nafion117 membrane showed 0.069±0.004 S/cm. The high proton conductivity of doped membranes was due to the effect of liquid electrolyte (sulfuric acid solution) penetrating in the membrane. It was found that the net negative charge of zeolite in chitosan-zeolite membranes as well as Pt particle in Pt-plated membranes could promote the proton transportation. However, those in cross section view of their MEA were as low as 0.013±0.002, 0.016±0.002, and 0.040±0.010 S/cm, respectively, as shown in Figure 3. This was due to the effect of component resistance in series of a cell not only the membrane itself. However, the transportation of proton in cross section view is more realistic in fuel cell operation.

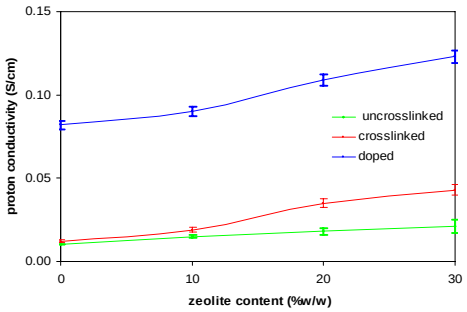

Figure 1. Proton conductivity in planar view of unplated membranes at 60°C

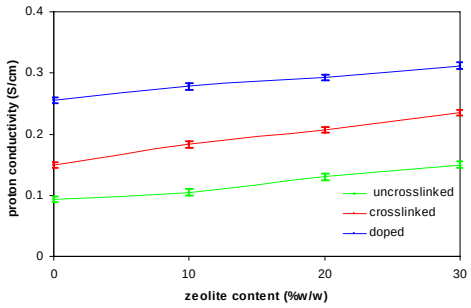

Figure 2. Proton conductivity in planar view of Pt-plated membrane at 60°C

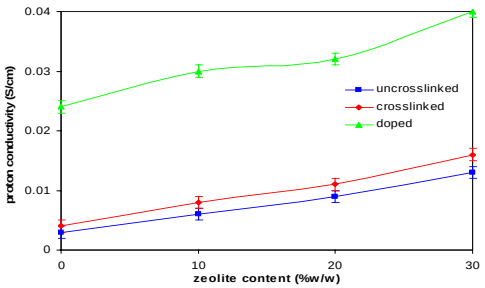

Figure 3. Proton conductivity in cross section view of a single cell at 60°C

4. Tensile strength

The tensile strength of crosslinked chitosan membrane was 62.5±0.9 MPa. It was decreased to 40.2±0.7 MPa for 30% zeolite-crosslinked chitosan membranes. However, it was still better than that of Nafion117 membrane having 28.4±2.3 MPa.

5. Cell performance

Figure 4 – 6 showed the single cell performance at 60°C of 30% zeolite of uncrosslinked, crosslinked, and doped crosslinked chitosan-zeolite membranes, respectively. It was found that the external humidifier could be eliminated by showing the highest polarization at RH 0%–0%. Their current density at 0.5 V for zero hydration was 2.9±0.1, 5.3±0.1, and 9.9±0.01 respectively.

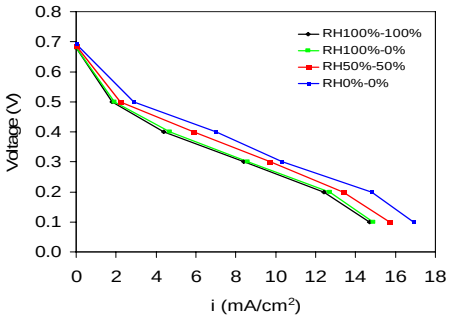

Figure 4. Single cell performance at 60°C of 30% zeolite-uncrosslinked chitosan membrane

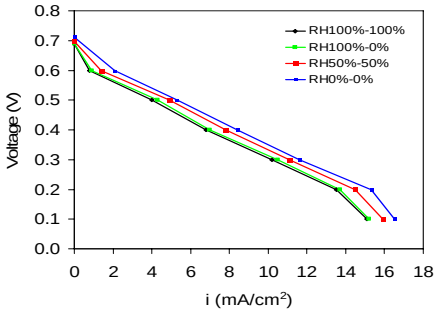

Figure 5. Single cell performance at 60°C of 30% zeolite-crosslinked chitosan membrane

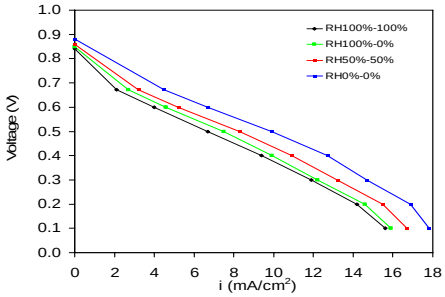

Figure 6. Single cell performance at 60°C of doped 30% zeolite-crosslinked chitosan membrane

Conclusions

This research studied the effects of relative humidity on performance of Pt/zeolite-chitosan membrane in PEM fuel cell. It was found that the ion exchange capacity, %water uptake and proton conductivity was increased with zeolite content however the tensile strength was decreased. It was found that the external humidifier was not necessary for chitosan based membranes because of its high hydrophilicity. The current density was highest at zero hydration in both sides.

References

[1] R.K. Ahluwalia, E.D. Doss and R. Kuman, *J. Power Sources*. **117**(2003)**,** pp. 45-60.
[2] K.T. Adjemian, S.J. Lee, S. Srinivasan, J. Benziger and A.B. Bocarsly, *J. Electrochem. Soc.* **149**(2002), pp. 356-364.
[3] V. Ramani, H.R. Kunz and J.M. Fenton, *J. Membr. Sci.* **232**(2004), pp. 31-40.
[4] C. Yang, P. Costamagna, S. Srinivasan, J. Benziger and A.B. Bocarsly, *J. Power Sources*. **103**(2001), pp. 1-9.
[5] M.V. Williams, H.R. Kunz and J.M. Fenton, *J. Power Sources*. **135**(2004), pp.122-134.
[6] S. Vengatesan, H-J. Kim, E.A. Cho, S.U. Jeong, H.Y. Ha, I.-H. Oh, S.A. Hong and T-H. Lim, *J. Power Sources*. **156**(2006), pp 294-299.
[7] J. Zhang, Y. Tang, C. Song, X. Cheng, S. Zhang and H. Wang, *Electrochim. Acta*.**52**(2007), pp.5095-5101.
[8] P. Mukoma, B.R. Jooste and H.C.M. Vosloo, *J. Power Sources*. **136**(2004), pp 16-23.

Design of hydrogen production system for application in polymer electrolyte membrane fuel cell vehicle

S. Boonkrue[1], W. Kiatkittipong[2], A. Arpornwichanop[1], N. Laosiripojana[3], A. Soottitantawat[1], W. Wiyaratn[4], and S. Assabumrungrat[1,*]

[1]Department of Chemical Engineering, Faculty of Engineering, Chulalongkorn University, Pathumwan, Bangkok, Thailand
[2] Department of Chemical Engineering, Faculty of Engineering and Industrial Technology, Silpakorn University, Thailand
[3] The Joint Graduate School of Energy and Environment, King Mongkut's University of Technology Thonburi, Thailand
[4] Department of Production Technology Education, Faculty of Industrial Education and Technology, King Mongkut's University of Technology Thonburi, Thailand

*E-mail: Suttichai.A@chula.ac.th

Abstract: This work focuses on the design of hydrogen production system fueled by methanol for application in polymer electrolyte membrane fuel cell (PEMFC) vehicle. The system consists of steam reformer (SR) and preferential oxidation (PROX) reactors. The former is for converting methanol to hydrogen while the latter is for reducing to the concentration of carbon monoxide in the SR effluent gas to less than 50 ppm before feeding to PEMFC to avoid the poisoning of PEMFC anode. In this work, the mathematical models of fixed-bed SR and PROX were developed in MATLAB program for designing and simulating the system performance. The simulations were based on one-dimensional and isothermal models. Effects of the reaction temperature and the reactor sizes (in term of catalyst weights) on performance of SR and PROX reactors were examined. Moreover, the effects of steam-to-methanol (*S*/*M*) ratio and oxygen-to-CO (O_2/CO) ratio in the SR and PROX reactor were considered. It is noted that the operating conditions of SR and PROX were performed under atmospheric pressure at varied temperatures from 450 to 525 K for SR and 423 to 523 K for PROX. The *S*/*M* ratio and O_2/CO ratio were evaluated from 1.0 to 2.0 and 0.5 to 2.0, respectively. According to our studies, it was found that the optimal condition for SR was at *T* = 525 K and *S*/*M* ratio = 1.5. As for PROX reactor, the optimal condition for PROX was at *T* = 473 K and O_2/CO ratio = 1.5. Finally, the total catalyst weight required for powering a 1 kW PEMFC was also determined.

Introduction

Fuels are very important for the public utilities especially in transportation section. Among several types of fuel, hydrogen is considered as a promising fuel for future applications. It is not only used as automotive fuel directly but also used for converting into many useful energy forms as environmentally friendly resource. It is well established that fuel cell is one of the most attractive power generation systems that use hydrogen and oxygen as reactants and produce the clean energy as products. In detail, fuel cell is an electrochemical device that can convert the chemical energy directly into electricity. Proton exchange membrane fuel cell (PEMFC) is one type of fuel cells that operates at low temperature with high efficiency and power density. Therefore, PEMFC is considered a suitable type of fuel cell for automotive system. However, the usage of pure hydrogen in vehicle system confronts the problems related to hydrogen storage and transportation. Therefore, the on-board fuel processor is preferred to liberate the hydrogen directly and methanol is often considered as a fuel source because it is stored as a liquid at atmosphere and can be reformed to hydrogen at relatively mild conditions [1]. Moreover, it has high hydrogen to carbon ratio.

The reforming technology intensively used for hydrogen production is currently based upon steam reforming, partial oxidation or autothermal reforming [2]. The steam reforming has an advantage of producing the highest hydrogen concentration when compared with partial oxidation and autothermal reforming, nevertheless, since this reaction is highly endothermic, it is required heat supply from external sources.

Typically, hydrogen produced from the steam reforming reaction always contain carbon monoxide, which easily poison the anode of PEMFC. Hence, the hydrogen-rich gas produced from the steam reformer (SR) must be treated in order to reduce carbon monoxide concentration to less than 50 ppm prior to use in the PEMFC [3]. One method to reduce carbon monoxide is the apply of sequential partial oxidation (PROX) as shown in Figure 1.

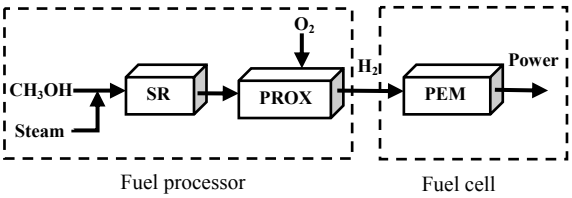

Figure 1. Schematic diagram of fuel processor and fuel cell system.

For designing of methanol reformer, Telotte et al. [4] presented a radial flow packed bed reactor to produce hydrogen for generating power in mobile application. This simulation studied effects of temperature, pressure and steam-to-methanol (*S*/*M*) ratio on hydrogen production. They showed that a reactor volume of 20 cm^3 at 202 kPa and *S*/*M* ratio of 1.5 is sufficient to generate the hydrogen for 24 W at 500 K and 72 W at 550 K. For the reducing of carbon monoxide by PROX reactor, Choi et al. [5] studied this

system and computed the temperature and oxygen-to-carbon (O_2/CO) ratio that suitable using to achieve low CO concentrations.

In this work, the mathematical models of steam reformer and preferential oxidation reactor were developed in MATLAB program for designing and simulating the system performance.

Materials and Methods

1. Steam reformer

Methanol is mixed with steam and fed to the SR that packed with Cu/ZnO/Al_2O_3. The feedstock is reformed to the mixture of H_2, CO_2 and CO. The three reactions that occur in the reformer include steam reforming, Eq. (1), methanol decomposition, Eq. (2), and water-gas shift, Eq. (3).

$CH_3OH+H_2O \leftrightarrow CO_2+3H_2$, ΔH=49 kJ/mol (1)
$CH_3OH \leftrightarrow CO+2H_2$, ΔH=90.1 kJ/mol (2)
$CO+H_2O \leftrightarrow CO_2+H_2$, ΔH=-41.2 kJ/mol (3)

$$r_R = \frac{k_R K^*_{CH_3O^{(1)}}(P_{CH_3OH}/P^{1/2}_{H_2})(1-P^3_{H_2}P_{CO_2}/K_R P_{CH_3OH}P_{H_2O})C^T_{S1}C^T_{S1a}}{(1+K^*_{CH_3O^{(1)}}(P_{CH_3OH}/P^{1/2}_{H_2})+K^*_{HCOO^{(1)}}P_{CO_2}P^{1/2}_{H_2}+K^*_{OH^{(1)}}(P_{H_2O}/P^{1/2}_{H_2}))(1+K^{1/2}_{H^{(1a)}}P^{1/2}_{H_2})} \quad (4)$$

$$r_D = \frac{k_D K^*_{CH_3O^{(2)}}(P_{CH_3OH}/P^{1/2}_{H_2})(1-P^2_{H_2}P_{CO}/K_D P_{CH_3OH})C^T_{S2}C^T_{S2a}}{(1+K^*_{CH_3O^{(2)}}(P_{CH_3OH}/P^{1/2}_{H_2})+K^*_{OH^{(2)}}(P_{H_2O}/P^{1/2}_{H_2}))(1+K^{1/2}_{H^{(2a)}}P^{1/2}_{H_2})} \quad (5)$$

$$r_W = \frac{k_w K^*_{OH^{(1)}}(P_{CO}P_{H_2O}/P^{1/2}_{H_2})(1-P_{H_2}P_{CO_2}/K_W P_{CO}P_{H_2O})C^{T\,2}_{S1}}{(1+K^*_{CH_3O^{(1)}}(P_{CH_3OH}/P^{1/2}_{H_2})+K^*_{HCOO^{(1)}}P_{CO_2}P^{1/2}_{H_2}+K^*_{OH^{(1)}}(P_{H_2O}/P^{1/2}_{H_2}))^2} \quad (6)$$

The rate expressions for the steam reforming of methanol applied in the present work are based on the empirical rate expression derived by Peppley et al. [6] using Cu/ZnO/Al_2O_3 catalyst as shown in Eqs. (4)-(6). The parameters for Eqs. (4)-(6) are given in Table 1. It is noted that the assumptions made are: the SR is operated at atmospheric pressure, temperature range from 433 to 533 K and *S*/*M* ratio are evaluated from 1.0 to 2.0 [6].

Table 1: The parameters for rate expression for steam reforming, decomposition and water-gas shift reaction (units are consistent with pressures in bar and overall rate in mol/kg_{cat} s) [6, 7]

Parameter	Expression
S_g (m^2kg^{-1})	$1.02x10^5$
$C_{s1} = C_{s2}$ (mol m^{-2})	$7.5x10^{-6}$
$C_{s1a} = C_{s2a}$ (mol m^{-2})	$1.5\ x10^{-5}$
k_{SR}	$7.4x10^{14}\exp(-102800/RT)$
k_{MD}	$3.8x10^{20}\exp(-170000/RT)$
k_{WGS}	$5.9x10^{13}\exp(-87600/RT)$
$K^*_{CH3O(1)}$	$6.55x10^{-3}\exp(20000/RT)$
$K^*_{CH3O(2)}$	$36.9\exp(20000/RT)$
$K^*_{OH(1)}$	$4.74x10^{-3}\exp(20000/RT)$
$K^*_{OH(2)}$	$36.9\exp(20000/RT)$
$K_{H(1a)}$	$5.43x10^{-6}\exp(50000/RT)$
$K_{H(2a)}$	$3.86x10^{-3}\exp(50000/RT)$
$K^*_{HCOO(1)}$	$2.30x10^{9}\exp(-100000/RT)$

2. Preferential oxidation reactor

As described, hydrogen-rich stream from steam reformer was mixed with oxygen and fed to PROX reactor to purify H_2 by eliminating CO. The reactions taken place in PROX reactor include CO oxidation, Eq. (7), H_2 oxidation, Eq. (8) and water-gas shift, Eq. (9).

$CO+0.5O_2 \rightarrow CO_2$, ΔH=-283 kJ/mol (7)
$H_2+0.5O_2 \rightarrow H_2O$, ΔH=-242 kJ/mol (8)
$CO+H_2O \leftrightarrow CO_2+H_2$, ΔH=-41.2kJ/mol (9)

The rate expressions for PROX reactor are based on Pt–Fe/γ-Al_2O_3 catalyst as shown in Eqs. (10)-(12) [5]. The operating condition of PROX reactor was investigated at atmospheric pressure, temperature range from 423 to 523 K and O_2/CO ratio are evaluated from 0.5 to 2.0.

$$r_{CO} = 3.528x10^2 \exp(\frac{-33092}{RT})P^{0.5}_{O_2}P^{-0.1}_{CO} \quad (10)$$

$$r_{H_2} = 2.053x10\exp(\frac{-18742}{RT})P^{0.5}_{O_2} \quad (11)$$

$$r_{WGS} = 4.402x10^3 \exp(\frac{-34104}{RT})(P_{CO}P_{H_2O} - \frac{P_{CO_2}P_{H_2O}}{K_p}) \quad (12)$$

where $K_P = \exp(\frac{4577.8}{T} - 4.33)$ (13)

3. Reactor model

The SR and PROX reactors are considered as one-dimensional reactor model and operated at isothermal condition. The flow rate of components in the exit gas-stream can be integrated along with the weight of catalyst by Eq. (14) [8].

$$\frac{dF_i}{dW} = \sum_j \nu_{ij} r_j \quad (14)$$

It is noted that this work is proposed to generate net power of 1 kW for PEMFC. The flow rate of methanol was kept at $3.0833x10^{-3}$ mol/s [5]. The effect of weight of catalyst, operating temperature on hydrogen production and methanol conversion were investigated for the SR as well as the PROX reactor. In addition, the effects of S/M and O_2/CO ratios were also evaluated for the SR and PROX reactors.

Results and Discussion

The SR packed with Cu/ZnO/Al_2O_3 catalyst (0.5 kg) was operated as a plug flow reactor. The methanol flow rate was kept at $3.0833x10^{-3}$ mol/s. This simulation was performed by MATLAB program. The effects of temperature and *S*/*M* ratio on the hydrogen production are shown in Figure 2. It can be seen that

hydrogen production is highly improved with increasing temperature but levels off after T = 500 K. The *S*/*M* ratio shows slight influence on hydrogen production. At higher temperatures, hydrogen production is favorable at high *S*/*M* ratio while the opposite trend is observed at lower temperatures. This can be described by the fact that increasing steam in the feed promotes hydrogen production from both reforming (Eq. 1) and water gas shift reaction (Eq. 3); however, the dilution effect from the presence of excessive steam retards the amount of hydrogen production, resulting in a lower hydrogen production especially pronounced at lower temperatures.

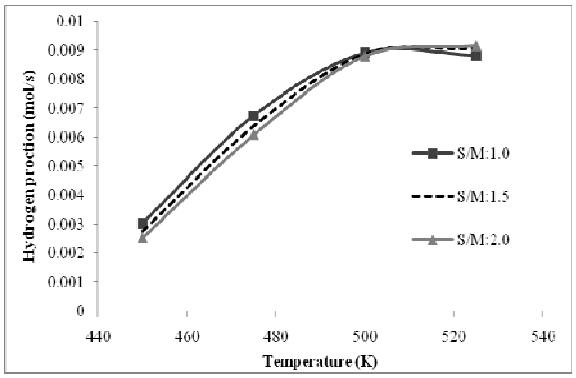

Figure 2. Effect of temperature and *S*/*M* ratio on hydrogen production.

Figure 3 shows that the methanol conversion increases with increasing temperature. The methanol conversion at operating temperature of 525 K, pressure of 1 atm and *S*/*M* ratio of 1.5 is up to 90% at the catalyst weight of 0.1 kg_{cat} as shown in Figure 4. At this condition, the methanol conversion rapidly increases with the amount of catalysts until reaching its equilibrium stage.

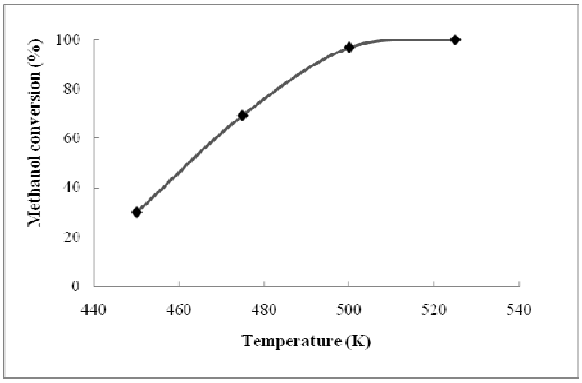

Figure 3. Effect of temperature on methanol conversion.

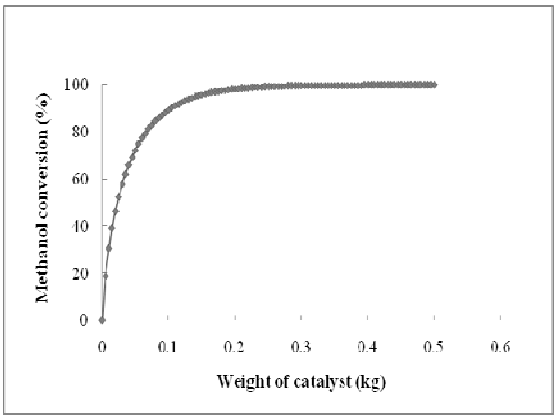

Figure 4. Effect of catalyst weight on the methanol conversion at 525 K and S/M ratio: 1.5.

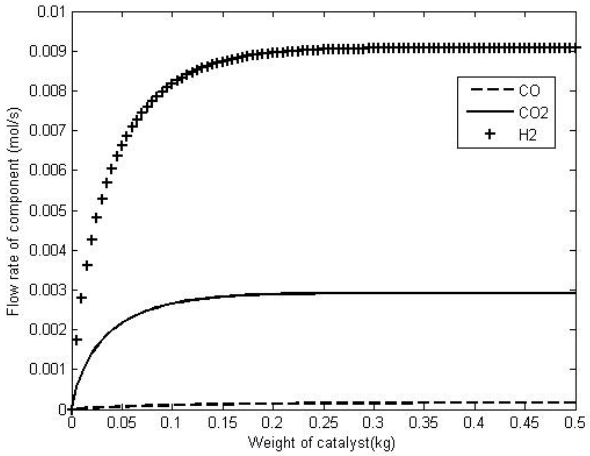

Figure 5. Effect of catalyst weight on the flow rates of CO, CO_2 and H_2 in outlet stream of the SR at T = 525 K and *S*/*M* ratio = 1.5.

Figure 5 clearly shows that the flow rates of CO, CO_2 and H_2 in the outlet stream from the SR are enhanced with increasing weight of catalyst. Considering CO concentration in hydrogen-rich stream, the value should be reduced to less than 50 ppm before feeding to PEMFC and therefore a PROX reactor is required. The concentrations of CO from the outlet streams of the SR were considered at different weights of catalyst (0.1, 0.2, 0.3, 0.4 and 0.5 kg_{cat}) in order to compare the reactor size by evaluating total weight of catalyst and the amount of hydrogen supply to PEMFC.

The temperature of PROX reactor shows slight effect on CO conversion as shown in Figure 6. However, the increasing of O_2/CO ratio has strongly effect on CO conversion when O_2/CO ratios are less than 1.5.

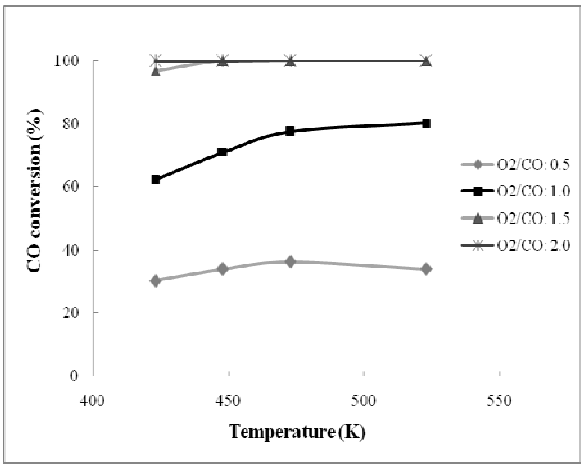

Figure 6. Effects of temperature and O_2/CO ratio on CO conversion in PROX reactor.

As the next step, the condition for PROX reactor was considered at T = 473 K and O_2/CO ratio = 1.5. It can be seen from Figure 7 that although at this condition the CO conversion is high, the hydrogen loss due to the oxidation of hydrogen becomes more significant.

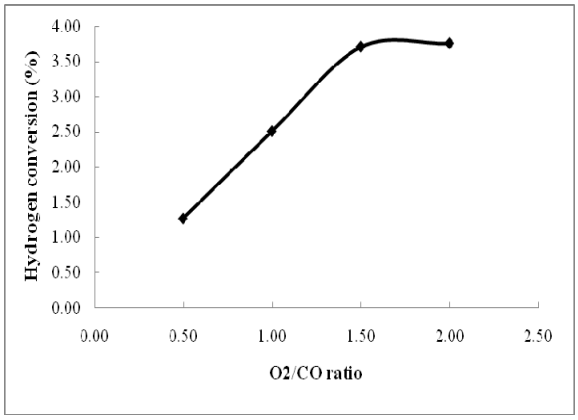

Figure 7. The effect of O_2/CO ratio on H_2 conversion in PROX reactor.

The inlet flow rate at different weights of catalyst of the SR contains 63-65% H_2, 21%CO_2, 1-2%CO, and 13%H_2O with insignificant amount of unreacted methanol. To diminish CO concentration to 50 ppm, the CO conversion should be higher than 99.5%. Consequently, at maximum CO conversion, the weight of catalyst for PROX reactor is determined as well as the hydrogen outlet stream from the PROX reactor.

The weights of catalysts for the SR and PROX reactors are determined by considering the amount of hydrogen outlet that should be enough for powering a 1 kW PEMFC. Figure 8 shows that the amount of PROX catalyst is considerably less than that of SR catalyst. From our simulation, SR catalyst of 0.2 kg_{cat} and PROX catalyst of 0.0112 kg_{cat} are sufficient for generating hydrogen for a 1 kW PEMFC.

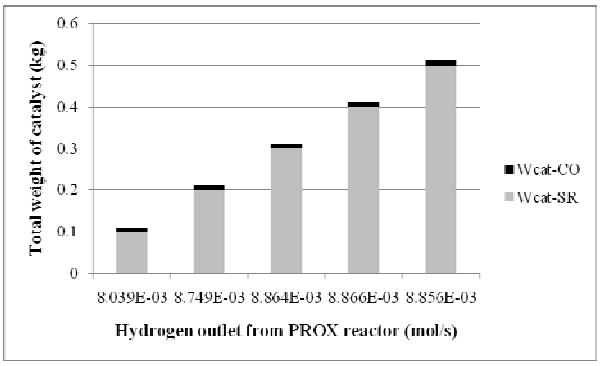

Figure 8. The H_2 outlet from PROX reactor with total weight of catalyst in the integrated SR and PROX reactor.

Conclusions

In this study, the SR and PROX reactors were modeled as one-dimensional, isothermal fixed bed reactors used for generating hydrogen for a 1 kW PEMFC. For the SR, the optimal conditions are at 525 K with *S*/*M* ratio of 1.5, in which shows high methanol conversion and sufficient hydrogen production. For PROX reactor, the condition is performed at 473 K and O_2/CO ratio of 1.5 to ensure that the CO concentration can be removed to less than 50 ppm. As for the amount of catalysts required for SR and PROX reactors, the uses of SR catalyst with the weight of 0.2 kg_{cat} and PROX catalyst with the weight of 0.0112 kg_{cat} can reduce CO concentration to X_{co} = 4.677×10^{-6} and produce sufficient hydrogen (8.770×10^{-3} mol/s) which is sufficient for supplying it to a 1 kW PEMFC.

Acknowledgement

This work is supported by the Thailand Research Fund and Commission on Higher Education.

References

[1] J.R. Lattner and M.P. Harold, *Appl. Catal., B*. 56 (2005), pp.149-169.
[2] C.D. Dudfield, R. Chen and P.L. Adcock, *Int. J. Hydrogen Energy*. 26 (2001), pp. 763-775.
[3] M. Ouzounidou, D. Ipsakis, S. Voutetakis, S. Papadopoulou and P. Seferlis, *Energy*. 34 (2009), pp. 1733-1743.
[4] J.C. Telotte, J. Kern, S. Palanki, *Int. J. Chem. Reactor Eng.* 6 (2008)
[5] Y. Choi and H.G. Stenger, *J. Power Sources*. 129 (2004), pp.246-254.
[6] B.A. Peppley, J.C. Amphlett, L.M. Kearns and R.F. Mann, *Appl. Catal., A*. 179 (1999), pp.31-49.
[7] J.R. Lattner and M.P. Harold, *Appl. Catal., B*. 56 (2005), pp.149-169.
[8] A.K. Avcı, Z.İ. Önsan and D.L. Trimm, *Appl. Catal., A*. 216 (2001), pp. 243-256.

Study on interaction of mixed plastic in steam gasification

E. Jamkrajang[1], L. Mekasut[1,2] and P. Kuchonthara[1,2*]

[1]Fuels Research Center, Department of Chemical Technology, Faculty of Science, Chulalongkorn University, Bangkok, Thailand.
[2]Center of Excellence for Petroleum, Petrochemicals, and Advanced Materials, Chulalongkorn University, Bangkok, Thailand.

* E-mail: pkuchonthara@gmail.com

Abstract: Gasification was a promising technology for converting wastes into useful gaseous fuel. Plastic waste was found to be a feedstock for the gasification, due to its high calorific value. Typically, plastic waste is found as a mixture of various types of plastics. There are a few data about the interaction of mixed plastic in gasification process. A better understanding of the interaction help suggest an optimal way for separation of plastics before introducing into a gasifier in order to approach the highest conversion of gas product. This research studied interaction of four types of plastics, including PP, PS, LDPE and HDPE, in steam gasification. Experiments were carried out in a drop tube fixed bed reactor. Effect of plastic type on gas yield and gas composition, especially CO and H_2, was investigated. The results of gasification of a single plastic indicated that HDPE gave the highest gas yield while PS gave the lowest. Hence PS was expected to possibly induce the most negative interaction when mixed with the others. In case of gasification of mixed plastic, gasification of the mixture of HDPE and PS, and of LDPE and PS showed negative interaction, on the other hand gasification of the mixture of PS and PP showed positive interaction.

Introduction

Recently, the growing rate of economic growth in Thailand has yielded the increasing amount of energy demand. Accordingly, the municipal solid wastes (MSW) have been increasing continuously. Approximately 14 million tonnes of MSW are generated throughout Thailand each year. About one-third of this solid waste is plastic. The average composition of plastic waste in Thailand is shown in Figure 1. The growing amount of plastic waste is generating more and more environmental problems.

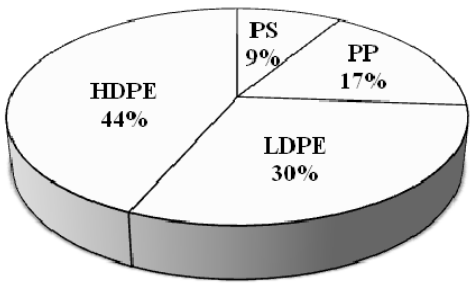

Figure 1. The average composition of plastic waste in Thailand

Nowadays there are typical three ways considered as disposal or utilization of plastic waste: landfilling, incineration and recycling. The largest amount of plastic waste is disposed of by landfilling and incineration (93%). Recycling is only about 7%. Moreover, the problem of wastes cannot be solved by landfilling and incineration, because suitable and safe depots are expensive, and incineration stimulates the growing emission of harmful, greenhouse gases, e.g. NO_x, SO_x, CO_x, etc. Thermochemical process is one of the prospective ways to solve this problem. The plastic wastes are converted into fuels or other valuable feedstocks for the petrochemical industry. Pyrolysis and gasification are now recognized as promising routes for the converting of plastic wastes to more usable and energy dense materials. Most of the pyrolysis products (liquid fuel) contains a large amount of complex compound. As the result, the liquid product must be distillated before use. Gasification can convert plastic waste to gaseous fuel that is directly usable, due to its high calorific value. Therefore, the converting plastic waste to gaseous fuel by gasification process is one of the prospective ways to utilize plastic wastes.

Gasification is a process that converts carbonaceous materials, such as coal, biomass, waste, into gaseous products by reacting the raw material or compost at high temperature with a controlled amount of oxygen and/or steam. The mainly gaseous products are carbon monoxide and hydrogen, are called synthesis gas or syngas and are themselves the fuel. Gasification is a method for extracting energy from many different types of organic materials. The advantage of gasification is that using the syngas is potentially more efficient than direct combustion of the original fuel because it can be combusted at higher temperature. Syngas may be burned directly in internal combustion engines, used to produce methanol and hydrogen, or converted via the Fischer-Tropsch process into synthetic fuel.

Plastic waste can be employed as a feedstock for the gasification process, due to its high calorific value. The major problem in plastic gasificion is high volatile, resulting in low conversion into gaseous product. This problem can be solved by employing a suitable catalyst. Another problem of plastic waste is that this waste is typically composed of various types of plastic. Each kind of plastic was observed to have different behavior in thermal composition as well as in

gasification process. Furthermore, there possibly is some interaction when more than one type of plastic is subjected to thermochemical process. There are a few data about the interaction of mixed plastic in gasification process. A better understanding of the interaction help suggest an optimal way for separation of plastic before introducing into a gasifier in order to approach the highest conversion of gas product. In our experimental work the four main plastics of the most occurring in plastic waste (high density polyethylene, low density polyethylene, polypropylene and polystyrene) were investigated individually and as mixed plastic. The gasification experiments were carried out in a drop tube fixed bed reactor at temperature of 850 °C with steam and oxygen as gasifying agents. Each of plastic was then mixed with each of the other three plastics in a ratio of 1:1 and gasified in the drop tube fixed bed reactor under the same condition. The interaction of plastic types in a mixture was investigated from yield and composition of the derived gases.

Materials and Methods

Plastic: A commercial high-density polyethylene (HDPE), low-density polyethylene (LDPE), polypropylene (PP) and polystyrene (PS) were used as raw materials in our studies. The results of ultimate and proximate analysis of plastic samples are listed in Table 1.

Table 1. Ultimate and proximate analysis of plastic samples.

Proximate analysis (wt%)				
Type	**HDPE**	**LDPE**	**PP**	**PS**
Ash	-	-	-	-
Volatile matter	100	100	100	99.8
Fixed carbon	-	-	-	0.2
Ultimate analysis (wt%)				
Type	**HDPE**	**LDPE**	**PP**	**PS**
C	85.4	85.56	85.19	92
H	14.6	14.44	14.81	8
O	-	-	-	-

Apparatus and procedure: The interaction of mixed plastic in steam gasification was investigated in a drop tube fixed bed reactor, as illustrated in Figure 2. In this study, the steam gasification of plastic was conducted on bench scale drop tube fixed bed reactor. The gasification system consists essentially of quartz tube (i.d. 20 mm, o.d. 22 mm, height 450 mm), a cooling system for the separation of water and condensable volatile (tar) from gaseous products, a bubble flow meter for assuring the desired unidirectional flow out from the reactor, and

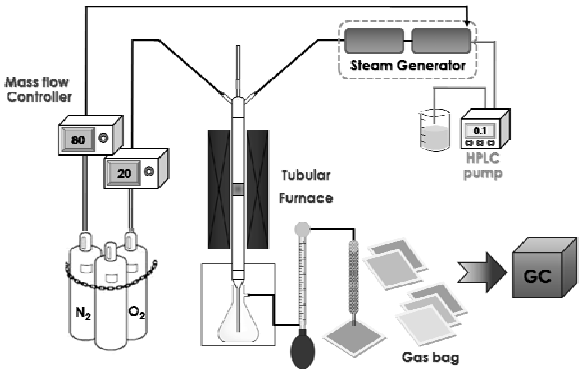

Figure 2. The schematic of drop tube fixed bed reactor.

a moisture absorber for drying the gaseous products.

The procedure for a typical steam gasification experiment is described below. When the desired carrier gas flow rate and temperature in the reactor were reached at the specific values, plastic sample (in case of both single and two mixed in a ratio of 1:1) and steam were fed into the reactor and plastic was reacted with steam and O_2 in N_2 atmosphere to produce gaseous products. The volatile and gaseous products were cooled in cooled trap and the produced gas was analyzed by a GC equipped with TCD detectors. the interaction of mixed plastics in steam gasification were carried out at 850°C, 1 atm with plastic weight 0.1 g and alumina ball height 25 mm. The steam content 52%vol, O_2 flow 20 mL/min was reacted gas and N_2 flow 80 mL/min was carrier gas.

Results and Discussion

Steam gasification of a single plastic: The results from single plastic steam gasification are shown in Figure 3a. The high gas yield was observed for HDPE, LDPE and PP, and gave quite similarly gas yields, while PS results the lowest gas yield and the highest tar yield. It could be expected that the radical fragments from preliminary degradation of PS may be occurred repolymerization to form polycyclic aromatic hydrocarbon (PAH) or tar, that retards steam gasification to produce gaseous products. Hence PS was expected to possibly induce the most negative interaction when mixed with the others.

The gas productions are shown in Figure 3b. The main compositions of gaseous product are H_2, CH_4 and C_2H_4. The HDPE, LDPE and PP gave more these gas, while PS provided significantly lower. PP results the highest CH_4. It can be explained by the fact that PP has been more easily cracked into small molecules than the other structures because of branched hydrocarbon chain structure of PP. In case of C_2H_4 production, the HDPE and LDPE provide higher results than PP, Since PE structure has strong intermolecular forces, the possible cracking of PE structure to longer hydrocarbon chains are higher. These hydrocarbon

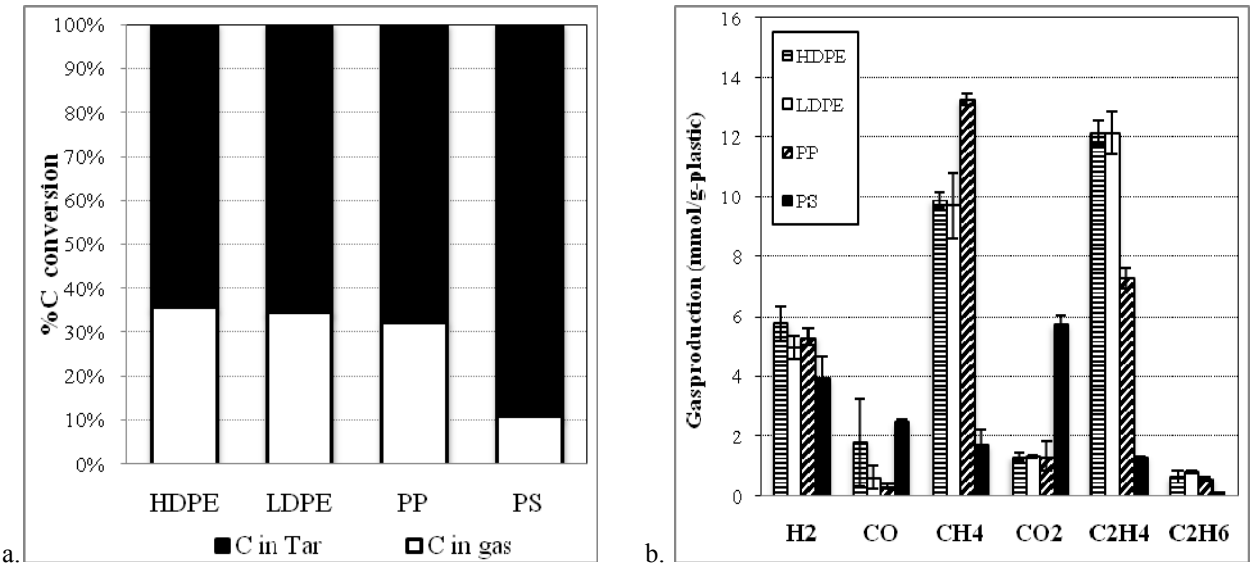

Figure 3. Gas production of single plastic in terms of a) % carbon conversion and b) gas production

chains would be reacted with steam and then reformed to smaller molecules by steam gasification.

Steam gasification of mixed plastic: The results from mixed plastic (in a ratio of 1:1) steam gasification are shown in Figure 4. The highest gas yield was observed for mixture of HDPE:LDPE, the very low gas yield was observed for mixture that contained with PS.

The gas productions of mixed plastic in steam gasification are shown in Figure 5. The main compositions of gaseous product are H_2, CH_4 and C_2H_4. The mixture that contained without PS gave more these gas, that can be explained by the structure of HDPE, LDPE and PP are easier cracked to small hydrocarbon chains than PS structure.

Interaction of mixed plastic can be considered from comparison of the predicted values with actual values obtained experimentally. The predicted values are obtained from weigh calculation using the value of gas production from single plastic steam gasification. The interaction of each plastic in the feed are shown in Figure 5. Steam gasification of the mixtures that contain with PS indicated negative interaction except PS mixed with PP, that shows positive interaction. Because PP consists of a branched hydrocarbon chain, and the carbon atoms in the ramification had lower thermal stability than the others. Therefore the PP structure has been more easily cracked than the PE structure [3]. Furthermore, it could be expected that the radical fragments from preliminary degradation of PS could react with remaining polymer chains and initiate the further cracking reactions. It is in agreement with the results of Kruse et al [4]. This results was proposed that low molecular weight radicals were diffusing into PP and abstracting hydrogen from PP, resulting in an enhanced degradation rate of PP, and resulted in higher yields of gaseous products [5]. In case of the PP showed the positive interaction when mixed with

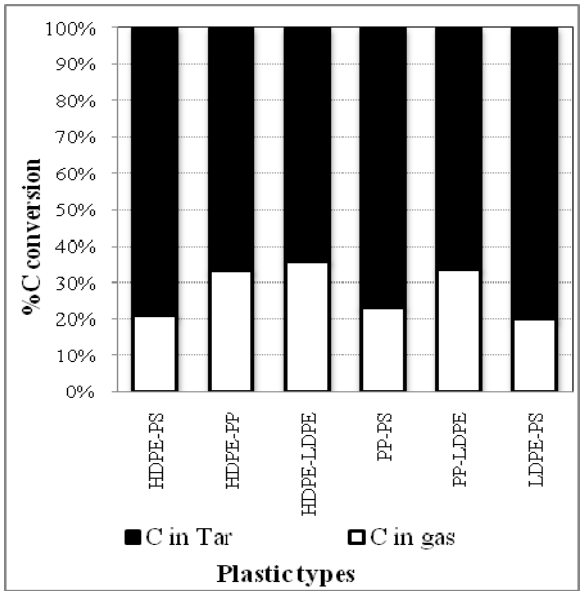

Figure 4. % Carbon conversion of mixed plastic in steam gasification

the others. The gas yield from steam gasification of PP:LDPE mixture was more than PP:HDPE mixture, because HDPE had little branching, giving it stronger intermolecular force than LDPE.

PS showed significantly negative interaction when mixed with the others, resulting in the relatively low gas yield. Therefore, it can be concluded that separation of PS of the mixed plastic waste before introducing into a gasifier is necessary in order to approach the high yield of gas product.

Conclusions

The interaction between plastics in the steam gasification was investigated in drop tube fixed bed

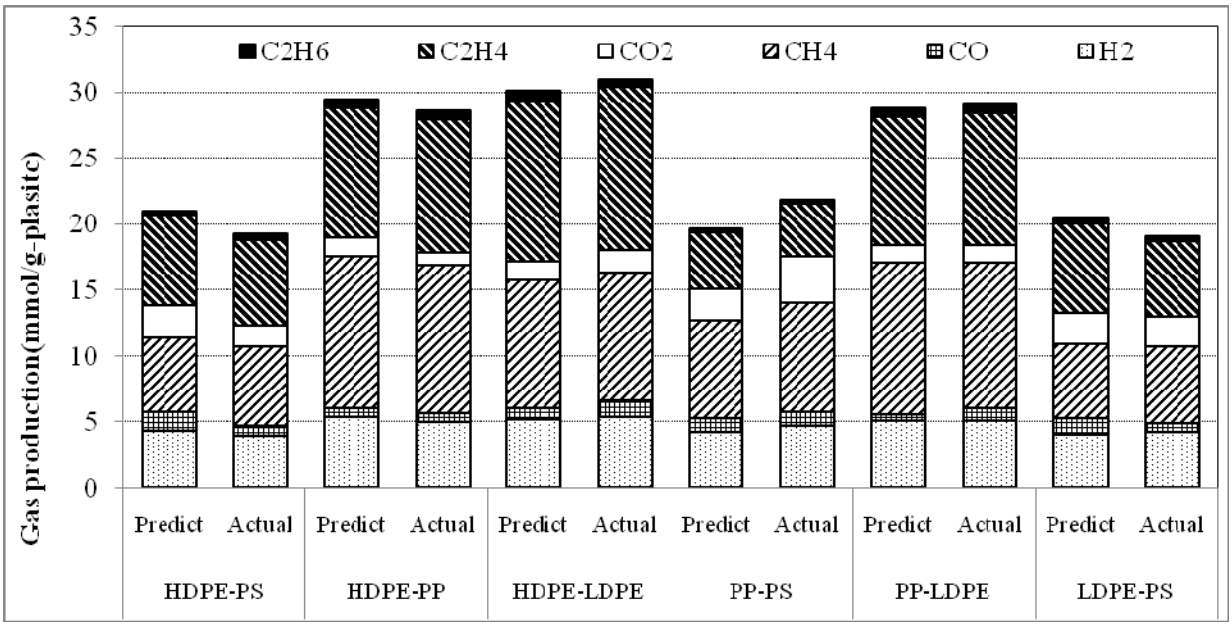

Figure 5. The gas production of two mixed plastic in steam gasification

reactor. The results of a single plastic gasification indicated that HDPE gave the highest gas yield while PS gave the lowest. PS was expected to possibly induce the most negative interaction when mixed with the others. In case of gasification of mixed plastic, Gasification of the mixture of HDPE and PS, and of LDPE and PS showed negative interaction. However, gasification of the mixture of PS and PP showed positive interaction. It was suggested that PS should be separated from the other plastics before introducing into a gasifier for high conversion into gaseous product.

Acknowledgement

The authors express gratitude to The Center of Excellence for Petroleum, Petrochemicals, and Advanced Materials and for providing financial support.

References

[1] M.N. Siddiqui and H.H. Redhwi, *Fuel Processing Technology*. **90** (2009), pp. 545–552.
[2] M. He, B. Xiao, Z. Hu, S. Liu, X. Guo and S. Luo, *International Journal of Hydrogen energy*. **34** (2009), pp. 1342–1348.
[3] N. Miskolczi, L. Bartha, G. Deak and B. Jover, *Polymer Degradation and Stability*. **86** (2004), pp. 357-366
[4] T.M. Kruse, S.E. Levine, H.W. Wong, E. Duoss, A.H. Lebovitz, J.M. Torkelson and L.J. Broadbelt, *J. Anal. Appl. Pyrolysis*. **73** (2005), pp. 342.
[5] A. Angyal, N. Miskolczi and L. Bartha, *J. Anal. Appl. Pyrolysis*. **79** (2007), pp. 409–414.
[6] I.I. Ahmed and A.K. Gupta. *Int. J. Hydrogen Energy*. **34** (2009), pp. 6253–6264.
[7] P.T. Williams and E.A. Williams, *Energy & Fuels*. **13** (1999), pp. 188-196
[8] http://www.dede.go.th/dede/index.php?id=126
[9] http://www.eppo.go.th/vrs/VRS80.pdf

Effect of temperature during thermal decomposition of biomass on catalytic steam reforming of released tar

S. Mahasuphab[1] , W. Suntornrangson[2] and P. Kuchonthara[1,3*]

[1] Fuels Research Center, Department of Chemical Technology, Faculty of science, Chulalongkorn University, Bangkok, Thailand
[2] Thailand Institute of Scientific and Technological Research (TISTR), Pathum thani, Thailand
[3] Center of Excellence for Petroleum, Petrochemicals, and Advanced Materials, Chulalongkorn University, Bangkok, Thailand

[*] E-Mail: prapan.k@chula.ac.th

Abstract: Effect of temperature during thermal decomposition of biomass on catalytic steam reforming of released tar was studied in this research. The pyrolysis of biomass was combined with the steam reforming in a two-stage fixed bed reactor. Pulverized biomass was fed into the first stage of rapid pyrolysis zone where nascent volatile and char were isolated from each other. Afterward, the volatile was mixed with steam and consequently introduced into the second stage of reforming zone at 800°C in which a catalyst was placed. The influences of pyrolysis temperature in range of 400 to 800°C on reforming reaction of released tar was investigated in terms of product gas composition and conversion. The characteristic of biomass was analyzed by CHN analyzer and also the product gas were analyzed by GC. Without catalyst, the trend of gas and tar yield were increased when the pyrolysis temperature was increased from 400 to 800°C. However, with catalyst, a minimum tar yield was obtained at pyrolysis temperature of 500°C. The results indicated that pyrolysis temperature affected the reactivity of released tar in catalytic steam reforming.

Introduction

Nowadays, the trend of population is increased continuously, resulting in an increase in energy consumption. However, energy production seems to be not enough to sustain the near-future consumer. The most of energy is presently produced from fossil fuels which are realized as rationale to give environmental, global warming issue. So, renewable energy sources are getting increased attention. Biomass is considered as a potential source of renewable energy. Moreover, biomass is neutral in carbon dioxide circulation. Biomass can be converted to energy via thermo-chemical conversion processes including combustion, pyrolysis and gasification.

Biomass gasification is gaining attention as route for biomass energy production, but producer gas from this process usually contains unacceptable levels of tar. Tar derived from biomass can cause operational problems in downstream processes by blocking gas coolers, and filter elements engine suction channels. Most producer gas applications also require removal at least part of tar before the gas can be used. Hence, tar degradation is a key issue for a successful application of biomass-derived producer gas.

As we know, the operating parameters play a very important role in tar degradation during biomass gasification. Ates and Isikdag [1] investigated alternative feedstock to obtain fuels from pyrolysis of corncob in fixed-bed reactor. They found that O/C ratio was reduced when the temperature was increased from 300 to 800°C. Phenolics compounds was also decreased from 33.31 to 29.28% but polycyclic aromatic hydrocarbon (PAHs), more than 2 aromatic rings, was increased with increasing temperature from 500 to 800°C.

Devi et al. [3] reported that biomass derived tar from bubbling-fluidised-bed gasifier is represented in terms of the following tar class; GC-undetectable tars (class 1), heterocyclic compounds (class 2), aromatic compounds (class 3), light polyaromatic compounds (class 4) and heavy polyaromatic compounds (class 5). They mentioned that the water-soluble heterocyclic compounds including phenolics compounds was found to be easiest converted by thermal treatment.

Hence, tar is a mixture of various compounds which have different reactivity in any thermal conversion processes, e.g. steam reforming. Furthermore, the temperature of pyrolysis step in which the tar is produced during the gasification seems likely influences variation of tar compounds. However, there is a few research investigating the effects of devolatilization temperature on ability of tar reforming. Therefore, the aim of this research is to study the influences of pyrolysis temperature on reforming reaction of released tar in two-stage fixed bed reactor.

Materials and Methods

Biomass: The Giant leucaena wood was employed as the biomass sample. Before the experimental, they were ground using a high-speed rotary cutting mill and then prepared to obtain a particle sizes about 250 to 425 μm. Table 1 shows the main characteristics of biomass sample: proximate and ultimate analysis.

Table 1. Poximate and ultimate analysis of biomass

Biomass	Proximate analysis (wt% as recieve)			
	Moisture	Volatile	Ash	Fixed C*
Giant leucaena wood	9.69	79.48	2.06	8.77
	Ultimate analysis (wt% daf)			
	C	H	N	O*
	37.35	5.13	0.54	56.98

* By difference

Catalyst preparation: $NiO/MgO/Al_2O_3$[5] catalyst was prepared by sequential impregnation. First, the magnesium nitrate $Mg(NO_3)_2$ 2 M (Mg 10%wt) was mixed with alumina power. The mixture solution was slowly evaporated water and dried in oven at 110°C for 24 hour. Second, the dried powder was brought to calcined in muffle furnace at 950°C for 6 hour and then MgO/Al_2O_3 was got. Third, the nickle acetate 0.5 M (Ni 10%wt) was mixed with the MgO/Al_2O_3 and later operated like MgO/Al_2O_3 preparation. Finally, $NiO/MgO/Al_2O_3$ was received.

Activities measurement: A two-stage fixed bed reactor [4] was developed for investigating tar degradation of volatiles from the pyrolysis of pulverized biomass. Figure 1 shows the schematic diagram of two-stage fixed bed reactor. The two-stage fixed bed reactor was made of quartz glass tube and consists of the first stage of rapid pyrolysis zone and the second stage of steam reforming zone.

In each experimental run, 0.12 g of biomass sample were fed into pyrolysis zone where nascent volatile and char were isolated from each other with N_2 flow rate 80 ml/min. Afterward, the volatile was mixed with steam flow rate 30 ml/min and consequently introduced into the second stage of reforming zone at 800°C in which a catalyst was placed. Among the volatile products from the fixed bed reactor were condensed in cold trap. Non-condensable gases passing through the cold trap was collected in the gas-bag. And the product gases collected in the gas bag were analysed with GC.

Characterization: Fundamental tests on pyrolysis for biomass sample were conducted using a thermo-gravimetric (TG) analyzer. The biomass 6 mg was heated from 30 to 800°C at heating rate of 50°C/min under N_2 atmosphere. The gas product is analyzed by gas chromatography (GC) with a Shimadzu GC-2014 under the following chromatographic condition: column: Unibeads C packed column; carrier gas: Ar; column temperature: 50 to 180°C; detector: thermal conductivity detector (TCD); injector temperature: 120°C.

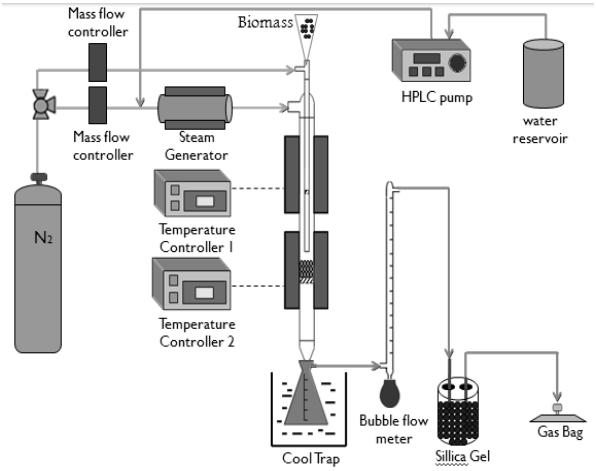

Figure 1. Show the schematic diagram of two-stage fixed bed reactor

Results and Discussion

Pyrolysis behavior of biomass

Typical TG curves of pyrolysis under N_2 atmosphere at heating rate 50 °C/min are shown in Figure 2 that represent %mass loss of Giant leucaena wood versus temperature. The results indicated that Giant leucaena wood is completely decomposed between 250 to 500°C (see Figure 2).

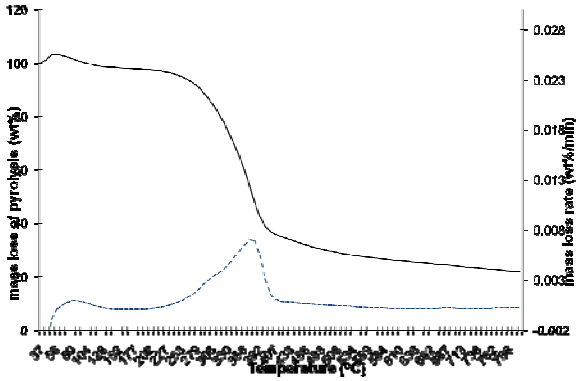

Figure 2. TG curves of Giant leucaena wood

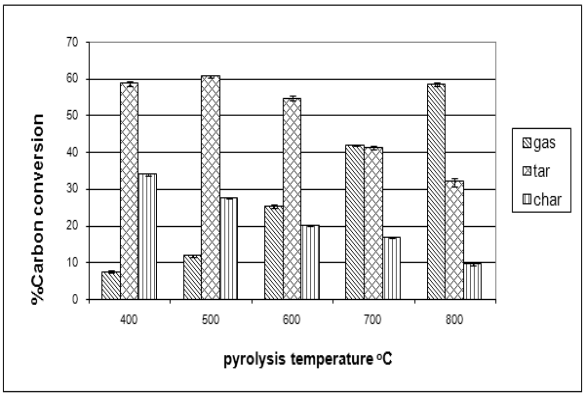

Figure 3. Effect of pyrolysis temperature on % Carbon production

Figure 3 depicts the effect of pyrolysis temperature on carbon conversion into each products including gas, tar, and char. When the pyrolysis temperature was increased from 500 to 800°C, the carbon conversion into tar was decreased from 60.7 to 31.9%. On the other hand, the carbon version into gas was increased from 11.77 to 58.4%. This is because the thermal cracking of biomass as well as tar is endothermic process which prefers high temperatre condition. I was observed that the carbon conversion into tar at 400°C is less than that at 500°C. An expalnation for this would be that the decomposition mechanism of the Leucaena wood is not yet completed at such a low temperature (see Figure 2). The influence of pyrolysis temperature on gas production is shown in Figure 4. The gradual increase in CO yield was observed with increasing pyrolysis temperature. This is because the oxygen content of the biomass sample is very high, as can be seen Table 1. So, the gradual increase in CO yield could be examined by decarbonylation of the

aromatic aldehydes of released tar. This explanation is as well as results of Ates and Isikdag [1] and Hosoya [2].

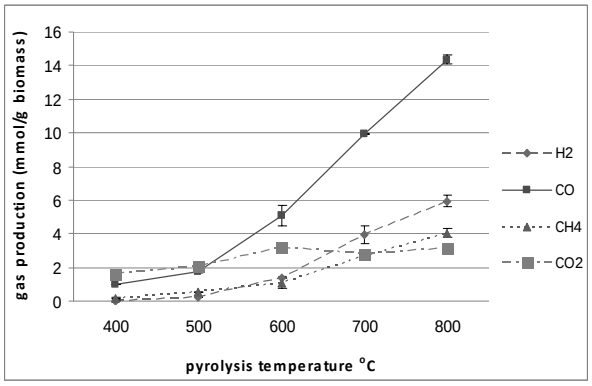

Figure 4. Effect of pyrolysis temperature on gas production for pyrolysis

Effect of pyrolysis temperature on reforming reaction of released tar with and without catalyst

Figure 5 shows the comparison of carbon conversion into tar obtained from pyrolysis, non-catalystic steam reforming, and catalytic steam reforming, at different pyrolysis temperatures. The carbon conversion into tar in case of steam reforming seems slightly increased with increasing pyrolysis temperature from 400 to 800°C. This trend is opposites to that in case of pyrolysis (see Figure 5). However, the trend %carbon in tar of catalytic steam reforming in case of catalytic reforming the pyrolysis temperature of 600°C was observed to give the highest carbon conversion into tar. It is speculated that the volatile or tar released at this temperature is composed of compounds that would be more stable and less reactivity in reforming reaction. In addition, it was possible that the catalyst activity was still low at this temperature, as discussed later.

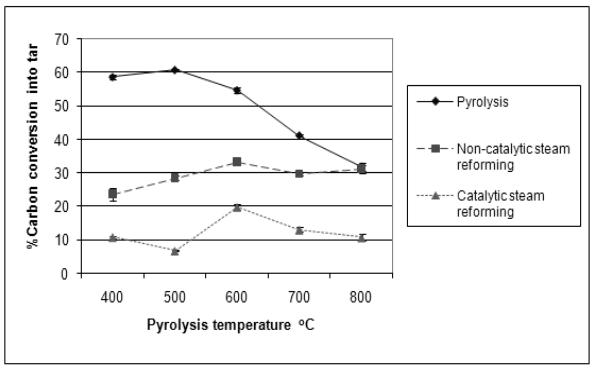

Figure 5. Effect of pyrolysis temperature on %carbon conversion into tar

The reactivity of tar could be examined by means of comparing conversion capability of tar released at a given temperature by steam reforming, as shown in Figure 6. The each of %tar conversion can be calculated by equation 1 and 2.

$$\frac{C_P - C_{NC}}{C_P} \times 100 \qquad \text{— 1}$$

$$\frac{C_{NC} - C_C}{C_{NC}} \times 100 \qquad \text{— 2}$$

where

C_P = %carbon conversion into tar of pyrolysis

C_{NC} = %carbon conversion into tar of non-catalytic steam reforming

C_C = %carbon conversion into tar of catalytic steam reforming

It was found that the %tar conversion with the absence of catalyst was decreased with increasing pyrolysis temperature. This result suggested that the released tar with increasing pyrolysis temperature is composed on less-reactive compounds. At relatively high pyrolysis temperature, free radical of tar can agglomerate to polycyclic aromatic hydrocarbon (PAHs) through condensation and re-polymerization [1]. This compound can be hardly decomposed in non-catalytic steam reforming.

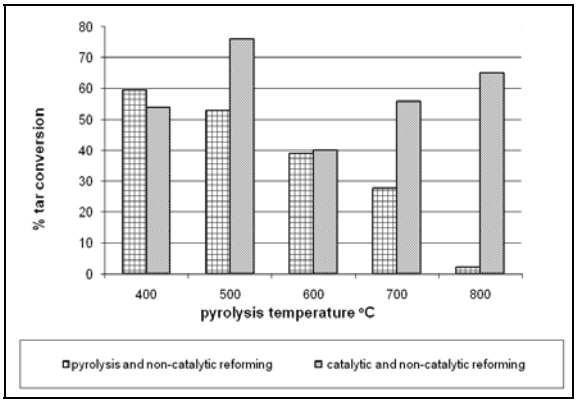

Figure 6. Effect of pyrolysis temperature on %tar conversion

Comparing the %tar conversion between non-catalytic and catalytic steam reforming, it was found that the highest %tar conversion was 76.14 at pyrolysis temperature of 500°C. This result indicated that the compositon of tar released at this temperaure could be easily decomposed in catalytic steam reforming. The tar conversion was increased from 40.25 to 63.35% when the pyrolysis temperature was increased from 600 to 800°C. This would be due to the catalytic activitiy of the $NiO/MgO/Al_2O_3$ which was employed as a catalyst in this work. The catalyst was prepared and calcined at relative high temperature and is likely active with released tar at high temperature operation.

Conclusions

In this study, the effect of pyrolysis temperature affected the reactivity of released tar in steam reforming. In case of non-catalytic steam reforming, the pyrolysis temperature was increased from 400^{o}C to 800^{o}C, the trend of tar conversion was decreased because the released compounds in tar at relatively high temperature can be hardly decomposed. Especially, the almost tar released at the pyrolysis temperataure of 800^{o}C cannot be decomposed by steam reforming with the absence of catalyst. On the other hand, the maximum tar conversion was observed at the pyrolysis temperaure of 500^{o}C. Employing catalyst can stimulate reaction rate and promote the steam reforming of tar. The released tar, even at 600 to 800^{o}C can be decomposed in catalytic steam reforming using the $NiO/MgO/Al_2O_3$ as the catalyst.

Acknowledgement

The authors express gratitude to Thailand Institute of Scientific and Technological Research (TISTR) and Center of Excellence for Petroleum, Petrochemicals, and Advanced Materials for providing financial support.

References

[1] F. Ates and M. Isikdag, *Influence of temperature and alumina catalyst on pyrolysis of corncob. Fuel.* **88** (2009), pp.1991-1997

[2] T. Hosoya, H. Kawamoto, S. Saka, *Pyrolysis gasification reactivities of primary tar and char fractions from cellulose and lignin as studied with a closed ampoule reactor*. J*ournal of Analytical and Applied Pyrolysis.* **83** (2008), pp.71-77

[3] L. Devi, K.J. Ptasinski, F.J.J.G. Janssen, S.V.B.V. Paasen, P.C.A. Bergman, J.H.A. Kiel, *Catalytic decomposition of biomass tars: use of dolomite and untreated olivine.* Renewable Energy **30** (2005), 565-587

[4] S. Hosokai, J.I. Hayashi, T. Shimada, Y. kobayashi, K. Kuramoto, C.Z. Li, T. Chiba, *Spontaneous generation of tar decomposition promoter in a biomass steam reformer.* Chemical Engineering Research and Design. **83** (2005), pp.1093-1102

[5] S. Krerkkaiwan and P. Kuchonthara, Syngas production from gasification of palm oil empty fruit bunchs, Master's Thesis, Chulalongkorn University, 2008.

Syngas production from a dual-bed gasifier

R. Sangboon[1] and P. Kuchonthara[1,2*]

[1] Fuels Research Center, Department of Chemical Technology, Faculty of Science, Chulalongkorn University, Bangkok, Thailand
[2] Center of Excellence for Petroleum, Petrochemicals and Advanced Materials, Chulalongkorn University, Bangkok, Thailand

[*] E-Mail: prapan.k@chula.ac.th

Abstract: Among the biomass conversion processes, gasification is one of the important and promising technologies. Conventional gasification typically employs a partial oxidation process using air. As a result, the calorific value of gaseous product is relatively low because of the dilution by inevitably substantial amount of nitrogen from air. To increase the calorific value of the gaseous product, dual-bed gasifiers (DBG) for biomass gasification based on a concept of separation of combustion zone and gasification zone have been developed recently by several researchers. The aim of this work was to design and construct a new gasifier based on the concept of DBG incorporated with integration of heat transfer between the two zones. This gasifier is called Indirect-Autothermal Dual Bed Gasifier (I-ADBG). The I-ADBG consists of a bubbling fluidized bed reactor serving as a combustor to provide necessary heat for endothermic gasification reactions and a two-stage moving bed reactor serving as a gasifier to produce gaseous product. The heat is transferred between two zone by circulation of bed materials. Sawdust was used as feedstock in the preliminary study. The result indicated that gaseous product has low nitrogen content, less than 10% by volume leading to high calorific value of gaseous product. In addition, high hydrogen content around 35-40% by volume was observed. These verify that the new designed gasifier, I-ADBG is beneficial for producing good quality gas product which can be used as syngas or hydrogen-rich gas.

Introduction

Recently, the utilization of biomass as an alternative of fossil fuels has been interested due to increasing of energy demand. However, most of biomasses are in solid form that unsuitable for using as direct fuel. Biomass conversion process is necessary for improve their efficiency. Many research activities were focused on the investigation and development of biomass utilization technology to meet high efficiency. There are many conversion technologies to convert biomass such as carbonization, pyrolysis, liquefaction and gasification. Among the biomass conversion technologies, gasification is one of the important and promising technologies which convert solid fuel into gaseous fuel with high conversion and overall energy efficiency. Moreover, the product gas can be used as direct fuel and feedstock to produce liquid fuel with higher selectivity than liquefaction. However, conventional gasification (fixed-bed, fluidized-bed) typically employs a partial oxidation process using air. As a result, the calorific value of gaseous product is relative low because of the dilution by inevitably substantial amount of nitrogen from air. To increase the calorific value of the gaseous product, dual-bed gasifiers (DBG) for biomass gasification based on a concept of separation of combustion zone and gasification zone have been developed recently by several researchers.

The basic idea of the dual-bed gasifier is to divide the reactor into two zones, a gasification zone and a combustion zone. A circulation loop of bed material is created between these two zones, while the gases should remain separated. The circulating bed material acts as heat carrier from the combustion zone to gasification zone. The basic principle of this process is illustrated in Figure 1.

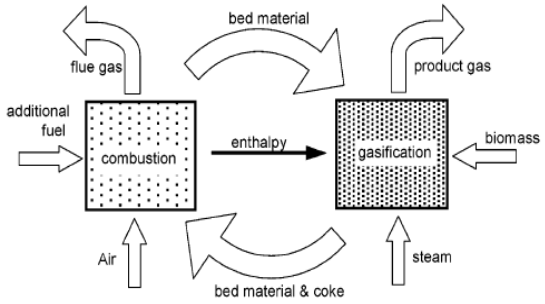

Figure 1. Principle of the dual-bed gasifier [1]

The aim of this work was to design and construct a new gasifier based on the concept of DBG incorporated with efficient integration of heat transfer between two zones to increase the calorific value of the gaseous product.

Design and construction

The autothermal gasification processes, in which air or air-steam mixtures act as the gasification agent, have been intensively investigated in the past decades. These processes will result in a large amount of N_2 in the produced gas, a lower heating value of the gas, and cold efficiency of the gasification process. Steam gasification is a promising technology for thermo-chemical hydrogen production from biomass. However, pyrolysis and steam gasification reactions of biomass are endothermic. The circulation of the solid heat carrier should be a good way to supply the energy required in steam gasification of biomass. It has actually been employed in various types of dual-bed gasifier (DBG) such as the FERCO SilvaGas process [2], the FICFB process [3], and the others [4, 5].

On the basis of the characteristics of biomass gasification and experiences reported in the literature, we propose in this paper a new dual-bed gasifier. The new dual-bed gasifier consists of a bubbling fluidized bed reactor serving as a combustor to provide the energy for endothermic gasification reactions in gasifier and a two-stage moving bed reactor serving as a gasifier with the concept of gas-solid countercurrently moving, where the produced tars in the lower stage of gasifier pass through hot bed in an upward direction and are greatly decomposed at the upper stage of gasifier. The circulation of bed material will make the steam gasification in a downdraft-moving bed are feasible. This new dual-bed gasifier is called Indirect-autothermal dual bed gasifier (I-ADBG). The basic idea of I-ADBG is illustrated in **Figure 2.**

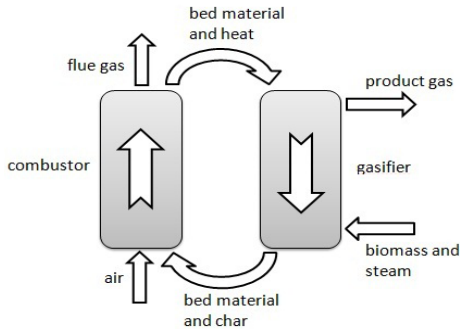

Figure 2. The basic idea of I-ADBG

Materials and Methods

Materials. Sawdust was employed as biomass samples for testing the I-ADBG system. The biomass samples were sieved and classified to fractions of particle size below 1.2 mm and dried for 2 hours at 100˚C before utilization. The properties of this sawdust are listed in Table 1. In this system, a silica sand was used as a bed material and heat carrier particles (HCPs). The samples were sieved and classified to particle size 250-425 μm.

A small amount of an additional fuel was used to control the temperature of combustion zone. Because of the amount of produced char from gasifier was insufficient to provide the energy supporting in the combustion process to obtain the conditioned temperature (800-900˚C). This additional fuel was charcoal.

Table 1. Properties of the sawdust

Proximate analysis (wt%, ad. basis)	
Moisture	9.10
Volatile matter	78.43
Fixed carbon	8.51
Ash	3.96
Ultimate analysis (wt%, daf. basis)	
C	43.14
H	5.07
N	0.00
O	51.79
HHV (MJ/kg, daf. basis)	12.59

Apparatus. I-ADBG is schematically shown in Figure 3, where steam gasification of biomass and combustion of the produced char can occur simultaneously. The unit consisted of a two-stage moving bed gasifier and a riser combustor. The riser was 50 mm in i.d. and 3500 m high, and the gasifier was 400 mm in i.d. and 1000 mm high. Both are made of steel. The thermocouples are placed at various points along the reactor to indicate the temperature.

The facility of an I-ADBG is composed of air compressor, scrubber, particle trap and vacuum pump.

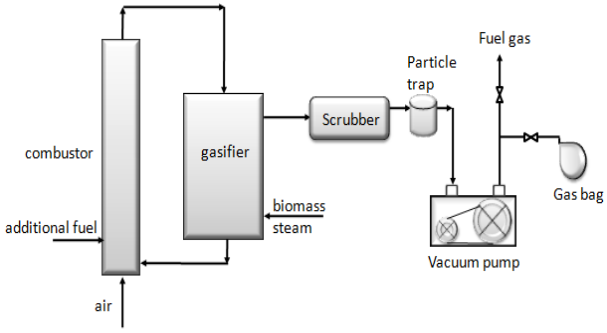

Figure 3. schematic of I-ADBG and facility

Methods. There are 2 experimental sections in this study. First section is the testing of the dual-bed gasifier concept. Second section is to study the I-ADBG system at the operating temperature.

Cold model test

The cold model test is to test the flowing of air and the circulation of bed material between combustor and gasifer. In the testing, we used a mixed gas of 25 vol% CO_2 balanced in air as a tracer. The tracer is fed into the bottom of combustor representing the fluidizing medium. And pure air is fed into the lower stage of gasifier representing the produced gas in the gasifier. The produced gas is taken at the top of gasifier (product gas outlet). The percentage of CO_2 in the sampling gas was analyzed using GC.

Hot run test

The combustor and the gasifier are heated up to desired temperature by LPG burner. Then steam is injected into the lower stage of gasifier and biomass is also fed into the gasifier by screw feeder at constant flow rate from hopper at the bottom of the gasifier. The produced tars and volatiles in the lower stage pass through hot bed together with steam. Steam reforming is partially occurred in the lower stage and continuously occurred in the upper stage that has higher temperature than the lower stage. The gaseous product was taken via a vacuum pump and cooled in the scrubber to separate the condensable components. The fine dust in the gaseous product is captured in the particle trap before the gaseous products are collected in gas bags.

The residual chars along with the bed material from the gasifier are transported to the riser combustor. In the combustor, the bed material is fluidized by air and the char is burned off. Additional fuel can be used to

control the temperature of combustor because the residual chars from the gasifier are insufficient to heat up the combustor to the require temperature. At the top of combustor, combustion gases are separated from the hot bed material, which is circulated into the gasifier, without mixing of the combustion and gasification product gases, providing the heat for the endothermic gasification reactions. The operating conditions are illustrated in Table 2.

Table 2. Summary of experimental conditions in hot run

Gasifier	
reactor temperature (˚C)	600-700
biomass feeding rate (kg/h)	3
circulating amount of bed material (kg/h)	140
steam to carbon ratio	1-3
pressure	atmospheric
Combustor	
Reactor temperature (˚C)	800-850
Amount of air supply (L/min)	300

The gaseous product was analysed by a gas chromatography (Shimadzu GC-2014) with a thermal conductivity detector (TCD) and Unibeads C column. Argon was used as a carrier gas. The temperatures of the injection port, column and detector were 120, 50 and 180 ˚C, respectively

Results and Discussion

From the cold model test, the produced gas in the gasifier has low carbon dioxide content (less than 1% by volume). The result verified that fluidizing air in combustor is not flow into the gasifier via the re-circulation line. Therefore, it is indicated that nitrogen from air combustion will scarcely contaminate in the product gas with the concept of dual-bed gasifer.

In the hot run test, the gas composition and the other experimental data when the representative sawdust is gasifed at 1.013 bar are shown in Table 3. It can notice that the I-ADBG gave high hydrogen content, about 35% by volume, while the nitrogen content was very low, less than 1% by volume.

Table 3. The data of hot run test

	I-ADBG
Gas composition (vol%, dry)	
H_2	34.63
CO	23.83
CO_2	26.00
CH_4	14.44
N_2	0.92
HHV (MJ/Nm^3)	13.20
C to gas conversion (%)	89.15
Cold gas efficiency (%)	52.63

Figure 4. show the gas composition of gaseous product of the I-ADBG compare with that of the other conventional gasifiers. Produced hydrogen in the I-ADBG is higher than the conventional gasifier and remaining nitrogen in the gaseous product is extremely low. The high hydrogen content in the gaseous product was mean that the I-ADBG process can also be used for toward Fischer Tropsch liquid fuels production and hydrogen separation in the longer term.

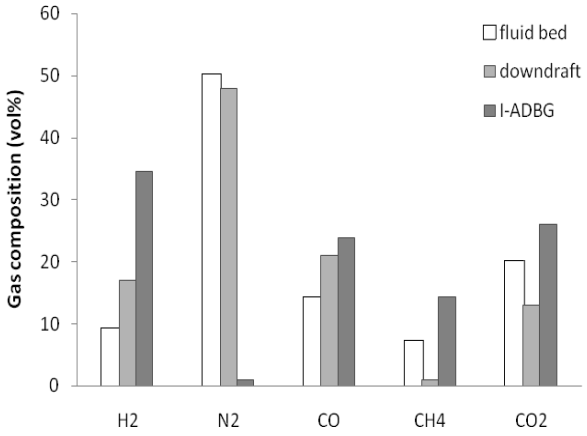

Figure 4. Gas composition of I-ADBG compared with other conventional gasifier.

In conventional gasification, Air-blown processes (Fixed-bed gasifier, Fluid-bed gasifier) produce low calorific value gases with a typical higher heating value (HHV) of 4–7 MJ/Nm^3, while oxygen- and steam-blown processes result in gases with a HHV of 10–18 MJ/Nm^3, In case of the I-ADBG, it gives the gaseous product with HHV of 13.20 MJ/Nm^3. This is attributable to the obviously low nitrogen content in the gaseous product. Therefore, the gaseous product from the I-ADBG could be use as a fuel gas in many types of industry.

Carbon to gas conversion of the I-ADBG process determined from the product gas composition and gas yield was very high (about 89%) because the residence time in the gasifier is adequate that most of produced volatiles could be completely gasified before leaving from gasification zone. In addition, the gasifier of the I-ADBG has sufficient heat to support the pyrolysis reaction, steam reforming reaction and the other endothermic reactions. Therefore, the produced volatiles and tars could be greatly decomposed into gaseous product that reducing the need for downstream processing.

However, the cold gas efficiency (CGE) of this I-ADBG system was found to be still low, 52.63%. This is due to the considerable amount of additional fuel which was supplied to the combustion zone in order to preserve the combustion temperature. This might be relevant to the insufficient char produced from gasification zone to be used as fuel in combustion. Hence, it has to increase the biomass feeding rate in order to produce sufficient char for using as fuel source in combustion zone.

Conclusions

The result indicated that gaseous product has low nitrogen content, less than 10% by volume, and high hydrogen content, 35-40% by volume leading to high calorific value of gaseous product. These verify that the new designed gasifier, I-ADBG is beneficial for producing good quality gaseous product which can be used as syngas or hydrogen-rich gas.

Acknowledgement

The authors express gratitude to The Research and technology institute of PTT public company and Center of Excellence for Petroleum, Petrochemicals, and Advanced Materials for providing financial support.

References

[1] H. Hofbauer, R. Rauch, G. Loeffier, S. Kaiser, E. Fercher, H. Tremmel, 12th European Conference and Technology Exhibition on biomass for Energy, Industrial and Climate Protection, Amsterdam, The Netherlands, 2002.

[2] M.A. Paisley, M.C. Farries, J.W. Black, J.M. Irving, R.P. Overrend, First World Congress and Exhibition on Biomass for Energy and Industry, Sevilla, Spain, 2000.

[3] C. Pfeifer, R. Rauch, H. Hofbauer, *Ind. Eng. Chem. Res.***43** (2004), pp. 1634-1640.

[4] L. Wei, S. Xu, J. Liu, C. Lu, S. Liu, C. Liu, *Energy & Fuels.* **20** (2006), pp. 2266-2273.

[5] G. Xu, T. Murakami, T. Suda, Y. Matsuzawa, H. Tani, *Fuel Process. technol*. **90** (2009), pp. 137-144.

[6] DR. Lide, *CRC Handbook of chemistry and physics*, CRC Press, Boca Raton, FL, USA (1994).

[7] X.T. Lia, J.R. Grace, C.J. Lim, A.P. Watkinson, H.P. Chen, J.R. Kim, *Biomass and Bioenergy.* **26** (2004), pp.171-193

Cyclone design for solid particles in circulating fluidzed bed

Natthaphong Imsaengchan[1*] and Lursuang Mekasut[1,2]

[1]Department of Chemical Technology, Faculty of Science, Chulalongkorn Universitsy, Phyathai Road, Patumwan, Bangkok, Thailand
[2]Center for Petroleum, Petrochemicals and Advanced Materials, Chulalongkorn University, Bangkok, Thailand

*E-mail:nor_nor_1106@hotmail.com

Abstract: In order to reduce the solid fuel lost in the circulating fluidized bed (CFB) system, cyclones have been widely used as gas-solid separator. Nowadays, cyclone design is one of an interesting topic to improve separation efficiency. In this work, the efficiency of cyclone with two different geometries, conventional and square cyclones, was studied in cold-flow CFB by varying primary air flow rate. Both sand and coal/sand mixture having different density and average particle size were tested in 6 meter-height CFB reactor equipped with 0.16 meter i.d. conventional cyclone. The results show that the collection efficiency of the conventional cyclone increased as the primary air flow rate was increased from 175 to 230 m^3/h. Modeling of computational fluid dynamics (CFD) using FLUENT 6.2.16 provides the preliminary results with the best collection efficiency for square cyclone.

Introduction

The Circulating Fluidized Bed (CFB) has been developed and applied into many industries using gas-solid direct contact processes in these days, because this system presents many advantages. The CFB gives higher production processes performance with lower emissions and consequently reduces production costs. Moreover, the CFB is very flexible for variety of solids fuel. Normally, the CFB is assembled by three main parts which are riser, cyclone and feedback system.

Cyclone is the key part of the CFB system that affects the economics of the process. In cyclone, after combustion, suspended solids are separated from gas by centrifugal force. The solids will attack the cyclone wall and fall into feedback system. In order to optimize the cyclone performance, it needs to be properly designed. Normally, the dimensions of cyclone are calculated following conventional ratios data. [1] After evaluation of pressure drop and separation efficiency, the cyclone dimensions were adjusted to improve the performance. Besides from the round shaped cyclone, the rectangular shaped cyclone has been developing recently. The inlet air velocity and the behavior of gas and solid are studied with the aim to improve the CFB particle separation performance improvement.

Materials and Methods

The experimental setup in this study is depicted in Figure 1. The riser section is constructed of acrylic of 10 cm i.d. 6 m height and a 6 cm i.d. standpipe (downcomer). The solid particles are fluidized and transported by upward flowing air into the cyclone at the top. Solids flow down vertically through the vertical standpipe while the air flows out from the cyclone. Twenty one pressure taps are equipped along the CFB system as shown in Figure 1, all connected to the Differential Pressure Transmitter (DPT) for pressure drop measurements. The geometry of cyclones is shown in Figure 2. This study is divided 2 main works. [1-3] First, the performance of the conventional cyclone is studied. The primary air feed rate is between 175 to 230 $m^{3/}$h. Flow pattern inside riser is tracked by measuring the pressure from the position 1 to 15. The effects of primary air velocity, pressure drop and separation efficiency at different air feed rate are also investigated. The physical properties of the solid particles (sand and the mixture of sand and coal) using in this experiment is summarized in Table 1 and the result of size distribution is given in Table 2.

In the second part, before building the actual square cyclone, the cyclone model is simulated by using Gambit program and compares the performance with conventional cyclone by using FLUENT 6.2.16 program. [4,5]

Table 1: Physical properties of sand and mixture

Property	sand	mixture
Particle density (kg/m^3)	2463	2354
Bulk density (kg/m^3)	1319	1277
Size range (μm)	<500	<500
Sauter mean diameter (μm)	109.5	273.4

Table 2: Size distribution of sand and mixture determined by screening

Mesh size (μm)	Mass fraction	
	Sand	Mixture
425 – 500	0.2	0.45
250 – 425	0.2	0.45
150 – 250	0.2	0.033
75 – 150	0.2	0.033
Lower 75	0.2	0.034

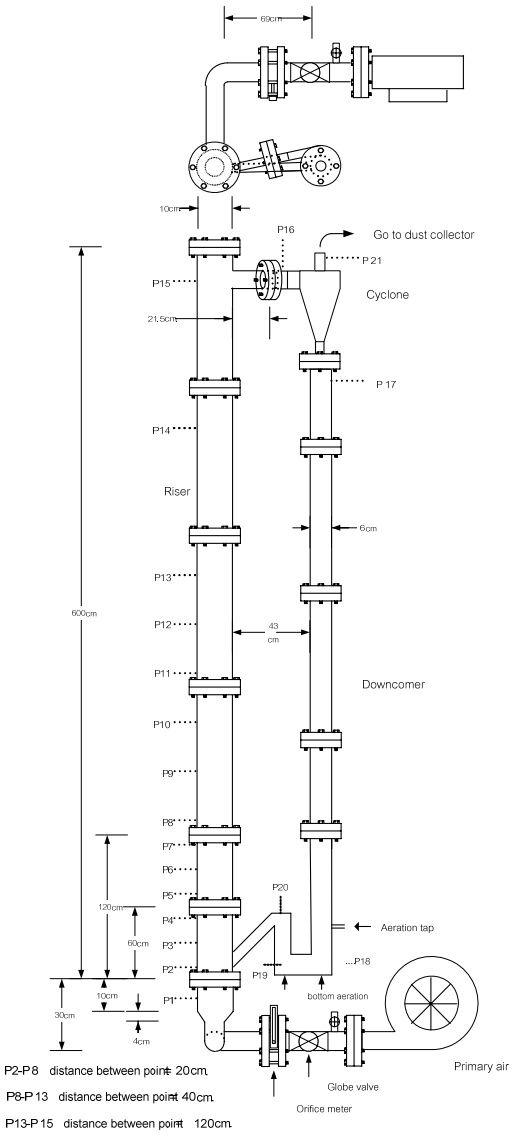

Figure 1. The CFB system

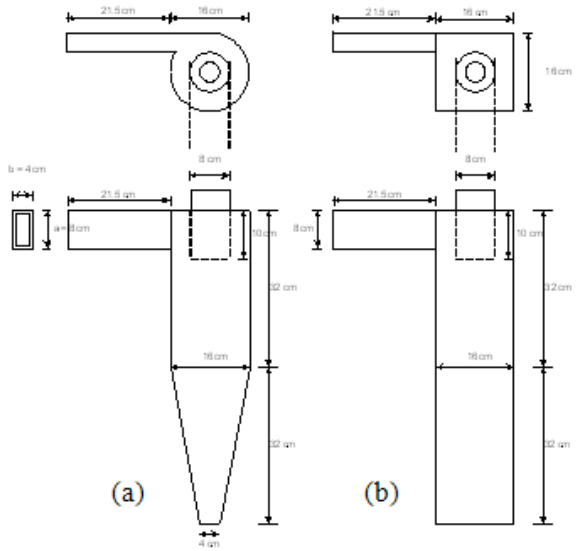

Figure 2. Cyclone separator (a) conventional cyclone and (b) square cyclone

Results and Discussion

Effect of primary air on flow pattern profiles

To study the flow pattern inside the riser of CFB system with different experimental conditions, the correlation between the voidage and the height of riser is illustrated in Figure 3. The voidage can be calculated from equation (1) and (2).

$$\varepsilon_s = \frac{\Delta P}{\Delta H g \rho_p} \quad (1)$$

$$\varepsilon = 1 - \varepsilon_s \quad (2)$$

The results show that the solids are very dense in the lower part of the riser, while the upper part has lower solid density. This flow pattern is called fast fluidization regime which is the general flow pattern for CFB system.

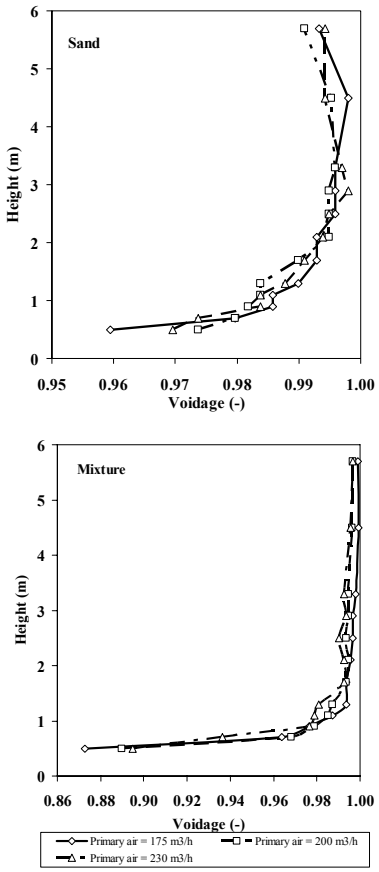

Figure 3. Flow pattern profiles of the CFB reactor using in this study

Effects of primary air on cyclone inlet velocity and pressure drop

From Table 3 and Figure 4, it can be seen that the air inlet velocity and the pressure drop increased as the primary air feed ratio is increased. The cyclone pressure drop is confirmed by using Shepherd and Lapple equation. The pressure drop equation of Shepherd and Lapple are as follow. [5]

$$\Delta P = \frac{1}{2}\rho_g V_g^2 N_H \tag{3}$$

$$N_H = K\frac{HW}{D_e^2} \tag{4}$$

The results display that the margin between the experimental data and the Shepherd and Lapple equation result is very large. Then the Muschelknautz and Greif (1997) equations are applied to the experimental results. The pressure drop equation of Muschelknautz and Greif (1997) are as follow. [6]

$$\Delta P = \Delta P_f + \Delta P_e \tag{5}$$

$$\Delta P_f = f_w \frac{A_R}{V_b}\frac{\rho_g}{2}(u_a u_i)^{1.5} \tag{6}$$

$$\Delta P_e = 2 + 3\left(\frac{u_i}{v_i}\right)^{\frac{4}{3}} + \left(\frac{u_i}{v_i}\right)^2 \frac{\rho_g v_i^2}{2} \tag{7}$$

The calculation results indicate the consistent with the experimental data.

Table 3: Comparison between cyclone inlet velocity and pressure drop of cyclone with various primary air flow rate.

Primary air (m^3/h)	Cyclone inlet velocity (m/s)	Pressure drop (Pa)	
		sand	mixture
175	10.9	205.76	205.76
200	13.1	323.33	372.32
230	15.3	421.31	431.11

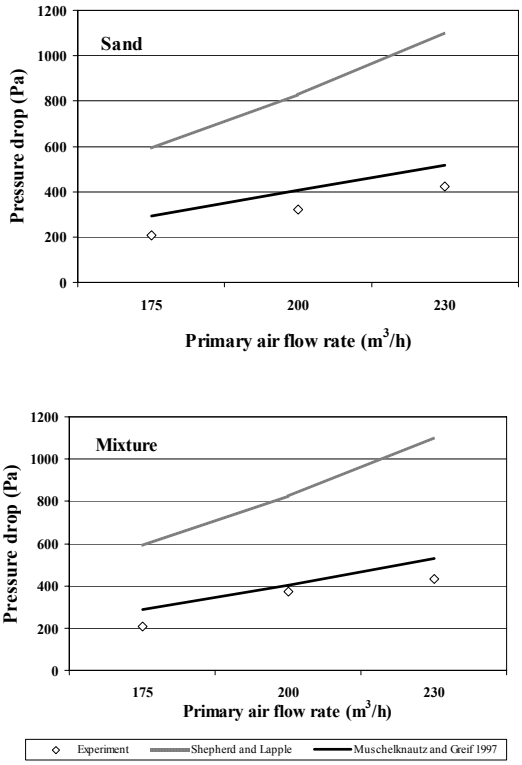

Figure 4. Effect of primary air on pressure drop in the cyclone

Effect of primary air on collection efficiency

For each experiment, the initial solid weight is 5 kilograms and it circulates for 2 hours in the system with air flow rate of 175-230 m^3/h. For different experimental conditions, the cyclone overall efficiencies are calculated and deduced from the amount of solid residue in each size range. Figure 5 shows the efficiency in each particle size range for different air flow rate. The result shows that the higher efficiency is obtained when using higher air feed rate.

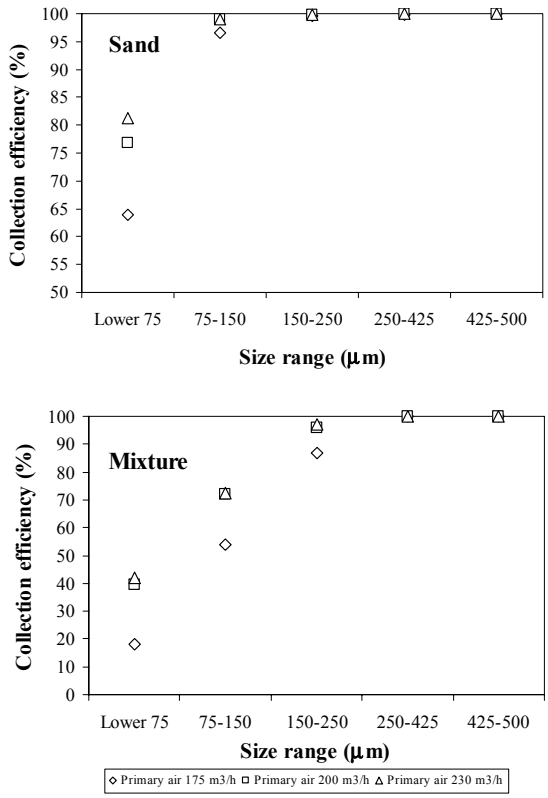

Figure 5. Size selective efficiency at different size ranges (sand and mixture) using various operating condition

Table 4: Amount of sand residue from experiments, Collection efficiency and mean diameter of cyclone leaving dust

Primary air (m^3/h)	Amount of sand residue (g)	Collection efficiency (%)	Mean diameter (μm)
175	4600.50	86.65	7.62
200	4750.10	91.09	13.65
230	4784.55	92.17	14.50

Table 5: Amount of mixture residue from experiments, Collection efficiency and mean diameter of cyclone leaving dust

Primary air (m^3/h)	Amount of sand residue (g)	Collection efficiency (%)	Mean diameter (μm)
175	4772.00	93.48	4.13
200	4846.45	95.32	3.96
230	4851.05	95.41	4.01

From the amount and size of sand residue and from the cyclone efficiency that are displayed in Table 4 and Table 5, it can be seen that the lowest efficiency is observed in the system with air feed rate of 175 m^3/h. This can be explained by the amount of solid residue. The highest residue gives highest efficiency.

The cyclone leaving dust are also collected and analyzed by particle size analyzer. The results show that the average particle size of the dust when using sand with high primary air flow rate is larger than that when using sand with low primary air flow rate. This is caused by the back pressure in the system. On the other hand, the experimental conditions don't affect the average particle size when using solid mixture in the system.

CFD studies

Table 6 shows the conventional and square cyclone simulation results. The actual velocity inlet from experiment is used as a simulation input. The results display that the square cyclone give better efficiency than conventional cyclone.

Table 6: Comparison between mass fractions at the gas exit and downcomer efficiency with various cyclone inlet velocity.

Velocity inlet (m/s)	Collection efficiency (%)	
	Conventional cyclone	Square cyclone
10.9	99.97	99.88
13.1	98.62	99.87
15.3	94.07	99.67

Conclusions

The effects of different variables for the circulating fluidized bed system had been studied in the present work. The conclusions may be summarized as follow:

1. The inlet velocity and pressure drop of cyclone are increased as the primary air increased, and result in higher collection efficiency.
2. Cyclone pressure drop in CFB system from experiment can be confirmed by calculation (Muschelknautz and Greif 1997).
3. From simulation, square cyclone gives better collection efficiency than the conventional cyclone.

List of symbols

A_R Area of cyclone wall including roof and outer surface of exit tube, m^2
D_e Vortex finder diameter, m
f_w Total wall friction coefficient
G Gas of density, kg/m^3
g Gravity force,m^2/s
H Gas inlet height, m
K 16 for tangential inlet cyclone
N_H Inlet velocity head number
u_a Tangential velocity at cyclone barrel radius, m/s
u_i Tangential velocity at exit radius, m/s
V_b $Vb \sim V_g$
V_g Gas velocity, m/s
v_i Mean velocity in exit tube, m/s
W Gas inlet width, m
ε_s Solid holdup
ε Voidage fraction
ρ_p Particle of density, kg/m^3

ΔH Different height, m
ΔP Pressure drop, Pa
ΔP_f Pressure drop due to friction on cyclone wall, Pa
ΔP_e Hydrodynamic loss in inner vortex, Pa

References

[1] K.W. Lee, K.S. Lim and H.S. Kim *Aerosol Science*. **35** (2004), pp. 743–754.
[2] S. Yaxin *Chemical Engineering Science*. **61** (2006), pp. 1395-1400.
[3] S. Yaxin and M. Yuru *Chemical Engineering Journal*. **121** (2006), pp. 51-58.
[4] S. Mehrzad, R. Arman and F. Meisam and E. Reza *Chemical Engineering and Processing*. **47** (2008), pp. 128-137.
[5] S. Mehrzad, R. Arman and K. Homayoon *Powder Technology*. **191** (2009), pp. 349-357.
[6] P. Basu, *Combustion and gasification in fluidized beds,* CRC Press, U.S.A. (2006)

Characteristics of microwave-assisted glycolyzed products from pet wastes using different glycols

S. Udomtawornsawat[1,2] and P. Potiyaraj[1,2*]

[1]Center of Excellence in Textiles, Department of Materials Science, Faculty of Science, Chulalongkorn University, Bangkok 10330, Thailand
[2]National Center of Excellence for Petroleum, Petrochemicals and Advanced Materials, Chulalongkorn University, Bangkok 10330, Thailand

*E-mail: pranut.p@chula.ac.th, Tel: +66 2218 5544

Abstract: Poly(ethylene terephthalate) (PET) from post-consumer soft-drink bottles was depolymerized in excess glycol using microwave energy source, as opposed to conventional thermal heating, with the presence of zinc acetate as a catalyst. The presences of –OH, -CH, C=O, C-O-C and C-OH were revealed by Fourier transform infrared spectroscopy (FT-IR). When ethylene glycol was used for the glycolysis reaction, bis-(2-hydroxyethylene) terephthalate (BHET) and some larger oligomers were recovered. It was found that, under a constant microwave power, the yield of the reaction was controlled by the irradiation time. PET was also depolymerized using propylene glycol and diethylene glycol in order to study the effects of different glycols on the characteristics of glycolyzed products. Thermal gravimetric analysis (TGA) pointed out that the thermal stability of glycolyzed products obtained using ethylene glycol was better than that of the products when propylene glycol and diethylene glycol were used for the glycolysis reaction.

Introduction

Poly(ethylene terephthalate) (PET) is one of the most widely-used polymers for domestic as well as industrial applications. High-performance fibers, photographic films, and soft-drink bottles were commonly manufactured from PET due to its superior properties such as high strength, toughness and clarity combined with low permeability to carbon dioxide, oxygen and water vapor. PET is usually synthesized either by reacting terephthalic acid (TPA) with ethylene glycol (EG) or dimethyl terephthalate (DMT) with EG. Both polymerization schemes first form the monomer, bis(hydroxyethyl) terephthalate (BHET). After adding stabilizers and additives, the polymer is polymerized through polycondensation by releasing EG as a by-product.

Due to its selective gas permeability, PET bottles are popularly used for carbonated beverages and other food products. In turn, the volume of post-consumer PET bottles has been rapidly increased. Like other petroleum based thermoplastic materials, spontaneously degradation of PET in nature is almost impossible inevitably causing plastic waste building up problem. Recycling of PET waste is one of the methods that can reduce this serious problem [1]. In general, PET waste can be recycled by different methods, namely, physical recycling and chemical recycling. Being the easiest method, physical recycling consists of grinding, washing and extruding of PET waste and reusing it to reduce new raw material usage. Unfortunately, during physical recycling, thermal degradation occurs thus lowering some usage properties of recycled products. In contrast, chemical recycling of PET can transform waste into other useful chemicals which can be used for synthesizing a new material with desired properties. However, chemical recycling of PET still needs a lot more research and development in order to make the technique more commercially feasible.

One of the most studied chemical recycling techniques is the depolymerization of PET in glycols. The reaction involves the molecular degradation of PET molecular chains by glycols, in the presence of trans-esterification catalysts, mainly metal acetates, where ester linkages are broken and replaced with hydroxyl terminals. PET can be depolymerized by glycolysis to obtain oligomeric diols and polyols, or glycolyzed into its monomeric units, bis-(2-hydroxyethylene) terephthlate (BHET) or dimethyl terephthlate [2, 3]. These glycolyzed products have been widely used in the production of unsaturated polyesters and rigid or flexible polyurethanes [4, 5]. It was found that zinc acetate was demonstrated as the most effective catalysts used for PET glycolysis [6]. Although the use of catalyst can improve depolymerization rate, the reactions still need hours to complete thus limit their commercial applications. The glycolysis reaction in excess EG in the presence of zinc acetate as a catalyst complete in 2 h at 190 °C [7,8].

The use of microwave energy as an energy source in chemical reactions requiring heat has received much attention in recent years. Microwave energy is supplied by an electronic field directly to the reaction system [9]. The main advantage of using microwave as an energy source in chemical reactions is the significantly decrease of reaction time while retaining, or even increasing, the reaction yields. PET glycolysis reactions characterized by short reaction times in which complete PET solubilization were achieved. It was clearly demonstrated that a domestic microwave oven of 800W was highly effective in completing the depolymerization reaction of PET in ethylene glycol

using zinc acetate as a catalyst. The time taken for completion of reaction was reduced drastically from 8 h to 35 min [10]. The method is compatible with the use of a wide range of glycol reagents as well as a variety of basic catalysts [11]. Microwave irradiation can be used as an energy source in hydroglycolysis. The process of hydroglycolysis reported here is economically viable since yields of recycled products are high, and it has potential for further improvement to produce useful products. Its can be recovered and used for virgin PET resin synthesis [12].

In this work, the use of microwave energy in PET glycolysis reactions using different glycols (EG, PG and DEG) with the presence of zinc acetate as a catalyst was investigated. The thermal properties and chemical structure analysis of glycolysis products were also discussed.

Materials and Methods

Materials

Post-consumer soft-drink PET bottles of the same brand were thorougly cleaned, cut into small pieces and oven-dried. The dried PET waste was pulverized and sieved in order to obtain PET waste powder with a particle size of less than 1.0 mm. Ethylene glycol (EG), propylene glycol (PG), diethylene glycol (DEG) were used as a glycol in the depolymerization reaction. Zinc acetate was used as a catalyst. All chemicals were purchased from Fluka and used without further purificatioin.

Glycolysis of PET waste

Pulverized PET waste was reacted with a glycol (EG, PG or DEG) with the molar ratio of PET repeating unit to glycol of 1:6. Zinc acetate was used as a catalyst at 0.5% by weight of PET. The glycolysis reaction was carried out in 600 W LG domestic microwave oven (Thailand). The oven was modified to equip with a reflux and teflon stirrer on the topside. The reaction was let to proceed for 40 min. The glycolyzed product was then precipitated in excess distilled water. Remaining solids were filtered from the liquid fraction, rinsed, dried to constant mass, and weighed.

Characterization of glycolyzed product

The onset thermal degradation temperature of glycolyzed products was determined by Mettler Toledo TGA/SDTA 851e thermal gravimetric analysis (TGA, Columbus, OH) at the heating rate of 20 °C/min from 50 to 1,00 °C under nitrogen atmosphere. The melting behavior was determined by Perkin Elmer Diamond differential scanning calorimeter (DSC, Waltham, MA) at the heating rate of 20 °C/min from 50 to 270 °C under nitrogen atmosphere. The glycolyzed products were also analyzed by a Perkin Elmer System 2000 Fourier transform infrared spectrometer (FT-IR, Waltham, MA).

Results and Discussion

A series of PET glycolysis reaction under microwave irradiation was performed to determine the effect of irradiation time at a constant microwave applied power. Times ranging from 10 to 40 min were used at a constant applied microwave power of 600 W. Figure 1 shows the yield of glycolyzed products obtained using different glycols at various irradiation times. The complete PET solubilization was achieved within 30 min when all residues cannot be visibly observed. The yield of glycolyzed products progressively increased until 30-35 min for all glycols at PET: glycol ratio of 1:6. Thereafter, with increase in the irradiation time, the yield of glycolyzed products slightly decreased. The system with DEG resulted in the higher yield than those with EG or PG. This result clearly shows that microwave irradiation is an effective energy source in PET glycolysis reactions characterized by substantial shorter reaction times comparing with the conventional heating.

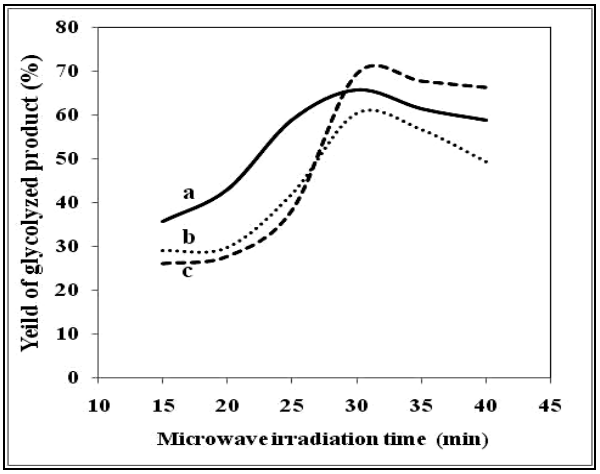

Figure 1. Effect of radiation time on the yield of glycolyzed product obtained using different glycol (a) EG (b) PG (c) DEG

As shown in Figure 2, the FTIR spectra of products obtained from glycolysis reaction of PET waste using EG, PG and DEG exhibit several peaks corresponding to –OH in the range of 3,400-3,600 cm^{-1}. The presence of peaks at 1950-1600 cm^{-1} indicats C=O stretching while peaks related to alkyl and C–H appear at 3000-2800 cm^{-1}. This implies that the glycolyzed products are compounds having hydroxyl and ester groups. [13]

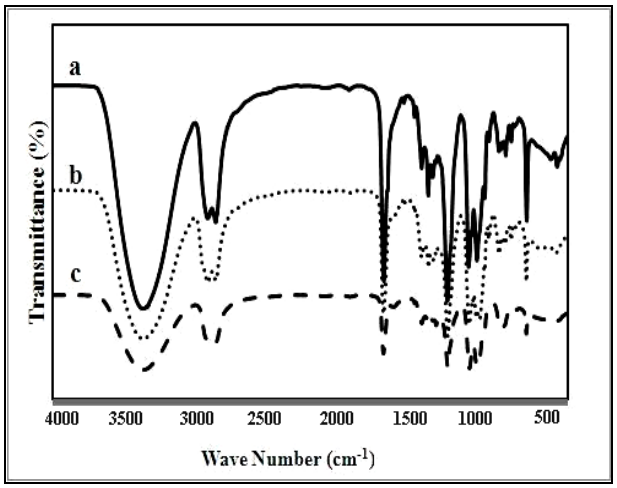

Figure 2. FT-IR spectra of glycolyzed products from (a) EG (b) PG (c) DEG

The DSC thermogram in Figure 3 shows melting temperatures of the glycolyzed products prepared from different glycols. The sharp endothermic peak at 109 °C is in agreement with the known melting point of BHET.

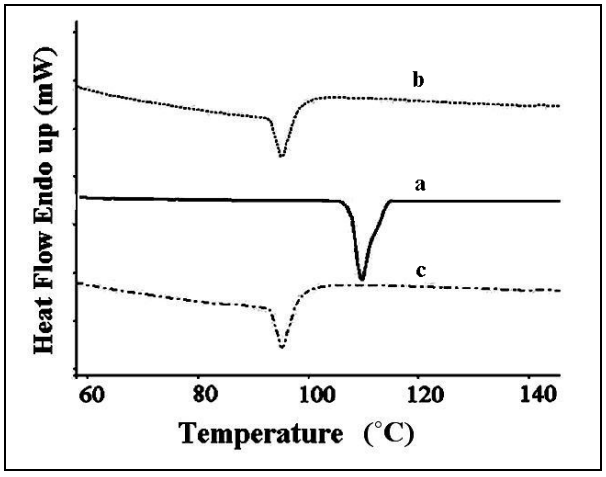

Figure 3. DSC thermogram of glycolyzed products prepared from different glycols (a) EG (b) PG (c) DEG

When all products were analyzed by TGA as revealed by the thermogram in Figure 4, it was found that the decomposition temperature of the glycolyzed product prepared with EG, PG and DEG was 423.94 °C, 401.61 °C and 412.73 °C, respectively. The results from these thermal analyses illustrate that the glycolyzed product prepared with EG has superior thermal stability than that prepared with PG and DEG.

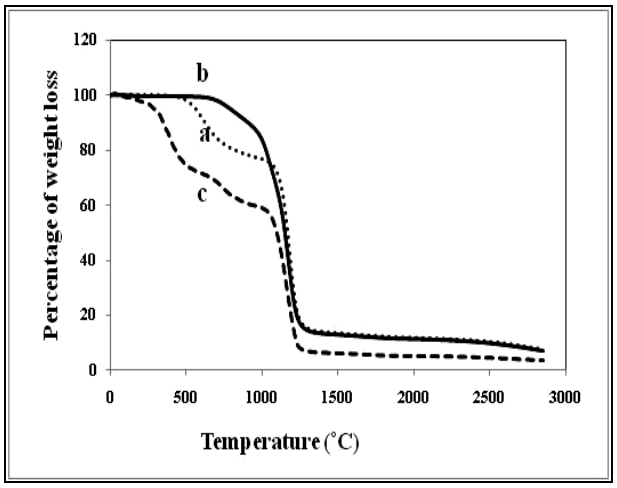

Figure 4. TGA thermogram of glycolyzed products from (a) EG (b) PG (c) DEG

Conclusions

The results show that the use of microwave radiation as the energy source in PET glycolysis resulted in the substantial shorter reaction times needed for complete PET degradation compared with conventional heating methods. Complete PET degradation in EG, PG and DEG was achieved within 30 min. The glycolysis reaction using DEG gave the higher yield than the others. However, the product obtained from the glycolysis reaction using EG possessed the maximum thermal stability.

Acknowledgements

The authors gratefully acknowledge National Metal and Materials Technology, NSTDA, Ministry of Science and Technology for the financial support.

References

[1] C. Lorenzetti, P, Manaresi, C. Berti and G. J. Barbiroli, *Polym. Environ*. **14** (2006), pp. 89-101.
[2] G. P. Karayannidis and D. S. Achilias, *Macromol. Mater.Eng*. **292** (2007), pp. 128–146.
[3] D. E. Nickles and M. S. Farahat, *Macromol. Mater. Eng.* **290** (2005), pp. 13-30.
[4] J. Kim, D. Jeong, C. Son, Y. Lee, E. Kim and I. Moon, *Korean J. Chem. Eng*. **24** (2007), pp. 1076-1083.
[5] D. Ratnasari, A. Bakar, I. Ahmad and A. Ramli, *Malaysian J. Chemistry*. **8** (2006), pp. 22-26.
[6] K. Li, X. Song and D. Zhang, *J. Appl. Polym. Sci*. **109** (2008), pp. 1298–1301.
[7] J. W. CHEN and L. W. CHEN, *J. Appl. Polym. Sci*. **73**, (1999), pp. 35–40.
[8] C. H. CHEN, C. Y. CHEN, Y. W. LO, C. F. MAO and W. T. LIAO, *J. Appl. Polym. Sci*. **80** (2001), pp. 943–948.
[9] E. T. Thostenson and T. W. Chou, *Composit*. **A30** (1999), pp. 1055-1071.
[10] N.D. Pingale and S.R. Shukla, *Eur. Polym. J.* **44** (2008), pp. 4151–4156.
[11] A. Krzan, *Polym. Adv. Technol*. **10** (1999), pp. 603-606.

[12] M. M. A. NIKJE and F. NAZARI, *Adv. Polym. Tech*. **25** (2006), pp. 242-246.
[13] O. Saravari, B. Vessabutr and V. Pimpan, *J. Appl. Polym. Sci*. **92** (2004), pp. 3040–3045.

Inorganic Chemistry

Synthesis of porphyrin-appended pyridine as a fluorescent chemosensor for Cd(II) and Hg(II)

K.Panpae[1]*, P. Nahom[1] and W. Yoosrijaroen[1]

[1]Department of Chemistry, Faculty of Science, King Mongkut's University of Technology Thonburi, Bangkok, Thailand 10140

*E-mail:kornvalai.pan@kmutt.ac.th

Abstract: A molecular fluorescent sensor for cations can be built through a modular approach, i.e. by covalently linking an appropriate photoactive fragment to the receptor displaying a satisfactory affinity towards the desired substrate. Following the receptor-cation interaction, an intercomponent process must take place, e.g. an electron transfer or an energy transfer process, that distinctly modifies the emission of the fluorophores, thus signaling the occurrence of the recognition event. In this research, specific molecular sensors are classified according to the type of receptor-cation interaction, that is ligand-metal interactions. Receptors are based on a multidentate protoporphyrin-appended pyridine platform, which leaves at least a vacant coordination site for the incoming metal ions. A protoporphyrin-appended pyridine, 2,5-pyridine dicarboxyamidyl-8,13-bis(vinyl)-3,7,18,17-tetramethyl-21H, 23H-porphyrin(P-PTP), was designed and synthesized. Its application as potential fluoroionophore for recognition of cadmium and mercury ions is reported. P-PTP shows chelation-enhanced fluorescence effect with Cd(II) and Hg(II) via the interruption of photoinduced electron transfer (PET) process, which has been utilized as the basis of the fabrication of the metal ions-sensitive fluorescent chemosensor. The analytical performance characteristics of the proposed Cd(II)- and Hg(II)- sensitive chemosensors were investigated. It shows a linear response toward Cd(II) and Hg(II) in the concentration range of 1.0 x 10^{-3} to 1.0 x 10^{-7} M with a limit of detection of 1.0 x 10^{-7} M and 0.5 x 10^{-7} M for Cd(II) and Hg(II), respectively. The chemosensor shows good selectivity for Cd(II) over a large number of other transition metal ions, i.e. Cu(II), Zn(II) and mixed metal ions.

Introduction

Cadmium and mercury are widely used in a variety of industrial processes including batteries, alloy and coloring matters as well as electroplating products. Cadmium is also frequently found in fertilizer production using phosphate minerals and sewage sludge. This element, unfortunately, has detrimental effects on human health as well as the environment accompanying with its wide use. Cadmium can accumulate in organs such as kidney, thyroid gland and spleen, which can induce physiological disorders and an increased incidence of certain cancer [1]. Mercury contamination is widespread and has a variety of natural and anthropogenic sources. Once introduced into the marine environment, bacteria convert inorganic mercury into methylmercury, which enters the food chain and accumulates in higher organisms. Methylmercury is neurotoxic and has been implicates as a cause of mercury pollution-related diseases. The development of simple methods for the determination cadmium and mercury is, therefore, of considerable research and practical significance.

Past decades have seen increasing interest in the development of fluorescent chemosensors for metal ions [2-5] due to the fact that such sensors demonstrate substantial advantages in sensitivity, selectivity and costs, and it is possible to perform remote detection with the application of fiber optics. In terms of sensitivity concerns, chemosensors exhibiting fluorescence enhancement on metal ion complexation are favored over those showing fluorescence quenching upon cation binding. By means of high sensitivity and simplicity, fluorosensor can be effectively used as a tool to analyze and measure the amount of metal ions as well as clarify their function in living system. The design and synthesis of fluorescent devices for recognition of metal ions are, therefore, currently of importance in chemical trace detection. Among the many reported fluorescent chemosensors with fluorescence enhancement for metal ions, only a few cases have been explored for Cd(II) and Hg(II) [1,6-8].

In order to recognize some metal ions which have two or more coordidation sites near from each other, it is necessary for a receptor to have functional groups for binding sites with certain metal ions. Thus, we designed and synthesized protoporphyrin- appended pyridine (P-PTP) as the receptor having 2,5-dicarboxylic groups for coordinating with cadmium and mercury ions. Protoporphyrin compound possesses fine optical characteristics with strong fluorescence, large Strokes shifts and relatively long exitation (> 400 nm) and emission (> 600 nm) wavelengths that minimize the effects of the background fluorescence. Pyridine is a good electronic acceptor.When protoporphyrin is concerned with pyridine derivative through a linking bridge, it could make up a ' donor-spacer- receptor' intramolecular photoinduced electron transfer (PET) system [1]. The fluorescence of P-PTP is quenched by the way of transfer of the exited state electron from protoporphyrin to pyridine. When P-PTP moiety is bound to cadmium and mercury ions, the chelate would abrogate the PET process and the fluorescence of protoporphyrin is recovered.

Materials and Methods

Reagents 2,5-pyridine dicarboxylic acid (PDC), 8,13-bis(vinyl)-3,7,18,17-tetramethyl-21H, 23H-

porphine -2,18-diprophynoic acid (protoporphyrin) and 4-dimethylaminopyridine (DMAP) were purchased from Aldrich-Fluka and used as received. 2-chloro-1-methylpyridiniumiodide (CMPI) and N,N-dimethylformamide (DMF), freshly distilled from CaH_2, were supplied by Aldrich Chemical Co. Except when specified, other chemicals were of analytical grade and used without furthed purification.

Synthesis of P-PTP The synthetic route for P-PTP is shown in *Figure 1*. The mixture of 2,5-pyridine dicarboxylic acid (19.0 mg, 0.114 mmol), 8,13-bis(vinyl)-3,7,18,17-tetramethyl-21H, 23H-porphine -2,18- diprophynoic acid (35.5 mg, 0.063 mmol), 2-chloro-1-methylpyridiniumiodide (51.0 mg, 0.270 mmol) and 4-dimethylaminopyridine (64.5mg, 0.253 mmol) in DMF was heated at 130°C for 5 h. The solvent was evaporated, and dichloromethane (100 mL) was added. Then the solution was washed with little water. The solvent was again evapolated, and the residue was purified by chromatograghy (silica gel, CH_2Cl_2, CH_2Cl_2: CH_3OH (50:1). The yield was 30.3 %. Spectral data of P-PTP : ^{1}HNMR(400MHz, $CDCl_3$), δ(ppm), 9.01(s,2H, pyridine), 8.56 (d, 2H, J = 4 Hz, pyridine), 8.43 (d,2H, J = 8Hz, pyridine). LC- MS; m/z $C_{41}H_{30}N_5O_8$ found 720 *(Figure 2)*.

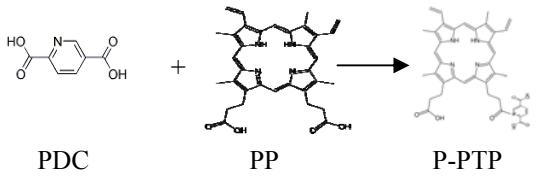

Figure 1. Scheme for P-PTP synthetic route.

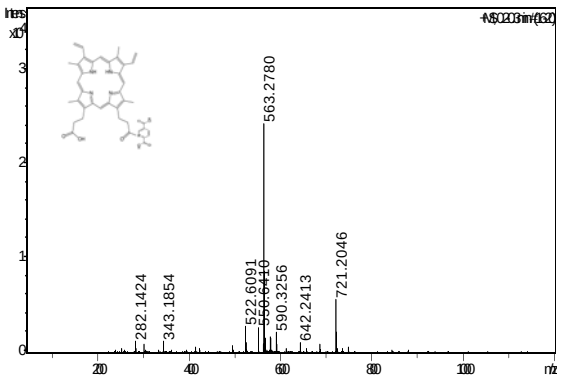

Figure 2. Liquid chromatograghy-mass spectrum of P-PTP.

Preparation of solutions The standard solutions of Cd(II) and Hg(II) were obtained by serial dilution of 1.0 x 10^{-3}M Cd $(NO_3)_2$ and 1.0 x 10^{-3}M $Hg(OAc)_2$ solutions with pH 10.83 tris-HCl buffer.

The complex solution of Cd(II) or Hg(II) and P-PTP was prepared by adding 2.0mL of the 1.0 x 10^{-5}M P-PTP and 2.0mL of the standard Cd(II) or Hg(II) solution. In the solution thus obtained, the concentrations were 5 x 10^{-6}M of P-PTP and 1 x 10^{-3} – 1 x 10^{-7}M of Cd(II) or Hg(II). Blank solution of P-PTP was prepared under the same conditions without Cd(II) or Hg(II).

Instrumentation All fluorescence measurements were carried out on a F-250C luminescence spectrometer (Hitachi) with excitation and emission slits set at 10.0 mm. The pH measurements were carried out on a Metler-Toledo 320 pH meter.

Procedures The fluorescence intensities were measured with the maximal excitation wavelength of 405.88 nm and at the maximal emission wavelength of 656 nm. Before each measurement, the solution was allowed to stand for 5 min to allow complete formation of metal-ligand complex.

Results and Discussion

Quench effect of P-PTP unit towards protoporphyrin unit The fluorescence spectra of PP and P-PTP are shown in *Figure 3 and 4,* respectively, where the PP and P-PTP units are excited at 405.88 nm.

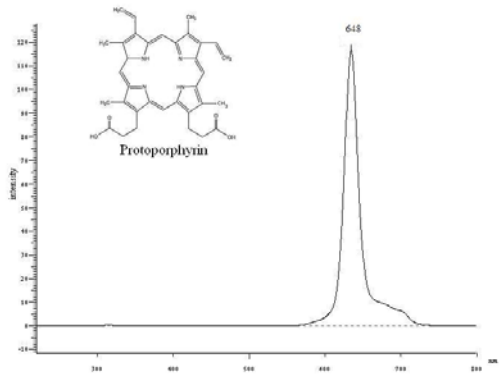

Figure 3. Fluorescence spectrum of 0.01mM protoporphyrin excited at 405.88 nm in DMF.

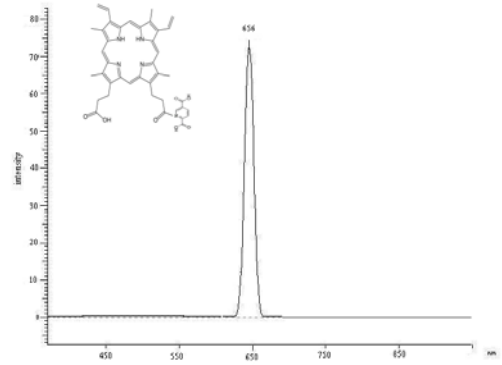

Figure 4. Fluorescence spectrum of 0.01mM P-PTP excited at 405.88 nm in DMF.

Spectral properties The fluorescence spectrum change of P-PTP when excited at 405.88 nm under various Cd(II) and Hg(II) concentrations are shown in *Figure 5 and 6,* respectively, which are recorded at λ_{ex} 405.88

nm, λ_{em} = 400-800 nm. The P-PTP exhibits fluorescence emission at 656 nm.

The ability of P-PTP to recognize Cd(II) and Hg(II) was further investigated. A great fluorescence enhancement accompanied with the increase of Cd(II) and Hg(II) concentrations. It is clearly that the detection limit of recognition are 1.0 x 10^{-7} M and 0.5 x 10^{-7} M for Cd(II) and Hg(II), respectively.

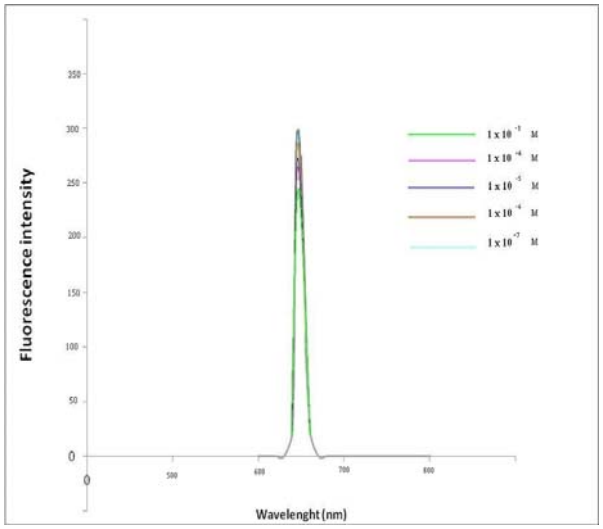

Figure 5. Changes of the fluorescence spectra of P-PTP (λ_{ex} 405.88 nm) at pH 10.8 as a function of added Cd(II) concentration.

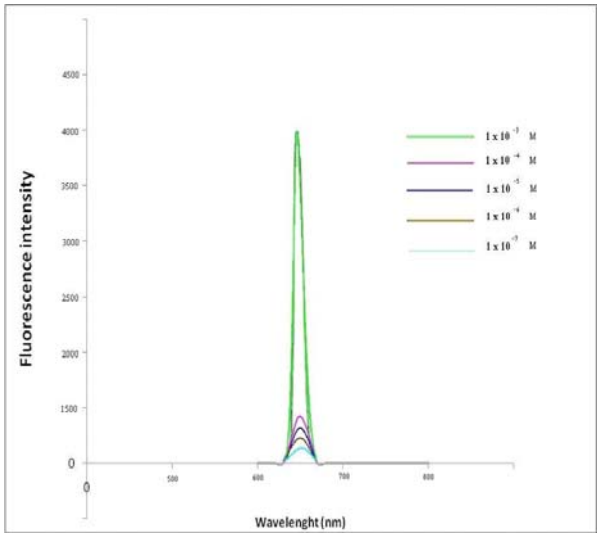

Figure 6. Changes of the fluorescence spectra of P-PTP (λ_{ex} 405.88 nm) at pH 10.8 as a function of added Hg(II) concentration.

Selectivity The other metal ions, Cu(II) and Zn(II), were used to evaluate the fluorescence enhanced effect of P-PTP. These results are shown in *Figure 7.* One notices that the fluorescence was quenched to some extent in the 1.0 x 10^{-4} mM of Cu(II) and Zn(II) solutions. Evidently, the protoporphyrin moiety participate in coordination to Cu(II) and Zn(II). Binding of the protoporphyrin moiety with these ions causes a great fluorescence quenching to the fluorophor. Cu(II) (74pm) and Zn(II) (74 pm) show more serious fluorescence quenching effect as compared to our ions with larger radii, e.g. Cd(II) (92 pm) and Hg(II) (110 pm). It is presumably due to the steric effect of the small radius in binding with the carboxylate group. These results suggested that P-PTP could be used as a potential Cd(II) and Hg(II) selective fluorescent chemosensor.

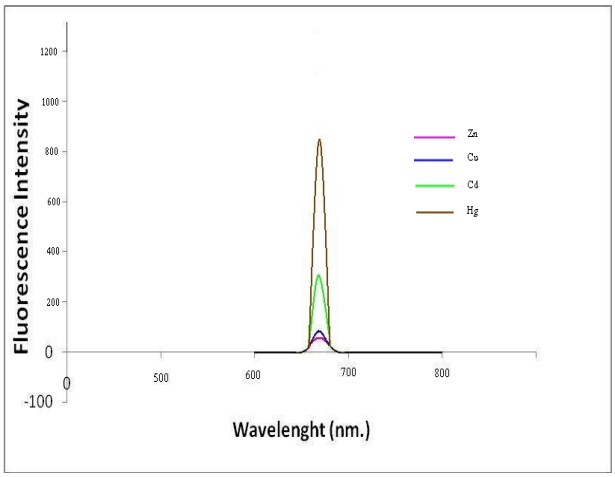

Figure7 (a) Fluorescence response of P-PTP (0.01Mm) to different metal ions : Hg(II), Cd(II), Cu(II) and Zn(II) at 1 x 10^{-4} mM , λ_{ex} 405 nm.

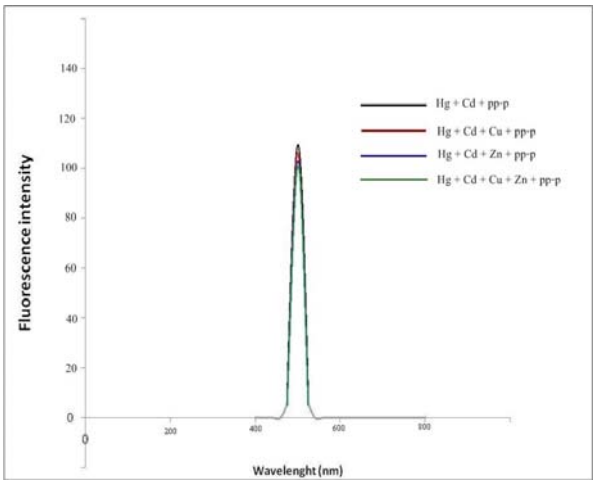

Figure7 (b) Fluorescence response of P-PTP (0.01Mm) upon the addition of mixed metal aqueous solution (Hg(II), Cd(II), Cu(II) and Zn(II) with each concentration at 1 x 10^{-6} mM) , λ_{ex} 405 nm.

Conclusions

Our study demonstrates the significance of ionophor – fluorophor interrelationship in the design of fluorescent

probes for the analytes of environmental concerns such as Cd(II) and Hg(II). It was routinely thought that , in the design of fluorescence chemosensors, the appropriately shorter the linkage between the fluorophor and the binding site, the better the performance of the designed molecule. We have synthesized a new protoporphyrin-appended pyridine. Using it, we have developed a fluorescent recognition method for Cd(II) and Hg(II), which shows fluorescent response to these in the range of 1 $x10^{-4}$ – 1 x 10^{-7} M with moderate selectivity. The remarkable enhancement of the fluorescence intensity in the presence of both ions is possible for this chelate abrogate the electron from the excited state of protoporphyrin to the pyridine. It is a new chemosensor for detecting Cd(II) and Hg(II).

References

[1] H-Y.Luo, J-H.Jiang, X-B.Zhang, C-Y. Li, G-L. Shen, and R-Q.Yu, *Talanta* **72** (2007), pp. 575-581.

[2] Y. Zheng, Q.Huo, P.Kele, F.M.Andreopoulos, S.M.Pham and R.M.Leblanc, *Organic Letter* **3** (2001), pp.3277-3280.

[3] A.Tong, H.Dong and L.Li, (2002). *Anal. Chim. Acta,* **466** (2002), pp. 31-37.

[4] Y.Zheng, X. Cao, J. Orbulescu, V. Konda, F.M. Andreopoulos, S.M. Pham and R.M. Leblanc, *Anal. Chem.* ***75*** (2003), pp. 1706-1712.

[5] W. Lin,Y.L. uan, Z. Cao, J. Feng and Y. Feng, *Dyes and Pigments* **83** (2009), pp.14-20.

[6] L. Feng and Z. Chen, *Sensors and Actuator B : Chemical* **122** (2007), pp. 600-604.

[7] Q. Y. Chen and C.F. Chen, *Tetrahedron Lett.* **46** (2005), pp. 165-168.

[8] X. Huang, Y. Xu, L. Zheng, J. Meng and Y. Cheng, *Polymer* **50** (2009), pp. 5996-6000.

[9] Y.F. Cheng, D.T. Zhao, M. Zhang, Z.Q. Lin, Y.F. Zhou, T.M. Shu, F.Y. Li, T. Yi and C.H. Huang, *Tetrahedron Lett.* **47** (2006), pp.6413-641

Nuclease activity studies of copper(II) complex containing *N*,*N*′-ethane-bis(amidino-*O*-methylurea)

A. Pinja[1], U. Chaveerach[1*] and Y. Trongpanich[2]

[1]Deparment of Chemistru, Faculty of Science, Khon Kaen University, Khon Kaen 40002, Thailand
[2]Department of Biochemistry, Faculty of Science, Khon Kaen University, Khon Kaen 40002, Thailand

[*] Corresponding Author E-Mail Sunchul@kku.ac.th

Abstract: Dichloro(*N*,*N*′-ethane-bis(amidino-*O*-methylurea))copper(II) complex, [CuL]Cl_2, was prepared by methanolysis of *N*,*N*′-bis(2-cyanoguanidine)-1,2-diaminoethane in the presence of copper(II) chloride. The complex was characterized by elemental analysis and spectroscopic techniques (infrared, mass, diffuse reflectance and UV-visible). Investigation on chemical nuclease activity of [CuL]Cl_2 toward plasmid pBR322 DNA was carried out by gel electrophoresis technique. The complex alone can partially cleave the supercoiled DNA. To enhance its cleavage ability, hydrogenperoxide was added to act as a reducing agent.

Introduction

In 1953, Watson and Crick firstly described the structure of deoxyribonucleic acid (DNA)[1], which is the most important macromolecule being the genetic material in living cell. DNA consists of two polynucleotide (nucleotides are the phosphate esters of nucleosides) chains, forming a helical structure, running in opposite directions. The outside of the helix consists of deoxyribose sugar moieties connected through phosphate groups. The nucleotides located on the inside of the helix and bound covalently to the sugar. Adenine (A) always binds to a thymine (T) via two hydrogen bonds, which guanine (G) is connected to cytosine (C) via three hydrogen bonds (Figure 1).

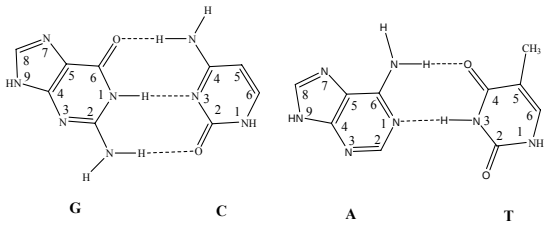

Figure 1. Schematic pictures showing complementary hydrogen bonds of DNA base pairs : guanine (G) – cytosine (C) and adenine (A) – thymine (T)

The DNA cleavage by synthetic metal complexes has become an importance filed due to the applications in development of anticancer drugs and antimicrobial agents. Especially, copper(II) complexes of various ligands were studied of their nuclease activity by many research groups. For example, the DNA binding and antimicrobial of polyethyleneimine copper(II) complex have been reported by Kumar R.S. et al.[2] This complex shows good antibacterial and antifungal activities against Gram +ve and Gram –ve bacteria and fungi. Moreover, it can bind to DNA mainly by electrostatic interaction. Also, the DNA cleavage activity of binuclear copper(II) complex with 1,1′-dimethyl-2,2′-biimidazole ligand was investigated by Li Y. et al.[3], in 2007. This binuclear complex can cleave DNA efficiently in the presence of ascorbic acid at pH 8.0 and 37°C. In 2008, the copper(II) complexes of oxindole-Schiff base were studied its DNA cleavage ability by Silveira V. et al.[4] They were able to cause double-strand DNA scissions, giving rise to nicked circular Form II and linear Form III species, in the presence of hydrogen peroxide.

Moreover, copper is one of metals containing in the bioessential properties to plants and animals. In the human body, the copper percentage composition by weight is 2 x 10^{-4} percent. It is well known that copper exists in various oxidation states, such as Cu(0), Cu(I) and Cu(II), which may serve various biological functions. It is found in a variety of enzymes, including cytochrome c oxidase in mitochondria and superoxide dismutase (containing copper and zinc) in red blood cells, used for electron transport. In many organisms, such as arthropods and molluscs, O_2 is transported by the Cu protein haemocyanin.

For dichloro (*N*,*N*′-ethane-bis(amidino-*O*-methylurea)) ligand, it has rich of hydrogen bonds. There are many reports that transition metal complexes containing ligands with versatile hydrogen-bonding capability have been deployed to bind DNA bases[2,6-8], to recognize anions, and to construct network of coordinated complexes connected through intermolecular interactions. In addition, the hydrogen-bonding interactions have long been considered to be of importance in biological systems, in molecular recognition and in crystal engineering.

In the presence work, we aimed to explore the nuclease activity of copper(II) complex, containing of dichloro(*N*,*N*′-ethane-bis(amidino-*O*-methylurea)) ligand ([CuL]Cl_2), previously synthesized and structurally studied by U. Suksangpanya[5] and coworkers in 2002. It contains the CuN_4 chromophore with square planar geometry (Figure 2).

Materials and Methods

All reagents were purchased commercially and used without further purification. Plasmid pBR322 DNA was purchased from Vivantis. Tris(hydroxymethyl)aminomethane was purchased from Acros Organic. Ethidium bromide was purchased

from Sigma. Agarose D-1 low EEO was purchased from Pronadisa.

For the nuclease activity studies, supercoiled pBR322 DNA (0.5 μg/μL) stock solution in Tris-HCl buffer (10 mM Tris-HCl/ 1 mM EDTA, pH 8.0) was performed by treating DNA (0.15 μg) with a different concentrations of the $[CuL]Cl_2$ complex (0,20, 40, 60, 80 and 100 μM) in the presence and absence of H_2O_2 (0, 60, 80, 100 and 140 μM). The total volume of 5 μL sample solution was incubated for 24 hours at 37°C, then 2 μL loading buffer was added. The analysis was performed by loading the reaction mixture on 1.0% agarose gel electrophoresis in 1x TAE buffer for 2.30 hours at 50 V. The gel was stained with 1.0 μg/mL ethidium bromide for 5 minutes, and then destained for 20 minutes. Bands were visualized and photographed by using BioRad Gel Doc 2000 System. The band intensity of DNA was quantified using Quantity One software (BioRad Laboratories).

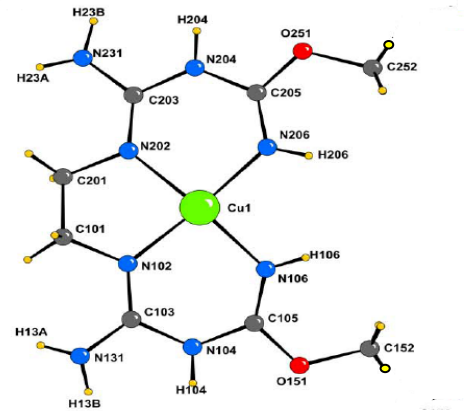

Figure 2. Molecular structure and numbering schemes for $[CuL]Cl_2$[5]

Results and Discussion

The nuclease activity of $[CuL]Cl_2$ complex was studied by using gel electrophoresis technique. This technique can separate DNA by size and shape[9]. When supercoiled plasmid pBR322 DNA is nicked by enzymes or metal complexes, the fast migration will be observed for the supercoiled form (Form I). If cleavage occurs on one strand (nicking), the supercoiled will relax to generate a slower-moving open circular form (Form II). If both strands are cut, a linear form (Form III) will migrates between Form I and Form II. Finally, the gels were analyzed after ethidium bromide staining.

Upon investigation of the nuclease activity of $[CuL]Cl_2$ complex, its DNA strand scission shows in Figure 3. Observe at bands intensity, the complex alone can partially cut DNA strand, the cleavage was increased with increasing of complex concentration (Lane 2-6). The result revealed that the $[CuL]Cl_2$ complex alone can cause the DNA cleavage activity.

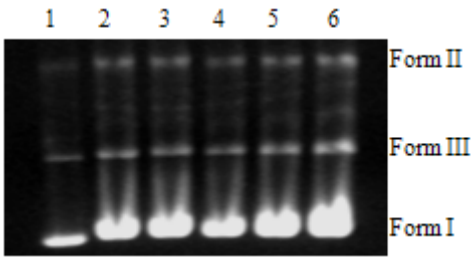

Figure 3. Agarose gel electrophoresis of pBR322 DNA incubated with $[CuL]Cl_2$ in 5 mM Tris-HCl/50 mM NaCl, pH 7.0 at 37°C for 24 hours. Lane 1: DNA control, Lane 2: DNA + $[CuL]Cl_2$ (20 μM), Lane 3: DNA + $[CuL]Cl_2$ (40 μM), Lane 4: DNA + $[CuL]Cl_2$ (60 μM), Lane 5: DNA + $[CuL]Cl_2$ (80 μM), Lane 6: DNA + $[CuL]Cl_2$ (100 μM)

The enhancement of DNA cleavage ability of complex by the addition of H_2O_2 was shown in Figure 4. In this path, 20 μM of complex was used, because it is the lowest concentration that effects on DNA strand scission. The cleavage of DNA was very interested at 1:1 (20 μM) ratio complex and H_2O_2 (Lane 4), respectively, Form III of DNA was extremely increment. This result suggests that supercoiled DNA was started to the degradation by the cleavage of $[CuL]Cl_2$ complex in the presence of H_2O_2. By contrast, increasing in the concentration of H_2O_2, linear form of DNA was constants (Lane 6, 8 and 10). At higher concentration of H_2O_2, it was effect in the cleavage of DNA (Lane 9).

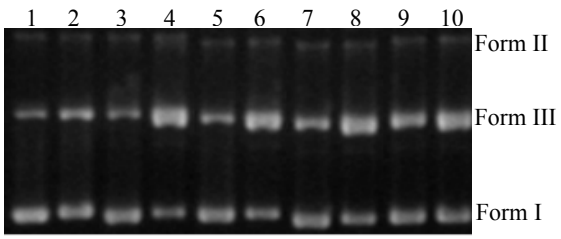

Figure 4. Agarose gel electrophoresis of pBR322 DNA incubated with $[CuL]Cl_2$ (20 μM) in the presence of H_2O_2, pH 7.0 at 37°C for 24 hours. Lane 1: DNA control, Lane 2: DNA + $[CuL]Cl_2$, Lane 3: DNA + H_2O_2 (20 μM), Lane 4: DNA + $[CuL]Cl_2$ + H_2O_2 (20 μM), Lane 5: DNA + H_2O_2 (60 μM), Lane 6: DNA + $[CuL]Cl_2$ + H_2O_2 (60 μM), Lane 7: DNA + H_2O_2 (100 μM), Lane 8: DNA + $[CuL]Cl_2$ + H_2O_2 (100 μM), Lane 9: DNA + H_2O_2 (140 μM), Lane 10: DNA + $[CuL]Cl_2$ + H_2O_2 (140 μM)

The DNA cleavage mechanism of $[CuL]Cl_2$ complex was proposed. In this case, H_2O_2 was acts as reducing agent[10], which is reduced the Cu(II) species to the Cu(I) species. This Cu(I) species can be generated the reactive oxygen species by redox reaction, these reactive oxygen species will be damaged the DNA strand. Generally, the hydroxyl radical is generated by a variety of chemical and physical processes. The Fenton reaction is one of the

most important metal mediated reactions, the metal ion acts as a catalyst for hydroxyl radical generation from H_2O_2[11]. In this studies, the propose mechanism of DNA cleavage by copper(II) complex as followed:

$$Cu(II) + H_2O_2 \longrightarrow Cu(I) + HOO^{\cdot} + H^{+}$$

$$Cu(I) + H_2O_2 \longrightarrow Cu(II) + HO^{-} + {}^{\cdot}OH$$

Conclusions

Copper(II) complex containing dichloro(*N*,*N*′-ethane-bis(amidino-*O*-methylurea)) shows artificial nuclease activity to cut DNA form I to Form III. The addition of H_2O_2 can enhance the DNA cleavage ability of the $[CuL]Cl_2$ complex. The best DNA strand scission by this complex was presented as 1:1 μM ratio complex and H_2O_2, respectively. Hence, this complex can act as DNA-cleavage agents.

References

[1] J.D. Watson and F.H. Crick, *Nature*. **171** (1953), pp. 737-738.

[2] R.S. Kumar and S. Arunachalam, *Polyhedron*. **26** (2007), pp. 3255-3262.

[3] Y. Li, Y. Wu, J. Zhao and Yang P, *J. Inorg. Biochem*. **101** (2007), pp. 283-290.

[4] V. Silveira ,J. Luz ,C. Oliveira, I. Graziani, M. Ciriolo and A. Ferreira, *J. Inorg. Biochem*. **102** (2008), pp. 1090-1103

[5] U. Suksangpanya, A.J. Blake, P. Hubberstey and C.Wilson, *CrystEngComm*. **4** (2002), pp. 552-563.

[6] B. Song, G. Oswald, J. Zhao, B. Lippert and H. Sigel, *Inorg. Chem*. **37 (**1998), pp. 4857-4864.

[7] R.S. Kumar and S. Arunachalam, *Eur. J. Med. Chem.* **44 (**2009), pp. 1878-1883.

[8] R.S. Kumar, S. Arunachalam, V.S. Periasamy, C.P. Preethy, A. Piyasdeen and M.A. Akbarsha. *Eur. J. Med. Chem.* **43 (**2008), pp. 2082-2091.

[9] S.I. Kirin, C.M. Happel, S. Hrubanova, T. Weyhermüller, C. Klein and N. Metzler-Nolte, *Dalton Trans*. 2004, pp. 1201-1207.

[10] H.L. Seng, K.W. Tan, M.J. Maah, W. T. Tan and H. Hamada, *Polyhedron*. **28** (2009), pp. 2219-2227.

[11] A. Gupte and R.J. Mumper, *Cancer Treat. Rev*. **35** (2009), pp. 32-46.

New polymorphs of lead(II) complex with 8-hydroxy-2-methylquinoline and KSCN

G. Mohammadnezhad[1], M. M. Amini[1]* and V. Langer[2]

[1] Department of Chemistry, General Campus, Shahid Beheshti University, Tehran 1983963113, Iran
[2] Environmental Inorganic Chemistry, Department of Chemical and Biological Engineering, Chalmers

* E-mail: m-pouramini@cc.sbu.ac.ir

Abstract: Two distinct polymorphs of Bis(μ_2-methylquinolin-8-olato)-κ^3N,O:O;κ^3O:N,O bis[(isothio cyanato-κN)lead(II)], [Pb($C_{10}H_8NO$)NCS]$_2$, forming a dinuclear complex from a methanolic solution containing lead(II) nitrate, 8-hydroxy-2-methylquinoline (M-Hq) and KSCN, were isolated simultaneously.

Introduction

Synthesis of novel organic-inorganic hybrid materials in the field of supramolecular and crystal engineering has been subject of rapid growth in recent years [1]. Bidentate ligands having soft and hard atoms have potential application in catalytic and stoichiometric reactions [2] as well as advanced materials [3]. Recent reports of 8-hydroxyquinoline and its derivatives with lead(II) salts includes [4-6].

As a part of our interest in exploring the effect of steric hindrance in lead(II) complexes with mixed ligands to dominate one coordination mode, we have examined thiocyanate (or isothiocyanate) due to its various coordination modes, single or bridging coordination through S-, N- or both, in the presence 8-hydroxy-2-methylquinoline. In this paper we report the crystal structure of two new polymorph of [Pb(M-Hq)NCS]$_2$.

Materials and Methods

All chemicals were purchased from Merck and used without further purification. Lead nitrate, 2-methyl-8-hydroxyquinoline and KSCN were loaded into a convection tube; the tube was filled carefully with methanol and kept at 333 K. Crystals were collected from the side arm after several days.

For both compounds, data collection: *SMART* [7]; cell refinement: *SAINT* [7]; data reduction: *SAINT* [7] & *SADABS* [8]; program(s) used to solve structure: *SHELXS97* [9]; program(s) used to refine structure: *SHELXL97* [9]; molecular graphics: *DIAMOND* [10]; software used to prepare material for publication: *SHELXTL* [9].

Results and Discussion

Polymorph (Ia) crystallized in the triclinic space group $P\bar{1}$ while polymorph (Ib) crystallized in the monoclinic space group $P2_1/c$. A perspective drawing of these compounds are shown in Figures 1 and 2, which Pb_2O_2 core lies on the crystallography inversion centre. In both structures lead(II) ion is four-coordinated and each metal centre is coordinated by two phenoxy bridged oxygens, one N atom from isothiocyanate ligand, and pyridyl N-donor atom from the M-Hq ligand. The direction of these four-coordinated atoms around the lead(II) centre in both complexes shows hemidirected geometry with a stereochemically active lone pair as expected. All of the bond distances in both structures are approximately the same.

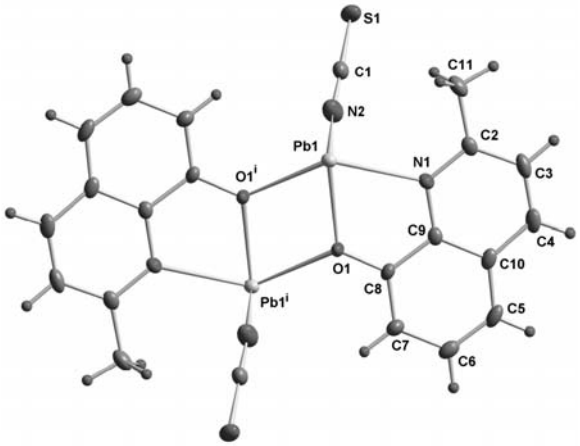

Figure 1. The atom numbering scheme for polymorph (Ia), with atomic displacement ellipsoids drawn at the 50% probability level.

Interestingly, on the contrast to previously reported coordination polymer [Pb(Hq)SCN]$_n$ [4], steric hindrance imposed by methyl group in C2 position prevent the coordination of SCN as a bidentate ligand. Indeed, the larger S1 atom could not coordinate to Pb1 in both cases and disrupt its polymeric nature and at the same time the coordination number is decreased to four. Nevertheless Pb-S interactions are formed for Pb1…S1^{ii} and Pb^{iv}…S1^{iii} with distances 3.6009(14) Å and for Pb1…S1^{iii} and Pb^{iv}…S1^{ii} with distances 3.6649(14) Å in compound (1a) (Fig. 3).

It is notable that the major structural difference between these two types of polymorph, which has influenced their structure, is the NCS coordination geometrical angle. In compound 1a, Pb1-N2-C1 angle is 149.7(4)° while in compound 1b is 136.8(6)°. All of the other angles except O1-Pb1-N2, N2-Pb1-O1^i and O1^i-Pb1-N1 are almost the same. In compound 1a, π- π interactions formed by quinoline rings overlap with a

perpendicular distance as shown in Fig. 4 and the overlap shown in Fig. 5.

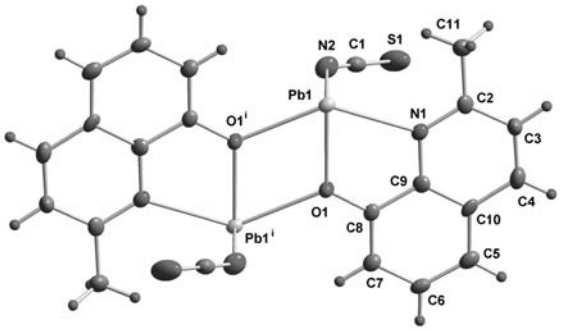

Figure 2. The atom numbering scheme for polymorph (Ib), with atomic displacement ellipsoids drawn at the 50% probability level.

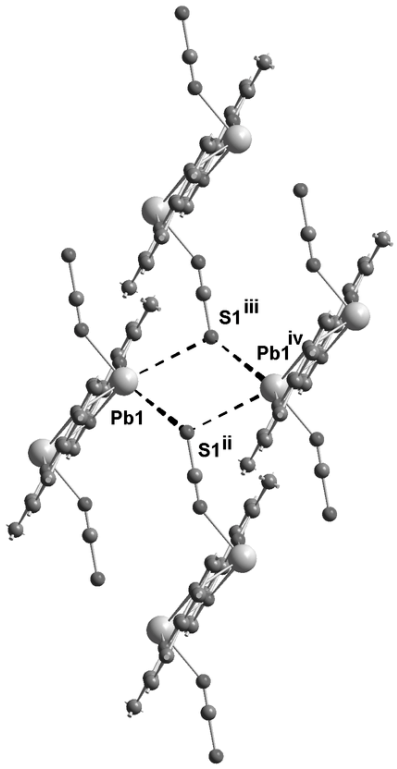

Figure 3. Pb···S interactions (dashed lines) in (Ia)

The upper part 3.288 Å and in the lower part is 3.377 Å. Different type of interactions is seen in compound (Ib) (Fig. 6). Despite of Pb…S interactions with distances of 3.506(3) Å, similar to compound (Ia), new interaction between S atom and phenyl ring is observed. The distance of the S atom to the centroid of the ring C5/C6/C7/C8/C9/C10 is 3.171 Å. Contents of the unit cell for both compounds are shown in Fig.4 and Fig.6. The Pb···Pb distances in these polymorph are 3.940 Å and 4.021 Å for Ia and Ib, respectively. Crystal data and refinement details are listed in Table 1.

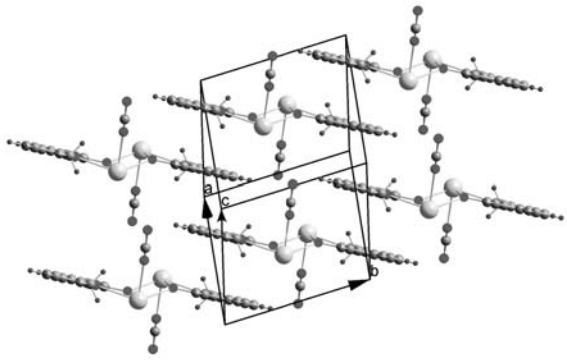

Figure 4. Contents of the unit-cell of (Ia) in a projection parallel with quinoline rings.

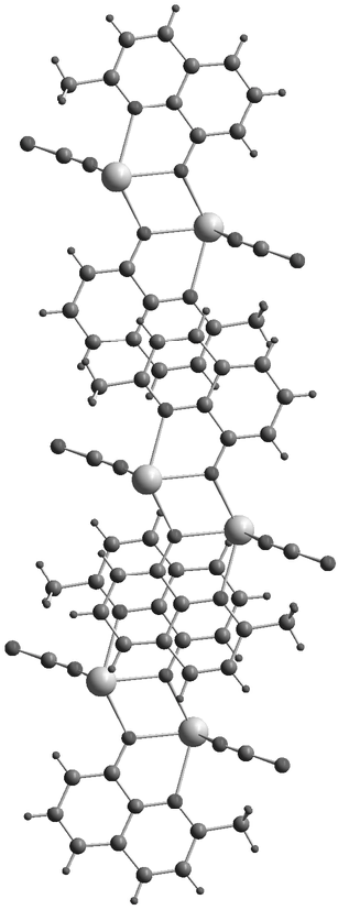

Figure 5. The π-π interactions in (Ia)

Conclusions

Two distinct polymorphs of dinuclear lead(II) complex were synthesized. Steric hindrance imposed by methyl group in C2 position of M-Hq prevents the coordination of SCN as a bidentate ligand. Indeed, the larger S atom could not coordinate to Pb in both cases and hence its polymeric nature is disrupted and the coordination number decreased to four. In polymorph (Ia), π- π interactions formed by quinoline rings. There are no π- π interactions formed by quinoline rings for the polymorph (Ib), but C—H···π interactions

mediated by C6—H6 to centroid of the ring C5/C6/C7/C8/C9/C10.

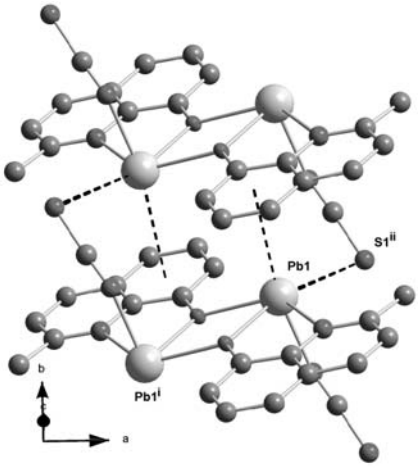

Figure 6. Pb···S interactions (dashed lines) in (Ib)

Table 1. Crystal data for Ia and Ib

Complex	Ia	Ib
Empirical formula	$C_{22}H_{16}N_4O_2Pb_2S_2$	$C_{22}H_{16}N_4O_2Pb_2S_2$
Formula weight	846.89	846.89
Temperature (K)	173	173
Crystal system	Triclinic	Monoclinic
Space group	$P\bar{1}$	$P2_1/c$
a (Å)	7.8556 (5)	12.037 (5)
b (Å)	8.4155 (5)	5.731 (2)
c (Å)	9.1550 (6)	16.327 (6)
α (º)	78.524 (1)	
β (º)	69.771 (1)	90.368 (7)°
σ (º)	82.813 (1)	
V (Å^3)	555.50 (6)	1126.3 (7)
Z	1	2
Abs. coeff. (mm^{-1})	15.35	15.14
Crystal size (mm)	0.43 × 0.21 × 0.06	0.96 × 0.04 × 0.02
Reflections collected	9987	12903
Unique reflections	3475	2528
R(int)	0.046	0.078
S	1.00	1.01
R [$I > 2\sigma(I)$]	$R_1 = 0.030$	$R_1 = 0.038$
	$wR_2 = 0.072$	$wR_2 = 0.090$

References

[1] B. Moulton and M. J. Zaworotko, *Chem. Rev.* **101** (2001), pp. 1629–1658.

[2] W. Kaim and B. Schwederski, *BioinorganicChemistry: Inorganic Elements in the Chemistry of Life*, Wiley, Chichester (1995).

[3] D. V. Soldatov, G. D. Enright, and J. A. Ripmeester, *Cryst. Growth Des.* **4** (2004), pp. 1185–1194.

[4] G. H. Shahverdizadeh, A. A. Soudi, A. Morsali, and P. Retailleau, *Inorg. Chim. Acta* **361** (2008), pp. 1875–1884.

[5] a) G. Mohammadnezhad, M. M. Amini, and S. W. Ng, *Acta Cryst.* **E65** (2009), p. 259. b) G. Mohammadnezhad, M. M. Amini, and S. W. Ng, *Acta Cryst.* **E65** (2009), p. 260. c) G. Mohammadnezhad, M. M. Amini, and S. W. Ng, *Acta Cryst.* **E65** (2009), p. 260.

[6] W.-Z. Zhang, , D.-Z. Wei, X.-F. Che, E.-J. Gao, K.-H. Wang, , H.-X. Yin, and X.-G. Gu, *Chin. J. Struct.Chem.* **27** (2008), pp.287–292.

[7] Bruker *SMART* (2003) (Version 5.63) and *SAINT* (Version 6.45). Bruker AXS Inc., Madison, Wisconsin, USA.

[8] G. M.Sheldrick, (2003) *SADABS*. Version 2.10. University of Göttingen, Germany.

[9] G. M. Sheldrick, *Acta Cryst.* **A64** (2008), pp. 112–122.

[10] K. Brandenburg, *DIAMOND* (2009) Version 3.2c. Crystal Impact GbR, Bonn, Germany

Immobilization of Cr(VI) in rice husk ash based geopolymer

K.S. Budiasih*, A.K. Prodjosantosa, and P.Utomo

Department of Chemistry Education, Yogyakarta State University , Indonesia

*)Email; ks_budiasih@yahoo.co.uk

Abstract: Geopolymer based on rice husk ash has been studied as an alternative eco-friendly cementitous material. Immobilization of Cr(VI) in its material was done for preventing toxicity effect of this species into human body. The rise husk ash based geopolimer was prepared using metakaolinite as alumina source and NaOH as the activator. The mixture of rice husk ask, kaolin and NaOH were autoclaving at temperature 115^{o}C and pressure 10 Psi for 5 hours. The NaOH concentration was varied of 8, 10 and 12 M. The Cr(VI) of K_2CrO_4 salt was introduced in resulting geopolymer material with concentration of 15 to 25 ppm. The final resulting material was characterized by X-Ray Diffraction, Fourier Transform Infra Red (FTIR) Spectrophotometer and Porosity Analyzer. X ray diffraction pattern of the geopolymer indicates that the material is amorphous. The FTIR spectra show several peaks at certain wavenumbers, indicating the vibration band of Si-O-Al at 1016-1006 cm^{-1}, Al-O at 875 cm^{-1} and Si-O at 440-450cm^{-1}, respectively. After introduction of Cr in the system, the vibration stretching band of Si-O-Si shifted from 1004.20-1006.12cm^{-1} to 1010.70cm^{-1}. Porosity analysis shows the highest porosity was 16.57 % reached by sample prepared at 10M NaOH. TCLP (Toxicity Characteristic Leaching Procedure) tests showed that Cr(VI) was stable in the geopolymer material during at least 10 days.

Keywords: ***geopolymer, rice husk ash, immobilization, Cr(VI), TCLP***

Introduction

Geopolymer, or Aluminosilicate Inorganic Polymers (AIPs) is a term of inorganic polymers group of aluminosilicates. Geopolymer shows the cement characters. It was designed to replace Portland cements in some applications. Development of geopolymer will also decrease the negative effect of cement production: emission of CO_2 which contributes to global warming [1].

Previous reports used the term of polysialate for describing the polymer structure of geopolymer. The sialate monomer represents SiO_4 and AlO_4 tetrahedra which connected by oxygen bridge [2,3]. Polisialate could be empirical formulated:

$$M_n\{-(SiO_2)_z-(AlO_2)-\}_n$$

The structure of geopolymer was also reported as SiO_4 and AlO_4 tetrahedra connected by oxygen bridge with hydrated Na^+ present in framework cavities. The structure is showed in Figure 1. [4,5]

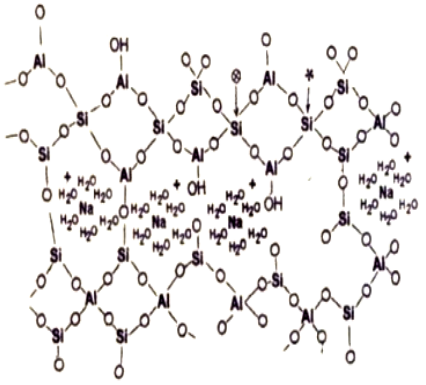

Fig.1. Proposed structure of a Na-polysialate polymer

Geopolymer will have advantages to replace Portland cement in ability of immobilization of toxic species from industrial waste water. Previous study of metakalonite based Geopolymer showed a high stability when exposed by aquadest, sea water, sodium sulphate and sulphuric acid [6].

Cr(VI) have known as a toxic species, with concentration of 10 mg/kg bodyweight can cause necrosis (breaking a part of tissues). Average Cr(VI) input in human body is 0,05 mg/day in their food consumption [7].

In this research, immobilization of Cr(VI) was applied in rice husk ash based geopolymer. Rice husk ash is an abundant waste from the rice production. The rice husk as based geopolymer have been prepared at the preliminary research. [8]

Materials and Methods

In the synthesis of geopolymers, there are two essentially types of raw materials, aluminosilicate-containing solids and alkali-silicate solutions. In this paper, rice husk ash were used as silica source and metakaolinite as alumina source.

The alkali-silicate solutions were prepared by diluting alkali-hydroxide solids in water, then added by rice husk ash to obtain certain silicate and alkali concentrations, expressed as SiO_2/M_2O and H_2O/M_2O ratios (where M = Na).[9]

Rice husk ash was made by calcinating dried rice husk at 800^{o}C. Rice husk consist of 85-98 % of SiO_2. NaOH pellets were obtained from Merck. The concentration of activating solutions was varied according to get the best result in order to apply in immobilization.

Geopolymer Synthesis and Characterization

Geopolymer materials were made by mixing of alumina source material (metakaolinite) with alkali-silicate solution. Alkali silicates were first prepared by mixing of rice husk ash (silica source) with alkali solution (NaOH 8,10 and 12M).

The geopolymer binders were synthesized in a plastic container by hand mixing of geopolymer slurries for 5 minutes or longer and then poured into 3x3x3 cm cubic plastic moulds. The samples were then sealed and placed immediately in an air-circulated oven or autoclave at 115^{o}C and 10 Psi for 5 hours.

The products (Na-geopolymer) were characterized by X-Ray Diffraction, Infrared Spectrophotometer and porosity test.

Immobilization of Cr (VI) in the Geopolymer

Immobilization of Cr(VI) was carried out similar to the preparation of the geopolymer. A portion of water used was replaced by simulation solution of 15,20 1nd 25 ppm Cr(VI) from K_2CrO_4. The resulting Cr-geopolymer were characterized by Infrared Spectrophotometer and TCLP test.

Results and Discussion

a.Geopolymer

Fig 2. Rice Husk Ash Based Geopolymer

Figure 2 showed the physical appearance of resulted Na-geopolymer in this research. It looks like a piece of chalk. The color of the material depends on the raw materials. Both rice husk ash and metakaolinite were resulting grayish white material. The shape of the geopolymer product came from the mould shape.

b.1.Characterization by X-Ray Diffraction (XRD)

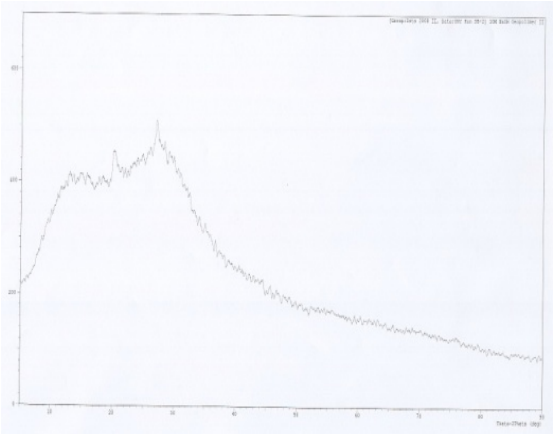

Figure 3. The XRD pattern of Na-geopolymer, made by NaOH 10M.

The XRD pattern showed that Na-Geopolymer is an amorphous material. There is no characteristic peaks correspond to the planes of crystalline solid.

b.2. Characterization by Infrared Spectrophotometer

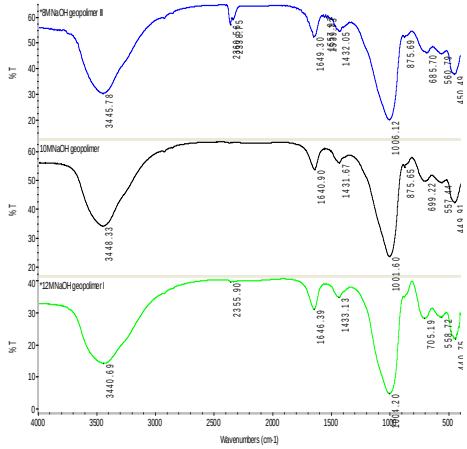

Fig.4. Infrared spectra of Na-Geopolymer made by 8,10,12 M NaOH**.**

In general, geopolymers consist of a short-range network of tetrahedrally-bonded Si-O-Si or/and Si-O-Al, loaded with water and carbonate species.The Infrared spectrophotometer spectra were shown at Figure 4. The characteristic wavenumbers of geopolymer was listed in Table 1.

Table 1. Assignment of wavenumbers (or frequencies) for molecular vibrations in absorption spectra of geopolymers.

Wavenumber (cm^{-1})	Vibrational assignments
3440-3480	Adsorbed O-H stretching
2855, 2930	Adsorbed O-H stretching
1650-1655	Adsorbed H-O-H bending
1420-1480	C-O stretching (carbonates)
865-875	O-C-O bending (carbonates)
950-1250	Asymmetric Si-O-Si and/or Al-O-Si stretching
950-980	Si-O stretching (Si-O-M), M = Na or K
870	Si-OH stretching
600-800	Al-O bands
797	Network Si-O-Si (or Si-O-Al) stretching
558	Network Si-O-Si (or Si-O-Al) symmetric stretching
461	Network Al-O-Si bending

b.3. Porosity Test

This test is based on the weight differences of the geopolymer before and after absorbtion of water. Porosity (P) was expressed by percentage as following equation:

$$P = \frac{\text{total weight-dry weight}}{\text{total weight-weight of geopolymer in water}} \times 100\%$$

The highest porosity of geopolymer material was 16.57 %, reached by Na-geopolimer with 10M NaOH. This product was applied in immobilization of Chromium (VI). The result was listed at Table 2.

Table 2. The result of the porosity test

Code	Dry weight (g)	Concentrated/ total weight (g)	Water weight (g)	Porosity (%)
Na-PS 8M	39,08	42,43	14,56	12,02
Na-PS 10M	38,76	43,48	15,0	16,57
Na-PS 12M	55,98	58,07	21,44	5,79
K-PS 8M	56,52	61,57	22,00	12,76
K-PS 10M	78,20	85,36	31,77	13,36
K-PS 12M	77,02	83,88	31,00	12,97

c. Immobilization of Cr(VI) in Geopolymer

The concentration of introduced Cr (VI) in the geopolymer matrix was varied by 15, 20 and 25 ppm. The resulting Cr-Geopolymers were characterized using Infrared spectrophotometer, giving 3 spectra as expressed at Fig.5a-5c:

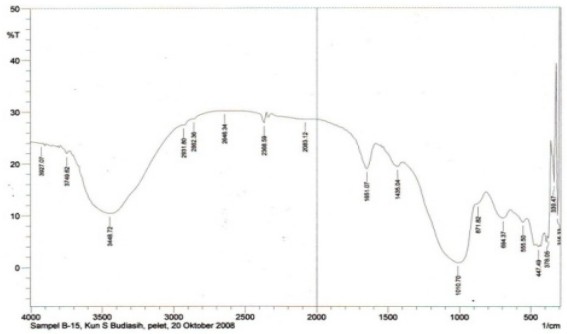

Fig 5.a. Infrared Spectra of Na-Geopolymer-Cr (15ppm Cr)

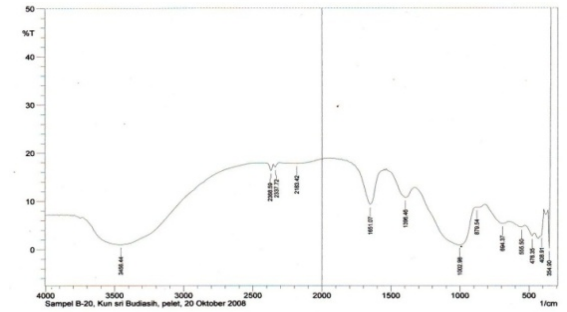

Fig 5b. Infrared Spectra of Na-Geopolymer-Cr (20ppm Cr)

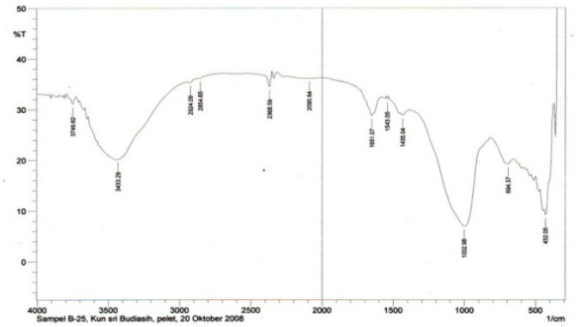

Fig 5c. Infrared Spectra of Na-Geopolymer-Cr (25ppm Cr).

There are no significant differences in infrared pattern of Na-Geopolymer-Cr compared to the original geopolymer, except a shifting of several peaks. For example,The strectching vibration peak of Si-O-Si was shifted from 1004,20- 1006.12cm^{-1} to 1010.70cm^{-1}.

There were two interpreted facts: First, there isn't a bond produced between Cr and geopolymer only physical interaction. The second, the Cr-O bonding was not detected until the wavenumber 500cm^{-1}. It coresponds to vibration of ionic bond which absorb higher energy and lower wavelength.

TCLP (Toxicity Characteristic Leaching Procedure) was done for determining the concentration of Cr (VI) diluted from the geopolymer matrix in a certain time. The procedure was adopted from Japan Environmental Agency [10].

The leaching agents were aquadest, well water, rain water and sea water. The effect of impregnated Cr(IV) concentration also studied. In 10 days, there is

no Cr (VI) detected in the leachate water. The result was listed at the Table 3.

Table 3. TCLP test of Cr (VI) in rice husk ash geopolymer (Na-Geopolimer for 10 days

Variables	code (ppm)	Amount of Cr
Cr (VI) introduced/ impregnated	C15 (15 ppm)	Undetected
	C20 (20 ppm)	Undetected
	C25(25 ppm)	Undetected
	C0 (blank)	Undetected
Leaching agents	A1 (well water)	Undetected
	A2 (rain water)	Undetected
	A3 (sea water)	Undetected
	A4 (aquadest)	Undetected

Conclusions

Immobilization of Cr(VI) in NaOH–rice husk ash geopolymer obtain a good result up to 25 ppm of Cr(VI). TCLP in 10 days showed that there is no Cr(VI) detected in the leachate water.

References

1) Davidovits,J., Geopolymers and Geopolymeric Materials, *Journal of Thermal Analysis*, vol. 35, no.2, 1989,p. 429-441.

2) Davidovits, J., Geopolymer : Inorganic Polymeric New Materials, *Journal of Thermal Analysis*, ,vol. 37, 1991 p. 1633-1656.

3) Rowles, M.R., The Structural Nature of Aluminosilicate Inorganic Polymers: A Macro to Nanoscale Study, thesis, Curtin University, , 2004

4) Sindhunata, *A Conceptual Model of Geopolymerisation*, Thesis, Department of Chemical and Biomolecular Engineering The University of Melbourne Australia, 2006.

5) Barbosa, V.F.F, Mac Kenzie, K.J.D., & Thaumaturgo, C.,, Synthesis And Characterisation of materials Based on Inorganic Polymer of Alumina and Silica, Sodium Polysialate Polymers, *International Journal of Inorganic Material*), vol 2, no 4, 2000, pp.309-317.

6) Palomo A & M. Palacios , Alkali-Activated Cementitious Materials: Alternative Matrices For The Immobilisation Of Hazardous Wastes Part II. Stabilisation Of Chromium And Lead, *Cement And Concrete Research* , Vol.33, iss 2, Feb 2003, 289-295.

7) Moore, JW: *Inorganic Contaminant of Surface Water*, Springer Verlag, New York, 1991.

8) Budiasih, KS., Prodjosantosa, A.K., *Preparation And Characterization Of Rice Husk Ash Based Geopolymer, ,*XIX International Chemistry Seminar *, Gadjah Mada University,* Yogyakarta, May ^{20}, 2009.

9) Kriven WM., & Jonathan L.Bell, Master Thesis, Effect of alkali choice on Geopolymer Properties, University of Illinois at Urbana Champaign Material Science and Engineering Bldg, 2004.

10) Japan Environmental Agency , TCLP for Toxic Species, 2007.

Anion-directed assembly dimerizations of *N,N′*-bis-(3,5-dinitro)isophthalamide: The DFT studies

R. Sawangsri[1] and K. Navakhun[1]*

[1]Department of Chemistry and Center of Excellence for Innovation in Chemistry, Faculty of Science, Ramkhamhaeng University, Huamark, Bangkapi, Bangkok 10240, Thailand

*E-mail: n_korakot@ru.ac.th, .

Abstract: The effects of anions, fluoride, chloride, and bromide ions, to the anion-directed assembly dimerizations procssses of *N,N′*-bis-(3,5-dinitro) isophathalamide, L, were studied with the density functional theory (DFT) calculation methods. Anion-directed assembly dimers of L co-existing with tetrabutylammonium ion (TBA^+) as [$L_2.F_2$].2TBA, [$L_2.Cl_2$].2TBA and [$L_2.Br_2$].2TBA and its 1:1 anion:receptor complexes co-existing with TBA^+ as [L.F].TBA, [L.Cl].TBA and [L.Br].TBA were obtained. Their optimized structures and structural energies were computed at the B3LYP/6-31G(d) level of theory in gas phase. The relative energy profiles confirm the previous X-ray crystallographic results that the fluoride ion can induce this compound to form the anion-directed assembly dimer.

Introduction

Anion-directed assembly dimerizations of compounds resulting to form the new noncovalently link molecular architectures via unusual processes have been immense interested by supramolecular chemists. Anion receptors containing isophthalamide backbone and electron withdrawing groups have been reported their formation of an anion-directed assembly dimers in the solid state. Functionalized isophthalamide with nitro-aromatic substitution as 3,5-dinitrophenyl groups revealed a double helix anion-directed assembly formed around two fluoride anions via NH···F^- hydrogen bonds and π-π interactions. To get more understand of these processes, in this work, the anion-directed assembly dimerizations procssses of *N,N′*-bis-(3,5-dinitro) isophthalamide, **L**, induced with halide ions have been studied *via* computational methods. Their optimized structures and energies have been computed using the density functional theory (DFT) at the B3LYP/6-31G(d) level of theory and compare to the previous X-ray crystallographic results.

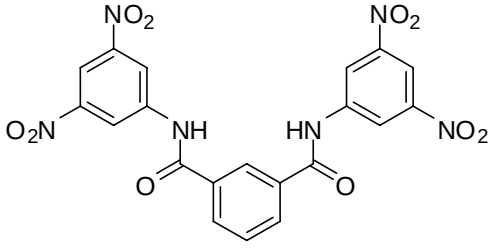

N,N′-Bis-(3,5-dinitro) isophthalamide, **L**.

Materials and Methods

Optimized and energies structures of *N,N′*-bis-(3,5-dinitro)isophthalamide, **L**, and its complexes with tetrabutylammonium fluoride (TBAF), tetrabutyl ammonium chloride (TBACl) and tetrabutylammonium bromide (TBABr) have been calculated using the density functional theory (DFT) at the B3LYP/6-31G(d) level of theory in gas phase with GAUSSIAN03 program. The complexes could be formed as 1:1 anion:receptor complexes which are 2[**L**.F].TBA, 2[**L**.Cl].TBA and 2[**L**.Br].TBA, equation 2, and 2:2 anion:receptor complexes, anion-directed assembly dimers co-existing with tetrabutylammonium ion (TBA^+), which are [$\mathbf{L}_2.F_2$].2TBA, [$\mathbf{L}_2.Cl_2$].2TBA and [$\mathbf{L}_2.Br_2$].2TBA, equation 3.

$$\underset{\text{(Host)}}{H} + \underset{\text{(Guest)}}{G} \rightleftharpoons HG \qquad (1)$$

Reaction of the system in presence of fluoride, chloride and bromide (X^-) are described by the following equations.

$$2\mathbf{L} + 2TBAX \rightleftharpoons 2[\mathbf{L}.X].TBA \qquad (2)$$

$$2\mathbf{L} + 2TBAX \rightleftharpoons [\mathbf{L}_2.X_2].2TBA \qquad (3)$$

Results and Discussion

The optimized structure of **L** is shown in Figure 1. From the relative energies of species in system **L** with TBAF, TBACl and TBABr computed at the B3LYP/6-31G(d) level of theory in gas phase shown in Table 1, It was found that the anionic self-assembly dimerization process is more prefer in the system with tetrabutylammonium fluoride. ΔE of this process is -122.25 kcal.mol^{-1} compare to ΔE of 1:1 anion:receptor complexes formation process which is -114.02 kcal.mol^{-1}. However, in the systems with tetrabutylammonium chloride and tetrabutylammonium bromide, 1:1 anion:receptor complexes formation processes are more preferable processes comparing to 2:2 anion:receptor complexes formation process. The systems with tetrabutylammonium chloride, ΔE of this process is -89.50 kcal.mol^{-1} compare to ΔE of 2:2 anion:receptor complexes formation process which is

-80.58 kcal.mol^{-1}. In the same way, the systems with tetrabutylammonium bromide, ΔE of 1:1 anion:receptor complexes process is -99.08 kcal.mol^{-1} compare to ΔE of the anionic self-assembly dimerization process which is -93.62 kcal.mol^{-1}. The B3LYP/6-31G(d) optimized structures of 1:1 anion:receptor complexes in gas phase, [**L**.F].TBA, [**L**.Cl].TBA and [**L**.Br].TBA, are shown in Figure 3 and the optimized structures of the anionic self-assembly dimers computed at the B3LYP/6-31G(d) level of theory in gas phase of [$\mathbf{L}_2$.F_2].2TBA, [$\mathbf{L}_2$.Cl_2].2TBA and [$\mathbf{L}_2$.Br_2].2TBA are shown in Figure 4.

.

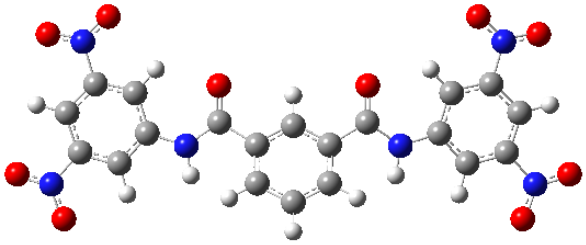

Figure 1. The optimized structures of *N,N′*-bis-(3,5-dinitro)isophthalamide, **L**.

Table 1. Relative energies of species in system **L** with TBAF, TBACl and TBABr computed at the B3LYP/6-31G(d) level of theory in gas phase.

1:1 Anion:Receptor complexes	**ΔE (kcal.mol^{-1})**
2[L.F].TBA	-114.02
2[L.Cl].TBA	-89.50
2[L.Br].TBA	-99.08
2:2 Anions:Receptors complexes	**ΔE (kcal.mol^{-1})**
[L_2.F_2].2TBA	-122.25
[L_2.Cl_2].2TBA	-80.58
[L_2.Br_2].2TBA	-93.62

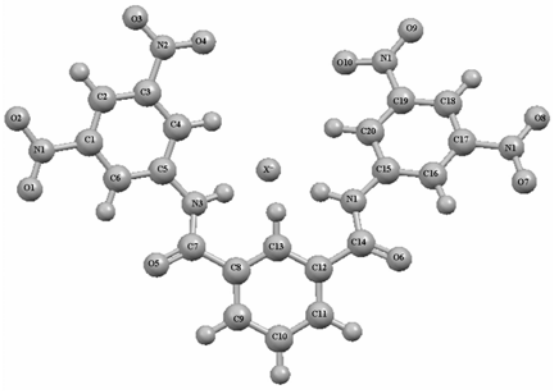

Figure 2. Atomic numbering of [**L**.X].TBA complexes.

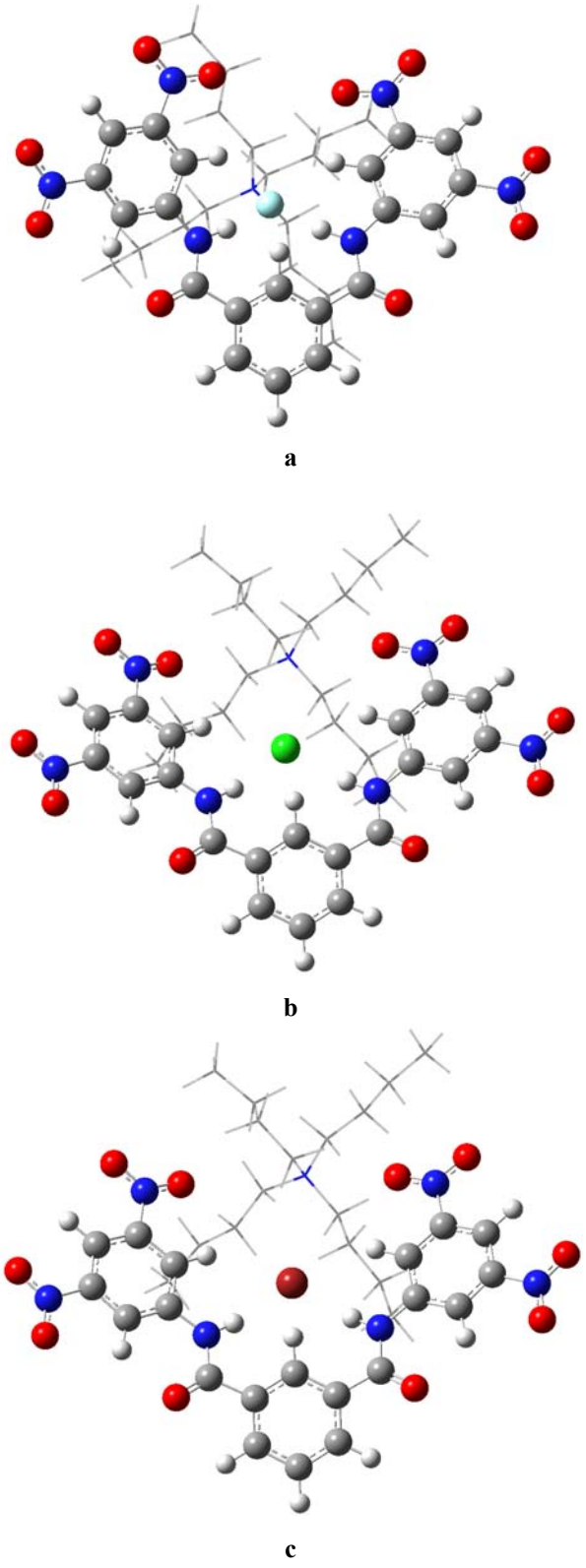

a

b

c

Figure 3. The optimized structures computed at the B3LYP/6-31G(d) level of theory in gas phase of **:** (a) [L.F].TBA, (b) [L.Cl].TBA and (c) [L.Br].TBA.

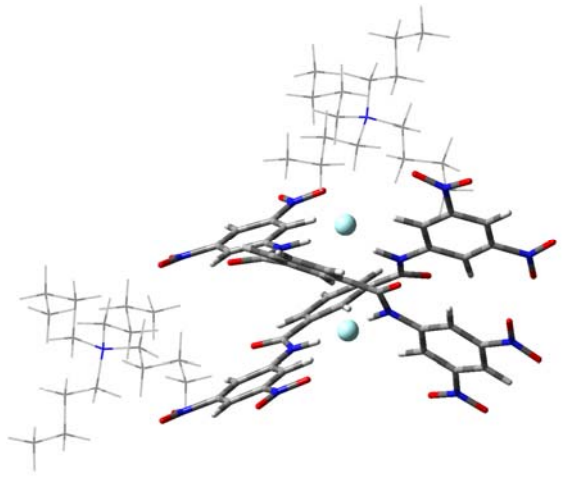

a

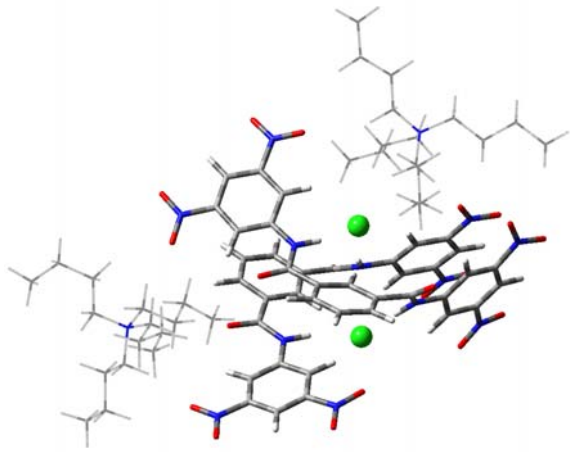

b

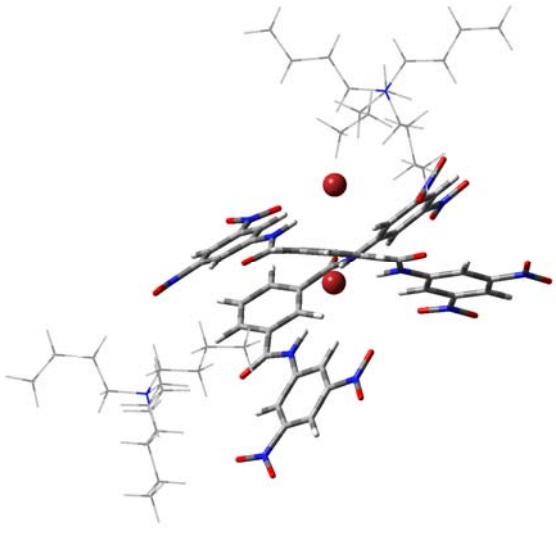

c

Figure 4. The optimized structures of the anionic self-assembly dimers computed at the B3LYP/6-31G(d) level of theory in gas phase of: (a) [**L**$_2$.F$_2$].2TBA (b) [**L**$_2$.Cl$_2$].2TBA and (c) [**L**$_2$.Br$_2$].2TBA.

Selected intermolecular bond-distances of [**L**.F].TBA, [**L**.Cl].TBA and [**L**.Br].TBA are shown is Table 2 and X-ray structure of [**L**$_2$.F$_2$].2TBA complex form the previous result is shown in Figure 5. The selected intermolecular bond-distances of [**L**$_2$.F$_2$].2TBA, [**L**$_2$.Cl$_2$].2TBA and [**L**$_2$.Br$_2$].2TBA are shown in Table 3. The geometrical data of the optimized structure of anion-directed assembly dimer of *N,N′*-bis-(3,5-dinitro)isophthalamide, [**L**$_2$.F$_2$].2TBA, computed with the density functional theory at the B3LYP/6-31G(d) level of theory in gas phase are in a good agreement with its X-ray crystallographic data.

Table 2. Selected intermolecular bond-distances of [**L**.F].TBA, [**L**.Cl].TBA and [**L**.Br].TBA.

Bond-distances	[**L**.F].TBA (Å)	[**L**.Cl].TBA (Å)	[**L**.Br].TBA (Å)
H4···X$^-$	2.4282	2.6819	2.7716
HN3···X$^-$	1.6944	2.3662	2.4676
H13···X$^-$	2.1343	2.6697	2.8424
HN4···X$^-$	1.7345	2.3623	2.4643
H20···X$^-$	2.3434	2.7154	2.7799

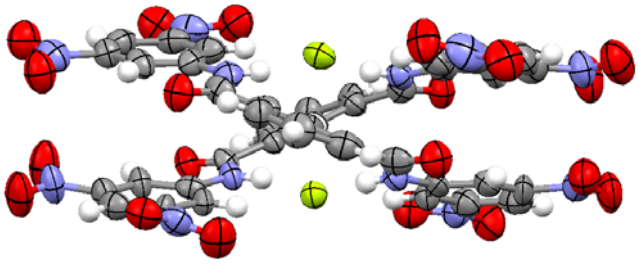

Figure 5. X-ray structure of [**L**$_2$.F$_2$].2TBA complex (TBA$^+$ are omitted for clarity).

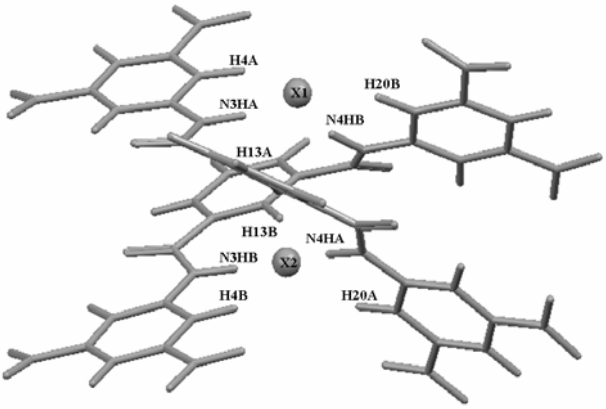

Figure 6. Partial atomic numbering of [**L**$_2$.X$_2$].2TBA complexes.

Table3. Selected intermolecular bond-distances of [$\mathbf{L}_2$.F_2].2TBA, [$\mathbf{L}_2$.Cl_2].2TBA and [$\mathbf{L}_2$.Br_2].2TBA.

Bond-distances (Å)	[$\mathbf{L}_2$.F_2].2TBA		[$\mathbf{L}_2$.Cl_2]. 2TBA	[$\mathbf{L}_2$.Br_2] .2TBA
	Cal.	X-ray		
H4A···X1	1.9926	2.4871	2.6309	2.7131
N3HA···X1	1.6158	1.7244	2.2570	2.3251
H13A···X1	2.8476	2.4962	2.6872	3.0145
N4HB···X1	1.6476	1.8139	2.4384	4.6107
H20B···X1	2.1568	2.4536	2.6998	3.1371
H4B···X2	2.1297	2.3861	2.5582	2.7198
N3HB···X2	1.5280	1.7813	2.1836	2.3326
H13B···X2	1.9562	2.4314	2.4656	2.7704
N4HA···X2	1.5897	2.3809	2.1686	2.5670
H20A···X2	2.1816	2.3678	2.8278	2.6747

Conclusions

The anion-directed assembly dimerizations procssses of *N,N'*-bis-(3,5-dinitro) isophthalamide, **L**, were studied with the density functional theory (DFT) calculation methods. The results show the fluoride ion can induce this compound to form the anion-directed assembly dimer.

Acknowledgement

This research is supported by the Thailand Research Fund (TRF). Center of Excellence for Innovation in Chemistry (PERCH-CIC), Commission on Higher Education, Ministry of Education and the Sila Cluster Computer Center, the Research and Development Institute, Ramkhamhaeng University are gratefully acknowledged.

References

[1]. K. Kavallieratos, S. R. de Gala, D. J. Austin and R. H.Crabtree, *J. Am. Chem. Soc.* **119** (1997), pp. 2325.

[2]. S. J. Coles, J. G. Frey, P. A. Gale, M. B. Hursthouse, M. E. Light, K. Navakhun and G. L. Thomas, *Chem. Commun.* (2003), pp. 568.

[3]. M. E. Light, P. A. Gale, K. Navakhun, *Acta. Cryst.* E62 (2006), pp. 1097.

[4]. K. Navakhun and V. Ruangpornvisuti, *J. Mol. Struct. (Theochem)* **864** (2008), pp. 26.

[5]. K. Navakhun and V. Ruangpornvisuti, *J. Mol. Struct. (Theochem)* **907** (2009), pp. 131.

Preparation of nanocrystalline TiO_2 for dye-sensitized solar cell (DSSC) applications

P. Pinpithak , P. Pakawatpanurat and J. Tantirungrotechai*

Center for Alternative Energy and Department of Chemistry, Faculty of Science, Mahidol University, Bangkok, Thailand

*E-mail: scjjp@mahidol.ac.th

Abstract: Morphology of titania (TiO_2) nanomaterial significantly affects the conversion efficiency of dye-sensitized solar cell (DSSC). Furthermore, metal dopants in titania influence the electrical properties of the electrode. In this work, TiO_2 has been synthesized via various routes. The titania products have diverse morphology such as nanospherical (NS-TiO_2), nanotubular (NT-TiO_2) and non-uniform (NU-TiO_2) particles depending on the synthetic method. These samples were characterized by x-ray diffraction (XRD), fourier transform infrared spectroscopy (FT-IR), diffuse reflectance UV-vis spectroscopy (DRS) and scanning electron microscopy (SEM). Distinctly, TiO_2 material presents anatase phase with crystalline size less than 20 nm. In addition, effect of Mg dopant was also investigated by photocatalysis experiment. The presence of MgO can deplete electron density on conduction band which can be evaluated via the oxidation rate of iodide solution. Photovoltaic performance was evaluated under simulated sun light intensity of 1000 wm^{-2}. The NU-TiO_2 and NS-TiO_2 sample present DSSC efficiency of 1.443 and 1.396% respectively which is better than P25.

Introduction

Conventional solar cell can effectively produce electrical current; however, the solar cell requires advanced technology in production. Therefore, lower cost solar cells are intensively developed. Since 1991, the dye-sensitized solar cell (DSSC) has been emerged and further developed in its photovoltaic performance [1]. Generally, the electron diffusion within photoanode can control electrical output of solar cell. So far, TiO_2 nanomaterial is a well-known candidate for the photoanode. Compatible energy gaps between the titania and sensitized dye facilitate the electron transfer. Nevertheless, the morphology of titania has been considered to affect the DSSC efficiency. Various kinds of TiO_2 such as nanotube nanosphere, and nanopore have been employed to investigate their photovoltaic performance. These morphologies presented unique properties, which may be appropriate for DSSC application.

Clearly, the different synthetic routes of titania result in different crystallinity and morphology. Interestingly, 1-dimensional (1-D) morphology such as nanotube, nanorod or nanowire can facilitate the electron transfer and provide high level adsorption of dye [2-3]. The 1-D product can be synthesized by several methods such as template assisted, electrochemical and hydrothermal treatment methods. The hydrothermal method has gained most attention because the product can be easily prepared with high thermal stability. In general, 1-D structure from the hydrothermal treatment can be obtained via the titanate layer formation and the rolling of the layers [4]. Attractively, spherical particles are widely utilized in electronic devices. Monodispersed particle size and well sintering of spherical particles have been expected. The synthetic routes for spherical titania generally proposed are relied on either sol-gel or co-precipitation route. Controlling the rate of $Ti(OH)_4$ coagulation during reaction is the key to the spherical particle preparation [5].

The DSSC efficiency can be raised by various strategies. Dark current or recombination process mainly reduces the photovoltaic performance. Distinctly, the introduction of metal oxide insulating layers to TiO_2 surface increases the efficiency. MgO and $Mg(OH)_2$ layers are potential species which can suppress recombination reaction [6-7].

In this research, TiO_2 samples were synthesized in three different methods: sol-gel, co-precipitation and hydrothermal. These methods led to different TiO_2 morphology. Furthermore, the effect of MgO to physicochemical properties of TiO_2 was examined. Photovoltaic performance of titania samples have been investigated under simulated sunlight intensity of 1000 wm^{-2} or 1 sun.

Materials and Methods

Synthesis materials: All reagents used were in analytical grade. Several Ti precursors were employed such as Titanium tetraisopropoxide (TTIP or $Ti(O^iPr)_4$, Fluka), Titaniumoxysulfate anhydrous (TOS or $TiOSO_4.xH_2O$, Riedel-de Haën) and TiO_2 powder (P25 or Degussa).

Preparation of NU-TiO_2 by sol-gel method: The method was reported by Warrier et al. [8]. Typical procedure, TTIP was slowly introduced to water with vigorous stirring. Then, glacial acetic acid was added to previous reaction mixture and continued stirring for 1 h. The milky solution was obtained. The solution was evaporated at 70°C to dryness. Finally, as-prepared product was calcined at 500 °C for 3h. In case of MgO doped TiO_2, the same procedure was followed, and $Mg(NO_3)_2$ aq. solution was added before the evaporation step.

Preparation of NT-TiO_2 by hydrothermal method: The synthesis was modified from Balkus, Jr. et al. [9]. Initially, P25 was treated in 10 M NaOH solution and

stirred for 10 min. Subsequently, the reaction mixture was transferred to teflon cup and closed in steel reactor. The reactor was aged in oven at 150 ^oC for 24 h. Then, milky solution was filtered and washed with 0.1 M HCl and water until the filtrate was neutral. The powder was dried at 90 ^oC for 10 h. The product was calcined at 400 ^oC for 2 h.

Preparation of NS-TiO_2 by co-precipitation method: This preparation method was followed from Lukáč et al. [10]. Firstly, TOS was dissolved in the H_2SO_4 solution which could be prepared from mixing in hot water and dense H_2SO_4. Consequently, the reaction mixture was diluted by water. Then, urea has been slowly introduced to previous reaction mixture while the reaction was heated at 98 ^oC. Milky solution immediately occurred after addition of co-precipitant. The reaction mixture was continuously heated for 7 h. The product was filtered and rinsed with water several times. Finally, as-prepared product was dried at 105 ^oC for 12 h and calcined at 500 ^oC for 3 h.

Characterization: X-ray diffractograms were recorded by Bruker D8 ADVANCE diffractometer using CuKα radiation (λ = 1.5406 Å). The operating condition was at 40 kV and 40 mA with a scanning speed and a step size of 1 sec/step and 0.075^o, respectively. The absorption spectra and band gap energy data of TiO_2 were collected by diffuse reflectance UV-vis spectrometer (DRS) UV-2401 Shimadzu. IR spectra were measured by fourier transform infrared spectrometer (FT-IR) Perkin-Elmer; model Spectrum EX FT-IR system. Morphological images were illustrated by scanning electron microscope (SEM) Hitachi S2500.

Photocatalysis experiment: Charge separation of TiO_2 was investigated by photocatalysis of iodide in aq. solution. Typical procedure, 100 mg of titania powder were dispersed in 20 mL of 0.2 M KI solution. Then, the suspension was stirred under UV light (80 W) in steel compartment at ambient temperature. The suspension was withdrawn every 10 min. for 1 h. Afterwards, precipitate was removed by centrifugation. The yellowish solution of triiodide was obtained. Concentration of triiodide was measured by UV-visible spectrometer (Jenway 2450) at 288 nm.

Dye capacity of titania: The dye capacity on TiO_2 surface was determined from amounts of desorped dye from titania powder. Initially, 20 mg of TiO_2 immersed in 10 mL of 0.3 mM N719 (dyesol). The suspension was kept in the dark for 24 h. Then, the powder was separated by centrifugation. Dried powder was rinsed with 5 mL of 0.1 M NaOH in 1:1 of EtOH to water. The dye was desorped out to solution phase in a few minutes. Desorped dye amount was measured by UV-visible spectrometer at 525 nm.

DSSC fabrication: The photoanode could be prepared by double-layer coating of titania film on fluorine-doped SnO_2 (FTO) glass (TEC15, dyesol). Initially, TiO_2 slurry was prepared by grinding the mixture of TiO_2 powder, Triton X-100 (Fluka) as binder, acetylacetone (BDH) as surface modifier and ethanol in motar until viscous slurry obtained. The slurry was dropped on FTO glass which masked the area by scott tape (3M Magic Tape). Slurry was pasted with glass rod until smooth film was obtained. Then, titania film was sintered at 450 ^oC for 30 min. The second layer coating employed the same method. In this experiment, P25 and synthetic samples was used as first and second layer, respectively. Afterwards, TiO_2 film was immersed in 5 mL of 0.3 mM N719 for at least 24 h. The immersed film on FTO glass was assembled with Pt printed FTO glass as counter electrode (dyesol) and the junction between the electrodes was sealed with Surlyn® at 100 ^oC for 2 h. Electrolyte of I^-/I_3^- system (EL41,dyesol) was injected through hole to the cell. Finally, aluminium foil tape was attached at the outer side of counter electrode to seal the hole.

Photovoltaic measurement: The photovoltaic performance of DSSC was measured under illumination of simulated sunlight intensity 1000 wm^{-2} or 1 sun calibrating with standard Si solar cell. UPTS software was used to control Keithley 2420 source meter to record the output current across a linear voltage sweep from 0.8 to -0.091 V.

Results and Discussion

Solid phase and crystallographic data of titania products have been examined by XRD technique. All synthetic samples have pure anatase phase with different crystallinity. The characteristics of NT-TiO_2 can be observed at 2θ of 14.5^o corresponding with the interlayer space of $H_3Ti_3O_7$ nanotube structure as shown in Figure 1.

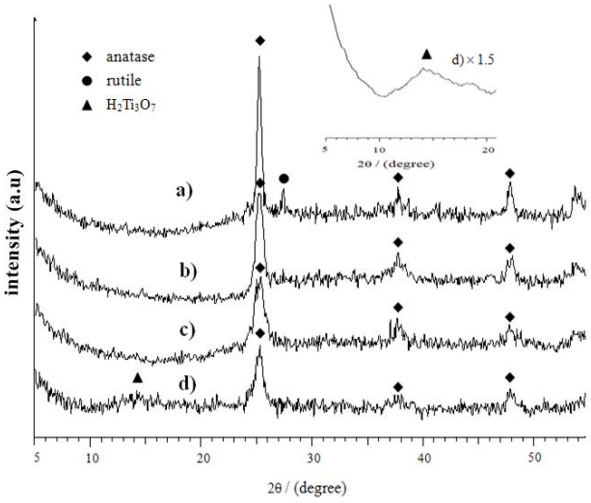

Figure 1. XRD pattern of titania samples a) P25-TiO_2 b) NS-TiO_2 c) NU-TiO_2 d) NT-TiO_2 and its 1.5 times magnified.

All titania samples reveal crystal size less than 20 nm. Distinctly, the NS-TiO_2 shows higher crystallinity with crystal size of 12.12 nm than other synthetic samples (Table 1). This indicates the well sintering of nanospherical morphology.

DRS technique was carried out to inform photoresponsibility and energy gap of titania. TiO_2

samples can absorp light in UV region (less than 400 nm) and thus the transition band in UV region can be observed as shown in Figure 2. Energy gap of NT-TiO_2 and NS-TiO_2 are in the same range with P25 (about 3.1 eV). NU-TiO_2 and its dope sample present negligible red shift with energy gap of 3.0 eV (Table 1). The oxygen vacancies in NU-TiO_2 may cause the shift in the spectra [11].

Dye capacity of the titania samples presents in the micromole level. The variation of adsorped dye content indicates that morpholology influences the surface area. Obviously, the NS-TiO_2 have low dye capacity because high sintering among spherical particles occurred reduces the surface area. Furthermore, effect of MgO clearly reduces the adsorption of dye as presented in Table 1.

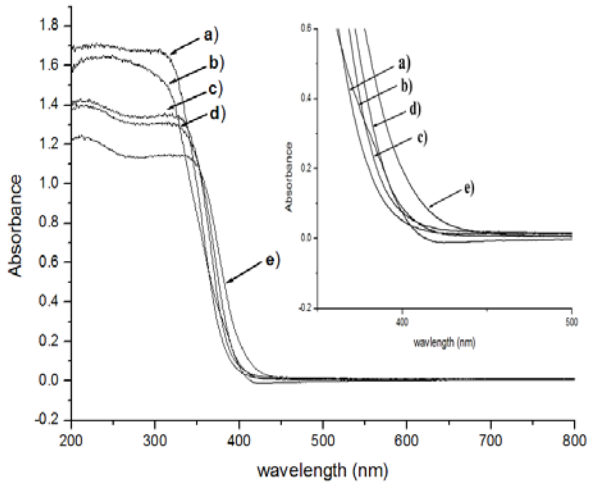

Figure 2. DRS spectra of a) NT-TiO_2 b) P25-TiO_2 c) NS-TiO_2 d) MgO/NU-TiO_2 e) NU-TiO_2 and their absorption edge in the inlet.

Table 1: Crystal size, band gap energy and amounts of adsorped dye on TiO_2 surface.

Samples	Crystal size [a] (nm)	E_g [b] (eV)	Covered dye ($\times 10^{-5}$ molg^{-1})
P25-TiO_2	22.68	3.13	5.96
NT-TiO_2	9.66	3.19	6.41
NS-TiO_2	12.12	3.12	3.96
NU-TiO_2	7.76	3.02	4.47
MgO/NU-TiO_2*	4.48	3.07	1.87

[a] Crystal size was calculated by Scherrer equation
[b] Band gap energy was extrapolated from absorption edge of TiO_2 and further converted by planck equation
* 2%wt MgO

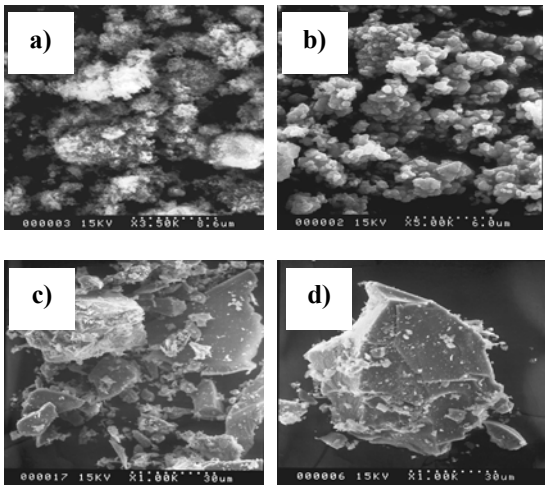

Figure 3. SEM images of various titania a) P25-TiO_2 b) NS-TiO_2 c) NU-TiO_2 d) 2%wt-MgO/NU-TiO_2

SEM images illustrate different morphology of the titania from various preparation methods. The NS-TiO_2 sample is rather monodispersed with a spherical shape and size less than 6 μm. Whereas, NU-TiO_2 and its doped sample reveal a non-orientated shape and size as shown in Figures 3c and 3d. NT-TiO_2 image is not shown in this report because the SEM cannot inform about its morphology. This sample will be further investigated by TEM technique.

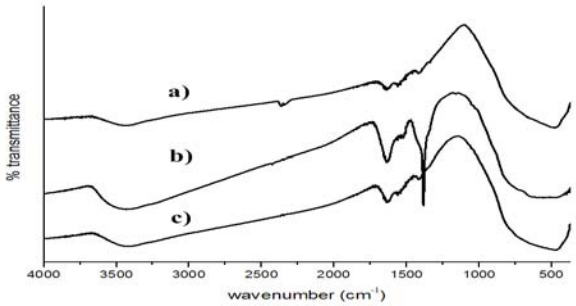

Figure 4. FT-IR spectra of a) NU-TiO_2 and b) as-prepared MgO/NU-TiO_2 and c) calcined MgO/NU-TiO_2.

Decomposition of dopant precursor to metal oxide species during calcination can be studied by FTIR technique. The results show that the $Mg(NO_3)_2$ salt completely decomposes under calcined temperature of 500 ^oC. This is confirmed by the disappearance of NO_3^- band at 1384 cm^{-1} in calcined sample. FTIR spectrum of the undoped sample has similar pattern: ν(-OH), δ(-OH) of adsorped water and fingerprint of 3300, 1630 and less than 900 cm^{-1}, respectively as presented in Figure 4.

The charge separation of titania significantly dominates in the electron transfer. Photocatalysis of the oxidation of iodide by titania was used to determine the corresponding recombination process with the rate of oxidation. Triiodide oxidized product has been rapidly generated by NU-TiO_2. On the other hand, the MgO/NU-TiO_2 slowly produces the

oxidation product. The charge separation can be shielded by MgO composite, which retards the rate of oxidation as illustrated in Figure 5.

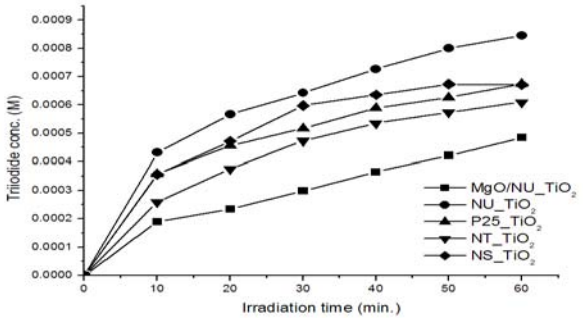

Figure 5. Photocatalysis of iodide by TiO_2 samples under UV irradiation for 1 h.

Finally, photovoltaic performance in of the titania samples, shown in Figure 6, were evaluated in terms of short circuit photocurrent (I_{sc}), open circuit photovoltage (V_{oc}), fill factor (FF) and overall efficiency (%η) as shown in Table 2. Particularly, NU-TiO_2 and NS-TiO_2 give efficiency of 1.443 and 1.396 % respectively which is better than P25 cell. Increasing of light harvesting of these layers are result in high output current. Even though, NU-TiO_2 and NS-TiO_2 indicate good efficiency but V_{oc} is significantly reduced to about 0.6 V. Recombination process mainly influences the diminished V_{oc}. Presumably, the defect in NU-TiO_2 drives the recombination which corresponds with DRS spectra. The MgO composite can clearly improve the photovoltage of NU-TiO_2 with V_{oc} of 0.764 V. Remarkably, the inverse rate of oxidation in photocatalysis of iodide is proportion to the V_{oc} value. Therefore, the electron density in the conduction band (CB) of TiO_2 relates with the recombination of photoelectron.

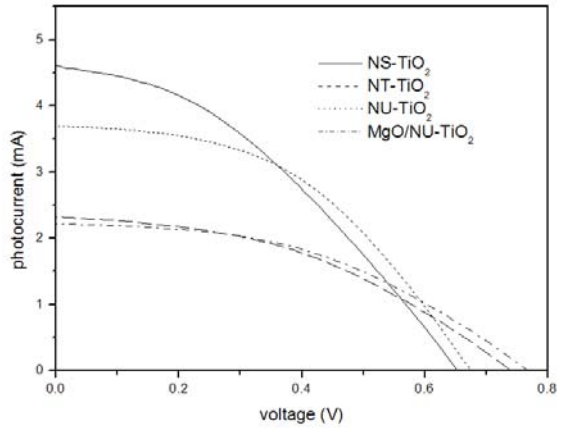

Figure 6. I-V curve measurement of TiO_2 samples under simulated sunlight power of 1000 wm^{-2} (1 sun)

Table 2 : Photovoltaic performance of titania samples

Samples	I_{sc} (mA)	V_{oc} (V)	FF[a]	%η[b]
P25-TiO_2	2.979	0.683	0.757	1.285
NT-TiO_2	2.323	0.737	0.722	0.902
NS-TiO_2	4.610	0.656	1.116	1.396
NU-TiO_2	3.696	0.674	0.463	1.443
MgO/NU-TiO_2	2.219	0.764	0.447	0.946

[a] Fill factor factor was calculated from the equation of $FF = (I \times V)_{max}/I_{sc}V_{oc}$.

[b]%η is overall efficiency which was from the equation of $\%\eta = (Isc \times Voc \times FF \times 100)/P_{input}$

Conclusions

Morphology of titania influences the electron transfer which directly affects the output current. NU-TiO_2 and NS-TiO_2 gives satisfied efficiency with strength of well light harvesting but easy recombination can occur. The defect of TiO_2 easily generates dark current. MgO composite effectively suppresses the recombination process which enhances the V_{oc} of the system. In addition, electron density in CB of TiO_2 corresponds well with the probability of electron recombination.

Acknowledgements

Financial support from the Center of Excellence for Innovation in Chemistry (PERCH-CIC), Comission on Higher Education, Ministry of Education is gratefully acknowledged. This work was also partially supported by Faculty of Science, Mahidol University.

References

[1] B. O' Regan, and M. Grätzel, *Nature*, **353** (1991), pp. 737-740.

[2] M. Adachi, Y. Murata, J. Takao, J. Jiu, M. Sakamato and F. Wang *J. Am.Chem. Soc.* **126** (2004), pp. 14943-14950.

[3] J. T. Jiu, S. Isoda, F. M. Wang and M. Adachi *J. Phys. Chem. B* **110** (2006), pp. 2087-2092.

[4] C-C. Tsai, H. Teng *Chem. Mater.* **18** (2006), pp. 367-373.

[5] T. Sugimoto, T. Kojima *J. Phys. Chem. C* **112** (2008), pp. 18760-18771.

[6] S-T. Bae, H. Shin, J. Y. Kim, H. S. Jung and K. S. Hong *J. Phys. Chem. C* **112** (2008), pp. 9937-9942.

[7] J-H. Yum, S. Nakade, D-Y. Kim and S. Yanagida *J. Phys. Chem. B* **110** (2006), pp. 3215-3219.

[8] C. P. Sibu, S. R. Kumar, P. Mukundan and K. G . K. Warrier *Chem. Mater.* **14** (2002), pp. 2876-2881.

[9] C. Ratanawanate, C. Xiong and K. J. Balkus, Jr. *ACS Nano*, 2 (2008), pp. 1682-1688.

[10] J. Lukáč, M. Klementová, P. Bezdička, S. Bakardjieva, J. Šubrt, L. Szatmáry and A. Grusková J. Mater. Sci. **42** (2007), pp. 9421-9428.

[11] V. N. Kuznetsov and N. Serpone *J. Phys. Chem. B* **110** (2006), pp. 25203-25209.

Oxidation of cyclohexane catalyzed by polyoxometalates supported on MCM-41

J. jatupisarnpong[1] and W. Trakarnpruk[1]*

[1] Petrochemistry and Polymer Science, Faculty of Science, Chulalongkorn University Bangkok 10330, Thailand.

E-mail: Wimonrat.t@chula.ac.th

Abstract: This work presents the results of synthesis, characterization of heteropolyoxometalate [(n-C_4H_9)$_4$N]$_4$H[$PW_{11}Co(H_2O)O_{39}$]= CoPOM supported on MCM-41. The supported catalysts were characterized by by DRUV, FT-IR, XRD and N_2 sorption technique. The catalytic efficiency was tested in the oxidation of cyclohexane using hydrogen peroxide as oxidant in the absence of solvent. It was found that there are only cyclohexanone and cyclohexanol products. The effects of temperature, amount of oxidant, reaction time and amount of catalyst on catalytic performance were investigated. The optimal condition of this reaction was at 80°C, 400 mg of catalyst and H_2O_2/cyclohexane molar ratio of 3.

Introduction

The selective oxidation of cyclohexane is of particular importance due to the large demand for its products such as cyclohexanone and cyclohexanol, which are important raw materials for the production of adipic acid and caprolactam, the intermediates in manufacturing Nylon-6 and Nylon6-6. In the commercial process, the reaction is carried out by using soluble cobalt salt as catalyst or without catalyst, at a temperature above 150°C in which the total conversion of cyclohexane is 3.9% and the selectivity of cyclohexanol and cyclohexanone at around 78%. However the catalyst separation is one of the important problems in the homogeneous systems. In order to avoid these problems heterogeneous catalysts are under intensive investigation. Recently, the use of heterogeneous catalysts such as molecular sieves or metal-containing molecular sieves has attracted a great interest due to their redox ability, shape-selectivity and recyclability [1-2].

In this paper, we report the synthesis of [(n-C_4H_9)$_4$N]$_4$H[$PW_{11}Co(H_2O)O_{39}$] supported on mesoporous molecular sieve MCM-41 by incipient wetness impregnation. It was used to catalyze oxidation of cyclohexane with hydrogen peroxide oxidant.

Materials and Methods

Preparation of catalysts[3].

[(n-C_4H_9)$_4$N]$_4$H[$PW_{11}Co(H_2O)O_{39}$] was prepared by mixing Na_2HPO_4 (1.52 mmol) and $Na_2WO_4{\cdot}2H_2O$ (16.67 mmol), after that metal nitrate (2 mmol) in 30 ml of water was add and the pH was adjusted to 4-5. An aqueous solution of [(n-C_4H_9)$_4$N]Br (7.5 mmol) in 3 ml was added dropwise, with stirring at 80°C. The precipitated salts were filtered off, washed with water and dried in vacuum at 50°C. The compound was recrystallized from acetonitrile.

Syntheses of MCM-41[4].

A composition of SiO_2:CTABr:NH_4OH:H_2O 1.0:0.12:8:114 was used. Ammonia and hexadecyl trimethyl ammonium bromide (CTABr) were dissolved in deionized. Tetraethyl orthosilicate (TEOS) was then added dropwise into the solution, after 2 h, gel was obtained. It was transferred into a Teflon bottle that was then heated at 110°C for 96 h. The solid was filtered, washed with deionized water until the filtrate was neutral, and finally dried. The removal of template was performed by extracting the as-synthesized product in a refluxing acidified methanol. The final product was obtained by centrifugal filtration, washed with ethanol and water and dried.

Incipient wetness impregnation[5].

A solution of CoPOM (0.2 g, 20 wt%) in CH_3CN (4 ml) was dropped to 1.0 g of MCM-41. Solvent was evaporated to leave solid which was further dried.

Characterization

The XRD pattern of catalysts were obtained on Rigaku, DMAX 2002 Ultima Plus X-ray powder diffractometer equipped with a monochromator and a Cu-target X-ray tube (40 kV, 30 mA) and angles of 2 Thetha range from 1.5-60 degree. Fourier transform infared spectra were recorded on a Nicolet FT-IR Impact 410 Spectrophotometer. The solid samples were prepared by pressing the sample with KBr. Infared spectra were recorded between 400-1400 cm^{-1} in transmittance mode. Diffuse reflectance UV-visible spectra were recorded at wavelengths between 200-800 nm on UV-vis 2550 spectrophotometer Shimadzu UV probe. The solid samples were prepared by pressing the sample into a specially designed cell. $BaSO_4$ was used as reference material. Nitrogen adsorption and desorption isotherms were obtained on a BELSORP mini instrument. Samples were degassed at 200°C under vacuum prior to measurements. Surface areas and pore

size distributions were calculated from the BET and the BJH methods.

Catalytic oxidation reaction

Oxidation reactions were carried out in a Parr reactor. 98 mmol of cyclohexane, H_2O_2 (30% aq) and supported catalyst were introduced into the reactor. The reactor was heated to desired reaction temperature and reaction time. After the reaction was completed the supported catalyst was separated by filtration using a filter paper. The products and recovered substrate were qualitatively analyzed by gas chromatography using the internal standard (cyclooctane) method.

Results and Discussion

X-ray diffraction patterns

For pure MCM-41(a), four peaks at low angle corresponding to four planes, (100), (110), (200), and (210) of an ordered hexagonal mesoporous structure. However a decrease in the intensity of the XRD peaks in the low angle region was observed for the CoPOM/MCM-41. This phenomenon is attributed to the filling of the pores of the mesoporous host by CoPOM. Fig. 1B shows the XRD patterns of the CoPOM/MCM-41(b) at higher angles (between 5° and 50°) compared to pure POM(c). In addition to the broad feature between 15° and 35°, which is due to scattering from amorphous silica. These results indicate that the CoPOM was well dispersed on the MCM-41 support at 20 wt% loading[6].

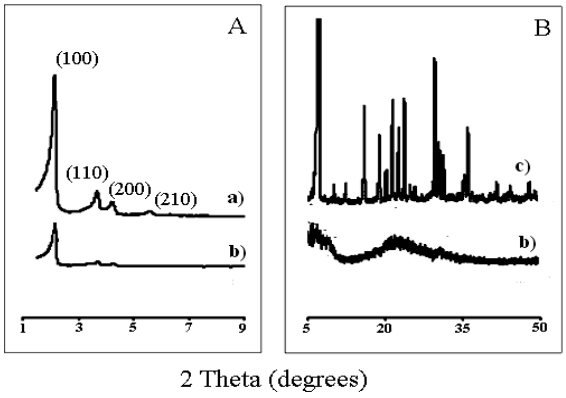

Figure 1. Powder XRD patterns in two different diffraction regions. (a) MCM-41, (b) CoPOM-MCM-41, (c) CoPOM.

FT-IR spectroscopy

The FT-IR spectra of the MCM-41, CoPOM/MCM-41 and bulk CoPOM are displayed in Fig. 2. In Fig 2(c) of CoPOM/MCM-41 show the absorption bands at 960 cm^{-1}, 891 cm^{-1} and 808 cm^{-1}. These characteristic peaks of Keggin ion confirmed the presence of CoPOM into MCM-41 framework[7].

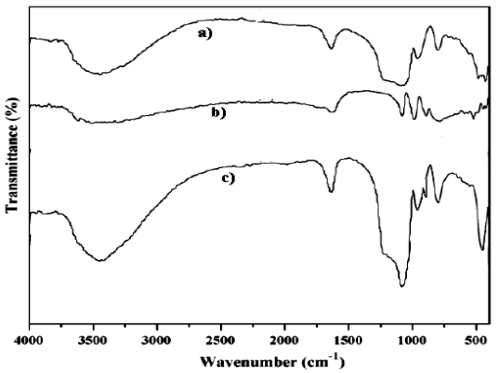

Figure 2. FT-IR spectra of the catalysts: (a) MCM-41 (b) CoPOM and (c) CoPOM/MCM-41.

DR-UV

The DR–UV–vis study was carried out to further confirm the presence of CoPOM in the supported catalyst. CoPOM linked to silica reveal peaks at 450 and 674 nm, indicating the formation of dative bonds of cobalt(II)[8].

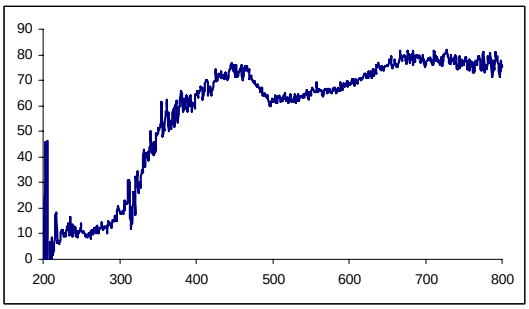

Figure 3. DRS–UV spectrum of CoPOM/MCM-41.

Nitrogen adsorption isotherms

Nitrogen adsorption isotherms of MCM-41 and CoPOM/MCM-41 show type IV character which is typical of mesoporous material. The BET surface area of the CoPOM/MCM-41 sample decrease from 1025 m^2/g (MCM-41) to 828 m^2/g.

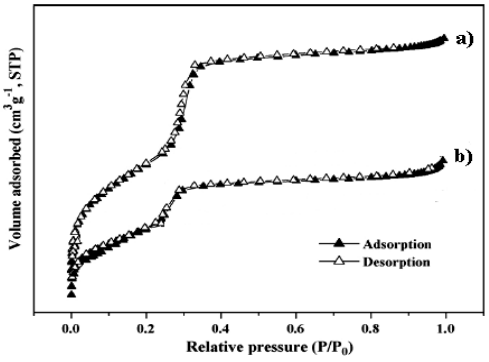

Figure 4. Nitrogen adsorption–desorption isotherms of the catalysts: (a) MCM-41, (b) CoPOM/MCM-41.

Table 1 Cyclohexane oxidation with hydrogenperoxide catalyzed by CoPOM/MCM-41

Entry	Cat(mg)	Oxidant(O/S)	time(h)	Temperature(°C)	Conversion(%)			
					Cyclohexanol(%)	Cyclohexanone(%)	Overall(%)	One/Ol
1	200	H_2O_2 (1)	8	80	0.18	0.67	0.85	3.72
2	300	H_2O_2 (1)	8	80	0.26	0.92	1.18	3.54
3	400	H_2O_2 (1)	8	80	0.44	1.67	2.11	3.80
4	500	H_2O_2 (1)	8	80	0.43	1.62	2.05	3.77
5	400	H_2O_2 (1)	8	70	0.37	1.41	1.78	3.81
6	400	H_2O_2 (1)	8	100	0.38	1.35	1.73	3.55
7	400	H_2O_2 (2)	8	80	0.64	2.29	2.93	3.58
8	400	H_2O_2 (3)	8	80	0.60	2.41	3.01	4.02
9	400	H_2O_2 (4)	8	80	0.53	2.00	2.53	3.77
10	400	H_2O_2 (3)	4	80	0.43	0.47	0.90	1.09
11	400	H_2O_2 (3)	12	80	0.74	3.16	3.90	4.27
12	400	H_2O_2 (3)	24	80	0.66	3.44	4.10	5.21

Catalyst = CoPOM/MCM-41

Effect of the amount of catalyst

From entries 1-4. The product increased with increasing amounts of catalysts. It reached a value of 2.11% with 400mg catalysts; Further increasing in catalyst amount resulted in the decrease in product yield an thus be concluded that the amount of catalyst required for the maximum conversion of cyclohexane was 400 mg[9].

Effect of the temperature

From entries 3, 5-6. It was observed that at 80°C, the highest yield of cyclohexanone and cyclohexanol. At the temperature lower than 80°C, H_2O_2 did not work well. This was probably because H_2O_2 was less homolytically dissociated to form a radical to initiate oxidation reaction. At higher reaction temperature (100 °C), the activity decreases, owing to a possible decomposition of H_2O_2 as well as to the formation by product**[**10**].**

Effect of the amount of H_2O_2

From entries 3, 7-9. When the ratio of H_2O_2/Cyclohexane was increased, conversions of products were increased. But when increase ratio of H_2O_2/Cyclohexane to 4, conversions of products was decreased. The result was affected of over oxidation turned product to by-product[11].

Effect of the reaction time

The ratio of cyclohexanone and cyclohexanol increased with reaction time. At 8 h one/ol ratio was 3.8 but at 24 h the rate of cyclohexanol production decreased and the ratio of one/ol was enchanced. This might be due to cyclohexanol being further oxidized to cyclohexanone[12].

Conclusions

CoPOM can be supported on mesoporous materials MCM-41 by incipient wetness impregnation method. In oxidation of cyclohexane by using CoPOM supported on MCM-41 provided highest mole of products, cyclohexanol and cyclohexanone, at 80°C, 400 mg of catalyst and H_2O_2/cyclohexane molar ratio of 3.

References

[1] Jian-Ying Wang, Feng-Yun Zhao, Run-Jing Liu , Yong-Qi Hu. *Journal of Molecular Catalysis A*(2007)*: Chemical,* **279**, pp. 153–158.

[2] Shahram Tangestaninejad,Valiollah Mirkhani, Majid Moghadam, Iraj Mohammadpoor-Baltork, Esmaeil Shams, Hossein Salavati. *Ultrasonics Sonochemistry*(2008)*,* **15***,* pp. 438-447.

[3] M.M.Q. Simoes, C.M.M. Conceicao, A.M.V. Cavaleiro, J.A.S. Cavaleiro, J.A.F. Gamelas, P.M.D.N. Domingues, A.J.V. Ferrer-Correia, R.A.W. Johnstone. *Journal of Molecular Catalysis A*(1998)*: Chemical,* **144**, pp. 461–468.

[4] Cui Zhang, Wei Zhou, and Shuangxi Liu. *J. Phys. Chem. B*(2005)**, 109***,* pp. 24319-24325.

[5] Piotr Michorczyk, Jan Ogonowski, Piotr Kus trowski , Lucjan Chmielarz. *Applied Catalysis A: General*(2008), **349**, pp. 62-69.

[6] HU Yongqi, WANG Jianying, ZHAO Ruihong, LIU Runjing and LI Yongdan. *Journal of Chemical Engineering*(2009), pp. 407-411.

[7] Aura Llanos, Luis Melo, Felix Avendano, Arturo Montes, Joaquin. *Catalysis today*(2008)*,* pp.133-135.

[8] N.V. Maksimchuk, M.S. Melgunov, Yu.A. Chesalov, J. Mrowiec-Bialon, A.B. Jarzebski, O.A. Kholdeeva. *Journal of catalysis*(2007),**246**, pp. 241-248.

[9] Andreia A. Costa , Grace F. Ghesti, Julio L. de Macedo, Valdeilson S. Braga,Marcello M. Santos, Jos´e A. Dias, S´ılvia C.L. Dias. *Journal of Molecular Catalysis A: Chemical*(2008) ,**282**, pp. 149–157.

[10] A.Sakthivel, P. selvam. *Journal of catalysis*(2002), **211**, pp. 134-143.

[11] S. Shylesh, Prinson P. Samuel, A.P. Singh. Applied Catalysis A: General(2007), **318**, pp. 128–136.

[12] H-X Yuan, Q-H Xia, H-J Zhan, X-H Lu, K-X Su.. *Applied Catalysis A: Genera*(2006), **304**, pp. 178-184.

Material Science and Nanotechnology

Synthesis of nanocrystalline N-doped TiO_2 and its application on high efficiency of dye-sensitized solar cells

C. Kusumawardani[1*], I. Kartini[2] and Narsito[2]

[1] Chemistry Department, Yogyakarta State University, Yogyakarta, Indonesia
[2] Chemistry Department, Gadjah Mada, Yogyakarta, Indonesia

[*] E-mail: irienuny@yahoo.com

Abstract: Nitrogen-doped TiO_2 (N-doped TiO_2) material with nanosize has been synthesized through the hydrolysis of N-substituted titanium isopropoxide precursors. The light absorption onset shifts to the visible region at 550 nm with N-doped TiO_2. The substitution of oxygen sites with nitrogen atoms in the titania structure was confirmed by X-ray photoemission spectroscopy (XPS). A clear decrease in the band gap on N-doped TiO_2 (compared to Degussa P25) is deduced from the optical absorption spectroscopy results. Application of synthesized nanocrystalline N-doped TiO_2 on dye-sensitized solar cells resulted 7.5% overall conversion efficiency, which was higher than the cell based on Degussa P25.

Introduction

Highly energy demand of our world onto fossil fuels have posed several drawbacks since fossil fuels are nonrenewable, cause many environmental problems and are likely not to continue to remain abundant for the next generations. Therefore, the search for alternative renewable energy technologies is of crucial importance for the sustenance and development of modern society [1]. One of the possible solution to the energy challenge is to make efficient use of solar energy, which is abundant, long lasting and clean. Solar cells are being most area of interest in solar energy utilization because it can directly convert the solar energy to electricity.

A new type of solar cells developed by O'Regan and Grätzel in 1991, dye-sensitized solar cells (DSSCs) have been attracting much attention over last decade as potential low-cost alternative to commercial solar cells based on silicon due to their ease of fabrication and high photoconversion efficiencies [2-5]. Despite low-cost, their system had a light-to-electricity conversion efficiency of around 12%, a level that is not easily obtained since the first concept firstly noticed in early 1970 [6]. It is necessary to further improve the energy conversion efficiency in order to commercialize DSSC successfully. Many methods for improving the conversion efficiency of the DSSC have been attempted [7-10], some considerable efforts have been devoted to find the most efficient dyes to increase the efficiency but effort to modify titania as the most efficient support for the dye have been overlooked.

Nanoparticles TiO_2 and thin films TiO_2 are easily produced, inexpensive and show good stability under illumination in most environments [11-13]. However, there is a major disadvantage for solar energy application that the bandgap energy, around 3 eV, only allows altraviolet (UV) absorption. To improve the photoelectro-chemical efficiency of the material it is desirable to red-shift the photoelectro-chemical onset to also include the less energetic but more intense visible part of the solar spectrum. Traditionally, this has been achieved by anchoring organic dyes as sensitiser, which are usually Ru(II) complexes, to harvest the visible light [2,9]. Although this method broadens the range of the visible light response effectively, the problem appear with organic dyes that they can detach from the surface when employed in aqueous solution and the long term stability of many dyes can be questioned. In addition, the semiconductors usually use pure TiO_2 in which there is some oxygen deficiency in the crystal structure [14-17]. It is known that oxygen deficiency can create electron-hole pairs and that the oxidizing holes can either react with the dye and destroy it and/or is scavenged by iodide ions [18], so the lifetime of the dye-sensitized solar cell may be shortened. Therefore, there is a need to increase the DSSC efficiency and stability by other approaches.

In this paper, we report a sol gel method for synthesizing of nitrogen-doped (N-doped) TiO_2 and its application into the DSSC system to enhance the efficiency of the solar cell due to the replacement of oxygen-deficient titania by visible-light-active N-doped TiO_2.

Materials and Methods

Materials: Titanium Tetra Isopropoxide, $Ti(OPr)_4$, 97% and acetylacetone were purchased from Aldrich. Dodecylamine 98 % and TritonX-100 were purchased from Fluka. Ethanol absolute and CH_3COOH were obtained from Merck. All materials were used as received. Di-tetrabutylammonium cis-di(isothiocyanato)bis(2,2'bipyridyl4,4'dicarboxylato) Ru(II) (N719 dye), Electrolyte EL-HSE, TEC 15 electrode glass plate and Pt-coated counter electrode are commercial products of Dyesol (Australia).

Synthesis of N-doped TiO_2: For synthesis of the N-doped TiO_2 powders, a mixture of 3 mL of $Ti(OPr)_4$, 10 mL dodecylamine, and 80 mL of ethanol absolute solution was stirred for 4 hours at 70^{o}C provided a clear solution. This precursor solution was then cooled to room temperature and 5 mL of CH_3COOH was added to neutralize the excess of dodecylamine.

Hydrolysis process was then achieved by adding 20 mL of distilled water dropwise into the solution under vigorous stirring, the solution continues stirred for 24 hours. The resulting yellowish precipitate was centrifuged and washed subsequently with distilled water and ethanol. Finally, the N-doped TiO_2 were vacuum-dried for 12 hours. The surfactant from the as-made N-doped TiO_2 powders was removed by calcining at a heating rate of 2°C/min in air atmosphere for 2 hours at 200, 300, 400, 450, 600 and 800°C.

N-doped TiO_2 thin film preparation: 2g of N-doped TiO_2 powder was mixed with 4 mL deionised water, 10 µL of acetylacetone and 50 µL of Triton X-100 in stepwise addition into a porcelain mortar to make slurries. The mixtures were ground until no lumps were observed. Then, using Scotch adhesive tape (as the spacer) to make 0.25 cm^2 active area, the slurries were deposited on electrode glass by a doctor blading technique. Before sintering at 400°C (heating rate of 20°C/min) for 30 min, the films were dried in air at room temperature for 10 min, and heated at 50°C for 10 min. For comparison a Degussa P-25 (Nippon Aerosil Co., Ltd.) thin film was made through similar way.

Characterization: The N-doped TiO_2 powder was analyzed by thermogravimetric analysis (TGA) with a Q500TGA Instrument using a 10°C/min ramp up to 800°C. The structure of the powder was examined with X-ray photoelectron spectroscopy (XPS, PHI-5300) and N_2 adsorption-desorption measurements at 77 K (NOVA Quantachrome). UV-visible diffuse reflectance spectra were obtained for N-doped TiO_2 using a UV-visible spectrophotometer (UV-2550, Shimadzu).

DSSC fabrication: To fabricate the DSSCs, the N-doped TiO_2 electrodes were immerse in 0.3mM solution of N719 dye in acetonitrile overnight. Cells were assembled by placing the Pt-counter electrode (CE) over the active area of N-doped TiO_2 working electrode. The electrolyte was introduced through drilled hole on CE by capillary action, the hole was then sealed. For comparison, DSSCs based on Degussa P25 thin film working electrode was also fabricated under the same conditions.

Current-voltage Measurement: Current-voltage measurements were done using a 450 W Xe lamp that was focused to provide 1000 W/m^2, equivalent to one sun at AM 1.5, at the surface of the cells. The spectral output of the lamp was matched in the region 350 – 800 nm with the aid of a Schott KG-5 sunlight filter so as to reduce the mismatch between the simulated and the true solar spectrum to less than 2%. The current-voltage characteristics of the cells were determined by biasing the cells externally and measuring the generated photocurrents. The overall photoconversion efficiency η is calculated from the integral photocurrent density (J_{sc}), the open circuit photocurrent (V_{oc}), the fill factor of the cell (ff), and the intensity of incident light (I_s) using the formula

$$\eta = J_{SC} V_{OC} ff / I_S \quad (1)$$

I_s = 1000 W/cm^2 at air mass (AM) 1.5, or under full sunlight. Fill factor (ff) is given by

$$ff = V_{\max} I_{\max} / (J_{SC} V_{OC}) \quad (2)$$

Results and Discussion

N-doped TiO_2 can be prepared in different ways. We found that complexation of organic amines on the Ti metal center creates highly efficient precursors for N-doped TiO_2 nanoparticles. Advantages of this route are high doping levels, controllable doping concentrations, and aqueous chemistry that results in a hydrophilic surface at low cost. The N-doped TiO_2 were synthesized by hydrolysis of N-substituted titanium isopropoxide precursors in alcohol solution. In the synthesis the nitrogen has been doped into the lattice and/or attached to the nanoparticles surface. However, at the same time, there is water and organic residue adsorbed on the surface and enclosed into the amorphous and porous N-doped TiO_2 powder.

The thermogravimetric analysis was used to study the weight loss of the N-doped TiO_2 in order to understand the loss of organic residues on the surface of the N-doped TiO_2 under calcinations. The TGA results of the N-doped TiO_2 in Figure 1 show that there is less weight loss, about 20% from room temperature up to 150°C, which is mostly due to the loss of physically adsorbed or embedded water and solvent on the surface of the N-doped TiO_2. From 150 to 200°C, there is about 40% weight loss of The N-doped TiO_2 sample. From 250 to 400°C there is much slower (about 5 %) weight loss of the N-doped TiO_2 sample in association with the crystallization of these nanoparticle. The latter weight loss is about the same as the nitrogen content in the N-doped TiO_2 calcined at 400°C. Above 400 °C, there is very little, about 3–5% weight loss of the N-doped TiO_2 sample in association with the crystallization of these nanoparticles.

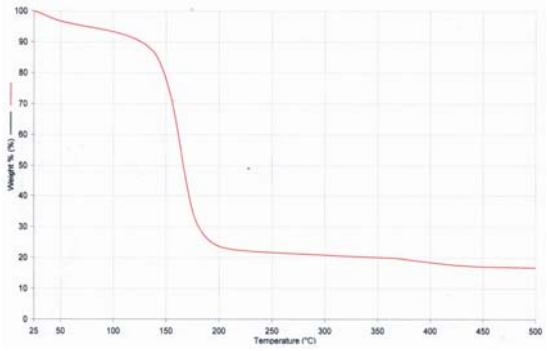

Figure 1. TGA graph of N-doped TiO_2

The substitution of the oxygen sites with nitrogen atoms in the titania structure was confirmed by X-ray photoemission spectroscopy (XPS), as shown in Figure 3. The nitrogen 1s core level of N-TiO_2 shows three peaks at 396.0, 399.4 and 400.5 eV, which is consistent with the reported results for N-TiO_2. The two peaks at higher binding energies may attributed to

molecularly adsorbed nitrogen species, whereas the peak at 396 eV was assigned to the substitutionally bound N^- species in the TiO_2 lattice [19]. Thereafter, Irie et.al. [20,21] and Diwald et.al. [22,23] reported that the peak at 396 eV in the XPS spectra was attributed to a chemically bound N^- species within the crystalline TiO_2 lattice. Most N species in the N-TiO_2 existed in the form of nitrides such as N in the O-Ti-N linkage, corresponding to the binding energy (BE) of 399.4 eV, while only small amounts of N were present in form of surface adsorbed ammonia, with the BE located at 396.0 eV.

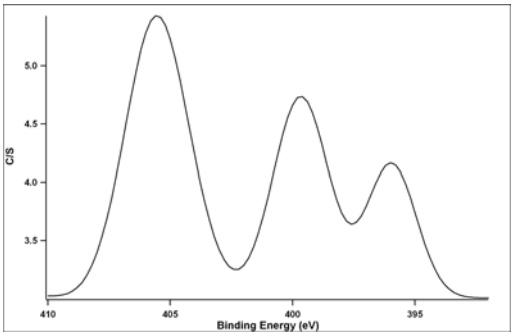

Figure 2. Nitrogen 1s XPS of N-doped TiO_2 calcined at 450°C

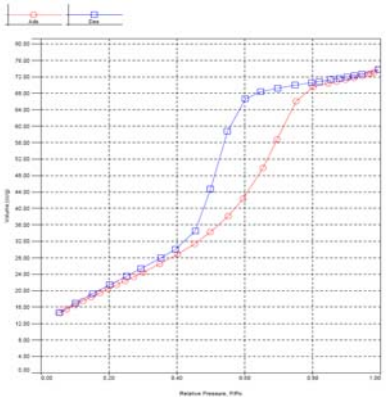

Figure 3. Isotherm curve of N-doped TiO_2

Figure 3 shows the typical nitrogen isotherm of N-doped TiO_2 spheres. It exhibits a type-IV isotherm curve with an H2 hysteresis loop according to IUPAC classification [24], which means the spheres have mesoporous structure. The N-doped TiO_2 show high BET surface areas 147 m^2/g because of the mesoporous structure and the large amount of nanometer crystallites.

The optical absorbance and reflectance was used to study the capability to photosensitize the TiO_2 nanoparticles. The absorbance shift of the N-doped TiO_2 NPs can be observed from the reflectance spectra of undoped (Degussa P25) and N-doped TiO_2 NPs in Figure 4. The yellowish N-doped TiO_2 sphere powders show good absorbance of visible light. It can be seen from Figure 5 that the visible light absorption is high and extended up to 550 nm in the case of N-doped TiO_2 calcined at 450°C compared to that of pure TiO_2 which could only absorb light in the UV range. It may be due to that nitrogen species occupy some of the oxygen positions in the lattice. This also rules out the occupancy of N in any other positions such as interstitial sites, which should give rise to a mid gap band/level between valence and conduction bands.

The band gaps of N-doped TiO_2 and Degussa P25 were calculated by the equation [2]

$$E_g = 1239.8/\lambda \qquad (3)$$

where E_g is the band gap (eV) and λ (nm) is the wavelength of the absorption edges in the spectrum. The band gap for N-doped TiO_2 and Degussa P25 as calculated for the absorption edge in the visible region was found to be 2.25 eV and 3.09 eV respectively.

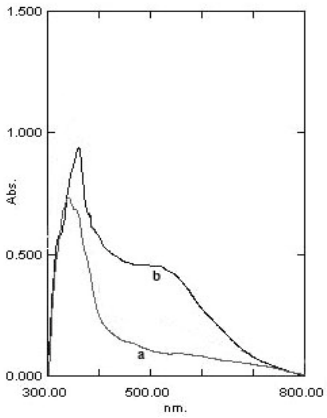

Figure 4. DRUV Spectra of N-doped TiO_2 (b) compared to Degussa P25 (a)

Figure 5 shows the current-voltage curves of the open cells based on the N-doped TiO_2 and Degussa P25 photoelectrodes. A pronounced increase in the photocurrent for the DSSC based on the nitrogen-doped titania was observed. The performance properties of the DSSCs are summarized in Table 1. A high-energy conversion efficiency of 7.5% was achieved, which was 25% higher than that of the P25, respectively. It is evident that the conduction band edge remains unchanged by nitrogen doping.

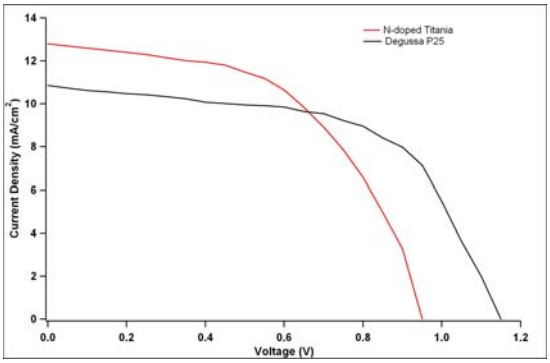

Figure 5. Current-voltage curves of the dye-sensitized cell based on the N-doped TiO_2 and Degussa P25

It assumed that occurrence of visible light absorption due to the nitrogen-doped titania support intrinsically increases the efficiency value due to the photoresponse of N-doped TiO_2 in the visible light region which is also supported by the results reported by Lindgren et. al. [19]. They have demonstrated that the photoinduced current due to the visible light activity of the best nitrogen-doped titania electrode prepared by reactive DC magnetron sputtering can increase significantly by approximately 200 times over those of the undoped titania electrodes. On the basis of these results, it can be expected that the optimization of the amount of nitrogen doping in titania nanoparticles and electrode can further improve the performance of the DSSCs. It also should be pointed out that a higher Ru dye uptake was observed on the N-doped TiO_2 film, compared to that for P25. It has been known that a larger surface area of the N-doped TiO_2 film can increase the amount of dye uptake and further lead to an increase in the conversion efficiency of the dye-sensitized solar cell.It is usual for the results to be presented first, followed by a discussion of their significance. Only strictly relevant results should be presented and figures, tables, and equations should be used for purposes of clarity and brevity. The use of flow diagrams and reaction schemes is encouraged. Data must not be reproduced in more than one form, e.g. in both figures and tables, without good reason

Table 1: DSSC characteristics

Character	N-doped TiO_2 DSSC	Degussa P25 DSSC
Jsc (mA/cm^2)	12.8	10.86
Voc (V)	0.95	1.1
Imax (mA/cm^2)	11.4	8.4
Vmax (V)	0.74	0.82
Ff (%)	0.61	0.58
η (%)	7.5	6.8

Conclusions

The N-doped TiO_2 nanocrystalline materials were synthesized successfully by a novel sol gel method. Three binding energy peaks were observed at 396.0, 399.4 and 400.5 eV in the N 1s region of the XPS. The first two signals were attributed to a chemically bound N^- species and the O-Ti-N linkages within the crystalline TiO_2 lattice, respectively. Whereas, the signal around 400.5 eV was assigned to the molecularly adsorbed nitrogen species. A new absorption was observed for the UV-vis spectrum of the nitrogen-doped TiO_2 in the visible light region. The action spectrum of the DSSC based on the N-doped TiO_2 was in agreement with the corresponding optical spectrum. The high energy conversion efficiency was achieved successfully for the DSSC based on the N-doped nanocrystalline titania electrode.

References

[1] Qiu, X. and Burda, C., Chem. Phys **339** (2007), pp. 1-10

[2] O'Regan, B. and Gratzel, M., *Nature* **353** (1991)**,** pp 737-739

[3] Gratzel, M., *Prog. Photovolt. Res. Appl*. **8** (2000), pp 171-185

[4] Hodgson and Wilkie, *Mater .World* **8** (2000), pp. 11-13, 2000

[5] Gratzel, M., *J. Photochem. Rev.* **4** (2003), pp. 145-153

[6] Gratzel, M., *J. Photochem. Rev.* **1644** (2004), pp. 3-14, 2004

[7] Miki, T.; Soga, T.; Umeno, M., *Sol. Energy Mater. & Sol. Cells*. **48** (1997), pp. 123-130

[8] Bach, U.D.; Lupo, P.; Comte, J.E.; Moser, F.; Weissortel, J.; Salbeck, H.; Spreitzer, H. and Gratzel, M., *Nature* **395** (1998), pp. 583-585

[9] Nazeeruddin, M.K.; Kay, A.; Rodicio, I.; Humphry-Baker, R.; Muller, E.; Liska, P.; Vlachopoulos, N. and Gratzel, M., *J. Am. Chem. Soc.* **115** (1993), pp. 6382-6390

[10]Yanagida, M.; Singh, L.K.; Sayama, K.; Hara, K.; Katoh, R.; Islam, A.; Sugihara, H.; Arakawa, H.; Nazeeruddin, M.K. and Gratzel, M., *J. Chem. Soc., Dalton Trans* (2000)., pp. 2817-2822

[11]Mills, A. and Hunte S.L., *J. Photochem. Photobiol. A: Chem.***108** (1997), pp. 1-35

[12]Linsebigler, A. L.; Lu, G. and Yates, J. T., *Chem. Rev.* 95 (1995), pp.735-758

[13]Weller, H. and Eychmuller, A., *Advances in Photochemistry*. **20** (1995), pp. 165-216

[14]Ihara, T.; Miyoshi, M.; Iriyama, Y.; Matsumoto, O.; Sugihara, S., *Appl. Catal., B: Environmental* **42** (2003), pp. 403-409

[15]Sathish, M.; Viswanathan, B.; Viswanath, R. P. and Gopinath., C., *Chem. Mater.* **17** (2005), pp.6349-6353,

[16]Chen, X.; Lou, Y.; Samia, A. C. S.; Burda, C.; Gole, J.L., *Adv. Funct. Mater* **15** (2005), pp. 41-49

[17]Burda, C.; Lou, Y. B.; Chen, X. B.; Samia, A. C. S.; Stout, J. and Gole, J.L., *Nano Lett.* **3** (2003), pp.1049-1051

[18]Chen, H.; Nambu, A.; Wen, W.; Graciani, J.; Zhong, Z.; Hanson, J. C.; Fujita, E.and Rodriguez, *J. Phys. Chem. C* **111** (2007), pp.1366-1372

[19]Lindgren, T.; Mwabora, J.M.; Avendan˜ o E., Jonsson, J., Hoel, A., Granqvist, C.G. and S.E. Lindquist, *J. Phys. Chem. B* **107** (2003), pp. 5709-5716

[20]Irie, H.; Watanabe, Y.; Hashimoto, K. J., *Phys. Chem. B* **107** (2003), pp. 5483-5486

[21]Irie, H.; Washizuka, S.; Yoshio, N. And Hashimoto, K., *Chem. Commun*. 11 (2003), pp.1298-1299

[22]Diwald, O.; Thompson, T. L.; Goralski, E. G.; Walck, S. D. and Yates, J. T.Jr., Photochemical Activity of Nitrogen-Doped Rutile TiO_2(110) in Visible Light, J. Phys. Chem. B, Vol. 108, pp. 6004-6008, 2004

[23]Diwald, O.; Thompson, T. L.; Goralski, E. G.; Walck, S. D. and Yates, J. T.Jr., *J. Phys. Chem. B* **108** (2004), pp. 52-57

[24]Rouquerol, F.; Rouquerol, J. and Sing, K., Adsorption by Powders and Porous Solids: Principles, Methodology, and Applications; Academic Press, San Diego,1999

Laminating PVC films on mulberry paper

A. Memon[1*] and S. Ithisophonakul[2]

[1,2] Center of Develop Innovation and Packaging for Village Products (CDiPV),
Department of Industrial Engineering, Faculty of Engineering,
Rajamangala University of Technology Thunyaburi, Phathumtani, Thailand

[*] E-mail: cdipv.rmutt@gmail.com

Abstract: This research project presents the laminating Polyvinylchloride (PVC) films on mulberry paper by latex glue. The objective of the research was developed the usage of mulberry paper for multifunction and widely used. A laminating machine was designed and constructed. It had size 68 x 98 x 60 centimeters. The mulberry paper used for the research had size 55 x 75 centimeters. The PVC films in this research had thickness 0.04 μm and tensile strength was 40.22 MPa. Latex glue was used as adhesive between mulberry paper and PVC films. The main results obtained as the follows. The mulberry paper was laminated with speed 75 meters per hour or coated 100 sheets per hour with continuous laminating. The appropriate temperature for laminate was 130 ^{o}C, and the motor speed was 10 rpm. The normal mulberry paper had average thickness 0.4 millimeter, it's bursting strength before laminated was 2.94 kg/cm^2 and after laminated was 7.26 kg/cm^2. The mulberry paper reinforcement by fiber of teak leaf had average thickness 0.25 millimeter, it had the bursting strength before laminate 0.70 kg/cm^2 and after laminated 3.66 kg/cm^2. The normal mulberry paper had tensile strength 37.07 MPa, after laminated it had 79.14 MPa. The reinforce mulberry paper had tensile strength before laminate 5.34 MPa and after laminated 56.69 MPa. Laminated mulberry paper was glossy and more attractive, strengthening, also protected water or humidity to decline them. The product from this process had smooth surface easily to screen printing and clean out the dirt.

Keyword: Mulberry paper, Laminating mulberry paper, Laminating machine, PVC films, Laminating mulberry paper by PVC films

Introduction

The mulberry paper was hand-made paper. Many product were used mulberry paper as main structure or used for decorated them. Now a day, mulberry papers were developed in many styles for made products as lantern, packaging, book cover, decoration product, office equipment etc,. Mulberry paper may decorate or reinforce by fiber of teak leafs and dried flowers, make it colorful and more attractive as shown in figure 1. Mostly, this paper was declined by water, humidity and light. Those environment make them had short life time and unattractive. One choice to improve this problem is laminating this paper by PVC films. This film has good strength, transparent and high temperature used.

This research aimed to develop the widely use of mulberry paper for produced modern products. After laminated, this paper had higher strength, more glossy, water and humidity proofed, smooth surface and protected dirt to decline them. Thus, we can design and develop many products from these laminated papers.

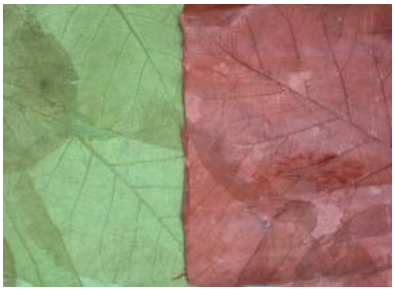

Figure 1. Mulberry paper reinforced by fiber of teak leafs

Dry laminate was the process to combine 2 materials together by adhesive. The first step, adhesive was coated on first materials and half dry the layer of adhesive by appropriate temperature. In the next step first materials and half dry layer were laminated with the second materials by roller. This process can used with many type of films and adhesive.

Anin Memon, et al. [1] designed a laminating machine size 0.45 x 0.9 x 0.8 meter for laminate the matter by Cellulose-propionate films and used Latex glue as adhesive. In this research used the matter from inject printing process because this process was wildly used in printing and suitable for infinitesimal matter, also had low cost and faster. The matter was printed on coated and uncoated papers 210 gram, size 297 x 420 millimeter (size A3). The laminating use temperature 160^{o}C for half dry latex glue, laminating speed was 45 second per sheet. The results obtained as the follows. The matter durable to scratched than non laminate matter. After dropped water on laminate matter, it could protect the color of matter as its original and the paper was not swell. The density tests of color in inject ink found the different 0.11% between laminated and non-laminated mater, test by Densitometers. This process could protect the evaporation of the water base ink, which keep colorful of the matter.

Wutinant Kongtud, et al. [2] studies physical properties of Thai hand-made paper from saa and rice straw pulp were studied. The ratio between saa pulp and rice straw pulp used in this experiment were 100:0, 90:10, 80:20, 70:30, 60:40, 50:50, 40:60, 30:70, 20:80, 10:90 and 0:100. Methods according to TAPPI standard were used for analysis of the resulting paper physical properties and the results showed that the

most appropriate ratio of saa pulp and rice straw pulp was to be 70:30. It was indicated that paper obtained from this ratio can be used as substitute of 100 % saa paper for handicrafts and packaging. Its physical properties were as follows: basis weight 64.23 g/m2. thickness 0.286 mm, density 0.224 g/cm3, brightness 78.88%, tensile index 27.76 Nm2/g, stretch index 3.63%, smooth index 11.38 sec, folding endurance 112 times, burst index 3.08 kPa.m2/g and tear index 588.22 mN.m2/g.

Pimanchan Rungrod and Nattakarn Hongsri-phan [3] investigate the effect of tackifier on tack and peel of natural rubber latex-based adhesives. Five ratios of NR latex to rosin-ester tackifier were mixed and coated on PET films to produce adhesive tapes samples for probe tack and 180° peel tests. Adhesive viscoelastic properties were also studied by using cone and plate rheometer. Adding tackifier into natural rubber latex decreases cohesiveness in natural rubber. Tack of NR adhesive increased up to 150 phr of tackifier. The decrease of tack after 150 phr of tackifier might due to phase separation of the mixture. The storage modulus of the mixture with tackifier was lower than NR latex indicting less flexibility of adhesive in presence of tackifier which improved wetting of adhesive on substrate. Higher concentration of tackifier increased peel strength of NR adhesive in the linear fashion

Somchai Maneewan [4] studied the physical properties of mulberry paper according to international organization for Standardization (ISO) and attempted to standardize the mulberry paper obtained from the north of Thailand. The mulberry papers from three sources were examined, including the mulberry paper from: Ban Naluang, Wiangsa, Nan; Ban Sanian, Muang, Nan; and ban Yang, Nachornthai, Phitsanulok. It was found that the maximum tensile strength for the dry mulberry paper was 16.811 kN/m. After the immersion in water, the maximum tensile strength was 1.089 kN/m. The water absorpveness was 3.500 g or 462 %. The basic weight, tickeness and density were 127.590 g/m^2, 0.372 mm, and 383.821 kg/m^3, respectively.Thus, it is concluded that the physical properties of the mulberry paper are appropriate to replace the imported celpads.

Materials and Methods

A laminating machine was constructed and it had size 68 x 98 x 60 centimeters. The components of this machine were shown in figure 2. Adhesive unit feed layer of latex glue on PVC films. Infrared heater was used to half dry adhesive on PVC films. The maximum temperature was 300°C. Laminating unit consist of rubber roller that used for compress films contact mulberry paper and steel roller used for support compression from rubber roller.

The components
1) Laminating films
2) Adhesive unit
3) Infrared heater
4) Laminating unit
5) Control system
6) Power unit

Figure 2. Laminating machine for laminated mulberry paper

The mulberry papers used for this research had size 55 x 75 centimeters. It was hand-made paper from Ban Thalore, Meoung district, Lampang. In this research used 2 type of mulberry paper. The first paper was a normally type, it had average thickness 0.4 millimeter as shown in figure 3a. The second was mulberry paper reinforce by fiber of teak leaf, average thickness 0.25 millimeter as shown in figure 3b. Latex glue was adhesive in this experimental. The laminate film was PVC film. It had thickness 0.04 μm, 60 centimeter width and length was 50 meter in a roll.

a) normally type b) reinforce by fiber of teak leaf

Figure 3. Mulberry papers

PVC film was coated by latex glue and half dry by infrared heater 130 °C. Motor speed was 10 rpm. Coated half dry film was compressed on mulberry paper by compression from rubber roller. The latex glue will spread out over paper and film was laminated on them. The mulberry paper was laminated with speed 75 meter per hour or coated 100 sheets per hour with continuous laminating. The testing of laminated mulberry paper was obtained as follows.

1) Water proof properties

The test was performed by drop water on laminated mulberry paper and wait for 5 minute. This property carried out using a visual examination.

2) Clean up the contaminate

Using Non-permanent pen drew a few lines on normal paper and laminated paper. Clean out those lines by tissue paper.

3) Bursting strength test

The bursting strength test was conducted according ASTM D774 with a bursting strength test (Mullen type) as shown in figure 4. The sample had size 10 x 10 centimeter. Each value obtained represented the average 5 samples.

Figure 4. Bursting strength tester

4) Tensile test

The tensile test was conducted according ASTM D882 with a tensile tester as shown in figure 5. The sample was cut size 2 x 10 centimeter. Each value obtained represented the average 5 samples.

Figure 5. Tensile tester

Results and Discussion

1) Water proof testing

Un-laminated mulberry paper absorbed water in a few second after dropped water on them. After 5 minute, the structure of paper was changed and very easy to wear and tear. While laminated mulberry paper still carried water on the surface longer than 5 minute. The visual examinations shown laminated paper proofed them from water.

2) Clean up the contaminate test

Laminated paper were drew lines on the surface by non-permanent pen. They are sharp and smooth line. After 10 minute, very easy to cleaned out those line by tissue paper. While un-laminated mulberry paper shown broken line and they adhered permanently on surface. Figure 6 shown the clean up contaminate on both papers. Laminated paper had smooth surface, which can apply other printing process on them such as screen printing and padding for logo brand of product.

3) Bursting strength testing

The bursting strength of un-laminate and laminated paper were shown in figure 7. Normal mulberry paper average thickness 0.4 millimeter had bursting strength 2.94 kg/cm^2, the busting strength was 7.26 kg/cm^2 while laminated this paper with PVC films. Mulberry paper reinforce by fiber of teak leaf with average thickness 0.25 millimeter had 0.70 kg/cm^2 and it was 3.66 kg/cm^2 after laminated. Un-laminate reinforcement mulberry paper had poor bursting strength than un-laminate normal paper because they are different thickness and structure. At the same time both of them had higher bursting strength after laminated by PVC film. Sample of bursting strength test were shown in figure 8.

a) Make a line on mulberry paper and can't clean out

b) Make a line on laminated mulberry paper and easy to clean out

Figure 6. Clean out contaminate testing

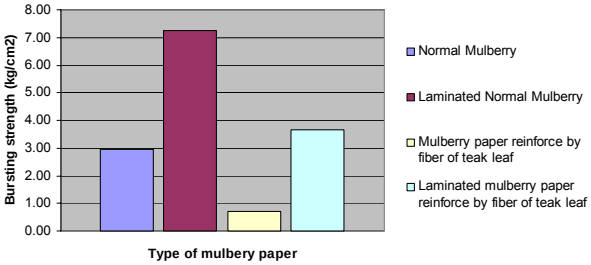

Figure 7. The bursting strength mulberry paper

a) Un-laminated mulberry paper

b) Laminated mulberry paper

Figure 8. Sample from Bursting strength test

4) Tensile strength testing

The tensile strength of un-laminate and laminated papers was shown in figure 9. PVC films 0.04 μm had tensile strength 40.22 MPa. Tensile strength of normal mulberry paper was 37.07 MPa, after laminated it was 79.14 MPa. At the same time un-laminate reinforcement mulberry was 13.87 Mpa, after laminated it was 56.69 MPa. Their tensile strength was increase due to PVC films in both paper but reinforcement mulberry had lower tensile strength because it thinner than normal mulberry paper as discussed in section 3.3. How ever, laminated mulberry had higher strength and elongation than un-laminate paper as shown the sample of tensile test in figure 10.

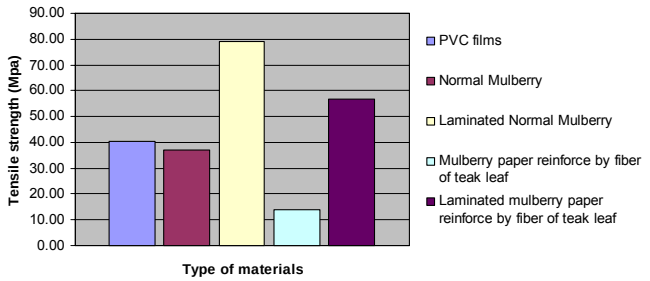

Figure 9. The bursting strength mulberry paper

a) Un-laminated reinforcement mulberry paper

b) Laminated reinforcement mulberry paper

Figure 10. Sample from tensile test

Conclusions

The laminating PVC films on mulberry paper by latex glue was developed the usage of mulberry paper for multifunction and widely used. The experimental used laminating machine size 68 x 98 x 60 centimeters. The mulberry paper used for the research had size 55 x 75 centimeters. They are 2 type of mulberry paper. The first paper was a normally type, it had average thickness 0.4 millimeter. The second was mulberry paper reinforce by fiber of teak leaf, average thickness 0.25 millimeter. The PVC film had thickness 0.04 μm and tensile strength was 40.22 MPa. Latex glue was used as adhesive between mulberry paper and PVC films. The main results obtained as the follows.

1) The mulberry paper was laminated with speed 75 meter per hour or coated 100 sheets per hour with continuous laminating.

2) The appropriate temperature for laminate was 130 ^{o}C, and the motor speed was 40 percents (10 rpm).

3) The bursting strength of normal mulberry paper before laminate was 2.94 kg/cm^2 and after laminated was 7.26 kg/cm^2. While mulberry paper reinforcement by fiber of teak leaf had the bursting strength before laminate was 0.70 kg/cm^2 and after laminated was 3.66 kg/cm^2.

4) The normal mulberry paper had tensile strength 37.07 MPa, after laminated it had 79.14 MPa. The reinforce mulberry paper had tensile strength before laminate 5.34 Mpa and after laminated was 56.69 Mpa.

The laminated mulberry paper was glossy and more attractive, strengthening, also protected water or humidity to decline them. The product from this process had smooth surface easily to screen printing and clean out the dirt. This materials could make products in different design and more attractive. The sample of these products were shown in figure 11.

Figure 11. Products from laminated mulberry paper

Acknowledgement

The author would like to acknowledge and thanks the Industrial and Research Projects for Under-graduate Students (IRPUS), Thailand Research Fund (TRF) for the budget of research in year 2008. Special thank you Supakorn Reungsri, Supachai Saladtook, Sarayut Surath and Suraphop Suparaseth for kind co-operation in this research.

References

[1] Anin Memon, Somsak Itthisophonakul, Sirichai Torsakul, Ekachai Tholuang and Janprapa Poungsuwan, Laminating for Publishing in Non Impact Printing by Latex Glue, 2nd Conference on Sustainable Community Development at Khon Kaen University, 29-30 January 2008 : p296-302.

[2] Wutinant Kongtud, Warunee Thanapase, Vichai H. Thanasan, Chaiyaporn Sampoompuang, and Pirun Srinuan, Physical properties of Thai hand-made paper from saa and rice straw pulp for handicrafts and packaging, Kasetsart Agriculture and Agro-Industrial Product Improvement Institute, Kasetsart University.

[3] Pimanchan Rungrod and Nattakarn Hongsriphan, Effect of tackifier on tack and peel strength of natural rubber latex-based adhesives, 31st Congress on Science and Technology of Thailand at Suranaree University of Technology, 18 – 20 October 2005.

[4] Somchai Maneewan, Investigation of Physical properties of mulberry paper for evaporative cooling system, Naresuan University Journal 2007; 15(2) : p63-67.

[5] Roongaroon Watthanawong and Supawadee Tewasano, 1997, 4th, Printing materials, Printing house of Sukhothai Thammatirat Open University, Nonthaburi.

[6] Supawadee Tewasano, 1997, Post-Press Techniques, Printing house of Sukhothai Thammatirat Open University, Nonthaburi.

[7] Bristow, J., and Kolseth, P., 1986, Paper Structure and Properties, New york: Marcel Dekker Inc.

[8] J.H. Briston and L.L. Katan, 1990 “Plastics Films”, Longman Singapore publishers (Pte) Ltd., Singapore.

Epoxy resin and epoxidised natural rubber blends by latex blending process: the effect of percent epoxidation and rubber contents on the tensile properties and related morphology

P. Ruamcharoen*, S. Umaree and Y. Chainarin

Rubber and Polymer Technology, Faculty of Science and Technology, Songkhla Rajabhat University, Songkhla, Thailand 90000

*E-mail: polphat@skru.ac.th

Abstract: The tensile properties of epoxy resin blended with epoxidised natural rubbers (ENRs) were investigated. The blending was performed in latex state which has been accepted to have more features than conventional solid state blending. The effect of percent epoxidation and ENR contents in the blends on tensile properties was studied. The percent epoxidations are 20, 45 and 60 and the contents of ENRs in the blends were 2, 4 and 6 parts per hundred of epoxy resin (phr). It was found that tensile strength, Young's modulus, and elongation at break decrease with the increasing of rubber contents in the blends but increase with the percent epoxidation of ENRs. The morphological study by optical microscope and scanning electron microscope suggests that the tensile properties of epoxy resin are controlled by compatibility between epoxy resin and ENRs and particle size of ENR globular nodules attached to the epoxy matrix. The epoxy blended with 2 phr of ENR with 60 percent epoxidation shows the best tensile properties. These results help towards a better understanding of the properties of final products in relation to percent of epoxidation and contents on the basis of latex blending process.

Introduction

Epoxy resins have many desirable properties such as modulus and tensile strength, excellent chemical and solvent resistance, dimentional and thermal stability, good creep resistance, and excellent fatigue properties. From these characteristics, epoxy resins are widely used in many applications, e.g. adhesives, high-performance matrix resin for composites and electronic encapsulants etc. The curing reaction with various curing agents such as acid anhydrides and amines leads to the formation of 3-dimensional network. However, when cured, the resins are generally brittle due to a high crosslink density and become brittle thermosets, therefore particular modification is necessary to improve this properties.

A lot of studies have been done on rubber modified epoxy resin. Most of them are blending with various synthetic polymers containing reactive functional groups at the chain end or even along the molecular structure.[1-4] However, the production of these polymers relies on petroleum oil. Nowadays, costs of polymeric raw materials have since risen steadily as a result of rising feedstock price. As the result of the problems mentioned previously, the epoxidised natural rubber (ENR) is a choice for the toughening the epoxy resin because ENR is a derivative of natural rubber (NR) which is renewable source. The introduction of the oxirane ring lets ENR have a higher polarity than natural rubber. The polar ENR usually leads to compatibility with lots of polar polymers such as nylon,[5] and phenolic resin.[6] Interestingly, few studies regarding the use of ENR latex in modifying the epoxy resin have been published.[7-8] Most of mentioned works have been done in solid state which requires high temperature and high energy consumption to achieve the best compatibility. To minimize the mentioned problems, the blending of epoxy pre-polymer and ENR in latex state was introduced in this report. It could be another simple technique as it would consume less energy and time.

The aim of this study was to investigate the effect of epoxidation level and ENR contents on tensile properties which are the universal properties and their relationship to the morphology.

Materials and Methods

Materials

The epoxy pre-polymer was diglycidyl ether of bisphenol A (DGEBA), (Epotec YD 127, Aditya Birla Chemicals (Thailand), Ltd). The curing agent was ethylene diamine (aldrich). High ammonia concentrated natural rubber latex with 60% DRC (Chana latex Co. Ltd.) was used. Formic acid (98%) and hydrogen peroxide were obtained from Merck. Terric-16A16 was employed as a stabilizer for preparation of epoxidised natural rubber.

In-situ epoxidation and characterization of NR latex

In this research, the *in-situ* epoxidation by performic acid was chosen. The latex (60% DRC) was diluted to 20% by adding distilled water and stabilized with 2 phr of Terric16A16 under continuous stirring. After heating to 50^{o}C, the required amount of formic acid and hydrogen peroxide were added dropwise. The formic acid in the molar ratios of 0.1-0.4 and hydrogen peroxide of 0.2-0.8 were varied with respect to a mole of isoprene unit. The achieved epoxide contents of ENR were calculated from the spectra of Fourier transform infrared spectroscopy (FTIR, Shimadsu 8900).[9]

Sample preparation and tensile testing

The NR and ENRs in latex state were mixed with epoxy pre-polymer. The contents of rubbers in the blends were 2, 4 and 6 phr. The mixtures were stirred at ambitent temperature for 30 min. Ethylene diamine in the stoichiometric molar ratio was added into the mixture and stirrered for 5 min. The sample was cured at the temperature of 60^{o}C for 3 h in the Teflon coated mould with tensile specimen cavities for testing. Tensile measurement was performed according to ASTM D 638.

Phase morphology studies

The information about the compatibility of polymer blends requires the use of an optical microscopy (OM) technique. The specimens obtained in thin sheet with aproximately 0.4 mm thickness were examined by bright field microscope (Nikon E600). Jeol (JSM-5800LV) scanning electron microscope (SEM) was used to investigate the tensile fracture surface of blends. The dispersed rubber phase was extracted using toluene for 96 h at ambient temperature. The dried samples were sputter-coated with gold prior to SEM examination. Several micrographs were taken for each sample.

Results and Discussion

Chemical structure analysis of ENRs

The structure of ENR obtained was investigated by FTIR spectroscopy. The adsorption bands at 1240 cm^{-1} and 870 cm^{-1} indicate that oxirane ring takes place on the rubber chain. The peak at 836 cm^{-1} is due to the C-H out of plane bending vibration of the cis-1,4 isoprene unit. The percent of epoxidation are 20%, 45% and 60% (i.e ENR20, ENR45 and ENR60 respectively).

Tensile properties

For tensile strength, as shown in Figure 1, this can be pointed out that as the epoxy resin was blended with NR and ENRs, tensile strength of all blends is lower than that of epoxy resin. However, the tensile strength increases with the percent epoxidation of ENRs. This could be implied the greater compatibility between epoxy and ENRs than NR.

Elongation at break of blended resins is shown in Figure 2. For epoxy/ENRs, elongation at break increases with epoxidation level. However, it was also found that increasing the rubbers from 2 phr to 6 phr results in lower elongation at break. This was also found in the other systems.[5, 8] It was assumed that rubber particle sizes are contributed to the elongation at break which will be explained by morphological detail later.

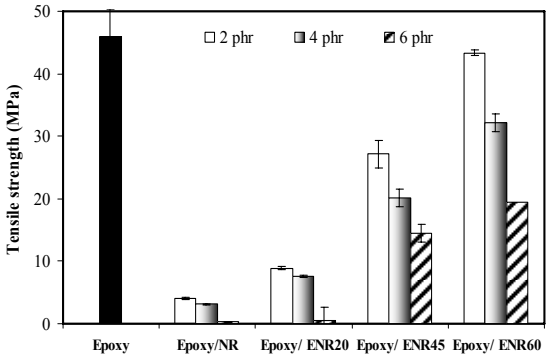

Figure 1. Tensile strength of epoxy resin and epoxy resin blends.

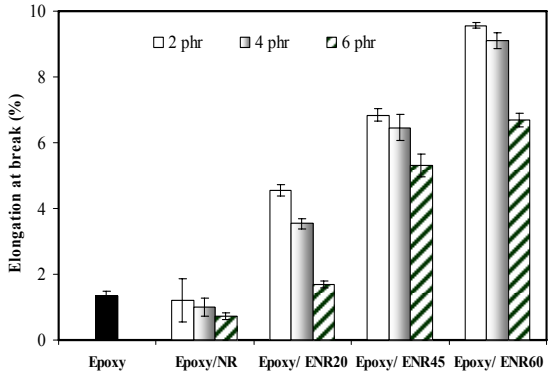

Figure 2. Elongation at break of epoxy resin and epoxy resin blends.

The results for Young's modulus of specimens are shown in Figure 3. The Young's modulus decreases when the rubbers are introduced into the epoxy resin. However, it is interesting to note that the percent epoxidation of ENRs leads to the increase Young's modulus. This may be related to the fact that the modulus of natural rubber is generally much lower than that of the epoxy resin but for ENRs, epoxide groups in ENRs help increase the rigidity of rubbers.

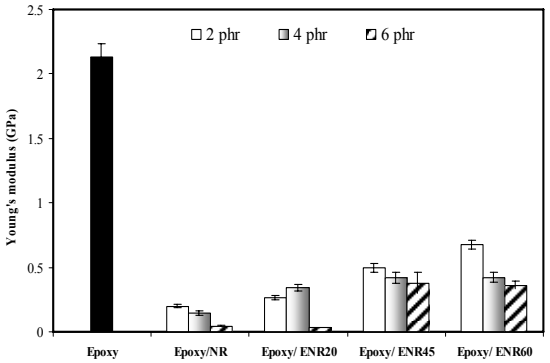

Figure 3. Young's modulus of epoxy resin and epoxy resin blends.

It is worthy to note that tensile strength, elongation at break and Young's modulus of epoxy/ENR blends increase significantly when epoxidation level increases. It should be assumed to result from excellent compatibility between epoxy and ENRs due to increasing epoxy content in ENR. This result agrees with the previous reports.[10]

Morphological Study and Relationship to the tensile properties

The morphology of blends was investigated by OM and SEM. The OM micrographs of NR blended epoxy were shown in Figure 4(a). The white spots represent the rubber phase in the dark epoxy matrix. When ENRs were introduced as shown in Figure 4(b), the white spots were dissapear. This could be clearly seen that epoxidation of natural rubber help improve the compatiblization between rubber phase and epoxy matrix.

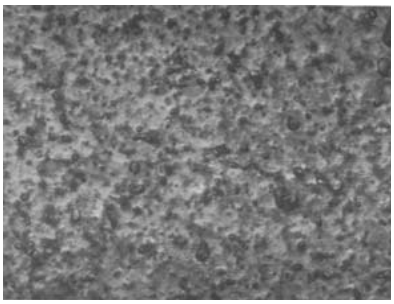

(a)

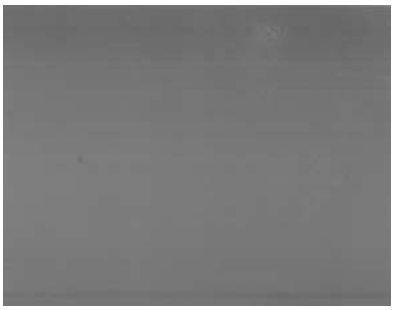

(b)

Figure 4. Optical micrographs of the blends containing 2 phr of (a) NR; (b) ENR60.

The SEM micrographs of epoxy/ENR blends are presented in Figure 5. The black holes represent rubber particles etched by solvent. This could be seen that the rubber phase appears as a spherical particle. Figures 5((a) and (b)) reveal that as the epoxidation level increases, the particle sizes of the rubber phase decrease. The final size of the rubber phase depends on whether phase separation takes place before or after gelation of one or both phases.[11] If gelation takes place before phase separation, the crosslink tends to hold the rubbers apart, and the pre-existing network will limit the size of the domains. On the other hand, if phase separation takes place before gelation, the crosslinks will tend to hold the phase domain together, and the rubber particle are likely to be larger. It has been known that the rate of phase separation depends on compatibility between rubber and epoxy resin. For this work, it was improved with epoxidation level. Consequently, good distribution of small globular nodules was achieved.

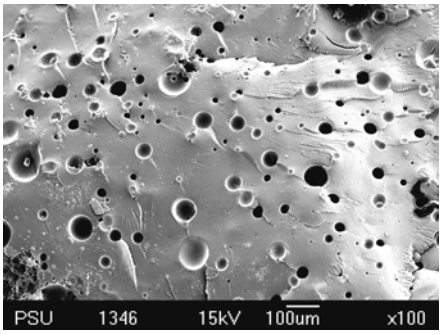

(a)

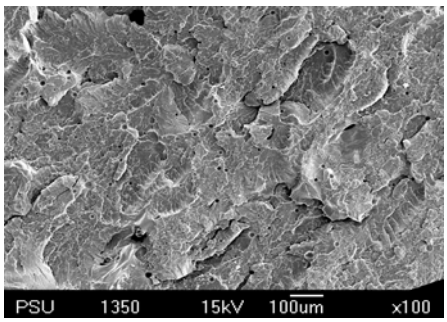

(b)

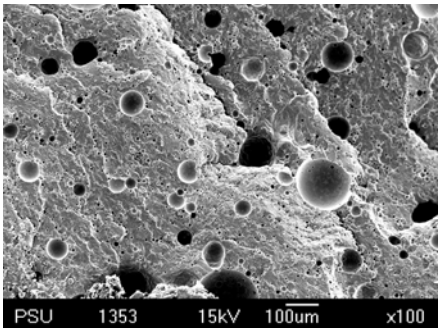

(c)

Figure 5. SEM micrographs of fracture surface of the Blends containing (a) 2 phr of ENR20; (b) 2 phr of ENR60; (c) 6 phr of ENR60.

This relates to the increase of tensile strength and elongation at break. In agreement with Jang et. al[12], the greater elongation at break has been achieved by the small particle size of rubber. However, the higher rubber contents in modified epoxy resins result in larger rubber particle size. As shown in Figure 5(c), the average diameters are larger.

The increase of particle sizes with the rubber content is also obtained in other rubber modified epoxy systems.[13-15] This leads to the decrease of tensile strength and elongation at break as shown in Figures 1 and 2.

Conclusions

Based on the results obtained and discussed previously, the following conclusions may be drawn. The blends of Epoxy resin and ENRs can be accomplished by latex blending. Blends of ENR and epoxy resin have been investigated. The influence of parameters such as rubber content, %ENR on tensile properties and morphology of these blends was established. Tensile strength and Young's modulus and elongation at break decrease with increasing of ENR content in the blends but increase with the percent epoxidation of ENRs. The morphological study shows that the epoxy/ENR blends were partially miscible blends. The particle sizes of rubber decrease with epoxidation level but increase with the rubber content in the blend. This result corresponds to the mechanical properties. It helps confirm that more compatibility is obtained with the increase of percent epoxidation. The epoxy blended with 2 phr of ENR with 60 percent epoxidation shows the best tensile properties. These new approach has the important advantage of better understanding of the properties of final products in relation to percent of epoxidation and contents on the basis of latex blending process.

Acknowledgements

The authors wish to express their deep gratitude to Thai Organic Chemicals Co. Ltd. for the epoxy resin, Deptartment of Industrial Engineering, Faculty of Engineering, RMUSTV for tensile tester, Science Center, SKRU for FTIR instrument.

References

[1] A. Ozturk, C. Kaynak and T. Tincer, *Eur. Polym. J.* **37**(2001), pp. 2353-2363.

[2] M. L. Auad, P.M. Frontini, J. Borrajo and M.I. Aranguren, *Polymer* **42**(2001), pp. 3723-3730.

[3] V. Nigam, D.K. Setua and G.N. Mathur, *Polym. Eng. Sci.* **39**(1999), pp. 1425-1432.

[4] D. Ratna, R.Varley, R.K.S. Raman and G.P. Simon, *J. Mater. Sci.* **38**(2003), pp. 147-154.

[5] V. Tanrattanakul, N. Sungthong and P. Raksa, *Polym. Test*. **27**(2008), pp. 794–800.

[6] J. K. Kallitsis, and N. K. Kalfoglou, *J. Appl. Polym.Sci*. **37**(1989), pp. 453-465.

[7] S-W Hong, and C.K.Chan, *Thermochim. Acta*. **417**(2004), pp. 99-106.

[8] S. Chuayjit, N. Soatthiyanon and P. Potiyaraj, *J. Appl. Polym. Sci.* **102**(2006), pp. 452-459.

[9] J. Davey and M.R. Loadman, *Brit. Polym. J*. **16**(1984), pp.134-138.

[10] S. Kannan, N.M. Mathew, G.B. Nando and A.K.Bhowmick, *Plast. Rub. Compos. Pro.* **24**(1995), pp.149-156.

[11] J-F. Hwang, J-A. Manson, R.W. Hertzberg, G.A. Miller, L.H. Sperling, *Polym. Eng. Sci*. **29**(1989), pp.1466-1476.

[12] B. Z. Jang, D.R. Uhlmann, V. Sande, *Polym. Eng. Sci.* **25**(1985), pp.643-651.

[13] S.C. Kunz, J.A. Sayre and R.A. Assink, *Polymer* **23** (1982), pp.1897-1906.

[14] P.Bussi and H. Ishida, *Polymer* **35**(1994), pp. 956-966.

[15] N. Chikhi, S. Fellahi and M. Bakar, *Eur. Polym. J.* **38**(2002), pp. 251-264.

Synthesis and characterization of quaternary ammonium salt on silica gel prepared from rice hull ash

D. Purwaningsih[1*], Nuryono[2] and R.T. Padmaningrum[1]

[1] Department of Chemical Education, Faculty of Mathematics and Natural Sciences, Yogyakarta State University, Karangmalang, Yogyakarta, Indonesia.
[2] Department of Chemistry, Faculty of Mathematics and Natural Sciences, Gadjah Mada University, Bulaksumur, Yogyakarta, Indonesia.

[*] E-mail: dyahuny@yahoo.com

Abstract: In the present work, synthesis of quaternary ammonium salt on silica gel prepared from rice hull ash (RHA) and used for anion exchanger was investigated. Sodium silicate (Na_2SiO_3) solution was prepared by destruction of rice hull ash with 4 M NaOH solution. The synthesis of ethylendiamino-silica hybrid (ESH) was carried out by adding 3 M HCl solution to the mixture of (3-etylenediaminoprophyl)-trimethoxysilane (EDAPTMS) and sodium silicate solution till pH 7. The gel was characterized by using infrared spectroscopy (FTIR), X-ray Diffraction (XRD) and Surface Area Analyzer (SAA). The ESH then was reacted using methyl iodide and sodium chloride solution to form quaternary ammonium salt (ESH^+/Cl^-). The salt was then characterized using infrared spectroscopy (FTIR), Thermogravimetry (TG), Kjehldahl analysis and potentiometric titration. Result of characterization with FTIR showed that ESH had been successfully synthesized, indicated by the presence of characteristic absorbance of functional groups silanol (Si-OH), siloxane (Si-O-Si), amine ($-NH_2$) and methylene ($-CH_2$). The XRD data showed amorphous structure of ESH. From SAA result, the specific surface area and total pore volume of ESH was obtained. The ESH^+/Cl^- had been successfully synthesized based on the data from FTIR, Kjehldahl analysis and potentiometric titration. From TG, it was discovered that ESH^+/Cl^- was thermically stable.

Keywords: ***synthesis, quaternary ammonium salt, silica gel, rice hull ash*.**

Introduction

Being an agricultural country, Indonesia has a side advantage due to the amount wastes from the farming activities such as rice hull ash (RHA) that can be utilized as a source of silica to make an adsorbent. Rice hull ash (RHA) contains over 90% silica and can be an economically viable raw material for the production of silicates and silica gel. Adsorbent has been prepared from RHA as a by-product of brick burning process. The use of RHA has more advantages than quartz, because of its high crystallinity and stability so the destruction must be done at high temperature (1300^OC) [1].

Silica is of particular interest as it doesn't swell and has good mechanical strength and thermal stability. Among the more promising highly developed surfaces are the-silica attached organosilanes which are widely used in various technologies. Silica gel can be synthesized through sol-gel process by the condensation of sodium silicate to an acid solution. Silica gel has silanol (Si-OH) and siloxan (Si-O-Si) that can be used for many adsorption processes. On the other hand, the capability of silica gel in adsorption is limited. It is because of the active sites, both functional groups of silica gel only adsorb hard metal ions [2].

Recently, the development of silica gels have become modified with suitable functional groups, with the purpose of application in the adsorption of metal ions from solutions, in preconcentration processes and further analysis of metal ions at trace levels in aqueous and non-aqueous solutions and as materials to pack columns for use in high-pressure liquid chromatography [3-4].

The application of these materials in chromatography includes adsoprtion, preconcentration, and ion-exchange techniques; in the latter, charged groups are introduced onto the silica surface by chemisorption. Thus, cation or anion exchangers are obtained depending on the immobilized functional group charge. The application of these materials in ion exchange is dependent on their exchange capacity, stability and selectivity [5]

The exchange capacity is governed by the concentration of surface hydroxyl groups before the modification, by extension in which the reactions occur between the silanol groups and the modifier, and by the nature of the kind of modifier [6]. An ion exchanger anchored onto silica gel is stable in solutions over the pH range 0-8 and shows much more rigidity than the organic matrices and swelling negligible [4]. The selectivity is usually expressed through the separation factor (derivative of the isotherms) and through the selectivity coefficient (retention time).

The anion exchangers immobilized onto silica gel containing primary, secondary or tertiary aminic groups show a behavior that is weakly acidic, while the quaternary salts are strongly acidic. In this paper, we report the synthesis and characterization of quaternary ammonium salts using silica gel from the sol-gel processing of rice hull ash and 3-ethylenediammine propyltrimethoxysilane (EDAPTMS).

Materials and Methods

Material: Rice hull ash (RHA), NaOH (Merck), HCl (Merck), CH_3I (Merck), NaCl (Merck), DMF (Merck), $AgNO_3$ (Merck), ethylenediaminopropyl-

trimethoxysilane (EDAPTMS), aquadest, filter paper Whatman 42, filter paper, pH indicator universal.

Instrumentation: Infrared spectra of the components were obtained on a FTIR spectrophotometer, Shimadzu FTIR-8201 PC. The crystallinity of the components was obtained using X-Ray Difractometer. The porosity and specific surface area was obtained by using Surface Area Analyzer (SAA). The TG analysis was made using a Shimadzu Model TGA 50 Thermobalance.

Preparation of Na_2SiO_3 *solution:* Rice hull ash was scrapped and sieved to obtain RHA 200 mesh. Here in after as much of 20 g RHA were then cleaned by 150 mL HCl 6M and neutralized by aquadest. The outcome was then dried in oven. The clean RHA taken about 20 g and enhanced by 167 mL NaOH 4M (stoichiometri), boiled at the same time swirled with the magnetic bar. After dried, condensation was infused by a porcelain cup and melted at temperature 500^{o}C for 30 minutes. After chilled, it was enhanced by 200 mL aquadest, let for one night and filtered by using Whatman 42. Filtrate yielded represent the condensation of sodium silicate solution (Na_2SiO_3) that will be ready to use as substance for preparing the material.

Hybridization: About 20 mL of sodium silicate solution was put into a plastic glass, enhanced by 1 mL of EDAPTMS. Here in after enhanced by HCl 3M dropwise swirled with the magnetic stirrer until a neutral pH. Gel was hushed for a night, cleaned by aquadest till neutral and dried in oven with the pressure reduction at a temperature of 70^{o}C. After dried, it was scrapped and sieved 200 mesh. The material then referred to as ethylenediamine-silica hybrid (ESH).

Synthesis: Twelve grams of ESH was suspended in 50 mL N,N-dimethylformamide and 4 mL methyl iodide was added gradually. The mixtures were stirred for 2 h in the dark, at room temperature. The solid products were filtered and washed with water, then with a 2% sodium bicarbonat solution, and again with water. The materials were dried under vacuum at 80^{o}C for 6 h. The methylation reactions were repeated four times to ensure a good yield of the desired quaternary ammonium product, $Si(CH_2)_3NH(CH_2)_2N^+(CH_3)_3I$. Finally, about 0.1 g of ESH^+/I^- was dispersed in 50 mL of 15% sodium chloride solution. The mixtures were slowly stirred for 5 h at a temperature of 25^{o}C. The solids were filtered, washed repeatedly with water, ethanol and diethyl ether, and then dried in air. The resulting derivative chloride, $Si(CH_2)_3NH(CH_2)_2N^+(CH_3)_3Cl^-$ then referred to as ESH^+/Cl^-.

Characterization: The nitrogen content of the aminated silica gels was determined by the Kjehldahl method. The chloride ion present on ESH^+/Cl^- was determined by potentiometric titration. About 0.2 g of ESH^+/Cl^- was shaken with 50 mL of 0.1 mol L^{-1} HNO_3 solution for 1 h. The solids were filtered and washed repeatedly with water until the chloride anion had disappeared. The amount of Cl^- present was determined by potentiometric titration with 0.01 mol L^{-1} $AgNO_3$ standard solution. This value corresponds to the limit amount of adsorbed Cl^- on the supports. The infrared spectra of the unmodified silica gel, ESH, ESH^+/I^- and ESH^+/Cl^- were performed by using the pure material pressed disk technique. To obtain information about the thermal stability of the studied materials, the analysis of TG was made by using the dynamic heating method.

Result and Discussion

Preparation of modified silica gel by ethylenediammine group: Preparation of modified silica gel was conducted in two steps, namely sodium silicate solution (Na_2SiO_3) preparation from RHA and the addition of hydrochloride acid solution to form gel. The anion species interaction of silicate with EDAPTMS was anticipated first of all by protonation to oxygen atom of methoxy (-OCH_3) from EDAPTMS and then followed by the anion attack of silicate to the inorganic compound through SN_2 mechanism. The protonated oxygen atom from methoxy going will cause the atom progressively positive polarize so that it has a tendency to be attacked by negative species of silicate anion. This will cause the formation of its siloxan bonding accompanied with the methanol release [7]. Simple model of the reaction of the formation of ethylenediamine-silica hybrid is described in Figure 1.

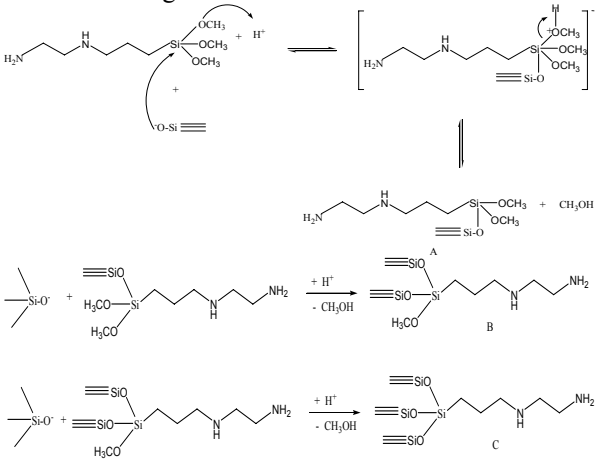

Figure 1: Reaction of the ESH formation

Infrared spectra: The characterization was to identify functional groups in ethylenediamine silica hybrid (ESH) is shown in Figure 2.

Table 1: Interpretation of infrared spectra of materials

Vibrational functional groups for each material (cm^{-1})		Interpretation
SG	ESH	
3425.3	3386.8	Stretching of –OH of Si-OH
-	2954.7	Aliphatic chain of $–CH_2-$
-	1461.9	Chain of C-C from methylene group (-CH2-)
1087.8	-	Asymmetric stretching Si-O from Si-O-Si
956.6	-	Stretching Si-O from Si-OH
802.3	-	Symmetric stretching Si-O from Si-O-Si
466.7	-	Bending Si-O from Si-O-Si

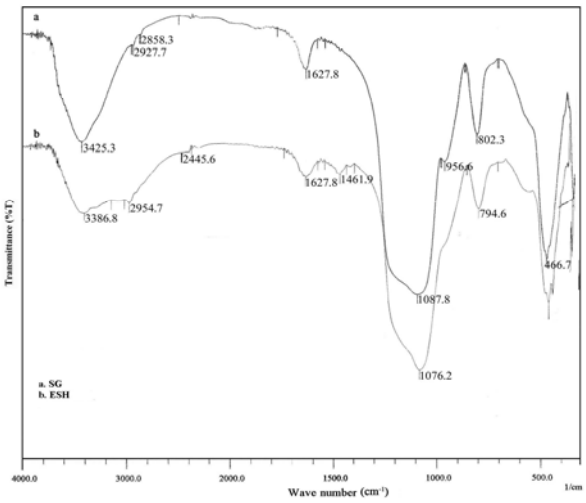

Figure 2: Infrared spectra SG (a) and ESH (b)

X-ray diffraction: The characterization is aimed to identify the crystallinity of materials, as shown in Figure 3.

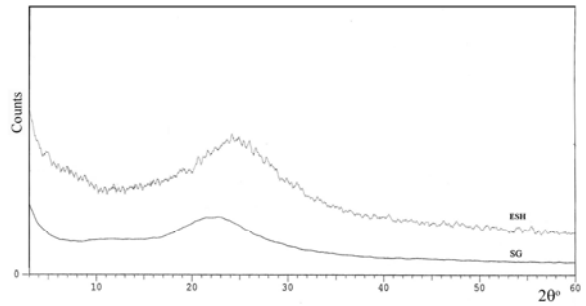

Figure 3. X-ray diffraction of SG and ESH

As shown in Figure 3, diffraction pattern of silica gel and ESH show the wide pattern around 2θ = 21-23°, which indicates that the silica gel and ESH are amorphous. The structure of modification of silica gel by organic ligand did not change the structure of silica gels.

Porosity and specific surface area: Determination of specific surface area and pores of the materials of silica gel and ESH can be seen from the results of analysis by using surface area analyzer (SAA). The results of the analysis are shown in Table 2.

Table 2: Data Analysis of Surface Area of Materials

Materials	Specific surface area (m^2/g)	Total pore volume (mL/g)	Pore diameter (Å)
SG	103,505	0.092	17,826
ESH	98,410	0,083	16,798

From the table above, it is clear that the total pore volume is proportional to the specific surface area of the material, thus, the larger the volume of the pores is, the larger the surface area will be. Silica gel has a surface area of 850 m^2/g and pore diameter of 22 Å [1]. The results showed a specific surface area and pore diameter of silica gel is relatively small. This is probably due to gel formation process so fast that the formation of pores decreases and tends to form a solid. The result of research shows that ESH has a specific surface area smaller than SG. This is possible because the binding occurs between ESH and EDAPTMS compounds that will block the pores so that the smaller the pore size and surface area produces a smaller. In general, both materials are at mesoporic scale 2-50 nm in pore diameter [8].

Synthesis of ESH^+/Cl^-: A total of 12 grams of ESH which is then mixed with *N,N*-dimethyl formamide and methyl iodide is added gradually. Then, the solution is stirred for 2 h in darkness at room temperature. Solids obtained then filtered and washed by using water, sodium bicarbonate and re-washed by water. The use of sodium bicarbonate solution is to remove organic impurities present in the ESH^+/I^-. Methylation is carried out four times. Formed solids dried at a temperature of 80°C. After it formed a solid solution of sodium chloride 15% is added, stirring for 5 h at a temperature of 25°C. The quaternary ammonium salt formed later referred to as ESH^+/Cl^-. The reaction that forms on the synthesis of the quaternary ammonium salts are as follows:

$$Si\text{-}O\text{-}Si\text{-}(CH_2)_3\text{-}NH(CH_2)_2NH_2 + CH_3I \longrightarrow Si\text{-}O\text{-}Si\text{-}(CH_2)_3\text{-}NH(CH_2)_2N^+(CH_3)_3I^-$$

(ESH^+/I^-)

$$Si\text{-}O\text{-}Si\text{-}(CH_2)_3\text{-}NH(CH_2)_2N^+(CH_3)_3I^- + NaCl \longrightarrow Si\text{-}O\text{-}Si\text{-}(CH_2)_3NH(CH_2)_2N^+(CH_3)_3Cl^-$$

(ESH+/Cl-)

Figure 4: Reactions for obtaining the quaternary ammonium salts (ESH^+/Cl^-).

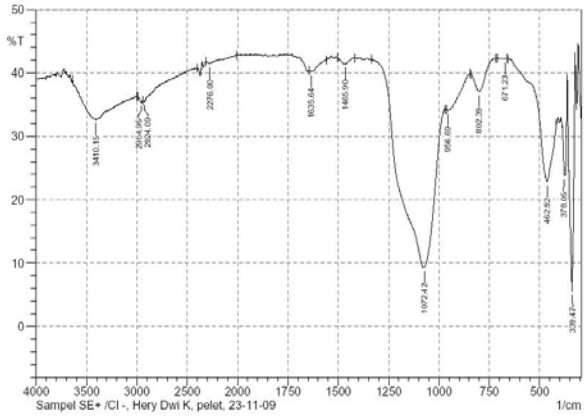

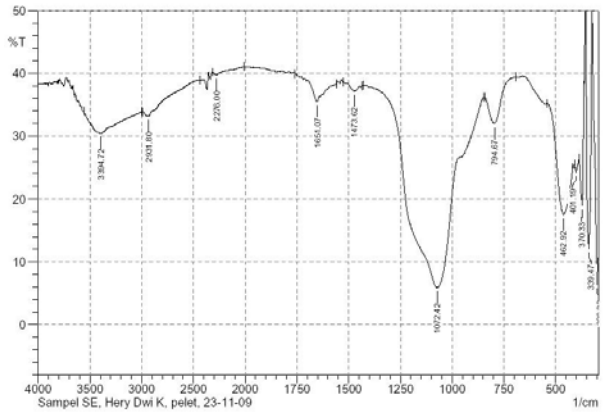

Figure 5: Infrared spectra of ESH^+/I^- (up) and ESH^+/Cl^- (bottom)

The main evidence from the infrared spectra is the strong band that observed at 1651 cm^{-1} in ESH^+/I^- which can be identified as bending vibrations of $-NH_2$ group. This frequency is disappeared in the ESH^+/Cl^-. The existence of a shift in absorption, changes in absorption intensity and the appearance of absorption at a particular wave number region shows that ESH^+/Cl^- have been formed.

To determine the characteristics of the ESH^+/Cl^- which produced are using analytical methods to determine total nitrogen and potentiometric titration to determine the presence or absence of Cl^- bound. The results of the chemical analysis for ESH^+/I^- and ESH^+/Cl^- are shown in Table 3.

Table 3: Nitrogen and Chloride Analyses of Materials

Materials	N (mmol g^{-1})	Cl^- (mmol g^{-1})
ESH^+/I^-	2.857	-
ESH^+/Cl^- (15%)	2.857	0.019

According to Thermogravimetric analysis (curves not shown) ESH^+/Cl^- presented a sudden weight loss at 140°C and a total moderate weight loss between 140°C and 800°C. Therefore, the material is thermically stable up to 140°C.

Conclusions

The material of quaternary ammonium salt (ESH^+/Cl^-) has been successfully made using rice hull ash (RHA) as silica source. ESH^+/Cl^- had been succesfully synthesized based on the data from FTIR, Kjehldahl analysis and potentiometric titration. From thermogravimetric analysis, it was discovered that ESH^+/Cl^- was thermically stable.

Acknowledgements

The financial support from the Directorate General of Higher Education, Government of Indonesia, through the Project of Strategi Prioritas Nasional (Contract No. 02/H.34.21/KTR.PHK.PINAS4/2009) is gratefully acknowledged.

References

[1] U. Schubert, and N. Hüsing. *Synthesis of Inorganic Material*, Willey-VCH Verlag Gmbh, Wernbeim, Germany (2000).
[2] J.F. Blais, B. Dufresne, and G. Mercier, *Rev. Sci. Edu* **12**(4) (2000), pp. 687-711
[3] C. Airoldi, and L.N.N. Arakaki, *Polyhedron* **20**, (2001) pp. 929-936.
[4] L.N.N. Arakaki and C. Airoldi, *Polyhedron* **19**, (2000) pp. 367-373.
[5] P.K. Jal, S. Patel and B.K. Mirsha, *Talanta* **62**, (2004) pp. 1005-1028.
[6] A.R. Cestari, E.F.S. Vieira, J.A. Simoni and Airoldi, *Thermochimia Acta* **348**, (2000) pp. 25-33
[7] D. Purwaningsih, Interaksi Cr(III) dan Cr(VI) dengan Gugus Etilendiamin yang Terimobilisasi pada Silika melalui Proses Sol-Gel, Master's Thesis, FMIPA UGM, Yogyakarta (2007).
[8] K. Ishizaki, S. Komarmeni, and M. Nanko, *Porous Material Process Technology and Aplications*, Kluwer Academic Pub., Dordrecht (1998).

Preparation and electrocatalysis of Pd on activated carbon cloth

S. Saipanya* and T. Sarakonsri

Department of Chemistry, Chiang Mai University, Chiang Mai, Thailand

*E-Mail Address: saipanya@chiangmai.ac.th

Abstract: Pd nanoparticles were simply prepared on activated carbon cloth (ACC). Pretreatment of ACC was performed by using oxidizing agent HNO_3 in order to introduce oxygen complex on the ACC surface. Pd nanoparticles were prepared by impregnation of palladium (II) chloride ($PdCl_2$) without reducing agents. Uniformly dispersed Pd nanoparticles with diameter 5-50 nm on the oxidized ACC support surfaces were observed. Morphology and composition were determined out by Scanning electron microscopy (SEM) and Energy dispersive spectroscopy (EDS), respectively. The activity of the prepared Pd/ACC was studied by Cyclic Voltammetry (CV) in methanol oxidation giving a hopeful indication for future applications.

Introduction

Precious metals (Pd, Pt and Rh) are well known as an exceptional element for automobile exhaust gas catalyst [1]. These metals are utilized in the catalytic converter as an active component for reducing the emission of hydrocarbons, carbon monoxide, and nitrogen oxides. In this work, we pay attention to the palladium metal nanoparticle as it can be used in other purposes for example vinylation of aryl bromide by heterogenous Pd/C, methane oxidation by Pd on mesoporous silica and fuel cell [2-4].

Many methods achieved for Pd nanoparticle preparation depend on applications and supports. Activated carbon cloth (ACC) is present used as a support of catalysis work as possessing high surface area and porous networks with plentiful functional groups with a uniform distribution of micropore providing a healthy host for adsorbates [5, 6].

Our aim is to plainly produce the Pd nanoparticles on the ACC substrate surface by means of impregnation method, characterize the nanoparticles and simple electrocatalytic test the activity by CV before further applications.

Materials and Methods

ACC as a support used in the current work was obtained from AmeriAsia (China Jiansu), coded as ACC MY-QW-025 with specific area of 1500 m^2g^{-1} and $PdCl_2$ precursor was from Merck.

ACC was cleaned by stirring the ACC in 6 M HCl (24 h), consequently washed with deionized water until pH is constant and then dried in the oven at 100 ^oC.

The pretreated ACC was stirred in 1.6 M HNO_3 solution for 24 h, and then washed with deionized water for neutralization and the oxidized ACC supports were dried at temperature 100 ^oC.

Pd adsorbed ACC was prepared by impregnation method (3% w/w Pd/ACC). The oxidized ACC were vigorously stirred for 30 min as the brown color solution turned to be colorless indicating Pd metal adsorbed on the surface of ACC support. After drying in the oven overnight, SEM (JEOL JSM-5910LV) and EDS (JEOL JSK-6335F) were used to characterize morphology and composition of nanoparticles, respectively.

The CV spectra were recorded using the voltammograph (BAS CV-50 W). The Pd/ACC catalyst ink was prepared by mixing suspension of Nafion with Pd/ACC powder in an ultrasonic bath. The mixed paste was dropped on top of glassy carbon electrode for working electrode. All electrochemical measurements were performed in three-electrode cell. A platinum wire and Ag/AgCl were used as counter and reference electrodes, respectively.

The electron-transfer properties of oxidized Pd/ACC were evaluated by running CVs in 1 M KCl containing 10^{-3} M $K_3Fe(CN)_6$.

The electrocatalytic activity of Pd/ACC electrode was studied in a solution of 1 M methanol in 1 M H_2SO_4 at room temperature. The solution was deaerated by nitrogen gas (N_2) bubbling in the mixed solution for 30 min. to remove impurities before CV experiment.

Results and Discussion

Pretreatment of ACC was performed by using 6 M HCl to get rid of some mineral impurities after that the surface of fabric was functionalized by oxidative treatment with HNO_3 in order to introduce oxide functional groups. The acid treatment launched oxygen components formed (such as carboxylic, anhydride, phenolic and carbonyl groups) which generate the surface of ACC to be such friendly host region to hold the metal to be well adsorbed on the oxidized ACC support.

SEM image in Figure 1. shows 3% w/w Pd/ACC. The mean particle size of metal adsorbed ACC support was ca. 5-50 nm. The results prove that nanoparticle size of Pd can simply be achieved by our method.

The color change of solution from brown color to colorless indicated that those Pd cations can be adsorbed on the porous activated carbon surface and then reduced to be Pd metal. The adsorption rate of

Pd metal on the ACC fiber is high as the color is clear in incredibly short time.

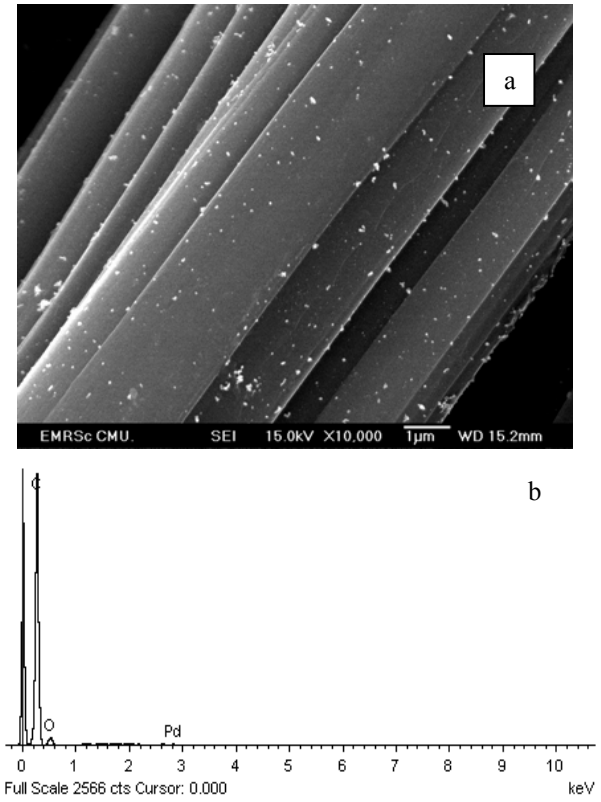

Figure 1. (a) SEM image (10,000x) and (b) EDS of 3% w/w Pd /ACC support.

It can also propose that Pd firstly deposits into the micropores and further aggregates to the outer surface of the ACC fibers as macroparticles are acquired on the surface. Figure 1. (b) confirmed that the Pd nanoparticle species adsorbed on the ACC surface by EDS spectra. EDS pattern of Pd/ACC shows that carbon(C) is a major element indicating that the Pd nanoparticles was distributed on the oxidized activated carbon cloth surface and oxygen peak is corresponding to oxide functional groups on the ACC surface. The Pd nanoparticles on the oxidized ACC with average nanoparticle size ca. 5-50 nm imply our simply method is such promising task to prepare Pd nanoparticles on porous carbons without using reducing agents for the future applications.

The ACC surface was treated by HNO_3 before Pd metal adsorption, the fiber surface of Pd/ACC needs to be checked whether it can be used as an electrode by determining the electron-transfer properties. The Pd/ACC and Nafion were mixed for working electrode preparation for cyclic voltammetry. It was studied by running CV in 1 M KCl containing 10^{-3} M $K_3Fe(CN)_6$. Both oxidation and reduction peak potentials of $K_3Fe(CN)_6$ (E_{pa} and E_{pc} respectively) were obtained at similar potential with different scan rate (20, 50 and 100 mV/s) although current intensity increases corresponding to higher scan rates (Figure 2.). Those results indicate that $K_3Fe(CN)_6$ undergoes redox reaction at the modified Pd/ACC electrode. This can be a promising sign for Pd adsorbed ACC for future applications.

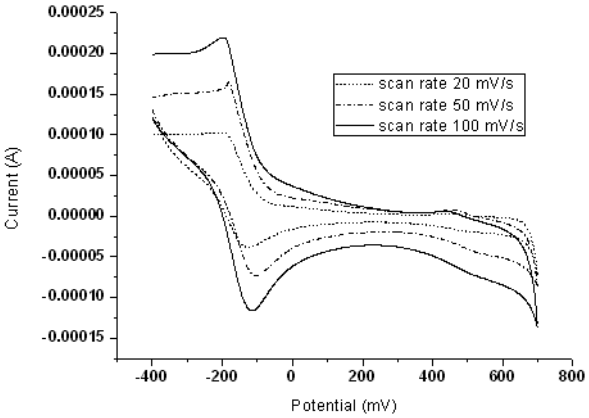

Figure 2. Cyclic voltammograms of 10^{-3}M $K_3Fe(CN)_6$ with 1 M KCl as the supporting electrolyte on Pd/ACC at scan rates of 20, 50 and 100 mVs^{-1}.

Methanol oxidation on Pd/ACC sample was characterized by cyclic voltammogram in Figure 3. The oxidation peak (280 mV) is corresponding to the oxidation of species generated from methanol chemical adsorption whilst the overturn peak (38 mV) is associated with the elimination of carbonaceous species which are not completely oxidized in the forward scan[7]. High current peak intensity of methanol oxidation indicates the electrocatalytic activity of the Pd/ACC catalyst in the methanol electrooxidation. The results imply the ability sign to apply prepared Pd/ACC catalysts to other applications. Variation of the amount of Pd on the oxidized ACC, time of acid treatment, size of metal nanoparticles and addition of N content to ACC have to be studied to get the better activity of the catalyst.

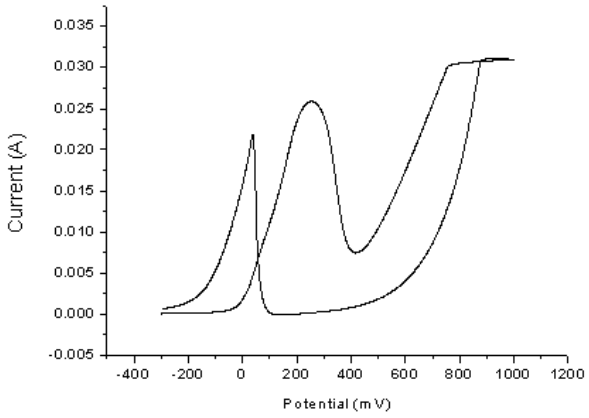

Figure 3. Cyclic voltammograms of methanol electrooxidation in N_2 saturated 1 M CH_3OH in 0.5 M H_2SO_4 solution on Pd/ACC electrode.

Conclusions

Activated carbon cloths were oxidized by HNO_3 and loaded with Pd nanoarticles by impregnation in $PdCl_2$ solution resulting in Pd nanoparticles adsorbed on the oxidized ACC surface. Uniformly dispersed Pd nanoparticles with diameter 5-50 nm on the ACC surfaces were achievd. The 10^{-3} M $K_3Fe(CN)_6$ in 1 M KCl has undergone a redox reaction at Pd/ACC electrode indicating good electron-transfer properties. Pd/ACC used as catalyst for electrode reactions in methanol oxidation also shows the promising sign for further catalysis applications.

Acknowledgement

This work was financially supported by Ministry of science and technology and Chiang Mai University, Thailand. Many thanks to Associated Prof. Jaroon Jakmunee for electrochemical experiment support.

References

[1] Y. Nishihata, J. Mizuki, H. Tanaka, M. Uenishi and M. Kimura, *J. Phys.Chem. Solids*. **66(2-4)** (2005), pp. 274-282.
[2] A.M. Venezia, R. Murania, G. Pantaleo and G. Deganello, *J.Catal.* **251(1)** (2007), pp. 94-102.
[3] L. Joucla, G. Cusati, C. Pinel and L. Djakovitch, *Appl. Catal. A*. **360(2)** (2009), pp.145-153.
[4] M. Gruber, S. Chouzier, K. Koehler and L., *Appl. Catal. A*. **265(2)** (2004), pp.161-169.
[5] P.J.M. Carrott, J.M.V. Nabais , M.M.L. Ribeiro Carrott and J.A. Pajares, *Carbon*. **39(10)** (2001), pp. 1543-1555.
[6] S.R. De Miguel, J.I. Vilella, E.L. Jablonski, O.A. Scelza, C. Salinas-Martinez De Lecea and A. Linares-Solano, *Appl. Catal. A*. **232(1-2)** (2002), pp. 237-246.
[7] C. Xu , Z. Tian, Z. Chen and S.P. Jiang, *Electrochem. Commun.* **10(2)** (2008), pp. 246-249.

Preparation of bacterial cellulose/high mw sericin/hydroxyapatite composites

K. Boonkitpatarakul, J. Jaipeaw and K. Mai-ngam*

National Metal and Materials Technology Center, Science Park, Klongluang, Pathumthani, Thailand 12120

*E-mail: katancv@mtec.or.th,

Abstract: Bones are mainly composed of inorganic hydroxyapatite (HA) nanocrystals and type I collagen. To mimic natural bone, bacterial cellulose (BC)/sericin composites were chosen as polymeric substrate materials for HA crystallization in this study because BC has an asymmetric structure composed of a fine network of nanofibrils similar to a collagen network and silk sericin protein can effectively induced HA nucleation. High molecular weight sericin protein, being poorly dissolvable, can non-reversibly adsorb on the BC surface. BC discs, created by *Acetobacter xylinum,* were soaked in various concentrations of sericin solutions. HA crystallization was then induced by soaking the obtained BC/sericin substrates in 1.5x simulated body fluid (SBF) at 37 °C. The resulting BC/sericin/HA composites were characterized by SEM. It revealed that HA crystals were uniformly formed on the bacterial cellulose/sericin substrate for all tested sericin concentrations. However, HA crystal precipitation rates increased with increasing sericin concentrations.

Introduction

Bone is a connective tissue largely composed of an inorganic mineral HA ($Ca_{10}(PO_4)_6(OH)_2$) and organic matrices such as collagen and some acidic proteins. During mineral formation, organic matrix plays an important role in terms of inducing the precipitation of HA. Bacterial cellulose (BC) is synthesized into a crystalline 3-D network by *Acetobacter xylinum.* The BC has high strength structure, high water content and an asymmetric structure composed of a fine network of nanofibrils similar to a collagen network. It does not cause any inflammation and irritation to the host. Moreover, BC has been successfully used as a novel polymer substrate for crystallizing HA (1, 2).

Sericin is a silk protein which is accounted for 25-30 percent of silk weight. It has molecular weight ranging from 5 to 400 kDa and composes of 18 proteins. It has been reported that mulberry sericin can effectively induced hydroxyapatite nucleation when it has high molecular weight (MW) and a β sheet structure. Moreover, another advantage of high MW sericin is its poor solubility which leads to nonreversible adsorption of the sericin on the BC surface. Therefore, the objective of this study is to investigate the utilization of high MW sericin/BC composite as a novel substrate for HA precipitation in a simulated body fluid (SBF).

Methods

Preparation of BC: Buffered Schramm and Hestrin (BSH) medium (pH 4.5) was prepared by dissolving glucose (10 g), peptone (2.5 g), Na_2HPO_4 (1.3 g), yeast extract (2.5 g) and citric acid (0.565 g) in deionized water. *Acetobacter xylinum* was grown in the sterile BSH under static culture at 37 °C for 7 days. BC pellicles were purified by soaking in deionized water at 90 °C for 2 h and then boiled in a 0.25 M NaOH for 1 h. After that the pellicles were washed with deionized water for several times to pH = 7 and stored in deionized water at room temperature prior to use.

Sericin preparation: Cocoon shells of *Bombyx mori* were degummed in an aqueous solution containing 4 M of urea and 0.1% of 2-mercaptoethanol at 80°C for 15 min. The insoluble residue was removed by filtration. The filtrate was thoroughly dialyzed against deionized water using Spectra/Por membrane (MWCO 3500) to obtain a high MW sericin solution with a concentration of ~ 2.1 mg/mL. MW of the obtained sericin was estimated by SDS-PAGE.

Preparation of BC/high MW sericin substrates: BC pellicles were immerged in 0.1% and 0.2% w/v sericin dilutions for 1 day and were stored at 4 °C for 14 day to change its conformation from random coil to β sheet structure and then washed with deionized water. The obtained substrates were signified as BC/0.1% and 0.2% w/v sericin, respectively.

Crystallization of HA on BC/sericin substrates: Pieces of BC were immerged in 0.1 M $CaCl_2$ solution at 37 °C for 1 day. To induce HA growth, $CaCl_2$-treated BC was soaked in a 1.5x SBF solution at 37 °C for 14 days. The obtained BC/sericin/HA composites were then rinsed thoroughly with deionized water.

Scanning electron microscopy (SEM): Morphology of the obtained HA containing composites was observed by SEM. The composite was lyophilized and subjected to gold sputtering.

Results and Discussion

Molecular weight of extracted sericin: Since the use of conventional elution methods using an acidic or alkaline aqueous solution or enzymatic treatment as means for isolating sericin of cocoon filaments results in reduction of molecular weight caused by hydrolysis. By using an aqueous urea solution, sericin having a high molecular weight of an average molecular weight of 100 kDa or more can be obtained efficiently. As seen that the extracted sericin solution exhibited distinct bands of two components at 150 kDa and > 500 kDa by SDS-PAGE analysis (Figure 1A). In contrast, the sericin solution was extracted by 0.5 % w/v of $NaHCO_3$ at 70 °C for 1 h providing an average molecular weight in range 50-70 kDa (Figure 1B).

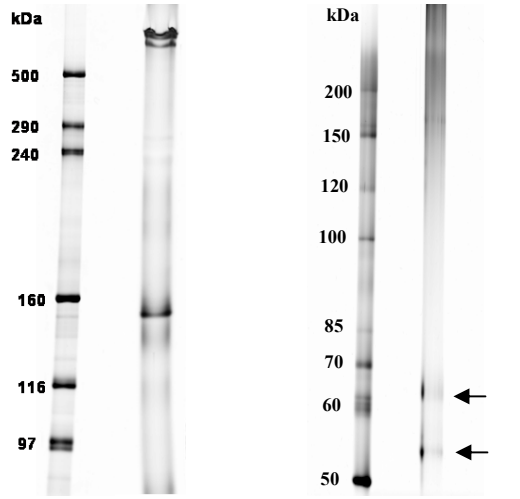

Figure 1 the pictures show SDS-PAGE pattern of the extracted sericin solution. The molecular maker is in the left lane. Right lanes are *Bombyx mori* sericin extracted with an aqueous solution containing 4M of urea in the presence of 0.1% of 2-mercaptoethanol at 80°C for 15 min (A) and extracted with 0.5 % w/v of $NaHCO_3$ at 70 °C for 1 h (B).

Scanning electron microscopy (SEM): Figure 2 showed SEM micrographs of freeze-dried pure BC, BC/0.1% and BC/0.2% high MW sericin samples obtained before HA precipitation in SBF. In both 0.1% and 0.2% sericin solution, the fiber structure of BC could be thoroughly concealed by the protein coating layer.

Figure 3A-C showed SEM micrographs of HA crystal precipitated on BC (no sericin coating), BC/0.1% and BC/0.2% high MW sericin substrates for 2 days. The presence of sericin on the BC surface could effectively accelerate HA crystallization. Growth rate of HA crystals increased as the concentration of sericin coating solution increased.

Figure 4A-C shows SEM image of HA crystal precipitated on BC (no sericin coating), BC/0.1% and BC/0.2% high MW sericin substrates after soaking in 1.5 SBF for 14 days. It was found that the thickness of HA layers increase with increase of soaking time and all of BC composites were fully covered with HA crystals.

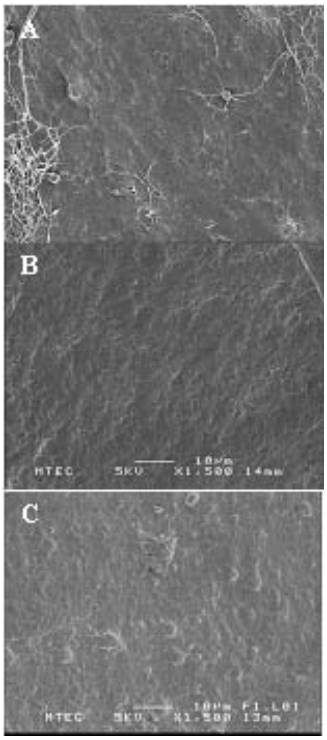

Figure 2 SEM micrographs of: (A) pure BC, (B) BC/0.1% and (C) BC/0.2% high MW sericin

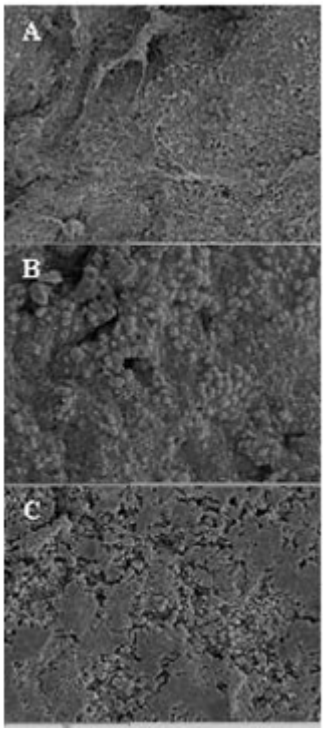

Figure 3 SEM micrographs of HA crystals formed on different substrates: (A) BC, (B) BC/0.1% and (C) BC/0.2% high MW sericin for 2 days.

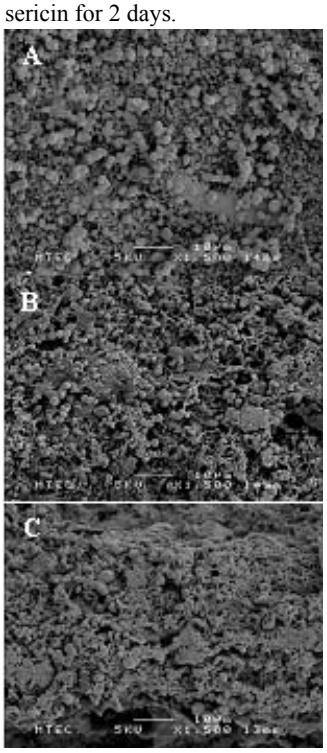

Figure 4 SEM micrographs of HA crystals formed on different substrates: (A) BC, (B) BC/0.1% and (C) BC/0.2% high MW sericin for 14 days.

Conclusions

In conclusion, high MW sericin was prepared by extraction with an aqueous urea solution at 80 °C. The high MW sericin coated BC substrate could successfully induce HA crystallization by soaking in SBF at 37 °C. HA crystal precipitation rate increased with sericin concentration.

Acknowledgments

We thank National Metal and Material Technology Center for financial support.

References

[1] Hong L., et. al., *Mater Lett*. **60** (2006), pp. 1710-1713.
[2] Stacy A.H., et. al., *Biomaterials*. **27** (2006), pp. 4661-4670
[3] Takeuchi, A., et. al., *J. R. Soc. Interface*. **2** (2005), pp. 373-378

Colorimetric detection of DNA by chemically treated silver nanoparticles : a preliminary evaluation

A. Thitimon[1], A. Sereemaspun[2] and R. Rojanathanes[1]*

[1]Department of Chemistry, Faculty of Science, Chulalongkorn University, Bangkok, Thailand 10330
[2]Genetic Unit, Department of Anatomy, Faculty of Medicine, Chulalongkorn University, Bangkok, Thailand 10330

*E-mail: rojrit@hotmail.com

Abstract: Recently, modified silver nanoparticles have been widely applied in many colorimetric DNA detection techniques based on the different adsorption efficiencies between single-stranded and double-stranded DNA's onto the silver nanoparticle surface. We also use this phenomenon to design a hybridization assay enhanced with an oxidation reaction of silver nanoparticles. With naked eye detection, the colour of silver colloids turns to colourless immediately after mixing with hydrogen peroxide with the presence of non-complementary DNA mixtures. On the other hand, the presence of complementary DNA mixtures prevents the colour changing of silver colloids from the chemically treatment process. The colorimetric response values can also be calculated from UV-visible spectra of the silver nanoparticles before and after exposing to hydrogen peroxide. The colour alterations exhibited from this method significantly improve the efficiency of metal-nanoparticles based detection of DNA.

Introduction

Nowadays, detection of specific DNA sequences is extremely important in clinical diagnosis, gene therapy, and a variety of biomedical studies. An easy way for the detection is the employment of metal nanoparticle labels on DNA. Metal nanoparticles offer excellent prospects for biological sensing because of their unique optical and electrical properties. Mirkin and co-workers were the first who developed an entirely new colorimetric detection scheme for DNA hybridization based on aggregation of oligonucleotide-functionalized gold nanoparticles.[1] Gold nanoparticles solution turns from red to purple (or blue) by aggregation. Later, Rothberg and co-workers reported the different aggregation of unmodified gold nanoparticles between ssDNA and dsDNA based on the differences of their electrostatic properties.[2] Silver nanoparticles also generates significant scientific and technological interests over gold nanoparticles in some applications due to the higher extinction coefficients compared with gold nanoparticles.[3] Consequently, the sensitivity of the technique can be improved. Until now, there are many colorimetric assays using unmodified silver nanoparticles based on the fact that the dispersed silver nanoparticles solution is yellow whereas the aggregated silver nanoparticles solution is brown.[4,5] Because silver nanoparticles' surface can be easily oxidized, thus we present another colorimetric DNA detection method apart from aggregation process, our novel oxidation process of unmodified silver nanoparticles exhibit higher degree of colour changing in naked eye detection method.

Materials and Methods

Silver colloids (5-20 nm in diameter) were obtained from *Department of Chemistry*, *Faculty of Science,* Chulalongkorn University. Probe1, Probe2 and Probe3 were purchased from BioDesign Co.,Ltd. Hydrogen peroxide were purchased from Thermo Fisher Scientific Inc. All other materials and reagents were reagent grade and purchased from Sigma-Aldrich, Co. The water used throughout all experiments was purified by a Milli-Q system. TEM images were taken using a Hitachi Model H-7650 transmission electron microscope and UV-vis spectra were taken using a DU 800 spectrophotometer.

Table 1: Probe sequences *

Probe	Sequence (5' to 3')
Probe1	GTAGTGTAACGACGAATAAA
Probe2	TTTATTCGTCGTTACACTAC
Probe3	CCGAGCAATAAATCTTTACC

*All probes have concentration of 20 μM

Hybridization Procedures: Typically, attempted hybridization of the target and the Complimentary target (DNA1) was conducted at room temperature for 30 min in hybridization buffer, 0.2xSSC containing 5% formamide and 1% dextran sulfate

Colorimetric detection of dsDNA and ssDNA with unmodified silver nanoparticle (AgNPs): Initially, 3 μl of DNA was added into 250 μl of 50 ppm AgNPs. Subsequently, 0.8 μl of 30% hydrogen peroxide was added. The colour of solution mixture was observed. Finally, the solution was mixed with 250 μl of water and the absorbance was measured by UV-VIS spectrophotometer.

Table 2: Ingredient of DNA by volume (Probe1 : Probe2 : Probe3 : hybridization buffer)

DNA1 (dsDNA) 3:3:0:2
DNA2 (ssDNA) 3:0:3:2

Colorimetric Measurements: UV-vis specta measurements were acquired between 300 and 600 nm. A quantitative measurement of the colour changing was given by the colorimetric response (CR).

Results and Discussion

Unmodified AgNPs used in this experiment are approximately in 5-20 nm in diameter. They exhibit an intense yellow colour with absorption maxima at 400 nm as shown in figure 1.

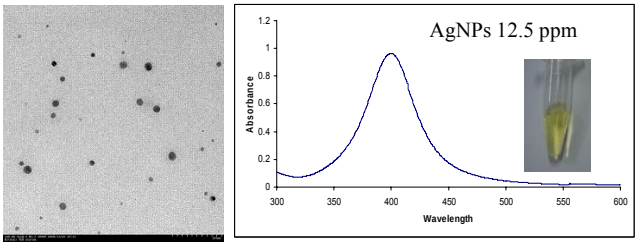

Figure 1. TEM image and UV-Vis spectrum of unmodified silver nanoparticles.

In this present study, we found that the higher concentration of peroxide, the higher degree of oxidization reaction. The oxidization was completed within 15 minutes, no further colour changing of AgNPs can be observed after this period.

Single and double stands DNA have different absorption efficiency on AgNPs due to their electrostatic properties. In figure3, AgNPs solution containing non complementary DNA (DNA2) was oxidized, the colour of solution mixture was then turned from yellow to colorless. On the other hand, complementary DNA (DNA1) prevented oxidation process.

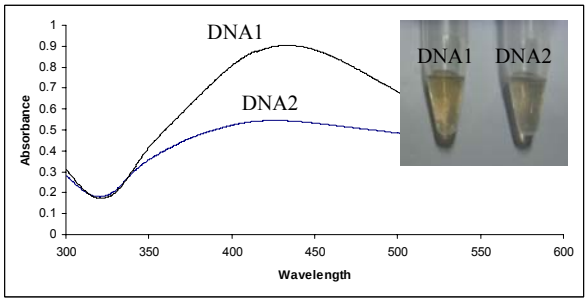

Figure 3. Shows the colour changing and the UV-vis spectra of unmodified AgNPs containing non complementary (DNA2) and complementary (DNA1) of oligonucleotide hybridization.

A quantitative value for the extent of the yellow-colorless colour transitions within the solutions is given by the colorimetric response (CR), which is defined as follows[6]

where $CR = (PB_0 - PB_I)/PB_0$

$PB = Ayellow/(Ayellow + Abasement)$

A is the absorbance at the "yellow(400 nm) and basement(320 nm)" in the UV-vis spectrum

PB_0 is the baseline/yellow ratio of the control sample (before induction of a colour changes), while PB_I is the value obtained after the colorimetric oxidization occurs.

In this experiment, the CR of unmodified AgNPs containing complementary and non complementary of DNA hybridization are 0.1151 and 0.2022 respectively. This difference is considered statistically significant.

Conclusions

We have developed a novel AgNPs-based colorimetric DNA detection method, using the oxidization behavior of unmodified AgNPs as the sensing element. Besides the common advantages of colorimetric assay such as simplicity, high sensitivity, and low cost, our method using unmodified AgNPs could further simplify the experimentation since it is a label-free design and provide an important and attractive alternative. Comparing with other colorimetric DNA detection, our new method exhibits stronger colour alterations than ever. This work can be used to create new avenues of research exploiting the advantages of AgNPs that are not currently possible using gold nanoparticles.

Acknowledgement

We thank the *Department of Chemistry*, *Faculty of Science and* Genetic Unit, Department of Anatomy, Faculty of Medicine, Chulalongkorn University for partial material and financial support to conduct this research.

References

[1] R. Elghnian, J.J. Storhoff, R.C. Mucic, R.L. Letsinger and C.A. Mirkin, *Science* **277** (1997), pp. 1078-1081.

[2] H. X. Li and L. J. Rothberg, *J. Am. Chem. Soc.* **126** (2004), pp. 10958–10961.

[3] G. Braun, S. J. Lee, M. Dante, T.Q. Nguyen, M. Moskovits, N. Reich, *J. Am. Chem. Soc.* **129** (2007), pp. 6378-6389.

[4] R. Kanjanawarut, and X. Su, *Anal. Chem.* **81** (2009), pp. 6122–6129.

[5] H. Wei, C. Chen, B. Han and E. Wang, *Anal. Chem.* **80** (2008), pp. 7051–7055.

[6] S. Kolusheva, R. Kafri, M. Katz and R. Jelinek, *J. Am. Chem. Soc.* **123** (2001), pp. 417-422.

Development of low-cost heterogeneous base catalysts from lime for biodiesel production

W. Roschat[1*], J. Khunchalee [1], B. Yoosuk[2], T. Tanachatchairutana[1]

[1] Chemistry program, Faculty of Science, Ubon Ratchathani Rajabhat University, Ubon Ratchathani, Thailand 34000
[2] National Metal and Materials Technology Center (MTEC),114 Thailand Science Park, Phahonyothin Road, Klong 1, Klong Luang, Pathumthani, Thailand 12120

* E-mail : Roschat1@gmail.com

Abstract: The present study reports the possibility for developing low cost solid catalyst for biodiesel production. Lime which is produced from hydration of thermal decomposed cheery shell was used as starting material for making cheap catalyst. The activity of synthesized catalysts was determined for transesterification of palm olein. The reactions were carried out in 200 ml batch reactor with theses conditions (temperature of 60^{O}C, molar ratio of methanol/oil of 15:1 and catalyst loading amount of 15 %wt.). Without modification, lime showed low activity for transesterification. 62.3 % methyl ester (ME) content was obtained within 4 h. After calcinations of lime at 900 ^{o}C, CaO was obtained as suggested from XRD. The ME content was increased up to 87.6%. The enhancement of activity after calcinations is likely associated with the evolution of H_2O, whose expulsion from the lattice during the calcinations of lime is expected to fracture the crystallites, with the concomitant formation of extra base sites in CaO. Interesting, the present of water at small amount could enhance the ME formation over lime catalyst. However, there was a limitation of the efficacy of water on the reaction. On the other hand, water showed the negative effect on the activity of CaO.

Introduction

In the recent years, there was being increased worldwide concern for the environmental protection and the conservation of non-renewable natural resources. In order to resolve these problems, biodiesel was alternative a source of renewable energy for diesel engines that is gaining attention in terms of the depleting fossil fuel resource of the world and the mitigating of greenhouse effect due to carbon dioxide [1].

Biodiesel was produced from direct transesterification of vegetable oils, where the corresponding triglycerides react with methyl alcohol in the presence of a catalyst (Eq.1). [2-4]

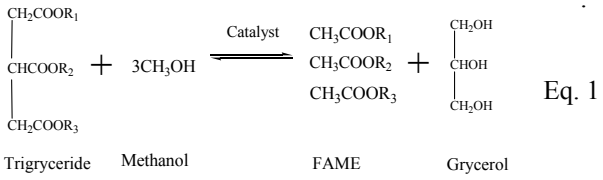

Eq. 1

Transesterification process with homogeneous base catalyst; NaOH, KOH and $NaOCH_3$, were extensively use in biodiesel production at 60-80 °C [5-6]. However, a large amount of water is required to transfer the catalyst from the organic phase to a water phase. Therefore, it is considerably costly to separate homogeneous catalyst [7].

Heterogeneous catalysis is an economically and ecologically important field in catalyst research because these catalysts have many advantages. They are non-corrosive, environmentally benign and present fewer disposal problems. They are also much easier to separate from liquid products and they can be designed to give higher activity, selectivity and longer catalyst lifetimes [8-9].

Unfortunately, the preparation of the highly effective solid catalysts is complex, costly, and requires experienced people to operate it. The cost of fabricating a catalyst can be a critical factor in its industrial applications. The production of biodiesel calls for an efficient and cheap catalyst to make the process economic and fully ecologically friendly, accordingly reducing its price and making it competitive with petroleum diesel

In the rural area of Thailand, lime (calcium hydroxide, $Ca(OH)_2$) was produced by local method. Cheery shell is thermally decomposed in the ground hole. Heat comes from the combustion of wood. After 3 hours day of the decomposition, the product was collected and mixed with water. In this present work, the possibility of using lime as cheap heterogeneous catalyst for biodiesel production was investigated in order to reducing the production costs of biodiesel and making the process to produce biodiesel fully ecologically friendly. The modification process was applied to enhance it's activity. The effect of water on the catalytic activity was also examined.

Materials and Methods

Chemicals and catalyst preparation: Palm olein oil was purchased from Morakot Industries PCL., Thailand. Composition of fatty acid in palm olein oil is given in Table 1. Methanol (QRec) used in this work was analytical reagent grade (AR). The lime which is produced from hydration of thermal decomposed cheery shell was used as starting material for making cheap catalyst. Lime was further modified by the thermal decomposition in a muffle furnace at 900 °C for 3 h. X-ray powder diffraction (XRD) patterns for lime and modified lime were analyzed.

Table 1 : Fatty acid Composition of Palm Olein Oil

Fatty acid	Composition (%wt)
Lauric acid (C12:0)	0.4
Maristic acid (C14:0)	0.8
Palmitic acid (C16:0)	37.4
Palmitoleic acid (C16:1)	0.2
Stearic acid (C18:0)	3.6
Oleic acid (C18:1)	45.8
Linoleic acid (C18:2)	11.1
Linoleic acid (C18:3)	0.3
Arachidic acid (C20:0)	0.3
Eicosenoic acid (20:1)	0.1

The mixture of methanol (32.8 ml) and catalyst (6.87 g) was stirred at 60 °C and then added into palm olein oil (50 ml). The reaction mixture was stirred at 60 °C for 4 hour. The fractionated sample was selected every hour and separated catalyst by centrifugation, and then excessive amount of methanol was evaporated before analysis of biodiesel yield.

The yield and composition of biodiesel were determined by a Gas chromatograph (GC-2010, Shimadzu) equipped with capillary column, DB-WAX (30 × 0.15 m) and a frame ionization detector. Methylheptadecanoate was used as internal standard for quantification, according to EN14103.

Results and Discussion

Fig. 1 shows the methyl ester (ME) content in the biodiesel product attained via the transesterification of palm olein over lime and modified lime. As can be seen, lime can act as solid catalyst for biodiesel production. The ME content was gradually increased during the reaction and ME content of 63.3 wt% was obtained within 4 h. After the modification with heat treatment, the catalyst showed higher activity. 93.2 wt% and 97.2 wt% of ME content were reached when lime was calcined at 800 ^{o}C and 900 ^{o}C, respectively. However, after the reaction was prolonged to 4 h, the decreasing in the ME content was observed. This may be due to the reverse transesterification reaction. Therefore, the reaction time required to obtain the highest amount of methyl esters is 180 min. The results indicate that the heat treatment is appropriated method to improve the activity of lime.

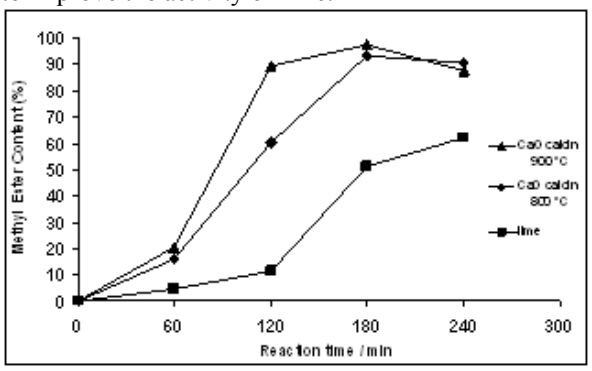

Figure 1. ME contenct obtained from transesterification over lime, CaO calcin 800 °C, and CaO calcin 900 °C. Reaction conditions: MeOH:Oil ratio of 15:1, catalyst weight of 15 wt%, Temperature of 60 °C.

The X-ray diffraction pattern of lime was shown in Fig. 2. The result shows that there are two major components in this starting material ($Ca(OH)_2$ and $CaCO_3$). $CaCO_3$ came from the incomplete decomposition of cheery shell. This implied that when the countryside people produced the lime, the using temperature was not high enough to make the cheery shell totally decomposed. Following the calcination, the reflections arising from $Ca(OH)_2$ and $CaCO_3$ were lost, coincident with the appearance of new crystalline phases that can be assigned to highly crystalline CaO (32.3◦, 37.4◦ and 53.9◦).

The XRD results agreed very well with the transesterification results showing that after calcination, the catalyst showed higher activity than lime. The enhancement of activity after calcinations is likely associated with the evolution of H_2O, whose expulsion from the lattice during the calcinations of lime is expected to fracture the crystallites, with the concomitant formation of extra base sites in CaO. This might be also due to the fact that, for alkaline earth metal, the oxide form has stronger basicity than does the hydroxide form.

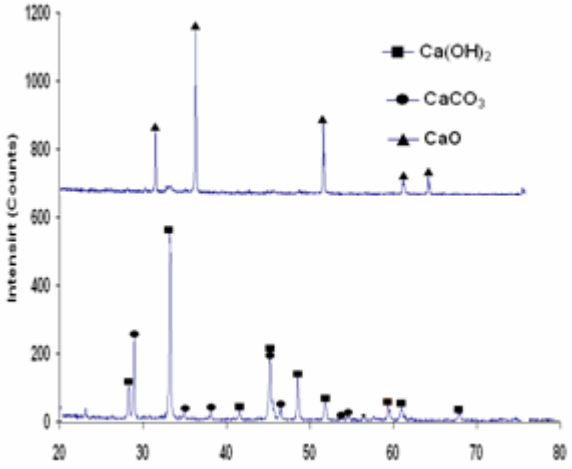

Figure 2. XRD patterns of lime and modified lime.

In the conventional transesterification of fats/vegetable oils for biodiesel production, free fatty acids and water always produce negative effects, since the presence of free fatty acids and water causes soap formation, consumes catalyst and reduces catalyst effectiveness, all of which result in a low conversion. The presence of water has a greater negative effect than that of the free fatty acids. So, the water content should be kept below 0.06% [10], much lower than the allowable free fatty acids content. These problems may hinder the most efficient utilization of waste vegetable oils and crude oils since they generally contain water and free fatty acids [11].

Water could pose a greater negative effect than presence of free fatty acids and hence the feedstock should be water free. Canakci and Van Gerpen [12] insisted that even a small amount of water (0.1%) in the transesterification reaction would decrease the ester

conversion from vegetable oil. Ellis et al. [13] found that even a small amount of water in the feedstock or from esterification reaction producing water from FFA might cause reduction in conversion of fatty acid methyl ester and formation of soap instead. At the same time, some researchers found that water has positive effect to transesterification. Zhang et al [14] found that water caused a significant increase in activity and selectivity of diacetone alcohol when MgO was used as a solid base catalyst. They proposed that basic OH-was an active site for aldol addition of acetone. Kusdiana and Saka [15] proposed that water could act as a stronger catalyst than methanol alone and the presence of a certain amount of water could enhance the methyl ester formation in the transesterification reaction with supercritical methanol.

Since water has important effect on the transesterification reaction, its effect on yield of methyl ester was studied in the present work. Fig. 3 shows the effect of water content in the mixture on the ME content obtained from transesterification over lime. Amount of water was calculated as follows:

wt% of water = (weight of water/ weight of catalyst)*100

The experiments were carried out under the conditions of 15% catalyst by weight of oil, 15:1 molar ratio of methanol to oil and 60 ^{o}C. From Fig. 3, it was observed that transesterification reaction rate can be accelerated and the ME content was increased with the rising water content. When the amount of water was increased from 0% to 30%, the ME content enchanted from 25.8 wt% to 80.8 wt% within the reaction time of 4 h. However, when the further increase in the amount of water to 40 wt%, the ME content decreased to 62.2 wt%.

From these results, it was evident that the transesterification reaction catalyzed by lime was promoted in the presence of moisture rather than was tolerant of moisture. But, there was a limitation of the efficacy of moisture, because an increase in the amount of the added water from 30 wt% to 40 wt% did not bring about the further promotion of the catalytic reaction.

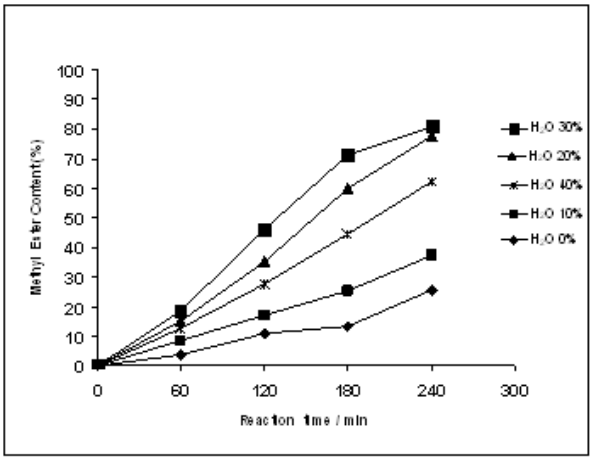

Figure 3. Effect of water content on biodiesel production using lime as catalyst. Reaction conditions: MeOH:Oil ratio of 15:1, catalyst weight of 15 wt%, Temperature of 60 °C.

Fig. 4 shows the effect of water content in the mixture on the ME content obtained from transesterification over modified lime (calcined at 900 ^{o}C for 3 h). The addition of water seemed to interfere with the catalytic reaction. Contrast with the lime. The presence of water results in the decrease of the ME content. The higher amount of added water, the lower ME content was obtained. At 3 h of the reaction time, the ME content decreased from 97.2 wt% to 92.7 wt% when the 5 wt% of water was added. No doubt that the additional water eroded the catalytic surface of catalysts by hydration. The decreasing in the ME content should be due to the hydrolysis of the fatty acid methyl ester with water under basic conditions to generate fatty acid which can react with catalyst to form soap.

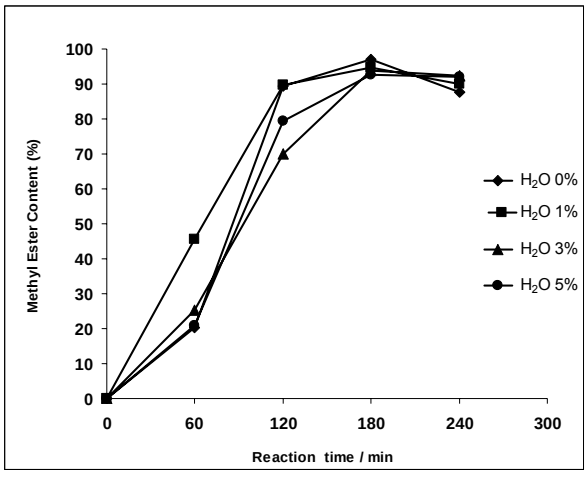

Figure 4. Effect of water content on biodiesel production useing modified lime as catalyst. Reaction conditions: MeOH:Oil ratio of 15:1, catalyst weight of 15 wt%, Temperature of 60 °C.

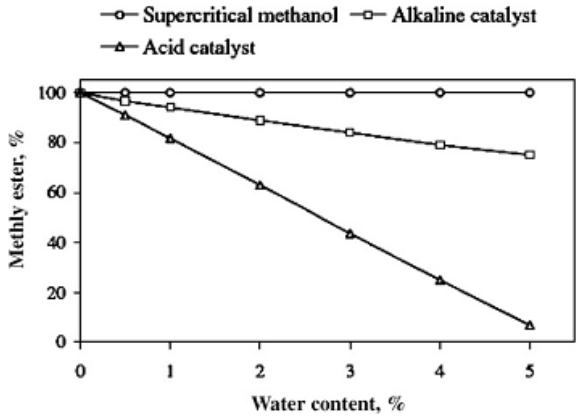

Figure 5. Plots for yields of methyl esters as a function of water content in transesterification of triglycerides. [16]

For the comparison purpose, Fig. 5 shows a direct comparison of the yield of methyl esters from various preparation methods as triglycerides with various water contents were treated. The alkaline catalyzed method used 1.5 % sodium hydroxide as a catalyst in methanol [17], while in the acid catalyzed method, 3 % sulfuric acid in methanol was added to the reaction system [18]. It is observed that acid catalyst is most prone to presence of water followed by alkaline catalyst. On the other hand, in the supercritical methanol method the amount of water added into the reaction system did not have any significant effect on the conversion, as a complete conversion was observed from any level of water content. This implies that the catalytic mechanism of the heterogeneous process is quite different from that of the traditional homogeneous process.

Conclusion

Lime was investigated in triglyceride transesterification with a view to determine its viability as a solid catalyst for use in biodiesel synthesis. Without modification, lime shows low activity. The results indicate that the heat treatment is appropriated method to improve the activity of lime. The catalyst with higher activity was obtained and 97.2 wt% of ME content was reached within 4 h of reaction time.

Water shows the difference effect on transesterfication over unmodified and modified lime. The reaction catalyzed by lime was promoted in the presence of water rather than was tolerant of water. But, there was a limitation of the efficacy of water. On the other hand, the negative effect was found when modified lime was used.

Acknowledgements

This work was supported by National Science and Technology Development Agency (NSTDA) under Young Science and Technologist Program (YSTP) and National Metal and Materials Technology Center, The author thanks Ubon Ratchathani Rajabhat University for partial supported.

References

[1] G. Vincent, A. Coteron, M. Martinez. *J. Aracil. Indu. Crop. Prod.* **8** (1998), pp. 29-35.
[2] M.P. Dorado, E. Ballesteros, M. Mittelbach. *Ener. Fuel.* 18 (2004), pp. 1457-1462.
[3] W. Zhou, S.K. Konar, D.G. Boocock, *J. Am. Oil. Chem. Soc.* **80** (2003), pp. 367-371.
[4] M. Iso, B. Chem, M. Eguchi, T. Kudo, S. Shrestha, *J. Mol. Catal.* **16** (2001), pp. 53-58.
[5] F. Ma, M. A. Hanna. *Bioresour. Technol.* **70** (1999), pp. 1–15.
[6] A.C. Pinto, L. L. N. Guarieiro, M. J. C. Rezende, N. M.Ribeiro. E. A. Torres, W. A. Lopes, P. A. de P. Pereira, J. B. de Andrade. *J. Braz. Chem. Soc.* **16** (2005), pp. 1313–1330.
[7] H. J. Kim, B. S. Kang, M. J. Kim, Y. M. Park, D. K. Kim, J. S. Lee, K. Y. Lee. *Cat. Today* **93** (2004), pp. 315–320.
[8] S. R. Watkins, K. F. A. Lee. *Green Chem.* **7** (2004), pp. 335-340.
[9] M. L. Granados, M. D. Z. Povas, D. M. Alonso, R. Mariscal. F. C. Galisteo, R. Moreno-Tost, J. Santnmaria, J. L. G. Fierro. *Appl. Catal. **B*** **73** (2007), pp. 317-326.
[10] F. Ma, L.D. Clements, M.A. Hanna. *Trans ASAE*. **41** (1998), pp. 1261–1264.
[11] A.V. Tomasevic, S.S.S. Marinkovic. Technol. **81** (2003), pp. 1–6.
[12] M. Canakci , J.V.Gerpan. *Trans Am Soc Agric Eng* . **42(5)** (1999), pp. 1203–1210.
[13] N. Ellis , F. Guan, T. Chen , C. Poon. *Chem Eng J*. 389 (2007), pp. 6-34.
[14] G. Zhang, H. Hattori, K. Tanabe. Appl Catal. **36** (1988), pp. 189–197.
[15] D. Kusdiana, S. Saka. *Bioresour Technol*. **91** (2004), pp. 289–294.
[16] Y.C. Sharma a, B.S.N. Singha. *A review Fuel*. **87** (2008), pp. 2355–2373
[17] F. Ma, L.D. Clements, M.A. Hanna. *Trans ASAE*. **41** (1998), pp. 1261–1264.
[18] M. Canakci. J.V. Gerven. *Trans ASAE*. **42** (1999), pp. 1203–1209.

Microfluidics for fuel cells: the preliminary study on proton transfer membrane and optical tweezers

C. Yunphuttha[1], W. Bunjongpru[2], S. Porntheeraphat[2], A. Wongchaisuwat[1], C. Hruanun[2], A. Poyai[2] and P. Viravathana[1*]

[1] Department of Chemistry, Faculty of Science, Kasetsart University, Bangkok, Thailand 10900
[2] Thai Microelectronics Center, Wangtakien District, Amphur Muang, Chachoengsao, Thailand 24000

[*] E-mail : fscipdv@ku.ac.th

Abstract: At present, the demand for energy consumption (electrical energy, fuel energy) increases and a need for a new energy resource to replace the energy from fossils is focused. Direct alcohol fuel cell, a type of micro fuel cell, is an alternative energy resource which generates electricity without fuel combusting. In this research, the direct alcohol fuel cell contains three parts of microchannels, electrodes, and membrane. For the proton transfer membrane, Nafion resin and polystyrene-block-poly(ethylene-ran-butylene)-block-polystyrene were employed as membrane polymers. These membrane polymers were composited with poly(methyl methacrylate). 36.5% w/v of PMMA solution was prepared in dichloroethane: propanol: acetone (3:1:0.5 by volume). Two mixtures, 5% w/w Nafion solution and the 36.5% w/v of PMMA solution as well as the mixture of 5% w/w polystyrene-block solution and the 36.5% w/v of PMMA solution, were sonicated for 2.5 h, poured 2 ml of each into a 4x4 cm^2 block, and baked in the controllable oven at 60^{o}C for 10 h. The conductivity of the two samples were measured by four-point probe, soaked with concentrated H_2SO_4 for 15 min and with DI-water for 1 h, then put in the oven at 80^{o}C for 1 h, and remeasured the conductivity. The results were compared to the conductivity of 5% w/w Nafion resin and 5% w/w polystyrene-block solution and showed that the two membrane polymers gave the conductivity higher than that of the two composited membrane polymers. To enhance the efficiency of micro fuel cell, optical tweezers is applied to this further study of direct alcohol fuel cell.

Introduction

Direct alcohol fuel cell [1], a type of micro fuel cell, is an alternative energy resource which generates electricity without fuel combusting. Attractive characteristics of direct alcohol fuel cell are high energy conversion efficiency, modular design, very low chemical and acoustical pollution, cogeneration capability, and rapid load response at room temperature [2]. The direct alcohol fuel cell, containing three parts of microchannels, electrodes, and membrane. Direct alcohol fuel cell contains polymer membrane like a key part to be improved its performance [3, 6-7]. In this research, microfluidics, dealing with volumes of fluid on the order of microliters to picoliters, was applied to fuel cell in order to reduce its size of products. For the proton transfer membrane, Nafion resin and polystyrene-block-poly (ethylene-ran-butylene)-block-polystyrene were employed as membrane polymers. These membrane polymers were composited with poly methyl methacrylate (PMMA). And then, composited membranes were compared with two membrane polymers by using four-point probe equipment (Model PMR 001) to measure conductivity.

Furthermore, we aimed to improve the capability of micro fuel cell with optical trapping or optical tweezer which was useful for scientific fields such as biology, chemistry, colloid science, polymer science, and membrane technology [4, 5, and 11]. This technique could be simply designed and has the advantage that a single microscope can be used to trap and view particles simultaneously without particle damage. Optical trapping can manipulate particles in three dimension of nanoscale to microscale, therefore, it is the most interesting technique for observation and improving the performance of micro direct alcohol fuel cell in the future.

Materials and Methods

1. Membrane

1.1 Polymer membrane resins

For membrane composition, Nafion resin (5wt% in lower aliphatic alcohols and water, containing 15-20%wt water, Sigma-Aldrich) and polystyrene-block-poly(ethylene-ran-butylene)-block-polystyrene (5wt% in 1-propanol and dichloroethane, Sigma-Aldrich) were used as membrane polymers.

1.2 Composited membrane with selected polymer

These polymer membrane resins, Nafion resin and polystyrene-block, were composited with PMMA which was the selected polymer based on its compatibility with the two polymer membrane resins. 36.5% w/v of PMMA solution was prepared in dichloroethane: propanol: acetone (3:1:0.5 by volume). Two mixtures, 5% w/w Nafion solution and the 36.5% w/v of PMMA solution as well as the mixture of 5% w/w polystyrene-block solution and the 36.5% w/v of PMMA solution, were sonicated for 2.5 h, poured 2 ml of each into a 4x4 cm^2 block, and baked in the controllable oven at 60 ^{0}C for 10 h.

1.3 Conductivity measurement

The conductivity of the two samples were measured by four-point probe, then soaked with conc. H_2SO_4 for 15 min and with DI-water for 1 h, put in the oven at 80 ^{0}C for 1 h, and remeasured the conductivity.

2. Optical trapping

2.1 Experimental setup

Optical trapping setup (Figure 1) was set up with three components of a Helium neon laser source (20 mW, Meredith instruments), a CCD colour video camera (SSC-DC138P, Sony), and a biological-microscope (Eclipse E200, Nikon). The Laser source gave the 5 mm-diameter red laser beam (λ 623 nm) which was reflected by a gold coated mirror down to the microscope.

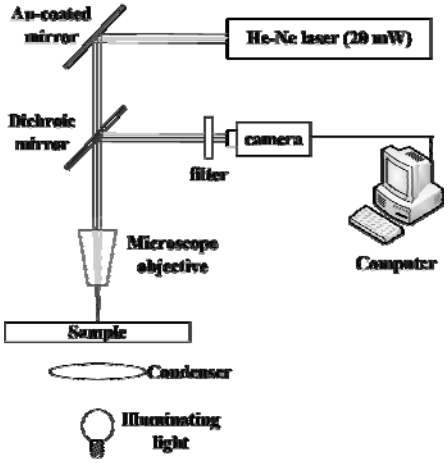

Figure 1. Experimental setup for optical trapping

2.2 Channel preparation for optical trapping

From preliminary studies on channel preparation, a cover slide was employed as a trapping window and to enhance the strength of channel. Channels were prepared from the fabricated silicon-wafer mold patterned by photolithography with SU-8 resist (SU-8 negative photoresist no.2150, Microchem). Some short tubes were adhered to the inlet-outlet of the pattern on silicon wafer mold before applying PDMS (Dow-Corning, Sylgard 184) mixed with its hardener at the ratio of 10:1 by weight. After pouring PDMS mixture over the fabricated silicon-wafer mold, the cover slide and a poly (acrylic acid) plate were put on, respectively. Then the silicon-wafer mold with PDMS was put in oven at 100 ^{o}C for 1h. PDMS channel with cover slide would be cut and peel from poly (acrylic acid) plate and silicon-wafer mold, then paste on a slide and ready for optical trapping.

In this work, 3μm-sized polystyrene was employed as suspended particles in DI-water. One drop of the polystyrene suspension was dropped into a PDMS channel with cover slide. The 100x microscope objective lens was used for particles trapping. The images of trapped particles were recorded by the CCD-camera which was connected to the computer.

Results and Discussion

1. Membrane: proton conductivity

To study the proton conductivity, the conductivity of 5% w/w Nafion resin (NR), 5% w/w polystyrene-block resin (PS), two composited membranes (as NR/PMMA and PS/PMMA), and blank PMMA were shown in Table 1. The results found that the conductivity of two composited membranes and blank PMMA could not be measured by four-point probe, whereas, the conductivity of Nafion resin and polystyrene-block resin could be detected. Before soaking in water, 5% w/w Nafion resin gave its conductivity higher than the conductivity of 5% w/w polystyrene-block resin but after soaking in water, the conductivity of 5% w/w polystyrene-block resin would be higher than the conductivity of 5% w/w Nafion resin. These phenomena happened because the swelling degree of Nafion resin was easily changed after immersing in water while the swelling degree of polystyrene-block resin was not affected [8]. Therefore, the conductivity of Nafion resin decreased. From the results, the swelling degree of polymer membrane was a factor that should be considered for application of membrane in micro direct alcohol fuel cell.

Table 1: Results of the conductivity of polymer membrane resins and composited membranes

Set	Samples, sample no.	Condition			Averaged conductivity(σ) x 10^{-6} cm/s
		H_2SO_4	H_2O	80^{o}C	
1	5%NR,1	N/A	N/A	N/A	7.96
	5%NR,2	N/A	3hr	1hr	11.30
2	5%RS,1	N/A	N/A	N/A	5.31
	5%RS,2	N/A	3hr	1hr	16.02
3	PMMA,1	N/A	N/A	N/A	*
	PMMA,2	15min	3h	1hr	*
4	30%w/v NR/PMMA, 1	N/A	N/A	N/A	*
	30%w/v NR/PMMA, 2	15min	3h	1h	*
	30%w/v NR/PMMA, 3	N/A	3h	1h	*
5	30%w/v RS/PMMA, 1	N/A	N/A	N/A	*
	30%w/v RS/PMMA, 2	15min	3h	1h	*
	30%w/v RS/PMMA, 3	N/A	3h	1h	*

Notices: * cannot be quantified

2. Optical trapping

From Figure 2, the microscope was modified by adding a dichroic mirror and a filter, also connected to the CCD camera which replaced the eyepieces of the microscope. In this work, trapping display was recorded by the CCD camera and the computer at room temperature.

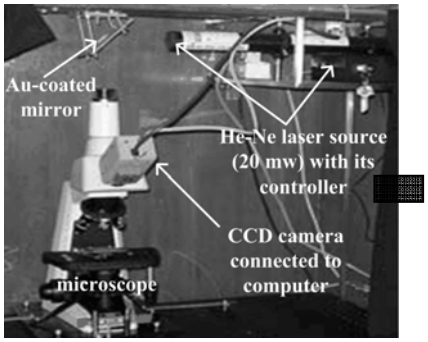

Figure 2. Experimental setup for optical trapping

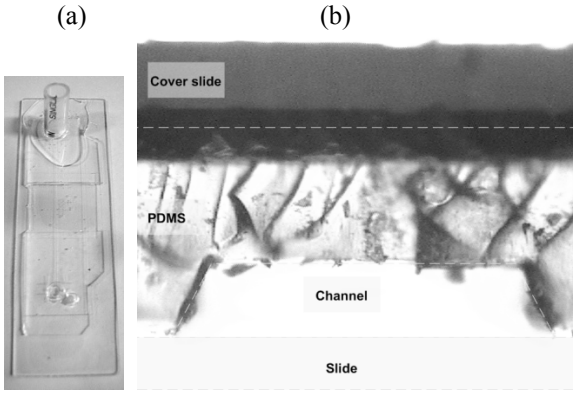

Figure 3. PDMS channel on slide for optical trapping
(a) top-view of PDMS channel on slide
(b) cross-section view of PDMS channel on slide from using 10x microscope objective lens.

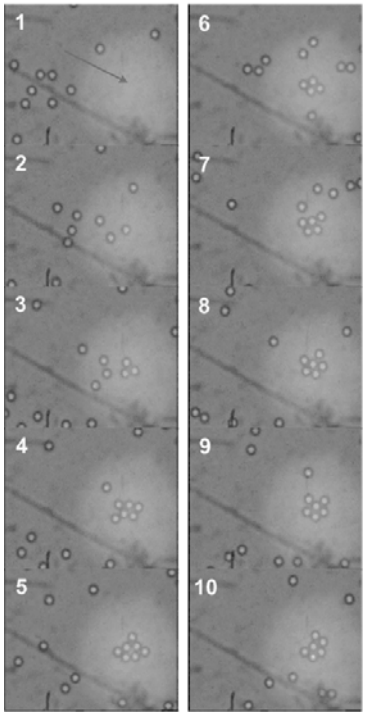

Figure 4. Particles trapping by optical trapping technique

PDMS channels on slide was prepared from photolithography as shown in Figure 3a; their cross-section view was observed by 10x-lens microscope as shown in Figure 3b. The image showed the PDMS layer between the cover slide and the channel. The thickness of PDMS layer was preferred to be as thin as possible in order not to affect the trapping power.

The polystyrene particle trapping was shown in Figure 4. In Figure 4-1, the red arrow was pointing at the trap with the highest laser beam intensity. Figures 4-2 to 4-5 showed that the laser beam could trap about 3-6 particles. When suddenly moving the stage of microscope, particles would be moved away from the trapping point. After not moving, the particles would gradually move back to the trap as shown in Figures 4-6 to 4-10.

In this work, many factors could have influences to the trapping force such as the suspension flow rate, the thickness of PDMS between a cover slide and a channel (as shown in Figure 3b), the adjustment of objective lens, and the laser scattering from lens in the microscope or mirrors. These factors should be considered in optical trapping which would be useful for micro direct alcohol fuel cell application in the future.

Conclusions

In preliminary study of membrane for direct alcohol fuel cell, Nafion resin and polystyrene-block showed the higher proton conductivity than two com-posited membranes of NR/PMMA and PS/PMMA. After being soaked in water, the proton conductivity of Nation resin was lower than that of polystyrene-block resin because of swelling effect. The optical trapping technique could be applied in micro fuel cell to ease the fabrication and enhance the capability of micro fuel cell.

Acknowledgements

Financial supports from the Thailand Research Fund (TRF) and Faculty of Science, Kasetsart University under co-funding window II (grant #MRG-WII515S019), Department of Chemistry, and Postgraduate Education and Research Program in Physical Chemistry (ADB KU–Chem) are acknowledged. The collaboration and instrumental supports from Thai Microelectronics Center (TMEC), National Nanotechnology Center (NANOTEC) and College of Nanotechnology, King Mongkut's Institute of Technology Ladkrabung are truly appreciated.

References

[1] T. Kobayashi, J. Otomo, C. Wen and H. Takahashi, *J. Power Source* **124** (2003), pp. 34-39.
[2] M. Wang., G. Huo and **C. Ma**, *Journal of Fuel Cell Science and Technology* **3** (2006), pp. 202-207.
[3] V. Mehta and J.S. Cooper, *J. Power Source* **114** (2003), pp. 32-53.
[4] C. Mio, T. Gong, A. Terray and D.W.M. Marr, *Rev. Sci. Instrum.* **71** (2000), pp. 2196-2200.
[5] S. Bleil, D.W.M. Marr and C. Bechinger, *Appl. Phys. Lett.* **88** (2006), pp. 263515.
[6] J. Kim, B. Kim and B. Jung, *J. Membr. Sci.* **207** (2002), pp. 129-137.
[7] J. Yuan, G. Zhou and H. Pu, *J. Membr. Sci.* **325** (2008), pp. 742-748.
[8] S.E. Nam, S.O. Kim, Y. Kang, J.W. Lee and K.H. Lee, *J. Membr. Sci.* **322** (2008), pp. 466-474.
[9] Y.A. Song, C. Batista, R. Sarpeshkar and J. Han, *J. Power Source* **183** (2008), pp. 674-677.
[10]M.A. Hickner, H. Ghassemi, Y.S. Kim, B.R. Einsla. and J.E. Mcgrath, *Chem. Rev.* **104** (2004), pp. 4587−4612.
[11]J. Oakey, J. Allely and D.W.M. Marr, *Biotechnol. Prog.,* **18 (**2002), pp. 1439-1442.

Utilization of leonardite and FGD gypsum for production of fired planting materials

R. Srisomang[1], W. Naksaka[1], S. Thiansem[2], P. Sooksamiti[3] and O. Arquero[1,*]

[1]Department of Chemistry and Center of Excellence for Innovation in Chemistry, Faculty of Science, Chiang Mai University, Chiang Mai, Thailand 50200
[2]Department of Industrial Chemistry, Faculty of Science, Chiang Mai University, Chiang Mai, Thailand 50200
[3]Department of Primary Industry and Mine Office Region 3, Chiang Mai, Thailand 50200

*E-mail: noi2495@hotmail.com

Abstract: Leonardite and flue gas desulfurization (FGD) gypsum, which are residues from coal mine and electric power plant in Mae Moh district, Lampang province, can be used to produce instant planting materials. The aim of this research is to fabricate an instant implant material by mixing the leonardite and FGD-gypsum with clay to replace the use natural planting materials. The production fired planting material was done by mixing raw materials in different proportions according to the triaxial diagram, forming and firing at various temperatures, respectively. The results showed that the percent weight ratio of leonardite : FGD-gypsum : clay soil at 70 : 20 : 10 and firing temperature at 650 °C were the appropriate conditions for production of fired planting material. It was found that the planting material obtained from this work did not slake after soaking at least 30 days in water. It has light weight, slightly acidic pH value, good water absorption and cation exchange capacity equal to 17.9 meq/100g, much higher than of the commercial planting material which had a cation exchange capacity in the range of 2-8 meq/100g.

Introduction

Planting materials are used as one kind of soil-less culture of growing plants without soil [1]. They are very popular and important for the production of many plants grown in containers because of their special characteristics such as light weight, low density, easy for use and high hardness. The disadvantage of commercial planting materials are high cost and imported from aboard [2]. There are many raw materials used for the production of planting materials, for example, coconut fiber, rice hulls, saw dust, sand, clay, diatomite, bottom ash and flue gas desulfurization (FGD) gypsum, etc [3]. In this work, Leonardite, FGD-gypsum and clay will be employed as raw materials for the production of fired planting materials. Leonardite, which is an organic material, is a soft coal-like deposit that occurred at shallow depth. It is more oxidized than lignite and naturally occurred in conjunction with deposits of lignite. Although leonardite has low heating content as a fuel, its high content of humic acids may make it useful as a soil amendment [4]. It is generally accepted that humic acids contain several major functional groups such as carboxyl (COOH), alcohol (OH) and carbonyl (C=O). These functional groups enable leonardite to be used as a wastewater treating medium to remove heavy metals. The low cost and the availability of this material make it a promising candidate for pollution remediation [5]. Humic substances are renowned for their ability to chelate soil nutrients, improve nutrient uptake, especially phosphorous, sulfur and nitrogen, stimulate soil biological activity, solubilize minerals, improve soil structure, improve water-holding capacity for better drought resistance and reduction in water usage, etc. [6].

FGD-gypsum is also known as scrubber gypsum. It is the byproduct of an air pollution control system that removes sulfur from the flue gas in calcium-based scrubbing systems. FGD-gypsum is produced by employing forced oxidation in the scrubber and is composed mostly of calcium sulfate. It has the ability to improve the physical properties of soil such as water infiltration, increased electrolyte concentration of water at the surface of the soil causing soil flocculation thus reducing sealing, help alleviate soil compaction and improved aggregate stability of soils [7]. Moreover, in this study, clay will be mixed to gain plasticity and strength with rather high cation exchange capacity (CEC) value after firing.

The goal of the research presented in this paper is to produce fired planting materials from leonardite and FGD-gypsum, which are residues from Mae Moh electric power plant in Lampang province, mixed with clay to replace the use of commercial planting materials and study their chemical and physical properties.

Materials and Methods

1. Production of fired planting material

As starting materials, leonardite and FGD-gypsum were provided by coal mine and electric power plant in Mae Moh district, Lampang province, Thailand. Clay was delivered by Paradon Company, Thailand. All materials (leonardite, FGD-gypsum and clay) were dried sequentially at 100 °C for 6 hours, 40 °C for 1 hour and 100 °C for 12 hours, in order to reach constant weight. Then the materials were crushed and sieved to different sizes by ball mill and sieving machine, respectively.

Three raw materials were dried and crushed to different sizes. These three solids were mixed in different proportions to produce mixtures whose

compositions correspond to the ternary diagram. From each mixture, a wet powder was produced by adding tap water and then compressed into the extrusion machine. All samples were dried at 100 °C for 12 hours. Then, they were fired at various temperatures (500, 600, 650, 700, 850, 900 and 1,000 °C). Finally, the physical and chemical properties such as pH, slake, water absorption, bulk density and cation exchange capacity of the fired samples were investigated.

2. Test physical and chemical properties of fired planting materials

2.1 Slake

Slake is an important parameter for the production of planting material. Samples were soaked in water for 30 days and the shape of the materials was investigated visually.

2.2 Water absorption (%WA) and bulk density

Water absorption is used to determine the amount of water absorbed under specified conditions. Factors affecting water absorption include: type of material, additives used, temperature and length of exposure. Bulk density is defined as the weight per unit volume of material. Variation in bulk density is attributable to the relative proportion and specific gravity of solid organic and inorganic particles and to the porosity of the soil. For the water absorption and bulk density test, samples were dried at 105 °C to constant weight, weighed at dry state (D), boiled in water for 2 h, cooled and weighed in water (S) and weighed at the saturated wet state in air (W) once more. The water absorption and bulk density of samples were calculated according to:

$$\%\text{Water absorption} = [(W-D)/D] \times 100 \quad (1)$$

$$\text{Bulk density} = [D/(W-S)] \quad (2)$$

2.3 pH

pH is the measure of the acidity or alkalinity of a solution. In this work, the pH value was measured by a pH meter using the ratio of material to distilled water at 1:3.

2.4 Cation exchange capacity (CEC)

CEC is the sum total of exchangeable cations that soil can absorb. The cations on the CEC of the soil particles are easily exchangeable with other cations and as a result, they are plant available. The CEC varies between different types of media. A high CEC is desirable as this means there will be a more even nutrient supply to the roots and less nutrients will be lost through over-watering. In this work, the CEC was measured to evaluate the adsorption capacity by the ammonium acetate method. The milli-equivalent value of ammonium ion in a 100 g sample was calculated by the formula:

$$\text{CEC (meq/100 g)} = \frac{[A \times B]}{C} \times 100 \quad (3)$$

where A = volume of acid used (mL)
B = normality of acid used (N)
C = weight of sample used (g)

2.5 *Morphology of the fired planting material and commercial planting*

To examine the microstructure of the fired planting materials and commercial planting material, the granules of samples were also subjected to a scanning electron microscopy (SEM) study. These samples were metal coated with a layer of gold and observed in a JSM-6335F SEM and the images of microstructure taken are shown in figures 1 and 2.

Results and Discussion

The effects of the different proportions of the admixtures on each of the properties of the fired planting materials made from the different mixes are discussed below.

From table 1, the results showed that the weight ratio of materials (leonardite : FGD-gypsum : clay) at 70 : 20 : 10 and firing at 650 °C was the suitable conditions. It has 58.3% water absorption, pH value was 5.3, bulk density 1.9 g/cm^3 and CEC value 17.9 meq/100 g. It is shown that this produced fired planting material has high water absorption content, acidic pH value and light weight. Furthermore, this fired planting material has a good characteristic from high quality unslaking which resulted from being soaked in water for at least 30 days. The commercial planting material used in this work was fired at higher temperature, i.e.1200 °C. It has pH value of 6.4, 22.3% water absorption, bulk density 1.3 g/cm^3 and CEC value in the range 2-8 meq/100 g.

Table 1: Properties of the fired planting material (fired at 650°C) compared with commercial planting material

Properties	The fired planting material (leonardite : FGD-gypsum : clay) 70 : 20 : 10	Commercial planting material
Firing	650 °C	1200 °C
Slake	not slake	not slake
pH	5.3	6.4
%WA	58.3	22.3
Density (g/cm^3)	1.9	1.3
CEC (meq/100g)	17.9	2-8

From the results, it can be seen that the fired planting material has the ability to absorb and retain large quantities of water for plant use between irrigations due to its high porosity. When compared with commercial planting material, it has higher porosity, so it should be able to absorb more water. Upon heating, the pore structure of planting material changes. When the FGD gypsum ($CaSO_4.2H_2O$) was heated at high temperatures, it might change from gypsum ($CaSO_4.2H_2O$) to hemihydrate ($CaSO_4.1/2H_2O$), to more spacious anhydrite III ($CaSO_4$ III), to more spacious anhydrite II ($CaSO_4$ II)

and to anhydrite I ($CaSO_4$ I), respectively [8]. For clay, the following changes were investigated upon heating at high temperature: water loss, combustion of organic matters, a change from α-quartz to β-quartz and decomposition of sodium carbonate [9]. According to the changes above, the generated gases inside the hot glowing body, such as carbon dioxide and carbon monoxide, caused the porous structure. In addition, it was found that firing at higher temperatures at 700, 850, 900 and 1000 °C could not improve the properties of the planting materials. The firing planting materials at 700, 850, 900 and 1000 °C had lower water absorption than those fired at 650 °C because at higher temperature the humic acid from leonardite was destroyed and the surface of the materials fused to decrease the surface area.

Water absorption rate has been used as an indication for porosity of the fired planting materials body. Generally, porosity increases with decreasing compressive strength but strength is also influenced by raw material composition and firing temperature. High values of water absorption obtained in this study indicated that the fired planting material produced was highly porous. Internal structure of the fired planting material is expected to be intensive enough to avoid intrusion of water. A significant linear relationship occurred between water absorption and firing temperature.

The CEC value of the fired planting material was 17.9 meq/100g. It has a higher CEC value than commercial planting material (2-8 meq/100g). The disadvantages of a low CEC include the limited availability of mineral nutrients to the plant and inefficient ability to hold applied nutrients. Plants can exhaust a fair amount of energy scrounging the the commercial planting material for mineral nutrients.

In this study, scanning electron microscopy was used to investigate and observe the small particle in each sample as shown in Figures 1 and 2. SEM of the surface of the fired planting material (Figure 1) it can be seen that the surface is coarse and porous, which structurally increased the surface area of the fired planting material. Therefore, when fired planting material is dipped in water, it can absorb water quickly than commercial planting material, which is responsible for the water-retention property of fired planting material.

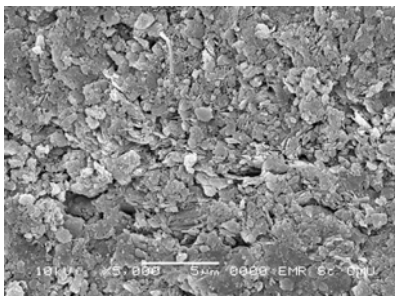

Figure 1. SEM micrograph of fired planting material (x5000; Scale bar = 5μm)

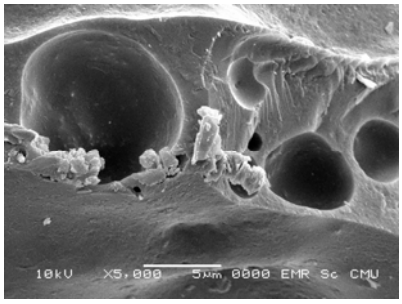

Figure 2. SEM micrograph of commercial planting material (x5000; Scale bar = 5μm)

Conclusions

Based on the experimental investigations reported in this research, the following conclusions can be drawn:

The compositions for materials used to produce fired planting material are 70% leonardite, 20% FGD-gypsum and 10% clay under the firing temperature of 650 °C. This prepared fired planting material did not slake after soaking in water. It had good water absorption and light weight. The results indicated that the fired planting material provided from this work has some properties that suitable for the plants grow. It is also an environmentally safe material.

Acknowledgments

The authors would like to thank the Center of Excellence for Innovation in Chemistry (PERCH-CIC) for the graduate scholarships, which relieved the author's financial burden and made it possible for me to complete this research. The authors also the thanks to coal mine and electric power plant in Mae Moh district, Lampang province, Thailand for leonardite and FGD-gypsum, respectively.

References

[1] J. Rogbeck, and A. Knutz, *Waste Manage*. **16** (1996), pp. 125-128.
[2] http://www.hydrogarden.com/hydro.html
[3] M. Schwarz, Editor, *Soilless culture management,* Springer-Verlag, Berlin Heidelberg, 1926, pp. 1-193.
[4] O. Akinremi, H. Janzen, R.L. Lemake and F.J. Larney, *J. Soil Sci*. **80** (2000), pp. 437-443.
[5] M. Sole, J.M. Casas and C. Lao, *Water, Air and Soil Pollut*. **144** (2003), pp. 57-65.
[6] http://www.acresusa.com
[7] L. D. Norton, *J. Am. Soc. Agron. Madison*. **58** (1995), pp. 87-105.
[8] H. Andrews, *The production, properties and uses of calcium sulfate Plasters*, London: building research congress, division 2, 1951, pp. 35.
[9] W.D. Kinggery, H.K. Bowen and D.R. Uhimann, *Introduction to ceramics*, Cambridge, Massachusetts, 1975.

Qualitative analysis of charcoal on some physical and mechanical properties of clay brick

N. Phonphuak[1,*], S. Thiansem[2], G. Rujijannagul[1] and K. Pengpat[1]

[1]Department of Physics and Materials Science, Faculty of Science, Chiang Mai University, Chiang Mai, Thailand 50200
[2]Department of Industrial Chemistry, Faculty of Science, Chiang Mai University, Chiang Mai, Thailand 50200

*E- mail: copper_red@hotmail.com

Abstract: This study was conducted to evaluate the effect of charcoal on some physical and mechanical properties of fired clay brick. Afterwards, in order to get comparable results, different ratios of the charcoal (0, 2.5, 5.0, 7.5 and 10.0% by weight) were added to the raw-brick and firing at 950 ^{o}C. The results shown that fired shrinkage: 1.80%, water absorption: 18.27%, apparent porosity: 31.45%, apparent density: 2.32 g/cm^3, bulk density: 1.72 g/cm^3 and compressive strength: 143.45 kg/cm^2. The results of clay brick-related word indicated that compressive strength: 105 kg/cm^2, apparent porosity: 21.61% and bulk density 1.54 g/cm^3. In conclusions, charcoal can be utilized in brick to save energy, which is the important issue of the world because of both economic and environmental concerns. Moreover, compressive strength, apparent porosity and bulk density of clay brick mixed with charcoal higher than clay brick-related word so that it can be used instead of clay brick-related word.

Introduction

Bricks are masonry units composed of inorganic non-metallic material and widely used as building components all over the world. The bricks could be sun-dried or burnt. Fired bricks are usually stronger than sun-dried bricks, especially if they are made of clay or clayey material. Because of fired bricks result of heat work about 800-1180 °C. Brick become homogeneous, harder and stronger from the ceramic bond from the fusion phase of the silica and alumina clay constituents [1]. Properties of bricks are affected as a result of physical, chemical and mineralogical alteration. Compressive strength and water absorption are two major physical properties of brick that are good predictors of brick's ability to resist cracking of face [2]. The additives, mixed in the clay bricks are burning out during the firing process producing extra energy, and decreasing the total energy need of the industrial furnace [3]. One of the most convectional ways to improve insulation capacity of a brick is to generate porosity in fired clay body [4]. Combustible, organic types of pore-forming additives are most frequently used for this purpose [5]. Jung, et al (2005), determined the feasibility of the use of coal wastes in clay brick production. Besides the composition of the waste, the feasibility also depends on the clay body's porosity and structure [6]. The most frequently used pore formers in clay brick manufacturing can be classified into two groups: Organic and inorganic pore generators [7]. Sawdust, polystyrene, paper sludge, coal, and coke are some examples of organic pore-forming materials. Perlite, diatomite, calcite, pumice, and vermiculite are inorganic agents. Organic pore formers are generally cheaper than inorganic ones and also have the advantage of ensuring a heat contribution to the firing furnace. However, CO_2 emission is the main drawback of the organic pore formers. Inorganic pore formers have less environmental problems but they may change the plasticity of the clay system negatively and increase the amount of water needed to maintain acceptable plasticity [8]. Organic product residues are extensively used as a pore former in the brick industry [9].

The main objective of this study is to investigate the effects of charcoal addition on the properties of fired building bricks.

Materials and Methods

In order to measure the physical and mechanical properties and feasibility of using charcoal material for brick production, the materials and methods are explained in this section.

1. Properties of brick raw material

Charcoal and Hang Dong clay used as raw materials which are obtained from Hang Dong district in Chiang Mai province, Thailand. The charcoal used in this research is mostly carbon present and the chemical components of clay such as SiO_2 (59.94%), Al_2O_3 (20.83%), Fe_2O_3 (4.87%) and K_2O (2.14%). Moreover, the other chemical components are TiO_2 and CaO. Qualitative determination of major crystalline phases present in the clay and charcoal was achieved by using an X-ray diffractometer (XRD - Bruker D8 Advance). The major crystalline phases found in clay are quartz, muscovite, kaolinite, alkali-feldspar and hematite, while charcoal contain quartz and cristobalite. The particle size distribution of the clay was analyzed by laser diffraction (Mastersizer, Melvern Instrument Ltd). The particles size of Hang Dong clay in the range of 27.19 - 43.96 micron.

2. Sample preparation

In order to determine the extent of the pore-forming effect of the charcoal particle size in the range of 2-3 mm. (size 1), 1-2 mm. (size 2) and less than 0.5 mm. (size 3). Then, they were added in to the raw-brick clay in different proportions (0, 2.5,

5.0, 7.5 and 10% by weight). After that forming or shaping, (mixing with about 20-30% water to a plastic condition to obtain the desired shape), soft-mud rectangle-shaped specimens of internal dimension of 5x9.5x3 cm. using hand-molding of the brick. Specimens were dried at 80 °C for 24 hrs. then, fired at 900, 950, 1000 and 1100 °C (soaking time 2 hr).

3. Testing method of the physical and mechanical properties for specimens

Tests were carried out on the clay brick samples to determine their shrinkage, apparent porosity, water absorption, apparent density, bulk density and compressive strength.

3.1 Shrinkage test

The firing shrinkage was calculated for each test specimen using the following formula

$$\% \text{ Avg. drying shrinkage} = [(OL-DL)/OL]\times 100 \quad (1)$$

$$\% \text{ Firing shrinkage} = [(DL-FL)/FL]\times 100 \quad (2)$$

$$\% \text{ Total shrinkage} = [(OL-FL)/OL] \times 100 \quad (3)$$

where : OL = original length, DL = stands for dry length and FL = fired length.

3.2 Bulk density, apparent density, apparent porosity and water absorption tests were calculated for each test specimen using the following formula

$$\text{Bulk density} = [D/(W-S)] \ (g/cm^3) \quad (4)$$

$$\text{Apparent density} = [D/(D-S)] \ (g/cm^3) \quad (5)$$

$$\% \text{ Apparent porosity} = [(W-D)/(W-S)] \times 100 \quad (6)$$

$$\% \text{ Water absorption} = [D/(W-D)] \times 100 \quad (7)$$

where : D = weight of fired specimen, S = weight of fired specimen suspended in water, and W = weight of soaked specimen suspended in air.

3.3 Compressive strength

The compressive strength is the most important parameter for assuring the engineering quality of a building material. In generally, the compressive strength depends on firing temperature, method of production, physical, chemical and mineral properties of the raw material. In this study the compressive strength was calculated for each test specimen using the following formula

$$\text{Compressive strength, } C = W/A \ (kg/cm^2) \quad (8)$$

where : C = compressive strength of the specimen (kg/cm^2), W = maximum load (kg), indicated by the testing machine, A = average of the gross areas of the upper and lower bearing surfaces of the specimen (cm^2)

Results and discussion

Effect of charcoal addition on the shrinkage, bulk density, apparent density, apparent porosity, water absorption and compressive strength properties of the clay bricks

Shrinkage in clay bricks can be explained as water leaving a body, which is used to shape a product. When water between clay particles leaves, particles come closer and shrinkage occurs. Then firing temperature is a key factor to be controlled to minimize the shrinkage in the firing process. Shrinkage of clay bricks increased with increasing firing temperature. In this research, it was found that when firing specimens at 500°C to 700°C, fired shrinkage decreases, that is, the specimens expand. (in all specimens, quartz changes phase and expands). From 700°C to 900°C small increases in shrinkage are seen. From 900°C up to 1200°C shrinkage was strongly increased that affects towards sintering and increasing of glassy phase.

The specimens were fired at 900, 950, 1000 and 1100°C. The results indicated that the shrinkage values of the specimens in the range of 2.00 - 3.05%; apparent porosity: 21.27 – 57.86%; water absorption: 13.54 – 41.40%; bulk density: 1.10 – 1.80 g/cm^3; apparent density: 1.85 – 2.38 g/cm^3; and compressive strength was 18.91 – 152.82 kg/cm^2. While at 950 °C the highest of shrinkage was 1.80% (charcoal size 3, 2.5 %) but the lowest, 1.42% (charcoal size 3, 7.5%). As density of clay bricks decreases, its strength and heat conductance also decreases, while its, water absorption increases. In this study, density of charcoal added clay bricks decreases as compared to clay bricks without charcoal fired under the same temperature.

Bulk density of a clay bricks depends on specific gravity of the raw material used, method of manufacturing and degree of burning. As density of a clay brick decreases, its strength and heat conductance also decreases, while its, water absorption increases.

Water absorption is the property of a material to be saturated with water. It is closely associated with the porosity of the material. Water absorption is an important factor for the durability of clay bricks. When water infiltrates the bricks, it decreases the durability of brick. Thus, the internal structure of the brick must be dense enough to void the intrusion of water. Water absorption of clay bricks decreased with increasing the temperature. However, amount of charcoal added increased the water absorption rate, linearly. Increasing water absorption causes clay bricks to adhere each other and this weakens the wall strength. Thus, resistance of clay bricks against frost also increases with decreasing water absorption. Water absorption is directly proportional to apparent porosity. Therefore, similar trends were observed in water absorption and apparent porosity. The apparent porosity of the specimens were obtained at 900 - 1100°C. The results indicated that the highest

porosity was 57.86% (charcoal size 1, 10 % at fired temperature 900°C). While showed the lowest was 20.27% (charcoal size 3, 2.5%). This indicates that high percentage of charcoal in a specimens leads to high porosity of the specimens that affect from the charcoal burning out during firing of pores in clay brick. These pores make clay brick porous. The more percentage of charcoal in clay brick, the more porous clay brick would be.

The compressive strength is a mechanical property used in clay brick specifications, which has assumed great importance for two reasons. Firstly, with a higher compressive strength, other properties like flexure, resistance to abrasion, etc., also improve. Secondly, while other properties are relatively difficult to evaluate, the compressive strength is easy to determine. The results indicate that the compressive strength is greatly dependent on the amount of charcoal in the clay bricks and the firing temperature. Increase in compressive strength is due to decrease in porosity and increase in bulk density with increasing temperature. The density of clay bricks increased as temperature. Fired shrinkage, bulk density, apparent density, apparent porosity, water absorption and compressive strength of fired sample (charcoal size 3) after firing at 950°C compared with clay brick-related word are shown in Table 1.

Table 1: The properties of fired sample (charcoal size 3) after firing at 950 °C compared with clay brick-related word

Properties	Charcoal (%)					**Clay brick-related word
	0	2.5	5.0	7.5	10.0	
Fired shrinkage (%)	2.0	1.80	1.70	1.42	1.80	-
Bulk density (g/cm^3)	1.78	1.72	1.63	1.60	1.40	1.54
Apparent density (g/cm^3)	2.56	2.32	2.30	2.24	2.15	2.38
Apparent porosity (%)	30.62	31.45	35.14	38.93	46.85	21.61
Water absorption (%)	17.88	18.27	26.60	29.78	35.48	15.73
Compressive strength (kg/cm^2)	152.60	143.45	90.57	85.70	78.59	105

** Clay brick-related word = commercial clay brick

The charcoals are applicable in clay brick production as combustible material designed to increase porosity. The results described in conclusion also be verified for other types of clay. With no necessary alteration of production operations, coarse as well as fine charcoal can be successfully utilized in the production of structural building bricks as backing bricks. Otherwise, the fired finished bricks produced with charcoal possess a similar or higher strength, a higher porosity (higher water absorption capacity) and lower density than those produced from a similar production clay.

Table 1 show that an increase in the amount of charcoal addition causes a reduction in the clay bricks bulk density and apparent density. But apparent porosity and water absorption were increases. The main reason for such a result is the burning of charcoal addition as an organic material which can easily burn out during the firing period. Depending on charcoal addition, apparent porosity increases continuously. From this table it can be seen that bulk density, apparent porosity and compressive strength of clay brick-related word, lower than clay bricks (charcoal size 3) at firing temperature at 950°C.

Conclusions

The following conclusions can be made from this study:

1. The effect of the addition of charcoal is mainly in producing lightweight and more porous burnt clay bricks.
2. An increase in the content of the charcoal addition leads to an increase in the fired shrinkage. Also an increase of additive leads to an increase in the water absorption. Bulk density and apparent density were increased as the amount of charcoal additive increased.
3. The compressive strength of clay bricks increases and water absorption decreases with increase in firing temperature (900-1100 °C). The density and firing shrinkage of clay brick fired at 900-1100 °C also increased with the increasing firing temperature.
4. According to test results, a mixture of up to 2.5% charcoal (particle size less than 0.5 mm, firing temperature at 950 °C) additives can be used in clay bricks production because of the fired shrinkage, bulk density, apparent density, apparent porosity, water absorption and compressive strength are higher than clay brick-related word.

Acknowledgments

The authors acknowledge the Office of the Higher Education Commission, Thailand for the graduate scholarships, which relieved the author's financial burden and made it possible for me to complete this research and Miss. Rungrudee Srisomang

References

[1] E.A. Okunade, *J. Applied Sci*. **8** (2008) (6), pp. 1042-1048
[2] S. Karaman, S. Ersahin and H. Gunal, *J. Sci Ind Res*. **65** (2005), pp. 153-159.
[3] B. Viktor and A.G. László, Mater Sci Forum, **589** (2008), pp. 1-6.
[4] I. Demir, M.S. Baspinar and M. Orhan, *Building and Environment*. **40** (2005), pp. 1533-1537.
[5] I. Demir, *Building and Environment*. **41** (2006), pp. 1274-1278.
[6] J.H. Jung, J.W. Yoo, J.U. Lee and H.T. Kim, *J. Ind. Eng. Chem.* **11** (2005) (2), pp. 175-179.
[7] I. Demir, *Waste Management*, **28** (2008), pp. 622-627.
[8] M. Dondi, M. Marsigli, B. Fabbri, *Tile and Brick International,* **13** (1997) (1), pp. 218-225.
[9] Ch. Schmidt-Reinholz, *Tile and Brick International,* **6** (1990) (3), pp. 23-27.

Effect of glass preparation on the compressive strength of glass ionomer cement for dental applications

W. Soodsawang*, S. Channasanon, S. Tanodekaew, N. Monmaturapoj

National Metal and Materials Technology Center (MTEC),
114 Thailand Science Park,

Abstract: Glass ionomer cements (GICs) are expansively applied as restorative materials in dentistry. Basically, they are made of fluoroaluminosilicate glass powder combined with a water-soluble polyacid. When the components are mixed together, the cements are set through a neutralization of acid-base reaction. Due to the broad chemical ranges of components, the series of glass ionomer cements are very extensive and the materials are considerably prospective for further investigation. Therefore in this study, several novel fluoroaluminosilicate glass compositions have been produced as potential cement components. The features such as crystalline structure, phase separation and particle shape of glass powder have been investigated with a view to improve the strength of glass ionomer cements. In this work, the spray drying method was used to produce spherical particle shape. XRD and SEM were used to characterized phase present and morphology in the glass ionomer samples, respectively. Particle size analysis of glass ionomer powder was detected by Mastersizer-S Malvern. The result shows the optimized compressive strength when the glass with phase separation was applied with a spherical particle shape at 120 MPa.

Introduction

Conventional glass ionomer cements (GICs) were firstly introduced to the dental material science 30 years ago as a restorative material by Wilson and Kent [1,2]. Originally, GICs consisted of an aqueous polyalkenoic acid such as polyacrylic acid which was reacted with a powder of calcium fluoroaluminosilicate glass under acid-base reaction. The GICs, which offers great properties, are particularly of interest due to their superior advantages such as adhesion to tooth structure, slow release of fluoride, good biocompatibility and a color close to enamel [3]. However, the performance of the original GICs was obstructed by the sensitivity to moisture and the appearance of relatively opaque cements [4]. Therefore, the several ways of GIC modifications were considerably investigated to improve their properties particularly strength and toughness for clinical applications.

In this study, three fluoroaluminosilicate glass compositions have been produced as potential cement components. The features such as crystalline structure, phase separation and particle shape of glass powder have been investigated in order to improve the glass ionomer cement strength. The spherical particle shape was produced by using the spray drying technique [5] to increase cement strength.

Materials and Methods

Glass preparation and characterization: The glass compositions of GI#1-GI#3 were modified from the original composition reported by Hurrell-Gillingham et al. [6] with an approximate Al_2O_3:SiO_2 weight ratio of 1.13 (GI#1) as shown in Table 1. The Al_2O_3:SiO_2 ratio was increased in glass GI#2 to induce phase separation. ZrO_2 was added followed by calcination of glass powder in glass GI#3 to achieve partial crystallization. The glass batches were melted at 1450°C for 2 hrs to make glass frits then ground to attain the mean particle size of 5 μm. Spherical powder was prepared by spraying the glass slurry using a spray dryer (Büchi Mini Spray Dryer, B-290). X-ray diffraction (XRD, JEOL JDX 3530) and X-ray fluorescence (XRF, Philips PW 2404) were performed to identify phase present and composition analyses of glasses, respectively. Particle size of glass powders was analysed using light scattering (Mastersizer). Morphologies of glass particle and cement surfaces were determined by scanning electron microscopy (SEM, JEOL JSM-5410). The commercial GIC, Fuji II, was used as a control throughout the study.

Polyacid preparation and characterization: A copolymers of acrylic acid (AA) and itaconic acid (IA) was produced by free radical polymerization at 90°C for 4 hrs under nitrogen atmosphere using a monomer feed ratio of AA:IA at 4:1. The copolymer (CAI) obtained Mw ≈34700 Dalton and 1.8:1 mole ratio of AA:IA as characterized by Gel Permeation Chromatography (GPC, Waters 600E) and Nuclear Magnetic Resonance Spectroscopy (NMR, Bruker DPX-300 spectrometer), respectively. The CAI solution at the concentration of 55 %wt was made as liquid components for GICs.

Cement fabrication and characterization: The glass powders were mixed with 55%wt of CAI solution, using the weight ratio of 8:3. The cylindrical specimens dimension 6 mm height x 4 mm diameter were made by placing the mixed materials into stainless steel molds. After being stored in an incubator at 37°C±2°C for 1 hr, the specimens were gently removed from the molds, dipped in deionized water and incubated at 37°C±2°C for 23 hrs. Universal Testing Machine (Instron Model 55R4502) at a cross-head speed of 0.75 mm/min was applied to measure the cement compressive strength (CS). The CS was determined by the following equation:

$CS = 4F/\pi d^2$, where F is the maximum applied load (N) and d is a diameter of the specimen (mm).

Results and Discussion

Glass compositions and Al_2O_3:SiO_2 ratios of GI#1-GI#3 before and after melting analyzed by XRF are reported in Table 1. XRF results verified a close similarity in molar composition between the pre- and post-melt, except a small increment of Al_2O_3 observed in post-melting because of the contamination of alumina content from alumina crucible during melting.

Table 1: Compositions of all glass formulae before and after melting coupled with Al_2O_3:SiO_2 ratios

Oxide	Pre-melt glass compositions (%wt)			Post-melt glass compositions (%wt)		
	GI#1	GI#2	GI#3	GI#1	GI#2	GI#3
SiO_2	24.16	22.00	22.24	23.10	21.06	23.16
Al_2O_3	27.26	30.00	20.59	29.64	33.66	25.46
P_2O_5	19.43	19.43	12.77	18.30	17.77	12.02
CaO	15.19	15.19	-	22.16	20.06	1.05
SrO	-	-	22.50	-	-	19.71
CaF_2	13.97	13.97	14.16	6.32	5.67	11.56
ZrO_2	-	-	6.93	-	-	4.45
Total	**100.00**	**100.59**	**99.19**	**99.52**	**98.22**	**97.41**
Al_2O_3: SiO_2	**1.13**	**1.36**	**0.93**	**1.28**	**1.60**	**1.10**

XRD patterns of all glasses presented in Figure 1 showed the amorphous phase of GI#1, phase separation as corundum (Al_2O_3, JCPDS No. 46-1212) of GI#2 and crystallization form of fluorapatite ($Ca_5(PO_4)_3F$, JCPDS No. 15-0876) in GI#3.

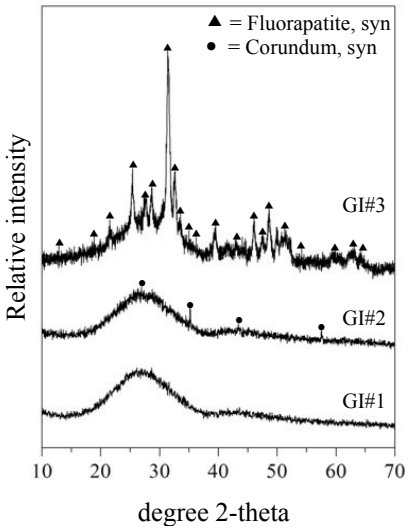

Figure 1. XRD patterns of all glasses

SEM images in Figure 2 illustrated the morphology of all glasses after spray drying as the spherical shape with the mean particle size around ≈25 μm, as reported in Table 2. The particle size of glass powder before spray drying was also measured and presented in Table 2.

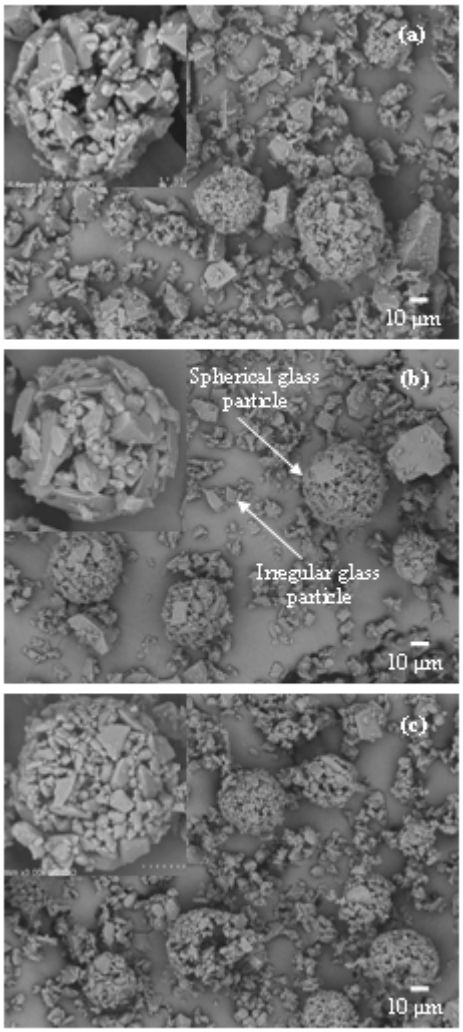

Figure 2. Morphology of glass powders after spray drying process a) GI#1, b) GI#2, and c) GI#3

Table 2: Mean diameter of glass powder

Glasses	Mean diameter/μm	
	Before spray dry	After spray dry
GI#1	7	26
GI#2	6	23
GI#3	6	29
Fuji II	5	57

Table 3 presents the compressive strengths of cements mixed between GI#1-GI#3 powders and 55%wt of CAI solution including the compressive strength of Fuji II cement as a control. The result revealed no trend of increasing in cement strength when the spherical particle was applied. However, the spherical particle eased in cement mixing and molding. The strongest cement with CS of 120 MPa was observed when the phase separation coupled with the spherical shape of GI#2 powder was applied in cement mixing. The partial crystalline glass does not improve the cement strength as expected.

Table 3: Compressive strengths of cements made of GI#1-GI#3; irregular and spherical shapes, and CAI 55%wt

Cements	Mean Compressive Strength/MPa	
	Irregular shape	Spherical shape
GI#1	96.94±6.40	72.30±10.41
GI#2	83.31±6.48	120.07±6.84
GI#3	102.70±14.84	99.32±12.13
Fuji II	89.81±25.26	

SEM images of all cement surfaces illustrated in Figure 3, show few gaps and cracks on the surface of all cements because of the dehydration of the cement samples. Some cracks were occurred around the glass particle-matrix (copolymer) interface, indicating that the interfacial bonding between the glass powders and the matrix was comparatively weak. In addition, some voids can also be observed on the fracture surface owning to air-bubble entrapment within the cements during transferring the mixed cement into the mould cavity. The presence of cracks and voids on the surface area of cements suggested that internal defects and weaknesses in the cements were most likely caused by weakness at the glass particle-matrix interface, leading to the low CS of the cement.

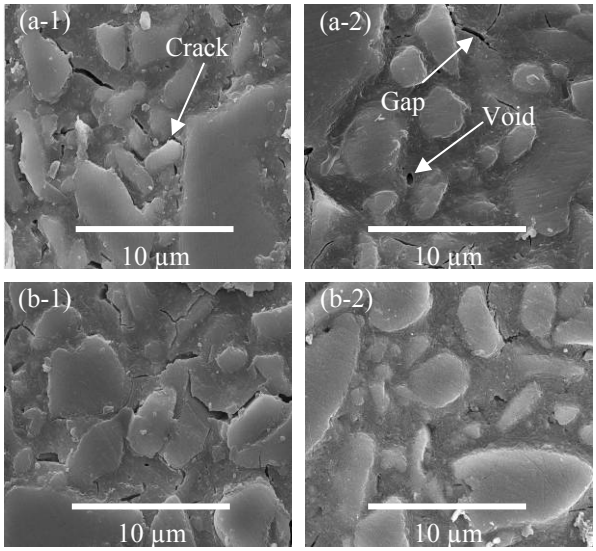

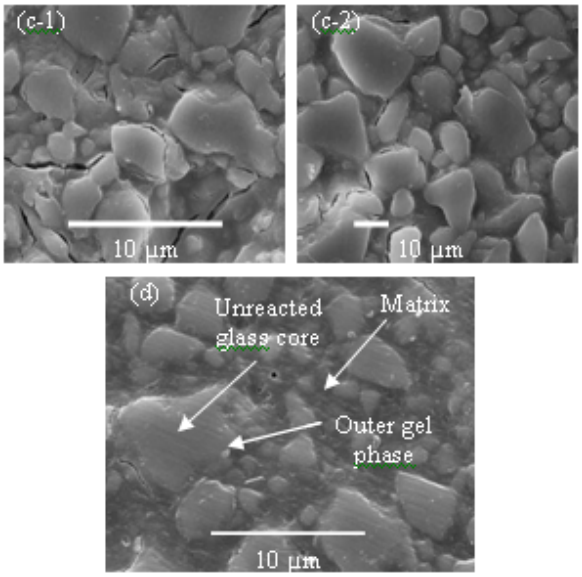

Figure 4. SEM images of cement surfaces: irregular glass particle (left) and spherical glass particle (right) a) GI#1, b) GI#2, c) GI#3, and d) Fuji II

Conclusions

Glass ionomer cement strength was directly affected by the phase present of glass in which phase separation was preferred. The spherical shape of glass powder was also improved the mixing characteristic. In this study, GI#2 which contained phase separation of spherical powder was the optimized glass formula, exhibiting the strongest cement of 120 MPa.

Acknowledgement

This work was performed under the support of National Metal and Materials Technology Center, the Ministry of Science and Technology of Thailand.

References

[1] A.D. Wilson and B.E. Kent, *J. Appl. Chem. Biotechnol.* **21** (1971), pp. 313-317.

[2] Y.W. Gu, A.U.J. Yap, P. Cheang and R. Kumar, *Biomaterials.* **25** (2004), pp. 4029-4035.

[3] S. Hübel and I. Mejàre, *Int. J. Paediat. Dent.* **13** (2003), pp.2-8.

[4] J.W. Nicholson, *Biomaterials.* **19** (1998), pp. 485-494.

[5] R. Vehring, W.R. Foss and D. Lechuga-Ballesteros, *Aerosol. Sci.* **38** (2007), pp. 728-746.

[6] K. Hurrell-Gillingham, I.M. Reaney, C.A. Miller, A. Crawford and P.V. Hatton, *Biomaterials.* **24** (2003), pp. 3153-3160.

Fabrication of fluorcanasite glass-ceramics by using sintered-powder method for biomedical applications

C. Yatongchai*, J. Jaipaew, K. Mai-ngam, N. Monmaturapoj

National Metal and Materials Technology Center (MTEC),114 Thailand Science Park, Pathumthani, Thailand 12120

*E-mail: chokchay@mtec.or.th

Abstract: Several fluorcanasite-based glass compositions had been reported in which obtained an excellent bioactive and biocompatibility, potentially used in hard-tissue augmentation. Previously, fluorcanasite-based glass-ceramics were fabricated by using glass melting process and no attempt to produce through sintered-powder route. In this study, therefore, sintered-powder method was applied on these glass-ceramics compositions for ultimate aim for easily fabricating the required shapes. Three fluorcanasite-based glass-ceramics were produced by controlled two stage heat-treatment of as-cast Glasses A-C. These glasses were modified from stoichiometric fluorcanasite composition ($Ca_5Na_4K_2Si_{12}O_{30}F_4$) by reducing the Na_2O concentration (A), adding excess CaO (B) and P_2O_5 (C). The uniaxial pressing was performed to fabricate the glass powder by varying the pressure from 1.5-8 MPa. Phases and microstructures of all glass-ceramics were examined after heat treatment, including density and shrinkage. The mechanical property was measured by using three-point bending testing. The result shows fluorcanasite, frankamenite, xonotlite, and in some cases fluorapatite were the dominant phase present in the glass-ceramics. The optimized mechanical property was observed in GC_C pressed at 7 MPa (186.40±4.69 MPa). Cell culture experiment shows good *in vitro* biocompatibility for all glass-ceramics.

Introduction

Chain silicate glass-ceramics such as enstatite, K-fluorrichterite and fluorcanasite glass-ceramics were reported in the 1980's to bulk nucleate and have good mechanical properties (BFS > 300 MPa and FT ~ 5 MPa $m^{1/2}$) [1]. More recently, there have been attempts to improve the osteoconductive potential of fluorcanasite glass-ceramics by Miller et al. [2-4] who reduced the Na_2O concentration, increased the CaO content and added in P_2O_5 in several different glass series. *In vitro* biocompatibilities in simulated body fluid (SBF) and in cell culture were subsequently demonstrated by Miller et al. [3] and Bandyopadhyay-Ghosh et al. [5] respectively. Kanchanarat et al. [6] investigated the early stages of nucleation and growth in the fluorcanasite compositions developed by Miller et al. [2-4] using transmission electron microscopy (TEM), which followed on from earlier detailed X-ray diffraction (XRD) work. However, to date, only conventional glass melting route has been applied to fabricate the glasses and there has been no attempt to perform through sintered-powder processing.

This paper, three fluorcanasite glass compositions were produced and fabricated by a uniaxial dry pressing the glass powder followed by sintering process. Not only were the phase present, physical and mechanical properties of the glass-ceramicss investigated but also *in vitro* biocompatibility properties.

Materials and Methods

Standard laboratory grade SiO_2 (Fluka,Belgium) $CaCO_3$, CaF_2 (Merck, Germany), K_2CO_3 (Riedel-de Haen, Germany) Na_2CO_3 (Fluka, Swizerland) and $CaHPO_4$ (Sigma-Aldrich, USA) were used to produce the glass batches listed in Table 1. Compositions were melted for 3 hrs at 1450 °C using an electric furnace in a Pt 2% Rh crucible and were then quenched in water to produce the frit which can subsequently be subjected to a grinding process. The frits were pulverized in zirconia ball mill to achieve the powder having an average particle size less than 15 μm determined by the Mastersizer S (Malvern, UK). After milling, the glass powder was uniaxial dry pressed in a stainless steel mold by varying the pressure from 1.5-8 MPa. The specimens were fabricated by having a dimension with 4x5x35 mm. The specimens were sintered in an electric furnace at the crystallization temperature of 550 °C held for 2 hrs and ramp up to the growth temperature at 850 °C held for 2 hrs with the heating rate of 300 °C/h.

Table 1: Glass compositions (wt%).

Compositions	GC_A	GC_B	GC_C
SiO_2	60.27	58.77	58.42
CaO	14.09	17.10	15.49
CaF_2	13.07	12.78	10.17
K_2O	7.87	7.62	7.57
Na_2O	4.70	3.73	3.74
P_2O_5	-	-	4.62

The physical properties such as firing shrinkage, bulk density and porosity of glass-ceramics specimens were tested by Archimedes' method in deionised water. The fracture strength of sintered samples was determined by three-point bending using a universal testing machine (Instron 55R4502) at a crosshead

speed of 0.5 mm/min. Powder X-ray diffraction (XRD, JOEL JDX3530) was used to identify phase present of specimens after sintering.

Proliferation of human SaOS-2 osteoblast-like cells on glass-ceramics surfaces was equivalent and morphological characteristics of SaOS-2 cells on all tested samples were observed by SEM (JEOL JSM-6301F).

Results and Discussion

Figure 1 shows XRD traces of GC_A, modified by reducing the Na_2O concentration, at different pressing loads. Canasite (JCPDS 13-553) and frankamanite (JCPDS 45-1398) are the major crystalline phase with a minor phase of xonotlite in samples with all pressing pressures. This is in agreement with Kanchanarat et al. [6] and Miller et al. [7] who reported the dominant phases of canasite and frankamanite in flourcanasite heat-treated at 750-950°C.

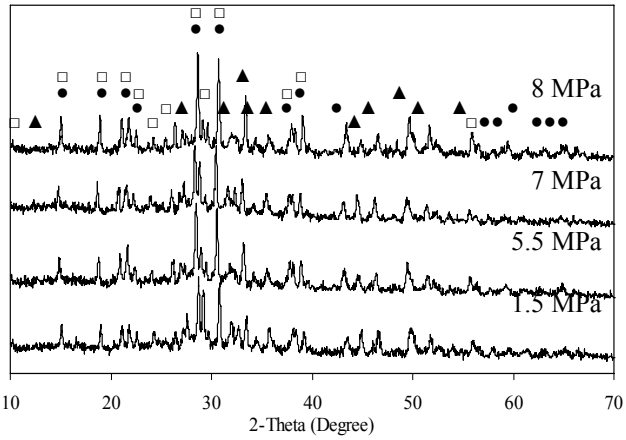

Figure 1. XRD pattern of GC_A, dry pressed at different load after sintering at 850 °C, ●: canasite, □: frankamanite and ▲: xonotlite.

XRD traces of GC_B, excess CaO, heat-treated at 850 °C with different applied loads during pressing show in Figure 2. The result presents the similar manner to GC_A in which canasite (JCPDS 13-553) and frankamanite (JCPDS 45-1398) are the dominant crystalline phase. However, the peaks of xonotlite phase appeared in GC_B are more intense than in GC_A.

Figure 3 presents the XRD patterns of GC_C, added in P_2O_5, at different applied loads during pressing. The major crystallization of canasite (JCPDS 13-553) and fluorapatite (JCPDS 15-0876) can be identified in GC_C including cristobalite (JCPDS 39-1425) coupled with xonotlite as a minor phase in consistent with the observation by Kanchanarat et al. [6] and Miller et al. [7].

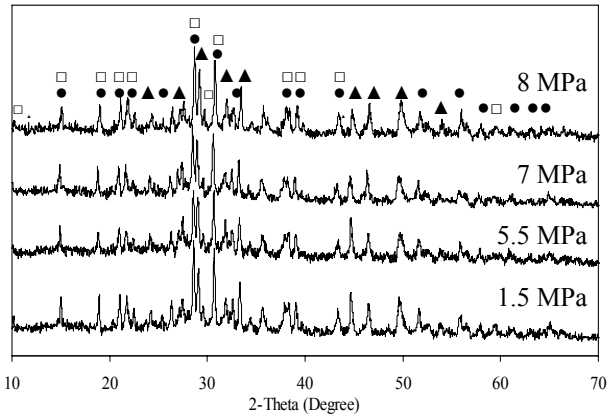

Figure 2. XRD pattern of GC_B, dry pressed at different loads after sintering at 850 °C, ●: canasite, □: frankamanite and ▲: xonotlite.

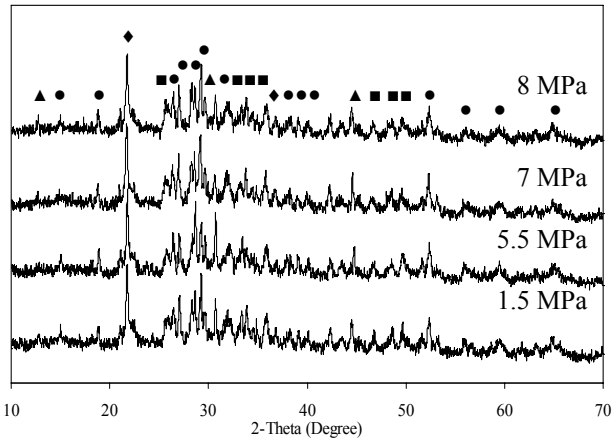

Figure 3. XRD pattern of GC_B, dry pressed at different loads after sintering at 850 °C, ●: canasite ■: fluorapatite, ♦: cristobalite, and ▲: xonotlite.

XRD results reveal the phase present for all glass-ceramics in consistent with the previous studied [6, 7]. This can be concluded that the fabrication of glass-ceramics by using sintered-powder method has no affects on the crystal formation of the studied glass-ceramics. Therefore, the phase formations reported here are the same as that investigated by the conventional glass melting process.

The physical and mechanical properties of glass-ceramics after sintering are shown in Table 2. All glass-ceramics show the decreasing in firing shrinkage when the load applied in dry pressing increased. Due to the increasing in pressing load was induced the packing ability of glass powder during making green samples, leading to the increases of the glass-ceramics bulk density. As a result of that, the density of GC_A also increased with the applied load increased and reached the maximum of 2.385 g/cm^3 at the applied load of 8 MPa.

Similarly, in GC_B and GC_C, the bulk density was increased with increasing the applied loads ranging from 1.5-7.0 MPa and unpredictably decreases when load of 8 MPa was applied. Therefore, the applied load in dry pressing of glass powder was limited less than 7 MPa in GC_B and GC_C.

Table 2: The physical and mechanical properties of all glass-ceramics.

Item	Load (MPa)	Shrinkage (%)	Bulk density (g/cm^3)	Fracture Strength (MPa)
GC_A	1.5	37.70	2.302	71.05
	5.5	35.36	2.359	113.74
	7.0	34.56	2.371	125.71
	8.0	32.70	2.385	138.26
GC_B	1.5	37.64	2.391	75.32
	5.5	36.41	2.423	104.37
	7.0	34.17	2.425	115.12
	8.0	33.03	2.423	102.85
GC_C	1.5	43.34	2.530	164.85
	5.5	38.64	2.532	180.48
	7.0	38.56	2.533	186.40
	8.0	36.37	2.526	178.41

The mechanical strength of all glass-ceramics also reports in Table 2 showing the analogous trend to the bulk density. The strongest GC_A, ≈138 MPa, is observed when the load of 8 MPa applied. Meanwhile, the maximum strength values of GC_B and GC_C were ≈115 MPa and ≈186 MPa, respectively, at the same pressure, 7 MPa. The strongest of GC_C is the result of an intragranular distribution of fluorapatite crystals in glass-ceramics GC_C [6].

It can also be implied that the sinterability of glass-ceramics which was fabricated from glass powder can be enhanced by using a proper applied load during pressing, consequently, the increases in mechanical strength of the glass-ceramics.

SEM images in Figure 4 illustrate the surface of all glass-ceramics before *in vitro* biocompatibility study . The micropores were occurred in the samples unlike the dense samples fabricated by glass melting process. This might be affected on the *in vitro* biocompatibility study.

Figure 4 shows growth curves of SaOS-2 cell on GC_A, GC_B and GC_C. The number of attached cells on all tested surface, represented by fluorescence intensities, were dramatically increased over the entire culture time and their rates of cell growth were equivalent. This is an evidence to indicate the good biocompatibility of all tested glass ceramic surfaces.

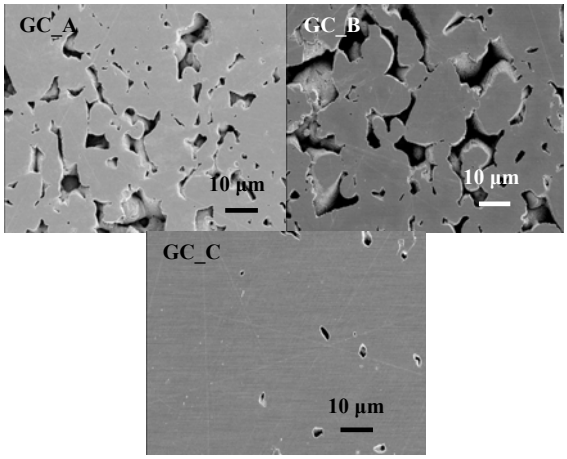

Figure 4. SEM images of all glass-ceramic surfaces.

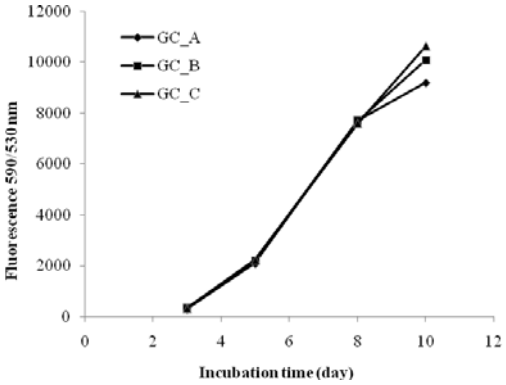

Figure 5. Saos-2 cell proliferation on all tested surface at 1 x 10^4 cells/well.

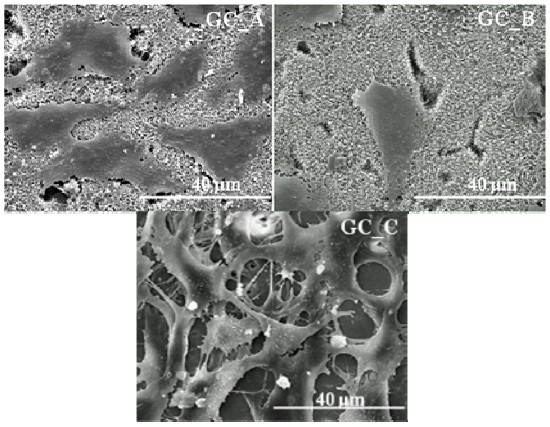

Figure 6. SEM images of SaOs2 cells cultured on glass-ceramic surfaces at day 10^{th}.

More insight in biological compatibility of glass-ceramic was obtained from the SEM observation of SaOS-2 cell morphology. Healthy osteoblast cells with a typical flatted, highly spread morphology were found on all tested GC.

Conclusions

Three fluorcanasite-based glass-ceramics can be successfully produced through sintered-powder route with controlled two stage heat treatment process. GC_A and GC_B have canasite and frankamanite as the major phase and xonotlite as minor phase. Canasite and fluorapatite are the major phases in GC_C with the minor phase of cristobalite and xonotlite. The increasing in applied load during dry pressing enhances the phsysical and mechanical properties of the studied glass-ceramics. The highest flexural strength of GC_A, GC_B and GC_C are ≈138, ≈115 MPa and ≈186 MPa, respectively. All glass-ceramics exhibit good *in vitro* biocompatibility in cells culture.

Acknowledgements

This work was performed under the support of National Metal and Materials Technology Center, the Ministry of Science and Technology of Thailand, under Project No. MT-B-49-BMD-07-131-I.

References

[1] G. H. Beall, J. Non-Cryst. Solids, **129** (1991), pp. 163-173.
[2] C. A. Miller, T. Kokubo, I. M. Reaney, P. V. Hatton and P. F. James, Int. Symp. On Crystallization in Glasses & Liquids, Glastech. Ber. Glass Sci. Technol., **73** (2000), pp. 154-161.
[3] C. A. Miller, I. M. Reaney, P. F. James, P. V. Hatton and T. Kokubo, Proc. Int. Congr. Glass, **2** (2001), pp. 601-602.
[4] C. A. Miller, T. Kokubo, I. M. Reaney, P. V. Hatton and P. F. James, J. Biomed. Mater. Res., **59** (2002), pp. 473-480.
[5] S. Bandyopadhyay-Ghosh, I. M. Reaney, K. Hurrell-Gillingham, I. M. Brook and P. V. Hatton, Key Eng. Mater., **284-286** (2005), pp. 557-560.
[6] N. Kanchanarat, C.A. Miller, P. V. Hatton, P. F. James and I. M. Reaney, J. Am. Ceram. Soc., **88** (2005), pp. 3198-3204.
[7] C. A. Miller, I. M. Reaney, P. V. Hatton and P. F. James, Chem Mater. **16** (2004), pp. 5736-5743

Synthesis and characterization of CuO nanorods by thermal decomposition of CuC_2O_4 precursor

P. Kasian[1*], S. Pukird[1]

Department of Physics, Faculty of Science, [1] Ubon Ratchathani University Ubon Ratchathani, Thailand 34190

[*] E-Mail : pristanuch@hotmail.com

Abstract: CuO nanorods prepared by thermal decomposition of CuC_2O_4 chemical reaction between $Cu(CH_3COO)_2{\cdot}H_2O$ and $H_2C_2O_4{\cdot}2H_2O$ in the presence of the ether $(C_2H_5)_2O_2$ and NaCl flux. The properties of the fabricated nanostructures were studied using scanning electron microscopy and X-ray diffraction. The diffraction peak indicated single phase monoclinic of CuO structure. The diameter of CuO nanorods varied from 100 nm to 200 nm and length of several 10 μm.

Introduction

Recently, quasi one-dimentional (1-D) solid nanostructures (nanowire or nanorods) have been very interesting in scientific research because of their importance with optical, electrical, and magnetic properties and their potential in nanodevice [1-2]. Difference methods have been synthesized nanomaterial, such as vapor liquid-solid (VLS) growth, laser-assisted catalytic growth and templating method[3, 8]. CuO is a p-type semiconductor with a norrow band gap (1.2 eV) [2-3, 5-6]. CuO nanowhisker synthesized by a novel and simple one-step, solid-state reaction in the presence of nonionic surfactant, PEG 400 [4]. The previous investigation reports, synthesis of copper oxide nanorods by thermal decomposition of the precursor of CuC_2O_4 use $Cu(CH_3COO)_2{\cdot}H_2O$ and $H_2C_2O_4{\cdot}2H_2O$ in the presence of surfactant nonyl phennyl ether (9)/(5) (NP-9/5) and NaCl flux. CuO nanorods with diameter of 30-100 nm, and lengths varied from 1 to 3μm [5]. The single crystalline $Cu_2(OH)_2$ nanoribbons precursor used for sacrifice-template via heat-treatments [6]. The CuO nanoribbon are formed a heat treatment of $Cu_2Cl(OH)_3$, which width and average diameter of 50 nm and several micrometer in length [7]. The synthesis CuO nanorods successfully were prepared circumstances of molten salt and heat treatment temperature [8]. CuO nanostructures are formed by simple thermal treatment of peanut-shaped nanoribbon of malachite ($Cu_2(CH)_2CO_3$) [9]. Recently, the synthesis and investigation of flower nanostructure prepared in domestic hydrothermal microwave oven was presented [10]. In this work, the CuO nanostructures were synthesized and characterized of by thermal decomposition of the precursor of CuC_2O_4.

Materials and Methods

In a typical synthesis, copper acetate $Cu(CH_3COO)_2{\cdot}H_2O$, oxalic acid $H_2C_2O_4{\cdot}2H_2O$, ether $(C_2H_5)_2O_2$ and NaCl. A total of 4g of $Cu(CH_3COO)_2{\cdot}H_2O$, 5g of $H_2C_2O_4{\cdot}H_2O$ were mixed with 10 ml of $(C_2H_5)_2O_2$, ground for about 30 min and heat in an oven at 50-60ºC for 6 h. After chemical reaction, we can observe that blue products. The product was washed several time with distilled water and acetone to remove remaining reactants in an ultrasonic bath, then dried in an oven at 70-80ºC for 12 h to get CuO nanoparticle and marked as sample A1. Two grams of A1 mixed with 8g of NaCl powder, and ground for several minutes, then we got sample A2. Sample A2 was annealed at 950ºC for 24 h in alumina crucible and loaded in the center of furnace. After heat treatment, it was cooled to room temperature. The product was washed with distilled water and ethanol several times in an ultrasonic bath. We can observe black color of products, sample A3. The product was characterized by X-ray diffraction (XRD) using X-ray diffractometer with Cu K_α radiation (λ = 1.5405 nm). A scan rate of 0.02º s^{-1} was applied record the pattern in the 2θ range of 20-80º. The morphology and size of nanostructures were investigated by scanning electron microscope (SEM), using voltage of 20 kV on a JEOL-5410 LV.

Results and Discussion

The prepared products were studied the morphologies and elements compound of nanostructures. Fig. 1 shows the XRD pattern of a sample of CuO nanorods prepared by thermal decomposition. The diffraction peak indicated single phase monoclinic of CuO structure, (a = 0.468 nm, b = 0.342 nm, c = 0.513 nm) and data of the JCPDS file no. 5-0661 without peak of impurities such as NaCl and ether $(C_2H_5)_2O_2$**.** The black powder products were prepared by thermal decomposition. The chemical reaction of this process explained by previous report as follows [5].

$$C_2O_4^{2-} + Cu^{2+} \rightarrow CuC_2O_4 \quad (1)$$

$$CuC_2O_4 \rightarrow CuO + CO + CO_2 \quad (2)$$

After heat-treatment, we can observe that the color of CuC_2O_4 changed from blue to black, may be indicate the formation of CuO nanostructures.

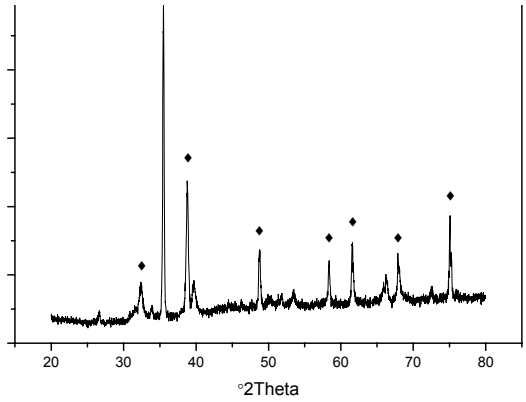

Figure 1. The XRD patterns of CuO nanostructures prepared by thermal decomposition (sample A3).

The SEM morphologies of the synthesized product are shown in Fig. 2. In this figure, we can observe nanorods-like structure of prepared products. The diameter of CuO nanorods varied from 100 nm to 200 nm and length of several 10 μm. This result was look like with previous report [5]. They synthesized by thermal decomposition of CuC_2O_4 from chemical reaction between $Cu(CH_3COO)_2{\cdot}H_2O$, oxalic acid $H_2C_2O_4{\cdot}2H_2O$, in the presence of surfactant nonyl phenyl ether (9)/(5) (NP-9/5) and NaCl CuO nanorods. The results showed the CuO nanorods with diameter of 30-100 nm, and lengths ranging from 1 to 3 μm, which CuO nanrods have size of diameter smaller than our work. But the lengths are longer than their results. CuO nanostructure have been synthesized many methods, Yu et al. [3] synthesized by thermal evaporation CuO nanostructures with diameter vary from about 20-150 nm and lengths several micrometer. However, we can successfully synthesized a large number of CuO nanorods, but some structures of CuO nanorods are also still big size in micrometer scale.

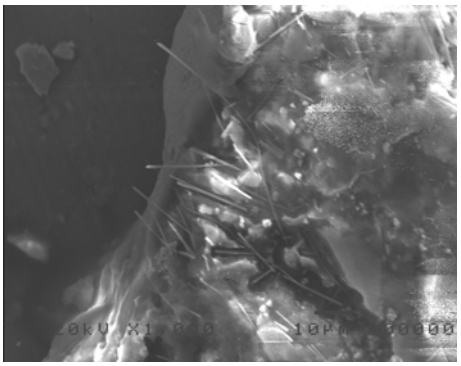

(a)

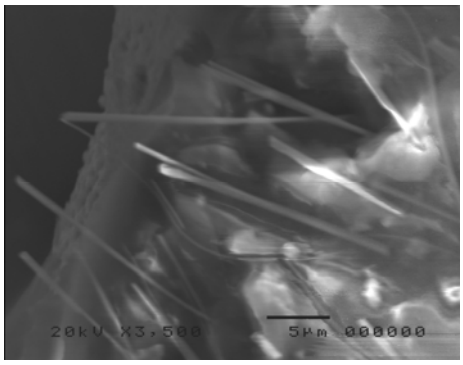

(b)

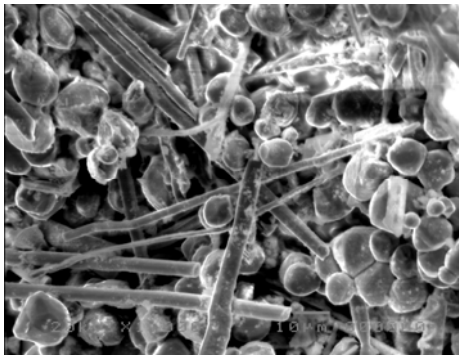

(c)

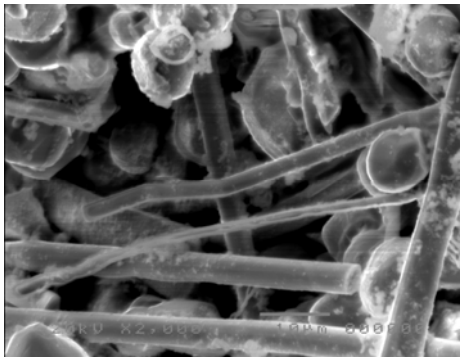

(d)

Figure 2. (a - d) SEM images of the synthesized products.

Conclusions

In summary, single crystal CuO nanorods have been successfully synthesized by thermal decomposition of CuC_2O_4 chemical reaction between $Cu(CH_3COO)_2.H_2O$ and $H_2C_2O_4.2H_2O$ in the presence of the ether $(C_2H_5)_2O_2$ and NaCl flux. The prepared products were studied using scanning electron microscopy and X-ray diffraction instrument. The diameter of CuO nanorods varied from 100 nm to 200 nm and length of several 10 μm. The diffraction peak indicated single phase monoclinic of CuO structure, (a = 0.468 nm, b = 0.342 nm, c = 0.513 nm). These CuO nanorods may be used in nanotechnology.

Acknowledgments

This work is supported by Thailand Research Fund (TRF-MRG-WII525S098) and Ubon Ratchathani University. The authors are grateful to them for financial support.

References

[1] M. Cao, C. Hu, Y. Wang, Y. Guo, C. Guo and E. Wang, *CHEM. COMMUN.* (2003), pp. 1884–1885.

[2] M.S Niasari and F. Davar, *Mater. Lett.* **63** (2009), pp. 441-443.

[3] T. Yu, X. Zhao, Z.X. Shen, Y.H. Wu and W.H. Su, *J. of Crystal Growth* **268** (2004), pp. 590-595.

[4] W. Wang, Y. Zhan, X. Wang, Y. Liu, C. Zheng and G. Wang, *Mater. Res. Bull*. 37 (2002), pp. 1093-1100.

[5] C. Xu, Y. Liu, G. Xu and G. Wang, *Mater. Res. Bull.* **37** (2002), pp. 2365-2372.

[6] C. Zhu, C. Chen, L.Y. Hao, Y. Hu and Z.Y. Chen, *Solid State Communications* 130 (2004), pp. 681-686.

[7] C.L. Zhu, C.N. Chen, L.Y. Hao, Y. Hu and Z.Y. Chen, *J. of Crystal Growth* **263** (2004), pp. 473-479.

[8] W. Jisen, Y. Jinkai, S. Jinquan and B. Ying, *Mater. and Design* **25** (2004), pp. 625-629.

[9] L. Zhang, J.C. Yu, A.W. Xu, Q. Li, K.W. Kwong and S.H. Yu, *J. of Crystal Growth* **266** (2004), pp. 545-515.

[10] D.P. Volanti, D. Keyson, L.S. Cavalcante, A.Z. Simões, M.R. Joya, E. Longo, J.A. Varela, P.S. Pizani and A.G. Souza , *J. Alloys and Comp.* **459** (2008), pp. 537-542.

(Chitosan/SDS)-stabilised emulsions

K. Phaenthong, R. Chantateyanont, P. Sunintaboon, and T. Vongsetskul*

Department of Chemistry, Faculty of Science, Mahidol University, Rama VI Road, Ratchathewee, Bangkok, 10400, Thailand

*E-mail: scthammasit_v@staff2.mahidol.ac.th

Abstract: Emulsions are thermodynamically unfavoured system. Normally, the emulsion is conventionally prepared using an emulsifier, which is normally a surfactant to improve the miscibility between two immiscible phases. However, the use of surfactants may result in unfavoured impact on human. Therefore, the reduction in the use of surfactant for preparing the emulsion has been one of the most interesting research topics in colloid science. In this study, the complexes between chitosan (CS), a biopolymer, and sodium dodecyl sulphate (SDS), the most commonly used surfactant, have been used. The effects of CS lengths (45 and 100 kD) and CS concentrations (50, 100, and 150 ppm) on the size and the stability of (CS/SDS)-stabilised emulsion have been studied using ζ-potential, droplet size and turbidity measurements. The ζ-potential results suggest that the CS/SDS complexes be surrounded the oil droplets as the ζ-potential became more positive (-33.7 mV at CMC for SDS-stabilised emulsions to 84.0 mV at CMC for (100 kD CS/SDS)-stabilised ones). These results were consistent with the droplet size ones in which CS/SDS-stabilised emulsions were slightly increased due to the layer of polymer/surfactant complexes. The turbidity results also suggest that the stability of (CS/SDS)-stabilised emulsions increased significantly. In conclusion, the particle size and the ζ-potential indicated that the presence of CS/SDS complexes around the emulsions result in the improvement of the emulsion stability significantly.

Introduction

An emulsion is a dispersion of one liquid in another liquid in which the two liquids are obviously immiscible. In general, emulsions consist of at least three components: two immiscible liquids and emulsifier, a substance enhancing a miscibility of two liquids. From all types of emulsions, the most common types of emulsions are oil-in-water emulsion stabilised by surfactants. These types of emulsions are macroscopically homogeneous mixtures which consist of individual domains of oil and water separated by a monolayer of amphiphile. These types of emulsions have been widely used in food, pharmaceutical and cosmetic applications [1]. Based on the emulsion composition, the most decisive factor determining the emulsion stability is emulsifier. Unfortunately, although emulsifier could improve the miscibility between two liquids, they tend to revert to the original states because of the thermodynamic driving force. Therefore, the stability of the emulsions has been one of the most studied topics in chemistry, engineering, and life sciences.

To overcome the above addressed problems, the use of polymer/surfactant complexes is one of the several approaches to increase the emulsion stability. There are several types of surfactants and polyelectrolytes standing as good candidates for improving the emulsion stability. In this study, sodium dodecyl sulphate (SDS) and chitosan (CS), a cationic biopolymer, have been studied because SDS is one of the most commonly used surfactants and CS, a biopolymer, shows several promising properties for further medical, food, and biological applications such as good biocompatibility, biodegradability, and low toxicity.

There are several studies on the use of CS/SDS as an emulsifier for preparing O/W emulsions. For examples, Mun *et al* [2] have studied the formation of O/W emulsion stabilized by CS/surfactants (SDS or Tween 20) layers to find the optimum conditions for preparing stable O/W emulsions. It was found that the droplet charge changed from negative to positive as the amount of CS in the emulsions increased. However, when the CS concentration reached a critical CS concentration (C_{Sat}), there is no change in the droplet charge because of the saturation of the droplet surfaces with CS. Extremely large droplet aggregates were formed when CS concentration was lower than $C_{Sat.}$ When CS concentration was higher than C_{Sat}, stable emulsions could be formed. Therefore, the droplet size was not large enough for depletion flocculation to occur. Also, interestingly, stable multilayer emulsions could also be formed when nonionic surfactant had been used instead of anionic one.

Djordjevic *et al* [3] studied comparatively between gum acacia-stabilised emulsions and SDS/CS-stabilised ones. It was found that SDS/CS complex outperformed gum acacia as measured by reduced *p*-cymene formation from citral over a period of time. CS had a net positive charge at pH 3.0 and could repel iron ions in solution.

Recently, alginate nanocapsules containing turmeric oil were prepared in a three-step procedure using emulsification, crosslinking with calcium chloride, and solvent removal by Lertsutthiwong *et al* [4]. They found that dissolution of turmeric oil in ethanol with the presence of Tween 80® were optimal for the preparation process. An increase in oil concentration or oil/alginate mass ration resulted in an increase in the average size of the nanocapsules. Besides, alginate nanocapsules showed good physical stability in long-term storage at 4°C. However, the

loading capacity of turmeric oil in the nanocapsules measured by HPLC was relatively low.

Even though, there are several studies on the preparation and characteriation of CS/anionic surfactant-stabilised emulsion, the study to understand some of the fundamental parameters is rare and the need to understand the effect of these factors is required. In this work, the effects of surfactant concentration, CS length, and CS concentration on emulsion size and emulsion stability have been studied.

Materials and Methods

2.1. Materials

Chitosan (CS) with molecular weights of 45 kD and 100 kD were purchased from Seafresh Chitosan (Lab) Company Limited, Bangkok, Thailand. Commercially available mineral oil (Drakeol® 7 LT MIN OIL NF) was purchased from Connell Brothers Company Limited (Thailand), Bangkok, Thailand. Acetic acid was purchased from Lab Scan Company Limited. Sodium dodecyl sulfate (SDS) was purchased from Fluka Chemicals. All chemicals were used as received.

2.2. Preparation of CS/SDS Mixtures

CS/SDS mixtures were prepared in acetic acid solution (pH = 2) to ensure that all amino groups in the CS structure were protonated. Both 45 kD and 100 kD CS were used to study the effect of CS length on CS/SDS interaction and on mineral oil-loaded emulsion stability. The CS concentrations were 50, 100, and 150 ppm, and the SDS ones were 5 x 10^{-5}, 10^{-4}, 5 x 10^{-4}, 10^{-3}, 5 x 10^{-3}, and 10^{-2} M.

2.3. Preparation of Emulsions

48.5 ml of all the mixtures mentioned above were mixed with 1.50 ml of mineral oil. Then, they were introduced to ultrasonicator (Sonopuls HD2200, Bandelin Electronic, Germany). The mixtures were sonicated for 5 minutes at a frequency of 20 kHz and an amplitude of 70 %. The emulsions were obtained as dispersion in aqueous solution and characterised further. It should be noted that the mineral oil-loaded emulsions were kept at room temperature to study the effect of CS length, CS concentration and surfactant concentration on emulsion stability.

2.4. Turbidity Measurements

First, the absorbance of the diluted mixtures (0.4%) was measured at 600 nm using a UV-visible spectrophotometer (Lamda 35, Perkin Elmer, USA). Then, the absorbance data was converted to turbidity via the equation (1).

$$T = 2.303 \times (A/l) \qquad (1)$$

where T = Turbidity
A = Observed Absorbance
l = Cuvette Pathlength (cm)

2.5. Zeta Potential Measurements

The electrical charge of the SDS-stabilised and (CS/SDS)-stabilised emulsions were measured using an electrophoresis machine (Zetasizer, model Nano-ZS, Malvern Instruments, England). Freshly prepared emulsions were diluted with distilled water. Then, the prepared emulsions were introduced to the instrument for measuring the emulsion surface charge.

2.6. Size Measurements

The average size of SDS-stabilised and (CS/SDS)-stabilised emulsions were determined using a dynamic light scattering instrument (Mastersizer 2000, Malvern Instruments, England) when distilled water was used as a background.

Results and Discussion

Three important results were presented here which are the sizes, the Zeta potentials, and the turbidity of prepared emulsions.

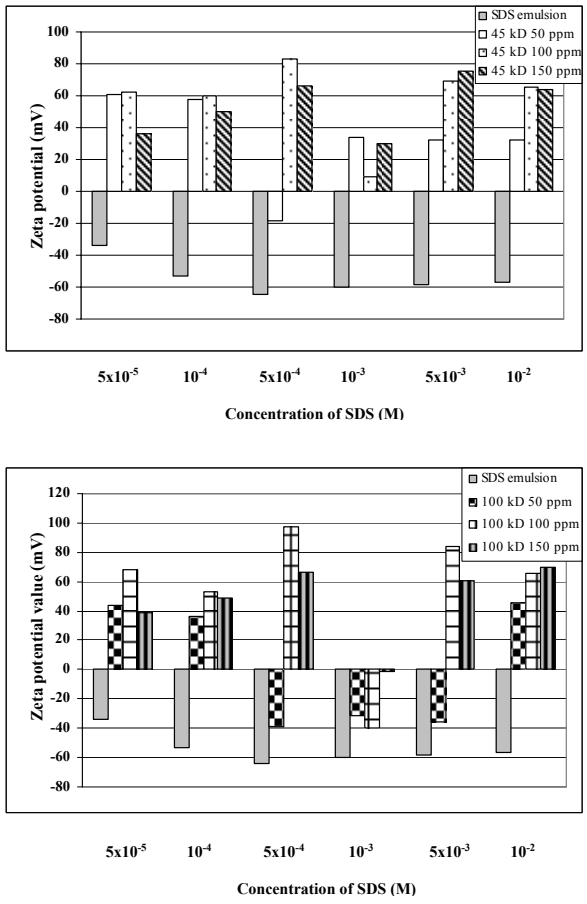

Figure 1. Shows the Zeta potentials of prepared emulsions when the emulsions were stabilised by 45 kD CS/SDS (upper) and by 100 kD CS/SDS (lower). The Zeta potential of SDS-stabilised emulsions was presented as a reference.

Figure 1 shows the negative electrical charges of the SDS-stabilised emulsion for the whole range of [SDS] which indicates the presence of negative charged species (SDS) on the emulsion surface. When the SDS was added, the potential of the surface became more negative as the SDS molecules were attached to the emulsions. However, when the SDS concentration reached the value of 5 x 10^{-4} M, the electrical charge of the emulsion surface became constant which suggest the saturation of SDS molecules on the emulsion surface.

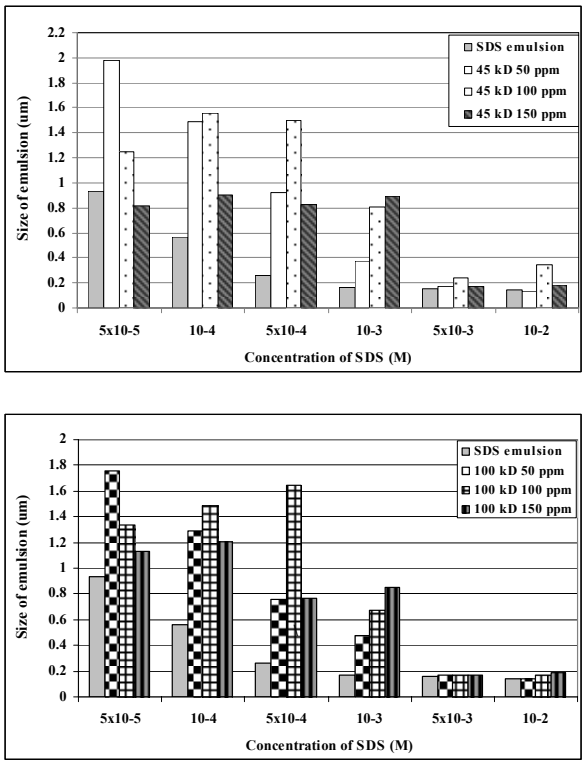

Figure 2. Shows the average sizes of prepared emulsions when the emulsions were stabilised by both 45 kD CS/SDS complexes (upper) and 100 kD CS/SDS complexes (lower).

Figure 2 shows the decrease of SDS-stabilised emulsion size when the SDS was added. Because of the saturation of SDS molecules on the emulsion surface, there is no change in the emulsion size when the SDS concentration reached the value of 5 x 10^{-4} M. Therefore, both size and Zeta potential results suggest that the SDS-saturated emulsion concentration was 5 x 10^{-4} M. The size of the obtained emulsions was about 0.20 micrometer.

Figure 3 shows the turbidity of the prepared emulsions. In general, the mixtures in which the oil droplets are emulsified well are cloudy. The mixtures, in which the miscibility between water and oil is poor, is clear and the phase separation can be observed. Therefore, the turbidity of the mixtures could be used as an indicator to measure the miscibility of the oil-in-water emulsion. The experimental data on the turbidity measurements will be discussed later for each SDS concentration. When CS was added, the CS molecules were absorbed at the emulsion surface as the Zeta potential became positive.

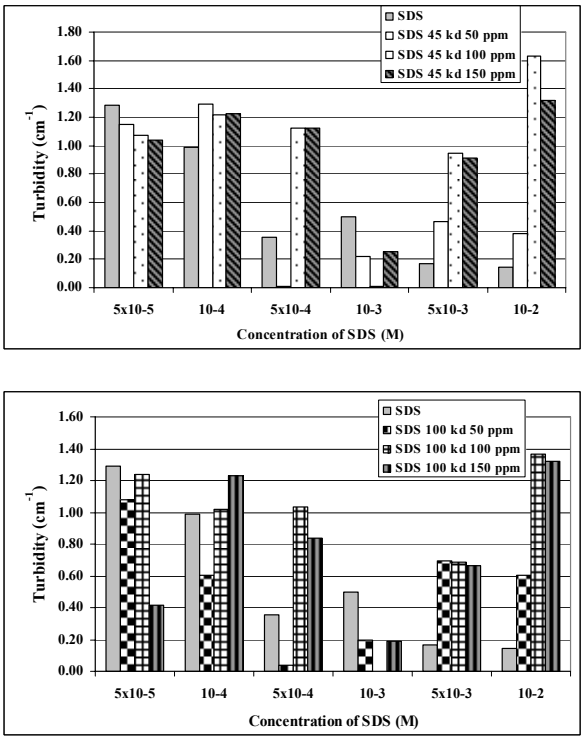

Figure 3. Shows the turbidity of (45 kD CS/SDS)-stabilised emulsion (upper) and turbidity of (100 kD CS/SDS)-stabilised one (lower). The size of SDS-stabilised emulsion was presented as a reference.

Figure 2 suggest the increase of the emulsion size when CS was added. This resulted from the adsorption of CS chain on the emulsion surface. Therefore, both the Zeta potential results and the size measurement ones suggest the presence of CS molecules surrounding the emulsions. In this paper, the effect of SDS concentration on the prepared emulsion would be discussed for each SDS concentration.

When the SDS concentration was in the range of 5 x 10^{-5} and 10^{-4} M, all the (CS/SDS)-stabilised mixtures behaved similarly. The sizes of the prepared emulsions increased and the electrical charges became positive because of the reasons as mentioned earlier. However, the turbidity of the (CS/SDS)-stabilised emulsions was lower than that of SDS-stabilised emulsion for the 5 x 10^{-5} M mixtures. Therefore, the miscibility of the (CS/SDS)-stabilised emulsions were lower than that of SDS-stabilised one which resulted from the added CS chains were not adsorbed on the emulsion surface totally. Some of the CS chains were in the bulk solution, for some SDS molecules were detached from the emulsion surface to form the complexes with SDS in the bulk solution. Surprisingly, when the [SDS] was 10^{-4} M, the turbidity of the (CS/SDS)-stabilised mixture was higher than that of SDS-stabilised one. These results suggest that the CS was adsorbed on the emulsion surface mainly which caused the increase of

size, electrical charge and turbidity (or miscibility) of the 10^{-4} M mixture.

When the SDS concentration was 5 x 10^{-4} M, the (CS/SDS)-stabilised emulsion shows two different types of behaviour. The (50 ppm CS/SDS)-stabilised emulsion's potentials became negative which resulted from the detachment of CS chains from the emulsion surface. The turbidity of the (50 ppm CS/SDS)-stabilised emulsions was lower than SDS-stabilised emulsions. These results suggest that the miscibility of two phases decrease when the CS was added at the concentration of 50 ppm. However, the sizes of the (CS/SDS)-stabilised emulsions were still larger than that of SDS-stabilised one. Therefore, all the results suggest the partial detachment of the CS/SDS complexes from the emulsion surface. These complexes were formed in the bulk solution instead. The (100 ppm and 150 ppm CS/SDS)-stabilised emulsions showed the different physical properties from the (50 ppm CS/SDS)-stabilised counterpart. The electrical charges of the emulsion surface became more positive which suggest that more CS chains were attached to the emulsion surface. The differences in the physical properties of these emulsions could be explained as follows. Normally, CS formed the complexes with SDS on the emulsion surface. However, when the SDS was added, the 'free' SDS in the bulk solution induced the CS chain to be detached from the emulsion surface and formed the complexes with SDS in the bulk solution instead. In these experiments, the more concentrated CS mixtures behaved differently because the number of CS chain is greater than that of SDS molecules. Therefore, there was no 'free' SDS in the bulk solution. As a result, all the added SDS molecules formed the complexes with CS at the emulsion surface. These explanations were also confirmed by the turbidity measurements. The turbidity (or miscibility) of (50 ppm CS/SDS)-stabilised emulsion was lower than that of SDS-stabilised one, while that of (100 ppm and 150 ppm CS/SDS)-stabilised emulsions was greater.

When the SDS concentrations were 10^{-3} and 5 x 10^{-3} M, all the (CS/SDS)-stabilised mixtures showed the destabilisation of the emulsions and the inhomogeneous mixtures. The charges of the SDS were neutralised by the CS charges and caused some of the CS/SDS complexes detaching from the emulsion surface. Therefore, the number of active SDS molecules stabilising the emulsions decreased. The Zeta potential results also suggest the detachment of the CS/SDS complex as the electrical charges of the emulsion surface decreased. However, the turbidity of the (CS/SDS)-stabilised emulsions was complex. The turbidity of (CS/10^{-3} M SDS)-stabilised emulsions was consistent with the other results which indicates the destabilisation of the emulsions. Even though the turbidity of the mixtures should be lower for (CS/5 x 10^{-3} M SDS)-stabilised emulsions than that of SDS-stabilised one theoretically, the turbidity of these mixtures was greater. This resulted from the presence of the large CS/SDS aggregates, which increase the turbidity of the mixtures greatly. The large CS/SDS started to form when the SDS concentration was not lower than the critical micelle concentration (CMC) value. These aggregates also occur in the (CS/10^{-2} M SDS)-stabilised emulsions.

When the SDS concentration was 10^{-2} M, the emulsion surface potential increased again. However, the electrical charges of the (CS/SDS)-stabilised emulsions at this concentration were slightly less positive when compared to those at low SDS concentrations (5 x 10^{-5} and 10^{-4} M). These results suggest the lower amount of CS/SDS complexes at the emulsion surface. Also, these results were consistent with the size measurement ones which the emulsion sizes of (CS/SDS)-stabilised emulsions were close to that of SDS-stabilised one. Therefore, the emulsions were now stabilised by SDS as well. This resulted from the competition in the CS/SDS complex formation between at the emulsion surface and in the bulk solution. Because SDS molecules occupied both on the emulsion surface and in the bulk solution, CS formed the complexes in both regions. It differs from surfactant-diluted mixtures which the SDS molecules occupied the emulsion surface mainly.

In conclusion, there are two main factors affecting the behaviour of emulsions which are CS concentration and CS length. The CS concentration affects the physical properties of the emulsions largely on the [SDS] in the range from 5 x 10^{-4} to 5 x 10^{-3} M as mentioned earlier. Figure 3 shows that the turbidity of (45 kD CS/SDS)-stabilised emulsions was slightly greater than that of (100 kD CS/SDS)-stabilised emulsions which suggest the better ability to form the complexes with SDS of 45 kD CS. This could be explained as follows. To form the complex with SDS, CS chains have to be stretched to maximise the interaction between CS and SDS and result in the loss of entropy. Therefore, the short CS formed the complexes with SDS at the surface better than the long CS did because the degree of order of stretched long chain is higher than that of stretch short one.

Conclusions

CS/SDS complexes improved the stability of prepared O/W emulsions significantly. Sonication is required for size homogeneity.The SDS concentrations, CS chain lengths, and CS concentrations have influenced the size and physical properties of the prepared emulsions.

References

[1] L. Payet and E. M. Terentjev, *Langmuir*. **24** (2008), pp. 12247-12252.

[2] S. Mun, E. A. Decker and D. J. McClements, *Langmuir*. **21** (2005), pp. 6228-6234.

[3] D. Djordjevic, L. Cercaci, J. Alamed, D. Julian McClement and E. A. Decker, J.Agric. Food Chem. **55** (2007), pp. 3585-3591.

[4] P. Lertsutthiwong, K. Noomun, N. Jongaroonngamsang, P. Rojsitthisak and U. Nimmannit, *Carbpohyd polym*. **74** (2008), pp. 209-214.

Effect of preparation method on mechanical properties of natural rubber-organoclay composites

A. Khamkhreung[1], S. Thanawan[2] and T. Amornsakchai[3*]

[1]Polymer Science and Technology Program, Faculty of Science, Mahidol University, Salaya, Nakhom Pathom, 73170.
[2]Institute of Molecular Bioscience, Mahidol University, Salaya, Nakhon Pathom, 73170.
[3*]Center for Alternative Energy, Department of Chemistry and Center of Excellence for Innovation in Chemistry, Faculty of Science, Mahidol University, Salaya, Nakhon Pathom, Thailand 73170.

[*] E-mail: sctam@mahidol.ac.th

Abstract: This study compared mechanical properties of natural rubber (NR) – organoclay composites prepared by mechanical mixing and solution mixing methods. The amount of organoclay was used varied from 0 to 8 phr and the effect of preparation method was investigated. It was found that solutions mixing provide composites with better clay dispersion than mechanical mixing as revealed by XRD. An exfoliated structure was observed for solution mixing while intercalated structure was observed for mechanical mixing systems. Moduli at 100% and 300% elongation and tensile strength were found to increase with increasing organoclay content. Solutions mixed composites were found to provide higher moduli at both elongations for all organoclay contents. However, no significant difference was observed for ultimate tensile strength among the two composites upto an organoclay content of 4 phr. At organoclay content of 8 phr, ultimate tensile strength for solution mixed composite still increased slightly while that of mechanically mixed composite dropped. An increase of 41.4% in tensile strength at organoclay content of 8 phr compared to control NR without clay was obtained for solution mixed system.

Introduction

Recently, polymer-clay composites have received a great deal of attention. However researches on rubber-clay, especially natural rubber, are much less reported. Clay minerals are composed of silicate layer 1 nm thick and about 200-300 nm in lateral directions. The structure contains one octahedral between two tetrahedral layers and weak intermolecular (Van der Waals) force occurs between them [1]. The very high aspect ratio of the structure is ideal for reinforcement. Generally, the Na^+ and Ca^{2+} cations are usually replaced by organic cation via ion exchange reaction to make the clay more hydrophobic and compatible with the polymer [2]. Polymer clay composites are divided into 3 types: phase-separated or conventional micro-composites, intercalated and exfoliated nanocomposites [3]. When incorporated into the polymer, the high aspect ratio nanocomposites are expected to enhance the polymer properties [4,5]. For many rubbery materials, such as styrene-butadiene rubber, polybutadiene rubber, nitrile butadiene and natural rubber, mechanical properties, barrier properties, flame resistance, electro-optical properties and cosmetic applications were improved through incorporating nanolayer of silicate [6].

In this work, the effect of preparation method, i.e. mechanical mixing and solution mixing, on mechanical properties of NR-organoclay composites were studied.

Materials and Methods

2.1. Materials

Natural rubber was STR 5L manufactured by MBJ Enterprise. An organoclay was Claytone HY, a Montmorillonites based organoclay manufactured by Southern Clay Product. Its specific gravity is 1.6. All other rubber chemicals were commercial grade and purchased from Flexsys.

2.2. Preparation of NR-organoclay composites.

Solution mixing: Predetermined amount of natural rubber was swollen in toluene for 1 day. In a separate container, predetermined amount of oranoclay was dispersed in 100 ml toluene with a homogenizer operating at 14,000 rpm. for 45 minutes. The organoclay dispersion was then poured into rubber/toluene solution. Vigorous stirring was maintained for 3 hour. The mixture was then poured into a metal tray. The solvent was allowed to evaporate in the fume hood until the weight of the NR-organoclay sample became constant. NR-organoclay compound was then obtained.

Mechanical mixing: NR was mixed with organoclay in an internal mixer for 15 minutes at 50 °C. Then, NR-organoclay compound was obtained.

Both types of NR-organoclay compound were mixed with curing agent in a two-roll mill according to formulation shown in Table 1. Vulcanization time for each composite was determined with a moving disk rheometer (MDR). For each composite, sheet with 1 mm thick was compression moulded at 155 °C and tested with tensile test.

The internal morphology of NR-organoclay composites was studied with SEM. The surface of the samples was removed with a microtome and then etched with a permanganic acid solution. The samples were then coated with gold and studied with a Hitachi S-2500 SEM operated at an accelerating voltage of 15 kV.

Table 1: Formulation of the organoclay filled natural rubber composites

Materials	Part per hundred rubber (phr)
Natural rubber	100
Zinc oxide	5
Stearic acid	2
CBS	1
TMTD	0.1
Sulfur	2
Organoclay	0, 2, 4, 8

Results and Discussion

X-Ray Diffraction (XRD)

XRD of NR-organoclay composites are shown in Figure 1. The pristine organoclay shows a strong peak at 2θ = 2.67° which corresponds to *d*-spacing of 3.27 nm. For mechanical mixing system, the main organoclay peak shifted to 2.1° which correspond to a wider *d*-spacing of 4.1 nm. In the case of solution mixing system, no strong peak is observed suggesting that the ordered structure in organoclay had been largely altered. It is believed that NR chains could diffuse in between the silicate layers of organoclay [2]. Therefore, it may be said that NR composite prepared by solution mixing shows exfoliated structure. For mechanical mixing systems, NR chains could only intercalate the organoclay structure [3].

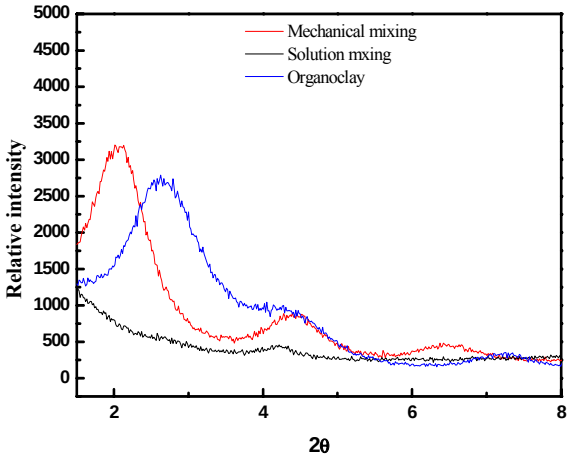

Figure 1. XRD patterns of NR-organoclay composites with 4 phr of organoclay

Mechanical Properties

Stresses at 100% (M100) and at 300% elongation (M300) of NR-organoclay composites are shown in Figure 2. It can be observed that both properties increase with the amount of organoclay. It clearly shows that organoclay is good reinforcing filler for NR. This is due to its characteristic of high aspect ratio [2]. When M100 and M300 of the two composites are compared, it is clear that composites prepared using solution mixing have higher M100 and M300. The greater improvement in solution mixed composites could be very well due to better dispersion of organoclay as seen in WAXD results.

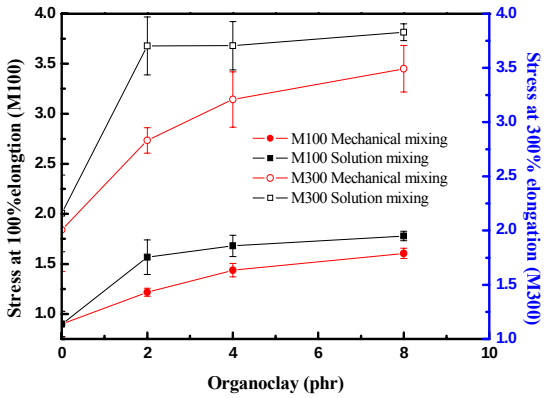

Figure 2. Stresses at 100% (M100) and 300% elongation (M300) of NR-orgaoclay composites prepared by different methods.

The tensile strength of organolcay-NR composites of various organoclay loading are shown in Figure 3. The tensile strength of both systems increased with increasing organoclay loading up to 4 phr. At 8 phr, the strength of solution mixing system continued to increase slightly while that of mechanical mixing system dropped significantly. It is believed that this drop is caused poor dispersion in which aggregation of clay was still remained in the composite [2]. It is clear that solution mixing system shows greater improvement than mechanical mixing system. The tensile strength of solution mixing system was approximately 41.4 % higher than that of NR (0 phr of clay).

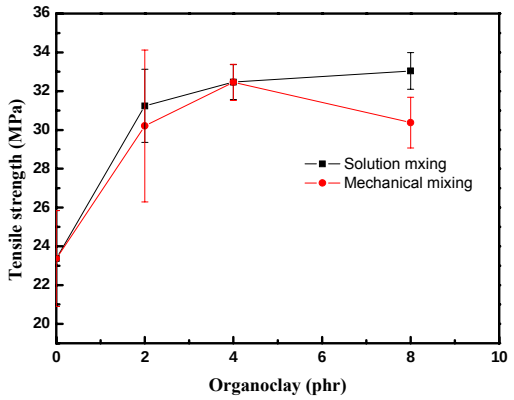

Figure 3. Tensile strength of NR-organoclay composites prepared by different methods.

Elongation at break of NR-organoclay composites are shown in Figure 4. It can be seen that the

elongation at break of both systems are very similar and slightly higher than that of NR. For both systems, elongation at break increased with increasing organoclay loading upto 4 phr and then dropped slightly at 8 phr. It may be due aggregations at high organoclay loading which could act as stress concentraters and cause the composites to fail [8]. However, the elongation at break of the composites is still higher than that of NR.

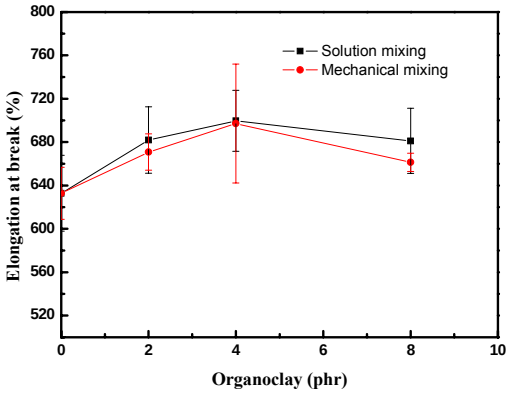

Figure 4. Elongation at break of NR-orgaoclay composites prepared by different methods.

SEM Study

The SEM images of controlled NR, NR-organoclay composites with 4 phr of organoclay loading prepared by mechanical mixing and solution mixing system are shown in Figure 5. NR shows very smooth surface. Organoclay particles can be seen in both composites. The dispersion of organoclay in mechanically mixed composite (Figure 5(b)) is not very good. Large aggregates can be clearly seen. On the other hand, the distribution and also dispersion of organoclay in solution mixed composite is much better. This is in agreement with the XRD results shown previously.

Conclusions

NR-organoclay composites were prepared by solution and mechanical mixing. The former method provides composites with better organoclay dispersion. Composites prepared by solution mixing also demonstrated higher stiffness, as seen from M100 and M300. However, both composites displayed similar improvement in tensile strength upto an organoclay content of 4 phr. Beyond this value, composites prepared by mechanical mixing displayed a significant drop in tensile strength while that prepared by solution mixing still increased slightly. The improvement was about 41.4 % at 8 phr of organoclay compared to NR without clay

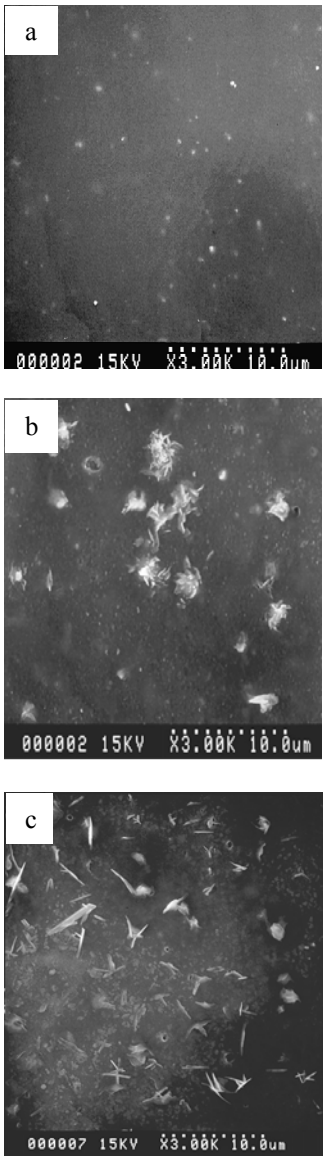

Figure 5. Surface morphology of controlled NR (a), NR-orgaoclay composites prepared by mechanical mixing (b) and solution mixing (c).

References

[1] B. Jurnowska, B. Jurkowski, M. Oczkowski, S.S. Pesetskii, V. Koval and Y.A. Olkhov, *J. Appl. Polym. Sci*. **106** (2007), pp. 360-371.

[2] H. Ismail and R. Ramli, *J. Reinf. Plast. Comp.* **27** (2008), pp. 1909-1924.

[3] U.N. Ratnayake and B. Haworth, *Polym. Eng. Sci*. **46** (2006), pp. 1008-1015.

[4] Y. Zhong, D. Janes, Y. Zheng, M. Hetzer and D.D. Kee, *Polym. Eng. Sci.* **47** (2007), pp. 1101- 1107.

[5] D.R. Paul and L.M. Robeson, *Polymer*. **49** (2008), pp. 3187-3204.

[6] M.S. Kim, G.H. Kim and S.R. Chowdhury, *J. Polym. Eng. Sci*. **47** (2007), pp. 308-313.

[7] A. Gaguly, M.D. Sarkar and A.K, Bhowmick, *J. Appl. Polym. Sci*. **100 (**2006), pp**.** 2040-2052.

[8] J.K. Mishr, K.J. Hwang and C.S. Ha, *J. Polym. Sci.* **46 (**2005), pp**.** 1995-2002.

Preparation of SiO_2 and Si from rice husk ask

S. Pukird[1*], P. Kasian[1], K. Noipa[1], S. Sumran[1], U. Tipparach[1] and P. Limsuwan[2]

[1]Department of physics, Faculty of science, Ubon Ratchathani University,Ubon Ratchathani, Thailand, 34190
[2]Department of Physics, Faculty of Science, King Mongkut's University of Technology Thonburi, Bangkok, Thailand, 10140.

[*] E-mail: supakorn@sci.ubu.ac.th

Abstract: High purity SiO_2 was prepared by burning rice husk in a furnace at temperature of 600°C in normal atmosphere. The rice husk firstly was soaked in 1 M hydrochloric acid solution for 1 hour, and then rinsed in distilled water and dried in air. The acid-treated rice husk was heated in the furnace with air circulation for 1 hour. The purity of SiO_2 in silica ash was studied. The silica ash mixed with Mg or Al and coconut shell charcoal were heated at various temperature and atmosphere in furnace again. After, the furnace was cooled down to room temperature, naturally. The products were treated by hydrofluoric acid and washed in distilled water several times, then filtered. The prepared products were investigated by X-rays diffraction instrument. The high purity of Si prepared from rice husk ash was observed.

Introduction

Rice husk (or rice hull) is an agricultural residue abundantly available in rice producing Thailand. The number of rice production of world is approximate 400 million metric tons per year. 10 % of rice husk is a by-product of rice milling process [1]. It consists 13-29 % inorganic components, of which 87-97 % is SiO_2 (silica) in an amorphous state [2]. The major contamination are metal oxides such as Na, K, Mg, Ca and Fe and silicates can vary from 3 to 13 % in ash. They can be eradicated easily by acid-leaching, while life-time killing impurities such as Mo, Ti, Ta, Ni, V, Cr are either absent or present in very low condensing and can also be similarly easily taken. The importance of rice husk used as a potential source for useful materials such as silica, silicon carbide, silicon nitride or pure silicon for solar cells solar-grade silicon [4-9]. The burning of rice husk in air takes to the production of silica ash, their color varies from black gray to white gray depending on temperature, air and the impurities. The temperature of heating also effected to structure or phase of amorphous silica or crystalline silica of rice husk ash. Amorphous silica can be easily transformed into the crystalline form [10]. The rice husk ash heated in the temperature range of 900 to 1200°C consisted of cristobalite and tridymite phase[2] .The amount of silica was increased after burning out the carbonaceous materials at different time and temperatures. A 95% silicon dioxide powder could be produced after heat-treating at 700°C for 6 hr, the specific surface area of particles was increased after wet milling from 54 to 81 m^2/g[11]. The silicon prepared from rice husk ash using magnesium metallothermic reduction heated at 620°C, the impurities of silicon sample also were appeared. Sodium, magnesium, potassium, calcium and iron were found in the range 50 to 150 ppm. Boron, aluminum manganese and titanium were very low concentration, less than 10 ppm [12]. Calcium was used for metallothermic reduction in rice husk silica, heated at about 720°C [3,7]. In this study, we prepared silicon from rice husk ash using magnesium or aluminum metallothermic reduction with charcoal carbon assisted.

Materials and Methods

The rice husks used in this work were obtained by product from rice mills and were washed with tap water to remove all adhering soil and dirt. They were dried in the sunlight.The dried husks were then washed with distilled water and dried again in an oven with temperature at 60°C. The dried husks were subjected to chemical treatment. The 37% HCl acid used in this study was produced by MERCK, Germany, and was used as received. A proper amount of the HCl was mixed with distilled water to form 1 molar of HCl. The rice husks were soaked with 1 molar of HCl in a glass beaker placed on hot plate at 90°C for 1 hr. The solution was filtered and the rice husks were washed with distilled water several times until they were acid free. The acid-leached rice husks were dried in an oven at 60°C. They were fired at 600°C for 1 hr. The rice husk ash was investigated by X-rays diffraction (XRD) and X-ray fluorescence (XRF) instruments. The coconut shell was cleaned by tap water and distilled water several times and dried in oven at 60°C. The cleaned coconut shell was burned at 400°C for form charcoal. The coconut shell charcoal was grounded to be fine powder (~90μm), and put in a glass beaker. The 1 molar of HCl was filled in the beaker and soaked for 1 hr. The solution was filtered and the charcoal powder was washed with distilled water several times until acid free. These processes were explained by previous report [13]. We prepared silicon from silica ash using 2 metallothermic reduction methods, (1) the silica ash, magnesium powder and charcoal powder were mixed with ratio of 2:1:0.1 by weight, the mixtures powder were grounded and put in alumina crucible, then heated at 600°C in the furnace chamber under atmosphere of nitrogen with flow rate of 2 L/min. The burn products were soaked in 1 M of HCl and H_2SO_4 for 1 hr. The solution was filtered and the burn products were washed with distilled water several times until acid free and dried in oven at 60°C. The burn products were soaked again in HF for 4 hrs. They were washed with distilled water several times

then, filtered and dried again. The prepared silicon was investigated by XRD instrument. (2) the silica ash, aluminum powder and charcoal powder were mixed with ratio of 3:0.5:0.1 by weight, the mixtures powder were grounded and put in alumina crucible, then heated at 1100°C in the furnace chamber under atmosphere of nitrogen with flow rate of 2 L/min for 2 hrs. The burn products were carried for production of silicon with the same process of method (1). The prepared product was investigated by XRD instrument.

Results and Discussion

The rice husk silica was taken from the furnace. The white color of silica ash can be observed by naked eye. The silica ash was characterized by XRD and XRF instruments, as shown in Figure 1, Figure 2 and Table 1.

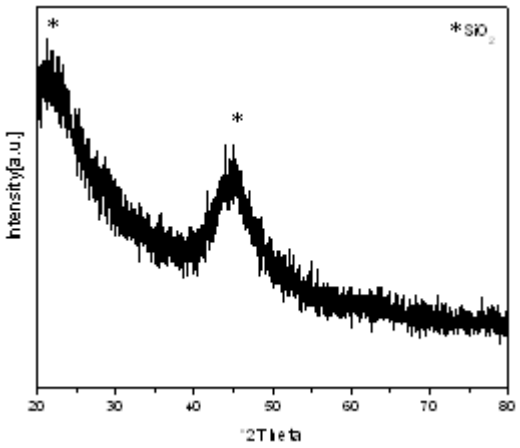

Figure 1. XRD curved of white rice husk ash.

Figure 1 show the broad peak XRD of white rice husk ash prepared form rice husk. The Figure 2 and Table 1 show the XRF curve of pure silicon dioxide from white rice husk ash. The white rice husk ash consist of silicon dioxide (SiO_2) 99.86 % and CaO 0.1419 %, GeO and FeO can not be observed.

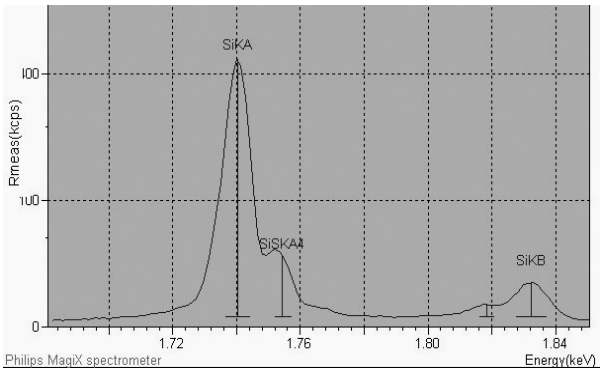

Figure 2. XRF curve of white rice husk ash.

Table 1: The composition of white rice husk ash

Compound Name	Conc. (%)	Compound Name	Conc. (%)
SiO_2	99.86	GeO	<<
CaO	0.1419	FeO	<<
Element Name	Conc. (%)	Element (%)	Conc. (%)
O	53.22	Ge	<<
Si	46.68	Fe	<<
Ca	0.1014		
Normalized to: 100 %			

After production of SiO_2, we carried thepreparation of silicon from white rice husk ash using metallothermic reduction process. Figure 3 shows the XRD curved burnt product before soaked in HF solution. We can see several peaks of the composition of burn product including of silicon.

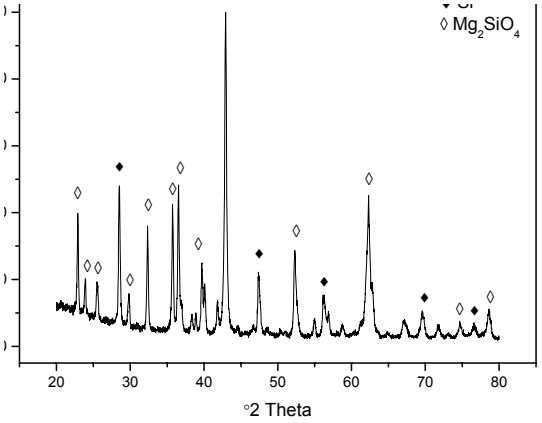

Figure 3. XRD curved of burn products before soaked in HF.

The burn product was soaked in HF solution for 4 hrs then, filtered and washed in distilled water many time. The dried product was studied by XRD instrument.

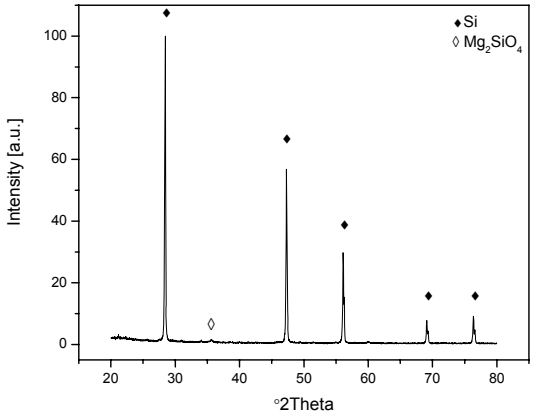

Figure 4. XRD curved of prepared silicon from rice husk ash using Mg metallothermic reduction.

After HF acid-treatment, the dried products were very clearly different form source materials before

reaction. Figure 4 shows XRD curved of silicon prepared from rice husk ash using Mg metallothermic reduction.

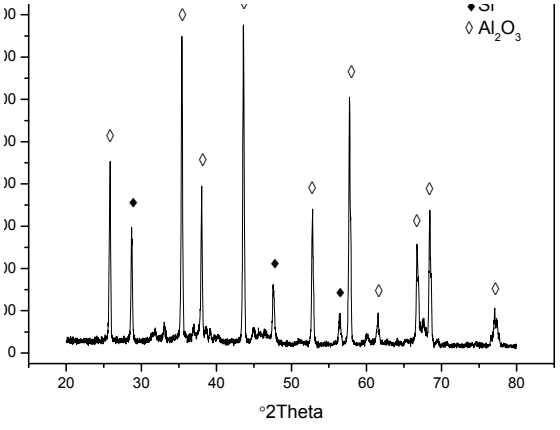

Figure 5. XRD curved of prepared silicon from rice husk ash using Al metallothermic reduction.

We studied the composition of the product from Figure 4 by using equation, $\%Si = [I_{Si} / I_{Mg2SiO4}]\times100$. From equation, we could calculate the percent of silicon in this prepared product. This prepared product consisted of silicon around 99.65 %. Figure 5 shows XRD curved of the prepared product after HF acid-treatment, this product prepared from rice husk ash using Al metallothermic reduction method. We found two peaks of Si and almost of Al_2O_3 structures, no other peaks. This result shows that Al metallothermic reduction can be produced silicon from rice husk ash.

Conclusions

In summary, high purity SiO_2 was prepared by burning acid-treated rice husk in a furnace at temperature of 600 °C in normal atmosphere for 1 hr. The XRD and XRF data show purity of SiO_2 in silica ash was around 99.86 **%**. The silicon was prepared from rice husk ash using Mg metallothermic reduction. The calculation from XRD curved showed around 99.65 % purity of Si from this process. The SiO_2 and Si prepared from rice husk ash may be used in materials technology.

Acknowledgements

This research is supported by Ubon Ratchathani University, the National Research Council Thailand (NRCT), the Commission on Higher Education (CHE) and the Thailand Research Fund (TRF). The authors gratefully thank them for financial support.

References

[1] R. Conradt, P. Pimkhaokham and U. Leela-Adisorn, *J. Non-Crystalline Solid.* **145** (1992), pp. 75-79.
[2] Y.Shinohara and N. Kohyama, *Industrial Health,* **42** (2004), pp. 277-285.
[3] D.N. Bose, P.A. Govindachargulu and H.D. Banerjee, *Solar Energy Materials.* **7 (**1982), pp. 319-321.
[4] J.A. Amick,*J.* Electrochem. Soc. **29(4)** (1982), pp. 864-866.
[5] L.P. Hunt, J.P. Dismukes and J.A. Amick, *J.* Electrochem. Soc. **131(7)**(1984), pp. 1683–1686.
[6] C. Real, M.D. Aleala and J.M. J. *American Ceramic Soc.* **79(8)** (1996), pp. 2012 – 2016.
[7] P. Mishra , A. Chakraverty and H.D. Banerjee, *J. Mater. Sci.* **20**(1985), pp. 4387 – 4391.
[8] Patel, M., Karera, A. and P. Prasanna, *J. Mater. Sci.* **22**(1987), pp. 2457 – 2464.
[9] A.Chakraverty, P. Mishra and H.D. Banerjee, *J. Mater. Sci.* **23**(1988), pp. 21–24.
[10] L.A. Zemnukhova, G..A. Fedorishcheva, A.G. Egorov, and V.I. Sergienko, *Russian J. Appl. Chem.* **78**(2005), pp.319-323.
[11] V. P. Della, I.Kuhn and D. Hotza, *Mater. Sci. For.* **416-418** (2003), pp.531-536.
[12] N. Ikram and M. Akhter, *J. Mater. Sci.* **23**(1988), pp. 2379-2381.
[13] S. Pukird, P.Chamninok, S. Sumran, P. Kasian, K. Noipa and L. Chow, *J. Mat., Mater. and Miner.* **19(2)** (2009), pp. 33-37.

Carbon-catalyst growth of SnO_2 nanowires and microfibers by thermal evaporation method

K. Noipa[1*], P. Chamninok[2] and S. Pukird[1]

[1]Department of physics, Faculty of science, Ubon Ratchathani University,
Ubon Ratchathani, Thailand, 34190
[2]Department of physics, Faculty of science, Ubon Ratchathani Ratchabhat University,
Ubon Ratchathani, Thailand, 34000

[*] E-mail: kiattisak_noipa@yahoo.com

Abstract: SnO_2 nanowires and microfibers have been synthesized using a thermal evaporation method of simple heating SnO_2 and carbon powders prepared from coconut shell charcoal at 800°C in one atmosphere of argon. The morphology of synthesized products was investigated by scanning electron microscopy (SEM). The crystal structures of prepared products were characterized by X-ray diffraction (XRD). XRD patterns shows that the products are tetragonal-structures with the lattice constant a = 0.4718 nm and c = 0.3187 nm. SEM images indicate that SnO_2 nanowires are about tens of micrometers in length, 80 nm to 500 nm in width. The widths of microfibers vary from 1 μm to 5 μm, and the lengths are about tens of micrometers.

Introduction

One-dimension nanoscale materials, such as nanowires, nanorods, nanobelts and nanofibers, have attracted significant attention of the researchers. Tin oxide (SnO_2) is n-type semiconductor, and for its potential application in gas sensors, transparent conducting electrodes, and optoelectronic devices [1-3], with a wide band gap (Eg = 3.6 eV, at 300 K). Recently, SnO_2 nanostructures have been successfully synthesized by thermal methods. For example, the single-crystalline SnO_2 nanostructures such as nanowires, nanobelts and nanodendrites were synthesized by a simple gas-reaction route on a large scale at 900°C [4]. The novel SnO_2 fishbone-like nanoribbons were synthesized, via a thermal oxidation of elemental Sn powder using $Fe_3(NO_3)_3$ as oxidizing agent at high temperature (1100°C). These products display a strong green emission at ~ 500 nm [5]. SnO_2 nanowires were prepared by thermal evaporation using SnO powder as the starting materials, was heated at 680°C for 8 hours under a argon gas flow at a rate of 15 sccm [6]. The single crystalline structures of SnO_2 nanowires and the branched nanowires were synthesized using the mixture of active carbon and SnO_2 powder at low temperature reaction [7], SnO_2 nanostructures in the forms of nanowires were fabricated using a simple method of rapid heating SnO_2 and graphite powders under a flow of high-purity nitrogen gas at 850°C, these products exhibited the difference of nanostructures materials in the Fourier transform infrared (FT-IR) [8]. Moreover, The uniform single-crystalline SnO_2 nanobelts that are smooth surface of the structural belt-like were fabricated by water-assisted growth at 850°C using high pure Sn powder as source materials [9]. SnO_2 nanoblets were fabricated by simply thermal evaporation process using metallic tin foil as source materials at 1000°C under normal atmospheric pressure. The products were high sensitivity and fast response time to ethanol gas [10]. Tetragonal phase SnO_2 nanocrystals were prepared by heating the mixture of Sn, S and NH_4Cl powders in air at 400°C for 2-5 hours [11]. The large-scale of SnO_2 nanoparticles were synthesized via a tin alkoxide ($Sn(OEt)_2$) hydrolysis process. The products demonstrated high sensitivity and good selectivity to ethanol and n-butanol at 220°C [12].The needle-shaped SnO_2 nanostructures were prepared on coated silicon substrates by thermal evaporation method at 900°C under a flowing oxygen (1 SCCM) atmosphere, using high purity metal Sn pellets as starting materials. These products were robust for field emission [13]. Ningthoujam et al fabricated SnO_2 nanoparticles by thermal decomposition of Sn-citrate-gel [14]. In the present paper, SnO_2 nanowires and microfibers were synthesized at 800°C in one atmosphere of argon by thermal evaporation method of SnO_2 and carbon powders prepared from coconut shell charcoal. The synthesized products were characterized by XRD and SEM instruments.

Materials and Methods

The synthesis process was carried out in a crucible furnace using the mixture of SnO_2 and active carbon powders with ratio of 1:1 by weight as source materials. The active carbon for source in this work was prepared in this process. Firstly, the coconut shell was cleaned with distilled water several times and dried in air then the cleaning coconut shell was heated in oven at 400°C for 2 hours to form charcoal. Finally, the coconut shell charcoal was grounded into powder (about 90 μm) [15]. The silicon substrate for collection nanostructures was cleaned with absolute ethanol several times. The starting materials were placed in alumina boat and the substrate for growth of nanostructures was put on the source materials. The alumina boat was placed in the middle of a crucible furnace. The furnace was heated to 800°C under a flowing argon (0.5 L/min) atmosphere and kept at 800°C for 2 hours. After evaporation, the furnace was

cooled down to room temperature, naturally. The prepared products were then studied by X-ray diffraction (XRD) and scanning electron microscope (SEM) instruments.

Results and Discussion

After the furnace was cooled down to room temperature, naturally. The source materials and substrate were taken from the crucible furnace. We observed that a white color materials formed on the silicon substrate surface, and the mophology of synthesized products was very obviously different form initial source materials. The crystal structures of synthesized products were characterized by X-ray diffraction (XRD), as shown in Figure 1. These XRD paterns of the products formed on source materials and on the silicon substrate after heat treatment is shown in Figure 1(a) and Figure 1(b) respectively. All these the XRD diffraction peaks of the (110), (101), (200), (111), (210), (211), (220), (022), (310), (112), (301), (202), and (321), which can be readily indexed to the tetragonal structure of SnO_2 with lattice constant of a = 0.4718 nm, c = 0.3187 nm. The mini peaks in Figure 1(b) can be attributed to silicon oxide formed in silicon substrate at high temperature. The morphology

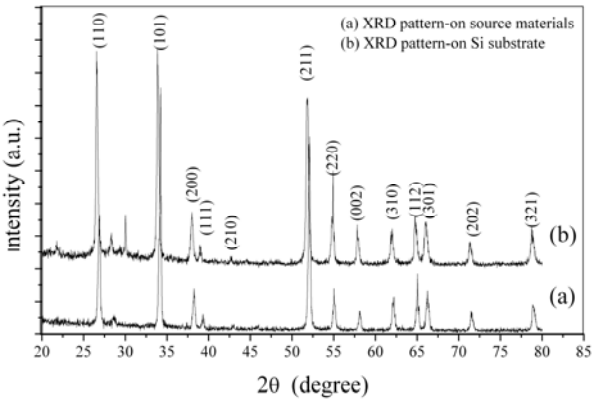

Figure 1. XRD curved of synthesized products formed (a) on source materials and (b) on silicon substrate.

of the prepared products was investigated by scanning electron microscope (SEM) instument. Figure 2. SEM image of source materials after evaporation. These products were very clearly different form source materials before reaction. We can be observed some nanoparticles and microfibers that showed in Figure 2, Figure 2 (b) a magnified image of Figure 2 (a) is shown. The morphology of the prepared products formed on silicon substrate was shown in Figure 3, we can be found that one-dimensional nanomaterials will be grown from one cluster particle to the other. These products were collected on the different regions of silicon substrate. Figure 3 shows the SEM image that SnO_2 nanowires appeared on the region I and microfibers formed on the region II, were presented in figure 4(b) and (5b). Figure 4 shows that SEM images of synthesized products formed on region I of silicon substrate. Figure 4(a) indicates that

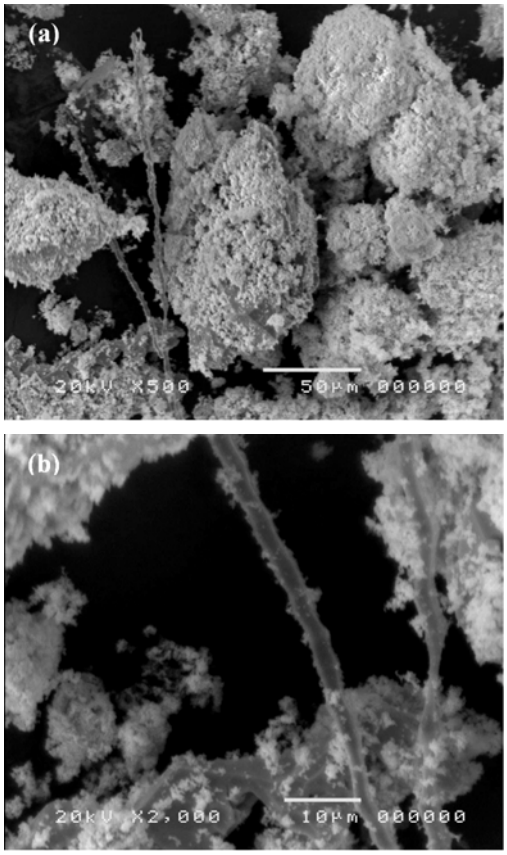

Figure 2. SEM image of products formed on the source materials, (a) as low magnification and (b) high magnification.

a low magnification SEM image of the nanostructures that consisted of nanowires and nanoparticles. Figure 4(b) displays a high magnification of SEM images, we can be observed that the SnO_2 nanowires are about tens of micrometers in length, 80 nm to 500 nm in width. Figure 5 shows the SEM image of microfibers synthesized on silicon substrate, which was placed over the starting materials. We noticed that the width microfibers vary from 1 µm to 5 µm, and the lengths are about tens of micrometers. In figure 5(b)

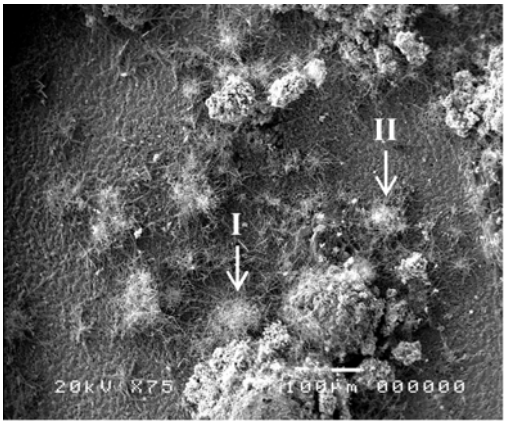

Figure 3. SEM image of the prepared products formed on the different regions of the silicon substrate, as SnO_2 nanowires (region I) and microfibers (region II)

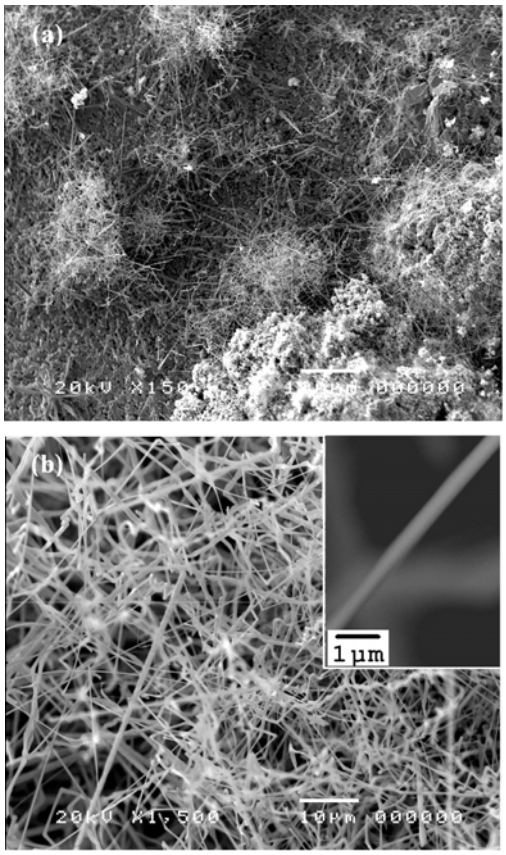

Figure 4. SEM image of SnO_2 nanowires synthesized at 800 ^oC for 2 hours on silicon substrate, (b) the magnified view of Figure 4(a)

a magnified image of figure 5(a) is shown. All these nanowires and microfibers are smooth in surface, as shown in the inset of the figure 4(b) and figure 5(b). The growth of the one-dimensional nanomaterials was described with vapor-liquid-solid (VLS) and vapor-solid (VS) mechanisms. Especially, the VLS mechanism is an important role in the growth of wires structures, which used to be obtained adding catalyst in the source materials. The growth of the SnO_2 nanowires and microfibers was described by the following chemical reaction [6-7].

$$C(s) + SnO_2(s) \rightarrow SnO(g) + CO(g) \quad (1)$$

$$CO(g) + SnO_2(s) \rightarrow SnO(g) + CO_2(g) \quad (2)$$

$$2SnO(g) \rightarrow Sn(l) + SnO_2(s) \quad (3)$$

When the temperature was elevated up to the reaction temperature, the source materials were continuously evaporated to form SnO vapor and CO gas, as the reaction (1) described. While SnO_2 powder was reduced by the CO gas formed form reaction (1) that was demonstrated with the reaction (2). Then a large amount of tin vapor was transported to the deposition zone by carrying gas, it will decompose into Sn and SnO_2, as indicated in reaction (3) and then Sn droplets fell on the substrate. Subsequently, the one-dimensional nanomaterials grow by precipitation of SnO_2 from the supersaturated droplets. These processes were explained by previous reports [6-9].

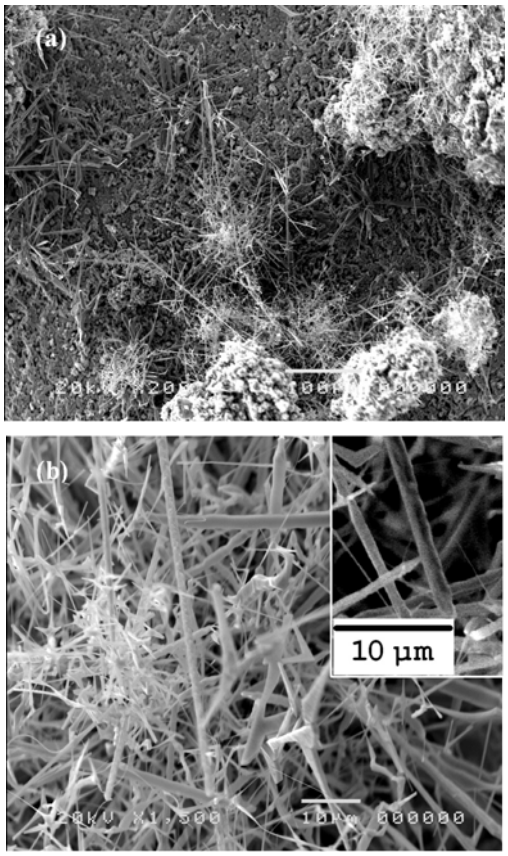

Figure 5. (a) Low magnification and (b) high magnification SEM image of SnO_2 microfibers on silicon substrate

Conclusions

In summary, SnO_2 nanowires and microfibers with tetragonal structure have been successfully synthesized by heating the mixture of SnO_2 powder and coconut shell charcoal with ratio of 1:1 by weight at 800 ^oC for 2 hours, under a flowing argon (0.5 L/min) atmosphere. The characteristics of synthesized products were investigated by X-ray diffraction (XRD) and scanning electron microscope (SEM) instruments. XRD pattern shows that the products are tetragonal-structures with the lattice constant a = 0.4718 nm and c = 0.3187 nm. SEM images indicate that SnO_2 nanowires are about tens of micrometers in length, 80 nm to 500 nm in width. The widths of microfibers vary from 1 µm to 5 µm, and the lengths are about tens of micrometers.

These prepared products can be used in future application in nanotechnology.

Acknowledgements

This research is supported by Ubon Ratchathani University and the Thailand Research Found (TRF-WindowII;MRG-WII525S099). The authors gratefully thank them for financial support.

References

[1] X. Kong and Y. Li , *Sens. Actuators*. **B 105 (**2005), pp. 449–453.
[2] H. W. Kim and S. H. Shim, *J. Alloys. Comp*. **426**(2006), pp. 286–289.
[3] H. W. Kim, S. H. Shim and C. Lee, *Ceram. Inter*. **32 (**2006), pp. 943–946.
[4] J. K. Jian, X. L. Chen, W. J. Wang, L. Dai and Y. P. Xu, *Appl. Phys*. **A 76** (2003), pp. 291–294.
[5] J. Q. Hu, Y. Bando and D. Golberg, *Chem. Phys. Lett*. **372** (2003), pp. 758–762.
[6] Y. Chen, X. Cui, K. Zhang, D. Pan, S. Zhang, B. Wang and J. G. Hou, *Chem. Phys. Lett*. **369** (2003), pp.16–20.
[7] J. X. Wang, D. F. Liu, X. Q. Yan, H. J. Yuan, L. J. Ci, Z. P. Zhou, Y. Gao, L. Song, L. F. Liu, W. Y. Zhou, G. Wang and S. S. Xie, *Solid State Common*. **130** (2004), pp 89-94.
8] L. Li, F. Zong, X. Cui, H. Ma, X. Wu, Q. Zhang, Y. Wang, F. Yang and J. Zhao, *Mater. Lett*. **61 (**2007), pp. 4152–4155.
[9] Z. Huang and C. Chai, *Mater. Lett*. **61** (2007), pp. 5113–5116.
[10] H. Xiangming, Z. Bing, G. Shaokang, L. Jindun, Z. Xiang, C. Rongfeng, *J. Alloys. Comp.* **461 (**2008), pp L26–L28.
[11] H. X. Bai, *Mater. Lett.* **63** (2009), pp 221–223.
[12] J. Zhang, S. Wang, Y. Wang, M. Xu, H. Xia, S. Zhang, W. X. Guo and S. Wu, *Sens. Actuators.* **B 139** (2009), pp 369–374.
[13] L.A. Ma and T.L. Guo, *Mater. Lett.* **63** (2009), pp 295–297
]14] R. S. Ningthoujam and S.K. Kulshreshtha, *Mater. Res. Bull.* **44** (2009), pp 57–62.
[15] P. Chumninok, P. Kasian, P. Limsuwan, U. Tipparach, S. Samran, L. Chow and S. Pukird, *Adv. Mater. Res*. **55** (2008), pp. 637- 640.

Preparation and evaluation of high efficiency dye-sensitized solar cells

Y. Poo-arporn[1], V. Vailikhit[2], D. Bashyal[3], K. Nakajima[4], P. Songsiriritthigul[1,5] and K. Mitsuke*[3]

[1]Synchrotron Light Research Institute, Nakhon Ratchasima, Thailand, 30000
[2] Faculty of Liberal Arts and Science, Kasetsart University, Nakorn Pathom, Thailand 73140
[3] The Institute for Molecular Science and Graduate University for Advanced Studies, Myodaiji ,Okazaki 444-8585, Japan
[4] Science Research Center, Hosei University, Chiyoda-ku, Tokyo 102-8106, Japan
[5] School of Physics, Suranaree University of Technology, Nakhon Ratchasima, Thailand, 30000

*E-mail: mitsuke@ims.ac.jp

Abstract: The high efficiency dye-sensitized solar cells (DSCs) were fabricated by using a screen-printing technique and a wet process. A TiO_2 anode was immersed for 3 days in the acetonitrile solution of ruthenium complex compound, triisothiocyanato-(2,2': 6',6"-terpyridyl-4,4',4"-tricarboxylato) ruthenuim(II) tris(tetra-butylammonium) dye (N719). The mixture of I_2, iodide salt, acetonitrile, and other ingredients was used as a redox electrolyte. The counter electrode was covered with thin platinum film. The I–V characteristics of DSCs were recorded under simulated sun light whose power density was set at 100 mW cm^{-2}. The highest overall energy conversion efficiency was found to be 5.78 %. The incidence photon to current conversion efficiency (IPCE) was calculated from the short current density and radiation power density as a function of the wavelength. The IPCE curve showed a peak of 0.73 at 535 nm. The performance and long-term stability of the DSCs were studied by changing the thickness of the TiO_2 film, the deposition method of the Pt film, and the compositions of the redox electrolyte.

Introduction

The photochemical property of titanium oxide (TiO_2) has been studied extensively due to its potential use in sensitization and remediation applications. TiO_2 is well known to be active under ultraviolet light of wavelengths shorter than 400 nm: the band gaps associated with optical absorption are 3.2 and 3.0 eV for the crystal structures of anatase and rutile, respectively [1]. Since the ultraviolet light contributes only a little to the radiation power of the sun light, the photovoltaic efficiency of TiO_2 is relatively low in its solar applications. Thus, we should modify TiO_2 to make it response to the visible light and enhance the efficiency.

After many years of efforts, a lot of methods have been invented to reduce the band gap of TiO_2 or to contact TiO_2 with materials having narrow band gaps [2]. Sensitization with the aid of dye is one of the most promising solutions to increase the photoabsorbance of solar cells [3]. In a dye-sensitized solar cell, DSC, photons are primarily absorbed by dye molecules which are tightly bound to the surface of TiO_2 nanoparticles. Then, the electrons excited to the LUMO level are injected into the conduction band of TiO_2, fed into an external circuit, and returned to the cell through the counter electrode on which Pt thin film is deposited. The liquid electrolyte (mostly an iodide/triiodide redox couple in an organic solvent) reduces the photo-oxidized dye molecules back to neutral.

In this work, DSCs were fabricated using N719 dye by employing a series of processes of screen-printing of TiO_2 paste, sintering, and soaking into dye solution. We investigated whether the performance and stability of DSCs are significantly influenced by the thickness of TiO_2 and Pt films and/or the compositions of redox electrolyte.

Materials and Methods

Fabrication of DSC: The TiO_2 paste (Catalysts & Chemicals Ind.) was coated onto a fluorine-doped tin oxide glass (FTO, Asahi Glass) by a screen printing technique. The coated TiO_2 was dried in air and sintered at 485 °C for 30 min. The TiO_2 pattern was a circle 0.564 cm in diameter and 0.25 cm^2 in area. The above printing and sintering were executed several times to increase the thickness of the TiO_2. Next the glass plate was immersed in acetonitrile solution of the N719 dye (Solaronix) in a petri dish and TiO_2 was subjected to dyeing for 3 days. A DSC was assembled from the photovoltaic electrode thus obtained, redox electrolyte, and the counter electrode (Figure 1). The redox electrolyte named AN-50 was purchased from Solaronix; Its principal ingredients are 50 mM I_2, iodide salt, pyridine derivative, ionic liquid and acetonitrile. The counter electrode was prepared by squeezing Pt paste (T/SP, Solaronix) onto another FTO glass and subsequent sintering at 400°C for 30 min. As an alternative method we adopted plasma discharge sputtering of Pt on an FTO glass. The

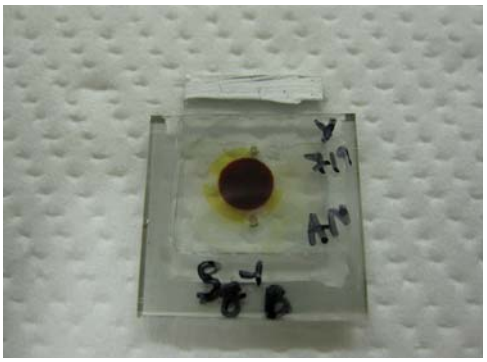

Figure 1. Dye sensitized solar cell.

sputtering was carried out in a quick coater for 10 min. at a discharge current of 8 mA.

DSC characterization: Photovoltaic measurements were conducted using a commercial solar simulator (PES-L11, Peccell Technologies) equipped with a xenon lamp. The wavelength-integrated radiation power density P_{int} was calibrated to be 100 mW cm^{-2} by using a standard Si photodiode. The I–V curves were obtained by applying an external bias to the cell and measuring the generated photocurrent with a digital source meter (model 2400, Keithley). The voltage step and delay time of photocurrent were 10 mV and 1 s, respectively. The IPCE curves were measured by a commercial action spectrometer (PEC-S20, Peccell Technologies).

Results and Discussion

The performance of DSC were judged by three important parameters, namely the open-circuit voltage V_{oc}, the short circuit photocurrent density J_{sc}, and the fill factor F. The fill factor is calculated by

$$F = \frac{V_m J_m}{V_{OC} J_{SC}} \quad (1)$$

where V_m and J_m are the voltage and current density, respectively, leading to a condition of maximum power. The overall energy conversion efficiency η can be estimated by

$$\eta = \frac{J_{SC} V_{OC} F}{P_{int}} \quad (2)$$

The IPCE can be calculated from

$$\text{IPCE} = \frac{J_{SC}(\lambda) \cdot hc}{P(\lambda) \cdot e\lambda} \quad (3)$$

where $J_{SC}(\lambda)$ is the short circuit photocurrent density as a function of the wavelength λ, while $P(\lambda)$ is the radiation power density as a function of λ. The other quantities $h\nu$ and e denote the photon energy and elementary charge, respectively.

We changed the thickness of TiO_2 by changing the number N of the cycles of the screen printing and sintering, and obtained the characteristics of DSCs with different TiO_2 thicknesses, as listed in Table 1. Here, all the counter electrodes were prepared by squeezing the Pt paste. The DSC with the TiO_2 layer triply piled up (N = 3) gives the largest values of J_{SC} and η, 12.67 mA cm^{-2} and 4.75 %, respectively. The smaller J_{SC} and η at N = 4 might be due to the increase in charge-transfer resistance in the TiO_2 film.

The largest IPCE of 0.693 was achieved at ca. 535 nm when the DSC was assembled with the doubly piled-up TiO_2 film (N = 2). This wavelength corresponds to the maximum of the absorption spectrum of the N719 dye [4]. The IPCE tends to decrease with increasing N at $N \geq 3$.

Table 1: Characteristics of DSCs with different TiO_2 thicknesses.

N^a	J_{sc} (mA cm^{-2})	V_{oc} (V)	F	η (%)	IPCE
1	8.49	0.66	0.64	3.65	0.633
2	11.37	0.65	0.53	3.94	0.693
3	12.67	0.64	0.58	4.75	0.668
4	11.89	0.65	0.61	4.70	0.557

[a] TiO_2 film was laminated by 1–4 cycles of screen-printing and sintering. Each cycle increases the thickness by ~ 8 μm.

Table 2: Comparison between the DSCs whose Pt thin films deposited on the cathode electrodes were prepared by different ways: (a) Squeezing and (b) plasma sputtering methods.

Method	J_{sc} (mA cm^{-2})	V_{oc} (V)	F	η (%)	IPCE
(a)	10.96	0.66	0.56	4.05	0.681
(b)	10.35	0.65	0.63	4.28	0.624

In Table 2 a comparison was made on the characteristics of the DSCs between the counter electrode (cathode) prepared by squeezing the Pt paste and that by depositing a Pt film using plasma sputtering. The photovoltaic electrodes of both the DSCs were fabricated by immersing the TiO_2 layer of N = 2 in the N719 dye solution for 2 days. A value of η was smaller for the squeezing than for the plasma sputtering method, though the former method revealed a higher IPCE at 535 nm than the latter. Conceivably $J_{SC}(\lambda)$ of the DSC is larger in the whole λ range when it was fitted with the cathode of the squeezed Pt than when with that of the plasma-sputtered Pt. On the contrary, the squeezed Pt results in only a small F value and therefore a poor energy conversion efficiency, as compared with the plasma sputtered Pt.

The effect of the redox electrolyte was studied by assembling DSCs with organic solvents containing the I^-/I_3^- couple called PN-50 and TG-50, other than AN-50. These redox electrolytes were purchased also from Solaronix. The principal ingredients of PN-50 are 50 mM I_2, pyridine derivative, ionic liquid and methoxypropionitrile, whereas those of TG-50 are 50 mM I_2, iodide salt, and tetraglyme. The TiO_2 film of N = 3 and Pt by the squeezing method were employed on the photovoltaic and cathode electrodes, respectively. The typical characteristics of the DSCs with the three redox electrolytes are summarized in Table 3.

Table 3: Characteristics of DSCs with different redox electrolytes.

Electro-lyte	J_{sc} (mA cm^{-2})	V_{oc} (V)	F	η (%)	IPCE
AN-50 [a]	12.67	0.64	0.58	4.75	0.668
PN-50	12.44	0.68	0.62	5.30	0.665
TG-50	10.42	0.62	0.37	2.40	0.324

[a] same as the results given in the N = 3 row of Table 1.

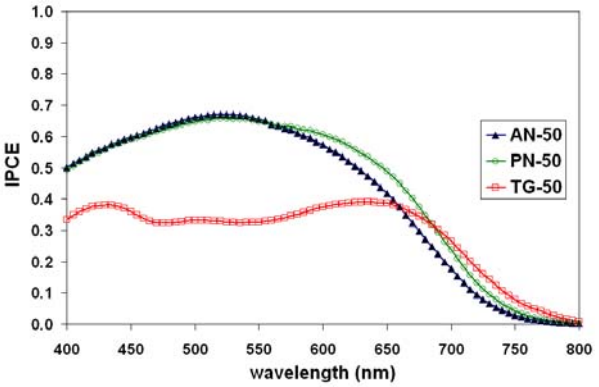

Figure 2. IPCE curves of the DSCs with three redox electrolytes containing the I^-/I_3^- couple: AN-50, PN-50 and TG-50.

In general, the largest η has been gained in the DSCs containing the PN-50 electrolyte. The best data that we have achieved so far using the TiO_2 film of N = 3 and PN-50 was η = 5.50 %. Figure 2 shows the IPCE curves of the DSCs assembled with AN-50, PN-50 and TG-50 at λ = 400 - 800 nm. It is clearly seen that PN-50 and AN-50 are more suitable redox electrolytes than TG-50, when the N719 dye is used as a photosensitizer of TiO_2. The DSC made of PN-50 was superior in IPCE to that made of AN-50 at λ > 570 nm, while, below 570 nm, the IPCE curves for the two redox electrolytes accord almost well with each other (~ 0.67 at 535 nm). It is worth while noting that TG-50 is well suited for DSCs which should be operated with much lower P_{int}. Another advantage of TG-50 is its less volatile nature, which will allow DSCs to run with no sealant of the cell, i.e. under the open cell condition.

Finally, the long-term stability of the DSC was inspected in the time scale of several weeks. Its constituents were a photovoltaic electrode made by immersing the TiO_2 layer of N = 3 in the N719 dye solution for 3 days, a cathode electrode with the squeezed Pt film, and AN-50. The time was measured with respect to the completion of assembling the DSC. Several hours later η reaches a maximum value of 4.75 % and then tends to decrease hour by hour (Figure 3b). However, the efficiency again starts to ascend on the third day, two days after assembling. The highest efficiency of 5.78 % was recorded on the eighth day, seven days after assembling. The three parameters were J_{sc} = 13.6 mA cm^{-2}, V_{oc} = 0.65 V and F = 0.63, respectively. After 8 days passed, both the IPCE and η

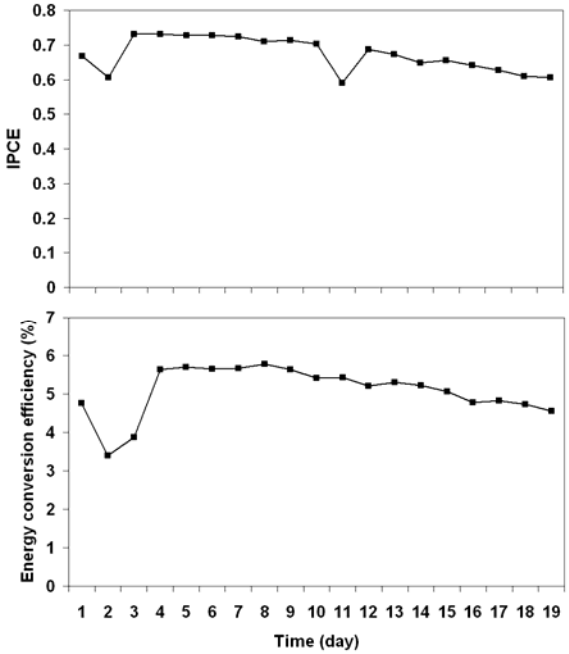

Figure 3. Long-term change in η and IPCE of the DSC.

curves again show decreasing trends. The degradation in the cell efficiency might be due to the leakage of liquid redox electrolyte from the DSC.

Conclusions

High efficiency dye-sensitized solar cells were fabricated by screen-printing the TiO_2 paste, sintering, and dyeing the TiO_2 film with N719 dye. The optimum results on the I-V characteristics were attained, when the cycle of the screen printing and sintering was repeated three times, corresponding to the thickness of the TiO_2 layer of ~ 24 μm. The best overall energy conversion efficiency was η = 5.5 % for the DSC that was assembled with the triply piled-up TiO_2 film, the N179 dye, the cathode with the squeezed Pt film, and the redox electrolyte of PN-50. When PN-50 was replaced with AN-50, η was found to drop to 4.75 %. This value, however, increased to 5.78 % on the eighth day, or seven days after assembling. The maximum IPCE value was obtained on the third day to be approximately 0.73 at 535 nm.

Acknowledgements

The authors acknowledge the support from the Japan-East Asia Network of Exchange for Students and Youths (JENESYS) Program 2009 conducted and organized by the Japan Society for the Promotion of Science and the Institute for Molecular Science.

References

[1] A. Hagfeldt, and M. Grätzel, *Chem. Rev.* **95** (1995), pp. 49-68.
[2] M. Shen, Z. Wu, H., Huang, Y. Du, Z. Zou, P. Yang, *Materials Letters* **60** (2006), pp. 693-697.
[3] M. Grätzel, *J. Photochem. Photobiol. C* **4** (2003), pp. 145-153.
[4] R. Katoh, *Chem. Phys. Lett.* **471** (2009), pp. 280-282.

Preparation and properties of EVA/nano-sized PS/ nanosilica hybrids

N.Piyawong[1,2*] and S.Chuayjuljit[1,2]

[1] Chulalongkorn University /Department of Materials Science, Faculty of Science,
[2] National Center of Excellence for Petroleum, Petrochemicals and Advanced Materials, Bangkok 10330, Thailand

*E-mail: nutnicha.p@gmail.com

Abstract: Organic-inorganic hybrid materials of ethylene vinyl acetate copolymer (EVA)/nanosized-polystyrene (PS)/nanosilica were prepared by latex compounding method. The PS nanoparticles were synthesized via a differential microemulsion polymerization using sodium dodecyl sulfate and azobisisobutyronitrile as a surfactant and an initiator, respectively. The resulting latex particles were observed under transmission electron microscope and dynamic light scattering analyzer. It is found that the spherical-shaped PS particles with diameter of less than 20 nm have been achieved. Blends of EVA and PS at EVA/PS dry weight ratios of 90/10, 80/20, 70/30 and 60/40 were mixed with nanosilica at the amount of 0.1 and 0.5 wt% using a mechanical stirrer at 100 rpm for 2 h. The blended latices were cast into sheets on a glass mold, air dried for 1 day and then in an oven at 70°C for 6 h. After that, the samples were examined for their tensile properties, thermal behavior and morphology using a universal testing machine, thermal gravimetric analyzer and scanning electron microscope, respectively. It is apparent that the PS and silica nanoparticles provide a good reinforcing effect on the EVA. However, the incorporation of high PS and nanosilica content results in its aggregation and poor dispersion.

Introduction

Polymer blends and composites are currently receiving great attention in industrial practices because they can modify their characteristics, reduce production cost, increase processability and broaden the applications of polymeric materials. Blending of ethylene vinyl acetate copolymer (EVA) and polystyrene (PS) are very attractive because of their excellent properties. EVA is available as rubbers, thermoplastic elastomers and plastics depending on the vinyl acetate content in the copolymer (9-18% VA = plastics; 28-33% VA = thermoplastic elastomers; 45% VA = rubbers) [1]. PS is one of the well known commodity polymers that can easily processed for making it a very useful and versatile manufacturing product. EVA/PS blends combine the excellent ageing and flex crack resistance of EVA [2] and the superior processing characteristic of PS [3]. However, most polymer blends are thermodynamically immiscible. In this work, PS nanoparticles have been utilized to blend with EVA under latex state in order to improve their miscibility on a molecular scale and form a homogeneous system. In recent years, differential microemulsion polymerization of styrene has been developed as a new technique for producing polystyrene nanoparticles with a diameter of less than 50 nm by using much smaller amount of surfactant than that used in conventional microemulsion polymerization [4]. The drawbacks of the microemulsion method are well-known, including the requirement of a much higher amount of surfactant and only a relatively low polymer content (< 10 wt %) in the produced latex, which raise concerns with cost required for materials and post-treatment to remove the surfactant after polymerization. These disadvantages have hindered the microemulsion process from scaling up to industrial level. In differential microemulsion process, styrene monomer was gradually fed in dropwise into the polymerizing system [4]. Moreover, one way of improving the properties of the blends is to introduce inorganic nanofillers into the systems. It has been found that the inorganic nanoparticles filled polymer composites often exhibit improvement of mechanicl, thermal and barrier properties when compared with pure polymers and their conventional composites, even at very low filler loading [7]. Among the inorganic nanofillers, silica has been extensively used to improve the mechanical and thermal properties of the polymer products because its hybrids can be widely used in many industrial areas ranging from paints and drug delivery to composite materials [8]. The purpose of this study was to investigate the tensile properties, thermal behaviors and morphology of EVA/PS/silica nanocomposites**.**

Materials and Methods

EVA latex was supplied by Eternal Resin. Styrene monomer was obtained from Dow Chemical. Sodium dodecyl sulfate (SDS) provided by Cognis was used as a surfactant. Azobisisobutyronitrile (AIBN) used as an initiator was donated by Siam Chemical Industry. Silica with particle size of 10-20 nm and specific area of 140-180 m^2/g was purchased from Sigma-Aldrich.

Nanolatex of PS was synthesized by differential microemulsion polymerization. SDS (8 g) and AIBN (0.12 g) were mixed in a 500 ml Pyrex glass reactor, which was equipped with a reflux condenser, a N_2 gas inlet and a dropping funnel for monomer feeding. A 60 ml of distilled water was thereafter added and the system was heated up to 70°C with stirring at 150 rpm using a magnetic stirrer under the circumstance of N_2 gas. After the temperature was raised to 70°C, the styrene monomer was fed slowly in a dropwise manner within 1.5 h. Afterwards, the reaction system was maintained at 70°C with constant agitation for an additional hour. Solid content (%*S*) of PS in the

nanolatex was detemined by the weighing method and calculated from the following equation, $\%S = W_1/W_2 \times 100$ (where W_1 and W_2 are the weights of dried PS and nanolatex, respectively). The number-average diameter (D_n) and morphology of the prepared PS nanoparticles were investigated using a dynamic light scattering analyzer (DLS, Zetasizer Nano ZS,Malvern Instrument Limited) transmission electron microscope (TEM, Jeol JEM-1230), respectively.

EVA latex was well mixed manually with the nanolatex of PS at EVA/PS dry weight ratios of 90/10, 80/20, 70/30 and 60/40. The mixtures were then blended with nanosilica at the amount of 0.1 and 0.5 wt% using a mechanical stirrer at 100 rpm for 2 h. The homogeneous latex was then cast into sheet on a glass mold (20 × 20 × 0.15 cm), air dried for 1 day and then in an oven at 60°C for 6 h. The tensile properties were measured with a LLOYD LR 100K Universal Testing Machine according to ASTM D 638. The load cell capacity and crosshead speed were 100 N and 50 mm/min, respectively. Thermal decomposition temperatures of the obtained nanocomposites were examined using a thermal gravimetry TGA (Mettler Toledo, TGA/SDTA 851°). The specimens were tested under nitrogen atmosphere using a temperature range of 50-1000°C and a heating rate of 20°C/min. The fractured surfaces of the specimens were observed by Jeol JSM-5410LV scanning electron microscope (SEM) after coating the broken surfaces with a thin layer of gold.

Results and Discussion

The obtained nanolatex had a solid content about 22%. The number-average diameter (D_n) of the nanoparticles was determined to be about 15 nm from the particle size analyzer. Figure 1 shows TEM image of spherical-shaped PS nanoparticles.

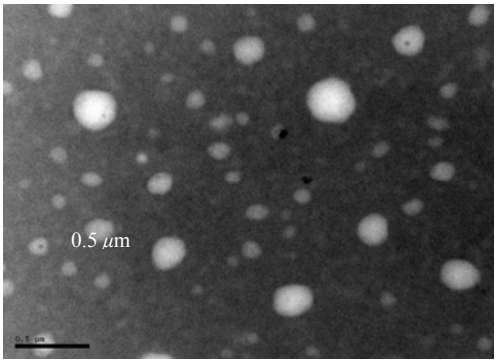

Figure 1. TEM image of PS nanoparticles.

Tensile properties of the test specimens are illustrated in Figures 2-4. The changes in tensile strength, Young's modulus and elongation at maximum load with the incorporation of PS and silica nanoparticles in EVA matrix were determined. As shown in Figure 2, the tensile strength of the neat EVA was 1.8 MPa and lower than all the EVA/PS blends. The 80EVA/20PS sample exhibits the maximum tensile strength of 4.5 MPa and shows a 150% increase in the tensile strength compared to the neat EVA. It is apparent that PS nanoparticles provide a good reinforcing effect on the EVA. However, the tensile strength of the blends shows a tendency to decrease along with an increasing amount of PS. This is because of the self aggregation and poor dispersion of the PS nanoparticles. Moreover, it was observed that by adding 0.1% nanosilica in the 70EVA/30PS blend, the increase in the tensile strength became apparent whereas the other hybrids showed the tendency to decrease with the incorporation of nanosilica. The result indicated the addition of PS and silica nanopaticles with appropriate content could remarkably improve the tensile strength of EVA.

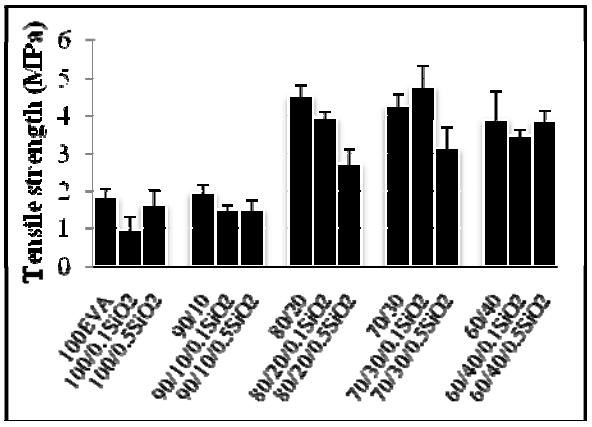

Figure 2. Tensile strength of EVA, EVA/PS blends and EVA/PS/silica hybrids.

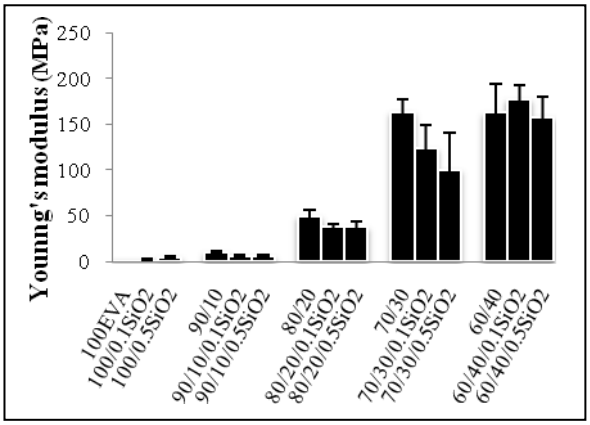

Figure 3. Young's modulus of EVA, EVA/PS blends and EVA/PS/silica hybrids.

Figure 3 shows that the Young's modulus of EVA/PS blends significantly increase with increasing PS content. This was expected due to the fact that the PS is stiffer in nature as compared to EVA. The increase in modulus may be due to the rigidity of the PS that restricts the EVA main chain movement. The blends of 70EVA/30PS and 60EVA/40PS exhibited a remarkable increase in the Young's modulus. However, it was observed that the modulus of the hybrid materials decreased with silica content due to

self aggregation and poor interfacial adhesion, the silica acting as defects and disturbing the continuity of the EVA/PS blend matrix.

Figure 4 shows the effect of PS and silica nanoparticles on the elongation at maximum load of EVA, EVA/PS blends and EVA/PS/silica hybrids. The result shows that the EVA filled with PS and silica nanoparticles exhibits lower elongation at break than the unfilled EVA. This is an expected result since it is well known that the addition of stiff particles can reduce the strain of the samples [7].

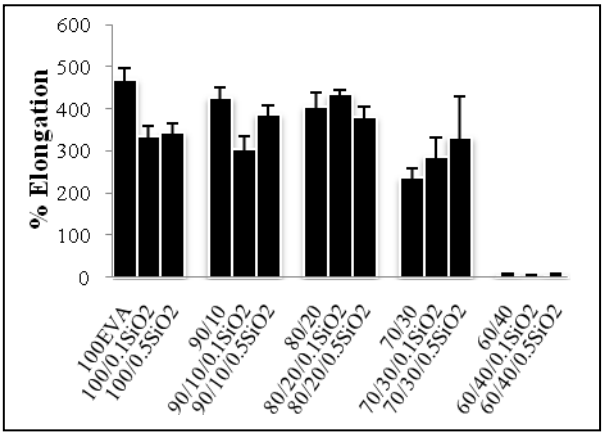

Figure 4. % elongation of EVA, EVA/PS blends and EVA/PS/silica hybrids.

Table 1 shows the changes in decomposition temperature of EVA, EVA/PS blends and EVA/PS/silica hybrids. It can be seen that the addition of PS and silica nanoparticles caused an increase in the decomposition temperature of EVA about 10-70°C.

Table 1: TGA of different polymeric systems.

Blend systems	50% Decomposition temperature (°C)
60EVA/40PS	445
60EVA/40PS/0.1Silica	447
60EVA/40PS/0.5Silica	448
70EVA/30PS	434
70EVA/30PS/0.1Silica	440
70EVA/30PS/0.5Silica	441
80EVA/20PS	395
80EVA/20PS/0.1Silica	400
80EVA/20PS/0.5Silica	404
90EVA/10PS	385
90EVA/10PS/0.1Silica	394
90EVA/10PS/0.5Silica	400
EVA	374
PS	413

Representative SEM micrographs (at 1000X magnification) of EVA, EVA/PS blends and EVA/PS/silica hybrids are presented in Figures 5. SEM micrographs that show low ridges and shallow grooves on the surface of the specimens indicate a ductile failure due to shearing whereas micrographs with smoother surface indicate a brittle failure. This is in good agreement with the result of percent elongation at maximum load.

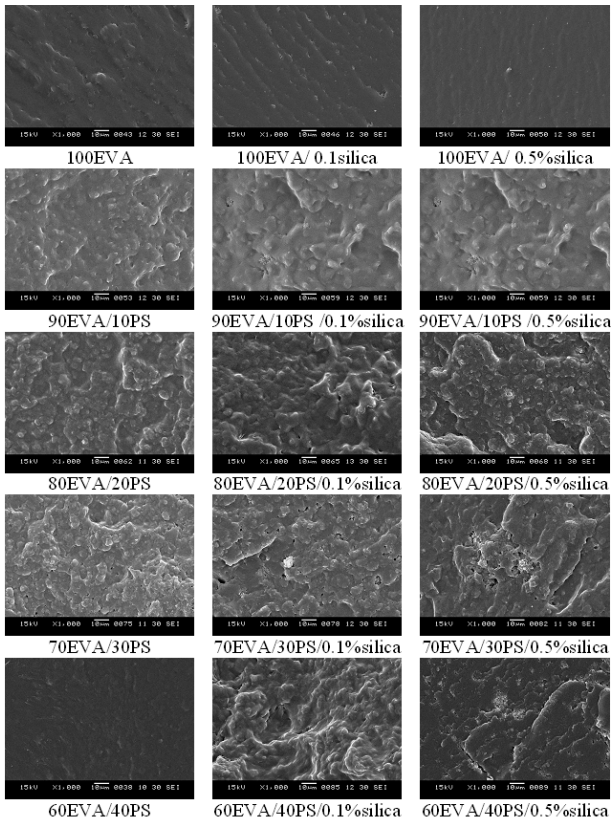

Figure 5. SEM micrographs of EVA, blends of EVA/PS and hybrids of EVA/PS/silica.

Conclusions

The tensile properties and thermal degradation temperature of EVA affected by additions of PS and silica nanoparticles were studied. The PS nanoparticles used in this work were synthesized by differential microemulsion polymerization using SDS and AIBN as the surfactant and initiator, respectively. The polymer blends and hybrid materials were successfully prepared by a latex compounding method. It was found that the tensile strength, Young's modulus and thermal stability of EVA were improved by adding the appropriate amount of PS and silica nanoparticles whereas the percent elongation at maximum load showed a tendency to decrease.

Acknowledgements

The authors gratefully acknowledge Faculty of Science, and National Center of Excellence for Petroleum, Petrochemicals and Advanced Materials, Chulalongkorn University for financial, material and instrument support.

References

[1] M. Pramanik, S.K. Srivastava and B.K. Samantaray, *J. Mater. Sci. Lett*. **20 (**2001), pp 1377-1380.
[2] A.T. Koshy, B. Kuriakose, S. Thomas and S. Varghese, *Polym. J*. **34** (1993), pp 3428-3426.
[3] R. Asaletha, M.G. Kumaran and S. Thomas, *Eur. Polym. J*. **35** (1999**),** pp 253-271.
[4] G. He, Q. Pan and G.L. Rempel, *J. Appl. Polym. Sci*. **105** (2007), pp 2129-2137.
[5] S.C. Tjong, *Mater. Sci. Eng. R* **53** (2006), pp 73-197.
[6] M. Chen, S. Zhou, L. Wu, S. Xie and Y. Chen, *Macromol. Chem. Phys.* **206** (2005), pp 1896-1902.
[7] L.Peterson and K. Oksman, *Compos. Sci. Technol.* **66** (2006), 2187- 2196.

Fabrication of mixed nonwoven and aligned nanofiber mat

C. Suwanboon[1,3], N. Chanunpanich[1,2*], W. Pinsem[1,2],
B. Boonyaphalanant[2], K. Boonthumsong[2], H. Byun[4], J. seo Park[5]

[1]Industrial Chemistry, Faculty of Applied Science, King Mongkut's University of Technology North Bangkok, Thailand
[2]Integrated Nano Science Research Center, Science and Technology Research Institute, King Mongkut's University of Technology North Bangkok, Thailand
[3]Chemistry, Faculty of Science and Technology, Suan Dusit Rajabhat University, Thailand
[4]Chemical System Engineering, Keimyung University, Daegu, Korea
[5]Chemical Engineering, Hankyong National University, Anseong, Korea

*Email : ncn@kmutnb.ac.th,

Abstract: Nanofiber mat produced by electrospinning technique, can be nonwoven and aligned morphology. Nonwoven nanofiber mat is fabricated by using aluminium foil as a collector. On the other hand, aligned nanofiber mat can be carried out using dual collector, but about 10x10 cm^2 size can be obtained. This paper announced new PLA and PVDF nanofiber mat patterns from nonwoven and aligned nanofiber. When these mats are used as protein support prior to MALDI-TOF mass spectrometry investigation. It is found that the higher alignment of the mat, the better for protein support.

Introduction

Electrospinning technique [1- 5] has been proved the easiest way to produce nanofiber with low cost and inexpensive machine. Various polymers can be made nanofiber via electrospinning, such as nylon 6 [6], polyurethanes (PU)[7], polyacrylonitrile (PAN) [8], polyvinyl alcohol (PVA) [9], polylactic acid (PLA)[10], polystyrene (PS) [11], polyamide (PA) [12], polyvinylchloride (PVC) [13] polyvinylidene fluoride (PVDF) [14-15], etc.

Electrospinning is a process, where a high voltage is applied to polymer solution or polymer melt, once the electrically charge overcomes surface tension, polymer solution is jet toward to the grounded target. Nanofiber morphology is affected by solution properties, processing properties- hydrostatic pressure in capillary tube, electric potential and the tip-to collector distance, and the chamber condition

Nanofiber mat can be nonwoven or aligned morphology. However, Chanunpanich and coworkers [15] found the mechanism of aligned nanofiber during fabricating nonwoven nanofiber on PET sheet. Hence, patterns of nanofiber mat, can be manipulated.

It is known that mass spectroscopy is not an easy method for protein characterization. However, with an assistance of ionizable matrix, so called MALDI-TOF (matrix-assisted laser desorption/ionization time-of-flight), mass spectroscopy has became a powerful technique in biochemical analysis[16]. The protein support is also play an important role on protein spectrum. The higher surface area of the protein support, the better result for MALDI-TOF ms. Hence, this paper announced using PLA and PVDF nanofiber mat patterns as protein supports for MALDI-TOF mass spectroscopy.

Materials and Methods

Preparation of PLA and PVDF nanofiber mat patterns:

Electrospinning of 8% PLA in DMAc/$CHCl_3$ with the ratio of 25:75 was carried out under high voltage of 8 kV, traveling distance between needle tip to target of 10 cm, and flow rate of 1 mL/h., while the electrospun PVDF was carried out using 19% PVDF in DMAc/acetone with the ratio of 4:6 was carried out under high voltage of 10 kV, traveling distance of 10 cm, and flow rate of 1 mL/h. Diameter size of nanofiber was determined using SEM (JSM-6480LV, JEOL). The nanofiber mats at various patterns were fabricated using man made moulds.

Preparation of protein solution:

20 mg/mL of DHB solution by weighing 5 mg of Dihydroxy Benzoic Acid and dissolving it in 245 µl of 0.1% TFA in 50% ACN followed by pipeting 5µl of 1nmol of Pepmix-1 (5 peptides standard from LaserBiolab). This will make 20 pmol/µl of Pepmix-1 in 20 mg/mL DHB matrix solution.

MALDI-TOF mass spectrometry:

PLA and PVDF fiber mats were cut with about equal size and placed onto 384 well MALDI target plate using conductive double sided tape. 1 µl of protein solution was spotted on the fiber mats prior to process on MALDI-TOF mass spectra technique. TOF MS spectrum of Pepmix1 sample was acquired from 800 to 3000 m/z using AXIMA –TOF MS, Shimadzu Biotech in positive reflectron with 337 nm nitrogen laser. The same acquisition parameters was applied with the following settings: laser power (90); raster type (regular circular, 2.8 mm diameter, 100 µm spatial distance); profiles per sample (500); laser rate (50Hz) and pulsed ion extract optimized at 1,800 m/z for resolution improvement. The resolved peaks were evaluated with 25% threshold peak detection and 0 mV threshold.

Results and Discussion

8% wt of PLA in $CHCl_3$ was first electrospinning on aluminum plate obtaining a nice fiber, but it doesn't work when the process spinned longer time. This is because the polymer solution was dried and blocked at the needle tip. This suggested that $CHCl_3$ exhibited low boiling point, once solution jetted, $CHCl_3$ evaporated very fast. To solve this problem, higher boiling point solvent, DMAc was mixed with various ratios. It was found that narrow distribution of PLA nanofibers was obtained at the ratio of 75:25 Hence, this condition was used to evaluate the processing condition and found that at 8 kV and traveling distance of 10 cm, the fibers exhibited quite narrow distribution with the fiber diameter range of 400-1000 nm and the average of 500 nm as shown in Figure 1 (a). The SEM morphology and its diameter size distribution of 19% PVDF in DMAc/acetone with the ratio of 4:6, shown in figure 1(b) was in the range of 400 - 1200 nm.

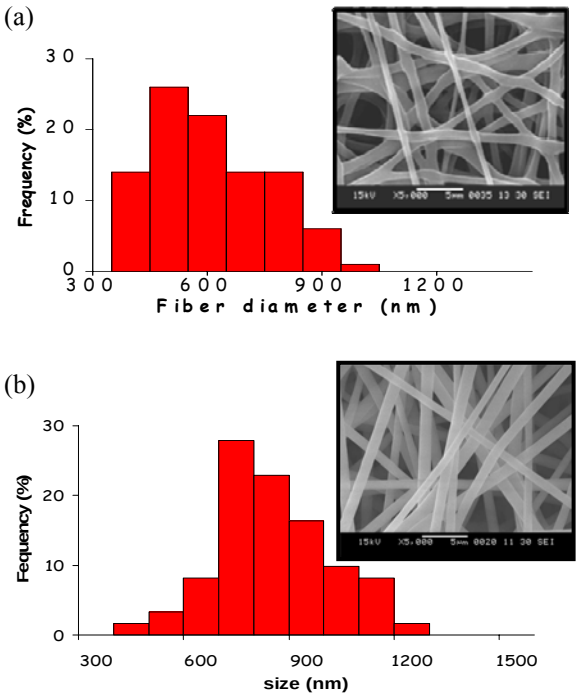

Figure 1: SEM images and diameter size distribution of (a) PLA and (b) PVDF electrospun nanofibers.

Nonwoven and aligned PLA and PVDF fiber mats have been fabricated for scaffold. It was found that the fiber mats were opaque, hence, it was difficult to observe cell growth under the optical microscope. On the other hand, aligned fiber mats were quite transparent but it can be made with a size of 10*10-13*10 cm^2 only. To make a better scaffold, nanofiber mat moulds were designed to manipulate mixed nanofiber mat between nonwoven and aligned fiber, hence, nanofiber patterns were obtained, as shown in table1.

Table 1: Percent alignment of PLA and PVDF nanofiber mats at various patterns.

Polylactic acid (PLA)		
Pattern	Image	% Alignment
L1		0.00±0.00
L3	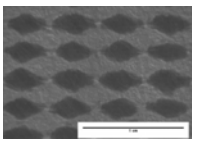	39.19±4.73
L4	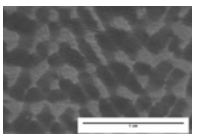	66.47±1.65
L6	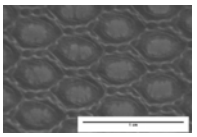	34.69±0.89
Polyvinyllidene fluoride (PVDF)		
Pattern	Image	% Alignment
F1		0.00±0.00
F3	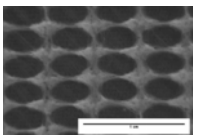	49.48±3.51
F4	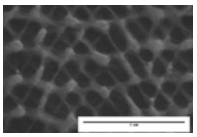	75.33±2.37
F6	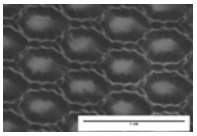	38.74±4.05

These patterns were pictured using a magnified lense on the black background, hence, the white area was nonwoven and the dark area was aligned nanofiber. PLA and PVDF nanofiber mats, L4 and F4, exhibited the highest alignment of 66.47% and 75.33% respectively.

MALDI-TOF ms is a well established mass spectrometry technique which has proved its abilities for identifying proteins, peptides and some other ionizable compounds in samplesref??. Sample support for MALDI-TOF MS should have high porosity and high surface area. It is expected that PLA and PVDF nanofiber mat patterns were met with this requirement. Therefore, these nanofiber mat

patterns were tested on standard protein Pepmix1, having 5 proteins: angiotensin II, angiotensin I, neurotensin, ACTH [1-17], ACTH [18-39]. Spectrum of Pepmix1 from conventional support was shown in Figure 2.

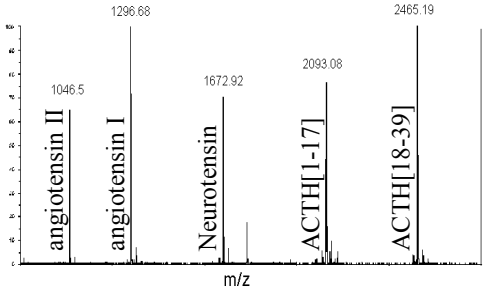

Figure 2: MALDI-TOF ms of standard pepmix-1 molecular weight 1000-2500 Da. (http://www.laserbiolabs.com/)

As seen in figure 3 and figure 4, The standard peptide sample was easily ionized on PLA fiber mat more than PVDF fiber mat. This is might be due to higher polarity of polymer. Although nanofibers mats L1, L3 and L6 exhibited high intensity of protein peak with low S/N ratio, the intensity at higher molecular weight proteins were quite low. On the other hand, L4 pattern obtained high intensity peaks for all proteins. This might be due to L4 pattern exhibited the highest aligned fiber, yielding higher surface area for protein absorption, then ionization was better carried out.

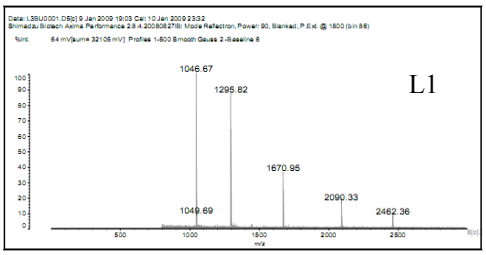

(a) L1 pattern

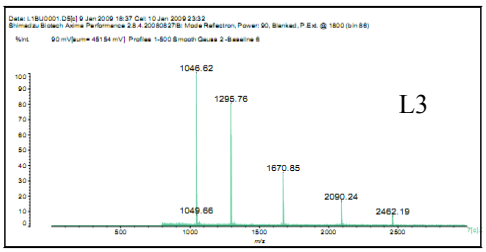

(b) L3 pattern

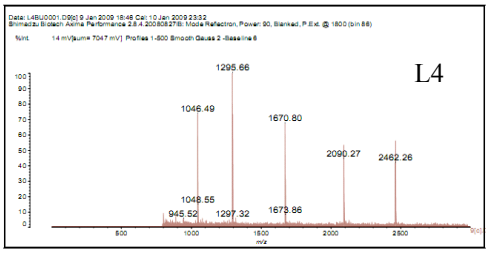

(c) L4 pattern

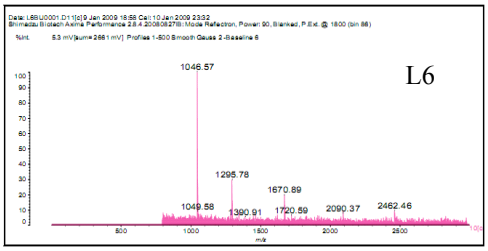

(d) L6 pattern

Figure3: MALDI-TOF ms of PLA nanofibers mat patterns.

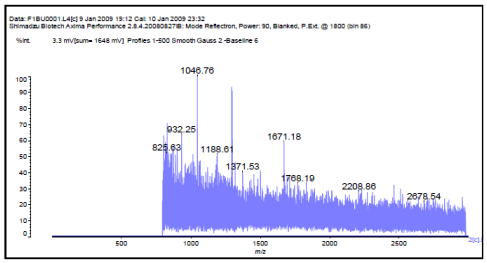

(a) F1 pattern

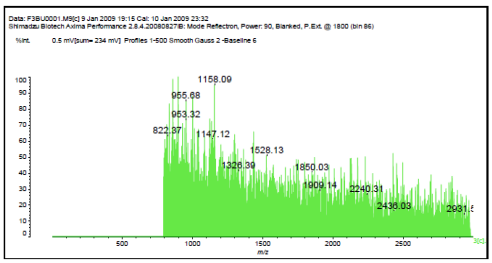

(b) F3 pattern

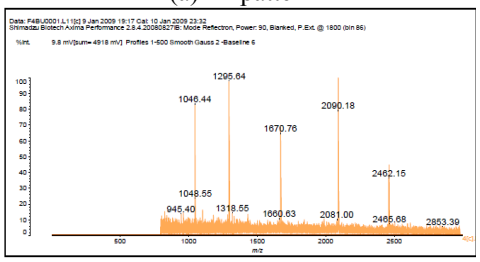

(c) F4 pattern

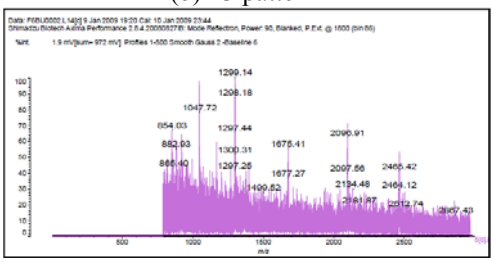

(d) F6 pattern

Figure 4: MALDI-TOF ms of PVDF nanofibers mat patterns

Conclusion.

PLA and PVDF nanofiber mat produced by electrospinning technique, can be nonwoven and mixed nonwoven and aligned morphology. These nanofiber mat patterns can be identified when they were used as protein supports prier to MALDI-TOF MS investigation. It was found that L4 pattern exhibited the highest intensity of protein spectrum. This is because this pattern displayed the highest percent of alignment fiber, as a result, protein can easily absorb and ionize.

References

1. Z.M. Huang, Y.Z. Zhang, M. Kotaki and S. Ramakrishna, *Composite science and technology*. **63** (2003), pp. 2223-2253.
2. F.Yanga, R. Muruganb, S. Ramakrishna, X. Wang, Y. X. Mac and S. Wang, *Biomaterials*. **25 (**2004), pp. 1891–1900.
3. M.G. Hajra, K. Mehta and G.G. Chase. *Separation and Purification Technology*. **30** (2003), pp. 79-88.
4. N.D. Luong, I.S. Moon, D.S. Lee, Y.K. Lee and J.D. Nam, *Materials Science and Engineering C*. **28** (2008)**,** pp. 1242–1249.
5. Y. Wang, S. Serrano and J.J.A Santiago. *Journal of Material Science Letters*. **21(13)** (2002), pp. 1055-1057.
6. H. Fong, W.D. Liu, C.S Wang and R.A. Vaia, *Polymer*. **43(3)** (2002), pp. 775-780.
7. F. Yanga, R. Muruganb, S. Wang and S. Ramakrishna. *Biomaterials*. **26** (2005**),** pp. 2603–2610.
8. W.P. Hsinu, J.Y. Cheng, Y.L. Chin, H.L. Yen and L.T. Wei, *J Am Soc Mass Spectrom*. **20** (2009), pp. 875–882.
9. B. Ding, H.Y. Kim, S.C. Lee, C.L. Shao, D.R. Lee and S.J. Park. *Journal of Polymer Science: Part B: Polymer Science*. **40** (2002), pp. 1261-1268.
10. E.R. Kenawy, G.L. Bowlin, K. Mansfield, J. Layman, D.G. Simpson and E.H. Sanders. *Journal of Controlled Release*. **81** (2002), pp. 5557-64..
11. S. Megelski, J.S. Stephens, J.F. Rabolt and C.D. Bruce. *Micro and nanostructured surface morphology on electrospun polymer fibers*. **35(22)** (2002), pp. 8456-8466.
12. K.H. Liland, B.H. Mevik, E.O. Rukke, T. Almøy, M. Skaugen and T. Isaksson, *Chemometrics and Intelligent Laboratory Systems*. **96 (**2009), pp. 210–218
13. S.H. Lee, B.C. Ku, X. Wang, L.A. Samuelson and J. Kumar. *Mat Res Soc Symp Pro*. **708** (2002), pp. 403-408.
14. S. Koombhongse, W.X. Liu and D.H.Reneker. *J Polymer Sci: Part B: Polymer Physics*. **39** (2001), pp. 2598-2606.
15. N. Chanunpanich, B. Lee and H. Byun. *Macromolecular Research*. **16** (2008), pp. 212-217.
16. Y. Wang, X. Xia and Y. Guo,. *J. Am. Soc. Mass Spectrom* . **16** (2005), pp. 1488–1492

A new narrow band gap polyfluorene copolymer for organic solar cells.

P. Piyakulawat, A. Keawprajak, U. Asawapirom*

National Nanotechnology Center, National Science and Technology Development Agency,
111 Thailand Science Park, Phahonyothin Rd., Klong 1, Klong Luang, Pathumthani, Thailand 12120

*E-mail: udom@nanotec.or.th

Abstract: A new copolymer, poly{[2,7-(9,9′-dioctyl) fluorene]-*co*-[5,5'-bis(3-dodecyl-2-thienyl)-2,2'-bithio phene]-*co*-[2,6-naphthalene-1,4,5,8-tetracarboxylic-N,N′-di(2-ethylhexyl)imide]}; PF4TFN was synthesized to limit the band gap widening by incorporating statistical donor and acceptor moieties in the main-chain of polyfluorene copolymer. The copolymer derived from 9,9'-dioctylflyorene, oligo-thiophene and naphthalene dicarboximide was polymerized through a Suzuki cross-coupling reaction using palladium complex as catalyst. The obtained copolymer showed absorption in wide range from 275-625 nm (solution) and 275-675 nm (film). The optical and electrochemical studied indicate that the band gap and energy level of the copolymer can be controlled by intramolecular electronic interactions character between the consecutive units. Polymer photovoltaic devices based on the blend of PF4TFN and PCBM in various ratios as an active layer was fabricated via spin-coating method. The best device performance was achieved at the copolymer/PCBM weight ratio of 1/4 under the illumination of A.M. 1.5, 100 mw/cm^2.

1. Introduction

In the past few years, the development of electroactive conjugated polymer for organic photovoltaic cells have attracted growing attention. Despite, one of the most successful donor polymer is poly(3-hexylthiophene) (P3HT). The devices made up of composites of P3HT:PCBM as active material have often been reported [1-3]. However, the upper limits of the power conversion efficiency (PCE) obtained by using P3HT seem to have been reached due to limitations of the polymer themselves. The one is the mismatch between the absorption spectrum of the photovoltaic layer and the solar radiation, which leads to only a small portion of solar energy, can be utilized. Another is poor charge transport properties of donor and acceptor materials [4-5]. Therefore, the design of novel photovoltaic polymer with broader absorption, low band gaps and high charge transport is one of the major challengers today.

As we known, polyfluorene (PF) show attractive properties in optoelectronic devices because of their properties such as good thermal and chemical stability, high fluorescence yield, good-film-forming and hole-transporting properties [6-7]. However, the large band gap made most polyfluorene copolymers less suitable for application in OPVs. Therefore, the modification of polyfluorene copolymers with large coverage of solar spectrum and low band gap were desirable [6,8]

In this work, a new copolymer based on polyfluorene and oligo-thiophene (as the electron donor) incorporating of naphthalene dicarboximide (as the electron acceptor) was synthesized for improvement of partial charge transfer and energy band gap. The chemical, optical and electrochemical properties of the copolymer were studies. The preliminary results of the devices based on the copolymer with PCBM as active layer are also presented.

2. Experimental section

2.1. Materials and Method

All reactions were carried out under an argon atmosphere. The starting materials and reagents were purchased from commercial sources and used without further purification. PCBM was synthesized from the reaction of fullerene and methyl-4-benzoylbutyrate-p-tosyl-hydrazone according to literature procedure [9]. The TiO_x precursor solution was prepared according to procedures previously reported [2]. Poly(3,4-ethylenedioxythiophene): polystyrene sulfonate (PEDOT:PSS) was received from Aldrich.

The synthesis compounds were characterized by NMR using $CDCl_3$ as the solvent. Chemical shifts were recorded in parts per million (ppm), and splitting patterns are designated as s (singlet), d (doublet), t (triplet) and m (multiplet). The molecular weights of polymers were evaluated by a Jasco Gel permeation chromatographic (GPC) analyzer. The UV/Vis spectra were recorded on a Perkin-Elmer Lambda 650 UV/Vis spectrophotometer. Fluorescence measurements were carried out on a Perkin-Elmer LS55 Fluorescence spectrometer with a xenon lamp as the light source. Cyclic voltammetry measurements were performed on an Autolab/Potentiostat galvanostat at room temperature under a nitrogen atmosphere. The measurements were carried out in an anhydrous acetonitrile solution containing 0.1 M of tetrabutyl ammoniumhexafluoro phosphate (Bu_4NPF_6) at a scan rate of 50 mV/s using a three-electrode cell with a platinum working electrode, a platinum wire counter electrode, and a Ag/AgCl reference electrode. Polymers to be measured were coated on the platinum working electrodes from dilute chloroform solutions and dried at 40°C in argon.

2.2. Synthesis

2,2′-Bis(trimethylstannyl)-5,5′-bithiophene (2): To stirred cooled solution (-50°C) of 2,2'-bithiophene (2.0 g, 12.03 mmol) and N,N,N′,N′-tetramethylethylene diamine (3.86 ml, 26.0 mmol) in anhydrous hexane/THF (40:40 ml) was added butyllithium solution (n-BuLi 1.6 M in hexane) (17.56 ml, 28.1 mmol) dropwise via a syringe. The solution was heated to reflux for 45 min and then cooled to -78°C. Trimethyltinchloride (26 ml, 26.0 mmol) was added dropwise and the mixture was stirred for 2 h at room temperature. The solution was then poured into aqueous NH_4Cl solution (2 M). The aqueous layer was extracted with diethyl ether (200 ml). The combine organic layers were washed with distillation water, dried over sodium sulfate (Na_2SO_4), and the solvent was removed. The residue was recrystallized from ethanol. The resulting product was obtained as brith solid. Yield: 4.13 g (70%)
^{1}H-NMR δ ($CDCl_3$): 7.25 (d, 2H), 7.07 (d, 2H), 0.36 (s, 18H).

3,3‴-Didodecyl-2,2′:5′,2″:5″,2‴-quaterthiophene (3): Compound **2** (0.87 g, 1.77 mmol), 2-Bromo-3-dodecylthiophene (1.17 g, 3.54 mmol), and tetrakis(triphenylphosphino)palladium [$Pd(PPh_3)_4$] (170 mg, 0.147 mmol) was mixed in anhydrous toluene (50 ml). The mixture was heated at 120°C for 18 h. and was then allowed to cool. The mixture solution was extracted with chloroform (50 ml) and aqueous HCl (2 M, 50 ml). The organic layer was isolated, washed with aqueous EDTA and $NaHCO_3$, respectively. The organic solution was dried over Na_2SO_4 and concentrated using a rotary evaporator. The product was purified by column chromatography on silica using hexane as the solvent. The compound **3** was obtained as a yellow solid. Yield: 0.43 g (36%)
^{1}H-NMR δ ($CDCl_3$): 7.15 (d, 2H), 7.10 (d, 2H), 7.00 (d, 2H), 6.93 (d, 2H), 2.76 (t, 4H), 1.63 (m, 4H), 1.23 (m, 36H), 0.85 (t, 6H).

5,5‴-Dibromo(3,3‴-didodecyl-2,2′:5′,2″:5″,2‴-quarterthiophene) (4): A mixture of compound **3** (0.605 g, 0.907 mmol) and n-bromosuccinimide (NBS, 0.162 g, 0.907 mmol) in hexane was heated to 50°C for 4 h to give a yellow precipitate. The precipitate was filtered off, washed with water/ethanol (1:1 v/v) and purified by column chromatography on silica using chloroform as the solvent. The pure product was obtained as orange solid. Yield: 2.2 g (67%).
^{1}H-NMR δ ($CDCl_3$): 7.08 (d, 2H), 6.95 (d, 2H), 6.88 (s, 2H), 2.68 (t, 4H), 1.55-1.23 (m, 40H), 0.85 (m, 6H).

2,6-Bisbromonaphthalene-1,4,5,8-tetracarboxylic acid anhydride (6): Bromine (1.68 g, 10.5 mmol) was poured into a solution of 1,4,5,8-naphthalenetetra carboxylic acid dianhydride (**5**) (2.68 g, 10 mmol) and iodine (6.5 mg, 0.03 mmol) in oleum (65% SO_3, 50 ml) and the reaction was stirred vigorously overnight at room temperature. The resulting orange suspension was poured into ice (200 g) and water was added (400 ml). The yellow precipitate was isolated by filtration and then sequentially washed with water, MeOH and dichloromethane. The compound was used in next step without further purification or analytical analysis due to its poor solubility in organic solvent. Yield: 4.02 g (94%).

2,6-Bisbromonaphthalene-N,N'-di(2-ethylhexyl)-1,4,5,8-tetracarboxylicdiimide (7): 2,6-Dibromonaph thalene (**6**) (2.0 g, 4.7 mmol) was stirred in glacial acetic acid (60 ml). Then 2-ethylhexylamine (2.3 ml, 14.1 mmol) was added dropwise and the reaction mixture was heated at 130°C overnight. After cooling to room temperature, the orange precipitate was recrystallized in acetic acid. The yellow-orange solid was isolated by filtration and then sequentially washed with distillation water and MeOH. Yield: 1.35 g (44%).
^{1}H-NMR δ ($CDCl_3$): 8.99 (s, 2H), 4.15 (m, 4H), 1.94 (m, 2H), 1.35 (m, 8H), 1.30 (m, 8H), 0.93 (t, 6H), 0.88 (t, 6H).

Poly{[2,7-(9,9′-dioctyl)fluorene]-co-[5,5‴-(3,3‴-didodecyl-2,2′:5′,2″:5″,2‴-quarterthiophene)]-co-[2,6-naphthalene-1,4,5,8-tetracarboxylic-N,N′-di(2-ethylhexyl)imide]}; PF4TFN:
Compound **4** (494.96 mg, 0.60 mmol), compound **7** (389.06 mg, 0.60 mmol), 9,9-dioctylfluorene-2,7-bis(trimethylborate) (989.93 mg, 1.2 mmol) and $Pd(PPh_3)_4$ (61 mg, 0.052 mmol) were refluxed in a mixed solvent of THF (25 ml) and toluene (25 ml) under argon atmosphere. The solution of Na_2CO_3 (5 ml, 0.2 g/ml) and n-butanol (5 ml) were added. The reaction mixture was stirred and heated for 3 days under protection from light. The suspension was allowed to cool down before aqueous (2M) HCl was added to stop the reaction. The polymer was extracted with chloroform. The organic phase was treated with an EDTA solution, $NaHCO_3$ solution and washed with water, respectively. The chloroform fraction was dried over Na_2SO_4, filtered and removed with a rotary evaporator. The polymer was solvated in $CHCl_3$ and precipitated into a mixture of methanol/ (2M) HCl (10:1 v/v). The precipitate was purified by Soxhlet extraction with methanol, acetone and chloroform, respectively. The chloroform phase was recovered, concentrated and crystallized in methanol/ (2M) HCl (10:1 v/v). The dark red precipitate was filtered off and dried under vacuum. Yield: 456 mg (78%).
^{1}H-NMR δ ($CDCl_3$): 8.79, 7.94-7.26, 7.17, 7.10, 4.05, 2.83, 2.02, 1.28-1.10, 0.79, 0.69.

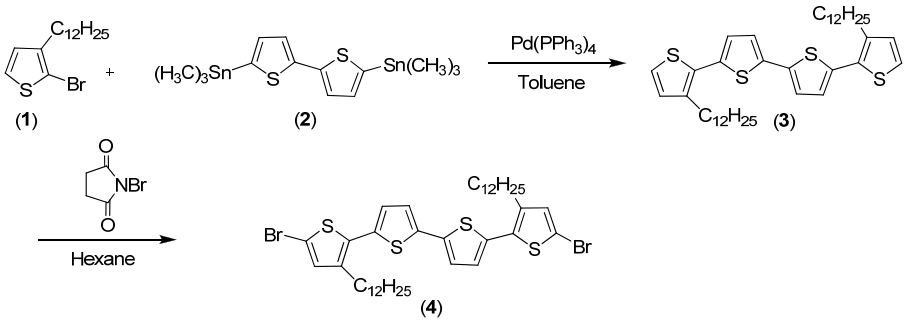

Scheme 1. Synthesis of oligo-thiophene monomer.

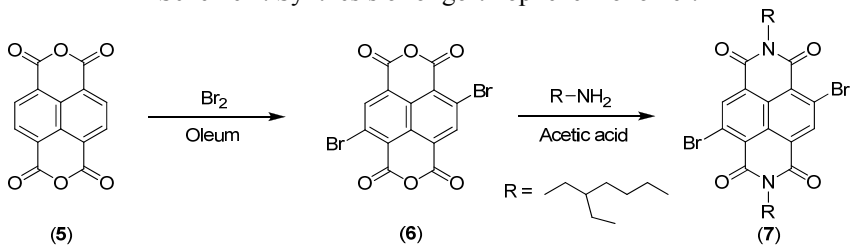

Scheme 2. Synthesis of naphthalenedicarboximide monomer.

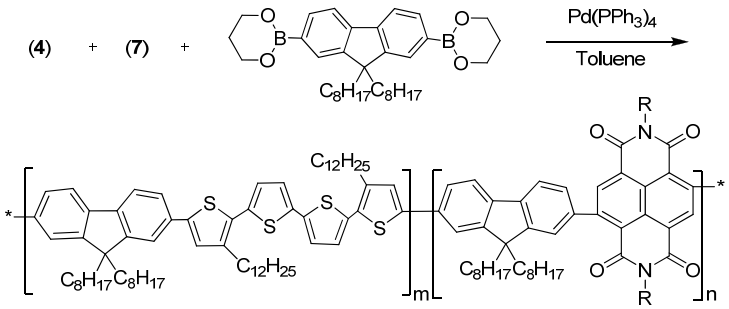

Scheme 3. Synthesis of PF4TFN copolymer.

2.3. Device Fabrication

Polymer solar cells were prepared according to the following procedure: The ITO-coated glass substrate (with a sheet resistivity of 15Ω/sq, Semiconductor wafer, Inc) was first cleaned. Onto the ITO glass, the conductive grade PEDOT:PSS (Aldrich; conductive grade) was spun-cast (2000 rpm) and dried at 110°C for 30 min under reduced pressure. The solutions of PF4TFN and PCBM in chlorobenzene were stirred for 12 h to ensure that all materials have completely dissolved and was spun-cast at 1500 rpm on the top of the PEDOT:PSS layer. The active layer was annealed at 165°C for 20 min under an argon atmosphere. Subsequently, TiO_x precursor solution was spun-cast on active layer, hydrolyzed in air for 30 min and dried at 150°C for 10 min. Finally, the samples were transferred into the vacuum chamber to deposit Al (~ 200 nm thick) on top of the spin-coated TiO_x film. The deposited Al electrode area defined the active area of the devices as 0.24 cm^2.

3. Results and Discussion

3.1. Synthesis and characterization

The synthetic routes toward the monomers and polymer are shown in Scheme 1-3. 2-Bromo-3-dodecylthiophene (**1**) and distannylated bithiophene (**2**) was coupled via Stille-type reaction to give quaterthiophene (**3**). Compound **3** was bisbrominated with NBS in hexane yielding oligo-thiophene monomer (**4**). Naphthalene-1,4,5,8-tetracar-boxylic acid anhydride (**5**) was converted under strong acidic condition into 2,6-bisbromonate (**6**) as outlined in Scheme 2. Bisbrominate (**6**) was then reacted with 2-ethylhexylamine by imidation reaction yielding naphthalenedicarboximide monomer (**7**). Lastly, 9,9-dioctylfluorene-2,7-bis(trimethylborate) was coupled with oligo-thiophene monomer (**4**) and naphthalene dicarboximide monomer (**7**) using $Pd(PPh_3)_4$ as the catalyst according to a Suzuki-type reaction to give the copolymer PF4TFN as summarized in Scheme 3.

The resulted copolymer is readily soluble in common organic solvent such as toluene, THF, chloroform and chlorobenzene. The average molecular weigth (M_w) of PF4TFN was determined by GPC analysis against polystyrene standards is found to be 19.200 g/mol with polydispersity index (PDI) of 1.35. The structure of PF4TFN was confirmed by NMR.

3.2. Optical and electrochemical properties

The optical properties of PF4TFN in dilute chloroform solution and the thin film are shown in Fig.1. The shape of the absorption spectrum in a film is similar to that in solution. The copolymer showed optical absorption in wide range from 275-625 nm (solution) and 275-675 nm (film). The red-shifted absorption spectra in solid film is presumably due to the increase in the coplanarity of polymer and the occurrence of intramolecular electronic interactions between the polymer molecules in the solid state. The optical band gap as 1.91 eV, estimated from the absorption onset (649 nm) of spectra in solid state.

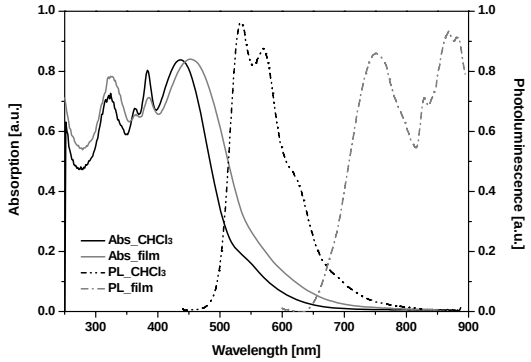

Figure 1. UV/Vis and PL spectra of PF4TFN in chloroform solution and solid state as film.

The emission spectrum of PF4TFN in thin films revealed red shifted and different in shape compared to the corresponding spectrum in solution. We attribute this to the presence of regions of more ordered, aggregated polymer chains within the film.

The electrochemical properties of PF4TFN (as film on Pt electrode) were investigated by CV. From the oxidation onset value of the copolymer at 1.09 V, the HOMO energy level was calculated according to the following equation; $E_{HOMO} = -(E_{ox} + 4.38)$ (eV), giving rise to the HOMO level of -5.47 eV. The LUMO energy level can be estimated from its HOMO energy level and optical energy gap with $E_{LUMO} = -3.56$ eV.

3.3 Solar cell characteristics

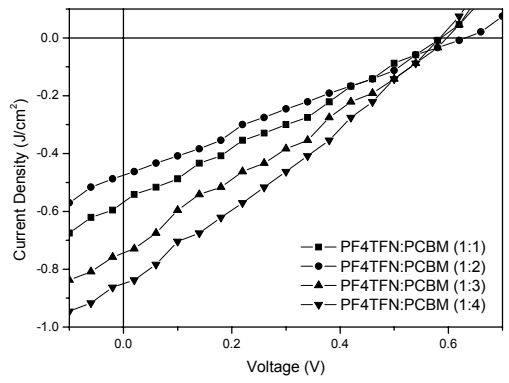

Figure 2. Current-voltage characteristics of PF4TFN:PCBM devices under illumination.

Bulk heterojunction solar cells were fabricated in the device configuration: ITO/PEDOT/PF4TFN:-PCBM/Al by solution processing. Weight ratios of PF4TFN:PCBM were varied from 1:1, 1:2, 1:3 to 1:4. The *J-V* characteristics of the produced devices were measured under AM 1.5 illumination with a calibrated solar simulator with an intensity of 100mW/cm^2. The results are presented in Fig. 2 and summarized in table 1. The J_{sc} and PCE, improves with increasing PCBM content in the composite film. The best device with PF4TFN:PCBM = 1:4 shows PCE 0.14% with V_{oc} of 0.58 V and J_{sc} of 0.85 mA/cm^2.

Table 1: Summary of performance for OPVs with various PF4TFN:PCBM ratios.

Device ratio	V_{oc} (V)	J_{sc} (mA/cm^2)	FF	PCE (%)
1:1	0.59	0.57	0.28	0.09
1:2	0.64	0.48	0.25	0.08
1:3	0.60	0.74	0.27	0.12
1:4	0.58	0.85	0.28	0.14

4. Conclusions

The synthesis of a narrow band gap copolymer PF4TFN based on fluorene was accomplished by Suzuki coupling reaction. The copolymer is readily soluble in common organic. The band gap of the copolymer is 1.95 eV, which indicate the band gap and energy level of the copolymer can be controlled by intramolecular electronic interaction between the consecutive units. The device with a PF4TFN:PCBM ratio of 1:4 (w/w) show the highest PCE 0.53% with V_{oc} of 0.66 V and J_{sc} of 2.48 mA/cm^2.

References

[1] E. Zhou, Z. Tan, Y. Yang, L. Huo, Y. Zou, C. Yang and Y. Li, *Macromolecules* **40** (2007), pp. 1831–1837.

[2] J. Y. Kim, S. H. Kim, H.-H. Lee, K. Lee, W. Ma, X. Gong and A. J. Heeger, *Adv. Mater.* **18** (2006), pp. 572–576.

[3] E. Perzon, X. Wang, S. Admassie, O. Inganäs and M. R. Andersson, *Polymer* **47** (2006), pp. 4261-4268.

[4] E. Wang, M. Wang, L. Wang, C. Duan, J. Zhang, W. Cai, C. He, H. Wu and Y. Cao, *Macromolecules* **42** (2009), pp. 4410–4415.

[5] A. Gadisa, F. Zhang, D. Sharma, M. Svensson, M. R. Andersson and O. Inganäs, *Thin Solid Films* **515** (2007), pp. 3126-3131.

[6] B. Zhao, D. Liu, L. Peng, H. Li, P. Shen, N. Xiang, Y. Liu and S. Tan, *Eur. Polym. J.* **45** (2009), pp. 2079-2086.

[7] M. S vensson, F. Zhang, O. Inganäs and M. R. Andersson, *Synth. Met.* **135-136** (2003), pp. 137-138.

[8] W. Mammo, S. Admassie, A. Gadisa, F. Zhang, O. Inganäs and M. R. Andersson, *Sol. Energy Mater. Sol. Cells* **91** (2007), pp. 1010-1018.

[9] J. C. Hummelen, B. W. Knight, F. LePeq, and F. Wudl, *J. Org. Chem.* **60** (1995), pp 532-538

The study of crystal structure and thermal decomposition of *Paphia undulate* using XRD, TGA and FTIR techniques

W. Siriprom[1*], M. Juntaropakorn[1], P. Donthuam[2] and P. Limsuwan[3]

[1]Faculty of Resources and Environment, Kasetsart University, Sriracha Campus, Chonburi ,Thailand.
[2] Department of Mechanical Engineering, Faculty of Engineering and Industrial Technology, Silpakorn University. Nakhon Pathom ,Thailand.
[3]Department of Physics, Faculty of Science, King Mongkut's University of Technology Thonburi, Bangkok 10140, Thailand.

*E-mail: w.siriprom@gmail.com , srcwcs@ku.ac.th

Abstract: The main purpose of this work is to study the structure of *Paphia undulate* shell sample and its structural transformation upon heat treatments. The sample was ground and characterized as powder throughout this work. Structural identifications of all samples were characterized, and determined qualitatively by using X-ray diffraction, thermogravimetry measurement (TGA), and FTIR spectroscopy. The powder sample was annealed at specific temperatures in the range of 200°C - 400°C and the effects of heat treatment on the structure of *Paphia undulate* shell samples were studied. The exact structures and quantities of phase at different annealing temperatures were studied by Rietveld refinement using the computer program FULLPROF SUITE-2000. The XRD patterns show that at 200°C *Paphia undulate* shell sample is pure aragonite phase as same as at room temperature. The aragonite begins to transform into calcite at the temperature of 300°C and completely transformed at 400°C. The TGA results show that the weight loss takes place at the temperature about 239 °C corresponding to expulsion of the water molecules. It indicates that at temperature 200°C the *Paphia undulate* shell sample is a reactive calcium carbonate. Hence, the *Paphia undulate* shell samples, after heat treatment at 200°C, is suitable to be used as a inorganic filler or calcium catalysis.

Introduction

Calcium carbonate like many other similar simple chemical compounds, forms different anhydrous polymorphs (aragonite, calcite and veterite) [1]. Marine skeletons may be composed of aragonite or calcite or a mixture of both structures. The marine mussel exoskeletons are expected to contain carbonaceous matter as they form themselves towards the carbonate exoskeletons by absorbing much of atmosphere emissions [2]. Although it is the major source and sink for atmospheric CO_2, there are major uncertainties about how it is stroed and how it might be released to the atmosphere in a cataclysmic eruptive cycle or impact event [3]. Calcium carbonate, a natural mineral with great biocompatibility, has been proven to intensify enzyme performance and has been widely used in industry, technology, medicine, microcapsule fabrication [4].

At the present time, inorganics fillers cooperate an important utility in plastic industry. Among the various mineral fillers, calcium carbonate ($CaCO_3$) has been the most utilized material, due partly to its availability and low cost, and other, have carried out research on two recurring issues that pertain to thermal reactivation. The first is related to calcium catalysis and has been addressed through the development of a new thermal reactivation protocol that overcomes the deleterious effects of calcium catalysis. The second issue is pH excursion: when reactivated carbon is returned to service, several water and waste water utilities have found that the pH of the subsequently treated water is excessively high [5].

The purpose of the present study is to investigate in detail the effect of temperature on crystal structure and phase transformation, It is of great importance to understand the formation and stability conditions for all crystal modifications of calcium carbonate, especially the formation of complex metamorphic for used as a filler for reinforcing thermoplastic.

Materials and Methods

The starting materials were the *Paphia undulate* samples, was obtained from the coastal area of Trad province, the eastern part of Thailand. First of all the soft parts inside the *Paphia undulate* samples were remove after opening the bivalve of the shell. The bivalve was brushed and washed with distilled water. Afterward the samples were cleaned by soaking in dilute HCl solution for less than 1 min, followed by washing thoroughly with distilled water. The cleaned sample was ground into fine powder to desired sizes by sieves and denoted as A-RT. Four powder samples were separately annealed at specific temperatures between 200 and 400^{o}C in a Carbolite furnace, model RHF 14/35. The heating rate was 5^{o}C /min until it reached the required temperatures and maintained at those temperatures for 4 h and then cooled down at 5 ^{o}C /min back to room temperature. The annealed samples are denoted as A-T200, A-T300, and A-T400 where the labeling numbers indicate the annealing temperatures. After the annealed sampled were kept in dessicator.

The crystal structure was characterized by a powder X-ray diffractometer. Powder diffraction data were recorded at room temperature using a Bruker AXS D8 Advance powder diffractomter [CuK_{α} (Ni

filtered) with scintillation detector; 2θ range, 20-80° step size 0.02°]. The minerals in each case were indentified from the diffractograms by reference to Joint Committee on Powder Diffraction Standard File (JCPDS).

The diffraction data were analysed by the Reitveld method using the computer program FULLPROF SUITE-2000. Reitveld (1969) introduced a technique to give the intensity by which crystal structure model can be refined from an experimental powder diffraction pattern using the method of least squares. Some 14 instrumental parameters were identified, including the mineral (phase) scaling factor, asymmetry, preferred orientation, half-width, instrument zero, line shape, and unit-cell parameter. It allows a calculated XRD profile of each mineral to be generate from its known crystal structure, and the sum of all calculated patterns to be fitted to the observed XRD profile of a multi-meneral sample by iterative least-squares analysis to find the individual phase scale. Then, these are used to estimate the mineral percentages in the sample.

Thermogravimetric (TGA) measurements were performed on Thermo Gravimetric Analyzer, Perkin Elmer TGA-7. Investigations were made while the samples were heated from 50 to 850°C at the rate of 5°C /min under atmosphere. The mass of the sample used for each measurement is about 5 mg.

Infrared analyses have been carried out on powdered shell. All spectra were recorded at 4 cm-1 resolution with 64 scans (measurement time > 4 min) with a Perkin Elmer Spectrum GX spectrometer Fourier transform infrared spectroscopy (FTIR), from 4000-370 cm^{-1}. For FTIR, 2 mg sample were dispersed in 300 mg KBr. All mixtures of the compound were pressed in pellet of cylindrical shape and carried out at room temperature.

Results and Discussion

When the *Paphia undulate* shell samples is heated up under an atmosphere, In thermogravimetric analysis, the TGA curve of aragonite phase is also observed that weight loss takes place at two stage of weight decreasing, its weight loss being observed as a function of temperature. The result of TGA (weight loss) and DTG (rate of weight loss, time differential of TGA) profiles is shown in Figure 1 and Figure 2.

From Figure 1 the weight loss started at around 200°C, and DTG curve showed a peak at 239°C corresponding to 1.65% of total weight loss, which is indicative of the maximum rate of weight loss. The thermal behavior in Figure 1 corresponds to expulsion of the water molecules. The thermogram in Figure 2 is shows a monotonous weight decreasing, weight loss started at around 600°C, and DTG curve showed a peak at 728°C corresponding to 42.60% weight loss. From temperature 600°C to 800°C as shown in Figure 1 and Figure 2, weight loss could be attributed to the dehydration and heat reactions of other organic compound and release of CO_2 gas present in the *Paphia undulate* shell samples. At temperature over 800°C indicate that decomposition of carbonates was produced.

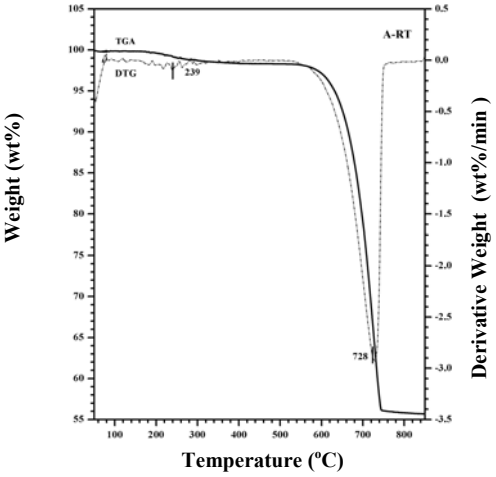

Figure 1. TGA and DTG plots of the *Paphia undulate* shell samples before annealing.

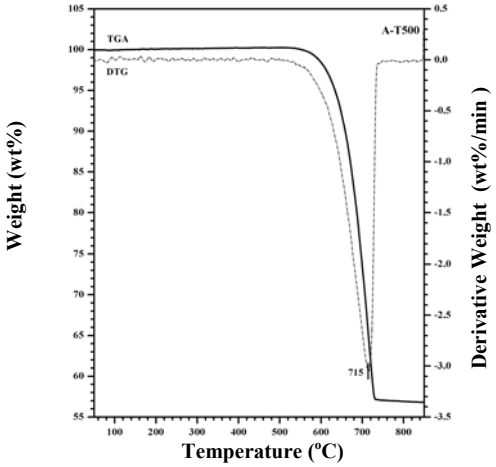

Figure 2. TGA and DTG plots of the *Paphia undulate* shell samples after annealing at 400°C.

The powder x-ray diffraction patterns of *Paphia undulate* shell samples before and after annealing at different temperatures and confirm by rietveld refinement are shown in Figures 3 – Figures 6. The powder X-ray diffraction pattern of A-RT in Figure 3 shows that the crystal structure of *Paphia undulate* shell samples was made of a pure aragonite phase, a common form of $CaCO_3$ mineral. For the common form of $CaCO_3$ mineral at room temperature, it indicated that the *Paphia undulate* shell samples are non – reactive calcium carbonate. X-ray diffraction patterns of *Paphia undulate* shell samples at temperature 200°C, it exhibited peaks characteristic of aragonite which the same as A-RT. Heating under atmosphere at temperature 200°C and the result of TGA involve that expulsion of the water molecules as shown in Figure 4. Transformation of aragonite to calcite starts at 300°C as shown in Figure 5. It can be concluded that A-T300 are composed of aragonite with a small fraction of calcite whereas at temperature

400^{o}C. A-T400 have pure calcite phase only as shown in Figure 6, suggesting that the phase transition is complete and seen that the greater weight loss corresponding to the release of CO_2 gas present in the *Paphia undulate* shell samples. The mineral phases at different temperature were identified from the diffractograms by reference to the Joint Committee on Powder Diffraction Standard file (JCPDS). For the JCPDS file number 01-083-0578, it corresponds to aragonite phase. The aragonite phase likely transforms into calcite phase at temperature above 200°C. Observed that the calcite phase corresponds to the JCPDS file number 01-077-2010.

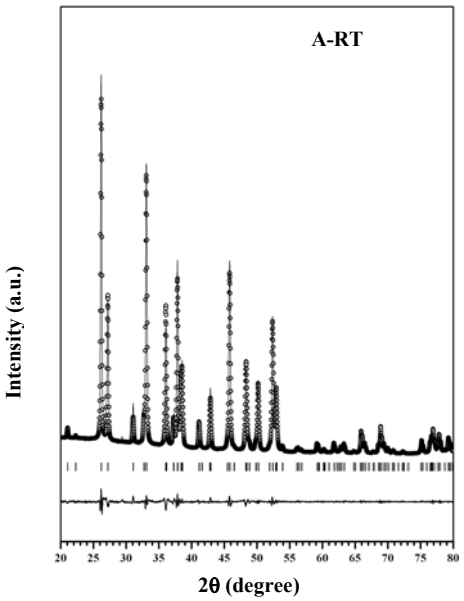

Figure 3. Difference X-ray diffraction profiles for the Rietveld refinement of *Paphia undulate* shell sample before heated-treatment. Experimental (○mark), calculated (solid line) and difference (bottom) powder diffraction profile.

XRD profiles with respect to corresponding structural parameters and instrumental parameters. For all refinements, lattice parameters and phase fractions of the *Paphia undulate* shell samples upon heat treatment are in good agreement. The percentage of phase fractions of the *Paphia undulate* shell samples upon heat treatment are reported in Table 1.

Polarized IR measurements were also carried out to confirm the structure of the *Paphia undulate* shell samples upon heat treatment. FTIR spectra of *Paphia undulate* shell samples are shown in Figure 7 the out of plane bending (ν2), the asymmetric stretching (ν3), and the in plane bending (ν4), modes of carbonate ion group are found to be active.

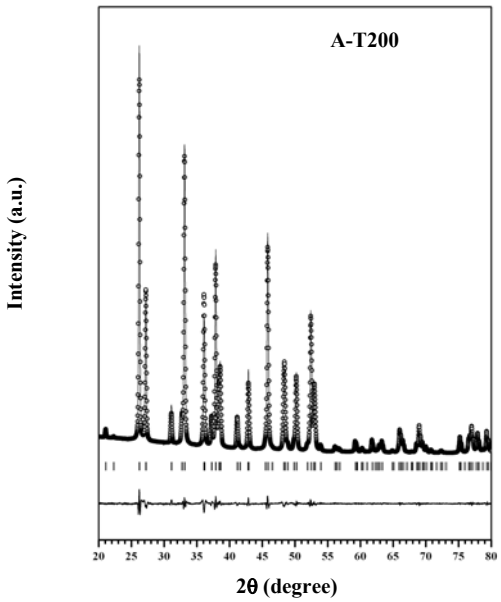

Figure 4. Difference X-ray diffraction profiles for the Rietveld refinement of *Paphia undulate* shell sample which heated at 200°C.Experimental (○mark), calculated (solid line) and difference (bottom) powder diffraction profile.

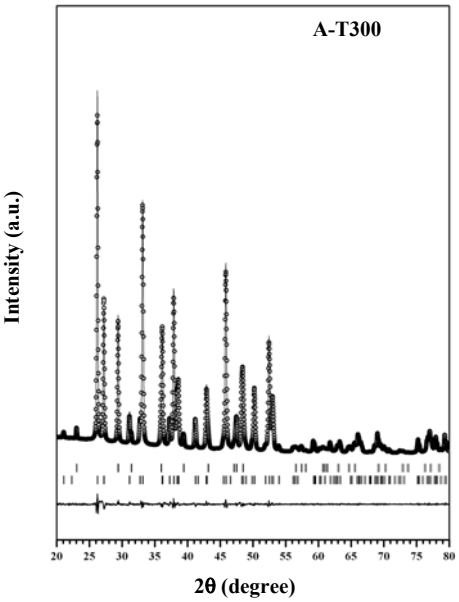

Figure 5. Difference X-ray diffraction profiles for the Rietveld refinement of Paphia undulate shell sample which heated a 300°C. Experimental (○mark), calculated (solid line) and difference (bottom) powder diffraction profile.

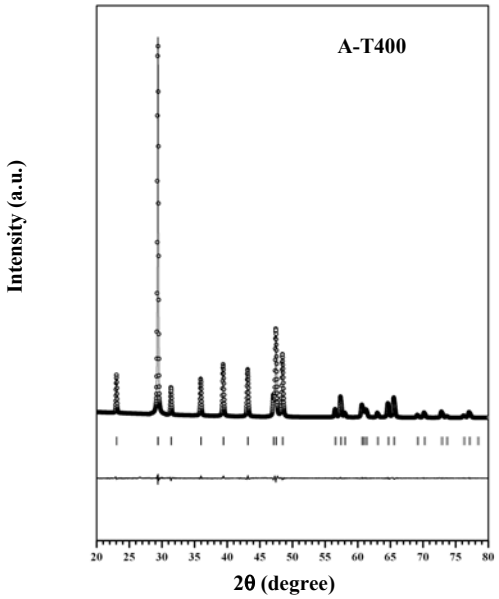

Figure 6. Difference X-ray diffraction profiles for the Rietveld refinement of Paphia undulate shell sample which heated at 400 °C. Experimental (○mark), calculated (solid line) and difference (bottom) powder diffraction profile..

Table 1: Relevant crystallographic data for the *Paphia undulate* shell samples, established from powder X-ray diffraction refinements before and after heat treatment.

Temperature/Type	% Composition		χ^2	Rwp	Rp
RT	Aragonite	100 %	1.37	8.17	6.14
T200	Aragonite	100 %	1.34	8.12	6.05
T300	Aragonite	94.73%	1.33	8.08	5.95
	Calcite	5.27%			
T400	Calcite	100%	1.23	7.48	5.15

Peaks located at 1788, 1471, 1082, 860, 713 cm^{-1} are assigned to the fundamental modes of vibration of CO_3^{2-} molecular ion. The broadband center at 1476 cm^{-1} in A-RT, A-T200 an A-T300 is assigned to asymmetric stretching mode of CO_3^{2-}. The molecular vibration of CO_3^{2-} ions gives frequency shift to about 876 cm^{-1} as seen in A-T400. The shift corresponds to the change of CO_3^{2-} structure coordinations, leading the change of carbonate. The band at ~1083 cm^{-1} of A-RT, A-T200 an A-T300 will be seen only in the aragonite lattice. The absence of the infrared inactive mode, ν1 (~1083 cm^{-1}) suggests that there is no breakdown of symmetry to that of free CO_3^{2-} radical, thus an indicative of the D3h symmetry corresponding to the calcite form of the $CaCO_3$. The absence band at ~1083 cm^{-1} observed from A-T400 indicates that there is a structural of calcite symmetry. While the FT-IR band between ~3500 cm^{-1} and ~3000 cm^{-1} of all sample have strong bands related to the presence characteristic broad band of OH stretching vibration.

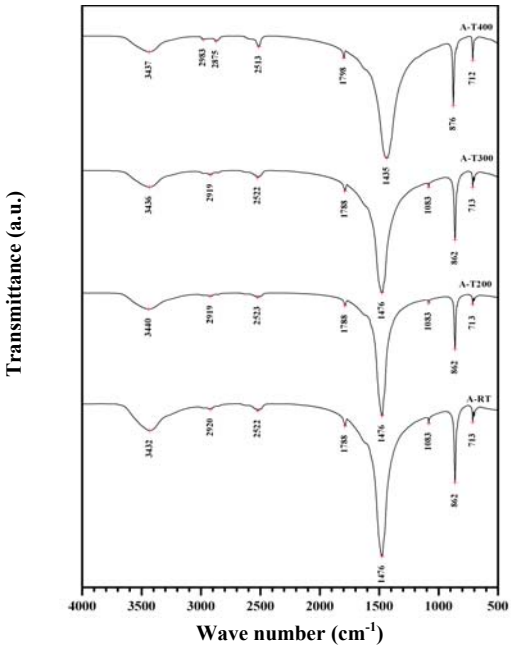

Figure 7. FTIR spectra of the *Paphia undulate* shell samples before and after annealing at 200, 300, 400, and 500˚C

Conclusions

The *Paphia undulate* shell sample obtained from the coastal area of Trad province, the eastern part of Thailand consists mainly of $CaCO_3$, aragonite structure. The heat treatment at temperature 200 °C on the powder sample has not induced the phase transformation from aragonite to calcite due to expulsion of the water molecules. This step is crucial for the quality of the final product, since the content in water molecule should be as low quality as possible. While the calcite phase begins at approximately 300 °C and is completed at about 500 °C.

References

[1] Perić, J.; Vučak, M.; Krstulović, R.; Brečević Lj.; Kralj, *J. Thermochim. Acta*. **277** (1996), pp. 175-186.
[2] Vongsavat, V.; Winotai P.; Meejoo S. *J. Nucl Instrum Meth B*. **43** (2006), pp. 167-173.
[3] Raju, C. L.; Narasimhulu, K.V.; Gopal, N.O.; Rao, J.L.; Reddy, B.C.V. J. Mol Struct. **608** (2002), pp. 201-211.
[4] Gunasekaran, S.; Anbalagan. G. *J. Spectrochim Acta A*. 69 (2008), pp. 1246-1251.
[5] Lau, S., Mohamed, M., Tan Chi Yen, A., and Su'ut, S., *The Science of The Total Environment*, **214** (1998), pp. 113-121.

Effect of using lignin extracted from pulping black liquor in polyethylene foam on physical and mechanical properties

A. Boonprasertpoh[1] D. Pentrakoon[1]* and W. Chavasiri[2]

[1]Department of Materials Science, Faculty of Science, Chulalongkorn University, Bangkok, Thailand 10330
[2]Department of Chemistry, Faculty of Science, Chulalongkorn University, Bangkok, Thailand 10330

*E-mail: duanghat@sc.chula.ac.th

Abstract: This research was conducted to assess physical and mechanical properties of polyethylene foam incorporating various amount of lignin from 5 to 20 parts per hundred. The lignin was extracted from pulping black liquor by precipitating with sulfuric acid at pH 3. A Fourier Transform Infrared Spectroscopy (FTIR) and Thermo Gravimetric Analyzer (TGA) were employed to characterize the extracted lignin. The preparation of polyethylene foam was carried out by a two stage process using two-roll mill and compression moulding. Visual inspection, density measurement, and Scanning Electron Microscope (SEM) were used to investigate physical properties while compression test and compression set were used to investigate mechanical properties. The SEM micrographs shows that cell size vary with amount of lignin. The addition of 10phr lignin in foam reveals maximum average cell size about 0.51 millimetres.

Introduction

Kraft pulping process, i.e. alkaline pulping process, is generally used in paper-making industry in Thailand since producing a strong pulp and chemical reagents being recycled [1, 2]. This Pulping process generates a great deal of black liquor containing sodium, sulfur, carbohydrate and lignin [1-3]. Generally, some of black liquor was treated via water treatment system, used as a fuel source for burning system in the pulping process, and also discharged as waste causing ecological dilemma. From previous studies [1, 2], it revealed that black liquor contains great amount of lignin, which can be isolated and used as the material for a series of useful products [1, 2]. Lignin can be utilized as an antioxidant for rubber and plastic [4, 5], processing stabilizer, light stabilizer [6], and flame retardant [7].

In this study, lignin extracted from pulping black liquor was incorporated in polyethylene foam by various amount of lignin. The effects of amount of lignin in polyethylene foam were investigated.

Materials and Methods

Materials: Low density polyethylene (LDPE) Grade MFI 2 and black liquor were kindly supplied by SCG Chemical and SCG Paper Plc, respectively. zinc oxide (ZnO), stearic acid, dicumyl peroxide (DCP), azodicabonamide (ADC), and sulfuric acid were purchased from S.R. LAB.

Preparation and Characterize of lignin: The lignin was extracted from pulping black liquor by precipitating with sulfuric acid at pH 3, filtered to obtain solid lignin. The solid lignin was washed in hot water several times, and then dried in an hot oven.

The chemical structure of the obtained lignin was characterized by FT-IR technique on Niccolet 6700 FT-IR. Lignin samples were mixed with KBr and pressed into a disc form by hydraulic compression. Each spectrum was recorded at a resolution of 4 cm^{-1} with 64 scans at a frequency range of 400-4000 cm^{-1}.

Thermo gravimetric analysis (TGA) were carried out on samples of about 7 mg in nitrogen atmosphere with a flow rate of 20 ml/min on a temperature range from 50 to 1000°C at a scanning rate of 20°C/min using METTLER TGA/SDTA 851^e.

Preparation of Polyethylene foam: Polyethylene foam was prepared by a two stage process using two-roll mill and compression moulding. Firstly, LDPE 100g, ZnO 5g, Stearic acid 1g, ADC 5g, DCP 0.5g and various amounts from 5 to 20g of lignin were mixed using two-roll mill. The obtained mixture was placed in compression moulding at press temperature 175°C and pressure 150 bar for 15 min, followed by cooling to 60°C.

Physical Properties of foam: Foam density was determined according to ASTM D 3575-08 suffix W method A. Besides, cell size and distribution were observed using SEM and SemAfore program. The foam sample was cut perpendicular to the rise direction and mounted on a aluminum stubs with nail polish. To obtain sufficient signal, the mounted foam samples were coated with gold-palladium under vacuum atmosphere. Foam samples were viewed using a JEOL JSM 6400 at a voltage of 15 kV.

Mechanical properties of foam: Compression set was conducted in line with ASTM D 3575-08 suffix B. The sample was compressed to 50% of its thickness for 22 hours, after that decompressed, and then measured the thickness after the specified recovery time – until 24 hours. The compression set (C_d) expressed as percentage of the original thickness was calculated as

$$C_d = [(t_0 - t_f) \times 100]/t_0$$

Where t_0 represents an original thickness (mm), and t_f represents thickness of the specimen after the specified recovery period (mm).

Compressive strength was performed using Universal Testing Machine Instron 5582 with the compressive speed of 12.5 mm/min according to ASTM D 3575-08 suffix D. The compression deflection force per unit of specimen area (CD) was calculated as

$$CD = F/A$$

Where F represents force required to compress the specimen 25% of the thickness (N) as measured, and A represents specimen compression contact surface area (m^2).

Results and Discussion

Figures 1 presents the spectra of extracted lignin (LIG), which shows relatively broad peak at 3420 cm^{-1} wavenumber designating O-H stretching peak, peaks at 2925 cm^{-1} and 2850 cm^{-1} wavenumber designating C–H stretching, peak at 1715 cm^{-1} wavenumber designating C=O nonconjugated, and peak between 1600 cm^{-1} and 1515 cm^{-1} wavenumber designating C–C bounds of aromatic skeleton. Some signals associated to syringyl (S) and guayacyl (G) groups in the lignin also exhibits at 1325–1265 and 1265–1130 cm^{-1} wavenumber, respectively.

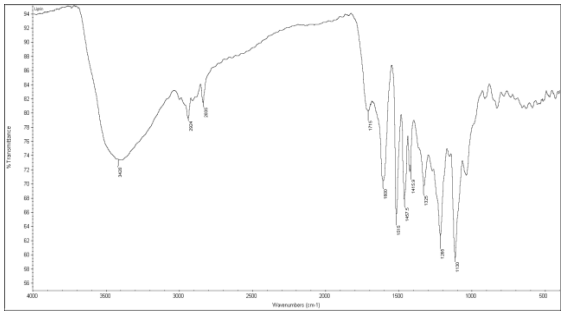

Figure 1. FT-IR spectra of extracted lignin.

The TG and DTG curves (weight loss of lignin in relation to the temperature of thermal degradation) as shown in Figure 2 demonstrates slow decomposition of extracted lignin in broad range of temperatures with maximal mass loss rate between 273°C and 403°C. Decomposition temperature was approximate 335°C.

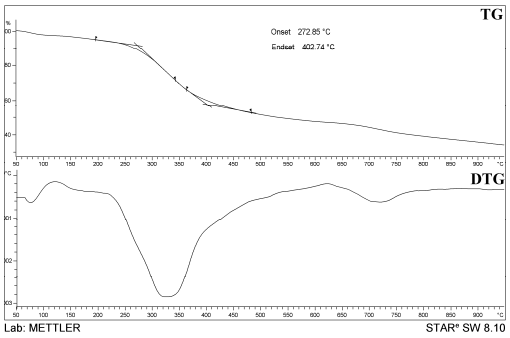

Figure 2. TG and DTG curve of extracted lignin

The SEM micrographs of PE foam sample with different ratios of lignin incorporation are presented at the same magnification of 30 times in Figures 3A-E. All micrographs show a closed-cell structure where average cell diameter measured using the SemAfore program presented in Table 1 denotes that PE foam incorporated 10 phr of lignin having the finest cell distribution with an average cell diameter of 0.506 mm.

Table 1: Average cell diameter

Foam specimens	Average diameter (mm)
PE	0.49±0.18
PE+ LIG 5phr	0.39±0.16
PE+ LIG 10phr	0.51±0.15
PE+ LIG 15phr	0.36±0.17
PE+ LIG 20phr	0.43±0.23

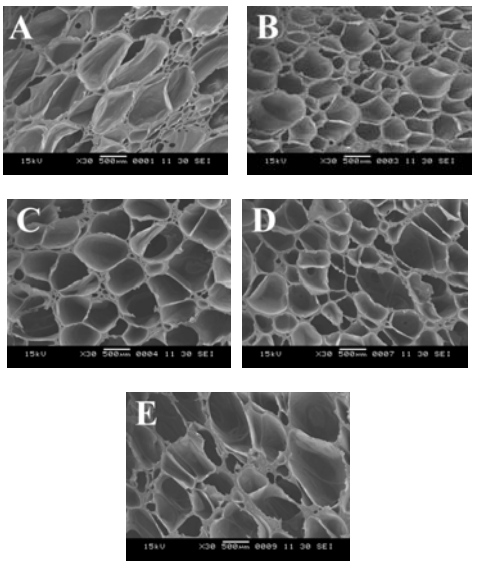

Figure 3. SEM micrographs of (A) PE foam, (B) PE foam+LIG 5phr, (C) PE foam+LIG 10phr, (D) PE foam+LIG 15phr lignin, and (E) PE foam+20phr lignin.

The density of each foam samples shown in Table 2, it is apparent that the density increases slightly with increasing amount of lignin.

Table 2: Foam density

Foam specimens	Density (kg/m^3)
PE	92.57±4.56
PE+LIG 5phr	102.65±4.11
PE+LIG 10phr	105.60±3.61
PE+LIG 15phr	111.85 ± 0.80
PE+LIG 20phr	115.63 ± 3.44

Compression set expressed as percentage of the original thickness (C_d) is presented in Table 3 where the recovery behaviour for each foam is shown in Figure 4.

Table 3: Compression set value (Cd) of PE foams

Foam specimens	Cd (%)
PE	3.58 ± 1.42
PE+LIG 5phr	5.37 ± 0.27
PE+LIG 10phr	6.85 ± 1.66
PE+LIG 15phr	7.80 ± 1.73
PE+LIG 20phr	8.79 ± 0.73

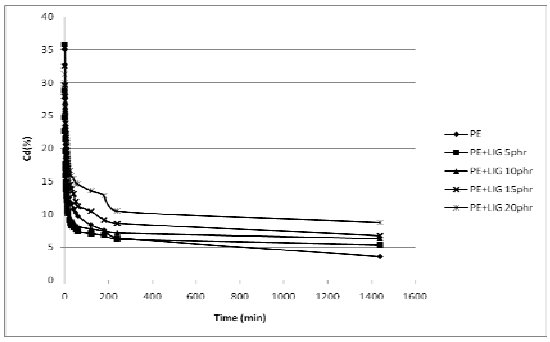

Figure 4 Compression set of PE foam samples with various amount of lignin.

It can be seen that the compression set increases with increasing amount of lignin where PE foam exhibits the finest recovery behaviour. Considering the recovery rate in Figure 4, it appears that PE foams incorporated with lignin 5 and 10 phr displaying improved recovery rate. This may be caused by more uniform cells size and cells distribution as described earlier by SEM micrographs.

As seen in Figure 5, the compressive strength increases gradually as increasing amount of lignin from 0 to 10 phr, subsequently the compressive strength declines. The explanation for this may be due to the cell structure and cell distribution of prepared foam samples. As PE foam incorporated 10 phr of lignin having the finest cell distribution, this would offer a better force distribution during the compression resulting in the highest compressive strength.

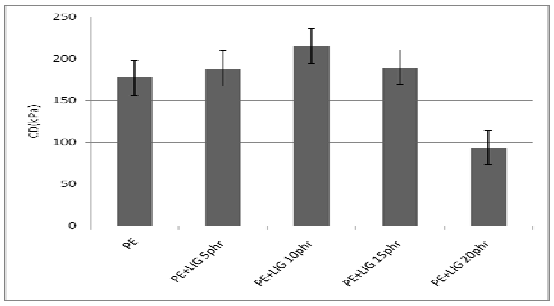

Figure 5. Compressive strength of PE foam samples with various amount of lignin.

Conclusions

It appears that the PE foam incorporated with 10phr lignin is likely to present the greatest physical and mechanical properties. At this proportion, the more uniform cell size and cell distribution of foam sample was detected. The improved recovery's capability from compression set testing and highest compressive strength were also perceived.

Acknowledgements

The authors would like to express gratitude to the SCG chemical and SCG paper Plc for supplying some materials, and also Department of Materials Science, Faculty of Science, Chulalongkorn University for financial, material and instrument support.

References

[1] Supachet Pongsai, Thesis Submitted in Partial Fulfillment of the Requirements for the Degree of Master of Science in Petrochemistry and Polymer Science Faculty of Science Chulalongkorn University. 2004.

[2] Witchar Pichainarong, Thesis Submitted in Partial Fulfillment of the Requirements for the Degree of Master of Science in Environmental Science Inter-department of Environmental Science Graduate school Chulalongkorn University. 2002.

[3] A. Garcia, A. Toledano, L. Serrano, I. Egues, M. Gonzalez, F. Marin, J. Labidi, Characterization of lignins obtained by selective precipitation, Separation and Purification Technology 68 (2009),pp 193–198.

[4] A. Gregorova, B. Kosikova, R. Moravcik, Stabilization effect of lignin in natural rubber, Polymer Degradation and Stability 91 (2006), pp. 229-233.

[5] A. Gregorova, Z. Cibulkova, B. Kosikova, P. Simon, Stabilization effect of lignin in polypropylene and recycled polypropylene, Polymer Degradation and Stability 89 (2005), pp. 553-558.

[6] P. Alexy, B. Kosikova, G. Podstranska, The effect of blending lignin with polyethylene and polypropylene on physical properties, Polymer 41 (2000), pp 4901–4908.

[7] A. De Chirico, M. Armanini, P. Chini, G. Cioccolo, F. Provasoli, G. Audisio, Flame retardants for polypropyplene based on lignin, Polymer Degradation and Stability 79 (2003), pp. 139-145

Preparation of electrospun fiber from polystyrene and poly (styrene-co-maleic anhydride) blends for lipase immobilization

R. Pudyenchuen[1], N. Chanunpanich[2], W. Chulalaksananukul[3], P. Opaprakasit[4], M. Opaprakasit[1,*]

[1]Department of Materials Science, Faculty of Science, Chulalongkorn University, Bangkok, 10330 Thailand
[2]Department of Industrial Chemistry, Faculty of *Applied Science*, King Mongkut's University of Technology North Bangkok, 10800 Thailand
[3]Department of Botany, Faculty of Science, Chulalongkorn University, Bangkok, 10330 Thailand
[4]School of Bio-Chemical Engineering and Technology, Sirindhorn International Institute of Technology (SIIT), Thammasat University, Pathumthani, 12121 Thailand

*E-mail: mantana.o@chula.ac.th, Tel: +66-2-2185559

Abstract: This study is aimed to develop an enzyme lipase catalyst system by immobilizing the enzyme on supporting materials. Feasibility of using spun fibers prepared via electrospinning of polystyrene/poly (styrene-co-maleic anhydride) blends as supporting materials for the lipase immobilization has been investigated. Effects of preparation conditions on morphology of the electrospun mats are investigated. It can be concluded from SEM results that types of solvent (DMF:THF at 1:1 and 2:1 weight ratio), concentration of polymer solution (10-15 %w/w), electrical potential (6-10 kV) and the distance between tip and collector (10-12 cm) significantly impose an influence on fiber appearance and their average diameter. It was found that the suitable conditions for e-spining PS/PSMA blend (1:1 weight ratio) are 8kV, 12%w/w in DMF mixed with THF at 1:1 weight ratio, and working distance at 10 cm. For PS/PSMA 4:1 blend, the optimal conditions are 6kV, 15% w/w in DMF mixed with THF at 2:1 and at the distance of 11 cm. These optimum conditions are defined as the spun fibers have bead-free structures and the smallest diameter. The study on the efficiency of lipase immobilization on the e-spun mats obtained at these optimal conditions is on-going and will be further discussed in separate communication.

Introduction

Utilization of enzymes as bio-catalysts has many advantages over chemical catalysts in many reactions. However, their high cost limits the use of enzymes in industrial scale process. Immobilization of enzyme [1-9] on supporting materials has been reported as a feasible and economically efficient approach for commercial use of the chemical, as the material's reusability results in a reduction of production cost. Therefore, various enzyme immobilization techniques have been researched for specific applications. Typically, high surface to mass ratio is a major property to generate high performance supporting materials. This can be achieved by reducing their dimensions to submicron scale. Electrospinning technique has recently proved as a potential process for producing polymeric nanofibers, which are suitable for use as supporting materials for enzyme immobilization [6-9].

Therefore, the main objective of this study is to develop an enzyme lipase catalyst system for use in production process of biodiesel by immobilizing the enzyme on electrospun nanofiber supporting materials produced from polystyrene/poly (styrene-co-maleic anhydride) blends. Effects of blend ratios and electrospinning conditions, i.e. type of solvents, concentrations, electrical potential and working distance, on morphology of the electrospun mats have been investigated. In addition, measurements of immobilization efficiency of the enzyme on the electrospun mats are ongoing.

Materials and Methods

Materials: Poly (styrene-alt-maleic anhydride) (PSMA, Mw 350,000) and polystyrene (PS, Mw 280,000) were supplied by Aldrich. Solvents, i.e. dimethylformamide (DMF) and tetrahydrofuran (THF), were obtained from Lab Scan. *Candida rugosa* lipase was purchased from Sigma-aldrich. Potassium dihydrogen phosphate (Carlo Erba), sodium hydroxide (Ajax Finechem) and tris-(hydroxymethyl)-aminomethane (Scharlau Chemie S. A.) were used in an enzyme immobilization process.

Preparation of electrospun fibers: Polymer solutions at various concentrations and different weight ratios of PS/PSMA were prepared in a mixed solvent of DMF and THF (Table 1). Electrospinning of a polymer solution was conducted at a flow rate of 1 ml/h using voltages and distances from needle tip to collector (screen covered with aluminum foil) as summarized in Table 1.

Table 1: Electrospinning conditions of PS/PSMA blend solutions prepared in mixed solvents at various concentrations.

PS:PSMA weight ratio	DMF/THF weight ratio	Conc^{n} (%w/w)	Voltage (kV)	Tip-to-collector distance (cm)
1:1	1:1	10-15	6 - 10	10
4:1	1:1 2:1	10-15 15	6 - 10 6	10 10-12

Characterisations: Morphology of the electrospun fibers was examined by a scanning electron microscope (SEM) (JEOL, JSM-6480LV). The average diameters were calculated from approximately 100 fibers observed in SEM images (2000X).

Results and Discussion

Effects of polymer concentration and an electrical potential on morphology of fibers prepared from PS/PSMA blend at 1:1 weight ratio are revealed in Figure 1 - 3. SEM images in Figure 1 obviously present that bead structures are obtained when a 10%w/w solution was spun with 6 - 10 kV. Figure 2 shows that bead-free fibers are successfully obtained when the e-spinning was performed in the range of 6 - 10 kV with the concentration of 12%w/w. Diameters of the e-spun fibers monitored from these images are plotted as histograms of the diameter distribution (Figure 2) and the average values are summarized in Table 2.

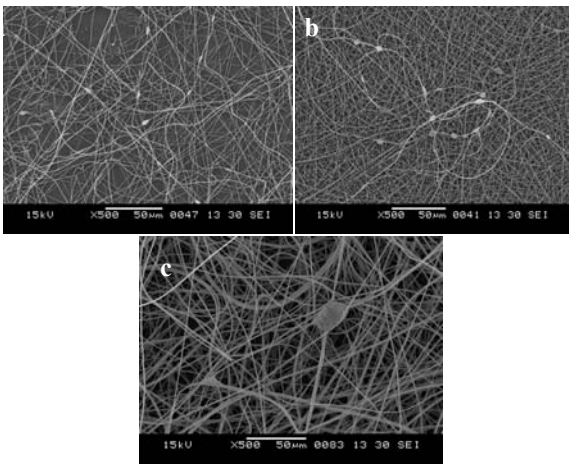

Figure 1. SEM images of fibers prepared from 10%w/w solutions of PS/PSMA blend (1:1) fabricated at (a) 6, (b) 8, and (c) 10 kV in a mixed DMF:THF (1:1) solvent.

It is clearly seen from these plots that the distribution is narrower when the spinning process was carried out at 8-10 kV (Figure 2b and 2c), compared to that prepared at 6 kV (Figure 2a). Results in Table 2 indicate that the increase in electrical potential from 6 to 8 kV results in a decrease in the average diameter of the fibers. However, upon increasing the potential further up to 10 kV, the resulting spun-fibers are thicker. It is observed from Figure 3 that fibers with bead-free structure are obtained only at 6 and 10 kV when the concentration of 15%w/w solution was employed.

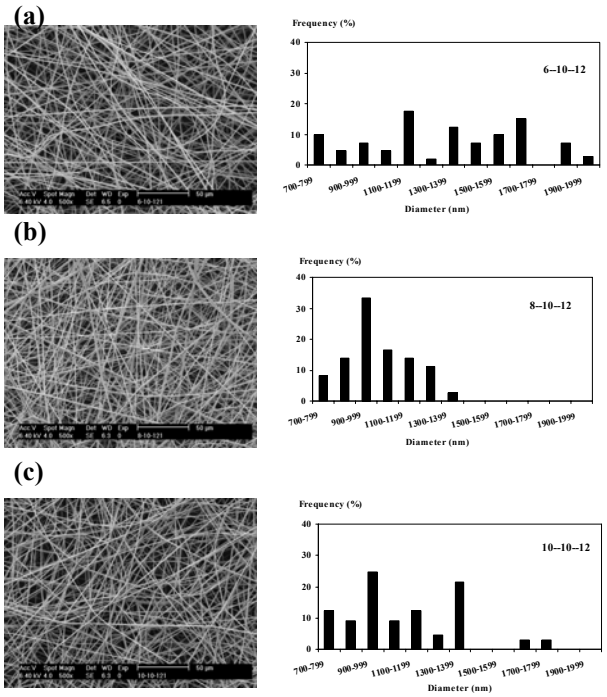

Figure 2. SEM images and diameter distribution of fibers prepared from 12%w/w solutions of PS/PSMA blend (1:1) fabricated at (a) 6, (b) 8, and (c) 10 kV in a mixed DMF:THF (1:1) solvent.

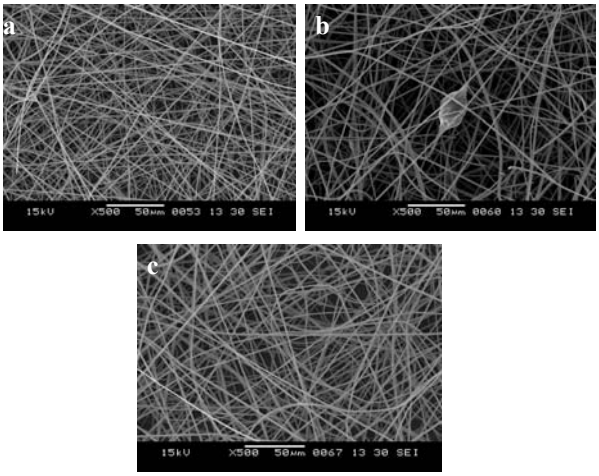

Figure 3. SEM images of fibers prepared from 15%w/w solutions of PS/PSMA blend (1:1) fabricated at (a) 6, (b) 8, and (c) 10 kV in a mixed DMF:THF (1:1) solvent.

Table 2: Average diameter of e-spun fibers obtained at 10 cm (distance of tip to collector) from PS/PSMA (1:1) blend solutions at a concentration of 12 %w/w.

Voltage (kV)	diameter ± SD (µm)
6	1.20 ± 0.29
7	1.04 ± 0.23
8	1.01 ± 0.16
9	1.05 ± 0.21
10	1.13 ± 0.29

For PS/PSMA blend at a 4:1 weight ratio, fibers with bead-free structure are not possibly obtained from solutions of DMF: THF (1:1) solvent at the concentration of 10 %w/w (Figure 4) in mixed solvent of, similar to what observed in the 1:1 PS/PSMA blend. However, production of bead-free fibers is feasible at 15%w/w concentration only when an electrical potential of 6 kV was applied (Figure 5a). E-spinning of the 4:1 PS/PSMA blend was also conducted with 2:1 DMF/THF mixed solvent. As evidenced in Figure 5a and 6a, the use of weight ratio of DMF/THF at 2:1 seems to provide much narrow diameter distribution than at 1:1 when similar spinning conditions and solution concentration were employed.

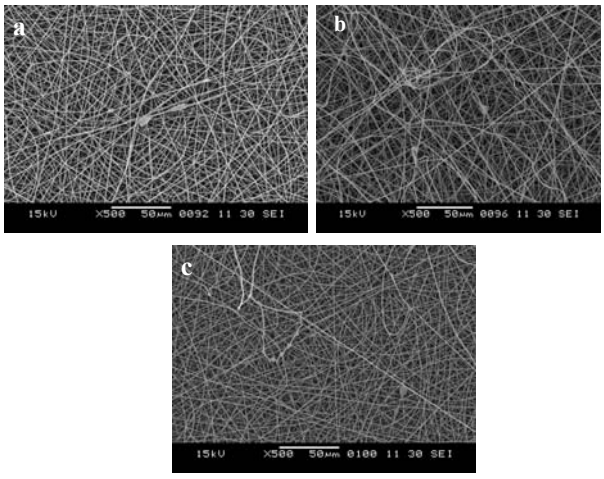

Figure 4. SEM images of fibers prepared from 10%w/w solutions of PS/PSMA blend (4:1) fabricated at (a) 6, (b) 8, and (c) 10 kV in a mixed DMF:THF (1:1) solvent.

Not only the electrical potential but a tip-to-collector distance also play significant role in morphology of the e-spun fibers. This can be verified by the distribution plots presented in Figure 6 and value of fibers average diameter (Table 3) which indicate that the thinner fibers are typically received by increasing the distance between need tip and collector.

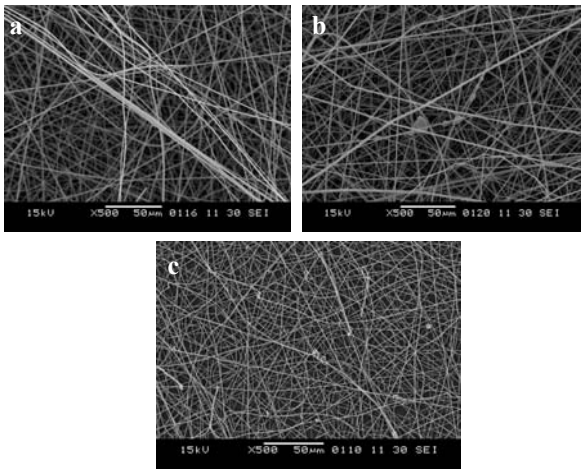

Figure 5. SEM images of fibers prepared from 15%w/w solutions of PS/PSMA blend (4:1) fabricated at (a) 6, (b) 8, and (c) 10 kV in mixed DMF:THF (1:1) solvent.

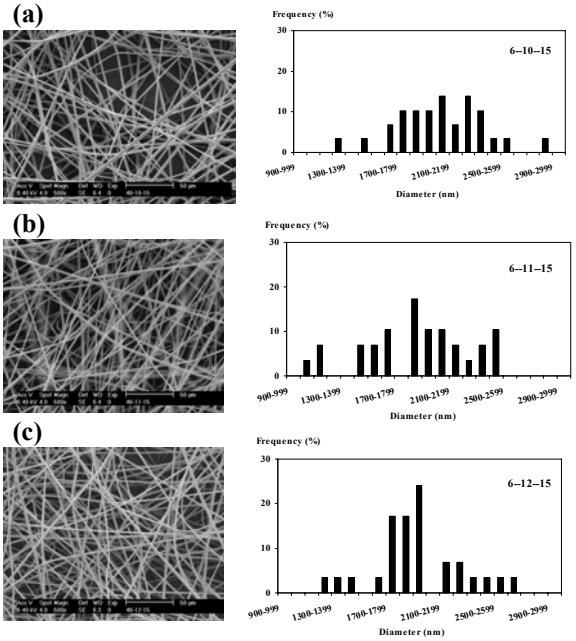

Figure 6. SEM images and diameter distribution of fibers prepared from 15%w/w solutions of PS/PSMA (4:1) fabricated at 6 kV using tip-to-collector distance at (a) 10, (b) 11 and (c) 12 cm.

Table 3: Average diameter of e-spun fibers obtained at 6kV from PS/PSMA (4:1) blend solution in 2:1 mixed DMF: THF at a concentration of 15%w/w.

Tip-to-collector distance (cm)	Diameter ± SD (µm)
8	2.08 ± 0.46
9	2.01 ± 0.39
10	2.03 ± 0.34
11	1.86 ± 0.38
12	1.93 ± 0.32

The preparation of e-spun fiber mat for use in lipase immobilization was carried out using a rotating steel cylinder (diameter x length: 30 cm x 57 cm) as a collector. The spinning was performed continuously for 2 hours. 3x3 cm^2 pieces cut from the electrospun mats were incubated at room temperature in 1ml lipase solution (2mg/ml) for 30 min and further kept overnight at 4°C. Subsequently, the samples were washed with phosphate buffer (pH 6.5) until no leaching of lipase was observed. Lipase contents of the remaining solution after immobilization and the washing solutions were measured and employed in the calculation of the amount of lipase immobilized on the electrospun fibers. Lipase concentration in these solutions was determined by measuring protein loading (BSA equivalent) according to Lowry method on a UV-vis spectrophotometer (Anthos Zenyth 200 rt). Study on effect of blend composition used in preparation of the fibers on the amount of immobilized enzyme is currently undergoing, and will be discussed further.

Conclusions

Electrospun fibers with bead-free structure are successfully fabricated from PS/PSMA blends with 1:1 and 4:1 weight ratio. Fibers with average diameter of 1.01 ± 0.16 μm were obtained from 1:1 PS/PSMA blend at 8 kV, 12%w/w solution in mixed DMF:THF (1:1) solvent and the distance from tip to collector of 10 cm. The corresponding fibers obtained from 4:1 blend show average diameter of 1.86 ± 0.38 μm with the following preparation conditions; 6 kV, 15%w/w in DMF mixed with THF at 2:1 weight ratio and the distance of 11 cm. Since high surface area is one of the most important properties required for supporting materials in enzyme immobilization application, the spun mats with smallest diameter prepared at these optimum conditions have been utilized in the immobilization of enzyme lipase. Efficiency of the immobilization process is under currently investigation.

Acknowledgement

The authors thank the Thailand Research Fund (granted no. MRG5280089) for financial support.

References

[1] Y. Wang and Y.-L. Hsieh, *J. Membr. Sci.* **309** (2008), pp. 73 – 81.
[2] Z. G. Wang, L. S. Wan, Z. M. Liu, X. J. Huang and Z. K. Xu, *J. Mol. Catal.B: Enzym.* **56** (2009), pp. 189-195.
[3] H. Filippusson, and W. E. Hornby, *Biochem. J.* **120** (1970), pp. 215–219.
[4] J. D. Page, R. Derango and A. E. Huang, *Colloids. Surf. A: Physico. Eng.* **132** (1998), pp. 193-201.
[5] V. V. Kuznetsov and S. V. Sheremet'ev, *J. Anal. Chem.* **62** (2007), pp. 270–278.
[6] S. Nair, J. Kim, B. Crawford and H. S. Kim, *Biomacromolecules.* **8** (2007), pp. 1266-1270.
[7] H. Jia, G. Zhu, B. Vugrinovich, W. Kataphinan, H. D. Reeneker and P. Wang, *Biotechnol. Prog.* **18** (2002), pp. 1027-1032.
[8] M. Ignatova, O. Stoilova, N. Manolova, D. G. Mita, N. Diano, C. Nicolucci and I. Rashkov, *Eur. Polym. J.* **45** (2009), pp. 2494-2504.
[9] C. Tand, S. Ye and H. Liu, *Polymer.* **48** (2007), pp. 4482-4491.

Preparation of MgO-Stabilized Na-β"-Alumina solid electrolyte using Na_3PO_4 as a sintering aid

K. Srisurat[1], W. Simsuay[1] A. Niyompan[1]* and R. Tipakontitikul[1]

[1]Department of Physics, Faculty of Science, Ubon Ratchathani University, Ubon Ratchathani, Thailand

* E-Mail: anuson@rocketmail.com

Abstract: This work is aimed to prepare the β"-aluminas solid electrolyte for application in electric vehicle battery system. The MgO-Stabilized Na- β"-alumina powder was prepared by calcination of the mixture of Na_2CO_3, MgO and γ-Al_2O_3 according to the formular $Na_{1-x}Mg_{2x}Al_{5-x}O_8$ with x = 0.175 at temperature 1200°C for 10 hours. Sintering temperature were selected in range 1450-1550°C for 4 hours and addition of Na_3PO_4 were varied from 1, 3, 5 and 10 mol% respectively. The XRD investigation on both powder and ceramics revealed that β"-alumina formed as a majority phase. The SEM results show that β"-alumina ceramic samples exhibit plate-like structure with strong packing and clustering arrangement. The highest density of 1.8358 g/cm^3 is found in ceramic sintered at 1550°C and with 10 mol% Na_3PO_4. Ionic conductivities values determined from AC impedance spectroscopy show that its highest value (measured at 300°C) was found in Na- β"-alumina sintered at 1550°C and with 5 mol% of Na_3PO_4.

Keywords: β"-Alumina, Solid Electrolyte, Conductivity, Liquid phase sintering.

Introduction

Sodium β"-alumina have been intensively studied for several decade because of its two-dimensional ionic conduction and high potential solid electrolytes for electrochemical applications, such as sodium sulfur battery, alkali metal thermoelectric converters, sodium sensors and electrochromic displays [1]. However, dense β"-alumina ceramics can be achieved only at high sintering temperature, i.e. 1600-1700°C [2, 3]. This temperature level normally lead to phase transformation because β"-alumina phase is a metastable at all temperature in the pure binary system. Therefore, it is usually stabilized by addition of MgO or Li_2O into system [2, 4]. In addition, high temperature sintering requires special skill and equipment. The other processing routes have been also attempted to reduce sintering temperature, e.g. sol-gel method [5] and microwave techniques [6-8] etc. But the latter mentioned methods displayed some disadvantages because of requiring complex starting materials and obtain only smaller quantity of the product. In this work, the attempt is to prepare MgO stabilized β"-alumina ceramic via conventional solid state reaction, and employing a so-called liquid phase sintering. Sintering behavior of the MgO-stabilized β"-alumina ceramics are then investigated. Phase formation is identified using XRD technique. The microstructure of β"-alumina ceramics were analyzed by SEM and ionic conductivities were determined using impedance analyzer.

Materials and Methods

Na-β"-alumina powders were prepared using conventional ceramics route with purity reagent chemical, i.e. Na_2CO_3, MgO and γ-Al_2O_3. A Mixture of starting materials was produced according to desired composition by ball-milling for 20 hours in ethanol solvent. The mixture was then subjected to calcination at 1200°C for 10 hours with heating and cooling rate of 5°C/min. Phase formation in calcined powders was identified using XRD technique. The calcined powders were then added with Na_3PO_4 in approximate concentration 1, 3, 5 and 10 mol% respectively, prior to sintering process. The ceramics pellets were formed using dry pressing technique and sintering were performed at temperature range 1450-1550°C for dwell time of 4 hours. The obtained ceramic was subjected to phase identification again. Densities of ceramics were determined using Archimedes principle. The microstructure of β"-alumina ceramics were analyzed by scanning electron microscopy (SEM). Finally, ionic conductivities of the ceramics were determined using impedance analyzer.

Results and Discussion

The XRD results of calcined powders are presented in Fig.1. The obtained powder shows that β"-alumina formed as a main phase with the composition $Na_{1.67}Mg_{0.67}Al_{10.33}O_{17}$. Moreover, it has been found that the β-alumina secondary phase with the composition $Na_2Al_{22}O_{34}$ also presents. These results reveal that both β and β" phase co-exist in this system which consistent to other reported [9, 10]. These two phase differ essentially only in their stacking sequence of close-packed layers. The result of XRD investigation on the ceramics samples sintered at 1550°C are shown in Fig.2. There is no phase change and high densification ceramic are obtained. These are the same as found in samples sintered at 1450 and 1500°C.

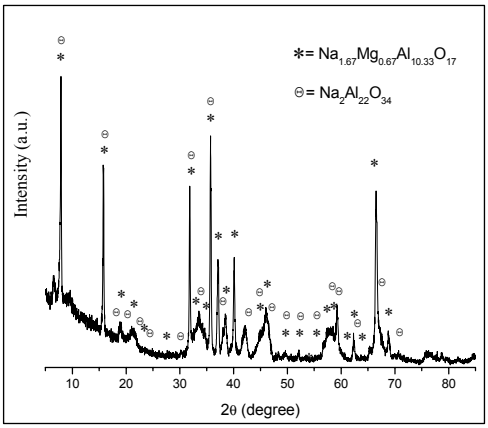

Figure 1. XRD pattern of calcined β" -alumina powder.

Bulk density of ceramics samples are summarized in Table1. It can be seen that higher density is found for sample sintered at 1550°C and added with 10 mol% of Na_3PO_4. It has been also seen that the density was not increased with increasing sintering temperature. However, the higher additive concentration promoted a higher densification of ceramics. The results of microstructural study of β"-alumina ceramics sintered at 1550°C are shown in Fig.3. It can be seen that packing of several plate-like structures and a cluster arrangement with roughly hexagon shape is clearly seen. This structure arrangement related to the densification of ceramics. It can be seen that the higher packing gives the higher density as found in the ceramic sintered at 1550°C added with 10 mol% of Na_3PO_4. The ionic conductivity measured at 300°C of ceramic samples are reported in Table1. High ionic conductivity of β"-alumina results from its layered crystal structure which consists of layers of four close-packed planes of oxygen and aluminium ions in spinel-like blocks which allow Na^+ to move freely in the channel between these blocks. From impedance spectra, the conductivity was identified. Fig.4 shows the temperature dependence of ionic conductivity in the Arrhenius representation for all dense Na-β" –alumina ceramics.

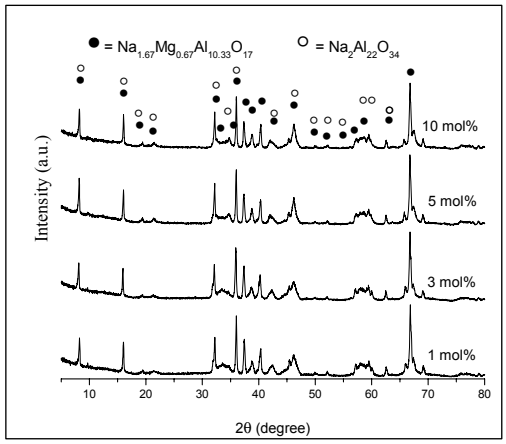

Figure 2. XRD pattern of the β" -alumina ceramics sintered at 1550°C with different additive concentrations.

Table 1: Ionic conductivity (σ_{DC}) measured at 300°C of the β"-alumina ceramics adding with Na_3PO_4 sintered at different temperature and their related bulk density.

sintering temperature (°C)	Conductivity (x 10^{-5} S.cm^{-1})				Density (g/cm^3)			
	1 mol%	3 mol%	5 mol%	10 mol%	1 mol%	3 mol%	5 mol%	10 mol%
1450	7.4989 (0.17)	5.8963 (0.16)	4.5671 (0.13)	9.5433 (0.13)	1.6900	1.6308	1.6954	1.4348
1500	2.1801 (0.14)	2.9199 (0.17)	2.2942 (0.16)	7.3562 (0.20)	1.6393	1.6391	1.6175	1.6384
1550	2.5723 (0.14)	3.6983 (0.14)	30.427 (0.18)	24.959 (0.17)	1.5740	1.5780	1.6886	1.8358

*Number in the bracket is activation energy of Na^+ migration calculated from the Arrhenius plot; Ea (eV)

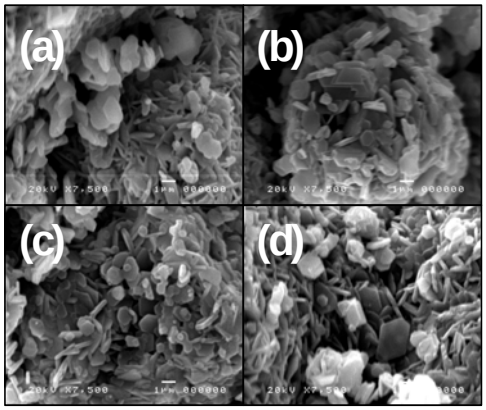

Figure 3. SEM micrographs of sintered pellet of β" -alumina ceramics sintered at 1550°C with additive 1(a), 3(b), 5(c) and 10(d) mol% of Na_3PO_4, respectively.

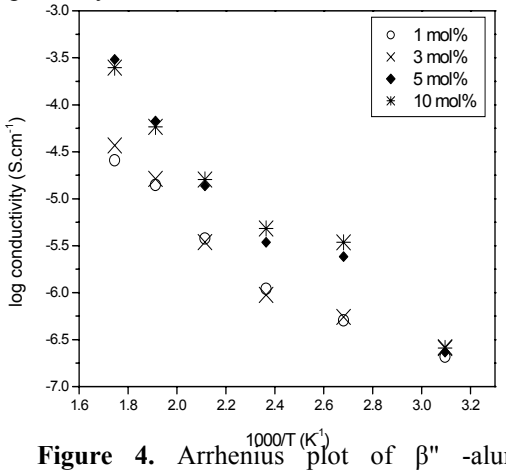

Figure 4. Arrhenius plot of β" -alumina ceramics samples sintered at 1550°C with different additive concentrations

From results in Fig 4, the activation energies were calculated according to the Arrhenius expression, given by, $\sigma = (A/T)\exp(-E_a/k_BT)$ Where σ is the conductivity at temperature in K, k_B is the Boltzmann's constants, E_a is the activation energy and A is the pre-exponential parameter [11]. The results of calculation are shown in Table 1. It can be seen that the activation energy for Na^+ migrations are in range 0.13-0.20 eV. There is no certain relation between activation energy for Na^+ migration and the content of Na_3PO_4.

Conclusions

The present study has reveal that calcination of MgO-stabilized β"-alumina gives β" phases with some β-phase impurity. The obtained ceramics exhibit high ionic conduction which is in order of 10^{-5} $S.cm^{-1}$. Their related activation energies are also quite low. Introduction of Na_3PO_4 as a sintering aid did not lead phase transformation but it promoted a denser ceramic which resulted to a better microstructure and higher ionic conduction.

Acknowledgements

This work was financially supported by National Research Council of Thailand.

References

[1] Beckers, J.V.L., K.J. Van der Bent, & S.W. De Leeuw, *Solid State Ionics.* **133**(2000), pp.217-231.
[2] A. Van Zyl, *Solid State Ionic.* **86-88**(1996), pp.883-889.
[3] C-H. Dustmann, *J. Pow. Sour.* **127**(2004), pp.85-92.
[4] R. Stevens, & J.G.P. Binner, *J .Mater. Sci.* **19**(1984). pp.695-715.
[5] S. Satori, A. Martucci, A. Muffato, & M. Guglielmi, *J. Eur. Ceram. Soc.* **24**(2004). pp.911-914.
[6] *T. Mathews, R. Subasri, & O.M. Sreedharan Solid State Ionic.* B78(2002). pp.135-143.
[7] R. Subasri, T. Mathews, O.M. Sreedharan, & V.S. Raghunathan, *Solid State Ionics,* **158**(2003). pp.199-204.
[8] R. Subasri, *Mater. Sci. and Eng.* **B112**(2004). pp.73-78.
[9] W.S. Kim, W. J. Kim, & S. K. Lim, *J. Ind .Eng. Chem.* 10 (2004). pp.78-84.
[10] P. Maass, M. Meyer, & A. Bunde, *Physica A*, 266(1999). pp.197-202.
[11] P. Padma Kumar, & S. Yashonath, *J. Chem. Sci.***118**(2006). pp.135-154.

Preparation and characterization of bimodal dextran based biosensor chips with carboxyl group variation for use in surface plasmon resonance biosensor

J. Sansatsadeekul[1], K. Boonkitpattarakul[2], N. Intaraprasit[2], J. Sakdapipanich[1] and K. Mai-ngam[2*]

[1]Department of Chemistry, Faculty of science, Mahidol University, Bangkok, Thailand
[2]National Metal and Materials Technology Center, Pathumthani, Thailand

[*] E-Mail: katancv@mtec.or.th

Abstract: Novel bimodal carboxylic dextran sensor chips with variation in surface density of carboxylic group were prepared by grafting of low (MW 1,500) molecular weight dextran aldonic and high (MW 100,000) molecular weight allyl dextran aldonic acid molecules to SPR chip surfaces. Allyl functional groups on the chip surface were then modified to be carboxylic acid by treatment of 6-mercaptohexanoic acid in the presence of ammonium persulfate. A series of high MW allyl dextran aldonic acid molecules was synthesized to possess the different allyl group contents along the long dextran chain. Such differences in allyl contents, sequencely resulting in hydrodynamic volume variation, caused differences in grafting density of high MW dextran molecuels on the sensor surface. Moreover, the working efficiency of all obtained sensor chips was tested by the SPR detection of the goat anti-mouse IgG with mouse IgG recognition system. Increases in immobilization capacity of IgG ligand and the binding capacity of IgG to its anti-IgG were found as the carboxylic surface density increased.

Introduction

Surface plasmon resonance (SPR) biosensors have been widely used as a label-free measurement system that can be performed in real time [1, 2]. It is sensitive to the changes in the thickness or refractive index of dielectric added layers above specific metals (e.g. gold and silver). Remarkable progress has been made in the development of SPR-based optical sensor and its applications in areas such as environmental monitoring, biotechnology, medical diagnostics, drug screening and food safety [3].

The CM5 carboxymethyl dextran chip (Biacore) is the most versatile and widely used SPR chip because of its high binding capacity and low non-specific binding [4]. The matrix is constructed from a composite of hydrophilic SAM and covalently bound carboxymethyl dextran (MW 500,000). Dextran matrix is generated on the chip surface by non-selectively reaction of the epoxy groups on the gold surface with the hydroxyl groups along the dextran chain, resulting in a loop-train-tail conformation. Subsequent reaction with bromoacetic acid results in the formation of carboxylic groups.

For an improvement of the sensing performance, the appropriate packing density of biomolecules on the sensing surface is necessarily required to readily detect a target molecule. The surface densities of functional groups for immobilization of the affinity ligand as well as the dextran molecules are needed to be optimized for the biomolecular recognition system with a specific size. The multi-point grafting reaction used for the CM5 sensor chip is hard to control the dextran brush density without changing the layer thickness. Therefore, we attempted to overcome the problem using a selective reaction to graft dextran brushes to the gold chip surface only through their terminal reducing ends (i.e., only one anchor point).

Novel bimodal carboxylic dextran SPR chips, consisting of two major layers, i.e., the inner layer and outer layer (Figure 1), have been successfully developed in our laboratory. The inner layer contains short- and some part of long-chain segments and provides polymeric repulsion against non-specific binding. The outer layer contains only long-chain segment with functional groups for ligand immobilization. The reducing ends of allyl dextran aldonic acid having MW of 100,000 and dextran aldonic acid with MW of 1,500 were selectively grafted to an SPR gold chip to generate the bimodal dextran chip. The allyl functional groups were then modified to carboxylic acid.

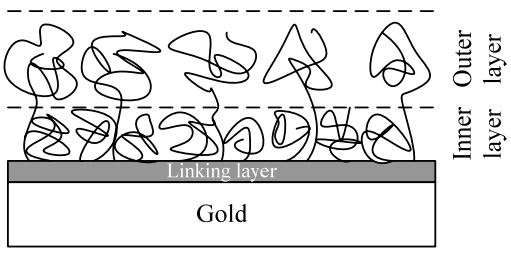

Figure 1. Bimodal dextran based SPR sensor chip

In this study, we attempted to control the carboxylic surface density of novel bimodal carboxylic dextran SPR chips through the allyl content of the high MW allyl dextran aldonic acid. Moreover, the sensing performance of each bimodal carboxylic dextran chip was evaluated by the SPR detection of the goat anti-mouse IgG with mouse IgG recognition system.

Materials and Methods

Synthesis of allyl dextran aldonic acid: The reducing ends of dextran (MW 100,000) were oxidized using an aq. solution of 0.1 M iodine and 0.4 M potassium hydroxide [5]. The obtained dextran aldonic acid (0.031 mole) was dissolved in 20 mL of deionized water containing 5 g of NaOH and 0.2 g of sodium borohydride. Allyl bromide (0.03, 0.15 and 0.61 mole) was added and allowed to react at 60 °C for 3 h. After neutralization with acetic acid, the product of allyl dextran aldonic acid with low allyl group content was precipitated in ethanol, while one with high allyl group content was precipitated using hexane and dried under vacuum. ^{1}H-NMR spectrum was utilized to evaluate the allyl content to be 0.64, 0.80 and 0.87 allyl groups per monomeric unit.

Modification of gold surfaces with 16-mercaptohexadecanoic acid and etheylenediamine: A piranha-cleaned SPR gold chip (Ssens) was immersed in 5 mM 16-mercaptohexadecanoic acid (16-MHA) solution in ethanol for 24 h. to form a carboxylic terminated SAM. After successively rinsing with deionized water and ethanol**,** the carboxylic terminated groups were activated by a 1:1 (v/v) mixture of 50 mM *N*-hydroxysuccinimide (NHS) and 200 mM 1-ethyl-3-(3-dimethylaminopropyl) carbodiimide (EDC) in 1 M sodium acetate buffer (pH 4.5) for 12 h. A 0.1 M ethylenediamine solution was added to the surface for 24 h and rinsed with deionized water.

Allyl dextran aldonic acid grafting and carboxylic formation: The obtained amine functionalized chip was soaked in 300 mg/mL of allyl dextran aldonic acid (MW 100,000) solution in 1 M sodium acetate buffer (pH 4.5) in the presence of EDC (0.2 M) and NHS (0.04 M) at room temperature for 24 h. The obtained sensor chip was washed with deionized water and the unreacted amine groups on the gold surface was then further grafted by low MW dextran aldonic acid (MW 1500; 1 mg/mL) with the similar procedure. The allyl groups were then reacted with 0.1 M 6-mercaptohexadecanoic acid in DMSO to generate carboxylic acid along the dextran backbone. This reaction was initiated by ammonium persulfate and performed at 50 °C under N_2 atmosphere for 3 h.

AFM experiment: The modified chip surface was spotted with aqua regia reagent, the mixture of concentrated nitric acid and concentrated hydrochloric acid in a volumetric ratio of 1:3, to remove the chromium, gold and dextran layer. The layer thickness of dextran modified gold surface was investigated with atomic force microscope (Seiko instrument, SPA 4000) in non-contact mode under fluid condition. AFM images were acquired at scan rate of 1 Hz with SI-DF-3 cantilevers (Seiko Instruments Inc.).

SPR experiments: An SPR imaging system builted by the Thailand National Electronics and Computer Technology Center (NECTEC, NSTDA) was employed. A 150 μL of testing fluid was loaded with a syringe injection system. The light emitting diode (LED) is used as a light source to make a monochromatic light with wavelength of 880 nm. The polarizer, which permits measurements with both p- and s-polarized light, is used as a reference. The prepared sensor chip was attached to a prism of the SPR device using a matching liquid. Moreover the SPR chip surface was equipped on the multi-channel flow cell to perform the multiple tests and the solution of 10 mM HBS (pH 7.4) was utilized as the mobile phase.

Ligand immobilization: The bimodal dextran chip was inserted into the SPR imaging system. The carboxylic groups on the modified chip surface were first activated by the aqueous solution of EDC (0.2 M)/NHS (0.05 M)/MES (0.05 M). Various concentrations (5, 10, 25, 50 and 100 μg/mL) of mouse IgG solution were prepared in 10 mM sodium acetate buffer pH 4.5 and injected into each flow cell channel for covalent immobization on the chip surface at 10 μL/min. Ethanolamine solution (1 M) was then injected at 25 μL/min.

Specific binding of analyte: Goat anti-mouse IgG was used as analytic substance of which stock solution was preserved in 50 mM HEPES buffer pH 7.5. The analytic substance solutions with various concentrations (0.1, 1, 5, 10, 25 and 50 μg/mL) were prepared by dissolving in PBS buffer (pH 7.4) and passed over the mouse immobilized surface at 50 μL/min. The capture event of antigen-antibody was measured as the change in SPR signal, in the percent of light reflectivity, before and after injection of anti-mouse IgG solution. After each measurement, the surface was regenerated by 10 mM of HCl solution.

Results and Discussion

1. Synthesis of bimodal carboxylic dextran sensor chips with different carboxylic content on chip surface

Surface carboxylic group densities on the chip surfaces grafted only with the high MW allyl dextran aldonic acid were evaluated using the toluidine blue-O (TBO) complex formation assay (Table 2). A series of high MW allyl dextran aldonic acid with three different allyl contents were used in this study. For clarity, the bimodal carboxylic dextran chip prepared from a long-chain dextran with 0.63 allyl groups per monomeric unit will be referred to 0.63Allyl-HMW Dex. It was found that the carboxylic groups increased from 0.54 to 1.40 nmol/cm^2 when the allyl group compositions on the high MW allyl dextran aldonic acid increased from 0.64 to 0.87 groups per monomeric unit. Furthermore, a surface density of glucose repeating

units of high MW allyl dextran aldonic acid on each chip was calculated from the resulting surface carboxylic density based on an assumption that all allyl groups were completely conversed to carboxylic acid. An increase in the surface coverage of long-chain dextran was found with the allyl content. This may be attributed to that the more hydrophobicity of the dextran molecules with greater allyl contents occupies less hydrodynamic volume and consequently allow higher chain packing density on the chip surface.

Table 1: Surface densities of carboxylic groups and glucose units on the bimodal carboxylic dextran chips

Bimodal carboxylic dextran SPR chips	Surface density	
	Carboxylic (nmol/cm^2)	Glucose unit (ng/mm^2)
0.64Allyl-HMW Dex	0.54 ± 0.26	1.39 ± 0.66
0.80Allyl-HMW Dex	1.11 ± 0.19	2.26 ± 0.38
0.87Allyl-HMW Dex	1.40 ± 0.94	2.61 ± 1.75

Table 2 lists the advancing contact angles of the dextran sensor chips measured after grafting of high MW allyl dextran aldonic acid (top row) and at the end of all reaction steps (bottom row). After grafting only with the high MW allyl dextran aldonic acid, the 0.64Allyl-HMW Dex has a significantly lower contact angle value than the 0.80 and 0.87Allyl-HMW Dex chips. This result well corresponds to the differences of surface allyl densities among the three obtained chips. Note that we assumed allyl groups were completely conversed to carboxylic acid, so that surface densities of carboxylic (Table 1) and allyl groups are equal.

After the high MW allyl dextran linked chips were further grafted with low MW dextran aldonic acid and the allyl groups were transformed into carboxylic acid, the contact angles became independent to high MW dextran packing density.

Table 2 : Advancing water contact angles for the products from each step in the bimodal carboxylic dextran chip preparation.

Substrate surface	Contact angles (degree)		
	0.64Allyl-HMW Dex	0.80Allyl-HMW Dex	0.87Allyl-HMW Dex
High MW dextran	55.2 ± 1.7	62.0 ± 1.0	62.4 ± 1.5
Bimodal carboxylic dextran	42.0 ± 0.6	40.6 ± 0.9	45.3 ± 2.5

2. AFM experiments

AFM was used to characterize surface thickness and roughness of the dextran matrix deposited on the chip surface. To determine the thickness of dextran layer, the step was produced on film with a mark of aqua regia reagent on the surface to remove the chromium, gold and dextran layer. This mark was then cleaned with DI water and the thickness subsequently determined by scanning across the revealed step. As seen in Figure 2, the step thickness of the bimodal dextran chip is larger than that of the bare gold chip, indicating the existence of dextran matrix with a thickness of about 25 nm.

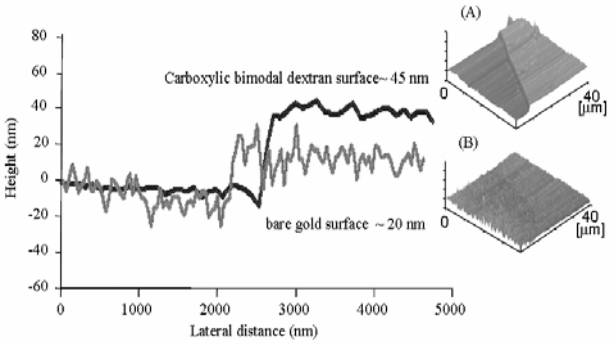

Figure 2. AFM images show film thickness of (A) carboxylic bimodal dextran surface and (B) bare gold surface under aqueous solution (40 μm scan). Z scale is 500 nm.

In addition, the AFM was also used to measure the rms roughness of the bimodal dextran modified surface. The scan size was made over area of 5 μm by 5 μm and this area was scanned to give the value for the rms roughness of biosensor chip surface (Figure 3 A-D). The 0.64, 0.80 and 0.87Allyl-HMW Dex chips
exhibited the rms roughness values of 11.87, 5.73 and 4.75 nms, while the rms roughness value of bare gold was only 1.94 nm. Owing to the high packing density of the dextran molecules (Table 1), a more smooth surface was obtained.

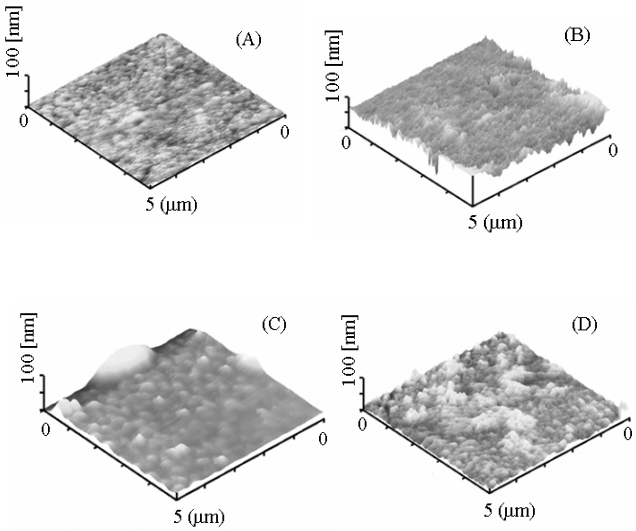

Figure 3. AFM 3-D topographic images of (A) bare gold surface (rms = 1.94 nm), (B) 0.64Allyl-HMW Dex (rms = 11.87 nm), (C) 0.80Allyl-HMW Dex (rms = 5.73 nm) and (D) 0.87Allyl-HMW Dex (rms = 4.75 nm).

3. SPR experiments

Surface plasmon resonance was used to evaluate the antibody immobilization and the capture event of antigen. Figure 4 shows the plots of reflectivity change of the immobilized mouse IgG against its concentration (5-100 μg/mL) obtained from all three prepared bimodal chips. As expected, the increase of ligands immobilization was found as the IgG concentration increased and the more reactive carboxylic acid groups available also lead to the more immobilized ligands. Note that a mouse IgG concentration of 50 μg/mL was chosen for all immobilization after this point.

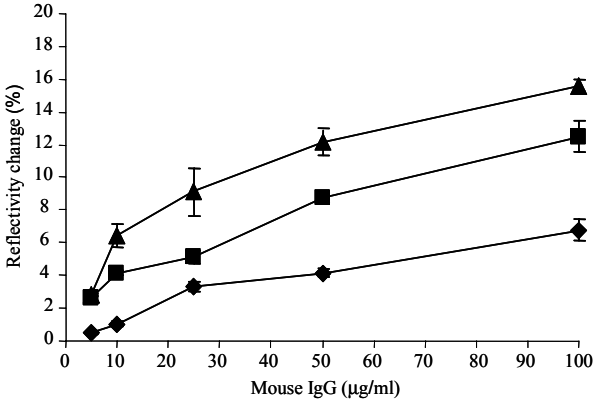

Figure 4. SPR analysis of mouse IgG immobilization on 0.64Allyl-HMW Dex (♦), 0.80Allyl-HMW Dex(■), 0.87Allyl-HMW Dex (▲) using the IgG concentration range from 5 to 100 μg/mL

After the immobilization, the different dilutions of analyte (goat anti-mouse IgG, 0.1-50 μg/mL) solutions in PBS buffer were passed over the surface and their response was investigated. Figure 5 shows the plots of goat anti-mouse IgG concentration against the percentage of reflectivity change obtained from the bimodal dextran chip surface with different carboxylic group contents. As expected, the level of protein capture well corresponded to the immobilized ligand density

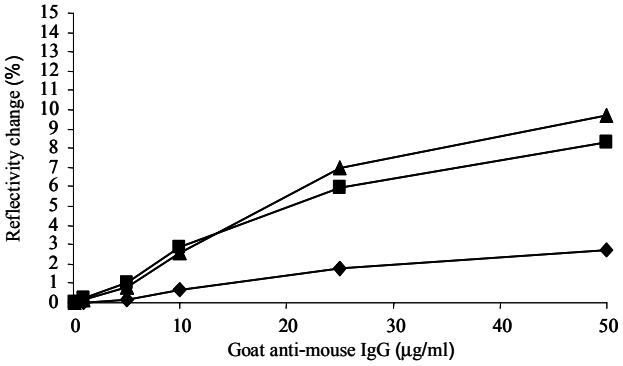

Figure 5. SPR analysis of specific binging of goat anti-mouse IgG after mouse IgG immobilization (at concentration of 50 μg/mL) on 0.64Allyl-HMW Dex (♦), 0.80Allyl-HMW Dex(■), 0.87Allyl-HMW Dex (▲).

Conclusions

Novel bimodal carboxylic dextran chips with different carboxylic group variation could be successfully prepared by controlling the allyl content of high MW allyl dextran aldonic acid. The present study suggests that, by varying the carboxylic content, our SPR chips with high carboxylic surface density shows the better results in both chemical linkage of ligand and biomolecular detection. Furthermore, this study will provide valuable background information for practical applications of these biosensor chip for bioaffinity studies.

Acknowledgements

This work was financially supported by the Thailand Graduate Institute of Science and Technology (TGIST), and National Metal and Materials Technology Center. The SPR imaging instrument was kindly supported by Dr. Boonsong Sutapan.

References

[1] R. J. Whelan, *et al.*, *J. Anal Chem*. **74** (2002), pp. 4570.

[2] F. Yu, *et al.*, *J. Anal Chem*. **76** (2004), pp. 1971.

[3] W. Jean, *et al.*, *J. Anal Biochem*. **270** (1999), pp. 201.

[4] S. Lofas, *et al.*, *J. Chem Soc Chem Commun*. **21** (1990), pp.1526.

[5] T. Zhang, *et al.*, *J. Macromolecules*. **27** (1994), pp. 7302.

Synthesis of Ni-doped mesoporous carbon by direct addition of Ni-salt to resocinol/formaldehyde gel

H. Khoomkhainum[1], n. Viriya-empikul[2], k. Faungnawakij[2], T. Charinpanitkul[1], a. Soottitantawat[1]*

[1]Center of Excellent in Particle Technology, Department of Chemical Engineering,
Chulalongkorn University, Pathumwan, Bangkok 10330, Thailand.
[2]National Nanotechnology Center (NANOTEC), National Science and Technology Development Agency (NSTDA),
111 Thailand Science Park, Phahonyothin Road, Klong 1, Klong Luang, Pathumthani 12120, Thailand

*E-mail:apinan_s@chula.ac.th

Abstract: This study shows a simple method to prepare the high content of Ni catalyst supported on the mesoporous carbon. The synthesis of Ni-doped meporous carbon materials were prepared by the sol-gel method through the polymerization of a resorcinol formaldehyde mixture containing nickel acetates. The soft-template of Pluronic F127 was used to promote the forming of meso-pores. The direct addition of metal to resorcinol/formaldehyde (RF) gel was novel strategy in reduction of synthetic time with the high content of Ni catalyst. The containing nickel acetates and Pluronic F127 of RF gel were carbonized at 800 °C for 3 hr. under inert condition to obtain Ni-doped mesoporous carbon. The effect of Ni acetate concentration in the RF gel on the porosity was investigated. The mesoporous carbon gel was obtained with the narrow pore size distribution and mean pore size diameter at 4.8 nm with the 444 m^2/g BET surface area which the ordered mesoporous structure was expected. When the Ni-acetate was added to the RF gel, the BET surface area, mesopore volume and means pores size were decreased. However, the porosity shows the optimum value with 15 %w/w of Ni loading with 153 m^2/g BET surface area with the mean pore size at 4.26 nm. However, even Ni was added to the carbon gel, the narrow pores size distribution was still observed. Therefore, the ordered mesoporous structure of carbon containing Ni catalyst was also expected.

Introduction

Mesoporous carbon (MC) materials, which were generally prepared by carbonization of carbon precursor gels, have recently attracted considerable attention due to their promising application in such fields as gas storage, energy storage, catalyst supports and electrode materials [1-3]. MC materials showed the properties of large surface area, large pore volume, chemical inertness, electrical conduction properties and well-tailored pore systems [1-4]. The using as the catalyst supports was interesting due to their chemical inertness as well as providing greater pore accessibility and facilitate molecular diffusion comparing to the conventional used of micropore activated carbon.

Recently, the syntheses of well ordered structure of mesopore carbon (OMC) have been achieved by the evaporation-induced self assembly (EISA) methods. The carbonizable polymer was used as the carbon precursor with pyrolyzable block copolymer inside which was self assembled to form the micelles as the template [5]. The controlled narrow pore size distribution, porosity and uniform pore connection of MC were obtained.

Generally, metal catalysts doped porous supports were prepared by impregnation methods which the soluble metal salt was adding to porous supporter. It generated via a multistep synthesis processes. Therefore, the methods to prepare the metal dope porous materials via sol-gel process have been reported. For the porous carbon supports, the researchers developed and discovered novel strategy for reduced steps of synthesis by adding metal salt in resorcinol-formaldehyde (RF) in aqueous solution (with acid or base catalyst) by so-gel method [1-7]. The metal catalysts, i.e. Fe and Ni [1, 3-4, 7], were observed to distribute through the porosity of the carbon phase which was obtained corresponding to carbon areogel synthesis. The advantages of simple and short period, low cost as well as the well disperse of metal catalysts were expected.

According to our knowledge, there were not the reports to prepare the metal doped MCs via the EISA technique. Therefore, in this study, the preparation of metal doped porous carbon will be investigated with the target of the well ordered of mesoporous properties as well as the well disperse of the metal nanoparticle in the pore structure. The soft templating and direct addition of metal to the carbon precursor gel, resorcinol/formaldehyde gel methods were used to obtain the target. The Ni ion was used as the model of transition metal. The resorcinol/formaldehyde is used as a carbonecous precursor and tri-block copolymer P127 is used as soft templates with base catalyst of NaOH for sol-gel reaction. The effect of Ni-metal concentration on the porous structure was investigated. The final products were characterized by N2 adsorption to evaluated the total specific surface area, pore size, pore size distribution and mesopore volume.

Materials and Methods

Materials: Triblock copolymer of Poly(ethylene oxide)-poly(propylene oxide)-poly(ethylene oxide) triblock copolymer (Pluronic F127, $EO_{106}PO_{70}EO_{106}$) was provided by BAFS Corp. Resorcinol, formaldehyde (37% methanol stabilized) and NaOH used in the sol-gel polycondensation were purchased from Fluka Crop. The nickel acetate and ethanol was

purchase from Aldrich Crop. The chemical used are in the research grade chemicals.

Preparation of mesoporous carbon containing Ni catalyst: Firstly, Pluronic F127 was dissolved in ethanol/water solution and stirred at 30 ° C over 20 min. Then resorcinol was added to the solution and then stirred for 30 min. Next, formaldehyde was dropped into the above mixture and the sample was stirred for 24 hr. After that, the Nickel acetate was added to the solution and stirred for 5 hr. NaOH was then added to solution as catalyst. The mixture was keep stirred and then separate into two phase layer. The upper phase was removed. The bottom phase layer was further kept aging for 24 hr and preheated at 90 ° C for 24 hr. Finally, the obtained RF gel was carbonized under nitrogen atmosphere by 800 ° C for 3 hr. The heating rate was 1° C/min. The molar ratio of F127:Ethanol:Water:Resorcinol: Formaldehyde were kept constant at 0.0027:9.6: 36.6:1.0:1.4:0.55. The amounts of added nickel acetate to the mixture were calculated to obtain the metal catalyst concentration in the MC at 0%, 5%, 10%, 15% and 20% w/w.

Characterization: The porous properties obtain MC and MC with Ni metal were examined by nitrogen-adsorption experiments using an adsorption apparatus (Belsorp Mini, Bel Japan Inc., Osaka, Japan). After the pretreatment, the adsorption and desorption isotherms of nitrogen were measure at 77 K. The BET (Brunauer-Emmett-Teller) surface areas and the mesopore volume were evaluated on the basis of nigrogen adsorption isotherms. The mesopore size diameter and size distribution were determined by applying the Barrett-Joyner-Halenda (BJH) model to the desorption isotherms.

Results and Discussion

Adsorption/Desorption Isotherm: The adsorption and desorption isotherms of nitrogen on the MC without any adding of Ni is shown in Figure 1. The isotherms are of Type IV (IUPAC classification), which indicates the development of mesoporosity in the sample and mesopore volumes were significantly larger than the micropore volumes. When the Ni ion was added to the RF sol-gel during the poly-condensation step, the adsorption/desorption isotherm of nitrogen of the obtained Ni-RF carbon gels are shown in Figure 2. The Type IV of isotherms could still be observed. However, the amounts of N_2 adsorbed were varied with the amount of adding Ni catalyst. These adsorption amount were used to evaluated the total specific surface area (BET-surface area) as shown in Table 1. The BET surface area of carbon gel without any Ni was 444 m^2/g. When the Ni was added, the BET surface area was decreased. The decreasing of surface area might be explained by the obstruction of Ni metal on the either entrance of the pores or inside the pores. However, the results was also shown that the BET surface area did not decrease relating to the amount of Ni. The BET surface area was shown the optimal value at 15 %w/w of Ni. These might be from the decreasing of synthesis pH from the acetate group (CH_3COO^-) from the nickel acetate. This make the different of polycondensation rate of the RF resulting in the difference of pore structure which mainly come from the micelles of Pluronic F127. Indeed, mesoporous for pH values should be about 6.00-7.00 [3-4].

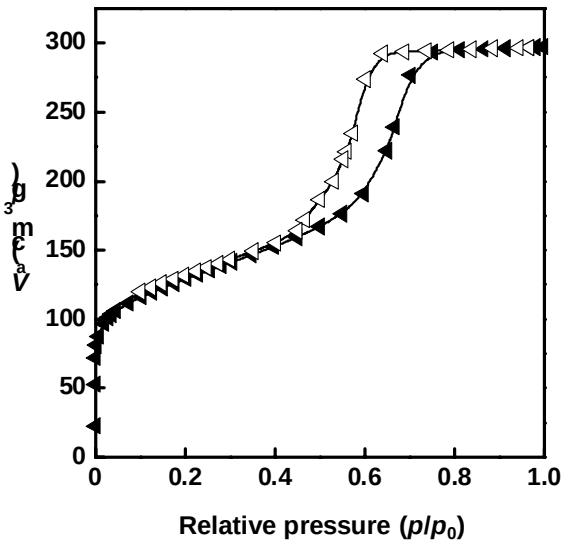

Figure 1. N_2 adsorption/desorption isotherms at 77 K of MC without Ni catalyst. (Closed symbols: adsorption isotherm, Opened symbols: desorption isotherm)

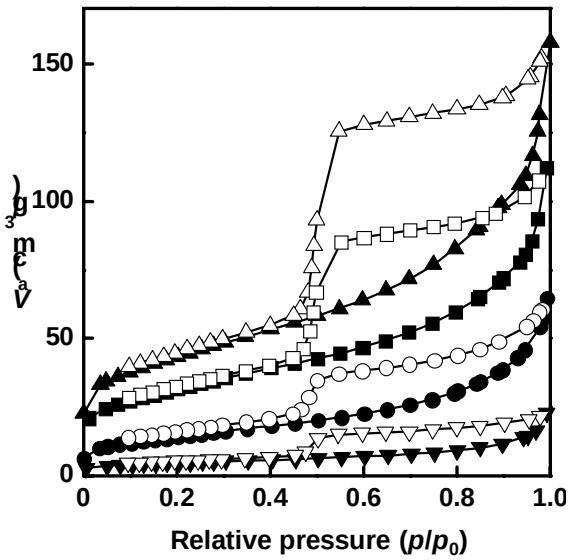

Figure 2. N_2 adsorption/desorption isotherms at 77 K of Ni doped mesoporous carbon gel for closed symbols as adsorption isotherm and opened symbols as desorption isotherm. (▽ 5 %w/w Ni, ○ 10 %w/w Ni, △ 15 %w/w Ni, □ 20 %w/w Ni)

Table 1: Porous properties of RF carbon gel

Sample	S_{BET} (m^2/)	V_{mes} (cm^3/g)	r_{peak} (nm)
RF carbon gel	444	0.378	2.41
RF carbon gel + 5 % Ni	17	0.039	1.88
RF carbon gel + 10 % Ni	52	0.095	1.88
RF carbon gel + 15 % Ni	153	0.256	2.13
RF carbon gel + 20 % Ni	112	0.178	1.88

Mesoporous properties and pore size distribution: The effect of concentration of Ni in the RF carbon gel on the mesopore volume, the mean pore size and the pore size distribution are shown in Table 1 and Figure 3, respectively. According to the BET surface area as discussed before, the mesopore volume was decrease with the addition of Ni. The optimal mesopore volume was observed at 15 %w/w Ni. Furthermore, for the size of pore, the diameter is about 4 nm ($2\times r_{peak}$) even the nickel acetate was added to the RF gel. The interesting results were shown in Figure 3 as the pore size distribution. The narrow size distributions of all prepared samples were observed. The order mesoporous structure of prepared RF carbon gel was expected. Furthermore, the addition of Ni to the structure did not make the much change of pore size distribution. The pore diameter trend to decrease with the adding of Ni.

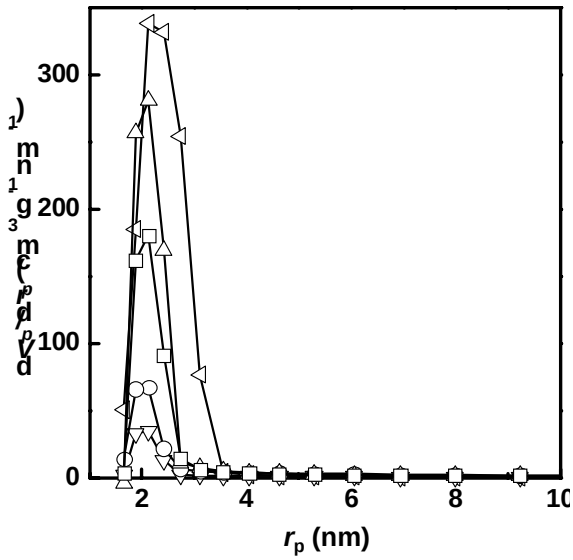

Figure 3. Pore size distribution of prepared RF carbon gel (◁ 0 %w/w, ▽ 5 %w/w Ni, ○ 10 %w/w Ni, △ 15 %w/w Ni, □ 20 %w/w Ni)

Conclusions

Ni-doped porous carbonaceous materials were prepared by the sol-gel method through the polymerization of a resorcinol formaldehyde mixture containing metal acetates and the soft-templating as Pluronic F127. It shown when metal concentration in system was increased, the porous properties as BET specific area and mesopore volume were decreased. It was found that initial synthesis pH strongly affects the size, porous, and uniformity of mesoporous occurred during self-assembly processing. However, the ordered mesoporous of prepared RF carbon were expected.

References

[1] Indrea, E.; Popescu, I. C.; Popp, J.; Baia, L.; Cotet, L. C.; Baia, M.; Cosoveanu, V.; Danciu, V.. Structural properties of some transition metal highly doped carbon aerogels. Journal of Alloys and Compounds, 2007, 434-435, 854-857.

[2] Jin, J.; Nishiyama, N.; Egashira, Y.; Ueyama, K.. Pore structure and pore size controls of ordered mesoporous carbonecouss preparedfrom resorcinol/formaldehyde/triblock polymers. Microporous and Mesoporous Materials, 2009, 18, 218–223.

[3] Job, N.; Pirad, R.; Marien, J.; Pirad, J. P.. Synthesis of transition metal-doped carbon xerogels by solubility of metal salts in resorcinol-formaldehyde aqueous solution. Carbon, 2004, 3217-3227.

[4] Job, N.; Vertruyen, B.; Colomer, J. F.; Pirard, J. P.; Marien, J.; Pirard, R.. Synthesis of transition metal-doped carbon xerogels by cogelation. Journal of Non-Crystalline Solids, 2007, 353, 2333-2345.

[5] Soler-Illia, G. J. de A.A.; Crepaldi, E.L.; Grosso, D.; Sanchez, C.. Block copolymer-templated mesoporous oxides. Current opinion in colloid and interface science 2003,8,109-126.

[6] Ueyama, K.; Nishiyama, N.; Tanaka, S.; Egashira, Y.. Synthesis of ordered mesoporous carbon materials with channel structure from an organic nanocomposite. Chemical communication. 2005. 2125-2127.

[7] Moreno-Castilla, C.; Maldonado-Hod'dar, F.J.; Pe'rez-Cadenas , A.F.. Physocochemical surface properties of Fe, Co, Ni and Cu-doped monolithic organic areogels. Langmuir, 2003 ,19, 5650-5655

.

Antibacterial performance evaluations for silver colloid incorporated thermoplastics

W. Pongnop[1], K. Sombatsompop[2], A. Kositchaiyong[1] and N. Sombatsompop[1,*]

[1]Polymer PROcessing and Flow (P-PROF) Research Group, School of Energy, Environment and Materials King Mongkut's University of Technology Thonburi (KMUTT), Thongkru, Bangkok, Thailand 10140

[2]Department of Civil and Environmental Engineering Technology, College of Industrial Technology, King Mongkut's University of Technology North Bangkok (KMUTNB), Bangsue, Bangkok, Thailand 10800

*E-mail: narongrit.som@kmutt.ac.th

Abstract: Anti-bacterial performance efficacies of various thermo-plastics, such as medium-density polyethylene (MDPE), polystyrene (PS), polyethylene terephthalate (PET) and polyvinyl chloride (PVC) containing nano-silver colloids were quantitatively assessed under a wide range of testing conditions. The effects of nano-silver colloid content and the silver-polymer contact time were of our main interests through a plate-count-agar (PCA) testing method using *Escherichia coli* as testing bacteria. Two different methods were used for incorporating the nano-silver colloids into the thermoplastics, these being spray-coating onto the thermoplastic surface, dry-blending in the thermoplastic matrices. The experimental results suggested that coating silver colloid onto all types of thermoplastic substrates could inhibit the growth of the *E. coli* bacteria up to 99%, different thermoplastics showing different optimum contents of nano-silver content to achieve the maximum bacterial inhibition. For a given nano-silver content, the spray-coating technique was much more effective than that dry-blending technique.

Introduction

In packaging applications, thermoplastics have been widely used and their microbial contaminations are recently of main concern. The application of antimicrobial agents into the polymer products is one of the methods to prevent the thermoplastic products from microbial contaminations **[1]**. Many antibacterial agents including nisin, nano-silver, triclosan and sorbic acid anhydride have been used in packaging thermoplastics for inhibition of the bacterial growth in various processing techniques **[2]**. Methods to incorporate the anti-bacterial agents into the polymer matrices could be done by either blending into the polymer matrices or coating onto the surface of the polymer products. The anti-bacterial efficacies are dependent on type, concentration and diffusability of the incorporated bacteria through the polymer matrices, as well as the testing methods used for such evaluations **[3-4]**. In this present paper, anti-bacterial performance efficacies of various thermo-plastics, such as medium-density polyethylene (MDPE), polystyrene (PS), polyethylene terephthalate (PET) and polyvinyl chloride (PVC) containing nano-silver colloids were quantitatively assessed under a wide range of testing conditions and the effects of nano-silver colloid content and the silver-polymer contact time.

Materials and Methods

Materials: Medium-density polyethylene (MDPE, M380RU/RUP, Thai Polyethylene Co., Ltd., BKK, Thailand), Polystyrene (PS, Styron 656D267; Siam Polystyrene Co., Ltd, BKK, Thailand), Polyethylene terephthalate (PET; Indorama Co., Ltd., BKK, Thailand), and polyvinyl chloride (PVC, VP Wood Co., Ltd., BKK, Thailand), were used as matrices. Nano-silver colloid (designated as SNSE, supplied by Koventure Co., Ltd, Bangkok, Thailand) was used as the anti-bacterial agent. *Escherichia coli* (ATCC 25922) was used as testing bacteria.

Incorporating method: The thermoplastics were incorporated with nano-silver colloid using two different techniques. For spray-coating, the polymeric substrates were pre-heated at 120^{o}C for 5 min before being spray-coated with nano-silver colloids using a constant spraying condition (spray distance of 10 cm, spraying temperature of 25^{o}C, spraying time of 10 sec and spray rate of 5 ml/min). The surface area covered by the nano-silver was 10x10 cm^2 for a required dosage. For dry-blending method, the thermoplastic powder were dry-blended with nano-silver colloid using a fluidized bed before being compression moulded to obtain the silver-incorporated thermoplastic film with 0.2mm thick. The resultant films from the two incorporating techniques were then cut into square samples of 2.5x5cm^2 for plate count agar (PCA) test.

Preparation of film specimens: The experimental procedure was commenced by compression moulding for making a film specimen of 0.2 mm thick. The mould pressure, temperature and time used in the compression moulding process were 150 kg.cm^{-3}, 160^{o}C and 5 min, respectively, for MDPE, 150 kg.cm^{-3}, 170^{o}C and 5 min, respectively, for PS, 50 kg.cm^{-3}, 255^{o}C and 1 min, respectively, for PET, and 180 kg.cm^{-3}, 180^{o}C and 2 min, respectively, for PVC.

Measurement of antibacterial performance: Plate Count Agar (PCA) was suitable for quantitative assessment of bacteria reduction, which follows the test standard of ASTM E-2149 (2001). 2 pieces of thermoplastic film sample of 2.5x5 cm^2 were used. Nutrient broth (NB) was used as a growing medium for *E. coli* bacteria and peptone solution (prepared by 1 g / L peptone, pH 6.8 – 7.2) was chosen as a testing medium. Bacteria were cultivated in 5 ml of NB at 37°C for 24 h. The film samples were placed into a 250 ml flask with peptone solution and the bacteria cell suspensions were diluted with 0.85% sodium chloride solution to the required initial bacteria density. In this work, the dilution factor (n) used was dependent on the preferred number of initial bacteria colonies (ranging from 30 to 300 colonies). The flask was shaken on a reciprocal shaker at a speed of 100 rpm at 37°C ± 0.5°C for a contact time of 30, 90, 150, and 210 minutes. 100 µL of bacterial suspension after shaking were placed over the agar into sterilized Petri dishes. The inoculated plates were cultivated at 37°C ± 0.5°C for 24 h before calculating the viable count of the testing bacteria and evaluating the anti-bacterial efficacies using Equation 1 **[5]**.

$$R = \frac{A - B}{A} \times 100 \qquad \text{(Equation 1)}$$

where: R is the percent reduction of bacteria (%).
A is average number of bacterial colonies from thermoplastics without nano-silver colloid (CFU/ml)
B is average number of bacterial colonies from thermoplastics incorporated with nano-silver colloid (CFU/ml)

Results and Discussion

Neat thermoplastics

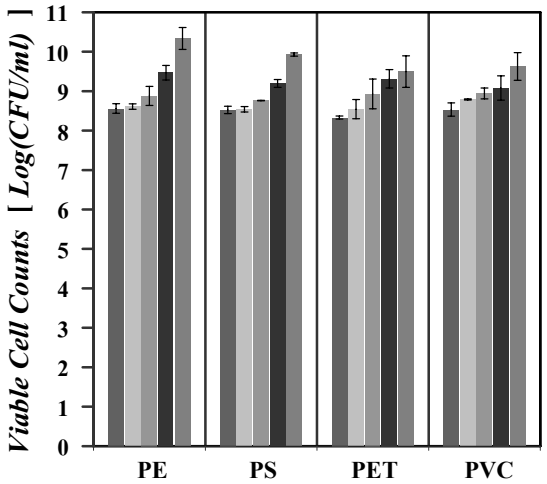

Figure 1. Viable *E. coli* colony count for various thermoplastics with different contact times 0 min (■), 30 min (■), 90 min (■), 150 min (■), and 210 min (■) without incorporation of nano-silver colloid

Figure 1 shows viable colony count for *Escherichia coli* for various thermoplastics under a wide range of contact times without incorporation of nano-silver colloid. It can be seen that all thermoplastics had similar viable count of *E. coli*, and the *E. coli* growth appeared to increase with increasing contact times. However, the increasing magnitude of *E. coli* growth with increasing contact times (differences in viable counts at 0 and 210min) for PET and PVC seemed to be smaller than that for other thermoplastics. The reason was related to polarity and halogen (chlorine atom) that had abilities to reduce *E. coli* population **[6].**

Nano-silver filled thermoplastics by spray-coating

Figure 2 shows the effects of nano-silver content and contact time on viable cell count and antibacterial efficacy for different thermoplastics. For all thermoplastics, it was observed that the viable cell count decreased with increasing the content of nano-silver colloid on the thermoplastic surfaces. This was obviously seen by the percentage reduction of *E. coli*. However, it was interesting to note that the optimum silver content to reach 99% reduction of *E. coli* for all thermoplastics were different. Overall, it was observed that the contact time of 150 min was sufficient for 99% reduction of *E. coli*. At 150 min contact time, 75 ppm nano-silver colloid was required for PE whereas 50 ppm nano-silver were required for PS, PET and PVC for achieving the maximum percentage reduction of *E. coli*. The differences in the silver dosages required for each thermoplastics were associated with a number of factors such as polarity of thethermoplastics used, embedding or diffusability of nano-silver colloid in the thermoplastic surfaces which were related with the softening temperatures of all thermoplastics, and possible formation of AgCl compound (in the case of PVC) during spray-coating.

Comparison of spray-coating and dry-blending techniques

Polyethylene (PE) was selected for studying the effect of incorporating technique on the anti-bacterial performance evaluation using nano-silver colloid. Figure 3 shows a comparison of viable cell count of PE sample having different dosages of nano-silver which were incorporated by spray-coating (a) and dry-blending (b) techniques. It was found that for a given nano-silver content, the spray-coating technique was much more effective than that dry-blending technique. This was simply explained that the silver concentration to contact with the *E. coli* by the spray-coating technique was greater. The nano-silver particles from the dry-blending were embedded and trapped in the PE matrix and they were not able to contact with the bacteria. This was why the concentration to reduce the viable bacteria in the dry-blending technique occurred at the silver content of 100 ppm whereas that in the spray-coating technique was 50 ppm.

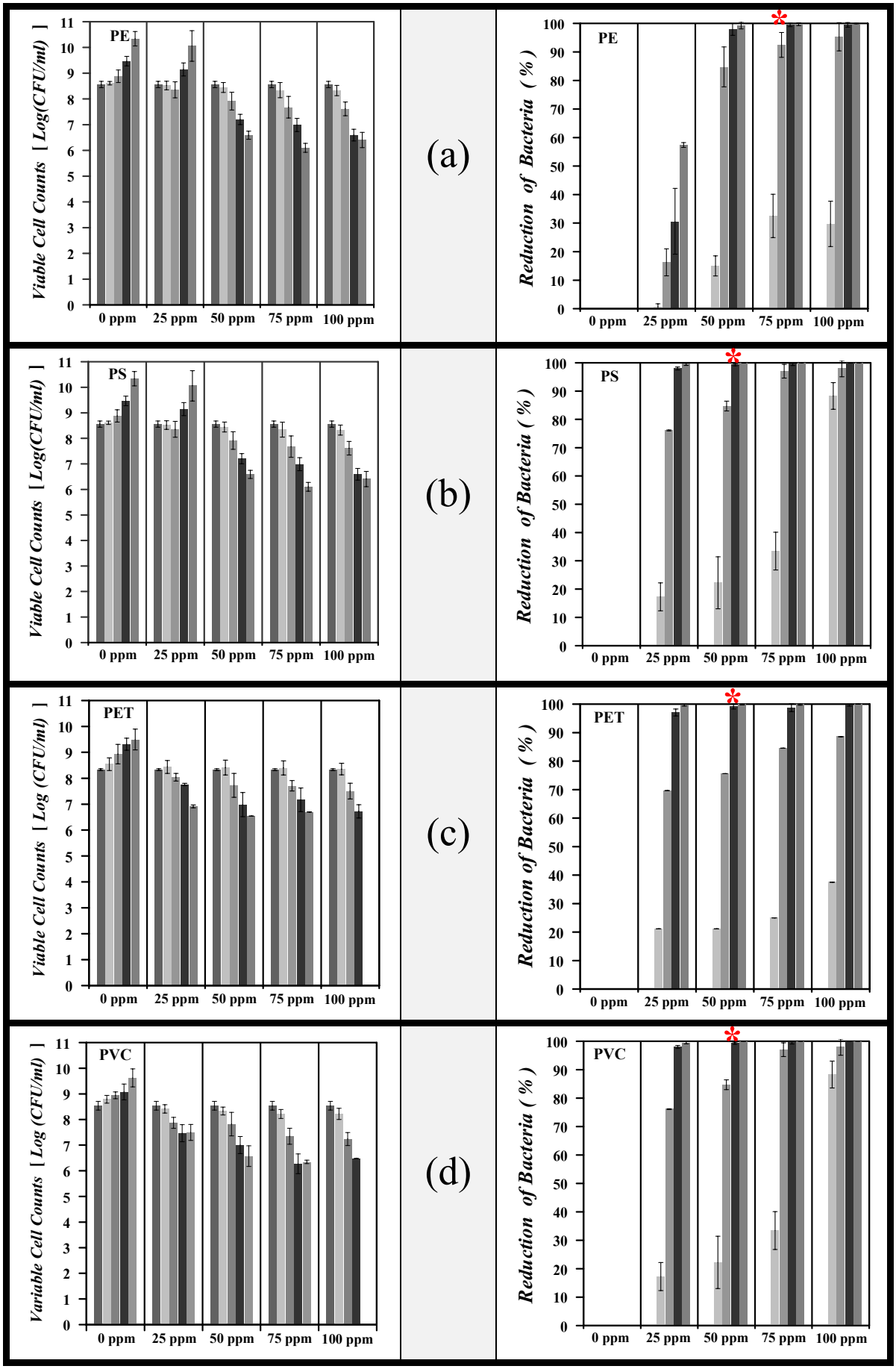

Figure 2. Effects of nano-silver content and contact times 0 min (■), 30min (■), 90 min (■), 150 min (■), and 210 min (■) on viable cell count and antibacterial efficacy of nano-silver colloid coated specimens: (a) PE (b) PS (c) PET (d) PVC

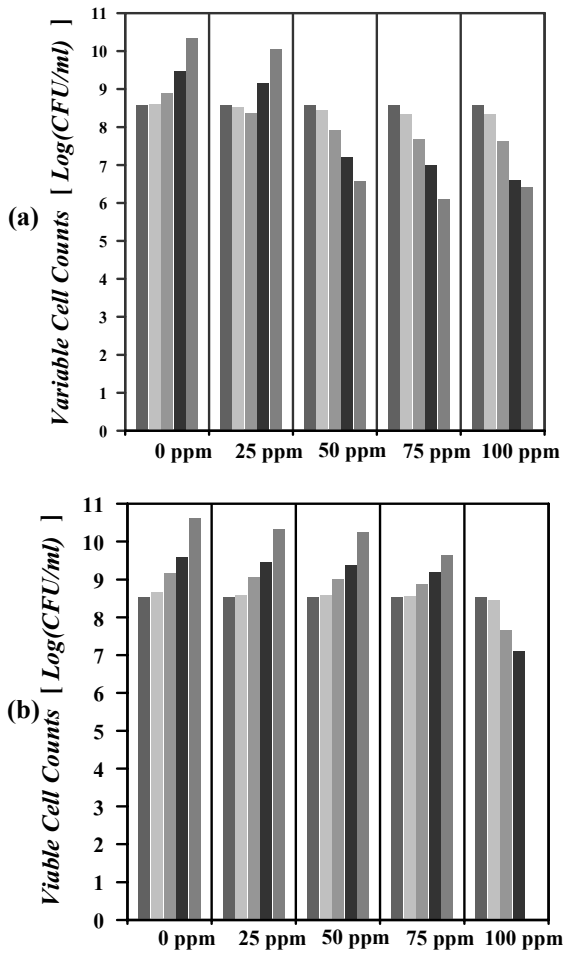

Figure 3. Comparison of viable cell count of PE sample having different dosages of nano-silver which were incorporated by spray-coating (a) and dry-blending (b) techniques with contact times 0 min (■), 30min (■), 90 min (■), 150 min (■), and 210 min (■)

Conclusion

In all thermoplastics used, it was observed that the viable cell count decreased with increasing the content of nano-silver colloid. The contact time at 150 min was sufficient for 99% reduction of *E. coli*. 75 ppm nano-silver colloid was required for PE whereas 50 ppm nano-silver were required for PS, PET and PVC for achieving the maximum percentage reduction of *E. coli* using the contact time of 150 min. For a given nano-silver content, the spray-coating technique was much more effective than that dry-blending technique

Acknowledgments

The authors would like to thank Jareonmitr Co., Ltd. and the Thailand Research Fund (TRF-MAG Research Grant Code: MRG–WI515S155). Sincere thanks are also expressed to Dr. Benjaphorn Prapagdee (Mahidol University) for her valuable comments and suggestions.

References

[1] Padgett, T., Han, I.Y. and Dawson, P. L., *Journal of Food Protection* **61** (1998), pp. 1330 – 1335.
[2] Appendini, P. and Hotchkiss, J.H., *Innovative Food Science and Emerging Technologies* **3** (2002), pp. 113–126.
[3] Pradeep, T. and Jain, P., *Biotechnology and Bioengineering* **90** (2005), pp. 59 – 63.
[4] Chammanee, P., Sombatsompop, K., Kositchaiyong, A. and Sombatsompop, N., *Journal of Macromolecular Science. Part B: Physics* **48** (2009), pp. 755 – 765.
[5] Lee, H.J. and Jeong, S.H., *Textile Research Journal* **75** (2005), pp. 551 – 556.
[6] Julia, B., Sonja, W., Peter. F. and Robert, P., *Postharvest Biology and Technology* **19** (2000), pp. 187 – 192.

Effects of fiber orientation and fiber content on physical properties of sisal fiber/epoxy composites

S. Srisuwan[1, 2], P. Chumsamrong[1, 2]*

[1] School of Polymer Engineering, Institute of Engineering, Suranaree University of Technology,Nakhon Ratchasima, Thailand 30000
[2] Center of Excellence for Petroleum, Petrochemicals and Advanced materials, Chulalongkorn University, Bangkok, Thailand 10330

* E-mail: pthongnoi@sut.ac.th

Abstract: Traditionally, synthetic fibers are used as reinforcing fiber in epoxy composites. However, increasing of environmental concern has resulted in a development of sustainable materials that can replace synthetic fibers. The natural fibers seem to be good alternative because they are high specific strength, low density and cost effectiveness [1]. Sisal fiber is one of the most interesting natural fibers that can be found in Thailand. The aim of this work was to investigate the effects of fiber orientation in woven form with different woven space and fiber content which varied from 1 wt.%, 3 wt.% and 5 wt.% of untreated sisal fiber on flexural and impact properties of sisal/fiber epoxy composites. The samples were produced by hand lay up process and they were cured at room temperatures for 24 hours in two plate moulds. After that the samples were subjected to flexural (three-point bending) and impact testing according to ASTM D790-02 and ASTM D256-02 respectively.

Introduction

The use of natural fibers as reinforcements in polymer composites is currently significance. This is due to the potential environmental benefits. One of the most interesting fibers is sisal fiber. Sisal plants can be found in Thailand especially in Nakhon Ratchasima. Sisal fiber is widely used in making ropes, mats, carpets because it has good mechanical properties such as low density, high specific strength [1-3]. In addition, it is renewable and low cost [4].

In this work, the investigation of mechanical properties of woven sisal fiber reinforced epoxy composites was focused. The influences of woven space and fiber content of sisal fiber on the impact and fractural properties of sisal fiber/epoxy composite were evaluated.

Materials and Methods

Sample preparation

Sisal fibers used in this study were obtained from Nakhon Ratchasima, Thailand. Woven sisal fibers were manufactured by hand weaving process. Two different woven patterns as shown in Figure 1 were used.

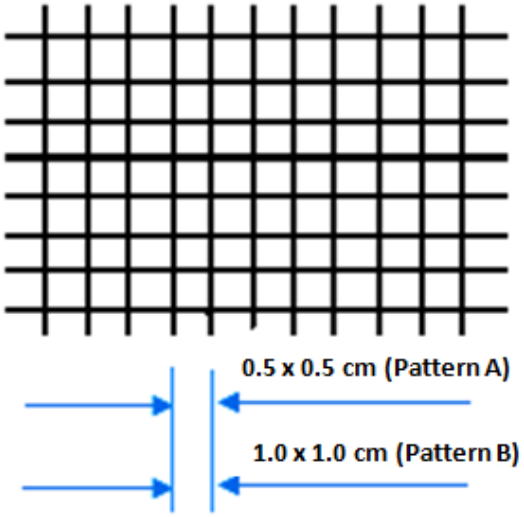

Figure 1. Schematic representation of woven sisal fibers used as reinforcement in epoxy matrix

The fiber content in epoxy composites was fixed at 1 wt.%, 2 wt.% and 3 wt.%. This was achieved by varying the number of woven plies. Weight per area and the number of woven plies of woven sisal fibers in composites are tabulated in Table 1.

Table 1: Weight per area of woven sisal fibers and the number of woven plies in composites

Woven pattern	Weight/area (g/cm^2)	wt.% of fiber in composite	The number of woven plies
A	5.649×10^{-3}	1%	1
		3%	4
		5%	7
B	3.286×10^{-3}	1%	2
		3%	7
		5%	12

To produce test samples, Epiclon 850 epoxy resin and Luckamide hardener supplied by Siam chemical industry co., ltd. were used. Stoichiometric ratio of epoxy and hardener was 100:40 by weight. The mixture was then carefully and slowly poured into the mould cavities about a half of mould depth after that the woven sisal fibers were slowly embedded to avoid the formation of voids. After all the remaining resin

was carefully poured into the mould cavities, the mould covers were tightened. The samples were allowed to cure at room temperatures for 24 hours in the mould and the samples were post cured at 120° C for 2 hour.

Sample testing

Determination of flexural strength and flexural modulus of samples was done at room temperature using an Instron testing machine following ASTM D790-02. Each sample was loaded over the support span length of 96 mm and crosshead speed of 2.56 mm/min until the sample fractures. The testing for impact strength was done using impact testing machine following ASTM D256-02. At least five samples were used for both impact and flexural testing.

Results and Discussion

The flexural and impact properties of pure epoxy resin and composites are summarized in Table 2.

Table 2: Flexural and impact properties for pure epoxy resin and epoxy/woven sisal fiber composites

Epoxy composites	Flexural		Impact
	σ (MPa)	E (GPa)	J/mm^2
Pure epoxy	100.95	2.323	0.053
Epoxy /1% pattern A	99.61	2.450	0.007
Epoxy /3% pattern A	82.73	2.666	0.009
Epoxy /5% pattern A	74.01	2.484	0.023
Epoxy /1% pattern B	97.95	2.526	0.012
Epoxy /3% pattern B	67.67	2.625	0.023
Epoxy /5% pattern B	63.00	2.690	0.007

For the flexural test, the results are graphically compared in Figures 2-3. It was found that the flexural strength of composites containing fiber with different woven pattern decreased when sisal fiber content increased. This could be because the natural fibers have the poor wettability and absorbability toward polymers resulting from the hydophilicity of plant fibers [5-7]. Nevertheless, the composites prepared from smaller woven space (pattern A) seemed to show slightly higher flexural strength than those prepared from larger woven space (pattern B). This might be because the number of plies of small woven space (pattern A) was lower than those of large woven space resulted in less interfacial weak points. From Figure 3, it was found that the flexural modulus of all composites were higher than that of pure epoxy resin. This is as expected because the modulus of sisal fiber is high. The composites containing woven fibers with woven space of 1x1cm (pattern B) increased with an increase of sisal fiber. The maximum flexural modulus was 2.69 GPa. In case of the composites prepared from woven fiber with woven space of 0.5x0.5cm (pattern A), the maximum modulus was about 2.67 GPa at 3 wt.% sisal fibers. However, when sisal fibers content was increased to 5 wt.% the flexural modulus of the composites prepared from woven fiber with woven space of 0.5x0.5cm slightly dropped to 2.48 GPa. This might be because more voids were trapped in sisal fiber and epoxy matrix when higher fiber content of small woven space was used.

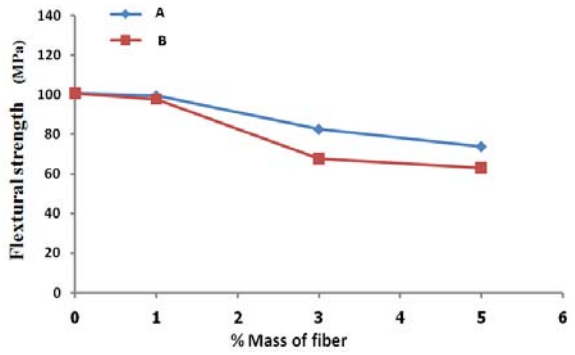

Figure 2. Variation of flexural strength of sisal fiber reinforced epoxy resin as a function of fiber content and woven pattern.

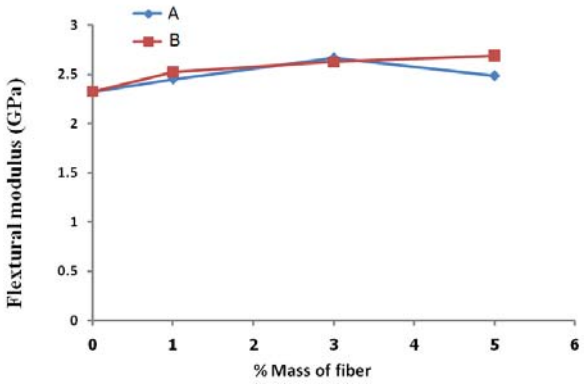

Figure 3. Variation of flexural modulus of sisal fiber reinforced epoxy resin as a function of fiber content and woven pattern

The results of impact strength are given in Figure 4. It was found that the impact strength of sisal fiber/epoxy composites made from both type of woven pattern was lower than that of pure epoxy samples. This could be due to poor interfacial adhesion between epoxy matrix and sisal fiber [8]. The gap between sisal fiber and epoxy matrix acted as stress concentrator leading to low impact strength. At 1 and 3 wt.% fiber content, the impact strength values of composites containing fibers with woven space of 0.5x0.5mm (pattern A) were lower than those of the composites containing fibers with woven space of 1x1mm (pattern B). This could be because small woven space was tighter and difficult to relax leading to more brittle characteristic. However, when fiber content was

increased to 5 wt.%, the present of more voids in composites containing fibers with woven space of 0.5x0.5mm (pattern A) led to more energy dissipation. The composite containing woven fiber with woven space of 1x1mm (pattern B) showed the lowest impact strength at 5 wt.% fiber. This might be because higher plies (12 plies) in composites containing 5 wt.% fibers with woven space of 1x1mm (pattern B) led to more weak point of interfacial adhesion between fiber and matrix. This is in agreement with the explanation given earlier.

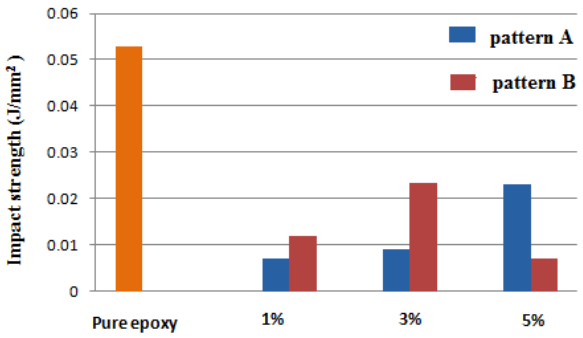

Figure 4. Variation of impact strength of sisal fiber reinforced epoxy resin as a function of fiber content and woven pattern

Conclusions

The flexural strength of all composites was lower than that of pure epoxy resin. However, the composites prepared from smaller woven space (pattern A) seemed to show slightly higher flexural strength than those prepared from larger woven space (pattern B). Flexural modulus of all composites was higher than that of pure epoxy resin. In addition, with an exception of the composites containing 5 wt.% woven fiber with woven space of 0.5x0.5cm (pattern A), the flexural modulus tended to increase with increasing fiber content. The impact strength of all composites was lower than that of pure epoxy resin. The highest impact strength of composite prepared from woven sisal fiber with woven space of 0.5x0.5cm (pattern A) appeared at 5 wt.% fiber but the highest impact strength of composite prepared from woven sisal fiber with woven space of 1x1 cm (pattern B) appeared at 3 wt.% fiber. The results obtained implied that both fiber content and woven pattern have affected the flexural and impact properties of the composites. Moreover, the interfacial adhesion between fiber and matrix also affected the properties of composites. Therefore, the modification of sisal fiber surface will be investigated in furthur study.

Acknowledgements

The authors gratefully acknowledge Suranaree University of Technology and Center of Excellence for Petroleum, Petrochemicals and Advanced materials, Chulalongkorn University for the financial support.

References

[1] Y. Li, Y. Mai,; and L. Ye, *Comp. Sci. Technol.*60,(2000), pp. 2037-2055.
[2] J. Kuruvilla, V. Siby, G. Kalaprasad**,** T. Sabu, L. Prasannakumari, P. Koshy and C. Pavithran, *Eur Polym J.* **32**(1996), pp. 1243-1250.
[3] P. S. Mukherjee and K. G. Satyanarayana, *J Mater Sci.* **19**(1984), pp. 3925-3934.
[4] X. Lu, MQ. Zhang, MZ. Rong, G. Shi, GC. Yang and HM. Zeng, *Adv Compos Lett.* **5**(1984), pp. 231-236.
[5] X. Lu, MQ. Zhang,MZ. Rong, DL. Yue and GC. Yang, *Compos Sci Technol.* **64**(2004), pp.1301–1310.
[6] J. Gassan and AK. Bledzki, *Polym Compos.* **18**(1997), pp.179–184.
[7] J. Kuruvilla, T. Sabu and C. Pavithran, *Compos Sci Technol.* **53**(1995), pp.99–110.
[8] MZ . Rong, MQ. Zhang, Y. Liu, GC. Yang and HM. Zeng, *Compos Sci Technol.* **61**(2001), pp.1437–1447.

Effect of carbonizing conditions on electrical resistivity of white popinac, bamboo, coconut shell and eucalyptus charcoal

S. Ruengsri*, T. Sripanlom and S.Thongngamdee

Department of Chemistry, Faculty of Science and Technology, Nakhon Pathom Rajabhat University, Muang Nakhon Pathom, Thailand

*E-mail:suwimonn@hotmail.com

Abstract: Electrical resistivity of *White Popinac, Bamboo, Coconut Shell* and *Eucalyptus* wood charcoal produced under different carbonizing conditions were determined. The results showed that electrical resistivity of the charcoal indicated strong and systematic dependence on the calcination temperature. The appropriate conditions for all were started from 400, 700 and up to 1000 °C. The soaking time at the highest temperature were 30 minutes for all samples, while the electrical resistivity of the charcoal powders were found to be 5.1, 9.7, 19.8 and 4.1 Ω for White Popinac, Bamboo, Coconut Shell and Eucalyptus, respectively. After that the prepared powders were placed in containers, electrical resisitivity were also determined.

Introduction

Wood charcoal is an important functional materials [1] which are widening use in structural applications such as carbon fibres [2], carbon fuel cells and carbon electrodes [3]. During 1970's, Stanford Research Institute (RSI) developed a coal base fuel cell in molten lead at temperature of 500 to 900 °C [4,5], while Gur and Huggins constructed a high temperature fuel cell (725 to 955 °C) that employed stabilized zirconia as a solid electrolyte and a graphite anode [6]. In 1810 carbonized charcoal electrodes were use in arc lamp, and in 1830 carbonized charcoal was used as an electrode for primary batteries. These electrodes were made from powdered charcoal or coke bonded with sugar syrup or coal tar, pressed and carbonized at high temperatures [7].

Charcoal is the carbon residue from thermal decomposition with insufficient oxygen. Good quality of charcoal has fixed carbon content, measured by ASTM D 1762-84, to about 70%. These charcoals prepared by heating up to 400-500 °C. Chemical formula for charcoal is $CH_{0.60}O_{0.13}$ [8]. Higher quality of charcoal corresponded to the higher carbon content, which prepared by treated higher carbonizing temperature to above 500 °C. Carbon content can have in excess of 94% in high temperature carbonized charcoal. Some carbonized charcoals are purer than natural graphite [9], and electrical properties are closely related to degree of graphitization in wood charcoals [10].

Accordingly, the objective of this work was to find out the suitable carbonizing conditions of White Popinac, Bamboo, Coconut Shell and Eucalyptus charcoal which affected to their electrical resistivity.

Materials and Methods

Wood samples of *White Popinac, Bamboo, Coconut Shell* and *Eucalyptus* were cut into 12 cm^2. The samples were carbonized from 30 to 400 °C at the starting rate of 4 °C/min and then to 600, 700, 800, 900 and 1000°C at the heating rate of 12°C/min and the holding time was 30 min. After that the charcoals were allowed to cool in the furnace, electrical resistivity were measured using digital multimeter.

The charcoal powders were ground and placed in pipette tips, which used as containers for voltammetric electrode. Mineral oil was used as binder. Electrical resistivities of the charcoal powders were determined. Two probes of multimeter were hold between the two copper wires. The first wire was touched to the contact surface to eliminate the resistant at the surface, while the other was inserted to the charcoal powders at the different height of 1 to 4 cm, as see in figure 1.

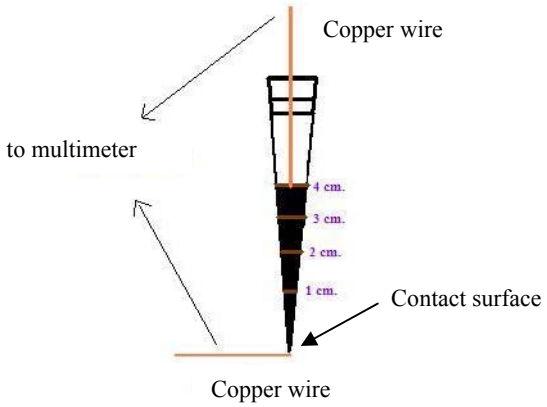

Figure 1. Apparatus for electrical resistivity measurement

Results and Discussion

The relation between carbonizing temperatures and electrical resistivity of *White Popinac, Bamboo, Coconut Shell* and *Eucalyptus* are shown in table 1.

Table 1: Electrical resistivity of wood charcoals at different carbonizing temperature

Type of wood charcoal	Temperature (°C)	Electrical resistivity (Ω)
White Popinac	400	-
	600	4.15×10^6
	700	3.72×10^2
	800	9.4
	900	7.4
	1000	5.1
Bamboo	400	-
	600	2.36×10^7
	700	1.75×10^5
	800	23.6
	900	10.5
	1000	9.7
Coconut Shell	400	-
	600	6.96×10^5
	700	1.51×10^4
	800	108.3
	900	26.3
	1000	19.8
Eucalyptus	400	-
	600	2.25×10^7
	700	1.76×10^5
	800	11.2
	900	5.6
	1000	4.1

From the table, the wood charcoals showed electrical resistivity decreases as increasing carbonizing temperature. At room temperature to about 400 °C, the removal of insulating volatile matters and breakage of C-H bonds has occurred. After the temperature increase to about 800 °C, C-H bonds are completely broken whereas the loss of volatiles predominates and results in an increase in both fixed and total carbon contents in wood charcoal [11]. Such reason depicts that electrical resistivity of wood charcoals had much decrease during carbonization temperature up to 800 °C.

Above 800 °C, electrical resistivity slightly decreases due to the breakage of the C-H bond resulting in the formation of free valence electron and appears to contribute to the electrical conductivity of wood charcoals. According to Neely [12], increase of carbonizing temperature affected to higher C/H ratio in wood charcoals. This means that the extent of aromatization increases with increasing carbonization temperature. The aromatization of wood charcoals leads to decrease in its resistivity of aromatic nuclei [13]. And from Kuma and Gupta [3], the soaking time (2 to 5 hours) is not the strong function to the carbon content in wood charcoals.

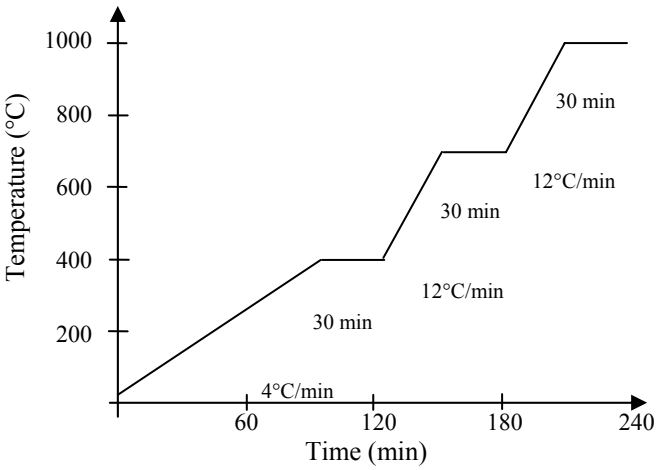

Figure 2. Suitable carbonizing conditions for wood charcoals

From table 1, electrical resistivity of *White Popinac, Bamboo, Coconut Shell* and *Eucalyptus* are close but slightly different due to the different in principal chemical constituents in wood. Cellulose, which has an electrical insulating effect, has higher electrical resistivity and energy gap than lignin [13]. The ratio of cellulose:lignin in wood indicated electrical resistivity, the higher ratio in wood, the high electrical resistivity in charcoals. *Bamboo, white popinac* and *coconut shell* have higher electrical resistivity due to their higher ratio of cellulose than *Eucalyptus*.

From these results, the suitable carbonizing temperatures to all wood charcoals were obtained. The heating temperature increases stepwise from room temperature to 400°C at the heating rate of 4 °C/min and from 400 - 700, 700 - 1000 °C at the heating rate of 12 °C /min (figure 2). Accordingly, the soaking time was 30 min for completing the reaction in each step.

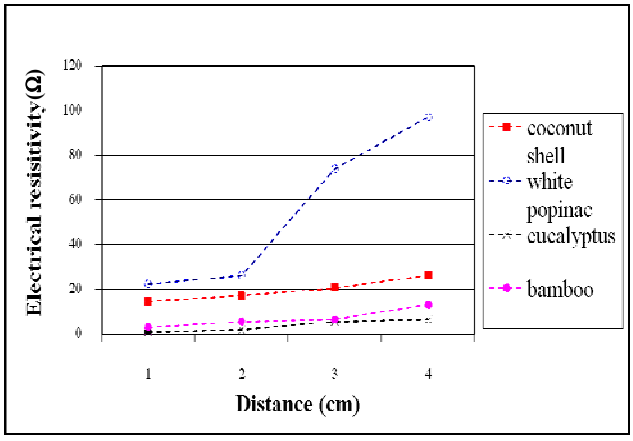

Figure 3. Electrical resistivity of wood charcoals after forming

After forming by placing the charcoal powders into the containers, electrical resistivity was observed, as shown in figure 3. Electrical resistivity increases with increasing distance between two copper wires in all samples.

Conclusions

Carbonizing conditions affected to the electrical resistivity of *White Popinac, Bamboo, Coconut Shell* and *Eucalyptus* wood charcoal. The suitable conditions were started from 400, 700 and up to 1000 °C. The soaking time at the highest temperature were 30 minutes for all samples. Electrical resistivity of the charcoal powders were found to be 5.1, 9.7, 19.8 and 4.1 Ω for *White Popinac, Bamboo, Coconut Shell* and *Eucalyptus,* respectively. After forming, electrical resistivity increases with increasing distance between two copper wires in all samples.

Acknowledgement

The researcher would like to thanks the research and development institute, Nakhon Pathom Rajabhat University for financial support.

References

[1] Y. Imamura, *Shokubai.* **41** (1991), pp. 254-258.
[2] http://acs.omnibooksonline.com/data/papers/1995.738.pdf
[3] M. Kumar and R.C. Gupta, *J. Mat. Sci.* **28** (1993), pp. 440-444.
[4] M. Anbar, D.E. McMillen, R.D. Weaver and P.J. Jorgensen, U.S. Pat. No. 3,940,474, 1996.
[5] M. Anbar, U.S. Pat. No. 3,741,809, 1973.
[6] T.M. Gur and R.A. Huggins, *J. Electrochem. Soc.* **139** (1992), p. L95.
[7] A.R. Ford, *Modern Aspects of Graphite Technology,* Academic Press, London, 1970, pp. 258.
[8] M.J. Antal and M. G. Gronli, *Ind. Eng. Chem. Res.***42** (2003), p. 1919.
[9] M.J. Antal, U.S. Pat. No. 7,405,020 B2, 2008.
[10] K. Nishiyama, T. Hata, H. Kikushi and Y. Imamura, *J. Wood. Sci.* **50** (2004), pp. 177-181.
[11] M. Kumar, Ph.D. Thesis, Banarus Hindu University, India, 1991.
[12] J.W. Neely, *ibid.* **19** (1981), p. 27.
[13] K. Ouchi, *Fuel.***46** (1967), p. 71.

Preparation of nanoparticles from pectin using ionotropic gelation method

Somkamol Manchun[1,2], Jurairat Nunthanid[1,2], Sontaya Limmatvapirat[1,2] and Pornsak Sriamornsak[1,2,*]

[1]Department of Pharmaceutical Technology, Faculty of Pharmacy, Silpakorn University, Nakhon Pathom, Thailand 73000
[2]Pharmaceutical Biopolymer Group (PBiG), Faculty of Pharmacy, Silpakorn University, Nakhon Pathom, Thailand 73000

*E-mail: pornsak@ su.ac.th.

Abstract: The aim of this research was to study factors affecting the formation of calcium pectinate (CP) nanoparticles through ionotropic gelation method. Fluorescein isothiocyanate dextran (FD4, MW 4000 Da) was used as a model macromolecule. The studied factors were type and concentration of pectin. The physicochemical properties of CP nanoparticles were characterized by particle size analysis and zeta potential measurement. The results showed that particle size of CP nanoparticles made of high degree of esterification (DE) pectin decreased to nano-sized and was smaller than those made of low DE pectin. Particle size was insignificantly changed when the concentration was increased. The zeta potential of CP nanoparticles tended to increase when low DE pectin was used. The encapsulation efficiency of FD4 was influenced by the type of pectin. The CP nanoparticles made of high DE pectin showed higher encapsulation efficiency than those made of low DE pectin. However, the encapsulation efficiency of FD4 changed insignificantly on increase of concentration. The results from this research provide the basic knowledge for preparation of calcium pectinate nanoparticles being a useful carrier for drug delivery system of macromolecule drugs.

Introduction

Macromolecules such as proteins and DNA play an increasingly important role in our arsenal of therapeutic agents. Delivery of these molecules to their site of action at the desired rate is a challenge. Their transport through compartmental barriers in the body is inefficient and they are readily metabolized[1]. In particular, nanoparticles are able to protect drugs from degradation, to improve permeation/penetration of the drugs across mucosal surfaces, and also to control the release of the encapsulated or adsorbed drug[2].

Nanoparticles can be prepared from biopolymer that is biodegradability, biocompatibility and non-toxicity[3]. Pectin is a naturally occurring biopolymer as a complex mixture of polysaccharides that makes up about one third of the cell wall dry substance of higher plants[4]. It also has bioadhesive properties towards other gastrointestinal tissues, which can be used as a drug delivery device on a specific site for targeted release and optimal drug delivery due to intimacy and duration of contact. [5] In this research , the factors affecting the formation of calcium pectinate (CP) nanoparticles through ionotropic gelation method were investigated. Fluorescein isothiocyanate dextran (FD4, MW 4000 Da) was used as a model macromolecule.

Materials and Methods

Materials: Two types of pectin with different degrees of esterification (DE) (i.e., 70% for high DE pectin and 43% for low DE pectin), Fluorescein isothiocyanate dextran (FD4), a hydrophilic and high-molecular weight molecule (MW 4000 Da) and calcium chloride were of reagent grade. All other chemicals were of standard analytical grade.

Preparation of CP nanoparticles: The CP nanoparticles were prepared by dissolving pectin in water with agitation. The 0.05 M solution of calcium chloride were dropped using a nozzle of 0.80 mm inner diameter into a 1% (w/w) pectin solution and homogenized using a homogenizer, at 9500 rpm for 20 min. The different amounts (i.e., 0.1, 0.25, 0.5, 0.75, 1 %) of dispersions were dropped using a nozzle of 0.80 mm inner diameter into cool distilled water and the mixture was stirred gently with magnetic stirrer. The CP nanoparticles formed were allowed to stand in the solution for 30 min.

Preparation of FD4-loaded CP nanoparticles: FD4 was dissolved in distilled water at a concentration of 0.5 mg/mL, and different amounts of CP nanoparticles were added. The mixture of nanoparticles and FD4 was protected from light and was stirred gently with magnetic stirrer at room temperature for 12 hours. Then, these nanoparticles were separated from the aqueous phase by centrifugation (Hettich Universal 320, Germany) at 14,000 rpm for 30 minutes. Next, the FD4-loaded nanoparticles obtained were washed with water.

Measurement of particle size, morphology and zeta potential: The average particle size and the zeta potential of the CP Nanoparticles were evaluated by a laser scattering particle size distribution analyzer (Horiba LA-950, Japan) and zeta potential analyzer (Zetaplus, Brookhavan, USA). The average particle size was calculated from 3 measurements. The average zeta potential value was also calculated. Morphology of CP Nanoparticles was observed with an inverted microscope (Model EclipseTE2000-U, Nikon, Japan) equipped with super high pressure mercury lamp (Model C-SHG1, Nikon, Japan)

Encapsulation efficiency of FD4: Each mixture of FD4-nanoparticles was centrifuged at 14,000 rpm for 30 minutes to separate the free FD4 in the supernatant from that loaded in the nanoparticles. The amount of free FD4 in the clear supernatant was measured by spectrofluorophotometer (Shimazu RF-1501, Japan) with excitation of 480 nm and emission of 520 nm. The encapsulation efficiency (EE %) of FD4 was calculated as the ratio between FD4 loaded into the nanoparticles with respect to the total amount of FD4 used for preparation of the original mixture as follows:

$$EE\ (\%) = (FD4_t - FD4_f)\ /FD4_t \times 100$$

where $FD4_t$ is the total amount of FD4 used for preparation in the original mixture and $FD4_f$ is the free amount of FD4 recovered in the supernatant.

Results and Discussion

Preparation and characterisation of CP nanoparticles: An aqueous solution of pectin was dropped into calcium chloride solutions and gelled spheres were formed instantaneously by ionotropic gelation in which intermolecular cross-links were formed between the divalent calcium ions and the negatively charged carboxyl groups of the pectin molecules. The result showed that the particles size depended on the type of pectin. The CP nanoparticles made of high DE pectin was decreased to nano-sized and smaller than of CP nanoparticles made of low DE pectin and Particle size were not significanty changed when the concentration was increased (Figure.1). The zeta potential of CP nanoparticles tended to increase when low DE pectin (Figure.2). As the low DE pectin contaiins higher amount of carboxyl groups that could dissociate to negative charge (e.g. COO^-), it could highly interact and form a complex with the positively charged calcium chloride, so the particle sizes were increased.

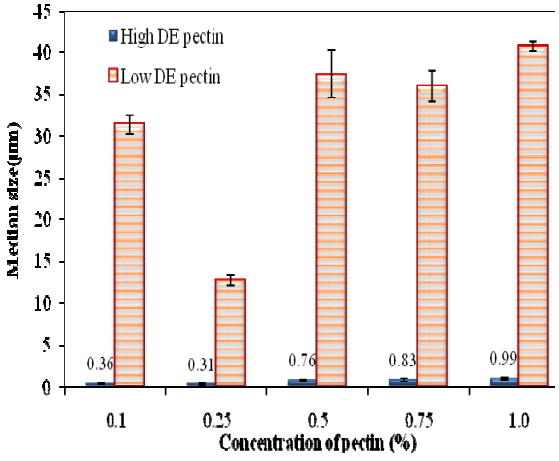

Figure 1. Median size (μm) of CP nanoparticles using various concentrations of pectin (n=3).

The fluorescence micrographs of the CP nanoparticles are shown in Figure 3. The CP nanoparticles made of low DE pectin (Figure 3A) showed an almost spherical shape. The CP nanoparticles made of high DE (Figure 3B) were also spherical with smaller size.

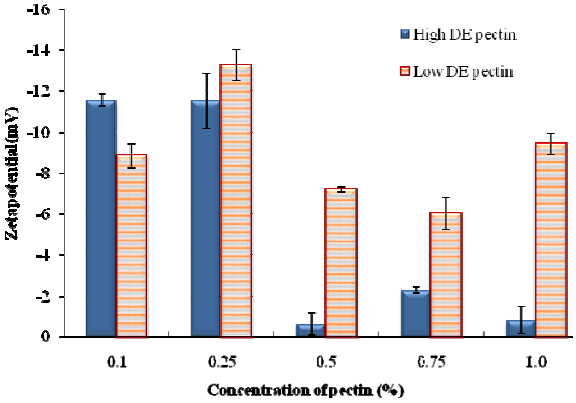

Figure 2. Zeta potential (mV) value of CP nanoparticles in various concentrations (n=3).

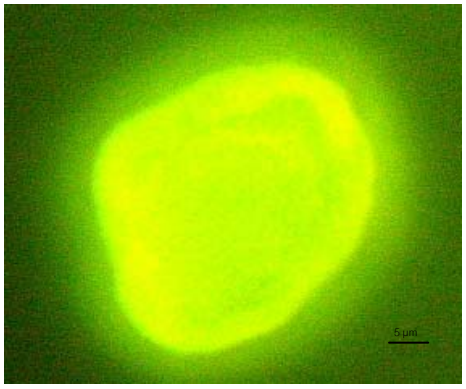

(A)

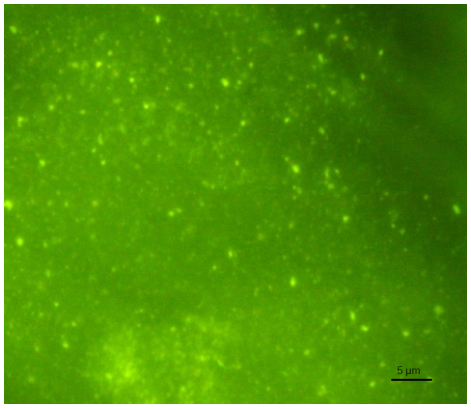

(B)

Figure 3. The fluorescence micrographs (40x) of the CP nanoparticles. (A) CP nanoparticles made of low DE ; (B) CP nanoparticles made of high DE.

Encapsulation efficiency of FD4 in CP nanoparticles: The encapsulation efficiency of FD4 was carried out by indirect assay of non-encapsulated FD4 in supernatant and then calculating the difference of FD4 amount in the CP nanoparticle suspension before and after centrifugation. The encapsulation efficiency were influenced by the type of pectin. The CP nanoparticles made of high DE pectin showed a higher encapsulation efficiency. This may be because the CP nanopaticles made of high DE pectin was nano-sized and smaller than of CP nanoparticles made of low DE pectin. Thus are more surface area to which FD4 can be adsorbed. As previously mentioned, low DE pectin can form complex by calcium ions in such nanoparticles, resulting in a rigid structure that caused lower FD4 encapsulation efficiency. Moreover, encapsulation efficiency were not significanly changed in each concentration and the maximum encapsulation efficiency was about 60% (Figure. 4).

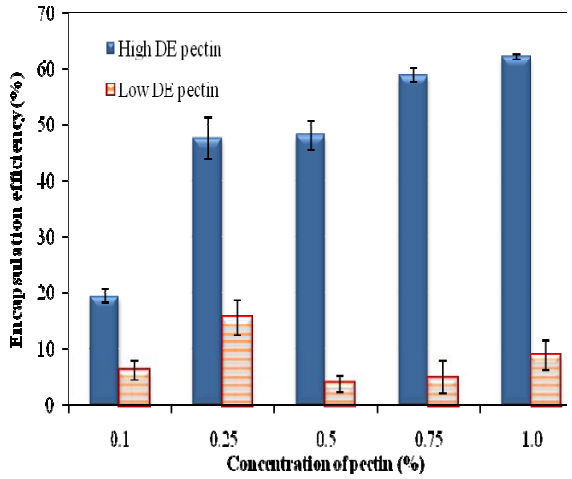

Figure 4. Encapsulation efficiency (%) of CP nanoparticles in various concentrations (n=3).

Conclusions

The particles size and encapsulation efficiency of CP nanoparticles prepared through ionotropic gelation method were influenced by the type of pectin. The CP nanoparticles made of high DE pectin showed a higher encapsulation efficiency and particle size was decreased to nano-sized and smaller than of CP nanoparticles made of low DE pectin. However, the encapsulation efficiency of FD4 insignificantly changed on the increase of pectin concentration. The results from this research provide the basic knowledge for preparation of CP nanoparticles for delivery of macromolecular drug.

References

[1] D. Crommelin, G. Storm, W. Jiskoot, R. Stenekes, E. Mastrobattista and WE. Hennink, J Control Release, 87(2003), pp. 81-87.

[2] H. Takeuchi, H. Yamamoto, Y. Kawashima, Adv Drug Deliv Rev. 47(2001), pp. 39-54.

[3] C. Reis, R. Neufeld, A. Ribeiro and F. Veiga, Nanomedicine. 2(2006), pp. 8-21.

[4] P. Sriamornsak, Silpakorn U Int J, 3(2003), pp. 206-228.

[5] N. Thirawong, RA. Kennedy and P. Sriamornsak , Carbohydr Polym, 71(2008), pp. 170-179

[6] K. Burapapadh and P. Sriamornsak, Preparation of indomethacin-loaded pectinmicroparticle by emulsification method. The 6th World Meeting on Pharmaceutics, Biophamaceutics and Pharmaceuticals Technology; Barcelona, Spain; 2008

[7] Z . Muhiddinov, D. Khalikov, T . Speaker and R. Fassihi, J Microencapsul, 21(2004), pp. 729-741.

Synthesis and structural characterization of pectin-deoxycholic acid chemical conjugates

K. Cheewatanakornkool[1,2], S. Niratisai[3], P. Sriamornsak[1,2,*]

[1]Department of Pharmaceutical Technology, Faculty of Pharmacy, Silpakorn University, Nakhon Pathom, Thailand 73000
[2]Pharmaceutical Biopolymer Group (PBiG), Faculty of Pharmacy, Silpakorn University, Nakhon Pathom, Thailand 73000
[3]Department of Pharmaceutical Chemistry, Faculty of Pharmacy, Silpakorn University, Nakhon Pathom, Thailand 73000

*E-mail: pornsak@su.ac.th

Abstract: Pectin, a water-soluble, non-toxic biopolymer, has been received more attention as carrier for drug delivery. In this study, citrus low methoxy pectin was hydrophobically modified by couping of deoxycholic acid (DOCA) onto the pectin molecule. The effect of the addition of N-hydroxysuccinimide (NHS) on the degree of substitution was investigated. Firstly, the hydrophobic segment was synthesized by cross-linking of DOCA with ethylenediamine (ETD) using 1-ethyl-3-(3-dimethyamino-propyl)carbodiimide hydrochloride (EDC) as a zero-length cross-linker. The N-deoxycholylethylenediamine (DOCA-NH_2) produced during the cross-linking reaction was checked by thin-layer chromatography. The structural characteristics of the resultant DOCA-NH_2 were confirmed by Fourier-transform infrared spectrometry and nuclear magnetic resonance spectroscopy (^{1}H-NMR and ^{13}C-NMR). The pectin-deoxycholic acid conjugates (PDAC) were then prepared by coupling DOCA-NH_2 onto the pectin molecules with or without NHS. The degree of substitution of DOCA-NH_2 onto pectin backbone was determined by titration method adapted from United State Pharmacopeia monograph. It was confirmed that DOCA-NH_2 was covalently attached to pectin in the presence of cross-linker. The addition of NHS yielded the PDAC with higher degree of substitution. The results from this study demonstrated the successful of structural modification of pectin by chemical conjugation.

Introduction

Pectin is a naturally occurring biopolymer makes up about one third of the cell wall dry substance of higher plants. Though it is a heterogenous polysaccharide, pectin contains linear chains of (1,4)-linked α-D-galacturonic acid residues (Fig. 1). The linear structure of pectin is partly interrupted by (1,2)-linked side chains consisting of L-rhamnose residues and some others neutral sugards, such as arabinose, galactose and xylose [1]. At present, commercial pectins are almost exclusively derived from citrus peel or apple pomace, both by-products from juice manufacturing. Apple pomace contains 10-15% of pectin on a dry matter basis. Citrus peel contains of 20-30%. The pectin classes based on the degree of esterification (DE) are high methoxyl (HM) pectins, and the low methoxyl (LM) pectins which are either the conventionally demethylated or the amidated molecule. DEs values for commercial HM-pectins typically range from 60 to 75% and those for LM-pectins range from 20 to 40% [2].

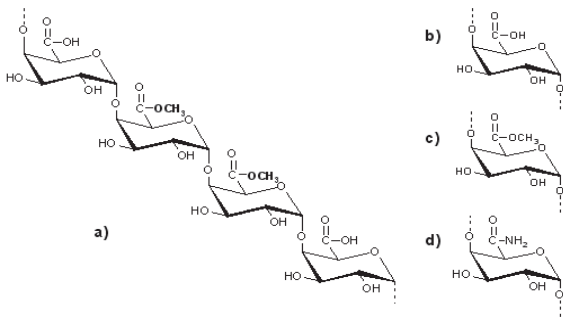

Figure 1. (a) A repeating segment of pectin molecule and functional groups: (b) carboxyl; (c) ester; (d) amide in pectin chain [2].

As a natural biopolymer, pectin has got increasing biotechnological and biomedical applications in view of its several advantages such as high biocompatibility, biodegradability, non-toxicity, non-immunogenicity, chelating ability, and the possibility of chemical modification [2]. In particular, the pectin hydrogels cross-linked by calcium ions are widely used for the encapsulation of drugs, cells and proteins (e.g. [3]). In general, biomolecules which do not interact ionically with the pectin are rapidly released (within a few hours), and the release profiles are often characterized by a more or less pronounced burst effect. Covalent modification of pectin by hydrophobic materials is an effective way for the increase of drug loading and the controlled release. Grafting polymerization is a well-established and powerful method for the development of natural–synthetic polymer hybrid materials. So far, the grafting of hydrophobic moiety onto pectin has not been carried out. Therefore, in this study, we aimed to prepare hydrophobically modified pectin molecules by coupling of deoxycholic acid (DOCA).

DOCA (Fig. 2) is one of the secondary bile acids, which are metabolic by-products of intestinal bacteria. In the human body, DOCA is used in the emulsification of fats for the absorption in the intestine. Outside the body it is used in experimental basis of cholagogues and is also used to prevent and dissolve gallstones. The free acid is soluble at 0.24 g/L in water at 15ºC, while the sodium salt is soluble at >333 g/L in water at 15ºC. Therefore, pH control is very important to the use of DOCA.

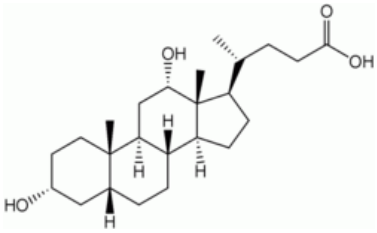

Figure 2. Chemical structure of deoxycholic acid.

In the present study, we have developed a hydrophobically modified pectin. DOCA has successfully been grafted onto pectin through coupling reaction. The physicochemical properties of pectin-DOCA chemical conjugates (PDAC) were also investigated.

Materials and Methods

Materials: Low DE (38%DE) pectin with the average molecular weight of 70,000 Daltons (grade CU701, Herbstreith & Fox KG, Germany), 99% deoxycholic acid (DOCA) (Fluka, USA), ethylene diamine (ETD) (Sigma-Aldrich, USA), N-hydroxy-succinimide (NHS) (Acros Organic, USA), thin layer chromatography sheet silica gel 60 F_{254} (TLC) (Merck, Germany), 1-ethyl-3-(3-dimethyaminopropyl) carbodi-imide hydrochloride (EDC) (Sigma-Aldrich, USA) were used. All other chemical reagents obtained from commercial sources were of analytical grade.

Synthesis of N-deoxycholyethylenediamine (DOCA-NH_2). The DOCA-NH_2 was synthesized using the method adapted from Hu et al. [4]. Briefly, DOCA and ETD were separately dissolved in methanol at the controlled temperature in ice bath. DOCA and ETD solution (ratio 1.5:1) was immediately mixed. The mixture was left to react for 3 h at control temperature and stirred at room temperature for 40 h. Solvent was then removed by using rotary evaporator (474 mbar, 40°C) until dry and product was separated by extraction with chloroform. The product was subsequently washed with distilled water, to remove by-product residues, until clear water was obtained. Finally, the solvent was removed by rotary evaporator. DOCA-NH_2 was purified by column chromatography using silica gel (0.040-0.063mm) as a stationary phase and chloroform-methanol mixture as a mobile phase. Solvent was removed and product was then dried and kept in dry place. In addition, sample was collected during reaction to check the if the reaction is completed. The sampling solution (2 µl) was spotted on to TLC sheet, compared with raw material DOCA and ETD. To check the complete reaction and impurity, spray regent (85% phosphoric acid and distilled water, ratio 1:1) was sprayed on the TLC plate that heated at 100°C for 15 minutes.

Preparation and conjugation DOCA–NH_2 on to pectin molecule (PDAC): DOCA–NH_2 was coupled using EDC or EDC with NHS as a zero-length cross-linker. Low methoxy pectin was dissolved in mixed solution of formamide and dimethyformamide, DOCA–NH_2 was dissolved in dimethyformamide, then EDC/NHS in formamide. The mixture solution was poured by order, gently mixed, stirred at room temperature under a nitrogen atmosphere for 24 h. After that the product was precipitated and washed by acetone and tetrahydrofuran. The product was filtered and washed again, and then dried at room temperature overnight. Finally, the product was dispersed in distilled water and exhaustively dialyzed using dialysis tube (molecular weight cut off 6,000-8,000) in distilled water (water change interval of 4 h, then overnight) and lyophilized to obtain the PDAC pure product.

Characterization: The chemical structure of DOCA-NH_2 and PDAC was confirmed by Furiour transform infrared spectroscopy (FT-IR) with KBr discs (Nicolet, USA) and nuclear magnetic resonance (Bruker, Germany) using tetramethylsilane (TMS) as internal standard and $CDCl_3$ as solvent.

Determination of degree of substitution of DOCA-NH_2: The degree of substitution of DOCA-NH_2 was determined by the method adapted from United State Pharmacopoeia monograph (USP26) [5]. Briefly, the samples (200 mg) were accurately weighed, moistened with alcohol, added carbon dioxide-free water, and swirled occasionally until the sample was completely dissolved. Two drops of phenolphthalein TS were added and then titrated with standard sodium hydroxide. The volume of standard sodium hydroxide used was recorded as initial titer, then 20 mL of standard sodium hydroxide were added and left standing for 15 minutes. Standard hydrochloric acid (20 mL) was added, shaken and then the mixture was titrated until a faint pink color was observed. The amount of titrant used was recorded as saponification titer (each mL of standard sodium hydroxide used in the saponification titer is equivalent to 15.52 mg of -OCH_3 (methoxyl group)).

Assay for galacturonic acid: From the above titration, each mL of standard sodium hydroxide used in the total titration (initial titer added to saponification titer) is equivalent to 97.07 mg of $C_6H_{10}O_7$.

Particle size and distribution measurement: The mean particle size and size distribution were measured using a static laser light scattering instrument (Horiba, Japan).

Results and Discussion

The product obtained from the synthesis of DOCA-NH_2 is white powder. The chemical structure of

DOCA-NH_2 was confirmed by FT-IR which showed amide linkages at 1647 and 1552 cm^{-1} (Fig. 3). The ^{13}C-NMR spectrum of DOCA-NH_2 also showed amide bond signal at chemical shift 175 ppm (Fig.4).

DOCA-NH_2 was covalently attached to pectin in the presence of EDC or EDC with NHS to improve the functional properties for pectin. The results from FT-IR demonstrated C-O stretching at 1,143 cm^{-1} and C=O stretching at 1,741.6 cm^{-1} according to the ester bond (Fig. 3E). The peaks of C=O stretching at 1,693 cm^{-1} and OH stretching at 2,850 to 2,900 cm^{-1} (referred to free carboxylic acid of pectin) disappeared in the PDAC structure. This confirmed that DOCA-NH_2 was conjugated on to pectin molecules.

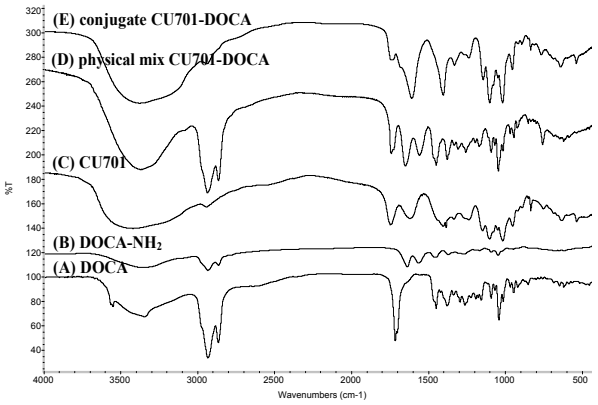

Figure 3. FT-IR spectra of (A) DOCA, (B) DOCA-NH_2, (C) pectin, (D) physical mixture of pectin and DOCA, and (E) pectin-DOCA conjugates (PDAC).

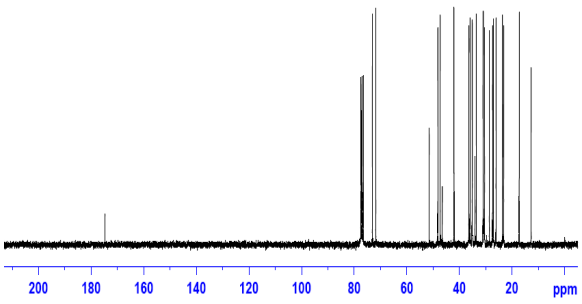

Figure 4. ^{13}C-NMR spectra of DOCA-NH_2.

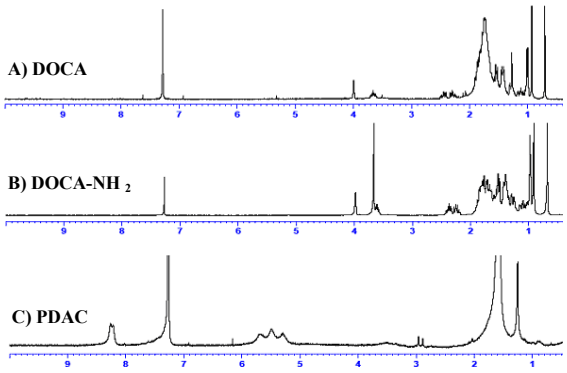

Figure 5. ^{1}H-NMR spectra of (A) DOCA, (B) DOCA-NH_2, and (C) pectin-DOCA conjugates (PDAC).

The results from ^{1}H-NMR spectrum demonstrated the characteristic peaks of DOCA appearing at 0.6-2.5 ppm (Fig. 5C). The ^{1}H-NMR spectrum of DOCA-NH_2 showed signals at chemical shift of 3.0-3.5 ppm (Fig. 5B). The PDAC dissolved slightly in $CDCl_3$ but its hydrophobic segment could dissolve and showed peaks at 0.6-2.9 ppm. The characteristic peaks of DOCA were still appeared in the spectrum of PDAC (Fig 5. C).

Excess reagent and isourea formed as the by-product of crosslink reaction. EDC reacted with carboxylic acid resulting in an active ester intermediate. In the presence of an amine nucleophile (i.e., ETD), an amide bond was formed with release of an isourea by-product. In the presence of both EDC and NHS, NHS ester intermediate was formed. The NHS ester intermediate has longer half-life which can increase the coupling of DOCA-NH_2 on to pectin molecules.

From Figure 6, the results showed a decrease value of galacturonic acid and free carboxylic group of pectin after coupling with DOCA. The free carboxylic group decreased from 67.61% to 24.38% when using EDC only, and to 19.24% when using EDC/NHS. The results indicated that DOCA-NH_2 coupled at the free carboxylic group of galacturonic acid in pectin chain. The presence of NHS may also increase the degree of substitution of DOCA on to the pectin chain.

Size and size distribution measurements of particles using static laser light scattering were performed. The size of PDAC was narrow distributed (Fig. 7) with the median size ranged from 35 to 53 µm, depending on the pH of medium (Table 1).

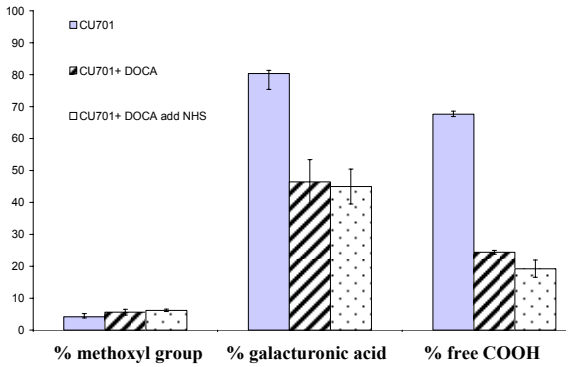

Figure 6. Chemical analysis of pectin and its derivatives showing % methoxyl group, % galacturonic acid and % free carboxylic acid in low methoxy pectin (CU701), PDAC that used EDC only (CU701+DOCA) and PDAC that used EDC/NHS (CU701+DOCA add NHS).

Table 1. Particle size of pectin-deoxycholic acid conjugates dispersed in different media.

Medium	Particle size (µm)	
	EDC	EDC/NHS
Basic (8.50-8.70)	43.26 ± 3.72	35.16 ± 4.17
Acidic (1.10-1.20)	precipitated	53.53 ± 3.89

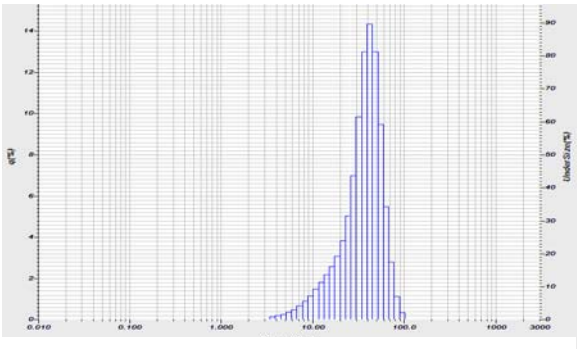

Figure 7. Size distribution of PDAC that used EDC/NHS as coupling reagent, in acidic medium.

Conclusions

Pectin-deoxycholic acid conjugates (PDAC) were synthesized by chemical reaction. The coupling reaction occurred at carboxylic acid position of both pectin and DOCA. The modification of pectin molecules can improve the properties of pectin while it is still water-soluble. The new developed materials may be used in biomedical and pharmaceutical applications as a carrier of a wide variety of biologically or other active agents.

Acknowledgements

The authors wish to acknowledge the Thailand Research Fund and Office of Small and Medium Enterprises Promotion, Thailand, for financial support (grant number IUG5080020). Thanks to Dr. Amornrat Chaidedgumjorn for her suggestion on some analytical experiments.

References

[1] G. B. Seymour and J. P. Knox, *Pectins and their Manipulation*, CRC press, UK , 2002.
[2] P. Sriamornsak, Chemistry of pectin and its pharmaceutical uses: A review. *Silpakorn U. Int. J.*, 2003, 3, pp. 206-228.
[3] P. Sriamornsak, Investigation of pectin as a carrier for oral delivery of proteins: using calcium pectinate gel bead. *Int. J. Pharm.*, 1998, 169, pp. 213-220.
[4] Y. Hu, X. He, L. Lei, S. Liang, G. Qui, X. Hu, Preparation and characterization of self assembled nanoparticles of the novel carboxymethyl pachyman-deoxycholic acid conjugated, *Carbohydr. Polym.,* 2008, 74, pp. 220-227.
[5] Authority of the United States Pharmacipeial Convention, *The United States Pharmacopeia*, Asian Edition, United States Pharmacopeial convention, Inc, USA, 2003, 26 pp. 1401.

Preparation and characterization of improved hydrophilicity poly(ether imide) ultrafiltration membrane by immobilization poly(ethylene glycol) on membrane

Watchanida Chinpa[1]* and Ratana Jiraratananon[2]

[1]Department of Materials Science and Technology, Faculty of Science, Prince of Songkla University, Hat-Yai, Songkhla, Thailand
[2] Department of Chemical Engineering, King Mongkut's University of Technology Thonburi,Bangkok, Thailand

Abstract: The hydrophilic porous of poly(ether imide) (PEI) membrane with ultrafiltration separation profile could be prepared by wet-chemical treatment. Poly(propylene oxide)/poly(ethylene oxide) monoamine, PEG-amine which predominates with ethylene glycol was used as surface modifier. PEI membrane was prepare via immersion precipitation method by using 16 wt% PEI in N-methyl pyrrolidone, using water as non-solvent. PEI membrane was treated with 10 wt% PEG-amine in water at 88ºC for 1, 3, 5 and 24h. The effect of the treatment time on the morphology (SEM, AFM), wettability (contact angle measurement), water permeability and mechanical properties of membrane were investigated. The chemical structure change during the modification process was monitored by FTIR-ATR, which indicated that imide groups were turned to amide group during this process. Water contact angle measurement indicated that treatment with PEG-amine resulted in a better wettability of PEI membrane and an increase in water permeability compared to parent PEI membrane. These characteristics offer a lower fouling useful for ultratiltration.

Introduction

Poly(ether imide), PEI is an attractive material for membrane fabrication because of its excellent film forming ability and mechanical properties as well as a good thermal and chemical resistance[1]. However, the hydrophobic character of PEI causes heavy fouling on the membrane surface with feed solutions containing substance like proteins entailing dramatic flux decline [2]. Increasing membrane surface hydrophilicity can effectively reduce membrane fouling [3]. Surface modification with chemical solution is an interesting route to make membrane surface more hydrophilic. This method presents the advantages of simplicity, versability and low cost operation.

Poly (ethylene glycol) (PEG) offers a hydrophilicity property, large excluded volume, and unique coordination with environmentally water molecule in an aqueous medium [4]. Many works used PEG to modify many polymeric membranes to resistance protein adsorption [5-8].

The aim of this work was the preparation of hydrophilic porous of poly(ether imide) membrane by using poly (propylene oxide)/poly(ethylene oxide) monoamine as surface modifier. The effect of the reaction time on the morphology, wettability (contact angle measurement), permeability (pure water flux, PWF), and mechanical properties of membrane were investigated

Materials and Methods

Materials: PEI (ULTEM 1000®) was kindly supplied by NOK Precision Component (Thailand) Ltd. PEG-amine or Jefamine M-2070 polyetheramine was kindly supported by Ethyoxy Chemical Co., Ltd. used as modifying agent. Anhydrous NMP was purchased from Aldrich and was used as a solvent. Bovine serum albumin (BSA) with an average molecular weight of 67 kDa was supplied from Fluka. All reagents were used without any further purification.

Membrane preparation and modification: Porous membranes were prepared by the classical phase inversion method in water as coagulant. 16 wt % PEI solutions was cast on a glass plate with a doctor blade fixed at 250 μm in an environment of 50 ± 5% relative humidity, 29 ± 1 ^{o}C. The cast films were then immediately immersed into a 25 ^{o}C water bath for complete precipitation.

For the modification, the PEI membranes were hold by the stainless support and all of them were then placed in the stainless steel cylinder containing PEG-amine modifying agent solution. This device was then immersed in the thermostat water bath controlled temperature at 88^{o}C. The studied concentration of PEG-amine solution was 10 wt%. Reactions were carried out for the indicated time of 1, 3, 5, and 24 h. The modified membranes were then thoroughly washed with distilled water to remove absorbed modifier and stored in wet state until use.

Surface Characterization: The surface of the film was carried out using Fourier Transform Infrared Spectrometer (FT-IR), Attenuated total reflection mode (ATR-FTIR: Equinox 55, Bruker).

*Membrane morphology observation:*The surface and cross-sectional morphology of the obtained membranes were characterized by SEM (JSM 5200). The membranes were cut into a piece of various sizes. These pieces were immersed in liquid nitrogen for a period of time and then broken in the case of cross-section morphology study. The fractured membranes were then coated with gold.

Hydrophilicity of membrane surface: The hydrophilic property of membrane surface was

characterized by using water contact angle measurement by using an automatic interfacial tensiometer (Data physic).

Ultrafiltration experiments: To measure the transport and separation properties of membranes, the UF experiments were carried out using a stirred dead-end filtration cell laboratory-scale system (Amicon 8050) with the active surface area of 13.4 cm^2. All experiments were conducted at room temperature using an operation pressure of 1 bar. The solute rejection of membranes was tested with 1g/L of BSA in phosphate buffer saline (PBS solution) with pH of 7. The protein concentration in the filtrate (C_p) and the feed (C_f) were measured by spectorphotometry (UV-model Lambda 25, Perkin Elmer) at a wavelength of 280 nm. The BSA rejection, R, was calculated according to the equation: $R = (1- C_p/ C_f) \times 100\%$.

Results and Discussion

Functionalization of PEI membrane

PEG-amine was chosen to modify PEI because of its molecular structure consisting of a reactive amine group and a chain predominately containing EO units. The amine group is expected to react directly with the electrophilic imide group of PEI as reported by Albrecth et al. [1]. The PO/EO chain is then linked to PEI by an amide function (Figure 1). The EO part of the grafted modifier is expected to improve the hydrophilicity of the PEI membrane surface.

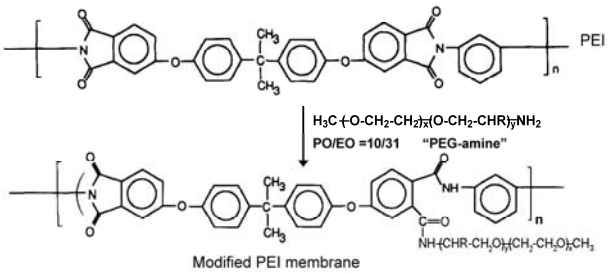

Figure 1. Surface modification of PEI membrane using PEG-amine

The surface modification was confirmed by FTIR-ATR (Figure 2). The main changes is the deformation vibration of the CONH group formed by functionalization arises between 1660 cm^{-1} (C=O stretch of CONH group band) and 1550 cm^{-1} (N-H band of CONH group). It can be concluded that the reaction between PEI with PEG amine results in a covalent binding of the modifier chain to the PEI surface.

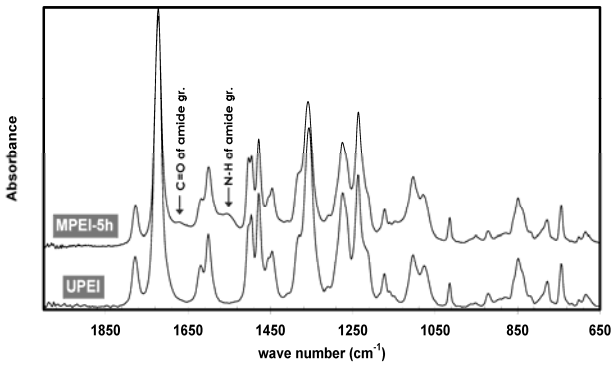

Figure 2. FTIR-ATR spectra of membrane surfaces: parent PEI membrane (UPEI) and PEI modified with PEG amine of 10 wt% for 5h.

Characterization of PEI membrane surface-modified PEG-amine

The cross-section of the unmodified PEI membrane and of modified membranes has similar morphologies (Figure 3). However, a change of surface aspect was detectable when PEI membrane was modified with PEG-amine for 3h and 5h. The presence of pores and a reduction of the thickness of upper layer could come from a partial degradation of the PEI membrane as reported by Santosa *et al*., [9]. No skin layer was observed for 24h. The thinner of upper layer usually provides a strongly increase in water permeability. However, it should be noted that the membrane modified for 24 h cannot measure the pure water flux under studied pressure because water can penetrate through the membrane without applied pressure. Therefore, it was not employed in the further work.

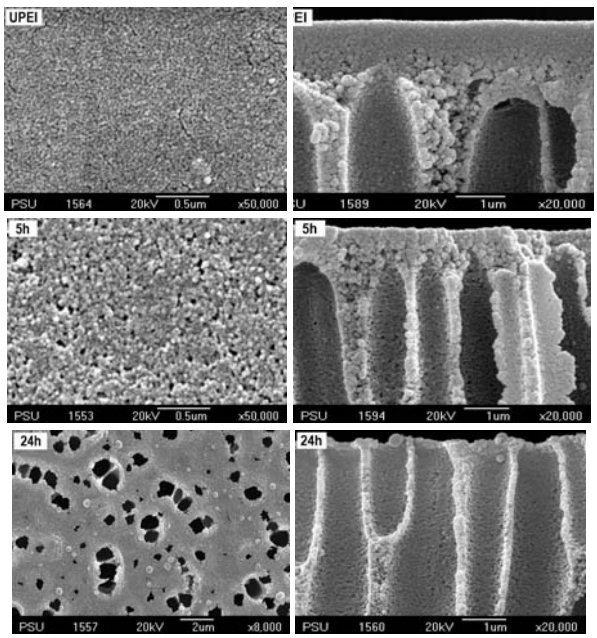

Figure 3. SEM micrographs of membrane surfaces (left) and cross sections near the membrane surface (right) at different modification times (0, 5 and 24 h).

AFM pictures (Figure 4) show that the surface modified membranes are not smooth and possess nodule-like structure. The nodules are seen as bright high peaks whereas the pores are seen as dark depression. For longer modification time, the membrane surface became rougher which was attributed to the change in chemical composition of membrane surface resulting from the presence of PEG covalently bound on the surface. The rougher membrane surface might result in the larger surface area contacting with water molecules, which resulted in higher flux [10].

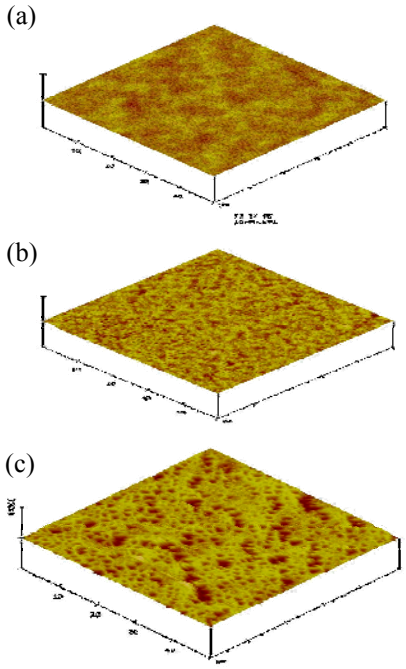

Figure 4. AFM photograph of unmodified PEI membrane (a) and PEI membrane modified for 5h (b) and 24 h (c).

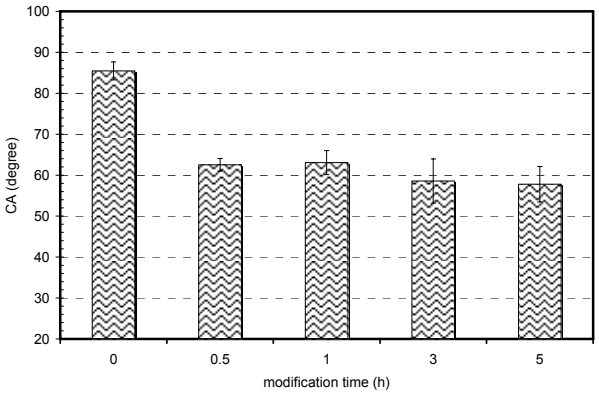

Figure 5. Contact angle of PEI membrane at different modification times

The water contact angle (CA) values are plotted as a function of the treatment time in Figure 5. As expected, the CA decreases after modification compared with that of the unmodified PEI. It can be concluded that modified PEI membrane surface is more hydrophilic. It should be noted that the modification time seems not to be a relevant parameter regarding CA.

Pure water flux and BSA rejection of PEI membrane surface -modified PEG-amine

The pure water flux with respect to the modification time is shown in Figure 6. An increase the modification time results in a significant enhancement of the pure water flux. On the other hand, BSA rejection presents the inverse trend with a high permeation enhancement beyond 1h (about 70 % after 5 h of reaction time).

It is assumed that at shorter reaction times (≤ 1h) only the surface is modified and the membrane keeps its initial rejection performances with a limitation of the protein fouling**.**

For longer reaction times, partial degradation of the upper surface takes place making the membrane surface more hydrophilic and enlarging the pores as showed by the microscopic observations.

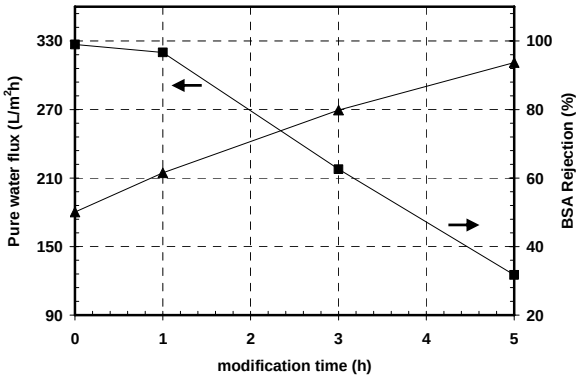

Figure 6. Pure water flux and BSA rejection of PEI membrane obtained for different modification times

Mechanical properties

Mechanical property of porous membrane is an important property due to during the filtration process; the operated pressure is needed to drive the filtration substance through to the porous membranes.

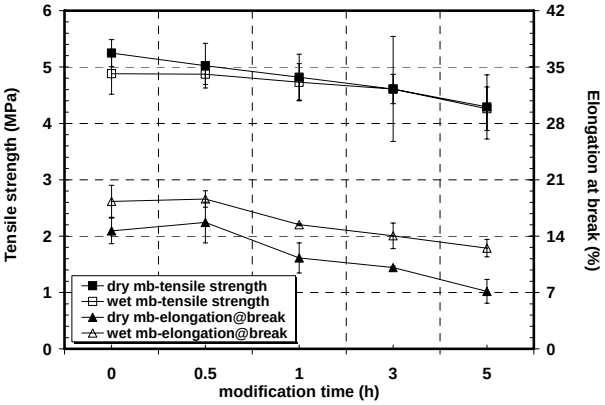

Figure 7. Mechanical properties of PEI membrane obtained for different modification times

Tensile strengths and elongation of the dry and wet membranes were then studied and shown in Figure 7. Figure 7 demonstrates that tensile strengths were lower than that of unmodified PEI membrane in wet and dry state. This result can be explained by considering the result of morphology change during modification. Although the tensile properties of modified membrane were lower, they can sustain the pressure normally applied during water permeability test.

Conclusions

Hydrophilic porous PEI membranes were prepared in a simple way by surface modification of PEI with PEG-amine/water solution. The chemical structure was monitored by FTIR-ATR that confirmed the grafting by PEG chain of the PEI membrane. Increasing the modification time resulted in an enhancement of the wetability of the membrane surface as showed by the decrease of the contact angle and the pure water flux increase. However, long modification time also entailed a degradation of the membrane surface with a enlargement of the pores as demonstrated by the decrease of the BSA rejection. Highly hydrophilic PEI surfaces can then be prepared using this route and it might be taken advantage of the degradation for adjusting the pore size to the desired application.

Acknowledgement

The authors are grateful for the financial support of this work provided by the Commission on Higher Education and the Thai Research Fund (TRF) contract no. MRG5080244. We also acknowledge King Mongkut's Institute of Technology North Bangkok for contact angle measurements, Ethoxy Chemical Co., Ltd, and NOK Precision Component (Thailand) Ltd. for the gift of PEG-amine and PEI ULTEM 1000, respectively.

References

[1] W. Albrecth, B. Seifert, T. Weigel, M. Schosssing, A. Holländer, T. Groth, and R. Hilke, *Macromol. Chem. and Phys*. **204** (2003), pp. 510-521.

[2] W. Albrecth, J. Schauer, Th. Weigel, K. Richau, Th. Groth, and A. Lendlein, *J. Membr. Sci*. **292** (2007), pp. 145-157.

[3] Y-Q Wang, T. Wang, Y-L Su, F-B Peng, H. Wu, and Z-Y Jiang, *J. Membr. Sci.* **291** (2007), pp.10-14.

[4] J.H. Lee, H. B. Lee, and J. D. Andred, *Prog. Polym. Sci*. **20** (1995), pp. 1043-1079

[5] M. Ulbricht, H. Matuschewski, A. Oechel, and H. G. Hicke, *J. Membr. Sci*. **115** (1996), pp. 31-47.

[6] M. S. Sheu, A.S. Hoffman, and J. Feijen, *J. Adhesion Sci. Technol.* **6** (1992), pp. 995-1009.

[7] J.P. Lens, P.F.H. Harmsen, E.M.T. Schegget. J. G. A. Terlingen, G.H.M Engbers, and J. Feijen, *J. Biomater. Sci. Polym. Ed.* **8** (1997), pp. 963-982.

[8] P. Wang, K.L. Tan, E.T. Kang and K.G. Neoh, *J. Membr. Sci* **195** (2002), pp. 103-114.

[9] F. Santoso, W. Albrecth, M. Schroeter, Th. Weigel, D. Paul, and R. Schomäcker, *J. Membr. Sci*. **223** (2003), pp. 171-185.

[10] L. Li, S. Zhang, X. Zhang, G. Zheng, *J. Membr. Sci.* **315** (2008), pp. 20-27.

Fabrication of hydrophilic and crosslinjed poly(ether imide) membrane

W. Chinpa

Department of Materials Science and Technology, Faculty of Science, Prince of Songkla University, Hat-Yai, Songkhla, Thailand 90112

*E-Mail Address: cwatchan@yahoo.com

Abstract: Poly(ether imide), PEI is an attractive material for membrane formation because it has excellent film forming ability, high mechanical properties as well as a good thermal and chemical resistance. However, the hydrophobic nature of PEI causes heavy fouling on the membrane surface when solution containing substance likes proteins. Membrane fouling leads to a flux decline and require an extra process of cleaning resulting in an increase the operation time and cost. Many studies demonstrate that increasing membrane surface hydrophilicity can availably reduce membrane fouling. In this work, PEI membrane was modified by using polyether diamine based on a predominantly polyethylene glycol backbone (PEG-diamine) due to two reactive primary amines could react directly with PEI and a dominant ethylene glycol part can improve hydrophilicity property of PEI membrane. The PEI membrane was prepared by casting the mixture solution of PEI and PEG-diamine in chloroform on the non-woven polyester support and heating at 90ºC for indicated times. A strong increase in absorption intensity at around 1660-1550 cm^{-1} of the amide groups formed by functionalization was observed. The formation of amide group identified as evidence that the amination reaction between PEI and PEG-diamine can be produced. It was also found that the crosslinked PEI membrane can be obtained as a longer reaction time which could be confirmed by measuring the gel content. A decrease in water contact angle and an increase in water uptake of membrane demonstrated that the PEI modified with PEG-diamine resulted in better wettabilty. The pure water fluxes of membrane decrease as a longer modification time. Base on the protein filtration experiments, the anti-fouling properties of the membrane were evaluated, and the results showed that the PEI membrane has an improved resistance to protein fouling

Introduction

It was well known that Poly(ether imide), PEI is a suitable material for fabrication membrane. However, the hydrophobic character of PEI is still greatly limited by membrane fouling, which reduces the flux and requires extra process of cleaning [2]. Increasing membrane surface hydrophilicity can effectively reduce membrane fouling [3]. Modification with chemical substance is an interesting route to make membrane more hydrophilic. This method presents the advantages of simplicity, versatility and low cost operation.

Poly (ethylene glycol) (PEG) offers a hydrophilicity property, large excluded volume, and unique coordination with environmentally water molecule in an aqueous medium [4]. Many works used PEG to modify many polymeric membranes to resistance protein adsorption [5-8]. Blending PEG or PEG-containing amphiphilic copolymer with the polymeric membrane was simplest and was widely used to improve the hydrophilicity of hydrophobic membrane [9], but PEG in the membrane matrix may not be retained on the membrane surface permanently. Photo-induced grafting polymerization [5] or plasma treatment [6-7, 10] is the method which induces covalently PEG grafting on the targeted polymer. The advantage of this method is the immobilization of PEG on the surface, however, this method need high operation cost.

Cross-linking has been used to resist the swelling and solvent of a membrane material during filtration process. Many researches prepared crosslinked membranes for gas separation [11-14]. The crosslinked membrane in waste water treatment rarely reported [15]. Ju and coworker [16] reported a crosslinked PEO fouling resistant coating materials for oil/water separation, and they had achieved promising results.

In this work, poly (propylene oxide)/poly (ethylene oxide) diamine (or PEG-diamine) predominately containing ethylene oxide (EO) units and two reactive amines was used as a modifier for PEI to prepare hydrophilic and crosslinked ultrafiltration membrane. It is expected that PEG-diamine can be directly react and further crosslinked with PEI. The effects of the reaction time on the wettability (contact angle measurement), gel content, permeability (pure water flux, PWF), and anti-fouling properties to bovine serum albumin (BSA) of membrane were investigated

Materials and Methods

Materials: PEI (ULTEM 1000®) was kindly supplied by NOK Precision Component (Thailand) Ltd. PEG-diamine (Jefamine ED-2003 polyetheramine) was kindly supported by Ethyoxy Chemical Co., Ltd. used as modifying agent. Chloroform was purchased from Fluka and was used as a solvent. BSA with an average molecular weight of 67 kDa was supplied from Fluka. All reagents were used without any further purification.

Membrane preparation: Modified membranes were prepared by casting the homogeneous of 8 wt% PEI/PEG-diamine/$CHCl_3$ solution on non-woven polyester. The casting film was left at ambient condition until dry; subsequently it was heated at 90°C for 1, 3, 5, 10 and 15 h for cross-linking reaction. The membrane was thoroughly then washed with distilled

water to remove absorbed modifier and stored in wet state until use.

Surface Characterization: The surface of the film was carried out using Fourier Transform Infrared Spectrometer (FT-IR), Attenuated total reflection mode (ATR-FTIR: Equinox 55, Bruker).

Solvent-resistant experiments: The solubility of modified membrane in $CHCl_3$ was preliminarily observed to confirm the cross-linking of PEI membrane by PEG-diamine. The gel content was also measure as described by Zhao et al., [17].

Hydrophilicity of membrane surface: The hydrophilic property of membrane surface was characterized by using water contact angle measurement by using an automatic interfacial tensiometer (Data physic).

The water uptake (WU) was also studied as reported by Zhu et al. [18]. The WU was calculated according to WU (%) = $(w_{wet}-w_{dry})/w_{dry}$ x 100%, where w_{wet} and w_{dry} represent the weights of dried membrane and membrane soaked in water at room temperature for 24 h, respectively.

Both measurements were carried out 5 times and the average values were reported.

Transport and separation properties: The UF experiments were carried out using a stirred dead-end filtration cell (Amicon 8050) with the active surface area of 13.4 cm^2. All experiments were conducted at room temperature using an operation pressure of 1 bar. The solute rejection of membranes was tested with 1g/L of BSA in phosphate buffer saline (PBS solution) with pH of 7. The protein concentrations in the filtrate (C_p) and the feed (C_f) were measured by spectorphotometry (UV-model Lambda 25, Perkin Elmer) at a wavelength of 280 nm. The BSA rejection, R, was calculated according to the equation: R = (1-C_p/ C_f) x 100%.

Anti-fouling properties: This property was investigated as described elsewhere [19-21]. Steady state pure water flux (J_{w0}) of prepared membranes was firstly measured. Then the feed solution of 1g/L of BSA solution (in phosphate buffer saline with pH = 7.4) was introduced and the filtrate at 0.1 MPa until the steady state flux was reached. Subsequently, the membrane was washed with distilled water on a vibrator for 2h, and then the water flux was reevaluated and the steady-state value was defined as J_{w1}.

Results and Discussion

According to Albrecth et al. [1], amination reaction between PEI and PEG-diamine could be possible (Figure 1). During this reaction, the imide group of PEI reacts with amine end groups; subsequently imide ring is opened forming new amide groups generated without breaking of the main chain. The PEG part could be covalently bound with PEI main chain. Furthermore, since the PEG-diamine have two amine end groups; the second amine can react with the large number of imide functional groups resulting in the formation of crosslinked structure

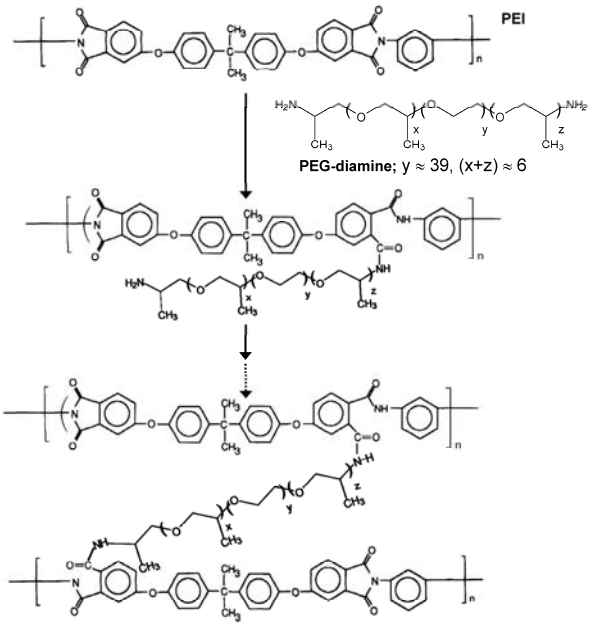

Figure 1. Scheme for the expected reaction of PEI and PEG-diamine.

ATR-FTIR was used to study the change in the reactive function group of PEI membrane before and after modification (Figure 2). The formation of new amide (-CONH-) group formed by functionalization arise between 1660 cm^{-1} (C=O stretch of CONH group band) and 1550 cm^{-1} (N-H band of CONH group) was generated. Moreover, a significant decrease in intensity of NC=O in imide ring around 1777 and 1720 cm^{-1} was observed. These changes are evidence that the amination reaction between PEI and PEG-diamine took place.

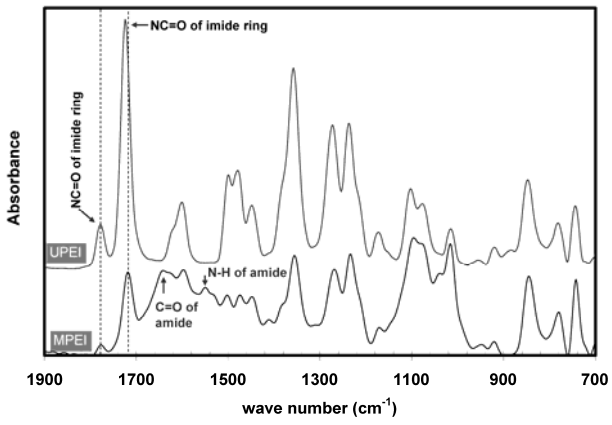

Figure 2. ATR-FTIR spectra of membrane surfaces: parent PEI membrane (UPEI) and PEI modified with PEG-diamine (MPEI).

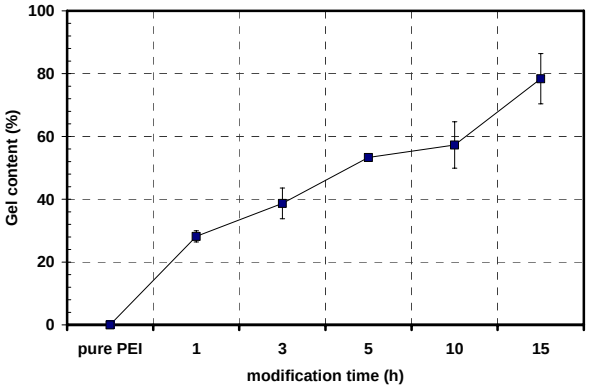

Figure 3. Gel content of modified PEI membrane for different modification time.

To verify the formation of crosslink of PEI membrane the solubility in chloroform and the gel content were studied.

Figure 3 presents the gel contents of the PEI membrane compared with unmodified PEI membrane. The gel contents of modified membrane increase as a longer modification time. It means that the cross-linking reaction between PEI and PEG-diamine is performed and forms the network structure thus resulting in decreasing the solubility of the cross-linked PEI in the chloroform.

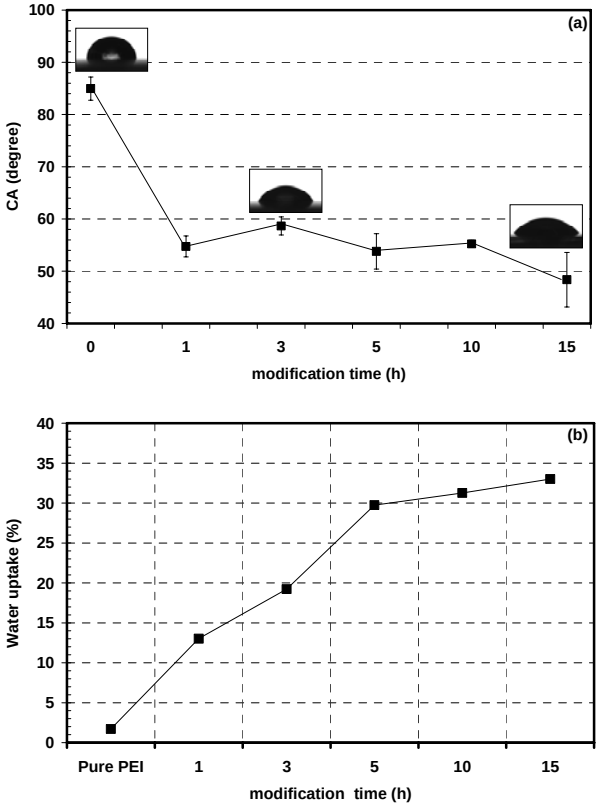

Figure 4. Static water contact angle (a) and water uptake (b) of PEI membrane at different treatment time compared with pure PEI membrane.

The surface hydrophilicity is an important factor affecting the anti-fouling property of membrane. One of widely used methods to evaluate the hydrophilicity is the water contact angle measurement [13]. The water contact angle (CA) values are plotted as a function of the treatment time in Figure 4 (a). As expected, the CA decreases after modification compared with that of the unmodified PEI. For the pure PEI membrane, CA is 85 ± 2°, showing a hydrophobic character. Compare to the pure PEI membrane, all modified membranes have smaller CA i.e. CA = 54.8 ± 2° for modification time of 1 h. The water uptake (WU) was studied as a supplement (Figure 14(b)). The result shows that WU increases compared with unmodified PEI and increases as a longer modification time. It can be concluded that modified PEI membrane surface is more hydrophilic.

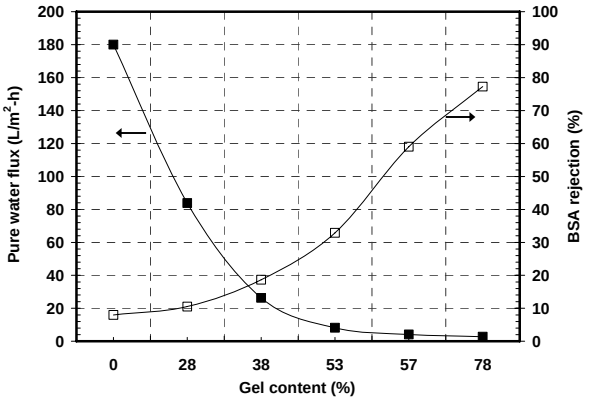

Figure 5. Pure water flux and BSA rejection of PEI membrane obtained for different gel content.

Membrane transport properties with respect to the gel content are reported in Figure 5. The result shows a significant decrease in water permeability while the BSA rejections showed an inverse trend. It can be explained that a decrease in permeation of water was due to the formation of crosslink structure. The longer modification time produce higher gel content. This means that modified PEI membrane has higher degree of cross-linking. A membrane with lower flux then exhibited a higher rejection for BSA.

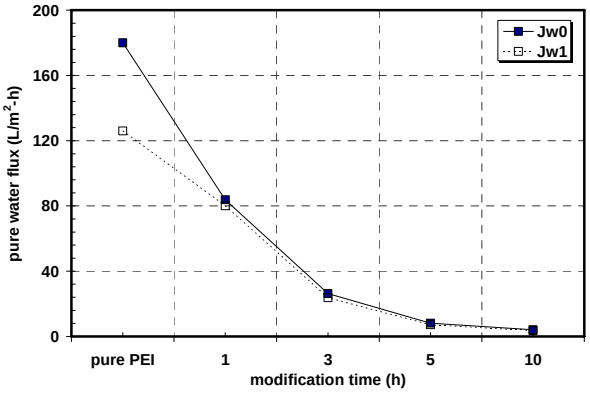

Figure 6. Water fluxes of the modified PEI compared pure PEI before and after protein filtration.

To investigate the fouling resistance of modified membrane, after measuring the pure water flux, a BSA

protein used a model protein was conducted. After that, the membranes were cleaned and measured again pure water flux. Figure 6 shows the anti-fouling property of PEG-modified PEI membrane. The pure PEI membrane protein fouling is observed. The water flux decreases about 34% after the protein filtration. For PEG-modified PEI membrane, the anti-fouling property improves because the water fluxes before and after protein filtration is almost the same value. This was due to the introduction of a hydrophilic PEG layer in the PGE-amine structure. This means that modified membrane is easy to clean with water.

Conclusions

PEG-diamine could be covalently immobilized and crosslinked with PEI by the simple fabrication. It was found that hydrophilicity of PEI membrane could be improved. The water flux decreased with the longer modification time corresponding to the higher gel content, while the increase in BSA rejection. BSA ultrafiltration experiments indicated that PEG-modified PEI membranes exhibited good anti-fouling property.

Acknowledgement

The authors are grateful for the financial support of this work provided by Department of Materials Science and Technology, Faculty of Science, Prince of Songkla University. We also acknowledge King Mongkut's Institute of Technology North Bangkok for contact angle measurements, Ethoxy Chemical Co., Ltd, and NOK Precision Component (Thailand) Ltd. for the gift of PEG-diamine and PEI ULTEM 1000, respectively.

References

[1] W. Albrecth, B. Seifert, T. Weigel, M. Schosssing, A. Holländer, T. Groth, and R. Hilke, *Macromol. Chem. and Phys*. **204** (2003), pp. 510-521.

[2] W. Albrecth, J. Schauer, Th. Weigel, K. Richau, Th. Groth, and A. Lendlein, *J. Membr. Sci*. **291** (2007), pp. 10-14.

[3] Y-Q Wang, T. Wang, Y-L Su, F-B Peng, H. Wu, and Z-Y Jiang, *J. Membr. Sci.* **291** (2007), pp.10-14.

[4] J.H. Lee, H. B. Lee, and J. D. Andred, P*rog. Polym. Sci*. **20** (1995), pp. 1043-1079.

[5] M. Ulbricht, H. Matuschewski, A. Oechel, and H. G. Hicke, *J. Membr. Sci*. **115** (1996), pp. 31-47.

[6] M. S. Sheu, A.S. Hoffman, and J. Feijen, *J. Adhesion Sci. Technol.* **6** (1992), pp. 995-1009.

[7] J.P. Lens, P.F.H. Harmsen, E.M.T. Schegget. J. G. A. Terlingen, G.H.M Engbers, and J. Feijen, *J. Biomater. Sci. Polym. Ed.* **8** (1997), pp. 963-982

[8] P. Wang, K.L. Tan, E.T. Kang and K.G. Neoh, *J. Membr. Sci* **195** (2002), pp. 103-114.

[9] H. Ma, J. Hyun, P. Stiller. A. Chilkoti, *Adv. Mater.* **16** (2004), pp. 338-314.

[10] P. Wang, K.L. Tan, E.T. Kang and K.G. Neoh. *J. Membr. Sci*. 195 (2002), 103-114.

[11] H.Q. Lin, E.V. Wagner, B.D. Freeman, L.G. Toy, R.P. Gupta, *Science.* **311** (2006), pp. 639–642.

[12] H.Q. Lin, T. Kai, B.D. Freeman, S. Kalakkunnath, D.S. Kalika, *Macromolecules*. **38** (2005), pp. 8381–8393.

[13] H.Q. Lin, E.V.Wagner, J.S. Swinnea, B.D. Freeman, S.J. Pas, A.J. Hill, S. Kalakkunnath, D.S. Kalika, *J. Membr. Sci.* **276** (2006), pp. 145–161.

[14] H.Q. Lin, and B.D. Freeman, *Macromolecules*. **38** (2005), pp. 8394–8407.

[15] G. Kang, Y. Cao, H. Zhao, Q. Yuan, *J. Membr. Sci*. **318** (2008), pp. 227-232.

[16] H. Ju, B.D. McCloskey, A.C. Sagle, Y.H. Wu, V.A. Kusuma, B.D. Freeman, *J. Membr. Sci.* **307** (2008) pp. 260–267.

[17] H-Y Zhao, Y-M Caoa, X-L Dinga, M-Q Zhoua, Q. Yuana, *J. Membr. Sci*. **323** (2008), pp. 176–184

[18] L-P Zhu, L Xu., B-K Zhu, Y-X Feng, Y-Y Xu, *J.Membr.Sci.* **294** (2007), pp.196-206.

[19] X. Ma, Y. Su, Q. Sun, Y. Wang, Z. Jiang, *J. Membr. Sci.* **292** (2007), pp.116-124.

[20] C. Arthanareeswaran, P. Thanikaivelan, and M. Raajenthiren, *Mater. Sci. Eng., C.* **29** (2009), pp. 246-252.

[21] W. Zhao, Y. Su, C. Li, Q. Shi, X Ning, Z. Jiang, J. Membr. Sci. **318** (2008), pp. 405-412.

Tensile properties and morphology of XSBR/NR blends filled with PS-encapsulated nanosilica

S. Chuayjuljit[1,2], W. Luecha[1,2*] and K. Boonkerd[1,2]

[1] Chulalongkorn University /Department of Materials Science, Faculty of Science,
[2] National Center of Excellence for Petroleum, Petrochemicals and Advanced Materials, Bangkok, Thailand 10330

[*] E-Mail : wasumint@hotmail.com

Abstract: This research aims to investigate the tensile properties and morphology of carboxylated styrene butadiene rubber (XSBR)/natural rubber (NR) blends filled with polystyrene (PS)-encapsulated nanosilica. The specimens were prepared by latex compounding method. The rubber blends of XSBR and NR at XSBR/NR dry weight ratios of 70/30, 50/50 and 30/70 were mixed with 3 phr of PS-encapsulated nanosilica. The nanolatex of PS-encapsulated nanosilica was synthesized via *in situ* differential microemulsion polymerization. The morphology and particle size of the encapsulated nanoparticles were investigated by transmission electron microscope and dynamic light scattering analyzer, respectively. The blended latices were cast into sheets on a glass mold, air dried and then cured in an oven at 80°C for 3 h. After that, the specimens were examined for their tensile properties and morphology using a universal testing machine and scanning electron microscope, respectively. The results showed that the tensile strength and elongation at break increased with increasing amount of NR in the rubber blends, but the Young's modulus decreased. However, the tensile properties have also been improved by adding the PS-encapsulated nanosilica. The rubber blend of 30/70/3 XSBR/NR/PS gave the optimum tensile strength and elongation at break, whereas the highest Young's modulus was attained from 70/30/3 XSBR/NR/PS blend. Moreover, the phase morphology of the blends could be understood from the scanning electron micrographs.

Introduction

This is the instruction for preparation of interest in polymer blend technology has rapidly increased. The appropriately combining two or more different polymers can provide a new material with desirable properties. Blending of rubbers is an important technique to improve certain properties not inherent in a single rubber. Moreover, rubber blends find widespread use in several applications. Natural rubber (NR) is characterized by good elastic properties, good resilience and damping behavior but poor chemical resistance and processability [1].

Carboxylated styrene butadiene rubber (XSBR) has been blended with NR in order to improve their thermal stability and mechanical properties [2]. However, the addition of reinforcing fillers in rubber blends is still required to obtain the appropriate properties for a variety of applications. In general, commercial carbon black and silica have been used successfully as reinforcing fillers in dry rubber but they are not so effective for rubber latex [3]. Consequently, it is necessary to exploit new approaches in order to increase the mechanical properties of the products processed from the rubber latex. Introduction of inorganic nanofillers at very low loading into rubber latex has currently received much attention. Among the inorganic nanofillers, silica has been extensively used to improve the mechanical and thermal properties of the rubber products [4]. However, silica contains a large number of silanol groups on the surface, which causes strong filler-filler interaction and high tendency for aggregation in the rubber matrix [5]. The heterogeneous dispersion of silica in the rubber matrix resulted in the reduction of the mechanical properties and thermal stability of the rubber composites [6]. Surface modification of silica nanoparticles has been widely studied in order to improve dispersibility and compatibility of silica in the rubber matrix. The most widely used method for filler surface treatment is *in situ* polymerization of organic monomers [7]. The resulted polymer shells covering on silica nanoparticles can improve the dispersion of filler in polymer matrix and cause more interaction between polymeric shells and matrices [8]. This present work aims to prepare nanolatex of PS-encapsulated silica by *in situ* differential microemulsion polymerization and subsequently incorporated into XSBR/NR blend in latex form. It is expected that the PS covered on the nanosilica could improve the application properties of the resulting rubber nanocomposites. The mechanical performance was evaluated using tensile testing and tear strength. The morphology of the rubber blend nanocomposites was also observed.

Materials and Methods

XSBR latex (52 wt% dry rubber content) and styrene monomer were provided by Dow Chemical Thailand. NR latex (60 wt% dry rubber content) compounded with potassium oleate solution (20 wt%), KOH solution (10 wt%), aqueous dispersions of sulfur (50 wt%), ZnO (50 wt%), zinc diethyl dithiocarbamate (50 wt%) and antioxidant (50 wt%) (the formulation is shown in Table 1) was supplied by Zmon Rubber. Silica with particle size of 10-20 nm was purchased from Sigma-Aldrich. Sodium dodecyl sulfate (SDS) powder provided by Cognis was used as a surfactant. AIBN used as an initiator was donated by Siam

Chemical Industry. MPTMS ($Si(OCH_3)_3(CH_2)_3SH$) from Dow Corning was used as a coupling agent.

MPTMS was applied to silica surfaces as a dilute aqueous solution (0.5% silane concentration) which was prepared by adjusting the pH of water (800 ml) from 3.5 to 4.5 with acetic acid and then adding MPTMS (4 g) while stirring. After adding MPTMS to the acidified water, the mixture was stirred for a minimum of 30 minutes before it hydrolyzed and formed a clear homogeneous solution. Dry silica (13.33 g) was then added to the MPTMS solution with stirring for 30 minutes.

PS-encapsulated silica was prepared via *in situ* differential microemulsion polymerization. The as-prepared surface-pretreated silica nanoparticles (0.4 g), SDS (8 g) and AIBN (0.12 g) were mixed in a 500 ml Pyrex glass reactor, which was equipped with a reflux condenser, a N_2 gas inlet and a dropping funnel for monomer feeding. A 60 ml of distilled water was thereafter added and the system was heated up to 70°C with stirring at 250 rpm using a magnetic stirrer under the circumstance of N_2 gas. After the temperature was raised to 70°C, the styrene monomer was fed slowly within 1.5 h. Afterwards, the reaction system was maintained at 70°C with constant agitation for an additional hour before a water cooling operation was applied. Solid content (%*S*) of the nanoparticles in the nanolatex was detemined by the gravimetric method. The number-average diameter (D_n) and morphology of the prepared PS nanoparticles were investigated using a dynamic light scattering analyzer (DLS) and transmission electron microscope, respectively.

Table 1 : Formulation of the rubber compound (based on dry weight).

Ingredient	Amount (phr)
Natural rubber	100
Potassium oleate	0.2
Potassium hydroxide	0.5
Sulfur	2.0
Zinc diethyl dithiocarbamate	1.0
Antioxidant (CPL)	1.0
Zinc oxide	1.0

XSBR/NR/PS-encapsulatedsilica nanocomposite sheets were prepared by mixing XSBR latex with NR latex at the XSBR/NR dry weight ratios of 70/30, 50/50 and 30/70. The mixtures were then blended with PS-encapsulated nanosilica at the amount of 3 phr (based on dry weight) using a mechanical stirrer at 60 rpm for 3 h. The homogeneous latex was then cast into sheet on a glass mold (20 × 20 × 0.15 cm), air dried for 24 h and then cure in an oven at 80°C for 3 h. The tensile and tear properties of the specimens were measured according to ISO 37-1 and ISO 34, respectively. Angle test pieces were used for determining tear strength whereas dumb-bell shaped samples were used for determining tensile properties. The measurements were carried out using a Universal Testing Machine with a load cell capacity of 1000 N and a crosshead speed of 500 mm/min. The fractured surfaces of the specimens were performed by a scanning electron microscope (SEM) after coating the broken surfaces with a thin layer of gold.

Results and Discussion

The solid content of the obtained nanolatex is about 22%. The number-average diameter (D_n) of the nanoparticles was determined to be about 33 nm. Figure 1 shows TEM image of the spherical-shaped PS-encapsulated nanosilica.

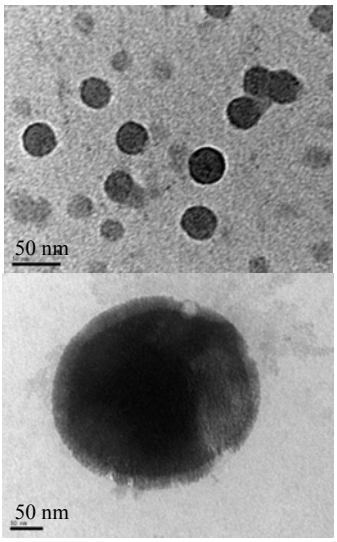

Figure 1. TEM image of PS-encapsulated nanosilica particles.

Tensile strength and elongation at break for all the compounds were shown in Figures 2 and 3, respectively. Among the rubber blends, blend of 30/70 XSBR/NR exhibits the highest tensile strength and elongation at break. The results indicated that these properties increased with increasing amount of NR. The increase in tensile strength may be due to the strain-induced crystallization ability of NR. The increase in elongation at break of the blend enriched with NR probably owing to the intrinsic chain flexibility of NR. Moreover, it can be seen that the incorporation of untreated nanosilica resulted in the reduction of tensile strength and elongation at break of the rubber blend. This may be due to the self aggreation of nanosilica and the lack of good interfacial adhesion between filler and matrix. To overcome these drawbacks, the PS-encapsulated nanosilica was introduced into the rubber blends. The results showed that the tensile strength and elongation at break of the blends filled with PS-encapsulated nanosilica were enhanced. This may attribute to the reinforcing effect of the PS-encapsulated nanosilica and the PS shell can improve the compatibility between nanosilica and rubber matrix.

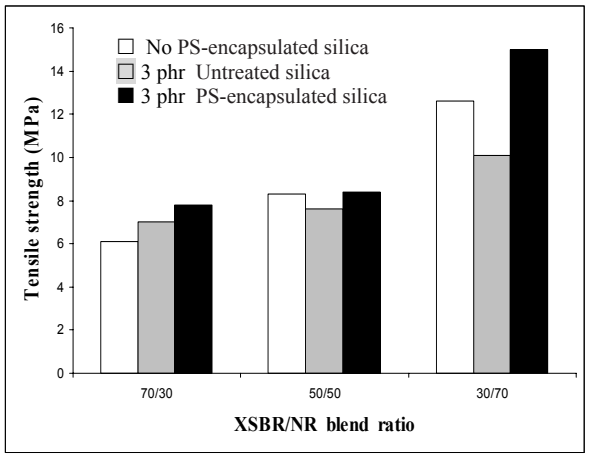

Figure 2. Tensile strength of XSBR/NR blends with and without nanosilica and untreated silica.

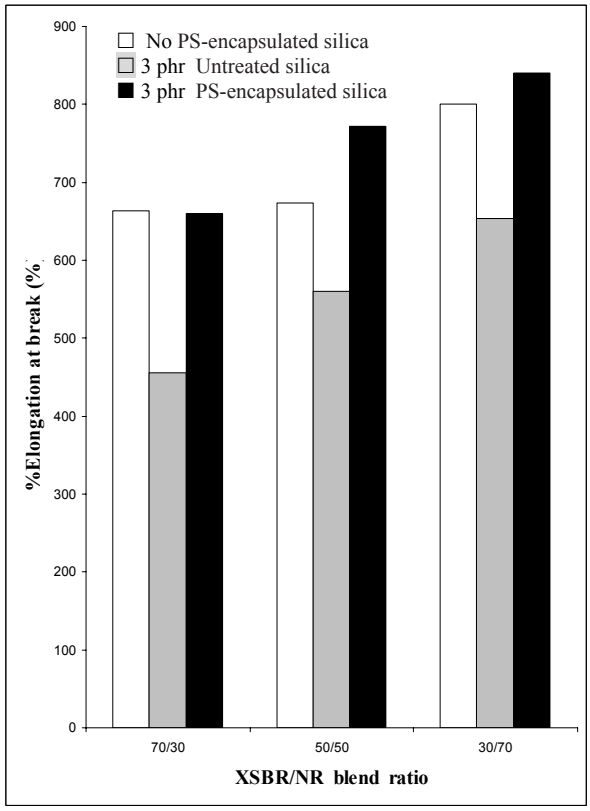

Figure 3. Elongation at break of XSBR/NR blends with and without nanosilica and untreated silica.

Figure 4 shows that the modulus at 300% strain was higher for the rubber blend enriched with XSBR (70XSBR/30NR). This may be due to the chain stiffness of the XSBR. In addition, the modulus was further improved by the incorporation of the untreated nanosilica and the PS-encapsulated nanosilica. The increase in the moduli of the rubber blends was caused by the fact that the nanosilica is more rigid phase as compared to the rubber phase. Moreover, the rubber blended with untreated silica is more stiff than the rubber blended with PS-encapsulated silica because flexibility of polystryrene covering on silica nanoparticles decreases the rigidity of silica. In addition, the nanosilica restricts the XSBR and NR main chain movement.

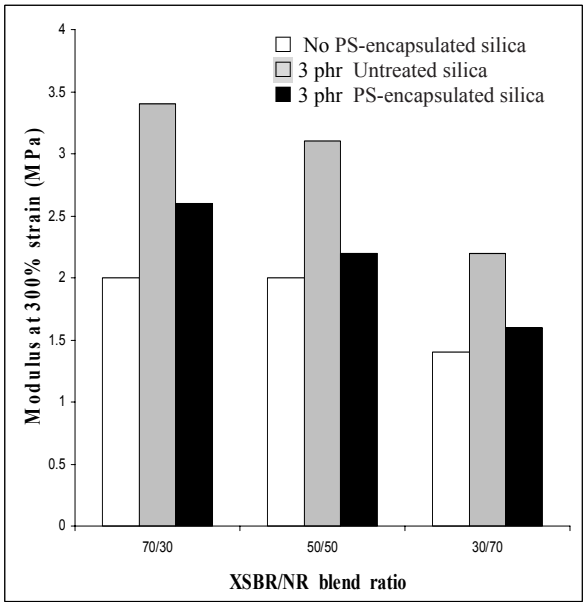

Figure 4. Modulus of XSBR/NR blends with and without nanosilica and untreated silica.

Figure 5 shows the tear strength of all the blend compounds. It is found that the blend of 30/70 XSBR/NR exhibits the highest tear strength. It should be noted that the tear strength tends to increase with increasing amount of NR in the blend. However, the incorporation of nanosilica into the rubber matrix could not much improve the tear strength of the vulcanizates.

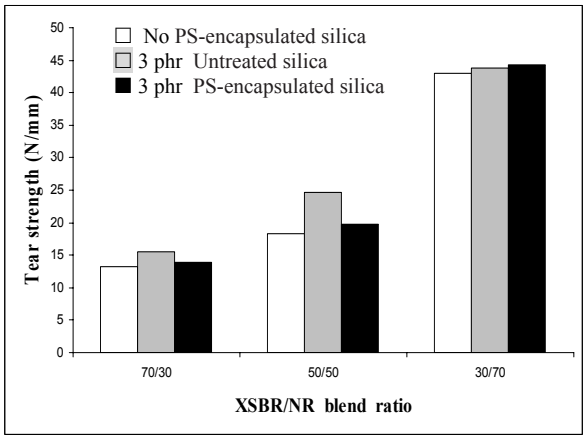

Figure 5. Tear strength of XSBR/NR blends with and without nanosilica.

Figure 6(a) shows the SEM micrograph of 30XSBR/70NR/3PS-encapsulat silica nanocomposite, in which XSBR is dispersed in continuous NR matrix. The blend 50/50 exhibits co-continuous morphology, Figure 6(b). In the case of 70XSBR/30NR/3PS-

encapsulated silicananocomposite (Figure 6(c)), NR phase is dispersed in the continuous XSBR matrix. However, the aggregation of the PS-encapsulated silica nanoparticles can be observed due to their very high surface area.

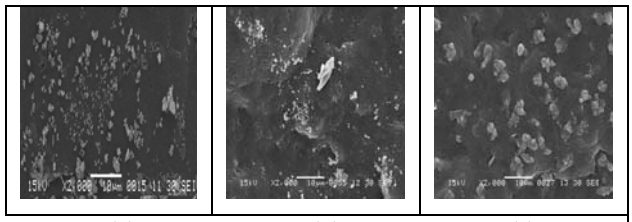

(a) **(b)** **(c)**

Figure 6. SEM micrographs of the nanocomposites:
(a) 30XSBR/70NR/3PS-encapsulated silica,
(b) 50XSBR/50NR/3PS-encapsulated silica and
(c) 70XSBR/30NR/3PS-encapsulated silica.

Conclusions

Blending of NR with the appropriate content of XSBR is an important technological method to improve the mechanical properties of the products. However, in commercial scale production, addition of reinforcing fillers is required to obtain the optimal properties for a variety of applications. It has been reported that the introduction of inorganic nanofillers at very low loading levels into rubbers has received much attention. The results in this work reveals that the incorporation of PS-encapsulated nanosilica (3 wt%) in rubber blends of NR and XSBR increases tensile strength,elongation at break and tear strength as well as decrease the modulus at 300% strain which provide final products of better mechanical properties..

Acknowledgement

The authors gratefully acknowledge the Department of Materials Science, Faculty of Science and National Center of Excellence for Petroleum, Petrochemicals and Advanced Materials, Chulalongkorn University for financial, material and instrument support.

References

[1] R. Asaletha, M.G.Kumaran and Thomas, S, *Eur. Polym. J* . **35** (1999), pp. 253-271.
[2] R. Stephen, S. Jose, K. Joseph, S. Thomas and Z. Oommen, *Polym. Degrad. Stab.* **91** (2006) , pp. 1717-1725.
[3] Z. Peng, L.X. Kong, S.D. Li, Y. Chen and H.F. Huang, *Comp. Sci.Tech.* **67** (2007), pp. 3130-3139.
[4] P. Liu, *Iran. Polym. J.* **14** (2005), pp. 968-972.
[5] A. Zhu, A. Cai, W. Zhou and Z. Shi, *Appl Surf Sci*. **254** (2008) pp.3745-3752.
[6] T.Wu and Y. Ke, *Thin Solid Films*, **515** (2007), pp. 5220-5226.
[7] X.L. Xie, R.K.Y. Li, Q.X. Liu and Y.W. Mai, *Polym*, **45**, pp. 2793-2802.
[8] T. Cui, J. Zhang, J. Wang, F. Cui, W. Chen, F. Xu, Z. Wang, K. Zhang and B.Yang, *Adv, Funct Mater*. **15** (2005), pp. 481-486.

Effect of heat annealing on crystal formation of metal phihalocyanine

T. Juagwon[1*], O. Chamlek[2], R. Jaisutti[2], A. Sinsarp[2] and T. Osotchan[1,2]

[1]Material Science and Engineering Program, Capability Building Unit of Nanoscience and Nanotechnology, Faculty of Science, Mahidol University, Rama VI Road, Bangkok, Thailand 10400
[2]Department of Physics, Faculty of Science, Mahidol University, Rama VI Road, Bangkok, Thailand 10400

[*]E-mail: t.juagwon@hotmail.com

Abstract: Metal phthalocyanine (MPc) is an organic semiconductor material which has several crystal forms depending on annealing temperature and metal ion in this metal organic complex. In this research, the X-ray diffraction (XRD) technique was used to investigate crystal structure of MPc powders including CoPc, CuPc, MnPc, MgPc and FePc before and after heated under Ar atmosphere. The lattice constant parameters of the MPc were evaluated by least square fit method and the obtained coefficient of determination values (R^2) are in the range of 0.998 to 0.999. The XRD pattern of MPc powders illustrated that these four MPc powders before and after annealing can be fitted with monoclinic crystal into two types. The beta phase has the β angle of about 120 degree while the alpha phase has the β angle of about 90 degree. The CuPc and CoPc powders are in the same β phase for both before and after heating at 530 °C. The fitted b lattice constants indicating the distance between the molecular planes are 5.001 and 4.836 Å and after annealing they exhibited the slight increase with the value of 0.08% and 0.21% for CuPc and CoPc, respectively. The as-received MnPc powder showed low crystalline with board XRD peak and the sharp XRD peaks of β phase appeared after heated at 530 °C with the obtained molecular inter-plane distance of 4.778 Å. For as-received FePc powders, the XRD patterns can be determined to be α phase with dominant (200) peak and fitted β angle of 89.89 degree. In FePc, the XRD patterns indicated the phase transformation from α to β phases clearly. At 250 °C the mixing of (200) peak in α phase became smaller and instead the peaks of (100) and ($\bar{1}02$) for β phase appeared and got larger at higher temperature. The molecular plane distance in FePc changed from 3.774 to 4.820 Å in α to β phases, respectively. The XRD pattern of as-recieved MgPc can be fixed with the monoclinic structure with the fitted β angle of 97.10 degree and after annealing at temperature higher than 250 °C, the XRD peaks is slightly shifted and the peak intensities were modified.

Introduction

The metal phthalocyanines are chemically and thermally stable organic semiconductors. The properties of material are attractive in organics transistor, photo-detectors and gas sensitivity sensors [1]. To understand it's behaviour in varies applications, the information on molecular and crystal structure are required. Since the crystals of the compound have more than one form, the crystal structure form of the compound is important. Metal phthalocyanine materials can generally exist in several crystalline polymorphs, including α, β, γ and χ structures [2]. The crystal structure of β and α phase are monoclinic structure type. The most well known are the thermally metastable α and stable β phases [2,3] The β form is the most stable phase and may be thermally derived from the α form [1]. The α phase can be converted into the β phase by heat annealing for a time long and depending on the temperature used. The criteria conversion of the α form into the β form can be identified by x-ray diffraction technique [4].

Materials and Methods

The MPc powders including CoPc, CuPc, MnPc, MgPc and FePc were supplied by Fulka with purity of 97, 80, 75, 90 and 80% respectively. Most MPc powders were heated under argon atmospheric at 150 250, 350, 450, and 530˚C for 60 mins to observe phase transformation of the material. The Bruker D8 advance x-ray diffractometer with Cu Kα wavelength of 1.5406 Å was used to investigate crystal structure of the MPc with step increment of 0.2deg/20s and 2θ range of 5˚-40˚. Finally, the fitted unit cell parameter of MPc powders were determined by least square fit method and the fitted values and determination values were examined.

Results and Discussion

The XRD patterns of as-received CuPc and CoPc powders can be identified to be β phase [1,3,5] with dominance peaks of (100) and ($\bar{1}02$). After heated at 530°C, the XRD peaks of both CuPc and CoPc powders became well defined with the same phase as shown in Figure 1 and 2.

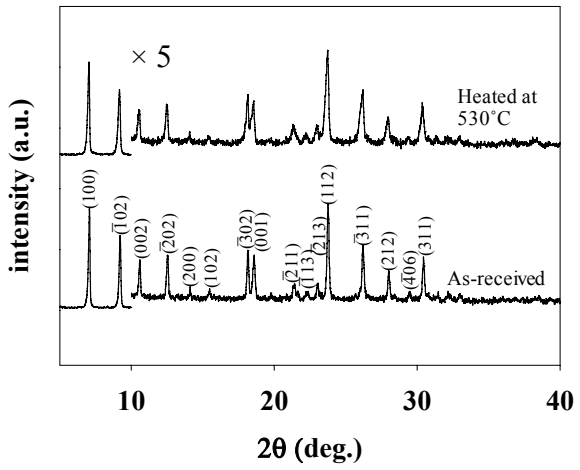

Figure 1. X-ray diffraction patterns of as-received and 530°C heated CuPc powders**.** The intensity in the range of 10-40 deg. was enlarged by 5 times.

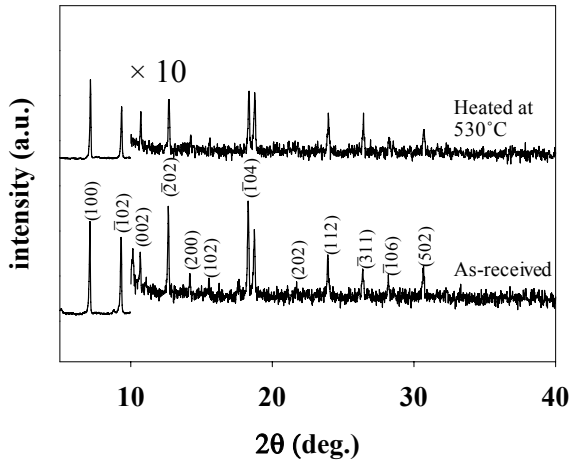

Figure 2. X-ray diffraction patterns of as-received and 530°C heated CoPc powders. The intensity in the range of 10-40 deg. was enlarged by 10 times.

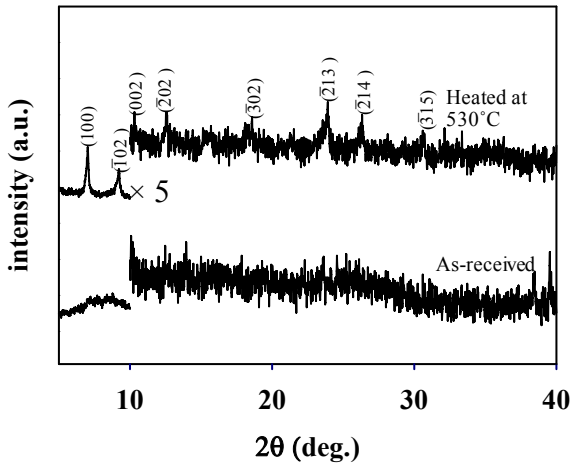

Figure 3. X-ray diffraction patterns of as-received and 530°C heated MnPc powders. The intensity in the range of 10-40 deg. was enlarged by 5 times.

The XRD pattern of as received MnPc powder, as demonstrated in Figure 3, showed broad diffraction peaks due to low degree of crystallization. After annealing at 530 ˚C, the sharp diffraction peaks appeared at 2θ = 7.02 and 9.24 degrees as a result of increase crystallization after annealing and can be matched with the diffraction peaks of β phase structure.

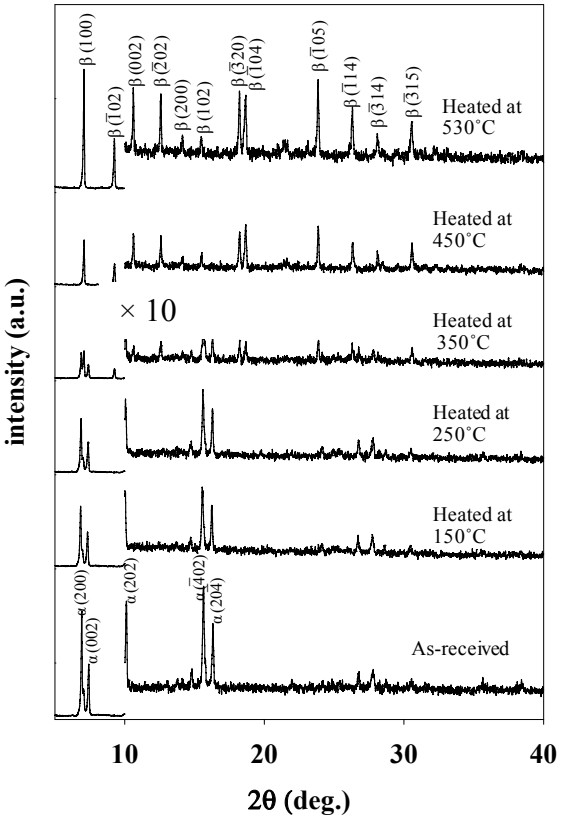

Figure 4**.** X-ray diffraction patterns of as-received and heated FePc powders at various temperatures. The intensity in the range of 10-40 deg. was enlarged 10 times.

The XRD pattern of as received FePc powder, as shown in Figure 4 indicates the mix phase between α and β phases. It clearly showed dominant diffraction peaks from planes (200) and (002) of α phase. The intensities of peaks were changed with increasing of heat annealing temperature. The intensity of (200) and (002) peaks of α phase [6,7] decreased when annealing temperature increased. After annealing at 250 °C, the peak characteristics of mixed phase of β phase and α phase occurred. The new dominate peaks were clearly appeared at 2θ values of 7.1 and 9.2 degrees corresponding to the peaks of the (100) and ($\bar{1}02$) of β phase [8].

Figure 5 shows the variation of these dominate diffraction peak intensities of FePc powder at various temperatures. When the annealing temperature increased, the intensity of β structure peaks significantly increased and the intensity of α phase significantly decreased. This result represented the crystal phase transformation in FePc by heat annealing. The FePc became β phase after heated at

higher than 250°C and it had a better β crystalline when annealing temperature was up to 530°C.

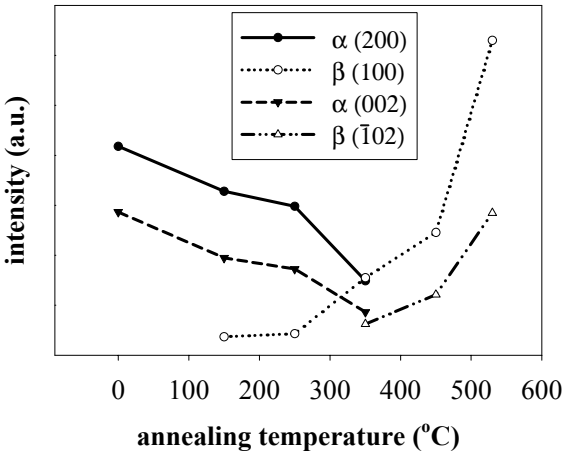

Figure 5. Intensity of peak diffraction from the plane of α(200), α(002), β(100) and β($\bar{1}$02) as a function of annealing temperature.

The XRD patterns of as received and annealed at various temperatures MgPc powder were depicted in Figure 6. The as-received peaks can be identified as those in Ref. [1] with monoclinic structure [1]. The fitted MgPc crystal structure can be matched with β angle of about 97˚ which did not consist with those of other MPc powders. A number of papers reported that the crystal of MgPc had an unusual behavior because Mg atom site was not planar with it's molecule [9,10]. After annealing at temperature more than 350 ˚C, the diffraction patterns of MgPc showed the dominant peak at 2θ of 6.8˚ consisting with previous reports [9,11,12]. This annealed MgPc powder was reported to be not pure MgPc but be the complex form of $(MgPc)N_2$ and $(MgPc)O_2$.

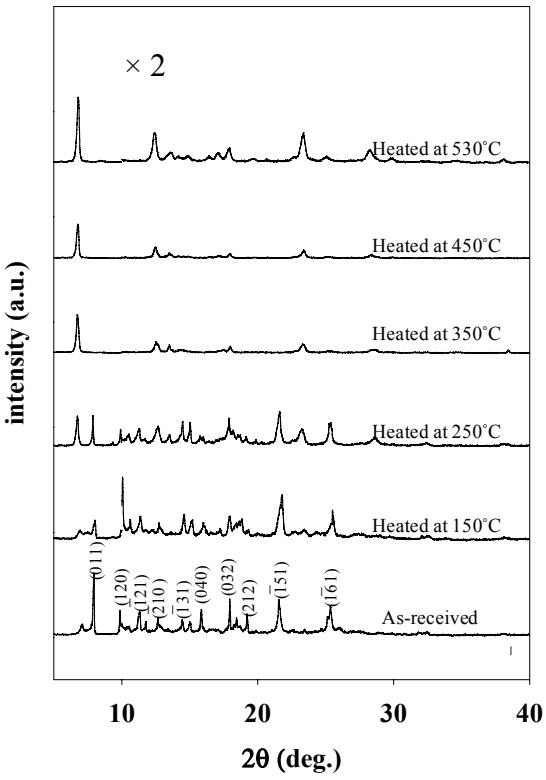

Figure 6. X-ray diffraction patterns of as-received and heated MgPc powder at various temperatures. The intensity in the range of 10-40 deg. was enlarged by 2 times.

The fitted lattice parameter of CuPc, CoPc, MnPc, FePc and MgPc were calculated from the results of XRD patterns and displayed in Table 1. The β phase crystal parameters of these CuPc, CoPc, MnPc, FePc powders were very similar. The molecular plane are along the b axis. The molecular packing distance slightly increased with increasing annealing temperature. The coefficient of determination values are in the range of 0.998-0.999 that advised the obtain lattice parameters were accurate values and consist with the literatures [2,3,7,8].

Table 1: Unit cell parameters obtained by least square fit method for as received and heated MPc powders.

MPC	a (Å)	b(Å)	c(Å)	β(deg.)	Phase	r^2
as received CuPc	14.711	5.001	19.902	121.68	β	0.999
heated 530 °C CuPc	14.727	5.005	19.760	121.75	β	0.999
as received CoPc	*14.904*	4.836	19.919	121.60	β	0.999
heated 530 °C CoPc	*14.890*	*4.846*	19.895	121.75	β	0.998
heated 530 °C MnPc	*14.575*	*4.778*	19.941	120.69	β	0.999
as received FePc	*25.774*	*3.774*	24.138	89.89	α	0.999
heated 530 °C FePc	14.574	*4.820*	19.382	120.76	β	0.999
as received MgPc	*15.274*	*22.314*	13.424	97.10		0.999

Conclusions

It was demonstrated that heat annealing can be affected on MPc crystal formation. The effects were different in different central metal of MPc molecules. The crystalline of MnPc powder increased after heat annealing. The obtained lattice parameters from least square fit method of CuPc, CoPc and FePc powders indicated that their β phase had similar crystal structures. The molecular inter-planar spacing of these MPcs in β phase slightly increased when the annealing temperature increased. The phase transition from α phase to β phase can be clearly observed after heated FePc powder at temperature higher than 250˚C. The quantity of phase transformation in FePc powder can be observed by intensity decreasing of dominate (200) and (002) peaks of α phase and intensity increasing of dominate (100) and $(\bar{1}02)$ peaks of of β phase after increasing annealing temperature. The crystal structure of MgPc can be fitted with unusual lattice parameters and the XRD pattern changed to impurity phase in the molecular forms of $(MgPc)N_2$ and $(MgPc)O_2$**.**

Acknowledgement

One of authors would like to acknowledge the Development and Promotion of Science and Technology Talents Project (DPST) for scholarship. This research was partially supported by National Nanotechnology Center.

References

[1] M.M. El-Nahass, A.A. Atta, H.E.A. El-Sayed and E.F.M. El-Zaidia, *Appl. Surf. Sci.* **254** (2008), pp. 2458–2465.

[2] O. Berger, W.-J. Fischer, B. Adolphi and S. Tierbach, *J. Mater. Sci. Mater.-El*. **11** (2000), pp. 331-346.

[3] B.N. Achar and K.S. Lokesh, *J. Solid State Chem*. **177** (2004), pp. 1987–1993.

[4] P. Ballirano, R. Caminiti, Ercolani, C. Maras and M.A. Orru, *J. Am. Chem. Soc.* **120** (1998), pp. 12798-12807.

[5] S. Liu, Z. Zhao and Z. Wang, *Photochem. Photobio. Sci.* **6** (2007), pp. 695-700.

[6] E. Kuzmann, A. Nath, V. Chechersky, S. Li, Y.Wei, X. Chen, J.Li, Z. Homonnay, M. gál4, V. K. garg, Z. Klencsár and A vértes, *Hyperfine Interact*. **139/140**, 2002. pp. 631–639.

[7] M. Ashida, N. Uyedia and E. Suito, *Bull. Chem. Soc. Jpn.* **39** (1966), pp. 2616-2624.

[8] K.P. Khrishnakumar and C.S. Menonr, *Mater. Lett.* **48** (2000), pp. 64–73.

[9] J. Jancza and R. Kubiak, *Polyhedron.* **202** (2001), pp. 901–2909.

[10] G. Guillaud, J.Simon and J.P. Germain, *Coord. Chem. Rev.* **178-180** (1998), pp. 1433-1484.

[11] R. Kubiak, J. janczak and K. Ejsmont, Chem. *Phys. Lett*. **254** (1995), pp. 249-252

[12] T.L. Bluhm, H.J. Wagner and R.O. Loutfy, *J. Mater. Sci. Lett*. **2** (1983), pp.85-87

Effect of nitrogen dioxide gas on various metal phthalocyanine thin film

R. Jaisutti[1*], O. Chamlek[1], T. Juagwon[2], W. Yamwong[3] and T. Osotchan[1, 2]

[1] Department of Physics, Faculty of Science, Mahidol University, Ratchathewi, Bangkok, Thailand 10400
[2] Material Science and Engineering Program, Capability of Nanoscience and Nanotechnology, Faculty of Science, Mahidol University, Ratchathewi, Bangkok, Thailand 10400
[3] Thai Microelectronic Center, Nantional Electronics and Computer Technology Center, National Science and Technology Development Agency, Chachoengsao, Thailand 20400

[*] E-mail: rawat_phytu@hotmail.com

Abstract: Effect of nitrogen dioxide (NO_2) gas on electrical resistance of metal phthalocyanine (MPc) thin films was investigated. The MPc thin films including CuPc, CoPc, ZnPc, MnPc and FePc thin film were prepared by thermal evaporation on aluminum interdigitated electrodes with 100 μm inter-electrode spacing. The respond and recovery characteristics of MPc thin films were investigated with various NO_2 gas concentrations at room temperature. The 100 ppm of NO_2 gas was used to dilute with ultra-high purity N_2 at a concentration between 0 ppm and 30 ppm. The total gas flow rate was fixed at 20 sccm controlled by mass flow controller. To investigate the responding and recovering characteristic, the device was maintained for 20 min in specific concentration of NO_2 gas and followed by 20 min of recovering period in N_2 atmosphere. The results show an increasing current of MPc thin film as the NO_2 concentration increases. After NO_2 exposing period, MPc thin film can not recover completely to the original state within 20 min due to the diffusion of NO_2 into the films especially in CoPc thin film. Phthalocyanine molecules with different metal ion have different responding and recovering characteristics. The responsivity of CoPc thin film to NO_2 gas exhibits higher than those others and it shows very slow recovery time. The responsivity of MPc thin films on NO_2 gas can be arranged in the order of high to low responsivity as CoPc, ZnPc, MnPc, FePc and CuPc, respectively.

Introduction

Nitrogen dioxide (NO_2) is dangerous toxic gas and major cause of environment pollution problem. It is an important product generated by high-temperature fossil fuel combustions especially in industrial activity and road traffic. The NO_2 is very noxious for humans even at very low concentration [1, 2]. Thus, the monitoring of NO_2 gas can be used to protect harmful effect on human health and control air pollutant quality. The simple method to detect gases is measuring the changes in electrical conductivity induced by the adsorption of gas molecules on the surface of semiconductor. Metal phthalocyanine (MPc) and their derivatives are organic semiconducting materials that have been widely used in the application of gas sensing [3-5]. This is due to the conductivity of MPc can be affected by the adsorption of oxidizing or reducing gas. Moreover, the variety of substituted metal ion in the phthalocyanine compound leads to various selectivity of sensitive layer such as cobalt, copper, zinc and manganese phthalocyanine (CoPc, CuPc, ZnPc and MnPc).

MPc has been found to be response on the presence of oxidizing gas such as NO, NO_2, NH_3, Cl_2 and O_3 [5-7]. In the gas sensing application, the MPc materials were usually prepared in the thin film form to increase the surface active area. The variation of conductivity of MPc thin film in the presence of gas is one of the most commonly used parameters in sensor devices [8, 9].

The present study demonstrates the effect of NO_2 gas sensing operation on different metal ion of phthalocyanine thin film including CoPc, CuPc, MnPc, ZnPc and FePc thin films. The changes in electrical conductivity of MPc thin films were measured under NO_2 atmosphere and followed by recovering period with flowing N_2 gas. Their responding and recovering characteristics were extracted to identify the sensing characteristics of each MPc thin film.

Materials and Methods

Interdigitated aluminum electrodes were prepared by thermal evaporation on glass substrate and used as the electrodes for studying the effect of MPc thin films to NO_2 gas. The electrodes had 5 fingers of 1000 μm width electrodes with 100 μm inter-electrode spacing as demonstrated in Figure. 1. The MPc powder including CoPc, CuPc, ZnPc, MnPc and FePc were used without further purification to prepare the thin film form on Al electrodes by thermal deposition. During deposition process the substrates were kept at room temperature with base pressure below 10^{-5} Torr.

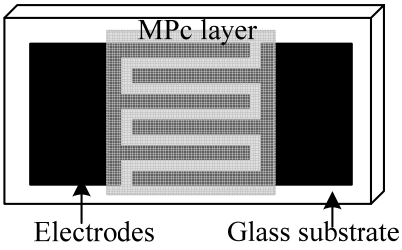

Figure 1. Interdigitated Al electrode structure prepared on glass-substrate and covered with an evaporated MPc thin films.

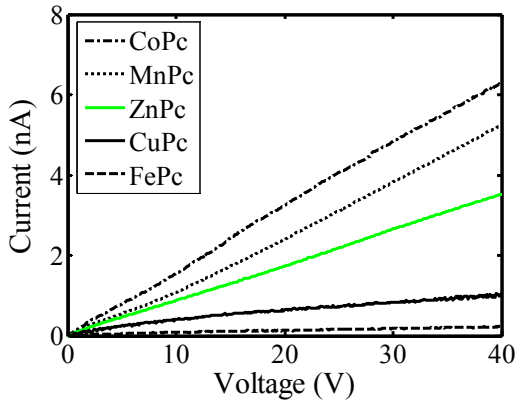

Figure 2. Linear current–voltage characteristics of MPc/Al planar structure in N_2 atmosphere before exposed to NO_2 gas.

A commercial gas mixture of 100 ppm NO_2 in N_2 was diluted at desired concentrations by ultra-high purity N_2 gas. The total gas flow rate was fixed at 20 sccm and the NO_2 concentration was varied at 10, 20 and 30 ppm. The MPc thin films were maintained in specific concentrations of NO_2 gas for 20 min and followed by N_2 gas flow for 20 min of recovering period. The conductivity changes of MPc thin films during exposed to NO_2 gas and cleaned by N_2 gas were measured by applying a constant bias voltage of 20V and monitoring the response current by using Keithley model 6517A electrometer.

Results and Discussion

The MPc thin films were measured on the steady state current-voltage characteristics in the N_2 atmosphere before exposing to NO_2 gas. The current of each sample was shown approximately linear dependence on applied voltage as indicated in Figure 2. The inverse slope of this characteristic yielded a resistance of the film as illustrated in Table 1. Different MPc thin films have different electrical conductivity. The FePc thin film showed the highest initial resistance value comparing to the other films, while the CoPc thin film showed that the carrier were easily transport through the film.

Figure 3 showed the dynamic response current of MPc thin films with three cycling process of NO_2/N_2 gas at varied NO_2 concentrations of 10, 20 and 30 ppm with 20 min exposure and 20 min cleaning periods. The results demonstrated that all investigated MPc thin films can be used to estimate NO_2 gas at room temperature. The rising and recovering period for most MPc thin films are almost changing as a function of NO_2 concentration. The response current started increase after a few minute of NO_2 gas was supplied to the films due to the effect of large chamber leads to slower equilibrium concentration inside the chamber. After that the response current also continuous increases but they show a slower increasing rate. There are no equilibrium state occur within the time periods investigated. When the NO_2 was switched off and N_2 was flowed through the film for cleaning process, the response shows a small decrease when NO_2 concentration was decreased leads to their recovering characteristics are slowly decreased. After NO_2 exposing period, MPc thin films can not be recovered completely to the original state within 20 min due to the diffusion of NO_2 into the films especially in CoPc thin film. However, full recovered response of MPc thin film can be achieved by using a long cleaning process which is different purging time depends on the strongly reacting effect between the film and NO_2 gas.

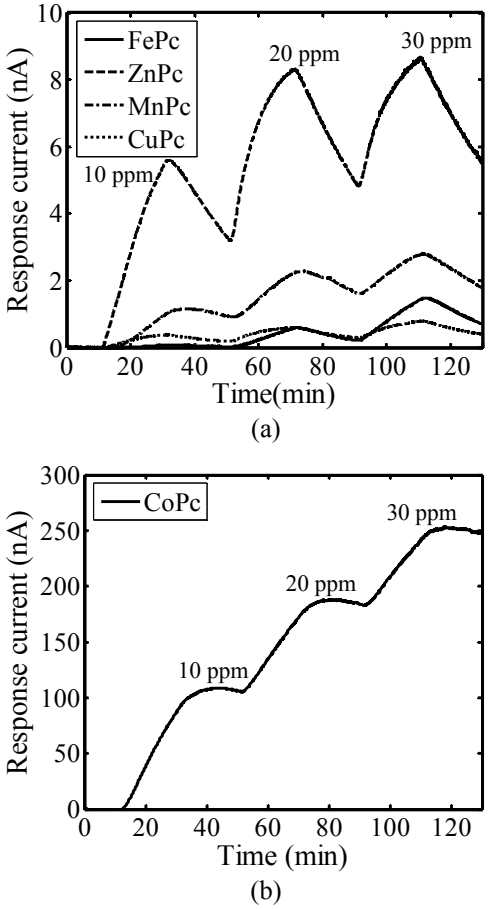

Figure 3. Response current of (a) FePc, ZnPc, MnPc, CuPc and (b) CoPc thin films with varied NO_2 concentrations of 10, 20 and 30 ppm.

Table 1: Resistance value of various MPc thin films deposited on interdigitated Al electrodes before and after exposed to NO_2 gas with the concentration of 10, 20 and 30 pppm.

Material	Resistance (Ω)			
	In N_2	In $[NO_2]$ (ppm)		
		10	20	30
FePc	102.56G	20.01G	3.19G	1.28G
CuPc	33.52G	2.85G	2.11G	1.74G
MnPc	0.99G	0.61G	0.43G	0.38G
ZnPc	2.56G	0.30G	0.20G	0.19G
CoPc	60.53M	11.86M	7.62M	5.90M

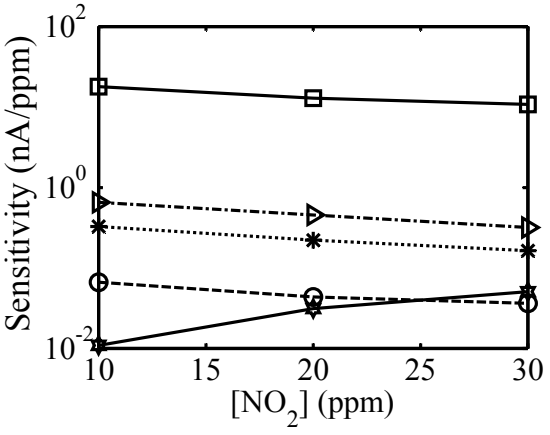

Figure 4. Sensitivity as a function of NO_2 concentration for CoPc, ZnPc, MnPc, CuPc and FePc thin film represented by the lines from bottom to top, respectively.

From the response current results, the resistance values of the MPc thin film under NO_2 atmosphere can be calculated from the ratio between applied voltages to the film and measured current at specific concentration. The calculated resistance values, as shown in Table 1, indicated that they are very large decreasing value when the NO_2 was supplyed to the films and a bit decreasing order when the concentration of NO_2 was increased from 10 ppm to 30 ppm.

Different metal ion substituted phthalocyanine molecules have different responding and recovering characteristics as indicated in Figure 2. It indicates very slowly changing for both in response and recovering periods. The result also shows that the response of CoPc thin film indicated the highest response than those from the other films as demonstrated their sensitivities in Figure 4. The sensitivity of MPc thin films on NO_2 gas can be ordered from high to low sensitivity as CoPc, ZnPc, MnPc, CuPc and FePc thin films, respectively. The sensitivity of CoPc, ZnPc, MnPc and CuPc thin films are about constant values for the measured NO2 concentration range at about the values of 200, 8, 5, and 0.8, respectively. In the case of FePc thin film, it was found that at NO_2 concentration greater than 20 ppm, the sensitivity is greater than the response of CuPc thin films. The ZnPc thin film indicated the fastest response during exposure to NO_2 gas.

Conclusions

The NO_2 gas affected on the conductivity of CoPc, ZnPc, MnPc CuPc and FePc thin fims. All studied MPc thin films show the response increased as NO_2 concentration increased. The sensitivity of CoPc thin film on NO_2 gas exhibits the highest value but it shows very slow responding and recovering rates. The sensitivity of MPc thin films on NO_2 gas can be ordered from the high to low values as CoPc, ZnPc, MnPc, CuPc and FePc, respectively. The ZnPc was showed the fastest responding and recovering rates while the transient responses of CuPc, MnPc, FePc and CoPc thin films are relatively slower.

Acknowledgements

This work was partially supported by National Nanotechnology Center, National Science and Technology Development Agency, Thailand. The author would like to acknowledge on the CHE-PhD-THA scholarship from the Commission on Higher Education, Thailand.

References

[1] A. Das, R. Dos, T. Richardson, M.Grell, J.J. Morrison and M.L. Turner, *Adv. Mater.* **19** (2007), pp. 4018–4023.
[2] Y.L. Lee, W.C. Tsai, C.H. Chang and Y.M. Yang, *Appl Surf. Sci.* **172** (2001), pp.191-199.
[3] M. Bouvet, G. Guillaud, A. Leroy, A. Maillard, S. Spirkovitch and F.G. Tournilhac, *Sens. Actuators B* **73** (2001), pp. 63-70.
[4] Y.L. Lee and C.H. Chang, *Sens. Actuators B* **119** (2006), pp. 174-179.
[5] M.I. Newton, T.K.H. Starke, G. McHale and M.R. Willis, *Thin Solid Films* **360** (2000), pp. 10-12.
[6] Y.L. Lee, W.C. Tsai and J.R. Maa, *Appl Surf. Sci.* **173** (2001), pp. 352-361.
[7] J. Brunet, V.P. Garcia, A. Pauly, C. Varenne and B. Lauron, *Sens. Actuators B.* **134** (2008), pp. 632-639.
[8] J. Brunet, A. Pauly, L. Mazet, J.P. Germain, M. Bouvet and B. Malezieux, *Thin Solid Films.* **490** (2005), pp. 28-35.
[9] R.D. Gould and N.A. Ibrahim, *Thin Solid Films.* **398-399** (2001), pp. 432-437.

Eeffect of fluorine doping in tin oxide films prepared by ultrasonic spray pyrolysis

P. Prachopchok[1*], C. Thanachayanont[2], K. Sriprapha[3], A. Heawchin[3]
S. Kaewket[3], P. Vijitjanya[3], C. Sac-kung[3] and T. Osotchan[1]

[1]Materials Science and Engineering Program, Capability Building Unit of Nanoscience and Nanotechnology, Faculty of Science, Mahidol University, Bangkok 10400
[2]National Metals and Materials Technology Center, National Science Technology Development Agency, Pathumthani 12120
[3]Institute of Solar Energy Technology Development National Science Technology Development Agency, Pathumthani 12120

[*] E-mail: p.t_physics@hotmail.com

Abstract: The transparent conducting oxide thin films of tin oxide doped fluorine (SnO_2:F) were prepared by ultrasonic spray pyrolysis. In order to obtain the good transparent conducting SnO_2:F thin film, the thin film is required to have proper crystallize size, high electrical conductivity and high optical transmission value. These can be modified by varying the amount of doping F in SnO_2 therefore the effect of doping F in SnO_2 was investigated in this study. Thin film of SnO_2:F was prepared by using 0.1 M of Tin (IV) chloride pentahydrate ($SnCl_4.5H_2O$) in 100 ml of methanol and deionized water. The amount of fluorine doping was varied by adding ammonium fluoride (NH_4F) with varied amount from 0 to 0.15 M into the solution. The 3 mm thick glass substrate was cut to the dimension of 75 x 75 mm^2 and cleaned in DI water and ethanol subsequently. During deposition process, the substrate temperature was kept at 450 °C while the flow rate of compressed air was fixed at 1.0 l/min. The solution was put in the glass tube with the diameter of 26 mm and covered by parafilm sheet then placed on the ultrasonic transducer. The glass substrate was placed 25 cm above the solution with double wall glass chamber. The crystalline of prepared SnO_2:F thin films was examined by x-ray diffraction (XRD) while the surface morphology of thin films was determined by atom force microscopy. The dominated XRD peaks of (110), (101), (200) and (211) can be identified as the crystal structure planes of SnO_2. The resistivity of thin films was determined by four-point probe technique while the mobility and carrier concentration of thin films were determined by Hall effect with Van der Pauw technique. The optical transmission of thin film was also examined by uv-visible spectrophotometer for various doping fluorine contents. The typical sheet resistance of SnO_2:F films is in the range of 110 ohm/ and modifying doping fluorine content affected the electrical and optical properties.

Introduction

Development of the transparent conducting oxide (TCO) in optoelectronic devices such as solar cells, liquid crystal displays, waveguide electron devices and light emitted diode, is very important. The TCO materials can be various kinds such as tin doped indium oxide (In_2O_3:Sn or ITO) and fluorine doped tin dioxide (SnO_2:F or FTO). The tin dioxide can be doped by other elements such as Mn, Pb, Fe and Ni. In case of undoped tin dioxide, the electrical property is similar to insulator therefore the doping is necessary. The tin dioxide has a tetragonal rutile structure with the wide energy gap of 3.67 eV, and behaves as an n-type semiconductor [1].

Thin films of fluorine doped tin dioxide can be prepare by vary techniques such as DC reactive sputtering [2], sol gel [3], and spray pyrolysis [4-7]. The spray pyrolysis method is most commonly used due to its simple process, ease in adding various doping materials and economic advantages [8-9]. Normally, the spray pyrolysis is used the nozzle to spray solution to the substrate while the ultrasonic spray pyrolysis was adapt to generate the fox of solution by ultrasonic transducer before it is spray on to substrate.

In this study, the crystal structure, surface morphology, electrical property were investigated on the undoped and fluorine doped tin dioxide thin films which were prepared by ultrasonic spray pyrolysis at various fluorine doping concentrations.

Materials and Methods

Thin film of SnO_2:F was prepared by using 0.1 M of tin (IV) chloride pentahydrate ($SnCl_4.5H_2O$) purchased from Sigma-Aldrich in 90 ml of methanol and of 10 ml of deionized water. The amount of fluorine doping was varied by adding ammonium fluoride (NH_4F) from Aldrich with varied amount from 0, 0.01, 0.05, 0.10 and 0.15 M in the solution. The 3 mm thick glass substrate was cut to the dimension of 75 x 75 mm^2 and cleaned in DI water and ethanol subsequently.

During deposition process, the substrate temperature was kept at 450 °C while the flow rate of compressed air was fixed at 1.0 l/min. The solution was put in the glass tube with the diameter of 26 mm which was covered by parafilm sheet then placed on the ultrasonic transducer. The glass substrate was placed 25 cm above the solution with double wall glass chamber as displayed in Fig. 1.

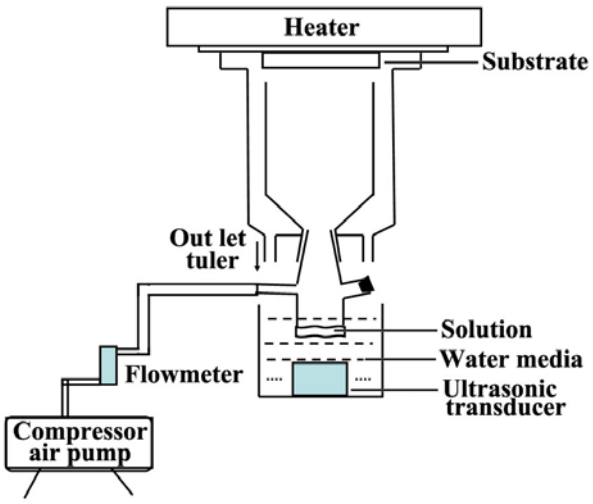

Figure 1. Schematic diagram of ultrasonic spray pyrolysis system for preparing SnO_2:F thin film.

After fixing the glass substrate on the heater, the setting heating temperature was slowly increased about 10°C/min until reached the temperature of 450°C then the substrate was maintained to this temperature for 5 mins before turn ultrasonic transducer on. The fox of the solution was carrier through the gradient of the temperature to the heated substrate by air flow for the period of 25 mins. During the solution pass through the temperature gradient, the oxide compound may be formed before and after deposition on the heated substrate. The water and residue vapours were carried out with the air flow through the outer chamber and outlet tube. After the ultrasonic transducer was turned off, the heater and air still maintained for other 5 mins to complete the reaction. Then the heater was slowly cooling down with the rate of 10°C/min with remain air flow.

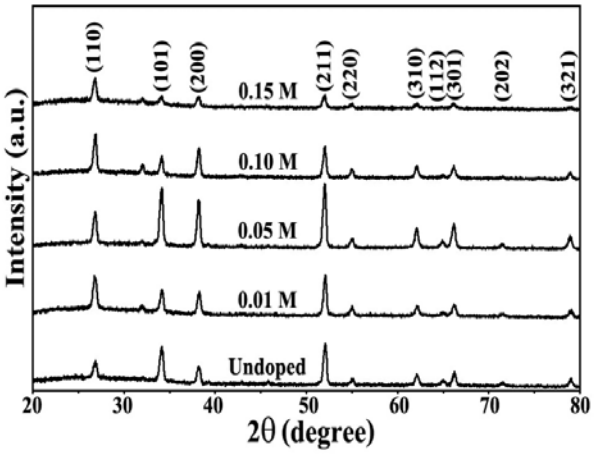

Figure 2. The XRD-patterns of SnO_2 and SnO_2:F thin films on glass substrate.

The crystallinity of prepared SnO_2:F thin films is examined by x-ray diffractometer model Advance D8 with copper Kα x-ray line, line focus and monochromator. While the surface morphology of thin films was determined by atom force microscopy (AFM) model SPA400 of Sieko Instruments. The thickness of films was determined by step profile. The resistivity of thin films was determined by four-point probe technique while the mobility and carrier concentration of thin films were determined by Hall effect using a van der Pauw technique with HMS-3000 Ecopia. Silver paste was used to make electrical contacts. The optical transmission of thin film was also examined by Hewlett Packard 8452A uv-visible spectrophotometer for thin film at various doping fluorine contents.

Results and Discussion

The obtained undoped SnO_2 thin film looked uniform but not clearly transparent while the doped SnO_2:F became uniform and clearly transparent film especially when the doping concentration was greater than 0.10 M. The crystal structure of the obtained SnO_2:F thin films at various doping concentration exhibited the same structure of tetragonal rutile phase as indicated in Fig. 2. The XRD pattern of SnO_2 and SnO_2:F thin films exhibits very sharp and high peaks. It indicates the well crystalline structure. The XRD peaks of undoped and doped of SnO_2 thin film are diffracted from the lattice planes of (100), (101), (200), (211), (220), (310), (112), (301), (202) and (321) as marked in Fig. 2.

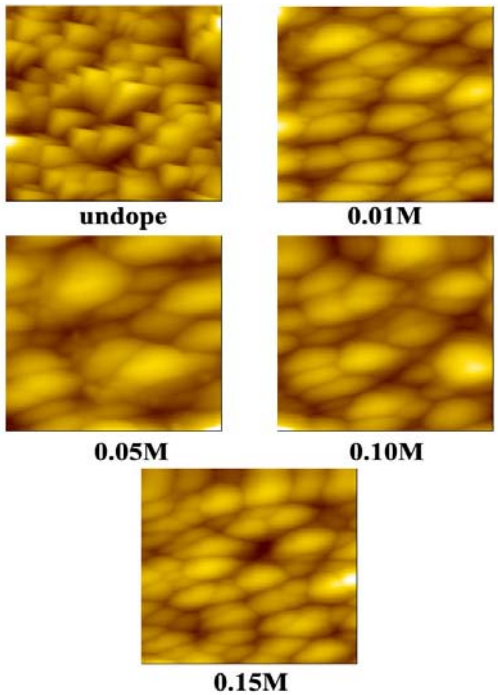

Figure 3. Surface morphology of SnO_2 and 0.01, 0.05, 0.10 and 0.15M SnO_2:F films on glass substrate. The sizes of images are 10x10 μm^2.

The dominate peaks of (110), (101), (200) and (211) are located at about 27, 34, 38 and 52 degree respectively. Although these peaks are at about the same angles, the relative intensities of these peaks are slightly changed. The (211) peak is the most dominant peak for undoped film while the intensity is relatively

smaller after the doping concentration is increase. The intensity of (211) peak becomes smaller than that of (110) peak after doping with concentration higher than 0.10M. At this doping region the (110) become most dominate peak. The intensity of (101) peak also decreases as increasing the doping concentration. This is similar to the case of (211) peak. While the (200) peak has the relative intensity almost constant for the whole entire doping range.

By comparing the intensity of whole XRD peaks, the peak of high doping thin film at 0.10 and 0.15M exhibit very small intensity probably due to low crystalline film. The extra peaks also can be noticed which may occur from the extra phase of Sn_5O_6 [6] in fluorine doped of SnO_2 or the phase of Sn_2O_5 occurring from the absent of oxygen atom.

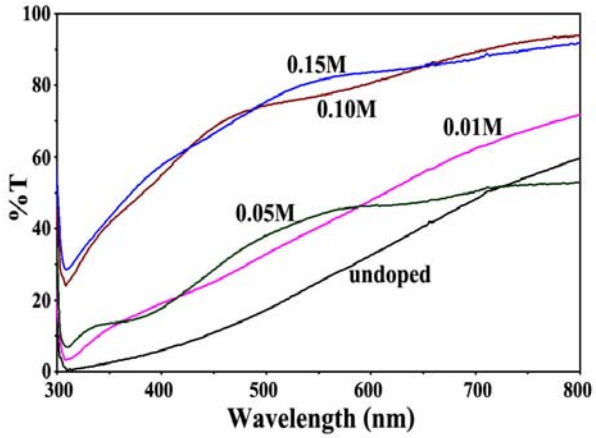

Figure 4. Optical transmission of SnO_2 and 0.01, 0.05, 0.10 and 0.15M SnO_2:F films on glass substrate.

The surface morphology of films SnO_2 and SnO_2:F show the high density films while the grain of SnO_2 film has triangle like edge shape. The shape of the grain for doped SnO_2:F film has smooth round shape. The grain size becomes large when the concentration increase up to 0.05M then grain size gets smaller after increase the concentration to 0.15M. These correspond to the result of the lower intensity of XRD peaks at the 0.15M film.

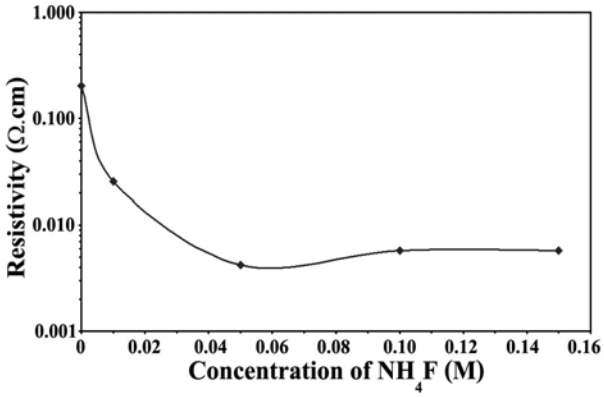

Figure 5. Resistivity of SnO_2 and 0.01, 0.05, 0.10 and 0.15M SnO_2:F films on glass substrate.

The optical transmission of undoped SnO_2 film exhibits the low transmission at about 40%. When the doping concentration increases, the optical transmission gets increase and the highest optical transmission at about 80% can be obtained at the doping concentrations of 0.1 and 0.15M, as shown in Fig. 4. The transmission spectra of fluorine doped films not only affect on the percent transmission but also modified the shape of spectra. The shape of 0.1 M doped film has linearly increase shape and similar to that of undoped film while the shape of the spectra for 0.05, 0.10 and 0.15M films become saturate value at wavelength higher than 550nm.

The resistivity of SnO_2 and SnO_2:F films was determined by four-point probe technique and the undoped film has high resistivity of about 0.203 Ωcm. The doped films have smaller resistivity and the lowest resistivity (0.004 Ωcm) films obtained from the film with the doping concentration of 0.05 M film. The higher doping concentration film cannot make the film with lower resistivity while at the increasing of the doping matter the resistivity has increased.

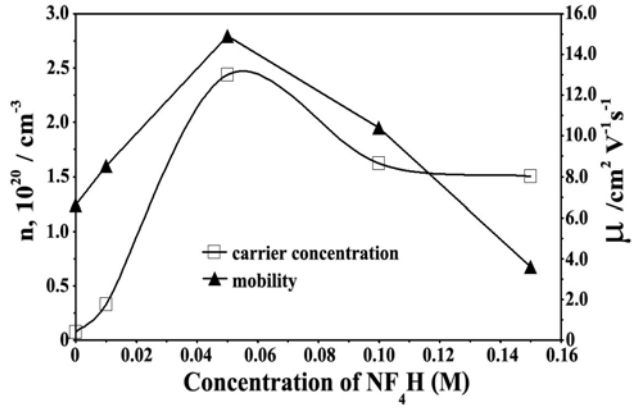

Figure 6. Carrier concentration and mobility as a function of doping concentration of SnO_2:F films on glass substrate.

By using van der Pauw technique, the carrier concentration and mobility were extracted from Hall measurement and the values as a function of doping concentration were evaluated, as indicated in Fig. 6. Hall effect results indicate the n-type carrier with the high carrier concentration of 2.4×10^{20} cm^{-3} from the film with the doping concentration of 0.05M. The carrier concentration for the higher doped film can have less carrier concentration and the carrier concentration of the film doped with 0.15M has less value than that in the undoped film. The highest mobility can also be obtained from the 0.05M doped film with the value of 3.6 cm^2/Vs. However the mobility value of highly dope film still has higher value than that in the undoped films.

Conclusions

The effect of fluorine doping in tin oxide films on the crystal structure, surface morphology, optical and electrical properties were studied systematically. It indicates that the strong effect of the fluorine doping films can cause higher crystallinity, larger grain size, higher optical transparence and higher electrical conductivity especially at the optimal dope concentration of 0.05M. This high electrical conduction originates from both of higher carrier concentration and higher mobility which probably dues to the better film structure.

Acknowledgement

This work was partially supported by National Nanotechnology Center, National Science and Technology Development Agency, Thailand. The author would like to acknowledge on the TGIST scholarship from National Science and Technology Development Agency, Thailand.

References

[1] A.V. Moholkar, S.M. Pawar, K.Y. Rajpure and C.H. Bhosale, *Materials Letters*. **61** (2007), pp. 3030-3036.

[2] A. Martela, F. Caballero-Brionesa, P. Bartolo-Perezc, A. Iribarrena,d, R. Castro-Rodrguezc, A. Zapata-Navarroa and J.L. Pena, *Surface and Coatings Technology*. **148** (2001), pp. 103–109.

[3] C.-H Hthan, S.-D Han, J. Gwak and S.P. Khatkar, *Materials Letters*. **61** (2007), pp. 1701–1703.

[4] D. Jadsadapattarakul, C. Euvananont, C. Thanachayanont, J. Nukeaw and T. Sooknoi, *Ceramics International*. **34** (2008), pp.1051-1054.

[5] M. Adnane, H. Cachet, G. Folcher and S. Hamzaoui, *Thin Solid Films*. **492** (2005), pp. 240-247.

[6] M.-M. Bagheri-Mohagheghi, N. Shahtahmasebi, M.R. Alinejad, A. Youssefi and M. Shokooh-Saremi, *Solid State Sciences*. **11** (2009), pp. 233-239.

[7] G.C. Morris and A.E. McElnea, *Applied Surface Science*. **92** (1996), pp. 167-170.

[8] S.-Y. Lee, B.-O. Park, *Thin solid films*. **510** (2006), pp. 154-158.

[9] C.-C. Lin, M.-C. Chiang, Y.-W. Chen, *Thin Solid Films.* **518** (2009), pp. 1241-1244.

Preparation of zinc oxide/butyl acrylate nanocomposite latex for coating application

P. Raksayot[1, 2], S. Phattanarudee[3], and V. Tangpasuthadol[1,2,4*]

[1]Center for Petroleum, Petrochemicals, and Advanced Materials, Chulalongkorn University
[2]Program of Petrochemical and Polymer science, Faculty of Science, Chulalongkorn University
[3]Department of Imaging and Printing Technology, Faculty of Science, Chulalongkorn University
[4]Department of Chemistry, Faculty of Science, Chulalongkorn University, Bangkok, Thailand 10330

*E-mail: varawut.t@chula.ac.th

Abstract: Nanocomposite latex of zinc oxide/poly(butyl acrylate) (ZnO/PBA) for coating on fabric was prepared by in situ emulsion polymerization of butyl acrylate in the presence of ZnO. The ZnO nanoparticles were first grafted with a silane coupling agent, 3-methacryloxy-propyltrimetoxysilane (MPS), in order to improve the interface compatibility between the ZnO and the organic PBA. One end of MPS was siloxyl group which could be bonded to the ZnO particle. The other end was the methacryloyl group that was facilitated as an initiating point for PBA grafting by using potassium persulfate as initiator in the presence of polyoxyethylene octylphenyl ether (OP-10) surfactant. The ZnO/BA composite latex encapsulation was assured by Fourier transform infrared spectroscopy (FT-IR) and transmission electron microscopy (TEM). In the latex, about 52% of ZnO nanoparticles were successfully grafted with PBA. The composite latex containing 0.3% by wt. of ZnO was fairly stable at room temperature for up to 3 weeks. Furthermore, antibacterial activities of the ZnO/BA composite latex were tested against Escherichia coli (Gram negative) and Staphylococcus aureus (Gram positive) cultures.

Introduction

ZnO nanoparticle has been used to suppress bacteria and block UV radiation[1-6]. Therefore it has been used increasingly as emulsion for coating on materials such as fabrics and construction materials. ZnO was reportedly encapsulated with many types of film forming polymer, for example, polystyrene [1]. The ZnO/polymer nanocomposites are usually in the form of emulsion, in which the nano ZnO/polymer particles must be dispersed homogeneously. One way to achieve this is to modify the ZnO particles by changing its polar surface (Zn-OH) to hydrophobic chemical groups. The method used is to graft an organic polymer on the metal-oxide surface. In general a coupling agent, such as 3-methacryloxypro-pyltrimethoxy silane (MPS), is needed as a link between the metal oxide and the organic polymer. The methoxy silane end of MPS can chemically link with ZnO, while the double bond end can become an initiating point for polymerization of the vinyl monomer in the emulsion; hence the process is called *in situ* emulsion polymerization.

The aim of this work was to prepare nano-composite latex between ZnO and butyl acrylate in the presence of MPS as a coupling agent by emulsion polymerization process.

Materials

Butylacrylate monomer and 3-methacryloxypro-pyltrimethoxy silane (MPS, AR) were purchased from Sigma-Aldrich. Zinc oxide (ZnO) type A (ZoNoP® Zinc Oxide Nano Particles) was obtained from Nano Materials Technology Co.,Ltd. ZnO type B (ZP 20L) was from Nanoscience Technology Co., Ltd. Potassium persulfate (KPS, production grade), polyoxyethylene nonylphenyl ether (IGEPAL CA-630, cmc = 0.083 mM or 0.005 % v/v, production grade, Rhodia), MeOH (AR), and isopropyl alcohol (AR) were purchased from Merck. Deionized water was used throughout this work.

Methods

Preparation of ZnO/PBA composite latex

Modification of nano-ZnO with MPS

ZnO nanoparticles (2 g) were mixed with a mixture (50 mL) of water and methanol (ratio 1:4), and then MPS (1 g) was added to the system. The mixture was first dispersed for 20 min through an ultrasonic instrument at room temperature and then the mixture was heated to reflux for at least 4 h. At the end of the reaction, the mixture was cooled down and diluted four or five times with iso-propanol. This mixture was filtered through membrane filter with suction system and the deposit was dried at 50 ˚C in vacuum for at least 8 h[2].

Emulsion polymerization of butyl acrylate

The aqueous solution of 0.004 % of surfactant (CA-630) was mixed with modified MPS-grafted nano-ZnO 0.3 % in a beaker. The beaker was then sonicated by ultrasonic instrument for 30 min at room temperature. The dispersion was then poured into a four-neck flask that equipped with a stirrer. The flask was heated to 65 ˚C under a N_2 atmosphere. BA monomer (5 %) was introduced by drill-feeding into the flask to react in 1.30 hr. The flask was then heated to 75 ˚C, followed by the addition of initiator solution (1% of monomer) [1]. During the polymerization, the reaction mixture was maintained at 75 ˚C for 3 h. After

that the latex was cooled down to room temperature, it was analyzed for stability, conversion, percentage of grafting, grafting efficiency and the other characterization methods. The emulsion polymerization recipe of ZnO/PBA nanocomposite latex is shown in Table1.

Table 1: The emulsion polymerization recipe of ZnO/PBA nanocomposite latex

Chemical Name	% wt
Butylacrylate monomer	5
Modifly ZnO	0.3
IGEPAL CA-630	0.004
KPS	0.05
Deionised water	94.7

Latex Stability determination

The latex was left standing in a clear screw thread vials (Size: 21×70mm, 15 mL tall) for 3 weeks. The depth of sedimentation from the surface of suspension was recorded periodically. The sedimentation percentage of the composite latex was determined by the following equation:

$$\% \text{ Sedimentation} = H/H_0 \times 100\%$$

where H (cm) is the depth of sedimentation from the surface of suspension, and H_0 (cm) is the total depth of suspension

Grafting efficiency

The monomer conversion was determined by conventional gravimetric method. Its result was calculated by the following equation:

$$\text{Conversion } (\%) = (A-B)/C \times 100$$

where A is the weight of total resulting particle, B is the weight of charged nano-ZnO particle, and C is the weight of charged monomer.

The resulting grafted ZnO particles was separated from the mixture by centrifugation at 15,000 rpm for 30 min and washed with water repeatedly. The amount of polymer grafted onto the nano-ZnO surface was determined after Soxhlet extraction, using acetone as solvent. The percentage of grafting and its efficiency of polymer onto the surface were calculated by the following equations:

$$\text{Grafting } (\%) = D/E \times 100$$

$$\text{Grafting efficiency } (\%) = D/F \times 100$$

where D (g) is the grafted polymer, E (g) is the charged nano-ZnO particles, and F (g) is the total polymer (grafted and ungrafted polymer) formed.

Antibacterial test

The antibacterial test was performed according to the agar dilution susceptibility method. *E. coli* and *S. aureus* were two bacterial strains selected for testing. Ampicillin 50 mg/mL was used as a positive control. First, Fresh culture of spawn raising under 37±1°C over 24 h was washed down by physiological saline and used as bacterial suspension. The growth medium was agar that mixed with the ZnO samples in different concentration. Second, The bacterial suspension of 100 µL was dropped on to the agar in growth medium plate. All plates were kept at 37±1°C. After 24 h, the bacteria were washed off using physiological saline. The colony forming units (CFU) of bacteria were taken count. The antibacterial concentration was calculated via the conventional calculation[6].

Other characterization and measurements

A Fourier transform infrared spectrophotometer (FT-IR) analysis was performed on IR spectrophotometer (Spectrum100, Perkin Elmer). FT-IR was used to characterize the functional groups of the nano-ZnO, modified nano-ZnO by KBr disc and nano-ZnO/PBA composite by casting on NaCl cell.

The morphology analysis of the ZnO particles and the composite was performed on transmission electron micrograph (TEM) analyzer.

Results and Discussion

Modification of nano-ZnO with MPS

In the order to obtain nanocomposite materials, the nano-ZnO must be modified by attaching hydrophobic group on the particle surface. In this work the surface of nano-ZnO particle was chemically linked with MPS via the Zn-O-Si bonding. On the other end, MPS molecule has a double-bond group that is able to bond with added monomers, BA.

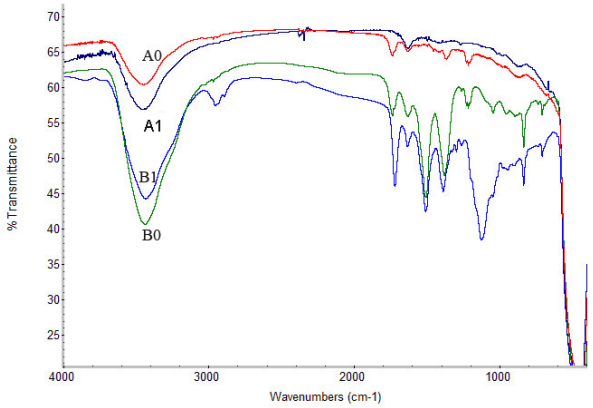

Fig. 1 FTIR of nano-ZnO particles type A (A0) and type B (B0); nano-ZnO particles modified by MPS in type A (A1) and type B (B1)

Two types of ZnO particles were compared for its ability to be grafted by MPS. ZnO type A was prepared by spray-drying process at 600-1,000 ºC, while the ZnO type B was obtained from the spray-drying at 600ºC. The two ZnO types, as analyzed by FTIR, possess different functional group feature especially at the region from 800-1,700 cm^{-1} (Fig. 1). It seems that there are more organic functional groups left in the ZnO type B than those in type A. This can be explained by the fact that both ZnO particles were prepared from zinc acetate that was subjected to pyrolysis process to prepare the ZnO particles[4]. At low temperature (600 ºC), more organic functional is therefore left in the particles type B.

Also from Fig. 1, the IR spectra of the modified nano-ZnO particle (A1 and B1) are compared with

those of its corresponding untreated particles (A0 and B0). It should be noted here that any non-bonded MPS was washed away from these two modified particles by extraction before the IR analysis. For type A ZnO, there is no signal feature indicating the presence of Zn-O-Si or Si-O-Si bond formation at 1,100 cm^{-1}. But a new and very distinct peak at 1,127 cm^{-1} shown in the spectrum of sample B1 can be clearly observed. In addition, an increase of C-H stretching signal (from CH_2) was observed at 2,955 cm^{-1}. These two evidences suggest the grafting of MPS on ZnO.

Emulsion polymerization of butyl acrylate on MPS-grafted ZnO nanoparticles

In the emulsion polymerization process, the surfactant (CA-630), used under its CMC, helps stabilize the grafted ZnO particles in the latex. During the polymerization, chain propagation should occur on the surface of the nano-ZnO resulting in an encapsulation of the ZnO particle by PBA

Figure 2 illustrates the spectrum that represents the frequency of absorbed band of PBA on the surface of the nano ZnO. It can be clearly seen that the carbonyl peak at 1,730 cm^{-1} and C-H stretching peak at 2,885 and 2,953 cm^{-1} increase dramatically. This is caused by the long chain length of PBA anchoring on the surface of nano-ZnO possibly via the grafted MPS molecules.

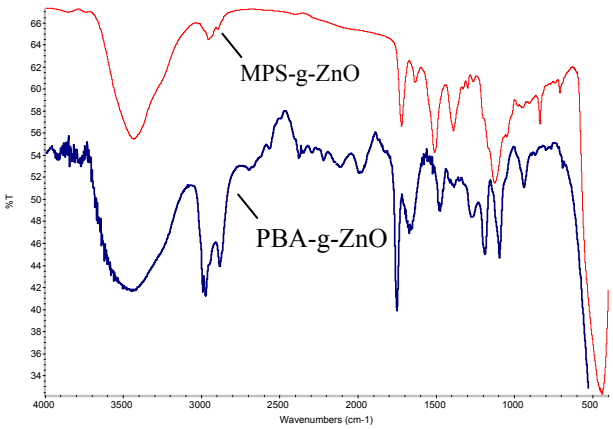

Fig. 2 FT-IR spectrum for nano-ZnO particles (type B) modified by MPS and ZnO/PBA composite particles.

It was found that upon using 5%wt of BA monomer in the polymerization, the grafting weight of PBA on the MPS-modified ZnO was 145%, with a grafting efficiency of 52%. The conversion of BA to PBA in this system is quite low (42%), possibly due to the fact that the BA monomer is rather hydrophobic and therefore does not mix well with the emulsion.

Micro-scale visualization of the nanocomposite ZnO particle was carried out by TEM (Fig. 3). Figures 3a, 3b and 3c show the spherical morphology of nano-ZnO particles type A, type B, and nano-ZnO particles modified by MPS type B with the mean size from 20–80 nm, respectively. In Figure 3d, light-toned shell layer surrounding the dark-toned ZnO particle in spherical morphology can be observed. This outer shell is most likely the PBA layer that was grafted on the ZnO particles via the MPS coupling agent. The mean size is ~100 nm.

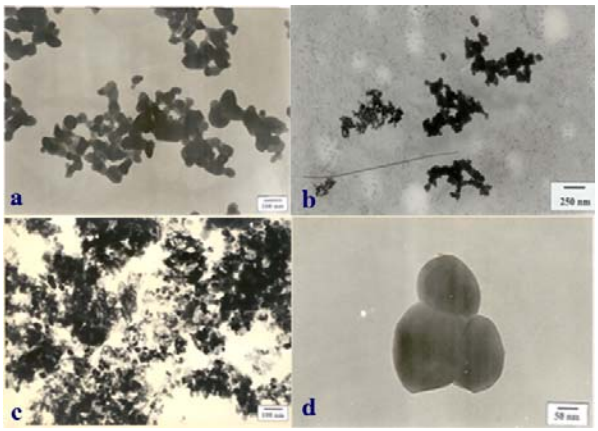

Fig. 3 TEMs of nano-ZnO particles type A (a), type B (b), nano-ZnO particles modified by MPS type B (b) and ZnO/PS composite particles (c).

Latex Stability determination

Higher BA content in the nanocomposite latex led to less stable latex. Therefore in this work, the optimal concentration of BA was fixed at 5%. The latex is stable at room temperature for as long as 3 weeks.

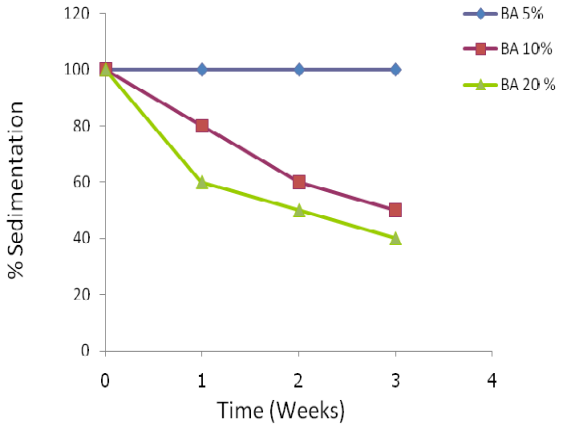

Fig.4 Stability curve of ZnO/PBA composite latex in driffent concentration of BA-monomers.

Antibacterial testing

The result of antibacterial test of ZnO/PBA nanocomposite latex is somewhat disappointing. It was found that the composite latex did not have any antibacterial properties against both S. aureus and E. coli bacteria strains (Table 2 and 3). However both untreated ZnO type A and B in fact show strong antibacterial effect. This finding can be explained by the fact that the ZnO particles in the ZnO/PBA nanocomposite are completely covered by the PBA. Therefore there is no contact between ZnO and bacteria [6].

Table 2 Results of antibacterial test by agar dilution susceptibility method against *S. Aureus*

S. aureus	**CFU/mL×10^6**
negative control	830
10% composite	927
20% composite	1270
30% composite	1283
40% composite	917
50% composite	823
10% ZnO A	0
20% ZnO A	0
30% ZnO A	0
40% ZnO A	0
50% ZnO A	0
10% ZnO B	0
20% ZnO B	0
30% ZnO B	0
40% ZnO B	0
50% ZnO B	0
positive control	0

Table 3 Results of antibacterial test by agar dilution susceptibility method against *E. Coli*

E. coli	**CFU/mL×10^6**
negative control	1183
10% composite	2093
20% composite	1987
30% composite	1963
40% composite	2033
50% composite	2047
10% ZnO A	1860
20% ZnO A	1780
30% ZnO A	1330
40% ZnO A	1383
50% ZnO A	1300
10% ZnO B	1220
20% ZnO B	613
30% ZnO B	0
40% ZnO B	0
50% ZnO B	0
positive control	0

Conclusions

The nanocomposite latex of PBA and ZnO nanoparticles was prepared by means of emulsion polymerization. The nano ZnO particles were enclosed by PBA shell with the help of MPS acting as a chemical link between the surface of ZnO and PBA. The latex remained stable up to 3 weeks of storage at room temperature. The ZnO/PBA nanocomposite did not exhibit any antibacterial activity. It is possible that the ZnO needs to be exposed from the PBA-coated particles in order to achieve antibacterial effect.

References

[1] Erjun, T.; Hong, L.; Liming, S.; Erli, Z.; Guoxiang C. *Eur. Polym. J.* **43** (2007), pp. 4210–4218.

[2] MA, S.; SHI, L.; FENG, Xin.; YU, W.; LU Bo. *J Shanghai Univ (Engl Ed)* **12(3)** (2008), pp. 278–282.

[3] Aiping, Z.; Aiyun, C.; Ziyi, Y.; Weidong, Z., *J. Colloid Interface Sci*. **322** (2008), pp. 51–58.

[4] Takao, T.; Lutz, M.; Sotiris, E. P, *J. Nanoparticle Res.* **4 (2002)**, pp. 337–343.

[5] Prafulla, K.S.; Ramakanta, S.; Sarat, K.S.; Pradeep, K.R. *Eur.Polym.J.* **44** (2008), pp 3522 - 3528

[6] Lingling, Z.; Yulong, D.; Malcolm, P.; David, Y. *Natural Sci.* **18** (2008), pp.939-944

Nucleation of polypropylene by organomodified-montmorillonite

P. Srisuwan[1], O. Saravari[1]*, N. Kerddonfag[2] and W.Chinsirikul[2]

[1] Department of Materials Science, Faculty of Science, Chulalongkorn University, Bangkok, Thailand 10330
[2] National Metal and Materials Technology Center, National Science and Technology Development Agency, Thailand

* E-mail: sonusa@chula.ac.th

Abstract:In this article,the nucleation of polypropylene (PP) by organomodified-montmorillonite (OMMT) was investigated. The PP/OMMT nanocomposites containing different OMMT content (0.1-2.5 wt%) were prepared by a melt blending process using an internal mixer. The nucleation effect of OMMT was characterized by X-ray diffraction (XRD) and differential scanning calorimetry (DSC) techniques. XRD indicated that the PP nanocomposites loaded with less than 1.5 wt% OMMT formed an exfoliated structure. The XRD patterns also showed that the addition of OMMT did not affect the crystal structure of PP. DSC studies revealed that OMMT was able to nucleate PP. The crystallization temperatures of the PP/OMMT nanocomposites were higher than that of neat PP. DSC results also showed that when the OMMT content was 0.1 wt%, the crystallization temperatures of the nanocomposite was the highest. Mechanical property tests indicated that the tensile and impact strengths of the PP/OMMT nanocomposites were better than those of neat PP when the OMMT content was below 1.5 wt%.

Introduction

Polypropene (PP) is a thermoplastic polymer used in a wide variety of applications, including packaging, textiles (e.g. ropes, thermal underwear and carpets), agriculture, automotive components, and polymer banknotes. Owing to the fact that the resulting physical properties are strongly dependent on the morphology formed and the extent of crystallization, studies related to the crystallization process of polypropylene are of great importance in polymer processing. Properties of polypropylene were often improved by fillers.

Crystallization is a process in which the molten polymer is cooled below its melting temperature such that the crystalline order begins to re-establish. Crystallization occurs essentially in two stages, nucleation and crystal growth. Nucleation is a process in which the loose coiled polymer chains orient themselves into the proper conformation and align into a perfect three-dimensional pattern. The site at which the nucleation starts is called the nucleus. During crystal growth polymer chains orient to the three-dimensional pattern on the nucleus and mostly form a spherical crystal cluster which is called a spherulite. Nucleation of polypropylene may be homogeneous or heterogeneous. Homogeneous nucleation occurs at high super-cooling in pure polymers. Heterogeneous nucleation occurs at relatively low super-cooling, when a foreign body is present in the melt which reduces the free energy barrier for nucleation. These foreign bodyies are called nucleating agents or nucleators. A third kind of nucleation called self-nucleation also occurs in polymer crystallization which is caused due to the presence of partially melted polymer, which acts as a nucleus. Nucleators raise the crystallization temperature and reducing spherulite size. Smaller evenly sized crystals improve the physical properties and mechanical properties

Several nucleators for polypropylene have been studied. Nagarajan et al.[1] observed an effect of nucleating agents in a commercial grade isotactic polypropylene. The results showed that nucleation by DBS was concentration dependent and DBS was effective as a nucleator even at a concentration as low as 0.014% by mass and the crystallization temperature was linearly proportional to the DBS concentration. Medeiros et al.[2] investigated the influence of talc concentration on the nucleation efficiency of polypropylene. Analysis of DSC curves showed that at 5% talc content, a nucleating efficiency of 42% was obtained. Kerddonfag et al.[3] observed an effect of disodium terephthalate (Na_2-TPA) and calcium terephthalate (ca-TPA) from waste PET bottles used as nucleating agents for isotactic polypropylene. The results indicated that both TPA salts could be used as nucleating agents for isotactic polypropylene. Osowiecka et al.[4] compared the nucleating effect of organic (Millard 3988, ADK NA21) and non-organic (talc) mediums in polypropylene. The results proved that the organic nucleation mediums are more efficient than the non-organic one.

Montmorillonite is a kind of layered silicates that is attracting great attention owing to its outstanding reinforcement for most polymers and its potential in the preparation of polymer/layered silicate composites. According to Mingliang et al.[5] the addition of montmorillonite did not affect the crystal structure of the polypropylene. DSC results showed that the addition of montmorillonite leaded to the acceleration of the crystallization rate of polypropylene.

In the present study, the nucleation of PP by organomodified-montmorillonite (OMMT) was investigated. The PP/OMMT nanocomposites containing different OMMT content were prepared by a melt blending process using an internal mixer. The nucleation effect of OMMT was characterized by X-ray diffraction (XRD) and differential scanning calorimetry (DSC) techniques. Tensile and impact strength properties were also investigated.

Materials and Methods

Polypropylene (PP) used in this study was the homopolymer grade HP420J from HMC Polymers Co., Ltd (Bangkok, Thailand). The organomodified-montmorillonite (OMMT) used was Cloisite 30B from South Clay Products, Inc. (TeXas, USA) .

PP and OMMT were melt blended using an internal mixer at 190°C for 10 min, with the OMMT content of 0.10, 0.25, 0.50, 0.75, 1.00, 1.50, 2.00 and 2.50% by weight. Prior to melt blending, PP and OMMT were dried in an oven at 80 °C for 12 hr. The mixtures were then compression molded into sheets at 190 °C and 1000 psi for 10 min, followed by cooling to room temperature.

The crystal structure and the clay dispersion in the nanocomposites were determined by X-ray diffraction using a Bruker D8 diffractometer (40 kV, 40 mA) equipped with CuKα radiation (λ = 0.1542 nm) at room temperature. The XRD patterns were obtained for a 2θ range of 2-30° at a rate of 1°/min. The interplanar spacing for any set for parallel planes passing through the crystal lattice is call d spacing. Bragg's equation permits the calculation of the interplanar d spacing from the X-ray diffraction data.

$$n\lambda = 2d \sin\theta \qquad (1)$$

Where n is an integer, λ is the wavelength of the X-ray beam, d is the spacing between reflecting planes and θ is the angle of incidence of the beam with the sample.

The nucleating efficiency was tested using a Perkin-Elmer DSC by heating the sample to 210°C, then holding for 3 min and cooling at the rate of 10° C/min. The degree of crystallinity (X_c) was determined from DSC curves. The enthalpy of fusion of the polypropylene sample (ΔH_f) was determined and divided by the enthalpy of a completely crystalline (100%) (ΔH_f°) sample. A value of 209.0 J·g^{-1} was used for the 100% crystalline iPP

$$X_c\,(\%) = 100\ \frac{\Delta H_f}{\Delta H_f^0} \qquad (2)$$

Mechanical properties were also tested by a Lloyd tensile tester using a crosshead speed of 50 mm· min^{-1}. Notched Izod impact test was conducted on a GOTECH GT-7045-MD impact tester.

Results and Discussion

Figure 1 displays the XRD patterns in the 2θ range of 2-10° of the OMMT and the PP nanocomposites containing different amounts of OMMT. The OMMT shows two diffraction peaks, the first of width 2θ = 2-4˚ of maximum intensity at 2.75˚ and the second one of 2θ =4-6˚ of maximum intensity at 4.86˚, corresponding to a d-spacing of 32.055 Å and 18.152 Å,

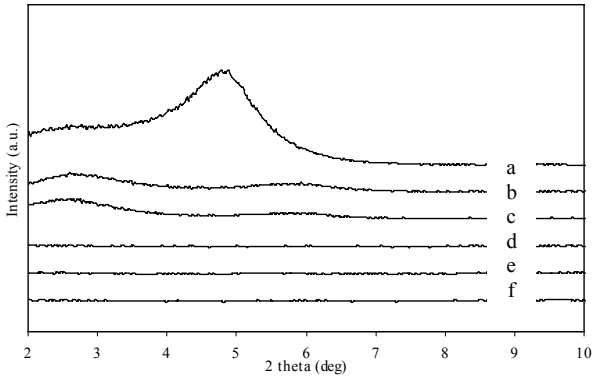

Figure 1. XRD patterns of OMMT (a), PP/2.5% OMMT(b), PP/1.5% OMMT(c), PP/1% OMMT (d), PP/0.5% OMMT (e), PP/0.1% OMMT (f)

respectively. It can be seen that the XRD patterns of the PP nanocomposites loaded with less than 1.5 wt% of OMMT have no diffraction peak which indicates that these nanocomposites formed an exfoliated structure. However, higher amount of the OMMT (1.5 and 2.5 wt%) in the nanocomposites resulted in less efficiency exfoliation of the nanoclay.

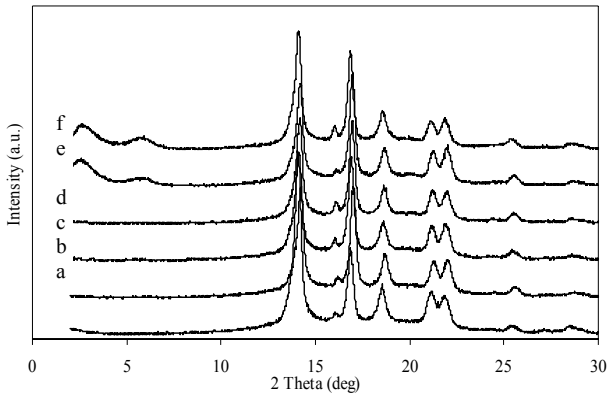

Figure 2. XRD patterns of PP(a), PP/0.1% OMMT(b), PP/0.5% OMMT(c), PP/1% OMMT (d), PP/1.5% OMMT (e), PP/2.5% OMMT (f)

The XRD patterns of neat PP and the PP/OMMT nanocomposites in the 2θ range of 2-30° are shown in Figure 2. It can be seen that there is no distinct difference between PP and the PP nanocomposites, both of them are α-phase crystallite. This indicates that the addition of OMMT did not affect the crystal structure of the PP .

The crystallization behavior of neat PP and the nanocomposites are shown in Table 1. The data in Table 1 show that the degree of crystallinity (X_c) of PP is enhanced by the addition of OMMT. The crystallization temperature of neat PP is 112.31 ˚C and the T_c of PP increase significantly with the addition of OMMT.

This indicates the nucleating effect of the OMMT in the crystallization of PP. DSC results also show that when the OMMT content was 0.1 wt%, the crystallization temperature of the nanocomposite was the highest.

Table 1. Crystallization temperature and degree of crystallinity of PP and the PP/OMMT nanocomposites

Sample	Crystallization temperature (˚C)	Degree of crystallinity (%)
PP	112.31	33.9
PP/0.1% OMMT	117.82	42.1
PP/0.5% OMMT	114.79	42.8
PP/1% OMMT	114.33	39.1
PP/1.5% OMMT	114.56	41.0
PP/2.5% OMMT	115.41	39.1

The mechanical properties of the PP/OMMT nanocomposites are measured and summarized in Table 2, Figures 3 and 4. When the OMMT content is below 1.5 wt%, both the tensile strengths and impact strengths of the PP nanocomposites were better than those of neat PP. The tensile strength increased from 31.50 MPa for neat PP to 33.56 MPa for the PP/OMMT nanocomposites while the impact strength increased from 1.812 kJ/m^2 for PP to 2.07 kJ/m^2 for the nanocomposites. However, when the OMMT content is 2.5%, both the tensile strength and impact strength decreased. This may be due to the less uniform dispersion of the OMMT in the PP matrix.

Table 2. Tensile strength and impact strength of PP and PP/OMMT

Sample	Tensile strength (MPa)	Impact strength (KJ/m^2)
PP	31.50	1.812
PP/0.1% OMMT	33.56	1.817
PP/0.5% OMMT	33.47	2.070
PP/1% OMMT	33.10	2.028
PP/1.5% OMMT	31.25	1.832
PP/2.5% OMMT	30.75	1.592

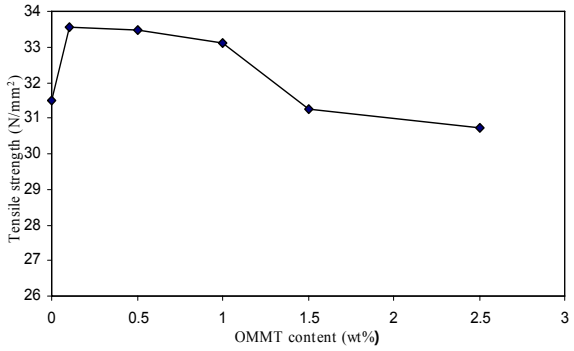

Figure 3. Tensile strength of PP and PP/OMMT nanocomposites.

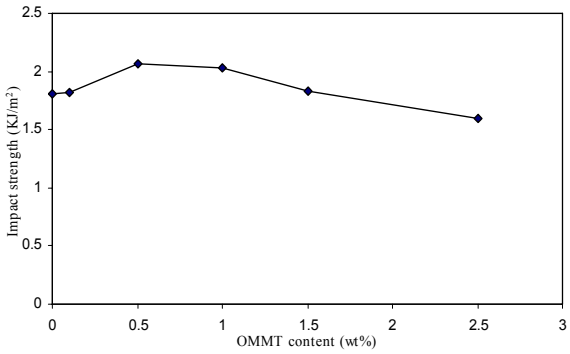

Figure 4. Impact strength of PP and PP/OMMT nanocomposites.

Conclusions

The X-ray diffraction patterns of PP and the PP/OMMT nanocomposites showed that the PP nanocomposites loaded with less than 1.5 wt% OMMT formed an exfoliated structure. The XRD patterns also indicated that the addition of OMMT did not affect the crystal structure of PP. DSC studies revealed that OMMT was able to nucleate PP resulting in a higher crystallization temperature, higher degree of crystallinity, and better mechanical properties.

Acknowledgements

The authors gratefully acknowledge Science and Technology Innovation Support Grant and HMC Polymers Co., Ltd for financial support. We are also thankful to National Metal and Materials Technology Center, Metallurgy and Materials Science Research Institute, and the Department of Materials Science, Faculty of Science, Chulalongkorn University for instrumental and material support .

References

[1] K. Nagarajan, K. Levon, and A.S. Myerson, Nucleating Agents in Polypropylene, *Journal of Thermal Analysis and Calorimetry*. **59** (2000), pp. 497-508.

[2] E.S. Medeiros, R.S. Tocchetto, L.H. Carvalho, I.M.G. Santos, and A.G. Souza, Nucleating Effect and Dynamic Crystallization of a Poly(propylene)/Talc System, *Journal of Thermal Analysis and Calorimetry*. **66** (2001), pp. 523-531.

[3] N. Kerddonfag, O. Saravari, W. Chinsirikul, and P. Supaphol, Nucleation of Isotactic Polypropylene by Nucleating agents Derived from Waste PET Bottles, *Asean Workshop on Polymer Processing,* National University of Singapore, Singapore, April 4-6. (2002).

[4] B. Osowiecka, A. Bukowski, J. Zielinski, W. Ciesinska, and T. Zielinski, Investigations on Nucleated Polypropylene with Using Thermal Analysis Method, *Journal of Thermal Analysis and Calorimetry,* **74** (2003), pp. 673-679.

[5] G. Mingliang, J. Demin, and X. Weibing, Study on the Crystallization Properties of Polypropylene/Montmorillonite Composites, *Polymer-Plastics Technology and Engineering,* **46 (**2007), pp. 985- 990.

Synthesis of deca- and dodecasilsesquioxana epoxides as nanobuilding blocks VIA metathesis and heck coupling

C. Samthong,[1*] J. H. Jung,[2] A. Somwangthanaroj[1] and R.M. Laine[2, 3]

[1] Department of Chemical Engineering, Faculty of Engineering, Chulalongkorn University, Bangkok, Thailand
[2] Department of Materials Science and Engineering, University of Michigan, Ann Arbor, USA
[3] Macromolecular Science and Engineering Center, University of Michigan, Ann Arbor, USA

[*] E-mail: s.chavakorn@hotmail.com

Abstract: Our work focuses on the preparation of new epoxy-functionalized decameric and dodecameric silsesquioxanes (SQs) with well-defined architectures as three-dimensional organic/inorganic nanobuilding blocks that can be used to process epoxy nanocomposites. The synthesis starts with the cage rearrangement of polyvinylsilsesquioxane $(vinylSiO_{1.5})_x$ using tetrabutylammonium fluoride as catalyst to obtain deca- and dodecavinylSQs. These SQs were reacted with *p*-bromostyrene via cross-metathesis using a first generation Grubbs catalyst to produce deca/dodeca(*p*-bromostyrenyl)SQs, and then further functionalized via Heck coupling with 4-vinyl-1-cyclohexene 1,2-epoxide to yield deca/dodeca (cyclohexylepoxidevinylstyrenyl)SQs. The chemical structures were characterized by FTIR, MALDI-ToF and ^{1}H NMR studies. The preparation of Heck coupling product did not work well as confirmed by both GPC and FTIR results; however, from the ^{1}H NMR data we find one or two arms of cross-metathesis product reacted with cyclohexene epoxide. We conclude that the incomplete Heck reaction comes from the low reactivity of cyclohexene epoxide compared to functionalized styrene compounds.

Introduction

Silsesquioxanes (SQs) are an attractive class of three-dimensional organic/inorganic hybrid compounds that have been used to prepare crosslinked epoxy [1-7] and polyimide composites [8,9] because of their intrinsic properties such as monodispersed size, excellent thermal stabilities, and controlled functionalities. SQs have silicon-oxygen cage cores with $(SiO_{1.5})_n$ where n = 8, 10, 12 covered externally by pendant organic functional substituents (R). The fully-condensed SQs, Q_x $[(ROSiO_{1.5})_x]$ and T_x $[(RSiO_{1.5})_n]$, have been used in numerous applications. Generally these SQs have highly symmetrical silica cores with diameters of 0.5-0.7 nm [10] and diverse numbers of reactive organic groups at vertices such as vinyl [10], epoxy [1-5], amine [6-9, 11], arylhalide [12,13] and so forth.

OctavinylSQ [OVS, $(vinylSiO_{1.5})_8$] is one of the more interesting functionalized SQs that can be synthesized via hydrolytic condensation of vinyltrichlorosilane ($vinylSiCl_3$) in ethanol/water solvents [14]. During the synthesis, the polymeric polyvinylSQ (PVS) is actually obtained as the major product in 50-60% yields but is highly insoluble and to date has been a useless by-product. To increase the value of PVS, we are interested in transforming PVS to decavinylSQ [dVS, $(vinylSiO_{1.5})_{10}$] and dodecavinylSQ [DVS, $(vinylSiO_{1.5})_{12}$], as shown in Figure 1. In comparison with OVS, dVS and DVS are less well-known because they are very difficult to prepare in high yields. In this work, the synthetic route to dVS and DVS from PVS was promoted by fluoride -catalyzed cage rearrangements.

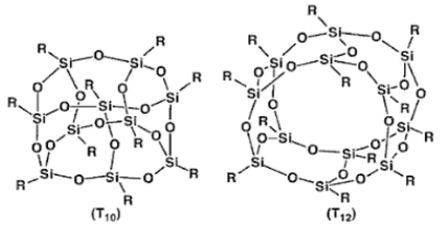

Figure 1. Structures of decasilsesquioxane (T_{10}) and dodecasilsesquioxane (T_{12}) [15].

Furthermore, we made an effort to synthesize the epoxy-functionalized decameric/dodecameric SQs deca/dodeca(cyclohexylepoxidevinylstyrenyl)SQs (dCSS/DCSS) as an approach to nanocomposite hybrid materials. Our idea was motivated by research of Sulaiman et al. [16] targeting the synthesis of perfectly symmetrical three-dimensional star molecules using OVS cores as starting points.

Various types of bases, such as sodium hydroxide [17] and tetrabutylammonium fluoride (TBAF) [18, 19], have been explored in efforts to promote cage rearrangement; however, we find that TBAF readily transforms PVS to dVS and DVS at room temperature in THF. Thereafter we are able functionalize them via cross-metathesis with *p*-bromostyrene reaction to obtain deca/dodeca(*p*-bromostrenyl)SQs (dBrSS/DBrSS). In turn, these compounds were further functionalized via Heck coupling with 4-vinyl-1-cyclohexene 1,2-epoxide to produce dCSS/DCSS. The synthetic approach is presented in Figure 2.

Materials and Methods

Materials. PVS is a by-product from the OVS synthesis according to the previous literature [14,16]. Dichloromethane was purified by distillation under nitrogen atmosphere and dried over CaH_2 prior used. 1,4-dioxane was refluxed over sodium potassium alloy under nitrogen atmosphere and distilled before used.

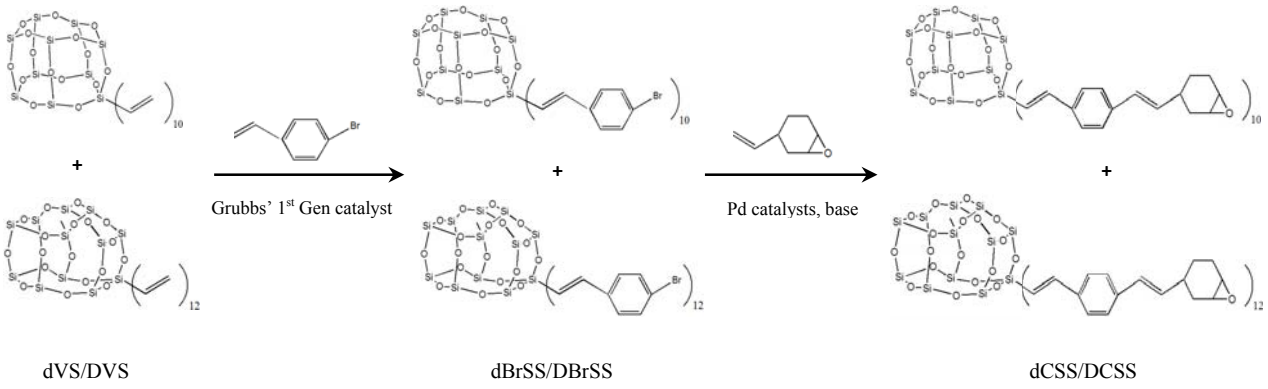

Figure 2. Synthesis of dBrSS/DBrSS and dCSS/DCSS.

Tetrabutylammonium fluoride (1.0 M TBAF solution in THF; water *ca*. 5 wt %) was purchased from Aldrich. All other chemicals were purchased from Aldrich or Fisher and use without purification.

Synthesis of dVS/DVS. To a dry 50 mL Schlenk flask under N_2 was added 1.00 g of PVS. THF (20 mL) was then added by syringe, followed by TBAF (118 μL,5 mol %). The reaction mixture was stirred at room temperature for 72 h and then transferred into 50 mL dry round-bottom flask containing 2.50 g of $CaCl_2$ to kill the remaining fluoride ion. The solution was stirred for 2 h, filtered and dried vacuum the filtrate for 3 h. The 0.95 g of white material was collected to give a yield of 63% based on DVS. FTIR (KBr, cm^{-1}): 3062-2958 (ν_{C-H}), 1602 ($\nu_{C=C}$), 1225-969 ($\nu_{Si-O-Si}$). MALDI-ToF (Ag^+ adduct, relative percentage): *m/z* = 896.3 (dVS, 82), 1056.7 (DVS, 100).

Synthesis of dBrSS/DBrSS. To a dry 50 mL Schlenk flask under continuous flow of nitrogen gas was added 1.00 g (12.6 mmol –CH=CH_2) of dVS/DVS and 104 mg (0.126 mmol, 1.0 mol %) of first generation Grubbs catalyst. Dry CH_2Cl_2 (15 mL) was added by syringe, followed by *p*-bromostyrene (25.0 mmol, 3.3 mL). The mixture was stirred at room temperature for 72 h and then precipitated into 150 mL of cold methanol. The solution was filtered and dried the residue in vacuo for 3 h, giving 2.50 g of products with an 84% yield based on DBrSS. FTIR (KBr, cm^{-1}): 3100-2840 (ν_{C-H}), 1604 ($\nu_{C=C}$), 1247-988 ($\nu_{Si-O-Si}$), 1008 (δ_{Ar-H}).

Synthesis of dCSS/DCSS. To a dry 50 mL Schlenk flask under N_2 was added 0.50 g (2.14 mmol–Br) of dBrSS/DBrSS, 14 mg (0.028 mmol) of Pd[P(*t*-Bu)$_3$]$_2$ and 13 mg (0.014 mmol) of $Pd_2(dba)_3$. 1,4-dioxane (10 mL) was then added by syringe, followed by NCy_2Me (4.16 mmol, 0.95 mL) and 4-vinyl-1-cyclohexene 1,2-epoxide (10.4 mmol, 1.4 mL). The reaction was stirred for 5 days and worked-up by filtering through Celite to remove the palladium catalysts. The solution was precipitated into 150 mL of cold methanol, filtered and redissolved in 10 mL of THF. The solution was then filtered though Celite and precipitate in 150 mL of cold methanol again. The residue was dried in vacuo for 3 h to remove remaining solvent. FTIR (KBr, cm^{-1}): 1605 ($\nu_{C=C}$), 1238-989 ($\nu_{Si-O-Si}$), 1009 (δ_{Ar-H}).

Analytical Methods. Fourier transform infrared spectra (FTIR) were conducted on a Perkin-Elmer SPECTRUM-2000 FTIR spectrometer. Infrared spectroscopic measurements were performed in the range of 4000-400 cm^{-1} with a resolution of ±4.0 cm^{-1}. Optical-grade, random cuttings of crystalline potassium bromide (KBr, International Crystal Laboratories, Garfield, NJ) was used as background. The analysis sample (5 mg) and KBr crystal (400 mg) were ground together using the alumina mortar and pestle. The ground powder was loaded into the sample holder and sliced off with glass plate to give a smooth surface. The holder was placed into a sample chamber and the spectrum was recorded under the continuous flow of dry nitrogen gas for at least 10 min before data collection to ensure the minima oxidation or degradation of sample. At least 100 scans were collected for each spectrum.

Matrix-assisted laser-desorption/time of flight mass spectra (MALDI-ToF) was obtained on a Micromass TofSpec-2E instrument equipped with a 337 nm-nitrogen laser in positive-ion reflectron mode using poly(ethylene glycol) as the calibration standard, dithranol as the matrix, and $AgNO_3$ as ion source. Samples were prepared by mixing solutions of 5 parts ditharol (10 mg/mL in THF), 5 parts sample (1 mg/mL in THF), and 1 part $AgNO_3$ (2.5 mg/mL in water), and blotting the mixture onto the target plate.

All ^1H NMR data were done in deuterated acetone (δ_H 2.05 ppm) and recorded on a Varian INOVA spectrometer at 400 MHz using a 6000 Hz spectral width, a relaxation delay of 3.5 s, 30k data points, a pulse width of 38°, and tetramethylsilane (TMS, 0.00 ppm) as the internal reference.

Gel permeation chromatographic (GPC) analyses were run on a Water 440 system equipped with Waters Styragel columns (7.8 x 300, HT 0.5, 2, 3, 4) with RI detection using Waters refractometer and THF as solvent, at a flow rate of 1.0 mL/min. The system was calibrated using polystyrene standards and toluene as a reference.

Results and Discussion

Synthesis Methods. The first step is cage rearrangement of PVS using TBAF containing 5% water as fluoride ion source. The mechanism is

unknown but seems to involve rapid cleavage and reformation of the Si-O-Si in SQ cores. This reaction is reversible and when it reaches the equilibrium, the cage fragmenats reassemble to form higher molecular weight silsesquioxanes such as T_{10} and T_{12} species.

Cross-metathesis reactions of dVS/DVS with *p*-bromostyrene were run in CH_2Cl_2 with a first generation Grubbs catalyst (72 h) produces dBrSS/DBrSS. This reaction is the reversible reaction with ethylene gas as by-product. Hence, by flowing nitrogen above the reaction to remove ethylene gas, the conversion of dVS/DVS reaches >99%.

Finally, the cross-metathesis products were then further functionalized via Heck coupling with 4-vinyl-1-cyclohexene 1,2-epoxide in 1,4-dioxane using palladium complexes as catalysts and using base for regenerating catalysts to form dCSS/DCSS. The Heck coupling was carried out at room temperature under nitrogen using a 2:1 molar mixture of $Pd[P(t\text{-}Bu_3)]_2$ and $Pd_2(dba)_3$ as catalysts and using NCy_2Me as base [20].

Characterization of dVS/DVS, dBrSS/DBrSS, and dCSS/DCSS. *MALDI-ToF Data*. Figure 3 illustrates the MALDI-ToF spectra for the products from cage rearrangement of PVS. It shows the two parent peaks of dVS and DVS at *m/z* equal to 896.3 and 1056.7 respectively, and traces of higher molecular weight vinyl-substituted cubes, e.g. T_{14}^V, T_{20}^V, T_{22}^V and T_{24}^V. Although we were not be able to collect the MALDI-ToF for dBrSS/DBrSS and dCSS/DCSS the ^{1}H NMR spectra confirm their chemical structures.

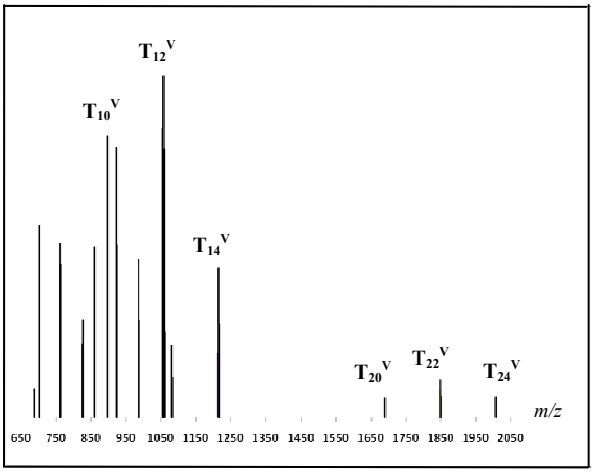

Figure 3. MALDI-ToF spectra for the products (Ag^+ ion) from cage rearrangement of PVS.

Gel permeation chromatographic (GPCs) analyses. Figure 4 compares the retention times of products from each reaction step. GPC data of (**a**) shows a major sharp peak and small broad peak **I** at *ca.* 33.3 and 31.5 min which expected that they are the mixture of deca/dodecavinylsilsesquioxanes (dVS/DVS) and T_{14}^V, and traces of T_{20}^V, T_{22}^V and T_{24}^V, respectively. After the cross-metathesis, the major peak (**a**) shifts to *ca.* 30.9 indicating that we obtained higher molecular weight products that we suggest are *p*-bromostyrenyl-substituted compounds. The GPC of Heck coupling product (**c**) does not differ from (**b**) that much. The maximum peak of (**c**) is at *ca.* 30.6 so the Heck coupling between dBrSS/DBrSS and 4-cyclohexene 1,2-epoxide is not particularly effective.

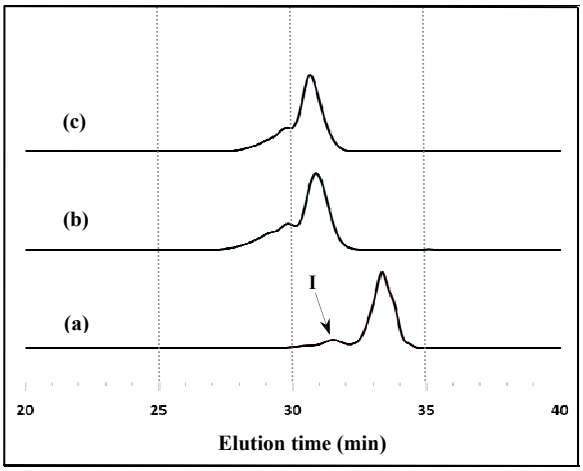

Figure 4. GPC results of the products from (a) cage rearrangement, (b) metathesis, (c) Heck coupling.

Fourier transform infrared spectrometry (FTIR). FTIR spectra are used to identify the functional groups on the deca- and dodecasilsesquioxanes and presented in Figure 5. dVS/DVS shows a weak peak at ~1604 cm^{-1} and a sharp strong peak at ~1125 cm^{-1}, which are characteristics of C=C bond and symmetric Si-O-Si stretching vibration, respectively. The symmetric and asymmetric C-H bands from the vinyl groups are observed at 2958-3062 cm^{-1} region. The peaks at 1400-1600 cm^{-1} and ~1008 cm^{-1} represent the aromatic C=C stretching bands and aromatic C-H in-plane bending, respectively, which indicate that there are *p*-bromostyrenyl arms on the SQs after cross-metathesis. However, no asymmetric stretching peaks are seen at 810-950 cm^{-1} that would suggest epoxy groups similar to the GPC results. The characteristic cage-structured νSi-O-Si vibration displays a similar intensity and position in the spectra for all compounds, which implies that the SQ cages remain intact during the reactions.

^{1}H NMR. ^{1}H NMR data for dBrSS/DBrSS and dCSS/DCSS are given in Figure 6. The chemical shift at 7.492 ppm is assigned to the aromatic protons. This spectrum confirms the presence of bromostyrenyl arms on the SQs; however, we cannot identify the exact number of these functional groups because we cannot separate dVS and DVS from each other. The Heck coupling product shows chemical shifts at 3.236 ppm which represent the protons on epoxide. However, the integration ratio between protons on epoxide and protons on aromatic ring is quite small (~ 1:19) which evidences the incomplete Heck coupling of dBrSS/DBrSS.

It appears that cyclohexene epoxide is relatively unreactive towards Heck cross-coupling compared with functionalized styrene compounds used in the previous paper [16].

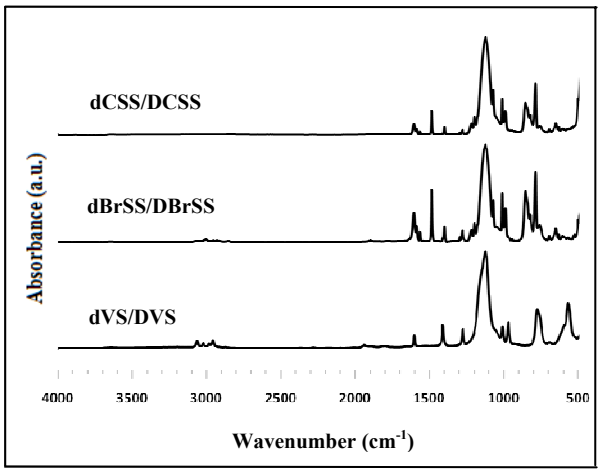

Figure 5. FTIR spectra of (a) dVS/DVS, (b) dBrSS/DBrSS, (c) dCSS/DCSS.

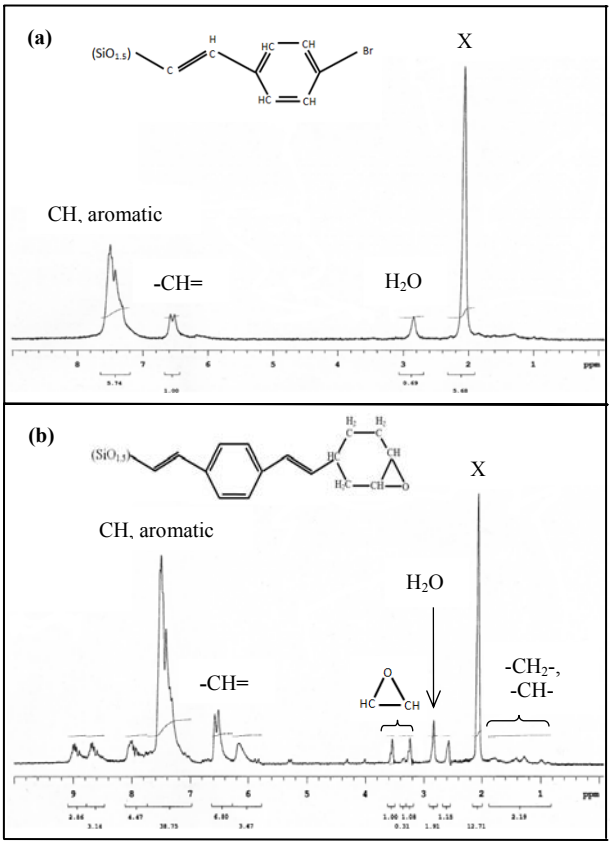

Figure 6. ^{1}H NMR spectra of (a) dBrSS/DBrSS, (b) dCSS/DCSS in Acetone (symbol X in the spectra).

Conclusions

The epoxy-functionalized decameric and dodecameric silsesquioxanes were prepared using cage rearrangement, cross-metathesis and Heck coupling for applying in organic/inorganic hybrid nanocomposites. The products dVS/DVS and dBrSS/DBrSS were characterized by FTIR, MALDI-ToF and ^{1}H NMR. However, dCSS/DCSS was difficult to produce via Heck coupling of dBrSS/DBrSS because of the low reactivity cyclohexene epoxide.

Acknowledgements

C. S. would like to thank department of Chemical Engineering, Chulalongkorn University for financial support. J.H. Jung and R.M. Laine thank the Office of Naval Research for partial support of this work.

References

[1] A. Lee and J.D. Lichtenhan, *Macromolecules* **31**(1998), pp. 4970-4974.
[2] J. Choi, J. Harcup, A.F. Yee, Q. Zhu and R.M. Laine, *J. Am. Chem. Soc*. **123**(2001), pp. 11420-11430.
[3] J. Choi, A.F. Yee and R.M. Laine, *Macromolecules* **36**(2003), pp. 5666-5682.
[4] J.C. Huang, Y. Xiao, K.Y. Mya, X. Liu, C.B. He, J. Dai and Y.P. Siow, *J. Mater. Chem.* **14**(2004), pp. 2858-2863.
[5] L.H. Lee and W.C. Chen, *Polymer*, **46**(2005), pp. 2163-2174.
[6] Y.J. Lee, J.M Huang, S.W. Kao, J.S. Lu and F.C. Chang, *Polymer* **46**(2005), pp. 173-181.
[7] K. Takahashi, S. Sulaiman, J.M. Katzenstein, S. Snoblen and R.M. Laine, *Aust. J. Chem*. **59**(2006), pp. 564-570.
[8] J. Choi, R. Tamaki, S.G. Kim and R.M. Laine, *Chem. Mater.* **15**(2003), pp. 3365-3375.
[9] J.C. Huang, C.B. He, Y. Xiao, K.Y. Mya, J. Dai and Y.P. Siow, *Polymer* **44**(2003), pp. 4491-4499.
[10] C. Zhang, F. Babonneau, C. Bonhomme, R.M. Laine, C.L. Soles, H.A. Hristov and A.F. Yee, *J. Am. Chem. Soc*. **120**(1998), pp. 8380-8391.
[11] S.G. Kim, J. Choi, R. Tamaki and R.M. Laine, *Polymer* **46**(2005), pp. 4514-4524.
[12] C.M. Brick, Y. Ouchi, Y. Chujo and R.M. Laine, *Macromolecules* **38**(2005), pp.4661-4665.
[13] M.F. Roll, M.Z. Asuncion, J. Kampf and R.M. Laine, *ACS Nano* **2**(2008), pp. 320-326.
[14] P.G. Harrison and C. Hall, *Main Group Met. Chem.* **20**(1997), pp. 515-529.
[15] R.H. Baney, M. Itoh, A. Sakakibara and T. Suzuki, *Chem. Rev.* **95**(1995), pp. 1409-1430.
[16] S. Sulaiman, A. Bhaskar, J. Zhang, R. Guda, T. Goodson and R.M. Laine, *Chem. Mater.* **20**(2008), pp. 5563-5573.
[17] E. Rikowski and H.C. Marsmann, *Polyhedron* **16**(1997), pp. 3357-3361.
[18] A.R. Bassindale, H. Chen, Z. Liu, I.A. MacKinnon, D.J. Parker, P.G. Taylor, Y. Yang, M.E. Light, P.N. Horton and M.B. Hursthouse, *J. Organomet. Chem.* **689**(2004), pp. 3287-3300.
[19] Z.H. Liu, A.R. Bassindale and P.G. Taylor, *Chem. Res. Chin. Univ.* **20**(2004), pp. 433-436.
[20] A.F. Littke and G.C. Fu, *J. Am. Chem. Soc.* **123**(2001), pp. 6989-7000.

Preparation of hydrophobic chitosan using complexation method for PLA/chitosan blend

P. Noknoi [1]*, K. Srikulkit [1,2] and K.Siralertmukul [3]

[1]Department of Materials Science, Faculty of Science, Chulalongkorn University, Bangkok, Thailand

[2]National Center of Excellence for Petroleum,Petrochemicals and Advanced Materials,Chulalongkorn University, Bangkok, Thailand

[3]Metallurgy and Materials Science Research Institute Chulalongkorn University, Bangkok, Thailand

*E-mail: phiangrawee@hotmail.com

Abstract: In this study, dioctyl sulfosuccinate-chitosan complex was prepared by a mechanical mixing of aqueous chitosan with sodium dioctyl sulfosuccinate. As a result, hydrophobic chitosan was achieved. Characterizations of the complex were carried out including XRD, DSC, TGA, and FT-IR in order to follow changes in the chitosan structure. Thus produced chitosan complex is hydrophobic and anticipated to be miscible with PLA. Melt blending of PLA and hydrophobic chitosan was then conducted using twin screw extruder in order to obtain flexible PLA. Characterization techniques including TGA, DSC and FT-IR were employed to investigate the structure of the polymer blend. The melting temperature of the PLA component in the blend was found to slightly decrease with increasing chitosan content. FTIR spectra show that the intensity ratio of the crystalline peak to that of the amorphous peak for blend is found to decrease from that of the pure PLA, indicating miscibility between chitosan and PLA.

1. Introduction

Poly(lactic acid) (PLA) is an aliphatic polyester. It is a biodegradable and compostable thermoplastic derived from renewable resources, such as starch and sugar cane [1]. PLA can be also synthesized by condensation polymerization of the lactic acid monomers or by ring opening polymerization of lactide monomer [2]. PLA have resulted in expanded use for consumer goods and packaging application. Because PLA is compostable and derived from renewable resources [1] but it is a high cost so polymer blend is an attractive route for producing new polymeric materials. Chemical and physical properties are very much dependent on state of mix and miscibility between the constituent components as well as phase morphology of the resulting blends [3]. So improve the chemical and physical properties of PLA by blending with chitosan.

Chitosan, a biodegradable copolymer of glucosamine and derived from renewable resources and low cost [4] is produce from deacetylation of chitin with a degree of deacetylation over 75% [5]. Due to the abundant of hydrophilic functional groups, chitosan is not compatible with thermoplastic polymers. In order to solve this problem, some chemical modifications to introduce hydrophobic moiety to chitosan such as hexanoylation [6]. As a consequence, the routes for blending of PLA with hydrophobic chitosan are possible [5-8].

In this study, preparation of hydrophobic chitosan using complexation method was investigated and the obtained hydrophobic chitosan was employed for PLA/chitosan blend. PLA/chitosan blend were prepared by melt blending technique using by twin screw extruder. The effect of blend composition on thermal properties, compatability and fine structure was presented .

2. Materials and Methods

2.1. Materials

Chitosan flake (MW=800,000) was bought Ebase (Thailand Co.Ltd) and it was pulverized into powder having the particle size about 0.5 mm prior to use. Its viscosity (η) measured by Brookfield viscometer (at 25^{o}C, speed 100 rpm) was found to be 138.6cps. Methanol was purchased from SK chemicals Ulsan, Korea. Toluene and acetic acid were purchased from Labscan Asia Co. Ltd, Thailand. Poly(lactic acid) under trade name of NatureWorks with melt index of 4-8g/10min was bought from a local supplier. Sodium dioctyl sulfosuccinate, an ionic surfactant, was commercial grade and kindly provided by Worldtex Commercial, Co. Ltd.

2.2 Methods

2.2.1 Preparation of dioctyl sulfosuccinate-chitosan complex

5 g (1% (w/v)) chitosan(CTS) in 500 ml of 1% (v/v) acetic acid solution was prepared. Then, 5 g of sodium dioctyl sulfosuccinate (DSS) equivalent to 1:1 wt ratio was slowly added under continuous homogenization for 30 minutes and left standing overnight. The insoluble DSS-CTS complex was filtrated and dried freely in open air. In a similar manner, DSS-CTS complexes of 3 : 1 and 5 : 1 DSS to CTS ratios were prepared.

2.2.2 Preparation of PLA/DSS-CTS blend

Blends of PLA with DSS-CTS were prepared by twin-screw extruder set processing temperatures of barrel zone 1, 2, 3, 4, and 5 at 130, 150, 155, 160, 165 ^{o}C, respectively and using screw speed of 100 rpm. PLA/DSS-CTS blends having the weight ratios of

PLA to DSS-CTS of 100/0, 95/5, 90/10, 85/15 and 80/20) were prepared. In this study, and fixed amount of 2 wt% heat stabilizer was added. The obtained blends were kept in a desiccator prior to characterizations.

2.2.3 Characterization techniques

FT-IR spectroscopy was employed to characterize the functional groups of chitosan, DSS-CTS, PLA and PLA/DSS-CTS blend. FTIR spectra measured on KBR pellet samples were recorded on Fourier Transform Infrared Spectrometer, PerkinElmer with 32 scans at a resolution of 4 cm^{-1}.

Thermal behavior of virgin chitosan, DSS-CTS complex, as-received PLA, and PLA/DSS-CTS blend was evaluated by TGA technique (METTER TOA/SDTA 851e). A heating rate of $10^oC\ min^{-1}$ under nitrogen atmosphere over the temperature range of 30–750°C was set. Sample weight of 5-10 mg was employed for this measurement. DSC analysis was carried out on Perkin Elmer PYRIS Diamond differential scanning calorimeter (DSC). The specimens were pack in aluminium pans, and heat from 50 to 220°C (Run 1) at a heating rate of 20°C/min under a nitrogen atmosphere and held for 3 min to destroy any residual nuclei, then they were cooled to 50°C at a rate of 20°C/min. The specimen were reheated to 220°C at a heating rate of 20°C/min (Run 2).

X-ray diffraction data was used to observe the crystal structure of the chitosan and DSS-CTS complex. XRD patterns were obtained on Philips PW 3710 X-ray diffractometer. The X-ray source was Cu Kα with a voltage of 40 kv and a current of 30 mv. The measurement was in the scanning range of 5–40^0 at a scanning speed of 50 s^{-1}.

3. Results and Discussion

3.1 Characterizations of DSS modified Chitosan

Thermal thermograms of virgin chitosan, DSS 3 : CTS 1, and DSS 5 : CTS 1 are presented in Fig. 1. As found, virgin chitosan exhibits the degradation temperature (Td) of 301°C. In case of DSS-CTS complexes, the corresponding Td exhibits relatively lower at 236 °C and 244 °C for DSS 3 : CTS 1 and DSS 5 : CTS 1. For virgin chitosan, loss of bound moisture is obviously observed due to hydrophilicity characteristic of chitosan. This phenomenon completely disappears in case of DSS-CTS complexes, indicating an increased hydrophobicity of the complexes. In addition, the decrease in Td is associated with the interuption of intermolecualr hydrogen bonding occuring during complexation of chitosan with dioctyl suffosuccinate.

XRD patterns of virgin chitosan and DSS modified chitosans are illustrated in Fig. 2. The XRD pattern of virgin chitosan exhibits broad diffraction peaks at 2θ = 10.0° and 19 ° which are typical fingerprint of semi-crystalline chitosan (Bangyekan et al., 2006). For the modified chitosan, peak intensity at 2θ = 19 ° notably decreases, indicating that the degree of chitosan crystallinity was partially destroyed due to the interruption of hydrogen (Zong et al., 2000).

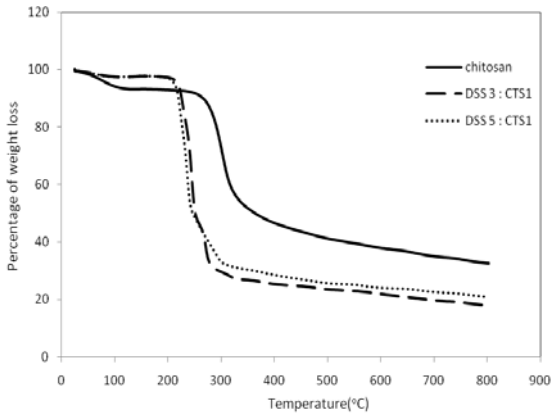

Figure 1. TGA curves for pure chitosan, DSS 3 : CTS 1 and DSS 5 : CTS 1. The heating rate used was $10^oC\ min^{-1}$.

Fig. 3 shows the DSC curves of pure chitosan, DSS 3 : CTS 1, and DSS 5 : CTS 1. DSC curve of chitosan shows the endothermic peak between 80 and 130°C, corresponding to the loss of water. On the other hand, this peak completely disappears from the thermograms of DSS-CTS complexes due to the absence of water. It could be concluded that DSS modified chitosan possesses the hydrophobic characteristic.

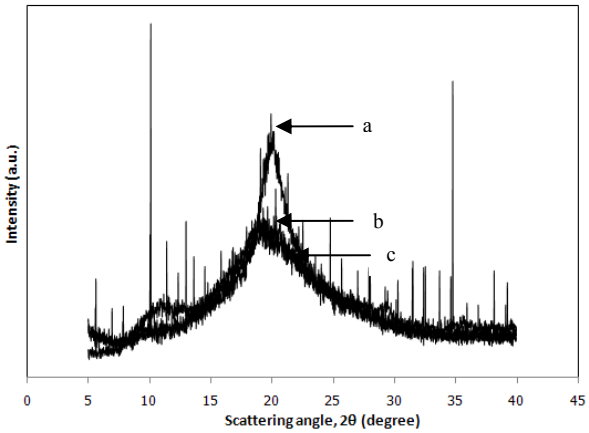

Figure 2. XRD patterns for pure pure chitosan and modified chitosan with surfactant in difference compositions.(a) pure chitosan; (b) DSS 3 : CTS 1; (c) DSS 5 : CTS 1

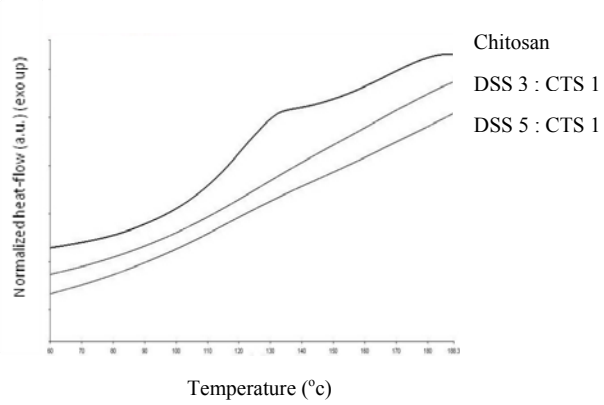

Figure 3. First heating thermograms for pure chitosan, DSS 3 : CTS 1, and DSS 5 : CTS 1. The heating rate used was 10°C min^{-1}.

FTIR spectroscopy was used to characterize the polymer-polymer interaction. Fig. 4 shows the FTIR spectrum of pure chitosan, DSS 3 : CTS 1, and DSS 5 : CTS 1. The chitosan amine band slightly shifted from 1655 cm^{-1} to 1737 cm^{-1}, arising from the interaction between chitosan NH_3^+ group and DSS-SO_3^- group. The broad absorption band in a region of 3286 to 3762 cm^{-1} corresponding to OH band decreases in the intensity with an increase in DSS content, further confirming changes in the property of chitosan from hydrophilicity to hydrophobicity.

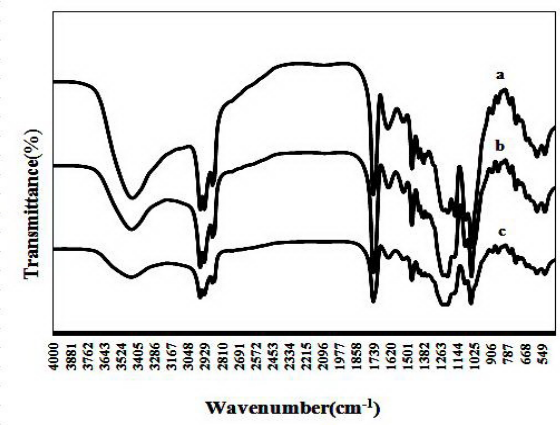

Figure 4. FTIR spectra of pure chitosan and modified chitosan with surfactant in difference compositions**.**(a) pure chitosan; (b) DSS 3 : CTS 1; (c) DSS 5 : CTS 1.

3.2 Characterizations of PLA/DSS-CTS blend

TGA thermograms of pure PLA and PLA/DSS-CTS blends (PLA/DSS-CTS 95/5, PLA/DSS-CTS 90/10, PLA/DSS-CTS 85/15 and PLA/DSS-CTS 80/20) are shown in Fig. 5. According to TGA curves, pure PLA begins to degrade at 380°C. PLA/ DSS-CTS 95/5 exhibits degradation profile similar to pure PLA. While other PLA/DSS-CTS blends exhibit two degradation steps (PLA/ DSS-CTS 90/10 at 265°C and 355°C, PLA/ DSS-CTS 85/15 at 240°C and 342°C, PLA/ DSS-CTS 80/20 at 238 °C and 341 °C). For blends, their degradation temperature smaller than those of pure components but PLA/ DSS-CTS 95/5 exhibited only one degradation peak at the same temperature of PLA.

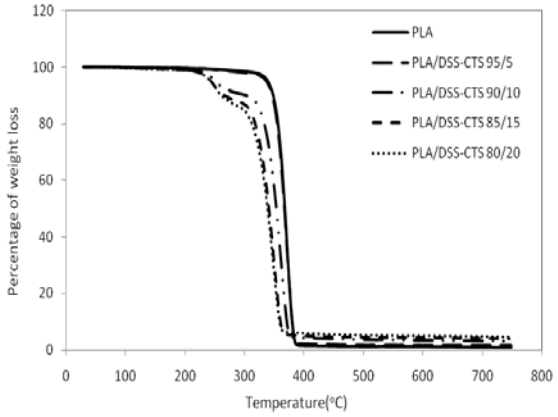

Figure 5. TGA curves for pure PLA and blends of PLA with chitosan (PLA/DSS-CTS 95/5, PLA/ DSS-CTS 90/10, PLA/ DSS-CTS 85/15 and PLA/ DSS-CTS 80/20). The heating rate used was 10°C min^{-1}.

Fig. 6 shows the DSC curves of pure PLA and blends of PLA with chitosan (PLA/DSS-CTS 95/5, PLA/ DSS-CTS 90/10, PLA/ DSS-CTS 85/15 and PLA/ DSS-CTS 80/20). In the DSC curve of chitosan and blends of PLA with chitosan appears low-temperature melting endotherm denotes T_{ml}, while that of the high-temperature denotes T_{mh}. For pure PLA, the observed T_{ml} and T_{mh} values are found at 144 and 170 °C. The thermogram reveals the apparent melting temperature of PLA at 170 °C (Manisara et al., 2005). With increasing chitosan content, both T_{ml} and T_{mh} values are found to slightly decrease from that of the pure PLA.

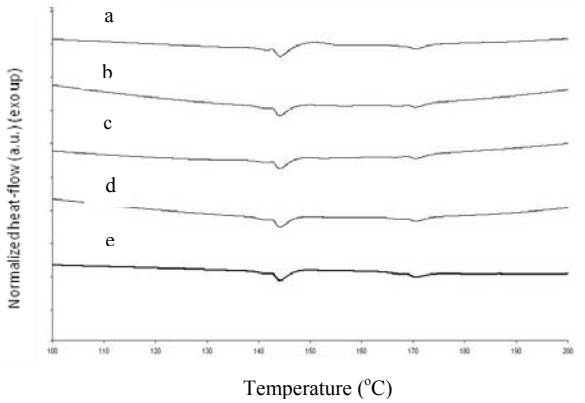

Figure 6. First heating thermograms for pure PLA and PLA/DSS-CTS blends. (a) pure PLA; (b) PLA/DSS-CTS95/5; (c) PLA/DSS-CTS 90/10; (d) PLA/DSS-CTS 85/15 and (e) PLA/DSS-CTS 80/20). The heating rate used was 10°C min^{-1}.

FTIR spectroscopy was used to characterize the interaction between pure PLA and DSS-CTS in the blend. Fig. 7 shows the FTIR spectra of PLA and its blends. The characteristic carbonyl stretching of PLA

at 1751 cm^{-1} is observed in all cases. It is interesting that the absorption peaks at 755 and 868 cm^{-1} corresponding to the crystalline/amorphous phase of PLA (Manisara et al., 2005) obviously decrease with increasing DSS-CTS content in the blends. The intensity ratio of the crystalline peak to that of the amorphous peak for blend is found to decrease from that of the pure PLA. Also, the decrease is associated with an increase in DSS-CTS content. The results present are indicative of the effect of DSS-CTS loading on the degree of PLA crystallinity which is worth investigating.

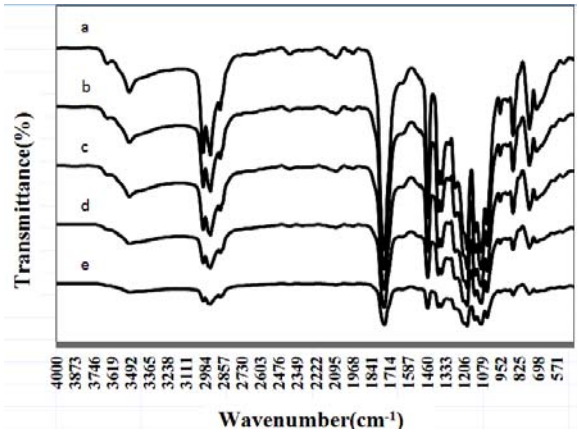

Figure 7. FTIR spectra of PLA and PLA/DSS-CTS blends in difference compositions. (a) pure PLA; (b) PLA/DSS-CTS 95/5; (c) PLA/DSS-CTS 90/10; (d) PLA/DSS-CTS 85/15; (e) PLA/DSS-CTS 80/20.

Conclusions

Hydrophobic chitosan was successfully prepared. Several techniques were employed to confirm the structural change from hydrophilicity to hydrophobilicity. The obtained hydrophobic chitosan was melt-mixed with polylactic acid using twin screw extruder. The results showed that hydrophobic chitosan was compatible with polylactic acid due to its hydrophobic similarity. Interestingly, the effect of hydrophobic chitosan loading on PLA crystallinity was observed. And the result show that the melting temperature of the PLA component in the blend was found to slightly decrease with increasing chitosan content. FTIR spectra show that the intensity ratio of the crystalline peak to that of the amorphous peak for blend is found to decrease from that of the pure PLA, indicating miscibility between chitosan and PLA.

Acknowledgements

The authors gratefully acknowledge National Science and Technology Development Agency and National Center of Excellence for Petroleum, Petrochemicals and Advanced Materials, Chulalongkorn University for financial support**.**

References

[1] L. Lim, R. Auras and M. Rubino, *Prog. Polym. Sci.* **33** (2008), pp. 820-852.
[2] T. Wu and C. Wu, *Polym. Deg. Sta.* **91** (2006), pp. 2198-2204.
[3] M. Peesan, P. Supaphol and R. Rujiravanit, *Journal of Applied Polymer Science*. **105** (2007), pp. 1844-1852.
[4] G. Luckachan and C. Pillai, *Carbohydra. Polym.* **64** (2006), pp. 254-266.
[5] C. Chen, L. Dong and M. Cheung, *Eur. Polym. J.* **41** (2005), pp. 958-966.
[6] M. Peesan, P. Supaphol and R. Rujiravanit, *Carbohydra. Polym*. **60** (2005), pp. 343-350.
[7] V. Correlo, L. Boesel, M. Bhattacharya, J. Mano, N. Neves and R. Reis, *Mater. Sci. Eng*. **A 403** (2005), pp. 57-68.
[8] F. Sebastien, G. Strphan, A. Copinet and V. Coma, *Carbohydra. Polym*. **65** (2006), pp. 185-193.
[9] C. Bangyekan, D. Ong and K. Srikulkit, *Carbohydra. Polym*. **63** (2006), pp. 61-71.
[10] Z. Zong, Y. Kimura, M. Takahashi and H. Yamane, *Polym*. **41** (2000), pp. 899.

Mechanical properties of rice husk silica (RHS)/ poly (butylene adipate-*CO*-terephthalate) (PBAT): effect of filter content

J. Phosee[1, 2], J. Wittayakun[3], N. Suppakarn[1, 2*]

[1] School of Polymer Engineering, Institute of Engineering, Suranaree University of Technology, Nakhon Ratchasima, Thailand 30000

[2] Center of Excellence for Petroleum, Petrochemicals and Advanced materials, Chulalongkorn University, Bangkok, Thailand 10330

[3]School of Chemistry, Institute of Science, Suranaree University of Technology, Nakhon Ratchasima, Thailand 30000

*E-mail: nitinat@sut.ac.th

Abstract: Poly (butylene adipate-*co*-terephthalate) (PBAT) is an interesting biodegradable polymer but it is expensive compared to other plastics with similar properties. To encourage the uses of PBAT and other biodegradable plastics, properties such as mechanical properties has to be improved to suit applications at the competitive cost. This work aimed to prepare a composite between PBAT and rice husk silica (RHS), PBAT/RHS. Amorphous silica with 97% purity was obtained after refluxing and burning rice husk. The amount of RHS in the range of 10-60 %wt was used as a reinforcing filler in the PBAT composites. Stress-strain curves of PBAT composites indicated the changes from ductile to brittle behaviors at the RHS content beyond 30%wt. Incorporation of the RHS into PBAT increased the modulus while decreased elongation at break, tensile strength and impact strength of PBAT composites. SEM micrographs of tensile fracture surfaces of the composites showed poor distribution of RHS and weak adhesion between RHS and PBAT matrix.

Introduction

Plastics materials are used vastly for various applications in daily basis but not many of them are biodegradable leading to environmental problems. Thus, it is necessary to develop biodegradable polymers with acceptable properties and reasonable cost.

Polyesters are good candidates because they consist of potentially hydrolyzable ester bonds. The aromatic polyesters exhibit excellent properties but are resistant to microbial attack. On the other hand, aliphatic polyesters are biodegradable but lack of important properties for applications [1-4]. To combine good material properties with biodegradability, a special type of biodegradable aliphatic–aromatic copolyester, poly (butylene adipate -*co*-terephthalate) (PBAT), was developed by BASF. PBAT is an alternative form of petrochemical plastics used mainly in biodegradable packaging [5-7]. Although PBAT is compostable, good water and tear resistant, high elongation at break, properties such as modulus of elasticity, thermal stability and gas barrier properties have to be improved to suit the applications. The mechanical properties of PBAT can be enhanced by either blending it with other biodegradable or non-biodegradable polymers [7] such as poly (lactic acid) (PLA) or mixing with a reinforcing filler such as montmorillonite (MMT), silica (SiO_2) to fabricate filler/polymer composites [7-9].

Rice husk, considered as an agricultural waste and abundantly available in Thailand, can be used as a silica source with high purity and low cost. [10-11]. Silica is widely used in various products in electronics, ceramic, and polymer material industries because it has good abrasion resistance, electrical insulation and high thermal stability. Silica has been proposed as an attractive filler for biodegradable polymer matrices because it can improve thermal and mechanical properties and increase gas barrier properties [12-14]. Such properties can be achieved by a homogeneous dispersion in polymer matrix and high interfacial adhesion between the filler and PBAT matrix due to micrometer size of silica [15].

The objective of this study is to improve properties of PBAT matrix by using rice husk silica (RHS) as a filler. Effect of RHS content on mechanical properties of the RHS/PBAT composite was studied.

Materials and Methods

Rice husk was obtained from a local rice mill in Nakhon Ratchasima, Thailand. Poly(butylene adipate-*co*-terephthalate) (PBAT, Ecoflex F111 BX 7011) was purchased from BASF. Hydrochloric acid (37%wt HCl) for RHS extraction was purchased from Carlo-Erba.

Rice husk was washed thoroughly with water to remove the adhered soil and dust, and dried in open air. The dried rice husk was refluxed in 3M HCl solution for 3 h, filtered and washed repeatedly with water until the filtrate was neutral. After the acid treatment, the rice husk was dried at 100 ^{o}C overnight and burned in furnace muffle at 550 ^{o}C for 5 h to remove organic contents.

PBAT / RHS composites were prepared using an internal mixer (Hakke Rheomix 3000P). The mixing temperature was 150 ºC, the rotor speed was 50 rpm and the mixing time was 15 min. PBAT pellets and

RHS were dried at 100 ºC for 4 h before mixing. The RHS content used in this study were 10, 20, 30, 40, 50 and 60 % wt. Then, test specimens were prepared by compression molding at a temperature and a pressure of 170°C and 130 MPa, respectively.

Chemical compositions of RHS, calculated as major oxides, were analyzed by energy dispersive XRF (Bruker AXS diffractometer D5005) with an array of 16 anodes analyzing crystals and Rh X-ray tube as target with a vacuum medium.

Phase and crystallinity of the RHS was confirmed by a powder XRD (EDS Oxford Instrument ED 2000) with Cu-Kα radiation. The instrument was operated at a voltage of 35 kV with a step size 0.02° and a scan speed 0.4°/min.

Impact properties of PBAT and PBAT composites were tested by an Atlas testing machine (model BPI) following ASTM D256.

Tensile properties of PBAT and PBAT composites were carried out using an Instron universal testing machine (model 5569) with a load cell of 50 kN, a crosshead speed of 50 mm/min, and a gauge length of 7.62 mm.

Morphologies of tensile fracture surfaces of PBAT and PBAT composites were examined using a scanning electron microscope (SEM, model JSM 6400). Samples were coated with gold before analysis.

Results and Discussion

XRD pattern of rice husk ash is shown in Figure 1. From the Figure, only a broad peak at 2θ = 22° was observed. Chemical compositions of RHS in the form of stable oxides are shown in Table 1. The major component was SiO_2 with purity approximately 97%wt along with small amounts of other inorganic oxides including Al_2O_3, K_2O, CaO, and Fe_2O_3. These results indicated that the obtained ash was amorphous silica. So, the ash was called rice husk silica (RHS) in the rest of this work.

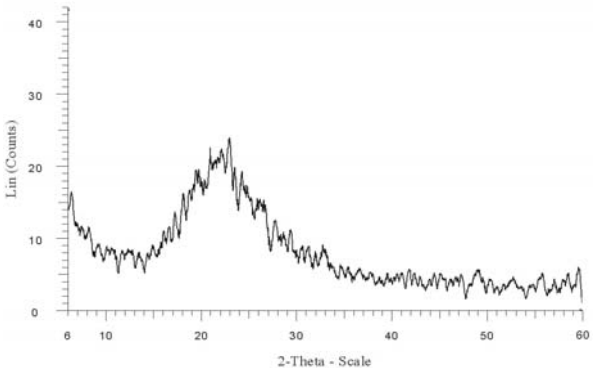

Figure 1. XRD pattern of rice husk ash.

Table 1: Chemical compositions of rice husk ash

Component	(% wt)
SiO_2	97.076
CaO	0.892
Al_2O_3	0.400
K_2O	0.066
Fe_2O_3	0.033

Stress-strain behaviors of PBAT and PBAT composites are shown in Figure 2. A gradual change in flexibility of the PBAT composites was observed with increasing RHS content. The neat PBAT showed abrupt yielding and necking, whereas the PBAT composites at 10-30 % wt of RHS showed gradual yielding without necking. Beyond 30 %wt of RHS, the stress-strain curves showed brittle behaviors of the composites.

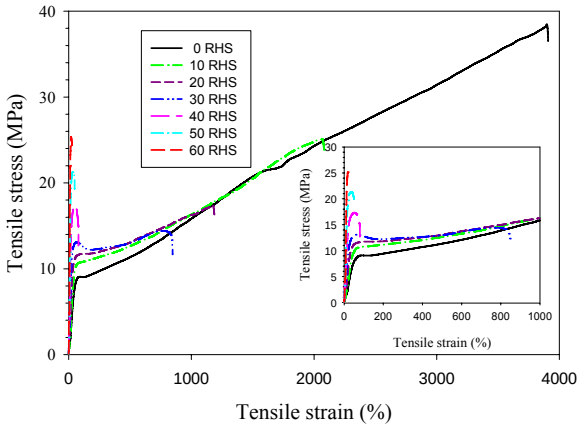

Figure 2. Stress-strain curve of PBAT and PBAT composites at various RHS contents.

As seen in Figure 3, tensile modulus of the composites significantly increased with increasing RHS content. In contrast, a rather precipitous drop of elongation at break of the composites was observed with the addition of RHS between 0 to 40 %wt thereafter a flat behavior was noticed. This observation indicates that the incorporation of RHS into the PBAT matrix improved the stiffness of the PBAT matrix.

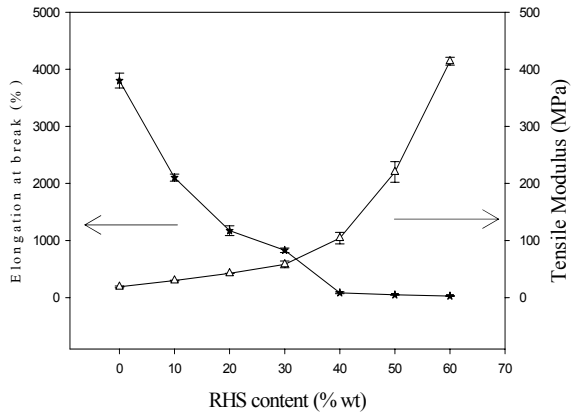

Figure 3. Tensile modulus and elongation at break of PBAT and PBAT composites at various RHS contents.

Figure 4. reveals that the composites with 30% wt of RHS had the lowest tensile strength. A gradual increase in strength was noticed with RHS content diverting either ways from 30% wt. When RHS content was below 30% wt, the reduction in tensile strength of the composites was due to the poor distributions and the agglomeration of RHS in the PBAT matrix as confirmed by SEM micrographs in Figure 6. However, the increase in tensile strength of the composites containing more than 30 %wt of RHS was due to the brittle behavior of the composites.

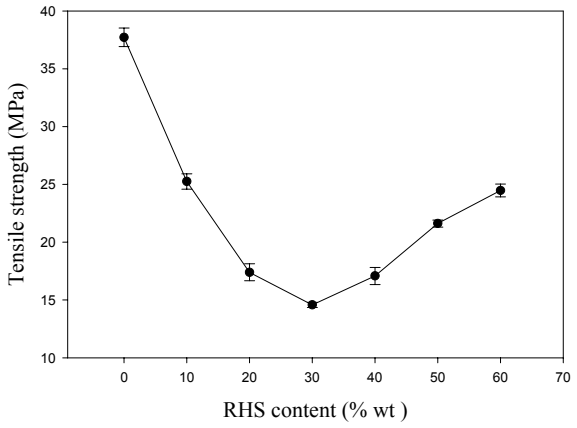

Figure 4. Tensile strength of PBAT and PBAT composites at various RHS contents.

Impact properties of PBAT composites are shown in Figure 5. Impact strength of the composites with RHS content between 0-20% wt was higher than 144 kJ/m^2 since the specimens did not break at testing load. Impact strength of the composites decreased with increasing RHS content. This suggested that RHS disturbed matrix continuity and acted as microcrack initiator. In addition, the decrease impact strength of the PBAT composites with increasing RHS content may indicate the poor distribution of RHS in PBAT matrix.

SEM micrographs of tensile fracture surfaces of PBAT and PBAT composites are shown in Figure 6. The micrographs clearly indicate structures consisting of fibrils. It was noted that the extended fibrils of PBAT composites were shorter than those of the neat PBAT. This suggested that the existence of the RHS filler in PBAT matrix tended to improve the stiffness of the PBAT matrix. This presumption was also supported by the tensile properties of the PBAT composites. In addition, gaps between filler and matrix were observed when more than 30% wt of RHS was added into PBAT matrix as shown in Figure 6 (c-d). This indicated critically weak surface adhesion between these two phases. Thus, it was clear that the dispersed RHS phases and surface adhesion played an important role in the properties of PBAT composites.

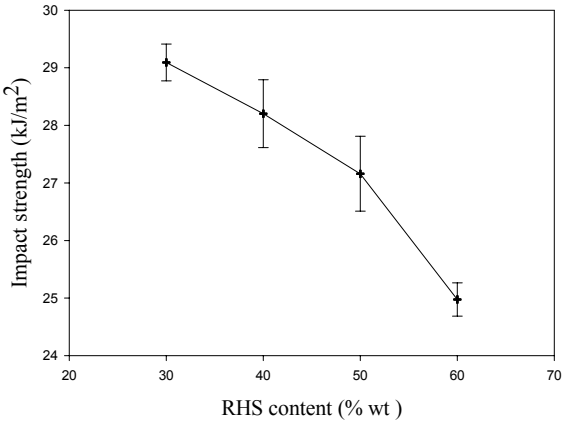

Figure 5. Impact strength of PBAT and PBAT composites at various RHS contents.

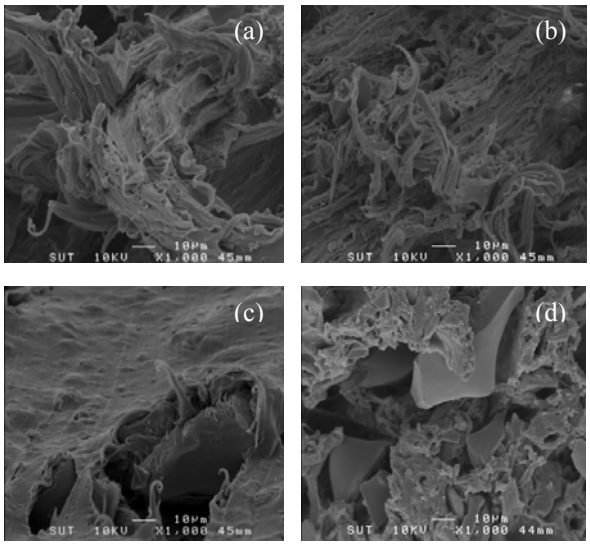

Figure 6. SEM micrographs of (a) PBAT and PBAT composites at various RHS contents: (b) 10% wt (c) 30% wt (d) 40% wt.

Conclusions

Amorphous silica with 97% purity was used as a filler for PBAT matrix. Stress-strain curved of PBAT composites indicated the changes from ductile to brittle behaviors with the addition of RHS. So, mechanical properties of PBAT/RHS composites can be adjusted through the mixing composition. The incorporation of the RHS into PBAT increased the modulus while decreased elongation at break, tensile strength and impact strength of PBAT composites. A gradually increase in strength was noticed with RHS content diverting either ways from 30% wt. Weak surface adhesion between RHS and PBAT was observed.

Acknowledgements

This research was financially supported by Suranaree University of Technology and Center of Excellence for Petroleum, Petrochemicals, and Advanced Materials.

References

[1] K. Van de Velde and P. Kiekens, *Polym. test.* **21**(2002), pp. 433-442.

[2] ***R.J. Mueller, I. Kleeberg*** and ***W.D. Deckwer*****, *J.* Biotechnol.** *86* **(*2001*),** pp. ***87–95*.**

[3] T. M. Wu and C.Y. Wu, Polym. *Degrad. Stab*. **91** (2006), pp. 2198-2204.

[4] O. Martin and L. Averous, *Polymer*. **42** (2001), pp. 6209-6219.

[5] Witt et al., *Chemosphere,* **44**(2001), pp. 289-299.

[6] F.T. Tan, D. G. Cooper, M. Maric and J. A. Nicell, *Polym. Degrad. Stab*. **93** (2008), pp. 1479-1485.

[7] F. Signori, M.-B. Coltelli and S. Bronco, *Polym. Degrad. Stab*. **94** (2009), pp.74–82.

[8] L. Jiang, M. P. Wolcott and J. Zhang *Biomacromolecules,* **7** (2006), pp. 199-207.

[9] L. Jiang, M. P. Wolcott, and J. Zhang, *Polymer*. **48** (2007), pp. 7632-7644.

[10] V.P. Della, I. Kuhn and D. Hotza, *Mater. Lett.* **57** (2002), pp. 818–821.

[11] N. Yalcin and V. Sevinc, *Ceram. Int.* **27**(2001), pp. 219-224.

[12] J. Wittayakun, P. Khemthong and S. Prayoonpokarach, *Korean J.Chem. Eng*. **25(**2008), pp. 861-864.

[13] S. Yan *et. al*., *Mater. Lett.* **61**(2007), pp. 2683–2686.

[14] S. Yan *et. al*., *Polymer*. **48** (2007), pp. 1688–94.

[15] X. Lu, X. Lv, Z. Sun and Y. Zheng, *Eur. Polym. J.* **44** (2008), pp. 2476–2481.

Phase transformation and vitrification mechanism of china clays from thailand

C. Saengthong[1*], D.Wattanasiriwech[1] S.Wattanasiriwech[1] and T. Panyathanmaporn[2]

[1] School of Science, Mae Fah Luang University, Chiang Rai, Thailand
[2] National Metal and Materials Technology Center, Pathumtani, Thailand

[*]E-Mail: ccst1540@yahoo.com

Abstract: Phase transformation and vitrification mechanism of two china clays with different illite contents were comparatively studied. High illite content was found in Lampang clay (LP) while high kaolinite content was found in Naratiwas clay (NR). Both clays were investigated in terms of phase transformation and microstructural change upon firing using X-ray diffraction spectrometry (XRD), differential thermal analysis (DTA), and scanning electron microscopy (SEM). Physical and mechanical properties including water absorption, bulk density, and flexural strength of the clay samples after firing at 900°-1350°C were also determined. The spinel phase was observed in both clays prior to transformation into mullite phase at 1000°C. In LP, crystalline peaks of mullite were observed after firing at 1000°C while in NR they were observed after firing at 1100°C. Crystalline peaks of illite disappeared at 1050°C, indicating the started of vitrification. The complete vitrification of LP was observed after firing at 1300°C. The size of mullite crystals observed in vitrified LP samples were larger than that observed in NR, indicating the higher degree of vitrification in LP samples. This was confirmed by the water absorption value of 0%, density value of 2.53 g/cm^3, and flexural strength value of 113.36 MPa from LP samples whereas the samples from NR showed the water absorption value of 6.28%, density value of 2.31 g/cm^3, and flexural strength value of 62.87 MPa.

Introduction

China clay is one of the raw materials which are widely used in traditional ceramic industries. China clay is mainly composed of kaolinite and other minerals such as quartz, illite, feldspar, hematite, and anatase of which proportion depends on their sources [1]. These mineral constituents have a major influence in phase transformations and microstructural development of ceramics during firing and consequently determine the final properties of the fired ceramics.

In Thailand, the major sources of china clay are in Ranong, Uttaradit, Naratiwas and Lampang. Although these china clays have been widely used in ceramic production, the detailed study on the sequence of phase and microstructural changes during firing stage of these clays have not been reported.

From our preliminary study, Naratiwas and Lampang china clays showed extreme difference in kaolinite and illite mineral contents. Thus, their phase and microstructural changes in response to the heat treatment were investigated. Finally, physical and mechanical properties after firing of both clays were also reported.

Materials and Methods

China clays from Lampang province (Lampang clay; LP) and Naratiwas province (Naratiwas clay; NR) were selected to study in this research. Both clays were sieved through a 325 mesh sieve. Chemical analysis of the clays was carried out prior to characterization by an X-ray fluorescence technique (XRF: Horiba Mesa-500w). Thermal analysis was performed using a Mettler TGA/SDTA 851^e (Metler Toledo corporation, Switzerland). The clays were heated from room temperature to 1300ºC with a heating rate of 20ºC min^{-1} in platinum crucibles. Clay powders were compacted at 50 MPa for 30 seconds into 25 mm diameter pellets by uniaxially pressing technique. The compacted clays were fired in a high temperature tube furnace at 900-1350ºC with a heating rate of 5ºCmin^{-1} for 30 min prior to quenching in water in order to freeze the phase formation. Phase transformations of the fired clays were examined by an X-ray diffraction technique (XRD: PaNalytical X'Pert PRO MPD, Netherland) in a 2θ range of 5-70° which step size 0.0084°. Microstructures of the fired clays were examined using a scanning electron microscope (SEM: JEOL JSM-5410LV). Water absorption and bulk density of the fired samples were measured following ASTM C 373-88. Three-point bending strength was determined using an universal testing machine, (UTM: Instron 5566 USA).

Results and Discussions

Characteristics of clay powders:

Chemical compositions of LP and NR are shown in Table 1. Both clays consist mainly of SiO_2 and Al_2O_3 which correspond to the presence of clay minerals and quartz. High content of K_2O (4.05%) in LP indicates the existence of illite mineral.

Figure 1 shows XRD patterns of LP and NR clay powders. Crystalline peaks corresponding to quartz, illite, and kaolinite minerals were clearly observed in LP. In NR, kaolinite peaks dominant. The rational analysis based on XRF and XRD [2] was used to estimate the content of these minerals provided that the formulae of kaolinite, illite, albite and microcline were $Al_2(Si_2O_5)(OH)_4$, $K_yAl_4Si_{8-y}Al_yO_{20}$ $(OH)_4$ with y=1.5 $Na(AlSi_3O_8)$ and $K(AlSi_3O_8)$ respectively [3]. The

estimated mineralogical compositions are shown in Table 2. LP clay contained a large amount of illite while NR clay has high content of kaolinite.

Table 1: Chemical analysis results for LP and NR clays.

Chemical compositions (wt%)	LP	NW
SiO_2	60.27	53.05
Al_3O_2	27.75	33.34
K_2O	4.05	0.83
Na_2O	0.46	0.00
CaO	0.16	0.04
Fe_2O_3	0.98	0.73
TiO_2	0.06	0.92
L.O.I	6.28	11.08

* L.O.I. = loss on ignition

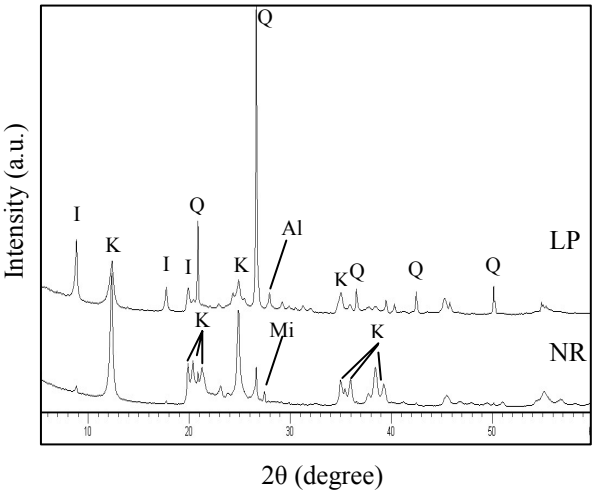

Figure 1. XRD patterns of LP and NR clays (I: illite, K: kaolinite, Q: quartz, Al: albite, Mi: microcline)

Table 2: The mineralogical compositions of LP and NR clays.

Mineral compositions (wt%)	LP	NR
Illite	33.43	trace
Kaolinite	37.78	82.13
Quartz	23.03	11.61
Albite	3.89	-
Microcline	-	4.89
Other	1.87	1.37

DTA curve of LP and NR clays are shown in Figure 2. Peaks corresponding to an endothermic reaction were found in both clays around 100°C and 520°C while, exothermic peaks were found at 1006°C and 1128°C. The first endothermic peak at 100°C corresponds to the loss of the weakly bound water while the second endothermic peak correspond to the loss of structural hydroxyl groups and the transformation of kaolinite to metakaolinite. The exothermic reaction observed at 1006°C was attributed to the latent heat of Al-Si spinel or mullite crystallization out of metakaolinite [4-7]. NR clay showed sharper peak than LP clay because of high amount of kaolinite. The exothermic peak at 1128°C indicated that mullite formed from illite [8]. LP clay showed dominant endothermic peak at 1128°C while in NR clay was observed small peak at this temperature due to small amount of illite.

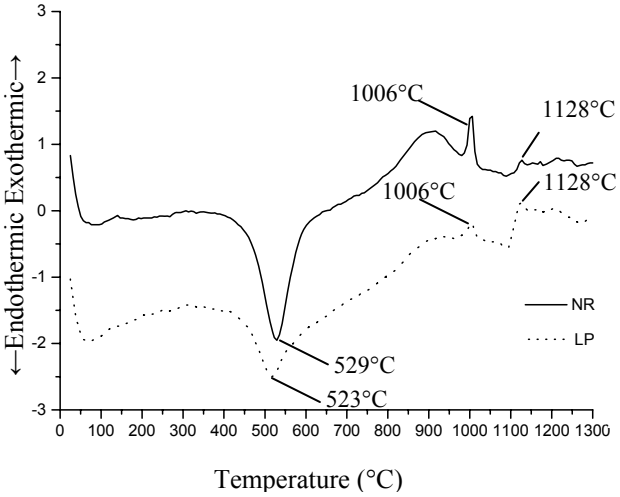

Figure 2. Differential thermal analysis of LP and NR clays.

Phase transformations of fired clays:

Figure 3 and 4 shows the XRD patterns of the LP and NR fired clays respectively. Crystalline peaks corresponding to kaolinite in both clays disappeared after firing at 900°C because of the transformation of the kaolinite into metakaolinite by the removal of the hydroxyl groups in the silicate lattice which occurred starting at 400°C as shown by in Figure 2. Broaden peaks between 2θ range of 15° and 30° found in NR clay correspond to amorphous silica ejected from Al-Si spinel formation [9]. Al–Si spinel was not observed in LP fired clay probably due to a small amount of kaolinite. Heated up to 1000°C in both clays, illite phase becomes progressively less crystalline. Peak intensity gradually decreases and disappears at 1050°C. In LP fired clays, mullite phase was developed at around 1000°C, while it was observed in NR clay after firing at 1100°C. Degree of mullite formation increases with increasing firing temperature up to 1350°C while quartz content decreases after firing at this temperature due to its partial dissolution. Cristobalite observed after firing at 1300°C only in NR clay, due to formation of cristobalite out of amorphous silica [6, 10].

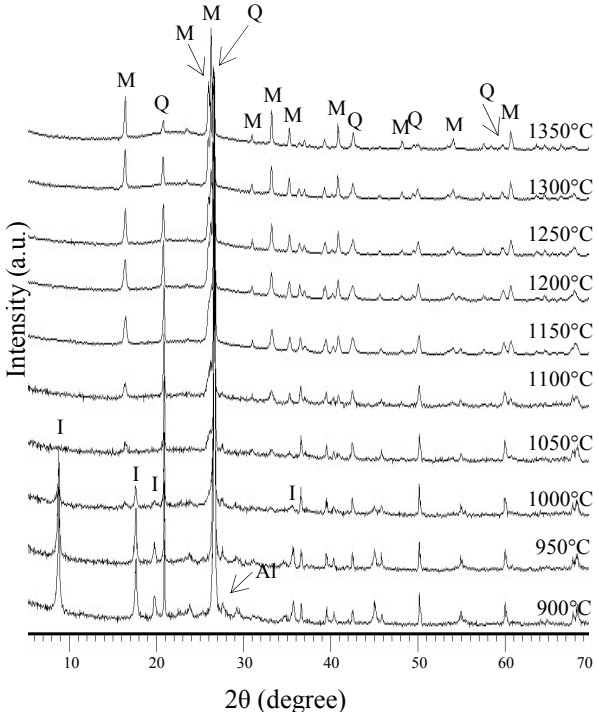

Figure 3. XRD patterns of LP fired from various firing temperature (I: illite, Q: quartz, M: mullite and Al: albite).

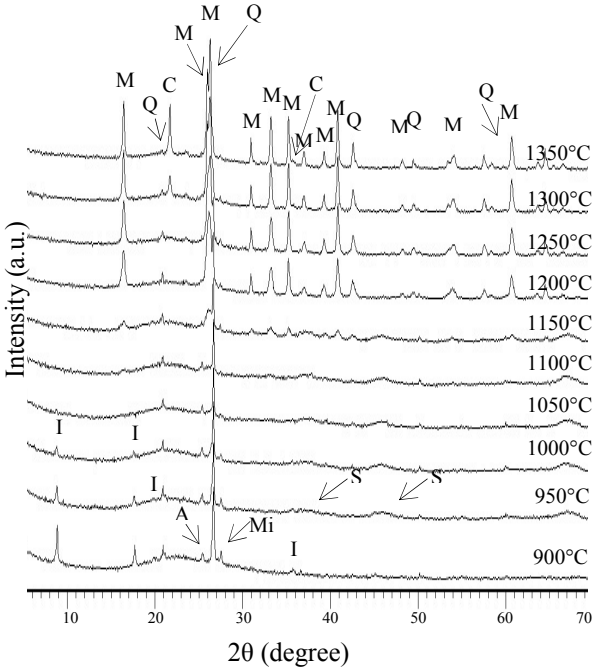

Figure 4. XRD patterns of NR fired clays from various firing temperature (I: illite, Q: quartz, M: mullite, C: cristobalite, Mi: microcline S: spinel and A: anatase).

Vitrification and physical properties:

Figure 5 shows water absorption and bulk density of LP and NR fired clays as a function of different firing temperatures. Water absorption values decreased with increasing firing temperatures, leading to an increase of bulk density. LP fired clay showed 0% water absorption with 2.53 g/cm^3 bulk density after firing at 1300°C. At this firing temperature, absorbed water in the NR fired clay is 6.28% while bulk density is 2.31 g/cm^3. The value of water absorption in LP decreased to 0% was due to the occurring of the glassy phase from illite and other feldspar minerals. Flexural strength values of LP and NR clays after firing at different temperatures are shown in Figure 6. The flexural strength in LP clay reached the highest value of 113.36 MPa after firing at 1300°C while NR fired clay showed value of 62.87 MPa. The higher value of flexural strength resulted from lower water absorption and higher bulk density of LP fired clay. The evidence indicated the complete vitrification in LP clay after firing at 1300°C, while the vitrification in NR clay was not completed at this firing temperature. Microstructure of LP and NR fired clays is shown in Figure 7. It was found that crystalline size of mullite in LP fired clay was larger than that of NR fired clay after firing at 1300°C. Such larger crystalline size of mullite was observed in LP fired clay leading to high flexural strength.

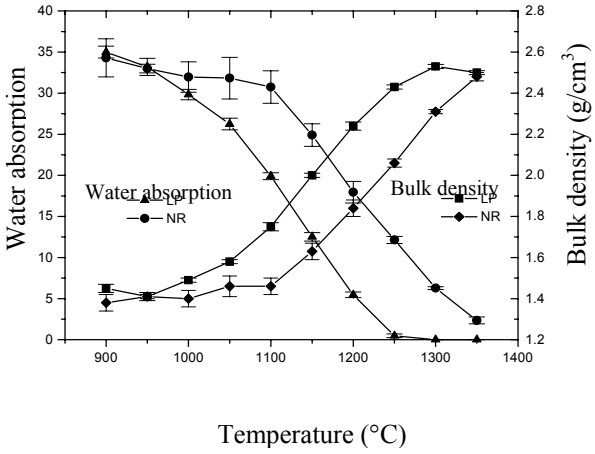

Figure 5. Variation in bulk density and water absorption with firing temperature.

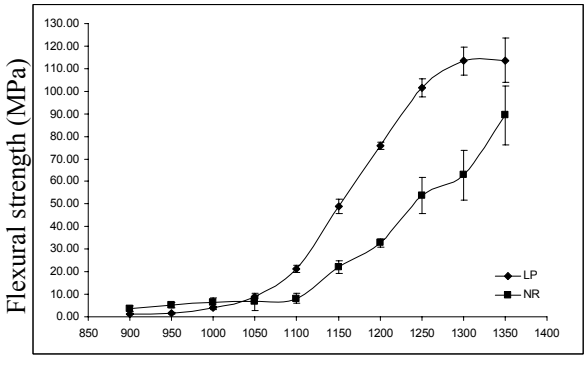

Figure 6. Variation in flexural strength with firing temperature.

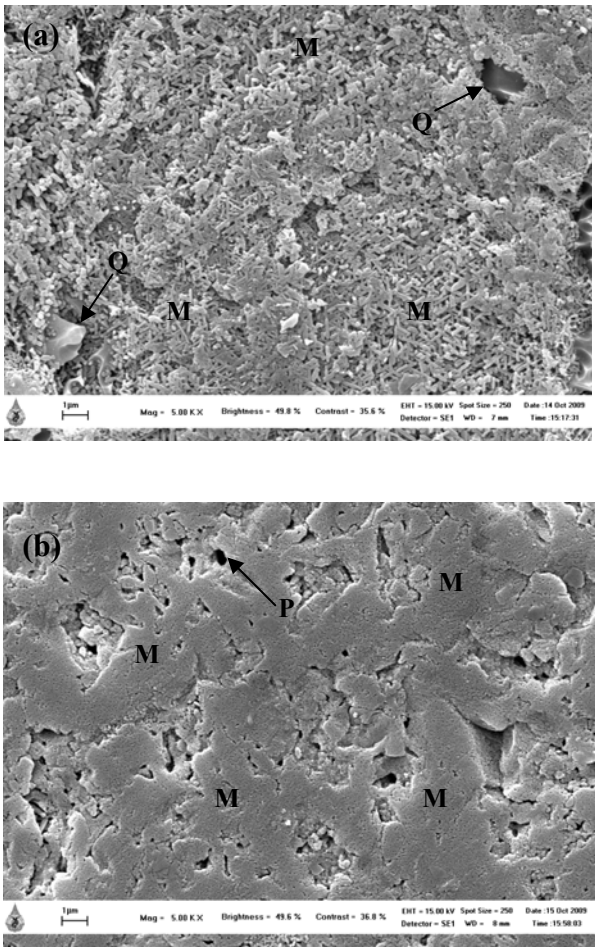

Figure 7. Microstructures of (a) LP and (b) NR clays fired at 1300°C (M: mullite, Q: quartz, and P: pore)

Conclusions

Difference of illite content in china clay was responsible for phase transformation, microstructure, and vitrification temperature of clays.

LP clay showed higher content of illite. Mullite formed after firing at 1000°C. Its crystalline size was larger than that of mullite observed in NR clay. Water absorption and bulk density of fired clay at 1300°C were 0% and 2.53 g/cm^3 respectively. Flexural strength of this sample was 113.36 MPa. Vitrification temperature was found to complete at 1300°C.

NR clay showed lower content of illite. mullite formed after firing at 1100°C. Water absorption and bulk density of fired clay at 1300°C were 6.28% and 2.31 g/cm^3 respectively. Flexural strength of this sample was 62.87 MPa. However, vitrification was not completed at 1350°C.

Acknowledgments

The authors would like to thank Thailand Graduate Institute of Science and Technology (TGIST) for the financial support of this work and Mae Fah Luang University.

References

[1] H. H. Murray, *Appied Clay Mineralogy, Elsevier*, Amsterdam, Natherland, (2007), pp. 21-22.
[2] R. Griffiths and C. Radford, *Calculations in Ceramics,* Livesey LTD, UK (1965), pp.116-119
[3] W. A. Deer, R. A. Howie, J. Zussman, *An Introduction to the Rock-Forming Minerals*, 2nd Pearson Prentice Hall, UK (1992).
[4] B. Sonuparlak, *J. Am. Ceram. Soc.* **70** [ll], (1987) pp. 837-842.
[5] K. Srikrishna, G. Thomas, R. Martinez, M. P. Corral, S. De Aza and J. S. Moya, *J. Mater. Sci.* **25** (1990), pp. 607-612.
[6] A. K. Chakraborty, *J. Therm. Anal*. **71** (2003), pp. 799–808.
[7] Y.F. Chen, *J. Eur. Ceram. Soc*. **24** (2004), pp. 2389–2397.
[8] T. Jiang and G. Li, *Appl. Clay Sci*. **40** (2008), pp. 81-89.
[9] C.J. McConville and W. E. Lee, *J. Am. Ceram. Soc.* **88** [8] (2005), pp.2267–2276.
[10] A. K. Chakraborty, *Therm. Acta*. **398** (2003), pp.203–209.

Self-organising nanostructures based on sorbitol derivatives

Supatra Wangsoub[1,2]*, Fred J Davis[2], Geoffrey R Mitchell[2] and Robert H Olley[2]

1 Department of Chemistry, Naresuan University, Phitsanulok, Thailand 65000
2 Polymer Science Centre, University of Reading, Whiteknights, Reading, RG6 6AF UK

*E-mail: supatraw@nu.ac.th

Abstract: Derivatives of sorbitol have a remarkable ability to form gels at very low concentrations in a wide variety of solvents. The levels of the gel forming material may be as low as 0.1% w/w. Transmission electron micrograph showed the formation of highly extended nanofibrils which relate to the extremely low levels of solute required for gelation. The fibril morphologies from a number of derivatives were investigated. The gel formation is strongly influenced by small-changes in the nature of the derivative and in the solvent. SEM and TEM of fibril from chloro and bromo substitutes show smaller in diameter than fibril from unsubstituted compound. Electron diffraction and x-ray diffraction reveal that these highly extended fibrils are crystalline and high anisotropic. Small amount of sorbitol derivatives dispersed in poly(ε-caprolactone) provide a very effective self-assembling nanoscale framework. The application of modest shear flow leads to extremely high levels of polymer crystal orientation. During modest shear flow of the polymer melt, the additive forms highly extended nano-particles which adopt a preferred alignment with respect to the flow field. On cooling, polymer crystallisation is directed by these particles. This ortho-chloro substituted dibenzylidene sorbitol is considerably more effective at directing the crystal growth of poly(ε-caprolactone) than the other substituted compounds. The intensity of equatorial section from the ortho-choro substituted increases approximately by 2.25 times compare to the unsubstituted compound. In contrast, the meta-chloro substituted dibenzylidene sorbitol shows the low level of preferred orientation compare to the unsubstituted compound.

Introduction

Di-benzylidene sorbitol (DBS) is a low molar mass gelator. In a variety of solvents at low concentrations it self-assembles into extended nano-fibrils and forms gel. In general, gels are viscoelastic solid-like materials comprised of an elastic cross-linked network and a solvent, which is the major component. The solid-like appearance of a gel is a result of the entrapment and adhesion of the liquid in the large surface area solid 3D matrix. In contrast to the formation of a gel in a polymer as a result of cross-linking of the polymer molecules by physical or chemical forces, gels derived from low molar mass compounds are formed through self-aggregation of the small gelator molecules to form entangled self-assembled fibrils. These gels are generally thermally reversible. DBS is an example of a low molar mass organic gelator [1] that can self-organise into nanoscale fibrils. At sufficiently high DBS concentrations, depending on factors such as temperature and matrix polarity, the nanoscale fibrils form a three dimension network that promotes physical gelation in a wide variety of organic solvents and polymers.

For polymer, row nucleation provides a powerful mechanism for templating or directing the growth of polymer lamellar crystals. A variety of such systems have been identified including macroscopic fibres,[2] discrete microscopic particles such as carbon nanotubes,[3] and molecular assemblies such as extended chains formed during flow,[4] We have recently shown that dibenzylidene sorbitol (DBS) coupled with modest flow fields can direct the crystallisation of polyethylene,[5] polypropylene,[6] and poly(ε-caprolactone) (PCL).[7] In essence, the low-molar-mass compound self-assembles into extended nano-particles which can be exploited to yield highly anisotropic crystal textures. On cooling, the aligned nano-particles direct the subsequent crystallisation of the polymer to yield highly aligned crystalline material. This process is dependent on the formation of nanoparticles in the polymer melt as well as the subsequent direction of the nucleation and growth processes of the polymer. These complex processes have been shown to occur in a number of synthetic polymers, and in this work we explore the effect of modifying the chemistry of the low molar mass compound on the subsequent particle formation and crystallisation processes by considering the chloro and bromo sorbitol derivatives.

Materials and Methods

Synthesis sorbitol derivatives

Dibenzylidene Sorbitol derivatives were prepared by the acid catalysed reaction of sorbitol with the appropriate aldehyde (4-chlorobenzaldehyde, 3-chlorobenzaldehyde, 2-chlorobenzaldehyde or 4-bromobenzaldehyde) in cyclohexane. The procedure for 1,3:2,4-di(4-chlorobenzylidene) sorbitol was as follows. An aqueous solution of D-sorbitol (0.1 mol, 70% w/v) was placed into a round bottom flask equipped with Dean-stark trap and condenser. To this was added 4-chlorobenzaldehyde (0.2mol) and methanesulfonic acid (1 ml), cyclohexane (200 mL) and dimethylsulfoxide (6 mL). The mixture was heated to reflux with constant stirring. The mixture of cyclohexane and water was condensed and separated in the Dean-Stark arrangement. Once no further water was produced the reaction was stopped, and following neutralisation with triethylamine the white precipitate

collected. Following purification by washing with methanol and water, the sorbitol derivative was obtained as a white powder. The chloro derivative was greater than 98% pure by ^{1}H NMR, yield 46 %, mpt. 201 °C while the bromo derivative sorbitol yield 49.39% , melting point 218 °C. Figure 1 show chemical structures of sorbitol derivatives where R= halogen group and p=1.

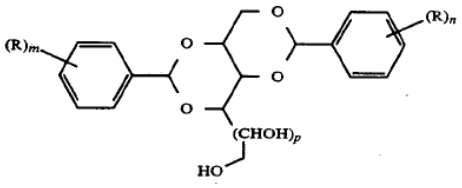

Figure 1 Chemical structure of sorbitol derivatives

Gel preparation

Gels were prepared by weighing and mixing sorbitol derivatives and solvents in a glass container which was then heated to 230°C to prepare a homogenous solution and subsequently cooled at various rates, normally 10°C/min to room temperature. The dissolution of the sorbitol derivatives in the solvent on first mixing was evaluated by visual inspection. In order to determine the sol-gel and the gel-sol points, the solutions were heated in a temperature controlled oven and subjected to a periodic tilting test in which the container was tilted by 45 degree to detect flow.

The samples for scanning electron microscopy (SEM) study were prepared by extracting the solvent from the gel by evaporating the solvent on a membrane filter for 1 week. The dry samples obtained in this manner were coated with gold and examined using a SEM Leo1455VP. Samples for transmission electron microscopy (TEM) were prepared from solutions of 0.01, 0.05,0.1, 0.5, 1 and 2 wt% sorbitol derivatives in tetradecane and deodecane were prepared by dropping the solution onto a carbon coated copper grid. The samples were left for the solvent to evaporate for 1 week. Samples were examined at room temperature using a Phillips Technai12 electron microscope, operating at 120 kV.

The sorbitol derivatives (1 to 5 wt%) were dispersed in PCL (MW=80,000 Da) by solution blending using butanone as the co-solvent. Preformed discs for use in the shear experiments were prepared by melt pressing at 80°C. Samples of PCL and PCL containing Cl-DBS, Br-DBS were subjected to controlled flow and thermal profiles using a specially designed parallel-plate shear-flow system described elsewhere[8]. Time resolved X-ray scattering experiments were performed at DESY.

Wide-angle X-ray Scattering (WAXS) were obtained using a symmetrical transmission diffractometer equipped with a graphite monochromator and pinhole collimation and a copper target x-ray source. The intensity was measured as a function of $|\underline{Q}|$ and α, the angle between the symmetry axis of the sample and the scattering vector Q. Data were obtained over a $|\underline{Q}|$ range of 0.16 to 6Å^{-1} in steps of 0.02 Å $^{-1}$and of α, over the range 0° to 90° in steps of 5°. Data was also recorded using a normal beam transmission arrangement with a graphite monochromator and pinhole collimation and a Cu K source coupled to a Photonic Science CCD camera providing 2-D scattering patterns with a $|\underline{Q}|_{max}$~ 2Å^{-1}

Results and Discussion

Table 1 shows the critical concentration of DBS and DBS derivatives in various solvents. The method mentioned in gel preparation section was used to determine the critical concentration. The critical gel concentrations of DBS and DBS derivatives in some solvents reproduced from [9] are displayed in Table 1. It can be seen that the solubility of DBS and its derivatives in polar solvents is higher than in non-polar solvent. The polarity of solvent can be measured as the dielectric constant or the dipole moment of a compound [10]. The polarity of a solvent determines what type of compounds it is able to dissolve and with what other solvents or liquid compounds it is miscible. The polarity shown in table 1 is given as dielectric constant. Solvents with large dielectric constants may act as dissociating solvents and are therefore called polar solvents in contrast to the nonpolar solvents with low dielectric constants. As an arbitrary guideline, a solvent is polar if it has a dielectric constant of 20 or greater. A solvent is nonpolar if it has a dielectric constant of less than 20 [11]. It can be seen that the alkane group of the solvents is classified as a nonpolar solvent due to presence of only carbon and hydrogen atoms. The polarity value of dodecane and tetradecane are assumed to be similar to the polarity of hexane. This type of solvent has low polarity compared to a polar solvent such as dimethyl sulfoxide or 1,4-dioxane. It is likely that chloro and bromo derivatives can form gel at lower concentration compare to DBS indicating a reduced solubility of DBS derivative in solvents. Therefore, the concentration of DBS and DBS derivatives required to form a gel is strongly dependent on the polarity of the solvents.

Table 1: Critical concentration

Solvent	Dielectric constant [11]	Critical Conc DBS w/w %	Critical Conc Cl-DBS w/w %	Critical Conc Br-DBS w/w %
Dodecane	2.0*	0.1	0.004	0.001
Tetradecane		0.1	0.006	0.004
DMSO	48.9	30	20	20
1,4-Dioxane	2.3	11	3	-

* assume dielectric constant similar to hexane[11]

SEM micrographs of 0.05wt% Cl-DBS in tetradecane in Figure 2 show that the fibril network is not homogeneous and consists of loosely connected fibrils and fibrillar bundles greater than 50 μm in length. The minimum diameter of the smallest

observed fibrils measures on the order of about 50 nm while the maximum diameter was found to be about 80 nm. Some of the larger fibrillar bundles consist of several fibril layers, each about 200 nm thick. The twisted fibrils of Cl-DBS are clearly seen. The helical pitch was about 170-180 nm compare to 4-5 μm of DBS. SEM micrograph of Br-DBS reveals similar fibrils network which their diameter are about 30-120 nm. We also considered the extracts from solutions of lower concentration of sorbitol derivatives in tetradecane but these did not reveal any identifiable objects in the SEM.

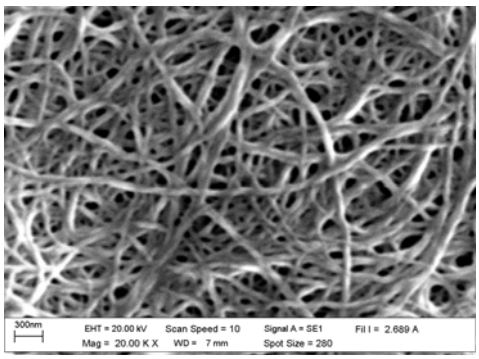

Figure 2 SEM micrograpgh of 0.05% Cl-DBS in Tetradecane

The use of TEM to study the fibrils requires the removal of the solvent and we have used the thin film approach to achieve this. No discernible features could be observed in the TEM for extracts obtained from solutions with low concentration of DBS derivatives in tetradecane. However, clear fibrils were observed in the extracted sample of 0.05wt% Cl-DBS in tetradecane as shown in Figure 3a. The image shows a fine, three dimensional network of Cl-DBS. The network consists mainly of fibrils and with a small number of fibrillar bundles. The networks appear electron opaque (dark). The network of fine, randomly oriented and shaped nanofibrils have a diameter of approximately 10-30 nm. Thicker DBS fibrils (darker) or possibly fibrillar bundles, measuring up to 70 nm in diameter are also observed. These fibrils are very long, more than 50μm in the length. At higher magnification, the internal structure appeared homogenous with no variation in contrast.

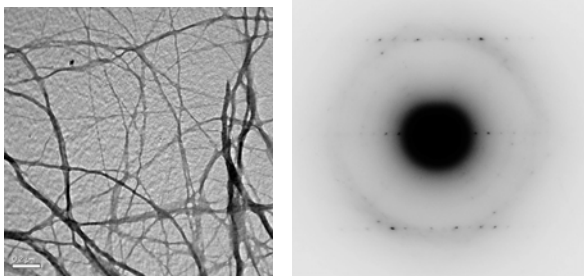

Figure 3 (a) TEM micrograpgh of 0.05% Cl-DBS in Tetradecane (b) Electron diffraction of DBS after solvent removal

The images displayed in Figure 2 and 3a confirm that DBS and DBS derivativs molecules self-organise into a nanofibrillar network in alkanes. We have used selective area electron diffraction method to ascertain whether these extracted DBS nanofibrils are crystalline. However, there is no result to provide any conclusive insight into the nature of the nanofibrils. Electron diffraction methods could be used to ascertain whether the DBS nanofibrils are crystalline. Thus electron diffraction technique has been examined in order to receive the electron diffraction pattern of DBS nanofibrils. Electron diffraction image of 5 wt% DBS in hexane is shown in Figure 3b. Many sharp spots are clearly seen from the pattern. The image reveals the diffraction of crystalline DBS.

Figure 4a and 4b show the SAXS and WAXS patterns for the system containing 3% Cl-DBS in a sheared melt. The samples were heated to and held at 80 °C and then subjected to a shear field of 10 s^{-1} for 1000su (shear units = shear rate x shear time). At cessation of shear flow, the sample was cooled at 10 °C /min to 20 °C. Analysis of the SAXS data gives a fibril diameter of 150Å and a length of over 800Å. Clearly the sorbitol derivative crystals are aligned preferentially parallel to the flow direction. The SAXS pattern of crystallised sample reveals a high level of lamellar crystal alignment normal to the flow direction. The long period is 185 A°; essentially the same as that for a system of DBS/PCL [12-13]. The WAXS pattern reveals the 110 and 200 crystalline peaks are most intense on the equatorial section and the 002 reflection is maximised on the meridional section indicating a preference for the c-axis alignment of the crystals parallel to the flow field. We have selected an intensity scale for the WAXS pattern which allows the much weaker scattering peaks from the Cl-DBS fibrils to be observed. This is most easily seen as series of sharp reflections on the equatorial section as well as a meridional peak. These indicate that the Cl-DBS is present in a crystalline and highly aligned form.

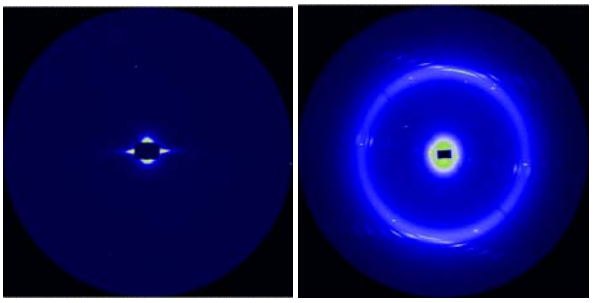

Figure 4 (a) SAXS and (b) WAXS pattern show highly align nanofibrils 3% chloro-derivative in polymer melt after subjected to shear flow. The flow direction is vertical.

Figure 5 shows azimuthal WAXS scans for the 110 crystal reflection in samples prepared using 3 wt% of Cl-DBS, Br-DBS and DBS for the same shear

condition. For Cl-DBS, the position of chloro substitution was investigated. It can be seen that the ortho and para substituted give the high level of preferred orientation of PCL crystal. The meta substituted shows low level of preferred orientation compare to the unsubstituted compound. Azimuthal WAXS scan in Figure 6 reveal the level of preferred orientation of PCL/Br-DBS is similar to that of PCL/DBS.

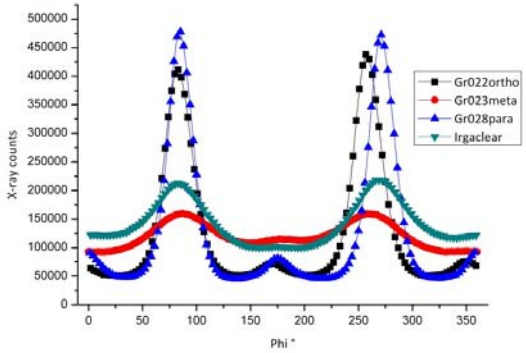

Figure 5 Azimuthal variation of the intensity for 110 crystal reflection of PCL/Cl-DBS samples. Irgaclear is trade name of DBS.

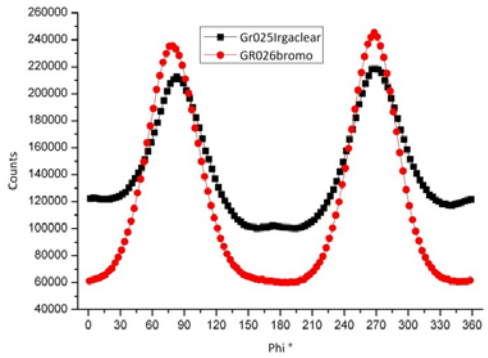

Figure 6 Azimuthal variation of the intensity for 110 crystal reflection of PCL/Br-DBS and PCL/DBS samples

Without the additive, PCL shows an isotropic distribution of lamellar crystals; presumably, any effects of the modest shear flow on the matrix polymer will have relaxed by the time the crystallisation point is reached[12]. Consequently these experiments probe only the effect of the aligned sorbitol derivatives fibrils on the crystallisation of the PCL matrix.

Conclusions

Chloro and bromo sorbitol derivativs can self-organise into a nanofibrillar network which give fibril diameter 50-80 nm and greater than 50 μm in length. Small amount of sorbitol derivatives disperse in the PCL matrix give a near perfect alignment of crystalline lamellae. The additive forms highly extended nano-particles which adopt a preferred alignment during shear flow. The nature of the particles means that this can be achieved with low shear rates and shear strains. On cooling, the crystallisation process of the PCL is directed by these particles. PCL without this additive shows an isotropic microstructure. The ortho and para chloro derivatives of dibenzylidene sorbitol show a reduced solubility in PCL which leads to an enhanced effectiveness of this additive in directing and nucleating the crystallisation of PCL compared with the unsubstituted compound. The bromo derivative gives the same level of preferred orientation as dibenzylidene sorbitol.

References

[1] P.Terech, R.G.Weiss, *Chem. Rev*., 1997, 97, 3133-3159
[2] D. C. Bassett*, Polymer*, 2006, 47, 5221.
[3] S. Zhang, M. L. Minus, L. Zhu, C.-P. Wong, S. Kumar, *Polymer*, 2008, 49, 1356.
[4] J. K. Keum, C. Burger, F. Zuo, B. S. Hsiao, *Polymer*, 2007, 48,4511.
[5] A. Nogales, R. H. Olley, G. R. Mitchell, *Macromol. Rapid Commun.,* 2003, 24, 496.
[6] A. Nogales, G. R. Mitchell, A. S. Vaughan, *Macromolecules*, 2003, 36, 4898.
[7] J. Siripitayananon, S. Wangsoub, R. H. Olley, G. R. Mitchell, *Macromol. Rapid Commun.*, 2004, 25, 1365.
[8] A. Nogales, S. A. Thornley, G. R. Mitchell, *J. Macromol. Sci.:Phys.* 2004, B43, 1161.
[9] S. Yamasaki, Y.Ohashi, H.Tsutsumi, K.Tsujii, *Bull. Chem. Soc. Jpn.,* 1995, 68,146-151
[10] J.Daintith, A Dictinary of Chemistry, 5th ed, Oxford University Press, 2004
[11] W.H.Brown, Organic Chemistry, Saunder College Publishing, 1995
[12] S. Wangsoub, R. H. Olley, G. R. Mitchell, *Macromol. Chem. Phys.,* 2005, 206, 1826.
[13] S.Wangsoub, Davis F.J., Mitchell G.R., Olley R.H., *Macromol. Rapid Commun*. 2008, 29, 1861–1865

http://www.paccon2010.sci.ubu.ac.th/ab_sub_guide

Preparation and characterization of melt free-radical grafting of maleic anhydride onto poly (lactic acid)

A.Teamsinsungvon[1, 2], Y. Ruksakulpiwat[1, 2], K. Jarukumjorn[1, 2*]

[1] School of Polymer Engineering, Institute of Engineering, Suranaree University of Technology, Nakhon Ratchasima, Thailand 30000

[2] Center of Excellence for Petroleum, Petrochemicals and Advanced materials, Chulalongkorn University, Bangkok, Thailand 10330

*E-mail: kasama@sut.ac.th

Abstract: Poly (lactic acid) (PLA), a biodegradable polyester, derived from renewable resources has been widely used in biomedical and packaging applications. However, the shortcomings for using PLA include its processing instability, low melt viscosity and low flexibility. The free-radical grafting of PLA has been reported to enhance physical and chemical properties and/or improve the processability of PLA. Moreover, PLA grafted with monomers containing functional groups such as anhydride, carboxylic acid is used to improve compatibility between PLA and other biodegradable polymers or PLA and natural fibers. In this study, maleic anhydride monomer (MA) was grafted onto PLA in the presence of dicumyl peroxide (DCP) in an internal mixer. The effects of initiator and monomer concentration on the grafting level were investigated. The quantity of grafted anhydride was determined by the titration method. In addition, Fourier transform infrared spectrometer (FTIR) and melt flow index (MFI) measurement were used to characterize the grafted PLA. Increasing monomer and initiator concentrations resulted in an increase in the grafting level and MFI.

Introduction

Poly (lactic acid) (PLA) is known as a biodegradable thermoplastic polymer with widely potential applications [1, 2]. PLA has a number of interesting properties including biodegradability, biocompatibility, high strength and high modulus [3-5]. For this reasons, PLA is an interesting candidate for producing package materials. However, its high brittleness, low toughness and high cost limit its application [6].

To overcome these limitations, combining PLA with nature materials and synthetic polymers provides ways of cost reduction and combined properties. Unfortunately, simple PLA composites with natural materials and polymer blends have poor mechanical properties because of the lack of interfacial adhesion [7].

PLA grafted with monomers e.g. anhydride, carboxylic acid has been used to improve the interfacial adhesion between PLA and other polymers [8, 9] or PLA and fillers [10]. It is common to use maleic anhydride (MA) monomer to graft onto PLA because of its good reactivity and controllability in free radical polymerization [11, 12].

The objective of this work was to investigate the effects of DCP as an initiator and MA monomer concentration on the grafting level of maleic anhydride-grafted-PLA (PLA-g-MA).

Materials and Methods

The materials used in this study were poly (lactic acid) (PLA Grade 4042, NatureWorks LLC), Maleic anhydride (MA, Sigma-Aldrich) and dicumyl peroxide (DCP, Aldrich Chemicals, 98%) as a free radical initiator.

The grafting reaction was carried out in an internal mixer (Haake Rheomix, 3000P). PLA pellets were dried at 70ºC for 4 hrs before mixing. The mixer temperature was kept at 170ºC. A rotor speed was 50 rpm and mixing time was 10 min. The MA contents were 0.5, 1.0, 1.5, 2.0 wt% and DCP contents were 0, 0.1, 0.25, 0.5 wt%.

The quantity of maleic anhydride content on PLA was determined by titration of acid groups derived from anhydride functions using phenolphthalein as an indicator. Samples were dissolved in chloroform and precipitated with methanol to remove residual MA and initiator. Then, the grafted PLA was accurately weighed and heated in xylene for 2 hrs and the hot solution was then titrated immediately with KOH (alcohol solution). The acid number and the grafting level (%G) were calculated using Eq. (1) and Eq. (2), respectively. Pure PLA without MA was also titrated under the same conditions to obtain blank values [13].

$$\text{Acid number (mg KOH/g)} = \frac{V_{KOH}(ml) - N_{KOH}(N)}{sample(g)} \times 56.1 \quad (1)$$

$$\text{G\%} = \frac{Acid\ number}{2 \times 561} - M_0 \times 98.06 \times 100\% \quad (2)$$

Where N is the normality (mol/l), V is the volume (ml), M_0 is the blank titration value of pure PLA and 98.06 is the molecular weight of MA.

The extracted samples were made into thin films by compression molding at 170ºC. The grafting

identification of MA onto PLA was determined by FTIR (BRUKER, TENSOR 27). The spectra were recorded in the 400-4000 cm^{-1} region with 4 cm^{-1} resolution.

Melt flow index (MFI) of grafted polymers were measured at 170ºC with a load of 2.16 kgs.

Results and Discussion

The FTIR spectra of PLA, MA and PLA-g-MA with various DCP and MA contents are shown in Figure 1 and 2, respectively. The characteristic transitions of PLA at 3300-3700, 1700-1760, and 500-1500 cm^{-1} appeared in the spectra of all PLA samples, while two extra shoulders at 1791 and 1851 cm^{-1} were observed in maleic anhydride spectrum [13, 14]. These features are characteristic of anhydride carboxyl groups [13, 15]. From Figure 1, the peaks of anhydride carbonyl group were found only in the grafted PLA with 0.25 wt% DCP (at 2.0 wt% MA). In addition, it can be observed these peaks in the grafted PLA with 1.5 and 2.0 wt% MA (at 0.5 wt% DCP) as shown in Figure 2. This confirmed that the discernible shoulder in the grafted PLA at 1791 and 1851 cm^{-1} demonstrated grafting of MA onto PLA.

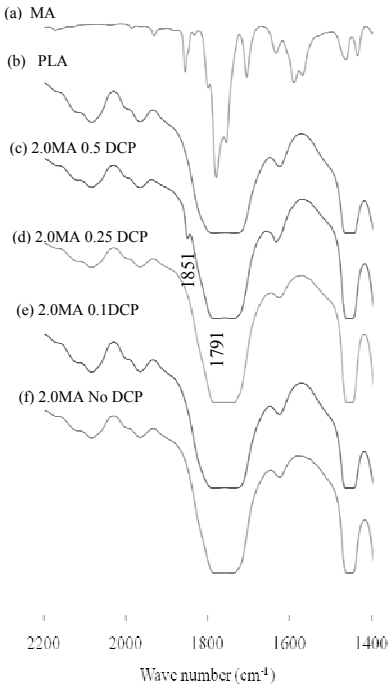

Figure1. FTIR spectra of PLA, MA and PLA-g-MA with different DCP contents.

The grafting levels of PLA-g-MA are shown in Table 1. No grafting level was found in the grafted PLA samples containing 0, 0.1 wt% DCP with 2.0 wt% MA and 0.5, 1.0 wt% MA with 0.5 wt% DCP. The result agreed with FTIR observation. Incorporating DCP into PLA generated more radical sites on PLA backbone for the grafting reaction [16]. With increasing the MA concentration, the probability of PLA macroradicals reacting with the MA is higher leading to increasing grafting level. The variation of MFI with the concentration of MA and DCP was illustrated in Table 1. MFI data showed that all the grafted samples had higher MFI (i.e. lower viscosity) than that of pure PLA (23.70 g/10 min). In addition, MFI of PLA-g-MA increased with increasing DCP and MA concentration. With the same amount of MA (2 wt%), the MFI of grafted PLA with adding DCP was higher than the grafted PLA without DCP because increasing DCP content might reduce chain of PLA macroradicals by chain scission [7]. Similarly, in the case of the modification of polypropylene (PP), the incorporation of peroxide caused chain scission of PP and the presence of MA also caused further chain scission of the PP chain [17]. On the other hand, this result was different from what was found in the modification of polyethylene (PE). The addition of peroxide caused branching and gelation and the presence of MA further promoted branching and gelation [18].

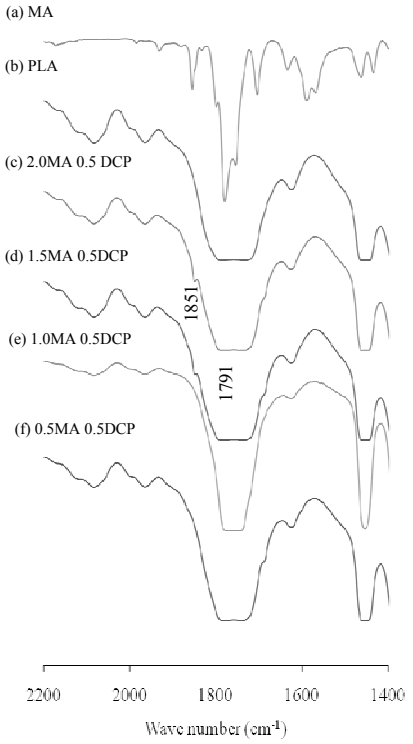

Figure 2. FTIR spectra of PLA, MA and PLA-g-MA with different MA contents.

Table 1: MFI of PLA and PLA-g-MA and grafting level PLA-g-MA.

ID No.	PLA sample		MFI (g/10 min)	%G
	Wt% MA	Wt% DCP		
1	Pure PLA		23.70	-
2	2.0	-	107.04	-
3	2.0	0.10	165.25	-
4	2.0	0.25	179.65	0.10
6	0.5	0.50	113.95	-
7	1.0	0.50	116.46	-
8	1.5	0.50	127.86	0.06
9	2.0	0.50	173.36	0.12

Conclusions

The grafting level was influenced by initiator and monomer concentrations. An increase in monomer concentration resulted in an increse in the grafting level of PLA-g-MA. MFI of the grafed PLA increased with increasing DCP and MA concentrations which indicated a decrease in viscosity by the chain scisson of PLA molecules.

Acknowledgements

The authors wish to acknowledge for financial support granted by Suranaree University of Technology and Center of Excellence for Petroleum, Petrochemicals and Advanced Materials and Dr. Wanwisa Pateeanasiriwisawa (National Synchrotron Research Center, NSRC) for assistance with FTIR measurements.

References

[1] M. Baiardo, G. Frisoni, M. Scandola, M. Rimelen, D. Lips and K. Ruffieux, *J. Appl. Polym. Sci*. 90 (2003), pp. 1731-1738.
[2] K. Arakawa, T. Madaa, S. Parka, and M. Todoa, *Polym.Test.* 25 (2006), pp. 628-634.
[3] N. Ljungberg, and B. Wesslen, *Polymer*. 44 (2003), pp. 7679-7688.
[4] N. Ljungberg and B. Wesslen, *Biomacromolecules*. 6 (2005), pp. 1789-1796.
[5] R. Auras, B. Harte and S. Selke, *Macromol Biosci*. 4 (2004), pp. 835-864.
[6] J. Yeh, C. Huang, W. Chai and K. Chen, *J. Appl. Polym. Sci,* 112 (2009), pp. 2757-2763.
[7] D. Carlson, L. Nie, R. Narayan and P. Dubois, *J. Appl. Polym. Sci.* 72 (1999), pp. 477-485.
[8] W. Jang, B. Shin, T. Lee and R. Narayan, *J. Ind. Eng. Chem*. 13 (2007), pp. 457-464.
[9] H. Yuan, Z. Liu and J. Ren, *Polym*. *Eng*. *Sci.*49 (2009), pp. 1004-1012.
[10]L. Jiang, B. Liu and J. Zhang, *Ind. Eng. Chem. Res*. 48 (2009), pp. 7594-7602.
[11]C. Jiang, S. Filippi and P. Magagnini, *Polymer.* 44 (2003), pp. 2411-2422.
[12]C. Chen, S. Peng, B. Fei, Y. Zhuang, L. Dong, Z. Feng, S. Chen and H. Xia, *J Appl. Polym. Sci.* 88 (2003), pp. 659-668.
[13]C. Wu, *Polym. Degrad. Stab.* 80 (2003), 127–134.
[14]F. Yao, W. Chen, H. Wang, H. Lin, K. Yao and P. Sun, *Polymer*. 44 (2003), pp. 6435-6441.
[15]J. John, J. Tang, Z. Yang and M. Bhattacharya, *J. Polym. Sci. Part A Polym. Chem.* 35 (1997), pp. 1139-1148.
[16]R. Maliger, S. McGlashan, P. Halley and L. Matthew, *Polym*. *Eng*. *Sci.* 46 (2006), pp. 248-263.
[17]P. Callais and R. Kazmierczak *ANTEC*' 90 (1990), pp. 1921-1923.
[18]A. Hogt, *ANTEC' 88* (1988), pp. 1478-1480.

Direct electrochemistry of methylene blue-carbon nanotubes nanohybrid modified glassy carbon electrode for hemoglobin detection

S. Pakapongpan[1], W. Surareungchai[1,2] and R. Palangsuntikul[1*]

[1] Biological Engineering Program, King Mongkut's University of Technology Thonburi, Bangmod Campus, Pracha-utit Rd., Bangkok, Thailand 10140

[2] School of Bioresources and Technology, King Mongkut's University of Technology Thonburi, Bangkhuntien Campus, Bangkhuntien-Chaitalay Rd., Bangkok, Thailand 10150

[*] E-mail: rungtiva.pal@kmutt.ac.th

Abstract: A biosensor for hemoglobin has been constructed by adsorbing the redox mediator, methylene blue (MB), onto multi-wall carbon nanotubes (MWNTs) through hydrophobic interaction. Nanohybrid (MB-MWNTs) was employed to establish the feasibility of fabricating highly effective biosensors for low-level hemoglobin determination. The electrochemical and electrocatalytic activity of the modified electrode were studied using cyclic voltammetry (CV), differential pulse votammetry (DPV) and flow injection analysis (FIA). The excellent electrocatalytic activity for reduction of hemoglobin and good stability resulted in the detection of hemoglobin with a wide range of determination from 5×10^{-9} to 2×10^{-6} M and with a detection limit of 3.7 nM (*S/N*=3).

Introduction

Hemoglobin (Hb) is an important protein in red blood cells, functions physiologically in the storage and transport oxygen in mammalian blood. As Hb is involved in many clinical diseases such as anemia, leukemia, thalassemia, heart disease, excessive loss of blood, it is one of the most important measurements required in clinical analysis. In general, the determination of Hb is carried out with spectrophotometric method (KCN method), however, this method often requires not only highly purified and very toxic reagents, but also time-consuming sample pretreatment [1].

There has been considerable interest in the electrochemical determination of hemoglobin. Electrochemical methods have been widely used for measuring various biological molecules due to their advantages such as high sensitivity, relatively low cost of realization, miniaturization, high rapid response time and also portability [2]. Most biomacromolecules exhibit slow electron transfer at the electrode. The electron transfer between protein and the electrode is difficult because of their extended three-dimensional structure. Thus, the use of a mediator as an electron transfer intermediate can enhance electron transfer [3]. To date, many compounds have been used as a mediator to enable efficient electrocatalytic reaction with Hb. The oxidation or reduction of Hb were catalyzed by many types of dyes such as methylene blue [1, 4, 5, 6], nile blue [7] and Prussian blue [8] and other types of mediators such as poly-β-aminoanthraquinone [9], riboflavin [10] and 9,10-anthraquinone [11]. From our knowledge, methylene blue (MB) is a type of blue dye which has been extensively used as a redox mediator because of its properties such as good stability, reversibility and its formal potential (E_0) is between −0.1 and −0.4 V which is very close to most of the biomolecular redox potentials. Thus the chemically modified electrodes based on this dye as an electron mediator system may be of great interest for developing biosensors.

In addition, the performance of biosensor is mainly affected by the electrocatalytic activity of modified electrode materials and composites. Nanomaterials have received great attention in recent years in different fields due to their enormous potentials. Carbon nanotubes (CNT) have recieved attention as electrochemical sensor due to their display attractive structural, mechanical, and electronic properties, including improved electrochemical activity and promote electron transefer [12].

In this study, a simple method for modification of the electrode for Hb detection was developed. The integration of multi-wall carbon nanotubes (MWNTs) with MB can be useful for amplifying the signal and enhancing its sensitivity since non-covalent immobilization of MB onto MWNTs modified electrode will endow the high stability to the resulting electrode. Moreover, the advantages of MB-MWNTs nanohybrid includes its stability of MB on CNT and its high electrocatalytic activities. Therefore, the challenge of using MB-MWNTs nanohybrid is applying as biosensor for detection of hemoglobin.

Materials and Methods

Reagents and materials: Hemoglobin (from human blood) was obtained from Sigma Chemical company, Methylene blue was obtained from Fluka, Multi-wall carbon nanotubes was obtained from Cheap Tube Inc. All solutions were prepared with double-distilled water. NaH_2PO_4 and Na_2HPO_4 containing KCl were mixed together to prepare the buffer solutions for all experiment.

Apparatus: All electrochemical experiments were carried out with Potentiostat (Autolab PGSTAT10, Ecochemie, the Netherlands) in a conventional three electrode electrochemical cell using glassy carbon as

working electrode, platinum electrode as counter electrode and Ag/AgCl saturated KCl as the reference electrode.

Preparation of the MB-MWNTs nanohybrid modified electrode: 2 mg of MWNTs and 5 mg of MB were dissolved in 10 ml of distilled water. MB was attached to the surface of MWNTs by sonicating for 2 hours at room temperature then the mixture solution was filtered with the filter paper and then washed with distilled water several times to remove non-absorbed MB. After that, the MB-MWNTs nanohybrid was dispersed in 250 µl of distilled water. The MB-MWNTs nanohybrid modified electrode was fabricated by casting 5 µl of the solution on the surface of a glassy carbon electrode and followed by air drying for 8 hours. The electrode with distilled water several times was rinsed before use. All solutions were deoxygenated by bubbling highly pure nitrogen for at least 10 minutes.

Results and Discussion

The stability and the electrochemical behavior of MB-MWNTs modified electrode were studied by cyclic voltammetry as shown in Figure 1. The result showed that the oxidation and reduction peak potentials appear at -0.25 V and -0.27 V and the redox peak current maintained the same original intensity after 100 scan cycles which indicated that the MB-MWNTs modified electrode is very stable and no leakage of MB from the electrode surface occurred.

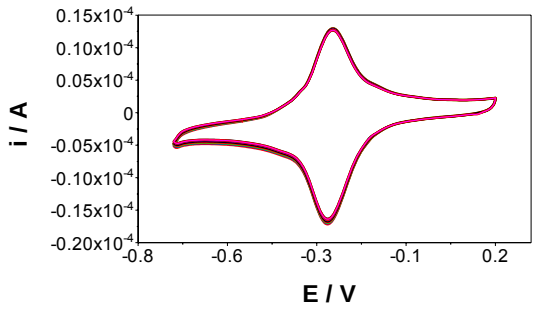

Figure 1. Cyclic voltammogram of MB-MWNTs modified electrode on continuously scanning 100 cycles at scan rate 50 mV/s.

Electrocatalytic reduction of hemoglobin at the MB-MWNTs modified electrode

In order to study the electrocatalytic response of MB-MWNTs modified electrode to Hb, the cyclic voltammetry was used to investigate. Figure 2 shows the cyclic voltammogram of MB-MWNTs modified electrode in the absence (curve a) and the presence (curve b) of 0.5 uM Hb. We found that the oxidation and reduction peak current are 1.1 uA and -1.25 uA, respectively. After addition of 0.5 uM of Hb to the solution, the reduction peak current was increased to -3.33 uA and the oxidation peak current was reduced. The result indicated that the MB-MWNTs modified electrode enhances the electrocatalytic response towards Hb reduction.

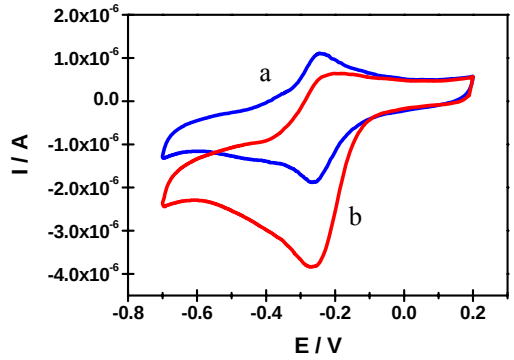

Figure 2. Cyclic voltammogram of MB-MWNTs modified electrode 0 M Hb(a) and 0.5 µM Hb(b). At scan rate 20 mV/s.

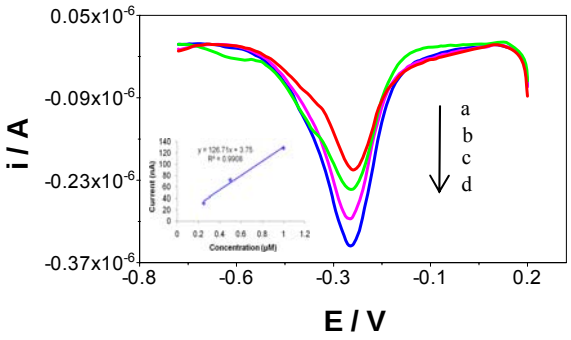

Figure 3. Differential pulse voltammograms of MB-MWNTs modified electrode with 0 M Hb (a) 0.25 µM (b) 0.5 µM(c) and 1 µM (d) Hb

Figure 3 shows the differential pulse votammogram of Hb on MB-MWNTs in the potential range from -0.7 V to +0.3 V. The reduction peaks currents were increased continually with increasing concentrations of Hb. The resulting catalytic peak currents are proportional to the concentration of Hb in the range of 2.5×10^{-7} to 1×10^{-6} M

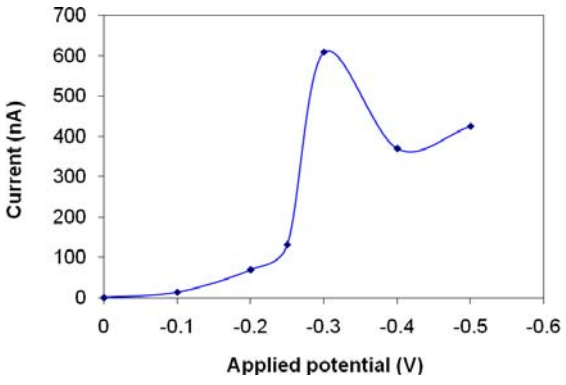

Figure 4. Hydrodynamic voltammogram for 1 µM Hb on the MB-MWNTs modified electrode

However, the electrode fouling from absorbed protein is the problem of electrochemical method. In order to solve this problem, flow injection analysis is an appropriate method as flow system can decrease the staying time of the protein and the electrode surface. 1 uM of Hb was injected to the flow injection analysis system at different potentials in the range of 0 to -0.5 V. The current increased when the potential was varied from 0 to -0.3 V and inclined to level off at -0.3 V and beyond. Therefore, -0.3 V was selected as the working potential for optimum signal.

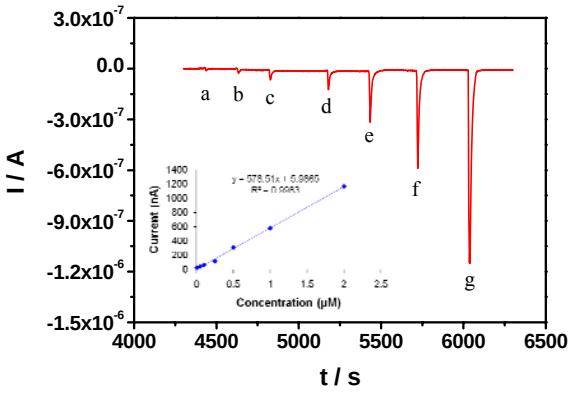

Figure 5. Flow injection amperometric response of Hb on MB-MWNTs modified electrode at -0.3 V. Injection concentration of Hb, a: 0.005, b: 0.05, c: 0.1, d: 0.25, e: 0.5, f: 1, g: 2 μM (Inset: linear plot of the currents and the concentration of Hb)

Linearity and detection limit of MB-MWNTs modified electrode

The analytical performance of MB-MWNTs modified electrode and the determination of Hb can be carried out with flow injection analysis. The working potential was fixed at -0.3 V. Flow injection response peak currents for increasing Hb concentration are depicted in Figure 5. The resulting calibration plot (inset) of the currents increases linearly with the concentration of Hb.

The sensor had a detection limit of 3.7 nM (*S/N*=3) with a linear range from 5×10^{-9} to 2×10^{-6} M for Hb. and the sensitivity determined from this plot was calculated to be 578.51 mA M^{-1}. The linear equation was y = 578.51x + 5.9865. The sensor showed excellent analytical performance, high stability, sensitivity and catalytic activity due to the properties of these nanohybrids which could promote the electron transfer between Hb and the electrode surface.

Conclusions

The MB-MWNTs nanohybrids have been successfully applied to determine Hb concentration. The developed sensor demonstrated good stability and high sensitivity. This platform could be advantageous for medical analysis and can be applied for different types of biosensor.

References

[1] H.Y. Chen, H.X. Ju, and Y.Q. Xun, *Anal. Chem.* **66** (1994), pp. 4538-4542.
[2] D.R. Thevenot, K. Toth, R.A. Dusrt and G.S. Wilson, *Biosens. Bioelecs.* **16** (2001), pp. 121-131.
[3] A. Chaubey and M.B. Malhotra, *Biosens. Bioelecs.* **17** (2002), pp. 441-456.
[4] J. Ye and R.P. Baldwin, *Anal. Chem.* 60 (1988), pp. 2263-2268.
[5] C.M.A.Brett, G. Inzelt and V. Kertesz, Anal. Chim. Acta. **385** (1999), pp. 119-123.
[6] Y. Xian, F. Liu, Y. Xian, Y. Zhou and L. Jin, *Electrochim. Acta.* **51** (2006), pp. 6527–6532.
[7] D.M. Zhou and H.Y. Chen, *Electroanalysis*. **9** (1997), pp. 399-402.
[8] Y. Xian, Y. Zhou, Y. Xian, L. Zhou, H. Wang and L. Jin, Anal. Chim. Acta. **546** (2005), pp. 139–146.
[9] H. Ju, H. Sun and H. Chen, Anal. Chim. Acta. **327** (1996), pp. 125-132.
[10] W. Sun, J. Kong and J. Deng, *Electroanalysis.* **9** (1997), pp. 115-119.
[11] Z. Zhu and N.Q. Li, *Electroanalysis.* **10** (1998), pp. 643-646.
[12] A. Lourdes, Y. Paloma and M.P. José, Anal. Chim. Acta. **622** (2008), pp. 11-47.

Detection of yellow head virus (YHV) by surface plasmon resonance

N. Intaraprasit[1], J. Sansatsadeekul[2], K. Boonkitpatarakul[1],K. Mai-ngam[1]

[1]National Metal and Materials Technology Center, Prathumthani, Thailand
[2]Department of Chemistry, Faculty of Science, Mahidol University, Nakornprathom, Thailand

Abtract:Yellow head virus (YHV) is one of the major viral pathogens that cause mortality in shrimp. In this study, surface plasmon resonance (SPR) analysis was selected to monitor biomolecular recognition system because a label-free detection can be done rapidly in real-time with high sensitivity. We prepared a bimodal dextran SPR sensor chip which can be divided into two regions: the inner and the outer layers. The inner layer containing both short- (MW 1,500) and long-chain (MW 100,000) dextran segments can serves as a barrier to non-specific protein adsorption as seen that the non-specific adsorption of non-diluted hemolymph protein solution could be completely eliminated. The outer layer containing only the longer chain segments can detect the specific binding interaction between anti-YHV and YHV. The detection limit of YHV was 5.4 x 10^7 varions/ml in PBS buffer.

Introduction

Surface plasmon resonance (SPR) biosensors exploit surface electromagnetic waves to probe the interactions between an analyst from solution and a biomolecular recognition element immobilized on the sensor surface. SPR is sensitive to the changes in the thickness or refractive index of dielectric added layers above specific metals (e.g. gold and silver). This label-free technique can be performed in real time, thereby allowing for kinetic as well as thermodynamic parameters to be determined. For more than a decade, remarkable progress has been made in the development of SPR-based optical sensor and its applications in areas such as environmental monitoring, biotechnology, medical diagnostics, drug screening and food safety [1].

The carboxymethyldextran-modified sensor chip (CM5; Biacore) is the most widely used SPR chip because it is designed to provide high binding capacity and low non-specific binding. The matrix is constructed from a composite of a hydrophilic SAM and covalently bound carboxymethyldextran brushes (MW 500,000). A hydroxyl-terminated self assembling monolayer (SAM) on gold surface is treated by epichlorohydrin to generate epoxy groups. Dextran matrix is then generated on the chip surface by non-selectively reaction of the epoxy groups with the hydroxyl groups along the dextran chain. Subsequent reaction with bromoacetic acid results in the formation of carboxylic groups.

Yellow-head virus (YHV) is one of viral pathogens in shrimp that has effect on mortality rate of shrimp in Thailand and the production decreased by about 5000 metric tons per year [2]. Therefore, diagnostic methods with rapid and sensitive detection are needed for management of shrimp disease.

In this paper, a novel design SPR chip having a bimodal molecular weight (MW) dextran composition (Figure 1) was chosen to quantitatively investigate specific binding of YHV to anti-YHV ligands and non-specific adsorption of hemolymph proteins from healthy shrimps to the sensor chip surface. The prepared dextran layer can be crudely divided into two regions: the inner and the outer layers. The inner layer, i.e., the layer adjacent to the sensing surface, contains both short- and long-chain segments and serves as a barrier to non-specific protein adsorption. The outer layer contains only the longer chain segments with functional groups for immobilization of the affinity ligands.

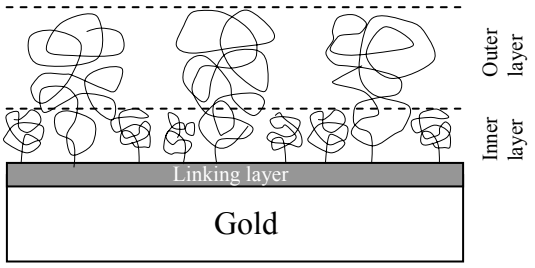

Figure 1. Dextran based SPR sensor chips: bimodal brushes with single anchor point.

Materials and Methods

Preparation of dextran aldonic acid: Dextran aldonic acid was prepared according to the method prescribed by Tianhong [3]. Briefly, a 30 ml aq. solution containing 5 g of dextran (MW 1,500 and 100,000) was added with iodine (0.1 M) and potassium hydroxide (0.4 M) and stirred at room temperature for 24 h. The crude product was treated with silver carbonate to precipitate excess iodine. The product was passed through a strong cationic exchange column packed with amberlite IR-120 to convert dextran silver aldonate to dextran aldonic acid. The solution was lyophilized.

Preparation of allyl dextran aldonic acid: The obtained dextran aldonic acid (1 g) was further reacted with allyl bromide with 1 to 1 equivalent in the presence of sodium hydroxide (0.5 g) and sodium borohydride (0.04 g) at 60 °C according to the method reported by Vera [4] with some modifications. After 3

h, the solution was neutralized with acetic acid. Subsequent to the reaction mixture cooling, the allyl dextran was precipitated with ethanol. The precipitate was redissolved in deionized water, dialyzed and lyophilized.

Immobilization of high MW allyl dextran aldonic acid on bare gold chip: A piranha-cleaned SPR gold chip (Ssens) was immersed in 10 mM 16-mercaptohexadecanoic acid solution in ethanol for 24 h to form a carboxylic terminated self assembled monolayer (SAM). The carboxylic groups were activated by 1-ethyl-3-[3 (dimethylamino)propyl] carbodiimide (EDC; 0.2 M), *N*-hydroxysuccinimide (NHS; 0.04 M) and 2-Morpholinoethanesulfonic acid monohydrate (MES; 0.5 M) for 12 h. After rinsing with deionized water for several times, the EDC/NHS/MES activated chip was reacted with 10 mM cysteamine aq. solution for 24 h to form an amine terminated self assembled monolayer (SAM). The obtained amine functionalized chip was soaked in allyl dextran aldonic acid solution (1 mg/mL; MW 100,000) in 1 M sodium acetate buffer pH 4.5 in the presence of EDC 0.2 M, NHS 0.05 M and MES 0.5 M at room temperature for 24 h. To terminate the reaction, saturated sodium hydrogencarbonate solution (pH 10) was added. The obtained sensor chip was washed with deionized water for several times.

Immobilization of low MW dextran aldonic acid on bare gold chip: The obtained chip was soaked in dextran aldonic acid solution (1 mg/mL; MW 1,500) in 1 M sodium acetate buffer pH 4.5 in the presence of EDC 0.2 M, NHS 0.05 M and MES 0.5 M at room temperature for 24 h. The obtained sensor chip was washed with deionized water for several times.

Amine functionalization of the bimodal dextran chip: The obtained chip was soaked in cysteamine (0.260 mM) and ammonium persulfate (0.018 mM) in DMSO to change allyl groups to active amine functional groups at 50 ^{o}C for 2 h. After the reaction, the obtained sensor chip was washed with deionized water for several times.

Determination of specific and non-specific binding on the biosensor chip using SPR: The modified sensor chip was placed in the SPR imaging instrument. An SPR imaging system builted by the Thailand National Electronics and Computer Technology Center was employed. Sample (300 µL) was loaded with a syringe injection system. The LED laser is used as a light source to make a monochromatic light with wavelength of 680 nm. The polarizer, which permits measurements with both p- and s-polarized light, is used as a reference. The prepared sensor chip was attached to a prism of the SPR device using a matching liquid. The mobile phase solution was a 10 mM HBS (pH 7.4).

The chip was equipped with a multi-channel polydimethylsiloxane (PDMS) flow cell to control the liquid flow. An anti-YHV solution (50 ng/ml) in 1 M sodium acetate buffer pH 4.5 in the presence of EDC (0.2 M), NHS (0.05 M) and MES (0.5 M) was injected at a flow rate of 10 µL/min in all flow channels. Activated carboxyl groups were then quenched by reaction with 1 M ethanolamine at 25 µL/min flow rate. To evaluate non-specific binding of hemolymph proteins to the sensor surface, healthy shrimp hemolymph with a protein concentration of 20 ng/ml was injected at a flow rate of 5 µL/min. The running buffer was passed over the sensor surface with a flow rate of 50 µl/min. The change in the SPR signal was recorded as non-specific binding. Finally, different concentrations of YHV in PBS (5.4×10^7 to 1.4×10^{10} varions/ml) were injected to unused flow channels at a flow rate of 5 µl/min to evaluate specific binding interaction.

Results and Discussion

The success of each modification step in the preparation of the bimodal carboxylic dextran sensors was characterized by ^{1}H-NMR (data not shown), FTIR (data not shown) and contact angle measurements. The contact angle of amine terminated SAM surface (54.2° ± 3.8°) was significantly lower than that of bare gold (75.0° ± 6.7°) due to the hydrophilicity of the amine end groups. Grafting of the high MW allyl dextran aldonic acid could be confirmed by the decrease in water contact angle to 59.7° ± 1.0°. After grafting of short chain dextran aldonic acid and further amine group generation, the contact angles became lower as 46.4° ± 4.0°.

Antibody was covalently immobilized onto biosensor chip surface via carbodiimide activation. The injection of anti-YHV at a concentration of 50 ng/ml resulted in an increase in reflectivity of 0.95 ± 0.19 %. Figure 2 shows a sensorgram of non-specific adsorption of healthy shrimp hemolymph proteins (without dilution) to the anti-YHV immobilized chip surface. The signal returned back to the baseline once the injected sample was eluted out of the flow cell, suggesting that the SPR signal variation is due to the refractive index difference between the running buffer and the shrimp hemolymph solution. The result showed that the inner dextran layer containing both short- and long-chain segments could completely prevent non-specific healthy shrimp protein adsorption (% reflectivity change = 0).

Figure 3 shows a sensorgram of specific binding of YHV (1.4×10^{10} virions/mL) in PBS to the anti-YHV immobilized chip surface. A shape characteristic of antigen–antibody interaction was found as a new baseline attaining at a higher reflectivity after the elution of the mixture of YHV. The specific YHV binding was simply evaluated using the change in the reflectivity before and after injected virus. The SPR signal due to YHV binding was found to be linearly dependent on the YHV concentration in the range of 5.4×10^7 to 1.4×10^{10} varions/ml with a R^2 value of 0.988 (Figure 4).

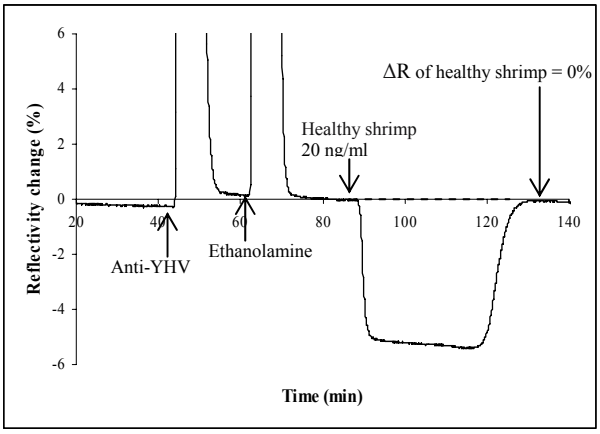

Figure 2. SPR signal for non-specific healthy shrimp protein binding at the concentration of 20 ng/ml.

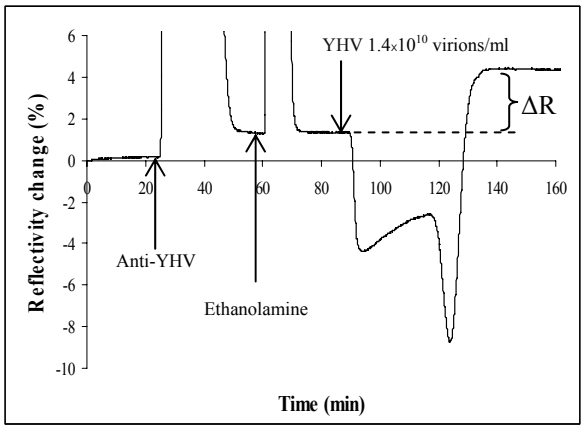

Figure 3. SPR signal for specific YHV binding at the concentration of 1.4 x 10^{10} varions/ml.

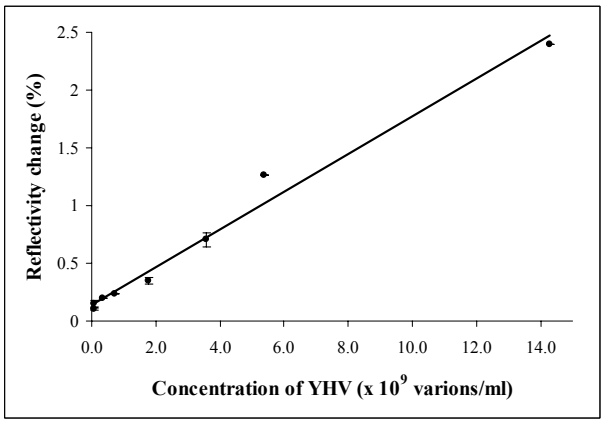

Figure 4. SPR signal for specific YHV binding in various concentration.

Conclusions

In this work, SPR instrument was used for detection of yellow head virus (YHV). We prepared a bimodal dextran sensor chip which was found to completely eliminate non-specific adsorption of non-diluted hemolypmh proteins. The specific interaction between anti-YHV and YHV rapidly in real time with high sensitivities (5.4 x 10^7 varions/ml). The SPR signal due to the specific YHV binding was found to be inearly dependent on the YHV concentration in the range of 5.4 x 10^7 to 1.4 x 10^{10} varions/ml.

Acknowledgement

This work was financially supported by National Metal and Materials Technology Center. The SPR imaging instrument was kindly supported by Dr. Boonsong Sutapan.

References

[1] W. Jean, *Analytical Biochemistry*, vol. 270, 1999, pp. 201–206.
[2] T.W. Flegel, *Aquaculture*, vol. 258, 2006, pp.1-33.
[3] Z. Tianhong and E.M Roger, *Macromolecules*, vol. 24, 1994, pp. 7302-7308.
[4] R.V. David, M.W. Anne, K.H. Carl and F.M. Robert, *Nuclear Medicine*, vol.42, No.6, 2001, pp 951-959.
[5] K. Ryoji, H. Yoshiki, Y. Soichi, Y. Yoshimi, K.Dai, S. Yukar, M.Fumio and N. Osamu, *Sensors and Actuators B*, vol. 130, 2008, pp. 320–325.
[6] Y. Lei, H. Chen, H. Dai, Z.Zeng,Y. Lin, F. Zhou, D. Pang, *Biosensors and Bioelectronics*, vol. 23, 2008, pp. 1200–1207

Hydrophilic property of galvanostatically prepared anodic oxide film on Ti-6Al-4V at a low current density

P. Whangdee[1, 2], D.P. Kashima[1, 2*] and V. Srimaneepong[3]

[1] Research Unit of Advanced Ceramics, Department of Materials Science, Faculty of Science, Chulalongkorn University, Patumwan, Bangkok, Thailand 10330
[2] Research Unit of Advanced Ceramic and Polymeric Materials, National Center of Excellence for Petroleum, Petrochemicals, and Advanced Materials, Chulalongkorn University, Patumwan, Bangkok, Thailand 10330
[3] Department of Prosthetic Dentistry, Faculty of Dentistry, Chulalongkorn University, Patumwan, Bangkok, Thailand 10330

[*]E-mail: dujreutai.p@chula.ac.th, dujreutai@gmail.com

Abstract: Anodic oxide film on Ti-6Al-4V prepared by galvanostatic method has been attracted our attention since it can be accomplished at wide ranges of current density. Due to the limitation of our potentiostat-galvanostat instrument which can be supplied at just only a low current density, we selected to prepare anodic oxide film on Ti-6Al-4V, a useful metal alloy in dental implant, at a low current density (-1 to -2 A/cm^2) and room temperature. The reactions were done in two different kinds of electrolyte, NaOH and H_3PO_4. The formation of anodic oxide film on Ti-6Al-4V included two processes of corrosion potential versus time curves. Firstly, the corrosion increased when the reaction time went by and finally the corrosion decreased due to the passive oxide formed on the surface. XRD patterns of the anodic oxide film using 1M H_3PO_4 as an electrolyte showed TiO on the surface, however, TiO could not be appeared when using 1M NaOH as an electrolyte. SEM micrographs revealed that surface roughness would increase after anodizing. Anodic oxide film formed in 1M H_3PO_4 showed better surface roughness than the other formed in 1M NaOH. The contact angle of both anodic oxide film formed in 1M NaOH and 1M H_3PO_4 were measured compared to the one before anodization. The best results of contact angle of as-anodized film were 46.8° (in 1M H_3PO_4, -1 A/cm^2), 64° (in 1M NaOH, -1.75 A/cm^2) and 88.8° (before anodization). It is indicated that galvanostatic method at a low current density could enhance the hydrophilic property of Ti-6Al-4V alloy. Anodic oxide film was activated by UV irradiation for various time periods up to 2 h and it was found that the contact angle would be decreased but the surface morphology and phase composition was not changed.

Introduction

Ti-6Al-4V alloy is used for dental implants due to the good mechanical properties, high corrosion resistance and excellent biocompatibility [1-5] but not bioactive [1, 6]. Therefore, surface properties of the anodic oxide film is much more important in biocompatibility of titanium implant than the bulk titanium itself [7-9]. Galvanostatic method is one of the important surface modification technique. It has become attractive for preparing oxide film on Ti-6Al-4V alloy because it is easily deposited, rapidly promoted surface roughness and not cost-consuming [10-11].

The surface roughness and wettability of implant may influence the contact between Ti-6Al-4V alloy and living tissues which is so called osseointegration [12]. Furthermore, UV which is not only clean energy science [13] but also enhance hydrophilic properties of TiO_2 [5, 14] and enhance titanium bioactivity. Generally, fluorides in term of NaF contained in commercial toothpastes were used orally and topically to prevent dental caries. Fluorides were harmful to all active metal such as titanium therefore, it would be essential to investigate the effect of corrosion on the titanium in fluoride containing solution [15] because soluble fluoride directly plays a role in enhancing of surface roughness of Ti implant.

The purpose of this study is to investigate the hydrophilic properties of anodic oxide film on Ti-6Al-4V prepared by galvanostatic method at a low current density (-1A/cm^2 to -2A/cm^2). The anodic oxide film formed at such low current density has not been paid much attention by researchers since it is composed of mixed anodic oxide such as TiO, Ti_2O_3, TiO_2, and etc [9]. Moreover, the effect of UV irradiation on the anodic oxide film formed at a low current density and the effect of corrosion on the titanium alloy in fluoride containing electrolyte were also investigated.

Materials and Methods

A working electrode was made from Ti-6Al-4V. The Ti-6Al-4V (1mm×8mm×20mm) was polished with No. 170 diamond plate, washed with distilled water in ultrasonic bath for 15 minutes and dried at a room temperature. Before anodizing, the working electrode was etched in 1 M HF for 1 minute, then washed in distilled water. The anodizing apparatus consisted of three electrode cell : a platinum plate was used as a counter electrode, Ag/AgCl electrode was used as a reference electrode and a Ti-6Al-4V was used as a working electrode. Alkaline solution of 1M NaOH and weak acid solution of 1M H_3PO_4 were used as electrolyte. The addition of different NaF concentration (0.5-3%) in 1M H_3PO_4 was also used as an electrolyte in order to study the corrosion behavior on Ti-6Al-4V surface. The electrochemical behavior was measured by a potentiostat-galvanostat connected to a computer and operated by GPEs program. The experiment was performed by galvanostatic method at a low current

density (-1A/cm^2 to -2A/cm^2). After anodizing, the Ti-6Al-4V was rinsed with distilled water and dried at room temperature.

The hydrophilic property of the anodic oxide film surface was determined by the contact angle of distilled water droplet, measured by a contact angle meters (CAM_PLUS Tantec). The phase component of the anodic oxide film was measured by X-ray diffraction (XRD : D8-Advance, Bruker, Germany). The surface of the anodic oxide film was measured by scanning electron microscope (SEM:JSM-6480LV, JEOL, Japan). The anodic oxide film was irradiated with UV for 2h using a 9W osram dulux s blue UVA (OSRAM, Korea). Finally, the surface roughness was also measured by a profilometer (Talyscan 150, Taylor Hobson, England).

Results and Discussion

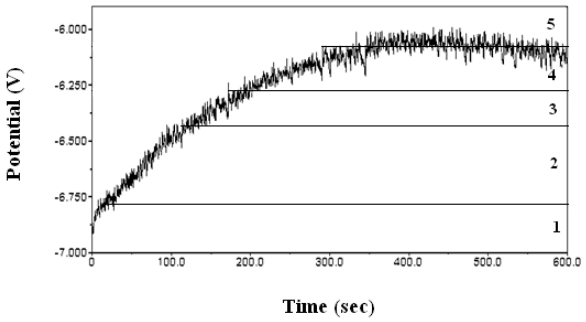

Figure 1. The open circuit potentials of Ti-6Al-4V in 1M H_3PO_4 at -1A/cm^2 during anodizing.

Ti metal which is the main component in Ti-6Al-4V alloy will always react with H_2O or air and become covered with a protective oxide layer. The native oxide film was formed on titanium when exposed to the atmosphere such as polishing or etching. During anodizing, the native oxide film was dissolved and then the selt-passivated film was formed [9].

There were two processes on the open-circuit potential versus time curves, as shown in Figure 1. The voltage-time responses for anodic oxide film in both 1M NaOH and 1M H_3PO_4 to various voltages. Five regions were separated as shown in the following. In the first region, the voltage up to -6.85V, the voltage increased linearly with time, with a slope 3Vs^{-1}. The second region, up to -6.51V, the voltage increased linearly with time, with a slope 1Vs^{-1}. The third region, up to -6.35V, the voltage increased linearly with time, with a slope 0.61Vs^{-1}. The fourth region, up to -6.19V, the voltage increased linearly with time, with a slope 0.37Vs^{-1}. Finally, the slope constant in the fifth region until the end of the experiment, which extended to -6.19V. Further anodizing was not carried out due to consumption of the titanium layer. Our results are similar to the reports of T.H. Tech, et.al. and M.A.M. Ibrahim, et.al. [16-17].

Therefore, this reactions were done in both NaOH and H_3PO_4. The formation of anodic oxide film on Ti-6Al-4V included two processes of corrosion potential versus time curves. Firstly, the corrosion increased when the reaction time went by and finally the corrosion decreased due to the passive oxide formed on the surface.

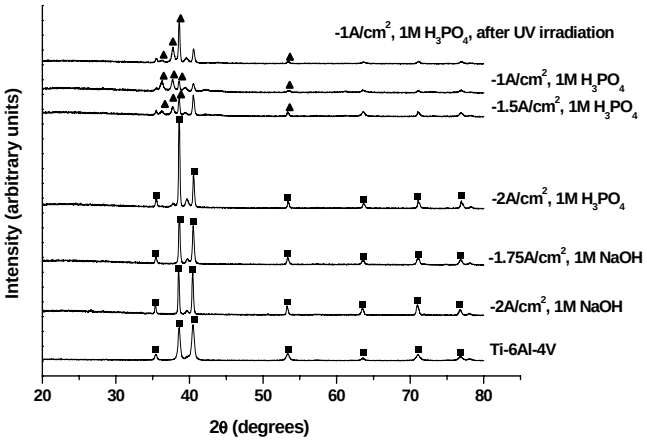

Figure 2. XRD patterns of anodic oxide film formed in both 1M NaOH and 1M H_3PO_4 at low current density ; ▪ Ti and ▲ TiO

XRD patterns of the anodic oxide film using 1M H_3PO_4 as an electrolyte showed TiO on the surface, however, TiO could not be appeared when using 1M NaOH as an electrolyte (Figure 2). It is indicated that the galvanostatic method at a low current density could formed TiO when using 1M H_3PO_4 at -1 A/cm^2 and -1.5 A/cm^2.

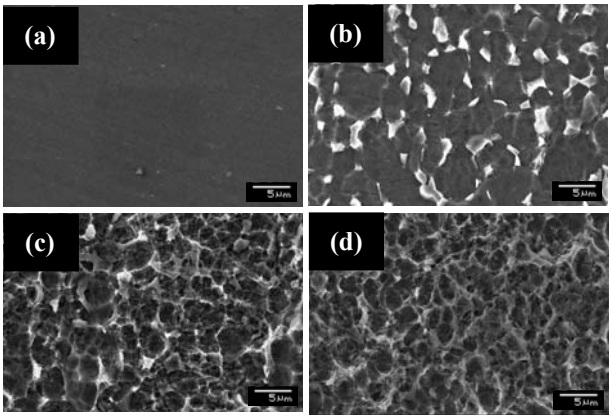

Figure 3. SEM micrographs of anodic oxide film on Ti-6Al-4V surface at various conditions : (a) Ti-6Al-4V before anodization (b) -1.75 A/cm^2, 1M NaOH (c) -1 A/cm^2, 1M H_3PO_4, before UV irradiation (d) -1 A/cm^2, 1M H_3PO_4, after UV irradiation

Figure 3. showed SEM micrographs of anodic oxide film on Ti-6Al-4V surface which revealed that surface roughness increase after anodizing in all samples. Anodic oxide film formed in 1M H_3PO_4 (Figure 3c) showed better surface roughness than the other formed in 1M NaOH (Figure 3b) which is according to the nature of Ti metal, a main component in Ti-6Al-4V alloy that will be rapidly dissolved by strong, and even weak acids [18]. It is indicated that

galvanostatic method could enhance the surface roughness on the Ti-6Al-4V surface.

Figure 4. showed the contact angle of both anodic oxide film formed in 1M NaOH and 1M H_3PO_4 were measured compared to the one before anodization. The best results of contact angle of as-anodic oxide film were 46.8° (in 1M H_3PO_4, -1 A/cm^2), 64° (in 1M NaOH, -1.75 A/cm^2) and 88.8° (before anodization). The present of TiO phase in anodic oxide film formed in 1M H_3PO_4 at a current density of -1 A/cm^2 showed the best contact angle of 46.8°. It is implied that even TiO phase (but not TiO_2) would take part in enhancing of the hydrophilic property. It is indicated that galvanostatic method at a low current density could enhance the hydrophilic property of Ti-6Al-4V.

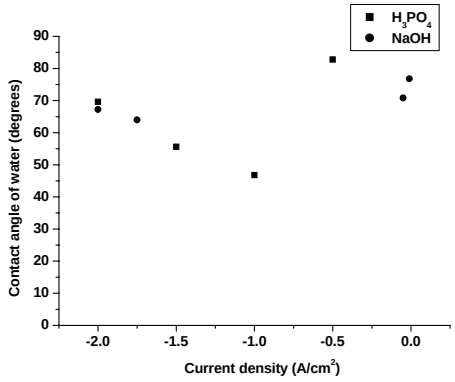

Figure 4. The contact angle of anodic oxide film in both 1M NaOH and 1M H_3PO_4 at different current density

After UV irradiation on the anodic film for 2h (Figure 5.), the contact angle of water droplets was decreased 14.29% and 22.51% for -1A/cm^2 and -1.5A/cm^2, respectively. However, the contact angle of Ti-6Al-4V was not changed after UV irradiation. Figure 6 showed that the hydrophilic status of anodic oxide film formed at -1A/cm^2 in 1M H_3PO_4 could be slightly retained even after storing in the dark environment. After storing the as-anodized film in the dark environment for two weeks, the contact angle increased but the phase composition (Figure. 2) and the surface morphology (Figure. 3d) were not changed [19]. It is indicated that UV could enhance the hydrophilic property of anodic oxide film on the surface.

SEM micrographs of Ti-6Al-4V surface after anodizing in 1M H_3PO_4 at a current density of -1A/cm^2 with different NaF concentration (0.5-3%) were shown in Figure 7. The results showed that surface roughness increased with increasing of NaF concentration (Figure 8). Due to adding fluoride into the electrolyte, it could promote the Ti-6Al-4V potential to be more active and also enhance the corrosion of the Ti-6Al -4V. However, at 3% NaF the surface roughness decreased due to the fluorides which were deposited on the Ti-6Al-4V surface (this results investigated by EDS, data are not shown in this paper).

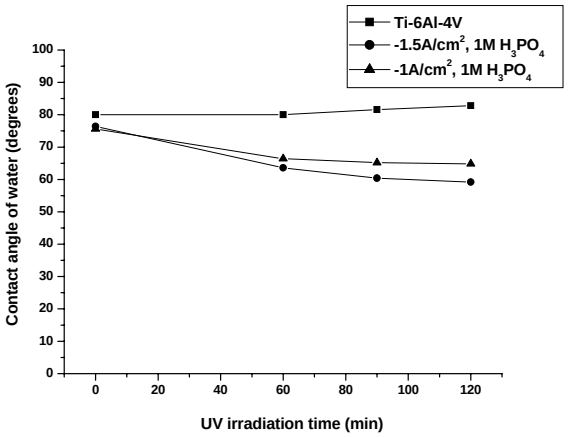

Figure 5. The contact angle versus the time which the water droplet falls on anodic oxide film after UV irradiation in Ti-6Al-4V, -1A/cm^2 and -1.5A/cm^2 in 1M H_3PO_4

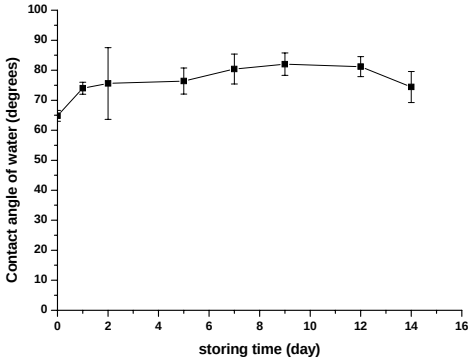

Figure 6. The contact angle versus time of anodic oxide film formed at -1A/cm^2 in 1M H_3PO_4 after storing in the dark environment

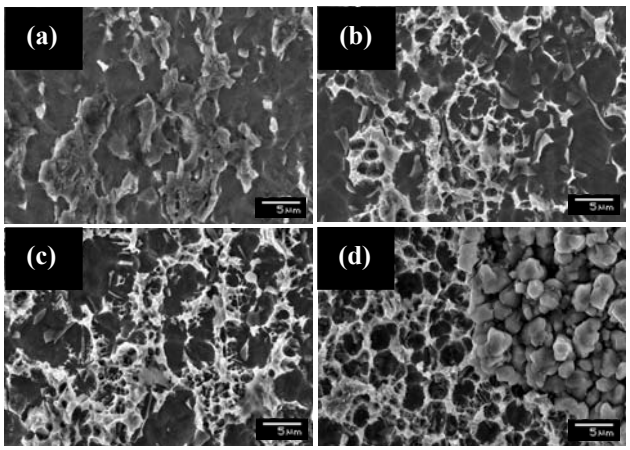

Figure 7. The SEM micrograph of Ti-6Al-4V surface after anodizing in (a) 1M H_3PO_4 + 0.5% NaF (b) 1M H_3PO_4 + 1% NaF (c) 1M H_3PO_4 + 1.5% NaF (d) 1M H_3PO_4 + 3% NaF at a current density of -1A/cm^2

As shown in Figure 9, increasing the NaF concentration (0.5-3%) led to decreasing in the contact angle due to effect of corrosion on Ti-6Al-4V surface

(Figure 7, 8). However, the best result of contact angle which represents the best hydrophilic property was the as-anodized Ti-6Al-4V at -1A/cm^2, in 1M H_3PO_4. The anodic oxide film formed on Ti-6Al-4V at this mentioned condition was TiO film (see XRD pattern in Figure 2). At 3% NaF adding, the contact angle was decreased compared to the one prepared at 0 (without NaF addition), 0.5, 1, and 1.5% of NaF addition due to fluoride effect in corrosion of Ti-6Al-4V surface. However, the surface roughness of as-anodized film on Ti-6Al-4V with 3% NaF addition was smoother than the others (see Figure 8) because high amount of fluoride was deposited on the as-anodized film as shown in Figure 7 d). After UV irradiation, the results showed that the contact angle decreased 8.65%. Therefore adding small amount of fluorides (0.5-1.5%wt) might enhance surface roughness and led to mechanical locking between titanium surface and bone tissue.

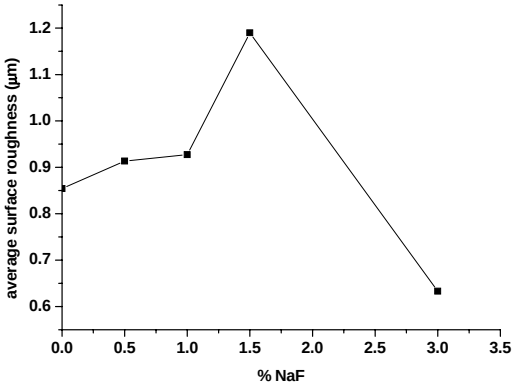

Figure 8. The average surface roughness of Ti-6Al-4V after anodizing in 1M H_3PO_4 with different NaF concentration (0.5-3%) at a current density of -1A/cm^2 in comparison with before NaF addition.

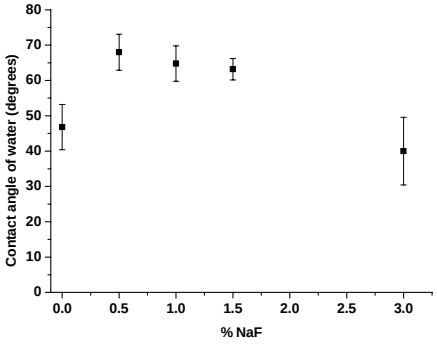

Figure 9. The contact angle of Ti-6Al-4V surface after anodizing in -1A/cm^2, 1M H_3PO_4 with different NaF concentration (0.5-3%)

Conclusions

The galvanostatic method at a low current density could form TiO when using 1M H_3PO_4 at -1 A/cm^2 and -1.5 A/cm^2, which included two process of corrosion potential versus time curves (corrosion and passivation). It could enhance the surface roughness and hydrophilic property of the Ti-6Al-4V alloy. Activated by UV could enhance the hydrophilic property of anodic oxide film on Ti-6Al-4V, the surface morphology and the phase composition were not changed. The fluoride ions adding in 1M H_3PO_4 electrolyte at different NaF concentration could enhance the surface roughness and led to mechanical locking for implants.

Acknowledgements

The financial supports from Research Unit of Advanced Ceramic and Polymeric Materials, National Center of Excellence for Petroleum, Petrochemical and Advanced Materials, Chulalongkorn University; Research Unit of Advanced Ceramics, Department of Materials Science, Faculty of Science, Chulalongkorn University; and Development and Promotion of Science and Technology Talents Project (DPST) were gratefully appreciated.

References

[1] X. Cui, H.-M. Kim, M. Kawashita, L. Wang, T. Xiong, T. Kokubo and T. Nakamura, *Dent. Mater.* **25** (2009), pp. 80-86.

[2] H.-H. Huang and T.-H. Lee*, Dent. Mater.* **21** (2005), pp. 749-755.

[3] Y.-H. Jeong, K. Lee, H.-C. Choe, Y.-M. Ko and W.A. Brantley*, Thin Solid Films*. **517** (2009), pp. 5365-5369.

[4] T. Sonoda and M. Kato, *Thin Solid Films*. **303** (1997), pp. 196-199.

[5] F. Guillemot, M.C. Porte, C. Labrugere and Ch. Baquey, *Colloid Interface Sci.* **255** (2002), pp. 75-78.

[6] B. Yang, M. Uchida, H.-M. Kim, X. Zhang and T. Kokubo, *biomaterials.* **25** (2004), pp. 1003-1010.

[7] E. Byon, S. Moon, S.-B. Cho, C.-Y. Jeoung, Y. Jeong and Y.-T. Sul, *Surf. Coat. Technol.* **200** (2005), pp. 1018-1021.

[8] Y.-T. Sul, C.B. Johansson, Y. Jeong and T. Albrektsson, *Med. Eng. Phys.* **23** (2001), pp. 329-346.

[9] Y. Oshida, *Bioscience and Bioengineering of Titanium Materials*, Elsevier BV, Oxford, UK (2007).

[10] R. Narayanan and S.K. Seshadri, *Corros. Sci.* **49** (2007), pp. 542-558.

[11] H.-J. Song, S.-H. Park, S.-H. Jeong and Y.-J. Park, *J. Mater. Process. Technol.* **209** (2009), pp. 864-870.

[12] C.N. Elias, Y. Oshida, J.H.C. Lima and C.A. Muller, *J. Mech. Behav. Biomed. Mater.* **1** (2008), pp. 234-242.

[13] H. Aita, N. Hori, M. Takeuchi, T. Suzuki, M. Yamada, M. Anpo and T. Ogawa, *Biomaterials***. 30** (2009), pp. 1015-1025.

[14] A. Fujishima, K. Hashimoto and T. Watanabe, *TiO_2 Photocatalysis Fundamentals and Application,* BKC, Tokyo, Japan (1999).

[15] L. Guo, X. Lui, Z. He, J. Gao, J. Yang and T. Guo, *Mater. Lett.* **62** (2008), pp. 2200-2202.

[16] M.A.M. Ibrahim, D. Pongkao and M. Yoshimura, *J. Solid State Electrochem.* **6** (2002), pp. 341-350.

[17] T.H. Teh, A. Berkani, S. Mato, P. Skeldon, G.E. Thompson, H. Habazaki and K. Shimizu, *Corros. Sci.* **45** (2003), pp. 2757-2768.

[18] A.J. Bard, editor, *Encyclopedia of electrochemistry of the elements* **vol. 5***,* Marcel Dekker, New York (1976), pp.305-395.

[19] Y. Han, D. Chen, J. Sun, Y. Zhang and K. Xu, *Acta Biomater.* **4** (2008), pp. 1518-1529.

Quantitative phase evaluation of antibacterial ceramic oxide powder against *E. COLI* and *S. AUREUS*

P. Preecha[1,2] , D. P. Kashima[1,2*] , S. Jinawath[1,2] and T. Singhaboonpong[3]

[1] Research Unit of Advanced Ceramics, Department of Materials Science, Faculty of Science, Chulalongkorn University, Patumwan, Bangkok, Thailand 10330
[2] Research Unit of Advanced Ceramic and Polymeric Materials, National Center of Excellence for Petroleum, Petrochemicals, and Advanced Materials, Chulalongkorn University, Patumwan, Bangkok, Thailand 10330
[3] Department of Microbiology, Faculty of Science, Chulalongkorn University, Patumwan, Bangkok, Thailand 10330

* E-mail: dujreutai.p@chula.ac.th, dujreutai@gmail.com

Abstract: The use of inorganic antibacterial agents has been attracted our attention since they are proved to be safe and stable even at high temperature, in comparison with organic antibacterial agents. There have been reported that CaO exhibited a strong bactericidal action and it can be obtained from calcium based natural wastes such as seashell and eggshell. In this work, antibacterial activities of CaO ceramic powder converted from eggshell after calcination at 500-900ºC against *Escherichia coli (E.coli)* and *Staphylococcus aureus (S.aureus)* were investigated. The effects of quantitative phase present of as-calcined powder were studied. XRD patterns of as-calcined powder showed $CaCO_3$, $Ca(OH)_2$ and CaO in various quantities. We found that as-calcined powder at 500, 600, 700, 800 and 900ºC showed the quantitative phase of $Ca(OH)_2$ at 0%, 16.23%, 94.75%, 92.83% and 45.09% respectively. Moreover, for as-calcined powder at 900ºC, CaO was also found at 54.05%. While the quantitative phase of $CaCO_3$ at 500, 600, 700, 800 and 900ºC were 100%, 83.77%, 5.25%, 7.17% and 0.86% respectively. The quantitative phase analyses had been computed by Rietveld refinement method. Antibacterial activities of as-calcined ceramic powder at 500-900ºC against *E.coli* and *S.aureus* were analyzed by spread plate technique. The results of antibacterial activities were shown as % reduction of bacteria after contact to as-calcined ceramic powder in nutrient broth for 6 hr. For antibacterial activities against *E.coli* of as-calcined ceramic powder at 500, 600, 700, 800, and 900 ºC were 0%, 35.71%, 99.99%, 99.99% and 100%, respectively which is in the same fashion of antibacterial activities against *S.aureus* that were 0%, 0%, 99.99%, 99.99%, 99.99%, respectively. The optimum condition for as-calcined ceramic powder from eggshell which showed the best antibacterial activities against both of *E.coli* and *S.aureus* was 700 ºC and the active phase for bactericidal action was $Ca(OH)_2$ and CaO.

1. Introduction

Recently, utilization of inorganic powder as the antibacterial agents has been attracted in development of new hygiene materials. The key advantages of inorganic antibacterial agents are the improving in the stability even at high temperature process and safety uses (Sawai., 2003). The fundamental data of antibacterial activity of 26 kinds of ceramic powder has been studied. There have been reported that 10 kinds of powder exhibited antibacterial activity. Among all of them, calcium oxide (CaO) exhibited a strong bactericidal action (Sawai et al., 2001). In the previous work, scallop-shell was selected as starting material because the main component is $CaCO_3$, and by heat treatment, $CaCO_3$ in the shell converted to CaO, which exhibited antibacterial activity. In our research, eggshell to be starting material because the main component is $CaCO_3$, like scallop-shell. The effects of calcined temperature at 500-900ºC and quantitative phase presents , which is a key factor role in enhancing the antibacterial activity were investigated.

2. Materials and Methods

2.1 Preparation of ceramic oxide powder

Eggshell was the starting material in this work. The eggshell, waste from restaurant or food court, was washed by tap water, let it dried under the sunlight. After that, cleaned eggshell was treated by calcination at 500-900ºC for 4 hr.

Table 1: Conditions for calcination temperature and soaking time of cleaned eggshell

Temperature (ºC)	Soaking time (hr)
500	4
600	4
700	4
800	4
900	4

2.2 Microorganism

Escherichia coli (E.coli) and *Staphylococcus aureus (S.aureus)* were the representative of gram-negative and gram-positive bacteria respectively. Since these two kinds of bacteria were the cause of diarrhea, so antibacterial activities against both *E.coli* and *S.aureus* were observed by spread plate technique

2.3 Characterization

X-ray diffraction (XRD) patterns obtained on X-ray diffractometer (Bruker AXS Model D8 Discover, operating at 40 kV, 40 mA, CuK_α radiation) were used to determine present phase of as-calcined powders. For the quantitative phase present had been computed by Rietveld analysis with Topas software (version 3.0) Bruker AXS. Scanning electron microscope technique (JSM-6480LV, JEOL, Japan) was used to investigate the microstructure of as-calcined ceramic powder. The particle size distribution of as-calcined ceramic powders were examined by laser light scattering technique (Malvern instrument 2000). BET technique was also used to measure the specific surface area (Coulter SA3100 with N_2 adsorption). Antibacterial activities of as-calcined ceramic powder at 500-900ºC against *E. coli* and *S.aureus* were analyzed by spread plate technique. The results of antibacterial activities were shown as % reduction of bacteria after contact to as-calcined ceramic powder in nutrient broth for 6 hr. The microstructure of as-calcined ceramic powders at 500-900ºC compared with commercial-grade CaO were investigated by scanning electron microscope (JSM-6480LV, JEOL, Japan, with operating voltage 15kV)

3. Results and disscussion

3.1 Determination of the qualitative and quantitative phase present

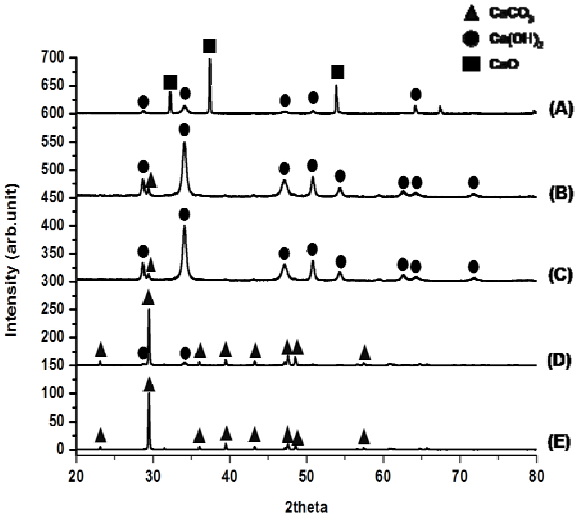

Figure 1. X-ray diffraction patterns of as-calcined ceramic powder at different calcined temperature (A) 900°C, (B) 800°C, (C) 700°, (D) 600°C, and (E) 500°C

From Figure.1, it could be found that when calcined temperature was 500°C, all diffraction peak attributed to $CaCO_3$ phase (JCPDS#01-086-2334). At 600°C, the most diffraction peaks of $Ca(OH)_2$, which is located at 2θ = 28.672 and 34.102° (JCPDS#00-044-1481) was slightly detected. At 700°C, corresponding to 800°C, all the $Ca(OH)_2$ peaks (JCPDS#00-044-1481) were clearly detected. When as-calcined ceramic powder was treated at 900°C, not only $Ca(OH)_2$ phase (JCPDS#01-084-1264) presented but also CaO phase (JCPDS#01-077-2376) was found.

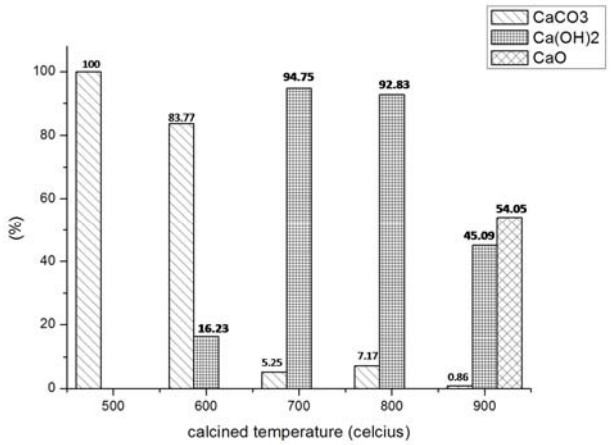

Figure 2. The quantitative phase present of as-calcined ceramic powder at various temperatures

Figure 2 is the quantitative phase present of as-calcined ceramic powders from eggshell at different temperature which was computed by Rietveld refinement method. At 500°C, there was 100% of $CaCO_3$. The quantity of $CaCO_3$ become decreasing with increasing calcined temperature that is 83.77%, 5.25%, 7.17% and 0.86% for 600, 700, 800 and 900°C respectively. While the quantity of $Ca(OH)_2$ was remarkably high at 700°C (94.75%), and 800°C (92.83%). Furthermore, CaO (54.05%) was found for as-calcined temperature 900°C.

As generally known that the main component of eggshell is $CaCO_3$, the reaction occurred in calcinations should be :

$$CaCO_3 \longrightarrow CaO + CO_2.$$

Calcium carbonate was converted to calcium oxide phase, which exhibited strong antibacterial activity and the optimum calcined temperature was 700°C.

3.2 Bactericidal action of as-calcined powder against E.coli and S. aureus

Figure 3 demonstrated the death of two kinds of bacteria after contact to as-calcined powder in nutrient broth for 6 hours shown as % reduction. It was obviously seen that the as-calcined ceramic powder at 700, 800 and 900°C exhibited strong antibacterial activity against both *E. coli* and *S. aureus*.

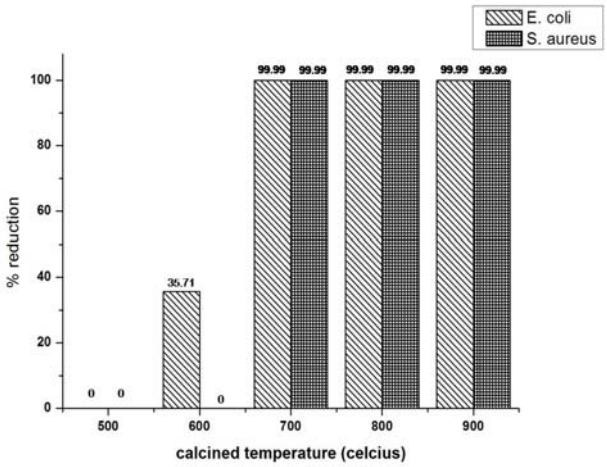

Figure 3. The death of *E.coli* and *S. aureus* after contact to as-calcined ceramic powder in nutrient broth for 6 hours shown as % reduction

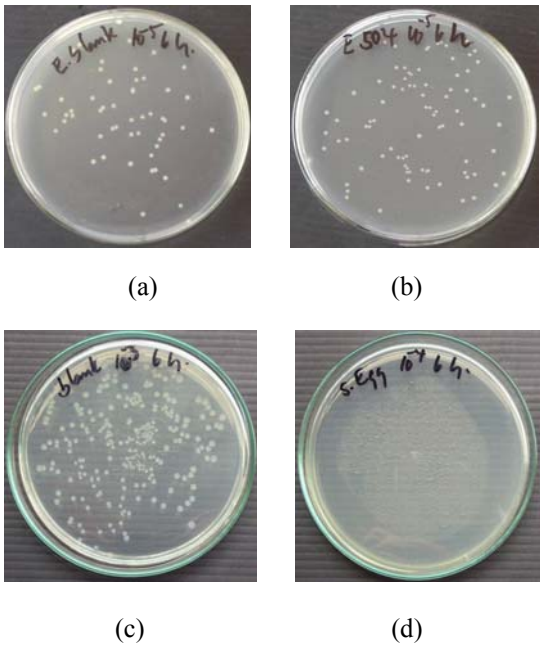

(a) (b)

(c) (d)

Figure 4 : Selected spread plate antibacterial results against *E.coli* of as-calcined powder at 500 °C (a), (b) and 700°C (c), (d).

Figure 4(a) demonstrated the test result of controlled sample is so called "blank" (without contact to as-calcined powder at 500ºC). It was shown that *E. coli* could spreadly grow in the nutrient broth. Figure 4(b) showed the test result of sample that contact to as-calcined powder at 500ºC and showed that the number of *E.coli* appeared as same as the one in blank (Figure 4(a)).

Figure 4(c) was also the test result of controlled sample is so called "blank" (without contact to as-calcined powder at 700ºC). It was shown that *E. coli* could spreadly grow. Figure 4(d) showed the test result of sample that contact to as-calcined powder at 700ºC. It was obviously seen that the number of *E.coli* was not appeared. It is indicated that the decreasing in population of *E. coli* was 100% and there was not any colony of *E. coli* in the nutrient broth.

From these results, it was considered that the bactericidal action of the as-calcined ceramic powder from eggshell is clearly related to the present of $Ca(OH)_2$ and CaO. On the hand $CaCO_3$ was not show any bactericidal action.

3.3 Microstructure of as-calcined ceramic powders

The particle morphology as-calcined powders at 500ºC compared to 700ºC were examined by scanning electron microscope (Figure 5).

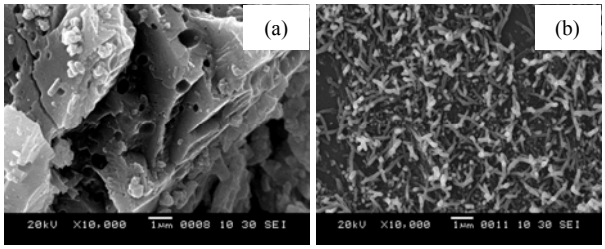

Figure 5. The morphology of as-calcined powder at 500ºC compared to 700ºC

It was found that SEM micrographs in Figure 5 (the same magnification) of as-calcined powder at 500ºC and 700ºC were different in both of morphology and size. As-calcined powder at 500ºC had platelet morphology and aggregated together. On the other hand, when calcined temperature was increase to 700ºC, the morphology of as-calcined powder turned to small rod shape with the uniform size (10 µm).

3.4 Particle size distribution

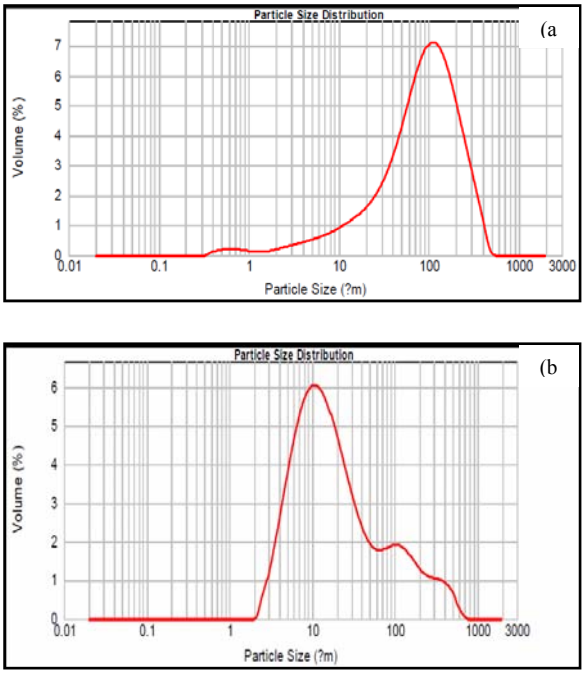

Figure 6. Particle size distribution of selected as-calcined powder at 500ºC (a) and 700ºC (b)

The particle size distribution of as-calcined powders were also investigated to confirm the results of SEM microstructure. Fig 6(a) showed that the mean particle size of as-calcined powder at 500ºC was around 100 µm. While the mean particle sized of as-calcined powder at 700ºC Fig 6(b) was about 10 µm.

3.5 The specific surface area

The specific suface area of as-calcined ceramic powders at 500ºC compared to 700ºC was measured.

Table 2: The specific surface area of selected as-calcined powder at 500ºC and 700ºC

Calcined temperature (ºC)	Specific surface area (m^2/g)
500	0.306
700	0.513

From the results of specific surface area of as-calcined powder at 500ºC, that is 0.306 m^2/g, and at 700ºC, that is 0.513 m^2/g, were corresponding to the results of SEM micrograph and particle size distribution. The first one, as-calcined powder at 500ºC, had bigger size and aggregated together, so the specific surface area was less than the as-calcined powder at 700ºC, which was uniformly small particle size.

4. Conclusions

This study showed the antibacterial activity of ceramic oxide powder from eggshell against *E.coli* and *S.aureus*. The active phase for bactericidal action was $Ca(OH)_2$ and CaO which converted from $CaCO_3$, the main component in eggshell. Calcined temperature directly affected the phase present of ceramic powder. $Ca(OH)_2$ and CaO phases presented at calcined temperature 700°C or above. The results of microstructure, particle size distribution and specific surface area of selected as-calcined ceramic powder at 500ºC and 700ºC were also confirmed. The optimum condition for as-calcined ceramic powder from eggshell which showed the best antibacterial activity against both of *E.coli* and *S.aureus* was 700°C**.**

Acknowledgements

The authors would like to thank Thailand Research Fund (TRF) for the research grant and National Center of Excellence for Petroleum, Petrochemicals and Advanced Materials, Chulalongkorn University for the financial support.

References

[1] J. Sawai, H. Igarashi, A. Kokugan and T. Shimizu, *J. Chem. Eng. Jpn* **28** (1995a), pp. 288-293.
[2] J. Sawai, H. Igarashi and H. Kojima, *Int. J. Food Microbiol.* **71** (2001), pp. 211-218
[3] J. Sawai, , *J. Microbiol. Methods*. **54** (2003), pp. 177-182.
[4] Y. Xu, J. Cheng, W. Zheng and D. Gao, *J Non-Cryst Solids*. **354** (2008), pp. 1341-1345.
[5] L. Zhang, Y. Ding, M. Povey and D. York, *Prog. Nat. Sci*. **18** (2005), pp. 939-944.
[6] Y. Du, Y. Zhao, S. Dai and B. Yang, *Innov. Food. Sci. Emerg*. **10** (2009), pp. 103-107

Dissolution enhancement of itraconazole using nanoemulsion template

K. Burapapadh[1,2] and P. Sriamornsak[1,2,*]

[1]Department of Pharmaceutical Technology, Faculty of Pharmacy, Silpakorn University, Nakhon Pathom, Thailand 73000
[2]Pharmaceutical Biopolymer Group (PBiG), Faculty of Pharmacy, Silpakorn University, Nakhon Pathom, Thailand 73000

[*] E-mail: pornsak@su.ac.th

Abstract: Itraconazole is poorly water-soluble and possessing extremely low water solubility (less than 1 µg/ml in aqueous solution) which causes limited bioavailability. Therefore, the aim of this study was to improve dissolution profile of itraconazole by nanoemulsion template. Nanoemulsions containing itraconazole and using pectin as emulsifier, was dried by lyophilization process. The dried products were pulverized into small pieces by simple grinding machine. The dried powder was then characterized. The dried powder showed porous, sponge-like structure with submicron-sized bulbs spreading over pectin flake. No itraconazole crystal was found when observing under scanning electron microscope. The thermal analysis using differential scanning calorimeter showed no melting peak of itraconazole in the formulation, indicating no crystalline structure. The powder x-ray diffractogram of the formulations demonstrated broad typical hump of amorphous material, indicating that itraconazole was changed from crystalline form to amorphous form by preparation process. The formulation of itraconazole prepared from nanoemulsion showed tremendous percent drug dissolved in simulated gastric fluid (pH 1.2), i.e., about 80 percent of drug dissolved within 2 hours. Itraconazole powder dissolved only 5% after 2 hours of dissolution study. From these results, dissolution profiles of itraconazole could be improved by changing of drug solid-state during preparation process.

Introduction

Itraconazole is an orally active triazole antimycotic agent. It actives against a broad spectrum of fungal species caused opportunistic infection in HIV infected patients, including Cryptococcus, Candida, Aspergillus, Blastomyces and *Histoplasma capsulatum* var. capsulatum [1]. It is a white to slightly yellowish powder. It has a molecular formula $C_{35}H_{38}Cl_2N_8O_4$ and molecular weight of 705.64. It is a weak basic drug (pK_a = 3.7) which is virtually ionized at only low pH, possessing extremely low water solubility (about 1 ng/mL at neutral pH and about 6 µg/mL at pH 1) [1]. According to the biopharmaceutics classification system (BCS), itraconazole is one of a class II compound suggesting that its oral bioavailability is determined by dissolution rate in gastrointestinal tract [2]. Various solubilization methods have been used to increase the drug solubility and dissolution properties, such as the use of water-soluble carriers, polymeric conjugates, solid dispersion, size reduction and crystal modification [3-7]. Among these methods, nanotechnology was widely used in many formulations. Nanoemulsion is normally referred to emulsion with droplet size in the nanometric scale which could be prepared by two major methods, high-energy emulsification and low-energy emulsification [8]. Generally, high-energy emulsification methods always achieved by high-shear stirring or high-pressure homogenizer which could damage long chain molecules when very high pressure conditions was used. High-energy emulsification by simple homogenization was adopted in the previous study [9]. In this work, the nanoemulsions were dried by lyophilization process, pulverized into small pieces and some properties related to drug dissolution profile were characterized.

Materials and Methods

All chemicals used in this study were of pharmaceutical grade. Itraconazole (Nosch Labs Private Ltd. India) was kindly donated by Pharma Nueva Co., Ltd. (Thailand). Pectins were the gifts from Herbstreith & Fox KG (Germany). Chloroform was purchased from Carl Roth GmbH (Germany). Purified water was used as aquous phase in all preparations.

Nanoemulsions were prepared by the method reported in previous study [9]. Briefly, twenty percent of chloroform, as an oil phase, were mixed with pectin solution using simple homogenizer at a speed of 24000 rpm for 20 minutes in an ice-bath to obtain chloroform-in-water emulsion. Three types of pectin with different degrees of esterification (DE) were used in this study, consisting of pectin with DE of 38 (low methoxylation pectin; LMP), 43 (amidated-low methoxylation pectin; ALMP) and 70 (high methoxylation pectin; HMP). Various concentrations of pectin were used to emulsify the mixtures.

The nanoemulsions were dried by lyophilizer (Freezone 2.5, Labconco, USA) at 0.280 mBar, -49ºC for overnight. Then, the dried products were pulvarized into small pieces by simple grinder and characterized. The morphology of dried powder was observed by scanning electron microscope (SEM). Thermal analysis and x-ray powder diffraction were also used to study the drug solid-state.

At the last step, dissolution profile of dried powder was tested. An appropiate drug amount was put into dissolution appataratus I (basket method), using simulated gastric fluid (SGF) pH 1.2 as a dissolution medium. The amount of drug dissolved was

investigated by high-performace liquid chromatogaphy (HPLC) at various time periods.

Results and Discussion

The morphology of dried emulsion powder was investigated by scanning electron microscope (SEM) as shown in Figure 1. The cross-section of dried powder showed porous, sponge-like structure with submicron-sized globules spreading over pectin flake. On the surface-side, minute round-shape particles were presented. No itraconazole crystal was observed in all formulations. These results could confirm the morphology of dried powder and also the unbroken conditions of the lyophilized emulsion. The size of nanoemulsion in all formulation were similar, around 500-600 nanometers before dried. However, after drying process, particle sizes were increased. The ALMP-based dried emulsion shown the largest droplet size, while LMP and ALMP formulations gave quite tiny particles with particle size of about 1 micrometer.

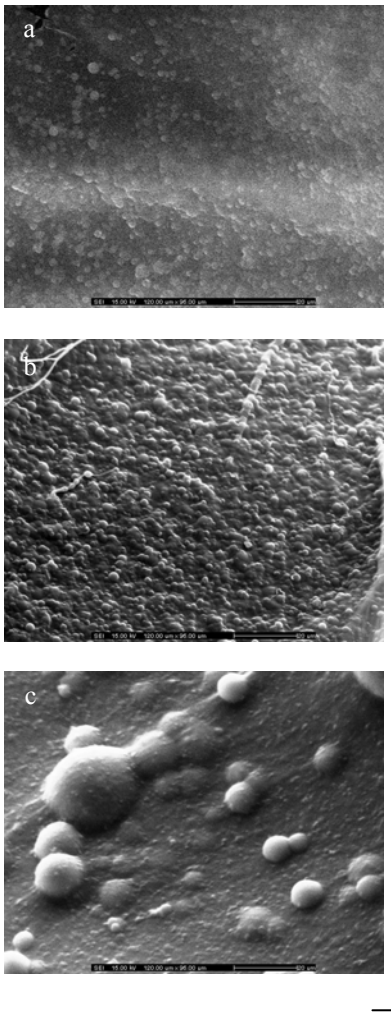

Figure 1. Morphology of dried emulsion powder investigated by SEM. (a) HMP-based dried powder; (b) LMP-based dried powder; (c) ALMP-based dried powder.

These may due to unsuitable properties of amide group in the pectin chain.

The thermal analysis results by differential scanning calorimeter (DSC) are shown in Figure 2. The melting peak of itraconazole crystal was manifested around 166-168ºC. The physical mixtures (PM) of itraconazole and various types of pectin also showed the same results. Nevertheless, no melting peak of itraconazole was found in all nanoemulsion formulations, indicating no crystalline structure.

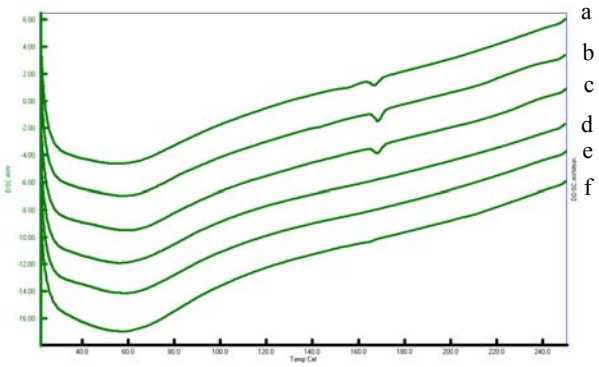

Figure 2. Thermal analysis by differential scanning calorimeter (DSC); (a) PM of LMP and itraconazole; (b) PM of HMP and itraconazole; (c) PM of ALMP and itraconazole; (d) ALMP-based dried powder; (e) HMP-based dried powder; and (f) LMP-based dried powder.

The drug solid-state in all formulations was confirmed by x-ray diffraction method, as presented in Figure 3. Itraconazole crystal shown very high crystallinity, the x-ray diffractogram of nanoemulsion formulations demonstrated broad typical hump of amorphous material, indicating that itraconazole was changed from crystalline form to amorphous form by preparation process.

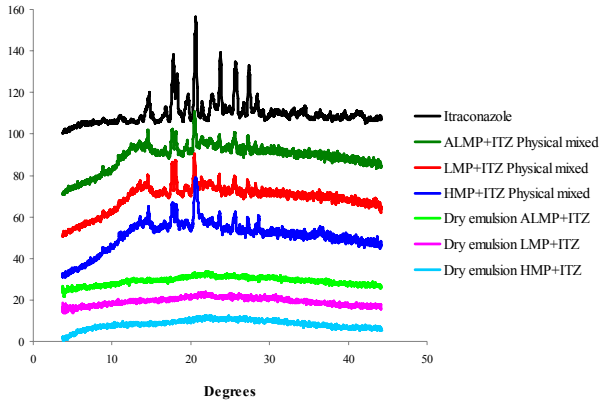

Figure 3. X-ray powder diffractogram of all formulations compare to itraconazole crystal.

The drug content and dissolution rate in simulated gastric fluid were evaluated. Figure 4 shows the dissolution profile of itraconazole from various formulations having different pectin types. In simulated gastric fluid, itraconazole powder dissolved only 3-5% in 2 hours while all lyophilized products shown tremendously advancement. Lyophilized product from HMP shown about 60% drug release within 2 hours while LMP and ALMP shown 66% and 80% drug release respectively. These results indicating that lyophilized product prepared from nanoemulsion could be used as an effective carrier in improvement of itraconazole dissolution properties

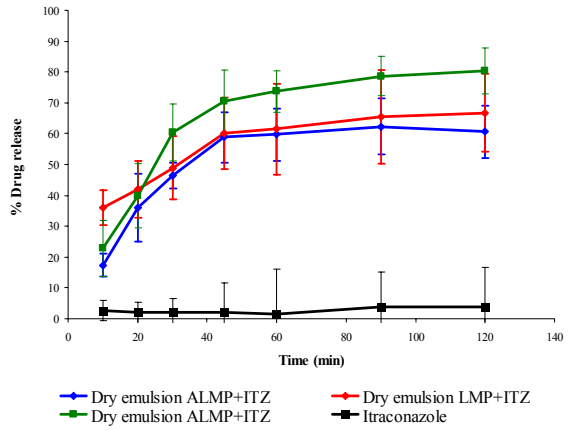

Figure 4. Dissolution profiles of itraconazole in SGF pH 1.2

Conclusions

After drying process, the particle size of dried emulsion was larger than the pre-treated one. The alteration of itraconazole solid-state was clearly observed from x-ray powder diffractogram. The formulation of itraconazole prepared from nanoemulsion template shown tremendous percent drug dissolved in SGF (pH 1.2), i.e., about 80 percent of drug dissolved within 2 hours, more than 10 folds over itraconazole powder. Dissolution profiles of itraconazole could be improved by changing of drug solid-state during preparation process.

Acknowledgements

This work is supported by The Royal Golden Jubilee Ph.D Program (RGJ) under agreement number PHD/2549/0029 and the Thailand Research Fund and Office of Small and Medium Enterprises Promotion, Thailand (grant number IUG5080020). We are very pleased to acknowledge Pharma Nueva (Thailand) who kindly donated itraconazole. Thanks also go to Mr. Witoon Sae-Ngow from Silpakorn University Scientific and Technological Research Equipment Centre for SEM imaging.

References

[1] M.S. Saag and W.E. Dismukes, *Antimicrob Agents Chemother.* **32** (1988), pp. 1-8.
[2] G.L. Amidon, H. Lennernäs, V.P. Shah, and J.R. Crison, *Pharm Res*. **12**(1995), pp. 413-420.
[3] M.H. Amaral, J.M. Sousa Lobo and D.C. Ferreira, *STP Pharm Sci* **13** (2003), pp. 191-194.
[4] R. Duncan et al. *J Control Release.* **74** (2001), pp. 135-146.
[5] G. Chawla and A.K. Bansel. *Acta Pharm.* **58** (2008), pp. 257-274.
[6] G.G. Liversidge and K.C. Cundy. *Int J Pharm* **125** (1995), pp. 91-97.
[7] A. Nokhodchi, N. Bolourtchian and R. Dinarvand. *J Cryst Growth.* **274** (2005), pp. 573-584.
[8] C. Solans et al. *Curr Opin Colloid Interface Sci.* **10** (2005), pp. 102-110.
[9] K. Burapapadh et al. *Itraconazole-loaded nanocapsules prepared from nanoemulsion templates by lyophilization.* Proceeding of the 17th International Symposium on Microencapsulation. Nagoya, Japan, 2009, pp. 115-116.

In situ synthesis of polyethyleneimine/silver-embedded poly(methyl methacrylate) composite particles

N. Jitjana[1] and P. Sunintaboon[1]*

[1] Department of Chemistry, Faculty of Science, Mahidol University, Bangkok, Thailand

* E-mail: scpsu@mahidol.ac.th

Abstract: In this present work, the *in situ* synthesis of composite particles based on poly(methyl methacrylate) (PMMA) core and silver-embedded polyethyleneimine (PEI) shell was carried out via an emulsifier-free emulsion polymerization. PEI, an amino-containing branched polymer, can act as both a reducing agent for converting silver ion (Ag^+) to metallic silver (Ag^0), and as a free radical co-initiator for propagating MMA monomer. The size and amount of embedded silver depended on the amount of $AgNO_3$ loaded, and had the effects on the optical properties of the composite particles. The mean particle size of the PMMA/PEI-Ag composite particles, measured by dynamic light scattering (DLS), displayed no significant difference from the neat PMMA/PEI latex particles (121-128 nm). UV-VIS spectra of the composites showed an absorption peak of surface plasmon resonance of silver in the range of 407-422 nm. In addition, the crystal structure of silver embedded in PEI shell corresponded to the face-centered cubic (fcc) crystal structure, determined by XRD. Moreover, the chemical composition of PMMA/PEI-Ag core-shell composite particles was characterized by ATR-FTIR.

Introduction

There are various synthetic routes that have been reported for preparation of silver nanoparticles with various sizes and shapes. A variety of stabilizers, including polymers, were used for the size and shape controlled synthesis of silver nanoparticles. Conventional polymers carrying functinal groups, such as poly[2-(N,N-dimethylamino)ethyl methacrylate] (PDMA), poly(2-vinylpyridine) (PVP), and poly(vinyl alcohol) (PVA) are able to coordinate to metal ions. Therefore, metal-polymer nanocomposites can be formed easily with these polymers. Moreover, systems with complicated architectures, such as block-copolymer micelles, dendrimers, microgels, etc., have also been used as stabilizers for the solution phase synthesis of silver nanoparticles [1,2]. Lei *et al*. synthesized Ag/PS-*b*-PAA composite particles by using PEI as a reducing agent. First, they let Ag^+ ions complex with PEI. Then, PEI-Ag^+ complex was immobilized on the surface of PS-*b*-PAA block copolymer micelles via electrostatic force and allowed Ag^+ to be reduced to Ag^0 [3]. Chen *et al*. prepared spherical silver-poly(4-vinylpyridine) (Ag-P4VP) hybrid microgels by a single-step emulsifier-free emulsion polymerization with the aid of γ-irradiation [4].

In the present work, we propose a new convenient route for a preparation of silver-polymer nanocomposites based on an emulsifier-free emulsion polymerization. The core-shell composite particles of poly(methyl methacrylate)-*g*-polyethyleneimine-silver (PMMA/PEI-Ag) were synthesized in one single step with mild condition. PEI, which is a water-soluble branched polymer, containing plenty of primary, secondary, and tertiary amine groups that can easily coordinate with metallic ions [1,3], acts as a reducing agent for reducing Ag^+ ions and also a redox co-initiator for grafting MMA. The resulting material would have some applications, for example, plasmonic sensors and anti-microbial agents.

Materials and Methods

Materials: Polyethyleneimine (PEI, M_w = 750,000) and methyl methacrylate (MMA) were purchased from Aldrich. PEI was used without further purification. MMA was distilled before used. *t*-Butyl hydroperoxide (TBHP) was purchased from Fluka and was used as received. Silver nitrate ($AgNO_3$) was purchased from AnalaR NORMAPUR.

Preparation of PMMA/PEI-Ag composite particles: PMMA/PEI-Ag composites were synthesized via the *in situ* emulsifier-free emulsion polymerization by using a redox-initiating system consisting of TBHP and amine groups on PEI chains. The preparation process was carried out in a 100-ml water-jacketed glass reactor equipped with nitrogen inlet, reflux condenser, water cooling system, and magnetic stirrer. 5 g of 10%wt. PEI aqueous solution and an appropriate amount of distilled water were added into the reactor and degassed with N_2 gas for 30 min with 600 rpm stirring rate. Reaction temperature was controlled at 80±1 °C by water pumped through the jacket from thermostat water bath. Then, 5%wt. of $AgNO_3$ aqueous solution was injected into the reactor and left for 10 min in order to allow Ag^+ ions to complex with amine groups of PEI. Weight ratio of PEI to $AgNO_3$ was varied from 1:0.5 to 1:1.5. After that, 2 g of MMA was injected into the mixture and followed by 1 g of TBHP (5×10^{-3} M) to start polymerization. The reaction took 2 h to complete and N_2 gas was bubbled throughout the reaction period. The resulting particles were purified by centrifugation for three times at 25,000 rpm for 35 min to remove unreacted starting materials [5].

Characterization: Mean particle size and particle size distribution were determined by dynamic light scattering (DLS, Malvern Instrument, Mastersizer 2000 model). The optical property of Ag nanoparticles embedded in the composite particles was characterized by UV-VIS spectroscopy using a PerkinElmer Lambda 35 spectrometer. All latex samples were diluted to 0.01% solid content for UV-VIS measurement. Crystal structure of silver was characterized by X-ray diffraction (XRD). XRD pattern was obtained by using Bruker D8 ADVANCE X-ray diffractometer operating with a Cu anode at 40 kV (acceleration voltage) and 40 mA (electric current) in the range of 2θ value between 10° and 80° with a speed of 1.5°/min. Chemical composition of latex was determined by FTIR (Bruker, EQUINOX55 model) using single reflection ATR mode.

Results and Discussion

After the PMMA/PEI-Ag composite latexes were purified by centrifugation, they were characterized for mean particle size and size distribution by DLS and the results were shown in Table 1. All PMMA/PEI-Ag composites displayed mean particle sizes in the same range and relatively smaller than that of the neat PMMA/PEI. This may be due to the existence of Ag nanoparticles in the PEI shell that can obstruct the expansion of PEI in aqueous medium, leading to shrinkage of the composite particles. Besides, PMMA/PEI-Ag0.5 to PMMA/PEI-Ag1 displayed similar particle size distribution to the neat particles as indicated by the uniformity and the distribution curves shown in Figure 1(a-d). While the last two samples, in which the higher amount of $AgNO_3$ was used, exhibited broader particle size distributions than the others, especially PMMA/PEI-Ag1.5 that showed quite asymmetric particle size distribution curve as displayed in Figure 1(f). When the $AgNO_3$ amount was increased beyond a certain value, the PEI, which has a constant amount, may not be sufficient to stabilize the Ag nanoparticles occurred. So some of the nanoparticles aggregated and caused the whole composite particle size to be larger.

Table 1: Mean particle size and uniformity of PMMA/PEI-Ag composite latexes with different amount of $AgNO_3$

Sample	Mean particle size (nm)	Uniformity
PMMA/PEI	128	0.253
PMMA/PEI-Ag0.5	122	0.263
PMMA/PEI-Ag0.75	121	0.258
PMMA/PEI-Ag1	123	0.261
PMMA/PEI-Ag1.25	124	0.323
PMMA/PEI-Ag1.5	122	0.481

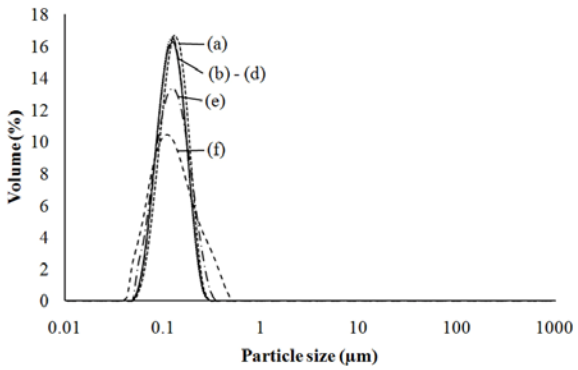

Figure 1. Particle size distribution curves of PMMA/PEI (a) and PMMA/PEI-Ag0.5 to PMMA/PEI-Ag1.5 composites (b-f)

UV-VIS spectra of the PMMA/PEI-Ag composite particles are demonstrated in Figure 2. Each composite displayed one absorption peak in the range of 407-422 nm except PMMA/PEI-Ag0.5 that had no absorption. These absorption peaks corresponded to the surface plasmon resonance of Ag nanoaparticles that embedded in PEI shell of the composite particles. Absorption peak intensity can be related the number of Ag nanoparticles and, from the spectra, it increased with increasing $AgNO_3$ amount. It can be assumed that at higher concentration of $AgNO_3$, there were more numbers of Ag nanoparticles formed in the composites [3,6].

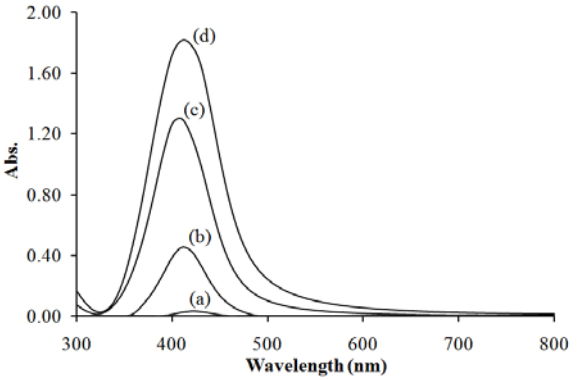

Figure 2. UV-VIS spectra of PMMA/PEI-Ag composites with different $AgNO_3$ amount (a-d are PMMA/PEI-Ag0.75 to PMMA/PEI-Ag1.5)

Ag nanoparticles embedded in composite particles had a face-centered cubic (fcc) crystal structure determined by XRD. The XRD pattern of the composite is shown in Figure 3. There were peaks at 2θ values of 38.02, 43.81, 64.30, and 77.35°, representing the (111), (200), (220), and (311) Bragg's reflections of fcc structure of silver (JCPDS No. 4-0783).

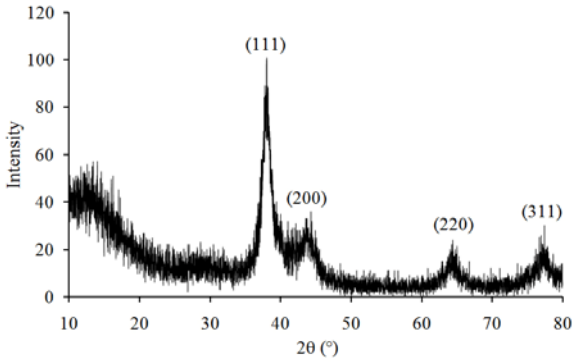

Figure 3. XRD pattern of PMMA/PEI-Ag1.5

FTIR spectra of PMMA/PEI neat particles and PMMA/PEI-Ag composites particles are illustrated in Figure 4. All samples had the same FTIR pattern. The peaks at 1729 and 1192 cm^{-1} corresponded to C=O stretching and C-O stretching, respectively. They were characteristic peaks of carboxylate groups of PMMA. C-N stretching of amine groups of PEI appeared at 1149 cm^{-1}. Thus, there were both PMMA and PEI in composite particles.

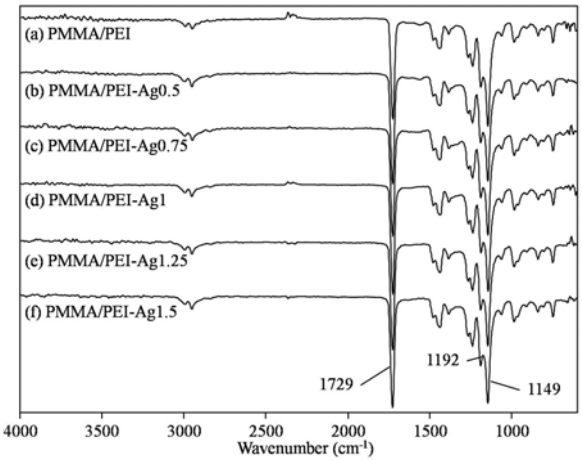

Figure 4. FTIR spectra of (a) PMMA/PEI and (b-f) PMMA/PEI-Ag composites with different $AgNO_3$ amount

Conclusions

PMMA/PEI-Ag composite particles were successfully synthesized by the *in situ* emulsifier-free emulsion polymerization with no additional reducing agent. The appearance of Ag nonaparticles did not affect the whole particle size significantly. Ag nanoparticles embedded in the composite particles displayed strong plasmon resonance, and they had face-centered cubic (fcc) crystal structure. This approach provided a new convenient method for synthesizing silver-polymer particle nanocomposites.

Acknowledgement

The authors thank the "Development and Promotion of Science and Technology Talents Project (DPST)" and Faculty of Graduate Studies, Mahidol University for funding.

References

[1] M. Manoth, K. Manzoor, M.K. Patra, P. Pandey, S.R. Vadera and N. Kumar, *Mater. Res. Bull.* **44** (2009), pp. 714-717.
[2] S.K. Jewrajka and U. Chatterjee, *J. Polym. Sci., Part A: Polym. Chem.* **44** (2006), pp. 1841-1854.
[3] Z. Lei, X. Wei, L. Zhang and S. Bi, *Colloids Surf., A* **317** (2008), pp. 705-710.
[4] Q. Chen, X. Shen and H. Gao, *Colloids Surf., A* **275** (2006), pp. 45-49.
[5] P. Li, J. Zhu, P. Sunintaboon and F.W. Harris, *Langmuir* **18** (2002), pp. 8641-8646.
[6] S.A. Vorobyova, A.I. Lesnikovich and N.S. Sobal, *Colloids Surf., A* **152** (1999), pp. 375-379.

Preparation and characterization of Li_2o-stabilized Na.β″-alumina solid electrolyte

A. Kamonlert[1], A. Niyompan[1*] and R. Tipakontitikul[1]

[1] Department of physics, Faculty of Science, Ubon Ratchathani University, Ubon Ratchathani, Thailand 34190

[*] E-Mail : anuson@rocketmail.com

Abstract: The Li_2O-stabilized Na.β″-alumina powder with composition $Na_{0.78}Li_{0.22}Al_5O_8$ was prepared via solid state reaction. The aim of the study is to find optimized conditions for its processing. Phase change and morphological evolution of Na.β″-alumina was carefully examined using TG/DTA, XRD and SEM techniques. Experimental results indicated that formation of the Na.β″-alumina started at 1100°C with presence of secondary phase ($NaAl_7O_{11}$). Calculated crystalline size of calcined powders increased with increasing dwell time. The maximum value of Na.β″-alumina phase purity of about 82 wt% was obtained at calcined temperature 1100°C with dwell time of 10 h. Microstructure of Li_2O-stabilized Na.β″-alumina particles are clearly seen as sheet morphology with hexagonal shape and consist of agglomerated randomly oriented nanocrystallites.

Introduction

Na.β″-alumina is a family of oxides that exhibits high sodium-ion conduction. It has been used as solid electrolytes known today. Na.β″-alumina is suitable for use in many applications, such as sodium sulfur battery, alkali metal thermoelectric converters, electrochromic displays and sodium sensor [1-2]. Usually β″-alumina has been prepared by conventional methods but the structure is not stable at temperature over 1400°C. A lot of methods have been also developed for the preparation of Na.β″-alumina such as sol-gel method [3-4], microwave processing [5-7] and co-precipitation method [8]. But those methods require complex starting material. The aim of this work is to prepare Li_2O-stabilized Na.β″-alumina powders by solid state reaction at lower temperature. The influence of the preparation parameters on Na.β″-alumina phase formation and microstructure were studied.

Materials and Methods

Powder of Li_2O-stabilized Na.β″-alumina with a composition $Na_{0.78}Li_{0.22}Al_5O_8$ was prepared from selected reagent substances, Na_2CO_3, Li_2CO_3 and γ–Al_2O_3. Mixing was carried using ball mill for 24 h at room temperature with YZT ball and ethanol as the wetting agent. Thermal behavior of the mixture was characterized by TG/DTA technique as to observed level of phase formation. To check information subtracted from DTA results, the mixtures were heat treated at several temperatures for 1 h following by XRD analysis. From information suggested by DTA and XRD, the calcinations process were performed at selected temperature for several dwell times, i.e. 5, 10 and 15 h, respectively. Phase characterization of calcined powders was performed by XRD (X'Pert X-ray diffractometer). The average crystalline size was calculated from the Scherrer equation as follows:

$$D = \frac{0.9\lambda}{\beta \cos\theta} \qquad (1)$$

where D is the crystalline domain size, λ is X-ray wavelength, β is full width at half maximum (FWHM)and θ is Bragg angle of the particles. Morphology of powder particles was analyzed by scanning electron microscope (SEM).

Results and Discussion

The thermal decomposition of precursors of Na.β″-alumina powder in the temperature range from 40 to 1300°C was investigated by themogravimetry (TG) and differential thermal analysis (DTA) as shown in Figure 1. It can be seen that the endothermic peak below 280°C accompanied with a weight loss of 4% was attributed to removal of physically absorbed water/ethanol. The significant endothermic peak presented at 280 to 550°C and 550 to 1100°C accompanied with a weight loss of 3.5% and 5% respectively, which was resulted from CO_2 evaporation of Na_2CO_3 and Li_2CO_3.

Phase formation of the Na.β″-alumina was analyzed by X-ray diffraction. Figure 2 shows the XRD patterns of powder heat treated at various temperatures. It was found that the powder heat treated at 280°C shows the Na_2CO_3, Li_2CO_3 and Al_2O_3 phase. Powders heat treated in the temperature rang of 750 to 850°C were mainly composed of transition phase, i.e. Na_2O, Li_2O and Al_2O_3. At temperature range from 850 to 1000°C, formation of the $LiAl_5O_8$, $LiAlO_2$ and $NaAlO_2$ phase are found corresponding to the reaction of Al_2O_3 with Na_2O and Li_2O, as described by the reaction

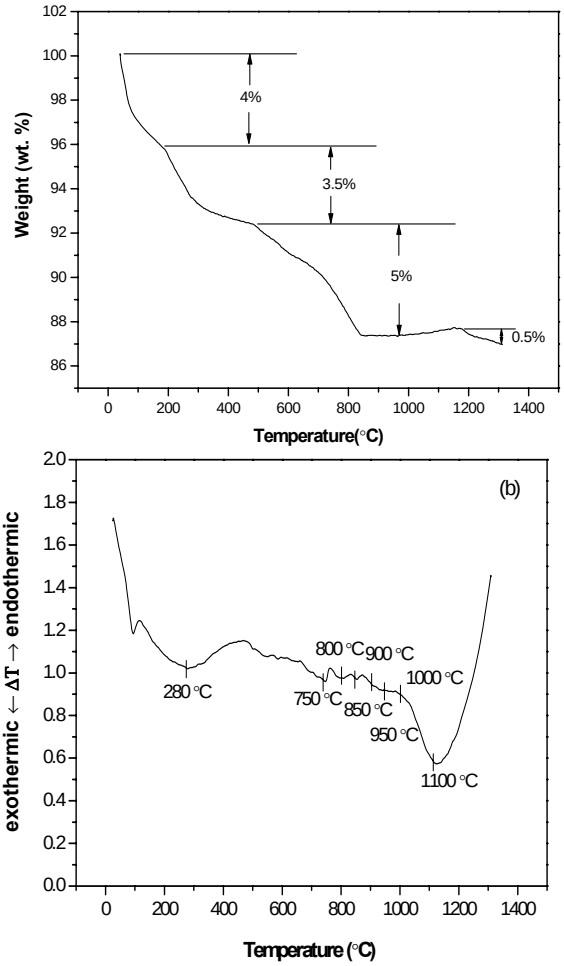

Figure 1. The result of mixture powders showing crystallization and phase transformation temperatures, (a) TGA and (b) DTA.

$$Na_2O + Al_2O_3 \rightarrow 2NaAlO_2 \qquad (2)$$

$$Li_2O + 5Al_2O_3 \rightarrow 2LiAl_5O_8 \qquad (3)$$

$$Li_2O + Al_2O_3 \rightarrow 2LiAlO_2 \qquad (4)$$

For treatment at 1100°C, crystallization of the β″-alumina and β′-alumina phase are clearly seen, the same as the previous report [9]. From results of DTA and XRD, It can be seen that transform from starting materials to the product β″-alumina was completed at 1100°C. Thus, this temperature level was selected for calcinations. Figure 3 shows the XRD pattern of the powders calcined at 1100°C for various dwell times. The results reveal that there are two co-existence crystalline phase, β″-alumina ($Na_{1.6}LI_{0.34}Al_{10.66}O_{17}$) and secondary β′-alumina ($NaAl_7O_{11}$). The same co-existence of two equilibrium phases has been reported previously [10]. The results of the averaged crystalline size of Na.β″-alumina samples were calculated from peak width (003) are summarized in Table 1. It was seen that crystalline size of particles increases with increasing calcination temperature and dwell time. To find yielding proportion, quantitative analysis using XRD data was also performed according to Eq. (5)

$$\beta''(wt\%) = \frac{I_{\beta''}}{I_{\beta''} + I_{\beta'}} \times 100\% \qquad (5)$$

where $I_{\beta''}$ and $I_{\beta'}$ are the intensity of X-ray reflection for β″-alumina and β′-alumina phase, respectively. The results of calculation are reported in Table1. At calcination of 1100°C with dwell time of 10 h, the phase purity of Na.β″-alumina is about 82 wt%.

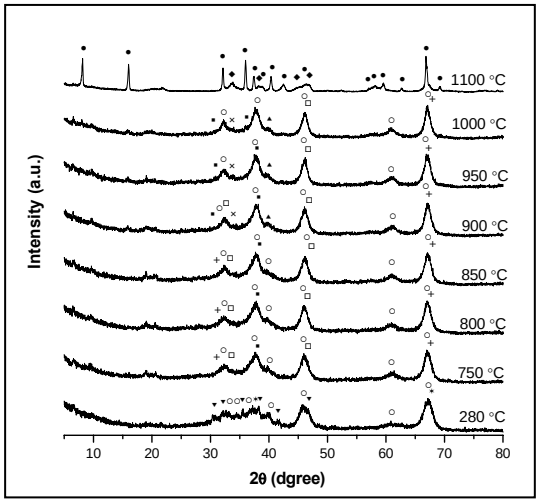

Figure 2. XRD patterns of powders heated at various temperatures for 1 h with heating rate and cooling rate 5°C/min: ❍ = Al_2O_3, ∗ = Li_2CO_3, ▼ = Na_2CO_3, ❒ = Na_2O, + = Li_2O, ■ = $LiAl_5O_8$, × = $LiAlO_2$, ▲= $NaAlO_2$, ● = $Na_{1.6}$ $Li_{0.34}Al_{10.66}O_{17}$ and ◆ = $NaAl_7O_{11}$

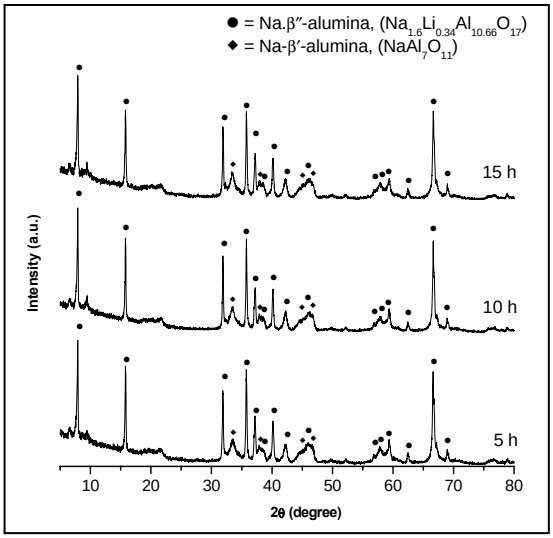

Figure 3. Powder XRD pattern of the samples calcined at 1100°C with for various dwell times.

Table 1. Crystalline size and proportion of β″-alumina phase at calcined temperature 1100°C.

Dwell time (h)	Crystalline size (nm)	Yielding of Na.β″-alumina phase (wt%)
1	34.1	79
5	40.3	79
10	46.5	82
15	49.4	81

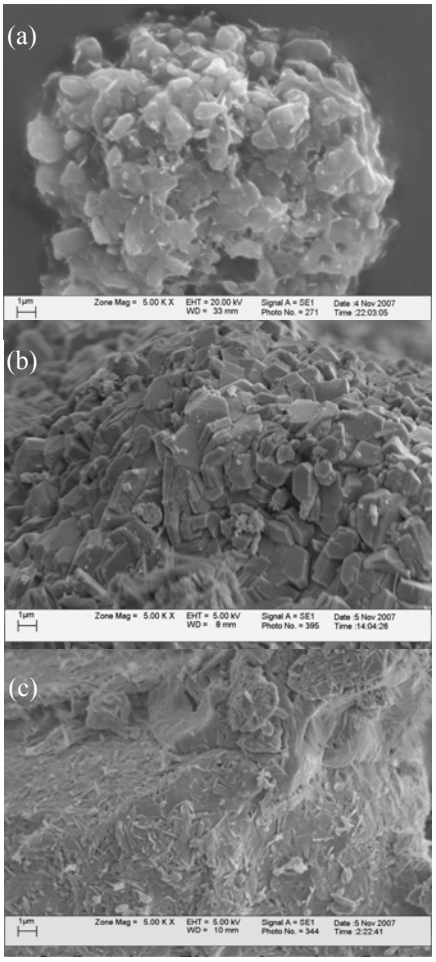

Figure 4. SEM images of heated powders of various temperatures at (a) 280°C, (b) 950°C and (c) 1100°C.

The results of SEM images of powders treatment at various temperatures for 1 h are shown in Figure 4. It can be seen that for treatment at 950°C, formation of plate-like particles with hexagonal shape characteristic and strong agglomeration (Fig. 4b). When treatment temperature increased to 1100°C, the powder particles observed as sheet morphology and consist of agglomerated randomly oriented nanocrystallites (Fig. 4c).

Conclusions

The present investigation has demonstrated that calcination of Li_2O-stabilized Na.β″-alumina gives a mixture of β′ and β″ phases at temperature 1100°C. Maximum value of β″-alumina purity phase was 82 wt% even at 1100°C for 10 h. The crystalline size increases with increasing dwell time. And also, microstructure of heated powders was seen as sheet morphology with hexagonal shape and consists of agglomerated randomly oriented nanocrystallites.

Acknowledgements

This work is supported by the National Research Council of Thailand.

References

[1] N. Li, Z. Wen, Y. Liu, X. Xu, J. Lin and Gu, Z, *J. Eur. Ceram. Soc.* 29(2009), pp. 3031-3037.
[2] J. H. Park and K. H. Kim, *J. Mater. Sci.* 33(1998), pp. 5671-5675.
[3] S. Sartori, A. Martucci, A. Muffato and M. Guglielmi, *J. Eur. Ceram. Soc*. 24(2004), pp. 911-914.
[4] V. Jayaraman, T. Gnanasekaran and G. Periaswami, *Mater. Lett.* 30(1997), pp. 157-162.
[5] T. Mathews, R. Subasri, and O. M. Sreedharan, *Solid State Ionics*. 148(2002), pp. 135-143.
[6] R. Subasri, T. Mathews, O. M.Sreedharan and V. S. Raghunathan, *Solid State Ionics*. 158 (2003), pp. 199-204.
[7] R. Subasri, *Mater. Sci. and Eng. B.* 112(2004), pp. 73-78.
[8] A. Pekararsky and P. S. Nicholson, *Mater. Sci. Res.* 15(1980), pp. 1517.
[9] N. Li, Z. Wen, X. Wu, J. Zhang and Y. Liu, *J.* Alloys. Comp. published by Elsevier B.V., (2009), inpress.
[10] H. Näfe, F. Meyer and F. Aldinger, *Electrochim. Acta.* 45(2000), pp. 1631-1638

Dye-sensitized solar cell with spray-coated TiO_2 electrode

C. Srisamanuwat[1*] and A. Sirisuk[2]

[1]Center of Excellence on Catalysis and Catalytic reaction, Department of Chemical Engineering, Faculty of Engineering, Chulalongkorn University, Bangkok 10330 Thailand

*E-mail: know_102@hotmail.com

Abstract: In this work, dye-sensitized solar cells (DSSC) with spray-coated TiO_2 electrode were studied. TiO_2 was prepared by a sol-gel method and was sprayed onto a conducting glass using an ultrasonic spray coater. Other components of the DSSC included N3 dye as a sensitizer, iodide/triiodide redox couple as an electrolyte, and a sputtered platinum film on conducting glass as a counter electrode. The effects of sintering temperature and thickness of TiO_2 were investigated. According to XRD results, only anatase phase was observed at a sintering temperature of 300°C. As sintering temperature was increased to 600°C, the rutile phase became the major component of TiO_2. At the same time, the specific surface area of TiO_2 decreased. The highest efficiency for a DSSC was obtained when sintering temperature was 400°C and the thickness of TiO_2 film was about 11.19 μm.

Keyword: Dye-sensitized solar cell, Spray-coated, Efficiency

1.Introduction

Dye-sensitized solar cell (DSSC) is an electrochemical solar cell that has been recognized for their high efficiency on converting light into electricity by using readily available and environmentally friendly materials. Generally, a DSSC was composed of three main components : a dye-covered nanocrystalline TiO_2 layer on a transparent conductive glass substrate, an electrolyte contained iodide/triiodide redox couple, and a platinized conductive glass substrate as a counter electrode. TiO_2 has been used as a working electrode for DSSC because it has a higher efficiency than any other metal oxide. TiO_2 film containing a large specific surface area increased light harvesting of the dye adsorbed on the TiO_2, leading to an improved efficiency of the solar cells.

TiO_2 can be synthesized via a number of techniques, including precipitation, chemical vapor deposition, solvothermal method, and glycothermal method. The techniques used for synthesis of titania in this study is a sol-gel method.

The objective of this work is to study of the effect of sintering temperature and thickness of TiO_2 film on the efficiency of dye-sensitized solar cell. The cell contained a spray-coated TiO_2 electrode prepared from titania sol.

2.Materials and Methods

TiO_2 was prepared using a sol-gel method. Typically, a solution of 70% nitric acid and distilled water was prepared. Titanium (IV) isopropoxide was added slowly to the solution while being stirred continuously at room temperature. The mixture was stirred for 3-4 days until clear sol was obtained. Next, the clear sol underwent dialysis in a cellulose membrane. The distilled water used for dialysis was changed daily until a pH of 3.5 was obtained. The resulting TiO_2 sol was kept in a refrigerator until needed.

The counter electrode for the DSSC is platinum coated on conducting glass. A platinum counter electrode was prepared by ion sputtering. A conducting glass to rectangular piece that was 1.0x1.5 cm^2 . Then, platinum was sputtered on the conducting glass using ion sputterer (JEOL JFC-1100E)

Anode electrode was a TiO_2 film on a conducting glass. To prepare the electrode, the glass was masked with aluminum foil containing a hole with a radius of 0.5 cm, as shown in Figure 1. The hole was located closer to one side of the foil than the other.

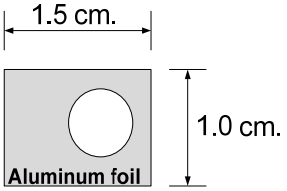

Figure 1. Aluminum foil used in preparation of an anode electrode before spray coating.

After masking, TiO_2 was coated on the glass using ultrasonic spray coater. The spraying liquid was placed in a syringe pump, which fed the liquid at a rate of 1 ml/min to an ultrasonic nozzle.

The film thickness was varied by changing of coats of TiO_2 at 200, 300, 400, 500 coats. After a few coats, TiO_2 film was dried by a hair dryer. The thickness of film was measured using profilemeter (Veeco Dektak 150). The coated glasses were sintered at a temperature ranging from 300°C to 600°C for two hours. The TiO_2 thin film electrode was immersed in solution of 0.3mM N3 dye for overnight in the dark.

3. Results and Discussion

3.1. Effect of sintering temperature for TiO_2 electrode

Figure 2 shows the typical X-ray diffraction patterns of TiO_2 films sintered at various temperatures. The anatase phase of TiO_2 started to forms at a sintering temperature of 300°C. When the sintering temperature reached 600°C, the rutile phase became the major component. Small amount of brookite was detected in all samples.

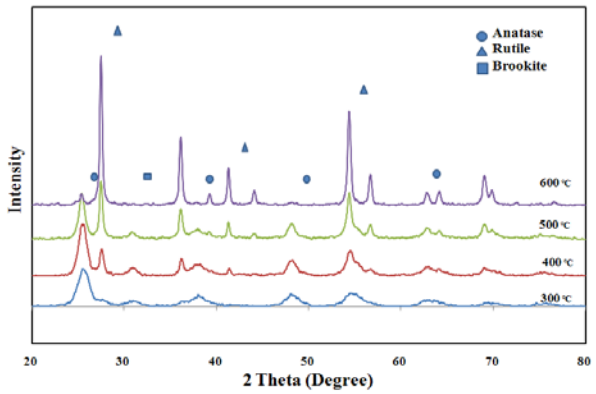

Figure 2. XRD pattern of TiO_2 powders sintered at various temperature

Crystallite size of anatase (as determined by Debye-Scherrer's equation) grew from 5.6 nm to 18.2 nm as sintering temperature was raised from 300°C to 600°C. The weight fraction of rutile phase of TiO_2 increased while the weight fraction of anatase and the specific surface area of TiO_2 decreased with increasing sintering temperature (see Table 1 and 2).

Table 1: Crystallite size and weight fraction of anatase, rutile and brookite phases of TiO_2 powders sintered at various temperatures.

Sintering Temperature (°C)	Crystallite size (nm)	W_A	W_R	W_B
300	5.6	0.62	0.22	0.16
400	7.6	0.50	0.37	0.13
500	10.1	0.44	0.47	0.09
600	18.2	0.09	0.90	0.01

W_A : weight fraction of anatase phase.
W_R : weight fraction of rutile phase.
W_B : weight fraction of brookite phase.

Table 2: Specific surface area of TiO_2 powders sintered at various temperatures.

Sintering Temperature (°C)	Surface area (m^2/g)
300	118.4
400	86.3
500	61.9
600	25.4

The PL measurement was carried out on a Fluorescence spectrophotometer (Perkin-Elmer LS-55) The PL spectra of TiO_2 sintered at various temperatures were shown in Figure 3. It can be seen that the PL intensity of TiO_2 decreased as the sintering temperature increased. These results suggested that the recombination rate of photogenerated electron and hole decreased when the sintering temperature increase, resulting in an increase of particle size.

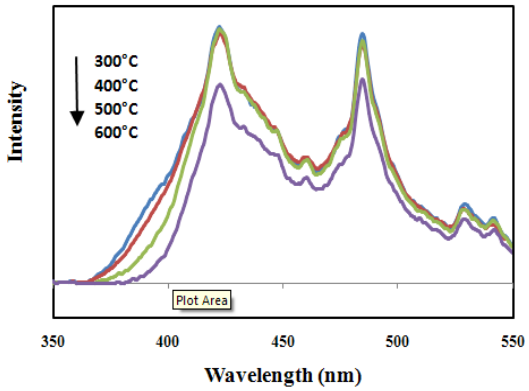

Figure 3. Photoluminescence spectra of TiO_2 sintered at various temperatures

The photovoltaic parameters of DSSC with a TiO_2 electrode that was calcined at various temperature are summerized in Table 3. We observed a maximum of short-circuit current density with a DSSC with a TiO_2 electrode calcined at 400°C for two hours. Similar trend was observed in fill factor and cell efficiency.

Table 3: Photovoltaic parameters of DSSC with TiO_2 electrode sintered at various temperatures. The film thickness was about 7.31 μm.

Sintering Temperature (°C)	V_{OC} (Volt)	J_{SC} (mA/cm^2)	Fill Factor	Efficiency (%)
300	0.71	3.43	0.69	1.68
400	0.74	4.44	0.82	2.69
500	0.71	3.92	0.77	2.14
600	0.68	3.58	0.73	1.80

3.2 Effect of thickness of TiO_2 film

We varied the thickness of TiO_2 electrode layer by varying number of coats of TiO_2 on the substrate. The number of coats of TiO_2 for this study were 200, 300, 400 and 500 coats. After coating, the electrode was sintered at 400°C for two hours. The film thickness was measured using step profilemeter. The highest cell efficiency of 3.06% were observed in a DSSC with the thickest TiO_2 electrode layer (ca. 11 μm). The cell efficiency increased as the TiO_2 film thickness increased.

Table 4: Photovoltaic parameters of DSSC with TiO_2 electrode sintered at 400°C for two hours.

Film Thickness (μm)	V_{OC} (Volt)	I_{SC} (mA/cm^2)	Fill Factor	Efficiency (%)
3.68	0.73	3.51	0.71	1.82
5.57	0.76	4.02	0.75	2.29
7.31	0.74	4.44	0.82	2.69
11.19	0.72	4.83	0.88	3.06

Conclusions

In conclusion, we have observed that the photovoltaic parameters of DSSC depends on sintering temperature and film thickness. We observed a maximum of short-circuit current density with a DSSC with a TiO_2 electrode calcined at 400°C for two hours. The highest cell efficiency of 3.06% were observed in a DSSC with the thickest TiO_2 electrode layer (ca. 11 μm). The cell efficiency increased as the TiO_2 film thickness increased.

Reference

[1].Liqianga, J., Yichuna, Q., Baiqia, W., Shudana, L., Baojianga, J., Libina, Y., Weia, F., Hongganga, F., and Jiazhong, S. Solar Energy Material & Solar Cells. 90 (2006): 1773-1787.

[2]. Lee, J. K., Jeong, B. H., Jang, S. I., Yeo, Y. S., Park, S. H., Kim, J. U., Kim, Y. G., Jang, Y. W., and Kim, M. R. J Mater Sci: Mater Electron (2008).

[3]. Hossain, M. F., Biswas, S., and Takahashi, T. Thin solid films 517 (2008): 1294-1300.

[4]. Lee, W. J., Ramasamy, E., and Lee, D. Y. Solar Energy Material & Solar Cells (2008).

[5]. Li, P., Wu, J., Lin, J., Huang, M., Huang, Y., and Li, Q. Solar Energy 83 (2009): 845-849.

[6]. Koo, H. J., Beomjin, J. P., Yoo, K., Kim, K., and Park, N. G. Inorganica Chimica Acta 361 (2008): 677-683.

[7]. Patrocinio, A. O. T., Paterno, L. G., and Iha, N. Y. M. Journal of Photochemistry and Photobiology A: Chemistry 205 (2009): 23-27.

[8]. Shi, J., Liang, J., Peng, S., Xu, W., Pei, J., and Chen, J. Solid State Sciences 11 (2009): 433-438.

[9]. Yu, H., Zhang, S., Zhao, H., Will, G., and Liu, P. Electrochimica Acta 54 (2009): 1319-1324.

[10]. Amornpitaksuk, P., and Leesakul, N Songklanakarin J. Sci. Technol 25(4) (2003): 535-551.

[11]. Zhoa, D., Peng, T., Lu, L., Cai, P., Jiang, P., and Bian, Z. The Journal of Physical chemistry C. 112 (2008): 8486-8494.

Investigation on the adsorption of an anionic dispersant on high rank and coal

N.Wongtanoi[1,2,3], T.Srikhirin[1,2,3,4]*, S. Jiwattayakul[5] , J. Kiatpattana[5] and N. Latthitham[5]

[1]Center of Intelligence Materials and Systems, [2]Materials Science and Engineering Programme, [3]NANOTEC Center of Excellence at Mahidol University ,[4]Department of Physics, Faculty of Science, Mahidol University, Bangkok, Thailand 10400
[5]SCT Company Limited, 1 Siam Cement Road, Bangsue Bangkok, Thailand 10800

*E-mail: sctsk@mahidol.ac.th

Abstract: Coal water mixture (CWM) is the suspension of coal particle in water with the high coal content, preferably in the range of 55 to 70%. CWM has received a lot of attention as an alternative source of energy because various problems associated with the conventional coal burning. The rheological property and stability upon storage are two of the most important parameters in CWM technology. The chemical agent, often referred as dispersant, is needed to provide sufficient viscosity and the desired stability. The aim of this work is to investigate the adsorption behavior of an anionic dispersant on the high rank (SCT-HR) and low rank (SCT-LR) coal surface is carried out in order to evaluate the amount of the surfactant needed for the stabilization of CWM. Sodium naphthalene sulfonate formaldehyde condensate was used as anionic dispersant. The higher effective dispersant adsorption was found in the high rank coal (SCT-HR) due to the hydrophobicity on coal surface which can be quantified as the hydrophillicity index (HI) and the presence of the higher ratio of the aliphatic and aromatic C-H stretching bands indicate that SCT-HR is more hydrophobicity from FTIR spectra. The SCT-LR is observed that less effective of dispersant adsorption. Therefore, more amount of dispersant is needed in order to provide the charge to the coal surface.

Introduction

After the increasing of oil price in the world, coal began to be reviewed as a substitute fuel for oil [1]. Coal has been emerged as an alternative source of the energy; however, the use of coal has long been associated with various environmental and safety concern. These include the dust particle, safety during storage, transportation [2] and requirement for the reduction of high sulfur emission. Coal water mixture (CWM) is the suspension of coal particle in water with the high coal content, preferably in the range of 55 to 70% and small quantities of additive. For successful utilization of CWM in commercial plants, a high coal concentration of CWM is desired, and it is necessary for CWM to display excellent fluidity and stability suitable for its handing preparation, storage, transport and production processes [3,4].

Since coal is mixture of carbonaceous materials and mineral matter, it has variety of surface properties depending upon its rank. The chemical agent, often referred as dispersant, is needed to be added to provide sufficient viscosity and the desired stability [5]. The dispersant is adsorbed onto the surface of the coal, thus modifying its surface properties. The amount of the adsorbed dispersant depends on various parameters which include the hydrophobic-hydrophillic balance of the dispersant molecule, nature of the coal surface, dispersant type and its concentration, pH, etc. As anionic dispersant, aromatic sulfate condensates are known to be effective dispersants for CWM due to they are able to disperse the coal particles in the water by preventing the flocculation and agglomeration [4].

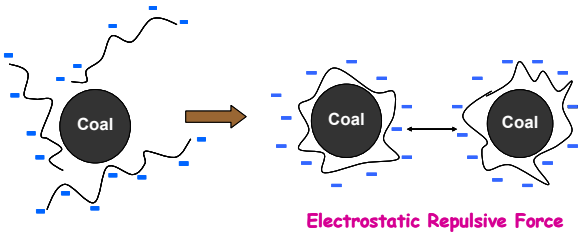

Figure 1. Schematic represents the adsorption of anionic polymer electrolyte, dispersant, on coal surface. The adsorption is taking place via the adsorption while the negative charge along the adsorbed polymer chain provide the electrostatic repulsion between the coal particle

The coal surface is hydrophobic by nature and the mechanism of adsorption of dispersant take place between the hydrophobic groups of coal and the hydrophobic chain of anionic dispersant. The negatively charge surface of the coal particles will provide the force for each particle to repel to each other by the action of electrostatic repulsive force. The flocculation is prevent while the dispersion of the coal particle is achieved [3,5]. It is very importance to examine the adsorption behavior of dispersant which is really necessary to make the coal particles disperse in water [4]. The aim of this investigation is to determine the adsorption behavior of anionic dispersant on the high rank (SCT-HR) and low rank coal (SCT-LR) surface is carried out in order to evaluate the amount of the surfactant needed for the stabilization of CWM.

Materials and Methods

The raw coals, high rank and low rank coals, were obtained from SCT co., ltd. (SCT-HR and SCT-LR respectively). The proximate analyses of the coal samples are given in Table 1.

Table 1: Proximate analysis of high rank and low rank coals.

Coal sample	Total moisture (%)	Volatile matter (%)	Fix carbon (%)	Gross calorific value (Kcal/kg)
SCT-HR	5.74	24.50	56.53	6,410
SCT-LR	25.39	42.31	41.60	5,878

The coal samples were ground by ball mill to the desired particle size distribution. Then, the grounded coals were sieved and particle size less than 75 µm. The dispersant used in this study is sodium naphthalene sulfonate formaldehyde condensate act as anionic dispersant.

The adsorption experiment were carried out at room temperature in glass vessels. Solid particle content in CWM was 20% (wt). Dispersant at different concentrations were prepared by a given amount of dispersant was mixed thoroughly with a given amount of distilled water. Then a certain amount of coal was added to the solution. This CWM was stirred at a speed of 600 rpm for given time at constant temperature. CWM was centrifuged and supernatant was analyzed to determine dispersant concentration by using UV spectrophotometer [6,7]. The concentration of dispersant in solution was determined from the absorbance at 296 nm using predetermined calibration curves.

Results and discussion

The nature of the coal surface can be quantified as the hydrophillicity index (HI) [8] which represents the amount of the polar group and non-polar group of the coal particle. It is well known that the polarity of the solid particle plays a major role in controlling the adsorption of the polymeric molecule onto the surface [8]. The HI can be calculated by using the adsorption intensity, obtained from fourier transform infrared (FTIR), following the equation 1.

$$HI = \frac{(C=O) + 2(-OH)}{(R-H) + (Ar-H)} \quad .....(1)$$

This FTIR spectrum of SCT-HR and SCT-LR were presented in Figure 2. Four major peaks are taken for the calculation of the HI are C=O stretching band at about 1616, 1620 cm^{-1}, the O-H band at 3317, 3233 cm^{-1}, the aliphatic and aromatic C-H stretching bands at 2849, 2849 and 2918, 2917 cm^{-1}, respectively. The calculated HI of the coal samples [4] are tabulated in table 2. The values indicate that SCT-LR is more hydrophilicity than SCT-HR on surface as evidenced from the presence of the higher ratio of O-H and C=O functionality on the coal particle. The aliphatic and aromatic C-H stretching bands indicate that SCT-HR is more hydrophobicity.

Table 2: Hydrophilicity index (HI) of coal samples.

Coal sample	Hydrophilicity Index (HI)
SCT-HR	1.2
SCT-LR	1.8

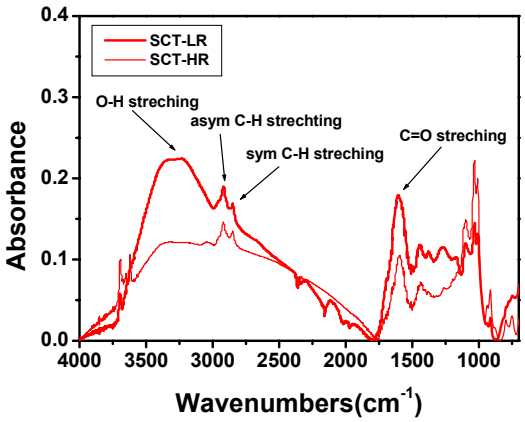

Figure 2. FTIR spectra of SCT-HR and SCT-LR coal samples.

Figure 3. shows that the amount of adsorption of dispersant on coal particles increases along with increase of concentration from the solution and reach the saturation due to the formation of the complete surfactant coverage on the surface. SCT-HR has higher adsorbed amounts of the dispersant than SCT-LR, for a given dispersant concentration, due to the balance of the hydrophobicity-hydrophilicity interaction between coal surface and the dispersant molecule. A less effective of the dispersant is observed for the SCT-LR, as a consequence more dispersant is needed in order to provide the charge to the surface.

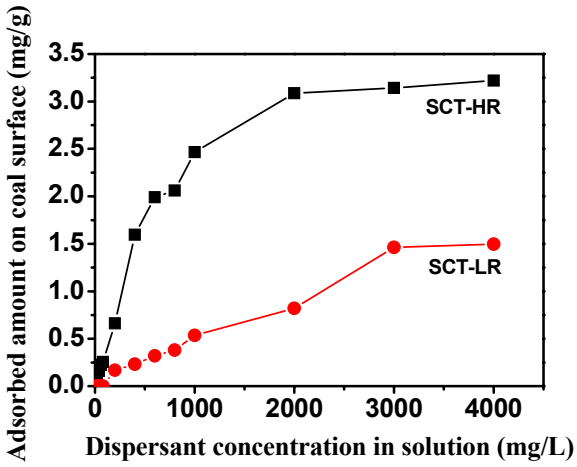

Figure 3. Adsorption isotherm of anionic dispersant on coal surface

Conclusions

Dispersant adsorption was found to be different for the high rank (SCT-HR) and low rank (SCT-LR) coal. The particle size distribution of both

coal samples does not have an effect on the dispersant adsorption; however, the degree of the hydrophilicity on coal surface is playing a major role in the dispersant adsorption. The SCT-HR shows a higher dispersant adsorption than SCT-LR and provide a higher negative charge to the surface of the coal.

Acknowledgements

This work is financially supported by SCT co., ltd through the development programme of the "clean coal technology".

References

[1] D.F. Umar, H. Usui, Y. Komoda, and Muta'alim, *Fuel Process Technol.* **90** (2009), pp. 611-615.
[2] A. Gürses, M. Açıkıldız, C. Doğar, S. Karaca, and R. Bayrak, *Fuel Process Technol*. **87** (2006), pp. 821-827.
[3] R. Yavuz and S. Küçükbayrak, *Energ Convers Manage*. **42** (2001), pp. 2129-2137.
[4] R. Yavuz and S. Küçükbarak, *Power Technology.* **119** (2001), pp. 89-94.
[5] H. Dinçer, F. Boylu, A.A Sirkeci, and G. Ateşok, *Int. J. Miner. Process*. **70** (2003), pp. 41-51.
[6] D. Yang, X. Qiu, M. Zhou, and H. Lou, *Energ convers Manage.* **48** (2007), pp. 2433-2438.
[7] Z. Aktaş and E.T. Woodburn, *Fuel Process Technol*. **62** (2000), pp. 1-15.
[8] F. Ohene, Correlation of stability/rheology relationship with coal, Master's Thesis, Grambling University, 1991.

Carbon-assisted growth of SiO_2 nanowires by thermal evaporation method

P. Chamninok[1, 2*], S. Pukrid[2]

[1] Department of Physics, Faculty of Science, Ubon Ratchathani Rajabhat University, Ubon Ratchathani, Thailand 34000
[2] Department of Physics, Faculty of Science, Ubon Ratchathani University, Ubon Ratchathani, Thailand 34190

[*] E-Mail: chamninok@hotmail.com

Abstract: SiO_2 nanowires had been synthesized by thermal evaporation method, using SiO_2 powder mixed with graphite powder ratio of 1:1 by weight, heated at 1200 degree Celsius for 6 hours in atmosphere of nitrogen and oxygen gas. The synthesized products and Si substrates were characterized by scanning electron microscopy (SEM) and X-ray diffraction (XRD) instruments. SEM images show SiO_2 nanowires have diameters in the range of 50-200 nm, and length up to several tens of micrometer.

Introduction

One-dimensional nanostructures materials have been synthesized due to these materials often show a unique physical properties that are different from those of the bulk ones and their potential uses in optoelectronic, nano-electronics devices and fundamental importance to the study of size-dependent chemical and physical phenomena [1-2]. Silicon-based nanoscale materials have attracted a lot of interest because of their valuable semiconducting, mechanical, and optical properties, and their potential applications in mesoscopic research and nanodevices [3]. Inorganic nanowires and nanorods have been fabricated by many different methods, such as thermal evaporation, laser ablation, chemical vapor deposition and solvothermal reactions. Nanorods and nanowires are distinguished in terms of the aspect ratio, which is far greater in the latter. The mechanism of formation of many of these nanostructures involves a vapor-solid (VL) or vapor-liquid-solid (VLS) growth process. There are two different synthesized methods have been mainly used: non-catalyst-based and catalyst-based methods [4]. Gundiah et al. [5] reported that silicon nanowires have been synthesized by heating a mixture of silicon powder and activated carbon or a carbon coated solid substrate at 1200-1350 $^\circ$C for 3 hours. in a mixture of Ar (50 sccm; standard cubic centimeter per minute) and H_2 (20 sccm). The formation of Si-nanowires can be explained as follows. Silicon is generally covered by an oxide layer. The oxide layer gets reduced by carbon into silicon monoxide by the reaction

$$Si_xO_2 + C \rightarrow Si_xO + CO \quad (x>1) \quad (1)$$

$$Si_xO \rightarrow Si_{x-1} + SiO \quad (2)$$

$$2SiO \rightarrow Si + SiO_2 \quad (3)$$

Crystalline silicon, formed in step (3). Yu, et al. [6] reported that the large-scale synthesis of high purity silicon nanowires of uniform diameters around 15 nm by heating silicon powder and mixed with 5 wt% of Fe powder, and hot-pressed to form a plate. Then heated at 1200 $^\circ$C for 20 hours under flowing argon (100 sccm) at a pressure of about 100 Torr. SiO_x nanowires are very interesting for applications in optical properties and its applications. The stable and bright blue emission of SiO_x nanowires used in sources of high-intensity light near-field optical microscope probes, waveguides, etc. [5]. The synthesis of mesoporous SiO_x nano-structures prepared from two stages: the sol-gel process with tetraethyl orthosilicate (TEOS) hydrolysis and the solvent-thermal process. The photoluminescence show that the SiO_x mesoporous structure has a stable and intensive blue emission [6]. The formation of nanowires of metal oxides and other materials can be prepared by using carbon catalysis. The synthesis and characterization of amorphous SiO_2 nanowires have been presented in many researches, but the theory on the nanowires formation mechanism is controversial [5-10]. Lately, crystalline SiO_2 nanowires have been synthesized by using fumed silica with activated carbon or activated charcoal at the temperature of 1300 $^\circ$C for 5 hours in a flowing Ar-H_2 atmosphere [9]. The previous paper reported that silicon dioxide nanowires could be synthesized by heating silicon powder and graphite at 1200 $^\circ$C under a mixture of Ar/O_2 (99.2/0.8mol%) for 30 min. Amorphous silica nanowires with lengths up to 500 micrometers and diameter in range 10-300 nm were been observed. A growth mechanism can be proposed. First, carbon dioxide is formed by the reaction of O_2 with the piece of graphite [$C(s) + O_2(g) \rightarrow CO_2$] and reacts with silicon to form silicon oxide. [$CO_2(g) + Si(s) \rightarrow CO(g) + SiO(g)$] The presence of O_2 (g), silicon oxide yields silicon dioxide, [$SiO(g) + (1/2)O_2(g) \rightarrow SiO_2(s)$] which aggregates to form nanowires [10]. In our case, we used the thermal evaporation process to grow SiO_2 nanowires through a vapor phase transport process via the vapor-liquid-solid mechanism.

Materials and Methods

SiO_2 nanowires can be synthesized by thermal evaporation method. The source materials in which SiO_2 (99.9%, Riedel-de Haren) was finely ground with graphite (99.99%, Alfa), keeping the ratio of 1:1 by weight. The finely ground mixture was taken in an alumina boat and silicon substrates were place on and next materials source. The alumina boat was put in a quartz tube furnace and then heated at 1200 $^\circ$C for 6 hours in a mixture of nitrogen (1 L/min) and oxygen

(0.5 L/min). When the temperatures reached the setting points, the switch was turned off and to cool down to room temperature naturally. The Figure 1, 2 and 3 show the results of products. The synthesized products on the silicon substrates were examined by scanning electron microscope (SEM), and X-rays diffraction (XRD) with appropriate manners.

Results and Discussion

The thermal evaporation of a commercial silicon dioxide powder with carbon-assisted under atmosphere of nitrogen and oxygen led to the formation of a large amount of nanowires. The product formed as a layer on the Si-substrate was grey or white in color. The morphology of the synthesized products can be characterized with SEM and XRD instruments. The low magnification SEM image (Figure 1.) shows the wires structure of the sample. According to this image, it is interesting to notice that the threads are aligned in a direction roughly parallel to that of the gas flow. They are very long and their length can estimate up to 500 micrometer. Figure 2. shows the SEM image of Figure 1. at higher magnification, indicates that the product is made of nanowires, which gathered to form bundles. Figure 3. shows the SEM image of the bundles of SiO_2 nanowires which silicon substrate was placed next materials source. We can see the growth nanowires form one cluster to the other. Figure 4. shows the XRD pattern of the synthesized product. This XRD peak indicates crystal state of SiO_2 structure.

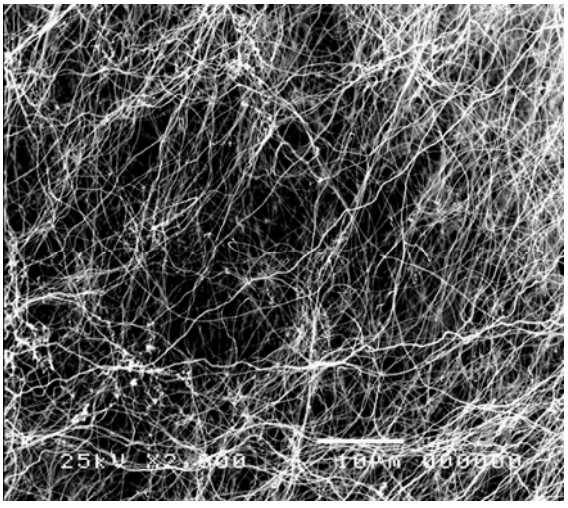

Figure 1. The low magnification SEM image of the SiO_2 nanowires on Si-substrate was placed on material source.

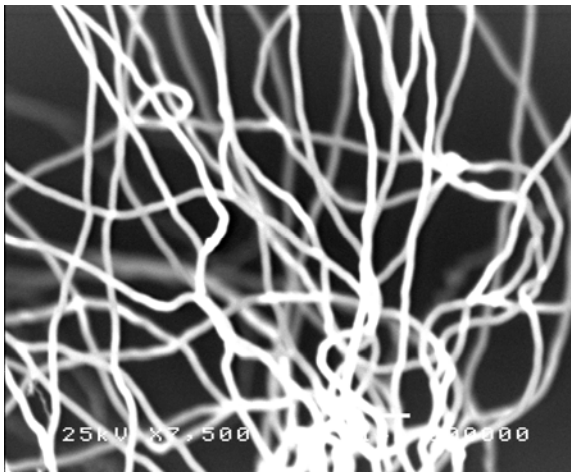

Figure 2. The SEM image of the SiO_2 nanowires from Figure 1. at higher magnification.

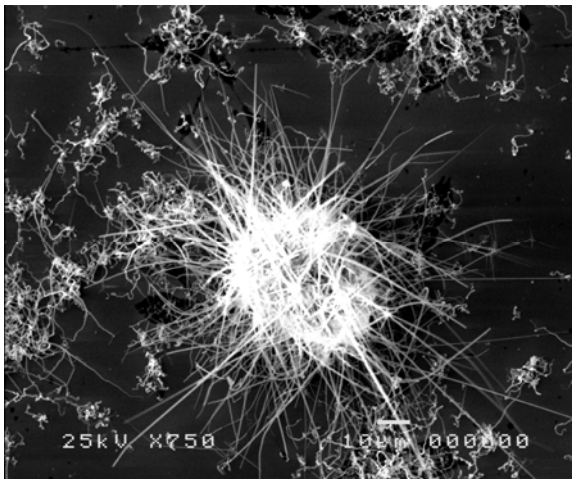

Figure 3. SEM image of the SiO_2 nanowires on silicon substrate was taken next materials source

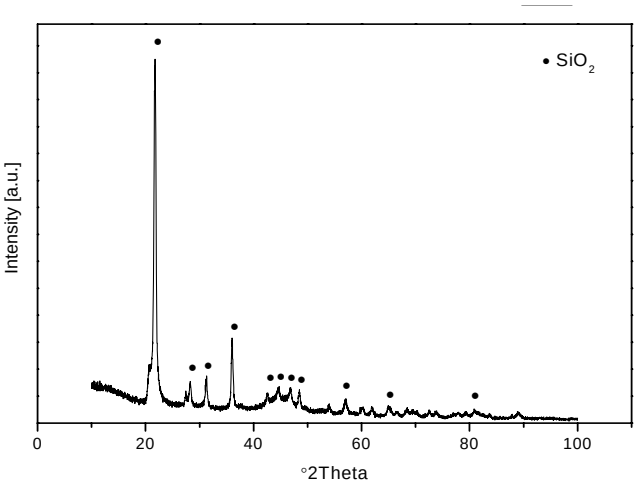

Figure 4. XRD spectrum of the SiO_2 nanowires

Conclusions

In summary, the formation of the silicon dioxide nanowires can be synthesized by thermal evaporation method at 1200°C for 6 hours under atmosphere of nitrogen and oxygen. The structures of these products have been characterized by scanning electron microscope (SEM) and X-rays diffraction (XRD). The SiO_2 nanowires have a uniform diameter in range 50-200 nm and length up to several tens of micrometers. The growth of SiO_2 nanowires is controlled by the vapor-liquid-solid (VLS) mechanism. This method is convenient and inexpensive for the synthesis. These nanowires could offer great opportunities for fundamental and applied research.

References

[1] J. C. Wang, C. Z. Zhang and F. G. Li, *Solid State Commun*. **125** (2003), pp. 629-631.

[2] K. H. Lee, S. W. Lee, R. R. Vanfleet and W. Sigmund, *Chem. Phys. Lett*. **376** (2003), pp. 498-530.

[3] Z. W. Pan, Z. R. Dai, L. Xu, S. T. Lee and Z. L. Wang, *J. Phys.Chem. B*. **105** (2001), pp. 2507-2514.

[4] C. N. R. Rao, Gautam Gundiah, F. L. Deepak, A. Govindaraj and A. K. Cheetham, *J. Mater. Chem.* **14** (2004), pp. 440-450.

[5] G. Gundiah, F. L. Deepak, A. Govindaraj and C. N. R. Rao, *Chem. Phys. Lett.* **382** (2003), *pp.* 579-583.

[6] D. P. Yu, Z. G. Bai, Y. Ding, Q. L. Hang, H. Z. Zhang, J. Wang, Y. H. Zou and W. Qian, *Appl. Phys. Lett*. **72** (1998), *pp.*3458-3460.

[7] Y. Xia, P. Yang, Y. Sun, Y. Wu, B. Mayers, B. Gates, Y. Yin, F. Kim and H. Yan, *Adv. Mater.* **15** (2003), pp. 353-389.

[8] S. –H. Li, X. –F. Zhu and Y. –P Zhao, *J. Phys. Chem. B.* **108** (2004). pp. 17032-17041.

[9] X. X. Li, Y. H. Tang, L. W. Lin and J. L. Li, *Micropor. Mesopor. Mater*., doi: 10.1016/j.micromeso.2007.09.004. in press. (2007).

[10] K. Saulig-Wenger, D. Cornu, F. Chassagneux, T. Epicier and P. Miele, *J. Mater.Chem.* **13** (2003). pp. 3058-3061.

Fabrication and characterization of nanocrystalline TiO_2 based solar cells with polymer gel electrolytes

S. Santhaveesuk, S. Wantawee, S. Pukird and U. Tipparach*

Department of Physics, Faculty of Science, Ubon Ratchathani University, Ubon Ratchathani,Thailand 34190

*E-mail: udomt@hotmail.com

Abstract: Polymer gel electrolytes were prepared by adding iodide salts XI (X = potassium, lithium or tetrapropylammonium (TPA)) and I_2 into γ–butyrolactone gelated with 1–methyl–3–propyl imidazolium iodide and 1,2,4,5–tetrakisbromomethyl benzene as a mixture solvent. The mixture with the ratio of XI:I_2 was 10:1. KI, LiI and TPA , poorly soluble in liquid electrolyte, can dissolve completely in polymer gel electrolytes. The maximum ionic conductivity of KI, polymer gel electrolytes was 2.37 mS/cm at 30 °C. The dye sensitized solar cells (DSSCs) with the polymer gel electrolytes were fabricated. The results showed that energy conversion efficiency of light to electricity were 1.90 %, 2.16 %, and 2.05 % where LiI, KI, and TPA electrolytes were used, respectively, under irradiation of 100 mW/cm^2.

Introduction

In between 2000 and 2030 demand the world energy increase will by about 70 %. Fossil fuels, supplying 80 % of all energy consumed worldwide, are facing rapid resource depletion. The resource reserves of fossil fuels throughout the whole world in 2002 were projected to last 40 year for oil, 60 year for natural gas and 200 years for coal. Because of a growing demand for energy, combined with the depletion of fossil resources, global warming and its associated climate change, there is an urgent need for environmentally sustainable energy technologies. Among all the renewable energy technologies, such as wind turbines, hydropower, wave and tidalpower, solar cells, solar thermal, biomass-derived liquid fuels and biomass-fired electricity generation, photovoltaic technology utilizing solar energy is considered as the most promising one. [1]. Dye-sensitized solar cells (DSSCs) has become an attractive and low production cost device for the conversion of solar light to electrical energy. The DSSCs consists of the working electrode including a dye-adsorbed nanocrystalline TiO_2 layer, an electrolyte containing redox couple I^-/I_3^- and a counter electrode. All these components affect the performance of the DSSCs. Photoexcitation of the dye leads to the electron injection from the excited state of the dye onto the conduction band of TiO_2. The oxidized dye receives electron from I^- and the resulting I_3^- is reduced back to I^- at the counter electrode [2]. The most effective electrolyte used for DSSCs at present is the liquid electrolyte of I^-/I_3^-. However it is not suitable for long term stability due to leakage and evaporation. Therefore, efforts have been made to replace the liquid electrolyte with organic hole transport materials (HTMs) [3,4]. p-type semiconductors [5,6]. and polymer electrolytes [7]. Dye-sensitized solar cells (DSSCs) based on TiO_2 porous films [8,9]. are one of the potential low-cost alternatives to traditional silicon solar cell and a maximal 1ight-electric power conversion efficiency of 11% [10]. was already achieved with liquid electrolyte containing a (I^-/I_3^-) redox couple in organic solution, such as acetonitrile, propylenecarbonate and ethylene carbonate. However, the volatility of organic solvent leads to a decrease in performance of DSSCs. This drawback limits practical application of DSSCs.

Efforts have been to overcome this problem. Substituting the gel liquid electrolyte for liquid electrolyte [11] is an efficient way to prevent the leakage and evaporate of electrolyte [12–17]. Recently, several types of polymers [18–20] as gelator have been used in gel electrolyte for DSSCs. For these electrolytes, the concentration of I^- ions is sufficient for reducing the oxidated sensitizer of DSSCs during operations, if the I^- ions are supplied by only adding the LiI or NaI in the gel electrolyte. However, it is interesting that the organic iodide salts containing large cation, such as N-methyl pyridine iodide [18] or 1, 3–dimethyl–3 - imidazolinium iodine [14] are also added into gel electrolyte to supply parts of I^- ions. The same strategy was adopted for DSSCs based on liquid electrolytes [21,22]. It implies that large cation in gel electrolytes contribute to improve the performance of quasi-solid-state DSSCs. In addition, LiI commonly used for DSSCs is deliquescent and more expensive than other alkali metal iodide salts, such as NaI, KI [23].

In this paper, Polymer gel electrolytes were prepared by adding iodide salts XI (X = potassium, lithium or tetrapropylammonium (TPA)) and I_2 into γ–butyrolactone gelated with 1–methyl–3– propyl imidazolium iodide and 1,2,4,5–tetrakisbromo methylbenzene as a mixture solvent. The mixture with the ratio of XI:I_2 was 10:1.

Materials and Methods

1. Materials

Iodide salts XI (X = potassium, lithium or tetrapropylammonium (TPA)) (A.R. grade), I_2, γ–butyrolactone, 1–methyl–3–propylimidazolium iodide and 1,2,4,5–tetrakisbromo methylbenzene were

used as received. Conducting glass substate (TCO glass, fluorine doped tin oxide over-layer, sheet resistance 8 Ω/sq) was purchased from Solaronix SA, Switzerland. Sensitizing dye bis (tetrabutylammonium) -*cis*-di (thiocyanato) -*N*,*N*- bis (4-carboxylato-4-carboxylic acid-2,2-bipyridine) ruthe nium(II) (or commercial name is N719 dye) was purchased from Solaronix SA, Switzerland. Other solvents and reagent were used as received.

2. Preparation of polymer gel electrolytes

A series of mixtures were prepared by adding iodide salts 0.5 g XI (X = potassium, lithium or tetrapropylammonium (TPA)), 0.05 g I_2, 1.0 ml 1–methyl–3–propylimidazolium iodide, and 0.1 g 1,2,4,5–tetrakisbromo methylbenzene into 2.0 ml γ–butyrolactone. The polymer gel electrolytes were obtained until the mixtures became homogenous and unflowable stering at temperature of 70-80 °C .

3. Measurement

The current-voltage characteristic curves were measured with Keithley 236 source meter. The active areas of the cells are about 0.25 cm^2. The Xenon arc lamp was used as an irradiation source and the intensity of the incident light was 100 mW/cm^2.

X-ray diffraction (XRD) spectra of KI, LiI, and TPA crystals and of polymer gel electrolytes with these three salts were tested by a X-ray diffraction XRD,Cu-tube (Philips X'Pert).

UV-visible spectrometer (Perkin) was used to measured absorbtion of polymer gel electrolytes with three salts.

The ionic conductivity of polymer gel electrolytes at temperature 30 °C was measured by Cyberscan PC 300. The photoelectronic performance [i.e. fill factor (FF) and overall light to electrical energy conversion efficiency (η)] were calculated by the following equation [24]. :

$$FF = \frac{V_{\max} J_{\max}}{V_{oc} J_{sc}}$$

$$\eta(\%) = \frac{V_{\max} J_{\max}}{P_{in}} \times 100 = \frac{V_{oc} J_{sc} FF}{P_{in}} \times 100$$

Where J_{sc} is the short-circuit current density (mA/cm^2), V_{oc} is the open- circuit voltage (V), P_{in} is the incident light power, $J_{\max}$ (mA/cm^2), $V_{\max}$ (V) are the current density and voltage at the point of maximum power output on the $J-V$ curve, respectively.

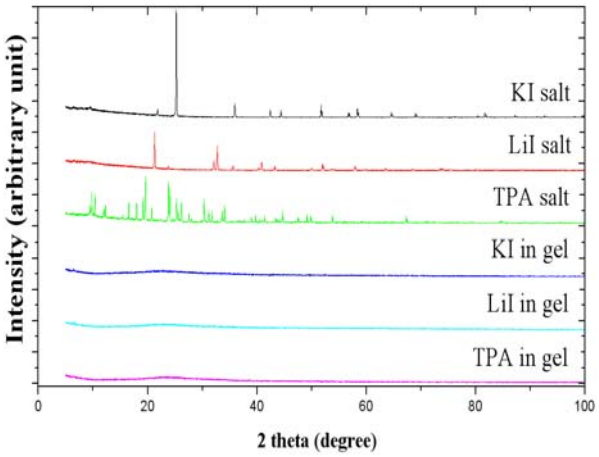

Figure 1. XRD spectra of KI, LiI, TPA salts and polymer gel electrolytes containing the three salts.

Methods

Titanium (IV) isopropoxide, $Ti[OCH(CH_3)_2]_4$ solution was obtained from Fluka and used as received. TCO glass substrates are F-doped SnO_2 thin films with 8 Ω/sq were purchased from Solaronix SA, Switzerland. Nanocrystalline TiO_2 thin flims were synthesized by sol-gel doctor-blade technique. The procedure of synthesis for sol-gel is described elsewhere [25]. To fabricated working electrodes for desensitized solar cells, we deposited TiO_2 on TCO glass substrates followed by sintering in air at 450 °C for 30 min. After cooling to 80 °C, the calcined films were immersed in ruthenium dye sensitizer bis(tetrabutylammonium)-*cis*-di(thiocyanato)-*N*,*N*-bis (4-carboxylato-4-carboxylicacid-2, 2-bipyridine) ruthenium(II) (or commercial name is N719 dye) 0.4 mM in acetonitrile for 24 hrs. Afterwards, the dye-sensitized TiO_2 electrode was rinsed with ethanol and dried in air. Finally, the working electrodes were dried in an oven and kept in oven at temperature of 80-90 °C. The crystal tructures of the resulting films were identified by X-ray diffraction (XRD) technique with X'Pert-MPD System. To obtain platinized counter electrodes with platinum colloidal nanoparticles, we prepared platinized counter electrodes using electrodeposition method as described by P. Li et al. [26]. Polymer gel electrolytes was synthesized by adding iodide salts 0.5 g XI (X = potassium, lithium or tetrapropylammonium (TPA)), 0.05 g I_2, 1.0 ml 1–methyl–3–propylimidazolium iodide, and 0.1 g 1,2,4,5–tetrakisbromo methylbenzene into 2.0 ml γ–butyrolactone. The polymer gel electrolytes were obtained until the mixtures became homogenous and unflowable stirling at temperature of 70-80 °C . Finally, the polymer gel electrolyte was obtained.

Dye-sensitized nonocrystalline solar cells were assembled according to the following stapes. The prepared gel electrolyte was casted onto the surface of

dry-absorbing TiO_2 working electrode. The platinized counter electrode was pressed on top of the working electrode to form a DSSCs. The active areas of the cells are about 0.25 cm^2. The photocurrent-potential characteristic curves were measured with Keithley 236 source meter. The Xenon arc lamp was used as an irradiation source and the intensity of the incident light was 100 mW/cm^2. The current density was calculated based on the current and the area of the cells.

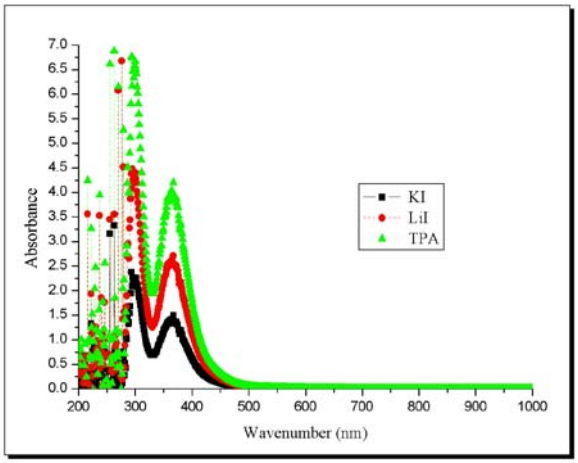

Figure 2. UV spectra of polymer gel electrolytes containing the KI, LiI and TPA.

Results and Discussion

The photovoltaic test of the dye-sensitized solar cells (DSSCs) composed of polymer gel electrolytes were prepared by adding iodide salts XI (X = potassium, lithium or tetrapropylammonium (TPA)) and I_2 into γ–butyrolactone gelated with 1–methyl – 3–propylimidazolium iodide and 1,2,4,5–tetrakis bromo methylbenzene as a mixture solvent. The mixture with the ratio of $XI:I_2$ was 10:1. were measured and experimental, and the results were summarized in (Table 1.). The overall light to electrical energy conversion efficiency (η) of polymer gel electrolytes of KI, LiI and TPA are 2.16 %, 1.90 % and 2.05 % respectively. In order to explain the complete dissolution of KI. LiI and TPA in polymer gel electrolytes, the interaction between three iodide salts and polymer gel electrolytes molecule was investigated by UV-visible spectrometer. (Fig 2.) show the UV spectra of polymer gel electrolytes with three iodide salts and polymer gel electrolytes. And coefficient absorbtion value of the dye-sensitized solar cells (DSSCs) with the polymer gel electrolytes of these three iodide salts are 367 nm. Prepared by adding iodide salts would dissolve were polymer gel electrolytes. In our experiment, by the complete solution of these three iodide salts in polymer gel electrolytes. Confirmed by the XRD spectra of their polymer gel electrolytes. (Fig 1.).

Table 1: Photoelectrochemical data of the DSSCs with different kinds of electrolytes*

Electrolytes	J_{sc} **(mA/cm^2)**	V_{oc} **(mV)**	FF	η (%)
LiI in gel	5.76	591	0.557	1.90
KI in gel	6.48	609	0.547	2.16
TPA in gel	6.42	589	0.543	2.05

*The electrolytes contain iodide salts XI and I_2 The mixture with the ratio of $XI:I_2$ was 10:1.

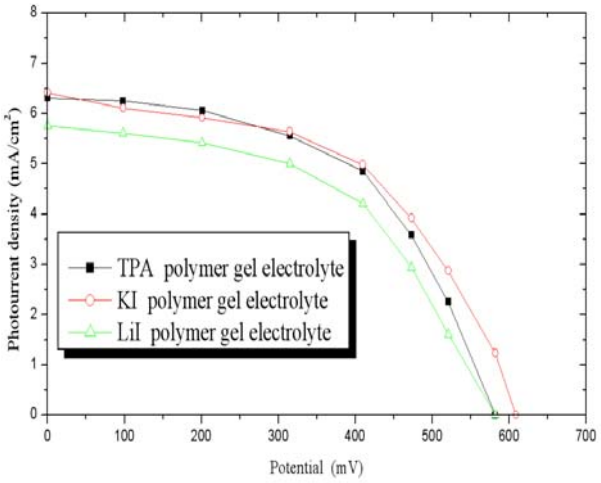

Figure 3. Photocurrent-potential curves for dye-sensitized solar cells (DSSCs) fabricated by using the polymer gel electrolytes containing the KI, LiI and TPA.

Figure 3. Shows the photocurrent-photovoltage characreristics curves of dye-sensitized solar cells (DSSCs) based on the polymer gel electrolytes by adding these three iodide salts : I_2. The mixture with the ratio of $XI:I_2$ was 10:1. The open- circuit voltage (V_{oc}), the short-circuit current density (J_{sc}), fill factor (FF) and overall light to electrical energy conversion efficiency (η) value of the dye-sensitized solar cells (DSSCs) with the polymer gel electrolytes of LiI are 591 mV, 5.76 mA/cm^2, 0.557, 1.90 %, respectively., (V_{oc}), (J_{sc}), (FF), (η) value of the dye-sensitized solar cells (DSSCs) with the polymer gel electrolytes of KI are 609 mV, 6.48 mA/cm^2, 0.547, 2.16 % respectively, and (V_{oc}), (J_{sc}), (FF), (η) value of the dye-sensitized solar cells (DSSCs) with the polymer gel electrolytes of TPA are 589 mV,6.42 mA/cm^2, 0.543, 2.05 % respectively.

Conclusions

In this work, dye-sensitized solar cell (DSSCs) composed of polymer gel electrolytes were prepared by adding iodide salts XI (X = potassium, lithium or tetrapropylammonium (TPA)) and I_2. The mixture with the ratio of XI:I_2 was 10:1. The system was optimized and the maximum ionic conductivity of KI polymer gel electrolytes was 2.37 mS/cm at 30 °C. The results showed that energy conversion efficiency of light to electricity were 1.90 %, 2.16 %, and 2.05 % where LiI, KI, and TPA electrolytes were used, respectively, under irradiation of 100 mW/cm^2.

References

[1] B. Li, L. Wang, B. Kang, P. Wang and Y. Qiu, *Solar Energy Materials & Solar Cells.* **90** (2006), pp. 549 - 573.

[2] M. Grätzel, *J. Photo.Chem. Photobiol. A: Chem.* **64** (2004), pp. 3-14.

[3] S.X. Tan, J. Zhai, M.X. Wan, L. Jiang, and D.B. Zhu, *Synthetic Metals.* **137** (2003), pp. 1511-1512.

[4] K. Murakoshi, R. Kogure, Y. Wada, and S. Yanagida, *Solar Energy Mater. Solar cells.* **55** (1998), pp. 113-125.

[5] V.P.S. Perera, P.K.D.D.P. Pitigala, M.K.I. Senevirathne, and K. Tennakone, *Solar Energy Mater. Solar cells*. **86** (2005), pp. 443-450.

[6] G.R.A. Kumara, S. Kaneko, M. Okuya, B. Onwona-Agteman, A. Konno, and K. Tennakone, *Solar Energy Mater. Solar cells*. **90** (2006), pp. 1220-1226.

[7] E. Chatzivasiloglou, T. Stergiopoulos, N. Spyrellis, and P. Falaras, *J. Mater. Processing Technol.* **161** (2005), pp. 234-240.

[8] B. O'Regan, and B.M. Grätzel, *Nature*. **353** (1991), pp. 737.

[9] M. Grätzel, *Nature*. **414** (2001), pp. 338.

[10] M. Grätzel, *J. Photochem. Photobiol.C: Chem.* **164** (2004), pp. 3–14.

[11] Y.J. Kim, J.H. Kim, M. -S. Kang, M.J. Lee, Y. Won, J.C. Lee, and Y.S. Kang, *Adv. Mater.* **16** (2004), pp. 1753.

[12] A.F. Nogueira, C. Longo, and M. -A. De Paoli, *Coordin Chem. Rev.* **248** (2004), pp. 1455.

[13] P. Wang, S.M. Zakeeruddin, P. Comte, I. Exnar, and M. Grätzel, *J. Am. Chem. Soc.* **125** (2003), pp. 1166.

[14] J. -B. Xia, F. -Y. Li, C. -H. Huang, J. Zhai, and L. Jiang, *Sol. Energ. Mat. Sol.* **C. 90** (2006), pp. 944.

[15] Y. -J. Ren, Z. -C. Zhang, S. -B. Fang, M. -Z. Yang, and S. -M. Cai, *Sol. Energ. Mat. Sol.* **C. 71** (2002), pp. 253.

[16] X. Zhang, H. Yang, H. -M. Xiong, F.-Y. Li, and Y. -Y. Xia, *J. Power Sources*. **160** (2006), pp. 1451–1455.

[17] Z. Lan, J.-H.Wu, D.-B. Wang, S.-C. Hao, J.-M. Lin, and Y.-F. Huang, *Sol. Energy*. **80** (2006), pp. 1483.

[18] Z. Lan, J.-H.Wu, D. -B.Wang, S.-C. Hao, J.-M. Lin, and Y.-F. Huang, *Sol. Energy*. **81** (2007), pp. 117.

[19] Z. Lan, J.-H. Wu, J.-M. Lin, and M.-L. Huang, *J. Power Sources.* **164** (2007),pp. 921.

[20] F.-J. Li, F.-Y. Cheng, J.-F. Shi, F.-S. Cai, M. Liang, and J. Chen, *J. Power Sources.* **165** (2007), pp. 911.

[21] S. Ito, S.M. Zakeeruddin, R. Humphry-Baker, P. Liska, R. Charvet, P. Comte, M.K. Nazeeruddin, P. Pechy, M. Takata, H. Miura, S. Uchida, and M. Grätzel, *Adv. Mater.* **18** (2006), pp. 1202.

[22] T. Horiuchi, H. Miura, K. Sumioka, and S. Uchida, *J. Am. Chem. Soc.* **126** (2004), pp. 12218.

[23] X. Shen, W. Xu, J. Xu, G. Liang. H. Yang, and M. Yao, *Solid State Ionics.* xxx (2008), pp. xxx-xxx

[24] M. Grätzel, *Prog Photovolt Res.* **8** (2000), pp. 171.

[25] M. Sreemany, and S. Sen, *Materials Research Bulletin.* **42** (2007), pp.177.

[26] P. Li, J. Wu, J. Lin, M. Huang, Z. Lan, and Q. Li, *Electrochimica Acta.* **53** (2008), pp. 41.

Preparation of silver nanoparticles in layered kaolinite by ascorbic acid-assisted reduction of Ag^+

U. Anglong[1, 2] and D. P. Kashima[1, 2*]

[1] Research Unit of Advanced Ceramics, Department of Materials Science, Faculty of Science, Chulalongkorn University, Patumwan, Bangkok, Thailand 10330
[2] Research Unit of Advanced Ceramic and Polymeric Materials, National Center of Excellence for Petroleum, Petrochemicals, and Advanced Materials, Chulalongkorn University, Patumwan, Bangkok, Thailand 10330

[*] E-mail: dujreutai.p@chula.ac.th, dujreutai@gmail.com.

Abstract: The synthesis of silver nanoparticles by chemical reduction of Ag^+ intercalated in layered kaolinite, a main mineral phase in kaolin clay: an important raw material in ceramic industries, using ascorbic acid as the reducing agent would be reported. Ascorbic acid was used instead of $NaBH_4$, a strong and widely used reducing agent. In general it is more demanding to find a weak reducing agent which is benign and environmentally friendly. Prior to the step of ascorbic acid-assisted reduction of Ag^+, the lamellae of kaolinite was enlarged by intercalation of dimethyl sulfoxide (DMSO), then it was suspended in aqueous $AgNO_3$ solution with various ratio of Ag to kaolin at 0.1%, 0.3%, 0.5% and 1.0%. Finally, the adsorbed Ag^+ was reduced to Ag by ascorbic acid, filtered and dried at room temperature. Then the phase analyses, morphologies, and the appearances of silver nanoparticles in layered kaolinite of as-received modified kaolinite powder were characterized by X-ray diffraction (XRD), scanning electron microscopy (SEM), and transmission electron microscopy (TEM), respectively. Finally, the inhibitory to Escherichia coli (*E.coli*) growth was also tested at 2 represented temperature; room temperature and high temperature (1200 ºC) to find the optimum inhibitory concentration of silver nanoparticles. Silver nanoparticles were intercalated in an interlamellar space between octahedral and tetrahedral sheets (OT sheets) of kaolinite. Based upon this concept, silver nanoparticles would be protected in a layer structure of kaolinite and they would not be decomposed even at the high temperature.

Introduction

In recent years, nanoparticle synthesis has been received considerable attention due to their unique physiochemical characteristics such as catalytic activity, optical properties, electronic properties, magnetic properties and antimicrobial activity which is superior than the large particle. Silver nanoparticle has been known well among the other heavy metal nanoparticle since it shows inhibitive and bactericidal effects. [1, 2] It is widely used in many applications of materials such as antimicrobial deodorant fiber and catalysts. However, the melting point of silver particle is about 960°C which is hardly appeared on ceramic body after sintering at 1200°C. Kaolin clay, an important raw material in ceramic industries, contains the layered structure of kaolinite as the main mineral would protect the silver nanoparticles in its layered kaolinite. The layered kaolinite is held together by hydrogen bond between hydroxyl group of AlO_2OH_4 octahedral sheet and SiO_4 tetrahedral sheet (OT sheet). Enlargement of the layered kaolinite by intercalation of dimethyl sulfoxide (DMSO) was primarily done [3], then intercalation of silver ion was performed by reducing agent-assisted reduction of silver ion (Ag^+) to silver nanoparticles (Ag). There are several methods to synthesize silver nanoparticles such as chemical reduction by $NaBH_4$ or ascorbic acid [4], radiolysis using a ^{60}CO radiation source [5], gas reduction process, microwave plasma synthesis hydrodynamic cavitations [6], and etc. Generally, $NaBH_4$ was used as the reducing agent because it is strong and high efficiency to reduce Ag^+ to Ag. The purpose of this work is to use ascorbic acid, a weak reducing agent but more environmentally friendly, instead of $NaBH_4$. The optimum concentration of ascorbic acid was investigated. Finally, the inhibitory to Escherichia coli (*E.coli*) growth of as-fired (1200°C) powder of the obtained silver nanoparticles in layered kaolinite was tested in order to confirmed the antibacterial activity at the high temperature.

Materials and Methods

1 Materials

Silver nanoparticles were prepared using $AgNO_3$ (Merck) as a source of Ag^+, $NaBH_4$ (99.7%, Laboratory Chemical) and ascorbic acid (Poch sa) as reducing agent, the fine fraction ($d \leq 2\mu m.$) of kaolin clay (Ranong, Thailand) was used as a source of layered kaolinite as well as a support (act as substrate) of silver nanoparticles. Prior to the step of reduction of Ag^+, the layered kaolinite was enlarged by primarily intercalation of dimethyl sulfoxide (DMSO, 99.5% Riedel- dehaën), and the excess of DMSO was removed by methanol (Merck).

2 Primarily enlargement of layered kaolinte with DMSO and non-enlargement of layered kaolinite

Comparative study of the synthesis of silver nonoparticles in layered kaolinite by primarily enlargement of kaolinite lamellae using DMSO (*with DMSO*) **VS** synthesis of silver nanoparticles in

layered kaolinite without primarily enlargement kaolinite lamellae by DMSO (*without DMSO*) was studied in order to find out the effect of DMSO in preparation process.

According to the process so called *with DMSO*, the layered kaolinite from raw kaolin clay was enlarged by intercalation of dimethyl sulfoxide (DMSO) at 65 °C (20 g. kaolin/100 cm^3 DMSO) under stirring time of 10 h, the redundant DMSO was removed from raw kaolin clay by sedimentation and repeatedly washed with methanol and decanting for 7 d, the starting powder so called *"with DMSO*" was obtained. On the other hand, the layered kaolinite from raw kaolin clay was directly used as the starting powder is so called *"without DMSO"*.

Both of *"with DMSO"* and "*without DMSO"* was individually transferred to suspend in aqueous 0.01 M $AgNO_3$ solution with various ratios of Ag to kaolin at 0.1%, 0.3%, 0.5% and 1.0% Ag (%wt /wt). The suspension was stirred for 1 h at room temperature. Finally the adsorbed Ag^+ was reduced to Ag by 0.04 M $NaBH_4$ solution. After that, the suspension was continuously stirred for 2 h, then filtered, double times washed by distilled water and dried at the room temperature. Both of *"with DMSO"* and "*without DMSO"* which is already intercalated with silver nanoparticles were characterized by XRD, SEM, TEM and the antibacterial activity to *E.coli* at high temperature was also performed.

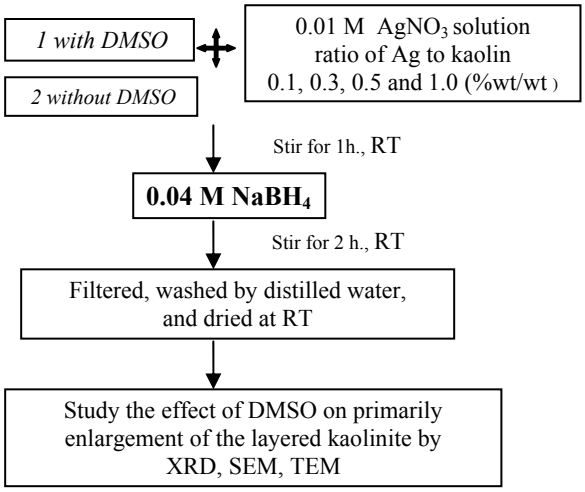

Figure 1 Flowchart of primarily enlargement of layered kaolinte with DMSO and non-enlargement of layered kaolinite.

3. Optimization for the optimum concentration of ascorbic acid in preparation of silver nanoparticles in layered kaolinite

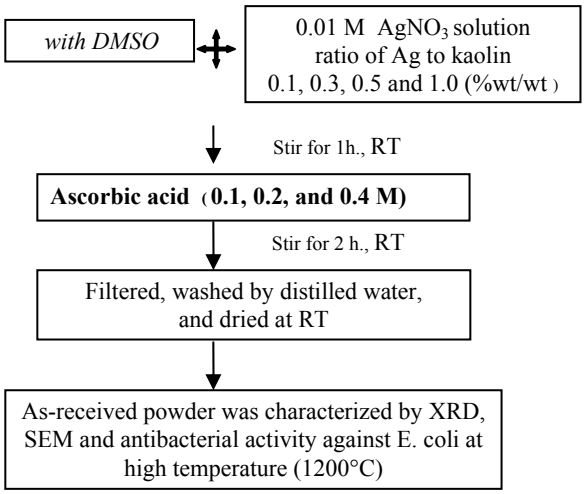

Figure 2 Flowchart of preparation of silver nanoparticles in layered kaolinite using ascorbic acid as a reducing agent.

4 Characterization

XRD analyses were carried out using a CuK_α radiation (λ=0.154 nm.) in a Bruker AXS diffractometer. XRD patterns were measured in the 2θ range from 5° to 70°. The basal distances d_L were calculated from the first (001) Bragg reflection. Morphology and the elemental composition of Ag nanoparticles which intercalated and dispersed on the plate of modified kaolinite were performed by SEM, JEOL (JSM 6400) and EDS, Oxford instrument 7573. Antibacterial activity of the Ag/kaolinite was tested on Escherichia coli ATCC 25922 according to dish susceptibility test by spread plate technique.

Results and Discussion

Phase analysis of raw kaolin clay intercalated by Ag prepared from the process is so called *"without DMSO*" was determined by x-ray diffraction, as shown in Figure 3. Raw kaolin composed of kaolinite and halloysite. The first (001) Bragg reflection of all conditions (Ag/kaolin 0.1-1.0%) from *"without DMSO*" was similar to the first (001) Bragg reflection of kaolinite at 2θ ~ 12.40°. From peak Ag(111) at around 2θ =39° (as indicated by dot line) implied that there was not Ag nanoparticle intercalated in the layered kaolinite but it might be appeared only on the plate of kaolinite. This is confirmed by TEM micrographs that all conditions from *"without DMSO*" process there was not any Ag nanoparticle intercalated in the layered structure of kaolinite (the data was not shown in this paper).

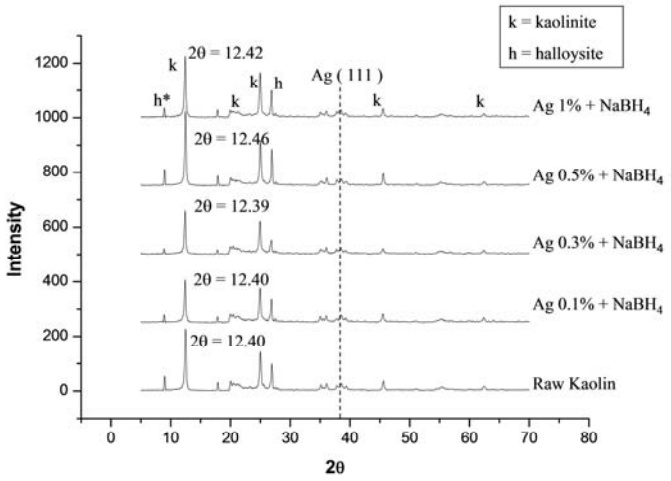

Figur e 3. XRD patterns of raw kaolin clay, layered kaolinite intercalated by Ag prepared from the process "*without DMSO"* with various ratios of Ag to kaolin at 0.1, 0.3, 0.5 and 1.0% using $NaBH_4$ as a reducing agent.

On the other hand, TEM results of 0.5% Ag/kaolin (Figure 4) prepared from *"with DMSO"* process showed Ag nanoparticles intercalated in the layered kaolinte even after firing at 1200°C (as-fired sample of 0.5% Ag/kaolin at 1200°C) The particle size of Ag found in layered kaolinite was around 17 nm.

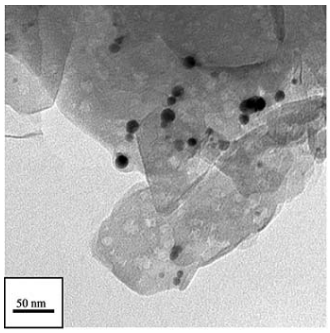

Figure 4. TEM micrograph of 0.5 % Ag/kaolin prepared from "with DMSO" process after firing at 1200°C.

The inhibition of *E.coli* growth was tested by spread plate technique, as shown in Table 1. We could interpret the antibacterial activity against *E.coli* of as-fired powder at 1200°C that the higher the content of Ag added, the stronger the antibacterial activity. The best antibacterial results was as-fired powder of Ag/kaolin at 1.0%Ag which was 99.94% reduction in the number of bacteria in comparison with blank. It was indicated that as-prepared powder of Ag/kaolin at 1.0%Ag from "*without DMSO"* process might be used as antibacterial agent in ceramic processing which is firing is needed in product forming. The previous study of U.Wongpratat, et.al. [3] found that as-fired (1200°C) powder of Ag/kaolin at 1.0 %Ag from "*with DMSO"* process which exhibited strong antibacterial effect against *E.coli.* contained much more Ag nanoparticles (observed by TEM) than the one from "*without DMSO"* This is implied that DMSO which was used in primarily enlargement of layered kaolinte played an essential role in the appearance of Ag nanoparticles in kaolinite layer. DMSO is an aprotic solvent which will deteriorate hydrogen bonding between each layers in kaolinite structure. Thus "*with DMSO"* process will promote the enlargement of layered kaolinite and finally, intercalation of Ag would easily occur by $NaBH_4$ assisted reduction of Ag^+ to Ag. We can summarize that primarily enlargement by DMSO was an important step for preparation of Ag nanopartcles in layered kaolinite and for this reason primarily enlargement "*with DMSO"* was selected to synthesize Ag nanoparticle in kaolinite layer by ascorbic acid assisted reduction of Ag^+ in the next step (topic 3).

Table 1 : Spread plate antibacterial results against *E.coli* of as-fired (1200°C) powder of Ag/kaolin at different silver contents reduced by $NaBH_4$ according to "*without DMSO"* process.

Sample 1200°C	The number of bacteria CFU/ml (6 h.)	% Reduction
Blank	9.5×10^7	-
Kaolin + 0.1% Ag	9.2×10^7	3.15
Kaolin + 0.3% Ag	7.9×10^7	16.84
Kaolin + 0.5% Ag	5.5×10^7	42.10
Kaolin + 1.0% Ag	5.0×10^4	99.94

Preliminary study on the optimum concentration of ascorbic acid used as reducing agent for preparation of Ag nanoparticles in layered kaolinite (topic 3) was performed without addition of raw kaolin clay in the experiment. SEM micrographs obviously showed that the particle size of Ag nanoparticles was 700 nm, 1 μm, and 1.3 μm when using ascorbic acid at 0.1, 0.2, and 0.4 M as reducing agent. Moreover, percent yield of Ag nanoparticles obtained from 0.1M ascorbic acid was highest compared to the one from 0.2, and 0.4 M ascorbic acid. Based upon these reasons 0.1 M ascorbic was used as an optimum concentration in preparation of Ag nanoparticles in layered kaolinite.

The first (001) Bragg reflection of kaolinite *with DMSO* shift to the left at 2θ = 8.10° that lower than the first (001) Bragg reflection of raw kaolinite at 2θ = 12.40°. When we add Ag particles, the first (001) Bragg reflection shift back to right at 2θ = 12.18°. For this reason,we can indicated that there were Ag nanoparticles intercalated in the layered kaolinite. Moreover, we could found the Ag peaks, when the precent of Ag increase, as shown in Figure 6.

Morphology of Ag/kaolinite (Figure 7) reduced by 0.1 M ascorbic acid observed by SEM. It is comprised of kaolinite (plate) and halloysite (rod) which is according XRD patterns in Figure 6. Eventhough, EDS results could not find any Ag element on as-received sample under reducing power of ascorbic acid but Ag(111) at around 2θ =39° (as indicated by dot line) from XRD pattern in Figure 6 was clearly shown that there were Ag incorporated in layered kaolinite.

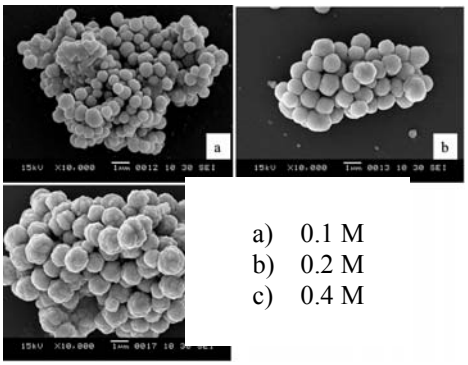

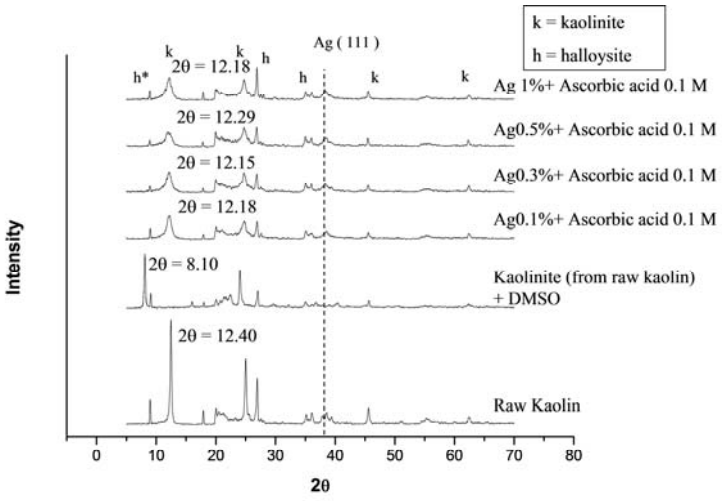

Figure 5. SEM micrographs of Ag nanoparticles reduced by ascorbic acid assisted reduction of Ag^+ to Ag at different concentrations of 0.1, 0.2, and 0.4 M ascorbic acid.

Figure 6. XRD patterns of raw kaolin clay, kaolinite (from raw kaolin) structure disrupted by DMSO and Ag/kaolinite prepared from "*with DMSO"* process with various ratios of Ag to kaolin at 0.1, 0.3, 0.5 and 1.0% using 0.1 M ascorbic as a reducing agent.

Antibacterial activities against *E.coli* ATCC 25922 was tested by spread plate technique, as shown in Table 2. We could interpret the antibacterial activity of as-fired powder at 1200°C that increasing in concentration of Ag led to a stronger antibacterial activity. The best antibacterial activity result was as-fired powder of Ag/kaolin at 0.5% Ag which was 99.75 % reduction in the number of bacteria in comparison with blank.

Table 2 : Spread plate antibacterial results against *E.coli* of as-fired (1200°C) powder of Ag/kaolin at different silver contents reduced by ascorbic acid according to "*with DMSO"* process

Sample 1200°C	The number of bacteria CFU/ml (6 h.)	% Reduction
Blank	4.0×10^7	-
Kaolinite + 0.1% Ag	2.5×10^7	37.5
Kaolinite +0.3% Ag	2.1×10^7	47.5
Kaolinite + 0.5% Ag	1.0×10^5	99.75
Kaolinite +1.0 % Ag	1.3×10^4	99.96

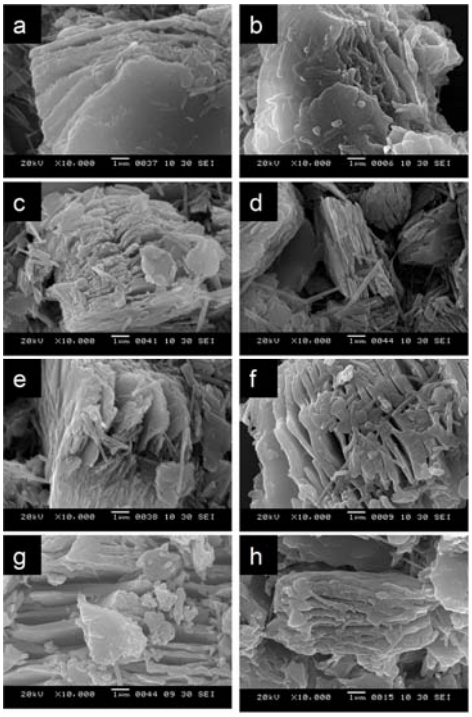

Figure 7 SEM micrographs of Ag/kaolinite (at RT) reduced by 0.1 M ascorbic acid with various ratios of Ag to kaolin (a) 0.1% Ag, (b) 0.3% Ag, (c) 0.5% Ag, (d) 1.0% Ag) and at 1200°C : (e) 0.1% Ag, (f) 0.3% Ag, (g) 0.5% Ag and (h) 1.0 % Ag

Conclusions

In this research, primarily enlargement of layered kaolinite by DMSO was an important step for preparation of Ag nanoparticles in layered kaolinite. Ag/kaolinite prepared from "*with DMSO"* process using 0.1 M ascorbic acid as a reducing agent showed good bacterial inhibition over the growth of *E.coli*. It is proven that percent reduction of the number of bacteria colonies grown were increased when increasing the concentration of Ag added. The best antibacterial results was at 0.5% Ag even at the high temperature, 1200°C.

Acknowledgements

The authors would like to thank National Center of Excellence for Petroleum, Petrochemicals and Advanced Materials, Chulalongkorn University for the financial support.

References

[1] A. R. Shahverdi, A. Fakhimi, H. R. Shahverdi and S. Minaian, *Nanomed-Nanotechnol* 3 (2007), pp. 168-171.

[2] K. H. Cho, J. E. Park, T. Osaka and S. G. Park, *Electrochim. Acta* 51 (2005), pp. 956-960.

[3] U. Wongpratat, D. P. Kashima and C. Prakitchaiwattana, *Pure and Applied Chemistry International Conference* (2009), pp. 328-330.

[4] A. Murugadoss, R. Pasricha and A. Chattopadhyay, *J. Colloid Interface Sci.* 311 (2007), pp. 303-310.

[5] R. Patakfalvi, A. Oszko and I. Dekany, *Colloids Surf.* 220 (2003), pp. 45–54.

[6] M. Zheng, Z .S. Wang, and Y. W. Zhu, Trans. Nonferrous Met. Soc. China 16 (2006), pp. 1348-1352.

Properties of elf-leveling underlayment in OPC-CAC-CS system

T. Tawong[1,2] , S. Jiemsirilers[1,2] , S. Jinawath[1,2]*

[1] Research Unit of Advanced Ceramics, Department of Materials Science, Faculty of Science, Chulalongkorn University, Patumwan, Bangkok, Thailand 10330

[2] Research Unit of Advanced Ceramic and Polymeric Materials, National Center of Excellence for Petroleum, Petrochemicals, and Advanced Materials, Chulalongkorn University, Patumwan, Bangkok, Thailand 10330

* E-mail: supatra.j@chula.ac.th

Abstract: The purpose of this work is to study the properties of self-leveling underlayments (SLUs) such as workability, rheology, drying shrinkage and compressive strength. The formulations were prepared in OPC-CAC-CS system with various OPC contents in the range of 36-42 wt.%, CAC contents in the range of 6-12 wt.% and CS content fixed at 6 wt.%. The mixtures belonged to the region of ettringite phase, the major modification of drying shrinkage/expansion and fresh property of SLUs. The results showed that the SLUs in OPC-CAC-CS base had an average linear expansion of about 1%. The rheological behavior was shear thickening (dilatant) with very low yield stress, and compressive strength was over 40 MPa at 28 day. Mineral phases and microstructures of the prepared SLUs were investigated by X-ray diffraction and scanning electron microscopy, respectively.

Introduction

Self-leveling underlayments (SLUs) are cement mortars used to produce level floors surface and used to repair surface on sub floors which are uneven or unfinished concrete. In generally, cement mortar is dumped to sub floor and a trowel is used to spread out the cement mortar, because it has a bad flow and hard to be leveled resulted from high viscosity. But SLUs can be spread out by gravity, hence they fill the holes and are self-leveling. [3]

SLUs must also have a good strength for the purpose of application. Good flowability is another important property which obtained by adding superplasticizers. Superplasticizers dissolved in water and is adsorbed on cement powder which is coating on aggregates (filler) such as limestone and sand grains. Therefore mixing water is reduced resulting in an increase in strength. [1,2,4]

SLUs are normally shear thickening, hence a suitable amount of superplasticizers has to be employed to reduce their yield stress. Moreover, SLUs must be self-leveling with suitable setting time, early strength and low shrinkage/expansion as well. [6,7]

Materials and Methods

Formulation of SLUs in this study is based on OPC-CAC-CS system in order to improve properties such as strength, flowability, setting time and shrinkage/expansion.[5] Experimental design, Taguchi method, is used in the formulation of the compositions of SLUs which are shown in Table 1.

The calculated contents of materials in each batch (Table 1.) were weighed and mixed in a Hobart mixer. The mixing sequence was as follows: cements, CS and filler combination were dry mixed for 3 min., then admixture dissolved in mixing water was poured in

Table 1. Formulation of SLUs

		OPC-CAC-CS System								
		A1	A2	A3	B1	B2	B3	C1	C2	C3
Materials (%)										
PC 1		36	36	36	39	39	39	42	42	42
CAC		12	12	12	9	9	9	6	6	6
Anhydrite		6	6	6	6	6	6	6	6	6
Limestone		6	6	6	6	6	6	6	6	6
Sand		40	40	40	40	40	40	40	40	40
Admixture (%)										
Plasticizer	Melflux	0.80	1.00	1.20	0.80	1.00	1.20	0.80	1.00	1.20
Accelerator	Li carbonate	0.1	0.1	0.1	0.1	0.1	0.1	0.1	0.1	0.1
Retarder	Citric acid	0.2	0.2	0.2	0.2	0.2	0.2	0.2	0.2	0.2
Stabilizer	Methocel	0.05	0.05	0.05	0.05	0.05	0.05	0.05	0.05	0.05
Water-powder ratio		0.20	0.22	0.24	0.22	0.24	0.20	0.24	0.20	0.22

and mixed for 1 min and stopped for 1 min for manual mixing with spatula, then the paste is remixed with a high speed for 2 min. [4]

The fresh properties such as flow ability and setting time were investigated by spread cone test and v-funnel test, and Vicat apparatus, respectively. Rheological behavior was investigated using a Brookfield viscometer. The properties of hardened specimens (5 cm^3 cube) such as shrinkage/expansion, compressive strength were measured using a micrometer and a universal testing machine, and mineral phases and microstructures of the cement pastes hydrated at 7 day and 28 day were characterized by X-ray diffraction (D8 Advance, Bruker, with Ni filter CuK_α radiation at 40 kV and 40 mA) from 5-60° and scanning electron microscopy (JSM-6480LV, JEOL), respectively.

Results and discussion

Fresh properties

The flow value [ASTM C1437] and setting time [ASTM C191] which were obtained for each formulation are shown in Table 2.

From Table 2, A2, B1 and C 2 have flow property (v-funnel time, spread diameter length), setting time and strength close to the target properties (v-funnel time ~3s, spread diameter length 300 mm, initial setting time ~60-90 min, final setting time ~120-180 min and strength at 28 d = 40 MPa)

Therefore, in the future samples A2, B1 and C2 are suitable for further improvement.

Table 2: Flow value and setting time

Mix.	V-funnel (s.)	Spread test (mm.)		Setting time (min.)	
		D1	D2	initial	final
A1	11	190	195	70	112
A2	3	260	255	96	128
A3	2	303	300	185	215
B1	3	275	273	140	179
B2	2	330	327	181	289
B3	3	250	255	115	165
C1	2	320	325	237	297
C2	3	275	273	122	155
C3	2	400	405	> 240	-

Compressive strength [ASTM C109] of hardened specimens

From Fig 1, the strength of most specimens at 7 d are over 20 MPa and all at 28 d are over 40 MPa. Generally the strength of SLUs at 28 day is reported as 40 MPa hence properties of the SLUs in this study are satisfactory.

Form Fig. 2. The percentage of shrikage/expansion was measured.[ASTM C426] It is found that on average, the linear dimensions of all specimens expands.

Specimens with higher PC content have higher %expansion than those of lower ones. This is probably due to the higher early strength of high CAC specimens. However, the %linear expansion is not large and is < 1% on average.

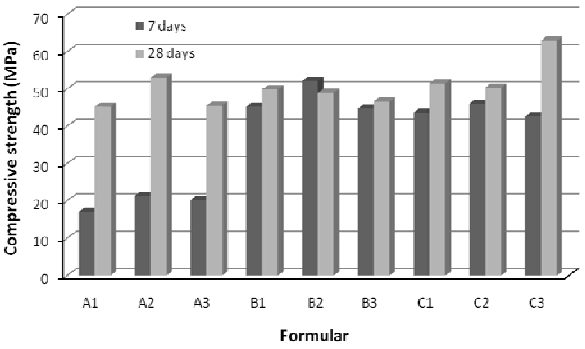

Figure 1. Compressive strength of batches A, B and C

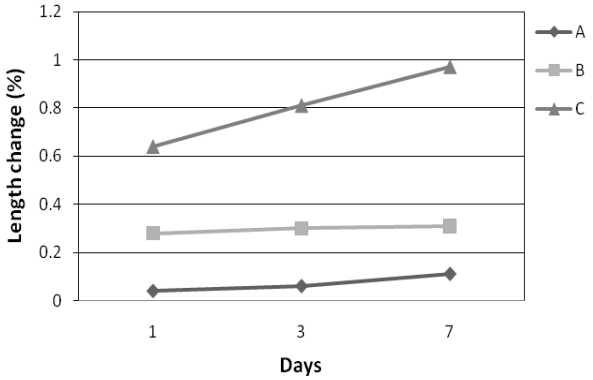

Figure 2. Shrinkage/expansion of A, B and C hardened mortar specimens

Fig. 3 shows the relationship between shear stress and shear rate fitted to power law, the value of n (from equation $y = kx^n$) is more than 1. Therefore the SLUs are dilatant or shear thickening with very low yield stress.

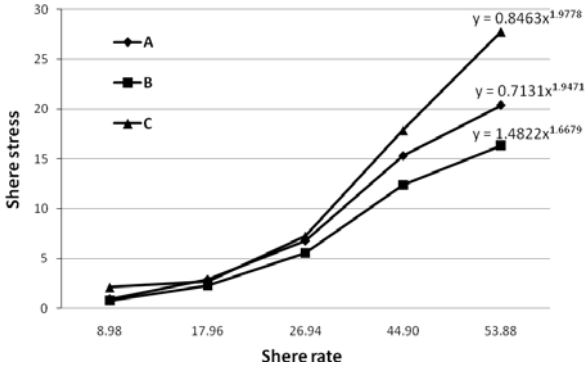

Figure 3. Relationship between shear stress and shar rate

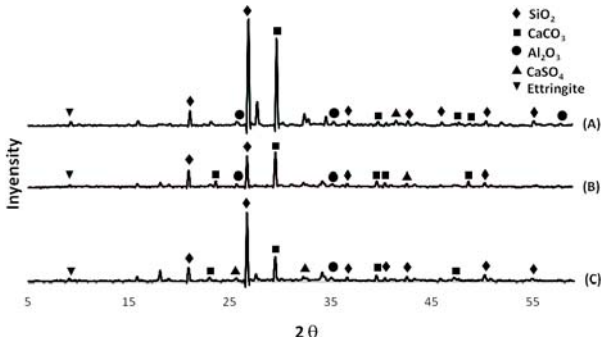

Figure 4. X-ray diffraction patterns of A, B and C hardened mortar specimens at 7 day

From Fig. 4. XRD patterns of SLUs at 7 day, the dominant peaks found were corresponded to SiO_2 $CaCO_3$, ettringite and traces of Al_2O_3 and $CaSO_4$. The mineral phases are also confirmed by the microstructures observed by SEM and the elements determined by EDS (results not shown).

Conclusion

The successful formulation of mortar for SLUs in the system PC-CAC-CS with satisfactory properties and shrinkage-free has been obtained. The mineral phases and microstructure of all the hardened mortar show the presence of filler, SiO2 and CaCO3, as the dominant phases, ettringite, C-S-H gel (EDX). and traces of Al_2O_3 and $CaSO_4$.

Acknowledgements

1. National Center of Excellence for Petroleum, Petrochemical, and Advanced Materials, Chulalongkorn University.
2. B.K. Mineral Co., Ltd.
3. The Siam Refractory Industry Co., Ltd.

References

[1] S. Hanehara and K. Yamada, *Cem. Concr. Res.* **29** (1999), pp. 1159-1165.
[2] M. Sahmaran, H.A. Christianto and I.O.Yaman, *Cem. Concr. Res.* **28** (2006), pp. 432-440.
[3] T. Emoto and T.A. Bier, *Cem. Concr. Res.* **37** (2007), pp. 647-654.
[4] B. Felekoglu, *Constr. Build. Mater.* **22** (2008), pp. 660-667.
[5] A.D. Gasparo, M. Herwegh, R. Zurbriggen and K. Scrivener, *Cem. Concr. Res.* **39** (2009), pp. 313-323.
[6] P. Nanthagopalan and M. Santhanam, *Mater. Struct.* doi:10.1617/s11527-009-9481-3
[7] M. Lachemi, K.M.A. Hossain, V. Lambros, P.C. - Nkinamubanzi and N. Bouzoubaa, *Cem. Concr. Res.* **34** (2004), pp. 917-926.

Encapsulation of biological molecule in chitosan-coated alginate microspheres by electrospraying

N. Kreua-ongarjnukool[1*], S. Thumsing[1],
D. Chartsathaporn[1], U. Ruktanonchai [2] and P. Supaphol [3]

[1]Department of Industrial Chemistry, Faculty of Applied Science,
King Mongkut's University of Technology North Bangkok, Bangkok, Thailand 10800

[2]National Nanotechnology Center, Thailand Science Park, Pathumthani, Thailand

[3] Technological Center for Electrospun Fibers and The Petroleum & Petrochemical college,
Chulalongkorn University, Bangkok, Thailand

[*] E-mail : nkk@kmutnb.ac.th

Abstract: In this research, Chitosan-coated alginate microspheres were prepared by electrospraying technique. The controlled realease of Calf thymus DNA from Chitosan-coated alginate microspheres was studied. Moreover, process parameters such as: alginate concentration, chitosan concentration and applied voltage were investigated. The most uniform microspheres in term of shape and size was obtained from alginate concentration of 0.1%w/v, chitosan concentration of 1.5% w/v, under 22 kV applied voltage and a solution flow rate at 1 ml/h. Diameters are in the range of 1.35±0.1 µm. Then, chitosan-coated alginate microspheres were prepared to encapsulate Calf thymus DNA. Microspheres were loaded with 1, 5, 10, 25, and 50% w of Calf thymus DNA. Diameter of chitosan-coated alginate microspheres containing 1 %w of Calf thymus DNA is in the range of 1.4±0.1 µm. Encapsulation efficiency is 47.76±0.70 % and release efficiency is 57.32 ± 0.62 % for 48 hr.

Keywords: Electrospray, Alginate, Chitosan, DNA, Microencapsulation

Introduction

Electrospraying is an interesting technique for making particles which could be used as drug delivery vehicles. Particles have diameter ranging from micrometers to nanometers from polymer solutions or melts. Electrospaying process have many potential application such as pharmacetical**,** food**,** etc. Electrospraying is a process of simultaneous droplet generation and charging by means of electrostatic. In this process, melt polymer flowing out from a capillary nozzle maintained at high potential, is subject to an electrical field, which causes elongation of the meniscus to a form of jet or spindle. The jet deforms and disrupt into droplet due mainly to electrical force [1]. In the electrospraying, on additional mechanical energy, other than that from the electric field alone, need for liquid atomization. Electrospraying allows generation of fine droplets of charge magnitude close to one-half of the Rayleigh limit. The Rayleigh limit is the magnitude of charge on a drop that overcomes the surface tension force, that leads to fission of the droplet. The charge and size of the droplet can be easily controlled to some extent by adjusting the flow rate and voltage applied to the nozzle. L. Reyderman et al. [2] studied the effect of using ring electrode for improving the stability of the drop from the nozzle in electrospraying technique and the result show that using ring electrode can stabilize the droplet generation of chlolesterol microsperes. M. Nithitanakul et al. [3] reported that an increasing of temperature was affected to reduce the average diameter of polyamide-6 electrospun fibers via electrospinning technique.

The encapsulation of biological molecules such as DNA, peptide and protein within biodegradable polymer is widely applied in food industy, phamaceutical and agrochemical fields. It is developed for the stability of bioactive component and controlled drug release. Sodium alginate is a sodium salt of alginic acid, a natural polysaccharide found in all species of brown algae. Chan et al. [4] reported that Ca^{2+} and Zn^{2+} for cross-linking of acid groups of alginate. However, Grant et al. [5] reported that Ca^{2+} is preferred as they selectively bind to the gluronic acid units to form an "egg-box" model. In the present study, alginate microspheres were produced by electrospraying technique. A.J. Ribeiro et al. [6] found that chitosan-alginate coated microspheres can obtain from oil/water/oil emulsification method and Y. Xu et al. [7] studied the effect of independent variable organic/aqueous phase volume ratio and weight ratio. Found that an increasing volume ratio in organic phase and decreasing the weight of PLA show a smoothess sphere paticle of BSA loaded PLA. Chitosan, deacetylated chitin, is highly specialized basic biopolymer established as the main industrial derivative of chitin [8,15]. Chitosan is a biocompatible and biodegradable cation polymer, non-toxic, and low-cost polymer, which has been used to improve controlled drug release. Therefore, chitosan has been used for bio-or medical – materials, such as a tissue engineering material, surgical tape, and artificial skin [9-13]. K.Anjani et al. [14] studied the controlled release of flavourzyme from chitosan-coated alginate microspheres by dipping method and the result show that using Ca^{2+} from 3%w/v calcium

chloride solution for cross-linking with alginic group within alginate solution to fabricate the chitosan coated alginate microspheres.

In this research, we prepared chitosan-coated alginate microspheres by electrospray technique. The process parameters (i.e. alginate concentration, applied voltage and chitosan concentration) were discussed. Our studied was aimed to prepared the melt uniform particles for potential application in encapsulation of biological molecules and the controlled release.

Materials and Experimental Procedures

Materials

Sodium Alginate powder (Viscosity 250 cp), Chitosan (M_w=72000) and Calf Thymus DNA was purchased from Sigma-Aldrich (Singapore). Calcium chloride dehydrate, Monobasic sodium phosphate and dibasic sodium phosphate were obtained from Ajax chemicals (Australia). All reagents were analytical grade and without further purification

Experimental Procedures

1) Effect of parameters upon microspheres

In the figure 1 chitosan-coated alginate microspheres were prepared by electrospraying technique. The effect of process parameters such as alginate concentration, chitosan concentration and applied voltage were investigated.

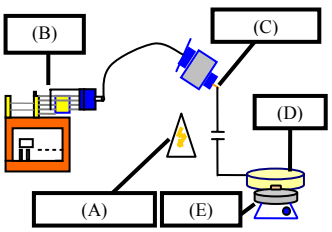

Figure 1 Schematic representation of the electrospray apparatus: (A) High Voltage Power Supply
(B) Syringe Pump (C) Syringe and Spinneret
(D) Solution bath (E) Magnetic Stirrer.

a) Alginate solutions were prepared at various concentrations at 0.1, 0.5, 1.0, 2.0, and 3.0% w/v, the applied voltage was kept at 22 kV and chitosan solution bath at 0.8%(w/v) were investigated.

b) Chitosan solutions were prepared at various concentrations at 0.1, 0.8, and 1.5%w/v, the applied voltage was kept at 22 kV and alginate solution at 0.5% w/v were investigated.

c) Various applied voltage ranging from 16, 18, 20, and 22 kV were used, the alginate and chitosan concentration at 1 and 0.8% w/v respectively were investigated.

d) $CaCl_2$ concentration of 3% w/v were dissolved into various concentrations of chitosan ranging from 0.1, 0.8, and 1.5% w/v , the applied voltage was kept at 22 kV and alginate solution at 0.1% w/v were investigated.

2) Electrospraying for Microspheres Preparation

Microspheres were prepared by Electrospray technique. The alginate, and $CaCl_2$ were weight separately and further dissolved in water to prepare stock solutions of alginate 0.1% w/v and $CaCl_2$ 3% w/v. Chitosan was dissolved by adding 1 %v of acetic acid and various concentration of DNA at 1, 5, 10, 25 and 50 %w. This setup use the applied voltage at 22 kV and flow rate at 1 ml/h. Microspheres were collected in $CaCl_2$ mixed chitosan then centrifuge and freeze dried.

3) Particle size analysis

The size fresh and dried microspheres was routinely measured by nanosizer (model Nano ZS, UK). The average diameter of 3 microspheres was considered as the mean particle size and photograph by scanning electron microscopy(SEM)(Model JSM 5400 LV, JEUL, Japan) using the magnification of 3500X.

4) Encapsulation efficiency of DNA loaded chitosan-coated alginate microspheres

DNA loaded microspheres were dissolved in chitosan 1.5% w/v and mixed with calcium chloride 3% w/v for 24 hr. Then centrifuge the mixture solution by centrifugation. Sampling 1 ml of mixture solution were measured the amount of DNA loaded microspheres by using UV-VIS spectrophotometer at wavelength 260 nm. Encapsulation efficiency (EE) was calculated as equation (1)

$$\%EE = 100 - \{[(A-B)/A\times100]+[C\times100]\} \quad \ldots(1)$$

Where A was a total amount of DNA, B the free amount of DNA in collection, and C The DNA was adsorped in solution bath.

5) Release profile of DNA from chitosan-alginate coated microspheres

DNA loaded microspheres were dried under vacuum oven. Each sample was soaked in phosphate buffer at pH 7.4 and was shaked at 37 °C. Sampling 5 ml of solutions at every minutes. In each time of sampling, 5 ml of phosphate buffer were added into the solution. The release of DNA was determined by using UV-VIS spectrophotometer at wavelength 260 nm.

Results and Discussion

1) Effect of alginate and chitosan concentration

Electrospraying parameters affected the average particle diameter in different extent. In order to find the extent of the impact on average particle diameter, the impact of two factors (concentration and applied voltage) on particle diameter was investigated. When the concentration of alginate and chitosan increases, the particle size will increase. Since the increasing the polymer concentration is to increase the viscosity of the solution and the viscosity of the solution is the molecular weight of the polymer. Similar to increasing the molecular weight, an increase in the concentration will result in greater polymer chain entanglements within the solution.

2) Effect of applied voltage

When the applied voltage is higher, the particle diameter will decrease. Since higher voltage will increase the columbic repulsive force. If the applied voltage is higher, the greater amount of charge will cause the droplet of microspheres to accelerate faster.

3) Cross-linking of Ca^{2+}

The addition of $CaCl_2$ was affected to decreasing of the particle size. Since the carboxyl group of alginate was cross-linked with Ca^{2+}.

4) Size and characterization of DNA from chitosan-coated alginate microspheres

The particle size of microspheres was obtained by Nanosizer and photograph by Scanning Electron Microscope. Show in Figure 2 and Table l. The microspheres without DNA have a smoother surface and were found to be less spherical in shape. (Table 1) Then, DNA-loaded chitosan-coated alginated microsphesres have a smoother surface and the shape of microspheres is bigger than microspheres without DNA. Because DNA is macromolecule structure. When concentration of DNA increase, the shape of DNA microspheres will increase respectively.

Table 1 Diameter of the DNA loaded chitosan-coated alginate microspheres

Type of Alginate microspheres	Diameter of the microspheres (μm)
Alginate + DNA 0%	1.35 ± 0.10
Alginate + DNA 1%	1.40 ± 0.19
Alginate + DNA 5%	1.54 ± 0.19
Alginate + DNA 10%	1.68 ± 0.01
Alginate + DNA 25%	1.86 ± 0.09
Alginate + DNA 50%.	2.34 ± 0.18

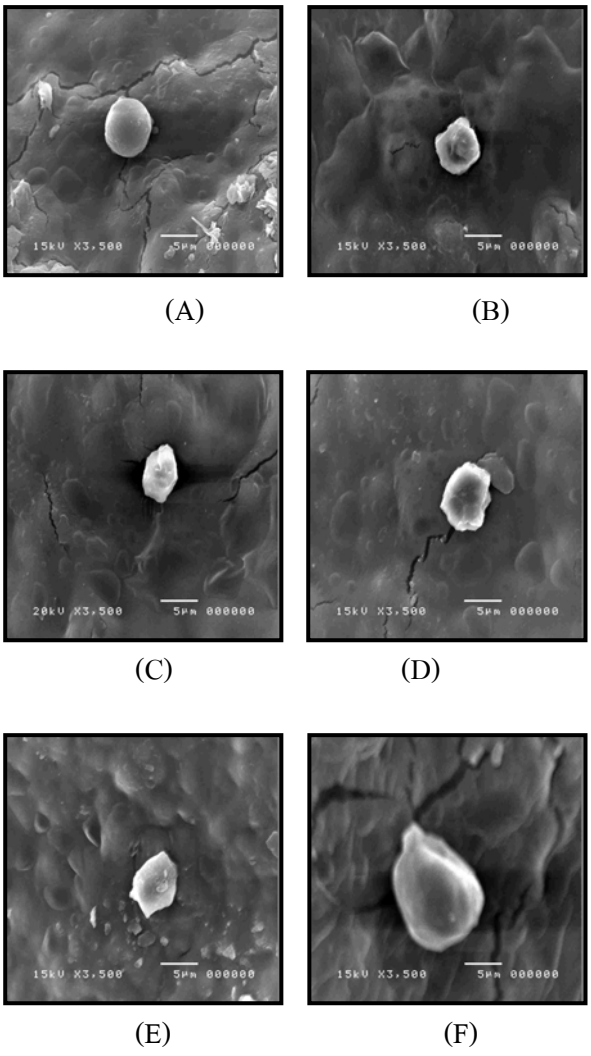

Figure 2 SEM micrographs of DNA loaded chitosan-coated alginate microspheres. (n=2)
(A) DNA 0 % (B) DNA 1% (C) DNA 5 %
(D) DNA 10% (E) DNA 25% (F) DNA 50 %
The applied voltage is 22 kV. Alginate concentration is 0.1% w/v and chitosan is 1.5% w/v mix with 3% w/v $CaCl_2$ in solution bath.

5) DNA Encapsulation Efficiency

1%w of DNA loaded chitosan-coated alginate microspheres has encapsulation efficiency equal to 47.76±0.70 %. For DNA concentration at 5.0, 10.0, 25.0 and 50.0 %w will decrease DNA encapsulation efficiency since DNA is a macromolecule. Therefore, the chitosan-coated alginate microspheres can not to encapsulate all DNA molecules.

6) The DNA release study from DNA loaded Chitosan-coated alginate Microspheres

Chitosan-coated alginate microspheres were load with 1, 5, 10, 25, and 50% w of DNA. The DNA release study was observed over a period of 48 hours. In the initial time, DNA releases very rapid. After 40 minutes the rate of release is slow. In figure 3 and 4

showed that the release behavior of DNA from microspheres. Cumulative release of DNA from DNA loaded chitosan-coated alginate microspheres as the percentage of the weight of DNA released divided by the actual amount of DNA is 57.32, 44.39, 34.35, 24.59 and 13.42%, respectively. From results, the percentage of the weight of DNA released divided by the actual amount of DNA and the actual weight of DNA loaded microspheres will decrease when the concentration of DNA increases. Due to generally seen that when microspheres of hydrophilic polymers are immersed in water, they swell and from a gel diffusion layer. Moreover, chitosan-coated alginate is a larger molecule compared with calcium ions, it is more efficient in blocking the pures in an alginate matrix, hence chitosan-coated alginated can be controlled the release of DNA [14].

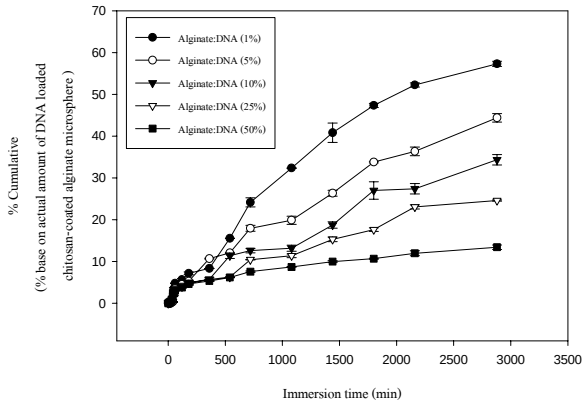

Figure 3 Cumulative release of DNA from DNA loaded chitosan-coated alginate microspheres as the percentage of the weight of DNA released divided by the actual amount of DNA over period 0-48 hours (n=3)

Conclusions

Chitosan-coated alginate microspheres were successfully by electrospraying technique. The results shown that the optimum conditions preparation of microspheres are alginate solution concentration of 0.1 %w/v, chitosan solution concentration of 1.5 %w/v and calcium chloride solution 3.0 %w/v. Microsphere was electrosprayed at 22 kV with flow rate 1.0 ml/hr. The DNA loaded chitosan-alginate coated microspheres use the same condition of chitosan-alginate coated microspheres. From the results, DNA encapsulation efficiency decreases when DNA concentration increases. Since DNA is the macromolecules structure, the chitosan-coated alginate microspheres can not encapsulate all DNA molecules. At 1%w of DNA loaded chitosan-coated alginate microspheres has higher encapsulation efficiency equal to 47.76±0.70 %. The DNA release study from DNA loaded chitosan-alginate coated microspheres has the maximum release of 56.23 ± 0.01 % at 1 %w of DNA over a period of 48 hr. The results from this research indicate that it is possible to fabricate DNA loaded chitosan-coated alginate microspheres by electrospray technique, and this technique can be applied to gene therapy and drug delivery.

Acknowledgements

The authors gratefully acknowledge the partial financial support from the National Nanotechnology Center (in house grant), The Petroleum & Petrochemical College, Chulalongkorn University and Department of Industrial Chemistry, Faculty of Applied Science, King Mongkut's University of Technology North Bangkok.

References

[1] E.H.Sanders, R. Kloefkorn, G.L. Bowlin, G.L. Simpsom, and G.E. Wnek, *Macromolecules*. **36**(2003), pp. 3803-3805.
[2] L.Reyderman, and S.Stavchansky, *International Journal of Pharmaceutics*. **124** (1995), pp. 75-85.
[3] C. Mit-uppatham, M. Nithitanakul, and P. Supaphol *Macromolecular Chemistry and Physics*. **205**(2004), pp. 2327-2338.
[4] L.W. Chan, Y. Jin, and P.W.S Heng, *International Journal of Pharmaceutics*. **242**(2002), pp. 255–258.
[5] G.T. Grant, E.R.Morris, D.A.Rees, P.J.C. Smith, and D.Thom, *FEBS Lett*. **32**(1973), pp. 195–198.
[6] A.J. Ribeiro, R. Neufeld, P. Arnaud, and J. Chaumeil, *International Journal of Pharmaceutics*. **187**(1999), pp. 115-123.
[7] Y.Xu, and M.A.Hanna, *International journal of Pharmaceutics*. **320**(2006), pp. 30-36.
[8] Y.Xu, W. J. Ng, L. Yeng,and C.H. Wang, *Journal of Colloids and Interface Science*. **317**(2008), pp. 469-476.
[9] M. Mochizuki, Y. Kadoya, Y. Wakabayashi, K. Kato, I. Okazaki, Masanori Yamada, T. Sato, N. Sakairi, N. Nishi and M. Nomizu, *FASEB J. published*. **17**(2003), pp. 875.
[10] K. Kato, U. A. Suzuki, N. Mochizuki, M. Yamada, M. Nishi, N. Matsuura, H. Shinkai, and M. Nomizu, *Biochemistry*. **41**(2002), pp. 10747-10753.
[11] J.K. F. Suh and H.W.T. Matthew, *Biomatials*. **21**(2000), pp. 2589-2598.
[12] M. Yamada, and I. Honma *Electrochimika Acta*. **50**(2005), pp. 2837-2841.
[13] I.V. Yannas**,** J.F. Burke, D.P. Orgill, and E.M. Skrabut *Science*. **215**(1982), pp. 174-176.
[14] K.Anjani, K.Kailasapathy, and M. Phillips *International Dairy Journal*. **17**(2007), pp. 79-86.
[15] K. Kanawung, W.Utok, N. Kreua-ongarjnukool, K. Panitchanapan, S.Puangmalee, R.Rangkupan, C.Meechaisue and P.Supaphol,*Polymer Journal.* **39**:4 (2007), pp. 369-378.

Preparation of stable water- and oil-repellent silica-based coating

O. Nimittrakoolchai and S. Supothina*

National Metal and Materials Technology Center, 114 Thailand Science Park,
Paholyothin Rd., Klong Luang, Pathumthani, Thailand 12120

*E-mail: sitthis@mtec.or.th

Abstract: The silica-based coating with water- and oil-repellent property and good stability has been deposited onto glass surface by a simple one-step dip coating technique. To achieve high water- and oil-repellency, surface roughness of the coating was enhanced by adding different amount SiO_2 nanoparticles of which the surfaces were hydrophobized with fluorosilane. At the highest surface roughness, the coating showed the highest contact angle of standard liquid droplets (water = 173°, glycerol = 173°, ethylene glycol = 147° and diiodomethane = 144°) and of seed oil droplet of 148°. The surface free energy of the most water- and oil-repellent coating calculated based on Owens–Wendt equation was 0.75 mJ/m^2. The achievement of water- and oil-repellency is also described based on the present of air trapped in micropores in the rough surfaces. The coating with solid and micropores was stable under ambient atmosphere for several months.

Introduction

Liquid-repellency has generated a lot of interest in the past two decades due to a great importance in daily life as well as in many industrial applications. Barthlott and Neinhuis [1] are the pioneers who discovered the water-repellent property on the lotus surface on which the water droplets can roll and rinsing off the dirt. This phenomenon is called "lotus effect" or "self-cleaning effect". Preparation of water-repellent surface with self - cleaning property has been investigated by many scientists [2-7]. However, such self-cleaning mechanism doesn't apply for hydrocarbon or oily liquids. Therefore, it is of great importance to further improve both water- and oil-repellent properties to fully utilize the lotus effect.

Generally, it is recognized that wetting of a solid surface by a certain liquid is governed by both a chemical composition and a geometrical microstructure of the surface [8]. The main approach for the chemical factor is modifying the surface with chemical groups that exhibit a low surface free energy. To obtain the surface with both water- and oil-repellent, the surface free energy of the solid (γ_s) must be smaller than a quarter of that of the liquid (i.e. $\gamma_l/4$) [9]. Only fluorinated compound can provide such a small surface energy because fluorine has a small atomic radius and biggest electronegativity [10-11]. The other aspect to further enhance water- and oil-repellency of the solid surface is the geometric factor which is governed by the formation of fractal or rough surface structure. One way of surface roughness enhancement is adding nano-sized particles in the coating in which the micropore providing more air resistance against wettability is formed [12-13]. By taking the approach described earlier, this present study aims to prepare nanocoatings exhibiting both water- and oil-repellent properties by mixing different ration of SiO_2 nanoparticles and fluorosilane. Effects of SiO_2 content on the surface roughness, the surface free energy, micropore ratio of the coating, and water- and oil-contact angles were investigated. Furthermore, long term stability of the coatings under condition of use was evaluated.

Materials and Methods

Preparation of water-and oil-repellent silica-based coating

Trichloro(1H,1H,2H,2H-perfluorooctyl) silane (Fluoro- or F-silane) was purchased from the Aldrich Chemical Company, Inc. while Aerosil® 200 silicon dioxide having an average particle size of 12 nm was purchased from JJ-Degussa Chemicals. The glass substrates were cut into 2.5 cm x 5 cm, then ultrasonically cleaned with ethanol, acetone and de-ionized water followed by Piranha solution, and then dried at 60 C. A precursor solution for film deposition was prepared as follow. 0.067M F-silane was dissolved in 2-propanol under ultrasonication. Then, the different amount of SiO_2 nanoparticles (0.005-1 g/30 ml of 2-propanol) were added into the F-silane solution and vigorously stirred for 1 h. The as-received solutions were deposited onto glass substrate by dip coating method by which the withdrawing speed was controlled at 0.1 mm/sec^{-1} to obtain the thin and uniform film. The coated substrate was dried in an oven at 120 ^oC for 1 h.

Surface characterization

Film's chemical functionality was analyzed by using an FT-IR spectrophotometer (Spectrum One, Perkin Elmer) by an Attenuated Total Reflection (ATR) mode. Surface morphology was observed by using a field-emission scanning electron microscope (SEM, JSM 6301F) and an atomic force microscope (AFM, SPA 400 Seiko instruments) performed in a non-contact mode. Surface's wettability was evaluated by measuring the contact angle of standard liquids (water, glycerol, ethylene glycol and diiodomethane) and seed oil by using a goniometer (ramé-hart instrument). A 5-µl droplet of all liquids was mounted onto the film's surface using

a microsyring. Photo of the liquid droplets was recorded using a CCD camera, and then a curvature profile was created and the contact angle measured. The measurement was repeated on at least five locations over the entire area. Stability of the film surfaces was evaluated by measuring the contact angle of water and ethylene glycol droplets on the surface for a period of 6 months. The tested samples were placed in the office room under ambient condition.

Calculation of surface free energy

The surface free energy of the coating was calculated based on Owens–Wendt equation (Eq. 1) by using the contact angles and surface free energy components of standard liquids listed in Table 1. [14]

$$\frac{\gamma_L(\cos\theta+1)}{2\sqrt{\gamma_L^D}} = \sqrt{\gamma_S^P}\times\sqrt{\frac{\gamma_L^P}{\gamma_L^D}}+\sqrt{\gamma_S^D} \qquad (1)$$

$$\gamma_S = (\sqrt{\gamma_S^D})^2 + (\sqrt{\gamma_S^P})^2 \qquad (2)$$

where, γ_S^D and γ_L^D are dispersive component of the surface free energies of solid and liquid, respectively, and γ_S^P and γ_L^P are polar component of the surface free energies of solid and liquid, respectively.

From Eq. [1], a plot of $\gamma_L(\cos\theta+1)/2\sqrt{\gamma_L^D}$ vs $\sqrt{\gamma_L^P/\gamma_L^D}$ for a set of standard liquid yields $\sqrt{\gamma_S^D}$ as the *y*-intercept and $\sqrt{\gamma_S^P}$ as the slope. Therefore, the solid surface energy can be derived from Eq. 2.

Table 1. Surface energy and surface free energy component of standard liquids used in the calculation

Standard liquid	γ_L	γ_L^D	γ_L^P
Water	72.8	21.8	51.0
Glyceral	64.0	34.0	30.0
Ethylene glycol	48.0	29.0	19.0
Diiodomethane	50.8	50.8	0

Results and Discussion

ATR-FTIR spectra of the glass substrate deposited with water- and oil-repellent silica-based coating, SiO_2 nanoparticles and pure fluorosilane are shown in Fig. 1. The absorption peaks at 1,250 and 1,150 cm^{-1} observed in Fig. 1(a) are a symmetric and an asymmetric stretching of CF_2, respectively. These peaks are weakly observed in the silica-based coating (Fig. 1(c)), resulting from interference of strong broad band peak at 1,000-1,300 cm^{-1}, corresponding to a Si-O-Si network. However, there is a peak at 1,316 attributed to a C-F stretching of the CF_3 group which indicated that the fluorosilane absorbed onto the SiO_2 surface.

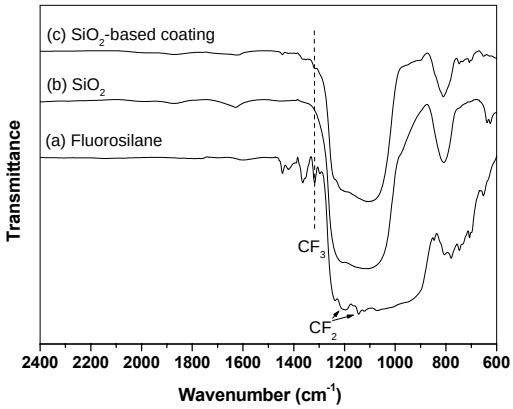

Figure 1. ATR-FTIR spectra of glass substrate coated with (a) fluorosilane, (b) SiO_2 nanoparticles and (c) water-and oil-repellent silica-based coating.

Figure 2 shows AFM images of the water- and oil-repellent coatings containing different SiO_2 content. At low SiO_2 content ($SiO_2 \leq 0.02$ g.), the film's surface was very smooth. The coverage of agglomerated SiO_2 nanoparticles increased with increasing amount of the SiO_2 content. At high SiO_2 content ($SiO_2 \geq 0.4$ g.), the film's surface consisted of hills and valleys and had double-scaled roughness: a micron-size roughness created by the deposition of agglomerated SiO_2 and a nanometer-sized roughness created by individual SiO_2 nanoparticle. This dramatic change in the surface morphology is responsible for the observed water- and oil- repellent properties (Table 2).

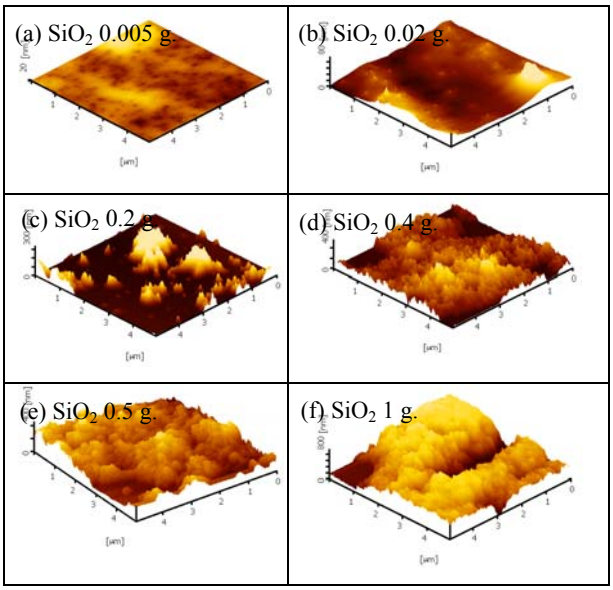

Figure 2. AFM images of the water- and oil-repellent coatings containing different SiO_2 content.

Values of the RMS surface roughness of all films are shown in Table 2. It was found that the average surface roughness increased with increasing the SiO_2 content leading to an increase of the wetting angle. Moreover, the increase of the SiO_2 content also had direct effect on surface free energy of the coatings.

Generally, the surface free energy of fluorinated compound on a flat surface is ~15 mJ/m^2 [10]. With the increase of the SiO_2 content, the apparent surface energy of the coatings (shown in Table 2) decreased to the order of several mJ/m^2, which was less than the surface energy of typical oils (20-30 mJ/m^2). Thus, at the high SiO_2 content, the coating exhibited not only water repellence but also oil repellence.

Fig. 3 shows SEM images of the glass substrate coated with pure fluorosilane and water- and oil-repellent coating prepared from 1 g. of SiO_2 hydrophobized with fluorosilane. The inset picture shows photos of water and ethylene glycol droplets. Surface of the fluorosilane-coated glass shown in Fig. 3(a) is quite smooth, giving the low contact angle of water and ethylene glycol of 111.3° and 94.3°, respectively. After coating with water- and oil-repellent film (Fig. 3(b)), many small spherical agglomerates and pores are observed on the surface. The diameters of those spherical agglomerates are about 0.1-0.3 μm, and the sizes of pores are in a range of 0.002-0.5 μm which can be classified into two kinds: micropore (< 2 nm) and mesopore (2-100 nm). This surface gave the high contact angle of water and ethylene glycol up to 173.2 and 146.7°, respectively. The achievement of water- and oil-repellent surface can also be attributed to air pockets trapped in the surface consisting of high fraction of these pores. Hsieh et al. [12] proposed that liquid droplets cannot penetrate or diffuse into micropores easily on a repellent surface because the air trapped in the micropores has a greater floating force to droplet, reflecting a higher air resistance against wettability.

The water- and oil- repellent properties on a composite surface consisting of solids and pores have been described by Cassie and Baxter model [15]. They proposed the equation in which the effective contact angle θ' is stated as:

$$\cos\theta' = f_1 \cos\theta_1 + f_2 \cos\theta_2 \quad (3)$$

where θ_1 and θ_2 are the contact angles corresponding to component 1 and 2, respectively, and f_1 and f_2 are the fractional areas of component 1 and 2, respectively.

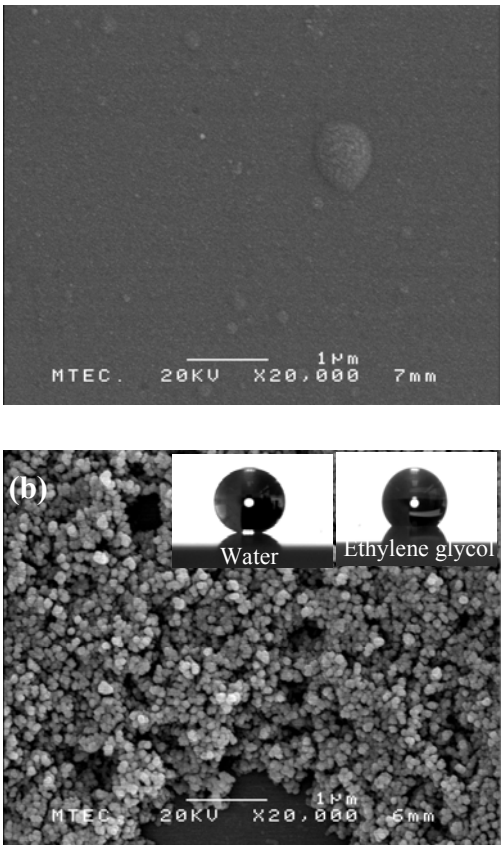

Figure 3. SEM images of glass substrate coated with pure F-silane (a) and water- and oil-repellent coating (b). The insets are photos of water and ethylene glycol droplets.

For a composite surface, f_1 and f_2 are the fractional areas of solid surfaces and air in contact with water, respectively. The contact angle of air is regarded to be 180° [16], thus the Eq. 3 can be rewritten as follows:

$$\cos\theta' = f_1 \cos\theta - f_2 \quad (4)$$

It is assumed that $f_1 + f_2 = 1$. The θ is the contact angle of water on fluorosilane-coated smooth glass surface, which is equal to 111.3°.

Table 2. Liquid drop contact angle, surface roughness and surface free energy

Sample no.	Contact angle (degrees)					RMS (nm)	γ_S (mJ/m^2)
	Water	Glycerol	Ethyltene glycol	Diiodo methane	Seed oil		
S-0.005	114.8	116.1	97.6	87.9	101.4	3.7	11.9
S-0.02	116.4	117.8	98.3	94.7	101.6	11.3	10
S-0.2	140.3	146.8	123.3	117.1	100.2	46.4	3.3
S-0.4	163.9	168.6	131.9	131.7	122.2	103	2.4
S-0.5	168.9	172.6	144.4	138.4	127.2	176.1	1.2
S-1	173.2	173.2	146.7	143.8	147.6	209.6	0.7

Thus, for our coatings, the fractional area of air (f_2) in the surface can be calculated from Eq. 4. The relationship between the fractional area of air and SiO_2 content is shown in Fig. 4. The fractional area of air increased with increasing SiO_2 content which in turn resulted to the increase in water and oil contact angles. The agglomerated SiO_2 nanoparticles deposited onto the surface gave rise to a large amount of air trapped in the micropores, creating a vast air coating against the water and oil droplets. Therefore, at the high SiO_2 content, the rough surfaces with high fraction of micropore can enhance water- and oil-repellency.

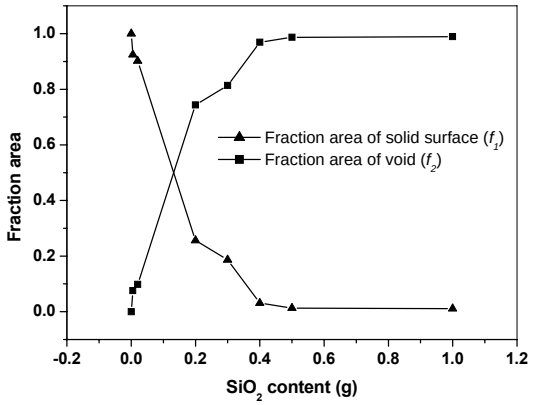

Figure 4. Calculated fraction of solid surface (f_1) and air (f_2) in contact with water

The environmental stability of the water- and oil-repellent coating evaluated in terms of a change of contact angle is illustrated in Fig. 5. It is obvious that values of the water and ethylene glycol contact angles remains constant for a period of 6 months indicating that the coatings are stable.

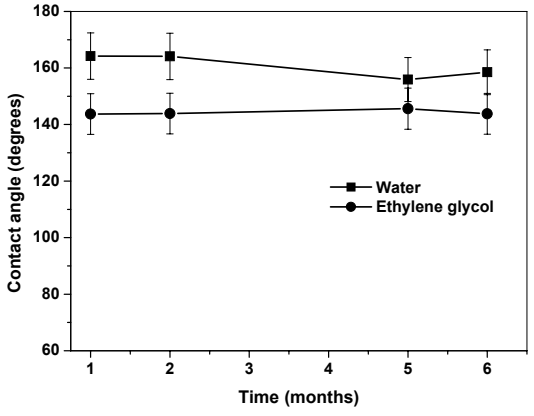

Figure 5. Environmental stability of the water- and oil-repellent coating.

Conclusions

The stable water- and oil-repellent silica-based coatings have been deposited onto glass surface. The coatings contained the SiO_2 nanoparticles as a surface roughness enhancer hydrophobized with the low surface free energy fluorosilane. At the highest surface roughness, the coating showed the contact angles of water and seed oil up to 173 and 148° , respectively, and low surface free energy of 0.75 mJ/m^2. The achievement of water- and oil-repellency is also attributed to the air trapped in the rough surfaces consisting of high fraction of micropore. The coating was stable under ambient atmosphere**.**

References

[1] W. Barthlott and C. Neinhuis, *Planta.* **202** (1997**)**, pp. 1.

[2] R. Furstner, W. Barthlott, C. Neinhuis and P. Walzel, *angmuir.* **21 (**2005), pp. 956–961.

[3] K. Kamitani and T. Teranishi, *J. Sol–Gel Sci. Technol.* **26** (2003), pp. 823–825.

[4] T.-S. Lin, C.-F. Wu and C.-T. Hsieh, *Surf. Coat. Technol.* **200** (2006), pp. 5253–5258.

[5] Z. Burton and B. Bhushan, *Nano Lett.*, **5** (2005), pp. 1607–1613.

[6] H. Zhang, R. Lamb and J. Lewis, *Sci. Technol. Adv. Mater.* **6** *(*2005), pp. 236–239.

[7] O. Nimittrakoolchai and S. Supothina, *J. Euro. Ceram. Soc.* **28** (2008), pp. 947.

[8] K. Tsujii, in *Surface Activity-Principles, Phenominoa, and Applications,* (Ed.: T. Tanaka), Academic Press, New York, 1998, pp. 52-54.

[9] K. Tsujii, T. Yamamoto and S. Shibuichi, *Angw. Chem. Int. Ed. Engl.* **36** (1997), pp. 1011.

[10] S. Shibuichi, T. Yamamoto, T. Onda, K. Tsujii, *J. Colloid Interface. Sci.* **208** (1998), pp. 287-294.

[11] T. Nishino, M. Meguro, K. Nakamae, M. Matsushita, and Y. Ueda, *Langmuir.* **15** (1999), pp. 4321-4323.

[12] C.T. Hsieh, J.M. Chen, R.R. Kuo, T.S. Lin, C.F. Wu, *Appl. Surf. Sci*. **240** (2005)**,** pp. 318-326.

[13] C.T. Hsieh, F.L. Wu and W.Y. Chen, *Surf. Coat. Technol.* **203** (2009), pp. 3377-3384.

[14] M-C, Michalski, Joe, Hardy and B.J.V. Saramago, *J. Colloid Interface Sci.* **208** (1998), pp.319-328.

[15] A.B.D. Cassie and S. Baxter, *Trans. Faraday Soc.* **40** (1994), pp. 546.

[16] L. Jiang, Y. Zhao and J. Zhai, *Angew. Chem., Int. Ed.* **43** *(*2004), pp. 4338-4341.

Electrochromic and photochromic properties of TiO_2-WO_3 nanocomposite

R. Rattanakam and S. Supothina*

National Metal and Materials Technology Center, 114 Thailand Science Park,
Paholyothin Rd, Klong 1, Klong Luang, Pathumthani, Thailand 12120

* E-mail: sitthis@mtec.or.th

Abstract: WO_3 is well-known for its application as electrochromic devices. TiO_2 on the other hand finds many applications through utilizing artificial or solar UV radiation. Incorporated with TiO_2, the WO_3 have been proposed to exhibit both electrochromic and photochromic phenomena due to electron injection from the TiO_2 to the WO_3 and hole injection in the opposite direction upon UV illumination. In this work, we present the alternative route to prepare TiO_2-WO_3 nanocomposite. Cyclic voltammetry and optical measurement revealed that coloration and bleaching processes of the nanocomposite resulted from the reduction and oxidation reactions, respectively, during the application of potentials. The coloring/bleaching ability of TiO_2-WO_3 nanocomposite was comparable to that of WO_3. However, the TiO_2-WO_3 nanocomposite exhibited photochromic characteristic which cannot be observed in case of WO_3.

Introduction

Since the discovery of the electrochromic (EC) effect in transition metal oxides in the mid-1960s, intensified research efforts to develop electrochromic devices have spread worldwide [1]. Among these devices, antiglare car rear view mirrors are already commercially available while solar control window have currently been under intensive developments. Tungsten oxide is found to be the most efficient candidate. Ions like H^+ or Li^+ in electrolyte are intercalated into WO_3 thin film to reduce WO_3 to M_xWO_3, blue-colored state, when negative electric field is applied. Under positive electrical field, oxidation state, the reduced M_xWO_3 is oxidized and return to WO_3 original from. However, for practical electrochromic device, the improvement in some properties such as electrochromic reversibility, life stability, switching rate, and contrast are required.

Several studies have been made on TiO_2-doped WO_3. It has been shown that reversibility of TiO_2-doped WO_3 films can be improved up to 91% [2]. It has been also observed that the coloration efficiency of TiO_2-WO_3 thin films decrease slightly but the lifetime can be five times longer than that of pure WO_3 [3-4]. In this present work, the TiO_2-WO_3 nanocomposite was prepared by mechanochemical technique using TiO_2 and $WO_3.H_2O$ as precursors. Its electrochromic properties were investigated. Additionally, thanks to the photoresponsive characteristic of the TiO_2, the photochromic effect of the TiO_2-WO_3 nanocomposite under UV irradiation was also studied.

Materials and Methods

The preparation of TiO_2-WO_3 nanocomposite was carried out in a planetary ball mill (Fritsch, Puluerisette 7). A commercial degussa P25 TiO_2 powder and synthesized $WO_3{\cdot}H_2O$ [5] with a weight ratio of 1:0.5 were introduced into a zirconia chamber containing zirconia balls and then mixing at the speed of 400 rpm 15 min. The yellow precipitate of TiO_2-$WO_3{\cdot}H_2O$ nanocomposite was obtained as a result.

Thick films of TiO_2-$WO_3{\cdot}H_2O$ nanocomposite were deposited by means of casting on indium tin oxide (ITO)-coated glass. The 4 mL of TiO_2-$WO_3{\cdot}H_2O$ aqueous suspension was dropped onto the ITO-coated glasses. The as-prepared films were dried in air for 2 h at 80 ºC to evaporate the solvent and then heated at 450 ºC for 2 h. Crystal structures of the WO_3 and TiO_2-WO_3 nanocomposite heated at 450 ºC were determined by using an x-ray diffractometer (XRD, JEOL JDX 3530).

In order to investigate the electrochemical properties, a quartz cell was used as an electrochemical cell, into which three electrodes were immersed. Therefore, the current and the light transmittance can be measured "*in situ*" as a function of applied voltage at different wavelengths. Cyclic votametry curves were recorded at room temperature within a -1.00 to +1.00 V range (vs. Ag/AgCl) at a scanning rate of 0.1 V/s by using $LiClO_4$ in propylene carbonate as an electrolyte and Li^+ source.

Photochromic behavior under UV irradiation of the TiO_2-WO_3 nanocomposite compared to that of pure WO_3 nanoparticle was carried out under UV for 1 h.

Results and Discussion

XRD patterns of the WO_3 and TiO_2-WO_3 composite are shown in Fig. 1. The nanocomposite film, Fig. 1(b), shows the peaks indexed to anatase TiO_2 (JCPDS file No. 21-1272), rutile TiO_2 (JCPDS file No. 21-1276) and WO_3 (JCPDS file No. 43-1035), corresponding to the XRD patterns of the starting materials (degussa P25 TiO_2 and WO_3). This result indicates that the TiO_2 and WO_3 formed a composite, not an alloying oxide compound or other new phases.

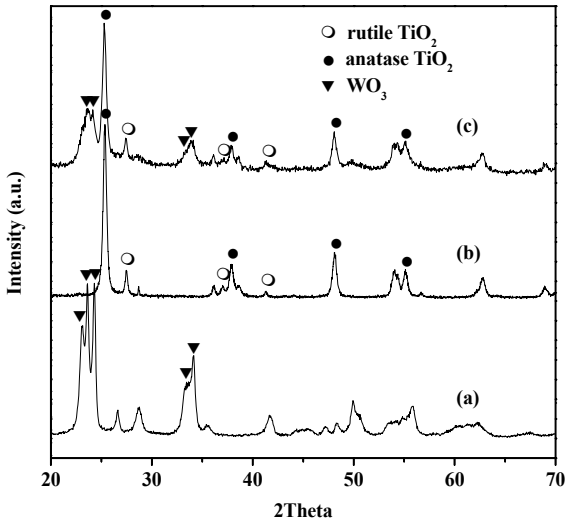

Figure 1. XRD patterns of WO_3 (a), P25 TiO_2 (b), and TiO_2-WO_3 nanocomposite (c).

Fig. 2 shows the cyclic voltamograms of the WO_3 and TiO_2-WO_3 nanocomposite, which were recorded with linear potential sweep between -1 and +1 V at the fixed scan rate of 0.1 V/s. The scan direction was indexed by the direction of the arrows. The potential scan was started at a negative potential. The cathodic coloration reaction peaks appear around the extreme value of the applied potential of -1.0 V, and the anodic peaks of bleaching reaction is saturated around -0.1 and -0.25 for WO_3 and TiO_2-WO_3 nanocomposite, respectively.

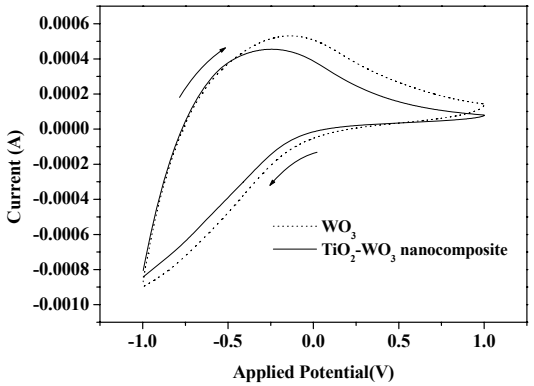

Figure 2. Cyclic voltamograms of the WO_3 and TiO_2-WO_3 nanocomposite deposited on ITO-coated glass. The applied potential was varied between -1.0 and +1.0 V at the sweep rate of 0.1 V/s.

A spectral switching of the TiO_2-WO_3 nanocomposite film was examined in the spectral region between 300 and 800 nm by applying coloring/bleaching voltages (-2.0 V/+2.0 V). Fig. 3 shows the transmittance spectra of the electrochromic film in the following states: as-prepared, colored, and bleached. The as-prepared film switched between deep blue and transparent after polarized at -2.0 V for 6 min and +2.0 V for 15 min, respectively. The electrochromic device showed cathodic coloration and considerable transmittance difference at the visible light spectrum (λ = 300-800 nm).

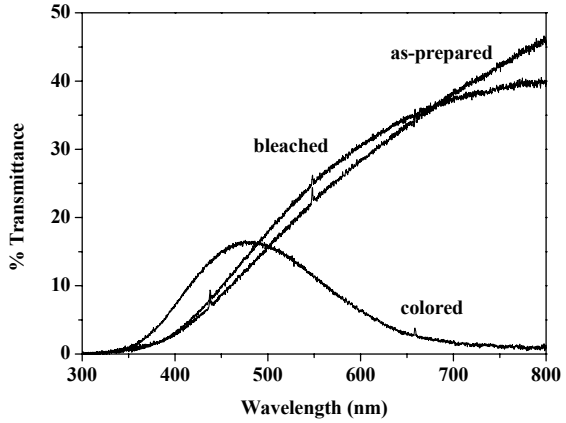

Figure 3. Transmittance spectra for an electrochromic device at as-prepared, colored, and bleached states.

Reversibility of the TiO_2-WO_3 nanocomposite film derived from the simultaneous optical modulation at λ = 630 nm is shown in Fig. 4. As shown in the graph, the switching of coloration and bleaching state is repeatable. However, further improvement is required to gain higher transmittance as well as faster beaching time.

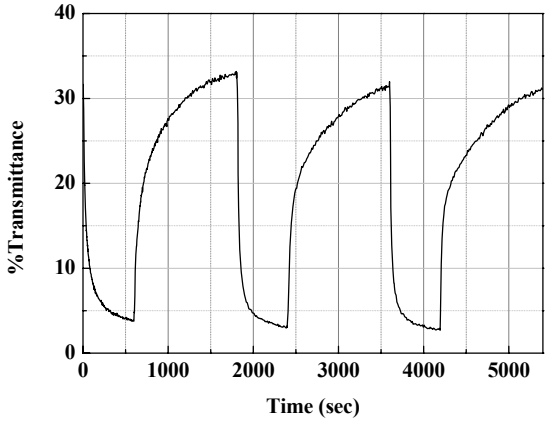

Figure 4. The *in situ* measurement of transmittance of the TiO_2-WO_3 nanocomposite film at 630 nm upon potential steps of -2.0 V (colored) and 2.0 V (bleached).

Fig. 5 shows photochromic behavior of the WO_3 and TiO_2-WO_3 nanocomposite powders exposed to UV illumination. It is evident that the WO_3 nanoparticle did not show photochromism by itself as its color remained yellow. Although some groups have reported photochromic behavior of the WO_3 colloids [6] and amorphous WO_3 [7-8], crystalline WO_3 is known to exhibit no photochromic characteristic [7]. On the other hand, the strong photochromic effect of the TiO_2-WO_3 nanocomposite to UV-irradiation was observed. The color of the TiO_2-WO_3 nanocomposite changed from pale yellow to blue in a few minutes. This is the result from charge separation at the large internal interface area.

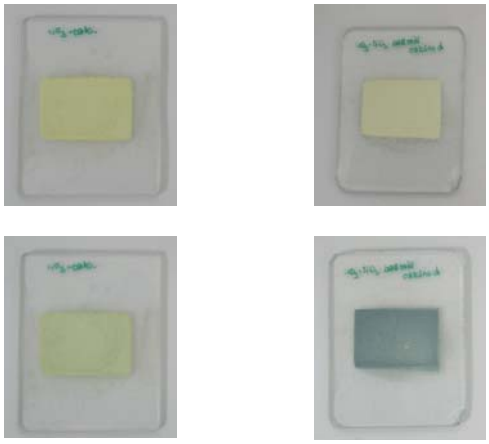

(a) (b)

Figure 5. Photochromic behavior in air of (a) WO_3 and (b) TiO_2-WO_3 nanocomposite at ambient condition (upper) and after irradiated with UV light (lower).

The electron transferring process that caused the color change can be proposed as follow. Under UV irradiation, an excited electron and a corresponding hole are generated on TiO_2 by

$$TiO_2 \xrightarrow{UV} TiO_2^*(e^- + h^+) . \quad (1)$$

The electron may be transported through TiO_2 and ITO (conductor) to WO_3, and if so, a cation should be intercalated into the WO_3 crystal. In air with humid atmosphere, adsorbed water layer should form on the film surface. This layer as well as the surface hydroxyl groups, of which dissociation should be facilitated by this water layer, should contribute to the ionic conduction which is necessary for the photo-electrochromical reduction of WO_3 as follow

$$WO_3 + xe^- + xH^+ \rightarrow H_xWO_3 . \quad (2)$$

Conclusions

TiO_2-WO_3 nanocomposite has been prepared by means of mechanochemical mixing of the commercial TiO_2 and synthesized WO_3 nanoparticles. Optical measurements performed during the electrochemical cycles showed that the TiO_2-WO_3 nanocomposite film deposited on the ITO-coated glass exhibited good electrochromic property. Photochromic behavior in air of the TiO_2-WO_3 nanocomposite revealed that the TiO_2-WO_3 nanocomposite can be a promising material for electro-photochromic application.

References

[1] S.K. Deb, *Sol. Energy Mater. Sol. Cell* **92** (2008), pp. 245-258.
[2] Z. Wang, X. Hu, *Electrochim. Acta.* **46** (2001), pp. 1951-1956.
[3] S. Hashimoto, H. Matsuoka, *J. Electrochem. Soc.* **138** (1991), pp. 2403-2408.
[4] S. Hashimoto, H. Matsuoka, *Surf. Interface Anal.* **19** (1992), pp. 464-468.
[5] O. Nimittrakoolchai and S. Supothina, *Mater. Chem. Phys.* **112** (2008), pp. 270-274.
[6] I. Bedja, S. Hotchandani and P.V. Kamat, *J. Phys. Chem.* **91** (1993), pp. 11064-11070.
[7] E. Kikuchi, K. Iida and A. Fujishima, *J. Electroanal. Chem.* **351** (1993), pp. 105-114.
[8] J. N. Yao, P. Chen and A. Fujishima, *J. Electroanal. Chem.* **406** (1996), pp. 223-226.

The optimum condition in lipase immobilization on carbon monolith prepared by continuous process

B. Luang-on[1,*] , P. Winayanuwattikun[2], A. Siyasukh[3], W. Tanthapanichakoon[1, 4] and N. Tonanon[1]

[1]Center of Excellence in Particle Technology, Faculty of Engineering, Chulalongkorn University, Bangkok, Thailand 10330
[2]Department of Biochemistry, Faculty of Science, Chulalongkorn University, Bangkok, Thailand 10330
[3]Department of Industrial Engineering, Faculty of Engineering, Naresuan University, Phitsanulok, Thailand 65000
[4] SCG Chemicals Co., Ltd. 10 I-1 Rd., Map Ta Phut Industrial Estate, Muang District, Rayong Province, Thailand 21150

*E-mail : Bordin.Lu@Student.chula.ac.th

Abstract: The hierarchical monolithic carbon is an interesting material for the enzymatic reactor due to high mass transfer rate. In this study the carbon monolith with hierarchical porous structure synthesized by sol-gel polycondensation of resorcinol with formaldehyde followed by carbonization is used as immobilized lipase supports. Physical absorption by continuous flowing enzyme solution through the column is applied for immobilization technique. The optimum condition in immobilization of lipase on the hierarchical porous carbon monolith is studied. The enzymatic activities of immobilized lipase and the effects of structure of carbon monolith on lipase immobilization are investigated.

Introduction

Hierarchical porous carbon monolith is an attractable materials containing combination pores of meso/micro pores on macroporous monolith [1] used as supports for enzyme immobilization due to their fairly uniform, adjustable pore sizes and structures, large surface area and pore volume.[2] This carbon monolith synthesized from resorcinol-formaldehyde gel by sol-gel polycondensation reaction. The ability to control pore size and characters of this materials is of immense advantage since these factors can exhibit direct impact on activity and stability of immobilized enzymes. Moreover, the macropore structure allows fluid flow under low back pressure and high convective mass transfer, which is an explanation for continuous process. Therefore, hierarchical porous monolith has a great potential for enzyme immobilization. [2, 3, 4]

Immobilization of free enzymes on a support facilitates the enzyme separation from product, improves biocatalysts stability, and be able to reuse for application in continuous operations, with a positive consequence on the process economy. [2] The supports must be made suitable for the technical applications by maintaining a high level of enzyme activity and preventing a possible leaching out during the reactions. Adsorption and covalent bonding are popular techniques for the preparation of immobilize enzyme. They have shown several advantages over enzymes in bulk solution.

The present work is an immobilization of *Candida rugosa* lipase onto a hierarchical porous carbon monolith in different pore characters. The optimization conditions and effects of pore characters for immobilization of lipase by physical absorption technique using circulating enzyme solution through the column packed carbon monolith are studied.

2. Experiment

2.1 Materials

Lipase from *Candida rugosa* and *p*-nitrophenol palmitate were purchased from Sigma. Resorcinol (C6H4(OH)2; 99%) was from purchased from Fluka. Formaldehyde (HCHO; 36.5%), *t*-butanol (95%), and sodium carbonate (Na_2CO_3) were obtained from Ajax Finechem.

2.2 Preparation of RF solutions

Resorcinol-formaldehyde (RF) solutions were prepared from resorcinol with formaldehyde in de-ionized water. Nitric acid solution 0.5 M is used as a catalyst. [5]

Firstly, resorcinol was dissolved into the de-ionized water and stirring it with magnetic stirrer until dissolution completely. Then, the resorcinol solution is added with formaldehyde solution and followed by adding the solution of 0.5 M of nitric acid. All solutions were then placed in a themostated bath and RF solutions were obtained.

The molar ratios of resorcinol to formaldehyde (R/F), and resorcinol to water (R/W), and the mole to volume ratio of catalyst to water (C/W) were fixed at 0.5 mol/mol, 0.15 mol/mol, and 0.20 mol/ml, respectively.

2.3 Formation of macroporous carbon beads

The macroporous carbon beads were used for finding the primary immobilization conditions. They were synthesized by RF solutions. Before RF solutions lost their fluidity, they were dispersed into a solution of nonionic surfactant (SPAN80) in cyclohexane. After that, the mixtures were agitated at 400rpm and 40 ^oC for 2 h. RF beads were then aged at 75 ^oC for another 24 h and drying at this temperature until the weight was constant.

Finally macroporous carbon beads were obtained by carbonization of RF beads. The RF beads were conducted by thermal activation under a 50 cm^3-STP flow of CO_2. Samples were heated up to 850 ^oC with

10 °C/min heating rate and kept at this temperature for 30 minutes.

2.4 Formation of macroporous carbon monoliths containing various pore characters

RF solutions were transferred into the cylindrical glass tube where RF gel was formed. After that the gel was sealed at the ends of the tube, followed by 24 h for aging in the oven at temperature of 75 ºC. After aging, the gel was moved from the tube and followed by drying with hot air at 75 ºC until the weight was constant. The macroporous carbon precursor in a monolithic form was obtained.

The RF monolith was carbonized in three different methods.

2.4.1 Carbonization with N_2

RF dried-monolith gels were carbonized with N_2 in a quartz tube reactor at 850 ºC for 30 min with 10 °C/min heating rate. RF carbon monoliths containing macro/micro porous structure were obtained.

2.4.2 Direct thermal activation with CO_2

RF dried-monolith gels were conducted by thermal activation with CO_2 in a quartz tube reactor at 850 ºC for 30 min with 10 °C/min heating rate. RF carbon monoliths containing macro/micro porous structure and having oxygen on surface were finally obtain after the process.

2.4.3 Direct chemical activation with CO_2-$Ca(NO_3)_2$

At first, the RF dried-monolith gels were soaked into the solution of $Ca(NO_3)_2$. After that, the $Ca(NO_3)_2$-impregnated RF monolith gels were dried until their weight were constant. Thermal activation was conducted in a quartz tube reactor with CO_2. The reactor was heated at 850 ºC for 30 min with 10 °C/min heating rate. The monolithic carbon products were soaked in the hydrochloric acid solution and then washed with deionized water to remove the residual chemical agent [9]. Then, the carbon monoliths were dried again until their weight were constant. Finally the activated carbon monoliths containing macro/meso and micro porous structure and having oxygen on surface were obtained.

2.5 Immobilization of lipase

2.5.1 Preparation of lipase immobilization on macroporous carbon beads

In preparation for immobilization, 0.1g of carbon bead supports were pre-wet with 3 ml *t*-butanol overnight to exclude the air within the carbon beads. Then, they were filtered for enzyme immobilization.

Upon immobilization, the prepared carbon bead was brought into contact with 3 ml lipase solution in a sealed vessel. The vessel was then placed in an orbital shaker at room temperature for 6 h. Next, the enzyme-loaded carbon beads were washed for five times with phosphate buffer solution. They were then filtered, dried, and stored at 4 °C.

2.5.2 Preparation of lipase immobilization on macroporous carbon monoliths

Immobilization was carried out by circulating lipase solution (under primary condition that find by using carbon beads) by peristaltic pump though macroporous carbon monolith in glass column (Fig.1) at various flow conditions and immobilization times. The immobilized enzyme was then washed by circulating phosphate buffer solution to remove the unbound enzyme. The supernatant and washing solution were assayed for protein loading in the supports.

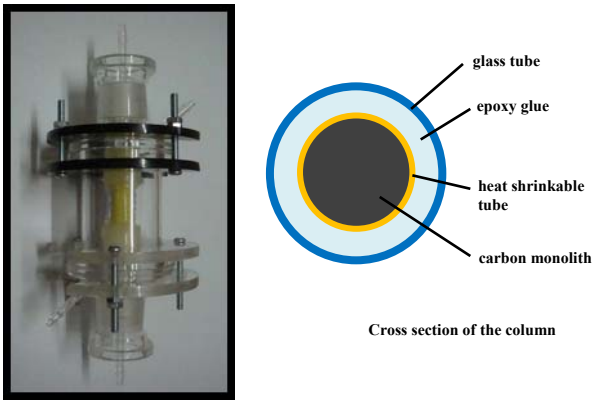

Fig.1 Column packing carbon monolith

3. Results and Discussions

3.1 Characteristic of the carbon beads and carbon monoliths

Fig.2 Photograph of carbon beads and carbon monolith

According to the Fig.2, the photograph of the macroporous carbon beads and carbon monoliths are shown.

The SEM images (Fig.3) show the porous texture of carbon beads (a,b) and the cross-section of RF monolith gels (c) ,carbon monoliths are conducted by carbonization with N_2 (d), thermal activation with CO_2 (e) and chemical activation with CO_2-$Ca(NO_3)_2$ (f).

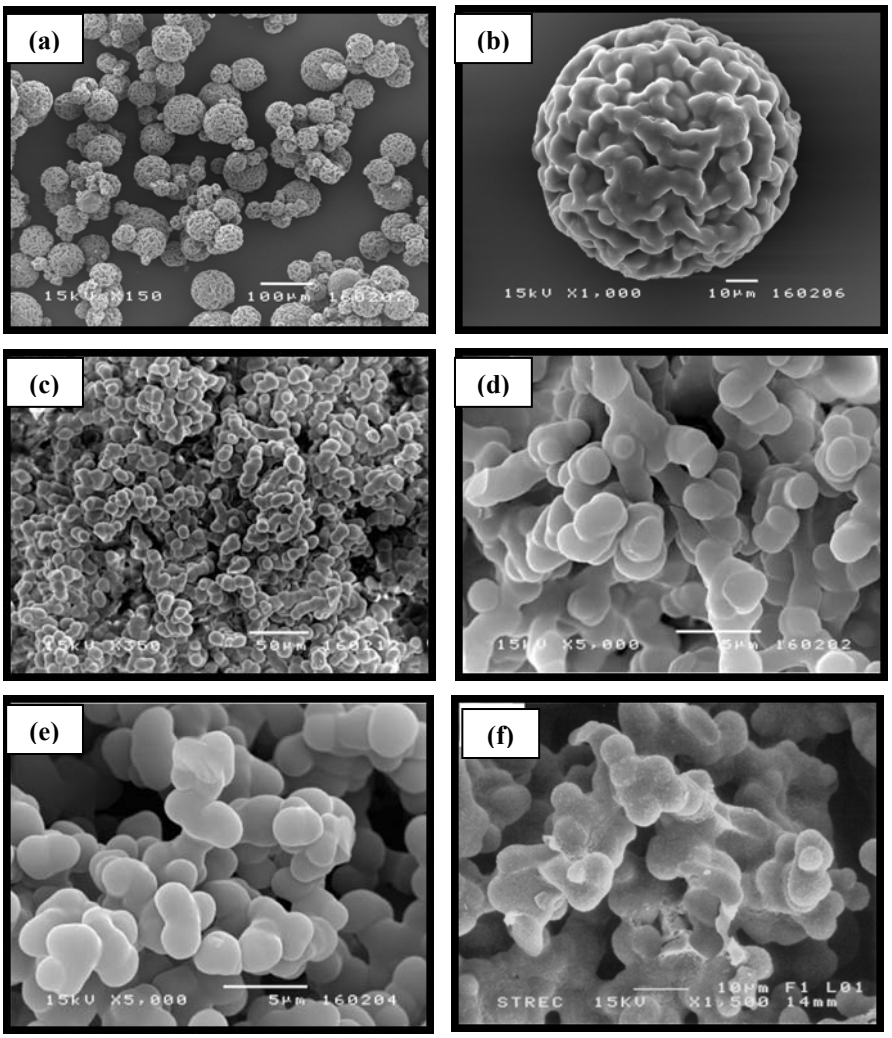

Fig.3 SEM micrograph of carbon beads and carbon monoliths

3.2 Optimization of immobilized lipase

3.2.1 Primary conditions for immobilization lipase

Macroporous carbon beads are used for primary conditions in order to decrease the amount of used enzyme. The effect of pH, ionic strength and protein loading for the immobilization of lipase are investigated.

3.2.1.1 Effect of pH on immobilization

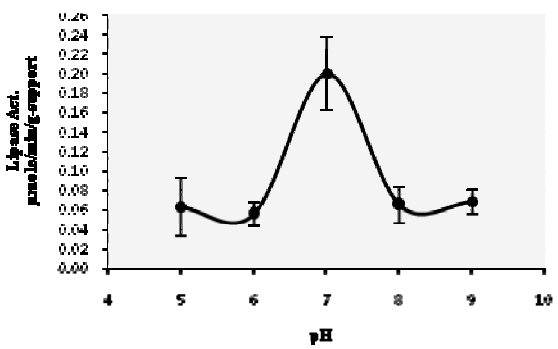

Fig.4 The effect of pH on the lipase activity of lipase immobilization

The activities of lipase at various pH are studied and the results are shown in Fig.4. The highest activity of lipase is obtained at pH 7. Thus, the optimal pH for the maximum of activity of lipase is fixed as 7.

3.2.1.2 Effect of ionic strength on immobilization

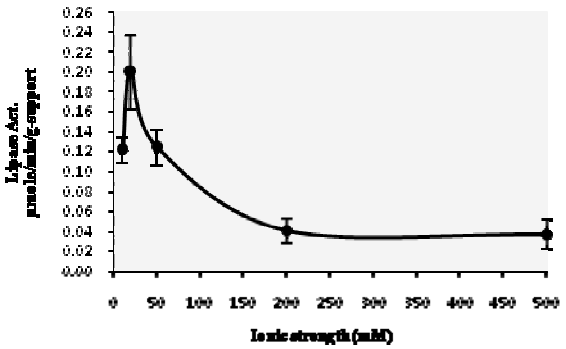

Fig.5 The effect of ionic strength on the lipase activity of lipase immobilization

When the optimal pH for immobilization is obtained, the phosphate buffer at various concentrations are prepared to study the effect of the

ionic strength on activity of immobilized lipase. The results are shown in Fig.5. The highest activity show at 20mM phosphate buffer. Therefore, the optimal concentration (20mM) of phosphate buffer pH 7 is used for study the effect of protein loading on activity of immobilized lipase.

3.2.1.3 Effect of protein loading on immobilization

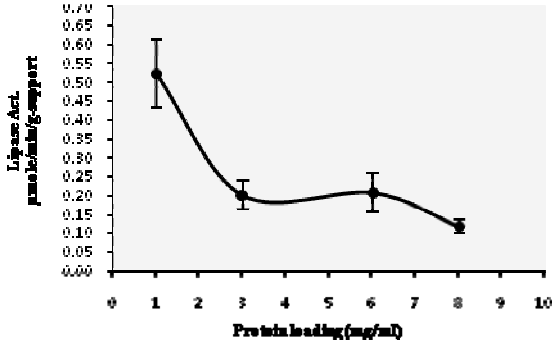

Fig.6 The effect of protein loading on the lipase activity of lipase immobilization

The effect of protein loading is studied by different quantities of enzyme from 1 to 8 mg/ml and the results are shown in Fig.6. It can be indicated that the highest activity of lipase at the lowest protein loading (1 mg/ml) is shown. Therefore, 1 mg/ml is used as optimal amount of protein loading. Hence, the selected optimal conditions (pH 7, 20 mM, 1mg/ml) are used for immobilization lipase on carbon monolith.

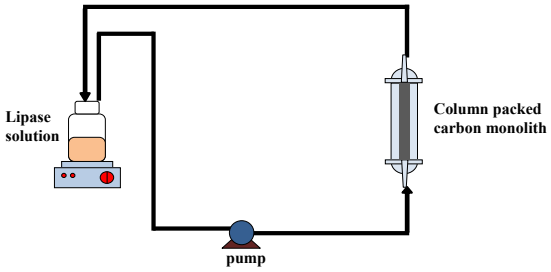

Fig.7 Experimental set up for the immobilization of enzyme

3.2.2 Immobilization of lipase by using column packed carbon monolith

The primary conditions obtained from using the carbon beads are applied for immobilization lipase by flowing the enzyme solution through the column. The model of the experimental set up is shown in Fig.7. The characteristics of carbon monoliths, flow conditions and times for immobilization are going to be studied.

4. Conclusions

Hierarchical porous carbon from resorcinol-formaldehyde gel (RF gels) of various pore characters are synthesized and used as a supports immobilization of *Candida rugosa* lipase. The primary conditions for preparing enzyme solution to immobilization lipase are pH 7, 20 mM of phosphate buffer solution and 1mg/ml protein loading. However, the immobilization enzyme on carbon monolith is going to be studied.

Acknowledgement

The authors would like to thank the fully supports from Thailand Research Fund (TRF).

References

[1] A. Siyasukh, P. Maneeprom, S. Larpkiattaworn, N. Tonanon, W. Tanthapanichakoon, H. Tamon, T.Charinpanitkul. "Preparation of a carbon monolith with hierarchical porous structure by ultrasonic irradiation followed by carbonization, physical and chemical activation". *Carbon*, 2008.

[2] Nadir Dizge, Coskun Aydiner, Derya Y. Imer, Mahmut Bayramoglu, Aziz Tanriseven and Bulent Keskinler. "Biodesel production from sunflower, soybean, and waste cooking oils by transesterification using lipase immobilized onto a novel microporous polymer". *Bioresource Technology 100 (2009)* 1983-1991.

[3] Leire Zubizarreta, Ana Arenillas, Jean-Paul Pirard, Jose Juan Pis, Nathalie Job. "Tailoring the textural properties of activated carbon xerogels by chemical activation with KOH". *Microporous and Mesoporous Materials, 2008.*

[4] T. Chaijitrsakool, N. Tonanon,W. Tanthapanichakoon, H. Tamon, S. Prichanont. "Effects of pore characters of mesoporous resorcinol–formaldehyde carbon gels on enzyme immobilization". *Journal of Molecular Catalysis B: Enzymatic 55, 2008*. pp. 137–141

[5] Cedric J. Gommes, Nathalie Job, Jean-Paul Pirard, Silvia Blacher and Bart Goderis. "Critical opalescence points to thermodynamic instability: relevance to small-angle X-ray scattering of resorcinol–formaldehyde gel formation at low pH". *Applied Crystallography, 2008*.

[6] Mozaffar Shakeri and Koei Kawakami. "Effect of the structural chemical composition of mesoporous materials on the adsorption and activation of the *Rhizopus oryzae* lipase-catalyzed trans-esterification reaction in organic solvent". *Catalysis Communications*, Volume 10, Issue 2, 15 November 2008, Pages 165-168

The influence of Mg-PSZ addition on microstructure and mechanical properties of Al_2O_3/WC composites

J. Boonpo[1,2,*], W. Buggakupta[1,2] and N. Chuankrerkkul[3]

[1] Research Unit of Advanced Ceramics, Department of Materials Science, Chulalongkorn University, Bangkok, Thailand

[2] Research Unit of Advanced Ceramics and Polymeric Materials, National Center of Excellence for Petroleum, Petrochemical and Advanced Material, Chulalongkorn University, Bangkok, Thailand

[3] Metallurgy and Materials Science Research Institute, Chulalongkorn University, Bangkok, Thailand

*E-mail: new_lionking@hotmail.com

Abstract: The study concerns microstructure and mechanical properties of the Al_2O_3/WC particulate composites, strengthened by Mg-PSZ. The samples were prepared from high purity powder precursors, i.e. alumina and tungsten carbide, along with Mg-PSZ particulates ranging from 0 to 6 wt%. The mixture was pressed and sintered at 1600 ^oC for 2 hours in an argon atmosphere. The density of the specimens was measured using liquid immersion. Hardness and fracture toughness were determined by Vickers indentation techniques. Phase content and microstructure of the composites were investigated by X-ray diffraction and scanning electron microscopy, respectively. It was found that the relative density of the Al_2O_3/WC composites with various Mg-PSZ content were over 95 %TD. The Al_2O_3 reinforced with WC particles has greater hardness than the monolithic Al_2O_3. A presence of the Mg-PSZ also contributed to slightly better fracture toughness even hardness is reduced. A comparison of the composites with and without Mg-PSZ additives were also reported and discussed.

Introduction

Nowadays, many materials were selected for superior and more efficient cutting tools. A combination of several desirable features, including high hardness and fracture toughness, excellent wear resistance, chemical inertness and high impact resistance, should be accomplished. Ceramic materials, such as, diamond, carbides and nitrides are candidates. Alumina (Al_2O_3), one of the most widely used engineering ceramics, also meets most of these significant requirements. The application of alumina as a cutting tool is possible, however, it is limited by low fracture toughness.

It is common that a composite material can improve mechanical properties and also enhance some properties as required for certain applications. The dispersion of hard carbide particles such NbC, TiC, WC and (W, Ti)C into Al_2O_3 matrix can be benefit to mechanical properties due to crack deflection. Although all carbides show relatively similar hardness, tungsten carbide (WC) has elastic modulus, flexural strength and fracture toughness higher than others, as shown in Table 1. It also provides chemical inertness and wear resistance. Therefore, the Al_2O_3/WC composites are expected to be another potential material for cutting tools [1-5].

Mechanical properties of the alumina matrix composite, especially fracture toughness, can be improved as a presence of zirconia. Pure ZrO_2 has a monoclinic crystal structure at room temperature and transforms to tetragonal and cubic at around 1170 ^oC and 2370 ^oC, respectively. It can be fully effective when using the dopants such as MgO, CaO, Y_2O_3 and CeO. These dopants control phase transformation by stabilizing tetragonal or cubic crystals at ambient temperature that can enhance fracture toughness [6,7]. The addition of Mg-PSZ to the Al_2O_3/WC composites may be possible to get higher toughness.

The aim of this work is to study the effects of Mg-PSZ on microstructure and mechanical properties of the Al_2O_3/WC composite, fabricated by pressureless sintering, for cutting tool applications.

Table 1: The mechanical properties of some engineering ceramic materials [1-3,8]

Material	H_v (GPa)	K_{IC} (MPa.$m^{1/2}$)	E (GPa)
C (Diamond)	30	1	1000
BN	27	1-2	700
Al_2O_3	18-20	2-4	310-410
ZrO_2	13-14	6-10	200-300
SiC	22	3-5	450
NbC	20-24	3-6	340-730
TiC	18-22	4-6	300-500
WC	17-24	11-12	520-700
Si_3N_4	16	4-7	320

Materials and Methods

The high purity alumina AKP30 (99.99% purity, Sumitomo Chemical Co., Ltd, Japan, D_{50} = 0.3 μm), WC powder (ATI Alldyne, United states, D_{50} = 1.2 μm) and Mg-PSZ powder (Fukushima, Japan, D_{50} = 17.8 μm) were used as starting materials. The Al_2O_3 matrix was reinforced by 10 wt% WC particles, accompanied by the addition of Mg-PSZ of 0-6 wt%. These powder mixtures were wet-mixed with ethanol for 4 hours in a polyethylene bottle, using alumina milling media. The slurry was dried in an oven at 60

°C, then crushed and sieved. Next, the powder was pressed into pellets of 13 mm in diameter at 30 MPa, using a uniaxially press. The pellets were placed in a BN-coated graphite die with a lid and sintered at 1600 °C for 2 hours in an argon atmosphere with a heating rate of 15 °C per minute.

The bulk density of the sintered samples were determined by liquid immersion and theoretical density (TD) was calculated by using the rule of mixture. Phase content were observed by X-ray diffractometer (D8 Advanced Bruker, with Ni filter Cu K_α radiation) from 20 to 80°. Microstructure of the composites was observed using scanning electron microscopy (SEM, JSM-6480LV, JEOL). The samples were polished and thermally etched at 1500 °C for 15 minutes in order to reveal the grain boundaries. The hardness and fracture toughness were obtained using Vickers hardness tester (HV-50A, Laizhou Huayin) with a load of 10 kg for 15 seconds, then the lengths of diagonal and cracks of indentation were measured. The hardness and fracture toughness were estimated from equation (1) and (2), respectively.

$$H_V = \frac{0.0018544(P)}{\bar{d}^2} \quad (1)$$

$$K_{IC} = 0.018 \left(\frac{E}{H_V}\right)^{1/2} \frac{P}{c^{3/2}} \quad (2)$$

Where H_v is the Vickers hardness (GPa), P the load (N), d the average length of two diagonals of the indentation (mm), K_{IC} the fracture toughness ($MPa.m^{1/2}$), E the elastic modulus (GPa) and c the crack length (mm). The elastic modulus of the composites were calculated from the rule of mixture with the following values: 401 GPa for Al_2O_3, 700 GPa for WC and 200 GPa for Mg-PSZ.

Results and Discussion

The values of green density of the composites were in the range of 52-56 %TD. After sintering, the monolithic Al_2O_3 of 99 %TD was achieved. The addition of WC and Mg-PSZ particles into alumina experimentally led to a slight decrease in relative density, as seen in Figure 1. The lower density of the sintered pellets may be caused by a porosity in the structure due to incomplete densification. It was also comparatively observed that the packing between different types of particles was low at the boundary regions (Figure 3).

A comparison of XRD patterns of the Al_2O_3/WC composites containing different Mg-PSZ contents was shown in Figure 2. This indicated a presence of alumina, tungsten carbide and tungsten sub-carbide (W_2C), along with a few number of unidentified peaks. The W_2C and the unidentified peaks appeared after sintering. The existence of W_2C was due to the decomposition of WC according to equation (3), and it was stable during the normal cooling process [9]. The

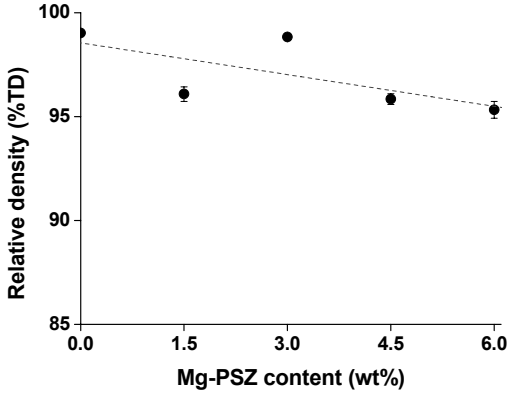

Figure 1. Relative density of the Al_2O_3/WC composites as a function of Mg-PSZ content.

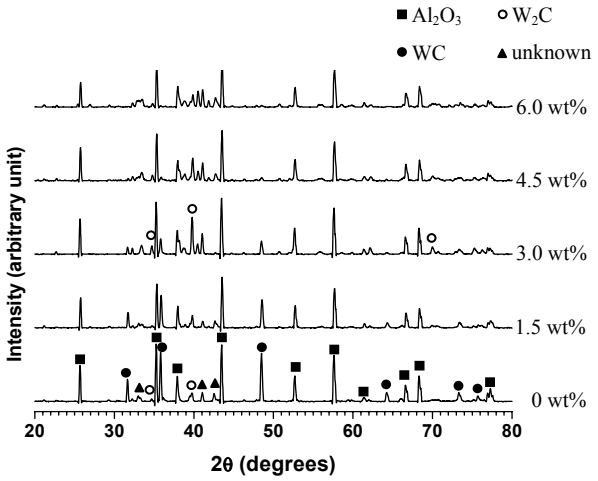

Figure 2. X-ray diffraction patterns of the Al_2O_3/WC composites containing various Mg-PSZ content.

phenomenon was found to be similar to Nb_2C in NbC system [10].

$$2WC \rightarrow W_2C + C \quad (3)$$

The intensities of the WC was decreased with increasing Mg-PSZ contents, whereas the unknown peaks were increased. There were no MgO or ZrO_2 peaks detected, which may be caused by a very small amount of MgO and ZrO_2 in the powder mixture.

The microstructures of the polished, thermally etched surfaces of monolithic Al_2O_3, Al_2O_3/WC composite with and without Mg-PSZ were shown in Figure 3(a), 3(b) and 3(c), respectively. The monolithic Al_2O_3 (Figure 3 (a)) had various grain size. Some were much larger than others, showing abnormal grain growth. Large grains of monolithic Al_2O_3 could result in poor strength. In Figure 3 (b). The bright phase was WC whereas the dark phase was Al_2O_3. The difference between WC and Mg-PSZ particles could not be defined, however, ZrO_2 can be observed by the mean of EDS analysis, as seen in Figure 4 and Figure 5. The composites showed that WC and Mg-PSZ particles randomly and evenly distributed, indicating that the powder mixtures were well blended. The WC

particles and Mg-PSZ particles were irregular and located along grain boundaries of the Al_2O_3 matrix, also at grain junctions. Moreover, the availability of WC particles can reduce the grain size of Al_2O_3 matrix when compared to the monolithic. These finer grains was likely to strengthen the whole system.

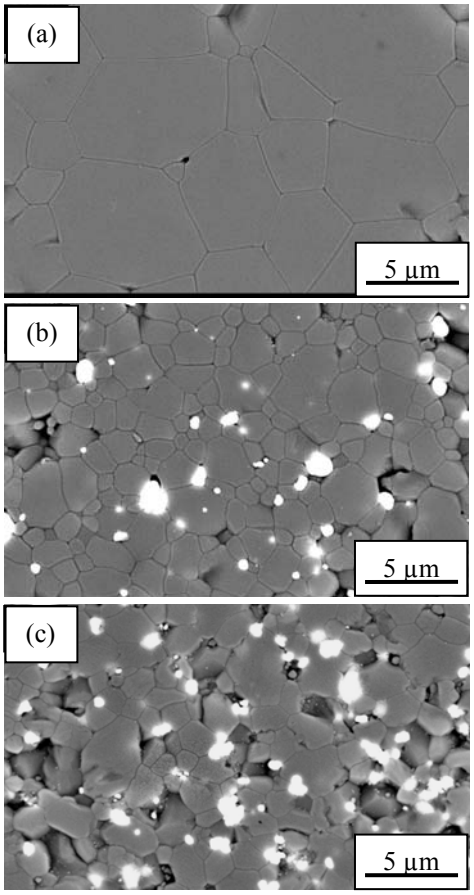

Figure 3. Backscattered electron micrographs of (a) monolithic Al_2O_3, (b) Al_2O_3/WC and (c) Al_2O_3/WC with 6 wt% Mg-PSZ, sintered at 1600°C for 2 hours.

Figure 4 showed crack propagation of the composite with 6 wt% Mg-PSZ. It was found that there were both transgranular and intergranular fractures. Moreover, crack deflection of the crack was also observed.

According to the EDS analysis, the dark field contained Al_2O_3 and carbon, dispersed into Al_2O_3 matrix. This confirmed the decomposition of WC to W_2C and carbon. Meanwhile, the bright field consisted of WC and ZrO_2. At region 2 and 3 (Figure 4), both WC and ZrO_2 particles were embedded in Al_2O_3 matrix so all elements e.g. Zr, Al, W, were detected. Gold (Au), which coated over the surface to enhance electrical conductivity and prevent charging were also detected.

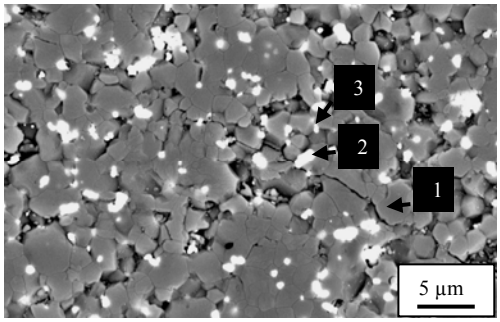

Figure 4. Crack propagation of the Al_2O_3/WC composites with 6 wt% Mg-PSZ.

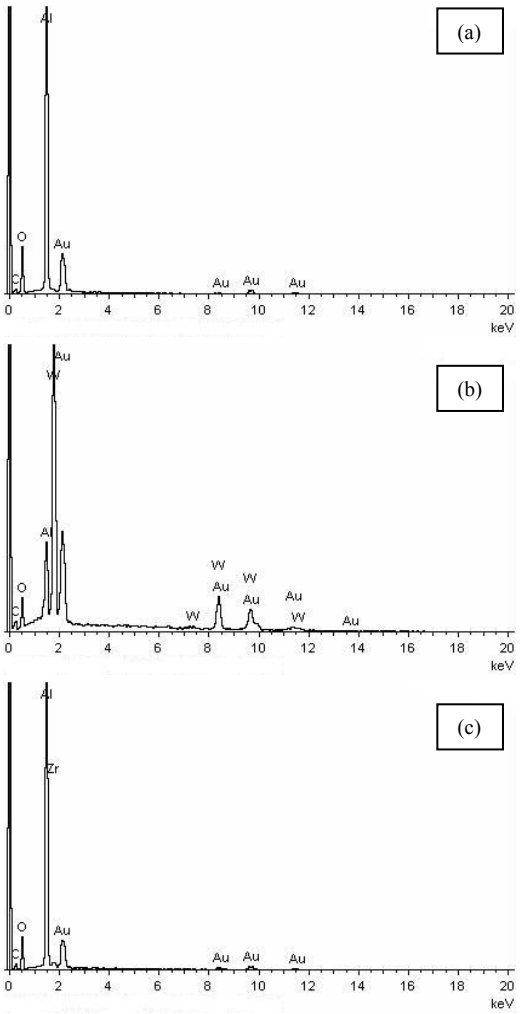

Figure 5. EDS analysis of the Al_2O_3/WC composite with 6 wt% Mg-PSZ (a) region 1, (b) region 2 and (c) region 3.

An indentation on the polished surface was shown in Figure 6, revealing that there was no plastic deformation around indentation zone. Instead, there were some cracks at the sharp corners of the indented marks, representing the degree of brittleness, in the other word, toughness of the material.

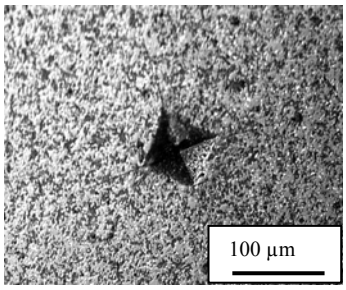

Figure 6. Optical micrographs of the indented surface of the Al_2O_3/WC composites.

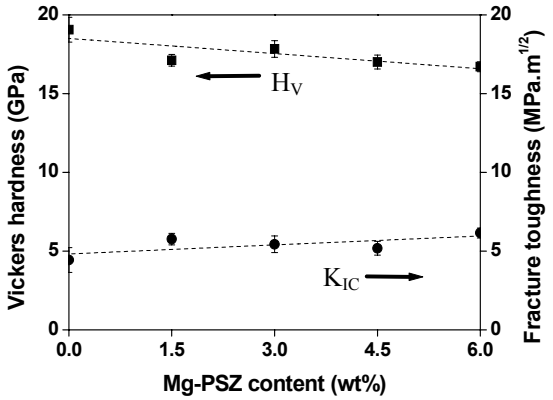

Figure 7. Vickers hardness and fracture toughness of the Al_2O_3/WC composites as a function of Mg-PSZ content.

The values of hardness of the Al_2O_3 and Al_2O_3/WC composites were 16.85±0.80 GPa and 19.05±0.79 GPa, respectively, showing that the hardness tended to increase with WC contents. In general, carbides are harder than alumina. The mixture between carbide and alumina is likely to have greater hardness with increasing carbide content. Main drawback of the greater hardness is that the system become more brittle and need to be toughened. As far as an addition of Mg-PSZ was concerned, the hardness was slightly less than that of the monolithic and the Al_2O_3 reinforced with WC particles. It can be seen that a presence of Mg-PSZ did not make any changes to hardness. However, Mg-PSZ may affects fracture toughness significantly.

As for the fracture toughness, the composites with Mg-PSZ rose up by 16-38% relative to the monolithic and Al_2O_3/WC ones. Actually, there are many mechanisms that offer higher strength, i. e. grain size reduction, phase transformation toughening and particle strengthening. Although, the addition of fine particles evenly distributed in a matrix usually hinder grain grown and improve strength, the WC powder used in this study was not likely to provide any much higher toughness. WC particles were too large to employ particle strengthening effectively even they took part in crack deflection and contributed to finer grains. This finding did not agree with the same composites fabricated by hot pressing [1-5]. Furthermore, it could notice that the microstructure of the Al_2O_3/WC with Mg-PSZ contained pores. These pores can reduce stress field developed during service and led to slightly higher toughness. An increase in fracture toughness of the Al_2O_3/WC composites resulted from a presence of Mg-PSZ rather than WC particle strengthening.

Conclusions

Mechanical properties and microstructure of the Al_2O_3/WC composites with Mg-PSZ prepared from a conventional powder processing have been focused. WC particles offered higher hardness but slightly lower fracture toughness. A presence of Mg-PSZ in the Al_2O_3/WC system provided better toughness as increasing Mg-PSZ content. An addition of Mg-PSZ to the Al_2O_3/WC system can possibly employ in order to improve fracture toughness and retain hardness.

Acknowledgements

The authors sincerely appreciated Prof. Shigetaka Wada, Dr. Thanakorn Wasanapiarnpong and Dr. Kuljira Sujirote for the powder precursors. Thanks to Research Unit of Advanced Ceramics, Department of Materials Science, Faculty of Science, Chulalongkorn University for all facilities. This work was financially supported by National Center of Excellence for Petroleum, Petrochemical, and Advanced Material, Chulalongkorn University.

References

[1] W. Acchar, C.A. Cairo and A.M. Segadães, *Mater. Sci. Eng., A*. **406** (2005), pp. 74-77.
[2] W. Achar, A.E. Martinelli, F.A. Vieira and C.A.A. Cairo, *Mater. Sci. Eng., A.* **284** (2000), pp. 84-87.
[3] W. Acchar and A.M. Segadães, *Int. J. Refract. Met. Hard Mater.* **xxx** (2008), pp. xxx-xxx.
[4] L. Wang, J.-L. Shi, J.-H. Gao and D.–S. Yan, *J. Eur. Ceram. Soc*. **21** (2001), pp. 1213-1217.
[5] L. Wang, J.-L. Shi, Z.-L. Hua, J.-H. Gao and D.-S. Yan, *Mater. Lett.* **50** (2001), pp. 179-182.
[6] D. Wittig, A. Glauche, C. G. Aneziris, T. Minghetti, C. Schelle, T. Graule and J. Kuebler, *Mater. Sci. Eng., A.* **488** (2008), pp. 580-585.
[7] J. A. Brito-Chaparro, A. Aguilar-Elguezabal, J. Echeberria and M. H. Bocanegra-Bernal, *Mater. Chem. Phys.* **114** (2009), pp. 407-414.
[8] C. Santos, L.D. Maeda, C. A. A. Cairo and W. Acchar, *Int. J. Refract. Met. Hard Mater*. **26** (2008), pp. 14-18.
[9] T. Li, Q. Li, J. Y. H. Fuh, P. C. Yu and C. C. Wu, *Mater. Sci. Eng., A.* **430** (2006), pp. 113-119.
[10] W. Acchar, D. Schwarze and P. Greil, *Mater. Sci. Eng., A.* **351** (2003), pp. 299-303.

Synthesis and characterization of allotrope carbon fiber from graphite apply for hydrogen fuel storage

C. Souvakon, and A. Vorasingha*

Department of Chemistry, Faculty of Science, Naresuan University, Phitsanulok, Thailand 65000

*E-mail: anusornv@nu.ac.th

Abstract : The Hydrogen storage based on physisorption potentially may have a higher energy efficiency. The very low boiling point of H_2 makes it necessary to apply temperatures of around 195 K to achieve sufficient amounts of adsorbed Hydrogen. The experiment was carried out to study the allotrope carbon which synthesis by using an arc-discharge apparatus, which induced with nickel metal, a common stationary charcoal rod as the source material was heated by moderate current to produce masses of the allotrope carbon. Morphology, particular structure and chemical compositions of the as-grown allotrope carbon samples (A) were characterized using scanning electron microscopy (SEM), transmission electron microscope (TEM) and X-ray diffraction (XRD). The allotrope carbon induced with nickel metal can be adsorbed hydrogen on material surface with large specific surface area, chemically bond in covalent and ionic compounds. All sample are used an arc-discharge apparatus whose major parts are nickel-bar electrodes, a DC power supply and a rod of common charcoal. The graphite rods, bought from commercial, mainly containing carbon were used as the source material. Each graphite rod used in the experiment was 6 mm in diameter and 150 mm in length and its two ends were polished for good electrical contacts with the copper electrodes. The prepared graphite rod was clipped between the moveable nickel electrode that were connected to the DC power supply with an appropriately slight force, which would result in longitudinal cracks on the rod after the processing as shown. The charcoal rod with the electrodes could be either housed in a small chamber equipped with argon gas. The allotrope carbon can be stored the hydrogen fuel 3.12% under condition 195 K and 1.5 bar.

Introduction

As supply of fossil fuels is limited and energy demand continues to rise, research is increasingly directed towards alternative renewable fuels. Biodiesel, as an alternative hydrogen fuel, is a promising non-toxic and clean renewable fuel comprised of hydrogen atoms of small molecules which are derived from water or hydrocarbon. Carbon nanofilaments, either nanotubes or nanofibers, have received increasing scientific and industrial interest during the last two decades owing to their exceptional physical and chemical properties. Large scale synthesis of carbon nanostructures, nanotubes and nanofibres, are today mainly conducted through a catalytic route due to the high yield, high selectivity and low cost, when compared to the traditional physical routes such as laser ablation or arc-discharge. Moreover, the control of the nanostructure morphology can be accurately realized through the tuning of the reaction parameters and the catalyst composition. The high selectivity of the catalytic method towards the formation of carbon nanostructures also avoids the need for a post-purification step, which is a time and cost-consuming process. Despite the significant amount of research, which has been initiated on this subject, the large scale synthesis of nanostructured materials with high purity for potential applications is still being investigated. In three recent studies of the reaction and synthesis parameters of carbon nanotubes, relatively high yields were reported. A high yield of multi-walled carbon nanotubes by fluidized bed has also been reported by Corrias et al. One of the highest reported in the open literature to date. The quality and the microstructure of the carbon nanotubes were investigated by scanning electron and transmission electron microscopy.

Hydrogen can be made available on-board vehicles in containers of compressed or liquefied H_2, in metal hydrides, or by gas-on-solid adsorption. Hydrogen can also be generated on-board by reaction or decomposition of a hydrogen containing molecular species. Although each method possesses desirable characteristics, no approach satisfies all of the efficiency, size, weight, cost and safety requirements for transportation or utility use. Gas-on-solid adsorption is an inherently safe and potentially high energy density hydrogen storage method that should be more energy efficient than either chemical or metal hydrides, or compressed gas storage. Consequently, the hydrogen storage properties of high surface area "activated" carbons have been extensively studied. However, activated carbons are ineffective in hydrogen storage systems because only a small fraction of the pores in the typically wide pore-size distribution are small enough to interact strongly with gas phase hydrogen molecules.

The gas adsorption performance of a porous solid is maximized when all pores are not larger than a few molecular diameters. Under these conditions the potential fields from the walls of the so called micropores overlap to produce a stronger interaction than would be possible for adsorption on a semi-infinite plane. At sufficiently low temperatures, where the escaping tendency of the gas is much less than the adsorption potential, the entire micropore may be filled with a condensed adsorbate phase. For the case of hydrogen with a van der Waals diameter of 2.89 Å

pores would be required to be smaller than ~40 Å, to access this nanocapillary filling regime. Sufficiently small pores would exhibit an adsorption potential strong enough to localize H_2 at relatively high temperatures. Ideally, the entire porous volume of an adsorbent would be of the microporous variety. In addition the volume and mass of the adsorbent skeleton would be the minimum necessary to develop the adsorption potential and provide sufficient thermal conductivity for management of heat fluxes associated with adsorption and desorption. We have been working on the idea that aligned and self-assembled single wall carbon nanotubes could serve as ideal hydrogen adsorbents since 1993. The concept was motivated by theoretical calculations which suggested that adsorption forces for polarizable molecules within SWNTs would be stronger than for adsorption on ordinary graphite. Thus, high H_2 storage capacities could be achieved at relatively high temperatures and low pressures as compared to adsorption on activated carbons.

Hydrogen atom is a kind of ideal energy source because of its clean end products and its abundancy in nature from which can be obtained in great quantity. However, the storage and safety problems are the main disadvantages because of its flammable nature. Four main types of techniques to store hydrogen are in use as well as under investigation. These are, compressed gas, liquefaction, metal hydrides and physorption. Particularly, metal hydrides, nanofibers, nanotubes and activated carbon materials have been in progressive development. Compressed gas storage requires the container to be very strong and bulky, whereas liquid storage of hydrogen requires very low but constant temperature. Storage in solid matrix offers the advantage of safer and easier handling of hydrogen due to some obvious reasons.

Due to their peculiar hallow texture in nanometer size and large specific surface area, carbon nano tubes should have higher hydrogen adsorption capacity than the ordinary adsorbent activated carbon. Many researchers have tried to investigate hydrogen storage capacity of carbon nanotubes and carbon nanofibers.

Methods and Experiment

The method named as current heating of charcoal rod is very simple and the relevant costs of the raw materials are fairly low. Based on using an arc-discharge apparatus, which is induced with palladium metal. Common stationary charcoal rod used as the source material were heated by moderate current to produce masses of fiber. All in all used are an arc-discharge apparatus whose major parts are only two thick copper-bar electrodes, a DC power supply and a rod of common charcoal. The charcoal rods, bought from local stationery shops (SIGMA-ALDRICH, USA), mainly containing carbon, were used as the source material. Each charcoal rod used in the experiment was 6 mm in diameter and 150 mm in length, and its two ends were polished for good electrical contacts with the copper electrodes. The prepared charcoal rod was clipped between the two moveable copper electrodes that were connected to the DC power supply with an appropriately slight force, which would result in longitudinal cracks on the rod after the processing (Fig. 1). The charcoal rod with the electrodes could be either housed in a small chamber equipped with gas inlet and outlet for atmosphere and pressure control, or simply opened to the air. In the experiment, the charcoal rod was preheated with a power supply for a few minutes, followed by main heating with the power of about 30 V, 120 A for only 1–2 min in the atmosphere of argon gas. During the main heating, the temperature of the charcoal rod was estimated to be about 1000 ^{0}C or higher from its white-bright red color. The products, formed on the charcoal rod surface as well as at the processing-induced cracks, were observed under an optical microscope and selected for further characterizations using scanning electron microscopy (SEM), X-ray diffraction (XRD). For comparison, nanofibers were also produced using a conventional arc-discharge technique. In the processing, two charcoal rods were attached to the anode and cathode of the arc-discharge apparatus, respectively,and the gap distance between the charcoal rods was adjusted to about a few millimeters for appropriate arc discharging in the air when a DC power of 30 V 120 A was supplied. The products were observed and characterized in the same ways as those for current heating of charcoal rod products.

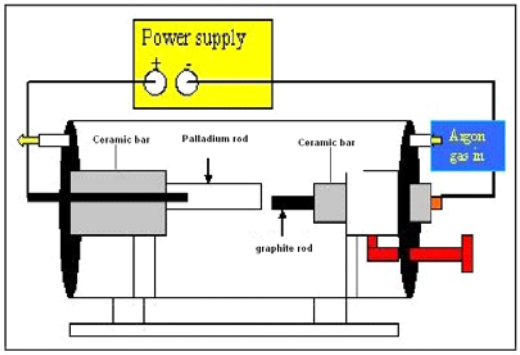

Figure 1. Eletronic system and schematic diagram of Arc-discharge apparatus

From the dryice-acetone physisorption data, obtained with a Micromeritics ASAP 2400 apparatus at 195 K, the BET surface area, total pore volume and micropore volume were derived. Prior to the physisorption measurements, the non-intercalated carbon fibers was evacuated at 300 °C. When intercalated samples were studied with dryice-acetone physisorption, they were evacuated at room temperature. Hydrogen adsorption experiments were performed in a conventional static volumetric adsorption apparatus, made of Pyrex glass, which could be operated at hydrogen pressures of up to 1.5 bar. The apparatus is displayed in figure 2.

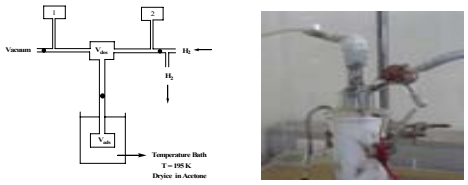

Figure 2. Hydrogen storage apparatus

Results and Discussion

Generally, mass of the current heating method produced allotrope nano carbon as formed black powder. The particular structures of the allotrope nano carbon observed by SEM, TEM and XRD are shown in figure 3, 4 and 5 respectively. It is seen that allotrope. Using this method we have made significant advances in the synthesis, allotrope nano carbon materials resulting in increased hydrogen adsorption on a sample wt% basis. We now can produce 1.5 g / day of material containing ~20–30 wt% allotrope nano carbon using the method of current heating of charcoal rod. Finally we have pioneered a gentle cutting process which enables 3.5 – 4.5 wt% hydrogen adsorption on our allotrope nano carbon materials. The adsorption occurs in two separate sites and conveniently, all of the adsorbed hydrogen is effectively capped by CO_2 resulting in the hydrogen's stability under atmospheric conditions for several weeks. The temperature at which hydrogen desorption occurs appears to vary with material and specific cutting conditions. In the future we will explore the hydrogen adsorption properties on materials with allotrope nano carbon of highly specific diameters, and we will also vary the parameters of our cutting scheme in order to further optimize Hydrogen adsorption properties.

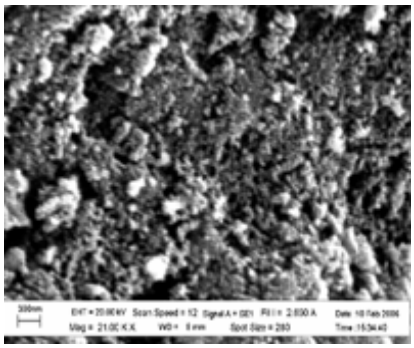

Figure 3. SEM image of allotrope nano carbon

The results of the TEM study show no systematic enlargement of the d-spacing. The XRD results show that a significant part of the fibers has not been intercalated and therefore does not show any enlargement of the d-spacing. Because with Electron Microscopy only a small part of the sample is studied it is possible that only non-intercalated parts were brought onto the grid and studied. On these parts it is still possible that K is present, between the fibers. It may also be possible that from the glovebox to the microscope the material had reacted slowly with air, de-intercalating the nikel metal. An explanation for the partial intercalation may be that fishbone fibers contain lots of defects inside the fibers and the graphite domains are usually quite small and angled upon each other. Lifting of the graphite planes in a system with a lot of those effects is more difficult.

When Hyperion carbon nanofibers are contacted with Nikel, they do show adsorption behavior, which is similar to fishbone fibers. After intercalation, when the material is contacted with air, they react in the same way as the fishbone fibers. This is surprising, because it would be expected that these parallel fibers cannot be intercalated in the same way as the fishbone fibers. Because these parallel fibers are shaped as rigid hollow tubes, surrounding each other, intercalation between these graphite planes would have to cause destruction of the fibers, because the tubes cannot enlarge easily and accommodate Paladium metal in between without destruction.

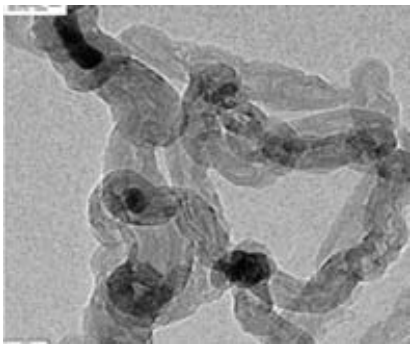

Figure 4. TEM image of allotrope nano carbon

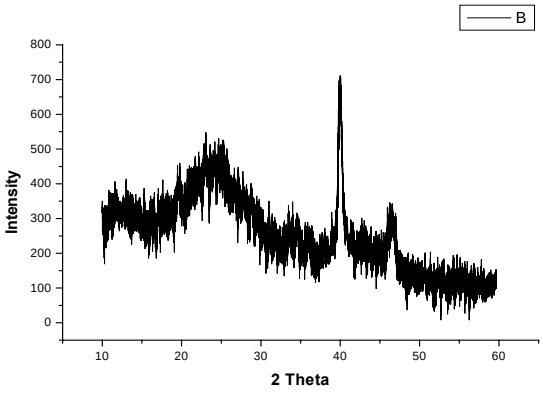

Figure 5. XRD of allotrope nano carbon with palladium metal

The hydrogen storage capacity of fishbone carbon nano fibers has been determined for several stages of intercalated compounds. In table 1 the materials and their adsorption capacities are summarized.

Table 1: Hydrogen storage capacities of several nikel-intercalated fishbone carbon nano fibers at 195 K and 1.5 bar.

Hydrogen Storage Capacity				
Sample	ml STP / $g_{adsorbent}$	ml STP / g_{carbon}	wt%	% adsorption
A50-Ni	10.2	9.4	0.1	1.64
A30-Ni	12.6	9.4	0.2	2.47
A15-Ni	16.1	8.6	0.3	2.91
A10-Ni	14.2	14.2	0.4	3.12
A05-Ni	10.7	7.1	0.5	2.62

The hydrogen uptake capacity of all these intercalated samples was tested repeatedly, each after 30 minutes of evacuation at 195 K. All samples were tested in at least 3 cycles, some in 6 cycles and still showed the same uptake capacity. The samples did not show any uptake at 273 and 298 K.

Tentatively, from the results can be concluded that most materials show hydrogen uptake related to the amount of K present, namely H/Ni ~1.6. This differs from the reported amount of H/Ni ~3.1. This can be explained because, firstly, we have not optimized this adsorption. Secondly, the structure and domain size of the CNF differs markedly from that of well-ordered graphite. Therefore, the structure of the intercalated compounds is also expected to be quite different. The XRD results showed that part of the fibers was not intercalated, and therefore, did not show an enlarged d-spacing. It is hard to determine how large this part is. It may be that the intercalated parts do adsorp H_2 with a H/Pd ratio of ~4. The samples for A15Ni and A05Ni show a different uptake, which cannot be explained. We did not find chemisorption of the hydrogen, as was reported for Ni-GICs, because from the results it is clear that the adsorbed hydrogen is physisorbed. Therefore, it is thought that enlargement of the d-spacing and an increased micropore volume can be assumed significant to the hydrogen storage capacity enlargement of the Ni intercalated CNFs.

Conclusions

In this study, we intended to examine with XRD we have shown that intercalation of nikel in as synthesized fishbone nano fibers does increase the d-spacing of the fibers. It was also shown that part of the fibers is not intercalated and remains graphitic, with a d-spacing of 0.32 nm. Results of SEM and TEM experiments did not show an enlarged d-spacing. This may be the result of only non intercalated parts being studied, or because of slow reaction with air and de-intercalation of Pd during insertion of the samples into the microscope. Many of small carbon nano fiber parts are observed in the microscope, so the intercalation procedure seems to negatively affect the strength of the fibers.

Intercalation of nikel in carbon nano fibers does significantly increase the hydrogen storage capacity of these materials. The observed adsorption is physisorption and the intercalated fibers do not show any hydrogen storage capacity at 273 and 298 K. The H_2 adsorption has not been optimized. The amount of H_2 stored is different (H/Ni ~1.6) than the amount mentioned for Ni intercalated graphite (H/Ni ~3.1). This may turn out different when the intercalation is optimised. XRD results show that only part of the fibers is intercalated, so it may be that the H_2 adsorption capacity of the intercalated fibers is closer to H/Pd ~3.1.

Acknowledgments

We wish to acknowledge Prof. Dr. Vichai Reutrakul from Department of Chemistry, Faculty of Science, Mahidol University and membered of Science Faculty and Technology Rajabhat Uttaradit University, delft for performing the electron microscopy investigations.. We thank MTEC for performing the XRD investigations. All helper are gratefully acknowledged. Work was funded by the Ministry of Energy Organization. Collaboration for this work was through the National Science and Technilogy Development Agency.

References

[1] S. Iijima, Nature (London) 354 (1991) 56.
[2] T.W. Ebbesen, P.M. Ajayan, Nature (London)358(1992) 220.
[3] J.W. Liu,D.Y. Zhong, F.Q. Xie, M. Sun, E.G.Wang, W.X. Liu, Chem. Phys. Lett. 348 (2001)357.
[3] Dillon, A.C., Bekkedahl, T.A., Cahill, A.F., Jones, K.M. & Heben, M.J. Carbon Nanotube Materials for Hydrogen Storage in 521-542 (1995).
[4] Noh JS, Agarwal RK, Schwarz JA. Hydrogen storage Systems using activated carbon. Int. J. of Hydrogen Energy 1987; 12 : 693-700.
[5] Amankwah KAG, Noh JS, Schwarz JA. Hydrogen storage on superactivated carbon at refrigeration temperatures. Int. J. Hydrogen Energy 1989; 14 : 437- 447.
[6] Chambers A, Park C, Baker RTK, Rodrigez N. Hydrogen storage in graphite nanofibers. J. Phys. Chem. B 1998 ; 102 : 4253-4256.
[7] Park C, Anderson PE, Chambers A, Tan CD, Hidalgo R, Rodrigez NM. Further studies of the interaction of hydrogen with graphite nanofibers. J. Phys. Chem. B 1999; 103 : 10572-10581.
[9] Fan YY, Liao B, Liu M, Wei YL, Lu MQ, Cheng H.M. Hydrogen uptake in vapor grown carbon nanofibers Carbon 1999; 37 : 1649-1652.
[10] Dillon AC. Jones KM, Bekkedahl TA, KiangCH, Bethune DS, Heben MJ. Storage of hydrogen in single-walled carbon nanotubes. Nature 1997;386 : 377- 379.
[11] Ye Y, Ahn CC, Witham C, Fultz B, Rinzler AG, Colbert D, Smith KA, Smalley RE. Hydrogen and cohesive energy of single-walled carbon nanotubes. Appl.Phys. Lett. 1999 ; 74(16) : 2307-2309.
[12] Chen P, Wu X, Lin J, Tan KL. High H2 uptake by alkali doped carbon nanotubes under ambidient pressure and moderate temperature. Science 1999 ; 285 : 91- 93.
[13] Chahine R, Bose TK. Low pressure Adsorption storage of hydrogen. Int. of Hydrogen Energy 1994;19 : 161- 164.
[14] Hynek S, Fuller W, Bentley J, Hydrogen storage by carbon adsorption Int J of Hydrogen Energy 1997;22: 601.

Preparation of Al-C composites film by magnetron sputtering technique

K. Boonchom[1] and A. Vorasignha[2*]

[1]Faculty of Science and Technology, Chiangmai Rajabhat University, Chiangmaix, Thailand 65000
[2]Faculty of science, Naresuan university, Phitsanulok, Thailand 65000

[*] E-mail: anusornv@nu.ac.th

Abstract: The composites film of aluminium and carbon were designed for coated on absorbing surface in solar thermal system. It was prepared by magnetron sputtering technique. The target of sputtering process was designed as carbon dish embed on aluminium dish. The surface area ratio of Al:C was 80:20. The condition of sputtering was setting the current at 800mA and argon flow rate at 29.2 sccm. The time was varying at 1, 2 and 3 hours. The characteristic of films were analyzed by X-ray diffractometer, Scanning probe microscope, UV-VIS spectrophotometer (wavelength 300-900 nm) and FT-IR spectrometer (2500-25000 nm). The results were found that the composites films as Aluminium Oxide Carbide (Al_2OC). The films have particle size between 0-50 nm. The average thickness was 295.40, 802.08 and 1164.33 nm. It related with time (1hr, 2hr and 3 hr). The solar absorptance of films was 0.5 at 1 hr but at 2hr and 3 hr cannot measure caused by film scattering. The thermal emittance of films was 0.20, 0.40 and 0.47, respectively.

Introduction

Solar collectors are special kind of heat exchangers that transform solar radiation energy to internal energy of the transport medium. The internal energy is converted into heat and transfers to a fluid flowing through the collector. Most of solar collectors need absorbing surface which has high absorptance at solar spectrum range and low emittance at infrared spectrum range to minimize heat radiation losses. It is called a spectrally selective surface. An ideal selective surface would be a material that would absorb all the solar radiation without emitting. There are several design options and physical mechanisms creating a solar selective by various compositions in the thin film of materials such as CuO, CrO_3, W-AlN, SS-Al_2O_3 etc. and different developing methods such as chemical vapor deposition, sol-gel, electroplating method, physical vapor deposition etc. [2,3,4,5] Composite media was interesting such as silica-carbon nanocomposites film prepared by Dahn Katzen et al [1]. It has excellent optical parameters, absorbance as 0.94 and IR emissivity of 0.15 at thickness 1000 nm.

The composites media of aluminum and carbon were interesting. Because of the materials were prepared from local material. Aluminum is prepared by recycle method and Carbon is prepared from graphite rod in old baterry. Magnetron sputtering technology was used to prepare the composites film. The characteristics of film were analyzed by these instruments: XRD, SPM, UV-VIS and FT-IR spectrophotometer.

Materials and Methods

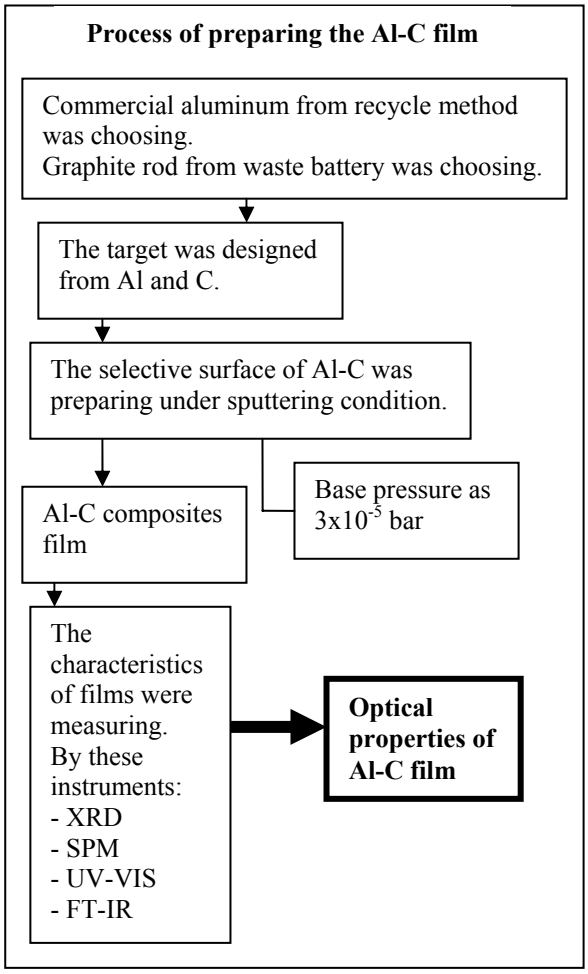

Figure 1. Diagram of process

The target of sputtering process was designed as dish. It is shown in figure 2.

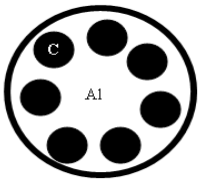

Figure 2. Schematic diagram of target

The target made from commercial aluminum dish has diameter 2 inch and thickness 3 mm. Graphite was embed in aluminum dish. It has diameter 8 mm. The

surface area ratio of Al and C is 80:20.The slide glass was substrate. It was setup in perpendicular direction of target. Two pieces of silicon was set on the slide glass for analyze properties of film. Size of glass substrate was 7.5 x 2.5 cm. and silicon 1x1 cm. The target and substrate were setting as shown in figure 3.

Figure 3. Substrate and target in the chamber

The sputtering condition was time of coating. The time was varying as 60, 120 and 180 minute. Current and argon flow rate are 800mA and 29.2 sccm (Standard Cubic Centimeters per Minute). The voltage was varying at 264 – 364 V. The film was coated on glass substrate and two pieces of silicon substrate. Size of glass substrate was 7.5 x 2.5 cm. and silicon 1x1 cm.

The basic principle of sputtering

The basic principle of sputtering is to knock out atoms from a source (target) and deposit them on a substrate. A vacuum chamber is containing a low pressure inert gas such as argon can set-up a glow discharge by applying a sufficiently large voltage between the target (raw material for coating) and the substrate inside the chamber. Energetic ions can bombard the surface of the target and knock out atoms or particles which are then transported and deposited on the substrate. The figure 4 showed sputtering technique [6].

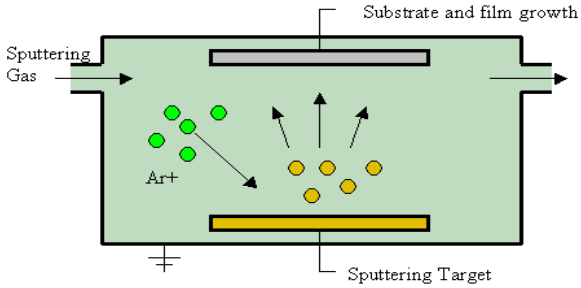

Figure 4. Schematic diagrams of Sputter depositions

Results and Discussion

The film was coated on glass substrate and silicon substrate. The sample of Al-C film on glass substrate and silicon substrate was shown in figure 5.

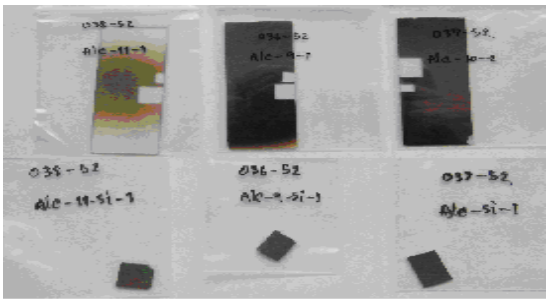

Figure 5. Film coated on glass and silicon substrate at 60,120 and 180 minute.

The silicon substrate was analyzing the structure of film by XRD. The thickness of film was analyzing SPM (Scanning Probe Microscope). The SPM can be observing the particle size and surface of film. The thickness of film was shown in table 1.

Table 1: Particle size and thickness of films at 60,120 and 180 minute

Time(min.)	Particle size (nm)	Average thickness(nm)
60	0-20	295.40
120	0-50	802.08
180	0-50	1164.33

The thickness of film related with time (60, 120 and 180 min.). Increasing of time was cause of collected particle. Then, particle size of film was increasing and the thickness of film was increasing. The surface of film was shown in figure 6.

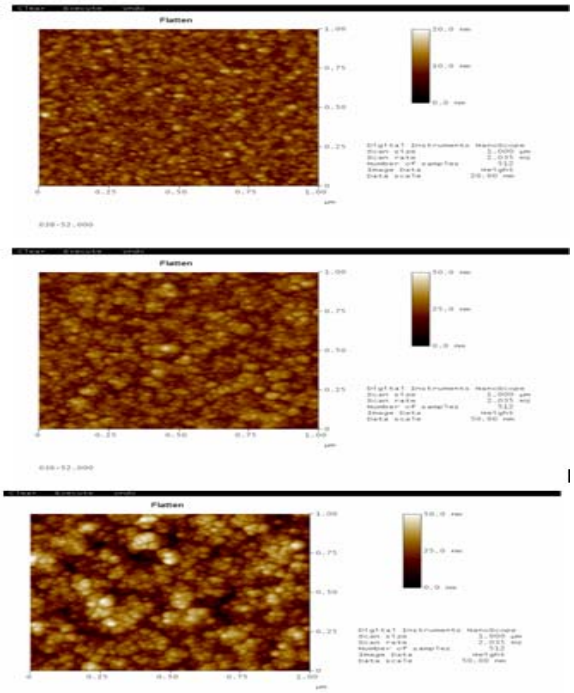

Figure 6. Surface of Al-C film at 60,120 and 180 min. from SPM

The film was analyzed the structure by X-ray diffractometer. The X-ray pattern of silicon substrate and X-ray pattern of Al-C film was shown in figure 7. The patterns were comparing with JCPDF file of Al-C compound.

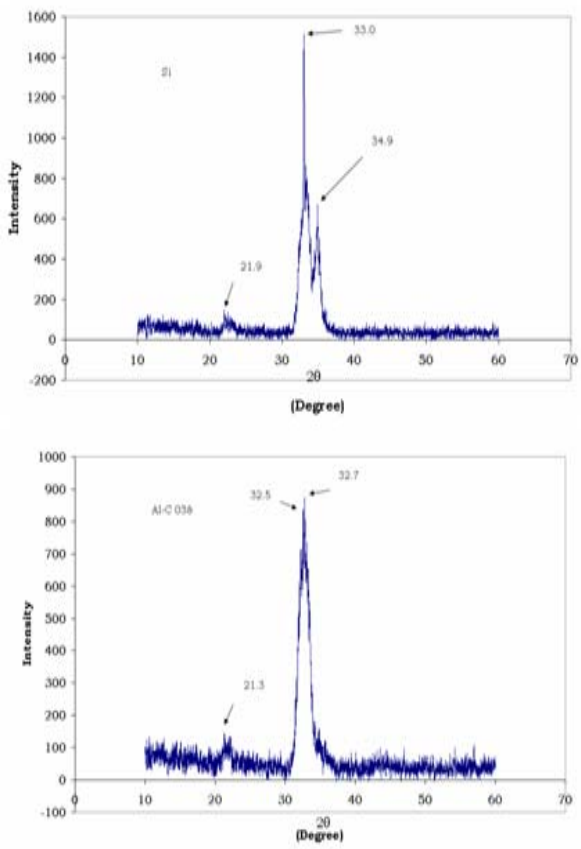

Figure 7. X-ray pattern of silicon and Al-C film

The main peak of silicon was 33 degree. The main peak of Al-C film was 32.7 degree. The peak of silicon at 21 degree corresponded with the peak of Al-C film. The x-ray pattern of Al-C was compared with JCPDF file. The main peak of Al-C film corresponded with the main peak of aluminium oxide carbide (Al_2OC) (09-0269).

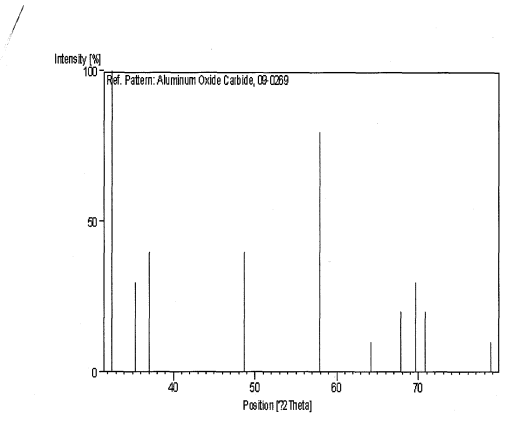

Figure 8: X-ray pattern of Al_2OC (09-0269)

From the X-ray pattern, the composites film was Al_2OC. Because of the materials were used to prepare the film not pure. Aluminum from recycle method or graphite rod may be compound with oxide. If the materials are pure, the film should be Al_4C_3.

The UV-VIS spectrophotometer was analyzed the solar absorptance of film. The film was evaluated the solar absorptance in wavelength 300-900 nm. Transmittance of film at 60,120 and 180 minute were shown in figure 9.

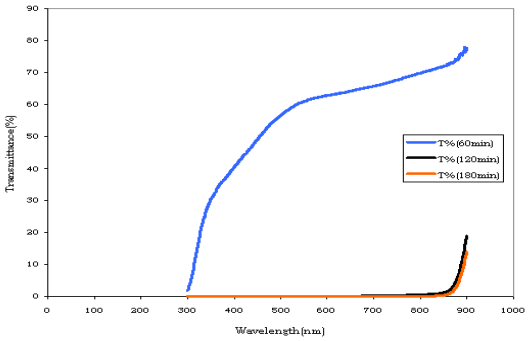

Figure 9. Transmittance of Al_2OC film

From transmittance of film in figure 9, the transmittance in solar spectrum 300-700 nm of Al-C film at 120 and 180 min. was flat. Because of the film was prepared by Al-C target. It has surface ratio as 80:20. Thus, probability of aluminum was embedding at the film more than carbon. As, the time is increasing, aluminum was increase embedding in film. Aluminum has high reflectance. Thus, the film was scattering caused by the film has high reflectance. The UV-VIS spectrophotometer can't measure the reflectance. Then, the value of solar absorptance at 120 and 180 minute can't accept. Because of increasing time, aluminum was embedding in film much more caused by film scattering. The film has high reflectance. The transmittance of solar spectrum at 300-700 nm was flat. The thermal emitance was analyzed by FT-IR spectrometer. The wavelength of thermal emittance was studied at 2500-25000 nm. The results of optical properties were shown in table 2.

Table 2: The characteristics of Al-C film

Time (min.)	Thickness (nm)	Solar absorbance	Thermal emittance
60	295.40	0.50	0.20
120	802.08	-	0.40
180	1164.33	-	0.47

For thermal emittance, the film at 60 min. has the value of thermal emittance lower than the film at 120 and 180 min. When, the time is increasing. The film will compose aluminum more than carbon. Thus, the film will transfer heat more than the film has low aluminum component. Because of aluminum has thermal conductivity more than carbon.

Conclusions

The composites film of aluminum and carbon were prepared by magnetron sputtering technique. The target of sputtering process was carbon dish embed on aluminum dish. The surface area ratio of Al:C was 80:20. The aluminum dish made from commercial aluminum from recycle method and graphite embeds on aluminum dish come from graphite rod from waste battery. The condition of sputtering was current at 800mA and argon flow rate at 29.2 sccm. The time was varying at 60, 120 and 180 minute. The characteristic of films were analyzed by XRD, SPM, UV-VIS spectrophotometer (wavelength 300-900 nm) and FT-IR spectrometer (2500-25000 nm). The X-ray pattern was shown the composites films from preparing as Aluminium Oxide Carbide (Al_2OC). The thickness of film relate with time in sputtering. The film has particle size between 0-50 nm. The average thickness was 295.40, 802.08 and 1164.33 nm. The solar absorptance of films was 0.5 at 60 minute. The value of solar absorptance cannot accept. Because of the film was high scattering. The film has thermal emittance of films was 0.20, 0.40 and 0.47, respectively.

References

[1] Dahn Katzen , Esthy Levy , Yitzhak Mastai , Applied Surface Science 248 (2005) pp. 514–517.
[2] P. Konttinena, P.D. Lunda, R.J. Kilpib, Solar Energy Materials & Solar Cells 79 (2003) pp.273–283.
[3] Andreas SchuK ler, Ivan R. Videnovic, Peter Oelhafen, Stefan Brunold, Solar Energy Materials & Solar Cells 69 (2001) pp. 271-284.
[4] Qi-Chu Zhang, Y.G. Shen, Solar Energy Materials & Solar Cells 81 (2004) pp.25–37.
[5] Kristina Gelin " Preparation and Characterization of Sputter deposited Spectally Selective Solar Absorber" Comprehensive Summaries of Uppsala Dessertations.
[6] www.kolzer.com "Applications of Vacuum Coating"

Synthesis and characterization of D-D-π-A type organic dyes for dye solar cells (DSCs)

S. Punsay[1]*, S. Numuangruk[2], R. Tarsang[1], T. Sudyoadsuk[1], T. Keawin[1], S. Jungsuttiwong[1], S. Saengsuwan[1] and V. Promarak[1]

[1]Center for Organic Electronics and Polymers, Department of Chemistry and Center of Excellence for Innovation in Chemistry, Faculty of Science, Ubon Ratchathani University, Warinchumrap, Ubon Ratchathani, Thailand
[2]National Nanotechnology Center, National science and Technology Development Agency, Pathumthani, Thailand

*E-mail: sakravee_noom@hotmail.com

Abstract: In this work, we investigated a series of new cabarzole-based D-D-π-A type organic dyes for DSCs. The designed dye compounds CCTnA (n = 1-3) compose of three parts: (1) carbazole donating group (D); (2) oligothiophene bridge (π); and (3) cyanoacrylic acid anchoring group (A). These organic dyes were synthesized using a combination of alkylation, bromination, Ullmann coupling, Suzuki cross-coupling and Knoevenagel condensation reactions. The electronic, electrochemical and thermal properties of these compounds can be tuned by varying the number of thiophene rings. These compounds exhibited a high molar absorptivity in the blue/green region of the solar light. Increasing number of thiophene ring in the molecules consequences in an increase of the π-electron conjugation length resulting red-shifted and broadened absorption spectra. These dyes can absorb very well on the TiO_2.

Introduction

Dye solar cells (DSCs) based on nanocrystalline TiO_2 photoelectrode have been actively studied since Grätzel and co-workers reported high solar energy to-electricity conversion efficiencies of up to 12% with a DSSC based on a Ru-complex photosensitizer. However, metal free organic dyes exhibit not only higher extinction coefficients, but simple preparation and low cost. The most efficient organic dyes give solar energy to-electricity conversion efficiencies of up to 9.5%. Most of the organic sensitizers applied in DSCs show the character with both the electron donor (D) and the electron acceptor (A) linked by a π-conjugation bridge, which is called the D-π-A structure. Generally, organic dyes for excellent DSCs are required to possess broad and intense spectral absorption in the visible light region, and have suited excited-state redox potential with the energy of the conduction band edge and have suited ground state redox potential with the redox potential of the electrolyte. The major factors for low conversion efficiency of DSCs based on organic dyes are the formation of dye aggregation on the semiconductor surface and the recombination of conduction band electrons with triiodide in the electrolyte.

In this work, we investigated on the design, synthesis and characterization of D-D-π-A type organic dyes that carbazole as donor and cyanoacrylic acid as acceptor is bridged by oligothiophene.

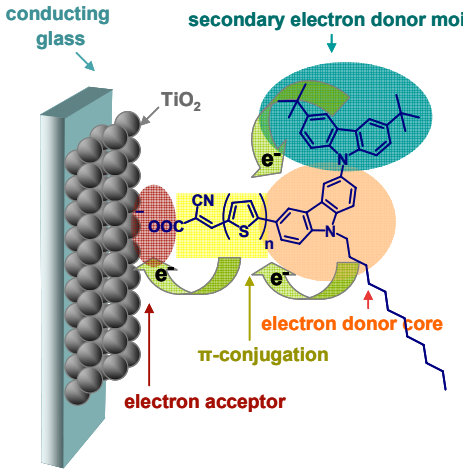

Figure 1. Organic dye structure of **D-D-π-A** type organic dyes.

Methodology

1. General methods

^{1}H-NMR spectra were recorded on Brüker AVANCE (300 MHz) spectrometer. ^{13}C NMR spectra were recorded on Brüker AVANCE (75 MHz) spectrometer and were fully decoupled. Chemical shifts (δ) are reported relative to the residual solvent peak in part per million (ppm). Coupling constants (*J*) are given in Hertz (Hz). UV-Visible spectra were measured in CH_2Cl_2 on a Perkin-Elmer UV Lambda 25 spectrometer. Analytical thin-layer chromatography (TLC) was performed with Merck aluminium plates coated with silica gel 60 F_{254}. Column chromatography was carried out using gravity feed chromatography with Merck silica gel mesh, 60 Å. Where solvent mixtures are used, the portions are given by volume. All calculated using density functional theory (DFT) at the B3LYP/6-31G(d,p) level, as implement in Gaussian 03 program. The excitation energies of the low lying states have been calculated using the time-dependent density functional theory (TD-DFT/B3LYP) at the same level.

2. Synthetic procedures

2.1 Synthesis of **CCT1A**

To a mixture of 1 (0.47 g, 0.55 mmol) and 2-cyanoacetic acid (0.09 g, 1.10 mmol) in $CHCl_3$ (25 ml) was added piperidine (0.05 ml, 0.55 mmol). The reaction mixture was heated at reflux under N_2 atmosphere for 6 h. After being cool to room temperature, the mixture was extracted with CH_2Cl_2 (50 ml x 2). The combined organic layer was washed successively with water (20 ml x 3), brine solution (20 ml x 2), dried over anhydrous Na_2SO_4 and evaporated to dryness. The residue was purified by column chromatography on silica gel eluting with CH_2Cl_2 increasing gradually to CH_2Cl_2:CH_3OH (3:1) to afford a yellow solid (0.25 g 57%).

2.2 Synthesis of **CCT2A**

To mixture **4** (0.46 g, 0.74 mmol) and 2-cyanoacetic acid (0.07 g, 0.86 mmol) in $CHCl_3$ (25 ml) was added piperidine (0.17 ml, 1.7 mmol). The reaction mixture was heated at reflux under N_2 atmosphere for 6 h. After being cool to room temperature, the mixture was extracted with CH_2Cl_2 (50 ml x 2). The combined organic layer was washed successively with water (20 ml x 3), brine solution (20 ml x 2), dried over anhydrous Na_2SO_4 and evaporated to dryness. The residue was purified by column chromatography on silica gel eluting with CH_2Cl_2 increasing gradually to CH_2Cl_2:CH_3OH (2:1) to afford a red solid (0.30 g 60%).

2.3 Synthesis of **CCT3A**

To a mixture of **5** (0.20 g, 0.23 mmol) and 2-cyanoacetic acid (0.04 g, 0.45 mmol) in $CHCl_3$ (30 ml) was added piperidine (0.08 ml, 1.7 mmol). The reaction mixture was heated at reflux under N_2 atmosphere for 6 h. After being cool to room temperature, the mixture was extracted with CH_2Cl_2 (50 ml x 2). The combined organic layer was washed successively with water (20 ml x 3), brine solution (20 ml x 2), dried over anhydrous Na_2SO_4 and evaporated to dryness. The residue was purified by column chromatography on silica gel eluting with CH_2Cl_2 increasing gradually to CH_2Cl_2:CH_3OH (1:1) to afford a dark red solid (0.14 g 67%).

Results and Discussion

The target **D-D-π-A** type organic dyes **CCTnA n = 1-3** were successfully formed as outlined in Scheme 1. Intermediate **1** was first synthesized by nucleophilic substitution reaction at 9-position of carbazole with $C_{12}H_{25}$ alkyl, selective bromination of the resultant at 3 and 6-positions with NBS in THF followed by mono-coupling of the resultant with 3,6-di-tert-butylcarbazole under Ullmann coupling conditions using CuI as a catalyst, (±)-*trans*-1,2-diaminocyclohexane as co-catalyst and K_3PO_4 as base. Intermediates **4** and **5** synthesized by using a combination of Suzuki cross-coupling and bromination reactions. Suzuki cross-coupling of either **1** or **4** with 2-thiopheneboronic acid with $Pd(PPh_3)_4$ as catalyst and Na_2CO_3 as base in THF/H_2O as solvent at reflux for 48 h to give **2** and **3** in good yields. NBS bromination of these resultants in THF afforded the intermediates **4** and **5** in excellent yields. The aldehyde intermediates **6**, **7** and **8** were then formed in reasonable yields by cross-coupling of he bromo **1**, **4** and **5** with formyl thiopheneboronic acid under the same Suzuki coupling conditions. Knoevenagel condensation of the resultant aldehydes **6**, **7** and **8** with 2-cyanoacetic acid in the presence of piperdine base in chloroform to give the desired organic dyes **CCTnA n = 1-3** as yellow, red and dark red solids, respectively in good yields. All compounds are well dissolved in most organic solvents. This is due to the use of long alkyl substitutent at the N-atom of the carbazole. This long alkyl chain may also play important role as hydrophobic shield to prevent the TiO_2 having a direct contact with the electrolyte which causes the dark reaction. This would give rise to more efficient dyes.

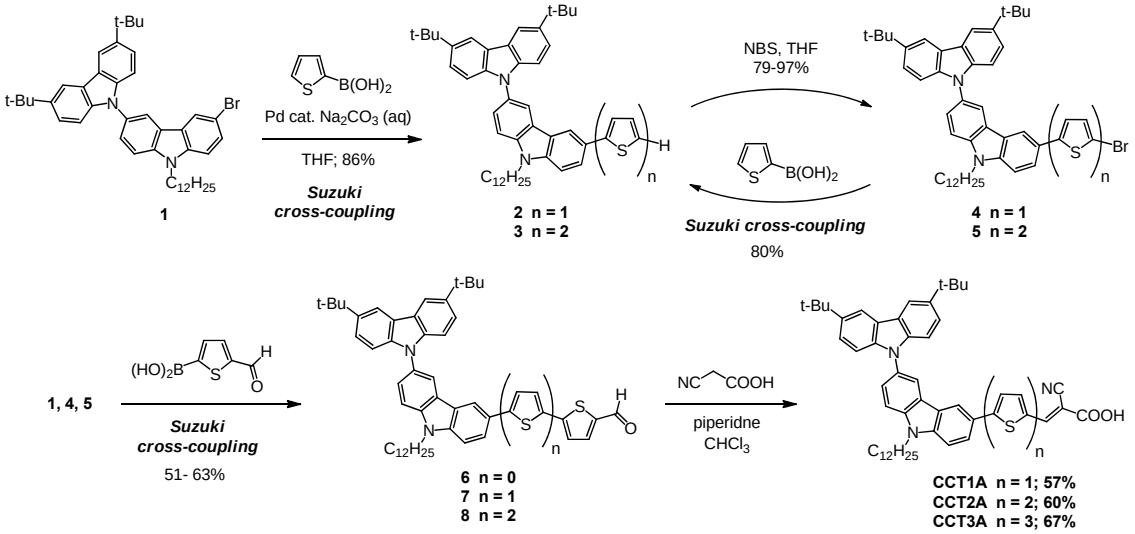

Scheme 1. The structures and preparation of **D-D-π-A** type organic dyes.

The absorption spectra of all of the **D-D-π-A** type organic dyes in dilute CH_2Cl_2 solution are shown in Figure 2. Dyes **CCTnA n = 1-3** exhibited broad absorption spectra ranging from 250 to 600 nm. The spectra exhibit two major absorption bands. The absorption bands at around 294 nm can be attributed to the π-π^* transition of the carbazole moieties and the absorption bands at longer wavelength around 450 nm corresponding to the intramolecular charge transfer (ICT) transition between the donor and the acceptor. This indicates that the molecules have a **D-D-π-A** character. As the number of thiophene units in the molecules increase, the spetra are red shifted and the molar extinction coefficients (ε) increase. Thier ε values range from 17,400 to 27,800 $M^{-1}cm^{-1}$. The broad absorption spectra and high ε value are the key requirments for best sentisizer for efficient DSC. Their energy gaps (E_g) calculated from the absorption edge range from 2.33 to 2.65 eV (Table 1).

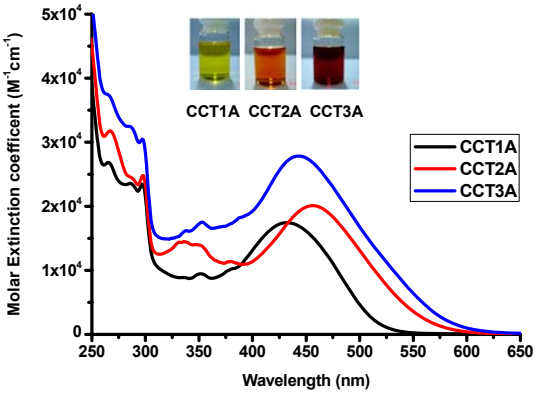

Figure 2**.** The absorption spectra of **CCTnA n = 1-3** in CH_2Cl_2 solution

The UV-vis absorption spectra of the **CCTnA n = 1-3** adsorped in TiO_2 film show a red shift and broader spectra when compare to their corresponding absorption spectra in solution (Figure 3). This is due to the dye aggregation and the formation of chemical bonding between dye molecule and TiO_2. The films have a very intense color.

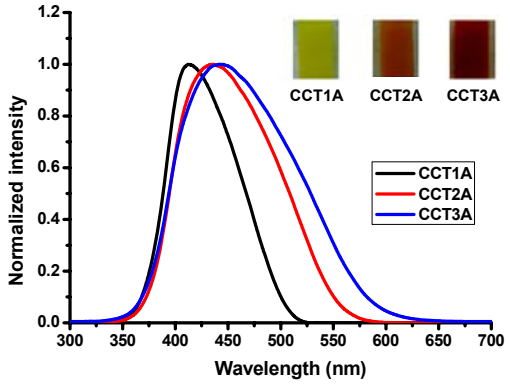

Figure 3. The normalized absorption spectra of **CCTnA n = 1-3** adsorped in TiO_2 film

The molecular geometries and electron distributions of **D-D-π-A** type organic dyes were obtained by using density function theory (DFT) calculations with Gaussian 03 program. The calculations were performed with the B3LYP exchange correlation functional under 3-21G(d) basis and the results are displayed in Figure 4. The electron distribution before the light irradiation (HOMO) is delocalized mainly over carbazole-carbazole donor and oligothiophene; whereas after light irradiation (LUMO) it moves to the acceptor units close to the anchoring groups, which favors the electron injection from the dye molecules to the conduction band edge of TiO_2.

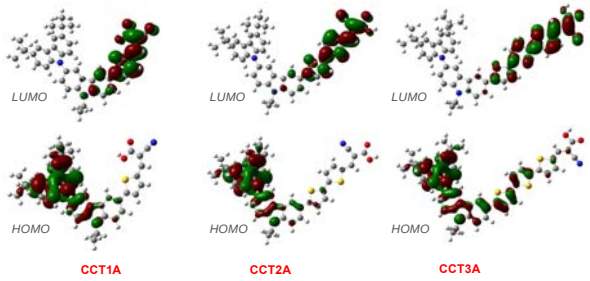

Figure 4. The frontier molecular orbitals of HOMO and LUMO calculated with TD-DFT on B3LYP/3-21G* of **CCTnA n = 1-3**

CV curves of all compunds showed one irreversible reduction of the cyanoacrylic acid acceptor and two oxidations. The reduction potentials increase when number thiophene units in the molecule increase (Figure 5). The first oxidation process can be attributed to the removal of electrons from the peripheral carbazole donors and the other corresponds to the removal of electrons from the interior thiophens backbone. The first oxidatio potential increase when number thiophene unit increase due to more delocalization of π-electron. The HOMO and LUMO energy levels of these dyes were determined using the onset positions of the oxidation and energy gap (E_g) and are summarized in Table 1.

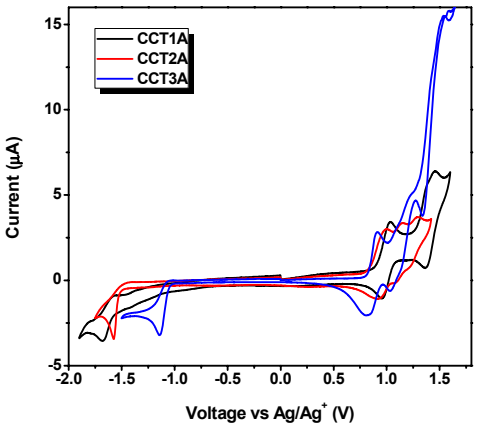

Figure 5. CV curves of **CCTnA n = 1-3** measured in CH_2Cl_2 solution with n-Bu_4NPF_6 as supporting electrolytes, scan rate of 50 mV/s

Table 1: The HOMO and LUMO energy levels of CCT1A, CCT2A and CCT3A dye.

Dyes	λ_{max} (ε) nm ($M^{-1}cm^{-1}$)[a]	E_{ox}(V)[b]	E_{re}^{pa}(V)[b]	E_g(eV)[c]	HOMO (eV)[d]	LUMO (eV)[f]
CCT1A	432 (17,461)	1.00	-1.68	2.65	-5.29	-2.64
CCT2A	457 (20,104)	0.96	-1.57	2.47	-5.24	-2.77
CCT3A	443 (27,866)	0.86	-1.14	2.33	-5.22	-2.89

[a] Measured in dilute CH_2Cl_2 solution.
[b] Measured using a glassy carbon electrode as a working electrode, a platinum rod as a counter electrode, and SCE as a reference electrode in CH_2Cl_2 containing 0.1 M n-Bu_4NPF_6 as a supporting electrolyte.
[c] Estimated from the onset of absorption ($E_g = 1240/\lambda_{onset}$).
[d] Calculated using the empirical equation: HOMO = -4.44 + E^{ox}_{onset}.
[e] Calculated from LUMO = HOMO- E_g.

The determined LUMO levels are in the range of -2.64 to -2.89 eV, which match well with the work function of TiO_2 favoring electron jumping from dyes to TiO_2. The determined HOMO levels are in the range of -5.22 to -5.29 eV, which match well with the redox potential of theI^-/I_3^- redox electrolytes favoring electron jumping from electrolyte to dye as illustrate in Figure 6.

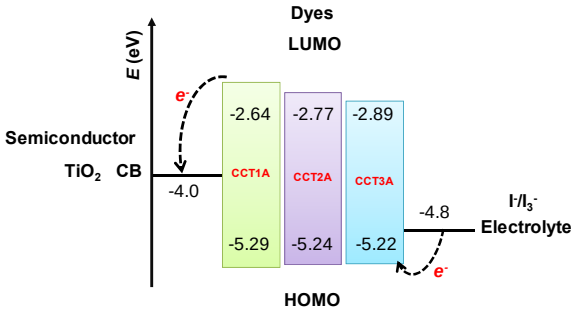

Figure 6. Schematic energy level diagram of the DSC based on **CCTnA n = 1-3** dyes

Conclusion

The designed dye compounds **CCTnA n = 1-3** composed of three parts: (1) cabarzole donating groups (D); (2) an oligothiophene (π); and (3) a cyanoacrylic acid anchoring group (A) were synthesized using a combination of alkylation, bromination, ullmann coupling, Suzuki cross-coupling and knoevenagel condensation reactions. The electronic, electrochemical, and thermal properties of these compounds can be tuned by varying the number of thiophene rings. These compounds exhibited a high molar absorptivity in the blue/green region of solar light. The number of thiophene increased the conjugation length of compounds resulting a red-shift and broad in absorption solution spectra. The DSCs cells using these dyes as sensitizers will be investigated.

References

[1] J. Pei, S. Peng, J. Shi, Y. Liang, Z. Tao, J. Liang and J. Chen, *Journal of Power Sources*, **248** (2004), pp.1363–1379
[2] F. Zhang, Y. Luo, J. Song, X.Guo, W.Liu, C. Y.Huang, M.Ge, Z. B and Q. Meng, *Dyes and Pigments* **81** (2009), pp. 224–230
[3] Y. J. Chang and T. J. Chow, *Tetrahedron* **65** (2009), pp. 4726–4734
[4] D. Kim, J. K. Lee, S. O.Kang and J. Ko, *Tetrahedron* **63** (2007), pp. 1913–1922
[5] S. Kim, H. Choi, D. Kim, K.Song, S. O. Kang and J.Ko, *Tetrahedron* **63** (2007), pp. 9206–9212
[6] D. Kim, M. S. Kang, K. Song, S. O. Kang and J.Ko, *Tetrahedron* **64** (2008), pp. 10417–10424
[7] H. Choi, J. K. Lee, K. Song, S. O. Kang and J. Ko, *Tetrahedron* **63** (2007), pp. 3115–3121
[8] S. Kim, H. Choi, C. Baik, K. Song, S. O. Kang and J. Ko, *Tetrahedron* **63** (2007), pp. 11436–11

Effects of hydroxyapatite and β-tricalcium phosphate on the physical properties of Thai silk fibroin/gelatin scaffolds

C. Dararutana[1], S. Honsawek[2] and S. Damrongsakkul[1]*

[1]Department of Chemical Engineering, Faculty of Engineering, Chulalongkorn University, Phaya Thai Road, Phatumwan, Bangkok, Thailand 10330
[2]Department of Biochemistry, Faculty of Medicine, Chulalongkorn University, Rama 4 Road, Phatumwan, Bangkok, Thailand 10330

*E-mail: siriporn.d@chula.ac.th

Abstract: Silk fibroin (SF), a major constituent of raw silk fiber, has been widely explored for many biomedical applications, due to its impressive biocompatibility, biodegradability, minimal inflammatory reactions and favourable mechanical properties. Gelatin (G), a denatured form of collagen, also shows interesting biological characteristics since it contains arginine-glycine-aspartic acid (RGD)-like sequence which promotes cell activities. In this study, silk fibroin from Thai yellow cocoon "Nangnoi-Srisaket1", and type A gelatin were used to prepare scaffold. In the application of bone tissue engineering, inorganic compound is another key consideration to modulate osteoconduction and improve mechanical properties of bone scaffold. The inorganic compound selected for this study included hydroxyapatite (HA) and β-tricalcium phosphate (β-TCP) were incorporated into SF/G scaffold.SF/G (50/50) scaffolds incorporated with various amount of inorganic HA or β-TCP were fabricated via freeze drying technique. The content of inorganic compound affecting on the properties of the composite scaffold was investigated. From the results, morphology of obtained scaffolds observed under scanning electron microscope (SEM) was porous and uniform. Pore size of all composite scaffolds was approximately 56–150 μm. Compressive modulus of the scaffolds was higher when increasing the amount of inorganic compound. It was also found that all scaffolds presented good swelling ability.

Introduction

Tissue Engineering is a multidisciplinary field which applies the principles of biology, materials, engineering, and medicine to develop tissue substitutes that can assist the regeneration and repair of damaged tissues[1]. Scaffolds play an important role in an accomplishment of tissue regeneration. Different tissues required biodegradable scaffolds with different physical and chemical characteristics. Gelatin and silk fibroin are examples of natural biodegradable materials that have been used as tissue engineered scaffolds due to their biocompatible and biodegradable characteristics.

Silk fibroin is from *Bombyx mori* silkworm has been used in many biomedical applications because of its impressive mechanical properties and biocompatibility [2,3].

Chamchongkaset et.al.[4] have introduced the concept of gelatin conjugation to Thai silk fibroin scaffold. Gelatin was shown to enhance the biological properties of Thai silk fibroin-based scaffolds. This was due to the fact that gelatin is a denatured form of collagen which contains RGD-like sequence that promotes cell adhesion and migration. Particularly, it does not exhibit antigenicity, and inherent biocompatibility and biodegradability.

Jetbumpenkul [5] has reported that the crosslinked Thai silk fibroin/gelatin scaffolds showed lower weight loss (%) and higher compressive modulus than those of non-crosslinked scaffolds. Interestingly, non-crosslinked Thai silk fibroin/gelatin scaffold at the weight blending ratio of 50/50 showed the lowest weight loss (%) with excellent mechanical strength as good as the crosslinked scaffold due to the suitable electrostatic interactions between silk fibroin and gelatin. The incorporation of hydroxyapatite into freeze dried Thai silk fibroin/gelatin scaffold was also preliminary reported to enhance the mechanical properties.

Recenly, the integration of two type of materials, inorganic compound and biodegradable materials such as hydroxyapatite/poly(L-lactic acid) [6], hydroxyapatite/poly-di-lactide [7], β-TCP/gelatin [8] and hydroxyapatite/silk were used to make a new material with desirable properties.[4] The result on the integration of biodegradable polymer or protein with inorganic compound showed the biocompatibility, biodegradability, ability to initiate osteogenesis and mechanical properties.[9] However, the effects of presented hydroxyapatite and β-TCP in Thai silk fibroin/gelatin system has not been investigated and compared yet.

It is the aim of this study to investigate the effects of inorganic compounds on the physical properties of Thai silk fibroin/gelatin scaffolds. Two types of inorganic compounds selected for this study are hydroxyapatite and β-TCP. Different ratios of inorganic compound were added in Thai silk fibroin/gelatin solution. The scaffolds will be fabricated via freeze drying technique and the mechanical properties, swelling property and pore size of obtained scaffolds were characterized and compared.

Materials and Methods

Cocoon of *Bombyx mori* Thai silk worm "Nangnoi-Srisaket 1" from Nakhonratchasima province, Thailand, and type A gelatin from Nitta Gelatin, Japan,

were used as raw materials. All chemicals used were analytical grade.

A. Preparation of Thai silk fibroin aqueous solution and silk fibroin/gelatin blended solution

Thai silk fibroin scaffolds were prepared as described by Kim et.al [10]. Briefly, cocoons were degummed by boiling in an aqueous solution of 0.02M Na_2CO_3 then rinsed with deionized water. The degummed Thai silk fibroin was dissolved in 9.3M LiBr solutions at 60ºC for 4 h to form 25wt% solution. The solution was dialysed against deionized water for 2 days by 3-time water changing per day. The final obtained concentration of Thai silk fibroin aqueous solution was 6.5wt%.

Silk fibroin solution were blended with gelatin solution at the weight blending ratio of 50/50. Various type and amount of inorganic compounds were added in the blended solution of silk fibroin/gelatin as shown in Table 1.

Table 1: Weight Ratio of Inorganic Compound/Protein (silk fibroin and gelatine) in scaffolds.

Inorganic Compound	**Weight Blending Ratio of Inorganic Compound with Protein (Silk fibroin and Gelatin)**
β-TCP	0/100,30/70,50/50,70/30
HA	0/100,30/70,50/50,70/30

B. Scaffold fabrication

All scaffolds were fabricated via freeze drying technique. The aluminium trays were pre-freezed at -80ºC for 20 min. The blended solution were homogenised at 10000 rpm for 45 sec then chloroform were added and further homogenize for 15 sec. The solution were immediately cast into the tray and freezed at -80ºC for 8 hours then the freezed solution were lyophilized at -55ºC for 2 days.

C. Morphological observation and Pore diameter measurement

The morphology of scaffolds was visualized by scanning electron microscopy (SEM). In order to observe the inner structure of scaffolds, the scaffolds were cut horizontally with razor blades. The cut scaffolds were placed on the copper mount and coated with gold prior to SEM observation.

The pore diameter of the scaffold was determined from SEM micrographs using ImageJ Launcher (n=100).

D. Mechanical test

The compression tests in a dry condition were performed on all scaffolds using a universal testing machine (Instron, 5567) at the constant compression rate of 0.5 mm/min. The compressive modulus of the scaffolds (dimension: d=12mm, h=3mm) was determined from the slope of the compressive stress-stain curves during the strain range of 5%-30%. The reported values were the mean±standard deviation (n=5).

E. Swelling property [11]

A scaffold with known weight was immersed in phosphate buffered saline (PBS) for 24 hours. After that, its wet weight was determined. The percentage of water absorption (W_{sw}) of the scaffold was calculated from the following equation.

$$W_{sw} = \left[\frac{W_{24} - W_0}{W_0}\right] \times 100$$

where W_{24} represents the wet weight of scaffold after 24 hours of incubation, and W_0 is the initial weight of the scaffolds. The values were expressed as mean ± standard deviation (n = 5).

Results and Discussion

A. Morphology of scaffolds

Morphology of Thai silk fibroin/gelatin scaffolds with various type and amount of inorganic compounds observed by SEM was shown in Figure 1. The pore sizes of all scaffolds were summarized in Table 2. It was found that the pore size of silk fibroin/gelatin scaffolds containing either β-TCP or HA. When silk fibroin and gelatin were added with inorganic compound, β-TCP/protein and HA/protein scaffolds obtained formed highly porous networks with smaller pore sizes compared to pure protein scaffolds. Both β-TCP and HA were well dispersed in silk fibroin/gelatin scaffolds.

Table 2: Pore Diameter of The Obtained Scaffold

Weight Percentage of Inorganic Compound (Compared to protein)	**Pore Diameter of The Obtained Scaffold with Inorganic Compound (μm)**	
	β-TCP	**HA**
0	150±26	150±26
30	92±15	112±13
50	92±12	105±16
70	56±6	81±12

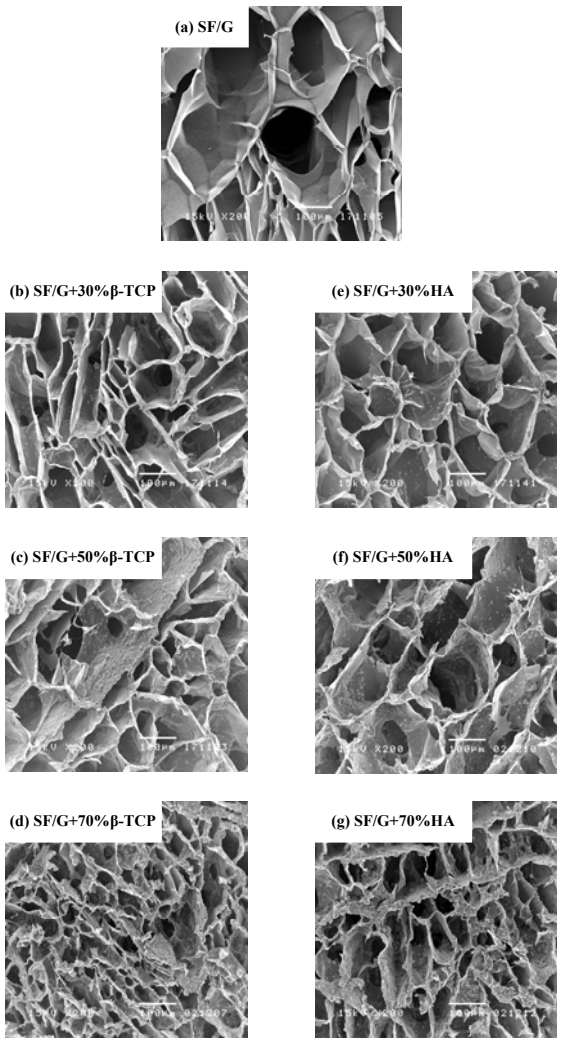

Figure 1. SEM micrographs of Thai silk fibroin/gelatin scaffolds incorporated with inorganic compound ; (a) SF/G (b) SF/G+30%β-TCP, (c) SF/G+50%β-TCP, (d) SF/G+30%β-TCP (e) SF/G+30%HA,
(f) SF/G+50%HA and (g) SF/G+70%HA
(scale bar : ⟝100 μm)

B. Mechanical property of scaffold

The compressive modulus of Thai silk fibroin/gelatin scaffolds with and without inorganic compound illustrated in Figure 2 indicated that the compressive modulus of Thai silk fibroin/gelatin scaffolds with inorganic compound was higher than Thai silk fibroin/gelatin scaffolds. The comperssive modulus was higher when increasing the percentage of incorporated inorganic compound. The result revealed that both inorganic compounds, β-TCP and HA, promoted the mechanical strength of scaffolds.Comparing at the same weight percentage of inorganic compound, β-TCP tended to be enhance the compressive mondulus of pretine scaffolds greater than HA.The scaffold with greates compressive modulus was found at 70% β-TCP incorporation.

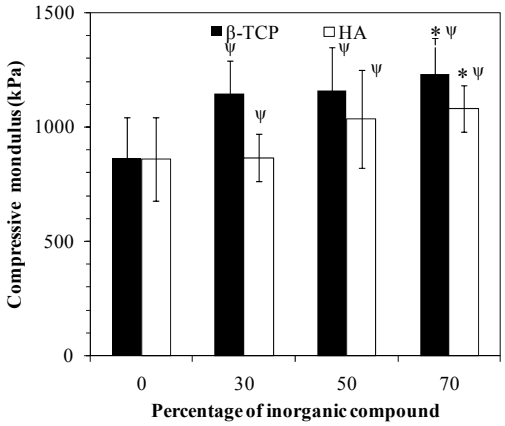

Figure 2. Compressive modulus of β-TCP/Thai silk fibroin gelatin and Hydroxyapatite/Thai silk fibroin gelatin scaffolds

* represent the significant difference ($p<0.05$) relative to Thai silk fibroin/gelatin scaffolds without inorganic compound.

$^{\Psi}$ represent the significant difference ($p<0.05$) between the pair at the same percentage of inorganic compound.

C. Swelling property of scaffolds

The result on water absorption of Thai silk fibroin/gelatin scaffolds with and without inorganic compound was demonstrated in Figure 4. It was found that an increasing of inorganic compound led to the slightly lower swelling ability of the scaffold. The incorporation of 70%β-TCP and 70%HA could decrease the swelling ability of SF/G scaffold by 5.24% and 7.73%, respectively

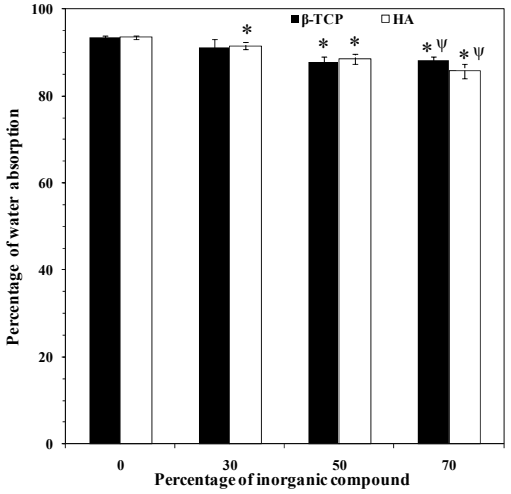

Figure 3. Percentage of water absorption of β-TCP/Thai silk fibroin gelatin and Hydroxyapatite/Thai silk fibroin gelatin scaffolds

* represent the significant difference ($p<0.05$) relative to Thai silk fibroin/gelatin scaffolds without inorganic compound

$^{\Psi}$ represent the significant difference ($p<0.05$) between the pair at the same percentage of inorganic compound.

Conclusions

Thai silk fibroin/gelatin (50/50) scaffolds incorporated with inorganic compound were prepared by freeze drying technique. Both inorganic compounds, β-TCP and HA, influenced on the morphology, compressive modulus and swelling property of Thai silk fibroin/gelatin scaffolds. Scaffolds incorporated with inorganic compound showed greater mechanical strength, smaller pore size, and lower swelling ability, comparing to Thai silk fibroin/gelatin scaffolds without inorganic compound. The biological property of these scaffolds will be further investigated in order to be applied in tissue engineering.

References

[1] X. Ma. Peter, *Mater Today*. **7** (2004), pp. 30-40.
[2] Y. Wang, H.J. Kim, G.V. Novakovic and D.L Kaplan, *Biomaterials*. **27** (2006), pp 6064–6082.
[3] N. Vachiraroj, J. Ratanavaraporn, S. Damrongsakkul, R. Pichyangkura, T. Banaprasertc, S. Kanokpanont, *Int J Biiol Macromol*.**45** (2009): 470–477.
[4] J. Chamchongkaset, S.Kanokpanont, D.L. Kaplan and S. Damrongsakkul, *J Adv Mate.r* **55-57** (2008), pp 685-688.
[5] P.Jetbumpenkul, Effect of chemical crosslink and hydroxyapatite on the properties of Thai silk fibroin/gelatin scaffold. Master's Thesis, Chulalongkorn University 2009.
[6] M. Fujimoto, M. Isobe, S. Yamaguchi, T. Amagasa, A. Watanabe, T. Ooya and N. Yui, *J Biomater Sci Polymer Ed.* **6**(2005), pp 1611–1621.
[7] M. Sato, E.B. Slamovich and T.J. Webster, *Biomaterials*. **26** (2005), pp 1349–1357.
[8] Y. Takahashi, M. Yamamoto and Y. Tabata, *Biomaterials* **26** (2005), pp 3587–3596.
[9] H.H. Lu, S. El-Amin, K.D. Scott and C.T. Laurencin, C. *J Biomed Mater Res Part A*. **64** (2003), pp 465–474.
[10] U.J. Kim, J. Park, H.J. Kim, M. Wada and D.L. Kaplan, *Biomaterials* **26** (2005), pp. 2775–2785.
[11] K. Tuzlakoglu, C.M. Alves, J.F. Mano and R.L. Reis, *Macromol Biosci.* **4** (2004), pp 811-819.

Development of low temperature ceramic glazes using MSW and borosilicate cullet

P. Ketboonruang[1,2], S. Jinawat[1,2], D. P. Kashima[1,2], T. Wasanapiarnpong[1,2], P. Sujaridworakun[1,2], W. Buggakupta[1,2], N. Traiphol[1,2] and S. Jiemsirilers[1,2*]

[1]Research Unit of Advanced Ceramics, Department of Materials Science, Faculty of Science, Chulalongkorn University.
[2]Research Unit of Advanced Ceramic and Polymeric Materials, National Center of Excellence for Petroleum, Petrochemicals and Advanced Materials, Chulalongkorn University, Bangkok, Thailand

[*]E-mail:sirithan.j@chula.ac.th

Abstract: Nowadays, people are interested in global warming and energy saving. Ceramic production is a high energy consumption process especially firing process. In this research, the utilization of industrial wastes to decrease firing temperature of ceramic glazes was studied. Raw materials selected were Municipal solid waste Phuket (MSW) and glass cullet. Chemical composition of MSW Phuket and cullet were analyzed by X-ray fluorescence. MSW Phuket is composed of CaO, Na_2O, and K_2O which are fluxing agents. The chemical composition of cullet shows that SiO_2 and B_2O_3 are major components which act as glass former oxides. The glaze compositions were designed using ternary phase diagram to study the relation of glass compositions and glaze properties. MSW Phuket, borosilicate glass cullet, and borax were used as raw materials. All formulas were ground in a high speed ball mill for 15 minutes and sieved through a screen. Properties of glaze slip; density, % residue were measured. Compound ceramic body was glazed then fired at 1000 and 1150°C. Fired properties for example water absorption, melting and flowing property, and coefficient of thermal expansion were analyzed. It was observed that the specimens with the ratio of MSW Phuket: cullet: borax is equal to 30:30:40 fired at 1000°C showed the appearance of matured clear glaze. The specimen fired at 1150°C shows good appearance as well. Municipal solid waste and cullet can be utilized as major raw materials for low temperature firing glazes without using commercial ceramic frit and high amount of expensive chemicals. The firing temperature and time can be reduced by using appropriate waste materials that have been processed. Firing of this low temperature glazes consumed lower energy because decomposition and some reactions were not necessary.

Introduction

Municipal solid waste (MSW) is one of the most critical environmental problems. The management and treatment of MSW has become and important due to the rapid population growth. [1] MSW can be reduced by many methods for example landfill or incineration. After incineration MSW produces a large amount of fly ash up to the proportion of 25-30 wt% of the original waste. [2] On the other hand, glass cullet is the waste that can be totally recycled can be used to substitute ceramic raw materials in order to reduce melting temperature or increase strength in ceramic body. [3] The chemical compositions of glass cullet were silica, alkaline and alkaline earth oxide which act as glass former and fluxing agents consecutively. [4] It was found that it can be used for replacing feldspar or frit in ceramic glaze. Normally low temperature ceramic glazes (900 - 1000°C) can be made by using more than 90% of commercial frit in glaze formula to produce ceramic wall tiles. [5] In this research, the utilization of industrial wastes to decrease firing temperature of ceramic glazes was studied. [6] The amount of reused materials used in this research was more than 50% in glaze formula. Beside reduction of production cost by firing at lower temperature, industrial wastes were eliminated resulting in less environmental problem.

Materials and Methods

Starting materials were Municipal Solid Waste (MSW) from Phuket waste incineration, borosilicate glass cullet, and borax. Glass cullet was obtained from Pyrex™ glass industry and commercial grade of borax. Figure 1 shows designed glaze compositions designed using ternary phase diagram to study the relation of glass compositions and glaze properties. All formulas were ground in a high speed ball mill for 15 minutes and sieved through a screen. Properties of glaze slip; density, % residue were measured. Compound ceramic body was glazed then fired at 1000 and 1150°C. Fired properties for example water absorption, melting and flowing properties and coefficient of thermal expansion were analyzed.

Glaze flow test was determined by placing glaze pellets on 45° C triangle molds then fired at 1000°C and 1150°C.

Melting property was studied. The powder glaze was pressed in a cone shape and fired at 1000°C and 1150°C.

Coefficient of thermal expansion glaze of specimen fired at 1000°C was measured by dilatometer (DIL 402C, Netzsch) using a heating rate of 10°C/min from 50 to 500°C.

Results and discussion

The chemical composition of MSW Phuket and cullet were analyzed by X-ray fluorescence. MSW Phuket was composed of CaO Na_2O and K_2O. The chemical composition of cullet showed that SiO_2 and B_2O_3 are major components.

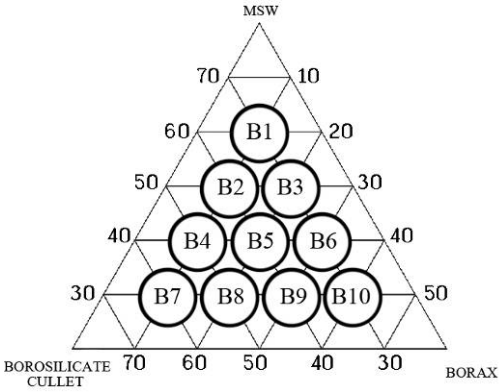

Figure 1. Ternary glaze compositions

Table 1: Density of glaze formulas

Formulas	Density (g/cm^3)	Residue on 325 mesh (%)
B1	1.41	0.95
B2	1.43	1.54
B3	1.43	1.33
B4	1.48	6.69
B5	1.40	4.72
B6	1.40	1.94
B7	1.42	10.70
B8	1.39	11.81
B9	1.41	5.21
B10	1.43	1.83

Table 1 shows density and % residue on 325 mesh of glazes. The average density of glaze slip was around 1.42 g/cm^3. The amount of % residue increased when the amount of cullet increased when milled at the same milling time. B8 shows highest % residue with the highest cullet content of 50%wt in composition.

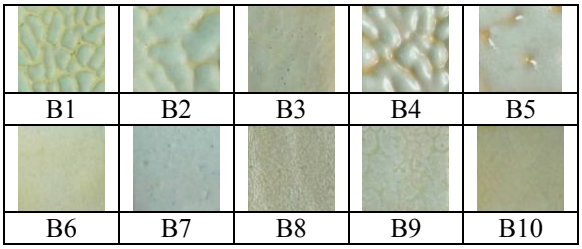

Figure 2. Appearance of glazes fired at 1000°C

B3 B6 B9 and B10 were matured when fired at 1000°C. B1 B2 B4 B7 and B8 were not matured and crawling defects existed.

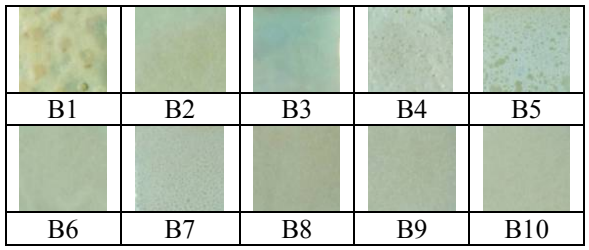

Figure 3. Appearance of glazes fired at 1150°C

The specimen in Figure 3 shows the appearance of matured glazes for most of compositions.

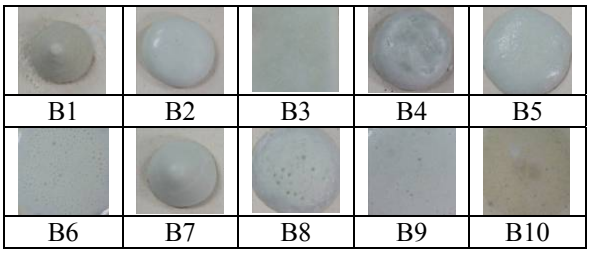

Figure 4. Melt Test at 1000°C

The specimen in Figure 4 that shows that B3, B6, B9, and B10 melted very well at 1000°C. On the other hand, B2, B4, and B5 started to melt at this temperature B1 did not melted at all. When glazes contain of at least 20 wt% borax glazes could be matured at 1150 °C if the amount of borax increased to 30 wt% all glazes could me matured at 1000°C as shown in Figure 5.

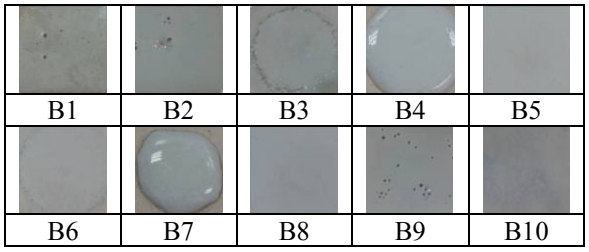

Figure 5. Melt Test at 1150°C

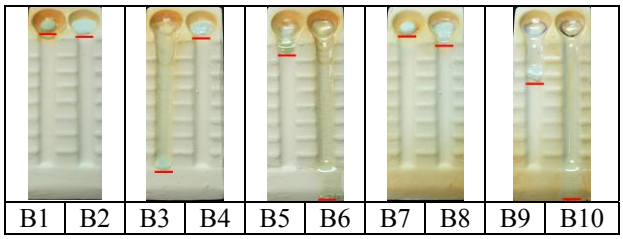

Figure 6. Melt flow test at temperature 1000°C

Figure 6 shows that the results of flow test are in the same trend as melt test in Figure 4 and 5. B1 and B2 glazes melted and flow very well when the firing temperature increased from 1000 to 1150 °C. At 1150° C B4 and B7 glazes are matured but can not cover

ceramic body well. The air bubbles can be detected in both glazes.

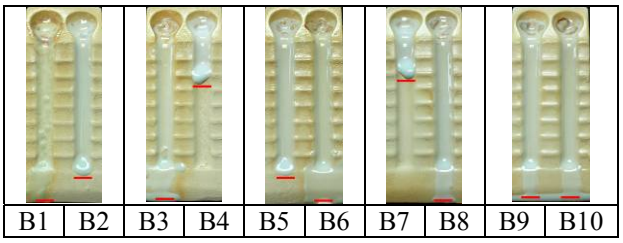

Figure 7. Melt flow test at 1150°C

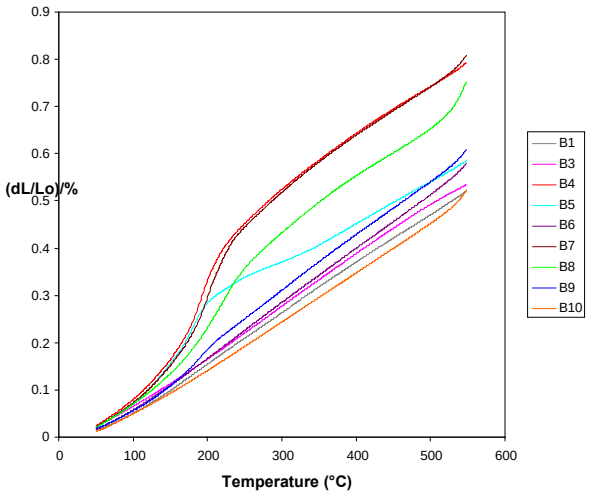

Figure 8. dL/dL_o vs temperature of various glazes

Table : 2 Thermal expansion coefficient of glaze

Formulas	Coefficient of Thermal Expansion	
	50-300°C	50-500°C
B1	$9.90x10^{-6}$	$10.12x10^{-6}$
B2	-	-
B3	$10.22x10^{-6}$	$10.46x10^{-6}$
B4	$20.02x10^{-6}$	$15.97x10^{-6}$
B5	$13.98x10^{-6}$	$11.54x10^{-6}$
B6	$10.74x10^{-6}$	$11.04x10^{-6}$
B7	$19.86x10^{-6}$	$15.99x10^{-6}$
B8	$16.48x10^{-6}$	$14.04x10^{-6}$
B9	$11.72x10^{-6}$	$11.61x10^{-6}$
B10	$9.26x10^{-6}$	$9.78x10^{-6}$
Stoneware Body	$4.69x10^{-6}$	$5.46x10^{-6}$

Thermal property of selected glazes was shown in Figure 8 and the coefficients of thermal expansion of glazes calculated at 50 -300 °C and 50 – 500 °C were shown in Table 2. In this stage of the research commercial stoneware body was used. The coefficient of thermal expansion of ceramic body and glazes are not match due to the low firing temperature is not suitable for this body. As can be seen in Figure 2 there are crawling defects in some glaze compositions (B1, B2, B4) due to high surface tension of glaze during firing. At higher firing temperature of 1150° C a few defects can be found due to lower of surface tension at higher firing temperature.

Table 2 shows thermal expansion coefficient of glaze from 50 – 300 °C and 50 – 500 °C. B4, B7, B8, and B5 shows effects of cristobalite formation. The coefficient of thermal expansion of theses glazes were very high at the temperature from 50 – 300 °C and decreased when the coefficients were averaged from 50 – 500 °C.

Conclusions

In the research, Municipal solid waste and borosilicate cullet can be utilized as major raw materials for low temperature firing glazes without using commercial ceramic frit and high amount of expensive chemicals. B10 glaze that contain of MSW Phuket: cullet: borax equals to 30:30:40 can be fired at 1000 °C. At 1150 °C, B3 glaze which contain of MSW Phuket: cullet: borax equals to 50:30:20 shows good appearance as well with lower content of borax. The firing temperature and time can be reduced by using appropriate waste materials that have been processed. Firing of this low temperature glazes consumed lower energy because the decomposition and some reactions were not necessary. The saving will be either in fuel consumption or in raw materials cost if inexpensive fluxes are used.

Acknowledgement

1. National Center of Excellence for Petroleum, Petrochemical, and Advanced Materials, Chulalongkorn University.

2. National Metal and Materials Technology Center for research funding Project Number MT-B-51-CER-09-210-G

References

[1] H. Shi and Li. Kan, *Constr.Build. Mater* **23** (2009), 2160-2166.

[2] Y. Lu, X. Wu and J. Guo, *Waste.Manage*. **29** (2009), 1152-1157.

[3] S. Maschio, E. Furlani, G. Tonello, N. Faraone, E. Aneggi, D. Minichelli, L. Fedrizzi, A. Bachiorrini and S. Bruckner, *Waste.Manage.* **29** (2009), 2880-2885**.**

[4] V. V. Gerasimov and O. V. Spirina, *Glass Ceram*. **61**. (2004), 11-12.

[5] I. G. Khizanishvili and R. A. Mamaladze, *Glass Ceram*. (1965), 33-34.

[6] C. Ferreira, A. Ribeiro and L. Ottosen, *J. Hazard. Mater*, **B96**. (2003), 201-216.

Calculated the spin hamiltonian parameters of Fe^{3+} ions in blue sapphires

Chittra Kedkaew[1,*], Treedej Kittiauchawal[2], Jakrapong Kaewkhao[3] Siwaporn Smith[4] and Pichet Limsuwan[1]

[1] Department of Physics, King Mongkut's University of Technology Thonburi, Bangkok, Thailand.
[2] Faculty of Science and Technology, Thepsatri Rajabhat University,Lopburi, Thailand.
[3] Glass and Materials Science Research Unit, Physics Program, Nakhon Pathom Rajabhat University, Nakhon Pathom, Thailand.
[4] Department of Chemistry, Mahidol University, Bangkok, Thailand.

[*] E-mail: chittra193@hotmail.com

Abstract: Electron spin resonance (ESR) spectroscopy was used to study the Fe^{3+} ions in blue sapphires. ESR measurements were performed on the crystal sample in X-band microwave frequency. In the experiment, the c-axis of crystal was perpendicular to the applied magnetic field direction and the sample was rotated from 0 to 180 degrees about c-axis. The ESR spectra were recorded every 15 degrees of rotation angle. It was found that three strong ESR absorption peaks at the magnetic field of 1360.21, 3444.23 and 7388.05 gauss were obtained. These ESR absorption peaks correspond to Fe^{3+} ions that replace the Al^{3+} ions of corundum structure (α-Al_2O_3). The conspicuous peaks of Fe^{3+} ions at various rotation angles were used to calculate the spin Hamiltonian parameters by least-squares fit method. The optimum spin Hamiltonian parameters of Fe^{3+} ions were then used to simulate the energy levels diagram of Fe^{3+} ions in sample.

Introduction

Electron paramagnetic resonance (EPR) spectroscopy, sometimes referred to as electron spin resonance spectroscopy (ESR), is a powerful tool used in several fields of physics, chemistry, and biochemistry Indeed, the low-level detection threshold (ppm) and the structural sensitivity of EPR allow analysis of the nature and localization of paramagnetic point defects as well as the atomic environment of paramagnetic ions, mainly first-row transition ions and lanthanide ions, in various solids and liquids. For instance, quantification of radiation-induced paramagnetic defects by EPR is used for dating and dosimetry. EPR is also used to study the site distribution of paramagnetic impurities in solids, as well as the relaxation processes related to their structural accommodation by the host matrix [1].

Single-crystal EPR analysis yields both the whole set of spin Hamiltonian parameters and the orientation of the principal axes of the local ligand field with respect to crystallographic axes. In polycrystalline solids, this relative orientation cannot be determined because an EPR powder spectrum is a summation over all orientations of the local ligand field with respect to the static applied field direction [1].

In the present work, we studied the ESR spectra of blue sapphire crystals both before and after heat treatment, to calculate the spin Hamiltonian parameters of Fe^{3+} ions.

Spin Hamiltonian Parameters of Fe^{3+} Ions

The ESR spectra of Fe^{3+} ions can be described by a spin Hamiltonian (H) incorporating with Zeeman interaction, hyperfine structure and crystal field operators. It is given by equation

$$H = H_{Zeeman} + H_{HF} + H_{CF} \qquad (1)$$

The first term corresponds to the Zeeman interaction arises from the interaction between electron spin angular momentum and external magnetic field. The Zeeman term is given by equation

$$H_{Zeeman} = \beta \mathbf{S} \cdot \mathbf{g} \cdot \mathbf{B}$$

$$= \beta \left[S_X, S_Y, S_Z\right] \cdot \begin{matrix} g_{xx} & g_{xy} & g_{xz} \\ g_{yx} & g_{yy} & g_{yz} \\ g_{zx} & g_{zy} & g_{zz} \end{matrix} \cdot \begin{matrix} B_X \\ B_Y \\ B_Z \end{matrix} \qquad (2)$$

where β, **S**, **g** and **B** are the Bohr magnetron; spin operators $\mathbf{S_x}$, $\mathbf{S_y}$, $\mathbf{S_z}$; gyromagnetic tensor, and magnetic field, respectively.

The second term is the hyperfine interaction term arises from the interaction between the electron spin and nuclear spin. The hyperfine term is written in the form

$$H_{HF} = \mathbf{S} \cdot \mathbf{A} \cdot \mathbf{I} \qquad (3)$$

where **I** and **A** are nuclear spin operator and hyperfine coupling tensor, respectively.

The third term is the crystal field term arises from the crystal field potential generated from the surroundings of the paramagnetic ion in sapphire. This term depends on the local symmetry of paramagnetic ion site and the electronic configuration of ion. It is the sum of spin angular momentum operators called Stevens' operators or equivalent operators (O_2^0 , O_4^0 and O_4^3) with their coefficients (B_2^0 , B_4^0 and B_4^3) as the crystal field parameters. The crystal field Hamiltonian is usually written in the spherical-tensor notation as the following relation

$$H_{CF} = B_2^0 O_2^0 + B_4^0 O_4^0 + B_4^3 O_4^3 \quad (4)$$

Therefore, the spin Hamiltonian is given by equation

$$H = \beta S \cdot g \cdot B + S \cdot A \cdot I + B_2^0 O_2^0 + B_4^0 O_4^0 + B_4^3 O_4^3 \quad (5)$$

However, the hyperfine term is small compared with the Zeeman term so that it can be neglected. Then, the spin Hamiltonian in Eq. (2.24) becomes

$$H = \beta S \cdot g \cdot B + B_2^0 O_2^0 + B_4^0 O_4^0 + B_4^3 O_4^3 \quad (6)$$

The parameters in Eq. (6) were calculated from the resonance magnetic field positions in the ESR spectra [1-6].

Materials and Methods

The natural Vietnamese blue sapphires were cleaned thoroughly with acid and solvent to remove all stains and other impurities on their surfaces. Next, the blue sapphires were heated at the temperatures of 1600 ^oC in oxygen atmosphere for 40 h with BeO. ESR measurements were performed on the unheated and heat treatment crystal samples in X-band microwave frequency (Bruker, Model E500 CW). In the experiment, the c-axis of crystal was perpendicular to the applied magnetic field direction; the sample was rotated from 0 to 180 degrees about c-axis. The ESR spectra were recorded every 15 degrees of rotation angle.

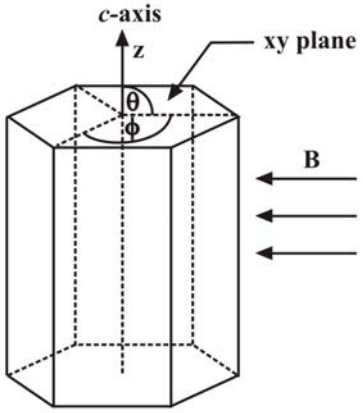

Figure 1. The direction of magnetic field, B and the rotation angle (ϕ).

Results and Discussion

Figure 2 shows ESR spectra of sample before (a) and after heat treatment (b) were performed in X-band microwave frequency. In the experiment, the c-axis of crystal was perpendicular to the applied magnetic field direction. It was found that three strong ESR absorption peaks at the magnetic field of 1360.21, 3444.23 and 7388.05 gauss were obtained. These ESR absorption peaks correspond to Fe^{3+} ions that replace the Al^{3+} ions of corundum structure (α-Al_2O_3) [7].

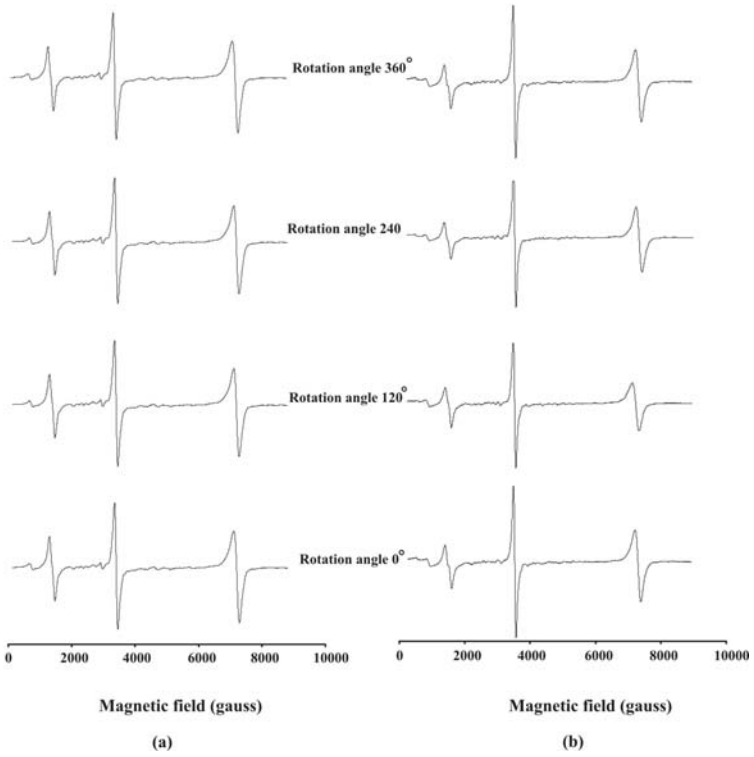

Figure 2. ESR spectra of crystal sample before (a) and after heat treatment (b).

Table 1: Calculated spin Hamiltonian parameters of Fe^{3+} ions in a blue sapphire crystal before and after heat treatment.

Sample	g		B_2^0 (mT)	B_4^0 (mT)	B_4^3 (mT)	RMSD* (mT)
	$g_{xx} = g_{yy}$	g_{zz}				
1. Before heat-treatment	2.005(1)	2.010(4)	68.543(2)	0.191(1)	0.003(4)	0.337(6)
2. After heat treatment	2.001(2)	2.007(6)	69.205(3)	0.197(3)	0.003(9)	0.159(0)

*RMSD = root mean sum of squares of weighted differences between observed and calculated line positions

The prominent peaks of Fe^{3+} ions at various rotating angles were used to calculate the spin Hamiltonian parameters by least-squares fit method with the help of an EPR-NMR computer program. The results of calculated spin Hamiltonian parameters of Fe^{3+} ions in blue sapphire crystal before and after heat treatment at various temperatures are shown in Table 1. From Table 1, it is seen that after heat treatment with BeO, the spin Hamiltonian parameters of Fe^{3+} ions in sapphire were changed in comparison with the unheated sapphire.

Conclusions

The heat treatments were carried out in an electric furnace at 1700 ^oC in oxygen atmosphere for 40 hours with BeO. It can be concluded that before and after heat treatments the Fe^{3+} ions replace the Al^{3+} ions sites on *c*-axis. This can be clearly seen that the resonant peak positions in ESR spectra at rotation angle (ϕ) of 120^o are exactly the same as those of original position (ϕ=0). The spin Hamiltonian parameters of Fe^{3+} ions in heat treatment were changed when compared with unheated sapphire. This resulted from the displacement Fe^{3+} ions during the heat treatment as well as the distortion of crystal structure.

References

[1] G. Morin and D. Bomin, *Journal of Magnetic Resonance,* **136** (1999), pp. 176-199.

[2] *V.Y. Nagy, P.N. Komozin and M.F. Desrosiers, Analytica Chimica Acta***, 339** (1997), pp. 31-51.

[3] C.P. Jr. Poll and H.A. Farach, *The Theory of Magnetic Resonnance*, John Wiley &Sons, New York. (1972).

[4] T.F. Yen, **Electron Spin Resonance of Metal Complexes,** Plenam Press, New York. (1969).

[5] Kittiauchawal, T.; Limsuwan, P.; Eitssayeam, S.; Tunkasiri, T., *Inter. J. Mod. Phys. B*, **22&23** (2008), pp.4730-4739.

[6] Die Dong ; Kuang Xiao-Yu ; Wang Hui ; Guo Jian-Jun ; Zhou Kang-Wei, *Chem. Phys. Let.*, **418** (2006), pp. 71–74.

[7] Limsuwan, P.; Meejoo, S.; Somdee, A.; Thamaphat, K.; Kittiauchawal, T.; Siripinyanond, A.; Krzystck, J., *Chin. Phys. Let.,* **25** (2008), pp. 1976-1979.

Electrochemical sensing properties characterization of as-grown carbon nanotubes

N. Punbusayakul[1*] and W. Surareungchai[2]

[1] School of Agro-Industry, Mae Fah Luang University, Chiang Rai, Thailand
[2] School of Bioresources and Technology, University of Technology Thonburi, Bangkok, Thailand

* E – mail: niramol@mfu.ac.th

Abstract: Electrodes from various as-grown carbon nanotubes (CNT) architectures, thread like single-walled CNT (T-SWNT), thread like double -walled CNT (T-DWNT) and long vertically aligned multi-walled CNT (L-MWNT), were fabricated and electrochemically characterized compared to the conventional glassy carbon electrode (GCE) using Ag/AgCl and Pt as reference and counter electrode respectively. Subsequently, hydrodynamic voltammetry at each electrode for hydrogen peroxide detection was performed. The potential providing the highest electrochemical response at each electrode was applied for sensitivity testing by amperometry. The results showed that the T-DWNT electrode reaction was more stable under the experimental condition than the T-SWNT electrode. Whereas, there was no well defined peak observed at the L-MWNT electrode. The potential providing the highest response at the T-SWNT electrode, the T-DWNT and the GCE were -0.6 V, -0.7 V, and -0.9 V respectively. Whereas, undefined with noisy response was observed at the L-MWNT electrode. Therefore, the potentials of -0.6, -0.7 and -0.9 V were chosen for sensitivity testing at T-SWNT, T-DWNT and GCE electrode respectively. It was found that both CNT electrodes exhibited better electrochemical properties than the GCE electrode. In addition, the T-DWNT electrode was found to electrochemically perform superior than the T-SWNT electrode by providing more sensitive to the interested species. These suggest that the T-DWNT electrode is promising for electrochemical sensing, consequently investigations toward biological molecules incorporation for biosensor applications are feasible.

Introduction

Electrodes with various oriented carbon nanotubes (CNTs) architectures have been applied for electrochemical analysis. Those include powder CNTs casting films, CNTs paste and polymer composites, as-grown CNTs, individual CNTs and CNTs arrays [1-9]. The most CNTs architecture used in electrochemical detection is CNTs casting films with various encountered problems including the limiting high background current due to the very high surface ratio of CNTs, the unstable of CNTs casting films during the measurement as a result of CNTs leaching out and the electrode manipulation difficulty as a result of the nano or micro-size of the CNTs bundles or fibers. Previously, our group has successfully applying the as-grown CNTs macro-architectures for electrochemical sensing [10-11]. Recently, there have been a number of different CNTs macro architectures producing, including long horizontally aligned single-walled (SW) and double-walled (DW) CNTs, long vertically aligned multi-walled (MW) CNTs. The electrode fabrication from these CNTs macro-architectures can be manipulated with bare hands or without any high technological tools. Some have not yet been applied for electrochemical analysis and there is no report on those architectures electrochemical properties comparisons. In addition, the electrodes from different CNTs architectures have been claimed to exhibit different electrode characteristics and their electrochemical properties and sensitivity are varied depending on the target species and the applied electrochemical probes [12]. This work, therefore, aimed to characterize the electrochemical properties of different forms of as-grown CNTs macro architectures. These include a thread-like SWNT (T-SWNT) and DWNT (T-DWNT) and long vertically-aligned MWNT (L-MWNT) compared to the conventional glassy carbon electrode (GCE). The as-grown CNTs will be able to further exploited for electrochemical sensing.

Materials and Methods

Materials: T-SWNT, T-DWNT and L-MWNT were grown by Lijie Ci, a post-doc fellow in Ajayan Research Group, with the permission from P.M. Ajayan (Rice University, TX, USA). Field-Emission Scanning Electron Microscope (FE-SEM, Hitachi S-4700) was used for morphological characterization of all CNTs materials.

Chemicals: All chemicals were analytical grade purchased from Sigma-Aldrich Company.

Electrode fabrication: A small CNTs strand was peeled out from the CNTs forest and placed on a flat substrate. One end of the strand was attached to an electrical wire using conductive silver paste and the other end as well as all of the conductive connection area was insulated by epoxy glue (Figure 1). The electrode was assembled in a standard three-electrode system as a working electrode (WE) with a Pt disk as a counter electrode (CE) and Ag/AgCl as a counter electrode (RE).

Electrochemical characterization: All electrochemical measurements were performed using the Autolab PBSTAT 12 with the GPES acquisition software. Cyclic voltammetry (CV) was carried out to

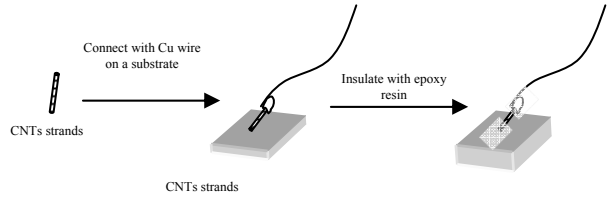

Figure 1. Schematic of electrode Fabrication.

observe the working potential at each electrode by scanning the potential from -3.0 to 3.0 V at a scan rate of 20 mV/s in 0.1 M KCl solution.

Hydrogen peroxide (H_2O_2) was selected as a model species for electrochemical characterization at the electrodes. For the reason that H_2O_2 is the product commonly obtained from the most oxidation biochemical processes and as a result of its very high electrocatalytic reduction, consequently causing the measurement difficulty [13]. Hydrodynamic amperometry was conducted in 2.0 mM H_2O_2 containing phosphate buffer solution (pH 7.0) in order to obtain an individual potential at each electrode providing the highest hydrodynamic response for further sensitivity testing.

Sensitivity testing was conducted in phosphate buffer (pH 7.0) bulk solution with the interval injection of H_2O_2 at the concentration of 200 µM to observe the detection range at each electrode with the optimal applied potential obtained from the hydrodynamic testing.

Results and Discussion

Material Characterization: Figure 1 shows the FESEM images of T-SWNT (Figure 2A), T-DWNT (Figure 2B) and L-MWNT (Figure 2C) at different magnifications. The T-SWNT strands was loosely packed and had wide-ranging diameter from 2.0-300.0 µm, while T-DWNT had all bundles densely packed together providing more consistent diameter for the whole strand about 10-20 µm. L-MWNT strands were vertically and orderly aligned. The diameter of the peeled CNTs for electrode fabrication did not only depend on the diameter of the original CNTs diameter, but also depended on how the bundles peeled or pulled out from the CNTs strands or the CNTs forest.

Electrochemical Characteristics of the electrodes: There was no well-defined peak obtained for all electrodes when the potential were cycling from -3.0 to 3.0 V in 0.1 M KCl at the electrodes vs. Ag/AgCl (Figure 3). These catalytic peaks may result from the naturally occurrences impurities' catalytic properties in the as-grown CNTs which claimed to contribute as a predominant catalytic activity of the electrode [14-17] and can be exploited for electroanalytical sensing [18-19]. Less oxidation peak was significantly observed at the T-DWNT electrode, whereas undefined peak was observed at L-MWNT (not shown). However, excessively high catalytic reaction could impair the catalytic response obtained by the species of interest.

Hydrodynamic response from current-time profile observed at the T-SWNT, T-DWNT and glassy carbon (GCE) electrodes, when H_2O_2 at a fixed concentration was injected to achieve the final concentration of 2.0 mM, was plotted against the applied potentials as shown in Figure 4a, 4b and 4c respectively. A very well-defined hydrodynamic current response with high current response was observed at T-DWNT electrode compared to the current response observed at T-SWNT and GCE electrodes (not shown).

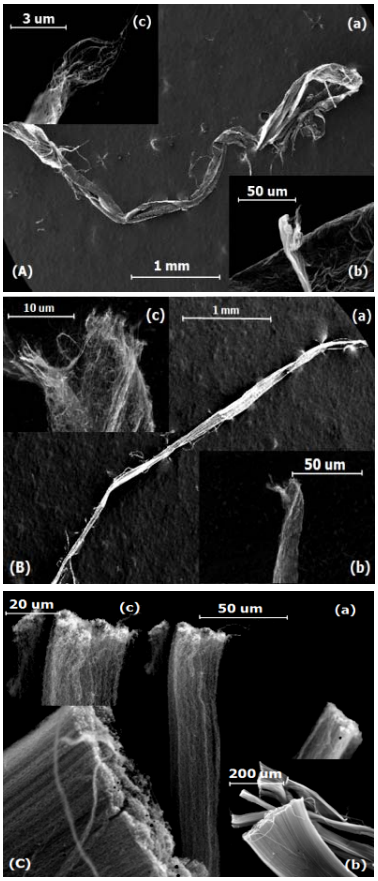

Figure 2. FESEM images of (A) T-SWNT (B) T-DWNT and (C) L-MWNT at (a) lower magnification (b) higher magnification (c) highest magnification

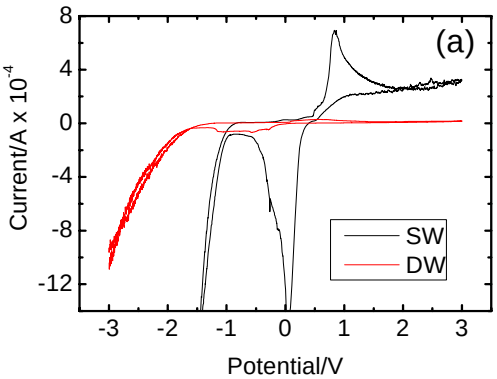

Figure 3. (a) CVs at T-SWNT & T-DWNT electrodes in 0.1 M KCl from -3.0 to 3.0 V at 20 mV/s *vs.* Ag/AgCl.

The potential providing the observed apparent highest hydrodynamic response at the T-SWNT, T-DWNT and GEC electrodes were -0.6, -0.7 and -0.9 V respectively. It was found that both CNTs electrodes performed superior electrocatalytic properties through the H_2O_2 hydrodynamic testing over the GCE electrode by providing the lower electrocatalytic reaction potential. In addition, lower catalytic reaction observed at both electrodes when the higher potential was applied to the electrodes compared to that of the GCE electrode. Among the CNTs, the lower reaction potential used for H_2O_2 detection was observed at the T-SWNT electrode compared to that of the T-DWNT electrode.

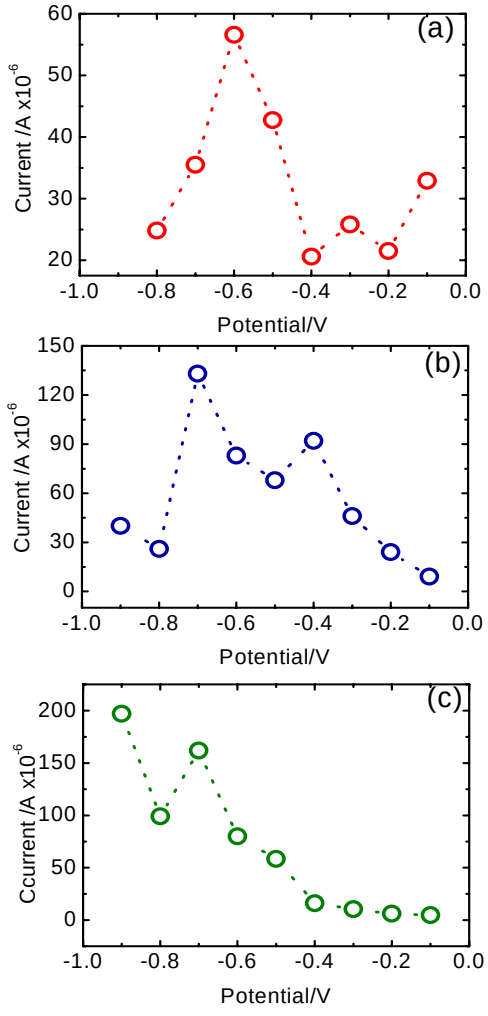

Figure 4. Hydrodynamic current response at different potentials at (a) T-SWNT, (b) T-DWNT and (c) GCE electrodes *vs.* Ag/AgCl with 2.0 mM H_2O_2 final concentration containing phosphate buffer solution (pH 7.0).

However, the current response obtained at the T-DWNT electrode was more than two times higher than the current response observed at the T-SWNT electrode. This suggests that the T-DWNT electrode exhibited the better electrochemical properties by providing faster electron transfer compared to the T-SWNT electrode which was also reported by other groups [6, 19]. These potentials were applied for further sensitivity testing as shown in Figure 5.

Sensitivity testing: The T-DWNT electrode exhibited more sensitive to H_2O_2 than the other electrodes indicating by the higher response obtained when the same concentration of H_2O_2 was injected to the bulk solution as shown in Figure 5. In addition, T-DWNT electrode illustrated a broader detection range by providing an observable signal for all ranges of H_2O_2 concentrations (~200-2000 nM) in the experiment. Whereas, the current response at both T-SWNT and GCE electrodes was apparently limited by the H_2O_2 concentration of ~1200 nM, indicating by the obtained plateau signal as shown in Figure 5.

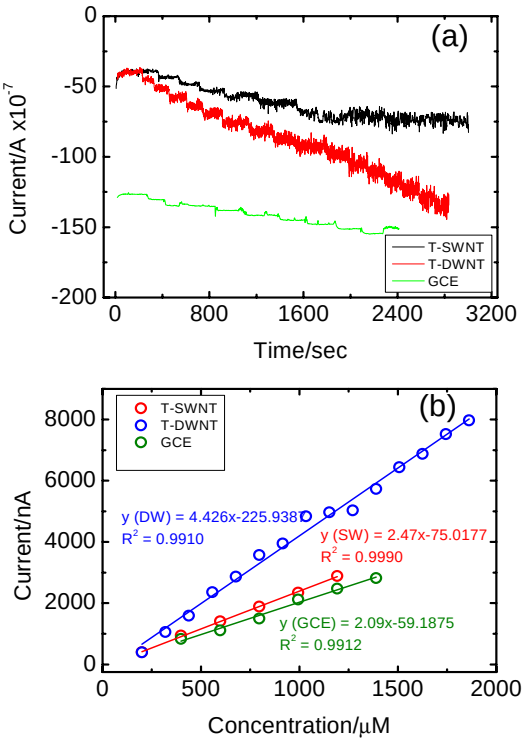

Figure 5. (a) Amperograms at T-SWNT (black), T-DWNT (red) & GCE (green) electrode vs. Ag/AgCl with 200 µM H_2O_2 addition using phosphate buffer solution pH 7.0 as a supporting electrolyte (b) A plot of H_2O_2 concentration against the obtained current response

The limit of detection (LOD) at T-SWNT, T-DWNT and GCE electrodes were 30.39, 28.97 and 28.80 µM based on signal to noise ratio of 3. T-DWNT exhibited the highest sensitivity (4.352 nA/µM) followed by T-SWNT (2.468 nA/µM) and GCE (2.09 nA/µM) respectively as indicating by the highest slope obtained shown in Figure 5b. The T-DWNT electrode superior electrochemical catalytic activity may due to the result of the dense bundles of the DWNT strands compared to that of the T-SWNT strands. This provides higher surface area contributing to the higher electron transfer rate at the T-DWNT electrode compared to the T-SWNT and GCE electrodes.

After six months storage at ambient temperature the electrode was tested again by amperometry to observe the electrode response to 2.0 mM H_2O_2. It was found that the electrode still provided a very exquisite signal with the consistent response over 16 times as shown in Figure 6.

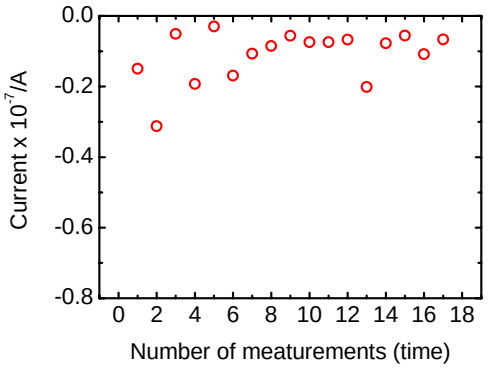

Figure 6. Amperometric response to 2.0 mM H_2O_2 at T-DWNT electrode stored at ambient temperature for over 6 month storage.

Conclusions

T-SWNT and T-DWNT electrodes exhibited higher electrochemical catalytic and electron transfer as compared to the GCE conventional electrode. Among CNTs electrodes, T-SWNT provided the lower catalytic potential for H_2O_2 detection compared to the T-DWNT electrode, however T-DWNT had wider detection range. T-DWNT electrode, therefore, is the most promising electrode for electrochemical analysis compared to the T-SWNT, L-MWNT & GCE conventional electrodes. Consequently, the T-DWNT could be further feasibility exploited for biosensor application to promote the analytical ability which will be further benefit in the various related fields.

Acknowledgements

NP would like to thanks Thailand Research Fund (TRF) for the financial support and P.M Ajayan (Rice University, TX, USA) allowing his fellow post-doc, Lijie Ci, growing CNT for the experiment.

References

[1] Z. Li, Z. Wu and K. Li, *J. Anal. Biochem.* **387** (2009), pp. 267-270.
[2] H. Xiong, H. Xu, L. Wang and S. Wang, *Microchim Acta*. **167** (2009), pp. 129-133.
[3] F. Berti, L. Lozzi, I. Palchetti, S. Santucci and G. Marrazza, *Electrochimica Acta.* **54** (2009), pp. 5035-5041.
[4] J. Zhang, J. Li, F. Yang, B. Zhang and X. Yang, *Sens. Actuators B.* **143** (2009), pp. 373-380.
[5] Y-H. Yun, Z. Dong, V.N. Shanov, A. Doepke, W.R. Heineman, H.B. Halsall, A. Bhattacharya, D.K.Y. Wong and M.J. Schulz, *Sens. Actuator B.* **133** (2008), pp. 208-212.
[6] M. Pumara, *Nanoscale Res. Lett.* **2** (2007), pp. 87-93.
[7] X-J. Huang, H-S. Im, O. Yarimaga, J-H. Kim, D-Y. Jang, D-H. Lee, H-S. Kim and Y-K. Choi, *J. Of Electroanal. Chem.* **594** (2006), pp. 27-34.
[8] P. Liu and J. Hu, *Sens. Actuator B,* **84**, (2002), pp. 194-199.
[9] J.M. Nugent, K.S.V. Santhnam, A. Rubio and P.M. Ajayan, *Nano Lett.* **1** (2001), pp. 87-91.
[10] N. Punbusayakul, S. Talapatra, L. Ci, W. Surareungchai, and P. M. Ajayan, *Electrochem. Solid-State Lett*. **10** (2007), pp. F13-F17.
[11] N. Punbusayakul, L. Ci, S. Talapatra, W. Surareungchai, P.M. Ajayan, *J. Nanosci. Nanotech.* **8**, (2008), pp. 2085-2090.
[12] K. Gong, S. Chakrabarti and L. Dai, *Angew. Chem. Int. Ed.* **47**, (2008), pp. 5446-5440.
[13] R. Stefan, J. F. Van Staden and H.Y.. Aboul-Enein. *Electrochemical sensors in bioanalysis.* Marcel Dekker, Inc. NY. (2001).
[14] C.E. Banks, A. Crossley, C. Salter, S.J. Wilkins, R.G. Compton, *Angewand. Chem.* **45** (2006), pp. 2533-2537.
[15] B. Sljukic, C.E. Banks, R.G. Compton, *Nano Lett.* **6** (2006), pp. 1556-1558.
[16] X. Dai, G.G. Wildgoose, R.G. Compton, *Analyst.* **131**, (2006), pp. 901-906.
[17] J. Kruusma, N. Mould, K. Jurkschat, A. Crossley and C.E. Banks, *Electrochem. Comm.* (2007), pp. 2330-2333.
[18] C.P. Jones, K. Jurkschat, A. Crossley and C.E. Banks, *J. Iran Chem Soc.* **5**, (2008), pp. 279-289.
[19] U. Anik and S. Cevik, *Microchim Acta.* **166**, (2009), pp. 209-213.

Effect of modification techniques of MMT on morphology and crystallization behavior of MMT/HDPE nanocomposite

C. Kulawong[1,2] and C. Thongpin[1,2,*]

[1]Materials Science and Engineering Department, Faculty of Engineering and Industrial Technology, Silpakorn University, Sanamchandra Palace Campus, Nakornpathom, 73000, Thailand
[2] Center of Excellent for Petroleum, Petrochemical, and Advanced Materials, Chulalongkorn University, Bangkok, 10330, Thailand

[*]E-mail:chanchai@su.ac.th, Tel: +66-3421-9363, Fax: +66-3421-9363

Abstract:-This research is aimed to chemically modify montmorrilonite (MMT) via ion exchanging Na^+ with n-hexadecyl trimethyl-ammonium bromide (CTAB), obtaining CTAB-MMT, and subsequently grafting with three different silanes which contain various carbon chain length. The ion-exchange process is enhanced by using ultrasonic wave in order to ease the swelling and exfoliation of the MMT. The modification method was carried under continuous stirring and using ultrasonic wave passing through the reactor via ultrasonic probe. After the treatment, the dried powder was characterized using X-ray diffraction (XRD) spectroscopy in order to evaluated silicate d-spacing in the modified MMT. The modified MMT was then grafted with the silane via the method explained elsewhere [1-2]. The silane grafted MMT/HDPE composites, in the present of virgin coconut oil as a plasticizer, were prepared in an internal mixer. The composites obtained were also characterized using XRD and transmission electron microscopy (TEM) to examine the exfoliation of the silane-g-MMT layers in HDPE matrix. It was elucidated that the mixture of intercalate and exfoliate were found in the HDPE matrix, however more exfoliation of the silicate layers were evident in this study. Moreover, further investigation the composites using differential scanning calorimetry (DSC) showed that HDPE exhibited higher crystallization temperature (T_c) but lower degree of crystallinity than virgin HDPE.

Keywords: nanocomposite, nanoclay, natural plasticizer

1.Introduction

In the majority of conventional polymer composites, i.e., immiscible systems, the weak interaction between organic and inorganic phase leads to not enhanced mechanical and thermal properties. On the other hand, strong interaction between the polymer and organically modified clay (organoclay) leads the dispersion on the inorganic phase in nanometer scale and this favor the nanocomposites formation. As a result, the nanocomposites present unique properties that not were observed in conventional composites. The small amounts used of organoclay in the polymer matrices enhance several properties significantly such as: mechanical, thermal, optical, electric, dimensional, flammability and barrier due to the large contact area between polymer and clay on a nanoscale.

The most commonly used clay is montmorillonite (MMT), which belongs to the general family of 2:1 layered silicates. Their structures consist of two fused silica tetrahedral sheets sandwiching an edge-shared octahedral sheet of either aluminum or magnesium hydroxide. The silicate layers are coupled through relatively weak dipolar and van der Waals forces. The Na^+ or Ca^{2+} residing in the interlayers can be replaced by organic cations such as alkylammonium ions via an ion-exchange reaction to render the hydrophilic-layered silicate organophilic. In most cases, the synthesis of polymer/MMT nanocomposites was reported via either an intercalated polymerization process or a melt-direct intercalation. The melt-direct intercalation process was more promise of the two ways because this process does not needany solvent. Therefore, it is easily applied in industry [3].

Polyethylene is one of the most widely used polyolefin polymers. Since it does not include any polar groups in its backbone, it is not thought that homogeneous dispersion of clay layers in PE would be realized. Alexandre and coworkers reported the preparation of polyethylene-layered silicate nanocomposites by the polymerization-filling technique [4]. Shin et al. used bifunctional organic modifiers to prepare PE/clay hybrid nanocomposites in situ polymerization [5].

The purpose of this work was to obtain organoclays and with them to produce PE nanocomposites. The organoclays were prepared using a montmorillonite and testing three different types of silane to investigate their performance. The morphology and the mechanism of formation of the resulting PE/organoclays nanocomposites were investigated.

2. Experimental

2.1. Materials

A high density polyethylene (PE, H5818J, density: 0.957 g/cm3, melting flow index: 15.0 g/10 min) was supplied by Thai Polyethylene Co.Ltd. and used as composite matrix. The used pristine clay was Na-montmorillonite (MMT) supplied by Kunimine Ind. Co. with a cation exchange capacity (CEC) of 115 meq/100 g and the interlayer spacing (d_{001}) obtained by XRD was 12.5 Å. Hexadecyltrimethyl ammonium (CTAB), isobutyl (trimethoxy) silane (C_4), hexadecyltrimethoxysilane (C_{16}) and trimethoxy

(octadecyl) silane (C_{18}) were provided from Fluka. And natural plasticizer is virgin coconut oil, provided from Pume Din Co.Ltd.

2.2 Preparation of OMMT

The CTAB-MMT was prepared by dispersion Na+MMT (5 g) was dispersed in 175 ml 80 °C water and stirred continuously. Meanwhile, CTAB (100% CEC) and 1M HCl 5 ml were dissolved together in 125 ml 80 °C water. This latter solution was poured into the hot clay slurry under vigorous stirring and using ultrasonic wave passing through the reactor via ultrasonic probe leave to stir for 2.5 hrs. to flocculate the clay. The precipitate was then filtered and washed with hot water of 80 °C to remove chloride anion. The CTAB-MMT was then grafted with silane in a mixed solvent of ethanol/water with the ratio of 25/75. 5 g of CTAB-MMT was firstly dispersed in 1000 ml mixed solvent, and then 1.5 g of silane was introduced into the mixture, stirred for 8 h at 80 °C. The obtained precipitate was washed using the mixture of ethanol/water in order to remove the residual silane and dried at 60 °C in a vacuum oven.

2.3 *Nanocomposite preparation*

The polymer pellets and the clay were dried in a vacuum oven at 60 °C overnight and were fed to a Brabender Plasticorder (Torque
Rheometer Haake). And add coconut oil, static mixer of 50 mL capacity, preheated to 160 °C. The rotor speed was maintained at 60 rpm for about 15 min. The molten composites were extracted from the mixer and cooled naturally in air.

2.4 Characterization techniques

X-ray diffraction analysis (XRD) was performed using Rigaku X-ray generation (CuK*a* radiation with α = 1.5406 Å) at room temperature. The diffractograms were scanned in 2θ ranges from 3° to 10° at a rate of 0.02 °/s. The interlayer distance of Org-MMT in composites was calculated from the (d_{001}) peak by using Bragg equation.

Differential scanning calorimetry (DSC) analyses were carried out using a TA instrument 2920 Modulated DSC. The temperature and energy readings were calibrated with indium at each cooling rate employed in the measurements. All measurements were carried out in nitrogen atmosphere. The materials were heated from 50 to 180 ° C at a rate of 5 ° C/min to eliminate the heat history before cooling at 5 °C/min.

And in isothermal crystallization, materials were heated up to 180 °C and after 1 min of annealing cooled down at the rate of 5 °C/min to the crystallization temperature of 124 °C.

3. Result and discussion

The basal spacing (d_{001}) from XRD measurement was calculated from Bragg's law: d =l/(2sinq). Fig. 1 shows the XRD pattern of primary Na-MMT, CTABMMT in the range of the diffraction angle 2θ = 3-10°. The basal spacing was found to be 1.24 nm, 1.99 nm which are the spacing of Na-MMT, CTAB-MMT respectively. The higher-order peaks of CTAB-MMT indicate that MMT can keep its layered structure upon the cation exchange with alkylammonium cation.

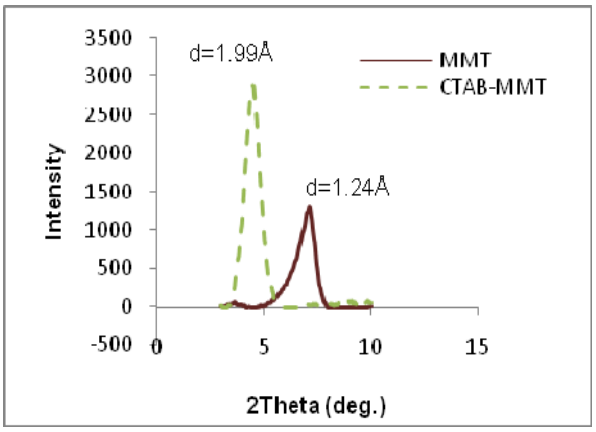

Fig.1. X-ray diffraction patterns of MMT and OMMT

In the present systems studied the best exfoliation was achieved from 2 phr of OMMT content, show in Fig.2. That is in the sample denoted as C16-2. However, a fraction of nonexfoliated but intercalated to various extent MMT particles still existed in this nanocomposite. The nonexfoliated particles show up on X-ray diffractograms for all other samples and their amount increases with the total MMT content.

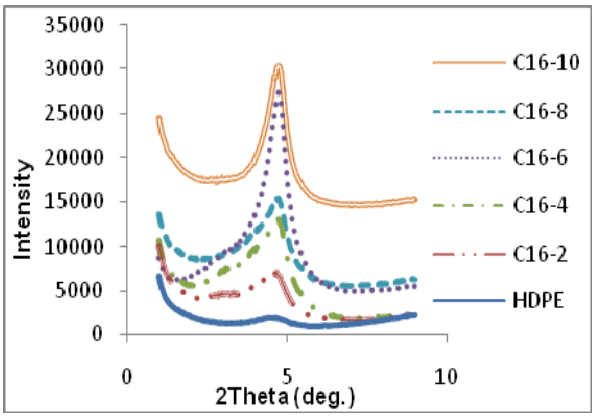

Fig.2. XRD diffractograms of HDPE based compositions with OMMT.

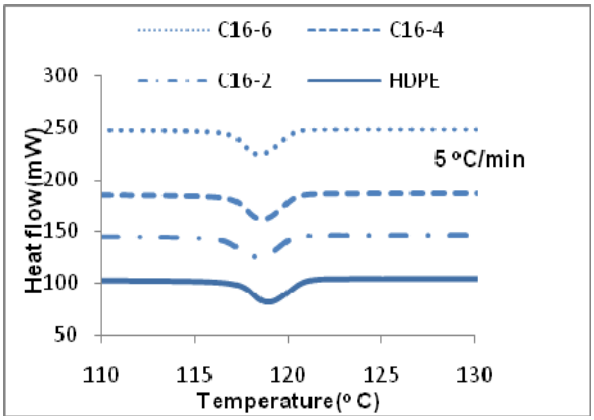

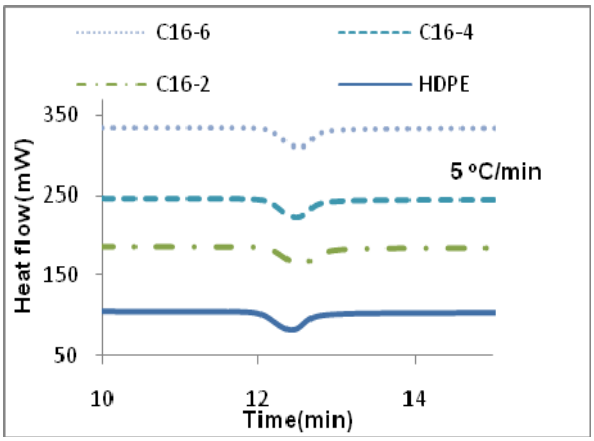

Fig. 3. DSC endothermic peaks recorded during nonisothermal crystallization at cooling rate of 5 °C/miin.

The endothermic crystallization peaks recorded during nonisothermal crystallization of HDPE and nanocomposites containing MMT, are shown in Fig. 3 and Table1. Nanocomposite having 2-6 phr of OMMT shows also the crystallization slower than pure HDPE. The nanocomposites having 8 and 10 phr of OMMT crystallize faster than neat HDPE. The crystallization peak temperature is slightly lower than pure HDPE. And composites have lower degree of crystallinity than virgin HDPE. In Ref [6] the acceleration of crystallization was observed only in those composites where nonexfoliated clay tactoids were present.

Table1 . Crystallization peak temperature; Tc, time and %crystallinity during cooling at rates 5 °C/min for materials studied.

Materials	T_c (5 ° C/min)	Time (min)	%Crystallinity (Xc)
HDPE	118.865	12.417	89.60
C16-2	118.353	12.517	86.41
C16-4	118.533	12.483	84.64
C16-6	118.380	12.517	80.35
C16-8	118.855	12.417	55.36
C16-10	118.867	12.104	58.58

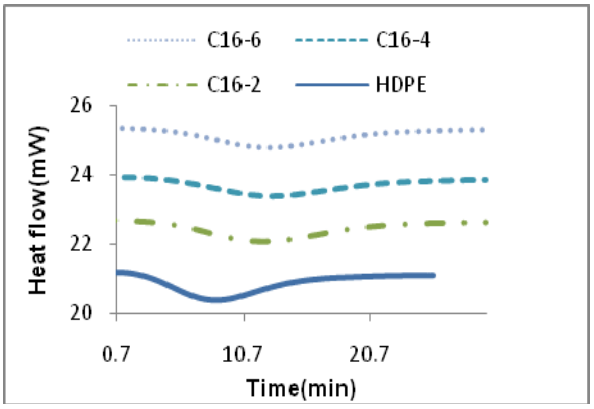

Fig 4. DSC endothermic peaks recorded during isothermal crystallization at 124 °C

Fig.4. nanocomposite having 2 and 4 phr of OMMT shows also slower rate of crystallization than that of pure HDPE. But the nanocomposites having 6 phr of OMMT show crystallization rate similar to that of neat HDPE.

4. Conclusions

Nanocomposites have been prepared in this work. It was elucidated that the mixture of intercalate and exfoliate were found in the matrix. However, almost exfoliated system would be obtained by ultrasonic wave method. Crystallization under static conditions show that the MMT exhibits low nucleation ability and the nucleation behavior increases with MMT content.

Acknowledgements

The authors gratefully acknowledge the financial support provided by the Department of Materials Science and Engineering, Faculty of Engineering and Industrial Technology, Silpakorn University; and the Center of Excellence for Petroleum, Petrochemical, and Advanced Materials, Chulalongkorn University, Thailand.

References

[1]. Thongpin, C.; Tangchantra, N.; Kositchaiyong, A.; Sagnuanmoo, R.; Jantham, J. and Sooksa-ard, A. *Advanced Materials Research*. **2008**, 55-57, 345-348.

[2]. Thongpin, C.; Tangchantra, N.; Kaewpetch, P.; Dejkun, J. and Chartsiriwattana, A. *Advanced Materials Research*. **2008**, 55-57, 341-344.

[3]. Hoai Nam P, Maiti P, Okamoto M, Kotaka T, Hasegawa N, Usuki A. Polymer **2001**, 42, 9633.

[4] Alexandre M, Dubois P, Sun T, Garces JM, Jerome R. Polymer **2002**, 42, 2123.

[5] Shin SYA, Simon LC, Soares JBP, Scholz G. Polymer **2003**, 44, 5317.

[6] Svoboda P, Zeng Ch, Wang H, Lee J, Tomasko DL. J Appl Polym Sci **2002**, 85, 1562.

Development of zinc tetra-tert-butyl-phthalocyanine (ZnTTBPc) blend in natural rubber as UV sensor

P. Promsuk[1], S. Pratontep[2], P. Sanguanthammarong[3], T. Kerdcharoen [1,4*]

[1]Materials Science and Engineering Programme, Faculty of Science, Mahidol University, Bangkok, 10400 Thailand
[2]KMITL College of Nanotechnology, King Mongut's Institute of Technology Ladkrabang, Bangkok, 10520 Thailand
[3] National Metal and Materials Technology Center (MTEC), NSTDA, 114 Thailand Science Park, Pathumthani 12120, Thailand
[4]NANOTEC Center of Excellence at Mahidol University, Rama 6 Road, Ratchathewi, Bangkok 10400, Thailand

* E-mail: teerakiat@yahoo.com

Abstract: Prolonged exposures to ultraviolet (UV) irradiation from sunlight and artificial sources can lead to sunburn and is a major cause for skin cancer. We report on the fabrication of a new UV colorimetric sensor in natural rubber matrix using zinc tetra-ter-butyl-phthalocyanine (ZnTTBPc) as a photochromic dye. Phthalocyanines play a major role in modern technology with applications in many fields. Complexation of a phthalocyanine molecules with various metal ions at its core center results in a diverse range of their photophysical properties. ZnTTBPc natural rubber thin films on clean glass substrates were prepared by the spin-coating technique, using chloroform as a solvent. The spin-coated thin films were placed in a black box under the 365 nm UV lamp irradiation with the light intensity of 1750 μW/cm^2. The optical absorption characteristics of UV-exposed films were measured by using UV-Vis spectrometer. The time of UV exposure was varied from 1, 5, 10, 30, 60, 120, 180 minutes. The results showed that the overall optical absorbance of the films was decreasing with increasing UV-exposure time. The UV label sensors were completely bleached out after 180 minutes. The stability of the UV label sensors under dark and ambient light was also investigated by storing them in a light-proof box and a transparent box over a long period of time. The optical absorbance of the UV sensors in the light-proof box remained almost unchanged over one month, whereas that of the UV sensors in the transparent box started to decrease after 7 days. This demonstrates that our low cost UV label sensor has promising sensitivity and stability characteristics for future applications in personal health care, such as personal UV dosimeter tags.

Introduction

Natural rubber (NR) is a natural polymer that is considered one of the most widely used with many attractive properties including low cost, excellent dynamic properties and high resilience [1]. Organic dyes and pigments such as metalloporphyrins and metallophthalocynanines have been discovered to introduce new functionalities, for example, epoxidation reaction in polymer [2]. NR blends have attracted the attention of researchers of polymeric materials due to the possibility of tailoring their properties by blending two or more polymers [3]. It is well known that the reactions induced in polymers by UV irradiation depend on different factors such as chain structure, internal and external impurities, physical state of the sample, type of radiation source, etc.

The purpose of this work was to develop UV sensitive materials from a blend of NR with zinc tetra-ter-butyl-phthalocyanine (ZnTTBPc), which was prepared into thin films by a spin-coating technique from solution. The optical absorption of the films was under controlled UV exposure. The stability of the films was examined by storing them in a light-proof box and a transparent box over a long period of time.

Materials and Methods

Natural rubber was provided from the National Metal and Materials Technology Center, Thailand. Zinc tetra-ter-butyl-phthalocyanine (ZnTTBPc) were purchased from Sigma Aldrich.

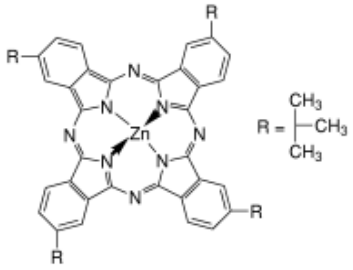

Figure 1. Structure of Zinc tetra-ter-butyl-phthalocyanine (ZnTTBPc).

NR- ZnTTBPc thin films on clean glass substrates were prepared by spin-coating using the ZnTTBPc : NR : chloroform concentration ratio of 2 mg/20 mg/1 ml, respectively. The spin-coating conditions were 2,500 rpm and 75 second spinning time at room temperature. The optical absorption of the thin films within the range 300-800 nm was recorded by using a Jenway UV-Visible spectrophotometer. The spin-coated thin films were placed in a black box under the 365nm UV lamp irradiation with the intensity of 1750μW/cm^2 for various exposure times: 1, 5, 10, 30, 60,120 and 180 minutes. The optical absorption properties of the films were re-measured after the UV irradiation. The stability was also investigated by keeping in a light-proof box and a transparent box over a long period of time: 1, 2, 7, 14, 30, 60 and 90 days.

Results and Discussion

UV irradiation has recently been a fast procedure for chemical synthesis. In this work, the ZnTTBPc -NR blend films as prepared appeared blue. After prolonged UV irradiation, the films of ZnTTBPc -NR films became almost colorless, as shown in Fig. 2.

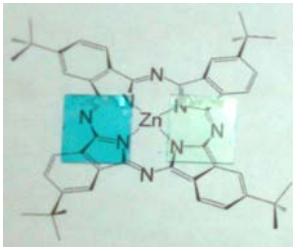

Figure 2. Color of NR-ZnTTBPc thin films before and after prolonged UV irradiation for 3 hour.

The optical absorption spectra of the films at various UV exposure times are shown in Fig. 3. The phthalocyanine displays characteristic absorption spectra with the Q (visible range) and B (near UV range) bands. The disappearance of the color should mean that ZnTTBPc molecules completely disintegrated rather than became de-metallized because metal free phthalocyanines would still have a light blue color. This is in accordance with the optical absorption results, which show only overall reduction of the peak intensities. Fig. 4. Average UV absorbance of NR-ZnTTBPc thin films in the Q band and B band regions. The peaks were slowly reduced over 2 hours exposed. The films became almost colorless after 3 hour UV exposure.

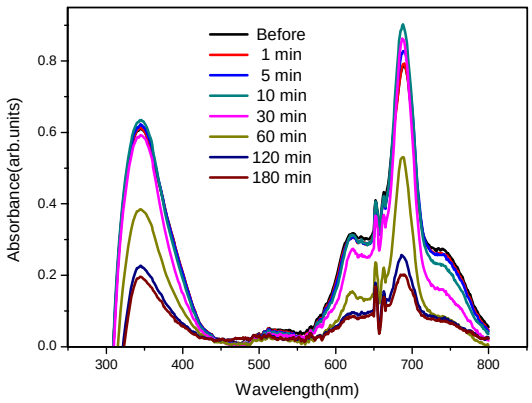

Figure 3. Optical absorption spectra of NR-ZnTTBPc thin films before and after UV irradiation.

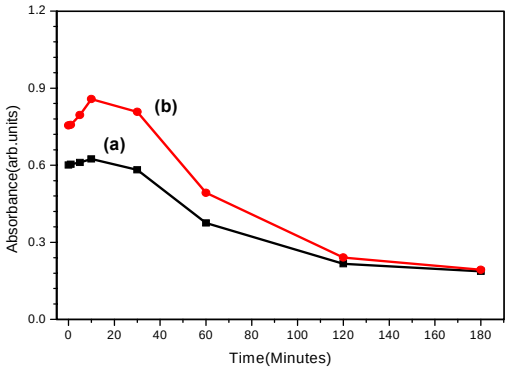

Figure 4. Average UV absorbance of NR-ZnTTBPc thin films in the region (a) 335-350 nm and (b) 680-695 nm.

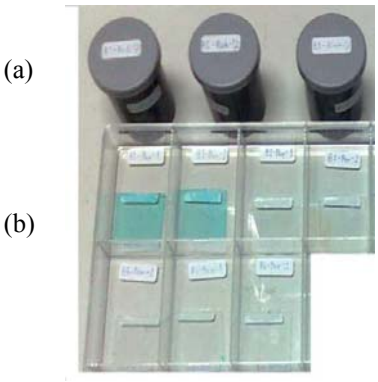

Figure 5. Containers used for storing the NR-ZnTTBPc films: (a) light-proof boxes (b) transparent boxes.

The stability of the NR-ZnTTBPc colorimetric UV sensor was investigated by monitoring the optical absorbance of the films over various storage times, as shown in Fig. 5. The ZnTTBPc-NR blend films were keeping in a light-proof box and a transparent box after the spin coating without UV exposure. It was found that the storage of the NR-ZnTTBPc UV sensors under dark conditions induced slow changes in the optical absorbance over a few months, whereas under the ambient light the sensors retained their characteristics for only a few days, as shown in Fig. 6 -7.

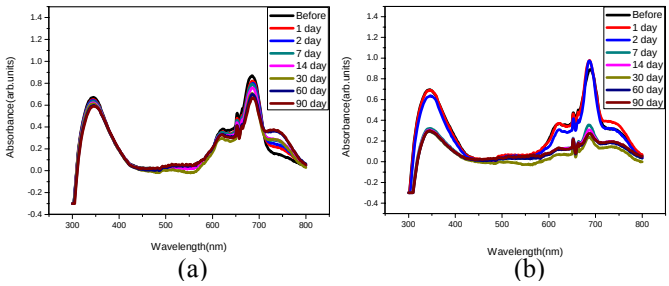

Figure 6. Optical absorption spectra of NR-ZnTTBPc thin films under storage in (a) light-proof boxes and (b) a transparent boxes.

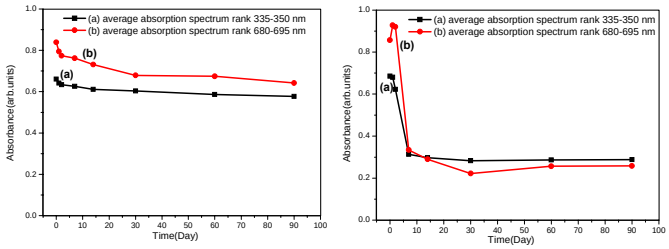

(a) (b)

Figure 7. Average optical absorbance of NR-ZnTTBPc thin films in the regions 335-350 nm and 680-695 nm, under storage in (a) a light-proof box and (b) a transparent box.

Conclusions

We have demonstrated that the NR-ZnTTBPc blend films prepared by spin coating can be used as low cost colorimetric UV sensors. At the dose rate of approximately 1750 $\mu W/cm^2$ the films appeared colorless after three hours of UV exposure. The stability of the sensors were also monitored. The sensors may be stored over a few month period in a dark condition. The NR-ZnTTBPc colorimetric UV sensors may be further developed for applications in personal health care, such as low cost personal UV dosimeter tags.

Acknowledgements

The authors thank NANOTEC (Project no. M09006) and Mahidol University for financial support.

References

[1] P. Sae-Oui, C. Sirisinha, T. Wantana, K. Hatthapanit, *J. Appl. Polym. Sci.* **104** (2007), pp. 3478-3483.
[2] E.M. Davoras, A.G. Coutsolelos, *J. Inorg. Biochem.* **94** (2003), pp. 161-170.
[3] S.H. El-Sabbagh, *J. Appl. Polym. Sci.* **90** (2003), pp. 1-11.
[4] M. Idowu, T. Nyokong, *J. Photochem. Photobiol. A.* **199** (2008), pp. 282-290.
[5] S.Y. Al-Raqa, A.S. Solieman, A.A. Joraid, S.N. Alamri, Z. Moussa, A. Aljuhani, *Polyhedron.* **27** (2008), pp. 1256-1261.
[6] C. Saron, F. Zulli, M. Giordano, M.I. Felisberti, *Polym. Degrad. Stab.* **91** (2006), pp. 3301-3311.
[7] W. Spiller, D. Wöhrle, G. Schulz-Ekloff, W.T. Ford, G. Schneider, J. Stark, *J. Photochem. Photobiol. A*. **95** (1996), pp. 161-173.
[8] Y. Kaneko, Y. Nishimura, T. Arai, H. Sakuragi, K. Tokumaru, D. Matsunaga, *J. Photochem. Photobiol. A.* **89** (1995), pp. 37-44.

Natural fibers in Thailand and its potential as geotextiles; I) structure and properties of the fibers

U. Weerawatsophon[1], P. Methacanon[1*], N. Sumransin[1], C. Prahsarn[1] and D.T. Bergado[2]

[1] National Metal and Materials Technology Center, 114 Thailand Science Park, Paholyothin Rd., Klong 1, Klong Luang, Pathumthani 12120 Thailand
[2] Geotechnical Engineering Program, School of Civil Engineering, Asian Institute of Technology, Paholyothin Rd., Klong 1, Klong Luang, Pathumthani 12120 Thailand

[*] E-Mail: pawadeem@mtec.or.th

Abstract: With increase in the environmental awareness and sustainability along with high cost of petroleum-based geotextiles, natural fiber geotextiles have emerged. The main purpose of the work is to assess the possibility of developing good performance woven geotextiles made of natural fibers. Initially, the composition, morphology and properties of four natural fibers (water hyacinth, reed, sisal, and roselle) were studied in order to select the most appropriate fiber for the next study steps; life expansion and field tests. It was found that total cellulose content of sisal and roselle was very close (76.55% and 75.06%, respectively) and higher than that of water hyacinth (62.43%) and reed (59.92%). Lignin content ranged from 11 to 24 %, with the highest content in reed. Water hyacinth possessed the highest ash content (14.70%). Moisture absorption at 95%RH of sisal and roselle was less than that of reed and water hyacinth. Tensile strength of dry sisal, roselle, water hyacinth and reed was 158.74, 111.72, 18.60, and 18.20 MPa, respectively, while elongation of each one was 12.70, 10.83, 8.81 and 13.31%, respectively. In addition, it was found that when the fibers were wet, their tensile strength and elongation increased. Morphology and fiber length of the fibers were determined using optical microscope. The results showed that there was a positive correlation between tensile strength and fiber length; the longer fiber length, the higher tensile strength. From all obtained results, roselle and water hyacinth were selected as a representative of long and short fibers, respectively for the further studies.

Introduction

In the recent years, the intensity of torrential rainfall and its subsequent destructive influencing on human community has become severe and unpredictable due to climate change including global warming. Landslide disaster is one of natural disasters resulting from the climate change. Ground improvement together with geosynthetic engineering has contributed greatly in undertaking scientific and systematic methodologies for declining the risk. Geotextiles derive their name from the two words "geo" and "textiles" and, therefore, mean the use of fabrics either woven or non-woven in association with the earth. Geotextiles, a core member of geosynthetic family, are widely used in civil engineering applications to improve soil structural performance. Their main functions are aggregate separation, soil reinforcement, filtration, drainage, and liquid barriers [1].

With the growing environmental concern all over the world, natural fiber geotextiles known as "Limited Life Geotextiles (LLGs)" have emerged in applications of temporary reinforcement and biological soil stabilization. In addition, they help to suppress extreme fluctuations of soil temperature [2]. Although the natural fibers are readily available and very low cost, only a few including jute [3], flax [4], coir [5, 6], sugarcane bagasse [7], palm-leaf [2] have been used as a raw material in geotextiles application. The market for geotextiles is growing, with world wide sales of over 700 million square meters annually of which about 2% is bio-fibers [8]. Therefore, there are many opportunities to expand the markets and develop new products.

The main purpose of the work, being presented here just a part, is to assess the possibility of developing good performance woven geotextiles made of the studied natural fibers; sisal, roselle, reed, or water hyacinth. Though, these natural fibers are one of the most natural fibers widely used in ropes, twines, rugs, mats, mattresses, and handcrafted articles, a large quantity of these economic and renewable resources is still under-utilized. In considering the aforementioned fibers for geotextiles, fiber chemistry and properties were a major consideration. Since the material composition of geotextiles determines their life in the field. This type of data is critical in order to determine if a selected fiber is suitable for geotextile application. In this paper, the detailed chemical composition and physical properties of the fibers were reported with the aim of providing knowledge of interest.

Materials and Methods

Materials: Natural fibers used for this study were water hyacinth (*Eichhornia crassipes*), reed (*Phragmites vulgaris*), roselle or Thai kenaf (*Hibiscus sabdariffa*) and sisal (*Agave sisalana* Perr.). Each fiber was obtained from the handicraft communities in Nakhon Pathom, Buriram, Khon Kaen and Petchburi Provinces, respectively. All analyses were carried out on the as received fibers, except where otherwise noted.

Fiber composition: Total cellulose content of the studied fibers was determined by Jenkins method [9]. Lignin content in the fibers was determined as Klason lignin in accordance with the standard method TAPPI

T 222 om-88 [10]. Ash content in the fibers was investigated according to ASTM method E 1755-01 [11]. Moisture content was determined by oven drying at 105 ^{o}C for 24 h. Each composition analysis was carried out in triplicates.

Morphology and fiber dimension: Surface and cross-section morphology of the fibers were investigated using a optical microscope. For investigation of fiber dimension, firstly, single cells of the fibers were obtained after the delignification process that was carried out at 80 ^{o}C for 6 h with the ratio hydrogen peroxide/acetic acid of 3/1, and repeated twice. After treatment, the samples were filtered and washed thoroughly with water. The average length and diameter of the fiber single cell were measured using the optical microscope.

Determination of moisture regain: The obtained fibers were twisted as yarns with a diameter of 2 mm, dried for 1 day at 50 ^{o}C and then placed at 23 $\pm$ 1 ^{o}C over saturated K_2SO_4 salt solution in a chamber having 95% relative humidity (RH). Weights of samples were measured as a function of time. All tests were conducted in triplicates.

Tensile properties: Tensile properties of dry and wet twisted fiber yarns in terms of tensile strength and elongation at break were determined using the Instron Universal testing machine (Instron 55R 4502) with a load cell of 10,000 N, a crosshead speed of 50 mm/min, and a gauge length of 15 cm. The length and diameter of specimens were approximately 40 and 0.2 cm, respectively. Measurements were performed in ten replicates. For the wet state, the twisted yarns were soaked in water for 16 h prior to tensile testing.

Results and Discussion

In general, chemical composition of lignocellulosics is inherent, according to the particular needs of the plants. Cellulose, hemicelluloses and lignin are the three main constituents of any lignocellulosic source, and the proportion of these components in a fiber depends on the age, source of the fiber and the extraction conditions used to obtain the fibers [12]. Cellulose is the main structural component that provides strength and stability to the plant cell walls. As shown in Table 1, cellulose is a main constituent of the fibers, ranging from 59 to 77 %. Sisal and roselle had a higher cellulose content compared with reed and water hyacinth. The results are in accordance with many previous studies [13, 14] even though there are some variations existing. Lignin is a highly crosslinked molecular complex with amorphous structure and acts as glue between individual cells. The lignin content of the fibers influences the structure, properties, morphology, flexibility and rate of hydrolysis [15]. It is worth noting that the reed possessed the highest content of lignin, making it coarse and less flexible. Water hyacinth contained the highest amount of ash. This was well supported by numerous works which reported that water hyacinth possesses the ability for the removal of toxic metals from wastewater [16, 17]. Moisture content present in reed and water hyacinth was approximately 1.5 times higher than that in sisal and roselle.

Table 1: Normalized chemical composition (% wt on dry basis) of the studied natural fibers

Natural fiber	A	B	C	D
Sisal	76.55	14.86	0.91	7.68
Roselle	75.06	16.45	0.79	7.69
Reed	59.92	23.50	5.52	11.06
Water hyacinth	62.43	11.41	14.70	11.45

A = cellulose, B = lignin, C = ash, and D= moisture

Figure 1 illustrates surface and cross-section morphology of the four studied fibers. The surface of all fibers looked uniform meanwhile, within the leaf, a sandwich structure was present. The diameter of fibers was in range of 0.05-0.10 mm for sisal and roselle. The cross-sectional images of both are very similar. In contrast, for reed and water hyacinth, the fiber diameters were significantly larger, ranging from 10.0 to 15.0 mm. In addition, a notable difference in the water hyacinth is hollow cavities which decrease the bulk density of the fiber making it lightweight.

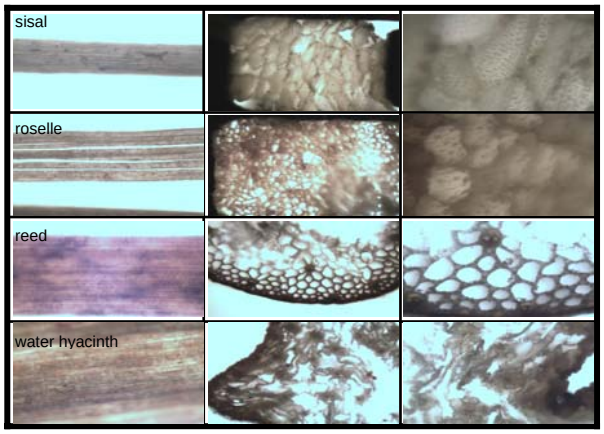

Figure 1. Optical mirographs of surface (1st column) and cross-section (4x, 2nd column and 40x, 3rd column) morphology of the studied natural fibers

Since lignocellulosic materials are composed of single cells of cellulose held together by lignin and the dimension and arrangement of unit cells in a fiber determine the structure and also influence the properties of the fibers. The dimension of individual fiber cell was determined and shown in Table 2. Individual cells in the studied fibers were approximately 0.1-0.3 mm long and 5-16 μm wide. Sisal had the longest single fiber cells, followed by roselle, reed, and water hyacinth, respectively, whereas the widest one belonged to water hyacinth, sisal, roselle, and reed, respectively. The presence of longer and smaller width single cells results in finer and

stronger fibers [18]. The dimensions of individual cells in natural fibers are dependent on the species, maturity and location of the fibers in the plant and also on the fiber extraction conditions [19].

Table 2: Fiber dimension of the studied natural fibers

Natural fiber	Length (mm)	Width (μm)
Sisal	0.26	12.09
Roselle	0.20	12.04
Reed	0.13	4.95
Water hyacinth	0.12	15.70

The fiber properties such as moisture regain, strength and elongation are measurable properties that are used to help comparing the fiber performance. Moisture absorption curve of the studied fibers is shown in Figure 2. The moisture absorption was more rapid at the initial stages and lower amount of water were absorbed as time increased until reached equilibrium. As predicted from the fiber morphology, the remarkable amounts of hollow cavity in water hyacinth fiber greatly contributed to the highest water regain (ca. 120%). The high moisture regain suggest ease of the microbial attack (biodegradation). The moisture sorption of sisal and roselle was very close (ca. 20%) and less than that of reed and water hyacinth.

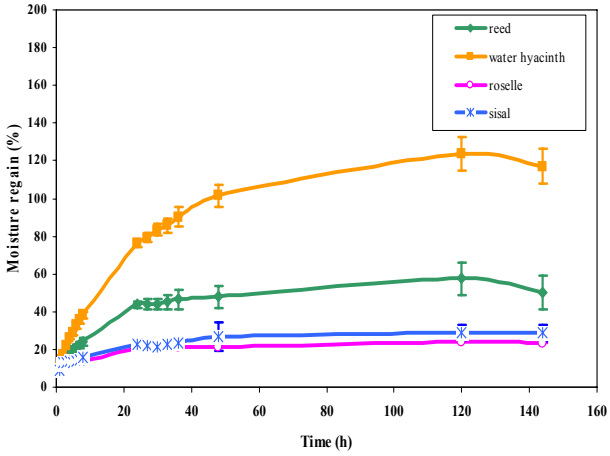

Figure 2. Moisture absorption of the natural fibers at 95%RH, 23 ºC

Mechanical properties in terms of tensile strength and elongation at break of the studied natural fibers in wet and dry states are shown in Figure 3. It is worth noting that both tensile strength and elongation of all wet fibers were higher than those of dry ones. This probably resulted from moisture in the fiber influencing the degree of crystallinity, crystallite orientation, and porosity of the fibers [12]. Tensile strength of reed was similar to that of water hyacinth (ca. 18-33 MPa) but much lower than that of roselle and sisal (ca. 112-180 MPa, Figure 3a). Although the strength of fibers cannot be exactly correlated to the cellulose content and microfibrillar angle, generally, fibers with higher cellulose content, higher degree of polymerization of cellulose, longer cell length and lower microfibrillar angle give better mechanical properties [12]. Elongation of the studied fibers was not significantly different (ca. 9-25%, Figure 3b). However, at wet state, the short fibers especially the water hyacinth showed remarkable increase in elongation. In general, natural fibers have a characteristic higher strength and lower elongation or *vice-versa*.

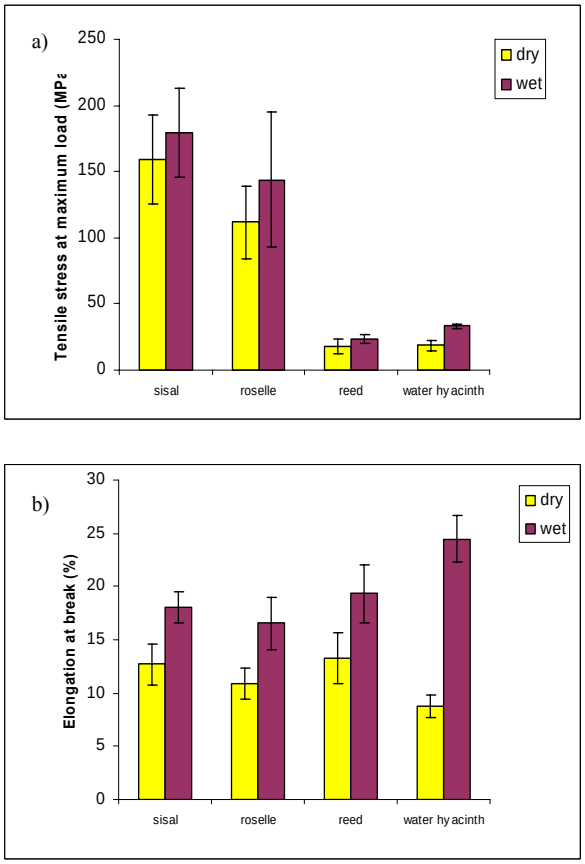

Figure 3. Mechanical properties of the natural fibers; a) tensile strength, and b) elongation at break

Conclusions

From composition and properties of the four studied fibers, they were classified into two groups; long (sisal and roselle) and short fibers (reed and water hyacinth). The unique properties such as low moisture absorption and high strength of roselle were similar to those of sisal, which would provide a good performance geotextiles. For reed and water hyacinth, it is worth to study further due to their availability, lower cost and high elasticity even though they have lower strength compared with sisal and roselle. Therefore, from many points of view, roselle and water hyacinth were selected as a representative of long and short fibers, respectively for the further studies in geotextile application.

References

[1] N.W.M. John, *Geotextiles*, Blackie & Son Ltd., London, UK (1987).
[2] R. Bhattacharyya, M.A. Fullen, K. Davies and C.A. Booth, *Agric. Ecosyst. Environ.* **130** (2009), 50-58.
[3] S.R. Ranganathan, *Geotext. Geomembr.* **13** (1994), pp. 421-433.
[4] A. Rawal and R. Anandjiwala, *Geotext. Geomembr.* **25** (2007), pp. 61-65.
[5] K.R. Lekha and V. Kavitha, *Geotext. Geomembr.* **24** (2006), pp. 38-51.
[6] E.A. Subaida, S. Chandrakaran and N. Sankar, *Geotext. Geomembr.* **26** (2008), pp. 384-392.
[7] I. Du and M. Saska, *J. Am. Soc. Sugar Cane Technol.* **27** (2007), pp. 36-47.
[8] B. English, *Geotextiles – A specific application of biofibers*, Research in industrial application of non food crops Conf. Proc., Copenhagen, Denmark, 1995, pp. 79-86.
[9] S.H. Jenkins, *Biochem. J.* **24** (1930), pp. 1428-1432.
[10] TAPPI Test Methods (1996), TAPPI T222 om-88 Klason Lignin.
[11] ASTM (2007), ASTM D1102-84 Standard test method for ash in wood.
[12] N. Reddy and Y. Yang, *Polym.* **46** (2005), pp. 5494-5500.
[13] C.C. Gunnarsson and C.M. Petersen, *Waste Manage.* **27** (2007), pp. 117-129.
[14] Y. Li, Y-W. Mai and L. Ye, *Compos. Sci. Technol.* **60** (2000), pp. 2037-2055.
[15] K. Sukumaran, K.G. Satyanarayana and S.G.K. Pillai, *Met. Mater. Process* **13** (2001), pp. 121-136.
[16] A. Milik, *Environ. Int.* **33** (2007), pp. 122-138.
[17] S.H. Hasan, M. Talat and S. Rai, *Bioresour. Technol.* **98** (2007), pp. 918-928.
[18] N. Reddy and Y. Yang, *Biotechnol. Bioeng.* **97** (2007), pp. 1021-1027.
[19] N. Reddy and Y. Yang, *Trends Biotechnol.* **23** (2005), pp. 22-27.

Effect of Ar and N_2 flow rate on structure of tin thin films deposited by reactive DC magnetron sputtering

N. Witit-anun* and S. Chaiyakun

Vacuum Technology and Thin Films Research Laboratory
Department of Physics, Faculty of Science, Burapha University, Chon Buri, Thailand

* E-Mail: nirun@buu.ac.th

Abstract: Titanium nitride (TiN) films possessing excellent mechanical properties, low electrical resistivity, high chemical and thermal stability, and interesting optical properties (colors varying from gold to dark brown), have been applied in many areas such as abrasion resistant coatings on tool steels, decorative coatings in architecture, diffusion barrier layers in semiconductor devices, and flat panel displays. The main objective of this research was studied the effect of gas flow rate, argon and nitrogen on structure of TiN thin films. The films were deposited on silicon wafer by reactive DC magnetron sputtering technique at different argon gas flow rates ranging from 1.0 sccm to 3.0 sccm and nitrogen gas flow rates from 1.0 sccm to 3.0 sccm. The crystal structure, surface morphology and films thickness were characterized by XRD and AFM, respectively. The crystalline of deposited films showed reflections corresponding to the (111), (200) and (220) orientation of TiN structure. There was no significant variation in the surface morphology with gas flow rate. It is noted that the roughness values and thickness varied from 2.8 nm to 2.9 nm and 372 nm to 387 nm, respectively.

Introduction

Recently, hard coatings such as TiN, TiCN, TiAlN, CrN, BN and DLC are used for cutting tools and wear applications. The use of these hard coatings has greatly improved the tribological performance of tool and machine elements [1–4]. Among these hard coatings, the TiN has been very successfully used and extensively studied for a long time because of its excellent properties such as high melting point, high hardness and high thermal conductivity as a protective coating material. In the tribological application of TiN coating, adhesion is the most important property and closely related to the lifetime of tools and dies exposed in severe environments [5]

TiN thin films possessing excellent mechanical properties, low electrical resistivity (18–25 μΩ-cm, better than that of Ti, 40–50 μΩ-cm), high chemical and thermal stability, and interesting optical properties (colors varying from gold to dark brown) [6,7], have been applied in areas such as abrasionresistant coatings on tool steels, decorative coatings in architecture, diffusion barrier layers in semiconductor devices, and flatpanel displays [8–10].

The crystal structure and properties of the deposited thin films were influenced by deposition parameters. For example, J. H. Huang et al. [11] reported that the effect of nitrogen flow rate on structure and properties of nanocrystalline TiN thin films produced by unbalanced magnetron sputtering. The (111) prefer orientation was observed initially and then changed to (200) with an increase in nitrogen flow rate.

The purpose of this study is to investigate the effect of argon and nitrogen flow rate on structure, colour and surface morphology of nanocrystalline TiN thin film deposited by reactive DC magnetron sputtering.

Materials and Methods

The TiN thin films were deposited on n-type silicon wafers (100) plane (for XRD and AFM characterization) and glass (for study colour and physical properties) without external heating by home-made reactive DC magnetron sputtering system as show in Figure 1. The substrates were cleaned in trichoroethylene, acetone and isopropanol using an ultrasonic for 5 min and dried, respectively. The films were prepared by high purity titanium (99.97%) and of 2 inch diameter and 0.125 inch thickness in a mixture of high purity argon (99.999%) and nitrogen (99.999%) atmosphere.

A diffusion pump with rotary pump was used to achieve the base pressure of 5.0×10^{-5} mbar. Prior to deposited, the Ti-targets were presputted for 5 min before each deposition in order to remove contaminates from Ti-targets surface. Then, the films were prepared by varying nitrogen flow rate ranging from 1 sccm to 3 sccm with fixed argon flow rate at 1 sccm consequently, fixed nitrogen flow rate at 1 sccm and deposited at different argon flow rate ranging from 1 sccm to 3 sccm. The total pressure was set at 5.0×10^{-3} mbar and target to substrate distance (ds-t) were kept fixed at 13 cm during the all depositions. The deposition conditions for the samples are listed in Table 1.

The crystal structure was characterized by x-ray diffractrometer (Riguku, Rint 2000) using Cu Kα radiation operated at 40kV and 40 mA with incidence angle (3°). The 2θ was scanned from 20^{O} – 65^{O} and scanning speed of 2°/min. The surface morphology, roughness values and thickness were evaluated by atomic force microscope (Nanoscope IV, Veeco Instrument Inc). The scan area was carried out of $1 \times 1\ \mu m^2$.

Table 1: Deposition conditions of TiN Film

Deposition parameters	Details
Target	Titanium (99.97%),
Base pressure (mbar)	5.0×10^{-5} mbar
Total pressure (mbar)	5.0×10^{-3} mbar
Substrate	Si-wafer and glass
Ar flow rate (sccm)	1, 2 and 3
N_2 flow rate (sccm)	1, 2 and 3
Current (mA)	800
Deposition time (min)	60
ds-t (cm)	13

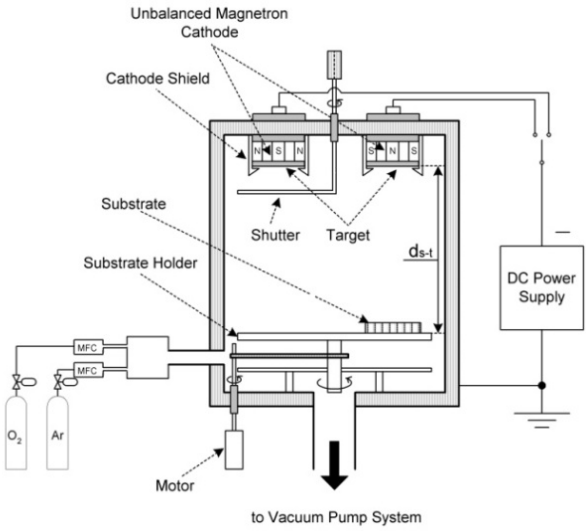

Figure 1. Schematic diagram of the DC magnetron sputtering system.

Results and Discussion

The physical properties of the films: The colour of TiN thin films deposited on glass by varying the argon and nitrogen flow rate were summarized in the Table 2 and Table 3, respectively. For the films prepared by varying the nitrogen flow rate, the film is yellow gold at 1 sccm. The film's color change from purple to dark purple (Figure 2) when increase of nitrogen flow rate to 2 and 3 sccm, respectively. In case of varying the argon flow rate, there was no change of film color. The yellow gold was observed for all films (Figure 3). It was noted that the nitrogen flow rate are strong influence to the color of the film.

Table 2: The color of TiN thin film deposited at various N_2 flow rate

Ar to N_2 ratio	Color
1:1	Yellow gold
1:2	Purple
1:3	Dark purple

Table 3: The color of TiN thin film deposited at various Ar flow rate

Ar to N_2 ratio	Color
1:1	Yellow gold
2:1	Yellow gold
3:1	Yellow gold

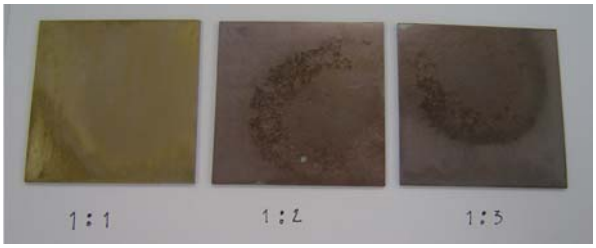

Figure 2. The color of TiN film deposited at various nitrogen flow rates.

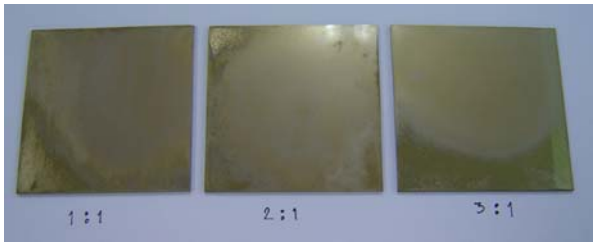

Figure 3. The color of TiN film deposited at various argon flow rates.

The influence of nitrogen flow rate on crystal structure: The XRD patterns of cubic TiN films deposited at different nitrogen flow rate at deposition time of at 60 min are shown in Figure 4. It was revealed that films exhibited reflection of (111), (200) and (220) planes at 2θ of 36.44°, 42.44° and 62.62°, respectively, which indicated that the film were cubic TiN structure. The XRD intensity of (111) plane was increased and decreased with increasing of argon flow rate whereas (200) plane was rapidly decreased when increase nitrogen flow rate but didn't change for (220) plane.

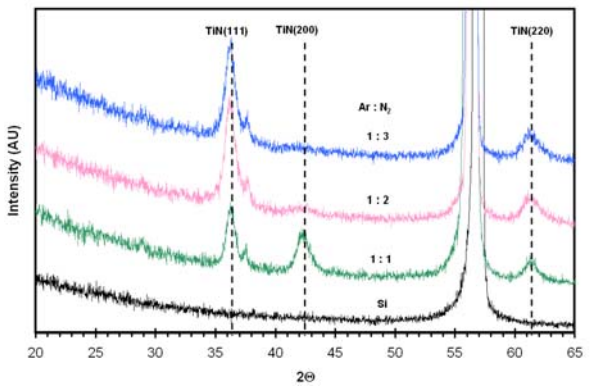

Figure 4. The XRD pattern of TiN film deposited at various nitrogen flow rates.

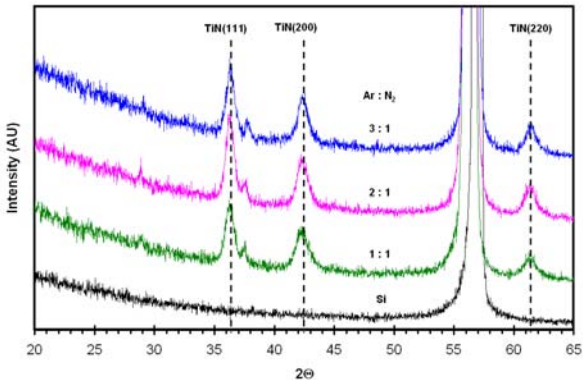

Figure 5. The XRD pattern of TiN film deposited at various argon flow rates.

The influence of argon flow rate on crystal structure: Figure 5. show the X-ray diffraction patterns of cubic TiN films deposited at various argon flow rate. It was revealed that films exhibited reflection of (111), (200) and (220) planes at 2θ of 36.44°, 42.44° and 62.62°, respectively, which indicated that the film were cubic TiN structure. It was observed that the peak intensity of (111) plane increased and decreased with increase flow rate. For the XRD intensity at (200) and (220) planes were insignificance change.

In addition, It was found that the color of the films depended on the crystal structure obtained from XRD results. The gold color films were observed when increased the argon flow rate but change from gold to purple with the nitrogen flow rate in the range of 2-3 sccm which respect to decreasing of XRD intensity at (200) plane. It can be concluded that to the gold color of the films were achieved at low nitrogen flow rate including the (111), (200) and (220) planes.

The surface morphology: The sample AFM images of surface morphology of deposited thin films are shown in Figure 6 with display three-dimensional representations (1x1 μm^2 surface plots), corresponding to the samples prepared at argon to nitrogen ratio of 1:1 sccm. The TiN grains were formed with mainly composed of individual grain and compact pattern which can be clearly identified but some areas were performed big grain (Figure 6b). It was revealed that the surface morphology had no significant change with gas flow rate. The root mean square roughness (rms) values of the film were varied from 2.8 nm to 2.9 nm, respectively. The average thicknesses are 372 nm to 387 nm with increasing gas flow rate.

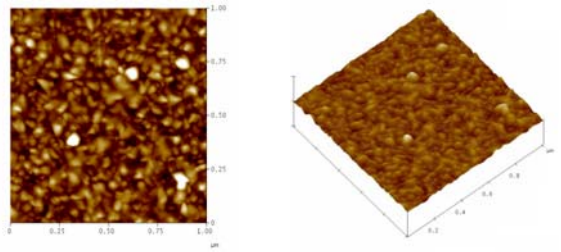

(a) (b)

Figure 6. Typical AFM images of TiN thin films (a) 2D (b) 3D

Conclusions

The nanocrystalline titanium nitride (TiN) thin films were successfully deposited on Si (100) wafers and glass by reactive DC magnetron sputtering system to investigate the effect of gas flow rate (Ar and N_2) on structure of TiN thin films. The colors of the films were strongly depended on nitrogen flow rates. The transformation from yellow gold to dark purple was investigated with increased nitrogen flow rate but the color still was yellow gold as increased argon flow rate. The XRD measurement identified that the polycrystalline cubic TiN structure with (100), (200) and (220) planes were observed. When increase the nitrogen flow rate, the XRD intensity at (200) plane was obviously changed. In case of increase the argon flow rate, it was found that the (111) plane increased and decreased. The results from AFM measurement indicated that the films insignificance change with argon and nitrogen flow rate. The roughness values and thickness were in the range of 2.8 nm – 2.9 nm and 372 nm – 387 nm, respectively.

Acknowledgment

The financial support from the Commission on Higher Education, Thailand, for this work is gratefully acknowledged.

References

[1] S.Y. Lee, J.W. Chung, K.B. Kim, J.G. Han and S.S. Kim, *Surf. Coat. Technol.* **86/87** (1996), pp. 325.
[2] S.Y. Lee, J.W. Chung, H.J. Park, J.G. Han, J.H. Lee and J. Kor, *Int. Met. Matter.* **35** (1997), pp. 1734.
[3] G.S. Kim, S.Y. Lee, E.Y. Lee andJ. Kor, *Int. Met. Matter*. **37** (1999), pp. 578.
[4] S.Y. Lee, J.W. Chung, J.G. Han, S.S. Kim and J. Kor, *Int. Met. Matter.* **34** (1996), pp. 1220.
[5] U. Wiklund, P. Hedenqvist and S. Hongmark, *Surf. Coat. Technol.* **97** (1997), pp. 773.
[6] W.D. Sproul, J.E. Green, J.A. Thornton (Eds.), *Physics and chemistry of Protective Coating*, 1999
[7] J.E. Sundgren, *Thin solid Films* **128** (1985), pp. 21.
[8] J.E. Sundgren and H.T.G. Hentzell, *J. Vac. Sci. Technol.* **A4** (1986), pp. 2259.
[9] M. Wittmer, *J. Vac. Sci. Technol.* **A3** (1985), pp. 1797.
[10] N.Y. Kim, Y.B. Son, J.H. Oh, C.K. Hwangbo and M.C. Park, *Surf. Coat. Technol.* **128-129** (2000), pp. 156.
[11] J.H. Huang, K.W. Lau and G.P. Yu, *Surf. Coat. Technol.* **191** (2005), pp. 17-24.

The influence of fruit bagging on beta-carotene content of *Mangifera indica*

K. Khongrat[1]*, C. Mukthung[2], S. Kongnium[1], J. Kruenate[1] and U. Wichai[2]

[1] National Metal and Materials Technology Center, 114 Thailand Science Park, Paholyothin Rd., Klong 1, Klong Luang, Pathumthani, Thailand 12120
[2] Department of Chemistry, Faculty of Science, Naresuan University, 99 Moo 9 Phitsanulok-Nakhonsawan Road Tambon Tapho, Muang, Phitsanulok, Thailand 65000

* E-Mail : grittabk@mtec.or.th

Abstract: The mango fruit (Nhamdokmai variety) was selected under this investigation due to its popularity among the consumer and its rich flavor. One of the interesting nutrition values in mango is beta-carotene due to its antioxidant activity which is good for health benefit. Currently, the commercial paper bag was introduced into the mango industry in order to provide the certain yellow color after bagging however, the sugar content was significantly decreased. In this investigation, the beta–carotene content was another interesting compound that can be affected under bagging condition because the beta-carotene formation is strongly affect by light. Under this study, the beta-carotene was determined between mango that bagged with the commercial paper bag and the blue PE bag containing UV blocking agent. Then, mangoes were harvested at approximately 45 day after bagging. After that, mangoes were stored at room temperature for 4 days and their beta-carotene contents were determined by using reverse phase HPLC. It was found that the beta-carotene concentration was ranged from 17.4 ± 1.3 - 33.3 ± 5.3 and 19.7 ± 2.8 - 33.1 ± 12.4 mg/100 g for blue PE bag and paper bag, respectively. Additionally, the sugar content in blue PE bag was higher when compared with paper bag. From this information, the PE photo-selection bag can be developed and can be employed as the commercial bagging fruit in the near future.

Introduction

Mangoes (*Mangiferaindica L.)* are one of the economic fruit that widely produced around the world. Following the data from the Food and Agricultural Organization for the year 2007, the world mango production was over 25 million tons. In Thailand, the planting area was approximately 726,970 rais (116,315.2 hectares) and the total production was roughly 563,663 tons, with the export value for both fresh fruit and caned was about 517.68 million Baht [1]. Mango is regarded as a rich source of carotenoids, which is responsible for the yellow to orange color of ripe mango, providing a high pro-vitamin A value and anti-oxidative capacity [2]. Beta-carotene (Fig. 1) which is a fat-soluble compound is one of the common carotenoid hydrocarbons that contains specific end groups or two-beta rings. Beta-carotene has also different applications in food, cosmetic, and pharmaceuticals industries as a colorant, antioxidant, and anti-cancer agent [3]. The practice of pre-harvest bagging has been used in several fruit crops to improve skin color and quality such as bananas, apple, grape, peach and pear [4-8]. Several researches have been reported that bagging treatment affected on fruit growth and development, maturity, skin color, and quality after harvest for different fruits [6, 9]. In this investigation, the beta–carotene content was another interesting compound that can be affected under bagging condition because the beta-carotene formation is strongly affect by light. Under this study, the beta-carotene was determined between mango that bagged with the commercial paper bag and the blue PE bag containing UV blocking agent.

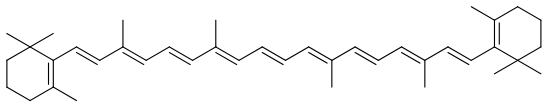

Figure 1. Chemical structure of beta-carotene.

Materials and Methods

Plant materials and Treatment

Mango fruit (Nhamdokmai variety) from an orchard in Aarng Thong Province was used in this experiments. Fruit were bagged with the commercial paper bag and the blue PE bag containing UV blocking agent. Fruit were bagged on the aged of 45 day after full bloom (DAFB) and using 9 replications per treatment. The mango samples were kept inside of the bag for 45 days before harvesting. Then, fruit were harvested at commercial maturity period, on the age of 90 DAFB. After that, the treated mango samples were transported to the laboratory within 2 hours and then storage at room temperature for 4 days and were collected. Ripe mangoes were washed with tap water, peeled and seed was also removed, the pulps were homogenized and freeze-dried and stored at 4^{o}C until analysis.

Extraction of beta-carotene

The extraction of beta-carotene was conducted according to previous report by Chen and et al [10] with modifications. About 0.1 g freeze dried powder was weighed into 50 mL centrifuge tube and extracted with 10 mL of acetone for 90 min with magnetic stirrer. The supernatants about 0.5 mL was filtered through a 0.45 μm filter before being injected into a liquid chromatography column.

HPLC analysis

The HPLC analysis of beta-carotene was conducted according to previous report by Emenhiser [11] and Hiranvarachat [12] with modifications. Twenty microlitres of extracts were analyzed in a Agilent 1100 Series HPLC system consisting of Photodiode Array detector (DAD) at 450 nm (reference off bandwidth 4 nm) and a VertiSep Bio C30 (5 µm, 4.6 x 250 mm; Vertical, Thailand), the experiments were performed using mobile phases containing a mixture of 80% of methanol and 20% of methyl *tert*-butyl ether (MTBE). The column was equilibrated for 30 min and its flow rate was set at 2 ml/min and temperature column set at 25°C. A DAD detector, operated at a wavelength of 450 nm, was used for detecting beta-carotene. The mobile phase was degassed using an ultrasonic generator. The calibration curve of beta-carotene was various concentrations form 1, 5, 10, 30 and 50 mg/L and injected into a HPLC.

Results and Discussion

The chromatogram of beta-carotene standard and sample extract in this study is shown in Fig. 2 and 3, the retention time of β-carotene were 15.87 min. The Calibration curves were constructed from five concentrations, each in three replicate. The regression equations of these curves and their correlation coefficients (R^2) were calculated as follows; $y = 7.7265x - 1.1007$ ($R^2 = 0.9998$), where y and x are the peak area and the concentration (mg/g) of the analyses, respectively. The beta-carotene content in mango samples is shown in Table 1 was ranged from 17.4 ± 1.3 - 33.3 ± 5.3 and 19.7 ± 2.8 - 33.1 ± 12.4 mg/100 g for blue PE bag and paper bag, respectively. It seems that the concentration of beta carotene from commercial bag was similar as the blue PE bag. Additionally, the data from previous study show the color skins and sugar content in blue PE bag was higher when compared with paper bag.

Conclusions

In conclusion, the blue PE bag showed several advantages in terms of reduction of diseases and cost of cultivation. From this information, the PE photo-selection can be developed and can be employed as the commercial bagging fruit in the near future.

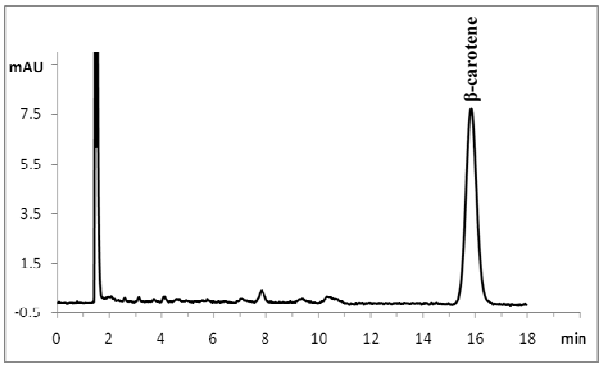

Figure 2. HPLC chromatogram of beta-carotene standard at a wavelength of 450 nm.

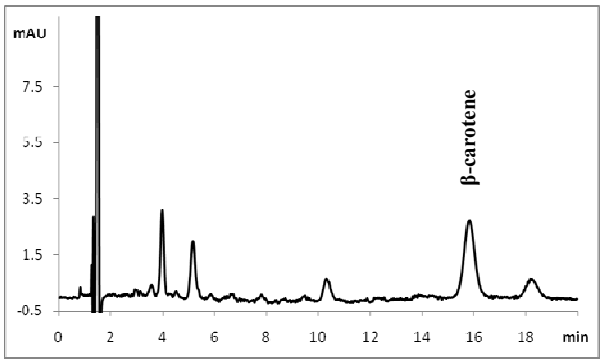

Figure 3. HPLC chromatogram of β-carotene of sample extract.

Table 1**:** The β-carotene contents of Blue PE bag and paper bag of all tree treatments.

No. Tree	Bag	beta-carotene contents (mg/100g)
1	TR3	17.4 ± 1.3
	TR4	28.6 ± 15.6
2	TR3	17.5 ± 0.7
	TR4	30.9 ± 1.1
3	TR3	24.3 ± 3.7
	TR4	23.3 ± 6.1
4	TR3	24.1 ± 2.1
	TR4	22.6 ± 5.8
5	TR3	33.3 ± 5.3
	TR4	32.5 ± 9.9
6	TR3	17.5 ± 1.2
	TR4	20.1 ± 4.3
7	TR3	18.7 ± 2.6
	TR4	19.7 ± 2.8
8	TR3	24.4 ± 0.2
	TR4	33.1 ± 12.4
9	TR3	18.8 ± 2.9
	TR4	25.3 ± 1.1

*TR3 = blue PE bag, TR4 = paper bag

References

[1] Department of Agricultural Extension. Production statistics: Mango. *available online* : http://www.doae.go.th/statistics roduction/mango.htm. 2007.

[2]. I. Pott, D. E. Breithaupt and R. Carlec, *Phytochemistry*. **64** (2003), pp. 825–829.

[3] G. Leach, G. Oliveira and R. Morais, *J Sci Food Agric*. **76** (1998), pp. 298-302.

[4] G. Johns, and K. J. Scott, *J. Exp. Agr*. **29** (1989), pp. 727-733.

[5] O. Arakawa, Y. Hori, and R. Ogata, *J. Jpn. Soc. Hort. Sci*. **54** (1986), pp. 424-430.

[6] I. M. Choi, J. S. Moon, C. J. Yun, S. B. Kim and N.H. Song, *J. Agr. Sci. Hort*. **38** (1996), pp. 687-693.

[7] R. L. Desond, J. Zhengwang and W. R. James, *J. Am. Soc. Hort. Sci*. **127(2)** (2000), pp. 88-193.

[8] A. Cassandro, N. H. Banks and S. Max, *J. Crop and Hort. Sci.* **30** (2002), pp. 99-107.

[9] Y. Kubo, S. Taira, S. Is Hhio, A. Sugiura and T. Tomana, *J. Jpn. Soc. Hort. Sci*. **57** (1988), pp.191-199.

[10]. X. Chen, J. Wu, S. Zhou, Y. Yang, X. Ni, J. Yang Z. Zhu and C. Shi, *Journal of Food Composition and Analysis*. **22** (2009), pp. 148-153.

[11]. C. Emenhiser, L. C. Sande and S. J. Schwartz, *Journal of Chromatography A*. **707** (1995), pp. 205-213.

[12]. B. Hiranvarachat, P. Suvarnakuta and S Devahastin, *Food Chemistry*. **107** (2008), pp. 1538–1546.

Effect of MCT-β-cyclodextrin to dye fixation on textile fabrics

T. Srikongkeaw[1] and W. Sricharussin[1,2*]

[1]Department of Materials Science and Engineering, Faculty of Engineering and Industrial Technology, Silpakorn University, Maung, Nakhonpathom, Thailand 73000
[2]National Center of Excellent for Petroleum, Petrochemical, and Advance Material, Chulalongkorn University, Bangkok, Thailand 10330

*E-mail: wimonrat@su.ac.th

Abstract: In this study, MCT-β-Cyclodextrins have been examinated as fixation agent. A disperse and reactive/disperse azo-dyes were prepared. The characterisation of the dye was performed by TLC Chromatography, ^{1}H and ^{13}C NMR, FT-IR, UV-Vis spectroscopies. The dye stuff were used to dye textile fabrics; synthetic fibres (PET), natural fibres (cotton) and cotton-polyester blend fibres. All fabrics were treated with MCT-β-Cyclodextrins before dyeing.Colour intensity and uniformity were evaluated by means of tristimulus colorimetry. It was found that, for the reactive-disperse dye, the treated MCT-β-Cyclodextrins fabrics show high colour intensity and uniformity than the untreated fabrics. For the disperse dye, treated polyester fabrics show excellent colour uniformity. The reactive-disperse dye show good wash fastness in all type of fabrics. MCT-β-Cyclodextrins improves uniformity of colour in polyester fabrics only.

Introduction

Cyclodextrins are cyclic oligosaccharides toroidal shaped with a hydrophilic outer surface and an internal hydrophobic hollow interior. The remarkable ability of cyclodextrins to include hydrophobic compounds has been exploited in several fields, spanning from food manufacturing to commodity, from pharmaceuticals to cosmetics. In textile field, a novel functional surface treatment of cotton based on the permanent fixation of β-cyclodextrins on fabric is receiving increased attention [1-8]. Some literatures have demonstrated that cyclodextrins fixed to cotton did not affect the hydrophilic properties of cellulose and the immobilized cavities of cyclodextrins did not lose their complexing power to form inclusion complexes with other molecules. Monochlorotriazinyl-β-Cyclodextrins (MCT-β-CD) is a reactive cyclodextrins capable of forming covalent bonds with nucleophilic groups [8-14]. For this reason β-cyclodextrins behave as hosts and the hydrophobic species are the guests. The driving force for such inclusion process is the enthalpic contribution that arises from non-covalent hydrophobic interactions. This complexation pheno-menon can modify some physico-chemical and chemical properties of the guest, for example enhancing its stability to oxidant agents and light and increasing its apparent aqueous solubility [6].

In the present work two novel dye structures, a disperse and a disperse-reactive dye, are proposed and prepared for the dyeing of cotton, polyester, cotton–polyester blend fabrics. Disperse dyes are commonly used in the dyeing of synthetic hydrophobic fabrics. Usually cotton cannot be directly dyed with this procedure for its hydrophilic nature. Possible applications of the reactive-disperse dye on cotton were also evaluated.

Materials and Methods

Materials

All Chemical and solvents used were purchased from Sigma-Aldrich (Thailand). Monochlorotriazinyl-β-Cyclodextrins (CAVATEX®W7 MCT) was kindly supplied by Wacker-Chemie (Germany). 2-(N-ethyl-N-phenylamino)ethyl chloride was prepared starting from 2-(N-ethylanilino)ethanol as reported by Boon [15]. Reacting the product with a solution of methylamine, as reported by Bach et al. [16], the coupling agent I was obtained.

^{1}H-NMR and ^{13}C-NMR spectra were performed on a Bruker Ultrashield 300 Spectrometer working at 300 MHz in DMSO-d_6 solution (2%) using the DMSO signal as a reference. NMR signals are described by use of *s* for singlet, *d* for doublet, *t* for triplet, m for multiplet and the chemical shifts with respect to TMS are expressed in δFT-IR spectra were performed on a Bruker Vertex spectrophotometer with KBr matrixes.

Preparation of Disperse azo-dye

4-Nitroaniline, 7 g, were treated with 12.5 ml of 37% hydrochloric acid and 25 ml of water. The solution was warmed just to complete dissolution of solids. Then the temperature was lowered to 0°C with precipitation of 4-nitroaniline hydrochloride. About 3.5 g of $NaNO_2$, dissolved in water, were slowly added to the mixture. After 30 min urea was added until unreacted nitrous acid was eliminated. The solution of diazonium salt was added dropwise into a 9 g of Coupling agent I dissolved in 35 ml of acetic acid at a temperature controlled between 0 and 5°C. After 1 hour the reaction mixture was neutralized with a solution of KOH. The solid was collected, stirred with a solution of 5% Na_2CO_3, filtered and washed with water. The product was crystallized from ethanol. Yield: 28.1%, Mp: 105-7°C, λ_{max} (ethanol) = 449 nm, ε = 33,000. TLC on silica gel, (acetone/methanol) 75/25, Rf = 0.25

^{1}H NMR ($CDCl_3$, the first number is related to the proton assignment, the second is the chemical shift in ppm, the third is the multiplicity of the signal and the integration): 14, 1.23, t 3H; 18 (NH), 1.42, s 1H; 17, 2.34, s 3H; 16, 2.79, t 2H; 13 + 15, 3.60, m 4H; 9 + 11, 6.74, d 2H; 2 + 6, 7.83, d 2H; 8 + 12,7.84, d 2H; 3 + 5, 8.35, d 2H.

^{13}C NMR ($CDCl_3$, the first number is related to the carbon assignment, the second is the chemical shift in ppm): 14, 12.19; 17, 37.16; 16, 44.98; 13, 49.56; 15, 50.51; 9 + 11, 110.34; 2 + 6, 123.17; 3 + 5, 124.88; 8 + 12, 126.02; 7, 143.57; 4, 146.63; 10, 152.31; 1, 155.90.

FT-IR spectrum of disperse dye are reported in Figure 1.

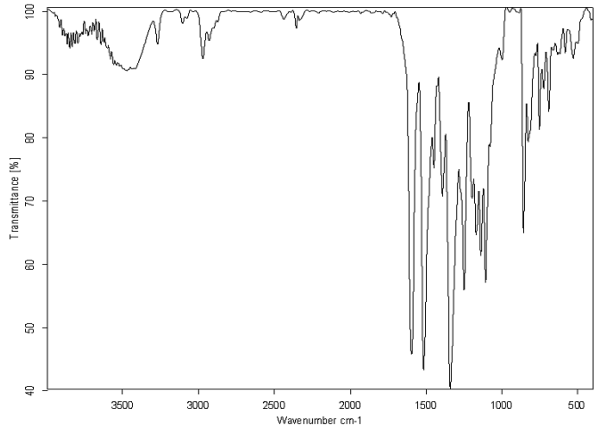

Figure 1. FT-IR spectrum of disperse dye

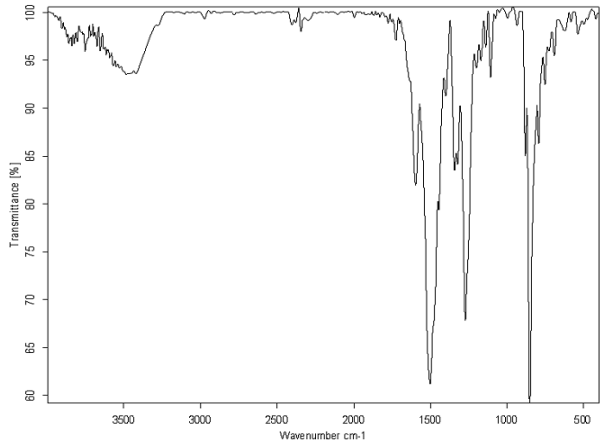

Figure 2. FT-IR spectrum of reactive/disperse dye

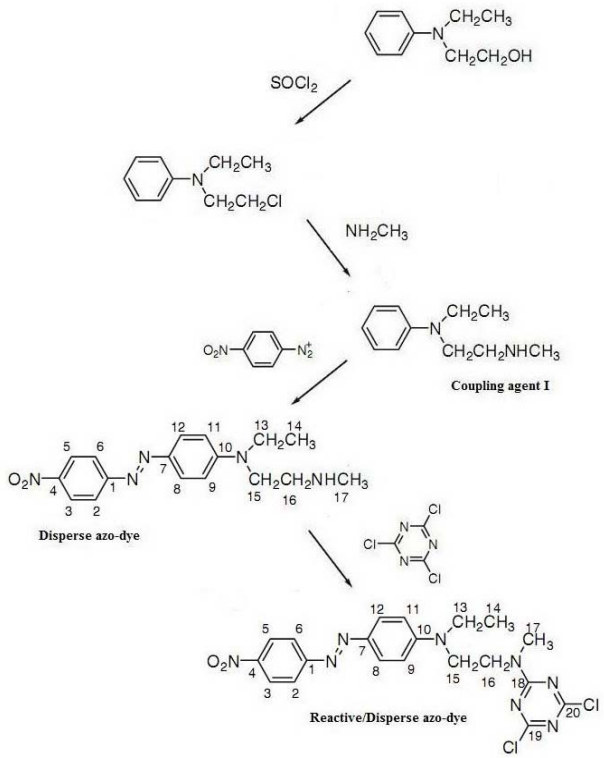

Figure 3. Dye synthesis process

Preparation of Reactive-Disperse azo-dye

Disperse azo-dye, 2.62 g dissolved in 100 ml of dichloromethane, was added to 0.97 g of collidine. After cooling at 0 °C, 1.47 g of trichlorotriazine were slowly added. The system was stirred at 0 °C for 2 h. The solid was filtered and washed three times with iced water. The product was then crystallized from dichloromethane reported by Parlati [17]. Yield: 22.7 %, Mp: 208-211 °C, λ max (ethanol) = 471 nm, ε = 26,000. TLC on silica gel , (ethyl acetate/petroleum benzene) 70/30, Rf = 0.78.

^{1}H NMR (DMSO d_6, the first number is related to the proton assignment, the second is the chemical shift in ppm, the third is the multiplicity of the signal and the integration): 14, 1.20, t 3H; 17, 3.31, s 3H; 16, 3.47, t 2H partially overlapped to the water signal; 15, 3.73, t 2H; 13, 3.69, q 2H; 9 + 11, 7.14, d 2H; 8 + 12, 7.80, d 2H; 2 + 6, 8.01, d 2H; 3 + 5, 8.29, d 2H.

^{13}C NMR (DMSO d_6, the first number is related to the carbon assignment, the second is the chemical shift in ppm): 14, 13.86; 17, 35.86; 13, 45.63; 15, 45.45; 16, 47.02; 9 + 11, 114.13; 2 + 6, 122.94; 3 + 5, 125.83; 8 + 12, 127.29; 7, 144.37; 4, 147.84; 10, 152.66; 1, 156.24; 18, 165.17; 19 and 20, 170.21 and 169.70. FT-

IR spectrum of reactive-disperse dye are reported in Figure 2. Dye synthesis process had showed in Figure 3.

Grafting of the fabrics with MCT-β-CD

The following approach to bond MCT-β-CD onto the fabrics was developed based on the method by Rehmann, et al [1]. Three types of fabrics (Cotton, Polyester, Cotton/polyester) were soaked for 10 min at room temperature in an aqueous solution of MCT-β-CD 60 g/L and catalyst Na_2CO_3 40 g/L (the liquor ratio is 1:20). The fabrics were then squeezed to remove the excess solution to wet pickup 80–100%, and dried at 80 °C for 10 min. The impregnated fabrics were cured in an oven at 150 °C for 3 min at atmospheric pressure (dry heat) for a thermal fixing reaction. The resulted fabrics was then washed under running water for 10 min to remove any unreacted MCT-β-CD and dried at 80 °C for 10 min. The quantity of MCT-β-CD bonded to the cellulose fabric was estimated by the weight difference of the sample of fabric before and after the fixing process described.

Dyeings

Dyeing tests were carried out on a Xaimen Rapid apparatus (China), using liquor ratio 40:1, dyeing intensity 1%, pH approximate 7-8 (basification from Na_2CO_3). Dyeings were performed on 3 types of fabrics. Dyeing condition for each fabrics are reported in Table 1. Dyed fabrics were then removed, washed at 50□C with water solution (liquor ratio 1:100) containing soap (2 g/L) for 30 min, rinsed and dried at room temperature. To evaluate colour uniformity tristimulus colorimetry was used [10]. Colour measurements were carried out with a Minolta CR 200 color reader. The colour difference between dyed and undyed specimen (ΔE) was measured on four different positions for each specimen (CIELAB : L*, a*, b* value). ΔE represents a mean value of the colour difference (Table 2). Washing fastness were performed at 60°C followed ISO 105 C06 C2S standard with multifiber AATCC No.1. Fastness to washing are displayed with an empiric scale ranging from the worst value (1) to the best value (5) which are reported in Table 3.

Table 1: Dyeing condition

Fabrics	Temperature (□C)	Time(min)
Cotton	70	90
Polyester	130	60
Blend	70	60

Results and Discussion

Dyeing

In opponent type system, Lightness represent by L* value. Redness or greeness can be expressed by a* value, and yellowness or blueness can be expressed by b* value.

Table 2: L*, a*, b*, Δ*E* value

Fabrics	Treated			Untreated			ΔE
	L*	a*	b*	L*	a*	b*	
Cotton							
Disperse	60.4	28.2	18.7	62.4	30.2	21.3	3.8
Reactive/Disperse	49.8	31.7	16.1	50.5	34.7	17.5	3.4
Polyester							
Disperse	33.3	43.3	21.5	29.5	35.8	15.5	10.3
Reactive/Disperse	47.2	44.7	28.8	51.6	47.0	32.6	6.3
Blend							
Disperse	56.8	33.2	23.8	55.3	34.8	24.4	2.3
Reactive/Disperse	43.8	32.7	16.3	45.3	36.2	19.5	4.9

It can be seen that ΔE of polyester dyed with disperse dye show the highest value. This means that treated fabric with CD can give high colour change. The dyeing uniformity is also better for all fabrics that grafted with MCT-β-CD before dyeing.

Wash fastness

Washing fastness test are reported in Table 3. Excellent fastness properties are reported for polyester fabrics. Cotton dyed with disperse dye show low wash fastness. Reactive/disperse dye can be used for all types of fabrics.

Table 3: Wash fastness value

Fabrics	Disperse		Reactive/Disperse	
	treated	untreated	treated	untreated
Cotton				
C	3	3	3/4	3/4
S_c	4	4/5	4	4
S_w	2	2	2/3	2/3
Polyester				
C	5	5	4/5	4/5
S_c	5	5	5	5
S_w	5	5	4/5	5
Blend				
C	3	3	4	3/4
S_c	3/4	4	4/5	4/5
S_w	3	2/3	3	3

C : colour change, S_c : staining on cotton
S_w: staining on wool

The presence of reactive groups of reactive-disperse dye systematically enhance washing fastness properties. This effect can be related to the reaction between reactive site of chlorotriazine and reactive site of cotton and blend fabrics. Moreover, there were no

difference between fastness value of treated and untreated fabrics in the same fabrics and the same dye stuff. This is because low amount of inclusion complex between dye and MCT-β-CD had been formed.

Conclusions

Novel reactive-disperse dye can be synthesized from disperse dye with this suggested route. This dye can be fixed on all type of fabrics. Treated polyester fabric with MCT-β-CD showed high colour change and also excellent wash fastness. Cotton fabric can also be dyed with disperse dye. In conclusion, grafting of MCT-β-CD on fabrics before dyeing can improve dyeing quality on all fabrics, especially polyester fabric.

References

[1] L. Rehmann, H. Yoshii and T. Furuta, *Starch/Starke,* **55** (2003), pp. 313.
[2] T. Vaios, K. & I. Mourtzinos, *Food Chem*. **101** (2007), pp. 652–653.
[3] J. Sanchez, *J. Anal. Chim*. **90** (1997), pp. 223–231.
[4] T. Nakajuma and M. Hirobasbi. *J. Chem & Phar*. **vol.2, 32** (1984) pp. 38.
[5] S. Scalia, R. Tursilli, A. Bianchi, P. L. Nostro, E. Bocci, F. Ridi and P. Baglioni, *J. Pharm*, 308 (2006), pp. 155–159
[6] J.H. Wang and Z. Cai, *Carbohydrate Polymers*, **72** (2008), pp. 695–700
[7] U. Denter. and E. Schollmeyer, *Surface modification of synthetic and natural fibres by fixation of cyclodextrin derivatives*. 8th of International Cyclodextrin Symposium, Budapest, Hungary, 1996, pp 559–564.
[8] H. J. Buschmann, U. Denter, and D. Knittel, *J. Text. Ins*.**89** (1988), pp.554–561.
[9] H. J. Buschmann, U. Denter, and D. Knittel, *Melliand Textiberichte* **Vol.9**, (1995), pp. 216–218.
[10] P. Lo Nostro, and L. Frantoni, *J. Incl. Phen. Mac. Chem*, **44** (2002), pp. 423–427.
[11] P. Lo Nostro, L. Frantoni, F. Ridi, *J. App. Poly*, **88** (2003), pp. 706–715.
[12] T. Loftsson, M.E. Brewster, *J. Pharm. Sci*. **85**, (1996), pp. 1017–1025.
[13] R.A. Rajewski and V.J. Stella, *J. Pharm. Sci*. **85** (1996.), pp.1142–1169.
[14] K. Uekama, F. Hirayama and T. Irie, *Chem. Rev*, **98** (1998), pp. 2045–2076
[15] W.R. Boon, *J. Chem. Soc*, (1947), pp. 307–308.
[16] F.L. Bach, H.S. Brabander and S. Kushner, *J. Am. Chem. Soc,* **79** (1957), pp. 2221–2225.
[17] S. Parlati, R. Gobetto, C. Barolo, A. Arrais, R. Buscaino, , C. Medana and P. Savarino, *J. Incl. Phen. Mac. Chem*, **57** (2007), pp.463–470.
[18] Methods of Test for Color Fastness of Textiles and Leather, the Society of Dyers and Colourists. Bradford, 4th Ed. (1978).

Development of biosensor for pesticide detection using methyl parathion hydrolase from recombinant MPD clone

A. Ekkhuntham[1], J. Wichitwechkarn[1], M. Somasundrum[2] and W. Surareungchai[3*]

[1] Department of Biotechnology, Faculty of Engineering and Industrial Technology, Silpakorn University, Nakhon Pathom 73000, Thailand.
[2] Biochemical Engineering and Pilot Plant Research and Development Unit, National Center for Genetic Engineering and Biotechnology , National Science and Technology Development Agency at King Mongkut's University of Technology Thonburi, 83 Moo 8 Thakham, Bangkhuntien, Bangkok, Thailand 10150
[3] School of Bioresources and Technology, King Mongkut's University of Technology Thonburi, 83 Moo 8 Thakham, Bangkhuntien, Bangkok, Thailand 10150

*E-mail: werasak.sur@kmutt.ac.th

Abstract: A high sensitive detection of organophosphate (OP) compounds was developed. Recombinant methyl parathion hydrolase (MPH) capable of hydrolyzing OP to generate *p*-nitrophenol (PNP) was need. The MPH was immobilized on multi-walled carbon nanotubes (MWNTs) via electrostatic self-assembly, and the detection was performed by direct oxidation of biocatalytically liberated PNP using amperometry. Under the optimized conditions, the biosensor exhibited responses to methyl parathion (MP), parathion, and paraoxon with the linear ranges of 10-90 nM, 20-240 nM, and 3.3-40 nM, and the detection limits of 10 nM, 20 nM, and 3.3 nM, respectively. The biosensor also provided high sensitivities to MP, parathion, and paraoxon at 616 nA/µM, 301 nA/µM, and 1547 nA/µM, respectively. Reproducibility assays using repetitive standards (n=15) of 200 nM showed the RSD of 9.19%, indicating high reproducibility. The response time was 10 s.

Introduction

Organophosphate (OP) compounds have been widely used as pesticides and insecticides in agriculture and as neuro-toxic chemical warfare agents in military practice, posing environmental problems to humans. Highly sensitive measuring devices for such compounds would facilitate the detection of OP pesticides in our food and water sources, providing an early warning of their environmental threat, and facilitating effective monitoring of detoxification processes [1].

Biosensor technology is so far considered to be well-suited for on-site environmental monitoring and rapid detection of these highly toxic agents. This work describes a device, based on the enzyme methyl parathion hydrolase (MPH), for the amperometric biosensing of OP nerve agents. With this enzyme, OP is hydrolyzed to produce PNP and diethylthiophosphoric acid. As PNP can be oxidized at an electrode it can be measured by amperometry. In this study, we report the development and the use of CNT modified electrode for OPs detection [2,3].

Materials and Methods

Apparatus **:** Amperometric experiments were performed with the PGSTAT 12 voltammetric analyzer and GPES software (Eco Chemie, Netherlands). The glassy carbon working enzyme electrode (BAS), Ag/AgCl (3M NaCl) reference electrode (BAS), and platinum counter electrode were used in a 3 ml cell. A magnetic stirrer and stirring bar were used to provide the desired convective transport.

Reagents **:** MPH (5250 IU/mg of protein, 9 mg of protein/ml; activity measured using MP as a substrate) [4,5]. MP, paraoxon, and parathion were obtained from Sigma and PNP was purchased from Aldrich.

Electrode Fabrication : Polyamine amide (PAA) was adsorbed by sonicating 0.5 mg ml^{-1} functionalized CNT in a 0.5 M NaCl solution containing 1 mg ml^{-1} PAA for 5 min, followed by shaking at regular intervals for 20 min. Subsequently, the PAA-coated CNT was centrifuged at 9,000 rpm for 15 min to remove the supernatant. One milliliter of deionized water was then added, and the nanotubes were redispersed by gentle shaking. The centrifugation/wash/redispersion cycle was repeated three times to ensure removal of the free polyelectrolyte from solution. Using the same procedure, a layer of the negatively charged MPH was adsorbed alternately with the positively charged PAA. Next, the CNT-PAA-MPH was dropped on the glassy carbon electrode. The modified electrode was subsequently dried completely at room temperature and kept in a refrigerator (at 4 °C) until use [6].

Amperometric Assay : All experiments, unless otherwise stated, were performed by applying a potential of +0.93 V onto the MPH modified electrode and allowing the transient background current to decay to a steady-state value, prior to addition of the OP substrates. A stirred solution was employed during the amperometric experiments, while a quiescent solution was used during the chronoamperometric testing. All experiments were carried out at room temperature.

Results and Discussion

MPH Immobilization : As expected, the surface loading of MPH had a profound effect upon the sensor's performance (Figure 1). The enzyme mass of 1.788 mg displayed the highest sensitivity with 697 nA/µM. On the contrary, the enzyme at the concentration of 0.894 mg yielded the lowest sensitivity, at 479 nA/µM for successive increments in the level of 1.0 x 10^{-7} M MP at +0.93 V.

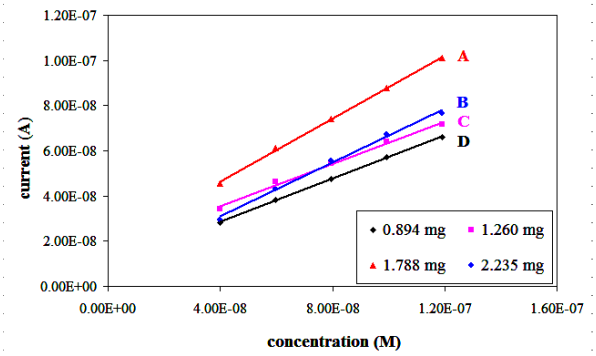

Figure 1. Effect of MPH surface loading upon the response to MP, using 0.894 (A), 1.260 (B), 1.788 (C) and 2.235 mg (D) of MPH. Operating potential, +0.93 V; electrolyte, phosphate buffer (0.05 M, pH 8.0).

Optimal Operating Potential : Figure 2 shows a hydrodynamic voltammogram (HDV) for successive increments in the level of 1.0 x 10^{-7} M MP over the 0.8-1.0 V potential range at MPH modified electrode. The oxidation of the enzymatically liberated PNP started at +0.90 V, with the response rising sharply up to +0.93 V, and then leveled off thereafter. All subsequent work was performed at +0.93 V.

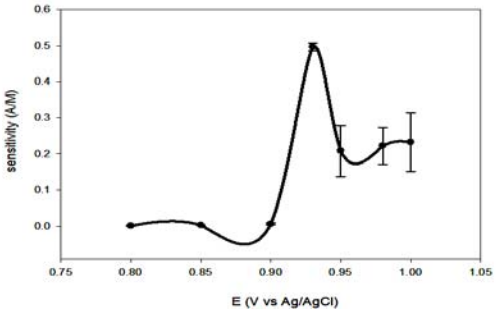

Figure 2. Hydrodynamic voltammograms for successive increments in the level of 1.0 x 10^{-7} M MP at the MPH-based amperometric biosensor

Performance Characteristics : Figure 3 displays current-time amperometric recordings obtained with the MPH electrode for MP (A), paraoxon (B), and parathion (C). Well-defined current signals were observed for these micromolar increments in the OP substrate concentration. No response was observed for bare (enzyme-free) electrode (data not shown).

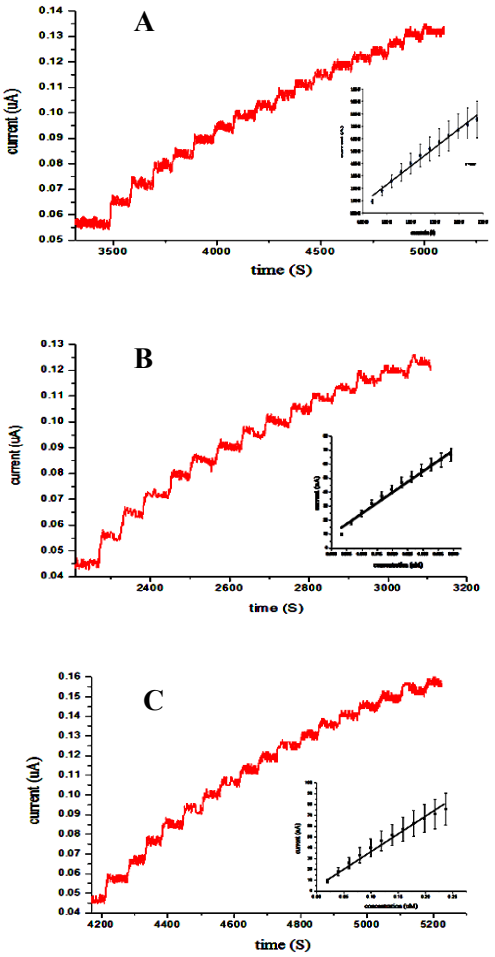

Figure 3. Current-time amperometric response to successive 5.0 x 10^{-6} M increments in the level of MP (A), 1.0 x 10^{-6} M increments in the level of paraoxon (B), and 1.0 x 10^{-5} M increments in the level of parathion (C). The insets showed the resulting calibration plots and the responses for 1.0 x 10^{-8} M MP (A), 3.3 x 10^{-9} M paraoxon (B), and 2.0 x 10^{-8} M parathion (C).

The resulting calibration plots (Figure 3) displayed high linearity for MP (slope, 616 nA/µM; r = 0.992), paraoxon (slope, 1547 nA/µM; r = 0.984), and parathion (slope, 301 nA/µM; r = 0.987). The data in Figure 3 also demonstrated that the MPH electrode offered attractive dynamic properties, with less than 10 s required to attain steady-state currents. Such a response was significantly faster than that of current inhibition (AChE)-based amperometric OP biosensors which require addition of the substrate and an incubation period [7].

Extremely low detection limits of 5.4 x 10^{-9} M MP, 8.6 x 10^{-10} M paraoxon, and 7.4 x 10^{-9} M parathion can be estimated from the signal-to-noise characteristics (S/N = 3) of the response to 1.0 x 10^{-8} M MP, 3.3 x 10^{-9} M paraoxon and 2.0 x 10^{-8} M parathion (Figure 3).

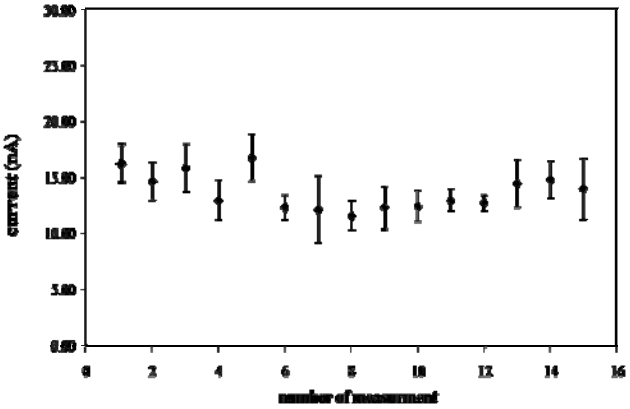

Figure 4. The reproducibility of MPH modified.

The response of the MPH biosensor was highly reproducible; a relative standard deviation of 9.29% characterized 15 repetitive chronoamperometric measurements of 1.0 x 10^{-7} M MP (Figure 4). This precision implies no problem with electrode poisoning from the oxidation of PNP. Hence, in addition to single-use applications, the new detecting device can serve as a reusable biosensor. This is not the case with inhibition OP biosensors that suffer from irreversible response.

Conclusions

The use of MPH for amperometric biosensing of OP compounds has been developed. This was done by immobilizing MPH onto carbon nanotubes which were then dropped into glassy carbon electrode transducer that offers favorable anodic detection of the liberated PNP product. Apart from having response for MP, the MPH modified biosensor is also responsive for other OP pesticides such as paraoxon and parathion that produce PNP upon hydrolysis. The electrode had a low detection limit, high sensitivity, high reproducibility, and rapid response. With all these good characteristics, this biosensor is suitable to be employed for field use with convenience and low cost.

Acknowledgment

This work was supported by grants from The National Nanotechnology Center of Thailand, and Thailand Research Fund - Master Research Grant (TRF-MAG, Window I).

References

[1] I.K. Konstantinou, D.G. Hela and T.A. Albanis, *Environ. Pollut.* **141** (2006), pp. 555-570.
[2] A. Mulchandani, W. Chen, P. Mulchandani, J. Wang and K.R. Rogers, *Biosens. Bioelectron.* **16** (2001), pp. 225-230.
[3] A. Mulchandani, P. Mulchandani and W. Chen, *Anal. Chem.* **71** (1999), pp. 2246-2249.
[4] A. Ekkunatham, and J. Wichitwechkarn, *Optimization of expression conditions for recombinant methyl parathion hydrolase production in Escherichia Coli*, 33th The Congress on Science and Technology of Thailand Conf. Proc., Bangkok, Thailand, 2007
[5] W. Suppaluknaree, Identification characterization and expression of genes in methyl parathion degradation pathway of Burkholderia Cepacia, Master's Thesis, Silpakorn University, 2006.
[6] B. Munge, G. Liu, G. Collins and J. Wang, *Anal. Chem.* **77** (2005), pp. 4662-4666.
[7] A.L. Simonian, E.N. Efremenko and J.R. Wild, *Anal. Chim. Acta.* **444** (2001), pp. 179–186.

Study of trehalose immobilization on Si surface

P. Pasakon[1*], S. Kiatisevi[2]

[1]Materials Science and Engineerings Program, Faculty of Science, Mahidol University, Ratchathewi, Bangkok, Thailand 10400
[2]Department of Chemistry, Faculty of Science, Mahidol University, Ratchathevi, Bangkok, Thailand 10400

[*] E-Mail: g5137455@student.mahidol.ac.th

Abstract: In this research, a new method to analyze metal ions in ultratrace amounts has been proposed in order to study the monitoring of trace metals in the environment and other real samples. Trehalose was chosen to be immobilized on a silicon surface because of its good divalent metal ion recognition. Self-assembled monolayer technique was used to modify the surface. The preliminary results based on FTIR spectroscopy and contact angle measurement show that trehalose could be immobilized on silicon and exhibit metal recognition ability.

Introduction

Analytical methods for detection of metal in nature and real samples are generally atomic absorption spectroscopy (AAS), inductively coupled plasma-mass spectroscopy (ICP-MS), and neutron activation analysis (NAA) which are complicated due to preconcentration before analyzing. Therefore, a new method that can determine metal ions in ultratrace amounts has been developed. This report describes the modification of silicon surface prepared for immobilization of trehalose. Trehalose will be employed because of its good divalent metal recognition. Starting from self-assembled monolayers (SAMs) of 11-acetoxyundecyl- l- trichlorosilane (**1**) on Si wafers, we could prepare electrophilic surfaces by reduction of the acetoxy to the hydroxyl group and transformation of the hydroxyl to a chloroformate group (figure **1**) by a reaction with triphosgene.

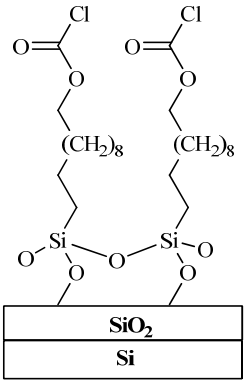

Figure 1. Schematic presentation of the chloroformate terminated monolayer on silicon surface.

The chloroformate-terminated monolayer obtained was then used for trehalose deposition. All modification steps mentioned above were followed by FTIR spectroscopy and water contact angle measurement.

Materials and Methods

1. Materials

The substrate used for assembly was 12 mm x 15 mm B-doped silicon wafer (100) (Wacker-Siltronic, Germany). Prior to SAM preparation, the silicon wafers were cleaned in the mixture of 70% sulfuric acid (Mallinckrodt Baker, Inc.) and 30% hydrogen peroxide (Merck), at 100°C for 45 min, washed with purified water (18 MΩ-cm^{-1}, Millipore-MilliQ water) and dried with nitrogen gas (Thai Industrial Gas (TIG)).

Reagents used for SAM preparation were toluene (Merck), methylene chloride (Lab-Scan), lithium aluminium hydride (Merck), tetrahydrofuran (Fluka), hydrochloric acid (Lab-Scan), triphosgene (Acros), pyridine (Lab-Scan), trehalose (Merck) and *N,N*-dimethyl formamide (Merck).

2. Methods

0.1 ml of compound **1** was dissolved with 20 ml of dried toluene in a reaction flask under nitrogen gas. The cleaned silicon wafer was then immersed in the reaction flask for at least 12 hours. The wafer was rinsed with methylene chloride and dried with nitrogen gas. The reduction of the ester into the hydroxyl terminal group was carried out by immersing the monolayer into a solution of lithium aluminium hydride in tetrahydrofuran, followed by diluted hydrochloric acid and purified water. For phosgenation, the hydroxyl terminated monolayer was immersed in a solution of triphosgene in dried toluene overnight. Finally, the wafer was rinsed with toluene and immersed in 0.3 M trahalose solution in *N, N*-dimethyl formamide.

Results and Discussion

1. FTIR characterization

The chloroformate terminated monolayer was successfully prepared on silicon which was characterized by FTIR spectroscopy as presented in Figure 2.

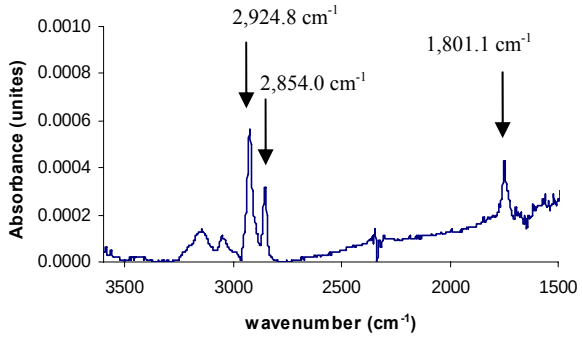

Figure 2. Transmission FTIR spectrum of the chloroformate terminated monolayer

IR peaks at 2,924.8 and 2,854.0 cm^{-1} correspond to asymmetric and symmetric stretchings of CH_2 groups. The C=O vibration of the chloroformate terminal group appeared at 1,801.1 cm^{-1}. In addition, Table 1 reveals additional IR data of the acetoxy and hydroxyl terminated monolayers.

Table 1: Transmission FTIR data of the monolayer of compound **1**, hydroxyl and chloroformate terminated SAM.

Wavenumber	Acetoxy terminated SAM of 1 (cm^{-1})	Hydroxyl terminated SAM (cm^{-1})	Chloroformate terminated SAM (cm^{-1})
ν_{as} (-CH_2)	2,923.2	2,923.9	2,924.8
ν_s (-CH_2)	2,855.6	2,853.0	2,854.0
ν (-C=O)	1,744.4	-	1,801.1

The immobilization of trehalose on chloroformate terminated monolayers was also studied by FTIR spectroscopy as shown in Figure 3. The vibration at 3,250-3,580 cm^{-1} was a result of hydroxyl groups of trehalose. The peaks at 2,918.0 and 2,846.6 cm^{-1} indicated asymmetric and symmetric stretchings of the CH_2 groups.

2. Water contact angle measurement

Table 2 includes results from water contact angle measurements of all modified surfaces. The water contact angles obtained are in accordance with the hydrophilic property of each surface. The trehalose modified surface exhibited a small contact angle comparable to the blank silicon wafer, whereas the acetoxy terminated monolayer gave the highest contact angle of 70 $\pm$ 1°.

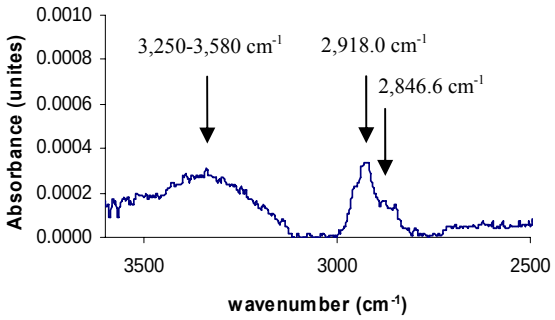

Figure 3. Transmission FTIR spectrum of trehalose immobilized on silicon that was subtracted from the spectrum of the monolayer of compound **1.**

Table 2: Water contact angle of Si, the monolayer of compound **1**, hydroxyl terminated SAM and trehalose terminated SAM.

	Water contact angle (°)
blank silicon wafers	33 $\pm$ 2
acetoxy terminated SAMs	70 $\pm$ 1
hydroxyl terminated SAMs	52 $\pm$ 1
trehalose modified monolayer	39 $\pm$ 3

Conclusions

The chloroformate terminated monolayer can be used to immobilize trehalose on Si surface with the results as shown in FTIR spectrum and water contact angles. In the future, we plan to apply the trehalose modified monolayers to determine ultratrace metals.

Acknowledgements

This work was supported by Department of Chemistry and Center for Alternative Energy, Faculty of Science, Mahidol University, and Center of Excellence for Innovation in Chemistry (PERCH-CIC).

References

[1] J. Xia, W. Wei, Y. Hu, H. Tao and L. Wu, *J. Anal. Chem.* **20** (2004), pp. 1037-1041.

[2] T. Higashiyama, *J. Pure Appl. Chem.* **7**, (2002), pp. 1263-1269.

[3] Y. E. Alekseev, A. D. Garnovskii and Y. A. Zhdanov, *Russ. Chem. Rev.* **67** (1998), pp. 649-669.

[4] N. K. Singhal, B. Ramanujam, V. Mariappanadar, and C. P. Rao, *Org. Lett.,* **8**, (2006), pp. 3525-3528.

Preparation and characterization of conducting polyaniline nanoparticle dispersions

Y. Pornputtkul*, R. Chatnantalouk, T. Reanthong, K. Maturos, N. Pussara

Department of Industrial Chemistry, Faculty of Applied Science, King Mongkut's University of Technology North Bangkok, Bangkok, Thailand

*E-mail: ypk@kmutnb.ac.th

Abstract: Electrically conducting polyaniline/poly(2-methoxyaniline-5-sulfonic acid) (PAn.PMAS) and polyaniline/poly(styrene sulfonic acid) (PAn.PSSA) nanoparticles dispersed in aqueous were prepared by chemically oxidative polymerization of aniline with ammonium peroxydisulfate (APS) in aqueous media containing PMAS and PSSA as both steric stabilizer and polymeric dopant. The polymer products were characterized by SEM, TEM, FTIR, UV-VIS, XRD, TGA, cyclic voltammetry (CV) and conductivity. SEM and TEM images showed that the uniform and well dispersion of spherical nanoscale particles, with diameters in the range of 50-100 nm, were prepared. The results from FTIR and UV-VIS spectra indicated that emeraldine salt form was obtained. Moreover, the UV-VIS spectrum of PAn.PMAS nanocomposite showed characteristic absorption peaks of both polymers. When the pH of the dispersions was changed, the UV-VIS spectra changes were observed. Chemical oxidation and reduction of the polymers to leucoemeraldine and pernigraniline can be performed by using hydrazine and APS, respectively. The conductivity of the polymer complexes measured by a four-point probe technique is around 10^{-2} S.cm^{-1}. CVs of the both PAn.PMAS and PAn.PSSA films recorded in aqueous acidic solution shows two main redox couples, indicating that the PAn.PMAS and PAn.PSSA nanoparticles were electroactive materials. Interestingly, when the CV was carried out in the dispersions of PAn.PMAS and PAn.PSSA nanoparticles, the cyclic voltammogram was gradually increased in current density during successive potential scanning due to deposition of the polyaniline nanoparticles at the electrode. This led to a facile fabrication of controlled thickness film on the electrode substrate.

1. Introduction

Polyaniline (PAn) is one of the most promising conducting polymers due to its good environmental stability and easy of synthesis, as well as its relative high conductivity and low price. PAn is also unique among organic conducting polymers in that its electrical properties are controlled by both its oxidation state and degree of protonation [1].

Consequently, PAn is widely used for various applications such as batteries, actuators, sensors, electrochromic device and anti-corrosion. However, like most of conducting polymers, PAn is infusible and insoluble in common solvents. The poor processability of these polymers has been limited theirs commercial applications. To improve the processability from aqueous media, preparation of nanoparticle dispersions is an option, since the colloidal dispersions of other polymers have been directly used in various industrial applications.

PAn nanoparticles have been prepared by a dispersion polymerization in the presence of a polymeric stabilizer such as poly(vinyl alcohol)[2,3], poly(vinyl methyl ether)[4,5] and poly(N-vinyl-2-pyrrolidone)[6].

In this work, poly(2-methoxyaniline-5-sulfonic acid) (PMAS) and poly(styrene sulfonic acid) (PSSA) were used as both steric stabilizer and polymeric dopant due to theirs acidicity. Similar researches have been reported [7-9]. However, it is different from our result in synthetic recipes and conditions. Therefore, we report the preparation and characterization of PAn.PMAS and PAn.PSSA nanoparticles.

2. Materials and Methods

*2.1 Materials:*Ammonium peroxydisulfate (APS), hydrochloric acid , and ammonium hydroxide were all purchased from Merck. Poly(4-styrenesulfonic acid) (PSSA) (M_w ~ 75 kDa) was obtained from Aldrich. All of these chemical were used as received without purification. Aniline (An) was supplied from BDH and distilled twice under atmospheric pressure prior to use. The poly(2–methoxyaniline–5- sulfonic acid) (PMAS) (M_w ~ 10-15 kDa) was obtained by chemical polymerization of 2-methoxyaniline-5-sulfonic acid (MAS), Tokyo Kasei Kogyo Co.Ltd, which was purified by recrystallaization before used. *The polymerization of MAS using APS as an oxidant (initiator) was carried out in NH_4OH solution (pH of the reaction solution ca. 4) in the present of LiCl at -10ºC, and subsequent dialysis with cellulose dialysis tubing (12 KDa MWCO, Sigma) against distilled water. The polymer was dried at 50ºC for 24 h.

*The procedure used to prepare PMAS was adapted from the method describe by Masdarolomoor et.al. [10].

2.2 Synthesis of PAn nanoparticals: A modified polymerization method similar to Choi et.al. [7,8] was used for preparation of PAn.PSSA. PSSA used as acidic dopant and polymeric stabilizer was dissolved

in distilled water with magnetic stirring. APS was used as oxidant was separately dissolved in distilled water. Polymerization was preformed by the addition of APS solution in the An/PSSA solution. Various synthetic conditions were studied. As the polymerization proceeded, the color of the solution changed to green, which indicates the formation of polyaniline emeraldine salt (ES). After 12 h, the polymerization solution was dialyzed with cellulose dialysis tubing (12 KDa MWCO) for 24 h to remove impurities such as unreacted An, APS and oligomers. The method used to synthesis PAn.PMAS was modified from the procedure described by Masdarolomoor et.al. [9]. PMAS was dissolved in distilled water or aqueous HCl solution. Greenish brown solution of PMAS was obtained. Then An was added to the PMAS solution. APS solution was added to the An/PMAS solution in one short, rigorously shaken for 2-3 min. The reaction mixtures were kept at room temperature without stirring for 12 h.

2.3 Characterization of polyanilines: The UV-vis spectra in the wavelength range 250-1100 nm of the PAn. nanodispersions were recorded using a UV-vis spectrophotometer (Perkin Elmer, Lambda 2S). FTIR spectra were measured using a Nicolet 6700 FT-IR, KBr pellet method. Cyclic voltammetry (CV) was carried out in a three-electrode cell using a glassy carbon (GC-disk) working electrode with a platinum mesh auxiliary electrode and $Ag/AgCl_{(3M\ NaCl)}$ reference electrode connected to a Multichannel Potentiostat (Biologic Science Instrument, VMP). Electrical conductivity was measured by a four-probe method using a four-point probe and a multimeter (Keithley 2700). Before measurement, the PAn powder was dried and ground with pestle in a mortar, then pressed to prepare pellet disk with a diameter of 1 cm. Particle size and morphology of the nanodispersions were examined via scanning electron microscopy (SEM, JEOL, JSM-6400) and Transmission Electron Microscopy (TEM, JEOL, JSM-2100). All samples were gold coated prior to analysis by SEM. The thermal stability was investigated using a thermogravimetric analyzer (TGA, TA Instrument 2950). The scan rate of temperature was 10ºC/min under N_2 atmosphere. The X-ray diffractometry was carried out on a Philips, X' Pert with a Cu detector using 1.54 ºA wavelength of the X-ray.

3. Results and Discussion

3.1 Synthesis of PAn.PSSA and PAn.PMAS dispersion

It is well known that polyaniline synthesized using the conventional chemical method in simple inorganic acid such as HCl is highly agglomerated. The large particles obtained are difficult to disperse. In order to make dispersible PAn, dispersion polymerization was carried out in the presence of stabilizer PSSA and PMAS which both also acted as a dopant. The PAn.PSSA and PAn.PMAS dispersions were stable for several months without precipitation.

3.2 UV-vis spectroscopy: UV-vis spectra of diluted samples were measured in the range between 300 and 1100 nm to determine doping characteristics of polyaniline. The UV-vis spectrum of PAn.PSSA (Fig.1,a) exhibited absorption bands at ca. 345, 420 and 760 nm, characteristic of polyaniline emeraldine salt. These bands are assigned to π-π*, polaron-π* and π-polaron transitions, respectively. Moreover, these polyaniline dispersions have compact coil conformation, as evidenced by well-defined polaron band at 800 nm. UV-vis spectra of PAn.PMAS dispersion (Fig.1,b) is compared to that of PMAS solution (Fig.1,c). A yellow-brown solution of PMAS exhibits a broad absorption band around 320-350 nm assigned to π-π* transitions and a strong sharp peak at ca. 472 nm assigned to a polaron transition. PAn.PMAS composites show characteristic absorption peaks of both polymers. The π-π* transition of benzenoid ring was observed at ca. 342 nm and two lower wavelength polaron bands at around 442 and 487 nm and higher wavelength polaron bands at ca. 837 nm and a free carrier tail in NIR region. A red-shift of the spectrum may be due to the inter-chain interaction. Therefore, theses results indicate that the incorporation of PSSA and PMAS in the polyaniline composite as a molecular template and a polymeric dopant.

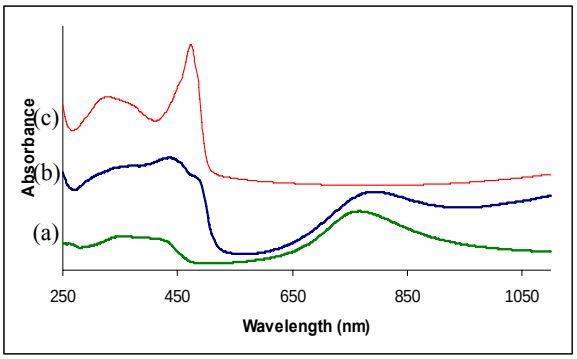

Figure 1.UV-vis spectra of (a) PAn.PSSA dispersion (b) PAn.PMAS dispersion and (c) PMAS solution.

When the pH of the dispersions was changed, the UV-VIS spectra changes were observed. It was also found that both large polymeric acid dopant PSSA and PMAS stabilized polyaniline against dedoping in basic medium. Chemical treatments of the polymers with hydrazine and APS, leucoemeraldine and pernigraniline form were obtained, respectively, as confirmed by the UV-VIS spectra.

3.3 FT-IR spectroscopy: FT-IR is often used to characterize the molecular structure, oxidation state and doping of polyaniline. It was found that PAn.PSSA and PAn.PMAS had characteristic peaks which are similar to that of polyaniline emeraldine salt. Therefore, the polymers obtained were in emeraldine oxidation state and doped form.

3.4 SEM and TEM: The shape and size distribution of polyaniline dispersion were examined using SEM and TEM. Fig.2 depicts SEM and TEM images of PAn.PSSA and PAn.PMAS particles. PAn.PSSA exhibits almost monodispersed sizes with spherical shape. Average particle diameters of PAn.PSSA and PAn.PMAS obtained by the TEM were 50-70 nm.

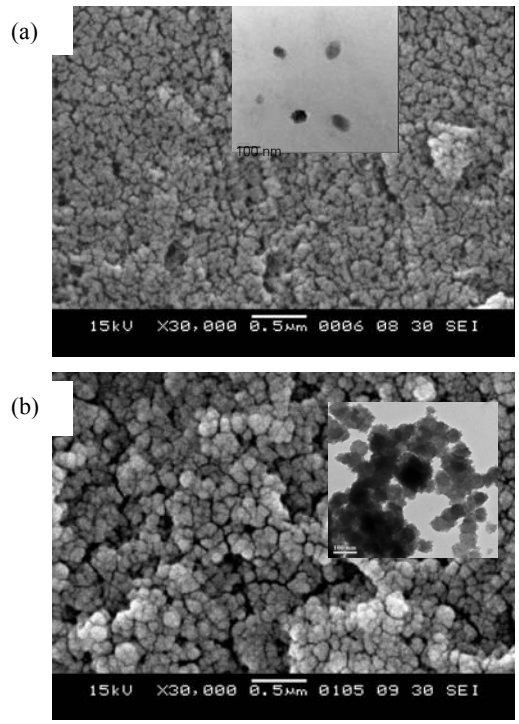

Figure 2. SEM and TEM images of (a) PAn.PSSA (b) PAn.PMAS nanoparticles (Inset : TEM)

3.5 Cyclic Voltammetry (CV): The CVs of PAn.PSSA and PAn.PMAS showed two main anodic peaks at *ca.* 0.2 and 0.65 V assigned as the oxidation from leucoemeraldine to emeraldine and emeraldine to pernigraniline, respectively. Two main cathodic peaks were also observed: a peak at *ca.* 0.57 V corresponding to reduction of pernigraniline to emeraldine, and a peak at *ca.* 0.05 V corresponding to reduction of emeraldine to leucoemeraldine. Interestingly, when the CVs were recorded in the as-synthesized PAn.PSSA and PAn.PMAS nanodispersions, the significant increase in a current response observed in successive cycles (Fig.3), indicated polymer films deposition onto the electrode, probably due to coagulation of the PAn nanoparticles. This led to a facile fabrication of controlled thickness film on the electrode substrate.

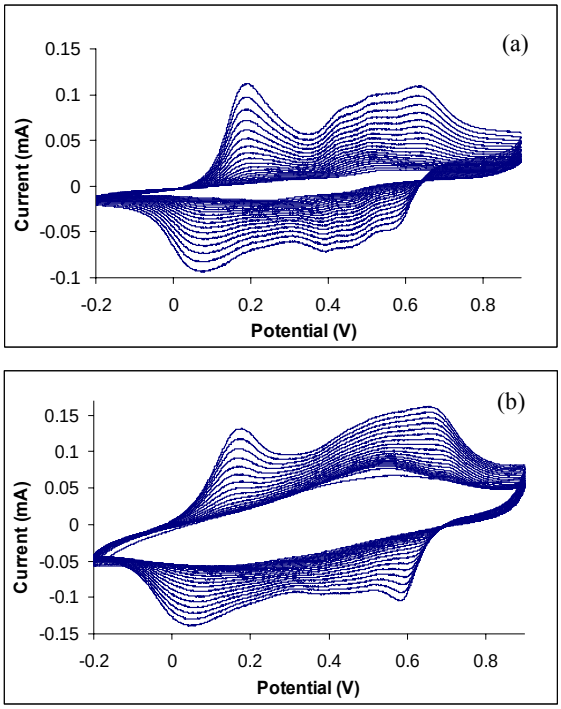

Figure 3. CVs of (a) PAn.PSSA dispersion (b) PAn.PMAS dispersion on GC-disk electrode at a scan rate of 50 mV/s

3.6 TGA: Thermal stability of the PAn was investigated using TGA. Typical three major stages of weight loss were observed for PAn.PMAS, at *ca.* 50-100, 200-270, and 400-520ºC results from moisture evaporation, loss of sulfonic acid and some structural decomposition of PAn backbone, respectively. While PAn.PSSA exhibited the 1st weight loss at 50-100ºC due to the evaporation of trace water, the 2nd weight loss at *ca*. 250-300ºC attributed to lost of sulfonic group, the 3rd weight loss around 350-400ºC assigned to structure decomposition of PSSA and the 4th weight loss at *ca*. 475-525ºC indicated partial degradation of PAn chain.

3.7 XRD: The XRD was used to study the crystalinity of the PAn. nanocomposites. The XRD patterns of PAn.PSSA and PAn.PMAS powder presented a broad peak centered at 2□ = 25º, suggested that the PAn. nanoparticles produced are nearly amorphous. A broader pattern (more amorphous) was observed for PAn.PSSA. The peak at 2□ = 25º may be ascribed to periodicity perpendicular to the polyaniline chain.

3.8 Electrical conductivity: Room-temperature d.c. electrical conductivity of PAn.PSSA and PAn.PMAS pellets is around 10^{-2} S.cm^{-1}, depending on synthesized condition. This is comparable to conductivity report for polyaniline nanoparticle powders.

4. Conclusions

Stabilized PAn.PSSA and PAn.PMAS nanoparticles can be successfully prepared in the wide range of synthetic conditions using oxidation polymerization of aniline in the presence of PSSA and PMAS act as steric stabilizer and dopant. PAn.PSSA nanodispersions can be obtained without any acid addition, while PAn.PMAS nanodispersions are obtained when small amount of HCl was added. It has been shown that both large polymeric acid dopant PSSA and PMAS stabilized polyaniline against de-doping in basic solutions. The TGA results indicate that PAn.PSSA and PAn.PMAS is relatively thermal stable under a nitrogen atmosphere. The conductivity of the polymer composites depended on the condition employed. Unusual electrochemical property of PAn nanoparticles was observed. Further studies by our laboratory are underway.

Acknowledgements

The authors would like to acknowledge the financial support from the Research, Development and Engineering (RD&E) Fund through National Nanotechnology Center (NANOTEC), National Science and Technology development Agency (NSTDA), Thailand (Project NN-B-22-FN3-22-50-17).

References

1. G.G. Wallace, G.M. Spinks, L.A.P. Kane-Maguire and P.R. Teasdale, *Conductive Electroactive Polymers : Intelligent Polymer Systems,* 3rd edition, 2009, Taylor & Francis Group, CRC Press, p.183-184.
2. J.Stejskal,P.Kratochvíl,N. Radhakrishnan, *Polyailine dispersions 2. UV-vis spectra*, Synthetic Metals, 61 (1993) 225-231.
3. A.Mirmohseni,G.G. Wallace, *Preparation and characterization of processable electroactive polyaniline-polyvinyl alcohol composite*, Polymer, 44 (2003) 3523-3528.
4. P.Banerjee,M.L.Digar,S.N.Bhattacharyya, B.M.Mandal,*Novel polyailine dispersions using poly(vinyl methyl ether) stabilizer*, European Polymer Journal, 30 (1994) 499-501.
5. B.M. Mandal, *Conducting polymer nanocomposites with extremely low percolation threshold*, Bulletin of Materials Science, 21, (1998) 161-165.
6. C. Dispenza, C.L. Presti, C. Belfiore, G. Spadaro, S. Piazza, *Electrically conductive hydrogel composites made of polyaniline nanoparticles and poly(N-vinyl-2-pyrrolidone)*, Polymer, 47 (2006) 961-971.
7. S.Y. Park, M.S. Cho, H.J. Choi, *Synthesis and electrical characteristics of polyaniline nanoparticles and their polymeric composite*, Current Applied Physics, 4 (2004) 581-583.
8. M. S. Cho, S. Y. Park, J. Y. Hwang, H. J. Choi, *Synthesis and electrical properties of polymer composites with polyaniline nanoparticles*, Materials Sciences and Engineering C. 24 (2004) 15-18.
9. F. Masdarolomoor, P.C. Innis, G.G. Wallace, *Electrochemical synthesis and characterization of polyaniline/poly(2-methoxyaniline-5-sulfonicacid) composites*, Electrochemical Acta, 53 (2008)4146-4155.
10. F. Masdarolomoor, P.C. Innis, G.G. Wallace,*Purification and characterization of poly(2-methoxyaniline-5-sulfonic acid)*, Electrochemical Acta, 53 (2008) 4146-4155.

Characterizations and mechanical properties of bentonite/natural rubber composites

S. Sakulkhaemaruethai[1*], P. Poptawee[2], N. Boonlert[2], S. Lenphet[2] and C. Kumnuantip[2]

[1] Department of Chemistry, Faculty of Science and Technology, Rajamangala University of Technology Thanyaburi, Klong 6, Thanyaburi, Pathumthani Thailand
[2] Department of Material and Metallurgical Engineering, Faculty of Engineering, Rajamangala University of Technology Thanyaburi, Klong 6, Thanyaburi, Pathumthani Thailand

[*] E-Mail : singto_rmutt@hotmail.com

Abstract: The objective of this work is to study the effect of bentonite loading on mechanical properties of natural rubber. The natural rubber composites at different bentonite loading from 0 to 10 phr (parts by weight per hundred parts of rubber) were prepared by using two-roll mill rubber mixing machine and compression molding process. Mechanical properties, which were tensile strength, elongation at break, modulus, tear strength, hardness and density, of the bentonite-natural rubber composites were investigated. It was found that the amount of bentonite loaded to natural rubber matrix has effected to the mechanical properties of prepared natural rubber. The tensile strength, elongation at break, modulus, tear strength, and hardness were decreased with increasing of the amount of bentonite.

Introduction

Natural rubber (NR) have been widely application in various areas due to its superior dynamic mechanical properties, abrasion resistance, elasticity, and flex crack resistance.[1-2] However, NR is susceptible to oxidative or thermal degradation and becomes loses mechanical integrity.

The development in natural rubber-nanocomposites gained a lot of interest from many research groups in order to achieve desired combination of properties in relation to conventional products.[3-4] In fact, the natural rubber-nanocomposites have been successfully prepared by several processing techniques, such as vulcanizing curing process, solution blending, etc.[5-6] For example, Pojanavaraphan and Magaraphan [7] reported the natural rubber latex/clay aerogel nanocomposites prepared via freeze-drying technique. The authors studied the effect of pristine clay in the NR matrix. The clay aerogel structure was formed at the 3 parts per hundred rubber (phr) clay loading.

In this study, incorporation of bentonite at different concentrations in natural rubber was done in order to achieve desirable combination of properties. The natural rubber was compounded with loaded bentonite and other ingredients to produce bentonite/natural rubber composites. The cure characteristics of various samples were also determined and reported.

Materials and Methods

Natural rubber (STR 5) used for this work was obtained from Thai Mac Company. Bentonite Mac-Gel, grade SAC (Treated bentonite, TB) and SAC-1 (Bentonite, B) were supplied by Thai-Nippon Chemical Co., Ltd. Composition and physical properties of both types of the commercial bentonite used are given in Table 1 and 2, respectively. All mixing ingredients were used as received.

Table 1: Composition of the commercial bentonite

Composition (%wt)	TB	B
SiO_2	55-60	65-70
Al_2O_3	14-18	13-17
Fe_2O_3	1-2	1-2
Na_2O	2.0-3.0	0.5-1.0
LOI	10-12	10-12
MgO	1.8-2.2	2.0-3.0
CaO	1.8-2.1	1.5-2.0
K_2O	0.3-0.5	0.4-0.8
TiO_2	0.2-0.3	0.2-0.3

Table 2: Physical properties of the commercial bentonite

Physical property	TB	B
Moisture content, %	8-12	8-12
5% Suspension, pH	9.5-11.0	9.0-10.5
Swelling index, ml per 2 g of clay	15 min	4 min
Viscometer dial reading @600 rpm	12-20	5-10

Preparation of Bentonite / Natural Rubber Composites

The bentonite/ natural rubber composites were compounded in an open two-roll mill (Labtech Engineering Co.,Ltd.) at room temperature and the blending time was 25 min. The ingredients were incorporated to the rubber before the addition of commercial bentonite. The formulation of the natural rubber compounds, NR-TB and NR-B, is complied in Table 3.

Table 3: Typical formulation of the natural rubber compound ingredients

Ingredients	NR-TB	NR-B
Natural rubber	100	100
Strearic acid	2	2
ZnO	5	5
MBT [a]	0.5	0.5
DPG [b]	0.2	0.2
Sulfur	3	3
Bentonite*	0-10	0-10

Note : The formulation of the compounds is expressed in phr (parts per hundred rubber).
[a] 2-Mercaptobenzothiazole.
[b] Diphenylguanidine.
* Bentonite loading: 0, 2, 4, 6, 8, and 10 phr.

Characterizations

The cure characteristics were measured using a Moving die rheometer following ASTM D5289. The moduli at 100% and 300% elongation, tensile strength and elongation at break (%) of the vulcanizates were determined using an universal testing machine (T5K Instron). Shore A hardness of the test pieces were measured using Durometer Shore A (PTC Instruments) in accordance with ASTM D2240. The Moony viscosity of the rubber was determined using the Mooney viscometer in accordance with standard method (ASTM D1646).

Results and Discussion

Figure 1 indicates the relationship between the Mooney viscosity of the natural rubber composites with bentonite loading from 0 to 10 phr for both types (TB and B). It was found that the Mooney viscosity slightly increased with the bentonite content increasing.

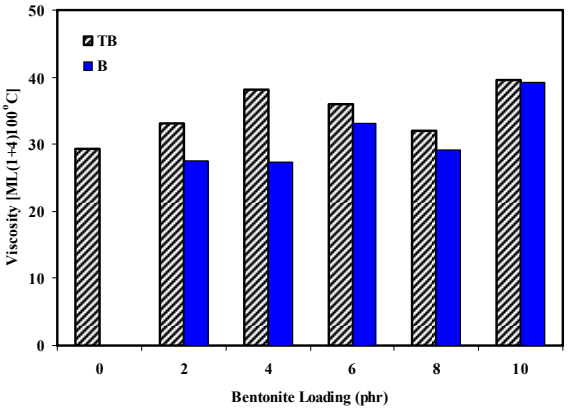

Figure 1. Mooney viscosity of various bentonite/ rubber composites.

Figure 2 shows the density of the various bentonite/natural rubber composites. The graph shows that the density increases with an increase in bentonite loading in all composites.

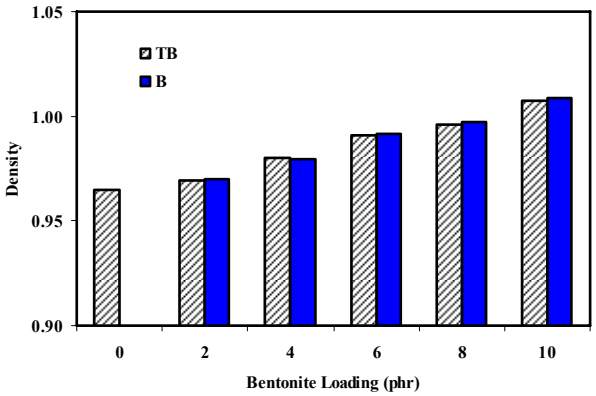

Figure 2. Density of various bentonite/natural rubber composites.

Figures 3, 4 and 5 show the cure characteristics of all composites at different bentonite loading. The results suggested that the scorch times, as shown in Figure 3, and the cure time (t_{c90}), as shown in Figure 4, increase with the bentonite content increasing. This indicates that the bentonite surface groups react with or absorb the vulcanizing agents and does not participate in the synergistic enhancement of the vulcanization reaction. The increase of cure times is explained by the interaction between the components of the cure system and the bentonite surface.[8] However, the 2 phr of the B type bentonite had lower cure time than the NR. This could be explained by the existence of MgO and CaO in the B type bentonite composition had higher than that in the TB type bentonite. The MgO and CaO probably acted as the activator for vulcanization reaction and resulted in the reduction of cure time. The cure rate decreases with bentonite loading, as shown in Figure 5, may be due to the loaded bentonite caused the vulcanization reaction to decrease and does not create any active cross link sites in the compound.[9]

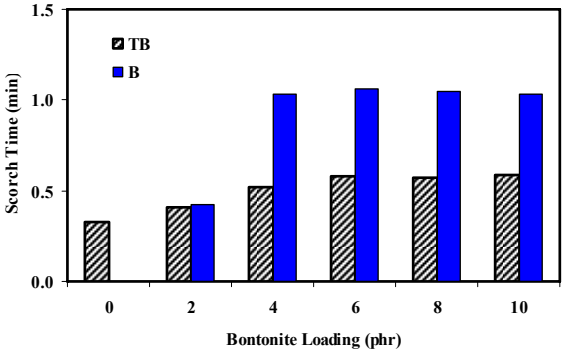

Figure 3. Scorch time of various bentonite/rubber composites.

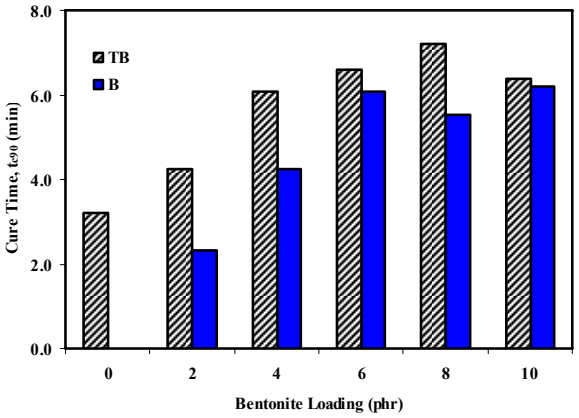

Figure 4. Cure time (t_{c90}) of various bentonite/rubber composites.

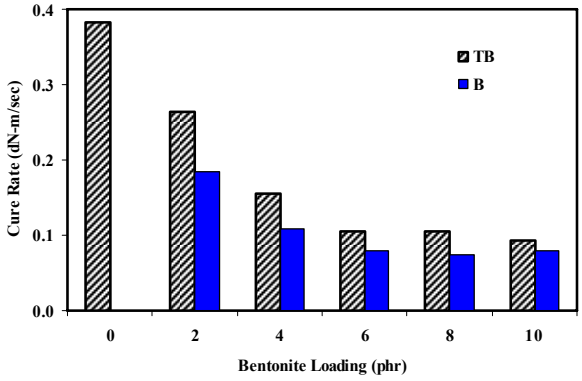

Figure 5. Cure rate of various bentonite/rubber composites.

The relationship between tensile strength and bentonite loading in all composites are shown in Figure 6. The tensile strength decreased when bentonite loading increased. The tear strength and 300% tensile modulus of various composites are displayed in Figures 7 and 8 respectively. It is apparent that the tear strength and modulus decrease with the bentonite loading. Addition of bentonite content to the NR composite decreased the mechanical properties. The formation of loaded bentonite aggregates reduces the interface area between rubber and bentonite layers, which decreases the mechanical properties.[10]

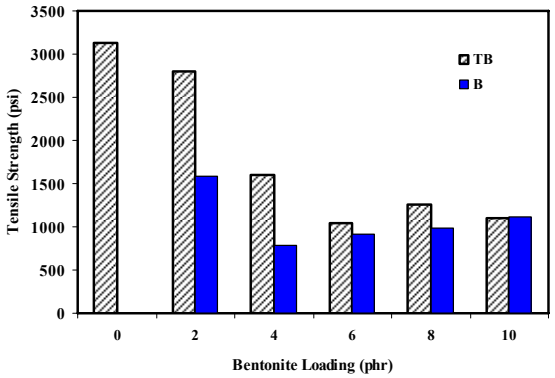

Figure 6. Tensile strength of various bentonite/rubber composites.

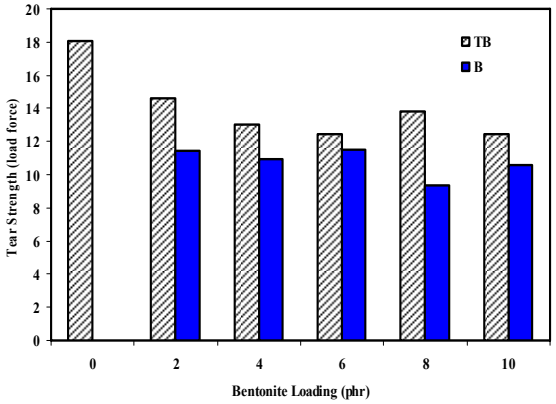

Figure 7. Tear strength of various bentonite/rubber composites.

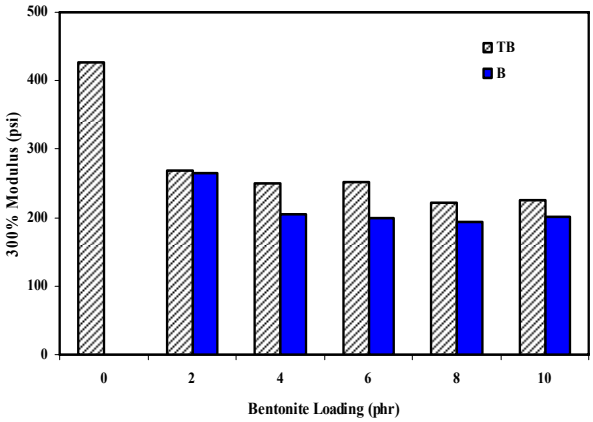

Figure 8. 300% Modulus of various bentonite/rubber compounds.

The influence of bentonite loading on the elongation at break and shore A hardness of all composites are displayed in Figures 9 and 10, respectively. It is apparent that all composites are not much different in the elongation at break and shore A hardness.

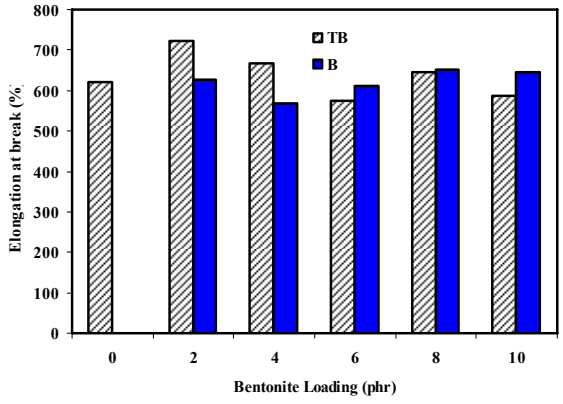

Figure 9. Elongation at break of various bentonite/rubber compounds.

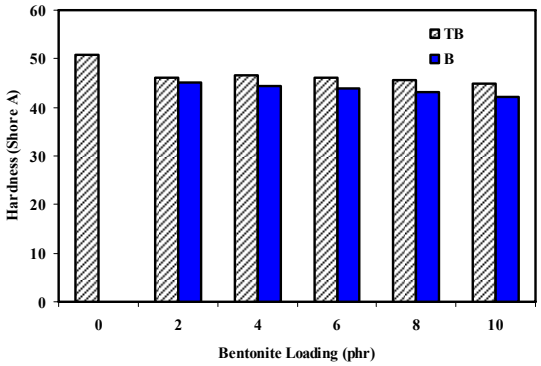

Figure 10. Shore A hardness of various bentonite/rubber compounds.

Conclusions

Bentonite/natural rubber composites were prepared by vulcanization and compression molding process. The mechanical properties produced by the presence of bentonite in vulcanized bentonite/natural rubber composites were investigated. It was found that the amount of bentonite loaded to natural rubber matrix has effected to the mechanical properties of prepared natural rubber. The tensile strength, elongation at break, modulus, tear strength, and hardness were decreased with increasing of the amount of bentonite. This research work has revealed the potentials of bentonite as filler in natural rubber compounds.

Acknowledgements

The authors would like to thanks the office of the Higher Education Commission for supporting by grant fund under the capacity building program. The authors also thanks Department of Chemistry, Faculty of Science and Technology and Department of Material and Metallurgical, Faculty of Engineering, Rajamangala University of Technology Thanyaburi (RMUTT), Thailand.

References

[1] H. Angellier, S. Molina-Boisseau and A. Dufresne, *Macromolecules* **38** (2005), pp. 9161-9170.
[2] P.L. Teh, Z.A.M. Ishak, A.S. Hashim, J. Karger-Kocsis and U.S. Ishiaku, *J. Appl. Polym. Sci.* **100** (2006), pp. 1083-1092.
[3] J.W. Gilman, *Appl. Clay Sci.* **15 (**1999), pp. 31-49.
[4] J. Zhu, A.B. Morgan, F.J. Lamelas and C.A. Wilkie, *Chem. Mater.* **13** (2001), pp. 3774-3780.
[5] Y.H. Sun, Y.F. Luo, and D.M. Jia, *J. Appl. Polym. Sci.* **107** (2008), pp. 2786-2792.
[6] R. Magaraphan, W. Thaijareon, and R. Lim-Ochakun, *Rubber Chem. Technol.* **76** (2003), pp. 406-418.
[7] T. Pojanavaraphan and R. Magaraphan, *Eur. Polym. J.* **44** (2008), pp. 1968-1977.
[8] M. Arroyo, M.A. Lopez-Manchado, J.L. Velentin and J. Carretero, *J. Compos. Sci. Technol.* **67** (2007), pp. 1330-1339.
[9] K. Pal, R. Rajasekar, D.J. Kang, Z.X. Zhang, S.K.Pal, C.K.Das and J.K. Kim, *Mater. Design.* **31** (2009), pp. 677-686.
[10] X. Shi and Z. Gan, *Eur. Polym. J.* **43** (2008), pp. 4852-4858.

Synthesis of Co-doped ZnO powders by mechanical milling method, Rietveld refinement and optical properties

S. Sujinnapram[1*], N. Rattanachoung[1] K. Naemchanthara[2], T. Nantawisarakul[2] and P. Limsuwan[2]

[1] Department of Physics, Faculty of Liberal Arts and Science, Kasetsart University, Kamphaeng Saen Campus, Nakhon Pathom, Thailand 73140
[2] Department of Physics, Faculty of Science, King Mongkut's University of Technology Thonburi, Bangkok, Thailand 10140

[*] E-Mail: supphadate@yahoo.com

Abstract: Co-doped ZnO, $Zn_{1-x}Co_xO$ powders were synthesized by the mechanical milling method at different cobalt concentration for 24 h under air atmosphere. The structural evolution of these powders as a function of cobalt concentration was analyzed by X-ray diffraction (XRD) and Fourier transmission infared (FT-IR) spectroscopy. The optical properties were investigated by Ultraviolet-visible (UV-vis) absorption spectroscopy and Photoluminescence (PL) measurements. XRD patterns, Rietveld refinement and FT-IR spectra indicated that the high-doped samples (x = 0.1 and 0.2) present the peaks of secondary phase CoO with a cubic structure, besides the main peaks of wurtzite-like structure the same as that of ZnO. UV-vis measurements suggested the presence of intermediary energy in disordered $Zn_{1-x}Co_xO$ powders, owing to the enhancement of *sp-d* exchange interactions and typical *d-d* transitions. Broad and narrow bands were observed in the PL spectra of these powders when excited with 325 nm wavelength. The broad bands were associated to the structural defects and optical quality in the ZnO.

Introduction

Zinc oxide is n-type semiconductor with a wide band gap of about 3.37 eV. The stable crystal structure of ZnO is wurtzite, in which each atom of zinc is surrounded by four atoms of oxygen in tetrahedral coordination [1]. ZnO is a unique position among semiconducting oxide because of its transparent conducting properties and dilute magnetic properties. Semiconductors in which cations are partially replaced by transition metal ions are called dilute magnetic semiconductors (DMS) [2]. Recent theories predicted [3,4] that the transition metal (i.e. Mn, Co, V, and Fe) doped ZnO diluted magnetic semiconductors exhibited ferromagnetic properties at room temperature. For example, Ueda et al. [5] reported that the Co-doped ZnO film prepared by a pulsed laser deposition exhibited ferromagnetic behavior with a Curie temperature at the room temperature. Moreover, Lee et al. [6] improved the Curie temperature of this material which grown by sol-gel method up to 350K. However, several studies also report the absence of ferromagnetism in films prepared with a similar method. There were indeed conflicting results among different authors and till now the exact nature of ferromagnetism in DMSs remains unclear [7].

The aim of this work is the preparation, structural and optical characterization of $Zn_{1-x}Co_xO$ powders. The samples were prepared by mechanical milling method, a known and versatile solid-state powder processing technique. We have previously used this technique to produce nanoparticles of ZnO and different cation substitutions in ZnO powders. Our purpose is to investigate the basic properties in materials in order to contribute to the comprehension of the magnetic character in these semiconductors.

Materials and Methods

The $Zn_{1-x}Co_xO$ powders were fabricated by the mechanical milling method. Zinc oxide powder (ZnO, 99.9% Aldrich), and cobalt oxide powder (CoO, 99% Aldrich) were used as starting materials. The powder mixture was milled in a polyethylene bottle with zirconia grinding media in ethanol for 24 h and then drying and sieving. The assynthesized $Zn_{1-x}Co_xO$ powders were characterized for crystal phase identification by powder X-ray diffraction (XRD) using a Philips X-ray diffractometer (PW3710) with CuKα radiation (λ = 0.15406 nm). We have analyzed the XRD patterns using the Rietveld technique with the FULLPROF [8]. The refinements were done using the wurtzite hexagonal space group $P6_3mc$ with (Zn, Co) atoms located at (2/3, 1/3, 0) and O atoms located at (2/3, 1/3, u). For both single-phase and multiphase samples (where impurity peaks were observed), this was the only phase refined. Fourier transform infrared (FT-IR) spectra of the powders (as pellets in KBr) were recorded using a Fourier transmission infrared spectrometer (PE2000, Perkin Elmer Instrument, USA) in the range 4000-500 cm^{-1} with a resolution of 1 cm^{-1}. The optical absorption spectra were measured in the range 200-800 nm using a UV-3101PC UV–VIS–NIR scanning spectrometer (Shimadzu, Japan). Photoluminescence measurement was carried out on a luminescence spectrometer (Perkin–Elmer, USA) using a Xenon lamp of 325 nm as excitation source at room temperature.

Results and Discussion

The Rietveld refinement analysis of XRD data of $Zn_{1-x}Co_xO$ samples by mechanical milling method for different compositions are presented in Figure 1. It was found that $Zn_{1-x}Co_xO$ samples were single phase with a wurtzite-like structure (space group $P6_3mc$) at low-doped sample (x = 0.01). The high-doped sample (x = 0.1 and 0.2) showed the secondary phase CoO with cubic structure. The crystal structure was obviously shown as x was between 0 and 0.01. This is because the Zn+2 ion site is replaced by Co+2 ions. As x was above 0.01, the CoO peaks started to show up and became dominant as x was equal to or greater than 0.10. The "*c*" parameter was decreased with the increasing of the x composition. The same behavior was also observed in the "*a*" parameter. The increase in the x lattice parameter to 0.01 indicated that the sample was a homogeneous solid solution. This means that Co^{2+} replaces the Zn^{2+} by occupying the 2b crystallographic site. As x became greater than 0.01, the lattice parameters remained the same because of over solubility

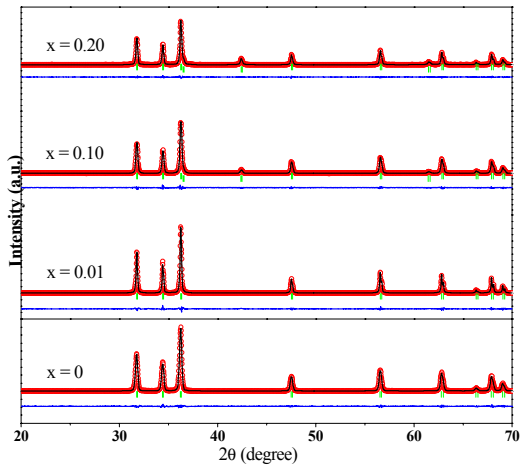

Figure 1. Experimental (o), calculated (solid line) and difference X-ray diffraction profiles for the Rietveld refinement of $Zn_{1-x}Co_xO$ (x = 0, 0.01, 0.1 and 0.2). The vertical tics below the all curve indicate that Bragg position.

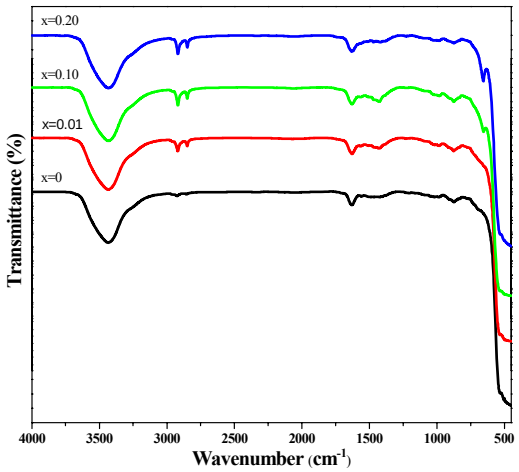

Figure 2. FT-IR spectra of of $Zn_{1-x}Co_xO$ (x = 0, 0.01, 0.1 and 0.2) by mechanical milling method.

The formation of ZnO wurtzite structure in the samples were further supported by FT-IR spectra in Figure 2. Similar spectra were obtained for $Zn_{1-x}Co_xO$ (x = 0, 0.01, 0.1 and 0.2) by ball milling method for 24 hours: absorption bands at ~3400 cm^{-1} represent O-H mode; those at ~2900 cm^{-1} are C-H mode; those at ~1380 and 1600 cm^{-1} are C=O mode, respectively, and that at ~490 cm^{-1} is the stretching mode of ZnO. The absorption peaks at 666 cm^{-1} are assigned to the ν (Co-O) modes, which confirms the formation of CoO structure.

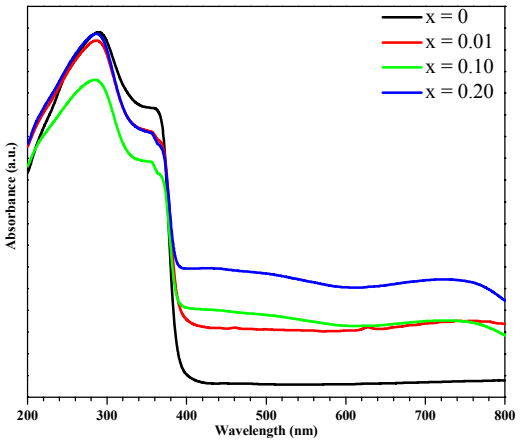

Figure 3. Optical absorbance spectra of $Zn_{1-x}Co_xO$ powders with x = 0, 0.01, 0.10 and 0.20 by ball milling method for 24 hours.

UV-vis spectroscopic measurements at room temperature were carried out to study the effect of Co doping concentration on the band gap of $Zn_{1-x}Co_xO$ in the range between 200-800 nm. Figure 2 shows the UV-vis absorption spectra of $Zn_{1-x}Co_xO$ powders with different Co doping concentration by ball milling method for 24 hours. The spectrum recorded for the ZnO reference sample was added for the comparison. As shown in Figure 2, there are absorption peaks in the 550-700 nm regions in the spectra of Co-doped ZnO samples. These peaks are assigned as typical *d-d* transitions of Co ions.

Zinc oxide is a direct gap semiconductor. Thus to allow interband transitions at photon energies above the band gap E_g, the absorption coefficient depends on the photon energy hν as follows: $\alpha h\nu = E_D(h\nu - E_g)^{1/2}$. Consistent with the behavior of a direct gap, the absorption spectra are plotted as $(\alpha h\nu)^2$, where E_D is a constant. We found that E_g decreases linearly with increasing Co concentration from 3.25 eV for pure ZnO down to 3.18 eV for $Zn_{0.8}Co_{0.2}O$. These results are in agreement with the gap narrowing with increase in Co for $Zn_{1-x}Co_xO$ doped at extremely high concentrations.

Room temperature PL spectrum of the $Zn_{1-x}Co_xO$ samples are shown in Figure 4. PL can be used for investigating the defects in the Co-doped ZnO. PL spectra showed the blue emission with the peak around 400 nm. The UV emission corresponds to the exciton recombination related near-band edge emission of ZnO. The weak blue emissions are

possibly due to defect in the ZnO powders as in the case of ZnO nanowires reported by Wang and Gao. The intensity of the blue emission can be used to qualitatively evaluate the oxygen vacancies concentration in ZnO. As the Co concentration increases, the intensity of the blue emission decreases strongly, which means that the oxygen vacancies concentration in Co-doped samples decreases with increasing Co concentration. This can be interpreted that the oxygen vacancies concentration in the Co-doped ZnO is strongly related to the Co concentration.

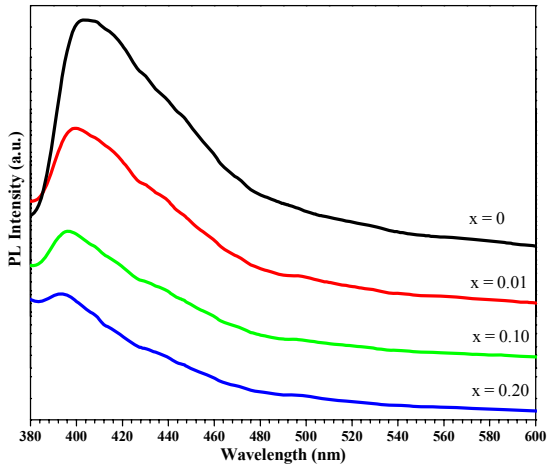

Figure 4 Room temperature PL spectra of $Zn_{1-x}Co_xO$ powders (x = 0, 0.01, 0.1 and 0.2) by ball milling method for 24 hours.

Conclusions

In summary, Co-doped ZnO samples have been prepared by mechanical milling method. Rietveld profile refinement analysis and XRD data of low doped (x = 0.01) samples showed the formation of a single-phase compound with wurtzite-like structure. However, XRD patterns of high doped (x = 0.1 and 0.2) samples showed the presence of an impurity phase, which has been identified as a variant of CoO. Rietveld refinement demonstrated that the Co cations had successfully entered into the hexagonal wurtzite structure and substituted for Zn cations sites in ZnO lattice. The UV-Vis were studied the red shift of E_g with increasing Co concentration. PL intensity due to the oxygen vacancies varies with the Co concentration.

Acknowledgements

The authors would like to thank the Department of Physics, Faculty of Science, Kasetsart University (KU) for XRD measurement. This work was also partly supported by the Department of Physics, Faculty of Science, King Mongkut's University of Technology Thonburi (KMUTT). Supphadate Sujinnapram wish to thank Dr. Taweesak Sudyoadsuk for the assistance with the Rietveld refinement method.

References

[1] R. Janisch, P. Gopal and N. A. Spaldin, *J. Phys.-Condens. Mat.* **17**(2005), pp. R657-R689.
[2] K. Ando, H. Saito, Zhengwu Jin, T. Fukumura, M. Kawasaki, Y. Matsumoto and H. Koinuma, *J. Appl. Phys*. **89**(2001), (11), pp. 7284-7286.
[3] K. Sato and H. Katayama-Yoshida, *Jpn. J. Appl. Phys*. **39**(2000), (6B), pp. L555-L558.
[4] T. Dietl, H. Ohno, F. Matsukura, J. Cibert and D. Ferrand, *Science*. **287**(2000), (5455), pp. 1019-1022.
[5] K. Ueda, H. Tabat and T. Kawai, *Appl. Phys. Lett*. **79**(2001), (7), pp. 988-990.
[6] H. J. Lee, S. Y. Jeong, C. R. Cho and C. H. Park, *Appl. Phys. Lett.* **81**(2002), (21), pp. 4020-4022.
[7] Z. Jin, T. Fukumura, M. Kawasali, K. Ando, H. Saito, T. Sekiguchi, Y.Z. Yoo, M. Murakami, Y. Matsumoto, T. Hasegawa and H. Koinuma, *Appl. Phys. Lett*. **78**(2001), (24), pp. 3824-3826.
[8] J. Rodriguez-Carvajal, *FULLPROF*. Laboratoire Leon Brillouin (CEACNRS) (2008).

Total and partial photon interactions of silicate glass system at 60 keV for shielding properties investigation: theoretical calculation

J. Kaewkhao[1*], C. Kedkaew[2], T. Kittiauchawal[3], N. Chanthina[2], K. Kirdsiri[2] and P. Limsuwan[2,4]

[*1]Glass and Materials Science Research Unit, Faculty of Science and Technology, Nakorn Pathom Rajabhat University, Nakorn Pathom, 73000, Thailand
[2] Department of Physics, King Mongkut's University of Technology Thonburi, Bangkok, 10140, Thailand
[3]Faculty of Science and Technology, Thepsatri Rajabhat University, Lopburi, 15000, Thailand
[4] Thailand Center of Excellence in Physics, CHE, 328 Si Ayutthaya Rd., Bangkok 10400, Thailand

*E-mail: mink110@hotmail.com

Abstract: Mass attenuation coefficients and partial photon interactions have been calculated theoretically at 60 keV photon energy for Bi_2O_3, PbO and BaO in xR_mO_n:(100-x)SiO_2 glass system, when x = 30 to 70 (by %weight) using WinXCom software. The values of these parameters have been found to significantly change with increasing of R_mO_n concentration. The mass attenuation coefficients were increased with increasing of R_mO_n concentration. This is due to increasing of photoelectric absorption, which dominant interaction in glass matrix at this energy. The Compton scattering and coherent scattering are rather small for these glass samples comparing with photoelectric absorption. This result reflecting the possibility to use Bi and Ba replaces Pb for development of lead-free radiation protecting glass at appropriated photon energy.

Introduction

The interaction of high-energy photons with matter is important in radiation medicine and biology, nuclear engineering, and space technology. Glass has the double function of being transparent to visible light and absorbing gamma rays and neutrons, thus providing a radiation shield for observers or experimenters. It may also be mentioned that vitrification is an interesting option for long-term storage of radioactive waste products. There is an increasing interest in heavy-metal oxide (HMO) glasses, based on for example PbO, because of their good gamma ray shielding properties **[1-3]**. However, a high Pb content lowers the melting point and the hardness of the glass. Moreover, it is desirable to replace Pb with other elements because of environmental considerations. Recently years, Bi and Ba based glass are playing an important role in radiation glass shielding replace lead due to environmental hazardous of lead **[3]**.

Silicon dioxide (SiO_2) is mainly for glass network former and most use in mass production in glass window. The good reviews on the development of radiation shielding glass have been published **[2-6]** from several authors, but there are almost no studies at lower and higher energies. In the present work, we have calculate theoretically the mass attenuation coefficients, partial interactions and effective atomic numbers for silicate glass system containing with BaO and Bi_2O_3 and compared with PbO at same glass system using photon interaction cross-sections from the WinXCom interpolation program **[7]** and the NIST database **[8]**. Moreover, calculation results from this work are also comparing with ordinary and ferrite shielding concrete.

Materials and Methods

In this section, we summarize theoretical relations used in the present work. The total probability of interaction is called the total linear attenuation coefficient, is equal to the sum of probabilities for each interaction, is given by

$$\mu = \tau + \sigma_{coherent} + \sigma_{incoherent} + \kappa \qquad (1)$$

Where τ, $\sigma_{coherent}$, $\sigma_{incoherent}$ and κ are the probability of photoelectric absorption, coherent scattering, Compton scattering) and pair production, respectively. Theoretical values of mass attenuation coefficients of chemical compound of mixture have been calculated using WinXCom **[7]**, based on the mixture rule **[9]**

$$\frac{\mu}{\rho} = \mu_m = \sum_i^n w_i (\mu_m)_i \qquad (2)$$

Where ρ, w_i and $(\mu_m)_i$ are density of glass samples, the weight fraction and mass attenuation coefficient of the i^{th} element in alloy, respectively. The total atomic cross-sections $(\sigma_{t,a})$ can be obtained using the values of mass attenuation coefficient by the following relation **[10]**,

$$\sigma_{t,a} = \frac{(\mu_m)_{alloy}}{N_A \sum_i^n (w_i / A_i)} \qquad (3)$$

Where N_A and A_i are Avogadro's number and atomic weight of the i^{th} element in alloy. Hence, the total electronic cross-sections $(\sigma_{t,el})$ for the i^{th} element is given by the following relation **[10]**,

$$\sigma_{t,el} = \frac{1}{N_A} \cdot \sum_i^n \frac{f_i A_i}{Z_i} (\mu_m)_i \qquad (4)$$

Where f_i is the number of atoms of the i^{th} element relative to the total number of atoms of all elements in alloy. From (3) and (4), the effective atomic number (Z_{eff}) can be given as **[10]**,

$$Z_{eff} = \frac{\sigma_{t,a}}{\sigma_{t,el}} \qquad (5)$$

Theoretical values for the total mass attenuation coefficient can be found in the tabulation by Hubbell and Seltzer. A lot of manual works can be saved by using suitable software. Berger and Hubbell developed XCOM for calculating total mass absorption coefficients or photon interaction cross-sections for any elements, compounds or mixtures at photon energy from 1 keV to 100 GeV. Recently, XCOM was transformed to the Windows platform by Gerward et al. **[7]**, called WinXCom.

Result and discussion

Table 1: Total mass attenuation coefficients and effective atomic numbers of Bi_2O_3, PbO and BaO in silicate glass samples

% composition	μ_m [cm^2/g]		
	Bi_2O_3	PbO	BaO
30	1.59	1.58	2.47
40	2.04	2.03	3.21
50	2.48	2.47	3.95
60	2.93	2.91	4.69
70	3.37	3.35	5.43

From table 1, although BaO has lower density compare with Bi_2O_3 and PbO. It has been found that the values of total mass attenuation coefficient for BaO glass samples are higher than that for Bi_2O_3 and PbO glass samples at this energy, this result show more attenuated photon in BaO glass than Bi_2O_3 and PbO glass. It was also found that the total mass attenuation coefficients increased along with increasing of Bi_2O_3, PbO and BaO concentration due to increasing of the photoelectric absorption which is dominant interaction at this energy. The photoelectric absorption values for BaO glasses are greater than the Bi_2O_3 and BaO glasses, reflecting more absorbed photon in BaO than Bi_2O_3 and PbO glasses. In the other hand, the Compton scattering and Coherent Scattering of BaO glass are lower than Bi_2O_3 and PbO glasses. The coherent interactions were increased and Compton scattering were decrease with increasing of Bi_2O_3, PbO and BaO concentration. However the both scattering are rather small for these glass samples at this energy (60 keV) comparing with photoelectric absorption. The pair production did not appear for all glass system due to the photon energy in this study is below 1.02 MeV. The partial interaction for all glass samples are show in table 2 along with composition of Bi_2O_3, PbO and BaO respectively.

Moreover, calculation results from this work are also comparing with ordinary and ferrite shielding concrete as show in figure 1. The results show that the total mass attenuation coefficients of all glass systems are better than ordinary and ferrite shielding concrete **[6]**, reflecting that the possibility to use glass in radiation shielding materials.

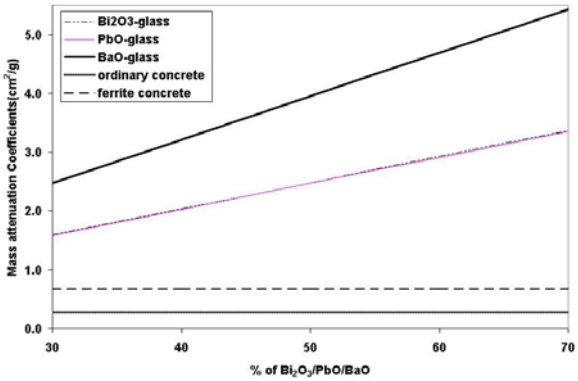

Figure 1. Mass attenuation coefficients of glass samples compare with ordinary and ferrite concrete at 60 keV

The effective atomic numbers of all silicate glass system are shown in Fig. 2. As the result, these parameters increased with increasing of Bi_2O_3, PbO and BaO concentration. In other words, the values for Bi_2O_3 and PbO glass samples are comparable, but the values of both glass samples are higher than BaO glass samples, which not agreement with mass attenuation coefficients values of this work. This could be the result of partial interactions contribute to total mass attenuation coefficients with the different glass components.

Table 2 : Partial interaction of Bi_2O_3, PbO and BaO in silicate glass samples

% composition	Photoelectric absorption [cm^2/g]			Coherent scattering($x10^{-1}$) [cm^2/g]			Compton scattering($x10^{-1}$) [cm^2/g]		
	Bi_2O_3	PbO	BaO	Bi_2O_3	PbO	BaO	Bi_2O_3	PbO	BaO
30	1.30	1.29	2.23	1.54	1.56	0.92	1.43	1.40	1.38
40	1.70	1.69	2.95	1.97	1.99	1.14	1.39	1.35	1.33
50	2.11	2.10	3.68	2.39	2.42	1.36	1.34	1.30	1.28
60	2.52	2.50	4.40	2.82	2.84	1.58	1.30	1.25	1.22
70	2.93	2.90	5.12	3.24	3.27	1.80	1.26	1.19	1.17

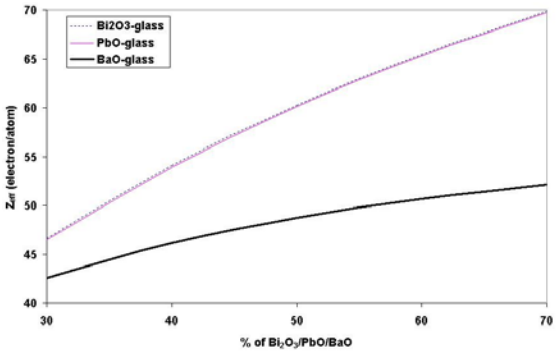

Figure 2. Effective atomic numbers of glass samples

Conclusions

In this work, the total mass attenuation coefficient, partial interaction and effective atomic number of Bi_2O_3, PbO and BaO in xR_mO_n:(100-x)SiO_2 glass system, when $30 \le x \le 70$ (by %weight) at photon energy 60 keV have been calculated using winXCom. The result found that the total mass attenuation coefficient and coherent interaction for all glass samples increased with increasing of Bi_2O_3, PbO and BaO concentration. The photoelectric effect is the dominant interaction of photon that contributes to the total mass attenuation coefficients for all glass samples. These results were varying useful for design radiation shielding glass and reflecting influence of Bi and Ba in shielding glass matrix. For this energy (60 keV) barium is appropriated materials than bismuth due to less toxic than both of Bi and Pb.

Further investigations of the development glass materials for radiation protection are in progress. Much more experimental works are clearly needed for the photon interactions with matter in the energy regions where significant variations occur especially near the absorption edges of elements present in the material.

Acknowledgement

The authors would like to thank Thailand Research Fund (TRF) and Commission of Higher Education (NRU project) for financial support to carry out this research work. Thanks are also due to the Research and Development Institute, NPRU for the facilities. J. Kaewkhao is thankful to Professor L. Gerward of Department of Physics, Technical University of Denmark for providing us with the WinXCom program.

References

[1] S.R. Manohara, S.M. Hanagodimath and L. Gerward, *J. Nucl. Mater.* **393** (2009), pp. 465-472.
[2] K. Kirdsiri, J.Kaewkhao, A. Pokaipisit, W. Chewpraditkul, and P.Limsuwan *Anna of Nucl. Ener.* **36** (2009), pp. 1360-1365.
[3] J. Kaewkhao and Limsuwan, *Nucl. Instr. and Meth. B.* (In Press, Corrected Proof)
[4] K. Singh, H. Singh, V. Sharma, R. Nathuram, A. Khanna, R. Kumar, S.S. Bhatti and H.S. Sahota, *Nucl. Instr. and Meth. B* **194** (2002), pp. 1-6.
[5] N. Singh, K.J. Singh, K. Singh and H. Singh, *Nucl. Instr. and Meth. B.* **225** (2004), pp. 305-309.
[6] N. Singh, K.J. Singh, K. Singh and H. Singh, *Radiat. Meas.* **41** (2006), pp. 84-88.
[7] L. Gerward et al., *Rad. Phys. and Chem.* **60** (2001), pp.23-24.
[8] M.J. Berger, J.H. Hubbell, XCOM: photon cross sections database, Web version 1.2, 1999, Available from: <http://physics.nist.gov/xcom>, originally published as NBSIR 87-3597: XCOM: Photon Cross Sections on a Personal Computer, Washington, DC, 1987.
[9] N.F. Jackson and D.J. Hawkes, *Phys. Rep.* **70** (1981), pp. 169-233.
[10] J. Kaewkhao, J. Laopaiboon and W. Chewpraditkul, *J. Quant. Spect. Rad. Trans.* **106** (2008), pp.1260-1265.

Effects of carbon black loading on reversion behavior of natural rubber compound cured with sulfenamide accelerators

W. Phasook[1], K. Boonkerd[1,2*] and C. Deeprasertkul[3]

[1] Department of Materials Science, Faculty of Science, Chulalongkorn University, Bangkok, Thailand
[2] Research Unit of Advanced Ceramic and Polymeric Materials, National Center of Excellence for Petroleum, Petrochemicals and Advanced Materials, Chulalongkorn University, Bangkok, Thailand
[3] Institute of Science and Technology for Research and Development, Mahidol University, Nakorn Phathom, Thailand

*E-mail: k.boonkerd@gmail.com

Abstract: Effects of carbon black loading on reversion behavior of natural rubber (NR) compounds cured with two different sulfenamide accelerators, including N-dicyclohexyl-2-benzothiazole sulfenamide (DCBS) and N-cyclohexyl-2-benzothiazole sulfenamide (CBS) were studied here. The amount of crosslink densities of the NR compounds cured with these two accelerated sulfur cure systems were controlled to be the same. For each accelerator, a series of six NR compounds at various carbon black (N330) loadings of 0, 10, 20, 30, 40, and 50 phr was prepared using an internal mixer. Then, the cure characteristics of compounds were carried out with a Moving Die Rheometer (MDR) at the different curing temperatures of 130, 140, 150, 160, 170, and 180 ^{o}C. The characteristics of both plateau region and slope of the decreasing MDR torque were used here to indicate the reversion behavior. The results showed that for both curing systems, the curing temperature and carbon black loading affected their reversion behavior similarly. The initial reversion temperature of unfilled NR compounds was observed at 160 ^{o}C. With the presence of carbon black 30 phr or more, this temperature was shifted downward to 150 ^{o}C. The time of the plateau region first decreased with increasing carbon black loadings and then levelled off. However, in the case of the rate of reversion, it was directly proportional to carbon black loading. It was clearly shown here that the presence of carbon black caused NR compounds higher reversion no matter DCBS or CBS accelerated sulfur cure system was used.

Introduction

Reinforcement is defined as an ability to increase the viscosity of unvulcanized compounds and to improve a variety of vulcanizate properties, example tensile strength, abrasion resistance and tear resistance. Most of engineering rubber products cannot be used without the addition of reinforcing filler. Carbon black is well-known reinforcing filler extensively used in rubber industry. The degree of reinforcement of carbon black depends strongly on the interaction forces between the rubber and carbon black surface. Thus, the smaller the size of primary particle is, the higher the degree of reinforcement is. Moreover, it has long been known that carbon black can also improve reversion resistance: thermal degradation of polysulfidic crosslinks leading to a reduction of crosslink density and an introduction of main chain modifications. The reversion behavior can be observed from cure curves. The decrease of torque after reaching maximum value indicated the initiation of reversion. Chen and coworker found that black filled NR compounds showed better reversion resistance [1]. The smaller the particle size, the greater the reversion improvement. It was proposed by them that the reversion improvement might be due to the adhere of rubber chains onto the carbon black surface, causing less desulfuration of polysulfidic linkages. The polysulfidic linkages now have greater thermal stability. So the reversion resistance is improved. Studebaker [2] and Porter [3] found that the network filled with carbon black consists of the higher proportion of stronger linkages, mono- and disulfidic linkages than one without carbon black. So this leads to higher thermal and reversion resistance. However, our previous studies showed that adding 50 phr of carbon black N330 into natural rubber cured with the DCBS accelerated sulfur cure system significantly increased in the reversion behavior [4].

According to above controversy, the study here will further investigate effects of carbon black on reversion behavior of natural rubber by varying carbon black loading and accelerated sulfur cure systems. It is expected here that the result from this study will give the suitable guideline to obtain a reversion-free rubber compound.

Materials and Methods

There were two accelerators including N, N-dicyclohexyl-2-benzothiazole sulfenamide (DCBS) and N-cyclohexyl-2-benzothiazole sulfenamide (CBS) used here. The amount of sulfur and accelerator used in these two accelerated sulfur cure systems were controlled to give these two unfilled rubber compounds the same crosslink density. The composition of unfilled natural rubber (NR) compounds cured with different accelerators was given in Table 1.

Table 1: The Composition of Unfilled NR Compounds

Ingredient (phr)	Compound	
NR	100	100
Stearic acid	1	1
ZnO	8	8
6PPD	1	1
TMQ	1	1
S/DCBS*	2.63/2.25	-
S/CBS*	-	1.60/1.35

* [5]

For each accelerator, a series of six NR compounds at various carbon black (N330) loadings of 0, 10, 20, 30, 40, and 50 phr was prepared using an internal mixer. All ingredients, except the curatives, were mixed with NR in a laboratory-size internal mixer at a set temperature of 50 °C with a rotor speed of 40 rpm and a fill factor of 0.7. The total mixing time of this step was seven minutes. After discharging, the mixed rubber compound was left at the room temperature until its temperature was equilibrated with the room temperature. Then, the mixed rubber compound was loaded back into an internal mixer again. Then, the curatives were added and mixed for four minutes. The compound was taken out and then placed onto a nip of a two roll mill. Then, 5 end-roll passes were made before sheeting off. The rubber sheet was kept at least 24 hours before the cure characterization step.

The cure characteristics of rubber compounds were determined using a moving die rheometer (MDR). Testing was conducted at different temperatures of 130, 140, 150, 160, 170, 180 ºC. From MDR curves, the effect of carbon black loading on the reversion behavior was characterized by two parameters: the time of plateau region and the rate of reversion indicated by the slope of the decreasing MDR torque after torque reached maximum.

Results and Discussion

Effect of the curing temperature on the reversion behavior of unfilled NR compounds was discussed first. As mentioned earlier, the reversion is the decrease of crosslink density when the compound is overcured. Therefore, this can be indicated by the decline of MDR torque. Figure 1 showed MDR curves of NR compounds cured at different curing temperatures. It was clearly seen that the reversion behavior depended strongly on the curing temperature. For both DCBS and CBS curing systems, the reversion of NR compounds was initially observed at the same temperature which was 150 °C. With further increasing curing temperatures, the reversion formed faster. This can be indicated by the shortening of the plateau region after torque reached maximum. Moreover, it was also found that the rate of reversion was also proportionally to the curing temperature. As seen in Figure 1, after reaching maximum, for both curing systems studied here, the slope of the decreasing MDR torque at the curing temperature of 180 °C was highest.

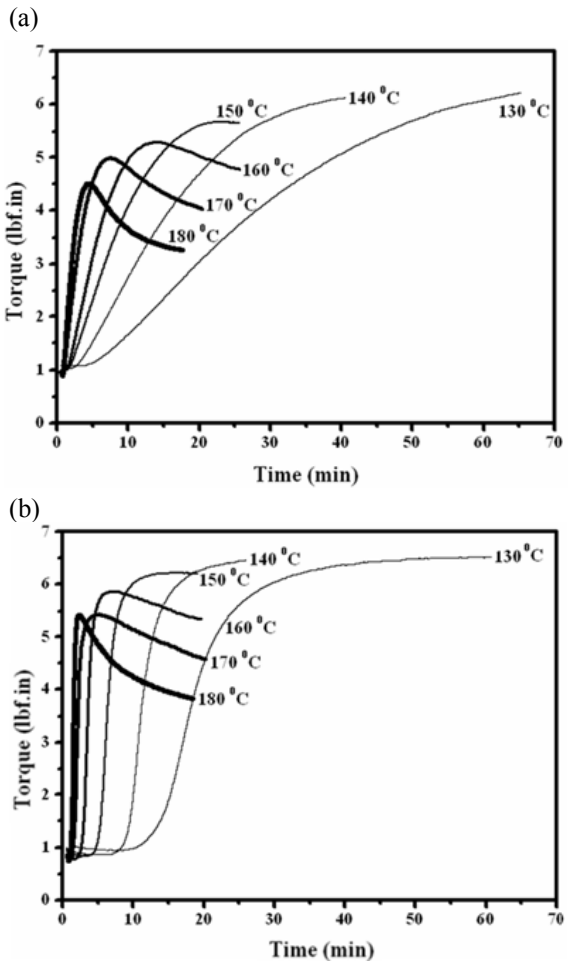

Figure 1. MDR curves at different curing temperatures of unfilled NR compounds cured with (a) DCBS (b) CBS

With the presence of carbon black, the change in the reversion behavior of NR compounds was observed. This significantly depended on carbon black loading. Firstly, it was found that when carbon black loading was increased up to 30 phr, the initial reversion temperature of NR compounds cured with both DCBS and CBS was shifted from 160 °C downward to 150 °C as shown in Figure 2. With the higher carbon black loadings, the initial reversion temperature was still 150 °C.

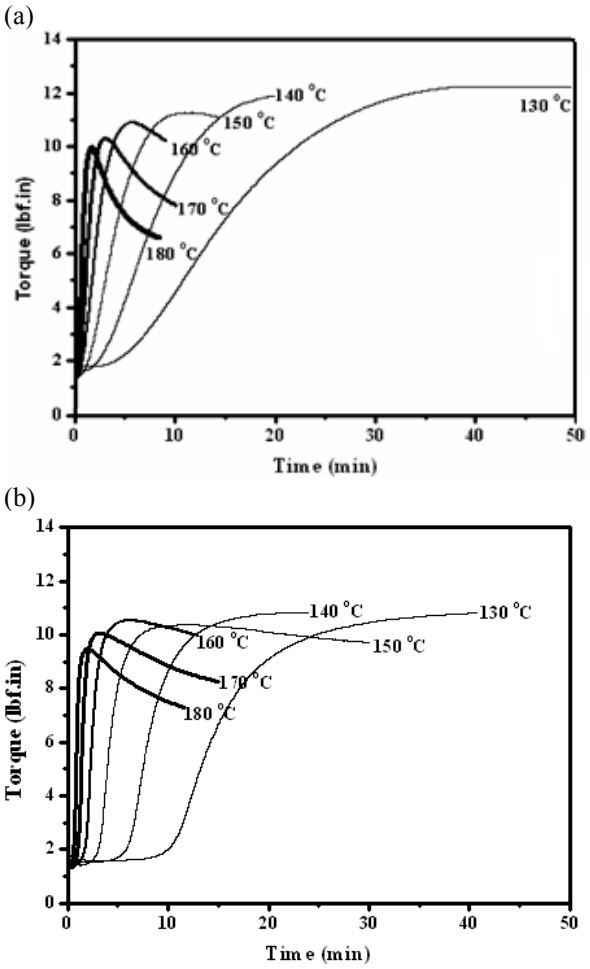

Figure 2. MDR curves at different curing temperatures of 30 phr black-filled NR compounds cured with (a) DCBS (b) CBS

Effect of carbon black loading was studied at the curing temperature of 160 °C. MDR curves of NR compounds filled with various carbon black loadings were shown in Figure 3. Cure characteristics including the scorch time (ts_2), time to reach 90% cure (tc_{90}), and time to reach 100% (tc_{100}) and the time of the plateau region from Figure 3 were ploted against carbon black loadings in Figure 4. Initially, it was observed the presence of carbon black affected the cure characteristics of NR compounds cured with DCBS and CBS in the same way. The ts_2, tc_{90}, and tc_{100} of NR compounds initially decreased with increasing carbon black loadings and then leveled off. Effect of carbon black loading on the time of the plateau region was similar to the cure characteristics. This might be due to the lack of desulfuration process when increasing cure rate. Therefore, there were a lot of polysulfidic crosslinks remaining in the network. According to their lowest bond energy, this resulted network in lower reversion resistance.

Effect of carbon black loading on the rate of reversion indicating by the slope of the decreasing MDR torque after reaching maximum in Figure 3 was given in Table 2.

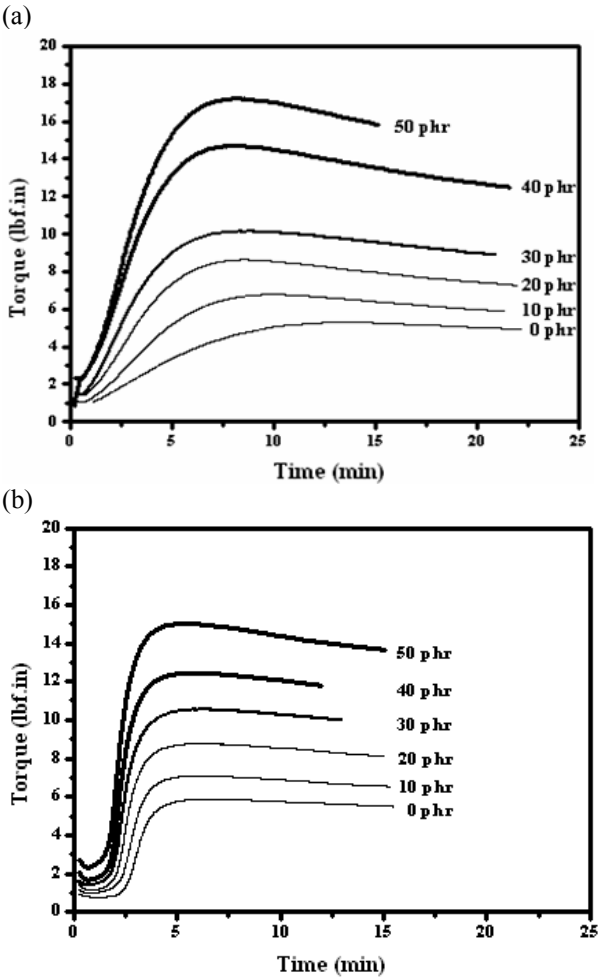

Figure 3. MDR curves at 160 °C of NR compounds with various carbon black loadings cured with (a) DCBS (b) CBS

Table 2: Rate of Reversion of NR compounds Cured at 160 °C

CB Loading (phr)	Rate of Reversion	
	DCBS	CBS
0	-0.042	-0.0009
10	-0.080	-0.0011
20	-0.112	-0.0014
30	-0.103	-0.0016
40	-0.184	-0.0019
50	-0.195	-0.0029

From Table 2, it was found that the rate of the reversion of NR compounds was proportional to carbon black loading. The higher carbon black loading was, the higher the reversion rate was.

Results here clearly showed that the presence of carbon black caused NR compounds higher reversion no matter DCBS or CBS was used. Moreover, the reversion tended to increase with the increase of carbon black loading.

(a)

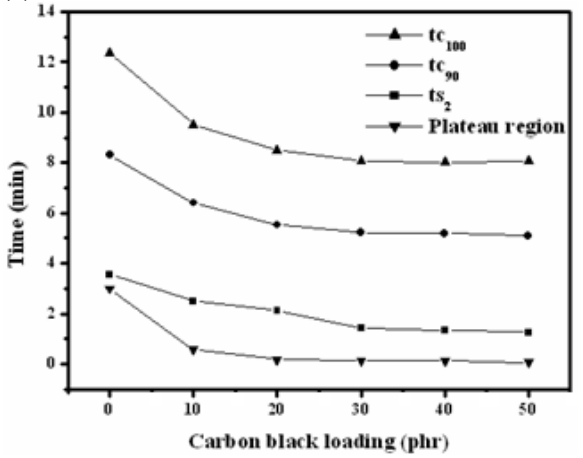

(b)

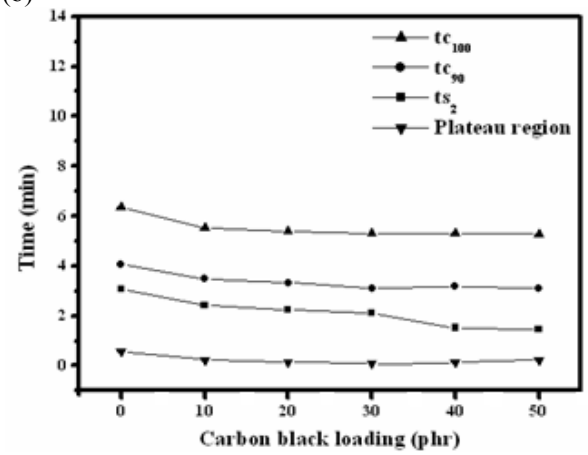

Figure 4. Cure characteristics and the time of the plateau region at 160 °C of NR compounds with various carbon black loadings cured with (a) DCBS (b) CBS

Conclusions

Effects of carbon black loading on reversion behavior of NR compounds cured with two different sulfenamide accelerators including DCBS and CBS were studied here. The preliminary results showed that for both curing systems, the initial reversion temperature of unfilled NR compounds was observed at 160 °C. With the presence of carbon black 30 phr or more, the initial reversion temperature was shifted downward to 150 °C. The time of the plateau region initially increased with increasing carbon black loadings and then levelled off. The rate of reversion was directly proportional to carbon black loading. Although there were a fair amount of researches showed that carbon black can enhance the reversion resistance, the results here clearly showed that the presence of carbon black caused higher reversion.

Acknowledgements

The authors would like to thank Research Unit of Advanced Ceramic and Polymeric Materials, National Center of Excellence for Petroleum, Petrochemicals and Advanced Materials, Chulalongkorn University for financial support.

References

[1] C.H. Chen, J.L. Koenig, J.R. Shelton and E.A. Collins, *Rubber Chem. Technol.* **55** (1982), pp. 103-115.
[2] M.L. Studebaker, *Reinforcement of Elastomers*, Interscience Publishers, New York, U.S. (1965).
[3] M. Porter, *Kautsch. Gummi. Kunst*. **22** (1969), pp. 419.
[4] K. Boonkerd, Effect of efficiency of sulfur vulcanization on properties of gum and black-filled natural rubber vulcanizates, Ph.D. Dissertation, The University of Akorn, 2006.
[5] K. Boonsomwong, Reversion behavior, mechanical and thermal aging properties of natural rubber vulcanizates cured with various accelerator ratios, Master's Thesis, Mahidol University, 2009.

Preparation and characterization of silver nanopaticles hydrogel polymer based on water soluble biopolymer based on water-soluble biopolymers and epoxidied natural rubber

W. Jindapon[1], S. Riyajan[1]* and T. Leejarkpai[2]

[1]Department of Material Science and Technology, Faculty of Science, Prince of Songkla University, Hat Yai, (Thailand) 90112
[2]National Metal and Materials Technology Center,114 Thailand Science Park Paholyothin Rd., Klong 1, Klong Luang, Pathumthani Thailand, 12120

*E-Mail: sa-ad.r@psu.ac.th, saadriyajan@hotmail.com

Abstract: At present, nanosilver polymer composite is widely used in biomedical application especially in antibacterial field. The aim of this work is the synthesis and characterization of nanosilver biopolymer semi interpenetrating polymer network (semi-IPN) hydrogel composite obtained from starch, poly(vinyl alcohol)(PVA) and natural rubber (NR) and silver nitrate via latex-solution method. The main factors including polymer blend ratio and silver contents affecting on the properties of the obtained sample were investigated. The resulting nanosilver semi-IPN hydrogel composite film is characterized using swelling in water, SEM, TEM, and UV spectroscopic. The diameter of nanosilver dispersed in biopolymer matrix was ranging between 4 and 10 nm observing from TEM. UV–Vis absorption spectra showed the peaks characteristic of the surface plasmon resonance of nano-sized silver. The swelling of polymer blend films decreased with increasing PVA contents in semi-IPN but the swelling ratio of semi-IPN increased as a function of increasing starch in sample. In addition, the contact angle of the semi-IPN sample loading with silver particle increased comparing to sample without silver particle due to hydrophobic of silver nano particle.

Introduction

Nowaday, polymer hydrogels have been interested in medical, pharmaceutics, agriculture field. Products of polymer hydrogels are contact lens, electrode sensors, adhesives, scaffold and plaster [1-5]. Because the advantage of polymer hydrogels is excellence in water absorption but it not dissolved in water [6-10]. The main polymer hydrogels are obtained from polyacrylamide, PVA, poly (vinyl pyrrolidone) and polyethylene glycol. Recently, natural polymers have attracted to use a raw material for preparing polymer hydrogel due to shortage of petroleum oil and environment pollution [8-9]. Among biopolymers, starch is mainly used the polymer hydrogel. The benefits of the starch are excellence biodegradability, low toxicity and biocompability. In addition, natural starch is available in Asia, especially Thailand due to renewable biopolymer. Many polymer scientists have modified the properties of starch through chemical modification, blend with other polymer and addition of polymer additive. For example, the modified starch was subjected to microwave to get ester group on the starch molecules. Results showed that the optimum condition for the modified starch were immobilized lipase and an oleic acid/starch molar ratio of 0.18 at 44^{o}C and 200 rpm. The property of modified starch shows the hydrophobic chatacteristic.

The aims of this work is study to the preparation and physical properties of the novel polymer hydrogel obtained from PVA, starch, and epoxided NR as well as silver.The resulting nanosilver semi-IPN hydrogel composite film is characterized using swelling in water, SEM, TEM, and UV-Vis spectroscopy.

Materials and Methods

Materials

High ammonia NR (HA-NR, Chalong Latex Industry Co.,Ltd.), hydrogen peroxide (Riede-de Haen Co.,Ltd., Germany), formic acid (Riede-de Haen Co.,Ltd., Germany), poly(vinyl alcohol) (PVA, commercials grades) with 87% hydrolysis, Terric 16A-16 (Lucky four), maleic acid (MA, Fluka Co.,Ltd., Switzerland). 200 g of HA-NR latex containing 20% DRC was blended with 10 g of 10% Terric acid as a non-ionic surfactant at ambient temperature while stirring for 1 h. The sample mixture was neutralized, then acidified with 12 g of formic acid (Fluka Co.,Ltd., Switzerland). After that, 80 ml of hydrogen peroxide (BHD, Analar) was added at 30^{o}C within 10-15 min. The epoxidation process was carried out at 70^{o}C for 5 h and the resulting ENR latex possessing a 20% of epoxided content was used in this paper.

Preparation of polymer hydrogel

The PVA solution (10% w/v) and starch solution (5% w/v), sodium alginate (2%w/w) were prepared in Millipore water by heating it on a water bath at 70 ºC while being continuously stirred. The 20 g of PVA, 40 g of starch**,**4 g of sodium alginate, 1.33 g of epoxided natural rubber, 1 g of glycerol were mixture together by magnetic stirrer. Then, the 5% glutaraldehyde and 0.10 g of silver was mixed with the solution at ambient temperature with the help of a mechanical stirrer. The mixture was poured in the form of a sheet on a glass surface. The sheet with an 0.55 mm thickness was dried at ambient temperature and subsequently cured in an oven at different curing times (eg 60 min) at 120 ºC.

The effect of PVA or starch contents and silver on the properties of polymer hydrogel was been investigated in this work.

Analysis of resulting polymer hydrogel

Polymer hydrogel samples of specific dimensions (2.5 cm × 2.5 cm) and with an average thickness of 0.5 mm were weighed and immersed in Millipore water for a period of 5 days at 32 ºC. The samples were then dried in an oven at 50 ºC for 24 h and weighed until a constant weight was achieved. The degree of swelling ratio was estimated from this equation (1)

$$\text{Swelling ratio} = (W_2 - W_1)/ W_1 \quad \ldots\ldots\ldots\ldots\ldots\ldots\ldots\ldots (1)$$

Where W_1 = the original weight of the sample

W_2= the weight of swollen sample

A scanning electron microscope (JMS-5800 LV, JEOL, and SEM) was used to investigate the morphologies of cross-sections of the samples at an accelerating voltage of 6 kV. Polymer hydrogel specimens were fractured in liquid nitrogen and the cross-sections were mounted on SEM stubs with double sided adhesive tape, and then coated with platinum under a 12 Pa vacuum. The thermogravimetric (TG) analysis was performed on a Pwein Elmer Thermobalance. The mass of each sample was about 6.00–7.00 mg. The carrier gas was N2 with a flow rate of 45 mL/min. The temperature rose from 50 to 800 ^{o}C at a heating rate of 10^{o}C/min.

UV–Vis spectra of semi-IPN hydrogel–silver nanocomposites (10 mg in 1 ml of distilled water) were carried out on a Shimadzu (Kyoto, Japan) 160A UV spectrophotometer. X-ray diffraction measurements were recorded using a Rikagu diffractometer (Cu radiation, λ=0.1546 nm) running at 40 kV and 40 mA. The thermal stabilities of the polymer hydrogel were evaluated by using the Mettler Toledo 851ethermal system (Zurich, Switzerland) at a heating rate of 10 °C/min under nitrogen atmosphere (flow rate, 10 ml/min). The dry hydrogel (coated with a thin layer of palladium gold alloy) and the semi-IPN hydrogel–silver nanocomposites were studied for morphological variations by using a JEOL JSM 840A (Tokyo, Japan) scanning electron microscope. Transmission electron microscopy images for the hydrogel–silver nanocomposites were recorded using a Tecnai F 12 transmission electron microscope operating at an acceleration voltage of 15 kV. For TEM measurements, samples were prepared by Microtone technique.

Results and Discussion

The silver nanoparticle formation within the hydrogel networks can be seen from the bulk gel disc, which became brown after the reduction reaction as shown in Figure 1. It is hypothesized that the silver nanoparticles are immobilized throughout the hydrogel networks due to a strong localization of the Ag+ ions within the network. This is caused by the complexation of the Ag+ ions by oxygen atoms (OH) of PVA or starch. Figure 2 represents the morphology of polymer hydrogel obtained from PVA, starch and epoxided natural rubber observed from TEM. It was found that the particle size of silver dispersed in polymer matrix was 10-25 nm. Figure 3 shows the morphology of polymer hydrogel observed from SEM. It is clear that the particle size of silver shows the many numbers of silver aggregations. The silver nanoparticle formation within the hydrogel networks can be seen from the bulk gel disc, which became brown after the reduction reaction. It is hypothesized that the silver nanoparticles are immobilized throughout the hydrogel networks due to a strong localization of the Ag+ ions within the network. This is caused by the complexation of the Ag+ ions by oxygen atoms (OH) of PVA or starch. The swelling of any polymeric film in a solvent depends upon the diffusion coefficient of the solvent, the relaxation rate of the amorphous regions of the polymer chain and its degree of crystallinity. Polymer gels may be classified into two different categories, i.e., physical gel and chemical gel. In a physical gel the junction points of the network arise owing to physical bonding like Van Der Waals interactions, hydrogen bonding, the presences of crystallites, etc.; hence, in a good solvent such networks exhibit a large extent of volume change owing to the facile penetration of the solvent. The swelling ratio of a semi-interpenetrating sample could be practically used to approximate the crosslinking density in sample.

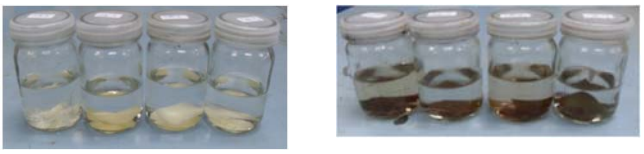

Without silver with silver

Figure 1 Appearance of polymer hydrogel without or with silver

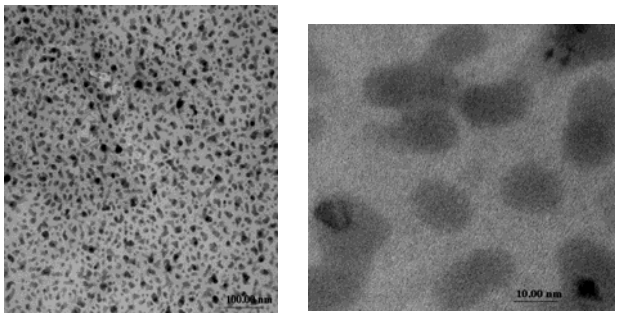

Expanded region

Figure 2 Morphology of polymer hydrogel containing silver particle observed from TEM

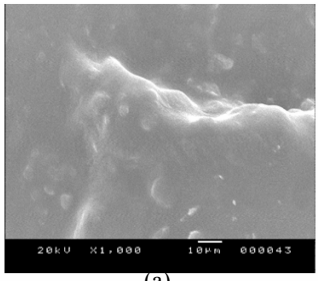

(a)

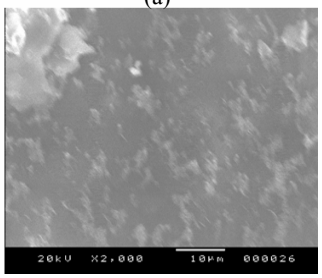

(b)

Figure 3 Morphology of polymer hydrogel observed by SEM (a) without and (b) with silver

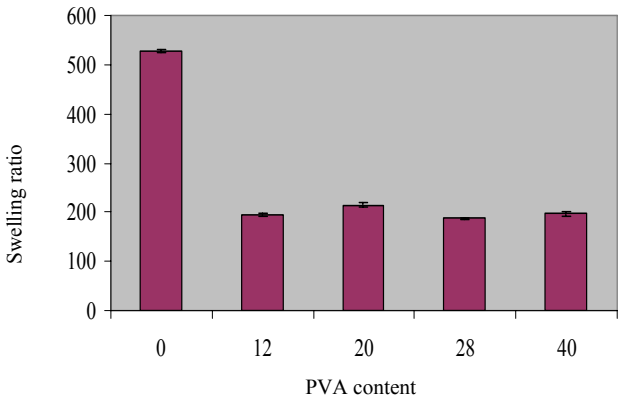

Figure4 Relationship between swelling and PVA content of polymer hydrogel

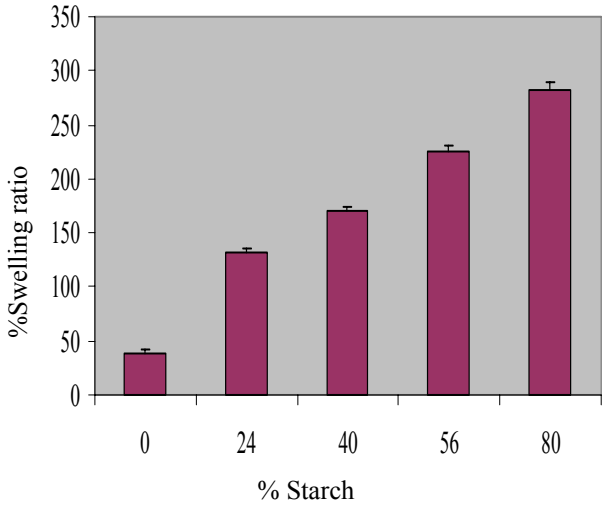

Figure 5 Relationship between swelling and starch content of polymer hydrogel

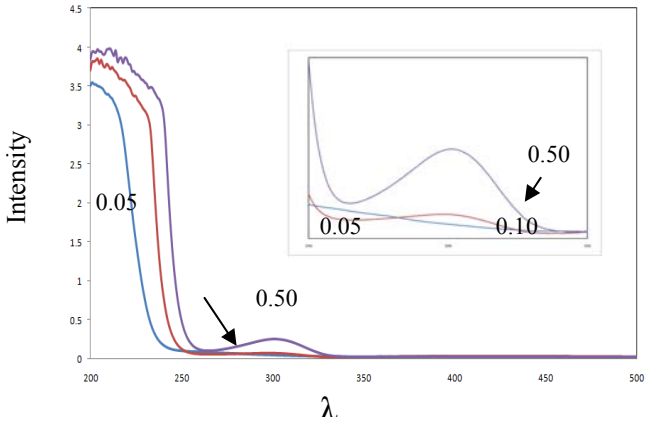

Figure 6 UV-Vis absorption of polymer hydrogel containing different silver contents

The influence of the PVA contents on the swelling ratio of polymer hydrogel was represented in Figure 5. Results showed that the swelling ratio of polymer hydrogel dramatically decreased after addition of PVA in polymer hydrogel. The swelling ratio of the sample containing PVA was about 200% whereas the %swelling ratio of starch alone was 890. The effect of starch on the swelling ratio of polymer hydrogel is shown in Figure 4. Results showed that the swelling ratio of polymer hydrogel increase as a function of starch due to its hydrophobic group content in polymer chain. The swelling ratio of polymer hydrogel containing 0, 24, 40, 56 and 80% of starch was 40, 130, 170, 230 and 280, respectively.

In order to inspect the formation of nanoparticles prepared using the contemporary approach, we have carried out UV–Vis absorption studies and the corresponding results are shown in Figure 5. It is very clear that an absorption peak at around 310 nm is noticed for the Ag particles due to the surface plasmon resonance effect originating from the quantum size of silver nanoparticles, whereas the 0.05 g $AgNO_3$ hydrogel showed no absorbance in this UV–Vis region

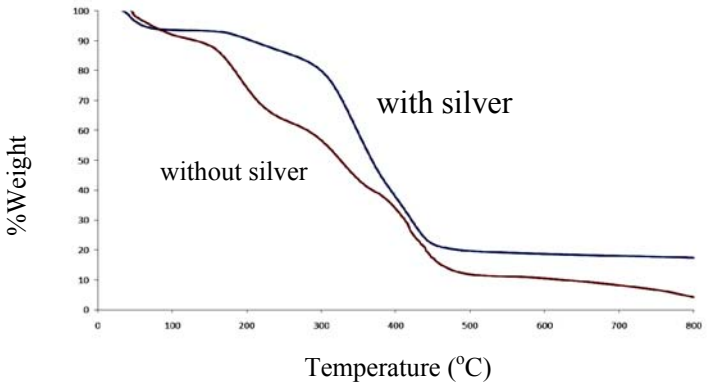

Figure 7 Thermal properties of polymer hydrogel without or with silver observed by TGA

Figure 7 shows the TGA of polymer hydrogel. Result shows that the hydrogel containing silver exhibits excellent thermal stability than semi-IPN hydrogels. In detail, semi-IPN hydrogels followed five degradation steps and 10 wt% degradation of the moisture in hydrogel chains occurred below 150 °C. The 50, 60, 85 and 95% degradation of polymer hydrogel chain occurred at below 220, 350, 450 and 800^{o}C, respectively. But in the case of semi-IPN hydrogel–silver composite it is noted as four degradation steps and only a 85% weight loss below 460 °C .

Conclusion

The novel biopolymer hydrogels were made from PVA, epoxided natural rubber and starch by glutaraldehyde as a crosslinking reagent. Effect of starch content and PVA contents on the swelling behavior of the new polymer hydrogel in distilled water was investigated in this paper. The swelling ratio of polymer hydrogel decreased as a function of PVA content, glycerol content while the swelling behavior of the new polymer hydrogel increased with increasing starch. The swelling ratio of polymer hydrogel was a range of 10-400 depending on the parameter conditions. The plasmon phenomenon of polymer hydrogel was analyzed by UV spectroscopy. The λ max of PVA in the presence of silver was observed at 310 nm and the intensity of λ_{max} increased with storage time of PVA solution.

Acknowledgement

The authors thank Department of Material Science and Technology, Prince of Songkla University for the use laboratory space. This study was supported by National Science and Technology Development Agency fund (SP52-MT10).

References

[1] W.W. Li, H. Li, Z.F. Liu, Q. Qiao, *Biomed. Envir. Sci*. **22** (2009), pp. 28-31**.**
[2] J. Chen, Y. Yang, P.Q.Z. Ma, W. Wu, P. Sung, X. Wang and, J.Li, *Radiat. Phy. Chem.* **42**(1993), pp.915-918.
[3] M.C. Chen, H.W. Tsai, C.T. Liu, S.F. Peng, W.Y. Lai, S.J. Chen, Y.C., H.W. Sung, Biomaterials **30**(2009), pp. 2102-2111.
[4] M. George, T.E. Abraham, *Inter. J. Pharm*. 335, (2007) pp.123-129.
[5] U. Shavit, M. Reiss, A. Shaviv, J.Control.Release, **88**(2003) pp. 71-83
[6] S. Riyajan, J.T. Sakdapipanich, Chem.Eng.J., **152** (2009) pp.591-597.
[7] S. Riyajan, J.T. Sakdapipanich, Polym. Bull. **63** (2009) pp.609-622
[8] H. Horchani, M. Chaâbouni,Y. Gargouri, A. Sayari, Carbohy. Polym. **79** (2010) pp. 466–474
[9] A.M.L. Huijbrechts, R.T.Haar, H.A. Schols, M. C.R. Franssen, C.G. Boeriu, E.J.R. Sudhölter, Carbohy. Polym. In Press, (2009)
[10] K.O. Adebowale, T. Henle, U. Schwarzenbolz, T. Doert, Food Hydrocolloids, 23(2009) pp.1947-1957.

Synthesis and Antibacterial Activity of Silica Quat-188 Prepared by Sodium Silicate Route

Sumet Lertpanyachokchai[1] Supawan Tantayanon[2]

[1]Program of Petrochemistry and Polymer Science, Faculty of Science
Chulalongkorn University, Bangkok, 10330 Thailand
[2]Green Chemistry Research Lab, Department of Chemistry, Faculty of Science,
Chulalongkorn University, Bangkok, 10330 Thailand

*E-mail: supawan.t@chula.ac.th

Abstract: Organic-inorganic hybrid materials have been widely investigated in order to improve their matrix properties. In this study, silica Quat-188 has been synthesized via sodium silicate route. The reaction involved the direct grafting of 3-chloro-2-hydroxyltrimethyl ammonium chloride (Quat-188) within the silicate matrix. The amount of Quat-188 was varied from 2.0 to 13.5 % weight by volume. After the unreacted Quat-188 was removed by washing with de-ionized water, the product was dried. It was characterized by FTIR, solid state ^{13}C-NMR and ^{29}Si-NMR. Then the silica Quat-188 was subjected to the antibacterial testing using both gram-positive bacteria (*Staphylococcus Aureus*) and gram-negative bacteria (*Escherichia Coli*). The determination of the incorporated Quat-188 and the antibacterial activity of silica Quat-188 will be discussed.

Introduction

The quaternary nitrogen functionality belong to the group of compounds, which exhibit high antibacterial activity both Gram-positive and Gram-negative bacteria, as well as against some pathogenic species of fungi and protozoa. They are widely used in many of domains such as environmental disinfection, equipment surfaces and disinfection in hospitals. Quaternary ammonium polymers are generally more active than their corresponding monomers, particularly against Gram-Positive bacteria. The higher alkyl group of quaternary ammonium materials having a higher molecular weight and multiple quaternary nitrogen exhibit increased activity as the charge density increases the attraction to the negatively charged cell membrane. However, these quaternary ammonium compounds, in general, have toxic effects toward mammalian cells. In humans and animals they are consider too toxic for systemic applications. To overcome these problems, anchoring the quaternary ammonium salt might be promising in developing materials which would have antibacterial activity by themselves [1,2].

Organic–inorganic hybrid materials prefer endless opportunities for tailoring chemical, physical, biochemical, optical, sensing, and chromatographic properties. General methodologies for the synthesis of such materials are therefore in constant need. The synergistic combination of organic polymer-inorganic silica via a sol-gel process has recently been attracted great attention in the field of material science because it has the potential for the development of new materials with design chemical, by structural manipulation at the molecular level[3].

We reported the synthesis of silica Quat-188 from sodium silicate (water glass) precursor employing an inexpensive and simple method involving the aging of a gel, washing with water, the subsequent surface modification of the gel, and finally drying at ambient pressure. This method is expected to produce organic-inorganic hybrid materials at low cost and high properties.

Experimental procedure

Material

Sodium silicate (Solid Content 44%, ratio SiO_2 : Na_2O 2.6-3.2 , Specific gravity 1.41-1.46) was purchased from Siri Kate Co.,LTD., 3-chloro-2-hydroxypropyl trimethylammonium chloride from Dow Chemicals Co.,Ltd. Other organic solvents were distilled before use. Tested microorganism included the Gram-negative bacteria *Escherichia Coli*(8099), Gram-positive bacteria *Staphylococcus Aureus* (ACTCC 6538). Bacteria was maintained on Sabouraud agar. Liquid broth medium was sterilized by autoclaving for 30 min at 121°C[2].

Synthesis of silica Quat-188

Sodium silicate solution 12.0 ml was added into 120 ml distilled water and mixed well using high speed dispenser for 5 min. Quat-188, at various amount as shown in Table 1, was then added while stirring. Then solution was kept at 50°C to allow for gel formation. The formed gels were aged for 3 h at 50°C to give strength to gel network [4]. The composite particles were then collected by filtration. The resulting silica Quat-188 was washed with de-ionized water several times to remove unreacted Quat-188 and then the product was dried at 110°C for 1 h.

Table 1. Preparation of Silica Quat-188

Sample (No.)	Quat-188		3M acetic acid(ml)	gel time (min)
	ml	mol ($\times 10^{-2}$)		
1	-	-	15.5	60
2	5	2	-	1300
3	8	3.2	-	570
4	14.5	5.9	-	155
5	20	8.1	-	30

Note : Na_2SiO_3 12 ml and water 120 ml were used in every entry.

Characterization of silica Quat-188

FTIR

Silica Quat-188 structure was studied by Fourier transform infrared spectroscopy (FTIR) using a Perkin-Elmer 2000.

NMR

All samples were characterized at room temperature (20+/- $^{\circ}$C) with solid state ^{13}C, ^{29} Si CP/MAS NMR. The spectra of ^{13}C, ^{29} Si CP/MAS NMR were recorded on a AVANCE 300 MHz Digital NMR Spectrometer Bruker Biospin DPX-300 at a frequency of 75 and 60 MHz, respectively.

Determination of the amount of incorporated Quat-188

The amount of Quat-188 incorporated on silica Quat-188 was determined by titrating with 0.00425 M silver nitrate, using potassium chromate as an indicator (0.250 g, 1.287 mmol in deionized water 20 ml).

Antibacterial activity

In order to assess antibacterial function of silica Quat-188, the suspension quantitative test was employed. The bacteria used were *E.Coli* (8099), *S.Aureus* (ATCC6538). Silica Quat-188 20 mg was added to a tube containing 1 ml of 10^7 cfu of *E. Coli* and 9 ml normal saline solution. The resulted solution was thoroughly mixed at 37°C by using a Burrell wrist action shaker for 16 hours, and left it stand for 30 min. 10 µl Supernatant of the mixture was diluted 50% gradiently. It was then added to agar plate and incubated at 37°C for 24 h. After incubation, the colonies of bacteria were counted to indicate antibacterial activity.

Results and Discussion

When Quat-188 reacted with sodium silicate in a medium at pH 5, the white solid was generated. It was possible that this solid could be the product because both Quat-188 and sodium silicate readily dissolved in water, while the white solid was not dissolved. It was then washed with water several times until the washed water was negative to silver nitrate solution. This indicated that no free Quat-188 was on the white solid. Silica was also prepared for comparison, by reacting sodium silicate with acetic acid solution. Figure 1 showed FTIR spectra of Quat-188 (a), silica (b) and silica Quat-188 (c). The presence of the absorption peak at 3429 cm^{-1} (SiOH stretching), 1633 cm^{-1} (SiOH bending), 1082 cm^{-1} (Si-O-Si stretching vibration), 1260 cm^{-1} (SiO stretching), 810 cm^{-1} (Si-O-Si), 1475 cm^{-1} (C H symmetric bending of $(CH_3)_3N+R$) [4,5] in Figure 1(c) clearly indicated that Quat-188 was grafted on silica.

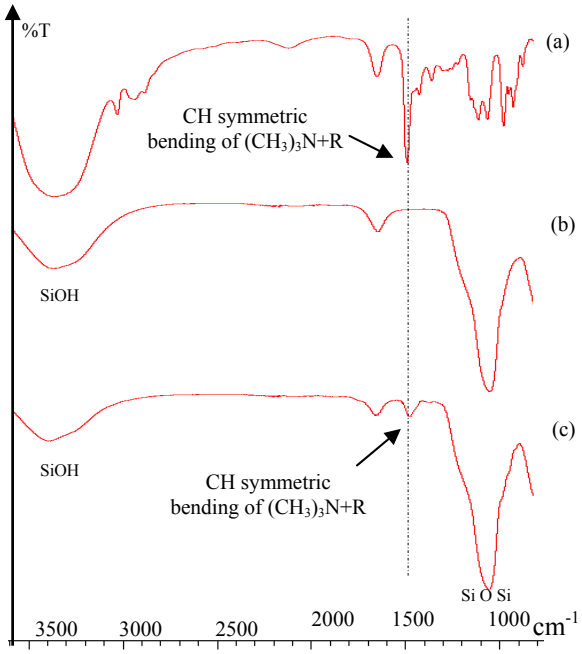

Figure 1. FTIR spectra(KBr) of Quat-188 (a), silica (b) and silica Quat-188 (c)

The structure of the white solid was further confirmed by ^{13}C and ^{29}Si CP/MAS NMR spectroscopy. The four signals in its ^{13}C NMR spectrum (Figure 2), at 69.269 ppm ($CH_2N+(CH_3)_3$, 67.418 ppm (CHOH), 64.792 ppm (CH_2OSi) and 55.29 ppm ($N+(CH_3)_3$) were belong to Quat-188 [1]. The three sigmals in the ^{29}Si NMR spectrum (Figure 3) at -110.507 ppm ($Si(OSi)_4$, siloxane), -100.95 ppm ($Si(OSi)_3OH$, silanol), -90,61 ppm ($SiO)_2Si(OH)_2$, geminal silanol) were observed. These results showed that quaternized silica was synthesized via the sodium silicate route [5].

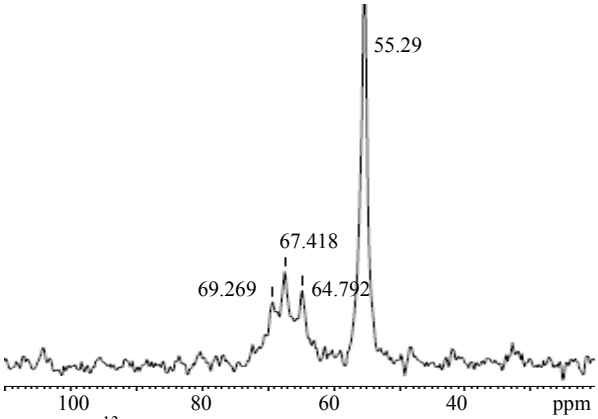

Figure 2.^{13}C solid state NMR spectrum of silica Quat-188

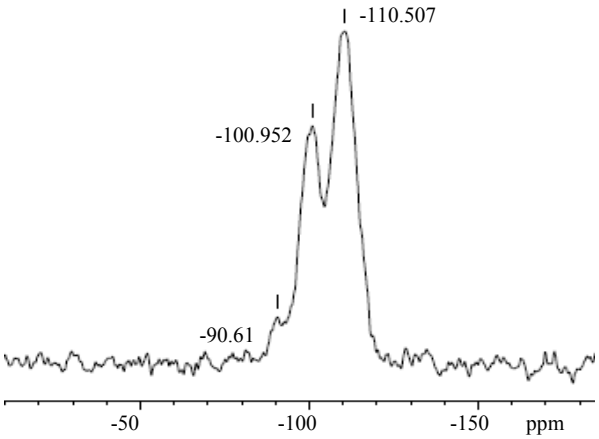

Figure 3. ^{29}Si solid state NMR spectrum of silica Quat-188

Incorporation of Quat-188 on silica Quat-188

Quaternization of Quat-188 on silica was determined by titration with $AgNO_3$ solution. Figure 4 exhibited that the amount of Quat-188 incorporated on silica Quat-188 depended on the added Quat-188 in the reaction mixture.

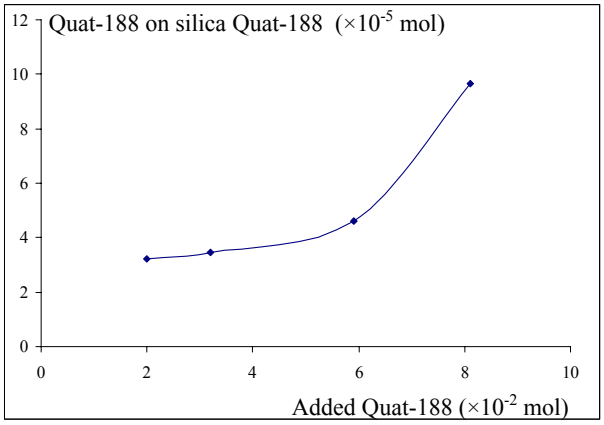

Figure 4. The incorporation of Quat-188 on silica Quat-188

From Table 1. The gel time of each reaction was also observed. When the amount of added Quat-188 was increased, the gel time decreased.

Antibacterial activity

Table 2 exhibited the antibacterial activity of silica Quat-188 comparing to Quat-188 at the same mole ratio. The results showed that silica Quat-188 had bacteriostatic rate of inhibiting the growth of both *S.Aureus* and *E.Coli* similar to Quat-188. However, silica Quat-188 showed the activity against *S.Aureus* higher than *E.Coli*.

Table 2. Antibacterial activity of silica Quat-188 after exposure 16 h.

Microorganism	Average bacterial count of control group	Average bacteriostatic rate(%)	
		Quat-188	silica Quat-188
E.Coli (x10^5)	14.2	64.79	50.7
S.Aureus(x10^7)	125	80.8	74.4

Conclusions

Silica Quat-188 at different degrees of quaternization were successfully synthesized by a sodium silicate route. They showed the antibacterial activity against both Gram-negative (*E.Coli*) and Gram-positive (*S.Aureus*), whereas higher bacteriostatic rate of silica Quat-188 of *S.Aureus* was observed.

References

[1] W. Sajomsang; P. Gonil; S.Tantayanon. *International Journal of Biological Macromolecules*. **2009**, 44, pp. 419-427.
[2] X. Xu; S. Li; F. Jia; P. Liu. *Life Science Journal.* **2006**, 3(1).
[3] H. Elimelech ; D. Avnir. *Chem Mater.* **2008**, 20(6), pp. 2224-2227.
[4] U. K. H. Bangi; A. Parvathy Rao; H. Hirashima ;A. Venkateswara Rao. *J Sol-Gel Sci Technol.***2009** 50, pp. 87-97.
[5] J. Vega-Baudrit; V. Navarro-Banon; P. Vazquez; J. Miguel Martin-Martinez. *International Journal of Adhesion & Adhesives*. **2006**, pp. 216, 378-387

Effect of nucleating agent on microcellular PP nanocomposite foam using super critical fluid (SCF)

J. Kruenate[1]*, T. Sooksomsong[1] and W. Phompan [1]

[1] National Metal and Materials Techology Center, Thailand Science Park, Pathumthani, Thailand

* E-mail: jittipk@mtec.or.th

Abstract: The effect of nucleating agent on the morphology of polypropylene (PP) foam was studied. Foaming of virgin polypropylene and polypropylene/ nano-$CaCO_3$ nanocomposite foams have been studied using a Supercritical Fluid technique. For preparing microcellular nanocomposite foams, 0.5%, 1% 3% and 5%wt. of nucleating agent were mixed with pure polypropylene. Morphology of cell size and cell size distribution of nanocomposite foams was compared. Solubility of scCO_2 under supercritical conditions in at saturation times of 1, 3, 6 and 12 hrs was investigated. The results showed that the nucleating agent nano-$CaCO_3$ improved the microstructure of the microcellular nanocomposite foam. The cell density increased and the cell size decreased while concentration of nano-$CaCO_3$ particles increased.

Introduction

Microcellular polymer has widely received attention in the past two decades due to its specific distinguished properties such as low material costs, a new range of insulating and good mechanical properties [1-3]. The term of microcellular polymers are generally defined as closed-cell polymers with cell density of 10^9-10^{13} cells per cubic centimeters and cell diameters in the range of 10-100 micrometers. It has been known that microcellular polymer containing a well define cell size and cell distribution are normally derived from the technique named Supercritical Fluids (SCF). The Super Critical Fluid has been developed in order to utilize the physical blowing agents (PBAs) to produce polymer foam[4]. Currently, from an environmental point of view CO_2 has been potentially used as physical blowing agent for producing microcellular polymers or foams. This technique can create highly functional materials with few features and dramatically improve the properties of finishing products such as impact strength, toughness, stiffness-to-weight ratio, high fatigue life, high thermal stability and low thermal conductivity[5]. There are various products can be produced with this process. Those are recycled-PET foamed coffee cups, automotive, aircraft part housings, building supplied, retail packaging, pipes and appliances goods[6].

Among those applications for utilizing microcellular material, semi-crystalline polymers are considered to possess desirable mechanical properties such as high stiffness and high strength [7]. However, semi-crystalline polymer produced via the SCF can rather be complicated in a sense of microcellular developing. This is due to owing crystal and lamellar structures. In the SCF foaming process, gas solubility and stiffness of material in different regions of polymer are major factors to be concerned. Baldwin et al. [8-9] studied a high density in semi-crystalline polymer such as polypropylene and found that interfaces between the crystalline and amorphous regions could be the preferential cell nucleation sites during the microcellular foaming process. Naguib et al. [10] have been able to obtain PP foams with a large volume expansion ratio by avoiding too rapid crystallization. It is conceivable that the reduction of crystalline structures in polymer can assist the solubility of the blowing agents especially in solid state batch foaming. Yuan et al. [4,11] studied the microcellular foaming behavior of PA6/clay nanocomposites. They found that nano-clays suppressed the α-form crystal structure of the PA6 which led to increase in CO_2 solubility throughout the PA6 matrix.

In PP processing, it is common practice that nucleating agents (i.e. nanometer inorganic particles) have been always introduced in order to improve both thermal and mechanical properties. According to Yuan's works, the nanometer particles can coincidentally improve the amount of CO_2 solubility in the semi-crystalline polymer.

Therefore, the purpose of this work is to present another attempt to obtain a well define cell distribution, uniform cell size and high CO_2 solubility of microcellular PP materials. This study aims to investigate the efficiency of cell formation in microcellular PP foams with and without adding nano-$CaCO_3$ particles via the super critical fluid technique.

Materials and Methods

Foamed PP/nano-$CaCO_3$ composite was prepared by the batch process. Firstly, mix polypropylene pellets with nano-$CaCO_3$ by twin screw extruder, then prepared samples in sheet form in the dimension of 5x5x0.5 cm^3 by using compression molding, after that placed the samples in the high pressure vessel, and saturated the sample with supercritical CO_2 at a given temperature and pressure above the critical point, followed by releasing CO_2 to atmospheric rapidly. After that, microcellular polypropylene/nano-$CaCO_3$ obtained at a wide range of saturation temperatures of 90°C -150°C with saturation times at 1, 3, 6, and 12 hrs via supercritical CO_2 were compared. Foamed samples were characterized by Scanning Electron

Microscopy (SEM) JEOL 6310 to investigate their morphology and cell size distribution.

Results and Discussion

Effect of Saturation Temperature

The effect of saturation temperature on the cell morphology was studied at a constant pressure of 15 MPa for 1 hour as shown in Fig.1 The operating temperature range was from 90 to 150^{o}C. From SEM images, it can be found that the proper temperature was very close to its melting temperature, because the gas could be easily diffused. When the saturation temperature was applied much lower than its melting temperature, the polymer chain moving was poor and CO_2 diffusion was hindered. In this case the suitable temperature was selected at 150^{o}C under saturation time of 1 hr and pressure of 15 MPa.

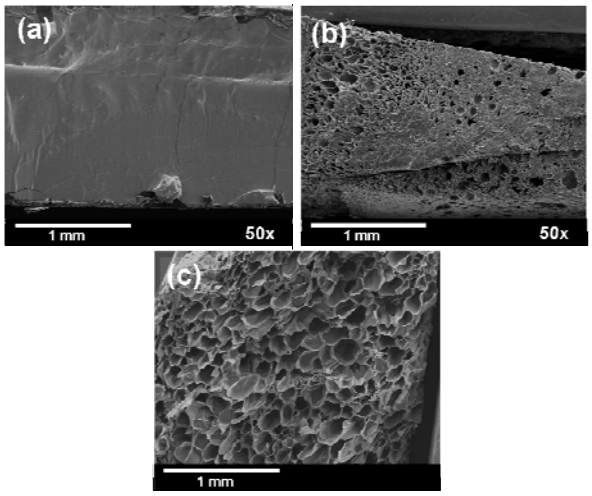

Figure 1. SEM micrographs showing effects of saturation temperature on PP foam structure at 1 hrs under 15 MPa: (a) 90 ^{o}C, (b) 125 ^{o}C and (c) 150 ^{o}C.

Effect of Saturation Time

The effect of saturation times on PP foams formation has been studied at constant saturation pressure (15MPa) and temperature (150^{o}C) under various saturation times at 1 3 6 and 12 hrs. Fig.2 displays the morphology of PP foam obtained from the batch process.

The volume of foam expansion was found to be at the highest size at saturation time of 1 hr. When the saturation time was increased more than 1 hour, the volume of foam was unable to further expand and the cell size distribution became non-uniform. From SEM micrograph, there was no significant difference in the size of cells.

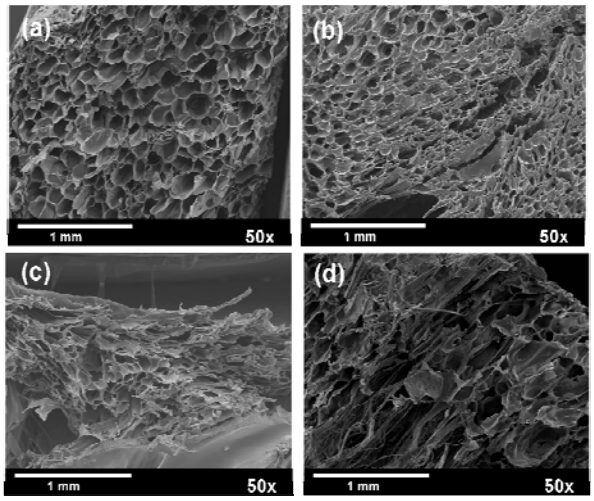

Figure 2. SEM micrographs showing effects of saturation time on CO_2 diffusion through virgin PP at temperature 150 ^{o}C under 15 MPa: (a) 1hr, (b) 3 hrs, (c) 6 hrs and (d) 12 hrs.

When the saturation time was increased the polymer's chains were freely moving which led to cell growth. When duration of the saturation time was too high, the viscosity of the polymer matrix was significantly increased which facilitating the cell growth until the coalescence of neighboring pores occurred. When duration of the saturation time was too short, the diffusion of CO_2 throughout the sample matrix was unable to complete resulting in non-uniformed cell size. In this experiment, saturation time at 1 hr exhibited the most uniform cell distribution with cell density approximately $8x10^{11}$ cell/cm^3.

Effect of nano-$CaCo_3$ content on PP foam morphology

Effect of various nano- $CaCO_3$ particles contents at saturation time of 1 hour, saturation temperature of 150^{o}C was shown in Fig.3. Figures 3(a), 3(b), 3(c) and 3(d) show microcellular foams such as virgin-PP and PPs with 0.5, 1, 3 and 5 %wt. nano-CaCO3. It has been widely known that the microcellular foamed produced via the $scCO_2$ process provided a majority of closed cell structure. The diffusion of $scCO_2$ under given pressure and temperature in polymer drove nucleation of a number of microcells while the nucleated cells continued to grow. Dispersion of nano-$CaCO_3$ created nucleating site for cell formation. For microcellular virgin-PP and PP/nano-$CaCO_3$ nanocomposite foams, it was found that the CO_2 solubility and the number of microcells increased with the nano-$CaCO_3$ particles contents. This phenomenon indicated that the addition of nano-$CaCO_3$ particles obviously increased the crystallinezation rate of PP which led to the reduction of spherulites structure and lamellae stacks (see Fig. 3a.).

These spherulite structures and the stacks of lamellae caused stiffness to virgin-PP which was very difficult to be molten at low saturation pressure and meting temperature.

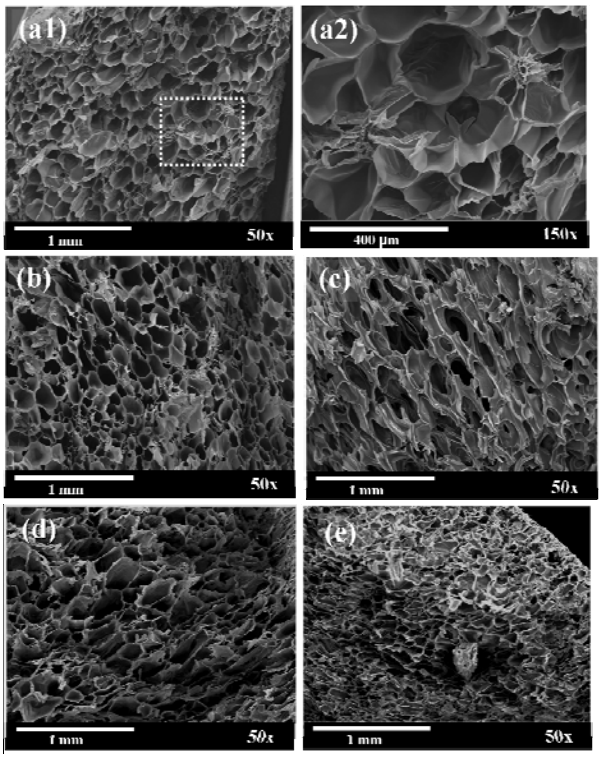

Figure 3. SEM micrographs of microcellular virgin-PP and PP/nano-$CaCO_3$ nanocomposite foams saturated by CO_2 under soaking pressure of 15 MPa at 150^oC and soaking time of 1 hour. : (a) virgin-PP (b) PP with 0.5 wt%nano-CaCO3 (c) PP with 1 wt%nano-CaCO3 (d) PP with 3 wt%nano-CaCO3 (e) PP with 5 wt%nano-CaCO3

At a given melting temperature, there was a lower limit for $scCO_2$ solubility which PP could not be completely foamed due to its stiffness [12]. Fig. 3(a) shows the cell morphology of the microcellular virgin -PP foam and fig. 3(b) showed the micrograph which taken from the center of fig. 3(a).

It can be observed that there were microcells filled with stretched fibrils which generated sporadically all over the virgin-PP matrix. These textures revealed as the architecture of the corresponding spherulite structure and lamellae stacks. As can be seen in the Fig. 3(b), there are uniform micro-size cells distributing around the microcells filled with stretched tie fibrils. The well defines uniform micro-size cells throughout the virgin-PP matrix indicated the interlamellar amorphous regions in which CO_2 could easily dissolved. The larger the amorphous area, the larger the amount of CO_2 dissolved in the area.

Figs.3 (b), (c) and (d) show the cell morphology of microcellular PP/nano-$CaCO_3$ nanocomposite foams. With adding of nano-$CaCO_3$ particles, the cell density was higher and cell uniformity was much improved. This may be because the nano-$CaCO_3$ particles can suppress the α-monoclinic crystal structure of virgin-PP. The α-monoclinic crystal structure of virgin-PP is one of the main factors for limiting of the CO_2 dissolved in the PP matrix. That is to say, the more the adding of nano-$CaCO_3$ particles contents the more the amount of CO_2 can dissolve in the virgin-PP matrix. This leads to uniform distribution of microcells and high cell density.

Conclusions

The PP/nano-$CaCO_3$ nanocomposite samples were foamed using $scCO_2$ as the foaming agent in a batch process. The addition of a small amount of nano-$CaCO_3$ contributed to the reduction of the crystallinity of the PP. The cell size distribution of the nanocomposite decreased while the amount of nano-$CaCO_3$ content increased. It can be concluded that high nucleation efficiency of the nano-$CaCO_3$ particles enabled the microcellular PP/nano-$CaCO_3$ nanocomposite foams to exhibit rather high cell density and uniform cell size distribution.

Acknowledgements

This research was supported by Nation Metal and Materials Technology Center grant.

References

[1] JE. Martini, N. Suh and FA. Waldman. U.S. Patent 4,473,665, 1984
[2] V. Kumar, *Cell Polym*. 12 (1993), pp. 23-207.
[3] V. Kumar, JE. I. Weller, *Polymeric foams: science and technology*, ACS Symposium Series 669. Washington: ACS, 1997, pp. 101-14 (Chapter 7).
[4] M. Yuan and L.-S. Turng, *Polymer*, 46(2005), pp. 7273-7292.
[5] J. Martini, FA. Waldman and N. Suh. ANTEC ,82. *SPE Tech Pap*. 28(1982), pp. 674-6.
[6] http://www.microgreeninc.com/
[7] X.-L. Jiang, T. Liu, Z.-M. Xu, L. Zhao, G.-H. Hu and W.-K. Yuan, *J. of Supercrit. Fluids*, 48(2009), pp.167-175.
[8] S. Doroudiani, C.B. Park and M.T. Kortschot, *Polym. Eng. Sci*. 36(1996), pp. 2645-2662.
[9] D.F. Baldwin, C.B. Park and N.P. Suh, *Polym. Eng. Sci*. 36 (1996), pp. 1437-1445.
[10] H.E. Naguib, C.B. Park, U. Panzer and N. Reichelt, *Polym. Eng. Sci*. 42(2002), pp. 1481-1492.
[11] M. Yuan, L.-S. Turng, S. Gong and A. Winardi, *J. Cell. Plast*, 40(2004), pp.397-409.
[12] Z.-M. Xu, X.-L. Jiang, T. Liu, G.-H. Hu, L. Zhao, Z.-N. Zhu and W.-K. Yuan, *J. of Supercrit. Fluids*, 41(2007), pp.299-310.
[13] D.L. Tomasko, A. Burley, L. Feng, S.-K. Yeh, K. Miyazono, S.N. Kumar, I.Kusaka and K. Koelling, *J. of Supercrit. Fluids*, 47(2009), pp. 493-499.

Preparation of microcellular EPDM/PP foams via superceitical CO_2 fluid (SCF) technique

N. Tangchantra[1]* J. Kruenate[1] and W. Phompan[1]

[1] National Metal and Materials Technology Center
National Science and Technology Development Agency
114 Thailand Science Park, Phanonyothn Rd.
Klong 1, Klong Luang, Pathumthani, Thailand 12120

*E-mail: nantavtt@mtec.or.th

Abstract: Blend of polypropylene (PP) and ethylene propylene diene rubber (EPDM) foam has been studied using a technique called high pressure supercritical fluid (SCF). For preparing microcellular EPDM/PP foam, PP was blended with 15, 30 and 50 wt % of EPDM via Brabender mixer and then prepared the sample as sheet-form using compression moulding. The SCF experiments were performed under 20 MPa foaming pressure and various foaming temperatures of 154°C. Solubility of supercritical CO_2 was directly affected foamed- polymer properties. Morphology of cell size and cell distribution at different concentrations of EPDM was compared. Characterization was accomplished by scanning electron microscopy (SEM), and Differential Scanning Calorimetry (DSC). The results revealed that the diffusion of supercritical CO_2 under given foaming pressure and foaming temperature in the EPDM/PP blends drove a nucleation of number of cells including the growth of nucleated cells. The influence of the EPDM content in PP matrix on rheological properties has also been investigated. The results showed that EPDM composition adding into EPDM/PP could improve the elastic behaviours of the polymer blend.

Introduction

Generally, Thermoplastic elastomers have been foamed using chemical blowing agents (i.e. low-boiling hydrocarbons, chlorofluorocarbons) as foaming agents [1]. All of these agents have drawbacks, base on inefficiency, high cost, difficulty of use, and, more recently, environmental considerations. Although the chlorofluorocarbons have been widely and effectively used in foaming thermoplastic elastomers, their perceived threat to the ozone layer has prompted a search for alternative foaming methods which do not process environmental hazards or present any of the other drawbacks.

These issues can be resolved by introducing the physical blowing agent via supercritical fluid technique. The supercritical fluid (SCF) has been developed for use as physical blowing agents (PBAs) in the production of polymer foams because they do not create chemical residues. Moreover, the SCF possess many advantage such as low cost, non-toxicity non-flammability and easily accessible supercritical conditions [2].

Thermoplastic elastomers used in this research are composed of polypropylene (PP) and ethylene propylene diene rubber (EPDM). PP is a commodity polymer with widespread applications due to its good mechanical and thermal properties but it has poor impact strength, whereas EPDM has proved to be the most effective impact strength.

In this work, we studied microcellular EPDM/PP foams prepared via supercritical CO_2 fluid technique. The influence of the EPDM contents in PP matrix on cell size, thermal and rheological properties had also been investigated.

Materials and Methods

Materials. The materials used in preparing the microcellular thermoplastic elastomeric foams consist of PP, supplied by LyondellBasell Industries, and EPDM, supplied by Silpakorn university.

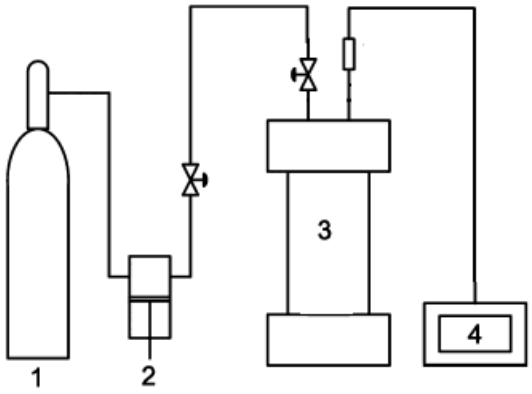

Figure 1. Schematic of the experimental setup for the batch foaming process. (1) CO_2 cylinder; (2) high-pressure liquid pump; (3) foaming reactor; (4) temperature controller.

Preparation of EPDM/PP compound. The PP was blended with 15, 30 and 50 wt % of EPDM by Brabender mixer at 190 °C for 6 min and then the sample was prepared as sheet-form using compression moulding.

Foaming process. A high-pressure vessel in stainless steel was used (Fig. 1). In EPDM/PP foaming process, The EPDM/PP blend was placed in high-pressure vessel. The high-pressure vessel was heated in temperature of 154 °C. Thereafter, the EPDM/PP blend was saturated under supercritical CO_2 at the pressure of 20 MPa with soaking time of 20 min. After

that the CO_2 in the high pressure vessel was released form the foaming pressure to the ambient one. The EPDM/PP foams were characterized cell morphology by JSM-5410 scaning electron microscopy (SEM). The samples were immersed in liquid nitrogen and then fractures

Thermal characterization. The melting temperature and crystallinity of the samples measured by differential scanning calorimetry (DSC, Mettler Toledo DSC822e) at a heating rate of 10°C/min and with scanning temperature range from 25°C to 190°C in N_2 atmosphere.

Rheological characterization. The melt flow index (MFI) of the samples were invatigated by melt flow indexer (MFI, Lloyd Instruments; Davenport model 10) at temperature of 190°C. Rheological properties of neat PP and EPDM/PP blends were invatigated by using a Rotational Rheometer (Gemini HR Nano) equipped with parallel plate geometry (diameter =25mm, gap = 1 mm). The frequency sweep tests were performed in the range of 0.1 – 100 s^{-1} at temperature of 190°C and with an amplitude of 1% in order to maintain the response of materials in the linear viscoelastic regime.

Results and Discussion

Thermal characterization. The melting temperature and percent crystallininity of PP and EPDM/PP blends are shown in Figure 2 and 3 respectively. Melting temperatures of crystalline polymers can be related to the size and perfection of their crystal units. The blends show a reduction in T_m value with greater effect for mixtures. The blending results in a decrease of the size and perfection of the PP crystals and in an increase of the amorphous regions [3]. The reason for the phenomenon can be explained as decreases in the crystallinity of PP phase may be arrived from an increasing of the amount of the EPDM elastomer.

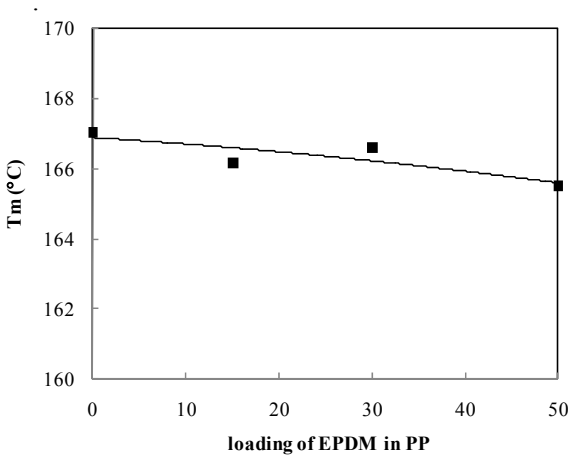

Figure 2. Effect EPDM on the melting temperature (T_m) of PP and EPDM/PP blends

Rheological characterization. The MFI of PP and EPDM/PP blends are show in Fig.4. The MFI values of the blends decrease as increasing the EPDM contents since EPDM possess a very high molecular weight and high viscosity.

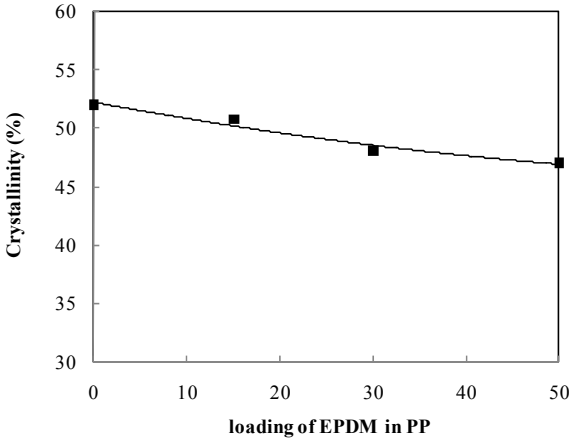

Figure 3. Effect EPDM on the crystallization of PP and EPDM/PP blends.

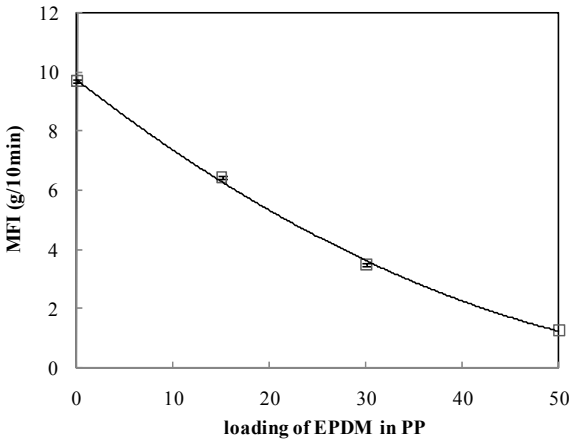

Figure 4. Effect EPDM on the MFI of PP and EPDM/PP blends.

The storage modulus(E′) and complex viscosity (η*) of the EPDM/PP blends have been attempted to be studied in order to assess the favorability of these blends for optimizing the performance for finishing products. In this case, the dynamic rheological analysis with storage modulus (E′) and complex viscosity (η*) parameters is a method that has been used to measure the elastic and strength of the blends. The results of storage modulus (E′) and complex viscosity (η*) as a functions of angular frequency (ω) obtained for various EPDM contents mixed with PP are shown in Figs. 5-6.

As seen in the Figs. 5 and 6, as the amount of the EPDM content increased, as expected, the storage modulus and the complex viscosity increased. This could be explained that the elastic behavior of EPDM plays a dominant role. Furthermore, the results also indicated that all the blends behaved as shear thinning materials. In low frequency region (low shear rate), the viscoelastic response of the blends could be used for evaluating of the interfacial interaction between the

EPDM and PP phases. The more the chain interfacial interaction between the EPDM and PP phases the higher the values of the modulus (E′) and complex viscosity (η*) are significantly increased.

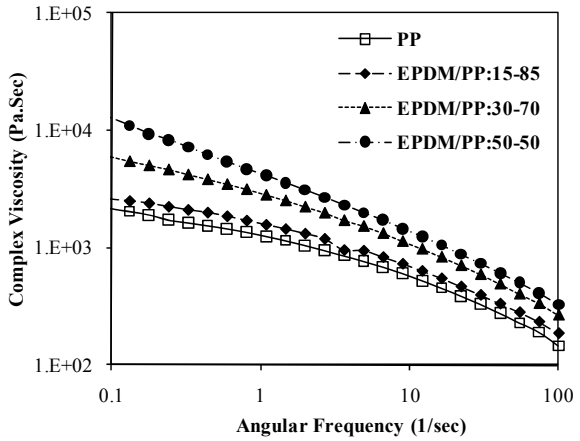

Figure 5. Complex viscosity versus angular frequency for different blends

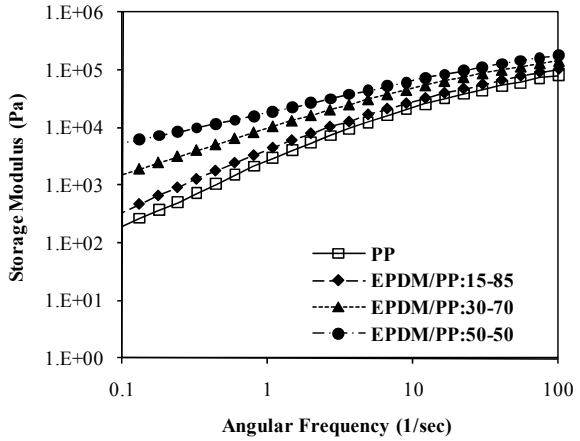

Figure 6. Storage modulus versus angular frequency for different blends

In addition, the EPDM mixed with PP is considered as one of special class of thermoplastic elastomer (TPEs). The microcellular EPDM/PP blends were foamed via the super critical fluid technique under fixed conditions: saturation pressure, temperature and time of 20 MPa, 154^{o}C and 20 min., respectively. These conditions of producing the microcellular TPEs foam are more favorable for obtaining a uniform cell size and cell distribution. From the high pressure $scCO_2$ point of view, the saturation pressure and the amount of EPDM contents are considered to be important processing parameters to control the foam structure of the microcellular TPEs [4].

Figs. 7-8 show a typical micrograph of microstructure of microcellular EPDM/PP blends obtained at different EPDM contents in PP matrix for given saturation temperature of 154 °C and saturation time of 20 min and depressurization time of 3 s.

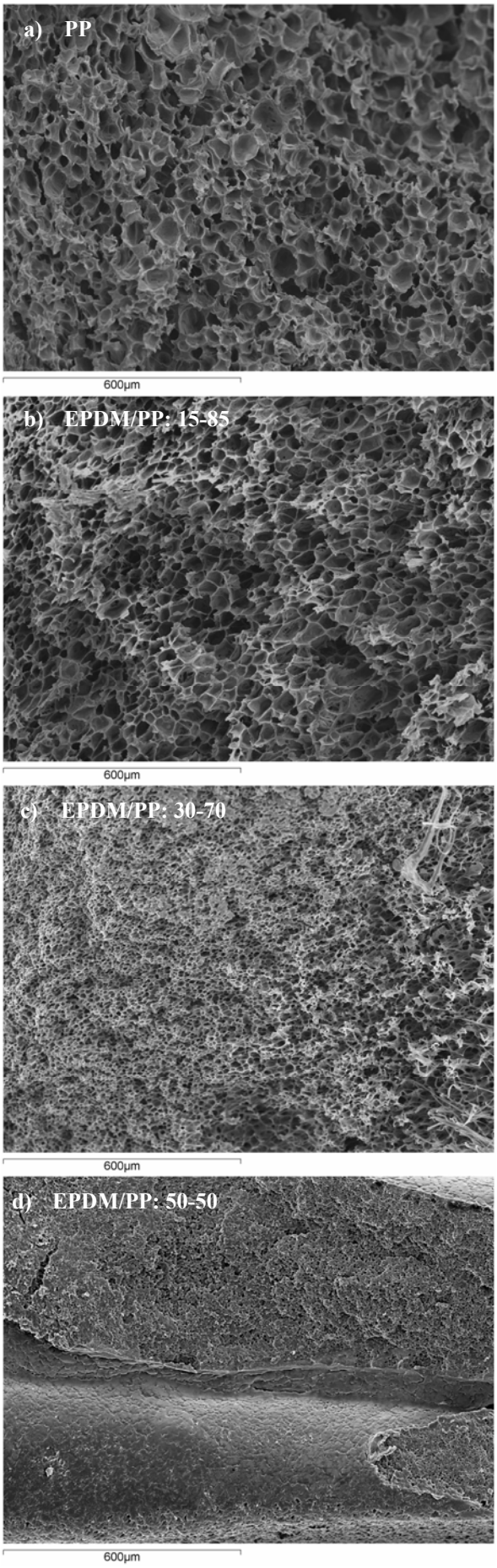

Figure 7. SEM micrographs of the specimens produced at different blends (×100)

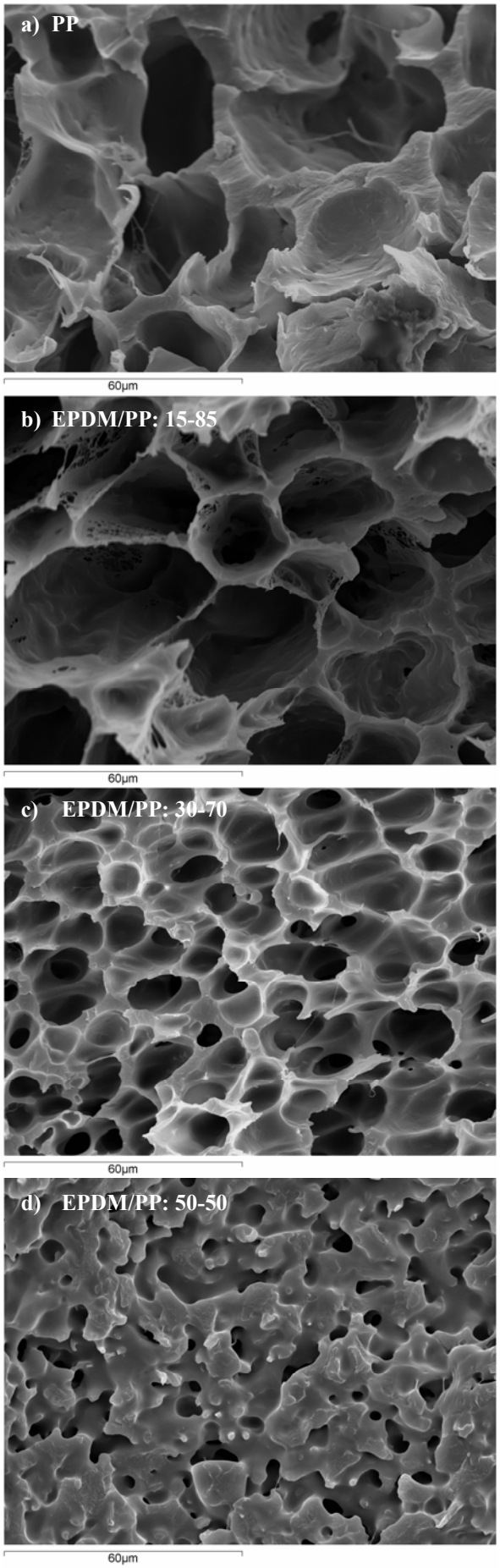

Figure 8. SEM micrographs of the specimens produced at different blends (×1000)

It is known that the saturated high pressure for foam formation significantly contributed to the solubility of CO_2 in the EPDM/PP blends matrix. The CO_2 can be more easily dissolved in the amorphous phase of PP matrix than in the crystalline phase[5]. As seen from the Fig.8(a), the cell walls of the PP's microcells are considerably thicker than those of EPDM/PP blends because of the PP containing a rather high portion of the crystals stacks. On the contrary, the cell wall of the EPDM/PP blend becomes thinner when a low content of EPDM was added. However, the average cell size and cell density of the blends dramatically reduced when the EPDM contents were increased up to 50%wt. It was conceivable that adding the EPDM increased the modulus and viscosity of the EPDM/PP blends and led to the limitation of solubility of the CO_2.

It can be clearly noticed that the microcells of EPDM/PP (50-50) blend were hardly observed (Fig. 8(d))

Conclusions

Solubility of supercritical CO_2 was directly affected foamed properties. Microcellular foam was produced via the supercritical fluid technique using CO_2 as physical blowing agent causing a number of closed cell foams. The diffusion of supercritical CO_2 under given pressure and temperature in polymer drove nucleation of number of micro-cells. The obtained microcellular EPDM/PP (known as TPE elastomeric foam) foam contained a uniformed cell distribution. The cell size of the obtained microcellular TPE foam decreased when the EPDM contents were increased.

References

[1] W. Yamsaengsung and N. Sombatsompop, J. Compositesb. 40 (2009), pp. 549–600.
[2] Kerem Goren, Limeng Chen, Linda S. Schadler and Rahmi Ozisik, *J. Supflu.* (2009).
[3] Helson M. da Costa, Vale´ ria D. Ramos and Marisa C.G. Rocha, *J. Polymertesting.* 25 (2006), pp. 498–503.
[4] Zhen Xiu Zhang, Shu Ling Zhang, Sung Hyo Lee, Dong Jin Kang, Daae-Suk Bang and JinKuk Kim, J. Matlet. 62 (2008), pp. 4396–4399.
[5] Zhi-Mei Xu, Xiu-Lei Jiang, Tao Liu, Guo-Hua Hu, Ling Zhao, Zhong-Nan Zhu, Wei-Kang Yuan, J. Supflu. 41 (2007), pp. 299–310.

Effect of plasticizers on the miscibility of low-density polyethylene/poly (ethylene-CO-vinylacetate) blends

C. Aumnate*, C. Gamonpilas and J. Kruenate

National Metal and Materials Technology Center (MTEC), 114 Thailand Science Park, Paholyothin Rd.,Klong 1, Klong Luang, Pathumthani 12120

Abstract: The effect of plasticizer on the miscibility of low-density polyethylene/poly (ethylene-co-vinylacetate) (LDPE/EVA) blends has been investigated. The plasticizer, namely Eastman168 (bis (2-ethylhexyl)-1,4-benzenedicarboxylate), was used in this study. All the blends filled with this plasticizer were prepared by using an internal mixer. The characteristics and physical properties of LDPE/EVA blends with varying Eastman168 contents (in phr) were determined through various experiments. Rheological data showed that all the blends exhibit shear-thinning behavior at high shear rates and Newtonian plateau at low shear rates. The viscosity of the blends decreases with the addition of plasticizers. DSC results show two melting temperature (T_m) peaks corresponding to the T_m of LDPE and EVA in all blends. However, the addition of the plasticizer did not significantly affect the thermal properties of these blends. Furthermore, the blend with 10 phr of Eastman168 showed the most improvement in their morphology and mechanical performance. These results indicated that the miscibility between the LDPE and EVA phases could be improved by adding plasticizers into the blending system.

Introduction

A blending of polymers is an alternative route to design final properties of the end products with improved specific properties and processability performances. Low Density Polyethylene (LDPE)/Ethylene Vinyl Acetate copolymer (EVA) blends are widely used in a range of applications such as multilayer films, packaging materials and agricultural applications. LDPE is the most common commercial polymer due to its good environmental stress, cracking resistance and thin film-forming properties. EVA is added into LDPE not only to enhance the capacity of additive carrying, but also to improve physical and mechanical performances. However, most polymer blends are immiscible, resulting in materials with multiphase morphology, weak interfacial interaction among phases, thus, leading to a poor mechanical performance. The final properties of polymer blends are directly related to their morphology, which in turn depends on the rheological properties and the compositions of the blend [1]. The viscoelastic behavior of polymer blends was necessary to recognise, not only for reaching optimum processing conditions, but also collecting precious information on the flow mechanism and its effect on both phase morphology and ultimate mechanical properties [2]. From our previous study, we found that the mismatch in viscosity of EVA and LDPE is considered to be the main factor that controls the miscibility of the LDPE/EVA blends [3].

Plasticizers are additives that increase the plasticity or fluidity of materials while decreasing their viscosity. They are normally used for increasing the flexibility of materials due to their ability to reduce internal hydrogen bonding between polymer chains while increasing molecular space. The objective of this work is to study effect of plasticizers on the miscibility of LDPE/EVA blends which can be used as the basic information to design the final properties of the end products.

Materials and Methods

Materials: Low-density polyethylene (LDPE), JJ4324 (MFI = 5.5 g/min; 190°C, 2.16 kg) and Ethylene Vinyl Acetate copolymer (EVA), N8038 (MFI = 2.3 g/min; 190°C, 2.16 kg with vinyl acetate content = 18%wt) from TPI Polene Co, Ltd, Thailand were used as received. Eastman168 (Bis (2-ethylhexyl)-1, 4-benzenedicarboxylate) were supplied by Eastman Chemical Company, US (see Fig. 1).

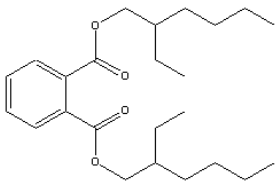

Figure 1. Molecular structure of Bis (2-ethylhexyl)-1, 4-benzenedicarboxylate

Sample preparation: The melt compounding of LDPE/EVA blend with varying plasticizer contents, e.g. 0, 5, 10 and 15 phr, were prepared using an internal mixer (Haake). The composition of all blends studied was 70% of LDPE and 30% of EVA.The blending conditions were at 150°C with the rotor speed of 100 rpm for 10 mins. LDPE/EVA blend sheet samples with a thickness of 150 μm were made using a compression moulding technique.

Rheological tests: Rheological experiments of the LDPE/EVA blend films were performed on a Gemini 200HR Nano rheometer (Malvem-Bohlin Instruments). Parallel plate geometry (25 mm diameter and 1 mm gap) was used. The frequency sweep tests were performed in the range of 0.01-100 Hz at a constant temperature of 180°C. A small strain amplitude of 1% was used in order to maintain the response of materials in the linear viscoelastic region.

Thermal analysis: Thermal behavior of LDPE/EVA blends was studied using a differential scanning calorimeter (DSC). Tests were performed in a nitrogen atmosphere at the heating rate of 20°C/min and with scanning temperature range from 30°C to 200°C.

Morphology tests: Morphology of LDPE/EVA blends were investigated using a scanning electron microscope (SEM). The cryo-fractured surfaces of the blends were etched with Xylene for 6 hours at 50°C in order to remove the EVA phase. Subsequently, the surfaces were gold sputtered and micrographs were taken at a magnification of 2000x [2].

Mechanical tests: Uniaxial tensile loading tests on LDPE/EVA blends were performed using an Instron 55R4502. A constant crosshead speed of 500 mm/min was used. Rectangular samples of 12 mm wide, 150 µm thick and a gauge length of 40 mm were employed. Four replicates were used for all blends.

Results and Discussion

Rheology: Fig. 2 shows the relationship between complex viscosity (η*) and angular frequency (ω) of LDPE/EVA blends with Eastman168 content from 0 to 15 phr. It can be seen that the complex viscosity decreases with increasing angular frequency for all blend compositions. All the blends exhibit shear-thinning behaviour at high shear rates and Newtonian plateau at low shear rates. Furthermore, the viscosity of the blends decreases with increasing the Eastman168 content.

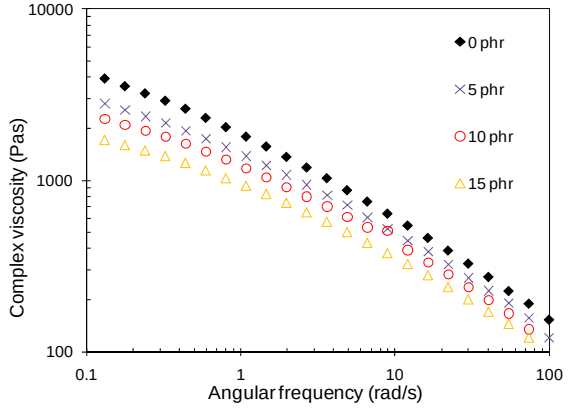

Figure 2. Relationships between complex viscosity versus angular frequency for LDPE/EVA blend with Eastman 168 content from 0 to 15 phr**.**

The decrease in the viscosity could be attributed to the presence of a polar carbonyl group within the Eastman168. Such polar functional group would interact with the acetyl group of EVA resulting in the reduction of polarity and, thus, reducing the intermolecular attraction of the polymer chains.

Thermal analysis: The effect of Eastman168 on the thermal properties of the LDPE/EVA blends is shown in Fig. 3 and 4. It can be seen from these figures that the thermal properties of the LDPE/EVA blends were not significantly affected by the addition of plasticizer. This could be due to weak dipole-dipole interactions formed between the carbonyl group of Eastman168 and the acetyl group of EVA.

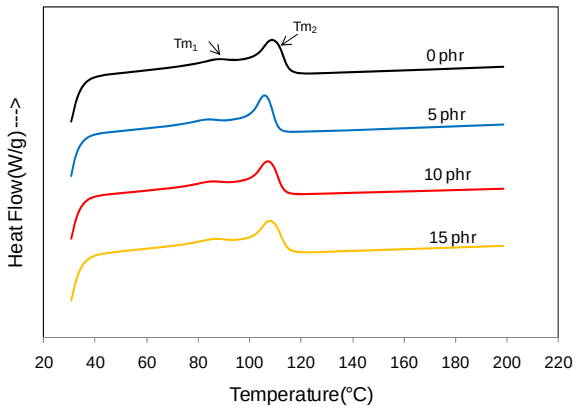

Figure 3. DSC thermogram for LDPE/EVA blends with various Eastman168 contents (phr).

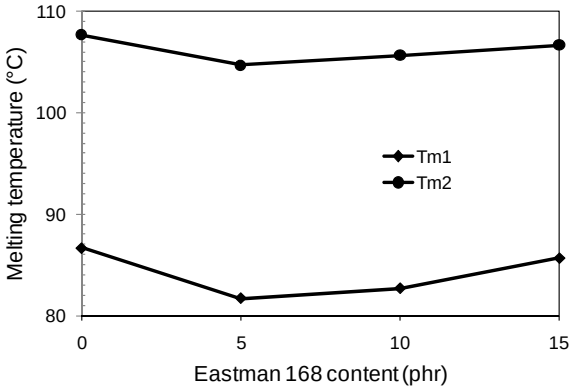

Figure 4. Effect of Eastman168 content (phr) on the melting temperature (T_m) of LDPE/EVA blends

Morphology: Fig.5 shows SEM micrographs of LDPE/EVA blends with 0, 5, 10 and 15 phr Eastman168, respectively. EVA phases were removed from the microstructure by Xylene solution. It is shown that the studied blends have two phase morphology, suggesting the immiscibility of the LDPE and EVA. However, the blend with 10 phr Eastman 168 revealed the best continuous phase of LDPE. This suggests that there was a better miscibility in the LDPE/EVA blend with 10 phr Eastman168 compared with other blends. It is hypothesised that the 10 phr of Eastman168 may provide the suitable amount of carbonyl group for incorporating with vinyl acetate group of the EVA. Beyond this point, the excess amount of carbonyl group may lead to more phase separation.

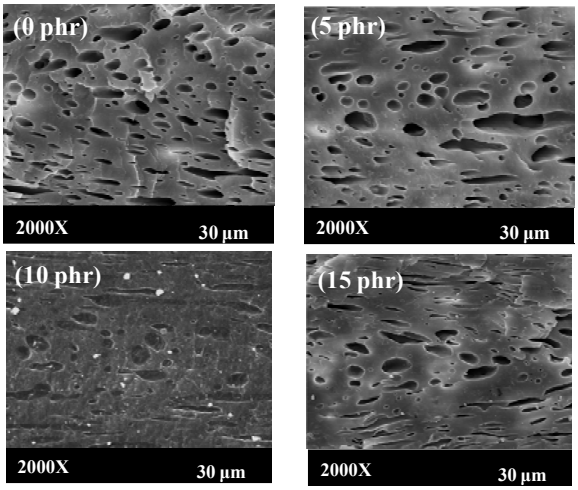

Figure 4. SEM micrographs of LDPE/EVA blends various concentration of Eastman168

Mechanical properties: The mechanical performance of LDPE/EVA blends with various concentrations of Eastman168 were evaluated by plotting their failure stress and failure strain with respect to Eastman168 contents in Fig. 5(a) and 5(b), respectively. From these figures, it can be seen that the blend with 10 phr Eastman168 showed the most superior mechanical properties i.e with the highest failure stress and strain. Above 10 phr of Eastman168, the mechanical properties were poorer. This could be due to the excessive amount of Eastman168 that could self-combine, thus, resulting in a more phase separation. This result was agreeable with the SEM result.

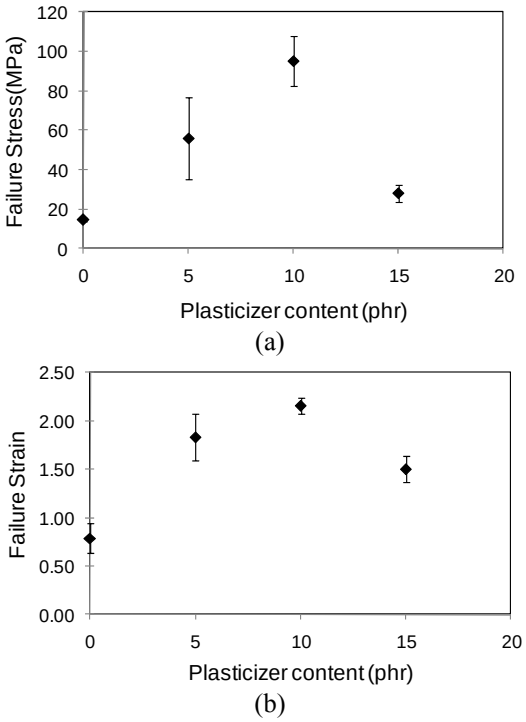

Figure 5. Mechanical performance of LDPE/EVA blends with various concentration of Eastman168 (a) failure stress (b) failure strain.

Conclusions

In this work, the effect of plasticizer on the miscibility of low-density polyethylene/poly (ethylene-co-vinylacetate) (LDPE/EVA) blends has been investigated. It was found that the blend with 10 phr Eastman168 showed a good compatibility with the EVA which in turn led to strong interfacial interaction between LDPE and EVA phases, thus, giving the best mechanical performance. From this study, the miscibility between the LDPE and EVA phases can be improved by adding the plasticizers into the blending system.

Acknowledgement

The funding from the Thailand Research Fund under funding code RDG 5120060 is gratefully acknowledged.

References

[1] Li. C., Kong, Q., Zhao, J., Fan, Q. & Xia, Y. Crystallization of partially miscible linear low-density polyethylene/poly (ethylene –co-vinylacetate) blends. *Materials Letters* **58**, 2004, 3613-3617

[2] Koning, C., Duin, M., Pagnoulle, C. & Jerome, R. Strategies for compatibilization of polymer blends. *Prog. Polym. Sci.* **23**, 1998, 707-757

[3] Aumnate, C., Gamonpilas, C. & Kruenate, J. *Advanced Materials Research* **93-94**, 2010, 475-478

[4] Iza, M., Bousmina, M. & Jerome, R. *Rheol Acta* **40**, 2001, 10-22

[5] Li, J., Shanks, R.A & Long, Y. *Polymer* **42**, 2001, 1941-1951.

[6] Elias, L., Fenouillot, F., Majeste, J.C.; Alcouffe, P. & Cassagnau, P. *Polymer* **49**, 2008, 4378-4385. [2] L. Frydman and J.S. Harwood, *J. Am. Chem. Soc.* **117** (1995), pp. 5367–5368.

Effects of carbon black and mixing parameters on capacity of expander

S. Meenakorn[1*], P. Termsuksawad[1], S. Phiboonkulsumrit[2] and O. Chailapakul[3]

[1] Integrated Product Design and Manufacturing Program, School of Energy, Environment and Materials, King Mongkut's University of Technology Thonburi, Thailand
[2] National Metal and Materials Technology Center, Thailand
[3] Sensor Research Unit, Department of Chemistry, Faculty of Science, Chulalongkorn University, Thailand

[*] somsak_me@hotmail.com

Abstract: Traction batteries are rechargeable batteries used in various types of vehicles. Service life of this battery depends on its capacity and working environment. Capacity of each battery relies on active materials used as negative electrode. One component in an active material is expander, whose function is to increase the capacity of the active material. Expander is a mixing of barium sulfate, sodium lignosulfonate and carbon black. In this study, effects of type of carbon black and expander preparation on capacity of pure lead were investigated. Two types of carbon black namely XE2B (high-structure carbon black) and N220 (medium-structure carbon black) were used. Applied mixing speed and mixing time for expander preparation are 500 and 1500 rpm, and 2 and 10 minutes, respectively. Cyclic voltammetry and transmission electron microscope were used to investigate the capacity of the lead electrode and to examine carbon black structure in the expander. The result showed that capacity of the electrode increases with carbon black addition. Interaction effect of type of carbon black and mixing parameter on capacity was found. For XE2B, the maximum capacity was obtained when applied mixing speed and mixing time are 500 rpm and 2 minutes. However, the appropriate mixing condition for N220 is mixing speed of 500 rpm and mixing time of 10 minutes.

Introduction

Traction batteries are rechargeable batteries used as power sources for various types of vehicles such as forklifts, wheelchairs, ships and subway trains. Service life of the batteries depends on their capacity and battery degradation during charge-discharge cycle. Capacity of each battery relies on composition of active materials, used as negative electrode for the battery. An active material consists of lead oxide, dynel flock, sulfuric acid, water, vaseline and expander. Function of expander is to increase the apparent volume of the active material, which results in increasing discharge rates and cyclability [1].

Expander is a mixing of barium sulfate, sodium lignosulfonate and carbon black. The role of carbon black is to cause an expander to be electrical conductive and to improve conductivity of the active materials during deep discharge. Carbon black can be classified by its structure as low, medium and high structure [2]. A low-structure carbon black refers to an aggregate of a relatively few carbon black primary particles. In contrast, high-structure carbon black is an aggregate consisting of many primary particles with considerable branching and chaining. The longer the carbon chain, the higher is the electrical conductivity [2]. Although effect of carbon black structure on electrical conductivity is obvious, its effect on capacity of active material is still questionable. In general, the recommended amount of carbon black in an expander equals to the amount of lignosulfonate [3].

To prepare an expander, carbon black will be mixed with barium sulfate and sodium lignosulfonate by a high speed mixer. Structure of carbon black may be destroyed during mixing; as a result, conductivity and capacity of the active materials may be altered. This study aims to study the effects of type of carbon black and mixing parameters: mixing speed and mixing time, on capacity of active materials.

Experiment

Materials

Two different types of carbon black namely; XE2B (high-structure carbon black) and N220 (medium-structure carbon black) were employed. Expander preparation was accomplished by mixing barium sulfate, sodium lignosulfonate and carbon black by a bench-top high speed mixer. The expander composition, mixing parameter and designation of all samples were shown in table 1. A commercial expander namely HE115 was also used in this study as a reference.

Testing

Cyclic voltammetry was carried out using Autolab PGSTAT 30. High purity lead was used as a working electrode with an exposed area of 1cm2. Before testing, the electrodes were mechanically polished by emery paper. In order to get rid of lead oxide on the surface, the electrode was then electrochemically cleaned using a constant potential of -0.90V (versus Ag/AgCl electrode), until a steady current of 0.1mA is reached.

The electrolyte for cyclic voltammetry is a sulfuric acid, whose concentration of 1.25 g-cm-3 density sulfuric acid was used as electrolyte. The prepared expander was added in sulfuric acid to obtain concentration of 20 ppm. Because expander is not directly dissolved in sulfuric acid, it was treated with a small amount of 0.1M NaOH before it was added in sulfuric acid.

Table 1: The expander composition (wt.%) and mixing condition for expander preparation

Batch Name	B.S. (%)	S.L. (%)	C.B.		Speed (rpm)	Time (min.)
			XE2B	N220		
1	94	6	-	-	1500	10
XE500-02	88	6	6		500	2
XE500-10	88	6	6		500	10
XE1500-10	88	6	6		1,500	10
N220500-02	88	6		6	500	2
N220500-10	88	6		6	500	10
N2201500-10	88	6		6	1,500	10

*B.S.: Barium sulfate
*S.L.: Sodium lignosulfonate
*C.B.: Carbon black

Cyclic voltammetry was conducted at the potential range of -0.90 to -0.30 V (versus Ag/AgCl electrode) with a scan-rate of 20 mV/s. Structures of carbon black in HE115 and in expander were investigated by JEOL JEM-2010 transmission electron microscope. TEM samples were prepared by ultrasonically dispersing 20 mg of HE115 or prepared expander in 50 ml of ethanol, then the dispersion was dripped on the sample grid and air dried for at least one hour prior to examination.

Results and Discussion

Figures 1 and 2 show the cyclic voltammogram of pure lead in 1.25 g-cm-3 density sulfuric acid without and with 20 ppm of expander batch no. 1 (without carbon black). From figure 1, the anodic peak-current increases to the limit extent after 400 cycles and then it remains constant. When expander was added, the maximum anodic peak-current was obtained at cycle 400. However, the anodic peak-currents of both cases are comparable. When carbon black is introduced in the expander, it is obvious that the maximum anodic peak-current increases (fig. 3). In addition, a considerable broadening of the anodic peak is observed with a shift of the peak-potential towards higher values. The amount of charge for each condition was estimated from the area under the anodic peak and was illustrated in figure 4.

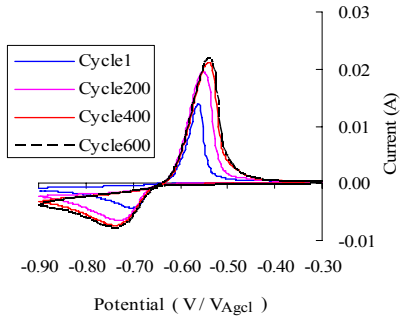

Figure 1. Cyclic voltammogram of a pure lead electrode in 1.25 g-cm^{-3} density sulfuric acid.

From figure 4, the amount of charge does not significantly change when expander batch no. 1 was added. This phenomenon indicated that barium sulfate and sodium lignosulfonate do not increase capacity of the lead electrode. Amount of charge reaches maximum at the cycle around 400 and remain slightly constant. However, effects of barium sulfate and sodium lignosulfonate individually are not studied in this work. When XE2B was added, the amount of charge significantly increased. The maximum charge was obtained at the cycle 100 and then it gradually decreases. However, the amount of charge in this case is higher than those of two previous cases for all cycles. Increasing amount of charge is due to XE2B addition.

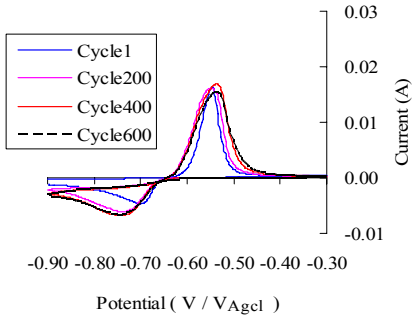

Figure 2. Cyclic voltammogram of a pure lead electrode in 1.25 g-cm^{-3} density sulfuric acid containing 20 ppm expander batch no. 1 (without carbon black).

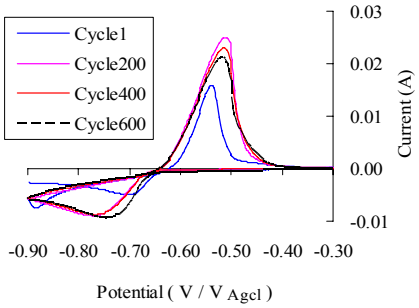

Figure 3. Cyclic voltammogram of a pure lead electrode in 1.25 g-cm^{-3} density sulfuric acid containing 20 ppm of XE500-02 (with XE2B).

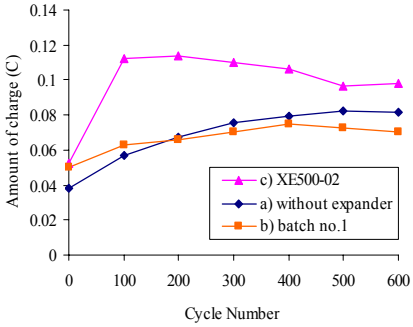

Figure 4. Amount of charge of the anodic peak and number of cycles for a pure lead electrode in 1.25 g-cm^{-3} density sulfuric acid: a) without expander, b) with 20 ppm of expander batch no.1 (without carbon black) and c) with 20 ppm of XE500-02.

Effects of types of carbon black and mixing parameter on amount of charge were illustrated in figures 5. The figure shows amount of charge when 20

ppm of HE115 and prepared XE2B-containing expander were introduced. HE115 is a commercial grade expander. HE115 in this study, analyzed by thermogravimetry (TGA), consists of 88 wt.% barium sulfate, 6 wt.% sodium lignosulfonate and 6 wt.% unidentified carbon black. From this figure, amount of charge in case that XE2B-containing expander was introduced is higher than that when HE115 is added. In addition, better charged stability was found for all cases when the XE2B-containing expander was employed.

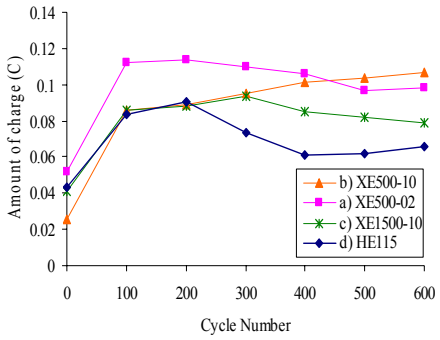

Figure 5. Amount of charge of the anodic peak and number of cycles for a pure lead electrode in 1.25 g cm-3 density sulfuric acid containing 20 ppm of a) XE500-02, b) XE500-10, c) XE1500-10 and d) HE115 (commercial expander)

Higher amount of charge when XE2B was employed may be explained by structure of carbon black. Transmission electron microscopy (TEM) has been used primarily to investigate the carbon black structure [4]. Figure 6 demonstrated the TEM images of HE115 and XE500-02. The black aggregate is barium sulfate and gray cluster is carbon black. From this figure, structure of carbon black aggregate in HE115 is shorter than that found in XE500-02 and there is no branch obviously indicated. The carbon black in HE115, therefore, may be defined as low-structure carbon black. This type of carbon black is less electrical conductive compared with that of high structure carbon. Surface area to volume ratio and void volume of carbon black in HE115 is also less than that of carbon black in XE500-02. Higher surface area and void volume means higher amount of charge can be stored. Therefore, higher amount of charge when XE500-02 is introduced is due to higher area to volume ratio and void volume of carbon black.

Effect of mixing parameter on amount of charge was also found in figure 5. Higher mixing speed reduced the amount of charge. When mixing speed is increased, torque increases and causes shearing of barium sulfate aggregate. The barium sulfate aggregates may be dispersed and no longer fuse with others to form long- chained aggregates (figure 7). It was also found that barium sulfate aggregate is coated by carbon black. Thus, as seen in figure 7, though structure of carbon black does not significantly change with higher mixing speed, electron path along carbon black chain may be reduced due to size reduction of barium sulfate aggregates. Total surface area of carbon black may also decreases because higher carbon black particles are required to coat on barium sulfate. Therefore, charge reduction may be resulted from size reduction and dispersion of barium sulfate aggregate. Increase mixing time does not reduce maximum charge capacity. However, it delays number of cycle in which amount of charge to reach the maximum. The cause of this delay is still unclear and requires further investigation.

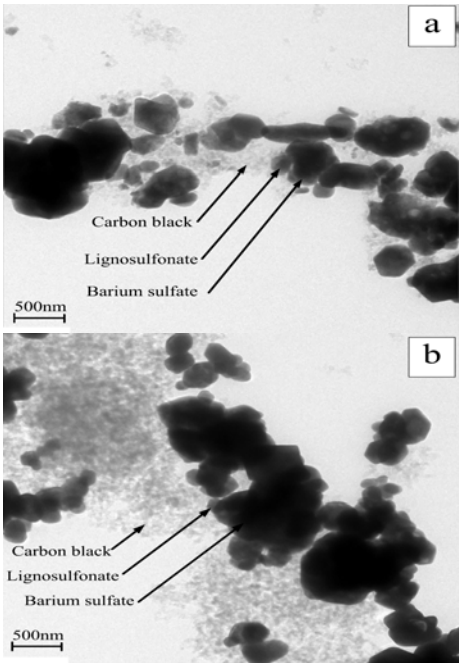

Figure 6. Images from transmission electron microscope (TEM) of (a) HE115 and (b) XE500-02

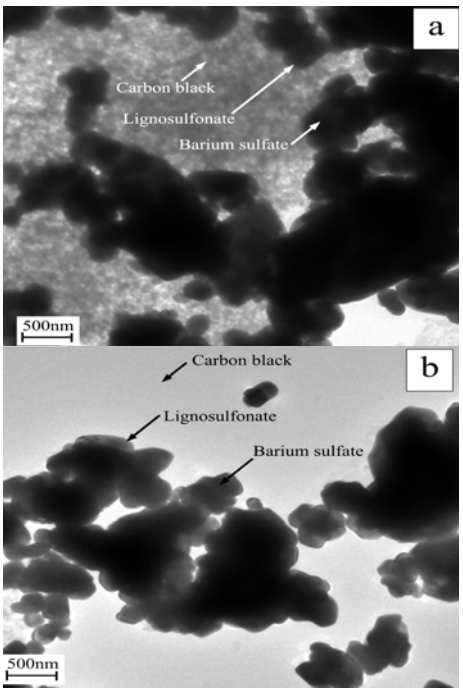

Figure 7. Images from transmission electron microscope (TEM) of (a) XE500-02 and (b) XE1500-10

Figure 8 shows the change of amount of charge corresponding to the anodic peak area with the number of cycles for expander containing N220. Unlike XE2B, N220 is medium-structure carbon black. Effect of mixing parameter on amount of charge in this case is then different from the XE2B case. For N220 addition, the appropriate mixing parameter is mixing speed of 500 rpm and mixing time of 10 minutes. Carbon black aggregates may not disperse all over expander when mixing time is low. As a result, amount of charge is small. In contrary, higher mixing speed may cause size reduction of barium sulfate aggregate and results in charge reduction.

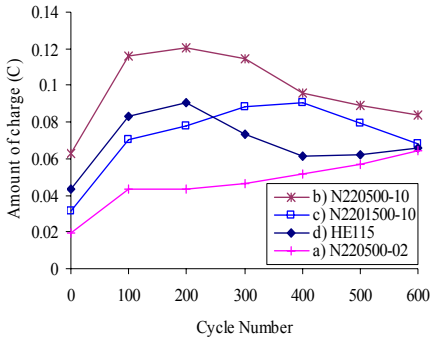

Figure 8. Amount of charge of the anodic peak and number of cycles for a pure lead electrode in 1.25 g cm-3 density sulfuric acid containing 20 ppm of a) N220500-02, b) N220500-10, c) N2201500-10 and d) HE115 (commercial expander)

From figures 5 and 8, it should be noted that amounts of charge in both XE500-02 and N220500-10 cases are equivalent. Charge stability of these cases also behaves similarly. Amount of charge reaches the maximum within 200 cycles and then decreases gradually. However, charge capacity of XE500-02 addition is slightly higher than that of N220500-10 after 400 cycles. This occurrence may be resulted from higher structure of XE2B than that of N220.

Conclusions

In this study, effects of carbon black and mixing parameter of expander preparation on charge capacity were investigated. It was found that carbon black addition increases amount of charge. Mixing speed and mixing time of expander containing different carbon black affect charge capacity differently. For high-structure carbon black, high mixing speed does not decrease the shape and size of carbon black structure but it reduces aggregate size of barium sulfate. This results in charge reduction. For medium-structure carbon black, longer mixing time increases charge capacity. It is believed due to dispersion of carbon black aggregate all over expander when mixing time increases. Finally, addition of high-structure carbon black was found to provide better charge stability than that obtained by addition of low-structure carbon black.

Acknowledgements

The authors would like to acknowledge the Metrohm Siam Ltd and the National Metal and Materials Technology Center for their supports on cyclic voltammetry testing and TEM characterization, respectively.

References

[1] C. Francia, M. Maja and P. Spinelli, *J. Power Sources*. **95** (2001), 119.
[2] J.K. Foster, *Effects of Carbon Black Properties on Conductive Coatings*, Presented in the 2nd international exhibition of paint industry suppliers, 1991.
[3] D.P. Boden, *J. Power Sources*, **73** (1998), 89.
[4] W. Xu, T.W. Zerda, H. Raab and D. Goritz, *Carbon*, **35** (1997), 471.

Preliminary studies on hydrotalcite-like synthesis using magnesium from desalination waste

E. Heraldy[1,2]* Triyono, S. J. Santosa, K. Wijaya, N. B. Alnavis, Rustina, E. S. Hardianti[2]

[1] Department of Chemistry, Faculty of Mathematics and Natural Sciences, Sebelas Maret University, Jl. Ir. Sutami 36A Kentingan, Surakarta 57126, Indonesia

[2] Department of Chemistry, Faculty of Mathematics and Natural Sciences, Gadjah Mada University, PO Box BLS 21, Sekip Utara, Yogyakarta 55281, Indonesia

* E-mail: eheraldy@gmail.com

Abstract: The preliminary studies on hydrotalcite-like (HTlc) synthesis using magnesium from desalination waste (brine water) and its characterization by FT-IR and XRD has been done. In preparation samples, 0.1 M Na_2CO_3 was added to calcium free brine water containing $AlCl_3$ with Mg/Al molar ratio of 2.0 until a pH 10.5 was obtained. The solution was then continuously stirred for 1 hour at 70^{0}C. The present study was able to show that the sample exhibit the (*003*) reflection around 7.583Á, typical for Mg/Al HTlc with carbonate interlayer.

Introduction

Hydrotalcite (HT) or hydrotalcite-like (HTlc) is a layered double hydroxides (LDH) with anion exchange property. HTlc have received much attention in view of their potential applications as adsorbents, as anionic exchangers, catalyst and catalyst support for a variety of organic transformations [1]. Therefore, there have been numerous studies on adsorption capacity and the catalytic activity of HTlc and several studies on their use for the preservation of water environment [2]. HTlc is usually produced by adding Na_2CO_3, solution or NaOH and Na_2CO_3, solutions to a mixed solution of $MgCl_2$ and $AlCl_3$ [3] but the production cost is quite high. There are few studies on the production of HTlc on a commercial scale production.

The aim of the present study is to examine the feasibility of a new inexpensive method to prepare HTlc using brine water, a waste from desalination process.

Materials and Methods

Materials: Original brine water ex Tanjung Jati B, Jepara, Central Java, Indonesia Coal Fired Power Plant (CFPP); magnesium chloride hexahydrate ($MgCl_2.6H_2O$); sodium chloride (NaCl); calcium chloride dihydrate ($CaCl_2.2H_2O$); potassium chloride (KCl); sodium carbonate (Na_2CO_3); sodium bicarbonate ($NaHCO_3$) and aluminum chloride hexahydrate ($AlCl_3.6H_2O$) were used for synthesis of hydrotalcite in p.a. grade. The redistilled water was used during the synthesis. The commercial HTlc from WAKO, Japan.

Synthesis of hydrotalcites by coprecipitation method.

Starting solution: (i) Original brine water ex Tanjung Jati B, Jepara CFPP and /or artificial brine water contained 0.710M NaCl, 0.411M $MgCl_2.6H_2O$, 0.056M $CaCl_2.2H_2O$ and 0.019M KCl. (ii) Filtrate was obtained by adding a mixed 0.1MNa_2CO_3-0.2M$NaHCO_3$, solution to (i) until the 1.2 equivalent of calcium ion in (i) and stirring for 1h at 95^{0}C.

Preparation of Mg/Al HTlc: One thousand milliliter of 0.10M Na_2CO_3 solution was added slowly to 50 mL of (ii) containing $AlCl_3.6H_2O$, with an initial Mg/Al molar ratio of 2.0 at constant pH 10.5 and then the solution was stirred for 1 h at 70°C. The product was centrifuged to recover the white solid at a speed of 2800 rpm for 15 min. The wet cake was washed with redistilled water until free of ion Chloride ($AgNO_3$ test) and dried overnight with oven. The structure of materials were characterized by X-ray diffraction and Fourier transform infrared spectroscopy (FT-IR).

Results and Discussion

XRD patterns of HTlc prepared with different brine water sources in Mg/Al molar ratio = 2 are shown in Figure 1 where all sample have the similar patterns that means the sample are hydrotalcite-like compounds.

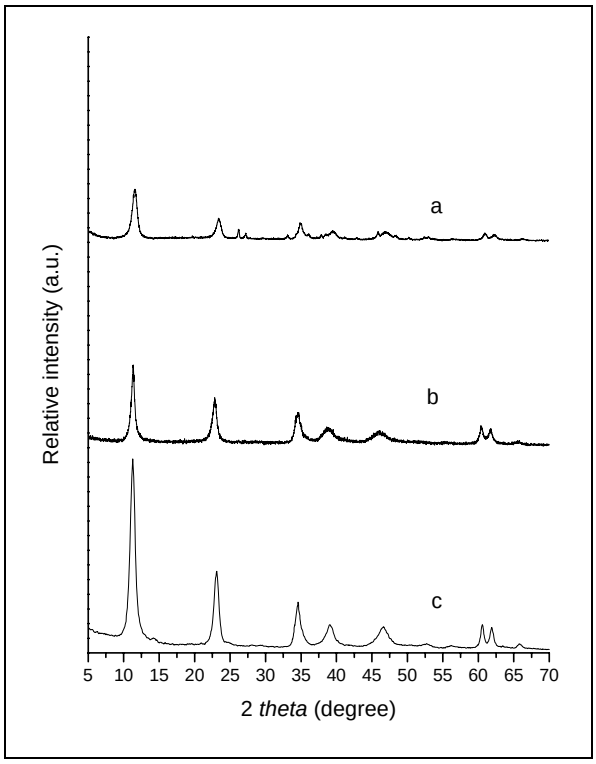

Figure 1. XRD patterns of Mg/Al HTlc prepared with (a) original brine water, (b) commercial ex. WAKO and (c) artificial brine water

The three strong peaks at 2θ values of about 11-12^0, 23-24^0 and 34-35^0 are characteristic of a layered structure and correspond to the (*00l*) reflections. The corresponding values of d_{003}, d_{006} and d_{009} are listed in Table 1. It was thought that CO_3^{2-} was intercalated into the precipitated HTlc since (*003*) reflection of HTlc intercalated CO_3^{2-} is around 7,54 - 7.83 Å. According to Kloprogge, the value of 7.83Å is characteristic for the (*003*) reflection of carbonate-bearing hydrotalcite [4] while Johnson and Glasser [5] and Xu and Lu [6] showed that the (*003*) reflection are 7.563Å and 7.540Å respectively. The diffraction peak near 61.0^0 corresponds to the (*110*) crystal plane. It can be seen in Figure 1 that the diffraction peaks are sharp, indicative of relatively well formed crystalline layered structures.

In addition, the FT-IR spectra obtained for three samples are in good agreement, with only slight variations in the peak positions as compared to the data available in the literature. FT-IR spectra of the HTlc samples are shown in Figure 2.

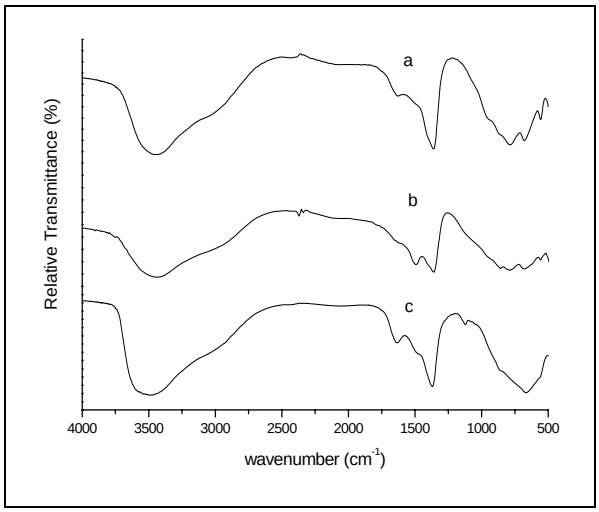

Figure 2. FT-IR spectra of Mg/Al HTlc with (a) artificial brine water, (b) original brine water and (c) commercial ex WAKO

The broad peak around 3500cm^{-1} are attribute to the stretching mode of OH groups in the brucite-like layer. The shoulder at 3000cm^{-1} is due to hydrogen bonding of interlayer water with interlayer CO_3^{2-} anions. The intensity of this shoulder increases with the crystallinity of Mg/Al HTlc, indicating stronger layer-interlayer interactions and a well ordered interlayer region.

A lower wavenumber band corresponds to Mg/Al HTlc lattice vibrations (Mg-O, Al-O, Mg-O-Al). The similarity of the spectrograms indicates that the structures of the three samples are the same.

Table 1: XRD data of d_{00l} of Mg/Al HTlc with different brine water sources

Mg/Al HTlc	Original bw	Artificial bw	Ex. WAKO	HT Std.
d_{003}(Å)	7.583	7.838	7.797	7.840
d_{006}(Å)	3.802	3.844	3.884	3.900
d_{009}(Å)	2.570	2.590	2.592	2.600

Conclusions

As prepared the other HT or HTlc, this sample exhibit the (003) reflection around 7.583 Å, typical for Mg/Al HTlc with carbonate interlayer.

References

[1] S.K. Sharma, P.K. Kushwaha, V.K. Srivastava, S.D. Bhatt and R.V. Jasra, *Ind. Eng. Chem. Res.* **46** (2007), pp. 4856–4865.
[2] T. Kameda, T. Yoshioka, M. Uchida and A. Okuwaki, *Mol. Cryst. Liq. Cryst.* **341** (2000), pp. 407–412.
[3] S. Miyata, *Clays Clay Miner.* **28(1)** (1980), pp. 50–56.
[4] J.T. Kloprogge, D. Wharton, L. Hickey and R.L. Frost, *Am. Mineral.* **87** (2002), pp. 623–629.
[5] C.A. Johnson and F.P. Glasser, *Clays Clay Miner.* **51(1)** (2003), pp. 1–8.
[6] Z.P. Xu and G.Q. Lu, *Chem. Mater.* **17** (2005), pp. 1055–1062.

Organic Chemistry and Medicinal Chemistry

Synthesis and activity test as antioxidant of two hydroxydibenzalacetones

S. Handayani[1,*], S. Matsjeh[2], C. Anwar[2] and S. Atun[1]

[1]Department of Chemical Education, Faculty of Mathematics and Natural Sciences,
State University of Yogyakarta, Karangmalang, Depok, Yogyakarta, Indonesia 55281
[2]Chemistry Departement, Faculty of Mathematic and Natural Science
Gadjah Mada University, Sekip, Yogyakarta, Indonesia

*Email: handayani137uny@yahoo.com

Abstract: Synthesis and antioxidant activity test of two hydroxydibenzalacetones have been conducted. 2,2'-Dihydroxydibenzalacetones and 3,3'-dihydroxydibenza--lacetones were synthesized by crossed aldol condensation in base condition with water-ethanol solvent from 2-hydroxybenzaldehyde and 3-hydroxybenzaldehyde as raw material respectively. The synthesize reaction was conducted in ice bath environment under stirring and followed by precipitation and purification by recrystalization with methanol-water as solvent. After filtration, 60.15% blackish green crystalline of 2,2'-dihydroxydibenzalacetone and 78.94% yellow crystalline of 3,3'dihydroxydibenzalacetone were obtained. The IC_{50} of two compounds were 791.62 and 196.56 µg/mL respectively.

Introduction

As curcumine analogue, dibenzalacetone is an attractive compound to be developed. Curcumine and dibenzalacetone structure was distinguished by a carbonyl and a methylene group so they have been predicted having similar activity. Itokawa et.al. [1] reported the relationship between structure and activity of curcuminoid compounds as antioxidant, anti-inflammatory, chemoprefentive and anti prostate cancer. Antiinflammatory and antioxidant activity was found not only in curcuminoid compounds, but also in dibenzalacetone [2]. Previous research was resulting that symmetric [3] and asymmetric dibenzalacetone also have antioxidant activity [4].

Dibenzalacetone could be synthesized by crossed aldol condensation easily.. Aldol Condensation is occured by a nucleophilic addition of the enolate ion to a carbonyl. Acetone also undergoes aldol condensation, but the equilibrium concentration of the product is generally small. Analogue benzalacetones still have a potential development based on previous reports of its biological activity. Some of researchers had reported dibenzalacetone synthesis by different method. Sardjiman had synthesized some of analogue hydroxydibenzalacetones using hydrochloric acid as acid catalyst while Pudjono [5] used sulphuric acid. Affandi [6] had synthesized 4-hydroxydibenzalacetone in base condition. Solvent also has a significant influence in benzalacetone synthesis [7].

2,2'-dihydroxydibenzalacetone and 3,3'-dihydroxydibenzalacetone will be synthesized in this research. Dihydroxydibenzalacetone compound has phenolic group that performing very reactive oxidative reaction and could produced free radical, so it was predicted that dihydroxydibenzalacetone has potency of an antioxidant activity.

Materials and Methods

General . All materials used was supplied from Merck, some of these are acetone, 2-hydroxybenzaldehyde, 3-hydroxybenzaldehyde, ethanol, chloroform, hexane, and ethyl acetate. The ^{1}H, ^{13}C-NMR, HMQC and HMBC Spectra were recorded on 500 MHz Jeol spectrophotometer. IR spectra were conducted using a Shimadzu 8300 FTIR spectrometer.

2,2'-dihydroxydibenzalacetones(4). Into a solution of acetone (0.01 mol, 0.58 g) in 5 mL ethanol that was prepared at ice bath environment, 2-hydroxybenzaldehyde (0.02 mol, 2.44 g) and NaOH (0.025 mol, 1 g) were added drop wise alternately. After stirring for 3 hours, the mixture was kept under 10^0C for 24 hours before filtering and purification by recrystalization using methanol as solvent. The obtained product was identified by thin layer chromatography, FTIR and NMR spectrophotometer.

3,3'-dihydroxydibenzalacetone (5). Into a solution of acetone (0.01 mol, 0.58 g) in aquades that was prepared at ice bath environment, NaOH (0.025 mol, 1 g) and 3-hydroxybenzaldehyde (0.02 mol, 2.44 g) were added drop wise alternately. After additional stirring for 3 hours, 3 mL HCl 37% and 5 mL aquades were added. The mixture was kept under 10^0C for 24 hours. Then, the mixture was filtered and followed by purification by recrystalization with ethanol-water as solvent. The yield was identified by thin layer chromatography, FTIR and NMR spectrophotometer.

Deoxyribose assay

The assay was performed by the following method as described by Halliwell [8]. All solutions were freshly prepared. Into a solution of 6 mM 2-deoxyribose (0.2 mL), 0.01 mM ascorbic acid (0.2 mL); buffer phosphate pH 7.4 (0.2 mL); 0.01 mM H_2O_2 (0.2 mL); 0.1 mM ferrosulphate (0.2 mL) and 0.02 mL of sample in various concentration (62.5; 125; 250; 500; 1000 µg/mL) were added. After an incubation period of 30 minutes at 310°K, the extent of deoxyribose degradation was measured by the TBA reaction. 3 ml of TBA and 3 ml of TCA were added to the reaction mixture and heated for 15 minutes at

353°K. After cooling, the absorbance of mixture was measured at 532 nm against a blank solution (the same solution but without sample). The percentage inhibition was calculated by the formula:

$$I(\%) = \frac{A_{blank} - A_{sample}}{A_{blank}} x100\%$$

The IC_{50} value represent the concentration of the compounds that caused 50% inhibition. BHT was used as a positive control.

Results and Discussion

The Synthesis of 2,2'-dihydroxydibenzalacetone (4). The preparation of compound **4** was initiated by the mixing of **1** and **3** with sodium hydroxide as catalyst in ethanol solvent (Figure 1). After stirring for 3 hours followed by filtration, 60.15% blackish green crystalline solid was obtained. The structure of **4** was determined by chromatographic and spectroscopic data: Rf (TLC; methanol: chloroform=1:9) 0.36; FTIR (KBr) cm^{-1}: 3425.58; 2939.52; 1589.34; 1543; 1458 and 1118.71.

The multiple bond correlation of HMBC supported the structure (Table 1, Figure 2). In the ^{1}H-NMR spectrum (500 MHz, CD_3OD), four equivalent protons with multiplicity as doublet and two equivalent protons with the multiplicity as triplet were observed. The doublet signal at δ = 8.4 ppm was assigned to H1 and H5, δ = 7.6 ppm to H6'and H6", δ = 7.1 ppm to H2 and H4 and δ = 6.69 ppm to H2' and H2". The triplet signal at δ = 6.47 ppm was assigned to H4' and H4" meanwhile δ = 7.06 ppm to H5' and H5". Support spectra data provided by the IR (KBr), which indicates the existence of C=O (1589.34 cm^{-1}), aromatic C=C (1543-1458 cm^{-1}) and CO (1118.71 cm^{-1}). Therefore, the structure of **4** was 2,2'-dihydroxydibenzalacetone.

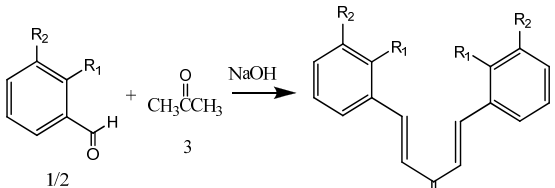

Figure 1. Synthesis reaction of **4** and **5** by crossed aldol condensation

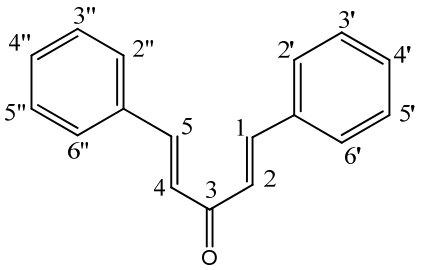

Figure 2. Numbering of dibenzalacetone structure for NMR data

Table 1: ^{1}H and ^{13}C-NMR data of compound **5** (CD_3OD)

C no.	δH (∑H; m;J Hz) ppm	δC ppm	HMBC (500 MHz)
1	8.42 (1 H; d; 15,9)	143	C3, C2', C6'
2	7.15 (1H; d; 15,9)	122	C3, C1'
3	-	193	-
4	7.15 (1H; d; 15,9)	122	C1", C3
5	8.42 (1H; d; 15,9)	143	C3, C4,C6''
1'	-	124	-
2'	-	169	-
3'	6.68 (1H; d; 15,9)	121	C1', C4'
4'	6.47 (1H; t; 8)	115	C3', C6'
5'	7.06 (1H; t; 8)	133	C2', C6'
6'	7.55 (1H; d; 8)	128	C2', C1, C5'
1''	-	124	-
2''	-	169	-
3''	6.68 (1H; d; 8)	121	C1'', C4''
4''	6.47 (1H; t; 8)	115	C3'', C6''
5''	7.06 (1H; t; 8)	133	C2", C6''
6''	7.55 (1H; d; 8)	128	C2'', C5, C5"

The Synthesis of 3,3'-dihydroxydibenzalacetone (5). The preparation of compound **5** was initiated by the mixing of **3** with sodium hydroxide as catalyst in aquadest as solvent (Figure 1). To this reaction mixture was directly added **2,** followed by stirring at ice bath for 3 hours. After additional stirring, provided yellow crystalline **5** in 78.94% was resulted. The structure of **5** was determined by chromatographic and spectroscopic data: Rf (TLC;methanol:chloroform = 1:9) 0.34; FTIR (KBr) 1/cm: 3379.29; 3248.13; 1620.21; 1581.63; 1450; 1211.30 and 1103.28.

The multiple bond correlation of HMBC supported the structure (Table 2, Figure 1). In the ^{1}H-NMR spectrum (500 MHz, CD_3OD), one set protons singlet, four set protons doublet and one set protons triplet were observed. Support spectra data were provided by the IR (KBr), which indicate the existence of C=O (1620.21 cm^{-1}), aromatic C=C (1581.63-1450 cm^{-1}) and CO (1103.28 cm^{-1}). Therefore, what can be concluded for the structure of **5** was 3,3'-dihydroxydibenzalacetone.

Table 2: ^{1}H and ^{13}C-NMR data of compound 6 (CD_3OD)

C no.	δH (∑H; m) ppm	δC ppm	HMBC (500 MHz)
1	7.68 (1 H; d; 15,9)	145	C3, C2', C2, C2'
2	7.16 (1H; d; 15,9)	126	C3, C1, C1'
3	-	191	-
4	7.16 (1H; d; 15,9)	126	C3, C1", C5
5	7.68 (1H; d; 15,9)	145	C3, C4, C1",C2''
1'	-	137	-
2'	7.1 (1H; s)	115	C1, C3', C6'
3'	-	159	-
4'	6.86 (1H; d; 8)	119	C3', C2', C6'
5'	7.2 (1H; t; 8)	131	C4', C3', C1'
6'	7.15 (1H; d; 8)	121	C1, C1'
1''	-	137	-
2''	7.1 (1H; s)	115	C5, C3'', C6''
3''	-	159	-
4''	6.86 (1H; d; 8)	119	C3'', C2'', C6"
5''	7.2 (1H; t; 8)	131	C4'',C3'',C1''
6''	7.15 (1H; d; 8)	121	C5, C1''

Deoxyribosa assay

Activity test as deoxyribose degradation inhibitor was done by fenton reaction. The IC_{50} value represented the consentration of the compounds, that caused 50% inhibition. All experiment were repeated for five times. Data of IC_{50} values were showed in Table 3.

Table 3: IC_{50} datas for compounds **4** dan **5**

No	Compound	IC_{50} (µg/mL)	activity
1.	4	791.62	Low
2.	5	196.56	active

Conclusions

In conclusion, two dihydroxydibenzalacetones, **4** and **5** were succesfully synthesized in 60.15 and 78.94% respectively. Compund **4** and **5** exhibited significant antioxidant activity with the IC_{50} of 791.62 and 196.56 µg/mL respectively. Compound **5** is more potent than **4** to inhibit deoxyribose degradation.

Acknowledment

This research had supported by "Hibah Doktor UGM 2009"

References

[1] Itokawa H., shi, Q., Akiyama, t., Morris, S.L and Lee K.H., 2008, Recent Advances in the Investigation of Curcuminoids, Chinese Medicine, 3,11.

[2] Sardjiman, 2000, *Synthesis of some New series of Curcumin Analogues, Antioxidative, Antiinflamatory, Antibacterial Activities and Qualitative-Structure Activity Relationship*, Disertasi, Fakultas Farmasi Gadjah Mada University, Yogyakarta

[3] Sri Handayani, Sabirin Matsjeh, Chairil Anwar and Sri Atun, *Synthesis and Activity Test As Deoxyribose Degradation Inhibitor of Two Asymmetric Dibenzalacetones*, Proc of International Chemistry Seminar, UGM, Yogyakarta, 2009

[4] Sri Handayani, Indyah Sulistyo Arty, *Journal of Physical Science,* Volume 19(2), 61-68, 2008

[5] Pudjono, Supardjan and Irawati, T, *Majalah Farmasi Indonesia*, 17(1), 45-49, 2006

[6] Muhammad Yusuf Affandi, *Sintesis p-hidroksibenzalde-hida dengan aseton,* Skripsi,FMIPA, UGM, 2008

[7] Pudjono, Sismindari and Widada, H., 2008, *Majalah Farmasi Indonesia,* 19(1), 48-55, 2008

[8] Halliwell, B., Gutteridge, J.M.C. & Aruoma, O.I., *Anal. Biochem.,* 1987, 165, 215–219

Phenolic content and cytotoxic properties of fermented black soybeans (*Glicine soja)* extract on human Hela-S3 and Raji cell lines

S. Atun[1*], R. Arianingrum[1], T. Yoshiaki[2] and N. Masatake[2]

[1] Department Chemistry education, Universitas Negeri Yogyakarta, Karangmalang, Depok, Sleman, Yogyakarta, Indonesia 55281
[2] Faculty of Pharmacy, Meijo University, Tempaku, Nagoya, Japan

*E-mail: Atun_1210@yahoo.com

Abstract: The purpose of this research are to determine total phenolic and flavonoids content from fermented black soybeans (*Glycine soja*) on various times (0; 2; 4; 6; and 8 days) by the micelium of *Rhizopus oligosporus*, the cytotoxic activity test on human cancer such as Hela S3 and Raji cell lines, and isolated the phenolic compounds from fermented black soybean.Total phenolics and flavonoids from some methanol extracts were determined by spectroscophy. The isolation of this compound was carried out by chromatographic method, whereas structure elucidation was performed by interpretation of spectroscopic data, including UV, IR, ^{1}H and ^{13}C NMR. The research showed that the highest content of total phenolic and flavonoids were found in 6 days fermented black soybean, which also displayed the highest cytotoxic activity against Hela S3 and Raji cell lines. Isolation and structure elucidation of phenolic compounds from fermented black soybean had also been done. From methanol extract of 4 days fermented black soybean, we isolated one known compound namely p-hydroxybenzoat.

Introduction

Cancer or tumor is one of the dangerous diseases nowadays. And until know, the medicine of this disease have not been found yet. So, the efforts to find the medicinal compounds which can be used to prevent and therapy cancer are needed [1]. It has been reported that black soybean is a type of soybean (*Glycine max*) with a black seed coat, contained numerous bioactive compounds and show radical-scavenging activity, anti-tumor activity and activity for improving the fluidity of the whole blood. The seeds of *Glycine max* (L.) Merr. (soybean) belongs to family Fabaceae is being used in Asia for many centuries to prepare a variety of fresh, fermented and dried foods [2-5]. It is one of the most economically important crop for the major source of high-quality protein and vegetable oil for animal and human nutrition in the world [5]. Seeds contain high amount of components with health benefits, such as proteins, isoflavones (genistein, daidzein, and glycitein), coumestrol, phytate, saponins, lecithin, phytosterols, vitamin E and dietary fiber. Isoflavones have been reported to play essential role in hyperlipidemia, cardiovascular diseases. Dietary fiber plays an important role in the reduction of cholesterol levels in some hyperlipidemic individuals [3-11]. The purpose of this research are to identification total phenolic and flavonoids content from fermented black soybeans (*Glycine soja*) on various times (0; 2; 4; 6; and 8 days) by the micelium of *Rhizopus oligosporus*, the cytotoxic activity test on human cancer such as Hela S3 and Raji cell lines, and identification the phenolic compounds from fermented black soybean.

Materials and Methods

Preparation of fermented methanol extract of black soybeans

The seeds of black soybeans (*Glycine max*) were purchased from local market in Bantul, Yogyakarta, Indonesia in February 2009. The seeds of black soybeans were identified by a staff at Department of Biology, UGM, Indonesia. The black soybeans were macerated for 24 hours, boiled for 2 hours, and then it was remacerated while peeling the seed coat, and washed it until clean. Next, the peeled black soybeans were boiled, and let it cool in a room temperature. After it was cool enough, approximately 2% of *Rizopus oligosporus* was added and wrapped it by using banana leaves. Then, it was fermented in 0; 2; 4; 6; and 8 days. The fermented black soybean was milled and added some methanol. As a result, the filtrate was collected and evaporated by using vacuum evaporator, so that we could get crude extract.

Determination of total phenolic and flavonoids content

Total phenolics were determined by the Folin-Ciocalteu procedure [12]. Aliquots (0.1 mL) of aqueous methanol extracts were transferred into test tubes and their volumes made up to 0.5 mL with distilled water. After addition of Folin-Ciocalteu reagent (0.25 mL) and 20% aqueous sodium carbonate solution (1.25 mL), tubes were vortexed and after 40 min the absorbance of the resulting blue colored mixtures was recorded at 725 nm against a blank containing only extraction solvent (0.1 mL). The amount of total phenolics was calculated as a galic acid equivalent from the calibration curve.

For the determination of flavonoids, powdered plant material (1 g) was homogenized with extracting solvent (140:50:10 MeOH-H_2O- CH_3COOH, 20 mL) and filtered into volumetric flasks. Volumes were adjusted to 100 mL by addition of additional extracting solvent. To prepare the solutions for analysis aliquots (2.5 mL) were transferred into 50 mL volumetric flasks and their volumes made up with water. To each 10 mL of analysis solution, water (2 mL) and $AlCl_3$

reagent (133 mg crystalline aluminium chloride and 400 mg crystalline sodium acetate dissolved in 100 mL of extracting solvent, 5 mL) were added and absorbances recorded at 430 nm against a blank (10 mL of analyzed solution plus 5 mL of water). The amount of flavonoids was calculated as a rutin equivalent from the calibration curve of rutin standard solutions, and expressed as g rutin/kg plant material [13].

Measurement of cytotoxic activity

All of methanol extracts we evaluated for *in vitro* cytotoxicity against a panel of human tumor Hela S3 and Raji cell lines. The *in vitro* cytotoxicity test was investigated using plate with 96 wells, with cell density $2x10^4$ cells per mL. Into each well was added 100 µL cells in culture medium (87,5% RPMI 10,4 g/L; 2% penstrep; and 10% FBS) which was then incubated in CO_2 incubator for 12-24 hours at 37^0C. Each sample was dissolved in culture medium containing 0,05% DMSO, and 100 µL of each sample in different concentrations was added into each well in triplicate and was then incubated in CO_2 incubator for 12-24 hours at 37^oC. MTT solution (10 µL per 100 µl medium) was added to all wells of an assay, and plates were incubated for 4 hours at 37^oC in CO_2 incubator. As much as 100 µl formazon (10% SDS and 0, 01 N hydrochloric acid) was added into each well and mixed on a shaker for 5 minutes. The wells were incubated in the dark room for 12-24 hours at room temperature. The absorbance was measured using multiwell scanning spectrophotometers (ELISA reader) at 595 nm. The absorbance is directly proportional to the number of living cells. So the dead cell could be calculated to determine LC_{50}. Doxorubicin, a medicine for lymphoma, leukemia and acute tumor, was also measured its cytotoxic activity as positif control comparison. The cytotoxic activity of the samples against Hela-S3 cell measured as LC_{50} were provided in Table 1. Hela-S3, a *continuous cell line* that lived as adherent cell, is a cell derivate of ephythell cell of human cervix cancer. Further investigation of cytotoxic activity of the samples was held against Raji cell (Table 1). The cell that resembles lymphoblast cell found by R.J.V Pulvertaft (1963) from *Burkitt's lymphoma* at the left of the upper jaw of a 11 year old negro boy.

Isolation phenolic compounds

The isolation of phenolic compounds from methanol extract of 4 day fermented black soybeans was done by using the chromatography. A portion (40 g) of the total methanol extract was fractionated by vacuum liquid chromatography (VLC) and purified by repeated column chromatography on silica gel eluted with various solvent systems. From this method we obtained one phenolic compounds, namely p-hydroxybenzoat (**1**) (30 mg). The structures of these compounds were established on the basis of their spectral data, including UV, IR, and NMR spectra.

Results and Discussion

The result of methanol extract of fermented black soybeans (*Glycine soja*) on various times can be seen on table 1. Rendemen methanol extract from fermented black soybean on various times show an increased, because that the more time we fermented the soybean, the more big compounds (polymer) which hydrolyze, so that it can easily soluble in methanol. The highest total phenolic and flavonoid were found in 6 days fermented black soybean, which also displayed the highest cytotoxic activity against Hela S3 and Raji cell lines.

Table 1: Rendemen methanol extracts, total phenolic content, total flavonoids, and cytotoxic activity against Hela S3 and Raji cell lines of fermented black soybeans (*Glycine soja*) on various times

Sample	Rende-men (M ± SD)%)	Total phenolic (M ± SD)%	Total flavonoids (M ± SD)%	LC_{50} µg/mL on Hela cell lines	LC_{50} µg/mL on Raji cell lines
Black soybean seed	0.06 ± 0.05	Not measu-red	Not measu-red	>> 1000 (not active)	>> 1000 (not active)
Black soybean fermented on 0 day	0.01 ± 0.04	3.67 ± 0.15	6.50 ± 0.24	>> 1000 (not active)	707,945 (less active)
Black soybean fermented on 2 days	0.11 ± 0.03	4.28 ± 0.19	4.54 ± 0.27	>> 1000 (not active)	>> 1000 (not active)
Black soybean fermented on 4 days	0.14 ± 0.03	3.56 ± 0.22	4.57 ± 0.11	977.237 (less active)	295,12 (active)
Black soybean fermented on 6 days	0.16 ± 0.01	4.61 ± 0.49	6.89 ± 0.29	316.228 (less active)	229,087 (active)
Black soybean fermented on 8 days	0.22 ± 0.04	3.73 ± 0.26	5.71 ± 0.61	416.869 (less active)	213,796 (active)
Doxoro bucin (positive control)				96,87 (active)	242,10 (active)

From the methanol extract of 4 days fermented black soybeans, after separated and repeatedly purification by extensive chromatography were

resulted one compound. Compound **1** was obtained as a white yellow powder, maxima of absorption were observed at 250 and 285 nm in the UV spectrum attributable to the phenol chromophor. The IR spectrum exhibited hydroxyl group (3445 cm^{-1}), C=O (1730; 1718 cm^{-1}), and C=C aromatic (1670-1454 cm^{-1}). The ^{1}H NMR spectra showed two sets of AA'BB' system of aromatic protons assignable to 1.4-disubstitutedbenzene at δ 5.45 (2H, *d, J* = 8.5 Hz) ppm and 7.38 (2H, *d, J* = 8.5 Hz). They also displayed two signal protons at δ 11.0 (2H, *br s*) exhibited of hydroxyl proton from phenol and carboxyl fungsional group. The ^{13}C NMR spectrum showed four signal carbon which exhibited of seven carbon atom. Furthermore, 7 signal carbon showed 1 carbon oxyaril at δ 164.3 (1 C) ppm, one carbon quarterner at δ 151.4 (2C) ppm, 4 carbon metin at δ 142.1 (2C) and δ 100.17 (1 C) ppm. Spectrum NMR (^{1}H and ^{13}C) of 1 has similar with p-hydroxybenzoat (Fig. 1). The isolation of the other compounds has been doing in my laboratory.

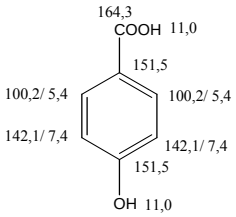

Figure 1. Structure of p-hydroxybenzoat

Some phenolic compounds have been isolated from soybean seeds such as chlorogenic acid, caffeic acid, ferulic acid, and p-coumaric acid. These have antioxidant effects that are beneficial to human health. Generally, these phenolic acids have contents ranging from 28 to 72% of the total phenol level in soybean seeds [4]. Many phenolic compounds found in plant tissues are potential antioxidants: flavonoids, tannins and lignin precursors may all work as ROS-scavenging compounds. The effects of dietary phenolics are of great current interest, due to their antioxidative and possible anticarcinogenic activities. A popular belief is that dietary phenolics are anticarcinogens because they are antioxidants, but direct evidence supporting this supposition is lacking [11]. Phenolics may inhibit carcinogenesis by affecting the molecular events in the initiation, promotion, and progression stages. Isoflavones and lignans from soybean may influence tumor formation by affecting estrogen-related activities. They also modulate the growth of benign and malignant prostatic epithelial cells *in vitro* [10].

Conclusions

The highest content of total phenolic and flavonoids were found in 6 days fermented black soybean, which also displayed the highest cytotoxic activity against Hela S3 and Raji cell lines. From methanol extract of 4 days fermented black soybean, we isolated one known compound namely p-hydroxybenzoat.

Acknowledgements

This work was supported by Indofood Research Nugraha 2009 (Indofood Sukses Makmur Tbk) Indonesia.

References

[1] Auroma O.I, *J. Nutr. Biochem*.Vol.5 (1994), p 370-381
[2] Dixon RA, Steele CL, *Trends Plant Sci*, 4, (1999), p394 - 400
[3] Galati G, O'Brien PJ., *Free Radic. Biol*. Med., 37(3), (2004), p287-303
[4] Kim E.H, Kim S.H, Chung J.I., Chi H.Y., Kim.J.A. Chung I.M., *Eur Food Res Technol*.222, (2006), p201-208
[5] Jha, H.C. *Asian Symposium Non-salted Soybean Fermentation*, Tsukuba, Japan, July 14-16., (1985)
[6] Lim H, Park H, Kim HP, *Arch. Pharm. Res*, 27(4), (2004), p 442-8.
[7] Moyers SB, Kumar NB, *Nutr. Rev*., 62(5), (2004), p 204-11.
[8] Murakami, H., Asakawa, T., Terao, J. dan Matsushita, S. *Agric. Biot. Chem*., 48 (12), (1984), p 2971-2975.
[9] Murata, K, *Asian Symposium on Non-salted soybean fermentation*, Tsukuba, Japan, July 14-16, 1985.
[10] Ralston L, *Plant physiology*, vol. 137, (2005), p 1375-1388
[11] Malencic D., Milan P., Jegor M., *Molecules*, 12, (2007), p 576-581.
[12] Hagerman, A.; Harvey-Mueller, I.; Makkar, H.P.S. *Quantification of Tannins in Tree Foliage Laboratory Manual*; FAO/IAEA: Vienna (2000).
[13] Marckam, K.R. 1989.*Methods in Plant Biochemistry*; Academic Press: London, (1989).

Chemical constituents of essential oil from *Solanum spirale* Roxb. and their biological activities

S. Keawsaard[1*], B. Liawruangrath[1], S. Natakankitkul[1], S. Chowwanapoonpohn[1], S. Liawruangrath[2], A. Teerawutgulrag[2] and S.G. Pyne[3]

[1]Faculty of Pharmacy, Chiang Mai University, Amphur Muang, Chiang Mai, Thailand 50200
[2]Faculty of Science, Chiang Mai University, Amphur Muang, Chiang Mai, Thailand 50200
[3]Department of Chemistry, University of Wollongong, Wollongong, Australia 2522

*E-mail:sukanya_k40@hotmail.com

Abstract: In this research, the antibacterial antioxidant activities and chemical constituents of *Solanum spirale* Roxb. were studied. The ripe fruit of this plant was extracted with methanol and concentrated under vacuum. The methanolic crude extract was screened for antibacterial by agar diffusion method. It was found that the crude extract also showed antibacterial activity against *Escherichia coli*, *Staphylococcus aureus* and *Pseudomonas aeruginosa*. This extract showed the highest antibacterial activity against *S. aureus*. The antioxidant activity of methanolic extract was determined by scavenging effect on 1-diphenyl-2-picrylhydrazyl radicals (DPPH$^{\bullet}$) method. The result showed that the extract was exhibited the antioxidant activity with IC_{50} = 2.43 mg/mL. The essential oil from the ripe fruit of this plant was isolated by hydrodistillation and analyzed by capillary gas chromatography-mass spectrometry (GC-MS). The essential oil obtained in 0.0037% yield as pale yellow liquid. Twenty-seven peaks were detected and seventeen compounds were identified. The oil was mainly consisted of carboxylic acids, esters (50%) and hydrocarbons (39%). The major compounds were linoleic acid (45.30%) and hexadecanoic acid (40.75%) which were firstly isolated from the ripe fruits of *S. spirale* Roxb.

Introduction

Solanum spirale Roxb. is in *Solanum* genus and *Solanaceae* family. This plant is local vegetable in many countries. It is distributed mainly in China, India, Vietnam, Burma Bengol, Thailand, Lao, Bhutan, Bangladesh, Indonesia, and Australia.[1,2] *S. spirale* Roxb. has been used as a folk medicine plant in many contries. The roots are employed as a narcotic, diuretic and anaesthetic.[3,4,5] The Vietnamese use the ripe fruits as vegetable and the leaves as folk medicine against beriberi and swollen stomach.[2,6] *S. spirale* Roxb. have been found some chemical constituents and found to contain mixture of steroidal alkaloid glycosides such as protodioscin,[2] 25-isosolafloridine, solacallinidine,[7] solasodine,[8] solaspiralidine, and 3-O-(β-D-glucopyranosyl) etioline [9,10]

According to our information, there are a few reports mentioned about the biological activities of *S. spirale* Roxb. Therefore, it seemed to be interesting to study the chemical constituents and biological activities of this plant. The aim of this study was carried out to investigate the biological activity of the methanol extract of *S. spirale* Roxb. The study was carried out to determine the chemical constituent of essential oil from the ripe fruits *vai* GC-MS technique.

Materials and Methods

Materials

Ripe fruits of *S. spirale* Roxb. specimen were collected from Phayao Province, Thailand in July 2008. A voucher specimen of this plant was deposited at the Herbarium of Queen Sirikit Botanic Garden, Chiang Mai, Thailand.

Extraction of materials

1 kilogram of powdered ripe fruits was extracted sequentially with 3 liters of hexane, chloroform and methanol. The extracts were filtered and concentrated under vacuum to crude residues. The percentage yield of methanolic extract was 3.93.

Antibacterial activity assay

The methanolic extract was screened for antibacterial activity by agar diffusion method. This extract was diluted with ethanol and screened for antibacterial activity against *Escherichia coli* ATCC 25922, *Staphylococcus aureus* ATCC 25923 and *Pseudomonas aeruginosa* ATCC 27853 by using 30 mg/ml concentrations of the extract. 100 microliters of solution was transfered to a 9 mm disk. The sample disk was placed on the microbe spread medium plate and then incubated at 37 °C for 24 hrs. After incubation, the diameter of the zones of complete inhibition was measured to the whole millimeter.

Antioxidant activity assay

Antioxidant activity was studied by DPPH method. 180 µL ethanolic solution of DPPH$^{\bullet}$ (10 µM) was mixed with 20 µL of test samples in a 96-well microtiter plate. After 30 min, the absorbance was measured at 540 nm. This experiment was carried out for concentration of sample that is 0.1, 0.2, 0.6, 1.0, 2.0, 4.0 mg/mL. The DPPH$^{\bullet}$ solution was used as control. The percentage inhibition of DPPH was determined by calculation as follows:

$$\text{DPPH scavenging activity (\%)} = \frac{Ac - As}{Ac} \times 100$$

where 'Ac' is absorbance of the control and 'As' is the absorbance of the test sample after 30 min.

From the result obtained a plot of percentage inhibition of DPPH against concentration and the IC_{50} determined.

Determination of chemical constituents

Fresh ripe fruits (934.97g) were cut pulp into small pieces, then subjected to hydrodistillation in Clevenger-type apparatus for 8 hours. The oil was separated and analyzed by capillary GC-MS. The essential oil was analysed on a Hewlett-Packard 6890 series on a HP-1 capillary column. It was 30 m x 0.32 mm id. with a 0.25 µm film thickness. The temperature of the HP-1 column was programmed starting at 50 °C and held for 5 min., the temperature was increased at a rate of 10°C/min from 50 to 280 °C and held there for 5 min. Helium gas was used as the GC carrier gas. The GC injector was in a split mode with a splitless. The injector temperature was set at 250 °C. The effluent from the capillary column went directly into the mass spectrometer and operated in the electron impact (EI) mode with an ionization voltage of 70 eV. The ion source temperature was 250 °C, and the GC-MS transfer line was set to 280 °C.

Results and Discussion

The results of the antibacterial screening are shown in Table 1 and Figure 1. The crude methanolic extract inhibited against all the bacteria tested. This extract showed highest antibacterial activity against *S. aureus* with a diameter of inhibition zone (13 mm). This result indicates that *S. spirale* Roxb. is highly effective in suppressing the growth of *S. aureus* and other bateria tested. It seems to be a good choice for the development of new strategies to treat staphylococcal infections, including those caused by methicillin-resistant *S. aureus* and others.

Table 1: Antibacterial activity of methanolic extract of *S. spirale* Roxb.

Bacteria	Diameter of inhibition zone (mm)
Escherichia coli	10
Staphylococcus aureus	13
Pseudomonas aeruginosa	12

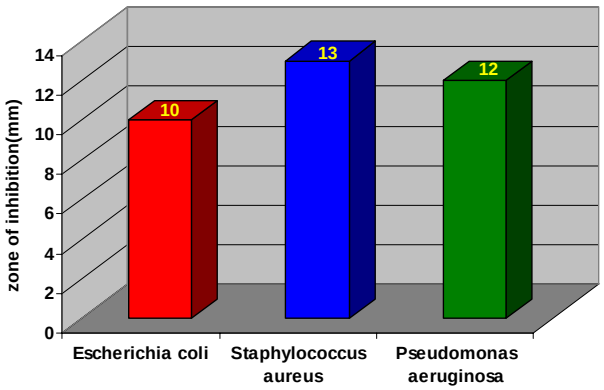

Figure 1. Antibacterial activity of methanolic extract of *S. spirale* Roxb

The antioxidant activity of methanolic extract of the ripe fruits of *S. spirale* Roxb. was investigated using DPPH method. The percentage inhibition of the methanolic extract at various concentrations are shown in Table 2. The plot of percentage remaining DPPH versus different concentrations of the extract is presented in Figure 2.

Table 2: Antioxidant activity assay of the ripe fruit of *S. spirale* Roxb.

Concentration of the extract (mg/ml)	% inhibition
0.1	12.97
0.2	14.24
0.6	19.17
1.0	26.83
2.0	40.74
4.0	76.79

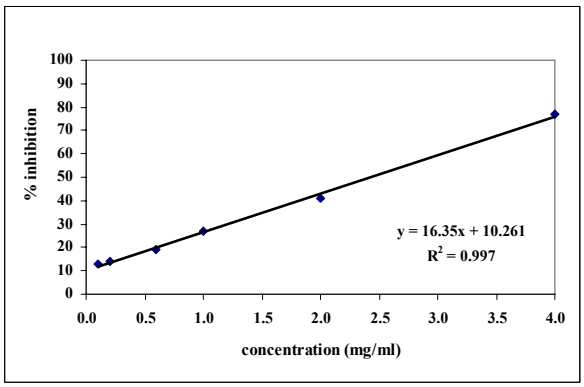

Figure 2. The plot of percentage inhibition of DPPH against concentrations of the extract

The methanol extract of the ripe fruits of *S. spirale* Roxb. possessed antioxidant activity with the IC_{50} of 2.43 mg/mL. The result from this study will be further investigated for the development of cosmetic and spa products for anti-aging.

The essential oil from *S. spirale* Roxb. was isolated by hydrodistillation and analyzed by gas chromatography-mass spectrometry (GC-MS). The content of essential oil was obtained in 0.0037 % yield as pale yellow liquid. Twenty-seven peaks were detected and the GC chromatogram of essential oil is shown in Figure 3.

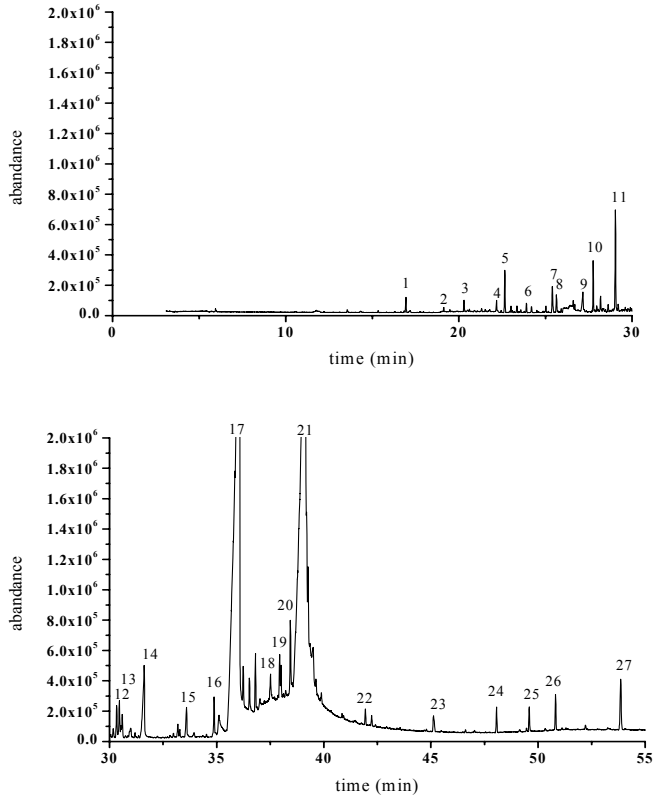

Figure 3. GC chromatogram of essential oil from *S. spirale* Roxb. obtained by GC-MS.

Lists of the essential oil were identified with their major ions from mass spectra. Compounds were identified by a comparison their mass spectra with the mass spectral data of the standard compounds in the WIELY and NIST literature data that yielded <90% matches were identified as unknowns and have not been included in Table 3. Eighteen components of the essential oil were identified and shown in Table 3.

Table 3: Structural assignments and EI-MS data obtained by capillary GC-MS of essential oil from *S. spirale* Roxb.

compound	*m/e* (% relative abundance)	peak
Hydrocarbons		
Beta.selinene	41 55 67 79 93 105(100) 121 133 147 161 175 189 204	7
Alpha.selinene	55 67 81 93 107 121 133 147 161 175 189(100) 204	8
Cyclohexane,1,5-diethenyl-3-methyl-2-methylene-,(1.alpha,3.alpha.,5.alpha.)-	41 53 67 79(100) 93 105 119 133 147 162	12
Patchoulane	39 55(100) 67 79 91 107 121 135 149 163 177 191 206	13
Pentacosane	41 57(100) 71 85 99 113 141 155 197 239 352	23
Eicosane	43 57(100) 71 85 99 113 169 282	24
Squalene	41 55 69(100) 81 95 137 191 231 341 410	25
Aldehydes and ketones		
2-butanone,4-(2,6,6,-trimethyl-1-cyclohexen-1-yl)-	43 55 67 79 93 105 121(100) 136 161 176 179 194	6
Carboxylic acids and esters		
Benzoic acid, 2-hydroxy-, methyl ester	50 53 65 81 92 93 120(100) 121 152	1
Dodecanoic acid	41 55 60 73(100) 85 97 101 115 129 143 157 171 200	9
Tetradecanoic acid	43 55 60 69 73(100) 85 97 115 129 143 171 185 199 228	14
Pentadecanoic acid	43 55 60 69 73(100) 83 97 115 129 143 157 171 180 185 199 213 242	15
Hexadecanoic acid, methyl ester	43 55 69 74(100) 87 143 185 227 239 270	16
hexadecanoic acid	43 55 60 73(100) 83 97 115 129 157 171 185 213 227 256	17
9,12-octadecadienoic acid (Z,Z)-, methyl ester	41 55 67(100) 81 95 109 150 178 263 294	18
9,12,15-octadecatrienoic acid, methyl ester (Z,Z,Z)-	55 67 79(100) 95 108 121 135 149 236 261 292	19
Linoleic acid	55 60 67 (100) 95 108 121 135 149 236 261 292	21
Aromatic compounds		
Trimethyl-tetrahydronaphthalene	65 91 105 117 131 144 159(100) 174	2

The oil was consisted of carboxylic acids and esters (50%) hydrocarbons (39%) aldehydes and ketones (5.5%) and aromatic hydrocarbons (5.5%). Results are shown in Figure 4.

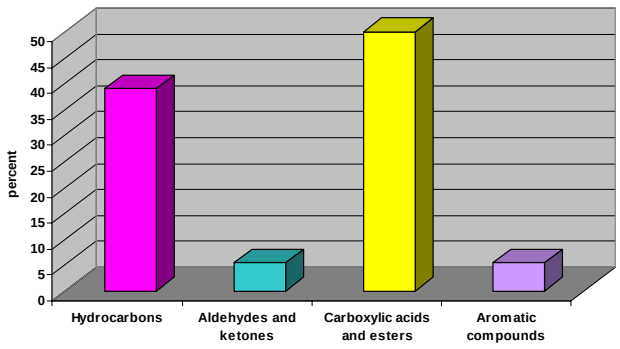

Figure 4. Volatile oil from the pulp of *S. spirale*.

The major compounds were linoleic acid (45.30%), hexadecanoic acid (40.75%) Tetradecanoic acid (2.13%) and 9,12-octadecadienoic acid (Z,Z)-, methyl ester (0.64%) . These compounds are reported for the first time in essential oil from the ripe fruits of *S. spirale* Roxb. Linoleic acid is a polyunsaturated fatty acid. It is abundant in many vegetable oils, especially safflower and sunflower oils. Linoleic acid has become increasingly popular in the beauty product industries because of its beneficial properties on the skin. Linoleic acid is effective properties when applied topically on the skin, i.e. acne reduction, moisture retention properties.[11,12]

Conclusions

From preliminary investigation, the results of the present study revealed that the methanolic extract of the ripe fruits of *S. spirale* Roxb. showed antibacterial and antioxidant activities. The essential oil, which was isolated by hydrodistillation from this plant, was analysed by GC and GC-MS. Linoleic acid which is the major component in *S. spirale* Roxb. might possibly plays an important role in drug development, health supplement and spa. Further chemical investigation is continuing undertaken using bioassay-directed isolation in order to determine bioactive compounds which are useful for new drug discovery. Since the plant showed significant antibacterial and antioxidant activities, it became necessary to expand the work so as to carry out chromatographic separation to isolate the active compounds and characterize their structure using UV, IR, Mass and NMR spectroscopic methods. In addition, toxicity assay is required to determine the safety level of the plant extract.

Acknowledgement

We would like to express their scincere thank to Department of Pharmaceutical Science, Faculty of pharmacy and the Graduate School, Chiang Mai University, Chiang Mai, Thailand for their partial support**.**

References

[1] K. Hu, A. Dong, Q. Sun and X. Yao, *Pharmaceutical Biology*, **39**(2001), pp 47-53.
[2] X.F. Teng, Y.J. Zhang, and C.R. Yang, *Acta Botanica Yunnanica.*, **30**(2008), pp. 239-242.
[3] P.P. Joy, J. Thomson, S. Mathew and B.P. Skaria, *Medical plants*, *Tropical Horticulture Vol. 2*.**,** Naya Prokash, Calcutta, 2001, pp 449-632.
[4] T. Ikeda, H. Tsumagari, T. Honbu and T. Nohara, *Biol. Pharm. Bull.*, **26**(2003), pp 1198-1201.
[5] Z.Y. Zhang, A.M. Lu and W.G. D′Arcy, *Flora of China*, Science Press, Beijing. **17**(1994), pp 300-302.
[6] L.T. Quyen, N.H. Khoi, N.N. Suong, K. Schreiber and H. Ripperger, *Planta Medica*, **52**(1987), pp 292-293.
[7] G.J. Bird, D.J. Collins, F.W. Eastwood and J.M. Swan, *Australian Journal of Chemistry*, **32**(1987), pp 597 609.
[8] E.W. Weiler, H. Krűger and M.H. Zenk, , *Planta Medica*, **39**(1980), pp 112-124.
[9] A. Rahman and M.I. Choudhary, *Nat. Prod. Rep*., **16**(1999), pp 619-635.
[10] H. Ripperger, *Phytochemistry*, **43**(1996), pp 705-707.
[11] C. Letawe, M. Boone, and G.E. Pierard, *Clinical & Experimental Dermatology* **, 23**(2)(1998), pp. 56–58.
[12] G.L. Darmstadt, G.L. Darmstadt, M. Mao-Qiang, E. Chi, S.K. Saha, V.A. Ziboh, R.E. Black, M. Santosham, and P.M. Elias, *Acta Paediatrica* **91** (5)(2002), pp. 546–550.

Antioxidant, antibacterial, antifungal and anticancer activities of *Ophiorrhiza aff. nutans.* Cl. *ex.* Hk. f.

N. Phoowiang[1], D. Santiarworn[1*], B. Liawruangrath[1], H. Takayama[2] and S. Liawruangrath[3]

[1]Departmement of Pharmaceutical Science, Faculty of Pharmacy, Chiang Mai University, Chiang Mai, Thailand 50200
[2]Department of Molecular Structure and Biological Function, Faculty of Pharmaceutical Sciences, Chiba University, Chiba, Japan
[3]Department of Chemistry, Faculty of Science, Chiang Mai University Thailand

[*]E-mail address: damrong@pharmacy.cmu.ac.th

Abstract: The antioxidant, antibacterial, antifungal and anticancer activities of the crude hexane, dichloromethane, ethyl acetate and n-butanol extracts of *Ophiorrhiza* aff. *nutans* Cl. *ex* Hk. f. were investigated. The antioxidant activity was evaluated by scavenging effect on 2,2´-diphenyl-1-picrylhydrazyl radicals (DPPH•) method. The antimicrobial activities were also determined by agar diffusion method. The cytoxicity and anticancer activity was determined by Sulforhodamine B (SRB) assay and Resazurin Microplate assay (REMA) method using African green monkey kidney (Vero) cells, small cell lung cancer, breast cancer and KB-Oral cavity cancer. All the crude extracts possessed antioxidant activities. The ethyl acetate extract showed the highest antioxidant capacity (IC_{50}=1.99 mg/mL). The crude hexane, dichloromethane, ethyl acetate and n-butanol extracts gave inhibition zone against *Pseudomonas aeruginosa*, *Staphylococcus aureus* and *Candida albicans*. All the crude extracts showed inhibition zones against *Trichophyton mentagophyte* except the crude n-butanol extract. Only the crude ethyl acetate extract gave inhibition zone against *Escherichia coli*. This extract also possessed anticancer activity.

Introduction

The genus *Ophiorrhiza* belongs to the family Rubiaceae, a small genus. Some species of *Ophiorrhiza* have been used in folk medicine as an antitussive, expectorant, analgesic, and for the treatment of amenorrhea and snakebite (Editorial Committee of the Flora of Taiwan, 1998). Members of this genus are well known for their production of alkaloids, in particular camptothecin derivatives and β -carbolines (Aimi *et al*., 1990; Kitajima *et al.*, 1997; Yamazaki *et al*., 2003). In order to discover new camptothecin-related alkaloids, investigations of the constituents of *Ophiorrhiza* plants that are distributed in Japan, that is, *Ophiorrhiza pumila* Champ., *Ophiorrhiza liukiuensis Hayata*, and *Ophiorrhiza japonica Bl.,* were carried out. As a result, it was found that *Ophiorrhiza pumila* produced camptothecin and its related alkaloids (Aimi *et al.*, 1989; Aimi *et al*., 1990; Aimi *et al*., 1992; Kitajima *et al*., 1997), whereas *Ophiorrhiza japonica* produced B-carboline-type alkaloids and no camptothecin-related alkaloids (Aimi *et al.*, 1985; Aimi *et al*., 1986). Another *Ophiorrhiza* plant, *Ophiorrhiza liukiuensis*, was found to produce both camptothecin-related alkaloids and β-carboline-type alkaloids (Kitajima *et al*., 2005). Recently the Camptothecin (Pizzolato and Saltz, 2003) was first isolated from *Camptotheca acuminate.* It is one of the most important alkaloids having inhibitory activities against tumor cells and HIV-I (Kitajima *et al*., 1997; Kitajima *et al*., 2002; kitajima *et al*., 2005). Recently, camptothecin derivatives such as topotecan® and irinotecan® were used as clinical antitumor agents (kitajima *et al.*, 1997; Kitajima *et al*., 2002; Yamazaki *et al*., 2003; Pizzolato and Saltz., 2003; Kitajima, 2007). In this research work, the bioactivity of each crude extract from *Ophiorrhiza* aff. *nutans* Cl. *ex* Hk.f. was investigated which may play an important role in drug development.

Material and Methods

Plant Materials

Whole dried plants of the *Ophiorrhiza* aff. *nutans* Cl. *ex* Hk. f. (Rubiaceae) family were collected from the Northern part of Thailand in Doitung Amphur Maephaloung, Chiang Rai Province during August to December 2007. Taxonomic identification of the collected plant was based on the specimen kept in Chiang Mai University (CMU) Herbarium, Biology department, Faculty of Science, Chiang Mai University, Chiang Mai, Thailand.

Chemical

2, 2´-diphenyl-1- picrylhydrazyl(DPPH•) and ascorbic acid were purchased from Sigma (St. Louis, USA). Trolox and quercetin were obtained from Aldrich (Milwaukee, USA). All the other chemicals and solvents used in this experiment were analytical grades.

A stock solution (5.0×10^{-4} mol L^{-1}) of DPPH• was prepared by dissolving the appropriate amount in ethanol. This solution was kept at 4 ˚C and protected from light. It was stable and can be used for a week. The DPPH• working solution containing 1.0×10^{-4} mol L^{-1} was prepared by measuring 50 mL of the stock solution. The volume was made up to 200 mL with ethanol. This working solution was prepared daily and protected from light. Ascorbic acid, Trolox and quercetin stock solutions were prepared by dissolving the appropriate amounts of the respective solids in

ethanol. Working standard solutions containing ascorbic acid, Trolox and quercetin in the concentration range of 0.5-5.0 μg mL^{-1} were prepared by dilution of the respective stock solution with ethanol.

Sample preparation

Whole plants of *Ophiorrhiza* aff. *nutans* Cl. *ex* Hk. f. were extracted with hot methanol by maceration. The combined methanolic extract was evaporated to dryness under reduced pressure which gave a crude extract. Afterword the crude methanol extract was dissolved in 5% sulfuric acid and partitioned by hexane and dichloromethane. Then the acid soluble extract was made alkaline to pH 10 by using ammonium hydroxide solution and partitioned by ethyl acetate and n-butanol respectively. After that each fraction was evaporated to dryness under reduced pressure which gave a crude extract.

Determination of antioxidant activity by Free Radical Scavenging Activity on 2, 2´-Diphenyl-1-picrylhydrazyl (DPPH•)

The test sample (20 μL) was added to 180 μL of 10 μM DPPH• solution in a 96-well microtiter plate. The reaction mixture was incubated at 37 °C for 30 min, and then the absorbance of each well was measured at 540 nm. The DPPH• solution was used as negative control. Trolox, ascorbic acid and quercetin were used as reference standards. For 50% inhibitory concentration (IC_{50}) evaluation of crude medicinal plant extracts, a graph showing concentration versus %DPPH• reduction was plotted (Thongchai *et al*., 2009). The IC_{50} was then calculated from the calibration curve and activity was expressed as percentage DPPH• scavenging relative to control using the following equation:

$$\text{DPPH}^{\bullet}\ \text{scavenging activity (\%)} = \frac{\text{Abs of control} - \text{Abs of sample}}{\text{Abs of control}} \times 100$$

Determination of antibacterial and antifungal activities

Antibacterial activity of the crude hexane, dichloromethane, ethyl acetate and n-butanol extracts was determined by the agar-well diffusion method (Musa *et al*., 2007). This extracts were diluted with ethanol and screened for antibacterial activity against *Escherichia coli* ATCC 25922, *Staphylococcus aureus* ATCC 25923 (Gram positive bacteria) and *Pseudomonas aeruginosa* ATCC 27853 (Gram negative bacteria) by using each concentrations of the extract. One hundred micro liters of sample solution were transferred to the well (9 mm in diameter) and the same volume of ethanol was used as a control. The inoculated plates were incubated for 24 hrs. After incubation, the diameter of the inhibition zone was measured. The measurements were done basically from the edge of the zone to the edge of the well. The antifungal activity of this crude medicinal plant extracts against yeast *Candida albican* and fungus *Aspergillus flavus* and *Trichophyton mentagrophyte*, which were also investigated using the procedure as described above.

Cytotoxicity and Anticancer studies

The cytotoxic effect of ethyl acetate extract of *Ophiorrhiza* aff. *nutans* Cl. *ex* Hk. f. was studied on normal African green monkey kidney (Vero) cells. The ethyl acetate extract was dissolved in dimethyl sulphoxide (DMSO) and the volume was made up to 10 mL with Dulbecco's Modified Eagle Medium (DMEM) to obtain 1 mg mL^{-1} concentration. Stock cells were cultured in minimum essential medium with 2% fetal calf serum supplemented with glutamine at 37 °C in an atmosphere of 5% CO_2 and 95% humidity. The medium was changed every 3 days. Monolayer cultures of Vero cells were trypsinzed and the cells were plated out at 6×103 cells/well in 96-well microtitre plate. The cell growth was found to be exponential during 2–3 days in the medium. The cultured cells were incubated with extracts of *Ophiorrhiza* aff. *nutans* Cl. *ex* Hk. f. at the concentrate rang 0-50 μg mL^{-1}. Control cells were incubated with DMSO (final concentration, 0.2%) at 37 °C, 5% CO_2, cell viability counts were made by sulforhodamine B assay (SRB) (Skehan *et al*., 1990). The percentage viability was calculated and plotted against concentration to get the IC_{50} values.

The anticancer activity of crude ethyl acetate extract against NCI-H187-Small cell lung cancer, MCF7-Breast cancer and KB-Oral cavity cancer were determined using the resazurin microplate assay (REMA) method (Brien *et al.,* 2000). Ellipticine and doxorubicin were used as positive controls. DMSO and sterile distilled water were used as negative controls. Cells at a logarithmic growth phase were harvested and diluted to105 cells/mL in fresh medium and gently mixed. Test compounds were diluted in culture medium in a ratio of 1:2 giving 8 concentrations. Five μL of the test sample and 45 μL of cells were put into 384-well microtiter plates with a total volume of 50 μL/well. Plates were incubated at 37 °C, 5% CO_2, for 72 hrs. for KB and MCF7 and 5 days for NCI-H187. After the incubation periods, 12.5 μL of resazurin solution was added to each well and the plates were incubated at 37 °C for 4 hrs. The plates were then processed for optical density absorbance analysis 538 using a Victor 3 Microplate reader at dual wavelengths of 530 and 590 nm.

Results and Discussion

Determination of antioxidant activity by Free Radical Scavenging Activity on 2,2´-Diphenyl-2-picrylhydrazyl (DPPH•)

The redical-scavenging activity on DPPH• was expressed as IC_{50}. This value was the concentration of the each crude extract of *Ophiorrhiza* aff. *nutans* Cl. *ex* Hk.f. required to inhibit 50% of the initial DPPH• free radical. The IC_{50} of all crude extracts are shown in Table 1.

Table 1: Antioxidant activities of crude extracts of *Ophiorrhiza* aff. *nutans* Cl. *ex* Hk. f. by DPPH$^{\bullet}$ assay.

Sample	IC_{50}(mg mL^{-1})
Crude extract of *O.* aff. *nutans* Cl. *ex* Hk. f.	
Hexane extract	5.17
Dichloromethane extract	3.36
Ethyl acetate extract	1.99
n-Butanol extract	2.35
Standard	
Ascorbic acid	0.05
Trolox	0.08
Quercetin	0.05

It is indicated that the ethyl acetate extract showed the highest antioxidant capacity (IC_{50} = 1.99 mg mL^{-1}), whereas the hexane extract showed the lowest antioxidant capacity (IC_{50} = 5.71 mg mL^{-1}) as shown in Table 1.

Table 2: Antimicrobial activities of each crude *Ophiorrhiza* aff. *nutans* Cl. *ex* Hk. f. extract compare with concentration of reference standard.

Sample	Inhibition activity (mg mL^{-1})			Inhibition activity (mg mL^{-1})		
	E. coli	***P.aeruginosa***	***S.aureus***	***C.albicans***	***A.flavas***	***T.mentagophyte***
Hexane Extract	0.0	10.0	30.0	30.0	0.0	30.0
Dichloromethane extract	0.0	30.0	30.0	30.0	0.0	30.0
Ethyl acetate extract	30.0	10.0	10.0	30.0	0.0	30.0
n-Butanol extract	0.0	10.0	30.0	30.0	0.0	0.0

Positive control of antibacterial=Gentamicin standard (75 µg mL^{-1})
Positive control of antifungal=Ketoconazole standard (250µg mL^{-1})
Minimum of inhibition zone= 11.00 mm.

The antibacterial activity of each crude extract of *Ophiorrhiza* aff. *nutans* Cl. *ex* Hk. f**.** were investigated by means of agar well diffusion method. The inhibition zones were measured. The crude ethyl acetate extract showed inhibition zone against all bacterias. But the crude hexane, dichloromethane and n-butanol extracts showed inhibition zones against *P. aeruginosa* and *S. aureus* but no activity against *E. coli* as shown in Table 2.

Antifungal activities studies

The antifungal activity of crude hexane, dichloromethane and ethyl acetate extracts gave inhibition zones against *C. albicans* and *T. mentagophyte* except *A. flavas.* But crude n-butanol extract showed only inhibition zone against *C. albicans* except *T. mentagophyte* and *A. flavas.* The results are presented in Table 2.

Table 3: Anticancer activity of crude ethyl acetate extract of *Ophiorrhiza* aff. *nutans* Cl. *ex* Hk. f.

Sample	Cytotoxicity against Vero cells IC_{50} (µg mL^{-1})	Anti cancer cell line IC_{50} (µg mL^{-1})		
		Small cell lung cancer	Breast cancer	KB-Oral Cavity cancer
Crude ethyl acetate extract	12.17	19.41	45.23	11.17

Cytotoxicity and anticancer activity studies

The cytotoxicity against normal Vero cell lines (African green monkey kidney) using standard SRB assay showed IC_{50} value of crude ethyl acetate extract 12.17 µg mL^{-1} against Vero cells. The anticancer activity of the crude ethyl acetate was investigated using NIC-H187-Small cell lung cancer, MCF7-Breast cancer and KB-Oral Cavity cancer. The crude extract showed activity against all of cell lines as follows: IC_{50} for KB-Oral Cavity cancer = 11.17 µg mL^{-1} for NCI-H187-Small cell lung cancer = 19.41 µg mL^{-1} and for MCF7-Breat cancer = 45.23 µg mL^{-1} respectively. Results are presented in Table 3.

Conclusions

The crude hexane, dichloromethane, ethyl acetate and n-butanol extracts of *Ophiorrhiza* aff. *nutans* Cl. *ex* Hk. f**.** possessed antioxidant activity. The ethyl acetate extract gave the highest antioxidant capacity (IC_{50}=1.99 mg mL^{-1}), whereas the hexane extract showed the lowest antioxidant capacity (IC_{50}=5.71 mg mL^{-1}). The crude hexane, dichloromethane, ethyl acetate and n-butanol extracts gave inhibition zones against *Pseudomonas aeruginosa*, *Staphylococcus aureus* and *Candida albicans*. The crude hexane, dichloromethane and ethyl acetate extracts showed inhibition zones against *Trichophyton mentagophyte* except the crude n-butanol extract. Only the crude ethyl acetate extract gave inhibition zone against *Escherichia coli*. This crude extract also showed cytotoxicity against vero cells and also inhibited against small cell lung cancer, breast cancer and KB-oral cavity cancer. Further studies on the crude extracts of *Ophiorrhiza* aff. *nutans* Cl. *ex* Hk. f. are required.

Acknowledgement

The authors are grateful for the Royal Forest Department of Doitung Mountain for support of plant. We also thank Mr. Banyong Khantawa, Microbiology Section, Central Laboratory, Maharaj Nakorn Chiang Mai Hospital, Chiang Mai, Thailand for kindly providing suggestions in the support microbiology laboratory. Considerably thanks go to then Ministry of University Affairs; Graduate School Chiang Mai

University and Faculty of Pharmacy, Chiang Mai University for partial support of this research work.

References

[1] N. Aimi, T. Tsuyuki, H. Murakami, S. Sakai and J. Haginiwa. Structure of Ophiorines A and B; novel type gluco indole alkaloids isolated from *Ophiorrhiza J.Tetrahedronletter.* 26(1985), pp.5299-5302.

[2] N. Aimi, H. Murakami, T. Tsuyuki, T. Nishiyama, S. Sakai and J. Haginiwa. Hydrolytic Degradation of β-Carbolin-type monoterpenoid glucoindole alkaloids: Apossible mechanism for Harman formation in *Ophiorrhiza* and related Rubiaceae plants. *J.Chem. Pharm. Bull*. 34(1986), pp. 3064 - 3066.

[3] N. Aimi, Nishimuram, A. Miwa, H. Hoshino, S. Sakai and J.Haginiwa. Pumiloside and deoxypumiloside; plausible intermediates of camptothecin biosynthesis. *J.Tetrahedron letters*. 30(1989), pp. 4991-4994.

[4] N. Aimi, H. Hoshino, M. Nishimura, S. Sakai and J. Haginiwa. Chaboside, first natural glycocamtothecin found from *Ophiorrhiza pumila*. *J. Tetrahedron Lett.* 31 (1990), pp. 5169-5172.

[5] N. Aimi, M. Ueno, H. Hoshino and S. Sakai. Synthesis and absolute configuration of chaboside, first natural glucocamptothecin. *J. Tetrahedron letter*. 33(1992), pp. 5403-5404.

[6] J.O. Brien, I. Wilson, T. Orton, and F. Pognan. Investigation of the alamar blue (resazurin) fluorescent dye for the assessment of mammalian cell cytotoxicity. *Eur. J.Biochem*. 267 (2000), pp. 5421-5426.

[7] F.Y. Lu, M.T. Kao, S.F. Huang and J.C. Wang. *Asclepiadaceae In: Editorial Committee of the Flora of Taiwan. Flora of Taiwan.* Vol. 4, 2nd ed (1998). Department of Botany, National Taiwan University, Taipei, pp.308.

[8] M. Kitajima, M. Nakamura, H. Takayama, K. Saito, J. Stöckigt and N. Aimi. Constituents of Regenerated Plants of *Ophiprrhiza pumila*; Formation of a New Glycocamptothecin and Predominant Formation of (*3R*) - Deoxypumiloside over (*3S*)-Congener. *J.Tetrahedron Lett*. 38(1997), pp. 8997-9000.

[9] M. Kitajima, S. Yoshida, K. Yamagata, M. Nakamura, H. Yakayama, K. Saito, H. Seki and N. Aimi. Camptothecin - related alkaloids from hairy roots of *Ophiorrhiza pumila. J. Tetrahedron letter*. 58(2002), pp. 9169-9178.

[10] M. Kitajima, N. Fujii, F. Yoshino, H. Sudo, K. Saito, N. Aimi and H. Takayama. Camptothecins and Two New Monoterpene Glucosides from *Ophiorrhiza liukiuensis*. *J.Chem.Pharm.Bull*. 53(2005), pp. 1355-1358.

[11] M. Kitajima. Chemical studies on monoterpenoid indole alkaloids from medicinal plant resources *Gelseminum* and *Ophiorrhiza*. *J.Nat Med*. 61 (2007), pp. 14-23.

[12] A. M. Musa, A.K. Haruna, I. Iliya and I. N. Akpul. Phytochemical and antimicrobial activity studies on *Indigofera pulchra*. *Int.Jor.P.App.Scs*. 1(2007), pp. 25-30.

[13] J.F. Pizzolato, L.B. Saltz. The camptothecin. *J.The Lancet*. 361 (2003), pp. 2235-2242.

[14] P. Skehan, R. Storeng, D. Seudiero, A. Monks, J. Mcmahon, D. Vistica, J. T. Warren, H. Bokesch, S. Kenny and M. R. Boyd. New colorimetric cytotoxic assay for anticancer drug screening. *J. National Cancer Institute*. 82 (1990), pp. 1107–1112.

[15] W. Thongchai, B., Liawruangrath and S. Liawruangrath. Flow injection analysis of curcuminoids content from turmeric and total antioxidant capacity using 2, 2-diphenyl-1-picrylhydrazyl assay. *Food Chemistry*. 112 (2009), pp. 494-499.

[16] Y. Yamazaki, A. Urano, H. Sudo, M. Kitajima, H. Takayama, M. Yamazaki, N. Aimi and K. Laito. Metabolite profiling of alkaloids and strictosidine synthase activity in camptothecin producing plants. *J.Phytochemistry*. 62 (2003), pp. 461-470.

Synthesis of oxazolidinones *via* acid-induced intramolecular cyclization

T. Chantra, M. Sukwattanasinitt and A. Ajavakom*

Organic Synthesis Research Unit, Department of Chemistry, Faculty of Science, Chulalongkorn University, Pathumwan, Bangkok, Thailand 10330

*E-mail: anawat77@hotmail.com

Abstract: Oxazolidinone is an important building block for chiral auxiliary and medicinal compounds. A novel synthetic approach for constructing a chiral oxazolidinone through acid-induced cyclization of arylepoxides has been investigated. Arylepoxides were synthesized from the alkylation of epichlorohydrin and arylcarbamates, which were readily prepared from the reaction between the corresponding arylamines and di-*tert*-butyl dicarbonate (Boc_2O). The acid induced cyclization of arylepoxides proceeded smoothly to give the desired *N*-aryloxazolidin-2-ones in excellent yields. Trifluoroacetic acid (TFA) was found to be superior to other acids such as acetic acid, $TiCl_4$, $AlCl_3$ and boron trifluoride diethyletherate ($BF_3{\cdot}OEt_2$) in cyclization step. This particular reaction can be conveniently applied to synthesis varieties of *N*-aryloxazolidin-2-ones.

Introduction

Oxazolidinone is a class of compound containing five memberd heterocyclic ring consisting of oxygen, carbonyl and nitrogen. They are useful as chiral auxiliaries in asymmetric synthesis [1-4]. One of the best known chiral auxiliaries of this class is Evans auxiliary used in enanyioselective Aldol reactions [5]. Some oxazolidinones also exhibit significant biological activities. Toloxatone (Humoryl) is an antidepressant and monoamine oxidase inhibitor (MAOI) activity [6]. Another major issue is the use of oxazolidinones as a new class of synthetic antibacterial drugs against gram-positive and anaerobic bacteria such as methicillin resistant *Staphylococcus aureus* (MRSA), methicillin resistant *Staphylococcus epidermitis* (MRSE) and Vancomycin resistant enterococci (VRE) [7-8]. Important examples are DuPont's compound DuP 721 [9-11], and the first commercial available oxazolidinone antibiotic, Linezolid (Zyvox®) [12-14]. Considerable attentions have thus been given to the synthesis of this class of compounds.

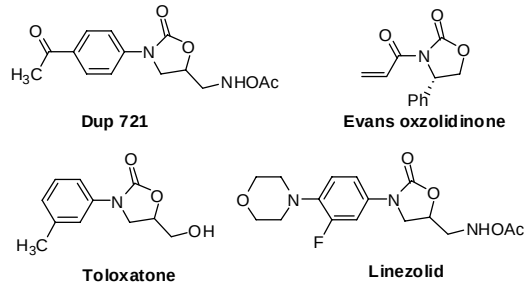

Figure 1. Oxazolidinone derivatives

In general, oxazolidin-2-ones derivatives can be synthesized from various compounds such as amino alcohol [15], isocyanate [16], β-lactam [17], alkynyl amide [18] and carbamate [19], aziridine [20-21] and epoxide [7, 22]. The epoxide is particularly of interest due to its possibility to be converted to oxazolidin-2-ones under either acid or basic condition. Several bases such as *n*-BuLi [7], and lithium hexamethyldisilazane (LiHMDS) [23] were used for epoxide ring opening and recycling to form oxazolidin-2-ones. In this proceeding, we would like to report the formation of oxazolidin-2-one from β-amidoepoxide under an acid conditions as an alternative effective method for synthesis of *N*-substituted aryloxazolidinones (Scheme 1).

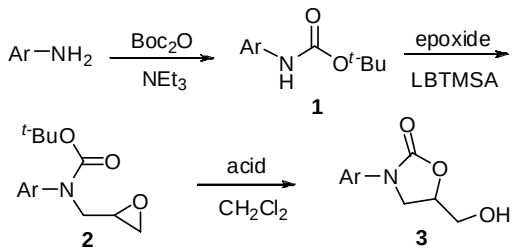

Scheme 1. Synthetic pathway of *N*-aryloxazolidin-2-one **3**

Materials and Methods

Aniline, 3-fluoroaniline, *m*-toluidine, 4-methoxy-aniline, di-*tert*-butyl dicarbonate and lithium bis(trimethylsilyl)amide were purchased from Aldrich (USA). Epichlorohydrin, trifluoracetic acid (TFA), boron trifluoride diethyletherate ($BF_3{\cdot}OEt_2$) and trichloride ($AlCl_3$) were purchased from Fluka (Switzerland). Acetic acid (CH_3COOH) and titanium(IV)chloride ($TiCl_4$) were purchased from Merck (Germany). Potassiumiodide was purchased from Riedel-de Haën. All other chemicals were reagent grade and used without additional purification unless state otherwise. Commercial-grade organic solvents were distilled prior to use. Column chromatography was performed using Merck silica gel 60 (70-230 mesh). ^1H and ^{13}C NMR spectra were recorded on a 400 MHz Varian Mercury NMR spectrometer using residual $CHCl_3$ as a reference at 7.26 ppm and 77.0 ppm, respectively.

Preparation of arylcarbamate (1a-1d): A mixture of arylamine (1 equiv.) and triethylamine (3

equiv.) in methanol (4 mL/mmol) was stirred. Di-*tert*-butyl dicarbonate (1.5 equiv.) was added into the mixture by a syringe. The mixture was stirred at ambient temperature under nitrogen atmosphere for 3 hours. The mixture was evaporated by a rotary evaporator to remove methanol and was then extracted with HCl solution (2 M) and dichloromethane. The combined organic layers were washed with brine, dried over anhydrous $MgSO_4$, filtered and evaporated *in vacuo.* The residue was eluted through a silica gel column by mixed solvent hexane/ethyl acetate (9:1).

***tert*-butyl phenylcarbamate (1a):** Aniline (2.00 mL, 2.10 mmol), was used as a starting amine to afford **1a** (400 mg, 94% yield). ^{1}H NMR (400 MHz, $CDCl_3$) δ (ppm): 7.35 (d, J = 8.0 Hz, 1H, Ar-H_{ortho}), 7.30 (m, 1H, Ar-H_{meta}) , 7.03 (t, J = 7.0 Hz, 1H, Ar-H_{para}), 6.45 (s, br, 1H, NH), 1.52 (s, 1H, CCH_3).

***tert*-butyl-3-fluorophenylcarbamate (1b):** 3-Fluoroaniline (1.00 g, 9.01mmol) was used as starting amine to afford **1b** (555 mg, 30% yield). ^{1}H NMR (400 MHz, $CDCl_3$) δ (ppm): 7.31 (d, J = 11.11 Hz, 1H, Ar-H_{ortho}), 7.21 (dd, J = 8.0, 15.0 Hz, 1H, Ar-H_{meta}), 6.97 (d, J = 8.0 Hz, 1H, Ar-H_{ortho}), 6.72 (dt, J = 2.0, 8.0, 8.0 Hz, 1H, Ar-H_{para}), 6.53 (s, 1H, NH), 1.52 (s, 9H, CCH_3).

***tert*-butyl-*m*-tolylcarbamate (1c):** *m*-Toluidine (0.500 mL, 4.67 mmol) was used as starting amine to afford **1c** (873 mg, 90% yield). ^{1}H NMR (400 MHz, $CDCl_3$) δ (ppm): 7.26 (s, 1H, Ar-H_{ortho}), 7.16 (t, J = 7.5 Hz, 1H, Ar-H_{ortho}), 7.09 (d, J = 8.0 Hz, 1H, Ar-H_{meta}), 6.85 (d, J = 7.5 Hz, 1H, Ar-H_{para}), 6.41 (s, 1H, NH), 2.32 (s, 3H, CH_3), 1.52 (s, 9H, CCH_3).

***tert*-butyl-4-methoxyphenylcarbamate (1d):** 4-Methoxyaniline (403 mg, 3.27 mmol) was used as starting amine to afford **1d** (737 mg, 97% yield). ^{1}H NMR (400 MHz, $CDCl_3$) δ (ppm): 7.26 (d, J = 8.0 Hz, 2H, Ar-H_{ortho}), 6.83 (d, J = 9.0 Hz, 2H, Ar-H_{mera}), 6.34 (s, 1H, NH), 3.78 (s, 3H, OCH_3), 1.51 (s, 9H, CCH_3).

Preparation of arylepoxide (2a-2d): A mixture of arylcarbamate **(1a-1d)** (1 equiv.), potassium iodide (3 equiv.), epichlorohydrin (3 equiv.) in *N,N'*-dimethyl formamide (DMF) (20 mL/mmol) was stirred. and lithium bis(trimethylsilyl)amide (LiHMDS) (2 equiv.) was added dropwise into the mixture by a syringe. The mixture was stirred at ambient temperature under nitrogen atmosphere for 18 hours. The reaction mixture was added with deionized water and extracted with ethyl acetate. The combined organic was washed with deionized water several times to remove DMF, dried over anhydrous $MgSO_4$, filtered and evaporated *in vacuo.* The residue was eluted through a silica gel column by mixed solvent hexane/ethyl acetate (9:1).

***tert*-butyl oxiran-2-ylmethyl(phenyl)carbamate (2a): 1a** (200 mg, 1.04 mmol) was used as a starting material to afford **2a** (210 mg, 81% yield). ^{1}H NMR (400 MHz, $CDCl_3$): δ (ppm) 7.40-7.20 (m, 5H, Ar-H), 3.87 (dd, J = 3.62, 14.5 Hz, 1H, NCH_2CH), 3.63 (dd, J = 5.48, 14.5 Hz, 1H, NCH_2CH), 3.24 (m, 1H, CH_2CHO), 2.79 (t, J = 4.5 Hz, 1H, CHCH_2O), 2.51 (dd, J = 2.5, 4.5 Hz, 1H, CHCH_2O), 1.44 (s, 9H, CCH_3).

***tert*-butyl-3-fluorophenyl(oxiran-2-ylmethyl)carbamate (2b): 1b** (103 mg, 0.486 mmol) was used as a starting material to afford **2b** (97.0 mg, 75% yield). ^{1}H NMR (400 MHz, $CDCl_3$) δ (ppm): 7.28 (m, 1H, Ar-H_{ortho}), 7.06 (m, 2H, Ar-H_{ortho}, Ar-H_{meta}), 6.91 (m, 1H, Ar-H_{para}), 3.94 (dd, J = 3.5, 14.5 Hz, 1H, NCH_2CH), 3.55 (dd, J = 5.5, 14.5 Hz, 1H, NCH_2CH), 3.24 (m, 1H, CH_2CHO), 2.82 (t, J = 4.5 Hz, 1H, CHCH_2O), 2.53 (dd, J = 2.5, 4.5 Hz, 1H, CHCH_2O), 1.46 (s, 1H, CCH_3).

***tert*-butyl oxiran-2-ylmethyl(*m*-tolyl)carbamate (2c): 1c** (200 mg, 0.965 mmol) was used as a starting material to afford **2c** (156 mg, 62% yield). ^{1}H NMR (400 MHz, $CDCl_3$) δ (ppm): 7.21 (t, J = 7.5 Hz, 1H, Ar-H_{ortho}), 7.10-7.00 (m, 3H, Ar-H_{ortho}, Ar-H_{meta},Ar-H_{para}), 3.83 (dd, J = 3.5, 14.5 Hz, 1H, NCH_2CH), 3.63 (dd, J = 5.5, 14.5 Hz, 1H, NCH_2CH), 3.23 (m, 1H, CH_2CHO), 2.79 (t, J = 4.5 Hz, 1H, CHCH_2O), 2.51 (dd, J = 2.5, 4.5 Hz, 1H, CHCH_2O), 2.34 (s, 3H, CCH_3), 1.45 (s, 9H, CCH_3).

***tert*-butyl 4-methoxyphenyl(oxiran-2-ylmethyl) carbamate (2d): 1d** (200 mg, 0.857 mmol) was used as a starting material to afford **2d** (181 mg, 76% yield). ^{1}H NMR (400 MHz, $CDCl_3$) δ (ppm): 7.15 (d, J = 5.5 Hz, 2H, Ar-H_{ortho}), 6.85 (d, J = 8.5 Hz, 2H, Ar-H_{meta}), 3.79 (m, 4H, OCH_3, NCH_2CH), 3.58 (dd, J = 4.5, 15.0 Hz, 1H, NCH_2CH), 3.21 (m, 1H, CH_2CHO), 2.78 (t, J = 4.5 Hz, 1H, CHCH_2O), 2.49 (dd, J = 2.5, 4.5 Hz, 1H, CHCH_2O), 1.42 (s, 1H, CCH_3).

Study of oxazolidinone formation by acid cyclization

The *tert*-butyl oxiran-2-ylmethyl(phenyl)carbamate **(2a)** (1 equiv.) in dichlorometane 20 mL was added with various acid (5 equiv.) (acetic acid (CH_3COOH), trifluoroacetic acid (TFA), boron trifluoride diethyletherate ($BF_3{\cdot}OEt_2$), titanium (IV) chloride ($TiCl_4$), or aluminium trichloride ($AlCl_3$) and then refluxed for 2 hours. The reaction mixture was quenched with aqueous solution of $NaHCO_3$ and extracted with dichloromethane. The combined organic were washed with brine, dried over anhydrous $MgSO_4$, filtered and evaporated *in vacuo.* The residuae was eluted through a silica gel column with mixed solvent hexane/ethyl acetate to give oxazolidinone derivatives.

5-(hydroxymethyl)-3-phenyloxazolidin-2-one (3a)): Use **2a** (209 mg, 0.822 mmol), TFA (0.315 mL, 4.11 mmol) to afford **3a** (146 mg, 92% yield). ^{1}H NMR (400 MHz, $CDCl_3$) δ (ppm): 7.55 (d, J = 8.5 Hz, 2H, Ar-H_{ortho}), 7.38 (t, J = 7.5 Hz, 2H, Ar-H_{meta}), 7.15 (dt, J = 1.0, 7.0, 7.0 Hz, 1H, Ar-H_{para}), 4.76 (m, 1H, CH_2CHO), 4.02 (m, 3H, NCH_2CH, CHCH_2OH), 3.77 (m, 1H, NCH_2CH), 2.14 (t, J = 6.5 Hz, 1H, OH).

From CH_3COOH: Use **2a** (161 mg, 0.648 mmol), CH_3COOH (0.200 mL, 3.49 mmol) to produce **3a** (28.8 mg, 23% yield).

From $BF_3{\cdot}OEt_2$: Use **2a** (210 mg, 0.844 mmol), $BF_3{\cdot}OEt_2$ (0.530 mL, 4.18 mmol) to produce **3a** (133 mg, 81% yield).

From $TiCl_4$: Use **2a** (112 mg, 0.450 mmol), $TiCl_4$ (0.25 mL, 2.27 mmol) to produce **3a** (71 mg, 82% yield).

From $AlCl_3$: Use **2a** (123 mg, 0.495 mmol), $AlCl_3$ (356 mg, 2.67 mmol) to produce **3a** (40.0 mg, 15% yield).

3-(3-fluorophenyl)-5-(hydroxymethyl)oxazolidin -2-one (3b): 2b (97.0 mg, 0.364 mmol) was used as a starting material to afford **3b** (71 mg, 93% yield). ^{1}H NMR (400 MHz, $CDCl_3$) δ (ppm): 7.44 (ddd, J = 2.0, 4.0, 11.0 Hz, 1H, Ar-H_{ortho}), 7.31 (m, 1H, Ar-H_{ortho}), 7.22 (d, J = 7.0 Hz, 1H, Ar-H_{meta}), 6.83 (m, 1H, Ar-H_{para}), 4.75 (m, 1H, CH_2CHO), 4.00 (m, 3H, NCH_2CH, $CHCH_2OH$), 3.75 (m, 1H, NCH_2CH), 2.73 (t, J = 6.0 Hz, 1H, O*H*).

5-(hydroxymethyl)-3-*m*-tolyloxazolidin-2-one (3c): 2c (68.0 mg, 0.258 mmol) was used as a starting material to afford **3c** (46.0 mg, 86% yield). ^{1}H NMR (400 MHz, $CDCl_3$): δ (ppm) 7.34 (s, 1H, Ar-H_{ortho}), 7.28 (d, J = 8.5 Hz, 1H, Ar-H_{ortho}), 7.22 (t, J = 7.5 Hz, 1H, Ar-H_{meta}), 6.93 (d, J = 7.0 Hz, 1H, Ar-H_{para}), 4.67 (m, 1H, CH_2CHO), 3.95 (m, 3H, NCH_2CH, $CHCH_2OH$), 3.73 (m, 1H, NCH_2CH), 2.44 (s, 1H, O*H*), 2.33 (s, 3H, CH_3).

5-(hydroxymethyl)-3-(4-methoxyphenyl)oxazolidin-2-one (3d): 2d (181 mg, 0.648 mmol) was used as a starting material to afford **3d** (109 mg, 76% yield). ^{1}H NMR (400 MHz, $CDCl_3$): δ (ppm) 7.44 (d, J = 8.0 Hz, 2H, Ar-H_{ortho}), 6.91 (d, J = 8.0 Hz, 2H, Ar-H_{meta}), 4.73 (m, 1H, CH_2CHO), 3.99 (m, 3H, NCH_2CH, $CHCH_2OH$), 3.77 (m, 4H, OCH_3, NCH_2CH), 2.19 (t, J = 5.5 Hz, 1H, O*H*).

Results and Discussion

The arylcarbamates **1** were generally obtained as the Boc protected compounds in excellent yield except for **1b** which was obtained relatively in poor yield (Table 1). The low yield is presumably due to the electron withdrawing fluoride which considerably decreased the nucleophilicity of the amino group. The arylepoxides **2** were prepared from the reaction of arylcarbamates **1** with epichlorohydrin in the presence of potassium iodide LiHMDS in DMF in satisfactory yields (Table 2).

Table 1: Synthesis of aryl carbamates **1**

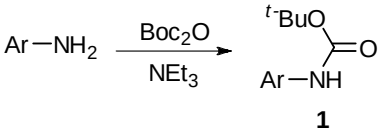

1

entry	Ar	product	yield[b]
1	C_6H_5	**1a**	94
2[a]	3-FC_6H_4	**1b**	30
3	3-$CH_3C_6H_4$	**1c**	90
4	4-$OMeC_6H_4$	**1d**	97

Conditions: arylamines (1 equiv), Boc_2O (1.5 equiv), NEt_3 (3 equiv) and MeOH, 3 h, rt.
[a]50 ℃ and overnight, [b] Isolated yield

The yield of the conversion of **2a** to oxazolidinones was optimized by using 5 equiv. of different acids, *i.e.* trifluoroacetic acid (TFA), acetic acid (CH_3COOH), boron trifluoride diethyletherate ($BF_3{\cdot}OEt_2$), titanium (IV) chloride ($TiCl_4$), and aluminium trichloride ($AlCl_3$), under reflux for 3 hours.

The corresponding oxazolidinone **3a** was obtained in high yields (Table 3) under the default conditions

Table 2: Synthesis of arylepoxide **2**

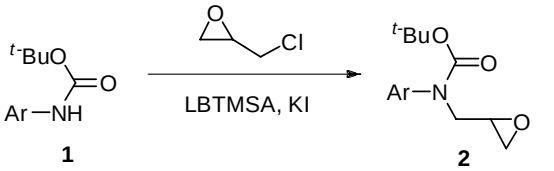

1 **2**

entry	Ar	product	Yield[a]
1	C_6H_5	**2a**	81
2	3-FC_6H_4	**2b**	75
3	3-$CH_3C_6H_4$	**2c**	62
4	4-$OMeC_6H_4$	**2d**	76

Conditions: arylcarbamate (1 equiv), LiHMDS (2 equiv), KI (3 equiv), DMF, 18 h, rt.
[a]Isolated yield

when strong acid ($BF_3{\cdot}OEt_2$, TFA and $TiCl_4$) was used. When relatively weaker acid (CH_3COOH and $AlCl_3$) was used, the reactions resulted in poor yields. The reaction induced by CH_3COOH was not completed under the condition and time allowed and the starting material was remained in the reaction mixture. However the longer reflux time did not significantly increase the yield. In the case of $AlCl_3$, long reflux time led to a complex unidentified mixture. According to the optimization results, TFA is the reagent of choice as it gives the highest yield, its ease of handling and relatively low cost.

Table 3: Optimization of acid induced oxazolidinone formation of arylepoxide

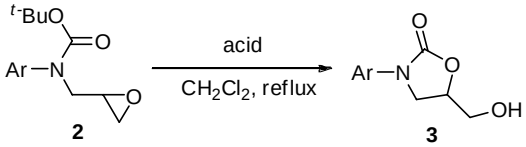

2 **3**

Entry	Ar	acid[a]	product	yield[b]
1	C_6H_5	$BF_3{\cdot}OEt_2$	**3a**	81
		$TiCl_4$		82
		$AlCl_3$		15
		TFA		92
		CH_3COOH		23
2	3-FC_6H_4	TFA	**3b**	93
3	3-$CH_3C_6H_4$	TFA	**3c**	86
4	4-$OMeC_6H_4$	TFA	**3d**	76

Conditions: arylepoxides (1 equiv.), acid (5 equiv.), CH_2Cl_2 , 2 h, reflux.
[a]Using 5 equiv. of acid, [b] isolated yield

Notably, TFA is commonly used for the deprotection of Boc group. However, in this particular β-(*N*-arylcarbamyl)epoxides substrates the Boc carbonyl oxygen intramolecularly attacks the epoxide ring in *5-exo-tet* fashion to give the oxazolidin-2-one derivatives.

It is also important to point out here that compound **3c** which is Toloxatone, a well known antidepressant and monoamine oxidase inhibitor (MAOI), was produced from **2c** in 86 %yield [6].

Conclusions

In conclusion, the TFA induced ring-opening/ring reclosure of β-(*N*-arylcarbamyl)epoxides provides a general and efficient route to *N*-substituted aryloxazolidin-2-ones under mild conditions in excellent yields. The method can be used for the economical synthesis of Toloxatone.

Acknowledgement

The authors gratefully acknowledge scholarship from TRF-Master Research Grants, The 90th Aniversary of Chulalongkorn University Fund (Ratchadaphiseksomphot Endowment Fund), ADB scholarship, and 100th year department of chemistry for financial support.

References

[1] L. M. Geary, P, G. Hultin, *Tetrahedron: Asymmetry*. **20** (2009), pp. 131–173.
[2] W. Adam, S. G. Bosio, and N. J. Turro. *J. Am. Chem. Soc.* **124** (2002), pp. 8814-8815.
[3] J W. Adam, S. G. Bosio, and N. J. Turro. *J. Am. Chem. Soc.* **124** (2002), pp. 14004-14005.
[4] J. E. Hein, L. M. Geary, A. A. Jaworski, and P. G.Hultin. *J. Org. Chem.* **70** (2005), pp. 9940-9946.
[5] G. Li, X. Xu, D. Chen, C. Timmons, M. D. Carducci, and A. D. Headley. *Org. Lett*. **5** (2003), pp. 329-331.
[6] Berlin, R. Zimmer, H. M. Thiede, *et al. British journal of clinical pharmacology.* **30** (1990), pp. 805-16.
[7] S. J. Brickner, D. K. Hutchinson, M. R. Barbachyn, P. R. Manninen, D. A. Ulanowicz, S. A. Garmon, K. C. Grega, S. K. Hendges, D. S. Toops, C. W. Ford, and G. E. Zurenko. *J. Med. Chem.* **39** (1996), pp. 673-679.
[8] J. V. N. Vara Prasad et al. *J. Med. Chem.* **50** (2007), pp. 5886-5889.
[9] A. M. Slee, M. A. Wunonola, R. J. McRipley, I. Zajac, M. J. Zawada, P. T. Bartholomew, W. A. Gregory, M.Forbes. *Antimicrob. Agents Chemother.* **31** (1987), pp. 1791.
[10] C-L. J. Wang, W. A. Gregory, M. A. Wuonola. *Tetrahedron.* **45** (1989), pp. 1323.
[11] C-H. Park, D. R. Brittelli, C. L-J. Wang, F. D. Marsh, W. A. Gregory, M. A. Wuonola, R. J. McRipley, V. S. Eberly, A. M. Slee, M. Forbes.*J. Med. Chem.* **35** (1992), pp. 1156.
[12] S. J. Brickner, M. R. Barbachyn, D. K. Hutchinson, and P. R. Manninen. *J. Med. Chem.* **51** (2008), pp. 1981-1990.
[13] S. J. Brickner. U. S. Patent 5, 231, 188, Jul 27, **1993**.
[14] S. J. Brickner. U. S. Patent 5, 247, 090, Sep 21, **1993**.
[15] D. J. Ager, I. Prakash, D. R. Schaad. *Chem. Rev*. **96** (1996), pp. 835–875.
[16] H. P. Buchstaller, *J. Comb. Chem.* **5** (2003), pp. 789-793.
[17] R. K. Mishra, C. M. Coates, K. D. Revell, and E. Turos. *Org. Lett*. **9** (2007), pp. 575-578.
[18] R. R-M. J. Adrio, and J. C. Carretero. *J. Org. Chem.* **71** (2006), pp. 5023-5026.
[19] W. R. Perrault, B. A. Pearlman, D. B. Godrej, A. Jeganathan, K. Yamagata, J. J. Chen, C. V. Lu, P. M. Herrinton, R. C. Gadwood, L. Chan, M. A. Lyster, M. T. Maloney, J. A. Moeslein, M. L. Greene, and M. R. Barbachyn. *Organic Process Research & Development.* **7** (2003), pp. 533-546.
[20] C. S. Park, M. S. Kim, T. B. Sim, D. K. Pyun, C. H. Lee, D. Choi, and W. K. Lee. *J. Org. Chem.* **68** (2003), pp. 43-49.
[21] R. M. Ramallal, R.Liz, and V. Gotor. *Org. Lett.* **9** (2007), pp. 575-578.
[22] G. Madhusudhan, G. O. Reddy, T. Rajesh, J. Ramanatham, P. K. Dubey. *Tetrahedron Lett*. **49** (2008), pp. 3060–3062.
[23] D. M. Gleave, and S. J. Brickner. *J. Org. Chem.***61** (1996), pp. 6470-6474.

Antioxidant antimicrobial activities and phenolic content of the extracts and chemical components of volatial oil from *Spondias pinnata* Kurz.

S. Keawsaard[1]* K. Pholsongkram[1]and S. Kongtaweelert[2]

[1]Faculty of Science, Payap University, Amphur Muang, Chiang Mai, Thailand 50000

[2]Faculty of Science King Mongkut's Institute of Technology Ladkrabung, Thailand 10520

*E-mail:sukanya_k40@hotmail.com

Abstract: The aim of this study was to investigate antioxidant antimicrobial activities and phenolic content of crude extracts from *Spondias pinnata* Kurz. The pulp of this plant were extracted with methanol and acetone. The extracts were concentrated under vacuum to yield yellow-brown crude residue. The antioxidant activity of the crude extracts were determined by scavenging effect on 2,2-diphenyl-1-picrylhydrazyl (DPPH) radical scavenging assay. The results showed that the methanol extract had the highest antioxidant activity with IC_{50} = 0.291 mg/mL. Total phenolic contents from methanol and acetone extracts were determined by Folin-Ciocalteu reagent method. The result showed that the total phenolic compounds contents of *S. pinnata* as gallic acid equivalents were found to be higher in methanol extract (80.45mg/g) than acetone extract (70.83mg/g). The antifungal activity of the extracts were against *Candida albican*, *Trichophyton mentagrophyte* and *Aspergillus flavus* by a disc diffusion method. The methanol extract showed the highest antifungal activity against *T. mentagrophyt*. The methanol and acetone extracts also showed antibacterial activity against *Escherichia coli*, *Staphylococcus aureus* and *Pseudomonas aeruginosa*. The methanol extract showed the highest antibacterial activity against *S. aureus*. The volatile components obtained by hydrodistillation of the pulp of this plant were analyzed by gas chromatography-mass spectrometry (GC-MS). The content of volatile oil was 0.0011%. A total of Thirty-four peaks were detected and twenty compounds were identified. The major compounds were 9,12,15-octadecatrien-1-ol (36.78%) hexadecanoic acid (25.27%) and furfural (19.77%). The antimicrobial activity of the volatile oil were studied. The oil also showed the highest antifungal activity against *T. mentagrophyt* and the highest antibacterial activity against *S. aureus*.

Introduction

Spondias pinnata Kurz or Makok is a genus of flowering plants of the family Anacardiaceae. It is a deciduous tree distributed in India, Sri Lanka and South-East Asian countries. [1] *S. pinnata* is a medical plant for several purposes in many East and Southest Asia countries. The stem barks are used in folk medicine in the treatment of antidiarrhoea , dysentery, rheumatism, gonorrhea and anti-tubercular. Barks are considered to be an anti-inflammatory, anthelmintic and antibacterial activities, fresh fruits eaten as a food and it promote the menses and dried fruits used as anti-tumour. [2,3] The methanolic extract of *S. pinnata* bark, which contains large amounts of flavonoids and phenolic compounds, exhibits high antioxidant and free radical scavenging activities.[4-6]

According to our information, the pulp of *Spondias pinnata* Kurz. has not been standardised and investigated for antioxdant and biological activity.

The purpose of this study was to investigate standardized methanol and acetone extracts of the pulp of *S. pinnata* Kurz. for phenolic contents, antioxidant, antibacterial and antifungal activities. In addition, this work was carried out to determine the the chemical constituents of essential oil from the pulp of this plant and their biological activity.

Materials and Methods

Materials

S. pinnata Kurz. specimens were purchased from Muangmai market, Chiang Mai Province, Thailand in November 2007. A voucher specimen of this plant was deposited at the Herbarium of Faculty of Pharmacy, Chiang Mai University, Chiang Mai, Thailand.

Extraction

The pulp of the plant was grinned and extracted with methanol and acetone. The extracts were dried under reduced pressure to yield a yellow-brown crude residue. The percentage yield of the methanol and acetone were 7.7 and 10.3.

Antioxidation activity Assay

6.6 mg/mL, DPPH in ethanol was prepared and stored in the dark before use. Various concentrations of the crude extracts were prepared using ethanol as solvent. 180 μL ethanolic solution of DPPH was mixed with 20 μL of test samples in a 96-well microtiter plate. After 30 min, the absorbance was measured at 540 nm. This experiment was carried out for concentration of sample that is 0.04, 0.06, 0.08, 0.10, 0.20, and 0.50 mg/mL. The DPPH solution was used as control. The percentage inhibition of DPPH was determined by calculation as follows:

$$\text{DPPH scavenging activity (\%)} = \frac{Ac - As}{Ac} \times 100$$

where 'Ac' is absorbance of the control and 'As' is the absorbance of the test sample after 30 min.

From the result obtained a plot of percentage inhibition of DPPH against concentration and the IC_{50} determined.

Estimation of phenolic contents

Total polyphenolic contents were determined by by Folin-Ciocalteu reagent method. The working solutions of the methanol and acetone extracts were prepared in a concentration of 0.12 mg/mL. The sample solution (1 mL) was mixed with 4 mL of Folin-Ciocalteu reagent thoroughly. After mixing for 8 min, 4 mL of 7.5% Na_2CO_3 was added and the mixture was allowed to stand for 2 h in dark. The absorbance was measured at 760 nm against a blank prepared in the same way except for the sample, and concentration of total polyphenolic contents was determined as mg of gallic acid equivalents by using equation obtained from gallic acid calibration curve. Concentrations of standard gallic acid in methanol were 0.02, 0.04, 0.06, 0.08, and 0.10 mg/mL. Linear regression equation ($Y = 5.2X-0.012$, $R^2=0.9959$).

Antimicrobial Activity test

The determination of antibacterial activity of crude methanol and acetone extracts by a disc diffusion method. This extracts were diluted with ethanol and screened for antibacterial activity against *Escherichia coli*, *Staphylococcus aureus* and *Pseudomonas aeruginosa* by using 35 mg/ml concentrations of the extract. 100 microliters of solution was transferred to a 9 mm disk. The sample disk was placed on the microbe spread medium plate and then incubated at 37 ^{0}C for 24 h. After incubation, the diameter of inhibition zone was measured and reported in the scale of millimeter.The antifungal activity of this curde extracts against yeast *Candida albican* and fungus *Aspergillus flavus* and *Trichophyton mentagrophyte* were also investigated using the procedure as described above.

Determination of Chemical Constituents

Pulp of this plant (1990g) and 3 liter of water were subjected to hydrodistillation in Clevenger-type apparatus for 8 hours. The oil was separated and analyzed by capillary GC-MS. The essential oil was analysed on a Hewlett-Packard 6890 series on a HP-5 capillary column. It was 30 m x 0.32 mm id. with a 0.25 µm film thickness. The temperature of the HP-5 column was programmed starting at 50 °C and held for 5 min., the temperature was increased at a rate of 10°C/min from 50 to 280 °C and held there for 5 min. Helium gas was used as the GC carrier gas. The GC injector was in a split mode with a splitless. The injector temperature was set at 250 °C. The effluent from the capillary column went directly into the mass spectrometer and operated in the electron impact (EI) mode with an ionization voltage of 70 eV. The ion source temperature was 250 °C, and the GC-MS transfer line was set to 280 °C.

Results and Discussion

The results of Table 1 show the percentage inhibition of the extracts at various concentrations.

Table 1: Percentage inhibition of methanol and acetone extracts of *S. Pinnata*.

Concentration of the extract (mg/ml)	% inhibition of methanol extract	% inhibition of acetone extract
0.04	12.85	12.15
0.06	15.39	14.27
0.08	18.54	15.36
0.10	22.56	19.76
0.20	40.17	31.09
0.50	79.20	65.15

The methanol and acetone extracts have exhibited different antioxidant activity. The result obtained a plot of percentage inhibition of DPPH against concentration and the concentration of the ethanol and actone extracts that causes 50% inhibition of DPPH (IC_{50}) were determined to be 0.291 and 0.368 mg/mL, respectively. The methanol extract have the highest antioxidant activity.

The total contents of phenolics in the methanol and acetone extract of *S. Pinnata*. that were measured by Folin-Ciocalteu reagent method. The result showed that the total phenolic compounds contents of *S. pinnata* as gallic acid equivalents were found to be higher in methanol extract (80.45mg/g) than acetone extract (70.83mg/g).

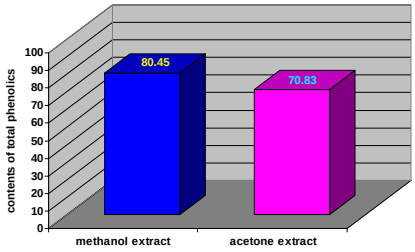

Figure 1. Total phenolic content in the methanol and acetone extract of the pulp of *S. Pinnata*.

As seen in Figure 1, the contents of total phenolics in methanol extract was higher than amounts found in acetone extract. The methanol extract has exhibited better antioxidant activity as compared to the acetone extract.. The contents of the phenolic derivatives in methanol extract was differed from those in actone extract such as a higher of number of OH group and has led to the result in higher antioxidant activity. *S. pinnata* Kurz. possessed antioxidant activity. The result from this study will be further investigated for the development of cosmetic and spa products for anti-aging.

The results of antimicrobial activity of the methanol and acetone extracts by a disc diffusion method are shown in Table 2 and Figure 2.

Table 2: Antimicrobial activity of the extracts and essntial oil of *S. Pinnata*.

Microorganism	Zone of inhibition (mm)		
	methanol extract	acetone extract	volatile oil
Escherichia coli	11.0	11.5	10
Staphylococcus aureus	20.0	19.0	14
Pseudomonas aeruginosa	12.0	12.5	10
Candida albican	11.0	13.0	11.0
Aspergillus flavus	11.0	12.0	12.0
Trichophyton mentagrophyte	19.5	19.0	21.0

The methanol extract was active against all the bacteria tested with *S. aureus* having the highest diameter of inhibition zone, while the lowest is shown by *E. coli*. The methanol extract showed antifungal activity against all the fungi tested and the highest antifungal activity against *T. mentagrophyt*. The acetone extract shown the highest antibacterial activity against *S. Aureus* and the highest antifungal activity against *T. mentagrophyt*.

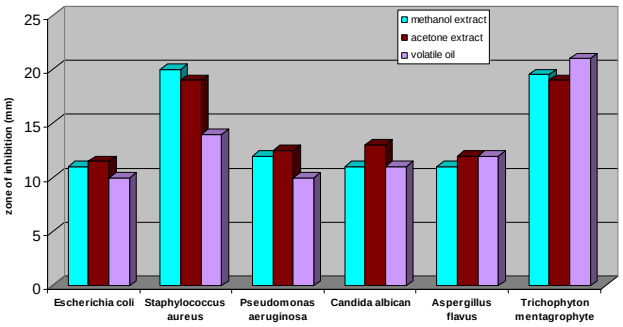

Figure 2. Antimicrobial activity of the extracts and essntial oil of *S. Pinnata*

The volatile components obtained by hydrodistillation of the pulp of this plant were analyzed by GC-MS. The yield of *S. Pinnata*. Essential oil was 0.0037%. Thirty-four peaks were detected. Identification of essential oil constituents was performed by a comparison their mass spectra with the mass spectral data of the standard compounds in the WIELY and NIST liberature data that yielded <90% matches were identified as unknowns and have not been included in Table 3. Twenty components of the essential oil were identified and shown in Table 3.

Table 3: Chemical components of valatile oil of *S. Pinnata.* were analyzed by GC-MS.

Chemical components	*T_R	Contents (%)
furfural	4.94	19.77
cis-3-hexenol	5.68	0.80
cis-6-methyl-2-(oxiran-2-yl) hept-5-en-2-ol	13.05	0.99
trans-6-methyl-2-(oxiran-2-yl) hept-5-en-2-ol	13.58	0.56
ethylbenzoate	16.19	1.17
methyl-2-hydroxybenzoate	16.92	0.36
1-methyl-4-propan-2-ylcyclohexa-1,3-diene	17.04	0.27
ethyldecanoate	22.48	0.10
ethyl-3-phenylpropenoate	24.34	0.13
4,7-dimethyl-1-propan-2-yl-1,2,3,5,6,8a-hexahydronaphthalene	25.66	0.08
(1S,4aR,8aR)-4,7-dimethyl-1-(propan-2-yl)-1,2,4a,5,6,8a-hexahydronaphthalene	26.15	0.07
tetradecanoic acid	31.27	0.30
ethyltetradecanoate	31.65	0.14
7,11,15-trimethyl-3-methylidenehexadec-1-ene	32.53	0.21
6,10,14-trimethyl-2-pentadecanone	32.68	0.33
methyl-14-methylpentadecanoate	34.40	0.49
hexadecanoic acid	35.58	25.27
ethylhexadecanoate	35.64	7.37
methyl (Z)-octadec-9-enoate	37.59	0.40
9,12,15-octadecatrien-1-ol	38.81	36.78

*T_R = retention time

The volatile oil was found to cantain hydrocarbons (10%) alcohols (20%) aldehydes and ketones (10%) carboxylic acids and esters (40%) and aromatic hydrocarbons (20%). Results shown in Figure 3

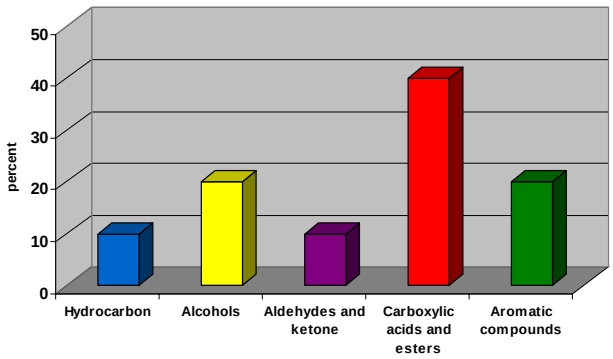

Figure 3. Volatile oil from the pulp of *S. Pinnata*.

The antibacterial and antifungal activities of volatial oil were also investigated using the procedure as described above. The results are shown in Table 3. The volatial oil shown the highest antibacterial activity against *S. aureus* and the highest antifungal activity against *T. mentagrophyt*.

Thus, *S. pinnata* Kurz. may play an important role in drug development and health supplement. Further chemical investigation is continuing undertaken using bioassay-directed isolation in order to determine bioactive compounds which are useful for new drug discovery.

Conclusions

The result report in this study may be considered as the preliminary report on the *in vitro* antibacterial and antifungal and antioxidant activities of *S. pinnata* Kurz.

Since the plant showed significant antimicrobial and antioxidant activities, it became necessary to expand the work so as to carry out chromatographic separation to isolate the active compounds and characterize their structure using UV, IR, Mass and NMR spectroscopic methods.

Acknowledgement

This research was supported by the research fund from Payap University, Chiang Mai, Thailand.

References

[1] B. Hazra, S. Biswas and N. Mandal, *BMC Complementary and Alternative Medicine,* **8** (2008).
[2] S. Hout, A. Chea, S. Bun, R. Elias, M. Gasquet, P.Timon-David, G. Balansard, and N. Azas, *Journal of Ethnopharmacology,* **107** (2006), pp 12–18.
[3] B. K. Panda, V. J. Patra, U. S. Mishra, S. Kar1, B.R.Panda, M.R.Hati, *Journal of Pharmacy Research,* **2**(5), (2009), pp. 825-827.
[4] P.A. Meléndez and V.A. Capriles, *Phytomedicine*, **13** (2006), pp 272–276.
[5] P. Maisuthisakul, S. Pasukb, and P. Ritthiruangdej, *Journal of Food Composition* and *Analysis* , **21** (2008), pp 229–240.
[6] P. Maisuthisakul, M. Suttajit, R. Pongsawatmanit, *Food Chemistry*, **100** (2007), pp 1409–1418.

Antimicrobial activities of various medicinal plant extracts in family Euphorbiaceae

D. Sanseera[1*], W. Niwatananun[1], B. Liawruangrath[1], S. Liawruangrath[2]
A. Baramee[2] and S. G. Pyne[3]

[1] Faculty of Pharmacy, Chiangmai University, Chiangmai, Thailand 50200
[2] Facultty of Science, Department of Chemistry, Chiangmai University, Chiangmai, Thailand 50200
[3] Department of Chemistry, University of Wollongong, Wollongong, Australia, NSW 2522

*Email: vanhappy@live.com, vanmeechai@yahoo.co.th

Abstract: The antibacterial activity of the hexane, chloroform and methanol extracts of three medicinal plants; *Acalypha indica* Linn., *Cleidion spiciflorum* Merr. and *Bridelia retusa* (L.) A. Juss. were studied. The extracts of these plants were tested *in vitro* against three bacteria : *Staphylococcus aureus* (ATCC25923), *Escherichia coli* (ATCC25922) and *Pseudomonas aeruginosa* (ATCC27553). The antifungal activity of these plant extracts were also investigated. The fungi employed were *Aspergillus flavus*, *Candida albican* and *Trichophyton mentagrophyte*. The agar diffusion method was used to screen both antibacterial and antifungal activities. The results indicated that the hexane, chloroform and methanol extracts of *A. indica* Linn. aerial part showed antibacterial activity against *S. aureus* and *P. aeruginosa*, but no activity against *E. coli*. Only methanolic extract of *C. spiciflorum* Merr. leaves exhibited antibacterial activity against *S. aureus*, *E. coli* and *P. aeruginosa,* respectively. However, the methanolic extract of the stems possed antibacterial activity against *S. aureus.* The chloroform extract of *B. retusa* (L.) A. Juss. fruits showed inhibition zones against *S. aureus*, *E. coli* and *P. aeruginosa*, but the methanolic extract showed antibacterial activity against *S. aureus* and *P. aeruginosa*. The methanolic extracts of *B. retusa* (L.) A. Juss. leaves and stems exhibited antibacterial activity against *S. aureus*, only the methanolic extract of the leaves showed inhibition zone against *P. aeruginosa*. The hexane, chloroform and methanol extracts of *A. indica* Linn. aerial parts showed antifungal activity against *T. mentagrophyte*, but the chloroform and methanol extracts showed inhibition zones against *A. flavus* and *C. albican* respectively. The methanolic extracts of *C. spiciflorum* Merr. stems, *B. retusa* (L.) A. Juss. leaves and stems exhibited antifungal activity against *T. mentagrophyte.* The hexane, chloroform and methanol extracts of *B. retusa* (L.) A. Juss. fruits showed antifungal activity against *C. albican*. The most active antimicrobial plant was *A. indica* Linn.

Introduction

Many plants in family Euphorbiaceae comprises about 300 genera and 5000 species distributed mainly in America and tropical Africa [1]. Some plants in family Euphorbiaceae are used in folk medicine to treat skin diseases, gonorrhoea, migraines, intestinal parasites and warts [2]. *Acalypha indica* Linn. (Thai name : Tam Yae Maeo) is a member of the family Euphorbiaceae. It is a weed. Different parts of the plants have been used traditionally for the treatment of many diseases. Fruits are used in asthma, cough, bronchitis and earache. The whole plant is used as an expectorant, laxative, diuretic, pneumonia and rheumatism. The leaves are used in skin diseases like scabies [3]. The petroleum ether extract of *A. indica* Linn. showed antimicrobial activity against *Aeromonas hydrophilla* and *Pseudomonas aeruginosa* [4], *Aspergillus niger* and *Escherichia coli* [5]. *Cleidion spiciflorum* Merr. (Thai name: Deemee) is a large shrub found in forests at low and medium altitudes from India to New Guinea [6]. In the Philippines, decoction of its leaves is reputed to cause abortion, whereas a decoction of the bark is given internally as stomachic. Its seeds were reported as an effective treatment for constipation [7]. Its stem has been employed as an analgesic, antipyretic and diaphoretic [8]. *Bridelia retusa* (L.) A.Juss. (Thai name : Tengnam) is a tree up to 10-20 m high. It is found in dry evergreen and deciduous forest and open land, e.g. India, Sikkim, Bhutan, Sri Lanka, Myanmar, Indochina, China, Thailand, Malay Peninsula and Sumatra [9]. It is used as traditional medicine in India, such as treatment of skin disease [10]. Eight compounds were isolated from the stem bark of *B. retusa.* They showed antifungal activity against *Cladosporium cladosporioides* [11]. In recent years, medicinal plants have been extensively investigated as a source of medicinal agents [12].Thus, it is anticipated that antimicrobial efficacy will be used for the treatment of bacterial and fungal infections [13].

The aim of this study was to evaluate the antimicrobial activity of selected medicinal plant extracts from three plants in family Euphorbiaceae which may possess antimicrobial activity.

Materials and Methods

Plant materials:

The plants in family Euphorbiacea were collected as follows :

1. The aerial parts of *Acalypha indica* Linn. were collected from Nakhonsawan, Thailand.

2. The leaves, fruits and stems of *Bridelia retusa* (L.) A. Juss. were collected from Chiang Mai, Thailand.

3. *Cleidion spiciflorum* Burm. f. Merr. (leave and stem) were collected from Chiang Mai, Thailand.

Voucher specimen of these plants were deposited at Queen Sirikit Botanic Garden Herbarium

(QBG) Prime Minister Office Flora of Thailand, Mae Rim Chiang Mai, Thailand.

Extraction:

The plants materials were dried and ground. The dried plants were macerated with hexane chloroform and methanol, respectively for 3 days and filtered. The filtrate of each solvent was evaporated by rotatory evaporator. Each crude extract was used for antimicrobial analysis.

Bacterial strains:

The microorganisms used were *Staphylococcus aureus* (ATCC25923), *Escherichia coli* (ATCC25922) and *Pseudomonas aeruginosa* (ATCC27553).

Fungal strains:

The microorganisms used were *Aspergillus flavus*, *Candida albican* and *Trichophyton mentagrophyte*.

Determination of antimicrobial activity:

The extracts were subjected to antimicrobial assay using the agar diffusion method [14]. The strains were maintained in agar conservation at room temperature. The strains inoculum were diluted in sterile 0.85% Saline to obtain turbidity visually comparable to a McFarland Nº 0.5 standard (10^{7-8} CFU/mL) for bacteria, but comparable to a McFarland Nº 1.0 standard (10^{15} CFU/mL) for fungi. Every inoculum was spread over plates containing Nutrient Agar (NA) for bacteria and Potato Dextrose Agar (PDA) for fungi. In each of these plates, 4 wells (9 mm) were cut out using sterile cork borer. One hundred µL (50 mg/mL)of each extract was carefully added into the wells by means of steriled dropping automatic pipette. The samples were then incubated at 37 ºC for 24 h for bacterial pathogens and 3 days for fungal pathogens. The antimicrobial activity was evaluated in mm by measuring the diameter of inhibition zone. A positive control was also assayed to check the sensitivity of the tested organisms using the following antibiotics : Gentamicin 100 µL (75 µg/mL) for bacterial and Ketoconazole 100 µL (250 µg/mL) for fungal.The experiments were repeated at least triplicate.

Results and Discussion

The antimicrobial activities of various medicinal plant extracts in family Euphorbiaceae were investigated by agar diffusion method. The crude extracts at 50 mg/mL concentration showed activity against the bacteria tested. The inhibitory zones were measured. Results are shown in Table 1. It is indicated that the hexane, chloroform and methanol extracts of *A. indica* Linn. aerial part showed antibacterial activity against *S. aureus* and *P. aeruginosa*, but did not inhibit *E. coli*. Only methanolic extract of *C. spiciflorum* Merr. leaves exhibited antibacterial activity against *S. aureus*, *E. coli* and *P. aeruginosa* respectively, but the methanolic extract of the stems possed antibacterial activity against *S. aureus*. The chloroform extract of *B. retusa* (L.) A. Juss. fruits showed inhibition zones against *S. aureus*, *E. coli* and *P. aeruginosa*, but the methanolic extract showed antibacterial activity against *S. aureus* and *P. aeruginosa*. The hexane extracts of *B. retusa* (L.) A. Juss. leaves, stems and fruits showed no inhibition zone against *S. aureus*, *E. coli* and *P. aeruginosa*. The methanolic extracts of *B. retusa* (L.) A. Juss. leaves and stems exhibited antibacterial activity against *S. aureus*, only the methanolic extract of the leaves showed inhibition zone against *P. aeruginosa*.

The crude extracts at the same concentration showed antifungal activity and the inhibitory zones were measured. Results are shown in Table 2. It is indicated that the hexane, chloroform and methanol extracts of *A. indica* Linn. aerial parts showed antifungal activity against *T. mentagrophyte*, but the chloroform and methanol extracts showed inhibition zones against *A. flavus* and *C. albican* respectively. The methanolic extracts of *C. spiciflorum* Merr. stems, *B. retusa* (L.) A. Juss. leaves and stems exhibited antifungal activity against *T. mentagrophyte*, but all the extracts of *C. spiciflorum* Merr. leaves showed no inhibition zone against all fungi tested. The hexane, chloroform and methanol extracts of *B. retusa* (L.) A. Juss. fruits showed antifungal activity against *C. albican*, but all extracts did not inhibit *A. flavus* and *T. mentagrophyte*. The most active antimicrobial plant was *A. indica* Linn.

In recent years, multi-resistant bacterial and fungal strains have increased, thus the treatment of several infections has become very difficult, reducing the therapeutic option [15].

However, the antimicrobial activity of various medicinal plant extracts in family Euphorbiaceae, offers an option to the pharmaceutical industry of new natural medicine sources with activity against these bacterial and fungal strains that represent an important public health problem.

Table 1: Antibacterial activity of crude hexane, chloroform and methanol extracts of selected medicinal plants.

Plant extracts	Part used	Zone of Inhibition (mm)[a]		
		S. aureus	*E. coli*	*P. aeruginosa*
A. indica Linn.	aerial parts			
Hexane extract		10	-	19
Chloroform extract		11	-	17
Methanol extract		10	-	17
C. spiciflorum Merr.	leaves			
Hexane extract		-	-	-
Chloroform extract		-	-	-
Methanol extract		25	15	14
C. spiciflorum Merr.	stems			
Hexane extract		-	-	-
Chloroform extract		-	-	-
Methanol extract		18	-	-
B. retusa (L.) A. Juss.	leaves			
Hexane extract		-	-	-
Chloroform extract		-	-	-
Methanol extract		10	-	14
B. retusa (L.) A. Juss.	stems			
Hexane extract		-	-	-
Chloroform extract		-	-	-
Methanol extract		15	-	-
B. retusa (L.) A. Juss.	fruits			
Hexane extract		-	-	-
Chloroform extract		10	12	12
Methanol extract		17	-	14
Gentamicin[b]	-	35	27	27

[a]: Inhibition zones are the mean cork borer (9 mm) diameter.
[b]: Possitive control = Gentamicin (75 µg/mL concentration).
(-) : No inhibition zone

Table 2: Antifungal activity of crude hexane, chloroform and methanol extracts of selected medicinal plants.

Plant extracts	Part used	Zone of Inhibition (mm)[a]		
		A. Flavus	*C. albican*	*T. mentagrophyte*
A. indica Linn.	aerial parts			
Hexane extract		-	-	15
Chloroform extract		11	-	14
Methanol extract		-	13	15
C. spiciflorum Merr.	leaves			
Hexane extract		-	-	-
Chloroform extract		-	-	-
Methanol extract		-	-	-
C. spiciflorum Merr.	stems			
Hexane extract		-	-	-
Chloroform extract		-	-	-
Methanol extract		-	-	11
B. retusa (L.) A. Juss.	leaves			
Hexane extract		-	-	-
Chloroform extract		-	-	-
Methanol extract		-	-	10
B. retusa (L.) A. Juss.	stems			
Hexane extract		-	-	-
Chloroform extract		-	-	-
Methanol extract		-	-	18
B. retusa (L.) A. Juss.	fruits			
Hexane extract		-	17	-
Chloroform extract		-	21	-
Methanol extract		-	14	-
Ketoconazole[b]	-	25	37	16

[a]: Inhibition zones are the mean cork borer (9 mm) diameter.
[b]: Possitive control = Ketoconazole (250 µg/mL concentration).
(-) : No inhibition zone

Conclusions

The screening results of antibacterial activity indicated that the methanolic extract of *C. spiciflorum* Merr. leaves and the chloroform extract of *B. retusa* (L.) A. Juss. fruits showed exhibited antibacterial activity against *S. aureus*, *E. coli* and *P. Aeruginosa*, respectively. The methanolic extract of *C. spiciflorum* Merr. leaves showed the highest inhibition zone against *S. aureus* (25 mm) and *E. coli* (15 mm). The hexane extract of *A. indica* Linn. aerial part showed the highest inhibition zone against *P. Aeruginosa* (19 mm) , compared with all the tested extracts. The screening results of antifungal activity indicated that the hexane, chloroform and methanol extracts of *A. indica* Linn. aerial parts showed antifungal activity against *T. Mentagrophyte*. The hexane, chloroform and methanol extracts of *B. retusa* (L.) A. Juss. fruits showed antifungal activity against *C. Albican*. Only chloroform extract of *A. indica* Linn. aerial part showed inhibition zone against *A. flavus* (11 mm). The chloroform extract of *B. retusa* (L.) A. Juss. fruits showed the highest inhibition zone against *C. Albican* (21 mm). The methanolic extract of *B. retusa* (L.) A. Juss. stems showed the highest inhibition zone against *T. Mentagrophyte* (18 mm).

The extracts will be further purified using bioassay-directed isolation and elucidated the bioactive compounds.

Acknowledgement

The authors would like to thank the Faculty of Pharmacy and the Graduate School, Chiangmai University, Chiangmai, Thailand, for their partial support.

References

[1] G. Webster, *Annal. Miss. Bot. Gard.* **83,** (1994), pp. 33-144.

[2] A. Singla and K. Pathak, *Fitoterapia.* **61,** (1990), pp. 483-516.

[3] A. Gurib-Fakim, M. Sewraj, J. Gueho and E. Dulloo, *J. Ethnopharmacol.* **39,** (1993), pp. 175-185.

[4] R. P. Samy, S. Ignacimuthu and D. P. Raja, *Journal of Ethnopharmacology.* **66,** (1999), pp. 235-240.

[5] R. D. J. Solomon., S. Kallidass and J. Vimalan, *World J. Microbiology & Biotechnol.* **21,** (2005), pp. 1231-1236.

[6] E. Quisumbing, *Medicinal Plants of the Philippines.* (1951), pp. 497.38.

[7] L. M. Perry, *Medicinal Plants of East and Southeast Asia.* (1980), pp. 139-140.

[8] N. Boonyaprapatsorn and A. Chokchaichareunporn, *Local medicinal plants (2).* (1996), pp. 28.

[9] S.Dressler, *Euphorb. Gen.* (1996), pp. 289.

[10] S. B. Vohora and G. V. Mishra, *Indian drugs.* **33 (1),** (1998), pp. 1-17.

[11] L. Jayasinghe , B. M. M. Kumarihamy, K. H. R. N. Jayarathna, N. W. M. G. Udishani, B. M. R. Bandara, N. Hara and Y. Fujimoto, *Phytochemistry.* **62,** (2003), pp. 637-641.

[12] A. V. Krishnaraju, T. V. N. Rao and D. Sundararaju, *Int. J. Appl. Sci. Eng.* **2,** (2005), pp. 125-134.

[13] M. F. Balandrin, A. J. Kjocke and E. Wurtele, *Science.* **228,** (1985), pp. 1154-1160.

[14] B. A. Adeniyi, H. A. Odelola and B.A. Osa, *Afr. J. Med. Sci.* **25,** (1996), pp. 221-224.

[15] P. Hsueh, L. Teng, W. Chen, H. Pan, M. Chen and S. Chang, *Antimicrob. Agents. Chemother.* **48,** (2004), 1361-1364.

Anticancer activity and chemical constituents of petroleum ether extract from *Lepisanthes Rubiginosa* (Roxb.) Leenh.

J. Chuangbanyat[1*], B. Liawruangrath[1], S. Liawruangrath[2], A. Teerawutgulrag[2] and S. G. Pyne[3]

[1] Faculty of Pharmacy, Chiang Mai University, Amphur Muang, Chiangmai, Thailand 50200
[2] Faculty of Science, Chiang Mai University, Amphur Muang, Chiangmai, Thailand 50200
[3]Department of Chemistry, University of Wollongong, NSW, Australia 2522

[*]Email: jitik@yahoo.com

Abstract: *Lepisanthes Rubiginosa* (Roxb.) Leeh. is one of Sapindaceae family, flowering shrub native to tropical southeastern Asia. It has been externally used as antipruritic; apply locally to forehead for fever, headache; decoction. Chemical investigation of the petroleum extract of the leaves of this plant was analysed by capillary GC and GC/MS. Eleven components were identified. The major component was Neophytadiene. The extract displayed cytotoxic effect on breast cancer cell lines (MCF7-breast cancer) with IC_{50} of 28.61 µg/mL (concentration that inhibit 50% of cell proliferation). However, the extract did not give any cytotoxic value against KB-oral cavity and NCI-H187-small lung cancer cell lines tested.

Introduction

Cancer is the second most common cause of death in Thailand after accident. Humans of all ages develop cancer and a wide variety of organs are affected. The incidence of many cancers increases with age, so that as people live longer more will develop the disease [1]. Each year in Thailand many patients are newly diagnosed with cancer. Most of these patients receive surgery, radiotherapy and/or chemotherapy to cure their disease. Some of the population is not so fortunate; even with these therapeutic treatments they will die within five years. Treatment itself may cause further morbidity. Intensive treatment with radiotherapy or chemotherapy is commonly associated with a range of adverse side effects from nausea to bone marrow failure. Those patients who receive intensive treatment may experience a decline in quality of life. Because of these and other reasons, a significant minority of cancer patients seek out alternatives to conventional care.

Natural products have played a significant role in drug discovery and development especially for agents against cancer and infectious diseases [2]. An analysis of new and approved drugs for cancer by the United States Food and Drug Administration over the period of 1981-2002 showed that 62% of these cancer drugs were of natural origin. Natural compounds possess highly diverse and complex molecular structures compared to small molecule synthetic drugs and often provide highly specific biological activities likely derived from the rigidity and high number of chiral centers. Ethnotraditional use of plant-derived natural products has been a major source for discovery of potential medicinal agents [3-5].

This study will focus on anticancer activity including structure elucidation of the isolated compounds.

Materials and Methods

Plant materials:

The fresh leaves of plant were collected from Kamphaengphet province, Thailand. A voucher specimen of the plant is deposited in Biology herbarium, Biology department, Faculty of Science, Chiang Mai University, Chiang Mai, Thailand for reference.

Extraction:

The leaves of the plant were cleaned, cut into small pieces and accurately weighed then the plant was macerated petroleum ether. The filtrate was evaporated by rotatory evaporator. The light white solid was obtained. This light white solid was then dissolved in small quantity of dichloromethane. The anticancer activity and the chemical constituents of this solution were investigated.

Determination of anticancer activity:

The anticancer activity of the petroleum ether extract was performed by using KB (Oral Cavity cancer), MCF 7 (Human breast adenocarcinoma) and NCI-H 187 (Human small cell lung carcinoma) and determined by resazurin microplate assay (REMA) following a modified method of the use of a fluorescent dye for mammalian cell cytotoxicity according to Brien *et al*. (2000) [6]. Ellipticine and doxorubicin were used as positive controls. DMSO and sterile distilled water were used as negative controls. Cells at a logarithmic growth phase were harvested and diluted to 10^5 cells/ml in fresh medium and gently mixed. Test compounds were diluted in culture medium in a ratio of 1:2 giving 8 concentrations. Five µl of the test sample and 45 µl of cells were put into 96 well microtiter plates with a total volume of 50 µL/well. Plates were incubated at 37 °C, 5% CO_2, for 72 hours for KB and MCF7 and 5 days for NCI-H187. After the incubation periods, 12.5 µl of resazurin solution was added to each well and the plates were incubated at 37 °C for 4 hours. The plates

were then processed for optical density absorbance analysis using a microplate reader at dual wavelengths of 530 and 590 nm.

Analysis of the extract by GC-MS

The extract was analysed on a Hewlett-Packard GC 6890/ MSD 5973 on a HP-5 capillary column (30m × 0.25 mm, 0.25 µm film thickness). The injector temperature was 250 °C, the petroleum ether extract of 0.2 µL was injected, using split mode (split ratio, 250:1). Helium was the carrier gas at a flow rate of 1.0 mL min^{-1}. The oven temperature was initially at 50 °C (3 min) and was then gradually increased at a rate of 7 °C min^{-1} up to 250 °C and held for 9 min. The ion source temperature of the MS unit was 230 °C, and the mass spectra were recorded at an ionizing voltage of 70 eV. The constituents were further identified and authenticated using their MS data compared to the wiley7n.l mass spectral library, as well as by comparison of their retention indices with literature values.

Results and Discussion

Preliminary testing showed that the extract had no anticancer activity against KB-Oral cavity cancer and NCI-H187-Small cell lung human cancer (% inhibition < 50%) but significant inhibition against MCF7-Breast cancer (IC_{50} = 28.61 µg mL^{-1}). The results are shown in Table 1.

Table 1: Anticancer activity of *Lepisanthes Rubiginosa* (Roxb.) Leeh. Extract.

Cancer	IC_{50} (µg mL^{-1})
KB-Oral cavity cancer	Inactive
NCI-H187-Small cell lung human cancer	Inactive
MCF7-Breast cancer	28.61

The extract was analysed by means of GC and GC-MS. Identification of extract constituents was performed by comparison of mass spectra with literature data (wiley7n.l) that yielded < 90% matches were identified as unknowns or with those in the literature [7-8]. Eleven compounds were identified and are listed in Table 2. A typical GC-MS chromatogram of the petroleum ether extract of *Lepisanthes Rubiginosa* (Roxb.) Leeh. is presented in Figure 1.

The constituents of the extract were devided in 3 groups 1) terpenes: neophytadiene and bistrimethylsilyl-N-acetyl eicosasphinga -4,11-dienine 2) fatty acids: palmitic acid acid and linoelaidic acid and 3) alkane hydrocarbon: tricosane pentacosane hexacosane eicosane and heneicosane. The major component, neophytadiene (36%) and fatty acids showed antimicrobial activity [9,10].

Table 2: Chemical composition of the extract of *Lepisanthes Rubiginosa* (Roxb.) Leeh.

Peak No.	R.T (min)	Compounds	% of total
1	20.968	Palmitic acid	6.07
2	22.950	Linoelaidic acid	19.86
3	23.291	Unidentified	7.57
4	24.232	Heneicosane	1.59
5	24.297	Hexacosane	3.74
6	25.456	Bistrimethylsilyl -N-acetyl eicosasphinga -4,11-dienine	2.76
7	28.009	Eicosane	3.01
8	29.937	Unidentified	4.47
9	30.132	Pentacosane	10.87
10	32.367	Neophytadiene	36.68
11	39.284	Unidentified	3.37

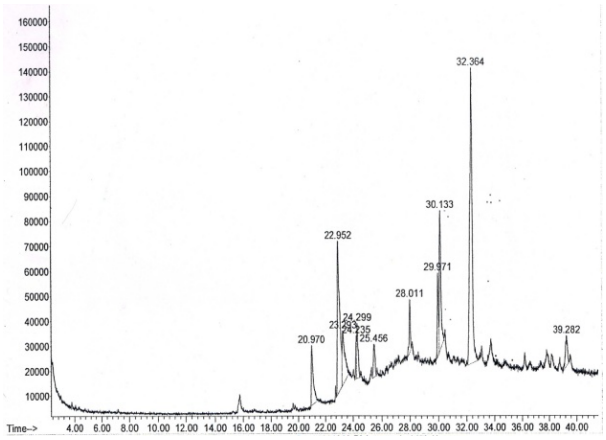

Figure 1. GC-MS chromatogram of *Lepisanthes Rubiginosa*(Roxb.) Leeh.

Conclusions

The petroleum ether of *Lepisanthes Rubiginosa* (Roxb.) Leeh. leaves exhibited anticancer activity against MCF7-Breast cancer but showed no activity against KB-Oral cavity cancer and NCI-H187-Small cell lung human cancer. This might be led to the isolation of lead compounds for drug development.

There are eleven chemical constituents present in the extract, only eight compounds were identified. The major components are neophytadiene and linoelaidic acid. Further studies are required to identify and search for bioactive compounds.

Acknowledgements

We would like to express our sincere thanks to Faculty of Pharmacy and the Graduate School, Chiang Mai University for partial support.

References

[1] John Boik. *Cancer Incidence and Mortality. In Cancer and natural medicine*, Oregon Medica Press United states of America,1996.

[2] Kimata H, Nakashima T., Kokubun S., Nakayama N., Mitoma Y., Kitahara T., Yata N., and Tanaka O. *Chemical and Pharmaceutical Bulletin*. 1983, **31**, pp. 1998-2005.

[3] Adesanya, S., Martin, M.; Hill, B., Dumontet, V., Van Tri, M., Sevenet, T., and Pais, M. *J. Elsevier Sci.* 1999, **51**, pp. 1039-1041.

[4] Ruangrungsi N. *Anticancer medicinal plants research*. Knowledge of Natural Products (Training Course2). 2002, pp. 70-110.

[5] Statz D. and Coon F.B. *J.Cancer Treat Rep.* 1976, **60**, pp. 999-1005.

[6] Brien, J.O., Wilson, I., Orton, T., Pognan, F., *Eur. J.Biochem*. 2000, **267**, pp. 5421-5426.

[7] Ahmad, A., Misra, L.N., Thakur, R.S., *Plant-Med*. 1989, **55**, pp. 199-200.

[8] GARG S. C., *Indian Perfumer*, 2000, **47**, 99-101.

[9] Plaza M, Santoyo S, Jaime L, García-Blairsy Reina G, Herrero M, Señoráns FJ, Ibáñez E. *J Pharm Biomed Anal.* 2009, **51(2)**, pp. 450-455.

[10] Rodríguez-Meizoso I, Jaime L, Santoyo S, Cifuentes A, García-Blairsy Reina G, Señoráns FJ, Ibáñez E. *J Agric Food Chem*. 2008, **56(10)**, pp. 3517-23.

Chemical constituent and biological activity of essential oil from Waan-Khun-Tha-Ma-La (*Curcuma* spp.) rhizome

O. Theanphong[1*], T. Songsak[1], W. Mingvanish[2] and C. Kirdmanee[3]

[1] Faculty of Pharmacy, Rangsit University, Patumtani, Thailand 12000
[2] Department of Chemistry, Faculty of Science, King Mongkut's University of Technology Thonburi, Bangkok, Thailand 10140
[3] National Center for Genetic Engineering and Biotechnology, National Science and Technology Development Agency, Patumtani, Thailand 12120

[*] Corresponding Author E-mail Address: theanphong@gmail.com

Abstract: Chemical constituent of essential oil from Waan-Khun-Tha-Ma-La (*Curcuma* spp.) rhizome was studied by GC-MS and its major chemical constituent was found to be germacrene B (24.57 %). The essential oil from Waan-Khun-Tha-Ma-La (*Curcuma* spp.) rhizome was evaluated for its *in vitro* scavenging effects on the DPPH, $OH^{\bullet}$, H_2O_2. The reducing power was also evaluated. Ascorbic acid was used as the positive control for all antioxidant activity experiments. The scavenging ability on DPPH and $OH^{\bullet}$ radicals of the essential oil had higher significance than that of ascorbic acid. The EC_{50} values for scavenging on DPPH and $OH^{\bullet}$ radicals of the essential oil were 8.88 and 82.68 μg/ml, respectively, and those for ascorbic acid were 18.87 and 218.25 μg/ml, respectively. The H_2O_2 scavenging activity of the essential oil and ascorbic acid was found to be indifferent significantly (EC_{50} = 539.03 μg/ml for essential oil and EC_{50} = 346.75 μg/ml for ascorbic acid). Based on the results obtained, the essential oil has not shown the reducing power properties as compared with ascorbic acid. Results of antimicrobial activity testing by agar diffusion method showed that the essential oil had strong activity against gram positive bacteria (*Staphylococcus aureus* ATCC 29213, *Enterococcus faecalis* ATCC 29212 and *Bacillus subtilis* ATCC 6633) with MIC 6.25, 6.25 and 200 mg/ml, respectively. In contrast, tetracyclin, the positive control for antimicrobial activity testing, exhibited stronger activity against gram positive and gram negative bacteria (*Escherichia coli* ATCC 25922) with MICs < 0.04 mg/ml. The essential oil has been also tested by Green Fluorescent Protein Reporter Microplate assay and it was found to be inactive toward *Mycobacterium tuberculosis* strain H37Ra.

Introduction

Curcuma species are rhizomatous herbs belonging to the family Zingiberaceae. The *Curcuma* species are widely distributed in the tropics and subtropics. The uses of the *Curcuma* species are commonly a natural food additive, cosmetic and folk medicine. *Curcuma* species contain terpenoids, diarylheptanoids, diphenylheptanoids and spirolactones [1]. Some of these compounds are reported to possess biological activities, such as antioxidant, anti-inflammatory, antimicrobial activities [1-6].

Waan-Khun-Tha-Ma-La, one unidentified member of this genus, is also used as folk medicine. Its fresh rhizome is used for a variety of therapeutic purposes such as the treatment of diarrhoea, dysentery, sore throat and abscess [2]. To the best of our knowledge, there is no available information reported about chemical composition and biological activities of the essential oil from the fresh rhizome of Waan-Khun-Tha-Ma-La. Thus, the aim of this study was to identify the chemical compositions of the essential oil of the fresh rhizome of Waan-Khun-Tha-Ma-La and to study *in vitro* antioxidant, antibacterial and antituberculosis activities of the essential oil.

Materials and Methods

Plant material

The fresh rhizomes of Waan-Khun-Tha-Ma-La (*Curcuma* spp., Zingiberaceae) were obtained in June 2008 from Ratchaburi province, Thailand.

Extraction of the essential oil

The fresh rhizomes of Waan-Khun-Tha-Ma-La were washed with tap water, air dried and then blended into small pieces with the blender. The ground rhizome of the plant was submitted to water-distillation. The distillate was dried over anhydrous sodium sulfate and after filtration, stored at 4°C for testing and analyzing.

Identification of the essential oil by GC-MS

Chemical constituents of the essential oil in ethanol (1 ml) were identified by Finnigan Trace GC ultra GC equipped with a Finnigan Trace DSQ quadrupole mass spectrometric detector (MSD). The BPX 5 Phenyl: Dimethylpolysiloxane (5:95) capillary column was 30 m in length, 0.25 mm i.d., and 0.25 μm in thickness. The gas carrier was Helium with the flow rate of 1 ml/min. The operating condition of GC oven temperature was: initial temperature 60°C for 1 min, heating rate 3°C/min up to final temperature 240°C with isotherm for 5 min. The GC injector and GC-MSD interface temperatures were set at 180°C and 290°C, respectively. The essential oil components were identified by comparing their mass fragmentation pattern with MS library from mainlib, replib and FICI2205. The amount of each oil component was compared using peak area measurement.

Antioxidant activity

DPPH scavenging assay

The DPPH free-radical scavenging activity of the essential oil was measured according to the method reported by Wang, *et al.* [7]. 1 ml of different concentrations of the essential oil in ethanol (0-5000 µg/ml) was mixed with 2 ml of 6×10^{-5} M DPPH solution in methanol. The reaction mixture was well shaken and kept it at room temperature in the dark for 30 min. The absorbance of the reaction mixture was measured at 517 nm against the blank, i.e. ethanol. *L*-ascorbic acid was used as a positive control. The percentage of DPPH elimination was calculated as follows:

$$\text{Percent inhibition} = [1-(A_1-A_2)/A_0]\times100\%$$

where A_0 is the absorbance of the control (without the essential oil), A_1 is the absorbance of the reaction mixture and A_2 is the absorbance without DPPH.

$OH^{\bullet}$ scavenging assay

$OH^{\bullet}$ scavenging assay was performed according to the method of Wang, *et al.* with some modifications [7]. 1 ml of different concentrations of the essential oil in ethanol (0-5000 µg/ml) was mixed with a mixture of 1.5 ml of 1.5 mM $FeSO_4$, 0.7 ml of 6 mM H_2O_2 and 0.3 ml of 20 mM sodium salicylate. The reaction mixture was incubated for 1 hr at 37°C. The absorbance of the reaction mixture was measured at 562 nm against the blank, i.e. ethanol. *L*-ascorbic acid was used as a positive control. The percentage of $OH^{\bullet}$ scavenging was calculated as follows:

$$\text{Percent inhibition} = [1-(A_1-A_2)/A_0]\times100\%$$

where A_0 is the absorbance of the control (without the essential oil), A_1 is the absorbance of the reaction mixture and A_2 is the absorbance without sodium salicylate.

H_2O_2 scavenging assay

H_2O_2 scavenging activity was determined according to the method of Wang, *et al.* with some modifications [7]. 1 ml of different concentrations of the essential oil (0-5000 µg/ml) in ethanol was mixed with 1 ml of 0.1 mM H_2O_2 and followed by 100 µl of 3% ammonium molybdate solution, 10 ml of 2 M H_2SO_4 and 7 ml of 1.8 M KI. The reaction mixture was titrated with 5 mM $Na_2S_2O_3$ until the violet color disappeared. The violet color results from the addition of 2% starch solution into the reaction mixture before titration. *L*-ascorbic acid was used as a positive control. The percent H_2O_2 scavenging activity was calculated as follows:

$$\text{Percent inhibition} = [(V_0-V_1)/V_0]\times100\%$$

where V_0 is the volume of $Na_2S_2O_3$ solution used to titrate the blank (without the essential oil) and V_1 is the volume of $Na_2S_2O_3$ solution used to titrate the reaction mixture.

Reducing power assay

The reducing power of the essential oil was carried out according to the method of Tsai, *et al.* with some modifications [8]. 2.5 ml of different concentrations of the essential oil in ethanol was mixed with a mixture of 2.5 ml of 200 mM PBS (pH 6.6) and 2.5 ml of 1% $K_3Fe(CN)_6$. The reaction mixture was incubated for 20 min at 50°C. After incubation, the reaction mixture was added with 2.5 ml of 10% w/v trichloroacetic acid then, centrifuged at 200 rpm for 10 min. After that, 5 ml of the supernatant was mixed with 5 ml of ethanol and 1 ml of 0.1% $FeCl_3$. The absorbance of the reaction mixture was measured at 700 nm against the blank, i.e. which did not contain the essential oil. The increased reaction-mixture absorbance indicates the increased reducing power. *L*-ascorbic acid was used as a positive control.

Antibacterial activity

All bacterial strains used for this study were obtained as lyophilized cultures from Department of Medical Science, Ministry of Public Health Thailand. Organisms were as follows: three species of gram positive *Staphylococcus aureus* ATCC 29213, *Enterococcus faecalis* ATCC 29212 and *Bacillus subtilis* ATCC 6633 and one species of gram negative *Escherichia coli* ATCC 25922. Antibacterial assay was determined by using the agar diffusion method. Microbial cultures for antimicrobial assay were freshly cultured on Tryptic Soy Broth (TSB) medium and incubated at 37°C for 24 hr. After that, the TSB medium was approximately adjusted to solution concentrations of 0.5 McFarland with 0.9% sterile normal saline solution. The mixtures were spread on Tryptic Soy Agar (TSA) plate with sterile cottons swab and allowed to dry. Sterilized paper filter discs with a diameter of 6 mm were impregnated with 20 µl of an essential oil solution in 5% v/v Dimethylsulphoxide (DMSO) in TSB and placed on the inoculated agar. The plates were left for 30 min at room temperature to allow the diffusion of the oil and then they were incubated at 37°C for 24 hr. Antimicrobial activity was evaluated by measuring the zone of inhibition against the test microorganisms. In this experiment, two controls were used, i.e. a control having microorganism but no test material and a control having 5 mg/ml standard tetracycline solution in 5% v/v DMSO in TSB. The tetracycline solution was used as a positive control. Experimental tests were performed in triplicate and the developing inhibition zones were compared with those of reference disc.

The minimum inhibitory concentration (MIC) for antibacterial assay was determined by the broth dilution method. The inocula of microorganisms were prepared from 24 hr broth cultures and suspensions were adjusted to 1 McFarland standard turbidity. The essential oil dissolved in 5% v/v DMSO in TSB were first diluted to the highest concentration (200 mg/ml) to be tested, and then serial two-fold dilutions were made in a concentration range from 200 to 1.56 mg/ml in 10 ml sterile test tubes containing nutrient broth. Solvent, antibiotic and microorganism controls were also analyzed. The mixture in each tube was incubated

at 37°C for 24 hr. The MIC of the essential oil was determined as the lowest concentration of the essential oil that completely prevent any turbidity or growth of the test organisms. All samples were tested in triplicate [9-10].

Antimycobacterial activity

Green Fluorescent Protein Reporter Microplate Assay (GFPMA) was used for the determination of antimycobacterial activity of the essential oil in question [11]. The tested mycobacterial strain used in this study was *Mycobacterium tuberculosis* strain H37Ra. 5 µl of various concentrations of the essential oil in 5% DMSO was added into each well containing 45 µl of cell suspension (2×10^4 - 1×10^5 cfu/ml/well). The antimycobacterial assay plate was incubated at 37°C for 7 days. After that, the fluorescence signals were measured using SpectraMax M5 microplate reader in the bottom-reading mode with excitation at 485 nm and emission at 535 nm. The fluorescence signals on day zero were used as a background. The percentage of growth inhibition was calculated according to the following equation:

$$\text{Percent inhibition} = [1-(FU_T/FU_c)] \times 100$$

where FU_T was the fluorescence units of cells treated with the essential oil and FU_c was the fluorescence units of cells untreated with the essential oil.

The minimum inhibitory concentration (MIC) for antimycobacterial assay was defined as the lowest concentration at which the growth inhibition of the test organisms by the essential oil was found to be 90%. Isoniazid was used as a positive control and 0.5% DMSO was used as a negative control. All samples were tested in triplicate.

Statistical analysis

All experiments were repeated at least three times. Results were reported as mean ± S.D. EC_{50} values were also calculated. Statistical comparison was made with Pair Sample T-Test at the confidence interval of 95%.

Results and Discussion

Chemical composition of the essential oil

Essential oil obtained from the water distillation of Waan-Khun-Tha-Ma-La rhizome was clear and colourless oil (%yield 0.40 %w/w). Totally, 24 components were identified and camphor (10.56%), germacrene B (24.5%) and atractylone (18.57%) were the major components in the essential oil. In addition, the results of GC-MS analysis revealed that the most of the 24 identified compounds in the essential oil were terpenoid compounds (Table 1).

Table 1: Essential oil components of fresh rhizome of Waan-Khun-Tha-Ma-La

RT[a]	Components	KI[b]*	Area %
5.67	α-Pinene	939	0.46
6.06	Camphene	954	1.97
6.85	β-Pinene	979	0.64
8.46	Limonene	1029	0.51
8.54	1,8-Cineole	1031	7.43
10.61	Terpinolene	1088	1.47
12.81	Camphor	1146	10.56
13.33	Isoborneol	1160	2.11
13.70	Borneol	1169	0.57
23.08	β-Elemene	1390	0.96
25.54	α-Humulene	1454	1.11
26.66	Germacrene D	1485	2.43
26.85	β-Selinene	1490	0.39
27.22	α-Selinene	1498	3.09
27.30	Curzerene	1499	6.83
27.61	Premnaspirodiene	1506	2.63
27.74	(*E*,*E*)-α-Farnesene	1505	1.87
28.32	β-Sesquiphellandrene	1522	2.59
29.60	Germacrene B	1559	24.57
32.17	Z-Asarone	1617	0.67
34.63	Atractylone	1658	18.57
34.76	Germacrone	1693	7.41
37.20	Benzene, 1,2,3,4-tetramethy l-4-(1-methylethenyl)	-	0.44
37.82	8-Hydroxy-eremophilone	1847	0.29
38.15	Nootkatin	1960	0.42

[a] retention time relative to n-alkanes on the BPX5 fused silica column
[b] Kovac index

Antioxidant activity

The results of the investigation of antioxidative activity of the essential oil were shown in Table 2. Obviously, the essential oil showed better scavenging ability on $DPPH^{\bullet}$ and $OH^{\bullet}$ radicals than ascorbic acid, whereas the essential oil was less effective for scavenging H_2O_2 as compared to ascorbic acid. The high free radical scavenging capacity of the corresponding essential oil may be caused by the presence of nonphenolic constituents in the essential oil such as α-pinene, β-pinene, limonene and camphene [12-13]. In case of the H_2O_2 scavenging assay, H_2O_2 is not as very reactive as $OH^{\bullet}$ radical, and so it may react very slowly with the nonphenolic compounds in the essential oil as compared to ascorbic acid. As seen in Table 2, the essential oil did not show the capacity of reducing the Fe^{3+}/ferricyanide complex to the ferrous form. It pointed out that the components existing in the essential oil may be weaker reducing agents for Fe^{3+}metal ion. The heavy metal reducing capacity of a compound may serve as a significant indicator of its potential antioxidant activity [14]. However, the

activity of antioxidants has been assigned to various mechanisms such as prevention of chain initiation, binding of transition-metal ion catalysts, decomposition of peroxides, and prevention of continued hydrogen abstraction, reductive capacity and radical scavenging [15-16].

Table 2: EC_{50} values of the essential oil of the fresh rhizome of Waan-Khun-Tha-Ma-La in various antioxidant systems as compared with the positive control ascorbic acid

Test	EC50 (μg/ml)	
	Essential oil	Ascorbic acid
DPPH radical scavenging assay	8.88 ± 2.82 [a]	18.87 ± 2.09 [a]
OH Scavenging assay	82.68 ± 4.90 [a]	218.25 ± 18.09 [b]
H_2O_2 Scavenging activity assay	539.03 ± 105.57 [a]	346.75 ± 142.79 [a]
Reducing power assay	> 1250 [b]	453.93 ± 13.78 [a]

Mean in the row followed by the difference latter are significantly different at the confidence interval of 95% probability level according to Pair Sample T-Test.

Antimicrobial activity

Antibacterial activity of the essential oil of the fresh rhizome of Waan-Khun-Tha-Ma-La against *S. aureus*, *E. faecalis*, *B. subtilis* and *E. coli* including its MIC values were tabulated in Table 3.

As seen in Table 3, the essential oil showed the close inhibition levels against *S. aureus* and *E. faecalis*. The MIC values for the inhibition of the growth of *S. aureus* and *E. faecalis* were 6.25 mg/ml. The lowest antibacterial activity of the essential oil was observed against *B. subtilis* with the MIC value of 200 mg/ml. In contract, it was not effective in inhibition of the *E. coli* growth (Table 3). The essential oil was also screened for antimycobacterial activity by using the GFP Microplate Assay (GFPMA). It was found that the essential oil had no the antimycobacterial activity against *Mycobacterium tuberculosis*. The positive control isoniazid for this test gave the MIC value of 0.023-0.046 μg/ml.

Table 3: Antibacterial activity and minimal inhibitory concentration (MIC) of the essential oil of Waan-Khun-Tha-Ma-La rhizome

Test	Zone of inhibition (mm) [a]		MIC (mg/ml)	
bacteria	Essential oil [b]	Tetracyclin [c]	Essential oil	Tetracyclin
E. coli	-	10 ± 0.8	-	< 0.04
S. aureus	10 ± 0.1	11 ± 0.8	6.25	< 0.04
B. subtilis	7.5 ± 0.1	8.7 ± 0.5	200	< 0.04
E. faecalis	13 ± 0.1	8.7 ± 0.6	6.25	< 0.04

Each value is expressed as means ± standard deviation (n=3).
[a] disk diameter 6.0 mm
[b] concentration of solution tested 200 mg/ml
[c] concentration of solution tested 5 mg/ml

Conclusions

This study is the first report on the essential oil from the fresh rhizome of Waan-Khun-Tha-Ma-La belonging to the family Zingiberaceae. The result of the present study showed that the essential oil contained high ratios of terpenoids. In addition, these nonphenolic compounds present in the essential oil showed the antioxidant and antimicrobial properties. Consequently, these results confirmed the use of the rhizome of Waan-Khun-Tha-Ma-La in traditional medicine for the treatment of diarrhoea, dysentery, sore throat and abscess.

Acknowledgements

This work was supported by program for Pharmaceutical senior project in Rangsit University in 2008 and National Center for Genetic Engineering and Biotechnology, National Science and Technology Development Agency. The authors would like to thank Dr. Thaya Jenjittikul; from Department of Plant Science Faculty of science, Mahidol University for her kindness, meaningful advice and valuable information.

References

[1] C. Leesuraplanon, S. Korsupphaisan and S. Amornrojworrawut, Chemotaxonomic study of Zingiberaceous plants, Bachelor degree of Pharmacy's thesis, Rangsit University, 2009.

[2] W. Chuakul and A. Boonpleng, *Thai Journal of Phytopharmacy*. **10**(2003), pp. 33-39.

[3] J. Miquel, A. Bernd, J.M. Sempere, J. Diaz-Alperi and A. Ramírez, *Arch. Gerontol. Geriatr.* **34**(2002), pp. 37-46.

[4] J.L. Mau, E.Y.C. Lai, N.P. Wang, C.C. Chen, C.H. Chang and C.C. Chyau, *Food Chem.* **82**(2003), pp. 583-591.

[5] B. Wilson, G. Abraham, V.S. Manju, M. Mathew, B. Vimala, S. Sundaresan and B. Nambisan, *J. Ethnopharmacol.* **99**(2005), pp. 147-151.

[6] J.K. Kim, C. Jo, H.J. Hwang, H.J. Park, Y.J. Kim and M.W. Byun, *Radiat. Phys. Chem.* **75**(2006), pp. 449-452.

[7] H. Wang, X.D. Gao, G.C. Zhou, L. Cai and W.B. Yao, *Food Chem.* **106**(2008); pp. 888-895.

[8] S.Y. Tsai, S.J. Huang and J.L. Mau, *Food Chem.* **98**(2006), pp. 670-77.

[9] A. Daud, A. Gallo and A.S. Riera, *J. Ethnopharmacol.* **99**(2005), pp. 193-197.

[10] I. Karaman, F. Sahin, M. Gulluce, H. Ogutcu, M. Sengul and A. Adıguzel *J. Ethnopharmacol.* **5**(2003), pp. 231-235.

[11] C. Changsen, S.G. Franzblau and P. Palittapongarnpim, *Antimicrob. Agents Chemother.* **47**(2003), pp. 3682-3687.

[12] B. Tepe, E. Donmez, M. Unlu, F. Candan, D. Daferera, G. Vardar-Unlu, *et al*. *Food Chem* **84**(2004), pp. 519-525.

[13] F. Deba, T.D. Xuan, M. Yasuda and S. Tawata, *Food Control* **19**(2008), pp. 346-352.

[14] S. Mei, J. Kanner, B. Akiri and S.P. Hadas, *J. Agric Food Chem.* **43**(1995), pp. 1813-1819.

[15] A. Yıldırım, A. Mavi, M. Oktay, A.A. Kara, O. F. Algur and V. Bilaloglu, *J. Agric. Food Chem.* **48**(2000), pp. 5030-5034.

[16] A.T. Diplock, *Free Radic. Res.* **27**(1997), pp. 511-532

Determination of some nutrient metals and bioactivity of some medicinal plants

J. Jeamjai[1], B. Liawruangrath[1]*, S. Liawruangrath[2], *S.* Vejabhikul[1], *A.* Baramee[2] and S. Satienperakul[3]

[1]Department of pharmaceutical Science, Faculty of Pharmacy, Chiang Mai University. Chiang Mai, Thailand 50200
[2]Department of Chemistry, Faculty of Science, ChiangMai University, Chiang Mai, Thailand 50200
[3]Department of Chemistry, Faculty of Science, Maejo University, Chiang Mai, Thailand 50290

*E-mail address: boonsom@pharmacy.cmu.ac.th

Abstract: Some nutrient metals from Leech lime (*Citrus hystrix* DC.), Wood apple (*Feronia limonia* Swing.), Bael-fruit (*Aegle marmelos* Corr.) and Lime (*Citrus aurantifolia* Swing) in family Rutaceae were investigated. The leaves of each plant were dried, ground and digested with 3:1 mixture of nitric acid and perchloric acid. The metals were determined by atomic absorption spectroscopy (AAS). There are Cu, Mn, Zn, Ca, Fe, Mg and Na present in young and old leaves of each plant. In addition, the hexane, chloroform, ethanol and methanol extracts of leaves from each plant showed antioxidant activity by the ABTS method. The antimicrobial activities of the hexane, chloroform, ethanol and methanol extracts from Lime leaves were determined by agar diffusion method. All crude extract of Lime leaves exhibited activities against *Escherichia* coli, Pseudomonas aeruginosa, *Staphylococcus aureus, Candida albicans* and *Trichophyton mentagophyte*.

Introduction

The family Rutaceae comprises about 150 genera and over 1600 plant species (1). In Thailand such as Leech lime(*Citrus hystrix* DC.), Wood apple(*Feronia limonia* Swing.), Bael-fruit(*Aegle marmelos* Corr.) and Lime(*Citrus aurantifolia* Swing). Leech lime,it was reported that the oil contained citronellal, citronellol and nerol. (2). Wood apple, the leaves are aromatic and carminative and used for the treatment of indigestion and minor bowel infection in children (3). Bael-fruit, It is claimed to be useful in treating pain, fever, inflammation, respiratory disorders, cardiac disorders, dysentery and diarrhoea (4). Lime is a highly polyembryonic species with the fruit surface smooth, greenish-yellow in colour and thin-skinned, core solid at maturity, and juice highly acidic. Lime is used for the extraction of juice, preparation of squash, concentrates, beverages and by-products, such as citric acid and pectin etc (5).

The aim of this study was to determine the nutrient metals and bioactivity of some plants in the family Rutaceae such as Leech lime, Wood apple, Bael-fruit and Lime.

Materials and Methods

Plant Materials: The Fresh leaves of C. *hystrix,* A. marmelos*, and* C. *aurantifolia* were purchased from commercial in Chiang Mai Province, Thailand and *F. limonia* was purchased from Phitsanulok Province, Thailand. A voucher specimen of C. *hystrix* (QBG No. 36963)*,* A. marmelos (QBG No. 33029)*, and* C. *aurantifolia* (QBG No. 36964) deposited in Queen Sirikit Botanic garden, Chiang Mai Province, Thailand and *F. limonia* (No.30252) is deposited in Biology herbarium, Biology department, Faculty of Science, Chiang Mai University, Chiang Mai, Thailand for reference.

Sample Preparation for Metal Analysis: The leaves of each plant were dried, ground. The leaves 5.0 g of each plant was digested with 3:1 mixture of nitric acid and perchloric acid and then adjusted with de-ionized water to 50 mL (final concentration = 100 mg mL^{-1}). The metals were determined by atomic absorption spectroscopy (AAS).

Analysis of metal: The metals such as Cu, Mn, Zn, Ca, Fe, Na and Mg were determined by atomic absorption spectroscopy (AAS; PerkinElmer AAnalyst 100, USA) using a mixture of acetylene-air flame and using respective hollow cathode lamps. The instrument was recalibrated using high purity grade salts of respective elements.

Sample preparation for antioxidant and antimicrobial activities determination on assay: The leaves of each plant were dried, ground and extracted with hexane, chloroform, ethanol and methanol by maceration. The extracts were filtered through Whatman No. 5 paper. Removal of the solvent with rotary evaporator to give sticky solid residues and were kept in the dark at 4 $^{\circ}C$.

ABTS radical scavenging activity: The antioxidant activity of the essential oil was investigated using the ABTS radical cation scavenging assay which was conducted according to the method of Roberta *et al.* [5], compared with vitamine C (final concentration 0.5-2.5 mM) and quercetin (final concentration 0.1-0.5 mM) standards. For the ABTS assay, 20 μL of crude extracts (5 mg mL^{-1}) was mixed with 2.0 mL of diluted ABTS solution (A_{734nm} = 0.700 ± 0.020) and the absorbance was determined at 734 nm after 5 min incubation at room temperature. Appropriate solvent blanks were run in each assay. All determinations were carried out at least three times, and in triplicate, on each occasion and at each separate concentration of the

standard and samples. Inhibition of free radical by $ABTS^{\bullet+}$ in percent (I%) was calculated as follows:

$$I\ (\%) = [(A_{blank} - A_{sample})/A_{blank}] \times 100$$

Where A_{blank} is the absorbance of the control reaction (containing all reagents except the test compound), and A_{sample} is the absorbance of the test compound. The percentage inhibition of absorbance at 734 nm is calculated and plotted as a function of concentration of antioxidants and of vitamine C and quercetin for the standard reference data. The concentration-response curve for 5 sequentially and separately prepared stock standards of Trolox is illustrated in Figure 1.

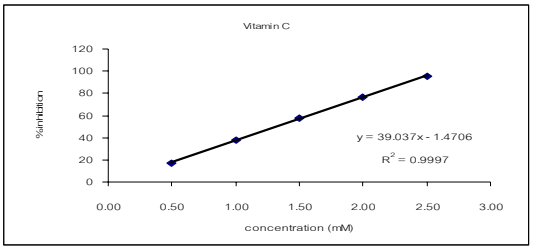

a

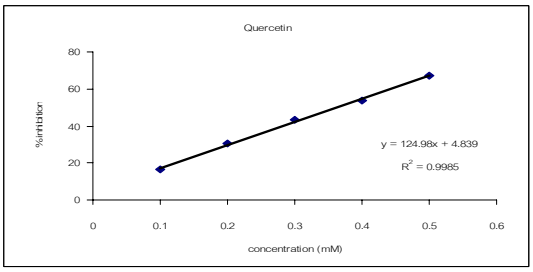

b

Figure 1. Concentration-response curve for the absorbance at 734 nm for $ABTS^{\bullet+}$ as a function of concentration of standard vitamine C (a) and quercetin (b) solution.

Antibacterial and Antifungal activity studies (agar well diffusion method): The determination of the inhibitory effect of the crude extracts on test bacteria was carried out by agar well diffusion method [6]. *Staphylococcus aureus* ATCC 25923, *Pseudomonas aeruginosa* ATCC 27853 and *Escherichia coli* ATCC 25922 were grown in Mueller-Hinton agar for 24 h, the culture suspensions were adjusted by comparing against 0.5 McFarland. *Candida albican*, *Aspergillus flavus* and *Trichophyton mentagrophyte* were grown in Sabouraud dextrose agar for 7 day, the culture suspensions were adjusted by comparing against 1.0 McFarland. Petri dishes with 20 mL of nutrient agar were prepared, previously inoculated with 200 µL of the culture suspension. The wells (9.0 mm in diameter) were made and the essential oil was diluted with ethanol then 150 µL of test concentration(50 mg mL^{-1}) was added to wells and the same volume (150 µL) of ethanol was used as a control. The inoculated plates were incubated for 24-72 h. After incubation, the diameter of the inhibition zone was measured. The measurements were done basically from the edge of the zone to the edge of the well.

Results and Discussion

The nutrient metals were determined by atomic absorption spectroscopy (AAS). There are Cu, Mn, Zn, Ca, Fe, Mg and Na present in young and old leaves of each plant. The results are shown in Table 1.

Table 1: Concentration of nutrient metals in each sample

Sample	Concentration (µg/g)						
	Ca	Mg	Na	Fe	Mn	Zn	Cu
A	16.43	89.95	3.55	1.48	0.19	0.44	0.03
G	33.91	96.68	3.94	2.65	0.22	0.45	0.08
C	12.04	90.63	2.30	2.67	0.67	0.78	0.14
D	30.69	96.72	1.88	3.06	0.89	0.75	0.07
E	12.15	154.24	2.07	2.22	0.24	0.56	0.06
F	41.92	128.63	2.21	1.96	0.46	0.88	0.05
G	7.67	89.43	1.32	3.32	0.38	0.56	0.08
H	25.17	85.64	5.18	5.45	0.32	0.54	0.05

A=Leech lime young leaves,B=Leech lime old leaves, C=Wood apple young leaves,D=Wood apple old leaves, E=Bael-fruit young leaves,F=Bael-fruit old leaves, G=Lime young leaves, H=Lime old leaves

Young and old leaves of each plant possessed the highest content of magnesium followed by calcium. Mg is an essential mineral for human nutrition. Excess magnesium in the blood is freely filtered at the kidneys, and for this reason it is difficult to overdose on magnesium from dietary sources alone. Calcium plays an important role in building stronger, denser bones early in life and keeping bones strong and healthy later in life. The human body cannot produce calcium on its own. That's why it's important to try to get enough calcium through the foods we eat. When the diet does not have enough calcium for our body's needs, calcium is taken from the bones. Therefore these metals play an important role for human health.

The antioxidant activities of the samples were determined by ABTS free radical-scavenging method. The percentage inhibition with the absorbance at 743 nm is calculated and plotted as concentration of standard vitamine C (final concentration 0.5-2.5 mM, $r^2 = 0.9997$) and quercetin (final concentration 0.1-0.5 mM, $r^2 = 0.9985$) solution as illustrated in Figure 1. The definition is mM of standard with the equivalent antioxidant capacity to 1 mg of sample. The results are presented in Table 2.

Table 2: Antioxidant activity

Sample	ABTS (mM/mg extracts)	
	Vitamine C	Quercetin
1. Leech lime leaves in various solvents :		
-Hexane ext.	0.100	0.021
-Chloroform ext.	0.213	0.056
-Ethanol ext.	0.299	0.083
-Methanol ext.	0.285	0.079
2. Wood apple leaves in various solvents :		
-Hexane ext.	0.079	0.015
-Chloroform ext.	0.159	0.040
-Ethanol ext.	0.303	0.084
-Methanol ext.	0.219	0.058
3. Bael-fruit leaves in various solvents :		
-Hexane ext.	0.064	0.010
-Chloroform ext.	0.083	0.016
-Ethanol ext.	0.177	0.045
-Methanol ext.	0.154	0.038
4. Lime leaves in various solvents :		
-Hexane ext.	0.065	0.010
-Chloroform ext.	0.094	0.019
-Ethanol ext.	0.218	0.058
-Methanol ext.	0.203	0.053

The results indicated that the leaves of Leech lime exhibited the highest antioxidant activity followed by Wood apple, Lime and Bael-fruit. The methanol extract showed the highest antioxidant capacity followed by the ethanol, chloroform and hexane extracts of each plant respectively. But methanol or ethanol extract in more preferable for medical use than chloroform or hexane extracts.

Table 3: Antibacterial activity

Sample	Antibacterial activity		
	E. Coli ($\mu g\ mL^{-1}$)	*P. aeroginosa* ($\mu g\ mL^{-1}$)	*S. aureus* ($\mu g\ mL^{-1}$)
Lime in various solvents :			
-Hexane ext.	0.208	0.229	0.177
-Chloroform ext.	0.208	0.208	0.193
-Ethanol ext.	0.229	0.229	0.161
-Methanol ext.	0.229	0.333	0.193

Positive control of antibacterial = Gentamicin standard (75 $\mu g\ mL^{-1}$)

The antibacterial activities of the crude extracts of L*ime leaves* were also investigated. Antibacterial studies were carried out *in vitro* against Gram-positive and Gram-negative organisms. Results are presented in Table 3. The hexane, chloroform ethanol and methanol extracts exhibited activities against *Escherichia* coli, Pseudomonas aeruginosa and *Staphylococcus aureus*.

The Antifungal activities of the crude extracts of L*ime* were investigated by means of agar well diffusion method. The inhibitory concentrations were calculated. Results are shown in Table 4. The hexane, chloroform ethanol and methanol extracts exhibited activities against *Candida albicans* and *Trichophyton mentagophyte*.

Table 4: Antifungal activity

Sample	Antifungal activity		
	C.albican ($\mu g\ mL^{-1}$)	*A.flavas* ($\mu g\ mL^{-1}$)	*T. mentagophyte* ($\mu g\ mL^{-1}$)
Lime in various solvents :			
-Hexane ext.	1.858	0	4.688
-Chloroform ext.	1.689	0	5.078
-Ethanol ext.	1.858	0	4.688
-Methanol ext.	2.027	0	4.883

Positive control of antifungal= Ketoconazole standard (250 $\mu g\ mL^{-1}$)

Escherichia coli, Pseudomonas aeruginosa and *Staphylococcus aureus*, *Candida albicans Trichophyton mentagophyte* are an important cause of persistent diarrhea, pneumonia and food poisoning respectively. *Candida albicans* and *Trichophyton mentagophyte* are an important cause of skin diseases.

Lime leaves can exhibit Gram-positive and Gram-negative organism's bacterea and it has antifungul activity. It begin that more study for may play an important role in medicine, food, health supplements and cosmetic industries.

Conclusions

There are Cu, Mn, Zn, Ca, Fe, Mg and Na are present in Leech lime, Wood apple, Bael-fruit and Lime leaves. In addition, the hexane, chloroform, ethanol and methanol extracts of leaves from each plant showed antioxidant activity by the ABTS method. Lime leaves can exhibit Gram-positive and Gram-negative organism's bacteria and it showed antifungal activity. Therefore, Leech lime, Wood apple, Bael-fruit and Lime leaves may play an important role in medicine, food, health supplements and cosmetic industries.

Acknowledgments

We would like to express our sincere thanks to Faculty of Pharmacy and the Graduate School, Chiang Mai University for partial support. We also thank Mr. Banyong Khantawa, Microbiology Section, Central Loboratory, Maharaj Nakorn Chiang Mai Hospital,

Chiang Mai, Thailand for kindly providing suggestions in the support microbiology laboratory.

We also would like to express our special thank to Center for Innovation in Chemistry: Postgraduate Education and Research Program in Chemistry (PERCH-CIC); Chemistry Department, Faculty of Science, Chiang Mai University; TRF and Commission on Higher Education for their partial support.

References

[1] S. Promjit, C. wongsatit, T. Rungravi, C. Terry, *Medicinal Plants in Thailand* **vol. 1**, Amaria P&P Public Co Ltd., Bangkok, Thailand (1996).

[2] The National Commission Organizing the Celebration of the 50th Anniversary of His Majesty's Accession to the Throne, *Medicinal plants garden in Phutthamonthon / the National Commission Organizing the Celebration of the 50th Anniversary of His Majesty's Accession to the Throne*, In commemoration of the Celebration of the 50th Anniversary of His Majesty's Accession to the Throne, Bangkok, Thailand (1996).

[3] C. Wongsatit, S. Promjit, P. Wichit, T. Rungravi, C. Terry, *Medicinal Plants in Thailand* **vol. 2**, Amaria P&P Public Co Ltd., Bangkok, Thailand (1997).

[4] A. Kumar, A.G.C. Nair, A.V.R. Reddy, A.N Garg, J. Phar. *Biomed. Anal.* **37** (2005), pp. 631-638.

[5] Roberta R., Nicoletta P., Anna P., Ananth P., Min Y., Catherine R.E. *J.* Free Rad *Biol* Med. **26** (1999), pp. 1231–1237.

[6] O. O. Igbinosa, E. O. Igbinosa, A. Aiyegoro, Afr. J. *Pharm. Pharmacol.* **3** (2009), pp. 058-062.

Antimicrobial activities of some Thai medicinal plants

S. Khamsan[1*], B. Liawruangrath[1], S. Liawruangrath[2], A. Teerawutkulrag[2], S. G. Pyne[3] and M. J. Garson[4]

[1]Department of Pharmacy, Chiang Mai University, Chiang Mai, Thailand 52000
[2]Department of Chemistry, Chiang Mai University, Chiang Mai, Thailand 52000
[3]Department of Chemistry, The University of Wollongong, Australia 2522
[4]School of Chemistry and Molecular Biosciences, The University of Queensland, Australia 4072

*Email:sorabond@hotmail.com

Abstract: The extracts derived from different parts of three medicinal plants were screened for their antibacterial and antifungal activities by the agar diffusion method. These plants are commonly used in Thai traditional medicine. The dried plants were extracted with petroleum ether and ethyl acetate (1:1). The extracts of *Lindenbergia philippensis* (cham.) Benth., *Barreria lavicaulis* (Miq.) Ridl *and Kyllinga nemoralis* (Rott.) C.B. Clarke were tested in vitro against three bacteria: *Escherichia coli* (ATCC25922), *Staphylococcus aureus* (ATCC25923), and *Pseudomonas aeruginosa* (ATCC27553). The antifungal activity of these plant extracts were also investigated against *Aspergillus flavus*, *Candida albican* and *Trichophyton mentagrophyte*. The results indicated that the extracts of *L. philippensis* (cham.) Benth. aerial part (9.1 mg/mL) and roots (10.7 mg/mL) showed antibacterial activity against *E. coli*., *S. aureus* and *P. aeruginosa*. They also showed antifungal activity against *A. flavus* and *C. albican*, but did not inhibit *T. mentagrophyte*. The extracts of *B. lavicaulis* (Miq.) Ridl aerial part (10.0 mg/mL) and roots (10.3 mg/mL) exhibited antibacterial activity against *S. aureus*, *E. coli* and *P. aeruginosa*, and also showed antifungal activity against *A. flavus* and *C. albican*, but did not inhibit *T. mentagrophyte*. The extracts of *K. nemoralis* (Rottb.) C.B. Clarke both aerial part (10.3 mg/mL) and roots (10.2 mg/mL) showed inhibition zones against *S. aureus*, *E. coli* and *P. aeruginosa*. They also showed antifungal activity against *A. flavus* and *C. albican*, but did not inhibit *T. mentagrophyte*. These extracts will be further purified and elucidated the bioactive compounds.

Introduction

Some diseases are caused by organisms such as bacteria and fungi. The conventional treatment of bacterial and fungal disease is limited, and part of the reason is due to the limited spectrum of the currently antibacterial and antifungal drugs, and the expensive treatment, particularly due to the need of prolonged therapy [1]. Thus, new drugs and alternative therapies are necessary, including natural products.

Nature has been utilized as a source of medicines and food throughout human history. For thousands of years, plants have formed the basis of sophisticated traditional medicine systems and more recently, natural products have been a good source of lead compounds, especially against infective diseases. Since the beginning with the isolation of morphine from opium in the early 19thcentury[2], drug discovery from nature led to important chemotherapeutic agents such as quinine, digitoxin and artemisinin[3-5]. It is estimated, however, that of the 250,000–500,000 species of major plant found on Earth, only 1% have been studied for their pharmaceutical potential [6]. The potential of higher plants as sources for new drugs is still largely unexplored.

The main objective of this study was to search for Thai medicinal plants which possess strong antimicrobial activity. In this study we report the antibacterial and antifungal activities of some Thai medicinal plant extracts.

Materials and Methods

Collection and preparation of plant material:

Fresh leaves and roots of the plants were collected and air-dried. Then the dried plants were ground into a powder, and fifty grams of each plants were subjected to soxhlet extraction with petroleum ether and ethyl acetate (1:1) for 72 h, followed by filtration. The filtrate was evaporated to dryness under reduced pressure to obtain the crude extracts. The results are shown in Table 1.

In vitro Bioassay studies:

The antibacterial activity of the extracts was determined using the agar diffusion method [7]. The bacteria used were: *Escherichia coli* ATCC25922, *Staphylococcus aureus* ATCC25923 (Gram positive bacteria), *Pseudomonas aeruginosa* ATCC27553 (Gram negative bacteria). The antifungal activity of the extracts against yeast *Candida albican* and fungus *Aspergillus flavus* and *Trichophyton mentagrophyte* were also investigated.

In brief, a measured amount of the crude extracts were dissolved in definite volumes of 10% dimethylsulfoxide (DMSO) to give solutions of known concentrations (mg/mL). In agar plates, bacteria and fungi were spread. In each of these plates, 4 wells (9 mm) were cut out using sterile cork borer and 20µL of each extracts were applied into the wells. 100µL of Gentamicin, 100 µL of Ketoconazole and 20 µL of 10% DMSO were used as a positve control. The plates were incubated at 37°C for 48-72 h. The antimicrobial activities were measured by the zone of inhibition expressed in mm. The experiments were repeated at least triplicate.

Results and Discussion

The antimicrobial of some Thai medicinal plant extracts were investigated by agar diffusion method. The crude extracts at 10 mg/mL concentrations showed activity against the bacteria tested. The inhibitory zones were measured. Results are shown in Table 2.

The crude extracts at the same concentration showed antifungal activity and the inhibitory zones were measured. Results are shown in Table 3.

The extracts derived from different parts of three medicinal plants showed the highest antibacterial activity against *P. aeruginosa*. The extracts also inhibited equal antibacterial activity against *E. coli* and *S. aureus*. The antibacterial activity against Gram negative bacteria was more pronounced than against Gram positive bacteria.

The crude extracts also showed antifungal activity against *A. flavus* and *C. albican* but showed no inhibition against *T. mentagrophyte*, because there was not enough active constituent in the crude extracts.

Table 1**:** The percentage yield of crude extracts from Thai medicinal plants

Thai Medicinal Plants	**Part used**	**%yield (w/w)**
Lindenbergia philppensis (cham*.)* Benth.	aerial roots	15.9 12.7
Barreria lavicaulis (Miq.) Ridl	aerial roots	13.9 13.0
Kyllinga nemoralis (Rott.) C. B. Clarke	aerial roots	10.9 10.7

Table 2**:** Antibacterial activity of Thai medicinal plant extracts

Plants	Part tested	Conc. mg/mL	Inhibitory zone (mm)[a]		
			E. coli	*S. aureus*	*P. aeruginosa*
L.philppensis (cham*.)* Benth.	aerial roots	9.1 10.7	13 12	11 10	15 13
B. lavicaulis (Miq.) Ridl	aerial roots	10.0 10.3	11 11	11 11	15 13
K. nemoralis (Rott.) C. B. Clarke	aerial roots	10.3 10.2	11 11	11 12	15 14
Gentamicin[b]	-	[c]	27	35	27
10% DMSO[d]	-	-	-	-	-

[a]: Inhibition zones are the mean cork borer (9 mm) diameter
[b]: Antibiotic for treatment of bacterial disease
[c]: (75 µg/mL concentration), [d]: positive control, -No inhibition zone

Table 3**:** Antifungal activity of Thai medicinal plant extracts

Plants	Part tested	Conc. mg/mL	Inhibitory zone (mm)[a]		
			A. flavus	*C. albican*	*T. mentagrophyte*
L. philppensis (cham*.)* Benth.	aerial roots	9.1 10.7	15 11	12 13	- -
B. lavicaulis (Miq.) Ridl	aerial roots	10.0 10.3	11 11	12 12	- -
K. nemoralis (Rott.) C. B. Clarke	aerial roots	10.3 10.2	11 12	12 14	- -
Ketoconazole[b]	-	[c]	25	37	16
10% DMSO[d]	-	-	-	-	-

[a]: Inhibition zones are the mean cork borer (9 mm) diameter
[b]: Antibiotic for treatment of fungal disease
[c]: (250 µg/mL concentration), [d]: positive control, -No inhibition zone

Conclusions

The antimicrobial activities of the petroleum ether and ethyl acetate (1:1) extracts of Thai medicinal plants commonly used in Thai traditional medicine were investigated. In this study, we focussed on screening of the crude extracts which possess antibacterial and antifungal activities. The screening results indicated that all the extracts showed antibacterial activity against *S. aureus*, *E. coli* and *P. aeruginosa* and showed the highest inhibition zone diameter against *P. aeruginosa* (15 mm), compared with all the tested organisms. All crude extracts showed antifungal activity against *A. flavus* and *C. Albican* but no inhibitory effects against *T. mentagrophyte*. The extract of the aerial part of *L. philppensis* (cham*.)* Benth. showed highest inhibition zone against *A. flavus* (15 mm). The extract of the roots of *K. nemoralis* (Rott.) C. B. Clarke showed highest inhibition zone against *C. albican* (14 mm).

The extracts will be further purified using bioassay-directed isolation and elucidated the bioactive compounds.

Acknowledgement

This research was supported by the research fund from The Thai Commission on Higher Education (CHE). Naresuan University, Phitsanulok, Thailand. We would like to thank the faculty of pharmacy and the Graduate School, Chiang Mai University for partial support.

References

[1] M. M. Cowan, *Clin. Microbiol. Rev.* **14**, (1999), pp. 564– 584.
[2] A. D. Kinghorn, *J. Pharm. Pharmacol.* **53**, (2001), pp. 135-148.
[3] D. J. Newman, G. M. Cragg, K. M. Snader, *Nat. Prod. Rep.* **17**, (2000), pp. 215-234.
[4] M. S. Butler, *J. Nat. Prod.* **67**, (2004), pp. 2141-2153.
[5] D. L. Klayman, *Science.* **228**, (1985), pp. 1049-1055.
[6] G. T. Prance, *Ann. Missouri Bot. Gard.* **64**, (1977), pp. 659-684.
[7] A. M, Janssen, J. J. C. Scheffer, A . B. Svendsen, *Plant. Med.* **53**, (1987), pp. 395–398.

Synthesis of molecularly imprinted polymers for isolation of dicyclohexylurea from peptide synthesis

S. Jaita, W. Kareuhanon, and M. Pattarawarapan*

Department of Chemistry and Center of Excellence for Innovation in Chemistry, Faculty of Science, Chiang Mai University, Chiang Mai, Thailand 50200

*E-mail: mookda@chiangmai.ac.th

Abstract: Dicyclohexylurea (DCU) is a common byproduct derived from dicyclohexylcarbodiimide (DCC) mediate coupling between an amine with a carboxylic acid. Due to its limited solubility in most solvents, it is difficult to remove from reaction mixtures using conventional techniques such as extraction or chromatography. Molecularly imprinted polymers (MIPs) have recently attracted the attention of researchers in a variety of disciplines because of their ease of preparation, versatility and stability. MIPs have been successfully used as separation media in chromatography applications and in solid phase extraction (SPE). Presented herein is the progress to date of using MIPs as a medium for the selective removal of DCU from peptide synthesis. MIPs were synthesized using DCU and a structure analog, diphenylurea (DPU), as the templates. Acrylamide was used as functional monomer. The conditions for MIPs synthesis were optimized by varying types of cross-linkers. The imprinted materials were characterized by FT-IR and SEM techniques. The binding performances of synthesized polymers were investigated by UV rebinding study. Because DCU has no chromophore present in its structure, DPU was chosen as a test substrate to ease quantification of concentration by UV spectroscopic method. Binding conditions was optimized to obtain specific binding of MIPs to urea derivatives. The MIPs of DPU and DCU were found to selectively bind to their corresponding target molecules and can be applied to remove byproducts, DCU, from peptide synthesis.

Introduction

In organic synthesis, the coupling reaction between amide and carboxylic acid generally suffer from the byproduct derived from coupling reagents such as diisopropylcarbodiimide (DIC), dicyclohexylcarbodiimide (DCC) which give the corresponding products, diisopropylurea (DIU) and dicyclohexylurea (DCU), respectively. Due to their limit solubility in most solvents, it is difficult to remove them from reaction mixtures using conventional techniques such as extraction or chromatography. Molecularly imprinted polymers (MIPs) are synthetic materials able to selectively recognize a guest molecule or related compounds[1]. It can be tailor-made to specifically bind to target analytes by means of imprinting process. Generally, a target analytes or its structurally analog is used as a template to direct the arrangement of the functional monomers which are then chemically fixed by co-polymerization with a cross-linker. Removal of the template reveals recognition sites in the rigid polymer matrix which are specific to the template and its close analogs. So far, MIPs have been used successfully as chromatographic separation media and in solid phase extraction (SPE).[1-5] However in the field of organic synthesis, less works have been investigated in the application of MIPs in byproduct removal.[6-8] MIP which is selective to DCU has previously been synthesized as a medium for the selective removal of DCU.[6] DPU was used as the template in a methacrylic acid (MAA)-ethylene glycol dimethacrylate (EDMA) copolymer matrix. The percent template bound (%) was found in range of 10-48%. Nevertheless, DCU has never been explored as the template in the preparate of MIPs. In this study, MIPs were synthesized using both DCU and DPU as the templates for selective removal of DCU from a reaction mixture.

Materials and Methods

Synthesis and binding study of MIPs

All imprinted polymers were synthesized by bulk polymerization method. Briefly, 0.25 mmol of template, 1 mmol acrylamide, 5 mmol of crosslinker and benzoyl peroxide were dissolved in acetonitrile. The solution was flushed with nitrogen for 5 min. Polymerization was started at 60°C and continued for 24 h. The imprinted bulk monolith was ground in mortar then washed with methanol, and dried in vacuum. Non-imprinted polymer (NIP), was also synthesized under the same conditions as that used for preparing MIP except that the template was omitted during the polymerization. The morphology of polymers were investigated by scanning electron microscope (SEM).

Assessment of MIP and NIP binding performances with template was performed by SPE experiments. Briefly, 100 mg of the polymers were packed in 5 mL extraction cartridges. After precondition with acetonitrile and 1,2-dichloroethane, 1 mL of test substrate solution, DPU, in 1,2-dichloroethane was loaded with 5x1 ml reloaded. The elution of the bound analytes was performed using MeOH (0.5 mL x 2). The combined eluate fraction was evaporated to dryness under N_2 and redissolved in 1,2-dichloroethane before analysis by UV-Vis spectrophotometer at λ 254 nm. Each experiment was done in duplicate.

The selectivity of MIPs towards the DPU and other amide containing substrates was investigated using the above described method. Quantification of the analytes concentration was done using UV spectroscopic method at λ 270, 230 and 273 nm for benzamide (BZM), benzylbenzamide (BBZM) and dipeptide I, respectively (Figure1).

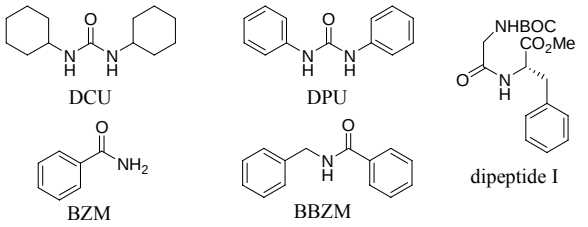

Figure 1. Structures of the templates and binding substrates

Loading capacity of **P4** was determined using the above described SPE procedure. The 1 mL solution of DPU at different concentrations (0.625-100 μgmL^{-1}) was loaded on the MIP cartridge. The eluent was collected and analyzed by UV and the amount of eluted DPU was plotted versus the amount of DPU loaded on SPE cartridge. Each experiment was done in duplicate.

Synthesis of dipeptide I (Scheme 1)

To a stirred suspension of phenylalanine methyl ester hydrochloride salt (1 equiv) and N-Boc-Gly-OH (1.1 equiv) in dichloromethane was added triethylamine (2 equiv) at 0 ^oC. DCC was then added and the reaction was stirred at 0 ^oC for 1 hour and at room temperature for 3 hours under N_2. The reaction was washed sequentially with 1 N aq. HCl, aqueous saturated $NaHCO_3$ and water. The organic phase was dried over Na_2SO_4 and concentrated under reduced pressure. The residue was purified by column chromatography, dried under vacuum and analyzed by ^{1}H-NMR.

The dipeptide I was obtained as colorless oil, 71%. ^{1}H NMR (400 MHz, $CDCl_3$) δ 7.32-7.25 (m, 3H, Ph), 7.11-7.13 (m, 2H, Ph), 6.54 (d, J = 7.2, 1H, NH), 5.12 (br s, 1H, NH), 4.90 (dd, J = 6, 2, 1H, NHCH_2), 3.82-3.78 (dd, 1H, CH_2Ph), 3.78-3.73 (dd, J = 6, 2, 1H, NHCH_2), 3.74 (s, 3H, OCH_3), 3.14 (m, 1H, CH_2Ph), 1.46 (s, 9H, $C(CH_3)_3$).

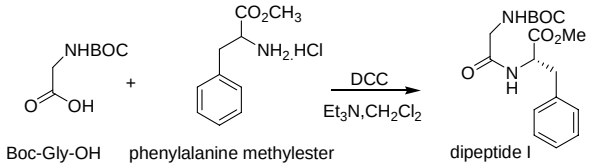

Scheme 1. Synthesis of dipeptide I

MIP-SPE to remove DCU byproduct in the synthesis of dipeptide I

The optimized MIP-SPE protocol was applied to remove DCU from the crude reaction mixture derived from coupling reaction between phenylalanine methyl ester and Boc-Gly-OH using DCC as a coupling agent (Scheme 1). The efficiency of removal byproduct was investigated by ^{1}H-NMR.

Results and Discussion

Synthesis of MIPs and their binding efficiency

Acrylamide was selected as functional monomer since it was known to interact with urea moiety presence in the templates.[6] All MIPs were thus prepared with bulk polymerization using DCU and DPU as the templates and the composition of MIPs were altered by varying types of cross-linkers. The white polymers were obtained in high percentage yield (80-90%) after grinding. Figure 2. is the SEM micrograft of the representative MIP, P4. The image shows the non-spherical morphology with pores on the surface.

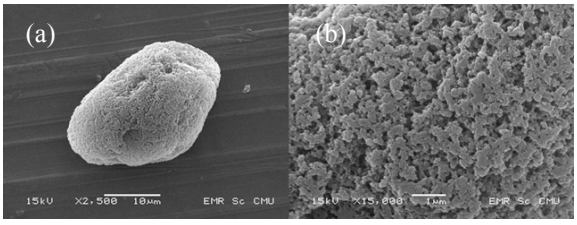

Figure 2. The SEM image of **P4** with (a) 2,500× and (b) 15,000× magnification

To investigate binding performance of synthesized polymers, MIPs were applied as a sorbent in SPE. Since DCU has no chromophore present in its structure, it would be difficult to analyze by UV spectroscopy. To overcome this problem, DPU was applied as a binding molecule in place of DCU.

For each polymer, the percentage bound (%Bound) and the imprinting factor (α) were calculated according to Eqs. (1) and (2), respectively.

$$\%Bound = \frac{Q}{Q_{initial}} \times 100 \qquad (1)$$

Where Q is the amount of analyte bound to the polymer and $Q_{initial}$ is the initial amount of analyte before loading in polymer

$$\propto = \frac{\%Bound_{MIP}}{\%Bound_{NIP}} \qquad (2)$$

Where $\%Bound_{MIP}$ and $\%Bound_{NIP}$ represent the percentage of bound analyte by MIPs and NIPs, respectively.

According to the Table 1, **P3** and **P4** show the high %Bound of DPU and also gave the high imprinting factor among the others MIPs, therefore, they were selected for further study.

Table 1: Compositions and binding characteristics of MIPs

MIP	Template	Cross-linker[a]	%Bound	α
P1	DPU	EGDMA	38.37±1.5	0.50
P2	DPU	DVB	56.60±1.2	0.84
P3	DPU	Bis-AA	92.24±4.7	1.99
P4	DCU	EGDMA	91.23±3.9	1.13
P5	DCU	DVB	56.64±1.7	0.87
P6	DCU	Bis-AA	62.08±1.1	0.92

[a] EGDMA=ethyleneglycol dimethacrylate, DVB=divinylbenzene, Bis-AA=bis-acrylamide.

DPU selectivity of imprinted polymers

The selectivity of **P3** and **P4** were evaluated by performing the SPE experiments using DPU and other amide containing substrates (Figure 1) as the analytes. Standard solution of analytes 25 μg mL^{-1} in 1,2-dichloroethane was applied. Figure 3 show the recovery of substrates after binding with P3 and P4 and the selectivity factors (ε) were calculated according to Eqs. 3 and listed in Table 2.

$$\varepsilon = \frac{\%Recovery_{DPU}}{\%Recovery_{substrate}} \qquad (3)$$

Where $\%Recovery_{DPU}$ represents the percentage of recovery DPU by MIP and $\%Recovery_{substrate}$ represents the percentage of recovery the dipeptideI and amide containing substrates.

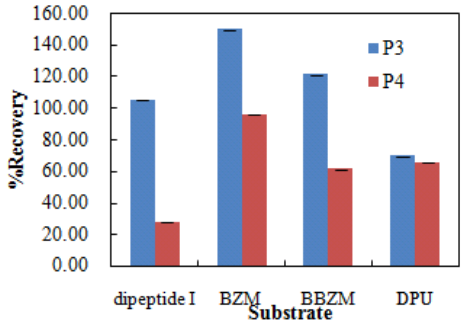

Figure 3. The %recovery of test substrates on **P3** and **P4**

According to Figure 3, all the amide containing compounds were bound to both imprinted polymers. **P3** exhibited higher recovery of the test substrates than its corresponding template, DPU. However, for **P4**, the polymer showed higher % recovery of DPU than that of dipeptide I. The highest selectivity factors for DPU over dipeptide I (ε = 2.38) indicated that this polymer can be used for effectively remove the byproduct, DPU, from the coupling reaction involving the preparation of the dipeptide I and other structurally related compounds.

It is noted that over 100% recovery were observed in many cases, especially for BZM. This probably was due to self aggregation of the compound causing an increase in the absorbance value after binding with the polymer.[9]

Table 2: The selectivity factors, ε, of **P3** and **P4**

substrate	selectivity factors (ε)	
	P3	P4
dipeptide I	0.66	2.38
benzamide	0.46	0.69
benzylbenzamide	0.57	1.07

Determination of MIP capacity

Capacity curve was plotted for **P4** to evaluate the maximum amount of DPU retain on a 100 mg MIP-SPE cartridge (Figure 4). The recovery of DPU sample during elution step was plotted against the loaded amount. From the result, the capacity curve of MIPs reaches a limit when the amount of loaded DPU is higher than 16 μgmL^{-1} which means that the MIP-SPE cartridge showed the maximum loading capacity at the amount of DPU 16 μgmL^{-1}.

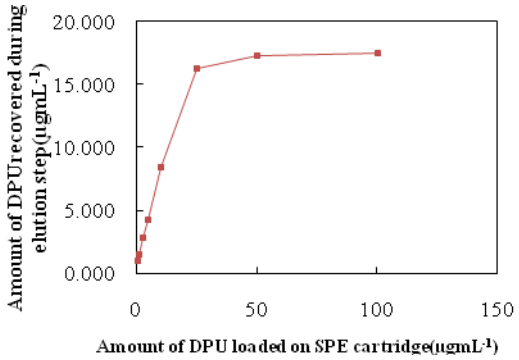

Figure 4. Loading capacity of **P4**

Application of MIP-SPE to amide coupling reaction

P4 was applied as a sorbent in SPE for selective removal of DCU byproduct in the synthesis of dipeptide I. The crude reaction mixture of the dipeptide synthesis was loaded on MIP-SPE protocol. The efficiency of **P4** for removal of byproduct was investigated using ^{1}H-NMR by comparison of the NMR spectra of crude mixture and the eluent after the MIP-SPE process. It was found that approximately 63% of DCU was removed from the crude mixture and dipeptide I was obtained in 82% yield. The data indicated that **P4** can selectively remove byproduct from the peptide synthesis using the DCC as coupling reagent.

Conclusions

In conclusion, a molecularly imprinted polymer has been synthesized. It was found to exhibit high binding affinity and selectivity toward DPU. The MIP was found to be efficiency to use in removal of DCU from the reaction mixture of the DCC mediate coupling reaction.

Acknowledgments

The authors gratefully acknowledge the Center of Excellence for Innovation in Chemistry (PERCH-CIC), the Thailand Research Fund (TRF) and Commission on Higher Education, Ministry of Education for financial support to this research.

References

[1] R. Arshadyand K. Mosbach, *Macromol. Chem. Phys.*, **182** (1981), pp. 687-692.
[2] C. Alexander, L. Davidsonand W. Hayes, *Tetrahedron.,* **59** (2003), pp. 2025-2057.
[3] K. Haupt, *Anal. Chem.*, **75** (2003), pp. 376A-383A.
[4] B. Sellergren, *Molecularly Imprinted Polymers: Man-Made Mimics of Antibodies and Their Applications in Analytical Chemistry.* Tech. Instrum. Anal. Chem., 2001.
[5] T. Takeuchiand J. Haginaka, *J. Chromatogr., B: Biomed. Sci. Appl.*, **728** (1999), pp.1-20.
[6] A. Mohammadi, T. Alizadeh, R. Dinarvand, M. R. Ganjaliand R. B. Walker, *Asian J. Chem.* **21** (2009), pp. 2875-2880.
[7] G. T. Rushtonand K. D. Shimizu, *Polym. Prepr. (Am. Chem. Soc., Div. Polym. Chem.)*, **45** (2004), pp. 811.
[8] L. Ye, O. Ramstroemand K. Mosbach, *Anal. Chem.*, **70** (1998), pp.2789-2795.
[9] S. Komkham, M. Pattarawarapan, W. Kareuhanon, C. Tayapiwatana, *e-Polymers*, **091** (2008) , pp.1-9.

Synthesis and pharmacological evaluation of capsaicin's analogues.

P. Kumboonma[1], C. Phaosiri[1*], T. Senawong [2], T. Saiwichai[2], K. Siriwong[1] and C. Yenjai[1]

[1]Department of Chemistry, Faculty of Science, Khon Kaen University, Khon Kaen, Thailand 40002
[2]Department of Biochemistry, Faculty of Science, Khon Kaen University, Khon Kaen, Thailand 40002

*E-mail:chapha@kku.ac.th

Abstract: Capsaicin, a natural compound from hot peppers, contains a similar structure to that of a potent anticancer, suberoylanilide hydroxamic acid (SAHA). Therefore, an array of capsaicin's analogues was designed and synthesized to investigate their anticancer activities based on histone deacetylase inhibitory activities. Histone deacetylase inhibitory activities of all compounds were evaluated *in vitro* by using HeLa nuclear extract in a fluorimetric assay. The pharmacological data in term of structure-activity relationship revealed that the non-polar aromatic region and the polar side chain were important for binding to the active site of histone deacetylase enzyme. A silyl-protected dihydrocapsaicin, an allylic hydroxyl derivative, a methyl ester derivative and a hydroxamic derivative were the most active histone deacetylase inhibitors among the synthesized compounds. Preliminary docking experiments on human HDAC8 enzyme showed partly consistent results to the *in vitro* experiments.

Introduction

Capsaicin (8-methyl-*N*-vanillyl-6-nonenamide, CAP, **3a**) and dihydrocapsaicin (8-methyl-*N*-vanillyl-6-nonanamide, DHC, **3b**), isolated from the fruits of *Capsicum* species or hot chilli peppers[1], contained partially mimic structure to that of the FDA approved histone deacetylase (HDAC) inhibitor, SAHA (**1**, Vorinostat®, Zolinza™) and trichostatin A (**2**, TSA)[2]. SAHA was approved to treat the rare cancer cutaneous T-cell lymphoma on patients who had progressive, persistent or recurrent disease.

Histone deacetyalse inhibitors can affect differentiation, growth arrest, or apoptosis in transformed cell cultures by blocking substrate access to the histone deacetylase active site[3]. These agents have been proposed not only as anti-cancer compounds but also therapeutic drugs to treat neurodegenerative diseases and inflammation[4]. Therefore, HDACs are popular targets in drug development and HDAC inhibitors are potential drug candidates for many diseases.

The results obtained from the X-ray crystallography and the structure-activity relationships of SAHA provided the structural characteristics of HDAC inhibitors as depicted in Figure 1.[3] The pharmacophore of HDAC inhibitors composes of a metal binding domain, a linker domain, and a surface recognition domain.

The molecular designs of the new HDAC inhibitors, derivatives of CAP/DHC, are based on the modification of the metal-binding functional group, surface recognition area and the hydrocarbon linker in order to improve HDAC inhibitory activities. In a previous report,[5] silyl ether (**4a, 4b**) derivatives showed good histone deacetylase inhibitory activities.

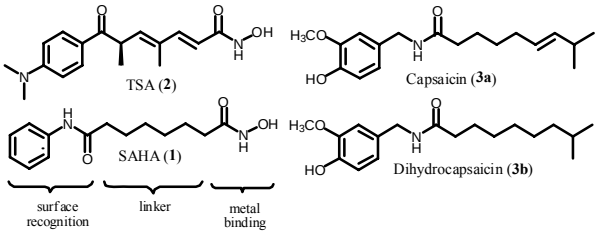

Figure 1. Structures of capsaicin (CAP, **3a**) / dihydro-capsaicin (DHC, **3b**), SAHA (**1**) and TSA (**2**).

In this present work, we further investigate the biological evaluation of capsaicin as HDAC inhibitor and the structural modifications of this lead compound to explore the potential inhibitory activities of capsaicin's derivatives. These results provide promising HDAC inhibitory for further studies in a molecular level using a molecular docking method.

Materials and Methods

General Experiment Procedures. Reagents were purchased from Sigma-Aldrich, Merck, and Carlo Erba. Solvents were purchased from Fisher Scientific. All solvents and volatile reagents were distilled prior to use. Tetrahydrofuran (THF) was distilled from sodium/benzophenone. "Dried and concentrated" refers to removal of residual amounts of water with anhydrous Na_2SO_4 followed by evaporation of solvent on a rotary evaporation. ^{1}H NMR, ^{13}C NMR were recorded in the indicated solvents on a Bruker AM400. When $CDCl_3$ was used as a solvent, the 77.00 ppm (center line) signal was the reference for ^{13}C NMR, and residual $CDCl_3$ (^{1}H NMR, 7.26 ppm) was used as an internal standard. IR spectra were recorded on Nicolet 5DXB FT-IR spectrophotometer using KBr pellets and NaCl cells. Silica gel 60 (230-400 mesh) were used as adsorbents.

Plant materials. Dried fruits of *Capsicum annuum.* (3 kg) were purchased in May 2009 at a local market in Khon Kaen, Thailand.

Extraction and Isolation. Dried fruits of *Capsicum annuum sp.* (3 kg) were extracted three times with

EtOAc. The EtOAc extracts were concentrated to give a residue 107 g. The EtOAc extract 40 g was dissolved in EtOAc 50 mL and extracted with 3 M NaOH 30 mL for three times. The basic extracts were collected, the process were repeated two more times. The basic extract was adjusted pH to be slightly acidic with concentrated HCl and extracted with EtOAc 20 mL for nine times. The combined EtOAc extracts were dried and concentrated in *vacuo* to yield a red mixture in 18.8 g. The red mixture (9.4 g) was purified by column chromatography using ethyl acetate/hexanes (50:50) to yield a mixture of CAP and DHC in 1:1 ratio (**3a**, **3b**, 2.7 g) as a red-orange oil.

Structural Modification

Preparation of hydroxyl-CAP (5). To a solution of compounds **3a, 3b** (30.8 mg, 0.1 mmol) in THF (1 mL) was added a solution of $Hg(OAc)_2$ (24 mg, 0.075 mmol, 1.5 equivalents) in water (0.5 mL). Catalytic amount of acetic acid was added and the reaction mixture was stirred at room temperature for 19 hr. Monitoring by TLC until all starting materials had been consumed, the reaction mixture was then treated with 3M solution of NaOH (0.5 mL) followed by $NaBH_4$ (14.7 mg, 0.008 mmol, 2 equivalents) solution in 3M NaOH (0.5 mL) and stirred further for 2 hr. The mixture was saturated with solid NaCl and extracted with EtOAc (3x20 mL). The combined organic layers were dried and concentrated. Purification by column chromatography (1:1 (v/v) ethyl acetate/hexanes) gave a yellow oil of compound **5** (15 mg, 91%) and recovered compound **3b** (14 mg, 91%).

Preparation of diacetyl-CAP (6) To a solution of compound **5** (12.8 mg, 0.04 mmol) in pyridine (2 mL) was added Ac_2O (0.01 mg, 0.098 mmol, 2.5 equivalents). The solution was stirred at room temperature for 24 hr. Then water 3 mL was added and the mixture was extracted with EtOAc (3x20 mL). The combined organic layers were dried and concentrated to give a yellow oil of compound **6** (10 mg, 73%).

Preparation of allylic hydroxyl-CAP (7) To a solution of compounds **3a, 3b** (60 mg, 0.14 mmol) in THF (3mL) was added SeO_2 (23 mg, 1.5 equivalents). Catalytic amount of pyridine was added and the reaction mixture was heated to reflux for 10 hr. Then water 3 mL was added and the mixture was extracted with EtOAc (3x20 mL). The combined organic layers were dried and concentrated. Purification by column chromatography (1:1 (v/v) ethyl acetate/hexanes) gave a yellow oil of compound **7** (25 mg, 80%) and recovered compound **3b** (28 mg, 93%).

Preparation of diacetyl allylic-CAP (8). To a solution of compound **7** (10.0 mg, 0.03 mmol) in pyridine (2 mL) was added Ac_2O (0.01 mg, 0.098 mmol, 2.5 equivalents). The solution was stirred at room temperature for 29 hr. Then water 3 mL was added and the mixture was extracted with EtOAc (3x20 mL). The combined organic layers were dried and concentrated, to give a yellow oil of compound **8** (11 mg, 86%).

Preparation of chloranil-DHC (9). To a solution of **3b** (35.0 mg 0.114 mmol) in 4 mL of THF at -40 ^{o}C under N_2 was added 42.0 mg (0.171 mmol) of *o*-chloranil. After 17 hr at rt, the solvent was removed in *vacuo* and 5% $NaHCO_3$ was added to the residue and the residue was extracted with EtOAc (3x20 mL). The combined organic layers were dried and concentrated. Purification by column chromatography (1:1 (v/v) ethyl acetate/hexanes) gave a brown gum of compounds **9** (36.3 mg, 92%).

Preparation of silyl bromo-DHC(10), **silyl bromo methyl ester (11) and silyl bromo dihydroxyl (12)**. Compounds **4a, 4b** (76 mg, 0.17 mmol) was dissolved in a mixture of THF (2 mL) and water (2 mL). A solution of potassium osmate dihydrate (3 mg, 0.04 mmol) in water 1 mL was added dropwise. After 1 hr, sodium periodate (71 mg, 0.34 mmol) was added and a mixture was allowed to stir at room temperature for 3 hr. After addition of water 3 mL, The mixture was extracted with EtOAc (3x20 mL). The combined organic extracts were washed with 1 N $NaHSO_3$, dried and concentrated to give 120 mg of brown oil. Without further purification, a 2.0 M bromine solution in 9:1 MeOH-H_2O 1 mL buffered with $NaHCO_3$ 0.2 g was added to a residue. After being stirred for 17 hr, solid sodium thiosulfate (0.1 g) was added to quench excess bromine. The undissolved material was removed by filtration and the filtrate was extracted with EtOAc (3x20 mL). The combined organic layers were dried and concentrated. Purification by preparative chromatography (1:1 (v/v) ethyl acetate /hexanes) gave a yellow gum of compound **10** (38.5 mg, 92%), a colorless compound **11** (30 mg, 73%), a colorless compound **12** (8 mg, 20%).

Preparation of bromo methyl ester (13). To a solution of **11** (28 mg, 0.065 mmol) in THF (2 mL) and H_2O (1 mL) at room temperature was added $NH_2OH.HCl$ (7 mg, 0.1 mmol, 1.5 equivalents) and Et_3N (0.25 mL). The mixture was refluxed for 5 hr. After the solution was cooled to ambient temperature, 2 mL of H_2O was added slowly to the reaction mixture which was extracted with EtOAc (3x20 mL). The combined organic layers were dried and concentrated. Purification by preparative chromatography (1:1 (v/v) ethyl acetate/hexanes) gave a colorless oil of compound **13** (20 mg, 82%).

Preparation of bromo hydroxamic acid (14). To a solution of compound **11** (16.5 mg, 0.039 mmol) in EtOH (3 mL) at room temperature was added $NH_2OH.HCl$ (8 mg, 0.12 mmol, 3 equivalents) and 20% KOH (2 mL). The mixture was refluxed for 4 hr. After the solution was cooled to ambient temperature, 2 mL of H_2O was added slowly to the reaction mixture which was extracted with EtOAc (3x20 mL). The combined organic layers were dried and concentrated. Purification by preparative chromatography (1:1 (v/v) ethyl acetate/hexanes) gave white sediments of compound **14** (10 mg, 69%).

Preparation of Silyl-DHC (4b) To a solution of compounds **4a**, **4b** (27.3 mg, 0.027 mmol) in CH_2Cl_2 (2 mL) was added a catalytic amount of palladium on charcoal. The solution was stirred with hydrogen gas at room temperature for 20 hr. The mixture was filtrated and evaporated in *vacuo* gave a yellow oil of compound **4b** (25.2 mg, 98%).

Histone Deacetylase Activity Assay. Capsaicin derivatives were evaluated for their ability to inhibit a commercially available assay (Fluor de Lys assay system). TSA was used as a positive control.[6] The reaction mixture contained a HeLa cell nuclear extract and a commercial substrate containing acetylated lysine side chains. The substrate and extract were incubated in the presence of the appropriate concentrations of the inhibitors. Deacetylation of the substrate followed by mixing with the obtained developer generated a fluorophore, and comparison of inhibitor *vs* control relative fluorescence using a standard plate reader was employed to determine percent HDAC activity remaining.

Results and Discussion

Structural modification of a CAP/DHC mixture is shown in Figure 2. A polar phenolic group of capsaicin should be converted into a less polar moiety to gain more surface recognition. Moreover, a hydrophobic double bond side chain of capsaicin may be performed to provide a compound with a better metal binding affinity. Oxymercuration[7] of a CAP/DHC mixture with $Hg(OAc_2)$ and $NaBH_4$ promoting specific addition of hydroxyl group to C-14 position of CAP gave hydroxyl-CAP (**5**) in a good yield and recovered DHC (**3b**). Diacetyl-CAP (**6**) was obtained in 73% yield when using Ac_2O as a reagent. Allylic oxidation[8] of CAP/DHC mixture with SeO_2 and pyridine promoting specific addition of hydroxyl group to C-13 position of CAP provided allylic hydroxyl-CAP (**7**) in 80% yield and recovered DHC (**3b**). An acetylation of allylic hydroxyl-CAP (**7**) with Ac_2O gave diacetyl allylic-CAP (**8**) in a good yield.

In the next step, attempts to oxidize the phenolic group of DHC (**3b**) to the ketone group with using *o*-chloranil were conducted. However, the unexpected chloranil-DHC (**9**) could be obtained.[9]

In a subsequent step, a double bond region of CAP (**3a**) was modified to promote a metal binding group at side chain. Silyl-CAP/DHC (**4a**, **4b**) were obtained in a good yield.[5] Oxidative cleavage[10] of silyl-CAP/DHC (**4a**, **4b**) by using potassium osmate and sodium periodate and following by oxidation with bromine[11] in methanol gave silyl bromo-DHC (**10**) in a good yield, silyl bromo methyl ester (**11**) in 73% yield and silyl bromo dihydroxyl derivative (**12**) as a minor product. In the final step, silyl bromo methyl ester (**11**) was reacted with $NH_2OH.HCl$ and Et_3N in a mixture of THF and water under a refluxing condition to give a compound **(13)** in 82% yield.[12] In contrast, using $NH_2OH.HCl$ and and 20% KOH in EtOH under a refluxing condition provided bromo hydroxamic acid (**14**) in 69% yield.

Histone Deacetylase Activity Assay. Capsaicin (**3a**), dihydrocapsaicin (**3b**) and their derivatives were screened *in vitro* by using HeLa nuclear extract in a fluorimetric assay. Trichostatin A (TSA) was used as the reference compound. The testing results of all compounds for inhibitory activity against HDAC *in vitro* are presented in Table 1. Ten compounds (**4a**, **4b**), **4b**, **5**, **6**, **7**, **8**, **9**, **11**, **13** and **14** showed inhibitory activities against HDAC in micro molar concentrations ranges. Even through the inhibitory activities were not comparable to that of TSA, these results provided valuable information regarding the binding to the active site of HDAC. The hydroxyl group at the side chain provided the better metal binding than a methyl ester group and the hydroxamic group was the best functional group. Nevertheless, a diol functional group provided a less efficient metal binding than only one hydroxyl group. It may be assumed that the hydroxyl of diol functional might not arrange itself in the same plane. Thus, the diol functional group might not be able to bind with the enzyme property. However, HDAC inhibitory activity of these derivatives guided that the very polar functional groups play important roles for the metal binding of the HDAC in cancer cells.

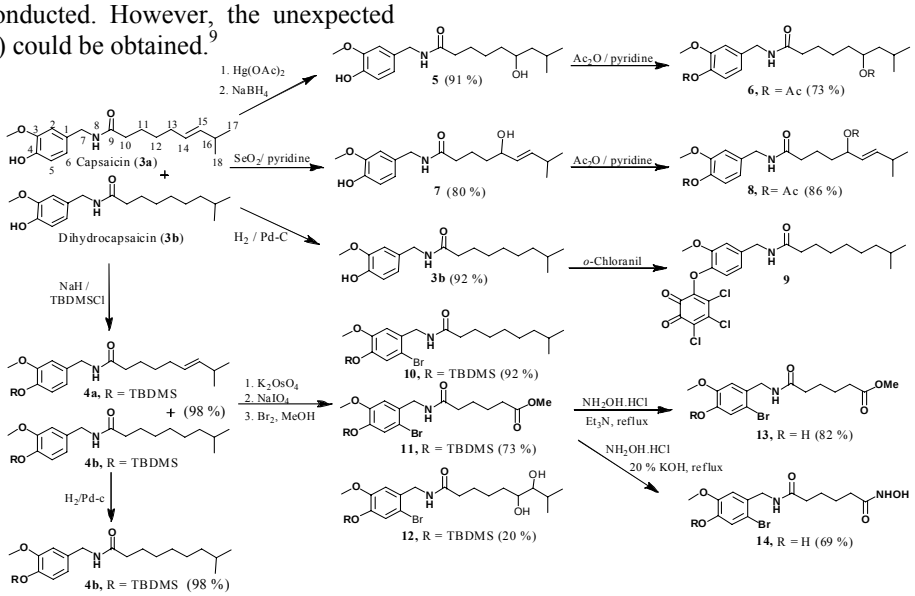

Figure 2. The structural modification of CAP and DHC (**3a**, **3b**).

Table 1: HDAC inhibition data for CAP and DHC analogues.

Compounds	% HDAC Inhibition	Conc. (μg/μL)	(μmol/μL)
TSA (**2**)	68.91	0.0073	0.025*
CAP/DHC (**3a**, **3b**)	inactive	40	0.13
DHC (**3b**)	35.1	40	0.13
silyl-CAP/DHC (**4a**, **4b**)	83.30	40	0.10
silyl-DHC (**4b**)	85.13	40	0.10
hydroxyl-CAP (**5**)	79.62	40	0.12
diacetyl-CAP (**6**)	82.72	40	0.10
allylic hydroxyl-CAP (**7**)	84.70	40	0.12
diacetyl allylic-CAP (**8**)	78.86	40	0.12
chloranil-DHC (**9**)	87.01	40	0.12
silyl bromo-DHC (**10**)	inactive	40	0.08
silyl bromo methyl ester (**11**)	55.53	40	0.08
silyl bromo dihydroxyl (**12**)	inactive	40	0.09
bromo methyl ester (**13**)	87.31	40	0.11
bromo hydroxamic acid (**14**)	90.03	40	0.11

* ; x 10^{-3}

Molecular Docking. To predict the predominant binding mode of some inhibitors (compounds **3b**, **4b**, **5** and **6** as well as TSA and SAHA for comparison) with HDAC enzyme, molecular docking studies were performed for 50 runs using AutoDockTools 1.5.4 and AutoDock 4.2 programs[13,14] with a grid box size of 66×66×66 points and Lamarckian genetic algorithm search. SAHA and TSA resulted in higher binding free energy and lower inhibition constant compared to others (Table 2). This result is consistent with higher inhibitory activity. Less efficient inhibition of capsaicin and their derivatives can be described from the indirectly orientation to zinc ion and less interaction with the HDAC binding site (Figure 3).

Table 2: Estimated binding free energy (ΔG) and inhibition constant (Ki) obtained from molecular docking studies.

Compounds	ΔG (kcal/mol)	Ki (μM)
SAHA (**1**)	–6.23	26.9
TSA (**2**)	–6.91	8.6
DHC (**3b**)	–4.76	325.3
silyl-DHC (**4b**)	–4.81	299.5
hydroxyl-CAP (**5**)	–5.41	108.7
diacetyl-CAP (**6**)	–5.46	99.5

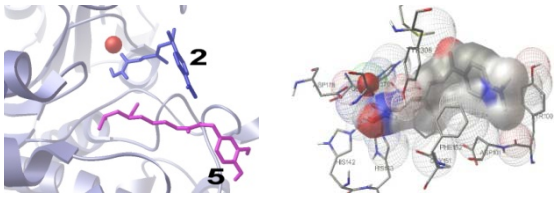

(a) (b)

Figure 3. (a) Orientation of TSA (**2**) toward HDAC binding site, compared with hydroxyl-CAP (**5**), and (b) surrounding residues of HDAC around **2**. The close contact displayed as spheres.

Conclusions

A mixture of CAP/DHC isolated from *Capsicum annuum.* was modified by various chemical reactions. All compounds were obtained in good yields. Structural modification based on the metal-binding functional group and surface recognition area. The side chain as hydrophilic groups in hydroxyl-CAP (**5**), diacetyl-CAP (**6**), allylic hydroxyl-CAP (**7**) and diacetyl allylic-CAP (**8**) showed the binding to the active site of HDAC. The methyl ester at side chain provided a less efficient metal binding than the hydroxamic group. The silyl-DHC (**4b**) and chloranil-DHC (**9**) showed the interaction to enzyme. Molecular docking study showed consistent results. Further detailed structure-activity relationship studies are currently in progress.

Acknowledgement

The Center of Excellent for Innovation in Chemistry (PERCH-CIC) and Khon Kaen University are acknowledged for their financial support of this work.

References

[1] P. M. Gannett, D. L. Nagel, P. J. Reilly, T. Lawson, J. Sharpe and B. Toth, *J. Org Chem.* **53** (1988), pp. 1064–1071.
[2] M. Paris, M. Porcelloni, M. Binaschi and D. Fattori, *J. Med. Chem.* **51** (2008), pp. 1505–1511.
[3] T. A. Miller, D. J. Witter and S. Belvedere, *J. Med. Chem.* **46** (2003), pp. 5097–5116.
[4] P. A. Marks, V. M. Richon, and T. Miller, *Adv Cancer Res*. **91** (1997), pp. 137–168.
[5] P. Kumboonma, C. Phaosiri, S. Misuna, T. Senawong and C. Yenjai, *paccon 2009*. (2009), pp. 397-400.
[6] S. Varghese, T. Senanayake, T. Murray-Stewart, K. Doering, A. Fraser, R. A. Casero and P. M. Woster, *J. Med. Chem.* **51** (2008), pp. 2447–2456.
[7] H. J. Wu, S. H. Tsai, J. H.Chern and H. C. Lin, *J. Org. Chem.* **62** (1997), pp. 6367–6373.
[8] H. Rapoport and U. T. Bhalerao, *J. Am Chem Soc.* **93** (1971), pp. 4835–4840.
[9] U. Wriede and H. W. Moore, *J. Org Chem*. **52** (1987) pp. 4485–4489.
[10] L. Chen and D. F. Wiemer, *J. Org. Chem.* **67** (2002), pp. 7561–7564.
[11] H. Kaknuma, Y. Tsuchiya, M. Tanaka, S. Horito and H. Hashimoto, *Carbohydr. Res.* **264** (1994), pp. 237–251.
[12] S. Hanessian, L. Auzzas, G. Giannini, M. Marzi, W. Cabri, M. Barbarino, L. Vesci and C. Pisano, *Bioorg. Med. Chem. Lett.* **17** (2007), pp. 6261–6265.
[13] M. F. Sanner, *J. Mol. Graphics Mod.* **17** (1999), pp. 57–61.
[14] G. M. Morris, , R. Huey, W. Lindstrom, M. F. Sanner, R. K. Belew, D. S. Goodsell and A. J. Olson, *J. Comput. Chem*. **30** (2009) pp. 2785–2791.

Chemical constituents of the bark of *Albizia lebbeck*(L.) Benth

C. Srisuwannaket[1*], S. Chaiyamat and S. Tungchaikij

Department of Chemistry, Faculty of Science, King Mongkut's University of Technology Thonburi, Bangkok, Thailand 10140

*E-mail: choladda@kmutt.ac.th

Abstract: Chemical constituents of crude dichloromethane extract of the bark of *Albizia lebbeck* (L.) Benth were isolated and their chemical structures were characterized using NMR spectroscopic technique. Based on the spectroscopic results obtained, two isolated chemical compounds were identified as methyl 4-hydroxybenzoate, methyl 3-hydroxy-4-methoxybenzoate. This is the first report for isolation of these compounds from *Albizia lebbeck* (L.) Benth. Furthermore, these isolated compounds show an antioxidant activity by scavenging DPPH radical.

Introduction

The genus *Albizia* belongs to the family Fabaceae which comprises approximately 150 species, which are mostly trees and shrubs native to tropical and subtropical regions of Asia and Africa. *Albizia lebbeck* (L.) Benth, a valued timber species, is widely distributed in India and is also found in South Africa and Australia. It was previously exported to Europe under the trade name East Indian Walnut. In Thailand, *Albizia lebbeck* is known as Ma-Room-Pa. It is used in folk remedies for abdominal tumors, boils, cough, eye ailments, flu and lung ailments. It is also reported to be astringent, pectoral, rejuvenant and tonic [1]. The ethanol extract of *Albizia lebbeck* leaves exhibited anticonvusant activity [2]. The methanol extract of *Albizia lebbeck* pods caused spermatogenic arrest in male albino rat [3]. The phytochemical investigation of *Albizia lebbeck* from the bark found saponins named albiziasaponins A, B, and C [4]. The phenolic glycoside and tannins were also isolated from the bark [5] and the two flavonol glycosides were isolated from its leaf as well [6]. However, there are no reports available on the antioxidant activity of its chemical constituents. The present study deals with the isolation and structural elucidation including antioxidant activity of the extract from the bark of *Albizia lebbeck.*

Materials and Methods

2.1 Plant material

The bark of *Albizia lebbeck* (1.8 kg) was collected in October 2006 from Chachoengsao Province, Thailand.

2.2 Chemical

All the chemicals and reagents were of analytical grade. 2,2-diphenyl-1-picrylhydrazyl (DPPH) radical and *n*-butanol were purchased from Sigma Chemical Co (USA). Solvents, i.e. hexane, dichloromethane, and methanol, were of chemical grade and purified prior to use by simple distillation.

2.3 Extraction and Isolation

The air-dried bark of *Albizia lebbeck* was powdered and macerated with methanol. The methanol extract was evaporated under vacuum and then partitioned with hexane, dichloromethane and *n*-butanol to afford 4.4 g, 7.1 g and 86 g extract, respectively.

The dichloromethane extract (7.1g) was chromatographed over silica gel column and was eluted with continuous hexane-CH_2Cl_2, CH_2Cl_2-MeOH. The eluates were identified by TLC technique to give 9 fractions. Fraction 5 (1.5 g) was purified by PTLC with the mobile phase hexane-CH_2Cl_2 (1:1), which afforded 4.1 mg of compound **1**. Fraction 4 (2.6 g) was purified by PTLC in the mobile phase hexane-EtOAc (93:7), which afforded 6.5 mg of compound **2**.

2.4 DPPH free radical scavenging activity

The stable 2,2-diphenyl-1-picrylhydrazyl (DPPH) radical was used for the evaluation of free radical-scavenging activity of the crude extracts [7]. Chemical constituents of plant extracts were analyzed by TLC technique using TLC plates (Silica gel 60 F254). Firstly, the TLC plates were developed with suitable mobile phases for isolation the compounds. To detect antioxidative capactivity of compounds, chromatograms were sprayed with 0.2% DPPH radical in methanol. The presence of antioxidant compounds was identified by observing yellow spots against a purple background.

Results and Discussion

Compound **1** was obtained as a white amorphous solid. The ^{1}H NMR ($CDCl_3$, 400 MHz) spectrum showed two symmetrical protons of benzene moiety. The present at δ_H 7.89 (2H, *d*, *J* = 8.7 Hz) and δ_H 6.08 (2H, *d*, *J* = 8.7 Hz), one methoxy group at δ_H 3.81 (3H, *s*). The spectral data of compound **1** were identical to that reported for methyl parabene [8]. Thus, compound **1** was identified to be methyl parabene.

Compound **2** was obtained as a pale yellow powder. The ^{1}H NMR ($CDCl_3$, 400 MHz) spectrum showed three aromatic protons at δ_H 7.64 (1H, *d*, *J* = 8.3 Hz, H-6), δ_H 7.54 (1H, *s*, H-2) and δ_H 6.94 (1H, *d*, *J* = 8.3 Hz, H-5), two methoxy groups at δ_H 3.95 (3H, *s,* OCH_3) and δ_H 3.89 (3H, *s*, OCH_3). The ^{1}H NMR data of compound **2** was very similar to that for methyl vanillate [8]. To confirm the chemical structure of

compound **2**, the ^{13}C NMR spectrum exhibited nine carbons signals including one carbonyl carbon at δ_C 167.0, two methoxy carbons at δ_C 52.0 and 56.1, six aromatic carbons at δ_C 150.0, 146.0, 124.2, 122.0, 114.0 and 111.7. The ^{1}H and ^{13}C NMR data were assigned from the ^{1}H-^{1}H COSY, HSQC, HMBC spectrum showed in table 1. As a result, compound **2** was determined as methyl vanillate.

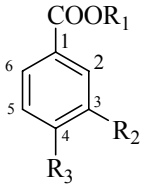

	R_1	R_2	R_3
1	CH_3	H	OH
2	CH_3	OH	OCH_3

Figure 1. The structure of compound **1** and **2** isolated from dichloromethane of *Albizia lebbeck*

Table 1: NMR data of compound **2** ($CDCl_3$, δ)

Position	^{1}H	^{13}C	HMBC (H→C)
1	-	122.0	-
2	7.54 (1H, *s*)	111.7	C-3, 4, 6, C=O
3	-	146.0	-
4	-	150.0	-
5	6.94 (1H, *d*, *J* = 8.3 Hz)	114.0	C-1, 3, 4
6	7.64 (1H, *d*, *J* = 8.3Hz)	124.2	C-2, 4, C=O
OCH_3	3.95 (3H, *s*)	56.1	C-3
C=O	-	167.0	-
$COOCH_3$	3.89 (3H, *s*)	52.0	C=O

The both isolated compounds, i.e. methyl parabene and methyl vanillate, showed antioxidative properties against DPPH radical as examined by TLC-DPPH screening method. Due to insufficient quantities of the test compounds, % inhibition and IC_{50} value were not determined.

Conclusions

The present study is the first report to exist methyl parabene and methyl vanillate in dichloromethane extract of the bark of *Albizia lebbbeck* (L.) Benth. Furthermore, these isolated compounds showed an antioxidant potential to scavenge DPPH radical.

References

[1] R.S. Gupta, R. Chuadhary, R.K. Yadav, S.K. Verma and M.P. Dobhal, *J. Ethnopharmacology* **96** (2005), pp. 31-36.

[2] V.S. Kasture, C.T. Chopde, V.K. Deshmukh, , *J. Ethnopharmacology.* **71** (2000), pp. 65-75.

[3] R.S. Gupta, J.B.S. Kachhawa and R. Chuadhary, *Asian J Androl.* **6** (2004), pp. 155-159.

[4] B.C. Pal, B. Achari, K. Yoshikawa and S. Arihara, *Phytochemistry.* **38** (1995), pp. 1287-1291.

[5] Y. Ma, S. Hsiao, H. Chen and F. Hsu, *Phytochemistry.* **46** (1997), pp. 1451-1452.

[6] A.M.D. El-Mousallamy, *Phytochemistry.* **48** (1998), pp. 759-761.

[7] M. Ondrejovic, Z. Ondrigova and J. Kubincova, *Nova Biotecnologica* **9-3** (2009), pp. 313-318.

[8] C. Chen, F. Chang, C. Teng and Y. Wu, *J. Chin. Chem. Soc.* **46** (1999), pp. 77-86.

Convenient esterification of alcohols via acylbenzotriazoles : efficient and stable esterifying agents

P. Teabsaen*, P. Theramongkol, V. Hahnvajanawong, and C. Phaosiri

Department of Chemistry, Faculty of Science, Khon Kaen University, Khon Kaen, Thailand 40002

*E-mail: p_teabsaen@hotmail.com

Abstract: Acylbenzotriazoles are known acylating agents for amines and carbonyl compounds due to the stability of the benzotriazolide anion which served as a good leaving group. However, the reagent failed to react with alcohols under previously known reaction conditions. This prompted us to the finding that esterification of alcohols with acylbenzotriazole could be realized only in the presence of K_2CO_3 in THF solution. Esterification of alcohols with acylbenzotriazoles gave the corresponding esters in good to excellent yields. The esterifying agents could easily be prepared in high yields from benzotriazole and the corresponding acid chlorides. Treatment of the crude esters from *N*-propionyl benzotriazole with methanol followed by extraction with 2 M Na_2CO_3 gave pure esters in good yields while those derived from *N*-benzoyl benzotriazole were isolated and purified by repeated extraction with 2 M Na_2CO_3 solution. This method thus served as an efficient and versatile alternative synthesis of ester under mild basic condition.

Introduction

Common route for ester synthesis is the treatment of carboxylic acid with alcohol in the presence of an acid catalyst such as concentrated sulfuric acid. However, the reaction takes a long period of time to reach its equilibrium and large excess of reagent is unavoidable in order to get high yield of ester. Although activated carboxylic acids such as acid chloride or acid anhydride give better results, they suffer from the problem of reagent handling and manipulating the reaction due to the highly reactive nature of the reagents. Exothermic reactions are always encountered and anhydrous conditions are required. In order to overcome these difficulties we have developed a much milder method for ester synthesis using *N*-acylbenzotriazoles as acylating agents which are stable solids that can easily be stored, handled and manipulated.

Materials and Methods

Preparation of Benzotriazole (1)

To a stirred cooled solution (15°C) of *o*-phenylenediamine (10.8 g, 0.1 mol) in glacial acetic acid (11.5 ml) was added a solution of sodium nitrite (7.5 g, 0.11 mol) in water (15 ml). Mild exothermic reaction commensed within a few minutes and rapidly subsided while the deep red colour faded into pale brown. Stirring was continue for 15 minutes until the temp dropped to 35-40°C and the mixture was then chilled in an ice-water bath for 30 minutes. The pale brown precipitates were collected by vacuum filtration and washed with ice-cold water. Highly colored crude product was purified by repeated recrystallization from water using activated charcoal as a decolorizing agent. Benzotriazole (**1**) was obtained as fine white needles (7.97 g, 0.07 mol, 67%), mp. 95-97 °C. (lit.mp. 96-97 °C)

Preparation of *N*-propionyl benzotriazole (2)

To a stirred mixture of benzotriazole (**1**) (1.20 g, 0.01 mol) and anhydrous K_2CO_3 (2.76 g, 0.02 mol) in CH_2Cl_2 (30 ml) was slowly added propionyl chloride (1.05 ml, 0.012 mol). The mixture was stirred for 30 minutes and filtrated under reduced pressure through a celite pad. The filtrate was evaporated using a rota-vaporator to dryness and the residue was purified by recrystallization from hexane to afford *N*-propionyl benzotriazole (**2**) as white crystals (1.65 g, 9.4 mmol, 94% yield).

Preparation of *N*-benzoyl benzotriazole (3)

To a stirred mixture of benzotriazole (**1**) (1.20 g, 0.01 mol) and anhydrous K_2CO_3 (2.76 g, 0.02 mol) in CH_2Cl_2 (30 ml) was slowly added benzoyl chloride (1.69 ml, 0.012 mol). The mixture was stirred for 30 minutes and filtrated under reduced pressure through a celite pad. The filtrate was evaporated using a rota-vaporator to dryness and the residue was purified by recrystallization from hexane to afford *N*-benzoyl benzotriazole (**3**) as white crystals (2.29 g, 9.8 mmol, 98% yield).

General method for preparation of ester using *N*-propionylbenzotriazole (2)

A mixture of *N*-propionyl benzotriazole (**2**) (0.21 g, 1.2 mmol) and alcohol (1 mmol) and anhydrous K_2CO_3 (0.28 g, 2.0 mmol) in THF (5 ml) was refluxed for 30-60 minute. The mixture was cooled to room temperature and the solvent was evaporated under vacuum to dryness. The residue was added CH_2Cl_2 (2-3 ml) and methanol (2 ml) and further stirred for 5 minutes. The resulting mixture was added 2M Na_2CO_3 (2 ml) and stirring was continued for 30 minutes then extracted with CH_2Cl_2 (2x5 ml). Combine organic layer were dried and concentrated under reduced pressure to give pure ester (57-89%).

General method for preparation of ester using *N*--benzoyl benzotriazole (3)

A mixture of *N*-benzoyl benzotriazole (**3**) (0.28 g, 1.2 mmol) and alcohol (1 mmol) and anhydrous K_2CO_3 (0.28 g, 2.0 mmol) in THF (5 ml) was refluxed

for 30-60 minute. The mixture was cooled to room temperature and the solvent was evaporated under vacuum to dryness. The residue was added CH_2Cl_2 (2-3 ml) and 2M Na_2CO_3 (2 ml) and stirring was continued for 30 minutes then extracted with CH_2Cl_2 (2x5 ml). Combine organic layer were dried and concentrated under reduced pressure to give pure ester (55-93%).

Results and Discussion

Benzotriazole was prepared from the reaction between *o*-phenylenediamine and sodium nitrite in acidic condition as shown below.

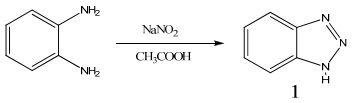

1

N-Acylbenzotriazoles were prepared from the reaction between acid chlorides and benzotriazole in basic condition with high yields as shown below.

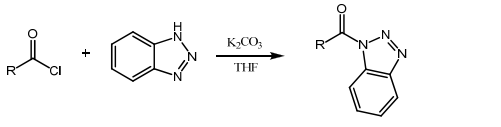

2 ; R=Et, 94%, mp. 79-80 °C (lit.80-82 °C)
3 ; R=Ph, 98%, mp. 113-115 °C (lit.112-113 °C)

N-Acylbenzotriazoles were allowed to react with 1° or 2° alcohols in THF in the presence of anhydrous K_2CO_3 at reflux to give the corresponding esters.

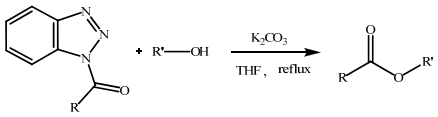

Crude esters derived from *N*-propionyl benzotriazole were easily purified by treatment with methanol followed by repeated extraction with 2M Na_2CO_3 while those derived *N*-benzoyl benzotriazole were isolated and purified by repeated extraction with 2M Na_2CO_3. *N*-propionyl benzotriazoles and *N*-benzoyl benzotriazole both gave esters from 1° and 2° aliphatic alcohols in good to excellent yields. In addition, phenols could also be esterifies with *N*-benzoyl benzotriazole in excellent yields.

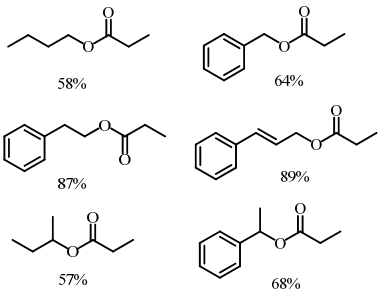

Figure 1. Esters from *N*- propionyl benzotriazole

In addition, *N*-benzoyl benzotriazoles with 1°, 2° and aromatic alcohols to give ester in good yields.

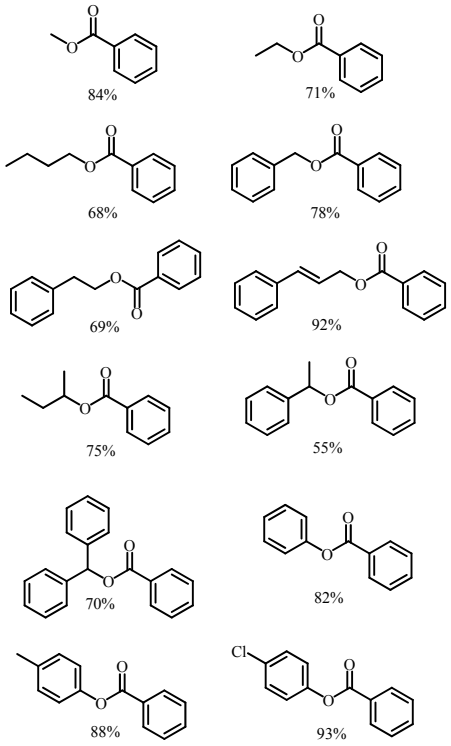

Figure 2. Esters from *N*- benzoyl benzotriazole

Conclusions

Benzotriazole was prepared in moderate yield. Purification was simply carried out by using water as a cheap and nontoxic solvent. Esters of 1° and 2° alcohols could be prepared using either *N*-propionyl benzotriazole or *N*-benzoyl benzotriazole in good to excellent yields. Product separation and purification could easily be achieved by basic extraction. An alternative mild and efficient method for ester preparation using *N*-acylbenzotriazoles as stable acylating solid reagents has been established.

Acknowledment

Financial support from the Center of excellence for innovation in Chemistry (PERCH-CIC)

References

[1] B. S.; Hannaford, A. J.; Smith, P. W. G.; and Tatchell, A. R. in Vogel's Textbook of practical Organic Chemistry; 5th ed., Longman Group UK Ltd, 1989.
[2] A. R. Katritzky, N. Shobana, J. Pernak, A.S. Afridi and W.-Q. Fan. *Tetrahedron*. (1992), 48, pp. 7817-7822.
[3] A. R. Katritzky, Hai-Ying He and K. Suzuki. *J. Org. Chem*. (2000), 65, pp. 8210-8213.
[4] A.R.Katritzky,*A.A.Abdel-Fattah, and M.Wang. *J. Org. Chem.* (2002), 30, pp. 1443-1446.

Coumarin derivatives : Novel acetylcholinesterase inhibitors

D. Aryuwananon[1], N. Chimnoi[2], K. Ingkaninan[3], and S. Techasakul[1,2*]

[1] Department of Chemistry and Center for Innovation in Chemistry, Faculty of Science, Kasetsart University, Chatuchak, Bangkok, Thailand
[2] Chulabhorn Research Institute, Vibhavadee-Rangsit Road, Laksi, Bangkok, Thailand
[3] Department of Pharmaceutical Chemistry and Pharmacognosy, Faculty of Pharmaceutical Sciences, Naresuan University, Phitsanulok, Thailand

*E-mail: fscispt@ku.ac.th

Abstract: A series of coumarin derivatives were designed, synthesized, and tested for studying their potential for treating Alzheimer's disease (AD). The novel coumarin derivatives were synthesized from scopoletin by acylation and alkylation reactions. Scopoletin was synthesized from commercially available esculin. Their anticholinesterase activity was tested using Ellman's method, with galanthamine as a reference compound. 6,7-Dimethoxycoumarin showed moderate inhibition against acetylcholinesterase (AChE) enzyme.

Introduction

Alzheimer's disease (AD), a progressive and degenerative disorder of the brain, is believed to be the most common cause of dementia among the elderly. AD is associated with the loss of the presynaptic markers of the cholinergic system in the brain areas related to memory and learning, and is characterized by the presence of amyloid deposits and neurofibrillary tangles in the brain of afflicted individuals.[1-2] Currently, the most widely accepted biochemical theory of the disease, known as the cholinergic hypothesis, is that the decline in cognitive and mental functions associated with AD is related to the loss of cortical cholinergic neurotransmission. One rational way to enhance cholinergic neurotransmission is to inhibit an enzyme responsible for the metabolic breakdown of acetylcholine (ACh). Thus, most of the drugs approved for the current treatment of AD are acetylcholinesterase (AChE) inhibitors (AChEIs), which can enhance cholinergic neurotransmission by increasing acetylcholine (ACh) availability in the synaptic cleft.[3-4] Acetylcholine (ACh) is a neurotransmitter in both the peripheral nervous system (PNS) and central nervous system (CNS) in many organisms including humans. In the PNS, acetylcholine activates muscles and is a major neurotransmitter in the autonomic nervous system (ANS). In the CNS, acetylcholine and the associated neurons form a neurotransmitter system, the cholinergic system, which tends to cause excitatory actions. Acetylcholine is one of many neurotransmitters in the ANS and the only neurotransmitter used in the somatic nervous system. It is also the neurotransmitter in all autonomic ganglia.[5]

Several AChE inhibitors are commercially available, for the example, donepezil, galanthamine, physostigmine, ensaculin, and tacrine. As mentioned above, scopoletin and scopolin have emerged as potential AChE inhibitors.[6] These two coumarins widely occur as secondary plant metabolites, especially in a number of the members of the Solanaceae family. Scopoletin has previously been described as an AChE inhibitory, anti-inflammatory, and antiproliferative agent that exhibits activities such as the inhibition of inducible nitric oxide synthase and prostaglandin synthase. Coumarin derivatives were designed and synthesized from scopoletin. Their anticholinesterase inhibitory activity was tested using Ellman's colorimetric method.[7]

Materials and Methods

Chemicals

Chemicals and solvents used for the synthesis were obtained from commercial sources (Merck, Fluka, Aldrich, and other companies)

Coumarin derivatives

All coumarin derivatives were synthesized from scopoletin using acylation and alkylation reaction.

Microplate assay for AChE activity

AchE activity was measured using a 96-well microplate reader base on Ellman's method. The enzyme hydrolyzes the substrate acetylthiocholine resulting in the product thiocholine. This product reacts with Ellman's reagent (DTNB) to produce 2-nitrobenzoate-5-mercaptothiocholine and 5-thio-2-nitrobenzoate, which can be detected at 405 nm. In 96-well plates, 25 μL of 15 mM ATCI, 125 μL of 3 mM DTNB, 50 μL of buffer, and 25 μL of coumarin derivative dissolved in buffer were added to the wells, followed by 25 μL of 0.28 U/mL AChE. The microplate was then read at 405 nm every 5 s for 2 min by a microplate reader. The rate of reactions was calculated by the Microplate Manager software. Any increase in absorbance due to the spontaneous hydrolysis of substrate was corrected by subtracting the rate of the reaction before adding the enzyme from the rate after adding the enzyme. Percentage of inhibition was calculated by comparing the rates for the sample with the blank. Every experiment was done in triplicate.[8]

Results and Discussion

Chemistry

Scopoletin was synthesized from the commercially available esculin in four steps, with a 37% overall yield. Scopoletin was prepared by esculin through the protection of hydroxyl group using benzyl bromide in the presence of potassium carbonate in methanol. Acid then catalyzed the hydrolysis of intermediate A using 5% H_2SO_4 in dioxane to produce phenol product B. Methylation of phenol B reacted with MeI to produce methylated product C and deprotection of C in the presence of concentrated HCl in glacial acetic acid yielded the scopoletin, as shown in Scheme 1.

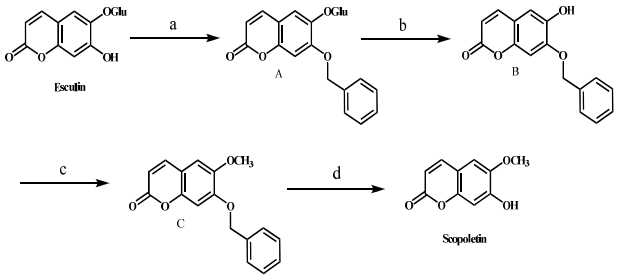

Scheme 1. Preparation of scopoletin. Reagents and conditions: (a) BnBr, K_2CO_3, MeOH, reflux; (b) 5 % H_2SO_4, Dioxane, reflux; (c) MeI, K_2CO_3, Acetone, reflux; (d) HCl, CH_3COOH, 100°C

Seven coumarin derivatives were designed and synthesized from scopoletin by acylation and alkylation reactions, as shown in Scheme 2. Ester series were prepared from carboxylic acid treated with $(COCl)_2$ and a catalytic amount of DMF in dry CH_2Cl_2 to give acyl chloride intermediate. They reacted with the scopoletin in the presence of DMAP and triethylamine in dichloromethane to produce the target compounds. Ether series were prepared from alkyl halide and scopoletin in the presence of potassium carbonate in acetone to produce the target compounds.

The structures of the target compounds were characterized by ^{1}H NMR, ^{13}C NMR, IR, and ESI-MS.

Scheme 2. Preparation of coumarin derivatives. Reagents and conditions: (a) RX, K_2CO_3, acetone, reflux; (b) RCOCl, Et_3N, DMAP, CH_2Cl_2, RT

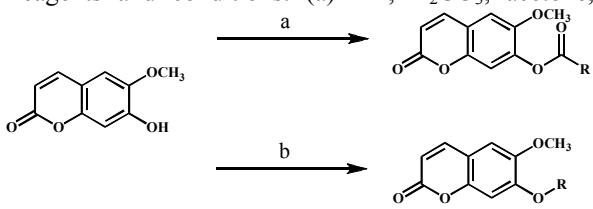

Inhibition of AChE

To determine the therapeutic potency of the new coumarin derivatives for treating AD, their anticholinesterase activities were assayed according to Ellman's method using galanthamine as reference compound. The inhibition of AChE activities of the synthesized compounds is shown in Table 1.

Table 1. Inhibition of AChE activities of the synthesized compounds

compound	Structure of Coumarin Derivatives	Percent Inhibition
1	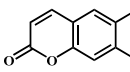	57.79
2	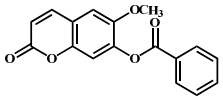	4.27
3	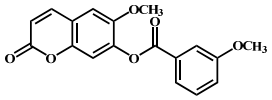	4.35
4	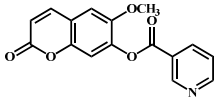	0.82
5	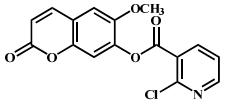	2.38
6	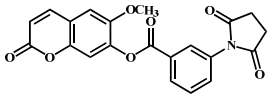	1.94
7	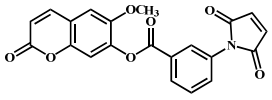	2.25

The data listed in Table 1 clearly show that the designed compounds exhibit moderate inhibitory activities towards cholinesterase.

Conclusions

Seven coumarin derivatives were designed, synthesized, and tested for inhibitory activity on AChE. 6,7-Dimethoxycoumarin (compound 1) showed moderate AChE inhibitory activity at a concentration of 0.1 mg/mL.

References

[1] A. V. Jr. Terry And J. J. Buccafusco. *J. Pharmacol. Exp. Ther.*, **306** (2003), pp. 821.

[2] D. Selkoe., *J. Physiol. Rev.* **81** (2001), pp. 741.

[3] A. Shvaloff, E. Neuman and D. Guez, *Physchoparmacol. Bull.*, **32** (1996), pp. 343.

[4] G. K. Wilcock, *Neurodegeneration*. **5** (1996), pp 505.

[5] X. Zhou, X. B. Wang, T. Wang and L. Y. Kong. *Bioorg. Med. Chem.*, **16** (2008) pp. 8011-8021.
[6] J. M. Rollinger, A. Hornick, T. Langer, H. Prast, and H. Stuppner, *J. Med. Chem.*, **47** (2004), pp. 6248-6254.
[7] G. L. Ellman, D. K. Lourtney, V. Andres and G. Gmelin, *Biochem. Pharmacol.* **7** (1961), pp. 88-95.
[8] K. Ingkaninan, P. Temkitthawon, K. Chuenchom, T. Yuyaem and W. Thongnoi. *J. Ethnophramacol.* **89** (2003), pp. 261-264.
[9] J. Trujillo-Ferrara, L. M. Cano and M. Espinoza-Fonseca. *Bioorg. Med. Chem. Lett.* **13** (2003), pp. 1825-1827.

Note RT is Room Temperature

Psalmopeotoxin I and II—anti-malarial peptides extracted from *Psalmopoeus cambridgei* : synthesis and thermal stability of their mutants

P. Sarnpitak[1], A. Tangpeerachaikul[2] and S. Deechongkit[1*]

[1] Chemical Biology Program, Chulabhorn Graduate Institute, Bangkok, Thailand 10210
[2] Department of Chemistry, Massachusetts Institute of Technology, Cambridge, Massachusetts, USA 02139

* E-Mail: songpond@yahoo.com

Abstract: Psalmopeotoxin I and II (PcFK1 & PcFK2) were recently isolated and characterized from tarantula's venom, *Psalmopoeus cambridgei*, by Camadro *et al*. These two peptides have good plasmodial activity against intra-erythrocyte stage of *Plasmodium falciparum in vitro* (IC_{50} ~ 1 µM), but do not exhibit any toxicity beside other structurally similar neurotoxins. Previously, both PcFK wild-types were chemically synthesized and thermal stability was studied. The thermal stability (fraction unfolding, f_u) of these peptides was reported in terms of mid-point of transition temperature (T_m) from Circular Dichroism (CD) studies. T_m of PcFK1 and PcFK2 were 18.3˚C and 29.5˚C, respectively. Based on thermal unfolding studies, both PcFKs were not thermally stable. At physiological temperature, 37˚C, which anti-plasmodial activities were determined, these two peptides were more than 50% unfolded. Therefore, it is not known either folded or unfolded that have the anti-plasmodial activities. The objective of this study is to determine the effect of mutations of PcFK1 and PcFK2 on the thermal stability whether positively or negatively. The designed mutations were based on the conserved-residues of PcFK1 and PcFK2 which are Val10, Pro13, and Pro17, these residues were mutated to alanine. These mutants were manually synthesized by Solid Phase Peptide Synthesis (SPPS) using Fmoc chemistry, regioselective disulfide bond formation and orthogonal thiol protecting group strategy. Tryptophan (Trp, W) was added to *N*-terminus in order to measure the amount of peptides. The resulting mutants were purified and identified by reversed-phase HPLC and ESI-TOF MS, respectively. Thermal stability was studied by Circular Dichroism spectroscopy (CD), fraction unfolding (f_u) curve was determined using baseline extrapolation method and mid-point of transition temperature (T_m) was calculated from fraction unfolding curve. Based on CD raw data, T_m of some mutants seems to be higher than their wild-types, for example, T_m of PcFK2-P13A is about 40˚C, while some other mutants are not folded.

Introduction

Psalmopeotoxin I and II (PcFK1 and PcFK2) have been isolated and identified from Trinidad chevron tarantula, *Psalmopoeus cambridgei*, by Camadro *et al.* These two peptides show good anti-plasmodial activity against intra-erythrocyte stage of *Plasmodium falciparum in vitro* with IC_{50} ~ 1 µM, but do not exhibit toxicity related to other structurally similar neurotoxins.[1] Both of them have three disulfide bridges (Figure 1) and are classified to Inhibitory Cysteine Knot (ICK) superfamily. Recently, PcFK1 and PcFK2 including their disulfide mutants were synthesized and characterized by our group to study the effects and relationships of disulfide mutation on their thermal stabilities and biological activities (unpublished results). Their thermal stabilities were showed in term of mid-point of transition temperature (T_m) which represents fraction unfold (f_u) of peptides. T_m for PcFK1 and PcFK2 wild-types were 18.3˚C and 29.5˚C, respectively. Therefore, both PcFKs were not thermally stable. At 37˚C, physiological temperature, where the anti-plasmodial activities were performed, these two peptides were more than 50% unfolded. We do not know either folded or unfolded that have anti-plasmodial activities.

This research will study the effects of mutating hydrophobic conserved-residues on the thermal stability of PcFKs. To design the sequences of PcFKs mutants, the hydrophobic-conserved residues among PcFK1 and PcFK2 which are Val10, Pro13, and Pro17 will be mutated to alanine (Ala, A). To synthesize these disulfide-complex peptides, the regioselective disulfide bond formation and orthogonal thiol protecting groups will be used. After the desired peptides are achieved, their thermal stabilities will be study by far-UV circular dichroism (CD).

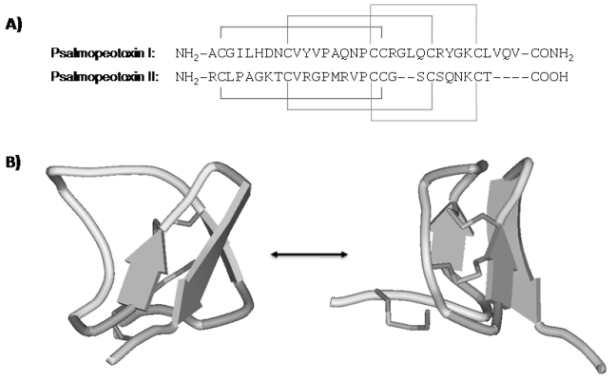

Figure 1. A) Sequences of wild-type Psalmopeotoxin I and II showing the three disulfide bonds and B) NMR structures of Psalmopeotoxin I (PDB ID: 1x5v), showing a 90º rotation around the z-axis

Materials and Methods

All Fmoc-protected amino acids, solid support, and other chemical reagents for peptide synthesis were purchased from Novabiochem, Aldrich Chemical Co., Fluka and Peptide Institute Inc.

General procedure for solid-phase peptide synthesis (SPPS) and sequence design

Productions of linear peptides (sequences shown in Table 1) were carried out by manual Fmoc solid phase peptide synthesis. All syntheses were performed on a 0.2 mmole scale, the coupling reaction was carried out using 4 equiv. of amino acid and the activating agent HBTU (2-(1*H*-benzotriazol-1-yl)-1,1,3,3-tetramethyluronium hexafluorophosphate, 4 equiv.) in the presence of diisopropylethylamine (DIEA, 8 equiv.) for 30 min. The *N*-terminal Fmoc deprotection was achieved using 20% piperidine in DMF for 30 min. Tryptophan (Trp, W) was added to the *N*-terminus in order to measure the amount of peptides. The three disulfide bonds were formed regioselectively by employing different cysteine's thiol protecting groups (Table 2): trityl (Trt), acetamiomethyl (Acm), and *tert*-butyl (*t*Bu) for the first, second, and third disulfide bond, respectively. Cleavage of linear peptides from resin and side-chain deprotection were achieved using 8 mL of reagent K (reagent K: 82.5% TFA, 5% thioanisole, 5% m-cresol, 5% water, and 2.5% ethanedithiol) for 4 h at room temperature. The peptides were precipitated by methyl *tert*-butyl ether (MTBE, < 0˚C) and centrifuged at 10,000 rpm for 10 min. The resulting crude peptides were purified by preparative reversed-phase HPLC as described above. Peptide identities were confirmed by ESI-MS.

Reversed-Phase HPLC and MS methods

RP-HPLC was performed on Young Lin Instrument Acme 9000 system (Seoul, Korea) equipped with binary pump and UV detector. Stationary phase was Vydac C_{18} column. The mobile phase system was water-acetonitrile (ACN)-trifluoroacetic acid (TFA). Flow rates were 1 and 10 mL/min for analytical and preparative HPLC, respectively. Chromatograms were monitored at 230 and 280 nm. The purified peptides and impurities were identified using Bruker microTOF ESI-HRMS (Bellerica, MA, U.S.A.).

Regioselective disulfide bond formation (Figure 2)

The first intramolecular disulfide bond formation (Monodisulfide, MDS). The two Trt side-chains protecting groups of Cys were removed at the same time as peptide cleavage from the resin by reagent K. The first disulfide bond can be formed using 0.95 equiv. of 2,2'-dithiodipyridine (PySSPy) and 1 mM peptide in 0.1% (v/v) TFA in water at room temperature. The oxidation was completed when left it overnight and product was purified by preparative RP-HPLC as described.

The second intramolecular disulfide bond formation (Didisulfide, DDS). The 1 mM peptide-MDS in 99% TFA and 1% anisole (v/v) was treated with 200 equiv. of silver trifluoroacetate (AgOTFA) and 200 equiv. of trifluorometanesulfonic acid (TfOH) which formed silver triflate (AgOTf) *in situ*, stirred for 2 h at room temperature. Peptide silver salt was precipitated in ice-cold *tert*-butyl methyl ether (MTBE, < 0˚C), centrifuged at 10,000 rpm for 10 min, re-dissolved in 30% ACN 0.1% TFA, and treated with 0.67 equiv. of PySSPy at room temperature, reactions was kept overnight. The resulting crude product was purified by preparative RP-HPLC.

The third intramolecular disulfide bond formation (Tridisulfide, TDS). The peptide-DDS in TFA was treated with TfOH and anisole (TFA:TfOH:anisole = 10:2:1, v/v), stirred at 0˚C for 1 h. After the reaction was completed, the reaction mixture was immediately purified in single injection by preparative RP-HPLC as described above. The third disulfide bond can be formed using 0.95 equiv. of PySSPy in 1 mM peptide 0.1% (v/v) TFA in water for 24 h at room temperature. The resulting crude product was purified by preparative RP-HPLC.

All purified peptides and impurities were identified by ESI-MS which corrresponding *m/z* ($[M+H]^+$) were shown in Table 3.

Table 1: Sequences for PcFKI and PcFKII wild-types and their mutants

Peptides	Sequences
PcFK1-wild-type	(W)ACGILHDNCVYVPAQNPCCRGLQCRYGKCLVQV
PcFK1-V10A	(W)ACGILHDNCAYVPAQNPCCRGLQCRYGKCLVQV
PcFK1-P13A	(W)ACGILHDNCVYVAAQNPCCRGLQCRYGKCLVQV
PcFK1-P17A	(W)ACGILHDNCVYVPAQNACCRGLQCRYGKCLVQV
PcFK2-wild-type	(W)RCLPAGKTCVRGPMRVPCCG--SCSQNKCT---
PcFK2-V10A	(W)RCLPAGKTCARGPMRVPCCG--SCSQNKCT---
PcFK2-P13A	(W)RCLPAGKTCVRGAMRVPCCG--SCSQNKCT---
PcFK2-P17A	(W)RCLPAGKTCVRGPMRVACCG--SCSQNKCT---

Table 2: Cysteine positions and corresponding thiol protecting groups used for synthesis of PcFKs

Protecting Groups	Cysteine residues	
	PcFK1	PcFK2
Trt (trityl)	Cys-9 and Cys-24	Cys-9 and Cys-22
Acm (acetamidomethyl)	Cys-18 and Cys-29	Cys-18 and Cys-27
*t*Bu (*tert*-butyl)	Cys-2 and Cys-19	Cys-2 and Cys-19

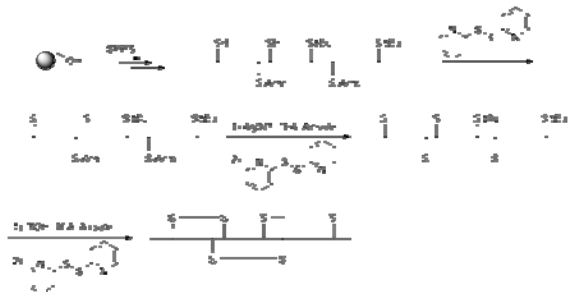

Figure 2**.** Regioselective disulfide bond formations

Table 3**:** Calculated and observed mass for PcFKs

Peptides	$[M+H]^+$	
	Calculated	**Observed**
PcFK1-wild-type	3802.7	3802.5
PcFK1-V10A	3774.7	3774.6
PcFK1-P13A	3776.7	3776.6
PcFK1-P17A	3776.7	3776.5
PcFK2-wild-type	3135.4	3135.2
PcFK2-V10A	3106.3	3106.1
PcFK2-P13A	3109.3	3109.0
PcFK2-P17A	3109.3	3109.1

Circular Dichroism studies

Circular dichroism (CD) experiments were performed on Jasco J-815 CD Spectropolarimeter (Tokyo, Japan) with peltier temperature-controlled cell holder using a 0.2 cm cuvette. Samples were 10.0 μM peptide in 0.1 M glycine-HCl (pH 3, NMR pH)[2] and 0.1 M phosphate buffer (pH 7.4, physiological pH). For the thermal unfolding experiments, wavelength/temperature scan macro was employed. Temperature scans of the samples were achieved by heating the samples from 0-100˚C using 2˚C/min heating rate. The change in protein characteristics was monitored at 214 nm with 8 s response time. In addition, wavelength scans for the samples were taken every 5˚C using a step-resolution of 0.1 nm, scanning speed of 20 nm/min, and 1 nm bandwidth. After the highest temperature was reached, samples were cooled to 0˚C. Fraction unfolding (f_u) curve was determined using the baseline extrapolation method.[3] The mid-point of transition temperature (T_m) was calculated from the fraction unfolding curve.

Results and Discussion

Peptide synthesis

The syntheses of linear PcFK peptides were achieved by manual Fmoc solid phase peptide synthesis. Then, their three disulfide bonds in the PcFKs' mutants were formed by regioselective disulfide bond formation method. The regioselective disulfide bond formation can be accomplished by using orthogonal thiol protecting group strategy. In this strategy, each disulfide bond was formed one at a time by choosing different protecting groups. The six cysteine residues were protected by three types of thiol protecting groups as shown in Table 2 (Trt, Acm, and *t*Bu) which can be removed under different conditions as described, allowing the three disulfide bonds to be formed, sequentially. When the pair of cysteines was deprotected, disulfide bond was formed using PySSPy in the presence of 0.1% TFA.

Thermal stability studies

To determine the effects of temperature on their structural changes, CD experiments were performed by monitoring the changes in ellipticity at 214 nm, where classical β-sheet CD minimum was at, while temperature was changed (from 0˚C to 100˚C). The thermal stabilities of each mutant were represented in terms of mid-point of transition temperature (T_m) which were obtained by using baseline extrapolation method.

The unfolding curves observed by CD demonstrated that PcFK1-V10A, PcFK1-P13A, and PcFK2-V10A were unfolded either pH 3 or pH 7.4, and PcFK2-P13A was also unfolded at pH 3. For PcFK1-P17A and PcFK2-P17A, they were folded at both pH's. Lastly PcFK2-P13A was folded only at pH 3. For the mutants which were folded, the fraction unfolding (f_u) could be calculated and used to construct thermal unfolding curve (Figure 3). The mid-points of transition temperature (T_m) of each folded mutant were obtained where the fraction unfolded was 0.5. The T_m determined for these mutants were shown in Table 4.

From the analysis of NMR solution structure, the unstructured region of PcFK2 is more compact than PcFK1. For this compactness could explain the stability of peptides that more compact peptides/proteins are more stable than less compact ones.[4] All mutants were not thermally stable for both PcFKs, possibly indicating that these residues (Val10, Pro13, and Pro17) which were mutated to alanine are important to the stability of PcFKs. When valine was replaced with alanine, the stability from hydrophobic interaction was reduced. For proline mutants, it is known that proline has more conformational rigidity than other amino acids, thus, playing an important role in protein folding and stability. According to thermal stabilities of these mutants, the mutations on Val10 and Pro13 had huge impact on the folding of PcFKs at both pHs, peptides were unfolded or had significant different T_m compared to their wild-types. On the other hand, Pro17 mutations had less impact to their stabilities which were shown in similar range T_m. When these prolines were mutated, only P17A mutants remained folded, suggesting that the conformational rigidity at this location of the flexible loop is not critical for stability. Interestingly, the PcFK2-P13A was more stable than pH 3 which suggest that at pH 3, the conformational rigidity at residue 13 destabilizes PcFK2.

Table 4**:** Mid-points of transition temperature of PcFK1 and PcFK2, their wild-types and mutants

Peptides	T_m (˚C)	
	pH 3	**pH 7.4**
PcFK1-wild-type	18.3	14.4
PcFK1-V10A	unfolded	unfolded
PcFK1-P13A	unfolded	unfolded
PcFK1-P17A	15.8	20.3
PcFK2-wild-type	29.5	15.9
PcFK2-V10A	unfolded	unfolded
PcFK2-P13A	43.8	unfolded
PcFK2-P17A	26.1	18.4

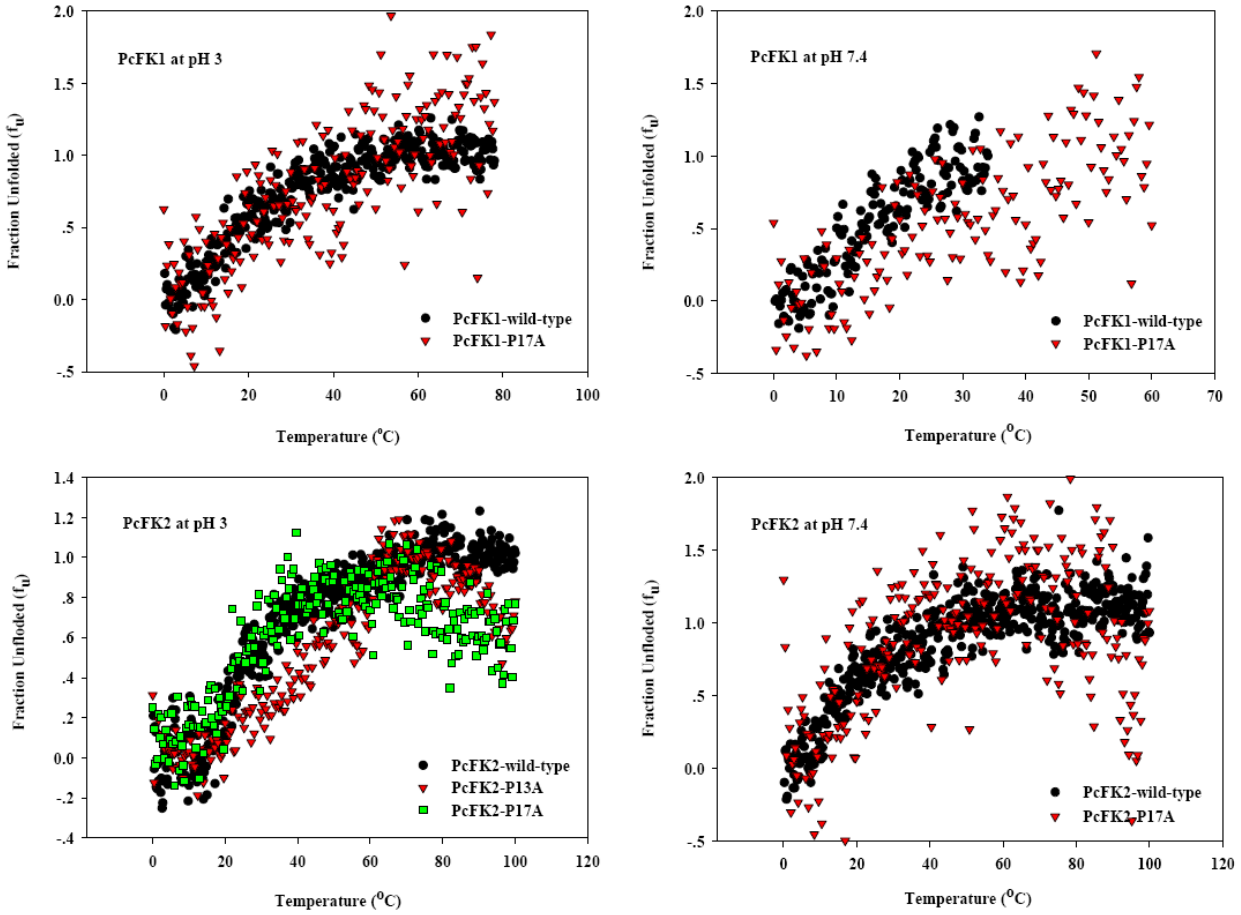

Figure 3. Thermal unfolding curve of PcFK1 at pH 3 (top-left), PcFK1 at pH 7.4 (top-right) and PcFK2 at pH 3 (bottom-left), and PcFK2 at pH 7.4 (bottom right). Showing overlaid curves between wild-types and mutants

Conclusion

From thermal unfolding studies, the results revealed that the mutants of PcFK1 and PcFK2 were thermally unstable peptides under physiological condition. As temperature increased, both PcFKs unfolded in a two-state fashion when monitored by far-UV CD. The effects of hydrophobic conserved-residue mutations (Val10, Pro13, and Pro17) caused peptides less stable than their wild-types (except for PcFK2-P13A which was more stable than PcFK2-wild-type at pH 3). Generally, PcFK2s were more stable than PcFK1s due to their compactness of unstructured region.

For the future works, it will be of significant interest to assess the biological activity of these mutants and to design other mutations in order to improve the stability and biological activity of PcFKs.

References

[1] S. J. Choi, R. Parent, C. Guillaume, C. Deregnaucourt, C. Delarbre, D. M. Ojcius, J. J. Montagne, M. L. Celerier, A. Phelipot, M. Amiche, J. Molgo, J. M. Camadro and C. Guette, *FEBS Lett* **2004**, *572*, 109-117.

[2] C. Pimentel, S. J. Choi, B. Chagot, C. Guette, J. M. Camadro and H. Darbon, *Protein Sci* **2006**, *15*, 628-634.

[3] S. Deechongkit and J. W. Kelly, *J Am Chem Soc* **2002**, *124*, 4980-4986.

[4] K. A. Dill and D. Shortle, *Annu Rev Biochem* **1991**, *60*, 795-825.

Synthesis of the novel piperine analogues

S. Phattanasarin*, C. Chokbundit and A. Baramee

Department of Chemistry, Chiang Mai University, Chiang Mai, Thailand 50200

*E-mail: guiassium@hotmail.com

Abstract: The natural amides piperine was isolated from *Piper nigrum Linn.* (piperaceae). Piperine was hydrolyzed into piperic acid (98% yield) which was converted into the six piperine derivatives in 28-49% yields. These derivatives of piperine have been synthesized and evaluated for their bioactivities, *e.g.* antibacteria and antioxidant. The synthetic process involves three steps from piperine, namely isolation of piperine from black pepper, alkaline hydrolysis of piperine to piperic acid, and the reactions of piperic acid with benzophenone oxime, 2-bromobenzaldehyde oxime, vanilline, eugenol, phenol, and ethanol using oxalyl chloride and triethylamine.

Introduction

Piperine (1-piperoylpiperidine), an alkaloid present in *Pipernigrum Linn* (black pepper), is use in the traditional system of medicine against intestinal ailments [1], against caecal amoebiasis of rats [2]. Piperine (Fig. 1) shows important pharmacological activity e.g. to possess promising pesticidal and antitumour properties [3-6], insecticidal [7], against phytopathogenic fungi [8]. In addition, piperine has also been shown to enhance the bioavailability of drugs like spateine, curcumin, barbiturates and oxyphenylbutazone, zoxazolamine, propanlol and theophylline in animal experiments [5,9,10].

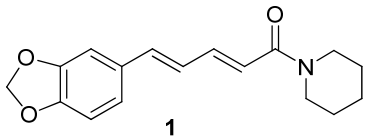

1

Figure 1. Piperine

The previously reported [11-12], it was demonstrated that an aromatic ring containing at least one ether function, carbonyl group and conjugated double bonds containing in side chain of piperine derivatives is essential for high activity in inhibition of CYP, stimulating melanocyte proliferation activity.

Recently, piperine and its derivatives can against some bacteria [10]. This research we focused on the preparation of ester derivatives of piperine for against bacteria.

Materials and Methods

Collection and preparation of plant material:

Dried fruits of *Piper nigrum Linn* were purchased from the local market in Chiang Mai province and were collected and air-dried. Then the dried fruits were ground into a powder.

The powder fruits material (100 g) was extracted with 95% ethanol and refluxed 24 h, filtered and concentrated by rotary evaporator until obtained a dark brown viscous liquid. Alcoholic potassium hydroxide 10 % (10 ml) was added to precipitate the residue, filtered and left it for one day to precipitate the crude piperine. The crude piperine was purified by crystallization from CH_2Cl_2: hexane (3:2) to give the pure piperine in 1.13 % yield [13].

Preparation of piperic acid (**2**) from piperine (**1**)

Piperine (2.853 g, 0.01 mol) was refluxed with ethanolic KOH (2 M, 10 ml) for 2-25 h. Ethanol was removed off by rotary evaporator to obtain the solid potassium salt of piperic acid, then follow by dissolved in hot water 50 ml, acidified with 35% HCl to give the yellow precipitate and recrystallization from ethanol to obtain piperic acid (**2**) in 35.45-98.98 % yield (Scheme1) [12].

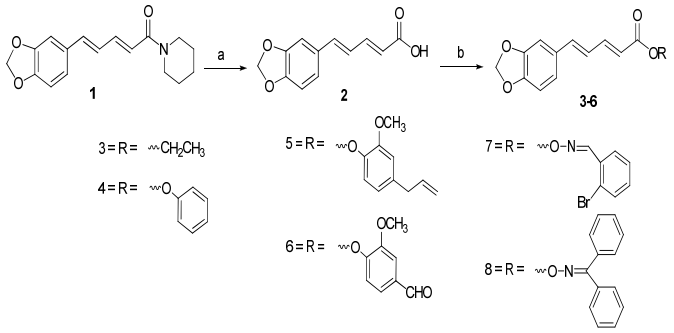

Scheme 1. Reagent: (a) 10% ethanolic KOH. (b) i. $(COCl)_2$, THF, RT, 6 h. ii. Alcohol or oxime, 70 ^oC, 5 h.

General procedure for preparation of oximes (9 and 10)

A mixture of aldehyde or ketone (1 mmol), sodium hydroxide (6 mmol) and hydroxylamine chlorohydrate (3 mmol) in EtOH (50 mL) was stirred at reflux for 3h. After cooling, the mixture was neutralized and extracted by CH_2Cl_2 (3x100mL). The organic layer was dried over Na_2SO_4 and the solvent was evaporated under vacuum pressure to give aldoxime (**9**) or ketoxime (**10**) (Scheme2) [14].

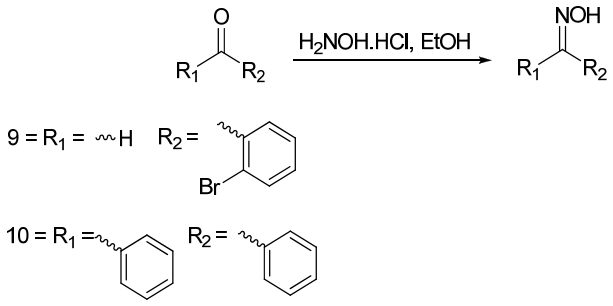

Scheme 2. Syntheses of oxime **9** and **10**.

General procedure for preparation of ester derivatives (3-8) of piperic acid

To a solution of piperic acid (**2**) (0.500 g, 2.29 mmol) in dried THF (4 ml) at room temperature under nitrogen atmosphere was added oxalyl chloride (1 ml, 11.5 mmol) and stirred at room temperature for 6 h. The reaction mixture was evaporated to give the crude piperic acid chloride as an orange residue. To the crude piperic acid chloride in dried THF (4 ml), was added the solution of ethanol, phenol, eugenol, vanilline, 2-bromobenzaldehyde oxime or benzophenone oxime (2.3 mmol) in dried THF (3 ml) followed by triethylamine (0.48 ml, 3.5 mmol) and stirred at 70 ºC for 5 h. The reaction mixture was evaporated to give the yellow crude product and then purified by column chromatography (silica gel; ethyl acetate in hexane, 1:4, as eluent) to obtain compound **3**-**8** in 48.75, 34.01, 37.09, 36.58, 29.27, 28.13 % yield respectively**.**

In vitro Bioassay studies:

The antibacterial activities of the extracts were determined using the paper disc method [15]. The bacteria used were: *Escherichia coli* ATCC25922, *Staphylococcus aureus* ATCC25923 (Gram positive bacteria)*, Pseudomonas aeruginosa* ATCC27553 (Gram negative bacteria).

In brief, a loop full of the strain was inoculated in 30 ml of nutrient broth in a conical flask and incubated on a rotary shaker for 24 h to activate the strain. Mueller-Hinton agar was prepared for the study. The media and the test bacterial cultures were poured into Petri dishes (Hi-Media). The test strain (0.2 ml) was inoculated into the media (inoculum size 108 cells/ml) when the temperature reached 40-42 ºC. Care was taken to ensure proper homogenization. The experiment was performed under strict aseptic conditions.

The compounds **1**, **2**, **3**, **4**, **5**, **6**, **7** and **8** were weighed and dissolved in dimethylsulfoxide (DMSO) to make a solution of concentration 0.005, 0.05, 0.1, 0.5, 1, 2 mg/ml. Sterilized filter discs were dipped in these solutions and subsequently dried to remove DMSO. Mueller–Hinton agar was prepared and allowed to solidify. One of these discs was kept free from antibiotic and served as growth control. Three different bacteria were selected and 1 ml of each bacterial culture broth were added in the Mueller–Hinton plates and spread with the help of sterile spreader. The filter paper discs soaked in above mentioned dilutions of compounds number **1**, **2**, **3**, **4, 5**, **6**, **7** and **8** were placed aseptically over the inoculated plates using sterile forceps. 0.75 mg/ml of Gentamicin and 20 µL of 100% DMSO were used as a positive control. The plates were incubated at 37 ºC for 24 h, in upright position. The zone of inhibition was measured.

TLC-DPPH separation and determination of radical scavenging activity

The compounds **1**, **2**, **3**, **4**, **5**, **6**, **7** and **8** were subjected to thin layer chromatography study. The plates were sprayed by 0.2 mM DPPH in methanol solution for 5 seconds and images were observed under visible light at exactly 2 min after spraying. The area of bright yellow bands against the purple background then determined radical scavenging activity [16].

Results and Discussion

Piperic acid (**2**) was used as a precursor for preparation of the piperine derivatives. Piperic acid (**2**) was obtained by alkaline hydrolysis of piperine (**1**). The conditions for alkaline hydrolysis of piperic acid from piperine were shown in Table 1.

Table 1**:** The reaction conditions for alkaline hydrolysis of piperic acid (**2**) from piperine (**1**)

Entry	Refluxed time (h)*	% yield
1	2	35.45
2	5	48.50
3	10	52.82
4	15	62.54
5	20	84.85
6	25	98.98

* Conditions: Piperine (2.853 g), ethanolic KOH (2 M,10 ml)

The results shown that the most effective method for alkaline hydrolysis of piperine (**1**) was refluxed with ethanolic KOH for 25 h to obtain piperic acid (**12**) in 98.98 % yield.

Antibacterial was determined by paper disc diffusion method. The reference compound, gentamycin, exhibited clear zone values 17, 23 and 24 mm, the synthetic compound, **3**, exhibited clear zone values 7 mm. For the synthetic compounds **2** and **8** exhibited inactive.

The biological activities of compounds **1**, **2**, **3**, **4**, **5**, **6**, **7** and **8** were shown in Table 2.

Result of the TLC-DPPH separation and determination of radical scavenging activity shown in Table 3.

Table 2: Antibacterial activity of compounds 1, 2, 3, 4, 5, 6, 7 and 8 (numerals show size of zone of inhibition in mm) of different dilutions (2, 1, 0.5, 0.1, 0.05, 0.005 mg/ml) against bacterial strains.

Name of bacteria	Inhibitory zone (mm)									
	1	2	3	4	5	6	7	8	DMSO	Gentamycin[a]
E.coli	-	-	7,7,7	-	-	-	-	-	-	17
S.aureus	-	-	7,7,7	-	-	-	8,8,8	-	-	23
P.aeruginosa	7,7,7,7	-	7,7,7,7,7,7	7,7,7,7,7,7	7,7,7,7	7,7,7,7	8,8,7,7,7	-	-	24

[a]: (0.75 mg/mL concentration)
- Resistant.

Table 3: DPPH radical scavenging activities of compounds **1**, **2**, **3**, **4**, **5**, **6**, **7** and **8** antioxidants SC_{50}

Compounds	SC_{50}*
1	-
2	-
3	-
4	-
5	-
6	-
7	-
8	-

*
Values obtained from logarithmic lines. SC_{50} is defined as the concentration sufficient to obtain 50 % of a maximum free radical scavenging capacity.
- Inactive

Conclusions

In conclusion, some ester derivatives of piperine have been synthesized and evaluated for their bioactivities. The synthetic process involves three reaction steps of piperine isolation from black pepper (1.1 %), alkaline hydrolysis of piperine to piperic acid (98.9%), and the reactions of piperic acid with benzophenone oxime, 2-bromobenzaldehyde oxime, vanilline, eugenol, phenol, and ethanol using oxalyl chloride and triethylamine to obtain esters **3**, **4**, **5**, **6**, **7** and **8** in 48.8, 34.0, 37.1, 36.6, 29.3, 28.1 % yield respectively. Then, these compounds were subjected to biological evaluations, namely antibacteria and antioxidant, using piperine and piperic acid as reference compounds for comparison. It was found that ester **3** was most effective in antibacterial activity . For the synthetic compounds **2** and **8** exhibited inactive. The compound **3** can against *E.coli*, compounds **3** and **7** against *S.aureus* and compounds **1**, **3**, **4**, **5**, **6** and **8** against *P.aeruginosa.* All these synthetic compounds were inactive antioxidant.

Acknowledgement

We would like to thank the faculty of chemistry and the Graduate School, Chiang Mai University for partial support and we also would like to thank Center for Innovation in Chemistry Postgraduate Education and Research Program in Chemistry (PERCH-CIC).

References

[1] G.V. Satyavati, A.K. Gupta and N. Tandon, *Medicinal Plants of India*, ICMR Publications, New Delhi, **2** (1987), pp. 426-456.
[2] S. Ghosshal, B.N.K. Prasad and V. Lakshmi, *J. Ethnopharmacology*, **50** (1996), pp. 167-170.
[3] F. Kiuchi, n. Nakamura, Y. Tsuda and H. Yoshimura, *Chem. Pharm. Bull*. **36** (1988), pp. 2452-2465.
[4] C.Y. Duh, Y.C. Wu and S.K. Wang, *J. Nat. Prod*. **53** (1990), pp. 1575-1577.
[5] A. Banerji, *J. Ind. Chem. Soc.* **69** (1991), pp. 53-67.
[6] D. Biswanath and P. Madhusudhan, *Tetrahedron Letters* **39** (1998), pp. 9099-9100.
[7] V. F. de Paula, L. C. de A barbosa, A. J. Demuner, D. Pilo-Veloso and M.C. Picanco, *Pest Manag. Sci.* **56** (2000), pp. 168-174.
[8] S.E. Lee, B.S. Park, M.K. Kim, W.S. Choi, H.T. kim, K.Y. Cho, S.G. Lee and H.S. Lee, *Crop Protection* **20** (2001), pp. 523-528.
[9] B.B. Aggarwal, A. Kumar, M.S. Aggarwal and S. Shishodia, *In Phyto chemicals in Cancer Chemoprevention*; D. Bagchi and H.G. Preuss, Eds., Culinary & Hospitality Industry Publications Services, 2003.
[10] S. Mishra, U. Narain, R. Mishra and K. Misra, *Bioorg. Med. Chem*. **13** (2005), pp. 1477-1486.
[11] S. Tsukamoto, B.C. Cha and T. Ohta, *Tetrahedron* **58** (2002) pp. 1667-1671.
[12] V. Radhakrishnan, F. Laura, R.Y. Anotony, R. Amala and C.H. Robert, *Bioorgan. Med. Chem.* **12** (2004), pp. 1905-1920.
[13] R. Jochen, X. Pei-Gen and B. Rudolf, *J.Ethnopharmacology* (2001), pp. 133-139.
[14] A. Baramee, A. Coppin, M. Mortuaire, L. Pelinski, S. Tomavoc and J. Brocard, *Bioorgan. Med. Chem.* **14** (2006) pp. 1294–1302.
[15] H. Chandarana, S. Baluja and S. V. Chanda, *J. Biol.* **29** (2005), pp. 83-87.
[16] S. Sreenivasan, D. Ibrahim and M. J. N. M. Kassim, *International Journal of Natural and Engineering Sciences 1,* **3** (2007), pp. 115-117.

Stilbenoids from the roots of *Shorea roxburghii*

W.Patcharamun[1], S. Tip-pyang[1*], J. Jong-aramruang[2] and S. Khumkratok[3]

[1]Natural products research unit, Faculty of Science, Chulalongkorn University, Bangkok, Thailand 10330
[2]Department of Chemistry, Faculty of Science, Burapha University, Chonburi, Thailand 20231
[3]Walai Rukhavej Botanical Research Institute, Mahasarakham University, Mahasarakham, Thailand 44000

[*]E-mail: Santi.Ti@chula.ac.th

Abstract: In phytochemical investigation for bioactive compounds from Thai medicinal plants in the family Dipterocarpaceae, acetone crude extract from the roots of *Shorea roxburghii* was selected for isolation, purification and structure elucidation. The chromatographic separation of this crude extract led to the isolation of a new stilbenoid, roxburghiol A (1), along with four known stilbenoids, resveratrol 2-*C*-glucoside (2), vitisinol G (3), gnetin C (4) and (-)-hopeaphenol (5). The structures of all isolated compounds were characterized by means of spectroscopic data as well as comparison with the previous literature data.

Introduction

Shorea roxburghii G.Don belongs to the Dipterocarpaceae family. It is widely distributed in many parts of Thailand. There are no reports on phytochemical investigation of this plant. Previous phytochemical study on the *Shorea* species revealed the presence of various stilbenoids[1]. Our phytochemical investigation of this plant has resulted in the isolation of a new stilbenoid dimer, roxburghiol A (**1**), and four known stilbenoids, resveratrol 2-*C*-glucoside (**2**) [2], vitisinol G (**3**) [3], gnetin C (**4**) [4], and (-)-hopeaphenol (**5**) [5] (Fig.1). This paper also describes the isolation and structure elucidation of a new stilbenoid dimer (**1**). The biological activities of all isolated stilbenoids are in progress.

Materials and Methods

^{1}H and ^{13}C NMR spectra were measured with a Varian model Mercury^{+} 400 spectrometer. HRMS were obtained with a Bruker MICROTOF mass spectrometer. Vacuum liquid chromatography (VLC), column chromatography (CC), centrifugal thin-layer chromatography (chromatotron) and preparative thin-layer chromatography (PTLC) were carried out using Merck Si gel 60 GF_{254}. For TLC analysis, precoated Si gel plates (Merck Kieselgel 60 GF_{254}, 0.25 mm) were used.

The roots of *S. roxburghii* were collected in May 2008 from Mahasarakham province, Thailand and identified by one of our co-auther (S. Khumkratok), a botanist at the Walai Rukhavej Botanical Research Institute, Mahasarakham University, Thailand where a voucher specimen is deposited.

The air-dried roots of this plant (2 kg) were soxhleted with acetone. The acetone extract was suspended into acetone solvent and left at room temperature over night. An acetone soluble part was

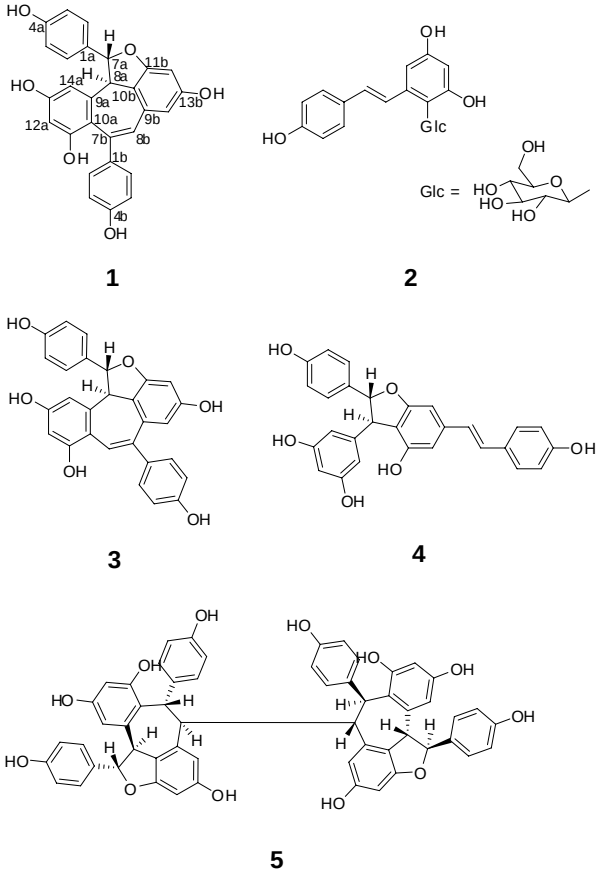

Figure 1. Structure of compounds **1-5** isolated from *S. roxburghii*.

fractionated using VLC on silica gel eluted with a mixture of CH_2Cl_2-MeOH increasing in the polarity to give six major fractions A-F. Fraction A was refractionated using Si gel CC [CH_2Cl_2-EtOAc-MeOH (80:10:10)] to yield fractions A1-A4. Repeated purification of fraction A3 using chromatotron [CH_2Cl_2-EtOAc-MeOH (70:20:10)] and PTLC [CH_2Cl_2-EtOAc-MeOH (70:20:10)] afforded compounds **1**, **3** and **4**. Similarly, fraction B was rechromatographed on Si gel CC [CH_2Cl_2-EtOAc-MeOH (70:20:10)] and then purified with chromatotron [CH_2Cl_2-EtOAc-MeOH (60:20:20)] and PTLC [CH_2Cl_2-EtOAc-MeOH (70:15:15)] to yield compounds **2** and **5**.

Roxburghiol A (**1**): brown powder; $[\alpha]^{25}_{D}$ -66° (*c* 0.20, MeOH); UV (MeOH) λ_{max} (log ε) 315 (5.45), 276 (5.40) nm; ^{1}H and ^{13}C NMR spectral data, see Table 1; HRMS m/z 452.1364 (calcd. for $C_{28}H_{20}O_6$ 452.1370).

Table 1. ^{1}H and ^{13}C NMR spectral data of **1**[a]

position	δ_H	δ_C
1a		133.7
2a, 6a	7.28 (d, 8.4)	126.9
3a, 5a	6.81 (d, 8.4)	115.4
4a (OH)	8.50 (s)	157.4
7a	6.38 (d, 4.4)	85.0
8a	4.05 (d, 4.4)	53.2
9a		134.0
10a		115.0
11a (OH)	7.39 (s)	157.0
12a	6.23 (d, 2.0)	101.3
13a (OH)	8.55 (s)	158.9
14a	6.73 (d, 2.0)	101.2
1b		135.9
2b, 6b	7.23 (d, 8.4)	127.6
3b, 5b	6.75 (d, 8.4)	115.0
4b (OH)	8.38 (s)	156.6
7b		141.8
8b	7.09 (br s)	127.1
9b		145.2
10b		122.0
11b		157.7
12b	6.25 (d, 1.6)	95.6
13b (OH)	8.38 (s)	156.9
14b	6.37 (d, 1.6)	105.0

[a]Measured in CD_3COCD_3 at 400 MHz (^{1}H NMR) and 100 MHz (^{13}C NMR).

Results and Discussion

The acetone extract of the roots of *S. roxburghii* was fractionated by VLC into six major fractions A-F. Fraction A and B were futher purified by combination of Si gel CC, chromatotron and PTLC to yield compounds **1-5**. Roxburghiol A (**1**), had a molecular formula of $C_{28}H_{20}O_6$, and its ^{13}C NMR spectrum showed 23 signals for 28 carbons. In the ^{1}H NMR spectrum of **1**, the signals at δ 6.38 (H-7a) and 4.05 (H-8a) with their HMQC correlated carbon signals at δ 85.0 (C-7a) and 53.2 (C-8a) showed the characteristics of a resveratrol derivative containing a 2,3-dihydrobenzofuran moiety [6]. In addition, one olefinic methine singlet due to H-8b appeared at δ 7.09. The HMBC experimental results (Fig. 2) showed that H-12a (δ 6.23) and H-14a (δ 6.73) correlated with an aromatic quaternary carbon C-10a (δ 115.0). The position of H-12b (δ 6.25) and H-14b (δ 6.37) were assigned by their correlation with an aromatic quaternary carbon C-10b (δ 122.0). Moreover, the presence of key correlations between H-8b and C-1b (δ 135.9)/C-14b (δ 105.0)/C-10a (δ 115.0)/C-10b (δ 122.0) resulted in the establishment of a seven-member ring. The NOE existed between H-2a (H-6a) and H-8a, suggesting a *trans* configuration for H-7a/H-8a [3].

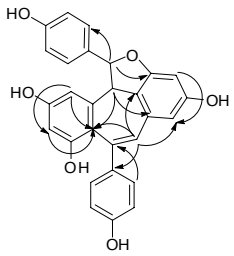

1

Figure 2. Key HMBC correlations of **1**. Arrows indicate correlation between hydrogen (point of origin) and carbon (arrowhead).

Conclusions

In conclusion, five stilbenoids, comprised of one new stilbenoid, roxburghiol A (**1**) and four known stilbenoids were isolated from the roots of *S. roxburghii*. All of isolated stilbenoids were elucidated by spectroscopic methods (MS, 1D and 2D NMR).

Acknowledgment

The authors are grateful to Assist. Prof. Tetsuro Ito, Gifu Pharmaceutical University, Japan, for his invaluable comments of the structure elucidation of the compounds in this work.

References

[1] Tukiran; Sjamsul, A.; Euis, H.; Lukman, M.; Kokki, S.; Kuniyoshi, S.; Yana, M. *Biochem. Sys. Ecol.* **2005**, 33, 631-634.

[2] Baderschneider, B.; Winterhalter, P. *J. Agric. Food Chem*. **2000**, 48, 2681-2686.

[3] Wen-Fei, C.; Chien-Chang, S.; Chien-Chih, C.; Chih-Hung, L.; Yu-Ling, H. *Planta Med*. **2009**, 75, 856-859.

[4] Iliya, I.; Ali, Z.; Tanaka, T.; Iinuma, M.; Furusawa, M.; Nakaya, K.; Murata, J.; Darnaedi, D. *Phytochemistry* **2002**, 61, 959-961.

[5] Kawabata, J.; Fukushi, E.; Hara, M. *J. Magn. Reson. Chem*. **1992**, 30, 6-10.

[6] Huang, Y.; Tsai, W.; Shen, C.; Chen, C. *J. Nat. Prod.* **2005**, 68, 217-220.

Syntheses of spirocyclopentanone-anthracene adduct *via* tandem Michael addition–Dieckmann condensation approach

R. Choommongkol[1], P. Meepowpan[1]*, T. Thongpanchang[2], and B. Tarnchompoo[3]

[1] Department of Chemistry and Center of Innovation in Chemistry, Faculty of Science, Chiang Mai University, Chiang Mai Thailand 50200
[2] Department of Chemistry and Center of Innovation in Chemistry, Faculty of Science, Mahidol University, Bangkok, Thailand 10400
[3] National Center for Genetic Engineering and Biotechnology (BIOTEC)/ National Science and Technology Development Agency (NSTDA), Pathumthani, Thailand 12120

* E-mail: puttinan@chiangmai.ac.th

Abstract: The tandem Michael addition–Dieckmann condensation reactions has become an active topic of research. In this approach, treatment of dimethyl itaconate-anthracene adduct and an *α,β*-unsaturated carbonyl compound with LDA resulted in Michael addition followed by a Dieckmann condensation. It is one of the most useful carbon–carbon bond reactions in organic synthesis. It is reported here a synthesis of novel antimalarial spirocyclopentanone–anthracene adducts from the racemic and optically active dimethyl itaconate–anthracene adducts and piperine via the tandem Michael addition–Dieckmann condensation reactions, as a key step. All adducts exhibited antimalarial activity with IC_{50} values of 3.4–4.7 μg/mL, and importantly displayed no cytotoxicity to vero cells. Spirocyclopentanone–anthracene adducts derived from the racemic dimethyl itaconate–anthracene adducts and derivatives of piperine, methylene-1,3-dioxy cinnamide and cinnamide have been successfully synthesized in the moderate yields.

Introduction

Malaria is one of the world's most serious, widespread and common diseases because of its prevalence, virulence and drug resistance. It is caused by a parasite called Plasmodium, such as *P. falciparum*, *P. vivax*, *P. ovale* and *P. malariae*, which are transmitted *via* the bites of infected mosquitoes. In the human body, the parasites multiply in the liver, and then infect red blood cells. According to recent estimates, malaria affects more than 2,400 million people that account for approximately 40% of the world's population and 300-500 million people suffer from this disease and 2-3 million people die of malaria every year. Thus, many research groups are interesting to study and synthesize of new class of antimalarial agents.

Dimethyl itaconate-anthracene adduct (**1**) was used as starting material and chiral auxiliaries for synthesize biologically active natural product activities such as sakomycin, methyl deepoxy-4,5-didehydromethyleno mycin A and methyl methylnomycin A. Piperine (**2**) is one of a major alkaloids from Piper nigrum it display a variety of pharmacological and biological such as antifungal, antidiarrheal, insecticidal, nematocidal activity, inhibition of live metabolism and anti-inflammatory.

In previous report, adduct **1** and piperine (**2**) were reacted via tandem Michael addition–Dieckmann condensation reactions to give spirocyclopentanone-anthracene adduct **3** and **4** (Scheme 1). Adducts **3** and **4** exhibited antimalarial activity against the parasite *P. falciparum* (K1, multi-drug resistance strain) with IC_{50} value of 4.7 and 3.4 μg/mL respectively. Interestingly, adducts **3** and **4** displayed non-cytoxicity against human epidermoid catcinima (KB), human breast cancer cells (BC-1) and *vero* cells. Therefore, aim of this work is to design and synthesis of novel antimalarial substances, spirocyclopentanone–anthracene adducts and their derivatives, using adduct **1** and amide compounds as starting materials.

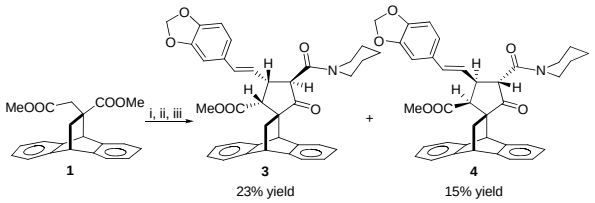

Scheme 1. Synthesis of spirocyclopentanone adducts *via* tandem Michael addition–Dieckmann condensation reactions. *Reagents and Conditions:* i) 1.2 equiv LDA, THF, –78 °C to 0 °C, 2 hr; ii) 1.2 equiv piperine (**2**), THF, 0 °C to rt, 3 days; iii) 30% aq. HCl.

Materials and Methods

All reactions were carried out under nitrogen or argon. Unless otherwise noted, materials were obtained from commercial suppliers and used without further purification. The ^{1}H and ^{13}C NMR spectra were recorded on Bruker DRX 400 MHz spectrometers and chemical shifts were given in ppm downfield from tetramethylsilane (TMS). Infrared spectra were taken with a FT-IR model TENSER 27 (Bruker) spectrometer and absorption frequencies were reported in reciprocal centimeters (cm^{-1}). Mass pectra (electrospray ionization mode, ESI-MS) were measured on a micromass Q-TOF-2^{Tm} (Waters) spectrometer. Flash column chromatography was performed employing Merck silica gel 60 and Merck silica gel 60H. Preparative thin layer chromatography (PLC) plates were carried out using Merck silica gel 60 PF_{254}. Solvents were dried over CaH2 and distilled

before used. Tetrahydrofuran (THF) was freshly distilled from sodium and benzophenone ketyl under nitrogen. Diisopropylamine was distilled over CaH_2 and stored under nitrogen. *n*-Butyllithium was purchased from Fluka and Across as solution in hexane and titrated periodically according to the 2,5-dimethoxybenzyl alcohol method.

Preparation of piperic acid (5) from piperine (2)

A solution of KOH (26.28 mmol) in H_2O (50 mL) was added to a solution of piperine (**2**) (17.52 mmol), in MeOH (100 mL) and heated to reflux for 2 hr. The cooled reaction mixture was diluted with water (15 mL) and acidified to pH 2-3 by 30% HCl, then extracted with CH_2Cl_2, dried over $MgSO_4$, filtered and evaporated to dryness. The crude product was crystallized from CH_2Cl_2/hexane to give the corresponding piperic acid (**5**) (3.75 g, 98% yield) as yellow solids.

General procedure for synthesis of (2E,4E)-5-(benzo [d][1,3]dioxol-5-yl)-1-(pyrrolidin-1-yl)penta-2,4-dien-1-one, amide 7

A mixture of piperic acid (**5**) (4.58 mmol) and oxalyl chloride (6.87 mmol) in CH_2Cl_2 (15 mL) was stirred at room temperature for 2 hr and the solvent was removed under reduced pressure. The mixture of the acid chloride obtained, CH_2Cl_2 (15 mL), triethylamine (5.50 mmol) and pyrrolidine (**6**) (5.50 mmol) was stirred at room temperature for 2 hr, filtered through Celite 545, diluted with H_2O and extracted with CH_2Cl_2. The solution was washed with H_2O, saturated NaCl solution, dried over $MgSO_4$, filtered and evaporated to dryness. The crude product was purified by flash column chromatography (silica gel) using EtOAc : hexane = 1 : 9 as eluent to give amide **7**.

General procedure for synthesis of spirocyclopenta none-anthracene adduct, 4'-(2'''-(benzo[c][1,3]dioxol yl)vinyl-3'-methoxy-carbonyl-5'-pyrrolidine-carbonyl -1'-cyclopentanone-2'-spiro-11-9,10-dihydro-9,10-ethanoanthracenes, 12 and 13

To a 50 mL round-bottomed flask equipped with a magnetic stirrer was fitted with a three-way stopcock with a septum cap and nitrogen inlet was added THF (8 mL) and dry diisopropylamine (4.28 mmol) *via* syringes. The mixture was cooled down to –78 °C, *n*-butyl lithium (1.4 N in hexane, 3.86 mmol) was added and the mixture left stirring at 0 °C for 1 hr. A solution of dimethyl itaconate–anthracene adduct, (**1**) (2.97 mmol) in THF (10 mL) was introduced to the LDA solution at –78 °C, then stirred at 0 °C for 2 hr. The solution of amide **7** (3.86 mmol) in THF (10 mL) was added to the anion solution at –78 °C after which the reaction mixture was left stirring at room temperature for 3 days. The reaction mixture was quenched with saturated aqueous ammonium chloride solution at 0 °C and the crude mixture was extracted several times with CH_2Cl_2. The dichloromethane solution was washed with H_2O, saturated NaCl solution, then dried over $MgSO_4$, filtered and evaporated to dryness. The crude product was purified by flash column chromatography (silica gel) using EtOAc : CH_2Cl_2 : hexane = 2 : 0.5 : 7.5 as eluent to give the spirocyclopentanone-anthracene adduct, **12** and **13** respectively.

Results and Discussion

Piperine (**2**) was hydrolyses with KOH in MeOH : H_2O (1 : 2) to give piperic acid in excellent yield, (Scheme 2).

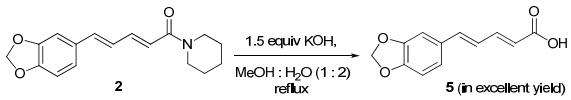

Scheme 2. Synthesis of piperic acid (**5**) from piperine (**2**)

Amide **7**, **9**, **11** were synthesized from acid **5**, **8**, and **10** respectively, in the present of oxalyl chloride and reacted with pyrrolydine (**6**) under N_2 gas (Scheme 3) and after purified by column chromatography to give amide **7**, **9** and **11** in good yields (Table 1).

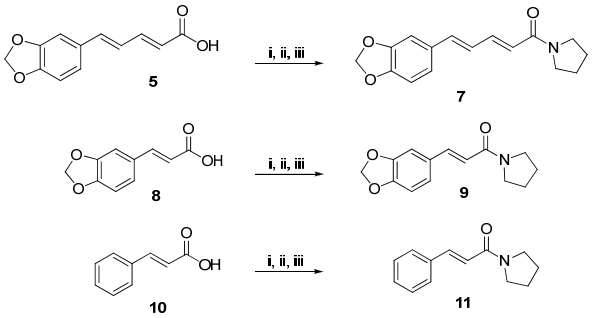

Scheme 3**.** Syntheses of amide **7**, **9** and **11**. *Reagents and Conditions:* i) 1.5 equiv $(COCl)_2$, 0 °C,15 min to rt 2 hr; ii) 1.2 equiv NEt_3, 0 °C 15 min; iii) 1.2 equiv pyrrolydine (**6**), 0 °C to rt, 2 hr.

Table 1: % Yields and % conversions of amide **7**, **9** and **11**

Compounds	Yield (%)	Conversion (%)
7	70	99
9	82	99
11	83	85

Then, the enolate anion of dimethyl itaconate–anthracene adduct (**1**) was generated by treated with LDA, at 0 °C for 2 hr and then reacted with amide **7** *via* tandem Michael addition–Dieckmann condensation reactions to give the spirocyclopentanone–anthracene adducts **12** and **13** in 9 % and 12 % yield, respectively (Scheme 4 and Table 2). Also amide **9** was allowed to react with the enolate anion of adduct **1** to give adducts **14** and **15** (in 23 % and 57 %), and adducts **16** and **17** (in 15 % and 15 %) were obtained from amide **11** whose results are shown in Table 2.

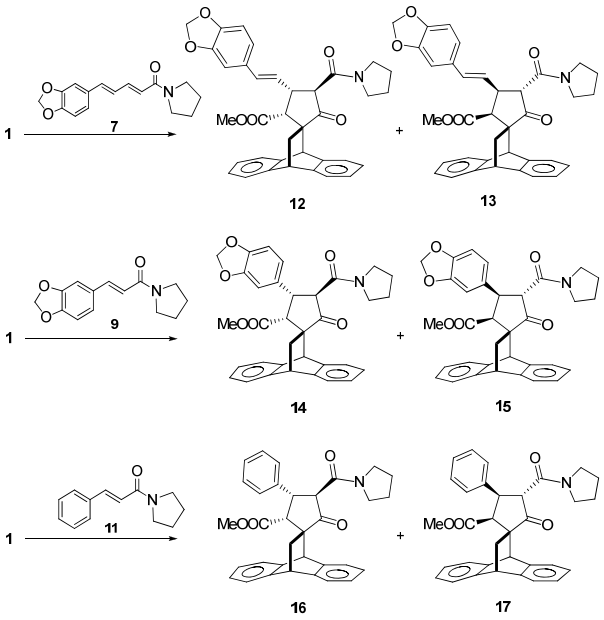

Scheme 4. Syntheses of spirocyclopentanone–anthracene adducts (**12**–**17**). *Reagents and Conditions:* i) 1.2 equiv LDA, THF, –78 °C to 0 °C, 2 hr; ii) 1.2 equiv amide **7** or **9** or **11**, THF, 0 °C to rt, 3 days; iii) 30% aq. HCl.

Table 2**:** % Yields of the spirocyclopentanone–anthracene adducts from tandem Michael addition–Dieckmann condensation reactions

Compounds	Yield (%)	Conversion (%)
12	9	70
13	12	
14	23	47
15	57	
16	15	80
17	15	

The relative stereochemistries of spirocyclopentanone–anthracene adducts (**12**–**17**) were determined on the basis of their analytical and spectroscopic data *e.g.* ^{1}H NMR, ^{13}C NMR and NOE experiment.

Conclusions

Amide **7**, **9** and **11** could be synthesized from piperic acid (**5**), methylene-1,3-dioxycinnamic acid (**8**), and cinnamic acid (**10**) reacted with pyrrolydine (**6**) in the present of oxalyl chloride in a good yield. Then, the spirocyclopentanone–anthracene adducts (**12**–**17**) could be synthesized using adduct **1** reacted with amides *via* tandem Michael addition–Dieckmann condensation reactions. In the future, all adducts **12**–**17** will be test antimalarial activity against the parasite *P. falciparum* (K1, multi-drug resistance strain) and cytoxicity against human epidermoid catcinima (KB), human breast cancer cells (BC-1) and *vero* cells.

Acknowledgement

I would like to thank the Office of the Higher Education Commission, Thailand for supporting by grant fund under the program Strategic Scholarships for Frontier Research Network for the Ph.D. Program Thai Doctoral degree for this research. We would like to thank the faculty of science and the Graduate School, Chiang Mai University and we also would like to thank Center for Innovation in Chemistry Postgraduate Education and Research Program in Chemistry (PERCH-CIC).

References

[1] Lertvorachon, J.; Meepowpan, P.; Thebtaranonth, Y. *Tetrahedron* **1998**, *54*, 14341–58.
[2] Kongsaeree, P.; Meepowpan, P.; Thebtaranonth, Y. *Tetrahedron: Asymmetry* **2001**, *12*, 1913–22.
[3] Tsukamoto, S.; Cha, B. C.; Ohta, T. *Tetrahedron* **2002**, *58*, 1667–71.
[4] Takahashi, M.; Ichikawa, M.; Aoyagi, S.; Kibayashi, C. *Tetrahedron Letters* **2005**, *46*, 57–9.
[5] Semler, U.; Gross, G. G. *Phytochemistry* **1988**, *27*, 1566–7.
[6] Rukachaisirikul, T.; Prabpai, S.; Champung, P.; Suksamrarn, A. *Planta Medica* **2002**, *68*, 853–5.

Synthesis and characterization of 3,4-di(pyridin-2-yl)-1,2,5-oxadiazole

K. Pattarith [1*], N. Pungwiwat[1], S. Khampiranon[1] and S. Laosooksathit[1]

[1]King Mongkut's University of Technology North Bangkok, Department of Industrial Chemistry, Faculty of Applied Science, Bangsue, Bangkok, Thailand 10800

[*]E-mail: spectro_aas@hotmail.com

Abstract: Oxadiazoles were nonnaturally occurring five-membered aromatic heterocycles, which are important structural components in many pharmaceuticals, agrochemicals, cosmetics, and plastics due to their topology and electronic properties. The 3,4-di(pyridin-2-yl)-1,2,5-oxadiazole was synthesized by dehydration of 1,2-di(pyridin-2-yl)ethane-1,2-dione dioxime, which was prepared from 1,2-di(pyridin-2-yl)ethane-1,2-dione and hydroxylamine hydrochloride. The structures of the products were deduced from their IR, ^{1}H-NMR and mass spectral data, and elemental analysis. The method developed gave the product in good yields.

Introduction

Most pharmaceuticals and biologically active agrochemicals are heterocyclic derivatives, as are numerous additives used in industries such as in cosmetics, reprography, information storage, and plastics[1–5]. Knowing the broad spectrum of biological activities and the significant applications of heterocyclic ring systems[6], nitrogen heterocycles are of special interest because they constitute an important class of natural and nonnatural products. Many of these heterocyclic compounds exhibit useful biological activities and unique electrical and optical properties[7-11]. Furthermore, the concern with five-membered heterocyclic derivatives has been growing because these compounds have a number of optical applications, such they are active as fluorescence compounds and dyes[12]. Oxadiazoles are important structural components in many pharmaceuticals and agrochemicals due to their topology and electronic properties[13-14]. In the field of medicinal chemistry, oxadiazoles are utilized as their ester or amide surrogates[15]. For optoelectronic properties, oxadiazole derivatives are good candidates for electron injection and transportation in organic and polymer light-emitting devices[16]. The purpose of this study was the synthesis of 3,4-di(pyridin-2-yl)-1,2,5-oxadiazole, and 2-pyridinecarboxaldehyde was used as a starting material in the synthesis. The structures of those products synthesized were confirmed by ^{1}H-NMR, IR spectroscopy and elemental analysis.

Materials and Methods

All chemicals were purchased from Sigma-Aldrich Company. IR spectra were recorded in KBr on a Nicolet 6700 FT-IR spectrophotometer. Elemental analyses were carried out in a Perkin–Elmer Series 2 CHNS/O analyzer 2400. ^{1}H-NMR spectra were recorded in $CDCl_3$ on a Bruker AVANCE-400 MHz NMR spectrometer using TMS as internal standard. Electron impact mass spectra were obtained at 70 eV using a Finnigan Mat GCQ spectrometer. Melting points were determined with an Electrothermal melting point apparatus.

Synthesis of 2-hydroxy-[1,2-di(pyridin-2-yl)]ethane-1-one(α-Pyridoin)

Sodium cyanide (10g, 0.2 mol) was dissolved in water (100 ml) in a 250-mL round-bottomed flask. Then over a period of 10 min, the 2-pyridine-carboxaldehyde (10 mL, 0.1 mol) was added drop wise to the reaction mixture. The mixture was magnetically stirred for 3 hr. at room temperature. After the addition, the reaction mixture gave precipitates, which were extracted with dichloromethane. The organic layer was separated, dried over anhydrous sodium sulphate and evaporated under vacuum yielding exclusively α-Pyridoin in 10.0 g, 93% yield; mp 155-158 ^{o}C; (Found: C, 67.02; H, 4.86; N, 13.10; O, 15.02. Calc. for $C_{12}H_{10}N_2O_2$: C, 67.28; H, 4.71; N, 13.08; O, 14.94). IR (KBr) 3455 cm^{-1}, ν O-H (broad); 1591 cm^{-1}, ν C=N (pyridine group); 1561 cm^{-1}, ν C=C (phenyl group); 1182 cm^{-1}, ν C-O (sharp band); 783 and 733 cm^{-1}, ν C-H (out of plane). Positive-ion EI-MS Calc. m/z for $C_{12}H_{10}N_2O_2$ 214.07; found m/z 214.0 (M^+, 76%), 108.2 ($pyCOH^+$, 100%), 78.0 (py^+, 50%). ^{1}H-NMR ($CDCl_3$) δ 8.65 ppm (d, 1H, J = 4.4 Hz); δ 8.57 ppm (dd, 1H, J_1 = 4.4 Hz, J_2 = 0.8 Hz); δ 8.20 ppm (t, 2H, J = 8 Hz); δ 7.92 ppm (m, 2H); δ 7.58 ppm (m, 1H)); δ 7.47 ppm (m, 1H).

Synthesis of 1,2-di(pyridin-2-yl)-ethane-1,2-dione (2,2'-pyridil)

α-Pyridoin was dissolved in ethyl acetate and filtered, producing a yellow solution which was then poured in to a closed vessel and kept at room temperature for a week. At the end of that time, yellow-brownish crystals were formed; filtered to gave a product with melting point 154-157 ^{o}C; (Found: C, 67.69; H, 4.07; N, 12.91; O, 15.33. Calc. for $C_{12}H_8N_2O_2$: C, 67.92; H, 3.80; N, 13.08; O, 15.08). The IR (KBr) was found 3060 cm^{-1} ν (C-H)(py); 1713 and 1691 cm^{-1} ν C=O ketone (-CO-CO-); 1583 cm^{-1} C=C (phynyl group); 897, 754 cm^{-1} ν CH(out of plane). Positive-ion EI-MS Calc. m/z for $C_{12}H_8N_2O_2$ 212.20; found m/z 212.0 (M^+, 30%), 156.0($2py^+$, 100%), 78.0 (py^+, 10%). ^{1}H-NMR($CDCl_3$) δ 8.45 ppm (d, 2H, J = 4.4 Hz); δ 7.89 ppm (t, 2H, J = 8 Hz); δ 7.82 ppm (dt, 2H, J_1 = 8 Hz, J_2 = 1.6 Hz); δ 7.17 ppm (m, 2H).

Synthesis of N,N'-(1,2-pyridin-2-yl)bis(hydroxyl-amine);(α-dioximes)

A mixture of 2,2'-pyridil (2.12g, 10 mmol), hydroxylamine hydrochloride (4.17 g, 60 mmol), sodium acetate (8.16g, 60 mmol) and methyl alcohol (25 mL) was refluxed on an oil bath for 8 hour. The precipitates formed from the solution were collected by filtration and the solvents were removed in vacuum and the residue was recrystallized from aceetonitile to give the product as white crystals in 2.17g, (90%); mp. 235-236 ^{o}C; (Found: C, 60.55; H, 3.64; N, 23.28; O, 12.53. Calc. for $C_{12}H_8N_2O_2$: C, 59.50; H, 3.64; N, 23.13; O, 13.21). IR (KBr) 3163 cm^{-1}, ν O-H (broad); 1624 cm^{-1}, ν C=N (oxime group); 1587 cm^{-1}, ν C=N (pyridine group); 1566 cm^{-1}, ν C=C (phenyl group). Positive-ion EI-MS: Calc. *m/z* for $C_{12}H_{10}N_4O_2$ 242.08; found *m/z* 242.0 (M^+, 2.61%), 224.0 (M^+ -H_2O, 22%), 207.0 (M^+-$2H_2O$, 100 %), 104.0 ($PyCN^+$, 10%), 78.0 (Py^+, 15%). ^{1}H-NMR (DMSO-d_6) δ 8.59 ppm (dd, 2H, J_1= 4.8Hz, J_2 = 0.8 Hz); δ 7.83 ppm (dt, 2H, J_1 = 7.6 Hz, J_2 = 1.6 Hz); δ 7.47 ppm (d, 2H, J = 7.6 Hz); δ 7.34 ppm (m, 2H).

Synthesis of 3,4-di(pyridin-2-yl)-1,2,5-oxadiazole

The above *α-dio*ximes (2.42 g 10 mmol) and 1M potassium hydroxide (2 mL) were placed in a moderate pressure vessels (dimensions 30 mm ID x 40 mm OD vol. 85 mL). The vessels was sealed and placed in an oil bath preheated to 180 ^{o}C and maintained at the temperature for 18 hours. The vessels was then allowed to cool to room temperature and opened carefully. The residual mixture was extracted with dichloromethane; the organic layer was separated and dried over anhydrous magnesium sulphate. Solvents were removed under reduced pressure to yield a light yellow solid which was recrystallized from 3 : 1 petroleum ether–ethyl acetate to yield 1.98 g (85%) of the expected product, mp 120–122 ^{o}C; (Found: C, 64.45; H, 3.45; N, 25.23; O, 6.87. Calc. for $C_{12}H_8N_2O_2$: C, 64.28; H, 3.60; N, 24.99; O, 7.14). IR (KBr) 1588 cm^{-1}, ν C=N (pyridine group); 1572 cm^{-1}, ν C=C (phenyl group); 890 cm^{-1}, ν N-O. Positive-ion EI-MS: Calc. *m/z* for $C_{12}H_{10}N_4O_2$ 224.22; found *m/z* 224.0 (M^+, 20%), 104.0 ($PyCN^+$, 31%), 78.0 (Py^+, 100%). ^{1}H-NMR (DMSO-d_6) δ 8.57 ppm (dd, 2H, J_1 = 4.4 Hz, J_2 = 0.8 Hz); δ 7.98 ppm (dt, 2H, J_1=7.6 Hz, J_2 = 1.6 Hz); δ 7.87 ppm (d, 2H, J = 7.6 Hz); δ 7.54 ppm (m, 2H).

Results and Discussion

Aqueous cyanide was employed as a catalyst for the condensation reaction of 2-pyridinecarboxaldehyde; which afforded hydroxy-[1,2-di(pyridin-2-yl)]ethane-1-one, (α-pyridoin) in 93% yield. It is worth to note that when the reaction run by following the reported procedure, which was heated at 140 $^{\circ}$C without solvent and catalyst, gave products in lower yield[17]. α-pyridoin so formed was further converted almost quantitatively to 1,2-di(pyridin-2-yl)ethane-1,2-dione (2,2'-pyridil) by dissolving in ethyl acetate for one week. This presumably a mild oxidation of α-pyridoin by trace oxygen has been taken place in ethyl acetate solution. The results of IR showed that the two sharp, strong bands around 1713 and 1691 cm^{-1} were assigned to the stretching vibration of C=O groups of 2,2'-pyridil, which also agreed with the disappearance of the O–H vibration stretching of α-pyridoin[18]. The 2,2'-pyridil was converted to the corresponding oxime, N,N'-(1,2-pyridin-2-yl)bis-(hydroxylamine) or α-dioxime, in 90% yield. The reaction was done by reacting with an excess of hydroxylamine in methanol at refluxing temperatures[19]. IR spectra showed the broad band at 3163 cm^{-1}, a weak band at 1624 cm^{-1}, and a sharp band at 1566 cm^{-1} which were assigned to the stretching vibration of OH, oximes and pyridine groups, respectively. The synthesis of 3,4-di(pyridin-2-yl)-1,2,5-oxadiazoles was performed on heating of the dioxime in potassium hydroxide solution at 185 ^{o}C for 18 hours; which effected the cyclization and yielding the product in 85% yield[20]. The ^{1}H-NMR resonance peaks appeared at δ 8.57, δ 7.98, δ 7.87, δ 7.54 ppm could be assigned to the contribution of aromatic protons. The elemental analysis was in good agreement with those calculated values for the expected molecular formula $C_{12}H_8N_4O$: C, 64.28; H, 3.60; N, 24.99; O, 7.14. Mass spectra showed the molecular ion peak at m/z 224.0 (M^+, 20%), 104.0 ($PyCN^+$, 31%), and 78.0 (Py^+, 100%), which agreed with the proposed structure.

Conclusions

We have successfully modified a procedure for the synthesis of 3,4-di(pyridin-2-yl)-1,2,5-oxadiazoles based on the published procedure. All the products were fully characterized by their IR, ^{1}H-NMR and mass spectral data as well as the data from the elemental analysis were found to be in good agreement with the proposed structures. In summary, the developed method gave the products in a high yields. Each step of syntheses gave products over 85% yields, and over all gave 70% yields.

Acknowledgements

The authors acknowledge with thanks the financial help from Graduate College King Mongkut's University of Technology North Bangkok.

References

[1] A. R. Katritzky, *Chem. Rev*., **104** (2004), pp.2125–2126.

[2] A. T. Balaban, D. C. Oniciu and A. R. Katritzky, *Chem. Rev*., **104** (2004), pp.2777–2812.

[3] A. D. Bond, A. Fleming, F. Kelleher, J. McGinley and V. Prajapati, *Tetrahedron,* **62** (2006), pp. 9577–9581.

[4] N. S. Sosnowska, *J. Org. Chem.,* **66** (2001), pp.8737–8743.

[5] G. I. Koldobskii and V. A. Ostrovskii, *Russ. Chem. Rev.* **63**(1994), pp.797–814.

[6] Ina´cio Luduvico, R. C. Mara, L.J. Couri, A. F.D. Santos, R. P. F. G. Maria Prado and B. A. Rosemeire *Carbohydrate Research* **343** (2008), pp.536–540.
[7] Y.F. Sun, H.C. Song, W.M. Li and Z.L. Xu, *Chin J Org Chem,* **23** (2003), pp.1286–90.
[8] F.Bellina, S.Cauteruccio and R. Rossi *Tetrahedron* **63** (2007), pp. 4571–624.
[9] Z.J. Hu, J.X. Yang, Y.P.Tian, H.P. Zhou, X.T.Tao and G.B Xu, *J. Mol Struct,* **839 (**2007), pp.50–7.
[10] Y.Z.Cui, Q. Fang, Z.L. Huang, G. Xue, W.T. Yu and H. Lei, *Opt Mater,* **27 (**2005), pp.1571–5.
[11] M.H. Tsai, Y.H.Hong, C.H.Chang, H.C.Su, C.C.Wu and A. Matoliukstyte, *Adv Mater,* **19** (2007), pp. 862–6.
[12] Y.F. Sun, W. Huang, C.G. Lu and Y.P. Cui, *Dyes and Pigments,* **81** (2009), pp.10–17.
[13] W. H. B. Sauer and M. K. Schwarz, *J. Chem. Inf. Comput. Sci.,* **43** (2003), pp. 987–1003.
[14] S. Cesarini, N. Colombo, M. Pulici, E. R. Felder and K.D. Wolfgang, *BrillTetrahedron,* **62** (2006), pp. 10223–10236.
[15] A. R.Hemaka, H. Zhu, M. B. Young and T. Bryan, *Mott Tetrahedron Letters*, **47** (2006), pp.4827–4830.
[16] G. Hughes and M.B. Bryce, *J. Mater. Chem.,* **15** (2005), pp.94.
[17] M. J. Percino, V. M. Chapela, S. Romero,C. Rodr´ıguez-Barbar´ın and J. Melendez-Bustamante, *Journal of Chemical Crystallography*, **36** (2006).
[18] W. S. Kim, B. J. Lee, N. M. Tuong, E.M. Son, K.S. Yang and Y.S. Kwon, *Current Applied Physics* **6** (2006), pp. 596–600.
[19] M. R. Yadav, S. T. Shirude, D. S. Puntambekar, P. J. Patel, H. B. Prajapati, A. Parmar, R. Balarman and R. Giridhar, *Acta Pharm*. **57** (2007), pp.13–30.
[20] C. Richardson, P.J. Steel, D.M.D. Alessandro, P.C. Junk and R.F.Keene, *J. Chem. Soc.,Dalton Trans*., (2002), pp. 2775–2785.

Isolation and structure elucidation of chemical components from branches of *Plumeria obtusa*

P. Mankong and P. Puangsombat*

Department of Chemistry, Faculty of Science, Chiang Mai University, Chiang Mai, Thailand 50200

* E-mail: pakawan@science.cmu.ac.th

Abstract : Chemical investigation on the ethyl acetate extract from branches of *Plumeria obtusa* has resulted in the isolation of an iridoid, namely plumericin, a coumarin, namely scopoletin together with methyl 4-hydroxycinnamate. All isolated compounds have been previously found in the fresh leaves of *P. obtusa.* The structures of these constituents were elucidated mainly by spectroscopic techniques including 1D and 2D NMR and mass spectrometry. All spectral data were corresponded with those reported in literatures. The ethyl acetate extract from branches of *P. obtusa* was found to exhibit moderate anti-tuberculous activity.

Introduction

Plumeria obtusa L. belongs to the family Apocynaceae, genus *Plumeria.* It originates from Central America and its many species are widely distributed in tropical countries. The plants in this genus have a medicinal value in the indigenous system of medicine and various species have shown antifouling, anticancer and antibiotic effects [1-3]. The compounds isolated from *P. rubra* were evaluated for biological activities and found useful against a number of cancerous celllines, *i.e.* breast, colon, fibrosarcoma, lung, melanoma and KB in humans [4].

As a part of our interests in chemical constituents and biological activities of natural sources, the branches of *P. obtusa* were collected for investigation. In the preliminary study, the crude extract of branches of *P. obtusa* was subjected to bioactivity screening and it was found that this extract was active against murine lymphocytic leukemia cell lines. This prompted us to investigate for the bioactive components. The phytochemistry of the plants in genus *Plumeria* is generally characterized by the occurrence of iridoid and coumarin, which were mostly found in roots or leaves. We report herein the isolation of some bioactive compounds; plumericin (**1**), scopoletin (**2**) and methyl 4-hydroxycinnamate (**3**) from branches of *P. obtusa.*

Materials and Methods

General Experimental Procedures: ^{1}H, ^{13}C-NMR and 2D spectra were measured with Bruker AVANCE 400 NMR spectrometer. Electron impact mass spectra were measured with Agilent-HP 5973 Mass spectrometer.

Plant Material: Branches of *P. obtusa* was collected in March 2008 from Chiang Mai University.

Extraction and Isolation: The fresh undried branches (3 kg) were ground and macerated in methanol for 2 days at room temperature followed by filtration. This process was repeated three times. After the methanolic extract was dissolved and shaken with EtOAc. The upper layer of EtOAc extract, after evaporated, yielded EtOAc crude extract as a dark brown viscous liquid (12.77 g). The EtOAc extract was subjected to flash column chromatography (silica gel, dichloromethane 100% to EtOAc 100%) to yield 12 fractions. Fractions 3 and 4 (eluted with dichlomethane:EtOAc 7:3) were combined and re-chromatographed (silica gel, Hexane:EtOAc 7:3) when 12 fractions were collected. Fraction 6 was subjected to flash column chromatography (silica gel, Hexane:EtOAc 9:1) to give 3 fractions, when fraction 3 was purified by preparative TLC (silica gel plates, Hexane:EtOAc 8:2) to afford **3** (6 mg). Fraction 7, which was eluted with dichloromethane was further purified by preparative TLC (silica gel plates, Hexane:EtOAc 8:2) to afford **1** (13mg). Finally, fraction 6 from the first column was re-chromatographed (silica gel, Hexane:EtOAc 8:2) to give 8 fractions, fraction 7 of which was re-chromatographed (silica gel, Hexane:EtOAc 7:3) to give 5 fractions. Fraction 2 was then purified by preparative TLC (silica gel plates, Hexane:EtOAc 6:4) to afford **2** (4 mg).

Plumericin (1): colourless powder; ^{1}H NMR ($CDCl_3$) δ 2.11 (d, J=7.2 Hz, 3H), 3.45 (dd, J=5.8, 9.4 Hz, 1H), 3.79 (s, 3H), 4.03 (dt, J=2.2, 9.4 Hz, 1H), 5.13 (s, 1H), 5.58 (d, J=5.8 Hz, 1H), 5.66 (dd, J=2.2, 5.4 Hz, 1H), 6.06 (dd, J=2.2, 5.4 Hz, 1H), 7.18 (dq, J=1.5, 7.2 Hz, 1H), 7.46 (s, 1H); ^{13}C NMR ($CDCl_3$) δ 16.0, 38.5, 51.9, 53.9, 80.5, 102.0, 104.8, 109.0, 126.5, 127.8, 141.2, 143.3, 153.0, 166.5, 168.2

Scopoletin (2): yellow powder; ^{1}H NMR ($CDCl_3$) δ 3.81 (s, 3H), 6.20 (d, J=9.4 Hz, 1H), 6.77 (s, 1H), 7.21 (s, 1H), 7.90 (d, J=9.4 Hz, 1H); ^{13}C NMR ($CDCl_3$) δ 56.0, 102.8, 110.5, 111.6, 111.7, 144.5, 145.3, 149.5, 151.2, 160.7; EI-MS (70 eV) m/z (rel. int. %) 192 (100), 177 (60), 164 (25), 149 (47), 121 (18), 69 (26), 51 (12), 39 (4).

Methyl 4-hydroxycinnamate (3): yellow powder; ^{1}H NMR ($CDCl_3$) δ 3.82 (s, 3H), 6.32 (d, J=15.9 Hz, 1H), 6.87 (d, J=8.7, 2H), 7.45 (d, J=8.5 Hz, 2H), 7.68 (d, J=15.5, 1H); ^{13}C NMR ($CDCl_3$) δ 51.6, 115.3, 115.9, 127.3, 130.0, 144.6, 157.7, 167.9; EI-MS (70

eV) m/z (rel. int. %) 178 (74), 147 (100), 119 (37), 91 (28), 65 (18), 39 (8).

Results and Discussion

The ethyl acetate extract of branches of *P. obtusa* was partitioned from methanolic extract. It was found that the crude EtOAc extract exhibited moderate anti-tuberculous activity with MIC value of 25 µg/ml. It was therefore subjected to successive chromato-graphic purifications to yield compounds **1**-**3**. The structures of the isolated compounds were elucidated mainly by routine spectroscopic methods including 1D, 2D NMR and MS and by comparison of the spectral data with those reported in literatures.

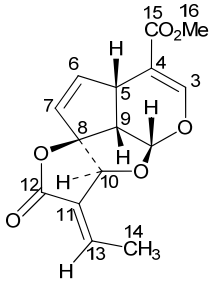

1

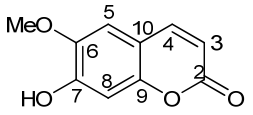

2

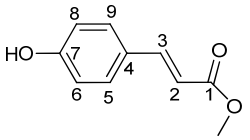

3

Compound **1** was obtained as a colorless powder, which was visualized on TLC as a black fluorescent spot under UV light (254 nm). Combination of ^{1}H, ^{13}C and various 2D-NMR spectra resulted in the formation of the methyl-substituted spirolactone-containing irridoid. Comparison of the spectral data with the reported values [5] suggested that **1** was one of major irridoids commonly found in *Plumeria spp*. Interestingly, there has been a report that plumericin (1) and isoplumericin (the Z-isomer of 1) which were found to have strong algicidal activity, were rarely found in aerial parts of *Plumeria spp* [6]. In fact, they were found only in the roots of *P. obtusa*, but not at all detected in any stem, leave and flower samples. It may well be noted that this is the first report of the isolation of plumericin from branches of *P. obtusa*.

The ^{1}H NMR spectrum (Table 1) displayed resonances of eight methine and two methyl protons. The signals of methine protons were observed in varied chemical shifts ranging from δ 7.46 to δ 3.45 ppm. The most low field signal at δ 7.46 ppm (C3-H, s) was attributed to the β-proton of the α,β-unsaturated ester whose signal was brought even more downfield by the neighborhood oxygen atom. On the other hand, the most high field signal at δ 3.45 ppm was corresponded with the bridge-head proton at C9. The AB coupling pattern appeared at δ 6.06 and 5.66 ppm with the *J* value of 5.4 Hz were assigned for the C6-C7 olefinic protons. The two signals of 3H resonated at δ 3.79 (s) and 2.11 (d) ppm were clearly characteristics of the methyl protons connected to an electron-withdrawing oxygen atom, assigned as methoxy protons at C16, and to the olefinic methine carbon (C13), which was assigned for C14 methyl group, respectively. In addition, ^{13}C-NMR also suggested that there were two carbonyl carbons resonated at δ 166.5 and 168.3 ppm together with other three quaternary carbons signaling at δ 127.8, 109.0 and 104.8 ppm which were assigned as C12, C15, C4, C11 and C8, respectively.

Table 1: ^{1}H and ^{13}C spectral NMR data ($CDCl_3$) of **1**

Position	δ_H (mult.)	δ_C
1	5.58 (1H, d, *J*=5.8 Hz)	102.4
3	7.46 (1H, s)	153.0
4	-	127.8
5	4.03 (1H, dt, *J*=2.2, 9.4 Hz)	38.5
6	5.66 (1H, dd, *J*=2.2, 5.4 Hz)	126.5
7	6.06 (1H, dd, *J*=2.2, 5.4 Hz)	141.2
8	-	104.8
9	3.45 (1H, dd, *J*=5.8, 9.4 Hz)	53.9
10	5.13 (1H, s)	80.5
11	-	109.0
12	-	166.5
13	7.18 (1H, dq, *J*=1.5, 7.2 Hz)	145.3
14	2.11 (3H, d, *J*=7.2 Hz)	16.0
15	-	168.3
16	3.79 (3H, s)	51.9

Compound **2** was obtained as yellow powder, which was visualized on TLC as a blue spot under UV light (254 nm) and exhibited a blue fluorescence under UV light (365 nm). It also appeared as a brown spot after being sprayed with anisaldehyde and heated at 100 ºC for 1 min. The molecular formula was confirmed as $C_{10}H_8O_4$ by EIMS, ^{1}H NMR and ^{13}C NMR experiments. The EI mass spectrum showed the basis molecular ion m/z 192. The initial GC analysis showed a peak with the retention time at 41.55 min. The compound was analyzed by a GC-MS method where its MS fragmentation pattern was compared with the mass spectra library [7] and was tentatively identified as scopoletin.

The ^{1}H NMR spectrum of compound **2** (Table 2) displayed signals which were characteristic of a 6,7-dioxygenated coumarin. The spectrum revealed two doublets with coupling constants of 9.4 Hz at δ 6.20

and δ 7.90 ppm , which were assigned as H-3 and H-4, respectively. The structure could be verified by the presence of two singlets at δ 7.21 and δ 6.77 ppm of aromatic protons and methoxy protons appeared as a singlet at δ 3.81 ppm. The hydroxyl proton was also detected as a broad singlet at δ 6.10 ppm. The position of substituents on the aromatic ring was confirmed by HMQC and HMBC experiments. The NMR data of the isolated compound was comparable to those reported earlier [8-10]. The compound inhibited AChE activity in a dose-dependent manner, and the IC_{50} values of scopoletin 10.0 µg/mL [11].

Table 2: ^{1}H and ^{13}C spectral NMR data ($CDCl_3$) of **2**

Position	δ_H (mult.)	δ_C
2	-	160.7
3	6.20 (1H, d, *J*=9.4)	111.7
4	7.90 (1H, d, *J*=9.4)	144.5
5	7.21 (1H, s)	110.5
6	-	145.3
7	-	151.2
8	6.77 (1H, s)	102.8
9	-	149.5
10	-	111.6
6-OCH_3	3.81 (3H, s)	56.0

Compound **3** was visualized on TLC as a black fluorescent spot under UV light (254 nm). Its molecular formula was analyzed as $C_{10}H_{10}O_3$ from its EIMS, ^{1}H NMR, ^{13}C NMR and 2D HMQC experiments.

The EI mass spectrum of **3** displayed molecular ion peak at m/z 178 with the best peak at m/z 147 which indicated the loss of CH_3O after fragmentation. The initial GC analysis showed a single peak with the retention time at 36.16 min. The compound was analyzed by a GC-MS method where its MS fragmentation pattern was compared with the mass spectra library [7] and was identified as methyl 4-hydroxycinnamate.

^{1}H and ^{13}C NMR spectral data of **3** are all in agreement with the identified compound. ^{1}H NMR spectrum (Table 3) exhibited a singlet signal attributed to the methoxy protons at δ 3.82 (s, 3H) whereas the corresponding methyl carbon resonated at δ 51.7 respectively. The expected set of AA'BB' aromatic protons resonated at δ 7.45 (2H, *J*=8.5 Hz, H-5 and H-9), δ 6.87 (2H, *J*=8.7 Hz, H-6 and H-8) was observed. The AB doublets at δ 7.68 (1H, *J*=15.5 Hz, H-2), δ 6.32 (1H, *J*=15.9 Hz, H-3) were assigned as the conjugated trans-coupled olefinic protons.

Methyl 4-hydroxycinnamate (**3**) is one of the widely known phytochemicals which usually present as a side chain of plants secondary metabolites. In *Plumeria spp*., it was found as a part of some iridoids [12] and pentacyclic triterpenoids [13].

Table 3: ^{1}H and ^{13}C spectral NMR data ($CDCl_3$) of **3**

Position	δ_H (mult.)	δ_C
1	-	167.9
2	7.68 (1H, d, *J*=15.5)	144.6
3	6.32 (1H, d, *J*=15.9)	115.9
4	-	127.3
5	7.45 (1H, d, *J*=8.5)	130.0
6	6.87 (1H, d, *J*=8.7)	115.3
7	-	157.7
8	6.87 (1H, d, *J*=8.7)	115.3
9	7.45 (1H, d, *J=8.5*)	130.0
1- OCH_3	3.82 (3H, s)	51.7

Conclusions

The isolation of three known bioactive compounds; plumericin (**1**), scopoletin (**2**) and methyl 4-hydroxycinnamate (**3**) from fresh branches of *P. obtusa* has been reported. The crude ethyl acetate extract was found to exhibit moderate activity in antituberculosis test system. The testing of the isolated compounds for the anti-TB as well as other bioactivities is in progress.

Acknowledgement

The graduate school, Chiang Mai University is thankful for PM's research grant.

References

[1] S. Siddiqui, B.S. Siddiqui, A. Naeed and S. Begum, *Phytochemistry.* **28** (1989), pp. 3143-3147.

[2] B. S. Siddiqui, F. Ilyas, M. Rasheed and S. Begum, *Phytochemistry* **65** (2004), pp. 2077-2084.

[3] B. S. Siddiqui, Firdous and S. Begum, *Phytochemistry* **52** (1999), pp. 1111-1115.

[4] M.P. Dobhal, A. M. Hasan, M.C. Sharma and B. C. *Phytochemistry* **51** (1999), pp. 319-321.

[5] M. S. Abdel-Kader, J. Wisse, R. Evans, H. van der Werff and D. G. I. Kingston, *J. Nat. Prod.* **60** (1997), pp. 1294-1297.

[6] J. J. W. Coppen and A. L. Cobb, **22** (1983), pp. 125-128.

[7] National Institute of Standards and Technology. *PC Version 1.7 of the NIST/EPA/NIH Mass Spectral Library*, Perkin-Elmer Corporation, Norwalk, USA (1999).

[8] M. C. Carpinella, C. G. Ferrayoli and S. M. Palacios, *J. Agric. Food Chem.* **53** (2005), pp. 2922-2927.

[9] A. El-Demeralash, A. M. Dawidar, E. M. Keshk and M. Abdel-Mogib, *Rev. Latinoamer. Quim.* **37** (2009), pp. 65-69

[10] S. M. Razari, H.Nazemiyeh, R. Hajiboland, Y. Kumarasamy, A. Delazar, L.Nahar and S. D. Saker, *Rev. Farm. Braz. J. Pharm* **18** (2008), pp. 1-5.

[11] J. H. Lee, K. T. Lee, J. H. Yang, N. J. Baek and D. K. Kim, *Arch. Pharm. Res.* **1** (2004), pp. 53-56.

[12] B. S. Siddiqui, A. Naeed, S. Begum and S. Siddiqui, *Phytochemistry* **37** (1994), pp. 769-771.

[13] S. Siddiqui, B. S. Siddiqui, A. Naeed and S. Begum, *Phytochemistry* **31** (1992), pp. 4279-4283.

A simple synthesis of isoxazole[3,4-*f*]quinolin-3-amine from quinoline used as an organic dye in dye-sensitized solar cells

K.Pattarith [1], N. Pungwiwat[1], S. Khampiranon [1*] and S. Laosooksathit[1]

[1]King Mongkut's University of Technology North Bangkok, Department of Industrial Chemistry, Faculty of Applied Science, Bangsue, Bangkok, Thailand

*E-mail: si_luck71@hotmail.com

Abstract: Some highly conjugated heterocyclic systems which are used as organic dyes in dye-sensitized solar cells were investigated. Isoxazolo[3,4-*f*]quinolin-3-amine, a highly conjugated heterocycle, was synthesized via intramolecular cyclization of 5-nitroquinoline-6-carbonitrile. Firstly, nitro group was smoothly introduced into the starting quinoline by simple nitration. The nitro group was further reduced to hydroxylamino intermediate and then cyclized to give isoxazole ring by the added potassium cyanide under refluxing methanol. Structures of the products were confirmed by IR, ^{1}H-NMR, ^{13}C-NMR and mass spectral data.

Introduction

Dye-sensitized solar cells have been intensively studied due to their importance as light harvesting tools. In general, dye-sensitized solar cells comprise of sensitizing dye, redox electrolyte, nanocrystalline metal oxide semiconductor film, and a counter electrode [1-2]. The sensitizing dye is a critical component in dye sensitized solar cells. Therefore, the design of the dye is one of the most important issues. In the development of dyes, both absorption in wide range of solar cell spectrum and high molecular extinction coefficient are required [3-4].

Quinoline system, a heterocyclic aromatic organic compound, has been considered as a good candidate for the purpose. Quinoline derivatives have long been used as starting materials in synthesis of many pharmaceutical products. On the other hand, these compounds have also been used as additive in electrolyte system for dye-sensitized solar cell [5]. However, there was little known about the use of quinoline derivatives as organic dyes. Extending conjugation of the quinoline system might be useful as light harvesting dyes. An investigation of the heterocyclic system was carried out and some of the interested compounds as light harvesting materials have been synthesized [5-8].

Materials and Methods

All melting points were measured on an Electrothermal melting point apparatus. IR spectra were recorded on Nicolet 6700 FT-IR. NMR spectra, 1D and 2D NMR spectra were measured with a Bruker AVANCE 400 NMR spectrometer. EI mass spectra were recorded on GCQ Finigan MAT GC-MS.

5-nitroquinoline (I)

To a solution of quinoline 12.9 g (0.10 mole) was added dropwise to 50 mL of concentrated sulfuric acid. The mixture was heated to 100 ºC and then a solution of 71% nitric acid 9.4 mL (0.15 mole) was added at such a rate to keep the temperature between 100 ºC and 110 ºC. Stirring was continued overnight at room temperature. The mixture was cooled slightly and poured onto a mixture of methylenechloride and ice. The temperature was kept below 25 ºC while the pH increased to 10 with concentrated ammonium hydroxide and extracted with methylene chloride (3x100 mL) dried over Na_2SO_4 and the solvent was removed to give the crude product which was purified by chromatography (SiO_2: 1:1, ethylacetate : hexane). The first fraction was collected and the solvent was removed under vacuo to give 8-nitroquinoline(II) as a slightly yellow solid 45 %yield, mp. 89-91 ºC. IR(KBr) υ_{max} 1357, 1529 (NO_2) cm^{-1} .^{1}H-NMR(400MHz,$CDCl_3$) : δ 6.66 (1H, t, J=8.5Hz, H_4), 6.70(1H, t, J=7.8Hz, H_6), 6.98(1H, d, J=7.8Hz, H_5), 7.27(1H, d J=7.8Hz, H_7), 7.86(1H, d, J=9.0Hz, H_4). m/z = 174

The second fraction was collected and the solvent was removed under vacuo to give 5-nitroquinoline(I) as a yellow solid in 55%yield.(melting point 71-73 ºC) IR(KBr) υ_{max} 1335, 1517 (NO_2) cm^{-1} ^{1}H-NMR(400MHz,$CDCl_3$): δ 6.64 (1H, t, J=8.1Hz, H_7), 7.10(1H, d, J=9.0Hz, H_3), 7.52(1H, d, J=8.1Hz, H_8), 7.77(1H, d J=8.1Hz, H_6), 7.86(1H, d, J=9.0Hz, H_4). Mass Spectrum : m/z = 174 (M^+ = 129).

Isoxazole[3,4-*f*]quinolin-3-amine

To a solution of 5-nitroquinoline 1.0 g (0.70 mole) in MeOH 25 mL and KCN 0.6 g (0.09 mole) was heated to reflux for 4 hrs. Then 25 mL water was added to the solution mixture. The solution was extracted with ethyl acetate (3x50 mL) and the organic layer was evaporated to dryness. The crude product so obtained was purified by chromatography (Al_2O_3 : 2:3 ethyl acetate :diethyl ether). The first fraction was obtained as an orange crystals identified as 5-methoxyquinoline-6-carbonitrile(IV) in 37 %yield IR(KBr) υ_{max} 2226.6 (CN)cm^{-1}. ^{1}H-NMR (400MHz,DMSO-d6):δ 4.23(3H, s, OCH_3), 7.65 (1H, dd, J=4.4 Hz, H_3) 7.83 (1H, d, J=8.8Hz, H_8), 7.91(1H, d, J=9.2Hz, H_7), 8.57(1H, dd, J=0.8Hz, H_4), 9.05(1H, dd J=1.6Hz, H_2). The second fraction was collected and identified as isoxazole[3,4-*f*]quinolin-3-amine(III) as a deep red solid (20% yield) IR(KBr) υ_{max} 3084,

3263 (NH_2)cm^{-1}.: ^{1}H-NMR (400MHz,DMSO-d6) δ 6.94(1H, d, J=9.2Hz, H_8), 7.44(1H, dd, J=4.4 Hz, H_3), 7.58 (1H, d, J=9.0 Hz, H_7), 8.1 (2H, s, NH_2), 8.8 (1H, dd, J=1.6Hz, H_4), 8.4(1H, dd, J=1.6Hz, H_2).

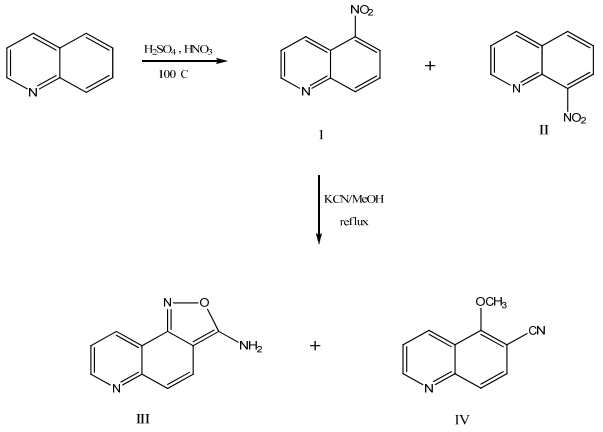

Figure 1. Synthetic pathway of nitroquinoline (I, II) and isoxazole derivative (III, IV)

Results and Discussion

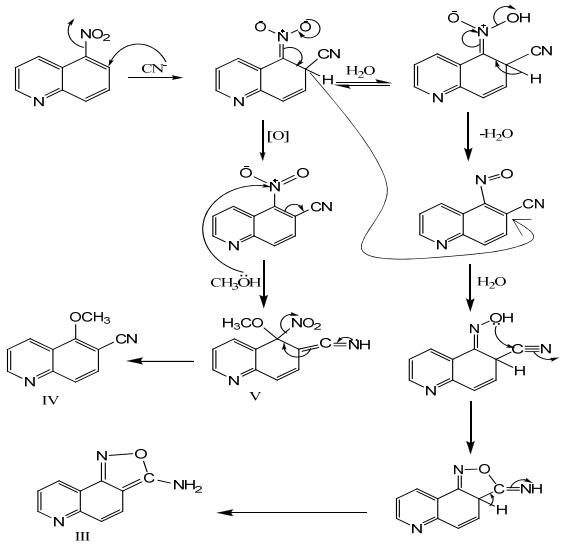

Figure 2. Mechanistic pathway of the isoxazole[3,4-f]quinolin-3-amine (III) and 5-methoxyquinoline-6-carbonitrile (IV).

It has been reported that quinoline was nitrated to give two nitro compounds; 5-nitroquinoline (I) and 8-nitroquinoline (II) in moderate yield. Our product investigation of the nitration gave higher yields by allowing the reaction to stay overnight [9-17]. The compounds were confirmed by their melting points and spectral data.

The reaction of 5-nitroquinoline with a solution of potassium cyanide in methanol gave isoxazole [3,4-*f*] quinolin-3-amine (III) and 5-methoxyquinoline-6-carbonitrile (IV) (see figure. 1). The products were comfirmed by their spectral data.

It has been reported that 5-nitroquinoline relate with potassium cyanide to give a similar result [18]. Formation of isoxazole[3,4-*f*]quinolin-3-amine (III) and 5-methoxyquinoline-6-carbonitrile (IV) was proposed to proceed *via* dihydro compound and through its dihydrigenation [18]. The intermediate V fromed was converted to (III). On the other hand, the dihydro-type intermediate was dehydrated to give the nitroso compound, successively reduced by the eliminated hydride ion to VI, and then intramolecular cyclization took place to form III (see figure 2).

Conclusions

Isoxazole[3,4-*f*]quinolin-3-amine was successfully synthesized from quinoline *via* a sequence of steps. All the spectral data and melting points agreed quite well with the proposed structures.

References

[1] B. O'Regan, M. Grätzel, Nature 353 (1991) 737.
[2] M.K. Nazeeruddin, A. Key, I. Rodicio, R. Humphry-Baker, E. M□ller, P. Liska, N.Vlachopoulos, M. Gr□tzel, *J. Am. Chem. Soc*. 115 (1993) 6382.
[3] Md. K. Nazeeruddin, C. Klein, P. Liska, M. Grätzel, *Coordination Chem. Reviews*, 249(2005)1460-1467.
[4] Keith R. Millington, Keith W. Fincher, A.Lee King, *Solar Energy Materials&solar Cells*. 91(2007)1618-1630
[5] H. Kusama, H. Arakawa, *J.Photo Chem. And Photo bio A : Chem* 165(2004)157-163
[6] Mark Wainwright, Jette E. Kristiansen. *J. Antimicrobial Agents*. 22(2003)479-486.
[7] E.Gondek, S. Calus, A. Danel, A.V. Kityk, Spectrochimica Acta part A, 69(2008)22-26.
[8] V.K. Gupta, Alok Mittal, Vibha Gajbe, J. Colloid and Interface Science 284(2005)89-98.
[9] M. Kimber, Pia I. Anderberg and Margarct M. Harding, *Tetrahedral* **56** (2000), 3575-3581.
[10] Boger, D.L. ; Yasuda, M.; Mitscher, L.A.; Drake, S.D.;Kitos, P.A.;Thompson. S.C. *J. Med.Chem*. 1987, 30, 1918-1928.
[11] Rao, K. V. *J. Heterocycl. Chem*. 1975, 12, 725-730.
[12] Rao, K. V. ; Kuo, H. *J. Heterocycyl. Chem*. 1979, 16, 1241-1248.
[13] Godard, A.; Rovera, J.; Marsais, F.; Ple, N.; Queguiner, G. *Tetrahedral* 1992, 48, 4123-4134.
[14] Godard, A.; Marsais, F.; Ple, N.; Trecourt, F.; Turck. A.; Queguiner, G. *Heterocycl.* 1995, 40, 1055-1091.
[15] Godard, A.; Rocca, P.; Pomel, V.; Thomas-dit-Dumont, L.; Rovera, J. C.; Thaburet, J.F.; Queguiner, G. *J. Organomet. Chem.* 1996, 517, 25-36.
[16] Fryatt, T.; Goroski, D. T.; Nilson, Z. D.; Moody, C. J.; Beall, H. D. Bioorg. *Med. Chem. Lett*. 1996, 2195-2198.
[17] Fourquez, J. M.; Godard, A.; Marsais, F.; Queguiner. G. *J. Heterocycl. Chem.* 1995, 32, 1165-1170.
[18] T. Okamoto and H. Takahashi, *Chem. Pharm. Bull* 16 (9)(1968), 1700-1704.

Synthesis of tricyclic orthoesters of mannose for ring-opening oligomerization toward d-mannopyranan

M. Sungsilp[1], C. Yongyat[1], S. Ruchirawat[2] and S. Boonyarattanakalin[1]*

[1]Department of Bio-Chemical Engineering, Sirindhorn International Institute of Technology, Thammasat University, Pathum Thani, Thailand 12121
[2]Laboratory of Medicinal Chemistry, Chulabhorn Research Institute, and Program in Chemical Biology, Chulabhorn Graduate Institute, Vipavadee-Rangsit Highway, Bangkok, Thailand 10210

* E-mail: siwarutt@siit.ac.th

Abstract: Oligo- and polysaccharides have recently been recognized for their various significant biological activities other than being the main energy sources. Polysaccharides found on bacterial surface have significant roles in immune response.[1-3] The intricate cell wall structure contributes to bacterial virulence, causing severe diseases in humans, such as tuberculosis and leprosy.[4] Although poly- and oligomannoses are available in nature, there are many limitations to access the homogeneous substances because of the difficulty in isolation, purification, and identification.[5] Therefore, chemical synthesis is employed as an reliable approach to obtain structurally defined oligosaccharides.[5,6] A more favorable method for the synthesis of oligosaccharide is controlled oligomerization rather than traditional stepwise synthetic method. Oligomerizations of monosaccharide building blocks create several glycosidic bonds in a single chemical reaction. Oligomerizations require much shorter time for chemical processing when comparing with the step by step synthesis. Furthermore, oligomerization can provide desired compounds in substantial quantity.

For rapid synthesis of oligomannosides, tricyclic orthoester building blocks of mannose provide suitable structural features for ring-opening oligomerizations. The building blocks 3,4-*O*-benzyl-β-D-mannopyranose 1,2,6-orthobenzoate (1) and 3,4-*O*-benzyl-β-D-mannopyranose 1,2,6-orthopivalate (2) were synthesized and for utilization as monomer in ring opening oligomerizations. The synthetic protocols for both building blocks were developed based on previous reports.[2,7] Orthoesters 1 and 2 were successfully prepared in six multiple-gram scale and high yielding chemical reactions. The whole synthesis requires only two purification steps. The transformation conditions were adjusted to fit the high humidity climate for versatility in possible industrial scale-up. Preliminary results from oligomerization of building block 1 and 2 proved that the substituent on the orthoester carbon of the building block 1 and 2 determine the diversity and size of oligomannoside products.

Introduction

In addition to macromolecules including proteins, DNA, and RNA, oligo- and polysaccharides play essential roles in biological systems other than being the main energy source. The oligo- and polysaccharides play crucial activities in various significant biological functions, such as, cell recognitions, cell differentiation, cell-cell adhesion, viral replication, parasitic infection, host-pathogen interactions, and immune responses.[8-10] Nowadays, the biological activities of these polysaccharides draw more attention from researchers in biochemical and medical fields due to their immunomodulatory and antitumor effects.[11]

Oligo- and polysaccharides have significant structural roles in immune response.[1-3] They are found on the envelope of pathogenic bacteria including *Mycobacterium tuberculosis* (*Mtb*), which has unique and complicated features.[4] This intricate cell wall structure contributes to bacterial virulence, causing severe diseases in humans.[4] The cell wall structure of *Mtb* consists of arabinogalactan (AG), lipoarabinomannan (LAM), mannose capped lipoarabinomannan (ManLAM) and lipomannan (LM).[4] AG, LAM, and also phosphatidylinositol mannosides (PIMs) play a critical role in interacting with host cells and moderating immune response.[4,12]

In spite of the availability of poly- and oligomannoses in nature, there are many limitations to access the homogeneous compounds because it requires multiple steps in order to isolate and purify them.[5] Therefore, chemical synthesis is considered to be a reliable approach to synthesize structurally-defined oligosaccharides.[5,6] Apart from traditional stepwise synthetic methods, automation and oligomerization are employed to be more favorable methods for the synthesis of oligosaccharide because they take much shorter time for chemical processing. Oligomerization of monosaccharide building blocks creates several glycosidic bonds in a single chemical reaction and gives desired products in a significant amount.

There are several reports on the synthesis of polysaccharide by ring-opening polymerizations of various building blocks, e.g. 3-*O*-benzyl-β-L-arabinofuranose 1,2,5-orthopivalate[13], 3,6-di-*O*-benzyl-α-D-glucopyranose 1,2,4-orthopivalate[14,15], 3-*O*-benzyl-6-*O*-pivaloyl-α-D-glucopyranose 1,2,4-orthopivalate[15], 3-*O*-benzyl-6-deoxy-α-D-glucopyranose 1,2,4-orthopivalate[16], and 3-*O*-benzyl-α-D-xylopyranose 1,2,4-orthopivalate[17]. Hori *et al.* (2000) reported that the ring-opening polymerization of 3-*O*-benzyl-β-L-arabinofuranose 1,2,5-orthopivalate by using $BF_3{\cdot}Et_2O$ as a catalyst gave the stereoregular polysaccharide (1→5)-α-L-arabinofuranan with DPn = 91.[13] The benzyl group at 3-*O* position and the pivaloyl group at 2-*O* position are necessary for

stereoregularity and regioregularity in the synthesis of arabinofuranan.[13] Moreover, stereoregular polysaccharide of glucose was synthesized by ring-opening polymerization of 3,6-di-*O*-benzyl-α-D-glucopyranose 1,2,4-orthopivalate or 3-*O*-benzyl-6-*O*-pivaloyl-α-D-glucopyranose 1,2,4-orthopivalate. Similar to the synthesis of arabinofuranan, the 3-*O*-benzyl group and 2-*O*-pivaloyl group of glucopyranose play a significant role in the stereospecificity and regiospecificity of the resulting polymer.[18,19] The resulting polymer contained only (1→4)-glycosidic bond, not (1→2)-bond.[19]

Apart from the substituents at 2-*O* and 3-*O* position, R group of CH_2OR at *C6*- position affected the stereo- and regioregularity of the resulting polymer due to electronic effect of the protecting group.[16] Therefore, the alkyl group at orthoester carbon should be electron-donating or slightly withdrawing group such as benzyl or pivaloyl group. Moreover, types of initiators and temperatures also affected the regioregularity of resulting polymers.[13-15]

In spite of many biological roles of oligomannosides, rarely there are accounts for one-step synthesis of poly- or oligomannose. The synthesis of mannopyranan will be useful contributions for biological studies. To serve this purpose, we have designed and synthesized tricyclic orthoester of mannose for the ring-opening oligomerization toward D-mannopyranan.

Materials and Methods

All chemicals used were reagent grade and used as supplied except where noted. All reactions were performed in oven-dried glassware under an inert atmosphere unless noted otherwise. Dichloromethane (CH_2Cl_2) was dried over calcium hydride (CaH_2) prior to use. Lutidine was treated by potassium hydroxide (KOH) and allyl alcohol was treated with potassium carbonate (K_2CO_3) prior to use. 4Å Molecular sieves were activated by a heat gun under high vacuum. Analytical thin layer chromatography (TLC) was performed on Merck silica gel 60 F254 plates (0.25mm). Compounds were visualized by dipping the plate in a cerium sulfate-ammonium molybdate (CAM) solution and phosphomolybdic acid (PMA) solution. Flash column chromatography was carried out using forced flow of the indicated solvent on Fluka Kieselgel 60 (230-400 mesh).

All new compounds were characterized by NMR chromatography (^1H, ^{13}C NMR and 2D NMR for some key intermediates), high resolution mass spectroscopy (HRMS), optical rotation activity, and melting point. NMR spectra were recorded on a Varian Gemini 2000 (200MHz) and Bruker AVANCE 400 (400MHz) in $CDCl_3$ with chemical shift reference to internal standards $CDCl_3$ (7.26 ppm for ^1H and 77.0 ppm for ^{13}C).

Results and discussion

The design of mannoside monomer: for a rapid synthesis of oligomannosides, tricyclic orthoester building blocks of mannose comprise suitable structural features for ring-opening oligomerizations. The building blocks 3,4-*O*-benzyl-β-D-mannopyranose 1,2,6-orthobenzoate (**1**) and 3,4-*O*-benzyl-β-D-mannopyranose 1,2,6-orthopivalate (**2**) were synthesized and utilized as monomer in ring opening oligomerizations. The monomers **1** and **2** contain highly strained tricyclic structure which is readily susceptible for ring opening oligomerization upon activation with Lewis acids.

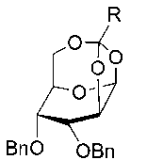

1: R = C_6H_5
2: R = $C(CH_3)_3$

Figure 1. The structures of tricyclic orthoester mannoside building blocks

The building block monomers for ring-opening oligomerizations are orthoesters of mannose sugars consisting of benzyl ether groups at 3-*O* and 4-*O* positions. The 1-, 2- and 6-*O* positions are masked in a form of tricyclic orthobenzoate and orthopivaloate in building blocks **1** and **2**, respectively. During the ring-opening oligomerization, the 3-*O* benzyl group will have a considerable effect on chemical activity because the benzyl group is an electron-donating group which is responsible for stabilizing the dioxalenium intermediate resulting in the formation of glycosidic bond via S_N2 attack of the next monomer after the activation by Lewis acid initiators.

Furthermore, the 4-*O* benzyl group will play important role in the regioregularity of the resulting polymer because it has a high electron-donating property. The electron donating group contributes to the high electron density of *C6*-oxygen of the monomers. It has been shown that when treated with BF_3Et_2O and allyl alcohol in CH_2Cl_2, the C-O bond between the orthoester carbon and the *C6*-oxygen atom was cleaved.[2] Therefore, we envisioned that during the oligomerization of monomer **1** and **2**, the C-O orthoester carbon - oxygen bonds will be selectively cleaved at the *C6*-oxygen atom and the resulting glycosidic bond formation will favor 1,6 linkage.

In addition to the benzyl groups at 3-*O* and 4-*O* positions, the alkyl substituent on the orthoester carbon of the building blocks **1** and **2** is essential for stabilization of cation intermediate on the orthoester carbon and thus promotes the growth of oligomer chains. During propagation step of oligomerization, the next monomer will favorably attack at the bottom face of anomeric carbon due to the steric effect from the acyl protected *C2* hydroxyl group that oriented out of the top face. Consequently, the incoming

nucleophilic oxygen is likely to form an α glycosidic bond with the anomeric carbon. Therefore, the stereospecificity in the oligomannoside product will be achieved by the acyl protecting group of the *C2*-hydroxyl.

The synthesis of mannoside building blocks: the synthesis of monomer **1** and **2** was developed based on the previously published report.[2,7] We found that the chemical reagents used in the previous report were not suitable for high humidity conditions in Thailand. The overall redesigned synthesis of monomers **1** and **2** was illustrated in Scheme 1. The synthesis was designed to be robust and scalable. We have developed short synthetic route that requires only six chemical transformations of which only two column purifications were necessary. Moreover, the same chemical conditions can be applied to produce both building blocks **1** and **2** in multiple-gram scale.

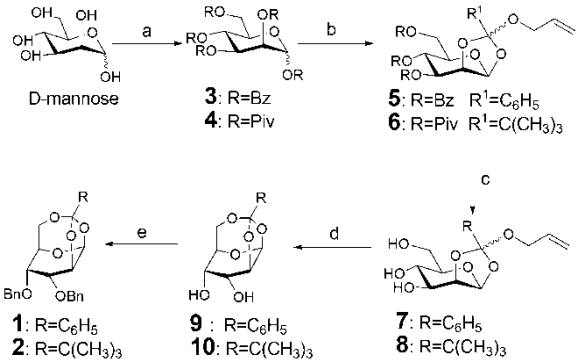

Scheme 1. Synthesis of building blocks **1** and **2**. Reagents and conditions: (a) BzCl, pyridine, 0 °C, 12 h or PivCl, pyridine, 125-130 °C, reflux, 24 h; (b) i) HBr/HOAc (33%), acetic anhydride, 24 h ii) AllOH, lutidine, 82.9% (3 steps) for compound **5**, 41.4% (3 steps) for compound **4**; (c) KOH, H_2O, MeOH, THF, rt, 24 h; (d) 30% CSA, 4Å MS, CH_3CN, 2 d; (e) BnBr, NaH, DMF, 0 °C to rt, 12 h at rt, 28% (3 steps).

The synthesis routes for building blocks **1** and **2** are different in the first step of global protection of hydroxyl groups in the native mannose. First, the native mannose sugar was globally protected with benzoate esters (Bz) and pivaloate esters (Piv) for the synthesis of building blocks **1** and **2**, respectively. More than twice of stoichiometric amount of the acid chlorides and high temperatures were required to drive the reaction to completion. The benzyl chloride (12 eq.) and pivaloyl chloride (12 eq.) were added dropwise to the sugar starting material suspended in pyridine (45 eq.) at 4 °C.

The reaction mixture was allowed to stir for 24 h at room temperature to afford **3** and refluxed for 16 h to yield **4**. The reaction mixture was filtered to remove suspended solid. The filtrate was concentrated *in vacuo* and extracted by EtOAc and 1 N HCl. The residual solid was extracted by H_2O/CH_2Cl_2 and 1 N HCl/CH_2Cl_2. The combined organic layer was washed with saturated $NaHCO_3$ solution, dried over Na_2SO_4, concentrated *in vacuo* and placed under high vacuum for at least 1 h. Compound **3** showed consistent NMR spectra with the published results.[7] Compound **4** was obtained as anomeric mixtures having the same molecular weight characterized by hi-resolution ESI mass spectrometry. The ^1H NMR of the major product showed the anomeric peak as doublet at 5.82 ppm (J = 1.0 Hz).

Without further purifications, compounds **3** and **4** were treated with acetic anhydride (8 eq.) and a solution of 33% HBr in AcOH (30 eq.). The reaction mixture was stirred at room temperature for 24 h and extracted with ice-cold water and CH_2Cl_2 for three times. The product obtained from this step was concentrated at rt and dried under high vacuum. The crude product was treated with 2,6-lutidine (6 eq.) and allyl alcohol (30 eq.). The reaction mixture was stirred at room temperature for 20 h and concentrated *in vacuo*. The crude product was co-evaporated with toluene (3x) and dried under high vacuum for 4 h. The dried crude product was extracted with H_2O/CH_2Cl_2, concentrated *in vacuo* and purified by flash silica gel column chromatography (hexanes / EtOAc) to obtain bicyclic orthoesters **5** and **6** as foamy syrup. The side products obtained from this reaction were 2,3,4,6-*O*-tetra-acyl D-mannopyranose which can be recovered by treatment with reaction condition b (Scheme 1) to give **5** and **6**. The anomeric doublet of **6** was at 5.51 ppm (J = 3.0 Hz).

To remove the acyl protecting groups which are benzoyl and pivaloyl, we initially performed the typical transesterification reactions which relied on the basic sodium methoxide generated *in situ* from the reaction between solid sodium and methanol. Under the transesterification conditions, benzoyl groups would be removed only at elevated temperatures. The amounts of NaOMe used ranged from catalytic (5%) to stoichiometric at reflux temperature (THF/MeOH ratio of 1:1) failed to remove the acyl protecting groups. The starting material was gradually decomposed by basic and heated conditions. We suspected that NaOMe was degraded under highly humid conditions in Thailand. NaOMe reacted with moisture (H_2O) to form NaOH which was too weak basic to catalyze the transesterification reactions. We then turned to hydrolysis reaction to remove the acyl groups. Moisture in the laboratory atmosphere was irrelevant during hydrolysis setup because water is one of the reagents used in this reaction. First, different equivalences of $LiOH{\cdot}H_2O$ were applied to compound **5** and **6** in MeOH and THF, but the desired products were not obtained and the starting material was decomposed. To a bicyclic orthoesters **5** and **6**, THF, MeOH and H_2O in the ratio of 12:24:1 were added at room temperature. KOH (4 eq.)/H_2O solution was prepared and added to the reaction mixture. After stirring for 24 h, the resulting mixture was extracted with CH_2Cl_2 and water, concentrated *in vacuo* and dried under high vacuum. Compounds **7** and **8** were obtained in quantitative yield and used in the next step without further purifications.

To obtain tricyclic orthoesters **9** and **10**, CH_3CN was added to a mixture of compounds **7** and **8** in 4Å molecular sieves and CSA (0.25 eq.). The reaction mixture was carried out at room temperature for 2 d and filtered by a celite plug to remove 4Å molecular sieves. The crude product was concentrated *in vacuo* and placed under high vacuum before the benzylation in the next step. The anomeric doublet of **6** was at 5.77 ppm (J = 5.8 Hz).

The final benzylation protection on compounds **9** and **10** were done by the treatments with BnBr (3 eq.) and NaH (4 eq.) in DMF at 0 °C. The reaction mixture was allowed to stir at room temperature for 24 h. The reaction mixture was quenched by MeOH and H_2O before extracted with Et_2O and water and washed with brine. The combined organic layer was concentrated *in vacuo*, and purified by flash silica gel column chromatography (hexanes / EtOAc) to obtain the compound **1** and **2** as white solids. The overall yields of orthoesters **1** and **2** from D-mannose were 25% and 12%, respectively. Compound **2** was characterized extensively by 1D and 2D NMR and the anomeric doublet was at 5.67 ppm (J = 5.8 Hz).

Conclusion

The building blocks 3,4-*O*-benzyl-β-D-mannopyranose 1,2,6-orthobenzoate (**1**) and 3,4-*O*-benzyl-β-D-mannopyranose 1,2,6-orthopivalate (**2**) were synthesized for utilization as monomers in ring opening oligomerizations for rapid synthesis of oligomannosides. The synthetic protocols of both building blocks were developed based on previous reports.[2,7] Orthoesters **1** and **2** were successfully prepared in six steps in multiple-gram scale and high yielding chemical reactions. The whole synthesis requires only two column purification steps. To be suitable for high humidity climate in Thailand, the removal of acyl protecting groups was done by hydrolysis reactions. The synthetic protocols were designed to be robust and scalable. Preliminary results from oligomerization of building block **1** and **2** proved that the building blocks monomers can form multiple glycosidic bonds upon single activation by Lewis acids. The more detailed studies on the oligomerization are under investigations.

Acknowledgement

This research was supported by Thailand Research Fund (TRF Grant # MRG5180240) and Thammasat University Research Fund. C. Yongyat and M. Sungsilp thank the National Science and Technology Development Agency (NSTDA) for the undergraduate scholarships from the Young Scientist and Technologist Program (YSTP). We thank CRI for chemical reagents and equipments.

References

[1] Ni, J.; Song, H.; Wang, Y.; Stamatos, N. M.; Wang, L.-X. *Bioconjugate Chemistry* **2006**, *17*, 493-500.
[2] Boonyarattanakalin, S.; Liu, X.; Michieletti, M.; Lepenies, B.; Seeberger, P. H. *Journal of the American Chemical Society* **2008**, *130*, 16791-16799.
[3] Wang, H.; Obenauer-Kutner, L.; Lin, M.; Huang, Y.; Grace, M. J.; Lindsay, S. M. *Journal of the American Chemical Society* **2008**, *130*, 8154-8155.
[4] Brown, J. R.; Field, R. A.; Barker, A.; Guy, M.; Grewal, R.; Khoo, K.-H.; Brennan, P. J.; Besra, G. S.; Chatterjee, D. *Bioorganic & Medicinal Chemistry* **2001**, *9*, 815-824.
[5] Wang, Z.-G.; Warren, J. D.; Dudkin, V. Y.; Zhang, X.; Iserloh, U.; Visser, M.; Eckhardt, M.; Seeberger, P. H.; Danishefsky, S. J. *Tetrahedron* **2006**, *62*, 4954-4978.
[6] Hattori, K.; Yoshida, T.; Uryu, T. *Carbohydrate Polymers* **1998**, *36*, 129-135.
[7] Liu, X.; Wada, R.; Boonyarattanakalin, S.; Castagner, B.; Seeberger, P. H. *Chem Commun (Camb)* **2008**, 3510-2.
[8] Li, B.-G.; Zhang, L.-M. *Carbohydrate Polymers* **2008**, *74*, 390-395.
[9] Singh, S.; Ni, J.; Wang, L. X. *Bioorg Med Chem Lett* **2003**, *13*, 327-30.
[10] Dwek, R. A. *Chemical Reviews* **1996**, *96*, 683-720.
[11] Gan, L.; Zhang, S.-H.; Liu, Q.; Xu, H.-B. *European Journal of Pharmacology* **2003**, *471*, 217-222.
[12] Nigou, J. m.; Gilleron, M.; Rojas, M.; Garča, L. F.; Thurnher, M.; Puzo, G. *Microbes and Infection* **2002**, *4*, 945-953.
[13] Hori, M.; Nakatsubo, F. *Macromolecules* **2000**, *33*, 1148-1151.
[14] Nakatsubo, F.; Kamitakahara, H.; Hori, M. *Journal of the American Chemical Society* **1996**, *118*, 1677-1681.
[15] Kamitakahara, H.; Hori, M.; Nakatsubo, F. *Macromolecules* **1996**, *29*, 6126-6131.
[16] Hori, M.; Nakatsubo, F. *Macromolecules* **2001**, *34*, 2476-2481.
[17] Hori, M.; Nakatsubo, F. *Carbohydrate Research* **2001**, *332*, 405-414.
[18] Hori, M.; Kamitakahara, H.; Nakatsubo, F. *Macromolecules* **1997**, *30*, 2891-2896.
[19] Kamitakahara, H.; Nakatsubo, F. *Macromolecules* **1996**, *29*, 1119-1122.

Chemical constituents of the volatile oil of *Laggera pterodonta*

T. Machan[1*], C. Phungpanya [1], and C. Thongpoon [2]

[1] Program of Applied Chemistry, School of Science, Mae Fah Luang University, Chiang Rai, Thailand 57100
[2] Program of Chemistry, Faculty of Science and Technology, Pibulsongkram Rajabhat University, Phitsanulok, Thailand 65000

*E-mail : theeraphan_mac@mfu.ac.th

Abstract: The essential oil from the aerial parts of *Laggera pterodonta* was extracted by hydrodistillation and analyzed by a combination of gas chromatography – flame ionization detector (GC–FID) and gas chromatography – mass spectrometry (GC–MS). The essential oil was obtained in 0.025% yield as a light yellow liquid. The major constituents of the volatile oil of *Laggera pterodonta* were thymohydroquinone dimethyl ether (21.3%), cubenol (15.2%), caryophyllene (6.8%), ∝-humulene (5.5%), and chrysanthenone (3.5%). In addition, the volatile oil inhibited some plant pathogenic fungi such as Lasiodiplodia *theobromae* and *Tricoderma resei* and human pathogenic bacteria such as *Micrococcus luteus,* MRSA OB10 and *Staphylococcus epidermidis* using agar diffusion technique.

Introduction

Laggera pterodonta (DC.) Sch. Bip. Ex Oliv. or *Laggera pterodonta* (DC.) Benth. is a weed, widely distributed from southwestern China to northern Thailand, especially in Chiang Mai and Chiang Rai provinces. The plant, commonly know as "Naad Leium or Naad Doi" in Thai, belongs to the family Asteraceae and has been used as traditional medicine by the natives for the treatment of a variety of conditions [1]. Pharmacological research revealed that extract of *L. pterodonta* has antibacterial, anti-inflammatory, anti-malarial and anti-leukaemia activities [2,3]. Several studies on the chemical constitutions of the crude extract from *L. pterodonta* have been reported [1-7], but the components and biological activities of *L. pterodonta* essential oil have not been studied previously. We report here the results of the identification of *L. pterodonta* essential oil components using a combination technique of GC-FID and GC-MS as well as its antifungal and antibacterial activity.

Materials and Methods

Materials: Fresh aerial parts of *L. pterodonta* were collected from Mae Rim, Chiang Mai, Thailand in March 2005. A voucher specimen number 25100 was deposited at CMU herbarium, Faculty of Science, Chiang Mai University, Chiang Mai, Thailand.

Extraction of Essential Oil: Fresh plant material (10 kg) was chopped into small pieces and subjected to hydrodistillation for 6 h, using a modified Clevenger-type apparatus to yield 2.5 mL of light yellow oil. The obtained essential oil was then dried over anhydrous sodium sulphate.

Analysis of Essential Oil: A chemical composition in the essential oil was analysed by a combination of GC-FID and GC-MS techneques.

GC-FID analysis was carried out using a Varian 3700 gas chromatograph coupled to a Shimadsu C-R3A integrator. Separation was achieved using H_2 as carrier gas (ca. 1 mL/min) with a fused silica capillary column (25QC/BP5) obtained from SGE, Australia (25 m × 0.25 mm i.d., 0.25 μm film thickness). The capillary column was connected to a Z guard column (2 m) of deactivated fused silica supplied by Phenomenex. Injector and detector temperatures were 260°C and 280°C, respectively; oven temperature programme, 2 min isothermal at 40°C, then at 4°C/min to 280°C (10 min isothermal).

GC-MS analysis was performed in electron impact mode (EI, 70 eV) with a Shimadzu QP5050A system, using the same temperature programme, with He as the carrier gas (1 mL/min) and a capillary column (BP-5) supplied by SGE, Australia (30 m × 0.32 mm i.d., 0.25 μm film thickness). For each analysis, programmed-temperature Kováts retention indices (RI) were obtained by analysis of the oil spiked with an *n*-alkane mixture containing each homologue from *n*-C_8 to *n*-C_{30}.

Antifungal and Antibacterial Assay: A preliminary bioassay on antifungal activity and antibacterial activity of the essential of *L. pterodonta* was performed by agar diffusion technique [8]. Tested plant pathogenic fungi and human pathogenic bacteria were Lasiodiplodia *theobromae* and *Tricoderma resei*, and *Micrococcus luteus,* Methicillin resistant *Staphylococcus aureus* OB10 (MRSA OB10) and *Staphylococcus epidermidis*, respectively.

Results and Discussion

Identification of the oil components was performed by a comparison of mass spectra with literature data (NIST, NISTREP) and by comparison of their retention indices (RI) with those reported in the literature [9]. Table 1 lists the identified compounds in the order of their elution on capillary column used for GC-FID analysis. A typical gas chromatogram of the essential oil from *L. pterodonta* is presented in Figure 1. The most prominent compounds found were thymohydroquinone dimethyl ether (21.3%), cubenol (15.2%), caryophyllene (6.8%), *α*-humulene (5.5%), and chrysanthenone (3.5%). respectively, with integrator raw peak areas expressed as a percentage of the total chromatographable components of the essential oil. These compounds accounted for

approximately 84.1% of total essential oil components. A number of components could not be indentified due to the lack of reference spectra and/or their relatively low abundance.

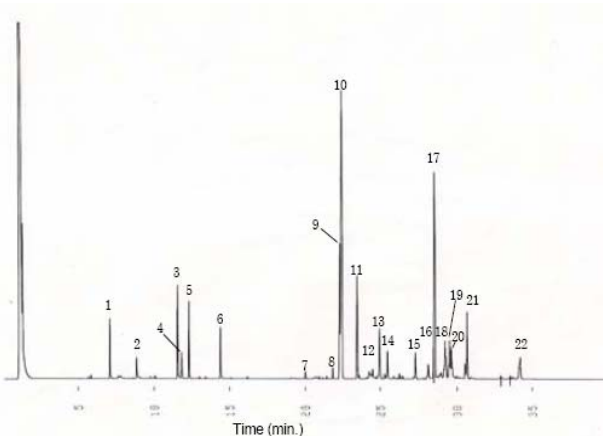

Figure 1. Gas chromatogram of the essential oil of *L. pterodonta.* See experimental for GC condition and Table 1 for peak identifications.

Bioassay screening showed the essential oil of *L. pterodonta* had antibacterial activity against *Micrococcus luteus*, Methicillin resistant *Staphylococcus aureus* OB10 (MRSA OB10) and *Staphylococcus epidermidis* and antifungal activity against Lasiodiplodia *theobromae* and *Tricoderma resei*.

Conclusions

The essential oil components of the aerial parts of *L. pterodonta* have been analyzed by GC-FID and GC-MS and 20/22 components have been identified. The major component was thymohydroquinone dimethyl ether (21.3%) and preliminary biological activity assay of the essential oil showed antifugal and antibacterial activity against Lasiodiplodia *theobromae* and *Tricoderma resei*, as well as *Micrococcus luteus*, Methicillin resistant *Staphylococcus aureus* OB10 (MRSA OB10) and *Staphylococcus epidermidi*, respectively.

Table 1: Chemical compositions of the essential oil of *L. pterodonta*.

No.	Compounds	RA[a](%)	RI[b](Exp)	RI[c](Lit)	MW	Identification[d]
1	Sabinene	2.50	966	976[T]	136	1,2
2	*p*-Cymene	1.17	1010	1026[T]	134	1,2
3	Unidentified	4.60	1097			
4	Eucarvone	1.39	1104		150	1,2
5	Chrysanthenone	3.52	1118	1123[T]	150	1,2
6	Terpinen-4-ol	2.50	1176		154	2
7	α-Longipinene	0.47	1338	1351[T]	204	1,2
8	β-elemene	0.59	1393	1391[T]	204	1,2
9	(*Z*)-Caryophyllene	6.78	1409	1404[T]	204	1,2
10	Thymohydroquinone dimethyl ether	21.28	1413		194	2
11	α-Humulene	5.48	1444	1454[T]	204	1,2
12	Germacrene D	0.66	1476	1480[T]	204	1,2
13	2-isopropenyl-4,4,7a-trimethyl-2,4,5,6,7,7a-hexahydrobenzofuran-6-ol	2.59	1492		222	2
14	δ-Cardinene	1.80	1509	1524[T]	204	1,2
15	Caryophyllene oxide	1.47	1569	1581[T]	220	1,2
16	γ-Eudesmol	1.03	1613	1630[T]	222	1,2
17	Cubenol	15.17	1633	1642[T]	222	1,2
18	Aristolene	2.91	1635		204	2
19	α-Cadinol	1.27	1643		222	1,2
20	Eudesma-3,7(11)-diene	2.23	1647	1653[T]	222	2
21	Eudesma-7(11)-en-4-ol	2.24	1686		222	2
22	Unidentified	2.41	1818			

[a] RA, Relative area (raw peak area relative to total peak area).
[b] RI (exp): Programmed temperature retention indices as determined on BP-5 column using a homologous series of *n*-alkanes (C_8-C_{30}) as internal standard and H_2 as carrier gas.
[c] RI (lit.): Value from literature data using He as carrier gas; T : Programmed temperature values; MW : Molecular weight.
[d] 1, Based on retention index; 2, Based on comparison of mass spectra with literature data (NIST, NISTREP).

References

[1] Y. Zhao, J. Yue, Z. Lin, J. Ding and H. Sun, *Phyto-chemistry*, **44** (1997), pp. 459-464.
[2] Y. B. Liu, W. Jia, W.Y. Gao, A. H. Zhao, Y.W. Zhang, Y. Takaishi and H.Q. Duan, *Journal of Asian Natural Products Research*, **8** (2006), pp. 303-307
[3] S. M. H. Ayoub and A. I. Babiker, *Fitoterapia*, 55 (1984), pp. 209-212.
[4] S. Li, J. Ding, B. Jiang and B. Na, *Phytochemistry*, **49** (1998), pp 2035-2036.
[5] Y. Zhao, J. M. Yue, Y. N. He, Z. W. Lin and H. D. Sun, *Journal of Natural Products*, **60** (1997), pp. 545-549.
[6] Y. Xiao, Q. Zheng, Q. Zhang, H. Sun, F. Gueritte and Y. Zhao, *Fitoterapia*, **70** (2003), pp. 459-463.
[7] Y. B. Liu, W. Jia, Z. Yao, Q. Pan, Y. Takaishi and H.Q. Duan, *Journal of Asian Natural Products Research*, **8** (2007), pp. 233-237.
[8] J.H. Jorgensen, , J.D. Turnidge, and J.A. Washington, Antibacterial susceptibility tests: dilution and disk diffusion methods. In Baron, E. J. (ed) *Manual of Clinical Microbiology*, 7th ed., Washington, D.C., ASM Press, 1999, pp. 1534-1535.
[9] R.P. Adams, Identification of Essential Oil Components by Gas Chromatography/Mass Spectrometry. Allured: Carol Strem, IL, 1995.

Synthesis of *n* - alkylaminoquinazoline derivatives and anticholinesterase evaluation

Y. Uetrongchit[1], S. Wacharasindhu[2] and P. Sawasdee[2*]

[1] Program in Biotechnology, Faculty of Science Chulalongkorn University, Bangkok, Thailand 10330
[2] Natural Products Research Unit, Faculty of Science Chulalongkorn University, Bangkok, Thailand 10330

*E-mail: spattara@windowslive.com

Abstract: In searching of pharmacophores for acetylcholinesterase (AChE) and butyrylcholinesterase (BChE) inhibitory activities, a serie of 4-aminoquinazoline derivatives (7 compounds, function-alized in position 4 by an alkyl- or arylamino substituent) were synthesized from 4-hydroxyquinazoline in one step. Of this serie, preliminary results found that 4-butylaminoquinazoline had mild effect against AChE and BChE. In order to enhance the cholinesterase inhibition activity, 4-butylaminoquinazolines carrying various substituents on the benzene ring moiety were prepared by Niementowski's reaction followed by BOP-mediated coupling reaction with *n*-butylamine. The results of activity test at a final concentration of 0.5 mM showed that 6-nitro-4-butylaminoquinazoline had the highest inhibition toward AChE of 91%. Moreover, 6,7-dimethoxy-4-butylaminoquinazoline exhibited the best inhibition toward BChE of 87%.

1. Introduction

Alzheimer's disease (AD) is a dementia that cause of losing memory and learning ability in the most of elderly. This degenerative neurological disorder was characterized by senile plaques containing amyloid β- peptide (Aβ) and loss of cholinergic neuromediators in the brain.[1] The most remarkable biochemical change in AD patients is low levels of neurotransmitter, acetylcholine (ACh), in the cortex and hippocampus. [2] Up to now, there are 5 drugs for healing AD patients that were approved by USFDA as AChE inhibitors; tacrine, donepezil, rivastigmine, galantamin and memantine. However these drugs have side effects e.g. nausea, diarrhea, vomiting, and weight loss. Especially The effect of higher doses was the cholinergic side effects. [3]

Quinazolines are pharmacological useful as antibacterial, anticancer, antimalarial, anticonvulsant and anti-inflammatory agents. [4] Moreover, quinazolines have the similarity of structure to tacrine which was one of the most potent acetylcholinesterase (AChE) as well as butyrylcholinesterase (BChE) inhibitors. [5] Thus quinazolines were synthesized and determined their cholinesterase (ChE) inhibitory activities against AChE and BChE.

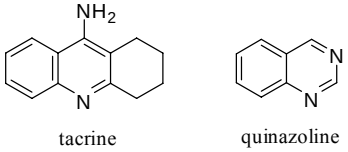

tacrine quinazoline

Figure 1 Chemical structure of tacrine and quinazoline

2. Experimental

2.1 General procedure for the synthesis of 4-substituted aminoquinazolines 1a-g [6]

A mixture of the commercially-available 4-hydroxyquinazoline**,** 1.1 equiv of BOP, 1.5 equiv of DBU and 1.5 equiv of amine in MeCN was stirred at room temperature for overnight **1a-c, 1e.** The other reactions of compound **1d-g, 1f** were stirred at room temperature for overnight, then heat to 80°C.
4-aminoquinazolines **1a-g** were gave after purify by Si gel column chromatography.

2.1.1 4-Butylaminoquinazoline (1a). Gray solid: 66 %yield. ^{1}H NMR (400 MHz, $CDCl_3$) δ (ppm) 0.94 (t, *J*=7.2 Hz, 3H), 1.44 (m, 2H), 1.69 (m, 2H), 3.63 (d, *J*=4.4 Hz, 2H), 6.47 (brs, 1H), 7.41 (m, 1H), 7.68 (m, 1H), 7.81 (m, 2H), 8.61 (s, 1H).

2.1.2 4-(methyl-2-aminoacetate)quinazoline (1b). Pale yellow solid: 12 %yield . ^{1}H NMR (400 MHz, $CDCl_3$) δ(ppm) 3.76 (s, 3H), 4.04 (d, *J*=5.6 Hz, 1H), 4.77 (s, 2H), 7.51 (m, 1H), 7.77 (m, 2H), 8.25 (d, *J*=7.6 Hz, 1H), 8.37 (s, 1H).

2.1.3 4-Benzylaminoquinazoline (1c). White powder: 62 %yield. ^{1}H NMR(400 MHz, $CDCl_3$) δ (ppm) 4.82 (d, 2H), 6.80 (brs, 1H), 7.27 (m, 3H), 7.37 (m, 3H), 7.65 (m, 1H), 7.82 (m, 2H), 8.58 (s, 1H).

2.1.4 4-Anilinoquinazoline (1d). White crystal: 11 %yield. ^{1}H NMR (400 MHz, $CDCl_3$) δ (ppm) 7.13 (t, *J*=7.2 Hz, 1H), 7.36 (m, 2H), 7.5 (s, 1H), 7.74 (m, 4H), 7.87 (d, *J*=6.4 Hz, 2H), 8.7 (s, 1H).

2.1.5 4-Piperidinoquinazoline (1e). Brown yellow oil: 89 %yield. ^{1}H NMR(400 MHz, $CDCl_3$) δ(ppm) 1.74 (s,6H), 3.68 (s, 4H), 7.39 (m, 1H), 7.67 (m, 1H), 7.83 (m, 2H), 8.66 (s, 1H).

2.1.6 4-Morpholinoquinazoline (1f). Pale yellow solid: 46 %yield. ^{1}H NMR (400 MHz, $CDCl_3$) δ(ppm) 3.73 (d, *J*=5.2 Hz, 4H), 3.81 (d, *J*=5.2 Hz, 4H), 7.40 (m, 1H), 7.69 (m, 1H), 7.80 (d, *J*=8.4 Hz, 1H), 7.86 (d, *J*=8.4 Hz, 1H), 8.68 (s, 1H).

2.1.7 4-(1*H*-Imidazol-1-yl)quinazoline (1g). White powder: 10 %yield. ^{1}H NMR (400 MHz, $CDCl_3$) δ(ppm) 7.57 (m, 1H), 7.64 (m, 1H), 7.81 (m, 3H), 7.95 (m, 1H), 8.25 (s, 1H), 9.33 (s, 1H).

2.2 General procedure for synthesis of substituted 4-butylaminoquinazolines 2a-d [7]

A mixture of substituted anthranilic acid and formamide was stirred in seal tube at 130-160°C for 6 h and cooled to room temperature. Water was added to the solution to get the product precipitate. The solid that formed was collect by filtration, washed subsequently with cold methanol, and dried to give pure substituted 4-hydroxyquinazoline. To obtain substituted 4-butylaminoquinazoline, the synthesized substituted 4-hydroxyquinazoline was then direct amination as procedure in 2.1.

2.2.1 4-butylamino-6-nitroquinazoline (2a). Yellow solid: 34 %yield. ^{1}H NMR (400 MHz, $CDCl_3$) δ(ppm) 0.94 (t, *J*=7.6,7.2 Hz, 3H), 1.43 (m, 2H), 1.70 (t, *J*=7.6,7.2 Hz, 2H), 3.66 (q, *J*=6.8 Hz, 2H), 6.36 (brs, 1H), 7.87 (d, *J*=9.2Hz, 1H), 8.42 (dd, *J*=1.6Hz, 1H), 8.68 (s, 1H), 8.74 (s, 1H).

2.2.2 4-butylamino-6,8-dichloroquinazoline (2b). Pale yellow crystalline needle shape: 23 %yield. ^{1}H NMR (400 MHz, $CDCl_3$) δ(ppm) 0.90 (t, *J* = 7.6, 7.2 Hz, 3H), 1.35 (m, 2H), 1.70 (m, 2H), 3.94 (d, *J*=0.8 Hz, 1H), 8.05 (s, 1H), 8.13 (s, 1H).

2.2.3 4-butylamino-6-fluoroquinazoline (2c). White solid: 98 %yield . ^{1}H NMR (400 MHz, $CDCl_3$) δ(ppm) 0.91 (t, *J*=7.6, 7.2 Hz, 3H), 1.40 (m, 2H), 3.59 (m, 2H), 5.70 (s, 1H), 7.31 (d, *J*=8.8 Hz, 1H), 7.41 (m, 1H), 7.77 (m, 1H), 8.57 (s,1H).

2.2.4 4-butylamino-6,7-dimethoxyquinazoline (2d). Red brown solid: 97 %yield. ^{1}H NMR (400 MHz, $CDCl_3$) δ(ppm) 0.90 (t, *J*=7.6,7.2Hz, 3H), 1.38 (m, 2H), 1.65 (m, 2H), 3.59 (m, 2H), 3.90 (s, 6H), 5.98 (s, 1H), 6.92 (s, 1H), 7.07 (s, 1H), 8.44 (s, 1H).

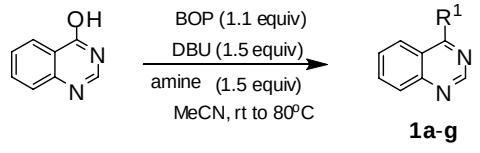

1a-g

Scheme 1.

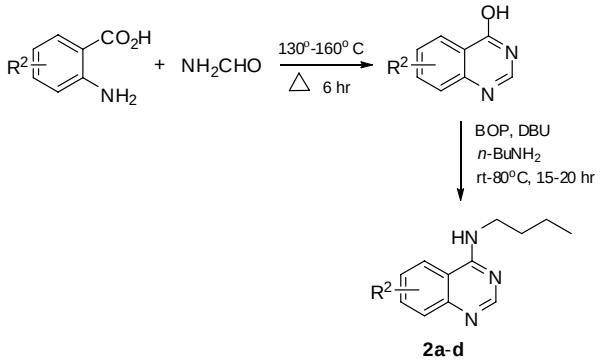

2a-d

Scheme 2.

2.3. Anticholinesterase test

Cholinesterase enzymatic activities were determined by the modified of Ellman's method. [8] Briefly, 125 µl of 3 mM DTNB in buffer C (50 mM Tris-HCl, pH 8, 0.1 M NaCl, 0.02 M $MgCl_2.6H_2O$), 25 µl of 0.22 U/ml of AChE (E.C.3.1.1.7, Type VI-S, from Electric eel) or BChE (E.C. 3.1.1.8, from equine serum) and 50 µl of buffer (50 mM Tris-HCl, pH 8, 0.1% bovine serum albumin) were mixed with 25 µl of sample in a 96-well microplate. Subsequently, 25 µl of 15 mM ATCI in MilliQ water were added and the absorbance was measured at 415 nm over 2 min with a 5s interval by a Sunrise microplate reader (P-Intertrade Equipments, Australia). Enzyme activity was calculated by comparing the rate of reaction for the samples relative to that for the blank (25 µl 10% methanol in buffer instead of sample). Percentage of inhibitory activity was calculated by substracting the percentage of enzyme activity from 100 percent. Eserine was used as standard compound.

3. Results and discussion

Our studies began with the synthesis of 4-substituted aminoquinazolines using the commercially available 4-hydroxyquinazoline as starting compound. The efficient one-step amination of 4-hydroxyquinazoline was promoted by using BOP and DBU as shown in Scheme 1. The inhibition activities of these synthesize quinazolines **1a-g** were evaluated for their AChE and BChE inhibitory activities (Table 1). The effect of substituents at the position 4 was observed. Compound **1e** with a *N*-piperidyl group showed the highest inhibition towards both enzymes. Interestingly, the displacement of a *N*-morpholinyl group (**1f**) resulted in a significant decrease in the affinity toward AChE but showed a slight decrease toward BChE compared with **1e.** Compounds **1a** and **1c** having a butylamino group and a *N*-benzylamino group, respectively, exhibited a moderate inhibition. Moreover, if a *N*-benzylamino group was replaced with a *N*-phenylamino group, the activity is drastically reduced in **1d**. From these results, **1a** was selected as the basic scaffold for the further study to determine how the substituents of the subunits affected the cholinesterase activity.

We next investigated the effects of the substituents on benzene ring of **1a**, 4-butylamino-quinazoline. Four derivatives of **1a,** compounds **2a-d,** were prepared by Niementowski's reaction followed by BOP-mediated reaction with *n*-butylamine as shown in Scheme 2. Inhibitory activities toward AChE and BChE *in vitro* of these compounds were determined and summarized in Table 2. The results indicated that a nitro group attached at position 6 (**2a**) caused two-folds better potency against AChE compared with none. Moreover, this substituent caused two-folds decreasing of the inhibition effect on BChE which led to enhance the selectivity of BChE over AChE. Similar tendency was also found in 4-

butylaminoquinazoline with either a 6,8-dichloro (**2b**) or a 6-fluoro (**2c**) substituents. On the other hand, when a 6,7-dimethoxy substituent was attached, the converse affect was observed. Starting with this evidence, we presuppose that the electron-withdrawing group attached on the benzene ring of quinazoline enhanced the selectivity towards AChE and the electron-donating group enhanced that of BChE.

Table 1. Anticholinesterase activity of 4-substituted aminoquinazolines.

Compound	R^1	Inhibition (%)[a]	
		AChE	BChE
1a	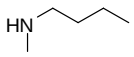	44.0 ± 1.8	66.0 ± 0.2
1b	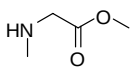	27.0 ± 2.8	24.0 ± 2.8
1c	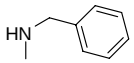	43.0 ± 2.8	46.2 ± 0.6
1d	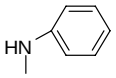	4.0 ± 0.7	11.0 ± 2.4
1e		84.6 ± 0.7	86.0 ±0.5
1f		29.2 ± 2.7	72.8 ± 1.8
1g	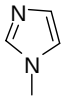	22.0 ± 2.2	27.6 ± 3.4
Eserine		93.2 ± 1.4	94.8 ± 1.5

[a] *final concentration 0.5 mM*

4. Conclusions

The prescreening cholinesterase inhibitory activitiy of 4-substituted quinazolines were examined by Ellman's method. The 4-piperidinoquinazoline (**1e**) showed the highest activity against both AChE and BChE. The best selectivity for BChE was reached for 4-morpholinoquinazoline (**1f**). However, 4-butylaminoquinazoline with moderate activities was chosen for further study the effect of substituents. The electron-withdrawing group in benzene ring of quinazoline increased the AChE affinity. The most active compound is 4-butylamino-6-nitroquinazoline (**2a**) with 91% inhibition and a selectivity of 2.5 toward AChE.

Table 2. Anticholinesterase activity of substituted butylaminoquinazolines.

Compound	R^2	Inhibition (%)[a]	
		AChE	BChE
2a	6-nitro	91.0 ± 0.8	37.0 ± 2.1
2b	6,8-dichloro	73.0 ± 3.5	43.0 ± 4.5
2c	6-fluoro	59.2 ± 1.1	36.1 ± 5.8
2d	6,7-dimethoxy	40.0 ± 5.0	86.5 ± 1.4

References

[1] V. Echeverria, S. Burgess, J. Gamble-George, G. W. Arendash, B. A. Citron, *Neurosci. Lett.* **444** (2008), pp. 92 - 96.

[2] M. Decker, F. Krauth, J. Lehmann, *Bioorg. Med. Chem.* **14** (2006), pp. 1966-1977.

[3] N. Mimica, P. Presecki, *Psy. Danub.* **21** (2009), pp. 108-113.

[4] V. Alagarsamy, V. R. Solomon, M. Murugan, R. Sankaranarayanan, P. Periyasamy, R. Deepa, T. D. Anandkumar, *Biomedicine. & Pharmacotherapy* **62** (2008), pp. 454-461.

[5] E. Giacobini, *Neurochem. Int.* **32** (1998), pp. 413-419.

[6] Z.-K. Wan, S. Wacharasindhu, E. Binnun, T. Mansour, *Org. Lett.* **8** (2006), pp.2425-2428.

[7] F.-R. Alexandre, A. Berecibar, T. Besson, *Tetrahedron Lett.* **43** (2002), pp. 3911-3913.

[8] K. Ingkaninan, P. Temkitthawon, K. Chuenchom, T. Yuyaem, W. Thongnoi, *J. Ethnopharmacology* **89** (2003), pp.261-264.

Molecular docking of 6-deoxyerythromycin-a to *Deinococcus radiodurans* 23S rRNA and the study of C-6 hydroxyl group presence to the binding capability of erythromycin-a to macromolecule target

W.Haryadi [1*], U.A. Jenie [2], R.S. Sudibyo [2], H.D. Pranowo[1] and F.R. Wibowo[3]

[1]Department of Chemistry, Faculty of Mathematics and Natural Sciences, UGM, Yogyakarta, Indonesia
[2] Faculty of Pharmacy, UGM, Yogyakarta, Indonesia
[3] Department of Chemistry, Faculty of Mathematics and Natural Sciences, UNS, Surakarta, Indonesia

*E-mail: winarto.hary@gmail.com, Tel: +62-8882710311

Abstract: Erythromycin-A is a broad spectrum macrolide antibiotic. This compound can be used to substitute penicillin because of the resistance of penicillin to microbes and its sensitivity to some patients. The disadvantage of the usage of erythromycin is the instability in stomach acid. The instability is caused by internal nucleophilic attack of C-6 hydroxyl group to protonated carbonyl (C-9) in the macrolide ring. 6-Deoxyerythromycin-A is an erythromycin-A derivative lacking the C-6 hydroxyl group. This compound is predicted to be more stable in acid condition because of absence of C-6 hydroxyl group. The molecular docking of 6-deoxyerythromycin-A were executed 10 times using AutoDock 4.0 to the experimentally erythromycin binding site of *Deinoccocus radiodurans* 23S rRNA. As a reference, molecular docking of erythromycin-A had been also conducted with the same method. Molecular docking of 6-deoxyerythromycin shows that this compound occupies the same cavity as of the experimental erythromycin-A and the binding energy of 6-deoxyerythromycin-A and erythromycin-A are not significantly different. These are evidences that the absence of C-6 hydroxyl group in the macrolide ring does not hamper the binding capability to the 23S rRNA. Therefore the presence of C-6 hydroxyl group in the macrolide ring does not cause an effect of any nature towards the pharmacological properties of erythromycin-A.

Introduction

Erythromycin-A is a broad spectrum macrolide antibiotic. This compound can be used to substitute penicillin due to the resistance of penicillin to microbes and its sensitivity to some patients. The disadvantage of the usage of erythromycin-A is the instability of this compound in stomach acid. The instability is caused by internal nucleophilic attack of hydroxyl group(C-6) to protonated carbonyl (C-9) in macrolide ring [1]. This reaction leads to decomposition of erythromycin-A and lack of its activity. The erythromycin-A decomposition can be prevented by chemical modifications, which are able to prevent the internal nucleophilic attack [2]. Some erythromycin-A derivative antibiotics produced by chemical modification are chlarithromycin, roxythromycin and azy-thromycin [3].

Δ^6-Anhidroeritromisin-A is new erythromycin-A derivative which is synthesized using biosynthetic engineering. This technique comprises of addition of isoniazide into *Sac. erythraea* fermentation [4]. The Δ^6-anhidroerythromycin-A molecule differs from of erythromycin-A due to the presence of Δ^6 double bond and unavailability of hydroxyl molecule (OH) at C-6 in erytronolide ring. The unavailability of hydroxyl molecule (OH) at C-6 is accustomed to increase its stability in acidic solution due to the hydroxyl molecule (OH) at C-6 which is an initiator of erythromycin-A decomposition [1]. The Δ^6-anhidroeritromisin-A molecule is experimen-tally proven to be stable and active until pH 3 [5]. Therefore, the absence of C-6 hydroxyl group in erythronolide ring can increase the structural stabilization, but the effect of the absence of this group has not been investigated.

The effect of C-6 hydroxyl group (OH) existence in erythronolide ring to the binding mode of erythromycin-A at macromolecule target can be investigated by interaction modeling of 6-deoxyerythromycin-A to the macromolecule target. 6-Deoxy-erythromycin-A is a molecular model of erythromycin-A derivative which has no C-6 hydroxyl group.

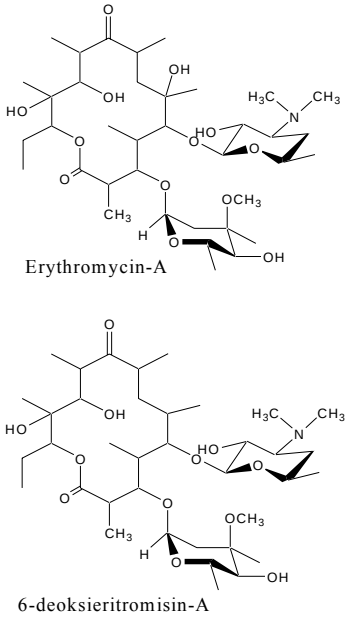

Figure 1: Chemical Structures of Erythromycin-A and 6-Deoxyeritromycin-A

The binding strength and binding mode of antibiotic molecule to the active site of macromolecule can be evaluate by molecular docking method [6]. The effect of C-6 hydroxyl group existence to the binding mode and strength of erythromycin-A can be studied by comparing the binding mode and strength of erythromycin-A and 6-deoxyerythromycin-A to the active site of rRNA 23S *D. radiodurans*[7,8]. The binding position of these molecules obtained from the docking calculation are compared with the binding site of erythromycin-A reported by X-ray crystallography [8] based on RMSD (root mean square deviation) calculations. The binding strength of these molecules to rRNA 23S macromolecule could be accessed on the basis of the binding free energy. Macrolide antibiotics have capability to inhibit elongation of oligopeptide synthesis in the cavity of rRNA 23S, named peptide exit tunnel [7].

Material and Methods

Main software packages for docking experiment research consisted of CentOS, Molden, Gaussian98, Chimera, Rasmol and Autodock Tools version 4.01., Protein data bank site (PDB) (www.RCSB.org) and from other sites which are relevant.

The complex structure of erytromycin-A and rRNA 23S *Deinococcus radiodurans* macromolecule is obtained from Protein Data Bank accessed via www.RCSB.org. The erythromycin-A structure was separated from antibiotic macromolecule using CHIMERA programme and then saved in PDB format. The structure of 6-deoxyerythromycin-A is drawn using MOLDEN programme and optimalized by *ab initio* method using Gaussian 98 software. The docking of erythromycin-A and 6-deoxyerythromycin-A on rRNA 23S macromolecule using Autodock version 4.0. The docking parameters used in this study were *Lamarckian Genetic Algoritm*, *grid box* 60 and total energy evaluation was 2,5 x 10^8. The *Genetic Algorithm* parameter were 150 initial population, 27.000 maximum generation, cross over rate of 0.8, and mutation rate of 0.02. Local search Solis parameter and Wet was 300 iterations of local search, consecutive successes before changing and 4 consecutive failures before changing.

Results and Discussion

The molecular docking of erythromycin-A and 6 deoxyery-thromycin-A molecules on the rRNA 23S were executed ten times at the active site of 23S macromolecule by X-ray crystallography [8]. The docking relative position to erythromycin-A (X-Ray) position of these three molecules based on RMSD is shown in Table 1.

Table 1: RMSD of Ten Docking of 6-Deoxyerythromycin-A (6-DEA) and Erythromycin-A (ERY-A) to The Position of Erythromycin-A (X-Ray) on 23S rRNA

Docking number	RMSD	
	6-DEA	ERY-A
1	8.25	9.39
2	9.06	9.89
3	8.24	9.31
4	**5.98**	9.30
5	10.37	9.88
6	8.60	8.59
7	8.59	8.45
8	8.25	**6.61**
9	10.38	9.89
10	10.36	9.28

Based on molecular docking result, the position of erythromycin-A, and 6-deoxyerythro-mycin-A does not exactly agree with experimental position of erythromycin-A, even though according to RMSD data, these molecules occupy a cavity in rRNA 23S which is similar to experimental erythromycin-A. From this fact, it could be expected that these molecules have capability to bind the peptide exit tunnel and inhibit the elongation of oligopeptide synthesis.

From Table 1, it clearly seen that the fourth docking result of 6-deoxyerythromycin-A and eighth of erythromycin-A are the closest docking molecule to the position of experimental erythromycin-A. Their binding position in the cavity of 23S rRNA are overlap each other. The relative position of fourth docking result of 6-deoxyerythromycin-A and eighth of erythromycin-A are ilustrated in fig.1.

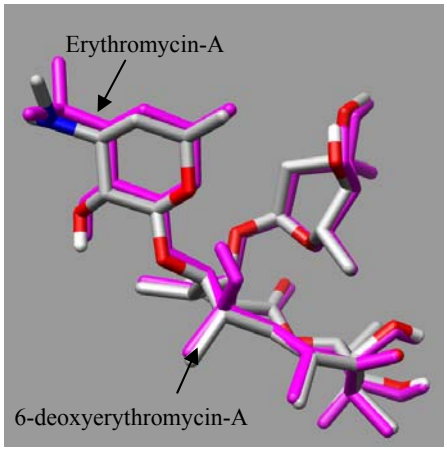

Fig 1: The Relative Position of 4th and 8th Docking Molecules for 6-Deoxyerythromycin-A and Erythromycin-A

It is clearly observed from fig 1, that the relative position of docking for 6-deoxyerythromycin-A and erythromycin-A are very close to each other. This result suggest that the inexistence of a hydroxyl group (C-6) in 6-deoxyerythromycin-A does not hindrance

the binding capabilities of this molecule to 23S rRNA, as it is not the case with erythromycin-A. Therefore, it may be concluded that both molecules have the same binding mode, i.e: in the cavity of 23S rRNA.

The binding strength of these molecules to the macromolecule target may be evaluated by observing their binding energy. The lower the binding energy, the stronger the binding [9]. The binding free energy(ΔG) obtained from molecular docking of 6-deoxyerythro-mycin-A and erythromycin-A are collected in Table 2.

Table 2: The Binding Free Energy (ΔG) of 6-Deoxyerythromycin-A, Erythromycin-A

Docking number	Binding free energy (ΔG) (kJ/mol)	
	6-DEA	ERY-A
1	-9.02	-8,78
2	-9.08	-9,41
3	-9.02	-9,20
4	-7.71	-9,19
5	-10.75	-9,40
6	-8.94	-8,66
7	-8.94	-8,25
8	-9.02	-8,14
9	-10.68	-9,41
10	-10.74	-9,17
Average	-9,39	-8,96

From Table 2, it is immediately emerged that the free binding energy of ten times docking result of 6-deoxyerythromycin-A and erythromycin-A on 23S rRNA are not significantly different. It is shown that the difference of their binding free energy less than 2 kkal/mol [6]. From these data, it may be concluded that 6-deoxyerythromycin-A and erythromycin-A have a relatively same binding strength. Based on their binding mode and binding energy, it has been demonstrated that the presence of hydroxyl group at C-6 does not affect significantly to the pharmacological properties of macrolide antibiotic and therefore, this group may be substituted or eliminated without any significant loss of their activity.

Conclusions

The binding position and mode of 6-deoxyerythromycin-A and erythro-mycin-A to rRNA 23S are similar to binding position and mode of real erythromycin-A. Based on the relative position and binding free energy in molecular docking, 6-Deoxyerythro-mycin-A and erythromycin-A have the same position and binding strength [10]. Therefore, the presence of hydroxyl group at C-6 is expected would not any significant effects towards their pharmacological properties of macrolide antibiotics. Consequently, this group may be substituted or eliminated without any significant loss of their activity.

References

[1] Sakakibara H. and S. Omura, 1984, *Chemical Modification and Structure-Activity Relationship of Macrolides* in Satoshi Omura (Ed) *:* Macrolide Antibiotics : Chemistry, Biology and Practise*,* Academic Press, Orlando

[2] Omura S. and Y. Tanaka, 1984, *Biochemistry, Regulation and Genetics of Macrolide Production* in Mura S (ed) : Macrolide Antibiotics : Chemistry, Biology and Practise, Academic Press, Orlando

[3] Fass, R.J., 1993, Erythromycin, Clarithromycin and Azithromycin: Use of Frequency Distribution Curves, Scattergrams and Regression Analyses to Compare in vitro Acvtivities and Describe Cross-Resistence, Antimicrob. Agents Chemother., 37, 10, 2080-2086.

[4] Sudibyo R.S., U.A. Jenie, and W. Haryadi, 1999*,* Biosynthesis of $\Delta^{6,7}$-Anhydro-Erythromycin via Enoyl Reductase Inhibition by Isonicotinic Hydrazide (INH), *Indo. J. Biotechnology., 311-316.*

[5] Sudibyo R.S., U.A. Jenie, and W. Haryadi, 1999b, Analysis of Acid Resistance of $\Delta^{6,7}$-Anhydro-erythromycin-D Using FT-IR Spectrometric Approach and Microbial Test, *Indo. J. Biotechnology*, 321-325.

[6] Morris, G.M., D.S. Goodsell, R.S. Halliday, R. Huey, W.E. Hart, R.K. Belew and A.J. Olson, 1998, Automated Docking Using a Lamarckian Genetic Algorithm and an Empirical Binding Free Energy Function, *Journal of Computational Chemistry,* Vol. 19, No 14, 1639-1662

[7] Lovmar, M, K. Nilson, V. Vimberg, T. Tenson, M. Nervall and M. Ehrenberg, 2005, The Molecular Mechanism of Peptide –mediated Erythromycin Resistence, *The Journal of Biological Chemistry* Vol 281. pp6742-6750

[8] Schlünzen F, R Zarivach, J Harms, A Bashan, A Tocilj[1], R Albrecht, A Yonath and F Franceschi, 2001, Structural Basis For The Interaction Of Antibiotics With The Peptidyl Transferase Centre In Eubacteria, *Nature* , **413**, 814-821

[9] Leach, A.R., 1996, Molecular Modelling Principle and Application, Addision Longman, London.

Petroleum Chemistry and Catalysis

Effect of variables on epoxidation of oleic acid using peracetic acid

T. Wattanakul, V. Chuenchom*

Department of Chemistry, Faculty of Science,
King Mongkut's Institute of Technology Ladkrabang, Bangkok, Thailand 10520

* E-mail: kcvancha@kmitl.ac.th

Abstract: 9,10-epoxystearic acid was synthesized by epoxidation of oleic acid with peracetic acid generated from hydrogen peroxide and acetic acid in the presence of H_2SO_4 catalyst. Two synthetic routes, namely two-step synthesis (generation of peracetic acid prior to epoxidation) and single-step synthesis (generation of peracetic acid during epoxidation) were compared. It was found that the two-step synthesis provided a relatively higher conversion of oleic acid and higher selectivity of epoxidized product, as compared to the single-step synthesis. In addition, water (presented in the 30% H_2O_2) and acetic acid in the presence of high H_2SO_4 content produced the by-products, namely diol and hydroxy-acetoxy compounds, from the ring-opening of epoxidized product. Experimental results showed that 76 % conversion of oleic acid and 95 % selectivity of epoxidized product were obtained by using 0.75 mol of hydrogen peroxide, 0.2 mol of acetic acid, 0.1 mol of oleic acid and 0.4 mL of H_2SO_4. The optimized reaction temperature for peracetic acid preparation and for epoxidation were 50 ^oC and 30 ^oC whereas the optimized reaction time for peracetic acid preparation and for epoxidation were 4 and 15 hours, respectively.

Introduction

Currently, vegetable oils make up the greatest proportion of the renewable raw materials consumed in the chemical industry for the manufacture of a variety of products. The vegetable oils are often modified to achieve the formulations with desired properties. Generally, vegetable oils with a high content of unsaturated fatty acid, which are rich in oleic (20-45%) and linoleic (10-60%) are used in the reaction to produce high epoxy functionality materials. Due to the high reactivity of the epoxy group, oxirane ring can also act as raw materials for synthesis of a variety of chemicals, such as lubricants, alcohols, glycols, alkanolamines, carbonyl compounds.

Epoxidation can be economically accomplished by reacting the double bonds with a peracid which is used for oxygen transfer [1]. The peracid is usually generated from hydrogen peroxide and acetic or formic acid using a strong mineral acid as catalyst [2-3]. However, their utilization prevents the achievement of high yields, because of the opening of the oxirane ring during the course of the main reaction [4-5]. An alternative process that is milder and more selective has also been reported by using enzyme as catalyst [6-7]. In addition, catalysts based on a homogeneous transition-metal were investigated in the presence of solvent such as benzaldehyde [8-9]. The use of volatile organic solvents in large-scale processes is undesirable as they require proper handling due to their toxic effects, and can further contribute to greenhouse effects unless solvent recycling is practiced.

The basic objective of this study is to explore the production of low-cost epoxidized fatty acid achieved by epoxidation of oleic acid with peracetic acid. Such fatty acid is chosen as a model reaction representing unsaturated fatty acids in palm oil which is one of the important agro-products in Thailand. Catalytic epoxidation using mineral acid as a catalyst is the most suitable technology to agro-industries countries like Thailand. In this work, various reaction parameters are optimized with respect to the conversion of the double bond to oxirane and their selectivity using the best-performing conditions. Therefore, the mild reaction condition, formation of stable peracid, high product selectivity, high conversion and an optimized content of sulphuric acid are investigated.

Materials and Methods

Synthesis of epoxidized oleic acid

Single-step synthesis

An (0.1-0.4 mol) acetic acid (100%, J.T. Baker), (0.4 mL) sulfuric acid (98%, J.T. Baker), and (0.1 mol) oleic acid (90%, Aldrich) were transferred into the 250 mL clean round-bottom flasks equipped with a mechanical stirrer and then placed in a water bath. To start the epoxidation, (0.30-0.75 mol) hydrogen peroxide (30%, Fisher) was gradually charged into the mixture. The system was kept at 30 ^oC and the mixture was continuously stirred for the desired time duration. The resulting of reaction mixture were then extracted with diethyl ether in order to separate oil product from water phase, washed with water successively to remove free acids. After that the lower aqueous phase was siphoned off and the retained product was dried to remove diethyl ether using vacuum oven at 40 ^oC.

Two-step synthesis

An (0.1-0.4 mol) acetic acid (100%, J.T. Baker), (0.4 mL) sulfuric acid (98%, J.T. Baker), and (0.3-0.9 mol) hydrogen peroxide (30%, Fisher) were transferred into the 250 mL of clean round-bottom flasks equipped with a mechanical stirrer and then placed in a water bath. The system was kept at a 50 ^oC (or 30 ^oC) and the mixture was continuously stirred for 2-6 hours. Then the mixture was cooled down to 30 ^oC and the 0.1 mol of oleic acid (90%, Aldrich) was gradually added. After the charging of oleic acid was

completed, the reaction continued by stirring it for the desired time duration.

Characterization of epoxidized oleic acid

The conversion of oleic acid and selectivity of epoxidized oleic acid were determined using the ^{1}H-NMR technique. The sample was dissolved in deuterated chloroform ($CDCl_3$). The measurement was performed on a Bruker (AVANCE DPX300 NMR spectrometer) with 300 MHz ^{1}H-resonance frequency. The conversion and selectivity were calculated as the peak percent value.

Results and Discussion

Effect of hydrogen peroxide

It is seen from Figure 1 that oleic acid can be converted to epoxidized product (9,10-epoxystearic acid), diol and hydroxy-acetoxy compound. The formation of epoxidized product from oleic acid was proposed by epoxidation with peracetic acid generated from acetic acid and hydrogen peroxide [10-11]. While the by-products, diol and hydroxy-acetoxy compounds, were derived by ring-opening of epoxidized product with water and acetic acid, respectively [5].

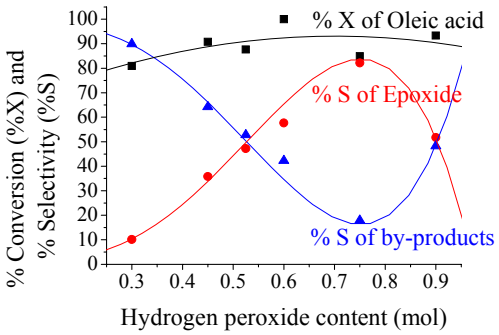

Figure 1. Effect of hydrogen peroxide content over two-step synthesis of 9,10-epoxystearic acid

(Acetic acid = 0.3 mol, Oleic acid = 0.1 mol, H_2SO_4 = 0.4 mL, Step 1: Temperature = 50 °C, Time = 4 hours, Step 2: Temperature = 30 °C, Time = 15 hours)

The effect of Hydrogen peroxide-to-oleic acid mole ratio on the conversion of oleic acid to epoxidized product was studied over two-step synthesis. Figure 1 shows that the conversion of oleic acid slightly increased as the concentration of hydrogen peroxide in the system increased. Interestingly, a dramatic increase in selectivity of epoxidized product was obtained by using 0.30-0.75 mol of hydrogen peroxide but was decreased at relatively higher hydrogen peroxide content (0.90 mol) and *vice versa* for the selectivity of by-products. In addition, water presented in 30% hydrogen peroxide and produced from the reaction of hydrogen peroxide together with acetic acid presented in the system and produced after epoxidation of peracetic acid can consecutively perform the ring-opening leading to the high yield of by-products. When the increase in hydrogen peroxide is up to 0.75 mol, the prior organic generation of peracetic acid not only reacts inside the phase, but also acts as an interphase layer between aqueous phase and organic phase. This can inhibit the water transferring to organic phase leading to the reduction of diol. This suggestion is consistent with several reports [12] that an excess hydrogen peroxide to the ethylenic unsaturation can minimize the formation of diol by-product through ring-opening reactions. Moreover, it is also suggested that some part of acetic acid generated after epoxidation can readily return to the aqueous phase to minimize hydroxy-acetoxy compounds and to reinitiate the peracetic acid. However, a decrease in selectivity of epoxidized product is obtained when using 0.9 mol of hydrogen peroxide. This is presumably explained that the use of 0.9 mol of 30% hydrogen peroxide can also increase the water content. The opportunity for such water to be in contact with the epoxidized product would be increased, resulting in the lower selectivity of epoxidized product and *vice versa* for the selectivity of by-products. From this result, it is interesting to note that the selectivity of desired product depends largely on the mass transfer across the interface between the aqueous phase and the organic phase.

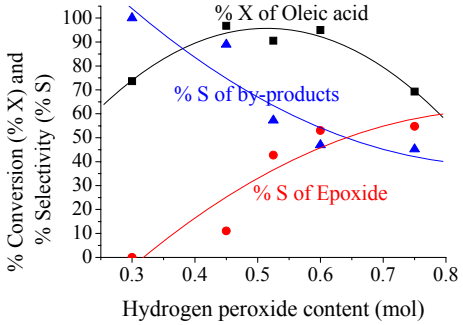

Figure 2. Effect of hydrogen peroxide content over single-step synthesis of 9,10-epoxystearic acid

(Acetic acid = 0.3 mol, Oleic acid = 0.1 mol, H_2SO_4 = 0.4 mL, Step 1: Temperature = 30 °C, Time = 15 hours)

Over the single-step synthesis (Figure 2), the selectivity of epoxidized product increases while the selectivity of by-products decreases when the increase in hydrogen peroxide content is from 0.30-0.75 mol. However, a dramatic decrease in conversion of oleic acid is obtained when using 0.75 mol of hydrogen peroxide. This implies that the reaction between oleic acid and peracetic acid may be diminished due to a decrease in concentration of peracetic which was generated *in situ* and/or a decrease in delivering into the organic phase. This shall not affect the conversion of oleic acid over two-step synthesis. This is because an excess concentration of peracetic acid which was previously generated during 4 hours preparation prior to epoxidation can be obtained in the system. It indicates that the rate of peracetic acid formation plays important role on the conversion of oleic acid. This is consistent with the previous report [13]. From the above result, the high conversion of oleic acid and high selectivity of epoxidized product can be obtained

when using 0.75 and 0.60 mol of hydrogen peroxide over the two-step and single-step synthesis, respectively. Further experiments were therefore carried out with these hydrogen peroxide contents to study the effects of acetic acid.

Effect of acetic acid

Acetic acid acts as the oxygen carrier and gets regenerated once the epoxidation reaction takes place [13]. Hence, acetic acid also acts as a catalyst in the epoxidation reaction. However, acetic acid can also hydrolyze the oxirane ring formed during the epoxidation [10-11]. The level of acetic acid should be such that both effects are balanced.

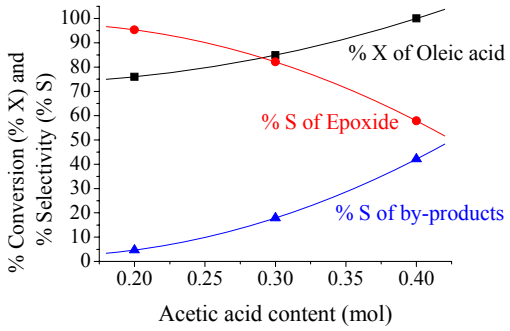

Figure 3. Effect of acetic acid content over two-step synthesis of 9,10-epoxystearic acid

(Hydrogen peroxide = 0.75 mol, Oleic acid = 0.1 mol, H_2SO_4 = 0.4 mL, Step 1: Temperature = 50 °C, Time = 4 hours, Step 2: Temperature = 30 °C, Time = 15 hours)

From Figure 3, it is clearly seen that as acetic acid content increases, the conversion of oleic acid increases over two-step synthesis. However, the increased acetic acid content has a detrimental effect on the epoxidized product, as the acid promotes the hydrolysis of the epoxide, hence decreasing its final selectivity. As can be seen from Figure 3, a 0.2 mol of acetic acid gives a moderately high conversion of oleic acid and a negligible rate of ring-opening.

Although an increase in conversion of oleic acid is initially obtained when increases acetic acid content in the case of single-step synthesis (Figure 4), a dramatic decrease in conversion of oleic acid is obtained when using acetic acid at 0.40 mol. Again, this implies that reaction between oleic acid and peracetic acid may be diminished, as earlier discussed in the effect of hydrogen peroxide. In addition, a slightly change of selectivity of epoxidized product can be observed when using acetic acid > 0.10 mol. From the above result, a relative higher conversion of oleic acid and selectivity of epoxidized product leading to the high yield of epoxidized product can be obtained over two-step synthesis, as compared to single-step synthesis. This is presumably due to the relative higher peracetic acid concentration generated at higher reaction temperature (50 °C). It is interesting to investigate the effect of peracetic preparation temperature.

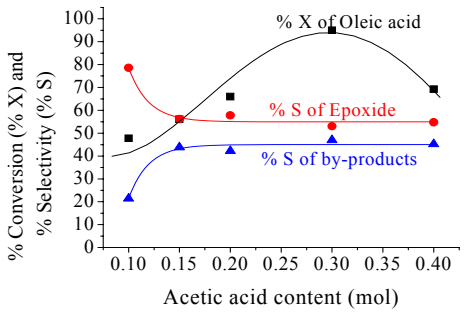

.

Figure 4. Effect of acetic acid content over single-step synthesis of 9,10-epoxystearic acid

(Hydrogen peroxide = 0.6 mol, Oleic acid = 0.1 mol, H_2SO_4 = 0.4 mL, Step 1: Temperature = 30 °C, Time = 15 hours)

Effect of reaction temperature and time over peracetic preparation

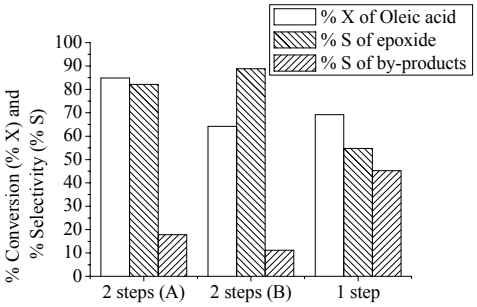

Figure 5. Data comparison between % conversion and % selectivity obtaining from single-step, two-step (A) and two-step (B) synthesis of 9,10-epoxystearic acid

(Acetic acid = 0.3 mol, Oleic acid = 0.1 mol, H_2SO_4 = 0.4 mL, H_2O_2 = 0.75 mol)
Single-step : Temperature = 30 °C, Time = 15 hours
Two-step (A) Step 1: Temperature = 50 °C, Time = 4 hours, Step 2: Temperature = 30 °C, Time = 15 hours
Two-step (B) Step 1: Temperature = 30 °C, Time = 4 hours, Step 2: Temperature = 30 °C, Time = 15 hours

In the case of two-step synthesis, the higher relative selectivity of epoxidized product (88.87%) is pronounced (Figure 5), although the lower relative conversion of oleic acid (64.21%) can be obtained when the preparation of peracetic acid was done at 30 °C, as compared to the preparation at 50 °C. It is interesting to note that two-step synthesis can provide the higher selectivity of epoxidized product, as compared to single-step synthesis. While a slightly change in conversion of oleic acid can be obtained. This implies that the prior generation of peracetic acid can stabilize the selectivity of epoxidized product and diminish the selectivity of by-products, as earlier discussed. Therefore, only two-step synthesis should be investigated over the other parameters.

As expected, the conversion of oleic acid increases when the preparation time of peracetic acid increases (Figure 6) due to an increase in concentration of peracetic acid. However, a marked drop of the selectivity of epoxidized product is obtained. This is

presumably because the water generated from the reaction of hydrogen peroxide and acetic acid can also be pronounced in the reaction system. Such water and acetic acid can consecutively carry out the ring-opening leading to the high yield of by-products, as earlier discussed.

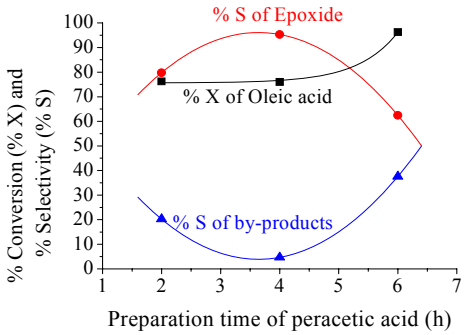

Figure 6. Effect of the preparation time of peracetic acid over the conversion of oleic acid and selectivity of 9,10-epoxystearic acid

(Acetic acid = 0.2 mol, Hydrogen peroxide = 0.75 mol, Oleic acid = 0.1 mol, H_2SO_4 = 0.4 mL, Step 1: Temperature = 50 °C, Time = 4 hours, Step 2: Temperature = 30 °C, Time = 15 hours)

Effect of sulfuric acid

To investigate the effect of H_2SO_4 content on the epoxidation reaction, the amount of acid was varied from 0.1 to 0.7 mL. Generally, with an increase in acid content, conversion of oleic acid increases (Figure 7). It is also observed that the selectivity of epoxidized product reaches the maximum when using 0.4 mL of H_2SO_4. It is evident that the relative higher sulfuric acid can promote the ring-opening reaction leading to the increase in the selectivity of by-products. This is consistent with the previous discussion that the by-products, diol and hydroxy-acetoxy compounds, were derived by ring-opening of epoxidized product with water and acetic acid, particularly under acid catalyzed condition.

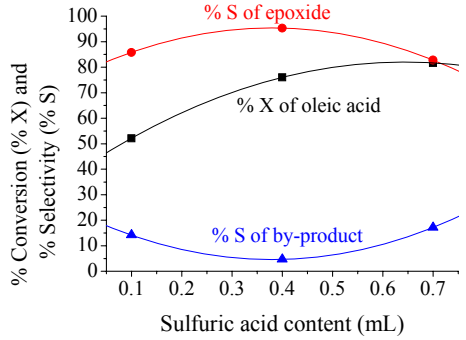

Figure 7. Effect of sulfuric acid over two step synthesis of 9,10-epoxystearic acid

(Hydrogen peroxide = 0.75 mol, Acetic acid = 0.2 mol, Oleic acid = 0.1 mol, Step 1: Temperature = 50 °C, Time = 4 hours, Step 2: Temperature = 30 °C, Time = 15 hours)

Conclusions

In summary, the epoxidation of oleic acid using hydrogen peroxide and acetic acid in the presence of H_2SO_4 was strongly affected by the reaction parameters studied in this work. It was observed that the epoxidized product derived by epoxidation of oleic acid with peracetic acid, consecutively performed the ring-opening to generate by-products namely, diol and hydroxy-acetoxy compounds. Two-step synthetic process provided the higher selectivity of epoxidized product, as compared to single-step synthesis. An excess amount of hydrogen peroxide was necessary in the reaction to achieve high reaction conversion and high selectivity. However, the water presented in the feed (30% hydrogen peroxide) and from the reaction of hydrogen peroxide and acetic acid in the presence of high H_2SO_4 content produced the by-products. In this investigation, 76 % conversion of oleic acid and 95 % selectivity of epoxidized product were achieved under the optimized condition.

References

[1] Swern D., *J Am Chem Soc,***69** (1947), pp.1692-1698.
[2] T.-C. Chou, J.-Y. Chang., *Chem. Eng. Commun.* **41** (1986). 253.
[3] Xuebing Zhao,Ting Zhang, Yujie Zhou, Dehua Liu., *J. Mol. Cat. A:Chem.* **271** (2007),pp. 246–252.
[4] B. Rangarajan, A. Havey, E.A. Grulke, P.D. Culnan., *J. Am. Oil Chem. Soc.* **72** (1995), pp. 1161–1169.
[5] A. Campanella, M.A. Baltanas., *Lat.Am. Appl. Res.***35** (2005), pp. 205–210.
[6] I. Hilker, D. Bothe, J. PruK ss, H. -J. Warnecke ., *Chem. Eng. Sci.* **56** (2000), pp. 427432
[7] Cecilia Orellana-Coca, Samuel Camocho, Dietlind Adlercreutz, Bo Mattiasson, Rajni Hatti-Kaul., *Eur. J. Lipid Sci. Technol.***107** (2005), pp. 864–870.
[8] Kuo, M. C. and T. C. Chou., *Ind. Eng. Chem. Research.* **26** (1987), pp. 277-284.
[9] Tse-Chuan Chou and Shan-Van Lee., *Ind. Eng. Chem. Res.***36** (1997), pp. 1485-1490.
[10] Srikanta Dinda, Anand V. Patwardhan , Vaibhav V. Goud , Narayan C. Pradhan., *Bioresource Technology.* (2008), pp. 3737–3744.
[11] Vaibhav V. Goud, Anand V. Patwardhan , Narayan C. Pradhan., *Bioresource Technology.* **97** (2006), pp. 1365–1371.
[12] Rubeena Mungroo, Narayan C. Pradhan, Vaibhav V. Goud, Ajay K. Dalai., *J. Am. Oil. Chem. Soc.* **85** (2008) , pp. 887–896
[13] Tse-Chuan Chou, Jy-Yang Chang., *Chem. Eng. Commun.* **41** *(1986)*, pp.253-266.

Hydrolysis of palm oil to fatty acids using Al_2O_3 catalyst

K. Sitanon, V. Chuenchom*

Department of Chemistry, Faculty of Science,
King Mongkut's Institute of Technology Ladkrabang, Bangkok, Thailand

*E-mail: kcvancha@kmitl.ac.th

Abstract: Hydrolysis reactions are important in the processing of fats and oils by the chemical industry. Fatty acids which produced from these reactions are widely used as raw material in food, cosmetics and pharmaceutical industries. In this work, hydrolysis reaction of palm oil was investigated at 220 to 240 ^oC in batch reactor using α-Al_2O_3 catalyst. The main products of this reaction were fatty acids and glycerol which immiscible in each other and automatically separated into 2 phases. The effects of the amount of catalysts, reaction temperature and reaction time in excess water were investigated to get the optimal condition toward the design product (fatty acids) comparing with those of non-catalytic system. It was found that the rate of hydrolysis was largely improved as the amount of catalysts increased from 2.0 to 5.0 wt.%. An increase in the reaction time from 30 to 180 min and the reaction temperature from 220 to 240 ^oC resulted in an increasing the fatty acid content. The conversion of palm oil to fatty acids with 4.0 wt.% Al_2O_3 using the reaction time of 90 min and reaction temperature at 240 ^oC gave 100% yield of fatty acids. This makes the process feasible for industrial practice.

Introduction

The hydrolysis or splitting of fats/oils to produce fatty acids and glycerol are important for chemical industries. Fatty acids and glycerol are widely used as raw materials in food, cosmetics and pharmaceutical industries [1-3].

Hydrolysis reaction of triglycerides for the production of fatty acids is as follows:

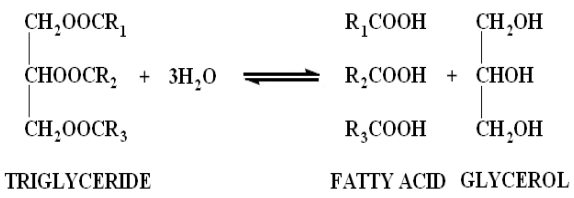

Crude palm oils in the existing industrial processes are usually hydrolyzed without catalyst to fatty acids and glycerol at 250 ^oC under 50 bar pressure within two hours to achieve 96–99% conversion [4, 5].

Recently, an alkali-catalyzed reaction for fatty acid production from oils has been reported. The final product obtained from this reaction gave a reduction in percent yield of fatty acid because it needed a sophisticated purification process to remove the saponified product [6].

A conventional method usually used an enzyme catalyzed process for oil hydrolysis. The advantages of the enzyme hydrolysis technique are that the reaction can be performed under a mild temperature and a simple operational process. Lipases have been successfully employed as biocatalysts in solvent media [7]. But the drawbacks are that the using solvents are expensive, flammable, toxic and involves higher investment costs to meet safety requirements.

In this work, hydrolysis reactions of palm oil to fatty acids were carried out in Parr reactor at 220 to 240 ^oC with varied reaction time from 30 to 180 min using Al_2O_3 as catalyst. The effects of the amount of catalyst, reaction temperature and reaction time in excess water were studied.

Materials and Methods

Materials and catalyst preparation: Refined palm oil was purchased from Lumsung (Thailand) Co, Ltd. Aluminum oxide powder was from J.T.Baker. Al_2O_3 catalyst was prepared by calcinations of α-Al_2O_3 in a muffle furnace at 500 ^oC for 4 h. Surface area of Al_2O_3 catalyst was determined by Gas Adsorption Analyzer (Autosorb-1C, Quantachrome). The nitrogen adsorption was measured at the partial pressure (P/P_0) ranged from 10^{-6} to 1.0 at 77.4 K. The BET surface area analysis of calcined Al_2O_3 at 500 °C is 21 m^2/g. Deuterochloroform, sodium sulfate anhydrous and diethyl ether (analytical grade) were purchased from Sigma Aldrich, Fisher Scientific and Carlo Erba, respectively. Air Zero gas and nitrogen gas were from TIG.

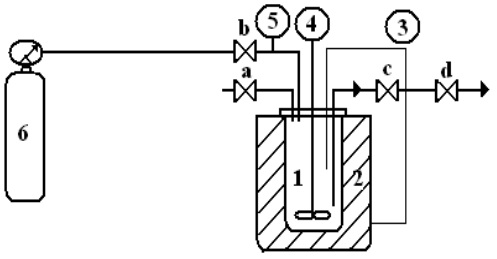

Figure 1. Schematic diagram of experimental apparatus. 1) autoclave; 2) oven; 3) temperature control monitor; 4) mechanical stirrer; 5) pressure control monitor; 6) nitrogen gas tank

Reaction procedures: Hydrolysis reactions were carried out in a 300 ml Parr series reactor which is shown in Fig. 1. The temperature of the reaction vessel can be measured by an iron-constant thermocouple

Table 1: Assignment of ^{1}H NMR Peaks of Oleic acid and Palm Oil

Proton(s)	Functional group	compound/chemical shift, δ (ppm)	
		oleic acid	palm oil
CH_3-C	terminal methyl group	0.88	0.85-0.88
-$(CH_2)_n$-	backbone CH_2	1.14-1.43	1.25-1.30
-CH_2CH_2COOH	β-methylene proton	1.54-1.69	1.61
=CH-CH_2-	α-methylene group to one double bond	1.92-2.11	2.01-2.05
-CH_2COOH	α-methylene group to acid	2.34	-
-CH_2COOR	α-methylene group to ester	-	2.28-2.33
=CH-CH_2-CH=	α-methylene group to two double bonds	-	2.74-2.76
-$COOCH_3$	methyl group of ester	-	-
-CH_2OCOR	methylene group ($C_1$and C_3) of glyceride	-	4.11-4.17
-CHOCOR	methine proton at C_2 of glyceride	-	-

inserted into a tube which was installed at about the middle of reactor. The reactor was placed in a temperature-controlled oven. The reaction procedure was as follows:

First, the catalyst was dispersed in 80 g of water under magnetic stirring. Then, 80 g of palm oil was added and the mixture was heated to a given temperature by oven for up to 90 min. After that, the samples were taken out from the Parr reactor and Al_2O_3 was separated by vacuum filtration. Next, the removal of the glycerol phase (bottom layer) was done and the water in the product (upper layer) was removed at 60-80 ^oC for half an hour. Finally, the product was dried over anhydrous Na_2SO_4 and was collected for chromatographic analysis.

Fatty acid determination by ^{1}H NMR Spectroscopy: The free fatty acid (FFA) products from palm oil were quantitatively determined by NMR spectroscopy [8]. Assignments of the ^{1}H NMR peaks are listed in Table 1.

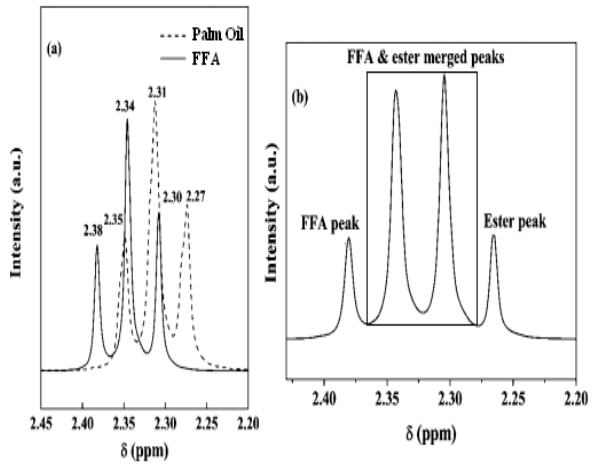

Figure 2. ^{1}H NMR spectrum in α-CH_2 region: (a) glyceryl (palm oil) esters and oleic acid (FFA) and (b) mixture of oleic acid and its glyceryl ester

α-CH_2 peaks of fatty acids appear at δ values higher than those of the glyceryl (palm oil) esters when the quantification of FFA content in palm oil was attempted by ^{1}H NMR. The difference in chemical shift between the fatty acids and ester is shown in Fig.2a. One of the triplet peaks of FFA shifts out of the α-CH_2 region of the ester with two peaks of the FFA triplet merged with the other two of ester as shown in Fig.2b. This can be used to determine the FFA content in palm oil is shown in Fig.3.

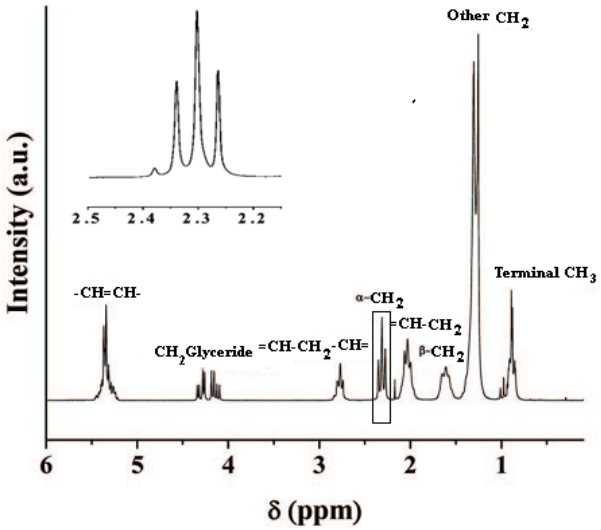

Figure 3. ^{1}H NMR spectrum and assignment of palm oil peak

The triplet peaks appear with an intensity ratio of 1:2:1. The total area corresponding to α-CH_2 of both FFA and ester can be determined by integrating the spectral region at 2.20-2.41 ppm. The area of the unmerged peak of the FFA triplet can be determined by integration of the spectral region at 2.37-2.41 ppm. The weight percentage of FFA in oil is thus

$$\text{Free fatty acids (FFA), \%} = \frac{4 \times \text{area of unmerged peak of } \alpha\text{-}CH_2 \text{ of FFA}}{\text{total area of } \alpha\text{-}CH_2 \text{ of both FFA and ester}}$$

Fatty acid determination by titration: The percentages of FFA in the collected samples were determined by titration [9]. The procedure can be described briefly as follows. First, 1.8–2.0 g of the sample was weighed and transferred to a 100 ml conical flask, and a mixture (50 ml) of ether-ethyl alcohol (2:1, v/v) was added to give a definite and sharp titration end point. Then phenolphthalein indicator was added, and the mixture was titrated against sodium hydroxide (0.1 N) until a permanent pink color persisted for at least 30 s. The weight percentage of FFA was calculated by the following equations.

$$\text{Free fatty acids (FFA), \%} = \frac{56.1 \times \text{ml of alkali} \times \text{N(conc. of NaOH)}}{\text{wt of sample}}$$

Results and Discussion

The effect of catalyst: In this work, the amount of catalyst was varied from 2.0 to 5.0 wt.% while the reaction temperature, calcinations temperature and reaction time were fixed at 220 °C, 600 °C and 60 minutes, respectively. The effect of the amount of catalyst on percent yield of fatty acids is shown in Fig. 4. The conversion was 22% when the reaction proceeded without catalyst. The hydrolysis rate was significantly improved as the amount of catalysts increased from 2.0 to 5.0 wt.%. However, since the percent yield of fatty acid increased a little when the amount of catalyst was further increased from 4.0 to 5.0 wt.%, therefore 4.0 wt.% of Al_2O_3 catalyst was chosen.

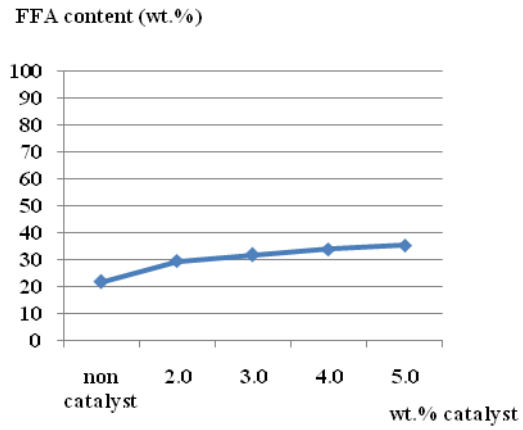

Figure 4. Effect of catalysts on hydrolysis of palm oil; reaction condition: 50% (w/w) water to oil ratio, reaction time = 60 minutes, reaction temperature = 220 °C

The effect of calcination temperature of catalysts: The effect of calcination temperatures on percent yield of fatty acid was investigated. In this work, the calcinations temperatures was varied within a range from 400 to 700 °C. The reactions were carried out with 4.0 wt.% of Al_2O_3 catalyst, reaction time of 60 minutes at 220 °C. The experimental results are shown in Fig. 5. The highest percent yield of fatty acids was achieved using the catalyst calcined at 500 °C.

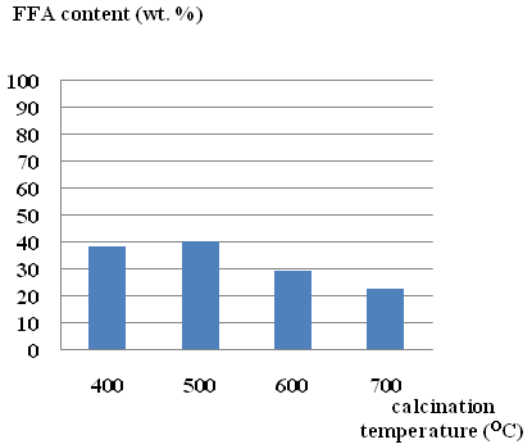

Figure 5. Effect of the calcination temperature on the hydrolysis of palm oil; reaction condition: 50% (w/w) water to oil ratio, 4.0 wt.% of catalysts, reaction time = 60 minutes, reaction temperature = 220 °C

The effect of reaction temperature: Reaction temperature can influence the reaction rate and percent yield of fatty acids. In this work, the reaction temperature was varied within a range from 220 to 240 °C. The experimental results are shown in Fig. 6. The reaction rate was slow at low temperatures and 59% yield of fatty acids were obtained at 220 °C after 90 min of reaction. The fatty acids conversion increased with the increase of reaction temperature to yield 100% of fatty acids at 240 °C.

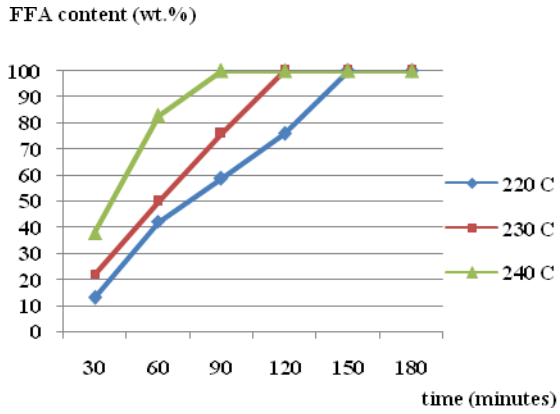

Figure 6. Effect of the reaction temperature on the hydrolysis of palm oil; reaction condition: 50% (w/w) water to oil ratio, 4.0 wt.% of catalysts, reaction temperature 220 °C, 230 °C and 240 °C

When considering both catalytic and non-catalytic reactions as shown in Fig. 7., Al_2O_3 catalyst gave 100% yield of fatty acid at 240 °C while non-catalytic reaction gave 88%. It was clear that the reaction with Al_2O_3 catalyst achieved higher conversion than non-catalytic reaction over the same reaction temperature.

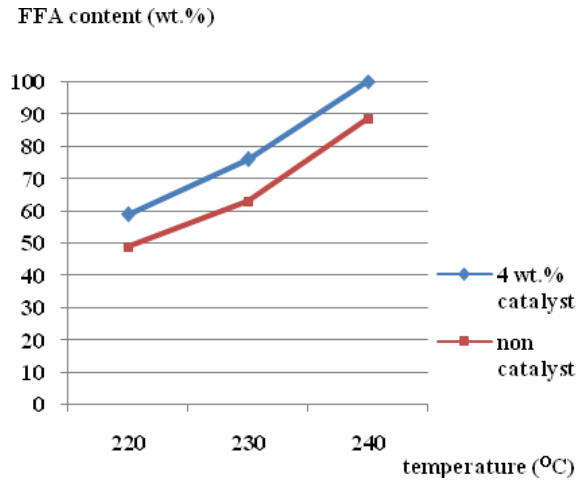

Figure 7. Effect of the reaction temperature on hydrolysis of palm oil; reaction condition: 50% (w/w) water to oil ratio, reaction time = 90 minutes, reaction temperature 220 °C, 230 °C and 240 °C

The effect of reaction time: The effect of reaction time on percent yield of fatty acids was investigated. In this work, the reaction time was varied within a range from 60 to 150 min. The experimental results are shown in Fig. 8. The results show that the percent yield of fatty acids increased with the increase of reaction time for both catalytic and non-catalytic reactions. It also shows that Al_2O_3 catalyst helps to improve the conversion comparing with the non-catalytic reaction over the same reaction time. Al_2O_3 catalyst gave 100% conversion within 90 minutes while non catalytic reaction gave 100% conversion after 120 minutes of the reaction.

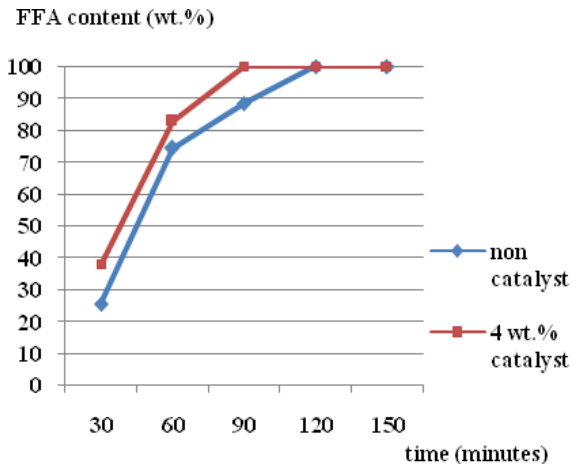

Figure 8. Effect of the reaction time on hydrolysis of palm oil; reaction condition: 50% (w/w) water to oil ratio, reaction temperature = 240 °C

Conclusions

Hydrolysis of palm oil with water was carried out over different amounts of Al_2O_3 catalysts. The results clearly demonstrated that Al_2O_3 catalyst had excellent catalytic activity. Within 90 minutes, 100% yield of fatty acids were obtained from palm oil at 240 °C with 4.0 wt.% of Al_2O_3 catalyst. In addition, the reaction was completed within a shorter time under milder temperature conditions than non-catalytic reaction. Al_2O_3 has potential for industrial application in hydrolysis of palm oil to fatty acids.

References

[1] H.T. Khor, N.H. Tan and C.L. Chua, *JAOCS* **63** (1986), pp. 538–540.
[2] A.N. Anozie and J.M. Dzobo, *Ind. Eng. Chem. Res.* **45** (2006), pp. 1604–1612.
[3] H. Hermansyah, M. Kubo, N. Shibasaki-Kitakawa and T. Yonemoto, *Biochem. Eng. J.* **31** (2006), pp. 125–132.
[4] N.A. Serri, A.H. Kamarudin, and S.N. Abdul Rahaman, *J. Phys. Sci.* **19** (2008), pp. 79–88.
[5] R. Alenezi, G.A. Leeke, R.C.D. Santos, and A.R. Khan, *Chem. Eng. Res. Des.* **87** (2009), pp. 867–873.
[6] E. Minami, and S. Saka, *Fuel* **85** (2006), pp. 2479–2483
[7] I.M. Noor, M. Hasan, and K.B. Ramachandran, *Process Biochem.* **39** (2003), pp. 13–20.
[8] J.K. Satyarthi, D. Srinivas, and P. Ratnasamy, *Energy & Fuels* **23** (2009), pp. 2273–2277.
[9] Y. Liu, Q. Jin, L. Shan, Y. Liu, W. Shen, and X. Wang, *Ultrason. Sonochem.* **15** (2008), pp. 402–407.

n-Pentane conversion over Pt/SiO_2: effect of calcination temperature

N. Peamaroon* and T. Sooknoi

Department of Chemistry, Faculty of Science, King Mongkut's Institute of Technology Ladkrabang, Bangkok, Thailand 10520

*E-mail: s9067151@kmitl.ac.th, jiiiiip@hotmail.com

Abstract: *n*-Pentane transformation to C_5 olefins over Pt/SiO_2 was investigated. The catalyst was prepared by incipient wetness impregnation with H_2Cl_6Pt solution on silica and calcined at (300-500°C). TPR suggested that some of Pt presumably embedded into SiO_2 after calcination. From TPD, Pt/SiO_2 possessed higher acidity, as compared to that of SiO_2; however, the same acid strength was observed. The reaction of *n*-Pentane carried by H_2 was performed in a fixed-bed quartz reactor at 500°C. The products of reaction were detected by an on-line gas chromatograph. It was found that with the same Pt loading (~1wt.%), the catalytic activity of Pt/SiO_2 (7-24% conversion) corresponded to the retaining Pt metal on the surface which was regulated by calcination temperature. Isomerization, cyclization and hydrogenolysis took place in parallel to form products. However due to the presence of acid site, 2-methyl-2-butene was observed as a main product (4-5% yield). At higher contact time, the reaction was significantly effected by H_2 promoting hydroisomerization and hydrocyclization.

Introduction

Pt supported on silica (Pt/SiO_2) was an active catalyst for converting various hydrocarbons to olefins [1-,2,3,4,5,6]. The Pt metal surfaces were effectively active sites which enhanced isomerization, cyclization, and hydronenolysis via alkylidyne intermediates [7], while SiO_2 acted as an inert support. To obtain high dispersion of such metal surfaces, the high surface area SiO_2 should be employed. However; with the flexible structure of SiO_2, some metals were able to penetrate into SiO_2 framework after heat treatment [8,9]. This presumably effected on a number of Pt metal surfaces available for reaction.

In this work, effect of heat treatment (i.e. calcination) on the formation of active Pt metal surfaces on SiO_2 support was investigated. The available Pt surfaces responsible to the catalytic activity for *n*-Pentane transformation will be discussed.

Materials and Methods

SiO_2 (BET = 363 m^2/g) was calcined at 500°C and used as a support. Pt/SiO_2 was prepared by incipient wetness impregnation of SiO_2 with H_2Cl_6Pt solution [10] to obtain ~1wt% Pt loading. The sample was subsequently dried and calcined at 300°C, and 500°C for 6 h.

Temperature programmed reduction (TPR) and temperature programmed NH_3 desorption (TPD) experiments were performed in a quartz micro-reactor. The H_2 consumption and NH_3 desorption were recorded by an on-line TCD detector.

The reaction was carried out at 500°C and ambient pressure. Before the reaction, the catalysts were activated in air (13 ml/min) at 300°C and 500°C for 1 h. After that, the catalysts were reduced by H_2 (15 ml/min) at 500°C for 2 h. The temperature was kept at the reaction temperature (500°C) [11], and a saturated vapor of *n*-Pentane (at -5°C) was carried by hydrogen (a total flow of 15 ml/min) through a fixed bed reactor made with quartz tube (O.D. = 8 mm). The products of the reaction were analyzed by an on-line gas chromatograph (BUCK Scientific Model 910) with FID detector using HP-PLOT column (ϕ = 0.53 mm, L = 30 m).

Results and Discussion

Catalyst Characterization

(a) Temperature Programmed reduction

TPR of Pt/SiO_2 catalysts calcined at 300°C and 500°C were shown in Figure 1. It was found that a major reduction peak was observed in all samples at about 100-200°C. This peak was in agreement with other reports [12,13] for the reduction of PtO to Pt metal.

It can be seen in Figure 1 that, with the same Pt loading (~1wt.%), the peak area for the reduction of PtO to Pt metal (at 100-200°C) decreases with an increase in calcination temperature. The H_2 consumption for reduction of PtO calculated proportionally to the peak area (standardized by CuO) were summarized in Table 1. It was suggested that although the same Pt loading (~1wt.%), the formation of PtO was limited by calcination temperature. The calcination at high temperature (500°C) produced low available PtO species (low H_2 consumption). It was possible that the most of Pt species would embed into SiO_2 [*ผิดพลาด! ไม่ได้กำหนดที่คั่นหน้า,ผิดพลาด! ไม่ได้กำหนดที่คั่นหน้า*]. In contrast, calcination at low temperature (300°C) produced corresponding amount of PtO on the surface (high H_2 consumption) with small amount of embedded Pt species. Such embedded species would be specifically reduced at high temperature as

observed > 500°C. Moreover, calcination at high temperature would not only leave low PtO contents on the surface, but also produce high dispersion of such species. Hence, smaller PtO cluster would be obtained and reduced at lower temperature (100°C), as compared to that of the PtO obtained from calcination at low temperature (reduced at 200°C).

Therefore it can be concluded that, the Pt metals (which was obtained from total PtO reduction and retained for *n*-Pentane transformation) are regulated by calcination temperature. It was calculated stoichiometically to the PtO and also summarized in Table 1.

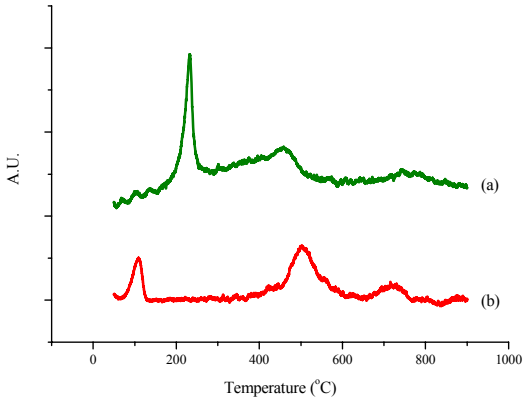

Figure 1. TPR of Pt/SiO_2 (impregnated ~1wt.%) calcined at (a) 300°C, and (b) 500°C.

Table 1. Retained Pt formed after reduction of catalysts calcined at 300°C and 500°C.

Calcination temperature (°C)	H_2 consumption (μmol)	Retained Pt (μmol/$g_{cat.}$)
300	2.41	12.05
500	1.06	5.30

(b) Temperature programmed ammonia desorption

The acidity and acid strength of Pt/SiO_2 and SiO_2 which were treated in the same condition (i.e. calcined at 300°C and then reduced at 500°C) were shown in Figure 2. It could be seen that acid site of SiO_2 was observed by ammonia desorption peak at 175°C. Such acid site contributed from its silanol group [14,15]. However, SiO_2 possessed lower acidity, as compared to that of Pt/SiO_2. This might be due to the interfacial between SiO_2 and Pt metal which was able to produce addition acidity.

Catalytic testing

Catalytic activity of Pt/SiO_2 calcined at 300°C and 500°C for *n*-Pentane transformation was shown in Table 2. It was found that high activity was observed when the catalyst was calcined at 300°C. This was in line with the retained Pt content (Table 1) which was regulated by calcination temperature, as mention previously. As the retained Pt was highly formed, the available Pt metal surfaces (active sites) would be proportionally produced with high contents. Therefore, high catalytic activity for *n*-Pentane transformation would be obtained.

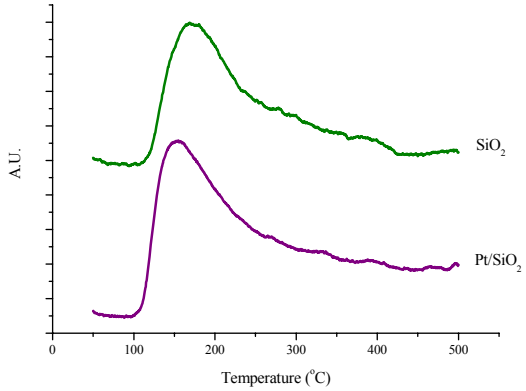

Figure 2. NH_3-TPD of Pt/SiO_2 and SiO_2 (calcined at 300°C and reduced at 500°C).

Table 2. Catalytic activities of Pt/SiO_2 calcined at 300°C and 500°C.

Calcination temperature (°C)	300	500
Reaction temperature (°C)	500	500
Contact time (g h/mol)	49.82	49.82
Conversion (%)	12.74	1.71
Yield (%)		
Ethylene	0.38	0
C_3	0.25	0
Cyclopentane	2.61	0
Isopentane	0.39	0
Cyclopentene	0.90	0
2-methyl-2-butene	4.98	1.03
1-pentene	1.05	0.28
Cyclopentadiene	1.95	0.40
C_6	0.23	0

Effect of contact time for *n*-Pentane transformation over Pt/SiO_2 calcined at 300°C was shown in Figure 3. It was found that all products (ethylene, C_3, cyclopentane, isopentane, cyclopentene, 2-methyl-2-butene, 1-pentene, cyclopentadiene, and C_6) were observed at low contact time. This revealed that isomerization, cyclization, and hydrogenolysis took place in parallel. However, isomerized product (i.e. 2-methyl-2-butene) was observed as a main product. This was due to the effect of acid site of Pt/SiO_2 (as observed from NH_3-TPD) to promote isomerization. As contact time increased, yield of 2-methy-2-butene, cyclopentene and cyclopentadiene

decreased (5.04, 1.67 and 1.94%, respectively) with an increase in isopentane and cyclopentane yield (2.69 and 6.07%, respectively). This revealed that at very high contact time H_2 would enhance hydroisomerization and hydrocyclization. Moreover as contact time increased, hydrogenolyzed products (i.e. ethylene and C_3) were also boosted.

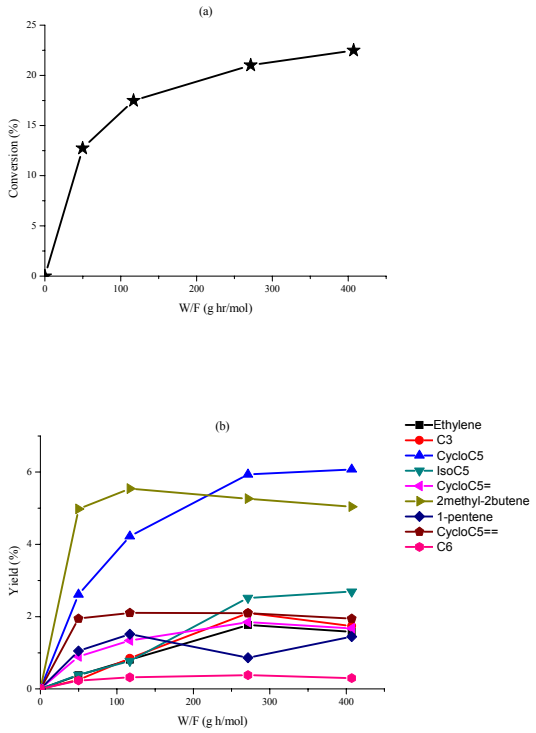

Figure 3. Effect of contact time for *n*-Pentane transformation, catalyst: Pt/SiO_2, pre-treatment: calcination at 300°C followed by H_2 reduction at 500°C, reaction temperature: 500°C, (a) conversion (%), (b) products yield (%).

Conclusion

n-Pentane transformation over Pt/SiO_2 was studied. TPR suggested that some of Pt presumably embedded into SiO_2 after calcination. From TPD, Pt/SiO_2 possessed higher acidity, as compared to that of SiO_2; however, the same acid strength was observed. It was found that with the same Pt loading (~1wt.%), the catalytic activity of Pt/SiO_2 corresponded to the retaining Pt metal on the surface which was regulated by calcination temperature. Isomerization, cyclization and hydrogenolysis took place in parallel to form products. However due to the presence of acid site, 2-methyl-2-butene was observed as a main product. At higher contact time, the reaction was significantly effected by H_2 promoting hydroisomerization and hydrocyclization.

Acknowledgement

The authors would like to thank the SCG chemicals Co., Ltd. for financial support.

References

[1] O.A. Barias, A. Holmen and E.A. Blekkan, *Catal. Today.* **24** (1995), pp.361-364.
[2] J.M. McNamara, S.D. Jackson and D. Lennon, *Catal. Today.* **81** (2003), pp.583-587.
[3] R.D. Cortright, J.M. Hill amd J.A. Dumesic, *Catal. Today.* **55** (2000), pp.213-223.
[4] H. Armendariz, A. Guzman, J.A. Toledo, M.E. Llanos, A. Vazquez and G. Aguilar-Rios, *Appl. Catal. A: Gen.* **211** (2001), pp. 69-80.
[5] Y. Park, F.H. Ribeiro and G.A. Somorjai, *J. Catal.* **178** (1998), pp. 66-75.
[6 Z. Karpinski and T. Koscielski, *J. Catal.* **63** (1980), pp. 313-323.
[7] B.C. Gates, *Catalytic Chemistry*, John Wiley & Son, Inc., USA (1992).
[8] G. Ghiotti, E. Garrone and A. Zecchina, *J. Mol. Catal.* **46** (1988), pp. 61-77.
[9] A. Zecchina, D. Scarano, S. Bordiga, G. Spoto and C. Lamberti, *Advances in Catalysis* **46** (2001), pp. 265-397.
[10] D. Radivojevic, K. Seshan and L. Lefferts, *Appl. Catal. A: Gen.* **301** (2006), pp. 51-58
[11] R.M. Dessau, *United States Patent*, Patent Number: 5,284,986.
[12] J. Arenas-Alatorre, A. Gomez-Cortes, M. Avalos-Borja and G. Diaz, *J. Phys. Chem. B* **109** (2005), pp. 2371-2376.
[13] J. Jia, J. Shen, L. Lin, Z. Xu, T. Zhang and D. Liang, *React. Kinet. Catal. Lett.* **64** (1998), pp. 255-260.
[14] E.F. Voronin, E.M. Pakhlov, A.A. Chuiko, *J. Appl. Spectro.* **64** (1997), pp. 315-318.
[15] Yu. I. Gorlov, M.M. Konoplya, A.A. Chuiko, *Theor. Experim. Chem.* **16** (1981), pp. 263-266.

Synthesis of biolubricant by transesterification and esterification using heterogeneous catalysts: double metal cyanides complexes

K. Sopachart[1], A. Sripusitto[2], C. Huntrakul[2], V. Punsuvon[3] and P. Viravathana[1]*

[1] Kasetsart University /Department of Chemistry, Chatuchak, Bangkok, Thailand
[2] Thai Lube Base Public Company Limited, Au-Udom, Sriracha, Chonburi, Thailand
[3]Center of Excellence-Oil Palm of Kasetsart University, Chatuchak, Bangkok, Thailand

* E-Mail Address: fscipdv@ku.ac.th

Abstract: Biodiesel and biolubricant of esters were typically prepared from palm oil by transesterification of its triglycerides or fatty acids, with alcohols. The higher molecular weight esters are often derived from the higher order of alcohols. In this study, the synthesis of biolubricant was attempted. Three starting materials, all derived from palm product (triglycerides from palm oil, its methyl esters or biodiesel, and free fatty acids from palm fatty acid distillate fraction (PFAD)) were reacted with oleyl alcohol using heterogeneous catalyst (double metal cyanides complexes (DMC)). Both transesterification and esterification means were applied as follows: transesterification of palm oil, and separately biodiesel, with oleyl alcohol; and esterification of palm fatty acid distillate (PFAD) with oleyl alcohol. The reaction was carried out in a batch reactor. The Fe-Zn DMC catalyst was prepared from three solutions, 0.01 mol of $K_4Fe(CN)_6{\cdot}3H_2O$, 0.1 mol of metal chloride ($ZnCl_2$), and tri-block copolymer. The prepared catalyst Fe-Zn DMC was characterized by X-ray diffraction, Fourier transform infrared spectroscopy, and surface analysis. From XRD, the result showed the structure of potassium zinc iron cyanide hydrate: $K_2Zn_3(Fe(CN)_6)_2{\cdot}9H_2O$. FTIR confirmed the bonding between Fe and Zn. From surface analysis, the Fe-Zn DMC catalyst has the BET specific surface area of 10.3 m^2/g, total pore volume of 1.3 cc/g, and average pore diameter of 496.0 Å. The catalytic activity of Fe-Zn DMC for the preparation of biolubricant was studied. The product was analysed by gas chromatography (GC-FID) and %conversion could be calculated except one using palm oil as the starting material due to the complication from unsuccessful removal of glycerol from the reaction mixture. Among three starting materials, PFAD gave 94.60 %conversion to biolubricant.

Introduction

Biodiesel obtained from transesterification of vegetable oil (triglyceride) was the process of employing an alcohol (usually methanol, ethanol, or butanol) in the presence of a catalyst to obtain methyl, ethyl, or butyl esters of the oil with glycerol as a byproduct. Biolubricant reaction was similar to the reaction of biodiesel with the use of higher alcohols to replace methanol or ethanol. Transesterification could be carried out catalytically in different routes namely [1]:

1) Base catalyzed transesterification of the oil with alcohol.
2) Direct acid catalyzed esterification of the oil with alcohol.
3) Hydrolysis of the oil to obtain the fatty acids and then converted to alkyl esters by acid or enzymatic catalysis.

To summarize the preparation, the scheme of transesterification of triglyceride [2] was written as a general equation (a). Transesterification reaction of biodiesel was presented in equation (b) and the esterification was shown in equation (c).

(a) Transesterification of palm oil

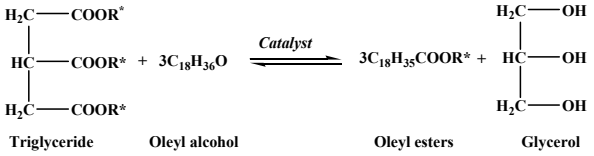

R*= palmitic acid, oleic acid, and linoleic acid in palm product

(b) Transesterification of biodiesel

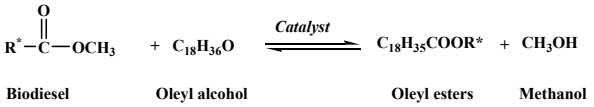

R*= palmitic acid, oleic acid, and linoleic acid in palm product

(c) Esterification of PFAD

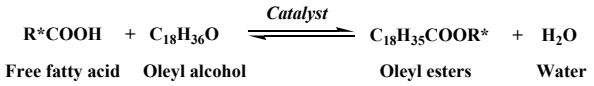

R*= palmitic acid, oleic acid, and linoleic acid in palm product

According to the study of P.S. Sreeprasanth [3], Fe-Zn DMC catalysts were Lewis acidic, hydrophobic (at reaction temperature of about 170 ^oC) and insoluble in most of the solvents including *aqua regia*. The Fe-Zn DMC catalysts could be recycled many times without loss in actively [3].

This work was focused on biolubricant preparation from palm products, including palm oil, biodiesel, and PFAD, as reactants with oleyl alcohol using Fe-Zn DMC as a catalyst. The reactants of biodiesel and PFAD, the byproduct from processed palm oil production, were obtained directly from the manufacturers. In order to report another use of PFAD as a reactant in biolubricant preparation, PFAD was used as obtained from the manufacturer without hydrolysis.

Materials and Methods

All materials such as potassium ferrocyanide ($K_4Fe(CN)_6{\cdot}3H_2O$) was from Merck; zinc chloride

($ZnCl_2$) was from Fisher Scientific; tri-block copolymer or poly(ethylene glycol)-block-poly(propylene glycol))-block-poly(propylene glycol) ($EO_{20}PO_{70}EO_{20}$), n-heptane, and oleyl alcohol (purity 65%) were from Aldrich. Palm products included palm oil, PFAD (Morakot Industries Public Co.,Ltd.), and biodiesel (vegetable oil Co., Ltd). Fatty acids composition in palm oil was 39-40% of palmitic acid, 4% of stearic acid, 40-45% of oleic acid, and 12% of linoleic acid. For methyl esters (purity 99%) using in the analysis of biodiesel, methyl laurate (purity 99%) used as internal standard in the gas chromatography analyses was obtained from Sigma-Aldrich. Oleyl palmitate, oleyl oleate, and oleyl linoleate used as standards in analysis of biolubricant were obtained from Sigma-Aldrich.

Catalyst preparation

Solution 1 was 0.01 mol of potassium ferrocyanide ($K_4Fe(CN)_6{\cdot}3H_2O$) dissolved in 40 ml of double-distilled water. Solution 2 was referred to the solution of 0.1 mol zinc chloride in 18 ml of distilled water and 20 ml of *tert*-butanol. Slowly add solution 2 to the solution1 over 1 h at 323 K under vigorous stirring. After precipitation occurred, add the solution of tri-block copolymer, which could be prepared by dissolving 15g of poly(ethylene glycol)-block-poly(propylene glycol))-block-poly(propylene glycol) ($EO_{20}PO_{70}EO_{20}$) in 2 ml of water and 40 ml of *tert*-butanol, over 5-10 min while stirring and have it stirred for another 1 h. The precipitate was filtered, washed thoroughly with 500 ml double-distilled water to remove the uncomplexed ions, and dried at 298 K for 24 h. The material was heated in oven at 453 K for 4 h.

Catalyst characterization

Powder X-ray diffraction technique was performed to verify the crystal structure of DMC catalysts with Cu Kα radiation. Fourier transform infrared (FTIR) spectroscopy (PERKIN ELMER Inst. Model: system 2000) was used to distinguish the chemical bonding and investigate the elemental composition of DMC. A BET surface area measurement was performed.

Reaction testing

The reaction setup consisted of a batch reactor was shown in Figure 1. To obtain the appropriate condition, the temperature, pressure, time, and molar ratio of palm product to higher alcohol (oleyl alcohol) were varied as shown in Table 1. The results showed the appropriate molar ratio of 1:3 for palm oil to alcohol and 1:2 for both biodiesel and PFAD to alcohol. The starting pressure of 1 bar, the reaction time of 9 h, and 20% wt catalyst were observed. The reaction temperature of 170 ^oC was found to be suitable for palm oil, biodiesel and PFAD as reactants. After the completion of reaction, the reactor was cooled down to room temperature, the Fe-Zn DMC catalyst was separated by centrifugation and filtration. The analysis method for all synthesized biolubricant was summarized as shown in Table 2.

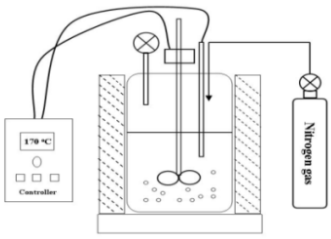

Figure 1. A batch reaction setup.

Table 1: Reaction condition for the synthesis of biolubricant

Palm product	Temperature ^oC	Pressure Bar	Molar ratio	time h	Catalyst % wt
Palm oil	170	1	1:3	9	20
Biodiesel	170	1	1:2	9	20
PFAD	170	1	1:2	9	20

PFAD = Palm fatty acid distillated

Analysis method of biolubricant (Oleyl esters)

GC analysis was conducted by Agilent gas chromatograph (GC6890) in a splitless mode equipped with a flame-ionization detector and capillary column DB-5ht 5%phenylpolydimethylsiloxane (30m x 0.32mm id.; film thickness 0.10 μm), also called GC method (Oleyl esters). Product identification was done by gas chromatography – mass spectrometry (GC-MSD Agilent GC 6890 N series auto sample, 5973 with inert mass selective detector).

Table 2: Summary of analysis methods for the composition of biolubricant and its % conversion

Palm product as reactants	method to analyst biolubricant	Method to calculate % conversion
Palm oil	GC method (Oleyl esters)	-, Identify by GC-MS
Biodiesel	GC method (Oleyl esters)	*GC method (methyl esters)
PFAD	GC method (Oleyl esters)	**Titrate 0.1 M NaOH

- unable to calculate %conversion
*Use eq.1 & eq.2 to calculate %conversion of biodiesel reactant
**Use eq.3 to calculate %conversion of PFAD reactant

For %conversion, when using biodiesel as a reactant, it could be analyzed by GC; in a splitless mode equipped with a flame-ionization detector and capillary column DB-5 MS (30m, 0.32mm, 0.10 μm), also called GC method (methyl esters). Using biodiesel as the reactant, % ester of methyl esters could be calculated from equation 1:

$$C_T = \left(\frac{\sum A - A_{SI}}{A_{SI}} \right) \times \left(\frac{C_{SI} \times V_{SI}}{m} \right) \times 100\% \text{(eq.1)}$$

C_T = % esters of methyl esters.
$\sum A$ = total peak area of methyl esters.
A_{SI} = peak area of internal standard (methyl heptadecanoate).
C_{SI} = concentration of internal standard.
V_{SI} = volume of internal standard.
m = weight of biodiesel (mg).
Also, %conversion can be calculated by equation 2;

$$\%\text{Conversion} = \frac{C_{T_{\text{biodiesel before reaction}}} - C_{T_{\text{biodiesel after reaction}}}}{C_{T_{\text{biodiesel before reaction}}}} \times 100 \quad \text{(eq.2)}$$

For PFAD, % conversion can be determined by titrating unreacted free fatty acid with 0.1 M NaOH.

$$\%\text{Conversion of oleyl esters} = \frac{\text{Vol. of NaOH used (without cat.)} - \text{Vol. of NaOH used (with cat.)}}{\text{Vol. of NaOH used (without cat.)}} \times 100 \quad \text{(eq.3)}$$

Results and Discussion

Fe-Zn DMC catalyst

Fe-Zn double-metal cyanide complexes catalyst after heating at the temperature of 453K for 4 hrs had the white appearance and powder-like.

Catalysts characterization

Powder XRD data for structural analysis was shown in Figure 2. The XRD pattern of Fe-Zn DMC complexes catalyst corresponded to a molecular formula of $K_2Zn_3(Fe(CN)_6)_2 \cdot 9H_2O$ (Potassium zinc iron cyanide hydrate) JCPDS # 33-1061 (at 2θ values (hkl): 16.92° (111), 20.16° (200), 22.33° (210), 24.77° (211), 29.10° (221)) and had the crystallite size of 35 nm.

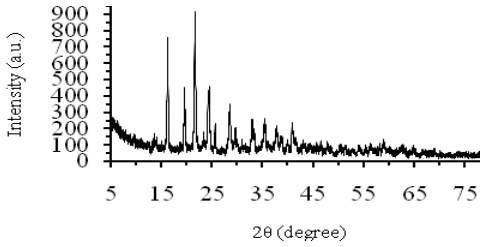

Figure 2. XRD pattern of Fe-Zn DMC complexes catalyst ($K_2Zn_3(Fe(CN)_6)_2 \cdot 9H_2O$).

Fe-Zn DMC complexes showed FTIR band at the wavenumber of 2094 cm^{-1} which corresponded to the reported Fe-Zn DMC complexes at 2096 cm^{-1} suggesting the formation of metal complex of cyanide moiety and Zn^{2+} ions was bridging cyanide ligands. The addition bands at 3632, 1611, 1083, 603, and 495 cm^{-1} and weak bands in the 1100-800 cm^{-1} region confirmed the presence of water molecules and coordinated tert-butanol (1083 cm^{-1}) [3,4]. The FTIR spectrum of the prepared Fe-Zn DMC complex catalyst was shown in Figure 3.

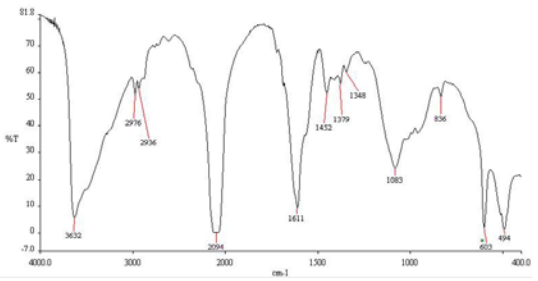

Figure 3. FTIR spectrum of Fe-Zn DMC complexes catalyst ($K_2Zn_3(Fe(CN)_6)_2 \cdot 9H_2O$).

Surface anlysis

The Fe-Zn DMC catalyst had the BET specific surface area of 10.3 m^2/g, total pore volume of 1.3 cc/g, and average pore diameter of 496.0 Å.

Reaction testing and analysis of biolubricant

As mentioned in the previous section on the appropriate condition for biolubricant synthesis, the results from each reactant with oleyl alcohol were as following.

Palm oil vs. oleyl alcohol

For the result of biolubricant synthesis using palm oil as a reactant by transesterification reaction, the product was analyzed by GC and GC-MS. The GC chromatogram of oleyl esters was depicted in Figure 4. The analysis was carried out by comparing the chromatogram to the authentic standard oleyl esters mixed with methyl laurate (internal standard, retention time 3.9 min). The synthesized biolubricant were oleyl palmitate, oleyl oleate, and oleyl linoleate which could be identified at retention time of 17.44, 21.32, and 21.67 min, respectively. The results of synthesized biolubricant from this reaction had the difficulty on byproduct (glycerol) removal. From GC, a large amount of unreacted oleyl alcohol was shown on the spectrum. To identify the presence of oleyl esters in the product, GC-MS was a selected tool. The peaks at 26.05, 34.54, and 35.36 min (Figure not shown here) were expected to be oleyl palmitate, oleyl oleate and oleyl linoleate, respectively. The selected peaks at 26.05 and 35.36 min were confirmed to be oleyl palmitate and oleyl linoleate by the mass spectrums at m/z of 506 and 534, respectively.

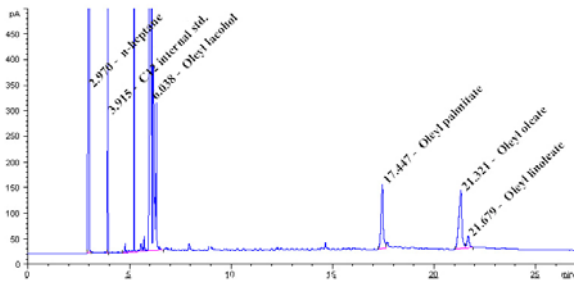

Figure 4. GC chromatogram of palm oil vs. oleyl alcohol [GC method (Oleyl esters)]

Biodiesel vs. oleyl alcohol

Another reaction was the transesterification of biodiesel with oleyl alcohol. The obtained product was the synthesized biolubricant and the byproduct was methanol. The reaction condition was similar to the palm oil vs. oleyl ester reaction except having the molar ratio of 1:2. The product could be analyzed by GC with GC method oleyl esters and the obtained GC chromatogram was shown in Figure 5.

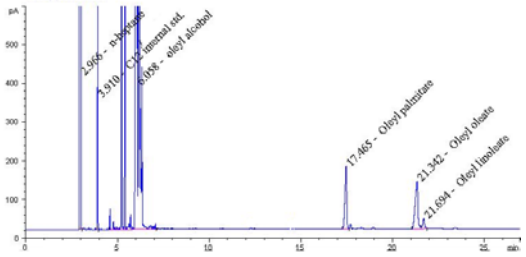

Figure 5. GC chromatogram of biodiesel vs. Oleyl alcohol [GC method (Oleyl esters)]

In order to study %conversion, the methyl esters composition in biodiesel before and after reaction were analysed (the figure of GC chromatogram of GC method (methyl esters) was not shown here). For the calculation, % methyl esters before and after reaction could be calculated by equation 1 and %conversion could be calculated from equation 2. At the reaction time of 9 h, 20%wt of catalyst and temperature at 170 ^{o}C, the result showed 23.8% conversion.

The PFAD reaction with oleyl alcohol

The other reaction was the esterification of PFAD vs oleyl alcohol. The obtained product was the synthesized biolubricant and the byproduct was water. The synthesized biolubricant was analyzed by GC method (Oleyl esters) compared to the standard esters as shown in Figure 6. The chromatogram showed major peaks of oleyl palmitate, oleyl oleate, and oleyl linoleate at the retention time of 16.91, 20.55, and 20.94 min, respectively.

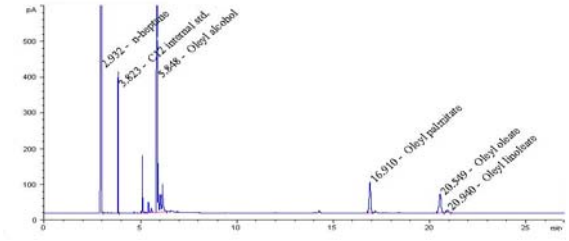

Figure 6. GC Chromatogram of PFAD vs oleyl alcohol [GC method (Oleyl esters)]

For the calculation, %conversion of PFAD could be obtained from equation 3 after titrating the reactants of PFAD mixed with oleyl alcohol and the obtained products with 0.1 M NaOH. The acidity of the reactants and products was corresponded to the volume of NaOH used in titration. With 20%wt Fe-Zn DMC catalyst, the result showed 94.6%conversion at the reaction temperature of 170 ^{o}C the reaction time of 9 h.

Conclusions

In the preparation of biolubricant from palm oil, biodiesel, and PFAD with oleyl alcohol and catalyzed by Fe-Zn DMC $K_2Zn_3(Fe(CN)_6)_2{\cdot}9H_2O$**,** the results showed that palm oil could be used to synthesize biolubricant confirmed by GC and GC-MS but unable to obtain %conversion due to the complication from unsuccessful removal of glycerol from reaction mixture. Biodiesel was also used to prepare biolubricant by transesterification having 23.8 %conversion when using 20 %wt catalyst, the reaction temperature of 170 ^{o}C, and the reaction time 9 h compared to 94.6 %conversion by esterification of PFAD at the same reaction condition.

Acknowledgement

We would like to thank Department of Chemistry, Faculty of Science, Kasetsart University, and Thai Lube Base (Public Company), Ltd for the funding support, Center of Excellence-Oil Palm of Kasetsart University for instrument support, and Postgraduate Education and Research Program in Physic Chemistry (ADB KU-Chem).

References

[1] B. Viswanathan and A.V. Ramaswamy, (2007) htt://203.199.213.48/1135/1/article_as_on_22nd_december.pdf.
[2] V.V. Bokade and G.D.Yadav, *Trans IChemE, Part B.* **85(B5) (**2007), pp. 372-377.
[3] P.S. Sreeprasanth, R. Srivastava, D. Srinivas and P. Ratnasamy, *Applied Catalysis A.* **314** (2006), pp. 148-159.
[4] R. Srivastava, D. Srinivas and P.Ratanasamy, *Journal of catalysis.* 241 (2006), pp. 34-44.
[5] L. Saikia, J.K. Satyarthi, R. Gonnade, D.Srinivas and P.Ratnassamy, *Catal Lett.* **123** (2008), pp. 24-31.
[6] J. Jitputti, B. Kitiyanan, P. Rangsunvigit, K. Bunyakiat, L. Attanatho and P. Jenvanitpanjakul, *Chemical Engineering Journal.* **116** (2006), pp. 61-66.
[7] S. Chen and L. Chen, *Colloid Polym Sci.* **282** (2004), pp. 1033-1038.
[8] S. Chen, P. Zhang and L. Chen, *Progress in organic coatings*. **50 (**2004), pp. 269-272.
[9] S.Chen, Z. Hua, Z. Fang and G. Qi, *Polymer.* **45** (2004), pp. 6519-6524.
[10] L. Reguera, et al, *J. Porous Mater*. **15** (2008), pp. 719-729.
[11] P. Bondioli, *Topics in Catalysis.* **27** (2004), pp. 77-81.
[12] S. Mat Radzi, et al, *J. Oleo Sci.* **54 No4** (2005), pp. 203-209.
[13] S. Mat Radzi, et al, *Journal of Biotechnology.* **8 No3** (2005), pp. 291-298.
[14] P.S. Keng, et al, *J. Bioresource Technology*. **99** (2008), pp. 6097-6104.
[15] P.S. Keng, et al, *J. Industrial crops and products.* **29** (2009), pp. 37-44.

Hydrodeoxygenation of phenol over unsupported $NiMOS_2$ catalysts

D. Tumnantong[1*], B. Yoosuk[2] and P. Prasassarakich[1,3]

[1]Department of Chemical Technology, Faculty of Science, Chulalongkorn University, Bangkok, Thailand
[2]National Metal and Materials Technology Center, 114 Thailand Science Park, Klong 1, Klong Luang, Pathumthani, Thailand
[3]Center of Excellence for Petroleum, Petrochemicals, and Advanced Materials, Chulalongkorn University, Bangkok, Thailand

*E-mail: kid_dee_t@hotmail.com

Abstract: Bio-oil from biomass fast pyrolysis or liquefaction usually consists of high oxygen content compounds (10-50 wt%) especially phenolic compounds. High oxygen content leads to deleterious properties, therefore, the oxygen in oil could be removed in the form of water via hydrodeoxygenation (HDO). Catalysts containing Mo as an active element and Ni or Co as a promoter have been used intensively for HDO process. In this present study, unsupported Mo based sulfide catalysts were prepared from ammonium tetrathiomolybdate (ATTM) and nickel nitrate by using a hydrothermal synthesis method involving water, organic solvent and hydrogen. The activity of these catalysts was investigrated for hydrodeoxygenation (HDO) of phenolic compounds as the major portion of oxygenated species in bio-oil. In this work, the HDO of phenol was carried out in a batch reactor. The results revealed that HDO of phenol proceeded through two major pathways (hydrogenolysis and hydrogenation) and their products were benzene, cyclohexanone, cyclohexene and cyclohexane. Phenol conversion and product distribution were strongly dependent on amount of promoter and HDO reaction conditions.

Introduction

With the depletion of fossil fuels and the growing greenhouse effect, interest in the exploitation of renewable energy has arisen in the past few decades all over the world. Biomass has proved to be a potential resource of renewable energy due to the advantages on its renewal, better quality exhaust emissions and biodegradability, etc., which may ultimately lead to the alternative fuels [1]. The bio-oils can be obtained from biomass by liquefaction or by pyrolysis. The product quality from the liquefaction is better but, as it gives lower yields at higher cost. The characteristics of the bio-oils obtained from the biomass pyrolysis are very different of that obtained from the conventional petroleum. The S-content is negligible while they are rich in oxygenated molecules from phenolic compounds in bio-oil which are responsible for some deleterious properties: high viscosity, low volatility, corrosiveness, immiscibility with fossil fuels, thermal instability and tendency to polymerize under exposure to air. To upgrade bio-oils, oxygen containing compounds have to be removed. [2,3].

The traditional hydrotreating processes used in oil refining can provide a solution for the upgrading of bio-oils. As the heteroatom to be removed from the oil is oxygen, and the oxygen is eliminated in the form of water in the presence of hydrogen, the process is called hydrodeoxygenation (HDO) [4]. The HDO of phenolic compounds also proceeds through hydrogenolysis and hydrogenation reactions [3]. Hydrogenation of the aromatic ring, the main reaction pathway on $CoMo/Al_2O_3$ catalysts, yields the corresponding cyclohexanol that is rapidly dehydrated to yield cyclohexane [5]. As methyl groups are added to phenol, the hydrogenolysis route (C–OH bond cleavage) becomes more important [6]. Direct hydrogenolysis yields monocyclic aromatics (toluene, benzene), hydrogenation of which proceeds with difficulty on Mo, CoMo and NiMo sulfide catalysts [5]. In this work the catalytic hydrodeoxygenation (HDO) with unsupported $NiMoS_2$ catalysts, prepared via hydrothermal method using decomposition of ammonium tetrathiomolybdate (ATTM), was studied using phenol HDO as a model reaction.

Materials and Methods

Catalyst preparation and characterization

The unsupported Mo based sulfide catalysts were synthesized by using hydrothermal method. High-purity ammoniumtetrathiomolybdate ($(NH_4)_2MoS_4$, ATTM) and nickelnitratehexahydrate ($Ni(NO_3)_2{\cdot}6H_2O$) were purchased from Aldrich Chemical Company and were used without further purification. ATTM was dissolved in deionized water in Parr reactor and organic solvent (decalin) was then added to this solution. $Ni(NO_3)_2{\cdot}6H_2O$ was dissolved in the minimum amount of water and was added to the solution to give an mole ratio of Ni/(Ni+Mo). The reactor was purged, then pressurized with hydrogen gas to an initial pressure of 2.8 MPa and heated to 350 ^oC. After 1 h, the unsupported catalysts synthesized were separated and immerged under an organic solvent. More detail on catalyst preparation was described in ref. [7].

Nitrogen adsorption measurements were performed on a Micromeritics ASAP 2020 (Accelerated Surface Area and Porosimetry System), which reported an adsorption – desorption isotherm, BET specific surface area and pore volume. Fresh samples were vacuum dried before the adsorption measurement. X-ray diffraction patterns were recorded on a Scintag Powder Diffractometer with Cu K_α emission, 30 mA 35 KV with a scanning speed of 2 degree/min.

Hydrodeoxygenation

HDO of phenol was carried out in a Parr reactor (250 mL). The reactor was charged with the phenol (0.3 g), decane (19.7 g) and catalyst. The reactor was purged with hydrogen and then pressurized up to initial pressure of 2.8 MPa and variable amount of catalyst (0.19-0.75 wt%). The reactor was heated to the specified temperature and maintained at that temperature for the desired reaction time. The stirring speed was 150 rpm. Then, the reactor was cooled down to room temperature, the gas inside was vented, and the solid and liquid products were rinsed from the reactor. The resulted suspension was filtered under vacuum through a Whatman No. 42 filter paper to recover the catalysts. The liquid products were identified by GC/MS (Agilent Technologies 5975C / inert XL EL/CI MSD 7890A) and quantitatively analyzed by a GC-FID (Shimadzu GC2010) with a DB-wax column. Both GC/MS and GC-FID were programmed from 40 to 230 ^{o}C at heating rate of 10 ^{o}C/min.

Conversions and product selectivities were calculated on molar basis. Phenol conversion was calculated as the ratio of converted phenol to phenol fed. The selectivity was calculated as the ratio of a product to the total products.

Results and Discussion

Phenomenon during catalyst preparation

During the catalyst preparation, the reaction occurred between ATTM and $Ni(NO_3)_2$ in the environment of hydrogen to form the bimetallic sulfide catalyst was suggested as follows [7]:

$$2(NH_4)_2MoS_4 + Ni(NO_3)_2 \rightarrow (NH_4)_2\{Ni(MoS_4)_2\} + 2NH_4NO_3 \quad (1)$$

In the presence of hydrogen, the bimetallic sulfide is formed according to the reactions

$$Ni(MoS_4)_2 + H_2 \rightarrow Ni(MoS_3)_2 + H_2S \quad (2)$$

$$Ni(MoS_3)_2 + H_2 \rightarrow Ni(MoS_2)_2 + H_2S \quad (3)$$

The chemical interaction between Ni and Mo atoms

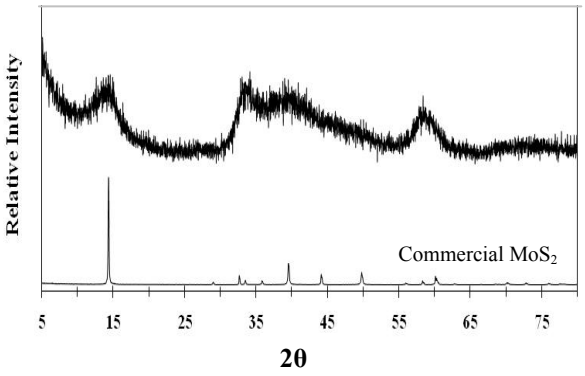

Figure 1. XRD patterns of unsupported NiMo sulfide catalyst and commercial MoS_2.

desired for effective NiMo catalysts implies that a good dispersion of the Ni promoter on MoS_2 is necessary for the formation of a large number of active NiMo sites.

Figure 1. shows the XRD patterns of the unsupported NiMo sulfided catalyst compared with a commercial MoS_2. The unsupported catalyst showed broad diffraction peaks characteristic of a poorly crystallized MoS_2 structure. It was composed of diffraction peaks of poorly crystalline MoS_2 only, indicating that the MoS_2 maintains its structure in the presence of amorphous Ni. The ternary Mo-Ni-S phases were not presented clearly in the NiMo sulfide catalyst prepared. It probably due to the fact that there is overlapping between MoS_2 and Mo-Ni-S phase. Another reason is that the active structures (Mo-Ni-S phase) are possibly presented as small nano-crystals, which cannot be characterized by diffraction method [8]. The BET specific surface area of the unsupported NiMo sulfide catalyst was 245 m^2/g with pore volume of 0.39 cm^3/g.

Hydrodeoxygenation mechanism

The reaction scheme for the HDO of phenol on sulfide catalysts was proposed to proceed through two pathways (hydrogenolysis and hydrogenation) as shown in Scheme 1 [4]. Hydrogenation of the phenol yields the corresponding cyclohexanol and cyclohexanone as intermediate that is rapidly dehydrated to form alicyclic hydrocarbons (cyclohexene and cyclohexane). Direct hydrogenolysis yields benzene.

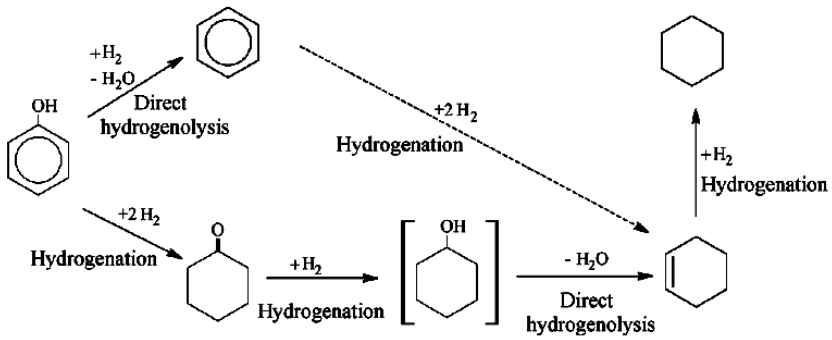

Scheme 1. Reaction scheme for the HDO of phenol on sulfide catalysts [4].

Effect of catalyst amount

The effect of catalyst amount on phenol conversion and product selectivity are shown in Figure 2. The catalyst amount was calculated as follows:

Catalyst amount (wt%) = (weight of catalyst/weight of solution)*100

In the absence of catalyst, 20.0% conversion of phenol was observed. The phenol conversion increased with increasing catalyst amount and 94.6% conversion was reached at the catalyst amount of 0.75 wt%. The products of phenol HDO over unsupported $NiMoS_2$ catalysts were benzene, cyclohexene, cyclohexane and cyclohexanone. The formation of intermediate cyclohexanol was not detected in the liquid products. For the product selectivity results, cyclohexanone was the major product of phenol HDO without catalyst. On the other hand, in the presence of catalyst, the main product was cyclohexane followed by benzene, cyclohexene and cyclohexanone. The total selectivity of free products (cyclohexane, benzene and cyclohexene) increased dramatically when the catalyst was used. These results implied that the $NiMoS_2$ unsupported catalysts help to eliminate oxygen from phenol molecule during HDO reaction.

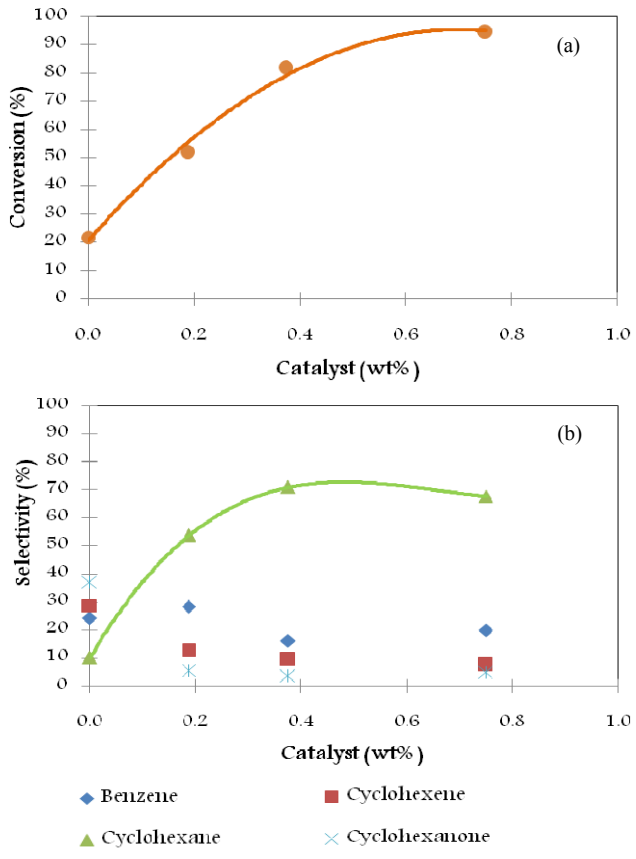

Figure 2. Effect of catalyst amount on phenol HDO over NiMo sulfide at 350°C for 3 h, H_2 pressure = 400 psia and Ni/(Ni+Mo) = 0.20; (a) conversion (b) product selectivity.

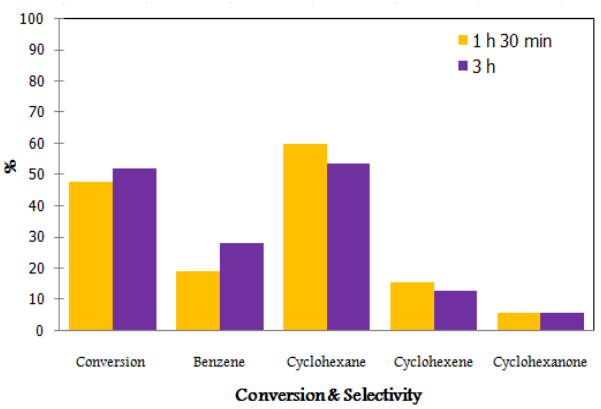

Figure 3. Effect of reaction time on phenol HDO over NiMo sulfide at 350°C, H_2 pressure = 400 psia, Ni/(Mo+Ni) = 0.20 and catalyst amount = 0.19 wt%.

Table 1 Carbon, hydrogen and oxygen amount (wt%) of liquid products from phenol HDO over NiMo sulfide.

Reactant and product	C (wt%)	H (wt%)	O (wt%)
Phenol	76.6	6.4	17.0
B,CH,$CH^{=}$,CHO (1 h 30 min)	86.4	12.5	1.1
B,CH,$CH^{=}$,CHO (3 h)	86.9	12.0	1.1

B = Benzene CH = Cyclohexane
$CH^{=}$ = Cyclohexene CHO = Cyclohexanone

Effect of reaction time

The effect of reaction time on phenol conversion and product selectivity are shown in Figure 3. The phenol conversion increased with increasing of reaction time. The product selectivity was in this order: cyclohexane > benzene > cyclohexene > cyclohexanone for both reaction time, 1.5 and 3 h.

Table 1 presents carbon, hydrogen and oxygen amount (wt%) of liquid products from HDO of phenol over NiMo sulfide. These results showed that unsupported $NiMoS_2$ catalysts was efficient to remove oxygen from phenol, this HDO reaction proceeded through hydrogenolysis and hydrogenation.

Effect of Ni/(Ni + Mo) mole ratio

The effect of Ni/(Mo+Ni) ratio on phenol conversion and product selectivity are shown in Figure 4 and 5. As can be seen, the Ni/(Mo+Ni) ratio of 0.2 showed the highest phenol conversion. However, the conversion decreased when the ratio was further increased. This likely because, excess Ni atoms may partly block the active phase of $NiMoS_2$ catalyst.

From Figure 4, for high catalyst amount and reaction time, selectivities of cyclohexane and benzene were about 68% and 19%, respectively for all Ni/(Mo+Ni) ratio in the range of 0.20-0.56. For low catalyst amount and reaction time, cyclohexane

selectivity was low (30-60%) while cyclohexene selectivity was increased (15-30%). This can be explained that the phenol conversion was low (25-50%) and the HDO was not complete to convert cyclohexene to cyclohexane due to the short reaction time.

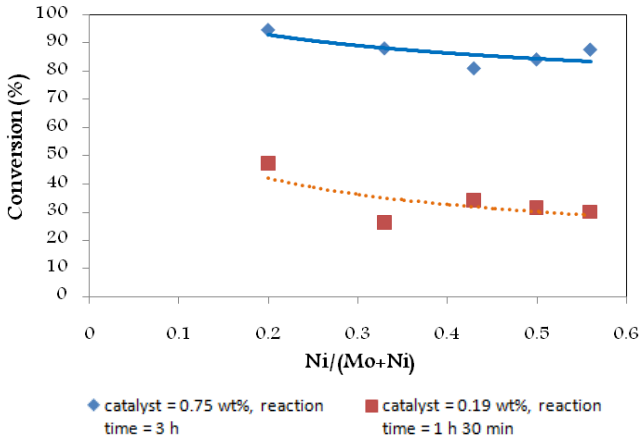

Figure 4. Effect of Ni/(Mo+Ni) mole ratio on conversion of phenol over NiMo sulfide at 350°C, H_2 pressure = 400 psia.

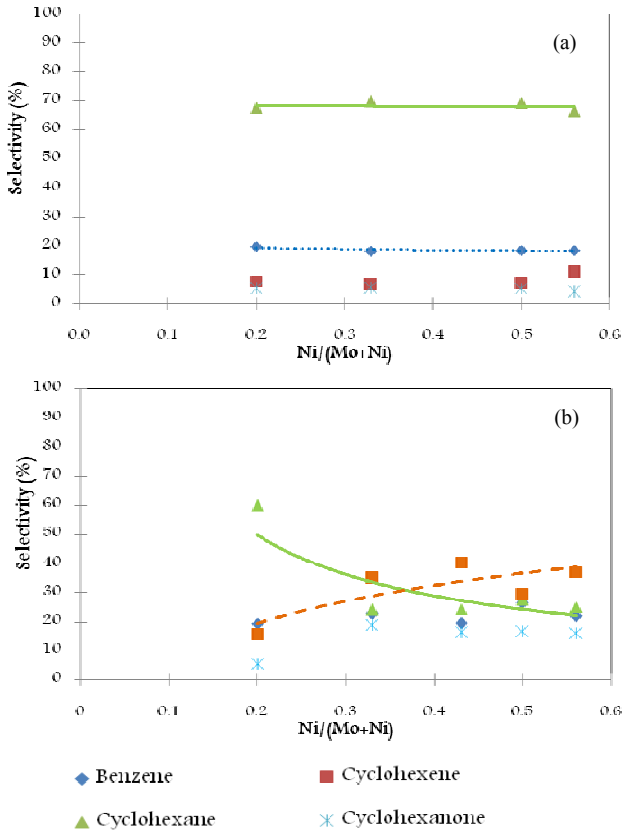

Figure 5. Effect of Ni/(Mo+Ni) mole ratio on product selectivity over NiMo sulfide at 350°C, H_2 pressure = 400 psia; (a) catalyst amount of 0.75 wt%, reaction time of 3 h (b) catalyst amount of 0.19 wt%, reaction time of 1 h 30 min.

Conclusions

The hydrodeoxygenation of phenol over unsupported $NiMoS_2$ catalysts prepared from ammonium tetrathiomolybdate (ATTM) and nickel nitrate by hydrothermal method was studied. The characterization results showed that the hydrothermal method leads to the catalyst with very high surface area. At the Ni/(Ni+Mo) ratio of 0.2, the Mo-Ni-S phases were not presented clearly and the MoS_2 maintains its structure in the presence of amorphous Ni.

The major products of HDO of phenol were benzene and cyclohexane. The results showed that HDO of phenol was proceeded through hydrogenolysis and hydrogenation pathways. Cyclohexanol was not detected in the products. In the presence of $NiMoS_2$ catalyst, HDO process variables affected the phenol conversion and product selectivities noticeably. The conversion increased with increasing catalyst amount and reaction time. The NiMo sulfide catalyst with the Ni/(Ni+Mo) ratio of 0.2 showed the highest activity among all catalysts tested.

Acknowledgement

The authors are gratefully acknowledge the funding support from Excellence Center for Petroleum, Petrochemical and Advance Materials (NCE-PPAM) and National Metal and Materials Technology Center (MTEC), National Science and Technology Development Agency.

References

[1] J. Li, L. Wu and Z. Yang, J. Anal. Appl. Pyrolysis **81** (2008), pp. 199–204.
[2] I. Gandarias, V.L. Barrio, J. Requies, P.L. Arias, J.F. Cambra and M.B. Guemez, Inter. J. Hydrogen Energy **33** (2008), pp. 3485 – 3488.
[3] E. Furimsky, Appl. Catal. A: Gen. **199** (2000), pp. 147.
[4] O.I. Senol, E.M. Ryymin, T.R. Viljava and A.O.I. Krause, J. Mol. Catal. A: Chem. **277** (2007), pp. 107-112.
[5] R. Wandas, J. Surygala and E. Sliwka, Fuel **75** (1996), pp. 687-694.
[6] F.E. Massoth, P. Politzer, M.C. Concha, J.S. Murray, J. Jakowski and J. Simons, J. Phys. Chem. B **110** (2006), pp. 14283-14291.
[7] B. Yoosuk, J.H. Kim, C. Song, C. Ngamcharussrivichai and P. Prasassarakich, Catal. Today **130** (2008), pp. 14–23.
[8] L.S. Byskov, B. Hammer, J.K. Norskov, B.S. Clausen and H. Topsoe, Catal. Lett. **47** (1997), pp.177-182.

Catalytic performance of gold catalyst supported on metal oxide for preferential CO oxidation

K. Tangpoonsinthana[1], A. Leungnaruemichai[3] and S. Pongstabodee[1,2*]

[1] Department of Chemical Technology, Chulalongkorn University, Phaya Thai, Bangkok, Thailand 10330
[2] Center for Petroleum, Petrochemicals, and Advanced Materials, Chulalongkorn University, Bangkok, Thailand
[3] The Petroleum and Petrochemical College, Chulalongkorn University, Bangkok, Thailand 12120

[*] E-mail: sangotib@gmail.com.

Abstract: Hydrogen is an effective clean fuel and generates low emission. Polymer Electrolyte Membrane Fuel Cell (PEMFC) systems use hydrogen as an energy source. However, trace amount of CO in hydrogen stream produced by hydrocarbon steam reforming process reduce the PEMFC efficiency. CO must be removed from the stream. The promising method is preferential oxidation (PROX). Therefore, the aim of this work is to study PROX of CO over monometallic Au, Cu and bimetallic Au-Cu supported on metal oxide. The experimental results elucidate that catalytic performance of bimetallic catalyst is better than monometallic catalyst. The experiments were done in a temperature range of 30 - 190 ^{o}C at atmospheric pressure.

Introduction

Polymer electrolyte membrane fuel cells (PEMFC) are one of interesting alternative applications due to their high efficiency and low emission. PEMFC fed with pure hydrogen can produce power to electrically [1]. The H_2 fuel is usually generated by steam reforming of hydrocarbon or alcohols followed by the water-gas shift (WGS) reaction. The composition of effluents obtained from such process contains about 1% of CO in a large excess of H_2 [2]. CO is a poisonous gas to Pt-electrode in the PEMFC. Therefore, CO must be removed from the feed stream. The preferential oxidation (PROX) is widely used to approach this milestone due to its potential and effectiveness on CO removal.

An effective PROX catalyst should express high activity for CO oxidation as well as low activity for hydrogen oxidation [3]. In recent years, many literatures revealed that supported gold catalyst is very active for PROX at low temperature [1,3 – 8]. In addition, it was demonstrated that the catalytic performance of bimetallic system of gold and other metals was higher CO conversion and selectivity than those of monometallic catalysts [4-7] Copper is an interesting metal to prepare bimetallic system with gold because of its activities and stability for CO removal with minimal loss of H_2 at high temperature [2-3,8].

CeO_2 has been of wide interest because it is thermally stable compound, promote metal dispersion, unique redox properties and high oxygen storage capacity [5,7]. In addition, TiO_2 is an interesting one due to it is unique redox properties.

The aim of the present work was to investigate the catalytic properties of bimetallic Au-Cu and monometallic Au, Cu supported on metal oxide in PROX reaction. Here, we present the effects of different supports, i.e CeO_2 and TiO_2, bimetallic and monometallic catalysts, on the catalytic performance of the prepared catalysts.

Experimental

Support preparation

The support was prepared by deposition-precipitation method. An aqueous solution of 0.1 M $Ce(NO_3)_3{\cdot}6H_2O$ (Merck) was adjusted to pH 9 by drop wise addition of Na_2CO_3 (Merck). The latter was heated to 80 ^{o}C for 1 h. Then, the precipitate was washed with deionized water. The support was dried overnight at 110 ^{o}C and calcined at 500 ^{o}C for 5 h in air.

Catalyst preparation

The 1 wt.% catalysts were obtained by deposition-precipitation. The appropriate amount of an aqueous solution of $HAuCl_4{\cdot}3H_2O$ (Merck) and $Cu(NO)_2{\cdot}3H_2O$ (Merck) were mixed with support then was adjusted pH to 9 by Na_2CO_3. The latter was heated to 80 ^{o}C for 1 h. Then, the precipitate was washed with deionized water. The support was dried overnight at 110 ^{o}C and calcined at 350 ^{o}C for 2 h in air.

Catalyst characterization

The Brunauer-Emmett-Teller (BET) method, using a Quantachrome Corporation Autosorb, was used to analyze the surface area and pore volume size of the prepared catalysts by N_2 adsorption/desorption at -196 ^{o}C. Prior to analysis, the samples were degassed at 300 ^{o}C for 2 h.

The scanning electron microscope (SEM) was used to indicate the crystal morphology of the catalysts.

Catalytic activity

Catalytic activity was carried out in a U-tube reactor (i.d. 6 mm) mounted in the constant temperature zone of an electric furnace. A sample of 100 mg was packed between two layers of glass wool.

Prior to reaction, the catalysts were treated in H_2 at 400 ^oC for 2h. The catalytic activity was investigated in temperature range of 30 – 190 ^oC. The feed stream contained 40% H_2, 1% CO, 1%O_2 and balance with He at the total flow rate of 50 ml min^{-1} under atmospheric pressure. The effluent gas was detected by an on-line gas chromatograph equipped with a carbosphere column and a thermal conductivity detector (TCD). The CO conversion was based on the carbon dioxide formation. The CO selectivity was defined as the ratio of O_2 consumption for the CO oxidation over the total O_2 consumption.

Results and Discussion

Catalyst characterization

Table 1. Characterization of the various supports

Support	BET surface area (m^2/g)	Pore size (nm)
TiO_2	8.8	7.96
Commercial CeO_2	1.6	11.74
Synthetic CeO_2	59.4	4.12

From Table 1, the results indicated that the order of surface area was synthetic CeO_2 >> TiO_2 > commercial CeO_2. The surface areas of synthetic CeO_2, TiO_2 and commercial CeO_2 were 59.4, 8.8 and 1.6 m^2/g, respectively. Considering pore size of these supports, it was found that pore size of the synthetic CeO_2 is only 4.12 nm whereas the pore size of TiO_2 and commercial CeO_2 are 7.96 and 11.74 nm, respectively.

The SEM images of these various supports are shown in Figure 1. Synthetic CeO_2 shows the smallest crystal shaped morphology. This can lead to the highest surface area, as shown in Table 1. Meanwhile, the commercial TiO_2 shows the largest crystal morphology.

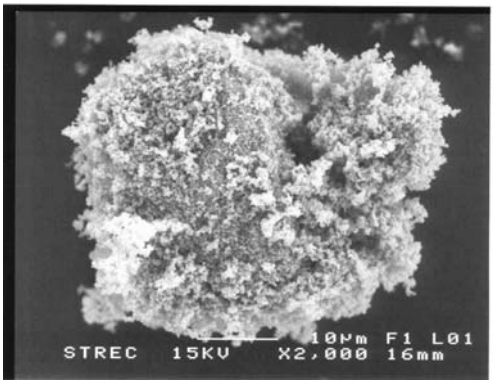

(a)

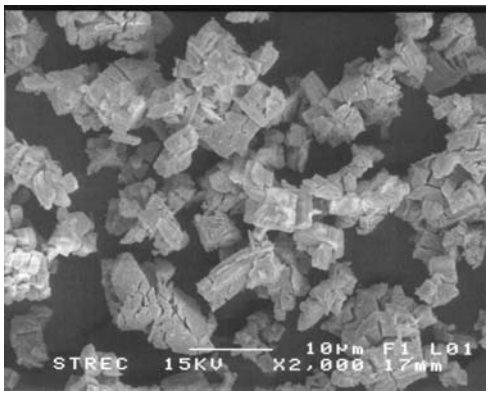

(b)

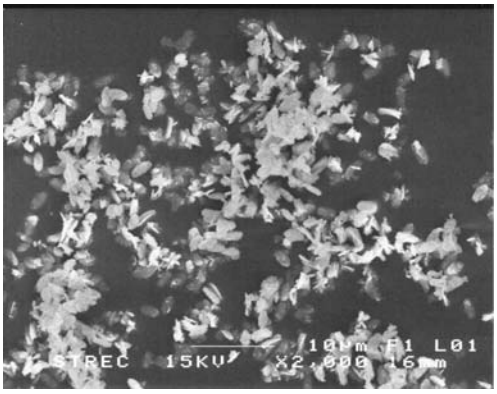

(c)

Figure 1. SEM images of various supports: (a) TiO_2 (b) commercial CeO_2 and (c) synthetic CeO_2.

Catalytic activities

Effect of support on the Au catalyst

A comparison of the catalytic performance of 1 wt.% Au catalysts supported on TiO_2 and synthetic CeO_2 in term of CO conversion and selectivity is shown in Figure 2. Higher CO conversion and selectivity was obtained when using Au/CeO_2 catalyst. The complete CO conversion was achieved in a range of reaction temperature of 30 – 50 ^oC for Au/CeO_2 catalyst. However, when the reaction temperature was increased from 50 to 190 ^oC, the CO conversion was decreased from 100% to 82%. This is due to a competition of H_2 oxidation on the same active site of the catalyst. The Au/TiO_2 catalyst showed the CO conversion less than 10% in a whole range of reaction temperature and the maximum CO selectivity was around 25% at 130 ^oC.

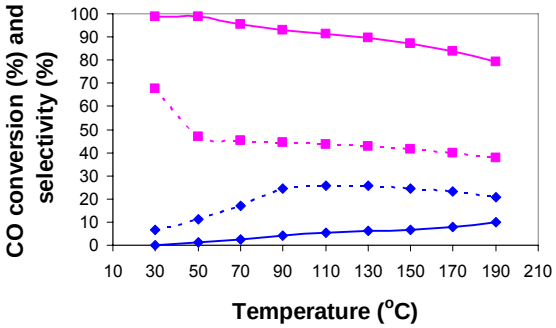

Figure 2. Catalytic activities of 1wt.% gold catalyst supported on (■) synthetic CeO_2 and (♦) TiO_2; (—) CO conversion; (---) CO selectivity.

Effect of support on the Cu catalyst

A comparison the catalytic activities of Cu/TiO_2 and Cu/CeO_2 is shown in Figure 3. We found that the results have a similar trend as previous results. The Cu/CeO_2 catalyst has higher catalytic activities than Cu/TiO_2 catalyst for a whole range of reaction temperature. The activity of catalysts increased with increasing temperature until reaching a maximum CO conversion and selectivity. The maximum CO conversions of catalysts were obtained at 150 – 170 °C for Cu/CeO_2, whereas only 50% conversion was obtained at 190 °C for Cu/TiO_2 catalyst. The selectivity for Cu/CeO_2 catalyst was increased from 10% to 100% when increasing temperature from 30 °C to 130 °C. After that the selectivity was then decreased dramatically at above 130 °C.

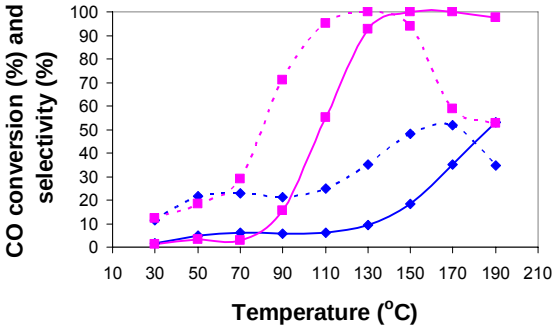

Figure 3. Catalytic activities of 1 wt.% Cu catalyst supported on (■) synthetic CeO_2 and (♦) TiO_2; (—) CO conversion; (---) CO selectivity

Effect of support on AuCu catalyst

Figure 4 shows the catalytic performance Au-Cu supported on TiO_2 and synthetic CeO_2 catalysts. The total metal loading was 1 wt.% at a Au:Cu ratio of 1:1. The result indicated that $AuCu/CeO_2$ catalyst expresses higher activities than $AuCu/TiO_2$ catalyst. Complete CO conversion was obtained at 70 °C for $AuCu/CeO_2$ catalyst while the maximum CO selectivity (96%) was achieved at 30 °C. Both CO conversion and selectivity were decreased with temperature due to H_2 oxidation.

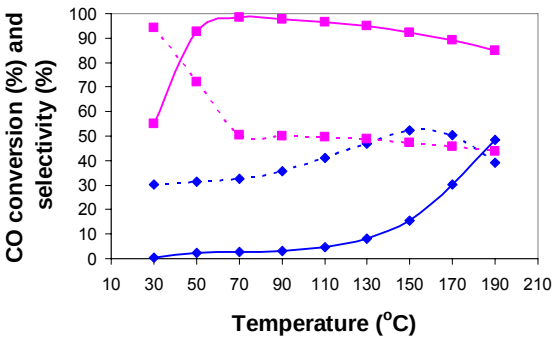

Figure 4. Catalytic activities of 1wt.%(1:1)AuCu catalyst supported on (■) synthetic CeO_2 and (♦) TiO_2; (—) CO conversion; (---) CO selectivity.

From above results, it can be concluded that the synthetic CeO_2 supported catalysts expresses higher catalytic performance than the TiO_2 supported catalysts due to its higher surface area.

Effect of metal on synthetic CeO_2.

Figure 5 shows the comparison CO conversion between monometallic (1% Au/CeO_2 and 1% Cu/CeO_2) and bimetallic (1%(1:1)$AuCu/CeO_2$) catalysts. These catalysts expressed complete CO conversion at different reaction temperature such as 30 – 50 °C for Au/CeO_2. 70 °C for $AuCu/CeO_2$ and 130 °C for Cu/CeO_2. For Au/CeO_2 and $AuCu/CeO_2$ catalysts, the activity for CO conversion is higher at low temperature and decreases with temperature. On the other hand, Cu/CeO_2 catalyst presented high activity at high temperature. The performances of Cu/CeO_2 catalyst increased with reaction temperature.

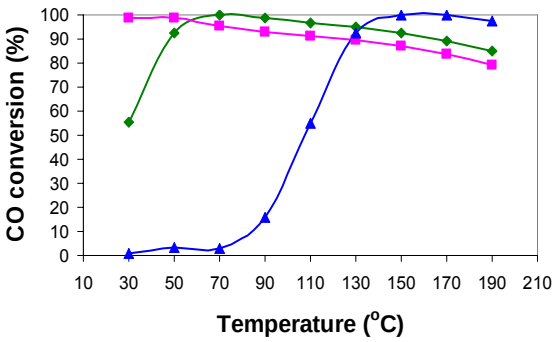

Figure 5. Catalytic performance on CO conversion of: (■) 1wt.%Au/CeO_2, (▲) 1wt.%Cu/CeO_2 and (♦) 1wt.%(1:1)$AuCu/CeO_2$.

The CO selectivity over Au/CeO_2, Cu/CeO_2 and $AuCu/CeO_2$ catalyst are shown in Figure 6. Cu/CeO_2 catalyst exhibited 100% CO selectivity at 130 °C. The selectivity for 1wt.%(1:1) $AuCu/CeO_2$ is higher than 1wt.%Au/CeO_2 at any temperature.

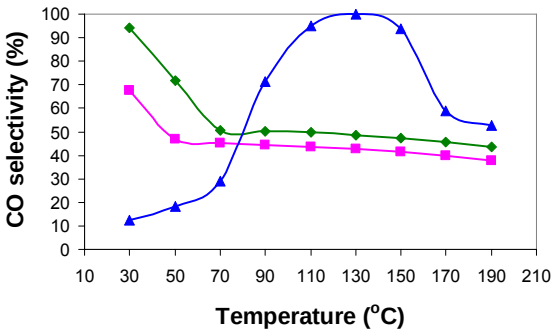

Figure 6. Catalytic performance on CO selectivity of: (■) 1wt.%Au/CeO_2, (▲) 1wt.%Cu/CeO_2 and (♦) 1wt.%(1:1)AuCu/CeO_2.

Effect of CeO_2 supported AuCu catalyst

The AuCu/CeO_2 catalysts were prepared with different CeO_2 supports, synthetic and commercial, at a Au:Cu ratio of 1:1. Figure 7 shows the CO conversion and selectivity of AuCu/CeO_2 catalysts as a function of temperature. It can be seen that CO conversion for AuCu supported on synthetic CeO_2 is higher than that of AuCu supported on commercial CeO_2 due to its higher surface area (see Table 1). Complete CO conversion was obtained at 70 °C for the synthetic CeO_2 supported catalyst meanwhile the maximum CO conversion for the commercial CeO_2 supported catalyst was 75% at 190 °C.

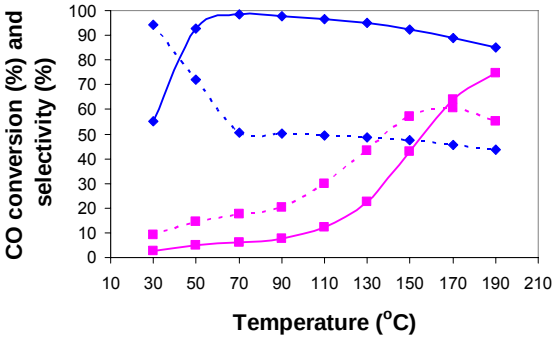

Figure 7. Catalytic activities of (♦) synthetic CeO_2 and (■) commercial CeO_2 supported 1wt.%(1:1)AuCu catalyst.; (—) CO conversion; (---) CO selectivity

Effect of commercial supported AuCu catalyst

Figure 8 shows the catalytic performance of bimetallic Au-Cu supported on commercial TiO_2 and commercial CeO_2 catalysts. The total metal loading was 1 wt.% at a Au:Cu ratio of 1:1. The result indicated that the activity of AuCu supported on commercial CeO_2 was higher than AuCu supported on commercial TiO_2 due to higher oxygen storage capacity.

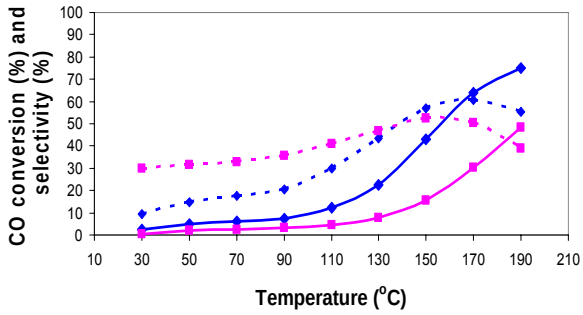

Figure 8. Catalytic activities of (♦) commercial CeO_2 and (■) commercial TiO_2 supported 1wt.%(1:1)AuCu catalyst.; (—) CO conversion; (---) CO selectivity

Conclusions

From the results, we can conclude the catalytic activities for preferential CO oxidation in the temperature range of 30 – 190 °C as follows.

The support which has smaller crystal shaped morphology and higher specific surface area expresses higher activities.

Complete CO conversion was achieved at 30 – 50 °C for 1wt.%Au/CeO_2, at 70 °C for 1wt.%(1:1)AuCu/CeO_2, at 130 °C for Cu/CeO_2 catalyst. The experimental results revealed that bimetallic catalyst (AuCu/CeO_2) displays higher performance than monometallic catalyst (Au/CeO_2) at low reaction temperature

Acknowledgement

This work was fully supported by the Center for Petroleum, Petrochemicals and Advanced Materials.

References

[1] C.Galletti, S. Fiorot, S. Specchia, G. Saracco, and V. Specchia, *Chem. Eng. J.* **134** (2007), pp. 45 – 50.

[2] A. Gómez-Cortès, Y. Márquez, J. Arenas-Alatorre and G. Díaz, *Catal. Today* **133 – 135** (2008), pp. 743 – 749.

[3] S. Kandoi, A.A. Gokhale, L.C. Grabow, J.A. Dumesic and M. Mavrikakis, *Catal. Lett.s* **93** (2004).

[4] S. Monyanon, S. Pongstabodee and A. Luengnaruemitchai, *J. Chin. Institure Chem. Eng.* **38** (2007), pp. 435 – 441.

[5] S. Monyanon, S. Pongstabodee and A. Luengnaruemitchai, *J. Power Sources* **163** (2006), pp. 547 – 554.

[6] P. Naknam, A. Luengnaruemitchai, S. Wongkasemjit and S. Osuwan, *J. Power Sources* **165** (2007), pp. 353 – 358.

[7] B. Zhu, Q. Guo, X. Huang, S. Wang, S. Zhang, S. Wu and W. Huang, *J. Mol. Catal.* **249** (2006) 211 – 217.

[8] G. Avgouropoulos, J. Papavasiliou, T. Tabakova, V. Idakiev and T. Ioannides, *Chem. Eng. J.* **124** (2006), pp. 41 – 45.

[9] E.D. Park, D. Lee and H.C. Lee, *Catal. Today* **139** (2009), pp. 280 – 290.

Effect parameter of coconut oil to biofuel by catalytic cracking

T. Piyanuch*, V. Tharapong

Department of Chemical Technology, Faculty of Science, Chulalongkorn University, Phayathai Road, Patumwan, Bangkok, Thailand 10330

* E-Mail: ka_pi@hotmail.com

Abstract: In this work, the catalytic cracking of coconut oil to biofuel using HZSM-5 catalyst in a batch reactor was investigated. The effects of reaction temperature (360-410 ^{o}C), residence time (30-60 mins), amount of catalyst (0.01-0.1 g)/ 20 g of coconut oil and initial hydrogen pressure (1-3 bar) were studied over the yield of gas and yield of liquid as fuel. Design of experimental method 2^k factorial was used to determine the parameter which affect to catalytic cracking of coconut oil to biofuel. The results showed that when increasing reaction temperature the yield of gas was increased from 13.7032 to 32.0407 wt%, the yield of liquid was decreased from 77.6001 to 61.4791 wt% and when increasing residence time the yield of gas was increased from 19.7134 to 26.0305 %wt, the yield of liquid was decreased from 71.4776 to 67.6016 wt%. The increasing amount of catalyst and initial hydrogen pressure are not significant for the yield of gas and yield of liquid.

Introduction

Biofuel is defined as gas or liquid fuel that can be produced from the utilization of biomass substrates and can serve as a (partial) substitute for fossil fuels. The production of biofuel such as diesel and gasoline fractions as an alternative fuel obtained from vegetable oils or fats are environmentally friendly since they are free of nitrogen and sulfur compounds. By-product of coconut-pulp such as coconut oil cab be convert to a usable fuel product is by catalytic cracking reactions [1-5].

There are several methods for the conversion of vegetable oils to biodiesel of which the most common is the transesterification process, in which an alcohol is reacted with the oil to form esters and glycerol. Another method for the conversion of vegetable oils to a usable fuel product is by catalytic cracking reactions.

In the case of production of biofuel from vegetable oils such as cottonseed oil [2], palm oil [3], cooking oil [4], canola oil [5].

The objective of this work is to study on the yield of gas and yield of liquid as fuel using method 2^k factorial to determine parameters affectting to catalytic cracking of coconut oil to biofuel in micro-reactor.

Materials and Methods

Starting material and chemicals

Coconut oil was obtained from Karnchanakaipani industry, Thapsakae, Prachuapkhirikhan, Thailand.

HZSM-5 powder micro porous catalyst with the ratio of Si/Al 39.

Hydrogen gas (purity 99.99%) used to trace the effected of initial pressure of hydrogen gas which supplied by Praxair Co., Ltd. Bangkok, Thailand.

The 250 cm^3 micro-reactor, SS 316 stainless-steel pressure cylindrical reactor was used for this study on catalytic cracking of coconut oil to biofuel and is shown in figure 2.1. The micro-reactor composed a pressure gauge, safety valve, valve for admitting and releasing gases.

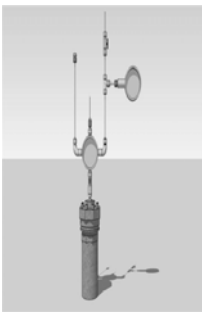

Figure 2.1. Stainless steel micro-reactor [6-7].

Reaction experimental unit with the rotating machine, a speed motor was used to control the shaking of cylindrical stainless steel micro-reactor at 80 rpm. The reactor was heated by 400 watt injection heater the temperature was measured by thermocouple type K having 1.6 mm. diameters with an accuracy of ± 20 ^{o}C by means of a programmable temperature controller.

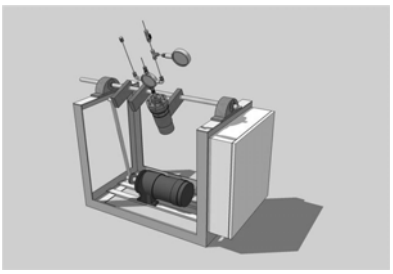

Figure 2.2. Reaction experimental unit [6-7].

Vacuum filtration and 40 nm sieve filter uses to filtrate the liquid products and solid products from vacuum pump.

Figure 2.3 Vacuum pump (left) and set of vacuum filter (right) [6-7].

Apparatus

20 grams of coconut oil were put in the 316-stainless steel cylindrical micro-reactor. 0.01-0.1 grams of HZSM-5 catalyst was added and hydrogen gas was filled into inside the reactor. The reactor with insulator was heated from room temperature to desired temperature and maintain temperature for any reaction times which shown as table 3.2. After outgassing at room temperature, the yield of gas, the yield of liquid and the yield of solid were calculated as equations 2.1, 2.2 and 2.3 respectively.(yield of solid was collected by vacuum filtration to separate from liquid)

$$Y_{Gas} = \frac{((W_1 + W_2 + W_3) - W_4)}{W_2} * 100 \quad 2.1$$

$$Y_{Solid} = \frac{W_5}{W_2} * 100 \quad 2.2$$

$$Y_{liquid} = 100 - (Y_{Gas} + Y_{Liquid}) \quad 2.3$$

Which W_1, W_2, W_3, W_4, and W_5 represented to weight of reactor, weight of coconut oil, weight of catalyst, weight of reactor and product after outgassing and weight of solid products respectively.

Results and Discussion

The 2^4 Experimental Design

2^k experimental design is an effective method to determine how various reaction parameters affect the system. It is very useful in the primary experimental study when there are many factor effects to determine. The interesting parameters in the study for catalytic cracking of coconut oil using HZSM-5 are temperature (A), residence time (B), amount of catalyst (C) and initial pressure hydrogen (D) each considered at three levels namely; low (-1), central (0), high (1) as shown in table 3.1. For the two level factorial design, the yield of gas, liquid, solid product were defined as the response by a change in the level of these factors. The treatment combination in standard order can be written as (1), a, b, ab, c, ac, bc, abc, d, ad, bd, abd, cd, acd, bcd, and abcd. The experiments were designed to run a double replicate to obtain the response data as the yield of gas, liquid and solid represented in table 3.2.

Accordingly, 35 experiments were conducted with the first 32 experiments organized in a factorial design and the remaining 3 involving the replication of the central points for each stage.

Table 3.1. Coded independent variables used in model.

Factor	Factor code	Unit	Low (-1)	Central (0)	High (1)
Reaction Temperature	A	^oC	360	385	410
Residence time	B	mins	30	45	60
Amount of catalyst	C	g	0.01	0.055	0.1
Initial hydrogen pressure	D	bar	1	2	3

Table 3.2. Yield of product from catalytic cracking of coconut oil using HZSM-5.

Treat-ment	Factor				%yield of gas	%yield of liquid	%yield of solid
	A	B	C	D			
1	-	-	-	-	14.74	75.15	10.11
	-	-	-	-	11.34	79.72	8.94
2	+	-	-	-	29.12	62.24	8.65
	+	-	-	-	27.26	65.25	7.49
3	-	+	-	-	23.72	71.86	4.42
	-	+	-	-	18.85	75.11	6.04
4	+	+	-	-	33.45	62.51	4.04
	+	+	-	-	29.92	64.57	5.51
5	-	-	+	-	14.40	78.01	7.60
	-	-	+	-	15.91	76.13	7.96
6	+	-	+	-	25.93	67.55	6.52
	+	-	+	-	27.16	67.39	5.44
7	-	+	+	-	12.83	74.99	12.18
	-	+	+	-	13.04	79.19	7.77
8	+	+	+	-	36.63	59.23	4.13
	+	+	+	-	38.54	53.57	7.90
9	-	-	-	+	5.52	83.15	11.33
	-	-	-	+	7.94	80.59	11.47
10	+	-	-	+	26.99	66.72	6.29
	+	-	-	+	27.01	65.93	7.06
11	-	+	-	+	13.28	77.48	9.24
	-	+	-	+	15.60	77.71	6.69
12	+	+	-	+	32.85	60.38	6.77
	+	+	-	+	35.88	56.66	7.46
13	-	-	+	+	6.68	80.39	12.93
	-	-	+	+	8.58	76.50	14.92
14	+	-	+	+	35.03	58.67	6.30
	+	-	+	+	31.80	60.25	7.95
15	-	+	+	+	16.10	79.44	4.46
	-	+	+	+	20.72	76.17	3.11
16	+	+	+	+	37.52	57.10	5.38
	+	+	+	+	37.56	55.64	6.79
17	0	0	0	0	23.98	70.68	5.33
	0	0	0	0	22.45	71.73	5.82
	0	0	0	0	20.63	72.85	6.52

The procedure to analyze the data from a single factorial design is providing through examination of a normal probability plot. The contrast constants for the 2^4 design were calculated and the normal probability plot of yield of gas is illustrated in figure 3.1. From the normal probability plot, all of the effects that lie along the line are negligible, whereas larger effects deviate from the straight line. Therefore, the important effects that emerge from this analysis are the main effect of reaction temperature (A) and residence time (B), as define in table 3.1.

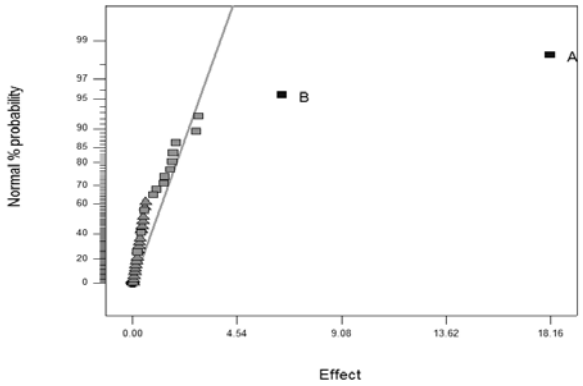

Figure 3.1. Normal probability plot of the effects which shows the effect of catalytic cracking of coconut oil using HZSM-5 to yield of gas.

The analysis of variance (ANOVA) display for this model is shown in table 3.3. and the test statistic F-Value shows the effect of reaction temperature, residence time are significant to yield of gas at 95 % confidence interval.

Table 3.3. Analysis of variance for 2^k experimental design in catalytic cracking of coconut oil using HZSM-5 to yield of gas.

Source of variation	Sum of squares	Degree of freedom	Mean Square	F Value	P Value
A	2639.26	1	2639.26	246.64	<0.0001
B	337.10	1	337.10	31.50	<0.0001
Error	331.73	31	10.7		
Total	3308.09	33			

ANOVA was carried out to establish its significance. The model for yields of gas in terms of coded factors and in terms of actual factor are shown in equations 3.1 and 3.2.

Gas = 22.87 + 9.17A + 3.16B 3.1
Gas = -127.80245 + 0.36675A + 0.21057 3.2

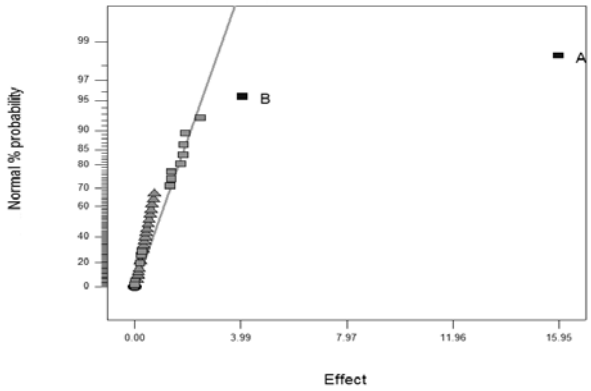

Figure 3.2. Normal probability plot of the effects which shows the effect of catalytic cracking of coconut oil using HZSM-5 to yield of liquid.

Figure 3.2. is a normal probability plot of the effects which shows the effect of reaction temperature (A) and residence time (B), are significant to the catalytic cracking of coconut oil to yield of liquid. The analysis of variance (ANOVA) display for this model is shown in table 3.4. and the test statistic F-Value shows the effect of reaction temperature, residence time are significant to yield of liquid at 95 % confidence interval.

Table 3.4. Analysis of variance for 2^k experimental design in catalytic cracking of coconut oil using HZSM-5 to yield of liquid.

Source of variation	Sum of squares	Degree of freedom	Mean Square	F Value	P Value
A	2034.43	1	2034.43	227.28	<0.0001
B	131.22	1	131.22	14.66	0.0006
Error	277.49	31	8.95		
Total	2443.14	33			

The model for yields of liquid in terms of coded factors and in terms of actual factor are shown in equations 3.3 and 3.4.

Liquid = 69.54 - 8.06A - 1.94B 3.3
Liquid = 199.48531 - 0.32242A - 0.12920B 3.4

Univariate study for the catalytic cracking of coconut oil using HZSM-5 on yield of gas and yield of liquid

The effect of reaction temperature

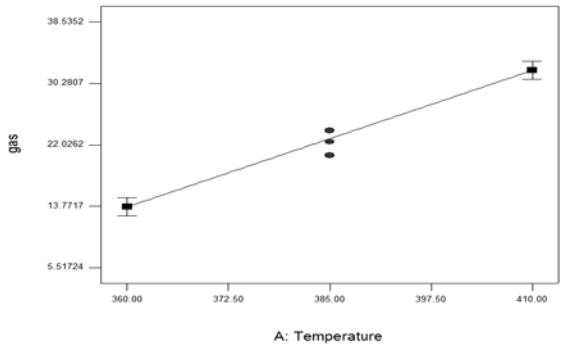

Figure 3.3. The effect of reaction temperature on yield of gas**.** (residence time = 45 mins, amount of catalyst = 0.06 g, initial hydrogen pressure = 2 bar)

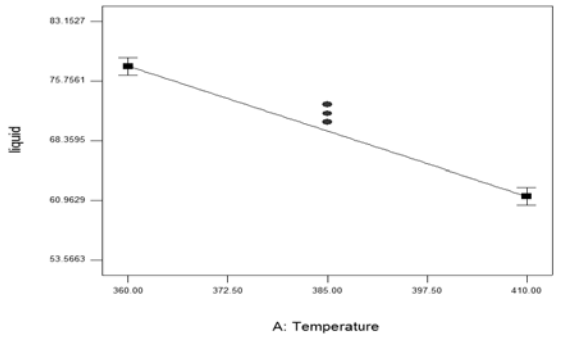

Figure 3.4. The effect of reaction temperature on yield of liquid**.** (residence time = 45 mins, amount of catalyst = 0.06 g, initial hydrogen pressure = 2 bar)

The effect of reaction temperature on the yield of gas shown in figure 3.3. and yield of liquid shown in figure 3.4. Yield of gas was increased from 13.7032 to 32.0407 wt% and yield of liquid was decreased from 77.6001 to 61.4791 wt% with an increase of reaction temperature. A possible reason for this behavior is that the higher temperature (410 ^{o}C) accelerated the thermal cracking and hence changing the long chain of hydrocarbon molecule from thermal cracking into a middle hydrocarbon molecule and light hydrocarbon molecules. Thereafter light hydrocarbon molecules were thermally and catalytically cracked converting them into gas product so liquid product was decreased [5].

The effect of residence time

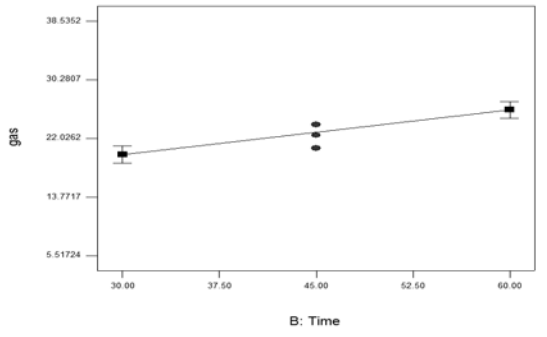

Figure 3.5. The effect of residence time on yield of gas. (reaction temperature = 385 ^{o}C, amount of catalyst = 0.06 g, initial hydrogen pressure = 2 bar)

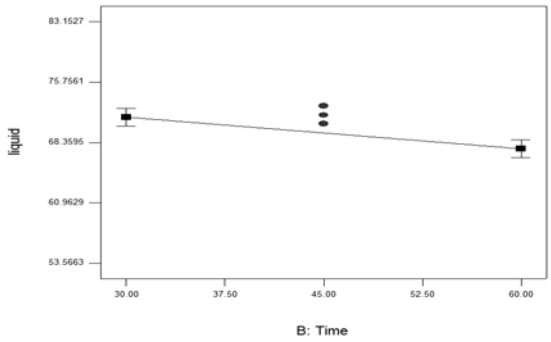

Figure 3.6. The effect of residence time on yield of liquid**.** (reaction temperature = 385 ^{o}C, amount of catalyst = 0.06 g, initial hydrogen pressure = 2 bar)

The effect of residence time on the yield of gas shown in figure 3.5. and yield of liquid shown in figure 3.6. When the residence time is continued the yield of liquid which consisted of the fraction of light hydrocarbon was continued cracking to the gas product. Hence, yield of gas was increased from 19.7134 to 26.0305 wt% and yield of liquid was decreased from 71.4776 to 67.6016 wt% with increasing the residence time.

Conclusions

The effect parameter of coconut oil to biofuel using HZSM-5 catalyst by catalytic cracking in a batch reactor was investigated. From normal probability plot, the main effect of reaction temperature and residence time are significant on yield of gas and yield of liquid. When increasing the reaction temperature, residence time the yield of gas was increased and yield of liquid was decreased whereas, the increasing amount of catalyst and initial hydrogen pressure are not significant for the yield of gas and yield of liquid.

Acknowledgements

The authors greatly acknowledge the support of Department of Chemical Technology, Faculty of Science, Chulalongkorn University. The authors also like to thank Center for Petroleum, Petrochemicals and Advance Materials Chulalongkorn University for funding support.

References

[1] Ooi, Y., Zakaria, R., Mohamed, A., Bhatia, S., *Biomass and Bioenergy* **27** (2004), pp. 477-484.
[2] Li, H., Shen, B., Kabalu, J.C., Nchare, M. *Renewable Energy* **34** (2009), pp. 1033-1039.
[3] Tamunaidu, P., Bhatia, S., *Bioresource Technology* **98** (2007), pp. 3593-3601.
[4] Bezergianni S., Kalogianni, A., *Bioresource Technology* **100** (2009) , pp. 3927–3932.
[5] Sadrameli, S.M., Green A., *J. Anal. Appl. Pyrolysis* **78** (2007),pp. 445–451.
[6] Mongkol, M., M.S. Thesis, Chulalongkorn University, Thailand 2003.
[7] Taepakdee, P., M.S. Thesis, Chulalongkorn University, Thailand 2004.

Effects of base-type-solution and pH-value on catalytic performance of Au/CeO_2 for preferential CO oxidation

T. Sakwarathorn[1], A. Luengnaruemitchai[2,3] and S. Pongstabodee[1,3*]

[1]Department of Chemical Technology, Faculty of Science, Chulalongkorn University, Phaya Thai, Bangkok, 10330, Thailand
[2]The Petroleum and Petrochemicals College, Chulalongkorn University, Phaya Thai, Bangkok, 10330, Thailand
[3]Center for Petroleum, Petrochemicals, and Advanced Materials, Chulalongkorn University, Bangkok, 10330, Thailand

[*] E-Mail Address: sangobtip@gmail.com

Abstract: Preferential CO oxidation is a promising reaction to remove carbon monoxide from the stream. In this work, preferential CO oxidation on Au/CeO_2 catalysts prepared by deposition-precipitation was investigated. Effects of base-type and pH values on preparing catalysts were studied. It observes that form of gold in the catalyst was Au^0 and Au^{3+} which were detected by TPR and UV-vis techniques. TEM images revealed that the smaller size of Au/CeO_2 was noticed when using by NaOH at as a precipitating agent to adjust pH values. Complete CO conversion with 51% selectivity was obtained when reaction temperature was kept at 40 ºC. When using Na_2CO_3 as the agent at pH 7 the maximum CO conversion was around 98.5% with 54% selectivity at 40 ºC. At given pH 9, the maximum CO conversion was approached at 96.5% with 53% selectivity. The performance of Au/CeO_2 decreased when the stream is contaminated by water. However, the complete CO conversion can be achieved when being pretreated in oxygen atmosphere at 110 ºC for 2 h.

Introduction

Catalytic oxidation of carbon monoxide has been of considerable interest recently and important research topic during the last decade due to relevance in many applications. The catalytic preferential CO oxidation is the simplest and most cost effective method for removing CO from H_2-rich fuels. Therefore, the content of CO in the H_2-stream must be reduced to the ppm level. In order to avoid technical problems associated with the use of pure H_2, especially in vehicle applications, a H_2-rich gas mixture can be obtained from liquid fuel such as methanol or natural gas, via a fuel processor. Goal of PROX researches include high conversion and high selectivity at an appropriate reaction temperature.

It is well documented that gold is not capable of chemisorbing detectable quantities of molecular hydrogen at room temperature due to the high activation energy required for dissociative adsorption of hydrogen. At higher temperatures, however, atomic hydrogen formation proceeds via a first order reaction having activation energy of 71 to 75 kJ/mole. The gold shows some very interesting properties which ensure continued study for catalysis field. In particular its remarkable high selectivity in some reactions and striking activity in oxygen transfer catalysis have received significant attention [1].

Supported gold catalysts found to be active for low temperature oxidation of CO include TiO_2 [2], ZrO_2 [2], MgO [3], Al_2O_3 [4,5]. The nature of the support plays a vital role in determining the activity of gold catalysts. Ceria is one of the relatively easily reducible metal oxides. It is currently used as a key component in the three-way automotive exhaust catalyst system. Among the metal-ceria systems examined in the literature [5-20], Au-ceria is particularly active and stable catalyst for low-temperature CO oxidation [6-10].

Many preparation method of catalyst were studied such as impregnation, coprecipitation, or deposition-precipitation method. In recent year, many researches used gold-ceria catalysts prepared by deposition-precipitation method for reducing carbon monoxide [2,8,10,13-15,17-19]. Deng et al. [9] reported that gold-ceria catalysts with a low gold content exhibit good catalytic properties for the water-gas shift and preferential CO oxidation reaction. They found that after prolonged reaction at 120 ºC, most of gold cations remained in ionic state. Pillai and Deevi [19] reported such a study, wherein a ceria supported catalyst prepared by deposition-precipitation method containing approximately 1%wt gold is found to be highly active for the room temperature oxidation of CO to CO_2. Fu et al. [6,11] further examine the gold-ceria interaction and evaluate the catalyst under realistic operating conditions. Avgouropoulos et al. [7,8] presented work in the comparative study of gold and copper oxide catalysts supported on ceria under realistic reaction conditions, the catalytic activity, selectivity and deactivation of these catalysts in the PROX reaction. Herein, we studied the catalytic performance of Au/CeO_2 catalysts, prepared by the deposition-precipitation method with base-type and pH values of in the terms of CO conversion and CO selectivity as a function of temperature. Moreover, stability of catalysts was studied.

Materials and Methods

The first step is that to prepare a pure support ceria by precipitation method. Aqueous solution of cerium nitrate precursor ($Ce(NO_3)_3 \cdot 6H_2O$) was added dropwise by sodium carbonate under stirring. It was kept a constant pH of 9.0 and temperature of 70 ºC. The precipitated ceria was aged for 1 h, washed by deionized water until no conductivity, dried at 110 ºC overnight and calcined in air at 500 ºC 5 h. The second step is to prepare gold-ceria catalysts were prepared by

deposition-precipitation method which containing 0.85%wt of gold. Gold precursor ($HAuCl_4 \cdot 3H_2O$) was dropped into a beaker that contained ceria in water. Gold hydroxide was deposited onto the support through sodium carbonate or sodium hydroxide and vigorous stirring at constant pH values (7 or 9). After 1 h of aging, the precipitated catalysts were washed by deionized water until no Cl^- ions, dried at 110 ºC overnight and calcined in air at 350 ºC for 2 h.

The catalysts, 100 mg, were packed in a fixed-bed, U-tube which had 0.6 mm diameter, micro-reactor for the PROX reaction. The activity was observed at various temperatures over the range of 37-110 ºC under gas mixture conditions, 40%H_2, 1%O_2, 1%CO in helium, and these tests were carried out at atmospheric pressure in a continuous-flow with 50 ml/min total flow rate. All the gases used were BOC certified with 99.99% purity. Mass flow controllers were calibrated for the above gases with a soap-bubble flow meter. No pretreatment was applied (an important advantage of this catalyst over catalysts prepared from salt precursors is the negligible amount of impurities and residuals). The effluent gas from the reactor was detected by auto-sampling in an on-line gas chromatograph equipped with a packed carbosphere column, 80/100 mesh, 10 ft x 1/8 in and a thermal conductivity detector (TCD).

Results and Discussion

Metal loading catalysts detected by XRF technique was reported in table 1. Using either Na_2CO_3 or NaOH at pH 7 and 9 for precipitated gold hydroxide less than 0.85%wt of gold was obtained because some gold ions in solution was not precipitated onto ceria. When washing the catalysts for eliminate anions (Cl^-, OH^- and CO_3^{2-}), some gold ions were flooded with washing water. Preparation catalysts by NaOH gave higher Au loading than Na_2CO_3 because of direct reaction between hydroxide ions and gold ions.

Table 1: Characterization of Au/CeO_2 catalysts

Condition	Au loading
Na_2CO_3, pH 7	0.59
Na_2CO_3, pH 9	0.44
NaOH, pH 7	0.63
NaOH, pH 9	0.60

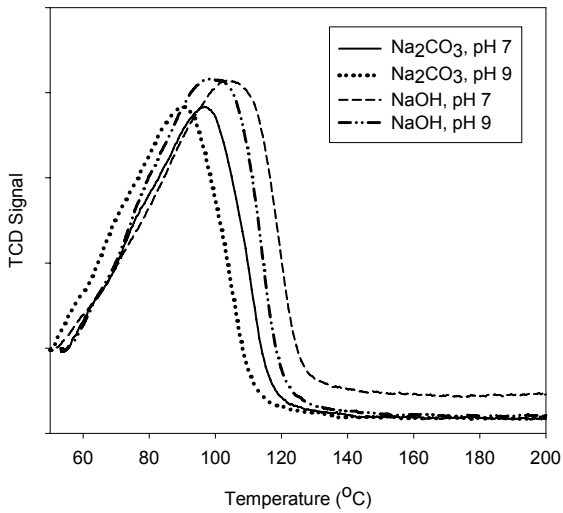

Figure 1. TPR profile of Au/CeO_2

Hydrogen temperature programmed reduction (TPR) is an effective technique to provide information on the characteristic of gold. All catalysts exhibit one reduction peak with a maximum temperature at 88-114 ºC (Fig. 1.). The reduction peak of catalysts can be ascribed to the reduction of gold ions. It is interesting to note that the corresponding peak around the reduction of gold ions of catalysts using NaOH as a precipitating agent expresses stronger bond than using Na_2CO_3. Furthermore, preparation catalysts at pH 7 gave a maximum peak at higher temperature than that at pH 9. This may be a possible reason for higher activity.

Higher temperature reduction means difficult to reduce of gold ions [6]. The catalyst using NaOH at pH 7 is a higher effective catalyst for preferential oxidation reaction because it exhibits higher reduction temperature and has the smallest particle size of gold. On the contrary, Fu et al. [11] said that containing of gold in catalysts can cause temperature reduction. When gold loading were increase, Hydrogen could reduce gold ions easily and the reduction temperature came down.

Light absorption of catalysts were investigated by UV-visible light technique, as shown in Fig. 2. The range of wavelength was around 200-800. At wavelength of 450-800 nm showed absorbance of gold metal or gold cluster and at wavelength less than 250 nm showed peak of gold ions [24]. Absorbance of catalysts related with particle size of gold. The catalyst using NaOH at pH 7 present less absorption at wavelength 450-800 nm and showed the smallest particle size than other. Thus form of gold in catalyst prepared by NaOH or Na_2CO_3 was gold metal and gold ions, which presence of $Au(OH)_3$ and Au_2O_3. Active site for CO PROX may be combination of Au^+-OH^- and Au^0, which Au^0 responsible for activation of O_2 molecule and hydroxyl containing Au cation provide the pathway for the conversion of CO to CO_2 [11].

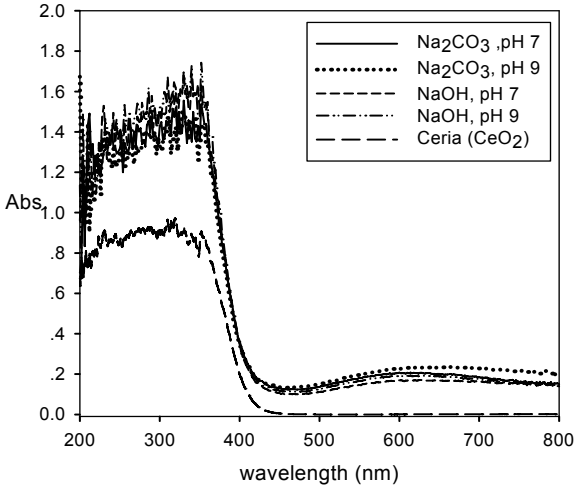

Figure 2. UV-vis spectra of catalysts

Fig. 3. showed the physical property of catalysts by TEM technique. Gold particles were black spot in TEM images and calculated particle size by SemAfore software. Distribution and mean size of gold particles was found that a small particle size effects on high reduction temperature. Using NaOH as the agent gave a narrower distribution gold particle size and smaller mean size. Moreover, pH condition has a significant effect on the particle size.

From characterization of catalysts, gold forms in catalysts have metal form (by UV-vis technique) and ions form (by TPR and UV-vis technique). The activities of gold metal were bonding with oxygen at surface area and gold ions were changing carbon monoxide to carbon dioxide [11].

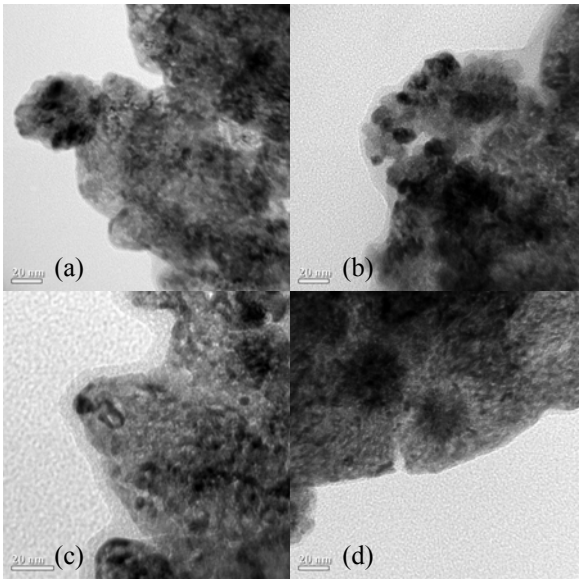

Figure 3. TEM image of Au/CeO_2 catalyst when using various precipitating agent at different pH conditions:
(a) Na_2CO_3–pH 7 (b) Na_2CO_3–pH 9
(c) NaOH–pH 7 (d) NaOH–pH 9

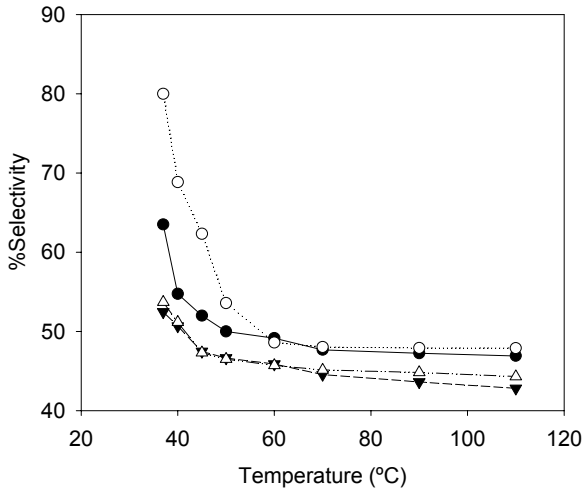

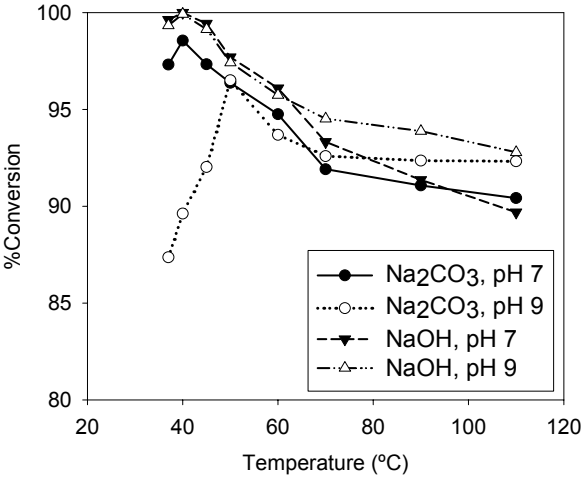

Figure 4. CO conversion and selectivity of Au/CeO_2 catalyst

Fig. 4. showed activities of prepared Au/CeO_2 at various condition. Using NaOH as the agent to adjust pH 7, a complete conversion and 51% selectivity was achieved at 40 ºC. While 98.5% CO conversion with 54% selectivity was obtained when using Na_2CO_3 as the agent at reaction temperature of 40 ºC. When temperatures increased, the conversion and selectivity were decreasing slightly because of competition reaction from hydrogen oxidation at higher temperatures. At constant pH 9, the prepared catalyst using NaOH as the agent gave complete conversion with 51% selectivity at 40 ºC. Whereas the prepared catalyst using Na_2CO_3 to prepare displayed 96.5% conversion and 53% selectivity at 50 ºC. The activity of catalysts prepared by NaOH is higher than the others because of the smaller particle size and higher reduction temperature.

From the activity of catalysts, the prepared catalyst using NaOH as the agent at pH 7 was recommended to be used in further study because of the smallest gold

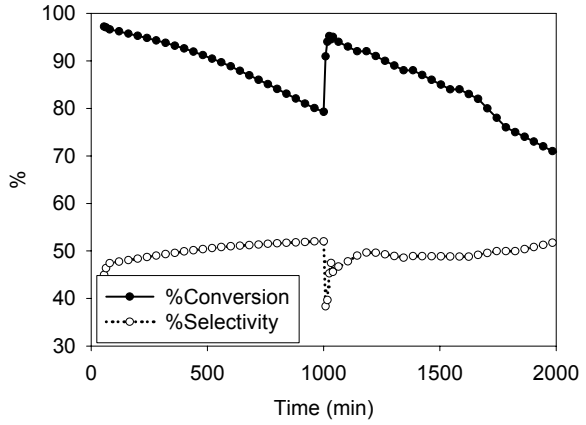

Figure 5. Stability of Au/CeO_2 catalyst

particle and narrow distribution of gold size. Moreover,the reduction temperature was higher than other which effecting high activity.

The catalysts was tested a stability at 45 ºC in Fig. 6. When reaction was running to 900 min, the activity was decreased (81% conversion) because of a deactivation of catalysts. A gold ions form, which converse carbon monoxide to carbon dioxide, was reduced by hydrogen to a metal form. Furthermore, hydrogen oxidation, which was a competition reaction, would produce water to cover an active site. From the result, water can cause very high deactivation of catalysts.

Water activity is an oxidizing agent to change a gold metal form to gold ions again. So, gold form in catalysts can be re-oxidized, re-reduced or redox phenomena [9]. However, the temperature of running stability test was not high enough to oxidized gold metal form to gold ions by water. When a form of gold ions was reduced to gold metal, the activity of gold ions to converse carbon monoxide would decrease. The activity of gold metal to promote selectivity would increase slightly. After 1000 min reaction, the deactivations of catalysts were regenerated by thermal treat with 5% oxygen in helium at 110 ºC for eliminating water. After regenerating the high activity increase again.

Conclusions

Gold in catalyst was in a form of Au^0 and Au^{3+} to promote CO oxidation in H_2-rich stream. Herein, prepared catalysts by NaOH at pH 7 gave higher activities because of the smaller particle size and higher reduction temperature. The catalyst was deactivated because of water molecule. However, the catalysts could regenerate with 5% oxygen in helium at 110ºC for eliminated water from an active site.

Acknowledgements

This work was fully supported by the Center for Petroleum, Petrochemicals and Advanced Materials.

References

[1] J. Schwank. *Gold Bull.* **16** (1983), pp. 103-110.
[2] C. Rossignol, S. Arrii, F. Morfin, L. Piccolo, V. caps and J.L. Rousset. *J. Catalysis* **230** (2005), pp. 476-483.
[3] L.-H. Chang, N. Sasirekha, B. Rajesh, Y.-W. Chen. *Sep. and Pur. Tech.* **58** (2007), pp. 211–218.
[4] E. Quinet, F. Morfin, F. Diehl, P. Avenier, V. Caps and J.L. Rousset. *App. Cat. B.* **80** (2008), pp. 195-201.
[5] D. Andreeva, I. Ivanov, L. Ilieva, J.W. Sobczak, G. Avdeev, T. Tabakova. *App. Cat. A*. **333** (2007), pp. 153–160
[6] Q. Fu, W. Deng, H. Saltsburg and M. F–Stephanopoulos. *App. Cat. B* **56** (2005), pp. 57-68.
[7] G. Avgouropoulos, J. Papavasiliou, T. Tabakova, V. Idakiev and T. Ioannides. *Chem. Eng. J.* **124** (2006), pp. 41-45.
[8] G. Avgouropoulos, M. Manzoli, F. Boccuzzi, T. Tabakova, J. Papavasiliou, T. Ioanides and V. Idakiev. *J. Cat.* **256** (2008), pp. 237-247.
[9] W. Deng, J.D. Jesus, H. saltsburg and M. F-Stephanopoulos. *App. Cat. A.* **l 291** (2005), pp. 126-135.
[10] M. Manzoli, G. Avgoruopoulos, T. Tabakova, J. Papavasiliou, T. loannides and F. Boccuzzi. *Cat. Today* **138** (2008), pp. 239-243.
[11] Q. Fu, S. Kudriavtseva, H. Saltsburg, M. F–Stephanopoulos. *Chem. Eng. J.* **93** (2003), pp. 41-53.
[12] A. Karpenko, R. Leppelt, V. Plzakb, R.J. Behma. *J. Cat.* **252** (2007), pp. 231–242.
[13] R. Leppelt, B. Schumacher, V. Plzak, M. Kinnea, R.J. Behma. *J. Cat.* **244** (2006), pp. 137–152.
[14] A. Karpenko, R. Leppelt, J. Cai, V. Plzak, A. Chuvilin, U. Kaiser and R.J. Behm. *J. Cat.* **250** (2007), pp. 139-150.
[15] H. Sakurai, T. Akita, S. Tsubota, M. Kiuchi, M. Haruta *App. Cat. A.* **291** (2005), pp. 179–187.
[16] D. Andreeva, V. Idakiev, T. Tabakova, L. llievaa, P. Falaras, A.Bourlinos and A. Travlos. *Cat. Today* **72** (2002), pp. 51-57.
[17] C. H. Kim, L. T. Thompson. *J. Cat.* **244** (2006), pp. 248–250.
[18] T. Tabakova, F. Boccuzzi, M. Manzoli, J.W. Sobczak, V. Idakiev, D. Andreeva *App. Cat. B.* **49** (2004), pp. 73–81.
[19] U. R Pillai and S. Deevi. *App. Cat. A.* **299** (2006), pp. 66-273.
[20] A. Gómez-Cortés, Y. Márquez, J. Arenas-Alatorre and G. Díaz. *Cat. Today* **133** (2008), pp. 743-749.
[21] J. Meilin, B. Haifeng, Zhaorigetu, S. Yuenain, L. Yanfeng *J. Rare Earths* **26** (2008), pp. 528
[22] Y. Shen, X. Yang, Y. Wang, Y. Zhang, H. Zhu, L.Gao, M. Jia. *App. Cat. B.* **79** (2008), pp. 142–148.
[23] L-C. Chung and C-T. Yeh. *Cat. Com.* **9** (2008), pp. 670-674.
[24] K.R. Souza, A.F.F. de Lima, F.F. de Sousa and L.G. Appel. *App. Cat. A.* **340** (2008), pp. 133-139.

Purification of biodiesel using adsorbents and saturated salt solution

M. Rungsiriworapong[1], S. Butnark[2*] and S. Pengprecha[3*],

[1] Program in Petrochemistry and Polymer Science, Faculty of Science, Chulalongkorn University, Bangkok, 10330 Thailand
[2] PTT Public Company Limited, Phahonyothin Rd., Sanubtub, Wangnoi, Ayutthaya, Thailand 13170
[3] Department of Chemistry, Faculty of Science, Chulalongkorn University, Bangkok, 10330 Thailand

*E-mail: somchai.pe@chula.ac.th

Abstract: Biodiesel has recently become one of the most promising alternative fuels from its environmentally concerning properties. The most effective method to produce biodiesel is the catalytic transesterification of vegetable oil to methyl ester using catalytic base as a catalyst. The common process of biodiesel purification is water washing, but this generates large amount of wastewater that causes environmental problems. The purpose of this research is to purify biodiesel and to remove the impurities especially glycerin content. Biodiesel production was performed by using standard condition (6:1 molar ratio of methanol:oil, 1 %wt of sodium hydroxide and reaction temperature of 60°C for 1.50 hours). After glycerin layer has been separated, the glycerin content in biodiesel was removed by saturated salt solution and adsorbents including silica gel, activated carbon and activated clay, respectively. The results show that this process can purify and reduce glycerin content in biodiesel and the amount of wastewater produced during the process to the acceptable level.

Introduction

Biodiesel is monoalkyl esters of long chain fatty acids derived from renewable feed stocks, such as vegetable oils or animal fats, which are composed of triglycerides. Since biodiesel has proper viscosity and boiling point, high cetane number and also free of sulfur and aromatics, it is considered as an environmentally friendly and nontoxic fuel[1-2]. The way to produce biodiesel is by the transesterification reaction between triglycerides and alcohol, mostly methanol because of its low cost. Transesterification of vegetable oils to biodiesel can be carried out using either heterogeneous or homogeneous catalysts, especially alkaline hydroxide [3]. After the separation process, the biodiesel contains several impurities such as glycerol, glycerides, soap, free fatty acids, methanol, catalyst, metals and water that must be removed from the product. The common process that widely use to purify biodiesel is water washing. However, the major problems in this process are large amount of wastewater produced from cleaning the products and the remained water-insoluble impurities. Moreover, soap can generate emulsion of water and biodiesel that cause separation problem [4-5]. To solve these problems, the application of adsorbents becomes attractive method of biodiesel purification. There are many adsorbents that use to purify biodiesel such as activated carbon, silica gel, magnesium silicate, clays and alumina [5-6]. The process using absorbents is more advantageous than water washing process because both the water-soluble and water-insoluble impurities are eliminated and this process doesn't generate wastewater. The objective of this research is therefore to develop biodiesel purification method using saturated salt solution and adsorbents as an environmentally favorable process.

Materials and Methods

All reagents were analytical grade.

Preparation of the saturated salt solution: Five hundred milliliters of water was added into a 1000-ml beaker and heated to 50 ^{o}C. Then, NaCl was added until the solution was saturated.

Transesterification of refined palm oil: Five hundred grams of palm oil was weighed and placed in a 1000-ml two-necked round bottom flask equipped with a reflux condenser and thermometer. After the oil was heated to 60 °C, the solution of 6 mol equivalent of methanol to palm oil and 1 wt% sodium hydroxide was slowly added into the reaction, then the mixture was stirred for 1.5 hours. The mixture was placed in a separatory funnel and allowed to stand for 30 minutes then glycerin layer at the bottom was removed.

Purification of crude biodiesel by using the saturated salt solution: To determine the efficiency of the saturated salt solution, the ratio between biodiesel and saturated salt solution and the temperature of washing were studied. After glycerin layer has been separated, 50 milliliters of biodiesel was washed three times with saturated salt solution at 2:1, 1:1 and 1:2 ratio of biodiesel and saturated salt solution in a separatory funnel for 30 seconds at 50 ^{o}C and room temperature. For conventional water washing process, 50 grams of biodiesel was successively washed with water in a separatory funnel until the washed water became clear. The amount of soap content was determined by titration method.

Purification of crude biodiesel by using the adsorbents: Three types of adsorbents including silica gel, activated carbon and activated clay were studied. After biodiesel has been washed with the saturated salt solution, 50 grams of biodiesel was treated with each of 0.1% wt of adsorbents at room temperature with

stirring rate at 150 rpm for 10 minutes. Then the adsorbents were removed by filtration. The biodiesel was subjected to determine the soap content by titration method.

Determination of soap content: 10 g of biodiesel sample was dissolved in 100 ml of isopropyl alcohol with 2 ml of 1% phenolphthalein as an indicator. The mixture was titrated with 0.01N hydrochloric acid until the color of the solution changed from red to clear color. This amount of 0.01N hydrochloric acid solution is referred as "A".

Then, 1 ml of 0.04% bromophenol blue was added into the mixture solution and titrated with 0.01N hydrochloric acid until the color of the solution changed from blue to yellow. This amount of 0.01N hydrochloric acid solution is referred as "B".

The amount of unreacted catalyst can be calculated by using the equation (1):

$$\text{g of catalyst / g of sample} = \frac{A \times 0.01 \times 40.0}{W \times 1000} \quad (1)$$

Where: A = volume of hydrochloric acid used in first step (mL)

W = weight of untreated biodiesel used (g)

And the amount of soap in the biodiesel can be calculated by using the equation (2):

$$\text{g of soap / g of sample} = \frac{B \times 0.01 \times 304.4}{W \times 1000} \quad (2)$$

Where: B = volume of hydrochloric acid used in second step (mL)

W = weight of untreated biodiesel (g)

Results and Discussion

Optimization of the saturated salt solution parameters:

Effect of the ratio between biodiesel and saturated salt solution: The effect of the ratio between biodiesel and saturated salt solution was studied in the range of 2:1, 1:1 and 1:2 ratio of biodiesel and saturated salt solution. Soap content remained in biodiesel was determined by titration method and the result was shown in Table 1.

Table 1: Soap content after washing with the saturated salt solution for 30 seconds three times at room temperature in various ratio.

Number of washing	Soap content (g soap/g biodiesel)		
	2 : 1	1 : 1	1 : 2
Before washing	0.0035386	0.0035386	0.0035386
1	0.0000968	0.0000554	0.0000551
2	0.0000548	0.0000552	0.0000548
3	0.0000415	0.0000415	0.0000417

The result from Table 1 showed that the saturated salt solution could be effectively used to remove soap in biodiesel. The soap content could be reduced from 0.0035386 to 0.0000554 g soap/g biodiesel by using 1:1 ratio of biodiesel and saturated salt solution, to 0.0000968 g soap/g biodiesel for 2:1 ratio and to 0.0000551 g soap/g biodiesel for 1:2 ratio, respectively. Therefore, the optimal ratio between biodiesel and saturated salt solution was 1:1 ration. The result also showed that only one time washing with the saturated salt solution was sufficient for this purpose because the number of washing for one, two or three times gave the similar results.

Effect of the temperature: The effect of the temperature was investigated at room temperature and 50 ^{o}C compared with water washing and the result was given in Table 2.

Table 2: Soap content after washing with the 1:1 ratio of biodiesel and saturated salt solution for 30 seconds three times in various temperatures compared with water washing.

Number of washing	Soap content (g soap/g biodiesel)		
	Room temp.	50 ^{o}C	Water washing
Before washing	0.0035386	0.0035386	0.0035386
1	0.0000554	0.0000690	0.0006812
2	0.0000549	0.0000691	0.0002789
3	0.0000414	0.0000688	0.0000917

The results from Table 2 showed that the soap content in biodiesel could be removed by using the saturated salt solution at room temperature better than at 50 ^{o}C. This was due to the solubility of soap in biodiesel in higher temperature was increased. Therefore, the suitable temperature to removed soap was room temperature. Moreover, the saturated salt solution was found to removed soap better than water washing process, and only one time washing with the saturated salt solution was sufficient to remove soap as compare to washing with water by three times.

In addition, the results showed that there is no washing problem since the emulsion was not generated in this process and the other impurities including glycerin, methanol, and catalyst were also removed.

Purification of biodiesel by using the adsorbents: Three types of adsorbents including silica gel, activated carbon and activated clay were studied. The result of the soap content in biodiesel was given in Table 3.

Table 3: Soap content after treated with the saturated salt solution and 0.1% wt of adsorbents at room temperature for 10 minutes compared with water washing.

Adsorbents	Soap content (g soap/g biodiesel)
Silica gel	0.0000280
Activated carbon	0.0000284
Activated clay	0.0000271
Water washing	0.0000277

The result showed that the soap content after treated with the saturated salt solution and adsorbents was similar to the soap content from water washing process and all value of soap content passed the specification of biodiesel standard.

Conclusions

The process for purifying biodiesel using adsorbents and saturated salt solution is successfully removed impurities including glycerin content. This process can also reduce the amount of wastewater and no emulsion occured.

References

[1] Marchetti, J.M.; Miguel, V.U. and Errazu, A.F. *J. Renew Sust Energy Rev.* **2007**, *11*, pp.1300-1311.
[2] Srivastava, A.and Prasad, R. *Renew Sust Energy Rev*. **2000**, *4*, pp.111–133.
[3] Kumar, S.; Gupta A. K. and Naik, S. *J. Sci. and Ind. Research.* **2003**, *62*, pp.124-132.
[4] Berrios, M. and Skelton, R.L. *Chem. Eng. J.* **2008**, *144*, pp.459-465.
[5] Munson, J.R.; Bertram, B.L. and Caldwell, J.D. *U.S. Patent 5597600.* **1997**.
[6] Bertram, B.; Abrams, C. and Cooke, B.S. *U.S. Patent Application 20050081436.* **2005**.

Reduction of benzene in reformate by olefin alkylation

W. Kiatkittipong[1,*], P. Khongjarern[2], S. Assabumrungrat[2]

[1] Silpakorn University, Department of Chemical Engineering, Faculty of Engineering and Industrial Technology, Nakhon Pathom 73000, Thailand

[2] Chulalongkorn University, Center of Excellence on Catalysis and Catalytic Reaction Engineering, Department of Chemical Engineering, Faculty of Engineering, Bangkok 10330, Thailand

[*] E-mail:kworapon@su.ac.th

Abstract: Benzene is a key aromatic hydrocarbon which is an important high octane component of motor gasoline; however, benzene is known as a human carcinogen and also has high vapor pressure thus high evaporative emissions. Thus benzene content will be limited to less than 1 vol.% follow Euro 5 standard which Thailand will be enforced on January 2012. Reformate is the largest portion of benzene in a gasoline pool and, therefore it was aimed to reduce benzene content prior to blending. Alkylation of reformate with ethylene was investigated in this research work. The reaction was performed in an autoclave reactor with the temperature of 225 °C and pressure of 45 bar for 20 h using β-zeolite as a catalyst. The original reformate poses benzene content of 9.84 vol% and research octane number (RON) of 95.9. Benzene conversion increases with lowering benzene:ethylene mole ratio and up to 31% benzene reduction could be obtained with increased of RON. This is due to ethylbenzene which has higher octane number and also less toxicity than benzene was produced.

Introduction

Currently, global awareness on environmental problems have been promoted via various environmental campaigns. The standards for vehicles will be further restricted in their emissions. The restriction not only applies to the vehicle manufacturers, but also refiners. Gasoline comprises of a mixture of numerous hydrocarbons including aromatics, olefins, naphthenes and paraffins. Benzene is a key aromatic hydrocarbon with high octane number, but benzene is a known human carcinogen and also has high vapor pressure and poses a constant health risk due to evaporative emissions. The benzene content in motor gasoline will be regulated to be less than 1 vol.% follow Euro 5 standard. For Thailand, the current benzene content is limited at 3.5 vol.% and the enforcement for reducing to 1 vol.% will begin on January 2012 [1]. Reformate is the largest blending stock for gasoline which constitutes up to 41.7 vol.% of the final product. Among the primary sources of benzene in gasoline pool i.e. reformate, isomerate, alkylated and FCC naphtha, reformate has the highest benzene content approx. 5 vol.% and therefore it contributes mostly of benzene presence in gasoline pool [2]. For this reason, many strategies for reducing benzene contents in gasoline have focused on removing a portion of benzene from reformate prior to blending.

The common strategies for reducing the benzene content in reformate include physical separation and chemical processes. There are many techniques of physical separations which can be used to remove benzene such as distillation, solvent extraction, extractive distillation and adsorption. Distillation is not suitable because benzene has azeotropes with normal hexane and naphthenes [3]. Solvent extraction process and extractive distillation process of benzene using sulfolane, n-methyl pyrolidone (NMP), n-formyl-morpholine (NFM) as solvent have been investigated. In spite of the advantages of high yield and selectivity, these methods have many drawbacks such as using of special equipment to resist the corrosion of solvent which result in high manufacturing cost.

There are many adsorbents which can be used in an adsorption process to separate aromatics such as alumino silicate zeolite, silica gel and molecular sieve etc. U.S. Pat. No. 5,294,334 [4] disclosed a process for reducing the benzene content by adsorption benzene using a zeolite layer and desorption of benzene is carried out using cyclohexane. But the adsorption-desorption operation in the zeolite adsorbent layer cannot be performed continuously. Moreover, all above benzene physical separation decreases in octane and volume of gasoline. Thus, these methods may not be satisfactory for reducing the benzene content [5-7].

A recent report proposes a method for converting benzene in gasoline into other compounds by a chemical reaction. For example, hydrogenation for converting benzene to cyclohexane has drawn many researches' attention to improve gasoline properties. However, cyclohexane has lower octane rating than benzene. In order to partially recover the octane number loss, Lee et al. [4] disclosed a process for reducing benzene in gasoline blending stock which uses a dual functional catalyst to hydrogenate benzene to cyclohexane and further isomerize to methylcyclopentane which has an octane rating between cyclohexane and benzene. Nevertheless, this method increases the refining cost and reduces the grade of gasoline blending stock [8].

To overcome these drawbacks, it has been found that benzene may be alkylated with olefins that improve both octane and volume of gasoline [5]. For example, Bellussi et al. [9] investigated the alkylation

of benzene with light olefins to produce alkylbenzene which is less toxic and desirable high octane blending compounds such as ethylbenzene, propylbenzene. One commercial process of this type is the Mobil Benzene Reduction (MBR) process which used a fluidized zeolite catalyst to convert benzene to alkylaromatics using olefins from sources such as fluidized catalytic cracking (FCC), excess LPG. The yield-octane uplift of MBR process makes processes become economically beneficial in petroleum refining [7].

This paper focused on alkylating of reformate with ethylene catalyzed β-zeolite. The composition and properties of alkylated reformate i.e. research octane number (RON), blending Reid vapor pressure (bRvp) and distillation temperature comparing to original reformate are also discussed.

Materials and Methods

Materials

The chemicals that used in this study are shown in Table 1.

Table1: Details of chemicals use in the study

Chemical materials	Purity	Supplier
Catalyst		
β-zeolite		Tosho
Chemical		
NH_4NO_3	> 99%	Fluka
Reformate (benzene 9.84vol%)		Bangchak Petroleum Public Company Limited.
Ethylene	> 99%	TIG
Benzene	99.7%	Merck

Catalyst preparation

Commercial of β-zeolite was purchased from Tosoh. β-zeolite was converted into H-form by the following procedure: β-zeolite and 2 M NH_4NO_3 solution (20 mg/g) were place in a flask. The mixture was stirred at 70 °C for 5.5 h to give NH_4β-zeolite. Then the material was filtered under suction and washed with distilled water. The filtered material was dried at 80 °C overnight. The exchange sample was further calcined in air at 550 °C for 4 h, the obtained crystals were Hβ-zeolite [10].

Characterization of reformate and product

Reformate and alkylation product were analyzed the benzene and ethylbenzene content by using gas chromatography. The standard analysis of RON, bRvp and distillation temperature were carried out by follows the standard methods of following the standard methods of ASTM D 2699, ASTM D 323 or D 4953 and ASTM D 86-05, respectively. All of analyses were tested by the laboratory of Bangchak Petroleum Public Company Limited.

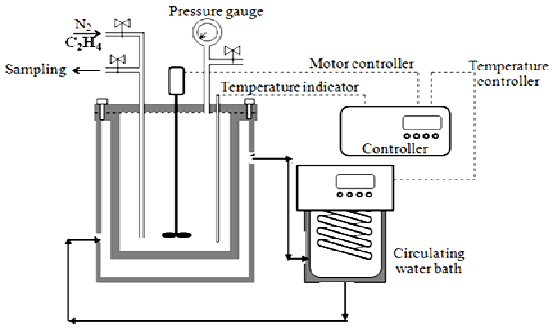

Figure 1. Schematic diagram of the autoclave reactor.

Alkylation of benzene in reformate with ethylene

The experimental set up is shown in Figure 1. Initially, 0.5 g of catalyst and 150 ml of reformate were added to the 300 ml reactor vessel. Ethylene was filled to desired benzene:ethylene mole ratio. Then N_2 was quickly charged to a pressure of 45 bar and stirred at 500 rpm. The temperature was raised to 225 °C and held 20 h for all run. At the end of reaction time, the reactor was left to room temperature before collecting the sample.

Alkylation of pure benzene with ethylene

The experiment with pure benzene feedstocks were carried out following a similar procedure of alkylation benzene in reformate.

Results and Discussion

The effect of benzene:ethylene (B:E) molar ratio was primarily investigated by using pure benzene. As shown in Fig. 2, benzene conversion is higher with lower B:E ratio. Similar tendency was obtained in the real sample of benzene constituent as shown in Table 2. The improvement of RON from 95.9 to 98.2 was obtained with B:E of 9:1. This might be mainly due to the increased of alkylated product i.e. ethylbenzene, di- and tri-ethylbenzene accompanied with decreased of benzene content. It should be noted that since many replicate was required to obtain sufficient amount for RON testing, the RON of the sample with B:E of 5:1 and 3:1 could not be determined yet. However, increasing of RON with lower B:E would be anticipated. This is because the RON of benzene and ethylbenzene are 99 and 124 [11] while that of o-, m-, p-diethyl benzene were estimated as 183, 154 and 209 [12]. Moreover, Rvp of alkylated reformate decreased and distillation temperature increased in all range of % evaporated (Figure 3). Therefore, evaporation loss lessens, resulting in reduction vapor lock problem.

Table 2: Effect of benzene:ethylene mole ratio for benzene in reformate alkylation with ethylene at 225 °C using β-zeolite

B:E mole ratio	Benzene (vol%)	Ethyl benzene (vol%)	1,2 *di*Ethyl benzene (vol%)	1,2,4 *tri*Ethyl benzene (vol%)	Rvp (psi	RON	% Benzene Conversion
Original reformate	9.84	2.08	-	-	5.7	95.9	-
9:1	8.21	3.53	0.49	0.03	5.5	98.2	16.57
5:1	7.38	3.80	0.41	0.07	5.4	N.D.	25.00
3:1	6.79	4.15	0.74	0.08	5.5	N.D.	31.00

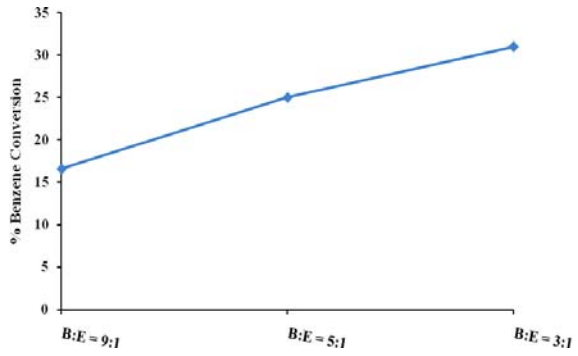

Fig 2 : Benzene conversion versus reaction time with different B:E ratio at temparature of 225 °C.

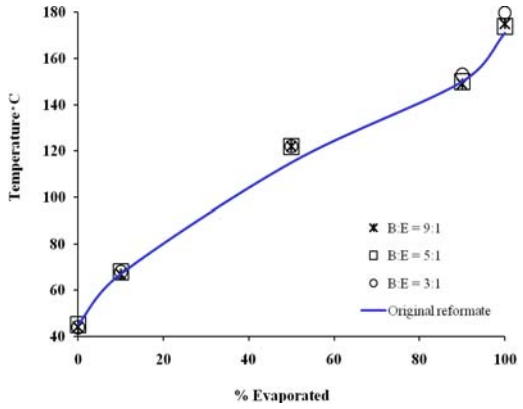

Figure 3. Distillation temperature of original reformate (—) and alkylated benzene with B:E mole ratio 9:1 (*), 5:1 (□) and 3:1 (o)

Conclusions

Benzene reduction in reformate by alkylation with ethylene catalyzed by β-zeolite was performed in a batch reactor at 225 °C and 45 bar. The benzene conversion increases with the lower benzene:ethylene mole ratio. The alkylated reformate increases in research octane number (RON), distillation temperature with decreasing in blending Reid vapor pressure (bRvp) because ethylbenzene is produced instead of benzene. The process improves gasoline quality in both term of technical and environmental viewpoint.

References

[1] Announcement of Department of Energy Business, 2007.

[2] W. Denis, S. Hiren, *Hydrocarbon Engineering*. 2004, 53-55.

[3] B.K. Kaul, D.W. Savage, and J.P. Dennis, *US patent 5,186,819*, to Exxon Research and Engineering Company, Patent and Trademark Office, 1993.

[4] C.H. Lee, C.H. Tsai, and J. Fung. *US patent 5,830,345*, to Chinese Petroleum Corp., Patent and Trademark Office, 1998.

[5] C.R. Hseieh, and R.C. Robinson, *US patent 5,210,348*, to Chevron Research and Technology Company, Patent and Trademark Office, 1993.

[6] T. Shimizu, *US patent 5,777,186*, to Cosmo Research Inst.; Cosmo Oil co., Ltd.. Patent and Trademark Office, 1998.

[7] B.S. Umansky, and M.C. Clark, *US patent 7,476,774 B2*, to Exxon Research and Engineering Company, Patent and Trademark Office, 2009.

[8] T.B. Lin, J.H. Hwang, H.C. Shen, and K.Y. Wu, *US patent 2007/0299294 A1*, to AMT International Inc.; Chinese Petroleum Corp., 2007.

[9] G. Bellussi, G. Pazzuconi, C. Perego, G. Girotti, and G. Terzoni, *J. Catal.*, **157** (1995), pp. 227-234.

[10] S. Siffert, L. Gaillard, and B.L. Su, *J. Mol. Catal. A: Chem.***153** (2000), pp. 267–279.

[11] G.D Hobson, Modern Petroleum Technology;5th Edition Part II, Wiley, 1984, p.786.

[12] O.M. Ramadhan, E.A. Al-Hyali, *Pet. Sci. Technol.*, **17** (1999), pp. 623-635.

Purification of biodiesel by adsorption with clays

B. Sriwichan[1], S. Butnark[2] and S. Pengprecha[3*]

[1]Program in Petrochemical and Polymer Science, Faculty of Science, Chulalongkorn University, Bangkok, Thailand 10330

[2] PTT Public Company Limited, Phahonyothin Rd., Sanubtub, Wangnoi, Ayutthaya, Thailand 13170

[3] Department of Chemistry, Faculty of Science, Chulalongkorn University, Bangkok, Thailand 10330

*E-mail: somchai.pe@chula.ac.th

Abstract: Biodiesel (fatty acid alkyl esters), which is derived from triglycerides by transesterification with alcohol in the presence of a suitable catalyst, has attracted considerable attention as a renewable, biodegradable, and nontoxic fuel. The crude biodiesel consists of fatty acid alkyl esters (FAAE) containing impurities that must be removed to meet the specification standards. Water washing is wildly used to purify biodiesel, however, it has many disadvantages especially for environmental problem. Therefore, the objective of this research is to purify biodiesel using natural adsorbents. The biodiesel was obtained from transesterification of crude palm oil with a 6:1 molar ratio of methanol to oil, 1%wt of sodium hydroxide as a catalyst and reaction temperature of 65°C for 1.50 hours. Biodiesel was further purified by using various natural adsorbents such as bentonite and diatomite etc. to remove glycerin, unreacted catalyst and soap. An amount of adsorbents, temperature and contact time were also investigated to determine the optimum conditions for purifying biodiesel. The results showed that by using 4%wt of adsorbents at 50°C for 10 minutes, the qualities of biodiesel meet the major specification of biodiesel standards.

Introduction

Rapid growth in population coupled with industrial and technological developments is leading towards the depletion of limited fossil fuel resources of the world. Currently, research is progressively more directed towards exploration of alternative renewable fuels. Biodiesel, an alternative diesel fuel, is a promising, non-toxic and eco-friendly clean fuel [1]. It could be regarded as petroleum-derived diesel substitute with many advantages including reduction of most exhaust emissions, biodegradability, high flash point, inherent lubricity, and domestic origin [2]. Biodiesel (fatty acid alkyl ester) is produced by transesterifying triglycerides, the main constituents of vegetable oils or animal fats with an excess alcohol, usually methanol, in the presence of a catalyst, usually a strong base such as sodium or potassium hydroxide [3]. The resulting product therefore can contain not only the desired alkyl ester product but also unreacted starting material (mono-, di- and triglycerides), residual alcohol, residual catalyst and soap. Glycerol is formed as a by-product and separated from the biodiesel in the production process, however, traces thereof can be found in the final biodiesel product [4]. To meet the requirements of biodiesel standards, removal of these impurities are especially important. Moreover, glycerol is especially undesired in the fuel because when heated it tends to polymerize by condensation with other molecules of glycerol or glycerides. The result is the formation of coke and tarnish on injectors and cylinders. Glycerides also increase the cloud point of biodiesel by forming small crystals at low temperatures [5]. In the usual industrial practice, water washing is wildly used to purified biodiesel but it has been lately critically objected on an environmental basis because of the relatively large amounts of process water that are issued as effluents. To eliminate these problems, the use of waterless process becomes the important role in removing biodiesel contaminants then conventional water washing could be replaced by using adsorbents with the associated reduction of effluent waters.

A study on the efficiency of natural adsorbents for the adsorption of biodiesel impurities were performed in this work. The main focus was put on the elimination of glycerin content in biodiesel obtained from refined palm oil. The optimum conditions for the adsorption of impurities were also investigated.

Materials and Methods

Transesterification of refined palm oil: 500 g of refined palm oil was added into 1000 ml of round bottom flask equipped with condenser. After the oil was heated to 65 °C, the solution of sodium hydroxide (5.0 g) in methanol (144.82 ml), 6:1 molar ratio of methanol to oil, was slowly added into the reaction and then the mixture was heated to 65°C for 1.50 h. The reaction mixture was transferred to a separatory funnel, and allowed glycerin to separate. The methyl ester layer was brought to purification process.

In order to investigate the effect of methanol on the adsorption, methyl ester was also synthesized by using 12:1 molar ratio of methanol to oil.

Purification of crude methyl esters: To determine the efficiency of natural adsorbents over the conventional purification process, two different treatments were utilized: (a) with various natural adsorbents and (b) with water-washing.

(a)Purification by using various natural adsorbents: Four types of adsorbents, diatomite, bentonite, activated clay and activated charcoal, were

studied. In an effort to adsorb glycerine content, five concentrations of each adsorbent: 1, 2, 3, 4 and 5 %wt were used. In 150 ml of flask, 100 g of untreated biodiesel was treated with each of adsorbents at 50°C, with stirring rate at 150 rpm and contact time at 10, 20, and 30 minutes in water bath. Then the adsorbents were removed by filtration.

(b) Purification with water-washing: The crude methyl esters were washed several times with warm deionized water (50°C) in a separatory funnel until the washed water became clear. The water in purified methyl esters was then removed by evaporation under atmospheric condition.

Analytical methods: Titration method was used to determine the amount of glycerin and unreacted catalyst.

Step A, 5 g of untreated biodiesel was dissolved in 100 ml of isopropyl alcohol with 2 ml of 1%phenolphthalein as an indicator. The mixture was titrated with 0.01N hydrochloric acid until the color of the solution changed from red to clear color. This amount of 0.01N hydrochloric acid solution is referred as "A".

Step B, then 1 ml of 0.04%bromophenol blue was added into the mixture solution and titrated with 0.01N hydrochloric acid until the color of the solution changed from blue to yellow. This amount of 0.01N hydrochloric acid solution is referred as "B" [6].

The amount of unreacted catalyst can be calculated by using the equation 1:

$$\text{g of NaOH/g of untreated biodiesel} = \frac{A \times 0.01 \times 40.0}{W \times 1000} \quad (1)$$

where:
A = volume of hydrochloric acid used in Step A (mL)
W = weight of untreated biodiesel used (g)

and the amount of glycerin content in the biodiesel can be calculated by using the equation 2:

$$\text{g of glycerin/g of untreated biodiesel} = \frac{B \times 0.01 \times 304.4}{W \times 1000} \quad (2)$$

where:
B = volume of hydrochloric acid used in step B (mL)
W= weight of untreated biodiesel used (g)

Results and Discussion

Optimization of the adsorption parameters:

Effect of contact time: The time-dependent behavior of the adsorption was measured by varying the equilibrium time between adsorbents and crude methyl ester in the range of 5–30 min. The experiment was carried out at 50°C with 3%wt of adsorbents and stirring rate at 150 rpm. As can be observed in Figure 1, at adsorbed time 5 min, glycerin contents were dramatically decreased more than 50% and they were appeared to be slightly reduced until 10 min of the adsorption. Afterwards, the significance of glycerin contents may not be great. Therefore, a 10 min contact time was found to be appropriate for maximum adsorption and it was used in all subsequent measurements.

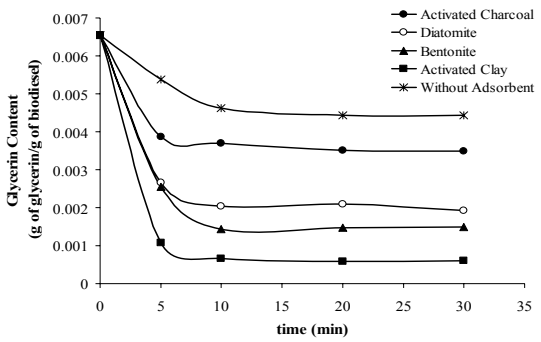

Figure 1. Effect of contact time (3%wt of adsorbents, 50°C, stirring rate 150 rpm)

Effect of amount of adsorbents: The effect of amount of adsorbents were studied in the range of 1-5%wt of adsorbents with stirring rate 150 rpm at 50°C. In Figure 2, the results showed that glycerin adsorptions were increased with increasing the amount of adsorbents up to 4%wt. Therefore, for all further studies 4%wt of adsorbents were used.

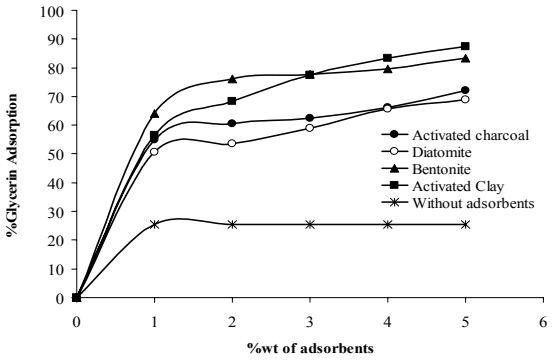

Figure 2. Effect of the amount of adsorbents (contact time 10 min, 50°C, stirring rate 150 rpm)

Effect of methanol on the adsorption: To investigate the effect of methanol on the adsorption, methyl ester was also synthesized by using 12:1 molar ratio of methanol to oil. The optimum conditions for adsorption were 4%wt of adsorbents at 50°C with 150 rpm stirring rate. As can be observed in Figure 3, methanol addition reduced the effective of all the adsorbents about 50%.

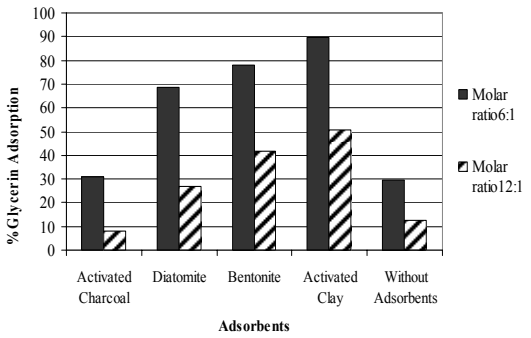

Figure 3. Effect of methanol on the adsorption (4%wt of adsorbents, 50°C, contact time 10 min, stirring rate 150 rpm)

From Figure 3, using 4%wt of activated clay, with the optimum conditions, gave the best result of removing of glycerin content. To perform as industrial practice, methanol was first removed before the adsorption was performed [7]. The result was shown in Table 1, without methanol, sorbent could removed glycerin better than sorbent with the presence of methanol. Moreover, the trace glycerin content by using this adsorption process was similar to the trace glycerin content of the conventional water washing process.

Table 1: Glycerin contents of 4%wt of activated clay and water washing process

Process	Glycerin Content (g glycerin / g biodiesel)
With methanol	1.06×10^{-3}
Without methanol	2.80×10^{-5}
Water washing	2.77×10^{-5}

Conclusions

The experimental study revealed that the optimum conditions for the purification of biodiesel by using various natural adsorbents were 4%wt of adsorbents, adsorption temperature 50° with stirring rate 150 rpm for a period of 10 min. Treating crude biodiesel, after methanol was removed, with 4%wt of activated clay gave the best result against the other adsorbents. Activated clay not only had an effective of removing glycerin content, but it also had an ability to neutralized the residual catalyst in biodiesel. The effective of removing glycerin content with activated clay offered similar result with water washing process and the level of glycerin content was lower than the specification of biodiesel standard.

References

[1] R. Umer and A. Farooq, *Fuel.* **87** (2008), pp. 265–273.
[2] A. Srivastava and R. Prasad, *Renew Sust Energy Rev.* **4** (2000), pp. 111-133.
[3] J.P. Zlatica, *Fuel.* **87** (2008), pp. 3522–3528.
[4] G. Knothe, *J Am Oil Chem Soc.* **83** (2006), pp. 823–833.
[5] V.A. Mazzieri, C.R. Vera and J.C. Yori, *Energy&Fuels*. **22** (2008), pp. 4281-4284.
[6] J. Van Gerpen, B. Shanks, R. Pruszko, D. Clements and G. Knothe, Biodiesel Analytical Methods, *National Renewable Energy Laboratory*, (2004), NREL/SR-510-36240.
[7] M. Berrios and R.L. Skelton, *Chem. Eng. J.* **144** (2008), pp. 459-465.

Biodiesel production from oilseed plants using ferric sulfate and sodium hydroxide

S. Issariyanate[1] and S. Pengprecha[2*] and K. Kangvansaichol[3]

[1]Program in Petrochemical and Polymer Science, Faculty of Science, Chulalongkorn University, Bangkok, Thailand 10330
[2]Department of Chemistry, Faculty of Science, Chulalongkorn University, Bangkok, Thailand 10330
[3]PTT Public Company Limited, Phahonyothin Rd., Sanubtub, Wangnoi, Ayutthaya, Thailand 13170

*E-mail: somchai.pe@chula.ac.th

Abstract: This research was aimed to study possibility of 10 new plant species in Thailand having 20% or more fixed oil in their seed/kernel to use as a raw material to produce biodiesel. The amount of oil, free fatty acid (FFA), saponification number (SN) and iodine value (IV) of oil of these plants were in the range of 20.96 to 54%, 0.65-5.47%, 150-187.79 mg KOH/g and 62.32-128.33 mg I_2/g respectively. By using the 12:1 molar ratio of methanol to oil for the FFA content less than 3%, or the 10:1 molar ratio followed by 12:1 molar ratio of methanol to oil for FFA more than 3%, the biodiesel of oils of these plant species could be conveniently synthesized. All of plant species gave ester conversion more than 90%. According to the methyl ester content, viscosity, density, acid value and flash point, the biodiesel produced from 4 plant species including *Lagenaria siceraria*, *Ocimum canum*, *Camellia oleifera* and *Moringa oleifera* could be potentially used and they meet the major specification of biodiesel standards.

Introduction

As the fossil fuels are depleting day by day, there is a need to find out an alternative fuel to fulfill the energy demand of the world. The petroleum fuels play a very important role in the development of industrial growth, transportation, agricultural sector and to meet many other basic human needs but these fuels are limited. Therefore, the alternative fuels are needed. Biodiesel, an alternative diesel fuel, is one of the alternative fuels can be used nowadays, it can be produced from biological sources such as vegetable oils and animal fats by transesterification reactions with alkali catalyst (e.g. NaOH, KOH), acid catalyst (e.g. H_2SO_4) or enzyme catalyst, however, the first two types have received more attention because of the short reaction times and low cost compared with the third one[1-3].

This research aimed to synthesize methyl ester compounds from 10 oilseed plants, containing 20% or more oil in their seed, fruit or nut, for using as biodiesel. The properties of biodiesel from oilseed plants were also studied.

Materials and Methods

All of reagents were analytical grade.

Extraction of oilseed plants and determination of physical and chemical properties of crude oil from oilseed plants: 500 ml of hexane was added to 500 g of the crushed kernel in 2000 ml of Erlenmeyer flask and allowed to shake overnight. The organic extract was filtered and evaporated to dryness by rotary evaporator. The amount of oil, %free fatty acid (FFA), saponification number (SN) and iodine value (IV) were determined according to ASTM D5555, ASTM D5558 and ASTM D5554 methods, respectively.

Optimization for one-step catalyzed process (base catalyzed).

Effect of free fatty acid to produce palm oil methyl ester: 20 g of palm oil with various amount of free fatty acid (0.14, 1.1, 2.1 and 3.3%wt) was added into 100 ml of round bottom flask equipped with condenser. After the oil was heated to 65 °C, the solution of sodium hydroxide (0.2 g) in methanol (5.79 ml) was added and then the mixture was heated to 65°C for 1.50 h. The mixture was transferred to a separatory funnel, allowed glycerol to separate for 2 h. The methyl ester layer (upper layer) was washed with hot water (5 x 100 ml), dried under vacuum (100±1 mmHg) at 60°C for 1 h. The percent conversion of methyl ester was analyzed by ^{1}H-NMR.

Effect of methanol to oil molar ratio and reaction time were studied following the method described above, by using molar ratio of methanol to oil equal to 3:1, 6:1, 9:1 and 12:1, the reaction times equal to 0.25, 0.5, 1, 1.5 and 2 h. The percent conversion of methyl ester was analyzed by ^{1}H-NMR.

Optimization for two-step catalyzed process (Acid – base catalyzed).

Effect of reaction time and amount of catalyst: 20 g of palm oil with 10% free fatty acid was added into 100 ml of round bottom flask equipped with condenser. After the oil was heated to 65 °C, various amount of ferric sulfate (1, 2, 3 and 4%wt) and methanol was added, then the mixture was heated to 65°C for 1, 2 and 3 h. The excess of methanol was removed by rotary evaporator, and the mixture was left to separate. The upper oil layer was subjected to determine the amount of FFA according to ASTM D 5555 and used in the second step following the method in optimization for one-step catalyzed process[4].

Effect of methanol to oil molar ratio and reaction time were studied following the method in optimization for two-step catalyzed process. The experiment was performed by using 6:1, 10:1 and 20:1 molar ratio of methanol to oil for 1 and 2 h.

Synthesis of methyl ester from oilseed plants via one-step catalyzed process (FFA< 3%): 20 g of *Basella alba* (BA), *Benincasa hispida* (BEH), *Caesalpinia crista* (CAC), *Camellia oleifera* (CAO), *Gardenia jasminodes* (GJ), *Hibiscus sabdariffa* (HIS), *Lagenaria siceraria* (LS) and *Passiflora foetida* (PAF) were synthesized following the optimization for one-step catalyzed process. The products were characterized by ^{1}H-NMR and GC techniques.

Synthesis of methyl ester from oilseed plants via two-step catalyzed process (FFA> 3%): 20 g of *Moringa oleifera* (MO) and *Ocimum canum* (OC) oils were synthesized following the optimization for two-step catalyzed process. The products were characterized by ^{1}H-NMR and GC techniques.

Analysis method: The analysis of %conversion of methyl ester of each samples were carried out by gas chromatography (GC). The condition of GC used was as follows: column: ZB-Wax plus; Zebron, 30m, 0.25mm ID, 0.25µm, injector temperature: 240 °C, detector: Flame ionization, detector temperature: 250 °C, column Oven: 50°C (hold 2 min), rate of 4 °C/min to 220 °C (hold 15 min), carrier gas: N_2, flow rate: 1.2 ml/min, volume injected: 1 µl.

Determination of the properties of biodiesel: The physical properties of biodiesel, viscosity at 40°C (cSt), flash point (°C), density at 15°C (kg/cm^3), acid number (mg KOH/g) and ester content (%wt) were determined according to ASTM D445, ASTM D93, ASTM D4052, ASTM D974 and EN 14103, respectively.

Results and Discussion

Extraction of oilseed plants and determination of physical and chemical properties of crude oil from oilseed plants: The amount of oil, the physical and chemical properties of crude oil from oilseed plants were listed in Table 1, % oil content, %FFA, SN and IV were in range of 20.96-54%, 0.65-5.47%, 150-187.79 mgKOH/g and 62.32-128.33 mgI_2/g, respectively.

Optimization for one-step catalyzed process (base catalyzed).

The effect of the amount of free fatty acid in palm oil: In Figure 1, the results showed that % conversion of methyl ester more than 90% could be achieved when FFA lower than 3%. Therefore, this process was suitable to synthesis of biodiesel from oil containing FFA less than 3%.

The effect of methanol to oil molar ratio and reaction time: In Figure 2, at higher molar ratio, the conversion of methyl ester was increased. Within 1.5h, the highest conversion of methyl ester was obtained. After that the reaction time had no significant effect on the conversion of triglycerides. Hence, the best result was 12:1 molar ratio of methanol to oil for 1.5 h.

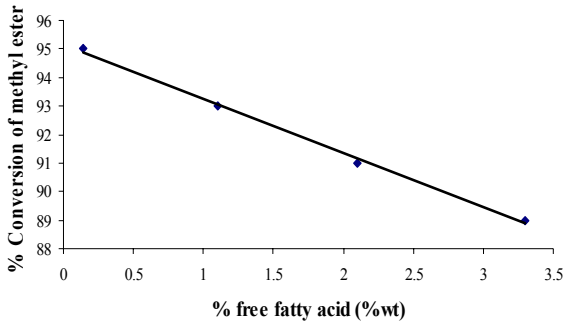

Figure 1. Effect of free fatty acid (at 65°C, 1%wt of NaOH and 6:1 molar ratio of methanol to oil).

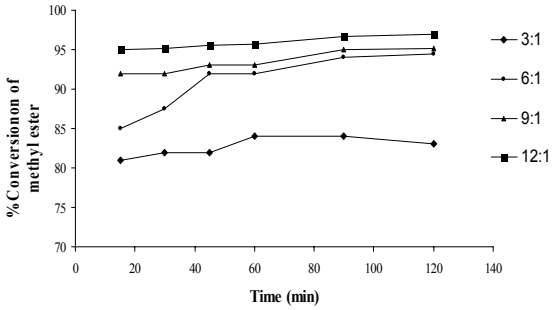

Figure 2. Effect of methanol to oil molar ratio and reaction time (at 65°C, 1%wt of NaOH).

Optimization for two-step catalyzed process (Acid – base catalyzed).

Effect of reaction time and amount of catalyst (ferric sulfate): In Figure 3, It could be seen that FFA less than 3% could be achieved by using 1% $Fe_2(SO_4)_3$ for 3 h, 2% $Fe_2(SO_4)_3$ for 2 h, 3 and 4% $Fe_2(SO_4)_3$ for 1 h. Therefore, 3% $Fe_2(SO_4)_3$ was used for synthesis of biodiesel from oil containing FFA more than 3%.

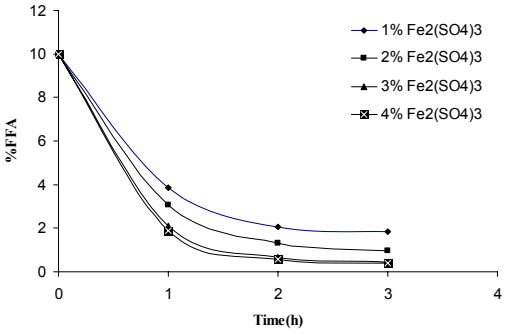

Figure 3. Effect of reaction time and amount of catalyst, $Fe_2(SO_4)_3$ (at 65°C and 10:1 molar ratio of methanol to oil).

Table 1. Summary of physical and chemical properties of crude oils from oilseed plants.

Oilseed plants	Codes	% Oil	% FFA	SN	IV
Basella alba	BA	27.40	0.65	167.55	76.78
Benincasa hispida	BEH	24.96	1.39	180.91	128.33
Caesalpinia crista	CAC	21	1.04	173.51	125.19
Camellia oleifera	CAO	36.51	0.65	168.21	115.29
Gardenia jasminodes	GJ	22.06	1.01	187.79	112.23
Hibiscus sabdariffa	HIS	22	1.40	150.00	81.11
Lagenaria siceraria	LS	54	2.77	161.13	119.24
Moringa oleifera	MO	36.57	3.13	156.03	62.32
Ocimum canum	OC	20.96	5.47	177.78	113.76
Passiflora foetida	PAF	22.63	1.40	159.37	127.32

Table 2. Summary of properties of biodiesel from oilseed plants and specification properties of biodiesel.

Oilseed plants	Codes	Viscosity at 40°C(cSt)	Flash point (°C)	Density at 15°C (kg/cm^3)	Acid number (mg KOH/g)	Ester content (%wt)
Basella alba	BA	4.47	>120	882.97	0.17	93.28
Benincasa hispida	BEH	3.92	>120	881.00	0.11	93.70
Caesalpinia crista	CAC	3.50	>120	862.30	0.20	94.65
Camellia oleifera	CAO	3.79	>120	880.55	0.18	97.09
Gardenia jasminodes	GJ	4.83	>120	884.24	0.45	94.73
Hibiscus sabdariffa	HIS	4.40	>120	882.60	0.19	91.57
Lagenaria siceraria	LS	3.50	>120	879.90	0.25	96.75
Moringa oleifera	MO	4.68	>120	883.75	0.34	96.55
Ocimum canum	OC	3.56	>120	879.72	0.22	96.61
Passiflora foetida	PAF	3.86	>120	880.80	0.22	95.13
Specification properties of biodiesel		**3-5**	**>120**	**860-900**	**<0.5**	**>96.5**

Effect of methanol to oil molar ratio and reaction time: As can be seen from Figure 4, FFA less than 3% was obtained by using 6:1 molar ratio of methanol to oil for 2 h, 10:1 and 20:1 for 1 h. However, concerning about cost and energy, 10:1 molar ratio for 1 h were found to be the optimum conditions for this process.

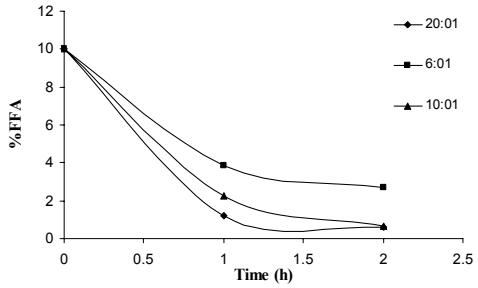

Figure 4. Effect of methanol to oil molar ratio and reaction time (at 65°C and 3% wt of ferric sulfate).

Synthesis of methyl ester from oilseed plants: The biodiesel from BA, BEH, CAC, CAO, GJ, HIS, LS MO, OC and PAF could be produced by either two-step catalyzed process or one-step catalyzed process depend on their %FFA. In Table 2, the results show that biodiesel from CAO, LS, MO and OC gave the percentage of methyl ester contents more than 96.5%.

Determination of the properties of biodiesel: From Table 2, it could be seen that the properties (viscosity, flash point, density and acid number) of all plants species are in the regimen of biodiesel standards. In the consideration of ester content, only 4 plant species, CAO, LS, MO and OC, could be used to produce biodiesel according to the regulation of biodiesel standards.

Conclusions

In this study, seed oils of 10 species were investigated as an alternative source for biodiesel production**.** The optimum conditions for one-step catalyzed process were studied and found to be 1%wt of NaOH, 12:1 molar ratio of methanol to oil, at 65°C for 1.5 h and the optimum conditions for two-step catalyzed process were 3%$Fe_2(SO_4)_3$, 10:1 molar ratio of methanol to oil, at 65°C for 1 h following by one-step catalyzed process. The biodiesel produced from 10 plant species under this optimum conditions gave high %conversion of methyl ester more than 90%. According to the properties of biodiesel and ester content, *Camellia oleifera, Lagenaria siceraria*, *Moringa oleifera* and *Ocimum canum* could be potentially used as raw material to produce biodiesel and they met the major specification of biodiesel standards.

References

[1] S. A. Basha, K. R. Gopal and S. Jebaraj, *Renewable and Sustainable Energy Reviews*. **13** (2009), pp. 1628–1634.

[2] Y. Watanabe, Y. Shimada and A. Sugihara, *JAOCS.* **78(7)** (2001), pp. 703–7.

[3] Y. Watanabe, Y. Shimada and A. Sugihara, *J Mol Catal B: Enzym.* **17** (2002), pp. 151–5.

[4] W. Yong, O. Shiyi, L. Pengzhan, X. Feng, and T. Shuze, *J Mol Catal A-Chem*. **252** (2006), pp. 107-112.

Modification method of calcined natural dolomite for transesterification acitivity improvment

P. Udomsap, B. Yoosuk*, B. Puttasawat and P. Krasae

National Metal and Materials Technology Center (MTEC)
114 Thailand Science Park, Phahonyothin Road, Klong 1, Klong Luang, Pathumthani 12120, Thailand

* E-Mail Address: boonyawy@mtec.or.th

Abstract: The present study provides an alternative technique for increasing the activity and improving the properties of calcined natural dolomite in order to make them highly suitable for use as heterogeneous catalysts for biodiesel production. Calcined dolomite was refluxed in water followed by the synthesis of the oxide from hydroxide species. The ensuing transformations of the dolomite during synthesis were monitored by XRD and TGA techniques. The characterization results indicate that the hydrated sample is composed of three phases: separate $Mg(OH)_2$, separate $Ca(OH)_2$ and magnesium-calcium hydroxide. Moreover, the hydration reduces calcination temperature required for the decomposition. Hydration and subsequent calcination also generates a new calcium oxide and magnesium oxide with less crystalline. Transesterification of palm olein was used to determine the activity of catalysts to show that the decomposed-hydrated calcined dolomite with Brønsted base sites exhibits higher catalytic activity than the decomposed dolomite. The methyl ester content was enhanced to 93.2 wt% from 80.8 wt% of calcined dolomite.

Introduction

The transesterification process with the homogeneous base catalysts, NaOH, KOH, and $NaOCH_3$, has been used extensively in biodiesel production. However, these homogeneous catalysis systems have many drawbacks. Heterogeneous catalysis is an economically and ecologically important field in catalysis research because the catalysts have many advantages. Many types of heterogeneous solid base catalysts, such as alkaline-earth metal oxides and hydroxides, have been studied in regard to the transesterification of vegetable, various alkali metal compounds supported on alumina, zeolite, hydrotalcites, anion exchange resins and polymer-supported guanidines [1]. The order of activity among alkaline earth oxide catalysts is BaO > SrO > CaO > MgO [2]. However, in most experiments using heterogeneous catalysts, the transesterification reaction proceeds at a relatively slow rate as compared to the transesterification reaction in those conducted with homogeneous catalysts. This typically slow reaction rate is due to diffusion problems accruing from the heterogeneous media's behavior as a three-phase system (oil/methanol/catalyst) [3]. Thus, the development of a solid basic catalyst capable of carrying the transesterification of oils proficiently under mild reaction conditions in short reaction times remains an intriguing and significant challenge.

Dolomite has a high natural abundance and low toxicity found in many areas of Thailand. Dolomite is comprised of alternating layers of $Mg(CO_3)$–$Ca(CO_3)$ and is structurally very similar to calcite ($CaCO_3$). Natural sources may also contain Ca-rich phases of magnesian calcite (Mg_xCa_{1-x} CO_3), which also adopt an alternating layered structure, in this instance of $Ca(CO_3)$ and mixed $Mg(CO_3)$–$Ca(CO_3)$. On reviewing temperature programmed experiments of fresh dolomite, the highly basic CaO and MgO are formed after the decomposition of carbonate groups in dolomite.

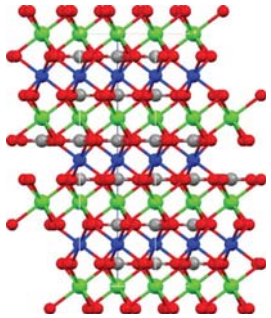

Scheme 1 Structure of dolomite $MgCa(CO_3)_2$ (C–grey, Mg^{2+}–blue, Ca^{2+}–green, O^{2-}–red) [4]

Dolomite is mainly used in agriculture and cement manufacturing. The catalytic application of dolomite in many processes such as gasification and reforming has attracted much attention as it is cheap high basicity and environmental friendly; however, there are not many studies of its applications that can be found in literature, particularly on a basic catalyzed chemical synthesis. Recently, a few works [4, 5] reported the success uses of calcined and/or modified dolomite as solid catalyst for biodiesel production. Nonetheless, its activity and surface area are not high as compared to liquid catalyst. More catalyst weight and longer reaction time are needed.

Thus, in this work, we have proposed techniques to improve activity and surface area of calcined natural dolomite by using hydration method. The influences of water on physical and chemical properties were reported by various characterization techniques. Transesterification reaction of plam olein was carried out to evaluate the activity of modified catalysts.

Materials and Methods

Chemicals and catalyst preparation: The dolomite used in the study was commercially available; in fact, it was purchased from an agricultural store. The elemental composition analysis with an X-ray fluorescence (XRF) spectrometer was showed in Table 1. Fresh dolomite was thermally decomposed at 1073 K for 3 h. The solid product ($CaMgO_S$) was refluxed in water at 333 K for 6 h, and the sample was filtered and heated at 393 K overnight. Prior to use, the product, referred to as $CaMgO_W$, was calcined at 923 K for 3 h in order to change the hydroxide form to an oxide form, the latter being the active form for a transesterification reaction. The solid product was designated $CaMgO_{650}$. The commercially available CaO (CaO_{com}), purchased from Ajax Finechem, was used for comparison purposes.

Table 1: XRF elemental composition analysis of fresh dolomite

	Concentration (wt%)[a]				
Sample	CaO	MgO	SiO_2	Al_2O_3	Fe_2O_3
Dolomite	45.0	13.3	0.3	0.3	0.1

[a] CO_2 balance

Transesterification reaction procedure: Palm olein oil was purchased from Morakot Industries PCL., Thailand. Composition of fatty acid in palm olein oil is given in Table 2. Methanol (Fluka) used in this work was analytical reagent grade (AR). The transesterification was carried out in batch reactor. A 500 ml round-bottom flask was equipped with a reflux condenser. Magnetic stirring rate of 500 rpm was adjusted and reaction temperature was controlled by hotplate with temperature sensor (Heidolph).

Table 2: Fatty Acid Composition of Palm Olein Oil

Fatty acid	Composition (wt%)
Lauric acid (C12:0)	0.4
Myristic acid (C14:0)	0.8
Palmitic acid (C16:0)	37.4
Palmitoleic acid (C16:1)	0.2
Stearic acid (C18:0)	3.6
Oleic acid (C18:1)	45.8
Linoleic acid (C18:2)	11.1
Linolenic acid (C18:3)	0.3
Arachidic acid (C20:0)	0.3
Eicosenoic acid (C20:1)	0.1

A 3.2 g of catalyst was mixed with 33 ml of methanol. The mixture was warm at 333 K. A 50 ml of palm olein oil was also warm at 333 K before being added to the mixture of methanol and catalyst. Temperature of the reaction was kept at 333 K by an oil bath. After the desired reaction time, the product of reaction was separated from catalyst by centrifugation, and then excessive amount of methanol was evaporated before analysis of biodiesel yield.

Determination of biodiesel yield: The yield and compositions of biodiesel were determined by a Gas chromatrograph (GC-2010, Shimadzu) equipped with capillary column, DB-WAX (30 x 0.15 m) and a flame ionization detector. Methylheptadecanoate was used as internal standard for quantification, according to EN14103.

Results and Discussion

The thermal decomposition of fresh dolomite and hydrated sample ($CaMgO_W$) is revealed in the Fig 1. The fresh dolomite shows 48.0 % weight loss at 923 – 1153 K. DTG curve of fresh dolomite shows two major peaks. The lower temperature peak represents the decomposition of the dolomite structure, releasing carbon dioxide from the carbonate ion associated with magnesium part of the structure accompanied by the formation of calcite and magnesium oxide. The higher temperature peak represents the decomposition of calcite with the evolution of carbon dioxide [6]. The phenomenon occurring during the thermal decomposition of fresh dolomite could be as follows:

$$MgCa(CO_3)_2 \rightarrow MgO - CaCO_3 + CO_2 \quad \text{Eq. 1}$$

$$MgO - CaCO_3 \rightarrow MgO - CaO + CO_2 \quad \text{Eq. 2}$$

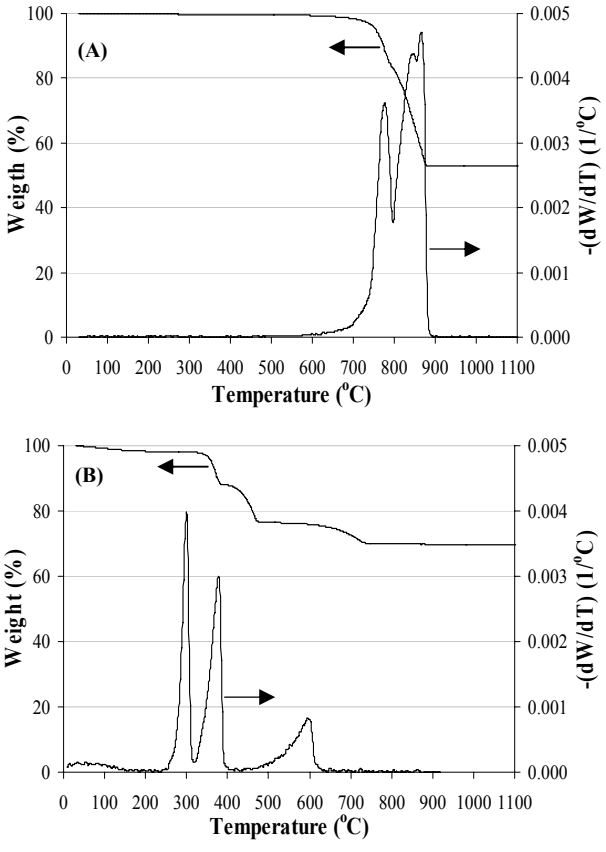

Figure 1. Thermalgravimatric analysis (TGA) of fresh dolomite (A) and CaMgOw (B).

$CaMgO_W$ shows three major weight loss peaks in temperature range of 523 – 593 K , 593 – 673 K and 733 – 933 K. By comparing with that of the authentic sample, the first two peak were attributed to the weight lose of $Mg(OH)_2$ to form MgO and $Ca(OH)_2$ to form CaO, respectively. These hydroxide species were formed from MgO and CaO species separate from magnesium-calcium oxide after calcination of fresh dolomite. This result was indicated that the $CaMgO_W$ is composed of three phases: separate $Mg(OH)_2$, separate $Ca(OH)_2$ and magnesium-calcium hydroxide.

The crystallinity of all the samples was probed by powder XRD. Fig. 2 shows the XRD patterns for fresh dolomite, CaMgOs, and $CaMgO_{650}$. The parent material exhibits major diffraction peaks at 29.4◦ and 30.9◦, characteristic of the reflections of calcite and dolomite, respectively. Weaker reflections between 35–55◦ are also consistent with both these phases, confirming our natural dolomite rock comprises a mixture of dolomite and calcite. Following calcination, the reflections arising from the dolomite and calcite were lost, coincident with the appearance of new crystalline phases that can be assigned to highly crystalline CaO (32.3◦, 37.4◦ and 53.9◦), and MgO (42.9◦ and 62.3◦).

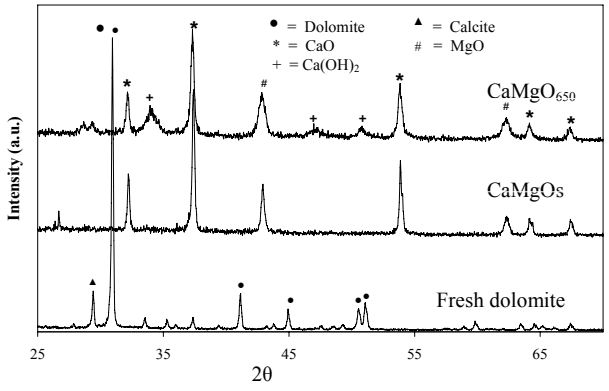

Figure 2. XRD patterns of fresh dolomite, CaMgOs and $CaMgO_{650}$, The peak intensity of fresh calcite was reduced 3.0 times.

The intensity of CaO and MgO peaks decreased significantly when the CaMgOs was hydrated and subsequently calcined. The results suggest that the water treatment has a strong effect on crystallinity of catalyst, which decreased considerably. This phenomenon has also been demonstrated previously in hydrotalcite-like compounds [7] and MgO [8].

The catalysts were subsequently examined for their activities in the transesterification of palm olein with methanol. The reactions were performed under these conditions: methanol/oil molar ratio of 15, catalyst weight of 7 wt%, and temperature of 333 K. Fig. 3 shows the methyl ester content in the biodiesel product attained via the transesterification for all samples as compared with commercial CaO. No methyl ester was observed when fresh dolomite was used. This suggests that the basicity of the carbonate form of calcium and magnesium is not high enough to catalyze the transesterification reaction. After the calcination of the fresh dolomite at 1073 K, the activity of the catalyst increased significantly. Within 1 h, 80.8 wt% of ME content had been obtained. The hydration without further calcination (CaMgOw) decreased the activity of the catalyst from 80.8 wt% to 18.3 wt% of ME content. This might be due to the fact that, for alkaline earth metal, the oxide form has stronger basicity than does the hydroxide form. However, CaMgOw showed higher activity than the fresh dolomite did.

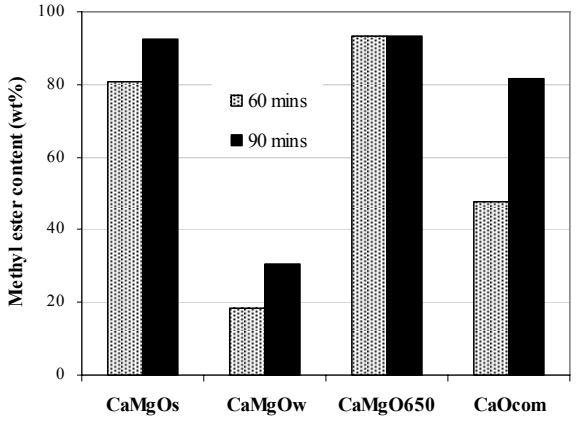

Figure 3. Methyl ester content obtained over fresh dolomite and various samples. (CaO_{com} represents commercial CaO).

Among all the samples, $CaMgO_{650}$ exhibited the greatest catalytic activity. For 1 h of reaction time, 93.2 wt% of ME content was observed. The commercial CaO showed less activity than both CaMgOs and $CaMgO_{650}$. The $CaMgO_{650}$ processed 12.4 wt% ME content higher than CaMgOs. It is clear that the hydration and subsequent calcination of the calcined dolomite is essential in order to get an active catalyst for this kind of reaction. This transesterification reaction study indicates that the reconstruction of decomposed dolomite by hydrating subsequent calcinations generates highly active CaO-MgO. During hydration, the charge-compensating carbonate anions were replaced by hydroxyl anions, thus forming Brønsted base sites. The decomposed-hydrated calcined dolomite with Brønsted base sites exhibited higher catalytic activity than the decomposed calcite for the transesterification reaction of the triglyceride with methanol.

Conclusions

The results obtained in this study show that hydration and subsequent calcination is a sufficient technique to improve the activity of calcined natural dolomite and contributes to the development of better heterogeneous catalysts for biodiesel production. This technique generates a new calcium oxide and magnesium with excellent textural properties and a large number of basic sites. The water treatment has a

strong effect on the crystallinity of the catalyst, which is considerably decreased as suggested from XRD.

The decomposed-hydrated calcined dolomite with Brønsted base sites exhibits a higher catalytic activity than the decomposed natural calcite does, as shown in the results of the palm olein transesterification with methanol. The $CaMgO_{650}$ processed 12.4 wt% ME content higher than the CaMgOs.

Acknowledgement

The authors gratefully acknowledge the support of National Metal and Materials Technology Center (MTEC).

References

[1] S.R. Watkins, F.A. Lee**,** *Green Chem*. **7** (2004), pp. 335–340.
[2] D.G. Cantrell, L.J. Gillie, A.F. Lee, K. Wilson, *Appl. Catal. A* **287** (2005), pp. 183.
[3] W.L. Xie, H. Peng, L.G. Chen, *Applied Catalysis a-General* **300** (2006), pp. 67-74.
[4] K. Wilson, C. Hardacre, A.F. Lee, J.M. Montero and L. Shellard, *Green Chem* **10** (2008), p. 654-659
[5] C. Ngamcharussrivichai, W. Wiwatnimit, S. Wangnoi, *J. Mol. Catal. A: Chem* **276** (2007), p. 24-33
[6] L.M. McInosh, J.H. Sharp, F.W. Willburn , Thermochim. Acta. 165 (1990), pp. 281-
[7] F. Cavani, F. Trifiro, A. Vaccari, *Catal. Today*. **11** (1991), pp. 173-301.
[8] M.A. Aramendia, J.A. Benitez, V. Borau, C. Jimenez, J.M. Marinas, J.R. Ruiz, F. Urbano, *J. Solid State Chem.*, **144** (1999), pp. 25-29.

Co/Tio$_2$ and Ce/Co/TiO$_2$ Fischer-Tropsch catalysts: preparation and characterization

S. Klaithong[1], S. Kityakarn[1], J. T-Thienprasert[2], S. Limpijumnong[3,4], A. Worayingyong[1*]

[1] Department of Chemistry, Faculty of Science, Kasetsart University, Bangkok 10900, Thailand
[2] Department of Physics, Faculty of Science, Kasetsart University, Bangkok 10900, Thailand
[3] School of Physics, Suranaree University of Technology, Nakhon Ratchasima 30000, Thailand
[4]Synchrotron Light Research Institute, Nakhon Ratchasima 30000, Thailand

*E-mail: fsciarw@ku.ac.th.

Abstract: Co/TiO$_2$ and Ce/Co/TiO$_2$, prepared by a sol-gel and a co-precipitation methods for Fischer-Tropsch synthesis, were characterized by X-ray diffraction (XRD) and X-ray absorption spectroscopy (XAS). Based on XRD results, Co/TiO$_2$ prepared by the sol-gel method calcined at 823 K, showed both anatase and rutile phases while Ce/Co/TiO$_2$ exhibited only the anatase phase. For comparison, commercial anatase-TiO$_2$ was used as the catalyst supports for Co/TiO$_2$ and Ce/Co/TiO$_2$ prepared by the co-precipitation method and showed only the anatase phase. Co *K*-edge XANES spectra indicated that Co in all catalysts are resembling the spectra of Co in Co$_3$O$_4$ and/or CoO with different percentages. Ti *K*-edge EXAFS spectra was used to determine the phase of TiO$_2$ in all catalysts, which is mainly anatase. The local states of Co in Co/TiO$_2$-SG and Ce/Co/TiO$_2$-SG determined by Co *K*-edge EXAFS spectra mainly substitute on Ti atoms.

Introduction

The Fischer-Tropsch synthesis (FTS) is a process used to produce liquid hydrocarbons from synthesis gas. It is the development of clean energy in renewable sources project. In this process, carbon monoxide (CO), green house gas, hydrogen and catalysts are used in the reaction. Therefore this process can be set up to reduce the introduction of polluted green house gas into atmosphere. The most effective catalysts for FTS are cobalt (Co), iron (Fe), and ruthenium (Ru). Cobalt catalyst has high activities for FTS based on natural gas, high selectivity to linear long-chain hydrocarbons, and low activity for the water–gas shift (WGS) reaction [1]. The most common catalyst supports used in FTS are alumina (Al_2O_3), silica (SiO_2), and titanium dioxide (TiO_2) [1-4]. In this research, titania was used as a support due to its ability to increase reduction [2]. During the past decades, titania-supported cobalt catalysts have been widely investigated [1,5]. This is because titania can be crystallized in three phases, i.e. anatase, rutile and brookite phases [1,5]. Each phase of titania plays an important role on catalytic properties. The active species of cobalt are mainly in the form of Co^0 [3,5,6]. The addition of various amounts of cerium dioxide affects strongly on the properties of Co/SiO_2 catalysts in Fischer-Tropsch synthesis under pressure [7]. It results in an increase in the methanation and orientation of the selectivity towards the C_5-C_{13} fraction (gasoline) at the expense of C_{22+} hydrocarbons (waxes) [7]. However, the addition of various amounts of ceria to 10 wt.% Co/γ-Al_2O_3 catalysts enhances the C_5-C_{10} selectivity and CO conversion while the methanation is decreased [8]. As a result, it would be interesting to investigate the effect of ceria promoted on titania supports containing different phases.

In this study, a series of titania-supported cobalt catalysts was prepared by the sol-gel and the co-precipitation methods to study the effect of preparation on the phase of the catalysts. X-ray diffraction (XRD) and X-ray absorption spectroscopy (XAS), were used to investigate the effect of cerium addition on phase of titania. The cobalt species (i.e. Co^0, Co^{2+}, or Co^{3+}) in the prepared catalysts were determined.

Experimental

Catalyst Preparation
Sol-Gel method

Titanium(IV) isopropoxide (Ti[OCH(CH$_3$)$_2$]$_4$, Fluka, analytical grade) in amount of 0.01 mol was slowly dropwised into 0.33 mol isopropanol (C_3H_8O, QRëC, analytical grade) with stirring. Ethylene glycol ($HOCH_2CH_2OH$, Fluka, 98%) in amount of 0.07 mol was added into the previous solution. Then, 0.04 mol deionized water was added and stirred until the solution was homogeneous. The sol was allowed to rest in an oven at 348 K until gel was formed, and then, dried at 383 K for 24 h. The dried sample was calcined at 823 K for 4h with ramp rate of 1.7 K/min in flowing of N_2/O_2 (70/30) gas with the flow rate of 100 cm^3/min to obtain the sample denoted as TiO_2-SG.

For a cobalt deposited TiO_2-SG catalyst, the sample was prepared with the same method as that described above with the addition of cobalt(II) nitrate hexahydrate ($Co(NO_3)_2.6H_2O$, Univar, analytical grade). The cobalt precursor in amount of 10% w/w dissolved in 0.04 mol deionized water was added into the sol solution. The obtained sample is denoted as Co/ TiO_2-SG.

Similarly, for a cerium and cobalt deposited TiO_2-SG sample, 10% w/w cobalt(II) nitrate hexahydrate and 1% w/w cerium(III) nitrate hexahydrate ($Ce(NO_3)_3.6H_2O$ (ACROS ORGANICS, analytical grade) were dissolved in 0.04 mol deionized water and added to the sol solution. The obtained sample is denoted as Ce/Co/ TiO_2-SG.

Co-precipitation

The catalysts were prepared from suspension of 0.038 mol titanium(IV) oxide (Aldrich, anatase ≥99%) in 10% w/w cobalt nitrate solution (cobalt(II) nitrate hexahydrate in 20.00 cm^3 deionized water). $Co(OH)_2$ was precipitated from NH_3 solution at pH 7.5 ± 0.2 at 368 K under vigorous stirring. Then, the suspension was heated for a short period, and filtered off at the boiling temperature. The filtered solid was washed and dried at 383 K in an oven. Then the prepared catalyst was calcined at 823 K for 2 h with ramp rate of 2.0 K/min in flowing argon with the flow rate of 40 cm^3/min to obtain the sample denoted as Co/TiO_2 (anatase).

For the cerium deposited TiO_2 (anatase), the preparation was the same as that described above with the exception that 1% w/w cerium(III) nitrate hexahydrate together with 10% w/w cobalt(II) nitrate hexahydrate were dissolved in 20.00 cm^3 deionized water. The sample is denoted as $Ce/Co/TiO_2$ (anatase).

Catalyst Characterization

X-ray diffraction (XRD)

XRD was performed to determine the bulk crystalline phases of the catalysts prepared in different conditions. It was conducted using a Philips X'Pert diffractometer with CuK_α (λ=1.54 Å). The spectra were scanned with step size of 0.01° in the range 2Θ = 10-80°.

X-ray absorption spectroscopy (XAS)

XAS measurements were performed in the transmission mode at the XAS beamline (BL-8) (electron energy of 1.2 GeV, beam current 150-80 mA) of Synchrotron Light Research Institutute, Thailand. Double crystal monochromator Ge (220) was used to scan with different energy step and energy range: (1) the photon energy step of 0.2 eV in the energy range of 7669-7819 eV for Co *K*-edge x-ray absorption near-edge spectroscopy (XANES) measurements, (2) the photon energy step of 1.0 eV in the energy range of 7600-8100 eV for Co *K*-edge extended X-ray absorption fine structure (EXAFS) measurements, and (3) the photon energy step of 1.0 (for pre-edge) and 0.5 eV (for post-edge) in the energy range of 4866-5366 eV for Ti *K*-edge EXAFS measurement.

Results and Discussion

X-ray Diffraction (XRD)

Figure 1 shows XRD patterns of TiO_2-SG, Co/TiO_2-SG and $Ce/Co/TiO_2$-SG calcined at 823 K. The XRD patterns of TiO_2-SG and Co/TiO_2-SG catalysts appear at 25°(major), 37°, 48°, 55°, 56°, 62°, 71°, and 75° corresponding to anatase phase of TiO_2 [5] and rutile phases of TiO_2 (the peaks appear at 28° (major), 36°, 42°, and 57° corresponding to rutile phase) [5]. However, $Ce/Co/TiO_2$-SG calcined at 823 K still shows only anatase phase of TiO_2.

As a comparison, the XRD patterns of commercial TiO_2 (anatase), which is used as a precursor, Co/TiO_2 (anatase), and $Ce/Co/TiO_2$ (anatase) were illustrated in Figure 2. The results indicate that only anatase phase of TiO_2 is observed. In addition, XRD patterns of Co/TiO_2 (anatase) and $Ce/Co/TiO_2$ (anatase) show a small peak at 59.5° which belongs to spinel Co_3O_4.

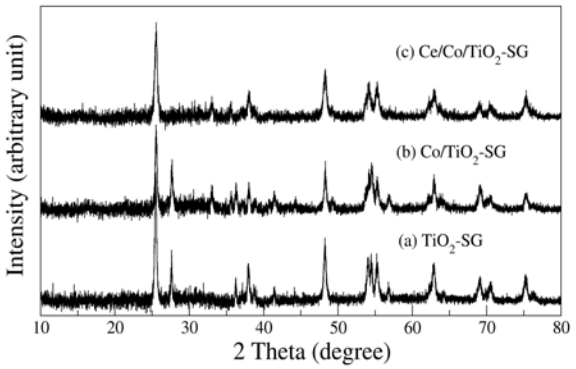

Figure 1 The XRD patterns of catalysts prepared by the sol-gel method and calcined at 823 K.

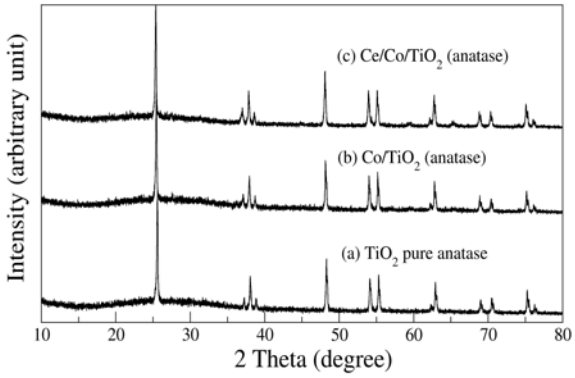

Figure 2 The XRD patterns of catalysts prepared by the co-precipitation method and calcined at 823 K.

From the XRD results, it can be concluded that the preparation methods have the effect on phase of TiO_2 in the catalysts, as shown in Figure 1 and 2.

Table 1: Linear combination of XANES spectra of sol-gel and co-precipitation catalysts (calcined at 823 K).

Catalysts	$\%Co_3O_4$	%CoO
Co/TiO_2-SG	4.6	95.4
$Ce/Co/TiO_2$-SG	7.6	92.4
Co/TiO_2 (anatase)	82.4	17.6
$Ce/Co/TiO_2$ (anatase)	83.5	16.5

X-ray absorption spectroscopy (XAS)

Co K-edge XANES analysis

In order to determine the cobalt species in all catalysts, Co *K*-edge XANES spectra of the catalysts and cobalt in other polymorphs, such as Co-metal, CoO and Co_3O_4, were performed. After that the pre-edge, post-edge, background subtraction and normalization were carried out for all measured spectra by using Athena program version 0.8.059 [9].

The normalized XANES spectra of all catalysts calcined at 823 K and reference compounds are presented in Figure 3. The edge-position and feature of measured spectra provide important information associated with the local structure of Co or the Co states in catalysts. With decreasing oxidation state, the pre-edge and absorption edge are expected to decrease in energy position [2,6]. It is quite clear that the spectra of Co/TiO_2 (anatase) and $Ce/Co/TiO_2$ (anatase) resemble the spectra of Co_3O_4. Whereas, the spectra of Co/TiO_2-SG and $Ce/Co/TiO_2$-SG calcined at 823 K show a mixture of both CoO and Co_3O_4. As a result, the linear combination method was further used to analyze these spectra.

From linear combination analysis, it reveals that the cobalt states in catalysts, which were prepared by sol-gel method and calcined at 823 K, are composed of 4.6% Co_3O_4 and 95.4% CoO for Co/TiO_2-SG, and 7.6% Co_3O_4 and 92.4% CoO for $Ce/Co/TiO_2$-SG. In co-precipitated catalysts, cobalt states in the Co/TiO_2 (anatase) are 82.4% Co_3O_4 and 17.6% CoO, in the $Ce/Co/TiO_2$ (anatase) are 83.5% Co_3O_4 and 16.5% CoO. The results of linear combination XANES are summarized in Table 1. The results of CoO which is easier reduction state [3,5,6] that we want in FTS, sol-gel catalysts contain CoO more than co-precipitation catalysts.

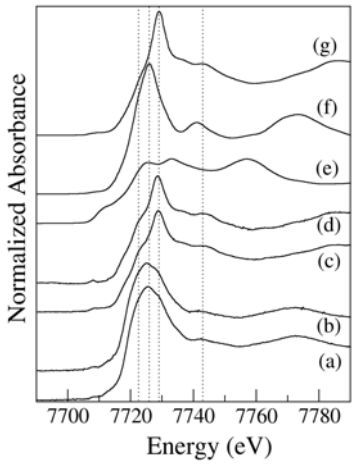

Figure 3 Nomalized Co *K*-edge XANES spectra of (a) Co/TiO_2-SG, (b) $Ce/Co/TiO_2$-SG, (c) Co/TiO_2 (anatase), (d) $Ce/Co/TiO_2$ (anatase), (e) Co-metal (Co^0), (f) CoO (Co^{2+}), and (g) Co_3O_4 ($Co^{2+/3+}$).

Ti and Co K-edge EXAFS analysis

Data analysis was performed following a standard procedure using the Athena program. In this manner, EXAFS over the range of 2-7 $Å^{-1}$ (for Ti *K*-edge) and 2-8 $Å^{-1}$ (for Co *K*-edge) in *k* space were extracted. To obtain the information in real space, Fourier transform with k^3 weight for Ti- and Co-edge and a hanning window function were performed.

In order to determine the phase of TiO_2 in catalysts, Ti *K*-edge EXAFS spectra of TiO_2-SG Co/TiO_2-SG, $Ce/Co/TiO_2$-SG and co-precipitated catalysts are performed. The Fourier transforms of these spectra are shown in Figure 4. It is clear that the features of all spectra resemble that of TiO_2-SG. These features are mainly composed of: (1) the main peak corresponding to the oxygen first-shell (Ti-O), (2) the second shell associated with Ti-Ti, and (3) the third shell associated with Ti-O [11]. This means that the phase of TiO_2 in these catalysts is mainly anatase which is in good agreement with the XRD results.

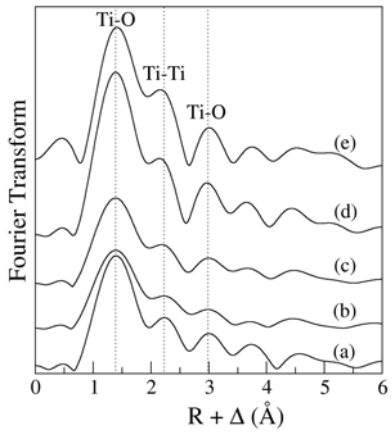

Figure 4 Fourier transforms of Ti *K*-edge EXAFS spectra for (a) TiO_2-SG (823K), (b) Co/TiO_2-SG (823K), (c) $Ce/Co/TiO_2$-SG (823K), (d) Co/TiO_2 (anatase), (e) $Ce/Co/TiO_2$ (anatase).

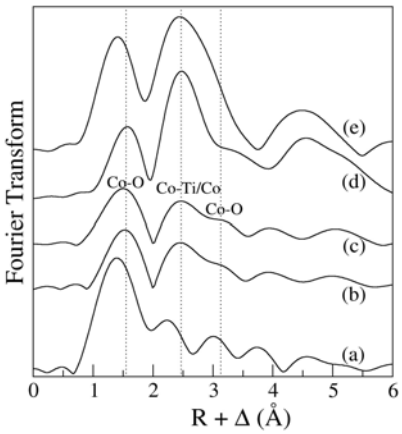

Figure 5 (a) Fourier transforms of (a) Ti *K*-edge EXAFS spectra for TiO_2-SG and Fourier transforms of Co *K*-edge EXAFS spectra for (b) Co/TiO_2-SG, (c) $Ce/Co/TiO_2$-SG, (d) CoO, and (e) Co_3O_4.

To determine the local state of cobalt in Co/TiO_2-SG, $Ce/Co/TiO_2$-SG and co-precipitated catalysts, Co *K*-edge EXAFS spectra of these catalysts and Co in other compounds were performed. The Fourier transforms of these spectra are illustrated in Figure 5. It is clear that the features of spectra obtained from catalysts are similar to that of TiO_2-SG. These features are mainly composed of the first-shell Co-O, second shell Co-Ti and/or Co-Co, and third shell Co-O in catalysts which agree well with the first-shell Ti-O, second-shell Ti-Ti, and third-shell Ti-O in TiO_2-SG. However, a small shift in the distances of the first, second, and third shells can be observed as expected. This is because the size of Co atom is larger than that of Ti atom [11,12], which means that the local structures of Co and Ti in catalysts are almost the same. It can be concluded that Co atoms mainly substitute on Ti atoms.

Conclusions

Based on XRD, the preparation method has the effect on phase of TiO_2 supported cobalt catalysts. At the calcined temperature of 823 K, TiO_2 from the sol-gel method will have the mixture phases of rutile and anatase phases with the exception of the cerium addition catalyst producing only the anatase. From linear combination analysis of XANES spectra, it reveals that the cobalt states in catalysts also depend on the preparation method. For those prepared from the sol-gel method; Co/TiO_2-SG are composed of 4.6% Co_3O_4 and 95.4% CoO and 7.6% Co_3O_4 and 92.4% CoO for $Ce/Co/TiO_2$-SG. In the co-precipitated catalysts Co/TiO_2 (anatase) and $Ce/Co/TiO_2$ (anatase), cobalt states are mainly Co_3O_4. The phase of TiO_2 in these catalysts is mainly anatase, which is determined by Ti *K*-edge EXAFS spectra and is in good agreement with the XRD results. The local states of Co in Co/TiO_2-SG, $Ce/Co/TiO_2$-SG are determined by Co *K*-edge EXAFS spectra and can be concluded that Co atoms mainly substitute on Ti atoms.

References

[1] B. Jongsomjit, T. Wongsalee, and P. Praserthdam, *Catal. Commun.* **6 (**2005), pp. 705-710.

[2] S. Storsæter, B. Tøtdal, J.C. Walmsley, B.S. Tanem, and A. Holmen, *J. Cata.* **236** (2005), pp. 139-152.

[3] G. Jacobs, Y. Ji, B.H. Davis, D. Cronauer, A.J. Kropf, and C. Marshall, *Appl. Catal., A.* **333** (2007), pp. 177-191.

[4] B. Jongsomjit, J. Panpranot, and Jr. G. Goodwin, *J. Catal.* **215** (2003), pp. 66-77.

[5] T. Wongsalee, B. Jongsomjit, and P. Praserthdam, *Catal. Lett.* **108** (2006), pp. 55-61.

[6] D. Grandjean, F. Morales, A. Mens, F. M.F. de Groot, and B. M. Weckhuysen, *AIP.* **882** (2007), pp. 666-668.

[7] B. Ernst, L. Hilaire, and A. Kiennemann, *Catal. Today.* **35** (1999), pp. 293-317.

[8] R. Gheitanchi, A.A. Khodadi, M. Taghizadeh, and Y. Mortazavi, *React. Kinet. Catal. Lett.* **88** (2006), pp. 225-232.

[9] B. Ravel and M. Newvile, *J. Synchrotron Rad.* **12** (2005), pp. 537-541.

[10] A.M. Saib, A. Borgna, J. Loosdrecht, P.J. Berge, and J.W. Niemantsverdriet, *Appl. Catal., A,* **312** (2006), pp. 12-19.

[11] S.H. Lim, N. Phonthammachai, T. Liu, and T.J. White, *J. Appl. Crystallogr*. **41** (2008), pp. 1009-1018.

[12] C.E. Rodrigues Torres, A.F. Cabrera, L.A. Errico, S. Duhalde, M. Renteria, F. Golmar, and F.H. Sánchez, *Physica B*. **398** (2007), pp. 219-222.

Mesoporous silica supported cobalt catalysts for Fischer-Tropsch synthesis

K. Prangtong[1] , S. Kityakarn[1] and A. Worayingyong[1*]

[1] Department of Chemistry, Faculty of Science, Kasetsart University, Bangkok 10900, Thailand

[*] E-Mail Address: fsciarw@ku.ac.th

Abstract: Cobalt deposited on mesoporous silica (MCM-41) with 10%, 20% and 40% loading were synthesized by the sol-gel method at ambient temperature and calcined at 823K. *N*-cetyltrimethylammonium bromide (CTABr) was used as a template. For comparison, cobalt deposited on commercial silica (aerosil 200) was prepared by the impregnation method and calcined at 823 K. X-ray diffraction (XRD), Raman spectroscopy, X-ray absorption near edge spectroscopy (XANES) and transmission electron microscopy (TEM) were used for catalyst characterizations. The XRD results showed the characteristic peak of MCM-41 at 2-theta 2.5 degree which decreased in intensity with increasing amount of cobalt incorporated in the silica framework. TEM images showed morphologies of the prepared catalysts with the hexagonal framework of MCM-41. XANES (Co *K*-edge) exhibited pre-edge peak at 7710 eV and white line at 7725 eV for all catalysts, which indicated that cobalt species on both supports were Co_3O_4 and CoO.

Introduction

Fischer–Tropsch (FT) synthesis is one of the most promising process for conversion of coal and natural gas to clean fuel. Cobalt-based catalysts are applied most widely for FT synthesis because of its high activity, low water–gas shift activity and high C_{5+} selectivity [1, 2]. Cobalt is mostly deposited on high surface area materials such as silica [3], alumina [4] and titania [5], to obtain a high metal dispersion. The catalysts should exhibit a wide range of properties, such as specific surface area, cobalt dispersion, reduction behavior, and catalytic activity.

MCM-41 is a highly ordered mesoporous silica, high surface area, uniform pore sizes with pore dimension between 1.5 to 10 nm and high thermal stability [6]. MCM-41 supported catalyst has a high surface area and high dispersion of a metal. Panpranot *et al*. [7] studied cobalt deposition on MCM-41 and commercial silica. They found that cobalt on MCM-41 catalysts showed stronger interaction of Co with the support than Co on commercial silica by lower reducibility of the catalysts during reduction. The Co dispersions were similar on MCM-41 to that on amorphous silica for a given Co loading.

This work aims to synthesize mesoporous MCM-41 as supported cobalt catalysts for Fischer-Tropsch synthesis. Two types of mesoporous silica were used, synthesized MCM-41 and commercial silica (aerosil), as catalyst supports for cobalt active species and were characterized by X-ray diffraction (XRD), Raman spectroscopy, X-ray absorption near edge spectroscopy (XANES) and transmission electron microscopy (TEM). Cobalt species on the mesoporous silica are also reported.

Experimental

Catalyst preparations

Preparation of MCM-41

The method of synthesizing MCM-41 was developed from Thachan's thesis [8]. *N*-cethylamonium bromide (CTABr, 98%, UNILAB) in the amount of 6.59 mmol was dissolved in 6.95 mol of deionized water. Ammonia solution (NH_3, 29%, J.T. Baker) 0.06 mol was added with stirring for 5 min and followed by the addition of tetraethyl orthosilicate (TEOS, 98%, Aldrich) 0.0438 mol. The suspension was stirred overnight at room temperature. The resulting solid was recovered by filtration, washed with deionized water and dried at 383 K overnight.

Preparation of MCM-41 supported cobalt by sol-gel method

MCM-41 supported cobalt catalysts were prepared using the method as that described above with the addition of cobalt(II) nitrate hexahydrate ($Co(NO_3)_2 \cdot 6H_2O$, 99%, UNIVAR). The cobalt precursors in the amount of 4.46 mmol (denoted as 10%Co/MCM-41), 8.92 mmol (denoted as 20%Co/MCM-41) and 1.78 mmol (denoted as 40%Co/MCM-41) in deionized water 5.74 mol were added after the addition of TEOS. The resulting solids were recovered by filtration, washed with deionized water and dried at 383 K overnight.

Preparation of aerosil supported cobalt by impregnation method

A suspension of 0.017 mol of aerosil 200 (SiO_2, 99%, EVONIX) in 0.017 mol of deionized water was stirred for 15 min. The sample denoted as 10%Co/aerosil was prepared by adding 17 mmol of cobalt(II) nitrate hexahydrate ($Co(NO_3)_2 \cdot 6H_2O$, 99%, UNIVAR) in 0.1700 mol of deionized water into the suspension and stirred for 15 min. The sample denoted as 20%Co/aerosil and 40%Co/aerosil were prepared by adding the cobalt precursors 33 mmol and 67 mmol, respectively in 0.1700 mol of deionized water into the suspension in the same way as that described above. The resulting solid was recovered by filtration, washed with deionized water and dried at 383 K overnight. All prepared catalysts were calcined at 823 K for 5 h.

Characterization

X-ray diffraction(XRD)

X-ray diffraction analysis was performed using a D8 discover Bruker AXS diffractometer. The X-ray is produced from Cu *Kα* radiation (λ = 0.1540 nm) operating with a current of 30 mA and an accelerating voltage of 40 kV. In all measurements, a scanning step of 0.02 degree was used. The identification of crystalline phases was accomplished by comparing the measured results with the JCPDS (Joint Committee on Powder Diffraction Standards) file numbers 74-1657 and 75-0419 for Co_3O_4 and CoO, respectively.

Raman spectroscopy

Raman spectra were recorded on Mk1 Renishaw Imaging Microscope model 166 series between 50 to 1000 cm^{-1} with the resolution of 4 cm^{-1}.

X-ray absorption near edge spectroscopy (XANES)

XANES measurements were performed in the transmission mode at the X-ray absorption spectroscopy beamline (BL-8) of Siam Photon Source (electron energy 1.2 GeV, beam current 150-80 mA), Synchrotron Light Research Institute (Public Organization), Thailand. Double crystal mono-chromator used Ge (220) that was used to scan the synchrotron x-ray with the photon energy step of 0.2 eV in the energy range 7680 to 7790 for Co *K*-edge measurements. To prepare the samples for measurement in the transmission mode, each powder sample was deposited on a Kapton tape. The absolute photon energy was calibrated by Co foil, showing the Co *K*-edge at 7709 eV.

Transmission electron microscope

TEM analysis of the samples was performed using a LaB_6 Hitachi H-8100 TEM operated at 200 keV. The powders were prepared for the TEM analysis by dropping the suspension of the powders in isopropanol on to a copper grid.

Results and Discussion

X-ray diffraction (XRD)

The XRD pattern of the unsupported MCM-41 in Figure 1 shows XRD peak at low 2-theta around 2.2 degree indicating the ordered structure which is confirmed by that reported in literature [7, 9, 10]. For the cobalt deposited MCM-41 samples, peaks appeared at 2.5 degree with decreasing in intensities. The cobalt loading increased, the ordering of MCM-41 structure was reduced. It indicates that cobalt incorporated into the silica network of MCM-41, destroys the MCM-41 framework [7, 11].

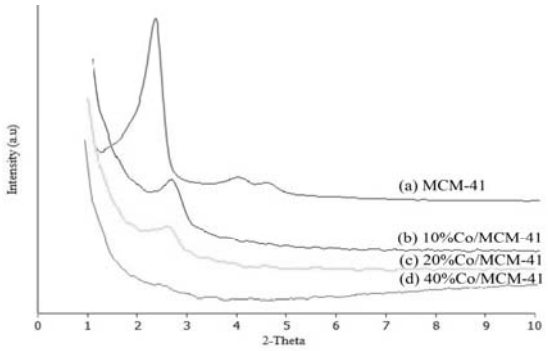

Figure 1. XRD patterns of (a) MCM-41, (b) 10%Co/MCM-41, (c) 20%Co/MCM-41 and (d) 40%Co/MCM-41 at low 2-theta

The XRD patterns at high 2-theta of cobalt loading on MCM-41 are shown in Figure 2. Co_3O_4 spinel with the 2-theta peaks at 31.5, 37.0, 45.1, 59.7 and 64.7 degree (JCPDS PDF No. 74-1657) appeared in both MCM-41 and aerosil.

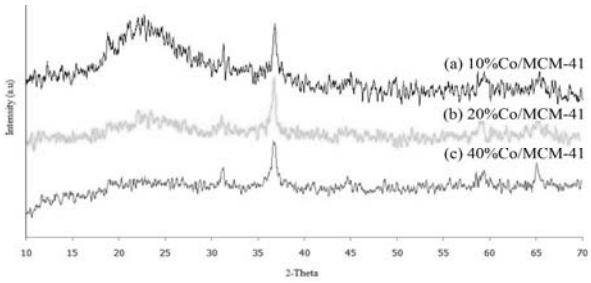

Figure 2. XRD patterns of (a) 10%Co/MCM-41, (b) 20%Co/MCM-41 and (c) 40%Co/MCM-41 at high 2-theta

Raman spectroscopy

The Raman shifts of the MCM-41 sample were observed as three broad bands at wavenumber 800, 610 and 485 cm^{-1} as shown in Figure 3. The band at 800 cm^{-1} is assigned to symmetrical stretching mode of siloxane (Si-O-Si) linkage and bands at 610 cm^{-1} and 485 cm^{-1} are assigned to 3-Si and 4-Si siloxane rings [12].

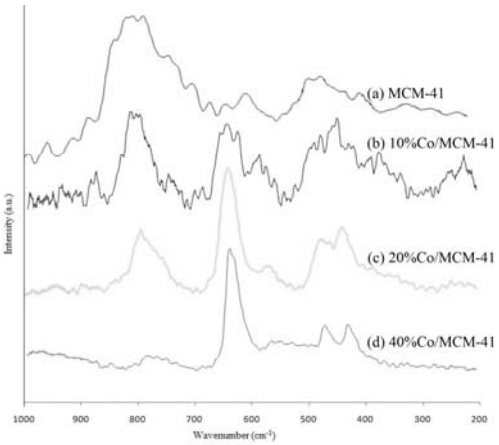

Figure 3. Raman spectra of (a) MCM-41, (b) 10%Co/MCM-41, (c) 20%Co/MCM-41 and (d) 40%Co/MCM-41

The Raman shifts of 10%Co/MCM-41 exhibit also the three broad bands at 800, 610 and 485 cm^{-1} as the characteristic peaks of the MCM-41 with the addition of peaks at 665 and 471 cm^{-1}, which are corresponded to Co_3O_4 [13, 14]. The intensities of the peaks at 665 and 471 cm^{-1} are more obvious when the cobalt percentages are higher. In contrary, for the high cobalt loading samples, the characteristic peaks of those for the siloxane rings decreased in intensity. This indicates that cobalt is incorporated into the silica framework of MCM-41 and decreases the Si-O-Si linkage, which is corresponded to the XRD results.

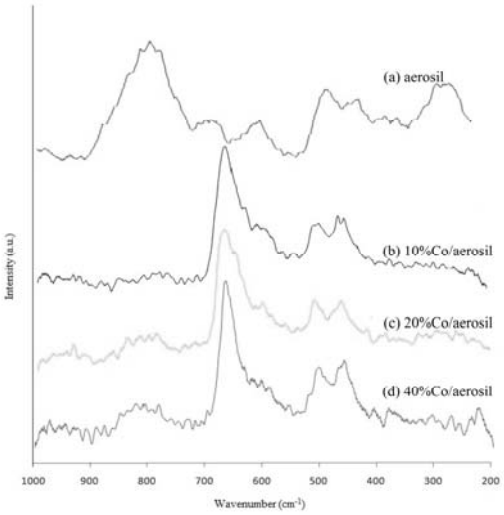

Figure 4. Raman spectra of (a) aerosil, (b) 10%Co/ aerosil, (c) 20%Co/aerosil and (d) 40%Co/aerosil

For the undeposited aerosil, a significant broad peak was observed at wavenumber 795 cm^{-1}, assigned to the symmetrical stretching mode of siloxane linkage, see Figure 4. In the 10%Co/aerosil sample, peaks at 667, 510 and 465 cm^{-1} corresponding to Co_3O_4 were observed clearly, with little shoulder of broad peak around 800 cm^{-1}. It is concluded that the small amount of cobalt formed Co_3O_4 on the aerosil surface without incorporation between the Si-O linkage.

X-ray absorption near edge spectroscopy (XANES)

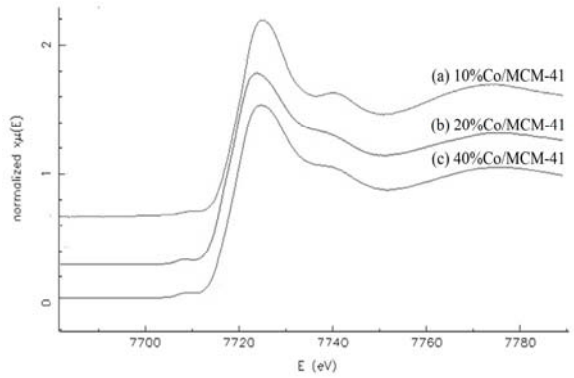

Figure 5. Co *K*-edge XANES spectra of (a) 10%Co/MCM-41, (b) 20%Co/MCM-41 and (c) 40%Co/MCM-41

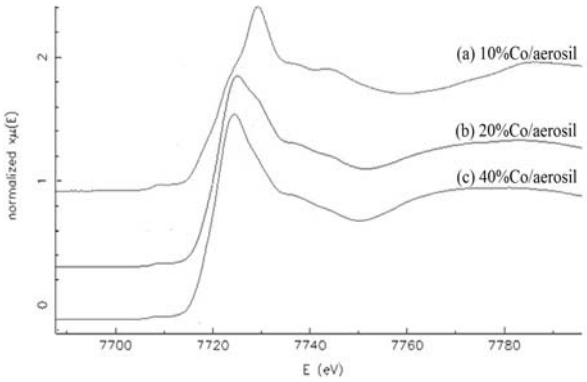

Figure 6. Co *K*-edge XANES spectra of (a) 10%Co/ aerosil, (b) 20%Co/aerosil and (c) 40%Co/aerosil

The normalized XANES spectra of 10%, 20% and 40%Co/MCM-41, shown in Figure 5, exhibit pre-edge peaks at 7710 eV and white line absorptions at 7725 eV. The XANES spectra of CoO and Co_3O_4 in literature have been reported that the pre-edge peak at 7710 eV can be observed in Co_3O_4 only [15]. This arises from *1s-3d* absorption transition and appears most strongly for tetrahedral cobalt environments. In CoO, Co^{2+} coordinates octahedrally to oxygen but Co_3O_4 has both tetrahedral Co^{2+} and octahedral Co^{3+} ions. It also reported that the white line peak of CoO appeared at 7725 eV and that of Co_3O_4 appeared at 7730 eV. Thus, it can be assumed that cobalt species on all MCM-41 samples are CoO and Co_3O_4.

The normalized XANES spectra of 10%, 20% and 40%Co/aerosil were shown in Figure 6, exhibit pre-edge peak at 7710 eV. The white line at 7725 eV was observed for 20% and 40%Co/aerosil and at 7730 eV for 10%Co/aerosil.

The active form of cobalt in cobalt catalysts for Fischer-Tropsch synthesis is the reduced cobalt metal, the reduction step is $Co_3O_4 \longrightarrow CoO \longrightarrow$ Co metal [7]. Percentages of CoO and Co_3O_4 in Co/MCM-41 samples are quantified by performing a linear combination fit using Athena program and XANES spectra of CoO and Co_3O_4 as the bases with the results shown in Table 1. For those samples of cobalt deposited on MCM-41, CoO was deposited with higher percentages than Co_3O_4. In contrast, the cobalt species on aerosil was mainly Co_3O_4 and decreased as the percentages of cobalt increased due to the cobalt species on MCM-41 were easier to reduce to cobalt metal than cobalt species on aerosil.

Table 1: Percentages of CoO and Co_3O_4 on catalysts

	%CoO	%Co_3O_4	R^2
10%Co/MCM-41	75.7	25.3	0.009249
20%Co/MCM-41	88.9	11.1	0.006811
40%Co/MCM-41	81.4	18.6	0.003656
10%Co/aerosil	13.5	86.5	0.008179
20%Co/aerosil	62.8	37.2	0.009240
40%Co/aerosil	84.8	15.2	0.010142

Transmission electron microscope

HR-TEM images of the MCM-41 samples in Figure 7(a) shows a well ordered structure of uniform hexagonal arrangement corresponding to that reported in literature as straight channels [16, 17]. Figure 7 (b) and (c) show the HR-TEM images of 10%Co/MCM-41 and 20% Co/MCM-41. The HR-TEM images confirm the XRD results that cobalt species incorporated in the Si-O-Si framework reduced the hexagonal arrangement of MCM-41.

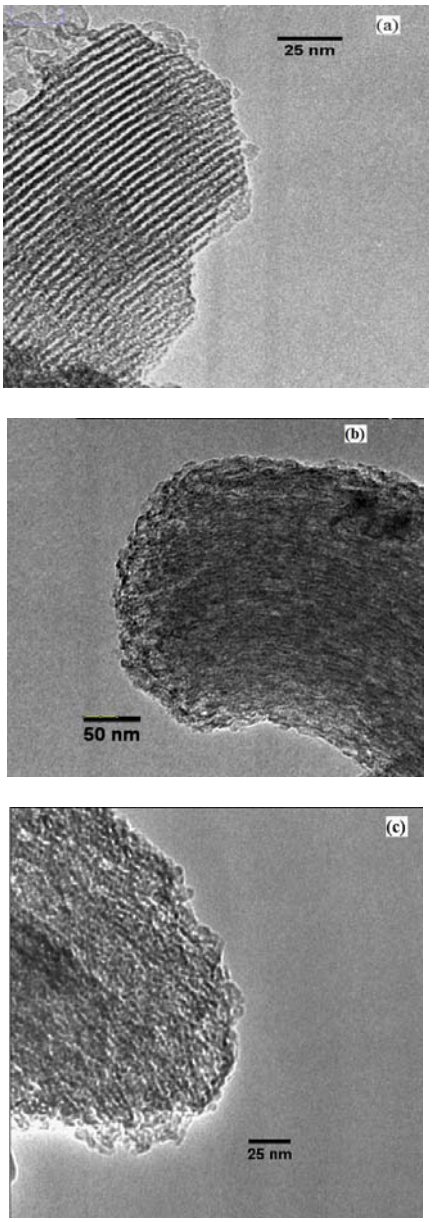

Figure 7. HR-TEM images of (a) MCM-41 (b) 10%Co/ MCM-41 and (c) 20%Co/MCM-41

Conclusions

MCM-41 could be synthesized by the sol-gel method at ambient condition, producing the hexagonal arrangement pores, which was characterized by XRD and HR-TEM. The prepared MCM-41 supported catalyst with 10% cobalt loading decreased in the well defined arrangement pores, which were totally destroyed with 40% cobalt loading. The Raman spectra showed that cobalt was incorporated in the hexagonal framework of Si-O-Si linkage in 10%Co/MCM-41.

XANES spectra were used to determine the cobalt species on MCM-41 and on aerosil being CoO and Co_3O_4. For those samples of cobalt on MCM-41, CoO was deposited with higher percentages than Co_3O_4, whereas the cobalt species on aerosil was mainly Co_3O_4, which decreased as the percentages of cobalt increased.

Acknowledgements

The authors gratefully acknowledge Prof. Dr. Supapan Seraphin, Department of Materials Science and Engineering, University of Arizona, USA, Chemistry Department, Faculty of Science, Kasetsart University and Synchrotron Light Research Institute (Public Organization), Thailand, for supporting this study.

References

[1] Q. Cai and J. Li, *Catal. Commun.* **9** (2008), pp. 2003-2006.

[2] R. Ravishankar, M. M. Li and A. Borgma, *Catal. Today.* **6** (2005), pp. 149-153.

[3] J.-S. Girardon, E. Quinet, A. Griboval-Constant, P. A. Chernavskii, L. Gengember amd A. Y. Khodakov, *J. Catal.* **248** (2007), pp. 143-157.

[4] T. K. Das, G. Jacobs, P. M. Patterson, W. A. Conner, J. Li and B. H. Davis. *Fuel* **82** (2003), pp. 805-815.

[5] N. N. Madikizela and N.J. Coville, *J. Mol. Catal.* **181** (2002), pp. 129-136.

[6] S. Storsæter, B Tøtdal, J. C. Walmley, B. S. Tanem and A. Holmen, *J. Catal.* **236** (2005), pp. 139-152.

[7] J. Panpranot, J. G. Goodwin Jr.and A. Sayari. *Catal. Today.* **77** (2002), pp. 269-284.

[8] W. Thachan, Synthesis and absorptivity of modified and unmodified MCM-41 mesoporous meterial, Master's Thesis, Kasetsart University, 2005.

[9] R. Srivastava, D. Srinivas and P. Ratnasamy, *Catal. Lett.* **91** (2003), pp. 133-139.

[10] H. Xiong, Y. Zhang, K.Liew and J. Li, *Fuel Process Technol.* **90** (2009), pp. 237-246.

[11] M. Selvaraj, A. Pandurangan, K. S. Seshadri, P. K. Sinba and K. B. Lal, *Appl. Catal. A: Gen.* **242** (2003), pp. 347-364.

[12] I.R. Lewis and G. M. Edwards, *Handbook of Raman Spectroscopy: from the Research and Laboratory to the Process Line*, Marcel Dekker, New York.

[13] M. Bouchard and D. C. Smith, *Spectrochim. Acta A.* **59** (2003), pp. 2247-2266.

[14] L. Mendoza, R. Baddour-Hadjean, M. Cassir and J. P. Pereira-Ramos, *Appl. Surf. Sci.* **225** (2004), pp. 356-361.

[15] A. M. Saib, A. Borgna, J. Van de Loosdrecht, P. J. van Berge and J. W. Niemantsverdriet, *Appl. Catal. A: Gen.* **312** (2006), pp. 12-19.

[16] S. Ramachandran, J. H. Ha and D. K. Kim, *Catal. Commun.* **8** (2007), pp. 1934-1938.

[17] S. Lim, D. Ciuparu, Y. Yang, G. Du, L. D. Pfefferle and G. L. Haller, *Micropor. Mesopor. Mater.* **101** (2007), pp. 200-206.

SrO/MgO heterogeneous catalysts for transesterification of soybean oil

S. Thepwatee[1], B. Yoosuk[2] and J. Tantirungrotechai[1,*]

[1] Department of Chemistry and Center for Innovation in Chemistry, Faculty of Science, Mahidol University, Bangkok, Thailand
[2] National Metal and Materials Technology Center (MTEC), Thailand Science Park, Pathumthani, Thailand

[*] E-Mail : scjjp@mahidol.ac.th

Abstract: The SrO/MgO mixed-oxide was used as a catalyst in transesterification under mind reaction conditions. The catalyst was prepared by wet impregnation method using $Sr(NO_3)_2$ and commercial grade MgO, then calcination at high temperature was performed to activate the catalyst. To investigate the catalytic activity, the transesterification was carried out by reacting the edible grade soybean oil with methanol under conditions: oil to methanol ratio of 1:12, a catalyst amount of 5 wt%, and reaction temperature of 65 ^{0}C. The biodiesel yield was followed by ^{1}H-NMR technique. The characteristics of the catalyst such as basic strength and crystalline phases were investigated by various Hemmett indicators and XRD, respectively. The results showed that the catalyst calcined at 600 ^{0}C yielded 93% biodiesel after 30 min. Moreover, the effect of Sr amounts on the MgO support and calcination temperatures were also studied to obtain the best catalyst for the biodiesel production. The catalyst calcined at 600 ^{0}C showed the highest catalytic activity when compared with that of the catalysts calcined at higher temperatures. In case of the effect of Sr loading amount, the highest catalytic activity occurred when the catalyst with 1:10 Sr/Mg molar ratio was used. The results correspond to its basic strengths. The higher basic strength results in higher catalytic activity, and the catalyst with the highest catalytic activity has basic strength in the range of $15 < pK_a < 18.2$. The transesterification reaction can be catalyzed by the SrO/MgO mixed-oxide. This catalyst system has a potential to be used in the biodiesel production. The studies on optimizing the reaction conditions such as oil/methanol ratio and catalyst amount are also investigated.

Introduction

Energy resources have been explored and developed to support the worldwide energy demands, and since 1850, primary energy resources change from wood to coal, then from coal to oil. Fossil oil, which is un-recycled, has been a primary energy resource since 1970 and its consumption is annually increasing. It was estimated that the oil will be depleted in the near future[1]. From this notice, many researches have focused on new energy resources. Biodiesel is an alternative energy resource for the future because of its recyclability and low toxicity. Besides, the properties of biodiesel are comparable to those of petroleum diesel and can be used in the diesel engines without engine modification [2]. There are many methods for biodiesel production such as direct use and blending, microemulsion, pyrolysis, and transesterification [3-4], . However, biodiesel is commonly produced by the transesterrification (also called alcoholysis) of vegetable oils or animal fats with methanol (or ethanol) in the presence of a catalyst. The reaction could be illustrated as shown in Figure 1 [4].

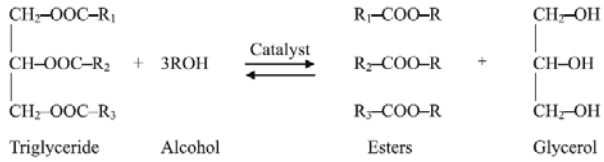

Figure 1. Transesterification of triglyceride with alcohol.

Generally, NaOH, a homogeneous catalyst, is added to improve rate of reaction and yield of biodiesel. Although, the biodiesel can be easily produced in the presence of the homogeneous catalyst, there are many problems in the production process, such as corrosion of reactor, difficulty of separation, soap formation, and large amount of chemical waste [5-6]. On the other hand, heterogeneous catalyst has low level of corrosion and chemical waste. Also, it can be used in a continuous process which is simpler in the industrial scale.

Alkaline earth oxides such as BaO, SrO, CaO,and MgO have been investigated as heterogeneous catalysts. BaO and SrO showed excellent activities but BaO is not considered to be used in transesterification because of its toxicity. Not only high activity but SrO also demonstrated an excellent lifetime, 10 cycles with merely a small gradually reduce of activity [7]. In comparison, CaO and MgO, both of them have lower catalytic activities than those of BaO and SrO.

Supported catalyst is a kind of catalyst that has gained much attention. Supports are used in order to improve catalyst's surface area and reduce cost of production. Various alkaline earth oxides supported on alumina [8], zinc oxide [8-9], zirconia [8], mesoporous silicas [10], and hydroxyapatite [11] have been developed according to those prospects.

In this study, SrO/MgO was used as a catalyst for transesterification of soybean oil. The catalyst was prepared by the conventional wet impregnation method and calcination at high temperature. The optimization of conditions in transesterification reaction and catalyst preparation such as reaction temperature, catalyst

amount, calcination temperature, and Sr/Mg molar ratio were studied.

Materials and Methods

Catalyst preparation: The SrO/MgO mixed oxide was prepared by the wet impregnation method using commercial grade $Sr(NO_3)_2$ and MgO as starting materials. To disperse Sr compound, corresponding amount of 0.1 M $Sr(NO_3)_2$ was stirred with MgO at room temperature for 2 h. After evaporation at 120 ^oC overnight, the dried powder was calcined at high temperature for 5 h in order to activate the catalyst. Various calcination temperatures such as 600 ^oC, 700 ^oC, and 800 ^oC were used to study the temperature effect. The calcined catalysts were then used in transesterification reaction and the catalytic activities were followed.

Transesterification reaction: To investigate the catalytic activity of the catalyst, the transesterification reaction was performed by refluxing methanol with soybean oil in the presence of the catalyst. The reaction was followed upto 3 h. The biodiesel yield at considered times were investigated by ^{1}H-NMR spectroscopy. The biodiesel yield is calculated by taking integration ratio between signal of methoxy group(A_1) and signal of α-carbon methylene (CH_2) group (A_2) as shown in eq.1 [12]. In addition, various parameters such as reaction temperatures, catalyst loading amounts, Sr loading amounts, and oil/methanol ratios were studied in order to optimize the reaction conditions.

$$\%\text{Yield} = (2A_1 / 3A_2) \times 100 \qquad \text{(eq.1)}$$

Catalyst characterizations: Various techniques were used to characterize the catalyst's properties. Thermo-gravimetric analysis (TGA) and differential thermal analysis (DTA) were performed to consider the catalyst's calcination temperature. The KBr pellet technique was applied for determining FT-IR spectra of the samples and powder X-ray diffraction was used to investigate the catalyst's phase components for both before and after the calcination. Moreover, to compare the basic strengths of the catalysts, various Hammett indicators such as Bromothymol Blue (pK_a = 7.2), Phenolphthalein (pK_a = 9.8), Nileblue chloride (pK_a = 10.1), Tropaeoline O (pK_a = 11.0), 2,4-dinitroaniline (pK_a = 15.0), and 4-nitroaniline (pK_a = 18.4) were used. With the different pK_a values of each of the indicators, the colour change after added to catalyst can be used to range the catalyst's basic strength.

Results and Discussion

1. *Catalyst characterizations*

1.1 XRD

Phase determination of the catalyst by powder XRD at wide angle is shown in Figure 2. Before calcination $Mg(OH)_2$ and $Sr(NO_3)_2$ were observed. After calcination at 600 ^oC, MgO and SrO were found indicating that $Mg(OH)_2$ and $Sr(NO_3)_2$ were converted to MgO and SrO, respectively.

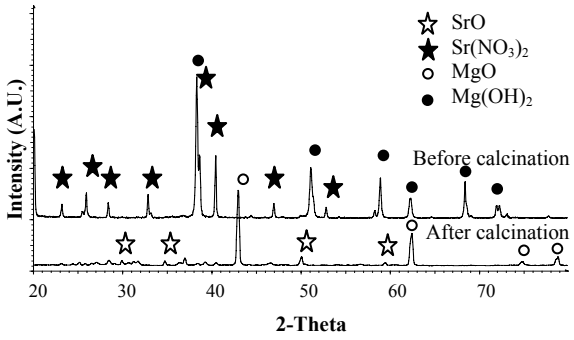

Figure 2. Powder XRD diffractogram of SrO/MgO before and after calcination at 600 °C.

1.2 FT-IR

FT-IR spectra of before and after calcinations are compared with the support and $Sr(NO_3)_2$. The spectrum of the sample before calcination SrO/MgO show peaks around 3,600 and 1,384 cm^{-1}, which were assigned to O-H(ν) of $Mg(OH)_2$ and N-O(ν) of NO^{3-}, respectively. After calcination at 600 ^oC, those two peaks disappeared which is consistent with the XRD results.

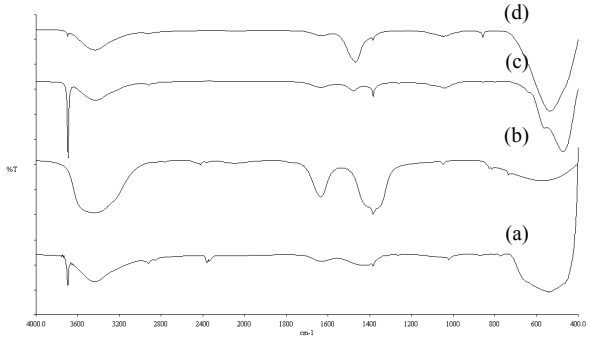

Figure 3. FT-IR spectra of MgO (a), $Sr(NO_3)_2$ (b), before calcination SrO/MgO (c) and after calcination SrO/MgO (d).

1.3 Hammett method

The basic strengths of the catalysts were determined by Hammett indicator method. The basic strengths were noted as pK_a range of the weakest indicator whose color changes and the strongest indicator with no color change. Table 1 shows that after doping of Sr element, the catalysts' basic strengths were improved

from the range of $9.8 < H_- < 15.0$ to the higher ranges. Entry 2 revealed the effect of calcination temperature. The higher temperatures do not affect the catalysts' basic strengths. In contrast, Entry 3, the higher the Sr amount, the higher basic strengths were observed. However, all catalysts with Sr:Mg molar ratio higher than 0.67:10 had the basic strength in the same range.

Table 1: Basic strength measured by Hammett method

Entry	Catalyst	Sr:Mg	T^c (^oC)	Basic strength (H_-)
1	MgO		800	$9.8 < H_- < 15.0$
	SrO/MgO		600	$15.0 < H_- < 18.4$
2	SrO/MgO	1:10	700	$15.0 < H_- < 18.4$
	SrO/MgO		800	$15.0 < H_- < 18.4$
	SrO/MgO	2:10		$15.0 < H_- < 18.4$
	SrO/MgO	1:10		$15.0 < H_- < 18.4$
3	SrO/MgO	0.67:10	600	$15.0 < H_- < 18.4$
	SrO/MgO	0.50:10		$11.0 < H_- < 15.0$
	SrO/MgO	0.25:10		$10.1 < H_- < 11.0$

* T^c is calcination temperature.

2. *Influence of catalyst preparation conditions on biodiesel yield:*

2.1 Sr:Mg ratio effect

The SrO/MgO was also investigated for the effect of Sr:Mg molar ratio to the catalytic activity by varying the molar ratio from 0.25:10 to 2:10. The results are showed in Figure 4. The increasing amount of Sr loading amounts results in the increasing of the catalytic activities which correspond well with the basic strength reported in Table 1. However, when the Sr:Mg ratios were higher than 1:10, the catalytic activity was only slightly improved as seen in Figure 4.

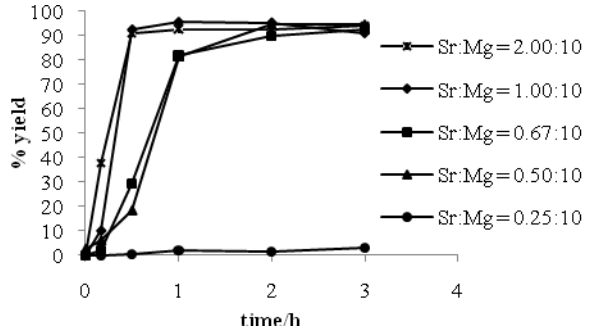

Figure 4. Effect of Sr:Mg molar ratio of the catalyst on biodiesel yield. Reaction conditions: methanol/oil molar ratio of 12:1, catalyst amount of 5 wt% (with respect to weight of oil), and reaction temperature of 65 ^oC.

2.2 Calcination temperature effect

To activate the catalyst, high temperature is required to change the catalyst to mixed-oxide form. Higher temperature could provide a catalyst with high basicity. However, surface area of the composite may be reduced at high temperature. The most suitable calcination temperature should provide the highest basic strength and catalytic activity. As the results shown in Figure 5 and Table 1, the catalysts calcined at temperatures 600 – 800 ^oC have the same basic strength, but different activities. The catalyst calcined at 600 ^oC showed the highest catalytic activity and provided yield over 90% within the first hour of reaction with basic strength of $15.0 < H_- < 18.4$. The surface areas of all samples will be further determined to confirm our hypothesis about the relation between surface area and calcinations temperature. At the moment, the calcination temperature at 600 ^oC was used to study other parameters here after.

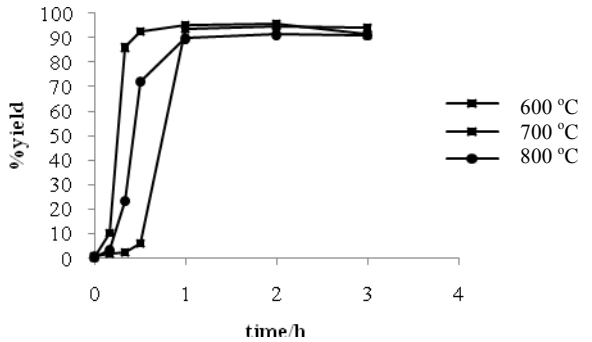

Figure 5. Effect of calcination temperature on biodiesel yield. Reaction conditions: methanol/oil molar ratio of 12:1, catalyst amount of 5 wt% (with respect to weight of oil), reaction temperature of 65 ^oC , and Sr:Mg molar ratio of 1:10.

3. *Influence of transesterification reaction conditions on biodiesel yield:*

3.1 Reaction temperature effect

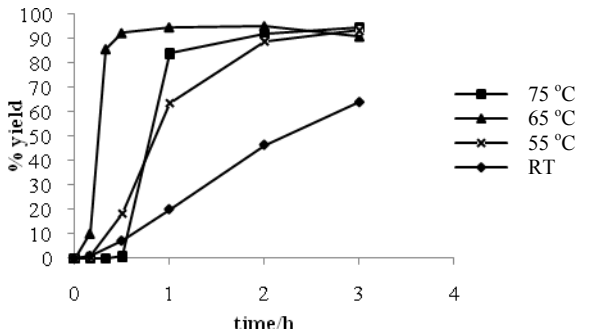

Figure 6. Effect of reaction temperature on biodiesel yield. Reaction conditions: methanol/oil molar ratio 12:1, catalyst amount 5 wt% (with respect to weight of oil), and Sr:Mg molar ratio of 1:10.

3. 2 Catalyst loading amount effect

The increasing of catalyst loading amount can improve the catalytic activity as seen in Figure 8. Biodiesel yielded over 90% when 5 wt% (respect to weight of oil) of catalyst was added. However, 7% of catalyst results in lower yield. The results suggest that 5 wt% of catalyst amount is the most suitable quantity for the transesterification in this work.

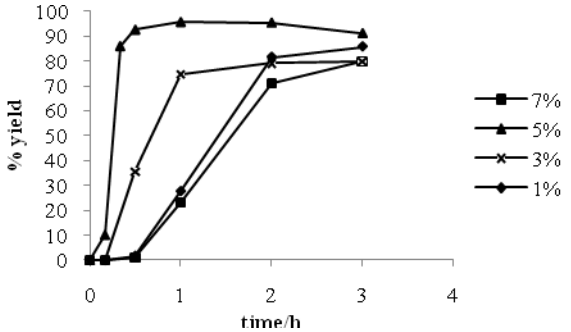

Figure 7. Effect of catalyst loading amount on biodiesel yield. The catalyst calcined at 600 ^{o}C was used. Reaction conditions: methanol/oil molar ratio of 12:1, reaction temperature of 65 ^{o}C , and Sr:Mg molar ratio of 1:10.

Conclusions

The SrO/MgO prepared by the wet impregnation method demonstrated an excellent catalytic activity for the transesterification of soybean oil. The biodiesel yield reached 90% after 30 min in the suitable conditions: (1) Sr:Mg molar ratio of 1:10, (2) reaction temperature of 65 ^{o}C, and (3) catalyst loading amount of 5 wt%. The catalyst showed the basic strength in the pK_a range of 15.0 and 18.4.

Acknowledgements

Financial support from Thailand Graduate Institute of Science and Technology (TGIST), Natioanl Science and Technology Development Agency (NSTDA), Ministry of Science and Technology, as well as from the Center for Innovation in Chemistry (PERCH-CIC), Commission on Higher Education, Ministry of Education are gratefully acknowledged. This work was also partially supported by Faculty of Science, Mahidol University.

References

[1] N.H. Afgan, D.A. Gobaisi, M.G. Carvalho, and M. Cumo, *Renew. Sust. Energ. Rev.* **2** (1998), pp. 2235-286.

[2] R. Jothiramalingam, and M.K. Wang, *Ind. Eng. Chem. Res.* **48** (2009), pp. 6162-6172.

[3] S.A. Basha, K.R. Gopal, and S. Jebaraj, *Renew. Sust. Energ. Rev.* **13** (2009), pp. 1628-1634.

[4] D.-W. Lee, Y.-M. Park, and K.-Y. Lee, *Catal. Surv. Asia* **13** (2009), pp. 63-77.

[5] Z. Helwani, M.R. Othman, N. Aziz, J. Kim, and W.J.N. Fernando, *Appl. Catal. A-Gen.* **363** (2009), pp. 1-10.

[6] Z. Wei, C. Xu, and B. Li, *Bioresource Technol.* **100** (2009), pp. 2883-2885.

[7] X. Liu, H. He, Y. Wang, and S. Zhu, *Catal. Commun.* **8** (2007), pp. 1107-1111.

[8] Z. Yang, and W. Xie, *Fuel Process. Technol.* **88** (2007), pp. 631-638.

[9] A.C. Alba-Rubio, J. Santamaría-González, J.M. Mérida-Robles, R. Moreno-Tost, D. Martín-Alonso, A. Jiménez-López, and P. Maireles-Torres, *Catal. Today* In Press, Corrected Proof.

[10] M.n.C.G. Albuquerque, I. Jimènez-Urbistondo, J. Santamaría-González, J.M. Mérida-Robles, R.n. Moreno-Tost, E. Rodríguez-Castellón, A. Jimènez-López, D.C.S. Azevedo, C.L. Cavalcante Jr, and P. Maireles-Torres, Appl.Catal. A-Gen. **334** (2008), pp. 35-43.

[11] W. Chen, Z. Huang, Y. Liu, and Q. He, Catal. Commun. **9** (2008), pp. 516-521.

[12] G. Gelbard, O. Brès, R.M. Vargas, F. Vielfaure, and U.F. Schuchardt, J. Am. Oil Chem.Soc. **72** (1995), pp. 1239-1241.

Production of amyl acetate from amyl alcohol and acetic acid in reactive distillation: comparison between Amberlist-15 and Dowex50Wx8-100 catalysts

A. Paethanom[1], W. Kiatkittipong[2,*], P. Praserthdam[1] and S. Assabumrungrat[1]

[1]Department of Chemical Engineering, Faculty of Engineering, Chulalongkorn University, Bangkok, 10330, Thailand
[2]Department of Chemical Engineering, Faculty of Engineering and Industrial Technology, Silpakorn University, Nakhon Pathom, 73000, Thailand

* E-Mail: kworapon@su.ac.th

Abstract: The catalytic esterification between acetic acid and amyl alcohol for the production of amyl acetate in reactive distillation has been studied. Two types of strong acid cation-exchange resins, Amberlyst 15 and Dowex 50Wx8-100 were used as catalysts. The kinetic parameters from the literature were used in an ASPEN PLUS simulator. The effects of reflux ratio, heat duty on the reactive distillation performance has been analyzed via simulation using ASPEN PLUS program. It was found that the effect of various operating parameters for both types of catalysts follows the same trend. However, this work shows that catalyst Dowex 50Wx8-100 is more attractive for the production of amyl acetate by reactive distillation due to its higher selectivity.

Introduction

In the chemical process manufactures and industries, dilute acetic acid is by-product in various chemical processes for instance; cellulose esters which are used in fiber processing and lacquers. Cellulose acetate is synthesized by acetylation of cellulose by acetic acid, acetic anhydride and sulfuric acid as a reagent. This reaction results the formation of a large amount by-product acetic acid containing waste, normally 35% w/w aqueous solution of acetic acid. Terephthalic acid production produces by-product containing 65% w/w of acetic acid in water. The synthesis of glyoxal from acetaldehyde and nitric acid generates by-product containing 13-20% w/w of acetic acid. The process of dimethyl terephthalate production which uses acetic acid as a surface coating chemical for resin preparation and dilute acetic acid occurs in an aqueous stream. In the production of vinyl acetate monomer (VAM), which is cracked from ethylidene duacetate (EDA) (generated by reaction of acetic acid anhydride with acetaldehyde), dilute acetic acid is also produced as by-product. Large amount of dilute acetic acid needs to be recovered.

There are several methods to recover acetic acid. Among these, the direct esterification reaction of acetic acid with various alcohols such as; methanol, ethanol, propanol, *n*-butanol, *n*-amyl alcohol and hexanol, etc. for accessing acetate esters is a well known procedure.

Amyl acetate has been used widely in industries as a solvent, an extractant, a polishing agent, etc. It is commonly synthesized in liquid phase through esterification of acetic acid with amyl alcohol catalyzed by strong acids. The reaction of producing amyl acetate is usually reversible and that is the difficulty in producing purity product as required. Besides, it is an equilibrium limited reaction. To improve separation and obtain enhanced conversion, simultaneous removal of products during the reaction is favorable. Various methods of product removal, such as reactive extraction and reactive distillation, have been widely studied.

Reactive distillation is the combination of distillation and reaction in a single vessel. The reaction undergoes at favorable pressure and temperature levels and needs to be catalyzed by strong acids or some solid acidic catalyst, e.g. ion exchangers. Reactive distillation offers many advantages for instance; improved selectivity, better temperature control, increased conversion, and effective utilization of reaction heat and avoidance of azeotrope. For this reaction, it is apparently that alcohol is soluble in water while ester is almost insoluble. This system is associated with the formation a minimum boiling ternary azeotrope of acetate ester, alcohol, and water in nonreactive zone, the heterogeneous azeotrope can be obtained as the distillate product. Moreover, after the vapor condensation, the aqueous phase is almost pure water and conveniently withdrawn as product while the organic phase can be recycled back as reflux.

In this work, an application of reactive distillation for esterification reaction of acetic acid with amyl alcohol was simulated. The simulations were carried out over two different types of catalyst which are Amberlyst 15 and Dowex 50Wx8-100. The commercial Aspen Plus program is used to simulate the performances of the different systems to find suitable operating conditions for the system.

Simulation

The esterification of acetic acid with amyl alcohol (Eq. (1)) is an elementary reversible and kinetically controlled reaction.

$CH_3COOH + C_5H_{11}OH \overset{H^+}{\leftrightarrow} C_5H_{11}COOCH_3 + H_2O$ (1)

The reaction is catalyzed by acidic cation-exchange resin, Amberlyst 15 and Dowex 50Wx8-100. The kinetic parameters for the synthesis of amyl acetate from acetic acid and amyl alcohol using Amberlyst 15 and Dowex 50Wx8-100 catalyst were obtained from literature.

The design parameters of reactive distillation (e.g., number of trays, number of reactive trays, feed locations, etc) were studied and shown in table 1. The reactive distillation apparatus for the amyl acetate process was shown in Figure 1. The heavy reactant (amyl alcohol) is fed to the column from the top section of the reactive zone, and the light reactant (acetic acid) comes in from the lower section of the reactive zone.

Table1: The design parameters of reactive distillation

Parameter	
Total number of trays	28
Number of trays in stripping section(N_S)	7
Number of trays in reactive section(N_{RXN})	15
Number of trays in rectifying section(N_R)	6
Reaction tray	7-21
AmOH feed tray	7
AcAc feed tray	21
Feed flow rate of AmOH, mol/hr	35
Feed flow rate of AcAc, mol/hr	35
Reflux ratio(RF), mol	6, 8, 10
Reboiler duty, watt	4600-7200

Amyl acetate is withdrawn from the bottom of the column as it is the highest boiling point as well as heaviest key component in the system. The overhead distillate consisting of amyl alcohol, water and amyl acetate is refluxed to the stage below the condenser at each reflux ratio. The order of column stages is assigned from the top to the bottom of the column, with stage 1 as the condenser and stage N as the reboiler. The feed locations of amyl alcohol and acetic acid are at the tenth and the fifteenth stages of the reactive section, respectively. The following parameters were kept as constant for all simulations: molar feed ratio of acetic acid and amyl alcohol = 1, the column pressure = 1 atm, feed stream pressure = 1 atm, pure amyl alcohol feed, feed temperature = 298 K and total condenser.

All simulations were carried out using the ASPEN PLUS program. The RADFRAC model was used for simulating the reactive distillation. All the separation stages of the reactive distillation columns were assumed at equilibrium.

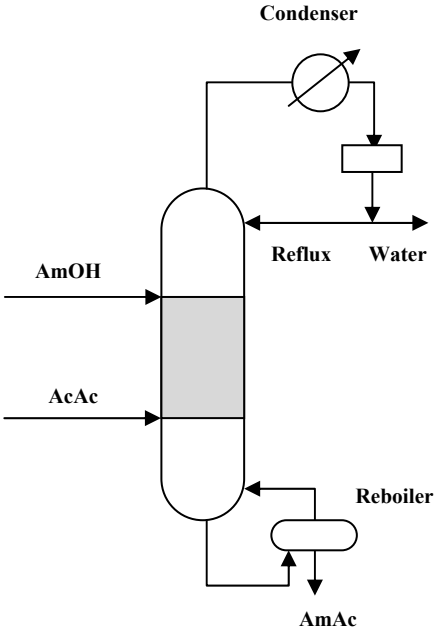

Figure 1: Schematic diagram of conventional reactive distillation

Results and discussion

Effect of reflux ratio and reboiler heat duty

The effects of reboiler heat duty on the reactive distillation performance with different reflux ratio were studied. Figure 2 presents the influence of reboiler heat duty on the conversion of acetic acid for various value of reflux ratio. It shows that increasing reboiler heat duty consequences in a decrease of the conversion of acetic acid for the entire value of reflux ratio. At the same time as reboiler heat duty is increased, more reactants are in the vapor phase and the esterification in the reactive zone is decreased. Thus, less yield and purity of the product, n-amyl acetate, at the bottom are observed as shown in Figure 3 and 4. It can be seen that even though the conversion of acetic acid is high at any specific value of reflux ratio and reboiler heat duty, the yield of n-amyl acetate at the bottom is very low. This can be explained that some n-amyl acetate product is lost in the distillate stream.

For the influence of reflux ratio, due to the higher reflux ratio, the more liquid is back to the column. Therefore, the distillation can be operated at a lower reboiler heat duty with decreasing reflux ratio. However, the mole fraction of n-amyl acwtate decreased with increasing of the reflux ratio and reboiler heat duty as shown in Figure 4. Comparing between Amberlyst 15 and Dowex 50Wx8-100, similar tendency can be obtained, however, Dowex 50Wx8-100 is more attractive as giving higher acetic acid conversion, n-amyl acetate yield and purity.

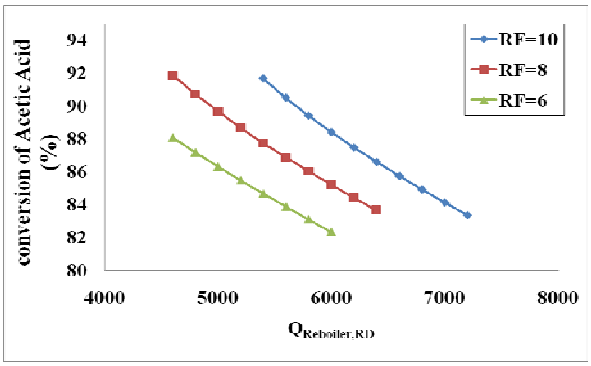

(a)

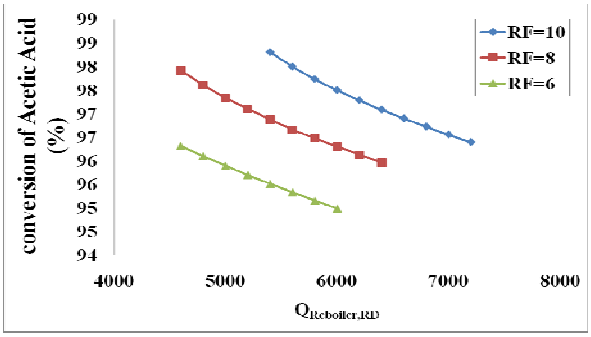

(b)

Figure 2: The conversion of acetic acid at each reflux ratio and reboiler duty in the use of (a) Amberlyst 15 and (b) Dowex 50Wx8-100 catalyst

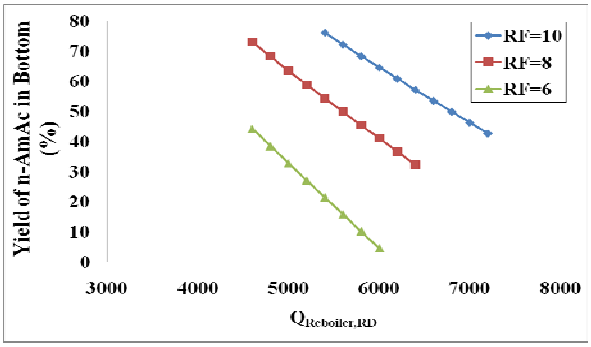

(a)

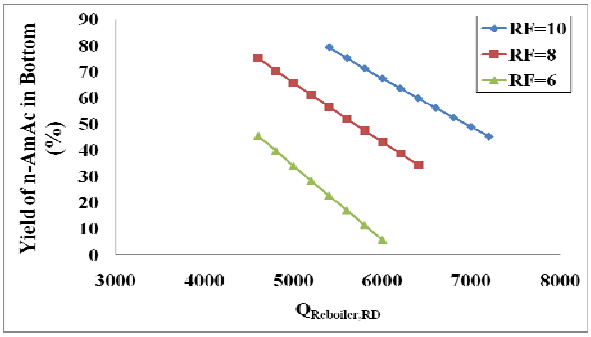

(b)

Figure 3: The yield of AmAc in bottom at each reflux ratio and reboiler duty in the use of (a) Amberlyst 15 and (b) Dowex 50Wx8-100 catalyst

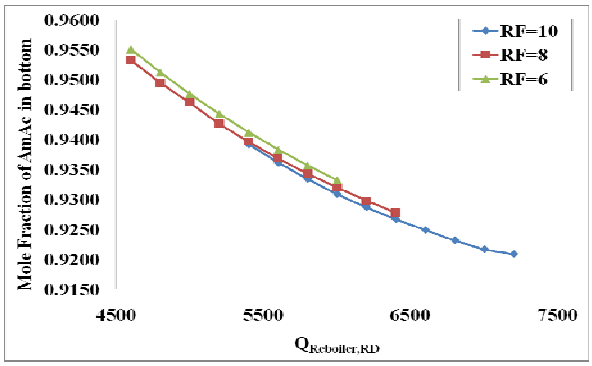

(a)

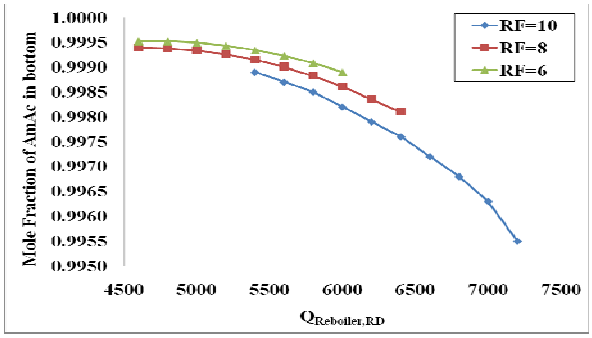

(b)

Figure 4: The mole of AmAc in bottom at each reflux ratio and reboiler duty in the use of (a) Amberlyst 15 and (b) Dowex 50Wx8-100 catalyst

Conclusions

In this work, the acidic cation-exchange resin catalyzed amyl acetate process was studied thoroughly. Two acidic catalyst, Amberlyst 15 and Dowex 50Wx8-100 were compared in an reactive distillation column using an ASPEN PLUS simulator. It was found that the effect of various operating parameters for both types of catalysts follows the same trend. However, this work shows that catalyst Dowex 50Wx8-100 is more attractive for the production of amyl acetate by reactive distillation due to its higher conversion, yield and mole fraction of the amyl acetate in the bottom.

Acknowledgement

Financial support from the Thailand Research Fund and Commission on Higher Education are gratefully acknowledged.

References

[1] S.F. Chiang, C.L. Kuo, C.C. Yu and D.S.H. Wong, *Ind. Eng. Chem. Res.* **41**(2002), pp. 3233-3246.
[2] H. Demiral and M.E. Yildirim., *Water Sci. Technol.* **47**(2003), pp. 183-188.
[3] W.J. Hung, I.K. Lai, S.B. Hung, H.P. Huang and M.J. Lee, *J. Mol. Catal. Chem.* **226**(2005), pp. 129–134.
[4] M.J. Lee, H.T. Wu, C.H. Kang and H.M. Lin, *J. Chin. Inst. Chem. Eng.* **30**(1999), pp. 117-122.

[5] M.J. Lee, H. T. Wu and H. M. Lin, *Ind. Eng. Chem. Res*. **39**(2000), pp. 4094-4099.
[6] B. Saha, S. P. Chopade and S. M. Mahajani, *Catal. Today*. **60**(2000), pp. 147-157.
[7] Y. T. Tang, S. B. Hung, Y. W. Chen, H. P. Huang, M. J. Lee and C. C. Yu, *AIChE J.* **51**(2005), pp. 1683-1699.

The effect of support on the catalytic dry reforming of methane over Ni based catalyst

S. Sawanglum[1*], S. Tungkamani[1], P. Narataruksa[2], K. Pana-Suppamassadu[2] and T. Sornchamni[3]

[1] King Mongkut's University of Technology North Bangkok, Department of Industrial Chemistry, Faculty of Applied Science, Bangkok, Thailand
[2] King Mongkut's University of Technology North Bangkok, Department of Chemical Engineering, Faculty of Engineering, Bangkok, Thailand
[3]PTT Research and Technology Institute, Department of Analytical & Petrochemical Research, Ayutthaya, Thailand

[*] E-mail my_marioh@hotmail.com

Abstract: Catalytic dry reforming of methane over 10%Ni/Al_2O_3, 10%Ni/MgO and 10%Ni/MgO-Al_2O_3 prepared by sol-gel method were investigated. Catalysts were characterized by BET, XRD H_2-TPRandCO_2-TPD. The catalytic reforming was carried out in the ratio of CH_4 and CO_2 15:25 at 500°C, 600°C and 700°C under atmospheric pressure for 6 h. All catalysts illustrated that the conversion of CH_4 increases with temperature enhancement. The catalytic reaction over 10%Ni/MgO gives the highest activity compared to the ones obtained from 10%Ni/MgO-Al_2O_3 and 10%Ni/Al_2O_3. The 10%Ni/MgO catalyst gives 95%CH_4 conversion at 700°C. This could be attributed to the stronger CO_2 adsorption on 10%Ni/MgO catalyst. In contrast, 10%Ni/Al_2O_3 catalyst gives the lowest activity because of the formation of nickel aluminate phase ($NiAl_2O_4$), which is not active and quite stable. However, the presence of MgO on the 10%Ni/MgO-Al_2O_3 catalyst, obviously demonstrates the higher activity compared to 10%Ni/Al_2O_3. This could be elucidated that the catalyst prepared by sol-gel technique could reduce the formation of nickel aluminate by forming a magnesium aluminate phase ($MgAl_2O_4$) instead, in which this phase is low acidity and more active phase than $NiAl_2O_4$.

Introduction

Catalytic dry reforming of methane to produce synthesis gas (H_2, CO) has been intensively focused of attention. Although methane and carbon dioxide are undesirable greenhouse gases, they could be converted to produce valuable feed stocks for production of petrochemicals and synthetic fuels. Synthesis gases obtained from the reforming of methane with carbon dioxide gives low molar ratio of H_2/CO ~ 1:1, which is favorable for the production of methanol and liquid hydrocarbons fuels via Fischer – Tropsch synthesis.

$$CH_4 + CO_2 \rightarrow 2H_2 + 2CO \quad \Delta H = 247.3 \text{ kJ/mol} \qquad (1)$$

The Ni-based catalyst is commonly used for dry reforming of methane, inspite of limited coking resistance. They are competitive metal catalyst compared to noble metal since they are relatively inexpensive catalyst with acceptable activity and selectivity criteria [1-3]. The scrutiny and development of Ni based catalyst could improve catalytic behavior and reduce coke formation.

The oxides supports were effective to improve the catalytic activity of catalyst [4]. Available Al_2O_3, MgO and CaO materials were generally used as support to prepare Ni-based catalysts for dry reforming of methane. It should be noted that the support with Lewis basic site might promote the carbon-resistant ability of the catalyst for the strong adsorption capacity of CO_2 [5].

In this research, the Ni-supported on Al_2O_3, MgO and Al_2O_3-MgO catalysts were prepared by sol-gel method, used in the catalytic dry reforming of methane over a temperature range 500 – 700°C. Catalyst characterisations were elucidated by BET surface area, XRD, H_2-TPR and CO_2-TPD.

Materials and Methods

Catalyst preparation

The Ni-based catalysts were prepared by the sol-gel method from a mixture of Aluminum isopropoxide Al[$(CH_3)_2$CHO], Magnesium ethoxide $Mg(C_2H_5O)_2$ as precursors of support and $Ni(NO_3)_2.6H_2O$. The loading amount of Ni fixed at 10 wt.%. The products dried at 45°C for 48 h in air and calcined at 450°C for 10%Ni/MgO and 10%Ni/MgO-Al_2O_3 and at 600°C for 10%Ni/Al_2O_3.

Catalyst characterizations

The total surface area (BET) of the catalysts were detected in a Belsorp-mini (Belsorp, Japan) by N_2 adsorption at -196°C.

The X-ray diffraction pattern (XRD) were obtained with PHILIPS X'Pert diffractometer operated at voltage 30 kV and current 30 mA and in a 2θ between 15° and 90°. Anode Co Kα was used as the X-ray source. The apparent diffraction peaks have been used to identify the surface structure of catalysts.

H_2-temperature programmed reduction (H_2-TPR) was performed to identify the catalyst reduction behavior. The amount of H_2 consumption were measured by gas chromatograph equipped with a thermal conductivity detector (TCD).

CO_2-temperature programmed desorption (CO_2-TPD) was carried out to investigate the desorption temperature of CO_2, reflecting the basicity of catalyst surface. After calcination, catalyst was pretreated under argon flow at 400°C then CO_2 was adsorbed at 50°C for 1 h. Temperature program desorption was performed under argon flow. The desorbed gas was analyzed by gas chromatograph equipped with a TCD detector.

Catalytic reaction

The catalytic reaction was performed by using 0.20 g of catalyst in a fixed-bed reactor. Catalysts were reduced at 600°C for 6 h in a flow of H_2 before the reaction proceeded. Feed ratio of CH_4 and CO_2 15:25 ml/min was allowed to flow over pretreated catalyst at 500, 600 and 700°C under atmospheric pressure for 6 h. During the reaction was carried out under steady state conditions, the desorbed products and reactants were analyzed by on-line gas chromatograph (Agilent 7890A) using a thermal conductivity detector. In this research, the catalytic activity was expressed in term of % CH_4 conversion.

Results and Discussion

Catalyst characterization

BET results

Total surface area of catalyst investigated is illustrated in Table 1. After calcination, 10%Ni supported on different support materials were observed to have different total surface area. 10%Ni/Al_2O_3 catalyst gives the highest surface area of 192 m^2 g^{-1}. The surface area of 10%Ni/MgO catalyst is approximately 92 m^2g^{-1} and 10%Ni/MgO-Al_2O_3 is 178 m^2 g^{-1}. It has to be mentioned that all support materials prepared by sol-gel technique have total surface area approximately 200, 211 and 251 m^2g^{-1} for Al_2O_3, MgO and MgO-Al_2O_3, respectively. Surface area of Ni supported catalyst, compared to the surface of support, seems to be slightly decreased for 10%Ni/Al_2O_3 and 10%Ni/MgO-Al_2O_3 catalysts. However, a significant decrease in total surface area of 10%Ni/MgO was observed. This could be due to low dispersion of NiO species over MgO support.

Table 1: BET surface area of fresh catalysts.

Supports/ Catalysts	Surface area (m^2 g^{-1})
Al_2O_3	251
MgO	200
MgO-Al_2O_3	211
10%Ni/Al_2O_3	192
10%Ni/MgO	92
10%Ni/MgO-Al_2O_3	178

XRD results

Figure 1 depicts XRD patterns of Ni based catalyst prepared by sol-gel method and calcined at 600 °C. XRD pattern obtained from 10%Ni/Al_2O_3 and 10%Ni/MgO-Al_2O_3 catalyst displays broad peaks indicating the amorphous structure of Al_2O_3 support, $NiAl_2O_4$ and $MgAl_2O_4$ solid solution. Ill defined peaks of MgO was also observed in 10%Ni/MgO-Al_2O_3.The result obtained from 10%Ni/MgO catalyst calcined at 450°C shows intense and sharp diffraction lines of MgO. No distinct diffraction lines were observed for NiO because of high dispersion of NiO on the catalyst surface and sensitive limit of apparatus [6].

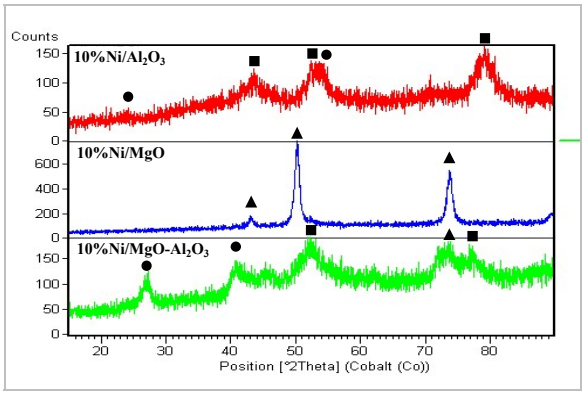

Figure 1. XRD patterns of fresh catalysts. (■)Al_2O_3; (▲)MgO; (●)$NiAl_2O_4$ or $MgAl_2O_4$.

H_2-TPR results

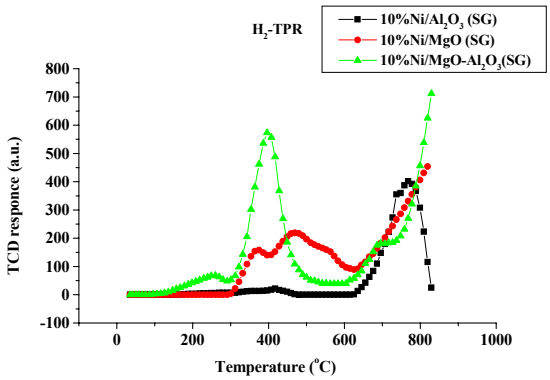

Figure 2. H_2-TPR profiles of fresh catalysts. (■)10%Ni/Al_2O_3; (●)10%Ni/MgO; (▲)10%Ni/MgO-Al_2O_3.

Figure 2 shows H_2-TPR profiles of all catalysts prepared. As could be seen, TPR profiles obtained from 10%Ni/Al_2O_3 , 10%Ni/MgO and 10%Ni/MgO-Al_2O_3 catalyst reveal more than one reduction peaks observed. The reduction profile of 10%Ni/Al_2O_3 shows a small and weak reduction peak at low temperature 420°C and a well defined reduction peak at higher temperature of 780°C. The higher temperature for the reduction could be indicated to

hardly reducible NiO species because of a stable nickel aluminate phase ($NiAl_2O_4$) [7,9]. For the 10%Ni/MgO catalyst, the reduction profile presents two unresolved peaks commencing at 360 ^oC and 480^oC, indicating the reduction of two different nickle oxidic species at low temperature. The profile was also observed to soar above 600^oC as a result of difficult reduction of nickel oxidic species. The reduction of 10%Ni/MgO-Al_2O_3 was observed at 260^oC, 390^oC and 680^oC. The profile shows a clear distinction at this temperature region. The peak temperature at 390 ^oC was recorded as an intense and distinct peak. The reduction behavior above 750^oC is similar to that reported for 10%Ni/MgO catalyst. The results could be explained in the same manner with others. The presence of more than one temperature peaks indicate the existence of more than one nickel oxidic species of different reducibility. Generally, reduction behavior obtained from TPR results could be concluded that lower reduction temperature range of 200-600 ^oC is assigned for easily reducible NiO particles, which are poor metal–support interaction. However, NiO particles strongly bonded to the support lead to difficult reducibilty. The readuction behavior of hardly reducible NiO species normally appears at higher temperatures, which is more than 750^oC [8,9].

CO_2-TPD results

Figure 3 shows CO_2-TPD profiles of Ni supported catalysts. The profile illustrates two temperature regions for CO_2 desorption. The lower temperature range of 50-350^oC is related to the desorption of CO_2 weakly adsorbed on basic site of catalyst surface, while the desorption of CO_2 observed above 400^oC is assigned to the strong chemisorption of CO_2 on the catalyst surface [10]. TPD profile of 10%Ni/MgO catalyst presents the highest amount of desorbed CO_2 in lower temperature range, compared to other catalysts, while TPD at high temperature range of 350-850^oC, gives the lowest amount of desorbed CO_2. This could reflect the existence of adsorbed CO_2 on strong basic site of catalyst surface. CO_2-TPD profiles of 10%Ni/Al_2O_3 and 10%Ni/MgO-Al_2O_3 catalyst show well defined peak at 500^oC. The amount of CO_2 desorbed from the surface of 10%Ni/Al_2O_3 and 10%Ni/MgO-Al_2O_3 catalyst is significant larger than that obtained from 10%Ni/MgO catalyst in temperature range of 350-850^oC, indicating the large amount of weakly adsorbed CO_2 on the basic site of 10%Ni/Al_2O_3 and 10%Ni/MgO-Al_2O_3 catalyst.

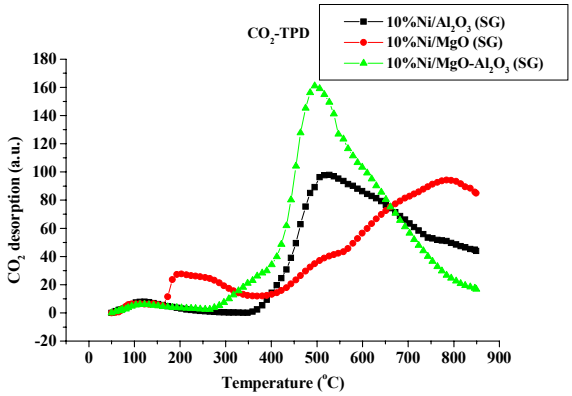

Figure 3. CO_2-TPD profiles of fresh catalysts. (■)10%Ni/Al_2O_3; (●)10%Ni/MgO; (▲)10%Ni/MgO-Al_2O_3.

Catalytic reaction

The activity of the Ni catalysts at different support for dry reforming of methane at temperature between 500 - 700^oC in the ratio of CH_4 and CO_2 15:25 ml/min for 6 h is summarized in Table 2. It was observed that the catalytic activity increases with rising the temperature of reaction [7,10]. The 10%Ni/MgO catalyst exhibited the highest activity and gives 95% CH_4 conversion at 700^oC. This could be attributed to the existence of strong CO_2 adsorbed on the 10%Ni/MgO at high temperature. The poor reforming activity was reported for 10%Ni/Al_2O_3 catalyst because of the formation of nickel aluminate phase ($NiAl_2O_4$) , which is not active and low reducibility.

The reaction over 10%Ni/MgO-Al_2O_3 catalyst obviously demonstrates the higher activity compared to 10%Ni/Al_2O_3**.** This could be elucidated that the catalyst prepared by sol-gel technique could reduce the formation of nickel aluminate by forming a magnesium aluminate phase ($MgAl_2O_4$) instead, in which this phase is low acidity and more active phase than $NiAl_2O_4$ [11].

Table 2: Catalytic results obtained from dry methane reforming reaction over all catalysts at temperature 500, 600 and 700^oC.

Catalysts	Reaction Temp. (^oC)	Conversion of CH_4 (%)	Selectivity of H_2 (%)	Selectivity of CO (%)	H_2/CO ratio
10%Ni/Al_2O_3	500	15	0	0	0
	600	10	0	0	0
	700	35	60	40	1.5
10%Ni/MgO	500	26	70	30	2.3
	600	53	52	47	1.2
	700	95	45	53	0.9
10%Ni/MgO-Al_2O_3	500	34	70	30	2.3
	600	45	52	48	1.1
	700	90	45	55	0.9

The selectivity of H_2 decrease with increase temperature for the reaction over 10%Ni/MgO and 10%Ni/MgO-Al_2O_3 catalyst. The H_2/CO ratio summarized in Table 2 ranges from 0.9 - 2.3. The ratio declines with temperature increase for 10%Ni/MgO and 10%Ni/MgO-Al_2O_3 catalyst. The stoichiometry of H_2 and CO products from the reaction should be equal to one. The H_2/CO ratio, which is lower than one, is due to the reverse water–gas shift reaction (RWGS)[4] and reverse Boudouard reaction and the ratio, which is higher than one could be because of methane decomposition reaction and steam reforming reaction.

Reverse-Water–gas shift reaction (RWGS)

$$CO_2 + H_2 \rightarrow CO + H_2O \quad \Delta H = 41.1 \text{ kJ/mol} \qquad (2)$$

Reverse-Boudouard reaction

$$C + CO_2 \rightarrow 2CO \quad \Delta H = 172 \text{ kJ/mol} \qquad (3)$$

Methane Decomposition reaction

$$CH_4 \rightarrow C + 2H_2 \quad \Delta H = 90.1 \text{ kJ/mol} \qquad (4)$$

Steam Reforming reaction

$$CH_4 + H_2O \rightarrow CO + 3H_2 \quad \Delta H = 206 \text{ kJ/mol} \qquad (5)$$

Conclusions

The conversion of CH_4 for all catalysts increases with temperature enhancement. The highest activity observed for 10%Ni/MgO catalyst could be attributed to the stronger CO_2 adsorption on the catalyst surface. In contrast, 10%Ni/Al_2O_3 catalyst gives the lowest activity because of the formation of nickel aluminate phase ($NiAl_2O_4$), which is not active and quite stable. However, the presence of MgO on the 10%Ni/MgO-Al_2O_3 catalyst, obviously demonstrates the higher activity compared to 10%Ni/Al_2O_3. This could be elucidated that the catalyst prepared by sol-gel technique could reduce the formation of nickel aluminate by forming a magnesium aluminate phase ($MgAl_2O_4$) instead, in which this phase is low acidity and more active phase than $NiAl_2O_4$.

Acknowledgements

The authors are grateful to thank the PTT, Thailand for financial support of this project, The authors also would like to thank Industrial Chemistry Department and Industrial Physics and Medical Instrumentation Department, Faculty of Applied Science, King Mongkut's University of Technology North Bangkok, Thailand, for catalyst characterisation.

References

[1] L. Feletto, W. Alves and L. Jahn, *J. Power Sources*. **161** (2006), pp. 531-534.
[2] J. Guo, H. Lou, and X. Zheng, *Carbon*. **45** (2007), pp. 1314-1321.
[3] E. Castro Luna and E. lriarte, *Appl. Catal. A*. **343** (2008), pp. 10-15.
[4] J. Guo, H. Lou, H. Zhao, D. C. and X. Zheng, *Appl. Catal. A*. **273** (2004), pp. 75-82.
[5] J. Ma, N. Sun, X. Zhang, N. Zhao, F. Xiao, W. Wei and Y. Sun, *Catal. Today*. **148** (2009), pp. 221–231.
[6] Z. Hou and T. Yashima, *Appl. Catal. A*. **261** (2004), pp. 205-209.
[7] A. Djaidja, S. Libs, A. Kiennemann and A. Barama, *Appl. Catal.* **113** (2006),pp. 194-200
[8] Y.-H.Wang, H.-M. Liu and B.-Q. Xua, *J. Mol. Catal. A: Chem.* **299** (2009), pp. 44–52.
[9] X. Zhu, P. Huo, Y.-ping Zhang, D.-guo Cheng and C.-jun Liu, *Appl. Catal. B*. **81** (2008), pp. 132-140.
[10] K. Y. Koo, H.-S. Roh, Y. T. Seo, D. J. Seo, W. L. Yoon and S. B. Park, *Appl. Catal. A*. **340** (2008), pp. 183-190.
[11] F. Frusteri, F. Arena, G. Calogero, T. Torre and A. Parmaliana, *Catal.Commun.* **2** (2001), pp. 49-56.

Improving cold flow properties of biodiesel produced from palm fatty acid distillate

K. Soontarapa[1,4*], N. Kongchom[2,4] and W. Chulalaksananukul[3]

[1*] Research Center, Department of Chemical Technology, Faculty of Science, Chulalongkorn University, Patumwan, Bangkok, Thailand 10330

[2] Program of Petrochemistry and Polymer Science, Faculty of Science, Chulalongkorn University, Patumwan, Bangkok, Thailand 10330

[3]Department of Botany, Faculty of Science, Chulalongkorn University, Patumwan, Bangkok, Thailand 10330

[4]Center of Excellence for Petroleum, Petrochemicals, and Advanced Materials, Chulalongkorn University, Patumwan, Bangkok, Thailand 10330

*E-Mail : khantong@sc.chula.ac.th

Abstract: Palm fatty acid distillate (PFAD), a byproduct from refining of palm oil, is of interest as an alternative feedstock for biodiesel production nowadays because of its low cost. However, its high free fatty acid (FFA) of 87±1.3% led the acid-catalyzed esterification to be selected in this study. The optimum conditions for acid esterification of PFAD with conventional methanol were at 1:8 molar ratios of PFAD:alcohol, 3wt% of conc. H_2SO_4, 60°C and 2 h. reaction time. The high FFA conversion of 98.4±0.003% was obtained. However, its cloud point and pour point were same as those of commercial B100; i.e., 297 K and 291 K, respectively. By using isopropanol in acid esterification step at 1:6 molar ratios, 10wt% of conc. H_2SO_4, 343 K and 5 h., the FFA content and conversion of 8.2±0.01% and 90.7±0.01%, respectively, were obtained. Their cold flow properties were decreased to 18±0 and 1.5±0.7°C, respectively. However, on duplicating esterification step by using optimum condition for methanol at 1:8, 3wt% of H_2SO_4, 333 K and 2 h.; the FFA content and conversion were 1.95±0.001% and 97.8±0.001%, respectively. Their cold flow properties were 291.5±0.7 and 273.75±1.8 K, respectively. After alkali purification, they were as low as 278±0 and 274±0 K, respectively.

Introduction

Recently, biodiesel is considered as a replacement to diesel fuel, due to its advantages such as biodegradable material, low emission, environmental benefit and nontoxic [1]. Biodiesel could be produced from many feedstocks. Palm fatty acid distillate (PFAD), a byproduct from refining of palm oil, is selected as raw material for biodiesel production in this work. Due to its high free fatty acids (FFA) contents, the esterification is usually carried out by using acid catalyst. However, its biodiesel still has poor cold flow properties (cloud point and pour point). Crystallization of the saturated fatty acid methyl ester components of biodiesel at low temperature causes operability problems as solidified material clog fuel lines and filters [2]. The present study is aimed to produce biodiesel from PFAD feedstock with satisfied low-temperature properties. The approach toward improving these properties in this work is the use of branch-chain alcohol (isopropanol) instead of methanol in acid-catalyzed esterification reaction.

Materials and Methods

Materials

PFAD consisted of 87±1.3% FFA analyzed by HPLC was purchased from local palm oil plant. Methanol (MeOH), isopropanol (IPA), sulfuric acid (H_2SO_4), and sodium hydroxide (NaOH) were commercial grade and used as received.

Acid-esterification

PFAD was preheated to about 313-323 K before adding the predetermined amount of IPA and H_2SO_4 catalyst. The mixture was heated to the desired temperature with stirring for a predetermined period of time. The reaction product was poured into a separating funnel for phase separation. The upper phase was residual alcohol, acid catalysts, water and traces of impurities. The bottom phase was biodiesel that would be washed with warm water for three times. The residual alcohol and water were finally removed by rotary evaporator.

The studied molar ratios of PFAD to IPA were 1:6, 1:8, and 1:10; the H_2SO_4 amount was 3, 5, and 10 wt%; the reaction temperature was 333, 343, and 353 K; and the reaction time was 3h, 5h, 7h, and 10h. For comparison, methyl ester was synthesized at molar ratios of 1:6, 1:8 and 1:10; H_2SO_4 in the range of 1–3wt%; reaction temperature in the range of 323–343 K; and the reaction time in the range of 1-3 hours. Acid value expressed in mg KOH required to neutralize 1 g of biodiesel was determined for %FFA [3]. %FFA conversion was then reported for investigation the effect of molar ratio, H_2SO_4 amount, reaction temperature and time.

Alkali-purification

To convert residual FFA to soap, the ester from the acid-esterification step was reacted with alkali. The procedure involved the reaction of ester layer from the acid esterification step with 4–5 %wt of NaOH solution in the amount of 4 mL/100 g of biodiesel at a

temperature of 333 K for 40 min. After washing with warm water for three times, the biodiesel product was in the top phase that be separated out and dried by rotary evaporator.

Cold flow properties

Cloud point and pour point were measured as cold flow properties of biodiesel following ASTM D2500 and ASTM D97, respectively [1].

Results and Discussion

The fatty acid profile of PFAD used in this study was shown in Table 1. To minimize the FFA effect in the alkali purification step, it was desired to select the optimum condition of acid esterification step from the residual FFA content that not more than 2% [4].

Table 1 Major fatty acid compositions in PFAD

Fatty acid		Wt%
Lauric acid	C12:0	0.46%
Myristic acid	C14:0	1.30%
Palmitic acid	C16:0	49.95%
Oleic acid	C18:1	35.38%
Linoleic acid	C18:2	8.97%

Acid-esterification of PFAD with methanol

The optimum conditions for acid esterification of PFAD with conventional methanol were at 1:8 molar ratios of PFAD:alcohol, 3wt% of conc. H_2SO_4, 333 K and 2 h. reaction time. The residual FFA content and FFA conversion of 1.4±0.002% and 98.4±0.003%, respectively, were obtained in acid esterification step. However, its cloud point and pour point were same as those of commercial B100; i.e., 297 K and 291 K, respectively. After alkali purification step at 4wt% NaOH, 4 mL/100 g, and 333 K for 40 min., the residual FFA content and FFA conversion were 0.4±0.03% and 99.5±0.1%, respectively.

Acid-esterification of PFAD with IPA

It could be stated that the optimum condition was at 1:6, 10wt% of conc. H_2SO_4, 343 K for 5 h. as shown Figure 1–4, respectively. The FFA content and conversion of 8.7±0.01% and 90.8±0.01%, respectively, were obtained at this condition. It was seen that the residual FFA content was still high. Although the cold flow properties were improved from those of commercial B100 to 291±0 and 274.5±0.7 K, respectively. The acid esterification was replicated. By using the above condition, the FFA content and conversion of 4.9±0.01% and 94.5±0.01%, respectively, were obtained. Their cold flow properties were 288.5±0.7 and 273.5±0.7 K, respectively. However, on duplicating the acid esterification by using methanol at 1:8 molar ratios, 3wt% of conc. H_2SO_4, 333 K and 2 h.; the FFA content and conversion of 1.95±0.001% and 97.8±0.001%, respectively, were obtained. Their cold flow properties as cloud point and pour point of 291.5±0.7 and 273.75±1.8 K, respectively, were not much affected. After alkali purification at 5wt% NaOH, 4 mL/100 g, and 333 K for 40 min., the residual FFA content and FFA conversion were as low as 278±0 and 274±0 K, respectively.

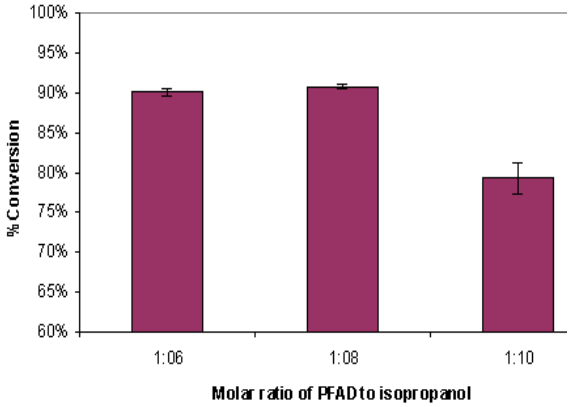

Figure 1. Effect of molar ratio of PFAD to isopropanol in esterification step at 343 K, 5h and 10wt% H_2SO_4

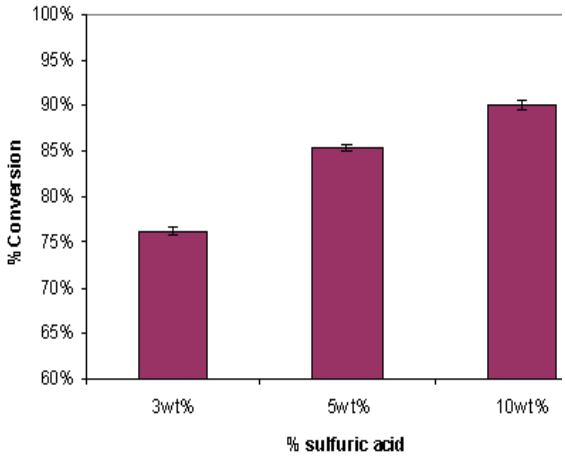

Figure 2. Effect of acid amount in esterification step at 343 K, 1:6 molar ratio and 5 h.

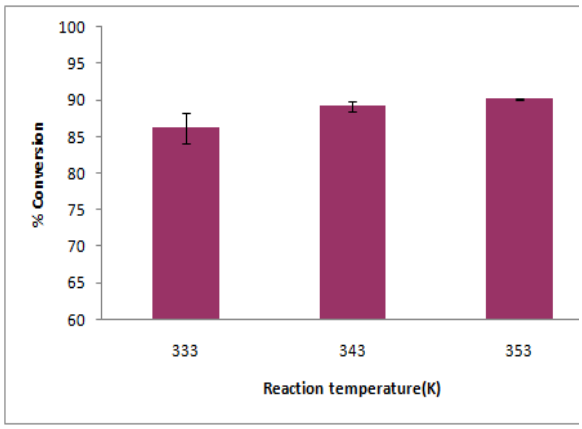

Figure 3. Effect of temperature in esterification step at 1:6 molar ratio, 10wt% H_2SO_4 and 5 h.

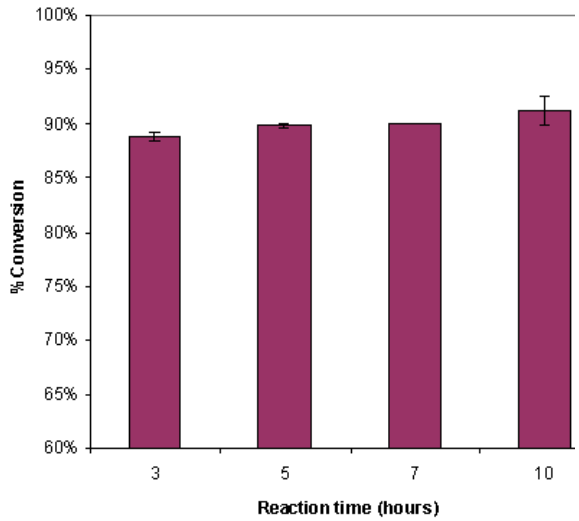

Figure 4. Effect of reaction time in esterification step at 1:6 molar ratio, 10wt% H_2SO_4 and 343 K

Conclusions

PFAD could be used as biodiesel production by acid catalyzed esterification. To improve its cold flow properties, IPA should be used in place of methanol. The optimum condition was at 1:6, 10wt% of conc. H_2SO_4, 343 K for 5 h. Their cold flow properties were improved from those of commercial B100 to 291±0 and 274.5±0.7 K, respectively. On high residual FFA content, two stages acid esterification could solve this to less than 2%. However, the esterification condition for the 2nd stage should be performed with methanol at 1:8 molar ratios, 3wt% of conc. H_2SO_4, 333 K and 2 h. The FFA content and conversion of 1.95±0.001% and 97.8±0.001%, respectively, were obtained. After modification method, their cold flow properties of 291.5±0.7 and 273.75±1.8 K, respectively.

References

[1] P.V. Bhale, N.V. Deshpande and S.B. Thombre, *Renewable Energy*. **34**(2009), pp. 794-800.
[2] I. Lee, L.A. Johnson and E.G. Hammond, *JAOCS*. **72**(1995), pp. 1155-1160.
[3] B. Saad, C.W. Ling, M.S. Jab, B.P. Lim, A.S.M. Ali, W.T. Wai and M.I. Saleh, *Food Chem.* **4**(2007), pp.1407-1414.
[4] A.S. Ramadhas, S. Jayaraj and C. Muraleedharan, *Fuel*. **84**(2005), pp. 335-340.

Support effect on the activity of cobalt based catalyst for CO hydrogenation

H. Sukkathanyawat[1*], S. Tungkamani[1], P. Narataruksa[2], K. Pana-Suppamassadu[2], B. Yoosuk[3], S. Nivitchanyong[3]

[1] Department of Industrial Chemistry, King Mongkut's University of Technology North Bangkok (KMUTNB)
1518 Piboonsongkram Road, Bangsue, Bangkok, Thailand, 10800
[2] Department of Chemical Engineering, King Mongkut's University of Technology North Bangkok(KMUTNB)
1518 Piboonsongkram Road, Bangsue, Bangkok, Thailand, 10800
[3]National Metal and Materials Technology Center (MTEC), National Science and Technology Development Agency (NSTDA)
114 Thailand Science Park, Paholyothin Rd., Pathumthani, Thailand 12120

*E-mail hsn.mic@hotmail.com

Abstract: The effect of support on the catalytic activity of cobalt based catalyst was investigated in CO hydrogenation by transient experiment using TPSR technique. 10%Co/MgO, 10%Co/Al_2O_3 and 10%Co/TiO_2 catalysts prepared by sol-gel method were characterized by BET, TPR and H_2-TPD. TPR profiles show the influence of support on the reduction behavior of cobalt based catalyst. The rate maximum for the reduction of Co supported MgO peaks at lower temperature (T_{max} 330°C) compared to Co/Al_2O_3 (T_{max} at 500°C) and Co/TiO_2 (T_{max} at 600°C). The catalytic results, obtained from TPSR experiment carried out after TPR of catalyst from ambient temperature to 800°C, demonstrates that temperature for hydrogenation of CO shifts to higher temperature in the order of 10%Co/Al_2O_3, 10%Co/MgO and 10%Co/TiO_2, respectively. This could indicate a decrease in the activity of Co supported on MgO and TiO_2. However, the rate maximum for the hydrogenation was observed on 10%Co/MgO. The result was related to H_2-TPD study, which the surface exposed of Co/MgO are much higher than Co supported on Al_2O_3 and TiO_2 catalyst. According to the determination, it could be concluded that Co/MgO catalyst is active and stable although it was treated during TPR at high temperature. On the other hand, Co/Al_2O_3 and Co/TiO_2 catalyst show inferior catalytic behaviors due to metal-support interaction of $CoAl_2O_4$ and $CoTiO_3$, which are inactive phase in the reaction.

Introduction

Fischer Tropsch synthesis (FTS) has been a topic of interest for production of liquid hydrocarbons from synthesis gas. Iron, cobalt, nickel and ruthenium have been commonly reported to be sufficiently active for Fischer Tropsch synthesis. Because of low cost compared to noble catalyst, iron and cobalt are practical catalyst for application in industrial scale, although they are active under high temperature or high pressure conditions to obtain desired products. Iron based catalysts are important for the formation of heavy hydrocarbon product with the desired olefin and oxygenate content and low CH_4 selectivity, whereas cobalt based catalysts predominantly present high activity and selectivity toward linear paraffins and low water-gas shift reaction [1-2]. For the production of liquid alkane hydrocarbons, cobalt catalysts are suitable for use in this purpose. The activity of cobalt for CO hydrogenation has been reported to depend on the support, preparation method, metal loading and dispersion [2]. Supported cobalt catalysts are important for the FTS, the role of support is to disperse the active phase. Bartholomew and Raul reported strong support effects in CO hydrogenation on cobalt catalyst. The support effect on activity of CO hydrogenation over cobalt based catalyst prepared by common technique decreases in the order of TiO_2 > SiO_2 > Al_2O_3 > C > MgO. The conventional technique used to prepared cobalt based catalyst is incipient wetness impregnation. The designed and prepared catalyst must have good mechanical properties and good thermal stability [3] Most of researches related to cobalt supported catalyst in FTS have been reported that the reaction over cobalt is active under severe reaction conditions to desired products. One attempt to develop the catalyst performance in this research is the improvement of the catalyst activity for FTS under mild reaction conditions. In order to obtain an active cobalt supported catalyst for low condition operation, cobalt supported Al_2O_3, MgO and TiO_2 catalyst were well prepared by modified solgel technique and used as catalysts in this study. The effect of support Al_2O_3, MgO and TiO_2 on the activity of cobalt based catalyst was investigated by transient experiment using temperature programmed surface reaction technique (TPSR).

Materials and Methods

Catalyst preparation

10%Co/Al_2O_3 catalyst was prepared by sol-gel method, using solution of $Al(OC_3H_7)_3$. Then HNO_3 solution was added in the precursor solution. The mixed solution was refluxed, stirred and controlled at 95-100°C for 12 h, following by addition of $Co(NO_3).6H_2O$ solution. The catalyst was dried and calcined in air at 400°C.

10%Co/MgO catalyst was prepared in the same method using of $Mg(OC_2H_7)_3$, The solution was refluxed, stirred and controlled at 80-85°C for about 2 h. Then, $Co(NO_3).6H_2O$ solution was added into the precursor solution. Portion of catalyst was dried and calcined in air at 400°C .

10%Co/TiO_2 catalyst was prepared using of 2M $Ti(OC_3H_7)_4$, dissolved in ethanol and stirred about 24 h. Addition $Co(NO_3).6H_2O$ was applied into the precursor solution. Then the catylyst was dried and calcined in air at 400°C.

Catalyst characterization

BET surface area, pore volume and average pore diameter were measured by N_2 physisorpsion at -196°C using a BELSORP-mini instrument. Sample were outgases at 350°C for 4 h before measurement.

The experiment of temperature programmed reduction (TPR) was carried out by using 0.200 g. catalyst packed in a tubular reactor. (4.5 mm, i.d.) Catalysts were first flushed with Ar at 200°C for 2 h and then cooled down to ambient temperature. Subsequently, the sample was heated to 800°C at a heating rate of 10°C/min under 5%H_2/Ar mixture at 30 ml/min. TCD signals were recorded from room temperature to 800°C.

Temperature programmed desorption (H_2-TPD) was performed after H_2 reduced and then cooled down to room temperature under the Ar atmosphere. Hydrogen was then chemisorbed on the catalyst for 30 min at ambient temperature, then flushed with Ar. The H_2-TPD profile was obtained by heating the sample to 800°C at a rate of 10°C/min under argon flow.

Catalytic reaction

Temperature programmed surface reaction (TPSR) experiment was carried out after TPR experiment. Before the TPSR was performed on 0.200 g of catalyst packed in the reactor (4.5 mm, i.d.), a flow of 10%CO/He was allowed to the catalyst bed at room temperature for 30 min, following by flushing under He flow. TPSR experiment was studied under the condition of H_2 flow (30 ml/min). Temperature of catalyst surface was increased by temperature programmed from ambient temperature to 800°C with heating rate of 10°C/min. Methane product was detected by FID detector.

Results and Discussion

Catalyst characterization

BET results

The BET results obtained from 10%Co/MgO, 10%Co/Al_2O_3 and 10%Co/TiO_2 catalyst were summarized in Table 1. The results indicate the difference in surface area, average pore diameter and pore volume of all catalyst. High total surface area of catalyst was observed for 10%Co/Al_2O_3 catalyst. 10%Co/MgO and 10%Co/TiO_2 catalyst give a similar total surface area. Average pore diameter of 10%Co/MgO is significant large compared to that observed for 10%Co/TiO_2 and 10%Co/Al_2O_3 catalyst. Pore volume of catalysts decrease in order of 10%Co/MgO, 10%Co/Al_2O_3 and 10%Co/TiO_2 catalyst.

Table 1. Surface area, average pore diameter and pore volume of all catalysts investigated.

Sample	Surface Area(m^2/g)	Average Pore	Pore Volume
10%Co/MgO	84.59	27.96	0.59
10%Co/Al_2O_3	127.06	6.21	0.20
10%Co/TiO_2	86.32	6.68	0.14

Temperature programmed reduction

The support effect on the reduction behavior of cobalt based catalysts was elucidated by transient experiment using temperature programmed reduction technique. Figure 1 shows the TPR profiles obtained for all catalyst. The rate maximum for the reduction of cobalt supported MgO peaks at lower temperature (T_{max} 330°C) compared to 10%Co/Al_2O_3 (T_{max} at 500°C) and 10%Co/TiO_2 (T_{max} at 600°C). 10%Co/MgO catalyst depicts the profile of unresolved peaks in lower temperature range of 200-500°C, compared to TPR profile of 10%Co/Al_2O_3 and 10%Co/TiO_2. It was reported that the reduction in this temperature region might be assigned to the easy reduction of Co_3O_4 to metallic cobalt phase [5]. The reduction behavior of Co/TiO_2 shows three peaks observed below 630°C. These could be attributed to the reduction of different species of cobalt oxides (Co_3O_4, CoO and/or CoTiO-like species). H_2 uptake for the reduction of cobalt oxides above 600°C is attributed to the partial reduction of TiO_2 to TiO_x [6]. The reduction profile of 10%Co/Al_2O_3 catalyst presents four peaks at 300, 400, 500 and 600°C. The first peak of the reduction process occurs between 180 and 330°C, due to the reduction of supported cobalt nitrate remaining after calcination at 400°C [7] Because calcination temperatures above 450 °C are needed to completely decompose the supported cobalt nitrate [8]. The reduction of catalysts in temperature range 350-450°C can be due to partial reduction of Co_3O_4 to CoO, whereas the reductions in temperature range of 450–550°C are assigned to the reduction of CoO to the cobalt metallic phase [1]. The shoulder with broad peak between 500-800°C is related to the reduction of cobalt oxide species, which strongly interact with the support [9] or the amorphous surface cobalt–support compounds [10].

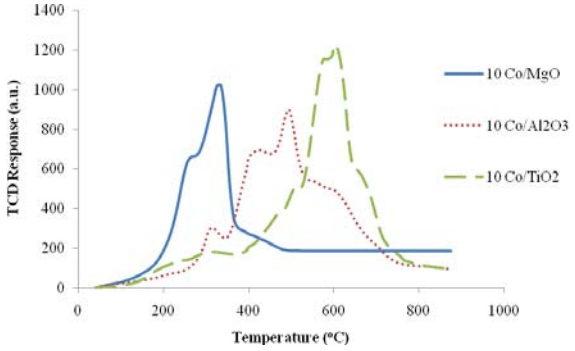

Figure 1. TPR profiles of 10%Co/MgO, 10%Co/Al_2O_3 and 10%Co/TiO_2 catalyst.

Temperature programmed desorption

Surface area of cobalt exposed and crystallite size of cobalt supported catalyst was investigated by H_2-TPD technique. Profiles of H_2-TPD for all catalysts were displayed in Figure 2. TPD profiles predominantly present broad peak at 250-800°C for all catalysts. The amount of H_2 desorbed from the catalyst surface was obtained from the area under the H_2-TPD profile. The information was used to calculate the surface area of cobalt exposed and metal crystallite size of catalysts. (Table 2). According to the results, it has to be mentioned that surface area of cobalt exposed decrease in the order of 10%Co/MgO > 10%Co/Al_2O_3 > 10%Co/TiO_2. Although, the total surface area of catalyst is not presented in the same trend and seems to be in contrast, the actual metal surface area exposed is obviously more importance than the total surface area reported by BET, because the reaction takes place in the metal site of the catalyst. The crystallite size of 10%Co/MgO catalyst is relatively smaller than that reported by other catalysts, indicating well dispersion of metal catalyst on MgO support. H_2-TPD results are obviously related to the results obtained from H_2-TPR.

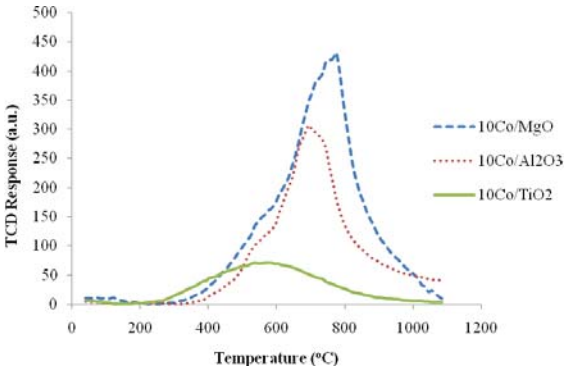

Figure 2. H_2-TPD profiles of 10%Co/MgO, 10%Co/Al_2O_3 and 10%Co/TiO_2 catalyst.

Table 2. Surface area of Co exposed and crystallite size.

Catalyst	Mole of H_2 (H_2 desorbed) (µmol/g of cat)	Surface area of Co exposed (m^2/g of Co)	Crystallite size (nm)
10%Co/MgO	473.32	207.20	3.25
10%Co/Al_2O_3	307.08	134.42	5.01
10%Co/TiO_2	114.68	50.20	13.43

Catalytic reaction

Temperature programmed surface reaction

The hydrogenation of pre-adsorbed CO over 10%Co/MgO, 10%Co/Al_2O_3 and 10%Co/TiO_2 catalyst was investigated by temperature programmed surface reaction technique (TPSR). The TPSR profiles present CH_4 formation as the result of CH hydrogenation reaction. TPSR profiles of all catalysts depicted in Figure 3. The initial temperatures for CO hydrogenation of 10%Co/Al_2O_3, 10%Co/TiO_2 and 10%Co/MgO catalysts starting about 150,180 and 240°C. The rate maximum for the hydrogenation was observed at 200, 390 and 300°C, respectively. The temperature for hydrogenation of CO shifts to higher temperature in the order of 10%Co/Al_2O_3, 10%Co/MgO and 10%Co/TiO_2, respectively. This could indicate a decrease in the activity of Co supported on MgO and TiO_2. However, the maximum amount of CH_4 from the hydrogenation was observed on 10%Co/MgO, summarized in Table 3. It has to be mentioned that the result is related to H_2-TPD study, which the metal surface exposed of Co/MgO are much higher than Co supported on Al_2O_3 and TiO_2 catalyst. This could be explained that high cobalt metal surface area obtained from 10%Co/MgO could be achieved by dispersion of cobalt on stable MgO with large average pore diameter. The activation energies for hydrogenation of pre-adsorbed CO is in the order of 10%Co/Al_2O_3< 10%Co/MgO < 10%Co/TiO_2. This data could also confirm the high activity of 10%Co/Al_2O_3 catalyst for CO hydrogenation.

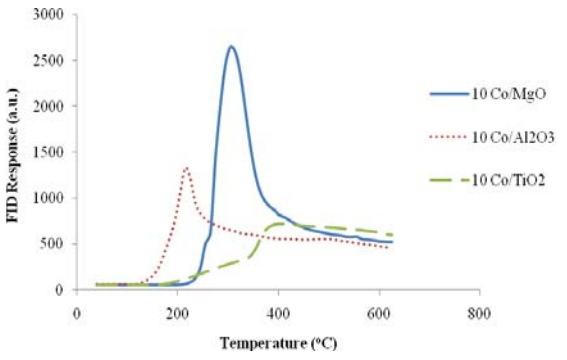

Figure 3. TPSR profiles of 10%Co/MgO, 10%Co/Al_2O_3 and 10%Co/TiO_2 catalyst.

Table 3. The Activation energies and amount of CH_4 produced over all catalysts obtained from TPSR profiles.

*Activation energy is calculated by the following formula:
= {E_a= R T_{max}[ln(A_r Tmax [H_2]/B)-3.9]} [11-12]

Catalyst	Initial Temperature (^oC)	T_{max} (^oC)	Ea* (kJ/mole)	mol of CH_4/g cat.
10%Co/MgO	240	300	98.8	1.86E-05
10%Co/Al_2O_3	150	200	80.8	7.20E-06
10%Co/TiO_2	180	390	115.1	1.03E-05

Conclusions

The physico-chemical properties and catalytic performance of cobalt supported catalysts depend on the features of support used. The activity of Co/Al_2O_3 are much higher than Co supported on MgO and TiO_2 catalyst. However, the metal surface exposed of Co/MgO, which plays a significant role for the catalytic reaction, are much higher than Co supported on Al_2O_3 and TiO_2 catalyst.

Acknowledgements

The authors would like to thank the Thailand Graduate Institute of Science and Technology (TGIST) and the National Science and Technology Development Agency (NSTDA) for scholarship and research funding. Industrial Chemistry Department and Industrial Physics and Medical Instrumentation Department, Faculty of Applied Science, King Mongkut's University of Technology North Bangkok, Thailand, are also gratefully acknowledged for catalyst characterisation.

References

[1] Ø. Borg, S. Eri, E.A. Blekkan, S. Stosater, H. Wigum, E. Rytter, A. Holmen, *J. Catal.* **248** (2007), pp.89-100**.**

[2] S. Li, S. Krishnamoorthy, A. Li, G.D. Meitzner, E. Iglesia, *J Catal,* **206** (2002), pp.202.

[3] D.I. Enache,B. Redours, M Ray-Auberger and R. Revel *J. Catal.* **205** (2002), pp.346-353.

[4] R.C.Raul and C.H.Bartholomew *J. Catal.* **85** (1984), pp.78.

[5] R. Bouarab, O. Akdim, A. Auroux, O. Cherifi, C. Mirodatos, *Appl. Catal.* **264** (2004), pp. 161-168.

[6] Nagaoka K ., Takanabe K . and K. Aika, *Appl. Catal. A: General* **268** (2004), pp. 151.

[7] A. Lapidus, A. Krylova, V. Kazanskii, V. Borovkov, A. Zaitsev, J. Rathousky, A. Zukal, M. Jan *Appl. Catal.* **73** (1991), pp. 65.

[8] Ø . Borg, E.A. Blekkan, S. Eri, D. Akporiaye, B. Vigerust, E. Rytter, A. Holmen, *Top. Catal.* **45** (2007), pp. 39-43.

[9] G. Jacobs, T.K. Das, Y.Q. Zhang, J.L. Li, G. Racoillet, B.H. Davis, *Appl. Catal. A: General* **233** (2002),pp. 63.

[10] W.J. Wang, Y.W. Chen, *Appl. Catal.* **77** (1991), pp. 223.

[11] M.C. Chan, R. Aris and W.H. Weiberg, *Appl. Surf. Sci.*, **1** (1978), pp. 360.

[12] P.A. Redhead, *Vacuum***, 12** (1962), pp. 203.

Effect of olefin pretreatment on Pd-Ag catalyst in selective hydrogenation of acetylene

P. Suttibut*, J. Panpranot, and K. Suriye

Center of Excellence on Catalysis and Catalytic Reaction Engineering, Department of Chemical Engineering, Faculty of Engineering, Chulalongkorn University, Bangkok 10330, Thailand

* Corresponding Author E-Mail Address: p_s_print_@hotmail.com

Abstract: The effect of catalyst pretreatment on the performance of a commercially obtained α-Al_2O_3 supported palladium-silver catalysts with metal loadings around 0.03 wt% has been investigated in the gas-phase selective hydrogenation of acetylene. The catalyst properties were modified by the catalyst pretreatment with olefin. Both acetylene conversion and ethylene selectivity were improved on the pretreated catalyst. At complete conversion of acetylene, ethylene selectivity was as high as 91.7% for the pretreated catalyst compared to 47.8% for the non-treated one. The FT-IR and TGA results indicated that green oil was produced during the reaction. However, the pretreated catalyst exhibited much smaller amount and shorter chain green oil. The pretreated catalyst was also stable during a test for more than 20 hours.

Introduction

The selective hydrogenation of acetylene in raw stream from a steam cracker is an important industrial process for the purification of ethylene. Ethylene selectivity is a key objective in this process [1]. In polyethylene industry, acetylene is a contaminant in the feedstock at approximately 0.35 wt.%, This impurity leads to a polymer with undesirable properties. There have been two general approaches to reducing the amount of acetylene from ethylene is very difficult and thus very costly. For this reason, the selective hydrogenation of this impurity to ethylene is the most attractive route [2]. A Small quantity of acetylene is a poison in the further process of ethylene polymerization [3]. Removal of trace amount of acetylene in ethylene feed stream is vital for the commercial product of polyethylene since acetylene acts as a poison to the polymerization catalysts. In order to prevent ethylene loss, when acetylene is catalytically hydrogenated, it is desirable that ethylene remains intact during hydrogenation [4].

The use of palladium as the active metal was studied by Cremer et al. [5] in a kinetic analysis. Work prior to 1963 has been summarized by Bond [6]. He showed that Pd was the most selective metal for this reaction. Industries still rely on this formulation to prepare the traditional Pd/α-Al_2O_3 catalyst, which is normally used for this reaction. It is usually prepared by either ion exchange or precipitation to produce a low-dispersion, low-metal content supported catalyst. The original idea was to prevent the re-adsorption of ethylene by using low metal content and to prevent the conjugation of adsorbed acetylene molecules to proceed towards either coke formation, C4 oligomers or C6's. The C4's are well known to industry as "green oil" [2]. Many researchers [7-11] have published papers about the selective hydrogenation of acetylene. It is well known that, among the metals of VIII B group, palladium dispersed on a support is the best catalyst, with good activity and selectivity for this reaction. But oligomers ('green oil') also form during acetylene hydrogenation on supported Pd catalyst, which shortens the recycle time and life of the industrial catalyst. In addition, Pd catalyst has poor selectivity at high levels of acetylene conversion. Supported Pd-based catalyst is known to be the best catalyst so far for such reaction with good activity and selectivity. The commonly used support for palladium catalyst in selective acetylene hydrogenation is α-Al_2O_3 [4]. At present all such catalysts are based on palladium using alumina as support, and palladium-based catalysts promoted by a second metal are now available.

The promoter improves selectivity or stability of the catalyst. Several attempts to improve ethylene selectivity of the palladium catalyst have been made by many researchers , including incorporation of a second metal such as Ag [12-15], Au [16,17], Cu [18], Si [19], K [20], and Co [21], pre-treatment with oxygen-containing compounds such as CO and N_2O [22-25], and modification of the catalyst supports [26,27]. Experimental results [28] indicated that Pd catalyst with addition of a group I B metal can increase the selectivity of acetylene hydrogenation to ethylene, reduce the yield of 'green oil', and improve the properties of the traditional catalyst. However, oligomer or green oil formation during reaction is inevitable over Pd/Al_2O_3 catalysts resulting in ethylene loss and shorten catalyst lifetime especially at high levels of acetylene conversion [29-34].

In this study, we concentrated the effect of olefin pretreatment on α-Al_2O_3 supported palladium-silver catalyst in selective hydrogenation of acetylene. The characterizations using BET, XRD, FT-IR and TGA methods have been taken to determine the catalyst properties. Based on the experimental results, some explanations of the catalyst improvements were illustrated for the selective hydrogenation of acetylene.

Materials and Methods

Gas and Pd-Ag/ α-Al_2O_3 catalyst:

The reactant gas used for the catalyst evaluation was the ethylene feedstream to the acetylene converter as supplied by the Rayong Olefins Co.,Ltd., Thailand. Ultra high purity hydrogen and high purity argon manufactured by Thai Industrial Gas Co., Ltd. (TIG) were used for reduction and cooling processes.

Catalyst was obtained from the SUD-CHEMIE CATALYSTS JAPAN, INC. that was used in this study. The size is 2-4 mm with spherical shape. The alumina support used balance with promoter and metal. The monometallic catalyst had a nominal weight loading of 0.03 wt% and 0.18 $\pm$ 0.03 wt% for promoter.

Methods:

Approximately 0.5 g of catalyst was packed in down flow reactor. The reactor was placed into furnace and argon was introduced into the reactor in order to remove air. Prior to the start reaction, the catalyst was reduced with 100 ml/min hydrogen flow at 150^{o}C and held at that temperature for 2 h. Afterwards, catalyst bed was switched into argon in order to remove the remaining hydrogen. If pretreatment with olefin was performed, catalyst bed must be cooled down to pretreatment temperature and known amount of olefin. Feed gas (Rayong Olefin Co.,Ltd.) was introduced at 60^{o}C temperature and 1 atm, sampling was taken every 20 minute. The composition of product and feed stream was analyzed by an Agilent 7890 GC equipped with TCD and FID detectors. Detail of the calculation of the catalyst activity to convert acetylene and the selectivity are given in Table 2. Acetylene conversion as used herein is defined as moles of acetylene converted with respect to a acetylene in feed. Ethylene selectivity is defined as the percentage of acetylene hydrogenated to ethylene over totally hydrogenated acetylene.

Characterization of catalysts:

The Brunauer Emmett Teller (*BET*) method continues to be widely used for evaluating the surface area, pore volume and pore size of catalysts and supports. The samples were determined by N_2 adsorption/desorption measurements using a Micromeritics ASAP 2020 automated system. Each sample was degassed under vacuum at < 10 μm Hg in the Micromeritics ASAP 2020 at 200^{o}C for 5 h prior to N_2 physisorption. The X-ray diffraction (*XRD*) spectra of the catalyst samples were measured from 20-80^o 2θ using a SIEMENS D5000 X-ray diffractometer and Cu Kα radiation with a Ni filter. Chemisorption and Fourier Transform Infrared Spectroscopy (*FT-IR*) with a NICOLET 6700 were used to detect the functional group. The thermal stability of catalyst was analyzed by thermal gravimetric analysis (*TGA*) using SDT Q6000.

Selective hydrogenation of catalysts:

The selectivity and conversion of Pd-Ag catalysts for ethylene hydrogenation was defined as:

$$\text{Selectivity} = \frac{\text{increase of ethylene (mol)}}{\text{decrease of acetylene (mol)}} \times 100\%$$

$$\text{Conversion} = \frac{\text{decrease of acetylene (mol)}}{\text{acetylene in feed (mol)}} \times 100\%$$

Results and Discussion

Characterization of catalysts:

The surface area, pore volume, and pore size of Pd-Ag/α-Al_2O_3 catalyst before and after pretreatment were not significantly different (see Table 1). The XRD patterns of commercial catalyst and catalyst after pretreatment are shown in Fig 1.

Table 1: Properties of Pd-Ag/ α-Al_2O_3 catalyst

Sample	BET surface area (m^2/g)	Pore Volume (cm^3/g)		Pore Size (nm)	
		Adsorption	Desorption	Adsorption	Desorption
NT*	27.4	0.14	0.15	19.3	16.5
PT**	29.2	0.17	0.17	20.7	17.4

* non treated catalyst
** pretreated catalyst

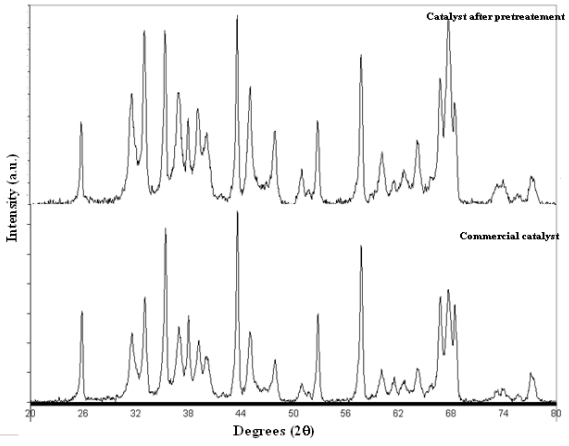

Figure 1. XRD results of commercial catalyst and catalyst after pretreatment

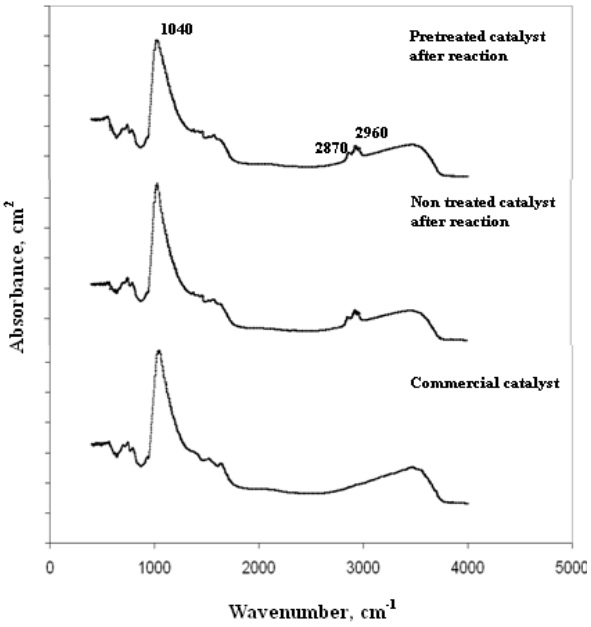

Figure 2. FTIR spectra of the commercial catalyst, non-treated catalyst after reaction and pretreated catalyst after reaction.

The FTIR results show that there was carbonaceous deposits/green oil formation after reaction.

The total weight loss during the reduction of spent catalysts was shown in Fig 3. The pretreated catalyst showed significantly lower weight loss than the non-treated one, indicating that much lower amount of green oil was produced on the pretreated catalyst. It is implied that we can prolong the catalyst lifetime by pretreatment the catalyst with olefin.

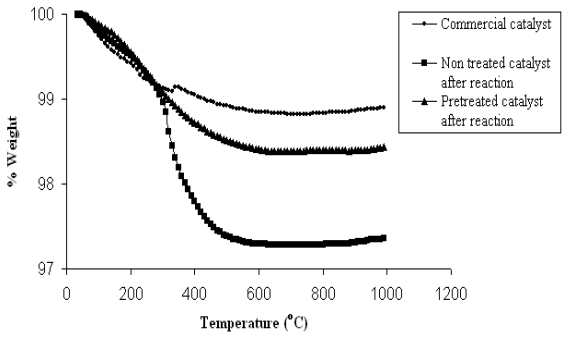

Figure 3. TGA results of commercial catalyst, non-treated catalyst after reaction and pretreated catalyst after reaction.

Table 2: Comparison of the amount of green oil after reaction between non-treated catalyst and pretreated catalyst.

Catalyst	% Total green oil in product
Non-treated	1.24
Pretreated	1.03

The total amount of green oil produced during reaction for the pretreated catalyst was less than that of the non-treated catalyst by ca. 17%. The comparison is shown in Table 3.

Catalytic performance of Pd-Ag/ α-Al_2O_3 catalyst

Performance of the pretreated catalyst in selective hydrogenation of acetylene has been compared with the non-treated one and the results are shown in Table 2. In this study, the ethylene selectivity at complete conversion of acetylene (100%) was of industrial interest. It was found that ethylene selectivity for the pretreated catalyst was higher than that of the non-treated one. In other words, the ethylene selectivity can be improved when the catalysts were pretreated with olefins. The selectivity improvement increases the ethylene yield in acetylene hydrogenation and also allows use of catalysts at high H_2/acetylene ratios, which extends the catalyst lifetime.

Table 3: Compare the selectivity and conversion of non-treated catalysts and pretreated catalyst.

Catalyst	Selectivity	Conversion
Non-treated	47.8 %	100%
Pretreated	91.7 %	100%

Moreover, the pretreated catalyst was stable during the reaction test for more than 20 hours.

Conclusions

The pretreatment of commercial Pd-Ag/α-Al_2O_3 catalyst with olefin prior to the reaction in the selective hydrogenation of acetylene gave higher selectivity towards ethylene (91.7%) at complete conversion of acetylene compared to the non-treated catalyst (47.8%). The improved catalyst performance of the pretreated catalysts was due to the smaller amount and shorter chain of green oil products being produced.

References

[1] Q. Zhang, J. Li, X. Liu and Q. Zhu, *Applied Catalysis A: General*. **197** (2000), pp. 221-228.
[2] M.J. Vincent and R.D. Gonzalez, *Applied Catalysis A: General*. **217** (2001), pp. 143-156.
[3] J. Hong, W. Chu, M. Chen, X. Wang and T. Zhang, *Catalysis Communications*. **8** (2007), pp. 593-597.
[4] J. Panpranot, K. Kontapakdee and P. Praserthdam, *Applied Catalysis A: General*. **314** (2006), pp. 128-133.
[5] E. Cremer, C.A. Knorr, H. Pleninger, Zeit, *Electrochem.* **47** (1994), pp. 737.
[6] G.C. Bond, *Catalyst by Metals, Academic Press, New York,* (1962), chapter 12.
[7] Q. Zhang, X. Liu and Q. Zhu, *Petrochem. Technol.* **27** (1998), pp. 53.
[8] G.C. Bond and P.B. Wells, *J. Catal.* **5** (1965), pp. 65.
[9] A.N.R. Bos, L. Van de Beld, H.J. Martens and K.R. Westerterp, *Chem. Eng. Comm.* **121** (1993), pp. 27.

[10] A.N.R. Bos, L. Van de Beld, H.J. Martens and K.R. Westerterp, *Chem. Eng. Comm.* **121** (1993), pp. 55.
[11] C. Gaudiness, A.L. Cabanes and G. Villora, *Can.J. Chem. Eng.* **74** (1996), pp. 84.
[12] J. Phillips, A. Auroux, G. Bergeret, J. Massardier and A. Renoupez, *J. Phys. Chem.* **97** (1993), pp. 3565-3570.
[13] D.C. Huang, K.H. Chang, W.F. Pong, P.K. Tseng, K.J. Hung and W.F. Huang, *Catal. Lett.* **53** (1998), pp. 155-159.
[14] Q. Zhang, J. Li, X. Liu and Q. Zhu, *Applied Catalysis A* **197** (2000), pp. 221-228.
[15] Y. Jin, A.K. Dayte, E. Rightor, R. Gulotty, W. Waterman, M. Smith, M. Holbrook, J. Maj and J. Blackson, *J. Catal.* **203** (2001), pp. 292-306.
[16] C. Visser, G.P. Zuidwijk and V. Ponec, *J. Catal.* **35** (1974), pp. 407.
[17] A. Sarkany, A. Horvath and A. Beck, *Applied Catalysis A*. **229** (2002), pp. 117.
[18] S. LeViness, V. Nair and A. Weiss, *J. Mol. Catal.* **25** (1984), pp. 131.
[19] E.W. Shin, C.H. Choi, K.S. Chang, Y.H. Na and S.H. Moon, *Catal. Today*. **44** (1998), pp. 137.
[20] Y.H. Park and G.L. Price, *Ind. Eng. Chem. Res.* **31** (1992), pp. 469.
[21] A. Sarkany, Z. Zsoldos, G. Stefler, W. Hightower and L. Guczi, *J. Catal.* **157** (1995), pp. 179.
[22] L. Cider and N.-H. Schoon, *Ind. Eng. Chem. Res.* **30** (1991), pp. 1437.
[23] P. Praserthdam, B. Ngamsom, N. Bogdanchikova, S. Phatanasri and M. Pramotthana, *Applied Catalysis A*. **230** (2002), pp. 41.
[24] B. Ngamsom, N. Bogdanchikova, M.A. Borja and P. Praserthdam, *Catal. Commun.* **5** (2004), pp. 243.
[25] R.N. Lamb, B. Ngamsom, D.L. Trimm, B. Gong, P.L. Silveston and P. Praserthdam, *Appl. Catal.* **268** (2004), pp. 43.
[26] J.H. Kang, E.W. Shin, W.J. Kim, J.D. Park and S.H. Moon, *J. Catal.* **208** (2002), pp. 310.
[27] A. Monzón, E. Romeo, C. Royo, R. Trujillano, F.M. Labajos and V. Rives, *Appl. Catal. A*. **185** (1999), pp. 53.
[28] M.M. Johnson, D.W. Walker, G.P. Nowack, US Patent 4,404,124.
[29] M.M. Johnson, D.W. Walker, G.P. Nowack, US Patent 4,484,015 (1984).
[30] G.C. Bond and P.B. Wells, *J. Catal.* **5** (1965), pp. 65.
[31] G.C. Bond and P.B. Wells, *Trans. Faraday Soc.* **54** (1958), pp. 1537.
[32] M. Larsson, J. Jansson and S. Asplund, *J. Catal.* **162** (1996), pp. 365.
[33] Y.-J. Huang, C.F. Shun, L.G. Daniel, E.L. Mohundro, J.E. Hartgerink, US Patent 5,332,705 (1994).
[34] K. Flick, C. Herion, H.-M. Allman, US Patent 5,856,262 (1999).


PACCON
Pure and Applied Chemistry International Conference 2010
Polymer Chemistry

Preparation of hydroxyl terminated natural rubber

L. Kaenhin[1,3*], P. Klinpituksa[2,3], A. Rungvichaniwat[1,3] and J.F. Pilard[4]

[1]Department of Rubber Technology and Polymer Science, Faculty of Science and Technology, Prince of Songkla University, Thailand 94000
[2]Department of Science, Faculty of Science and Technology, Prince of Songkla University, Thailand 94000
[3]Center of Excellence in Natural Rubber Technology, Prince of Songkla University, Thailand 94000
[4]LCOM-Chimie des Polymères, UMR CNRS 6011, Université du Maine, Le Mans Cedex9, France 72085

[*] Corresponding Author E-Mail Address: g4920330101@pn.psu.ac.th

Abstract: Natural rubber (NR) is high molecular weight and non-polar polymer. The chemical modification of NR molecular structure can be easily modified by introducing some special functional groups at the chain-ends and also the molecular weight can be decreased by chemical reactions. The present work was an attempt to study the degradation of NR to develop to a controlled molecular weight polymer with reactive terminal groups. The oxidative degradation of NR was performed through the reaction between epoxidized natural rubber (ENR) and periodic acid, leading to obtain carbonyl terminated natural rubber (CTNR). ENR was first prepared in latex phase using performic acid generated *in situ* by reaction of hydrogen peroxide and formic acid. It was found that percentages of epoxidation had effect on a number average molecular weight of degradation reaction in CTNR. The selective reductive amination of CTNR using sodium triacetoxyborohydride as reducing agent was carried out. After that, carbonyl groups of CTNR were reduced to hydroxyl terminated natural rubber (HTNR) by sodium borohydride. HTNR can also be modified by adding epoxy groups into its molecular structure. The resulting HTNR number average molecular weight of 600-3500 was obtained. The molecular structure of chemical modification of NR was characterized using proton nuclear magnetic resonance spectroscopy (^{1}H-NMR) technique.

Introduction

Chemical modifications or functionalizations of NR are of wide interest to research scientists. The aim of chemical modifications is to improve the properties of NR for specific applications or to convert NR to the new material. Epoxidation represents a particularly attractive and convenient method of transforming NR into a new polymer with interesting properties. The epoxide group in the modified NR structure is also active to various chemical reactions involving hydrogen donor atoms, such as amines, alcohols, and carboxylic acids. Periodic acid is an effective scission agent with NR and partially with epoxidized natural rubber (ENR). It can select oxidation at epoxide group in ENR [1] and also decrease the molecular weight of NR latex [2] as well as ENR. The selective oxidation of high molecular weight NR to obtain carbonyl end group has been the center of the preparation of new hydroxyl and amino terminated *cis*-1,4-polyisoprene (isoprene rubber; IR) [3,4,5,6]. The reactive oligomers such as carbonyl or hydroxyl terminated ones and macromonomer are attractive interest as intermediates for use in surface coatings, adhesives and synthesis of block and graft copolymers.

The present work was focused on a preparation of hydroxyl terminated NR (HTNR) through the oxidative degradation reaction of ENR. The chemical modifications of HTNR were further carried out by adding epoxide and amino groups onto the HTNR molecular structure. The obtained chemical structure was characterized by ^{1}H-NMR technique.

Materials and Methods

Materials

High ammonia concentrated natural rubber latex (HA-NRL, Yala Latex Industry Co., Ltd), formic acid (Merck, 98%), hydrogen peroxide (Merck, 30%), periodic acid (Merck), sodium borohydride (Merck), diethanolamine (Sigma-Aldrich, 99%), sodium triacetoxyborohydride (Acros Organics, 97%), *m*-chloroperbenzoic acid (*m*-CPBA, Fluka, 70%) sodium hydroxide (Carlo Erba, 97%) and glacial acetic acid (J.T. Baker) were used without purification. Tetrahydrofuran (THF, Lab-Scan), dichloromethane (Lab-Scan) and dichloroethane (Ajax Finechem) were used as solvent in the reactions.

Methods

Synthesis of epoxidized natural rubber (ENR): 60%DRC of HA-NRL (1 mole) was diluted to 20%DRC in reaction kettle, stabilized with Terric N-10 3 phr and stirred at room temperature to eliminate ammonia. Then, the latex was heated to 60 °C. Added drop by drop of formic acid (0.3 mole). Hydrogen peroxide (0.3 mole) was then added. The reaction was stopped at various interval times for sampling to characterize the epoxide contents. ENR latex was coagulated in methanol, washed with water several times and dried in hot air oven at 40 °C. The resulting ENR was analyzed by ^{1}H-NMR technique for determining percentage of epoxidation reaction.

Synthesis of carbonyl terminated natural rubber (CTNR): ENR (1 mole) was dissolved in THF and reacted with periodic acid (1.1 mole) at 30 °C for 6 hours in reaction kettle with controlling of stirrer speed at 300 rpm. Solvent was removed from CTNR solution by evaporator.

Synthesis of hydroxyl terminated natural rubber (HTNR): Sodium borohydride (6 mole) was dissolved in THF in a reaction kettle at 30 °C. Added drop by

drop of the solution of CTNR (1 mole) in THF, heated to 60 °C and continued the reaction for 6 hours. When the solution was cool down, hydrolysis was performed by adding cool water. THF was then evaporated from the reaction mixture under vacuum.

Synthesis of α-hydroxy, ω-N,N-amino dihydroxy ethyl natural rubber (nHTNR): CTNR (1 mole) and diethanolamine (2.1 mole) were dissolved in dichloroethane in reaction kettle. Solution was then treated with sodium triacetoxyborohydride (2.8 mole) and glacial acetic acid (1 mole) at ambient temperature for 24 hours. Organic phase was washed with 1 N NaOH and dried under vacuum. Then the product (α-methyl ketone, ω-N,N-amino dihydroxy ethyl natural rubber; nCTNR) was reduced with sodium borohydride according to the experimental above.

Synthesis of epoxidized hydroxyl terminated natural rubber (eHTNR): HTNR (1 mole) was dissolved in dichloromethane and reacted with the solution of *m*-CPBA (1 mole) in dichloromethane in three necked round bottom flask with magnetic stirrer at 0 °C for 3 hours. After that the solvent was removed.

Samples of ENR, CTNR, nCTNR, HTNR, nHTNR and eHTNR were characterized by ^{1}H-NMR technique (Fourier Transform NMR Spectrometer 500 MHz, Model UNITY INOVA, Varian).

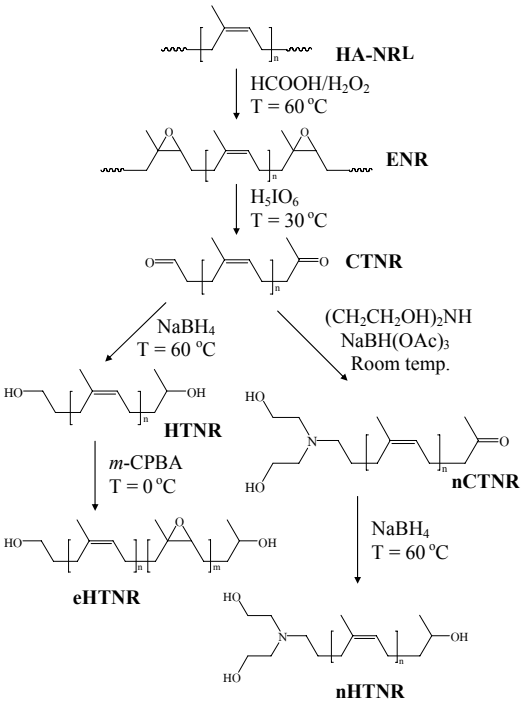

Figure 1. Idealized reaction scheme for chemical modifications of NR

Results and Discussion

HTNR ($\overline{M}_n$ = 1200 g mol^{-1} from 7% epoxide contents of ENR) (Figure 2.) was obtained by selective reduction of CTNR resulting from controlled degradation of high molecular weight of NR according to a method previously described [1, 3, 4]. All of ^{1}H-NMR spectra in Figure 2 shows the same methyl (C*H*$_3$), methylene (C*H*$_2$) and methine protons (C=C*H*) at 1.67, 2.04 and 5.12 ppm, respectively. The different signals of each spectrum were observed at 2.70 ppm (epoxide methine proton: C-O-C*H*) of ENR, 9.80 ppm of CTNR (*H*C=O), 3.63 ppm (C*H*$_2$OH) of HTNR and 3.80 ppm (C*H*OH) of HTNR.

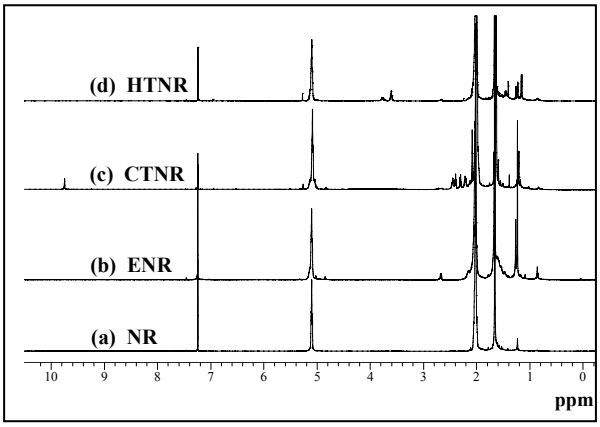

Figure 2. ^{1}H-NMR spectra of (a) NR, (b) ENR, (c) CTNR and (d) HTNR

2, 4, 7 and 14% epoxide contents in ENR were cleaved epoxide units by periodic acid to form CTNR. After that, the carbonyl end groups in CTNR was reduced by sodium borohydride to obtain HTNR of $\overline{M}_n$ = 3500, 2000, 1200 and 600 g mol^{-1}, respectively (Figure 3).

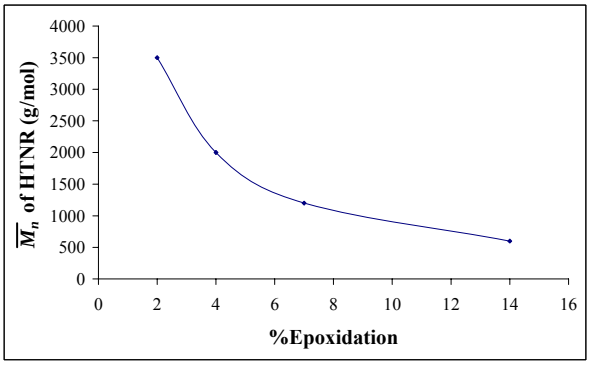

Figure 3. %Epoxidation versus the number average molecular weight ($\overline{M}_n$) of HTNR

The $\overline{M}_n$ can be obtained by the signals of ^{1}H-NMR using the following formulas:

$$\overline{M}_n(HTNR) = \left[\frac{I(C=CH)}{I(CHOH)}\right] \times 68 + 104$$

$$\overline{M}_n(eHTNR) = \left[\frac{I(C=CH)}{I(CHOH)}\right] \times 68 + \left[\frac{I(CHepoxide)}{I(CHOH)}\right] \times 84 + 104$$

$$\overline{M}_n(nHTNR) = \left[\frac{I(C=CH)}{I(CHOH)}\right] \times 68 + 191$$

HTNR ($\overline{M}_n$ = 1200 g mol^{-1}, Figure 1) were modified to obtain amine and epoxide groups in the main chain. The main signals of ^{1}H-NMR spectra of nHTNR (Figure 4(c)) are at 2.54 (CH_2 connect to nitrogen atom) and 2.69 (HO-CH$_2$-CH_2-N) ppm [6]. The eHTNR signals (Figure 4(d)) of the epoxide proton of epoxidized unit was shown at δ = 2.70 ppm and of the ethylenic proton of isoprene unit was shown at δ = 5.12 ppm.

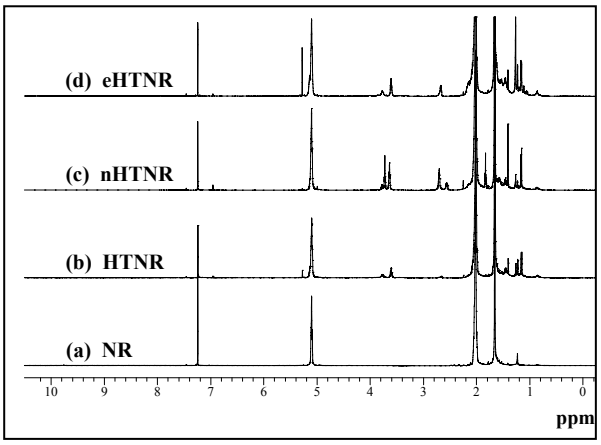

Figure 4. ^{1}H-NMR spectra of (a) NR, (b) HTNR, (c) nHTNR and (d) eHTNR

Conclusions

Chemical modification of NR to obtain HTNR, nHTNR and eHTNR can be effectively prepared through the oxidative degradation of ENR in latex phase using periodic acid. The $\overline{M}_n$ of HTNR depends on the epoxide contents in ENR. The higher of epoxide contents of ENR, the lower of $\overline{M}_n$ of HTNR are founded. The evident end groups of HTNR, nHTNR and eHTNR obtained from ^{1}H-NMR technique are clearly observed.

Acknowledgements

The financial support of the Graduated Education at Prince of Songkla University is gratefully acknowledged. LCOM-Chimie des Polymères at Université du Maine is greatly appreciated for technical support.

References

[1] S. Gillier-Ritoit, D. Reyx, I. Campistron, A. Laguerre and R.P. Singh, *J. Appl. Polym. Sci*. **87** (2003), pp. 42-46.

[2] P. Phinyocheep, C.W. Phetphaisit, D. Derouet, I. Campistron and J.C. Bross, *J. Appl. Polym. Sci*. **95** (2005), pp. 6-15.

[3] N. Kébir, G. Morandi, I. Campistron, A. Laguerre and J.F. Pilard, *Polymer*. **46** (2005), pp. 6844-6854.

[4] N. Kébir, I. Campistron, A. Laguerre, J.F. Pilard, C. Bunel, J.P. Couvercelle and C. Gondard, *Polymer*. **46** (2005), pp. 6869-6877.

[5] N. Kébir, I. Campistron, A. Laguerre, J.F. Pilard, C. Bunel and T. Jouenne, *Biomaterials*. **28** (2007), pp. 4200-4208.

[6] G. Morandi, N. Kébir, I. Campistron, F. Gohier, A. Laguerre and J.F. Pilard, *Tetrahedron Letters*. **48** (2007), pp. 7726-7730.

Effect of carbon black loading on the mechanical properties and gasohol resistance of the filled natural rubber

S. Khongvittaya[1] and W. Keawwattana[1*]

Department of Chemistry, Faculty of Science, Kasetsart University, Jatuchak, Bangkok, 10900 Thailand

[*]E-mail: fsciwyk@ku.ac.th

Abstract: Effect of the addition of carbon black (CB) loading on the mechanical properties, thermal and gasohol resistance of the natural zeolite, rice husk ash (RHA) and perlite-filled natural rubber (NR) was studied. The amount of fillers (natural zeolite, RHA and perlite) filled in the vulcanizates has been fixed at 20 phr, while CB loading was varied in a range of 0-45 phr. It was found that the tensile strength, % elongation at break, modulus and hardness of the vulcanizates filled with all kinds of fillers increased with the increase in CB loading, while there was no significant change in the compression set. Moreover, at this particular filler loading (20 phr), the addition of perlite has significant effect on gasohol resistance of the vulcanizates in which gasohol resistance (various ethanol ratio) of the vulcanizates was significantly improved with perlite loading compared with others.

Introduction

Gasohol is substitute energy for gasoline. Gasohol was formed from mixture of gasoline with 99.5% purified ethanol (ethyl alcohol). The purified ethanol was produced from agricultural plants via fermentation process, distillation and purification process. The gasohol product was occurred in 1985 from His majesty the king's genius (King Bhumipol). He realized that Thai people encountered petroleum oil shortage and receive lower price of their agricultural product. Thus, the royal created his project (Suan Jitlada project) to study ethanol production from sugar cane. This ethanol was then mixed with gasoline to obtain gasohol. Gasohol is socially useful such as helping farmer gain more money from their agricultural products so they will have better quality life and can solve poverty problem in lower income level of farmers.

It is widely known that some part of engine component produced from rubber such as gasket cover, sealing and hoses. These parts will be contacted with oil for several times. Generally, rubber product has high polarity such as acrylonitrile butadiene rubber (NBR). When NBR contact with diesel oil having hydrocarbon and non-polar solvent, it shows non-effect to rubber product. For gasohol, a gasoline containing ethanol is a polarity. The polarity behavior of gasohol will depend on ethanol ratio in mixing gasohol. Therefore, when gasohol having ethanol as a mixture contact with rubber part, it can act as solvent to dissolve rubber part. Hence, changing from diesel to gasohol will affect on rubber product that contact with gasohol. The physical properties such as rubber swelling and duration use of rubber will decrease.

In this research work, we expected to modify and improve natural rubber to prevent gasohol corrosion (at various ethanol ratios). We thus aim to study not only the influence of ethanol ratio in gasohol but also the effect of filler types (natural zeolite, RHA and Perlite) at a particular loading (20 phr) on mechanical properties, thermal aging and gasohol resistance of natural rubber. Moreover, the effect of carbon black loading (5-45 phr) on aforementioned properties will be disscussed.

Materials and Methods

Natural rubber (STR5L) and gasohol were supplied by S.M.P Rubber (Bangkok, Thailand) and PTT Public Company Limited (Bangkok, Thailand), respectively.

Rubber compound formulae are given in Table 1. The mixing was carried out on two-roll mill, a circulating water temperature of 70°C, and a rotor speed of 55 rpm for 2 min, then further mixed with a specific content of filler for 20 min. The compounds were then kept at room temperature before further use. Finally, vulcanization was performed using a compression molding machine (G30H-15-CX, Wabash, USA). The cure characteristics were assessed by Moving Die Rheometer (MDR). The various rubber compounds were compression molded at 160°C according to their respective optimum cure time.

Table 1: Formulation of the rubber compounds

Ingredients	Function	Contents (phr)
NR	matrix	100
Fillers*	filler	20
carbon black	filler	0-45
ZnO	activator	5.0
Stearic acid	activator	2.0
Rubber oil	processing aid	2.0
TBBS	accelerator	2.4
TMQ	antioxidant	1.5
Sulfur	crosslink agent	0.2

Note* (Natural Zeolite, RHA and Perlite)

Results and Discussion

1. Filler characterization

Table 2: Physical properties of fillers

Fillers	Surface area (m^2/g)	Pore volume (cm^3/g)
Natural zeolite	14.9752	0.0003
RHA	66.3699	0.0068
Perlite	4.6177	0.0055
Carbon black (CB)	71.8423	0.1654

It was found in Table 2 that the BET surface area of RHA and CB was greatly greater than that of zeolite and perlite. It shows that pore volume of CB is high compared with others while that of natural zeolite is quite low.

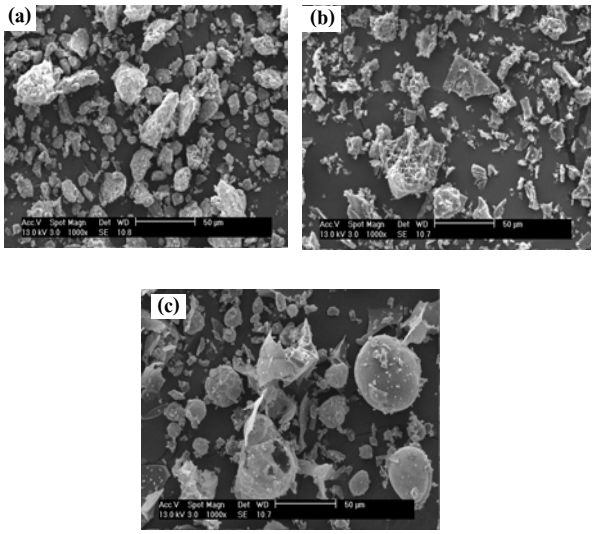

Figure 1. SEM images of (a) natural zeolite (b) RHA and (c) perlite at 1000x.

It can be seen from Figure 1 that the particle size of perlite is quite large compared to natural zeolite and RHA which is in accordance with the result of BET surface area as shown in Table 2.

2. Effect of types of fillers (without CB) at 20 phr

2.1 Cure characteristics

Table 3: Cure characteristics of compounds

NR (phr)	Type of fillers (20 phr)	Cure characteristics			
		t_{S2} (min)	t_{C90} (min)	M_H (lbf.in)	M_L (lbf.in)
100	Zeolite	10.58	13.45	2.87	0.29
	RHA	7.55	11.58	3.61	0.45
	Perlite	9.33	13.05	3.29	0.38

Table 3 represents the value of torque, scorch time (t_{s2}) and optimum curing time (t_{c90}) of the rubber compounds filled with various fillers at specific loading (20 phr). The high values of minimum (M_L) and maximum torques (M_H) for RHA-filled rubber compounds indicate that there is a high restriction to the molecular motion of the macromolecules, probably caused by the greater interaction between RHA and the rubber matrix. This is possibly due to the higher surface area of RHA compared to natural zeolite and perilte as seen from Table 2.

2.2 Mechanical properties

Table 4: Mechanical properties of vulcanizates

NR (phr)	Filler (20 phr)	TS (MPa)	300% Mod (MPa)	EB (%)	Hardness (Shore A)	Set (%)
100	Zeolite	5.4	0.96	626	27.0	24.67
	RHA	7.0	1.2	695	29.0	33.92
	Perlite	8.0	1.1	680	32.0	21.68

It can be seen from Table 4 that NR filled with natural zeolite gave lower values of tensile strength (TS), modulus, elongation at break (EB) and hardness than that filled with RHA, possibly due to the lower surface area giving the decrease in filler-rubber interaction. Eventhough perlite has the lowest surface area, perlite-filled vulcanizates showed the highest TS and hardness compared with natural zeolite- and RHA-filled vulcanizates, probably as a result of the layer structure of perlite as shown in Figure 1.

2.3 Thermal and gasohol resistance

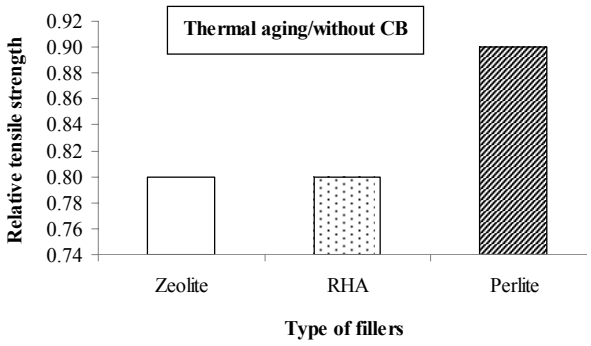

Figure 2. Relative tensile strength of filled vulcanizates after thermal aging

It is shown in Figures 2 and 3 that perlite-filled vulcanizate gives not only the highest relative tensile strength after thermal aging at 100°C for 22 hrs but also the greatest gasohol resistance as can be seen from the highest relative tensile strength after gasohol immersion at almost all ethanol ratios. In general, tensile strength decreases after gasohol immersion. The higher the relative tensile strength, the higher the gasohol resistance is. The result of relative tensile strength is in good correlation with the percentages of

swelling as seen in Figure 4. That is to say the lower the swelling in gasohol, the higher the relative tensile strength, higher the gasohol resistance will be. It was also observed that natural zeolite-filled vulcanizates show the lowest relative tensile strength and obviously the highest percentage of swelling. It could be explained by the fact that natural zeolite has low pore volume compared with other fillers as seen in Table 2, resulting in less diffusion of gasohol through the particles.

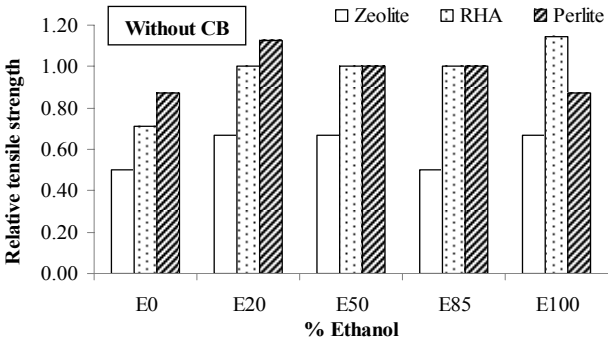

Figure 3. Relative tensile strength of filled vulcanizates after immersion in gasohol

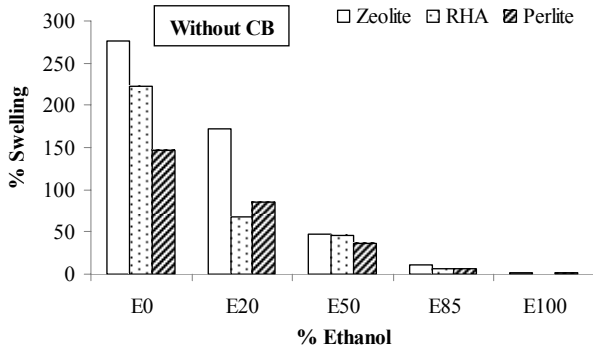

Figure 4. Swelling of filled vulcanizates after immersion in gasohol

3. Effect of carbon black loading

3.1 Cure characteristics

It can be seen from Table 5 that t_{s2} and t_{c90} of natural zeolite-, RHA- and perlite-filled compounds decrease with the increase in carbon black loading from 5 to 45 phr. While the addition of carbon black leads to the increment in minimum and maximum torques of the compounds, as a result of high restriction to the molecular motion of the macromolecules.

Table 5: Cure characteristics of filled compounds with various CB loadings

NR (phr)	Fillers (20 phr)	CB loading (phr)	Cure characteristic			
			t_{s2} (min)	t_{c90} (min)	M_H (lbf.in)	M_L (lbf.in)
100	Nat. zeolite	5	7.07	10.38	3.79	0.56
		10	5.51	9.11	4.03	0.56
		15	5.32	9.12	4.20	0.61
		35	4.06	8.18	5.08	0.72
		45	3.48	7.41	5.94	1.04
	RHA	5	5.25	9.33	4.36	0.53
		10	5.04	8.46	4.31	0.59
		15	4.42	8.33	4.71	0.75
		35	3.40	7.41	6.36	1.02
		45	3.18	7.23	7.84	1.53
	Perlite	5	5.29	9.27	3.95	0.45
		10	4.51	8.17	4.46	0.64
		15	4.40	8.21	4.80	0.72
		35	3.28	6.48	6.29	0.99
		45	3.12	7.11	7.79	1.44

3.2 Mechanical properties

The increase in CB amount from 0 to 45 phr can promote the mechanical properties, namely TS, modulus and hardness of the all filled-vulcanizates as shown in Table 6, possibly due to the fact that CB shows reinforcement effect and also it has high surface area (Table 2), leading to better filler-rubber interaction.

Table 6: Mechanical properties of filled vulcanizates with various CB loading

Filler (20 phr)	CB (phr)	Mechanical Properties				
		TS (MPa)	300%Mod (MPa)	EB (%)	Hardness (Shore A)	Set (%)
Nat. Zeolite	5	7.6	1.1	672	31.3	21.4
	10	8.7	1.8	545	35.2	22.7
	15	11.8	2.3	570	36.8	27.2
	35	12.2	5.0	460	39.7	22.0
	45	13.8	7.3	456	46.5	20.8
RHA	5	9.8	1.7	589	34.0	25.7
	10	10.0	2.1	600	37.3	27.5
	15	9.6	2.5	582	39.7	30.7
	35	11.7	6.2	430	47.5	16.5
	45	11.7	9.1	389	54.7	21.0
Perlite	5	9.0	1.7	606	35.6	26.4
	10	11.4	2.5	557	37.4	30.6
	15	16.2	3.6	558	41.7	28.6
	35	17.2	6.0	540	50.4	24.1
	45	16.9	9.6	439	56.9	27.5

3.3 Thermal and gasohol resistance

The amount of CB loading shows no significant effect on the relative tensile strength of 20 phr RHA-, zeolite-, and perlite filled-vulcanizates after thermal aging as seen in Figure 5.

It was found from Figures 6 and 7 that the vulcanizate filled with perlite show the better gasohol resistance than that filled with RHA and natural zeolite as can be seen from the higher relative tensile strength and lower percentage of swelling after immersion in gasohol (various ethanol ratios). It was in accordance with the earlier results of the vulcanizates without carbon black (from Figure 4). Moreover, as compared with Figure 4, it was observed that the addition of CB (at 35 phr) could promote the gasohol resistance as a result of decreasing percentage of swelling, possibly due to the fact that CB has great pore volume as seen in Table 2.

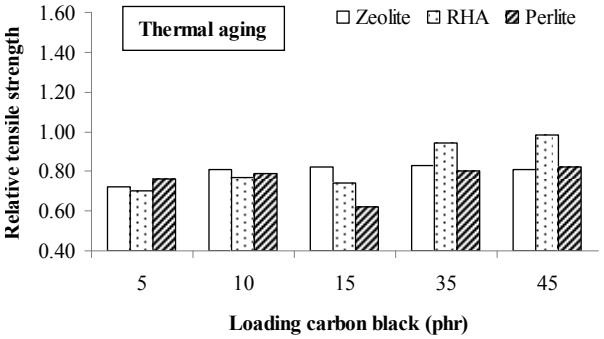

Figure 5. Relative tensile strength of filled vulcanizates with various CB loadings after thermal aging

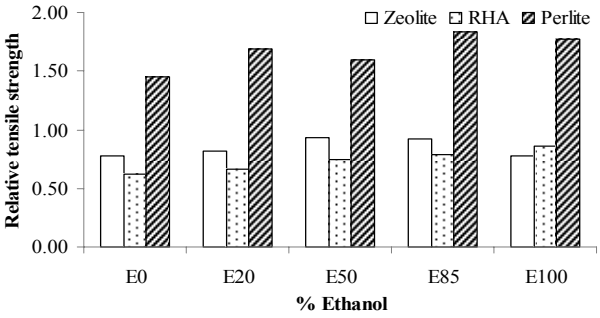

Figure 6. Relative tensile strength of filled vulcanizates with 35 phr CB loading after gasohol immersion

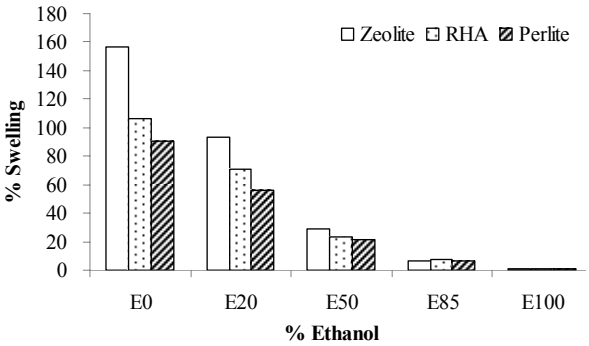

Figure 7. Swelling of filled vulcanizates with 35 phr CB loading after immersion in gasohol

Conclusions

The purpose of this study was to verify the effect of CB loading on the mechanical properties, thermal and gasohol resistance of the vulcanizates filled with fixed amount of RHA, natural zeolite and perlite (20 phr). It was turned out that TS, modulus and hardness of all filled vulcanizates increase with increasing CB loading as a result of reinforcement effect of CB. However, the amount of CB does not seem to have significant effect on the thermal resistance of the filled-vulcanizates. It should be noted here that the addition of CB at 35 phr could increase the gasohol resistance of the filled-vulcanizates as can be seen from the decrease in percentage of swelling after gasohol immersion (various ethanol ratio). It should be also pointed out here that perlite particles seem to give the best benefit to natural rubber compared with other fillers.

References

[1] S. Thongsang and N. Sombatsompop, *ANTEC*. 2005, pp. 3282.

[2] S. Chakrit, S. Pongdhorn, and J. Guaysomboon, *Journal of Applied Polymer Science*. **84** (2002), pp. 22-28.

[3] S. Chakrit, S. Limcharoen and J. Thunyarittikorn, *Journal of Applied Polymer Science*. **87** (2003), pp.83-89.

[4] W. Douglas Ming and A. Frederick, *Mumpton. Brockport, NY.* (1995).

[5] H. Donald, and Y. Lauriente, Inoguchi, *CEH Marketing Research Report,"Zeolites"*.

Characteristics of microwave-assisted glycolyzed products from PET wastes using different catalysts

P. Phanwiroj[1,2] and P. Potiyaraj[1,2*]

[1]Center of Excellence in Textiles, Department of Materials Science, Faculty of Science, Chulalongkorn University, Bangkok 10330, Thailand
[2]National Center of Excellence for Petroleum, Petrochemicals and Advanced Materials, Chulalongkorn University, Bangkok 10330, Thailand

*E-mail: pranut.p@chula.ac.th

Abstract: The target of this research is to seek a more eco-friendly approach to chemically recycle poly(ethylene terephthalate) (PET) wastes using glycolysis reaction. Under microwave radiation, PET was depolymerized by excess diethylene glycol with different catalysts. An 800W domestic microwave oven was modified in order to carry out the reaction. Apart from zinc acetate which is a common catalyst for PET glycolysis, more eco-friendly catalysts, that are sodium bicarbonate and sodium carbonate, were also employed. The rate of depolymerization and yield of the reaction were quantitatively determined. The glycolyzed products were investigated using Fourier transform infrared spectroscopy (FT-IR), differential scanning calorimetry (DSC) and thermal gravimetric analysis (TGA) in order to study the effects of type of catalyst on characteristics of the glycolyzed products. The advantage of using microwave radiation is the much shortening of reaction time. Excessive reaction time led to lower yield and the gelation of the reaction mixture. $NaHCO_3$ which is not a good catalyst in the conventional heating reaction can be used effectively in the microwave-assisted reaction comparable to zinc acetate. Na_2CO_3 can also be used as a catalyst but with a slower rate of depolymerization

Introduction

Wide spread applications and non-biodegradable of poly(ethylene terephthalate) or PET have created a large amount of waste and disposal which tends to create critical environmental problems. Recovery of recyclable PET is processed from two sources that are manufactured wastes and the post-consumer waste. Primary recycling involves reprocessing of manufactured wastes. Post-consumer PET may also be recycled with physical reprocessing methods, i.e. grinding, melting and reforming. This method is called secondary recycling. Alternatively, it may process with chemical recycling and feedstock recycling. This method is called tertiary recycling. The last method is quaternary recycling which involves the recovery of the energy content of plastic waste [1].

Chemical recycling though depolymerization leads to the formation of monomers or oligomers which can react to form a new polymer. PET ester chain cleavage can possibly be occurred by reagents, such as water (hydrolysis), alcohols (alcoholysis), amines (aminolysis), acids (acidolysis) [2]. However, one of the most studied chemical recycling techniques is the depolymerization of PET in glycols. The reaction involves the molecular degradation of PET molecular chains by glycols, in the presence of catalysts, mainly heavy metal acetates, where ester linkages are broken and replaced with hydroxyl terminals. PET can be polymerized by glycolysis reaction to obtain oligomeric diols and polyols, or glycolyzed into its monomeric units, bis-(2-hydroxyethylene) terephthlate (BHET) or dimethyl terephthlate. These glycolyzed products have been widely used in the production of unsaturated polyesters, acrylate/ methacrylate-terminated oligoester and rigid or flexible polyurethanes. It was found that zinc acetate was the best catalysts in term of glycolyzed products [1,2]. C-H Chen studied the factor affecting the glycolysis reaction in detail with conventional heat and his conclusion was the optimum glycolysis condition to reach 100% conversion would be at the temperature of 190°C for 2 hours with zinc acetate as a catalyst at 0.5% concentrate (w/w) [3].

The use of microwave energy as an energy source in chemical reactions has received more attentions in the recent years because of its high efficiency. Two fundamental mechanisms for transferring energy from microwaves to substance being heated are the dipole rotation (dipole polarization) and ionic conduction [4]. The main advantages of microwave over conventional heating sources are noncontract, well heat distribution into the bulk of material and decreasing the reaction time. It was reported that PET can be glycolyzed under microwave radiation replacing conventional heating [5].

In this article, we attempt to use microwave energy as a replacement for conventional heating for PET depolymerization in DEG. Characteristics of glycolyzed products obtained from the reaction using different catalysts were determined. It was expected that, apart from minimizing the energy used, the heavy metal catalyst can be replaced by a more eco-friendly catalyst.

Materials and Methods

Materials

Post-consumer PET bottles from local market were procured. Labels and caps were removed. The bottles

were thoroughly cleaned with water. The bottles were then dried and pulverized into powder.

Diethylene glycol (DEG) and all the chemicals including zinc acetate, sodium bicarbonate, sodium carbonate, sodium chloride, and calcium chloride were purchased from Fluka and all of them were of laboratory grade and used without further purification.

Glycolysis of PET waste

An LG domestic microwave oven was modified in order to carry out the glycolysis reaction. A condenser and a Teflon mechanical stirrer were fitted on the top of the oven as shown in Figure 1. PET waste powder and DEG were charged into a round-bottom flask at the molar ratio of PET:DEG of 1:6. A catalyst, that is, zinc acetate, sodium bicarbonate, sodium carbonate, sodium chloride or calcium chloride was also used at the weight ratio of 0.5% by weight of PET. The glycolysis reaction proceeded for the time periods up to 25 min at the irradiation power of 600 W. At each selected time period, if the reaction was not completed, filtrated to separate PET residue which was weighed in order to calculate depolymerization rate. When PET residue was not able to visually observe, excess distilled water was added to the reaction mixture with vigorous agitation. The mixture was then left to precipitate in a refrigerator for 1 day and filtered in order to obtain the glycolyzed product. The filtrate was dried an oven and weighed to determine the yield of the reaction.

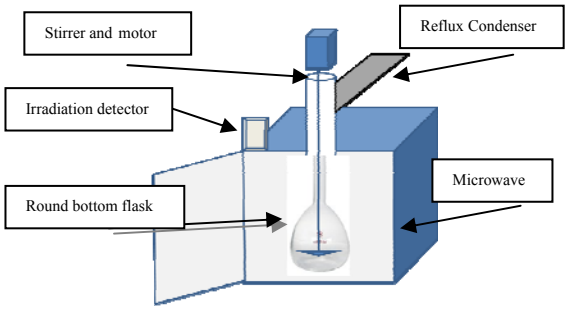

Fig.1 Modified microwave reactor

Characterization of glycolyzed product

Functional group analysis was performed using a Perkin Elmer System 2000 Fourier transform infrared spectrometer (FT-IR, Waltham, MA). The degradation temperature was determined by thermal gravimetric analysis (TGA, Netzsch type 409, Selb, Germany) at the heating rate of 10 °C/min from 50 to 500 °C under nitrogen atmosphere. The melting temperature was determined by Perkin Elmer Diamond differential scanning calorimeter (DSC, Waltham, MA) at the heating rate of 10 °C/min from 50 to 250 °C also under nitrogen atmosphere.

Results and Discussion

The depolymerization reaction occurred under the optimal experiment conditions obtained from previous experiments, with the microwave power of 600 W and the reaction time ranging from 5 to 25 min. Figure 2 shows the unsolubilized PET remain solid after the selected reaction times. Complete PET depolymerization was achieved within 10 min when zinc acetate and sodium bicarbonate were used and within 12 min when sodium carbonate was used. However, it was not possible to complete the depolymerization reaction when sodium chloride and calcium chloride were used as a catalyst.

Among the catalyst used, zinc acetate was found to be the most effective catalyst for the reaction in the previous studies using conventional heating method[3]. However, it was found that, in the microwave-assisted depolymerization of PET, the efficiency of $NaHCO_3$ is somewhat comparable to that of zinc acetate.

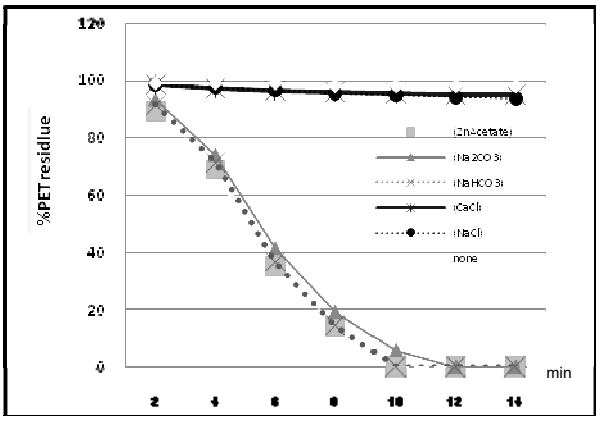

Fig.2 Depolymerization rate of the glycolysis reaction of PET with DEG using various catalyst

The effect of reaction time on the yield when different catalysts were used was in agreement with the previous result. Figure 3 indicates that the yield of glycolyzed product increased till 14 min for all the catalyst at 0.5% concentration (w/w) and PET:DEG molar ratio 1:6. After 14 min, the yield of the reaction was found to be decreased. The glycolysis of PET is a reversible equilibrium reaction. With increase in time, its reverse reaction starts predominating thereby decreasing the glycolyzed product yield [5]. According to previous studies [2], this implies that the substantial decrease in reaction time of depolymerization reaction comparing with conventional heating method attribute to the fact that microwave do not affect the activation energy of the reaction but provide the momentum to the reactant molecules to overcome the barrier to reach the higher state helping in completion of reaction at a faster rate than the conventional heating.

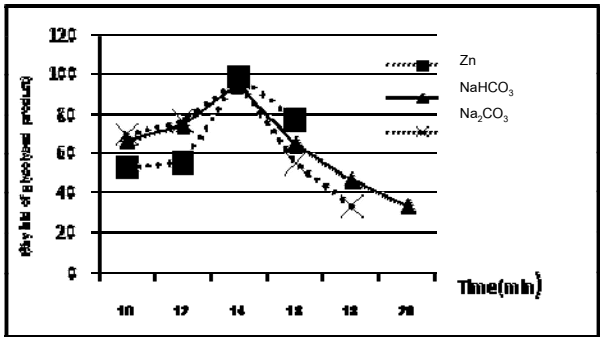

Fig.3 Effect of glycolysis time on the yield of glycolyzed product

The FTIR spectrograph in Figure 4 shows that all obtained glycolyzed products showed –OH band range at 3388 cm^{-1} and 1126 cm^{-1}, alkyl C-H at 2877 cm^{-1} and 2931 cm^{-1}, C=O ester stretching at 1717 – 1719 cm^{-1}, aromatic C-H at 1409 – 1457 cm^{-1} and C-H position para in aromatic at 732 cm^{-1}. The results on FTIR spectra of the glycolyzed products are similar to previous reports.

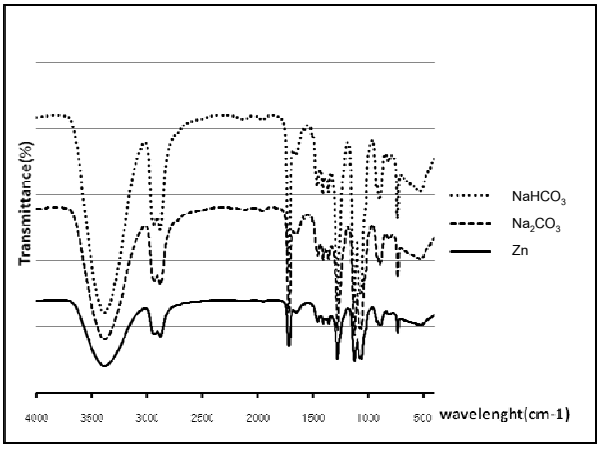

Fig.4 FT-IR spectra of the glycolyzed products with DEG using various catalysts

From DSC thermogram in Figure 5, the melting of glycolyzed product was found between 140 °C and 180 °C. From the previous studies, this implies that the glycolyzed products show melting behavior between those of monomer and dimer. According to the previos work [4], pure monomer melts at about 140 °C, and the dimer melts in the temperature range 170–174 °C.

TGA thermogram of glycolyzed product shown in Figure 6 indicates the first onset degradation around 290 °C was monomer and the second onset degradation temperature around 440 °C was oligomer. This result show that the glycolyzed products consist of not only monomers but also higher degree oligomers. Thus, one could suppose that the main part of this glycolyzed product is oligomers.

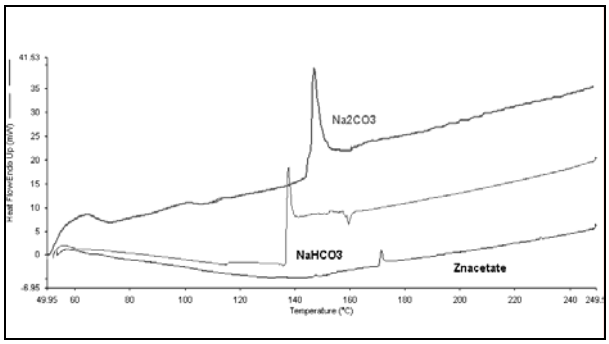

Fig.5 The melting of the glycolyzed products with DEG using various catalysts

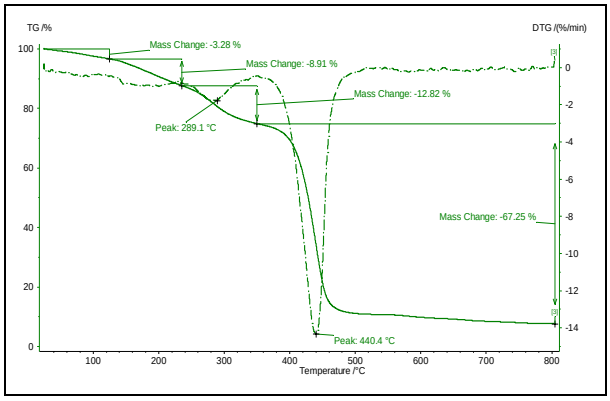

Fig.6 TGA thermogram of the glycolyzed products

Conclusions

The experiments were done to study the efficiency of various catalysts in the PET glycolysis reaction using microwave radiation as the energy source instead of the conventional heating method. PET waste from post-consumer bottles was depolymerized in DEG under microwave radiation. Glycolyzed products were successfully obtained when zinc acetate, sodium bicarbonate or sodium carbonate was used as a catalyst in the microwave-assisted depolymerization reaction. The advantage of using microwave radiation is the much shortening of reaction time. Excessive reaction time led to lower yield and the gelation of the reaction mixture. However, it was found that sodium chloride and calcium chloride were not efficient catalysts. Zinc acetate which is the most common catalyst used in the conventional heating reaction was still found to be a decent catalyst in the microwave-assisted reaction. Furthermore, it was found that, in term of depolymerization rate, $NaHCO_3$ which is not a good catalyst in the conventional heating reaction can be used effectively in the microwave-assisted reaction comparable to zinc acetate. Na_2CO_3 can also be used as a catalyst but with a slower rate of depolymerization. The results also imply that the degree depolymerization may be higher when zinc acetate was used as a catalyst.

Acknowledgements

The authors gratefully acknowledge National Metal and Materials Technology, NSTDA, Ministry of Science and Technology for the financial support.

References

[1] G. P. Karayannidis and D. S. Achilias, *Macromol. Mater.Eng*. **292** (2007), pp. 128–146.
[2] D. E. Nickles and M. S. Farahat, *Macromol. Mater. Eng.* **290** (2005), pp. 13-30.
[3] C. H. CHEN, C. Y. CHEN, Y. W. LO, C. F. MAO and W. T. LIAO, *J. Appl. Polym. Sci*. **80** (2001), pp. 943.
[4] N.D. Pingale and S.R. Shukla, *Eur. Polym. J.* **44** (2008), pp. 4151–4156.
[5] A. Krzan, *Polym. Adv. Technol*. **10** (1999), pp. 603-606.

Characteristics of microwave-assisted glycolyzed products from PET wastes using different glycols

S. Udomtawornsawat[1,2] and P. Potiyaraj[1,2*]

[1]Center of Excellence in Textiles, Department of Materials Science, Faculty of Science, Chulalongkorn University, Bangkok 10330, Thailand
[2]National Center of Excellence for Petroleum, Petrochemicals and Advanced Materials, Chulalongkorn University, Bangkok 10330, Thailand

*E-mail: pranut.p@chula.ac.th

Abstract: Poly(ethylene terephthalate) (PET) from post-consumer soft-drink bottles was depolymerized in excess glycol using microwave energy source, as opposed to conventional thermal heating, with the presence of zinc acetate as a catalyst. The presences of –OH, -CH, C=O, C-O-C and C-OH were revealed by Fourier transform infrared spectroscopy (FT-IR). When ethylene glycol was used for the glycolysis reaction, bis-(2-hydroxyethylene) terephthalate (BHET) and some larger oligomers were recovered. It was found that, under a constant microwave power, the yield of the reaction was controlled by the irradiation time. PET was also depolymerized using propylene glycol and diethylene glycol in order to study the effects of different glycols on the characteristics of glycolyzed products. Thermal gravimetric analysis (TGA) pointed out that the thermal stability of glycolyzed products obtained using ethylene glycol was better than that of the products when propylene glycol and diethylene glycol were used for the glycolysis reaction.

Introduction

Poly(ethylene terephthalate) (PET) is one of the most widely-used polymers for domestic as well as industrial applications. High-performance fibers, photographic films, and soft-drink bottles were commonly manufactured from PET due to its superior properties such as high strength, toughness and clarity combined with low permeability to carbon dioxide, oxygen and water vapor. PET is usually synthesized either by reacting terephthalic acid (TPA) with ethylene glycol (EG) or dimethyl terephthalate (DMT) with EG. Both polymerization schemes first form the monomer, bis(hydroxyethyl) terephthalate (BHET). After adding stabilizers and additives, the polymer is polymerized through polycondensation by releasing EG as a by-product.

Due to its selective gas permeability, PET bottles are popularly used for carbonated beverages and other food products. In turn, the volume of post-consumer PET bottles has been rapidly increased. Like other petroleum based thermoplastic materials, spontaneously degradation of PET in nature is almost impossible inevitably causing plastic waste building up problem. Recycling of PET waste is one of the methods that can reduce this serious problem [1]. In general, PET waste can be recycled by different methods, namely, physical recycling and chemical recycling. Being the easiest method, physical recycling consists of grinding, washing and extruding of PET waste and reusing it to reduce new raw material usage. Unfortunately, during physical recycling, thermal degradation occurs thus lowering some usage properties of recycled products. In contrast, chemical recycling of PET can transform waste into other useful chemicals which can be used for synthesizing a new material with desired properties. However, chemical recycling of PET still needs a lot more research and development in order to make the technique more commercially feasible.

One of the most studied chemical recycling techniques is the depolymerization of PET in glycols. The reaction involves the molecular degradation of PET molecular chains by glycols, in the presence of trans-esterification catalysts, mainly metal acetates, where ester linkages are broken and replaced with hydroxyl terminals. PET can be depolymerized by glycolysis to obtain oligomeric diols and polyols, or glycolyzed into its monomeric units, bis-(2-hydroxyethylene) terephthlate (BHET) or dimethyl terephthlate [2, 3]. These glycolyzed products have been widely used in the production of unsaturated polyesters and rigid or flexible polyurethanes [4, 5]. It was found that zinc acetate was demonstrated as the most effective catalysts used for PET glycolysis [6]. Although the use of catalyst can improve depolymerization rate, the reactions still need hours to complete thus limit their commercial applications. The glycolysis reaction in excess EG in the presence of zinc acetate as a catalyst complete in 2 h at 190 °C [7,8].

The use of microwave energy as an energy source in chemical reactions requiring heat has received much attention in recent years. Microwave energy is supplied by an electronic field directly to the reaction system [9]. The main advantage of using microwave as an energy source in chemical reactions is the significantly decrease of reaction time while retaining, or even increasing, the reaction yields. PET glycolysis reactions characterized by short reaction times in which complete PET solubilization were achieved. It was clearly demonstrated that a domestic microwave oven of 800W was highly effective in completing the depolymerization reaction of PET in ethylene glycol using zinc acetate as a catalyst. The time taken for completion of reaction was reduced drastically from 8

h to 35 min [10]. The method is compatible with the use of a wide range of glycol reagents as well as a variety of basic catalysts [11]. Microwave irradiation can be used as an energy source in hydroglycolysis. The process of hydroglycolysis reported here is economically viable since yields of recycled products are high, and it has potential for further improvement to produce useful products. Its can be recovered and used for virgin PET resin synthesis [12].

In this work, the use of microwave energy in PET glycolysis reactions using different glycols (EG, PG and DEG) with the presence of zinc acetate as a catalyst was investigated. The thermal properties and chemical structure analysis of glycolysis products were also discussed.

Materials and Methods

Materials

Post-consumer soft-drink PET bottles of the same brand were thorougly cleaned, cut into small pieces and oven-dried. The dried PET waste was pulverized and sieved in order to obtain PET waste powder with a particle size of less than 1.0 mm. Ethylene glycol (EG), propylene glycol (PG), diethylene glycol (DEG) were used as a glycol in the depolymerization reaction. Zinc acetate was used as a catalyst. All chemicals were purchased from Fluka and used without further purificatioin.

Glycolysis of PET waste

Pulverized PET waste was reacted with a glycol (EG, PG or DEG) with the molar ratio of PET repeating unit to glycol of 1:6. Zinc acetate was used as a catalyst at 0.5% by weight of PET. The glycolysis reaction was carried out in 600 W LG domestic microwave oven (Thailand). The oven was modified to equip with a reflux and teflon stirrer on the topside. The reaction was let to proceed for 40 min. The glycolyzed product was then precipitated in excess distilled water. Remaining solids were filtered from the liquid fraction, rinsed, dried to constant mass, and weighed.

Characterization of glycolyzed product

The onset thermal degradation temperature of glycolyzed products was determined by Mettler Toledo TGA/SDTA 851e thermal gravimetric analysis (TGA, Columbus, OH) at the heating rate of 20 °C/min from 50 to 1,00 °C under nitrogen atmosphere. The melting behavior was determined by Perkin Elmer Diamond differential scanning calorimeter (DSC, Waltham, MA) at the heating rate of 20 °C/min from 50 to 270 °C under nitrogen atmosphere. The glycolyzed products were also analyzed by a Perkin Elmer System 2000 Fourier transform infrared spectrometer (FT-IR, Waltham, MA).

Results and Discussion

A series of PET glycolysis reaction under microwave irradiation was performed to determine the effect of irradiation time at a constant microwave applied power. Times ranging from 10 to 40 min were used at a constant applied microwave power of 600 W. Figure 1 shows the yield of glycolyzed products obtained using different glycols at various irradiation times. The complete PET solubilization was achieved within 30 min when all residues cannot be visibly observed. The yield of glycolyzed products progressively increased until 30-35 min for all glycols at PET: glycol ratio of 1:6. Thereafter, with increase in the irradiation time, the yield of glycolyzed products slightly decreased. The system with DEG resulted in the higher yield than those with EG or PG. This result clearly shows that microwave irradiation is an effective energy source in PET glycolysis reactions characterized by substantial shorter reaction times comparing with the conventional heating.

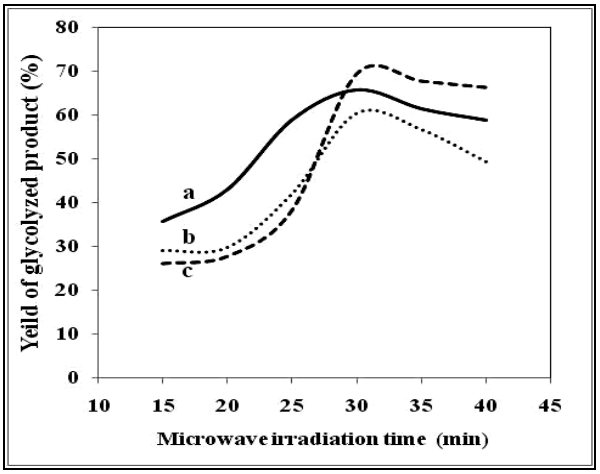

Figure 1. Effect of radiation time on the yield of glycolyzed product obtained using different glycol (a) EG (b) PG (c) DEG

As shown in Figure 2, the FTIR spectra of products obtained from glycolysis reaction of PET waste using EG, PG and DEG exhibit several peaks corresponding to –OH in the range of 3,400-3,600 cm^{-1}. The presence of peaks at 1950-1600 cm^{-1} indicats C=O stretching while peaks related to alkyl and C–H appear at 3000-2800 cm^{-1}. This implies that the glycolyzed products are compounds having hydroxyl and ester groups. [13]

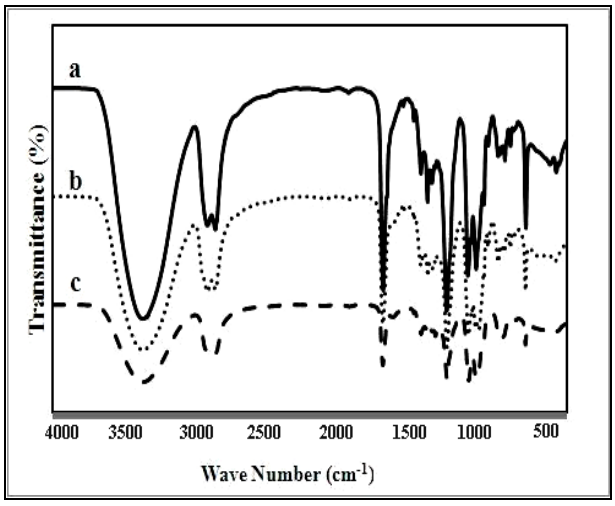

Figure 2. FT-IR spectra of glycolyzed products from (a) EG (b) PG (c) DEG

The DSC thermogram in Figure 3 shows melting temperatures of the glycolyzed products prepared from different glycols. The sharp endothermic peak at 109 °C is in agreement with the known melting point of BHET.

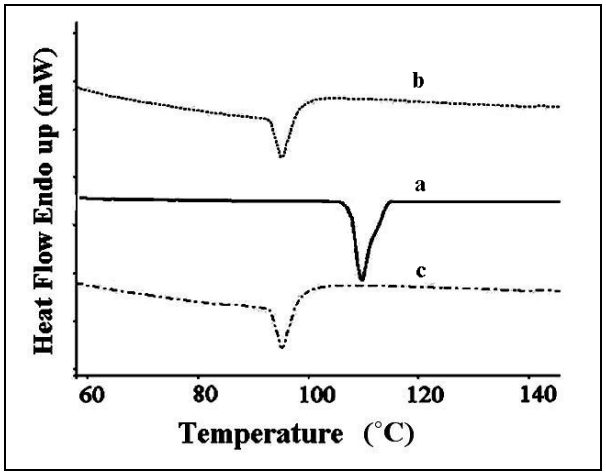

Figure 3. DSC thermogram of glycolyzed products prepared from different glycols (a) EG (b) PG (c) DEG

When all products were analyzed by TGA as revealed by the thermogram in Figure 4, it was found that the decomposition temperature of the glycolyzed product prepared with EG, PG and DEG was 423.94 °C, 401.61 °C and 412.73 °C, respectively. The results from these thermal analyses illustrate that the glycolyzed product prepared with EG has superior thermal stability than that prepared with PG and DEG.

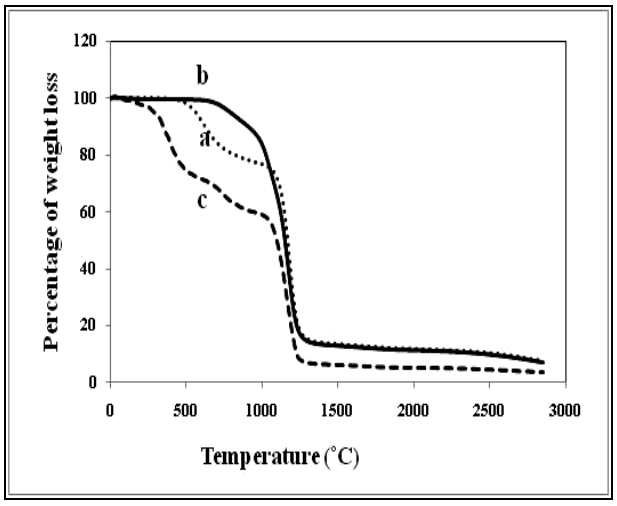

Figure 4. TGA thermogram of glycolyzed products from (a) EG (b) PG (c) DEG

Conclusions

The results show that the use of microwave radiation as the energy source in PET glycolysis resulted in the substantial shorter reaction times needed for complete PET degradation compared with conventional heating methods. Complete PET degradation in EG, PG and DEG was achieved within 30 min. The glycolysis reaction using DEG gave the higher yield than the others. However, the product obtained from the glycolysis reaction using EG possessed the maximum thermal stability.

Acknowledgements

The authors gratefully acknowledge National Metal and Materials Technology, NSTDA, Ministry of Science and Technology for the financial support.

References

[1] C. Lorenzetti, P, Manaresi, C. Berti and G. J. Barbiroli, *Polym. Environ*. **14** (2006), pp. 89-101.
[2] G. P. Karayannidis and D. S. Achilias, *Macromol. Mater.Eng*. **292** (2007), pp. 128–146.
[3] D. E. Nickles and M. S. Farahat, *Macromol. Mater. Eng.* **290** (2005), pp. 13-30.
[4] J. Kim, D. Jeong, C. Son, Y. Lee, E. Kim and I. Moon, *Korean J. Chem. Eng*. **24** (2007), pp. 1076-1083.
[5] D. Ratnasari, A. Bakar, I. Ahmad and A. Ramli, *Malaysian J. Chemistry*. **8** (2006), pp. 22-26.
[6] K. Li, X. Song and D. Zhang, *J. Appl. Polym. Sci*. **109** (2008), pp. 1298–1301.
[7] J. W. CHEN and L. W. CHEN, *J. Appl. Polym. Sci*. **73**, (1999), pp. 35–40.
[8] C. H. CHEN, C. Y. CHEN, Y. W. LO, C. F. MAO and W. T. LIAO, *J. Appl. Polym. Sci*. **80** (2001), pp. 943–948.
[9] E. T. Thostenson and T. W. Chou, *Composit*. **A30** (1999), pp. 1055-1071.
[10] N.D. Pingale and S.R. Shukla, *Eur. Polym. J.* **44** (2008), pp. 4151–4156.

[11] A. Krzan, *Polym. Adv. Technol*. **10** (1999), pp. 603-606.
[12] M. M. A. NIKJE and F. NAZARI, *Adv. Polym. Tech*. **25** (2006), pp. 242-246.
[13] O. Saravari, B. Vessabutr and V. Pimpan, *J. Appl. Polym. Sci.* **92** (2004), pp. 3040–3045.

Thermomechanical properties of organic-inorganic nanocomposites involving epoxy resins and POSS epoxides

A. Somwangthanaroj, K. Suwanchatchai*, P. Praserthdam, and S. Thongyai

Chulalongkorn University /Department of Chemical Engineering, Faculty of Engineering, Bangkok, Thailand 10330

* E-Mail : beau_jung28@hotmail.com

Abstract: Epoxy resins are important thermosetting materials and widely used in polymer nanocomposites because of their high moduli and high thermal properties. Polyhedral oligomeric silsesquioxane (POSS) is a potential nanofiller which is often used in organic-inorganic hybrid to reinforce the polymer matrix. The present research aims to improve thermomechanical properties of epoxy nanocomposites by investigating the effect of the types of POSS namely epoxycyclohexyl POSS, glycidyl POSS, and glycidylphenyl POSS. The composites were prepared by adding POSS particles into diglycidyl ether of bisphenol A and 4 – methylhexahydro phthalic anhydride. To enhance the properties, six compositions from 5% to 40% by weight of POSS were investigated. The storage modulus of POSS/epoxy nanocomposites at 40 °C was slightly increased when POSS particles were added because POSS was dispersed and reinforced in epoxy matrix. However, at high loading of glycidyl POSS, the moduli of hybrids were decreased. The tan delta peak shows the glass transition temperature (T_g) of the hybrid composites. The T_g value increased with increasing POSS concentration. The increasing of T_g was obvious from neat epoxy to 40 wt% of glycidylphenyl POSS from 92°C to 143°C. This is due to high crosslink density of POSS composites and the presence of phenyl groups in glycidylphenyl POSS molecules. The coefficient of thermal expansion (CTE) of nanocomposites were examined by means of thermal mechanical analysis. Although the crosslink density in the nanocomposites increase with increasing POSS content, the CTE of POSS/epoxy nanocomposites are nearly the same or increased from neat epoxy because of soft interphase around the POSS cages as a result of flexible tether of POSS structure in the epoxy nanocomposites. In addition, the rigidity of POSS molecules leads to lower CTE of nanocomposites when compared with neat epoxy.

Introduction

Nowadays, electronic products are becoming important in our life. Many electronic processes are developed same as the flip chip technology. Underfill is layer of adhesive that is applied between the chip and the substrate in the flip chip packaging [1]. Underfill is composed of epoxy-based, filler, and hardener. Epoxy resins, high-performance thermosetting polymers, are widely utilized in the electronic industries for electronics' packaging due to their good thermal and mechanical properties, easy in processing, and low cost materials. Polyhedral oligomeric silsesquioxanes (POSS) is used as filler to improve the properties of underfill. POSS was attracted many researchers because POSS is a potential nanofiller which is often used in organic-inorganic hybrid compounds to reinforce the polymer matrix.

In several years, the organic-inorganic hybrids involving epoxy resins and POSS become popular because they can solve the problem of epoxy usage that is the coefficient of thermal expansion (CTE) mismatch between epoxy and metal component. OctaaminophenylPOSS (OapPOSS), was synthesized, characterized and incorporated into epoxy resins. The storage moduli were higher than the controlled epoxy and the CTE of OapPOSS nanocomposites are decreased from 60 to 25 ppm/°C when using tetraglycidyl-m-xylenediamine (TGMX) as an epoxy resins [2-3].

Chen et al. synthesized octakis(dimethylsiloxypropyl glycidyl ether) silsesquioxane (OG) and then reacted with meta-phenylenediamine (mPDA). Their results show that the glass transition temperature (T_g) of OG/mPDA is significant higher than that of DGEBA/mPDA because of the presence of POSS cages [4]. Therefore, POSS can be incorporated into epoxy resin to improve thermal and mechanical properties of POSS/epoxy nanocomposites.

In this work, POSS has been used as filler for epoxy-based substrate. The POSS contained three different types of functionalities that is epoxycyclohexyl POSS, glycidyl POSS, and glycidylphenyl POSS. These POSS monomers were incorporated into thermosetting epoxy resins. The amount of POSS content and effect of POSS on mechanical and thermal properties of POSS/epoxy nanocomposites were investigated.

Materials and Methods

Materials: Epoxy monomer used, diglycidyl Ether of Bisphenol A (DGEBA) was purchased from Dow Chemical Company. 4-methylhexahydrophthalic anhydride (MHHPA) was purchased from Aldrich Chemical. Epoxycyclohexyl POSS, glycidyl POSS, and glycidylphenyl POSS were purchased from Hybrid Plastics Inc. The POSS structures are presented in Figure 1.

Preparation of nanocomposites: The composites were prepared by the following steps: POSS particles were mixed with epoxy resin using mechanical stirrer. 4-methylhexahydrophthalic anhydride were added into the solution and stirred until homogeneous dispersion was achieved. Then, the homogeneous solution was put into vacuum oven for 2 h at temperature 50°C to

release air bubbles. After that, the mixture was poured into a Teflon mould and cured at 230 °C for 30 min.

Dynamic mechanical analysis (DMA): The thermomechanical properties of POSS/epoxy nanocomposites were measured using DMA operated under the three point bending mode with the temperature range from 30 to 250°C under nitrogen atmosphere. The heating rate and nominal frequency was set at 5°C/min and 1 Hz, respectively. The specimen dimension was 10 x 2 x 50 mm^3.

Thermomechanical analysis (TMA): Coefficient of thermal expansion (CTE) of POSS/epoxy nanocomposites were measured using TMA in expansion mode. All measurements were made under nitrogen atmosphere at a heating rate of 5°C/min from 30°C to 200°C. The specimens' length was set between 2 and 5 mm, the width and the thickness were 2-3 mm.

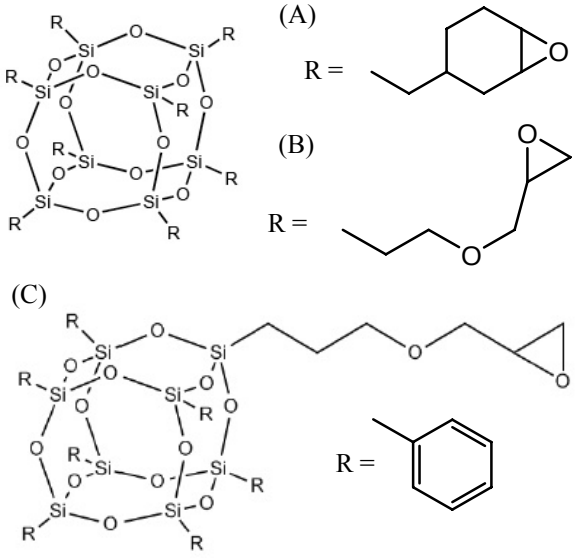

Figure 1. The chemical structure of POSS monomer used in this research: (A) epoxycyclohexyl POSS; (B) glycidyl POSS; (C) glycidylphenyl POSS

Results and Discussion

The effects of POSS on storage moduli were investigated by dynamic mechanical analysis (DMA). Figure 2 demonstrates the storage modulus for the different weight ratios of epoxycyclohexyl POSS, glycidyl POSS, and glycidylphenyl POSS added in DGEBA. The storage modulus of epoxycyclohexyl POSS epoxy hybrid was increased when POSS particles were added because POSS was dispersed and reinforced in epoxy matrix. It is of interest that the storage modulus of glycidyl POSS epoxy hybrid was significantly higher than the control epoxy at 15 wt% loading. However, at high loading of glycidyl POSS, the moduli of hybrids were decreased. A possible explanation is that at high amount of glycidyl POSS, the crosslinking of nanocomposites is not complete, therefore the storage moduli of hybrids were dropped. The addition of glycidylphenyl POSS in epoxy matrix will enhance the storage moduli of nanocomposites. This can be due to the fact that the POSS cages were bonded with the epoxy resins, so the crosslinking densities were increased.

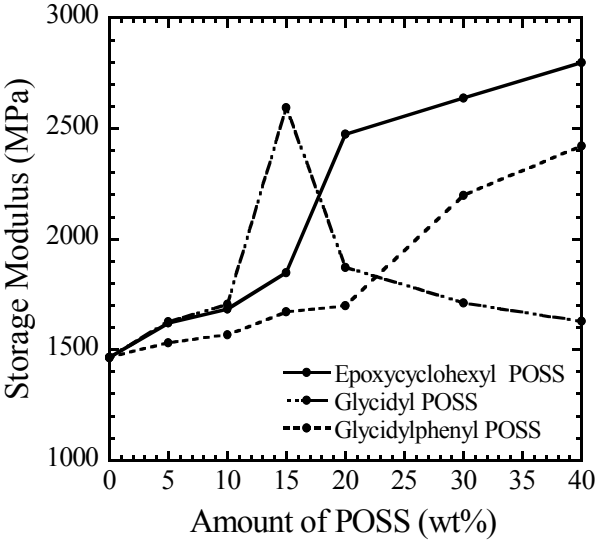

Figure 2. Influences of POSS content on the storage modulus of the POSS/epoxy nanocomposites

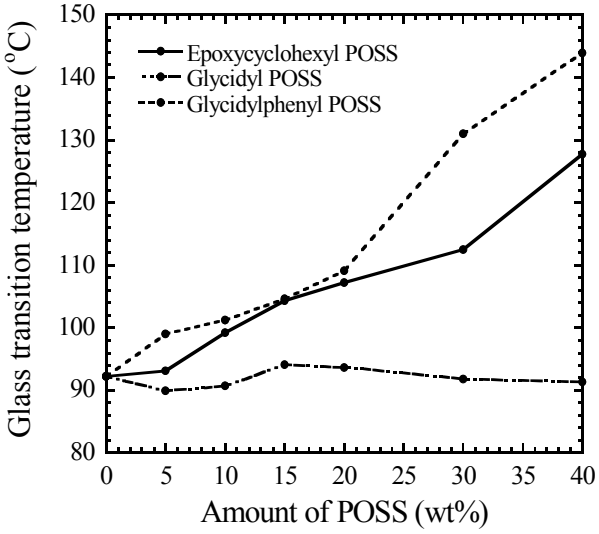

Figure 3. Influences of POSS content on the glass transition temperature of the POSS/epoxy nanocomposites

The glass transition temperature, T_g, is defined as the peak temperature in tan δ curves. Figure 3 exhibits the relationship between the T_g value and the amount of POSS. The T_g value of epoxycyclohexyl POSS hybrids were increased with increasing POSS content. Addition of glycidyl POSS in epoxy matrix, the T_g value of nanocomposites are nearly the same or slightly increased when compared with neat epoxy because of the presence of ether linkage in their chains.

The steadily increasing of T_g was obvious from neat epoxy to 40wt% glycidylphenyl POSS from 92°C to 143.9°C. It is therefore possible to explain this result by the rigidity of linkage that is phenyl group in the glycidylphenyl POSS molecules leads to high energy for chain movement therefore the T_g values of nanocomposites were increased.

Table 1: The coefficient of thermal expansion of POSS/epoxy nanocomposites

Amount of POSS	CTE (ppm/ºC)		
	Epoxycyclo hexyl POSS	Glycidyl POSS	Glycidyl phenyl POSS
5 wt%	72±3	81±4	77±2
10 wt%	81±2	83±5	85±3
15 wt%	80±2	89±2	86±2
20 wt%	81±2	90±3	89±1
30 wt%	85±5	90±1	88±2
40 wt%	88±3	90±1	89±1

* The CTE of neat epoxy is approximately 80±1 ppm/ºC

The CTE of nanocomposites were examined by means of thermal mechanical analysis (TMA). Table 1 summarizes the results of functionalities and loading POSS on the CTE values. The epoxy hybrid containing 5 wt% epoxycyclohexyl POSS exhibited a CTE value lower than controlled epoxy because of the rigidity of POSS molecules. The CTE of glycidyl POSS/epoxy nanocomposites are nearly the same or slightly increased from neat epoxy because of soft interphase around the POSS cages as a result of flexible tether of POSS structure in the epoxy nanocomposites. At 5 wt% of glycidylphenyl POSS, the CTE value of hybrid is slightly decreased when compared with neat epoxy. The reason for this would be related with the phenyl group in their chains resulting in the linkage are difficult to move, therefore the CTE of nanocomposite is reduced.

Conclusions

Three functionalities of POSS monomers were manipulated to prepare POSS/epoxy nanocomposites. The amount of POSS content was varied and investigated. Epoxycyclohexyl POSS can improve the thermal and mechanical properties including the CTE value of hybrid composites which is an important factor for electronic devices. For glycidyl POSS/epoxy nanocomposites, the storage modulus was significantly higher than that of the neat epoxy. Interestingly, glycidylphenyl POSS can increase the T_g value of nanocomposites obviously from neat epoxy. From the results, POSS/epoxy nanocomposites have potential to use for any applications which are used in high temperature.

Acknowledgements

The authors are grateful to Mektec Manufacturing Corporation (Thailand) Ltd. for financial support.

References

[1] Y. Sun, Z. Zhang, and C.P. Wong, *IEEE Trans. Comp. Packag. Technol*. **29**(2006), pp. 190-197.
[2] Y. Ni, S. Zheng, and K. Nie, *Polymer*. **45**(2004), pp. 5557-5568.
[3] S. Sulaiman, C.M. Brick, C.M. De Sana, J.M. Katzenstein, R.M. Laine, and R.A. Basheer, *Macromolecules*. **39**(2006), pp. 5167-5169.
[4] W.Y. Chen, Y.Z. Wang, S.W. Kuo, C.F. Huang, P.H. Tung, and F.C. Chang, *Polymer*. **45**(2004), pp. 6897-6908.

Study on thermal and mechanical properties of silicon carbide filled epoxy nanocomposites

A. Somwangthanaroj*, P. Praserthdam, S. Luangon and S. Thongyai

Department of Chemical Engineering, Faculty of Engineering, Chulalongkorn University, Bangkok 10330, Thailand.

*E-Mail: anongnat.s@chula.ac.th

Abstract: Epoxy resins for using in micro electronics packaging had quite low thermal conductivity (0.2 W/mK). Therefore, the incorporation of nano sized silicon carbide (SiC) in epoxy to improve thermal conductivity was investigated. In this work, the thermal and mechanical properties of epoxy filled nano sized silicon carbide (about 50 nm) were studied by thermo-mechanical analysis (TMA), dynamic-mechanical analysis (DMA) and laser flash method. The results showed that coefficient of thermal expansion (CTE) of SiC filled epoxy nanocomposites was changed by filler content. Nano SiC content at 4 vol% was the maximum concentration in which filler begin to highly contact with each other. Adding 4 vol% of nano-sized filler decreased CTE of neat epoxy from 80 ppm/°C to 68 ppm/°C. Glass transition temperature (T_g) and storage modulus of nano sized SiC filled epoxy nanocomposites slightly increased when increasing SiC loading. The T_g of epoxy nanocomposite increased from 87 °C to 91 °C when adding 1 vol% of SiC. Thermal conductivity of epoxy nanocomposites was measured with the laser flash method. The experimental results showed that the thermal conductivities of epoxy nanocomposite increased with increasing the amount of nano sized SiC. The highest thermal conductivity of epoxy nanocomposite filled with SiC was obtained with 4 vol% SiC. Furthermore, silane coupling agent treatment of nano sized SiC particles had a beneficial effect on improving the thermal conductivity. Therefore, silane treatment of nano sized SiC by using aminopropyltrimethoxy silane (amino silane) were investigated.

Introduction

Today's world is filled with electronics products such as computer, mobile phones, and digital cameras. All of these systems, electronics packaging presents an important role by supplying power to chips, increasing signals between chips and other devices through interconnects, helping heat dissipation, and protecting components from environmental effect. Nowadays, interesting electronics packaging are flip chip technology. This technology has many advantages over the conventional one. It has much higher input/output (I/O) signal because the area under the chip can be used for interconnection. The shorter signal path between chip and board increases signal, speed and greatly enhances electrical performance. Main problem of flip-chip interconnection technique is the mismatch in the coefficient of thermal expansion (CTE) between a silicon chip (2.5 ppm/°C) and an organic substrate (18–24 ppm/°C). The problem with coefficient of thermal expansion (CTE) mismatch can be solved by using underfill.[1-2] Underfill is a liquid encapsulate, which usually is silica filled epoxy resins that is applied between the chip and the substrate to reinforce the mechanical properties of the solder joints. Unfortunately, underfill has low thermal conductivity (0.03 W/mK). Therefore, the incorporation of highly thermal conductive fillers in epoxy to improve thermal conductivity of epoxy has been desired. There are many candidates for high thermal conductivity fillers such as diamond (2000 W/mK), boron nitride (BN) (300 W/mK), aluminum nitride (AlN) (150 W/mK), and aluminum oxide (Al_2O_3) (30 W/mK), silicon nitride (Si_3N_4) (150 W/mK), and silicon carbide (SiC) (390 W/mK). [3-5] Diamond has the highest thermal conductivity, but it is too expensive while alumina has lowest thermal conductivity. SiC is the most attractive filler with respect to other fillers because it has higher thermal conductivity than AlN, BN and Si_3N_4 filler.

In this work, nano-sized SiC particles were treated by aminopropyltrimethoxy silane (amino silane) because silane coupling is used to enhance the compatibility between the nano- sized SiC particles and the epoxy matrix, as well as preventing the agglomerations of the nano-sized SiC particles. The amount of nano-sized SiC content and effect of silane coupling on mechanical and thermal properties of SiC/epoxy nanocomposites were investigated.

Materials and Methods

Materials

Diglycidyl ether of Bisphenol A (DGEBA) was purchased from Dow Chemical Company. β-SiC particles with average particle size of 50 nm were purchased from Aldrich Chemical Company, Inc. γ-aminopropyltriethoxy silane were supplied by Dow Corning Corporation (Thailand). The curing agent, 4-methylhexahydrophthalic anhydride (MHHPA) 96%, catalyst for epoxy curing, 2, 4, 6 Tris-(dimethylaminomethyl) phenol 95% and ethanol 99% was purchased from Aldrich Chemical Company, Inc.

Surface modification of SiC nanoparticles

Silane-absolute ethanol solution at a selected concentration, and the required amounts of silane coupling agent used were 1-5% by weight of the nano-sized SiC particles. SiC particles were added to the

solution. The solution was stirred with a magnetic stirrer for 30 min and sonicated for 60 min. Ethanol were removed by filtration. SiC particles were dried by oven at 60 °C for 12 h. Then the silane treated particles were stored in desiccators.

Preparation of SiC/epoxy nanocomposites

DGEBA was stirred at 80 °C with magnetic stirrer for 1 h. Surface treated or untreated SiC particles was added to DGEBA. The solution was stirred for 30 min and sonicated for 1 h to ensure good homogeneity. MHHPA was added depending on the weight of DGEBA to the mixture and continuing stir for 10 min. 2, 4, 6 Tris-(dimethylaminomethyl) phenol was then added to the mixture, and the mixture was poured in a mould. Air bubble appeared on the surface of the mixture was removed by vacuum pump. The mixture was cured in an oven at 230 °C for 30 min and cooled to room temperature, then demoulded.

Characterization

The coefficient of thermal expansion (CTE) of the sample was measured on a thermomechanical analyzer (TMA, Perkin-Elmer Diamond). The dimensions of the sample were about 2×5×2 mm. The sample was heated in the TMA furnace at 5 °C/min from room temperature to 150 °C.

The dynamic mechanical properties of SiC/epoxy nanocomposites were measured using DMA. A specimen for DMA test was a rod of a size about 10×50 ×20 mm. The test was performed on a dual Cantilever bending mode under 1 Hz sinusoidal strain loading and the temperature was increased from room temperature to around 200 °C in a heating rate of 5 °C/min.

Thermal conductivity (λ, W/mK) of the nanocomposites was given by the product of thermal diffusivity (δ, mm2/s), specific heat (Cp, J/gK) and bulk density (ρ, g/cm3). Thermal diffusivity (d) was measured on disk samples (∅ 12.7 × 1.0 mm) by laser flash method (NETZSCH Co., LFA 447TM Nanoflash). Furthermore, specific heat (Cp) was measured on disk samples by DSC (Perkin–Elmer Co, Pyris Diamond). Also, bulk density (ρ) of specimen was measured by water displacement. For each measurement, three samples were tested three times. After that, thermal conductivity (λ) was calculated by equation: $\lambda = \delta \times Cp \times \rho$

Results and Discussion

Dynamic mechanical Properties

The effect of SiC content and amino coupling agent on the Dynamic mechanical Properties of SiC/epoxy nanocomposites is shown in Figure 1. The storage modulus of SiC/epoxy nanocomposites slightly increased when increasing SiC content because SiC can remedy the defects from epoxy self-curing and reinforce in epoxy matrix. [6] The storage modulus of SiC/epoxy nanocomposites filled with amino silane coupling agent treated SiC is higher than that of untreated SiC. It is due to the fact that silane coupling agent improved SiC dispersion and interfacial interactions between SiC particles and epoxy matrix. [7]

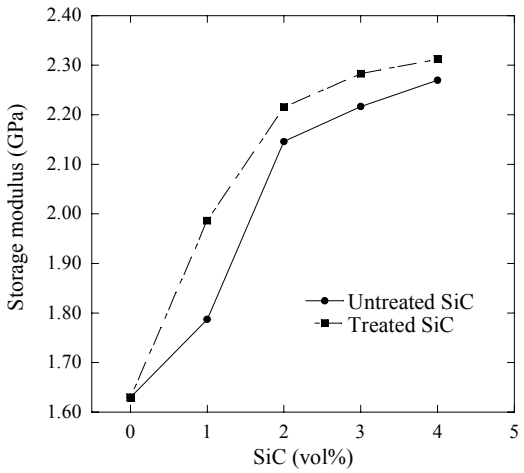

Figure 1. The storage moduli of SiC/epoxy nanocomposites

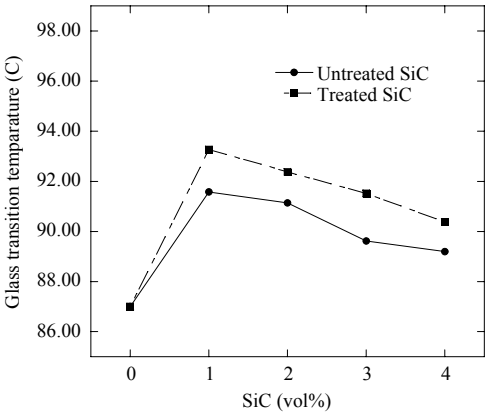

Figure 2. The glass transition temperature of SiC/epoxy nanocomposites

The glass transition temperature of SiC/epoxy nanocomposites was determined using DMA. T_g of SiC/epoxy nanocomposites was defined using peak temperature of tan δ curves. From Figure 2, the results showed that the content of SiC slightly affect T_g of SiC/epoxy nanocomposites. The T_g of SiC/epoxy nanocomposites increased from 87 °C to 91 °C when adding 1 vol% of SiC, but decreased at high volume fraction content. The decreasing of T_g can be due to the agglomeration of SiC nanoparticles. T_g of silane coupling agent treated SiC is higher than that of untreated SiC, because silane coupling agent increase the interfacial interaction between particles and epoxy. Therefore, it is harder for the polymer chains to move.

Thermomechanical Properties

The coefficient of thermal expansion (CTE) of SiC/epoxy nanocomposites was determined using TMA. The result was summarized in Table 1. Adding 4 vol% of nano-sized SiC decreased CTE of neat epoxy from 80 ppm/°C to 68 ppm/°C and decreases

from 80 ppm/°C to 64 ppm/°C when using treated nano-sized SiC particles. CTE of SiC/epoxy nanocomposites was decreased by rigidity of SiC and effect of silane coupling agent that enhances the interface adhesion between SiC and epoxy.

Table 1: The coefficient of thermal expansion of SiC/epoxy nanocomposites

SiC vol%	CTE (ppm/°C)	
	Untreated SiC	Treated SiC
0%	80	80
1%	72	70
2%	70	68
3%	69	66
4%	68	64

Thermal Conductivity

From Figure 3. shows the thermal conductivity of treated and untreated SiC/epoxy nanocomposites. Thermal conductivity of treated and untreated SiC/epoxy was increased by increasing SiC content. The highest thermal conductivity of epoxy filled with SiC was obtained with 4 vol%. It may be due to high thermal conductivity of SiC. Adding a treated nano-sized SiC particle to epoxy is greater enhanced thermal conductivity than untreated nano-sized SiC particles because silane treatment reduces high surface energy of SiC and improved dispersion and compatibility of SiC in epoxy nanocomposites. [8-10]

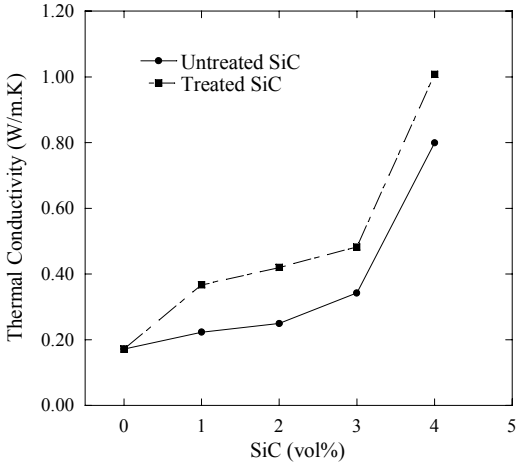

Figure 3. The thermal conductivity of SiC/epoxy nanocomposites

Conclusions

Mechanical and thermal properties of SiC/epoxy nanocomposites were studied by thermo-mechanical analysis (TMA), dynamic-mechanical analysis (DMA) and laser flash method. The results showed that coefficient of thermal expansion (CTE) of SiC/epoxy nanocomposites was changed by filler content. Nano SiC content at 4 vol% was the maximum concentration. Glass transition temperature and storage modulus of SiC/epoxy nanocomposites slightly increased when compared with neat epoxy. Thermal conductivity of SiC/epoxy was increased by increasing SiC content. Silane coupling agent treatment of nano sized SiC particles slightly enhanced mechanical and thermal properties of SiC/epoxy nanocomposites.

Acknowledgements

The authors would like to thank the financial support of Mektec Manufacturing Corporation (Thailand) Ltd.

References

[1] H.Y. Li, L.J. Wang, K. Jacob, C.P. Wong, *Journal of Polymer Science Part a-Polymer Chemistry* **40** (2002), pp. 1796-1807.
[2] C.P. Wong and L. J. Wang, *Journal of Applied Polymer Science* **81** (2001), pp. 1868-1880.
[3] E.S. Lee, S.M. Lee, D.J. Shanefield, W.R. Cannon, *Journal of the American Ceramic Society* **91** (2008), pp. 1196-1174.
[4] C.P. Wong and R.S. Bollampally, *IEEE Transactions on Advanced Packaging* **22** (1999), pp. 54-59.
[5] W.S. Lee, J. Yu, *Diamond and Related Materials* **14** (2005), pp. 1647-1653.
[6] J. Gu, Q Zhang, J. Dang, J. Zhang, S. Chen, *Polymer Bulletin* **62** (2009), pp. 689-697
[7] J. Abenojar, J.C. del Real, M.A. Martinez, M. Cano de Santayana, *The Journal of Adhesion* **85** (2009), pp.287 - 301
[8] Y. J. Lou, J Dang, H. Y. Qi, H. R. Li, *Polymer-Plastics Technology and Engineering* **48** (2009), pp.877-881
[9] T. Zhou, X. Wang, G.U. Mingyuan, X.H. Liu, *Polymer* **49** (2008), pp. 4666-4672.
[10] T. Zhou, X. Wang, G.U. Mingyuan, D.S. Xiong, *Polymer Journal* **41** (2009), pp. 51-57.

The effect of silicon nitride filler on mechanical and thermal properties of epoxy composites

A. Somwangthanaroj, M. Suwan*, P. Praserthdam and S. Thongyai

Chulalongkorn University/Department of Chemical Engineering, Faculty of Engineering, Bangkok, Thailand 10330

* E-Mail: mootune_nd@hotmail.com

Abstract: Epoxy resin is a high performance thermosetting polymer which is used as underfill material for the flip-chip packages. Materials used in microelectronic systems require high thermal conductivity. Generally, epoxy has low thermal conductivity. To achieve high thermal conductivity, using ceramic powder with high thermal conductivity as thermal conductive filler is an effective way. In this work, silicon nitride (Si_3N_4) filled epoxy, DGEBA, composites was prepared. The effects of particle size (10 μm and 50 nm) and the amount of Si_3N_4 filler on mechanical and thermal properties of epoxy composites were investigated. The storage modulus and glass transition temperature (T_g) of Si_3N_4 filled epoxy composites were slightly increased with increasing Si_3N_4 loading. Adding only 1 vol% of nano-sized Si_3N_4 can enhance T_g of epoxy composites higher than adding 10 vol% of micron-sized Si_3N_4. The coefficient of thermal expansion (CTE) of epoxy composites were decreased by increasing filler concentration. CTE was changed by filler content at the same particle size. At the same filler content, nano- sized Si_3N_4 filled epoxy composites showed lower CTE than that with micron-sized Si_3N_4. Thermal conductivity of the composites increased as the filler content increased. At the same filler content, the thermal conductivity of epoxy composites was increased with decreasing the Si_3N_4 particle sizes. These results indicate that, nano-sized Si_3N_4 filler can improve properties of epoxy composites better than the micron-sized ones at low filler loading in the composites.

Introduction

With fast development of the electronic industry, electronic products are smaller, thinner, lighter weight, faster and less expensive with more functionality and better performance. These properties of electronic products have driven the advanced electronic packaging to a new level. The flip-chip technology has been a promising candidate for microelectronics in the next generation of electronic packaging. Flip chip microelectronic assembly is the direct electrical connection of face-down electronic components onto substrates, circuit boards, or carriers, by means of conductive bumps on the chip bond pads [1]. The underfill material is a layer of polymeric adhesive used in flip chip packaging and employed in flip-chip assemblies to enhance solder joint reliability performance and environmental protection. In general, epoxies are known for their excellent adhesion, high thermal stability and excellent mechanical properties. Therefore epoxy resin is widely desirable to be used as underfill material for flip chip packaging. There are several requirements for underfill material, which include high modulus, high glass transition temperature, coefficient of thermal expansion (CTE) matched to the solder joint, low moisture absorption, and good adhesion with various interfaces [2]. However, the thermal conductivity of epoxy is very low. Thus, underfill material with higher thermal conductivity is continuously required, so many researchers tried to improve their properties by adding the filler into epoxy resin. Extensively, silica (SiO_2) filled epoxy is the most prevalent studied because of their low coefficient of thermal expansion, only 0.5 ppm/°C [3]. Nevertheless, its thermal conductivity is still poor due to the low thermal conductivity of the silica itself, only 1.5 W/mK [4]. Therefore, finding the new filling material which has better thermal conductivity than traditional filler, SiO_2, is necessary. Thus, other fillers obtained high thermal conductivity must be added when their several requirements for underfill material are maintained.

The thermal conductivity of composites is controlled by the thermal conductivity of filler, matrix and the interface conductance between filler and matrix. Approach to increase heat dissipation is using filler with high thermal conductivity. There were several researchers employed ceramic material with high thermal conductivity as fillers within encapsulants. These were alumina [5,6], boron nitride [7], and aluminum nitride [8-10]. One of alternative particle is silicon nitride (Si_3N_4), with a higher thermal conductivity, higher than 150 W/mK [11], than SiO_2 and low value of CTE (about 4 ppm/°C). Moreover, it has much higher mechanical and thermal properties compared with other ceramics. Among the commonly used ceramic fillers, Si_3N_4 particles were considered to be an ideal candidate due to their high thermal conductivity and more commercially available. Moreover, the thermal conductivity of Si_3N_4 is much larger than that of the epoxy resin. These outstanding properties of silicon nitride suggest that Si_3N_4 might be a good choice to be used in epoxy composites as a filler to improve the mechanical and thermal properties without having effect on electrical properties.

In previous works, researchers were studied on the effect of Si_3N_4 filled various polymer composites, however only a few investigation studied the Si_3N_4 filled epoxy composites. In this work, two different sizes of Si_3N_4 filled epoxy composites is prepared and their mechanical and thermal properties of composites are investigated.

Materials and Methods

Materials: The epoxy resin used, diglycidyl ether of bisphenol A (DGEBA), was purchased from Dow Chemical Company. The curing agent, hexahydro-4-methylphthalic anhydride (MHHPA), and catalyst, 2, 4, 6 Tris-(dimethylaminomethyl) phenol, were purchased from Aldrich Chemical Company, Inc. Si_3N_4 particles used as filler with micron-sized Si_3N_4 (<10 μm) and nano-sized Si_3N_4 (<50 nm) were purchased from Aldrich Chemical Company, Inc.

Preparation of Si_3N_4 filled epoxy composites: The composites were prepared by the following steps: the epoxy resin was heated to 80 °C to reduce its viscosity. Si_3N_4 particles were mixed with epoxy resin using mechanical stirrer and sonicator. MHHPA and catalyst were added into the solution and stirred until homogeneous dispersion was achieved. Then, the solution was poured into a teflon mold. For curing the composites, the specimen was placed in an oven at 230 °C for 30 minutes after well releasing of air bubbles.

Dynamic mechanical analysis (DMA): The glass transition temperature and storage moduli of Si_3N_4 filled epoxy composites were measured by using Dynamic Mechanical Analyzer (DMA). The cured sample was measured using DMA operated under the bending mode with the temperature range from 30 to 200 °C. The frequency used was 1.0 Hz and the heating rate 5.0 °C/min. These samples were in the form of strips having dimensions of about 10x2x50 mm^3.

Thermomechanical analysis (TMA): The coefficient of thermal expansion (CTE) of Si_3N_4 filled epoxy composites was measured by using thermomechanical analyzer (TMA). The cured sample was mounted on the TMA using an expansion probe and heated from 30 to 150°C at a heating rate of 5°C/min. The sample had a size of 4×4×2 mm^3.

Thermal conductivity analysis: Thermal diffusivity was measured by the laser flash at various temperatures. Specific heat was measured by Differential Scanning Calorimetry (DSC). Also, the density of the specimen was measured by water displacement. The measurement of thermal diffusivity, specific heat capacity and bulk density of the samples, thermal conductivity was calculated as following equation:

$$\kappa = \alpha \rho C_P \qquad (1)$$

where, K is the thermal conductivity, α is the thermal diffusivity, ρ is the bulk density and C_P is the specific heat capacity.

Results and Discussion

Dynamic mechanical analysis: Storage modulus, which tells us how elastic the material is, of epoxy composites filled with Si_3N_4 was increased when filler content increased as shown in Figure 1. Adding only 2.5 vol% of nano-sized Si_3N_4, storage modulus of epoxy composites was nearly the same as that with adding 15 vol% micron-sized Si_3N_4. The T_g of composites filled with two different particle sizes of Si_3N_4 were increased by increasing Si_3N_4 content, but were decreased at high Si_3N_4 filler content as listed in Table 1. It shows that adding only 1 vol% of nano-sized Si_3N_4 can enhance T_g of epoxy composites higher than adding 10 vol% of micron-sized of Si_3N_4. Furthermore, we observed that low loading addition of micron-sized Si_3N_4 did not change the T_g of composites significantly; however, incorporating the nano-sized Si_3N_4 slightly increased the T_g of composites. The presence of Si_3N_4 particles restricted mobility of polymer chains in composites attributed to the T_g increment of composites. From the experimental results indicate that nano-sized Si_3N_4 can restrict the chain mobility better than micron-sized Si_3N_4 because the amount of nano-sized particles is higher than that with micron-sized at the same filler contents due to a high surface area of nanoparticles. However, T_g of composites were decreased at high filler content that was possibly due to the agglomeration of particles.

Table 1: T_g of Si_3N_4 filled epoxy composites with different particle sizes

Si_3N_4	**Amount of Si_3N_4 (Vol%)**	**T_g** (°C)
Neat epoxy	-	88
Nano-sized Si_3N_4	0.5	94
	1	104
	1.5	98
	2	94
	2.5	90
Micron-sized Si_3N_4	1	89
	5	89
	10	101
	15	89

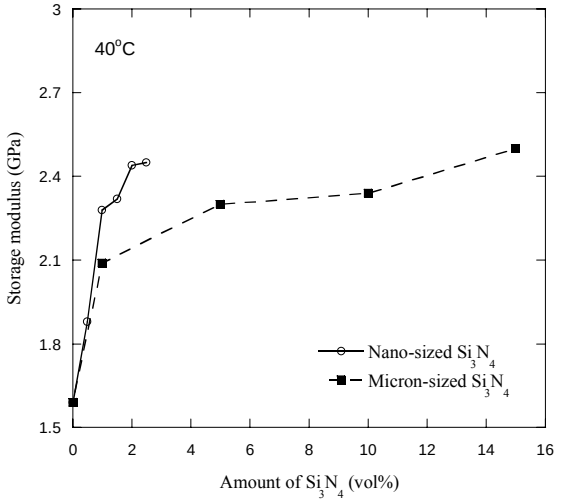

Figure 1. Storage moduli of the composites as a function of Si_3N_4 content with different particle sizes

Thermomechanical analysis: The TMA results are shown in Figure 2. With the increase of filler content, the CTE tends to decrease gradually. In this regard, only small amount of nano-sized filler resided in epoxy matrix, the CTE of the composites significantly reduced when compared with epoxy filled with micron-sized filler. For example, the CTE of composites with only 2.5 vol% nano-sized Si_3N_4 was 62 ppm/℃ while that with 10 vol% micron-sized Si_3N_4 was 66 ppm/℃. Moreover, the CTE of composites with nano-sized Si_3N_4 was lower compared to that of micron-sized Si_3N_4 at the same filler loading. By adding the filler in composites material, the filler binds the matrix and prevents it from expanding as much as it would on its own. Subsequently, this would affect the thermal expansion of the composites. The result generally agreed with the trend observed by Lee and Yu [4] who studied the effect of fillers in underfill for the electronic components. The studies have shown that material with higher filler content leads to a lower CTE.

Thermal conductivity analysis: Thermal conductivity of samples as a function of the volume fraction of the filler is shown in Figure 3. We can see that thermal conductivity of the epoxy filled with Si_3N_4 composites increases with the volume fraction of the filler. Furthermore, the result indicates that the composites containing smaller Si_3N_4 particles show higher thermal conductivity than that with larger filler particles. For example, the epoxy composites filled with only 2.5 vol% of nano-sized Si_3N_4 particle exhibited a higher thermal conductivity than that of the composites filled with 15 vol% of micron-sized Si_3N_4. The result generally agreed with the trend observed by Zhou et al. [12] who investigated the effect of Si_3N_4 size on thermal conductivity of polyethylene composites. These can be due to the number of filler particles increased with decreases in the particle size at the same volume fraction. The smaller particle size would give the higher specific surface energy. Also, the surface absorption energy between the smaller filler powder and matrix particles is higher than that between the larger filler particles and matrix, due to the presence of many unsaturated chemical bonds existing on the surface of the smaller filler particles.

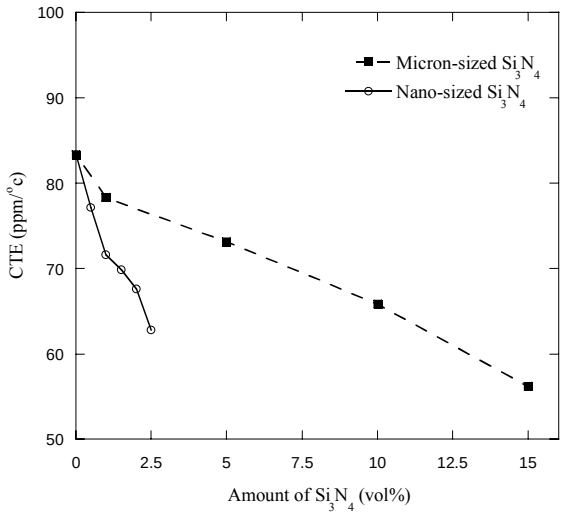

Figure 2. CTE of the composites as a function of Si_3N_4 content with different particle sizes

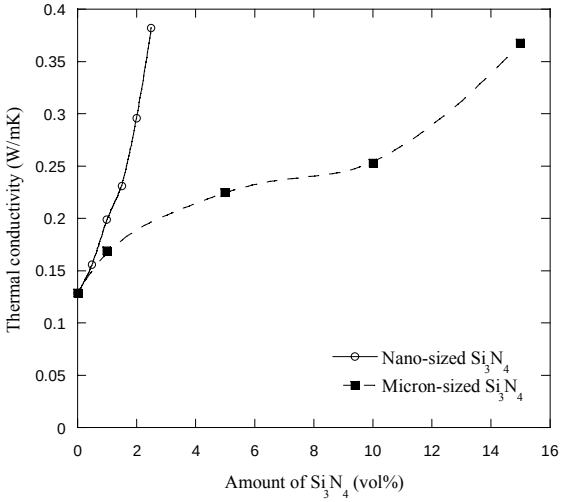

Figure 3. Thermal conductivity of the composites as a function of Si_3N_4 content with different particle sizes

Conclusions

Two different particle sizes of Si_3N_4 filler were manipulated to prepare Si_3N_4 filled epoxy composites. The particle sizes and the amount of Si_3N_4 content were varied and investigated. Adding only small amount of nano-sized Si_3N_4 in epoxy composites can improve the mechanical and thermal properties, including the storage modulus, T_g, CTE and thermal conductivity of epoxy composites which is an important factor for underfill material. It can be concluded that, nano sized Si_3N_4 filler can improve properties of epoxy composites better than the micron-sized ones at low filler loading in the composites.

Acknowledgements

The authors are grateful to Mektec Manufacturing Corporation (Thailand) Ltd. for financial support.

References

[1] M.B. Vincent and C.P. Wong, *Solder Surf Mt Tech.* **11** (1999), pp. 33-39.
[2] S.J. Luo and C.P. Wong, *IEEE. T. Compon. Pack. T.* **28** (2005), pp. 88-94.
[3] Y.Y. Sun, Z.Q. Zhang, and C.P. Wong, *IEEE. T. Compon. Pack. T.* **29** (2006), pp. 190-197.
[4] W.S. Lee and J. Yu, *Diam. Relat. Mater.* **14** (2005), pp. 1647-1653.
[5] W.S. Lee, I.Y. Han, J. Yu, S.J. Kim and K.Y. Byun, *Thermochim. Axta.* **455** (2007), pp. 148–155.
[6] P. Bujard, G. Kuhnlein, S. Ino and T. Shiobara, *IEEE. T. Compon. Pack. A.* **17** (1994), pp. 527-532.
[7] K.C. Yung, J. Wang and T.M. Yue, *J. compopos. Mater.* **42** (2008), pp. 2615-2627.
[8] K.C. Yung, J. Wu, T.M. Yue and C.S. Xie, *J. Compos. Mater.* **40** (2006), pp. 567-581.
[9] K.C. Yung, B.L. Zhu, J. Wu, T.M. Yue, and C.S. Xie, *J. Polym. Sci. Pol. Phys.* **45** (2007), pp. 1662-1674.
[10] C.Y. Hsieh and S.L. Chung, *J. Poly. Sc.* **102** (2006), pp. 4734-4740.
[11] H. He, R. Fu, Y. Han, Y. Shen and D. Wang, *J. Electron. Packaging.* **39** (2007), pp. 469-472.
[12] W. Zhou, C. Wang, T. Ai, K. Wu, F. Zhao and H.Gu, *Compos. Part. A-Appl. S.* **40** (2009), pp. 830-836.

Properties of novel composite from natural rubber, sugar cane bagasse and plaster

S. Riyajan*[1], S.Thaiprasansup[1], and V. Distarote

[1] Department of Material Science and Technology, Faculty of Science, Prince of Songkla University, Hat Yai, (Thailand) 90112

* E-Mail : sa-ad.r@psu.ac.th, saadriyajan@hotmail.com

Abstract: The sugar cane bagasse was modified with sodium hydroxide and silane. The characterization of the modified sugar cane bagasse was achieved with FTIR, and SEM. Results showed that the presence Si-CH_3 group occurred on sugar cane bagasse surface after chemical modification. In addition, the roughness of the modified sugar cane bagasse was higher than that of unmodified sugar cane bagasse due to chemical modification from sodium hydroxide. Two polymer composite types, namely (1) natural rubber(NR)/sugar cane bagasse and (2) NR/plaster via two-roll mill method were prepared. The optimum cure (t_{90}) and torque of the NR/plaster increased with increasing plaster loading in composite. In case of NR/sugar cane bagasse, the t_{90} of this sample decreased as a function of sugar cane bagasse while torque of this sample increased with increasing sugar cane bagasse. The modulus of the resulting composite increased with increasing both plaster and sugar cane bagasse but the tensile strength and elongation at break of the composite decreased as a function of both plaster and sugar cane bagasse in composite.

Introduction

Recently, many works have studied the utilization of natural fibre as reinforcement of polymer matrix including both natural polymer and synthetic polymer [1]. Since the advantages of natural fiber are available in Asia country, cheap, biodegradable polymer and easily degradation in soils with many microorganisms leading to a good environment in the further. For example of the natural fibre, bagass is the solid lignocellulosic residue left after extraction of juice from the sugar cane stalk. Nowadays, the application of bagasse are used in burnt for energy supply in sugar cane factory, pulps, board materials and composites [3], [4], [5] and [6]. In the previous work, bagasse being a raw material blended with poly (vinyl alcohol) [2], polypropylene [4], phenol formaldehyde (PF) resin [3] waste gelatin [7] and polystyrene [8]. For example, poly (vinyl alcohol), PVA composites sheet [2] was prepared from PVA, and lignocellulosic fillers, corn starch, presence of water and glycerol by compression molding. Results shows that the resulting polymer composite based on PVA and starch with apple wastes and sugarcane bagasse fillers were much harder than samples prepared with orange wastes. Chiellini, E and co-worke [9-10] studied the preparation and mechanical properties of composite films from biorelated agro-industrial waste including sugar cane (SC) and apple (AP) and orange (OR) fruit juice extraction and PVA cast from PVA aqueous solutions. Result shows that composite obtained from OR gave to be suitable for blending in higher amounts by weight than that SC and AP. To the best of our knowledge, this is the first study of its kind wherein the preparation of polymer composite obtained from natural rubber, sugar cane bagasse and plaster. The obtained polymer composite from NR, sugar cane bagasse and plaster was prepared by two-roll mill method. In addition, the modified sugar cane bagasse with sodium hydroxide and silane treatment was analyzed by ATR-FTIR, SEM and AFM were studied. The characterization of novel polymer composite was studied through curing properties and tensile strength.

Materials and Methods

Materials

Natural rubber grade STR 5L was supplied by Chalong Latex Industry Co.,Ltd. Sugar cane bagasse was obtained from local in Thailand. Then, sugar cane bagasse fibers were obtained by milling using a laboratory blender. Plaster was purchased from Siam Nakarin Co.,Ltd. All other ingredients used were a commercial grade. The commercial Bis-(3-triethoxysilyl propyl)-tetrasulfide, which is a coupling reagent was provided by Sigma-Aldrich Company. The vulcanizing agent including zine oxide, steric acid, sulfur and tetramethyl thiuram disulfide (TMTD) were reagent grade and were obtained commercially.

Modified sugar cane bagasse

The resulting sugar cane bassage was immersed in 10% sodium hydroxide solution for 24 h. After sugar cane bagasse treated with sodium hydroxide, it was washed with water for many times reached to neutral pH. Thus, the resulting sugar cane bagasse was coated with silane by stiring an immersion of 10 g of sugar cane bagasse in silane for 5 h.

Preparation of polymer composite

Formulation of mixes used for polymer composite from NR/sugar cane bagasse and NR/plaster in this the present work is shown in Table 1 and Table 2, respectively. NR was masticated on the mill for 5 min followed by addition of the ingredients as shown in Table 1 and Table 2. The resulting polymer composite materials were prepared in a two-roll mill. The condition of operation including the nip gap, speed ratio, mill roll and the number of passes for two-mill

was controlled at the same in all the mixes at 50°C. The resulting samples were milled for sufficient time to disperse the sugar cane bagasse or plaster with different loading in the NR matrix at a mill opening of 1.55 mm. The silane as a coupling agent was added in NR compound during mixing to improve the interaction between sugar cane bagasse/plaster and NR matrix. Then, the resulting NR composite was kept at 28±2°C for overnight in a closed container before cure analysis using an Alpha Moving Die rheometer (MDR 2000). The t_{90}, cure time and max torque were measured from the MDR 2000. Then, each specimen was placed in a mold (140×140×1.5 mm) and the NR compounds were vulcanized at 150°C and the pressure of 6.89 MN/m^2 for 20-30 min for a optimum cure (t=90)or tc_{90}). The polymer composite was compressed by compression molding machine to give the polymer composite sheet.

Characterization of modified sugar cane bagasse and testing of polymer composite

The chemical structure of the modified sugar cane was observed by FTIR-ATR. ATR-FTIR spectra were studied with Fourier transformed infrared; FTIR (Bruker, EQUINOX 55) spectral data, taking 100 scans for each sample with resolution 3 cm^{-1}, and raging from 400-4000 cm^{-1} and the ATR-FTIR of samples were obtained to detect any chemical interactions between silane and sugar cane bagasse. The aim of the SEM study was to obtain a topographical characterization of the modified and unmodified sugar cane bagasse. In addition, the morphology of fractured polymer composite sheet was analyzed by SEM. The sample was deposited on a brass hold and sputtered with platinum. SEM photographs were taken with a JSM 6400 Scanning Microscope (Japan) at the required magnification at

room temperature. SEM was performed at an accelerating voltage of 20 kV. The height and deflection images were recorded with the resolution of 512 lines. Then, the resulting polymer composite was kept at 28±2°C for overnight in a closed container before cure analysis using an Alpha Moving Die rheometer (MDR 2000). The t90, cure time and max torque were measured from the MDR 2000. The testing crosshead speed of 500 mm/min was applied with load cell of 1 kg-N. The physical testing of dried latex film was analyzed by universal testing machine Gotech brand model TCS 2000 based on ASTM D 412. Five dumbbell test pieces were cut from each film and the average thickness was calculated and then attached between the grips of a tensile testing machine and pulled at a rate of 500 mm. The thermogravimetric (TG) analysis was performed on a TGA7, PERKIN ELMER: TGA. The mass of each sample was roughly 5.00–6.00 mg. The carrier gas was air with a flow rate of 50 ml/min. The temperature rose from 50 to 800 °C at heating rates of 10 °C/ min.

Results and Discussion

3.1 Characterization of modified sugar baggage

The characterization of modified sugar cane bagasse was investigated by SEM and FTIR. The chemical structure of modified sugar cane bagasse was analyzed by FTIR as shown in Figure 1. The ester-linkage or OC=O stretching of modified sugar cane was observed at 1085 and 1238 cm^{-1}. In addition, the wavelength at 1321 cm^{-1} of modified sugar cane bagasse are indicated the stretching C-O. The new peak of modified sugar cane was observed at 1180 and 1225 cm^{-1} referred to Si-O-Si and Si-O-cellulose, respectively. This result responds with this reference [1]. These results are revealed that the successfully modified surface of sugar cane bagasse. The morphology of modified sugar cane and unmodified sugar cane bagasse is shown in Figure 2. It is clear that the surface of unmofidified sugar cane bagasse exhibited lower roughness comparing to sample with modified with sodium hydroxide treatment as shown in Figure 2. This result is explained that the fat acid on surface of sugar cane was removed by sodium hydroxide. The diameter of sugar cane was roughly 0.1 mm.

Table 1 Formulation of polymer composite obtained from NR and sugar cane bagasse

Chemical	Formulation			
	1	2	3	4
STR 5 CV60,phr	100	100	100	100
Wigstay L, phr	2	2	2	2
Sulfur,phr	2	2	2	2
Steraric acid	2	2	2	2
ZnO,phr	3	3	3	3
TMTD,phr	1.3	1.3	1.3	1.3
DPG,phr	0.7	0.7	0.7	0.7
Sugar cane bagasse,phr	2	5	10	20
Silane, phr	0.5	0.5	0.5	0.5

Table 2 Formulation of polymer composite obtained from NR and plaster

Chemical	Formulation				
	1	2	3	4	5
STR 5	100	100	100	100	100
CV60,phr	2	2	2	2	2
Wigstay L, phr	2	2	2	2	2
Sulfur,phr	2	2	2	2	2
Steraric acid	3	3	3	3	3
ZnO,phr	1.3	1.3	1.3	1.3	1.3
TMTD,phr	0.7	0.7	0.7	0.7	0.7
DPG,phr	5	30	50	70	100
Plaster ,phr	0	0.18	0.3	0.42	0.60
Silane, phr					

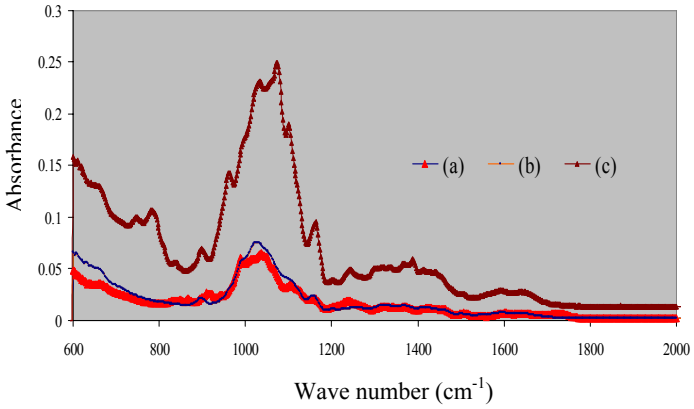

Figure 1 FTIR spectra of surface of (a) unmodified sugar cane bagasse, and modified sugar cane with (b) sodium hydroxide and (c) silane treatment, (A) expand region between 600-2000 cm^{-1}

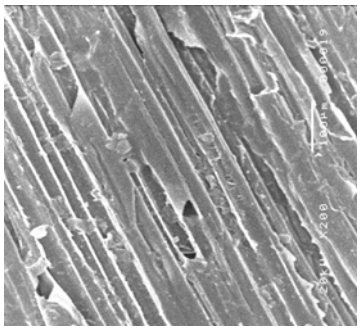

(a)

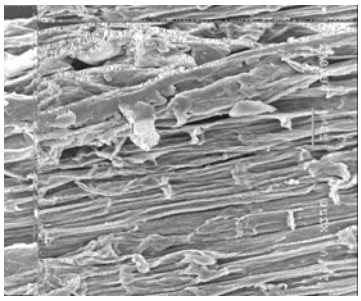

(b)

Figure 2 SEM image of surface of (a) unmodified sugar cane and modified sugar cane with (b) sodium hydroxide

3.2 Curing properties of polymer composite.

When the addition of plaster in NR matrix was subjected to tc_{90} of sample containing and polymer composite at 30, 50, 70 and 100 phr of plasters was 2.33, 2.51, 2.42 and 2.41 min, respectively as shown in Figure 3 (a). Torque of polymer composite containing 0 phr of plaster was about 2 dNm while the torque of this polymer composite in the presence of 30, 50 and 70 phr plaster was 3, 6 and 11 dNm, respectively as shown in Figure 3(b). Moreover, when plaster was added in polymer composite, the properties of the resulting polymer composite exhibited a hardness behavior due to elastic modulus of plaster observing from torque.

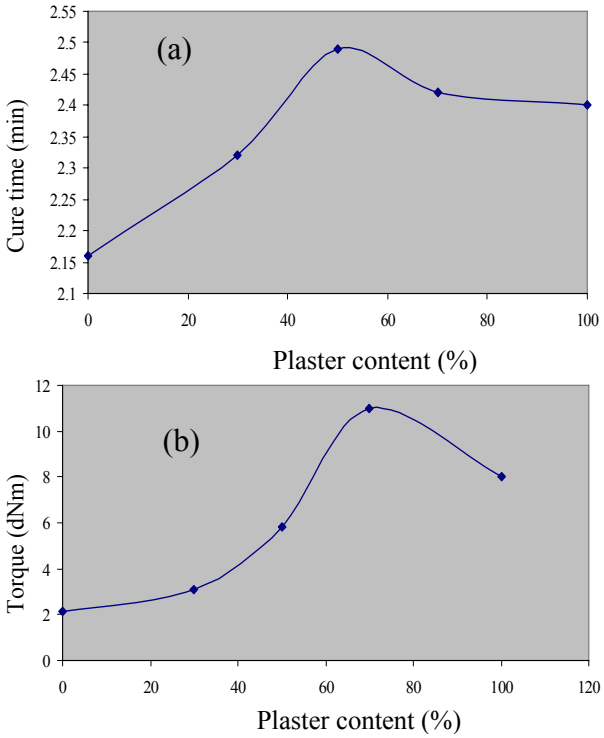

Figure 3 Effect of plaster on (a) the cure property and (b) torque of composite

3.3 SEM of polymer composite

The morphology of polymer composite is a relationship with the physical properties of polymer composite. The morphology of polymer composite was obtained from NR and sugar cane bagasse contents and plaster contents as shown in Figure 4. It is clear that the plasters and sugar cane bagasse are hard to disperse in NR matrix due to difference in surface component between NR and plaster. The morphology of polymer composite showed the more roughness as a function of amount of plaster content in polymer composite. In the case of polymer composite containing 70 phr of plaster, a large number of voids were clearly visible on the fracture surface leading to poor adhesion between NR matrix and plaster. In addition, the sugar cane bagasse is difficulty to disperse in NR matrix due to difference in polar groups between sugar cane bagasse and NR matrix.

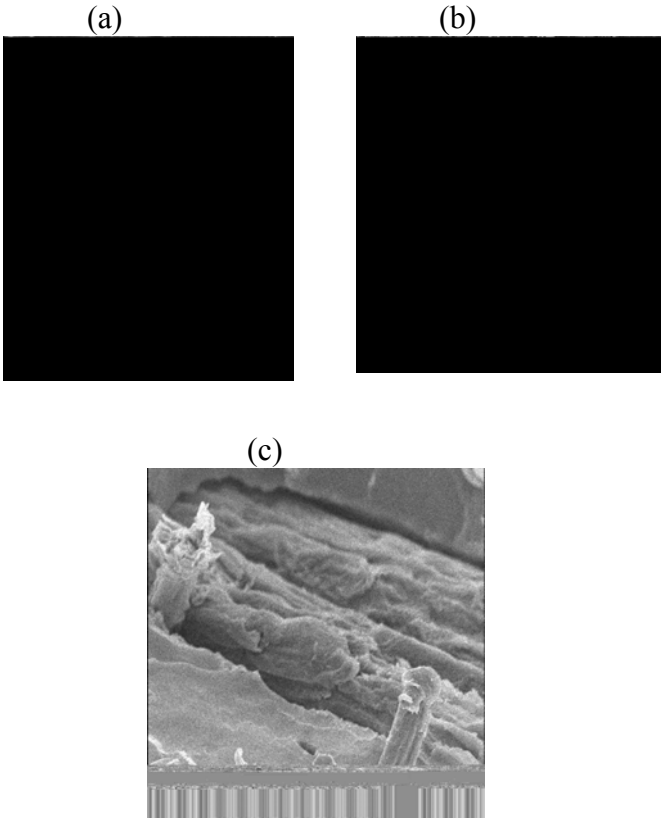

Figure 4 Morphology of natural rubber alone (a), composite in the presence of (b) 50 plaster and (c) 20 phr of sugar cane bagasse observed from SEM

3.4 Mechanical properties

The modulus of NR filled with plaster and bagasse increased with increasing percentage of plaster and bagasse loading as shown in Figure 5 (A). It is noted that the maximum of modulus was observed in sample in the presence of 20 phr of sugar cane bagasse and 70 phr of plaster. Figure 5 (B) shows the influence of both sugar cane bagasse and plaster on the tensile strength of polymer composite. The tensile strength of the polymer composite containing 70 phr of plaster was about 2 MPa. The elongation at break of polymer composite dramatically decrease after addition of more amount of sugar cane bagasse and plaster as shown in Figure 5(C). This result is explained that the reduction of the tensile strength can be attribution to the more dewetting of NR matrix at the interface between NR and filler and more amount of agglomeration of plaster leading to generation of weak to structure due to creating stress concentration [8].

Figure 6 (a) and Figure 6 (b) exhibit the effect of sugar cane bagasse on modulus and tensile strength of polymer composite. Results show that the modulus of polymer composite increased as a function of sugar cane bagasse. But the tensile strength of this sample decreased after addition of more amount sugar cane bagasse.

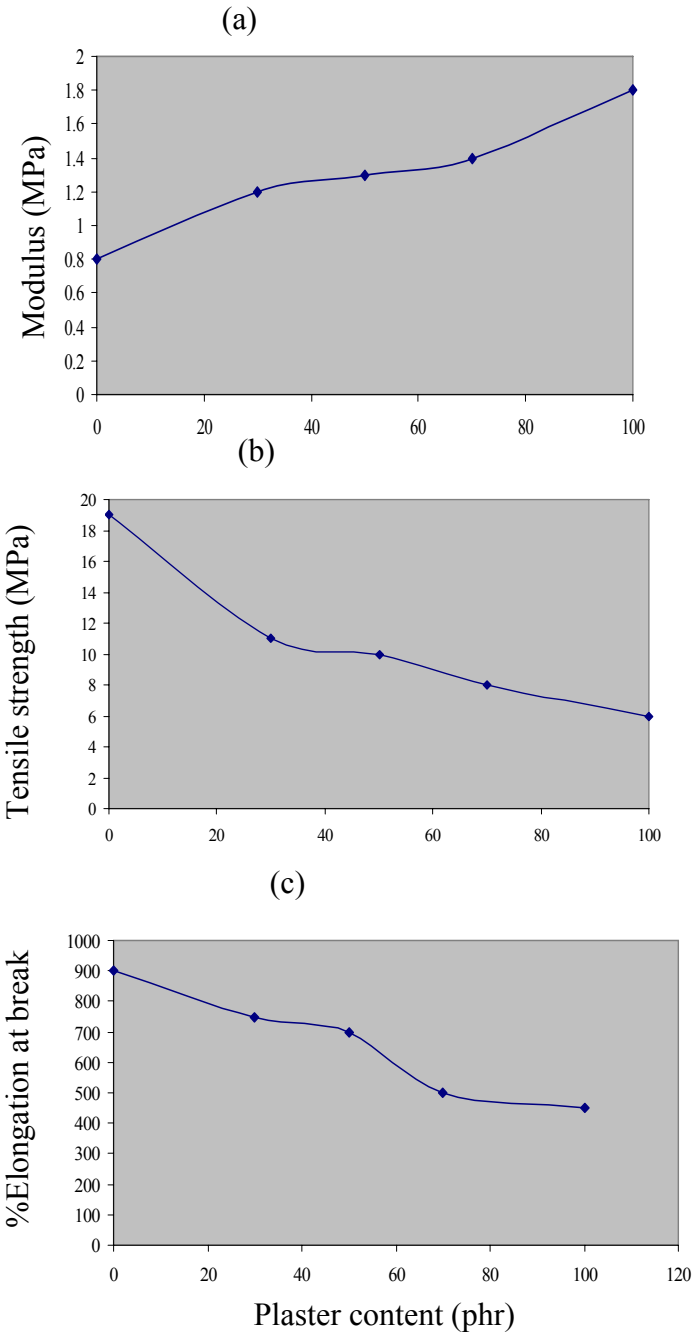

Figure 5 Effect of plaster on (a) modulus, (b) tensile strength and (c) elongation of composite

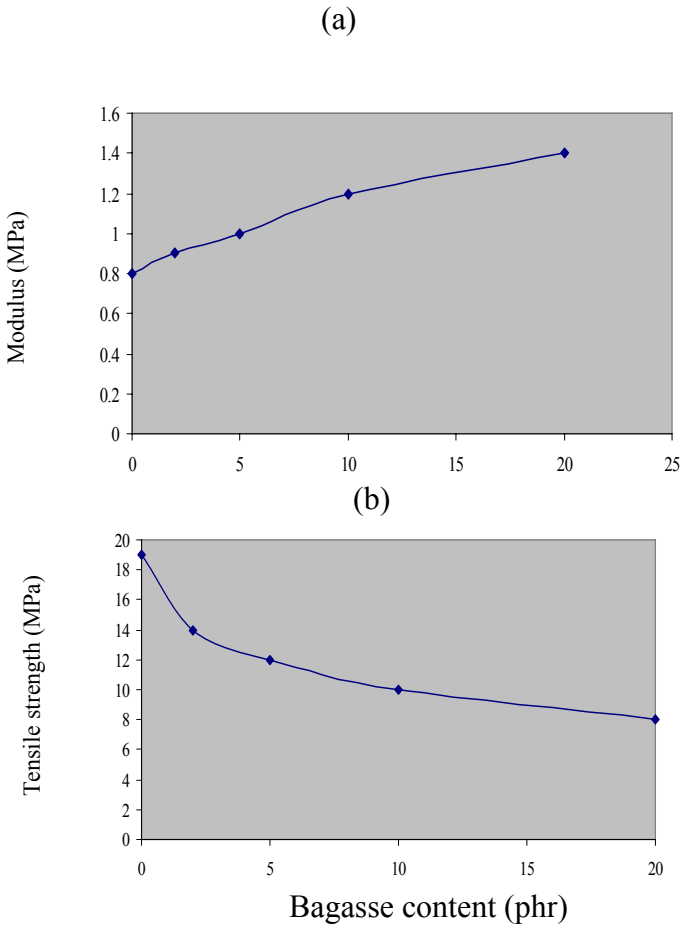

Figure 6 Effect of sugar cane bagasse on (a) modulus, and (b) tensile strength

Conclusions

The achievement in the preparation of polymer composite was obtained from natural rubber, sugar cane bagasse and plaster. The chemical stretching of the modified sugar cane bagasse showed the occurrence of Si-CH_3 group after chemical modification. The roughness of sugar cane bagasse modified with sodium hydroxide was higher than that of unmodified bagasse, leading to removing fatty acid from sugar cane. The torque of the polymer composite increased with increasing both plaster content and sugar cane bagasse. The modulus of the polymer composite increased as a function of the both sugar cane bagasse and plaster contents in polymer composite.

Acknowledgement

The authors thank Department of Materials Science and Technology, Prince of Songkla University for the use laboratory space. This study was supported by Thailand Research Fund

References

[1] S.M. Luz, J. Del Tio, G.J.M. Rocha, AR Gonçalves, J.A.P. Del'Arco, *Comp. Part A: Appl. Sci. Manuf.* **39** (2008), pp.1362-1369.

[2] P. Cinelli, E. Chiellini, S.H. Imam, *J. Appl. Polym. Sci.* **109** (2008), pp.1684-1691.

[3] C.N. Zarate, M.I. Aranguren and M.M. Reboredo *J .Appl. Polym. Sci*. **107**(2008), pp.2977-2985.

[4] S.M. Luz, A.R. Gonçalves, J.A.P. Del'Arco, *Comp. Part A: App.l Sc.i Manuf*. **38** (2007) pp.1455-1461.

[5] N. Kiattipanich, N. Kreua-ongarjnukool, T. Pongpayoon and C. Phalakornkule. J. Polym. Eng. **27** (2007), pp. 411-428.

[6] F.J.F. Talavera, J.A.S. Guzmán, H.G. Richter, R.S. Dueñas and J.R. Quirarte, *Indus.Crop.Prod.* **26** (2007), pp.1-7.

[7] E..Chiellini, P. Cinelli, E.G. Fernandes, E.R.S. Kenawy and A.Lazzeri, Biomacromolecules **2** (2001),pp. 806-811.

[8] L.T. Furlan, M.A. Rodrigues, M.A. De Paoli. *Polym.Degrad. Stab* . **13** (1985), pp.337-350.

[9] E. Chiellini, P. Cinelli, S.H. Imam, and L. Mao, *Biomacromolecules* **2** (2001), pp.1029-1037.

[10] E. Chiellini, P. Cinelli, R. Solaro, and M. Laus, *J .Appl. Polym. Sci.* **92** (2004), pp. 426-432.

Preparation of porous polyimide films from polyimide films from polyimide grafted poly(methyl methacrylate) on polyimide by ultraviolet light cleavage

R. Atthapornrangsri, S. Thongyai*, P. Praserthdam

Center of Excellence on Catalysis and Catalytic Reaction Engineering, Department of Chemical Engineering, Faculty of Engineering, Chulalongkorn University, Bangkok, Thailand 10330

*E-mail: tsupakan@chula.ac.th

Abstract: A study to generate nanoporous polyimide films with low dielectric constants has been proposed. The preparation was consisted of two steps. Firstly, the graft copolymers have been synthesized by atom transfer radical polymerization (ATRP) via reaction with 2-bromo-2-methyl propanoyl bromide that attached on polyimide. The polyimide has been synthesized by one step polymerization of 4,4'-(hexafluoroisopropylidene) diphthalic anhydride (6FDA) , 4,4-oxydianiline (ODA) and dihydroxy dianiline by the ratio of 6FDA:ODA:dihydroxy dianiline of 120:119:1. The chemical composition and structure of the graft copolymers have been characterized by nuclear magnetic resonance (NMR). From results of ^{1}H-NMR and ^{13}C-NMR spectroscopy found that the ^{1}H-NMR peak of the OH group at 10.1 disappeared due to the substitution of the OH group with a 2-bromo-2-methypropanoyl bromide group. The structure of graft copolymers was confirmed by the disappearance of chemical shifts of ^{13}C-NMR at 9.1, 27.9, 46.1 ppm and appearance at 17.7, 30.6, 50.0 ppm. Secondly, graft copolymers of polyimide and poly(methyl methacrylate) (PMMA-g-PI) films have been prepared by spin coating and nanoporous polyimide films will be prepared by a cleavage of PMMA-g-PI by ultraviolet irradiation. The films prepared from the solution casting of these graft copolymer with N-Methyl-2-pyrrolidone (NMP) as solvent were opaque.

Introduction

Porous polymer membranes have various applications in biotechnology and electronics in the field of separation and/or filtration of gases, biomolecules, and environmentally hazardous materials, and in function as insulating materials with low dielectric constants [1]. Especially, the demand for low dielectric constant (low-κ) materials in the microelectronics industry has recently led to considerable interest in porous materials, in particular, nanoporous materials. Polyimides (PI's) have been widely used as dielectric and packaging materials in the microelectronics industry because of their good mechanical, thermal and dielectric properties. However, with dielectric constants in the range of 3.1–3.5, conventional polyimides are insufficient to meet the requirement of $\kappa < 2.5$ [2].

The electrical performance of PIs in these applications is dictated by its dielectric constant, and can be further improved by reducing the dielectric constant. Moreover, lower dielectric constant materials reduce crosstalk between adjacent circuit lines and transmission delay time. There are many ways to reduce the dielectric constant of PIs. They are incorporation of hexafluoroisopropylidene linkages or perfluoroalkyl groups, synthesis of block copolymer (where one of the blocks has a low dielectric constant), introduction of alicyclic rings instead of aromatic rings into the PI structure, and chemical modification of the polymer backbone to reduce chain-chain interactions. A new approach, which has developed considerable interest recently, is the generation of a nanoporous structure in PIs [3].

Here, the reduction in dielectric constant is achieved by replacing a proportion of the polymer with air, which has a dielectric constant of one($\kappa \sim 1$). However, there are restraints on these materials. Firstly, it is quite obvious that the pore size must be smaller than the film thickness. Secondly, it is necessary that the pores be closed cell i.e., the connectivity between pores must be minimal. Thirdly, the volume fraction of voids must be as high as possible. Each of the above can alter the mechanical properties of the film and its structural stability. Failure to meet these restrictions will lead to limited use of the nanoporous PI film. Apart from its use as low dielectric insulators, PI film is also being used in other applications such as gas separation membranes and lightweight heat insulators.

Nanoporous polymers are prepared in various ways: by using blowing agents, by utilizing chemically generated blowing agents, inclusion of glass or carbon microspheres, by microwave processing, by phase inversion of cast films and by decomposing the thermally labile domain in a phase separated block or graft copolymer [3]. The pore size and size distribution are of great importance to the mechanical and dielectric properties of the porous materials. A better control of the pore size and pore size distribution in nanoporous PI film can probably be achieved through a better control of the molecular weight and polydispersity of the thermally labile components in various copolymers.

In the present work, the synthesis porous polyimide films to reduce low dielectric constant. Porous polyimide films prepared via UV cleavage of poly(imide-graft-methyl methacrylate) copolymer prepared using atom transfer radical polymerization.

Materials and Methods

Materials

4,4-hexafluoroisopropylidene diphtalic anhydride (6FDA), Oxydianiline (ODA), Triethylamine (TEA), Toluene, Methanol, 4-dimethylaminopyridine (DMAP), copper(I)bromide (CuBr), *N*,*N*,*N*′,*N*″,*N*″-pentamethyldiethylenetriamine (PMDETA), and 2-bromo-2-methylpropanoyl bromide was purified the Sigma-Aldrich Chemical Co., Methyl methacrylate (MMA) was purchased from the Sigma-Aldrich Chemical Co. was distilled under reduced pressure before use. The solvent, *N*,*N*-dimethylformamide (DMF), was purchased from Fisher Scientific Co. Leics, UK, and was used as received. Tetrahydrofuran (THF, from Aldrich Chemical Co.) was distilled under nitrogen. *N*-Methyl-2-pyrrolidone (NMP) was purified by distillation under reduced pressure.

ODA-dihydroxy dianiline/6FDA polyimide(1)

A one step polymerization technique was employed to synthesize ODA-6FDA-dihydroxy dianiline polyimide. A 100 mL three-neck flask fitted with an overhead stirrer and charged with (1.22 g, 2.75 mmol) of 6FDA and 5 mL of NMP was stirred under an argon blanket to dissolve the diamine. After a homogeneous solution was obtained, the flask was added (0.55 g, 2.75 mmol) of ODA and (0.005 g, 0.029 mmol) of dihydroxy dianiline and washed into the flask with 10 mL of NMP. The mole ratio and solid content of diamine/dianhydride mixture were 1:1 and 15 wt.%, respectively. The reaction mixture was reacted for 2 h at 180 °C in Ar atmosphere. The reaction mixture was then added to toluene solution and was stirred for 2 h at the same temperature in Ar atmosphere. The resulting polymer solution was cooled to room temperature and precipitated into 200 mL of water/methanol, filtered, and vaccumn-dried for overnight at 60 °C to obtain the solid of polyimide.

Bromide functionalized polyimide(2)

A 100 mL round-bottomed flask was equipped with a stir bar, PI**(1)** (500 mg, 10.997 mmol), and 4-dimethylaminopyridine (DMAP, catalytic amount, ~50 mg). After the flask was capped with a rubber septum, the flask was filled with dry argon by three vacuum-argon cycles. Dichloromethane (10 mL) was added to the flask via a syringe to dissolve the mixture. Then, triethylamine (TEA, 150 μL) and 2-bromo-2-methylpropanoyl bromide (17.28 μL, 0.1398 mmol) were sequentially added. The resulting solution was stirred for 20 h at room temperature. After 20 h, the reaction was quenched by the addition of methanol (200 μL) and was diluted with THF. The filtrate was dripped in diethyl ether to precipitate the polymer. The precipitates were collected by filtration and dried under vacuum overnight to provide the bromide functionalized polyimide **(2)** as a white solid.

Synthesis of PI-g-PMMA(3)

Bromide functionalized polyimide **(2)** (300 mg, 12.676 mmol) and CuBr (9 mg, 0.063 mmol) were placed in a Schlenk flask. After the flask was filled with dry argon by three vacuum-argon cycles, *N*,*N*-dimethylformamide (DMF) (5 mL,) and methyl methacrylate (58 μL, 5.424 mmol) was added. Then, three freeze pump-thaw cycles were repeated, and *N*,*N*,*N*′,*N*″,*N*″-pentamethyldiethylenetriamine (PMDETA, 36 μL,0.18 mmol) was added. The mixture was heated to 90 °C for 8 h. The filtrate was precipitated by dripping in distilled water. After filtration and vacuum drying, PI-g-PMMA was obtained as white powder.

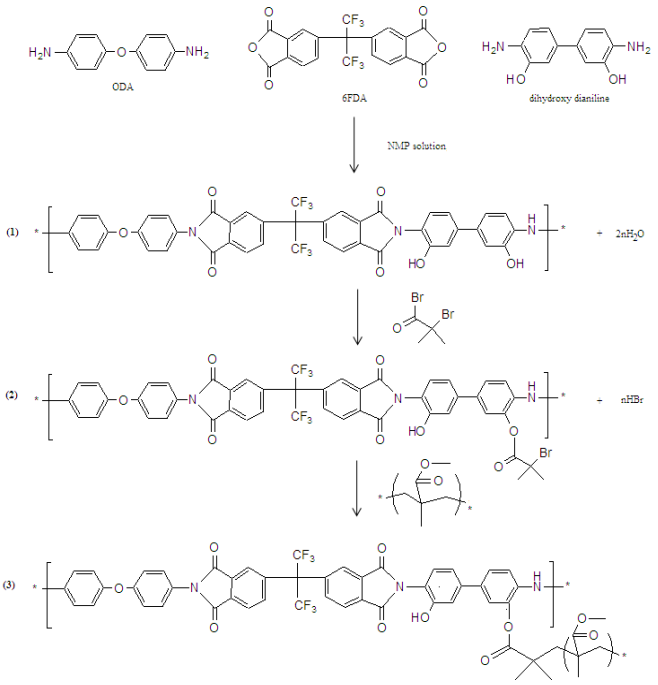

Scheme 1. Synthesis of the PI-g-PMMA with ATRP

Method to produce porous polyimide films

Initially, the graft copolymer was dissolved in NMP to a concentration of 15 wt%. PI-g-PMMA graft copolymer was spin-cast onto a glass substrate. After spin coating (3000 rpm, 50 s), the thin film substrates (thickness in nanometer) were annealed for 2 h via solvent annealing procedure. Then, the thin films were exposed to UV light (350 nm) for 2 h in a UV reactor After the UV exposure, the films were rinsed with Toluene to remove PMMA domains.

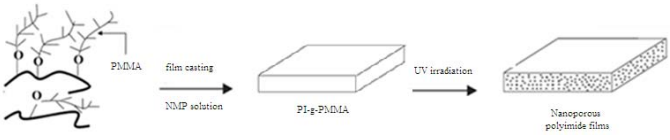

Figure 1. The preparation of a porous PI film

Results and Discussion

Bromide functionalized polyimide **(2)** was prepared in 81% yield by treatment of OH functionalized PI (1) with 2-bromo-2-methylpropanoyl bromide in the presence of TEA and DMAP.

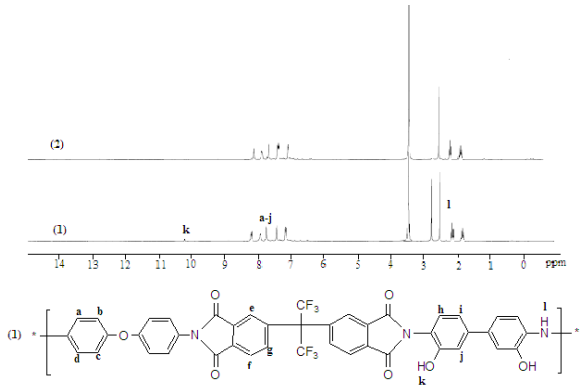

Figure 2. ^{1}H-NMR spectra of functionalized PI **(1)** and **(2)** (400 MHz, DMSO)

Figure 2. shows the 1H-NMR spectra of polyimide and bromide functionalized polyimide in DMSO. As expected, all hydrogen peaks in the ^{1}H-NMR were in good agreement with the proposed polymer structure. The aromatic protons were detected around 7.1–8.1 ppm, depending on the position in the aromatic ring [4]. The sharp single peak observed at about 2.5 ppm meant the proton in N–H stretching. After substitution of the OH group with an 2-bromo-2-methypropanoyl bromide group, the peaks of the OH group at 10.1 ppm was disappeared [5].

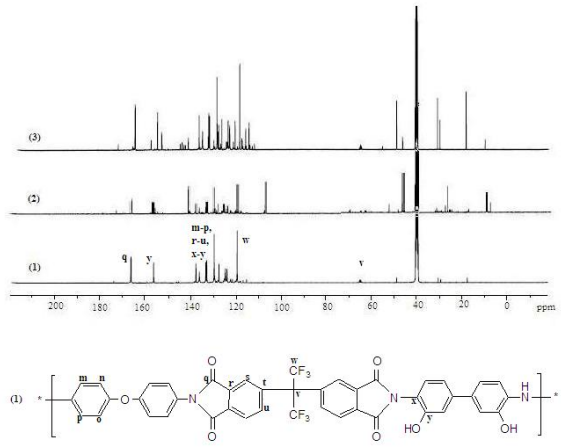

Figure 3. ^{13}C-NMR spectra of functionalized PI **(1)**, **(2)**, and **(3)** (400 MHz, DMSO)

Having synthesized PI-g-PMMA graft copolymers **(3)** , we prepared PI-*g*-PMMA graft copolymers by using the typical ATRP conditions (CuBr, PMDETA). Figure 3 shows the ^{13}C-NMR spectra of polyimide, bromide functionalized polyimide and PI-g-PMMA graft copolymer in DMSO. The aromatic carbon were detected around 110-140 ppm, depending on the position in the aromatic ring [4]. The single peak observed at about 158 ppm meant the carbon in C-OH strength. Another single peak at about 168 ppm assigned the carbon in amide C=O strength of polyimide. ^{13}C-NMR of bromide functionalized polyimide **(2)** also indicates complete functional group transformation, which is inferred from the chemical shift appearance of the singlet peak at 9.1, 27.9, 46.1 ppm and the appearance of a new resonance at 17.7, 30.6, 50.0 ppm for after polyimide grafting with polymethyl methacrylate.

In the addition, the films prepared from the solution casting onto a glass substrate of these graft copolymer with 15% w/w of N-Methyl-2-pyrrolidone (NMP) as solvent were opaque and viscous.

Conclusions

We have successfully synthesized PI-*g*-PMMA graft copolymer using atom transfer radical polymerization. The key in the design of this unique graft copolymer was to incorporate a bromide functional, in the middle of the graft copolymer. the films prepared from the solution casting onto a glass substrate with NMP as solvent were opaque and viscous.

References

[1] W. Kim and M.K. Lee, *Mater. Lett.* 63 (2009), pp. 933–936.

[2] Y.W. Chen, W.C. Wang, W.H. Yu, E.T. Kang, K.G. Neoh, R.H. Vora, C.K. Ong and L.F. Chen, *J. Mater. Chem.* 14 (2004), pp. 1406-1412.

[3] P.S.G. Krishnan, C.Z. Cheng, Y.S. Cheng, J.W.C. Cheng, *Macromol. Mater. Eng.* 288 (2003), pp. 730-736.

[4] X. Han, Y. Tian, L. Wang, C. Xiao, B. Liu, *Eur Polym. J.* 43 (2007), pp. 4382–4388.

[5] M. Kang and B. Moon, *Macromolecules*. 42 (2009), pp. 455-458.

Synthesis of amine functional groups upon surface of polyimide

W. Sorratuyawit[1], S. Thongyai [1]*, and P. Praserthdam [1]

[1]Center of Excellence on Catalysis and Catalytic Reaction Engineering, Department of Chemical Engineering, Faculty of Engineering Chulalongkorn University, Bangkok 10330, Thailand

*E-Mail : tsupakan@chula.ac.th.

Abstract: Polyimide, which has an amine functional on the surface, enhances high temperature resistance and enhances many reactions at surface of polyimide including an adhesion at surfaces because of the strong covalent bond generated from amine interaction. Special polyimide film were prepared by two-step method using 3,3',4,4'-benzophenone tetracarboxylic dianhydride (BTDA) and 4,4'-oxydianiline (ODA) in NMP solvents to form poly(amic-acid) (PAA), followed by the thermal imidization at 250°C. The mole ratio of dianhydride to diamine was 1:1 to obtain the highest molecular weight of polyimide that can be achieved from polymerization step. Surface modification of polyimide films were first carried out by changing the ketone group (C=O) on polyimide surface to oxime group (C=N-OH) and then changing to be the ammonium chloride (C-NH_3^+ Cl^-) and finally to amine group (C-NH_2) respectively. The surface functional was characterized by ATR FTIR Technique. The IR spectrum of the first step films shows the peak 3350 cm^{-1} and 2333 and 2320 cm^{-1} corresponded to OH and overtone of C=N at vibrations of oxime respectively. The absorbances of oxime at various reaction times of 3, 5, and 7 days showed progressing increase of oxime functional. After the reactions of the second steps for 7 days, the compositions of the modified PI surfaces by amine functional were characterized by ATR FT-IR technique. The reaction of oxime groups to amino was confirmed by IR spectrum by a presence of N-H stretching at 2800 and 3100 cm^{-1}.

1. Introduction

Polyimide is one of the most important high-temperature polymers. With high thermal stability, excellent mechanical and electrical properties, as well as radiation resistance, this class of polymer has found broad commercial applications ranging from household and automotive uses to separation membranes and electronic devices[1,2]. Polyimide is used as high flexible circuit board which has resistances of heat, chemical, and corrosion, and good mechanical properties. However, polyimide has low adhesion with other materials. Therefore, epoxy glue is used between the layers of multilayer printed circuit board which melts and flows out the circuit board at high temperature. Polyimide, which has an amine functional on the surface, enhances adhesion because the covalent bond is stronger than the epoxy adhesion and enhances high temperature resistance.

From the research has been studies, the desirable functionalities onto PI films can be accomplished via several surface modification such as chloramethylation [1,2], ion implantation [3], deposited metal [4], surface-grafting [5-8] gamma rays irradiation [9,10] plasma treatment[11,12] hydrolysis reaction [13], acid ething [14] basic ething [15]. The amine group is expected that it can interact with the main chain of polyimide and don't disturb the strength of structure as other methods which is used for increasing surface interaction of polyimide.

The amine functional on the surface of polyimide is made by changing the ketone group (C=O) in polyimide, which made from special monomer such as BTDA, to be oxiem group (C=N-OH) on the surface and then changing to be the amine group (C-NH_2). The reaction which made the amine group in monomer of polyimide or other polymer is only used in a laboratory of Chulalongkorn University [16].

2. Materials and Methods

2.1. Materials

3,3',4,4'-benzophenonetetracarboxylic dianhydride (BTDA) was used as received from Merck. 4,4' -Oxydianiline (ODA) purchased from Aldrich. N-Methyl-2-pyrrolidinone (NMP) were purified by sublimation under vacuum which purchased from Merck. Hydroxylamine hydrochloride and stannous chloride were used as received from Aldrich.

2.2. Preparation of the polyimide films

PAA solution in NMP of 14% (w/w) content was prepared from BTDA/ODA which the mole ratio of dianhydride to diamine was 1:1. The weight of BTDA 4.2893 g was dissolved in 80 mL of NMP and ODA 6.9107 g. The mixture was stirred at room temperature to get a homogeneous solution. The obtained viscous PAA was cast on well cleaned glass substrates. The cast film was thermally treated at 3°C/min heated rate and cured according to the holding time temperature procedure of 100°C and 150°C for 0.5 h and 250°C for 1h. Then polyimide film was removed from the glass substrate by immersing into water and dried at 100°C for 24 h.

2.3 Surface modification of polyimide

The reactions involved were illustrated schematically in Figure 1. Surface modification of polyimide films, the first step was carried out by changing the ketone group (C=O) on polyimide surface to oxime group (C=N-OH). Add a solution of hydroxylamine hydrochloride (7.84 g, 0.01 mol) in 80

mL of ethanol in the bottom flask containing 500 mL to contain polyimide film 2.6 g in 160 mL of ethanol. The solution was heated to reflux. The second step, polyimide films in 140 mL of ethanol with stirring were added with a solution of stannous chloride (7.42 g, 0.03 mol) in 20 mL of concentrated hydrochloric acid. The mixture was heated to reflux to changing to be the ammonium chloride (C-NH_3^+ Cl^-) and to amine group (C-NH_2) by extracted chloride ion with 1 M NaOH. The modified polyimide surface was washed with distillation water and dried in oven night.

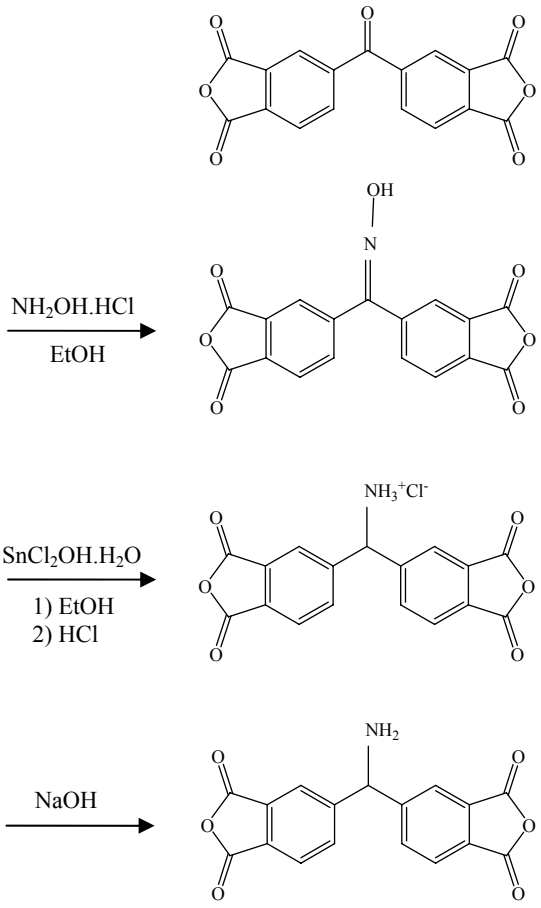

Figure 1. Synthesis of amine functional group.

2.3 Surface Characterization

The chemical composition of the modified polyimide surfaces was determined by the attenuated total reflectance Fourier transform infrared (ATR-FTIR) spectra of the films with a diamond ATR cell. Amine functional groups were determined by reacted with 4,4'-diphenylmethane diisocyanate (MDI).

3. Results and Discussion

3.1. Preparation of the polyimide films

The highest molecular weight of polyimides were prepared by the reactions of ratio of diamine : dianhydride to 1:1. The poly(amic-acid) will be imidized to obtain polyimide at the highest temperature of 250°C. The IR spectrum of polyimide film as shown in Figure 2.

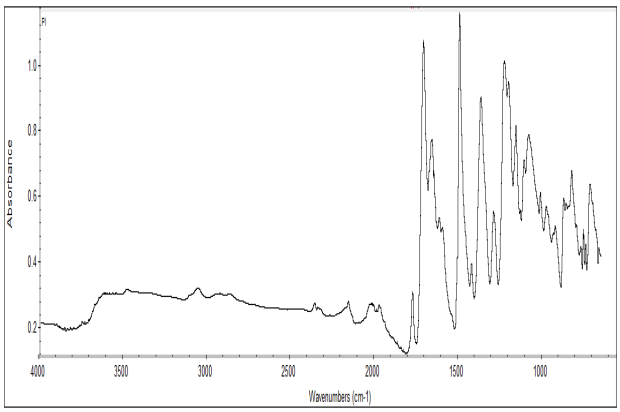

Figure 2**.** The IR spectrum of polyimide film.

3.2. Synthesis of amine functional groups

The IR spectrum of the first step films shows the peak 3350 cm^{-1} and 2333 and 2320 cm^{-1} corresponded to OH and overtone of C=H at vibrations of oxime respectively as shown in figure 3. From figure 4 shows the absorbances of oxime at various reaction times of 3, 5 and 7 days showed progressing increase of oxime functional group. For the reactions of the second steps various reaction times 3, 5 and 7 days and the extraction chloride ion steps with 1 M NaOH cannot characteried by using ATR-FTIR. We determine the amine functional groups on polyimide surface by reacting the modified polyimide surfaces with methylene diphenyl diisocyanate (MDI) [17] which shows the peak 2277.8 cm^{-1} in figure 5.

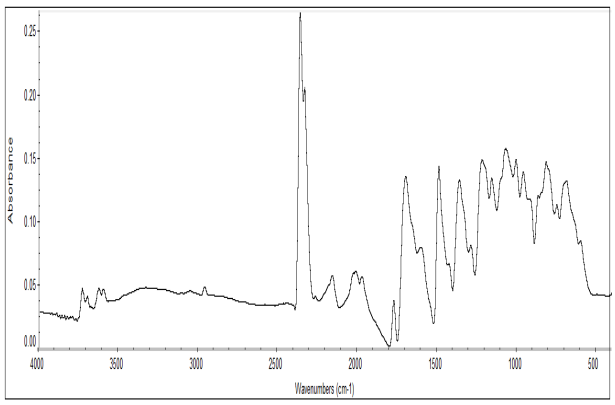

Figure 3. The IR spectrum of the first step of modified polyimide surface.

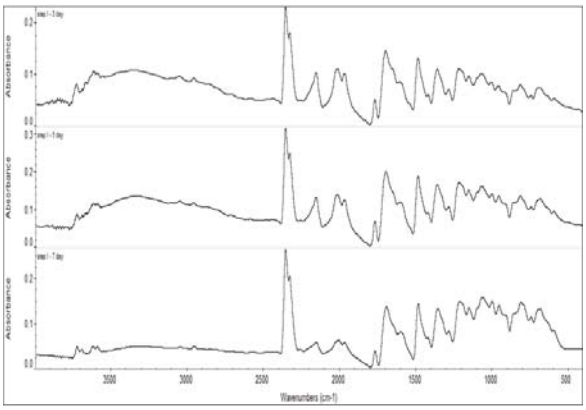

Figure 4. The IR spectrum various the reaction times of the first step of modified polyimide surface. a) 3 days b) 5 days c) 7 days.

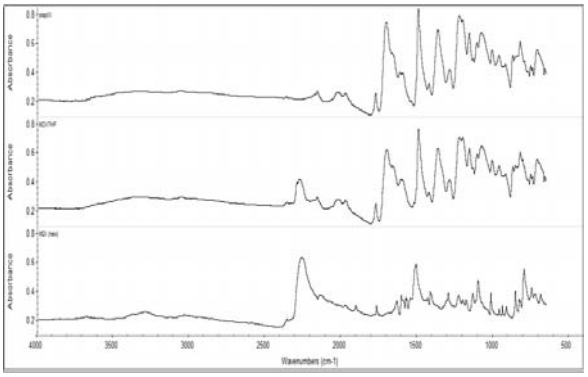

Figure 5. The IR spectrum of a) the final step b) modified polyimide surface were reacted with MDI c) MDI.

Conclusions

The synthesis of amine functional groups upon polyimide surface can be successful by changing the ketone group on polyimide surface to be oxime group which is determined by reacting the modified polyimide surfaces with methylene diphenyl diisocyanate (MDI) as shows the peak at 2277.8 cm^{-1}.

The polyimide films were prepared by a two-step reaction between BTDA and ODA, then changing to be the amine group.

References

[1] L.Li, G.Yan, J.Wu, X.Yu, Q.Guo and E.Kang, *Appl. Surf.* Sci. **254** (2008), pp. 7331-7335.

[2] F.J.Xu, J.P.Zhao, E.T. Kang and K.G. Neoh, *Ind. Eng. Chem.* Res. **46** (2007), pp. 4866-4873.

[3] S. Koytepe, S. Erdogan and T. Seckin, *Jour. of Haz. mat.* **162** (2009), pp. 695-702.

[4] W.V. Dumas, D.F. Foust,Patent 4775449 (1988).

[5] M.R. Tomlinson and J. Genzer, *Jour. Pol. Sci.* **49** (2008), pp. 4837-4845.

[6] Y.G. Ko and P.X. Ma, Jour. *Coll.* Int. Sci. **330** (2009), pp. 77-83.

[7] D. Li, J. Chen, M. Zhai, M.Asano, Y.Maekawa, H. Oku and M.Yoshida, Nucl. Instr. Meth. Phys. Res. xxx (2008)

[8] M.F.A. Taled, G.A. Mahmoud, S.M. Elsigeny and El-S.A. Hegazy, *Jour. of Haz. mat.* **159** (2008), pp. 372-379.

[9] M. Zhai, S. Hasegawa, J.Chen and Y. Maekawa, Jour. of Fluor. Chem. **129** (2008), pp. 1146-1149.

[10] T.A. Sherazi, S. Ahmad, M.A. Kashmiri and M.D. Guiver, Jour. of Mem. Sci. **325** (2008), pp. 964-972.

[11] S.J. Park, E.J. Lee and S.H. Kwon, *Bull. Korean. Chem.* **28** (2007) pp.188-192.

[12] S.J. Park, E.J. Lee and S.H. Kwon, *Sol. Stat. Phen.* **119** (2007), pp. 123-126.

[13] N.C. Stoffel, M. Hsieh, S. Chandra and E.J. Kramer, *Chem. Mater.* **8** (1996), pp. 1035-1041.

[14] W.B. Lindsey and N.Y. Tonawanda, Patent 3361589 (1968).

[15] J. Hermes, M. Va, Patent 3770528 (1973).

[16] C. Apithanawat, S. Thongyai, P. Praserthdam, B. Pulpoka and N. Chantarasiri, *Technology and Innnovation for Sustainable Development Conference(TISD)*, Faculty of Engineering, Khon Kaen University, Thailand (2008).

[17] D.A. Wicks and P.E. Yeske, *Prog. Org. Coat.* **30** (1997), pp. 265-270.

Preparation of soluble bulky side chain polyimide

C. Chanthana[1,2*] ,S.Thongyai [1,2], P. Praserthdam[1,2]

[1] Department of Chemical Engineering, Faculty of Engineering
Chulalongkorn University, Bangkok, Thailand 10330
[2] Center of Excellence on Catalysis and Catalytic Reaction Engineering
at Chulalongkorn University, Bangkok, Thailand 10330

[*] E-Mail : kab_wy@hotmail.com

Abstract: In this study, aiming at synthesis the new polyimide with increases the solubility without scarifying their thermal stability and mechanical properties by synthesis of new diamine monomers which is incorporation of bulky side chain into polyimide backbone. The new symmetrical aromatic diamine (1,2,4,5-Tetrakis([1,1′-biphenyl]-2-oxy)-3,6-bis(4-amino-phenoxy)benzene) was synthesized by the aromatic nucleophilic substitution reaction between 4-amino phenol and hexafluorobenzene in DMF solvent gave the yellow-green powder of 1,2,4,5-Tetrafluoro-3,6-bis(4-aminophenoxy)benzene as a first product. The compound was collected to react with 2-phenylphenol which required a high temperature and long reaction time become a new symmetrical aromatic diamine. The resulting brown solid was collected and purified by column chromatography on a silica gel. ^{1}H NMR were used to confirm the structures of the first product monomer and diamine monomer. Polyimide film derived from the new symmetrical aromatic diamine dipolar aprotic solvents such as NMP, DMF, DMAc and DMSO at room temperature. The thermal properties was investigated by TGA.

Introduction

Polyimides have attracted a lot of scientific and commercial interest because of their excellent thermal stability, mechanical and electric properties. High optical transparency is one of the most attractive properties of polyimides materials for a variety of applications such as electrics, optical waveguide. However, the widespread applications of polyimides are often limited by processing difficulties because of their poor solubility, infusible and high processing temperature, this makes them difficult to process unless they are carefully tailored for improvement in the solubility of these materials in wide range of polar and non-polar solvents. Therefore, much research has been devoted to synthesize highly soluble polyimides without affecting their basic properties [1].

Polyimides (PIs) are a class of thermally stable polymers that are often prepared from dianhydride and diamine monomers. They are usually prepared by the so called one-step or two-step polycondensation method in which a dianhydride and a diamine are allowed to undergo condensation polymerization to form a polyamic acid (PAAs) precursor and subsequently, the precursor is converted thermally or chemically to the final polyimide. Then, they have a number of outstanding properties such as high thermo resistance, dimension stability, excellent electrical and mechanical properties [2].

In order to increase the solubility of polymers, several research groups have explored the possibility of incorporating various of diamine and dianhydride into polymer matrixes to improvement solubility and a variety of concepts for structural modifications such as flexible alkyl side chains, bulky lateral substituents, noncoplanar biphenylene moieties, as well as flexible alkyl or aryl ether spacers, have been used to enhance the solubility and lower the phase transition temperatures. Moreover, for the processing of polyimides many copolyimides such as poly(amide imide)s, poly (ester imide)s, poly(amide ester imide)s, and poly (imide carbonate)s have been prepared for the same reason[3-5]. It is one of important progresses that fluorine-containing polyimides have been synthesized by polycondensation of 4,4'-(hexafluoroisopropylidene) diphthalic dianhydrides (6FDA) with aromatic diamine monomers [6] and the resulting polyimides have been widely employed in the fields that need high-performance materials, e.g. aerospace, electricity, electronic encapsulation and so on, because of their excellent thermal and chemical stabilities, as well as good mechanical properties at high temperature. However, the 6FDA is too expensive to be used for common materials because of hardness to synthesize it [7],so that, the molecular design and synthesis of new dianhydride or diamine monomers containing fluorine and corresponding polyimides containing fluorine will still be very important for further development of polyimides [8-9]. However, fluorine has been prohibit from electrical appliance in Europe, so the driven for cheaper and green chemistry of soluble polyimide is urgently needed.

In this study, synthesized the new polyimide with increases the solubility without scarifying their thermal stability and mechanical properties by synthesis of new diamine monomers not containing fluorine instead of uses 6FDA as a dianhydride and also incorporation of bulky side chain into polyimide backbone will be examined. The solubility and thermal properties was investigated by TGA.

Materials and Methods

4-amonophenol, 2-penylpenol, Hexafluorobenzene (99.9%) , Benzene-1,2,4,5-tetracarboxylic dianhydride (PMDA), 4,4'-Diaminodiphenyl Ether(ODA), 1,3-

dimethyl-2-imidazolidinone(DMI),N-Methyl-2-pyrrolidinone (NMP) , N,N-di- methylacetamide (DMAc), N,N-Dimethylformamide(DMF), dimethyl sulfoxide (DMSO), Tetrahydrofuran(THF),m-Cresol, pyridine, acetone , cyclohexane, methanol and toluene were purchased from Aldrich and used as received.

Synthesis of 1,2,4,5-Tetrafluoro-3,6-bis(4-amino phenoxy)benzene(1)

0.5 ml(4.332 mmol) of Hexafluorobenzene was reacted with 0.9455 g (8.664 mmol) of 4-aminophenol. DMF and K_2CO_3 were used as solvent and catalyst respectively. The mixture was stirred at 50 ^oC for 6 h. then was cooled and stirred overnight at room temperature. The mixture was filtered for removing unreacted catalyst. The filtrate was poured into an excess amount of water. The precipitate was collected by filtration, washed with water, and dried in vacuo oven at 50^oC for 12 h. The obtained yellow-green powder which yield was 2.5932 g (90.67%).The structral formula was confirmed by ^{1} H NMR.

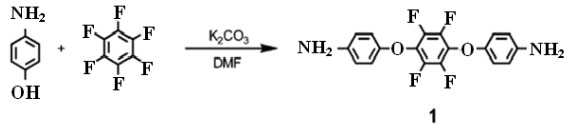

Scheme 1.Synthesis of 1,2,4,5-Tetrafluoro-3,6-bis(4-amino phenoxy)benzene(1)

Synthesis of 1,2,4,5-Tetrakis([1,1'-biphenyl]-2-oxy)-3,6-bis(4-aminophenoxy)benzene(2).

To a round-bottomed flask equipped with a Dean-Stark trap, a mixture of 0.728 g (2 mmol) of *(1)*, 2.7233 g (16 mmol) of 2-phenylphenol and K_2CO_3 2.2114 g (16 mmol) were charged. Then, 8 mL of 1,3-dimethyl-2-imidazolidinone and 5 mL of toluene were added into the flask under nitrogen. The reaction mixture was stirred at 150 °C for about 2 h. until about 4 mL of water had distilled off azeotropically via a Dean-Stark trap. After complete removal of water, the residual toluene was distilled off under reduced pressure,next,the reaction temperature was increased to 220°C, and the reaction was continued for 48 h.After cooling to room temperature, the mixture was trickled into 10 wt % NaOH(aq). The resulting precipitate was collected and was washed several times with distilled water. The resulting solid was collected by filtration and purified by column chromatography on a silica gel (EtOAc:hexane=1:1) to yield a brown powder. The yield was 1.9272 g (55.84%).

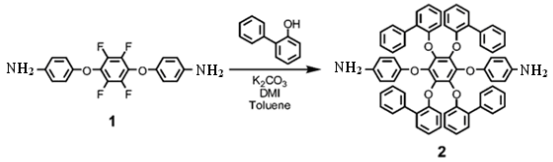

Scheme 2. Synthesis of 1,2,4,5-Tetrakis([1,1′-biphenyl]-2-oxy)-3,6-bis(4-aminophenoxy)benzene (2).

Preparation of the polyimide films

A polymer solution of approximately 15% was made by dissolving PMDA : ODA : Synthesized Diamine with different ratio in NMP. The solution was poured into a square glass culture dish 10x10 cm. that was then placed in a 100,150,200°C vacuum oven each for 30 minutes and further dried to remove the solvent and closed aromatic rings at 250 ^oC for 1 h.

Results and Discussion

Synthesis of Diamine

According to a new synthesized diamine start with synthesis of compound (1) *1,2,4,5-Tetrafluoro-3,6-bis (4-aminophenoxy)benzene* which was designed and pre pared as shown in Scheme 1. The aromatic nucleophilic substitution reaction between 4-aminophenol and hexafluorobenzene gave disubstituted compound (1). Compound *(2)*, *1,2,4,5-Tetrakis([1,1'-biphenyl]-2-oxy)-3,6-bis(4-aminophenoxy)benzene* was prepared by the reaction of 2-phenylphenol with (1), which required a high temperature (220 °C) and a long reaction time (48 h.) due to the steric hindrance of 2-phenylphenol.Compound (2) was a new synthesized diamine .The structure of compound (1) and (2) was confirmed by NMR spectroscopy. Figure 1. shows the ^{1}H NMR spectrum of compound(1) consist of a singlet peak at 4.696 ppm and two doublets at 6.667-6.856 ppm that are assigned to NH_2 and aromatic protons, respectively. The ^{1}H NMR spectrum of synthesized diamine is shown in Figure 2. All signals were well assigned, and the expected copolymer structure was confirmed. The multiplets of the peaks at 6.310-7.713 ppm are relative to aromatic protons.

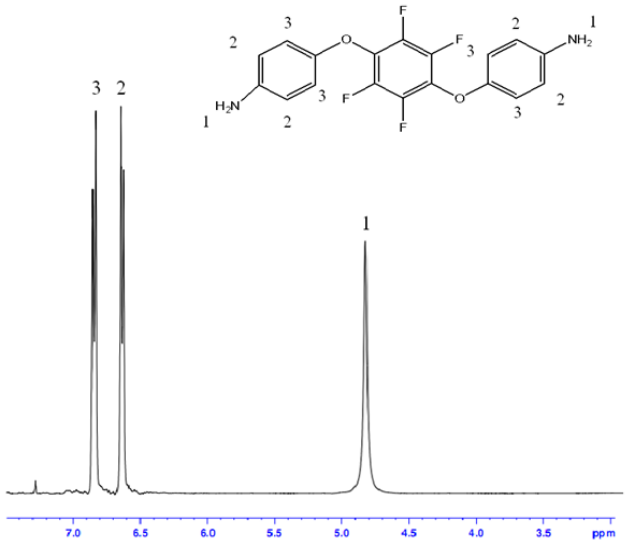

Figure 1. ^{1}H NMR spectrum of compound 1.

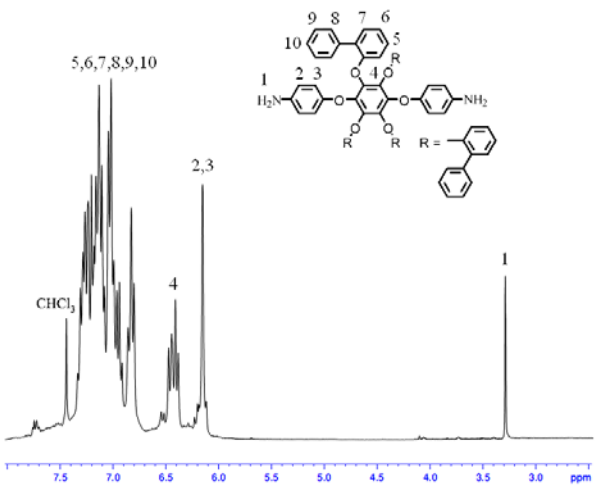

Figure 2. ^{1}H NMR spectrum of sisthesized diamine.

The solubility of polyimides film

The solubility of polyimides film that were prepared by two-step chemical-imidization procedures was determined in the common organic solvents, and the results summarized in Table 1. The resulting polyimides at ratio of PMDA:ODA:Synthesized Diamine = 2:1:1 had excellent solubilities in both aprotic dipolar solvents and common organic solvents, such as N-methyl-2-pyrrolidinone (NMP), N,N-dimethylacetamide (DMAc), N,N-Dimethylformamide (DMF), dimethyl sulfoxide (DMSO), Tetrahydro furan(THF), m-cresol, pyridine, acetone and toluene at room temperature but insoluble in methanol and cyclohexene while PMDA:ODA polyimide was insoluble in every solvent .When the composition of Synthesized Diamine in polyimides was decreased, cause to poor solubility. Nevertheless, they can be also dissolved when it was heated at 80 ^{o}C.The excellent solubility of the polyimides should result from the symmetrical penylphenol group. The construction of aromatic compound makes the chain distance of polymers that was apart-off and decreased the interaction of molecule.

Table 1: The solubility of polyimides film**.**

Solubility : measured at a polymer concentration of 0.02 gml^{-1};(+) soluble at room temperature; (±) partially soluble, (-) insoluble and (Δ) soluble on heating at 80 ^{o}C

Ratio of cast film PMDA:ODA: Synthesized Diamine	Solvent										
	NMP	DMAc	DMF	DMSO	m-Cresol	Py	THF	Acetone	Toluene	Cyclohexane	MeOH
1:1:0	-	-	-	-	-	-	-	-	-	-	-
2:1:1	+	+	+	+	+	+	+	+	+	-	-
3:2:1	+	+	+	+	±Δ	±Δ	±Δ	±Δ	±Δ	-	-
4:3:1	+	+Δ	+Δ	+Δ	±Δ	±Δ	±Δ	-	-	-	-
5:4:1	+Δ	+Δ	+Δ	+Δ	±Δ	±Δ	±Δ	-	-	-	-
6:5:1	+Δ	+Δ	+Δ	+Δ	-	-	-	-	-	-	-

Table 2: The thermal properties of polyimides film.

Ratio of cast film PMDA:ODA: Synthesized Diamine	TGA		
	$T^{a}_{5\%}$ (°C)	$T^{a}_{10\%}$ (°C)	Char yeild[b] (%)
1:1:0	575	589	57.26
2:1:1	391	456	44.12
3:2:1	482	513	50.99
4:3:1	413	494	50.69
5:4:1	390	500	51.61
6:5:1	519	551	53.25

[a]Temperature at 5% and 10% weight loss were recorded by TGA at a heating at10 ^{o}C/min in nitrogen.
[b]Residual weight (%) when heated to 800 ^{o}C.

Thermal properties of polyimides

The thermal stability of soluble polyimide was evaluated by TG analysis. A three-step weight loss was observed from 30 to 400 °C, from 420 to 600 °C, and above 600 °C approximately . The first weight loss is due to the evaporation of solvent, and the second and third ones are attributed to the decomposition of the polymer main chains.TGA data presented in Table 2 shows that the temperature of 5% and 10% weight loss of the polyimides film were measured at 211–413 and 342–559 ^{o}C in nitrogen, respectively, while the residue of weight at 800 ^{o}C was measured at 44.12–59.72 %. It was an evidence that polyimides shown all excellent thermal stability as shown in Figure 3.

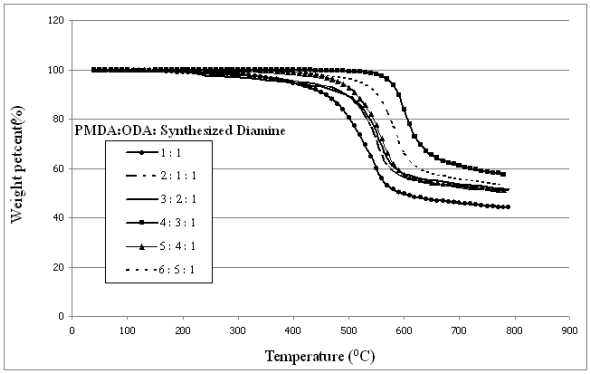

Figure 3. TGA curves of the polyimides.

Conclusions

The new soluble bulky side chain polyimide was successfully synthesized through the synthesis of new diamine which had a construction of aromatic compound and increased the free volume of polymer to provide enhanced solubility. In addition, these polymers are characterized by excellent thermal stability as well as high transition temperatures ; need high temperature to decompose, demonstrating a good combination of properties and processability.

References

[1] L. Yu, Z. Yunhe, *Polymer*.**49** (2008), pp.5439-5445.

[2] W. Lihua, L. Jiding, Z. Zhiping, C. Cuixian, *Journal of Macromolecular Science.* **43** (2006), pp.305–314.

[3] D.J. Liaw, B.Y. Liaw, C.W. Yu, *Polymer*. **42** (2001) , pp.5175–5179.

[4] K.U. Jeong, J.J. Kim, T.H. Yoon, *Polymer*. **42** (2001) , pp.6019–6030.

[5] C.S. Wang, T.S. Leu, *Polymer*. **41** (2000), pp. 3581–3591.

[6] D.Yin , Y.Li, Y.Shao , X. Zhao , S. Yang , L. Fan, *Journal of Fluorine Chemistry*.**126**(2005), pp. 819–823.

[7] S.Z. Zhu, J.W. Zhao, Y.X. Zhang, *Journal of Fluorine Chem*. **123** (2003) , pp.221–225.

[8] A.J. Hu, J.Y. Hao T. , He, S.Y. Yang, *Macromolecules*. **32** (1999), pp. 8046–8053.

[9] K. Xie, J.G. Liu, H.W Zhou., S.Y. Yang, *Polymer*. **42** (2001), pp. 7267–7274.

Synthesis and characterization of methacrylate-modified poly(alkenoic acid)

S. Channasanon, W. Soodsawang, N. Monmaturapoj and S. Tanodekaew*

National Metal and Materials Technology Center (MTEC),
114 Thailand Science Park, Pathumthani 12120, Thailand

* E-Mail : Siriporn@mtec.or.th

Abstract: The objective of this research was to synthesize and characterize methacrylate-modified poly(alkenoic acid) for dental application. Poly(alkenoic acid) which chemically forms cement with a fluoroaluminosilicate glass has shown high potential for dental restorative use since 1970. Subsequent studies in this area have been concentrated to improve mechanical properties of materials by introducing light curing mechanism to harden cement. In this study, poly(alkenoic acid) based on copolymer of acrylic acid (AA) and itaconic acid (IA) having AA/IA molar ratio of 6 was synthesized under nitrogen using potassium persulfate as an initiator. The resulting copolymer was further reacted with glycidyl methacrylate (GMA) in tetrahydrofuran using pyridine as a catalyst to obtain pendant free-radical polymerizable double bond, randomly attaching onto its backbone. Such reaction conditions as reaction temperature and concentration of copolymer were varied to investigate their effects on the degree of methacrylation as well as to find the optimum reaction condition. The methacrylate functionalized copolymer after purification was characterized by ^{1}H-NMR and FT-IR spectroscopy. ^{1}H-NMR spectra showed the existence of vinyl resonance indicating successfully attaching methacrylate active sites onto copolymer chains. FT-IR spectra also confirmed the occurrence of active sites. The degrees of methacrylation were investigated and compared by ^{1}H-NMR. After photo-initiator incorporation, the properties affected by methacrylation degree were determined and discussed.

Introduction

Poly(alkenoic acid) which chemically forms cement with a fluoroaluminosilicate glass has performed high potential for dental restorative since 1970[1]. Due to its unique advantages such as anticariogenic properties, low thermal expansion, low shrinkage and biocompatibility, this chemical-cured cement, so-called conventional cement, has been extensively applied in dentistry. However, its low mechanical strength has made this cement unsuitable for high stress areas.

Considerable efforts for strength enhancement have been made in several aspects, including incorporation of polymerizable components into poly(alkenoic acid). 2-Hydroxyethyl methacrylate (HEMA), one of polymerizable components, has been either simply blended or grafted onto poly(alkenoic acid) backbone. HEMA is a water soluble monomer, so it acts as a cosolvent and a comonomer. However, its cytotoxicity has been reported[2-3]. Glycidyl methacrylate (GMA) is an alternative of polymerizable components which can be functionalized onto poly(alkenoic acid) [4-5]. The light-initiated polymerization of methacrylate functionalized poly(alkenoic acid) in combination with the chemical hardening would play an important role in improving mechanical properties of the cement.

In this study, methacrylate-modified poly(alkenoic acid) was synthesized using various reaction conditions. The resulting products were characterized and their application as dental cement was investigated.

Materials and Methods

Synthesis

Poly(alkenoic acid): Copolymer of acrylic acid (AA, Acros Organics Co.) and itaconic acid (IA, Aldrich Chemical Co.) having AA/IA feed molar ratio of 6 was synthesized in aqueous solution using potassium persulfate (Fluka Chemicals) as an initiator and isopropanol (Lab-scans Ltd.) as a chain transfer agent. The reaction was carried out at 80 ºC for 4 h under nitrogen atmosphere. The synthesized copolymer (CAI) was concentrated by rotary evaporator and dried by lyophilizer.

The methacrylate-modified poly(alkenoic acid): The CAI was further reacted with various amount of glycidyl methacrylate (GMA, Aldrich Chemical Co.) in tetrahydrofuran (Lab-scans Ltd.) using pyridine (Aldrich Chemical Co.) as a catalyst and butylated hydroxytoluene (BHT, Fluka Chemicals) as an inhibitor. Under a nitrogen atmosphere, the reaction was carried out at 60 ºC (or 40 ºC) for 5 h and then kept at room temperature overnight. The methacrylate-modified CAI (MA-CAI) was precipitated in diethyl ether (Lab-scans Ltd.) and dried in a vacuum oven at room temperature. The chemical structure of MA-CAI was characterized in comparison with that of the original CAI by the techniques of proton nuclear magnetic resonance (^{1}H NMR, Bruker DPX-300 spectrometer) and Fourier transform-infrared (FT-IR, Perkin-Elmer).

Cement preparation and characterizations

Powder: Fuji II powder (GC Corporation, Japan) was used in this study.

Liquid: The 50 wt-% aqueous solutions of CAI and MA-CAI were added with 2 wt-% tartaric acid (Ajax Chemicals). The MA-CAI solutions were further added with camphorquinone (CQ, Esschem Inc.) and

N,N'-dimethylaminoethyl methacrylate (DMAEMA, Fluka Chemicals) as a photoinitiator and a reducing agent, respectively.

Cement preparation: Fuji II glass powder was mixed with different kinds of liquid using the powder to liquid weight ratio of 2.7:1. The rod-shape specimens were fabricated using stainless steel moulds. The top and bottom of specimens prepared from MA-CAI liquid were exposed to visible light (wavelength 470 nm, 3M ESPE device) for 40 seconds each. After being stored in an oven at 37 ºC for 1 h, the specimens were removed from the moulds, immersed in distilled water and kept in an oven at 37 ºC for 23 h before testing.

Working time: The working time was tested as described in BS 6039:1981[6]. The mixed cement (powder to liquid weight ratio of 2.7:1) was filled to a level of acrylic mould surface at room temperature within 2 min after start of mixing. Three minutes after start of mixing, the indentor (mass 28 ± 0.25 g, flat-end diameter 2.0 ± 0.05 mm) was lowered onto the surface of the cement for 5 s. The test was repeated at 10 s intervals until the needle failed to make a complete circular indentation in the cement. The time elapsed between start of mixing to the time when the needle failed to make a complete indentation was recorded as the working time of the cement.

Compressive strength: The compressive strength (CS) was tested according to the method described in ISO 9917-1:1998[7] using a Universal Testing Machine (Instron Model 55R4502) at a crosshead speed of 0.75 mm/min. Six cylindrical specimens with a dimension of 4 mm diameter by 6 mm height were tested for each of cement formulation. The CS was calculated using the following equation:

$$CS = 4F/\pi d^2$$

where F is the maximum applied load (N) and d is a diameter of the specimen (mm).

Results and Discussion

Copolymer of AA and IA (CAI) was synthesized and further modified with GMA as illustrated in Figure 1.

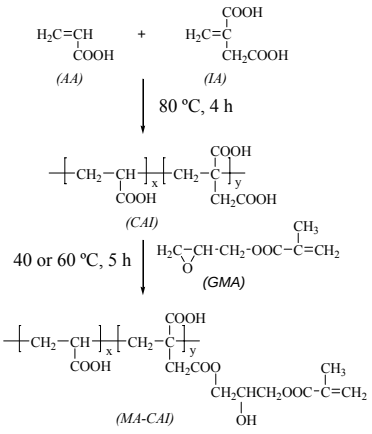

Figure 1. Synthesis of MA-CAI

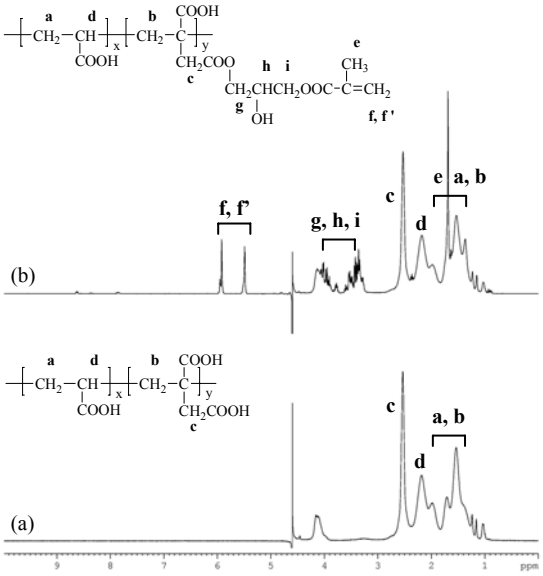

Figure 2. ^{1}H-NMR spectra of CAI (a) and MA-CAI (b)

The ^{1}H-NMR spectrum of MA-CAI was compared with that of CAI as shown in Figure 2. In MA-CAI spectrum (Figure 2b), new peaks at the ranges of 5.6-6.0 ppm and 3.3-4.6 ppm corresponding respectively to $=CH_2$ protons and CH_2-O, CH-O protons of GMA were observed, indicating the incorporation of GMA onto CAI chains. The success in methacrylation of CAI was also confirmed by FT-IR. As seen in Figure 3, the peak at 1637 cm^{-1} corresponding to C=C absorption band was intensified as feed molar ratio of GMA to CAI increased.

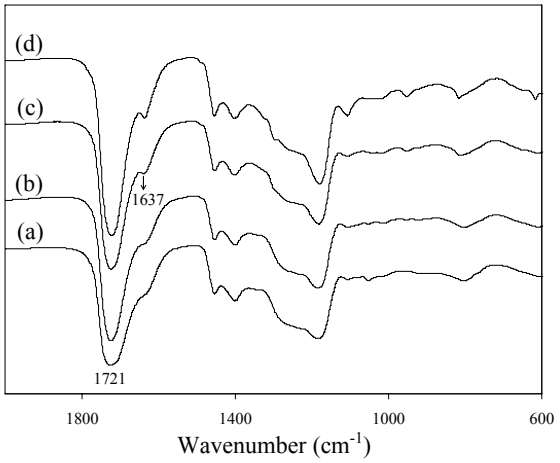

Figure 3. FT-IR spectra of CAI (a), and MA-CAI with feed molar ratio of GMA to CAI = 0.20 (b), 0.35 (c) and 0.50 (d)

The ratios from band heights at 1637 (C=C) and 1721 cm^{-1} (C=O) were used to investigate the effects of reaction temperature and CAI concentration on degree of methacrylation. The results are shown in Table 1 in comparison with the degree of methacrylation determined from NMR.

Table 1: The Effects of Reaction Conditions on Degree of Methacrylation

Reaction Condition	FT-IR C=C/C=O Peak Height Ratio	NMR Degree of Methacrylation (%-mole)
1. Reaction Temperature		
40 °C	0.0045	2.88
60 °C	0.0297	7.12
2. CAI Concentration		
5 wt-%	0.0080	1.08
15 wt-%	0.0297	7.12
30 wt-%	0.0273	8.80
3. Feed Molar Ratio of GMA to CAI		
0.20	0.0297	7.12
0.35	0.0184	6.01
0.50	0.0531	13.50

An increased peak height proportion of C=C to C=O implied a greater number of methacrylate groups attaching onto CAI. These ratios were correspondent with methacrylation degree determined by NMR. The optimal conditions for the synthesis of MA-CAI in this study were found at reaction temperature of 60 °C, using 15 wt-% of CAI. These conditions were used to synthesize MA-CAI series with different feed molar ratios of GMA to CAI.

Working time and compressive strength at 24 h of cements prepared from MA-CAI with different methacrylation degrees are summarised and compared with those of CAI cement in Table 2.

Table 2: Working Time and Compressive Strength of Cements

Cements	Working time (min)	CS (MPa)
CAI	3.53 ± 0.03	106.24 ± 7.00
MA-CAI(0.2)*	4.13 ± 0.03	110.03 ± 2.86
MA-CAI(0.35)*	4.08 ± 0.08	114.23 ± 8.02
MA-CAI(0.5)*	4.10 ± 0.10	104.14 ± 3.13

* feed molar ratio of GMA to CAI

When subjected to light exposure, the presence of methacrylate groups would help to harden cement in addition to the conventionally hardening cement by chemical reaction. Consequently, the increasing in CS was expected as methacrylation degree increased. The CS results, however, showed no significant difference between CAI and MA-CAI cements. The MA-CAI liquid was found poorer miscibility or even phase separation as increased degree of methacrylation. Its immiscibility may impede the chemically hardening mechanism of cement, resulting in a lower CS than that expectation. The height of specimen (6 mm) was also too deep for the light-curing completion, explaining insignificantly increased in CS strength.

The working time of MA-CAI cements was 10-20 seconds longer than that of CAI cement. The extended working time resulted in convenient cement-mixing that led to a better cement preparation.

Conclusions

The methacrylate modified poly(alkenoic acid) (MA-CAI) was successfully synthesized as evidenced from ^{1}H-NMR and FT-IR spectroscopy. The reaction temperature at 60 °C using 15 wt-% of CAI was found to be the optimal reaction condition for the synthesis of MA-CAI. A higher feed molar ratio of GMA to CAI led to a higher degree of methacrylation. The compressive strength was insignificantly affected by incorporation of vinyl pendant groups on CAI backbone. However, the working time was found prolonged that would ease cement handling.

Acknowledgement

This research study was financially supported by National Metal and Materials Technology Center (MTEC), Thailand.

References

[1] A.D. Wilson and B.E. Kent, *Br. Dent. J.* **132** (1972), pp. 133-135.
[2] W. Guerten, W. Spahl and G. Leyhausen, *J. Dent. Res.* **77** (1998), pp. 2012-2019.
[3] J.W. Nicholson and B. Czarnecka, *Dent. Mater.* **24** (2008), pp. 1702-1708.
[4] B.M. Culbertson, *J. Dentistry.* **34** (2006), pp. 556-565.
[5] D. Xie, J-G. Park and J. Zhao, *Dent. Mater.* **23** (2007), pp. 395-403.
[6] BS 6039:1981 Specification for dental glass ionomer cements.
[7] ISO 9917-1:1998 Water-based cements (powder/liquid acid-base cements).

Effect of nitrogenous substances in natural rubber on grafting efficiency of S/MMA copolymer

N. Kreua-ongarjnukool [1]*, P. Pittayavinai[1] and S. Tuampoemsab[2]

[1]King Mongkut's University of Technology North Bangkok, Department of Industrial Chemistry, Faculty of Applied Science, Bangkok, Thailand

[2]King Mongkut's University of Technology North Bangkok, Department of Mechanical Engineering Technology, College of Industrial Technology, Bangkok, Thailand

*E-mail: navika_t@hotmail.com, nkk@kmutnb.ac.th

Abstract: Nitrogenous substance, mostly meaning to protein, is known as one of the naturally occurring components in the natural rubber (NR) latex and is always suspected to interfere many chemical reactions as well as modifications of NR. Since free-radical species in the system of graft polymerization of NR may be terminated by protein. The removal of some proteins from the NR latex was the main reason for the different characteristics of the NR graft copolymers. Therefore, the purpose of this work is to elucidate the effect of nitrogenous substance included in NR on the grafting efficiency onto the styrene/methyl methacrylate copolymer (S/MMA). Deproteinized Natural Rubber (DPNR) used in the experiment was carried out by adding sodium dodecyl sulphate (SDS) into the high-ammoniated NR latex (HANR) and washed by centrifugation at 9,000 and 12,000 rpm, respectively. The DPNR was characterized by FT-IR spectrometer and CHNS/O analyzer to clarify the decreasing of nitrogen content. Thereafter, the DPNR was grafted with styrene and methyl methacrylate via emulsion polymerization using CHP/TEPA (cumenehydroperoxide /tetraethylenepentamine) as an initiator. The DPNR grafted with S/MMA copolymer was characterized by FT-IR spectroscopy and solvent extraction for analyzing the grafting efficiency. FT-IR spectra of the DPNR showed the peak of N-H stretching at the wave number of 1560 and 3500 cm^{-1}, which were clearly decreased with increasing the amount of SDS. Finally, FT-IR spectra of the grafted DPNR demonstrated the peak at wave number 810, 1492 and 1709 cm^{-1} which indicated that of R_2C=CHR of isoprene unit in the DPNR, C=C conjugated stretching of benzene ring in the styrene and C=O stretching in the methyl methacrylate, respectively. It should be noted that the grafting efficiency of S/MMA copolymer onto the DPNR was the highest at 94.55% with 1.00 phr both of initiator and SDS. The core-shell of graft copolymer was confirmed again by Transmission Electron Microscopy (TEM).

Keywords : Grafting DPNR / DPNR-g-S/MMA

Introduction

Natural Rubber from *Hevea brasiliensis* is an unsaturated elastomer with excellent physical properties includes high resilience, high elongation at breaks and good fatigue resistance. However, NR is very sensitive to heat and oxidation because of the double bonds in the chain of isoprene unit as well as ozonization [1,2]. One method to modified the NR is graft copolymerization with a given vinyl monomer. Graft copolymerization has attracted much attention and is applicable to a new class of specialty polymers with an expanded useful range. It can improve the properties and compatibility with other polymers but the grafting efficiency of NR with vinyl monomer is low because the nitrogenous substance existing in the protein can terminated free-radical species in graft copolymerization [3-7]. Many researchers have noted that removal protein can improve higher grafting efficiency. C. Nakason *et al.* reported that grafting efficiency of DPNR with MMA has higher than NR because proteins play an important role in free-radical polymerization. That is, the free-radical species may be terminated by proteins during graft copolymerization [3]. S. H. C. Man *et al.* reported graft polymerization of vinyl monomer in DPNR latex using ammonium peroxy disulfate was successfully prepared with more than 99% conversion [4]. S. Kawahara *et al.* reported that DPNR may be possible to achieve not only high conversion but also high grafting efficiency of monomer for the NR graft copolymerization in latex form [5]. N.pukkate *et al.* reported that grafting of urea deproteinized natural rubber (U-DPNR) was carried out with tert-butylhydroperoxide/tetraethylenepentamine as an initiator in latex stage. The highest conversion and grafting efficiency of styrene for U-DPNR-*g*-PS copolymer were achieved at 1.5 mol/kg-rubber feed of styrene to be about 90 and 90 w/w% [6].

There are many methods for removing protein from NR. S. Kawahara *et al.* prepared DPNR by using proteolytic enzyme with surfactant followed by centrifugation called enzymatic deproteinization [5]. N. Pukkate *et al.* reported using urea with surfactant followed by centrifugation can decreased nitrogen content from 0.35 to 0.02%w/w similar with enzyme [6]. J. Sakdapipanich reported using surfactant with centrifugation at high speed can removed protein from NR and was similar to that of an enzymatic treatment [9].

Materials and Methods

Materials

High Ammoniated Natural rubber latex (HANR) (60% DRC) was produced by Thai Rubber Latex Co.,Ltd. Sodium dodecyl sulfate was obtained from Ajax Finechem. Cumenehydroperoxide, potassium hydroxide, tetraethylenepentamine, isopropanol and ethanol were the products of Fluka. Acetone and petroleum ether were purchased from Fisher Scientific. Methyl methacrylate and styrene were supplied by Pan Asia Industrial Co., Ltd.

Methods

In this research, DPNR was prepared by adding Sodium dodecyl sulfate (SDS) with various conditions and washed by centrifugation at 9,000 and 12,000 rpm then grafting DPNR with S/MMA via emulsion polymerization using CHP/TEPA as an initiator [10-12]. The grafted DPNR with styrene and methyl methacrylate (DPNR-*g*-S/MMA) was characterized by FT-IR spectroscopy and solvent extraction method was used for analyzing the grafting efficiency.

Preparation of deproteinized natural rubber latex

HANR with 60% DRC was added SDS (0.25, 0.50, 0.75 and 1.00 phr) and washing three times at 9,000 and 12,000 rpm by Supreme 21 High speed refrigerated centrifugator. The cream fraction was re-dispersed with distilled water to make DPNR latex.

Preparation of grafted copolymerization DPNR

The graft copolymerization of styrene and methyl methacrylate onto DPNR was carried out in 500 ml five-necked, round-bottomed flask equipped with mechanical stirrer, thermometer, reflux condenser and gas inlet tube. The 150 g DPNR latex was introduced into the glass reactor with SDS as an emulsifier, isopropanol as the stabilizer and potassium hydroxide to maintain the pH of the system. The system was stirred under nitrogen atmosphere at room temperature. The monomer mixture (S/MMA=25/75 w/w) was charged into the reactor. When temperature was heated up to 70 °C, gradually dropped redox initiator (CHP/TEPA). The reaction was allowed to proceed for 8 h with under continuous stirring. The latex was coagulated with ethanol and dried in vacuum oven at 60 °C.

Characterization DPNR and DPNR-g-S/MMA

The nitrogen content of DPNR was characterized by elemental, CHNS/O analyzer 2400 (Perkin Elmer series 2) and Fourier Transform – Infrared Spectrophotometer (Thermo Scientific Nicolet 6700).

The grafting efficiency of DPNR-*g*-S/MMA was determined by Soxhlet extraction method using petroleum ether and acetone (for extracted free DPNR and copolymer) [13,14]. The grafting efficiency was determined gravimetrically by the relationship following as the equation (1)

$$\%GE = \frac{\text{weight of grafted S/MMA}}{\text{weight of total S/MMA}} \times 100 \quad .....(1)$$

when GE is the grafting efficiency

The DPNR-*g*-S/MMA from soxhlet extraction method was characterized by Fourier Transform – Infrared Spectrometer (Thermo Scientific Nicolet 6700) and investigated core-shell particles by Transmission Electron Microscopy technique (JEOL JEM-1230).

Results and Discussion

Characterization of deproteinized natural rubber

From elemental analysis the CHNS/O, it was found that nitrogen content was the lowest at SDS 1.00 phr by centrifugation at 12,000 rpm as shown in Table 1.

Table 1 Nitrogen content from CHNS/O analyzer

SDS (phr)	Nitrogen content (%w/w)	
	Centrifuge at 9000 rpm	Centrifuge at 12000 rpm
0.00	0.442±0.01	0.331±0.01
0.25	0.394±0.01	0.213±0.01
0.50	0.244±0.01	0.153±0.03
0.75	0.209±0.01	0.078±0.01
1.00	0.136±0.01	0.034±0.01
1.50	0.135±0.02	0.033±0.02

The FT-IR spectra of DPNR at 12,000 rpm showed N-H stretching at wave number 1560 and 3500 cm^{-1}. It was found that when increasing amount of SDS, the nitrogen content was decreased as showed in Figure 1.

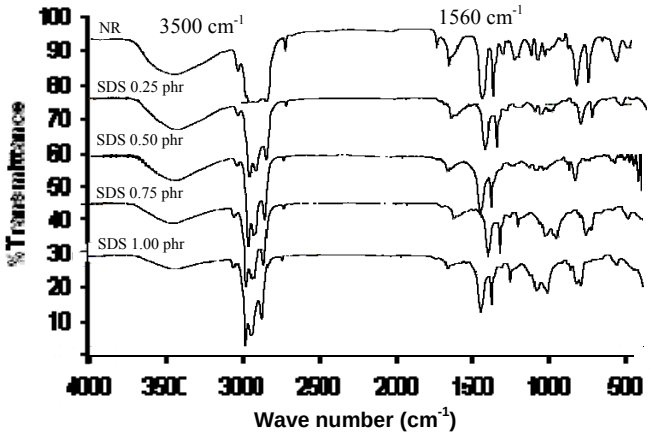

Figure 1 FT-IR spectra of DPNR with various of SDS.

The results from FT-IR spectra and CHNS/O analysis were shown decreasing the nitrogen content with increasing the amount of SDS. It was assured that SDS can remove protein from NR similar to enzyme and urea [5-7,9].

Characterization DPNR-g-S/MMA

The grafting efficiency of NR-*g*-S/MMA and DPNR-*g*-S/MMA were indicated in Figure 2. The highest grafting efficiency was 94.55% from emulsion polymerization with initiator at 1.00 phr.

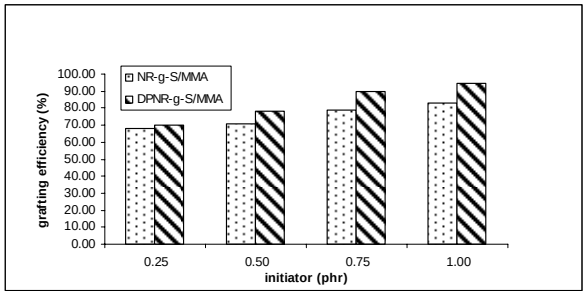

Figure 2 Grafting efficiency of NR-*g*-S/MMA and DPNR-*g*-S/MMA

FT-IR spectra of DPNR-*g*-S/MMA with initiator at 1.00 phr was shown in Figure 3. which indicated that of R_2C=CHR of isoprene unit in the DPNR at 810 cm^{-1} C=C conjugated stretching of benzene ring in the styrene at 1492 cm^{-1} and C=O stretching in the methyl methacrylate at 1709 cm^{-1}. FT-IR spectra was confirmed the grafting of styrene and methyl methacrylate onto DPNR.

The grafting efficiency of DPNR-*g*-S/MMA was higher than NR-*g*-S/MMA because of removing protein from NR was increased more radicals in initiator. Thus, there were more transfer of radicals to the rubber chain and produced more of the graft copolymer [8].

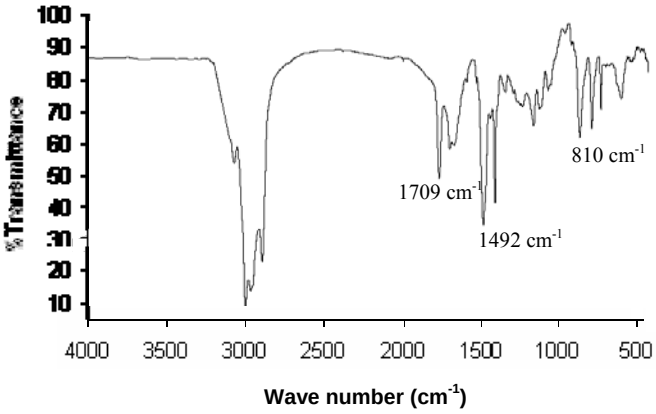

Figure 3 FT-IR spectra of DPNR-g-S/MMA

Transmission Electron Microscopy

The particle morphology of DPNR-*g*-S/MMA was supposed consisting of DPNR as core and S/MMA as shell from emulsion polymerization. The morphology of the core-shell formation of grafted DPNR latex is shown in Figure 4, which indicates the complete closed shell [10,15-17].

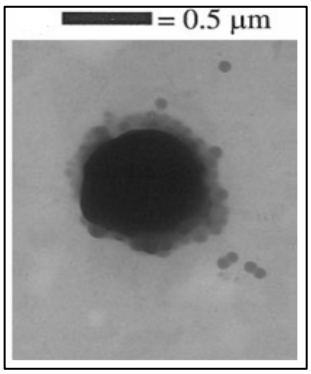

Figure 4 Transmission electron micrographs of DPNR-*g*-S/MMA (×3000)

Conclusions

DPNR was successfully prepared by adding surfactant at SDS 1.00 phr, centrifugation at 12,000 rpm. FT-IR spectra of DPNR showed N-H stretching at wave number 1560 and 3500 cm^{-1} with increasing SDS, the nitrogen content was decreased. The lowest nitrogen content from elemental, CHNS/O analyzer was 0.03%w/w. DPNR was used to prepare graft copolymer with styrene and methyl methacrylate via emulsion polymerization using CHP/TEPA as redox initiator. Grafting efficiency of DPNR was higher than NR because protein in NR can terminate free-radical species during graft copolymerization [3,5,6]. FT-IR spectra was confirmed DPNR-*g*-S/MMA which was indicated R_2C=CHR of isoprene unit in the DPNR at 810 cm^{-1}, C=C conjugated stretching of benzene ring in the styrene at 1492 cm^{-1} and C=O stretching in the

methyl methacrylate at 1709 cm^{-1}. The morphology of DPNR-*g*-S/MMA was supposed core-shell of grafted DPNR by DPNR as core and S/MMA copolymer as shell.

Acknowledgements

The authors acknowledge with thanks for partial financial support from the Graduate College, Industrial Chemistry Department, Faculty of Applied Science King Mongkut's University of Technology North Bangkok. The authors wish to thank Pan Asia Industrial Co., Ltd. for supplying the materials used in this research.

References

[1] W. Hofmann, *Rubber Technology Handbook*, Hamser Publishers, New York, (1989), pp.20-25.
[2] B. Rodgers, *Rubber Compounding : Chemistry and Applications,* Marcel Dekker, (2004), pp.50-52.
[3] C. Nakason, A. Kaesaman and N. Yimwan, *J. of App. Polym. Sci,* **87** (2003), pp. 68–75.
[4] S. H. C. Man, A. S. Hashim and H. M. Akil, *J Polym Res.*, **15** (2008), pp.357–364.
[5] S. Kawahara, T. Kawazura, T. Sawada and I. Yoshinobu, *J. Polym,* **44** (2003), pp.4527-4531.
[6] N. Pukkate, T. Kitai, Y. Yamamoto, T. Kawazura and J. Sakdapipanich, S. Kawahara, *European Polymer Journal,* **43** (2007), pp. 3208–3214.
[7] N. Pukkate, Y. Yamamoto and S. Kawahara, *J. Colloid. &. Polym. Sci*, **286** (2008) , pp. 411-416.
[8] W. Kangwansupamonkon, R.G. Gilbert and S. Kiatkamjornwong, *J. Macromolecular Chemistry & Physics,* **206** (2005)**,** pp. 2450-2460.
[9] J. Sakdapipanich, *J. of Bioscience and Bioengineering*, **103** (2007), pp. 287–292.
[10] W. Arayapranee and G. L. Rempel, *J. of App. Polym. Sci.,* **93** (2004) , pp. 455–463.
[11] N. Hinchiranan, B. Suppaibulsuk, S. Promprayoon and P. Prasassarakich, *Materials Letters,* 61 (2007), pp. 3951–3955.
[12] P.C. Oliveira, A. Guimaraes, J.Y. Cavaille, L. Chazeau, R.G. Gilbert and A.M. Santos, *Polymer,* **46** (2005), pp. 1105–1111.
[13] B.George, S. N. Maiti and I. K. Varma, *J. of elastomers and plastics,* **38** (2006), pp.319-331.
[14] P.C. Oliveira, A.M. Oliveira, A. Garcia, J. C. S. Barboza, C.A.C. Zavaglia and A. M. Santos, *European Polymer Journal*, **41** (2005), pp.1883–1892.
[15] A. Hassan and B. Haworth, *J. of Mat. Processing Technology,* **172** (2006), pp.341–345.
[16] F. Ramsteiner, W. Heckmann, G.E. McKee and M. Breulmann, *Polymer*, **43** (2002), pp.5995–6003.
[17] K. Wang, Y. Chen and Y. Zhang, *Polymer,* **50** (2009), pp.1483–149.

Prepration of antibacterial hydrogels from *N,O*-[(2-hydroxy-3-trimethyl ammonium) propyl] chitosan chloride modified with glycidyl methacrylate

P. Intaraksa[1], P. Ngamviriyavong[2], P. Tanjak[2], A. Kleawkla[1] and W. Janvikul[2*]

[1] Department of Chemistry, Faculty of Science, Maejo University, Chiang Mai, Thailand 50290
[2] National Metal and Materials Technology Center, Pathumthani, Thailand 12120

[*]E-Mail : wanidaj@mtec.or.th

Abstract: The synthesis of antibacterial hydrogels from chitosan (CS) containing both trimethyl ammonium salt and methacrylate groups was carried out. The modified chitosan was prepared via two reverse synthetic routes. Firstly, chitosan was chemically modified with glycidyl trimethyl ammonium chloride (GTMAC), yielding trimethyl ammonium salt-containing chitosan (CS-GTMAC) which was subsequently reacted with glycidyl methacrylate (GMA) to yield *N,O*-[(2-hydroxy-3-trimethyl ammonium) propyl] chitosan chloride modified with glycidyl methacrylate (CS-GTMAC-GMA). Secondly, chitosan was reacted with GMA, yielding glycidyl methacrylate-containing chitosan (CS-GMA) which was then reacted with GTMAC to result in *N,O*-[(2-hydroxy-2-methacrylate) ethyl] chitosan modified with glycidyl trimehtyl ammonium chloride (CS-GMA-GTMAC). The chemical structure and degrees of substitution of trimethyl ammonium salt and methacrylate groups in each modified chitosan were determined by ^{1}H NMR spectroscopy. The hydrogels were prepared through the polymerization of the methacrylate pendant groups in both CS-GTMAC-GMA and CS-GMA-GTMAC using potassium persulfate as an initiator at 80^{o}C. The results revealed that CS-GTMAC-GMA could completely dissolve in weak acid solution, whereas CS-GMA-GTMAC could partially dissolve, indicating that the sequence of etherification of chitosan by either GTMAC or GMA played an important role on the solubility of the chitosan intermediates. As a result, only CS-GTMAC-GMA was selected and employed in the preparation of the antibacterial hydrogels. It was noted that the % gel fraction of the hydrogels was directly proportional to the amount of methacrylate pendant groups present in the modified chitosan. The antibacterial activities of each modified chitosan and hydrogel were assessed against *Staphylococcus epidermidis*. The minimum inhibitory concentrations (MIC) of the tested samples were found in the range of 32-1034 µg/mL. The cytotoxicity of the modified chitosans and hydrogels were evaluated by an MTT assay. The results demonstrated that all samples were non-cytotoxic to human dermal fibroblasts.

Introduction

Chitosan has been widely accepted as a material for several biomedical uses, owing to its biodegradable, biocompatible, and bioactive properties [1]. Some chitosan derivatives have been previously reported to demonstrate antibacterial activities, e.g., chitosan salts from amino acids [2,3] and quaternary chitosan salts from glycidyltrimethyl ammonium chloride (GTMAC) used as an etherifying agent [4].

Hydrogels are three-dimensional networks of hydrophilic polymers that can hold a large amount of water while maintaining the solid state. High swelling ratio or water-keeping ability of hydrogels is one of the basic requirements for being used as biomaterials [5]. Hydrogels from glycidyl methacrylated chitosan (CS-GMA) and *N*-isopropylacrylamine (NIPAAm) were prepared by the free radical photopolymerization through the methacrylates of CS-GMA and NIPAAm [6]. The objective of this study was to synthesize antibacterial chitosan hydrogels containing both trimethyl ammonium salts from GTMAC and methacrylate groups from GMA. Their antibacterial activity were assessed against *Staphylococcus epidermidis*.

Materials and Methods

Materials: Chitosan (CS), from shrimp shells, having MW ≈ 700 kDa (determined by GPC) and deacetylation of 95.5%, (determined by solid state ^{13}C-NMR) was purchased from A.N. lab. Glycidyl methacrylate (GMA) and potassium persulfate were purchased from Fluka, whereas glycidyl trimethyl ammonium chloride (GTMAC) was purchased from Aldrich. All reagent-grade chemicals were used as received.

Preparation of trimethyl ammonium salt-containing chitosan (CS-GTMAC): The modified chitosans were prepared using GTMAC as an etherifying agent with two different mole ratios of CS to GTMAC, 1:1 and 1:4. Typically, CS (2.0 g) was dissolved in 100 mL of 2% v/v acetic acid aqueous solution. Then, 1.57 or 6.29 mL of GTMAC (1 or 4 mole equivalent based on CS unit) was added, and the solution was stirred at 60^{o}C for 6 h. The reaction mixture was ultimately precipitated with 50% v/v acetone in methanol. The resulting precipitate was repeatedly washed with acetone and then dried under reduced pressure.

Preparation of glycidyl methacrylate-containing chitosan (CS-GMA): The modified chitosans were prepared using GMA as an etherifying agent with two different mole ratios of CS to GMA, 1:1 and 1:4. Typically, CS (2.0 g) was dissolved in 100 mL of 2% v/v acetic acid aqueous solution. Then, 1.55 or 6.20 mL of GMA (1 or 4 mole equivalent based on CS unit) was added, and the solution was stirred at 60^{o}C for 6 h. The reaction mixture was finally precipitated with acetone. The resulting precipitate was repeatedly

washed with acetone and then dried under reduced pressure.

Preparation of chitosans containing both trimethyl ammonium salt and methacrylate groups: The modified chitosans, CS-GTMAC or CS-GMA, were subsequently reacted with GMA or GTMAC to yield CS-GTMAC-GMA or CS-GMA-GTMAC, respectively. CS-GTMAC (1.0 g) was dissolved in 50 mL of 2% v/v acetic acid aqueous solution. To the solution, 0.77 mL of GMA (1 mole equivalent based on initial CS unit) was added. Meanwhile, CS-GMA (1.0 g) was dissolved in 50 mL of 2% v/v acetic acid aqueous solution and subsequently added with 0.79 mL of GTMAC (1 mole equivalent based on initial CS unit). Both reaction solutions were stirred at 60°C for 6 h. The reaction mixtures were precipitated with acetone. The resulting precipitates were repeatedly washed with acetone and then dried under reduced pressure.

Preparation of hydrogels from chitosans containing both trimethyl ammonium salt and methacrylate groups: The hydrogels were prepared via the polymerization through the methacylate groups of GMA in the modified chitosans using potassium persulfate as an initiator. Typically, CS-GTMAC-GMA (1 g) was dissolved in 20 mL of 2% v/v acetic acid aqueous solution. Then, 10 mg of potassium persulfate was added, and the solution was stirred at 80°C for 2 h. The hydrogel was dried at 80°C. The dried hydrogel was washed with an excess amount of deionized water.

Chemical structure analysis: The chemical structures of the modified chitosans (CS-GTMAC, CS-GMA, CS-GTMAC-GMA and CS-GMA-GTMAC) were confirmed by ^{1}H NMR spectroscopy (Bruker DPX-300 spectrometer), and the degrees of quaternization and methacrylation were also determined by ^{1}H NMR spectroscopy.

Swelling behavior: The dried hydrogels were initially weighed (W_o) and subsequently immersed into deionized water. At a given time (t), the swollen hydrogels were re-weighed (W_t) after they were wiped with soft paper tissue. The degree of swelling of the samples at time t was calculated by using the expression: $(W_t - W_o)/W_o$, where W_t and W_o were the weights of the hydrogels at time t and the dry state, respectively.

Antibacterial activity assessment: The antimicrobial activities of the modified chitosans were evaluated using a shake flask method. The *S. epidermidis* bacteria were first overnight cultured in nutrient broth (NB) (Difco) at 37°C before use. The bacterial cultures were subsequently diluted with NB to a concentration of approximately 10^6 CFU/mL. Meanwhile, the modified chitosans were dispersed in NB at final concentrations of 2048, 1024, 512, 256, 128, 64, 32 and 16 μg/mL in flasks. The NB without sample was used as a blank. After 24 h of incubation, the whole dispersions of the samples in the bacteria cultures were analyzed by a Spectrophotometer, at 600 nm, to determine a minimum inhibitory concentration (MIC) of each modified chitosan. MIC was defined as the lowest concentration of an antimicrobial agent which could completely inhibit the growth of a given microorganism after overnight bacterial incubation with the material.

Cytotoxicity assessment: Normal human dermal fibroblasts were seeded into 96-well microplates at a concentration of 3×10^3 cells/well in Dubelco's modified Eagle medium (DMEM) supplemented with 10% fetal bovine serum and incubated at 37°C. After 48 h of incubation, the medium was replaced with a fresh medium containing various concentrations of the modified chitosans and reincubated for an additional 48 h. Subsequently, a fresh medium and 3-(4,5-dimethyl thiazol-2-yl)-2,5-diphenyl-tetrazolium bromide (MTT) were added into the wells, and the whole microplates were again incubated at 37°C for 4 h. The collected purple formazan products were ultimately dissolved in dimethyl sulfoxide (DMSO) and glycine buffer for the measurement of optical density values, later converted to the percentage of viability of cells (% cell viability), using a Microplate Reader at 570 nm.

Results and Discussion

The antibacterial hydrogels from the modified chitosans containing both trimethyl ammonium salt and methacrylate groups were prepared via two reverse synthetic routes, as schematically shown in Figure 1.

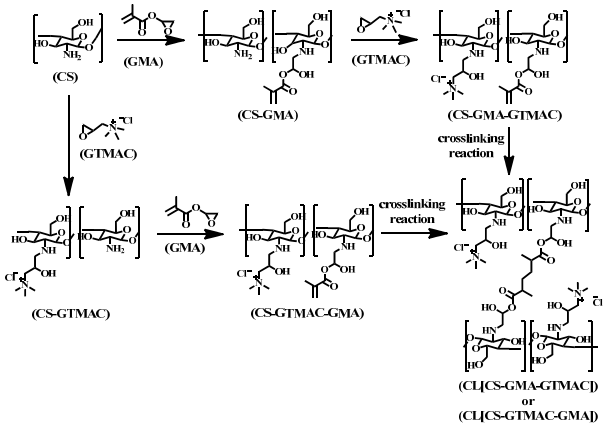

Figure 1. The schematic preparation of antibacterial hydrogels from modified chitosans containing both trimethyl ammonium salt and methacrylate groups.

After quaternization, the presence of positive charge of 2-hydroxy-*N*-trimethylammonium propyl groups, (-N(CH_3)$_3^+$), in the modified chitosan was markedly observed in the spectra of the CS-GTMAC samples at 3.13 ppm in Figure 2 (b and c). The degree of quaternization (DQ) was directly determined from the ^{1}H NMR spectra. The calculated % DQ values of CS-GTMAC (1:1) (prepared by using mole ratios of CS to GTMAC = 1:1) and CS-GTMAC (1:4) (prepared by using mole ratios of CS to GTMAC = 1:4) were 37 and 109, respectively, as shown in Table 1.

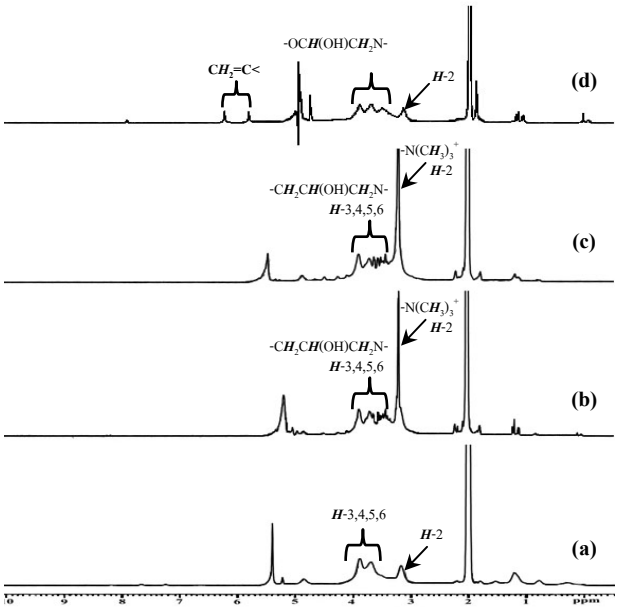

Figure 2. The ^{1}H NMR spectra of (a) CS, (b) CS-GTMAC (1:1), (c) CS-GTMAC (1:4), and (d) CS-GMA (1:1) in D_2O/CD_3CO_2D.

Table 1: % DQ and % DM of All Modified Chitosans Determined by ^{1}H NMR Spectroscopy.

Samples	Mole Ratios			% DQ	% DM
	CS	GTMAC	GMA		
CS-GTMAC (1:1)	1	1	-	37	-
CS-GTMAC (1:4)	1	4	-	109	-
CS-GMA (1:1)	1	-	1	-	23
CS-GTMAC-GMA (1:1:1)	1	1	1	37	22
CS-GTMAC-GMA (1:4:1)	1	4	1	109	33

After methacrylation, the unsaturated methylene protons of 2-hydroxy-2-methcrylate ethyl groups in the CS-GMA sample were observed at 5.8 and 6.2 ppm in the spectrum shown in Figure 2(d). The degree of methacrylation (DM) was directly determined from the ^{1}H NMR spectra. The calculated %DM of CS-GMA (1:1) was 21. The % DM of CS-GMA (1:4) could not be determined as it was hardly soluble in acid solution (D_2O/CD_3CO_2D).

The chemical structure of the modified chitosans containing both trimethyl ammonium salt and methacrylate groups, CS-GTMAC-GMA and CS-GMA-GTMAC, was elucidated by ^{1}H NMR spectroscopy. As shown in Figure 3 (b and c), the ^{1}H NMR spectra of CS-GTMAC-GMA (1:1:1) and CS-GTMAC-GMA (1:4:1) revealed both characteristic absorption peaks of trimethyl ammonium protons at 3.13 ppm and unsaturated methylene protons at 5.8 and 6.2 ppm. The calculated %DM values of CS-GTMAC-GMA (1:1:1) and CS-GTMAC-GMA (1:4:1) were 22 and 33, respectively, as shown in Table 1.

As revealed in Figure 3 (a), the ^{1}H NMR spectrum of CS-GMA-GTMAC (1:1:1) only displayed the absorption peak of trimethyl ammonium protons at 3.13 ppm. Some methacrylate groups of GMA in the modified chitosan might selt-react to one another upon the quaternization, leading to the crosslinking reaction of CS-GMA-GTMAC; the CS-GMA-GTMAC sample could partially dissolve in weak acid solution. The solid state ^{13}C NMR spectrum of the insoluble CS-GMA-GTMAC sample displayed the residual peak of the unsaturated methylene carbon of 2-hydroxy-2-methcrylate ethyl groups at 142.5 ppm (data not shown).

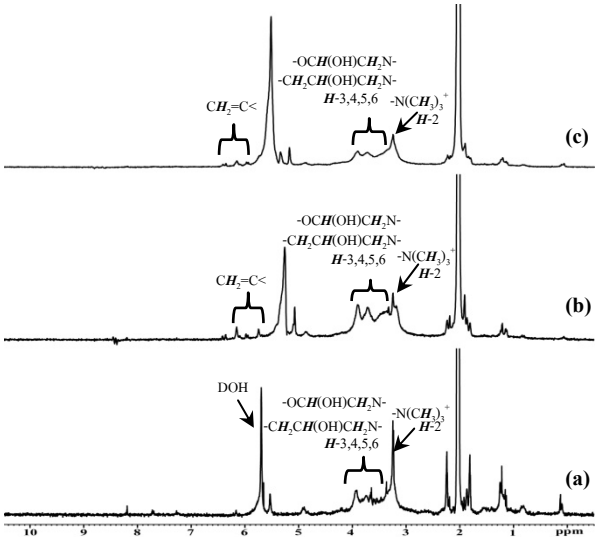

Figure 3. The ^{1}H NMR spectra of (a) CS-GMA-GTMAC (1:1:1), (b) CS-GTMAC-GMA (1:1:1), and (c) CS-GTMAC-GMA (1:4:1) in D_2O/CD_3CO_2D.

The CS-GTMAC-GMA samples were readily susceptible to the free radical polymerization by potassium persulfate at elevated temperature, yielding hydrogels, CL[CS-GTMAC-GMA]. It was noted that the %gel fraction of the CL[CS-GTMAC-GMA] samples increased as a function of the degree of methacrylation of the CS-GTMAC-GMA samples, as shown in Tables 1 and 2.

Table 2: %Gel and %Sol Fractions of the Modified Chitosan Hydrogels.

Hydrogel Samples	%Gel Fraction	%Sol Fraction
CL[CS-GTMAC-GMA (1:1:1)]	44	56
CL[CS-GTMAC-GMA (1:4:1)]	64	36

The swelling ability of the CL[CS-GTMAC-GMA] hydrogels was determined as a function of immersing time. As shown in Figure 4, although CL[CS-GTMAC-GMA (1:1:1)] possessed a lower gelation, its swelling ability was smaller, indicating a greater crosslinking density.

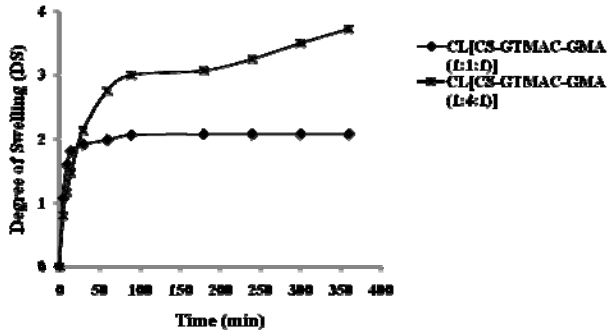

Figure 4. Degree of swelling of CL[CS-GTMAC-GMA] samples.

The antibacterial activities of the modified chitosans and the hydrogels against *S. epidermidis* were evaluated and reported in terms of MIC values, with respect to that of chitosan, the starting material. As reported in Table 3, the modified chitosans and the hydrogel samples presented the MIC values in the range of 32-1024 μg/mL. Both CS-GTMAC (1:1) and CS-GTMAC (1:4) demonstrated higher antibacterial activities than CS due to the presence of the positive charge of quaternary ammonium salts. After GMA was incorporated into CS-GTMAC, yielding CS-GTMAC-GMA, the antibacterial activity became somewhat deteriorated; slightly greater MIC values were resulted. This was attributed to the chain bulkiness. The antibacterial activity of the modified chitosan hydrogels was about that of the chitosan; their MIC values were 1024 μg/mL.

Table 3: The MIC Values of Chitosan, Modified Chitosans and Hydrogels.

Samples	MIC (μg/mL)
CS	1024
CS-GTMAC (1:1)	64
CS-GTMAC (1:4)	32
CS-GMA (1:1)	64
CS-GTMAC-GMA (1:1:1)	1024
CS-GTMAC-GMA (1:4:1)	254
CL[CS-GTMAC-GMA (1:1:1)]	1024
CL[CS-GTMAC-GMA (1:4:1)]	1024

The % cell viability of normal human dermal fibroblasts after being exposed to the modified chitosans and the hydrogel samples at concentrations of 128-1024 μg/mL for 48 h was higher than 50%, indicating that all the tested samples were non-cytotoxic to the normal human dermal fibroblasts.

Conclusions

The antibacterial hydrogels were successfully prepared via the free radical polymerization of GMA in the modified chitosans, CS-GTMAC-GMA. Their antibacterial activities were attributed to the presence of the positive charge of trimethyl ammonium salt. Only CS-GTMAC-GMA was selected and employed in the preparation of the antibacterial hydrogels as the sequence of etherification of chitosan by either GTMAC or GMA played an important role on the solubility of the chitosan intermediates. The % gel fraction of the CL(CS-GTMAC-GMA] samples was increased with an increasing methacrylate content in the CS-GTMAC-GMA samples. The lower swelling ability of the hydrogel samples was attributed to the higher crosslinking density of the hydrogels. The MTT assay also revealed that the hydrogels appeared non-cytotoxic to normal human fibroblasts.

Acknowledgements

This research was co-financially supported by Young Scientist and Technologist Programme (YSTP) and National Metal and Materials Technology Center (project code: MT-B-52-BMD-07-174-I).

References

[1] G. Lu, L. Kong, B. Sheng, G. Wang, Y. Gong and X. Zhang, *Eur. Polym. J.* **43** (2007), pp. 3807-3818.
[2] P. Ngamviriyavong, P. Uppanan and W. Janvikul, *Study on biocompatibility and antimicrobial activity of water-soluble chitosan salts*, Pure and Applied Chemistry International Conference Proceeding, Bangkok, Thailand, 2008.
[3] P. Tanjak, P. Uppanan, R. Chainoy, P. Ngamviriyavong, and W. Janvikul, *Effect of environmental pH and MW of chitosan salts on their biological properties*, Pure and Applied Chemistry International Conference Proceeding, Pitsanulok, Thailand, 2009.
[4] H. Seong, H.S. Whang and S. Ko, *J. Appl. Polym. Sci.* **76** (2000), pp. 2009-2015.
[5] L. Liu, D. Liu, M. Wang, G. Du and J. Chem, *Eur. Polym. J.* **43** (2007), pp. 2672-2680.
[6] J. Han, K. Wang, D. Yang and J. Nie, *Int. J. Biol. Macromol.*, 44(2009), pp. 229-235.

Preparation of alkylphosphonic acid modified microcrystalline cellulose/polypropylene composite

S.Phomsurin[1,2] and K.Srikulkit[1,2]*

[1] Department of Materials Science, Faculty of Science, Chulalongkorn University
[2] National Center of Excellence for Petroleum, Petrochemicals and Advanced Materials, Bangkok 10330, Thailand

* E-mail: kawee.s@chula..ac.th

Abstract: In this study, the alkylphosphonic acid modified microcrystalline cellulose(PMCC)/ polypropylene composite was prepared. In the first step, the surface modification of MCC with alkylphosphonic acid was carried-out in order to obtain the PMCC having good compatibility with PP matrix. For MCC preparation, the cotton fabric was hydrolyzed with 3 M hydrochloric at 80 °C for 1 hour and MCC powder was achieved. Characterizations including SEM, FT-IR, XRD and TGA were employed to analyze the structure of PMCC. Primary investigation by SEM revealed that MCC surface was successfully treated by alkylphosphonic acid. In the next step, the obtained PMCC was mixed with PP powder using twin-screw extruder. The compatibility was achieved, as evidenced by SEM micrographs and TGA thermograms. Finally, the flame retardancy property of the composited was presented and discussed.

Introduction

Polypropylene (PP) is a thermoplastic polymer which is widely used such as packaging, automotive, and textile due to its excellent mechanical properties, low cost, low density and high water and chemical resistance. However, the incorporation of additives is required in order to enhance its properties [1]. Natural fillers are one of candidates offering cost effective and renewable advantages. One of the most used reinforcement fillers is microcrystalline cellulose. It was reported that the addition of microcrystalline cellulose into NR.[1] Microcrystalline cellulose is easy to prepare, renewability, biodegradability and non-toxicity. However, microcrystalline cellulose is hydrophilic and tends to aggregate when incorporated into polymer matrix, causing poor compatibility. To solve this problem, surface modification of microcrystalline cellulose is required. It was reported that the microcrystalline was surface treated with maleic anhydride and stearic acid.[2] Mainly, the application of microcrystalline cellulose for polymer composites is to improve the mechanical properties of polymer composites. It was reported that the addition of lignin into polypropylene In other aspect, it was reported that the addition of lignin into polypropylene could promote char formation and reduce the rate of heat release[3] . Therefore, the utilization of cellulose bases as a flame retardant for polypropylene is worth investigation.

The aim of this study was to prepare PP-microcrystalline cellulose (MCC) composites having a flame retardancy and anti-dripping properties. MCC surface was midified with alkylphosphonic acid prior to application. Polypropylene loaded with surface modified MCC was melt blended using twin screw extruder. The obtained PP/modified MCC composite was characterized by XRD, FTIR and TGA. The results were discussed.

Materials and Methods

Materials: Bleached woven cotton fabric as a source of microcrystalline cellulose was bought from a local textile weaving factory. 37 % (wt/v) hydrochloric acid and 28 % ammonia solution was purchased from JT Baker Company. Dodecylphosphonic acid was synthesized in our laboratory.[4] Dicyandiamide was bought from Fluka. Isotactic polypropylene resin (Moplen® HP 561R) was from HMC Polymers Company Limited, Polypropylene wax from Clariant Chemical Company and heat stabilizer from Global Connections Public were used as recieved.

Method: Preparation and modification microcrystalline cellulose were carried out as follows: 40 g cotton fabric was hydrolyzed in 400 ml of 3 M hydrochloric at 80 °C for 1 hour. The obtained white MCC powder was washed repeatedly with distilled water until pH value was neutral. The MCC powder was dried at 60 °C. For surface modification, dodecylphosphonate ammonium (prepared from 100 g dodecylphosphonic acid and ammonia) was mixed with 100 grams of MCC and dicyandiamide (10 wt% based on MCC). The mixture was sonicated for 30 minutes to maximize the good dispersion and then dried at 60 °C for 24 hr and followed by curing at 170 °C for 3 minutes. Dodecylphosphonate microcrystalline cellulose (PMCC) was obtained. The PP/PMCC composite was prepared by twin screw operating at 180-210°C and 100 rpm using corrotating mode.

Characterizations

Scanning electron microscopy (SEM) was used to observe the morphology. Fourier transform infrared (FTIR) spectroscopy was used to characterize the functional group composition of pure and treated MCC. XRD analysis was carried out to investigate the fine structure of polypropylene and MCC. TGA analysis was performed to study the thermal behavior.

Results and Discussion

The morphology of MCC and PMCC was observed by SEM. Fig. 1 (a) and (b) show the morphology of MCC and the morphology of PMCC**,** respectively**.** As seen, it is evident that the coating as a result of dodecylphosphonic acid treatment is clearly observed on the MCC surface.

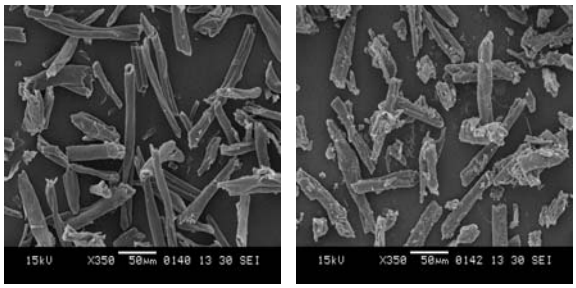

(a) MCC 350x (b) PMCC 350x

Figure 1. SEM micrographs of (a) MCC and (b) dodecylphosphonate-MCC

FTIR spectra of MCC and PMCC are shown in Fig. 2. In case of PMCC, the strong absorption band at 2900 cm $^{-1}$ is responsible for methylene groups (-CH_2-) of dodecylphosphonate chain. The Phosphonate ester bands are located in the region of 1050-1100 cm^{-1}. In addition, the carbonyl band of urea residue is found in the region of 1600-1700 cm^{-1}. The remaining urea is derived from the conversion of dicyandiamide to urea during the modification reaction.:

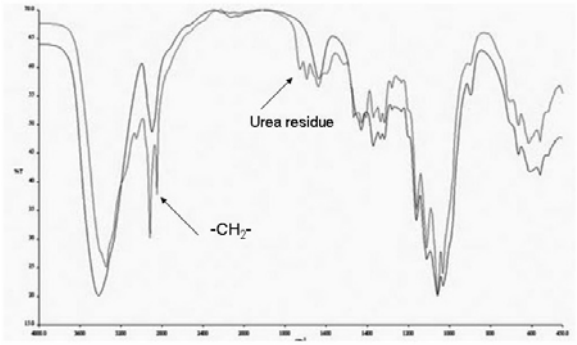

Figure 2. FTIR spectra of (a) MCC and (b) PMCC

XRD pattarns of MCC, PMCC and PP/PMCC composites are shown in Fig. 3. The XRD pattarn of MCC exhibits a sharp peak at 2θ = 22.8 ^{o} and broad peak at 2θ = 16.5 ^{o}. For PMCC, the strong peak still shows up strongly but the broad peak greatly lost in the intensity due to structural change arising from the modification. The presence of PMCC in PP/PMCC composite could be detected by XRD when the applied amounts of PMCC loading higher than 8 %. Based on XRD evidence, the addition of PMCC into polypropylene produces no change in the fine structure of the PP matrix.

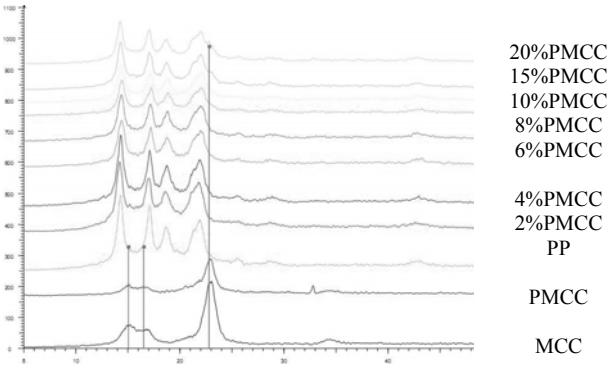

Figure 3. XRD patterns of MCC, PMCC, PP/ 2wt%MCC, and PP/PMCC composites (2-20 wt% PMCC)

TGA thermograms of MCC and PMCC is shown in Fig. 4(a) and 4(b), respectively. MCC exhibits the degradation temperature (Td) at 313.54 oC while PMCC exhibits two degradation steps with Td at 287.36 oC and 406.96 oC, respectively. As seen, PMCC begins to degrade at lower temperature to give rise to char formation. This is a phenomenon of flame retardancy of cellulose containing phosphorus compound. In the following TGA analysis of PP/PMCC composites, the results show that PP/PMCC composites start to decompose faster than neat PP and PP/MCC composite (Fig. 5), producing a char. A char formed is a basic aspect of flame retardant additives since the char reduced the combustion rate of polymeric materials. These indicate that PP/PMCC exhibit flame retardancy property when compared to PP/MCC and neat PP.

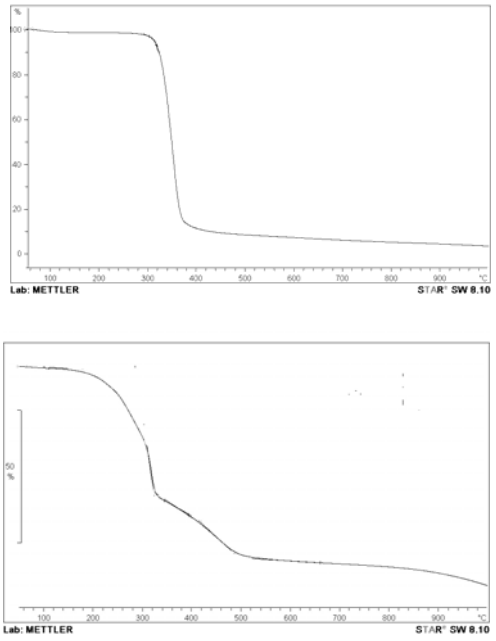

Figure 4. Thermogravimetric mass loss curves for MCC and modified MCC

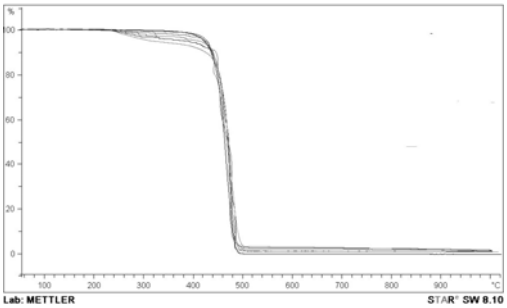

Figure 5. Thermogravimetric mass loss curves

Conclusions

Phosphonate microcrystalline cellulose (PMCC) was successfully prepared. The PMCC surface was hydrophobic. The prepared PMCC was employed as flame retardant additive for polypropylene. The loading of PMCC into polypropylene was achieved by twin screw extruder. The TGA results showed that PP/PMCC composites degraded at lower temperature and consequently were transformed into char. The formation of char by PMCC additive indicated that PP/PMCC composite exhibited flame retardacy property.

Acknowledgements

The authors gratefully acknowledge National Science and Technology Development Agency and National Center of Excellence for Petroleum, Petrochemicals and Advanced Materials, Chulalongkorn University for financial support**.**

References

[1] S. Chuayjuljit, S. Su-uthai, C. Tunwattanaseree, and S. Charuchinda, Preparation of Microcrystalline cellulose from waste-cotton fabric for biodegradability enhancement of natural rubber sheets, *Journal of Reinforced Plastics and Composites,* **28** (2009), pp. 1245-1254.

[2] K. Boonaree, Modification of cotton from waste fabric as a filler for polypropylene composites, Department of Materials Science, Faculty of Science, Chulalongkorn University, (2001).

[3] A.D. Chiroco, M. Armnini, P. Chini, and G. Ciocolo, Flame Retardants for Polypropylene Based on Lignin, *Polymer Degradation and Stability* **79** (2003), pp. 139-145.

[4] P. Punyacharoennon, S. Charuchinda, and K. Srikulkit, Grafting and Phosphonic Acid Functionalization of Hyperbranched Polyamidoamine Polymer onto Ultrafine Silica, *Journal of Applied Polymer Science*, **110** (2008), pp. 3336-3347.
Crystallization Properties of Polypropylene/Mont-morillonite Composites, *Polymer-Plastics Technology and Engineering,* **46 (**2007)*,* pp. 985- 990.

.

http://www.paccon2010.sci.ubu.ac.th/ab_sub_guide.

Effect of ozone on the reduction of proteins present in the natural rubber latex

P. Watthusintu[1] , C. Watthusintu[1], N. Phaonakrop[2], J. Jaresitthikunchai[2], S. Roytrakul[2], P. Boochathum[1], S. Angkaew[1] and B. Sukhummek[1*]

[1] Division of Polymer Chemistry, Department of Chemistry, King Mongkut's University of Technology Thonburi, Bangkok, Thailand

[2] Proteomics Laboratory, Genome Institute, National Center for Genetic Engineering and Biotechnology, Patumthani, Thailand

[*] E-Mail: b.sukhummek@gmail.com

Abstract: To understand the effect of ozone on the proteins content in the natural rubber latex, the label free proteomic analysis of serum, which was separated from the latex by using centrifugation, after ozonolysis for 0, 30, 60, 180 and 300 min was conducted. Mass spectrometry was utilized for protein quantification and identification. A total of 7 proteins with MW of 14-20 kDa were identified. Due to lack of the genome database, only 1 protein from *Hevea brasiliensis* was found. Proteins in latex showed different resistance toward ozone uptake. Of these, 4 proteins decreased after ozonolysis for 300 min, other 2 proteins decreased after ozonolysis for 180 min while ozone had no effect on 1 protein. This result confirmed that ozone is capable to reduce a number of proteins in the natural rubber latex especially Hev b1, an allergic protein.

Introduction

Natural rubber latex (NRL) is obtained principally from rubber-producing trees of the species *Hevea brasiliensis*. Natural rubber products from latex have been used widely. There are several products made from concentrated latex such as glove, condom, tip, catheters, endotracheal tubes, latex balloon, baby bottle nipples, and dental cofferdams. Besides, some products are made from solid rubber such as tire, shoes, adhesives, elastic rubber, and medical products [1].

Fresh latex is a polydisperse system in which negatively charged particles of various types are suspended in aqueous serum. The two main particulate phases in latex are lutoid particles and rubber particles. The latter, constituting 30-45% of the latex composition [2], contains polymers of cis-1,4 polyisoprene coated with a hydrophilic layer of proteins, lipid and phospholipids [3-5]. The total protein content of fresh field latex is about 1.0-1.8%. They are distributed in three major fractions; the rubber phase (27%), the C-serum (48%) and within the lutoid or the B-serum (25%) [6-7]. The major proportion of water soluble proteins in fresh latex is derived from the B-serum and C-serum; majorities are anionic proteins with molecular weights between 14.0 to 100.0 kDa [8].

The presence of proteins in the natural rubber has been reported to have resulted in some undesirable properties such as poor creep, stress-relaxation and reduces modulus. Some authors believe that proteins of 14.6 kDa (Hev b1) and 24 kDa (Hev b3) are particularly important in spina bifida children. While Hev b5 and Hev b6.02 are especially in many health care workers [9-11].

There are several attempts to produce a rubber product with a very low protein content which can be divided into three groups; 1) centrifugation or washing of latex with surfactants. 2) by enzymatic reaction and 3) by chemical reaction [12-13]. However, products from these methods have some disadvantages and limitations such as chemical residues, lower latex stability and high cost.

Another way for protein removal is ozonolysis reaction. S. Wiboonkul, studied the effect of ozone on the reduction of the allergenic proteins in the skim and the serum by Lowry method and Fit kit. It was found that lower level of all heveins after ozonolysis was observed. Besides, Hev b5 is the only protein allergen remained after ozone uptake for 5 hours [14]. However, more studies are needed to understand those phenomena. So this research work aims to analyse the allergenic proteins present in the natural rubber latex, especially Hev b1, Hev b3, Hev b5 and Hev b6.02 including other allergenic proteins by SDS-PAGE and LC-MS/MS.

Materials and Methods

Ozonolysis

Ozone was applied into the 30.0 ml NRL. The flow rate of ozone was kept constant and the reaction time intervals were varied from 0, 30, 60, 180 and 300 minutes. The excess ozone in the ozonolysis reaction was trapped by KI solution and then was determined by titration with Na_2SO_3. The end point showed the colour change from yellow to colourless. The ozone uptake in mole unit was calculated from the mole number of ozonolysed rubber divided by the total mole number of the rubber used in the reaction; the equation as shown below.

$$\text{Ozone uptake (\% mol/mol)} = \frac{\text{Mole number of ozonolysed rubber}}{\text{Mole number of rubber before ozonolysis}} x100$$

Protein analysis

Protein contents in the serum, which was separated from the latex using centrifugation, before and after ozonolysis were determined using Lowry method with BSA as a standard protein [15]. Proteins were separated by SDS-PAGE (12.5%) according to Laemmli (1970) [16] and detected by silver staining [17]. Thereafter, the protein bands with the MW of 14-20 kDa were excised and subjected to in-gel digestion. Tryptic peptides were extracted and directly injected into Ultimate 3000 LC System (Dionex, USA) coupled to ESI-Ion Trap MS (HCT Ultra PTM Discovery System (Bruker, Germany)) with electrospray at flow rate of 300 nl/min to a nanocolumn (Acclaim PepMap 100 C18, 3 □m, 100A, 75 □m id x 150 mm). A solvent gradient (solvent A: 0.1% formic acid in water; solvent B: 80% 0.1% formic acid in 80% acetonitrile was run in 40 min. The relative protein quantity was analyzed using DeCyder MS Differential Analysis software (DeCyderMS, GE Healthcare) [18, 19]. The acquired LC-MS raw data were converted and the PepDetect module was used for automated peptide detection, charge state assignments, and quantitation based on the peptide ions signal intensities in MS mode. The analyzed MS/MS data from DeCyderMS were submitted to database search using the Mascot software (Matrix Science, London, UK) [20].

Results and Discussion

The contact time of ozone in the NRL was varied as the time intervals of 0, 30, 60, 120, 180, 240 and 300 minutes. The ozone uptake and the protein concentration from each time point were determined. The rates of ozonolysis of the NRL at 0, 30 and 60 min were proportional related to the decrease of protein content as shown in Figure 1.

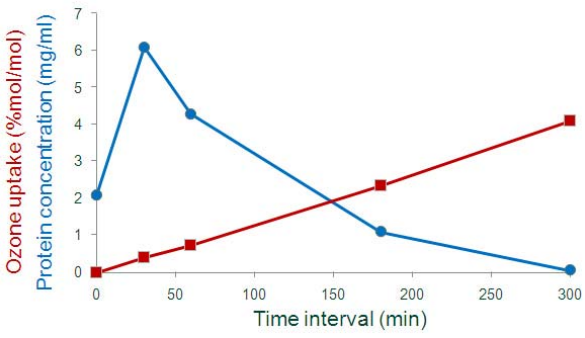

Figure 1. Protein concentration in natural rubber latex at the various time intervals of ozonolysis.

Surprisingly, the protein content significantly increase after ozone uptake for 30 min. There is possibility that the ozone reacted with not only proteins solubilized in the latex, but also with the proteins present on the surfaces of lutoids, suspending in the latex. After ozonolysis reaction for longer time, most proteins were decomposed and short peptide chains were produced resulting in lower protein concentration determined by Lowry method.

Proteins from serum fractions were separated using SDS-PAGE (Figure 2). The sizes of the proteins in rubber serum phase were 14, 17, 24, 27, 30 and 43 kDa. Two major bands of about 14 and 24 kDa proteins had earlier been reported as the major rubber particle protein in Heavea rubber particle proteins [21]. The 43 kDa allergenic latex protein was frequently observed [22]. The staining intensity of 14-30 kDa abundant protein bands decreased after ozonolysis treatment for 300 minutes (Figure 2).

The proteins with molecular mass of 14-20 kDa before and after ozone treatment was preliminarily studied by label free proteomics analysis. The amount of the four proteins, including Hev b1 protein was downed to zero at 300 min of ozonolysis. Besides, the amount of the two proteins was downed to zero at 180 min. Interestingly, only 1 protein (Glycine-rich RNA-binding protein GRP1A) was left at 300 min of ozone treatment (Table 1). Berlett et al., (1996) demonstrated that during exposure to ozone, the methionine and aromatic amino acid residues are oxidized rapidly in the order Met > Trp > Tyr = His > Phe [23]. Strongly tolerance to oxidation by ozone of GRP1A protein (Table 1) may be dependent on its primary, secondary, tertiary, and quaternary structures as suggested by Berlett et al. (1996).

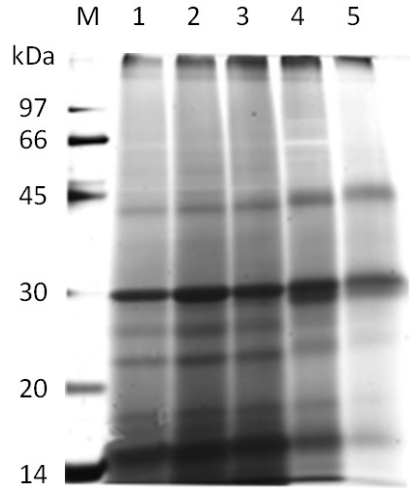

Figure 2. Silver stained 12.5% SDS-PAGE analysis of the ozonolyzed natural rubber latex proteins. Lane M: standard proteins; lane 1: natural rubber latex proteins; lane 2-5 as in 1 but after further ozonolysis treatment for 30, 60, 180 and 300 minutes, respectively.

Conclusions

Ozone is capable to reduce the number of proteins present in the NRL especially an allergenic protein, Hev b1. Its content was undetectable at the exposure time of 300 minutes. However, the sensitivity of proteins to oxidation by ozone varies from one protein to another. Besides their sizes, the tolerance to oxidation by ozone of the proteins may probably be caused by differences in their primary, secondary, tertiary and quaternary structures.

Table 1 List of differentially expressed proteins identified in the natural rubber serum after ozonolysis for 0, 30, 60, 180, and 300 minutes.

Accession No.	Name of identified proteins	Source	Relative intensity (%)				
			0	30 min	60 min	180 min	300 min
gi|132270	Hev b 1	*Hevea brasiliensis*	100	95.83	94.72	95.12	0
gi|7630036	Putative protein	*Arabidopsis thaliana*	100	95.83	94.72	95.12	0
gi|52077142	Dragline silk protein-like	*Oryza sativa*	100	90.82	89.45	84.86	0
gi|18419557	Transposase	*Triticum aestivum*	100	91.44	85.58	85.58	0
gi|147823253	DNA-binding protein-related	*Arabidopsis thaliana*	100	113.54	104.84	0	0
gi|226496916	Hypothetical protein	*Zea mays*	100	98.73	100.98	0	0
gi|225428473	Glycine-rich RNA-binding protein GRP1A	*Oryza sativa*	100	103.56	97.44	96.59	100.31

References

[1] K.A. Loos, Latex Allergy, University of Pacific Dental School, 1998.

[2] J.L. Jacob, d' Auzac., and J.C. Prevot, The composition of latex from *Hevea brasilliensis*, *Clin Rev Al.* **11** (1992), pp. 327-337.

[3] O. Vandenplas, J.P. Delwiche, G. Evrard, P. Aimont, X. Vanderbrempt, J. Jamart and L. Delaunois, Prevalence of occupational asthma due to latex among hospital personnel, *Am J Res Critic Care Medicine.* **151** (1995), pp. 54-60.

[4] P. Rattanaleklai, Effect of chemical reagents on coagulation of natural rubber latex, Thesis, Chulalongkorn University, 2000.

[5] F.A. Rueggeberg, From vulcanite to vinyl, a history of resins in restorative dentistry. *J Prosthet Dent.* **87** (2002), pp. 79-364.

[6] C.S. Fong, Protein in natural rubber concentrated latex, *J nat Rubb.* **7** (1992), pp. 102-112.

[7] http://gotoknow.org/blog/akesilly/291782

[8] http://www.allergen.org/List.htm

[9] E.M. Warshaw, Latex allergy, *Am. Acad. Dermatol.* **39** (1998), pp. 1-24.

[10] H. Alenius, T. Palosuo, K. Kelly, V. Kuruv, T. Reuncla and S. Makinen-Kiljunen, IgE reactivity to 14 kDa and 27 kDa natural rubber protein in latex-allergic children with spina bifida and other congenital anomalies, *Int Arch Allergy Immunol.* **102** (1993), pp. 61-66.

[11] D.R. Ownby, A history of latex allergy, *J. Allergy Clin. Immunol.* **110** (2002), pp. 41-67.

[12] M.Y.A. Hashim, in: *Latex protein workshop of the international rubber techonology conference*, Rubber Research Institute of Malaysia, Kuala Lumpur, Malaysia, 1993.

[13] A. Subramanian, in: *Immonulogy and Allergy Clinics of North America,* Saunders, Philadelphia, USA, 1995.

[14] S. Wiboolkul, S. Nonkeaw, P. Boochathum and B. Sukhummek*, Effect of Ozone on the Reduction of the Allergenic Proteins Present in the Skim and the Serum",* Commemorative International Conference of the Occasion of the 4th Cycle Anniversary of KMUTT Sustainable Development to Save the Earth : Technologies and Strategies Vision 2050 : (SDSE 2008), 7-9 April, Bangkok, 2009, pp. 713-716.

[15] O.H. Lowry, N.J. Rosbrough, A.L. Farr, and R.J. Randall. Protein measurement with the folin phenol reagent. J. Biol. Chem. ***193*** *(1951), pp* 265.

[16] U.K. Laemmli, Cleavage of structural proteins during the assembly of the head of bacteriophage T4. *Nature* **227** (1970), pp. 680–685.

[17] H. Blum, H. Beier, H.J. Gross, Improved silver staining of plant protein, RNA and DNA in polyacrylamide gels. *Electrophoresis* **8** (1987), pp. 93–99.

[18] C. Johansson, J. Samskog, L. Sundstrom, H. Wadensten, L. Bjorkesten, J. Flensburg, Differential expression analysis of *Escherichia coli* proteins using a novel software for relative quantitation of LC-MS/MS data. *Proteomics* **6** (2006), pp. 4475-85.

[19] A. Thorsell, E. Portelius, K. Blennow, and B.A. Westman, Evaluation of sample fractionation using microscale liquid-phase isoelectric focusing on mass spectrometric identification and quantitation of proteins in a SILAC experiment. *Rapid Commun Mass Spectrom* **21** (2007), pp. 771-778.

[20] D.N. Perkins, D.J.C. Pappin, D.M. Creasy, J.S. Cottrell, Probability-based protein identification by searching sequence databases using mass spectrometry data. *Electrophoresis* **20** (1999), pp. 3551-3567.

[21] R. Wititsuwannakul, K. Rukseree, K. Kanokwiroon, and D. Wititsuwannakul, A rubber particle protein specific for Hevea latex lectin binding involved in latex coagulation. *Phytochemistry* **69** (2008), pp. 1111–1118.

[22] D.H. Beezhold, Paper presented at International Conference on Latex Protein Allergy: The Latest Position, Paris, France, 11 January 1995.

[23] B.S. Berlett, R.L. Levine, E.R. Stadtman, Comparison of the effects of ozone on the modification of amino acid residues in glutamine synthetase and bovine serum albumin *J. Biol. Chem.* **271** (1996), pp. 4177-4182.

Preparation of cotton fabric bound with β-cyclodextrin and its derivative for controlled release of pyrethrum

H.Leekmek[1,2], A. Sittattrakul[1,2], and W. Lerdwijitjarud[1,2*]

[1]Department of Materials Science and Engineering, Faculty of Engineering and Industrial Technology, Silpakorn University, Nakorn Pathom 73000, Thailand
[2]National Center of Excellence for Petroleum, Petrochemicals, and Advanced Materials, Chulalongkorn University, Bangkok 10330, Thailand

[*] E-mail : wanchail@su.ac.th

Abstract: Pyrethrum is a natural insecticide extracted from the chrysanthemum flowers. The advantages of pyrethrum are low toxicity to human and warm blooded animals, but fast action against a wide variety of insects. This work aims to study the preparation of cotton fabrics bound with β-cyclodextrin and benzylated β-cyclodextrin with cyanuric chloride for controlled release of pyrethrum. Benzylated β-cyclodextrin was prepared by using phase transfer catalyst. The chemical structures of β-cyclodextrin, benzylated β-cyclodextrin, β-cyclodextrin bound with cyanuric chloride, and benzylated β-cyclodextrin bound with cyanuric chloride were characterized by FT-IR and ^{1}H-NMR techniques. The thermal stability of cotton fabric bound with β-cyclodextrin and benzylated β-cyclodextrin were tested by using thermogravimetric analysis (TGA) technique. TGA curves of cotton fabrics bound with β-cyclodextrin and benzylated β-cyclodextrin showed a two-step weight loss. Based on the derivative thermogravimetric (DTG) curves, the contents of β-cyclodextrin and benzylated β-cyclodextrin onto cotton fabrics were at approximately 29 and 25 weight percent, respectively. The level of pyrethrum entrapped in the unmodified cotton fabrics and modified cotton fabrics were determined by UV spectrophotometry. For a period of 10 days on standing at atmospheric environment, the cotton fabric bound with benzylated β-cyclodextrin has more pyrethrum left than cotton fabric bound with β-cyclodextrin and unmodified cotton fabric.

Introduction

Cyclodextrins (CDs) are cyclic oligosaccharides built from glucopyranose units linked by α-(1,4)-glucosodic bounds. The three most common cyclodextrins are α-cyclodextrin, β-cyclodextrin, and γ-cyclodextrin, which consist of six, seven, and eight glucopyranose units in the ring structures, respectively[1]. Cyclodextrins are shaped like a truncated cone with a hydrophobic cavity in the interior and a hydrophilic outer surface. Cyclodextrin molecules can entrap a large number of organic molecules such as drugs, volatile molecules, and insecticides into their hydrophobic cavity[2].

During recent years, textile applications of cyclodextrins have been developed [3]. Some results indicate that cotton fabrics bound with β-cyclodextrin can used for controlled release of drugs, antibacterial agent (miconazole nitrate) [4], sunscreen agent (octyl methoxycinnamate) [5], and insect repellent (cypermethin and prallethrin) [6].

Pyrethrum is a natural insecticide extracted from the chrysanthemum flowers and has been in use for more than 60 years. Pyrethrum is considered to be biodegradable. It shows fast action against a wide variety of insects and low toxicity to warm blooded animals. Pyrethrum is used for household and agricultural applications. However, pyrethrum breaks down quickly in sunlight, moisture, or oxygen [7]. The stability of pyrethrum against light can be enhanced by the complexation with cyclodextreins [8].

This research involves the preparation of cotton fabrics bound with β-cyclodextrin and benzylated β-cyclodextrin with cyanuric chloride for controlled release of pyrethrum. Benzylated β-cyclodextrin was prepared by using phase transfer catalyst [9]. Its cavity has less polarity than that of β-cyclodextrin. The performance of cotton fabrics bound with β-cyclodextrin and benzylated β-cyclodextrin for controlled release of pyrethrum is investigated.

Materials and Methods

Materials

Pyrethrum extract with 25% of pyrethin I (Sigma-Aldrich, U.S.A) was used as insecticide for this study. β-cyclodextrin (purum > 99%) and Cyanuric chloride 98.0% were supplied by Fluka (Switzerland). N,N-dimethylformamide (analytical reagent) was purchased from Ajax Finechem Pty Ltd (Australia). 100% cotton fabric was obtained from a local store (133 g/m^2).

Preparation of Cotton Fabrics Bound with β-Cyclodextrin and Benzylated β-Cyclodextrin

The first step is the preparation of β-cyclodextrin bound with cyanuric chloride. Cyanuric chloride was dissolved in dried N,N-dimethylformamide (DMF) at the temperature of 2°C under nitrogen atmosphere. Subsequently, a homogeneous solution of β-cyclodextrin dissolved in dried N,N-dimethylformamide was added into a solution of cyanuric chloride. The reaction mixture was further stirred at 2°C for 20 h under nitrogen environment. Finally, the product was obtained by adding excess

acetone, filtered, washed with acetone several times, and then dried under vacuum oven at 40°C for 48 h.

In the second step, cotton fabrics (3 cm x 3 cm) were soaked in a 5 M NaOH at room temperature for 2 h under magnetic stirring, and then dried at room temperature. Dried NaOH-treated cotton fabrics were soaked in a solution containing β-cyclodextin grafted with cyanuric chloride in dried DMF at room temperature for 24 h under atmosphere of nitrogen. Modified cotton fabrics were washed under running water for 10 min to remove unreacted substance and dried at room temperature.

The preparation of benzylated β-cyclodextrin bound with cyanuric chloride is similar to that of β-cyclodextrin bound with cyanuric chloride excuse using benzylated β-cyclodextrin in place of β-cyclodextrin. Benzylated β-cyclodextrin was prepared from β-cyclodextrin by using phase transfer catalyst [9].

The contents of β-cyclodextrin and benzylated β-cyclodextrin bound onto cotton fabrics were characterized by using thermogravimetric analysis (TGA) technique. The chemical structures of β-cyclodextrin bound with cyanuric chloride and benzylated β-cyclodextrin bound with cyanuric chloride were characterized by FT-IR and ^{1}H-NMR techniques.

Encapsulation of Pyrethrum to Cotton Fabric and Testing of Controlled Release Performance of Entrapped Fabric

Unmodified and modified cotton fabrics (cotton fabrics bound with β-cyclodextrin and benzylated β-cyclodextrin) were immersed in a solution containing pyrethrum (2 mmol) in mixed solvent (ethanol (20 ml) : water (1.35 ml)) at room temperature for 12 h under stirring, and then air dried for 4 h.

For testing the controlled release performance, the pyrethrum-entrapped fabrics were standing at atmospheric environment for 10 days.

In order to investigate the amount of pyrethrum entrapped in the cotton fabric, pyrethrum-entrapped fabric was cut into small pieces (1.5 cm x 1.5 cm). The cloth strip was accurately weighted and extracted with ethanol (30 ml) under stirring at 50°C for 6 h. The extraction process was repeated with fresh solvent for 4 times. The level of pyrethrum entrapped in the unmodified and modified cotton fabrics were determined by UV spectrophotometry.

Statistical Analysis

Statistical analyses were performed by using the one-way ANOVA test and Scheffe's test. The *p*-values < 0.05 were considered significant.

Results and Discussion

Characterization of Benzylated β-Cyclodextrin, β-Cyclodextrin Bound with Cyanuric Chloride, and Benzylated β-Cyclodextrin Bound with Cyanuric chloride

The FT-IR spectra of β-cyclodextrin (Fig. 1(a)) shows peaks at wave number 3392 cm^{-1} (O-H stretching), 2925 cm^{-1} (CH_2 stretching), 1417 cm^{-1} (C-H bending) and 1027 cm^{-1} (C-O-C stretching). Characteristic peaks assignment of benzylated β-cyclodextrin (Fig. 1(b)) appear at 3087 cm^{-1}, 3062 cm^{-1}, and 3030 cm^{-1} (=C-H stretching), 1953cm^{-1},1879 cm^{-1}, and 1811 cm^{-1} (mono-substitution), 1618 cm^{-1}, and 1497 cm^{-1}(C=C ring stretching) and 912 cm^{-1} (=C-H bending), which can be referred to the successfulness of the preparation of benzylated β-cyclodextrin by using phase transfer catalyst.

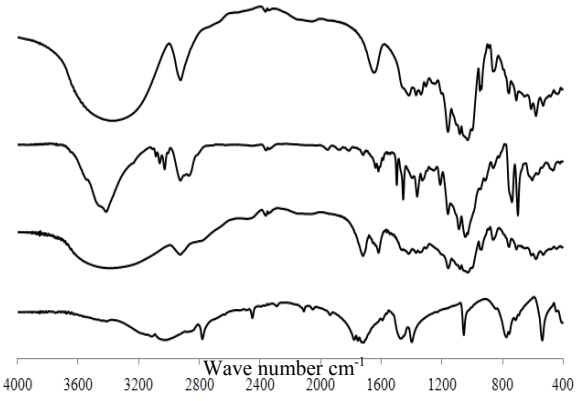

Figure 1. FT-IR Spectra of (a) β-Cyclodextrin; (b) Benzylated β-Cyclodextrin; (c) β-Cyclodextrin bound with Cyanuric Chloride; and (d) Benzylated β-Cyclodextrin bound with Cyanuric Chloride

Fig. 1(c), and 1(d) illustrate the characteristic peak of β-cyclodextrin bound with cyanuric chloride and benzylated β-cyclodextrin bound with cyanuric chloride, respectively. The peak at wave number 1719 cm^{-1} indicates the C=N stretching of cyanuric chloride molecule.

The ^{1}H-NMR spectrum of β-cyclodextrin (dissolved in d_6-DMSO) is shown in Fig. 2(a). For ^{1}H-NMR of benzylated β-cyclodextrin (Fig. 2(b)), the chemical shift of benzylated group appears at δ = 7.3-7.0 ppm which refer to the proton of benzene ring in the benzylated β-cyclodextrin structure.

The degree of substitution of the reactive chlorine in the triazine group was calculated from ^{1}H-NMR spectrum after the reaction of β-cyclodextrin bound with cyanuric chloride (or benzylated β-cyclodextrin bound with cyanuric chloride) with diethylamine in water at room temperature for 20 h [10]. The ^{1}H-NMR (Fig. 2(c) and Fig. 2(d)) signal at δ = 0.5-1.75 ppm can be attributed to the methyl protons of the diethylamine and the signal at δ = 2.75-2.81 ppm is

assigned to a methylene protons of diethylamine. Thus, the higher the intensity of signal at δ = 2.75-2.81 ppm, the higher the amount of reactive chloride in the structure.

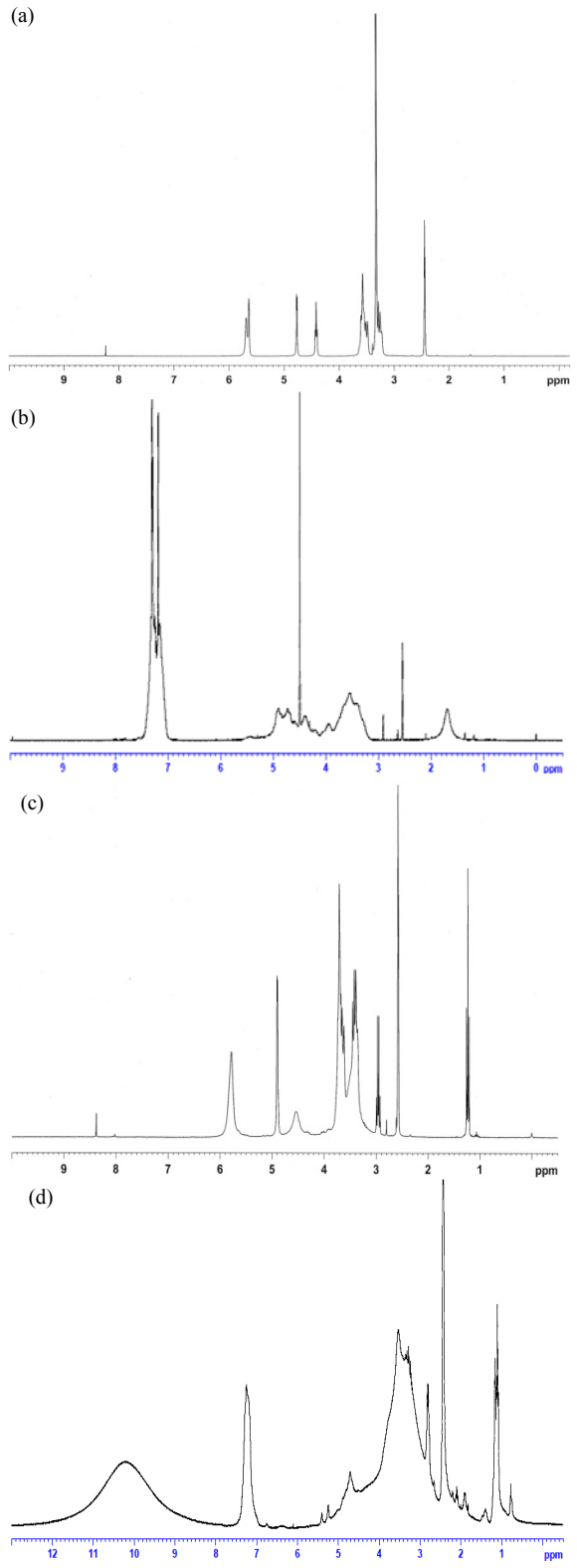

Figure 2. ^{1}H-NMR Spectra of (a) β-Cyclodextrin; (b) Benzylated β-Cyclodextrin; (c) β-Cyclodextrin bound with Cyanuric Chloride reacted with Diethylamine; and (d) Benzylated β-Cyclodextrin bound with Cyanuric Chloride reacted with Diethylamine

The thermal stability of cotton fabrics bound with β-cyclodextrin and benzylated β-cyclodextrin were obtained by using thermogravimetric analysis (TGA) technique. One step weight loss characteristic was obtained for TGA curve of unmodified cotton fabric, whereas TGA curves of cotton fabric bound with β-cyclodextrin and cotton fabric bound with benzylated β-cyclodextrin showed two steps weight loss. This phenomenon implies the occurrence of covalent bond between cyclodextrin derivatives and cotton fabric, which results from the reaction between the triazinyl chloride atom of cyclodextrin derivatives and the hydroxyl group of cotton fabric.

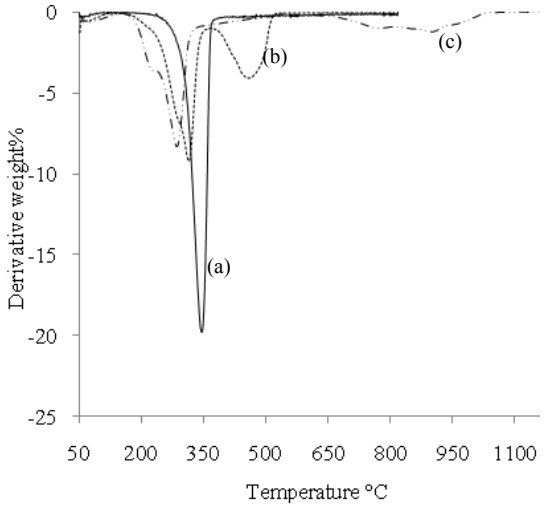

Figure 3. Derivative thermogravimetric (DTG) curves of (a) —— Pure Cotton Fabric; (b) ····· Cotton Fabric bound with β-Cyclodextrin; and (c) – · · – Cotton Fabric bound with Benzylated β-Cyclodextrin

Based on the derivative thermogravimetric (DTG) curves (Fig. 3), the contents of β-cyclodextrin and benzylated β-cyclodextrin bound onto cotton fabric were at approximately 29 and 25 weight percent, respectively.

Performance of Cotton Fabrics Bound with β-Cyclodextrin and Benzylated β-Cyclodextrun for Controlled Release of Pyrethrum

The actual amount of pyrethrum entrapped into the different cotton fabrics (unmodified cotton fabric, cotton fabric bound with β-cyclodextrin and cotton fabric bound with benzylated β-cyclodextrin), was determined by UV spectrophotometry after extraction process. Table 1 shows the amount of pyrethrum extracted from different cotton fabrics. Initially, the amount of pyrethrum entrapped into unmodified cotton fabric was 15.67±0.68 (x 10^{-6} mol/g of fabric), while these of cotton fabric bound with β-cyclodextrin and cotton fabric bound with benzylated β-cyclodextrin were 15.86±0.86 (x 10^{-6} mol/g of fabric) and 19.88±0.42 (x 10^{-6} mol/g of fabric), respectively. The pyrethrum succeedingly released form the fabric as shown in Table 1 and Fig. 4.

Table1: The amount of Pyrethrum Extracted from Cotton Fabrics (x 10^{-6} mol/ 1 g of Cotton Fabric).

Sample	Amount of Pyrethrum (x 10^{-6} mol / 1 g Cotton Fabric)		
	Started day	Period of 5 days	Period of 10 days
Pure cotton	15.67±0.68[a]	9.46±0.62[a]	5.23±0.23[a]
Cotton bound with β-cyclodextrin	15.86±0.86[a]	10.16±0.43[a]	7.31±0.11[b]
Cotton bound with benzylated β-cyclodextrin	19.88±0.42[b]	14.89±0.29[b]	12.58±0.65[c]

*one-way ANOVA test at significant at the 0.05 level.

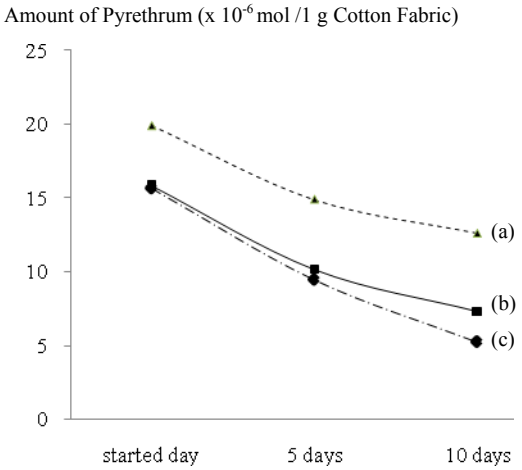

Figure 4. The level of Pyrethrum extracted from Cotton Fabrics (x10^{-6} mol)/ 1 g of Cotton Fabric.; (a)-----Cotton Fabric bound with Benzylated β-Cyclodextrin; (b) —— Cotton Fabric bound with β-Cyclodextrin; and (c) - - - -Pure Cotton Fabric

For a peroid of 10 days on standing at ambient condition, the cotton fabric bound with benzylated β-cyclodextrin had more pyrethrum left (12.58±0.65 x 10^{-6} mol/g of fabric; 63.19±2.53 % from initial amount) than that of cotton fabric bound with β-cyclodextrin (7.31±0.11 x 10^{-6} mol/g of fabric; 46.57±2.40 % from initial amount) and unmodified cotton fabric (5.23±0.23 x 10^{-6} mol/g of fabric; 33.78% from initial amount). The slowest rate of releasing pyrethrum from cotton fabric bound with benzylated β-cyclodextrin may due to the strong interaction between low-polarity cavity of benzylated cyclodextrin and pyrethrum molecule.

Conclusions

β-cyclodextrin and benzylated β-cyclodextrin could be successfully bound onto cotton fabrics with cyanuric chloride for controlled released of pyrethrum. Pyrethrum could be entrapped into the cotton fabric bound with benzylated β-cyclodextrin with highest amount and this fabric has the lowest rate of releasing pyrethrum after a peroid of 10 days on standing at atmospheric condition.

Acknowledgement

The authors gratefully acknowledge the financial support provided by the Department of Materials Science and Engineering, Faculty of Engineering and Industrial Technology, Silpakorn University; and the Center of Excellence for Petroleum, Petrochemical, and Advanced Materials, Chulalongkorn University, Thailand.

References

[1] P.J. Hauser and J. Niu, *Covalently bound Cyclodextrin: A New Functional Finish for Cellulosics,* North Carolina State University, Raleigh, NC.

[2] C.H. Lin, C.Y Chen, S.W. Chang, J.C. Wu, and C.E. Lin, *Analytica Chimica Acta.* **576** (2006), pp. 84-90.

[3] H.J. Buschmann, D. Knittel, E.J Schollmeyer, *J. Inc. Phenom. Macrocyclic. Chem*. **40** (2001), pp. 169-172.

[4] J.H. Wang and Z. Cai, *Carbohydrate Polymers.* **72** (2008), pp. 695-700.

[5] S. Scalia, R. Tursilli, A. Bianchi, P.L. Nostro, E. Bocci, F. Ridi, and P. Baglioni. *Int. J. Pharm.* **308** (2006), pp. 155-159.

[6] F.A. Abdel-Mohdy, Moustafa M.G. Fouda, M.F. Rehan, and A.S. Aly, *Carbohydrate Polymers.* **73** (2008), pp. 92-97.

[7] D.W. Connell, *Basic concepts of Environmental Chemistry,* Lewis publishers, New York (1997), pp. 194-197.

[8] R. Biebel, E. Rametzhofer, H. Klapal, D. Polheim, and H. Viernstein, *Int. J. Pharm.* **256** (2003), pp. 175-181.

[9] P. Limsophathum, Preparation of β-Cyclodextrin Bound onto Cotton Fabrics for Textile Application, Master's Thesis, Slipakorn University, 2007.

[10] H. Reuscher and R. Hirsenkon, *Beta W7 MCT-New ways in surface modification,* Wacker-Chemie Gmbh, Germany.

Preparation of microcellular EPDM/PP foams *via* supercritical CO_2 fluid (SCF) technique

N. Tangchantra[1]* J. Kruenate[1] and W. Phompan[1]

[1] National Metal and Materials Technology Center
National Science and Technology Development Agency
114 Thailand Science Park, Phanonyothn Rd.
Klong 1, Klong Luang, Pathumthani, Thailand 12120

*E-mail : nantavtt@mtec.or.th

Abstract: Blend of polypropylene (PP) and ethylene propylene diene rubber (EPDM) foam has been studied using a technique called high pressure supercritical fluid (SCF). For preparing microcellular EPDM/PP foam, PP was blended with 15, 30 and 50 wt % of EPDM by Brabender mixer and then prepared the sample as sheet-form using compression moulding. The SCF experiments were performed under 20 MPa foaming pressure and various foaming temperatures of 154°C. Solubility of supercritical CO_2 was directly affected foamed polymer properties. Morphology of cell size and cell distribution at different concentrations of EPDM was compared. Characterization was accomplished by scanning electron microscopy (SEM), and Differential Scanning Calorimetry (DSC). The results revealed that the diffusion of supercritical CO_2 under given foaming pressure and foaming temperature in the EPDM/PP blends drove a nucleation of number of cells including the growth of nucleated cells. The influence of the EPDM content in PP matrix on rheological properties has also been investigated. The results showed that EPDM composition adding into EPDM/PP could improve the elastic behaviours of the polymer blend.

Introduction

Generally, Thermoplastic elastomers have been foamed using chemical blowing agents (i.e. low-boiling hydrocarbons, chlorofluorocarbons) as foaming agents [1]. All of these agents have drawbacks, base on inefficiency, high cost, difficulty of use, and, more recently, environmental considerations. Although the chlorofluorocarbons have been widely and effectively used in foaming thermoplastic elastomers, their perceived threat to the ozone layer has prompted a search for alternative foaming methods which do not process environmental hazards or present any of the other drawbacks.

These issues can be resolved by introducing the physical blowing agent via supercritical fluid technique. The supercritical fluid (SCF) has been developed for use as physical blowing agents (PBAs) in the production of polymer foams because they do not create chemical residues. Moreover, the SCF possesses many advantages such as low cost, non-toxicity non-flammability and easily accessible supercritical conditions [2].

Thermoplastic elastomers used in this research are composed of polypropylene (PP) and ethylene propylene diene rubber (EPDM). PP is a commodity polymer with widespread applications due to its good mechanical and thermal properties but it has poor impact strength, whereas EPDM has proved to be the most effective impact modifier.

In this work, we studied microcellular EPDM/PP foams prepared via supercritical CO_2 fluid technique. The influence of the EPDM contents in PP matrix on cell size, thermal and rheological properties had also been investigated.

Materials and Methods

Materials. The materials used in preparing the microcellular thermoplastic elastomeric foams consist of PP (HP553R), supplied by Lyondell Basell Industries, and EPDM (keltan 512), supplied by DSM elastomer.

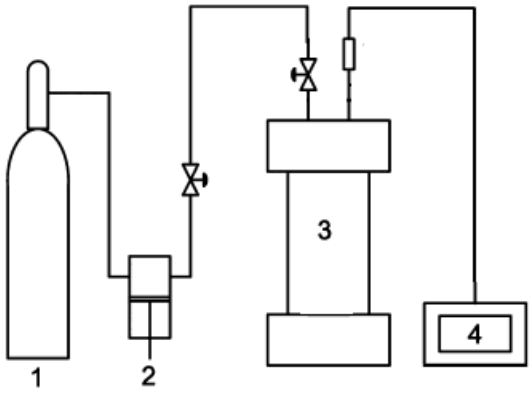

Figure 1. Schematic of the experimental setup for the batch foaming process. (1) CO_2 cylinder; (2) high-pressure liquid pump; (3) foaming reactor; (4) temperature controller.

Preparation of EPDM/PP compound. The PP was blended with 15, 30 and 50 wt % of EPDM by Brabender mixer at 190 °C for 6 min and then the sample was prepared as sheet-form using compression moulding.

Foaming process. A high-pressure vessel in stainless steel was used (Fig. 1). In EPDM/PP foaming process, The EPDM/PP blend was placed in high-pressure vessel. The high-pressure vessel was heated in temperature of 154 °C. Thereafter, the EPDM/PP blend was saturated under supercritical CO_2 at the pressure of 20 MPa with soaking time of 20 min. After that the CO_2 in the high pressure vessel was released

form the foaming pressure to the ambient one. The EPDM/PP foams were characterized cell morphology by JSM-5410 scaning electron microscopy (SEM). The samples were immersed in liquid nitrogen and then fractures

Thermal characterization. The melting temperature and crystallinity of the samples measured by differential scanning calorimetry (DSC, Mettler Toledo DSC822e) at a heating rate of 10°C/min and with scanning temperature range from 25°C to 190°C in N_2 atmosphere. The crystallization degree (X_c) was determined according to the next relation: $X_c = 100 (\Delta H=\Delta H_0)$; where ΔH is the enthalpy of fusion of the polypropylene as calculated from the DSC results, and ΔH_0 is the enthalpy of fusion of the 100% crystalline polypropylene. In all calculations a crystal heat of fusion of 209 J/g has been taken for the polypropylene [3]

Rheological characterization. The melt flow index (MFI) of the samples were invatigated by melt flow indexer (MFI, Lloyd Instruments; Davenport model 10) at temperature of 190°C. Rheological properties of neat PP and EPDM/PP blends were investigated using a Rotational Rheometer (Gemini HR Nano) equipped with parallel plate geometry (diameter =25mm, gap = 1 mm). The frequency sweep tests were performed in the range of 0.1 – 100 s^{-1} at temperature of 190°C and with an amplitude of 1% in order to maintain the response of materials in the linear viscoelastic regime.

Results and Discussion

Thermal characterization. The melting temperature and percent crystallinity of PP and EPDM/PP blends are shown in Figure 2 and 3 respectively. Melting temperatures of crystalline polymers can be related to the size and perfection of their crystal units. The blends show a dramatic reduction in T_m value and PP crystallinity with greater effect for mixtures. It can be deduced that PP crystallization is more difficult as EPDM content in the blend increases which is attributed to restrictions created by the EPDM on the mobility of PP segments, as suggested above. [4].

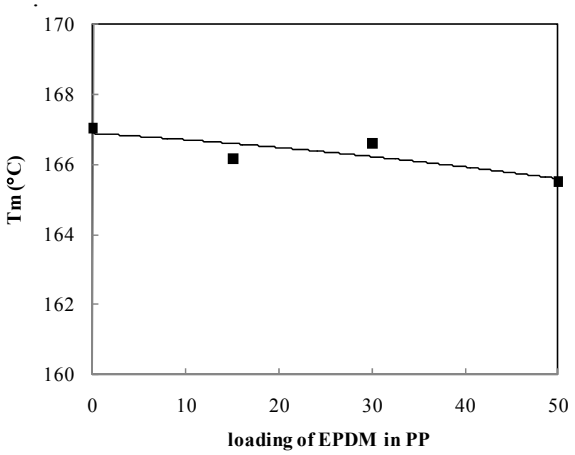

Figure 2. Effect EPDM on the melting temperature (T_m) of PP and EPDM/PP blends

Rheological characterization. The MFI of PP and EPDM/PP blends are shown in Fig.4. The MFI values of the blends decrease as increasing the EPDM contents since EPDM possess a very high molecular weight and high viscosity.

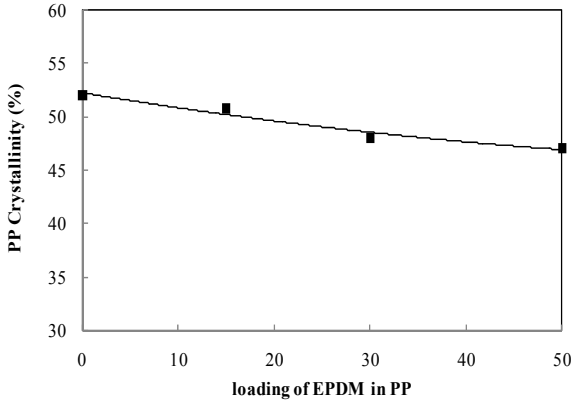

Figure 3. Effect EPDM on the crystallization of PP and EPDM/PP blends.

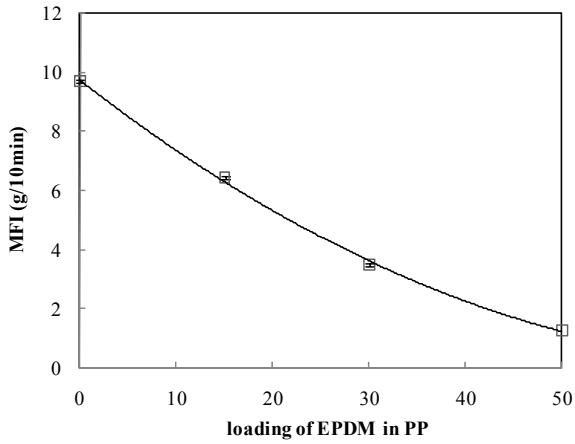

Figure 4. Effect EPDM on the MFI of PP and EPDM/PP blends.

The storage modulus and complex viscosity of the EPDM/PP blends have been attempted to be studied in order to assess the favorability of these blends for optimizing the performance for finishing products. In this case, the dynamic rheological analysis with storage modulus (E′) and complex viscosity (η*) is a method that has been used to measure the elastic and strength of the blends. The results of storage modulus (E′) and complex viscosity (η*) as a functions of angular frequency (ω) obtained for various EPDM contents mixed with PP are shown in Figs 5-6.

As seen in the Figs 5 and 6, as EPDM content increased, as expected, the storage modulus and the complex viscosity increased. This could be explained that the elastic behavior of EPDM plays a dominant role. Furthermore, the results also indicated that all the blends behave as shear thinning materials. The linear viscoelastic behaviour of the TPE blends in the melt can be explained by changes in the composition. The

increase of EPDM phase volume results in a increasing of the storage modulus and complex viscosity at low frequencies. The values of the storage modulus at low frequencies depend on the amount and on the structure of the elastomer phase [5].

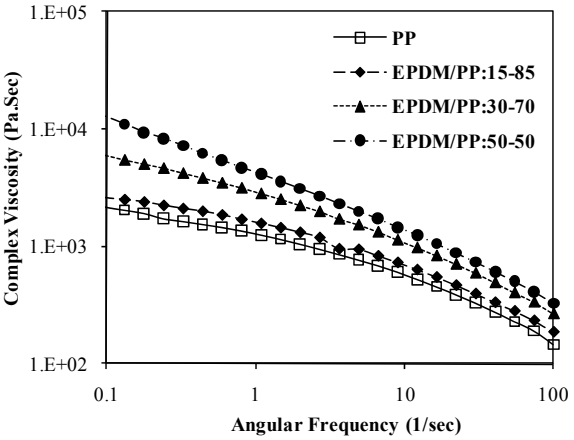

Figure 5. Complex viscosity versus angular frequency for different blends

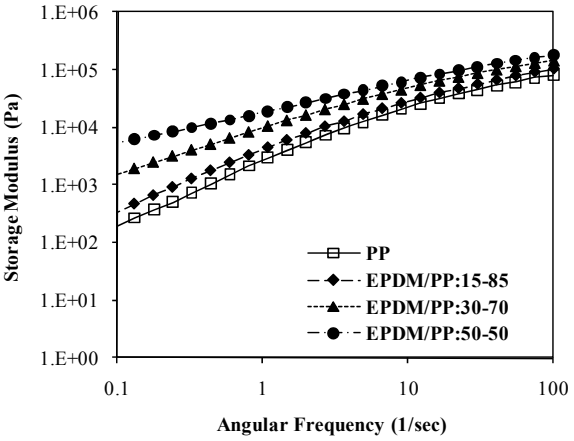

Figure 6. Storage modulus versus angular frequency for different blends

The EPDM mixed with PP is one of special class of thermoplastic elastomer (TPEs). The microcellular EPDM/PP blends were foamed via the super critical fluid technique under fixed conditions: saturation pressure, temperature and time of 20 MPa, 154 ^{o}C and 20 min, respectively. These conditions of producing the microcellular TPEs foam are more favorable for obtaining a uniform cell size and cell distribution. From the high pressure $scCO_2$ point of view, the saturation pressure and the amount of EPDM contents are considered to be important processing parameters to control the foam structure of the microcellular TPEs [6].

Fig. 7-8 shows a typical micrograph of microstructure of microcellular EPDM/PP blends obtained at different EPDM contents in PP matrix for given saturation temperature of 154 °C and saturation time of 20 min and depressurization time of 3 s.

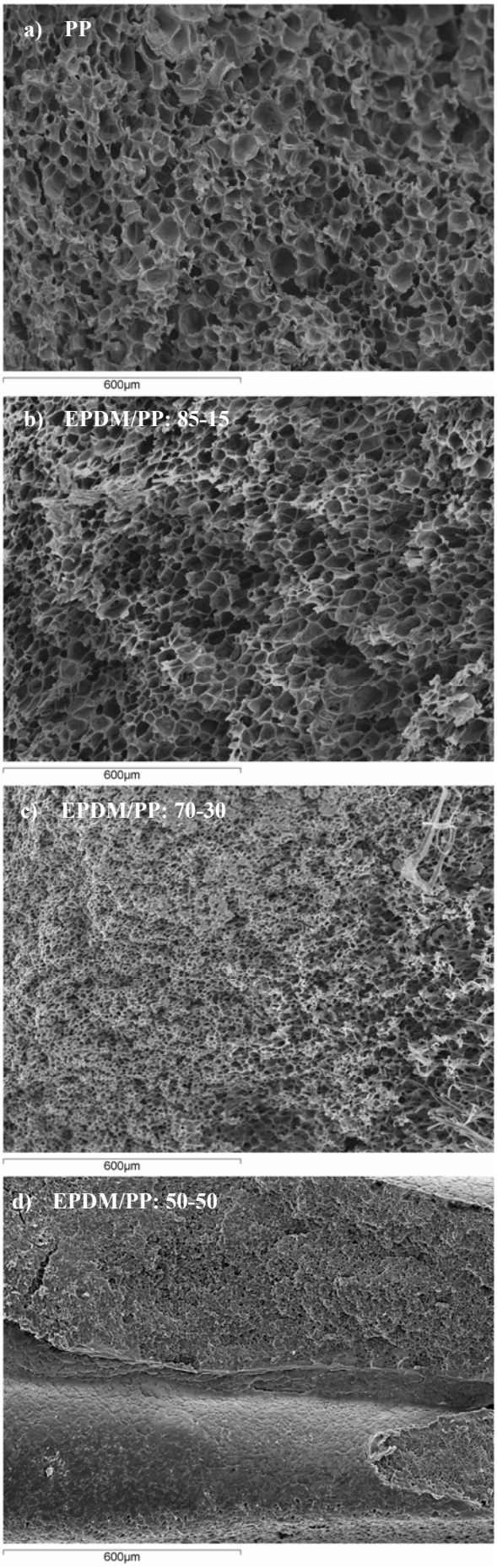

Figure 7. SEM micrographs of the specimens produced at different blends (×100)

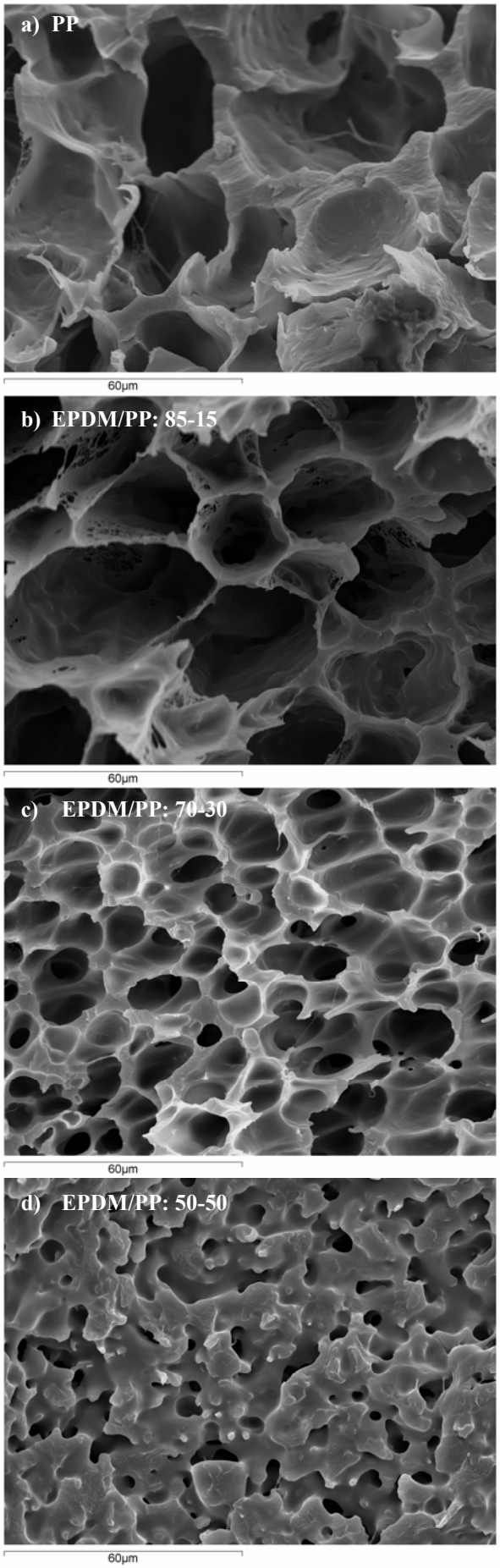

Figure 8. SEM micrographs of the specimens produced at different blends (×1000)

The saturated high pressure for foam formation contributed to the solubility of CO_2 in the EPDM/PP blends matrix. The CO_2 could be dissolved in the PP, PP chains in the amorphous phase gained mobility to the point that they re-organized themselves to form crystallites. Since CO_2 was not soluble in the crystalline regions [7]. This work studied the effect of various EPDM contents in PP foam. In this case of the CO_2 could was soluble in PP amorphous phase more than EPDM phase because molecular weight of PP amorphous chains lower. It was found that the average cell size decreases with increasing in the EPDM contents. It was conceivable that adding the EPDM could increase viscosity of EPDM/PP blend, which caused the CO_2 was difficultly dissolved in amorphous phase. Thus, EPDM/PP (50-50) blend, the cells were hardly observed (Fig. 8d)

Conclusions

Solubility of supercritical CO_2 was directly affected foamed properties. Microcellular foam produced via the supercritical fluid using CO_2 as physical blowing agent caused closed cell foam. The diffusion of supercritical CO_2 under given pressure and temperature in polymer drove nucleation of a number of micro-cells. The obtained microcellular EPDM/PP foam, thermoplastic elastic (TPE) foam, containing uniform cell distribution. The cell size of the obtained microcellular TPE foam decreased with increasing EPDM contents.

References

[1] W. Yamsaengsung and N. Sombatsompop, *J. Compositesb.* **40** (2009), pp. 549–600.
[2] Kerem Goren, Limeng Chen, Linda S. Schadler and Rahmi Ozisik, *J. Supflu.* (2009).
[3] M. Arroyo, R. Zitzumbo and F. Avalos, *Polymer.* **41** (2000), pp. 6351–6359.
[4] Helson M. da Costa, Vale´ ria D. Ramos and Marisa C.G. Rocha, *J. Polymertesting.* **25** (2006), pp. 498–503.
[5] W.G.F. Sengers, P. Sengupta, J.W.M. Noordermeer, S.J. Picken and A.D. Gotsis, *Polymer*, **45** (2004), pp. 8881–8891.
[6] Zhen Xiu Zhang, Shu Ling Zhang, Sung Hyo Lee, Dong Jin Kang, Daae-Suk Bang and JinKuk Kim, *J. Matlet.* **62** (2008), pp. 4396–4399.
[7] Zhi-Mei Xu, Xiu-Lei Jiang, Tao Liu, Guo-Hua Hu, Ling Zhao, Zhong-Nan Zhu, Wei-Kang Yuan, *J. Supflu.* **41** (2007), pp. 299–310.

Poly(lactic acid)/lignocellulosic filler from rice straw biocomposites

T. Soonthornwatanasiri[1] and C. Noomhorm[1*]

[1] Kasetsart University, Department of Chemistry, Faculty of Science, Jatuchak, Bangkok 10900, Thailand

*E-mail: fscictn@ku.ac.th

Abstract: Biocomposites were obtained by the combination of biodegradable poly(lactic acid) (PLA) matrix and biodegradable lignocellulosic filler (LCF). Among biodegradable polymers, PLA has a great potential to replace petroleum–based plastics, however, PLA has some limitations such as high cost, high glass transition temperature, brittleness and low crystallization rate. To improve these properties, composites with renewability, environmental friendly, low cost and low density lignocellulosic filler were investigated. The LCF used was from rice straw. The objective of this study was to process and to characterize thermal and mechanical behaviors of PLA/LCF biocomposites. The matrix PLA and the LCF were mixed in chloroform, followed by drying, kneading and hot pressing into sheet. The biocomposites thermal stability behavior has been investigated by TGA (thermal gravimetric analysis) and DSC (differential scanning calorimeter). PLA/LCF biocomposites showed an addition crystallization (T_c) peak at 106.2-115.8°C from the DSC measurements. The impacts of the cellulose fiber content (5%, 10%, 15% and 20 wt%), size (>40 mesh and <60 mesh) on the mechanical of the biocomposites have been investigated. It was found that tensile modulus of PLA/LCF biocomposites was increased by adding of LCF, whereas the tensile strength was decreased by adding the LCF.

Introduction

Over the last two decades, polymers from renewable resources or bio-based polymers have attracted an increasing amount of attention predominantly due to two major reasons: firstly environmental concerns, and secondly the realization those petroleum resources are finite. Generally, polymers from renewable resources can be classified into three groups: (1) natural polymers, such as starch, protein and cellulose; (2) synthetic polymers from natural monomers, such as poly(lactic acid) (PLA); and (3) polymers from microbial fermentation, such as polyhydroxyalkanoate (PHA). A large number of these biodegradable polymers are commercially available. They show a large range of properties and at present, they can compete with non-biodegradable polymers in different industrial fields (e.g., packaging, agriculture, hygiene, and cutlery).

Biodegradable polymers are rarely used by themselves. Generally, fibers, such as carbon fibers and glass fibers are widely used to improve their mechanical properties. However, these fiber-reinforced polymeric composites cause environmental problems upon disposal. Reinforcements of biodegradable polymers by utilizing renewability, environmentally friendly, low cost and low density natural lignocellulosic fibers are required to obtain fully biodegradable composites together with to improve mechanical properties. Since both components are biodegradable, the biocomposites (biodegradable composites) are also expected to be biodegradable. A large number of biocomposites have been investigated in association with diverse lignocellulosic fibers from various origins such as bleached cellulose fibers, bamboo fibers or flax, oil palm, jute or ramie fibers [1-5].

Rice straw is principally used as animal feed, and as raw material for fiber in paper industry. Burning is still the most common practice for rice straw disposal resulting in emissions to air that have a deleterious effect on air quality and human health [6-7]. Utilization of rice straw as an alternate for reinforcements of biocomposites is not only reducing greenhouse gas emission from open burning the rice straw but also gaining monetary value of these agricultural wastes.

Among biodegradable polymers, poly(lactic acid) (PLA) has a great potential to replace petroleum-based plastics because of its high stiffness and strength. Thailand is the world's top producer and exporter of tapioca, derived from cassava, and its second biggest sugar exporter, two crops in demand for the production of lactic acid, the precursor for production of poly(lactic acid). As Thailand is an agricultural country, it is a potential base to produce biomass plastic material and this would be a new business opportunity for the country. Development of new technologies, emergence of new end-use applications, and evolution of new markets are all expected to offer opportunities for future growth.

This paper described thermal and mechanical properties of biocomposites based on biodegradable poly(lactic acid) (PLA) and rice straw lignocellulosic filler (LCF) with the goal to obtain fully biodegradable composites together with to improve mechanical properties.

Materials and Methods

PLA used was Polymer 2002D from NatureWorks ($\overline{M}_W$ = 155741). LCF used was from rice straw. It was washed and dried in oven at 60±5°C for 2 days, milled, sieved with a 40 mesh (425 μm) for LCF >40

mesh (STL). The LCF <40 mesh was further sieved with a 60 mesh (250 µm) for LCF < 60 mesh (STP).

Preparation of PLA/LCF biocomposites

PLA and 5%, 10%, 15% or 20 wt% of LCF were mixed in chloroform, cast and the solvent was evaporated at room temperature for 24 h followed by vacuum drying for another 24 h. The mixture from which the solvent had been removed was kneaded by two roll mill (Model YFCR 6, Chor.Sri-Anan Co., Ltd.) at 120°C by varying the roll gap from 1.6-0.2 mm which the roll gap would decrease by 0.2 mm at every 4 rounds. The PLA/LCF biocomposites were cut into small pieces and compression molding into sheets at 190°C in three steps: pre-heating for 15 min, compression at 10 MPa for 10 min, and cooling for 15 min.

Thermal properties

Differential scanning calorimetry (DSC) measurements were performed on a DSC7 (Perkin Elmer) from 0-200°C. The heating rate and the cooling rate were 10°C/min and 5°C/min respectively. Thermogravimetric analysis (TGA) measurements were performed on TGA7 (Perkin Elmer) from 30-550°C with heating rate of 10°C/min in a nitrogen atmosphere.

Mechanical properties

Shore D hardness of the PLA/LCF biocomposites was measured using hardness tester (ZWICK , Model 3102) according to ASTM D 2240. The tensile properties of PLA/LCF biocomposites samples were carried out according to ASTM D638 using the Universal Testing Machine (Instron 5566). An average of the five measurements was taken for each sample.

Results and Discussion

The results of DSC heating scans for the PLA/ LCF (STL, LCF >40 mesh) biocomposites were presented in Figure 1and Table 1 and for PLA/ LCF (STP, LCF <60 mesh) biocomposites were presented in Figure 2 and Table 2. The glass transition temperature (Tg) of PLA was about 61.9°C. Both LCF (>40 mesh and <60 mesh) contents slightly decreased the Tg in the PLA/LCF biocomposites. The melting temperature (Tm) of PLA was about 151.5°C and LCF were about 173.5°C and 165.9°C for LCF >40 mesh and LCF <60 mesh respectively. Both LCF (>40 mesh and <60 mesh) contents also slightly decreased the Tm in the PLA/LCF biocomposites. In addition, exothermic peaks (Tc) at about 106.2-115.8°C which may be attribute to crystalline reorganization during heating were found in all PLA/LCF biocomposites [8]. These newly formed crystallites melted on continuous heating. The presence of LCF can act as nucleating agent on the crystallization of PLA.

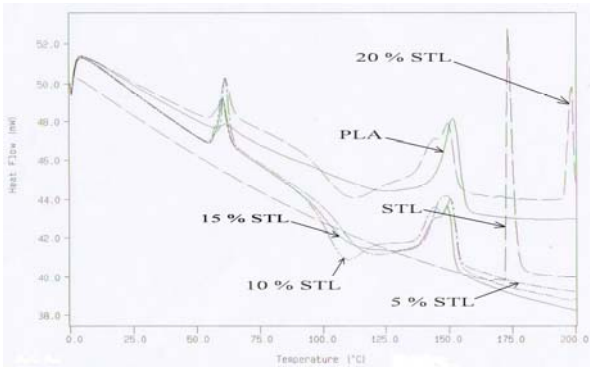

Figure 1. DSC thermogram of PLA/LCF biocomposites (STL= LCF >40 mesh)

Table 1: DSC measurements of PLA/LCF biocomposites (STL= LCF >40 mesh)

Sample	Tg (°C)	Tm (°C)	Tc (°C)
Pure PLA	61.9	151.5	-
LCF(STL)	-	173.5	-
5% STL	61.4	149.1	115.8
10% STL	60.2	150.6	108.3
15% STL	60.4	149.2	109.7
20% STL	61.5	149.4	110.2

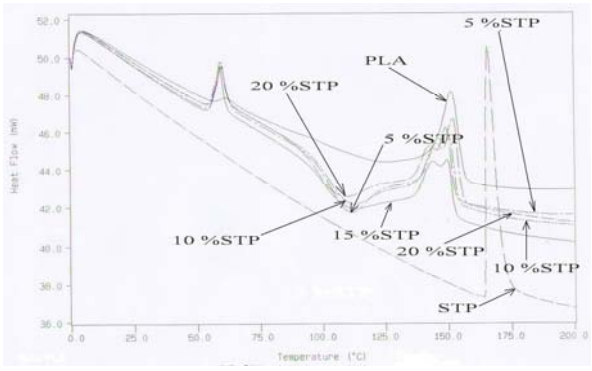

Figure 2. DSC thermogram of PLA/LCF biocomposites (STP = LCF <60 mesh)

Table 2: DSC measurements of PLA/LCF biocomposites (STP = LCF < 60 mesh)

Sample	Tg (°C)	Tm (°C)	Tc (°C)
Pure PLA	61.9	151.5	-
STP	-	165.9	-
5% STP	60.0	152.0	110.5
10% STP	59.8	150.5	110.4
15% STP	59.4	149.7	108.8
20% STP	60.1	149.2	106.2

Figure 3 and Table 3; Figure 4 and Table 4 showed the results of thermogravimetric analysis (TGA) for PLA/LCF biocomposites under nitrogen atmosphere for LCF >40 mesh and <60 mesh respectively. Increasing the LCF contents decreased both the decomposition onset and maximum temperatures in the PLA/LCF biocomposites and the decreasing of decomposition onset and maximum temperatures of the PLA/LCF biocomposites showed slightly higher value than the of pure LCF.

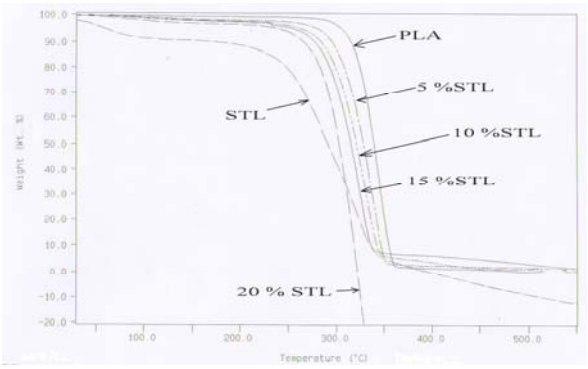

Figure 3. TGA thermogram of PLA/LCF biocomposites (STL= LCF >40 mesh)

Table 3: TGA measurements of PLA/LCF biocomposites (STL= LCF >40 mesh)

Sample	Onset Temp. (°C)	Maximum Temp. (°C)
Pure PLA	304.0	345.4
STL	225.0	286.2
5% STL	287.7	341.7
10% STL	278.8	330.4
15% STL	272.7	324.9
20% STL	268.2	322.5

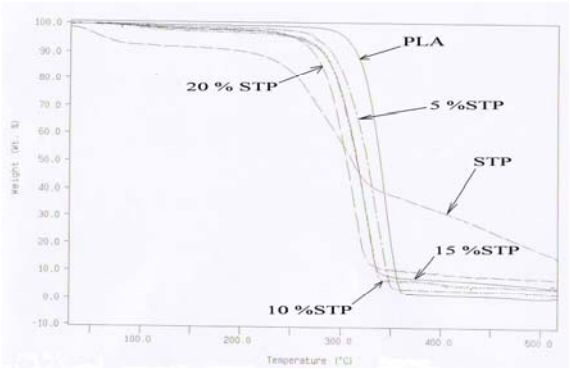

Figure 4. TGA thermogram of PLA/LCF biocomposites (STP = LCF <60 mesh)

Figure 5 and Table 5; Figure 6 and Table 6 showed hardness, tensile strength, % elongation at break and tensile modulus of PLA/LCF biocomposites for LCF >40 mesh and <60 mesh respectively. Hardness of all PLA/LCF biocomposites slightly increased with increasing the LCF contents but tensile strength and elongation at break slightly decreased as the LCF contents increased for both LCF >40 mesh and <60 mesh. However, the tensile modulus was increased by adding of LCF and at 20 wt% LCF contents, the tensile modulus increased much higher than pure PLA.

Table 4: TGA measurements of PLA/LCF biocomposites (STP = LCF < 60 mesh)

Sample	Onset Temp (°C)	Maximum Temp. (°C)
Pure PLA	304.0	345.4
STP	221.2	311.4
5% STP	287.9	336.6
10% STP	286.4	329.1
15% STP	272.7	326.0
20% STP	259.1	312.8

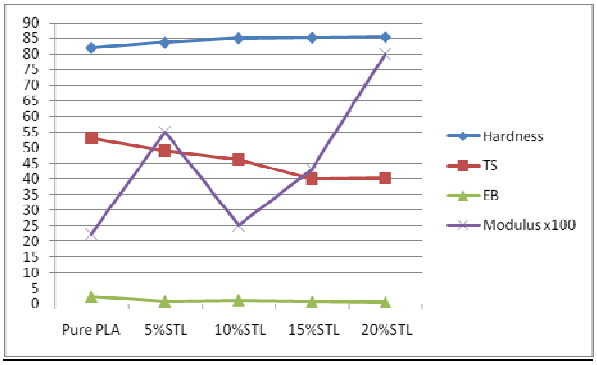

Figure 5. Results of the mechanical properties of PLA/LCF biocomposites (STL = LCF >40 mesh)

Table 5: Results of the mechanical properties of PLA/LCF biocomposites (STL = LCF >40 mesh)

Sample	Hardness (Shore D)	Tensile strength (MPa)	Elongation at break (%)	Modulus x100 (MPa)
Pure PLA	82	52.9	2.3	22.3
5%STL	83.6	48.8	0.9	55
10%STL	85	46.2	1.2	25
15%STL	85.2	39.9	0.8	42.8
20%STL	85.4	40.0	0.6	80

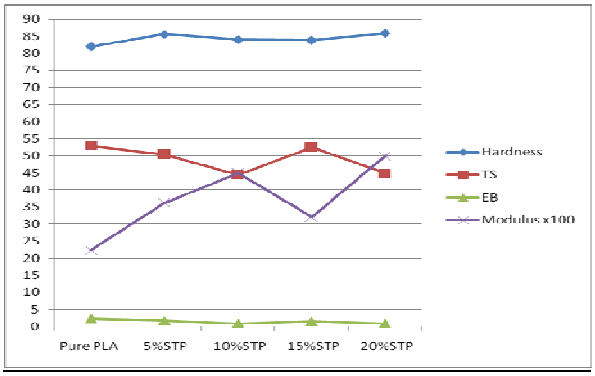

Figure 6. Results of the mechanical properties of PLA/LCF biocomposites (STP = LCF <60 mesh)

Table 6: Results of the mechanical properties of PLA/LCF biocomposites (STP = LCF <60 mesh)

Sample	Hardness (Shore D)	Tensile strength (MPa)	Elongation at break (%)	Modulus x100 (MPa)
Pure PLA	82	52.9	2.3	22.3
5%STP	85.6	50.4	1.7	36.1
10%STP	84	44.4	0.9	45
15%STP	83.8	52.5	1.5	32
20%STP	85.8	44.9	0.9	50

Conclusions

PLA/LCF from rice straw biocomposites were carried out by kneading and hot pressing into sheet using two roll mill at 120°C. For the operation of the two roll mill, the roll gap was varied from 1.6 mm to 0.2 mm and the roll gap was decreased by 0.2 mm for every 4 rounds of the two roll mill. The study of thermal properties revealed that both LCF (>40 mesh and <60 mesh) contents slightly decreased the Tg and Tm in the PLA/LCF biocomposites. In addition, exothermic peaks (Tc) at about 106.2-115.8°C which may be attribute to crystalline reorganization during heating were found in all PLA/LCF biocomposites. The presence of LCF can act as nucleating agent on the crystallization of PLA. Increasing the LCF contents decreased both the decomposition onset and maximum temperatures in the PLA/LCF biocomposites and the decreasing of decomposition onset and maximum temperatures of the PLA/LCF biocomposites showed slightly higher value than that of pure LCF. The study of mechanical properties showed that hardness of all PLA/LCF biocomposites slightly increased with increasing the LCF contents but tensile strength and elongation at break slightly decreased as the LCF contents increased for both LCF >40 mesh and <60 mesh. However, the tensile modulus was increased by adding of LCF and at 20 wt% LCF contents, the tensile modulus increased much higher than pure PLA

References

[1] M. Shibata, K. Takachiyo, K. Ozawa, R. Yosomiya and H. Takeishi, *J. Appl. Polym. Sci*. **85** (2002), pp. 129–138.
[2] K.Oksman, M. Skrifvars and J.F. Selin, *Compos. Sci. Technol*. **63** (2003), pp. 1317–1324.
[3] F. Le Digabel, N. Boquillon, P. Dole, B. Monties and L. Averous, *J. Appl. Polym. Sci*. **93** (2004), pp. 428–436.
[4] L. Averous and F. Le Digabel, *Carbohydr. Polym*. **66** (2006), pp. 480-493.
[5] L. Suryanegara, A.N. Nakagaito, and H. Yano, *Compos. Sci. Technol*. **69** (2009), pp. 1187-1192.
[6] B.C. Gadde, C. Menke and R. Wassmann, *Biomass Bioenergy*. **33** (2009), pp. 1532-1546.
[7] DEDE (Department of Alternative Energy Development and Efficiency). *Rice in Thailand*. (2003), in DEDE, ed., pp. 43.
[8] S.M. Lee and J.W. Lee, *Korea-Australia Rheology J*. **17** (2005), pp. 71-77.

Thermal characterizations and thermal decomposition kinetics of polycarbonate/ABS-polybenzoxazine blends

S. Tiptipakorn[1*], S. Rimdusit[2], P.Suwanmala[3], and K. Hemvichian[3]

[1*] Department of Chemistry, Faculty of Liberal Arts and Science, Kasetsart University, Kamphaensaen, Nakorn Pathorm 73140, Thailand.
[2] Department of Chemical Engineering, Faculty of Engineering, Chulalongkorn University, Pathumwon, Bangkok 10330, Thailand.
[3]Thailand Institute of Nuclear Technology, Ongkarak, Nakorn-nayok 26120, Thailand.

[*] E-mail: otiptipak@yahoo.com

Abstract: Thermal behaviors of the polymeric blends between Polycarbonate/ABS (Bayblend® T85, high impact commercial grade) and common-type benzoxazine monomer (BA-a) were studied using Differential Scanning Calorimetry (DSC) and Thermogravimetric Analysis (TGA). The blended samples were prepared at various BA-a ratios (0 wt%, 25 wt%, 50 wt%, 75 wt%, and 100 wt%). The processing programs of 180°C (4 hours) and 200°C (4 hours) were performed in order to ensure full curing. The DSC thermograms reveal that the blends provided the glass transition temperatures which differed from the original polymers. Interestingly, the synergistic behavior of glass transition temperature was found at some ratios of BA-a. In addition, the TGA results reveal that the char yield of the blends was increased with the increase of BA-a, while the peak of first derivative of thermogravimetry curves (DTG) was increased with increasing the amount of PC/ABS. The DTG thermograms of the blends exhibited four sub-stages of thermal decomposition reaction. Moreover in this study, the apparent activation energies (E_a) of each decomposition step were determined using Kissinger method. From the calculation of the blend at 50wt% BA-a, the Ea values are approximately 150 kJ/mol, 356 kJ/mol, 403 kJ/mol, and 430 kJ/mol, respectively.

Introduction

Polycarbonate/ABS is the thermoplastics widely used in many applications such as electrical & electronics (E&E) devices and automotive parts due to its unique properties i.e. high impact resistance, high stiffness, good dimensional stability. However, its shortcomings are its low chemical resistance to hydrocarbon, fuel, and alcohol. Furthermore, its char yield is rather low.

Polybenzoxazine is the novel thermosetting polymer which renders the outstanding properties, i.e. it could be synthesized via solventless technique without need of catalyst. Moreover, its near zero shrinkage, with high chemical resistance.

The objectives of this study are to determine thermal behaviors of the PC/ABS-polybenzoxazine blends, and study the effects of BA-a contents on the thermal stability of the blends. In addition, the thermal decomposition kinetics of the blends was studied as well.

Materials and Methods

Polycarbonate/ABS (Bayblend® T85, high impact commercial grade) was supplied from Bayer Thai Co., Ltd. The benzoxazine monomer bis(3-phenyl-3,4-dihydro-2H-1,3-benoxzinyl) isopropane (BA-a) was prepared from 2,2'-bis(4-hydroxyphenyl)-propane (Bisphenol-A) with aniline and formaldehyde according to the reported method [1] . Bisphenol-A (commercial grade) provided by Thai Polycarbonate Co., Ltd. (TPCC) was used as received. Para-formaldehyde (AR grade) and aniline (AR grade) were purchased from Merck and APS Finechem Companies.

Polycarbonate/ABS was blended with BA-a monomer at various BA-a ratios ratios (0wt%, 25wt%, 50wt%, 75wt%, and 100wt%). The heating programs was 180°C (4 hours) and 200°C (4 hours).

FTIR analysis was performed via Thermo Nicolet FT-IR Spectrometer (model NEXUS670FTIR). The spectra were recorded with a resolution of 4 cm^{-1} and 32 scans.

Differential Scanning Calorimeter (DSC) of TA instruments (model DSC2910), calibrated with Indium standard, was used. A sample of about 10 mg was used for each test. In order to erase any thermal history, the samples were heated at 5°C/min. Then, they were cooled to the ambient temperature, and scanned again using the same heating rate as before. The glass transition temperatures (T_g) of the blends were measured.

The decomposition temperature (T_d) and char yield of the blends were studied using TGA Instruments (model TGA/SDTA 851^e). The experiments were performed using a heating rate of 10°C/min from 40 to 700°C under nitrogen atmosphere. The flow of purging nitrogen was kept at 80 ml/min. The sample mass was approximately 20 mg. Kinetics analysis via Kissinger method was carried out at various heating rates, i.e. 5, 10, 15, and 20°C/min.

Kissinger method (differential method) [2-4] uses Eq. (1) to determine the E_a of solid state reactions.

$$\ln(\frac{\beta}{T_p^2}) = \ln\frac{AR}{E_a} + \ln\left[n(1-\alpha_p)^{n-1}\right] - \frac{E_a}{RT_P} \quad \ldots(1)$$

,where T_p and α_p are the absolute temperature and weight loss at maximum weight-loss rate $(d\alpha/dt)_p$,

respectively, and n is the reaction order. From the slope of the straight $\ln(\beta/T_p^2)$ versus $1/T_p$, the E_a can be obtained. The advantage of the Kissinger model is that the E_a can be obtained without the knowledge of any thermal degradation reaction mechanism in advance.

Results and Discussion

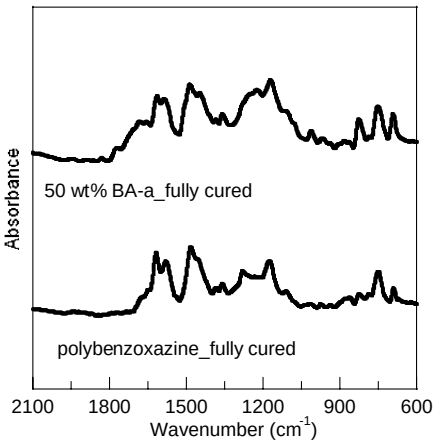

Figure 1. FTIR spectra of polybenzoxazine and the blend at 50wt% BA-a

Figure 1 shows the comparison between the FTIR spectra of polybenzoxazine and the blend at 50wt% of BA-a. The spectra of the blend indicate the hydrogen-bonded carbonated band of PC at the wavenumber in the range between 1772 cm^{-1} and 1720 cm^{-1}. The result is correlated to the system that was found in the PC/epoxy blends and PC/benzoxazine blends [5-6].

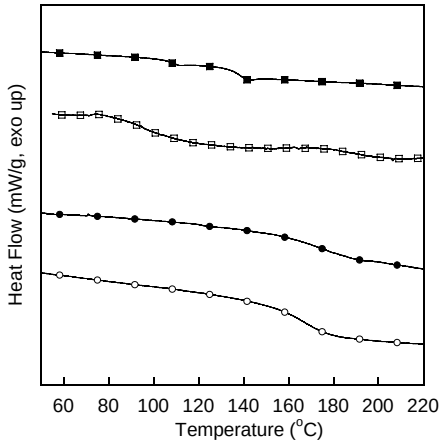

Figure 2. DSC thermograms of the PC/ABS/BA-a blends at various BA-a contents: (○) pure BA-a, (●) 75wt% BA-a, (□) 50wt% BA-a, (■) pure T85.

The DSC thermograms of the blends are shown in Figure 2. It can be observed that the glass transition temperature (Tg) of pure polybenzoxazine was around 165°C, while the Tg values of pure PC/ABS were approximately 100°C and 140°C. Interestingly, the value of the blend at 75wt% BA-a was shifted to around 180°C. In case of the blend at 50wt% BA-a, two Tg values were found at ca. 105°C and ca. 190°C. The phenomenon of not following the Fox's Equation was also found in the similar system of PC/benzoxazine blends. However, it could be noticed that the synergistic behaviour of Tg values was found in PC/ABS-benzoxazine blends but not found in PC/benzoxazine system. [6]

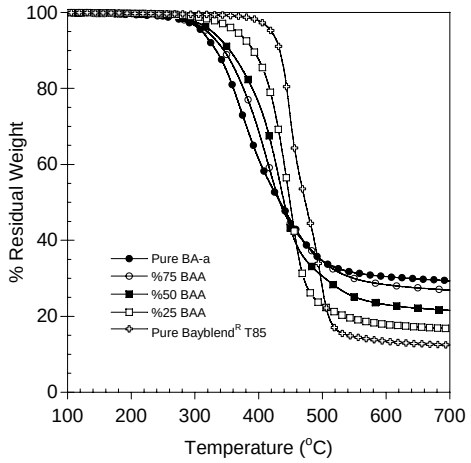

Figure 3. TGA thermograms of the PC/ABS/BA-a blends at various BA-a contents in the nitrogen atmosphere (heating rate of 10°C/min)

The temperatures at peak of derivatives thermogravimetric (DTG) curves and the char yields of the blends from Figure 3 could be tabulated in Table 1.

Contents of BA-a	T_{peak} of DTG curve at 10°C/min	Char Yield @ 700°C
100wt% (Pure polybenzoxazine)	390	30
75wt% BA-a	414	27
50wt% BA-a	424	21
25wt% BA-a	436	16
0wt% BA-a (Pure Bayblend®T85)	441	12

Table 1. Temperatures at DTG peak of the blends of various BA-a ratios (heating rate of 10°C/min).

From Figure 3 and Table 1, it could be noticed that the temperatures at peak of DTG curves were increased with the increase of PC/ABS contents. It was contributed to the fact that pure PC/ABS renders higher thermal stability than pristine polybenzoxazine. Furthermore, the char yield of the blends was increased with increasing the amount of BA-a content because this kind of thermosetting provide higher char yield than PC/ABS.

To investigate the thermal degradation kinetics, the DTG curve of the 50wt% BA-a blended was selected to deconvolute via Peak Fit program as shown in Figure 4.

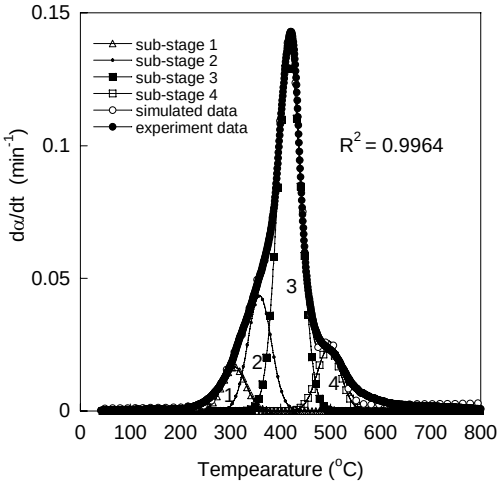

Fig. 4 DTG curve and individual contributions of the blends with 50wt% of BA-a (10°C/min), R^2=0.9964: (●) experimental data, (○) simulated curve.

Table 2 Activation energies of each sub-stage decomposition of the blend at 50wt% BA-a calculated via Kissinger Method

Sub-stage of decomposition	E_a (kJ/mol)
1	149.7
2	355.5
3	403.4
4	429.8

Conclusions

The blends of PC/ABS and benzoxazine were prepared and studied in this study. FTIR spectra reveal the interaction between hydrogen atoms of benzoxazine and carbonate groups in PC. DSC thermograms presented the synergistic behaviour of Tg values in some compositions. The thermal stability of the blends increased with increasing PC/ABS, while the char yield of the blends increased with the increase of BA-a. The thermal decomposition of the blends exhibited four sub-stages.

Acknowledgements

This work was supported by the Research Promotion and Technology Transfer Center Grant for year 2009 from the Faculty of Liberal Arts and Science, Kasetsart University.

References

[1] Low HY, Ishida H., *Polymer*, **40** (1999), pp.**4365-4376**.
[2] Barral L, Cano J, Lopez J, Lopez-Bueno I, Nogueira P, Ramirez C, et al., *J Therm Anal Calorim* **51** (1998), pp. **489-501**.
[3] Kissinger HE., Anal Chem **29** (1957), **pp.1702-1706**.
[4] Liaw DJ, Shen WC., *Polym Eng Sci* **34** (1994), **pp.1297-1303**.
[5] Don, T,Bell, J.P. *Polym Eng Sci* **36** (1996), **pp.2601-2613.**
[6] Ishida H. Lee Y.-H., *J. Appl. Polym. Sci.* 81, 4, (2001) **pp.1021-1034.**

Reactive extrusion and characterization of maleic anhydride-grafted poly(lactic acid) as an interfacial compatibilizer in biopolymer composite

S. Ouajai[1]*, A. Reung-u-rai[1], W. Prissanaroon-Ouajai[1], T. Leejarkpai[2] and R.A. Shanks[3]

[1]Department of Industrial Chemistry, Faculty of Applied Science,
King Mongkut's University of Technology North Bangkok (KMUTNB), Bangkok, Thailand 10800
[2]National Metal and Materials Technology Center (MTEC), Pathumthani, Thailand 12120
[3]School of Applied Sciences, RMIT University, Melbourne, Australia 3001

*E-mail: soj@kmutnb.ac.th

Abstract:Good interfacial adhesion between fiber and matrix is an expected requirement for composites. The maleated poly(DL-lactic acid) (PLA) has been prepared as a compatibilizer in oil palm empty fruit bunch cellulose fiber (OPEFB) and PLA biopolymer composite. Maleic anhydride (MAH) has been grafted on the PLA structure using benzoyl peroxide (BPO) as an initiator. PLA and MAH have been mixed at different ratios by reactive twin-screw melt extrusion at 175 °C. Qualitative characterization of the maleated PLA has been done by various techniques including FT-IR, ^{13}C NMR, XPS, DSC, TGA and SEM. The glass transition and decomposition temperatures of the maleated PLA have been influenced by MAH contents. PLA/OPEFB composite containing 10 phr of the maleated PLA has been prepared by an extrusion process. The SEM micrographs showed an improvement of interfacial adhesion between OPEFB and PLA in the composite.

Introduction

Biopolymer composites of natural cellulose fiber are increasing an attention. Advantages of these materials are biodegradable property and origin from renewable resources [1]. Inter-phase between reinforcing material and polymer matrix influences the performance of the composite. Modification of reinforcing materials and addition of compatibilizer can improve the interfacial adhesion [2-3].

Poly(lactic acid) (PLA) or polylactide is a biodegradable polymer produced from renewable resource via ring-opening polymerization of lactides. Maleic anhydride grafted PLA (MAH-g-PLA), also called maleated PLA, is a potential compatibilizer for PLA and reinforcing materials i.e. layer silicate and wood fiber [3-4]. The anhydride group is available for reaction with cellulose during the compounding by extruder. The production of MAH-g-PLA was initiated by peroxide radical i.e. benzoyl peroxide and dicumyl peroxide [5]. Reactive extrusion process was conducted in the research since it is easy in operation and large scale of modified PLA could be obtained. Several characterization techniques were employed in order to gain more information on modified PLA using MAH.

Materials and Methods

Polymer: Poly(DL-lactic acid) 4042D resin was obtained from Nature Work. MAH was purchased from Sigma-Aldrich.

Cellulose fiber: Oil palm empty fruit bunch was purchased from a factory in Krabi province, Thailand. The OPEFB fibers were treated with 8 %wt/v NaOH solution for one hour at 30 °C. The fibers were washed and oven dried before mixing with the PLA resin.

ATR FT-IR: The measurements were performed using a Nicolet 6700 FT-IR spectrometer. The 64 scans were taken with a resolution of 4 cm^{-1} for each sample.

^{13}C CP/MAS NMR: The OPEFB fibers were characterized at 20 °C with Bruker Biospin-300 solid state ^{13}C CP/MAS NMR.

XPS: X-ray photoelectron spectra were generated using an Axis Ultra spectrometer (Kratos Analytical, UK), equipped with a monochromatised X-ray source (Al Kα, hν =1486.6 eV) operating at 150 W. The spectrometer energy scale was calibrated using the Au $4f_{7/2}$ photoelectron peak at binding energy of 83.98 eV. High resolution spectra were acquired using a pass energy of 20 eV.

Thermal Analysis: Differential scanning calorimetry (DSC) was performed using a TA instruments DSC 2910. Temperature programs for the tests were from 0-240 °C at a heating rate of 20 °C/min. Thermogravimetric analysis (TGA) was conducted using a TA instruments TGA 2950. The samples were heated from 40 to 800 °C at the heating rate of 20 °C/min. The measurements were conducted under nitrogen gas (100 mL/min).

Surface Morphology: Scanning electron microscope (SEM, JEOL JSM-6480LV) was used to observe morphology of the PLA composites.

Reactive extrusion: The reactive extrusion of MAH and PLA containing 5, 10 and 20 %wt of MAH and 0.1 %wt of BPO were carried out in a twin-screw extruder (Prism TSE16TC). The speed of screw rotation was set at 10 rpm. Temperatures of screw barrel were maintained at 175, 165 and 150 °C for the metering zone, compression zone and feed zone, respectively. The extrudate was collected after air cooling and

palletized into granulates. The extrudate was purified by dissolving in chloroform and precipitated in methanol. The precipitate was rewashed and oven dried at 60 °C.

Composite preparation: Dried PLA resin, 20 phr of ground OPEFB and extrudate pellet of 10 phr MAH-g-PLA were mixed and fed into a twin-screw extruder using the similar temperature profile as an reactive extrusion procedure.

Results and Discussion

ATR-FTIR: FTIR measurements were conducted to investigate the functionalised PLA. Fig. 1 shows IR spectra of PLA, MAH and MAH-g-PLA extrudate. The C=O stretching at 1759 cm^{-1} is the characteristic of ester bond in PLA. The streching of MAH (1780 cm^{-1}) is presented in an PLA extrudate indicating the existing of MAH. Nevertheless, only weak absorbance of this peak is observed. This peak overlaps with the carbonyl band.

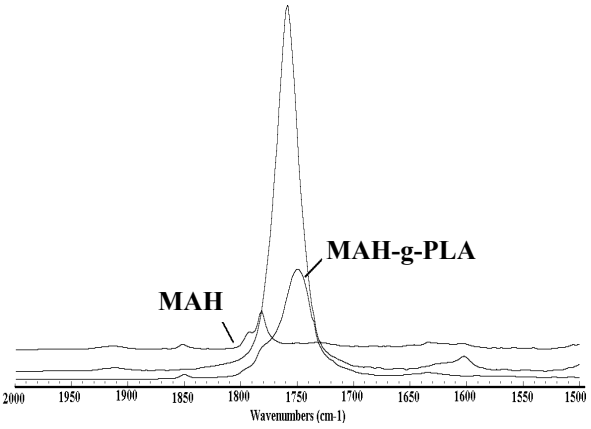

Figure 1. FTIR absorbance spectra of PLA, MAH and MAH-g-PLA.

XPS analysis: To study the surface composition of a MAH-g-PLA, XPS was carried out and exhibited the expected elemental composition of carbon and oxygen. High resolution C 1s and O 1s photoelectron spectra for the MAH-g-PLA are shown in Fig. 2. The C 1s spectrum (Fig. 2a) may be decomposed into four components. Three main components are attributed to C-C (C1= 285.0 eV). C-O (C2 = 286.9 eV) and O-C=O (C3 = 289.2 eV), corresponding to PLA structure as illustrated in Fig. 3. The last two components may also originate from MAH structure since MAH contains both C-O and O-C=O. The appearance of small peak at 286.1 eV assigned to the C-C=O (C4) may indicate the presence of MAH [6]. Fig. 2b shows that the O 1s spectrum for the MAH-g-PLA is resolved into three components. The peaks located at 532.5 eV and 533.7 eV are associated with C=O (O1) and C-O (O2), respectively, which arise from both PLA and MAH structures (see Fig. 3). The high binding energy side of the O 1s spectrum centred at 534.3 eV is due to O=C-O-C=O (O3) in MAH structure [6]. The presence of C-C=O and O=C-O-C=O described by XPS may indicate the existence of MAH-g-PLA structure.

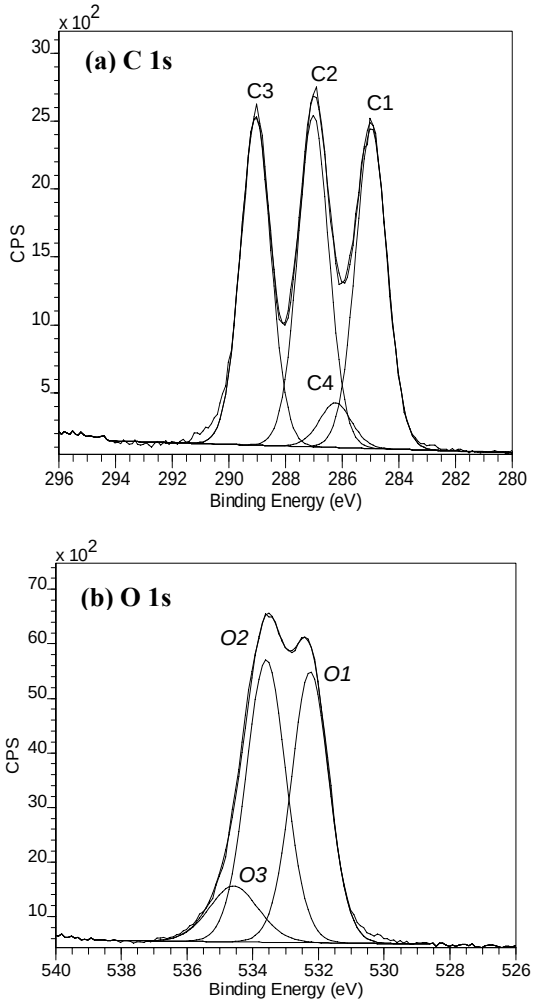

Figure 2. High resolution photoelectron spectra of (a) C 1s and (b) O 1s for MAH-g-PLA.

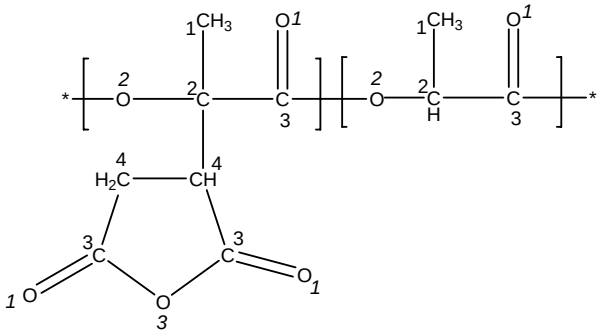

Figure 3. Proposed structure of MAH-g-PLA.

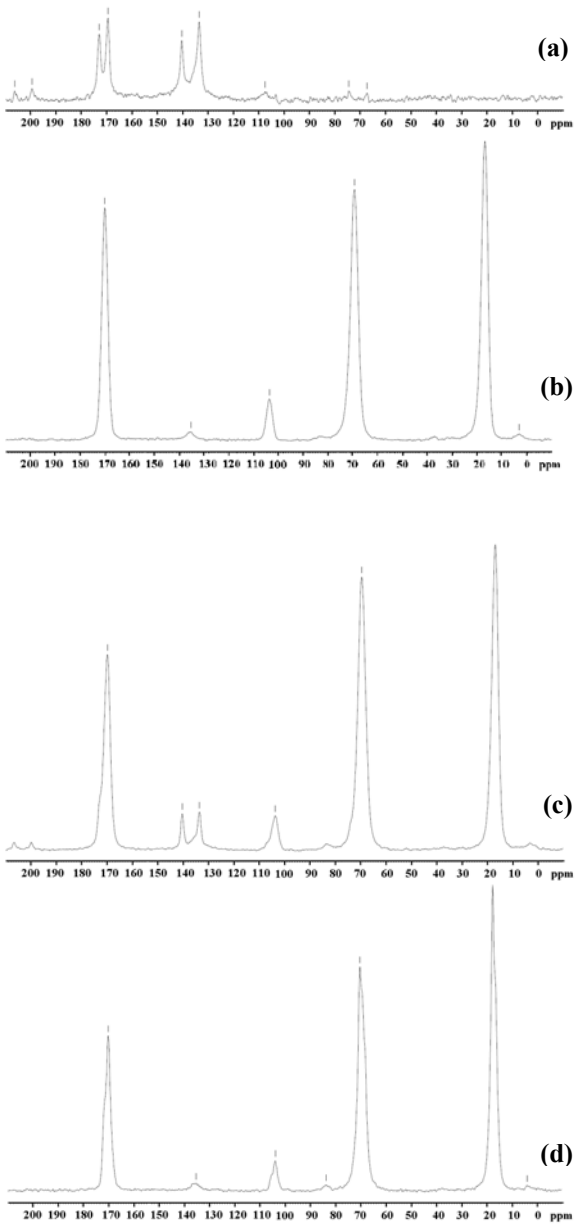

Figure 4. ^{13}C NMR spectra of (a) MAH, (b) PLA (c) MAH-g-PLA extrudate and (d) purified MAH-g-PLA.

^{13}C CP/MAS NMR: Solid state ^{13}C NMR spectrum of PLA (Fig. 4(b)) shows signals at chemical shifts of 17.1, 69.6, 103.9, 135.4 and 170.0 ppm. After grafting with MAH, the shoulder of peak at 170.0 ppm is observed in Figs. 4(c)-(d). This shoulder is assigned to a carboxylic carbon of MAH. In addition, the MAH-g-PLA extrudate shows the signals at 133.5 and 140.3 ppm attributed to the chemical shifts of unreacted MAH or low molecular weight fraction of MAH-g-PLA. The unreacted MAH has been removed after the purification process confirming by the decrease of these two signals in Fig. 4(d). The existing of the shoulder of peak at 170.0 ppm after the purification confirms a successful grafting of MAH onto PLA by reactive extrusion.

Thermal Analysis: Differential scanning calorimetry technique was employed to study the thermal property of the MAH-g-PLA. The first scan was conducted to remove thermal history of PLA and the results of second heating scan were used for characterization. In Fig. 5, glass transition temperature (T_g) of pure PLA, PLA grafted with 10%MAH and PLA grafted with 20% MAH decreased from 62.2 °C to 50.2 °C and 39.6 °C, respectively. Only a high loading of MAH (20%) shows cold crystallization peak at ~110 °C and melting peak at 134.4 °C. These peaks cannot be seen at low percentage of MAH loading (10%). The lowering of T_g may be attributed to the plasticizing effect of MAH molecules since the purification of the grafted PLA by precipitation and washing with methanol results in increasing of T_g.

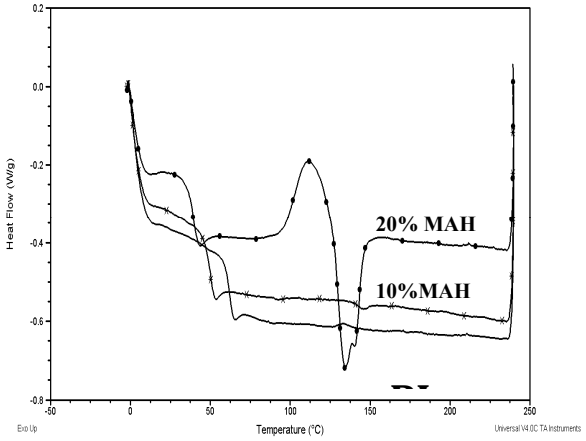

Figure 5. DSC thermograms of (—) PLA, MAH-g-PLA using 0.1%BPO and (-*-) 10%MAH and (-●-) 20%MAH .

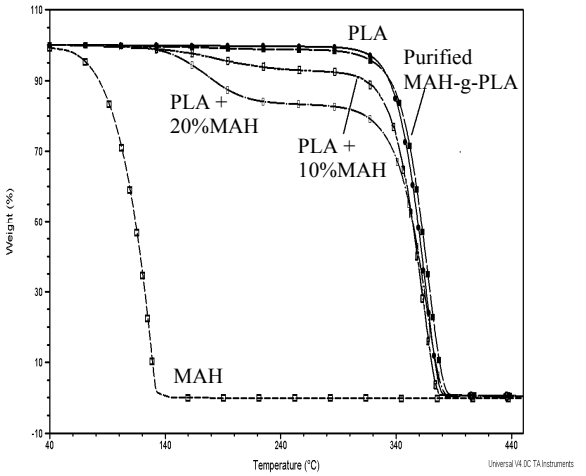

Figure 6. TGA thermograms of MA (□---), PLA (●—) PLA grafted with 10%MAH (▯— --), 20%MAH (▯—..) and purified MAH-g-PLA (■—).

Thermal stability of the MAH-g-PLA was studied by thermogravimetry technique. TGA thermograms of PLA and MAH show degradation temperatures at 366 °C and 126 °C, respectively (Fig. 6). Degradation temperature of the MAH-g-PLA is slightly shifted to lower temperature (362-365 °C) indicating decrease in thermal stability of the MAH-g-PLA. An increase in BPO content above 0.1% reduced the degradation temperature of PLA to 356 °C (no thermogram present). The molecular weight reduction during a grafting reaction was thought to be a reason, since the yellowing of the extrudate was observed.

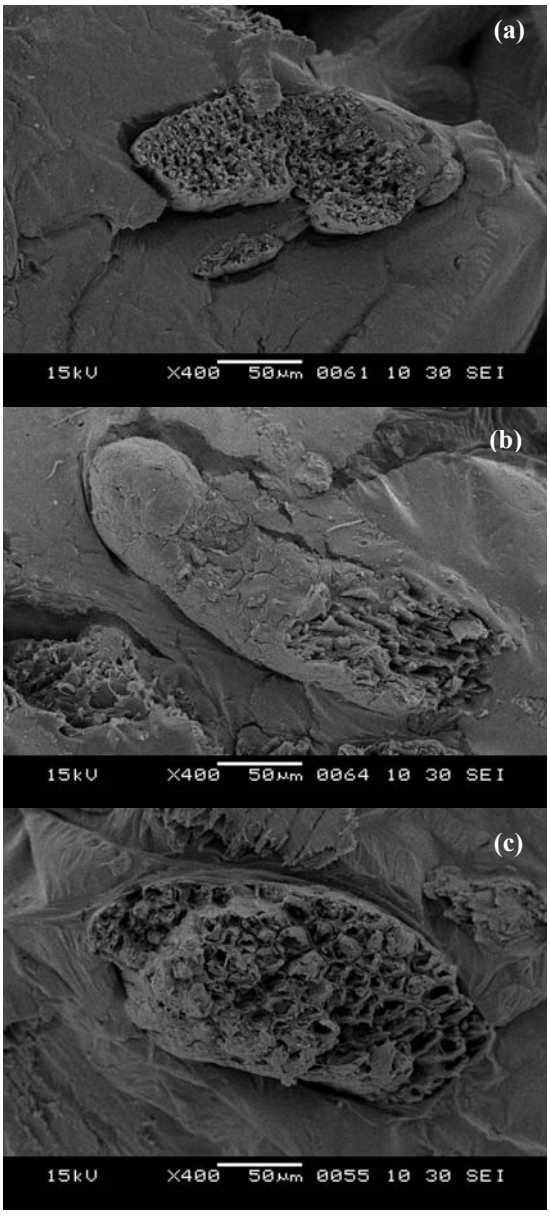

Figure 7. SEM images of (a) 8 %wt/v NaOH treated OPEFB-PLA composites, (b) untreated OPEFB-PLA composites containing 10 phr MAH-g-PLA and (c) 8 %wt/v NaOH treated OPEFB-PLA composites containing 10 phr MAH-g-PLA.

Morphology of OPEFB-PLA composite: The inter-phase between OPEFB fiber and PLA matrix was observed by SEM technique. A gap between 8% wt/v NaOH treated OPEFB fiber and PLA matrix (Fig. 7(a)) is observed on the fracture surface of the composite without MAH-g-PLA implying poor inter-phase adhesion. An improvement of interfacial adhesion between OPEFB fiber and PLA in the composite exhibits after an inclusion of 10 phr MAH-g-PLA for both raw OPEFB fiber (Fig. 7(b)) and 8 %wt/v NaOH treated OPEFB fiber (Fig 7(c)). This indicates the effectiveness of MAH-g-PLA as a biopolymer composite plasticizer.

Conclusions

Reactive extrusion is a novel technique for MAH-g-PLA production. The MAH-g-PLA influences the glass transition temperature and thermal stability of PLA. The obtained compatibilizer enhances inter-phase adhesion between OPEFB fiber and PLA in the composite. The influenece of MAH-g-PLA on the thermal properties of the biocomposite is under investigation.

Acknowledgments

This project was financially supported by the Thailand Research Fund (Grant number MRG5080157). The scholarship for Amparat Reung-u-rai from Thailand Graduate Institute of Science and Technology (TGIST) has been acknowledged. Assoc.Prof. Paul J. Pigram is acknowledged for the use of XPS instrument.

References

[1] R. A. Shanks, A. Hodzic and D. Ridderhofd, *J. Appl. Polym. Sci.* **101** (2006), pp. 3620-3629.
[2] M. S. Huda, L. T. Drzal, A. K. Mohanty and M. Misra *Comp. Sci Tech*. **68** (2008), pp. 424–432.
[3] L. Petersson, K. Oksman and A. P. Mathew, *J. Appl. Polym. Sci.* **102** (2006), pp. 1852-1862.
[4] D. Plackett, *J. Polym. Envir.* **12**(3) (2004), pp. 131–138.
[5] D. Carson, L. Nie, R. NaraYan and P. Dubois*, J. Appl. Polym. Sci.* **72** (1999), pp. 477-485.
[6] G. Beamson, and D. Briggs, High Resolution XPS of Organic Polymers, The Scienta ESCA 300 Database, John Wiley, Chichester (1992).

Thermoplastic starch/biodegradable polyester blends by using reactive blending

S. Uasopon[1], N. Euaphantasate[1], P. Methacanon[1]* and P. Prachayawasin[1]

National Metal and Materials Technology Center, 114 Thailand Science Park, Paholyothin Rd., Klong 1, Klong Luang, Pathumthani 12120 Thailand[1]

* E-mail: pawadeem@mtec.or.th

Abstract: Since petroleum based packaging increases the waste problems including people' growing concern for environmental protection, finding plastic substitutes based on sustainability especially for short-term packaging and disposable applications has attracted scientific interest for many years. Starch is a naturally occurring biopolymer that can be a substitute for petroleum based plastics. However, it shows severe limitations due to its water sensitivity and rather low mechanical properties. To overcome the weakness and to maintain the material biodegradability, blending of thermoplastic starch (TPS) with other biodegradable polymers is a good way. In this research work, binary blend with thermoplastic starch (TPS) and poly(butylene adipate-co-terephthalate) (PBAT), a flexible biodegradable copolymer, was prepared using the reactive extrusion. Two parameters as the thermoplastic starch content (0 – 50%) and maleic acid content (0 – 1%) were studied. Maleic acid as a compatibilizer was used to improve the interfacial affinity between TPS and PBAT. The morphology and properties of both compatibilized and non-compatibilized blends were investigated. The results showed that the addition of compatibilizer (maleic acid) increased the mechanical properties of the blends. The mechanical properties of the blend film with the ratio of 80:20 by weight (PBAT : TPS) were the best compared to others. Morphological study by SEM revealed that TPS particles were well dispersed in the polyester matrix.

Introduction

Plastic packaging is now subjected to strong pressure from environmental and disposal regulations in the design of single-use disposable packaging [1]. Obviously, there is a need for the development of environmentally friendly and biodegradable products derived from renewable resources, which retain all of the current plastics performances [2]. Because of the biodegradable character, natural abundance and low-cost, many researchers have attempted to incorporate starch into a great variety of plastic materials. Native starch may be added as unmodified filler [3] in melt-blends with, e.g. poly(hydroxybutyrate-co-hydroxyvalerate). However, the use of unmodified granular starch as a particulate filler cannot provide any appreciable reinforcement due to the poor adhesion of the polymer-granule interface [4].

The main uses of starch have been as a binder, as a thermoplastically processable constituent within thermoplastic polymer blends, and as a thermoplastic material by itself. In general, thermoplastic starch (TPS) is obtained from native starch in the presence of a plasticizer when heated and sheared [2]. Glycerol and water are the most used plasticizers. Unfortunately, the main limitation to use TPS as commodity plastics is due to its moisture sensitivity and thermal instability. It is well understood that TPS has to be combined in melt-blend with hydrophobic polymeric materials to produce high-performance TPS-based products [5]. At the earliest stage, polystyrene, polyethylene, poly(methy methacrylate) and others have been largely studied [6]. However, from an environmental viewpoint, the residues from nondegradable polymers are not environmentally friendly after biodegradation of starchy fraction. In this respect, some authors have preferred biodegradable hydrophobic polymers such as poly (caprolactone) and cellulose acetate to manufacture biodegradable products. Recently, poly (butylene adipate-co-terephthalate) (PBAT), a biodegradable aliphatic-aromatic copolyester, has shown to be an interesting polymeric partner in the starch-based melt-blends. This is due to its interesting thermomechanical properties [7]. However, because of the large difference in the hydrophilic balance, it is necessary to carry out a chemical functionalization on the biodegradable hydrophobic polymers in the preparation of starch-based polymer melt-blends [8].

Grafting of maleic anhydride onto the polymer backbone is currently used for functionalization. These grafted reactive functions can then react with the hydroxyl groups from starch to form covalent bonds; and thus, to provide better size control of the dispersed phase and stronger interfacial adhesion [9]. In a similar way, we have reported chemically modified TPS, called maleated TPS (MTPS). MTPS was prepared, through reactive extrusion processing of starch in the presence of glycerol (plasticizer) and maleic acid (MA, esterification agent).

This article aims at reporting the utilization of TPS in the reactive extrusion melt blending with PBAT. The ultimate objective of this work is to use the resulting (reactive) melt-blends in blown film applications. The effects of both MA and TPS contents by acid-promoted transesterification reactions on mechanical and morphology properties were studied.

Materials and Methods

Materials

The following materials were obtained from commercial suppliers and used as received. The tapioca starch was supplied by Tongchan Co., Ltd.

Poly(butylene adipate-co-terephthalate) (PBAT, T_g = - 29 °C, T_m = 110 -115 °C, Ecoflex F BX 7011) was supplied by BASF. The chemical structure is shown in Figure 1. Maleic acid (98%) and glycerol were obtained from Sigma-Aldrich.

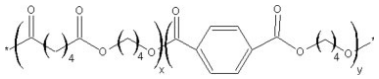

Figure 1. Chemical structure of poly(butylene adipate-co-terephthalate)

Processing

TPS (Thermoplastic starch) can be obtained by processing granular starch at low water or other plasticizer content using thermal and mechanical forces [10]. In this work, TPS was prepared by a food mixer (K5SS, Kitchen aid Co., Ltd., USA) in the following proportions: 100 g of starch and 35 g of glycerol. TPS/polyester binary blends were prepared by melt mixing TPS and PBAT using a twin-screw extruder (LTS 20-32, L/D Labtech Engineering Co., Ltd., Thailand). The compositions of the blends are shown in Table 1. Before extrusion, PBAT pellet was dried in a hot oven at 70 °C for 3 h. The extrusion temperature was independently controlled at eight zones along the extruder barrel and a strand die to achieve a temperature profile in the range of 160–175 °C. The screw speed was set at 80 rpm.

Blown film processing was accomplished in a blown film extrusion (HAAKE PolyLab,Germany). Test specimens for tensile testing were obtained according to ASTM D882 (USA). The binary blends follow the following processing conditions: barrel temperature 150-175 °C and screw speed 80 rpm. All samples were conditioned at room temperature at 50% relative humidity for at least 1 day before testing.

Mechanical properties.

All the mechanical property measurements were performed at room temperature on blown film samples. Both tensile strength and elongation at break properties were measured on a universal testing machine (Instron model 55R4502, USA) according to ASTM D882. A crosshead speed of 500 mm/min was used. At least five specimens were used for each blend condition.

Scanning electron microscopy (SEM analysis)

Impact samples were gold coated and observed under a JEOL JSM-5410 scanning electron microscope (SEM).

Table 1 : The formulation used in the preparation of a polyester blend films.

Formula	PBAT (%wt)	TPS (%wt)	MA (%wt)
20STMA0	80	20	0
30STMA0	70	30	0
40STMA0	60	40	0
50STMA0	50	50	0
20STMA0.5	80	20	0.5
30STMA0.5	70	30	0.5
40STMA0.5	60	40	0.5
50STMA0.5	50	50	0.5
20STMA1	80	20	1
30STMA1	70	30	1
40STMA1	60	40	1
50STMA1	50	50	1

Results and Discussion

Mechanical properties of the films

Mechanical properties of blends are shown in Figure 2. The blend film at 80:20 PBAT:TPS showed higher mechanical properties compared to others. The results showed that, although the incorperation of TPS in the PBAT led to lower tensile strength, the binary blends are still operational. On the other hand, the incorporation of TPS had no pronounced effect on elongation at break. When a small amount of compatibilizer was added to the blend, increases in both tensile strength and elongation at break were observed throughout the studied composition ranges. These increases could be ascribed to the poor interfacial adhesion between TPS and PBAT being improved after the compatibilizer was added. The reaction of the ester groups of the PBAT with the hydroxyl groups of the TPS formed ester linkages. Maleic acid as a compatibilizer was used to promote the transesterification reactions between TPS and PBAT. So compatibilized blends had better interfacial adhesion between the blend components, thus resulting in a relatively compact phase structure and an increase mechanical properties.

For the compatibilized blends, as TPS content increased, the tensile strength of the blends tended to decrease, as well as the uncompatibilized ones. Meanwhile, elongation at break of the blends was not significantly affected as TPS content increased. For compatibilizer effect, the tensile strength of the blends increased when 0.5% MA was added. Conversely, when the MA content reached to 1%, it decreased. The results implied that there was an optimum amount of maleic acid used in the studied system. For elongation, the higher content of MA, the higher elongation.

Film morphology

The SEM micrographs of blend films were displayed in Figure 3 (a-f). Phase separation of PBAT and TPS can be seen clearly in blend without MA (Figure 3b). Many TPS were pulled out from the matrix.

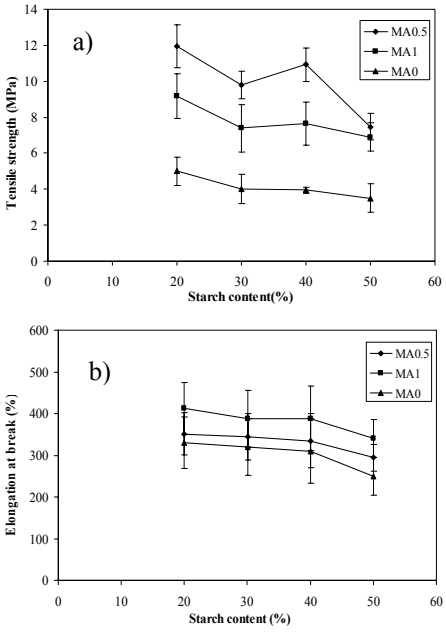

Figure 2. Mechanical properties of PBAT : TPS at various maleic acid contents (a) Tensile strength (b) % Elongation at break

These results indicated poor interfacial adhesion between PBAT and TPS. Therefore, the blends without MA showed poor mechanical properties compared to those of compatibilized ones as described earlier. These results indicated that the MA acted as compatibilizer and increased the interfacial adhesion between PBAT and TPS. There after, the SEM results of blends with MA exhibited few holes in two phases. So, it was confirmed that TPS particles were dispersed homogeneously in PBAT matrix.

Conclusions

Biodegradable binary blends of TPS and PBAT gave good properties when small amount of compatibilizer (0.5% MA) was added. For the PBAT : TPS binary blends the tensile strength increased about 100% after addition of compatibilizer. The elongation was no pronounced decrease as the percentage of TPS increased.The MA functionalized polyester reduced size of the dispersed phase, thus enhancing the interaction the two phases; TPS and polyester.

Acknowledgements

This work was financially supported by the National Metal and Materials Technology Center (MTEC).

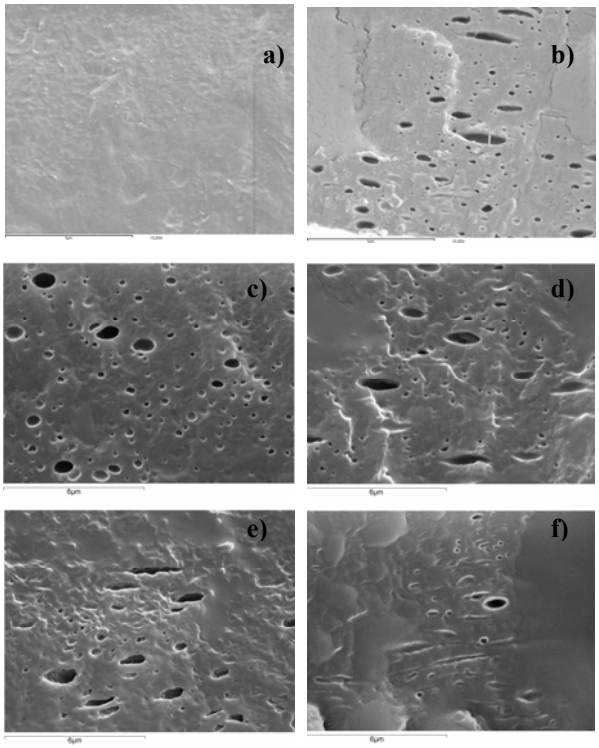

Figure 3. SEM micrographs of PBAT : TPS : MA blends at different blend ratios (a) 100:0:0 (b) 80:20:0 (c) 80:20:0.5 (d) 70:30:0.5 (e) 60:40:0.5 (f) 50:50:0.5

References

[1] C. Reddy, R. Ghai, and V. Rashmi, *Bioresour Technol* **87** (2003), pp. 137.

[2] R. Narayan, *Commercialization Technology: A Case Study of Starch Based Biodegradable Plastics in Paradigm for Successful Utilization of Renewable Resources*, AOCS Press, Champaign, IL, 78 (1998).

[3] G.J.L. Griffin, *Chemistry and Technology of Biodegradable Polymers*, Blackie Academic and Professional, Glasgow, UK (1992).

[4] B.A. Ramsay, V. Langlade, P.J. Carreau, and J.A. Ramsay, *Appl. Environ. Microbiol*, **59** (1993), pp. 1242.

[5] P. Nayak, *J. Macromol. Sci. Rev. Macromol. Chem. Phys*, **C39** (3) (1999), pp. 481.

[6] R. Chinnaswamy and M.A. Hanna, U.S. Patent 5,496,895 (1996).

[7] Y. Nabar, J.-M. Requez, P. Dubois, and R. Narayan, *Biomacromolecules*, **6** (2005), pp.807.

[8] G. Ruggeri, M. Aglietto. A. Petramani, and F. Ciardelli, Eur. Polym. J, **19** (1983), pp. 863.

[9] J.-M. Raquez, Y. Nabar, P. Dubois, and R. Narayan, *Carbohydr. Polym*, (2008), in press.

[10] P. Myllarinen, R. Partanen, J. Seppala and P. Forssell, *Carbohydrate Polymers* **50** (4) (2002), ppA.355–36

Effect of plasticizers on mechanical properties of cassava starch films

W. Kumpapong and S. Lumlong*

Department of Chemistry, Faculty of Science, Ubon Ratchathani University, Ubon ratchathani, Thailand 34190

*E-mail : g3936619@hotmail.com Tel. +66-4-528-8381 ext 4119

Abstract: This work studied the effect of types and quantities of plasticizer on physical properties and mechanical properties of cassava starch film. Three types of plasticizers had been investigated: glycerol, urea, and ethylene glycol. The plasticizers were used as individual and mixed plasticizers. Moreover, we studied the effect of lignin on physical properties and mechanical properties of cassava starch film. The results showed that the starch film was less brittle when increased the amount of glycerol or urea. The modulus and tensile strength of plasticized films were lower than that of un-plasticized film. However, the elongation at break of plasticized film was higher than that of un-plasticized film. The starch film with ethylene glycol was still brittle. The starch film with lignin was less brittle than that of un-plasticized film. The mixed plasticizers were glycerol and urea, glycerol and ethylene glycol, urea and ethylene glycol. The starch film with mixed plasticizers showed the same trend. The modulus and tensile strength of plasticized films were lower than that of un-plasticized film. However, the elongation at break of plasticized film was higher than that of un-plasticized film.

Introduction

Over the past few years, there has been an interest in film made from renewable and natural polymers such as starch. Several studies have analyzed the properties of starch-based films. Edible or biodegradable films are not meant to totally replace synthetic packaging films; however, they do have the potential to replace the conventional packaging in some applications. Starch is considered one of the most promising natural polymers for packaging applications because of its low cost, renewability and biodegradability. Unfortunately, starch-based products have some major limitations when compared to conventional petroleum-derived films, due to their poor mechanical properties [1].

Starch is polysaccharide composed of amylose, a linear or sparsely branched polymer, and amylopectin, a highly branched polymer [1]. Starch, a natural renewable polysaccharide, obtained from a great variety of crops, was one of the promising raw materials for the production of biodegradable plastics. However, native starch commonly existed in granule structure with about 15–45% crystallinity and starch-based materials were susceptible to aging and starch recrystallization (retrogradation). The properties of starch film can be modified by the addition of various chemicals in minor amounts. For example, plasticizers, such as glycerol and sorbitol are often used to modify the mechanical properties of the film. These compounds decrease intermolecular attractions between adjacent polymeric chains, thus increasing film flexibility. Incorporation of these additives may, however, cause significant changes in the barrier properties of the film. Thermoplastic starch (TPS) plasticized with glycerol, a conventional TPS, was thought to tend to retrogradation after being stored for a period of time, and this retrogradation embrittled TPS. Urea was proven to prevent starch retrogradation. It was, however, a solid with little internal flexibility and hence urea-plasticized TPS became rigid and brittle [1-5].

In this work, we studied the effect of types and quantities of plasticizer on physical properties and mechanical properties of cassava starch film. Three types of plasticizers had been investigated: glycerol, urea, and ethylene glycol. The plasticizers were used as individual and mixed plasticizers. Moreover, we studied the effect of lignin on physical properties and mechanical properties of cassava starch film.

Materials and Methods

Materials

Cassava starch was purchased from Thai Wah Food Products Public Company Ltd. Glycerol, urea, ethylene glycol, hydrochloric acid (HCl) and sodium hydroxide (NaOH) were used without further treatment.

Lignin extraction

Lignin was extracted from banana stem. First, the banana stem was clean and cut into 1x1 cm pieces and dried at 45°C. Then, the dried banana stem was soaked with 1M NaOH and stirred at 80°C for 3 h to extract lignin. The aqueous phase with extracted lignin was neutralized by 1M HCl. The obtained lignin was dried at 60°C

Preparation of starch films

Starch films were prepared by the casting method. Starch was mixed and dispersed in water. The mixture contained 2 g of starch/100 g of water. The film-forming suspension was heated with continuous stirring and kept at 70°C for 1 hr. The film-forming solution was casted on a polystyrene tray. Starch films were obtained by evaporating water in an oven at 45°C.

Preparation of plasticized starch films

Plasticized starch films were obtained by the casting method. Starch and plasticizer were first mixed and dispersed in water. The mixture contained 2 g of starch/100 g of water and 10, 20, 30 and 40 g of plasticizer/100 g of starch. The film-forming suspension was heated with continuous stirring and kept at 70°C for 1 hr. The film-forming solution was casted on a polystyrene tray. Starch-based films were obtained by evaporating water in an oven at 45°C. For mixed plasticizers, the ratios of glycerol:urea, glycerol:ethylene glycol and urea:ethylene glycol were 1:1.

Mechanical testing

Mechanical properties of samples were determined by tensile testing (LR series, Lloyds) at a crosshead speed of 50 mm/min. The data were averages of 5 specimens.

Results and Discussion

Starch films with different glycerol contents were shown in Figure 1. Starch film without glycerol was stiff and brittle, in Figure 1a. Starch film with 10% w/w glycerol was still brittle, in Figure 1b. Starch film with 20% w/w glycerol was softer than that of starch film with 10% w/w glycerol, in Figure 1c. Increasing the amount of glycerol to 30% w/w, the starch film was softer and tougher than that of starch film with 20% w/w glycerol, in Figure 1d. The starch film with 40% w/w glycerol was very soft, tough, and sticky, in Figure 1e. Therefore, the starch film was changed from stiff and brittle to soft and tough when increasing the glycerol content. This result indicated that glycerol acts as a plasticizer for starch. The highest amount of glycerol for starch film was 30%w/w of starch.

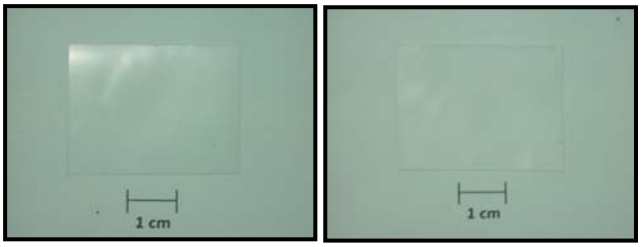

(a) (b)

(c) (d)

(e)

Figure 1. Starch films with different glycerol contents (a) 0%, b) 10%, (c) 20%, (d) 30% and (e) 40%.

Figure 2 showed the stress-strain curves of starch film with different glycerol contents. The mechanical properties of starch films without glycerol and with 40%w/w glycerol could not be measured because they were too brittle (starch films without glycerol) and too soft (films with 40%w/w glycerol) to be cut. The tensile strength of starch film was decreased when increasing the amount of glycerol. However, the elongation at break of the starch film was significantly increased when increasing the amount of glycerol.

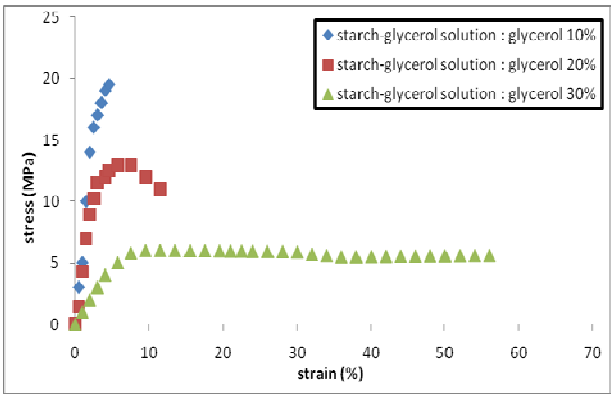

Figure 2. Stress-strain curves of starch films with various glycerol contents from 10% - 30%.

Starch films with different urea contents were shown in Figure 1. Starch film without urea was stiff and brittle, in Figure 3a. Starch film with 10% w/w urea was still brittle, in Figure 3b. Starch film with 20% w/w urea was softer than that of starch film with 10% w/w urea, in Figure 3c. Increasing the amount of urea to 30% w/w, the starch film was softer and tougher than that of starch film with 20% w/w urea, in Figure 3d. The starch film with 40% w/w urea was very soft, tough, and sticky, in Figure 3e. Therefore, the starch film was changed from stiff and brittle to soft and tough when increasing the urea content. This result indicated that urea acts as a plasticizer for starch film. The highest amount of urea for starch film was 30%w/w of starch.

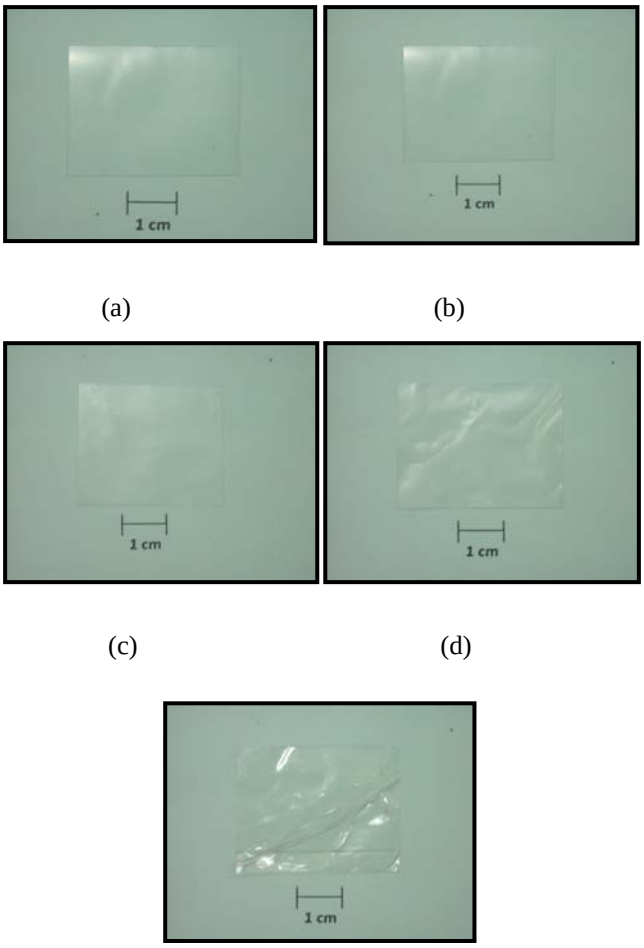

Figure 3. Starch films with different urea contents (a) 0%, b) 10%, (c) 20%, (d) 30% and (e) 40%.

Figure 4 showed the stress-strain curves of starch film with different urea contents. The mechanical properties of starch films without urea and with 40%w/w urea could not be measured because they were too brittle (starch films without urea) and too soft (films with 40%w/w urea) to be cut. The tensile strength and modulus of starch film were decreased when increasing the amount of urea. However, the elongation at break of the starch film was increased significantly when increasing the amount of urea. Urea also acts as plasticizer for starch.

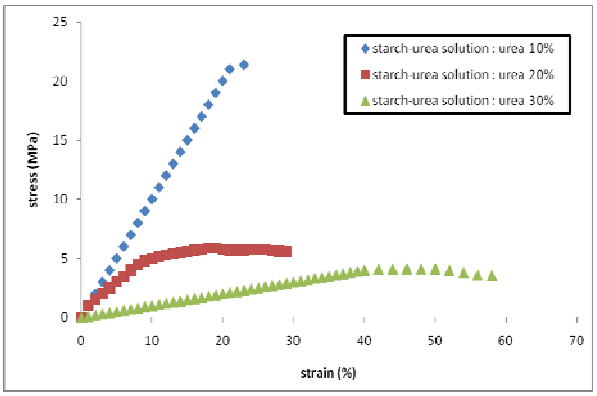

Figure 4. Stress-strain curves of starch films with various urea contents from 10% - 30%.

Starch films with different ethylene glycol contents were shown in Figure 5. Starch film without ethylene glycol was stiff and brittle, in Figure 5a. Starch film with 10% w/w ethylene glycol was still brittle, in Figure 5b. Increasing the amount of ethylene glycol up to 40%, the starch film was still brittle. The physical properties of starch film with ethylene glycol were almost the same. Therefore, ethylene glycol was not a plasticizer for starch.

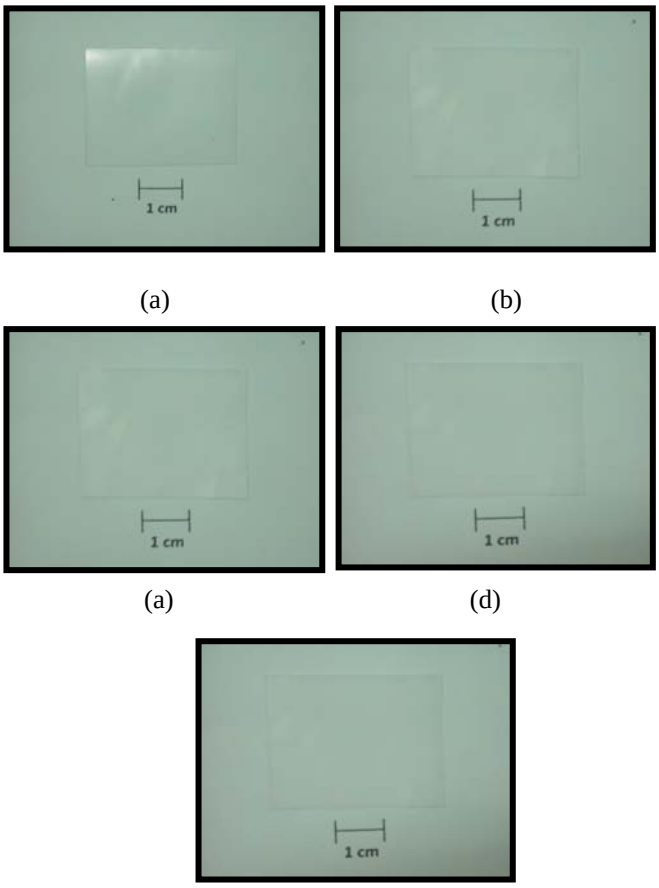

Figure 5. Starch films with different ethylene glycol contents (a) 0%, b) 10%, (c) 20%, (d) 30% and (e) 40%.

Figure 6 showed the stress-strain curves of starch film with different lignin contents. The mechanical properties of starch films without lignin could not be measured because they were too brittle to be cut. The tensile strength of starch film was decreased when increasing the amount of lignin. The elongation at break of the starch film was increased when increasing the amount of lignin from 5% to 20% w/w. However, the elongation at break was decreased when increased the amount of lignin. Lignin also acts as plasticizer for starch. However, it was less effective than that of glycerol or urea.

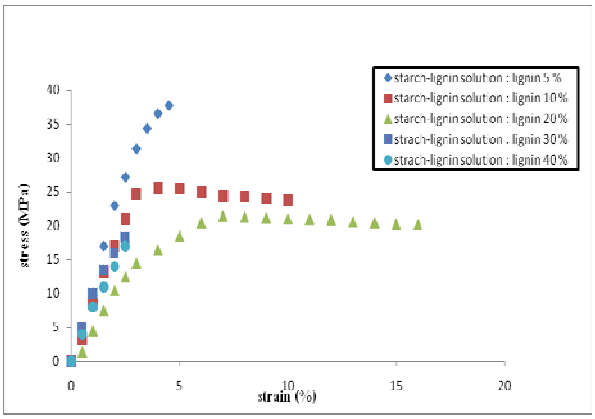

Figure 6. Stress-strain curves of starch films with various lignin contents from 5% - 40%.

Table 1 showed the modulus, tensile strength, and elongation at break of starch film with various amount of urea:glycerol mixed plasticizer ratio of 1:1. The modulus and tensile strength of starch film were decreased when increasing the amount of urea:glycerol mixed plasticizer. The elongation at break of the starch film was increased when increasing the amount of urea:glycerol mixed plasticizer from 10% to 20% w/w.

Table 1. The modulus, tensile strength and elongation at break of starch films with various amount of urea:glycerol mixed plasticizer ratio of 1:1.

Amount of urea:glycerol (1:1) (%)	Modulus (MPa)	Tensile strength (MPa)	Elongation at break (%)
10	8.63 ±1.27	17.43±3.84	2.31 ± 0.19
20	2.66 ±1.18	6.49 ±0.99	24.07 ±6.44

Table 2 showed the modulus, tensile strength, and elongation at break of starch film with various amount of urea:ethylene glycol mixed plasticizer ratio of 1:1. The modulus and tensile strength of starch film were decreased when increasing the amount of urea:ethylene glycol mixed plasticizer. The elongation at break of the starch film was increased when increasing the amount of urea:ethylene glycol mixed plasticizer from 10% to 20% w/w.

Table 2. The modulus, tensile strength and elongation at break of starch films with various amount of urea:ethylene glycol mixed plasticizer ratio of 1:1.

Amount of urea: ethylene glycol (1:1) (%)	Modulus (MPa)	Tensile strength (MPa)	Elongation at break (%)
10	8.02 ±0.48	21.37±1.12	3.40 ± 0.51
20	388 ±0.52	8.34 ±3.94	11.66 ±2.24

Conclusions

The starch film was less brittle when increased the amount of glycerol or urea but the starch film with ethylene glycol was still brittle. Therefore, glycerol and urea acted as plasticizer for starch. The tensile strength of plasticized films was lower than that of un-plasticized film. However, the elongation at break of plasticized film was higher than that of un-plasticized film. The starch film with lignin was less brittle than that of un-plasticized film. The tensile strength of mixed plasticized films was lower than that of un-plasticized film. However, the elongation at break of plasticized film was higher than that of un-plasticized film.

Acknowledgements

The authors gratefully acknowledge Department of Chemistry, Faculty of Science, Ubon Ratchathani University for the equipment and chemical reagent support.

References

[1] H. Dai, , P. R. Chang, J. Geng, J. Yu, X. Ma, *Carbohydr. Polym.* **79** (2010), pp. 306-311.
[2] P. Veiga-Santos, L.M. Oliveira, M.C. Cereda, A.R.P. Scamparini, *Food Chem.* **103** (2007), pp. 255-262.
[3] X.F. Ma, J.G. Yu, J.J Wan, *Carbohydr. Polym.* **64** (2006), pp. 267-273.
[4] M. Rodriguez, J. Oses, K. Ziani, J.I. Mate, *Food Res.Int.* **39** (2006), pp. 840-846.
[5] A.L. DaRoz, A.J.F. Carvalho, A. Gandini, A.A.S. Curvelo, *Carbohydr. Polym.* **63** (2006), pp. 417-424.

Physical and Theoretical Chemistry

Computer-aided molecular design of arylamide as the novel direct inhibitors of the enoyl ACP reductase (InhA) from *M. tuberculosis* based on molecular docking calculations and QSAR studies

A. Punkvang[1], P. Saparpakorn[2], S. Hannongbua[2], P. Wolschann[3], H.Berner[3] and P. Pungpo[1*]

[1]Faculty of Science, Ubonratchathani University, Ubon Ratchathani, Thailand
[2]Faculty of Science, Kasetsart University, Bangkok, Thailand
[3]Institute for Theoretical Chemistry, University of Vienna, A-1090 Vienna, Austria

[*] pornpan_ubu@yahoo.com

Abstract: The enoyl ACP reductase enzyme (InhA) involved in the type II fatty acid biosynthesis pathway of M. tuberculosis is the attractive target enzyme for antitubercular drug development. A series of arylamide derivatives is the novel class of potent InhA inhibitors that can address the drug-resistant problem of isoniazid, the frontline line drug for tuberculosis treatment. To model the potential binding modes of arylamide derivatives in InhA binding pocket, molecular docking calculations using Glide program were utilized. Molecular docking calculations reveal high reliability to reproduce the X-ray bound conformation with the rmsd value of 0.73 Å and could be successful to carry out the important drug-enzyme interactions. To clearly delineate the linear relationship between structure and activity of these inhibitors, CoMFA and CoMSIA models were set up based on molecular alignment of the reliable conformations gained from the Glide docking. The selected CoMFA and CoMSIA models are satisfying based on the good r^2_{cv} of 0.68 and 0.64, respectively. Structural requirements that can be utilized for structural modification to improve the activity of arylamide inhibitors could be highlighted through CoMFA and CoMSIA contour maps. Moreover, to reveal the molecular fragment contribution to the inhibitory activity of arylamide derivatives, HQSAR was also performed. Finally, the obtained computational results from all approaches in the present study are well consistent with each other. Therefore, the combined results gained from structure-based and ligand-based design approaches could provide the insight into drug-enzyme interactions and the structural requirement of arylamide derivatives and should be useful for designing the new and more potent InhA inhibitors in class of arylamide derivatives.

Introduction

The enoyl-acyl ACP reductase (InhA) involved in mycolic acid biosynthesis is the potential enzyme targets for developing antibacterial drug. Subsequently, InhA has been identified as the primary target of isoniazid (INH), the frontline drug for tuberculosis chemotherapy [1]. As a prodrug, INH must first be activated by catalase-peroxidase (KatG) to generate the reactive acyl radical [2]. Then, the reactive specie binds covalently to nicotinamide adenine dinucleotide (NAD+) to form the active adduct (INH-NAD adduct) that functions as the highly potent inhibitor of InhA [3]. Mutations in katG, the most commonly found in *M. tuberculosis* clinical isolates, give high levels of resistance to INH [4]. To address the resistance to INH associated with mutations in the katG enzyme, compounds that directly inhibit InhA enzyme but do not require activation by KatG would be introduced as novel antitubercular agents. A series of arylamides were identified as the novel class of potent InhA inhibitors [5]. Arylamides target InhA directly without a requirement for KatG activation that functions as the direct InhA inhibitors. However, the majority of arylamides exhibit high minimum inhibitory concentrations against *M. tuberculosis* strain H37Rv. Therefore, the basis information for structural modification to improve the antibacterial activity of arylamide compounds is essential. In present study, molecular docking calculations were employed to carry out the important drug-enzyme interactions for binding of arylamides in InhA binding pocket. Moreover, to gain insight into the structural requirement of arylamide compounds for enhancing antibacterial activity, the relationship between structure and activity of these compounds was elucidated by CoMFA, CoMSIA and HQSAR methods. These data should aid in the rational design of direct InhA inhibitors with highly potential antitubercular activity.

Materials and Methods

The general structure of arylamide is shown in Figure 1. All chemical structures of 28 arylamide derivatives were constructed using Gaussview 3.07 program and then were fully optimized using HF/3-21G method in Gaussian 03 program. Molecular docking calculations were performed by using Glide program. CoMFA and CoMSIA based on the docked structural alignment were applied to 28 arylamide derivatives. HQSAR was also performed by using Sybyl program.

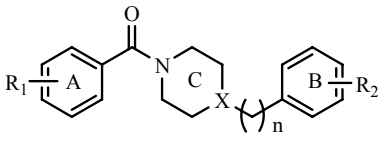

Figure 1. General structure of arylamide

Results and Discussion

Molecular Docking Calculations: The potential binding modes of arylamide derivatives in InhA binding pocket were carried out by molecular docking calculations with the program Glide. The root mean-square deviation (rmsd) between the docked and crystallographic conformations of arylamide is 0.73 Å indicating that molecular docking calculations with the Glide program reveal high reliability for reproducing the binding mode of arylamide in the InhA binding pocket.

The analysis on the predicted binding modes of arylamide derivatives reveals the key interactions of these inhibitors for inhibiting InhA enzyme. Two hydrogen bonds of the amide carbonyl group oxygen with hydroxyl group of the nicotinamide ribose and the hydroxyl group of Tyr158 play important rule for inhibitor binding as shown in Figure 2. Other important interactions for reinforcing the inhibitor binding is hydrophobic interactions of the substituent B formed with hydrophobic residues of Ala157, Met199, Pro193, Val203, Ile215, Leu218, Ile202, Trp222 and Met232.

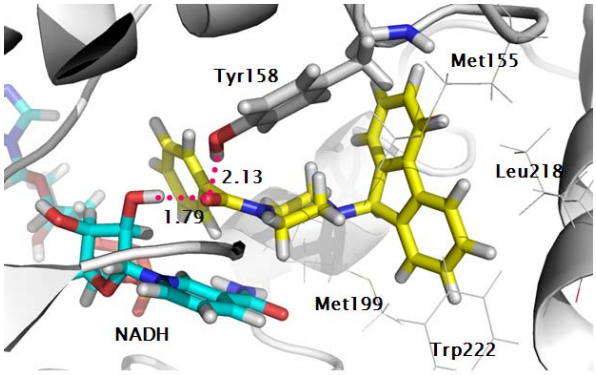

Figure 2. The most active compound (yellow) in InhA binding pocket obtained from docking calculations.

CoMFA and CoMSIA models:

The best CoMFA and CoMSIA models generated based on molecular docking alignment are satisfying with the cross-validation (r^2_{cv}) of 0.68 and 0.64, respectively. From CoMFA steric contours as shown in Figure 3, two large yellow contours located near the meta- and para-substituents on the aryl ring A indicate that these region must not contain bulky substituents. Another interesting large green contour is located near ring B. Therefore, introducing a bulkier group to ring B within the large green region would enhance the activity of these compounds. Figure 4 presents the electrostatic CoMFA contour map. A blue contour appears near the hydrogen atoms at the ortho-position of the aryl ring A indicating that a more positively charged substituent is favored in this position for increased affinity. Additionally, two large blue contours situated near the meta- and para-substituents on the aryl ring A of these compounds imply that electron deficient substituents were preferred in these region. In another area, CoMFA model shows that a large electronegatively favored region is located above the aromatic fluorene ring B implying that the aromatic ring at this position would enhance the inhibitory potency. In case of CoMSIA steric and electrostatic contours (not shown), these contours are similarly to those of CoMFA contours.

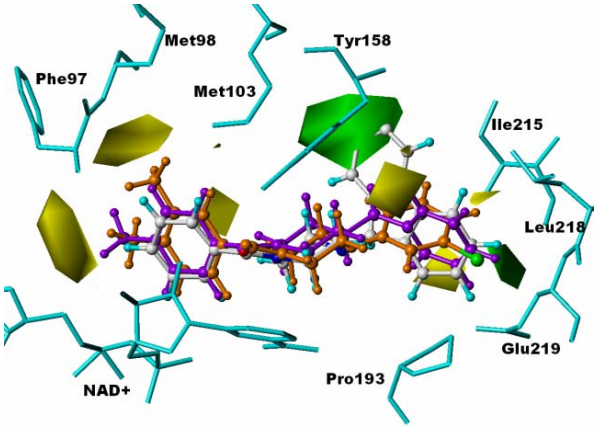

Figure 3. CoMFA steric contours. Favorable and unfavorable steric regions are displayed in green and yellow contours, respectively.

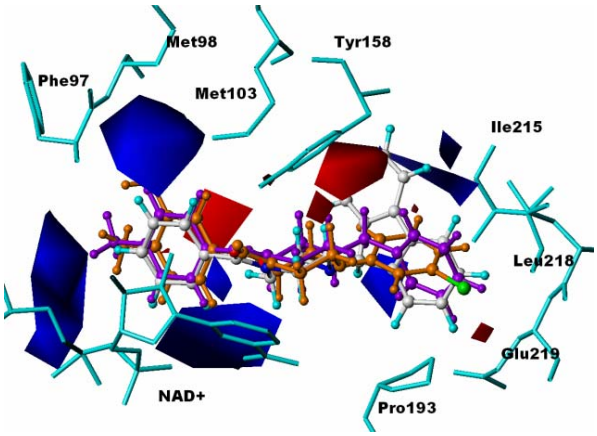

Figure 4. CoMFA electrostatic contours. Blue and red contours illustrate the regions that favor the positive and negative charge, respectively.

The CoMSIA model indicating hydrophobicity is shown in Figure 5. Two hydrophobic unfavorable white contours appear near the meta- and para-substituents on the aryl ring A. The combined results from CoMFA and CoMSIA contour maps indicate that electron donating group with less steric demand and more hydrophilicity in these regions would be helpful to enhance the binding affinity of arylamide derivatives in the InhA pocket. Two hydrophobic favorable magenta contours are located near ring B. Therefore, the hydrophobic group matches two favorable hydrophobic magenta contours of ring B and thence should enhance activity of arylamides.

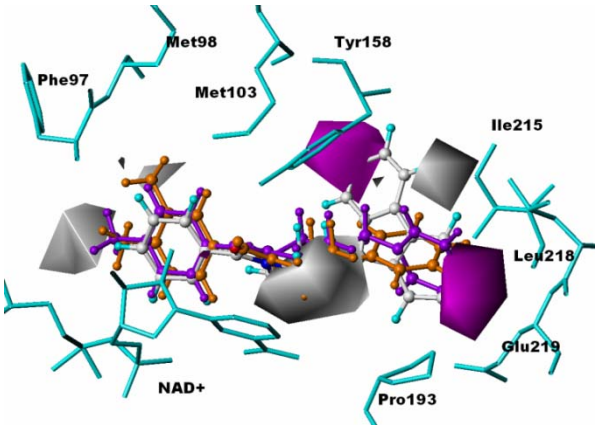

Figure 5. CoMSIA hydrophobic contours. Magenta and white contours represent the favorable and unfavorable hydrophobic regions, respectively.

HQSAR model:

Molecular fragments of arylamides which are directly contributing to biological activity can be visualized through HQSAR contribution maps as shown in Figure 6. The different contributions of all atoms in a molecule to the biological activity are discriminated by a color code. Atoms with negative contributions are represented at the red end of the spectrum, whereas atoms with positive contributions are presented by the colors at the green end of the spectrum. The white colored atoms are giving intermediate contributions. As seen from Figure 10, the fragments of the fluorene ring B of the most active compound are positively correlated with the biological activity of this compound. These observations confirm the previous CoMFA and CoMSIA results which suggest that the bulky volume of ring B would enhance the biological activities of arylamide derivatives. With regard to the aryl ring A, this fragment of this compound is positively related to the biological activities.

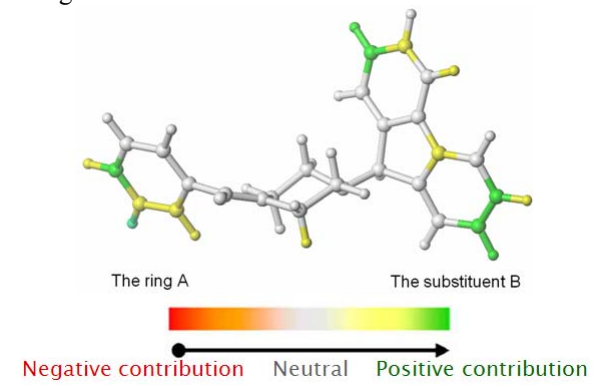

Figure 6. The HQSAR contribution map for the most active compound

Conclusions

Molecular docking calculations using Glide program were successful to carry out the crucial interactions for binding affinity of arylamide inhibitors in InhA binding pocket. Only the steric electrostatic and hydrophobic field descriptors were considered in the best CoMFA and CoMSIA models implying that three molecular field descriptors play the dominant rule on biological activity of arylamide inhibitors. Successfully, the HQSAR contribution maps could nicely reveals the individual contribution of the atoms to the inhibitory activity of arylamide derivatives. Overall, the integrated results from molecular docking and QSAR analysis in this study could provide the valuable computational tools that can be utilized for designing novel and more active antitubercular agents in the series of arylamide derivatives.

References

[1] B. Saint-Joanis, H. Souchon, M. Wilming, K. Johnsson, P.M. Alzari, S.T. Cole, *Biochem. J.* **338**(1999), pp.753-760.
[2] X. Zhao, H. Yu, S. Yu, F. Wang, J.C. Sacchettini, R.S. Magliozzo *Biochemistry* **45**(2006), pp.4131-4140.
[3] C.W. am Ende, S.E. Knudson, N. Liu, J. Childs, T.J. Sullivan, M. Boyne, H. Xu, Y. Gegina, D.L. Knudson, F. Johnson, C.A. Peloquin, R.A. Slayden, P.J. Tonge, *Bioorg. Med. Chem. Lett.* **18**(2008), pp.3029-3033.
[4] X.Y. Lu, Y.D. Chen, Y.J. Jiang, Q.D. You. *Eur. J. Med. Chem.* **44** (2009), pp.3718-3730.
[5] X. He, A. Alian, P.R. Ortiz de Montellano, *Bioorg. Med. Chem.* **15**(2007), pp.6649–6658

Feasibility study on the mass-selected velocity map imaging of polyatomic molecules and fullerenes

H. Katayanagi[1,2], B.P. Kafle[1], C. Huang[1], Md.S.I. Prodhan[1,2], H. Yagi[1], K. Mitsuke[1,2]*

[2]Department of Photomolecular Science, Institute for Molecular Science, Myodaiji, Okazaki, 444-8585,Japan
[3]Department of Structural Molecular Science, Graduate University for Advanced Studies, Myodaiji, Okazaki, 444-8585,Japan

*E-mail: mitsuke@ims.ac.jp

Abstract: A photoionization spectrometer for velocity map imaging (VMI) has been developed for measuring the scattering distribution of fragment ions from polyatomic molecules. The spectrometer contains a mass gate and an ion reflector which can discriminate ions with a particular mass-to-charge ratio *m/z*. The basic functions and feasibility of these devices were tested experimentally and theoretically. First, the photoions from Kr and C_{60} were extracted into a time-of-flight (TOF) mass spectrometer by pulsed or continuous electrostatic fields. When the pulse-application timing on the mass gate was tuned to a specific *m/z*, the peak of the selected ions alone was present on a TOF spectrum. Second, the performance of the mass gate in the VMI spectrometer was investigated by the computer simulations of the ion trajectories of fragments from C_{60}. The initial three-dimensional velocity distribution of C_{58}^+ was projected onto the image plane with an energy resolution better than 10 meV. The C_{58}^+ image was free from the contamination of other ions, e.g. C_{60}^+ and C_{56}^+.

Introduction

In the velocity map imaging (VMI) technique, the three-dimensional (3D) scattering distribution of photoions is projected onto the surface of a position sensitive detector (PSD). The obtained image allows us to gain valuable insight into the dynamics of photoionization and photodissociation of diatomic and triatomic molecules [1]. General applications of VMI for polyatomic molecules should however await a practical solution to the problem that image data are contaminated by multiple fragments with different mass to charge ratio *m/z*. Some authors [2] applied a pulsed high voltage to the front plate of the microchannel plate multipliers (MCP) just on time for the arrival of the ionic fragments with a particular *m/z*. This MCP switching is not so advantageous to large molecules, because the time of flights (TOFs) of various kinds of fragments come close to one another. Furthermore, applying the pulsed high electric field brings about distortion of the equipotential surfaces inside a drift tube which prevents a part of ion trajectories from reaching a PSD.

In this paper, we will discuss the feasibility of the mass gate and ion reflector inside the drift tube designed for VMI of photofragments from large molecules such as clusters, fullerenes, and biopolymers. The capability of these elements for discriminating the ions with a particular *m/z* from other unnecessary species will be demonstrated in two ways. First, the mass gate and ion reflector will be tested experimentally by TOF mass spectrometry of Kr and C_{60}. Second, we will use computer simulation of the trajectories of fragment ions from C_{60} to show the performance of the two elements in discriminating particular ions, in the prospect of adaptation to the VMI studies. We will examine whether the pulsed operation of the mass gate has a negligible effect on the trajectories of the selected ions and whether the image on a PSD closely reflects their primary 3D velocity distribution.

Experimental Methods

We used a conventional lens system of Wiley-Mclaren type [3] including the electrodes of the repeller (R), ion extractor (E) and tube entrance (T) as shown in Fig. 1. The voltages applied to the respective electrodes and their dimensions are summarized in Table 1. Central holes drilled in these electrodes were covered with tungsten or copper meshes. The tube-entrance electrode was fitted to a cylindrical drift tube. Monochromatized synchrotron radiation (SR) supplied from the bending magnet beamline BL2B in the UVSOR [4] was focused onto the center of the volume across which the repeller and ion-extractor electrodes face each other. When Kr and C_{60} were introduced, the pressures of the experimental chamber were 2×10^{-6} and 7×10^{-8} Torr, respectively. The detailed explanation on our C_{60} beam source was given elsewhere [5]. The photoions produced by SR irradiation were extracted by either (a) a pulsed electric field in the pulsed extraction (PEX) mode or (b) a continuous electrostatic field in the photoelectron photoion coincidence (PEPICO) mode. The ions were

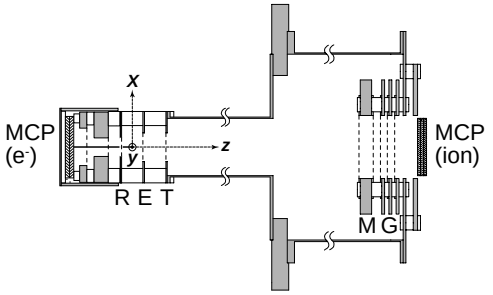

Figure 1. TOF mass spectrometer and electron analyzer. Synchrotron radiation was introduced along the *y*-axis. R, repeller; E, ion extractor; T, tube entrance; M, mass gate; G, ion reflector.

mass-separated by a double-focusing TOF mass spec-

Table 1. Voltages applied to the respective electrodes and their dimensions with internal diameter Φ.

	Voltages (in V)		**Dimensions (**in mm)	
Electrode	**base line value**	**top line value**[a]	**shape**	**thick-ness**
Repeller, R	0 [b,c] 75 [c,d]	V_R=75 [b,c] - [c,d]	racetrack[e] Φ20	1
Ion Ex-tractor, E	1.0 [b-d]	-	racetrack[e] Φ10	1
Tube En-trance, T	–340 [b-d]	-	racetrack[e] Φ15	1
Drift Tube	–340 [b-d]	-	cylinder Φ40, Φ130	340
Mass Gate, M	–340 [b,d] –340 [c]	V_G=100[b,d] - [c]	cylinder Φ44	10
Retarding Grid,[f] G2	80 [b,d] 0 [c]	- [b,d] - [c]	cylinder Φ44	1

[a] Voltage at the top line of the pulse waveform. Not applicable in the case of a DC operation. [b] For the PEX mode. [c] For the control experiments. [d] For the PEPCO mode. [e] axes of 50×66, [f] Second disk electrode of the ion reflector G.

trometer, and detected with a *z*-stack MCP detectors (ϕ27, Hamamatsu, F1552). The signal from MCP was processed by conventional pulse counting system and a time-to-digital converter with a minimum bin width of 1 ns (FastComtec, P7888).

In the PEX studies of Kr and C_{60}, a pulsed voltage rising from the ground level to V_R = 75 V was applied to the repeller electrode as a start trigger for the TOF measurement. The duration and frequency of the pulsed voltage were 4.5 μs and 0.5 – 1.5 kHz, respectively. In the PEPICO of Kr, photoelectrons and photoions were accelerated in the opposite directions by a continuous electrostatic field between the repeller and ion extractor. Then the electrons passed through the central hole of the repeller were detected with another MCP (ϕ27, Hamamatsu, F1552). The electron signal was amplified, discriminated and fed into the start input of the time-to-digital converter.

The mass gate (M) and ion reflector (G) were installed in the end of the drift tube (see Figure 1); their symmetry axes agree with that of the drift tube. Their dimensions and positions were optimized by ion-trajectory simulation. The optimum distances from the ionization region were 335.5 and 360.5 mm to the center of the mass gate and the MCP, respectively. Thin meshes with 85% transmission were mounted on the both ends of the mass gate, so that we could avoid the distortion of the equipotential surfaces due to a fringe effect. The ion reflector consists of a triplet of disk electrodes that have central holes covered with fine meshes. The second disk electrode G2 named "retarding grid" was placed 5 mm apart from the first and third electrodes (G1 and G3) that were kept at -340 V. These two electrodes made the equipotential surfaces flat and parallel inside the ion reflector.

The retarding grid was biased to 80 V in both the PEX and PEPICO modes. Eventually, all ions were forced back there and cannot enter the MCP. We then applied a pulse voltage changing from –340 to V_G = +100 V to the mass gate by using a home made pulse generator. Instantaneously the potential energies of the ions were elevated. The ions of interest were made to pass through the retarding grid and reach the MCP, if we had adjusted the application timing of V_G to their arrival time into the mass gate. For the control experiment we applied DC voltages of -340 and 0 V to the mass gate and retarding grid, respectively. This combination resulted in no *m/z* discrimination and allowed all the ions to go beyond the ion reflector.

Performance tests of the mass gate

1. PEX of Kr

Figure 2 shows the TOF mass spectra of Kr^{z+} (z = 1 - 3) from Kr measured at $h\nu$ = 90 eV. Panel (a) was obtained by the control experiment with the V_R pulse to the repeller. Indeed all the species were observed with the MCP. In contrast, the voltage settings for the PEX of Kr^{2+} were adopted in Panel (b). The difference in application timing was 9 μs between the pulse voltages of V_R and V_G. The duration of V_G was 2 μs. The TOF position of the single peak of Kr^{2+} was nearly equal to the corresponding peak in Panel (a). Similarly any ion could be discriminated according to its charged state using the mass gate and retarding grid.

2. PEPICO of Kr

Figure 3 shows the TOF mass spectra of Kr^{z+} from Kr measured at $h\nu$ = 90 eV. Panel (a) was obtained by the control experiment with the continuous 75 V to the repeller, and no *m/z* discrimination was discernible. Here, the start triggers were taken from the photoelectron signals. The rate of background counts is higher in Figure 3(a) than in 2(a), which is due to the false coincidence counts arising from the ion signal which has no time correlation with the electron triggers. In Figure 3(b), the voltage settings for the PEPICO mode were employed. The timing of V_G was so chosen that the time lag with respect to the photoelectron trigger agrees with the flight time of the

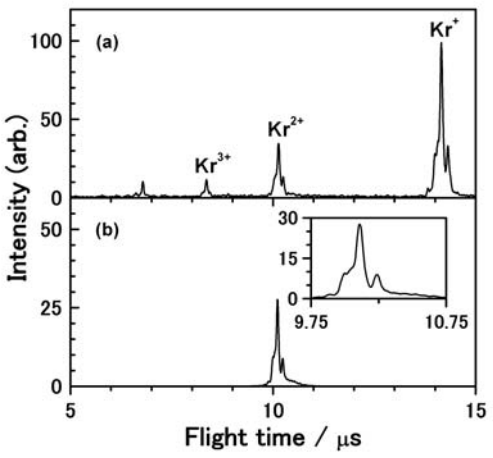

Figure 2. TOF spectra of Kr at $h\nu$ = 90 eV. (a) The control experiment with the V_R pulse; (b) the discrimination of Kr^{2+} by the PEX mode.

ions of interest. Indeed, the three spectra in Figure 3(b) obtained at the time lag of 6.2, 8.0 and 12.0 μs contain sharp peaks of Kr^{3+}, Kr^{2+} and Kr^{+}, respectively. The mass resolving power in Figure 3(b) appears to be a little lower than that in 2(b). The better mass resolution in the PEX mode arises from the so-called time-lag focusing [3] that is effective in the TOF mass spectrometer of Wiley-Mclaren type.

The ratio between the intensity of Kr^{z+} (z = 2 or 3) to that of Kr^{+} was found to be higher in Figure 3(b) than the reported value [6] at $h\nu$ = 90 eV. This is reasonably interpreted in terms of the difference in the number of detectable photoelectrons. In addition the above discrepancy is probably ascribable to the dependence of the photoelectron detection efficiency on the electron kinetic energy.

3. PEX of C_{60}

Figure 4 shows the TOF mass spectra of C_{60} measured at $h\nu$ = 90 eV. Panel (a) was obtained by the control experiment with the V_R pulse to the repeller. There are various photofragments, such as C_{58}^{2+}, C_{56}^{2+} and C_{54}^{2+}, in addition to the strong peaks of C_{60}^{z+} (z = 1 - 3). In contrast, the voltage settings for the PEX mode were adopted in Panels (b) and (c). The difference in application timing was 24 μs between V_R and V_G. The durations of V_G were 3 and 0.7 μs in Panels (b) and (c), respectively. The parent and fragment ions in doubly charged state alone remain in Panel (b). With the narrower duration, the fragment peak of C_{54}^{2+} could be selected in Panel (c). Obviously we have achieved the mass resolving power high enough to discriminate a particular species from the mixture of the multiple fragment ions.

Trajectory simulations of C_{58}^{+} from C_{60} in the VMI spectrometer

1. Basic idea of the simulation

In this section the performance of the mass gate inside the VMI spectrometer is investigated by the computer simulation of the ion trajectories. Taking an example of C_{58}^{+} from C_{60} we have studied the influence of the mass gate on the position resolution of the PSD and the purity of the *m/z* discrimination.

For the trajectory simulation the MCP was replaced with a PSD of 40 mm in diameter. The arrangement of the lens system used for the simulation is similar to that in Figure 1, though we dismissed the meshes attached on the electrodes to realize a open-hole structure (see below). The repeller, ion extractor and tube entrance electrodes were assumed to have the dimension listed in Table 1. The latter two electrodes have central holes of 20 mm in diameter with no mesh. Such open-hole structure of the two electrodes enables us to bend the equipotential surfaces simply by manipulating the ion-extractor voltage and to achieve the excellent focusing of the velocity map image on the PSD [1,7]. The optimized separation between the ion extractor and the other electrodes was found from the simulation to be 15 mm.

2. Method of the simulation

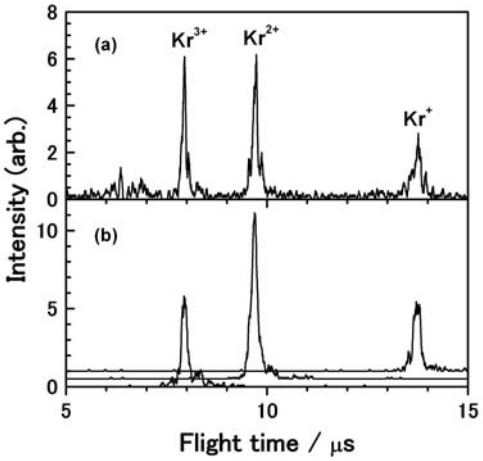

Figure 3. TOF spectra of Kr at $h\nu$ = 90 eV. (a) The control experiment with the photoelectron triggers; (b) the discrimination of Kr^{z+} by the PEPICO mode.

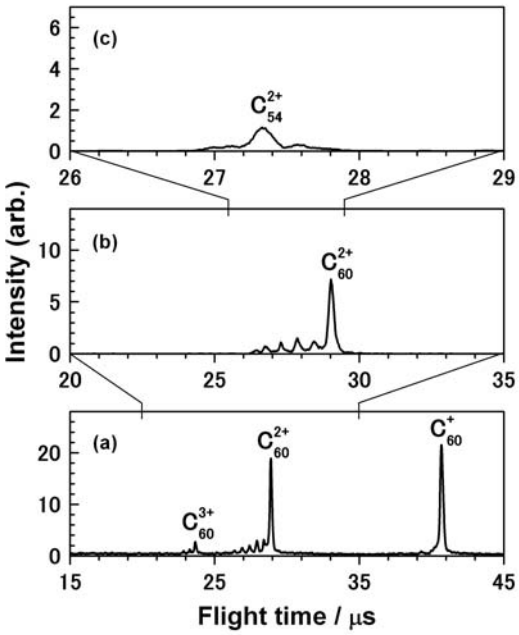

Figure 4. TOF spectra of C_{60} at $h\nu$ = 90 eV. (a) The control experiment with the V_R pulse; (b) and (c) the discrimination of all species in doubly charged state and C_{54}^{2+}, respectively, by the PEX mode.

We performed ion trajectory simulations utilizing the SIMION 3D software (ver. 7.0) [8] to optimize the dimensions of the electrodes. The grid size of 0.5 or 1 mm was adopted in the simulations to keep a good scale factor. Here, dissociative ionization of C_{60} was considered to take place within a region of rectangular parallelepiped $\Delta x\Delta y\Delta z$ = 1×3×1 mm^3. The y-direction was assigned to the passage of SR, so that it ranges from -1.5 to +1.5 mm. In the trajectory simulations the eight corners and center of the ioni-zation region were chosen for the starting points of the ion flights. From each point 171 trajectories were generated in the range of the elevation angle θ from – 90° to + 90° at intervals of 22.5° and in the range of the azimuth angle ϕ from 0° to + 180° at intervals of 10°. The definition of the two angles is given in [7].

Application of the pulse voltages of V_R and V_G was realized by means of a "user program" of SIMION [8]. The base line values of all the pulse voltages were 0 V. The amplitude and duration of V_R were 300 V and 7 μs, respectively. At the same time a pulse voltage with the amplitude of 214 V was applied to the ion extractor. Such applications permit the ions produced during the past 13 μs to be guided into the drift tube. To filter C_{58}^+ ions we set the timing of V_G at 44.5 μs later than that of V_R. At the mass gate the spread of the TOF of C_{58}^+ was estimated to be 0.65 μs which arises from the finite volume of the ionization region and distribution of the kinetic energy of the fragment ions. Thus, the amplitude and duration of V_G were set to 120 V and 1 μs, respectively. A continuous voltage of 320 V was applied to the retarding grid of the ion reflector.

3. Simulation results on C_{58}^+ from C_{60}

The simulated trajectories of C_{58}^+ at initial kinetic energies of 0.1 eV are illustrated in Figure 5(b), while those of C_{60}^+ and C_{56}^+ are in 5(a) and 5(c), respectively. Most of the trajectories of C_{58}^+ are found to go beyond the retarding grid and reach the PSD, whereas the trajectories of C_{60}^+ and C_{56}^+ are reflected completely. This observation may provide evidence for exclusive imaging detection of C_{58}^+ without interference from the neighboring ions, C_{60}^+ and C_{56}^+, with the same kinetic energies.

Figure 6 shows the simulated velocity map images of C_{58}^+ ions on the PSD at the kinetic energies of 0.1 eV (○) and 0.11 eV (■). It should be noted that these images result from momentum distributions of the ions in the laboratory system. We took into account the ion trajectories generated in the elevation and azimuth angle ranges of 0° to +90° and 0° to +180°, respectively, which cover only one quarter of the full three-dimensional trajectories over the 4π solid angle. The trajectories with a given elevation angle form a horizontal stripe, and the envelope of all the stripes makes an arc, which clearly demonstrates that scattering distribution in spherical symmetry can be successfully projected on an image plane. It is likely that C_{58}^+ fragment ions with kinetic energy difference of 0.01eV are almost separable. Comparison between the simulations with and without the mass gate and ion reflector confirmed that the images are not distorted in the presence of these devices.

Conclusions

The results of the mass spectrometric experiments of Kr and C_{60} and the ion trajectory simulations of C_{60} have clearly demonstrated the capability of the mass gate and ion reflector in discriminating specific ion species. The VMI for photofragmentation of large molecules is feasible by the use of the imaging spectrometer equipped with these two devices.

Acknowledgements

This work has been supported by Grants-in-Aid for Scientific Research (Grant Nos. 17750023, 18350016, 18045031, 20550029) from the Ministry of Education, Culture, Sports, Science and Technology, Japan.

References

[1] A. Eppink and D.H. Parker, *Rev. Sci. Instrum.* **68** (1997), pp.3477-3484.

[2] F. Aguirre and S.T. Pratt, *J. Chem. Phys.* **118** (2003), pp.6318-6326.

[3] W.C. Wiley and I.H. McLaren, *Rev. Sci. Instrum.* **26** (1955), pp.1150-1157.

[4] M. Ono, H. Yoshida, H. Hattori and K. Mitsuke, *Nucl. Instrum. Methods Phys. Res., A* **467** (2001), pp.577-580.

[5] T. Mori, J. Kou, M. Ono, Y. Haruyama, Y. Kubozono and K. Mitsuke, *Rev. Sci. Instrum.* **74** (2003), pp.3769-3773.

[6] N. Saito and I. H. Suzuki, *Int. J. Mass Spectrom. Ion Proc.* **115** (1992), pp.157-***.

[7] B.P. Kafle, H. Katayanagi and K. Mitsuke, 9th International Conference on Synchrotron Radiation Instrumentation, Conf. Proc., Am. Inst. Phys. **CP879** (2007), pp.1809-1812.

[8] D.A. Dahl, SIMION 3D ver. 7.0, Boise Idaho, Scientific Instrument Services Inc., 2000.

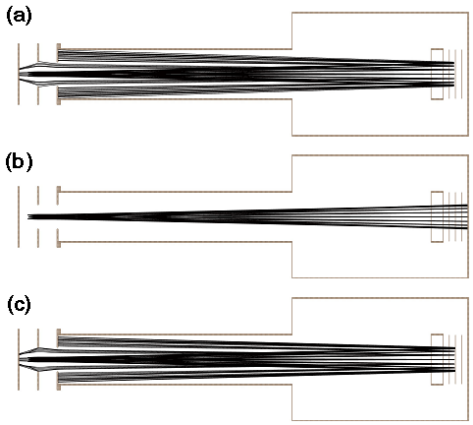

Figure 5. Simulated trajectories of (a) C_{60}^+, (b) C_{58}^+ and (c) C_{56}^+ produced from C_{60}. The initial kinetic energies of the ions were set to 0.1 eV. Only the trajectories of C_{58}^+ can reach the PSD.

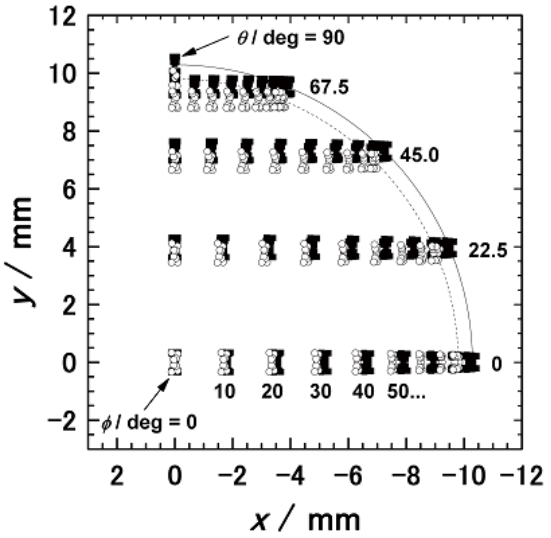

Figure 6. Simulated two-dimensional images of the 3D velocity distribution of C_{58}^+ from C_{60} projected on the PSD. The initial kinetic energies of C_{58}^+ were set to 0.1 (○) and 0.11 eV (■).

Adsorption behavior of copper (II) ion on leonardite prepared from coal waste

S. Katanyoo[1] O. Arquero[1*] W. Naksata[1] S. Thiansem[2] and P. Sooksamiti[3]

[1]Department of Chemistry and Center of Excellence for Innovation in Chemistry, Faculty of Science, Chiang Mai University, Chiang Mai, Thailand 50200
[2]Department of Industrial Chemistry, Faculty of Science, Chiang Mai University, Chiang Mai, Thailand 50200
[3]Department of Primary Industry and Mine Office Region 3, Chiang Mai, Thailand 50200

*E-mail: noi2495@hotmail.com,

Abstract: The sorbent, leonardite, was obtained from Mae Moh power plant in Lampang province, Thailand, and used without any additional pre-treatment except of grinding and size classification by sieving. The elemental mass percent compositions of leonardite were investigated using XRD and XRF techniques. The factors such as pH, contact time and sorbent amount were studied by batch experiment carried out by shaking a known amount of the sorbent with solutions of copper (II) ion of desired concentrations. The adsorption capacity of leonardite was then determined. From XRD and XRF data, an elemental mass percent composition of leonardite contained mainly compounds of SiO_2 29.4 %, Al_2O_3 15.5 %, Fe_2O_3 4.5 % and CaO 2.7 %. Non-negligible amounts of K, Na, Mg, Ti, and P were also detected in low concentration. The content of humic substances in the sorbent was approximately 41.3%. The optimum pH for adsorption of Cu(II) was in the range of 5-6. Batch experiment showed that equilibrium was reached after 2 h, at 0.4 g of leonardite quantity. Moreover, the Langmuir and Freundlich isotherms are used to fit the experimental data in equilibrium concentration range 1.39 to 10.75 mg/L. The results show that both isotherms fitted the experimental data very well. The maximum adsorption capacity (q_{max}) of Cu(II) from Langmuir isotherm is 23.92 mg/g .

Introduction

Environmental pollution by heavy metals is a serious and complex problem that has been, and still is, a focus of attention all over the world. Heavy metals are among the chief pollutants of surface and groundwater. Industrial and municipal wastewater frequently contains metal ions that can be harmful to aquatic life and human health [1]. Cu(II) can be found in many wastewater sources including, printed circuit board manufacturing, electronics plating, plating, wire drawing, copper polishing, paint manufacturing, wood preservatives and printing operations. Cu(II) is essential mineral but too much is not beneficial, and symptoms of Cu(II) poisoning are very similar to those produced by arsenic. Fatal cases are generally terminated by convulsions, palsy, and insensibility [2].

Leonardite or oxihumolite or a young brown coal is a frequency used name for a certain kind of oxidatively altered young brown coal that originated on the surface of lignite deposits by post-sedimentary oxidation [3]. The oxihumolites, similarly to the related organic deposits such as humalites, are exploited for an industrial preparation of humic acids as well as additives to agricultural fertilizers. Humic materials are complex organic molecules that contain a wide variety of functional groups, which can be involved in chemical binding. Because of these properties, leonardite tends to have a high cation exchange capacity. The low-cost and the availability of this material make it a promising candidate for pollution remediation in both soils and groundwater [4, 5, 6]. Therefore, in this work the adsorption of Cu(II) on untreated leonardite obtained from the Mae Moh mine in Lampang province has been studied. The adsorption capacities were estimated from the parameters of the adsorption isotherms, and factors influencing the adsorption were investigated.

Materials and Methods

The sorbent—leonardite obtained from the Mae Moh mine in Lampang province, Thailand, was used without an additional pre-treatment except of grinding and size classification by sieving. All reagents used are AR grade and all solutions have been prepared with deionized water. Stock standard solutions of Cu(II) at concentration of 1000 mg/L were obtained from (Fluka, Buches, Switzerland). Working standard solutions were obtained by appropriate dilution of the stock standard solution. Solutions of NaOH 0.5 M and HNO_3 0.5 M were used for pH adjustment. Determination of Cu(II) in the initial and remaining solutions was carried out by flame atomic absorption spectrophotometer, series AA-275, Varian Company, Australia.

Influence of pH on Cu(II) adsorption

The initial pH of Cu(II) aqueous solutions (5 and 20 mg/L) was adjusted to pH 2-6. Control test solutions (10 mL) were filtered and analyzed after pH adjustment to ensure that no precipitates formed prior to contact with the sorbent. Then 0.4 mg of the leonardite was added to flasks containing 50 mL of the Cu(II) solutions. The flasks were maintained under

continuous agitation for 24 hr, at room temperature and 130 rpm. Then, the mixture was centrifuge and filtered, and the remaining concentrations of Cu(II) were determined.

Effect of contact time

Batch experiments were conducted to determine the time needed to reach equilibrium at the optimum pH (pH 6). 0.4 mg leonardite was added to flasks containing 50 mL of the two Cu(II) aqueous solutions (5 and 20 mg/L). The experimental conditions used were the same as those mentioned above. After various periods of time (10-1440 min), each mixture was centrifuged and filtered, and the remaining concentrations of Cu(II) were determined.

Effect of leonardite quantity

Various amounts of leonardite in the range of 0.4 to 3 mg were added to 50 mL of 5 and 20 mg/L Cu(II) at optimum pH 6 and shaken until equilibrium. Then, residual metal ions concentrations were determined.

Adsorption Isotherm

To test the adsorption capacity of leonardite, 50 mL of six Cu(II) aqueous solutions between 5 and 100 mg/L were mixed in triplicate with a constant 0.4 mg leonardite dose. The flasks were kept in the same conditions as described above until equilibrium time, and the Cu(II) concentrations were determined in the remaining solutions.

Results and Discussion

Effect of pH

The sorption of Cu(II) on leonardite was studied over the pH range 2–6. Fig. 1 shows the removal of ions versus initial pH for a fixed adsorbent dose and initial metal concentrations of 5 and 20 mg/L Cu(II). The analysis of Cu(II) in blank solutions showed that there was no leaching of this metals from the adsorbent. The results show that, the removal of Cu(II) from aqueous solutions by sorption on leonardite was pH dependent. It was observed that the removal percentage was maximum at pH 6. At pH 2 the adsorption of Cu(II) on leonardite was practically negligible. The pH effect of adsorption on leonardite can be explained by the surface characteristics of the adsorbent. Hydrogen ions affect metal complexation because they have a great affinity for many complexing and ion-exchange sites. At very low pH (<2) functional oxidized groups (hydroxyl, carboxyl, phenol, methoxyl, etc.) of humic acids are protonated. As the pH increases metal ions will replace hydrogen ions from the surface of the leonardite and therefore the extent of the adsorption will increase [2].

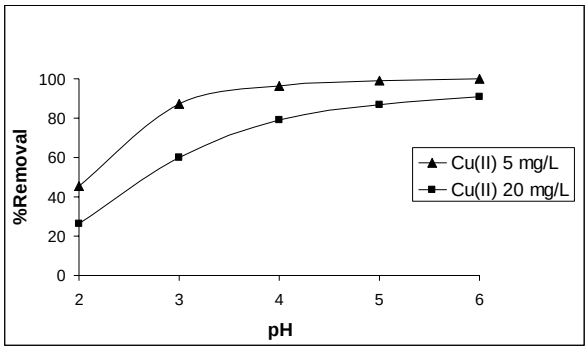

Fig. 1 pH effect on Cu(II) removal by leonardite

Contact time

The percentages of Cu(II) removal and the amount of Cu(II) adsorbed against contact time at the optimum pH 6 and with initial concentrations of 5 and 20 mg/L are shown in Fig. 2a and 2b. These data indicated that after 120 min, the amount of Cu(II) adsorbed becomes asymptotic to the time axis, nearly representing an equilibrium pattern. After 120 min, the removal percentages were greater than 90% for both concentrations. Therefore, for practical purposes this time was assumed to represent the equilibrium time.

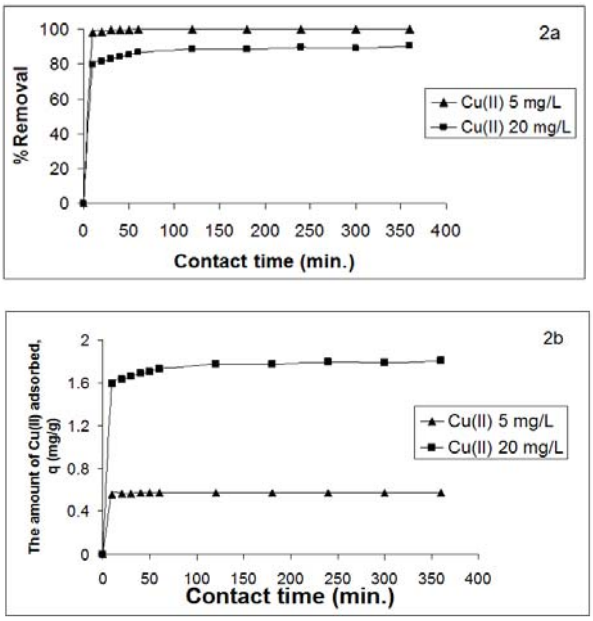

Fig. 2 Contact time
a. %Removal of Cu(II) vs. Contact time
b. The amount of Cu(II) adsorbed vs. Contact time

Effect of leonardite quantity

Fig. 3a and 3b show the percentage of Cu(II) removal and the amount of Cu(II) adsorbed as a function of adsorbent dose at the optimum pH 6 and with initial concentrations of 5 and 20 mg/L. Increase of leonardite quantity, in the range of 0.4 to 3 mg slightly increased in the percentage removal and the amount of Cu(II) adsorbed.

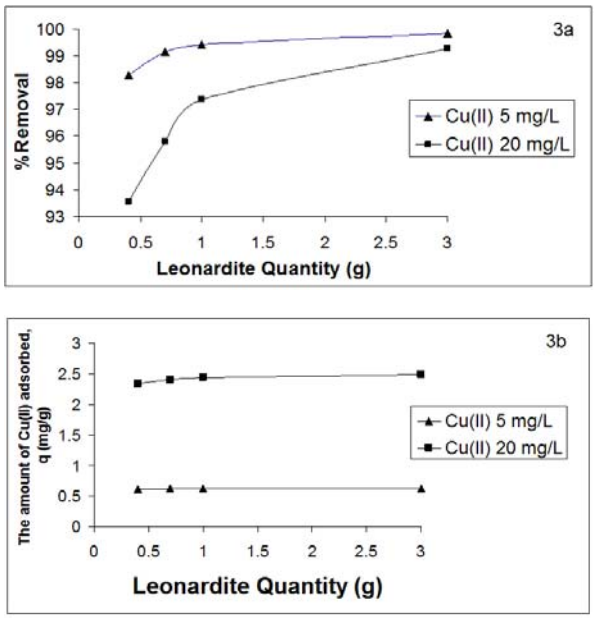

Fig. 3 Effect of leonardite quantity
a. %Removal of Cu(II) with leonardite quantity
b. The amount of Cu(II) adsorbed with leonardite quantity

Adsorption Isotherm

Fig. 4 shows the relationship between the different amounts of metal ion adsorbed per unit mass of leonardite (X mg/g) and the equilibrium concentration of Cu(II) (C_e) at room temperature. The leonardite quantity was kept at a constant value of 0.4 mg/50 mL of solution and a contact time of two hours was employed.

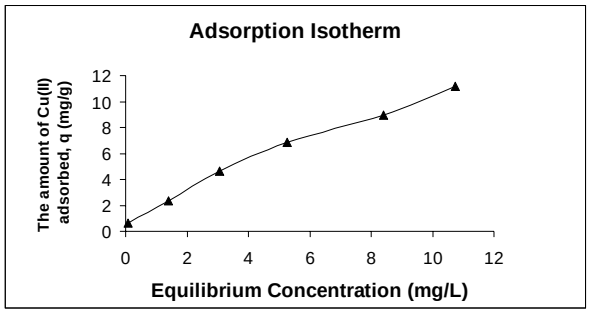

Fig. 4 Adsorption Isotherm of Cu(II) on leonardite

Langmuir and Freundlich isotherms applicable to aqueous solutions adsorption processes, were used to determine the adsorption capacity of leonardite. Heavy metal adsorption on heterogeneous sorbents has been interpreted using both isotherms on various occasions in the environmental literature. Although the basic assumptions for these models were not fulfilled due to the heterogeneity of the sorbents' surface, they were quite successful in predicting the experimental saturation capacities of the sorbents. However, the adsorption data in the linearized forms gave satisfactory correlation coefficients for a part of the covered concentration range as shown in Figs. 5a and 5b. The Langmuir values q_{max} and b and Freunlich values K and n were then calculated and are shown in Table 1.

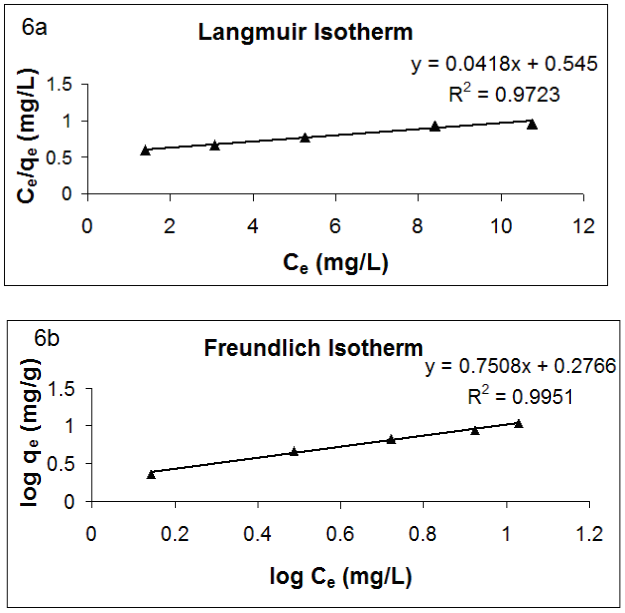

Fig. 5 Graphical representation
a. Langmuir Isotherm b. Freundlich Isotherm
for adsorption Isotherm of Cu(II) on leonardite

Table 1 Langmuir and Freundlich constants

Cu(II)	Langmuir			Freundlich		
	q_{max} (mg/g)	b (L/g)	r^2	K (mg/g)	n	r^2
	23.923	0.077	0.9723	1.891	1.332	0.9951

The adsorption data of Cu(II) was correlated with the Langmuir and Freundlich isotherms in equilibrium concentration range 1.39 to 10.75 mg/L. From the Langmuir plot, an adsorption capacity (q_{max}) of 23.92 mg Cu(II)/g of leonardite was determined.

Conclusions

Leonardite has been shown to be effective for the removal of Cu(II) from aqueous solutions. The adsorption in these systems is highly dependent on pH. The uptake of Cu(II) increases with increasing pH, the maximum percent removal being obtained at pH 6. At pH 2 the adsorption was negligible. The adsorption isotherms were obtained in the linearized forms (both Langmuir and Freundlich equations). The sorption data was correlated with the Langmuir and Freundlich isotherms in equilibrium concentration range 1.39 to 10.75 mg/L. The adsorption capacity was 23.92 mg of Cu(II) per g of leonardite.

Acknowledgements

The authors wish to thanks Mae Moh Coal Mine in Lampang province for leonardite, the National Research University, the Center of Excellence for Innovation in Chemistry (PERCH-CIC), Commission on High Education, Ministry of Education and the

Graduate School, Chiang Mai University for financial support.

References

[1] C. Lao, Z. Zeledon, X. Gamisans and M. Sole, *Sep. Purif. Technol*., **45** (2005) 79-85.

[2] Z. Zeledon, C. Lao and F. X. Heras, *Chemosphere*, **67** (2007) 505-512.

[3] A. Santos, W. Botero, I. Bellin, L. Oliveira, J. Rocha, A. Mendonca and A. Godinho, *J. Braz. Chem. Soc.*, **18** (2007) 824-830.

[4] I. Christl, A. Metzger, I. Heidmann and R. Kretzschmar, *Environ. Sci. Technol*., **39** (2005) 5319-532.

[5] M. Kurkova, Z. Klika, C. Klikova and J. Havel, *Chemosphere*, **54** (2004) 1237-1245.

[6] M. Sole, J. Casas and C. Lao, *Water*, *Air and Soil Pollut*., **144** (2003) 57-65.

Simple synthesis, FTIR/FT Raman Spectroscopic studies and non-isothermal dehydration kinetics of $CaHPO_4 \cdot 2H_2O$

B. Wondee[1,2], C. Danvirutai[1,2]*, T. Srithanratana[1]

[1]Department of Chemistry, Faculty of Science, Khon Kaen University, Maung, Khon Kaen, Thailand 40002
[2]Center of Excellence for Innovation in Chemistry (PERCH-CIC), Khon Kaen University

*E-mail: chanai@kku.ac.th

Abstract: A rapid chemical process to synthesize dicalcium phosphate dihydrate (DCPD or brushite, $CaHPO_4 \cdot 2H_2O$) will be presented. The title compound was synthesized by using disodium hydrogen phosphate and calcium chloride at room temperature, followed by air dried in a desiccator. On calcination in air, the powder samples were transformed into triclinic monetite (DCPA: dicalcium phosphate anhydrous, $CaHPO_4$) first, and then into $Ca_2P_2O_7$ (calcium pyrophosphate). DCPD is known to crystallize in the monoclinic (*Cc*) space group. The results from X-ray diffraction (XRD) agree well with the Fourier transform infrared and Raman (FTIR/FTRaman) spectra. The kinetic parameters such as activation energy and reaction order of the thermal dehydration of brushite were determined by thermogravimetry (TG) with different heating rates (5, 10, 15 and 20 °C min^{-1}) using Ozawa's approach based on empirical Arrhenius-type equation.

Introduction

Many metal phosphates have been extensive studied[1] due to their wide application such as catalysts for a variety of organic processes, industrial, commercial, science and health sectors. Especially, anhydrous calcium hydrogen phosphates, ($CaHPO_4$, monetite) and dicalcium phosphate dihydrate ($CaHPO_4 \cdot 2H_2O$, DCPD or brushite) have been studied for decades as their mineral forms. As members of the series of calcium phosphates, they have considerable biological importance with respect to the biomineralization processes in bones and teeth, and find practical uses in dental cements and restorative materials. The structure of brushite has been described as either a non-centrosymmetric, monoclinic with space group I_a, $Z = 4$, or as the centrosymmetric space group $I_{a/2}$.[2] DCPD powders can easily be synthesized in aqueous solutions at room temperature by using soluble calcium (e.g., $Ca(NO_3)_2 \cdot 4H_2O$, $CaCl_2 \cdot 2H_2O$, or $Ca(CH_3COO)_2 \cdot H_2O$) and phosphate (e.g., $NH_4H_2PO_4$, $(NH_4)_2HPO_4$, Na_2HPO_4, NaH_2PO_4, KH_2PO_4, or K_2HPO_4) salts on adjusting the Ca/P molar ratio to 1.[3] $CaHPO_4 \cdot 2H_2O$ crystallizes at room temperature in the monoclinic *Cc* (C_s^4) space group. All the structural parameters were refined by Curry and Jones[4] using neutron diffraction data: a = 6.359 Å , b = 15.177 Å , c = 5.81 Å , β = 118.54°, Z = 4.[3,5,6] Its crystal structure contains compact sheets consisting of parallel chains, in which calcium ions are coordinated by six oxygens, two oxygen atoms belonging to the water molecules, while another four oxygen atoms belong to anion. Two kinds of water molecules exist in brushite[5] and three types of proton species can be found. The protons in this compound bound to the PO_4^{3-} group, the two lattice H_2O molecules and the adsorbed surface molecules.[5] The first dehydration step, most of the adsorbed water molecules were eliminated, at about 105 °C. At 195 °C brushite gives rise to the well known monetite $CaHPO_4$. A further step of dehydration at 700 °C gives the pyrophosphate $Ca_2P_2O_7$.[6]

The monetite crystallizes in a triclinic unit cell a = 6.910 Å, b = 6.627 Å, c = 6.998 Å, α =96.34°, β = 103.82°, and γ = 88.33° at 25 °C, with Z = 4. Its structure consists of $CaHPO_4$ chains bonded together by Ca-O bonds and three types of hydrogen bonds. But the vibrational behavior is more complex than in brushite. Two distinct sets of pairs of PO_4^{3-} units are found in each primitive cell and induce a band splitting. Differences in the bonding between H atoms and the phosphate PO_4^{3-} ions of the two different sets perturb the band splitting pattern of the vibrational spectra.[5]

However, although many studies of the anhydrous and calcium phosphate hydrates, little studies on their thermal properties were reported. The aim of the present study is to report the simple synthetic method, vibrational spectroscopies and the kinetic parameters calculated from the thermogravimetric (TG) data.

Materials and Methods

Preparation of $CaHPO_4 \cdot 2H_2O$ powder

The synthesis of brushite ($CaHPO_4 \cdot 2H_2O$) was carried out by adding dropwise of 0.3 M $CaCl_2 \cdot 2H_2O$ solution into 100 cm^3 of 0.3 M Na_2HPO_4 solution. After 30 min, the precipitate was filtered and washed with de-ionized water, followed by air dried in a desiccator.

Characterization

The crystal structure was analyzed by XRD (D8 Advance powder diffractometer, Bruker, Karlsruhe, Germany) with CuK_α radiation (λ = 0.15406 Å). FTIR and FT-Raman spectra of $CaHPO_4 \cdot 2H_2O$ were recorded in the range of 4000–370 cm^{-1} on an FTIR/FT-Raman spectrophotometer (Perkin-Elmer Spectrum GX) with a resolution of 4 cm^{-1} and 8 scans

using KBr pellets (spectroscopy grade, Merck). The FT-Raman spectra were also recorded on the same range and instrument. The thermal properties of the synthesized sample was investigated by thermal gravimetric and differential thermal analyzer (TG/DTA Perkin Elmer Pyris Diamond).

Theoretical approach and calculation procedures

Consider a solid material undergoing thermal decomposition according to the reaction A(solid) + B(solid) → C(gas). If the composition starts at an initial temperature (T_o) and is linearly increased ($T = T_o + \beta t$) by thermogravimetrically at a constant rate, β (where $\beta = dT/dt$), then the rate of conversion of the solid A, ($d\alpha/dt$) can be defined by

$$\frac{d\alpha}{dt} = f(\alpha)k(T) \quad \text{or} \quad \frac{d\alpha}{f(\alpha)} = k(T)dt \tag{1}$$

where the degree of conversion $(\alpha) = \frac{m_0 - m}{m_0 - m_f}$ being the fraction of A that undergoes decomposition, m_o and m_f are the sample masses at the beginning and at the particular end of the weight loss due to thermal decomposition at any time t. The functions $f(\alpha)$ and $k(T)$ are, respectively, functions of conversion and temperature. In the usual manner, the temperature dependence of the rate of weight loss is assumed to formulate the rate constant through an Arrhenius relationship given by

$$k(T) = A \exp\ \frac{-E_a}{RT} \tag{2}$$

where A is the pre-exponential factor, E_a the activation energy, and R the gas constant. The simplest and most frequently used method for $f(\alpha)$ determination is

$$f(\alpha) = (1-\alpha)^n \tag{3}$$

where n is the order of reaction. Insertion of the equations (2) and (3) into equation (1) results

$$\frac{d\alpha}{dt} = \beta\frac{d\alpha}{dT} = (1-\alpha)^n A \exp\ \frac{-E_a}{RT} \tag{4}$$

Integration of this equation from an initial temperature (T_0), corresponding to initial degree of conversion (α=0), to a temperature (T), which corresponds to any degree of conversion ($\alpha > 0$), results equation (5):

$$\int_0^\alpha \frac{d\alpha}{f(\alpha)} = \int_0^\alpha \frac{d\alpha}{(1-\alpha)^n} = \frac{A}{\beta}\int_{T_0}^{T} \exp\ \frac{-E_a}{RT}\ dT \tag{5}$$

where $g(\alpha)$ is the integral form of the reciprocal of the $f(\alpha)$. The right hand side of equation (5) may be solved using the following power series expansion, which results in

$$g(\alpha) = \int_0^\alpha \frac{d\alpha}{f(\alpha)} = \frac{AE_a}{\beta R}\ \int_x^\infty \frac{e^{-x}}{x^2}dx$$

$$\cong \frac{AE_a}{\beta R}\ \frac{e^{-x}}{x^x}\ \frac{1}{(x+1)} - \frac{1}{(x+1)(x+2)} + \frac{2}{(x+1)(x+2)(x+3)} + \ldots \tag{6}$$

Where $x = E_a/RT$. The logarithm of the previous expansion was used by Doyle[7] to obtain the equation

$$g(\alpha) = \int_0^\alpha \frac{d\alpha}{f(\alpha)} = \frac{AE_a}{\beta R}\ \int_x^\infty \frac{e^{-x}}{x^2}dx\ \cong \frac{AE_a}{\beta R}\ p(x) \tag{7}$$

The term $p(x)$ in equation (7) is the Arrhenius temperature integral defined by Doyle for $20 < x < 60$. Since this equation involves an exponential integral which is still complicated and involves a succession of mathematical steps, the integral method of Ozawa uses Doyle's linear approximation of $p(x)$ given by Eq.(8), then Eq.(9) can be obtained as:

$$\ln p(x) = -5.3305 - 1.0516\frac{E_a}{RT} \tag{8}$$

$$\ln \beta = \ln\ \frac{AE_a}{R}\ - 5.3305 - 1.0516\frac{E_a}{RT} - \ln f(\alpha) \tag{9}$$

Thus, for a constant degree of conversion (α=constant), the plot of $\ln(\beta)$ versus $1/T$, obtained from thermograms recorded at several constant heating rates (β) should result in straight line whose slope is approximately $-1.0516E_a/R$.

In order to determine the reaction order, Ozawa extended the Avrami theory to describe non-isothermal cases, defining the following equation for the variation of the degree of conversion with temperature and heating rate as given in Eq.(10).

$$\alpha(T) = 1 - \exp\ \frac{-k(T)}{\beta^n} \tag{10}$$

By taking double logarithm in both sides of equation (10) and noting that $k(T)$ is the same parameter as defined in equation (2), the following expression is obtained:

$$\ln\{-\ln[1-\alpha(T)]\} = \ln(A) - \frac{E_a}{RT} - n\ln(\beta) \tag{11}$$

Hence, a plot of $\ln\{-\ln[1-\alpha(T)]\}$ versus $\ln(\beta)$, which is obtained at the same temperature from a number of isotherms taken at different heating rates, should yield straight lines whose slopes are the Ozawa's exponent (n).[8]

Results and Discussion

Characterization

The X-ray diffraction pattern of the synthesized compound has matched with that of $CaHPO_4{\cdot}2H_2O$ in JCPDS file (PDF # 720713), belongs to monoclinic system with space group $I_a(9)$ (Fig. 1.). The lattice parameters of $CaHPO_4{\cdot}2H_2O$ were calculated using Bragg's equation and found to be: a = 6.008 Å, b = 14.715 Å, c = 6.697 Å, β = 111.10°, Z = 4 and the cell volume V = 552.37 Å^3. The thermogravimetric (TG) data suggested that the elimination of crystallization water were observed in two stages. The first stage from 106 °C to 206 °C, the mass loss is about 18.15 %, which correspond to 1.7 mol of water of crystallization loss from the structure, while the second stage from 206 °C to 484 °C, the mass loss is about 3.04 %, which due to 0.3 mol of crystallization water loss from the structure and indicating that hydrated phosphate becomes anhydrous. Thereafter, at 588 °C,

$CaHPO_4 \cdot 2H_2O$ turns into calcium pyrophosphate ($Ca_2P_2O_7$).

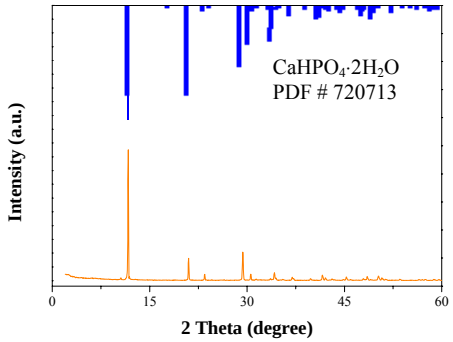

Fig.1. Powder X-ray diffraction pattern of synthesized $CaHPO_4 \cdot 2H_2O$ compared with the standard PDF # 720713

FTIR and FT Raman analysis of the product

The FTIR/FT Raman spectra of $CaHPO_4 \cdot 2H_2O$ and FTIR spectra of $CaHPO_4$ are reported in Fig. 2, Fig. 3 and Fig. 4, respectively. The attributions of the main vibrational modes of $CaHPO_4 \cdot 2H_2O$ and $CaHPO_4$ are reported in Table 1. The ν_{OH} stretching observed at 3191, 2862 cm^{-1} and 2406 cm^{-1} for (P)O-H on the IR spectrum (Fig. 4) of $CaHPO_4$ seems to be strongly dependent on the three types of hydrogen bonds. These bands are broad, due to the disorder introduced by the different hydrogen bond strengths. The H bonds are stronger in $CaHPO_4$ than in $CaHPO_4 \cdot 2H_2O$, which agree with to the reported data.[5]

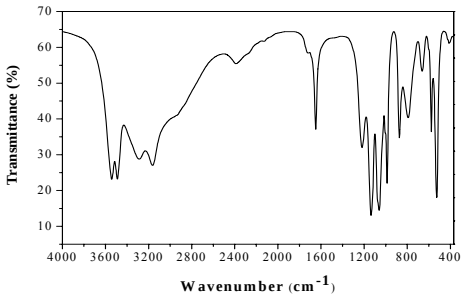

Fig.2. FTIR spectrum of the synthesized $CaHPO_4 \cdot 2H_2O$

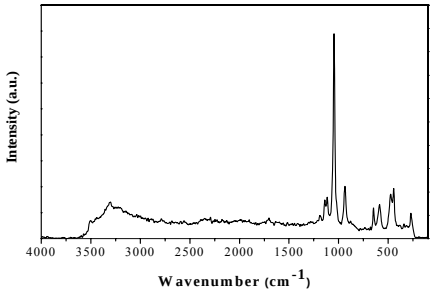

Fig.3. FT Raman spectrum of the synthesized $CaHPO_4 \cdot 2H_2O$

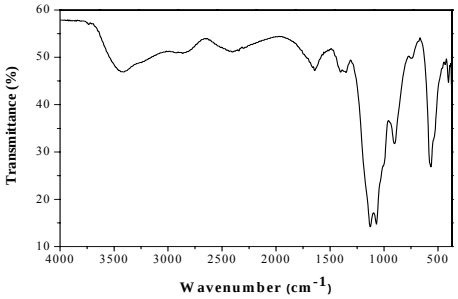

Fig.4. FTIR spectrum of dehydration product in form of $CaHPO_4$

Table 1 Main Vibrational Modes of $CaHPO_4 \cdot 2H_2O$ (brushite) and $CaHPO_4$ (monetite) (FTIR/FT Raman)

IR brushite (cm^{-1})	Raman brushite (cm^{-1})	IR monetite (cm^{-1})	Assignments
3162-3542	3196-3313	3410	O-H stretching of lattice water molecule
		3191	(P)-OH stretching
		2862	(P)O-H stretching
		2406	(P)O-H stretching
2390			Combination
1649-1727		1644	H-O-H bending
		1353-1399	P-O-H in-plane bending
1219			P-O-H in-plane bending
	1190		P-O-H in-plane bending
1135	1139	1128	$\nu_3(F_2)PO_4^{3-}$
	1112	1070	$\nu_3(F_2)PO_4^{3-}$
1059	1043	1039	$\nu_3(F_2)PO_4^{3-}$
986			$\nu_1(A_1)PO_4^{3-}$
	933	903	$\nu_1(A_1)PO_4^{3-}$
873			H_2O Libration
791		751	P-O-H out-of-plane bending
662	650		H_2O Libration
576	584	576	$\nu_4(F_2)PO_4^{3-}$
		564	$\nu_4(F_2)PO_4^{3-}$
526		534	$\nu_4(F_2)PO_4^{3-}$
	474		$\nu_2(E)PO_4^{3-}$
	442		$\nu_2(E)PO_4^{3-}$
	286		Lattice mode

Kinetic Studies

The TG curve of $CaHPO_4 \cdot 2H_2O$ (Fig. 5) was obtained by heating a sample from 30 °C to 700 °C, in an atmosphere of nitrogen, with various heating rate (5, 10, 15 and 20 °C min^{-1}) using alumina as standard reference.

The values of Ozawa's exponent (Table 2) is considerably low at the beginning of the dehydration process and not constant at the early increasing temperature until at 463 °C, by which the Ozawa's exponent is maximum and is about unity. After that, the Ozawa's exponent decreases to the value close to zero at the completion of the reaction. This indicates that both the early and the latter stages of $CaHPO_4 \cdot 2H_2O$ dehydration follow zero or pseudo-zero order kinetics, whereas the intermediate stages follow a first order kinetics. The Plots of $\ln\{-\ln[1-\alpha(T)]\}$

versus ln(β) for the $CaHPO_4 \cdot 2H_2O$ for computation of Ozawa's exponent (n) as a function of the temperature are shown in Fig. 6.

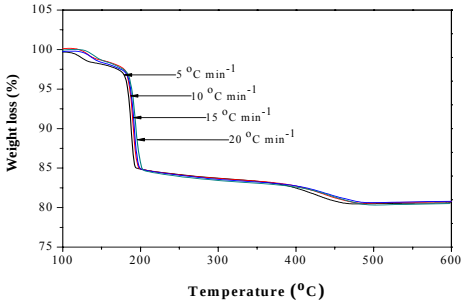

Fig. 5. TG curves for thermal decomposition of $CaHPO_4 \cdot 2H_2O$ in nitrogen atmosphere at various heating rates (5, 10, 15 and 20 °C min^{-1}).

The activation energy values decreased with increasing degree of conversion in the range of 10 to 70 % (Table 3). The highest activation energy value at α=80, is suggested to be due to the synthesized $CaHPO_4 \cdot 2H_2O$ transformed into $CaHPO_4$. The Plots of ln(β) versus $10^3/T$ for the $CaHPO_4 \cdot 2H_2O$ are shown in Fig. 7.

Table 2 The values of Ozawa's exponent as a function of temperature for the synthesized $CaHPO_4 \cdot 2H_2O$.

Temperature (K)	Ozawa's exponent (n)
423	0.10±0.03
433	0.06±0.02
443	0.05±0.01
453	0.15±0.03
463	0.77±0.05
673	0.04±0.01
683	0.07±0.01
693	0.10±0.01
703	0.14±0.01
713	0.18±0.01
723	0.24±0.01

Table 3 Values of activation energy as a function of the conversion degree for the synthesized $CaHPO_4 \cdot 2H_2O$.

α (*T*) (%)	Activation energy, E_a (kJ/mol)
10	851.65±11.84
20	500.40±3.48
30	453.70±3.59
40	403.86±3.36
50	387.88±5.63
60	371.90±7.18
70	322.61±4.75
80	1335.81±19.72
90	285.97±9.49

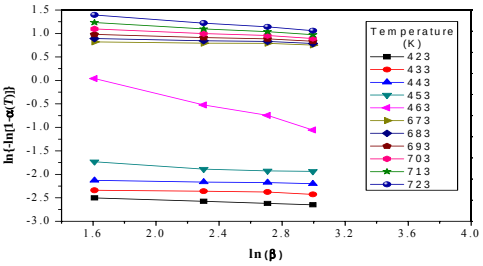

Fig. 6. Plot of ln{-ln[1-$\alpha(T)$]} versus ln(β) for the $CaHPO_4 \cdot 2H_2O$

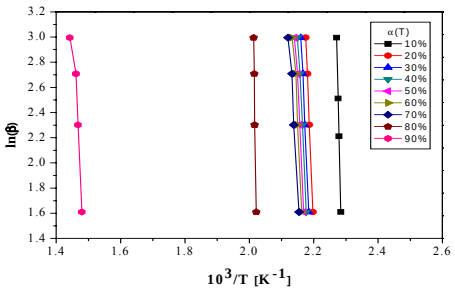

Fig.7. Plot of ln(β) versus $10^3/T$ for the $CaHPO_4 \cdot 2H_2O$

Conclusions

The $CaHPO_4 \cdot 2H_2O$ was successfully synthesized by the simple method at ambient temperature. The results from FTIR/FT Raman spectra, X-ray diffraction data and the thermogravimetric (TG) data confirm that the synthesized compound is $CaHPO_4 \cdot 2H_2O$. The synthesized $CaHPO_4 \cdot 2H_2O$ was found to transform into $CaHPO_4$ and $Ca_2P_2O_7$ at 193 °C and 588 °C, respectively. The Ozawa's exponent indicates that both the early and the latter stages of $CaHPO_4 \cdot 2H_2O$ dehydration follow zero or pseudo-zero order kinetics, whereas the intermediate stages follow the first order kinetics. The activation energy values decrease with increasing the degree of conversion. The highest activation energy value at α = 80 of 1335.81 kJ mol^{-1} is suggested to be due to the synthesized $CaHPO_4 \cdot 2H_2O$ transformed into $CaHPO_4$.

References

[1] B. Boonchom and C. Danvirutai, *Ind. Eng. Chem. Res.*, 47 (2008), pp. 5976-5981.

[2] J. Xu, I.S. Butler and D.F.R. Gilson, *Spectrochim. Acta.*, Part A **55** (1999), pp. 2801–2809.

[3] A.C. Tas and S.B. Bhaduri, *J. Am. Ceram. Soc.*, **87** [12] (2004), pp. 2195–2200.

[4] N.A. Curry and D. W. Jones, *J. Chem. Soc*., *A* 3725 (1971).

[5] L. Tortet, J.R. Gavarri, G. Nihoul and A.J. Dianoux. *J. Solid State Chem.*, **132** (1997), pp 6-16.

[6] L. Tortet, J.R. Gavarri and G. Nihoul, *Solid State Ionics.* 89 (1996), pp. 99-107.

[7] C.D. Doyle, Nature, 207 (1965), pp. 290-291.

[8] E.S. De Medeiros, R.M.B. Moreno, F.C. Ferreira, N. Alves, E.J. Aldo, P.S. Goncalves, and L.H.C. Mattoso, *Plastics and Recycling Technology*. **19** (2003), pp. 189-204.

Photocatalytic degradation of direct blue 98 dye in the presence of ZnS suspensions

H. Puttraruksa[1], E. Sanmerng[1] and B. Sangchakr[1*]

[1] Department of Chemistry, Faculty of Science, King Mongkut's University of Technology Thonburi, 126 Pracha-utis Rd., Thung-Kru, Bangkok, 10140 Thailand

[*] E-mail : benchang.san@kmutt.ac.th

Abstract: Photocatalytic degradation of a textile dye, Direct Blue 98, was studied under an irradiation of a high pressure mercury lamp using ZnS as the catalyst. The photodegradation activity was followed by periodically monitoring residual concentration of the dye using UV-visible spectrometer. The results showed that the photodegradation kinetics of Direct Blue 98 on ZnS follows the pseudo-first order rate according to the Langmuir-Hinshelwood equation with the rate constant (k), and the adsorption constant (K) of 22.47 mgl^{-1} min^{-1} and 8.51x10^{-3} l mg^{-1}, respectively. It was also found that the photodegradation was inhibited by ethanol. From the inhibitive effect of ethanol, it indicated that hydroxyl radicals played a significant role in the photodegradation of the dye.

Introduction

Wastewater from textile, paper and some other industries contain residual dyes, which is very difficult to treat. This is because dyes usually have complex aromatic molecular structures which make them more stable and more difficult to be biodegradable [1, 2]. Dye wastewater is usually treated by physical and chemical treatment processes. These include adsorption and chemical coagulation processes. However, these methods are usually inefficient in the removal of color and require further treatment. Advanced oxidation processes (AOPs) are alternative techniques of destruction of dyes and other organics in wastewater and effluents. These processes generally involve UV/H_2O_2, UV/O_3, or UV/Fenton's reagent for the oxidative degradation of contaminants. Semiconductor photocatalysis is other developed AOP, which can be applied to remove organic pollutants [3-6]. The advantage of photocatalytic process is its mild operating conditions and it can be activated by sunlight, thus reducing the elective power required and therefore the operating cost [7].

Titanium dioxide (TiO_2) is generally considered to be the best photocatalysts, and has the ability to mineralize wastewater [8, 9]. However widespread use of TiO_2 is uneconomical for large scale water treatment, thereby interest has been drawn towards the search for suitable alternatives to TiO_2. Many attempts have been made to study photocatalytic activity of different semiconductors such as SnO_2, CdS and ZnO [10,11]. Our present study provides results describing the photocatalytic decolorization and mineralization of Direct Blue 98 (DB-98), an azo dye used for dyeing of cotton fibers over ZnS powders under various experimental conditions. Its structure is shown in Figure 1. Since DB-98 has azo groups, it is also toxic and even carcinogenic and this poses a serious hazard to aquatic living organisms [12,13]. Azo dyes are resistant to biological treatment and they are reduced under anaerobic conditions to hazardous aromatic amines. Thus, there is a need for developing treatment methods that are more effective in eliminating dyes from wastewater.

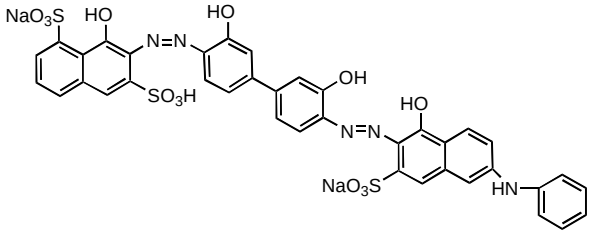

Figure 1. Molecular structure of DB-98

Materials and Methods

Materials

Direct Blue 98 (DB-98) was obtained from Dystar (Thailand) and was used without further purification. ZnS and ethanol (95%) were purchased from Fluka (Switzerland). Solutions were prepared by dissolving appropriate amount of the dye in deionized water.

Photoreactor

All experiments were carried out in a 100 ml Pyrex glass bottle. The radiation source was a 200W high pressure mercury lamp (Applied Photophysics, England), which was placed about 20 cm behind a Pyrex glass bottle.

Procedure

For the photodegradation of DB-98, a solution containing known concentration of the dye and ZnS was prepared and the solution was stirred during irradiation. Irradiation was carried for a specific period. Subsequently, the suspension was filtered through 0.45μm Millipore membrane to remove the particles before analyzed.

Analysis

The degradation was monitored by measuring the absorbance on a UV-VIS spectrophotometer at 580nm.

The decolorization efficiency (%) has been calculated as:

$$Efficiency\,(\%) \;=\; \frac{C_0 - C}{C_0} \times 100$$

where C_0 is the initial concentration of dye and C is the concentration of dye after photoirradiation.

Results and Disscusion

Effect of UV Irradiation and ZnS

The change in the dye concentration versus time during the photocatalytic degradation of DB-98 is shown in Figure 2. The removal of DB-98 was negligible in the absence of ZnS. It can be seen from the figure that in the presence of ZnS and light, about 90% of dye degraded within 90 min of irradiation time. These results reveal that both UV light and photocatalyst, such as ZnS, were needed for the effective destruction of DB-98. When ZnS is exposed to UV radiation, an electron-hole pair is produced [14].

$$ZnS + h\nu \longrightarrow e^-_{cb} + h^+_{vb} \qquad (i)$$

where, e^-_{cb} and h^+_{vb} are the electrons in the conduction band and valence band holes, respectively. The photogenerated holes can react easily with surface bound H_2O to produce hydroxyl radicals, whereas, e^-_{cb} can react with O_2 to produce superoxide radical anion [15].

$$e^-_{cb} + O_2 \longrightarrow O_2^{\bullet-} \qquad (ii)$$

$$h^+_{vb} + H_2O \longrightarrow {}^{\bullet}OH + H^+ \qquad (iii)$$

The hydroxyl radical is extremely strong oxidant that leads degradation of organic dye.

$$O_2^{\bullet-} + H_2O + H^+ \longrightarrow H_2O_2 + O_2 \qquad (iv)$$

$$H_2O_2 \longrightarrow 2\,{}^{\bullet}OH \qquad (v)$$

$${}^{\bullet}OH + \text{dye} \longrightarrow \text{degradation of the dye} \qquad (vi)$$

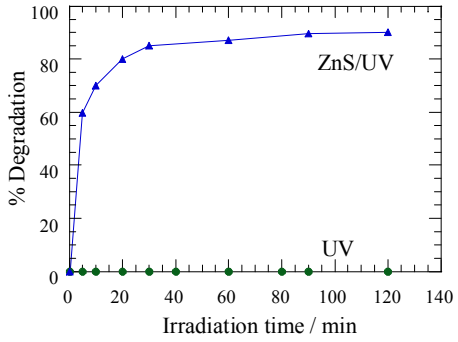

Figure 2. Effect of UV light and ZnS on photocatalytic degradation of DB-98. $[DR\text{-}98]_0$ = 50 mgl^{-1}; [ZnS] = 3 gl^{-1}; pH = 6.

Effect of the Amount of ZnS

The effect of the amount of ZnS on the degradation of DB-98 was investigated using different concentrations of ZnS varying from 1-5 gl^{-1}. Figure 3 shows the degradation efficiency of DB-98 at irradiation time of 90 min. It can be seen that the photodegradation efficiency increases with an increase in ZnS concentration up to 3 gl^{-1} and is then almost constant. The increase in the amount of catalyst enhances the number of active sites on the photocatalyst surface, thus causing an increase in the number of hydroxyl radicals which can take part in decolorization of the dye [16].

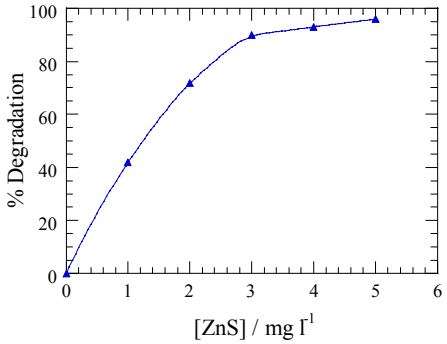

Figure 3. Effect of ZnS amount on photocatalytic degradation efficiency of DB-98 at irradiation time of 90 min. $[DB\text{-}98]_0$ = 50 mgl^{-1}; pH = 6.

Effect of Initial Dye Concentration

The effect of the initial dye concentration on the photocatalytic degradation is an important aspect of the study. The photodegradation of various initial concentrations of DB-98 in the presence of 3 gl^{-1} ZnS is illustrated in Figure 4. It was found that percentage degradation decreases with increasing amount of dye concentration. The effect of altering the initial concentration of the dye (C_0) on the initial rate (r_0) of photodegradation is shown Figure 5. The rate of photodegradation first increases sharply and then reaches saturation value at high concentration of the dye. This may be due to the fact that as the initial concentration of the dye increases, the color of the solution becomes more intense which presents penetration of light to the surface of the catalyst. Therefore, less hydroxyl radicals are formed, thus causing a decrease in percentage degradation.

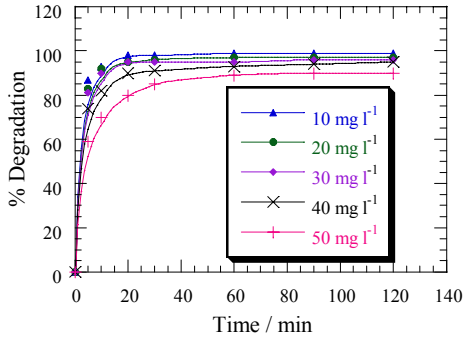

Figure 4. Effect of initial dye concentration on photocatalytic degradation efficiency of DB-98. [ZnS] = 3 gl^{-1}; pH = 6.

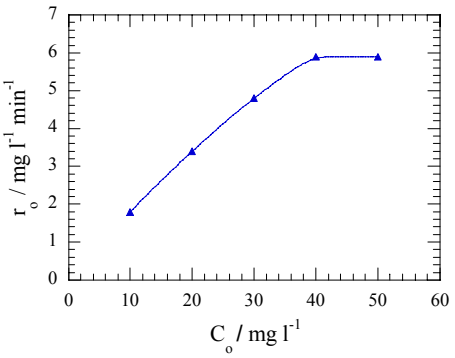

Figure 5. Plot of r_0 versus C_0 for photocatalytic degradation of DB-98. [ZnS] = 3 gl^{-1}; pH = 6

Kinetics of Photocatalytic Degradation of DB-98

The influence of the initial concentration of the solute to the photocatalytic degradation rate of most organic compounds is described by a pseudo-first kinetic order according to the Langmuir-Hinshelwood model, modified to a reaction occurring at solid-liquid interface [17].

$$1/r_o = 1/k + 1/(kKC_0)$$

where k is the rate constant and K is the adsorption coefficient. The dependence of r_o^{-1} values on the respective inverse initial concentrations of DB-98 for constant concentration of ZnS at 3 gl^{-1} is shown in Figure 6. The k and K values were calculated from the slope and the intercept of the straight line, respectively. The values were k = 22.47 mgl^{-1}min and K = 8.51x10^{-3} lmg^{-1}.

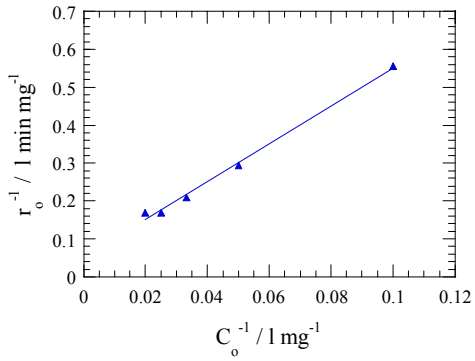

Figure 6. Plot of r_0^{-1} versus C_0^{-1} for photocatalytic degradation of DB-98. [ZnS] = 3 gl^{-1}; pH = 6

Effect of Addition of Ethanol

The change in DB-98 degradation in the presence of ethanol is shown in Figure 7. It was observed that small amount of ethanol inhibited the photocatalytic degradation of DB-98. This can be explained by the competitive reactions of hydroxyl radicals with DB-98 and ethanol. The ethanol can react with hydroxyl radicals in solution (k = 1.9x10^9 $M^{-1}s^{-1}$) thus decreasing their concentration which result in less degradation [18]. This result showed that hydroxyl radicals play a major role in the UV/ZnS process.

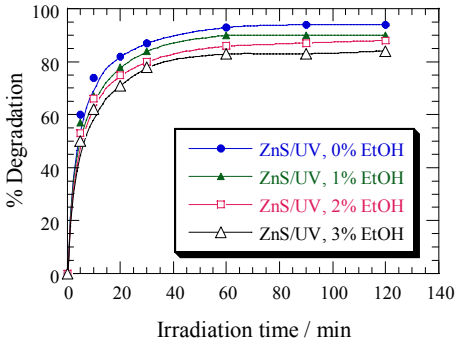

Figure 7. Inhibition of photocatalytic degradation of DB-98 by ethanol. $[DB\text{-}98]_0$ = 50 mgl^{-1}; [ZnS] =3 gl^{-1}; pH = 6.

Conclusions

Effective destruction of DB-98, an azo dye, is possible by photocatalysis in the presence of ZnS suspension and UV light. The kinetics of the photocatalytic degradation follows the Langmuir-Hinshelwood model. Addition of ethanol can inhibit the photodegradation of the dye.

Acknowledgements

The authors thank the Chemistry Department, King Mongkut's University of Technology Thonburi for financial and other supports.

References

[1] C.A. Fewson, *Trends Biotechnol*. **6** (1988), pp.148-153.
[2] S. Seshadri, P.L. Bishop, and A.M. Agha, *Waste Manag*. **15** (1994), pp.127-137.
[3] S.Chakrabati, B.K. Dutta and R. Thampi, *J. Hazard. Mater*. *B* **112** (2004), pp.269-278.
[4] V. Kandavelu, H. Katieu, and R. Thampi, *Appl.Catal. B: Environ*. **48** (2004), pp. 101-111.
[5] A.A. Khodja, T. Sehili, J. Pilichowski and P.J. Boule, *J. Photochem. Photobiol.A:Chem*. **141** (2001), pp. 231-239.
[6] N. Daneshvar, D. Salari, and A. Khataee, *J. Photochem. Photobiol. A: Chem.,* **162** (2004), pp. 317-332.
[7] D.Y. Goswami, *Advance in Solar Energy* **10** (1995), pp. 165-209.
[8] I. Poulios and I. Aetopoulou, *Environ. Technol*. **20** (1999), pp. 479-487.
[9] J. Saien, and A.r. Soleymani, *J. Hazard. Mater*. **144** (2007), pp. 506-512.
[10] S.K. Kansal, M. Singh, and D. Sud, *J. Hazard. Mater*. **141** (2007), pp. 581-590.
[11] X. Wang, B.Q. Xu, J. Zhao, B. Mai, P. Peng, G. Sheng and J. Fu, *J. Photochem. Photobiol. A: Chem*. **168** (2004), pp. 47-52.
[12] C. O'Neil, F.R. Hawles, D.L. Hawkes, N.D. Lourenco, H.M. Pinheiro, and W. Dele'e, *J. Chem. Technol. Biotechnol.* **74** (1999), pp. 1009-1018.
[13] P.C. Vandevivere, R. Bianchi, and W. Verstraete, *J. Chem. Technol. Biotechnol*. **72** (1998), pp. 289-302.
[14] M.A. Rauf, S.B. Bukallah, A. Hammadi, A. Soliman, and F. Hammadi, *Chem. Eng. J.* **129** (2007) pp. 167-172.

[15] N.M. Mahmoodi, M. Arami, N.Y. Limaee, and N.S. Tabrizi, *J.Colloid Interface Sci.* **295** (2006), pp. 159-164.
[16] I.K. Konstatinou, and T.A. Albanis, *Appl. Catal. B: Environ*., **49** (2004), pp. 1-14.
[17] H. Al-Ekabi, and N. Serpone, *J. Phys. Chem.* **92** (1982), pp. 5726-5731.
[18] N. Daneshvar, D. Salari, and A. Khataee, *J.Photochem. Photobiol. A: Chem*. **157** (2003), pp. 111-116.

Growth of diamond-like carbon films on alumina by MW-PECVD technique

C. Rattanasatien[1], N. Tonanon[1] and B. Paosawatyanyong[2,3*]

[1] Center of Excellence in Particle Technology, Department of Chemical Engineering, Faculty of Engineering, Chulalongkorn University, Bangkok, Thailand 10330
[2] Department of Physics, Faculty of Science, Chulalongkorn University, Bangkok, Thailand 10330
[3] ThEP Center, Commission on Higher Education, Bangkok, Thailand 10400

[*] E-mail: paosawat@sc.chula.ac.th

Abstract: Diamond is one of the best grinding and cutting tool materials because of its superior properties such as hardness and wear resistance. Alumina has been considered as one of materials for grinding balls, cutting tool and orthopedic implants. However, it has a low resistance against wear after specific length of time. Therefore, the deposition of diamond-like carbon (DLC) films is a promising solution to this problem. In this research, microwave plasma enhanced chemical vapor deposition (MW-PECVD) technique was used to deposit DLC films on alumina substrates using methane (CH_4) and hydrogen (H_2) gas mixture as plasma media. In order to increase the nucleation density of diamond, the alumina substrates were scratched with diamond powder. The influence of methane concentrations from 0.5 to 5% and deposition pressure in the range 10 to 50 torr were investigated. The input microwave power was kept constant at 700 W with total deposition time of 30 h. All samples were characterized by scanning electron microscope (SEM), Raman spectroscopy and nano indentation testing. The surface morphology of DLC films showed cauliflower-like type. With increasing deposition pressure, dense DLC films could be formed on the substrate. Moreover, the morphology of the films changed from ballas-like to cauliflower-like with CH_4 concentration of 3%. Raman investigations indicated the spectra of DLC films which clearly verified the occurrence of diamond and graphite phases as related to D band and G band respectively. Results of nano indentation tests performed that the hardness of alumina after coated with DLC films were increase.

Keywords: alumina, DLC, MW-PECVD, hardness

Introduction

Alumina has a high potential for use in many refractory materials because of its high hardness (7-9 GPa), wear resistance, low thermal expansion and high melting point. It has been considered as one of the most promising advanced materials for variety of applications such as grinding balls, wear resistance material, cutting tools and orthopaedic implants. However, alumina could wear after the long term use. Hence, it is highly desirable to improve the hardness and wear resistance of alumina by coating with diamond-like carbon (DLC) thin films. DLC has found to be used in many applications including hard coating, cutting and grinding tools and as electronic devices due to its extreme hardness, high wear resistance and good chemical inertness [1]. In order to grow DLC films on alumina substrates, it is necessary to increase the nucleation density of diamond at first. Generally, alumina substrates have a low nucleation density of diamond. Several processes are proposed to improve the nucleation density as such scratching with diamond powder, applying negative bias voltage and chemical etching [2]. Therefore, in this research the substrates are improved the nucleation density by scratching with diamond powder. Most of the DLC synthesis processes have been carried out using microwave plasma enhanced chemical vapor deposition (MW-PECVD) technique. The synthesis of DLC films can be realized by modifying the deposition parameters commonly used in producing the films, such as the deposition pressure and the gas composition. Thus, we have investigated the effects of the deposition pressure and the gas methane concentrations of the formation of DLC films on alumina by MW-PECVD technique in this research.

Materials and Methods

Before deposition began, the alumina substrates were scratched with 0.1 μm diamond powder, followed by ultrasonic cleaning and rinsing in acetone, methanol and de-ionized water respectively. A description on the MW-PECVD system used to deposit the DLC coatings has been given elsewhere [3]. The MW-PECVD technique, using gaseous mixture of methane and hydrogen was applied to deposit DLC films on alumina substrates. In order to investigate the effects of the deposition pressure and the methane gas concentration on the formation of DLC films on alumina, the deposition pressure was varied from 10 torr to 50 torr and the gas methane was concentrated in the range of 0.5% to 5%. The microwave power was held constant at 700 W for all depositions and the substrate temperature during the deposition was measured by a thermocouple embedded within the substrate holder.

The investigations of surface morphology were observed with a JEOL, JSM-6480LV Scanning Electron Microscope (SEM) and the raman spectra

were obtained using a Renishaw invia raman microscope operated at a laser wavelength of 514.5 nm. The r.m.s. surface roughness was evaluated with a Veeco NanoScope IV Atomic Force Microscope (AFM). The hardness of the DLC films was evaluated by nano indentation tests using (NHT, CSM instruments) nano indentation tester with a diamond Berkovich indenter.

Results and Discussion

Effect of deposition pressure on the formation of the DLC films

A comparison of the surface roughness of the films deposited at various deposition pressures was carried out by AFM. Fig 1(a) and (b) illustrate the AFM image of the films grown at 10 torr and 50 torr respectively. The r.m.s. surface roughness is found to increase from 23 to 45 nm with increasing deposition pressure from 10 to 50 torr. At higher deposition pressure, the amount of secondary nucleation decreases, leading to an increase the grain size and the surface roughness [4, 5]. As the hardness of the alumina substrates evaluated by nano indentation tester under a load of 5 mN. It can be preliminary shown that the hardness of the films deposited with DLC films have an increase in all deposition conditions. With increasing deposition pressure from 10 to 30 torr, the hardness is found to increase from 17 to 49 GPa.

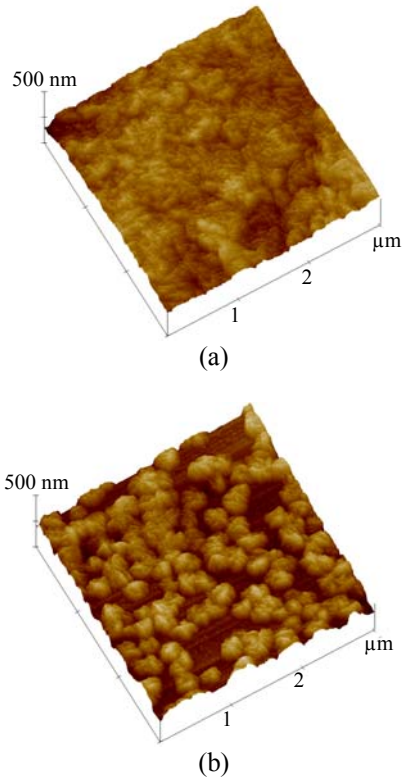

Figure 1. AFM images of DLC films grown under CH_4 concentration of 1%, deposition pressure at (a) 10 torr and (b) 50 torr.

The SEM images of the DLC films grown on alumina prepared at different deposition pressure are shown in Fig 2 for (a) 10 torr, (b) 30 torr, and (c) 50 torr, respectively. Obviously, it can be shown that by increase deposition pressure from 10 to 50 torr, the grain sizes increase gradually with nanostructure. The smaller grains are formed as a result of the enhanced secondary nucleation during the deposition process. According to kinetic theory of gas, the mean free path of active species decrease at higher pressure. This leads to an increase in collision frequency and number of active species in plasma, which are more favorable for diamond growth [6, 7]. Moreover, the DLC films are dense and continuous, which indicates a very high nucleation density.

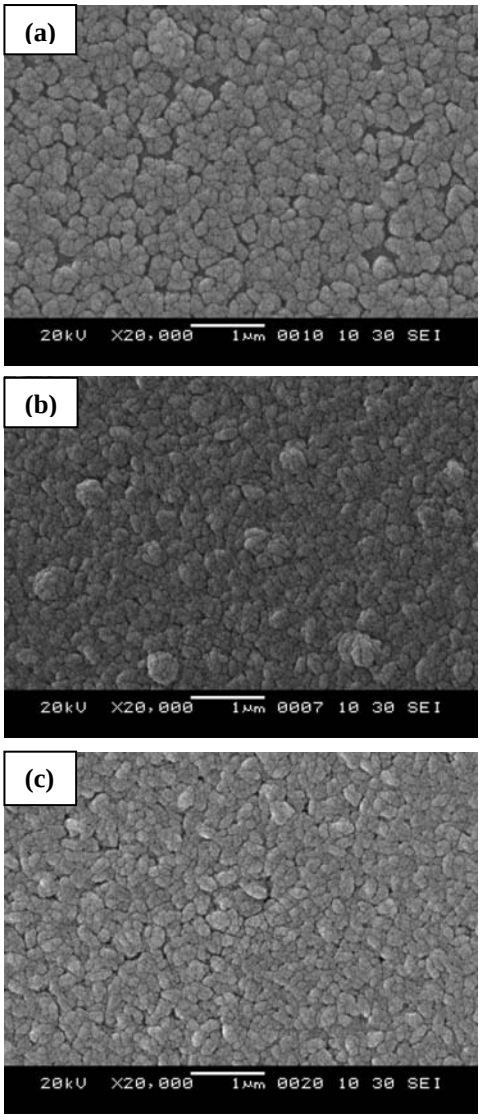

Figure 2. SEM images of DLC films deposited on alumina grown at 1 % CH_4 concentration under various deposition pressure, (a) 10 torr, (b) 30 torr, and (c) 50 torr

The raman spectra of the DLC films on alumina grown at various the deposition pressure as shown in Fig 3. The raman peak around 1332 cm^{-1} assigned to D band, clearly demonstrates the presence of diamond phase in the deposited films. The broad hump peak around 1450-1600 cm^{-1} assigned to G band, can be attributed to graphite phase. With decreasing deposition pressure, the intensity of D band becomes weaker for the films grown at 10 torr. As the grain sizes decrease gradually at low deposition pressure speculatively due to the increase of amorphous carbon content in the deposited films [6].

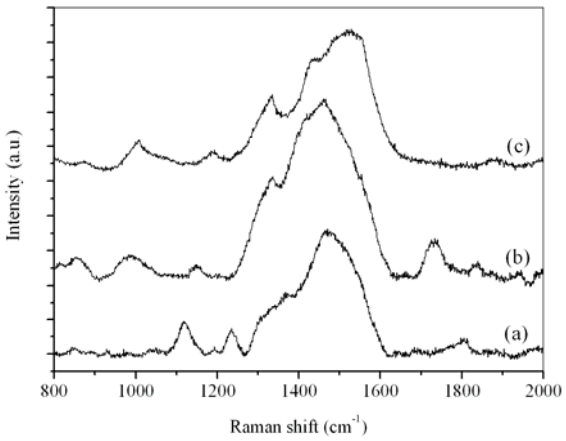

Figure 3. Raman spectra of the DLC films deposited at 1 % CH_4 concentration under different deposition pressure, (a) 10 torr, (b) 20 torr, and (c) 30 torr.

Effect of the CH_4 concentrations on the formation of the DLC films

Fig. 4 presents SEM images of the DLC films grown for 30 h at deposition pressure of 30 torr. Under a low CH_4 concentration of 0.5%, the ballas-like shape particle can be seen in the films as illustrated in Fig. 4(a). With increasing CH_4 concentration to 3%, a smooth and fine grained surface similar to cauliflower-like morphology is observed as shown in Fig. 4(b)-(c). As mentioned above, the surface morphologies of the films change from ballas-like to cauliflower-like with the increase in CH_4 concentration of 3%. An increase in CH_4 concentration can lead to an increase in the secondary nucleation effect. This can repress the former crystals completely, resulting to a decrease in the grain size [8, 9].

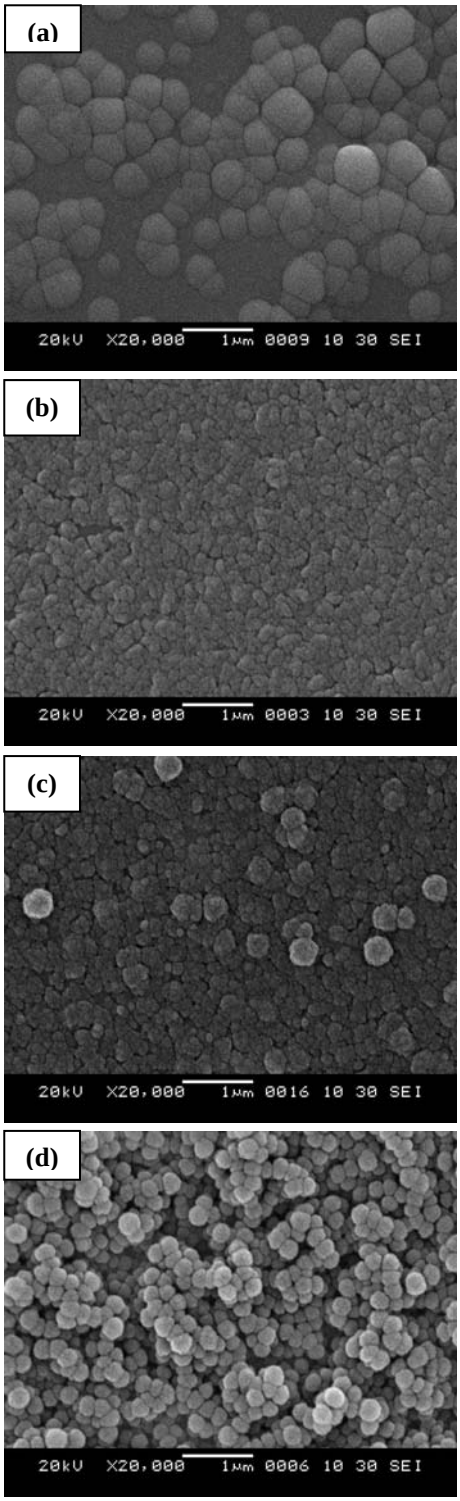

Figure 4. SEM images of DLC films grown on alumina under different CH_4 concentration, (a) 0.5%, (b) 1%, (c) 3%, and (d) 5%.

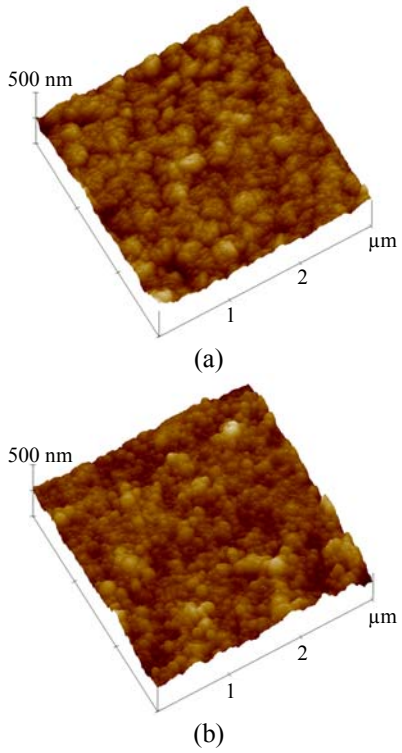

Figure 5. AFM images of DLC films grown under the deposition pressure of 30 torr, CH_4 concentration at (a) 1% and (b) 5%.

The surface roughness of the films grown at deposition pressure of 30 torr under various CH_4 concentrations as shown in Fig 5. It can be seen that with increasing CH_4 concentration from 1% to 5%, the r.m.s surface roughness decrease from 47 to 38 nm. As related above, the surface roughness decrease because of a very small grain or secondary diamond nuclei scatter among the large grain boundaries with higher pressure [4].

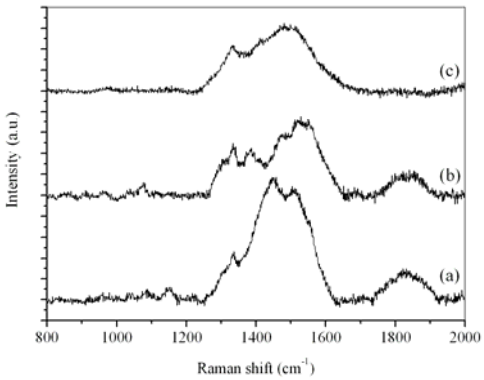

Figure 6. Raman spectra of the DLC films grown at deposition pressure of 30 torr under various CH_4 concentrations, (a) 1%, (b) 2%, and (c) 3%.

The raman spectra of the DLC films at different CH_4 concentration are illustrated in Fig 6. The raman peak is performed with respect to the graphite and diamond phase. The diamond band around 1332 cm^{-1} is significant broadened, which caused by decreasing the grain size [5]. Particularly, at CH_4 concentration of 3%, a very broad peak around 1450-1600 cm^{-1} can be observed. Furthermore, the hardness of alumina after coated with DLC films are increase, according to measure by nano indentation tester under various CH_4 concentrations. It can be found that the hardness in the range of 39-43 GPa. It is indicated that there is significant improvement on the hardness of alumina surface coated with DLC films.

Conclusion

DLC thin films on alumina have been investigated using MW-PECVD technique in a methane and hydrogen gas mixture. It was found that by decreasing the deposition pressure, the grain sizes increase gradually with nanostructure. In contrast, the surface roughness of the films increased with increasing deposition pressure, whereas the increase of CH_4 concentration to 3%, the surface roughness decreased and the films were observed to change from ballas-like to cauliflower-like morphology. The raman spectra showed peak of D band around 1332 cm^{-1} and broad hump of G band around 1450-1600 cm^{-1}. Furthermore, the hardness of alumina could be found to increase after coated with DLC films in the range of 17-49 GPa. Demonstrating the significant improvement on the hardness of the coated alumina.

Acknowledgement

This research was supported by Chulalongkorn University. The authors gratefully acknowledge the nano indentation instrument support of Nano Shield Co. Ltd. and CSM instruments Co. Ltd.

References

[1] P. W. May, *Philosophical Transactions of The Royal Society* A **358** (2001), pp. 473-495.
[2] D.S. Dandy and M.E. Coltrin, *Daimond Thin Films Handbook*, New York:Marcel Dekker, 2002, pp.227-281.
[3] B. Paosawatyanyong, K. Honglertsakul and D.K. Reinhard, *Solid State Phenomena* **107** (2005), pp.75-80.
[4] N. Rujisamphan, Design and construction of microwave-PECVD and preliminary characteristics of synthesized polycrystalline diamond film, Master' Thesis, Chulalongkorn University, 2006.
[5] X.M. Meng, W.Z. Tang, L.F. Hei, C.M. Li, S.J. Askari, G.C. Chen and F.X. Lu, *International Journal of Refractory Metal and Hard Materials* **26** (2008), pp.485-490.
[6] X. Liang, L. Wang, H. Zhu, and D. Yang, *Surface and Coatings Technology* **202** (2007), pp.261-267.
[7] K. E. Spear, and J. P.Dismukes, *Synthetic diamond: Emerging CVD science and technology*, New Jersey: John Wiley & Sons, 1994.
[8] K. Mallika, R. Komanduri, *Thin Solid Films* **396** (2001), pp.145–165.
[9] S.J. Askari, G.C. Chen and F.X. Lu, *Materials Research Bulletin* **43** (2008), pp.1086–1092.

Calculation of partition coefficient (Log P) of synthesized cinnamic acid and cinnamate derivatives

S. Sukiattichaisakul [1,2], K. Noytanom [1,2], W. Jungtanasombut [1,2], T. Karpkird [1], W. Parasuk[1] and S. Hannongbua [1,2*]

[1]Department of Chemistry, Faculty of Science, Kasetsart University, Chatuchak, Bangkok, Thailand 10900
[2] Center of Nanotechnology KU, and NANOTEC Center of Excellence at Kasetsart University, Kasetsart University,Chatuchak, Bangkok, Thailand 10900
*E-mail: fscisph@ku.ac.th

Abstract: Cinnamic and cinnamate derivatives are the popular UV-B screening compounds which are widely used in various cosmetic formulations in sunscreen products. So, it is necessary to study the effect of these chemicals on human and environmental systems. The n-octanol/water partition coefficient (log P_{ow}) is one of the most important physicochemical properties that represents the distribution of chemical in environmental system and capability of bioaccumulation in human or animal. Thus, the purpose of this study is to calculate the log P_{ow} of new 24 synthesized cinnamic and cinnamate derivatives by using MOE and MODEL programs and compare the obtained log P_{ow} values from both calculations. From estimation of the log P_{ow} of these compounds, we found that the range of log P_{ow} values are between 1.5 and 2.7. While, the range of cinnamate derivatives are 4.8 to 5.7. These indicate that cinnamate derivatives have polar less than cinnamic acid derivatives. The calculated log P_{ow} of these 24 compounds from MOE program correlated well with the calculated log P_{ow} from MODEL program which supported by correlation coefficient (r^2 = 0.99).

Introduction

Cinnamic acid and cinnamate derivatives are important UV-B absorbing compounds[1]. They are widely used in the cosmetic industry especially in sunscreen products and non-cosmetic products such as household cleaners and detergents[2]. And under the new legal framework for management of chemicals within the European Union (EU) called Registration Evaluation and Authorization of Chemicals (REACH), which announced. "increase the protection of human health and environment from exposure of chemicals." (EU 2006) . Then, the effect of these chemicals on human health and environment are very important and to be investigated. The octanol/water partition coefficient that usually expresses as log P_{ow} can be indicated the behavior of hydrophobic of organic compounds. When log P_{ow} >1, compounds are hydrophobic while log P_{ow} < 1, compounds are hydrophilic[3]. Therefore, log P_{ow} is one of the necessary physicochemical parameters that can indicate the distribution of chemical in environment, chemical persistence and ability of bioaccumulation. Besides, log P_{ow} is correlative to the toxicity of chemical[4-7].

The log P_{ow} is defined as the ratio of equilibrium concentrations of chemicals in n-octanol and water system[6]. Log P_{ow} value can be calculated as following equation :

$$\log P_{ow} = \log \frac{C_{n\text{-octanol}}}{C_{water}} \quad (1)$$

$C_{n\text{-octanol}}$ and C_{water} are the concentration of test chemical in octanol and water phase, respectively. The log P_{ow} can be indicated the behavior of hydrophobic of organic compounds.

There are various methods to determine the log P_{ow} values, such as shake-flask method, slow-stirring method, chromatography method, and so on[8-10]. Therefore, log P_{ow} calculation of these compounds by computational method is very needful to find a good method to mesure the log P_{ow} of compounds. So the aim of this work is to calculate log P_{ow} of 24 synthesized cinnamic and cinnamate derivatives shown as Figure 1 by using Molecular Descriptor Lab program (MODEL) and Molecular Operating Environment program (MOE). It is already known that the physicochemical property predictions from different molecular descriptors can give different predicted values, therefore, the calculated log P_{ow} values for all new synthesized derivatives from both programs are compared.

Computational Methods

Structures of all 24 cinnamic and cinnamate derivatives were constructed by Gaussian view 03 program. The geometry of each molecule was optimized and calculated atomic net charge by SYBYL 7.0 program[11]. Afterward, log P_{ow} values of each compounds was calculated by using the MODEL program and MOE program. And the obtained calculated values from both programs were compared.

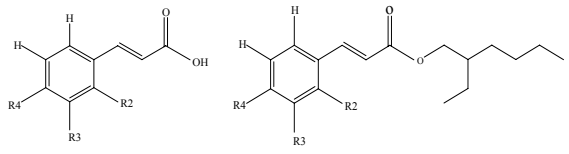

(a) (b)

Figure 1. General structure of (a) cinnamic acid derivatives (b) cinnamate derivatives

Results and Discussion

The structures and calculated log P_{ow} 24 cinnamic and cinnamate derivatives are shown in Table 1. Log P_{ow} of cinnamate derivatives that obtained from the MOE and MODEL programs are in the range of 4.8 to 5.7. While, cinnamic acid derivatives are in the range 1.5 to 2.7. These indicate that cinnamate derivatives are preferred to dissolve in n-octanol more than cinnamic derivatives. And the obtained log P_{ow} values form both programs were compared by finding the correlation between them shown as Figure 2. We found that calculated log P_{ow} values from MOE and MODEL programs are silightly different supported by correlation coefficient ($r^2 = 0.99$)

Table 1: Structures and calculated log P_{ow} using MOE and MODEL programs of 24 cinnamic acid and cinnamate derivatives

No.	Compound			Log P_{ow}	
	R2	R3	R4	**MOE**[1]	**MODEL**[2]
Cinnamic acid derivatives					
1	**OCH_3**	H	H	2.44	1.77
2	H	**OCH_3**	H	2.48	1.77
3	H	H	**OCH_3**	2.45	1.77
4	**OH**	H	H	2.18	1.52
5	H	**OH**	H	2.22	1.52
6	H	H	**OH**	2.18	1.52
7	**F**	H	H	2.64	1.99
8	H	**F**	H	2.68	1.99
9	H	H	**F**	2.64	1.99
10	**NO_2**	H	H	1.95	1.73
11	H	**NO_2**	H	1.99	1.73
12	H	H	**NO_2**	1.95	1.73
Cinnamate derivatives					
13	**OCH_3**	H	H	5.53	5.11
14	H	**OCH_3**	H	5.56	5.11
15	H	H	**OCH_3**	5.53	5.11
16	**OH**	H	H	5.26	4.86
17	H	**OH**	H	5.30	4.86
18	H	H	**OH**	5.26	4.86
19	**F**	H	H	5.72	5.30
20	H	**F**	H	5.76	5.30
21	H	H	**F**	5.72	5.30
22	**NO_2**	H	H	5.50	5.06
23	H	**NO_2**	H	5.54	5.06
24	H	H	**NO_2**	5.51	5.06

[1]Molecular Operating Environment[12] [2]Molecular Descriptor Lab[13]

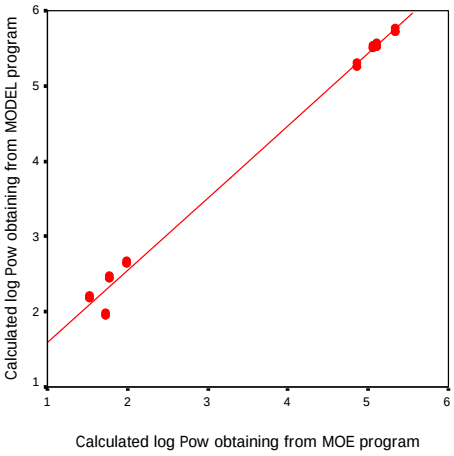

Figure 2. The correlation between predicted log P_{ow} values obtaining from MOE program and MODEL program.

Conclusions

The n-octanol/water partition coefficient (log P_{ow}) of 24 cinnamic and cinnamate derivatives were calculated by computational method (MOE and MODEL programs) and found that cinnamic and cinnamate derivatives have calculated log P_{ow} between 1.5 to 2.7 and 4.8 to 5.7, respectively. From both programs for log P_{ow} calculation, we found that they gave closely log P_{ow} values which shown as correlation coefficient ($r^2 = 0.98$). And for further work, we will measure log P_{ow} of these compounds using experimental methods (Shake-flask and HPLC) and set up Quantitative Structure-Property Relationships (QSPR) model for predicting the partition coefficient of the other new synthsized cinnamic and cinnamate compounds.

Acknowledgments

This research was supported by the Thailand Research Fund (RTA5080005, TRF-MRG5180279, RDG5230004), National Nanotechnology Center under the National Science and Technology Development Agency, NANOTEC Center of Excellence, Kasetsart University and the Project for the Promotion of Science and Mathematics Talented Teachers (PSMT.). The Computer Center at University of Vienna is acknowledged for providing MOE calculations.

References

[1] G.-S. Lee, A. Widjaja and Y.-H. Ju., *Biotechnology Letters*. **28**(2006), pp.581-585
[2] S. P. Bhatia, G. A. Wellington, J. Cocchiara, J. Lalko, C. S. Letizia and A. M. Api, *Food. Chem. Toxicol.* **45** (2007), pp. S90-S94.
[3] G.-N. Lu., X.-Q. Tao., Z. Dang., X.-Y. Yi., C. Yang., *Cent. Eur. J. Chem.* 6(2)(2008), pp. 310-318.
[4] Y. Dai, J.-L. Jiang, Z.-Y. Wang, and Q. Xue., *Chinese J. Struct. Chem.* **vol.26** (2007), pp. 1449-1454.

[5] L. Li, S. Xie, H. Cai, X. Bai, and Z. Xue., *Chemosphere.* **72**(2008), pp. 1602-1606.
[6] P.Y. Lee and C.Y. Chen, *Journal of Hazardous Materials*. **165**(2009), pp. 156-161.
[7] Y.-z. Sun., Z.-j. Li., X.-i Yan., L. Wan., F.-h. Meng., *Med Chem Res*. Article in press (2009), pp. 1-13
[8] OECD Guidelines for Testing of Chemicals No. 107. 1995.
[9] OECD Guidelines for Testing of Chemicals No. 117. 2004.
[10] OECD Guidelines for Testing of Chemicals No. 123. 2006.
[11] http://www.nectec.or.th/
[12] http://www.univie.ac.at/ZID/services/
[13] http://jing.cz3.nus.edu.sg/cgi-bin/model/model.cgi

Adsorption of sodium dodecylbenzene sulfonate on ceramic glaze

S. Satchawan,[1] O. Arquero,[1*] W. Naksata,[1] S. Thiansem,[2] and P. Panya[3]

[1]Department of Chemistry and Center of Excellence for Innovation in Chemistry, Faculty of Science, Chiang Mai University, Chiang Mai 50200, Thailand.
[2]Department of Industrial Chemistry, Faculty of Science, Chiang Mai University, Chiang Mai 50200, Thailand.
[3]Department of Chemistry, Faculty of Science and Technology, Kamphaengphet Rajabhat University, Kamphaengphet 62000, Thailand.

[*]E-mail: noi2495@hotmail.com

Abstract: The rheological behavior of ceramic glaze suspensions containing limestone, quartz, feldspar and kaolin, has been improved by the addition of surfactant. Underdosing may result in high viscosity due to hydrophobic attraction between particles while overdosing may result in high viscosity possibly due to micelles in the solution. The adsorption of anionic surfactant (sodium dodecylbenzene sulfonate, SDBS) on a ceramic glaze mixture in the presence of 1% ferric oxide has been investigated. The adsorption isotherm has been studied in order to understand the suspension stability as a function of pH and anionic surfactant concentration. The adsorbed amount of SDBS increases with increasing added surfactant concentration at pH 7 and 9 in a fixed electrolyte. However, the adsorbed amount of SDBS at pH 7 was more than at pH 9 because anionic surfactant could adsorb on the positively charged edge of kaolin and on the positive site of limestone. The maximum adsorbed amount of SDBS at pH 7 and 9 are 136 and 60 µmol/g, respectively.

Introduction

The colloidal processing of submicron sized ceramics is necessary to control the inter-particle forces because colloidal ceramic particles will naturally aggregate together. If the particles in this slurry quickly settle when coating or dipping the ceramic body into this slurry, the surface of each ceramic product after coating will not be smooth and uniform. To control the inter-particle forces, it is possible to eliminate these aggregates. There are two methods of imparting stability to the particles so that they do not aggregate. The first is the charged groups on the surface of the particles. The surface groups can be positively or negatively charged depending on the pH condition. The second is the adsorption of surfactant onto the particle surface [1]. Surfactants are found widespread applications in many industrial processes. An important property of surfactants is their tendency to adsorb onto solid surfaces. The surfactants are used in many fields in order to regulate the stability and flocculation properties of dispersion systems [2-4]. If too little of surfactant is added, then some flocculation will persist as suspension and if too much of is added then destabilization may occur [5]. Another factor that affects the adsorption of surfactant from solution onto ceramic particles is the ionic strength of the suspension [6]. In the case of ionic surfactant, adsorption at the solid/liquid interface will also affect the interfacial electrical properties, and the interactions between particles [7]. The adsorption of single surfactants at solid/liquid interactions is fundamentally important for many technical applications.

Materials and Methods

All minerals were sourced locally in Thailand: the kaolin (85%) from Ranong, the feldspar (99%) and quartz (>99%) from Tak and limestone (97%) from Sara Buri. Ferric oxide (AR grade, Sigma-Aldrich), soduim dodecylbenzene sulfonate (AR grad, Sigma-Aldrich), hydrochloric, HCl (AR grade, Lab-Scan), sodium hydroxide, NaOH (AR grade, Caro Erba) and magnesium chloride, $MgCl_2$ (AR grade, Caro Erba) were used as supplied. All water used was deionized water.

The quartz and feldspar were ground by dry ball milling and mixed to homogeneous. The final compositions of the glaze of each component are presented in Table 1.

Table 1: Composition of ceramic glaze mixture

Materials	Formula	Mass fraction %
Limestone	$CaCO_3$	28
Kaolin	$Al_2O_3{\cdot}2SiO_2{\cdot}2H_2O$	27
Quartz	SiO_2	20
Feldspar	$KNaO{\cdot}Al_2O_3{\cdot}6SiO_2$	25
Ferric oxide	Fe_2O_3	1

Adsorption isotherms were measured at 30 °C. To prepare the ceramic glaze with 1% ferric oxide suspension, 0.50 g of ceramic glaze was added to a solution containing magnesium chloride and surfactant. The pH was checked and adjusted, if necessary, using 0.01 or 0.1 M HCl or NaOH, to a total volume 25 ml. The mixtures were shaken for 24 hrs and then centrifuged. The clear supernatant was removed for determination of the equilibrium surfactant concentration by UV-VIS spectrometer (UV Lambda 25 spectrometer). The UV absorption of

dodecylbenzene sulfonate ion in the supernatant was measured at 223 nm. A calibration curve of SDBS surfactant concentration shown in Figures 1-2 (at the necessary pH and $MgCl_2$ concentration) was prepared for each experiment to permit the supernatant concentration to be determined. The amount of surfactant adsorbed was calculated with following equation:

$$\Gamma = \frac{(C_i - C_{eq}) \times V}{1000 \times m}$$

where Γ is the amount of surfactant adsorbed; C_i and C_{eq} are initial concentration and equilibrium concentration of surfactant respectively; V is final volume of solution; and m is mass of ceramic glaze mixture.

Results and Discussion

The adsorption isotherm for anionic surfactant, SDBS, on ceramic glaze mixture in the presence of 1% ferric oxide particle as a function of ionic strength at pH 7 and pH 9 are shown in Figures 3-4, respectively.

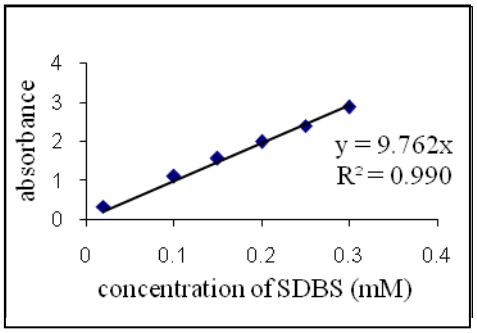

Figure 1. Standard curve of SDBS in 0.001 M $MgCl_2$ at pH 7

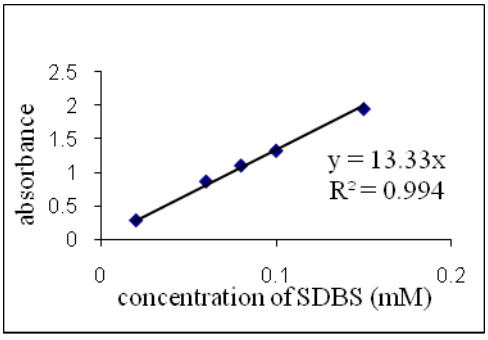

Figure 2. Standard curve of SDBS in 0.001 M $MgCl_2$ at pH 9

At pH 7 the adsorbed amount of SDBS increased at equilibrium concentration from 0.03 to 1.2 mM SDBS and the maximum adsorption of SDBS reached 136 µmoles/g. At pH 9 the trend is the same as that observed for the adsorption at pH 7 and the maximum adsorption of SDBS was about 60 µmoles/g. At higher SDBS concentrations, the adsorbed amount decreased after the maximum adsorbed amount of SDBS for both pH might be due to micelle formation.

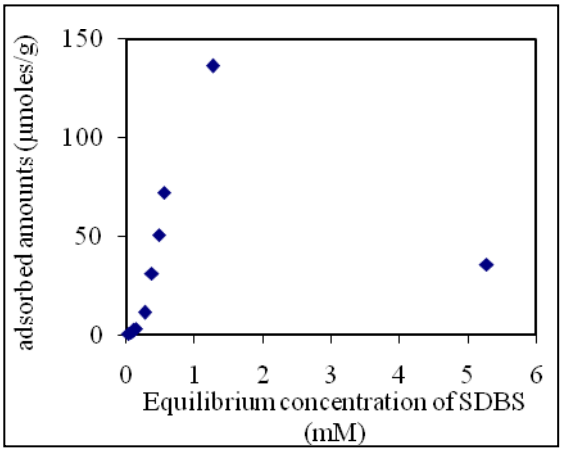

Figure 3. Adsorption isotherm of SDBS on ceramic glaze mixture with 1% ferric oxide in 0.001 M $MgCl_2$ at pH 7

The maximum adsorbed amount of SDBS on the ceramic glaze was more at pH 7 than at pH 9 because there might be more positively charged surface sites on kaolin that dodecylbenzenesulfonate ions could be adsorbed. At pH 9, almost all surface sites of the ceramic glaze mixture with 1% ferric oxide particle become negative charge.

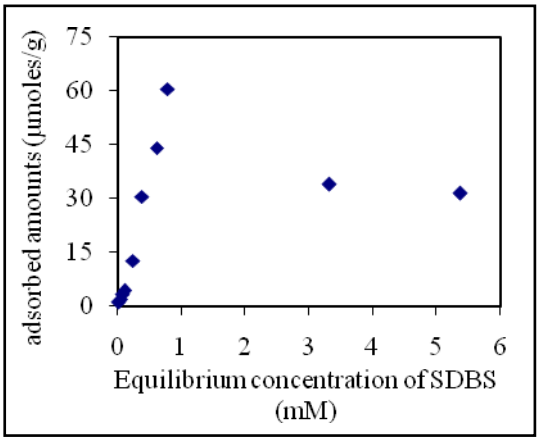

Figure 4. Adsorption isotherm of SDBS on ceramic glaze mixture with 1% ferric oxide in 0.001 M $MgCl_2$ at pH 9

Conclusions

The adsorption isotherm of SDBS onto ceramic glaze mixture particle including limestone, feldspar, quartz, kaolin and 1% ferric oxide has been investigated as a function of pH, ionic strength and surfactant concentration. Adsorption of SDBS to ceramic glaze mixture with 1% ferric oxide increases with added anionic SDBS concentration. However, the adsorbed amount of SDBS decreases with increasing pH values.

Acknowledgments

The authors acknowledges the Graduate School of Chiang Mai University, Department of Chemistry Faculty of Science Chiang Mai University, National Research University, and the Center of Excellence for Innovation in Chemistry : PERCH-CIC, Thailand, for partial finacial support of this research.

References

[1] R. Greenwood and K. Kendall, *Powder Technol*., **113** (2000), pp. 148-157.
[2] S. Schwarz, K. Lunkwitz, B. Kebler, U. Spiegler, E. Killmann and W. Jaeger, *Colloids Surf. A: Physicochem. Eng. Aspects,* **163** (2000), pp. 17-27.
[3] S. Thongphrom. "Factors affecting colloidal stability of ceramic glazes". Ph.D. Thesis, Chiang Mai University, 2003.
[4] P. Panya, O. Arquero, G.V. Franks and E.J. Wanless, *J. Colloid Interface Sci*., **279** (2004), pp. 23-37.
[5] S.B. Johnson, G.V. Franks, P.J. Scales, D.V. Boger and T.W. Healy, *Int. J. Miner. Process.,* **58** (2000) 267-304.
[6] P. Marco and J. Llorens, *Colloids Surf. A: Physicochem. Eng. Aspects,* **270** (2005), pp. 291-297.
[7] K. E. Bremmell, G. J. Jameson and S. Biggs, *Colloids surf. A: Physicochem. Eng. Aspects,* **146** (1999), pp. 75-87.

Azo dyes as photosensitizers for organic solar cells

K. Nakajima[1,2], K. Ohta[1], H. Katayanagi[2,3], K. Mitsuke[2,3]*

[1]Science Research Center, Hosei University, Fujimi, Chiyoda-ku, Tokyo, Japan 102-8160
[2]Department of Photomolecular Science, Institute for Molecular Science, Myodaiji, Okazaki, Japan 444-8585
[3]Department of Structural Molecular Science, Graduate University for Advanced Studies, Myodaiji, Okazaki, Japan 444-8585

*E-mail: mitsuke@ims.ac.jp

Abstract: Fabrication and performance tests are reported on dye sensitized solar cells (DSCs) containing azo dyes as photosensitizers. Fundamental properties of the DSCs were obtained on the energy conversion efficiency η, short current and photoabsorbance in the wavelength range of 300 to 800 nm. Various azo dyes were synthesized in such a way that the positions and numbers of carboxylate and hydroxy groups differ from one dye to another. The carboxylate groups are considered to form strong linkages with the surface of TiO_2 nanoparticles to promote rapid electron injection from dye molecules to the conduction band of TiO_2. We could demonstrate a remarkable correlation between the performance of the DSCs and the energy level of the lowest unoccupied molecular orbital (LUMO) of the azo dye: no dye whose LUMO energy is lower than −1.5eV could allow the authors to make DSCs with η > 0.1%. This finding is consistent with the necessary condition for the DSC that the LUMO level should be higher than the lower bound of the conduction band of TiO_2.

Introduction

The dye sensitized solar cell (DSC) has attracted universal attention because of its high-solar-energy-to-electricity conversion efficiency and relatively low cost of its manufacturing [1]. Panchromatic sensitizers which can efficiently absorb the sunlight are in the stage of research and development. So far the best photovoltaic performance has been achieved with ruthenium complex dyes, but organic dyes have also stimulated intensive research efforts [2]. Indeed high energy conversion efficiency can be obtained with coumarin, polyene, thiophene, and other dyes. In the present study, we focused our attention on azo compounds which have been widely used for dyes and pigments with excellent lightfastness. The main advantage of azo dyes is their facile introduction of various substituents onto the main chromophore R-N=N-R′ where R and R′ are either aryl or alkyl group, permitting us to easily modify their electronic and spectroscopic properties.

Materials and Methods

To fabricate DSCs with azo dyes we followed the same procedure as we have established for those with ruthenium complex dyes which showed the energy conversion efficiency η of ca. 7%. We designed various azo dyes having carboxylate and hydroxy groups whose positions and numbers differ from one dye to another. Only nine azo dyes listed in Table 1 were found to show appreciable photovoltaic capability among 25 azo dyes that we actually synthesized. All the dyes were obtained by using diazo coupling between diazonium compounds and β-naphthol or naphthoic acid derivatives. The diazonium salts were obtained in advance from aniline, *p*-amino-benzoic acid (ABA), *p*-amino-salicylic acid (ASA), and other primary amines. The dyes were carefully purified by alkali dissolution, precipitation with acid solution, centrifugal filtration, stirring in water, ultrasonication, three centrifugal filtrations, dissolution in ethanol, reversed phase chromatography, and evaporation to dryness. Paste of TiO_2 nano-particles in average diameter of 18 μm was screen-printed on a plate of electrically conductive glass. The TiO_2 patterns were made to be typically circular (0.564 cm in diameter and 0.25 cm^2 in area) and occasionally rectangular (1.5×2 cm^2). We sintered this glass plate covered with TiO_2 and immersed it into dye solution to form an anode electrode. We assembled a DSC by combining this plate with another conductive glass deposited with thin platinum film. A volume between the two plates was filled with redox electrolyte solution containing iodide. Two sorts of redox electrolyte solution were used: (i) AN-50 purchased from Solaronix Inc. the principal ingredients of which are 50mM I_2, iodide salt, pyridine derivative, ionic liquid and acetonitrile and (ii) the homemade solution prepared with I_2, lithium iodide and acetonitrile.

Photovoltaic measurements of the DSCs thus fabricated were performed using a solar simulator equipped with a xenon lamp (Peccell Technologies, PEC-L11). We calculated η from the product of the fill factor F, open circuit voltage V_{OC}, and short current density $J_{SC,int}$ integrated over the whole wavelength range; these three quantities were obtained by measuring the I-V curves under the condition of AM 1.5, i.e. the integrated radiation power density of the light of P_{int} = 100 mW/cm^2. The incidence photon to current conversion efficiency IPCE was obtained from

$$\mathrm{IPCE} = J_{SC} \Big/ I_P e = J_{SC} \cdot h\nu \Big/ Pe \qquad (1)$$

where I_P, $h\nu$ and e denote the intensity of incident light, photon energy and elementary charge, respectively. We measured the short current density J_{SC} and radiation power density P as a function of the

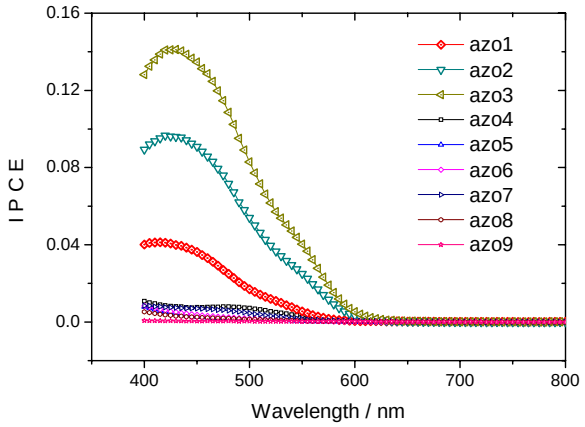

Figure 1. IPCE curves of 9 azo dyes measured with the action spectrometer.

wavelength λ of the light dispersed from two types of monochromator. One is the commercial action spectrometer equipped with a xenon lamp (Peccell Technologies, PEC-S20) and the other is the 3m-normal incidence monochromator connected to a visible to near-infrared beam line of the synchrotron radiation facility (UVSOR) at the Institute for Molecular Science [3]. At λ = 532 nm *P* at the sample point was 20 mW/cm^2 and 150 nW/cm^2 in the action spectrometer and normal incidence monochromator, respectively. We have monitored J_{SC} at λ ~ 532 nm of many DSCs containing Ru535 and Ru535-bis-TBA dyes and demonstrated that their respective IPCEs do not change in a wide *P* range from 100 nW/cm^2 to 100 μW/cm^2 if AN-50 was adopted as the redox electrolyte. Moreover, $J_{SC,int}/P_{int}$ was found to remain almost constant between P_{int} ~ 100 μW/cm^2 to ~ 100 mW/cm^2, when the power of the solar simulator was attenuated stepwise by three orders of magnitude (The data on the power dependence will be published in a separate paper). Hence, for every DSC, we can confidently anticipate a close resemblance between the IPCE curves measured by the above two monochromators. The optical densities of the dye molecules adsorbed on TiO_2 were evaluated from $\log_{10}(I_{blank}/I_{cell})$, where I_{blank} and I_{cell} are the intensities of the transmitted synchrotron radiation through a blank cell and a DSC, respectively. The blank cell was fabricated in the same manner as DSCs except for omitting the soaking process of the glass in dye solution.

Results and Discussion

The I-V characteristics of 9 DSCs filled with AN-50 electrolyte are summarized in Table 1. Values of η larger than 0.1% have been achieved for DSCs containing three dyes, azo1, 2 and 3, which were synthesized by diazo coupling of β-naphthol with ABA, ASA and *p*-amino-cinnamic acid, respectively. In contrast, we found lower η values for the dyes from naphthoic acid derivatives: azo4, 5 and 6 from 3-hydroxy-2-naphthoic acid, and azo7 and 8 from 6-hydroxy-1-naphthoic acid. Also azo9 from 2,7-dihydroxynaphthalene gives low η.

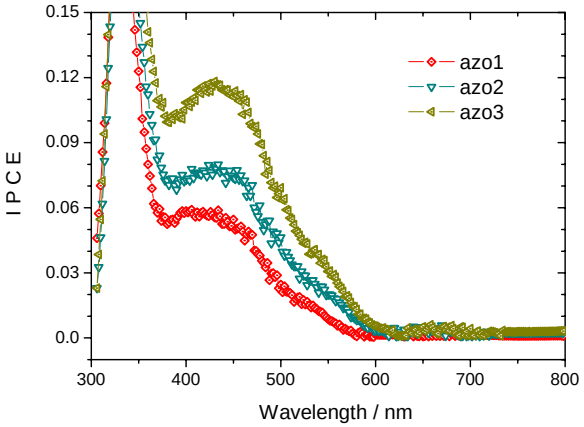

Figure 2. IPCE curves of 3 azo dyes measured by using the 3-m normal incidence monochromator.

We measured J_{SC} in the λ-range of 400 to 800 nm using the action spectrometer. Figure 1 shows the IPCE of 9 DSCs containing AN-50 electrolyte. The three DSCs having larger η (azo1, 2 and 3) exhibit noticeable peaks between λ = 410 and 430 nm and weak shoulders at ~ 540 nm. The IPCE curves of these three DSCs were measured under the condition of their being exposed to low intensity synchrotron radiation dispersed from the UVSOR's 3m-normal incidence monochromator. In addition to the above two features, each curve of Figure 2 shows a very weak peak encompassing the λ region of 600 - 700 nm.

We next measured the optical densities of the dye molecules adsorbed on TiO_2 using monochromatized synchrotron radiation. The optical densities plotted in Figure 3 are considered to be roughly equal to the photoabsorbance *A* of the adsorbed dye, i.e.

$$A \approx \log_{10}(I_{blank}/I_{cell}) \qquad (2)$$

as long as the attenuation of the light due to scattering at dye molecules can be disregarded. All the three dyes have broad and intense absorption maxima at around 500 nm, which may partially give rise to the shoulders at ~ 540 nm in Figure 2. In contrast, absorption peaks at ~ 410 nm appear to be smeared out by the above stronger maxima at ~ 500 nm. The IPCE curve is determined essentially by the quantum yield Y_{inj} for electron injection from the excited dye to TiO_2 [1]:

$$\mathrm{IPCE} = 10^{-A'}(1-R)(1-10^{-A}) \cdot Y_{inj}$$

$$\approx (1-R)(1-10^{-A}) \cdot Y_{inj} \qquad (3)$$

Here, *R* indicates the reflectivity of the electrically conductive glass plate of the incident-light side which is measurable from the optical density of a glass plate. The photoabsorbance A' of the TiO_2 and the two glass plates is known to be negligible at 600 > λ > 380 nm. Instead, light scattering due to TiO_2 nanoparticles was found to be appreciable at ~400 nm or lower wavelengths from the measurements of the optical

density of the blank cell. In the present analysis we made a plausible assumption that this scattered light fully contributes to irradiation of the adsorbed dyes but

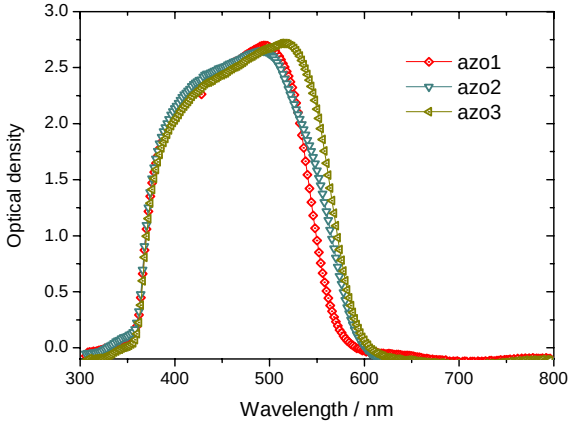

Figure 3. Optical densities of 3 azo dyes measured by using the 3-m normal incidence monochromator.

not to the monitored intensity of I_{cell}. Then, equations (2) and (3) allowed us to calculate the approximate Y_{inj} curves (see Figure 4). The Y_{inj} values are much higher at the absorption peak of ~ 410 nm than at that of ~ 500 nm. The true Y_{inj} curves may shift to the upper direction a little because all of the scattered light is not shone on the dye molecules.

Following the abrupt decrease in the optical densities above ~ 530 nm, the IPCE curves in Figures 1 and 2 descend sharply and drop close to zero at ~ 600 nm. Such spectroscopic behaviors may be responsible for the fact that η values of the DSCs are much lower for the azo dyes than for the ruthenium complexes. In the prospect of much higher η we should develop a new azo dye, which has a longer conjugating system, in order to realize wide-range absorption of the visible and near infrared light.

It is well documented in the literature dealing with photovoltaic mechanism of DSCs that the electron injection from excited dye to TiO_2 proceeds efficiently when the LUMO level of the dye is located above the lower bound of the conduction band of TiO_2 [4]. Since nothing is known about the unoccupied orbitals of the present azo dyes, we estimated the LUMO levels of isolated dye molecules with the help of the software package MOPAC7 for the semiempirical quantum chemistry program [5]. The resultant LUMO energies are listed in Table 1 and the plot of these energies versus $J_{SC,int}$ experimentally obtained are depicted in Figure 5. There is a salient correlation between $J_{SC,int}$ and the LUMO energies, that is, the three dyes with the LUMO energies of ca. -1.5eV give higher $J_{SC,int}$ than the other dyes having the energies of < -1.5 eV. This observation suggests that the performance of the present DSCs is dominated crucially by the quantum yield of the electron injection from the excited dyes. An only exception is DSC made of azo7 whose calculated LUMO level is as high as -1.390 eV. Explanation for the low-performance of the DSC with azo7 might be its possible incompatibility with AN-50. When homemade redox electrolyte solution was

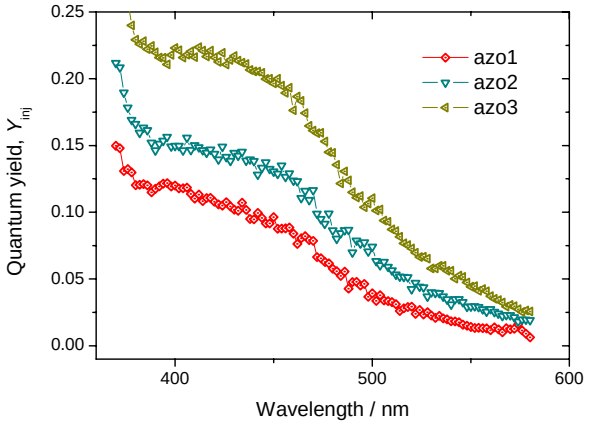

Figure 4. Approximate curves of the quantum yields for electron injection from the excited level of the dyes.

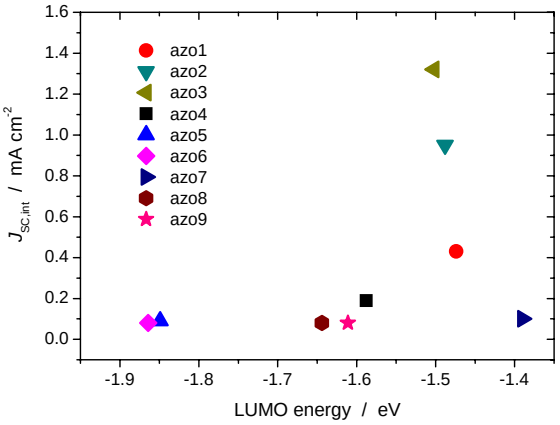

Figure 5. Correlation between the experimental data of the short current density of DSCs and the theoretical energy levels of the LUMO of the solitary azo dyes.

employed in place of AN-50, $J_{SC,int}$ for azo7 was found to be improved and become almost comparable with that for azo2. It is therefore possible that one of the ingredients in AN-50 plays a role of prohibiting a rapid electron injection from azo7 by promoting either unwanted dye aggregation or chemical reactions.

References

[1] B. O'Regan and M. Grätzel, *Nature* **353** (1991), pp. 737-740.

[2] Y. Ooyama and Y. Harima, *Eur. J. Org. Chem.* **2009** (2009), pp. 2903-2934.

[3] H. Yagi, K. Nakajima, K.R. Koswattage, K. Nakagawa, C. Huang, Md.S.I. Prodhan, B.P. Kafle, H. Katayanagi and K. Mitsuke, *Carbon* **47** (2009), pp. 1152-1157.

[4] K. Hara, H. Horiuchi, R. Katoh, L.P. Singh, H. Sugihara, K. Sayama, S. Murata, M. Tachiya and H. Arakawa, *J. Phys. Chem. B* **106** (2002), pp. 374-379.

[5] Stewart Computational Chemistry, Colorado Springs, CO, USA, http://openMOPAC.net/ (2008).

Table 1: Summary of the azo dyes available for the photosensitizers of the DSC and their formulae. Their short current density $J_{SC,int}$, the open circuit voltage V_{OC}, the fill factor F, and the energy conversion efficiency η were obtained from the I-V curves measurements. The energy levels of the HOMO and LUMO of solitary dye molecules were calculated by using the MOPAC package software and given in the last two columns.

Dye	structural formula	$J_{SC,int}$	V_{OC}	F	η	ε_{HOMO}	ε_{LUMO}
azo1	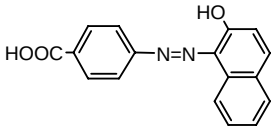	0.43 mA/cm^2	0.43 V	0.55	0.10 %	-8.792 eV	-1.474 eV
azo2	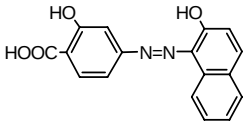	0.95	0.43	0.62	0.25	-8.780	-1.488
azo3	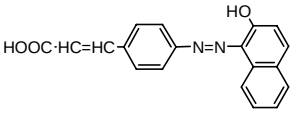	1.32	0.45	0.59	0.35	-8.727	-1.502
azo4	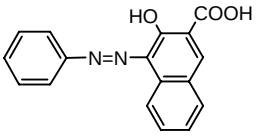	0.19	0.34	0.60	0.04	-9.056	-1.588
azo5	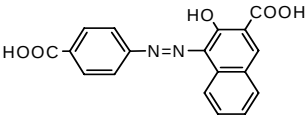	0.09	0.27	0.45	0.01	-9.213	-1.849
azo6	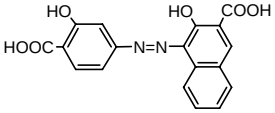	0.08	0.23	0.42	0.01	-9.209	-1.864
azo7	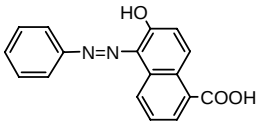	0.10	0.26	0.37	0.01	-8.842	-1.390
azo8	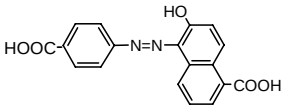	0.08	0.32	0.49	0.01	-9.033	-1.644
azo9	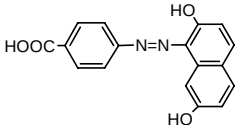	0.08	0.26	0.49	0.01	-8.921	-1.611

Molecular modeling of inclusion complexes of non-nucleoside reverse transcriptase inhibitors with beta-cyclodextrin

K. S. Boonyarattanakalin, A. Klomjitr, D. Phatravinij, K. Krutkhuntode, P. Pimantape, and L. Lawtrakul *

School of Bio-Chemical Engineering and Technology, Sirindhorn International Institute of Technology, Thammasat University, P.O.Box 22, Thammasat Rangsit Post Office, Pathum Thani, Thailand 12121

*E-mail: luckhana@siit.tu.ac.th

Abstract: Docking techniques and quantum calculations were used to study interactions of beta-cyclodextrin (BCD) with non-nucleoside reverse transcriptase inhibitors (NNRTIs): Nevirapine, Efavirenz, HBY097, and PHI443. The starting geometries of NNRTIs were taken from the Protein Data Bank. Docking was performed using AutoDock 4.2 program. The solutions with the best energy assigned by the AutoDock were selected to further investigated in details by *ab-initio* (HF/3-21G) method which implement in the Gaussian03 software. The results allowed us to explain the BCD-NNRTI interactions when the crystallographic or NMR structural data is not available.

Introduction

Beta-cyclodextrin (BCD) is a cyclic oligosaccharide and naturally contains seven glucose residues linked by α(1-4) glycosidic bonds, with a hydrophilic outer surface and a relative hydrophobic central cavity, which can form complexes with appropriate guest molecules. The chemical structure of BCD is shown in Fig. 1. It has received increasing attention in the pharmaceutical field, to modify drug physicochemical properties, such as solubility, stability and bio-availability, reducing their toxicity and side effects, and suppressing unpleasant taste or smell [1, 2].

The development of non-nucleoside reverse transcriptase inhibitors (NNRTIs) has drawn much attention from researcher due to its promising outcome for HIV/AIDS treatment. One major problem to the development stems from the typically low oral availability of the inhibitor molecules [3]. Generally, NNRTIs are extremely poor water solubility. BCD complexation technique may provide an effective method to overcome the aqueous solubility challenge for NNRTIs [4].

Theoretical understandings of how NNRTIs interact with and behave in the presence of BCD will aid in formulating anti-HIV drugs with desired oral availability. Inclusion complexes of four NNRTIs in the host BCD were investigated.

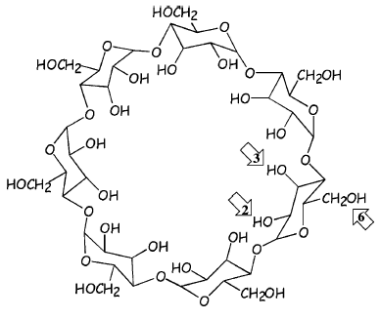

Figure 1. Chemical structure of BCD, the primary hydroxyl group (O6-H) and the secondary hydroxyl groups (O2-H, O3-H) located on the edge of BCD ring.

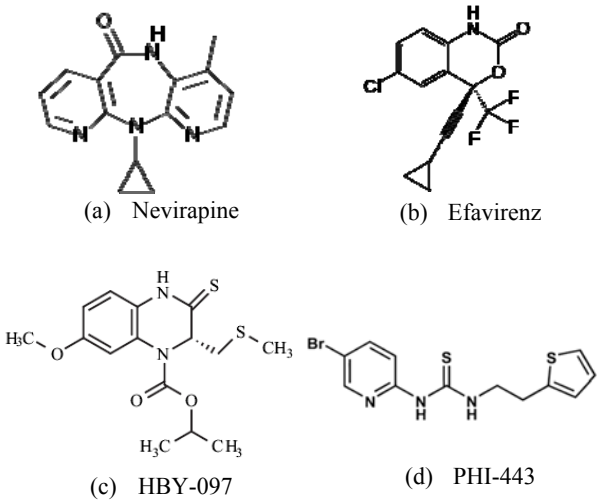

(a) Nevirapine (b) Efavirenz

(c) HBY-097 (d) PHI-443

Figure 2. Chemical structures of NNRTIs selected in this study: **(a) Nevirapine**: 11-cyclopropyl-4-methyl-5,11-dihydro-6*H*- dipyrido[3,2-*b*:2′,3′-*e*][1,4]diazepin-6-one; **(b) Efavirenz**: (4*S*)-6-chloro-4-(2-cyclopropylethynyl)-4-(trifluoromethyl)-2,4-dihydro-1*H*-3,1-benzoxazin-2-one; **(c) HBY-097**: (S)-7-Methoxy-3,4-dihydro-2-[(methylthio) methyl]-3-thioxo-2(1H)-quinoxalinecarboxylic acid, isopropyl ester; **(d) PHI-443**: (N′-[2-(2-thiophene) ethyl]-N′-[2-(5-bromopyridyl)]-thiourea)

The aim of the present study is to establish a molecular model which able to simulate the behavior of BCD-NNRTI inclusion complex by applying the techniques of molecular docking and quantum calculations.

Materials and Methods

The BCD structure with C7 symmetry was obtained from the calculations of Wolschann's group [5]. This structure was fully geometry optimized with symmetry restriction with the density functional theory, B3LYP/6-31G(d,p) calculation using Gaussian03 program package [6]. The obtained geometry was taken for further modeling of the inclusion complexes with NNRTIs.

The starting geometries of Nevirapine, Efavirenz, and HBY-097 were taken from the Protein Data Bank (PDB) with PDB code: 3HVT, 1FKO, and 1BQM, respectively [7-9] and fully geometrically optimized at the HF/3-21G level by the Gaussion03 program. The initial conformation of PHI-443 [10], which not available in PDB, was constructed by GaussView and fully optimized at the basis set HF/3-21G as well.

The computer simulated automated docking studies were performed using the widely distributed molecular docking software, AutoDock 4.2 program [11]. The inclusion complex conformation that has minimum binding energy was optimized using basis set HF/3-21G to obtain the global minimum energy and observed the host-guest interaction, where the BCD is assigned to be a rigid host conformation, the NNRTIs are assigned to be a flexible guest conformation.

Results and Discussion

The results from the molecular docking calculations by using AutoDock program provide the most stable conformation for each of NNRTI-BCD inclusion complexes with the lowest binding energy. The geometry corresponding to the most stable conformation of each NNRTI-BCD inclusion complexes were used as the initial structure for the quantum study by using HF/3-21G in order to investigate the interaction between drug and BCD molecule. The binding energies of the minimum conformations are presented in Table 1 and the configurations are shown in Fig. 3.

Table 1: Binding energies of the NNRTIs inclusion complexes with BCD obtained from HF/3-21G calculations.

NNRTI	Binding energy ($kcal \cdot mol^{-1}$)	Number of intermolecular hydrogen bond
Nevirapine	-24.84	2
Efavirenz	-14.27	1
HBY-097	-20.45	1
PHI-443	-2.72	2

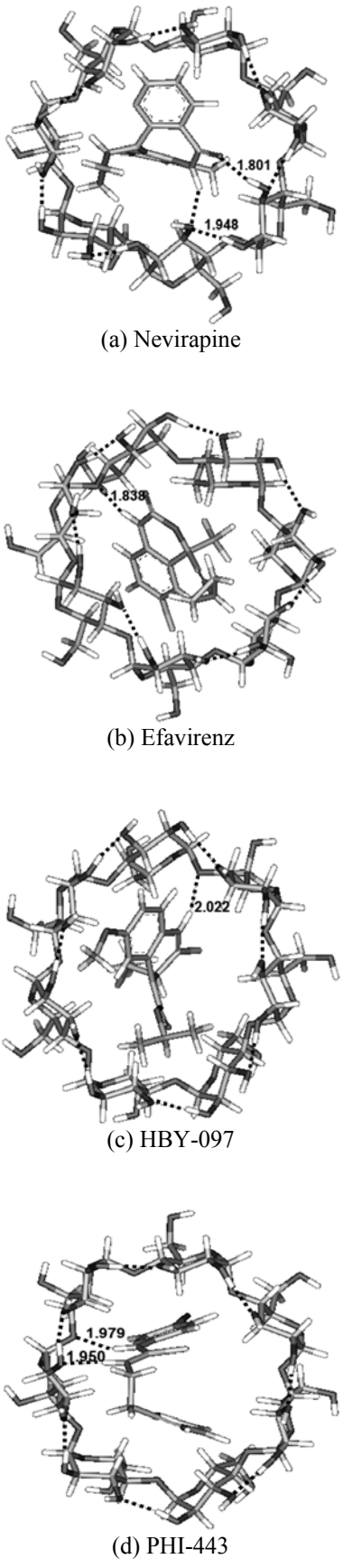

(a) Nevirapine

(b) Efavirenz

(c) HBY-097

(d) PHI-443

Figure 3. The optimized structure of NNRTI-BCD inclusion complexes of (a) Nevirapine, (b) Efavirenz, (c) HBY-097, and (d) PHI-443.

There are hydrogen bonding formations between the inhibitors, which is a proton donor, and the oxygen atoms of BCD glycosidic linkage in all inclusion complex structures except in Nevirapine-BCD complex. In contrast, there are two hydrogen bonding formations between Nevirapine and the secondary hydroxyl groups (O2-H, O3-H) of BCD in order to stabilize the Nevirapine-BCD inclusion complex and yield the lowest binding energy among all complexes in this study.

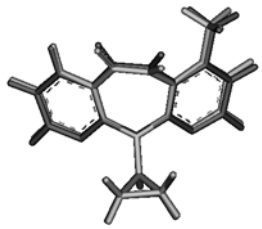

(a) Nevirapine

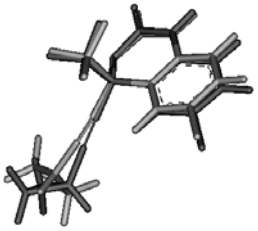

(b) Efavirenz

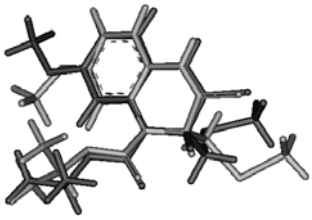

(c) HBY-097

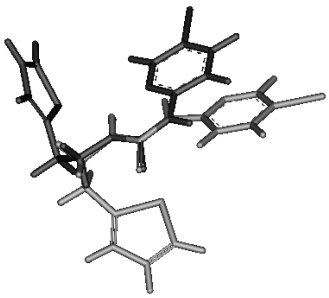

(d) PHI-443

Figure 4. Lowest energy conformation of NNRTIs calculated by *ab initio* method (HF/3-21G, black) superimposed with the structure of NNRTIs in the inclusion complex with BCD (grey).

Conclusions

The predictive capabilities of the methods could provide considerate satisfactory, even though they are not well established in the accuracy of the BCD's mobility and the solution effect. It is clear that the present work should still be considered only in the scope of preliminary study. However the results from this work could provide the possibility of using BCD complexation method in order to increase the solubility of these HIV-1 reverse transcriptase inhibitors in the aqueous solution. This work also could lead to the further study in related topics.

Acknowledgements

The financial support of the Thailand Research Fund (Grant RSA5080001) and the scholarship from the Office of the Higher Education Commission (Grant 139/2551) are gratefully acknowledged.

References

[1] J. Szejtli, *Chem. Rev.* **98** (1998), pp. 1743-1753.

[2] K. Uekama, F. Hirayama, and T. Irie, *Chem. Rev.* **98** (1998), pp. 2045-2076.

[3] M.-P. de Béthune, *Antiviral Res*. (2009), doi:10.1016/j.antiviral.2009.09.008

[4] H. Yang, M. A. Parniak, C. E. Isaacs, S. L. Hillier, and L. C. Rohan, *AAPS*. **10** (2008), pp. 606-613.

[5] W. Snor, E. Liedl, P. Weiss-Greiler, A. Karpfen, H. Viernstein, and P. Wolschann, *Chem. Phys. Lett.* **441** (2007), pp. 159-162.

[6] M.J. Frisch, G.W. Trucks, H.B. Schlegel, G.E. Scuseria, M.A. Robb, J.R. Cheeseman, J.A. Zakrzewski, J.J.A. Montgomery, R.E. Stratmann, J.C. Burant, S. Dapprich, J.M. Millam, A.D. Daniels, K.N. Kudin, M.C. Strain, O. Farkas, J. Tomasi, V. Barone, M. Cossi, R. Cammi, B. Mennucci, C. Pomelli, C. Adamo, S. Clifford, J. Ochterski, G.A. Petersson, P.Y. Ayala, Q. Cui, K. Morokuma, D.K. Malick, A.D. Rabuck, K. Raghavachari, J.B. Foresman, J. Cioslowski, J.V. Ortiz, B.B. Stefanov, G. Liu, A. Liashenko, P. Piskorz, I. Komaromi, R. Gomperts, R.L. Martin, D.J. Fox, T. Keith, M.A. Al-Laham, C.Y. Peng, A. Nanayakkara, C. Gonzalez, M. Challacombe, P.M.W. Gill, B. Johnson, W. Chen, M.W. Wong, J.L. Andres, C. Gonzalez, M. Head-Gordon, E.S. Replogle and J.A. Pople, GAUSSIAN 03, Revision C.02, Gaussian Inc., Wallingford, CT (2004).

[7] PDB ID: 3HVT
S. J. Smerdon, J. Jager, J. Wang, L. A. Kohlstaedt, A. J. Chirino, J. M. Friedman, P. A. Rice, and T.A. Steitz, *Proc. Nat. Acad. Sci. USA* **91**(1994), pp. 3911-3915.

[8] PDB ID: 1FKO
J. Ren, J. Milton, K. L. Weaver, S. A. Short, D. I. Stuart, and D. K. Stammers, *Structure* **15**(2000) pp. 1089-94.

[9] PDB ID: 1BQM
Y. Hsiou, K. Das, J. Ding, A. D. Jr Clark, J. P. Kleim, M. Rösner, I. Winkler, G. Riess, S. H. Hughes, E. Arnold, *J.Mol.Biol.* **284**(1998), pp. 313-323.

[10] J. Osmond, P. S. D'Cruz, and F. M. Uckun, *Biol. Reprod.* **71** (2004), pp. 2037–2047.

[11] G. M. Morris, R. Huey, W. Lindstrom, M. F. Sanner, R. K. Belew, D. S. Goodsell, A. J. Olson *J. Comput. Chem.* 30 (2009), pp. 2785-2791.

Theoretical calculations of vibrational spectrum and conformational analysis of bis(2-hydroxyphenyl)methane

K. S. Boonyarattanakalin and L. Lawtrakul*

School of Bio-chemical Engineering and Technology, Sirindhorn International Institute of Technology, Thammasat University, P.O. Box 22, Thammasat Rangsit Post Office, Pathum thani, 12121,Thailand

E-mail: d5222300013@studentmail.siit.tu.ac.th, luckhana@siit.tu.ac.th*

Abstract: The potential energy surfaces of bis(2-hydroxyphenyl) methane (B2HPM) were calculated by *ab initio* method at the HF/3-21G level and the density functional theory at B3LYP/6-31G(d) level. The optimized structures were examined in details by using *ab initio* method: HF/3-21G, MP2/6-31G(d), and MP2/6-31+G(d,p) levels and the density functional theory: B3LYP/6-31G(d) and B3LYP/6-31+G(d,p) levels. All calculations provide the almost identical structure that has only one conformational structure- *cis* isomer of B2HPM. In this work theoretical calculation of infrared spectrum for this minimum energy structure was carried out at the B3LYP/6-31G(d) level of theory. A comparison between the calculated and experimental spectra was made aiming to attribute the intra-molecular hydrogen bond characteristic of the molecule. The structure was stabilized by two types of hydrogen bond formation. The first one is the strong intra-molecular hydrogen bond between the *ortho-ortho* hydroxyl groups. The second one is the weak intra-molecular hydrogen bond between the oxygen atom of the hydroxyl group and the hydrogen atom of the methylene linkage. Both of them influence B2HPM conformation.

Introduction

Phenolic resins are the first synthetic polymer produced commercially, which are widely used in adhesive industry. The adhesive properties of this class of materials are strictly related to hydrogen bonding formed by their hydroxyl groups [1]. The linear structure p-cresol/ formaldehyde (PCF) resins exhibit an unusual thermal transition due to the intra-molecular hydrogen bonding in the form of calixarene-like structures which cannot be formed in the branched structured phenolic resins [2,3].

Calixarenes are macrocyclic compounds consisting of phenol rings that are connected via the ortho positions by methylene groups. Calixarenes derivatives are increasingly being employed in the complexation of cations, anions and neutral molecules [2,4]. When heated up to a transition temperature, the calixarene-like structure in PCF is destroyed and apparently largely replaced by intermolecular hydrogen bonding. Once destroyed, the cyclic structure cannot be recovered by simply cooling down or annealing. However, the original structure can be obtained by dissolving and recasting the sample from solution. This suggests that in these materials there is an interesting coupling of the conformational freedom of the chains with intra- and intermolecular interactions.

In order to understand this phenomenon, we investigate the nature of hydrogen bonding formed between phenolic hydroxyls by studying the simple calixarene building blocks, bis(2-hydroxyphenyl) methane. The conformational analysis and vibrational spectra of B2HPM was determined by using chemical quantum calculations, then compare with the experimental data.

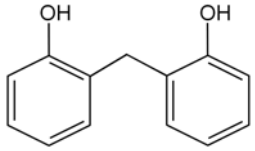

Figure 1. Structure of bis(2-hydroxyphenyl)methane (B2HPM)

Materials and Methods

An initial conformation for B2HPM, was generated by GaussView and was fully optimized by the Gaussian03 package on an Intel Core 2 Quad Q9550/2.83 GHz personal computer. The vibrational frequencies calculations were performed on the Cluster of Digital Alpha Servers (2100 4/275).

Results and Discussion

Molecular calculation on the geometry of B2HPM: The potential energy surface of B2HPM around α torsion angle (C1'-C6'-C7-C6) and β torsion angle (H1-O1-C1-C6) was investigated by partial optimization with a step-size of 30 degrees, based on an *ab initio* calculation at the HF/3-21G level was presented in Figure 3.

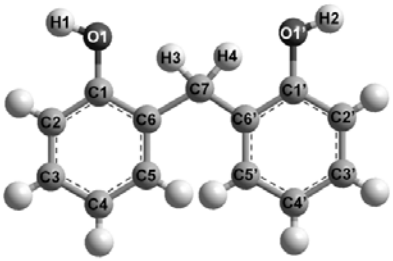

Figure 2. Atomic numbering of B2HPM

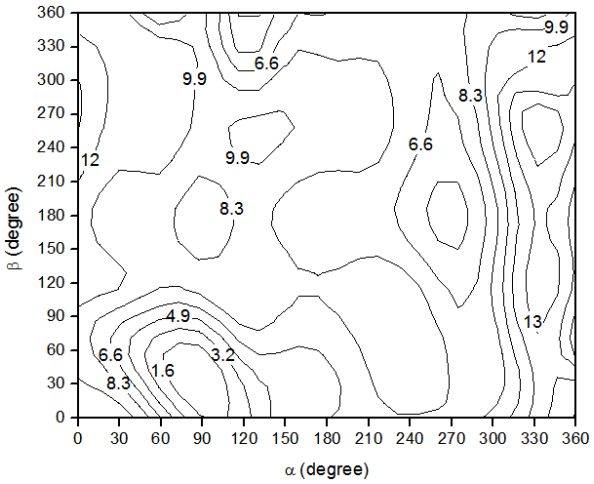

Figure 3. The potential energy surface for B2HPM with α and β torsion angles, obtained from HF/3-21G calculation. The relative energies are in kcal·mol^{-1}.

The geometry corresponding to the minimum energy of B2HPM (with 90 and 30 degrees for α and β torsion angles, respectively) was then fully optimized using the HF/3-21G and the density functional theory B3LYP/6-31G(d), respectively. The minimum conformation was shown in Figure 4 with α = 98.9 degrees and β = 10 degrees.

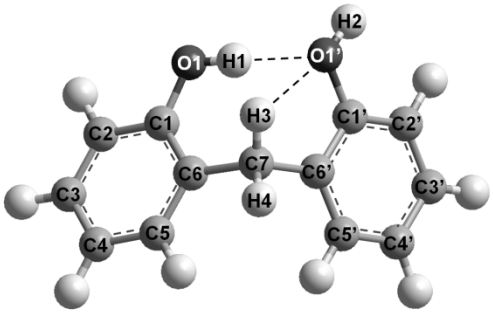

Figure 4. The optimized structure of B2HPM

The optimized structures were examined in details by using *ab initio* method: MP2/6-31G(d) and MP2/6-31+G(d,p) levels and the density functional theory: B3LYP/6-31+G(d,p) levels. All calculations provide the approximately identical structure that has only one conformation in *cis*-isomer (*ortho-ortho* hydroxyl groups). The results show the unequal lengths of the hydroxyl groups (O-H). The O1-H1 bond length (0.973-0.979 Å) is longer than the bond length of O1'-H2 (0.964-0.975 Å). These can be explained by the effect of two intra-molecular hydrogen bonding. The first hydrogen bond occurs between O1'···H1 within the distance 1.747-1.884 Å.

The weaker hydrogen bonding occurs between the oxygen atom of the phenyl group and the hydrogen atom of the methylene linkage (O1'···H3). The distance is in the range of 2.385-2.478 Å.

Calculated vibrational spectra of B2HPM: The B2HPM vibrational spectra are calculated by B3LYP/6-31G(d). The results are presented in Table 1. The experimental infrared spectra of B2HPM were taken from Katsyuba, S. et al. [5].

Table 1: The experimental and calculated vibrational spectra of B2HPM

Assignment[a]	Experiment	Calculation	
	ν (cm^{-1})	Unscaled ν	Scaled ν
νOH_{free}	3602	3755	3599
$\nu OH\cdots O_{intra}$	3472	3625	3473
νCH_{ar}	3071	3214	3078
		3214	3077
νCH_{ar}	3047	3204	3068
		3199	3063
νCH_{ar}	3034	3186	3051
		3184	3049
νCH_{ar}	3016	3168	3033
		3167	3032
$\nu_{as}CH_2$	2938	3099	2967
$\nu_{s}CH_2$	2873	3061	2930

[a] ν, stretch; s, symmetrical; as, asymmetrical

The difference of OH frequencies is the result of the strong O1'···H1-O1 intra-molecular hydrogen bonding. The calculated red-shift of the OH frequency obtained from B3LYP/6-31G(d) show excellent agreement with the experimental data.

Conclusions

The conformational analysis of B2HPM yields one energy minimum with respect to the orientation of the phenyl rings in the *ortho-ortho* hydroxyl groups or *cis*-isomer. The comparison of calculated vibrational spectra with the experiment indicates the *cis*-isomer is the preferred conformation in solution which corresponds also to the calculated gas phase conformational minimum. The structure was stabilized by two types of hydrogen bond formation. The first one is the strong intra-molecular hydrogen bonds between the *ortho-ortho* hydroxyl groups. The second one is the weak intra-molecular hydrogen bond between the oxygen atom of the hydroxyl group and the hydrogen atom of the methylene linkage.

Acknowledgements

The financial support of the Thailand Research Fund (Grant RSA5080001) and the scholarship from the Office of the Higher Education Commission (Grant

139/2551) are gratefully acknowledged. Generous supply of computer time on vibrational frequencies calculations on the Cluster of Digital Alpha Server of the computer center of the University of Vienna; is highly appreciative. The authors wish to thank Prof. Peter Wolschann and Asst.Prof.Dr.Pakorn Opaprakasit for helpful discussions.

References

1] A. Knop and L. A. Pilato, *Phenolic Resins*, Springer-Verlag, Newyork, (1985).

[2] C. D. Gutsche, *Calixarenes*, The Royal Society of Chemistry, St. Louis, (1989).

[3] P. Opaprakasit, A. W. Scaroni, and P. C. Painter, *J. Mol. Structure* **570**, (2001), pp.25.

[4] Z. Asfari, V. Bohmer, J. M. Harrowfield and J. Vicens, *Calixarenes 2001*, Kluwer Academic Publishers, Dordrecht, (2001).

[5] S. Katsyuba, A. Chernova, R. Schmutzler and J. Grunenberg, *J. Chem. Soc., Perkin Trans.* **2**, (2002), pp. 67.

An influence of Pt/Au bimetallic nanoparticles on the interaction of DNA base pairs

M. Amnuaysopon[1], O. Kongkwamjaraen[1] and C. Kritayakornupong[1,*]

[1]Department of Chemistry, Faculty of Science, King Mongkut's University of Technology Thonburi, Bangkok, Thailand 10140.

*E-Mail: chinapong.kri@kmutt.ac.th

Abstract: The optimized structures of bimetallic nanoparticles (Pt/Au and Pt/Au_2) coordinated at N7 site of G-C and A-T base pairs were studied using the B3LYP method. The 6-31G(d) basis set was employed for G-C and A-T base pairs, while the LANL2DZ basis set was applied for Pt and Au atoms. For the Pt/Au dimer located near the N7 site of G-C base pair, the interaction energies of -28.2 and -27.8 kcal/mol were obtained from the complexes of Au and Pt coordinated at N7 site of G-C base pair, respectively. These values are almost the same as that determined from the isolated G-C base pair. The H-bond interactions of G-C base pair were increased by ~6 kcal/mol as increasing Au composition. However, the different trend was observed for A-T base pair. In addition, the interaction energy between the bimetallic nanoparticles and DNA base pairs was also elucidated, indicating that the Pt plays an important role for the interaction between bimetallic and DNA base pairs.

Introduction

Nanoparticles have been an interesting area for experimental and theoretical investigations to evaluate their physical and chemical properties [1]. Recently, the Pt/Au bimetallic nanoparticles has been demonstrated to have significantly better catalytic activity than pure Pt or Au clusters [2]. In the present study, structural properties and interaction energies between Pt/Au clusters and DNA base pairs and that between DNA base pairs complexed with Pt/Au bimetallic nanoparticles have been studied using *ab initio* quantum mechanical calculation at the B3LYP level of theory.

Methods

The complexes of Pt/Au bimetallic nanoparticles coordinated at the N7 site of DNA base pairs were fully optimized at the B3LYP level of theory. The 6-31G(d) basis set was used for DNA base pairs, while the LANL2DZ ECP basis set was applied for Pt and Au atoms. The geometries of the complexes were performed using the Gaussian 03 program [3]. The basis set super position error (BSSE) corrected interaction energy was calculated using the Boys-Bernardi counterpoise correction scheme [4]. Interaction energy of complex was defined as

$$E_{\text{int}} = E_{AB} - E_{A(AB)} - E_{B(AB)}$$

where E_{int} represents the interaction energy, E_{AB} is the total energy of complex AB, $E_{A(AB)}$ represents the total energy of complex A of the respective complex with ghost atoms in place of complex B, and $E_{B(AB)}$ represents the total energy of complex B of the complex with ghost atoms for the rest of the system. The H-bond interactions of DNA base pairs complexed with Pt/Au bimetallic nanoparticles and that between Pt/Au clusters and DNA base pairs were elucidated to reveal the influence of Pt/Au bimetallic nanoparticles on chemical properties of the DNA base pairs. In addition, structural parameters were also characterized in terms of bond distances and bond angles.

Results and Discussion

Table 1: Hydrogen bond distances in bimetallic clusters (Pt/Au and Pt/Au_2) coordinated at N7 site of DNA base pairs

Complex	Bond distances (Å)		
	O6-N4	**N1-N3**	**N2-O2**
G-C	2.82	2.95	2.93
Pt/AuG-C	2.85	2.93	2.89
Au/PtG-C	2.85	2.93	2.89
Pt/Au_2G-C	2.85	2.93	2.89
Au_2/PtG-C	2.87	2.87	2.90

Complex	Bond distances (Å)	
	N6-O4	**N1-N3**
A-T	2.95	2.88
Pt/AuA-T	2.93	2.89
Au/PtA-T	2.94	2.89
Pt/Au_2A-T	2.92	2.90
Au_2/PtA-T	2.95	2.89

Table 2: Hydrogen bond angles for bimetallic clusters (Pt/Au and Pt/Au_2) coordinated at N7 site of DNA base pairs

Complex	Bond angles (°)		
	O6-HN4	**N1H-N3**	**N2H-O2**
G-C	179.6	178.3	180.0
Pt/AuG-C	177.9	177.4	178.7
Au/PtG-C	177.9	177.6	178.9
Pt/Au_2G-C	178.3	177.8	179.0
Au_2/PtG-C	174.7	173.0	175.2

Complex	Bond angles (°)	
	N6H-O4	N1-HN3
A-T	174.8	179.3
Pt/AuA-T	176.6	179.0
Au/PtA-T	175.8	179.2
Pt/Au_2A-T	177.2	179.0
Au_2/PtA-T	175.2	179.2

Structural properties of Pt/Au bimetallic nanoparticles coordinated at the N7 site of DNA base pairs computed by the B3LYP/6-31G(d) level of theory are shown in the Tables 1 and 2. The interatomic distances of O6-N4, N1-N3, and N2-O2 bonds obtained from the isolated G-C base pair were 2.82, 2.95, and 2.93 Å, respectively. The Pt/AuG-C, Au/PtG-C, and Pt/Au_2G-C complexes reveal the similar values of the O6-N4, N1-N3, and N2-O2 bond distances, resulting in 2.85, 2.93, and 2.89 Å, respectively. Furthermore in the Au_2/PtG-C complex the Pt site of the bimetallic cluster bound with the N7 site of guanine predicts the maximum change in the O6-N4, N1-N3, and N2-O2 bond distances of 2.87, 2.87, and 2.90 Å, respectively. These results show that the interaction between Pt site in Pt/Au_2 cluster plays an important role for presenting a slight opening of the H-bond observed for the O6-N4 hydrogen bonding. In the case of A-T base pair, the N6-O4 bond distances evaluated from Pt/AuA-T, Au/PtA-T, and Pt/Au_2A-T complexes were found to be 2.93, 2.94, 2.92 Å, which are slightly shorter than the value of 2.95 Å obtained from the isolated A-T base pair. For the Au_2/PtA-T complex, the corresponding value of 2.95 Å was predicted, which is the same as that determined from the isolated A-T base pair. In contrast, the calculated values of the N1-N3 bond distances obtained from all A-T base pairs complexed with bimetallic cluster are slightly larger than the value of 2.88 Å elucidated from the isolated A-T base pair. As shown in Table 2, the isolated G-C base pair gives O6-NH4, N1H-N3, and N2H-O2 bond angles of 179.6, 178.3, and 180.0°, respectively. It is clear that consequent to the interaction with the bimetallic clusters the O6-NH4, N1H-N3, and N2H-O2 hydrogen bond angles are decreased, compared to that resulted in the isolated G-C base pair. In contrast, the N6H-O4 hydrogen bond angle obtained from the A-T base pair attached with bimetallic cluster are increased, while the similar values of the N1-HN3 hydrogen bond angles were presented compared with the isolated A-T form.

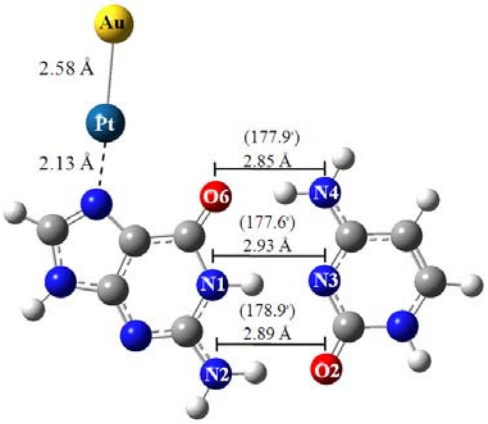

(a.) (Au/Pt)G-C

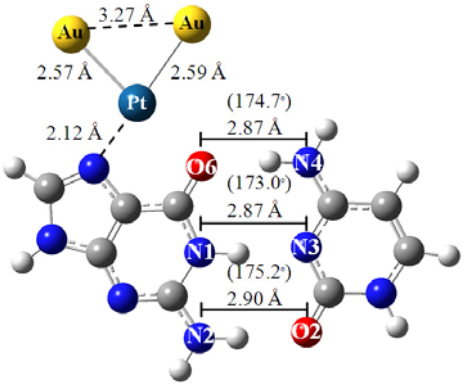

(b.) (Au_2/Pt)G-C

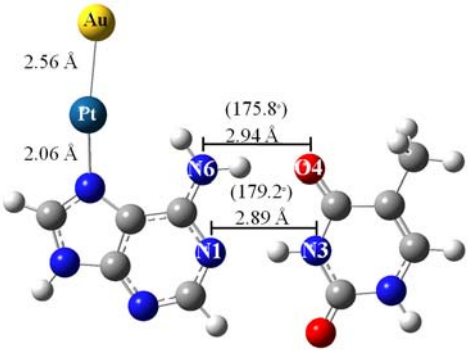

(c.) (Au/Pt)A-T

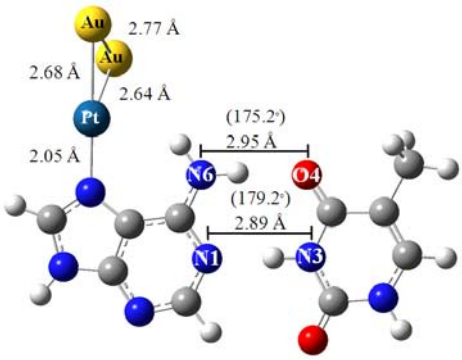

(d.) (Au_2/Pt)A-T

Figure 1. The Pt/Au bimetallic nanoparticles coordinated at the N7 site of DNA base pairs

Table 3: Interaction energy (E_{int}) between DNA base pairs complexed with bimetallic nanoparticles and that between bimetallic nanoparticles and DNA base pairs

Complex	E_{int} (kcal/mol)
G···C	-29.1
Pt/AuG···C	-28.2
Au/PtG···C	-27.8
Pt/Au_2G···C	-30.1
Au_2/PtG···C	-33.5
Pt/Au···GC	-20.8
Au/Pt···GC	-22.0
Pt/Au_2···GC	-15.6
Au_2/Pt···GC	-29.1

Complex	E_{int} (kcal/mol)
A···T	-13.5
Pt/AuA···T	-9.3
Au/PtA···T	-7.6
Pt/Au_2A···T	-8.0
Au_2/PtA···T	-6.9
Pt/Au···AT	-18.9
Au/Pt···AT	-24.8
Pt/Au_2···AT	-15.9
Au_2/Pt···AT	-25.5

Interaction energies between DNA base pairs complexed with bimetallic nanoparticles and that between bimetallic nanoparticles and DNA base pairs obtained from the B3LYP level of theory. Interaction energies between G-C base pairs in Pt/AuG···C and Pt/Au_2G···C complexes were found to be -28.2 and -30.1 kcal/mol, respectively, while the corresponding values of -27.8 and -33.5 kcal/mol were obtained from Au/PtG···C and Au_2/PtG···C structures. These predicted values revealed that the H-bond energies are increased as increasing Au composition in the bimetallic clusters. The different trend was pronounced in the case of A-T base pair in which interaction energies of A-T base pair are decreased with increasing Au composition (corresponding values of -9.3, -8.0, -7.6, and -6.9 kcal/mol evaluated from Pt/AuA···T, Pt/Au_2A···T, Au/PtA···T, and Au_2/PtA···T complexes, respectively).

For the interaction energies between bimetallic clusters and DNA base pairs, it was found that the interactions between Pt site of bimetallic cluster and DNA base pairs are stronger than those evaluated from Au site. For the Pt/Au cluster complexed with G-C base pair, the interaction energy of -22.0 kcal/mol was determined from the Au/Pt···GC structure, which is slightly higher than the value of -20.8 kcal/mol evaluated from the Pt/Au···GC structure. The similar result was also detected in the case of A-T base pair. The corresponding values of -24.8 and -18.9 kcal/mol were calculated from the Au/Pt···AT and Pt/Au···AT complexes, respectively. With increasing Au composition in the bimetallic clusters, the Au_2/Pt···GC and Au_2/Pt···AT complexes were found to be about 15 and 10 kcal/mol more stable than the respective Pt/Au_2···GC and Pt/Au_2···AT complexes. These results prove that the Pt site and additional Au composition in bimetallic clusters play a significant role on the interaction between Pt/Au bimetallic nanoparticles and DNA base pairs.

Conclusions

Our results reveal that the Pt/Au bimetallic nanoparticles in various compositions form stable complexes with DNA base pairs. It can be concluded that the Pt site of bimetallic cluster interacts more strongly with the DNA base pairs than Au site.

References

[1] D. W. Yuan, Y. Wang and Z. Zeng, *J. Chem. Phys.* **122** (2005), pp. 114310-11.

[2] C. Song, Q. Ge and L.Wang, *J. Phys. Chem. B* **109** (2005), pp. 22341-22350.

[3] M.J. Frisch , G. W. Trucks, H. B. Schlegel, G. E. Scuseria, M. A. Robb, J. R. Cheeseman, J. A. Montgomery, Jr., T. Vreven,. N. Kudin, J. C. Burant, J. M. Millam, S. S. Iyengar, J. Tomasi, V. Barone, B. Mennucci, M. Cossi, G. Scalmani, N. Rega, G. A. Petersson, H. Nakatsuji, M. Hada, M. Ehara, K. Toyota, R. Fukuda, J. Hasegawa, M. Ishida, T. Nakajima, Y. Honda, O. Kitao, H. Nakai, M. Klene, X. Li, J. E. Knox, H. P. Hratchian, J. B. Cross, C. Adamo, J. Jaramillo, R. Gomperts, R. E. Stratmann, O. Yazyev, A. J. Austin, R. Cammi, C. Pomelli, J. W. Ochterski, P. Y. Ayala, K. Morokuma, G. A. Voth, P. Salvador, J. J. Dannenberg, V. G. Zakrzewski, S. Dapprich, A. D. Daniels, M. C. Strain, O. Farkas, D. K. Malick, A. D. Rabuck, K. Raghavachari, J. B. Foresman, J. V. Ortiz, Q. Cui, A. G. Baboul, S. Clifford, J. Cioslowski, B. B. Stefanov, G. Liu, A. Liashenko, P. Piskorz, I. Komaromi, R. L. Martin, D. J. Fox, T. Keith, M. A. Al-Laham, C. Y. Peng, A. Nanayakkara, M. Challacombe, P. M. W. Gill, B. Johnson, W. Chen, M. W. Wong, C. Gonzalez, and J. A. Pople, Gaussian Inc., Pittsburgh PA, 2003.

[4] S. F. Boys, F. Bernardi, *Mol. Phys.* **19** (1970), 533.

[5] T. Matsui, Y. Shigeta and K. Hirao, *Chem. Phys. Lett.* **423** (2006), pp. 331-334.

[6] A. Kumar, P. C. Mishra and S. Suhai, *J. Phys. Chem. A* **110** (2006), pp. 7719-7727.

[7] M. K. Shukla, M. Dubey, E. Zakar and J. Leszczynski, *J. Phys. Chem. C* **113** (2009), pp. 3960-3966.

Proton-transfer processes in guanine-cytosine base pair by coordination of gold nanoparticles

O. Kongkwamjaraen[1], K. Kunsutha[1], J. Wicheandee[1] and C. Kritayakornupong[1,*]

[1] Department of Chemistry, Faculty of Science, King Mongkut's University of Technology Thonburi, Toongkru, Bangkok, Thailand 10400

[*] E-Mail:chinapong.kri@kmutt.ac.th

Abstract: The interactions of gold nanoparticles with the guanine-cytosine (GC) Watson-Crick DNA base pair were investigated using the density functional theory (DFT). Geometries of the GC base pair complexed with one, two, and four gold atoms each were fully optimized using the B3LYP method in conjunction with 6-31+G(d,p) basis set for all atoms except gold. For gold atoms, the Los Alamos effective core potential (ECP) basis set LANL2DZ was utilized. The result shows that double proton-transfer reaction in the GC base pair complexed with gold nanoparticles is more favorable than that for the isolated GC base pair. The complexes of one gold atom located near the N7 and N3 sites of guanine provide the activation energies of 13.4 and 13.8 kcal/mol, respectively, which are slightly higher than those evaluated from the corresponding structures complexed with a pair of gold atoms (~13 kcal/mol). It was found that the lowest energy barrier of 9.6 kcal/mol was obtained from the GC-Au_4 structure, in which a pair of gold atoms is bound to the N7 and N3 sites of guanine.

Introduction

It is well-known that the proton-transfer ability in Watson-Crick base pair plays a crucial role in DNA replication [1]. Recently, numerous studies have revealed the complexity of interactions involving DNA fragments with gold surfaces [2]. However, the basic question as to how proton-transfer processes occurs between DNA base pairs complexed with gold nanoparticles should be answered.

Materials and Methods

An influence of gold nanoparticles on the double proton-transfer reactions in Watson-Crick base pairs has been investigated using the density functional theory (DFT). A combination of Becke's three-parameter hybrid exchange functional and the Lee-Yang-Parr correlation functional (B3LYP) was chosen since it includes the exchange functional as a linear combination of Hartree-Fock and gradient-corrected exchange terms. The 6-31+G(d,p) basis set was employed for all atoms except gold. For gold atoms the Los Alamos effective core potential (LANL2DZ ECP) was applied. The mixed basis set employed will be denoted by 6-31+G(d,p)∪LANL2DZ. In the present work, full geometry optimizations of one, two, and four gold atoms each attached to N7 and/or N3 sites of the G-C base pair, including their double proton-transfer processes were evaluated. All calculations were performed using the Gaussian 03 program [3].

Results and Discussion

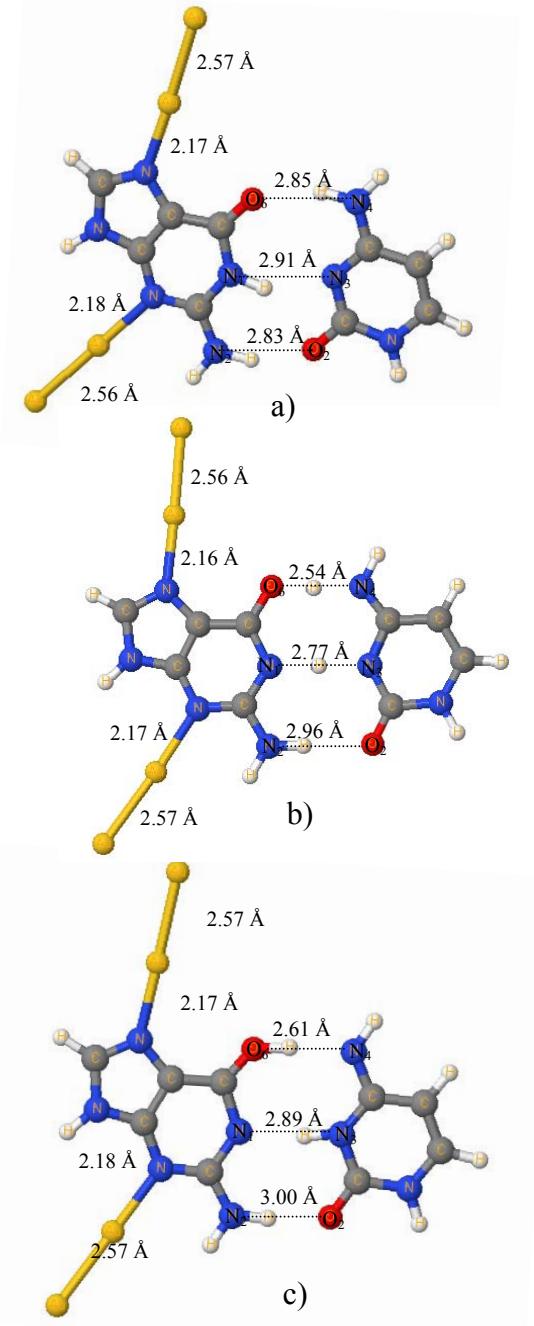

Figure 1. Optimized structures of Au_4-GC in a) ground state (GS), b) transition state (TS), and c) double proton-transfer (DPT) forms.

Table 1: Structural parameters of GC base pair complexed with gold nanoparticles in ground state (GS), and double proton-transfer (DPT) forms obtained from the B3LYP/6-31+G(d,p)∪LANL2DZ method.

Complex	GS (Å)			DPT (Å)		
	O6-N4	N1-N3	N2-O2	O6-N4	N1-N3	N2-O2
Isolated GC	2.79	2.95	2.93	2.69	2.90	3.00
Au-N3(G)-C	2.82	2.93	2.85	2.65	2.90	2.99
Au-N7(G)-C	2.81	2.93	2.91	2.66	2.89	3.00
Au_2-N3(G)-C	2.82	2.92	2.86	2.66	2.90	2.98
Au_2-N7(G)-C	2.83	2.92	2.89	2.64	2.89	3.00
Au_2-N3_Au_2-N7(G)-C	2.85	2.91	2.83	2.61	2.89	3.00

Interesting information could be obtained from the analysis of the geometrical parameters. Optimized structures of Au_4-GC in ground state, transition state, and double proton-transfer complexes evaluated from the B3LYP/6-31+G(d,p)∪LANL2DZ method are depicted in Figure1. A comparison of the hydrogen-bonding distances in the isolated GC base pair and the GC base pair complexed with the one, two and four gold atoms each are summarized in Table 1. The hydrogen-bonding distances O6-N4, N1-N3, and N2-O2 were found to be 2.79, 2.95, and 2.93 Å evaluated from the isolated GC base pair. With increasing size of the gold cluster the N1-N3 and N2-O2 bond distances are generally decreased for all complexes, while the O6-N4 bond distances are all increased. In the Au-N3(G)-C complex, the calculated O6-N4, N1-N3, and N2-O2 bond distances are 2.82, 2.93, and 2.85 Å, while the Au atom coordinated at N7 site of GC base pair show the corresponding values of 2.81, 2.93, and 2.91 Å, respectively. For Au_2 cluster, the predicted O6-N4, N1-N3, and N2-O2 bond distances of 2.82, 2.92, and 2.86 Å were yielded from the Au_2 cluster attached to N3 site of GC base pair, while the Au_2-N7(G)-C complex gives the corresponding values of 2.83, 2.92, and 2.89 Å. The maximum change in the O6-N4 and N2-O2 bond distances is observed for the Au_2-N3_Au_2- N7(G)-C complex, representing the calculated O6-N4 and N2-O2 bond distances of 2.85 and 2.83 Å, respectively. For the double proton-transfer complexes, the O6-N4 bond distances are all decreased with respect to the corresponding hydrogen-bond distance in the isolated GC base pair. However, the N1-N3 and N2-O2 bond distances are almost the same as those obtained from the isolated GC base pair.

Table 2: Binding energy (BE) and activation energy (E_a) of GC base pair complexed with gold nanoparticles in ground state (GS), transition state (TS), and double proton-transfer (DPT) forms obtained from the B3LYP method.

Complex	GS	DPT	TS
	BE (kcal/mol)	BE (kcal/mol)	E_a (kcal/mol)
Isolated GC	-26.2	-18.8	14.9
Au-N3(G)-C	-23.5	-15.0	13.4
Au-N7(G)-C	-23.5	-15.5	13.8
Au_2-N3(G)-C	-24.4	-16.0	12.6
Au_2-N7(G)-C	-24.3	-16.4	12.9
Au_2-N3_Au_2-N7(G)-C	-27.0	-18.3	9.6

Table 2 presents the binding energy and activation energy of GC base pair complexed with gold nanoparticles obtained from the B3LYP/ 6-31+G(d,p)∪LANL2DZ method.

The hydrogen-bonding energy of -26.2 kcal/mol was predicted for the isolated GC base pair obtained from the B3LYP/6-31+G(d,p)∪LANL2DZ method, while the corresponding value of -18.8 kcal/mol was evaluated from the double proton-transfer (DPT) reaction in GC base pair. Its reaction barrier amounts to 14.9 kcal/mol for the DPT reaction without the gold nanoparticles. For the a gold atom attached to N3 site of GC base pair, the hydrogen-bonding interaction decreases by 2.7 kcal/mol, which is same as that calculated from the Au-N7(G)-C complex. However, the reaction barriers of 13.4 and 13.8 kcal/mol were resulted from the Au-N3(G)-C and Au-N7(G)-C complexes, which is lower than that evaluated from the DPT reaction in GC base pair. The reaction barrier decreases by ~2 kcal/mol for the Au_2 cluster coordinated at N3 or N7 sites of GC base pair. For the GC base pair complexed with the Au_2 clusters coordinated at N3 and N7 sites, the lowest reaction barrier of 9.6 kcal/mol was predicted, corresponding to the hydrogen-bonding energies of -27.0 and -18.3 kcal/mol determined from neutral and DPT forms, respectively. These results indicate that consequent to the interaction with the gold nanoparticles the reaction barrier of the double proton-transfer process in GC base pair is decreased.

Conclusions

The hydrogen-bonding interactions between GC base pairs complxed with the gold nanoclusters were estimated using the B3LYP/6-31+G(d,p)∪LANL2DZ method. It was revealed that the consequent to the interaction with gold nanoparticles the GC base pair may slightly open the hydrogen-bond. Our calculations

show that the reaction barrier of the double proton-transfer process in GC base pair complexed with gold clusters is decreased with respect to the isolated GC base pair.

References

[1] L. Gorb, Y. Podolyan, P. Dziekonski, W. A. Sokalski and J. Leszczynski, J. Am. Chem. Soc. 126 (2004), pp. 10119-10129.

[2] A. Kumar, P. C. Mishra and S. Suhai, J. Phys. Chem. A 110 (2006), pp. 7719-7727.

[3] M.J. Frisch , G. W. Trucks, H. B. Schlegel, G. E. Scuseria, M. A. Robb, J. R. Cheeseman, J. A. Montgomery, Jr., T. Vreven,. N. Kudin, J. C. Burant, J. M. Millam, S. S. Iyengar, J. Tomasi, V. Barone, B. Mennucci, M. Cossi, G. Scalmani, N. Rega, G. A. Petersson, H. Nakatsuji, M. Hada, M. Ehara, K. Toyota, R. Fukuda, J. Hasegawa, M. Ishida, T. Nakajima, Y. Honda, O. Kitao, H. Nakai, M. Klene, X. Li, J. E. Knox, H. P. Hratchian, J. B. Cross, C. Adamo, J. Jaramillo, R. Gomperts, R. E. Stratmann, O. Yazyev, A. J. Austin, R. Cammi, C. Pomelli, J. W. Ochterski, P. Y. Ayala, K. Morokuma, G. A. Voth, P. Salvador, J. J. Dannenberg, V. G. Zakrzewski, S. Dapprich, A. D. Daniels, M. C. Strain, O. Farkas, D. K. Malick, A. D. Rabuck, K. Raghavachari, J. B. Foresman, J. V. Ortiz, Q. Cui, A. G. Baboul, S. Clifford, J. Cioslowski, B. B. Stefanov, G. Liu, A. Liashenko, P. Piskorz, I. Komaromi, R. L. Martin, D. J. Fox, T. Keith, M. A. Al-Laham, C. Y. Peng, A. Nanayakkara, M. Challacombe, P. M. W. Gill, B. Johnson, W. Chen, M. W. Wong, C. Gonzalez, and J. A. Pople, Gaussian Inc., Pittsburgh PA, 2003.

Gas adsorption in covalent organic frameworks (COFs): the ONIOM approach

P. Ariyageadsakul[1], P. Thampravit[1] and C. Kritayakornupong[1,*]

[1]Department of Chemistry, Faculty of Science, King Mongkut's University of Technology Thonburi, Bangkok 10140

*chinapong.kri@kmutt.ac.th

Abstract: The ONIOM (B3YP/6-31g(d,p):AM1) and ONIOM (MP2/6-31g(d,p):AM1) denoted as ONIOM-B and ONIOM-M methods have been performed to evaluate the adsorption energies of gases (H_2, O_2, CO and NO) in Covalent Organic Framework (COF). The B_3O_3 ring was treated as the high model, while $(C_6H_4)_3$ rings was calculated as low model in the ONIOM methods. The adsorption energy trend obtained from the ONIOM-B method is in good agreement with that evaluated from the ONIOM-M method. However, the underestimated values were pronounced from the ONIOM-B method in comparison with the ONIOM-M method. For the ONIOM-B, the interaction energies of -1.9, -0.1, -1.4, and -2.8 kcal/mol were calculated from O_2, H_2, CO and NO, respectively. In contrast the highest binding energy of -3.4 kcal/mol was determined for O_2 obtained from ONIOM-M method, which is much stronger than that calculated for H_2 (-0.4 kcal/mol). For homogeneous gas, the corresponding values of -2.6 and -2.8 kcal/mol were elucidated from CO and NO respectively. The result of ONIOM-M method seems to be a suitable level of theory for evaluating such weak interaction energies of gases in COF.

Introduction

The Covalent Organic Frameworks (COFs) have been developed to be a new class of materials for storage of H_2. The COFs are composed of strong covalent bonds between light elements such as C, B and O with a high porosity (4210 m^2/g for COF-103) and extremely low crystal density (0.17 g cm^{-3} for COF-108) [1-3], These materials present all the advantages of MOFs considering hydrogen storage (surface area, pore volume, rigidity of the structure) [1]. It has been reported that the hydrogen storage capacity in the COFs is higher than that determined from the MOFs[4]. However, the capacity of gas absorptions such as CO and NO is quite interesting subject since the processes involving CO and NO are important in environment control of exhaust fumes from combustion.

In the present work, adsorptions of gases such as H_2, O_2, CO, and NO in the covalent organic frameworks have been performed using the ONIOM approaches.

Methods

The two-layer ONIOM method has been used to study the adsorption energy of gases (H_2, O_2, CO, and NO) in the covalent organic frameworks. A boroxine (B_3O_3) ring attached to three benzene (C_6H_4) rings is considered to be the simplest model system for representing the binding site of the COF-1. (see Figure 1).

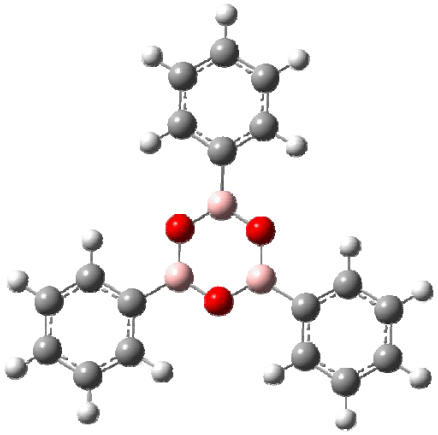

Figure1. Structure of Covalent Organic Framework

According to the ONIOM technique, the $(B_3O_3)(C_6H_4)_3$ model is divided into two layers, namely, a high level and a low level. The high level contains the critical part of the absorption site (B_3O_3), which was treated at the B3LYP/6-31g(d,p) and MP2/6-31g(d,p) levels of theory. Three C_6H_4 rings were treated at the low level of theory using the AM1 method. The ONIOM (B3YP/6-31g(d,p):AM1) and ONIOM (MP2/6-31g(d,p):AM1) were denoted by ONIOM-B and ONIOM-M methods, respectively. All calculations were performed using the Gaussian 03 program [5].

The binding energy between absorbed gas (H_2, O_2, CO, and NO) and the COF-1 was defined by

$$\Delta E_B = E_{(Complex)} - (E_{(COF)} + E_{(Free\ gases)})$$

where $E_{(Complex)}$, $E_{(COF)}$ and $E_{(Free\ gas)}$ are the total energies of the COF containing adsorbed homogeneous gas or heterogeneous gas, the intrinsic COF, and a isolated gas molecule, respectively.

Finally, structural properties of adsorbed gases in the COF were analyzed in terms of bond distances and bond angles.

Results and Discussion

The distances between the B_3O_3 ring plane and the closer atom of H_2, O_2, CO, and NO obtained from the ONIOM-B and ONIOM-M methods are summarized in Table1.

Table1: Distances between the B_3O_3 ring plane and the closer atom of H_2, O_2, CO, and NO obtained from the ONIOM-B and ONIOM-M methods

Notation	Method	
	ONIOM-B[a] (Å)	ONIOM-M[a](Å)
$B_3O_3\cdots H_2$[b]	3.46	3.28
$B_3O_3\cdots O_2$	3.26	3.09
$B_3O_3\cdots CO$	3.29	3.15
$B_3O_3\cdots NO$	3.38	3.10
	Angle (°)	
$B_3O_3\cdots H$-H[c]	84.6	107.1
$B_3O_3\cdots O$-O	80.3	80.3
$B_3O_3\cdots C$-O	179.9	180.0
$B_3O_3\cdots N$-O	177.4	176.4

[a]ONIOM-B and ONIOM-M represent ONIOM (B3YP/6-31g(d,p):AM1) and ONIOM-M: (MP2/6-31g(d,p):AM1), respectively.
[b] Distance between the absorbed gas molecule and the B_3O_3 plane
[c]Angle between center of B_3O_3 plan and absorbed gas molecule.

Figure 2 displays optimized structures of hydrogen molecule, oxygen molecule, carbon monoxide, and nitrogen monoxide adsorbed on the $B_3O_3(C_6H_4)_3$ ring obtained from the ONIOM-B and ONIOM-M methods. For H_2, the energetically most favorable structure is on the oxygen site where the axis of a dihydrogen molecule aligns almost parallel to the B_3O_3 plane with the bond length and bond angle of 3.46 Å and 84.6° evaluated from the ONIOM-B, respectively. It is evident that the ONIOM-M method presents the structure of the hydrogen molecule pointing toward the oxygen atom of B_3O_3 ring, showing the bond length and bond angle of 3.28 Å and 107.1°, respectively. The similar result for O_2 absorbed on the B_3O_3 ring was predicted from the ONIOM-B and ONIOM-M methods. The most stable absorption site is the boron site of B_3O_3 ring in which a axis of oxygen molecule is parallel to the B_3O_3 plane. For heterogeneous gases, the most favorable site for CO molecule is a position where the axis of CO molecule is perpendicular to the B_3O_3 plane and points to the middle of the ring. The calculated bond angles are 179.9 and 180.0° elucidated from the ONIOM-B and ONIOM-M methods, respectively. The bond distance of 3.29 Å obtained from the ONIOM-B method is larger than the value of 3.15 Å determined from the ONIOM-M method. In the case of NO molecule, the axis of the NO molecule is perpendicular to the B_3O_3 plane and points to about the B-O bond of the B_3O_3 ring obtained from the ONIOM-B method, while the NO molecule pointing to a middle of the B_3O_3 ring was evaluated from the ONIOM-M method.

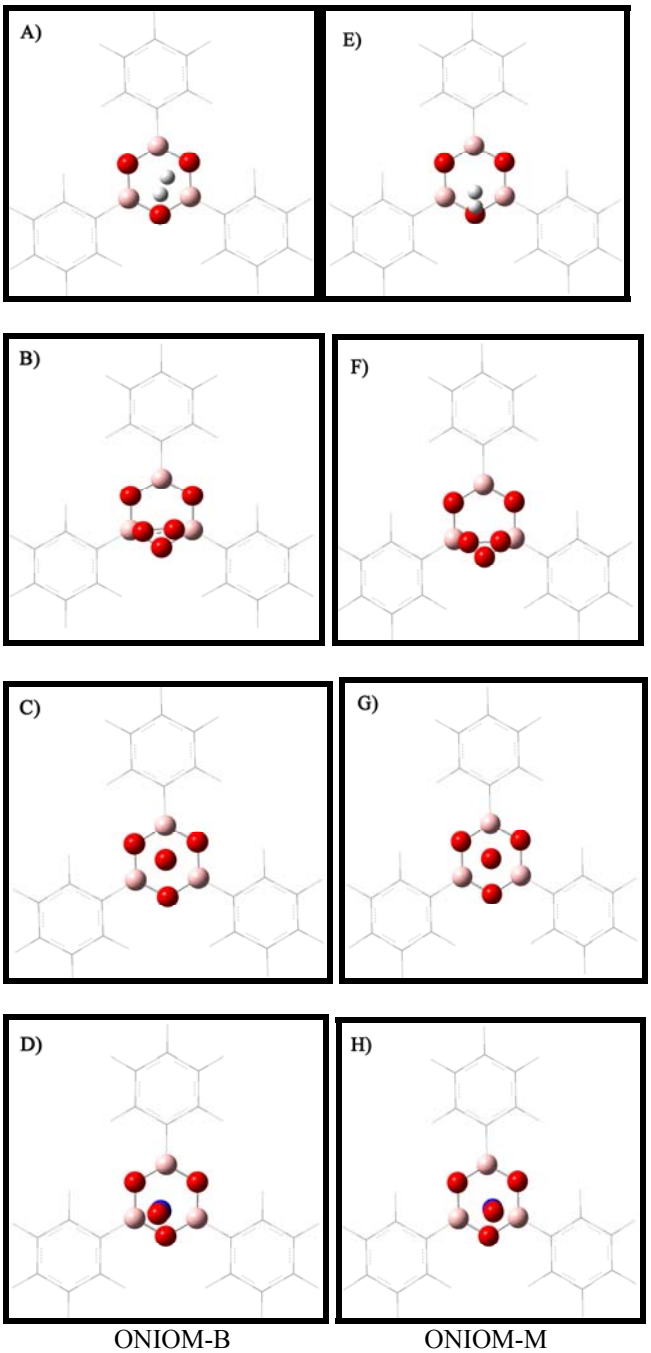

Figure 2. Structures of A) hydrogen molecule, B) oxygen molecule, C) carbon monoxide and D) nitrogen monoxide adsorbed on the $B_3O_3(C_6H_4)_3$ ring of the COF-1 evaluated from the ONIOM-B method. E) hydrogen molecule, F) oxygen molecule, G) carbon monoxide and H) nitrogen monoxide adsorbed on the $B_3O_3(C_6H_4)_3$ ring of the COF-1 evaluated from the ONIOM-M method.

Table 2: Binding energy (kcal/mol) between gases and COF obtained from the ONIOM-B and ONIOM-M methods

Notation	Method	
	ONIOM-B	ONIOM-M
H_2	-0.1	-0.4
O_2	-1.9	-3.4
CO	-1.4	-2.6
NO	-2.8	-2.8

The binding energies between gases and the $B_3O_3(C_6H_4)_3$ ring evaluated from the ONIOM-B and ONIOM-M methods are listed in Table2. The highest binding energy of -3.4 kcal/mol was elucidated for O_2 determined from the ONIOM-M method, which is much higher than that observed from the ONIOM-B (-1.9 kcal/mol). For NO molecule, ONIOM-B and ONIOM-M methods provide the similar value of -2.8 kcal/mol. These were also observed for H_2 molecule where the corresponding values of -0.1 and -0.4 kcal/mol were determined from the ONIOM-B and ONIOM-M methods, respectively. The value of -0.4 kcal/mol obtained from ONIOM-M method is in good agreement with the value of -0.3 kcal/mol evaluated from RI-MP/2def2-TZVPP calculation [1]. The ONIOM-M binding energy between CO molecule and the $B_3O_3(C_6H_4)_3$ ring amounts to -2.6 kcal/mol, which is much larger than the value of -1.4 kcal/mol evaluated from the ONIOM-B method. These results pronounced that the ONIOM(B3LYP/6-31g(d,p):AM1) method shows the underestimated binding energies for the absorbed gases in the COF, while the ONIOM(MP2/6-31g(d,p):AM1) method seems to be a suitable level of theory for describing weak van der Waals interaction energy.

Conclusion

It can be concluded that the most favorable adsorption position of heterogeneous gases (CO and NO) on the $B_3O_3(C_6H_4)_3$ ring places the heterogeneous gases above the $B_3O_3(C_6H_4)_3$ ring with the axis pointing toward the middle of the ring, while the homogeneous gases align parallel to the B_3O_3 plane. The ONIOM(MP2/6-31g(d,p):AM1) method is considered to yield appropriate estimates for this kind of weak van der Waals interaction energy.

Reference

1. Klontzas, E.; Tylianakis, E.; George, E. *J. Phys. Chem. C* **2008**, 112, 9095-9098.
2. Han, S.; Furukawa, H.; Yaghi, O.; Goddard, W. J. AM. CHEM. SOC. **2008**,130, 11580-11581.
3. Garberoglio, G. *Langmuir* **2007**, 23, 12154-12158.
4.Yang Q.; Zhong C. *Langmuir* **2009**, 25, 2302-2308.
5. M.J. Frisch , G. W. Trucks, H. B. Schlegel, G. E. Scuseria, M. A. Robb, J. R. Cheeseman, J. A. Montgomery, Jr., T. Vreven,. N. Kudin, J. C. Burant, J. M. Millam, S. S. Iyengar, J. Tomasi, V. Barone, B. Mennucci, M. Cossi, G. Scalmani, N. Rega, G. A. Petersson, H. Nakatsuji, M. Hada, M. Ehara, K. Toyota, R. Fukuda, J. Hasegawa, M. Ishida, T. Nakajima, Y. Honda, O. Kitao, H. Nakai, M. Klene, X. Li, J. E. Knox, H. P. Hratchian, J. B. Cross, C. Adamo, J. Jaramillo, R. Gomperts, R. E. Stratmann, O. Yazyev, A. J. Austin, R. Cammi, C. Pomelli, J. W. Ochterski, P. Y. Ayala, K. Morokuma, G. A. Voth, P. Salvador, J. J. Dannenberg, V. G. Zakrzewski, S. Dapprich, A. D. Daniels, M. C. Strain, O. Farkas, D. K. Malick, A. D. Rabuck, K. Raghavachari, J. B. Foresman, J. V. Ortiz, Q. Cui, A. G. Baboul, S. Clifford, J. Cioslowski, B. B. Stefanov, G. Liu, A. Liashenko, P. Piskorz, I. Komaromi, R. L. Martin, D. J. Fox, T. Keith, M. A. Al-Laham, C. Y. Peng, A. Nanayakkara, M. Challacombe, P. M. W. Gill, B. Johnson, W. Chen, M. W. Wong, C. Gonzalez, and J. A. Pople, Gaussian Inc., Pittsburgh PA, 2003.

Theoretical study on the geometry around an impurity ion in corundum

C. Jaiklam, S. Prompid and A. Saksaengwijit*
Department of Chemistry, Faculty of Science, King Mongkut's University of Technology Thonburi, Bangkok, Thailand

* E-mail: aimorn.sak@kmutt.ac.th

α-Aluminium oxide (Al_2O_3) is one of important geological materials, also called corundum. It is known that pure aluminium oxide is colour-less and the colour of corundum is caused from some trace impurities inside. In gem industrials, the value of corundum almost depends on its optical properties; therefore the main focus in many gem-researches is to study the physics of impurities in corundum [1-3]. In this work, we attempt to gain more information in the atomic scale on the geometry around an impurity ion in corundum. The density-functional theory (DFT) techniques is employed to model the aluminium oxide (Al_2O_3) and the doped aluminium oxide with Ti^{3+}, Cr^{3+} and Mn^{3+} ion ($M:Al_2O_3$). The exchange correlation function BLYP together with the plane-wave basis set and pseudopotentials in the Kleinman-Bylander form is used. All paramagnetic ions are treated with the spin polarized local density approximation. All calculations are done in the periodic manner by using the CPMD program [4]. The results are mainly focused on energetic and structural properties. Linear effect of the impurity ion-size on the asymmetry of M-O trigonal bipyramidal unit (M= Ti^3+, Cr^{3+}, Mn^{3+}) is found. The reduction of energy band gap upon doped impurity ion is also reported. Moreover, the change in the environment around an impurity ion at high temperature is also discussed.

Introduction

In the crystalline state, the most widespread and important phase of aluminum oxide (α-Al_2O_3) is corundum. Pure α-Al_2O_3 is colorless; the various color of corundum is caused from some trace impurities inside its crystal. Due to numerous applications of corundum and doped corundum as optical materials, ceramics and semiconductors in the gemstone and electronic industries [1-3], there is an increasing need to understand the physics of impurities and their electronic structures. However, the knowledge on the nature of impurities and the local electronic structures around them is still lacked, even many experimental researches have been attempted to obtain more information on the microscopic level [5-6]. From the theoretical way, one of the effective techniques developed in a few decades is a computational simulation based on quantum chemistry approaches.

Recently, many calculations on α-Al_2O_3 and doped Al_2O_3 by the first principle calculation had been published. T.V. Perevalov et al. [7] reported the reliable value of energy band gap of pure α-Al_2O_3 obtained from the density functional theory (DFT) calculation in comparison with XPS and UPS experimental results. The relaxation of some paramagnetic impurities in α-Al_2O_3 had been studied theoretically by E. Gaudry et al. [5]. They found that structural relaxation of an impurity ion is much localized in their site. C. Verdozzi et al. [8] studied on the α-Al_2O_3 doped with some rare-earth ions (La^{3+}). They found that substituting aluminum ion with a rare-earth ion has strong structural and energetic effect on α-Al_2O_3 crystal. Therefore, it is interesting to know more on the effect of some common impurities such as Ti^{3+}, Cr^{3+} and Mn^{3+} on the structural and energetic properties of corundum.

Materials and Methods

We have investigated the electronic and energetic properties of pure α-Aluminium oxide (corundum) and the doped aluminum oxide, $M:Al_2O_3$ where M stands for the transition impurity ion; Ti^{3+}, Cr^{3+} and Mn^{3+}. In this study we have carried out the first principle calculation of Al_2O_3 and $M:Al_2O_3$ by using the plane wave basis set and the combination of the norm-conserving Godecker and Troullier-Martins pseudo-potentials in the Kleinman-Bylander form based on the Density Functional Theory (DFT) as implemented in the CPMD code [4]. Calculations based on the known BLYP functional. All transition metals are treated with the spin polarized local density approximation (LSDA). The cut-off for the pseudopotentials in this work is 180 Ryd. The periodic crystal structure is taken into account by using the periodic boundary conditions at the unit cell boundaries. The generalized gradient approximation (GGA) is not used in this simulation since it had been reported that it does not improve geometries for this case [9].

The structural model of pure aluminium oxide (α-Al_2O_3) is constructed by using the lattice parameters recieving from the Inorganic Crystal Structure Database (ICSD) published by Maslen *et al*. The crystal of Al_2O_3 belongs to the space group R3c. The hexagonal unit cell parameters are a = b = 4.7540, c= 12.9820 Å and α = ß = 90°, γ = 120°, which contain 12 six-coordinated Al atoms and 18 four-coordinated O atoms. Then, calculations were performed with relaxation of all atomic position. For doped aluminum oxide ($M:Al_2O_3$), the structural model is constructed by substituting one of Al atom with an impurity ion (M) in the unit cell of pure aluminum oxide after optimization. The Ab Initio molecular dynamics simulation of doped aluminum oxide had been done in the canonical ensemble with the Hoover-Nose's thermostat after equilibrating at the temperature of 300K and 1000K.

Results and Discussion

The crystal structure of Al_2O_3 has hexagonal symmetry. The geometric properties of its electronic structure are summarized in table 1.

For reasons of structural analysis, the following notation O1 and O2 are used to classify neighbouring oxygen ions around the considered aluminium ion (Al^{3+}) site. Aluminum ions are bonded with six oxygen ions in distorted octahedron along the C3 direction. Three neighboring oxygen ions, which are closed to the considered aluminum site are labeled O1, while the others in octahedron unit are denoted O2. This nomenclature also applies to doped aluminum oxide ($M:Al_2O_3$), when we consider an impurity ion instead of the considered aluminum ion. In our supercell, the O1 ions are reciprocally coplanar and lie above the impurity site, while the O2 ions lie below (see figure 1).

The difference between Al-O1 and Al-O2 bond lengths is agreed with the presence of distorted octahedron in the crystal of natural aluminum oxide (α-Al_2O_3). This distortion causes an asymmetric trigonal bipyramid in octahedron unit. Therefore, the O1-Al-O1 bond angle is larger than O2-Al-O2 bond angle. The values of bond length and bond angle are similar to those values reported in the previous experimental and theoretical works [5,8].

Table 1: Geometric properties of α-Al_2O_3 and $M:Al_2O_3$

M	$O_1\widehat{M}O_1$ (degree)	$O_2\widehat{M}O_2$ (degree)	d_{M-O_1} (Å)	d_{M-O_2} (Å)
Al^{3+}	100.14	80.30	1.82	1.95
Ti^{3+}	115.50	82.97	1.90	2.19
Mn^{3+}	100.71	78.90	1.87	2.04
Cr^{3+}	101.59	84.77	1.98	2.01

*The value is averaged over all sides of the trigonal pyramid.

The starting structural model of doped aluminum oxide ($M:Al_2O_3$) is constraint, since it is generated from simply substituting an impurity ion at an aluminum site in the relaxed structure of pure α-Al_2O_3. After simulation, all atomic positions are freely relaxed. The electronic structure of $Ti^{3+}:Al_2O_3$ is shown in figure 1. The geometric properties of all doped alumina are summarized and compared with those values of pure alumina in table 1. The influence of impurity ion on the M-O bond length is not much. MO2 bond length is still larger than MO1 one. The values of MO1 and MO2 bond lengths are quite similar to those of AlO1 and AlO2. However, the impurity ion affects significantly on an asymmetric trigonal bipyramidal unit in octahedron site. The O1-M-O1 bond angle is much broader than O2-M-O2 bond angle. Therefore, the impurity ions enhance the

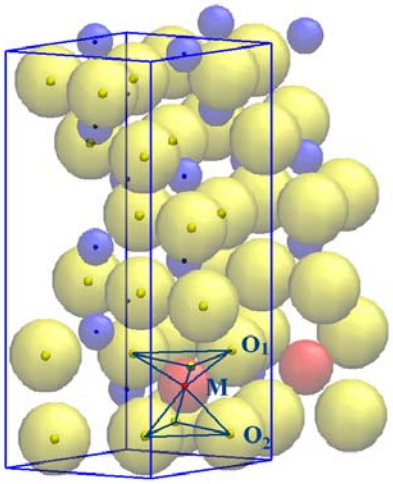

Figure 1. Relaxed crystal structure of $Ti^{3+}:Al_2O_3$, The large circle represents the O atom, the medium one represents impurity atom ($M=Ti^{3+}$ for this figure) and the small one represents aluminum atom. A sketch shows a distorted octahedron at an impurity site. Three closed oxygen atoms are denoted O1 and the rest of oxygen in octahedron unit are O2.

distortion of octahedron unit in α-Al_2O_3 crystal. This effect relates somehow linearly with the ionic radius of impurity ion (r_{Ti3+} = 0.67 Å > r_{Cr3+} = 0.62 Å> r_{Mn3+} = 0.58 Å). Mn^{3+} ion has the least effect in this work (O1-Mn-O1 ≈ O1-Al-O1 and O2-Mn-O2 ≈ O2-Al-O2) since its ionic radius is similar to Al^{3+} (r_{Al3+} = 0.54Å).

In gem industrials, the heat treatment is used as a common method to improve the quality of corundum, especially on the optical properties. It is interesting to see that how the temperature affects on the crystal structure around the impurities (Mn^{3+}, Ti^{3+}). The ab initio molecular dynamics simulations of doped aluminum oxide have been performed at equilibrium at low temperature (300K) and high temperature (1000K). We investigated the distorted octahedron around an impurity ion comparing with one around an aluminum ion. With the statistic analysis, we found that the distortion of the octahedron around impurity get less pronounced at high temperature. However the octahedron around an impurity site is still more distorted comparing with the one around aluminum ion at the same temperature. The difference of impurity environment at high temperature might yield some change in the crystal structure after annealing, which give raise a change in the crystal field around the impurity ion.

Recently, doped aluminum oxide is widely used in electronic industry. It is served as semiconductor materials [3]. Therefore, it is interesting to study the effect of impurity ion on an energy band gap of pure α-Al_2O_3. In this work, we have investigated the influence of substituted impurity ion on the energy band gap of α-Al_2O_3. The band gap has been

calculated based on the Kohn-Sham scheme of density functional theory (DFT). The value of the energy band gap for pure aluminum oxide is 6.65 eV and for doped ones are 5.70 eV, 4.31 eV for Mn^{3+}:Al_2O_3 and Cr^{3+}:Al_2O_3, respectively.

The energy band gap of pure aluminum oxide is smaller than the experimental value [10] (8.7 eV). This discrepancy is evidently associated with the fact that DFT systematically underestimate the band gap width in solids. However, it is closed to the value reported in previous calculation [7]. Substituting an aluminum ion with a paramagnetic impurity ion (Mn^{3+}, Cr^{3+}) decreases the band gap in α-Al_2O_3.

Conclusions

In summary, we have studied some structural and energetic properties of the crystal of pure aluminum oxide (α-Al_2O_3) and doped aluminum oxide M:Al_2O_3, where M=Ti^{3+}, Cr^{3+}, Mn^{3+}. Substituting an aluminum ion with an impurity ion in the unit cell of α-Al_2O_3 crystal increases the distortion of its octahedron site; i.e O1MO1 bond angle is wider than O1AlO1 bond angle. The distortion of the octahedron site around an impurity ion decreases at the high temperature. For energetic aspect, the energy band gap of α-Al_2O_3 is calculated from the Kohn-Sham energy. An impurity ion affects some decrease in the energy band gap of α-Al_2O_3. It tends to have more semiconductor behavior in doped α-Al_2O_3.

References

[1] A. I. Kingon, J. P. Maria, and S. K. Streiffer, Nature **406** (2000), pp 1032.

[2] P. Rey, A. Souto, C. Santos and F. Guitian, *J. Euro. Ceram. Soc.*, **23** (2003), pp 2983-2986.

[3] Yu. N. Novikov, V. A. Gritsenko, and K. A. Nasyrov, *JETP Lett.*, 98 (2009), pp 506-509.

[4] CPMD V3.13 Copyright IBM Corp. 1990-2008, Copyright MPI fuer Festkoerperforschung Stuttgart 1997-2001.

[5] E. Gaudry, D. Cabaret, P. Sainctavit, C. Brouder, F. Mauri, *J. Phys.: Condens. Matter,* **17** (2005) 5467–5480

[6] E. Lo´ pez-Navarrete, A. Caballero, A.R. Gonza´ lez-Elipe, M. Ocan˜, *J. Euro. Ceram. Soc.*, **24** (2004), pp 3057–3062

[7] T. V. Perevalov, A. V. Shaposhnikov, V. A. Gritsenko, H. Wong, J. H. Han, and C. W. Kim, *JETP Lett.,* **85** (2007), pp. 165–168.

[8] C. Verdozzi, D. R. Jennison, P. A. Schultz, M. P. Sears, J. C. Barbour, and B. G. Potter, *Phys. Rev. Lett.* **80** (2003), pp 5615-5618.

[9] I. Frank, D. Marx, and M. Parrinello, *J. Chem. Phys.* **104** (1996), pp 8143

[10] R. H. French, H. Mullejans, and D. J. Jones, *J. Am. Ceram. Soc.* **10** (1998), pp 2549.

Molecular dynamics simulations of tuberculosis agents in class of arylamide derivatives with Inha from *M. tuberculosis*

A. Punkvang[1], P. Wolschann[2], A. Beyer[2] and P. Pungpo[1]*

[1]Faculty of Science, Ubonratchathani University, Ubon Ratchathani, Thailand
[2]Institute for Theoretical Chemistry, University of Vienna, A-1090 Vienna, Austria

* E-mail:pornpan_ubu@yahoo.com

Abstract: Arylamides are the novel inhibitors of the enoyl ACP reductase enzyme (InhA) involved in the type II fatty acid biosynthesis pathway of *M. tuberculosis*. Arylamides could be directly bound to InhA without mycobacterial enzymatic activation. Therefore, this inhibitor can address the resistance mechanism in the enzymatic activation process of antitubercular prodrugs such as isoniazid and ethionamide. In order to study the binding of arylamide derivatives in the InhA binding pocket, molecular dynamics (MD) simulations were performed wusing Gromacs. The results show that the binding modes of arylamides in InhA binding pocket are successfully simulated by Gromacs. Investigation of arylamide/InhA complexes reveals that only Tyr158 and NADH are within distances for forming hydrogen bond interaction with the carbonyl oxygen of arylamides. These results indicate that arylamides are tightly held in InhA binding pocket by these hydrogen bonds. Therefore, the obtained results might be helpful for better understanding the binding mechanism of arylamide derivatives in InhA binding pocket.

Introduction

Tuberculosis (TB) caused by *M. tuberculosis* still remains a serious public health problem. Accordingly, to address these problems the design of novel and more potent antitubercular agents is necessary.

The enzymes involved in the bacterial fatty acid biosynthetic pathway, the type II fatty acid synthase (FAS II) system, are attractive targets for designing novel antibacterial agents and for improving the existing antibacterial agents [1]. One of the potential enzyme targets in FAS-II pathway for developing antibacterial drug is the enoyl-acyl ACP reductase (InhA). InhA has been identified as the primary target of isoniazid (INH), the frontline drug for tuberculosis chemotherapy [2]. As a prodrug, INH must first be activated by catalase-peroxidase (KatG) to generate the reactive acyl radical [3]. Then, the reactive specie binds covalently to nicotinamide adenine dinucleotide (NAD+) to form the active adduct (INH-NAD adduct) that functions as the highly potent inhibitor of InhA [4]. However, the high potency of INH for tububerculosis treatment is diminished by the drug resistance. High levels of resistance to INH are caused by mutations in katG, most commonly found in *M. tuberculosis* clinical isolates [5]. To address the resistance to INH associated with mutations in the katG enzyme, a series of arylamides were identified as a novel class of potent InhA inhibitors [6]. Arylamides target InhA directly without a requirement for KatG activation and function as direct InhA inhibitors. Therefore, to understand the important drug-enzyme interactions for binding of arylamides toward InhA and to get some information about the dynamics behaviour, molecular dynamics simulation were employed in the present study. The obtained results should provide us some information on the correlation of arylamide structures and their inhibition activities, the binding modes and the binding free energies.

Materials and Methods

Arylamide/InhA model: Two arylamides, compounds B3 (IC_{50} = 5.16 μM) and A10 (IC_{50} > 100 μM), complexed with InhA were used for MD simulations. Compounds B3 and A10 complexed with InhA was taken from Protein Data Bank (PDB code 2SND) and from molecular docking studies, respectively, as the initial structures for MD simulations.

Molecular simulations: GROMOS96 43a2 force field was applied for MD simulation. Gromacs 4.0.4 software package was used for MD simulations. Arylamides/InhA complexes were immersed in a box that extends at 3 nm from all atoms of these complexes and it was then solvated by SPC216 water molecules. The energy minimization with 2000 steps using the steepest descent algorithm was performed for these systems with all bonds constrained. After energy minimization, position restraining simulation of this system was performed. Then, 6 ns MD simulations with time step of 0.002 ps were performed. The leapfrog algorithm in the NVT ensemble at 300 K was used for simulation. To calculate the binding free energy, MD simulations of arylamides in water were also performed. Last 1 ns simulation (5 to 6 ns) was selected for detailed analysis.

Calculation of binding free energy: The linear interaction energy (LIE) method was employed to estimate the relative binding free energy for arylamides in InhA enzyme. The binding free energy of an inhibitor to a receptor target based on LIE method can be expressed using the following equation.

$$\Delta G_{bind} = \alpha(V_{LJ})_{bond} - (V_{LJ})_{free} + \beta(V_{CL})_{bond} - (V_{CL})_{free} \quad (1)$$

Where

$(V_{LJ})_{bond}$ = average Lennard-Jones energy for ligand/protein interaction

$(V_{LJ})_{free}$ = average Lennard-Jones energy for ligand/water interaction

$(V_{CL})_{bond}$ = average electrostatic energy for ligand/protein interaction

$(V_{CL})_{free}$ = average electrostatic energy for ligand/water interaction

α, β = Scaling factors with $\alpha = 0.18$ and $\beta = 0.50$

Results and Discussion

Root mean square deviation: The root mean square deviations (RMSD) of all atoms of InhA/NADH/B3 and InhA/NADH/A10 complexes compared with initial coordinates as a function of the simulation time were examined. RMSD values of InhA, NADH and B3 were more stable over the entire simulation time after increasing of RMSD about 0.35, 0.08 and 0.10 nm, respectively as shown in Figure 1. These results reveal that the complex structure obtained from MD simulations is well consistent with X-ray crystal structure. Regarding to InhA/NADH/A10 complex, RMSD values of InhA and NADH are similar to those of InhA/NADH/B3 complex as shown in Figure 2. RMSD value of compound A10 was more stable after increasing of RMSD in range of 0.1-0.15 nm. Compounds B3 and A10 in InhA binding pocket taken from average structure at last 1 ns of simulation time is shown in Figures 3 and 4.

Hydrogen bonding: The hydrogen bonds for compounds B3 and A10 in complex structures at the last 1 ns of the simulation time were investigated. Two hydrogen bonds could be observed for compound B3. The hydrogen bonds between carbonyl oxygen of compound B3 and hydroxyl group of Tyr158 is strongly formed with a distance and an angle of 1.68 Å and 165 degrees, respectively, as shown in Table 1. Another hydrogen bond is formed between this oxygen atom of compound B3 and the hydroxyl group of nicotinamide ribose of NADH with a distance and an angle of 1.76 Å and 163 degrees, respectively. In case of compound A10, no hydrogen bond is formed to Try158 as shown in Table 1 and Figure 4.

Table 1: Average hydrogen bond distances and hydrogen bond angles for compounds B3 and A10 with Tyr158 and NADH

Compound	Tyr158		NADH	
	distance (Å)	angle	distance (Å)	angle
B3	1.68	165	1.76	163
A10	6.89	24.35	1.67	161

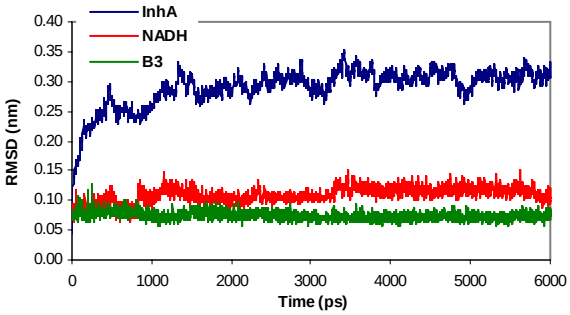

Figure 1. RMSD of InhA, NADH and B3 with respect to their initial configurations as a function of simulation time

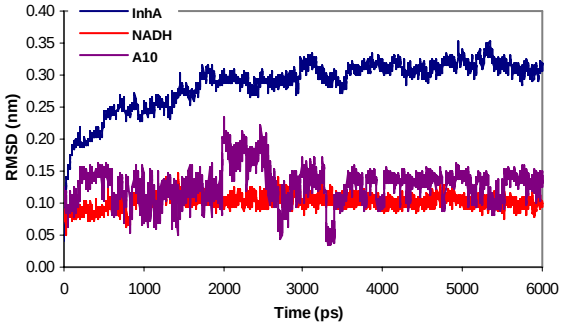

Figure 2. RMSD of InhA, NADH and A10 with respect to their initial configurations as a function of simulation time

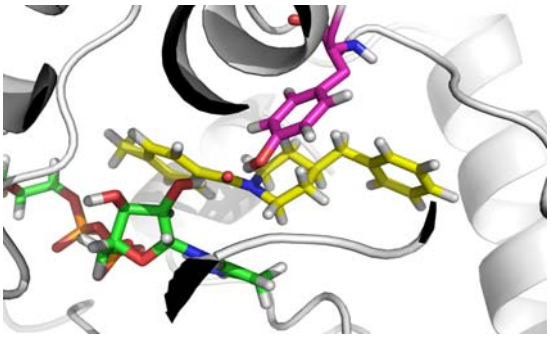

Figure 3. Compound B3 (yellow) in InhA binding pocket obtained from MD simulation. NADH and Tyr158 represented in green and pink, respectively.

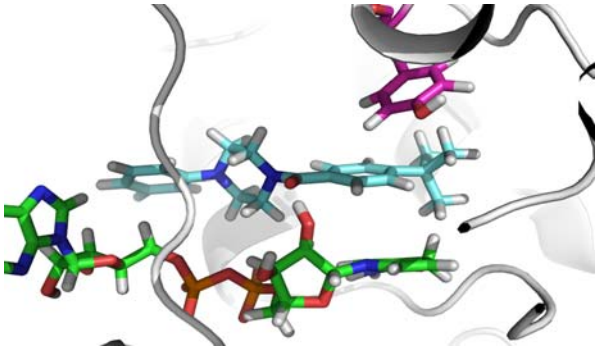

Figure 4. Compound A10 (blue) in InhA binding pocket obtained from MD simulation. NADH and Tyr158 represented in green and pink, respectively.

The binding free energy and particular interaction energy: The estimate binding free energies of these compounds were calculated by LIE equation. The calculated binding energies of compounds B3 and A10 are -21.91 and -15.80 kJ/mol, respectively, indicating the better binding of compound B3 compared with compound A10. These results are consistent with the higher activity of compound B3 (IC_{50} = 5.16 μM) as compared with compound A10 (IC_{50} > 100 μM). To reveal key inhibitor-enzyme interaction, interaction energies between compounds B3 and A10 and each amino acid residue in InhA binding pocket were calculated. Interactions between compound B3 and NADH and Tyr158 show highest attractive interaction energies of 68.36 and 98.69 kJ/mol, respectively, as shown in Table 2. These high attractive energies are consistent with two strong hydrogen bonds among them. For compound A10, it shows the highest attractive interaction energy with NADH, whereas, a lower attractive interaction energy with Tyr158 than that of compound B3 is observed, because of the loss of the hydrogen bond. These results reveal that two hydrogen bonds are important to hold arylamides in InhA binding pocket.

Table 2: Average interaction energies between compound B3 and residues in InhA binding pocket

Residue	Interaction energy (kJ/mol)	
	B3	**A10**
NADH	-98.69	-149.46
Gly96	-6.49	-12.56
Phe97	-5.17	-3.72
Met98	-2.64	-1.75
Met103	-15.15	-12.69
Phe149	-20.94	-9.89
Met199	-20.46	-21.86
Ile202	-13.69	-10.30
Val203	-7.97	0.00
Tyr158	-68.36	-27.21
Met155	-11.80	-7.09
Ala157	-2.76	-0.11
Pro193	-8.92	-10.37
Ile215	-5.35	-11-16
Leu218	-4.08	0.00
Trp222	-4.43	0.00

Conclusions

MD simulations with Gromacs program are convenient to simulate the binding mode of arylamides in InhA binding pocket. The binding free energies of arylamides to InhA estimated by LIE equation correlate well with their inhibition activities. Moreover, the important drug-enzyme interactions are also delineated. These results provide insights into the dynamics of arylamide and InhA which may be useful for rational drug design.

References

[1] J.W. Campbell, J.E. Cronan, Jr. *Annu. ReV. Microbiol.* **55** (2001), pp. 305-332.

[2] D.A. Rozwarski, G.A. Grant, D.H. Barton, W.R. Jacobs Jr., and J.C. Sacchettini. *Science* **279** (1998), pp. 98–102.

[3] B. Lei, C.-J. Wei and S.-C. Tu. *J. Bio. Chem.* **275** (2000), pp. 2520–2526.

[4] C. Vilcheze, F. Wang, M. Arai, M.H. Hazbon, R. Colangeli, L. Kremer, T.R. Weisbrod, D. Alland, J.C. Sacchettini, and W.R. Jacobs Jr. *Nat. Med.* **12** (2006), pp. 12:1027–1029.

[5] A.I. De La Iglesia and H.R. Morbidoni. *Rev. Argent Microbiol.* **38** (2006), pp. 97-109.

[6] X. He, A. Alianc and P.R. Ortiz de Montellano, *Bioor. Med. Chem.* **15** (2007), pp. 6649–6658L.

Understanding the binding interaction of diarylpyrimidine derivatives in wild type and double mutant type HIV-1 RT based on computer aided molecular design

A. Kumkong[1], A. Punkvang[1], N. Kuntiya[1], C. Kheawsod[1], P. Saparpakorn[2], S. Hannongbua[2] and P. Pungpo[1*]

[1]Faculty of Science, Ubonratchathani University, Ubon Ratchathani, Thailand
[2]Faculty of Science, Kasetsart University, Bangkok, Thailand

*Email: pornpan_ubu@yahoo.com

Abstract: Molecular docking simulations and quantum chemical calculations were performed to investigate the essential interactions for binding of diarylpyrimidine derivatives (DAPY) in the allosteric binding site of wild type (WT) and double mutant type (K103N/Y181C, L100I/K103N HIV-1 RT. All DAPY derivatives were docked into each HIV-1 RT binding site by Autodock 3.05 program. RMSD between the docked and X-ray conformations for each binding site less than 1.0 Å suggests that this approach shows high ability to model the potential binding mode of DAPY. For quantum chemical calculations, the interaction energies of the docked conformations of the lowest and highest active compounds with the individual amino acids in the WT and mutant type HIV-1 RT binding pockets were calculated at the MP2/6-31G(d) level of theory. Both approaches are successful to reveal the meaningful information for describing the binding interactions of DAPY derivatives in each HIV-1 RT binding pocket. Hydrogen bond interactions of DAPY derivatives with Lys101 and Glu138 play the important role for binding. Moreover, hydrophobic interactions with Tyr181 and Tyr318 are also crucial for binding of these inhibitors. Consequently, the acquired results base on molecular docking and quantum chemical calculations provide valuable information in the drug-enzyme interactions of DAPY derivatives toward the designing of new more potent inhibitors for WT and K103N HIV-1 RT.

Introduction

Because of the rapid emergence of mutant forms of HIV-1 RT, the successful treatment of HIV-1 infection with non-nucleoside reverse transcriptase inhibitors (NNRTIs) is undermined. Accordingly, the development of new highly effective drug against wild-type and drug-resistance of HIV-1 remains essential. Diarylpyrimidine derivatives (DAPY) have been proven to be a new potential class of NNRTIs that are extremely potent against both wild-type (WT) and mutant type HIV-1 RT [1,2]. Therefore, the inhibitory mode and main interactions of DAPY at the molecular level have become essential to investigate. In the present study, molecular docking calculations were performed on a series of DAPY derivatives to achieve the insight into the inhibitor-enzyme interactions of DAPY in wild-type and two double mutant types (L100I/K103N and K103N/Y181C) of HIV-1 RT.

Materials and Methods

All DAPY derivatives were constructed by Gaussview 3.07 program and then, fully optimized by HF/3-21G method. The starting geometries of DAPY in complex with wild-type and two double mutant types (L100I/K103N and K103N/Y181C) were taken from X-ray crystallographic data (pdb codes 2ZD1, 2ZE2, 3BGR, respectively). Docking studies of DAPY derivatives in wild-type and two double mutant types of HIV-1 RT binding pockets were carried out using Autodock 3.05 program. Three X-ray structures of DAPY were selected to calculate the interaction energies at MP2/6-31G (d) level of theory by Gaussian03 program.

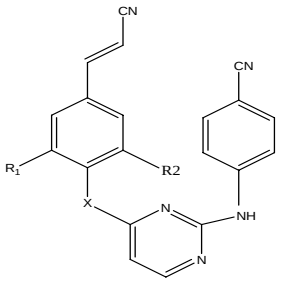

Figure 1. General structure of DAPY derivatives

Results and Discussion

Molecular docking calculations

Molecular docking calculations enable to nicely simulate the potential binding modes of DAPY with rmsd less than 1.0 Å for all binding pockets. From the molecular docking analysis, DAPY compounds could adapt their conformation and position for each pocket, to retain potency against wild-type and mutant-type HIV-1 RT. Most of the top-ranking active compounds present the hydrogen bond interactions with Lys101 and Glu138, the π-π interactions with Tyr181 and the hydrophobic interaction with Tyr188, Trp229 and Phe227 as shown in Figure 2(a). In K103N/Y181C HIV-1 RT, the conformational change of DAPY compounds to form nicely hydrophobic interaction

with Tyr188, Tyr183 and Trp229 enable to compensate for the loss of interactions caused by Y181C mutation as shown in Figure 2(b). For L100I/K103N HIV-1 RT, the ability to reposition of DAPY compounds helps them to reduce the mutation effect shown in Figure 2(c).

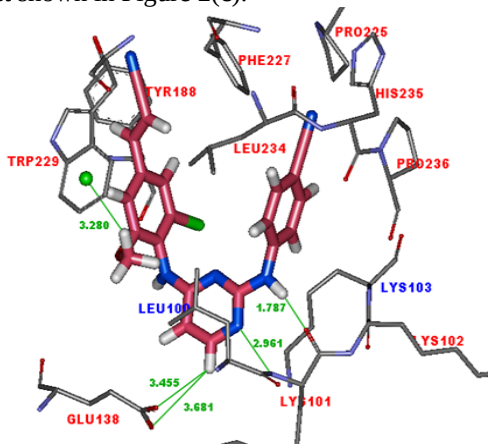

(a) Cpd. 11, EC_{50} = 0.1 nM

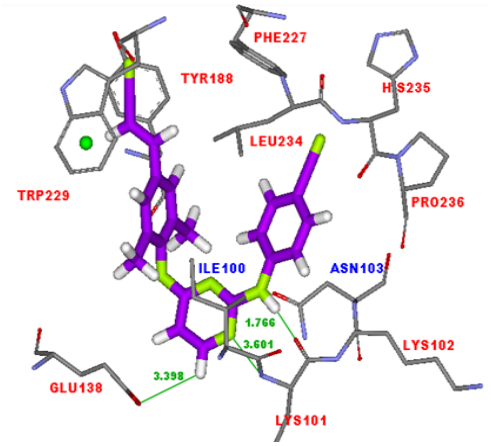

(b) Cpd.5, EC_{50} = 3.7 nM

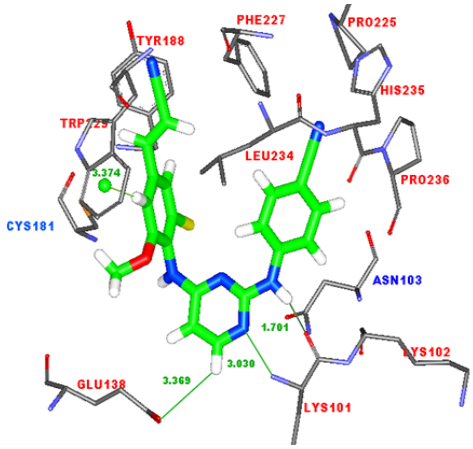

(c) Cpd. 11, EC_{50} = 2.0 nM

Figure 2. Docked conformations of the best active compounds for each pocket in WT (**a**) and L100I/K103N (**b**) and K103N/Y181C (**c**) HIV-1 RT

Quantum chemical calculations

In WT HIV-1 RT binding pocket, the interaction between DAPY and Glu138 shows the highest attraction energy of 12.2 kcal/mol. This attraction energy corresponds with electrostatic interaction of negative side chain of Glu138 and ligand. Two hydrogen bond interactions with Lys101 give the attraction energy of 8.9 kcal/mol. The pi-pi interaction with Tyr181 shows the interaction energy of -2.8 kcal/mol. The hydrophobic interaction with Trp229, Tyr188 and Phe227 shows attraction energies of 3.3 - 4.3 kcal/mol. Because of L100/I100 mutation in L100I/K103N binding pocket, the attraction energy of DAPY and I100 is decreased about 2.3 kcal/mol. For Lys103/Asn103 mutation, the attraction energy is decreased about 10.9 kcal/mol because the electrostatic interaction of TMC278 with Asn103 is deleted. In K103N/Y181C HIV-1 RT pocket, the attraction energy with Cys181 is decreased about1.6 kcal/mol, because of Tyr181/Cys181 mutation. For Lys103/Asn103 mutation, the attraction energy is decreased about 4.8 kcal/mol. Therefore, the main interactions and the mutation influence are elucidated based on the quantum chemical calculation results

Table 1: Interaction energy with BSSE correction of DAPY in WT and L100I/K103N and K103N/Y181C HIV-1 RT

Amino acid	**Interaction energy (kcal/mol)**		
	WT	**K103N/Y181C**	**L100I/K103N**
Glu138	-12.24	-12.35	-12.15
Gly190	-0.62	-0.70	-0.43
His235	-2.72	-2.40	-1.37
Leu100/I100	-1.61	-1.88	0.67
Leu234	-0.17	-0.04	1.72
Lys101	-8.90	-3.32	1.21
Lys103/Asn103	-4.90	-0.14	6.01
Phe227	-3.27	-2.41	-3.96
Pro226	-0.83	-0.69	-0.79
Pro225	-1.31	-1.16	-1.39
Pro236	-1.89	-2.21	-1.15
Pro95	-0.33	-0.41	-0.11
Trp229	-4.28	-4.40	-1.20
Tyr181/Cys181	-2.84	-1.20	-3.62
Tyr188	-4.18	-2.29	-4.32
Tyr183	-0.71	-1.40	-1.26
Tyr318	-1.51	-1.40	-1.23
Val106	-1.22	-1.31	-1.44
Val179	-1.03	0.76	-0.60
Val189	-0.07	-0.20	-0.31

Conclusions

The results derived from molecular docking calculations provide the significant insight into the strategy of DAPY compounds for reducing the drug-resistance mutation effect. The ability of DAPY compounds to adapt their conformation and position for each pocket could retain the potency against wild-

type and mutant-type HIV-1 RT. This information can be useful to utilize for designing new more effective HIV-1 RT inhibitors active against WT and mutant HIV-1 RT strains.

References

[1] Y. Van Herrewege, G. Vanham, J. Michiels, K. Fransen, L. Kestens, K. Andries, P. Janssen, Lewi, P. *Antimicrob. Agents Chemother.* 48(2004), pp. 3684-3689.

[2] K. Das, A.D. Jr. Clark, P.J. Lewi, J. Heeres, M.R. De Jonge, L.M. Koymans, H.M. Vinkers, F. Daeyaert, D.W. Ludovici, M.J. Kukla, B. De Corte, R.W. Kavash, C.Y. Ho, H. Ye, M.A. Lichtenstein, K. Andries, R. Pauwels, M.P. De Béthune, P.L. Boyer, P. Clark, S.H. Hughes, P.A. Janssen, Arnold, E. *J. Med. Chem.* 47(2004), pp. 2550-2560

Binding investigation of azanaphthoquinone annelated pyrrole derivatives as cytostatic compounds in DNA using molecular modeling approaches

C. Kheawsod[1], A. Punkvang[1], N. Kuntiya[1], A. Kumkong[1], P. Wolschann[3], P. Saparpakorn[2], S. Hannongbua[2], N. Pongprom[1] and P. Pungpo[1]

[1]Department of Chemistry, Faculty of Science, Ubonratchathai University, Ubonratchathani, Thailand
[2]Department of Chemistry, Faculty of Science, Kasetsart University, Bangkok, Thailand
[3]Institute for Theoretical Chemistry, University of Vienna, A-1090 Vienna, Austria

[*]E-mail: pornpan_ubu@yahoo.com,

Abstract: Azanaphthoquinone annelated pyrrole derivatives act as the synthetic DNA intercalating agent. In order to investigate the binding interaction of these compounds in DNA binding site, molecular docking calculations with Glide and Gold programs were employed. Moreover, quantum chemical calculations based on MP/6-31G(d) method were also applied. The results shows that molecular docking calculations with Glide and Gold programs enable to model the potential binding modes of azanaphthoquinone annelated pyrrole derivatives with RMSD values less than 1 Å. From molecular docking, the azanaphthoquinone scaffolds are sandwiched between hydrophobic sides of two base pairs of DNA strains. In addition, strong hydrogen bond interactions of oxygen of deoxyribose with inhibitors are also observed. Based on the calculated interaction energy, azanaphthoquinone annelated pyrrole derivatives show high attraction energy with two base pairs of DNA strains. Therefore, the integrated results from both approaches should be helpful for understanding the binding modes and the important interactions of azanaphthoquinone annelated pyrrole derivatives in DNA binding site.

Introduction

Azanaphthoquinone annelated pyrrole derivatives act as the synthetic DNA intercalating agent [1-2]. They were synthesized and screened for cytotoxic activity against at least four different cell lines KB/HeLa, NCI-H460, SKOV-3 and SF-268. They exhibit promising cytotocity. In order to investigate the binding interaction of these compounds in DNA binding site, molecular docking calculations with Glide and Gold programs were employed. Moreover, quantum chemical calculations based on MP2/6-31G(d) method were also applied.

Materials and Methods

All azanaphthoquinone annelated pyrrole derivatives were constructed by Gaussview 3.07 program and then, fully optimized by HF/3-21G method. The starting geometry of azanaphthoquinone annelated pyrrole in complex with DNA binding site was taken from X-ray crystallographic data (pdb codes 1Z3F). Docking studies were carried out using Glide and Gold programs. The structures of azanaphthoquinone annelated pyrrole derivatives in DNA binding site were selected to calculate the interaction energies at MP2/6-31G (d) level of theory by Gaussian03 program.

Results and Discussion

Molecular docking results

RMSD of X-ray crystal structure and docked structure obtained from Gold and Glide programs are 6.04 and 0.20 Å, respectively. This result shows that Glide program is more efficient to model the binding mode of azanaphthoquinone annelated pyrrole than Gold program. Therefore, the binding modes of azanaphthoquinone annelated pyrrole derivatives obtained from Glide program were selected to analyze binding interactions of these compounds. From molecular docking, the azanaphthoquinone scaffolds are sandwiched between hydrophobic sides of two base pairs of DNA strains, G6-C1, C5-G2. This hydrophobic interaction is the main interaction for binding of azanaphthoquinone annelated pyrrole derivatives as shown in Figures 2 and 3. Moreover, hydrogen bonding interaction between R group and oxygen atom of deoxyribose is also observed.

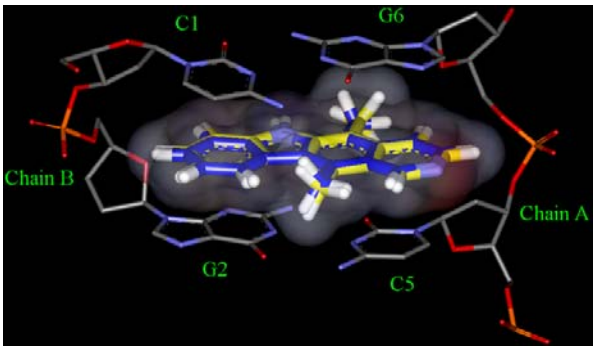

Figure 1. X-ray pose orientation (blue) and the docked conformation obtained from Glide docking (yellow) of inhibitor in DNA binding site

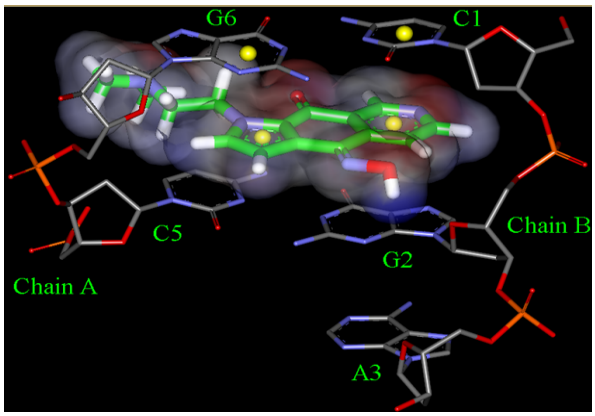

Figure 2. Docked conformations obtained from Glide docking of compound 18 (IC_{50} = 0.66 µM) in DNA binding site

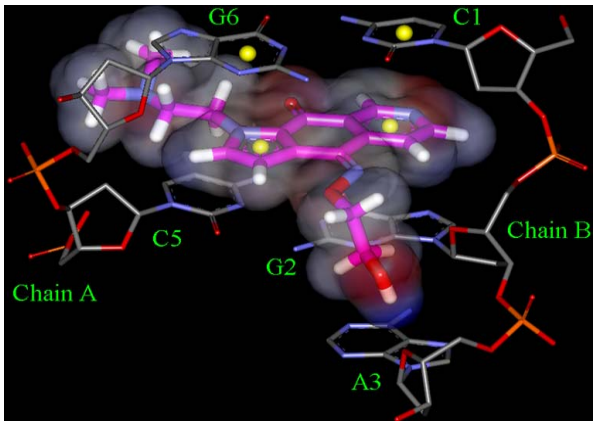

Figure 3. Docked conformations obtained from Glide docking of compounds 16 (IC_{50} > 12 µM) in DNA binding site

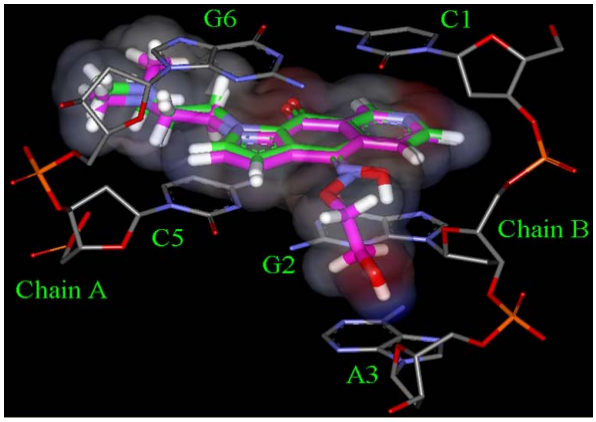

Figure 4. Superimposition of docked conformations of compounds 16 (green) and compound 18 (pink) in DNA binding site

Quantum chemical calculation results

Based on the calculated interaction energy, azanaphthoquinone annelated pyrrole derivatives show attraction energies with two base pairs of guanine (G6)-cytosine (C1) and cytosine (C5)-guanine (G2). Interaction energy of hydrogen bonding interaction between R group of compound 16 and adenine sugar chain B shows higher than that of compound 18 indicating the importance of this interaction.

Table 1 Calculated interaction energy between compound 16 and compound 16 in DNA binding site

DNA	**Interaction energy (kcal/mol)**	
	Compound 18	**Compound 16**
Guanine Chain A (G6)	-4.32	-3.32
Guanine Sugar Chain A	-3.06	-2.73
Guanine Phosphate Chain A	-6.63	-7.05
Cytosine Chain A (C5)	2.04	-2.23
Cytosine Sugar Chain A	1.72	4.99
Cytosine Phosphate Chain A	-3.51	-0.91
Cytosine Chain B (C1)	-3.63	-3.90
Cytosine Sugar Chain B	-0.53	-0.50
Guanine Chain B (G2)	-4.35	-2.53
Guanine Phosphate Chain B	-2.86	-2.41
Guanine Sugar Chain B	-4.95	-3.39
Adenine Chain B (A3)	-0.36	-0.48
Adenine Phosphate Chain B	-2.12	-1.91
Adenine Sugar Chain B	-0.30	-5.62

Conclusions

The integrated results from molecular docking calculations using Glide program and interaction energy based on quantum chemical calculations should be helpful for understanding the binding modes and the important interactions of azanaphthoquinone annelated pyrrole derivatives in DNA binding site. These results are fruitful information for improving the binding efficiency of these inhibitors toward to gain new and more cytotoxic activity anti-cancer agents.

References

[1] N. Pongprom, G. M ller, P. Schmidt, W. Holzer, H. Spreitzer, *Monatsh Chem.* 140 (2009), pp.309–313.
[2] K. Shanab, N. Pongprom, E. Wulz, W. Holzer, H. Spreitzer, P. Schmidt, B. Aicher, G. Muller, E. Guntherb, *Bio. Med. Chem. Lett.*, 17 (2007), pp.6091–6095

.

Molecular modeling and quantum chemical calculations of InhA inhibitors as anti-tuberculosis agents in class of arylamide

N. Kutiya[1], A. Punkvang[1], A. Kumkong[1], C. Kheawsod[1], P. Saparpakorn[2], S. Hannongbua[2], P. Wolschann[3] and P. Pungpo[1*]

[1]Department of Chemistry, Faculty of Science, Ubonratchathai University, Ubonratchathani, Thailand
[2]Department of Chemistry, Faculty of Science, Kasetsart University, Bangkok, Thailand
[3]Institute for Theoretical Chemistry, University of Vienna, A-1090 Vienna, Austria

[*]E-mail: pornpan_ubu@yahoo.com,

Abstract: The emergence of drug resistant strains and the synergy between tuberculosis (TB) and HIV are the major problems for tuberculosis treatment. The enoyl-ACP reductase enzyme (InhA) from Mycrobacterium tuberculosis is the favoable target for tuberculosis treatment. Arylamides are the novel inhibitors of InhA that can directly bind in InhA binding pocket. To elucidate the important interactions of arylamides in InhA binding pocket, molecular docking calculations using Autodock 3.0.5 and Gold programs were performed. Moreover, quantum chemical calculations based on MP/6-31G(d) method was also applied. The results shows that molecular docking calculations with Autodock 3.0.5 and Gold programs could nicely model the potential binding modes of arylamides with RMSD values less than 1 Å. The important interactions between arylamides and InhA were carried out based on molecular docking calculations and quantum chemical calculations. The obtained results from both methods agree well that two hydrogen bonding interactions between carbonyl group of arylamide with hydroxyl group of Tyr158 and nicotinamide ribose are the crucial interaction for binding in InhA enzyme. Therefore, hhese results are beneficial for improving the binding efficiency of these inhibitors leading to gain new more potent InhA inhibitors.

Introduction

An enoyl-ACP reductase (InhA) from *M.tuberbulosis* has been validated as the primary molecular target of isoniazid (INH), the frontline drug for tuberculosis [1-3]. INH requires the activation process from KatG enzyme to generate InhA inhibitor form. The number of the strains resistant to INH arises from mutations in KatG [4]. Therefore, the development of direct InhA inhibitors should solve the INH-resistant problem. Arylamides, a novel series of direct InhA inhibitors, can bypass the mycobacterial enzymatic activation [5]. To evaluate the specific interactions of arylamides in InhA binding pocket, molecular docking calculations using Autodock 3.0.5 and Gold programs and quantum chemical calculations based on MP2/6-31G(d) method have been performed in this work.

Materials and Methods

The X-ray structures of arylamide B3 in InhA enzyme (2NSD pdb code) was selected for the molecular docking calculations. All arylamide structures were constructed by Gaussview 3.07 program and then, partially optimized by HF/3-21G method. Gold and Autodock 3.05 programs were employed to investigate the potential binding orientations of all arylamide derivatives in InhA binding pocket. To calculate interaction energies formed between arylamides and the surrounding amino acids, single point calculations at MP2/6-31G (d) levels of theory by using Gaussian03 program were performed.

Results and Discussion

Molecular docking results

RMSD values between the docked conformation and the X-ray structure of arylamide obtained from Autodock 3.05 and Gold programs are 1.07 and 0.71 Å. This result shows that Gold program is more efficient to simulate the binding mode of arylamide than Autodock 3.05. Therefore, the binding modes of arylamides obtained from Gold program were selected to study binding interactions of these compounds. Based on the binding modes obtained from docking calculations, carbonyl amide group of all arylamides form two hydrogen bonds with hydroxyl group of Tyr158 and hydroxyl group on nicotinamide ribose of NADH. This result implies that two hydrogen bonds of carbonyl amide group are crucial for binding of arylamide in InhA binding pocket. Moreover, the hydrophobic interactions of arylamide with Ala157, Pro156, Ile215, Leu218, Pro193, Val203, Met199, Met232 and Glu219 also are helpful for binding of inhibitors.

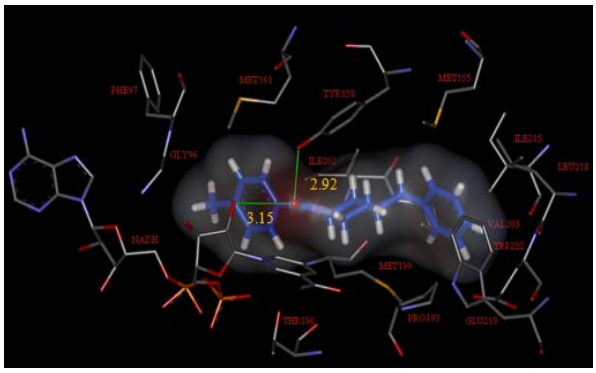

Figure 1 Docked conformation of arylamide B3 (IC_{50}= 5.16 µM) in InhA binding pocket

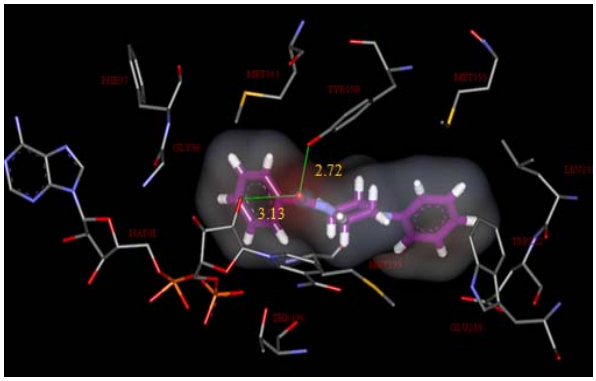

Figure 2 Docked conformation of arylamide A1 (IC_{50} = 38.86 µM) in InhA binding pocket

Quantum chemical calculation results

Interaction energies of two arylamides, A1 and B3, in InhA were calculated. Two compounds show the high attractive energy with Tyr158 and nicotinamide ribose corresponding with strong two hydrogen bond interactions. This result confirms the importance of these interactions for arylamide binding which correlates well with the docking results. Moreover, more Van der Waal interaction with Gly96 and Phe97 also important for inhibitory activity. Arylamide B3 shows higher attractive energies with Gly96 and Phe97 than those of arylamide A1 corresponding with the higher activity of arylamide B3. Therefore, more Van der Waal interaction of the substituent on left aromatic ring of arylamide may enhance its inhibitory activity.

Regarding on the right phenyl ring, interaction energies of this part and the hydrophobic residues of Ile215, Leu218, Val203 and Phe149 show attractive interactions responding well with the hydrophobic interactions of the right phenyl ring.

Table 1 Calculated interaction energy between aryamides A1 and B3 and amino acids in InhA binding pocket

Amino Acid	Interaction energy (kcal/mol)	
	A1	B3
Ala198	-0.92	-1.05
Leu218	-1.35	-2.60
Met161	-2.11	-2.10
Met199	-3.05	-3.00
Phe149	-4.48	-7.24
Glu219	-9.03	-4.78
Val203	-1.26	-1.10
Gly96	-1.10	-2.15
Ile215	-2.55	-1.15
Lys165	-9.75	-10.53
Phe97	-0.59	-1.51
Pro193	-3.01	-2.75
Thr196	-0.83	-0.59
Tyr158	-12.58	-13.65
nicotinamide ribose	-11.46	-12.31

Conclusions

Molecular docking calculations using Gold program show more efficient to simulate the binding mode of arylamide than Autodock 3.05. The obtained results from molecular docking calculations using Gold program and interaction energy based on quantum chemical calculations provide the significant insight into inhibitor-enzyme interactions of arylamide derivatives. Hydrogen bonding interactions of these inhibitors with Tyr158 and nicotinamide ribose are important for arylamide binding. Therefore, these results are fruitful information for improving the binding efficiency of these inhibitors toward to gain new and more potent anti-tuberculosis agents.

References

[1] L. Kremer, L.G. Dover, H.R. Morbidoni, C. Vilche`ze, W.N. Maughan, A. Baulard, S.C. Tu, N. Honore, V. Deretic, J.C. Sacchettini, C. Locht, W.R. Jacobs Jr. and G.S. Besra, *J. Biol. Chem.* 278(2003), pp. 20547–20554.

[2] M.H. Larsen, C. Vilche`ze, L. Kremer, G.S. Besra, L. Parsons, M. Salfinger, L. Heifets, M.H. Hazbon, D. Alland, J.C. Sacchettini, W.R. Jacobs Jr., *Mol. Microbiol.* 46(2002), pp. 453–466.
[3] A. Que´mard, J.C. Sacchettini, A. Dessen, C. Vilcheze, R. Bittman, W.R. Jacobs Jr., J.S. Blanchard, *Biochemistry.* 34(1995), pp. 8235–8241.L.
[4] A. Argyrou , M.W. Vetting, J.S. Blanchard, *J. Am. Chem. Soc.* 129(2007), pp. 9582-9583.
[5] X. He, A, Alian, PR.Ortiz de Montellano, *Bioorg. Med. Chem.* 15(2007), pp. 6649-6658.

Synthesis and characterization of enlarged pore zeolite beta by mixed template system

N. Wongsawatgul[1]*, S. Chaianansutcharit[2, 3]

[1] Program of Petrochemistry and Polymer Science, Faculty of Science, Chulalongkorn University, Bangkok, Thailand 10330
[2] Department of Chemistry, Faculty of Science, Chulalongkorn University, Bangkok, Thailand 10330
[3] Center for Petroleum, Petrochemicals and Advanced Materials, Chulalongkorn University, Bangkok, Thailand 10330

* Corresponding Author E-Mail Address: hachiku_z@hotmail.com

Abstract: The enlarged pore zeolite beta (en-h-BEA) was synthesized under hydrothermal condition from hexagonal mesoporous silica (HMS). The effects of mixed template, TEAOH-HDA, and crystallization time were investigated. The samples were characterized by powder X-ray diffraction (XRD), nitrogen adsorption analysis, scanning electron microscopy (SEM) and ^{27}Al-NMR techniques. The analysis data indicated that enlarged pore zeolite beta can be prepared and ZSM-12 is a coexisting phase. The latter phase was predominated with increasing the crystallization time. The synthesized samples were tested for catalytic cracking of heavy fuel oil to produce lighter hydrocarbon fuel.

Introduction

Zeolite beta was first synthesized in 1967 [1], possessed a 3-dimensional system of interconnected channels with two different pore sizes (5.5x5.5 Å and 6.4x7.6 Å diameters). It has high acidiy and thermal stability, so this material can be a potential catalyst for fluid catalytic cracking [2], hydrothreating, and aromatic alkylation with alkenes [3]. In spite of zeolite beta is well-defined large microporosity, it cannot be applied to treat the relatively large molecules present in heavy fuel oils [4]. In 1992 Mobil Oil researchers announced the synthesis of the first broad family of mesoporous molecular sieves (denoted M41S) [5]. Recently, there are many families of mesoporous materials, such as, MCM-41, HMS (Hexagonal Mesoporous Silica) and SBA-15, with hexagonal structure. These materials exhibit large pore volumes and a monomodal narrow distribution of pore sizes.

Although, mesopores are higher accessibility of reactants as compared to zeolites and are capable of cracking large size molecules, these materials have low acidity and hydrothermal stability because of their crystallinity in pore walls and frameworks. That limits their use as catalysts in a wide range of industrial processes and reactions.

Since, there has been increasing interest in expanding the pore size of zeolite materials from micropore to mesopore region for fundamental studies and applied in oil industry [6]. This research is aimed on synthesizing enlarge pore size zeolite beta with HMS (Hexagonal Mesoporous Silica), as silica source and using mixed template, TEAOH-HDA, by hydrothermal method. By controling the operation condition, such as crystallization time, the materials will be achieved and tested a beneficial performance as catalyst in cracking process of heavy fuel oil (HFO).

Materials and Methods

Firstly, HMS, a starting material, was obtained by mixing hexadecylamine (HDA, 0.05 mole) with EtOH (1.66 mole) and water (11.01 mole) under stirring until it becomes a clear mixture. Then tetraethyl orthosilicate (TEOS, 0.20 mole) and water (8.99 mole) were added to the mixture in stirred to age for 20 h with gel mole composition of $1SiO_2$: 0.25 HDA: 8.3 EtOH: 100 H_2O. After that the HMS product was filtered, washed with water to neutral pH value and dried at room temperature, as-synthesized HMS was obtained. After calcination at 550°C for 10 h, the calcined HMS was produced. It was then used as silica source for synthesizing enlarged pore zeolite beta.

The enlarged pore zeloite beta (denote en-h-BEA) was prepared by modifying the method from Aguado *et al*. [7] with Si/Al ratio of 60. Calcined HMS (0.20 mole) were hydrolyzed with HCl ($6.0x10^{-4}$ mole) under stirring for 45 min. Then the mixture was added with a homogeneous mixture of HDA ($2.0x10^{-3}$ mole), EtOH (0.067 mole) and water (0.45 mole). After that the mixture was converted into a cogel by dropwise addition of tetraethylammonium hydroxide (TEAOH) ($2.0x10^{-3}$ mole) under continuous stirring. Then the cogel was dried overnight at a temperature of 110°C to obtain xerogel. In the crystallization stage, aluminium isopropoxide (AIP, $3.33x10^{-3}$ mole) was mixed with TEAOH (0.06 mole) at 0°C and stirred, denoted Al-TEAOH solution. The other homogeneous mixture of HDA (0.01 mole), EtOH (0.34 mole) and water (2.23 mole) was poured into the xerogel under stirring. After that Al-TEAOH solution was slowly added into the mixture at 0°C, and stirred for 18 h to obtain gel mole composition of $1SiO_2$: $0.0083Al_2O_3$: 0.3148TEAOH: 0.06HDA: 1.685EtOH: $16.965H_2O$. Then the gel was charged into Teflon-lined autoclaves and crystallized at 140°C for 6-15 days. The crystalline product was separated by centrifugation, washed with water to neutral pH value and dried at 110°C to obtain as-synthesized enlarged pore zeloite beta. After calcination at 550°C for 10 h, the calcined enlarged pore zeolite beta was obtained.

The zeolite beta prepared from HMS (denote h-BEA) and the comparative zeolite beta (denote BEA) were also synthesized using Aguado's method [7] with

the same Si/Al ratio and gel mole composition of $1SiO_2$: 0.0083 Al_2O_3: 0.37 TEAOH: 16 H_2O. By substituting TEOS, a silics source in preparation of xerogel in BEA, with HMS the h-BEA was obtained.

To determine the structure of HMS, BEA, h-BEA and en-h-BEA, X-ray diffraction patterns were recorded. The powder X-ray diffraction measurements were carried out by a Rigaku, Dmax 2200/Ultima$^+$ diffractometer using a monochromator and Cu Kα radiation. The tube voltage and current were set at 40 kV and 30 mA, respectively. XRD patterns were collected in the 2-theta ranges from 5 to 50 degree with scan speed of 5 degree min^{-1} for zeloite beta and from 1.2 to 10 degree applied for HMS.

Nitrogen adsorption isotherm measurements were carried out using a BEL Japan BELSORP-mini 28SP adsorptometer for characterization of catalyst porosity. Before analysis, each calcined sample was degassed at 400°C for 3 h under vacuum. Adsorption isotherms were measured at 77 K (liquid nitrogen) using nitrogen of 99.999% purity as an adsorbate.

Morphology and particles size of BEA and en-h-BEA samples were determined by scanning electron microscope (SEM), on JSM-5410 LV scanning electron microscope with 15 kV of acceleration voltage.

To test the catalytic activity of enlarged pore size zeolite beta, heavy fuel oil (HFO) was selected as feedstock. The catalytic cracking was performed in a glass reactor. The reactions were carried out at 380°C with a heating rate of 20°C/min and the temperature was kept constant for 40 min. The pure nitrogen gas was purged through the reactors with a flow rate of 20 ml/min during the experiment. In each experiment, 1.00 g of catalyst was loaded for 10.00 g of HFO. For thermal reaction, no catalysts were added.

Results and Discussion

Fig. 1 demonstrated XRD patterns of calcined sample: HMS, zeolite beta and enlarged pore zeolite beta. The XRD pattern of calcined HMS, as a silica source, was shown in Fig. 1 (inset). HMS has a prominent diffraction peak of (100) at the 2θ range of 1.5-2.0° indicating the hexagonal mesoporous structure of HMS, as reported by Tanev *et al.* [8]. The h-BEA illustrated a broad diffraction peak of (101) plane at 2θ of 7.5°. The most intense sharp peak at 22.4° was assigned to the diffraction of (302) plane, suggesting the high craystallinity of the zeolite beta [7]. The h-BEA also did not show (100) plane, which is the characteristic peak of HMS at low 2θ angle, suggesting that the HMS structure was completely changed to zeolite beta structure. Thus, it is concluded that zeolite beta can be prepared by using HMS as silica source.

The enlarged pore zeolite beta prepared from HMS and the mixed template was investigated by varying the crystallization time for 6, 9, 12, and 15 days (denoted en-h-BEA-9, en-h-BEA-12 and en-h-BEA-15, respectively). The XRD patterns of en-h-BEA samples were also illustrated in Fig. 1. After crystallization for 9 days a crystalline enlarged pore zeolite beta was obtained. With increasing crystallization time, the crystallization of zeolite beta was rapidly taken place by ZSM-12 after 12 days and increasing more crystallinity in 15 days. The phase change was indicated by a splitting of the beta peak at 7.5° to peaks at 7.5, 7.6, 8.9°, a fading of the peak at 22.4°, and an emerging of a new peak at 21°. With more crystallization time there is an increase in the crystallinity of ZSM-12 phase [9].

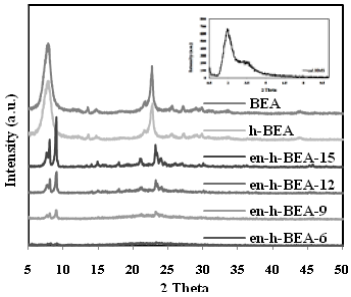

Figure 1. XRD patterns of calcined HMS, BEA, h-BEA, en-h-BEA-9, en-h-BEA-12 and en-h-BEA-15.

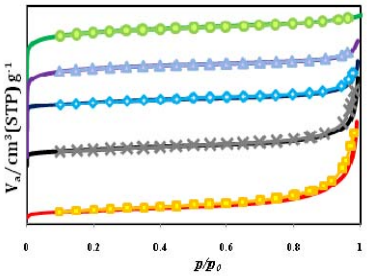

Figure 2. N_2 sorption isotherms of (a) BEA, (b) h-BEA, (c) en-h-BEA-15, (d) en-h-BEA-12 and (e) en-h-BEA-9.

The N_2 sorption isotherms of en-h-BEA-9, en-h-BEA-12 and en-h-BEA-15, compared with BEA and h-BEA, were shown in Fig. 2. It can be seen that both en-h-BEA-9 and en-h-BEA-12 samples showed an increase in adsorbed nitrogen and hysteresis loop when the relative pressure (p/p_0) was higher than 0.8, which means that there are monolayer and multilayer sorption characteristics, processed micropore and mesopore characteristics [10]. While BEA, h-BEA and en-h-BEA-15 gave N_2 sorption isotherms type I with high adsorption at low relative pressure (p/p_0) and a plateau at relative pressure higher than 0.02, which is the characteristic of micropore.

Table 1 presents specific surface area, diameter and total pore volume, calculated from a BET plot of adsorption isotherms. The BEA exhibits specific surface area 743 m^{-1}g^{-1} and pore diameter 0.59 nm. For en-h-BEA, even though pore diameter of each sample was increased and larger than BEA, the specific surface area of BET model was decreased. This result was caused by ZSM-12 coexisting phase. ZSM-12 consists of 12-membered ring pore openings of 5.7 x 6.1 Å in size (large pore zeolite) like BEA but uni-dimensional channels. These properties lead specific surface area of en-h-BEA to decrease. Notice that the

samples with mixed template system were decreased in the average pore diameter when increased crystallization time.

Scanning electron micrographs of HMS, en-h-BEA and BEA were shown in Fig. 3. Morphology of HMS exhibits an agglomeration of semi-crystalline material, whereas BEA presents a uniform round granular and shape. The en-h-BEA-9, en-h-BEA-12 and en-h-BEA-15 samples exhibit mixed morphology between crystalline particles and amorphous materials. However, the agglomerations of small amorphous particles were mainly observed. With more crystallization time, their morphology was become to increase in crystallinity. There were in corresponding with their medium intensity XRD peak.

Generally, the mechanism for zeolite synthesis is commonly understood as a solution-mediated process with two main steps: nucleation through the formation of very small crystalline entities and crystal growth through the progressive incorporation of soluble species around these nuclei previously formed. Therefore, when the temperature is raised during hydrothermal treatment in the mixed template system, secondary building units of zeolite beta can be further developed to be nuclei and transformed into small zeolite crystals [12]. Some HDA template can be enriched at the liquid-solid interface through the H-bond interaction between the neutral inorganic precursor and the surfactant head group. Obviously, the crystal growth process in mixed template system is more difficult than that in single template system. In addition, a H-bond interaction between the inorganic precursor and the surfactant head group existing in the synthesis media may weaken the incorporation abilities of template and inorganic precursor during the crystallization. All mentioned above may prevent the zeolite crystals growing.

Catalytic cracking of HFO over BEA, en-h-BEA catalysts, compared with thermal (no catalyst), were conducted at 380°C. The conversions, presented in Table 2, have been calculated into account only the products those leave the reactor with the N_2 stream. The residue remaining inside the reactor has not been considered as a reaction product.

The amounts of gas and liquid products increased with the all of enlarged pore catalysts, while the amounts of residue fractions decreased. This may be due to the acidity of catalyst. In addition, h-BEA and en-h-BEA gave higher liquid yield than BEA. That was affected by pore size of catalyst. With increasing pore size diameter, large molecules of HFO can diffuse through the pore and degrade in pore to increase liquid product. Note that, liquid yield of en-h-BEA-15 was lower than h-BEA, whereas pore size of en-h-BEA-15 was larger than h-BEA. It is probably because en-h-BEA-15 has small pore volume. So, the large diffused molecules cannot degrade in limited pore volume.

Table 1. Properties of materials.

Zeolite	S_{BET} (m^2g^{-1})	Pore diameter (nm)	Micropore volume (cm^3g^{-1})
BEA	743	0.59	170.84
h-BEA	721	0.62	165.55
en-h-BEA-15	245	0.66	21.62
en-h-BEA-12	164	0.63	37.76
en-h-BEA-9	94	0.63	56.31

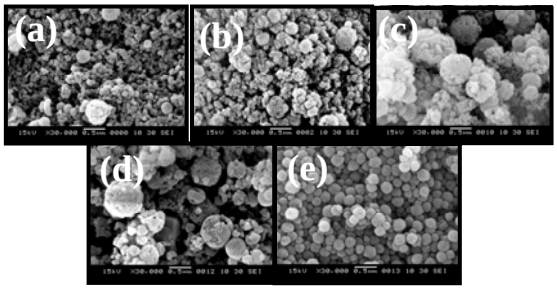

Figure 3. SEM image of (a) Si-HMS, (b) en-h-BEA-9, (c) en-h-BEA-12, (d) en-h-BEA-15 and (e) BEA.

The liquid product was then distillated to separate light oil from heavy oil. It was found that en-h-BEA-9, en-h-BEA-12 and en-h-BEA-15 catalysts produce heavy oil and less distillate oil, comparing with BEA and h-BEA, which produces more distillate oil. With increasing pore size diameter, the selectivity to distillate oil is decreased.

The compositions of light oil and heavy oil were analyzed by GC. It was found that light oil is mainly composed of C_5-C_{11} hydrocarbons or gasoline range, while heavy oil is distributed in C_{10}-C_{18}, or kerosene range. Kerosene can be used as fuel for jet engines, tractors and starting material for making other products. It can conclude that the enlarged pore size zeolite beta had higher ability for cracking large molecules into liquid more than BEA.

Table 2. Catalytic cracking of heavy fuel oil over various catalysts

	thermal	BEA	h-BEA	en-h-BEA-9	en-h-BEA-12	en-h-BEA-15
% Conversion (%wt) *	44.55	55.79	60.97	66.52	63.49	61.17
% Yield (%wt) *						
1. Gas	10.74	12.79	14.54	17.29	16.33	15.34
2. Liquid	33.82	43.01	46.43	49.22	47.15	45.53
- % Distillate oil	0.42	1.83	3.62	0.17	0.32	0.60
- % Heavy oil	33.40	41.18	42.80	49.05	46.83	49.93
3. Residue	55.44	44.21	39.03	33.48	36.51	38.17
Liquid fraction density (g/cm^3)	0.83	0.83	0.85	0.85	0.84	0.85

Condition: 10 wt% of catalyst to HFO, N_2 flow of 20 cm^3/min, reaction temperature of 380ºC, and reaction time of 40 min. *Deviation within ±0.50 for conversion, ±0.20 for yield of gas fraction, ±0.60 for yield of liquid fraction, and ±0.50 for yield of residue.

Conclusions

In summary, the enlarged pore size zeolite beta has been prepared in a mixed template system: TEAOH-HDA by hydrothermal method using HMS as silica source. The pore diameter can be controlled by varying crystallization time under suitable conditions. When applied in catalytic cracking of HFO, enlarged pore size zeolite beta catalysts enhanced the cracking of large molecules in heavy fuel oil to lighter hydrocarbon liquid in range of kerosene.

References

[1] Wadlinger, R. L., Kerr, G. T., & Rosinski, E. J. (1967). A crystalline zeolite with improved adsorption and catalytic properties. *U.S. Patent*, 3308069.

[2] Zhang, H., & Li, Y. (2008). Preparation and characterization of Beta/MCM-41 composite zeolite with a stepwise-distributed pore structure. *Powder Technology,* 183, 73-78.

[3] Reddy, K. S. N., Rao, B. S., & Shiralkar, V. P. (1993). Alkylation of benzene with isopropanol over zeolite beta. *Appl. Catal.,* 95(1), 53-63.

[4] Groen, J. C., Abelló, S., Villaescusa, L. A., & Pérez-Ramírez, J., 2008. A new family of mesoporous molecular mieves prepared with liquid crystal templates. *Microporous and Mesoporous Materials*, 114, 93–102.

[5] Beck, J. S., Vartuli, J. C., Roth, W. J., Leonowicz, M. E., Kresge, C. T., Schmitt, K. K., Chu, C. TW., Olson, D. H., Sheppard, E. W., McCullen, S. B., Higgins, J. B., & Schlenker J. L., (1992). A new family of mesoporous molecular mieves prepared with liquid crystal templates. *J. Am. Chem. Soc.*, 114, 10834-10843.

[6] Zhao, L., Shen, B., Gao, J., & Xu C., (2008). Investigation on the mechanism of diffusion in mesopore structured ZSM-5 and improved heavy oil conversion. *Journal of Catalysis*, 258, 228–234

[7] Aguado, J., Serrano, D. P., Escola, J. M., Garagorri, E., & Fernández, J. A., 2000. Catalytic conversion of polyolefins into fuels over zeolite. *Polymer Degradation and Stability*, 69, 11-16.

[8] Tanev, P. T., & Pinnavaia, T. J., (1995). A neutral templating route to mesoporous molecular sieves. *Science*, 267, 865-867.

[9] Gopal, S., Yoo, K., & Smirniotis P.G., (2001). Synthesis of Al-rich ZSM-12 using TEAOH as template. *Microporous and Mesoporous material*, 49, 149-156.

[10] Wei, X., & Smirniotis P. G., (2006). Development and characterization of mesoporosity in ZSM-12 by desilication. *Microporous and Mesoporous material*, 97, 53-63.

[11] Kong, L., Chen, H., Tai J., Shen J., Zhang, S., & Chen, J., (2009). Synthesis of small crystal zeolite beta in a biphasic H_2O–CTAB–alcohol system. *Materials Letters*, 63, 343–345

Structural characterization and environmental application of natural zeolites in removal of arsenic ions from aqueous solution

P. Pungpo[1*], M. Puengpan[1], C. Kortprom[1], S, Pakapol[1], U. Traklang[1], P. khamsri[1], T. Siriream[1], S. Lumlong[1], C. kanapan[1], M. Kacha[1], D. Sattayaku[1], M. Projuabsuk[1], T. Panyathanmaporn[2] and U. Onthong[3]

[1]Department of Chemistry, Faculty of Science, Ubonratchathani University, Ubon Ratchathani Thailand
[2] National Metal and Materials Technology Center, 114 Thailand Science Park, Paholyothin Rd, Klong 1, Klong Luang, Pathumthani, Thailand
[3]Department of Chemistry, Faculty of Science, Taksin University, Songkla Thailand

*E-mail: pornpan_ubu@yahoo.com, Tel: +66-4528-8379

Abstract: In the present study, Environmental Application of Natural Zeolites in Arsenic (V) Adsorption from Aqueous Solution. Four natural zeolites, Mordenite, Kaolinite, Kaolinite-1MD and Clinoptilolite, have been applied to adsorp arsenic (V) ions form sample water on laboratory. The results show that natural zeolites of Kaolinite-1MD and Kaolinite are successfully used to significantly reduce arsenic (V) ions form sample water. The adsorption efficiency are 79.17% and 68.19% respectively, at the initial concentration of 5 mg/L and an hour adsorption time and 50 g/L of the ratio of zeolite usage per water sample volume. The optimum of the ratio of zeolite per water sample is 50 g/L with one hour optimum adsorption time. The increase of arsenic (V) ions initial concentration from 100, 200, 300, 400 and 500 µg/L, respectively, results in efficient adsorption increase. Based on the adsorption capacities isotherm of arsenic ion, the obtained isotherm corresponds well to the Freundlich isotherm more than the Langmiur isotherms. These natural zeolites, Kaolinite-1MD and Kaolinite are recommended adsorption for high removal arsenic (V) ions from wastewater with low cost treatment and environmentally friendly chemical processes.

Introduction

Arsenic exists ubiquitously and it is well known that arsenic is toxic to humans [1]. Various minerals include arsenic, but arsenic contamination in groundwater is mainly caused by agricultural activities and industrial wastes [2]. Recently, arsenic contamination has come into the spotlight, because of its negative impact on humans and the environment. There will be an increase in the global cycling of arsenic due to the progressive industrialization of developing nations, which will pose potentially serious environmental problems throughout the world. Zeolites have a three-dimensional structure constituted by $(Si,Al)O_4$ tetrahedra connected by all their oxygen vertices forming channels where H_2O molecules and exchangeable cations counterbalancing the negative charge generated from the isomorphous substitution are present. Zeolites have many applications, mainly based on their structural characteristics, their sorbent properties and their relatively high specific surface area. The objectives of the present work are to study the applicability of natural zeolites on removal of arsenic ion from aqueous solution.

Materials and Methods

Four natural zeolites were applied for removal of arsenic ions from aqueous solution. Figure 1 shows the appearance of natural zeolites, defined as no. A, B, C and D, respectively, used in this study. For characterization of natural zeolites, the X-ray diffraction (XRD) patterns were acquired on a Philips X'Pert MPD, using CuK_α radiation source (λ=1.54 nm) at 45 kV and 35 mA. Each sample was measured in the range of $5^o \leq 2\theta \leq 120^o$ with scanning rate 0.04 2θ/sec at room temperature. The X-ray fluorescence (XRF) were performed on a Philips MagiX WDXRF. For water samples used in this study, the 10 ppm concentration of ammonium solution was prepared in de-ionized water. To measure the exact concentration of the metal ions before and after treatments by zeolite, atomic absorption spectroscopy (Perkin Elmer Model Analyst 800) was used.

Figure 1. Natural zeolites, no.A,B,C,D, respectively.

Results and Discussion

Structural characterization of natural zeolites

In order to characterize the structure of four natural zeolites, XRD analysis was performed. The XRD pattern is shown in Figure 2. The obtained XRD patterns were compared with the patterns given in the ICDB number. The results reveal that the profiles correspond to Mordenite, Kaolinite, Kaolinite-1MD

and Clinoptilolite compounds for natural zeolites no.A, no.B, no.C and no.D, respectively. For XFR results, the elemental compositions of the zeolites were analyzed. It was found that the information obtained XRF analysis could support the structural data derived by the XRD pattern.

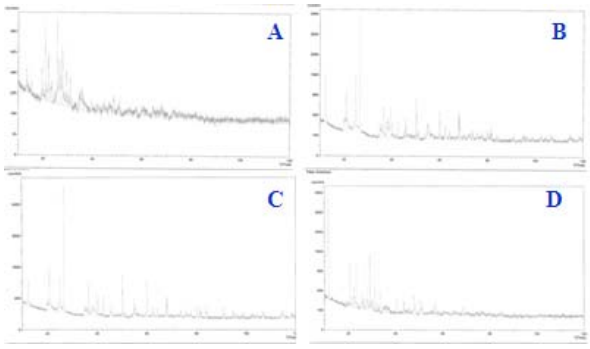

Figure 2. X-ray diffraction pattern of four natural zeolites, no.A,B,C,D, respectively.

Table 1. The element compositions of four natural zeolites, derived by XRF spectroscopy.

Elements	Concentration (%)			
	No.A	No.B	No.C	No.D
O	49.47	50.36	50.80	50.32
Si	33.52	28.37	31.34	24.36
Al	6.726	18.31	15.18	4.829
Ca	4.405	0.0561	0.1478	7.857
K	2.451	0.5501	0.4484	1.861
Fe	1.394	0.9589	0.7995	0.8847
S	1.003	<<	0.06787	9.140
P	0.4226	0.4668	0.4590	0.3131
Mg	0.3719	<<	<<	0.3153
Ti	0.1810	0.8301	0.5987	0.1172
Mn	0.05526	-	-	<<
Au	0.0000	0.0000	0.0000	0.0000
Zr	0.0000	0.0000	0.0000	0.0000
Sr	0.0000	-	-	0.0000
Rb	0.0000	0.0000	0.0000	-
Se	0.0000	0.0000	0.0000	0.0000
Y	<<	<<	-	-
Ce	-	-	-	-
Cl	-	<<	-	-

The efficiency of aresenic removal using natural zeolites

As the metal removal efficiency was affected by adsorption time and ratio of zeolite usage per water sample volume, the optimal parameters for the adsorption have to be determined. Modernite was selected to use for the adsorption preliminary study. To study the effect of zeolite amount, Kaolinite-1MD was weighted and varied from 1.00, 1.50, 2.00, 2.50 and 3.00 g. Then, all suspension were carried out in 50 mL of each 5 mg/L metal solution. All batch adsorptions were performed for an hour. The removal efficiency of arsenic ion from aqueous solutions is 64.5%, 66.26%, 66.59%, 74.53% and 79.19%, respectively. The result showed that 2.5 g of Kaolinite-1MD was optimum amount for the arsenic adsorption. To study the effect of contact time for adsorption, the natural zeolite was weighted as the optimum amount obtained from from the previous step. Then, all suspension were carried out in 50 mL of metal solution. All batch adsorptions were varied from 1, 2, 6 and 12 hours, respectively. The arsenic ion removal efficiency of 69.21 %, 75.07 % and 75.46 % were derived, respectively. The optimum contact time for arsenic adsorption is an hour. Therefore, an hour adsorption time and 50 g/L of the ratio of zeolite per water sample are chosen as optimal adsorption parameters for further step.

Four natural zeolites, namely, Mordenite, Kaolinite, Kaolinite-1MD and Clinoptilolite were used as adsorbents for arsenic ions removal from sample water. Based on adsorption parameters derived from the preliminary study with an hour adsorption time and 50 g/L of the ratio of zeolite amount per water sample volumn, the results show that arsenic ions with concentration of 5 mg/L were adsorped from water samples with average removal efficiency of 56.94%, 68.19%, 79.17%, and 56.29 %, respectively. The order of removal efficiency can be given as B, Kaolinite-1MD > C, Kaolinite > A, Mordenite ≈ D, Clinoptiolit.

Adsorption isotherm of arsenic ions from aqueous solution on the natural zeolites

The sorption data of arsenic by the natural zeolite have been subjected to two sorption isotherms, namely, Freundlich and Langmuir isotherms to study the effect of initial metal ion concentration for adsorption behavior onto natural zeolite. Kaolinite-1MD was used as the highest effective adsorbent in this study. The results show that the Freundlich model effectively described the sorption data with high R^2 values (0.994) compared with that obtained from Langmuir adsorption isotherm. It is clearly seen that Freundlich have a better correspondence with the experimental findings rater that Langmuir isotherm.

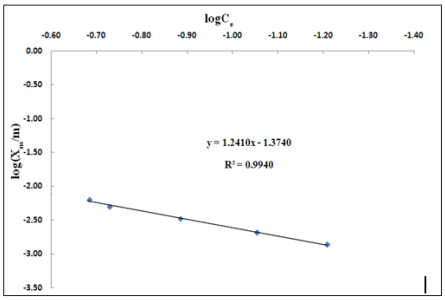

Figure 3. Freundlich adsorption isotherm for *aresenic* ions on the natural zeolite Kaolinite-1MD

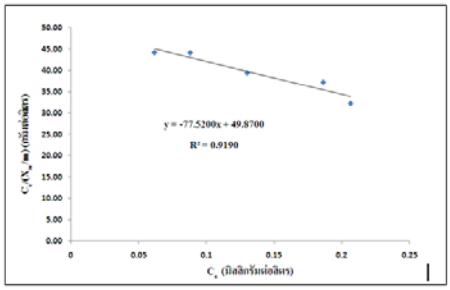

Figure 4. Langmuir adsorption isotherm for *aresenic* ions on the natural zeolite Kaolinite-1MD

Conclusion

In summary, the fundamental study on arsenic removal efficiency from sample water based on models on laboratory scale by using natural zeolites as adsorbents were reported. Kaolinite-1MD and Kaolinite shows very high effectiveness of the natural adsorbent. The results can suggest that the use of the natural zeolites are capable of arsenic treatment from industrial wastewater. Moreover, the natural zeolite is great potential adsorbents due to its availability and its low cost.

Acknowledgements

Research supports from National Research Council of Thailand and Faculty of Science, Ubonratchathani University are gratefully acknowledged.

References

[1] Y. Li, J. Wang, Z. Luan, Z. Liang,, *J. Hazardous Materials* , 177 (2010), pp. 131–137.
[2] Buschmann, J.; Berg, M.; Stengel, C.; Sampson, M.L. *J. Envir. Science & Tech.*, 41(2007), pp.2146-2152.
[3] Inglezakis, V.J.; Stylianou, M.A.; Gkantzou, D.; Loizidou, M.D. *J. Desalination*, 210(2007), pp. 248-256.
[4] Erdem, E.; Karapinar, N.; Donat, R. *J. Colloid and Interface Science*, 280(2004), pp. 309-314.
[5] Y. Xu, T. Nakajima, A. Ohki, *J. Hazardous Materials* , B92 (2002), pp. 275–287.
[6] C.Jeona, K. Baeka, J. Parkb, Y. Ohc, S.D. Leec, *J. Hazardous Materials*, 163(2009), pp. 804–808.

Structural characterization of natural zeolites and its application in adsorption of ammonium ion from aqueous solution at laboratory scale

M. Prajuabsuk[1], L. Promlek[1], P. Wangkapan[1], W. Anomnual[1], N. Napong[1], C. kanapan[1], D. Sattayakul[1], R. Tipakontitikul[2], A. Niyompan[2], U. Onthong[3], T. Panyathanmaporn[4] and P. Pungpo[1]

[1]Department of Chemistry, Faculty of Science, Ubonratchathani University, Ubon Ratchathani Thailand
[2]Department of Physics, Faculty of Science, Ubonratchathani University, Ubon Ratchathani Thailand
[3] Department of Chemistry, Faculty of Science, Taksin University, Songkla Thailand
[4]National Metal and Materials Technology Center, 114 Thailand Science Park, Paholyothin Rd, Klong 1, Klong Luang, Pathumthani, Thailand

*E-mail: malee_pr@sci.ubu.ac.th, Tel: +66-4528-8379

Abstract: Three natural zeolites, namely, Kaolinite 1Md, Kaolinite, Clinoptilolite, have been applied to adsorp ammonium ion from aqueous solution at laboratory scale using batch method. The results show that natural zeolites of Kaolinite 1Md, Kaolinite and Clinoptilolite are successfully used to reduce significantly ammonium ion with the adsorption efficiency of 79.46%, 77.25% and 50.78%, respectively, at the initial concentration of 10 mg/L, one hour adsorption time and 40 g/L of the ratio of zeolites usage per water sample volume. The optimum conditions for adsorption of ammonium ionis an hour for Kaolinite-1Md. The optimunm ratio of Kaolinite-1Md per aqueous solution is40 g/L. Based on the adsorption isotherm studies of ammonium ions using the natural zeolites, the obtained isotherm corresponds well to the Langmuir isotherms more than the Freundlich isotherm. The results show that three natural zeolites are recommendable adsorbents for highly ammonium ion adsorption from wastewater treatment with economically and environmentally friendly chemical treatment processes

Introduction

Natural zeolites are low cost aluminosiliates, with a cage-like structure suitable for ion exchange due to isomorphous replacement of Al^{3+} with Si^{4+} in the structure, giving rise to a deficiency of position charge in the framework. This is balanced by mono and divalent exchangeable cations such as Na^+, K^+ and Mg^{2+}. Zeolites show extraordinary adsorption properties for metal cations, particularly, has high affinity for NH_4^+. The main objectives of the present work are to characterize natural zeolites and to study the applicability of the natural zeolites as an effective adsorbent of ammonia removal from aqueous solution. ted the application of Thai natural zeolites

Materials and Methods

Three natural zeolites, defined as no.1, 2 and 3, were applied for removal of arsenic ions from aqueous solution. For characterization of natural zeolites, the X-ray diffraction (XRD) patterns were acquired on a Philips X'Pert MPD, using CuK_α radiation source (λ=1.54 nm) at 45 kV and 35 mA. Each sample was measured in the range of $5^o \leq 2\theta \leq 120^o$ with scanning rate 0.04 2θ/sec at room temperature. The X-ray fluorescence (XRF) were performed on a Philips MagiX WDXRF. For water samples used in this study, the 10 ppm concentration of ammonium solution was prepared in de-ionized water. To measure the exact concentration of the metal ions before and after treatments by zeolite, atomic absorption spectroscopy (Perkin Elmer Model Analyst 800) was used.

Results and Discussion

Structural characterization of natural zeolites

In order to characterize the structure of three natural zeolites, XRD analysis was performed. The XRD pattern is shown in Figure 1. The obtained XRD patterns were compared with the patterns given in the ICDB number. The results reveal that the profiles correspond to Kaolinite-1MD, Kaolinite, and Clinoptilolite for natural zeolites no.1, no.2, and no.3 respectively. For XFR results, the elemental compositions of the zeolites were analyzed. It was found that the information obtained XRF analysis could support the structural data derived by the XRD pattern.

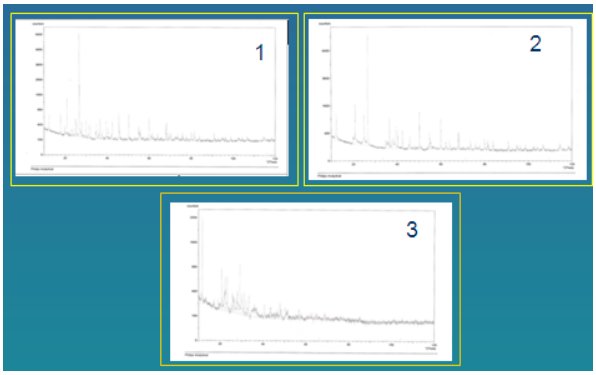

Figure 1. X-ray diffraction pattern of four natural zeolites, no.1,2 and 3, respectively.

Table 1. The element compositions of four natural zeolites, derived by XRF spectroscopy.

Elements	Concentration (%)		
	No.1	No.2	No.3
O	50.36	50.80	50.32
Si	28.37	31.34	24.36
Al	18.31	15.18	4.829
Ca	0.0561	0.1478	7.857
K	0.5501	0.4484	1.861
Fe	0.9589	0.7995	0.8847
S	<<	0.06787	9.140
P	0.4668	0.4590	0.3131
Mg	<<	<<	0.3153
Ti	0.8301	0.5987	0.1172
Mn	-	-	<<
Au	0.0000	0.0000	0.0000
Zr	0.0000	0.0000	0.0000
Sr	-	-	0.0000
Rb	0.0000	0.0000	-
Se	0.0000	0.0000	0.0000
Y	<<	-	-
Ce	-	-	-
Cl	<<	-	-

Table 2. Comparison of ammonia solution removal efficiency using three natural zeolites.

Types of natural zeolites	Removal efficiency (%)
Kaolinite	77.25
Kaolinite-1MD	79.46
Clinoptilolite	50.78

The adsorption efficiency of ammonium ions using natural zeolites

In this study, the adsorption of ammonia in aqueous solution by using three natural zeolites, Kaolinite, Kaolinite-1MD and Clinoptilolite, were used as the adsorbent to adsorb ammonium solution by batch method. The results show that natural zeolites are able to adsorb ammonium ion significantly reported in Table 2. The order of ammonium ion removal efficiency can be given as Kaolinite-1MD > Kaolinite > Clinoptilolite with adsorption efficiency of 77.25%, 79.46% and 50.78% respectively, at the initial concentration of 10 mg/L, an hour contact time and the adsorption dosage of 40 g/L. As Kaolinite-1MD shows the highest effective adsorbent, the natural zeolite was used for furthur study. The optimum parameters for using Kaolinite-1MD were investigated. The obtained results are that the optimum dosage ratio of zeolites per water sample volume is 40 g/L with an hour adsorption time as reported in Table 3 and 4, respectively.

Table 3. Efficiency of ammonia solution removal using Kaolinite-1MD by varying ratio of zeolites per water sample volume

Ratio of zeolites per water sample volume (g/L)	Removal efficiency (%)
20	74.69
40	79.46
80	83.22
120	84.59
160	85.41

Table 4. Efficiency of ammonia solution removal using Kaolinite -1MD by varying adsorption time.

Adsorption time (hrs)	Removal efficiency (%)
1	75.23
2	79.46
6	77.32
12	76.52
24	75.83

Adsorption isotherm of ammonium ions from aqueous solution on the natural zeolites

The sorption data of ammonium ion by the natural zeolite have been subjected to two sorption isotherms, namely, Freundlich and Langmuir isotherms to study the effect of initial metal ion concentration for adsorption behavior onto the natural zeolite. Kaolinite-1MD, the highest effective adsorbent in this study, was used to study adsorption isotherm. The increase of initial concentrations of ammonium ion of10 mg/L, 20 mg/L, 30 mg/L, 40 mg/L and 50 mg/L, respectively, results in efficient adsorption decrease. The isotherm results as shown in Figures 2 and 3 reveal that the Langmuir model effectively described the sorption data with high R^2 values (0.999) compared with Freundlich isotherm. It is clearly seen that Langmuir is a better correspondence with the experimental findings rater that Freundlich isotherm.

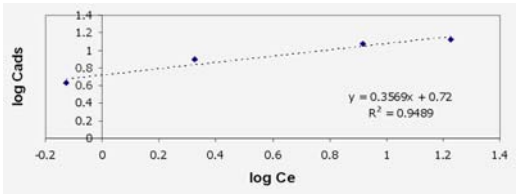

Figure 2. Freundlich adsorption isotherm for ammonium ions on Kaolinite-1MD

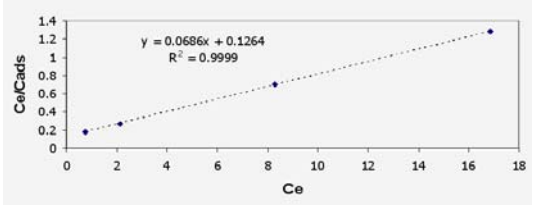

Figure 3. Langmuir adsorption isotherm for ammonium ions on Kaolinite-1MD

Conclusion

In the present study, the fundamental study on the ammonia removal efficiency from aqueous solution using natural zeolites have been reported. Kaolinite-1MD shows the highest effective adsorbent. On the basis of the study, the obtained results can suggest that the use of the natural zeolite as the adsorbent is an efficient and cost-effective method for ammonia treatment from wastewater. Consequently, its application would significantly reduce the cost of wastewater treatment with environmentally friendly chemical process.

Acknowledgements

Research supports from National Research Council of Thailand and Faculty of Science, Ubonratchathani University are gratefully acknowledged.

References

[1] A.H. Englert and J. Robio, *Int. J. Miner.Process.* 75(2005), pp. 21-29

[2] D. Wen, Y.S. Ho and X. Tang. *Hazardous Materials*, 133(2006), pp. 252-256.

[3] D. Karadag, S. Tok, E. Akgul, M. Turan, M. Ozturk and A. Demir, *Hazardous Materials*, 153(2008), pp. 60-66.

[4] R.M.A. Tehrani , A.A. Salar, *Applied Surface Science* , 252 (2005), pp. 866–870.

[5] J. Buschmann, M. Berg, C. Stengel, M.L. Sampson, *J. Envir. Science & Tech.*, 41(2007), pp. 2146

A comparative study of Pt/C and PtPd/C electrocatalyst for catalytic loading on GDL and on membrane

S. Thanasilp[1*] M. Hunsom[1,2]

[1]Fuel Research Center, Department of Chemical Technology, Faculty of Science, Chulalongkorn University, Bangkok, Thailand 10330
[2]Center for Petroleum, Petrochemicals, and Advanced Materials, Chulalongkorn University, Bangkok, 10330, Thailand

*E-mail: oomaamy@hotmail.com, Tel: +66-89-920-1847

Abstract: Effect of the MEA fabrication including the conventional direct spray on gas diffusion layer (GDL) with hot-pressing and catalyst-coated membrane (CCM) with direct spray deposition and decal transfer procedure was carried out for PEM fuel cell under identical condition of Pt/C and PtPd/C electrocatalysts loading. The preliminary results indicated that the fabrication method had very slightly effect on the ohmic resistance of the PEM fuel cell while it had significantly effect on charge transfer resistance for both types of electrocatalyst. In addition, the cells prepared by CCM procedure exhibited a significantly higher active surface area, electrochemical performance and power density than those prepared with the conventional procedure. In addition, by using the cyclic voltammetry with H_2 adsorption method, it was found that the active surface area of Pt/C and PtPd/C prepared by the CCM procedure was higher than the conventional method of around 1.92 and 1.76 times, respectively. In a H_2/O_2 system at 0.6 V, the cells with Pt/C and PtPd/C prepared by the decal transfer procedure provided the highest cell performance of around 458 and 310 mA/cm^2, greater than those prepared by the conventional direct spray on GDL of around 171 and 129 mA/cm^2 and also greater than the direct spray on membrane of approximately 48 and 32 mA/cm^2, respectively.

Introduction

Fuel cells are attractive for their high-energy conversion efficiency and low emission. Proton exchange membrane fuel cells (PEMFC) known as a clean alternative energy devices for generating electricity in many applications such as vehicular, portable and small stationary application with good efficiency. They can be operated under atmospheric pressure and low temperature (60^{o}C-80^{o}C) with feeding of hydrogen and oxygen or air. Due to the fact that PEMFC electro catalyst need precious metals such as Pt which is very expensive, in order to lower the PEMFC cost the amount of Pt is need to be reduce. The key to reducing the loading of precious metals and maintaining the performance is to increase the catalyst utilization of the membrane electrode assemblies (MEA) of a PEMFC. The MEA comprises a polymer electrolyte membrane and catalyst electrodes for hydrogen oxidation (anode) and oxygen reduction (cathode).

In a fuel cell system, the electrochemical reaction can only occur at "Three phase boundaries", where the electrolyte, reaction material, and electrically connected catalyst particles contact together in a MEA[1,2]. The three phase boundary area in turn depends significantly on the fabrication procedure of MEA in addition to other important parameters such as catalyst loading and ionomer loading[3-5]. Primarily two fabrication methods may be used to prepare MEAs, conventional catalytic loading on GDL and on membrane by direct spray deposition and decal transfer method are called CCM. In the case of MEA by conventional method, the Pt or Pt alloy catalyst mixing with a PTFE suspension is spread onto the carbon paper or porous cloth support, and sintered to produce the electrodes. The electrodes are sandwiched between a proton exchange membrane and then hot pressed to form a MEA[6,7]. On the other hand, MEA can also be prepared by a CCM method [8-10]. In the CCM is classified into 2 techniques. The first technique is catalytic loading on membrane by direct spray, this technique is the fussy operation process, which may be a practical problem for a large-scale application[11]. The CCM is then sandwiched between porous carbon paper or cloth supports. The second technique is catalytic loading on membrane by decal method, the Nafion containing catalyst ink is spread on a Teflon support and then transferred to the proton exchange membrane by hot pressing. The Teflon support is then peeled away and the CCM is sandwiched between porous carbon paper or cloth supports. It is reported that the MEA prepared by the CCM method provides better power density due to an extended catalyst/ionomer interface and improvement of catalyst utilization[12]. Thus it is important to investigate the performance and electrochemical activity of the MEA by the hot-press and CCM methods under identical experimental conditions. The results in the present study clearly show that the MEAs prepared by the CCM method not only have high catalyst utilization, but also have a smaller contact resistance and charge-transfer resistance which makes the fuel cells have a promising power output.

Materials and Methods

Prior to fabricating the electrodes, a homogeneous suspension composed of PTFE and carbon powder was sprayed onto carbon cloth to form the GDL with a sublayer [13]. The proton exchange membranes (PEM,

Nafion 115, DuPont) were treated according to the standard procedure of 1 h in 3 wt.% H_2O_2 solution at 80 °C, 1 h in DI water at 80 °C, 1 h in 8 wt.% H_2SO_4 solution at 80 °C and finally 1 h in DI water at 80 °C again. Commercial Pt/C is used as anode catalysts and Commercial Pt/C or PtPd/C is used as cathode catalysts. The catalyst ink is composed of 0.025 g Pt/C catalyst powder, 6 ml 1,2-dimethoxyethane and 0.284 ml Nafion solution. The mixture was sonicated for 1h, then 0.375ml ethylene glycol was added and sonicated for another 1h to form catalyst ink.

To prepare the MEA by the conventional method, the catalyst ink was spray onto the GDL to form the electrode layer. The electrode layer was dried at 100 °C for 30 min. The pretreated membrane and electrode layers were bonded together by hot pressing under 65 kg/cm^2 for 2.5 min, maintaining the temperature at 137 °C. The Pt or PtPd loading was controlled by weight and the value for both the anode and cathode was 0.15 mg/cm^2.

For the MEA fabrication was the CCM by decal method, the same catalyst ink was applied to Mylar film by spraying, After dried at 100 °C for 30 min, the catalyst layer was then transferred onto the membrane at 137 °C and 65 kg/cm^2 by the decal method to form the CCM. The GDL was placed on the anode and cathode side of the CCM to form the MEA. The Pt or PtPd loading was controlled by weight and the value for both the anode and cathode catalyst layer was 0.15 mg/cm^2.

For the MEA fabrication was the CCM by direct spray method, the same catalyst ink was applied to membrane by spraying, After dried at 100 °C for 30 min. The membrane with catalyst layer and electrode layers were bonded together by hot pressing under 65 kg/cm^2 for 2.5 min, maintaining the temperature at 137 °C. The Pt or PtPd loading was controlled by weight and the value for both the anode and cathode was 0.15 mg/cm^2.

Single cells were assembled with the prepared MEA. The active area of the cell was 5 cm^2. The experiments were operated in a fuel cell mode. For H_2/O_2 test, the flow rate of pure hydrogen, oxygen are controlled at 100 sccm. The test was carried out at ambient temperature with zero back pressure. Performance of the single cell was evaluated by measuring the I–V curves using a fuel cell test station (PGSTAT30 potentiometer). Polarization resistance of the single cells was investigated by electrochemical impedance spectroscopy (EIS). The impedance spectra were recorded in the 10 mHz to 100 kHz frequency range. The oxygen and hydrogen gas were supplied into the cathode and anode, respectively. Due to the much faster reaction kinetics of the H_2 oxidation reaction on the Pt/C electrocatalysts as compared to that of the O_2 reduction reaction [14], the cell impedance would be mainly dominated by the cathode impedance. The anode at which hydrogen oxidation takes place was used as the reference and also as the counter electrode of the AC measurements (the cathode was used as the working electrode). The electrochemical active surface area or activity of the cell was estimated from cyclic voltammegrams measured at scan rate of 20mV/s and at ambient temperatures. During the measurement, dry H_2 at a flow rate of 100 sccm was fed to the anode (which served as the counter and reference electrodes) and N_2 to the cathode at 100 sccm, which served as working electrode. The potential was scanned between 0.05 and 1.2V versus the cathode (working electrode). Relative electrochemical active surface areas were obtained by comparing the area of hydrogen oxidation peaks from the cyclic voltammograms. Morphologies of the MEA after the performance evaluation were investigated with a JEOL JSM 5800 LV scanning electron microscope (SEM).

Results and Discussion

Fig. 1 and Fig. 2 show the single cell performance and power density curves of the two different cathodes with the Pt/C and PtPd/C electrocatalyst using same Pt/C anode. The MEAs were prepared by the conventional direct spray on gas diffusion layer (GDL) with hot-pressing and catalyst-coated membrane (CCM) with direct spray deposition technique and decal transfer technique. The single cell with Pt/C cathode shows a maximum open circuit potential (OCV) prepared by CCM method with both techniques were 1.020 V and 0.987 V , respectively higher than 0.968 V observed on the fuel cell with the conventional MEA. To confirm that the single cell with PtPd/C cathode has a maximum open circuit potentialprepared by CCM method with both techniques were 1.009 V and 0.971 V , respectively higher than 0.943 V observed on the fuel cell with the conventional MEA. In the case of CCM, this method may decrease the gas crossover due to reduce pore size of catalyst layer. The CCM method can be reduced contact resistance between catalyst layer and membrane. The cell performance of the CCM with direct spray deposition and decal transfer with Pt/C and PtPd/C cathode are clearly better than the conventional MEA under identical test condition of H_2/O_2. The single cell with the Pt/C and PtPd/C cathode show a maximum power of the cell made by decal transfer technique are 230 mWcm^{-2} and 307 mWcm^{-2} , respectively, which are 38% and 36%, respectively higher than the conventional MEA. And current density of 350 mAcm^{-2} and 458 mAcm^{-2} , respectively, which are 74% and 60%, respectively higher than the conventional MEA. at a fuel cell voltage of 0.6 V. The results indicated that the fabrication method had very slightly effect on the ohmic resistance of the PEM fuel cell while it had significantly effect on charge transfer resistance.

The catalyst utilization or electrochemical active surface area can also be estimated from the charge of hydrogen oxidation peak observed on cyclic voltammograms(CV). Fig.3 and Fig.4 shows the cyclic voltammegrams of the cells of the two different cathodes with the Pt/C and PtPd/C electrocatalyst using same Pt/C anode made from CCM with both techniques and conventional MEA. During the

measurement of cyclic voltammegrams, nitrogen was fed to the working electrode (cathode) and hydrogen was fed to the counter and reference electrode (anode). Thus, the electrochemical active surface area estimated from the cyclic voltammetric could be mainly

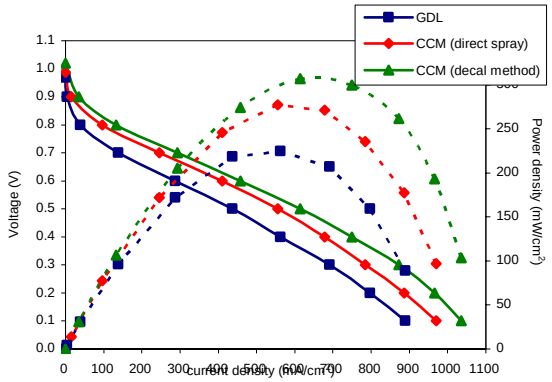

Fig. 1 Current density–voltage and current density–power density curves of single cells with Pt/C both anode and cathode made from CCM with both technique and conventional MEA under H_2/O_2 atambient temperature.

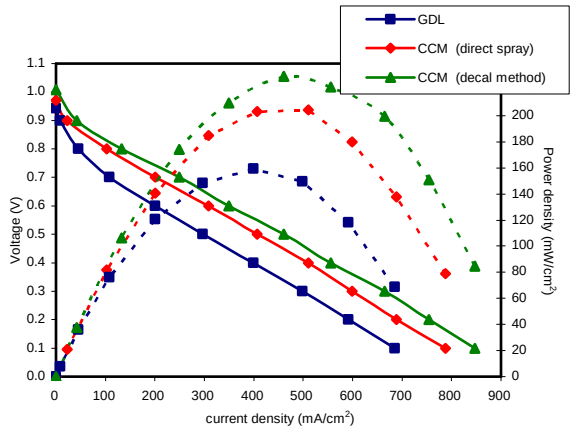

Fig. 2 Current density–voltage and current density–power density curves of single cells with Pt/C anode and PtPd/C cathode made from CCM with both technique and conventional MEA under H_2/O_2 atambient temperature.

associated with the cathode catalyst layer. The cyclic voltammetric studies from 0.05 to 0.4V provides information on the hydrogen adsorption and desorption which occurs on the platinum surface. The region from 0.4 to 0.5V is regarded as the double-layer region. The electrochemical surface area of the CCM with decal transfer with Pt/C and PtPd/C cathode were higher than the conventional method of around 1.92 and 1.76 times, respectively. As can be seen, the cell made from CCM exhibit significantly larger hydrogen desorption peak than that prepared by the conventional MEA. This shows that CCM has higher electrochemical surface area than that MEA prepared by the conventional method. The CV results confirm the higher electrochemical performance of the PEM fuel cells made by the CCM (Fig. 1).

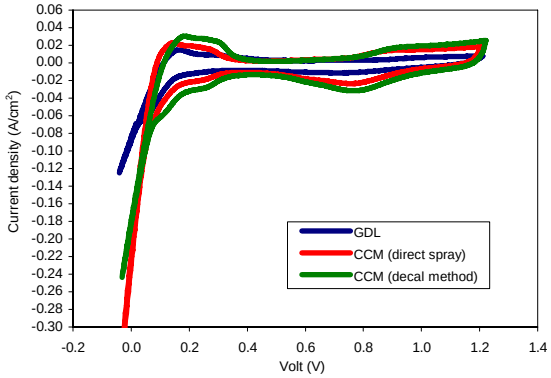

Fig. 3 CV of the single cells made with Pt/C both anode and cathode from CCM with both techniques and conventional MEAs.

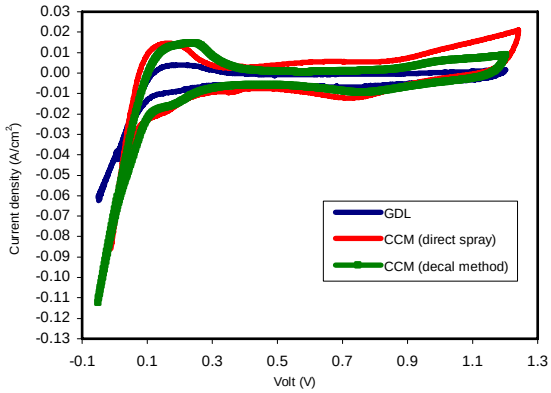

Fig. 4 CV of the single cells with Pt/C anode and PtPd/C cathode made from CCM with both technique and conventional MEAs.

Fig. 3. is the impedance responses of the single cells prepared by CCM and conventional MEA under H_2/O_2 cell potential of 0.70 V. In the figure, the symbols are the experimental results and lines are the fitted data using the equivalent circuit is shown in Fig. 7. In the equivalent circuit, R_1 represents the total ohmic resistance of the cell which includes ohmic resistances of various cell components and also the end plates and the contacts between them. R_2 is usually associated with the charge transfer resistance across the catalyst/electrolyte interface, and CPE is a constant phase element related to the double-layer capacitance of the porous electrode.The impedance responses were characterized by a semi-circle at low overpotentials (i.e.,at a cell potential of 0.70 V). Nevertheless, as expected, the impedance arc for the reaction on the cell made from CCM is much smaller that observed on the cell made form conventional MEA . As the cell impedance is kinetically dominated by the oxygen reduction at the cathode [18], the much smaller impedance arc for the cell prepared by the CCM demonstrates that the oxygen reduction reaction on the catalyst layer of the CCM is significantly faster than that of the conventional MEA . This is consistent with that of the cyclic voltammetric studies.

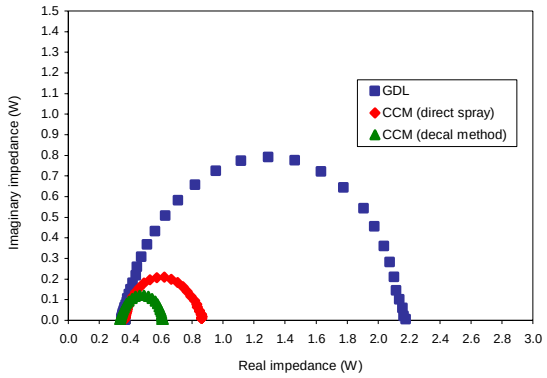

Fig. 5 Impedance curves of the single cells with Pt/C both anode and cathode with conventional MEA and CCM with both techniques, measured at 0.70V under H_2/ O_2.

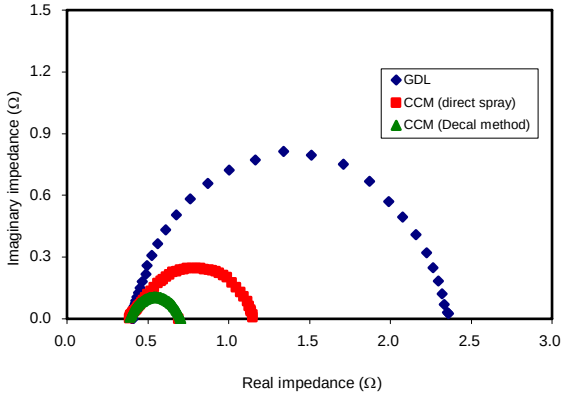

Fig. 6 Impedance curves of the single cells with Pt/C anode and PtPd/C cathode with conventional MEA and CCM with both techniques, measured at 0.70V under H_2/ O_2.

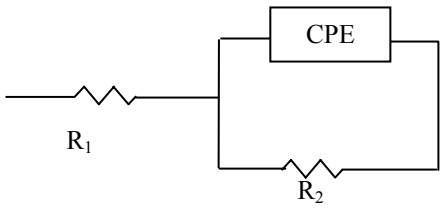

Fig. 7. Equivalent circuitused for the impedance analysis

The fit between the observed and calculated data was reasonable, indicating that the equivalent circuit may be applicable though the real reaction pathways could be very complicated. The fitting results are given in Table 1 and Table 2. The ohmic resistance R_1 for each test cell is relatively constant. In general, the cell with the CCM has a smaller R_1 than the cell with the conventional MEA at the same voltage under the same test conditions. As the gas diffusion layer, membrane and assembly pressure were equal for cells with either CCM or conventional MEA, the differences in R_1 appear to show that the catalyst layer made by the CCM method has much better contact with the polymer electrolyte membrane than that of the hot-pressed MEA. The much smaller charge transfer resistance, R_2, indicates a faster charge-transfer reaction for the oxygen reduction at the electrode and electrolyte interface of the cell with CCM. This again shows that CCM have a much more efficient electrochemical active layer than that of the conventional MEA.

Table 1
Fitted impedance parameters of the single cells with Pt/C both anode and cathode made from conventional MEA and CCM with both techniques at cell voltage of 0.7 V

Test Condition	MEA	R_1 (Ωcm^2)	R_2 (Ωcm^2)
H_2/O_2	Conventional MEA	0.3743	1.7834
	CCM (direct spray)	0.3664	0.4824
	CCM (decal transfer)	0.3384	0.2700

Table 2
Fitted impedance parameters of the single cells with Pt/C anode and PtPd/C cathode made from conventional MEA and CCM with both techniques at cell voltage of 0.7 V

Test Condition	MEA	R_1 (Ωcm^2)	R_2 (Ωcm^2)
H_2/O_2	Conventional MEA	0.3817	1.9722
	CCM (direct spray)	0.3681	0.5097
	CCM (decal transfer)	0.3585	0.3148

Morphology analysis was investigated in this comparative study to give an direct comparison between these six MEAs. Fig. 8 shows SEM micrographs of cross-section MEA of the two different cathodes with the Pt/C and PtPd/C electrocatalyst using same Pt/C anode prepared by the conventional method and CCM method with both techniques. The result reveals very different microstructures in the membrane–electrode interface. For the MEA of the two different cathodes with the Pt/C and PtPd/C electrocatalyst using same Pt/C anode prepared with CCM method, the catalyst electrode has been integrated with the Nafion membrane due to the close contact between the catalyst layer and the membrane (8b and 8c) and (8e and 8f), respectively. In contrast, the interface between the catalyst electrode and the Nafion membrane is clearly visible and most region of the catalyst layer has not been directly contacted with the membrane in the hot-pressed MEA (8a) and (8d), respectively. The catalyst layer on the membrane is reasonablely beneficial to fuel cell performance since the catalyst

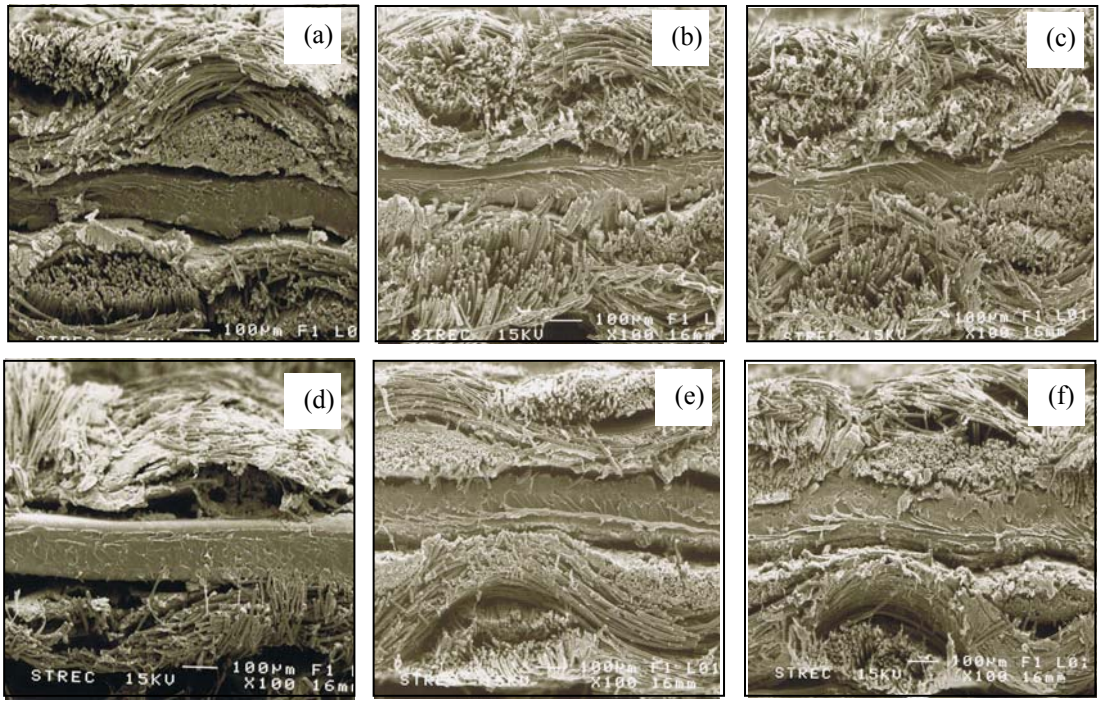

Fig. 6 SEM micrographs of cross-section MEA of the two different cathodes with the Pt/C and PtPd/C electrocatalyst using same Pt/C anode prepared by CCM method (band c) and (e and f) and conventional method (a) and (d).

Conclusions

The best MEA fabrication was the catalyst-coated membrane (CCM) by decal method. It exhibited a significantly higher active surface area (EAS), electrochemical performance (458 mA/cm^2) and power density (307 mW/cm^2) than those fabricated with the direct spray on GDL and on membrane. The fabrication method had very slightly effect on the ohmic resistance of PEM fuel cell while it had significantly effect on charge transfer resistance for both types of electrocatalyst as cathode.

Acknowledgements

The authors greatly acknowledge the support of Department of Chemical Technology, Faculty of Science, Chulalongkorn University. The authors also like to thank the Petroleum and Petrochemical Technology Consortium for funding support.

References

[1] S.D. Thompson, L.R. Jordan and M. Forsyth, *Electrochim. Acta.* **46** (2001), pp.1657.
[2] M.Pan, H. Tang, S. Mu and R.Yuan, *J. Mater. Res.* **19** (2004), pp. 2279.
[3] E. Antolini, L. Giorgi, A. Pozio and E.Passalacqua, *J. Power Sources* **77** (1999), pp. 136.
[4] Z. Qi and A. Kaufman, *J. Power Sources* **113** (2003), pp. 37.
[5] P. Gode, F. Jaouen, G. Lindbergh, A. Lundblad And G. Sundholm, *Electrochim. Acta* **48** (2003), pp. 4175.
[6] X.M. Ren, P. Zelenay, S. Thomas, J. Davey and S. Gottesfeld, *J. Power Source* **86** (2000), pp. 111.
[7] A. Lindermeir, G. Rosenthal, U. Kunz and et al., *On the question of MEA preparation for DMFCs, J. Power sources* **129 (2)** (2004), pp. 180–187.
[8] M.S. Wilson and S. Gottesfeld, *J. Appl. Electrochem.* **22** (1992), pp. 1.
[9] S.Q. Song, Z.X. Liang, W.J. Zhou, et al., J Power sources **145** (2005), pp. 495.
[10] Hu Mingruo, Sui Sheng, Zhu Xinjian and et al., Int. *J. Hydrogen Energy* **31** (2006), pp. 1010.
[11] M.S.Wilson,J .A. Valerio and S.Gottesfeld,*Electrochim. Acta* **40** (1995), pp. 55–363.
[12] M. Prasanna, H.Y. Ha, E.A. Cho, S.-A. Hong and I.-H. Oh, *J. Power Sources* **137** (2004), pp. 1.
[13] H.L. Tang, S.L. Wang, M. Pan and R.Z. Yuan, *J. Power Sources* **166** (2007), pp. 41.
[14] H.A. Gasteiger, W. Gu, R. Makharia, M.F. Mathias, B. Sompalli, in: W. Vielstich, A. Lamm, H.A. Gasteiger (Eds.), *Handbook of Fuel Cells: Fundamentals, Technology, and Applications*, *Wiley*, **vol. 3** (2003), pp. 593, Chapter 46.

Nanocomposites of EVA/polystyrene nanoparticles/montmorillonite

C. Worawas[1,2*] and S. Chuayjuljit[1,2]

[1] Chulalongkorn University /Department of Materials Science, Faculty of Science,
[2] National Center of Excellence for Petroleum, Petrochemicals and Advanced Materials, Bangkok, Thailand

[*] E-mail : c.worawas@gmail.com

Abstract: This research aims to prepare nanocomposites from ethylene vinyl acetate copolymer (EVA), polystyrene (PS) nanoparticles and montmorillonite (MMT). PS nanoparticles were synthesized by differential microemulsion polymerization using sodium dodecyl sulfate and *2,2'*-azobisisobutyronitrile as a surfactant and an initiator, respectively. Solid content in the nanolatex was determined by gravimetric method. Morphology of the obtained nanoparticles was explored using a transmission electron microscope. The polymer blends of EVA and PS at EVA/PS dry weight ratios of 90/10, 80/20 and 70/30 were mixed with MMT at the amount of 1, 3 and 5 wt% using a high speed mixer at 3000 rpm for 5 min. The homogeneous latex mixtures were cast on a glass mold and then compressed into thin sheets. After that, the samples were examined for their tensile properties, thermal behaviors and morphology using a universal testing machine, thermal gravimetric analyzer and scanning electron microscope, respectively. The results showed that the stress at maximum load and Young's modulus of the blends were improved with the incorporation of MMT at 3 and 5 wt%. The TGA analysis showed that the thermal stability of the nanocomposites was improved by the adding of MMT.

Introduction

Polymer-clay nanocomposites have been studied extensively for several years because they exhibit superior properties when compared to the virgin polymers or pristine composites. The incorporation of nanoclay into the polymer domain leads to higher mechanical properties, dimensional stability and heat distortion temperature and lower gas permeability [1]. In addition to the observed improvements in performances, very low loading of nanoclay (< 5 wt%) are required in comparison to microparticle fillers to achieve the same desired effect, resulting in lighter weight materials but superior properties [2]. Clays are comprised of silicate layers having a planar structure of 1 nm thickness and up to 500 nm length [3]. Montmorillonite (MMT) belonged to smectite group of clay minerals is the most commonly used layered silicate because of its natural abundance, its commercial availability, high aspect ratio (100-500) and great specific surface area (as high as 800 m^2/g) [4,5]. Recently, blends of ethylene vinyl acetate copolymer (EVA) and polystyrene (PS) have gained a lot of interest. These materials combine the excellent ageing and flex crack resistance of EVA [6] and the superior processing characteristic of PS [7]. However, a polymer blend often produces a material with poor mechanical properties as most polymer pairs are thermodynamically immiscible with each other [8,9]. Many studies have focused on enhancing the compatibility of the two components. The nanosized PS and inorganic fillers incorporated into an EVA matrix are expected to provide a synergistic combination of individual organic/inorganic component properties. To the best of our knowledge, polymer blend of EVA and PS nanoparticles reinforced by MMT has not been reported so far. In the present work, our objecive was to blend EVA with PS nanoparticles and MMT in order to improve the mechanical properties of the neat EVA. The PS nanoparticles prepared by differential microemulsion polymerization were used in this work. A reaction system is composed of water, surfactant, styrene monomer (water insoluble monomer) and a water-soluble initiator and requires a certain temperature to initiate polymerization and suitable agitation to form an emulsion. This method uses a much smaller amount of surfactant than that of the pristine microemulsion polymerization. It has been confirmed to be useful for synthesizing nanosized polystyrene particles [10]. The tensile properties, thermal behavior and morphology of EVA/PS/MMT nanocomopsites were investigated by the universal testing machine, thermal gravimetric analyzer (TGA) and scanning electron microscope (SEM), respectively.

Materials and Methods

EVA latex was supplied by Eternal Resin Company. Styrene monomer was obtained from Dow Chemical Co., Ltd. Sodium dodecyl sulfate (SDS) provided by Cognis Co., Ltd. was used as a surfactant. *2,2'*-Azobisisobutyronitrile (AIBN) used as an initiator was donated by Siam Chemical Industry Co., Ltd. MMT was obtained from Metallurgy and Materials Science Research Institute, Chulalongkorn University.

Nanolatex of PS was synthesized by mixing SDS (8 g) and AIBN (0.12 g) in a 500 ml Pyrex glass reactor, which was equipped with a reflux condenser, a N_2 gas inlet and a dropping funnel for monomer feeding. A 60 ml of distilled water was thereafter added and the system was heated up to 70°C with stirring at 150 rpm using a magnetic stirrer under the circumstance of N_2 gas. After the temperature was raised to 70°C, the styrene monomer was fed slowly in a dropwise manner within 1.5 h. Afterwards, the reaction system was maintained at 70°C with constant agitation for an additional hour. Solid content (%*S*) of PS in the nanolatex was detemined by the gravimetric method and calculated from the following equation,

$\%S = W_1/W_2 \times 100$ (where W_1 and W_2 are the weights of dried PS and nanolatex, respectively). Morphology of the prepared PS nanoparticles was investigated using a transmission electron microscope (TEM, Jeol JEM-1230).

EVA latex was mixed manually with the obtained PS nanolatex at the EVA/PS dry weight ratios of 90/10, 80/20 and 70/30. The mixtures were then blended with MMT at the amount of 1, 3 and 5 wt% using a high speed mixer at 3000 rpm for 5 min. The homogeneous latex was cast into sheet on a glass mold (20 × 20 × 0.15 cm), air dried for 24 h and then in an oven at 60°C for 6 h. The sample was subsequently compressed into thin sheet at 110°C for 7.5 min. The tensile properties were measured with a LLOYD LR 100K universal testing machine on dumb-bell shaped samples according to ASTM D 882. The load cell capacity and crosshead speed were 100 N and 50 mm/min, respectively. Thermal decomposition temperatures of the nanocomposites were carried out using a thermal gravimetry TGA (Mettler Toledo, TGA/SDTA 851^e). The specimen was tested under nitrogen atmosphere using a temperature range of 50-1000°C and a heating rate of 20°C/min. The fractured surfaces of the specimens were performed by a Jeol JSM-5410LV scanning electron microscope after coating the broken surfaces with a thin layer of gold.

Results and Discussion

The solid content of the prepared PS nanoparticles is about 22%. Figure 1 shows a TEM image of spherical shape PS nanoparticles.

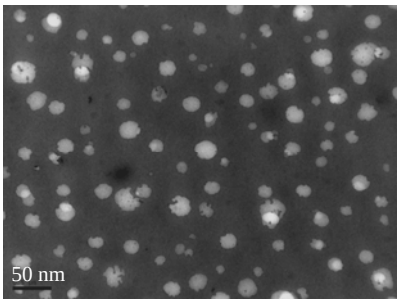

Figure 1. TEM image of the spherical nano-clusters of PS particles.

Figures 2-4 show the tensile properties of the prepared nanocomposites. The changes in stress at maximum load, Young's modulus and strain at maximum load with the incorporation of PS nanoparticles and MMT in the EVA matrix were determined. Figure 2 displays that the stress at maximum load of the EVA/PS blends without MMT was found to decrease along with the increase in PS content. This may be due to the low interfacial interaction between EVA and PS, which would lead to mechanical rupture at the blend interface. Moreover, the incorporation of high PS content results in its aggregation and poor dispersion. However, this property could be improved by the addition of MMT. The nanocomposite at the blend composition of 80EVA/20PS/5%MMT exhibited the highest stress at 4.2 MPa. This improvement may be due to the filler (MMT) dispersion and filler/matrix adhesion where delamination of the layered MMT is probably favored by the shear force during compounding.

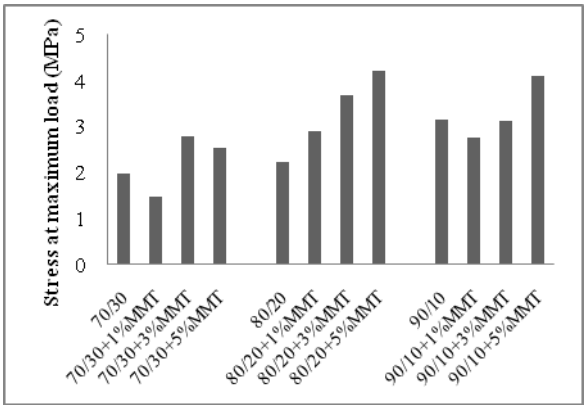

Figure 2. Stress at maximum load of EVA/PS blends and EVA/PS/MMT nanocomposites.

With respect to the Young's modulus of the samples, as expected this increased with increasing loadings of PS and MMT in the nanocomposites (Figure 3). The increase in modulus is due to the high modulus of PS and clay platelets themselves. Thus the nanocomposite with high Young's modulus could be found in PS and MMT-rich blends.

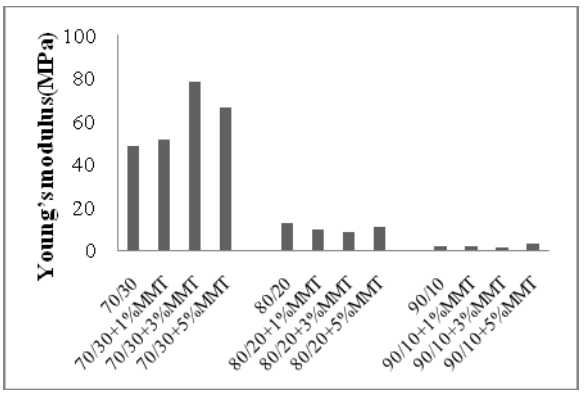

Figure 3. Young's modulus of EVA/PS blends and EVA/PS/MMT nanocomposites.

Finally, considering the strain at maximum load of the samples, this was observed to markedly decrease with the incorporation of increasing level of PS, which shows a minimum value of strain at maximum load at the blend composition of 70/30 EVA/PS. However, an enhancement in the strain at maximum load was observed through the incorporation of MMT

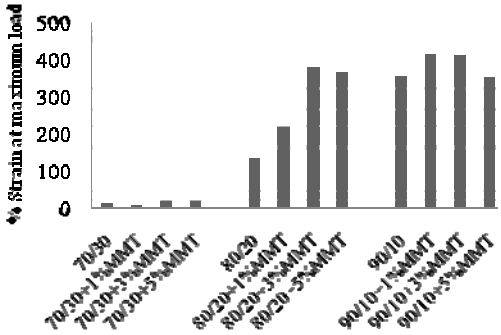

Figure 4. Strain at maximum load of EVA/PS blends and EVA/PS/MMT nanocomposites.

TGA results are summarized in Table 1. The on set temperatures and 50% decomposition temperature of EVA, PS, EVA/PS blends, and EVA/PS/MMT nanocomposites were investigated. The thermal degradation temperature of EVA undergoes two stages. The first stage is assigned to the loss of acetic acid (319°C) and the second stage is the main-chain degradation (436°C). The main stage of polystyrene degradation is at 415°C, attributed to the main chain pyrolysis with the evolution of aromatics (styrene, toluene, methyl styrene, etc) [11]. The thermogravimetric analysis shows that the MMT had an influence on enhancing the stability of the nanocomposites

.

Table 1: TGA of different polymeric systems.

EVA/PS/MMT	Onset temperature (°C) 1	2	50% Decomposition temperature (°C)
70/30	318	432	425
70/30/1%MMT	319	433	430
70/30/3%MMT	318	430	440
70/30/5%MMT	316	431	445
80/20	314	430	385
80/20/1%MMT	315	432	395
80/20/3%MMT	319	438	420
80/20/5%MMT	318	436	431
90/10	319	433	378
90/10/1%MMT	320	437	380
90/10/3%MMT	317	432	380
90/10/5%MMT	319	435	395
EVA	319	436	
PS	415		

Representative SEM micrographs (at 1500× magnification) of EVA, EVA/PS blends and EVA/PS/MMT nanocomposites are presented in Figure 5. It can be seen that the compatibility between EVA and PS decreased with the increasing amount of PS. However, the compatibility has been improved by the incorporation of the MMT. This is because the MMT can act as a compatibilizer for immiscible polymer blends [8].

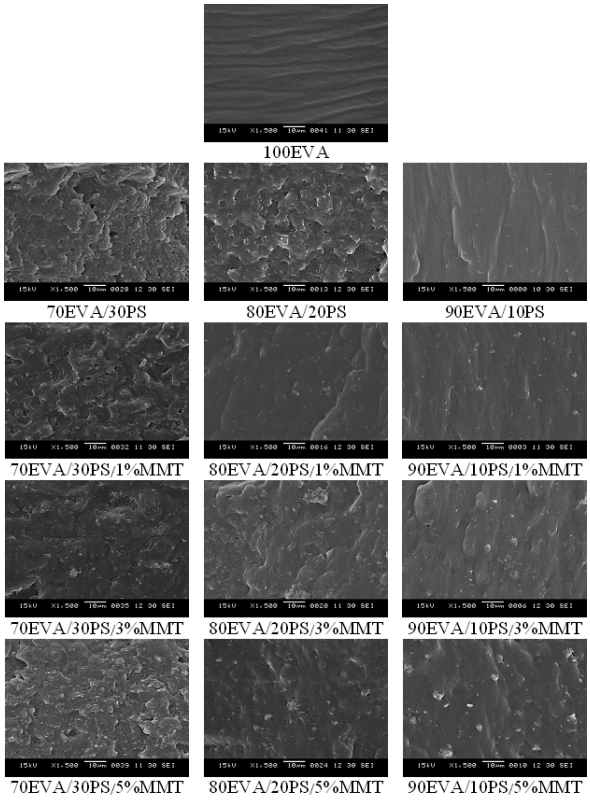

Figure 5. SEM micrographs of EVA, EVA/PS blends and EVA/PS/MMT nanocomposites.

Conclusions

The novel nanocomposites of EVA, PS nanoparticles and MMT were successfully produced by a latex compounding followed by the simple compression molding process. The synergistic effects of PS nanoparticles and MMT on tensile properties were observed. The stress at maximum load and Young's modulus of EVA/PS blends were improved by the introduction of the MMT, with the highest stress at maximum load and Young's modulus being attained from the nanocomposites with compositions 80EVA/20PS/5%MMT and 70EVA/30PS/3%MMT, respectively. However, the PS nanoparticles and MMT had slightly influence on the stability of the blends and the nanocomposites.

Acknowledgements

The authors gratefully acknowledge Faculty of Science, and National Center of Excellence for Petroleum, Petrochemicals and Advanced Materials, Chulalongkorn University for financial, material and instrument support.

References

[1] J. Shen, X. Cao and J. Lee, *Polym. J*. **47** (2006), pp. 6303-6310.

[2] M. Alexandre, G. Beyer, C. Henrist, R. Cloots, A. Rulmont, R. Jerome and P. Dubois, *Chem. Mater*. **13** (2001), pp. 3830-3832.

[3] S. Varghese and J.K. Kocsis, *Polym. J*. **44** (2003)**,** pp. 4921-4927.

[4] S. Chuayjuljit, B. Nonthaboonlert and S. Limpanart, *Polym. Polym. Compo.* **16** (2008), pp. 277-282.

[5] T. Peprnicek, J. Duchet, L. Kovarova, J. Malac, J.F. Gerard and J. Simonik, *Polym. Degrad. Stabil*. **91** (2005) , **pp.** 1855-1860.

[6] A.T. Koshy, B. Kuriakose, S. Thomas and S. Vaghese, *Polym. J*. **34** (1993), pp.3428-3436.

[7] R. Asaletha, M.G. Kumaran and S. Thomas, *Eur. Polym. J*. **35** (1999)**,** pp 253-271.

[8] G.X. Chen, H.S. Kim, E.S. Kim and J.S. Yoon, *Polym. J*. **46** (2005), pp. 11829-11836.

[9] H.H. Ismail and M. Nasir, *Polym. Test*. **21** (2002), pp. 163-170.

[10] G. He. and Q. Pan, *Macromol. Rapid. commun*. **25** (2004), pp. 1545-1548.

[11] A.P. Mathew, S. Packirisamy and S. Thomas, *Polym. Degrad. Stabil*. **72** (2001), pp. 423-439.

Author Index

Author Index

Author Index

Author Index

L

Author Index

Author Index

Author Index

Author Index

Author Index

Author Index

T

Author Index

Author Index

Challenges in Chemistry for Sustainable Development

UBON RATCHATHANI UNIVERSITY
UBON RATCHATHANI
THAILAND